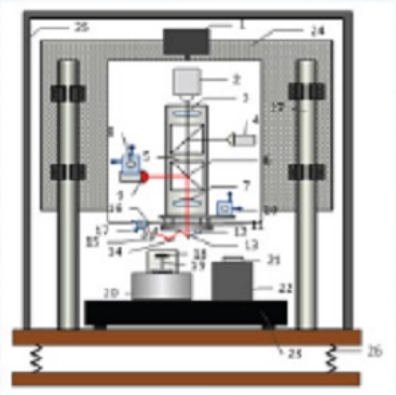
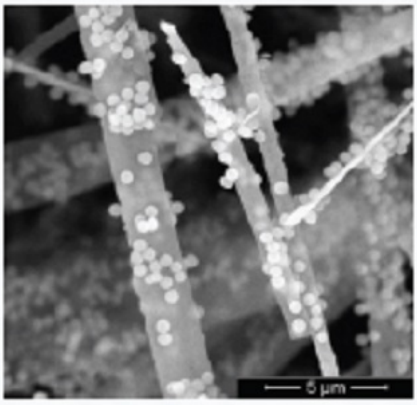
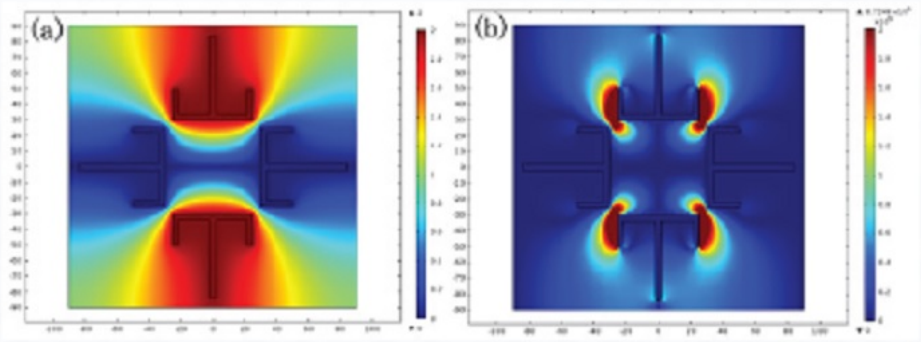
Micro-Nano Technology XVI







Edited by
Fei Tang

TRANS TECH PUBLICATIONS

Micro-Nano Technology XVI

Edited by
Fei Tang

Micro-Nano Technology XVI

Selected, peer reviewed papers from the
16th Annual Conference and
5th International Conference of the
Chinese Society of Micro-Nano Technology
(CSMNT 2014),
August 31-September 3, 2014, Chengdu, China

Edited by

Fei Tang



Copyright © 2015 Trans Tech Publications Ltd, Switzerland

All rights reserved. No part of the contents of this publication may be reproduced or transmitted in any form or by any means without the written permission of the publisher.

Trans Tech Publications Ltd
Churerstrasse 20
CH-8808 Pfaffikon
Switzerland
http://www.ttp.net

Volumes 645-646 of
Key Engineering Materials
ISSN print 1013-9826
ISSN cd 1662-9809
ISSN web 1662-9795

Full text available online at *http://www.scientific.net*

***Distributed** worldwide by*

Trans Tech Publications Ltd
Churerstrasse 20
CH-8808 Pfaffikon
Switzerland

Fax: +41 (44) 922 10 33
e-mail: sales@ttp.net

and in the Americas by

Trans Tech Publications Inc.
PO Box 699, May Street
Enfield, NH 03748
USA

Phone: +1 (603) 632-7377
Fax: +1 (603) 632-5611
e-mail: sales-usa@ttp.net

Preface

This book collects papers selected from the 16th Annual conference and 5th International Conference of the Chinese Society of Micro-Nano Technology.
Micro-nano is considered as an emerging high technology for the 21th century. It involves various high-tech fields including electronics, machinery, materials, manufacturing, testing, and disciplines of physical, chemical and biological. A lot of remarkable achievements have been made in the past few years. Still it is expected that the emerging novel ideas will change people's way of thinking. The conference brings together leading scientists and engineers in Micro- and Nanotechnology to exchange information on their latest research progress. The conference provides a perfect forum for scientist and engineers of different disciplines to meet and discuss. 16th Annual conference and 5th International Conference of the Chinese Society of Micro-Nano Technology have been held in Chengdu, China. Southwest China, is one of the most modern and prosperous cities in China. The fertile Chengdu Plain, on which Chengdu is located, is also known as the "Country of Heaven". Being the birthplace of China's 4 leading cuisines in China-Sichuan Cuisine, Chengdu is widely recognized as the " Land of Abundance and Capital of Great Food" and was crowned the UNESCO City of Gastronomy of the World in 2010, the first one in Asia. With a city history of 2,300 years, Chengdu is one of the first historically and culturally famous cities nominated in China and a permanent venue for China.
In this conference, eight top level MEMS and NANO technology researchers were invited to make plenary presentations. They are:

● Horacio Dante Espinosa, the Director of the Theoretical and Applied Mechanics Program at the McCormick School of Engineering, Northwestern University;

● Qing-An Huang, the Founding Director of the Key Laboratory of MEMS of the Ministry of Education, Southeast University;

● Tianhong Cui, an Affiliate Senior Member of the graduate faculty in Department of Electrical and Computer Engineering and Department of Biomedical Engineering at the University of Minnesota;

● Quanshui Zheng, the Founding Director of Center for Nano and Micro Mechanics, Tsinghua University;

● Shangjr (Felix) Gwo, the Vice President for Research and Development in NTHU;

●SU Wei, a Ph.D supervisor and a deputy director of Institute of Electronic Engineering of CAEP;

● Jiwang Yan, a professor of mechanical engineering at Keio University, Japan;

● K.K. Jain, serves as a CEO of Jain PharmaBiotech as well as a consultant to the biopharmaceuticals industry;

Thanks the staff of Electronic Science and Technology University, China Academy of Engineering Physics and CSMNT Secretary for the efforts they have made, and thanks all honored attendees. Their contributions in all aspects are indispensable to the conference's success.
Thanks to Trans Tech Publications (TTP) for their work on publishing the special volume for selected papers of this conference. We have a good experience for cooperation, and hope that we can continue this cooperation in coming conferences in the future.
The 17th Annual conference and 6th International Conference of the Chinese Society of Micro-Nano Technology will be held in October11-14, 2015, Shanghai, China.

Shanghai is a municipality under the direct jurisdiction of the central government. It is the city of extreme contrasts that reflect not only in its architecture or landscape, but also in its social and cultural milieu. Shanghai is an ideal "shopping paradise" in the mainland of China; Nanjing Road, known as "China's No.1 Street", and Huaihai Road are packed with rows of shops arrayed with large collections of merchandise that are a feast to the eyes. It is also a paradise for gourmets. There are over a thousand restaurants serving the famous 16 styles of Chinese food. There are also French, Italian, Japanese, Indian and other kinds of foreign flavored cuisine.

See you in Shanghai!

Zheng You

Chairman of Organizing Committee

Table of Contents

Preface

Chapter 1: Materials and Technologies in the Scale of Micro and Nano

Study of PSG Thickness Uniformity Influencing Factors in LPCVD
W.L. Lü, Z. Zhan, X.H. Du, R.H. Zhou, H.E. Zhang, L.Y. Wang and D.H. Sun 3

Anisotropic Elastic Properties of Chiral Sculptured Thin Films at Micro-Scale Evaluated by Resonance Frequency Spectra
H. Fang, K. Matsumoto, T. Sumigawa and T. Kitamura 9

The Dilute Magnetic Properties of Monolayer MoS_2 Doped with Transition Metal Fe and VA Atoms
L. Lan, J.M. Cao, Y.J. Cao, D.S. Xu and J. Zhou 15

Strategies for Defect-Free and Deep Wet Etching of Pyrex 7740
Z. Zhan, L.K. Yu, C. Zheng, J.F. Cai, D.H. Sun and L.Y. Wang 21

Effect of Hydrophilic and Hydrophobic SiO_2 Particles on Performances of PI/Al_2O_3 Composite Films
Y.Y. Li, L.Z. Liu, H. Shi, L. Weng and W.W. Cui 26

Synthesis and Characterization of Topological Insulator Bi_2Te_3 Nanowires
Z. Guo, L. Lu, J.Y. Wang and Y.J. Xing 32

Electronic and Magnetic Properties of Rare-Earth Atoms Absorbed on Graphene Sheet: A Theoretical Study
Q.X. Zhou, Z.B. Fu, C.Y. Wang, X. Yang, L. Yuan and Y.J. Tang 40

Melt Electrohydrodynamic Direct-Writing Micro/Nano Fiber with Restriction of Heated Sheath Gas
Z.J. Yu, L.J. Wang, L.L. Sun, Y.H. Lin, W. Wang, G.F. Zheng and D.H. Sun 45

Experimental Study on WEDM Machining of PCD and PCBN Compacts
M.C. Song, J.L. Zhang, C. Yu, M.J. Wang, C. Liu and Y. Liu 52

Wet Anisotropic Etching Characteristics of Si{100} in TMAH+Triton at near the Boiling Point
M.Q. Yao, B. Tang, W. Su and G. Tan 58

Hierarchically Ordered Porous Carbon as a Host Material for Energetic Composites
J. Chen, S.M. He, H.Q. Cai, Q.L. Hao and H. Huang 64

TCAD Study of the Raised SiGe Source/Drain in 40nm PMOS
M. Zhong, Y.H. Zhao, S.M. Chen, M. Li, S.H. Zeng and W. Zhang 70

Adsorption of Silver Nanoparticles on Modified Surfaces
C. Gao, T. Guo, X.S. Ye, H.F. Zhang, H.N. Liu and Z.J. Wu 75

W-Band Quadrupler Based on Multi-Chip Module and Schottky Barrier Diodes
Y. He, X.J. Deng, C. Wang and B. Lu 80

Intermediate Layer Bonding for Silicon and Piezoelectric on UV Adhesive
X.Y. Wang, H. Liu, R. Lei and W.G. Liu 86

Quantitative Production of Charges with a Carbon Nanotubes Coated Electrode Based on Trichel Pulses
F.C. Deng, L.Y. Ye and K.C. Song 92

Band Engineering of Graphene Nanomesh Field Effect Transistor under Multiscale Simulation Framework
Y.W. Lv, H. Wang, S. Chang, Z.H. Yu, J. He and Q.J. Huang 98

Growth and Magnetic Properties of Three-Dimensional Firtree-Like Cobalt Microcrystals with Hierarchical Dendritic Superstructures
X. Yang, Z.B. Fu, L. Yuan, C.Y. Wang and Q.W. Chen 104

The Thermal Decomposition Behavior of Graphene Oxide/HMX Composites
G.Y. Zeng, J.H. Zhou and C.M. Lin 110

Facile Fabrication of Super-Hydrophobic Surfaces by Spray PTFE
Y. Wang, H.F. Zhang and X.W. Liu 115

Frequency Characteristics Research for the Negative Resistance Oscillations Phenomenon of a Silicon Magnetic Sensitivity Transistor
X.F. Zhao, Y.F. Li, M.W. Lv, D.Z. Wen and H.Q. Zhang 120

Large-Scale Synthesis and Microwave Absorption Properties of $CoFe_2O_4$/ $Co_{0.4}Zn_{0.6}Fe_2O_4$ Hollow Nanospheres
Q.G. Ren, X.J. Qiao, Y. Li, Z.G. Sun, X.D. Guo and S.Z. Zhang 126

Research of Magnetic Characteristics of the Split-Drain MAGFET Based on Nano-Polysilicon TFTs
X.F. Zhao, H.Y. Guan, M.W. Lv, Y.N. Bai and D.Z. Wen 132

Graphene Field Effect Transistor's Circuit Modeling and Radio Frequency Application Study
R. Zhu, Y. Zhang, J. Luo, S. Chang, H. Wang, Q. Huang and J. He 139

Synthesis and Dispersity of YBCO Powder Produced by Oxalic Acid Precipitation Method
A.Q. Wang, H.H. Han, M. Li, J.P. Xie, Q.J. Wu and D.Q. Ma 145

Influence of Defects on the Young's Modulus of [110] Silicon Nanowires with Different Cross Sections
F. Gu, J.H. Zhang, M. Li, L.Y. Liu and J. Su 151

Sintering Behavior and Electrical Property of Surface Treated Silver Nanoparticle for Electronic Application
H. Xie, N.N. Xiong, Y.Z. Zhao and Y.H. Wang 157

Study on the Etching Technique of Non-Photosensitive Polyimide
R. Lei, W.G. Liu, C.L. Cai, S. Zhou, J. Nie and X.Y. Wang 163

An Investigation on Resistive Switching Characteristics Induced by HfO_x and Electrode Interfaces
X.R. Chen and J. Feng 169

Study on Internal Stress in Micro-Electroformed Layer
L.Q. Du, Z.C. Tan, C. Song, Z. Zhao, Q.F. Li and P.H. Yin 178

Low Temperature Eutectic Alloy Bonding Used in MEMS-Based Solid Propellant Microthrusters Array
C.B. Ru, Y.H. Ye, J.B. Xu, Z.Y. Zou, J. Dai, P. Zhu and R.Q. Shen 184

Simulation and Test of through Silicon Vias Impacted by Large Current Pulse
X.R. Ding, Y.B. Wang, W.Z. Lou and F.Y. Liu 190

Preparation of Strongly Hydrophobic Film with Large Area and Flexibility Based on Micro Fabrication
Y.B. Zeng, T.T. Wang, J.Y. Wang and H. Guo 195

Preparation of TiO_2 Nano-Film by Anodic Oxidation Method and its Hydrophobic Modification
F.B. Liu and B. Jing 201

Fabrication and Thermal Performance of Copper Pillars Modified Micro Heat Pipe (MHP)
L.L. Zou, Y. Luo, J.G. Liu, B.K. Yu, Q. Shan and X.D. Wang 208

Research on TSV Dry Etching Technology
G.Q. Jiang, L. Kuang and J. Zhu 216

Research on Microstructure and Wear Resistance of Cast-Penetrated Layer Strengthened by Nano-Sized TiN Intermediate Alloy
J.P. Xie, X.H. Shao, S. Liu, F.M. Wang, A.Q. Wang and D.Q. Ma 221

Research on Delamination of Plastic Packaging Device during Reflow Soldering
P.S. Liu, Y. Lu, J.X. Huang and L.L. Yang 226

Preparation of Nano α-Fe_2O_3 Powders and Characterization of their Photo-Catalysis Capacities
N.Y.S. Zhang, Y.A. Zen, S.B. Wang and B. Zhu 232

Research on the Preparation of Nanoporous Copper Using Taguchi Method
K.C. Li, X.G. Liu, Y. Chen and M.X. Chen 238

Preparation of Mn-Zn Ferrite Flake Absorbent by Self-Reactive Spray Forming Technology
H.T. Gao, J.J. Wang, H.F. Lou, X.D. Cai and Y.S. Hou 246

Intermolecular-Interaction and Mechanical Properties of MNs-Plasticizer Modified 2,4,6-Trinitrotoluene/1,3,5-Trinitrohexahydro-1,3,5-Triazine Molten-Energetic-Composite(MEC)
Q. Ma, M.P. Wen, B.H. Zheng, H.J. Huang, D.B. Liu and J.S. Li 252

Research Survey of Electroformed Nickel Material Properties Used in MEMS
G.Z. Li, G.C. Shi, L. Sui, F.T. Yi and B. Wang 259

The Effect of Thermal Accumulation to the Field Emission Properties of the Carbon Nanotubes
F. Yan, N.N. Li, L. Chen, D.Z. Jin and W. Xiang 265

Effect of Ammonia as an Inert Solvent on Structure and Separation Performance for Oil/Water Mixtures of PVDF Porous Membranes
W.W. Cui, J.Q. Liu, L.Z. Liu, W.H. Xu, Y.Y. Li and Z.Q. Gao 269

Size Effect of Piezoelectricity in ZnO Nanowires: A First-Principles Study
C.Q. Qin, Y.S. Gu, X. Sun, C. Li and Y. Zhang 275

Ejection and Motion Behaviors Simulation for Multi-Jet Electrospinning
W.W. Li, Z.W. Luo, X. Wang, J.Y. Zheng, G.F. Zheng and D.H. Sun 281

Measurement on the Mechanical Properties of SiC Thin Films Based on Square Thin Films Theory
Y.M. Chen, P.T. Dong, X.Z. Wu and Y.L. Wu 287

Optimization of Chemical Mechanical Planarization Process of High Enrichment Slurry Under Low Pressure
Y. Li, Y.L. Liu, H.B. Li, A.C. Wang, W.J. Liu and J. Hong 291

Effect of Reaction Inhibitors on Synthesized Silver Nanostructures via Solvothermal Method
H. Xie, N.N. Xiong, J.Z. Liu, Y.Z. Zhao and Y.H. Wang 297

Effects of NaOH Concentration on Section Structures of Oxide Films Based on TC4 by Anodic Oxidation Process
J.K. Yan, G. Yang, Z. Shi, W.X. Tang and Y.F. Wu 303

A Novel High Precision Analytic Potential Function for Diatomic Molecules
C.F. Yu 313

The Simulation and Analysis of Current Crowding and Joule Heat in Flip Chip Solder Bumps
P.S. Liu, L.L. Yang, J.X. Hang and Y. Lu 319

Effects of n-Type Dopants on Electronic Properties in 4H-SiC
J.L. Tang, J.N. Zhong and C. Wen 325

Fabrication of Ultrasmooth Polymer Films by Concentration Control and Spin Speed Adjustment
Y. Guo, W.G. Liu, H. Liu, S. Zhou, L. Wu and F. Li 330

Nanopore in C-S-H Gel Stability Analysis of Hardened Cement Pastes
L. Wu, N. Xiong and F.Y. Yu 335

Simulation and Typical Application of Multi-Step Diffusion Method for MEMS Device Layers
L.Y. Wang, R.H. Zhou, Y.F. Liu, C. Zheng, J.F. Cai and Y. He 341

Synthesis of Nano-Al with Fe_2O_3 Nanowires to Realize Core-Shell Composite Materials Arrays Based on Colloidal Templates
S.M. He, J. Chen, K. Fang, Z.Q. Qiao and J.S. Li 347

Evaluation of the Stability on the New Alkaline Copper Bulk Slurry
J. Wang, R. Wang and G.D. Chen 352

Research on Low Temperature Anodic Bonding Based on Interface Pretreatment of Dielectric Barrier Discharge Plasma
M.Q. Pan, L.N. Sun, Y.J. Wang, J.Z. Liu, T. Chen, H.C. Liu and L.G. Chen 356

The Study on the Selectivity Ratio of SiC/Epoxy Resin Based on ICP Etching
J. Hu, S. Zhou, C.L. Cai, Y.F. Zhu, S. Hu and W.G. Liu 362

High-Efficiency Preparation of N-Doped Titania with High Visible Light Photocatalytic Activity Using Composite N Precursor
Y.L. Hu, X.D. Zhang, H.F. Liu and X.P. Guo 368

UV Photocatalytic Digestion Utilizing TiO_2 Nano-Fiber for the Determination of Total Phosphorus
Q. Zhang, J.H. Tong, C. Bian and S.H. Xia 375

Research of Thin Film for Laser Polarization Beam Splitter
X.H. Fu, Y.G. Pan, D.M. Liu, J. Zhang and X.J. Wang 381

Micro Laser Joining between Dissimilar Materials of 200μm Thick TiNi Alloy and Stainless Steel and the Joint's Electrochemical Behavior
Y.H. Chen, J.L. Xie and W.H. Gong 388

Electrokinetic Research on the Dispersion Behavior of Nano-Ceria Particles in Concentrated Suspensions
W. Gao, Q.L. Wei, L. Ding, X.Y. Li, C. Wang, G.P. Tang and J.G. He 394

Study of SiC's Mechanical Property Variance Caused by Film Thickness
Z.L. Jiao and J. Zhu 400

Experimental Study on the Relationship between Dislocation Density and Internal Stress in Micro Electroforming Layer
C. Song, L.Q. Du, T. Yang, L. Luo, Y.S. Tao and X. Zhang 405

Influence of Hybrid Fibers on Flexural Properties of Ultra High Toughness Cementitous Composites with Nano-SiO_2
X. Gao, Q.H. Li and S.L. Xu 411

The Influence of Polyhedral Oligomeric Silsesquioxane on Heat Resistance and Curing Kinetics of Potting Materials
J.H. Fan, H. Jing and J.Y. Wu 416

Study on Mechanism of Phase Forming in Ni^+ Implantation into Ti6Al4V at Elevated Temperature
Y. Wang, X.H. Yu and H.L. Yang 421

Preparation and Mechanical Properties of Ultra-Fine Grain Medium-Carbon Steel Based on Equal-Channel Angular Pressing
J.M. Wang, W.T. Hou and L. Lu 427

Chapter 2: Micro/Nanofluids Research and Technologies

Tribological Properities of Oil-Based ZnO Nanofluids
X. Ran, X.Y. Yu, Y. Wang and Z. Xiao 437

Performance Investigation of TiO_2 Nanofluid Coolant for Automobile Cooling Applications
J.M. Chen, X.Y. Sun, G.J. Leng and J.H. Feng 444

The Simulation and Experimental Analysis of Hydrodynamic Focusing Effect inside a Rectangular Microchannel
S.J. Feng, X.Q. Shi, J. Zeng, Y. Peng and M. Liu 449

Threshold Model of Micro-Fluidic Inertial Switch Based on Orthogonal Regression Design
T.T. Liu, W. Su, C. Wang and T. Yang 455

Effect of Flow Rate of Slurry in Micro-Channels on the Consistency of Polishing Rate
Y. Li, M. Sun, Y.L. Liu, A.C. Wang, J.Y. Tang and S.Y. Fan 462

Discrimination of Low-Grade Oil from Edible Oil by a Microfluidic Device
M. Liu, S.J. Feng, X.Q. Shi, Y. Peng and Z.Z. Wu 469

Effect of Elliptical Dimples on Hydrodynamic Lubrication
J.H. Ji, H. Wang and Y.H. Fu 474

Chapter 3: Measurements, Sensors and MEMS

Study of Bandwidth Expansion Based on Electrochemical Vibration Sensor
Z.Y. Zhang, J.B. Wang, D.Y. Chen and Y.A. Li 483

A Novel Micro-Machined Out-of-Plane Resonant Accelerometer with Differential Structure of Different-Height Resonant Beams
S.M. Zhao, Y.F. Liu and J.X. Dong 488

The Research of Turn-On Time for Silicon Micromechanical Gyroscope on a Chip
Y. Bian, Q. Shi and G.M. Xia 492

3D Indoor Positioning System Based on MEMS Sensors
J.L. Zhu, B. Mo, C.D. Ling and W.Y. Fu 498

Analysis Temperature Characteristics of Atmosphere Pressure Sensor Caused by Residual Gas
L.D. Du, Z. Zhao, S.H. Wu and Z. Fang 504

Q-Factor Improving of Film Bulk Acoustic Wave Resonator for Chip-Scale Atomic Clocks
Z.S. Zhang, L. Tang and L. Ji 509

Study on a Planar Interdigitated MEMS Supercapacitor Using Modeling and Simulation Method
K.R. Dai, X.F. Wang, W.S. Lv and Z. You 513

Passive Acoustic Localization Based on MEMS Microphone Arrays
X.M. Dai, W.Z. Lou, M.R. Guo, F.F. Wang and X. Jin 517

An Electromagnetic Vibrating Ring Gyroscope Using SOI-MEMS Technology
Y.X. Li, D.Y. Chen, G. Huang and Q. Li 522

The Research on MEMS Micro Capacitance Sensor Detection Based on MS3110
H.J. Yu, Z.Q. Ding, X.P. He, L.M. Du, H. Qu, W. Zhou and B. Peng 528

The Influence of Die-Attach Adhesives on the Packaging of MEMS Accelerometer
P. Peng, X.P. He, L.M. Du, W. Zhou, H.J. Yu and B. Peng 533

High Resolution Micro-Displacement Sensing Circuit for Rotor Micro-Gyroscope
M.Y. Ren, X.W. Liu, H.F. Zhang and Z.G. Mao 538

Simulation and Experimental Verification of Silicon Microgyroscope's Closed-Loop Driving Circuits Based on Cadence
W.F. Tang, G.M. Xia, A.P. Qiu and Y. Su 543

Design of 16 bit 200kHz Feedforward Sigma-Delta ADC Applied in Silicon Gyroscope
F.X. Huang, Z.Q. Gao and X.W. Liu 548

Advancements in Micro-Structure with Multiple Stress Concentration Region for Bionic Vector Hydrophone
G.J. Zhang, P. Zhao and W.D. Zhang 555

High-Precision Quadrature Signal Generator for Digital Demodulation of MEMS Gyroscope
D.H. Chen, L. Chen, H. Zhou and Y. Tian 561

Study of Thin Film Pressure Sensor by Magnetron Sputtering
D.P. Hu and X.L. Wang 566

FPGA-Based Test Equipment for System-Level MEMS Switch Series
P. Liu, W.Z. Lou, Y.F. Lu and X.Y. Feng 572

Design and Analysis of Capacitive Micromachined Ultrasonic Transducers Based on SU-8
Y.P. Li, C.D. He, J.T. Zhang, J.L. Song, W.D. Zhang and C.Y. Xue 577

Passive Wireless Multi-Parameter Sensor System for Hermetic Environment Monitoring
D. Tang, L.F. Wang and Q.A. Huang 583

Statistical Analysis and Yield Enhancement of MEMS Devices by Considering Multi-Process Variations
L.L. Gao, W.H. Li and Q.A. Huang 589

Effects of Hall Output Probes Shape on Magnetic Characterization of Hall Magnetic Field Sensor Based on MOSFET
X.F. Zhao, Q.R. Lin, A.L. Mu, D.Z. Wen and H.Q. Zhang 595

Chip-Level Active Temperature Control for Improving Temperature Robust of a Micro-Gyroscope
Z.H. Chen, L.L. Liu, D.B. Xiao, H.J. Cui and X.H. Wang 600

A 16 Bits 500 kHz Sigma-Delta DAC for Silicon Micro Gyroscope
Y.K. Zhao, L. Yin, Z.T. Liu, W.P. Chen and X.W. Liu 605

An Integrated Pressure and Magnetic Field Sensor Based on Piezoresistance Effect
T. Wu, X.F. Zhao, X.H. Yang, D.Z. Wen and G. Li 610

The SOI Micro-Accelerometer Fabricated by Sacrificial Process
Z.Y. Zhang, W. Su, Z.G. Shi, B. Tang, Z. Xiong, Y.H. Chen and B. Peng 616

Noise Analysis of Silicon Microgyroscope's Transimpedance Amplifier Interface Circuit
W.F. Tang, A.P. Qiu, G.M. Xia and Y. Su 624

Micromachined Tri-Axis Capacitive Accelerometer Based on the Single Mass
F. Yuan, L.G. Chen, T. Chen and L.N. Sun 630

Multi-Chip Module Design of a MEMS Air Pressure Sensor
G.X. Yao, H.Y. Du, Q.A. Huang and M. Nie 636

A Modulated Feedback Approach to Improve Closed Loop MEMS Accelerometer Bias Instability
M.J. Ma, Z.H. Jin and Y.D. Liu 640

A Second Differential Bandpass Filter with Tuning Center Frequency and Constant Q
Y.X. Zhao, W.R. Zhang, H.Y. Xie, X. Huang and L.H. Zhang 646

Trajectory Guidance Law for MAV Based on MEMS Sensor/GPS
Y. Cai, W. Xiong, X.T. Cao and Z.Y. Zhou 653

A Feed-Forward Sigma-Delta Modulator Applied in Silicon Gyroscope
Q. Shao, Q.Y. Lv, H. Meng, Q. Fu and X.W. Liu 657

A Novel Capacitive Temperature Sensor for Real-Time Monitoring of Temperature in the Silicone Oil Fan Clutch
Q.Y. Ren, L.F. Wang, J.Q. Huang and Q.A. Huang 662

Active Disturbance Rejection Control Design for Fast AFM
D.X. Chen, B.H. Yin, J.B. Liu, W.P. Li, L.Q. Wu and H. Li 670

Plastic Strain Effect in Progressive Multi-Cycle Nano-Indentation Measurement
Q.L. Wei, X.Y. Li, X.B. Yue and D.J. Lei 675

Micro-Fabricated Pre-Concentrator Filled with Single-Walled Carbon Nanotubes as Adsorbent Material
X.F. Zhu, Z.W. Ning, J.H. Sun, T.J. Ma, Y.N. Zhang and J.H. Liu 681

Research on Rapid Detection and Accounting of Small Particles in Marine Hydraulic Oil
L. Zeng, H.P. Zhang, E.C. Liu, H.Q. Chen and F.Y. Cui 687

Dissemination of Micro-Gram Weights from 500 μg to 50μg Based on Automatic Mass Measuring System
X.P. Ren, J. Wang, L. Dong and O. Wilson 693

Design and Fabrication of High Vacuum Gauge Based on Micro Hotplate
F.T. Zhang, Y.B. Zheng, B. Tang, W. Su and Z. Tang 698

Analysis of Impact of Bottom Electrode Position on Dynamic Pull-In Parameters of Microcantilevers
S.K. Chang, G.F. Zhang and Z. You 706

Fabrication and Formaldehyde-Sensing Property of Quartz Crystal Microbalance (QCM) Coated with PVP-MWCNTs Composites
Y.F. He, Y.D. Jiang, H.L. Tai and G.Z. Xie 719

A Micro Direct Formic Acid Fuel Cell with PDMS Fluid Flow Plates
T.T. Wang, Y.B. Zeng, Z.G. Zhao and H. Guo 724

A Novel Microfluidic Time Gate for Controlling Flow of Liquids
L. Gan, C. Liu, J.M. Li, Y.H. Ma, L.J. Zhou, H. Zhang, T. Li and L. Wang 730

Microfluidic Amperometric Detection Sensor with Integrated Ag/AgCl Reference Electrode
H. Zhang, X.W. Liu, L. Tian, X.W. Han and T. Dai 736

Optimization of Microfluidic Chip Bonding Technology Based on Polydimethylsiloxane
J. Mao, W. Chen, L. Zhao, L.X. Yang and B.Z. Zhang 741

Applied Research on Self-Sensing Micro-Flow Injection Device Based on Piezoelectric Ceramics
J. Huang, L.P. Shi, H.M. Zhou, X.W. Wei and Y.B. Wei 746

Iron Wear Particle Content Measurements in Process Liquids Using Micro Channel – Inductive Method
Z. Bo, X.M. Zhang, H.P. Zhang, E.C. Liu and H.Q. Chen 756

Fluid Dynamic Analysis on Solar Heating Error of Radiosonde MEMS Humidity Measurement
X.L. Mao, J.H. Zhang, M. Li, S.R. Xiao and Q.Q. Liu 761

Experimental Study on Velocity of Flyer Based on Silicon
Q.B. Fu, Y. Wang, M. Wang, W.Z. Qin and F. Guo 766

A New Method of Design and Verification of Digital Silicon Gyroscopes Closed-Loop Driving System Based on MicroBlaze
P. Sun, Q. Shao, Y.Y. Liu and W.P. Chen 771

Design and Fabrication of a SOI Optical Waveguide Sensing Platform for Biochemical Sensor Application
Y.J. Liu, Y. Dong, D.P. Yuan and T.J. Li 777

The Research on Electroplating Technology Used for RF Micro Inductor Coil
R.K. Bi, X.Y. Wei, J.L. Wu and H. Guo 783

Study on Magnetization and Detection the Metal Particle in Harmonic Magnetic Field
X.M. Zhang, H.P. Zhang, Z. Bo, H.Q. Chen and Y.Q. Sun 790

The Buckling Simulation of Planar W-Form Micro-Spring in MEMS Safety and Arming Device
F.F. Wang, W.Z. Lou, F.Y. Liu, D.K. Wang, J. Lu, J. Wu, X.H. Guo and Z. Zhang 796

Design, Optimization and Simulation of an Electric Field Microsensor Based on PZT Piezoelectric Interdigitated Cantilevers
K. Feng, J.H. Tong, Y. Wang and S.H. Xia 800

Design and Application of Digitally-Programmable Delay-Time Microchip in Detonating System
Y.F. Lu, W.Z. Lou, X.R. Ding and Y.B. Wang 806

A Traceable Metrological Method with Nanometer Scale Resolution for Micro-Structure
B.H. Yin, D.X. Chen, H. Xue, Y.S. Lin, S.T. Gao, W. Li and L. Han 810

Accurate and Traceable Calibration of the Stiffness of Various AFM Cantilevers
Y.W. Zhao, Y.P. Song, S. Wu and X. Fu 817

Design of Minimal Capacitance Detect Circuit for MEMS Capacitive Sensor
H. Qu, H.J. Yu, W. Zhou, X.P. He, L.M. Du and B. Peng 824

Micro-Spring's Variable Stiffness Design and Characteristics Analysis
G.H. Liu, L. Sui, G.C. Shi and X.H. Guo 830

Fabrication Process and Electro-Thermal Modeling for the Cathode of the CMOS-Compatible Hot-Filament Vacuum Gauge
J.Q. Wang and J. Yu 836

A New Design of a Piezoelectric Triaxial Micro-Accelerometer
J.Y. Wang, T.T. Wang and H. Guo 841

UVC-Thermal Coupled Digestion without Oxidant for the Detection of Total Phosphorus
L. Li, C. Bian, J.H. Tong, H. Li and S.H. Xia 847

Fabrication of SU-8 Microneedle Based on Backside Exposure Technology
L.Q. Du, Z.Z. Wang, X.P. Ruan, S.L. Chen and Q. Shan 853

Analysis on the Effect of Machining Error on the Vibration of MEMS Device
H. Wang, W.H. Li and L.L. Gao 859

A Variable Resistor Micro System Based on Electro-Explosion
X.R. Ding, Y.B. Wang, W.Z. Lou and Y.L. Guo 865

Design and Experimental Study of a Composite Materials Micro-Deformation Measurement Device
Y. Yuan, H. Bao, H. Xu and Z.L. Li 869

A Low-Frequency Filter in Inertial Applications
Q. Li, X.W. Liu, L. Yin and J.J. Zhou 875

Experimental Investigations on New Characterization Method for Giant Piezoresistance Effect and Silicon Nanowire Piezoresistive Detection
J.H. Zhang, M. Yang, Q.Q. Liu, F. Gu, M. Li and Y.X. Ge 881

Application of Magnetic Filter Technology in Improving the Precision of a Micro Attitude Reference System
G.M. Yuan, X.R. Cao, Y.M. Zhao, P. Wang, J.B. Xie and H.L. Chang 888

Intelligent Logistics Monitoring Microsystem Based on STM32
F. Wang, W.Z. Lou, M.R. Guo and Y.F. Lu 896

Nondestructive Microscopy Test on Damage of Waterproof Material in Underground Engineering
Q.G. Wang, Q.X. Yang, Y.J. Jiang and J. Yang 900

A Robust Adaptive Angle Algorithm for Imaging Bionic Polarization Navigation Sensor
B. Li, L. Guan, S.Y. Li, J.K. Chu and Y. Cui 906

A Nano-Cantilever Bending Method for Interface Cracking in Nanoscale Materials
X.Y. Wang and Y.B. Yan 912

The Displacement Characteristics of Piezoelectric Ceramic Micro Actuators Evaluated by Laser Interferometer
H. Wu, L.B. He, J.L. Zhou and P. Yang 920

On the Temperature-Related Mechanical Properties of UV-LIGA Nickel Material
S.S. Yuan, G. He, M. Zhang and G.Z. Li 926

Design and Experiment Research on MEMS Vector Hydrophone Vibration Damping Structure
N. Guo, G.J. Zhang and W.D. Zhang 931

The Test and Simulation Modeling of Micro Scale Solid Particles Fuel Cloud Dispersal under High Dynamic
X. Jin, W.Z. Lou, M.R. Guo and X.M. Dai 942

Chapter 4: Micro Actuators and Devices

Performance-Enhanced Heat Converter Used in FPA Utilizing a SiOx/Al Corrugated Micro-Cantilever Actuator
Y.M. Kong, R.W. Liu, B.B. Jiao, D.K. Lu, E.C. Zhu, Q.S. Fu and D.P. Chen 951

Modeling of Hysteresis in Piezoelectric Actuator Using Linear Play Operator Adaptive Filter
R. Xiong, X.D. Liu and F.M. Shan 957

The Dynamic Characteristics Research of MEMS V-Shaped SiO_2/Al Electrothermal Actuator
Y.Y. Shen, R.C. Song, H.M. Tang, Q.S. Chen and P. Guan 963

The Parametric Analysis of the Threshold Value Judging Mechanism in MEMS Safety and Arming Device
F.F. Wang, W.Z. Lou, F.Y. Liu, D.K. Wang, M.R. Zhang and C.G. Xu 968

The Error Analysis of Micro-Flow Self-Sensing Actuator
Y.B. Wei, L.P. Shi and H. Zhou 972

Analysis of Harmonic Distortion of Sigma-Delta Modulator
D. Yan, W.N. Jiang, S.Q. Tao, J. Yang, L. Yin and X.W. Liu 980

The Parametric Analysis of the Lock-Releasing Mechanism in MEMS Safety and Arming Device
F.F. Wang, W.Z. Lou, F.Y. Liu, D.K. Wang, J. Lu, J. Wu, X.H. Guo and Z. Zhang 986

Theoretical Investigation of the Electronic Properties in BN Nanowires
C.C. Zhuang, L. Li, S.D. Fan, C.C. Ban and X.W. Liu 990

Dynamic Modeling and Output Characteristic Analysis of a Micro Bistable Piezoelectric Generator
X.H. Mao, Q. He and T.T. Huang 995

Impact of Cross-Section and Size on Vibration of Silicon Nanowires
P. Zhang, H.B. Chen and H. Yu 1004

Controlled Encapsulation of Micron-Sized Beads in a Droplet Based on Pulse Inertia Force Driving of Micro-Fluids
H.C. Wang, L.J. Yang, J. Liu and Z.D. Dai 1009

Interference Fit Assembly of Micro-Parts Based on Microscopic Vision and Force
J. Zhang, W.R. Wu, F. Shen and Y.J. Deng 1016

Scalable Electrical Model and Performance Analysis of a Novel Bar TSV Structure
Z.S. Li, M. Miao, S.C. Yang and D.C. Yang 1024

Experimental Investigation of Thermal Conduction Performance on Silicon-Based Micro Flat Heat Pipe
C.M. Li, Y. Luo, C.P. Zhou, L.L. Zou, X.D. Wang and Q. Shan 1032

Analysis of Effective Field Emitting Angle for Spindt Cathode
N.N. Li, S.C. Pang, F. Yan, D.Z. Jin, W. Xiang, D. Zhang, J.Y. Dai and B.Q. Zeng 1038

Fabrication of Convex Plate-Shaped Micro Tool Electrode and its Application in Micro Hole Machining by ECM
Z.W. He, M.H. Wang, L. Zhang and W. Peng 1043

Design of Micromachining System Based on Nanosecond Pulsed Laser
D. Xu, Y. Yao, X. Fu and C. Wang 1049

Experimental Research on Nanostructure Fabricated by AFM Probe Combining with a CW Laser
L.J. Yang, B. Cheng and Y. Wang 1054

Constructing Dual Band Metamaterial Absorbers at Mid-Infrared by Employing Multi-Resonant Structures
W. Ma, Y.Z. Wen, R. Zhao and X.M. Yu 1059

Structure Design of Large Travel One-Arm Bridge Type Z-Axis Nano-Positioning Stage
W. Fan, Z.S. Li and S.Y. Jiang 1064

Effect of Undercut on the Characterization of the Mechanical Properties of Silicon Nanocantilevers with Dynamic and Static Test
J.H. Zhang, F. Gu, X.L. Zhang, M. Li, Y.X. Ge and X.L. Mao 1072

Implementation of Convolutional Encoder in Quantum-Dot Cellular Automata
M.L. Zhang, L. Cai, X.K. Yang, H.Q. Cui and Z.C. Wang 1078

Chapter 5: Optics in the Scale of Micro and Nano

Theoretical and Experimental Studies on Microcavity Organic Light-Emitting Diodes with Different Emitters
C.Y. Peng, M.J. Wei, R.J. Huang, K.P. Guo, Y.L. Jing, T. Xu and B. Wei 1087

A Method to Fabricate Thin Micro Silicon Cantilever Based on Optical Lithography with AZ 1518
C.Z. Tang 1093

Design and Experiment of Phase Laser Ranging System Based on MEMS Mirror for Scanning Detection
C. Zhang and H. Huang 1099

High-Frequency InP-InGaAsP Heterojunction Phototransistor Employing a UTC Structure
Z.Y. Jiang, H.Y. Xie, W.R. Zhang and L.H. Zhang 1105

A Compact Infrared Gas Sensor Based on an Asymmetry Gas Cavity
A.J. Ming, Y.H. Ren, Y. Zhang, L. Zhang, W.B. Zhang, Z.X. Tan, W. Ou, Q.L. Tan, H.Y. Mao, J.J. Xiong and D.P. Chen 1111

Surface Micromachined Mirror Based on Pre-Stress Comb-Drive Actuator
W.M. Wang, S.M. Yan, Q. Wang, C.K. Qiu, Z.X. Chen and B. Fan 1115

Design and Simulation of MEMS Mirror Based 3D Shape Measurement System
C. Zhang 1120

Chapter 6: Energy Harvesting, Power Supply and Technologies for Fuel Cells

The Design of an Interface Circuit for Micro-Electrostatic Vibration Energy Harvesters and Super-Capacitor
S. Chen, Y.X. Lu and X.H. Wang 1127

Fabrication of Aluminum Nitride Films by Reactive Pulse DC Magnetron Sputtering for Vibration Energy Harvester
Z.G. Shang, D.L. Li and S.Q. Wang 1133

Novel Wind Energy Harvesting Device for City Building Based on ZnO Films Array
S.H. Wu, L.D. Du, Z. Zhao, D.Y. Kong and Z. Fang 1139

VCu_xO_y Thin Film by Magnetron Sputtering as Cathode Material for Thin Film Lithium-Ion Microbatteries
J. Lin, J.L. Guo, C. Liu and H. Guo 1145

High Performance Supercapacitor Electrode Materials Based on Activated Carbon and Conducting Polypyrrole
W.T. Yuan, Y.J. Yang, Y.L. Qiu, J.H. Xu, W.Y. Yang and S. Xia 1150

Electrohydrodynamic Atomization Deposition of Fuel Cell Catalyst-Coated Membrane with Structure and Material Gradient Variation
D.Z. Wang, W. Zha, X.H. Zhu, Y. Li, J.S. Liang, T.Q. Ren, Y. Luo, X.D. Wang and C. Liu 1156

Secondary Synthesis of Microporous Heteroatoms Y Zeolite and their Hydrodesulfurization Properties for Model Fuel
X. Hong and K. Tang 1163

A 3D All-Solid-State Thin Film Microbattery with Inverted Pyramid Arrays
J. Lin, J.L. Guo, C. Liu and H. Guo 1170

Formation of Membrane Electrode Assembly for High Temperature Methanol Fuel Cells
D.Z. Wang, X.H. Zhu, W. Zha, T.Q. Ren, M.Q. Li, J.S. Liang and C. Liu 1175

Asymmetric Design of Anode and Cathode Current Collectors for Micro Direct Methanol Fuel Cells
Y.F. Zhang, S.B. Zhang, Z.Z. Ma, H.L. Chen and X.W. Liu 1181

Study on the Energy Harvesting Performance of PE Cantilever Beam
H.P. Liu, S.Q. Gao and L. Jin 1189

To Improve Micro-Planar-Magnetic Generator Performance Based on Addition of Magnetic Material
L. Du, G.C. Shi and J.J. Zhao 1195

Electrospun PVDF/PMMA/SiO_2 Membrane Separators for Rechargeable Lithium-Ion Batteries
X.L. Wu, J. Lin, J.Y. Wang and H. Guo 1201

Electrospun SnO_2-Graphene Composite Nanofibers as High Performance Anode for Lithium Ion Batteries
Y.L. Wu, J. Lin, J.Y. Wang and H. Guo 1207

Numerical Optimization Approach of the Gap between the Magnet and Coil for Electromagnetic Vibration Energy Harvesters Design
Y.M. Lei and Z.Y. Wen 1214

Design and Comparison of Micro Electromagnetic Vibration Energy Harvesters
Y.M. Lei, Z.Y. Wen and L. Chen 1223

Corrosion Behavior of SAMs Modified Silver-Coated 316LSS as PEMFC Bipolar Plates
X.J. Yan, J.B. Zhuang, N.B. Huang, C.H. Liang, H.T. Wang and L.S. Xu 1233

Chapter 7: Bioresearch and Biomedical Engineering

Stabilization of Pickering Emulsions by Bacterial Cellulose Nanofibrils
W. Fu, Y. Liu, C. Yang, W.H. Wang, M. Wang and Y.Y. Jia 1247

Enrichment Efficiency Optimization of Dielectrophoresis Cell Chip Based on Interdigitated Microelectrodes Array
W.W. Gu and J. Huang 1255

Functionalization of Mesoporous SBA-15 with APTES by Co-Condensation and its Effect on Immobilization of *Candida rugosa* Lipase
X.Y. Li, Y.Q. Xu and G.W. Zhou 1261

Fabrication of a Pendulous Resonant Micro-Machined Biosensor for Direct Liquid Detection
G. Huang, Y.X. Li, L. Qian and Q. Li 1267

***In Situ* Synthesis of the Hollow Silica Microspheres with Porous Surface by Using Chemical Modified Pollen Grains as Biotemplate**
F. Cao, D.X. Li and Z.Y. Wu 1273

CMOS Amplifier for Neural Signal Recording Applications
Z. Zhang, Z.X. Cheng and Y.W. Zhuang 1279

Analysis and Simulation of a Planar Microelectrode Structure for Dielectrophoretic Manipulation of a Single Cell and Cell Cluster
P. Chen, X.L. Ma, H. Zhang, M.J. Han, Y.C. Wang, B.B. Li and H.X. Zhu 1285

A Biological 3D Printer for the Preparation of Tissue Engineering Micro-Channel Scaffold
Y.N. Zhang, Y.Y. Liu, Y. Li, S. Li and Q.X. Hu 1290

Specific Detection of Staphylococcus Enterotoxin B in Milk Using Piezoresistive Cantilever Aptasensor
R. Zhao, Y.Z. Wen, W. Ma, J.C. Yang and X.M. Yu 1298

Biological CAD/CAM/3D Printing Integrated Molding Platform and System Building
Y.M. Ma, Y.Y. Liu, H.P. Chen and Q.X. Hu 1303

A CMOS Automatic Gain Control Circuit for Biomedical Applications
Z.Q. Gao, F.X. Huang, J. Li, L. Yin and X.W. Liu 1308

Facile Preparation of Cu/TiO_2 Nanocomposite via Photocatalysis and their Antibacterial Performance
B.X. She, J.B. Long, Y.M. Deng, X.J. Wan, K.J. Zhu and J.N. Tang 1314

Design of a Microfluidic Chip for Enrichment of Circulating Tumor Cells
X.X. Ling, D.H. Ren and Z. You 1320

Biological Effect of Single Wall Carbon Nanotubes on *Skeletonema costatum* and *Prorocentrum donghaiense* in Seawaters
F.F. Li, J.T. Wang and L.J. Tan 1326

Expansion Performance of Novel Balloon-Expandable Stent for Tapered Vessel
X. Shen, Y.Y. Sun and B.B. Wu 1333

Synthesis of Silica Modified Large-Sized Hydroxyapatite Whiskers by a Hydrothermal Co-Precipitation Method
Y.T. Yin, Q.H. Chen, T.T. Yan and Q.H. Chen 1339

Flow Field Analysis for Plant Vessel and Bionic Structural Microfluidic Chip
C. Zheng, C.Y. Guo, J.W. Xue, S.B. Liu and T. Chen 1345

The Application of Micro-Flow Extrusion Forming Technology in the Denture Preparation
J. Zhou, G.L. Duan, D.B. Zhu and J. Cai 1351

Yeast Cells Immobilization in Microfluidic Channels Based on a Self-Polymerized Nano-Film of Poly(Dopamine)
X. Chen, L.L. Zhang, J.H. Sun, H. Li and D.F. Cui 1357

An Ultrasonic Micro Knife Based on Triangular Silicon Horn Chip
T.T. Wang, J. Wu, K.M. Ying, W.G. Li and H. Guo 1363

Preparation and Characterization of Tissue Engineering Scaffolds by Composite Molding of 3D Printing and Electrospinning
Y.M. Ma, Y.Y. Liu, H.P. Chen and Q.X. Hu 1368

Pretreatment with Huperzine A-Loaded Poly(lactide-co-glycolide) Nanoparticles Protects against Lethal Effects of Soman-Induced in Mice
R.H. Zhang, L.Q. Li, C. Wang, X.J. Lu, T. Shi, J.F. Xu, L.C. Song and H.F. Wang 1374

CHAPTER 1:

Materials and Technologies in the Scale of Micro and Nano

Key Engineering Materials Vols 645-646 (2015) pp 3-8
© (2015) Trans Tech Publications, Switzerland
doi:10.4028/www.scientific.net/KEM.645-646.3

Submitted: 2014-10-28
Accepted: 2014-12-23

Study of PSG Thickness Uniformity Influencing Factors in LPCVD

Wenlong Lü[1,2,a], Zhan Zhan[2,b],Xiaohui Du[2,c],Ruhai Zhou[2,d],

Haoer Zhang[2,e], Lingyun Wang[2,f]， Daoheng Sun[2,g*]

[1]Micro-Electro-Mechanical Systems Research Center, Xiamen University, Xiamen,Fujian, China

[2]Department of Mechanical and Electrical Engineering, Xiamen University, Xiamen,Fujian, China

[a]lwl1980@xmu.edu.cn,[b]zhanzhan_snow@163.com,[c]772745108@qq.com,[d]345325749@qq.com,

[e]693406356@qq.com,[f]rabitwangly@yahoo.com.cn,[g]sundh@xmu.edu.cn

Keywords: LPCVD; PSG thickness uniformity; Surface velocity uniformity; Flow distribution

Abstract. In the fabrication of SiC high-temperature sensors, the phosphosilicate glass film (PSG) is deposited on the SiC wafer as the intermediate layer, achieving the bonding of two SiC wafers. The ease of bonding is affected by the PSG film thickness uniformity. In this paper, the flow field distribution in the LPCVD tube is simulated under different deposition conditions，obtaining the wafer surface uniformity of gas flow distribution, which was verified by the experiment, The aim of this work is to study the impact of several deposition conditions such as the location of SiC wafers, wafer inclination and wafer spacing on the thickness uniformity of PSG film. Experimental results show that SiC wafer position in the tube and its own inclination and wafer spacing affect gas flow field on the SiC wafer surface，leading to uneven distribution of gas flow, thus affect the thickness uniformity of PSG.

1.Introduction

Phosphosilicate-glass (PSG), as a kind of mid-layer, is needed to be deposited on the surface of SiC wafer in order to accomplish the bonding between two SiC wafers in the manufacturing process of sensors applied in high temperature condition[1]. While to some extent, the PSG thickness uniformity will affect the subsequent bonding process.

In this paper, PSG film is deposited with LPCVD (Low-pressure Chemical Vapor Deposition). LPCVD has a series of advantages over APCVD and PECVD in quality, thickness uniformity and mechanical property of the deposited film[2,3]. It is easier to obtain PSG film with better thickness uniformity, since diffusion coefficient of gas increases dramatically with the decrease of pressure, making reactants and by-products diffuse faster.

In essence，the process of LPCVD is a kind of gas phase transportation and reaction which includes reacting gas flow, diffuse and a series of surface chemical reaction[4]. Since gas diffusion coefficient is big under low pressure, the deposition process is mainly dominated by diffusion mechanism which could be explained by Monte Carlo method[5]. In fact, the direct flux is not completely isotropic and the supplementary reacting gas flow will also affect the thickness uniformity of deposited film. We have analyzed the gas flow distribution in the tube and the velocity uniformity change in the area on the wafer surface.

On the one hand, gas mixture flow into the tube from inlet. Macroscopic gas flow should not be ignored, even though the reactants transportation is mainly dominated by diffusion[6]. The reactants flow is not completely isotropic in the area between wafers. When gas flow velocity in the area is relatively faster, the deposition velocity is tend to be faster as well, because of the faster exchange

of reactants and by-products[7]. So in the process of PSG deposition, the uniformity of gas flow velocity will affect the deposition velocity as well as the final PSG thickness uniformity.

On the other hand, though the gas flux is very small, the PSG thickness is from several hundred nanometers to 1.5 microns usually and only several decade nanometer deviations can be tolerated. Therefore, improving the uniformity of gas flow velocity is significant to PSG thickness uniformity.

2. Simulation

The STAR-CD software is applied to simulate the gas flow field in the tube of LPCVD system, which is the special simulation software used for computational fluid dynamics.

During the former PSG deposition experiments, the inner diameter of the tube is 0.16m, and the gas flow rate is 2.3×10^{-4}m/s. According to Eq.(1), the Reynolds number of gas mixture is 4.17, belonging to laminar flow. In addition, the pressure in the tube is only 33.25Pa, so the deposition of PSG in the tube is mainly dominated by the diffusion of PH_3.

$$R_e = \frac{\rho \cdot v \cdot D}{\eta} \quad (1)$$

In the Equation， ρ is fluid density; v is fluid velocity; D is geometric limitation of object; η is fluid viscosity.

Though the chemical reaction in the process of PSG deposition would consume gas, creating negative pressure zone. According to Eq.(2) and the deposition rate---12nm/min obtained from the former deposition experiments, total gas consumption rate on each SiC wafer (double sides) is 4.47×10^{-6}mol/min while the total supply amount is 1.25×10^{-2}mol/min, based on the amount of substance. So the supply amount is far more than the consumption amount. Therefore, we could regard the pressure in the tube as a constant during deposition process, ignoring the influence of chemical reaction on the pressure in the tube[8,9].

$$Si(OC_2H_5)_4 + O_2 + PH_3 \rightarrow SiO_2 : P + by - products \quad (2)$$

When we take the trace chemical reaction into the simulation, the simulation will become extremely complicated. So we ignore the consumption of PH_3 in our simulation.

In order to calculate the surface velocity uniformity of SiC wafer, we choose five square areas (5×5mm) on the surface of each wafer, and each area contains 100 grids. The average velocity of these nodes in 100 grids is calculated according to Eq.(3), marked as the velocity of each area[10,11]. Then the surface velocity uniformity of the SiC wafer surface is calculated according to Eq.(4).

The average velocity of each square area: $\bar{V} = \frac{V_1 + V_2 + V_3 + \cdots + V_n}{n}$ (3)

The surface velocity uniformity of SiC wafer: $\sigma = \frac{(V_{max} - V_{min})}{\bar{V}_0}$ (4)

2.1 The location of SiC wafer

The distribution of flow field on the SiC wafer surface is affected by the location of SiC wafers in the tube, in which exist the uneven distribution of gas flow. In our simulation, SiC wafers locate the lower part of the tube, in which the deviation is 15 mm, and the wafer inclination is 0.6°.

Fig.1(a) shows that gas flow in the upper part is significantly larger than the lower part. Fig.1(b) shows the airflow velocity in the upper part in the furnace was faster, resulting in an uneven uniformity of the flow field in the upper part between SiC wafers, and a larger velocity gradient.

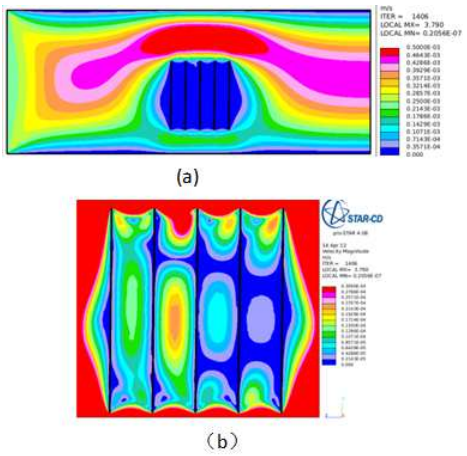


Fig.1 Cross-sectional view of gas flow field (a)The entire region, (b)Local region between SiC wafers

2.2 Different wafer inclinations

During LPCVD process, SiC wafers are arranged on a carrier, and the different supporting modes will affect the wafer inclination, and then affect the flow field uniformity which will finally influence the PSG thickness uniformity[12]. In our simulation, two different supporting modes are usually adopted. The schematic sectional views of two supporting modes are shown in Fig.2.

The slot widths of two supporting modes are 1mm and the wafer spacing is 12mm. The wafer inclination is 6.58° in Fig.2(a) and 1.15° in Fig.2(b).

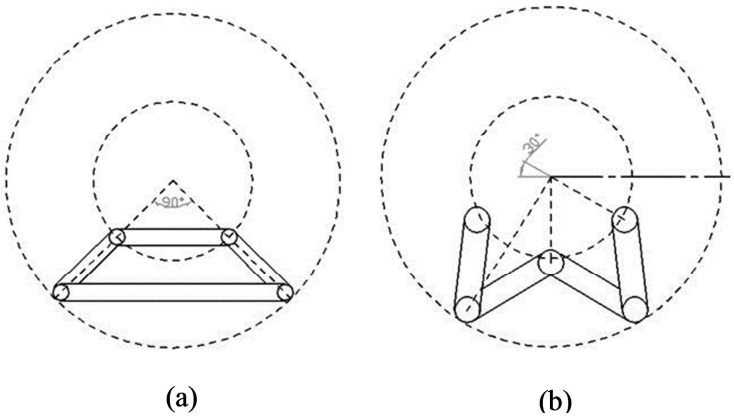


Fig.2 Schematic of different supporting modes (a)2-point supporting (b)3-point supporting

When the slot width of 3-point supporting mode is reduced further, the wafer inclination becomes smaller. When the wafer is strictly perpendicular to supplementary reactants flow, SiC wafers will be in the ideal situation. As we know, the slot width is always larger than wafer thickness, ensuring wafers placed in the quartz slots. So it is impossible to accomplish. When the slot width is reduced from 1mm to 0.6mm, the wafer inclination changes from 1.15° to 0.6°, bringing better reactants flow uniformity.

From the simulation results (Fig.3) we could easily recognize the difference of gas flow field uniformity. Different inclinations cause significant differences of the flow in upper region and lower region between wafers and tube wall. When the inclination is 6.58°, there are twice more reactants supply in the upper part than the lower part (Fig. 3(a)). When the inclination is 1.15°, the reactants flow is obviously more uniform and the velocity uniformity in the region between wafers is much better (Fig. 3(b)). When the wafer inclination changes from 1.15° to 0.6°, the uniformity of reactants supply flow and the velocity uniformity will be in the best condition.

The calculated result of the uniformity of reactants flow velocity on the wafer surface is represented in Fig.4.

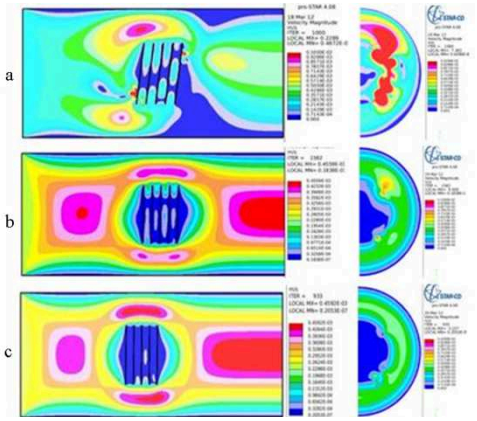


Fig.3 Distribution of reactants flow velocity at different wafer inclinations

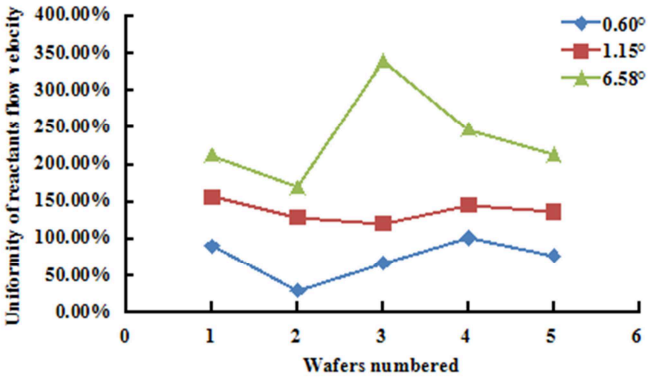


Fig.4 Uniformity of reactants flow velocity on the SiC wafers surfaces

When the wafer inclination is 0.6°, the surface velocity uniformity on the wafer surface is below 100%. As the inclination increases, the velocity uniformity becomes worse. When wafer inclination is 6.58°, the surface velocity uniformity is generally over 200%, some even more than 300%

When the SiC wafer inclination is 0.6°, both the uniformity of the flow field distribution in the tube and the velocity uniformity on the SiC wafer surface are relatively optimal.

2.3 Different wafer spacing

Wafer spacing is another critical parameter in the LPCVD system. Large spacing is not necessary for satisfying PSG thickness uniformity. Though it is apparently helpful to the exchange of fresh reactants and by-products, it could be disadvantageous to the uniformity of the reactants flow distribution. We can easily figure out the difference from the simulation results as shown in Fig.5. Wafer spacing given in simulation is 6mm, 9mm and 12mm. The max flow velocity in these three conditions is 0.45×10^{-3}m/s, 0.45×10^{-3}m/s and 0.44×10^{-3}m/s. There is no big difference in the value of max flow velocity. However, the uniformity calculated is obviously different as shown in Fig.6. When wafer spacing is 9mm, the uniformity of reactants flow distribution is from 30 to 40 percent, While the uniformity in other two conditions is almost over 50 percent. Therefore, 9mm should be a relatively appropriate wafer spacing for PSG deposition.

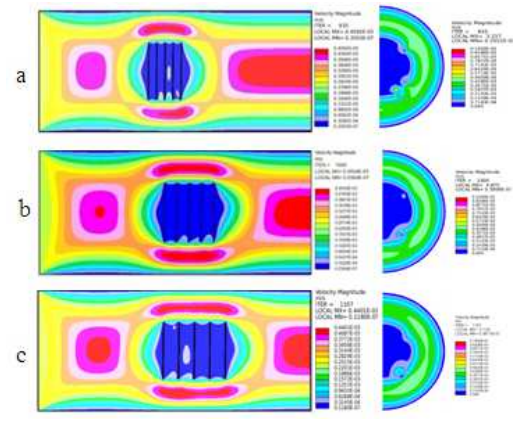


Fig.5 Distribution of reactants flow velocity at different wafer spacing (a)6mm,(b)9mm,(c)12mm

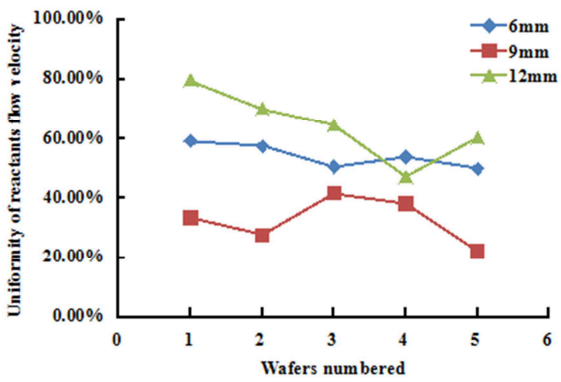


Fig.6 Uniformity of reactants flow velocity on the wafer surface

3. Experiments and discussion

Starting wafers were 75mm in diameter, double-sided polished SiC wafers which were 350 microns in thickness. The deposition is conducted at 900K and the composition of gas mixture in LPCVD deposition process is listed in Tab.1.

TAB 1 LPCVD gases flow

Gas	O_2	N_2	PH_3
Flow	200ml/min	76ml/min	4ml/min

In order to obtain the optimum contrasting results, two kinds of supporting mode are both adopted. The slot spacing is 3mm, making it easy to obtain different SiC wafer spacings discussed in simulation. When the 3-point supporting mode is adopted and the slot width is 0.6mm, the wafer inclination is 0.6°. When the 2-point supporting mode is adopted and the slot width is 1mm, the wafer inclination is 6.58°. The SiC wafers arranged on 3-point supporting quartz boat is shown in Fig.7.

Using different carriers, two batches of SiC wafers were deposited in the condition mentioned above to verify the influence of wafer inclination.

The PSG thickness was measured by ellipsometer and the uniformity was calculated according to Eq.(5).

$$\sigma = \frac{(x_{\max} - x_{\min})}{\bar{x}} \tag{5}$$

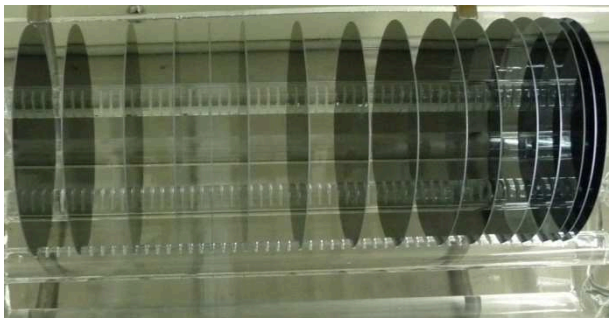


Fig.7 SiC wafers arranged on 3-point supporting quartz boat

When the wafer inclination is 6.58°, the PSG thickness uniformity is around 8%. While the uniformity is mostly around 5% when the wafer inclination is 0.6° (Fig.8). The PSG thickness uniformity is significantly improved.

Selecting different wafer spacings, four batches of SiC wafers were deposited in the condition mentioned above to verify the influence of wafer spacing on the thickness uniformity of PSG films. The thickness uniformity of deposited PSG films is shown in Fig.9. When the wafer spacing is 9 mm, the thickness uniformity is about 5%, which is most suitable for the PSG deposition.

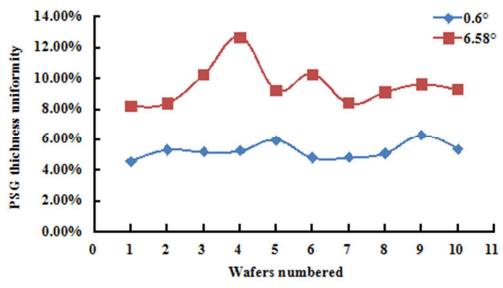


Fig.8 PSG thickness uniformity at different support modes

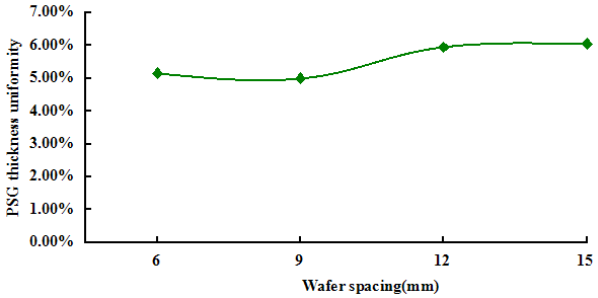


Fig.9 PSG thickness uniformity at different spacings

4. Conclusion

In PSG deposition, the transport of reactive substances is mainly depended on diffusion. However, the effect of the gas flow has also a significant impact on the uniformity of PSG film thickness.

The simulation results shows that SiC wafers should be located in the centerline of the tube as vertical as possible in order to obtain a good uniform of gas flow field in the different parts between SiC wafers.

Simulation and experimental results show that different inclination of SiC wafer and the wafer spacing affect the uniformity of the flow field velocity between SiC wafers, and affect the transmission rate of the reactants and byproducts, and then affect the thickness uniformity of PSG

The best deposition conditions is that adopting 3-point supporting mode, setting the wafer inclination as 0.6° and the wafer spacing as 9 mm, in which the thickness uniformity of PSG film on SiC wafers is about 5%.

5. Acknowledgments

This work funding is supported by China Aviation produce-learn-research projects (cxy2011XD25) and (cxy2013XD31).

References

[1] L. Hu, F. Yang, Q. Shang, et al, Application of TEOS LPCVD technique in SiC power devices process, Semiconductor Technology, 36(2011) 439-442.

[2] C. Liu, Y. Tai, Sealing of micromachined cavities using chemical vapor deposition methods: characterization and optimization, Journal of Microelectromechanical Systems, 8(1999) 135-145.

[3] J. Wang, L. Tong, Y. Li, et al, Study on preparation of the SiO_2 film thickness by LPCVD, Equipment for Electronic Products Manufacturing, 6(2011) 24-26.

[4] D. Adalsteinsson, J. A. Sethian, A level set approach to a unified model for etching, deposition, and lithography, Journal of Computational Physics, 138(1997) 193–223.

[5] J. Dai, Z. Zhou, Q. Huang, et al, LPCVD process simulation based on Monte Carlo Method, Solid-State and Integrated Circuit Technology (ICSICT), (2010) 1907-1909.

[6] K. Zhu, L. Chen, W. Yuan, Modeling and analysis of LPCVD reactors, Journal of Chemical Industry and Engineering, 5(1989) 540-548.

[7] H. Huppertz, W. L. Engl, Modeling of low-pressure deposition of SiO_2 by decomposition of TEOS, IEEE Transactions on Electron Devices, 26(1979) 658-662.

[8] J. M. Olson, Analysis of LPCVD process conditions for the deposition of low stress silicon nitride. Part I: preliminary LPCVD experiments, Materials Science in Semiconductor Processing, 5(2002) 51–60.

[9] J. Wang, S. Zhang , H. Wang, et al, Three dimensional computer simulation of low pressure chemical vapor deposition, Journal of Semiconductors, 5(1984) 621-630.

[10] E. Bar, J. Lorenz, 3-D Simulation of LPCVD using segment-based topography discretization, IEEE Transactions on Semiconductor Manufacturing, 9(1996) 67-73.

[11] M. Shenasa, B. O'Toole, B. Stueve, et al, Optimization of LPCVD silicon nitride process in a vertical thermal reactor: use of design of experiments, Advanced Semiconductor Manufacturing Conference and Workshop (ASMC), (1992) 216-219.

[12] K. F. Jensen, E. O. Einset, D. I. Einset, Flow phenomena in chemical vapor deposition of thin films, Annual Review of Fluid Mechanics, 23(1991) 197-232.

Key Engineering Materials Vols 645-646 (2015) pp 9-14
© (2015) Trans Tech Publications, Switzerland
doi:10.4028/www.scientific.net/KEM.645-646.9

Submitted: 2014-10-28
Accepted: 2014-12-23

Anisotropic elastic properties of chiral sculptured thin films at micro-scale evaluated by resonance frequency spectra

H. Fang [1,2, a], K. Matsumoto [2, b], T. Sumigawa [2, c], and T. Kitamura [2, d]

[1] Institute of System Engineering, China Academy of Engineering Physics, Mianyang 621900, China

[2] Department of Mechanical Engineering and Science, Kyoto University, Yoshidahommachi, Sakyo-ku, Kyoto 606-8501, Japan

[a] fanghui@caep.cn (H. Fang), [b] matsumoto @mbox.kyoto-inet.or.jp,

[c] sumigawa @mbox.kyoto-inet.or.jp, [d] takasan@mbox.kyoto-inet.or.jp

Keywords: Chiral sculptured thin films, Mechanical anisotropy, Vibration testing, Micro-scale.

Abstract. Chiral sculptured thin films (STFs) Glancing-angle deposition (GLAD) thin films are nano-engineered to meet the requirements of a variety of applications such as micro filters, sensors, and waveguides due to their unique frequency characteristics which cannot be achieved by conventional solid materials. For the design, it is necessary to understand the elastic properties of STFs. To facilitate this, we report on our newly developed advanced micro-scale vibration testing process. In the testing, specially designed micro-specimens with surface areas of tens by tens of microns are excited using a piezoelectric (PZT) actuator and the resonance frequencies are detected by a laser device in the vertical or lateral directions successfully. The anisotropy elastic modulus of STFs composed of helical nano-springs are identified on the basis of vibration testing. The thin film shows strong characteristic anisotropy that the solid one hardly can attain. The micro-scale testing technique can be extended to other materials and microstructures.

Intorduction

Chiral sculptured thin films (STFs) are compose of numerous parallel nano-scale spring-units that have helicoid, zigzag, pillar, and other shapes[1]. Accordingly, for engineering purposes, a micro-size STF is a unidirectional and anisotropic module that can be used in vibration, wave, and acoustic micro-devices at low (less than 1 MHz) and high (more than 100 MHz) frequencies, which depend on material, geometric characteristics of unit element and structural features of the entire film. Determining the anisotropic elastic properties of micro-size STFs through dynamic methods is challenging and remains a subject of scientific and technological interest in the micro-scale components, i.e., from a scientific point of view, they allow extension of dynamic techniques and models to other materials/microstructures, while the derived properties are also important for device designs, particularly to address compliance issues. In this paper, we report on the development of advanced Frequency-Sweep Vibration technique based on Laser Doppler, which can excite and measure the vibration of STFs comprised of helical nano-springs with thickness 1.0 μm. In our study, we prepared two specimens with surface areas of 30 × 30 μm2 and 15 × 15 μm2, respectively. Additional mass would be put in a certain place of the specimens, which would change the resonance frequency of specimens and be a significant marker for laser focusing. With this method, we detect the resonance frequency at the vertical and lateral directions, which make it possible to successfully measure the elastic constants of the STFs.

STFs GLAD thin films composed of helical nano-springs

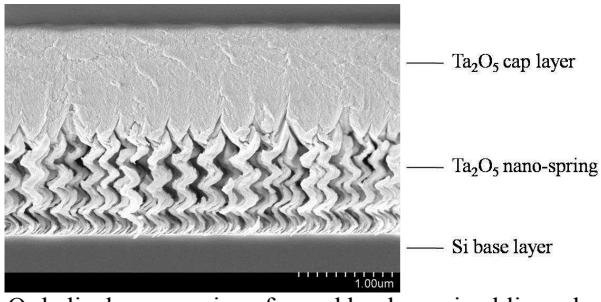


Fig. 1. STFs that consist of Ta_2O_5 helical nano-springs formed by dynamic oblique deposition technique: SEM image

Table 1 Size of Ta_2O_5 nano-springs

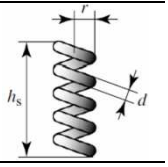
n	h_s (nm)	r (nm)	d (nm)	N_s (No./ μm^2)	illustration
4	1030	126	93	15	

Figure 1 shows a field emission scanning electron microscope (FE-SEM) (Hitachi, S-5500) image of a STF that consists of tantalum oxide (Ta_2O_5) helical nano-springs. The nano-springs are grown on the Si substrate via the DOD technique using electron beam (EB) evaporation. The incidence angle, defined as that between the incident flux and the normal to the substrate, is set at 87°, and the substrate is rotated during the deposition so that the number of turns *n* is four. The average size of nano-springs is listed in Table 1. Here, *N*s is the number of nano-springs contained in a unit area, which is evaluated by removing the cap layer and observing from the top. The springs uniformly distributes. Here, h_s, *r*, and *d* represent the scale of spring as illustrated in Table 1. A Ta_2O_5 cap layer with a thickness of h_c = 1030 nm is deposited by EB evaporation after the nano-springs are grown. Thus, the STF of nano-springs is sandwiched between the Ta_2O_5 cap and Si base layers. Because of the in-plane symmetry of the film, the elastic stress-strain matrix of the film is in the form

$$\mathbf{C}_{film} = \begin{bmatrix} 0 & 0 & 0 & 0 & 0 & 0 \\ 0 & 0 & 0 & 0 & 0 & 0 \\ 0 & 0 & c_{zzzz} & 0 & 0 & 0 \\ 0 & 0 & 0 & 0 & 0 & 0 \\ 0 & 0 & 0 & 0 & c_{yzyz} & 0 \\ 0 & 0 & 0 & 0 & 0 & c_{xzxz} \end{bmatrix}, \quad (1)$$

in which $c_{yzyz} = c_{xzxz}$. The major mechanics of material of STFs are found in their out-of-plane anisotropy, which plays a very important role in the mechanical behavior of multi-layered components. For example, Sumigawa et.al (2009)[2] proved that STFs inserted on a bi-material interface release stress concentrations and this prevents interface fractures.

Experimental and analytical procedure

We prepared two specimens with dimensions of 30 × 30 μm^2 (Specimen A, FE-SEM image shown in Fig. 2) and 15 × 15 μm^2(Specimen B), which were cut using a focused ion beam (FIB) processing system (Hitachi, FB-2200). A nano-scale component usually has a resonance frequency of GHz order. As the vibration at such high frequencies is very small, precise measurement is very difficult even using the modern techniques. Thus, it is necessary to reduce the resonance frequency for the evaluation of small elements. To accomplish this, we emplace Au (Gold) block onto the thin films using of the FIB system. The block is fixed on the Ta_2O_5 cap layer by deposition of Tungsten. The dimensions of the specimens used for evaluating the elastic properties of the STFs are listed in Table 2.

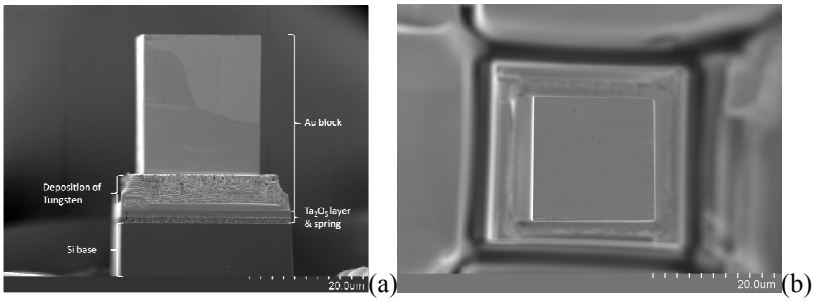
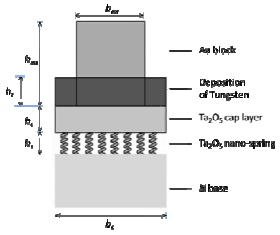


Fig. 2 Specimen A for evaluating the elastic properties of the STFs, Specimen configuration; specimen is a brick consisting of a Au block (top view surface measuring 20×20 μm^2), a Ta_2O_5cap layer (top view surface measuring 30×30 μm^2), a nano-springs layer, and a Si base layer; brick is fabricated from multilayered thin films by FIB. (a) side view, (b) top view.

Table 2 Dimensions of the specimens used for evaluating the elastic properties of the STFs

Specimens	b_{au} (μm)	b_c (μm)	h_{au} (μm)	h_t (μm)	h_c (μm)	h_s (μm)	illustration
A	20	30	30	6.18	1.03	1.03	
B	10	15	10	2.65	1.03	1.03	

The Frequency-Sweep Vibration system assembled is shown schematically in Fig. 3. The specimen is affixed with a piezoelectric actuator, which provides a frequency sweep vibration (DC: 0 Hz to 40 MHz) via a signal generator (Polytec: MSA-500 Processing Unit). This enables us to excite lateral or vertical vibration to the STF [3]. The actuator is mounted on an X–Y–Z stage so that it can make relative movements to accomplish spectra measurement. To minimize extraneous vibrations, the system is mounted on a vibration isolation table. The vibrational response of the specimen is then monitored using a laser Doppler vibrometer (LDV) (Polytec: MSA-500), which can measure displacements over a frequency range of 0 Hz–24 MHz.

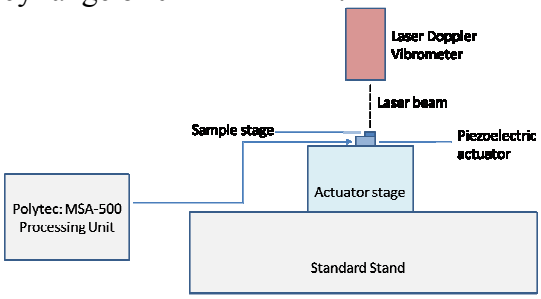


Fig. 3 Schematic representation of Frequency-Sweep Vibration system based on Laser Doppler.

To evaluate the elastic property of thin film, resonance frequencies under different modes must be measured. In this study, the vertical (axis z) and bending (axis y) vibrations of the specimens are actuated at room temperature. The Si subtrate of Specimen A is actuated vertically, and the vertical displacement (the axis z in the specimen coordinate system) at the top surface is measured, which is designated as "Task one" in the paper. The Si subtrate of Specimen B is then actuated laterally, and the lateral displacement (the axis y) at the side surface is measured, which is designated as "Task two". Tasks one and two are designed to identify the elastic property c_{zzzz} and c_{xzxz}.

Numerical analysis is conducted using a commercial software of finite element method (FEM), ABAQUS 6.5-1. The configuration is constructed based on the three-dimensional (3D) images of the SEM micrographs. Because (when compared with the specimen) the Si substrate is a "giant" solid, the substrate deformation can be neglected. This allows the substrate to be treated as a 3D analytic rigid shell. In contrast, the STFs are treated as orthotropic elastic materials, and the elastic

stress-strain matrix and density (2.38×10^3 kg/m^3) are defined by Eqs. (1) and $\rho_{film}=\rho_{Ta_2O_5}\times\pi\left(\frac{d}{2}\right)^2\times2\pi\left(r-\frac{d}{2}\right)\times\frac{1}{\cos\theta}\times n\times N_s$, respectively. The interaction between the Si substrate and the STF is defined as surface-to-surface contact ("rough" tangential and "hard" normal). The Ta_2O_5 cap layer, W and Au block are treated as 3D deformable solids. The interaction between the Ta_2O_5 cap layer and deposited W is defined as surface-to-surface contact ("rough" tangential and "hard" normal). Because the deposited W is non-uniform, the actual interaction is complex, which would cause noise in the experiment. However, since the STF is very "soft" and the Au block is very "heavy", these characteristics govern the vibration behavior. In this study, we focus on the dominating vibration, which allow us to eliminate noise when comparing between the experiment and analytical results.

Results and discussion

Task one: Vertical vibration and Vertical elastic property. Since the specimen is small, its displacement is dominated sample stage movement. Accordingly, it is necessary to compare the swept-frequency spectra of both the sample stage and the specimen in order to identify the resonance frequency. Figure 4 shows the swept-frequency spectra observed for specimen (black solid line) and sample stage (red dash line). The Savitzky-Golay method is used to smooth the original data[4]. The peaks around 0.5 MHz overlap each other, which mean the vibration entire sample stage. On the other hand, one significant solid line peak is only found at 1.31 MHz on the specimen. This is the resonance frequency of the vertical vibration. There are some small peaks during 0.5MHz and 2 MHz, which include the fixture, spurious or local modes due to the experimental ambiguity. Due to unavoidable errors in instrumentation and measurements, vibration data are often contaminated with noise. A 5% change in mode shape data is often introduced by researchers[5]. And it is well know that resonance frequencies can be measured with more ease and accuracy than mode shape. So, the rationale of the error of resonance frequency is less than 5%.

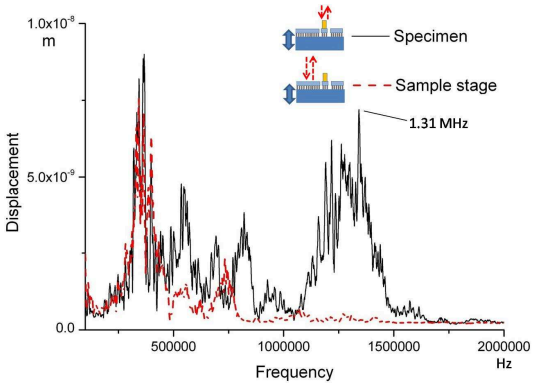


Fig. 4 Task one: swept-frequency spectra of Ta_2O_5 cay layer and specimen

Numerical analysis was then conducted on Model. Because the amplitude of the force does not influence the resonance frequency, a vertical load along the axis z with an amplitude of 1×10^{-6} N is used for the analysis. To identify the vertical elastic properties, the FEM model was conducted changing the magnitude of c_{zzzz} under $c_{xzxz}=0.03$ GPa ($k_l=2.05$ N/m[6]). The swept-frequency was set from 0.5 MHz to 2 MHz. When c_{zzzz} is between 0.085GPa and 0.090GPa, the resonance frequency is close to the experimental result. When $c_{zzzz}=0.087$ GPa, as shown in the Fig. 5, the significant peak is 1.33 MHz. Thus, c_{zzzz} is inversely extracted to be 0.087GPa. Although we set different c_{xzxz} values and repeated the above simulation, little changes were observed.

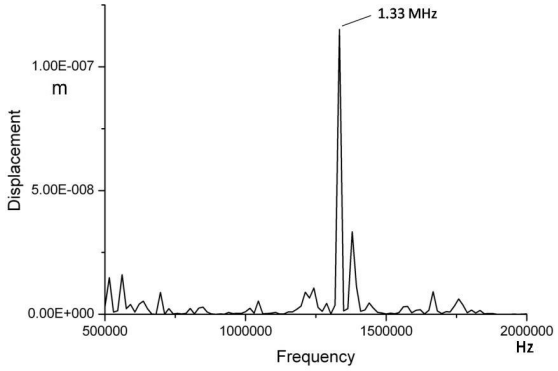


Fig. 5 Task one: Simulation results of specimen

Task two: Bending vibration and Lateral elastic property. In this task, the initial situation of the specimen is different from Task one, in which the substrate is anchored to the transducer, and sticking out sideways is the film followed by the weight. Based on the mechanics of vibration, the initial situation would not influence the resonance vibration because the resonance frequencies of specimens are determined by the mass and stiffness. Figure 6 shows the swept-frequency spectra observed for the specimen (black solid line) and the sample stage (red dash line). The Savitzky-Golay method is used to smooth the original data. The significant peaks (0.93 MHz and 1.35 MHz) present the resonance frequencies of bending vibration in the specimen.

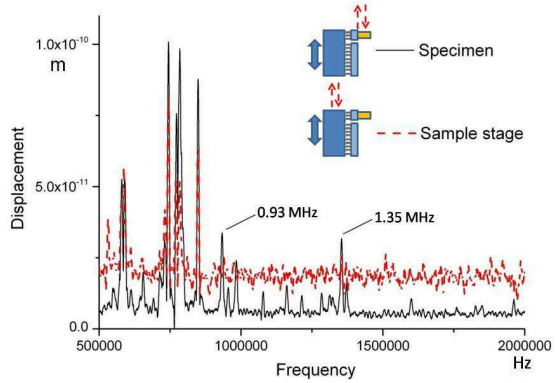


Fig.6 Task two: swept-frequency spectra of Si base and specimen

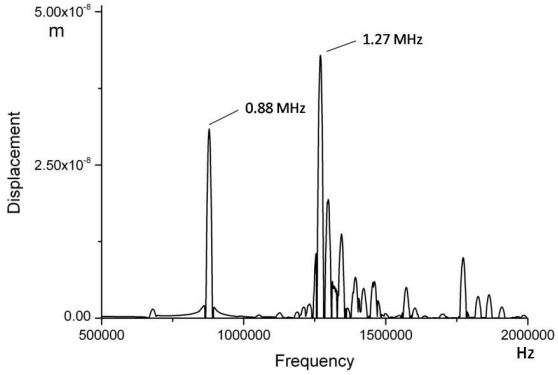


Fig7 Task two: Simulation results of specimen

To identify the lateral elastic property, an FEM simulation was conducted. Changing the magnitude of c_{xzxz} under c_{zzzz} = 0.087 GPa, the swept-frequency was then applied from 0.5 MHz to 2 MHz. c_{xzxz} = 0.036 GPa ~ 0.040 GPa, provides reasonable correspondence of the resonance frequency to the experimental result. Figure 7 shows spectra obtained by the FEM under c_{zzzz} = 0.087 GPa and c_{xzxz} = 0.038 GPa. The significant peaks are at 0.88 MHz and 1.27 MHz. The elastic properties of the STF were also obtained and are listed in Table 3.

Table 3. The elastic property of this STF

E (GPa)	G (GPa)
0.087	0.038

Conclusion

Sculptured thin films (STFs) are unidirectional and anisotropic modules which can be used in vibration, wave and acoustics micro-devices. To evaluate the anisotropic elastic properties of STFs at the micron-scale, we designed a vibration testing system, which can provide a frequency sweep vertical and bending vibration and monitor the displacement of micro-specimens over a frequency range at MHz. In our study, two micro-specimens with design of 30×30 μm^2 and 15×15 μm^2, on the top of which added mass are fixed to decrease the resonance frequency to MHz order, are fabricated. Based on the swept-frequency spectra obtained by the testing and numerical analysis, the anisotropic elastic properties of STF were identified (Table 3). The micro-scale testing technique could be extended to other materials/microstructure.

Acknowledgements

This work was supported in part by a Grant-in-Aid for Scientific Research (S) (Grant No.21226005) from the Japan Society for the Promotion of Science, by a Grant-in-Aid for International cooperation from China Academy of Engineering Physics, by RONPAKU Program from the Japan Society for the Promotion of Science, by Special Fund from Institute of Systems Engineering at China Academy of Engineering Physics (2013KJZ02), and by National Natural Science Funds of China (No. 11002133).

Reference

[1] M., Suzuki, Y., Taga, 2001. Integrated sculptured thin films. Jpn. J. Appl. Phys. 40, 358–359.
[2] T., Sumigawa, T., Sueda, Y., Futamura, M., Suzuki, T., Kitamura, 2009. Effect of interface layer consisting of nanosprings on stress field near interface edge. Eng. Fract. Mech. 76, 1336–1344.
[3] T., Sumigawa, K., Matsumoto, T., Tsuchiya, T., Kitamura, 2012. Fatigue of 1μm-scale gold by vibration with reduced resonant frequency. Mater. Sci. Eng. A. 556, 429–436.
[4] P., Gorry, 1990. General least-squares smoothing and differentiation by the convolution (Savitzky-Golay) method. Anal. Chem. 62, 570–573.
[5] M., Ge, M., Liu, 2005. Structural damage identification using system dynamic properties. Comput & Struct. 83, 2185-2196.
[6] H., Hirakata, S., Matsumoto, M., Takemura, M., Suzuki, T., Kitamura, 2007. Anisotropic deformation of thin films comprised of helical nanosprings. Int. J. Solids Struct. 44, 4030–4038.

Key Engineering Materials Vols 645-646 (2015) pp 15-20
© (2015) Trans Tech Publications, Switzerland
doi:10.4028/www.scientific.net/KEM.645-646.15

Submitted: 2014-10-29
Accepted: 2014-12-23

The dilute magnetic properties of monolayer MoS_2 doped with transition metal Fe and VA atoms

Lan Lan[1, a *], Jiamu Cao[2,b], Yijiang Cao[3,c], Dianshuang Xu[4,d] and Jing Zhou[5,e]

[1,2,3,4] Department of Electronic Science and Technology, College of Applied Science, Harbin University of Science and Technology, Harbin, Heilongjiang, China

[5]School of Electronics and Information Engineering, Harbin Institute of Technology, Harbin, Heilongjiang, China

[a]lanlan_goodluck@163.com, [b]leocaojiamu@126.com, [c]caoyijiang@hrbust.edu.cn, [d]376919517@qq.com, [e]453513521@qq.com

Keywords: First-principles theory. Diluted magnetic semiconductor (DMS). MoS_2

Abstract. The two-dimensional material MoS_2 has attracted a growing attention due to its potential applications in electronic devices in recent years [1,2,3], and the monolayer MoS_2 is a direct gap semiconductor with a band gap of 1.8eV [4]. In the existing studies, it has indicated that MoS_2 can get an available magnetism with doping transition metal atoms [5], and is expected to be a new generation of diluted magnetic semiconductor (DMS) [6,7]. Moreover, we found that Fe-doped MoS_2 could present a strong magnetism but a semimetal characteristic, losing its original semiconductor properties while obtaining magnetism. Therefore, it is necessary to explore some methods to make monolayer MoS_2 exhibit both magnetic and semiconductor properties. In this paper, we propose the method of N, Fe atoms co-doping to achieve this objective. The structural, electronic and magnetic properties of MoS_2 doped with transition metal Fe and VA atoms have been investigated by first principle calculations based on density functional theory. The 3×3×1 supercell of monolayer MoS_2 as a calculation model has been used. The result shows that pure MoS_2 has no magnetism, while Fe-doped MoS2 exhibits a good magnetism about 1.849μB but a semimetal characteristic. This is due to that Mo-4d, S-2p, Fe-3d states has a strong coupling around the Femi energy for the introduction of Fe atom, and the Femi energy only pass through the spin-up density of states. For the co-doping with VA atoms and Fe atoms, it is found that the magnetic moment of Fe-N, Fe-P and Fe-As co-doped MoS_2 is 0.956μB, 0.775μB, 0.782μB. Moreover, the Fe-N co-doped MoS_2 presents semiconductor characteristics, in contrast, Fe-P and Fe-As co-doped MoS_2 appear semimetal properties. It indicates that the semimetal characteristic of Fe-doped MoS_2 could change into indirect band gap semiconductor due to the introduction of N atom. The band gap is 0.2eV. Our study demonstrate that the method of Fe, N co-doping could make MoS_2 have good magnetic and also semiconductor properties at the same time.

Introduction

Spin electronic devices become a hot topic in recent years, because of its electron is the carrier of spin and also charge. Compared with the traditional silicon based electronic devices, it has the advantages of small size, high speed, low energy consumption, non-volatile etc [8]. Diluted magnetic semiconductors (DMS) as the core material of spin electronic devices, having the function of information processing of semiconductor material and information storage of magnetic material, it also has been highly concerned [6,7]. Substituting the cations in semiconductor material with the magnetic transition metal is usually the most intuitive way to obtain diluted magnetic semiconductor material.

Molybdenum disulfide (MoS_2) is a new kind of two-dimensional semiconductor material emerging in recent years. The single layer MoS_2 is a direct band gap semiconductor with band width of 1.8eV, while the block MoS_2 is an indirect band gap semiconductor with band width of 1.29eV [3,4]. The characteristics of adjusting band gap by layer numbers decided its application potential in

the microelectronic, optoelectronic and nano electronic devices [9,10]. At the same time, the research on MoS_2 magnetic properties has been aroused people's attention gradually. For example, J.Karthikeyan explored the edge magnetism and electronic structure of monolayer MoS_2 thin slices of different sizes [11]. Hongliang Shi used stress tuning hydrogen adsorbed monolayer MoS_2 to obtain the stable magnetism [12]. Feng studied the properties monolayer MoS_2 doped with Fe-X_6, in which X represents C, N, O, and F [13]. Cao Juan and others doped part of the transition metal atoms into monolayer MoS_2 and drew a conclusion that Mn doped MoS_2 could obtain stable ferromagnetism [14].

However, for doping monolayer MoS_2 with transition metal atoms, it is seldom reported in this respect for how to adjust band structure of the doped system to obtain characteristics of good semiconductor. Pan of National University of Singapore (NUS) obtained stable diluted magnetic semiconductor with C non-magnetic atom doping ZnO [15].

Whether it will get stable magnetism and good semiconductor properties if we dope monolayer MoS_2 with transition metal Fe atom, if the answer is not, what effects will get on electronic properties and magnetism properties while we doping non-magnetic atoms, these questions are worthy our concern. Therefore, we calculated and analyzed electrical properties and magnetic properties of pure MoS_2 and Fe doped MoS_2, then we doped VA family nonmagnetic atoms into Fe-doped MoS_2. The calculation results show that the pure MoS_2 has no magnetism, Fe-doped MoS_2 has magnetic properties and appears some semimetal characteristics at the same time. Among Fe and VA family atoms co-doped systems, Fe-N co-doping MoS_2 has good magnetism and semiconductor properties, the introduction of N atom effectively regulate the semimetal properties of Fe doped MoS_2. This paper can provide theoretical reference for the expectation of MoS2 as diluted magnetic semiconductor material in the future.

Method and Calculation Details

In the framework of the density functional theory (DFT), first principle calculations were carried out using an ultra-soft pseudo-potential plane wave to describe the ion-electron interaction as implemented in Material Studio5.5. The exchanging interaction of coherent energy between electrons was handled by the Perdew-Burke-Ernzerh function of generalized gradient approximation (GGA-PBE). The cutoff energy for the plane wave is set at 320eV. The Brillouin zone (BZ) sampling based on Monkhorst-Pack scheme using a 3×3×1and a 9×9×1 grid for Geometry optimization and Energy calculation respectively. In the process of optimization, the atomic complete relaxation, where energy convergence precision is 1.0e-5eV/atom, the inter atomic forces do not exceed 0.03eV/Å.

In order to avoid the doping concentration is too large to guarantee the original properties of material, we take a 3×3×1 super cell with a total of 27 atoms including 9 Mo atoms and 18 S atoms as the research object. The supercell parameter is set as a=b=9.48Å according to the experimental, a vacuum layer of 14 Å at c direction is used to prevent interaction between the supercells caused by periodic calculation. In the calculation, the doping position of transition metal Fe atom and VA family nonmagnetic atoms doping position as shown in Figure 1.

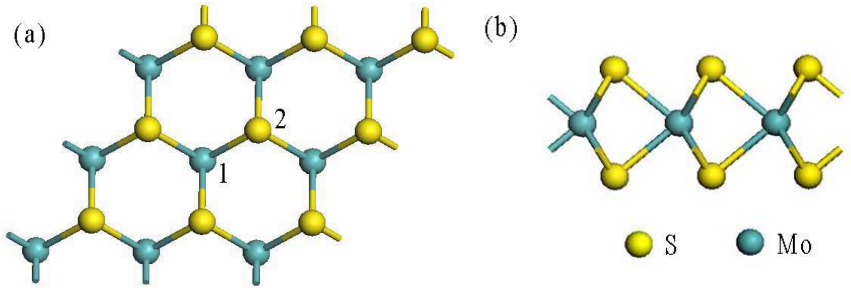


Figure 1. (a) The 3×3×1 supercell of the top view for monolayer MoS2，the transition metal atom Mn was doped in position 1，the IVA atoms was doped in position 2. (b) The side view of the supercell.

Results and Discussion

The properties of pure MoS_2 and Fe doped MoS_2. The structure parameters of pure MoS_2 and Fe doped MoS_2 after optimization are given in Table 1. In the pure monolayer MoS_2, S-Mo-S bond angle is 82.338 °, Mo-S bond length is 2.405 Å, the calculation results are consistent with Wu et al [14]. The total magnetic moment of pure MoS2 is 0 μ B under the energy calculation with the consideration of spin. In order to further explain the reasons of pure MoS_2 does not show magnetism, the analysis of band structure and density of state analysis for pure MoS_2 has been taked, the band structure and the density of states as shown in in Figure 2. The conduction band minimum (CBM) and the valence band maximum (VBM) of pure MoS_2 are all located in the G point, it is a direct band gap semiconductor of 1.724eV band gap, the gap value is consistent with Mak KF et al [4].We can know it from the density of States, CBM energy are mainly contributed from the Mo-4d state, the energy of VBM is determined by the Mo-4d state and the S-3p state together, S-3p state make a smaller proportion, overall, spin up and down spin density of States is completely symmetrical, therefore, the magnetic moment of the system is 0μB, does not show magnetism.

Table 1. The structure parameter of pure and doped MoS_2, band angleθ, band length d and magnetic moment M of all systems.

type	Band angle Θ[°]			Band length d[Å]		$M_{tot}[\mu_B]$
	$\Theta_{S\text{-}Mo\text{-}S}$	$\Theta_{S\text{-}Fe\text{-}S}$	$\Theta_{Mo\text{-}X\text{-}Mo}$	$d_{S\text{-}Mo/Fe}$	$d_{Fe\text{-}S/X}$	
MoS_2	82.338	-	82.338	2.405	-	0
Fe	82.668	80.709	83.551	2.305	2.307	1.849
Fe, N	79.836	74.846	96.929	2.330	1.965	0.956
Fe, P	82.054	80.036	81.178	2.290	2.370	0.775
Fe, As	82.320	81.697	78.764	2.284	2.473	0.781

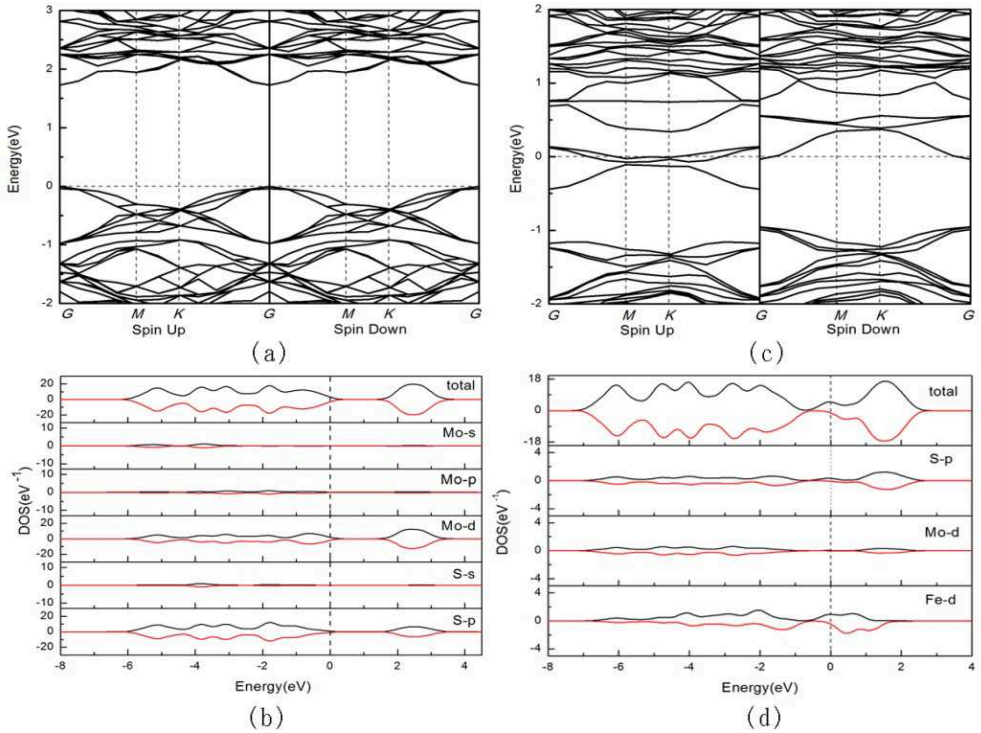


Figure 2. (a),(c)is the band structure and corresponding DOS of pure MoS_2 respectively. (b),(d)is the band structure and corresponding DOS of Fe-doped MoS_2 respectively. Black and red means spin up and down.

The structure parameters of Fe doped MoS_2 are given in Table 1 after optimization and energy calculation, doping position as shown in Figure 1. Among them, S-Mo-S bond angle is 82.668°, S-Fe-S bond angle is 80.709°, the bond length of S-Mo is 2.407 Å, S-Fe bond length is 2.307 Å. The

total magnetic moment of the system is 1.849μB, the local magnetic moment of Fe atom is very big contrast to Mo atoms and S atoms. In order to observe the spin distribution of doping system more intuitively, the spin density map is given in Figure 3, it can be seen from the figure, the magnetic moment is mainly localized around the dopant Fe atom and six Mo atoms around the Fe atom, they are in the same spin direction, and a minute quantity localized at three S atoms nearest Fe atom, which shows the opposite spin direction with Fe atom. Combining with the band structure and the density of states in Figure 2 (b), (d), it is asymmetric between spin up density and spin down density, furthermore, appeared some impurities bands composed of Mo-4d, S-3p and Fe-3d states around Fimi energy, it is the main reason for the system magnetic of strong coupling actions in these impurities states. But the Fimi energy of system only pass through the spin up density of states curve, system will show some semimetal characteristics.

The whole energy band of system moving down about 1.2eV comparing with pure MoS_2. In order to analyze the reason for doping system moving down, we give a difference charge density about pure MoS_2 and doped MoS_2 in Figure 4. From the graph, it is not difficult to see that, when Fe atom substituting for Mo atom, the charge density between Fe and S is smaller than Mo and S, S obtain more less electrons from Fe atom compared to Mo atom. Therefore, when S bonding with Mo and Fe separately, the electrons of S will prefer Mo, which leads the density between S and Mo increase comparing to the undoped system, thus, the unit energy of system will reduce, and Mo-4d state will move downward to low energy. From the density of states of Fe doped MoS_2, we can know that Mo-4d state has a large proportion in VBM and CBM, therefore, lead to the whole band of doped system shift to lower energy.

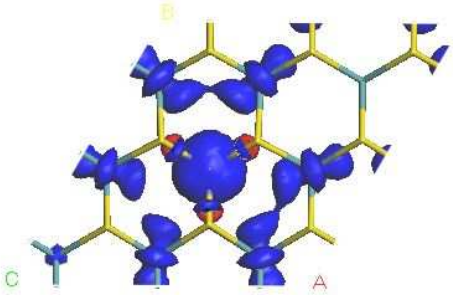


Figure 3. The spin density isosurface plot of Fe doped monolayer MoS_2, blue means spin up while red means spin down.

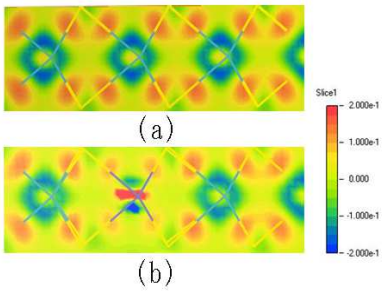


Figure 4. (a) The difference charge density of pure MoS_2. (b) The difference charge density of Fe doped MoS_2.

The properties of VA family atoms doped MoS_2. The above results show that doping MoS_2 with transition metal Fe atom, could obtain better magnetic properties, but lose the semiconductor properties of MoS_2 itself, doped MoS_2 exhibit semimetal characteristics. In order to adjust semimetal properties of Fe doped MoS_2, we continue to dope atoms into the doped system. According to the charge transfer theory, in MoS_2 material, Mo atoms must lose 4 electrons on the adjacent S atoms in order to get a stable S^{2-} when the Mo atoms bonding with S atoms, the electronic configuration of Mo is $4d^5 5s^1$, while the electronic configuration of Mo which lose 4 electrons is $4d^2$. When Fe atom bonding with S atom substituting for Mo atom in MoS_2, the electronic configuration of Fe is $3d^6 4s^2$, and the electronic configuration of Fe which lose 4 electrons is $3d^4$, but these electrons in 3d shell did not arrange in symmetry spin, as the result, Fe doped MoS_2 appears some obvious magnetic moment. In order to maintain the magnetism of Fe doped MoS_2, we select VA atoms as the step dopant. The outermost shell of VA family atoms locate 5 electrons, they must capture 3 electrons from Fe atom to form a stable negative ions. Therefore, Fe atom will be captured a total of 5 electrons by S atom and VA atoms, the electronic configuration will be $3d^3$, the remaining 3 electrons of d shell could not arrange in spin symmetry, thus, Fe and VA atoms co-doped MoS_2 will still exist magnetic moment.

The structure of Fe and VA family atoms co-doping MoS_2 has been calculated, VA atoms were N, P and As, doping position as shown in Figure 1. The structure parameters after geometry optimization are given in table 1. The bond length of Fe-N, Fe-P and Fe-As is 1.965 Å, 2.370 Å, 2.473 Å respectively, showing an increasing trend. This is mainly cause of the increasing of covalent radius. When VA atoms bonding with Fe atom, the adjacent S-Fe bond are squeezed for the increasing of

Fe-VA bond length, the bond length of S-Fe in three co-doped systems is 2.330 Å, 2.290 Å, 2.284 Å, in a decreasing trend. The S-Mo-S angle which is the nearest of VA atoms is 79.836°, 82.054°, 82.320°, the angle of Mo-N-Mo, Mo-P-Mo and Mo-As-Mo is 96.929°, 81.178°and 78.764°, showing a decreasing current. The calculation results are consistent with facts.

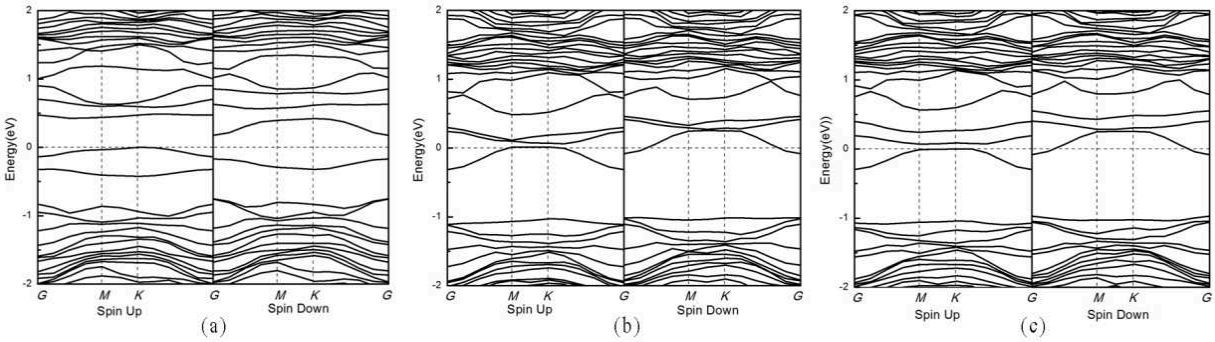


Figure 5. (a), (b), (c) is the band structure of Fe-N, Fe-P, Fe-As co-doped MoS_2 respectively.

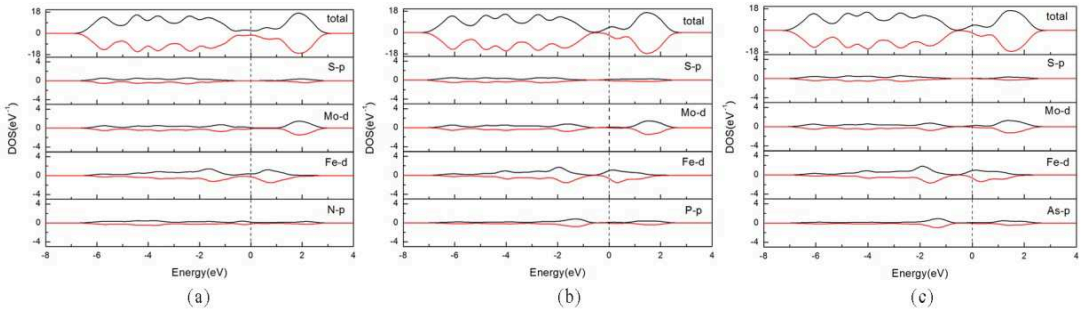


Figure 6. (a), (b), (c) is the density of states for Fe-N, Fe-P, Fe-As co-doped MoS_2 respectively. Black and red means spin up and down.

After energy calculation, the band structure and the density of states about Fe-N, Fe-P and Fe-As co-doped MoS_2 is shown in Figure 5 and Figure 6. It can be seen from Figure 5(a), the band structure of Fe-N co-doped MoS_2 move 0.4eV upper than Fe doped MoS_2, this is due to the introduction of N atom, adjusting the charge density between S and Mo in Fe doped MoS_2, resulting in the change of overall energy. Combining with Figure 6(a), it is known that impurity bands below Femi energy are consist of Mo-4d state, Fe-3d state and N-2p state, while impurity bands above Femi energy is mostly originate from Fe-3d state, the part of Fe-3d state passing through Femi energy in Fe doped MoS_2 is changed for the introduction of N atom, it makes impurity bands distribute at both sides of Femi energy clearly. VBM locates at K point and CBM locates at G point, Fe-N co-doped MoS_2 is a narrow band gap semiconductor with band gap of 0.2eV. For Fe-P co-doped MoS_2, it can be seen from Figure 5(b) and Figure 6(b), the impurity bands in band gap still mostly come from Fe-3d state. The introduction of P atom did not make any other impurity bands, and the band structure did not show any significant movement in energy-axis, and the Fermi level only pass through the curve of spin down density of state, reflecting Fe-P co-doped system has some semimetal characteristics. As for Fe-As co-doped MoS_2, the band structure in Figure 5(c) and density of states in Figure 6(c) are similar to Fe-P co-doped system, showing some semimetal properties.

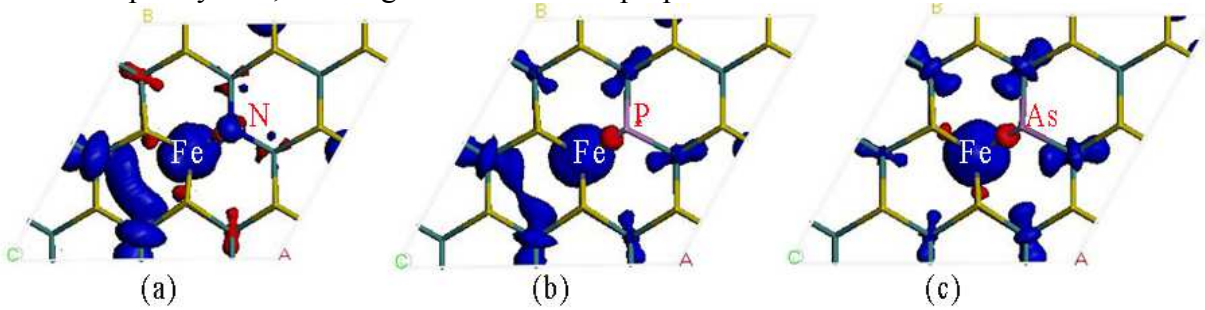


Figure 7. (a), (b), (c) is the spin density isosurface plot of Fe-N, Fe-P, Fe-As co-doped monolayer MoS_2, blue means spin up while red means spin down.

Magnetic moment of three kinds of co-doped system is given in Table 1, Fe-N, Fe-P and Fe-As co-doped MoS_2 were 0.956μB, 0.775μB and 0.781μB. The spin density of three co-doped systems is given in Figure 7. In Figure 7(a), Fe and N atoms local magnetic moment, furthermore, they got a same spin direction, which is known as ferromagnetic coupling. In addition, 6 Mo atoms around the Fe atom have local magnetic moment, too. They divided into two types, the two Mo atoms which are far from N atom have a bigger magnetic moment, and the same spin direction with Fe atom. There are small amount of magnetic moment on remaining four Mo atoms, they have the opposite direction of Fe atom. In the system, S atoms have rarely magnetic moment. In the Fe-P, Fe-As co-doped system, the magnetic moment is mainly distribute in Fe atom and 6 Mo atoms around Fe, P and As atom have a small amount, they form a ferromagnetic coupling with the former. Therefore, only the Fe-N co-doped system has good magnetic and semiconductor properties.

Conclusion

In this paper, by using the first principles method based on density functional theory, electrical properties and magnetic properties of monolayer MoS_2 and Fe doped MoS_2 is calculated, results show that the monolayer MoS_2 is a direct band gap semiconductor does not show magnetism, Fe doped MoS_2 has good magnetic properties, but due to the introduction of impurity atoms and the split of impurity levels near the Fermi level, showing a semimetal properties. According to the charge transfer theory, we use VA family atoms N, P, As and Fe as co-doping calculation with pure MoS_2. The calculation results show that Fe-P, Fe-As co-doped system have magnetism and semimetal characteristics, Fe-N co-doped MoS_2 has magnetism and semiconductor properties at the same time, N atom could adjust the position of impurity level caused by the introduction of Fe atom, so that it is no longer through Femi level, changing the semimetal properties of Fe doped MoS_2, while preserving the magnetism. Fe-N co-doped MoS_2 is an indirect band gap semiconductor with band gap of 0.2eV. Our study indicates that the method of using Fe, N atoms co-doping, could get MoS_2 with semiconductor properties and magnetic properties at the same time, MoS_2 is very promising in diluted magnetic materials.

References

[1] Z. Haiqing, Y. Fang, L. Yuanyue, Nano Res, 6 (2013) 703-711.
[2] B. Radisavljevic, A. Radenovic, J. Brivio, Nat Nanotechnol, 6 (2011) 147-150.
[3] S. Kim, A. Konar, W.S. Hwang, Nat Commun, 3(2012) 1011.
[4] K.F. Mak, C. Lee, J. Hone, J. Shan, T.F. Heinz, Phys Rev Lett, 105 (2010) 136805.
[5] A. Ramasubramaniam, D. Naveh, Phys Rev B, 19 (2013) 195201.
[6] K. Sato, L. Bergqvist, J. Kudrnovsky, Rev Mod Phys, 82 (2010) 1633-1690.
[7] J.K. Furdyna, J. Appl. Phys, 64 (1988) R29.
[8] J.F. Gregg, Nat Mater, 6 (2007) 798-799.
[9] E. Goki, Y. Hisato, V. Damien, F. Takeshi, C. Mingwei, C. Manish, Nano Lett, 11 (2011) 5111-5116.
[10] Y. Youngki, G. Kartik, S. Sayeef, Nano Lett, 11 (2011) 3768-3773.
[11] J. Karthikeyan, Vijay Kumar, P. Murugan, Phys. Chem. Chem. Phys, 15 (2013) 13077-13082.
[12] S. Hongliang, P. Hui, Z. Yong-Wei, Boris I.Yakobson, Phys Rev B, 88 (2013) 205305.
[13] F. Nan, M. Wenbo, C.Yingchun, G. Zaibing, U. Schwingenschlogl, B. Haili, Sci Rep-UK, 4 (2014) 3987.
[14] C. Juan, C. Lei, J. Pan, Acta Phys. Sin, 62 (2013) 187102.
[15] H. Pan, J.B. Yi, L. Shen, R.Q. Wu, J.H. Yang, J.Y. Lin, Y.P. Feng, J. Ding, L.H. Van, J.H. Yin, Phys. Rev. Lett, 99 (2007) 127201-127204.

Key Engineering Materials Vols 645-646 (2015) pp 21-25
© (2015) Trans Tech Publications, Switzerland
doi:10.4028/www.scientific.net/KEM.645-646.21

Submitted: 2014-10-29
Accepted: 2014-12-23

Strategies for Defect-free and Deep Wet Etching of Pyrex 7740

Zhan Zhan[1], Lingke Yu[1], Cheng Zheng[1], Jianfa Cai[1], Daoheng Sun[1] and Lingyun Wang[1a]

[1]Dept. of Mechanical and Electrical Engineering, Xiamen Univ., Xiamen, China

[a]email: wangyl@xmu.edu.cn (corresponding author)

Keywords: Pyrex 7740, Wet etching, Pre-annealing, Mask Process.

Abstract. In this paper, two aspects in the wet glass etching, the pre-annealing of the glass and the mask process, are taken into consideration to achieve the deep and defect-free wet etching of Pyrex glass. Compared with the conventional strategies, i.e., *HF* solution component and mask kinds, our experiment results prove the pre-annealing is another key role to obtain theoretical isotropy character in wet etching. Besides, the high temperature pre-annealing dramatically improves the structure profiles and reduces the notching defects. Additionally, a novel multilayer mask process is proposed. With 1.5μm *PR*/ 100nm *Au*/ 100 nm *Au*/ 20 nm *Cr* mask and > 450 °C pre-annealing, > 150 μm deep and non-pin-holes Pyrex glass structures are achieved and the roughness of etched surface is lower than 1 nm.

Introduction

Pyrex 7740 glass is one of the most common material in MEMS for its good mechanical and optical properties, high electrical insulation, and thermal compatibles with silicon, hence it has been widely used in MEMS wafer-level packaging [1] and micro fluid chip [2].

Compared with dry process such as sandblasting [3] or ICP [4], conventional wet etching by *HF* etchant is a faster and low cost method. Thus, it is the most common process to micro-machine for Pyrex glass. However, there are still a few issues remaining in defect-free and deep wet etching, particularly in the following three categories: (a) large and non-uniform lateral undercutting with difficulties to achieve the theoretical isotropy etching; (b) the notching defects at the pattern edges; (c) pin-holes caused by the poor mask layer.

To achieve defect-free and deep glass structure, some researchers focus on the mask and the etchant, in which masks mainly affect the quality of the non-etched glass. The component of masks includes the bonded silicon [5], LPCVD *Si* [6] or *SiC* [7], *PR* [8], *Cr/Au/PR* [9], *Ni* [10] et al, and some of them are with the high efficiency such as the *Cr/Au/Cr/Au/PR* mask [11]. With 20.9 μm mask, the etching depth can reach 300 μm, and the ratio between etched depth and the mask depth reaches 14.3 μm:1 μm. Besides that, Corman [5] shows that the specific mask will result in different undercut rate, which affects the isotropy of the etching. In the case of etching etchant, the *HF* solution is added with *HCl* or HNO_3 to improve the roughness of the etched surface [12]. And *HCL* is more suitable than HNO_3 for Pyrex glass defect-free and deep etching [13].

Aiming at the three issues, compared with the non-crystal property of glass, pre-annealing is introduced to improve the isotropy of the material. Moreover, since the pin-hole of the sputtering mask can be wipe off by the several times individual process, a new mask process is proposed for defect-free and deep structure implementation.

Experiment

In this work, Pyrex 7740 glasses (TECNISCO CO., LTD, SUZHOU, and thickness 510 μm) are prepared for the experiments. The wafers are cleaned in RCA 3 (H_2SO_4: H_2O_2= 3:1) for 15 min, then rinsed in DI water and spun-dried. Based on the two strategies, the whole process is illustrated in Fig. 1.

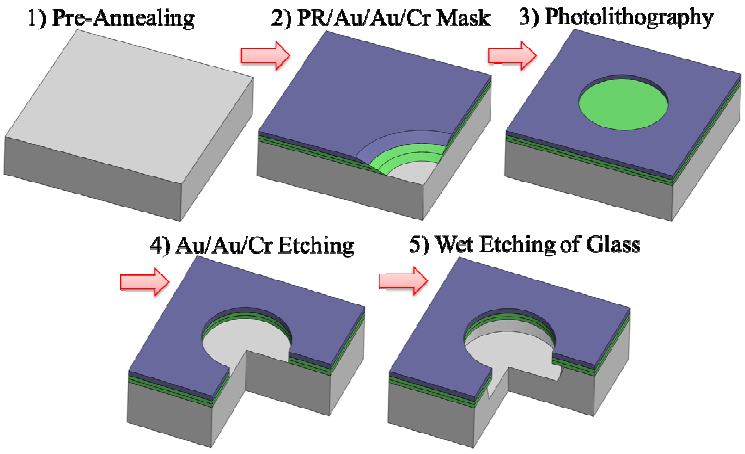


Fig.1: Flowchart for HF wet etching

1) Pre-annealing;

The bared glass wafers are selective to anneal from 250 °C to 590 °C, respectively. Then, the samples cool down to room temperature naturally.

2) PR/Au/Au/Cr Mask deposition;

The annealed wafers are sputtered with 20 nm *Cr*, 100 nm *Au*, 100 nm *Au*. Then, the glass is spunned with the 1.5 μm Photoresist (BP212).

3) Photolithography;

4) Patterned metal;

Wet etch the *Au* layers (*KI* based solution) and *Cr* layer ($Ce(NH_4)_2(NO_3)_6$ based solution).

5) Wet etching of glass.

With the same solution stirring, all the samples are etched for 60 min and then the masks are lifted off. layer. After the whole process, SEM (LEO-1530) and Profiler (Dektak-3) are used to measure the etching morphology and depth.

Result and Discussion

Inevitably, the awful results are likewise attained as shown in Fig. 2 in our preliminary experiments. With optimized etchant component (*HF: HCL: NH_4F*=5.5 mol/L: 4 mol/L: 2.5 mol/L), the minimum ratio between the vertical and lateral etching rate remains 1: 2.8, which is still much lower than the theoretical. In addition, large numbers of the notching defects merge along the structure edge as plotted by groove etched with a circle mask. Even worse, the undercut of the structure isn't uniform ($D_1 \neq D_2$). In whole, the wet etching process completely shows the anisotropy. On the other hand, the conventional *PR/Au/Cr* mask can't resist *HF* etchant once the etching depth exceeding 50 μm as shown in (b).

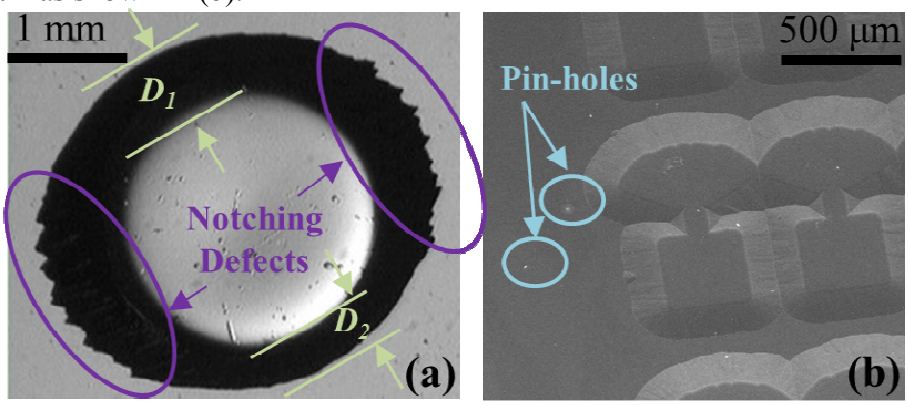


Fig.2: The disadvantages in the wet etching of the Pyrex 7740, (a) Notching defects and anisotropy; (b) Pin-holes

Fig. 3 demonstrates the etching rate in two directions, the vertical and lateral of the glass, with the pre-annealing from 250 to 590 °C for Pyrex 7740. Compared with the different annealed samples, the etching rate variation indicates that the thermal process has dramatically influence on the lateral etching rate, but slight effect on the vertical. When pre-annealing is lower than 250 °C, the wet etching rates in two directions are almost the same with the none-annealing samples. While the pre-annealing is higher than 450 °C, the ratio of vertical and lateral etching rate is trend to be theoretical isotropy 1:1. The comparison results show that the improvement of the annealing on the etching rate ratio can be 150%. The same variation can also reflect by the inserted SEM image of cross section of the etched structure. The angle of undercut decreases from 153 ° to 139 °

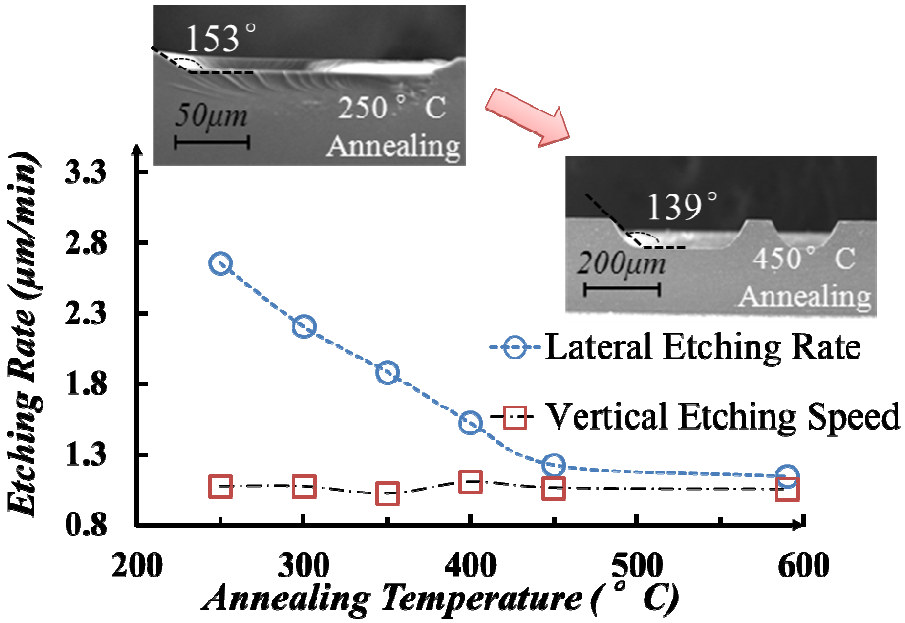


Fig.3: The etching rate of two directions (lateral and vertical) with different pre-Annealing, inset: the SEM of the cross section of the etched structure

Post the annealing, not only the rate difference of the vertical and lateral etching is adjusted, but also the morphology of the structure edge can be improve. As shown in Fig. 4, the notch-defects, once spread along the structure edges, are found to be eliminated. With the same trend of lateral rate variation, the notching defect is vulnerable to the wet etching under annealing temperature below 250 °C. And defects can be wiped off when the samples are annealed higher than 450 °C. This is because that the notching defects can also be regard as the partial etching acceleration along the lateral direction. Thus, similar slow down effect of annealing mentioned above also works on the notching area, correspondingly, the lateral etching rate tend to be equal with vertical. Compared with Fig 2 (a), the circle groove on the annealed glass are shown in fig 4 (d), it is with uniform undercut and perfect edge. In a whole, both the etching rate adjustment and notching defects elimination prove that annealing is a efficacy way to promote etching quality. And compared with the mask and etching solution component, the core problem of the isotropy etching is the isotropy of materiel.

In addition, the SEM results also proves that the glass with multilayer mask, i.e., 1.5 μm *PR*, 100 nm *Au*, 100 nm *Au*, 20 nm *Cr*, can achieve > 150 μm structure without pin-holes in the HF based solution. Our work provides a more efficacy mask components, and the ratio between etched depth and the mask depth improve to 88 μm:1 μm.

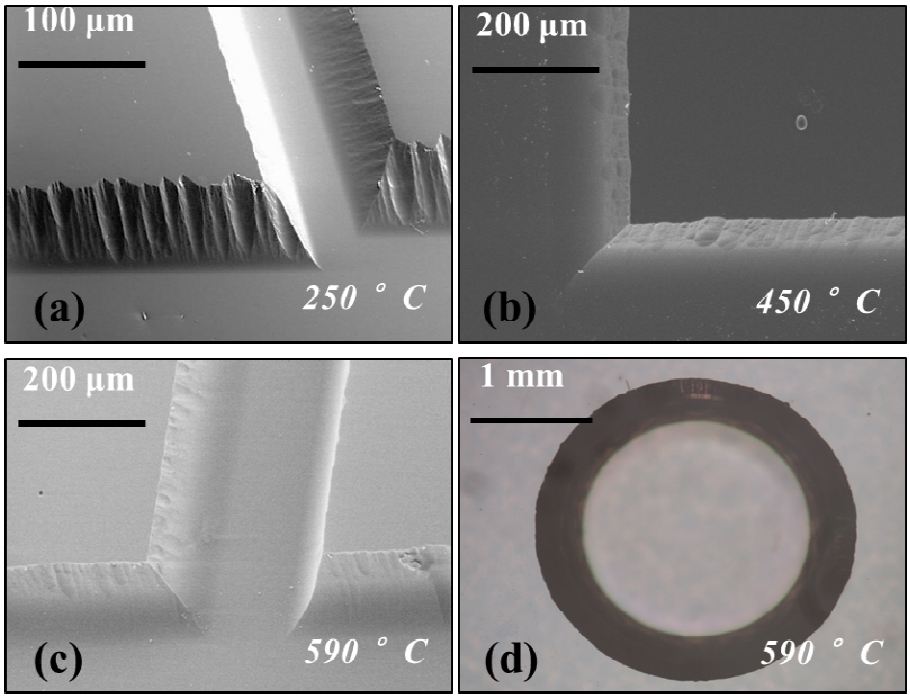


Fig.4: The SEM of etched glass with multilayer at different pre-annealing temperature, (a) 250 °C pre-annealing; (b) 450 °C pre-annealing, (c) and (d) 590 °C pre-annealing

Fig 5 indicates the etched Pyrex surface roughness scanned by the AFM (SPA-400). In the 10×10 μm random test area, the roughness of etched surface is lower than 1 nm. The AFM results manifest that the annealing is not harmful for surface quality of the etched surface and the optimized process is suitable for defect-free and deep wet etching of Pyrex glass.

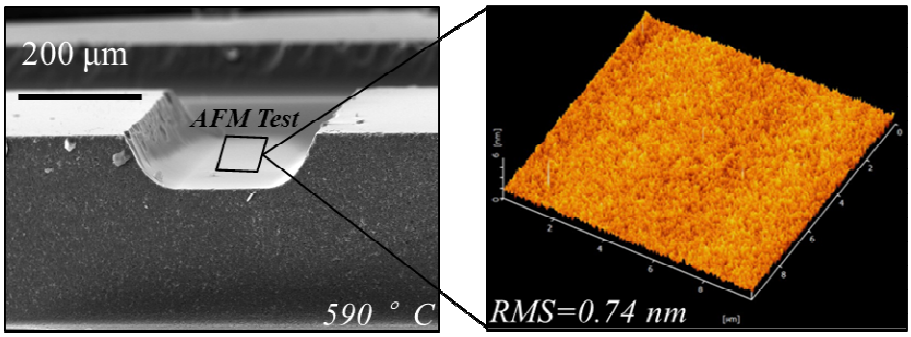


Fig.5. The AFM test of HF wet etched surface

Summary

In this work, pre-annealing of the glass and a new mask process, are proposed to obtain the deep and defect-free wet etching of Pyrex glass. The experiments results show that pre-annealing is another key role to obtain theoretical isotropy character in wet etching, and confirms the high temperature pre-annealing dramatically improves the structure profiles and reduces the notching defects. Additionally, with a novel multilayer, the process the > 150 μm deep, < 1 nm roughness etched surface and non-pin-holes Pyrex glass structures. The optimized process is suitable for defect-free and deep wet etching of Pyrex glass.

Acknowledgement

This work funding was supported by China Aviation produce-learn-research projects (cxy2013XD31).

References

[1] Z. Zhan, *et al.*, "Application of Aerosol Jet technology in through-via interconnection for MEMS wafer-level packaging," *Microsystem technologies,* pp. 1-5, 2014.

[2] C. Rusu, *et al.*, "Direct integration of micromachined pipettes in a flow channel for single DNA molecule study by optical tweezers," *Microelectromechanical Systems, Journal of,* vol. 10, pp. 238-246, 2001.

[3] E. Belloy, *et al.*, "The introduction of powder blasting for sensor and microsystem applications," *Sensors and Actuators A: Physical,* vol. 84, pp. 330-337, 2000.

[4] X. Li, *et al.*, "Fabrication of high-density electrical feed-throughs by deep-reactive-ion etching of Pyrex glass," *Microelectromechanical Systems, Journal of,* vol. 11, pp. 625-630, 2002.

[5] T. Corman, *et al.*, "Deep wet etching of borosilicate glass using an anodically bonded silicon substrate as mask," *Journal of Micromechanics and Microengineering,* vol. 8, p. 84, 1998.

[6] C. Iliescu, *et al.*, "Optimization of an amorphous silicon mask PECVD process for deep wet etching of Pyrex glass," *Surface and Coatings Technology,* vol. 192, pp. 43-47, 2005.

[7] A. F. Flannery, *et al.*, "PECVD silicon carbide for micromachined transducers," in *Solid State Sensors and Actuators, 1997. TRANSDUCERS'97 Chicago., 1997 International Conference on*, 1997, pp. 217-220.

[8] J. Zhang, *et al.*, "Polymerization optimization of SU-8 photoresist and its applications in microfluidic systems and MEMS," *Journal of Micromechanics and Microengineering,* vol. 11, p. 20, 2001.

[9] I. Schneegaß, *et al.*, "Miniaturized flow-through PCR with different template types in a silicon chip thermocycler," *Lab on a Chip,* vol. 1, pp. 42-49, 2001.

[10] Y. Mourzina, *et al.*, "The evaporated metal masks for chemical glass etching for BioMEMS," *Microsystem technologies,* vol. 11, pp. 135-140, 2005.

[11] M. Bu, *et al.*, "A new masking technology for deep glass etching and its microfluidic application," *Sensors and Actuators A: Physical,* vol. 115, pp. 476-482, 2004.

[12] C. Iliescu, *et al.*, "Characterization of masking layers for deep wet etching of glass in an improved HF/HCl solution," *Surface and Coatings Technology,* vol. 198, pp. 314-318, 2005.

[13] W. Tao, *et al.*, "Comparison of glass etching properties between HCl and HNO 3 solution," in *Nano/Micro Engineered and Molecular Systems (NEMS), 2012 7th IEEE International Conference on*, 2012, pp. 562-566.

Key Engineering Materials Vols 645-646 (2015) pp 26-31
© (2015) Trans Tech Publications, Switzerland
doi:10.4028/www.scientific.net/KEM.645-646.26

Submitted: 2014-10-29
Accepted: 2014-12-23

Effect of Hydrophilic and Hydrophobic SiO_2 Particles on Performances of PI/Al_2O_3 Composite Films

Yuanyuan Li[1], Lizhu Liu[1, 2, a *], Hui Shi[1], Ling Weng[1], Weiwei Cui[1]

[1]College of Materials Science and Engineering, Harbin University of Science and Technology, Harbin 150040, China

[2]Key Laboratory of Engineering Dielectric and Its Application, Ministry of Education, Harbin University of Science and Technology, Harbin 150080, China;)

[a]email: mrliulizhu@163.com (corresponding author)

Keywords: PI；Al_2O_3；SiO_2；Hydrophilic；Hydrophobic

Abstract. In this paper, we mainly analyzed the different influence of hydrophilic SiO_2 particles and hydrophobic SiO_2 particles on the properties of PI/Al_2O_3 films. PI/Al_2O_3/SiO_2(hydrophilic) films and PI/Al_2O_3/SiO_2(hydrophobic) films with 16 wt% content of Al_2O_3 and 3 wt‰, 5 wt‰, 7 wt‰ content of SiO_2 respectively were prepared by in-situ polymerization method. Firstly, the hydrophilic SiO_2 particles and hydrophobic SiO_2 particles were investigated by transmission electron microscopy(TEM), infrared spectroscopy(FTIR) and X-ray diffraction(XRD). The results showed that the average sizes and infrared characteristic peaks of two kinds of SiO_2 particles were similar, and two kinds of SiO_2 particles were amorphous inorganic particles. Then the morphology of the composite films was characterized by scanning electron microscopy(SEM), and the mechanical properties, the breakdown field strength and corona resistant time were tested and analyzed. Results indicated that inorganic particles added to PI/Al_2O_3/SiO_2(hydrophilic) films dispersed better than that of PI/Al_2O_3/SiO_2(hydrophobic) films. When the content of SiO_2 particles was 5 wt‰, the mechanical properties and corona resistance of PI/Al_2O_3/SiO_2(hydrophilic) films were best, the tensile strength, elongation at break and corona resistance times of the films were: 132.44 MPa, 12.64%, 378 min, respectively. The breakdown field strength of PI/Al_2O_3/SiO_2(hydrophilic) films was only 211.15 kV/mm, and inferior to that of PI/Al_2O_3/SiO_2(hydrophobic) films(232.08 kV/mm).

Introduction

Polyimide(PI) has been applied in the aerospace, microelectronics industry, lightwave communications, gas separated and other industries widely because of its' outstanding thermal stability, good mechanical properties, dielectric properties, solvent resistance and radiation resistance[1,2]. Most of polyimide products are used for the production of polyimide films, which are mainly used in two areas including insulation and flexible copper clad laminate(FCCL)[3,4]. Polyimide films are key materials of electrical insulating materials, and are widely used in transmission and distribution equipment manufacturing, wind power equipment, frequency conversion motor, high-speed traction motor and high voltage transformers. Therefore, PI films with excellent corona resistant performance have been required.

In recent years, researchers attempted to improve corona resistant performance of PI films by the introduction of inorganic particles, such as Al_2O_3, SiO_2, TiO_2, and obtained some success[5-7]. However, the overall performance of PI films have been affected by the inorganic particles. Researchers have tried to use two or more kinds of inorganic particles to improve PI films, for example: X. Xu [8] prepared a series of PI/SiO_2@TiO_2 composite films, and found that the corona resistant time of composite films with 25% content of inorganic particles was 20 times of that of

pure films; The polyimide/MMT-AlN composite films were prepared by M. H. Chen[9], the corona resistant time of composite films with 7% content of inorganic particles was 40 times of corona resistant time of the pure PI films; L. Z. Liu[10] prepared PI/SiO_2-Al_2O_3 hybrid films by sol-gel method, and found that the addition of inorganic components significantly improved mechanical properties and thermal stability of the hybrid films. Our team improved the properties of PI/Al_2O_3 composite films by the introduction of trace amount of SiO_2 particles, and achieved some interesting results. Hydrophilic SiO_2 particles have much larger surface energy and contain more hydroxyl groups, but also have strong adsorption. Hydrophobic SiO_2 particles have a low moisture absorption and good dispersibility. Therefore, the effects of different kinds of SiO_2 particles on the properties of the films are different. In this paper, we used hydrophilic SiO_2 particles and hydrophobic SiO_2 particles to improve the properties of PI/Al_2O_3 films, and analyzed the effects of different kinds of SiO_2 particles on properties of PI/Al_2O_3 films.

Experimental

Materials

4,4'-Oxydianiline(ODA) and Pyromellitic diananocomposite(PMDA) were industrial grade and purchased from BR Leheng Chemical Co. N,N-dimethylacetamide (DMAc) was analytical grade and purchased from Tianjin Basifu Chemic al Co. Hydrophilic and hydrophobic SiO_2 particles with 20 nm average diameter and Al_2O_3 particles with 20 nm average diameter were obtained from Shandong Zhengyuan nanomaterials engineering.

Fabrication of composite films

In this paper, PI/Al_2O_3/SiO_2(hydrophilic) films and PI/Al_2O_3/SiO_2(hydrophobic) films with 16 wt% content of Al_2O_3 and 3 wt‰, 5 wt‰, 7 wt‰ content of SiO_2 respectively were prepared by in-situ polymerization method. First, nano-Al_2O_3 and SiO_2 were weighed accurately according to the composite proportion and a certain amount of N, N-dimethylacetamide solvent were added to three-opening flask and stirred vigorously. After 30 min, ODA was added to the mixture. PMDA was added into this solution with a certain time sequence until completely dissolved of ODA, and the mixture was stirred to get a yellow PAA/inorganic particles solution. Then, the solution was stirred mechanically at a high speed for 3 hours to form homogeneous PAA/inorganic particles solution. Then the solution was casted on clean glass substrate. Through complete imidization of the solution, the PI films were obtained after the films peeled off the glass substrate.

Measurements and Characterization

The morphology and particle size of SiO_2 particles were characterized by Tecnai G220 transmission electron microscopy(TEM). The molecular aggregation morphology of SiO_2 particles was characterized by Rigaku D/max-γB rotating anode X-ray diffraction(XRD). Fourier Transform Infrared(FTIR) spectra of SiO_2 particles were recorded at room temperature in the range of 4000-500 cm^{-1} on a BRUKER EQUINOX55 spectrophotometer.

The section microstructure of PI films was scanned by the FEISirion200 type of scanning electronic microscopy. The tensile strength and elongation at break of the composite films were tested according to the standard of GB/T13524.2-2009 using AGS-J type electronic tensile testing machine. Breakdown field strength was tested using HT-5/20 type breakdown voltage test machine at booster speed of 1kV/s in the air medium. The corona resistant time of the composite films was measured using HP-3kV high frequency pulse voltage test machine manufactured by Guilin Institute of Science Research. The voltage value and pulse frequency of corona resistant test are 2.0 kV and 20 kHZ, respectively.

Characterization of hydrophilic SiO_2 particles and hydrophobic SiO_2 particles

The TEM images of hydrophilic SiO_2 particles and hydrophobic SiO_2 particles were shown in Figure 1, the dark areas were nanopowders. It seems that the shape of the hydrophilic SiO_2 particles is spherical and the average particle size is 20~25nm. From TEM images of hydrophilic SiO_2

particles and hydrophobic SiO_2 particles, we know that the shapes of two kinds of particles are spherical and the average particle sizes of that are similar.

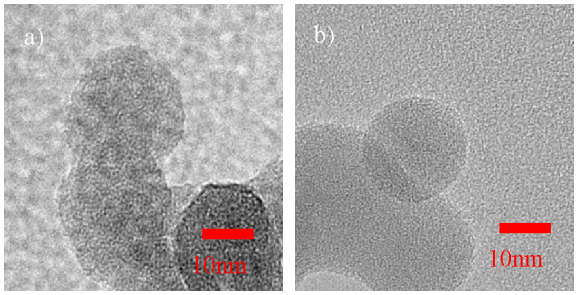


Fig. 1 TEM images of SiO_2 particles a) hydrophilic SiO_2 particles b) hydrophobic SiO_2 particles

FT-IR spectra of hydrophilic SiO_2 particles and hydrophobic SiO_2 particles are shown in Figure 2. In the spectra of the hydrophilic SiO_2 particles, the peaks at about 1102 cm^{-1}, 800 cm^{-1}, 471 cm^{-1} are the characteristics peaks of the asymmetric stretching vibration, symmetric stretching vibration and bending vibration of Si-O bond, respectively. The characteristic peak of O-H stretching is visible at 3423 cm^{-1}. FT-IR spectra of the hydrophobic SiO_2 particles is similar to that of hydrophilic SiO_2 particles, but the absorption peak(2360 cm^{-1}) of CO_2 appear in the FT-IR spectra of hydrophilic SiO_2 particles, but does not appear in that of hydrophobic SiO_2 particles. So the surface adsorption of hydrophilic SiO_2 particles is stronger than that of the hydrophobic SiO_2 particles.

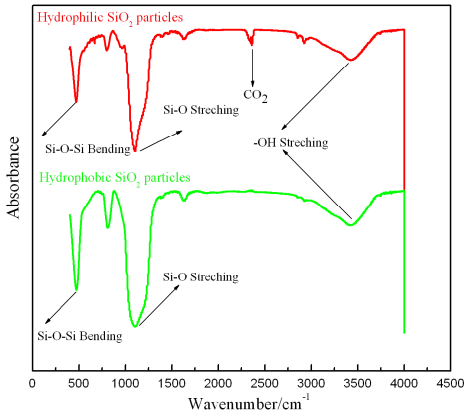


Fig. 2 FT-IR spectra of SiO_2 particles

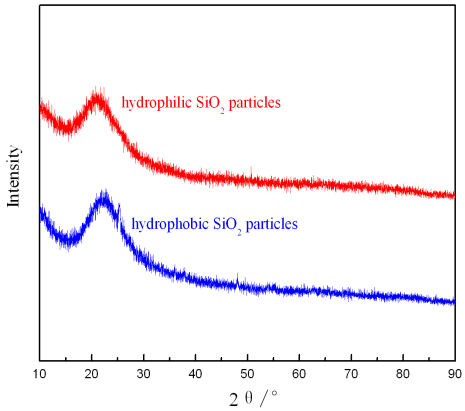


Fig. 3 XRD spectra of SiO_2 particles

The X-ray diffraction (XRD) patterns of hydrophilic SiO_2 particles and hydrophobic SiO_2 particles are shown in Figure 3. From the XRD pattern of the hydrophilic SiO_2 particles, there is only a bread peak at $2\theta=22°$, it seems that hydrophilic SiO_2 particles is totally amorphous in nature due to XRD patterns of hydrophilic SiO_2 particles without any sharp diffraction peaks. The XRD pattern of the hydrophobic SiO_2 particles is similar to that of the hydrophilic SiO_2 particles, which indicates that the structures of hydrophilic SiO_2 particles and hydrophobic SiO_2 particles are similar, and they are non-crystalline inorganic particles.

Characterization of composite films

SEM analysis

SEM images of cross-section of PI/Al_2O_3/SiO_2(hydrophilic) films and PI/Al_2O_3/SiO_2(hydrophobic) films are shown in Figure 4. It can be seen from the Figure 4 that the fibrous materials are PI matrix and the particulate materials are inorganic particles. The figures show that inorganic particles in composite films dispersed more evenly without significant agglomeration, and the combination interfaces of PI matrix and inorganic particles are good. When the content of hydrophilic SiO_2 particles is 5 wt‰, the dispersion of the inorganic particles in the films is the optimal. Comparison of PI/Al_2O_3/SiO_2(hydrophilic) films and PI/Al_2O_3/SiO_2(hydrophobic) films, we know dispersion of the inorganic particles in the PI/Al_2O_3/SiO_2(hydrophilic) films are better. If PI/Al_2O_3 films are modified by the moderate amount of the hydrophilic SiO_2 particles, the hydrogen bonds or other

chemical bonds between -OH groups of hydrophilic SiO_2 particles and -OH groups of Al_2O_3 particles can promote the dispersion ability of inorganic particles.

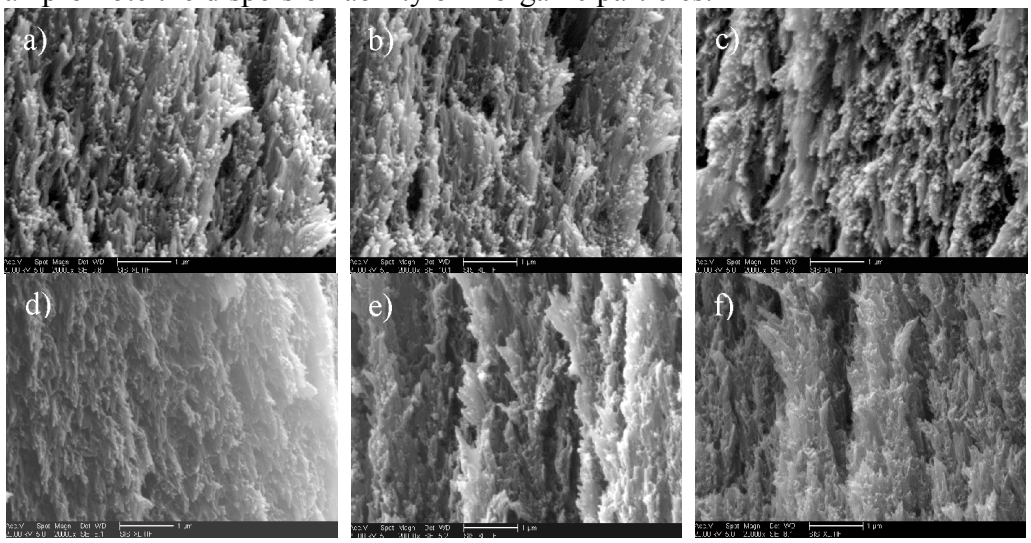


Fig. 4 SEM images of composite films a)3wt‰-hydrophilic b)5w‰-hydrophilic c)7wt‰-hydrophilic d)3wt‰-hydrophobic e)5wt‰-hydrophobic f)7wt‰-hydrophobic

Mechanical performance analysis

The tensile strength and elongation at break of the composite films are shown in Figure 5 and Figure 6. For $PI/Al_2O_3/SiO_2$(hydrophilic) films, the mechanical properties of the films with 5 wt‰ content of SiO_2 particles are best. Tensile strength and elongation at break of that are 132.44 MPa, 12.64%, respectively. When the content of SiO_2 particles is 5wt‰, the dispersion of inorganic particles in $PI/Al_2O_3/SiO_2$(hydrophilic) films and the combination interface of PI matrix and inorganic particles are better, so the energies required for the scission of PI segments are larger and the mechanical properties of the films are the optimal. For $PI/Al_2O_3/SiO_2$(hydrophobic) films, the mechanical properties of the films increase with increasing of the content of SiO_2 particles. If the dispersion of inorganic particles is homogeneous in PI matrix, the effect of inorganic particles on the order degree of PI segments is small, the energies required for the scission of PI segments are larger due to resistance of inorganic particles and interface, so the mechanical properties of the films increase.

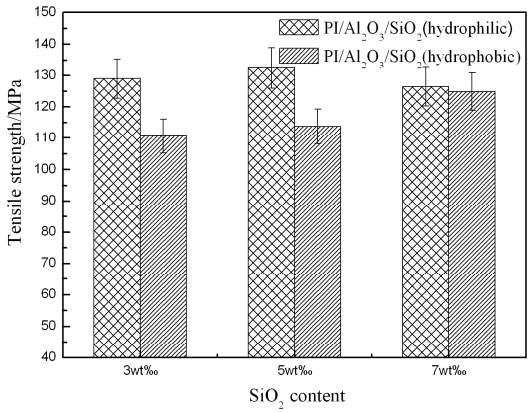


Fig. 5 Tensile strength of composite films

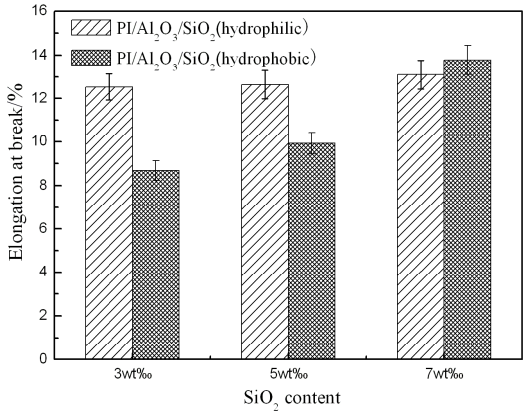


Fig. 6 Elongation at break of composite films

The mechanical properties of $PI/Al_2O_3/SiO_2$(hydrophilic) films are better than that of $PI/Al_2O_3/SiO_2$(hydrophobic) films. When the content of hydrophilic SiO_2 particles is appropriate, more -OH groups can facilitate dispersion of the inorganic particles and improve the interface bonding between PI matrix and inorganic particles due to hydrogen bonds or other chemical bonds between -OH groups of SiO_2 particles and -OH groups of Al_2O_3 particles. Under the action of external force, it is not easy to break for PI segments, therefore, the mechanical properties of the films is better.

Breakdown field strength analysis

Breakdown field strength of composite films is shown in Figure 7. Breakdown field strength of PI/Al_2O_3/SiO_2(hydrophilic) films with 3 wt‰, 5 wt‰, 7 wt‰ content of SiO_2 particles are similar. Breakdown field strength of PI/Al_2O_3/SiO_2(hydrophobic) films decreases with increasing of the contents of SiO_2 particles. The interfaces and defects increase with increasing of the contents of SiO_2 particles, so the breakdown field strength of the films decreases.

Breakdown field strength of PI/Al_2O_3/SiO_2(hydrophilic) films is inferior to that of PI/Al_2O_3/SiO_2(hydrophobic) films. More -OH groups of hydrophilic SiO_2 particles can facilitate dispersion of the inorganic particles and improve the interface between organic phase and inorganic phase due to hydrogen bonds or other chemical bonds. Therefore, it is easier to form a conductive channel under continuous voltage, the breakdown field strength of composite films is low.

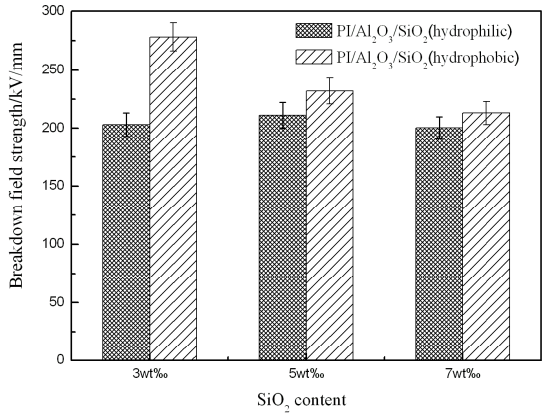


Fig. 7 Breakdown field strength of composite films

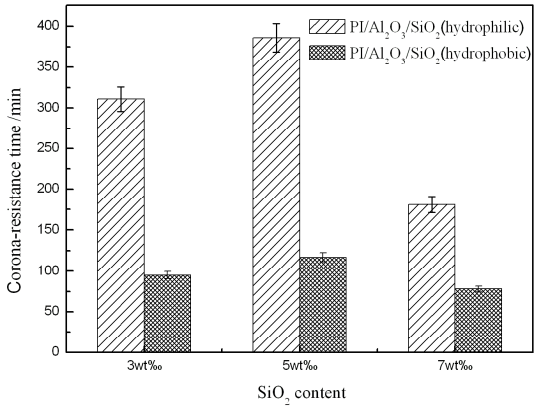


Fig. 8 Corona resistant time of composite films

Corona resistant performance analysis

Figure 8 shows the corona resistant time of composite films. Corona resistant performance of PI/Al_2O_3/SiO_2(hydrophilic) films is superior to that of PI/Al_2O_3/SiO_2(hydrophobic) films. Corona resistant time of PI/Al_2O_3/SiO_2(hydrophilic) films with the 5 wt‰ content of SiO_2 particles is optimal and up to 378min.

Polyimide/inorganic particles nanocomposite films have excellent corona resistant performance, it is mainly because of that the induction of inorganic materials makes deep traps within the films into shallow traps and reduces the accumulation of space charge. In addition, it is easier for space charge to move between the interfacial region of inorganic phase and organic phase, and the interfacial region reduce the chance of charge trapped, so it is difficult for space charge to gather, thereby improve the corona resistance performance of the films[11,12]. Compared with the hydrophobic SiO_2 particles, the surfaces of hydrophilic SiO_2 particles contain more hydroxyl, hydrogen bonds or other chemical bonds between -OH groups of SiO_2 particles and -OH groups of Al_2O_3 particles can promote the dispersion of the inorganic particles. And the interface of PI matrix and the inorganic particles improve effectively due to interactions of hydroxyl groups of the inorganic particles and carboxyl groups or acid anhydride of PI segment through hydrogen bonds or other chemical bonds. Thus deep traps of the films become shallow traps, which reduce the accumulation of space charge and make difficult for space charge to gather. Therefore, corona resistant properties of PI/Al_2O_3/SiO_2(hydrophilic) films are more excellent.

Conclusions

(1) In this paper, the hydrophilic SiO_2 particles and hydrophobic SiO_2 particles are investigated by TEM, FTIR and XRD. The results show that the average size, infrared characteristic peaks and molecular state of aggregation of two kinds of SiO_2 particles are similar.

(2) Inorganic particles disperse evenly without significant agglomeration in PI composite films, and the combination interface of PI matrix and inorganic particles is good. The dispersion of the inorganic particles in the PI/Al_2O_3/SiO_2(hydrophilic) films is superior to that of PI/Al_2O_3/SiO_2(hydrophobic) films.

(3) The mechanical properties and corona resistant performance of PI/Al_2O_3/SiO_2(hydrophilic) films are better than that of PI/Al_2O_3/SiO_2(hydrophobic) films. When the content of SiO_2 particles is 5wt‰, tensile strength and elongation at break of PI/Al_2O_3/SiO_2(hydrophilic) films are: 132.44 MPa, 12.64%, increased 16.46%, 27.29% compared with PI/Al_2O_3/SiO_2(hydrophobic) films. Corona resistant time of PI/Al_2O_3/SiO_2(hydrophilic) films is 378 min, and 2 times of that of PI/Al_2O_3/SiO_2(hydrophobic) films. The breakdown field strength of the films is only 211.15 kV/mm, and inferior to that of PI/Al_2O_3/SiO_2(hydrophobic) films(232.08 kV/mm).

Acknowledgement
The authors wish to acknowledge the generous support of Natural Science Foundation of China (51177030, 50137010), Key Projects of Science Research of the Education Department of Heilongjiang Province(12511z007) and Key Basic Research Development Program of China (2012CB723308).

References

[1] M. Ree, High performance polyimides for applications in microelectronics and flat panel displays, Macromol. res. 14 (2006) 1-33.
[2] C. Linda, D. Virginie, F. Odile, (Semi-)Interpenetrating polymer networks as fuel cell membranes, J. membrane sci. 368 (2011) 1-17.
[3] S.H. Bang, K.K. Kim, H.Y. Jung, et al, Application of NiMoNb adhesion layer on plasma-treated polyimide substrate for flexible electronic devices, Thin solid films. 558 (2014) 405-410.
[4] B. Noh, J.W. Yoon, J.H. Choi, et al, Effect of Cr Thickness on Adhesion Strength of Cu/Cr/Polyimide Flexible Copper Clad Laminate Fabricated by Roll-to-Roll Process, Mater. Trans. 51 (2010) 85-89.
[5] M.H. Chen, J.H. Yin, D.J. Song, et al, Fabrication and Characterization of Polyimide/AlN Nanocomposite Films, Polym. Polym. Compos. 22 (2014) 221-226.
[6] Y.N. Kong, J.H. Yin, W.L. Tie, et al, Preparation and Corona Resistant of Polyimide/TiO_2 Nanocomposite Films, J. Inorg. Mater. 29 (2014) 98-102.
[7] L.Z. Liu, H. Shi, L. Weng, et al, The Effects of Particle Size on the Morphology and Properties of Polyimide/nano-Al_2O_3 Composite Films, Polym. Polym. Compos. 22 (2014) 117-121.
[8] X. Xu, J.H. Yin, G.Y. Li, Study on the Corona Resistant Property of Polymide/TiO_2@SiO_2 Films.Strategic Technology (IFOST), 1 (2013) 101-104.
[9] M.H. Chen, J.H. Yin, W.B. Bua, Microstructure changes of polyimide/MMT-AlN composite hybrid films under corona aging, Appl. Surf. Sci., 263 (2012) 302-306
[10]L.Z. Liu, L. Weng, W.W. Cui, et al, Preparation and properties study of PI/SiO_2-Al_2O_3 films by sol-gel progress, Polym. Mater. Sci. and Eng. 26 (2010) 131-134.
[11]J.W. Zha, H.T. Song, Z.M. Dang, et al, Mechanism analysis of improved corona-resistant characteristic in polyimide/TiO_2 nanohybrid films, Appl. Phys. Lett. 93 (2008).
[12]L.R. Zhou, G.N. Wu, B. Gao, et al, Study on Charge Transport Mechanism and Space Charge Characteristics of Polyimide Films, IEEE T. DIELECT. AND EL. IN. 16 (2009) 1143-1149.

Key Engineering Materials Vols 645-646 (2015) pp 32-39
© (2015) Trans Tech Publications, Switzerland
doi:10.4028/www.scientific.net/KEM.645-646.32

Submitted: 2014-10-30
Accepted: 2014-12-23

Synthesis and Characterization of Topological Insulator Bi_2Te_3 Nanowires

Zhen Guo[1]，Lan Lu[1]，Jingyun Wang[1], Yingjie Xing [1,a*]

[1]Key Laboratory for the Physics and Chemistry of nanodevices and Department of Electronics, Peking University, Beijing, China

[a]xingyj@pku.edu.cn

Keywords: Bi_2Te_3, Topological Insulator, Hydrothermal Method.

Abstract. Bi_2Te_3 nanowires are prepared by a low-cost and facile hydrothermal method without any surfactant. The structure and morphology of the nanowires are characterized by X-ray diffraction, field emission scanning electron microscopy, and transmission electron microscope. The influences of experimental conditions on the products are investigated. The growth mechanism is proposed based on the experimental results. This work is promising for the synthesis of Bi_2Te_3 nanowires with less impurity.

Introduction

Bi_2Te_3 is well-known for its outstanding thermoelectric property, which shows the highest thermoelectric figure of merit *ZT* at room temperature. Nanostructured bismuth telluride compounds have been synthesized and treated via various techniques during the last decade and some progresses have been achieved in their thermoelectric performances, because the small size and low dimensionality are believed helpful to induce lower densities of phonon states and to increase the phonon scattering at multiple grain boundaries [1]. However, no significant improvement of power factor is obtained in these bottom-up prepared nanomaterials when comparing with the bulk Bi_2Te_3 materials [2]. From the view point of structure and transport, it seems that the nanocrystals of Bi_2Te_3 are the main reason for the enhancement of the thermoelectric performance and therefore, the nanomaterials with particular morphology, including nanowires and nanoplates, does not become the star candidate in this research arena.

Recently, Bi_2Te_3 is predicted and proved as a 3D topological insulator [3]. Some literatures reported the gapless electronic surface states from Bi_2Te_3 nanowires and nanoplates [4]. In these experiments, because the contribution of bulk conductivity is hard to suppress completely, the clear identification of surface transport is highly benefited from the particular shape of the nanowires or nanoplates. In other words, both a large surface-to-volume ratio and a continuous surface of the nanowires or nanoplates make the behavior of electronic surface states more prominent. This finding opens a new field for the application of Bi_2Te_3 nanowires. In order to promote the study of this material, more simple way to prepare Bi_2Te_3 nanowires in large scale is needed.

Among various approaches to fabricate Bi_2Te_3 nanowires, wet chemical strategy is attractive because of its low cost and the large quantity of products [2]. Bi_2Te_3 nanowires were prepared via electrochemical deposition by employing an anodized aluminium oxide (AAO) template [5]. A more successful method to grow Bi_2Te_3 nanowires is the hydro- or solvo-thermal synthesis, which is a technique that crystallizes materials under high pressure and elevated temperature in a sealed flask [6-8]. Several groups reported the hydrothermal synthesis of Bi_2Te_3 nanowires in the last

decade. Other than the diversity of the chemical agents and experimental conditions, a common key factor in these experiments is the addition of surfactants, which influences the stacking style of nanocrystals and then controls the morphology of the final products [7,8]. For example, Zhang et al. observed one-dimensional growth promoting by proper surfactants during hydrothermal synthesis [8]. Nonetheless, the surfactants residing at the heterostructured interfaces demonstrated some negative influences on the thermoelectric performance of Bi_2Te_3 nanostructures, and a surfactant-free method was developed to further enhance the thermoelectric figure of merit [9]. Here we present a hydrothermal synthesis of Bi_2Te_3 nanowires without any surfactant. We believe that this method can eliminate the effect of surfactants on Bi_2Te_3 nanowire as a topological insulator and an ideal performance of the topological insulator may be obtained because of the controlled compositions at Bi_2Te_3 nanowire surface. We also study the dependence of Bi_2Te_3 nanowire growth on experimental conditions detailedly in this work.

Experimental

Chemicals. All the chemicals used for the synthesis of Bi_2Te_3 nanowires in this work are analytical grade without further purification. Bismuth chloride ($BiCl_3$, 98%), potassium tellurite (K_2TeO_3, 98%), sodium hypophosphite monohydrate ($NaH_2PO_2 \cdot H_2O$, 98%), polyvinyl alcohol (PVA, 99%), polyvinyl pyrrolidone (PVP) K30, polyethylene glycol (PEG) 20000, and sodium dodecyl sulfate (SDS,98%), were purchased from Sinopharm Chemical Reagent Beijing Co.,Ltd.

Preparation of Bi_2Te_3 nanowires. In a typical synthesis, 0.126 g (0.4 mmol) of $BiCl_3$,0.152 g (0.6 mmol) of K_2TeO_3, 5g of $NaH_2PO_2 \cdot H_2O$, were dissolved in 40 mL deionized water with sufficiently stirring (about 10 min) and transferred into a 60 mL Teflon-lined stainless-steel autoclave. The autoclave was heated at 180 °C in an electric oven for 12 h and then cooled to room temperature naturally. The black powders were collected by centrifugation and were washed several times with distilled water and ethanol, and finally dried at 70 °C in vacuum for 12 h. The effect of the heating temperature, the reaction time, and the different kind of alkali surfactants (PVP, PVA, SDS, and PEG) were systematically studied in order to clarify the growth mechanism of Bi_2Te_3 nanowires.

Characterizations. The structure of the final products was investigated by X-ray diffraction (XRD) on a DMAX-2400 diffractometer with Cu-Kα radiation (60 Kv × 200 mA). The overview morphologies of the samples were obtained by a FEI Quanta 600 field emission scanning electron microscope (FESEM) at an acceleration voltage of 20 kV. Transmission elctron microscope (TEM) images, high resolution transmission electron microscope (HRTEM), selected area electron diffraction (SAED), and energy dispersive X-ray spectroscopy (EDS) patterns were recorded on a Tecnai F20 S-Twin transmission electron microscope using an accelerating voltage of 200 kV.

Results and Discussion

Structure and Morphology of Bi_2Te_3 Nanowires. The method employed here is a simple hydrothermal treatment of $BiCl_3$ and K_2TeO_3 in the presence of $NaH_2PO_2 \cdot H_2O$ at 180 °C for 12 h. The structure of the products was examined by XRD and the result is shown in Figure 1a, which reveals a pure rhombohedral phase of Bi_2Te_3 with a space group $R\bar{3}m$ (166) (JCPDF #15-0863). Figure 1b shows a FESEM image of Bi_2Te_3 nanowires. The morphologies of the nanowires were observed by FESEM and the nanowires demonstrated a large distribution of diameters (40−200 nm) and lengths (from several hundred nanometers to several microns). Figure 1c shows a

low-magnification TEM image of the Bi_2Te_3 nanowires. A slight variation of the diameter even in a single nanowire is revealed in this figure. This morphology was also observed in other similar solvothermal experiment [6]. The SAED pattern of a nanowire (shown in the inset of Figure 1c) indicates the polycrystalline nature of these hydrothermal-synthesized nanowires. This result can partly be explained by the anisotropy growth of rhombohedral-structured Bi_2Te_3 crystal. The HRTEM image of a nanowire is shown in Figure 1d. A single crystalline region is clearly demonstrated and the spacing of the lattice fringes is 3.685 Å, which is in good agreement with the d value of the (012) planes of rhombohedral structured Bi_2Te_3 crystal (3.685 Å).The top inset of Figure 1d is the fast fourier transform of the framing area of Figure 1d. The bottom inset of Figure 1d shows the EDS spectrum of the nanowires, in which a element ratio (Bi:Te) of approximately 2:3 is detected.

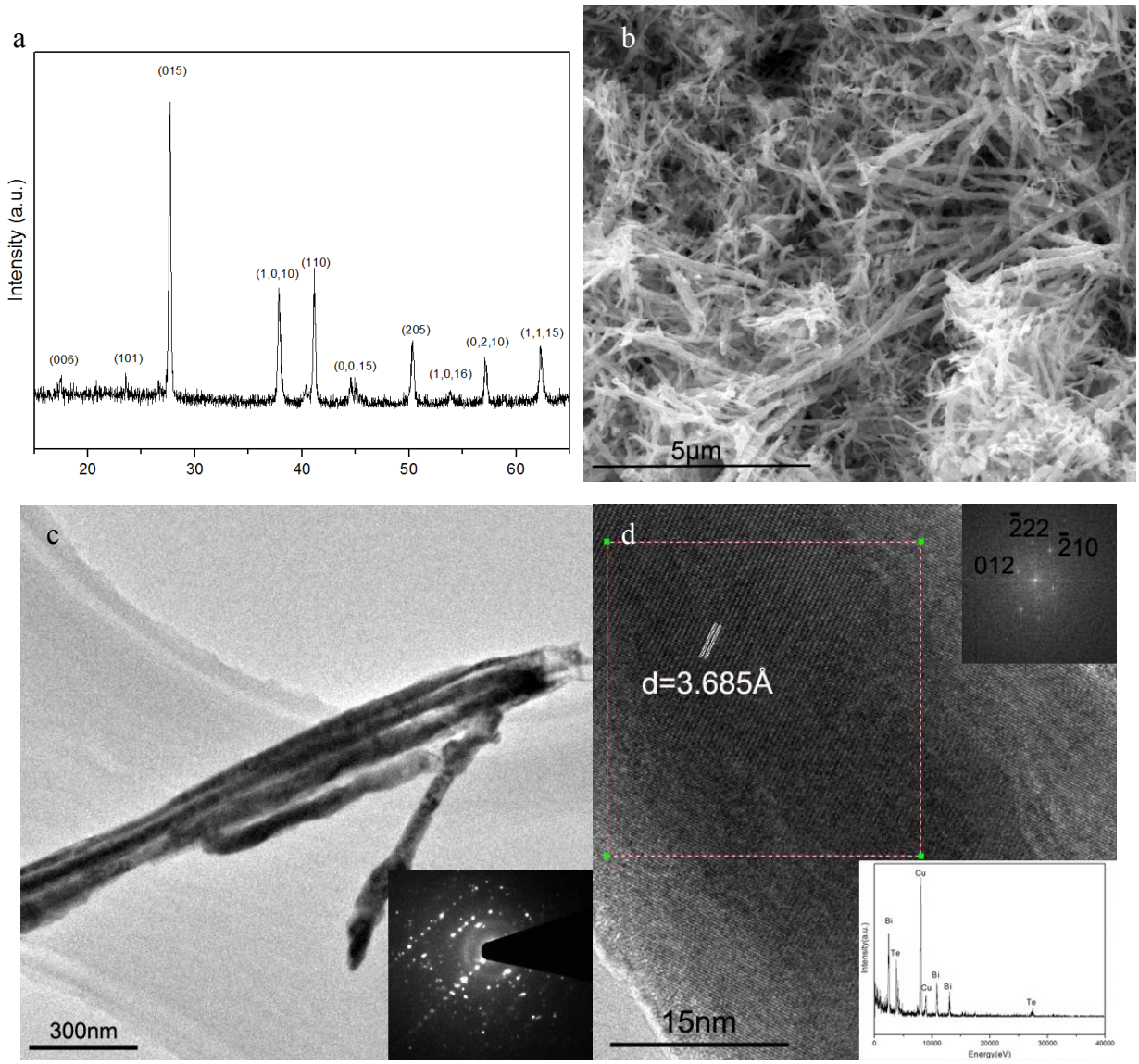


Figure 1. (a) XRD pattern, (b) FESEM image, (c) TEM image, (d) HRTEM image of the Bi_2Te_3 nanowires. The inset of Figure 1c is the SAED pattern of a nanowire. The insets of Figure 1d are EDS spectrum (bottom) and FFT result (top).

Effects of $NaH_2PO_2 \cdot H_2O$. We found that the structure and morphology of the products were influenced by some experimental parameters, including the reduction agent, temperature, and reaction time.

In our material system, we found that $NaH_2PO_2•H_2O$ not only served as a reduction agent, but also influenced the morphology of the products significantly. In order to clarify the effect of $NaH_2PO_2•H_2O$ in the reaction, we conducted a series of experiments with different amount of $NaH_2PO_2•H_2O$ (1, 2, 3, 4 and 5 g) while fixing all other conditions. When $NaH_2PO_2•H_2O$ concentration was not high enough (1, 2 and 3 g), the products were disk-like nanostructures (shown in Figure 2a). As the amount of $NaH_2PO_2•H_2O$ increased to 4 g, the products contained a large amount of twisting nanowires and some large ribbon-like nanostructures (shown in Figure 2b). The optimal amount of $NaH_2PO_2•H_2O$ was 5 g in our experiments, with which the products were pure nanowires (shown in Figure 1b). More insights of the effect of $NaH_2PO_2•H_2O$ was probed by XRD analysis. The reducing power of $NaH_2PO_2•H_2O$ was confirmed by adding only 1 g of $NaH_2PO_2•H_2O$ into the solution. XRD pattern of the products (shown in the inset of Figure 2a) reveals the appearance of Bi_2Te_3 crystal. When 4 g of $NaH_2PO_2•H_2O$ was used, sharp and high peaks in the inset of Figure 2b means that the products are pure Bi_2Te_3 crystals. These results indicate that as a reducing agent, $NaH_2PO_2•H_2O$ controls the formation of Bi_2Te_3 crystals effectively. Although we do not exactly understand its action mechanism on one-dimensional growth, it is clear that $NaH_2PO_2•H_2O$ has great importance in forming Bi_2Te_3 nanowires in the case of no surfactant.

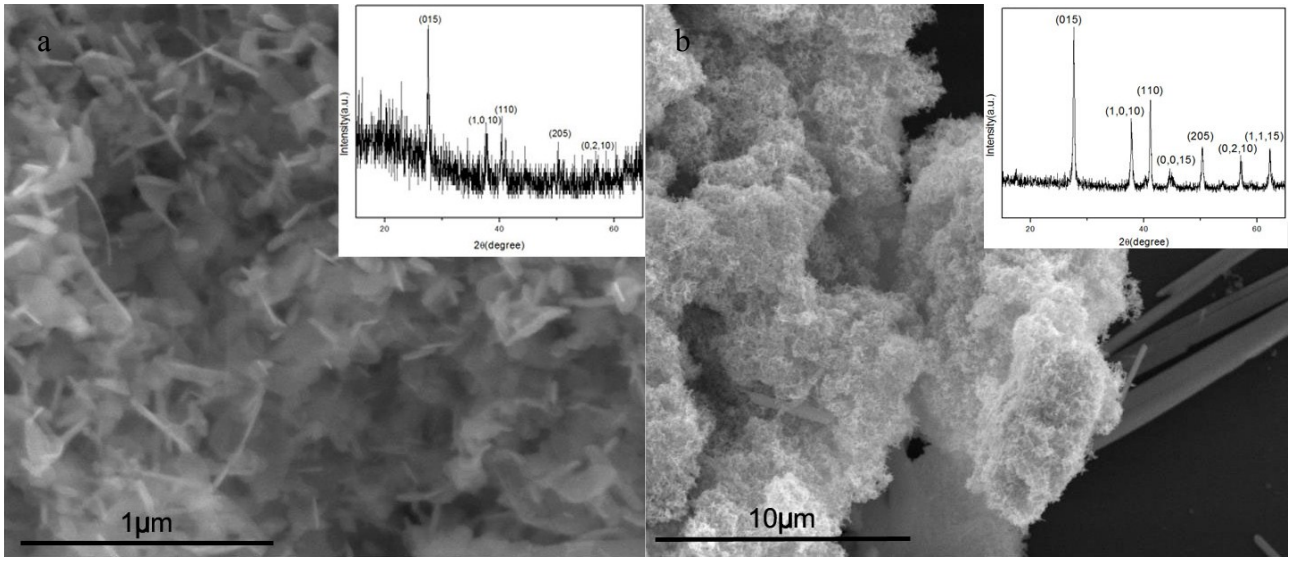


Figure 2. FESEM images and the XRD patterns (inset) of the products prepared with different amount of $NaH_2PO_2•H_2O$. (a) 1 g, (b) 4 g.

Influences of Reaction Temperature. The reaction temperature was found as another crucial factor to obtain Bi_2Te_3 nanowires with good morphology. We compared the products synthesized at a series of temperatures (120, 150 and 180 °C) while keeping all other conditions unchanged. The morphology of the products prepared at 120 °C is shown in Figure 3a. We found that the nanowires become longer and thicker when the reaction temperature increases. This phenomenon can be explained by the Gibbs-Thomson effect, in which the tiny crystal particle is more unstable because of its bigger Gibbs free energy than that of a large particle. When Gibbs free energy of the system increases at a higher temperature, the size of the nanowires enlarges to keep the system stable. XRD characterization shows one more benefit of the high reaction temperature. Figure 3b shows that in the products prepared at 120 and 150 °C, a small amount of Te is detected besides Bi_2Te_3. In contrast, there is only Bi_2Te_3 in the 180 °C sample. So we choose 180 °C as the optimal temperature.

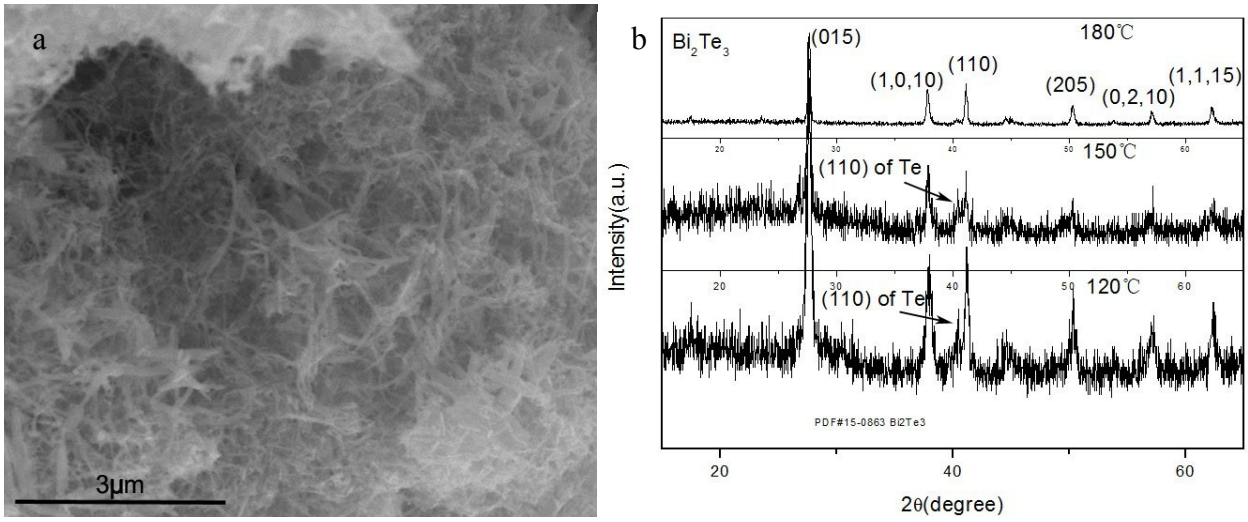
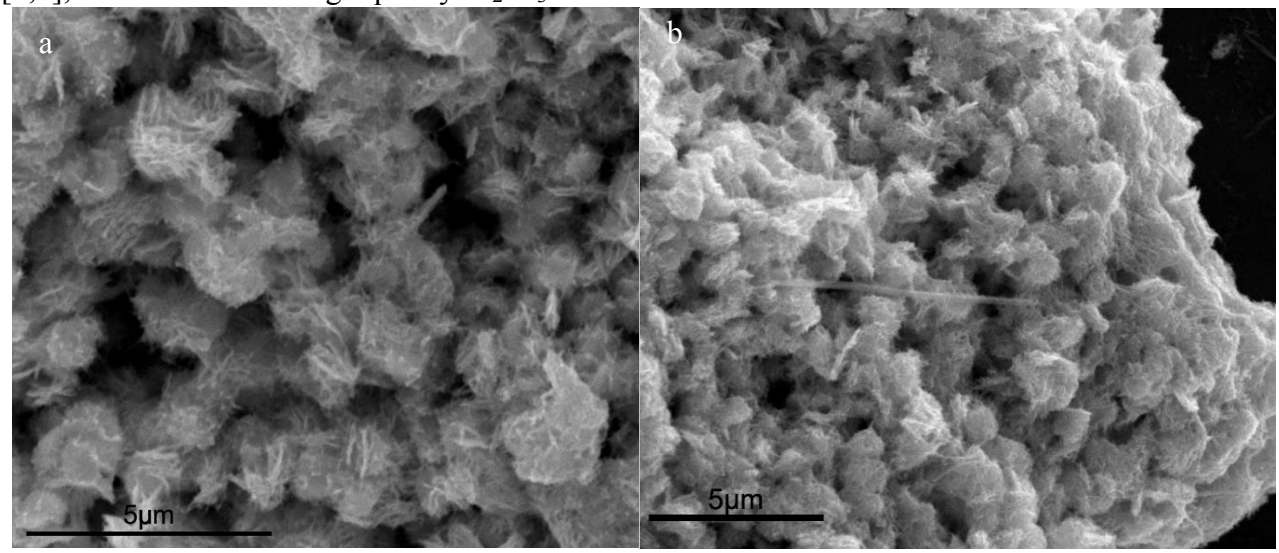


Figure 3. FESEM image of nanocrystals synthesized at 120 °C (a), XRD patterns of the products prepared at different temperatures (b).

Influences of surfactants. As reported in literatures [7,8], the surfactants play an important role in a typical hydrothermal process. We added four kinds of surfactants (PVA, PVP, PEG, and SDS) in our hydrothermal experiments to determine their influence on the products. The corresponding FESEM images of the products are shown in Figure 4a-d, respectively. With the present of PVA or PVP (Figure 4a, 4b), similar morphologies of nanoballs were observed. Further analysis revealed that the nanoballs composed of many Bi_2Te_3 nanowires. However, the degree of crystallinity of these nanowires was poor. In the case of adding PEG or SDS (Figure 4c, 4d), we can find many straight nanowires and some spherical nanostructures. XRD analysis showed that the products contained both Bi_2Te_3 and Te. Although some surfactants have been used to synthesize one-dimensional Bi_2Te_3 nanomaterials by restraining crystal growth in some particular directions [7,8], we do not obtain high quality Bi_2Te_3 nanowires with above surfactants.



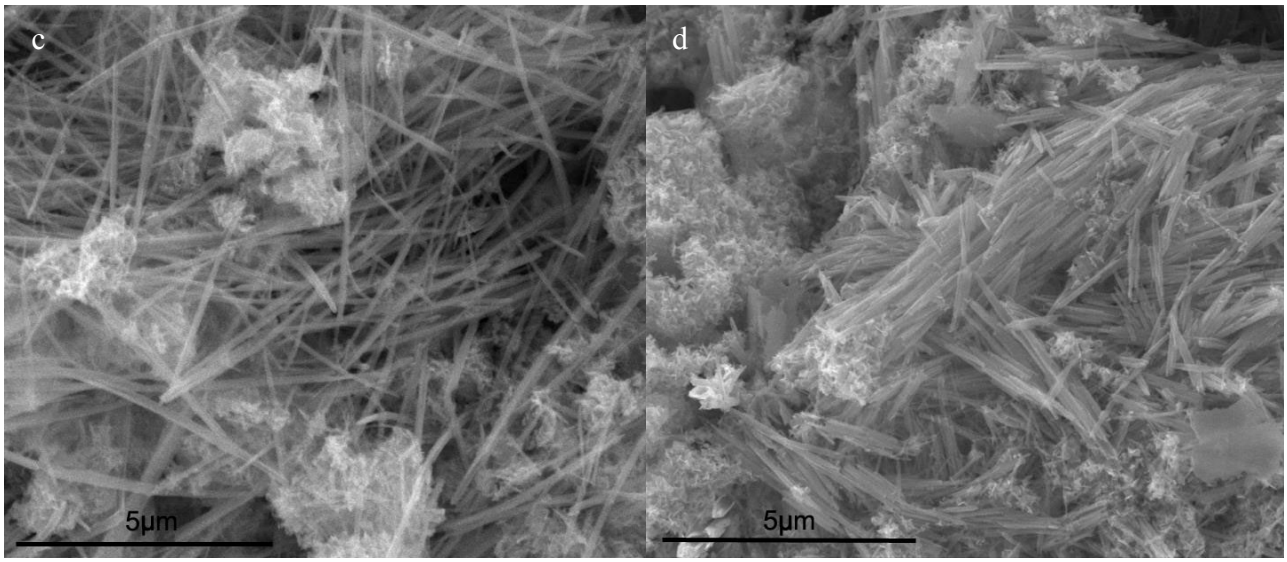


Figure 4. FESEM images of nanocrystals synthesized with different surfactants. (a) PVA, (b) PVP, (c) PEG, (d) SDS.

Growth mechanism. There are two typical growth mechanisms for the formation of Bi_2Te_3 nanowires in hydro- or solvo-thermal synthesis. The more popular approach employs some surfactants in the synthesis, by which the selectively covering with surfactant molecules on some specific crystal facets hinders the nucleus enlargement in these directions [7,8]. However, in our experiments, this template effect was not observed with four kinds of surfactants and the best products were obtained without any surfactant. It is obvious that the growth mechanism in our hydrothermal synthesis should be a different one. Song et al. proposed a two-step route to prepare Bi_2Te_3 nanowires, in which Te nanowires generated firstly and transformed to Bi_2Te_3 nanowires consequently in a solvothermal synthesis [6]. We think that a similar mechanism may exist in our experiments. In order to further understand the formation process of Bi_2Te_3 nanowires without surfactant, different intermediate products were collected and investigated. The products after 2 h of reaction contained a lot of flocculent nanostructures and some large and thick nanostructures (Figure 5a). From the XRD pattern shown in the inset of Figure 5a, Te and Bi_2O_3 were characterized in this sample. FESEM observation revealed that there were also flocculent nanostructure and some rod-like nanostructure in the products after 3 or 4 h of reaction (figure not shown). When the reaction time extended to 5 h, some nanowires appeared as shown in Figure 5b. XRD analysis proved that Bi_2Te_3 rhombohedral phase existed in the products after 5 h of reaction (shown in the inset of Figure 5b). According to above results, we propose that the growth mechanism of the Bi_2Te_3 nanowires includes two steps: First, $NaH_2PO_2 \bullet H_2O$ works as the reducing agent and Te and Bi_2O_3 are generated in the solution, and then Bi_2Te_3 nanowires are transformed from Te nanostructures. It seems that Te component is generated easily in solution but the generation of Bi_2Te_3 nanowires needs enough temperature and time. This assumption can be deduced from Te peaks in above XRD patterns. We note that the morphology of intermediate products changes significantly as the reaction time prolongs. Therefore we suggest that the formation of Bi_2Te_3 nanowires is not a simple reaction between Te nanostructures and surrounding Bi ions as the mechanism proposed in Ref. 6. An additional process of continually stacking Te on the original nanostructures and then converting to Bi_2Te_3 is highly possible in our hydrothermal synthesis, resulting in the disappearance of pure Te in the final products after long enough reaction (12 hours) at 180 °C.

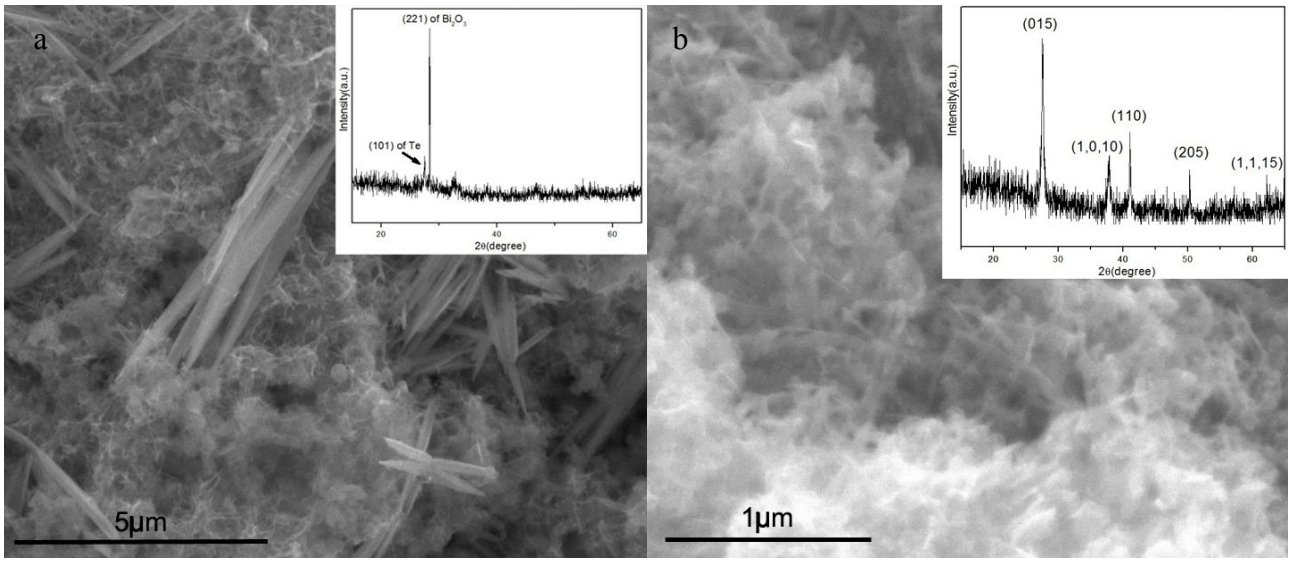


Figure 5. Intermediate products at different time. FESEM images and XRD patterns (inset) of the products after (a) 2 h and (b) 5 h of reaction.

We tried to fabricate field-effect-transistors with Bi_2Te_3 nanowires. However, the rate of successful devices was not satisfied. Some nanowires were deteriorated by the process of device fabrication. More treatments of nanowires and devices are ongoing.

Conclusions.

A simplified hydrothermal process to synthesize Bi_2Te_3 nanowires without any surfactant was developed. The growth of Bi_2Te_3 nanowires were investigated under different reaction temperature and time. The growth mechanism was discussed and a continually stacking and converting process was proposed. Our results provide a new approach for preparing Bi_2Te_3 nanowires in large scale.

Acknowledgements

This work is supported by the National Natural Science Foundation of China (Grant Nos.61376059,91221202) and the National Basic Research Program of China (“973”Program) (Grant Nos.2012CB932701,2011CB933001).

References

[1] Hilaal Alama, Seeram Ramakrishna, A review on the enhancement of figure of merit from bulk to nano-thermoelectric materials, Nano Energy. 2 (2013) 190–212.

[2] Yixin Zhao, Jeffrey S. Dyck, Clemens Burda, Toward high-performance nanostructured thermoelectric materials: the progress of bottom-up solution chemistry approaches, J. Mater. Chem. 21 (2011) 17049–17058.

[3] M. Zahid Hasan and Joel E. Moore, Three-Dimensional Topological Insulators, Annu. Rev. Condens.Matter Phys. 2 (2011) 55–78.

[4] Xiu Fa-Xian and Zhao Tong-Tong, Topological insulator nanostructures and devices, Chin. Phys. B. Vol. 22, No. 9 (2013) 096104.

[5] Z. Aabdin, N. Peranio, O. Eibl, W. Tollner, K. Nielsch, D. Bessas, R.P. Hermann, M. Winkler, J. Konig, H. Bottner, V. Pacheco, J. Schmidt, A. Hashibon, C. Elsasser, Nanostructure, Excitations, and Thermoelectric Properties of Bi_2Te_3-Based Nanomaterials, Journal of Electroni Materials. 41(2012) 1792–1798.

[6] Shuyan Song, Jipeng Fu, Xiyan Li, Wei Gao, and Hongjie Zhang, Facile Synthesis and Thermoelectric Properties of Self-assembled Bi_2Te_3 One-Dimensional Nanorod Bundles, Chem. Eur. J. 19 (2013) 2889–2894.

[7] T. Sun, X.B. Zhao, T.J. Zhu, J.P. Tu, Aqueous chemical reduction synthesis of Bi_2Te_3 nanowires with surfactant assistance, Materials Letters. 60 (2006) 2534–2537.

[8] Yanhua Zhang, Guiying Xu, Pan Ren, Ze Wang, Changchun Ge, Effects of Various Reductants and Surfactants on the Nanostructure of Bi_2Te_3 Synthesized by a Hydrothermal Process, Journal of Electronic Materials. 40 (2011) 835–839.

[9] Yichi Zhang, Heng Wang, Stephan Kräemer, Yifeng Shi, Fan Zhang, Matt Snedaker, Kunlun Ding, Martin Moskovits, G. Jeffrey Snyder, and Galen D. Stucky, Surfactant-Free Synthesis of Bi_2Te_3−Te Micro−Nano Heterostructure with Enhanced Thermoelectric Figure of Merit, ACS Nano. 5 (2011) 3158–3165.

Key Engineering Materials Vols 645-646 (2015) pp 40-44
© (2015) Trans Tech Publications, Switzerland
doi:10.4028/www.scientific.net/KEM.645-646.40

Submitted: 2014-10-30
Accepted: 2014-12-23

Electronic and magnetic properties of Rare-Earth atoms absorbed on graphene sheet: A theoretical study

Qingxiao Zhou[1,a], Zhibing Fu[1,b],Chaoyang Wang[1,2,c], Xi Yang[1,d], Lei Yuan[1,e], Yongjian Tang[1,2,f]

[1]Research Center of Laser Fusion, China Academy of Engineering Physics, Mianyang 621900, People's Republic of China

[2]Science and Technology on Plasma Physics Laboratory, China Academy of Engineering Physics, Mianyang 621900, People's Republic of China

[a]zhouqingxiao1989@163.com, [b]fuzhibingcn@aliyun.com, [c]wzxhw@tom.com, [d]xingxingysx@163.com, [e]yuanlei0211@163.com, [f]fgmh2000@163.com(corresponding author)

Key words: Graphene; Density functional theory; Adsorption; Rare-Earth atom.

Abstract: The electronic and magnetic properties of graphene functionalized by 4f-orbital RE-metal atoms (Ce, Nd, Sm and Eu) were investigated by the density functional theory (DFT) calculations. The results of binding energy and geometry parameters showed that the hollow site, the center of a carbon hexagon, was the most stable adsorption structure. Furthermore, the PDOS results suggested that the electronic hybridization between the RE-adatoms and C atoms was mainly contributed by the 5d orbitals, whereas the 4f-orbital of the metal adatoms dominated the net magnetic moments of the systems significantly.

Introduction

Graphene, one-atom thick sheet of carbon atoms arranging in hexagonal lattice, has attracted enormous interest, since it was discovered in 2004 [1-2]. Because of its unique physical and chemical properties, such as giant mobility of charge carriers, anomalous quantum Hall effect, and Dirac-type quasiparticles [3,4], it has attracted many scientists to except for making a breakthrough in some new research areas. Moreover, carbon-based materials doped by transition-metal atoms introduced many interesting properties which have been observed and explored [5-7]. To our best knowledge, the Rare-Earth catalysts play an important role in the process of the graphene or CNTs growth. The groups of Suzuki and Deng have investigated the geometry and electronic structures of Sm and Eu decorated C_{60} [8-9]. However, the interaction between the RE-metal atoms and graphene was few. In order to model the electronic and magnetic properties, the understanding of the effect by the adatoms was indeed to be explored.

In our paper, the interaction between the RE-metals (Ce, Nd, Sm and Eu) and the graphne were investigated by the density functional theory (DFT) method. We performed the corresponding results of geometry parameters, binding energy, magnetic and electronic properties detaily describing the adsorption configurations. It is expected that our results could provide useful information for the application based on the RE-metals decorated graphene.

Computational method

All calculations were performed using the density functional theory (DFT) methods, as implemented in the $DMol^3$ package [10]. The electron exchange and correlation were treated within

the generalized gradient approximation (GGA) with the Perdew, Burke and Ernzerhof (PBE) function. In contrast to the local-density approximation (LDA), the GGA tends to improve total energy, atomization energy, and energy barrier. Generally, it yields chemical bonds slightly longer and weaker than LDA, an effect that corrects LDA predictions. So it is starting to replace the LDA in applications. Particularly, as the additional cost of GGA computation is rather small. For accurately calculating the interaction energies of transition metal atoms on graphene, the Double Numerical plus polarization (DNP) function basis set [11] was selected. The internal coordinates for all the atoms in the unit cell were fully relaxed without any constraint, and the DFT semicore psendopotential (DSSP) replaced core electrons as a single effective potential [12].

In our calculations, the system was modeled by one RE-adatom in a 5×5 graphene supercell substrate plus a vacuum layer of 20 Å along the z axis and a 5×5×1 Monkhorst-pack scheme for K-points of the Brillouin zone was set. The optimization will continue until the energy fluation was not greater than 2×10^{-5} Ha and the forces on each atom was less than 0.004Ha/ Å. For comparison, the same conditions were used in all computations.

To calculate adsorption energies, the total energy of an isolated atom was approximated by the computation with a single atom in a cubic supercell of length 13 Å and only Gama K-points of the Brillouin zone was set in this case. For RE-adatoms adsorption on the systems, the binding energy is defined as:

$E_b(A) = E_t(AG) - E(A) - E_t(G)$

Where $E_t(AG)$, $E(A)$ and $E_t(G)$ is the total energies for the optimized configuration of the relaxed graphene with an adsorbed RE-adatom, the isolated RE-atom and the isolated graphene sheet, correspondingly.

Results and discussion

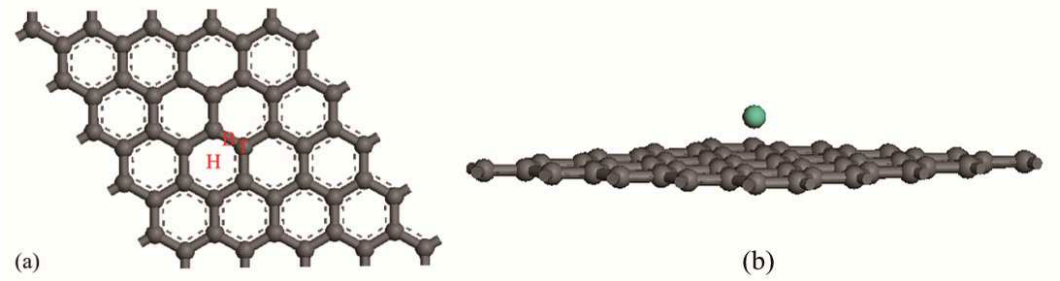


Fig.1 (a) Optimized configurations of graphene, and the three adsorption sites are labeled: bridge (B), top (T), and hollow (H) sites; (b) the optimized atomic structure of Eu-adatom on the hollow site.

Considering the symmetry of graphene, we calculated three adsorption sites, namely, the bridge site at the midpoint of a C-C bond (B), the top site above a carbon atom (T), and the hollow site at the center of a hexagon (H). The geometry structures are obtained from the positions of these atoms after optimized. Furthermore, the corresponding parameters describing the geometry structures and magnetic properties were summarized in Table 1. It can be obtained that the hollow sites were the most favorable adsorption sites for the RE-adatoms (Ce, Nd, Sm and Eu). The E_b of the Nd adsorbed on the hollow site was the largest with the value of 2.205 eV, and the Eu-adatom exhibited the smallest binding energy (0.952 eV). The distance between the adatoms and the nearest carbon atom varied from 2.740 Å to 2.866 Å, which was consistent with the results reported by Chan et al. (2.11 Å ~ 3.80 Å) [13] exploring the adsorptions of 12 different metal atoms on the graphene.

To deeply understand the interaction mechanism, the charge transfer between the RE-metal atoms and the graphene-support was investigated by Mulliken population analysis. The Nd adsorbed on H site of the graphene, the most stable configuration, was taken as an example for analysis. The electronic configuration of Nd is [Xe] $4f^{3.896}5d^{1.066}6s^{1.938}$ before absorbed and it became [Xe] $4f^{3.943}5d^{1.315}6s^{0.682}$ upon the adsorption. As for the pure graphene, the electronic configuration of C atom is [He] $2s^{1.325}2p^{2.650}$. After absorbing the Nd-adatom, the nearest C atoms changed to [He] $2s^{1.494}2p^{2.882}$. There were about 0.756e electrons of Nd-6s orbital transferring to the graphene, but the 5d orbital increased slightly as a contribution of back-donation for the occupied orbitals of graphene. As for other cases, the similar phenomena existed. Therefore, the interaction between the RE-metal atoms and the graphene was primarily ionic resulted from the charge transfer from the 6s orbital of RE-metals atoms and to C-2p orbital. In addition, we also calculated the magnetic moment of the free RE-metal atoms and the adsorption complexes. As we know, the RE-metal atoms owned magnetic characters due to the presence of unpaired electrons. As shown in Table 1, the RE-atoms exhibited different magnetic moments as free atoms. Upon adsorptions on the graphene, the magnetic properties of adatoms changed obviously and there presented distinct difference for various adsorption sites. Above results was due to the interaction between the adatoms and the graphene affected the configurations of unpaired electrons.

Table 1
Summary of results for RE atoms adsorbed on three sites of graphene. The properties listed are the binding energy (E_b), the smallest adatom-carbon distance (d_{AC}), magnetic moment of the isolated RE-atom (μ_{RE}), magnetic moment of the RE-adatoms adsorbed on the graphene ($\mu_{RE/adsorbed}$), magnetic moment of adatom-graphene system (μ_{REG}), and Mulliken charge of RE-adatoms (Q).

Atom	Site	E_b (eV)	h (Å)	d_{AC} (Å)	μ_{RE} (μ_B)	$\mu_{RE/adsorbed}$ (μ_B)	μ_{REG} (μ_B)	Q (e)
	T	1.660	2.279	2.742	-2.000	2.609	2.903	0.675
Ce	H	1.720	2.212	2.740		2.626	2.957	0.672
	B	1.670	2.380	2.627		4.764	4.744	0.496
	T	1.745	2.366	2.582	4.000	4.868	4.936	0.428
Nd	H	2.205	2.332	2.820		4.861	4.960	0.409
	B	1.040	2.451	2.704		7.037	7.024	0.611
	T	1.035	2.459	2.632	-6.038	7.046	7.042	0.601
Sm	H	1.164	2.421	2.853		7.050	7.034	0.576
	B	0.957	2.478	2.719		-8.055	-8.017	0.604
	T	0.952	2.481	2.648	7.000	8.052	8.019	0.606
Eu	H	1.056	2.457	2.866		8.075	8.033	0.569
	B	0.874	2.460	2.741		8.060	8.036	0.595

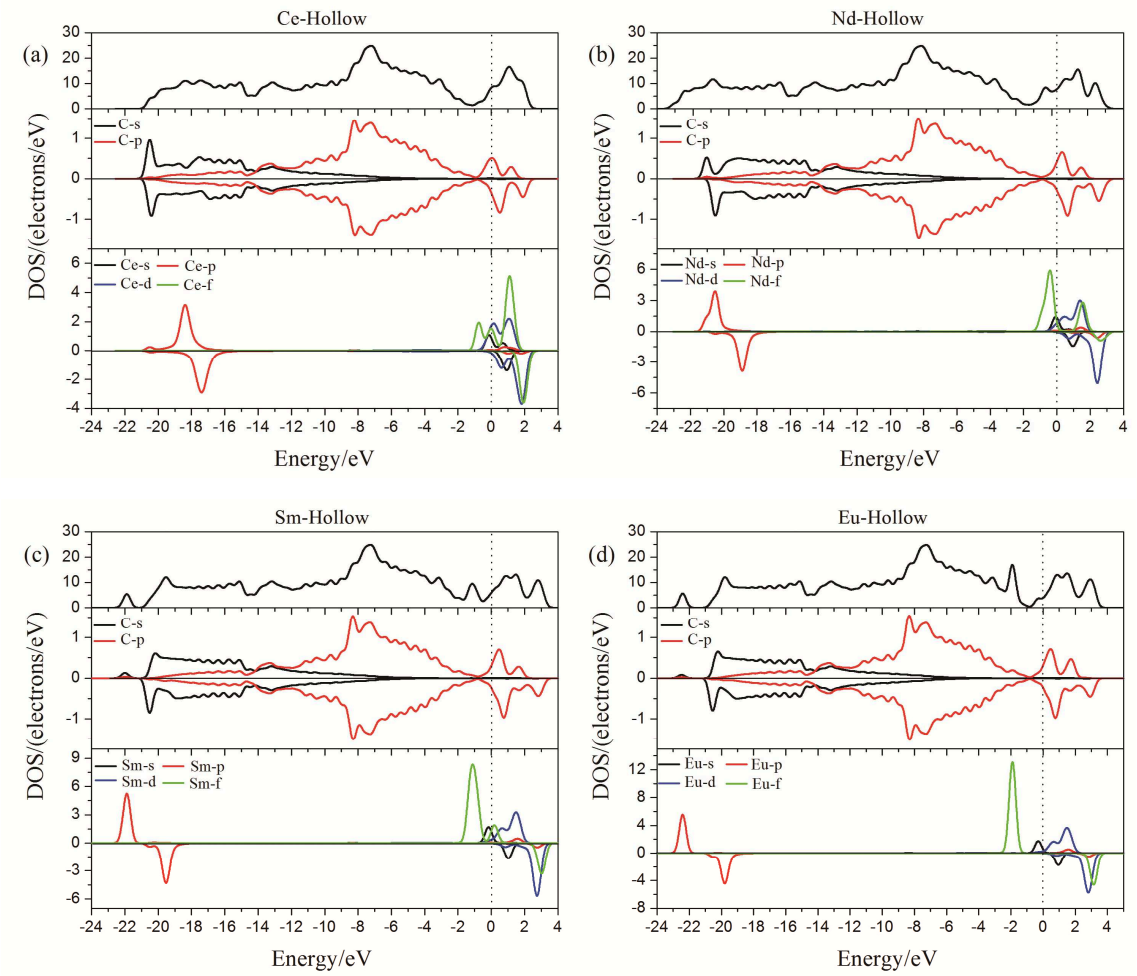


Fig.2 The total density of states of adatom-graphene system, the project density of states of adjacent C atoms to the adatom, and the partial density of states of adatom: (a) Ce adsorbed on the hollow site, (b) Nd adsorbed on the hollow site, (c) Sm adsorbed on the hollow site, and (d) Eu adsorbed on the hollow site.

In order to deeply understand the electronic and magnetic properties of the adsorption systems, the total density of states (TDOS) and partial density of states (PDOS) of the RE-metal atoms absorbed on the hollow site of graphene were performed in Fig.2. As shown in Fig.2a, the overlaps between the C-2p and the Ce-5d orbitals happened ranging from -0.853 eV to 2.344 eV through the Fermi level, but there little hybridizations appeared between the Ce-4f orbital with the C atoms. For other cases (Nd, Sm and Eu), the 4f orbitals exhibited the similar behavior with the case of Ce. Nevertheless, the magnetic moment of the RE-adatoms was mainly contributed by the 4f orbitals with the spin-up and spin-down electronic states mismatching significantly.

Summary

In conclusion, the interaction between the RE-metal atoms (Ce, Nd, Sm and Eu) and graphene were studied via the density functional theory (DFT) method. We explored the stability of the adsorption systems for different adsorption sites, and the results indicated the hollow site was favorable. According to the Mulliken charge analysis, it was found that the charge transfer from 6s orbitals of RE-adatoms to the graphene. The results of PDOS indicated that the hybridization between the RE-metal atoms and the graphene mainly appeared between the RE-5d and C-2p orbitals, and the RE-4f orbitals acted an important role in the magnetic moment of the systems. We hope our work could be useful for the application of graphene coated by RE-metals.

Acknowledgement

This work was supported by the National Natural Science Foundation of China (11074176, 10976019 and 51101141), the Research Fund for the Doctoral Program of Higher Education of China (20100181110080), and the Research Found from Science and Technology on Plasma Physics Laboratory (9140C680502C68254).

References

[1] K.S. Novoselov, A.K. Geim, S.V. Morozov, D. Jiang, Y. Zhang, S.V. Dubonos, V. Grigorieva, A.A. Firsov, Science 306 (2004) 666-668.
[2] K.S. Novoselov, A.K. Geim, S.V. Morozov, D. Jiang, M.I. Katsnelson, I.V. Grigorieva, S.V. Dubonos, A.A. Firsov, Nature 438 (2005) 197-204.
[3] A.K. GEIM, K.S. NOVOSELOV, Nature Mater. 6 (2007) 183-189.
[4] A.H.C. Neto, F. Guinea, N.M.R. Peres, K.S. Novoselov, A.K. Geim, Rev. Mod. Phys. 81 (2009) 109-215.
[5] Y. Zhang, N.W. Franklin, R.J. Chen, H. Dai, Chem. Phys. Lett. 331 (2000) 35-39.
[6] B.C. Regan, S. Aloni, R.O. Ritchie, U. Dahmen, A. Zettl, Nature 428 (2004) 924-930.
[7] A. Javey, J. Guo, Q. Wang, M. Lundstrom, H. Dai, Nature 424 (2003) 654-659.
[8] S. Suzuki, M. Kushida, S. Amamiya, S. Okada, K. Nakao, Chem. Phys. Lett. 327 (2000) 291-298.
[9] G.L. Lu, K.M. Deng, H.P. Wu, J.L. Yang, X. Wang, J. Chem. Phys. 124 (2006) 054305-1.
[10] B.Delley, Chem. Phys. 92 (1900) 508-518.
[11] J.P. Perdew, K. Burke, M. Ernzerhof, Phys. Rev. Lett., 77 (1996) 4.
[12] B. Delley, Phys. Rev. B, 66 (2002).
[13] K.T. Chan, J.B. Neaton, M.L. Cohen, Phys. Rev. B, 77 (2008) 235430-1.

Key Engineering Materials Vols 645-646 (2015) pp 45-51
© (2015) Trans Tech Publications, Switzerland
doi:10.4028/www.scientific.net/KEM.645-646.45

Submitted: 2014-11-01
Accepted: 2014-12-23

Melt Electrohydrodynamic Direct-Writing Micro/Nano Fiber with Restriction of Heated Sheath Gas

Zhaojie Yu[a], Linjie Wang[b], Lingling Sun[c], Yihong Lin[d], Wei Wang[e], Gaofeng Zheng [f]*, Daoheng Sun[g]**

Department of Mechanical and Electrical Engineering, Xiamen University, China, 361005

[a] 307224162@qq.com, [b] 258494581@qq.com, [c] 602968671@qq.com,
[d]kuangbiaohudie@foxmail.com, [e] 373491075@qq.com,
[f] zheng_gf@xmu.edu.cn (corresponding author), [g] sundh@xmu.edu.cn(corresponding author)

Keywords: Electrohydrodynamic Printing, Melt Electrospinning, Micro/Nano-Structures, Direct-writing Technology, Heated Sheath Gas

Abstract. Melt electrospinning is a novel technology in the field of 1D micro/nano structure fabrication. Decreasing the diameter and promoting surface morphology of melt fiber are the key for the application of melt electrospinning technology. Heated sheath gas is introduced to build up melt electrospinning direct-write technology, and then orderly micro/nano fibers can be direct-written. The heated sheath gas provided a good way to increase the temperature of melt jet, by which solidification can be slowed. With the help of heated sheath gas, the diameter of melt fiber can be decreased. The affects of process parameters on the diameter of melt electrospinning fiber was investigated, the diameter of melt electrospinning fiber increased with the increasing of temperature of spinneret and feed rate, but decreased with the increasing of voltage and distance between spinneret and collector. Heated sheath gas is an excellent method to promote the application of melt electrospinning.

Introduction

Polymer nanofibers have large surface area to volume ratio and excellent mechanical properties, which have been widely used in various areas such as biomedical, flexible electronic, sensor, reinforcing material, nano channel, and nano optical fiber [1,2]. Electrospinning is a convenient method to fabricate nanofibers [3], which has attracted great attention from all over the word. During the electrospinning process, polymer solution was stretched into the Taylor cone under the electrical field, and then a jet ejected from the tip of Taylor cone. By now, there are more than 100 kinds of polymers have been successfully electrospun into fibers by this technique directly [4].

At present, polymeric micro/nano fibers can be electrospun both from solution and melt [5~7]. Solution electrospinning is the common method used to fabricate nanofiber. However, polymer solution preparation is a great obstacle for the solution electrospinning. The solvent evaporation would introduce hydrodynamic stability into the ejection process of charged jet, which resulted in non-uniform structure and poor surface morphology. On the other hand, the organic solvent may produce environmental pollution and human harm. Melt electrospinning doesn't required solution preparation, uses polymer melt as injection materials. A heating apparatus is introduced into electrospinning system to melt polymer. Without the interferences of solvent evaporation, charged jet in melt electrospinning displayed greater stability than that in solution electrospinning. Uniform polymer micro/nano fiber with smooth surface can be fabricated directly, and has wild application potential in lots of fields [8,9].

In conventional melt electrospinning system, the heating apparatus installed in the electrospinning spinneret. The air temperature decreases quickly under the nozzle, then the melt electrospinning jet would be solidified and can't be stretched into finer one. Decreasing the diameter of jet is a key role for the application of melt electrospinning, which requires to increase the air temperature during the jet ejection and prevent the fast solidification of jet during the ejection process [10]. Increasing the environmental temperature is a good method to prevent the solidification and decrease the diameter of jet. But the environmental temperature controlling is a complex process, which would also enhance the instability of charged jet and decrease the quality of electrospun fiber [11]. At present, heated sheath gas has become a good and simple way to increase the controlling level electrospinning, which also provides an excess stretching and restriction force on the charged jet [12]. The sheath gas would decrease the diameter of liquid jet as well as the voltage required for the jet ejection.

Based on near-field electrospinning theory [13], heated sheath gas is introduced into melt electrospinning to direct-write orderly micro/nano fiber. And then, the affects of process parameters on the jet ejection and melt electrospinning fiber are also investigated.

Experiment

Melt electrospinning direct-write device with heated sheath gas is showed in figure 1 and figure 2 respectively, which including a melt electrospinning spinneret, a thermal spray gun, a DC-voltage power source (Sanchuan high technology development production, Tianjin), a roller collector (collecting rotation speed 0~4500 rpm, diameter of roller is 60mm), a host computer and a temperature controller.

The inner nozzle diameter of spinneret is 400μm. Melt electrospinning spinneret is connected to the ground, and roller collector is connected to the cathode of DC-voltage power source. The distance from spinneret to collector can be adjusted from 0cm to 5cm. Melt electrospinning spinneret is equipped with a heater, the polymer can be heated and melted. The heated gas from thermal spray gun is guided into the spinneret to form sheath gas, which increase the air temperature under the nozzle of spinneret and decrease the diameter of charged jet.

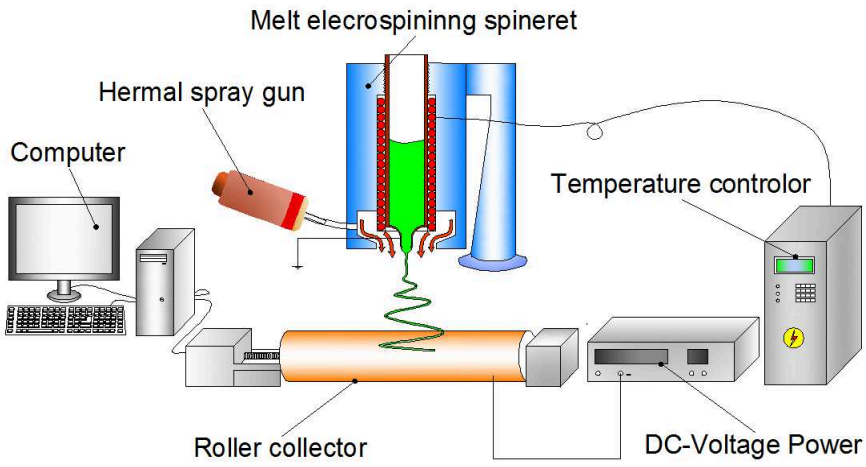


Figure 1. Schematic of melt electrospinning direct-write device with heated sheath gas

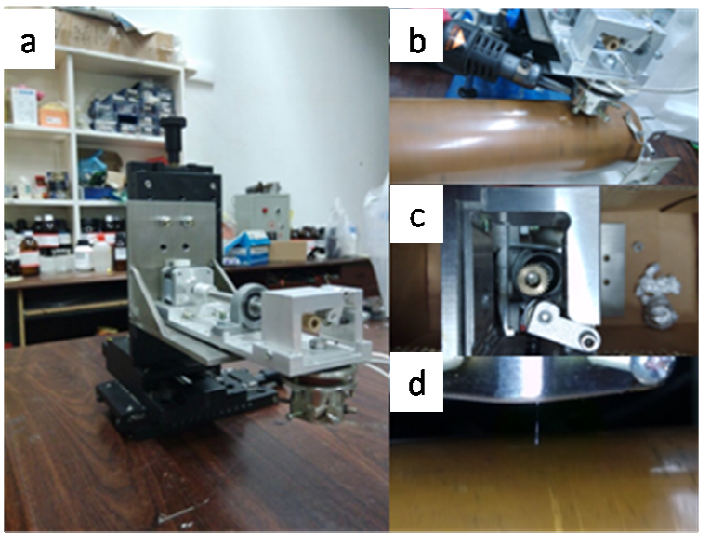


Figure 2. (a) Melt electrospinning direct-write device with heated sheath gas; (b) Roller collector; (c) Material delivery system; (d) Melt charged jet with the restriction of heated sheath gas.

Electrospinning Materials

Polymethylmethacrylate (PMMA, ρ=1.19g/cm, Taiwan Chimei Chemical Products Co., Ltd., China) rod was used as melt electrospinning materials. The melting temperature of PMMA rod is 240℃~270℃, then PMMA rod would be soften when the temperature reached 160℃, and decomposed when temperature higher than 270℃.

The heated gas around the nozzle would provide additional heating function, which can slow the solidification speed of melt jet and promote the jet stretching refinement. With the restriction of heated sheath gas, straight stable melt jet is shown in figure 2 (d). The heated sheath gas provides excess stretching and restriction force on the melt jet, which also provide a good way to restrict the instability behaviors of melt jets. Then, the charged jet can be stretched into uniformity and finer ones. With the help of sheath gas, the stable straight jet can be direct-written on the roller collector as orderly fiber, as shown in figure 3. The direct-written fiber with diameter ranged from 5~50μm under the restriction of heated sheath gas can be gained. However, the diameter of direct-written fiber was 50~250μm without the restriction of heated sheath gas. Then, the affects of process parameters on the diameter of melt electrospinning fiber are investigated further.

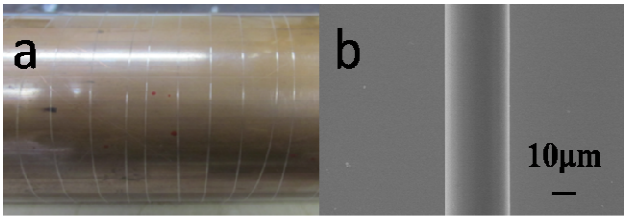


Figure 3. (a) PMMA fiber in the roller collector; (b) SEM image of PMMA fiber.

Results and Discussions

(1) Temperature

Firstly, the melt electrospinning without heated sheath gas was investigated, as shown in figure 4. With the temperature of spinneret increased from 240℃ to 270℃, the average diameter of melt electrospinning fiber increased from 47.81μm to 215.60μm.

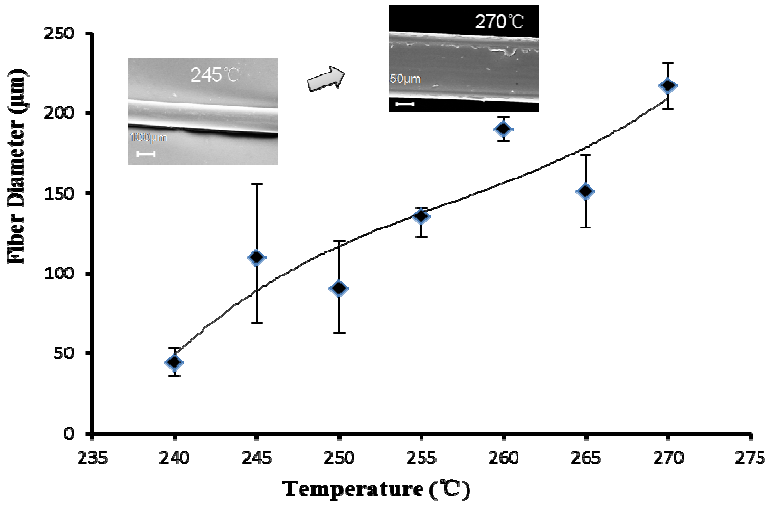


Figure 4. The relationship between average diameter of melt electrospinning fiber and temperature of spinneret (without heated sheath gas). The feed rate, voltage, distance between spinneret and collector was 5.15mm/min, 12kV and 6mm, respectively.

Attribute to the environmental temperature is 25℃, the melt jet would be solidified quickly and can't be stretched fully, the melt electrospinning fiber have larger diameter. With the help of heated sheath gas, the cooling rate and solidification speed was decreased. And then, the melt jet with higher temperature can be stretched fully and decreased the diameter of charged jet.

The relationship between average diameter of melt electrospinning fiber and temperature were shown in figure 5. As the temperature of spinneret increased from 230℃ to 270℃, the average diameter of melt electrospinning fiber increased from 16.90μm to 75.24μm.

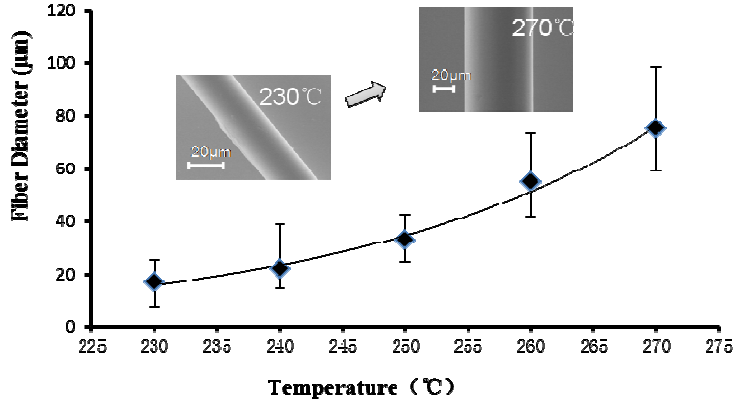


Figure 5. The relationship between average diameter of melt electrospinning fiber and temperature of spinneret (with the restriction of heated sheath gas).The feed rate, voltage, distance between spinneret and collector was 5.15mm/min, 12kV and 6mm, respectively.

(2) Voltage

Electrical field force is the main force for the stretching process of charge jet, larger electrical field force can stretch melt jet into finer ones. The relationship between average diameter of melt electrospinning fiber and voltage was shown in figure 6. As the voltage increased from 10kV to 16kV, the average diameter of melt electrospinning fiber decreased from 112.33μm to 98.51μm.

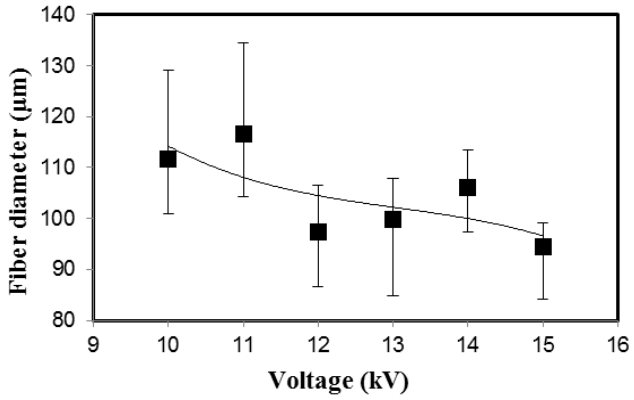


Figure 6. The relationship between average diameter of melt electrospinning fiber and voltage. The feed rate, spinneret temperature, distance between spinneret and collector was 5.15mm/min, 270℃, and 6mm, respectively.

(3) Feed rate

The increasing of feed rate would will increase the internal pressure of melt jet, and increase the diameter of melt electrospinning fiber. The relationship between average diameter of melt electrospinning fiber and feed rate was shown in figure 7.

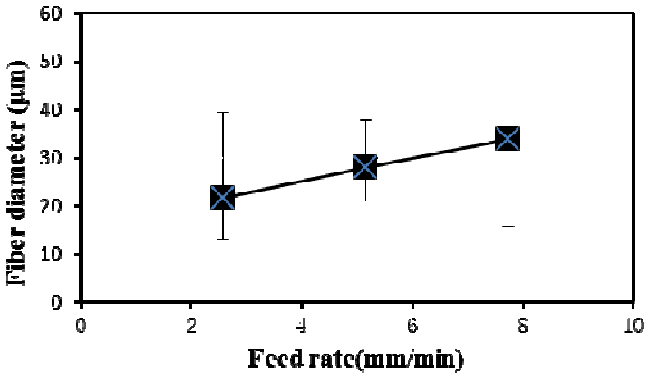


Figure 7. The relationship between average diameter of melt electrospinning fiber and feed rate. The voltage, temperature, distance between spinneret and collector was 12kV, 240℃ and 6mm, respectively.

(4) Distance between spinneret and collector

Smaller distance between spinneret and collector increased the space electric field strength, and enhanced the tensile effect imposed on the jet. Moreover, when the distance between spinneret and collector was decreased, the temperature between spinneret to the collector was increased, which would prevent the rapid solidification of melt jet. Therefore, the diameter of fiber increased from 16.90μm to 24.47μm, when the distance between spinneret and collector increased 6mm to 10mm, as shown in figure 8.

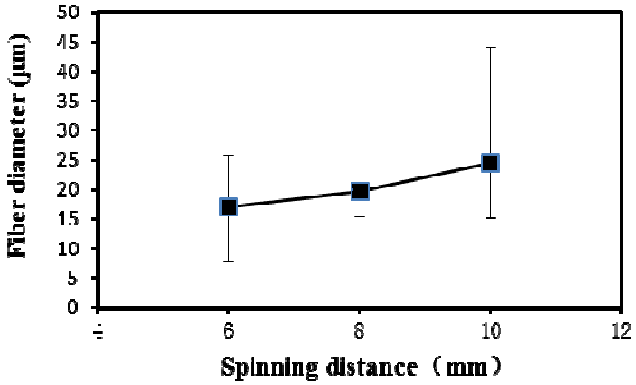


Figure8. The relationship between average diameter of melt electrospinning fiber and spinning distance. The voltage, temperature, feed rate was 12kV, 240℃ and 5.15mm/min, respectively.

Summary

The heated sheath gas was introduced into the melt electrospinning, and increases the temperature of melt jet. And then, the rapidly solidification was prevented and the stretching of melt jet can be promoted, by which the orderly polymer fiber with finer diameter of 5~50μm can be direct-written. Experiment results showed that the heated sheath gas was a valid way to decrease the diameter of melt fiber. The affects of process parameters on the diameter of melt electrospinning fiber was also investigated, the diameter of melt electrospinning fiber increased with the increasing of temperature of spinneret and feed rate, but decreased with the increasing of voltage and distance between spinneret and collector.

Melt electrospinning direct-write with heated sheath gas provides an effective technology to increase the stability and deposition precision of melt charged jet, which would promote the application of electrospinning technology in the fields of micro/nano system integration manufacturing.

Acknowledgement

This work is supported by the National Natural Science Foundation of China (No. 51305373, 51475398), Major Science and Technology Projects of Fujian Province of China (No. 2012H6022), Natural Science Foundation of Fujian Province of China (No. 2013J05083).

References

[1] T. Subbiah, G.S. Bhat, R.W. Tock, S. Parameswaran, S.S. Ramkumar. Electrospinning of nanofibers, J. Appl. Polym. Sci. 2005, 96 (2) 557-569.

[2] D. Li, Y. Xia. Electrospinning of Nanofibers: Reinventing the Wheel, Adv. Mater. 2004, 16 (14) 1151-1170.

[3] D. Li, J.T. McCann, Y. Xia, M. Marquez. Electrospinning: a simple and versatile technique for producing ceramic nanofibers and nanotubes, J. Am. Ceram. Soc. 2006, 89 (6) 1861-1869.

[4] Z.M. Huang, Y. Z. Zhang, M. Kotaki, S. Ramakrishna. A review on polymer nanofibers by electrospinning and their applications in nanocomposites, Compos. Sci. Technol. 2003, 63 (15) 2223-2253.

[5] L.M. Bellan; H.G. Craighead. Nanomanufacturing using electrospinning, J. Manuf. Sci. E-T Aams. 2009, 131 (3) 034001.

[6] L. Persano, A. Camposeo, C. Tekmen, D. Pisignano. Industrial upscaling of electrospinning and applications of polymer nanofibers: a review, Macromol. Mater. Eng. 2013, 298 (5) 504-520.
[7] A. Frenot, I.S. Chronakis. Polymer nanofibers assembled by electrospinning, Curr. Opin. Colloid. In. 2003, 8 (1) 64-75.
[8] N. Bhardwaj, S.C. Kundu. Electrospinning: a fascinating fiber fabrication technique, Biotechnol. adv. 2010, 28 (3) 325-347.
[9] T.D. Brown, P.D. Dalton, D.W. Hutmacher. Direct writing by way of melt electrospinning, Adv. Mater. 2011, 23 (47) 5651-5657.
[10] T.D. Brown, P.D. Dalton, D.W. Hutmacher. Melt electrospinning in a direct writing mode, J. Tissue Eng. Regene. M. 2012, 6 383-384.
[11] S. De Vrieze, T. Van Camp, A. Nelvig, B. Hagstrom, P. Westbroek, De Clerck K. The effect of temperature and humidity on electrospinning, J. Mater. Sci. 2009, 44 (5) 1357-1362.
[12] Y. Srivastava, I. Loscertales, M. Marquez, T. Thorsen. Electrospinning of hollow and core/sheath nanofibers using a microfluidic manifold, Microfluid. Nanofluid. 2008, 4 (3) 245-250.
[13] D.H. Sun, C. Chang, S. Li, L.W. Lin. Near-field electrospinning, Nano Lett. 2006, 6 (4) 839-842.

Key Engineering Materials Vols 645-646 (2015) pp 52-57
© (2015) Trans Tech Publications, Switzerland
doi:10.4028/www.scientific.net/KEM.645-646.52

Submitted: 2014-11-01
Accepted: 2014-12-23

Experimental Study on WEDM Machining of PCD and PCBN compacts

SONG Mancang[a], ZHANG Jianlei[b] , YU Chao[c] , WANG Minjie[d] , LIU Chong[e] , Liu Ying[f]

Key Laboratory for Precision and Non-traditional Machining Technology of Ministry of Education,

Dalian University of Technology, Dalian 116023，China

[a]mcsong@dlut.edu.cn, [b]skdzjl_001@126.com, [c]smiletofacelife@163.com,[d]mjwang@dlut.edu.cn, [e]chongl@dlut.edu.cn, [f]liuying@dlut.edu.cn

Keywords: polycrystalline diamond(PCD); polycrystalline cubic boron nitride(PCBN); processing quality; wire electric discharge machining(WEDM)

Abstract. Some typical kinds of PCD and PCBN compacts are selected to be machined by WEDM, and a series of processing tests are taken. After machining, the surface roughness of cutting section, the processing quality of cobalt-rich interface layer and the edge of superhard material layer are measured by surface profiler and 3D microscope. The results show that processing quality is affected by superhard particle size and concentration greatly, and better processing quality can be obtained after several cutting of WEDM. The minimum sharpening allowance of PCD cutting tools can be controlled within 4~15μm after WEDM, and within 10μm for PCBN BNX20, while BZN6000 needs larger follow-up workload of sharpening.

Intorduction

The conventional manufacturing method of PCD and PCBN cutting tools can be divided into three steps roughly: (1) cutting PCD and PCBN compacts; (2) welding compacts with cutter bodies; (3) sharpening tools. Laser is used to cut compacts usually. Though laser has good ability to cut compacts, considering its high cost and unsatisfactory processing quality, many manufacturing enterprises use WEDM to cut compacts. Because the superhard particles in the compacts don't conduct electricity, the difficulty of discharge machining is increased, and the wire is easily broken in WEDM. Domestic and foreign scholars have made much research on the WEDM for compacts. Zhang[1] et al. studied the processing mechanism for PCD. Wang[2] indicated that when the wire electrode can work under the premise of maximum current, the best combination of process parameters can be found out after a series of experiments, which is an effective method to improve the cutting efficiency in the WEDM for superhard cutting tool material. Suzuki[3] and Olsen[4] added boron into PCD to improve its electrical conductivity, and got good WEDM processing quality. In addition, Tso[5] and Jia[6] were also engaged in the research of this field.

As for superhard cutting tool materials machining, the QWD series of products is one of representatives abroad, made by Vollmer Ltd., German. PCD and PCBN compacts are cut by WEDM in the machine, which has the advantage of high automatic processes and precision, but the machining surface roughness is worse than the one of grinding, in addition, the machine is very expensive. In China, NHT series of products of NINGHUA Ltd., BEIJING is one of representatives. After a lot of processing contrast tests, it's proved the NHT has advantages of high efficiency, small consumption, processing stability in machining of PCD and PCBN compacts.

In conclusion, the WEDM plays a very important role in machining of PCD and PCBN cutting tools, and its processing quality directly affects the production efficiency and quality of the tools. With the development of the WEDM technology, the improvement of the WEDM technology, it's expected that the ordinary commercial WEDM can be used to finish the most of manufacturing work for the cutting tools, and even replace the final grinding process, in order to reduce the manufacturing cost of the cutting tools. In this paper, a series of WEDM tests on two kinds of superhard cutting tools of PCD and PCBN compacts are made, and the roughness of the cutting surface, the cobalt-rich interface layer and the cutter edge are observed and measured. From the test results and theoretical

analysis, a kind of method to increase cutting efficiency, reform machining surface quality and reduce the grinding allowance is summarized, also provides supports and references for tools manufacturing.

Equipments, materials and methods of experiments

The machine for the tests is NA2400 WEDM with a 0.2mm brass wire electrode, and the measure equipments include NewView5200 surface profiler, VHX-600E three-dimensional microscope and digital image tool microscope. NA2400 is the latest WEDM machine for Chinese market by the Mitsubishi Electric Ltd., which can guarantee the ±2μm dimensional accuracy, and the optimal surface roughness is claimed up to *R*a0.03μm and corner shape accuracy can be controlled within 1μm.

The cutting tool materials in the experiments are listed in Table 1.CTB010 and CTH 025 are PCD compacts. BNX20 and BZN6000 belong to PCBN compacts.

Table 1 Materials of experiments

Model	Company	Material description	Thickness
CTB010	Element Six	Mass fraction: Diamond 80% , Cobalt 20% The average size of diamond particle: 10μm	Total thickness: 2.0mm PCD layer: 0.5mm
CTH025	Element Six	Mass fraction: Diamond 80%, Cobalt 20% The average size of diamond particle: 25μm	Total thickness: 2.0mm PCD layer: 0.5mm
BNX20	Sumitomo	Mass fraction: CBN 60% The average size of particle: 3μm. Binder: TiN	Total thickness: 2.0mm PCBN layer: 0.8mm
BZN6000	GE	Mass fraction: CBN 90% The average size of particle: 2μm. Binder: Metal	Total thickness: 1.6mm PCBN layer: 0.8mm

The most effective method of improving the processing precision and the surface quality is cut by several times, which can do finish machining on the cutting surface while the discharge energy is lowered each time. In this experiment, as shown in Fig.1[3], the material is cut five times with one time clamping. The results of wire cutting experiments are reserved and analyzed after the first cutting, the second cutting and the Nth cutting. From the second cutting to the fifth cutting, the offsets of wire electrode are 30μm, 15μm, 8μm, 8μm, respectively.

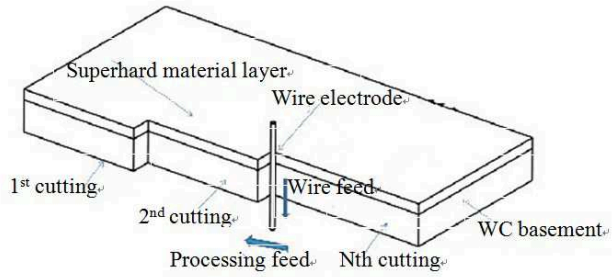


Fig.1 The machining model for compacts

Experimental results and analysis

Surface roughness of superhard material layer. Roughness of the cutting surface is measured by surface profiler, and the results are shown in Fig.2. From the test results, it's found that with the processing times increasing, better surface roughness can be obtained. In a word, ideal surface roughness can be obtained after several cutting by WEDM. After the first cutting the surface roughness of CTH025 is equal to *R*a1.96μm, and after the fifth cutting which is dropped to *R*a0.85μm, while the values of CTB010 are *R*a1.29μm and *R*a0.57μm respectively. So after cutting, the surface

roughness of CTB010 is better than CTH025, and the process stability of CTB010 is better than CTH025 during the machining. Meanwhile, after the first cutting the surface roughness of BNX20 is equal to *R*a1.35μm, and after the fifth cutting which is dropped to *R*a3.51μm, while the values of BZN6000 are *R*a3.91μm and *R*a3.51μm respectively. So after cutting, the surface roughness of BNX20 is better than the one of BZN6000, and the process stability of BNZ20 is better than the one of BZN6000 during the machining.

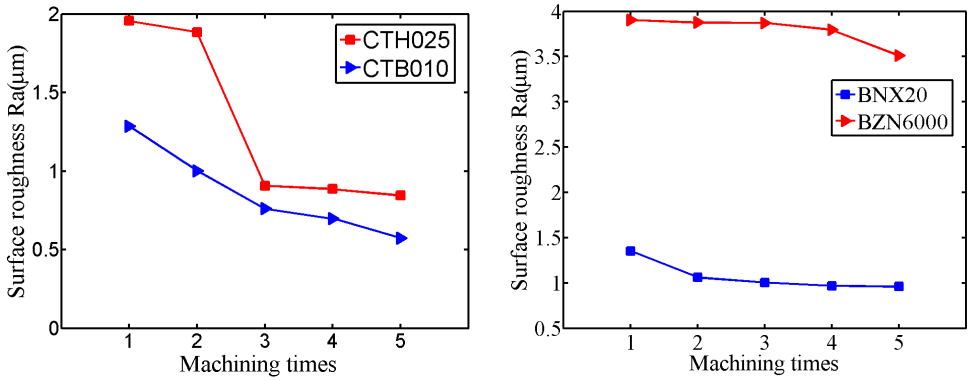


Fig.2 The relationship between surface roughness and machining times

The EDM removal mechanism of the PCD layer includes two aspects. One is that the high temperature of the discharge gap can make the local diamond particle graphitization, melting and vaporization, and the melt is thrown from the weld pool by the discharge explosion on the condition of small pulse energy. The other is that the conductive binder is melted and boiled away by the high discharge temperature, and the diamond particles are dropped off on the condition of high pulse energy. Owing to the higher energy of the first cutting, the diamond particles are struck, broken and dropped off, leaving a larger depression on the machining surface. With the decrease of the machining energy, the removal model of the diamond particles has been changed and the surface roughness becoming better. Considered the diamond particles are larger, its removal pattern could directly influence the machining surface quality. However, several cutting is helpful to improve the machining surface quality. The depression left by the first cutting has a great effect on finishing surface, which is the reason why the surface roughness of CTB010 is better than the one of CTH025. The removal mechanism of PCBN layer is similar to the one of PCD layer, while the CBN particles are smaller, it is easy to drop off relatively and its removal pattern has a little influence on surface roughness. Therefore, there is less improvement on the surface roughness with the increase of the cutting times. When the mass fraction of CBN for PCBN compacts is smaller, its cutting performance is better. So BNX20 compact has the most stable condition in cutting of the four kinds of compacts. However, with the increase of the mass fraction of CBN, the cutting difficulty is increased and its cutting state is not stable. So the processing quality of the BZN6000 compacts is very poor.

Processing quality of cobalt-rich interface layer. In the sintering process of the PCD and PCBN compacts, cobalt in the substrate of cemented carbide has tendency to infiltrate into the PCD and PCBN layers, and there is a cobalt-rich interface layer between the PCD and PCBN layers. According to the difference of the material composition, the compacts can be divided into three layers in terms of the WEDM research, namely superhard material layer, cemented carbide substrate layer and cobalt-rich interface layer. Because material composition, melting point, evaporating point and electrical conductivity for each layer are different, the needed processing parameters for WEDM are different too. Under same processing parameters, material removal rate of each layer should be different, so the surface will have height difference after cutting. Some scholars find that there is a groove in the cobalt-rich interface layer of PCD compacts and a significant step between PCBN layer and cemented carbide substrate layer of PCBN compacts after cutting. The depth of the grooves directly determines the workload of the follow-up sharpening and polishing. Thus efforts should be made to reduce the groove depth in the processing.

After cutting the cobalt-rich interface layer are observed by three-dimensional microscope (Magnification of 500 times). Fig.3 and Fig.4 are the grooves generated after cutting for CTB010 and

CTH025 respectively. The depth of the groove is 16.3μm and the width is 99.4μm for CTH025 after fifth cutting. The depth of the groove is 5.7μm and the width is 72.6μm for CTB010 after fifth cutting. The cutting surface of BNX20 is shown in Fig.5, and there is a significant step between PCBN layer and cemented carbide substrate layer. And after first cutting, the step height is 31.9μm, after fifth cutting, the step height is dropped to 7.4μm. Compared with BNX20, there would generate a groove in the cobalt-rich interface layer of BZN6000 after cutting, shown in Fig.6. And the groove depth by first cutting is 27.6μm, while the groove depth is dropped to 11μm after fifth cutting.

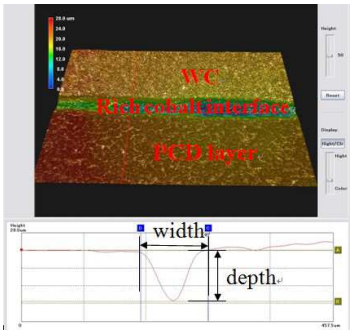


Fig.3 Cobalt-rich interface for CTH025

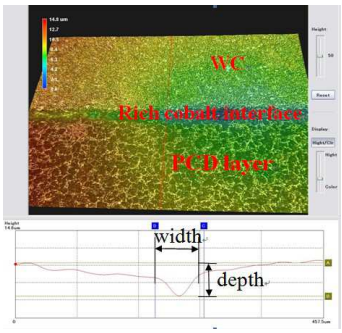


Fig.4 Cobalt-rich interface for CTB010

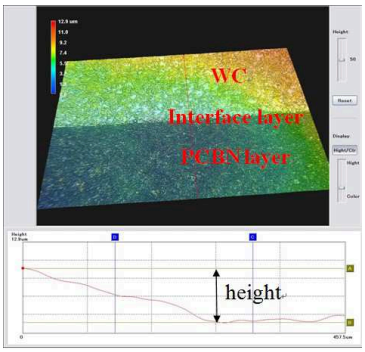


Fig.5 Cobalt-rich interface for BNX20

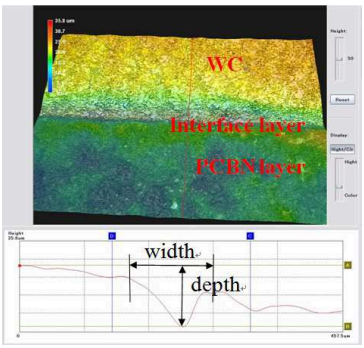


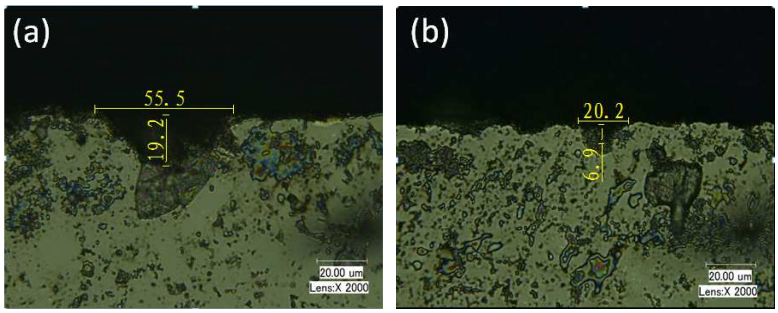
Fig.6 Cobalt-rich interface for BZN6000

As the melting point and evaporating point of the material are relatively lower, meanwhile their electroconductibility is better, the material can be removed largely by single pulse discharge, even in the relatively bigger discharge gap. As a result, there will be excessive removal phenomenon. Conversely, the less material is removed. Shown in Table1, the diameter of CTH025 diamond particles is larger than the one of CTB010. The remove for larger diamond particles requires higher energy, using the same process parameters, the cutting speed has to be reduced, but the slower cutting speed increases the excess removal phenomenon, a deeper groove is formed. The mass fraction of CBN for BNX20 is lower, and the binder is TiN, PCBN layer shows better processing ability than the substrate layer in WEDM. So PCBN layer easily appears to excess removal phenomenon. The mass fraction of CBN for BZN6000 is 90%, and the binder is metal. Although its processing ability is better than the substrate layer, but not as cobalt-rich layer, so there appeared a step on the cutting surface, and a groove on the cobalt- rich interface layer.

Quality of PCD cutting tool edge. The quality of cutting tool edge is one of major factors that influence cutting tool life[4]. In the process of the producing of cutting tools, it is very important to ensure the quality and efficiency of cutting tool edge. In the WEDM of PCD and PCBN compacts, because of their special position at the cutting tool edge, diamond particles being located on the surface of PCD compacts are not firmly fixed, they are easy to drop off wholly and then incision defects are formed during the WEDM cutting.

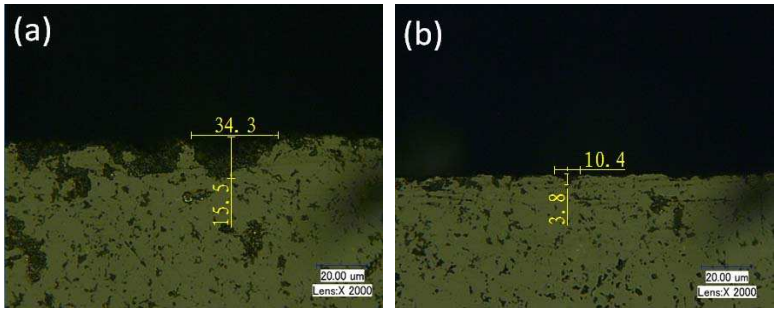
The cutting tool edge of PCD compacts after machining is shown in Fig.7 and Fig.8. For CTH025, after first cutting, its maximum incision defect is 55.5μm wide and 19.2μm deep. After fifth cutting, the width is reduced to 20.2μm, the depth is 6.9μm. For CTB010, after fifth cutting, its maximum incision defect is 34.3μm wide and 15.5μm deep. After fifth cutting, the width is reduced to 10.4μm, and the depth is 3.8μm.

In first cutting, the pulse discharge energy is higher, resulting in the excessive removal of the binder and the probability of falling off for the diamond particles is increased, so larger incision defect is formed. With continuous cutting, pulse energy is dropped smaller and the incision defect gets corrected. After finish cutting the size of defects is the same as the one of diamond particles, so the size of incision defect got from CTB010 is less than the one got from CTH025. But to eliminate the cutting edge defect, the next working procedure of sharpening is needed. Considering the various measurement results and the thickness of metamorphic layer formed in WEDM, the groove depth of cobalt-rich interface layer has a bigger influence on grinding allowance. It's found that the grinding workload of PCD compacts may be controlled within the range of 4~15μm after WEDM and the processing efficiency is raised greatly.



（a）First cutting　　b）Fifth cutting

Fig.7 The processing quality of CTH025 edge



（a）First cutting　　（b）Fifth cutting

Fig.8 The machining defects of CTH010 edge

The processing situation of BNX20 edge is depicted in Fig.9, and its surface quality is better after fifth cutting. While the processing situation of BZN6000 edge is shown in Fig.10, and its surface quality is poorer. Due to higher mass fraction of CBN, the machining process is not stable, so the quality of the cutting tool edge can't be guaranteed well. In Fig.10, there is a width of 34.4μm and depth of 66.8μm incision defect, meanwhile, a larger range of impact area will be left because of unstable cutting.

Generally, CBN particles of the PCBN layer are smaller, regardless of being overall dropped off or partial broken in WEDM, which have a little influence on processing quality. Therefore BNX20 can get a better processing quality. With the increase of the mass fraction of CBN, the cutting difficulty will increase and the cutting will become unstable, there are large incision and impact area left in the cutting tool edge. The incision defect is mainly caused by a large number of CBN particles falling off, and the cutting impact area is caused by the instability of discharge. A greater depth of the heat affected layer will be formed if the discharge energy is too large. Considering the various measurement results, the metamorphic layer of BNX20 compacts can be controlled below 10μm after finish cutting. Therefore its follow-up grinding workload is decided by the step height and can be controlled below 10μm. However, the grinding quantity of BZN6000 compacts largely depends on the incision defects, large grinding workload is required.

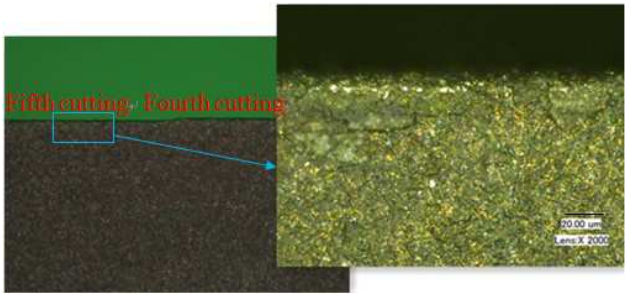


Fig.9 The edge quality of BNX20

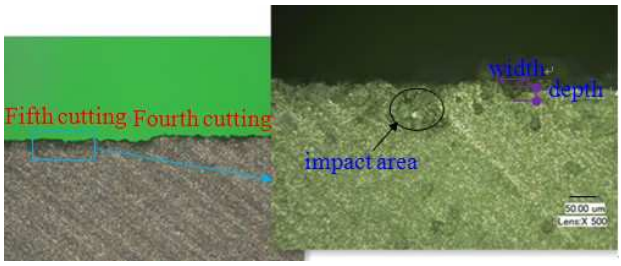


Fig.10 The edge quality of BZN6000

Summary

(1) PCD and PCBN compacts can get better surface quality by WEDM. But with the increase of diamond particles diameter, it is more difficult to machine PCD compacts and the processing quality is decreased. Meanwhile, with the increase of CBN concentration, the difficulty of machining PCBN compacts is increased and the processing quality is also decreased.

(2) The groove on the cobalt-rich interface layer in PCD compacts is inevitable, but it can be reduced by several processing by WEDM.

(3) There will be incision defects in PCD compacts edge after WEDM. After several cutting, the size of the defects in the edge of PCD compacts is matched with the size of diamond particles. Because CBN particles are smaller, to PCBN compacts, BNX20 can get good edge quality after several cutting, while BZN6000 edge quality is poorer. But for the elimination of edge defects, next grinding process is still needed.

Acknowledgement

The authors gratefully acknowledge the support given by the National High Technology Research and Development Program of China (No: 2012AA040406), the Fundamental Research Funds for the Central Universities of China (No: DUT13JB05) and Natural Science Foundation of Liaoning Province of China (No: 201202036).

References

[1] G. F. Zhang, Z. H. Deng. Cutting mechanism and surface appearance of PDC with WEDM. China Mech. Eng.， 18(6)(2007) 671-675(in Chinese).

[2] J. Wang. The way to improve super-hard cutting tool material wire-cutting processing efficiency. Electromach. Mould，(4)(2004) 59-60(in Chinese).

[3] K. Suzuki, Y. Shiraishi, N. Nakajima, et al. Development of new PCD made up of boron doped diamond particles and its machinability by EDM. Adv. Mater. Res.， (76-78) (2009) 684-689.

[4] R. H. Olsen, R. C. Dewes, D. K. Aspinwall. Machining of electrically conductive CVD diamond tool blanks using EDM. J. Mater. Process. Technol.， (149)(2004) 627-632.

[5] P. Tso, Y. Liu. Study on PCD machining. Int. J. Mach. Tools Manuf., (42)(2002) 331-334.

[6] Y. Jia, B. S. Kim, D. J. Hu, J. Ni. Parametric study on near-dry wire electrodischarge machining of polycrystalline diamond-coated tungsten carbide material. J. Eng. Manuf.， 224(2009) 185-194.

Key Engineering Materials Vols 645-646 (2015) pp 58-63
© (2015) Trans Tech Publications, Switzerland
doi:10.4028/www.scientific.net/KEM.645-646.58

Submitted: 2014-11-02
Accepted: 2014-12-23

Wet anisotropic etching characteristics of Si{100} in TMAH+Triton at near the boiling point

Mingqiu Yao [1,2,a]*, Bin Tang [1,b] , Wei Su [1] and Gang Tan[1]

[1] China Academy of Engineering Physics, Mianyang, Sichuan Province, China

[2] Nanjing University of Science and Technology, Nanjing, Jiangsu Province, China

[a]email : ivykaiser@163.com

[b]email : john46311@hotmail.com

* Mingqiu Yao as the corresponding author

Keywords: Silicon; near boiling point; TMAH; Triton X-100; etching rate; surface morphology; convex corner

Abstract. The anisotropic silicon etching characteristics of TMAH(tetramethyl ammonium hydroxide)+Triton at near the boiling point were investigated. The etch rate of Si{100}, the convex corners, and the roughness of the etched surface contact with the fabrication of bulk microstructures and thus micromechanical devices in silicon. This study presents that the etch rate of Si{100} in 25 wt.% TMAH with 0.1% Triton at near boiling point(112°C) is 1.37μm/min, it is three times higher than it at 80°C. The surface roughness and convex corners of Si{100} after etching at different temperature were investigated by optical microscope, scanning electron microscope (SEM) and atomic force microscope (AFM). The etching rate and smoothness of an etched surface can be improved simultaneously at near boiling point, meanwhile, the undercutting on convex corner should be accepted.

Introduction

The wet anisotropic etching of silicon is a wide technology for manufacturing microstructures. This method can do to form membranes, to make cantilever for sensors, or to make holes, grooves on one side of a wafer. The anisotropic etchants that we most commonly used are TMAH and KOH(Potassium hydroxide). Depending on the requirement of technics and microstructures, we select one etchant from these two etchants which have different etching characteristics to fit. KOH provides a higher value of the etch rate for the (100) crystal plane than TMAH. But the silicon oxide is always used the photomask in bulk silicon micromachining, TMAH is the best choice for anisotropic etching[1]. TMAH solution is very good selectivity because of the compatibility when manufacture COMS (complementary metal oxide semiconductor). In order to optimize the etched surface morphology, the additives like NC-200，Triton X-100，PEG（non-ionic poly(ethylene glycol)），ASPEG(cationic ammonium salt of poly(ethylene glycol)), IPA(isopropyl alcohol) have been used. For example, IPA-mixed TMAH solution is used to improve the etch rates and the undercutting convex corners[2,3,4], but the change of morphology was unconspicuous. Triton X-100 initially used to control the surface roughness, it can reduce the undercutting at convex corner. Triton X-100 is the best choice recently as an additive to TMAH solution in order to obtain minimum undercutting[5]. These changes are very useful for fabricating 3D silicon microstructures.

In the previous study, the etch rate, roungnees and convex corners of Si{100} wafers in pure TMAH solution and surfactant-added TMAH solution at the range of 60-80°C were reported, but the characteristic of anisotropic etching in TMAH or in TMAH+Triton at near boiling temperature has not been performed. In this paper, we describe the character of anisotropic etching of single crystal silicon using 25wt.% TMAH solution including different concentrations of the surfactant Triton X-100 at different temperature. the ranges of temperature are at near the boiling point of TMAH solution.

Experimental method

The common silicon wafer with 1-10Ω·cm resistivity, 4-inch diameter and p-type (100) were used in this study. The 1μm silicon oxide was grown in the silicon wafers for thermal oxidation as masking layer. Etching process is performed in a cylindrical polytetrafluoroethylene barrel. A reflux condenser is used to avoid changing the concentration of the etchant because of any factor like water evaporates during etching. We used 25wt.% TMAH solution, the Triton X-100 concentration for TMAH is 0.1%v/v. In order to obtain the etching result, the wafers are immersed completely in TMAH+Triton and keeping them in the solution bath for 120min. Before immersion in the solution, the wafers are dipped in 5% HF acid solution for 1 min at room temperature to remove the native oxide, and then rinse them with DI water for a few minutes.

During etching, the temperature of solution is at 90-120°C to study the etching micromorphology and etching rates. We tested the boiling point of 0.1%v/v Triton added TMAH by making the solution seething. The boiling point in our experimental condition is 116°C.

The etching at concave corners stops at the intersections about (111) and (100) orientation on (100) silicon, but convex corners are undercut. In the beginning, the surfactant as a additive is used to improve the roughness of the etched surfaces. But they could reduce undercut of convex corner.

The etching rate, roughness and convex corners are investigated in the following section.

Results and Discussion

Etching rate. The etching was performed in the Triton-mixed TMAH solution bath at 90°C, 100°C, 106°C, 112°C and 116°C respectively, and the result is shown in figure 1.

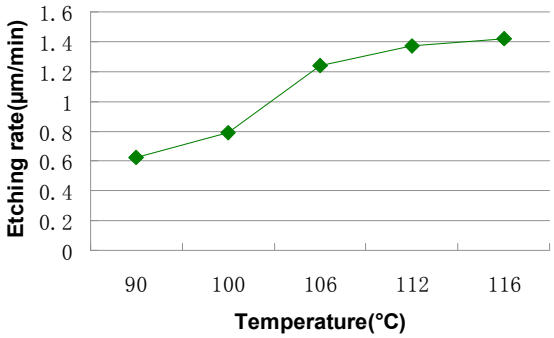


Figure 1. Effect of temperature on etching rate of (100) in TMAH(25 wt.%) with Triton(0.1% v/v)

The etching temperature affects the etching rate of silicon {100} wafers, it keeps a order that a 10 degrees increase in temperature is associated with 0.15 increase in etching rate at 60-80°C [6]. As can be seen in Fig. 1, the etching rate for Si{100} provides the same order at 90°C and 100°C respectively, but it changes remarkably at 106°C. The growth extent of etching rate becomes 0.45μm instead of 0.15μm. The etch rate of Si{100} at near boiling point(112°C) is 1.37μm/min, it is three times higher than it at 80°C. The etching rate is always affected by temperature. As well known for Arrhenius behavior, The chemical reaction rate is proportional to the activation energy. With the temperature increased, the number of molecules raised and the actual number of reactants increased. So we can obtain a high etching rate at high temperature.

Roughness. The surface roughness of Si{100} after etching in 25 wt.% TMAH with 0.1% Triton added at different temperature were investigated by optical microscope, scanning electron microscope (SEM) and atomic force microscope (AFM). Fig. 2 shows the result of optical microscope measurements, the smoothness of specimens etched at different temperature are compared. The etch surface roughness was clearly affected by the temperature, the increase in temperature can reduce the number and dimension of hillocks in a certain range. A very smooth etched surface for Si{100} was been obtained at near boiling point(see figure 2(d)). At boiling point, the hillocks on facet were disappeared, but many little pits form the surface morphology(see figure 2(f)).

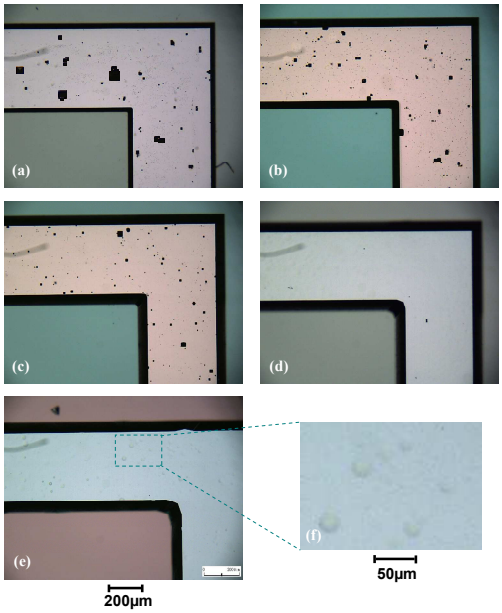


Figure 2. Optical micrographs of effect of temperature on surface roughness of (100) in TMAH(25 wt.%) with Triton(0.1% v/v). (a) at 90°C (b) at 100°C (c) at 106°C (d) at 112°C (e) at 116°C

SEM measurements are presented in figure 3, the hillocks are clearly square-based pyramids. At near the boiling point(see figure3(d)), no pyramids were formed. The pyramids disappeared at near boiling point due to the growth values are likely to differences for different crystal orientations by the increase of temperature and the disparity in etching rates of three principal crystal surfaces lessens markedly. The very smooth etched surfaces with an average roughness 3-6 nm was shown in figure 4, the result was measured by AFM.

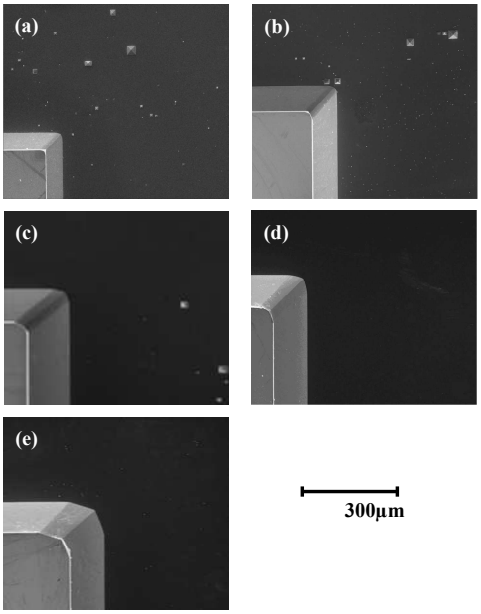


Figure 3. SEM results of effect of temperature on surface roughness of (100) in TMAH(25 wt.%) with Triton(0.1% v/v). (a) at 90°C (b) at 100°C (c) at 106°C (d) at 112°C (e) at 116°C

The etching of silicon process in high TMAH concentration(25 wt.%) with 0.1% v/v Triton X-100.

At high TMAH concentration, Si{110} orientation has the fastest etching rates, followed by Si{100} and Si{111}. As a result, the micro-pyramids were formed. With the temperature raise, the etching rate ratio of three orientations strongly reduce.

the surfactant added can adsorb on silicon surface and improve the roughness. Triton as an non-ionic surfactant, is not electrostatically or chemically adsorbed, but physically. Different surface orientations have different surfactant adsorption, Si{100} surface has an inherently low surfactant adsorption density, and Si{111} is the most surfactant concentration of the three main surfaces. Triton can strongly reduce etch rate of Si{110}[7], but Si{100} and Si{111} have weak effect. In addition,

The adsorption of surfactants general involves single ions rather than micelles, and the adsorption is relative to many factors such as concentration, temperature, or molecular structure of the surfactant. A change in temperature can lead to a very different result on the adsorption. The number of surfactant ions on the silicon surface increase with increasing temperature[8]. The adsorption density increased dramatically on {110}surface, moderately on {100} and {111} surfaces. It presumes that chemisorption as a function may effect mostly the adsorption mechanism, because of the apparent activation energies for {100}, {110} and {111} are 0.01eV, 0.16eV and 0.05eV, respectively[7]. Si{110} is most reactive at high TMAH, with the temperature raise, etch rate reduce very rapidly. Because of three reasons above mentioned, the hillocks size and amount decrease.

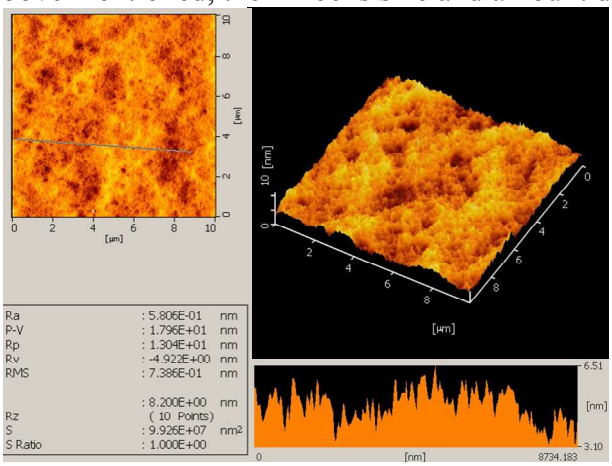


Figure 4. AFM result of the very soomth surface for Si{100} at near boiling point

Convex corner. A very regular mesa structure is necessary for some devices, such as accelerometer and esthesiometer. Because of the structure of silicon, the etching surface shape is generally not quadrangle, it is generally eight-square or dodecagon. the effective area decrease by the undercutting of convex corner and severe convex corner undercutting can not obtain designed structure. Corner compensation is a common method to realize desired shape of convex corner. It must distinguish the orientation of oblique surface with convex corner and calculate corner compensating structures. In addition, extra mask and processing steps are used. But the methods mentioned are complex or expensive.

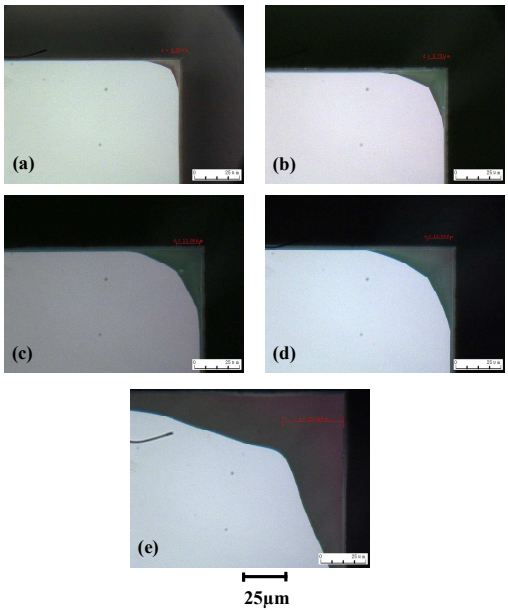


Figure 5. optical microscope results of effect of temperature on convex corners of (100) in TMAH(25 wt.%) with Triton(0.1% v/v). (a) at 90°C (b) at 100°C (c) at 106°C (d) at 112°C (e) at 116°C

The effect of temperature on the undercutting at the convex corners of (100) were been studied, the temperature of etchant is at 90-120°C. It is not increased significantly at near boiling point, as shown in Fig.4(d). But a big change of the shape of convex corner appeared at boiling point(116°C), as

shown in Fig.4(e). This is explained by a reduction in the number of surfactant ions on the exposed silicon surfaces. The adsorption mechanism of surfactant is physical process, the forces between the ions of surfactant and the surface silicon surface are van der waals(VDW), it is very weak. A lot of bubbles were produced in solution at the boiling point, making the molecules keep stirring. The physical motion can breaks a number of VDW contacts and influences the adsorption density bring the undercutting increasing significantly.

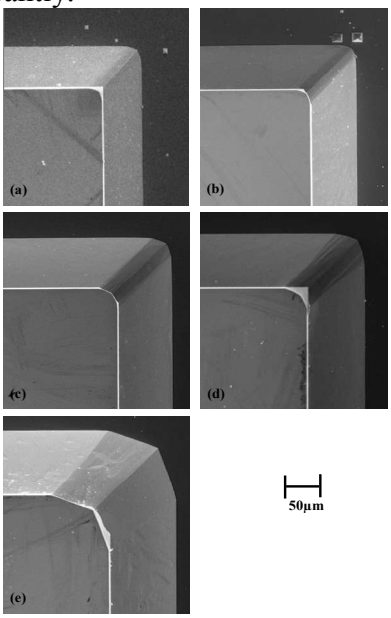


Figure 6. SEM results of effect of temperature on surface roughness of (100) in TMAH(25 wt.%) with Triton(0.1% v/v). (a) at 90°C (b) at 100°C (c) at 106°C (d) at 112°C (e) at 116°C

Summary

The values of etch rate, roungness and convex corners are extremely dependent on the chemical composition, concentration, and temperature of the etchant solutions used.

In this paper, the etching characteristic of Si{100} at near the boiling point was been investigated. We can get the conclusion that the etching rate is connect to the heating temperature. A very smooth surface and little undercutting of convex corner were obtained at near boiling point, the etching rate improve very obviously either. Si{110} is most reactive at high TMAH, followed by Si{100} and Si{111}. The different etching rates make a roughened surface in the process of wet etching. Increasing with the temperature, the difference of etch rate among three primary surfaces is reduced. Otherwise, the etching rate was affected by surfactant on silicon surface. And with the increase of temperature the surfactant adsorption density increase, but the growth values are differences for different crystal orientations. The adsorption density of Si{110} is strongly enhanced, meanwhile, leading to etch rate of Si{110} declines significantely, Si{100} and Si{111} are weakly increased by temperature. Thus, the temperature paly an important role to close the gap of etch rate. At near the boiling point, etching rate of three principal silicon facets are weakly different, then no hillocks modify the surface morphology. The wet anisotropic etching of silicon is commonly used to fabricate mechanical microstructures. The study is very useful for engineering application.

Acknowledgement

This work is supported by the Natural Science Foundation of China (NSFC) project (51305412) and the Funding Support by Laboratory of Ultra Precision Manufacturing Technology (CAEP) project (2012CJMZZ00003).

References

[1] P. Pal, M. A. Gosálvez, K. Sato, Etched profile control in anisotropic etching of silicon by TMAH+Triton, Journal of micromechanics and microengineering. 22 (2012) 065013.

[2] I. Zubel, M. Kramkowska, The effect of alcohol additives on etching characteristics in KOH solutions, Sens. Actuators A. 101 (2002) 255-261.

[3] M. Sekimura, Anisotropic etching of surfactant-added TMAH solution, IEEE Int. Conf. Micro Electro Mech. Syst., Tech. Dig.. Institute of Electrical and Electronics Engineers, New York, N. Y. 12 (1999) 650-655.

[4] A. Merlos, M. Acero, M. H Bao, J. Bausells, J. Esteve, TMAH/IPA Anisotropic Etching Characteristics, Sensors and Actuators A. 37-38 (1993) 737-743.

[5] P. Pal, K. Sato, Various shapes of silicon freestanding microfluidic channels and microstructures in one step lithography, J. Micromech. Microeng. 19 (2009) 055003.

[6] B. Tang, M. Shikida, K. Sato, P. Pal, H. Amakawa, H. Hida, K. Fukuzawa, Study of surfactant-added TMAH for applications in DRIE and wet etching-based micromachining, J. Micromech. Microeng. 20 (2010) 065008.

[7] M. A. Gosálvez, B. Tang, P. Pal,K. Sato,Y. Kimura, K. Ishibashi, Orientation- and concentration-dependent surfactant adsorption on silicon in aqueous alkaline solutions: explaining the changes in the etch rate, roughness and undercutting for MEMS applications, J. Micromech. Microeng. 19 (2009) 125011.

[8] B. Tang, P. Pal, M. A. Gosalvez, M. Shikida, K. Sato, H. Amakawa, S. Itoh, Ellipsometry study of the adsorbed surfactant thickness on Si{110} and Si{100} and the effect of pre-adsorbed surfactant layer on etching characteristics in TMAH, Sensors and Actuators A. 156 (2009) 334-341.

Key Engineering Materials Vols 645-646 (2015) pp 64-69
© (2015) Trans Tech Publications, Switzerland
doi:10.4028/www.scientific.net/KEM.645-646.64

Submitted: 2014-11-02
Accepted: 2014-12-23

Hierarchically Ordered Porous Carbon as A Host Material for Energetic Composites

Jin Chen[1 2, a], Simin He[2, b], Huaqiang Cai[1, c], Qingli Hao[1, d*] and Hui Huang[1 2*, e]

[1] School of Chemical Engineering, Nanjing University of Science and Technology, Nanjing 210094, China

[2] Institute of Chemical Materials, China Academy of Engineering Physics, Mianyang 621900, China

[a]cjyeying@sina.cn, [b]ljshan245@163.com, [c]caihuaqiang@caep.cn, [d]qlhao_nust@163.com, [e]hhuang_icm@sina.com (corresponding author)

Keywords: Hierarchically ordered porous carbon; Impregnation; Host-guest chemistry; Energetic composites; CL-20.

Abstract. Hierarchically ordered macro-/mesoporous carbon (HOPC) was synthesized via a dual-template approach and used as the host matrixes to design the host-guest energetic composites. Monodisperse silica colloidal crystals were used as a hard template, amphiphilic triblock copolymer Pluronic F127 as a soft template, and soluble resols as a carbon source. The obtained HOPC is composed of highly ordered fcc macropores (225 nm), interconnected macropore windows (40 nm), and large mesopores (11.6 nm), resulting in high surface area (503.6 m^2/g) and large pore volume (0.833 cm^3/g). A high energy material (CL-20) had been encapsulated in HOPC by impregnation process, and the maximum loading amount was around 63 wt.%. The synthesized CL-20/HOPC host-guest energetic composites exhibit much lower thermal decomposition temperature than that of pure CL-20 and their physical mixture.

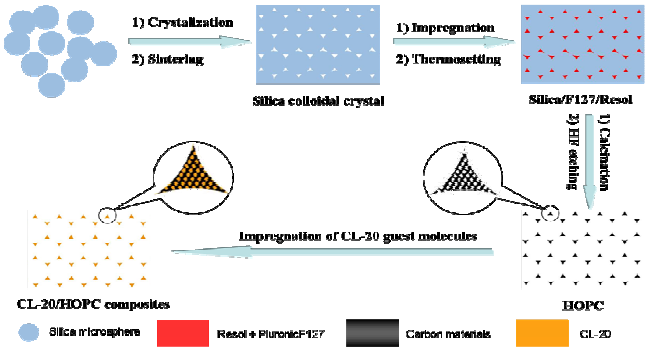
Introduction

Hierarchically ordered porous materials, combining different length-scale pores from micropore (< 2 nm) to mesopore (2-50 nm) to macropore (> 50 nm), have attracted enormous attentions because of their appealing features such as highly ordered, large pore volume, high surface area, molecule selectivity and efficient mass transportation [1-3], and as a result, diverse potential applications in catalysis [4-5], adsorption [6], electrode materials [7-8], sensors [9], and many others. Extensive works have been done to design hierarchically ordered porous materials with various framework compositions, including silica, carbon, metal oxide, and so on. And the dual-template approach using colloidal crystals and surfactants has been considered as an efficient strategy to synthesize hierarchically ordered porous materials with ordered arrays of macropores and mesopores, interconnected windows, high surface area and large pore volume [10-14].

Recently, hierarchically ordered porous carbon (HOPC), especially those possessing well-defined macropores and interconnected meso- and/or micropores, is of particularly great interest due to the efficient mass transport from macropores, high surface area from micro-/mesopores [2], and their excellent chemical, mechanical and thermal stability [15]. All The above mentioned properties should make such materials ideal candidates for extensive applications, for example, for the promising host matrixes of host-guest chemistry. HOPC materials can allow the guest molecules to diffuse more easily in the entire bimodal pore system and fill them via a variety of strategies. Then the physicochemical properties of the guest molecules could be tailored through orientation and/or conformation inside the hierarchically porous structure [16]. Herein, we choose high energy density material as the guest molecules to design host-guest structure energetic composites with HOPC, in order to improve its explosive properties. The influence of ordered space structure on energetic properties of high energy density material has been discussed in our earlier works with using ordered mesoporous materials as the host matrixes [17-19]. However, HOPC has rarely been explored for host matrixs of energetic composites up to date.

In this paper, we used the dual-template approach to synthesize hierarchically ordered macro-/mesoporous carbon, using monodisperse silica colloidal crystals as the hard template,

amphiphilic triblock copolymer Pluronic F127 as the soft template, and soluble resols as the carbon source. The host-guest energetic composites were prepared by the impregnation method with selecting 2,4,6,8,10,12-hexanitro -2,4,6,8,10,12-hexaazaisowurtzitane (CL-20), which is considered as the most powerful explosive today [20], as the guest and HOPC as the host. The HOPC has a large effect on the exothermal property of CL-20 due to its superior hierarchically ordered space structure, thus it is a useful platform to clarify the roles of ordered porous structures in the host-guest energetic composites.



Scheme 1. Synthesis procedure for the HOPC via dual-templating approach, and the impregnation of CL-20 in the HOPC to form CL-20/HOPC host-guest energetic composites.

Experimental Section

Chemicals. Triblock copolymer Pluronic F127 ($EO_{106}PO_{70}EO_{106}$, Mw = 12600) was purchased from Sigma-Aldrich. Phenol (AR), formaldehyde solution (37 wt.%), sodium hydroxide, tetraethyl orthosilicate (TEOS) (AR), ethanol, aqueous ammonia (25-28 wt.%), and acetone were purchased from Sinopharm Chemical Reagent Co. Ltd. CL-20 was provided by our group. All chemicals were used as received without further purification. Deionized water was used in all experiments.

Preparation of Hierarchically Ordered Porous Carbon. The HOPC was synthesized according to the reported dual-templating approach with silica colloidal crystals as the hard template and the amphiphilic triblock copolymer Pluronic F127 as the soft template, and soluble resols as the carbon source (Scheme 1) [12]. Monodisperse silica microspheres with a mean size of 240 ± 5 nm were synthesized according to Stöber's method [21]. The as-made silica microspheres were repeatedly washed with an ethanol/water mixture (50/50 volume ratio) by centrifugation and then redispersed in ethanol for a week to form colloidal crystals sediment. After careful removal of the supernatant, the remaining solvent was further evaporated for 24 h at 25 ^{o}C and the monoliths were then heated at 100 ^{o}C for 24 h. The 20 wt.% resol solution in ethanol, derived from phenol and formaldehyde, was prepared by a basic polymerization method [22]. In a typical process, a piece of colloidal crystal monolith was immersed in a homogeneous ethanol solution of resol and F127 (mass ratio of resol: F127: ethanol is 2: 1: 20). After the impregnation and evaporation for 24 h at 25 ^{o}C, the composite monolith was further heated at 70 ^{o}C for 4 h. The obtained silica/PF/F127 composite was calcined in N_2 at 600 ^{o}C for 3 h to remove F127 templates. The resulting silica/carbon composite was then treated with HF solution (10 wt.%) to etch the silica, followed by washing with water and drying at 60 ^{o}C in a oven to obtain HOPC.

Preparation of CL-20/HOPC Host-Guest Energetic Composites. The CL-20/HOPC host-guest energetic composites were synthesized by impregnation method (Scheme 1). Prior to use CL-20 was dried at 50℃ for 5 h. 140 mg of CL-20 was dissolved in 4.0 g of acetone, then 80 mg of HOPC was added to the solution, and the mixture was stirred for 5 min. After that the solvent was slowly evaporated for 4 h at room temperature. The final products were black-green solid and were dried above 60℃ under vacuum. The weight percent of CL-20 in the sample was 63.6 wt.%.

Characterization and Measurements. The morphology of HOPC was examined by using the Apollo 300 and Philips XL30 scanning electron microscopies (SEM). Transmission electron microscopy (TEM) images were obtained with a JEOL 2011 microscope. Small-angle X-ray

scattering (SAXS) and X-ray diffraction (XRD) patterns were collected on a Bruker D4 Endeavor diffractometer with Cu K_α radiation ($\lambda = 0.15406$ nm). Nitrogen sorption isotherms were measured at 77 K with a Quadrasorb SI analyzer after the samples were degassed in a vacuum at 180 ^oC for at least 6 h. The Brunauer-Emmett-Teller (BET) method was utilized to calculate the specific surface area (S_{BET}). By using the BJH model, the pore volume and pore size distribution were derived from the adsorption branches of isotherms. The total pore volumes (V_t) were estimated from the adsorbed amount at a relative pressure P/P_0 of 0.991. Differential scanning calorimetry (DSC) and thermogravimetry (TG) analyses were carried out by using a NETZSCH STA 449C simultaneous thermal analyzer from 50 to 350 ^oC with a heating rate of 10 ^oC/min in a flowing nitrogen atmosphere.

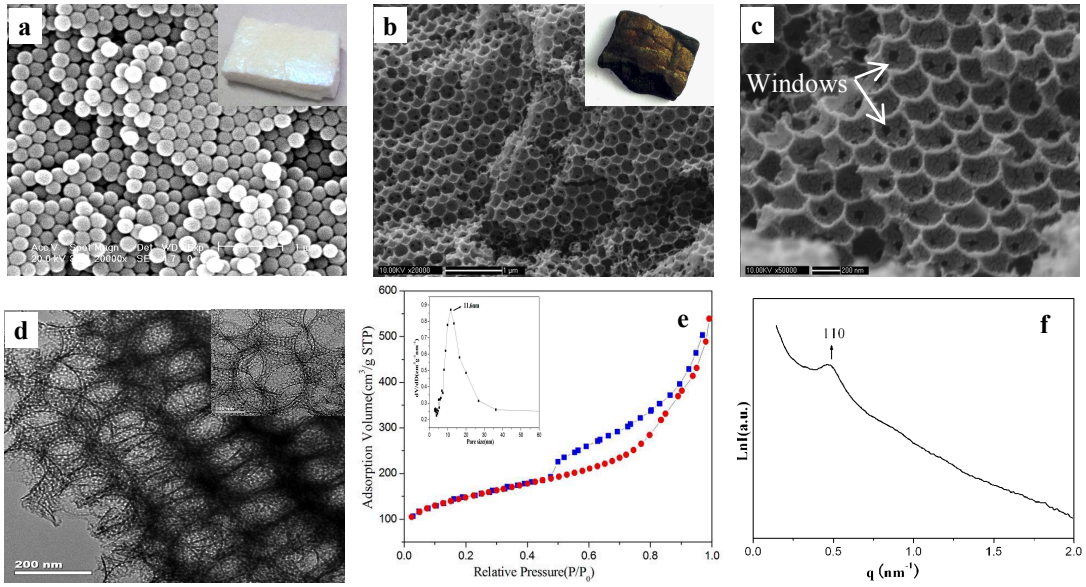


Fig. 1. SEM images of (a) the as-made silica colloidal crystals, (b, c) HOPC. The insets in a and b are the photographs of the colloidal crystal monoliths and the replicated HOPC, respectively. TEM images (d), N_2 sorption isotherms and pore size distribution (inset) (e), and SAXS pattern (f) of HOPC.

Results and Discussion

The Architectural Characterization of HOPC. The as-made silica microspheres have a mean diameter of 240 nm with a standard size deviation of less than 5%, and pack into highly ordered colloidal crystals with face-centered cubic (fcc) structure after the sedimentation (Fig. 1a). The ordered colloidal crystal monolith shows pearlescent color due to the light diffraction (Fig. 1a inset). After the impregnation with the sol solution of resol precursors and F127, and further thermosetting treatment, the interstitial voids in the as-made colloidal crystals are filled, and the formation of the mesostructure can be achieved by the organic-organic self-assembly of the resins and F127. After calcination in N_2 at 600 ^oC and HF etching, the F127 and the silica microspheres can be removed, and black monolith (Fig. 1b inset) with highly ordered macropores can be clearly observed (Fig. 1b), indicating that the ordered macrostructure of silica colloidal crystals is faithfully replicated. All the macropores are well-connected by the large windows of ~ 40 nm (marked by arrows, Fig. 1c). The diameter of the macropores measured from TEM images is about 225 nm, suggesting a small shrinkage compared with the colloidal crystals template, and numerous large mesopores surrounding the macropores with the size of about 11.6 nm are clearly observed (Fig. 1d). It is noteworthy that the thermosetting treatment of the silica colloidal crystals at 70 ^oC is necessary for preventing the collapse of the macrostructures and the formation of the interconnected windows [12].

Nitrogen adsorption/desorption isotherms (Fig. 1e) of HOPC exhibit similar type IV curves with a clear H2-type hysteresis loop due to the existence of irregular mesopores formed on the microspheres surface. The sharp capillary condensation at relative pressure of 0.74-0.87 indicates a uniform large mesopore. In addition, further N_2 uptake is observed at high relative pressure of 0.93-1.00, suggesting the presence of macropores. The mesopore size calculated from the adsorption branch by the BJH model is 11.6 nm (Fig. 1f, inset). The HOPC materials possess a BET surface area of 503.6 m^2/g and

a large pore volume of 0.833 cm^3/g, suggesting the ability of efficient adsorption and high loading level for guest molecules. The SAXS pattern of the obtained HOPC sample only shows a broad scattering peak at 0.48 nm^{-1}, corresponding to 110 reflection of cubic mesostructure (Fig. 1f). It suggests that the sample has a relatively low periodicity of mesostructure because the ordered mesostructure is retained in small domains. Therefore, the synthesized HOPC materials exhibit superior hierarchical porosities, which can provide a fast mass transport and diffusion pathways for guest molecules in host-guest chemistry.

The CL-20/HOPC Host-Guest Energetic Composites. Since the HOPC materials have 3D macropores of about 225 nm with large window size of 40 nm and numerous mesopores of 11.6 nm, host-guest energetic composites were synthesized to study the application possibility of HOPC as host matrixes in host-guest chemistry. The ε-phase of CL-20 is selected as the raw compound because of its excellent stability and high density under ambient conditions. The CL-20/HOPC energetic composites were synthesized by the impregnation method: firstly, CL-20 is dissolved in acetone and enters the macro-/mesopores of HOPC by capillary forces at ambient temperature; secondly, CL-20 can be dispersed in pores driven by hydrogen bonds during the evaporation of acetone. Based on the density of ε-CL-20 (2.03 g/cm^3) and the pore volume of HOPC, the theoretical maximum loading amount of CL-20 in the CL-20/HOPC composites is up to around 62.9%, much higher than that of ordered mesoporous carbon FDU-15 (~ 43 wt.%) [18-19].

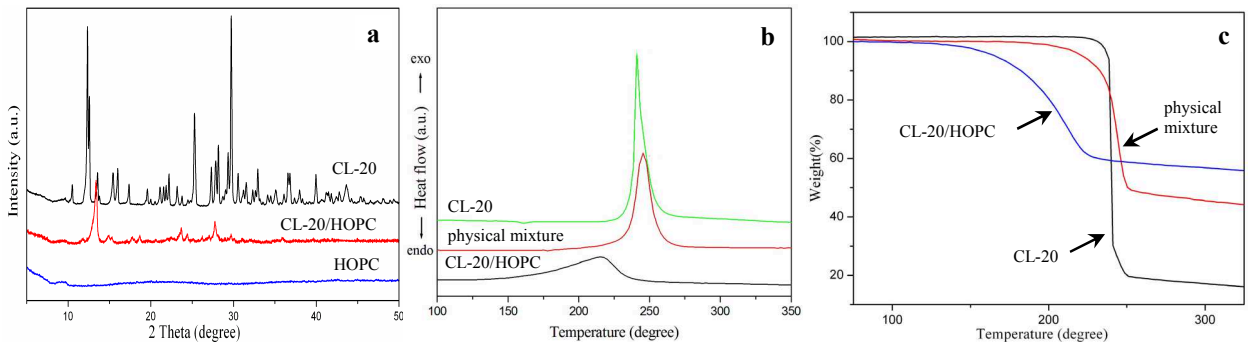


Fig. 2. (a) XRD patterns of HOPC, CL-20/HOPC composites and pure CL-20, (b) DSC patterns and (c) TG curves of CL-20/HOPC composites, physical mixture and pure CL-20.

To confirm the formation of CL-20 crystals inside HOPC, XRD patterns (Fig. 2a) have been observed for HOPC, pure CL-20 and their composites. The sharp diffraction peaks of the composites show that the CL-20 is well-crystalline in HOPC host after impregnation. However, the diffraction patterns of the composites cannot be indexed strictly to that of bulk crystals for large shift and absentation of some diffraction peaks, which may be caused by the preferred orientation growth of CL-20 crystals within hierarchically porous structure induced by hydrogen bonds between CL-20 and HOPC [23]. And the broaden diffraction peaks imply the nanosizd CL-20 crystals.

The exothermal property is one of the most important explosive properties because it can demonstrate complete phase transformation and explosion process of energetic materials. The exothermal behavior of pure CL-20, CL-20/HOPC composites and physical mixture of HOPC and CL-20 (63.6 wt.%) were studied by DSC (Fig. 2b). The DSC patterns of the pure CL-20 and their physical mixture both show an endothermic peak and an exothermic peak, which can be attributed to the ε - λ phase transition and the characteristic peak for the thermal decomposition of CL-20, respectively [24]. For CL-20/HOPC composites, only a single exothermic peak at 215 ^oC is observed, which shifts to lower temperature approximately 25 ^oC compared with that of pure CL-20 (240 ^oC) and their physical mixture (243 ^oC), and even 14^oC lower than that of CL-20/SBA-15 composites (229 ^oC) reported in our previous work [17]. Furthermore, the TG measurements (Fig. 2c) show that the weight loss of the pure CL-20 and the physical mixture take place at about 220 °C, while that of the composites decreased by 50 ^oC to 170 ^oC. It is apparent that HOPC has a great effect on the exothermal property of CL-20 confined in its macro-/mesopores because of its superior hierarchically porous structure that have not been found in other porous materials. Moreover, the tremendous improvement of thermal

decomposition property of CL-20 also relates to the decreased particle size induced by the confinement effect of support.

CONCLUSION

In this study, we demonstrated the synthesis of hierarchically ordered macro-/mesoporous carbon monoliths via a dual-templating approach using silica colloidal crystals and amphiphilic triblock copolymer PEO-PPO-PEO as templates for applications in designing the host-guest energetic composites. The synthesized HOPC possesses high surface area (503.6 m^2/g) and large pore volume (0.833 cm^3/g), with highly ordered fcc macropores (225 nm), interconnected macropore windows (40 nm), and large mesopores (11.6 nm). A high energy material (CL-20) has been encapsulated in HOPC host by impregnation method. The obtained CL-20/HOPC host-guest energetic composites exhibit lower thermal decomposition temperature than that of pure CL-20 and their physical mixture, suggesting that the HOPC is a superior candidate for host matrixes to design energetic composites. By taking advantage of HOPC-based materials, this concept can be extended to potential applications in energetic materials or other various systems.

ACKNOWLEDGMENTS

This work was financially supported by the Science and Technology Innovation Fund of the Institute of Chemical Materials, China (KJCX-201302), and National Science Foundation of China (11172275, 11172276, and 11372288).

References

[1] T. Sen, G.J.T. Tiddy, J.L. Casci, M.W. Anderson, One-pot synthesis of hierarchically ordered porous-silica materials with three orders of length scale, Angew. Chem. Int. Ed. 42 (2003) 4649-4653.

[2] G.S. Chai, I.S. Shin, J.S. Yu, Synthesis of ordered, uniform, macroporous carbons with mesoporous walls templated by aggregates of polystyrene spheres and silica particles for use as catalyst supports in direct methanol fuel cells, Adv. Mater. 16 (2004) 2057-2061.

[3] Z.Y. Yuan, T.Z. Ren, A. Vantomme, B.L. Su, Facile and generalized preparation of hierarchically mesoporous-macroporous binary metal oxide materials, Chem. Mater. 16 (2004) 5096-5106.

[4] G. Collins, M. Blömker, M. Osiak, J.D. Holmes, M. Bredol, C. O'Dwyer, Three- dimensionally ordered hierarchically porous tin dioxide inverse opals and immobilization of palladium nanoparticles for catalytic applications, Chem. Mater. 25 (2013) 4312-4320.

[5] T.S. Li, A.J. Duan, Z. Zhao, B.J. Liu, G.Y. Jiang, J. Liu, Y.C. Wei, H.F. Pan, Synthesis of ordered hierarchically porous L-SBA-15 material and its hydro-upgrading performance for FCC gasoline, Fuel 117 (2014) 974-980.

[6] Z.K. Sun, Y.H. Deng, J. Wei, D. Gu, B. Tu, D.Y. Zhao, Hierarchically ordered macro-mesoporous silica monolith tuning macropore entrance size for size-selective adsorption of proteins, Chem. Mater. 23 (2011) 2176-2184.

[7] B. Ding, C.Z. Yuan, L.F. Shen, G.Y. Xu, P. Nie, X.G. Zhang, Encapsulating sulfur into hierarchically ordered porous carbon as a high-performance cathode for lithium-sulfur batteries, Chem. Eur. J. 19 (2013) 1013-1019.

[8] X. Huang, H. Yu, J. Chen, Z.Y. Lu, R. Yazami, H.H. Hng, Ultrahigh rate capabilities of lithium-ion batteries from 3D ordered hierarchically porous electrodes with entrapped activenanoparticles configuration, Adv. Mater. 26 (2014) 1296-1303.

[9] W. Zhu, S.Y. Tao, C.A. Tao, W.N. Li, C.X. Lin, M. Li, Y.Q. Wen, G.T. Li, Hierarchically imprinted porous films for rapid and selective detection of explosives, Langmuir 27 (2011) 8451-8457.

[10] C.G. Oh, Y.Y. Baek, S.K. Ihm, Synthesis of skeletal-structured biporous silicate powders through microcolloidal crystal templating, Adv. Mater. 17 (2005) 270-273.

[11] C.Z. Li, J.H. He, Easy replication of pueraria lobata toward hierarchically ordered porous γ-Al_2O_3, Langmuir 22 (2006) 2827-2831.

[12] Y.H. Deng, C. Liu, T.Yu, F.Q. Zhang, Y. Wan, L.J. Zhang, C.C. Wang, B. Tu, P.A. Webley, H.T. Wang, D.Y. Zhao, Facile synthesis of hierarchically porous carbons from dual colloidal crystal-block copolymer template approach, Chem. Mater. 19 (2007) 3271-3277.
[13] S.L. Zhang, L. Chen, S.X. Zhou, D.Y. Zhao, L.M. Wu, Facile synthesis of hierarchically ordered porous carbon via in situ self-assembly of colloidal polymer and silica spheres and its use as a catalyst support, Chem. Mater. 22 (2010) 3433-3440.
[14] T.C. Chou, C.H. Huang, R.A. Doong, C.C. Hu, Architectural design of hierarchically ordered porous carbons for high-rate electrochemical capacitors, J. Mater. Chem. A. 1 (2013) 2886-2895.
[15] L.H. Yu, N. Brun, K. Sakaushi, J. Eckert, M.M. Titirici, Synthesis of hierarchically porous carbon monoliths and their application in lithium-sulfur batteries, Carbon 61 (2013) 245-253.
[16] U. Suryavanshi, T. Iijima, A. Hayashia, Y. Hayashi, M. Tanemura, Fabrication of ZnO nanoparticles confined in the channels of mesoporous carbon, Chem. Eng. J. 179 (2012) 388-393.
[17] H.Q. Cai, R.J. Yang, G.C. Yang, H. Huang, F.D. Nie, Host–guest energetic nanocomposites based on self-assembly of multi-nitro organic molecules in nanochannels of mesoporous materials, Nanotechnology 22 (2011) 305602 (6pp).
[18] H.Q. Cai, L. Tian, H. Huang, J.S. Li, J.G. Deng, G.C. Yang, The formation of energetic composites by embedding multi-nitro organic molecules in an ordered mesoporous carbon, Micropor. Mesopor. Mater. 163 (2012) 110-114.
[19] H.Q. Cai, L. Tian, B. Huang, G.C. Yang, D.B. Guan, H. Huang, 1,1-Diamino-2,2-dintroethene (FOX-7) nanocrystals embedded in mesoporous carbon FDU-15, Micropor. Mesopor. Mater. 170 (2013) 20-25.
[20] U.R. Nair, R. Sivabalan, G.M. Gore, M. Geetha, S.N. Asthana, H. Singh, Hexanitrohexaazaisowurtzitane (CL-20) and CL-20-based formulations, Combust. Explos. Shock Waves 41 (2005) 121-132.
[21] W. Stöber, A. Fink, E. Bohn, Controlled growth of monodisperse silica spheres in the micron size range, J. Colloid Interface Sci. 26 (1968) 62-69.
[22] Y. Meng, D. Gu, F.Q. Zhang, Y.F. Shi, H.F. Yang, Z. Li, C.Z. Yu, B. Tu, D.Y. Zhao, Ordered mesoporous polymers and homologous carbon frameworks amphiphilic surfactan templating and direct transformation, Angew. Chem. Int. Ed. 44 (2005) 7053–7059.
[23] M. Beiner, G.T. Rengarajan, S. Pankaj, D. Enke, M. Steinhart, Manipulating the crystalline state of pharmaceuticals by nanoconfinement, Nano Lett. 7 (2007) 1381-1385.
[24] R. Turcotte, M. Vachon, Q.S.M. Kwok, R.P. Wang, D.E.G. Jones, Thermal study of HNIW (CL-20), Thermochim. Acta 433(2005) 105-115.

Key Engineering Materials Vols 645-646 (2015) pp 70-74
© (2015) Trans Tech Publications, Switzerland
doi:10.4028/www.scientific.net/KEM.645-646.70

Submitted: 2014-11-03
Accepted: 2014-11-20

TCAD Study of the Raised SiGe Source/Drain in 40nm PMOS

M. Zhong[1, 2, a*], Y.H. Zhao[2, b], S.M. Chen[2, c], M. Li[2, d], S.H. Zeng[2, e], W. Zhang[1, f]

[1]State Key Laboratory of ASIC and System, School of Microelectronics, Fudan University, Shanghai, China

[2]Shanghai IC R&D Center Ltd., Shanghai, China

[a]zhongmin@icrd.com.cn, [b]yhzhao@icrd.com.cn, [c]shoumian@icrd.com.cn, [d]liming@icrd.com.cn, [e]zengshouhai@hlmc.cn, [f]dwzhang@fudan.edu.cn

Keywords: SiGe, strain engineering, TCAD simulation

Abstract An embedded SiGe layer was applied in the source/drain areas (S/D) of a field-effect transistor to boost the performance in the p channels. Raised SiGe S/D plays a critical role in strain engineering. In this study, the relationship between the SiGe overfilling and the enhancement of channel stress was investigated. Systematic technology computer aided design (TCAD) simulations of the SiGe overfill height in a 40 nm PMOS were performed. The simulation results indicate that a moderate SiGe overfilling induces the highest stress in the channel. Corresponding epitaxial growth experiments were done and the obtained experimental data was in good agreement with the simulation results. The effect of the SiGe overfilling is briefly discussed. The results and conclusions presented within this paper might serve as useful references for the optimization of the embedded SiGe stressor for 40 nm logic technology node and beyond.

Introduction

Due to the continuing trend of downscaling of semiconductor devices, strain engineering is now widely adopted in complementary metal–oxide–semiconductor (CMOS) device fabrication. The introduction of strain in a metal-oxide-semiconductor field-effect transistor (MOSFET) can increase the carrier mobility in the channel. An embedded SiGe (eSiGe) layer is usually applied in the source/drain areas (S/D) to boost the p channel MOSFET (PMOS) performance in the advanced technology nodes. This eSiGe technique enhances the hole mobility in the PMOS by inducing an uniaxial compressive strain in the channel due to the lattice mismatch between Si and eSiGe. Capable of achieving considerable strain enhancement and low sheet resistance, applying a high Ge concentration and in-situ Boron doping during SiGe epitaxial growth has attracted more and more attention in the past decade [1-4]. It has also been reported that a raised SiGe S/D can play a critical role in strain engineering [5], i.e., the SiGe film is overfilling the S/D trench after the SiGe deposition process. However, the effect of the SiGe overfilling on the channel stress is yet not fully understood. Therefore, this study focused on the correlation between SiGe overfilling and the potential improvement in channel stress by systematic technology computer aided design (TCAD) simulations of the SiGe overfill height in a 40 nm PMOS. Corresponding experiments were designed and carried out on Si wafers to compare with TCAD simulation results. In addition, the SiGe overfilling mechanism is briefly discussed.

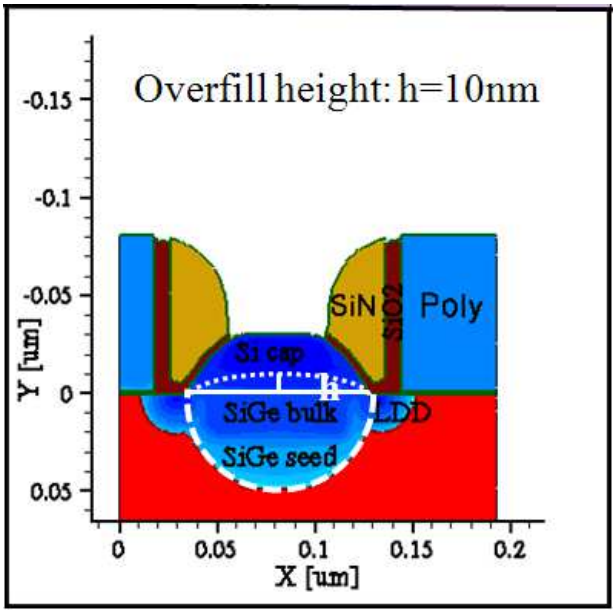


Fig. 1. Schematic diagram of a raised SiGe S/D PMOS device.

Methods and experiments

TCAD simulation provides a convenient way to analyze the changes in stress in a PMOS device during SiGe deposition process. In this work, the 2D simulations were based on a typical 40 nm CMOS process and the simulations were conducted using Sentaurus Sprocess software (Synopsis, version 2013.03-SP1). Fig. 1 shows the schematic diagram of the S/D in a 40 nm PMOS transistor. The planar PMOS devices were fabricated on a bulk silicon substrate according to the following procedure: At first, the channel implantation was performed before the formation of the gate dielectric and the gate electrode. Secondary, the dopants for the lightly doped drain (LDD) were implanted. After that, a 50 nm U-shape trench was etched and a triple-layer epitaxial S/D structure consisting of a SiGe seed layer, a SiGe bulk layer and a Si cap layer was consecutively deposited via a selective epitaxy process followed by S/D implantation. Key features of the tri-layer, such as nominal Ge concentration, layer thickness, and doping concentration, were summarized in Table 1. Finally, electrodes were formed on the gate, source and drain. The SiGe overfill height (h) is defined as the height difference between the SiGe bulk layer top surface and the poly gate/silicon substrate interface. The height h was varied by changing the deposition time while keeping the other parameters fixed. In order to improve the accuracy of the simulation, Ge chemical effects model, the stress effect model and the segregation at the silicon/SiGe interface model, as well as the Monte Carlo implantation model, were taken into account. The detail information of the above models is provided in the user guide of the TCAD software [6].

To verify the simulation results, SiGe deposition experiments were performed. Epitaxial SiGe layers were grown on 300 mm diameter patterned Si (100) substrates in an AMAT Centura reduced pressure-chemical vapor deposition (RP-CVD) reactor at 650°C at a growth pressure of 10 torr. Dichlorosilane (SiH_2Cl_2), 10% germane (GeH_4), with H_2 as carrier gas, and 1% diborane (B_2H_6), also with H_2 as carrier gas, were used as Si, Ge, and B sources, respectively. HCl was used as the etchant for necessary selectivity during the SiGe deposition process. The deposited eSiGe at PMOS S/D regions was further analyzed by TEM (JEOL JEM-2100F microscope).

Table 1. Key features of the deposited SiGe films and the Si cap layer.

Layers	Ge content [%]	B doping concentration[cm^{-3}]	Thickness [nm]
SiGe seed	20	0	25
SiGe bulk	40	6E19	25
Si cap	0	8E20	20

Results and discussions

Fig. 2 shows the simulated stress curves obtained along the channel direction of the PMOS devices with different *h*. The longitudinal Sxx stress curves exhibit a W-shape profile (Fig. 2a), which is in agreement with the previous results reported in the literature [7]. The maximum value of the Sxx curves was found near the Si/SiGe interface because the SiGe in the S/D region compressed the Si in the channel. The smallest position of the compressive stress induced by the SiGe layers on the Si region was found at the center of the channel (x = 0) because the distance to the S/D regions is largest here. The stress value obtained at a distance of 5 nm to the channel surface represents the average channel stress. As shown in Fig. 2b, the simulation results indicate that the highest stress in the channel was obtained for the PMOS with 10 nm overfilling. Compared to the PMOS with the completely flat SiGe ($h = 0$), the stress increased from 0.93×10^9 Pa to 1.02×10^9 Pa. With overfilling *h* increasing from flat to 20nm, the channel stress increases until it reaches to a peak value, and then decreases. These observations were partly as expected. In a previous paper reporting on TCAD simulation results [5], the channel stress was found to increase with the SiGe overfill height. It can be readily explained that a higher SiGe overfilling means a larger SiGe volume, which would result in a more highly strained silicon channel. However, such theory cannot explain the drop in channel stress when the overfill height exceeded 10 nm however.

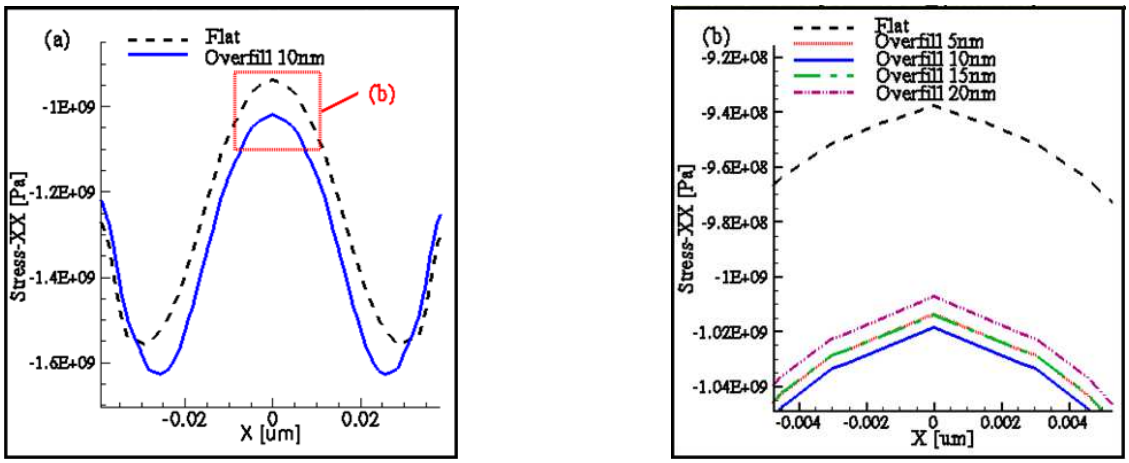


Fig. 2. Sxx stress curves simulated by TCAD (at a distance of 5 nm from the channel surface).

To further investigate the mechanism behind these new observations, stress distribution in the PMOS transistor with 0 nm, 10 nm and 20 nm overfilling was simulated and the results are shown in Fig. 3. It was found that the tensile stress was enhanced in the raised SiGe/Si cap interface or the bulk SiGe (Area 1) when *h* was increased from 0 nm to 20 nm. This tensile stress may affect the strain in the PMOS channel and lead to a reduction of the channel stress if *h* is higher than 10 nm. In conventional simulation models, the channel stress was increased by a higher amount of SiGe overfilling and defect formation in the SiGe was not considered. However, in an actual SiGe epitaxial growth process, if the thickness of the SiGe layer exceeds the critical thickness, the formation of defects, such as threading dislocations, occurs [8]. These defects will lead to strain relaxation, thereby effectively decrease the stress in the channel. Therefore, the simulation model was modified by taking into the account of both the critical thickness and Ge/B implantation-induced extended defects [9]. As a result, an accumulation of tensile strain was found in the designated Area 1 for $h > 0$. Consequently, the effect of the overfilling on the channel stress can now be explained completely.

However, it should be noticed that due to the large range of stress proximity effects in CMOS materials, the modeling of an isolated devices is not sufficient to predict the final circuit behavior. In general, it is expected that a higher compressive stress Sxx in the channel leads to a better PMOS performance.

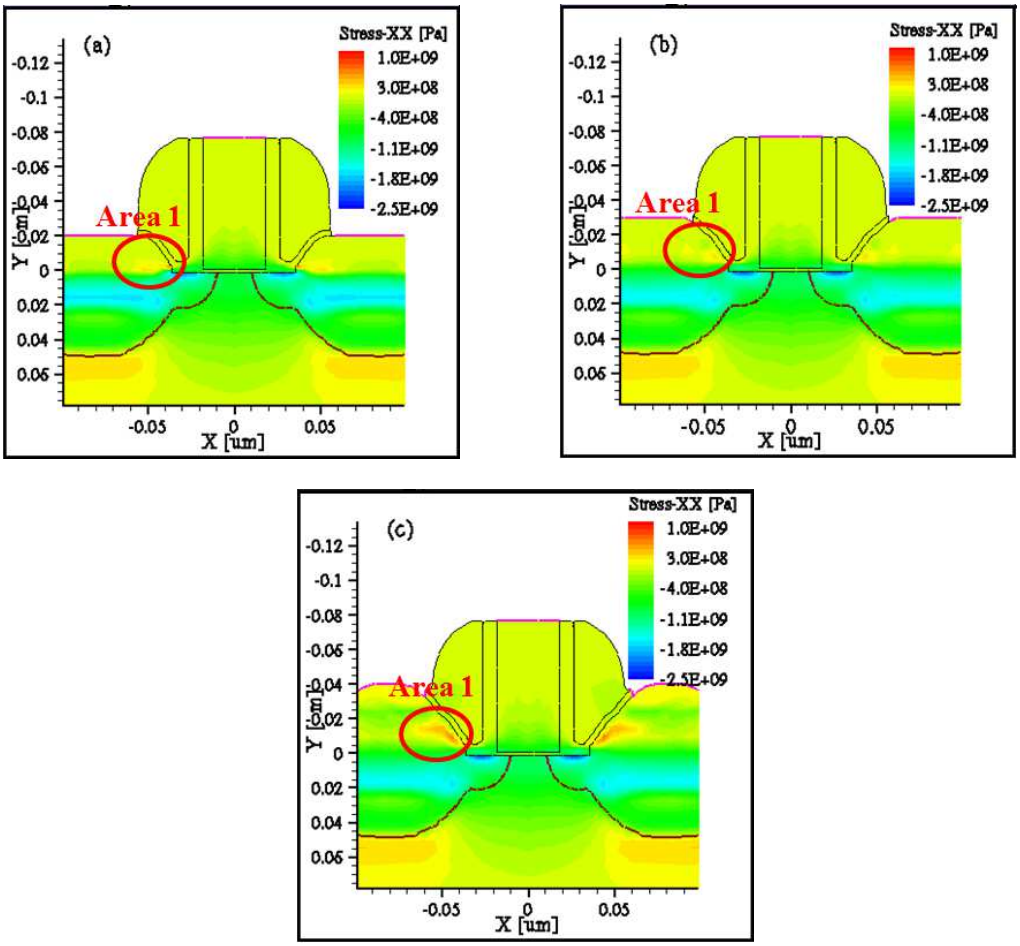


Fig. 3. TCAD images showing the strain distribution for an overfill height of (a) 0 nm, (b) 10 nm, and (c) 20 nm, respectively.

The simulation results suggest that a moderate SiGe overfilling induces the highest stress in the channel. To verify the effectiveness of these simulations, SiGe epitaxial growth experiments on Si wafers were performed. In actual device fabrication, a slight SiGe overfilling in the regions with narrow micro-features is essential to ensure that the SiGe completely fills the wider micro-features. Fig. 4 and Fig. 5 show TEM images of SiGe S/D regions with a different amount of SiGe overfilling. The TEM micrographs reveal that the SiGe film with 10 nm overfilling has a good crystalline quality without presence of defects, whereas threading dislocations were found in the SiGe film with 16 nm overfilling. These dislocations probably contributed to the stress relaxation in the layer since the SiGe film thickness exceeded the critical thickness. This experimental data is in good agreement with the simulation results. Therefore, our TCAD model was demonstrated to be accurate and valid for this particular 40 nm PMOS device.

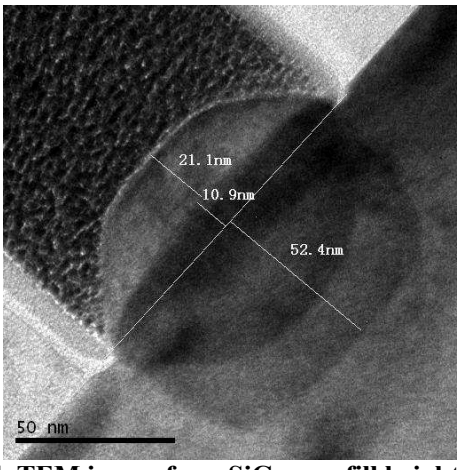


Fig. 4. TEM image for a SiGe overfill height of 10nm.

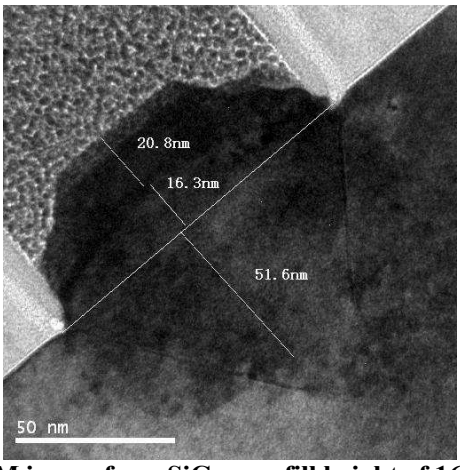


Fig. 5. TEM image for a SiGe overfill height of 16nm.

Conclusions

In summary, the influence of the SiGe overfilling on the channel stress in a 40 nm PMOS device was successfully explored by modifying the existing TCAD simulation such that the critical thickness of the SiGe epitaxial growth process was taken into account. The simulation results were consistent with TEM analysis on epitaxial SiGe samples of 10nm and 16nm overfilling. The effect of the SiGe overfilling was briefly discussed. The results and conclusions presented within this paper might serve as useful references for the optimization of the eSiGe stressor for the 40 nm logic technology node and beyond.

Acknowledgement

This work is sponsored by the Shanghai Postdoctoral Scientific Program (14R21421600), the Program of Shanghai Subject Chief Scientist (14XD1400900) and the Program for Changjiang Scholars and Innovative Research Team in University (IRT13013).

References

[1] M.Kolahdouz, P.Tabib Zadeh Adibi and A.Afshar Farniya, Journal of the Electrochemical Society. 157(2010) H633-H637.
[2] J.P.Han, H. Utomo and L.W. Teo, Electron Devices Meet.. (2006) 1-4.
[3] A.V.-Y. Thean, D.Zhang and V. Vartanian, Symposium on VLSI Technology. (2006) 101-103.
[4] D.Lee, M.Sakuraba and T. Matsuura, Device Research Conference. (2002) 83-84.
[5] H. Wu and Z.C Pan, ECS Transactions. 52 (2013) 61-66.
[6] Advanced Calibration for Process Simulation User Guide, Sentaurus, Version I-2013.12
[7] C.Y. Cheng, Y.K. Fang and J.C. Hsieh, Electron Devices. IEEE Trans. Magn. 56 (2009) 1618-1623.
[8] D.C. Houghton, Journal of Applied Physics. 70 (1991) 2136-2151.
[9] E.M. Bazizi, A. Zaka and G. Dilliway, ECS Transactions. 53 (2013) 27-32.

Key Engineering Materials Vols 645-646 (2015) pp 75-79
© (2015) Trans Tech Publications, Switzerland
doi:10.4028/www.scientific.net/KEM.645-646.75

Submitted: 2014-11-03
Accepted: 2014-11-28

Adsorption of Silver Nanoparticles on Modified Surfaces

Can Gao[1,2], Tan Guo[1,2], Xiushen Ye[1], Huifang Zhang[1], Haining Liu[1*, a], Zhijian Wu[1*, b]

[1]Key Laboratory of Salt Lake Resources and Chemistry, Qinghai Institute of Salt Lakes, Chinese Academy of Sciences, Xining, Qing Hai, CHINA

[2]University of Chinese Academy of Sciences, Beijing, CHINA

[a]liuhn@isl.ac.cn, [b]zjwu@isl.ac.cn

Keywords: Silver nanoparticles; Adsorption; Modified surfaces.

Abstract. Uniform films of silver nanoparticles (Ag NPs) were fabricated by self-assembly on 3-aminopropyltriethoxysilane (APTES) and [3-(2-aminoethyl)aminopropyl]trimethoxysilane (AEAPTES) modified glass slides. A stable Ag NPs suspension was synthesized via the reduction of silver nitrate using sodium citrate. Bulk characteristics of Ag NPs in aqueous solution were carried out by measuring their absorption spectrum, morphology and particle shape using the UV-vis absorption spectroscopy and transmission electron microscopy (TEM), respectively. The average diameter of Ag NPs is about 50 nm. The coverage of adsorbed particles on the modified glasses was measured by scanning electron microscopic imaging (SEM). The SEM images indicate that the Ag NPs films on the glasses are uniform. It is supposed that the adsorption processes are mainly controlled by electrostatic interactions. The adsorption amount of Ag NPs on APTES modified glass slides is much more than the amount on AEAPTES modified glass slides.

Introduction

Nanotechnology is considered as the most advanced technology in the 21st century. Ag NPs have been widely used in recent years due to their unique properties and application potentials in catalysis [1], opto-electronics [2] and surface-enhanced Raman scattering (SERS) [3]. The characteristics of the Ag NPs are closely related to their size, shape and surface charge. Therefore, great efforts have been contributed to studying methods for the preparation of Ag NPs, including chemical reduction [4], thermal decomposition [5], and laser ablation [6]. Chemical reduction is the most frequently approach to synthesis Ag NPs using sodium borohydride or citrate as reducing and protecting agents, because it is relatively simple and efficient.

Ag NPs films on various solids substrates have been wildly investigated due to their excellent electric, optical, catalytic, and antibacterial properties [7-9]. The main routes to prepare Ag NPs films include chemical vapor deposition (CVD) [10], chemical bath deposition (CBD) [11], sputtering and evaporation [12], etc. However, these techniques require expensive, specialized equipments and hard experimental conditions [13]. Moreover, the poorly controlled purity and coverage is another issue [13]. These problems can be avoided by using the colloid self-assembly methods based on diffusion controlled deposition of silver particles from stable suspensions [14].

C.Y. Flores et al [15] studied a method to modify Ti/TiO_2 surfaces with citrate-capped Ag NPs by spontaneous adsorption. The modified AgNP-Ti/TiO_2 surface exhibited a good resistance to colonization by Pseudomonas aeruginosa, a model system for biofilm formation.

K. Nishioka et al [16] reported the formation of antireflection nanostructure using single nano-sized silver particle. The Ag NPs dispersion solution was coated onto Si(100) substrate with polished surface. The conversion efficiency of solar cell with antireflection structure was significantly increased.

S. Zhu et al [17] described the uniform and reproducible substrates for SERS were fabricated by self-assembly of Ag NPs on APTES modified glass. Ag NPs films exhibited an excellent SERS activity.

Because of the importance of silver films, the goal of our work is to find a simple and easy way to fabricate silver films on different silanes modified glass slides and discuss the difference of adsorption behaviors.

Experiment

Materials

Silver nitrate ($AgNO_3$), (Tianjin Tian Gan Chemical Industry), sodium citrate ($Na_3C_6H_5O_7 \cdot 2H_2O$), (Beijing Chemical Works), sulfuric acid (H_2SO_4), (Baiyin Liangyou Chemical Co., Ltd), hydrogen peroxide (H_2O_2), (Tianjin Fuyu Fine Chemical Co., Ltd), 3-Aminopropyltriethoxysilane (APTES, 97%), (Nanjing Capatue Chemical Co., Ltd), [3-(2-Aminoethyl)aminopropyl]trimethoxysilane (AEAPTES, 97%), (WD Silicone Co., Ltd), were used as perchased without further purification. Methylbenzene (C_6H_6), (Sinopharm Chemical Reagent Beijing Co., Ltd) was distilled before use. All reagents were of analytical grade and all aqueous solutions were prepared with distilled water.

Surface modification of glass slides

The glass slides were soaked in chromic-sulfuric acid overnight in order to clean the surface and enhance their hydrophilicity and washed extensively with distilled water. After that they were treated in piranha solution (H_2O_2/H_2SO_4=3:7, v/v), boiling at 98 ^oC for 1 h, and at last washed with distilled water again. The surface-activated glass slides were vertically placed in a 2% (v/v) solution of APTES and a 2% (v/v) solution of AEAPTES in methylbenzene for 4 h at room temperature, respectively. After that, the slides were washed with copious amounts of methylbenzene and ethanol, and then dried under a gentle stream of nitrogen.

Preparation of Ag nanoparticles

The Ag nanoparticle suspension was prepared by the method reported by Lee and Meisel [4]. Firstly, distilled water (150 ml) was placed in a 250 ml beaker and heated to 70 ^oC. Then 18 mg silver nitrate was added. The solution was heated to boiling point and 2 ml 1% solution of sodium citrate was added rapidly under vigorous stirring. The solution was kept at boiling point for 1.5 h, and then cooled down to room temperature with continuous stirring.

Preparation of Ag NPs films

The modified glass slides were vertically immersed into the Ag nanoparticles suspension for 24 h to prepare the self-assembled substrates, on which the silver films were obtained.

Characterization and mesurement methods

The contact angle of the silanized glass substrates was measured by a Dataphysics OCA20 contact angle measuring device. UV-vis adsorption spectra of silver nanoparticle suspension was taken by using a Purkinje TU-1810 ultraviolet-visible spectrophotometer. For transmission electron microscopy (TEM) observation, the aqueous silver nanoparticle suspension was added dropwise onto copper grids and allowed to dry overnight in air. TEM images were recorded on a FEI TECNAI G2 TF20 TEM. Characterizations of the self-assembled Ag NPs films were performed by a JEOL JSM-5610LV/INCA scanning electron microscopy (SEM).

Results and Discussion

Characterization of modified glass slides

Contact angles at room temperature of the surfaces of the glass substrates to water at different stages of the functionalization have been measured and shown in Table 1. Reference to the table reveals that the contact angle decreased significantly from 23.74±0.7 ° to 13.51±0.3 ° and 24.29±0.3 ° to 11.05±0.6 ° after treatment with the “piranha solution”, respectively. Further treatment with APTES and AEAPTES results in sharp increase in the data 52.2±0.5 °and 42.37±1.0 °, respectively, indicating that the wettability of the surfaces have changed.

Table 1. Contact angles of different surfaces

Surface	APTES	AEAPTES
Untreated	23.74±0.7 °	24.29±0.3 °
Hydroxylated	13.51±0.3 °	11.05±0.6 °
After Silanization	52.20±0.5 °	42.37±1.0 °

Characterization of Ag NPs

The average size of Ag NPs measured by TEM is around 50 nm shown in Fig. 1. UV-vis absorption spectroscopy of silver nanoparticle suspension was recorded on a UV-vis spectrophotometer. Aliquot of the silver nanoparticle suspension was taken out and cooled down to the room tempreture. Then this sample was diluted 10 times before being measured. Fig. 2 shows that the absorption band of the silver nanoparticle suspension appeared at 431-442 nm.

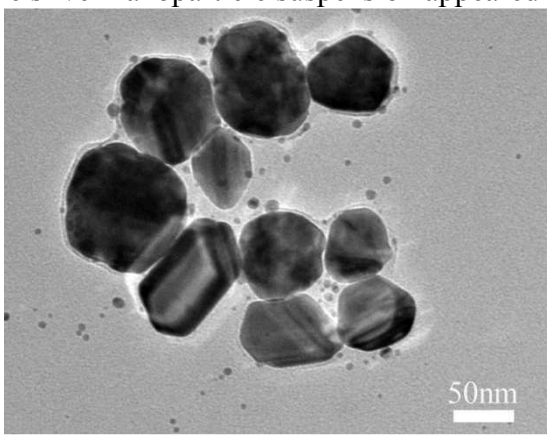


Fig. 1. TEM image of the Ag nanoparticles

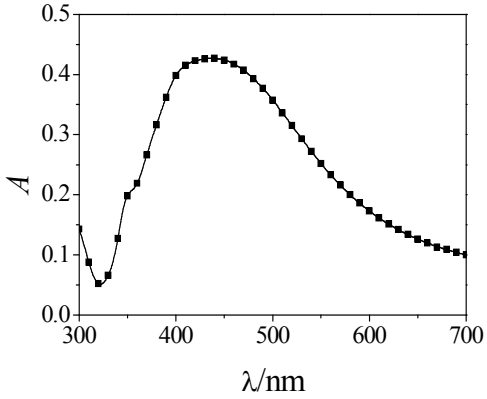


Fig. 2. UV-visible absorption spectroscopy of Ag nanoparticle suspension diluted 10 times

Adsorption of Ag NPs on the modified glass slides and adsorption mechanism

The glass slides were dipped into the APTES and AEAPTES solution, respectively, after cleaned by the piranha solution, where the ethoxy groups of APTES and AEAPTES were easily hydrolyzed into Si-OH, then interacted with the Si-OH of glass surface to form hydrogen bond. After washing out the APTES and AEAPTES without interacting with the Si-OH on the glass surface, silanol groups would be dehydrated to form Si-O-Si bond and a film with terminal amino-group was formed. The surface of the silanized glass is positively charged, which favors the negative-charged Ag NPs to adsorb through electrostatic interactions. Finally, Ag NPs films were realized on APTES and AEAPTES modified glass slides [17]. The adsorption kinetic curves of Ag NPs adsorbed on APTES and AEAPTES modified glass slides are illustrated in Fig. 3 and 4, respectively. The maximum absorbance of Ag NPs adsorbed on APTES is about 0.68, meanwhile, which on AEAPTES is about 0.30. The SEM images of APTES-modified glass slides and AEAPTES-modified glass slides with self-assembled Ag NPs are shown in Fig. 5 and 6,

respectively. The distribution of Ag NPs both on APTES-modified glass slides and AEAPTES-modified glass slides are uniform. However, the adsorption amount of Ag NPs on APTES modified glasses was much more than the amount on AEAPTES modified glasses. Because the electronegativity of amino group in AEAPTES is stronger than which in APTES, therefore, the interaction force between amino group in APTES and Ag NPs is stronger than which in AEAPTES. This is in agreement with the results of the adsorption kinetic curves and the SEM images.

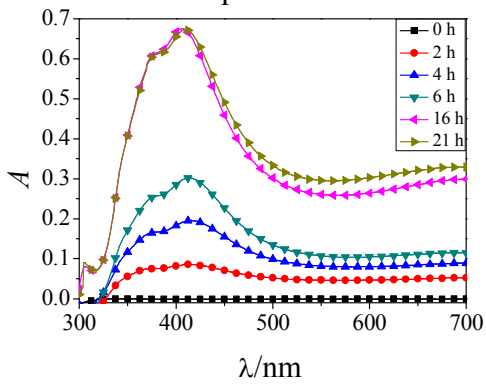


Fig. 3 Adsorption of Ag nanoparticles on APTES modified glass slides

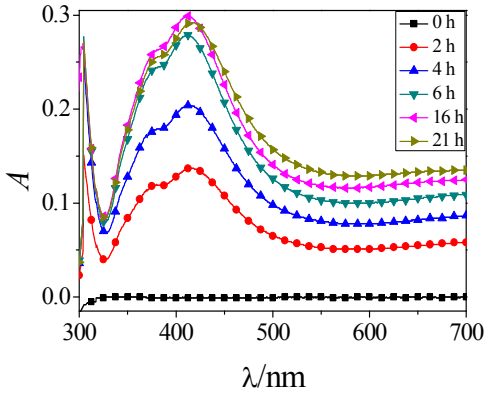


Fig. 4. Adsorption of Ag nanoparticles on AEAPTES modified glass slides

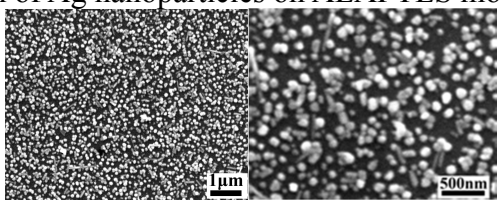


Fig. 5. SEM images of the Ag nanoparticles adsorbed on the APTES modified glass slide

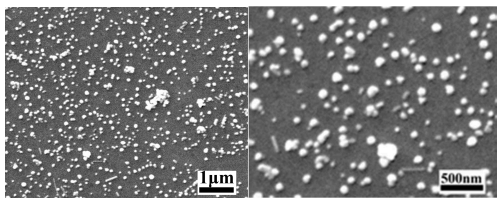


Fig. 6. SEM images of the Ag nanoparticles adsorbed on the AEAPTES modified glass slide

Conclusion

In this paper, we describe a simple and efficient method to fabricate Ag NPs films on APTES and AEAPTES modified glass slides via electrostatic interactions. The SEM images show that Ag NPs are uniformly distributed on two types modified glass slides, however, the adsorption amounts of Ag NPs on APTES and AEAPTES modified glass slides are different. The APTES modified glasses adsorb much more Ag NPs because of stronger interaction force between amino group in APTES and negative-charged Ag NPs. Such films can be used efficiently in SERS and antibacterial, and also they may have other interesting potential applications.

Acknowledgement

This work was supported by the Foundation of Knowledge Innovation Program of Chinese Academy of Sciences (KZCX2-EW-QN309), National Natural Science Foundation of China (51002164), the Talents Program of the Youth Innovation Promotion Association, Chinese Academy of Sciences and the Foundation of Basic Research for Application of Qinghai Province (2013-Z-706).

References

[1] M. Steffan, A. Jakob, P. Claus, H. Lang, Silica supported silver nanoparticles from a silver(I) carboxylate: Highly active catalyst for regioselective hydrogenation, Catal. Commum. 10 (2009) 437-441.

[2] N.J. Borys, J.M. Lupton, Surface-Enhanced Light Emission from Single Hot Spots in Tollens Reaction Silver Nanoparticle Films: Linear versus Nonlinear Optical Excitation, J. Phys. Chem. C. 115 (2011) 13645-13659.

[3] H. Kang, J. Yim, S. Jeong, J.K. Yang, S. Kyeong, S.J. Jeon, J. Kim, K.D. Eom, H. Lee, H.I. Kim, D.H. Jeong, J.H. Kim, Y.S. Lee, Polymer-mediated formation and assembly of silver nanoparticles on silica nanospheres for sensitive surface-enhanced raman scattering detection, ACS Appl. Mater. Interfaces. 5 (2013) 12804-12810.

[4] P.C. Lee, D. Meisel, Adsorption and Surface-Enhanced Raman of Dyes on Silver and Gold Sols, J. Phys. Chem. 86(1982), 3391-3395.

[5] Y. Yang, S. Matsubara, L. Xiong, T. Hayakawa, M. Nogami, Solvothermal Synthesis of Multiple Shapes of Silver Nanoparticles and Their SERS Properties, J. Phys. Chem. C. 111 (2007) 9095-9104.

[6] A.V. Simakin, V.V. Voronov, N.A. Kirichenko, G.A. Shafeev, Nanoparticles produced by laser ablation of solids in liquid environment, Appl. Phys. A. 79 (2004) 1127-1132.

[7] Y. Saito, J. J. Wang, D. A. Smith, D. N. Batchelder, A Simple Chemical Method for the Preparation of Silver Surfaces for Efficient SERS, Langmuir. 18 (2002) 2959-2961.

[8] E. Grantscharova, D. Dobrev, Catalytic activity of ion-bombarded silver films, Thin Solid Films. 196 (1991) 163-169.

[9] D. Lee, R.E. Cohen, M.F. Rubner, Antibacterial properties of Ag nanoparticle loaded multilayers and formation of magnetically directed antibacterial microparticles, Langmuir. 21 (2005) 9651-9659.

[10] Y. Chi, E. Lay, T.Y. Chou, Y.H. Song, A.J. Carty, Deposition of silver films using the pyrazolate complex, Chem. Vapor Depos. 11 (2005) 206-212.

[11] I.C. Estrada-Raygoza, M. Sotelo-Lerma, R. Ramirze-Bon, Structural and morphological characterization of chemically deposited silver films, J. Phys. Chem. Solids. 67 (2006) 782-788.

[12] M. Levin and A. Laakso Evaporation of silver thin films on mica, Appl. Surf. Sci. 171 (2001) 257-264.

[13] Y. Yan, S.Z. Kang, J. Mu, Preparation of high quality Ag films from Ag nanoparticles, Appl. Surf. Sci. 253 (2007) 4677-4679.

[14] M. Ocwieja, Z. Adamczyk, M. Morga, A. Michna, High density silver nanoparticle monolayers produced by colloid self-assembly on polyelectrolyte supporting layers, J. Colloid Interface Sci. 364 (2011) 39-48.

[15] C.Y. Flores, C. Diaz, A. Rubert, G.A. Benítez, M.S. Moreno, M.A. Fernández Lorenzo de Mele, R.C. Salvarezza, P.L. Schilardi, C. Vericat, Spontaneous adsorption of silver nanoparticles on Ti/TiO2 surfaces. Antibacterial effect on Pseudomonas aeruginosa, J. Colloid Interface Sci. 350 (2010) 402-408.

[16] K. Nishioka, T. Sueto, N. Saito, Formation of antireflection nanostructure for silicon solar cells using catalysis of single nano-sized silver particle, Appl. Surf. Sci. 255 (2009) 9504-9507.

[17] S. Zhu, C. Fan, J. Wang, J. He, E. Liang, Self-Assembled Ag Nanoparticles for Surface Enhanced Raman Scattering, Optical Review, 20 (2013) 361–366.Reference an article:

Key Engineering Materials Vols 645-646 (2015) pp 80-85
© (2015) Trans Tech Publications, Switzerland
doi:10.4028/www.scientific.net/KEM.645-646.80

Submitted: 2014-11-07
Accepted: 2014-12-23

W-band Quadrupler based on Multi-Chip Module and Schottky Barrier Diodes

Yue He[1, a], Xianjin Deng[1], Cheng Wang[1] and Bin Lu[1,b*]

[1] Institute of Electronic Engineering, Terahertz Research Center, China Academy of Engineering Physics, Mianyang, Sichuan, 621900, P. R. China

[a]heyue1109@163.com,[b*]shirelylubin@sina.com

Keywords: Millimeter Wave, Frequency Quadrupler, Schottky Diodes, power-combining.

Abstract. This paper reports a W-band solid-state quadrupler based on multi-chip module and nonlinear schottky barrier diodes. The quadruple consists of Q-band doubler and amplifier, branched-guide coupler and two parallel W-band doublers that are power-combined in-phase using T-juntion at output waveguide, and each W-band doubler channel includes two schottky barrier diodes featuring two anodes on a 127um-thick quartz substrate. The power-combined strategy decreases the size of W-band quadrupler to 56mm×33mm×20mm and increases the maximum stable output power by twice with regard to the traditional W-band doubler. The measured output power of the quadrupler is greater than 20mW over the 80 to 90 GHz and 40mW within 80.6 to 86.6 GHz with above 12% 3dB bandwidth when driven with 2mW input power at 300K. The spectrum of output signal is tested and analyzed to obtain the purity and noise performance of signal.

I. Introduction

Local oscillator sources are a crucial part of all high-frequency receivers and transmitter. Solid-state harmonic multipliers is a main way to obtain higher frequency[1]. Compared with others approaches, Solid-state harmonic multipliers offer the possibility to produce high stable, high power capacity, low phase noise and broadband millimeter wave signals[2]. Nearly, there are many reports about frequency doubler or tripler based on schottky barrier diodes[3,4,5]. However, single frequency doubler or tripler always generates limited conversion efficiency and output power, as dedicated in equation (1), not enough to pump cascading terahertz frequency doubler.

$$\frac{P_{nf}}{P_f} \le \frac{1}{n^2}, \; n \text{ is harmonic order} \tag{1}$$

To solve this problem, researchers have attempted lots of technologies[6,7,8,9,10], while power–combined frequency multiplier based on T-junction or hybrid coupler is the reliable approaches. For efficient power combining, the increasing attention must be paid to keep two parallel paths well-matched despite fabrication and assembly tolerances and to minimize losses in dividing and recombining the signal. In this context, we present the design, fabrication and test results of a W-band quadrupler that includes Q-band doubler chip and amplifier chip, branched-guide coupler and two parallel W-band doublers with a total of four Shottky barrier diodes. The W-band quadrupler produces 40mW within 80.6 to 86.6 GHz when pumped with 2mW input power.

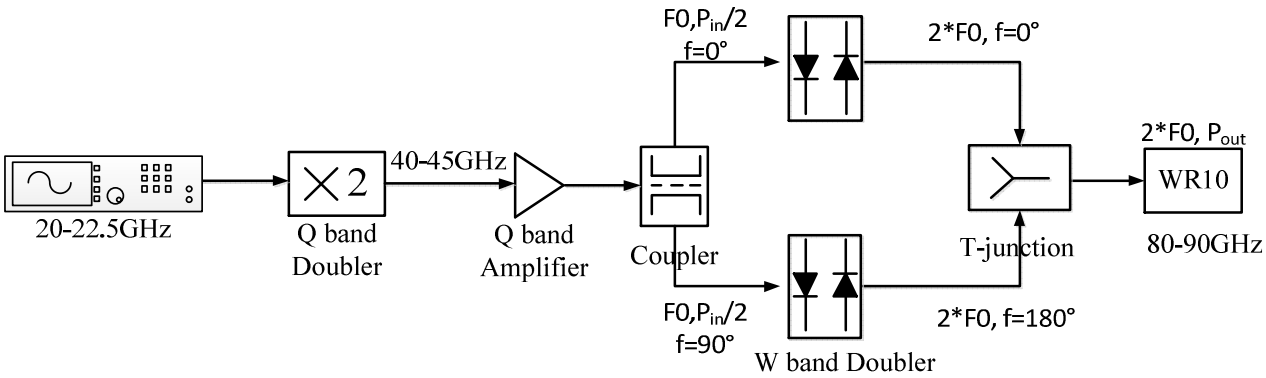
II. Scheme

The W-band quadrupler is based on multi-chip such as Q-band doubler and Q-band amplifier, and W-band schcotty diode doubler in a split-waveguide block design shown Fig. 1. The 20-22.5GHz input signal is doubled and amplified by Q-band doubler and amplifier chip aiming to increase the input power of W-band doubler. Meanwhile, due to series resistance, power saturation and thermal effect of Schottky diode, the conversion efficiency η of frequency doubler is limited[11].

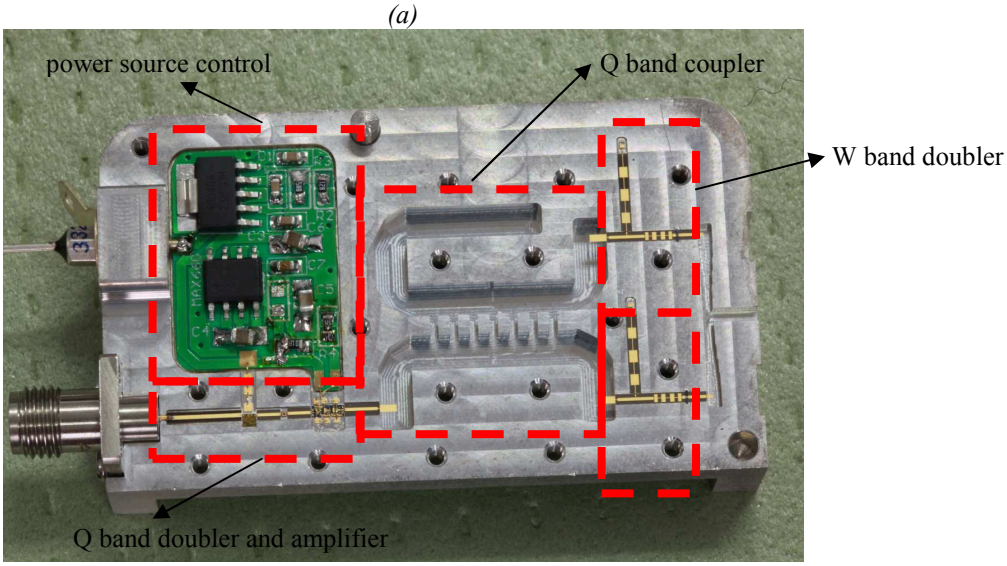
$$\eta = \exp\left(-a \cdot f_{out} / f_c\right) \tag{2}$$

where f_{out} is the output frequency, f_c is the dynamic cutoff frequency and a is a parameter related to the harmonic order of output and to the input drive level.

The amplified input signal is split into two paths by branched-guide coupler to evenly feed two identical W-band doublers each featuring two Schottky planar barrier diodes. The two W-band doublers are mounted in two independent and parallel channels that run between their respective input and output waveguides as shown in Fig. 1(b). The two output waveguides of two W-band doublers are combined by a compact T-junction. The T-junction is completed with a succession of waveguide step to provide broadband impedance matching.



(a)



(b)

Figure 1. (a) Schematic drawing.(b) the bottom half of the W-band quadrupler

In the input channel, Q-band doubler and amplifier chip both need the +5V bias voltage provided bias circuit. The output power at 1dB compression point of Q-band amplifier is 23dBm through 475mA bias current. An E-plane probe located in the input channel couples nearly 400mW signal in the Q-band frequency to branched-guide coupler. The 3dB coupler has seven sections and the simulated flatness and insertion loss is less than 0.2dB and 0.15dB within 40-45GHz. The 400mW signal evenly pumps two identical W-band doublers by another two Q-band E-plane probes. The second harmonic produced by the diodes is coupled to the output waveguide by a W-band E-plane probe. The detail introduction of W-band doubler will be present in next section.

III. Design And Simulation OF W-band Doubler

The W-band schottky diode doubler is based on quartz microstrip circuit designed originally for the 0.14THz frequency doubler[5]. The design methodology combines Agilent ADS non-linear harmonic balance simulation to optimize the performance of the circuit, with Ansoft HFSS 3-D EM simulation to accurately model the diode geometry and waveguide structure, as in [5]. The high-low impedance low-pass filter between E-plane probe and the diodes prevents the second harmonic from leaking into

input waveguide. To improve the doubler bandwidth, the real impedance matching in input and output port of varactor is implemented. Simultaneously, the DC bias needs to be applied to the diode by a low-pass filter and gold wire. According to [5], the DC bias voltage is fixed to 0V and DC port is connected to the ground directly without worsening the performance of the doubler and simplifying structure instead. The diodes are located on 127um-thick quartz substrate, as shown in Fig. 2(a). 13.5% peak simulated efficiency of W-band doubler is achieved with this topology as depicted in Figure 2(b).

To avoid the risk of overdriving an anode and investigate the balancing of the anodes in input frequency, the input coupling efficiency of each anode is simulated, as shown in Fig. 3. The input coupling efficiency is defined as following[8],

$$\text{Coupling efficiency} = \frac{P_{\text{anode(i)}}}{P_{\text{in}}/N} \times 100\% \tag{1}$$

where N is the numbers of the anodes. $P_{\text{anode}}(i)$ is the driving power of each anode at pumped frequency f_p which can be defined by Fourier series of the anode voltage V_t and the diode current i_t.

$$P_{\text{anode(i)}} = \frac{1}{2} V_t(f_p) \cdot i_t(f_p) \tag{2}$$

Fig. 3 clearly indicates the coupling efficiency of each anode almost approximates to ideal taking into account the loss of circuit. That is the input signal is poured into schottky diode furthest in order to produce more second harmonic signal. Fig. 4 shows that the power combining of W-band doubler is consummate so that the power-combined douber perform with almost identical conversion efficiency as the single W-band doubler expect with twice the output power.

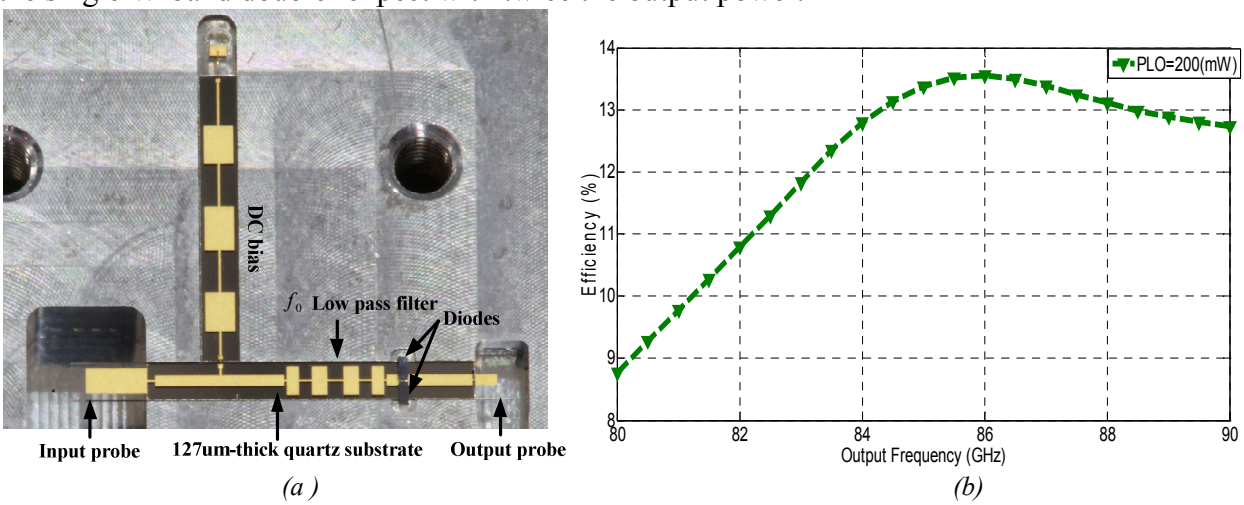


Figure 2. (a) Close-up photograph of single W-band doubler. (b) Simulated efficiency with 200mW of input power.

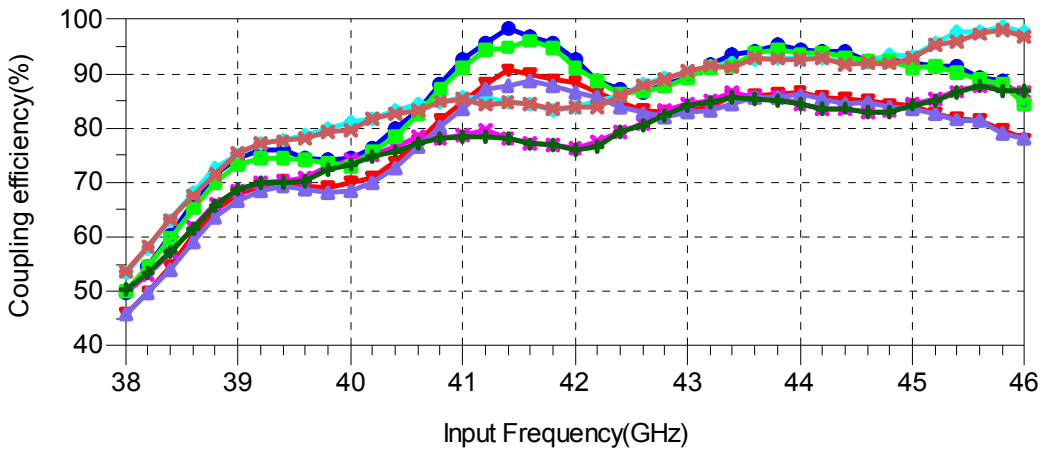


Figure 3. Input power coupling efficiency of each singnal anode

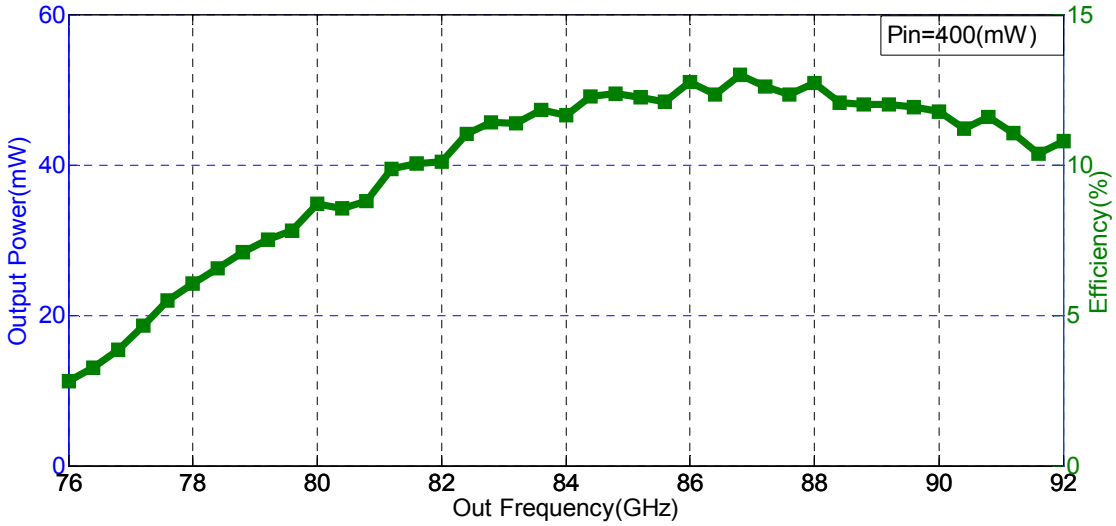


Figure 4. Simulated output power and conversion efficiency of power combined W-band doubler

IV. Quadrupler Measurements

We assembled and tested two quadrupler blocks. The source used to test the quadrupler consisted of a synthesizer tuned in the 20-22.5GHz band with 3dBm(the input power has been correct for the loss of coaxial RF cable). For all the measurements, the input power of the quadruplers was limited on 3dBm and DC voltage bias circuit was kept on 6V.

A. Frequency sweep

The output power of the quadrupler was measured using the power meter. Their output powers range from 20mW to 50mW across 80-90GHz band, shown in Fig. 5. A 57mW peak output power at 83.5GHz and a 12% 3dB bandwidth have been measured when pumped with a 2mW constant input power across the measured frequency band. Form the measured data, the center frequency of the quadrupler slipped slight. The discrepancy of two blocks in output power attributed to the bias current variation of the Q-amplifier, of which one is 540mA and another 570mA. In table 1, there was some research result about the power-combined strategy of frequency multiplier. [6] and [7] in overseas research indicated the power-combined method could be feasible in higher frequency and compared with [8], [9] and [10], this work had distinct advantage on conversion efficiency and output power which built more powerful source in microwave oscillator to drive terahertz component.

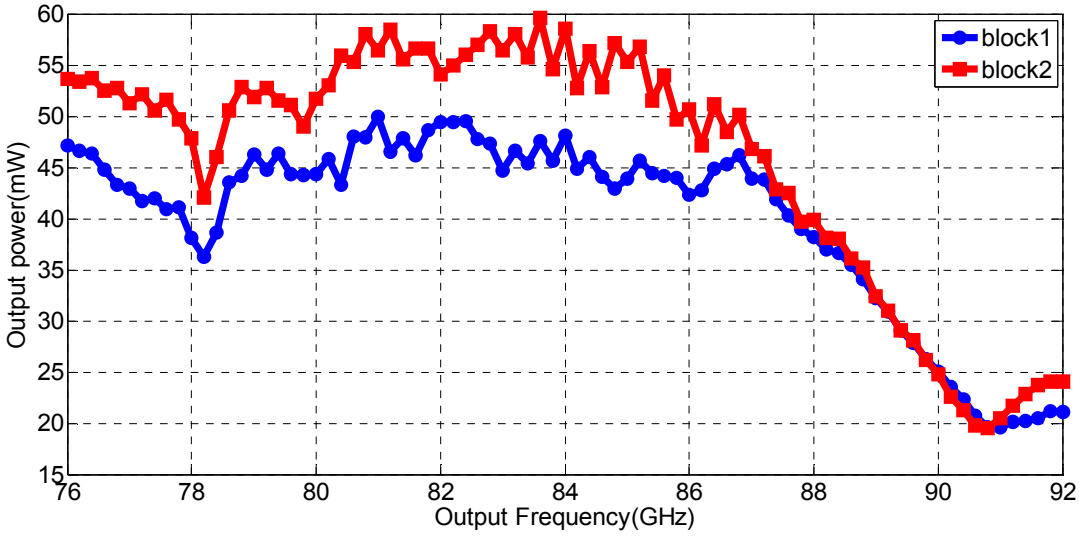


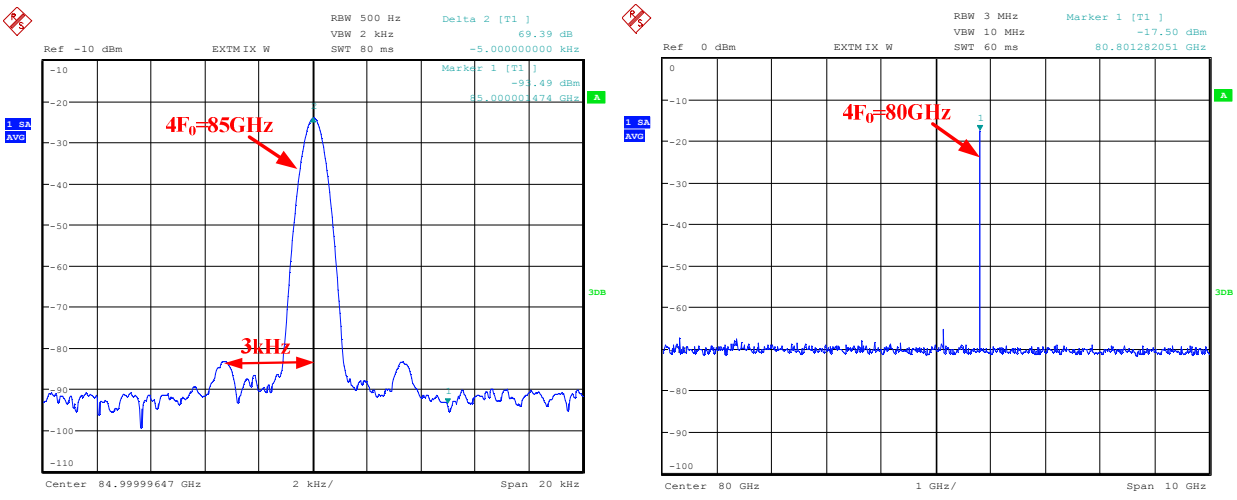
Figure 5. Measured output power of two W-band quadruplers

Table 1 State of the art power-combined schottky multipliers or tripler

Design	Year	Frequency	Pout(mW)	Conversion Effciency(%)
[6]	2011	177-202GHz	10mW	6-10%
[7]	2008	265-330GHz	15-20mW	5-15%
[8]	2013	75-110GHz	6-10mW	1.2-3.8%
[9]	2012	50-75GHz	2.5-7mW(simulation)	2.5-7%
[10]	2012	86-96GHz	4-8	3-8%
This paper	2014	76-90GHz	20-50mW	8-13%

B. Spectral Analysis

The spectrum of the output signal was analyzed with Agilent spectrum analyzer and an external W-band mixer used as down converter. Since the input power of the mixer was limited to 3dBm, the input power of the W-band quadrupler was adjust to -6dBm corresponding when we analyzed the spectral characteristic of the quadrupler. Figs 4(a) and (b) show the spectral line of the output signal in 85GHz and 80GHz.Theoretically, the phase noise of natural circuit would be degraded $20\times\log(N)$, where N is the order of multiplication. According to the measurements, the quadrupler had low phase noise across the measurement band. While in Figs 4(a), at an offset of 3 KHz, there was a parasitic and indelible clutter signal. The existing clutter signal may degrade the THz signal purity pumped by the quadrupler. When THz mixer is used to the front of the receiver, the purity of LO signal is fatal for the sensitivity. There are the following reasons of the clutter signal: (a) the purity of DC current is not enough to be block to RF signal and leak into RF channel. (b) the Q doubler chip introduces the clutter signal when doubles the input signal.



(a) *(b)*

Figure 4.Specturm of the output signal (a) 85GHz.(b) 80GHz.

V. Summary

The W-band quadrupler based on multi-chip module and schotty diodes has been successfully accomplished with nearly 50mW output power and 12% 3dB bandwidth. Two W-band power combined doubler produces approximately twice as much power without sacrificing efficiency or bandwidth compared with single W-band doubler. This approach represents an important steps towards increasing the LO power at W-band and reducing the size of solid-state LO chains. It could be potentially applied to higher frequency.

References

[1] C. Goutam, S. Erich, S. John, etc. "An all-solid-state broad-band frequency multiplier chain at 1500 GHz", IEEE transactions Microwave Theory techniques, vol.52, no.5, 1538–1547, 2004.

[2] D.W. Porterfield, T.W. Crowe, R.F. Bradley, N.R. Erickson, "A high-power, fixed-tuned, millimeter-wave balanced frequency doubler", Microwave Theory and Techniques IEEE Transactions, vol. 47, no. 4, 419-425, 1999.

[3] J. V. Siles and J. Grajal, "Physics-based design and optimization of Schottky diode frequency multipliers for terahertz applications," IEEE Trans. Microw. Theory Tech., vol. 58, no. 7, 1933–1942, Jul. 2010.

[4] D.W. Porterfield, "High-Efficiency Terahertz Frequency Triplers," IEEE MTT-S International Microwave Symposium, Honolulu, Hawaii:[s.n.], 337-340, Jun 2007.

[5] L. Miao, X.J. Deng, etc. "The Design and Simulation of A 0.14 THz Frequency Doubler", 2012 International Conference on Microwave and Millimeter Wave Technology, ICMMT 2012 – Proceedings, 379-382, May 2012.

[6] V.S. Jose, M. Alain, A. Byron, etc. "A Single-Waveguide In-Phase Power-Combined Frequency Doubler at 190 GHz", IEEE Microwave and Wireless Components Letters, vol. 16, no. 6, 332-334, Jun. 2011.

[7] M. Alain, S. W. John, T.C. Charlotte, etc. "In-Phase Power-Combined Frequency Triplers at 300 GHz", IEEE Microwave and Wireless Components Letters, vol. 17, no. 3, 219-220, Mar. 2008.

[8] Z.H. Chen and J.P. Xu, "Design and characterization of a W-band power-combined frequency tripler for high-power and broadband operation", Progress in Electromagnetics Research, vol. 134, 133-150, 2013.

[9] Z.H. Chen and J.P. Xu, "Design of a V-band single-substrate single-waveguide power-combined frequency doubler covering 50-75 GHz band", IEEE MTT-S International Microwave Workshop Series on Millimeter Wave Wireless Technology and Applications, IMWS 2012 - Proceeding, 149-152, 2012.

[10] J. Guo, J. Xu, Y.J. Cui and C. Qian, "Design of a W-band single-substrate single-waveguide power-combined frequency doubler", 2012 International Conference on Microwave and Millimeter Wave Technology, ICMMT 2012 – Proceedings, 1997-2000,2012.

[11] J.W. Gewartawsk, "Microwave Semiconductor Devices,Circuits,and Applications", Watson, H. A., editor, Chap. 8, McGraw Hill, 1969.

Key Engineering Materials Vols 645-646 (2015) pp 86-91
© (2015) Trans Tech Publications, Switzerland
doi:10.4028/www.scientific.net/KEM.645-646.86

Submitted: 2014-11-10
Accepted: 2014-11-14

Intermediate Layer Bonding for Silicon and Piezoelectric on UV Adhesive

Xuanyang wang[1,2,a], Huan liu[1,2,b], Rui lei[1,2,c],Weiguo liu[1,d*]

[1]Xi'an Technological University, Micro-optoelectronic System Labs, Xi'an,China.
[2]Science and Technology on Low-light-level Night Vision Laboratory, Xi'an, China.
[a] wangxuanyang@163.com,[b]liuhuan360@163.com,
[c]280124564@qq.com,[d*]wgliu@163.com

Keywords：UV adhesive；wafer bonding；Piezoelectric；

Abstract: During making the surface acoustic wave devices and integrated circuit hybrid integrated electronics, it needs to put the piezoelectric crystal and silicon wafer bonding together. By selecting a certain wavelengths of UV curing adhesive, then exposing with 300-436nm wavelength of exposure machine, 8mm×8mm bonding chips are got. Bonding $LiNbO_3$, quartz and silicon wafer respectively, measured maximum shear force is 116.2 N and 117.9 N with shear force test machine. The fracture energy is 5.831 J/m^2 measured by crack-opening method test $LiNbO_3$ bonding chips. The results show that piezoelectric crystal and silicon wafer bonding interface level off and the bonding of the middle layer thickness for about 3 microns observed the bonding section with SEM.

1. Introduction

In recent years, the microelectronic technology has been applied widely. Wafer bonding is one of the important MEMS production and packaging technologies, it has key technology for microelectronics. Piezoelectric crystal is mainly used in SAW devices, bonding silicon and piezoelectric crystal make SAW devices and IC hybrid integrated together, so as to improve the integration of IC technology.

Lord Rayleigh had released paper about bonding in 1936. The main bonding methods are anodic bonding, polymer bonding, direct bonding. Advantages of polymer bonding are pressure is not required, it use a simple process can quickly achieve low-temperature bonding between different materials. For example, Jilin University got thermo-optic switch device with Norland optical adhesive[1], Ghent University conducted the research about BCB as bonding intermediate layer of semiconductor material bonded III-V and Si[2], Huazhong University of Science and Technology with UV adhesive bonding silicon and glass to achieve the bonding tensile strength of 26MPa[3], China Electronics Technology Group corporation with BCB bonding MEMS sensors, key combined shear force greater than 49N etc.

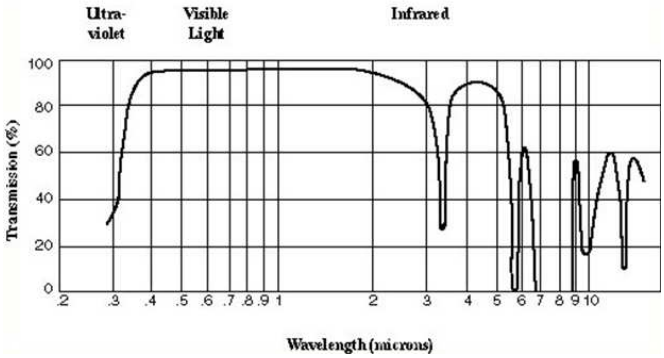
2, Process experiment

This article use the material are $LiNbO_3$, quartz XT cut, silicon, UV adhesive. Their properties shown as following table.

Table. 1 Properties of the material

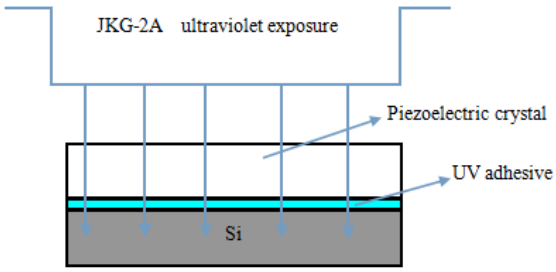
	cut	diameter	thickness	roughness
$LiNbO_3$	YX128°	2 **inch**	500 μ m	<1nm
quartz	XT	2 **inch**	500 μ m	<1nm
silicon	<100>	2 **inch**	500 μ m	<1nm

UV adhesive is made by Norland company. It is transparent, colorless liquid, can be cured quickly as long as the adhesive can be UV exposed. It shows many outstanding advantages when bonding optical components and sensitive to the ultraviolet light wavelength from 350 to 380 nm. NOA61 light transmission curve as follow.



Curve.1 Optical transmission of NOA61

The light source is JKG-2A type ultraviolet exposure machine, its spectral range is 300-436 nm. The transmit rate of $LiNbO_3$ and quartz in this band is about 75% -80%[4] and 80% [5]respectively. Apparently the source meet the needs the UV illumination of UV adhesive curing, the schematic diagram of the machine is shown in figure 1.



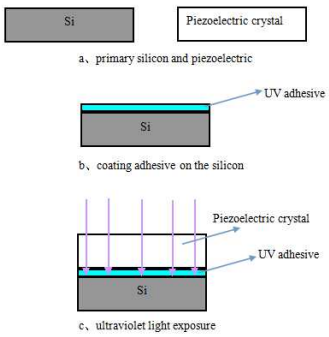


Fig.1 Schematic of UV curing set-up Fig.2 Schematic of wafer bonding process

The process of experiment are as follows: (1) cut $LiNbO_3$ and quartz crystal into 8 mm×8 mm square slice with WXQH160 diamond cylindrical cutter, shown in figure 3. (2) ionized water flushing crystal then with acetone wiping it. (3) heating crystal 5 min on the 150 ℃ heating plate, makes the surface evaporation. (4) we need to keep the temperature of NOA61 to room temperature before use it, then coating the adhesive in the surface of silicon wafer, can make the piezoelectric crystal infiltration as standard.(5) press the piezoelectric crystal on the adhesive, put the crystal shake a little on silicon wafer surface, one is able to make silicon and crystal infiltration better, other to cast out large bubbles from the adhesive. (6) implement pre-bonding before bonding completely, put the objects in 15cm distance the ultraviolet light source exposure 10s. (7) finally curing completely. The adhesive curing completely when UV light illuminate piezoelectric crystal for 8 min.

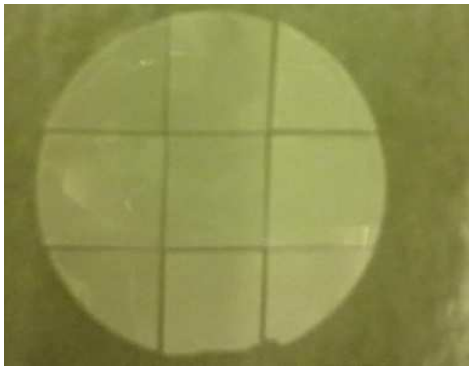


Fig.3 The cut of $LiNbO_3$ wafer

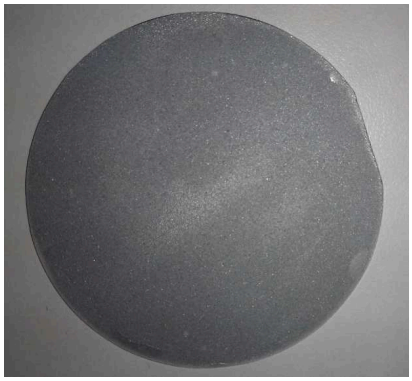


Fig.4 Bonded Si-$LiNbO_3$ pair

First we research effects of bonding use different illumination time. We found that UV adhesive lighted for 8min achieve good curing. Poor bonding effect if the time is less than 8min, and curing insufficient. While the exposure time for 8min, UV adhesive has completely polymerization and cross linking reaction, bonding effect get best. Bonding effect did not improve when the light time is longer than 8 min.

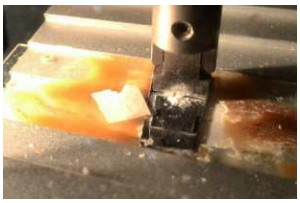
Second we research effects of bonding use different pressure on the crystal. We use transparent glass with different weight pressure on the crystal bonded when the crystal lighted ultraviolet light. Study the the bonding effect implement different pressure. We cut glass into pieces with seven kinds of weight. We can get pressure 5N, 10N, 15N, 20N, 25N, 30N, 35N respectively by the gravity of the glasses. Every kind of gravity has two experiments. Then test the bonded respectively.

3. Test and results

We use three methods to test $LiNbO_3$ and quartz bonding respectively. Firstly test bonding shear stress with DAGE4000 push-pull test machine. Secondly test fracture energy by the method of crack-opening test. Thirdly observe the thickness of the intermediate layer with SEM, and discuss the influence of shear force different pressure on their bonding effect. The bonding has been bonded shown as figure 4. It has less air bubbles.

3.1, Shear forces test

Shear forces test: Fixed silicon/piezoelectric crystals bonding on the steel plate of DAGE4000 push-pull test machine. Then test the shear forces of the samples with the tester. Results shown as in figure 6,7 ,which has 14 data respectively. Set of data A and B is $LiNbO_3$ experimental results under the same test conditions in the figure 6. Set of data C and D is quartz experimental results under the same test conditions in the figure7. We get maximum tension further, calculates the average tension corresponding. Sometimes the bad fixed plate and base plate will cause the experiment failure in the test. Eliminate the part of the data test failure. The test results shown in figure 6 and 7.



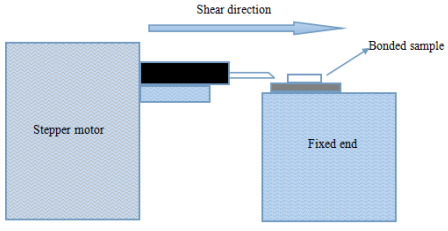


Fig.5 Shear force test for bonded piezoelectric wafer

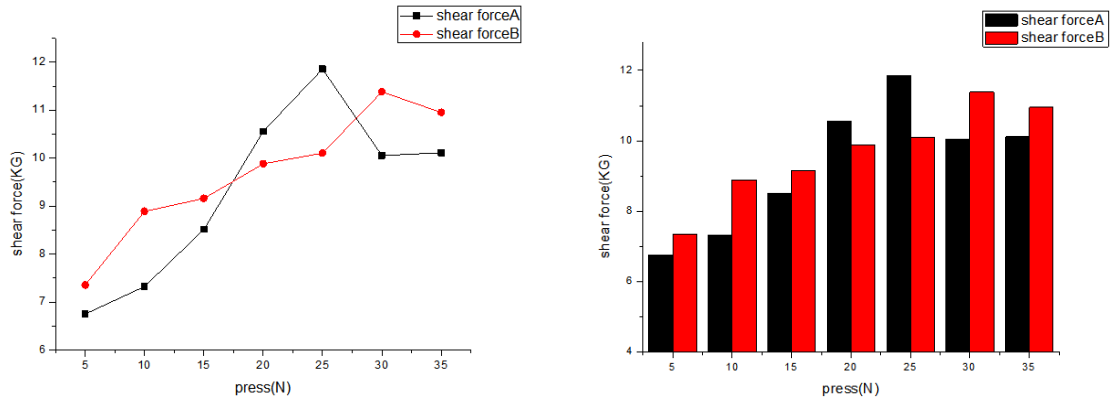


Fig.6 The results of shear force test for bonded $LiNbO_3$ wafer

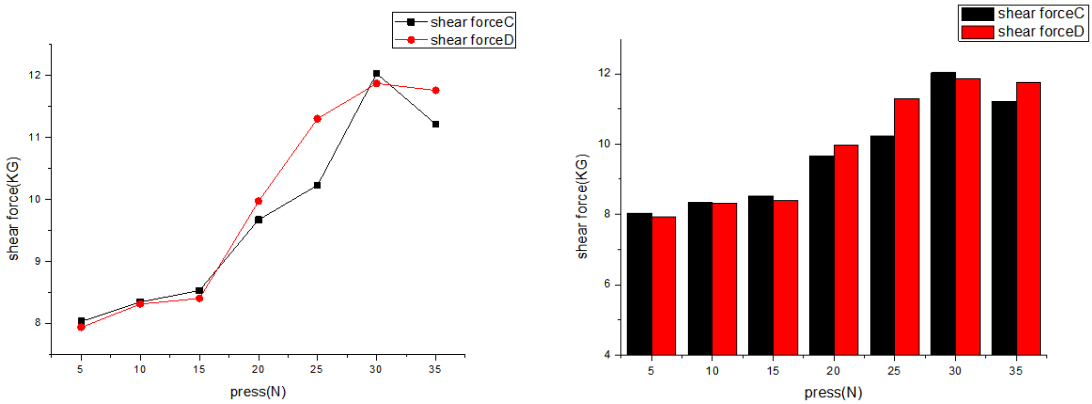


Fig.7 The results of shear force test for bonded SiO_2 wafer

The shear forces and pressure exists proportional relationship a certain draw from the result. The shear force got the biggest value when the pressure is about 30N, shear force decreased slightly when the pressure continued to increase. The biggest shear force of $LiNbO_3$ bonding wafer is 116.2 N (F=mg), the average shear force got 91.24 N by calculated. The biggest shear force of quartz bonding wafer is 117.9 N (F=mg), the average shear force got 96.35 N. The thickness of the adhesive is thicker when we implement a low pressure, the cross linking reaction is incomplete because the transmittance of adhesive, and the bonding strength is weak. The thickness of the adhesive is thinner with the gain of the pressure we implement, the adhesive get exposure abundant in the same exposed time, and bonding strength get enhanced. The bonding strength get decrease slightly when we implement a excessive pressure. because the adhesive is pressured to both sides of the crystal at the time, leading to the intermediate layer get excessive little. We found the shear force of $LiNbO_3$ is bigger than quartz when comparison between different crystal. The reason is that they have different roughness in bonding surface and UV light transmittance. $LiNbO_3$ and quartz in the band of transmittance about 75%-85%[4] and 90%[5] respectively.

3.2, Fracture energy test

Test the fracture energy of bonding wafer by the method of crack-opening, shown as figure 7, t_b represents the thickness of the blade; w represents the width of the bonding wafer; $t_{w\,1}$ represents the thickness of the bonded wafer 1;$t_{w\,2}$ represents the thickness of the bonded wafer 2; E_1 represents the Young's modulus of the wafer 1; E2 represents the Young's modulus of the wafer 2; L

represents the length of the crack. This method uses the bonded elastic force of separate pieces and the bonding force of cracking at the top to establish equilibrium equation and obtains the average fracture energy of bonding[6].

$$\gamma = \frac{3t_b^2 E_1 t_{w1}^3 E_2 t_{w2}^3}{16L^4(E_1 t_{w1}^3 + E_2 t_{w2}^3)}$$

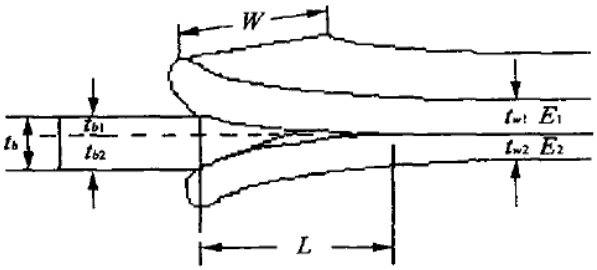


Fig.8 Crack-opening method

To $LiNbO_3$ bonded wafer as an example make crack-opening test, find the value of E_1 is 160Gpa, E_2 is 72.8Gpa, t_{w1} and t_{w2} is 500 μ m, the value of t_b is 2mm, the width of the wafer w is 8mm. We use the wafer fabricated in the bonding wafer experiment implement 30N pressure do crack-opening test, measured the length of crack is 9.3mm. Calculated the fracture energy of $LiNbO_3$ bonded wafer is 5.831J / m^2.

3.3, Research for thickness of intermediate layer

Cut the $LiNbO_3$ bonded wafer into 5mm×5mm square sample with diamond cutting machine, then scanning the intermediate layer by SEM. The results are shown as figure 9. The thickness of the intermediate layer is approximately 3 microns and uniformity well. Table 2 shows some foreign researchers for thickness range of intermediate layer bonding material. In comparison, intermediate layer bonding based on UV curing can obtain uniform, thinner layer and its thickness less than other similar curing photosensitive material. The bonding can meet bonding strength better and to minimize the effects of layer thickness to the device at the same time.

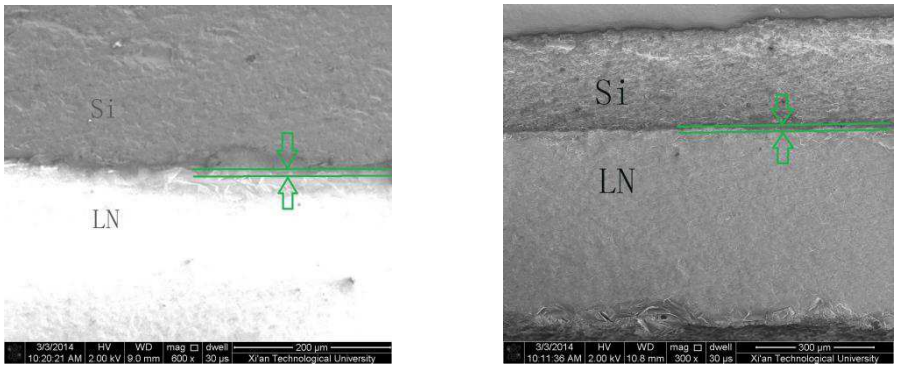


Fig.9 SEM photographs of the bonding cross-section

Table. 2 Thickness of common material intermediate layer[4]

Interface materials	thickness / μm
SU-8	20~30
BCB	15~25
JSR-137N	20~30
AZ-4620	10~20

4. Conclusions

This paper realized piezoelectric crystal and silicon wafer bonding by using new polymer materials NOA61. Working out the optimum process of intermediate layer bonding. Get 8 mm×8 mm bonding wafer, then test the shear stress of the sample, results shown: The shear strength of $LiNbO_3$ bonded wafer is greater than 116.2 N. The fracture energy get 5.831 J/m^2 by the method of crack-opening test. The thickness of the intermediate layer about 3 microns observed with SEM. UV adhesive curing can be applied in piezoelectric crystal and silicon layer bonding successfully.

Acknowledge:Project supported by High-end CNC machine tools and basic manufacturing equipm ent technology major projects(2013ZX04006011), The fund of the Key Laboratory of Science and Technology on Low-light-level Night Vision (No.J20130203), Shanxi Provincial Department of education study abroad personnel funded projects (608-000030)

References

[1]wang qi.Thermo-optic switch device based on Norland optical adhesive [J], Chinese Optics, 2012:194-197

[2]Brouckaert J, Roelkens Getal . Silicon-on-insulator nanophotonic waveguide circuit for fiber-to-the-home transceivers[J],Optics Express, 2008, 13(25) :21-25

[3]Cheng wen-jin, Tang zi-rong, Intermediate Layer Bonding for Silicon and Glass Based on UV[J], Journal of seminconductors, 2008:181-182

[4]Yan tao, Growth, Structure and property of high quality of $LiNbO_3$ and $LiTaO_3$ crystal[D], Shan Dong University, 2011

[5]Wang Qiangtao, Stria observation and its influence and transmittance in quartz crystal[J], Journal of Chinese ceramic society, 2010:193-195

[6]Chen Li-Guo, Sun Li-Ning, Measurement system for wafer bonding strength[J], Journey of test and measurement technology, 2005:137-140

Key Engineering Materials Vols 645-646 (2015) pp 92-97
© (2015) Trans Tech Publications, Switzerland
doi:10.4028/www.scientific.net/KEM.645-646.92

Submitted: 2014-11-13
Accepted: 2014-12-23

Quantitative production of charges with a carbon nanotubes coated electrode based on Trichel pulses

Fucheng Deng[a], Lingyun Ye[b*] and Kaichen Song[c]

College of Biomedical Engineering and Instrument Science, Zhejiang University, Hangzhou 310027, China

[a]dunfen@zju.edu.cn, [b]lyye@zju.edu.cn, [c]kcsong@zju.edu.cn

Keywords: quantitative charges, carbon nanotubes, Trichel pulses.

Abstract. This paper presents a novel method of quantitative production of charges with a carbon nanotubes (CNTs) coated electrode. It is based on the Trichel pulse (TP) discharge which is characterized as highly regular current pulses. The charge-per-pulse transported in the discharge gap is nearly constant for a given condition. The total charges produced in unit time are an integer times of charge-per-pulse. The amount of charges and production velocity can be easily and quantitatively controlled, which may be of importance for some particular applications, such as electro-fluid-dynamic (EFD) actuator, reaction control in plasma-chemical synthesis and lab-on-a-chip. The effects of humidity and temperature on the charge-per-pulse also have been experimentally investigated and extensively analyzed.

Introduction

Since the discovery of carbon nanotubes (CNTs) by Ijima in 1991 [1], publications and patent filings on CNTs have increased exponentially and many potential applications have been proposed, such as conductive composites, electrochemical devices, hydrogen storage, field emission devices, nanometer-sized electronic devices, sensors and actuators [2-4]. It has been demonstrated that carbon nanotubes could be used to fabricate miniaturized gas ionization sensors, which work by fingerprinting the electrical breakdown characteristics of distinct gases [5]. To some extent, this kind of gas ionization sensors is essentially based on corona discharge which has been extensively used in many applications, including electrostatic precipitation, electro-photography, static control in semiconductor manufacture, destruction of toxic compounds, production of ozone, and so on [6, 7].

Specifically, Trichel pulse (TP) discharge is the initial regime of negative corona discharges, which is characterized as highly regular current pulses. This rather peculiar discharge phenomenon was first studied by Trichel [8] and further improved by Loeb [9, 10]. Lama and Gallo [11] carried out a systematic study and presented the electrical characteristics of the TPs as functions of the applied voltage, gap spacing and tip radius. It is of great interest that the charge-per-pulse, charges produced and transported in the gap during a discharge pulse, is nearly constant. Theoretically, since Morrow [12] proposed a one-dimensional (1D) model to successfully explain the development of the TPs, many researchers have worked on the subject to get an improved understanding of the mechanism of TPs [13-17].

In this paper, we report a novel method of quantitative production of charges with a carbon nanotubes coated electrode based on TPs. A needle-to-plate structure is implemented with a CNTs coated sharp electrode and a plate electrode. The amount of total charges and the velocity of production can be conveniently and quantitatively controlled, which may be of importance for some particular applications, such as electro-fluid-dynamic (EFD) actuator [18], reaction control in plasma-chemical synthesis [19] and lab-on-a-chip[20].

Experimental Setup

It is well-known that carbon nanotubes are good materials for cathode or electron emission devices. Acid-treated multi-walled carbon nanotubes (MWCNTs) were used to make the cathode in the present experiments. The MWCNTs sample (purchased from Beijing BOYU GAOKE new materials

Co., Ltd.) was with a purity of over 95%. The length of the nanotube was 10–30 μm and the diameter was less than 8 nm. 1 mg of the sample was dispersed in 1 mL of absolute ethyl alcohol and then an ultrasonic processing was performed for 15 min, forming a well-distributed black suspension of MWCNTs with a concentration of 1 mg/mL.

An inexpensive sewing needle made of nickel-plated steel was used as support electrode. The electrode was firstly polished and then cleaned with ultrasound for 20 min in absolute ethyl alcohol and deionized water, respectively. After the electrode had been dried, a droplet of the MWCNTs suspension (about 1 μL) was dripped on the tip of the electrode. After the ethyl alcohol had volatilized, a film of MWCNTs was coated on the tip of the electrode. The CNTs modified needle tip was observed with microscope and the curvature radius of the tip was about 20 μm.

The experimental scheme is shown in Fig. 1. The CNTs coated electrode was used as cathode and the ITO (Indium Tin Oxide) glass was used as anode. The ITO glass was a round plate with a thickness of 1mm and a diameter of 15mm. The needle-to-plate system was placed in a temperature/ humidity chamber (ESPEC, SH-261) which could provide an environment with specific temperature and relative humidity (RH) at atmospheric pressure. An adjustable high voltage DC source (GAMMA, RR10-2R/DDPW) was used to apply a particular constant negative voltage to the cathode. The micro ammeter could monitor the average discharge current. The waveform of TPs could be monitored with an oscilloscope (Agilent, Infiniium 54832D MSO). A microcontroller (TI, TMS320F2810) based system has been designed to continuously measure the repetition frequency of TPs, control the electronic switch, communicate with a computer and upload the measurement results.

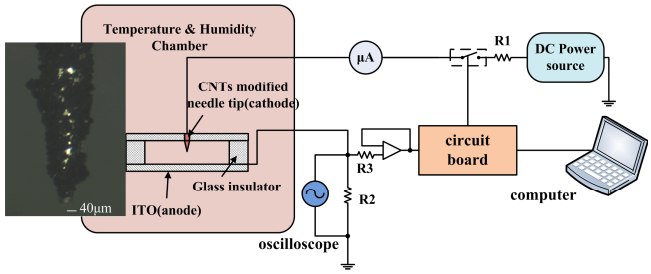


Fig.1 Schematic diagram of experimental setup.

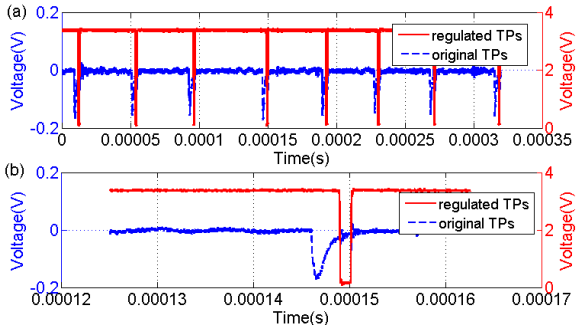


Fig. 2 Typical waveforms of TPs (a) TPs sequence; (b) zoomed view of one typical TP.

Results and Discussions

Quantitative Production of Charges. In the experiments, the gap spacing was set to 2 mm. The gas in the chamber was room air. The temperature and RH set to 20 °C and 60%, respectively. No current was detected until the voltage applied to the cathode increased to a threshold. The current abruptly rose from zero to 1 or 2 μA. At this time, unstable pulses were observed by the oscilloscope. When the applied voltage increased further and the average discharge current increased to several μA, the current pulses became stable. That is so called the regular TPs. In the present work, the measurements were taken when the current pulses were relatively regular.

The typical waveforms of TPs are shown in Fig. 2. A single TP has a sharp falling edge and a relatively slower rising edge and the pulse width is in the order of 10 ns. The observed duration of a TP is limited by the electrical characteristics of the discharge circuit and the oscilloscope and could be even shorter [10]. On the other hand, the interval of TPs is relatively much longer, in the order of 1 μs. TP regime is the initial stage of negative corona discharge and main ionizations take place only in a very small area close to the tip of cathode. The space charges, especially positive ions and electrons, are rapidly accumulated due to avalanche process. When enough negative ions are formed near the cathode due to attachment process, the ionizations are distinguished quickly. Then, the electrons swiftly reach the anode while the negative ion cloud and positive ion cloud slowly move to the anode

and the cathode, respectively. Especially, it is a relatively long way for negative ions to travel towards the anode. Once the negative ion cloud moves away from the critical ionization area, the ionization process will restart. Thus, it is the time took by the negative ion cloud to move away that primarily determines the interval of TPs. Furthermore, it can be found that the total charges produced during a pulse are nearly constant. That is so called charge-per-pulse which can be obtained in a simple method described later. In order to measure the repetition frequency of TPs conveniently, the TP signal was magnified and regulated, as is shown in Fig. 2. Then, it was further processed in the microcontroller, which could measure the TP frequency in real-time and control the electronic switch according to instructions to produce quantitative charges.

The time-averaged current of the discharge can be expressed as

$$I_{\text{mean}} = FQ_{\text{pulse}}, \tag{1}$$

where I_{mean} is the time-averaged current, F is the TP repetition frequency and Q_{pulse} is the charges-per-pulse. It is obvious that the charge-per-pulse Q_{pulse} can be obtained by computing the proportionality of average current and TP frequency. Then, the total charges produced during a period of time are

$$Q_{\text{total}} = I_{\text{mean}}\Delta t = NQ_{\text{pulse}}, \tag{2}$$

where Q_{total} is the total charges, Δt is a period of time and N is the number of pulses. Since the charge-per-pulse Q_{pulse} is a constant, a quantitative production of charges can be achieved by controlling the value of N. The number of pulses N can be counted by the microcontroller. When the number reaches the preset, the microcontroller can control the electronic switch to shut down. The frequency F represents the production velocity of charges and it is related to the applied voltage. Thus, the production velocity can be easily adjusted by changing the applied voltage.

Therefore, the value of charge-per-pulse Q_{pulse} is of importance and must be determined firstly. The measurements of the repetition frequency of TPs varying with the applied voltage were taken, as is shown in Fig. 3. Generally, the frequency increases quickly as the applied voltage grows. This can be readily understood. The larger the applied voltage is, the more intense the avalanche is, and the faster the negative ions move toward the anode. In other words, a higher voltage speeds up the recovery of electric field weakened by the space charges and shortens the interval of TPs. The relationship between the frequency and the applied voltage is obtained by a least-square fitting method and it can be expressed as

$$F = k_1 V_{\text{applied}}(V_{\text{applied}} - V_0) = 444.7 V_{\text{applied}}(V_{\text{applied}} - 2.28), \tag{3}$$

where k_1 is a constant coefficient and equals to about 444.7 kHz kV^{-2} in the experiments, V_{applied} is the applied voltage (kV) and V_0 is the threshold voltage (kV) and equals to about 2.28 kV in the experiments. The TP frequency and the average current are linearly related as is shown in Fig. 4. It can be explained that a higher frequency means a less time for the transportation of charges per pulse

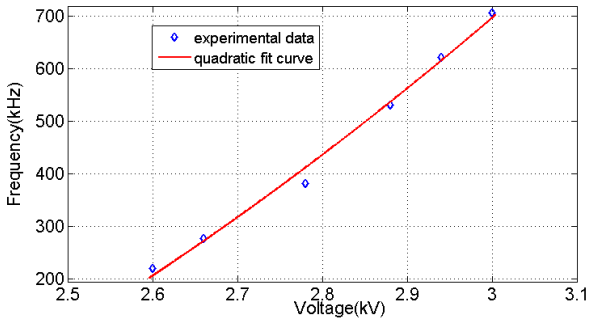


Fig. 3 TP Frequency varies with applied voltage.

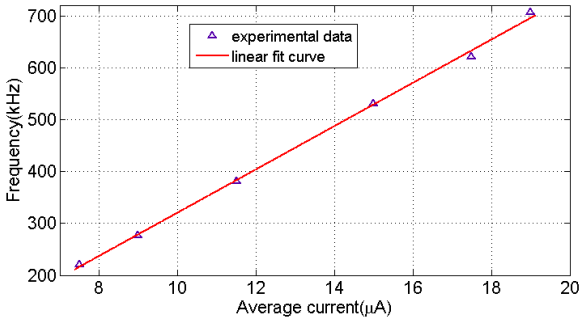


Fig. 4 TP frequency varies with average current

and thus a bigger rate of change for charge-per-pulse, i.e., a greater average current. In Fig. 4, the linear fit expression is

$$F = k_2(I_{\text{mean}} - I_0) = 34.83(I_{\text{mean}} - 4.2), \tag{4}$$

where k_2 is a constant coefficient (kHzμA^{-1}) and I_0 is the threshold current (μA). The charge-per-pulse Q_{pulse} can be easily deduced from Eq. 4 and the value is about 2.87×10^{-11} C. Therefore, it can be argued that the charges produced during a discharge are constant and transported in a quantized form in the gap. If the applied voltage is unchanged, the total charges transported per unit time are constant, which are an integer times of Q_{pulse}. The transportation velocity for the quantized charges can be conveniently accelerated by increasing the applied voltage. In other words, it is equivalent to speed up the frequency of pulses. This means that both the total charges and the velocity can be easily controlled, which is of importance for the applications.

Effect of Humidity. In this section, the effects of RH on the charge-per-pulse are studied. The gap spacing was set to 2.5 mm and the temperature was kept at 20 °C. RH continually changed from 30% to 75% in the chamber. Figure 5 depicts the TP frequency F as a function of average current with different RHs. The linear fit expressions are as follows.

$$\begin{cases} F = 41.15(I_{\text{mean}} - 3.67), \ (\text{RH=30\%}), \\ F = 37.88(I_{\text{mean}} - 1.65), \ (\text{RH=45\%}), \\ F = 41.79(I_{\text{mean}} - 2.32), \ (\text{RH=60\%}), \\ F = 31.46(I_{\text{mean}} - 3.94), \ (\text{RH=70\%}), \\ F = 22.09(I_{\text{mean}} - 3.35), \ (\text{RH=75\%}). \end{cases} \tag{5}$$

It is noted that the effect of RH on the threshold current I_0 is not obvious. The values of threshold current obtained from Eq. 5 are approximately consistent with the experimental observations. Figure 6 shows the variation of charge-per-pulse with different RHs. It can be found that the humidity did not have a great influence on the charge-per-pulse except for the cases of high humidity. In other words, the effect of humidity on charge-per-pulse becomes evident only when the relative humidity is high. Since the ionization energy of H_2O (12.59 eV) is a little greater than that of O_2 (12.06 eV) and smaller than that of N_2 (15.58 eV), water molecules in the air tend to lead to more electrons. Specifically, when the content of water molecules is large, charges are more likely to get through the gap, decelerating the accumulation velocity for space charge, especially the negative ions. Thus, more charges will produce during the interval of pulses, leading to a bigger charge-per-pulse. On the other hand, plenty of water molecules may change the characteristics of CNTs and enhance the electron emission from the cathode tip.

Moreover, it was observed in the experiments when the RH was as high as 85% and even higher, the TPs became unstable. The TPs may never appear as the RH was close to 100%. The discharge current was steady instead of a pulsating one. This can be understood that when the RH is very high

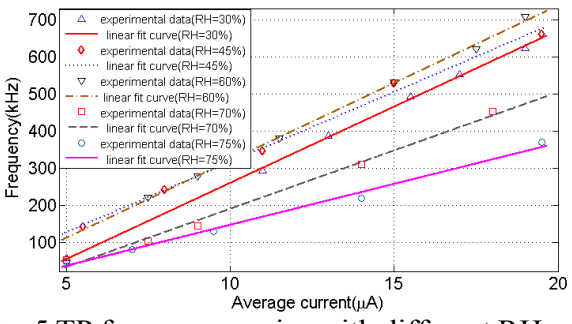


Fig. 5 TP frequency varies with different RHs

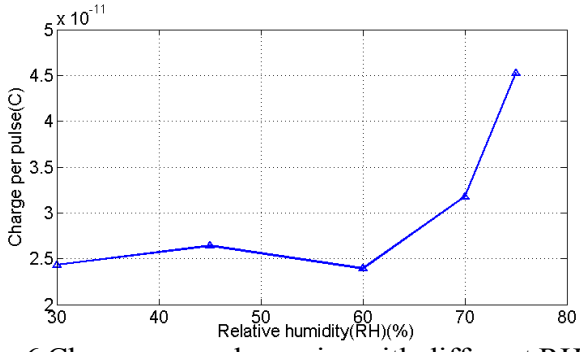


Fig. 6 Charge-per-pulse varies with different RHs

and close to the saturation point, the insulation of the air gap greatly declines. The air gap is likely to be breakdown at a small applied voltage. The discharge transforms to another form instead of TPs.

Effect of Temperature. Temperature is usually an important physical parameter concerned in applications. The effects of temperature on the charge-per-pulse were also investigated. In the experiments, the temperature T was continually changed from 40 ^{o}C to 10 ^{o}C. The Fig. 7 shows the TP frequency varies with increasing average current at different temperatures. The linear fit expressions are as follows.

$$\begin{cases} F = 19.17(I_{\text{mean}} - 1.50), \ (T{=}40^{o}\text{C}), \\ F = 22.30(I_{\text{mean}} - 2.68), \ (T{=}30^{o}\text{C}), \\ F = 23.78(I_{\text{mean}} - 2.55), \ (T{=}20^{o}\text{C}), \\ F = 41.46(I_{\text{mean}} - 4.02), \ (T{=}10^{o}\text{C}). \end{cases} \tag{6}$$

It can be noted from Eq. 6 that the threshold current I_0 increases approximately as the temperature declines. It was also found in the experiments that the TP were more likely to build up at a higher temperature. The relationship of charge-per-pulse and temperature is shown in Fig. 8. As the temperature rises, the charge-per-pulse gradually increases. It is expected that the motion of molecules and ions will be accelerated at a higher temperature. Electron avalanche is more intense. More charges need to be produced and more space charges need to accumulate, especially negative ions, to periodically extinguish the discharge in higher temperature. On the other hand, the electron emission from the CNTs coated cathode gets enhanced as the temperature increases.

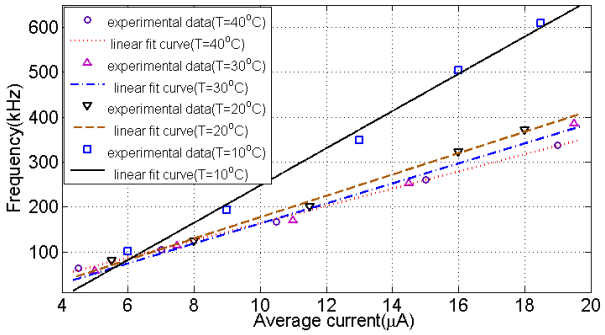


Fig. 7 TP frequency varies with temperature.

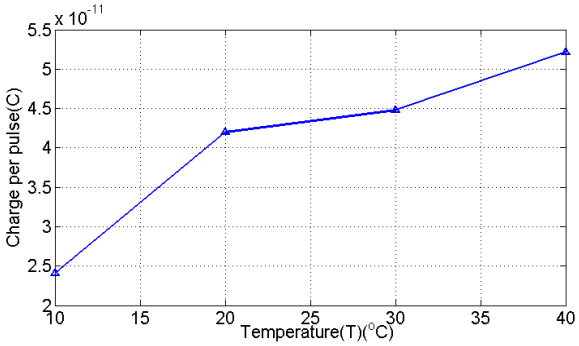


Fig. 8 Charge-per-pulse varies with temperature

Summary

A method of quantitative production of charges with a carbon nanotubes coated electrode has been proposed. It was based on the TP discharge. The charge-per-pulse transported in the discharge gap was nearly constant for a given condition. The amount of charges could be easily controlled by counting the number of pulses and the production velocity could be conveniently adjusted by changing the applied voltage with a microcontroller.

The charge-per-pulse is the most important parameter and should be predetermined in applications. It can be conveniently determined by the relationship of average current and the TP frequency. They were linearly related and the proportionality constant was the charge-per-pulse. The effects of RH and temperature on the charge-per-pulse have been investigated. It was found that the humidity did not have a great influence on the charge-per-pulse except for the cases of high humidity. The charge-per-pulse is relatively larger for higher humidity. In addition, it was observed that as the temperature rises, the charge-per-pulse gradually increases.

Moreover, the needle-to-plate structure is very simple and easy to implement. We also bring forward to the readers' attention that micro-nano technology can be considered to fabricate the structure and micro-scale device may be implemented.

Acknowledgement

This work was supported in part by the ministry of education of China under grant No. 62501040204.

References

[1] S. Iijima, Helical microtubules of graphitic carbon, Nature, 354 (1991) 56-58.
[2] R. H. Baughman, A. A. Zakhidov and W. A. de Heer, Carbon nanotubes-the route toward applications, Science, 297 (2002) 787-792.
[3] S. Geier, T. Mahrholz, P. Wierach and M. Sinapius, Carbon nanotube array actuators, Smart Mater. Struct., 22 (2013) 94003.
[4] U. Kosidlo, M. Omastová, M. Micusík, G. Ćirić-Marjanović, H. Randriamahazaka, T. Wallmersperger, A. Aabloo, I. Kolaric and T. Bauernhansl, Smart Mater. Struct., 22 (2013) 104022.
[5] A, Modi, N. Koratkar, E. Lass, B. Q. Wei and P. M. Ajayan, Miniaturized gas ionization sensors using carbon nanotubes, Nature, 424 (2003) 171-174.
[6] J. S. Chang, P. A. Lawless and T. Yamamoto, Corona discharge processes, IEEE Trans. Plasma Sci., 19 (1991) 1152-1166.
[7] G. E. Georghiou, A. P. Papadakis, R. Morrow and A. C. Metaxas, Numerical modeling of atmospheric pressure gas discharges leading to plasma production, J. Phys. D: Appl. Phys., 38 (2005) 303-328.
[8] G. W. Trichel, The mechanism of the negative point to plane corona near onset, Phys. Rev., 54 (1938) 1078-1084.
[9] L. B. Loeb, A. F. Kip, G. G. Hudson and W. H. Bennett, Pulses in negative point-to plane corona, Phys. Rev., 60 (1941) 714-722.
[10] L. B. Loeb, The mechanism of the Trichel pulses of short time duration in air, Phys. Rev., 86 (1952) 256-257.
[11] W. L. Lama and C. F. Gallo, Systematic study of electrical characteristics of Trichel current pulses from negative needle-to-plane coronas, J. Appl. Phys., 45 (1974) 103-113.
[12] R. Morrow, Theory of negative corona in oxygen, Phys. Rev. A, 32 (1985) 1799-1809.
[13] A. P. Napartovich, Y. S. Akishev, A. A. Deryugin and I. V. Kochetov, A numerical simulation of Trichel-pulse formation in a negative corona, J. Phys. D: Appl. Phys., 30 (1997) 2726-2736.
[14] Y. S. Akishev, I. V. Kochetov, A. I. Loboiko and A. P. Napartovich, Numerical simulations of Trichel pulses in a negative corona in air, Plasma Phys. Rep., 28 (2002) 1049-1059.
[15] C. Soria-Hoyo, F. Pontiga and A. Castellanos, Paritcle-in-cell simulation of Trichel pulses in pure oxygen, J. Phys. D: Appl. Phys., 40 (2007) 4552-4560.
[16] T. N. Tran, I. O. Golosnoy, P. L. Lewin and G. E. Georghiou, Numerical modeling of negative discharges in air with experimental validation, J. Phys. D: Appl. Phys., 44 (2011) 015203.
[17] P. Sattari, C. F. Gallo, G. Castle and K. Adamiak, Trichel pulse characteristics-negative corona discharge in air, J. Phys. D: Appl. Phys., 44 (2011) 155502.
[18] E. Moreau, L. Leger and G. Touchard, Effect of a DC surface-corona discharge on a flat plate boundary layer for air flow velocity up to 25 m/s, J. Electrostat., 64 (2006) 215-225.
[19] G. Vissokov, I. Grancharov and T. Tsvetanov, On the plasma-chemical synthesis of nanopowders, Plasma Sci. Technol., 5 (2003) 2039-2050.
[20] H. A. Stone, A. D. Stroock and A. Ajdari, Engineering flows in small devices: microfluidics toward a lab-on-a-chip, Annu. Rev. Fluid. Mech., 36 (2004) 381-411.

Key Engineering Materials Vols 645-646 (2015) pp 98-103
© (2015) Trans Tech Publications, Switzerland
doi:10.4028/www.scientific.net/KEM.645-646.98

Submitted: 2014-11-14
Accepted: 2014-12-23

Band Engineering of Graphene Nanomesh Field Effect Transistor under Multiscale Simulation Framework

Yawei Lv[1,2,a], Hao Wang[1,2,b*], Sheng Chang[1,2], Zhihao Yu[1,2], Jin He[1,2], Qijun Huang[1,2]

[1]School of Physics and Technology, Wuhan University, Wuhan, Hubei, China

[2]Suzhou Institute of Wuhan University, Suzhou, Jiangsu, China

[a]lvyawei@whu.edu.cn, [b]wanghao@whu.edu.cn

Keywords: multiscale simulation, graphene nanomesh, band structure, transport.

Abstract. In this paper, we investigate the impact of the size of holes in graphene nanomesh. A multiscale simulation framework is utilized to simulate different structures flexibly. These structures include an intact graphene nanoribbon (GNR), a graphene nanomesh with 4 atoms missing periodic (4-atom holes GNM), and a graphene nanomesh with 6 atoms missing periodic (6-atom holes GNM). Simulation results indicate that a subband appears in the conduction band in 6-atom holes GNM. In addition, interface states which come from the interactions among dangling bonds can significantly reduce the bandgaps of GNMs and induce a pinning effect to their Fermi energies.

Introduction

Graphene has significant potential for application in electronics, but cannot be used directly for digital logic device because it is a semimetal with a zero bandgap [1]. When it is tailored as a graphene nanoribbon (GNR) with width of less than 10nm, bandgap will appear [2]. If some atoms are removed from the ribbon periodically, a graphene nanomesh (GNM) can be obtained [3]. Since graphene nanoribbon's bandgap is inversely proportional to its width and the nanomesh's width changes periodically [4], the bandgap of graphene nanomesh can be enlarged by decreasing neck widths [5]. In this paper, this phenomenon is studied in detail with numerical simulation, and the performance of graphene nanomesh field effect transistor (FET) is studied under an open source multiscale simulation framework [6]. The results show that obvious band structure discretization appears, and interface states are also investigated in order to explain the bandgap narrowing effect in 4-atom holes GNM. The IV characteristic of GNM FET shows an appropriate size of hole can be used to enlarge the bandgap in GNR and induce a subband causing negative resistance effect.

Device Structure and Simulation Approach

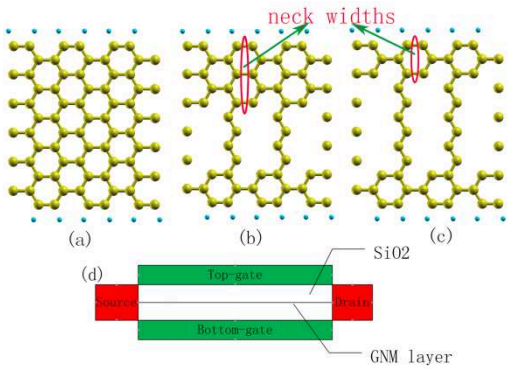


Fig. 1. Channel structure of GNR (a), 4-atom holes GNM (b) and 6-atom holes GNM (c). Three unit cells are shown respectively. The whole transistor is displayed in (d).

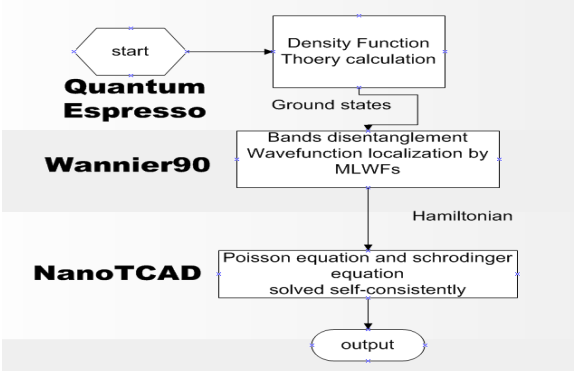


Fig. 2. Flowchart of the multiscale simulation framework.

Fig. 1 shows the structure of double gate graphene field effect transistor with GNR channel and GNM channels. Based on a 12-aGNR saturated by Hydrogen atom in Fig. 1 (a), a 4-atom holes GNM is obtained by removing four carbon atoms periodically in Fig.1 (b). And similarly, a 6-atom holes GNM is attained by removing six carbon atoms periodically in Fig.1 (c). The neck width is defined as the width of Carbon layer at the top of the hole as shown in Fig. 1 (b) and (c). It changes with the size of holes. A whole structure of the transistor is shown in Fig.1 (d). A 1nm SiO_2 layer is used as the gate oxide layer and the channel length is 30nm.

The devices are simulated with the following open source simulation tools: Quantum Espresso [7], Wannier90 [8], and NanoTCAD ViDES [9,10] as depicted in Fig. 2. The key point is to find out a tight-banding (TB) Hamiltonian *H* of the channel to study the transport characteristics. An ab-initio calculation with Quantum Espresso using density functional theory (DFT) [11] and Hartree-Fork approximation [12] gives the energy bands and wave functions of the channel structure. The wave functions are obtained from ab-initio calculation in Bloch representation. Then a transformation was made to translate them into a representation based on maximally localized Wannier functions (MLWFs) as shown in Eq. 1. The centers of MLWFs are on the actual positions of atoms or bonds in the crystal.

$$\omega_{n\vec{R}}(\vec{r}) = \frac{V}{(2\pi)^3}\int_{BZ} e^{-i\vec{k}*\vec{R}}\psi_{n\vec{k}}(\vec{r})d\vec{k}\,. \tag{1}$$

where *V* is the real-space unit cell volume of the crystal, $\vec{k}$ is the wave vector, *BZ* is the first Brillouin zone over which the integral is performed, $\vec{R}$ is Bravais lattice vector, and *n* is the band index. The phases of the Bloch function $\psi_{n\vec{k}} = e^{i\vec{k}*\vec{r}}u_{n\vec{k}}$ are arbitrary and the shapes or spatial extents are sensitive to the phases [13]. So a unitary transformation then can be carried out with Eq. 2 to minimize Ω in Eq. 3

$$u_{n\vec{k}} = \sum_{m=1}^{N} U_{mn}^{(\vec{k})} u_{m\vec{k}}\,. \tag{2}$$

$$\Omega = \sum_{m}[\langle r^2\rangle_n - \bar{r}_n^2]\,. \tag{3}$$

where U^k is a unitary matrix for mixing the bands at wave vector $\vec{k}$. Ω is a measurement of the space spread of Wannier function in analogy with Boys' definition of localized molecular orbitals [14]. Once the wavefunction is maximally localized, the TB-like orbitals can be acquired and also the TB Hamiltonian. Finally, the transport problem can be solved using Green's function [15] with the Hamiltonian obtained from Wannier function in Eq. 4

$$G(E) = [ES - H - \Sigma_S - \Sigma_D]^{-1}\,. \tag{4}$$

where *E* is the energy, *S* is overlap matrix, Σ_S and Σ_D are the self-energies of the source and drain, respectively. Note that electron-phonon interaction is not considered in this paper under ballistic transport theory. Together with Poisson equation, the whole transport characteristics are obtained within the NanoTCAD ViDES code.

Results and Discussions The band structures and their MLWF interpolation of GNR and GNMs are shown in Fig. 3. It can be observed that the interpolations match original calculations from DFT methods accurately. The 4-atom holes GNM has a narrower bandgap of 0.057eV compared with the

bandgap 0.56 eV of GNR though it has a small neck width. And the lowest one of the conduction bands in Fig, 3 (b) shows a tendency of discretization. Further enlarging the size of holes leads to a significant increase in bandgap up to 0.602eV in the 6-atom holes GNM. Furthermore, as shown in Fig. 3 (c), a sub-bandgap of 0.117eV appears between -2.746eV and -2.629eV as the result of conduction band discretization. And it can be observed that the Fermi energies of the two GNMs drop into the valence band.

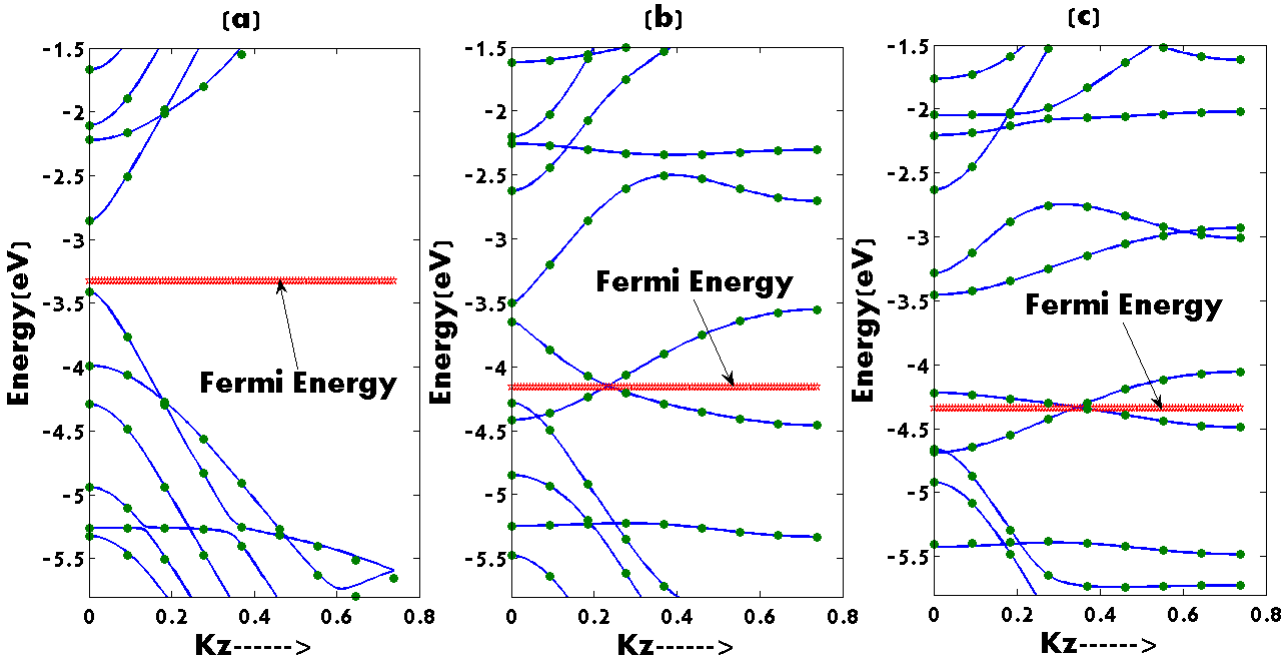


Fig. 3. Band structures (green dots) and the MLWF interpolations (blue line) of GNR (a), 4-atom holes GNM (b) and 6-atom holes GNM (c). The red lines denote Fermi energy respectively.

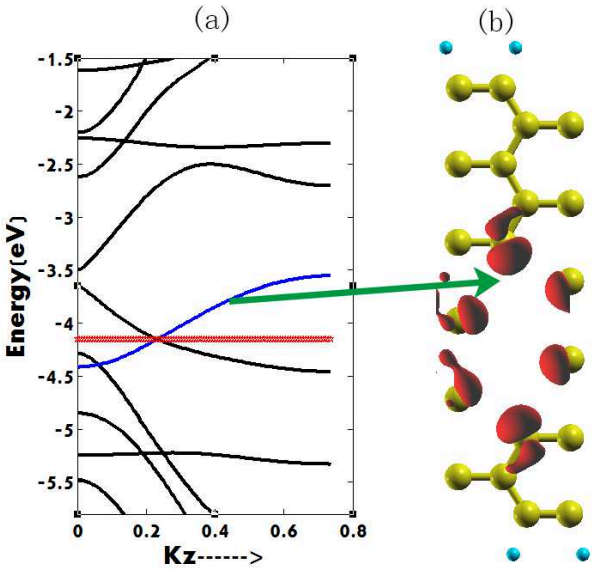


Fig. 4. Real space probability locations of states near the bandgap in 4-atom holes GNM. Yellow dots denote Carbon atoms, blue balls denote Hydrogen atoms and the red color in (b) denotes contour surface which the probability is 0.005.

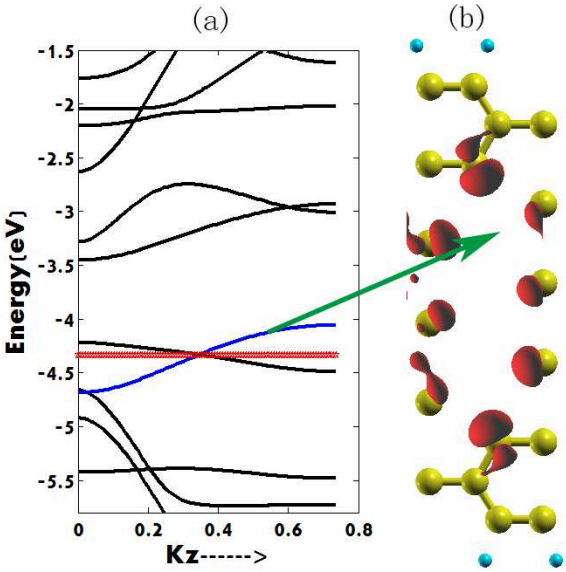


Fig. 5. Real space probability locations of states near the bandgap and the sub-bandgap in 6-atom holes GNM. Yellow dots denote Carbon atoms, blue balls denote Hydrogen atoms and the red color in (b) denotes contour surface which the probability is 0.005.

In order to investigate the reason of Fermi energies going into valence band in 4-atom holes GNM and 6-atom holes GNM and the bandgap narrowing effect in 4-atom holes GNM, the probability

$|\Psi(\vec{r})|^2$ at given wave vectors, is calculated in a periodic supercell. Fig. 4 and Fig. 5 show the real space location of the band of blue color in the two GNMs respectively. All states in these two bands are confined within the holes of each structure. These states come from the interactions of dangling bands. Therefore, they can be identified as interface states. And they cause a Fermi energy pinning effect that the Fermi energies of 4-atom holes GNM and 6-atom holes GNM move into the valence band. The holes in 4-atom holes GNM are small so that the interactions among dangling bonds become significant. A large energy rang is occupied by the interface states coming from the dangling bonds. Consequently, the bandgap is reduced in spite of a small neck width. On the other hand, the holes in 6-atom holes GNM become larger compared to 4-atom holes GNM. This leads to a weaker interface states effect as shown in Fig. 5 (a). The energy rang occupied by interface states is smaller and the neck width is also narrower than that of 4-atom holes GNM's. Thus, the bandgap is enlarged in 6-atom holes GNM.

After the translation from Bloch presentation to Wannier presentation, it is convenient to obtain the Hamiltonian matrix of tight binding model. Then the transport characteristics are calculated with Green's Function. The energy bands should be translated by a constant to fit the Green's Function calculation in order that the zero energy point is at the middle of bandgap in each structure. The transmission coefficient of 6-atom holes GNM (blue line) plotted in Fig. 6 is near zero at the energy within two black ellipses. Therefore, these ellipses denote where bandgap and sub-bandgap exists. No obvious sub-bandgaps appear in the curves of other two structures.

Fig. 7 gives the IV curves of transistor made by intact GNR terminated by Hydrogen atoms. The Ion/Ioff ratio of the GNR transistor is low to 700 when the drain voltage increases to 0.3V. Fig.7 (b) also shows a large on current which implies a good transport capability.

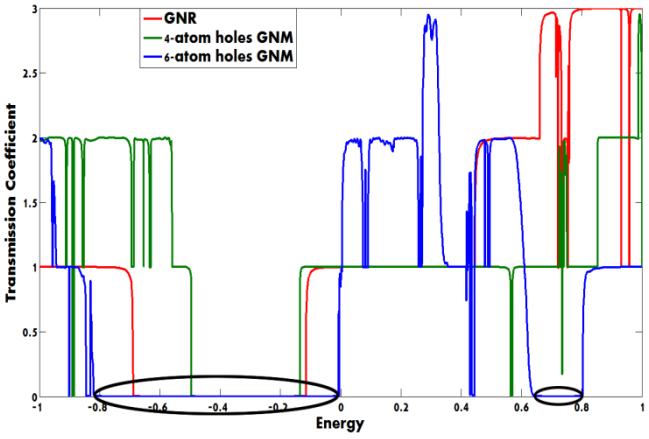


Fig. 6. Transmission coefficient of all the three structures drawn at gate voltage is 1V and drain voltage is 0.1V. It is obvious that 6-atom holes GNM has a bandgap in the bigger ellipse and a sub-bandgap in the smaller one.

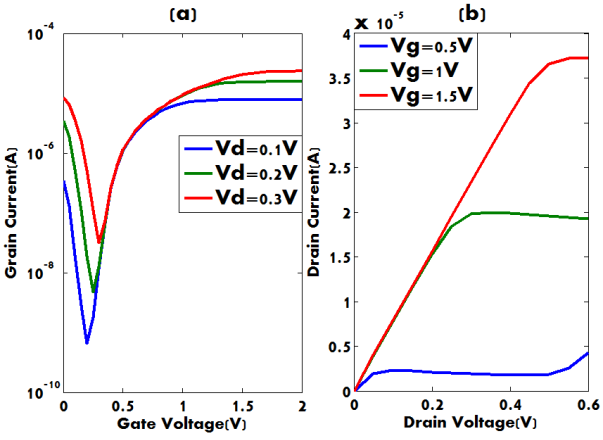


Fig. 7. Transfer characteristic curves (a) and output characteristic curves (b) of the transistor made by GNR.

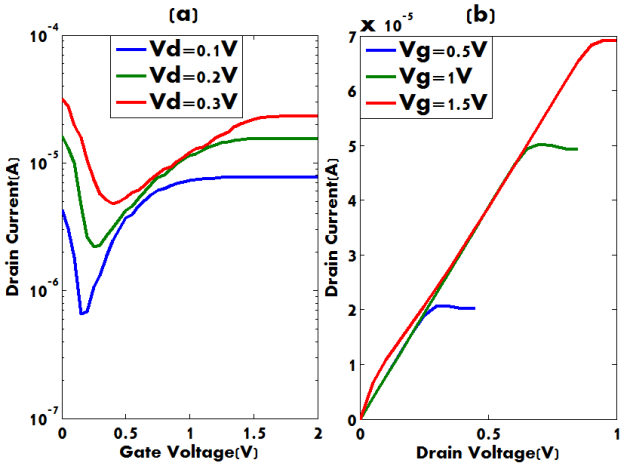


Fig. 8. Transfer characteristic curves (a) and output characteristic curves (b) of the transistor made by 4-atom holes GNM.

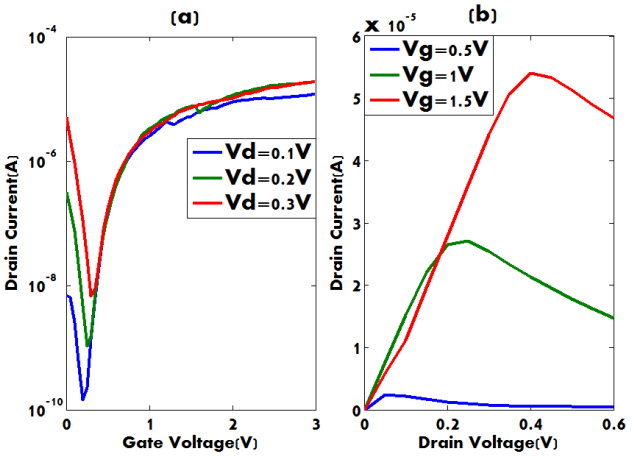


Fig. 9. Transfer characteristic curves (a) and output characteristic curves (b) of the transistor made by 6-atom holes GNM.

The transport characteristics of 4-atom holes GNM and 6-atom holes GNM are shown in Fig. 8 and Fig. 9 respectively. The 4-atom holes GNM's poorer cut off behavior and low Ion/Ioff ratio in contrast with GNR is shown in Fig. 8 (a) as a result of smaller bandgap. On the other hand, 6-atom holes GNM shows a better cut off behavior as shown in Fig. 9 (a). The Ion/Ioff ratio of this structure is 4 times of the GNR transistor at the drain voltage of 0.3V. It is worth noting that the output characteristic curves of 6-atom holes GNM in Fig. 9 (b) show a strong negative resistance effect which is similar with [16]. This phenomenon can be well explained by the sub-bandgap appearance in the bands structure of 6-atom holes GNM in Fig. 3 (c).

Summary

We have proposed and studied a novel channel structure of graphene nanomesh field effect transistor using multiscale simulation tools based on an ab-initio calculation. Band structures and transport characteristics of GNMs with different sizes of holes show that the effect of interface states can reduce the bandgaps of GNMs remarkably. Moreover, a sub-conduction band and a sub-bandgap can be induced when there is an appropriate size of holes in GNM. The proposed structures and effects show that it is straightforward to modulate the band structure of GNM FET by removing atoms, which gives it a potential application for low power consumption or high performance devices in the future.

Acknowledgement

This work was supported by the National Natural Science Foundation of China (grant Nos. 61204096 and J1210061), the Specialized Research Fund for the Doctoral Program of Higher Education of China (grant No. 20110141120074), the Fundamental Research Funds for the Central Universities, Wuhan University (grant No. 2042014kf0238), and the Science Foundation of Jiangsu Province, China, (grant No. BK20141218).

References

[1] H.S.P. Wong, D. Akinwande, Carbon nanotube and graphene device physics, Cambridge University Press, Cambridge, 2011.
[2] X. Li, X. Wang, L. Zhang, Chemically derived, ultrasmooth graphene nanoribbon semiconductors, Science. 319 (5867) 1229-1232.
[3] J. Bai, X. Zhong, S. Jiang, Graphene nanomesh, Nat. Nanotechnol. 5 (2010) 190-194.

[4] Y.W. Son, M.L. Cohen, S.G. Louie, Energy gaps in graphene nanoribbons, Phys. Rev. Lett. 97 (2006) 216803.
[5] X. Liang, Y.S. Jung, S. Wu, Formation of bandgap and subbands in graphene nanomeshes with sub-10 nm ribbon width fabricated via nanoimprint lithography, Nano. Lett. 10 (2010) 2454-2460.
[6] S. Bruzzone, G. Iannaccone, N. Marzari, An Open-Source Multiscale Framework for the Simulation of Nanoscale Devices, IEEE Trans. Electron Dev. 61 (2014) 1-1.
[7] P. Giannozzi, S. Baroni, N. Bonini, QUANTUM ESPRESSO: a modular and open-source software project for quantum simulations of materials, J. Phys.: Condens. Matter. 21 (2009) 395502.
[8] A.A. Mostofi, J.R. Yates, Y.-S. Lee, wannier90: A tool for obtaining maximally-localised Wannier functions, Comput. Phys. Commun. 178 (2008) 685-699
[9] G. Fiori, G. Iannaccone, Simulation of graphene nanoribbon field-effect transistors, IEEE Electron Dev. Lett. 28 (2007) 760-762.
[10] H. Wang, S. Chang, Y. Hu, A Novel Barrier Controlled Tunnel FET, IEEE Electron Dev. Lett. 35 (2014) 7.
[11] R.M. Martin, Electronic structure: basic theory and practical methods, Cambridge university press, Cambridge, 2004.
[12] R.G. Parr, W. Yang, Density Functional Theory of Atoms and Molecules, Oxford University Press, Oxford, 1989.
[13] N. Marzari, A.A. Mostofi, J.R. Yates, Maximally localized Wannier functions: Theory and applications, Rev. Mod. Phys. 84 (2012) 1419-1475.
[14] I. Souza, N. Marzari, D. Vanderbilt, Maximally localized Wannier functions for entangled energy bands, Phys. Rev. B. 65 (2001) 035109.
[15] A. Martinez, M. Bescond, J.R. Barker, Svizhenko, A self-consistent full 3-D real-space NEGF simulator for studying nonperturbative effects in nano-MOSFETs, IEEE Trans. Electron Dev. 54 (2007) 2213-2222.
[16] V.H. Nguyen, F. Mazzamuto, J. Saint-Martin, Graphene nanomesh-based devices exhibiting a strong negative differential conductance effect, Nanotechnology. 23 (2012) 065201.

Key Engineering Materials Vols 645-646 (2015) pp 104-109
Submitted: 2014-11-24
© (2015) Trans Tech Publications, Switzerland
Accepted: 2014-12-23
doi:10.4028/www.scientific.net/KEM.645-646.104

Growth and magnetic properties of three-dimensional firtree-like cobalt microcrystals with hierarchical dendritic superstructures

Xi Yang[1, 2, a *], Zhi-bing Fu[1, b], Lei Yuan[1, c], Chao-yang Wang[1, d], Qian-wang Chen[2, e]

[1]China Academy of Engineering Physics, Rearch Center of Laser Fusion, Mianyang, 621900
[2]Hefei National Laboratory for Physical Sciences at Microscale, Department of Materials Science & Engineering, University of Science and Technology of China, Hefei 230026

[a]xingxingysx@163.com, [b]fuzhibingcn@aliyun.com, [c]yuanlei0211@163.com, [d]wzxhw@tom.com, [e]cqw@ustc.edu.cn

Keywords: Magnetic materials; Chemical synthesis; Crystal growth

Abstract. Novel ordered three-dimensional (3D) firtree-like hexagonal cobalt microcrystals with hierarchical dendritic superstructures have been obtained by using cobalt bis (4-pyridine carboxylate) tetrahydrate as the precursor of Co. The 3D dendrite has a main axis and the leaves arrange layer by layer in parallel along the axis, which exhibit the radiate hexagonal arrangement from the axis in a layer. The main axis of the dendrite grows along the [001] direction of hexagonal Co and the leaves grow parallel to the (001) plane. The hysteresis loop of the sample shows a ferromagnetic behavior with the saturation magnetization of 134.0 emu/g and the coercivity of 184.9 Oe. It is noted that the coercivity is relatively low compared with that of the cobalt dendritic crystallites reported previously, which may result from the lower total morphology anisotropy of our sample.

Introduction

Cobalt nanomaterials have attracted great attention for their interesting magnetic, electrical, optical, and catalytic properties [1]. It is well known that these properties depend on the size and morphology of nanomaterials significantly; so much attention is focused on the fabrication of Co nanomaterials with specific structures and shapes recently. Several methods are available for this, such as template methods [2], physical routes [3] and chemical methods [4]. Cobalt materials with various morphologies have been prepared with chemical methods, such as disks [5], wires [6], belts [7], spheres [8], chains [9], dendrites [10] and so on. Dendritic materials are important topics because they are significant in physics studies and have potential applications in the catalysis and technological fields [10-11]. Cobalt hierarchical structures with dendrites were obtained by liquid-phase reduction [12-20]. For example, Large-scale dendritic cobalt was successfully obtained via solution synthetic route at room temperature firstly [12]. The highly ordered snowflakelike hexagonal cobalt microcrytals were prepared through a controlled slow-release precipitation process under mild conditions, in which it is easy to control the morphology and structure of crystals by adjusting the reaction parameters such as reaction time and the concentration of reductant [13]. Zhu et al. synthesized the flowery three-dimensional (3D) Co dendritic superstructures via a hydrothermal reduction route and suggested the superstructures were formed by self-assembly of Co dendrites [14].

As reported previously, they suggested Co dendrites grew and then the superstructures were formed by self-assembly of these dendrites [13-15]. However, the formation process of the 3D firtree-like dendritic superstructures we prepared can not be explained by this self-assembled mechanism due to the experiment results. Herein, a metal organic complex cobalt bis (4-pyridine

carboxylate) tetrahydrate ($CoL_2(H_2O)_4$) was selected as the precursor of Co and the ordered 3D firtree-like hierarchical dendritic crystallites were obtained, on which there were few reports. Meanwhile, a possible growth mechanism and magnetic properties are studied. The products have relatively low coercivity compared with other cobalt dendritic crystallites [12-18].

Experimental details

All the reagents were of analytical grade and used without further purification. In the first step, the metal organic complex $CoL_2(H_2O)_4$ was synthesized by a hydrothermal method according to the literature [15]. In a typical synthesis, 0.1 mmol of $CoL_2(H_2O)_4$ was dispersed into 20 ml 25wt% Ammonia solution (NH3). A brown-yellow solution was prepared after vigorous magnetic stirring for half an hour. Then 3 mmol of sodium hypophosphite (NaH_2PO_2) was added with constant stirring. The final mixture was transferred into a Teflon-lined stainless steel autoclave (50 ml capacity), which was closed tightly and maintained at 160 ℃ for 24 hours. After the autoclave was cooled to room temperature, the black powders were settled at the bottom of the autoclave and collected by using a magnet. And then the solid product was rinsed with distilled water and ethanol several times respectively and finally dried in air at room temperature.

Results and discussion

The chemical composition and the phase of the obtained products were determined by X-ray diffraction (XRD). The XRD pattern of the typical sample is shown in Figure 1, in which all the diffraction peaks are well consistent with the standard card (JCPDS 89-4308, P63/mmc, a = 2. 505 Å, c = 4. 089 Å). This designates that the samples can be identified as hexagonal cobalt, and no other phases can be detected. Compared with the neighboring peak (101), the relative intensity of peak (002) in patterns increases significantly, indicating the oriented growth of the products.

The FESEM was used to investigate the morphologies and structure of the products. Figure 2a-2c show the SEM images of the as-prepared sample. As what can be observed from Figure 2a, the product consists of a majority of 3D firtree-like dendritic microcrystals, whose size is in the range of tens of micrometers. Figure 2b is a high magnification image of an individual 3D dendrite. It displays that the 3D hierarchical superstructure has a main axis and the leaves arrange layer by layer in parallel along the axis. Seen from the tip of the axis (Figure 2c), the leaves exhibit the radiate hexagonal arrangement from the center. Some isolated small corncob-like crystallites are also observed from Figure 2b, which may be the initial form of the firtree-like 3D dendritic crystals. This can be demonstrated by the sample obtained for 1h (Figure 2d). It is observed that the 3D crystallites heated for 1h are similar to the corncob-like crystals. The boxed area reveals that the main axis is a hexagonal prism and the flakes grow on the columnar facets. Figure 2e displays the image of the sample synthesized by using $CoCl_2$ as the precursor of Co. The products are some irregular microflakes. This means that the metal complex $CoL_2(H_2O)_4$ is the key to the formation of 3D cobalt dendritic superstructures.

The growth orientation of the 3D superstructures was characterized by the HRTEM. Figure 3a is the TEM image of a leaf shed from the 3D dendrite by ultrasonication, which shows a clear vein-like structure. The SAED patterns in Figure 3b and 3d illustrate a single crystal nature of the leaf, which indicates that the normal orientation of the leaf is [001] of hexagonal cobalt. The corresponding HRTEM images (Figure 3c and 3e) show a lattice spacing of 0.22nm, which can be indexed to {100} planes of hexagonal Co. These results conform to the characteristics of the XRD

pattern in Figure 1. The normal direction of the leaf flake is along the main axis (Figure 2b), so the main axis of the 3D dendrite grows along the [001] direction of hexagonal Co and the leaves grow parallel to the (001) plane.

Based on the studies above, the formation of the 3D superstructures could not be formed through the self-assembly of dendrites. It is suggested that the $CoL_2(H_2O)_4$ precursor plays a structure-directing role in the formation process of the hierarchical structures due to the experiment results and previous literature [21]. The possible schematic illustration of the formation process is shown in Figure 4. The strong coordination between cobaltous ion and ligands may lead to two results. One is that the isonicotinate groups bind to certain crystal faces of the cobalt nuclei [6-7], and this varies the surface energy of these planes. Then the varieties yield anisotropies in the kinetic limit [1], which induces the anisotropic growth of the cobalt nuclei. In the initial reaction stage, the cobalt (II) was reduced by NaH_2PO_2, and the cobalt nuclei were generated. The oriented growth of the cobalt nuclei led to the formation of main axis along the [001] direction. The relatively rapid growth would induce the tapered morphology, which can explain the experiment phenomenon that the primary axis of the corncob-like crystals is tapered (Figure 2b) [22-23]. Then the selective adsorption of the isonicotinate groups would guide the formation of a few layers of the precipitation on the columnar surface of the primary axis [21]. As a result, the new crystals grew on the columnar facets of the main axis as the secondary growth and initiated the hierarchical growth process. In addition, the Co^{2+} is not easily ionized out into the solution, resulting in the slow reaction rate [24]. And this can regulate the growth of Co nanoparticles and further control the structure and morphology of the products. On the basis of the diffusion limited aggregation (DLA) model, the interaction between the stochastic diffusive force and directive force may induce the formation of branch structures [25]. These secondary crystals would grow into leaf-like flakes perpendicular to the main axis. Finally, the ordered firtree-like dendritic superstructure is formed.

Figure 5 displays the hysteresis loop of as-synthesized sample measured at room temperature (300K), which demonstrates a ferromagnetic behavior of the sample. The saturation magnetization (Ms) and the coercivity (Hc) are 134.0 emu/g and 184.9 Oe, respectively. Both of the values are lower than those of bulk cobalt (Ms=168 emu/g, Hc= 1500Oe) [26]. The inevitable surface-oxidation may be a reason for the decrease of saturation magnetization [27]. Furthermore, the moment fluctuation of the surface moments is larger than the interior and this moment fluctuation effect in the layer under the surface-oxide layer would reduce the Ms [28]. It is noticed that the coercivity of the sample is lower than those of the cobalt dendrites previously reported (above 200Oe) [12-18]. The reason may lie in that the assembly manner of our 3D dendrite has lower shape anisotropy as a total than that in previous literatures (From Figure 2c, it is observed that the leaves show a radiate hexagonal arrangement from the axis.) [29].

Conclusions

In summary, ordered 3D firtree-like hexagonal cobalt dendritic superstructures have been prepared with a metal complex precursor $CoL_2(H_2O)_4$ by hydrazine reduction. The dendrite has a main axis along the [001] direction and the leaves, which grow parallel to the (001) plane, arrange layer by layer along the axis. The complex ligands are proposed to be responsible for the formation of 3D dendrite. The hysteresis loops measured at 300 K reveals a ferromagnetic behaviour with saturation magnetization of 134.0 emu/g and coercivity of 184.9 Oe. The coercivity is lower than that of other cobalt dendritic crystallites, which may result from the lower total morphology anisotropy of our sample.

Acknowledgement

This work was supported by the Natural Science Foundation of China (No. 51101141).

Figures:

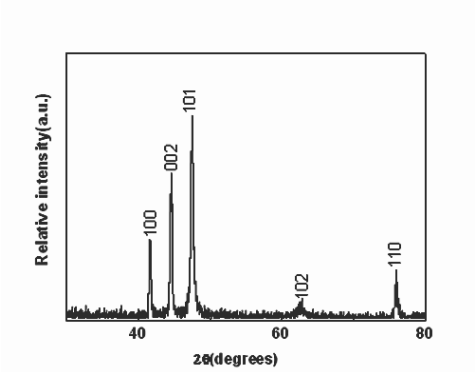


Figure 1. XRD pattern of a typical sample

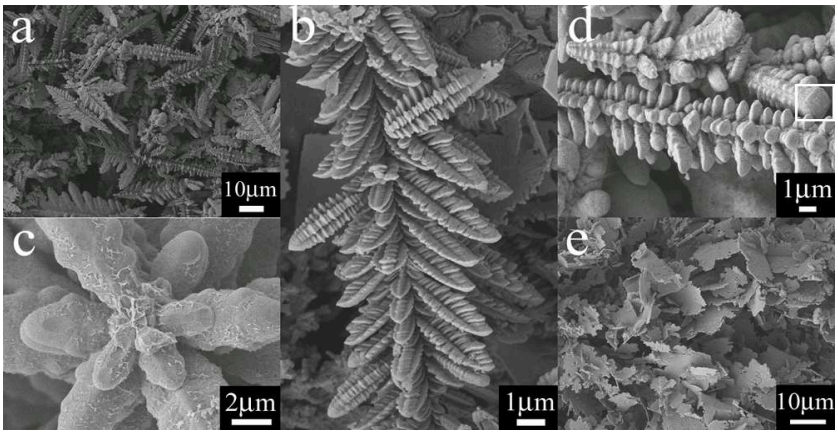


Figure 2. (a-c) SEM images of the sample prepared for 24h at different magnifications; (d) SEM images of the sample obtained for 1h; (e) SEM image of the sample synthesized by using $CoCl_2$ as the precursor of cobalt

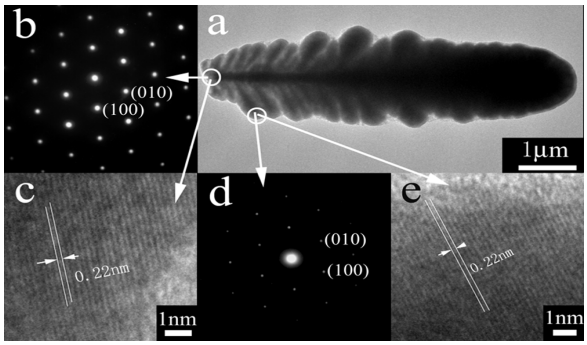


Figure 3. TEM images at low resolution (a) and high resolution (c, e) of the leaf; (b, d) SAED patterns taken from the white circled areas in (a).

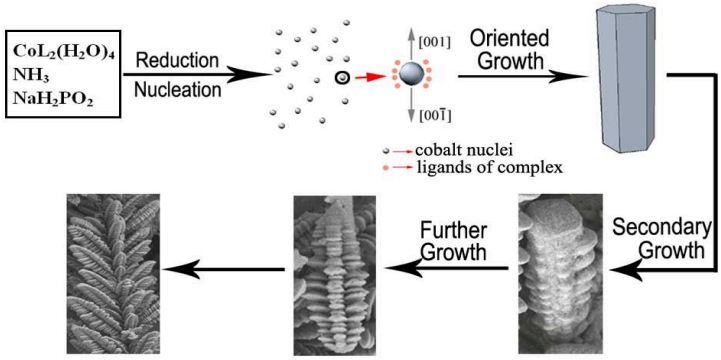


Figure 4. Schematic illustration of the formation process of the ordered firtree-like dendritic superstructures.

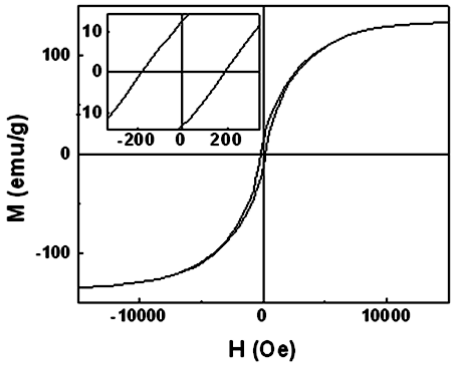


Figure 5. Magnetic hysteresis loop of the sample measured at room temperature.

References:

[1] V.F. Puntes, D. Zanchet, C.K. Erdonmez, and A.P. Alivisatos, Synthesis of hcp-Co Nanodisks, J. Am. Chem. Soc. 124 (2002) 12874-12880.

[2] A.K. Srivastava, S. Madhavi, T.J. White, and R.V. Ramanujan, Template assisted assembly of cobalt nanobowl arrays, J. Mater. Chem. 15 (2005) 4424-4428.

[3] Z.Q. Liu, H. Hashimoto, E. Sukedai, M. Song, K. Mitsuishi, and K. Furuya, In situ observation of the formation of Fe_3O_4 in Fe_4N (001) due to electron irradiation, Phys. ReV. Lett. 90 (2003) 25504.

[4] Y.L. Hou, H. Kondoh, and T. Ohta, Self-Assembly of Co Nanoplatelets into Spheres: Synthesis and Characterization, Chem. Mater. 17 (2005) 3994-3996.

[5] V.F. Puntes, K.M. Krishnan, and A.P. Alivisatos, Colloidal Nanocrystal Shape and Size Control: The Case of Cobalt, Science 291 (2001) 2115-2117.

[6] Q. Xie, Y.T. Qian, S.Y. Zhang, S.Q. Fu, and W.C. Yu, A Hydrothermal Reduction Route to Single-Crystalline Hexagonal Cobalt Nanowires, Eur. J. Inorg. Chem. 12 (2006) 2454-2459.

[7] Q. Xie, Z. Dai, W.W. Huang, J.B. Liang, C.L. Jiang, and Y.T. Qian, Synthesis of ferromagnetic single-crystalline cobalt nanobelts via a surfactant-assisted hydrothermal reduction process, Nanotechnology 16 (2005) 2958-2962.

[8] L.P. Zhu, W.D. Zhang, H.M. Xiao, Y. Yang, and S.Y. Fu, Facile Synthesis of Metallic Co Hierarchical Nanostructured Microspheres by a Simple Solvothermal Process, J. Phys. Chem. C 112 (2008) 10073-10078.

[9] Y.J. Zhang, Q. Yao, Y. Zhang, T.Y. Cui, D. Li, W. Liu, W. Lawrence, and Z.D. Zhang, Solvothermal Synthesis of Magnetic Chains Self-Assembled by Flowerlike Cobalt Submicrospheres, Cryst. Growth & Des. 8 (2008) 3206-3212.

[10] X. M. Liu, W.L. Gao, S.B. Miao, and B.M. Ji, Versatile fabrication of dendritic cobalt microstructures using CTAB in high alkali media, J. Phys. Chem. Solids 69 (2008) 2665-2669.

[11] R. Qiu, X.L. Zhang, R. Qiao, Y. Li, Y.I. Kim, and Y.S. Kang, CuNi Dendritic Material: Synthesis, Mechanism Discussion, and Application as Glucose Sensor, Chem. Mater. 19 (2007) 4174-4180.

[12] Y.C. Zhu, H.G. Zheng, Q. Yang, A.L. Pan, Z.P. Yang, and Y.T. Qian, Growth of dendritic cobalt nanocrystals at room temperature, J. Cryst. Growth 260 (2004) 427-434.

[13] X.H. Liu, R. Yi, Y.T. Wang, G.Z. Qiu, N. Zhang, and X.G. Li, Highly ordered snowflakelike metallic cobalt microcrystals, J. Phys. Chem. C 111 (2007) 163-167.

[14] L.P. Zhu, H.M. Xiao, W.D. Zhang, Y. Yang, and S.Y. Fu, Synthesis and Characterization of Novel Three-Dimensional Metallic Co Dendritic Superstructures by a Simple Hydrothermal Reduction Route, Cryst. Growth & Des. 8 (2008) 1113-1118.
[15] Y.L. Li, J.Z. Zhao, Y.C. Zhu, D.C. Ma, Y. Zhao, S.N. Hou, F. Yan and Z.C. Wang, Controlled synthesis of rice ear-like cobalt microcrystals at room temperature, Colloids Surf. A: Physicochem. Eng. Aspects 356 (2010) 156-161.
[16] H.Y. Chen, R.H. Zhou, C.J. Xu, Y.Q. Liu, G.Z. Zhao, Cobalt microtrees assembled by dendrites: Hydrothermal synthesis and their enhanced magnetic properties, Mater. Lett. 99 (2013) 1-4.
[17] Y.J. Zhang, S.W. Or, Z.D. Zhang, Hydrothermal self-assembly of hierarchical cobalt hyperbranches by a sodium tartrate-assisted route, RSC Advances 1 (2011) 1287-1293.
[18] R.H. Wang, J.S. Jiang, M. Hu, Metallic cobalt microcrystals with flowerlike architectures: Synthesis, growth mechanism and magnetic properties, Mater. Res. Bull. 44 (2009) 1468-1473.
[19]C. Wang, X.J. Han, X.L. Zhang, S.R. Hu, T. Zhang, J.Y. Wang, Y.C. Du, X.H. Wang, P. Xu, Controlled synthesis and morphology-dependent electromagnetic properties of hierarchical cobalt assemblies, J. Phys. Chem. C 114 (2010) 14826-14830.
[20] R. Qiu, P. Wang, D. Zhang, J.J. Wu, One-step preparation of hierarchical cobalt structure with inborn superhydrophobic effect, Colloids Surf. A: Physicochem. Eng. Aspects 377 (2011) 144-149.
[21] T.R. Zhang, W.J. Dong, M.K. Brewer, S. Konar, R.N. Njabon, and Z.R. Tian, Site-Specific Nucleation and Growth Kinetics in Hierarchical Nanosyntheses of Branched ZnO Crystallites, J. Am. Chem. Soc. 128 (2006) 10960-10968.
[22] Y.H. Tong, Y.C. Liu, C.L. Shao, R.X. Mu, Structural and optical properties of ZnO nanotower bundles, Appl. Phys. Lett. 88 (2006) 123111.
[23] A. Taubert, C. Kubel, D.C. Martin, Polymer-Induced Microstructure Variation in Zinc Oxide Crystals Precipitated from Aqueous Solution, J. Phys. Chem. B 107 (2003) 2660-2666.
[24] Y. Tang, and Q.W. Chen, A Simple and Practical Method for the Preparation of Magnetite Nanowires, Chem. Lett. 36 (2007) 840-841.
[25] T.C. Halsey, B. Duplantier, and K. Honda, Multifractal Dimensions and Their Fluctuations in Diffusion-Limited Aggregation, Phys. ReV. Lett. 78 (1997) 1719-1722.
[26] H.L. Niu, Q.W. Chen, H.F. Zhu, Y.S. Lin, and X. Zhang, Magnetic field-induced growth and self-assembly of cobalt nanocrystallites, J. Mater. Chem. 13 (2003) 1803-1805.
[27] X.M. Ni, D.G. Li, Y.F. Zhang, and H.G. Zheng, Complexant-assisted Fabrication of Flowery Assembly of Hexagonal Close-packed Cobalt Nanoplatelets, Chem. Lett. 36 (2007) 908-909.
[28] J.G. Li, Y. Qin, X.L. Kou, H.Y. He, and D.K. Song, Structure and magnetic properties of cobalt nanoplatelets, Mater. Lett. 58 (2004) 2506-2509.
[29] D.L. LesliePelecky, and R.D. Rieke, Magnetic properties of nanostructured materials, Chem. Mater. 8 (1996) 1770-1783.

Key Engineering Materials Vols 645-646 (2015) pp 110-114
© (2015) Trans Tech Publications, Switzerland
doi:10.4028/www.scientific.net/KEM.645-646.110

Submitted: 2014-12-03
Accepted: 2014-12-23

The thermal decomposition behavior of graphene oxide/HMX composites

Zeng Guiyu[1,a], Zhou Jianhua[1,b], Lin Congmei[1,c*]

[1] Institute of Chemical Materials, CAEP, Mianyang, China

[a]guiyuzeng@sina.com, [b]zhoujh@caep.cn, [c]lincmei2009@163.cn (corresponding author)

Keywords: HMX; Graphene oxide (GO); thermal decomposition; activation energy

Abstract. Graphene oxide(GO) was prepared by Hummers method and GO/1,3,5,7-tetranitro-1,3,5,7- tetrazocine (HMX) composite was prepared via an ultrasonic compounding method. The structure of GO was characterized using XRD and SEM, the thermal decomposition of HMX and GO/HMX composite was analyzed by DSC/TG test. The results show that interlayer space of GO increases markedly, the thermal decomposition process of HMX can be promoted with the nanolayer structure of GO, resulting the reduced thermal decomposition activation energy of about 50 kJ/mol with 1% GO.

Introduction

Graphene is an outstanding functional material with many advantages, it is the thinnest known material in the universe and the strongest ever measured. Its charge carriers exhibit giant intrinsic mobility, have zero effective mass, can travel for micrometers without scattering at room temperature, and can sustain current densities six orders of magnitude higher than that of copper, etc. [1]. Graphene has been widely concerned in all aspects for its excellent properties, considerable works have been reported in the last decade. Simultaneously, graphene is potential to be used in many fields for these properties, such as transistors, sensors, energy storage, ultra capacitors [2-5]. However, grapheme is neither hydrophilic nor lipophilic and cannot be used in specific application.

Graphene oxide (GO) is a derivative of graphene bearing oxygen functional groups on its basal planes and edges, an individual sheet is relatively thin, with only several layers which enable diffusion distance smaller than most other nanoparticles or nanostructures [6,7]. GO exhibits good performance such as high energy and thermal stability [8].The tunable oxygen functional groups facilitate the modification on the surface and make it a promising material for preparing composites with other materials, for example, graphene oxide can be compounded with organic energetic material to form energetic composite and presents an opportunity for nanoscale energetic materials, improving the performances of energetic materials.

1,3,5,7-tetranitro-1,3,5,7- tetrazocine (HMX) is an energetic material with high energy density, good thermal stability and proper mechanical sensitivity. It is frequently used as an important component of high-power missile ordnances, pyrotechnics and solid propellants. The thermal decomposition of HMX has significant influence on its application performance. With a small quantity of GO added, the thermal decomposition of HMX may be affected by the nanostructure and heat transfer property of GO. However, there are few studies focused on the effect of GO on the thermal decomposition of HMX. Herein, the influence of GO on the thermal decomposition of HMX was studied by differential scanning calorimetry (DSC) and thermogravimetry (TG).

Experimental

Materials. HMX (mean particle size is 25.6μm) was purchased from Gansu Yinguang Chemical Industry Group Co., Ltd of China, graphite(D_{90} is 40μm) was provided by Qingdao Yingshida graphite Co., Ltd, concentrated H_2SO_4 (98%), potassium permanganate ($KMnO_4$), sodium nitrate ($NaNO_3$),hydrogen peroxide (H_2O_2, 30%), concentrated Hydrochloric acid (HCl, 37%), $NaBH_4$, $BaCl_2$ were purchased from Tianjin Chemical Reagent Co.

Sample Preparation. Graphite oxide was synthesized from powdered flake graphite (40μm, 400 mesh) according to Hummers method [9]. The 1000ml three-necked flask was placed in an ice-water mixture, then concentrated H_2SO_4 (98%, 120ml) was put into the flask, the solution was under stirring and the temperature was kept at 0 ^oC. $NaNO_3$ (2.0g) and flake graphite (5.0g) were then added while stirring. After mixing, $KMnO_4$ (15.0g) was added slowly and mixed well. The reactants reacted for 2h under 10-15 ^oC and stirring strongly, then heated to 35 ^oC and stirred for 1h. Add 230ml de-ion water slowly and heat to about 98 ^oC. Stir for 40min, and add H_2O_2 (50ml, 30%) and deionized water (300ml). The mixture was filtered, washed with dilute HCl (5%) and deionized water until no $SO4^{2-}$ can be detected from the filtrate (validated by $BaCl_2$). The product after washing was dried at 60 ^oC for 24 h under vacuum and finally GO sample was obtained.
GO/HMX composite was prepared by ultrasonic compounding with a mass ratio of 1:99. Typically, 0.1g GO and 9.9g HMX were added into a beaker, 50g ultrapure water was then added to the mixture under stirring. After stirring for a few minutes, the suspension was ultrasonicated (220V, 250W) for 1h. The product was solid-liquid separated and dried at 60 ^oC for 12h under vacuum. GO/HMX composite was then obtained.

Characterization Methods. The crystal structure of GO was determined by Bruker D8 Advance X-ray diffraction (XRD). Granularity was characterized using a Malvern 2000 Laser Sizer. The particle morphology was analyzed by scanning electron microscopy (SEM, JEOL JSM-6380LV). The thermal decomposition experiments were carried out using SAT 449C synchronous thermal analyzer (NETZSCH), the experimental conditions were as follows: sample mass was 2.0-2.5 mg, measuring temperature range was 20-400 ^oC, heating rate was 2, 5, 10, and 20 K/min, respectively, and the nitrogen flow rate was 30 ml/min.

Results and Discussion

Structure of GO. The XRD patterns of GO and graphite are shown in Fig.1, their SEM images are shown in Fig.2.

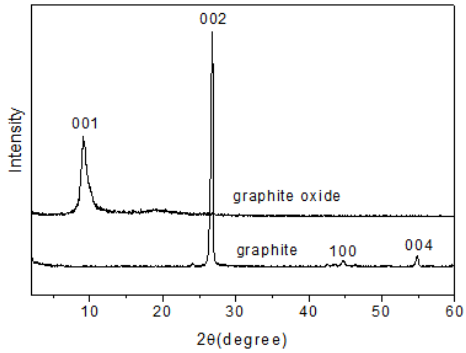


Fig.1 The XRD patterns of graphite and GO

From Fig.1, it can be seen that graphite flakes have a layered structure and the layer distance is 0.331nm (2θ=26.8º). During the oxygenation process, the new forming functional group of -OH,

-COOH, epoxy inserted the layers, so the characteristic peak (002) of graphite has disappeared after oxygenation, and GO has a new characteristic peak (001), the layers' distance of GO is increased to 0.964nm (2θ=9.15º).

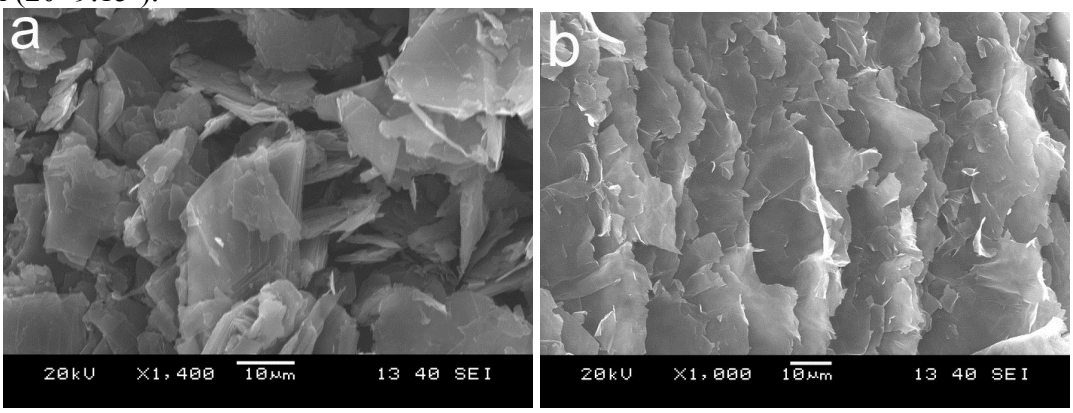


Fig.2 The SEM images of graphite (a) and GO (b)

SEM images reveal that the GO material has a lamellar structure and the exfoliated layered structure exhibits an agglomerated state, the film layer is thin, indicating the separation between the graphite layers is better and lower layer lamellar structure has been formed.

Thermal Property. The TG curves of HMX and GO/HMX are shown in Fig.3, the thermal property data are listed in table 1.

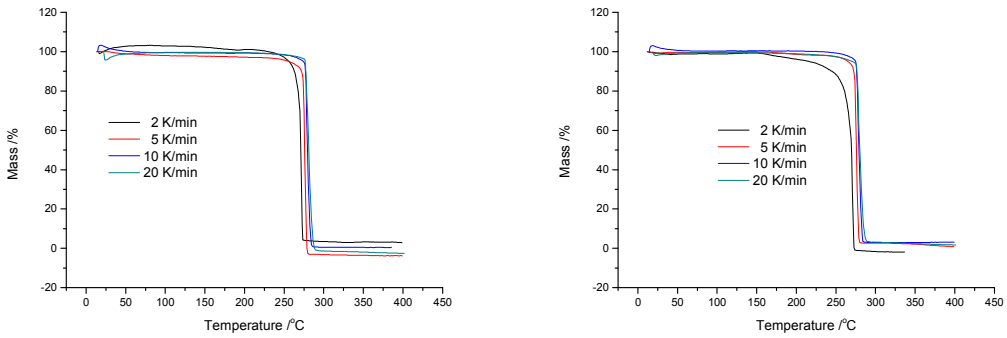


Fig.3 The TG curves of HMX (left) and GO/HMX composite (right) at different heating rate

It can be seen from fig.3 that HMX and GO/HMX composites exhibit similar orderliness to heating rate, i.e., with the increase of heating rate from 2K/min to 10K/min, the decomposition temperature gradually occurred in advance, TG curve shifts to higher temperature direction. But the shape of TG curve maintain unchanged when GO was added, indicating a negligible effect of GO on the general thermal decomposition behavior of HMX.

Table 1 The endothermic and exothermic temperature of HMX and GO/HMX at different heating rate

heating rate [K.min^{-1}]	samples	Endothermic peak [^{o}C]	Exothermic temperature at 20% decomposition [^{o}C]
2	HMX	191.9	266.5
	GO/HMX	188.5	260.9
5	HMX	196.0	274.4
	GO/HMX	193.7	272.2

It can be seen from table1 that GO can decrease the phase transformation temperature and thermal decomposition temperature of HMX, the decrease value can reach above 2 °C and 5 °C respectively for phase transformation and 20% HMX decomposition under the heating rate of 2K/min, showing GO can promote the thermal process of HMX.

The activation energy. When calculating activation energy, Ozawa method does not consider the reaction mechanism, so it will not bring miscalculation for different reaction mechanism and often be used to validate the reliability of activation energy calculated by other methods. Based on the TG curves of different heating rate, the equation for calculating thermal decomposition activation energy via Ozawa kinetic method is as follows:

$$\lg \beta = \lg\left[\frac{AEa}{RF(\alpha)}\right] - 2.315 - 0.4567\frac{Ea}{RT} \quad (1)$$

Where:

β is the heating rate, $K \cdot min^{-1}$; A is the pre-exponential factor,s^{-1}; Ea is the activation energy, $J \cdot mol^{-1}$; R is the universal gas constant, 8.314 $J \cdot mol^{-1} \cdot K^{-1}$; $F(\alpha)$ is the thermal decomposition mechanism function; α is the decomposition degree or transform ratio,%; T is the temperature, K.

For Eq.1, a straight line is obtained when $lg\beta$ is plotted against $1/T$, the activation energy (Ea) of the samples can be calculated from the slope. From the TG curve, the temperature can be achieved when decomposition degree α is 0.2, 0.3, 0.4, 0.5, 0.6, 0.7, 0.8, 0.9 under given heating rate, the data are listed in table 2 and table 3.

Table 2 The decomposition activation energy of HMX under different decomposition degree

α	Temperature[°C]				Ea
	β= 2 K/min	β= 5 K/min	β= 10 K/min	β= 20 K/min	[kJ/mol]
0.2	266.5	274.4	276.6	278.6	416.6
0.3	269.1	275.1	278.2	279.5	488. 1
0.4	270.2	275.5	278.7	280.3	515.5
0.5	270.9	275.9	279.3	281.1	515.3
0.6	271.2	276.4	279.9	281.9	492.4
0.7	271.6	276.9	280.7	283.0	473.2
0.8	272.1	277.5	281.5	284.2	447.0
0.9	272.7	278.4	282.7	285.8	416.7
mean					470.6

Table 3 The decomposition activation energy of GO/HMX under different decomposition degree

α	Temperature[°C]				Ea
	β= 2 K/min	β= 5 K/min	β= 10 K/min	β= 20 K/min	[kJ/mol]
0.2	260.9	272.2	275.1	277.8	262.9
0.3	265.6	274.9	277.7	278.6	363.4
0.4	268.2	275.4	278.3	279.3	441.1
0.5	269.6	275.8	278.9	280.1	480.5
0.6	270.3	276.3	279.6	280.9	479.8
0.7	270.8	276.8	280.2	281.9	470.7
0.8	271.4	277.5	281.1	283.1	452.2
0.9	272.1	278.3	282.1	284.9	421.9
mean					421.6

Table 2 and Table 3 show the influence of GO and heating rate on the thermal decomposition of HMX. The heating rate is an important factor for the thermal decomposition of HMX, the decomposition peak shifts to a higher temperature with the heating rate increases. At a constant

heating rate, this decomposition temperature will also increase as the decomposition degree enhances. The mean thermal decomposition activity energy *Ea* of HMX is 470kJ/mol, while *Ea* of GO/HMX composite is 421 kJ/mol and decreases by about 50kJ/mol. This shows GO can decrease the energy barrier of HMX during thermal decomposition and promote the thermal decomposition reaction. The GO provided catalysis is obvious for thermal decomposition of HMX, probably due to the good heat-transfer property of GO, which can transfer the heat produced by the thermal decomposition of HMX to the reaction system rapidly and promote the thermal decomposition. Furthermore, the nanostructure of GO can form lots of localized hotspots where energy is localized, consequently, this nanostructure also cause the thermal decomposition process occur in advance.

Summary

In this study, we produced the graphene oxide (GO) by Hummers' method and GO/HMX composite using ultrasonic compounding method. The prepared GO has a layer distance of 0.964nm which is higher than that of graphite (0.331nm). The heating rate is an important factor in the thermal decomposition of HMX, the decomposition peak shifts to a higher temperature as the heating rate increases. 1% GO has obvious influence on the thermal decomposition of HMX , it can decrease the decomposition temperature and activation energy by 5 ^{o}C and 50kJ/mol respectively, GO provides obvious catalysis effect on the thermal decomposition of HMX.

Acknowledgment. This work was supported by Natural Science Foundation of China and China Academy of Engineering Physics (NSAF found No.U12301054).

References

[1] A K Geim. Graphene: status and prospects. Science, 324(2009)1530-1534.

[2] Gilje S, Han S, Wang M, et al. A chemical route to graphene for device applications. Nano letters, 7(2007)3394-3398.

[3] W Yang, K R Ratinac, S P Ringer, et al. Carbon nanomaterials in biosensors: should you use nanotubes or graphene?. Angewandte Chemie International Edition, 49(2010)2114-2138.

[4] Hu Y H, Wang H, Hu B. Thinnest Two‐Dimensional Nanomaterial—Graphene for Solar Energy. ChemSusChem, 7(2010)782-796.

[5] Celebi K, Buchheim J, Wyss R M, et al. Ultimate Permeation Across Atomically Thin Porous Graphene. Science, 6181(2014) 289-292.

[6] Krishnan D, Kim F, Luo J, et al. Energetic graphene oxide: challenges and opportunities. Nano Today, 2(2012)137-152.

[7] Yang G W, Xu C L, Li H L. Electrodeposited nickel hydroxide on nickel foam with ultrahigh capacitance. Chem. Commun., 48 (2008)6537-6539.

[8] Sarah Claypool, Kaushik Kalaga, Arava Leela Mohana Reddy,et al. Graphene Based Energetic Materials: A Case Study. Graphene, 1(2013)11–15.

[9] Kovtyukhova N I, Ollivier P J, Martin B R, et al. Layer-by-layer assembly of ultrathin composite films from micron-sized graphite oxide sheets and polycations. Chemistry of Materials, 3(1999) 771-778.

Key Engineering Materials Vols 645-646 (2015) pp 115-119
© (2015) Trans Tech Publications, Switzerland
doi:10.4028/www.scientific.net/KEM.645-646.115
Submitted: 2014-12-05
Accepted: 2014-12-23

Facile Fabrication of Super-hydrophobic Surfaces by Spray PTFE

A. Yang Wang[1] B. Hai Feng Zhang[1*] C.Xiao Wei Liu[1]

[1]MEMS Research Center , Harbin Institute of Technology, China, Harbin

Keywords: hydrophobic polytetrafluoroethylene tin oxide water contact angle coating

Abstract. We have developed a combination of electro –deposition and spraying methods to prepare water-repellent tin oxide/ polytetrafluoroethylene(SnO_2/PTFE) coating. The coating has a high water contact angle. The resulting porous and lowest surface energy hydrophobic groups ($-CF_3$) has a water contact angle of 165° and a sliding angle of 7°, showing super-hydrophobic property. The coating with good adhesion on substrates and the long-term stability can be fabricated on various metal substrates.

Introduction

In recent years, many papers were published dealing with the preparation of super-hydrophobic surfaces, with water contact angles (WCAs) higher than 150℃,[1-5] because of their importance in daily life and industrial processes, such as self-cleaning coatings, in microfluidic devices and for drag reduction in fluid flow.[4] It is well known that geometric factor and surface roughness are two factors which governed hydrophobic property. For example, there is the unusual phenomenon of super-hydrophobicity, such as the lotus leaf, taro and the wings of cicada, which is usually called the "lotus effect". [5]

Artificial super-hydrophobic surfaces with WCAs larger than 150° and very low WSAs have been prepared by various processing methods through increasing the surface roughness and changing surfaces with hydrophobic material.[6-9] Previously, many methods have been studied to prepare super-hydrophobic surfaces with WCAs larger than 150, using techniques such as sol-gel, plasma treatment, electro-deposition and spraying.[13-15] However, it is well known that the various super-hydrophobic surfaces are either weak which can be scraped off easily, or expensive which cannot be applied in the large-are coatings. Polytetrafluoroethylene (PTFE) with many characters, such as low surface adhesion, low surface energy, high gas permeability, low toxicity, climate hardiness, and excellent chemical stability, is an ideal material to prepare super-hydrophobic surfaces.[16] In this paper, tin oxide/polytetrafluoroethylene (SnO_2/PTFE) super-hydrophobic coatings are demonstrated, which possess long-term stability and high adhesion on substrates. We fabricated super-hydrophobic surface using electro-deposition of thin oxide to enhance surface roughness and then spraying PTFE to the coating to optimize surface roughness and energy, which have micrometer-nanometer-scale binary structure roughness and lowest surface energy hydrophobic groups (-CF3).[17] The SnO2/PTFE super-hydrophobic surface coatings have mild temperature, high combination strength fabricated, which can be applied in the industry widely.

Experimental

Super-hydrophobic surfaces were fabricated on stainless steel（30mm×20mm×0.8mm） by electroplating tin in solvent and spraying PTFE solvent (distilled water/ethanol/isobutyl alcohol in a volume fraction of 2:5:1). 6 g of stannous chloride and 0.3 g gelatin were added to 200 ml of 1:19 mixture (by weight) of HCL and distilled water, which was called solution A. Solution B was 200 ml of 3:1:16 mixture of hydrochloric, H2O2 and distilled water. The stainless steel (2J85) includes 0.03 wt % carbon, 0.20 wt % manganese, 0.020 wt % sulfur, 0.02 wt % phosphorus, 25 wt % chromium, 11.5 wt % cobalt, 1.10 wt % silicon and margin.

The method of fabricating the stable super-hydrophobic surface is as follows: The stainless steel were dipped in solution B for 50 min to eliminate oxide layer of metal surfaces at room temperature and then cleaned with acetone in an ultrasonic bath for 5 min. The sheets which were placed at cathode were electroplated in the solution A at 0.1Adm-2 and the pure tin placed at anode. After a deposition time of 15 min, the samples were taken out of solution and dried at 160in the vacuum oven for 12 hours to form tin oxide coating. Then the coatings were sprayed PTFE solvent with 0.2MPa nitrogen gas and curing 150 for 1 h.

Morphologies of the coatings were observed on a FEI-430 scanning electron microscope (SEM) at 20 kV. The composition of the product was also characterized by an axis ultra X-ray photoelectron spectrometer (XPS). Sessile water contact angle (CA) values were acquired using a JC-2000C1 optical contact angle meter (Zhong Chen Company, China) at room temperature (20). The average CA value was determined by measuring the same sample at five different positions. The image of the droplet was obtained by digital camera (Canon).

Results and discussion

First, the film of PTFE is deposited on the substrate by spraying process. A typical scanning electron microscopy (SEM) image is shown in Fig 1a. The WCA on the surface is about 110°, because there is no obvious micrometer-scale or nanometer-scale structure on the substrate. Second, we prepared film of SnO_2 on stainless steel by electroplating tin and dried the film over 150 for 12 hours. Fig. 1b shows the particle morphology of these porous materials synthesized by the proposed process observed from scanning electron microscopy (SEM). As can be seen, the samples are composed of SnO_2 particles with irregular shapes, which results provide the rough surface coatings. The micro-particles on top of micrometer sized particles provide roughness. Herein, the SnO_2 particles affect the super-hydrophobic of coatings by changing surface roughness and lowing surface energy with strong strength between the particles and the substrate. Although the water contact angle on this surface coating is about 145°, the coating with only micro-roughness and surface energy are not enough to form super-hydrophobicity.

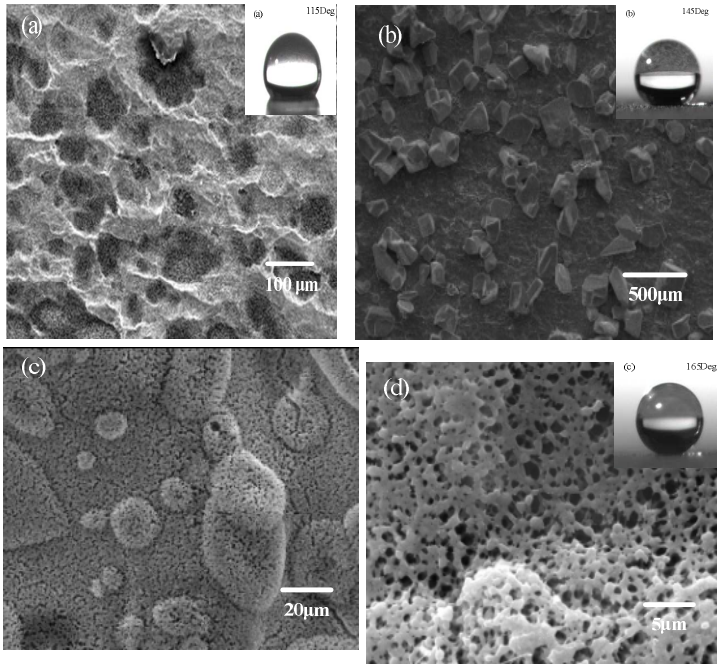


Figure.1. SEM images at different magnification of surface microstructures. Pure PTFE coating (a), SnO_2 coating (b), SnO_2/PTFE coating (c), SnO_2/PTFE coating at high magnification.

Finally, we fabricated super-hydrophobic coatings by electro-deposition of tin oxide and spraying PTFE to fabricated micrometer-nanometer-scale binary structure roughness and lowed surface energy. The WCAs of composite coatings increased from 145°to 165°. Fig. 1c clearly shows porous

structures and more detailed morphology is shown in Figure. 1d. The composite coating surfaces not only have over the WCAs of 160° but also low the WSAs, implying that the water droplets could be moved upward easily. These results provide strong evidence that SnO_2/PTFE coating surface with the hierarchical micrometer-nanometer-scale binary structure roughness, which achieve the super-hydrophobic surfaces. Consequently, a rough hydrophilic surface will become super-hydrophilic, as can be seen in the Cassie and Wenzel modes [19]. In the Cassie mode, the water droplets do not penetrate into the surface cavities in the roughness regime and sit partially on the surface air pockets. The apparent contact angle can be calculated using the following Cassie equation [20].

$$\cos\theta = u_1 \cos\theta_1 + u_2 \cos\theta_2 \quad (1)$$

where θ_i and u_i are the Young angle and the fraction of surface relative to phase, respectively. θ is the apparent contact angle in the Cassie mode.

In the Wenzel case, liquid completely fills the grooves of the rough surface where they contact. The apparent contact angle can be described by the following equation [21]:

$$\cos\theta_w = r\cos\theta \quad (2)$$

where θ_w is the apparent contact angle and is the intrinsic contact angle. r is the area ration between the effective and the geometric areas.

X-ray photoelectron spectroscopy (XPS) analysis is used to investigate the composition and structure of the prepared the SnO_2/PTFE. Fig. 2a shows the XPS survey spectrum of the SnO_2 coating surface by electroplating and it can be seen that elements of Sn, O and C are detected. Fig. 2b shows the XPS survey spectrum of the SnO_2 coved by PTFE and F, C and O are indicated, implying that the coating is covered by PTFE. Therefore, the SnO_2/PTFE coatings are vital to fabricate the porous structure, which form super-hydrophobic surfaces on stainless steel.

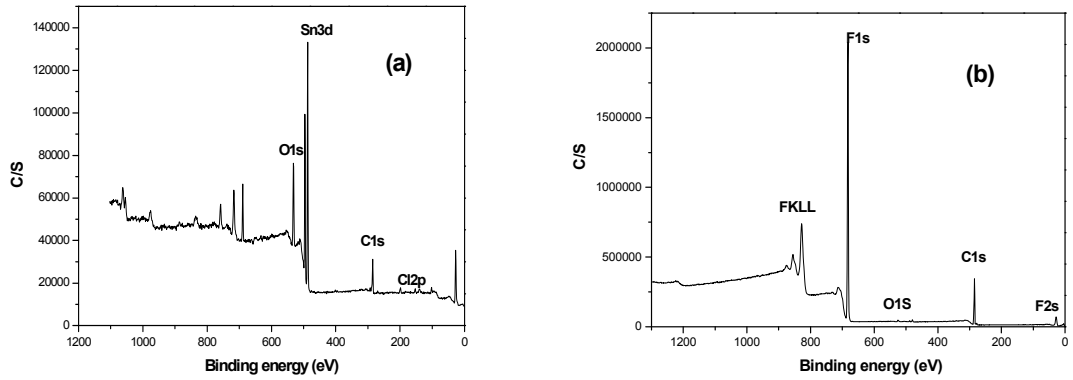


Fig.2. XPS survey spectrum of (a) SnO_2 coating and (b) SnO_2/PTFE coating

The shapes of water droplets on SnO_2/PTFE composite coating surfaces are shown in Fig. 3, which shows that the water droplets on the coating can remain almost perfect sphere. The water droplet can slide easily downward when the surface is only slightly titled. Furthermore, its super-hydrophobic is tested at different time. After several weeks of storage in air, the value of water contact angle and sliding angle remain essentially constant, showing that super-hydrophobicity has long-term stability.

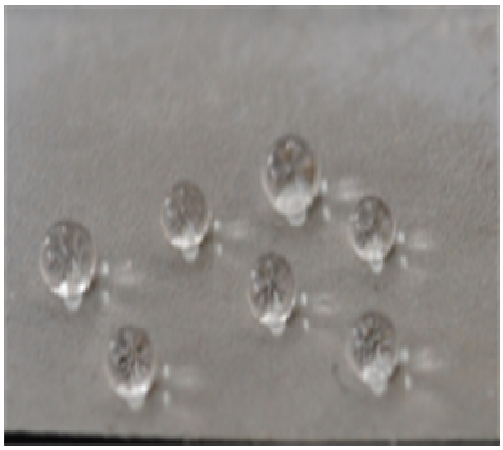


Fig.3. Optical images of water droplets floating on the SnO_2/PTFE coating surface.

Interestingly, the fabricated SnO2/PTFE coating shows the super-hydrohobicity not only for pure water but also corrosive liquids. Fig.4 shows the relationship between different PH and contact angle on the coating surface with experimental error, keeping a value larger than 155°. These results are very useful that shows the SnO2/PTFE coating can be used in various conditions to prevent engineering materials from corrosive liquid.

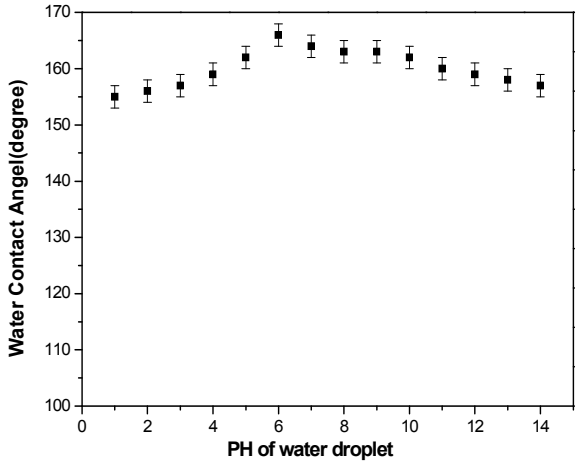


Fig.4. Relationship between pH of water droplets and water CA on the coating surface.

Conclusions

In conclusion, we report a simple and conventional process to obtain a super-hydrophobic SnO_2/PTFE composite coating using electro-deposition and spraying process. The coating surface with both micrometer- nanometer-scale binary structure and lowest surface energy was fabricated on the stainless steel with water contact angles lager than 155° and long-term stability over wide pH range when exposed to the environment for corrosive water. It is expected that this economical technique can be employed in a wide variety large area super-hydrophobic materials with both industrial and scientific applications.

Acknowledgments

The authors would like to thank National Basic Research program of China (No. 2012CB934104) and National Science Foundation of China (No. 61071037) for financial support.

References

[1] X.T. Zhu, Z.Z. Zhang, X.H. Men, J. Yang, X.H. Xu, ACS Applied Materials & Interfaces 2 (2010) 3636–3641.

[2] M. Ma, R.M. Hill, Colloid & Interface Science 11 (2006) 193–202.

[3] C.R. Crick, I.P. Parkin, Chemistry: A European Journal 16 (2010) 3568–3588.

[4] Z. Genzer, K. EFimenko, Biofouling 22 (2006) 339–360.

[5] M. Zielecka, E. Bujnowska, Prog. Org. Coat. 55 (2006) 160–167.

[6] T. Kako, A. Nakajima, H. Irie, Z. Kato, K. Uematsu, T. Watanabe, K. Hashimoto, Mater. Sci. 39 (2004) 547–555.

[7] W. Barthlott, C. Neinhuis, Planta 202 (1997) 1–8.

[8] M. Lejeune, L.M. Lacroix, F. Bretagnol, A. Valsesia, P. Colpo, F. Rossi, Langmuir 22 (2006) 3057–3061.

[9]K. Tadanaga, J. Morinaga, A. Matsuda, T. Minami, Chemistry of Materials 12 (2000) 590–592.

[10] Y. Wang, Y.F. Mo, M. Zhu, M.W. Bai, Surface and Coatings Technology 203 (2008) 137–141.

[11] M.K. Tiwari, I.S. Bayer, G.M. Jursich, T.M. Schutzius, C.M. Megaridis, ACS Applied Materials & Interfaces 2 (2010) 1114–1119.

[12] H.Y. Erbil, A.L. Demirel, Y. Avci, O. Mert, surface, Science 299 (2004) 1377–1380.

[13] X.D. Wu, L.J. Zheng, D. Wu, Langmuir 21 (2005) 2665–2667.

[14] W.C. Wu, X.L. Wang, D.A. Wang, M. Chen, F. Zhou, W.M. Liu, Q.J. Xue, Chemical Communications (2009) 1043–1045.

[15] S. He, M. Zheng, L.Yao, X.Yuan, M. Li, L. Ma, W. Shen, Applied Surface Science 256 (2010) 2557–2562.

[16] X. Zhang, Y.G. Guo, P.Y. Zhang, Z.J. Zhang, Z.S. Wu, ACS Applied Materials & Interfaces 4(2012)1742–1746.

[17] J.M. Xi, L. Jiang, Industrial & Engineering Chemistry Research 47 (2008) 6354-6359.

[18] Zhuang. Zhu Luo, Zhao zhu Zhang, Adv. Mater 28（2008）970-975.

[19] Li, X.-M, Reinhoudt, D, Crego-Calama, M. Chem, Soc. Rev 26(2007) 1350-1354.

[20] X.J. Feng, L. Jiang, Adv. Mater 18(2006) 3063-3067.

[21] R.N. Wenzel, Ind. Eng. Chem 28(1936) 988-993.

Key Engineering Materials Vols 645-646 (2015) pp 120-125
© (2015) Trans Tech Publications, Switzerland
doi:10.4028/www.scientific.net/KEM.645-646.120

Submitted: 2014-12-07
Accepted: 2014-12-23

Frequency Characteristics Research for the Negative Resistance Oscillations Phenomenon of a Silicon Magnetic Sensitivity Transistor

Xiaofeng Zhao [a], Yifan Li, Meiwei Lv, Dianzhong Wen [b], Hongquan Zhang

Key Laboratory of Electronics Engineering, College of Heilongjiang Province, Heilongjiang University, Harbin, China

[a]zhaoxiaofeng@hlju.edu.cn, [b]wendianzhong@hlju.edu.cn (corresponding author)

Keywords: silicon magnetic sensitivity transistor; negative resistance oscillations; frequency characteristics; MEMS technology;

Abstract. A silicon magnetic sensitivity transistor (SMST) with negative resistance oscillations phenomenon is presented in this paper, which is constituted by emitter (E), base (B) and collector (C). The SMST chip is fabricated on <100> orientation high resistivity C-type silicon cup by using MEMS technology. Experiment results show, when external magnetic field B=0 T, base injection current I_b is the scope of 1.5mA to 1.7mA and V_{CE} is greater than 4.0V, the collector current I_c appears negative resistance oscillation phenomenon, the oscillation frequency will increase with the increase of the V_{CE}. I_c changes with external magnetic field B, where V_{CE} and I_b are constant. With the condition of the I_b=1.5 mA and V_{CE}=9.0 V, the oscillation frequency of B=0 mT *and* B=-150 mT are 5.88 kHz and 7.60 kHz, respectively.

Introduction

The silicon magnetic sensitivity transistor chip is fabricated on rectangular silicon membrance with high resistance using MEMS technology in 2003, the collector current relative magnetic sensitivity up to 227%/T[1-2]. When supply voltage V_{CE} and base current I_b are constant, the collector current Ic appears negative resistance oscillation phenomenon. Further discussi on the principle of negative resistance oscillations shows, in case of collector $n^+\pi$ junction and $p^+\pi$ formed between base and π regions being biased, and an avalanche multiplication effect occurring in the π region, base injunction occurs corresponding to $V_{p+\pi}$ biased voltage in the *V-I* curve of the magnetic sensitive transistor and the collector current shows negative resistance oscillations characteristics [3-6].

In this paper, based on the collector current oscillation characteristics of the SMST, studying the external magnetic field influences on the negative resistance oscillation phenomenon and the oscillation frequency.

Basic structure and working principle

Basic Structure. The SMST chip is fabricated on <100> orientation high resistivity C-type silicon cup by using MEMS technology[7]. Figure 1 shows basic structure of the SMST. The cubic structure of the silicon magnetic sensitivity transistor includes the base, the collector region, the emitter region, the collector junction and the emitter junction. But the collector（C）and the base（B） are formed on the surface of the C-type silicon cup，the emitter（E）is formed on the inside of the C-type silicon cup. L is length of the base, and W is width of the base.

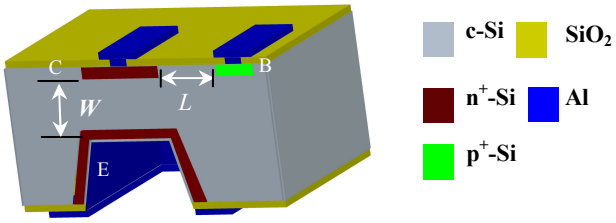


Figure 1 Basic structure of the silicon magnetic sensitivity transistor.

Working principle. As shown in Fig.2 (a), common emitter connection, the electrons injected from the emitter (E) are transported to the collector (C) to form the collector current I_c, where the external magnetic field B=0 T. Because that most of the electrons are acted by transverse field, the electrons will be combined with the holes injected from the base to form the base current I_b. Current gain is defined as[1-2]:

$$I_c = \beta I_b \tag{1}$$

Where, β is the common emitter magnification and β<1, I_b is the base injection current. As shown Fig.2 (b), when external magnetic field is along the direction of +y axis defined as positive magnetic filed (B>0 T), under the action of Lorentz force, carriers deflect to the recombination region，due to the the modulation role of the composite area, the lifetime of the carriers reduce, the I_c would be decreased. As shown Fig.2 (c), when external magnetic field is along the direction of -y axis defined as negative magnetic filed (B<0 T), similarly, owing to the the modulation role of the composite area, the I_c would be increased.When applied the magnetic field, the relative magnetic sensitivity of the I_c is shown as Eq.2[1-2]:

$$S_c = \frac{1}{Ic}\frac{\partial I_c}{\partial B} = \frac{1}{\beta_B}\frac{\partial \beta_B}{\partial B} + \frac{1}{I_b}\frac{\partial I_b}{\partial B} = S_\beta + S_{I_b} \tag{2}$$

In which, β_B is the magnification after the external magnetic field, S_β is the current gain relative magnetic sensitivity, S_{I_b} is the base injection current magnetic sensitivity. The current relative magnetic sensitivity of the long-base magnetic sensitive transistor is equal to the current gain plus the relative magnetic sensitivity of the base current, the device is used to detection the positive or negative external magnetic field.

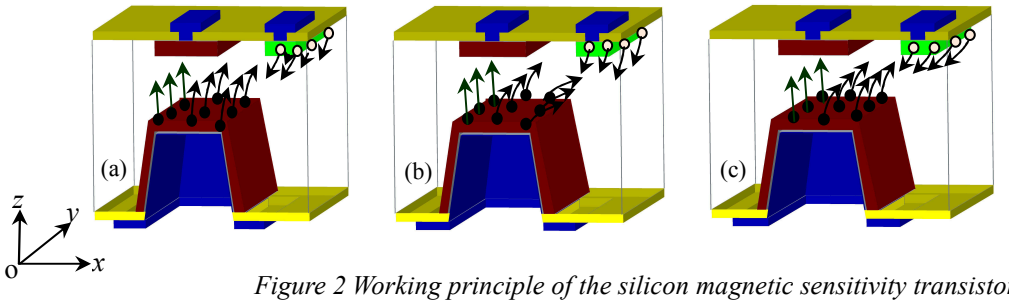


Figure 2 Working principle of the silicon magnetic sensitivity transistor.
(a) B=0 T (b) B>0 T (c) B<0 T

Fabrication technology of the sensor chip

The fabrication process of the SMST is shown as Fig.3. The main fabrication process steps are as follows[8-10]: (a) cleaning the p-type <100> orientation with high resistance silicon wafer; (b) growing SiO_2 layer and depositing Si_3N_4 and etching SiO_2 and Si_3N_4 ; (c) etching C-type silicon cup by KOH anisotropic etching technique; (d) etching SiO_2 and Si_3N_4 , and then diffusing phosphorus

to fabrication the collector and the emitter; (e) etching SiO_2 and Si_3N_4, and then diffusing boron to fabrication the base; (f) etching all the layer of Si_3N_4 and then growing the layer of SiO_2 on the upper surface, etching contacts; (g) evaporating aluminum electrodes, metalizing at 420 ℃ for 30 min to achieve ohmic contacts of E, B and C. Figure 4 shows packaging photograph of the SMST chip, the SMST chip includes emitter (E), colletor (C) and base (B).

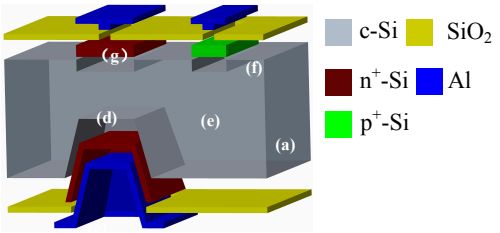


Figure 3 Fabrication technology steps of the silicon magnetic sensitivity transistor.

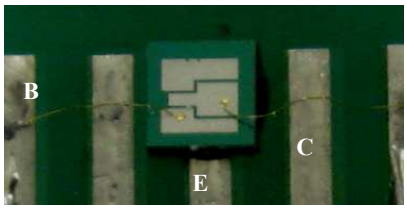


Figure 4 Packing photograph of the silicon magnetic sensitivity transistor chip.

Experimental results and discussion

In this paper, the characteristics of the SMST were measured at room temperature by using semiconductor characterization system (KEITHLEY, 4200) and magnetic field generator (CH-100), the oscilloscope (Agilent MSO7032B).

Oscillations phenomenon. Figure 5 (a), (b), (c) and (d) show negative resistance oscillations phenomenon of the SMST when the external magnetic field B is 0 mT, -300 mT, -600 mT and 150 mT, respectively. At the room temperature, the base injection current I_b is the scope of 0 mA to 4 mA, and the collector voltage V_{CE} is the scope of 0 V to 15 V. In the Fig.6, abscissa represents the collector voltage, ordinate represents the collector current. Figure 5 (a) shows that appears oscillation phenomenon, where the external magnetic field B=0 mT and the collector voltage V_{CE} is greater than 4 V; Figure 5 (b) shows that appears oscillation phenomenon, where the external magnetic field B=-300 mT and the collector voltage V_{CE} is less than 3V; When the negative external magnetic field is larger(B= -600 mT), the oscillation phenomenon is more significant; In the Fig.5 (d), with the condition of the positive external magnetic field B= +150 mT, the oscillation phenomenon disappear. According to the Fig.5 (a), (b), (c) can understand that with the increase of the external magnetic field, oscillation phenomenon gets significant. Through the Fig.5 (d) can realize that plus the opposite magnetic field (B=150 mT) relative to the Fig.5 (a), (b), (c), oscillation phenomenon significantly decline.

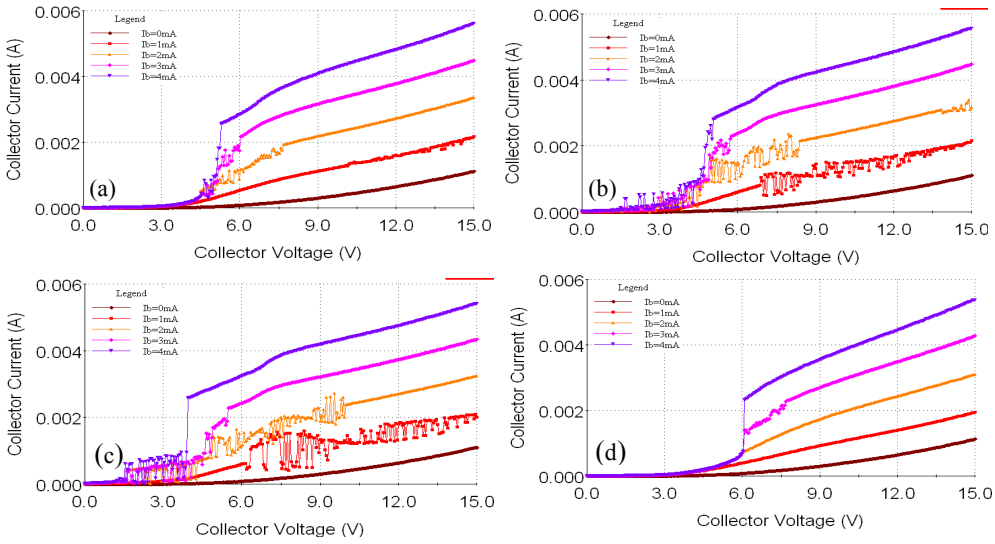


Figure 5 Oscillations phenomenon of the SMST.
(a) B=0 mT (b) B=-300 mT (c) B=-600 mT (d) B=+150 mT

Frequency characteristics. Figure 6(a) shows the test principle of the oscillation frequency. In the Fig.6(a), R_L is load resistance, C is capacitance, V_{out} is the output voltage, V_{CE} is the supply voltage . V_{DD} is power supply. Figure 6(b) shows the system figure.

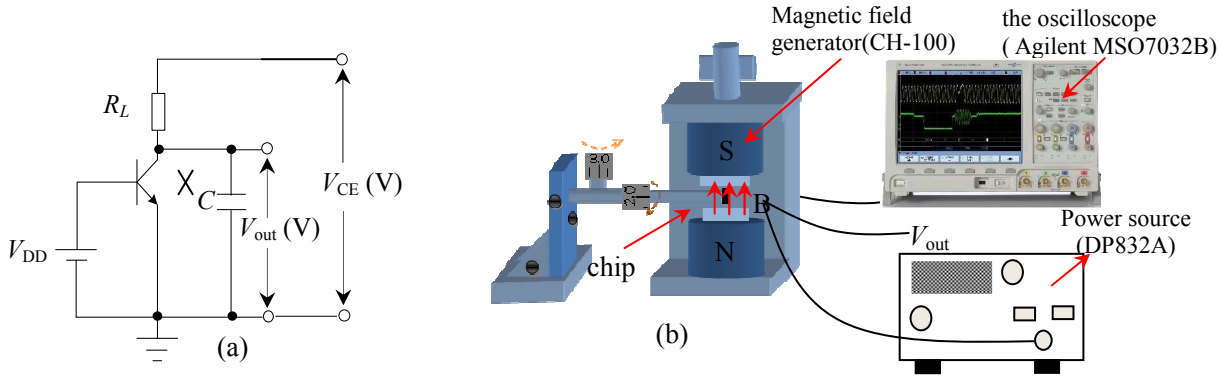


Figure 6 Testing principle of the silicon magnetic sensitivity transistor chip.

In the Fig.7, abscissa represents the time, ordinate represents the collector voltage. Figure 7 (a), (b) and (c) show corresponding oscillation frequency characteristics, where B=0 T，collector voltage V_{CE}=8.8 V and I_b=1.9 mA, 1.7 mA and 1.5 mA, respectively. The experimental results show that the oscillation frequency is 7.6 kHz at I_b=1.9 mA and increases with I_b.

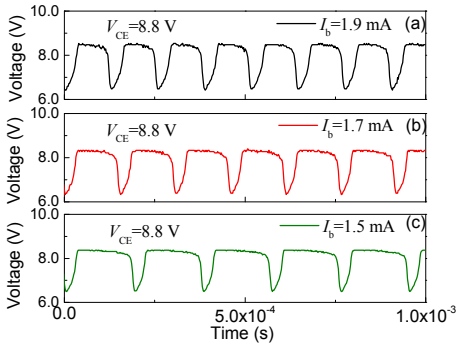


Figure 7 Oscillation characteristic curves with V_{CE}=8.8 V. (a) I_b=1.9 mA (b)1.7 mA (c) 1.5 mA

When I_b=1.5 mA, Fig.8 shows oscillation frequency characteristic curves of the SMST under different collector voltage V_{CE} of 8.2 V, 8.4 V, 8.6 V, 8.8 V and 9.0 V, respectively. Considering the effect V_{CE} on oscillation frequency, Fig.8 shows that the oscillation frequency increases with V_{CE} and the oscillation frequency is 5.56 kHz at V_{CE}=9.0 V. In the Fig.8, abscissa represents the time, ordinate represents the collector voltage. From the Fig.8 to know that when the collector voltage ranges from 8.2 V to 9.0 V, the electrons of the composite area increase, lead to the frequency enhance.

When V_{CE}=9.0 V and I_b=1.5 mA, Fig.9 (a), (b), (c), (d) and (e) show oscillation frequency characteristic curves under different external magnetic field B of -600 mT, -150 mT, -50 mT, 0 mT and 50 mT, respectively. With the condition of B>0 mT, the oscillation frequency decreases with the external magnetic field increases, however, when B<0 mT, the oscillation frequency decreases firstly with the external magnetic field increases, the oscillation frequency reaches maximum value of 7.6 kHz at B=-150 mT, then decrease gradually. The oscillation frequency reaches 5.58 kHz, where B=0 mT.

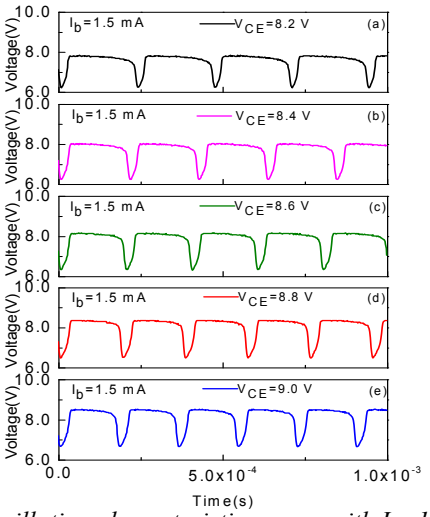


Figure 8 Oscillation characteristic curves with I_b=1.5 mA. (a) V_{CE} =8.2 V (b) V_{CE} =8.4 V (c) V_{CE} =8.6 V (d) V_{CE} =8.8 V (e) V_{CE} =9.0 V

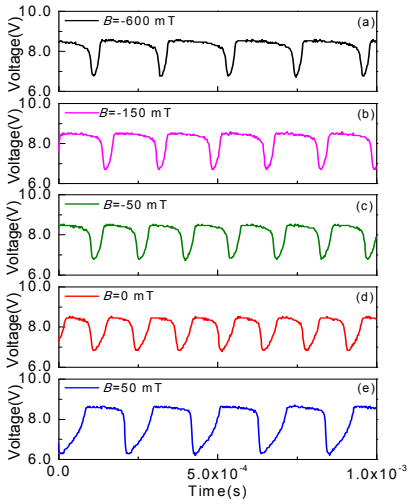


Figure 9 Oscillation characteristic curves with V_{CE}=9.0 V and I_b=1.5 mA. (a)B=-600mT (b)B=-150mT (c)B=-50 mT

Conclusion

In summary, through the analysis of the negative resistance oscillation phenomenon of the SMST, under certain working conditions, the collector current I_C changes with the external magnetic field, the collector current I_C appears oscillation phenomenon. Experimental results show that the oscillation frequency of I_C is relative to V_{CE} and I_b. When B=0 T, collector voltage V_{CE}=8.8 V, the oscillation frequency is 7.6 kHz at I_b=1.9 mA and increases with I_b. The oscillation frequency is 5.56 kHz at V_{CE}=9.0 V and increases with V_{CE}, where B=0 T, I_b=1.5 mA. With the condition of V_{CE} and I_b are constant, the oscillation frequency changes with external magnetic field B. When V_{CE}=9.0 V and I_b=1.5 mA, B=-150 mT, the oscillation frequency reaches maximum value of 7.6 kHz. It is possible to detect the external magnetic field and lays a foundation for research of the digital magnetic sensor.

Acknowledgements

This work is supported by the National Natural Science Foundation of China (Grant No. 61471159, 61006057), the China Postdoctoral Science Foundation (Grant No. 2013M530163), the Heilongjiang Province Natural Science Foundation of China (Grant No. F201433), the Special Funds for Science and Technology Innovation Talents of Harbin in China (Grant No. 2014RFQXJ007), the Modern Sensor Technology Innovation Team for College of Heilongjiang Province in China (Grant No.2012TD007).

References

[1] Wen Dianzhong, Mu Changsheng, Zhao Xiaofeng. Silicon magneto transistor by MEMS technology silicon transistor[J]. Journal of Transducer Technology,2001,20(5):49-52.

[2] Zhao Xiaofeng, Wen Dianzhong. Negative-resistance oscillations characteristics of a new type silicon magnetic sensitive transistor on MEMS [J]. Chinese Journal of Semiconductor, 2005,26(6):1214-1219.

[3] Wen Dianzhong. Study on a new magnetic-transistor on a SOI substrate[J]. Chinese Journal of Electron Devices,2006,29(3): 609-612.

[4] Victor Zieren, Bart P.M. Duydam. Magnetic-field-sensitive multicollector n-p-n transistors[J]. IEEE Transactions on Electron Devices,1982,29(1):83-90.

[5] Tian Fengjun, Wen Dianzhong. New type of P^+-I-N^+ double injection magneto-sensitive difference circuit developted on SOI[J]. Journal of Transducer Technology.2005,24(4):84-86.
[6] Zhao Xiaofeng, Li Lei, Wang ping, et al. Simulation research of the long-base silicon magnetic sensitive diode negative-resistance characteristics on the base of ATLAS[J]. Key Engineering Materials,2013.562-565:465-470.
[7] Agnes Nagy, Hector Trujillo. Highly sensitive magneto transistor with new topology[J]. Sensors and Actuators A,1998,65:97-100.
[8] Zhao Xiaofeng, Wen Dianzhong. Fabrication technology research of new type silicon magnetic-sensitive transistor[J]. Rare Metal Materials and Engineering,2006,35(12):492-494.
[9] Zhao Xiaofeng, Wen Dianzhong, Pan Dongyang, et al. Differential structure and characteristics of a new-type silicon magnetic sensitivity transistor[J]. Chinese Physics Letters, 2013,30(8) : 088501(1-4).
[10] Wen Dianzhong. Study on laser etching emitter region-groove approach of magnetic-sensitive silicon transistor[J]. Chinese Journal of Lasers, 2003, 30(5):454-456.

Key Engineering Materials Vols 645-646 (2015) pp 126-131
© (2015) Trans Tech Publications, Switzerland
doi:10.4028/www.scientific.net/KEM.645-646.126

Submitted: 2014-12-17
Accepted: 2014-12-23

Large-scale Synthesis and Microwave Absorption Properties of $CoFe_2O_4$/ $Co_{0.4}Zn_{0.6}Fe_2O_4$ hollow nanospheres

Ren Qingguo[1,a]，Qiao Xiaojing[1,b*]，Li Yan[2,c]，Sun Zhigang[1,d]，
Guo Xiaodang[1,e]，Zhang Shuaizhong[1,f]

[1] 5 South Zhongguancun Street, Haidian District, Beijing, China

[2] 52 Yongding Road, Haidian District, Beijing, China

[a]370690256@qq.com, [b]lan6603@sina.com, [c]470569768@qq.com, [d]375408644@qq.com
[e]905693503@qq.com , [f]252965365@qq.com

Keywords: hollow nanospheres; ferrite ; electromagnetic wave; absorption; solvothermal.

Abstract. Monodisperse $CoFe_2O_4$ and $Co_{0.4}Zn_{0.6}Fe_2O_4$ hollow nanospheres were synthesized in large scale by solvothermal method in ethylene glycol solution. The structure, shape and size of the samples were investigated by Fourier Transform infrared, X-ray powder diffraction and scanning electron microscopy. The results indicate that the products are spherical with an average diameter less than 200 nm. Magnetic studies revealed that the saturation magnetization of $Co_{0.4}Zn_{0.6}Fe_2O_4$ is 78.6 emu/g, higher than the $CoFe_2O_4$, which is 69 emu/g, while the coercivity of the $Co_{0.4}Zn_{0.6}Fe_2O_4$ is 184 Oe , obviously lower than that of $CoFe_2O_4$ which is 832 Oe. The electromagnetic parameters were measured at 2-18 GHz using HP8722ES vector network analyzer and then the microwave absorption properties were calculated through the transmission line theory. As to the $Co_{0.4}Zn_{0.6}Fe_2O_4$, the absorption bandwidth with reflection loss below -10 dB is up to 3GHz, from 10GHz to 13GHz with a thickness of 2 mm. A maximum reflection loss -45.6 dB was found at 12.9 GHz for the $CoFe_2O_4$ with a thickness of 1.8 mm. As a result, the as-prepared hollow nanospheres show good prospects of being applied in EM wave absorption materials.

Intorduction

In recent years, electromagnetic (EM) waves have been used in various applications, such as satellite broadcasting, local area network systems and mobile phones, so that the utilization of GHz range microwaves has drastically increased and some EM interference problems have become serious[1]. In order to solving the expanded EM interference problems, considerable theoretical and experimental investigations have been focused on effective EM-wave-absorption materials[2,3,4,5,6]. Among the candidates for EM-wave absorbers, magnetic materials have attracted a great attention for their high saturation magnetization and complex-permeability values, for which it is possible to make thinner absorbers[7,8,9]. Monodisperse magnetic microspheres with sizes of hundreds of nanometers are currently attracting considerable interest because of their large specific area, low density, large saturation magnetization and excellent EM-wave absorption properties [10,11,12] . Much effort has been devoted to the synthesis of diverse magnetic hollow spheres such as Ni,Co,$CoFe_2O_4$, Fe_3O_4 ,etc [13,14,15,16].The purpose of this study is to synthesize monodispersed hollow ferrite spheres in low temperature from EG solution with simple template free solvothermal method.

Experimental Section

Sample preparation. All chemicals (purchased from Beijing Chemical Co., Ltd) used in this experiment were analytical grade and were used without further purification. The starting materials include hydrated iron chloride ($FeCl_3$ •$6H_2O$), cobalt chloride hexahydrate ($CoCl_2$•$6H_2O$), zinc chloride ($ZnCl_2$), urea, ethylene glycol (EG) and polyvinylpyrrolidone(PVP). $CoFe_2O_4$ and $Co_{0.4}Zn_{0.6}Fe_2O_4$ nanospheres were synthesized by a template-free solvothermal method. In a typical procedure,10.81 g $FeCl_3$•$6H_2O$ and 4.76 g $CoCl_2$•$6H_2O$ were dissolved into 80 mL EG. 5 g urea and

0.5 g PVP were added into the solution and stirred under room temperature to form a homogeneous brown solution. The solvothermal synthesis was carried out in a 100mLTeflon-lined stainless-steel autoclave cell . The autoclave was sealed and maintained at 180 ℃ in an oven for10h before being left to cool to room temperature naturally . After the reaction was completed, the resulting black solid powder was obtained. The products were thoroughly washed with distilled water and ethanol three times respectively, and then dried at 50℃ for 6h. For the $Co_{0.4}Zn_{0.6}Fe_2O_4$, 2.76 g $ZnCl_2$ was added along with the 4.76 g $CoCl_2$•$6H_2O$. Other procedures were the same.

Characterization. The X-ray powder diffraction (XRD) pattern of the as-prepared products was collected by a Rigaku D/max-2500 X-ray diffractometer with Cu Kα radiation. IR transmittance spectra of these hollow ferrite powders were measured on Bruker Equinox 55 infrared spectrophotometer (KBr pellets) in the range of 4000-400cm^{-1}. The microstructures of the powders were observed by scanning electron microscopy (SEM) and transmission electron microscopy (TEM). Magnetic studies were carried out by using a HH-15 vibrating sample magnetometer (VSM) with fields up to 15000 Oe at room temperature. The complex permeability and complex permittivity in 2-18 GHz frequency range were measured with an s-parameter Network Analyzer (Agilent8722ES).

Results and Discussion

FTIR spectroscopic characterization. FT-IR spectra of the as prepared samples are presented in Figure 1. Theoretically, spinel ferrites have four infrared active modes. These vibrations occur in the v_1 (650~550cm^{-1}), v_2 (525~390cm^{-1}), v_3 (380~335cm^{-1}) and v_4 (300~200cm^{-1}) regions [17], The $v_1$and v_2 bands are generated owing to intrinsic vibrations of tetrahedral and octahedral coordination compounds. Absorption of v_1 is caused by the bond stretching of tetrahedral metal ions and oxygen, while v_2 vibration is observed due to the vibration of oxygen in the direction perpendicular to the axis joining the tetrahedral ions and oxygen; The v_3 mode is obtained from the Fe^{3+}-O complexes at octahedral sites. The frequency of v_4 vibration depends on the mass of tetrahedral metal ion complexes, which gives information about the vibration of ions occupying at tetrahedral site.

The absorptions at 3409 and 1633cm^{-1} are ascribed to the antisymmetric stretching of –OH. The broadness of stretching mode is attributed to the existence of EG absorbed on the surface of hollow spheres. Weak bands of C–H symmetric stretching and antisymmetric stretching of –CH_2– groups are recorded at 2856 and 2921cm^{-1}. The appearance of these peaks in the spectrum confirmed the presence of PVP and adsorbed EG on the surface of particles. The absorption at 592cm^{-1}and 422cm^{-1} ascribed to characteristic peaks of tetrahedral and octahedral Fe-O stretching, which indicate the formation of spinel ferrites.

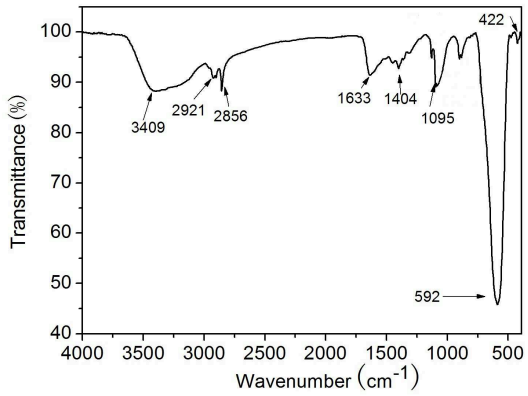


Fig. 1. FTIR spectra of the products

X-ray diffraction analysis. Figure 2 shows the X-ray diffraction pattern of the prepared $CoFe_2O_4$ and $Co_{0.4}Zn_{0.6}Fe_2O_4$ hollow nanospheres. The strong diffraction peaks at 30.2° , 35.5° , 43.3° , 53.6° , 57.4° and 62.7° correspond to (220), (311), (400), (422), (511) and (440) crystal planes of spinel structures with face centered cubic phase. The sharp peaks indicate that the products were well

crystallized. All the peaks perfectly match with the cubic structure. No impurity peak was observed, which indicated that high purity crystalline spinel ferrite was successfully synthesized by this approach.

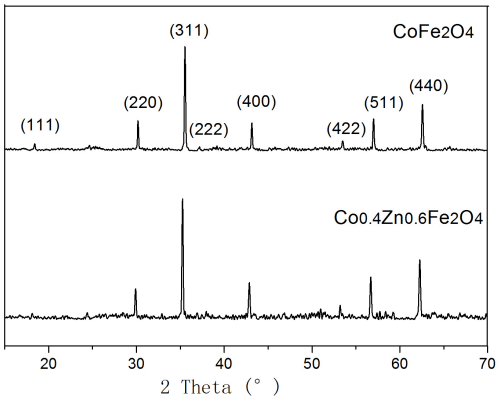


Fig. 2.XRD patterns of the synthesized products

Morphology Observation. The size and morphology of the synthesized products were characterized by SEM and TEM. Figure 3 shows the SEM and TEM of the $CoFe_2O_4$ hollow nanospheres. As seen in Figure 3, most of the particles are fully spherical. It can be seen that the diameter of the hollow spheres are in the range of 150-200nm with average size of 180nm. The inset of Figure 3c is the TEM of some individual particles, from which we can see that the inside of the $CoFe_2O_4$ is hollow.

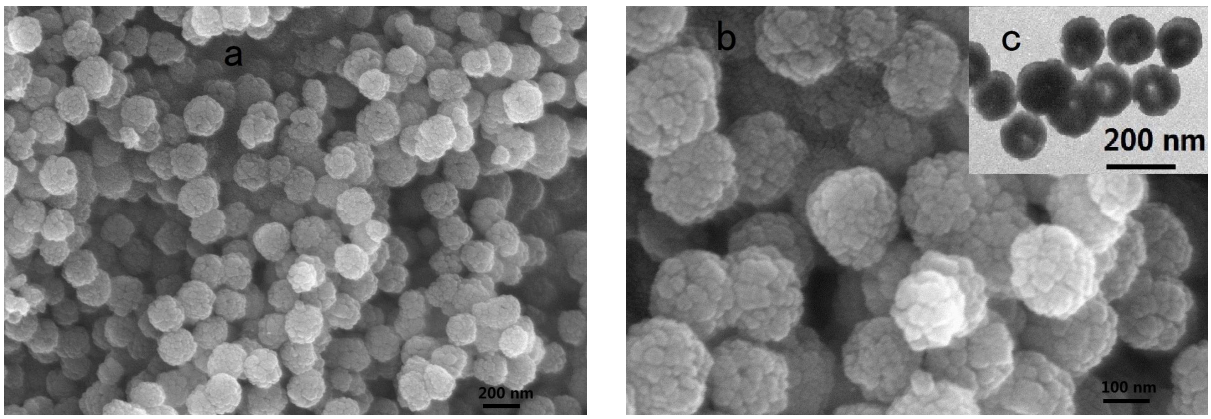


Fig. 3.SEM and TEM of the CoFe2O4

The SEM and TEM of the $Co_{0.4}Zn_{0.6}Fe_2O_4$ hollow nanospheres are shown in Figure 4. Comparing with Figure 3, it can be seen that the surface morphologies are more smooth. These spheres are generated by small crystalline structures and have a mean size of about 200 nm, and there exist many broken spheres, which shows that they are hollow inside, too. From the TEM (inset of Figure 4c), the hollow inside can be clearly observed.

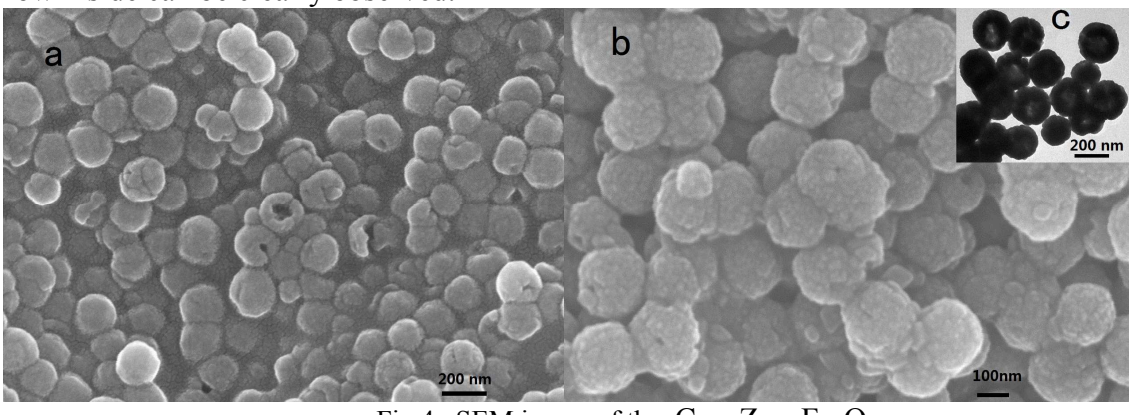


Fig.4. SEM image of the $Co_{0.4}Zn_{0.6}Fe_2O_4$

VSM. The magnetic properties of the as-prepared $CoFe_2O_4$ and $Co_{0.4}Zn_{0.6}Fe_2O_4$ nanospheres were investigated with a vibrating sample magnetometer at 300 K. The magnetic hysteresis loops for the samples are shown in Figure 5. Figure 5A and B correspond to $CoFe_2O_4$ and $Co_{0.4}Zn_{0.6}Fe_2O_4$ hollow nanospheres, respectively. The results show the saturation magnetization (Ms), remanent magnetization (Mr), and coercivity (Hc) values of $CoFe_2O_4$ were 69 emu/g , 23 emu/g and 832 Oe. While the values of the $Co_{0.4}Zn_{0.6}Fe_2O_4$ hollow nanospheres were 78.6 emu/g , 4.9 emu/g and 184 Oe respectively. Herein, it is obvious that when some Zn^{2+} is added, the saturation magnetization of the hollow spheres get higher. The remanent magnetization and coercivity value of the $Co_{0.4}Zn_{0.6}Fe_2O_4$ is drastically lower than the $CoFe_2O_4$.

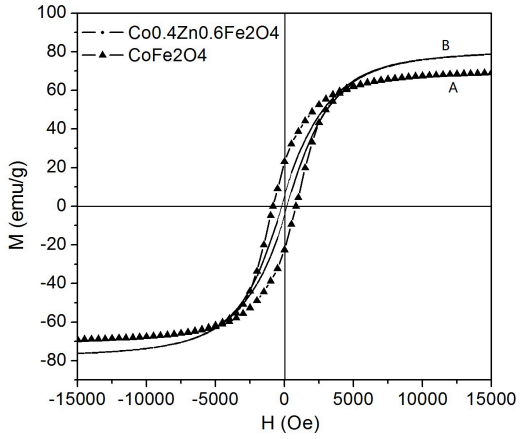


Fig. 5 Hysteresis loops of the samples

Microwave Absorption Properties. The complex dielectric permittivity ($\varepsilon_r = \varepsilon' - \varepsilon''$) and magnetic permeability ($\mu_r = \mu' - \mu''$) represent the dynamic dielectric and magnetic properties of electromagnetic materials. The real components of the complex dielectric permittivity and magnetic permeability symbolize the storage capability of electric and magnetic energy. The imaginary components represent the loss of the electric and magnetic energy. In this work, electromagnetic parameters were tested with 60% of the titled materials and 40% of paraffin wax composites by using HP8722ES vector network analyzer.

Figure 6 shows the complex permittivity and permeability of the $CoFe_2O_4$ and $Co_{0.4}Zn_{0.6}Fe_2O_4$. As shown in the figure 6, the adding of Zn^{2+} has an obvious effect on all of the four electromagnetic parameters. In the range of 2-5 GHz, both real and imaginary part of permittivity of $Co_{0.4}Zn_{0.6}Fe_2O_4$ are lower than those of $CoFe_2O_4$. The permittivity value of $CoFe_2O_4$ decreases deeply from 2 to 5 GHz. After 8 GHz, the value of both real and imaginary part of permittivity of $CoFe_2O_4$ get lower than those of $Co_{0.4}Zn_{0.6}Fe_2O_4$. According to free-electron theory[18], it can be speculated that the lower ε'' values indicate a higher electric resistivity with respect to other microwave absorbing materials.

The right curves show the real and imaginary parts of complex permeability for the two ferrite hollow nanospheres, respectively. It is observed that the real parts of permeability (μ') of $Co_{0.4}Zn_{0.6}Fe_2O_4$ hollow spheres are larger than those of $CoFe_2O_4$ in the low frequency region (f <5 GHz). The imaginary parts (μ'') are much larger than the values of the $Co_{0.4}Zn_{0.6}Fe_2O_4$ before the 9GHz, indicating that the hollow $Co_{0.4}Zn_{0.6}Fe_2O_4$ spheres have higher magnetic energy loss in these frequencies. The values of permeability are approximately equal in the high frequencies of 9-18GHz.

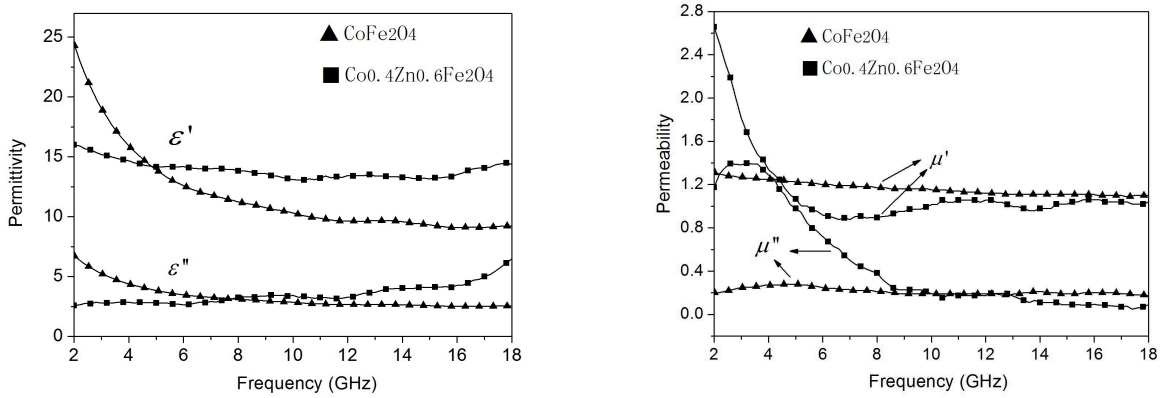


Fig. 6 Electromagnetic parameters of the hollow nanospheres

The EM wave-absorbing performances usually can be evaluated by the following equation [19]:

$$RL = 20\log\left|(Z_{in} - Z_0)/(Z_{in} + Z_0)\right| \tag{1}$$

where the RL denotes the reflection loss in dB unit. Z_0 is the characteristic impedance of free space, which equals $120\pi\ \Omega$. Zin is the input characteristic impedance at the absorber/free space interface, which can be expressed as

$$Z_{in} = Z_0\sqrt{\mu_r/\varepsilon_r}\tanh\left\{j(2\pi fd/c)\sqrt{\mu_r\varepsilon_r}\right\} \tag{2}$$

where c is the velocity of light, ε_r is the complex relative permittivity and μ_r is the complex relative permeability of the material. d is the thickness of the absorber.

Figure 7 shows the frequency dependence of the reflection loss for the samples at the desired thicknesses of 2 mm. The maximum magnitudes of the reflection are -38.3 dB at 11.4 GHz for $CoFe_2O_4$ sample and -23 dB at 10.4 GHz for the $Co_{0.4}Zn_{0.6}Fe_2O_4$ hollow spheres, respectively. RL values of less than −10 dB were obtained at 9.2-13.6 GHz for $CoFe_2O_4$ absorber. In the low frequency, the $Co_{0.4}Zn_{0.6}Fe_2O_4$ hollow spheres exhibit strong absorption properties. The reflection is lower than -5dB between 3.8-14 GHz.

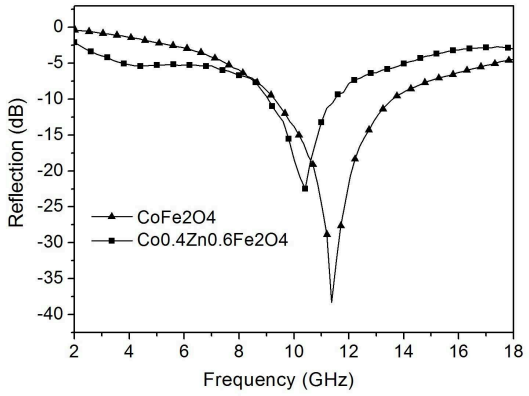


Fig. 7 Microwave reflection loss RL of the samples at the thickness of 2 mm

Reflection loss of $CoFe_2O_4$ at different thickness is presented in figure 8. The minimum RL clearly shifts to lower frequencies with increasing the thickness of the layer. The hollow nanospheres exhibit strong EM-wave absorption properties (RL < −10 dB) in the 5.4-18 GHz range for absorber thicknesses of 1.5-3.0 mm and a minimum reflection of −45.6 dB is observed at 12.9 GHz for a thickness of 1.8 mm. When the absorber is 1.5 mm, the hollow nanospheres possess excellent EM-wave absorption properties with reflection lower than -10dB in the high frequency from 13.2 to18 GHz.

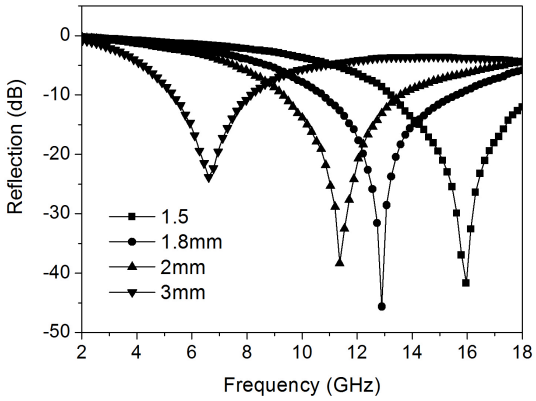


Fig. 8 Reflection loss of Co0.4Zn0.6Fe2O4 at different thickness

Summary

In conclusion, monodisperse $CoFe_2O_4$ and $Co_{0.4}Zn_{0.6}Fe_2O_4$ hollow magnetic nanospheres with diameter less than 200nm have been successfully synthesized in large scale via a solvothermal method. Magnetic studies revealed that the saturation magnetization of $Co_{0.4}Zn_{0.6}Fe_2O_4$ is higher than the $CoFe_2O_4$, while the coercivity of the $Co_{0.4}Zn_{0.6}Fe_2O_4$ is obviously lower than that of $CoFe_2O_4$. The microwave absorbing properties of the $Co_{0.4}Zn_{0.6}Fe_2O_4$ nanospheres is excellent in the low frequency. The reflection loss is lower than -5dB in the range of 3.8-14 GHz. The maximum RL of the $CoFe_2O_4$ was −45.6 dB at 12.9 GHz and the RL less than −10 dB was found to exceed 5 GHz between 10.8 GHz and 15.8 GHz for a thickness of 1.8 mm.

Acknowledgement: This work was supported by General Armament Department and School of Mechatronical Engineering, Beijing Institute of Technology.

References

[1] K. Miura, M. Masuda, M. Itoh, J. Alloys Compd. 1391(2006)408-412.
[2] X. Li, D. Zhang, J. Chen, J. Am. Chem. Soc.128(2006) 8382-8383.
[3] C. Su, H. Sheu, C. Lin, C. Huang, Y. Lo, Y. Pu. J. Am. Chem. Soc. 129(2007)2139-2146.
[4] X.M. Feng, H.Y. Wen, Y.F. Shen, J. Alloys Compd. 555 (2013) 145-149.
[5] W.C.Li, X.J.Qiao, H.Zhao, J. Nanosci.Nanotech.13(2013)793-798.
[6] C.R. Li, M.Y. Cui, Q.T. Sun, J. Alloys Compd. 504 (2010) 498–502.
[7] J. Bai, J. P. Wang, Appl. Phys. Lett.87(2005)152502-152506.
[8] S. Y.Tong, M.J. Tung, W.S. Ko, J. Alloys Compd.550 (2013)39-45.
[9] M. Penchal Reddy , W. Madhuri. J, Electroceram. 28(2012)1-9 .
[10] A.Yan, X.H. Liu, R.Yi, J. Phys. Chem. C.112 (2008) 8558-8563.
[11] Z.H. Yang, Z.W. Li, L. Liu, L.B. Kong. J. Alloys Compd. 509(2011)3038-3041.
[12] P M PRITHVIRAJ SWAMY, S BASAVARAJA1.Bull. Mater. Sci. 34 (2011) 1325-1330.
[13]N. Wang, X. Cao, D. Kong, J. Phys. Chem. C.112(2008) 6613-6619.
[14] Lin Guo,Fang Liang, Xiaogang Wen,Adv. Funct. Mater. 17(2007) 425–430.
[15] W.C.Li, X.J.Qiao, Q.Y.Zheng, J. Alloys Compd. 509(2011)6206-6211.
[16] J. Huang,W.M. Chen, W. Zhao, J. Phys. Chem. C. 113 (2009) 12067-12071.
[17] C. Julien, M. Massot, C. Perez-Vicente, Mater. Sci. Eng. B 75 (2000) 6-12.
[18] X. G. Liu, D. Y. Geng, H. Meng, Appl. Phys.Lett. 92(2008)173117-173122.
[19] T. Maeda, S. Sugimoto, T. Kagotani, J. Magn. Magn. Mater. 281 (2004) 195.

Key Engineering Materials Vols 645-646 (2015) pp 132-138
© (2015) Trans Tech Publications, Switzerland
doi:10.4028/www.scientific.net/KEM.645-646.132

Submitted: 2015-01-06
Accepted: 2015-01-12

Research of Magnetic Characteristics of the Split-drain MAGFET based on Nano-polysilicon TFTs

ZHAO Xiao Feng[1,2,a], GUAN Han Yu[1,b], LV Mei Wei[1],

BAI Yin Nan[1], WEN Dian Zhong[1,c*]

[1]Key Laboratory of Electronics Engineering, College of Heilongjiang Province, Heilongjiang University, Harbin, China 150080

[2]The 49th Research Institute of China Electronics Technology Group Corporation, Harbin, China 150001

[a]zhaoxiaofeng@hlju.edu.cn, [b]guan.han.yu@163.com,

[c]wendianzhong@hlju.edu.cn (corresponding author)

Keywords: nano-polysilicon TFTs; split-drain MAGFET; magnetic sensitivity characteristics; channel shape; CMOS technology

Abstract. The split-drain magnetic field effect transistor (MAGFET) based on nano-polysilicon thin film transistor (TFT) is fabricated on <100> high resistivity silicon substrates by (complementary metal oxide semiconductor) CMOS technology in this paper. It contains source (S), drain1 (D_1), drain2 (D_2) and gate (G), and adopts nano-polysilicon thin films and nano-polysilicon/high resistivity silicon heterojunction interfaces as the magnetic field sensing layers. The influence of the channel size and shapes on the transistor, are studied to further improve its magnetic sensitivity. When the ratio of channel length and width (L/W) of MAGFET is 80 μm/160 μm, V_{DS}=5.0 V, the MAGFET with convex channel has higher magnetic sensitivity than the rectangle and concave, the absolute current magnetic sensitivity S_I and the absolute voltage magnetic sensitivity S_V of the proposed sensor reach the maximum values, and are 0.021 mA/T and 55 mV/T, respectively.

Introduction

In 1966, R.C.Gallagher and W.S.Corak proposed magnetic field effect transistor (MAGFET) that the drain was divided into two. When the external magnetic field $\boldsymbol{B}$ is applied to the MAGFET using channel layer of MOSFET as sensing layer, a induced Lorentz force is exerted on the carriers to cause deflection of carriers, the current difference occurs between the two drains, it is possible to realize the detecting for $\boldsymbol{B}$ [1,2]. Since then, a lot of influence factors on the magnetic sensitivity of MAGFET's such as the channel width, length, shapes, the gap between drains, the cover ratio of polysilicon, the conductive type (n type or p type) of channel layer, the number of drains (two or three drains), etc. were studied. In 1997, Dirk Killat fabricated the MAGFET by CMOS technology to study the influence of geometric parameters on magnetic characterization of the MAGFET and optimized the design[3]. In 2005, the sector split-drain MAGFET based on standard CMOS technology was fabricated in Zhejiang University, and the max relative sensitivity of the sensor is 3.77%[4]. The current relative sensitivity of integrated sectorial MAGFET is 3.61 %/T, the output voltage magnetic sensitivity is 2.62 V/T[5]. Recently, with the further study of the influence factors

on the characterization of the split-drain MAGFET, the magnetic sensitivity characterization has been significantly improved[6]. The MAGFET are widely used, not only in detecting the magnetic field, but also in non-contact switching, magnetic memory reading, contactless mechatronic and so on[7].

Based on the previous research on nano-polysilicon TFT[8,9], and combining with the theoretical analysis and experimental results of nano-polysilicon TFT, this paper proposed the split-drain MAGFET based on the nano-polysilicon TFT. Due to of the novel sensing layers of the nano-polysilicon thin films and nano-polysilicon/high resistivity silicon heterojunction, it is possible to improve the carrier mobility by the action of carrier tunnel effect and heterojunction structure, and increase magnetic sensitivity of the MAGFET. The channel size and shape are studied to improve the characterization of the MAGFET in this paper. Through further research on the rectangle, concave and convex shapes of the channels, the magnetic sensitivity of the sensor is increased, significantly.

Basic structure and operation principle

Basic Structure. Fig. 1 shows the basic structure of split-drain MAGFET based on nano-polysilicon TFT, which contains the source (S), drain1 (D_1), drain2 (D_2) and gate (G), and the thickness of nano-polysilion thin film is 120 nm, the gap (d) between D_1 and D_2 is 10 μm, the width (W) of channel is 160 μm, the lengths (L) of channels are 80 μm, 160 μm, 320 μm and 640 μm, respectively. The layouts of proposed sensor with different channel shapes (rectangle, concave and convex) are shown as Fig.2, where W_S and W_D are the width of the source and drain, L_S and L_D are the length of the source and drain, respectively.

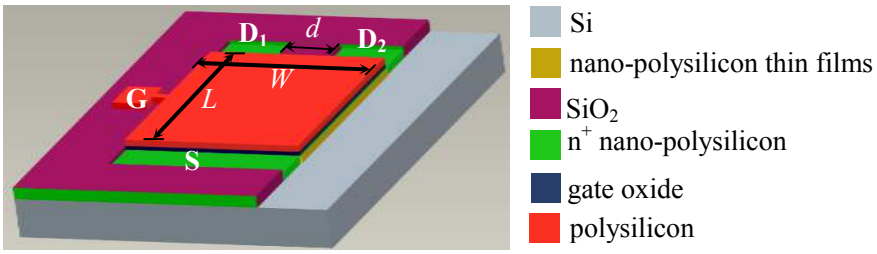


Fig. 1 Basic structure of the split-drain MAGFET based on nano-polysilicon TFT.

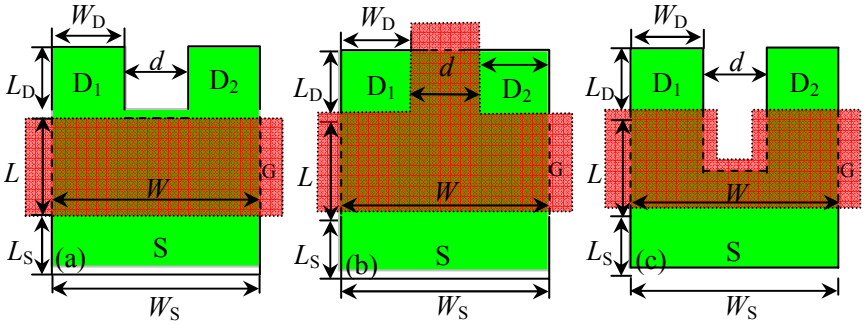


Fig. 2 Layout of the split-drain MAGFET based on nano-polysilicon TFT.
(a) rectangle channel (b) convex channel (c) concave channel

Operation Principle. The operation principle of the MAGFET based on nano-polysilicon TFT is shown as Fig. 3. As shown in the Fig. 3 (a), without the external magnetic field ***B***, no carriers deflection in the channel of split-drain MAGFET under ideal conditions, the current difference ΔI_D between D_1 and D_2 equals to zero, which can be expressed as

$$\Delta I_D = I_{D1} - I_{D2} = 0 \tag{1}$$

As shown in the Fig. 3 (b), (c), the external magnetic field ***B*** (***B***≠0 T) is applied perpendicular to the chip surface, the channel carriers of the MAGFET will be deflected due to the action of Lorentz

force, I_{D1} and I_{D2} change with the external magnetic field $\boldsymbol{B}$, and the current difference ΔI_D between D_1 and D_2 can be expressed as

$$\Delta I_D = I_{D1} - I_{D2} \neq 0 \tag{2}$$

The positive external magnetic field (B>0 T) applied perpendicularly to the chip surface, is defined as Fig. 3 (b), and the negative external magnetic field (B<0 T) applied perpendicularly towards the outside of the chip surface, is defined as Fig. 3 (c).

From the above discussion, the external magnetic field can be detected by the split-drain MAGFET, the absolute current magnetic sensitivity (S_I) and absolute voltage magnetic sensitivity (S_V) of the split-drain MAGFET can be defined as fllows[10]

$$S_I = \frac{|I_{D1} - I_{D2}|}{B} = \frac{|\Delta I_D|}{B} \tag{3}$$

$$S_V = \frac{|V_{D1} - V_{D2}|}{B} = \frac{|\Delta V_D|}{B} \tag{4}$$

where B is the external magnetic field, I_{D1} and I_{D2} are the drain currents of D_1 and D_2, V_{D1} and V_{D2} are the voltages of D_1 and D_2, respectively.

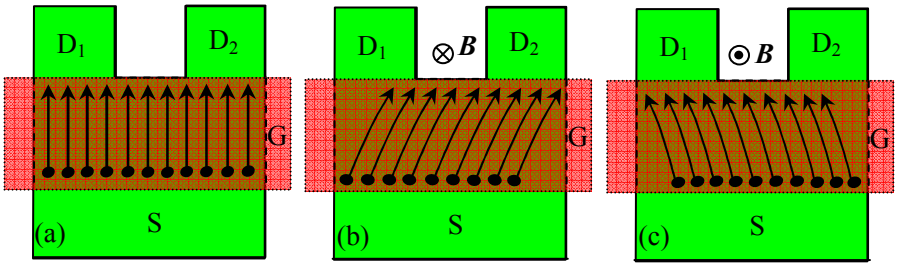


Fig. 3 Operation principle of the split-drain MAGFET based on nano-polysilicon TFT. (a) B=0 T (b) B>0 T (c) B<0 T

Fabrication technology

The split-drain MAGFET based on nano-polysilicon TFT was fabricated on <100> orientation high resistivity silicon substrates by CMOS technology[11]. Fig. 4 shows the main fabrication processes of split-drain MAGFET: (a) cleaning the <100> orientation high resistivity silicon wafer; (b) the first oxidization, SiO_2 thin films with thickness of 450 nm were grown on the substrates by thermal oxidization; (c) the first lithography, forming active region windows of the nano-polysilicon TFT, where the nano-polysilicon thin films with thickness of 114 nm were deposited on the high resistivity silicon substrates by the low pressure chemical vapor deposition (LPCVD), and the crystal orientation are <111>, <220> and <311>[11], respectively, then injecting phosphorus atoms by an ion implantation machine, where the energy and the dose of the implanted ions are 60 keV and 5.0×10^{13} atom/cm^2, respectively; (d) the second lithography and oxidization, etching nano-polysilicon thin films and depositing gate oxide with thickness of 50 nm on the nano-polysilicon thin films by LPCVD, then depositing polysilicon with thickness of 960 nm by the LPCVD; (e) the third lithography, etching polysilicon to form polysilicon gate; then injecting phosphorus atoms by the ion implantation machine, where the energy and the dose of the implanted ions are 60 keV and 6.0×10^{15} atom/cm^2, respectively; (f) the fourth lithography, forming contact

holes; (g) aluminum electrodes with thickness of 1μm were formed by the magnetron sputtering; (h) fifth lithography, etching aluminum, followed by metalized at 420 ℃ for 30 minutes to form ohmic contacts of source (S), drain1 (D_1), drain2 (D_2) and gate (G). Fig. 5 (a), (b) and (c) show the photographs of the split-drain MAGFET chips with L/W=80 μm/160 μm, where the shapes of the channels are rectangle, concave and convex, respectively.

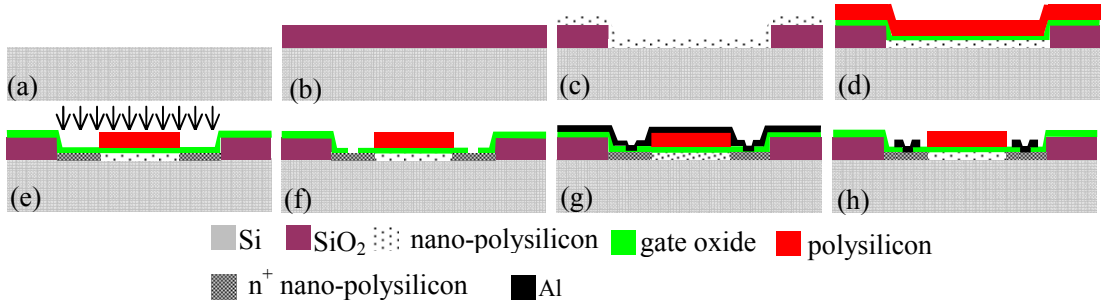


Fig. 4 Main fabrication steps of the split-drain MAGFET based on nano-polysilicon TFT.

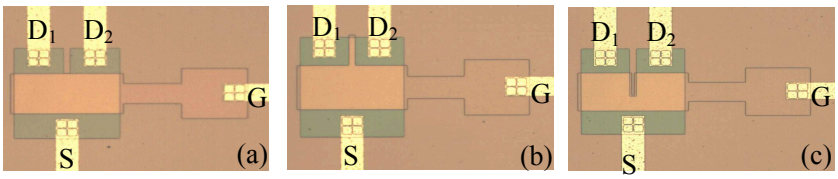


Fig. 5 Chip photographs of the split-drain MAGFET based on nano-polysilicon TFT with L/W=80 μm/160 μm. (a) rectangle channel (b) convex channel (c) concave channel

Experimental results and discussion

***I*$_D$-*V*$_{DS}$ Characterization.** I_D-V_{DS} characterization of the proposed sensor was measured by semiconductor characteristic analysis system (KEITHLEY 4200) at room temperature. The drain-source voltage V_{DS} ranged from 0 V～10.0 V with voltage step of 0.5 V, the gate-source voltage V_{GS} were 0.0 V, 4.0 V and 8.0 V, respectively.

When there is no external magnetic field ***B*** and the channel width and length are 160 μm and 80 μm, respectively, the I_D-V_{DS} characterization for the two drains (D_1 and D_2) of the split-drain MAGFET that the shapes of the channels are rectangle, concave and convex are shown as Fig.6 (a), (b) and (c). The curves in Fig.6 are different from the normal field effect transistor which has saturation region while the proposed MAGFET doesn′t have, and the I_D-V_{DS} characterization of D_1 and D_2 are similarly same. The drain currents of D_1 and D_2 approximately are equal (I_{D1}= I_{D2}), and increase with the drain-source voltage V_{DS}. Moreover, when the thickness of the nano-polysilicon thin films and the ratio of L/W are constant, under the same voltages of V_{DS}, the sequence of drain current I_D for the split-drain MAGFET changes from high to low: $I_{Dconcave}$> $I_{D\ rectangle}$> $I_{Dconvex}$.

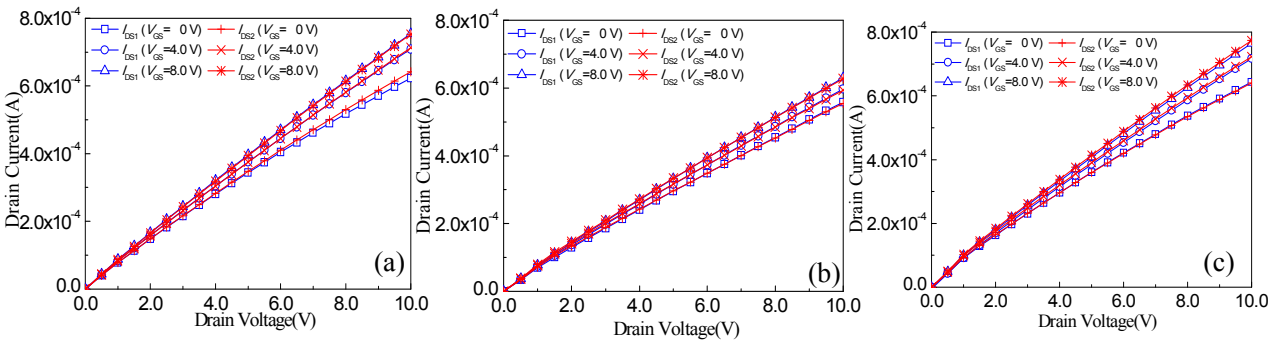


Fig. 6 I_{DS}-V_{DS} characterization curves of split-drain MAGFET with different shapes of the channel. (a) rectangle channel (b) convex channel (c) concave channel

Magnetic characterization. At room temperature, the characterization of the sensor were measured by magnetic field generator (CH-100), power supply (BJ1790B), and multimeter (34401A, Agilent). The external magnetic field B ranged from -0.60 T to 0.60 T with magnetic field step of 0.05 T, and the experiments were repeated for three cycles.

Fig. 7 shows the testing principle of magnetic characterization of the sensor chip, where the sensor chips are drawn in the dotted line box, I_{D1} and I_{D2} are drain currents for D_1 and D_2 as shown in Fig. 7(a), R_1 and R_2 are drain load resistances for D_1 and D_2 as shown in Fig. 7 (b). When B=0 T and V_{DS} is constant (the gate of the MAGFET is suspended), V_{D1} and V_{D2} don't have the same value owing to the influence of the fabrication technology. By modulating R_1 and R_2, when studied the magnetic characterization of the MAGFET, the value of V_{D1} and V_{D2} are the same.

Fig. 8 shows the relative curves of the drain currents difference ΔI_D (I_{D1}-I_{D2}) and B of the rectangle channel MAGFET with different L/W, where the V_{DS} is 5.0 V. The relative curves of the drain voltages difference (V_{D1}-V_{D2}) and B of the rectangle channel MAGFET with different L/W is shown as Fig.9, where V_{DS} is 5.0 V. According to the experimental results, the main reason for the difference between I_{D1} and I_{D2} is the uneven distribution of current density in the channel layer caused by fabrication technology, where $B\neq0$ T and V_{DS} is constant. The absolute value of (I_{D1}-I_{D2}) is approximately linear increasing with the increase of both the positive and negative external magnetic field B. R_1 and R_2 are modulated to realize the same value for V_{D1} and V_{D2}, so that the absolute value of (V_{D1}-V_{D2}) is approximately linear increase with B. This structure can realize the detection of positive or negative B, and the magnetic characterization of the MAGFET is distinguished when L/W is 80 μm/160 μm.

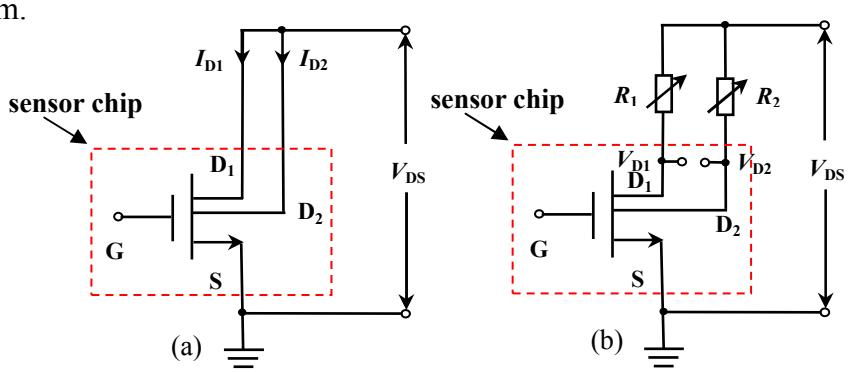


Fig. 7 Testing principle of the magnetic characterization of the split-drain MAGFET based on the nano-polysilicon TFT (a) testing principle of ΔI_D (b) testing principle of (V_{D1}-V_{D2}).

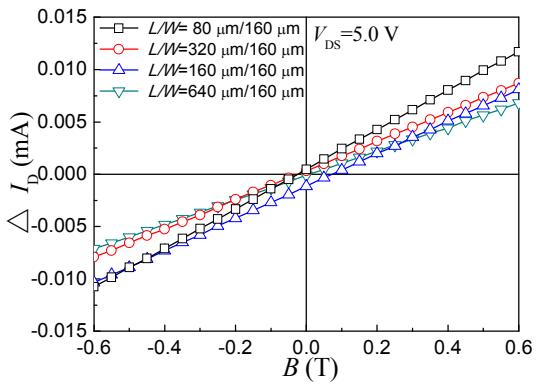


Fig. 8 Relational curves of ΔI_D and B of split-drain MAGFET with rectangle channel with different L/W.

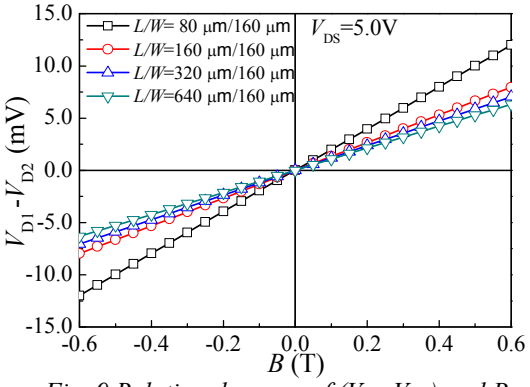


Fig. 9 Relational curves of (V_{D1}-V_{D2}) and B of split-drain MAGFET with rectangle channel.

Fig. 10 shows the relative curves of the drain currents difference ΔI_D and B of the MAGFET, the ΔI_D of convex is higher than the concave's with the same L/W, V_{DS} and B. The relative curves of (V_{D1}-V_{D2}) and B of the MAGFET with channel shapes of convex and concave are shown as Fig.11. The proposed MAGFETs were fabricated and the test results show that the L/W has the effect on

drain currents when V_{DS} is constant. Moreover, the MAGFET with convex channel has higher magnetic sensitivity than the others, when V_{DS}=5.0 V, L/W=80 μm/160 μm, the current magnetic sensitivity S_I and the voltage magnetic sensitivity S_V of the convex MAGFET reach the maximum values, and are 0.021 mA/T and 55 mV/T, respectively.

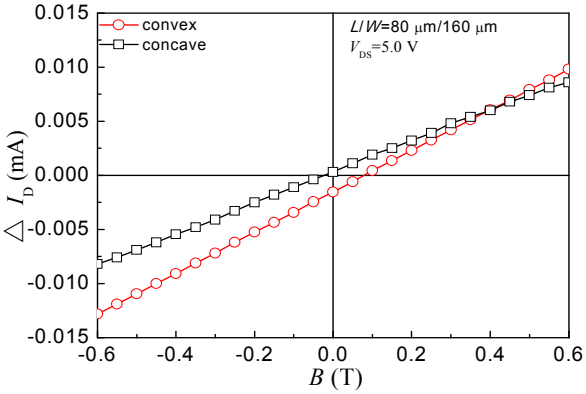


Fig. 10 Relational curves of ΔI_D and B of split-drain MAGFET.

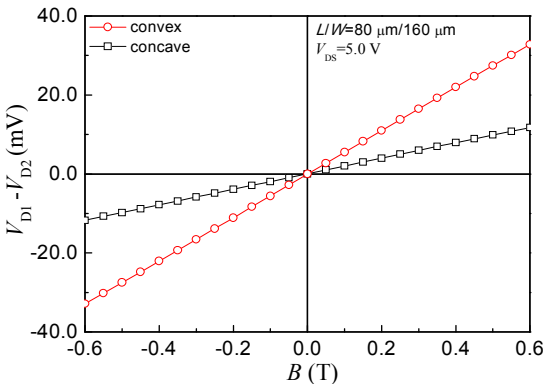


Fig. 11 Relational curves of (V_{D1}-V_{D2}) and B of split-drain MAGFET with different shapes of the channel.

Summary

The fabrication and characterization of the split-drain MAGFET based on nano-polysilicon TFT were discussed in this paper, and the MAGFET adopts the channel layer of nano-polysilicon TFT and nano-polysilicon thin films/high resistivity silicon heterojunction interfaces as magnetic sensing layer. The channel shapes of rectangle, convex and concave are analyzed emphatically to improve the magnetic sensitivity. The experimental results show that the magnetic sensitivity of the split-drain MAGFET is improved significantly and the MAGFET with convex channel has higher magnetic sensitivity than the others, when V_{DS}=5.0 V, L/W=80 μm/160 μm, the current magnetic sensitivity S_I and the voltage magnetic sensitivity S_V of the convex MAGFET reach the maximum values, and are 0.021 mA/T and 55 mV/T, respectively. The channel size and shape of the split-drain MAGFET based on the nano-polysilicon TFT are optimized in this paper, and it also lays a foundation for the design and manufacture of magnetic sensor.

Acknowledgements

This work is supported by the National Natural Science Foundation of China (Grant No. 61471159, 61006057), the China Postdoctoral Science Foundation (Grant No. 2013M530163), the Heilongjiang Province Natural Science Foundation of China (Grant No. F201433), the Special Funds for Science and Technology Innovation Talents of Harbin in China (Grant No. 2014RFQXJ007), the Modern Sensor Technology Innovation Team for College of Heilongjiang Province in China (Grant No.2012TD007).

References

[1] Feng Ning, Erik Bruun. An offset-trimmable array of magnetic-field-sensitive MOS transistors (MAGEFTs) [J]. Sensors and Actuators A, 1997, 58(2):109-112.

[2] Johannes W.A. von Kluge, Werner A. Langheinrich. An analytical model of MAGFET sensitivity including secondary effects using a continuous description of the geometric correction factor G [J]. IEEE Transactions on Electron Devices, 1999, (1):89-94.

[3] Dirk Killat, Johannes v.Kluge, Frank Umbach, et al. Measurement and modeling of sensitivity and noise of MOS magnetic field-effect transistors [J]. Sensors and Actuators A, 1997, (61):346-351.

[4] Yao Yunruo, Zhu Dazhong, Guo Qing. Sector split-drain magnetic field-effect transistor based on standard CMOS technology[J]. Sensor and Actuators A, 2005, 121(2):347-351.

[5] Guo Qing, Zhu Dazhong, Yao Yunruo. CMOS magnetic sensor integrated circuit with sectorial MAGFET[J]. Sensor and Actuators A, 2006, 126(1):154-158.

[6] Guo-Ming Sung. Error correction for transformed concave and convex MAGFETs with DC supply voltage[J]. Sensor and Actuators A, 2005, 117(1):41-49.

[7] S.M. Rezaul Hasan. A novel 0.7 V high sensitivity complementary differential MAGFET sensor for contactless mechatronic applications[J]. Sensor and Actuators A, 2010, 163(1):138-149.

[8] Zhao Xiaofeng, Wen Dianzhong, Zhuang Cuicui, et al. High sensitivity magnetic field sensors based on nano-polysilicon thin-film transistors[J]. Chinese Physics Letters, 2012, 29(11): 118501(1-4).

[9] Zhao Xiaofeng, Wen Dianzhong, Zhuang Cuicui, et al. Fabrication and characterization of the magnetic field sensors based on nano-polysilicon thin-film transistors[J]. Journal of Semiconductors, 2013, 34(3): 036001(1-6).

[10]Zhao Xiaofeng, Wen Dianzhong. Fabrication and characteristics of the nc-Si/c-Si heterojunction MAGFET [J]. Journal of Semiconductors, 2009, 30(11):114002(1-4).

[11]Zhao Xiaofeng, Wen Dianzhong, Lv Mwiwei, et al. Fabrication and characterization of the split-drain MAGFET based on the nano-polysilicon thin film transistor [J]. Journal of Semiconductors, 2014, 35(9):094004(1-6).

Key Engineering Materials Vols 645-646 (2015) pp 139-144
© (2015) Trans Tech Publications, Switzerland
doi:10.4028/www.scientific.net/KEM.645-646.139

Submitted: 2015-01-08
Accepted: 2015-01-15

Graphene Field Effect Transistor's Circuit Modeling and Radio Frequency Application Study

R. Zhu[1,2,a], Y.Zhang[1,2,] J.Luo[1], S.Chang[1,2,b],*, H.Wang[1,2], Q.Huang[1,2] and J.He[1]

[1]School of Physics and Technology, Wuhan University, Wuhan, Hubei, CHINA

[2]Suzhou Institute of Wuhan University, Suzhou, Jiangsu, CHINA;

[a]zhurh@whu.edu.cn, [b]changsheng@whu.edn.cn

Keywords: GFET, Verilog-A, GFET frequency multipliers, GFET subharmonic mixers

Abstract. In this paper, a large signal circuit model of graphene field effect transistor (GFET) is described accurately by Verilog-A language, which is suitable for radio frequency circuit design and can be applied in HSPICE and ADS directly. Then two typical radio frequency (RF) circuits, frequency multiplier and mixer, are based on this GFET circuit model. The proposed circuits' performance are analyzed respectively in 10GHz, 15GHz and 20GHz, and GFET's application foreground in radio frequency area is discussed.

Introduction

Since its discovery in 2004 [1], graphene has attracted great attention with its unique structures and properties. Extremely high intrinsic carrier mobility, low contact resistance and high Fermi velocity make it a potential material for high-frequency electronics. Since the first top-gated GFET was manufactured in 2007, great effort has been made for its circuit application. As it is lack of intrinsic band gap (patterning graphene into nanoribbon is a way of obtaining band gap [2]), GFET is hard to be turn off, which means it is suitable for analog circuit rather than digital application. Up to now, GFET is utilized as a kernel on frequency doubler [3], radio frequency (RF) mixer [4], digital modulator, multiplier phase detector, and so on. In this paper, a GFET circuit model [5] is realized in Verilog-A language [6], and the performance of two typical RF circuits (frequency multiplier and subharmonic mixer) which are constructed by GFET, are discussed in detail.

Ambipolar transport characteristic of GFET

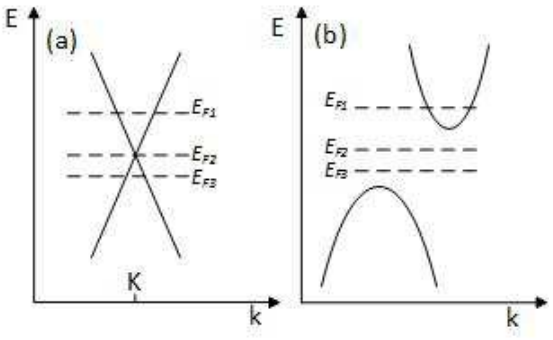


Fig.1 (**a**)Schematic band diagram of gapless large-area graphene. (**b**) Band diagram of an indirect semiconductor, e.g., Si.

Natural large-area graphene is gapless. Its cone-shaped valence and conduction bands touch each other at the K points of the Brillouin zone, as shown in Fig. 1a. When a positive (negative) voltage is applied on gate electrode, the Fermi level E_{F2} shifts to the conduction (valence) bands and therefore the electron (hole) is dominant in channel current, namely a pronounced n-type (p-type) conduction. Assuming a proper voltage is applied on the gate, carriers in the channel of a GFET can be changed between electron and cavity [7]. This phenomenon is called ambipolar transportation of GFET. This ambipolar transportation characteristics are different from traditional semiconductor devices (Fig.1b), resulting in the special features of GFET's application circuits.

GFET circuit model

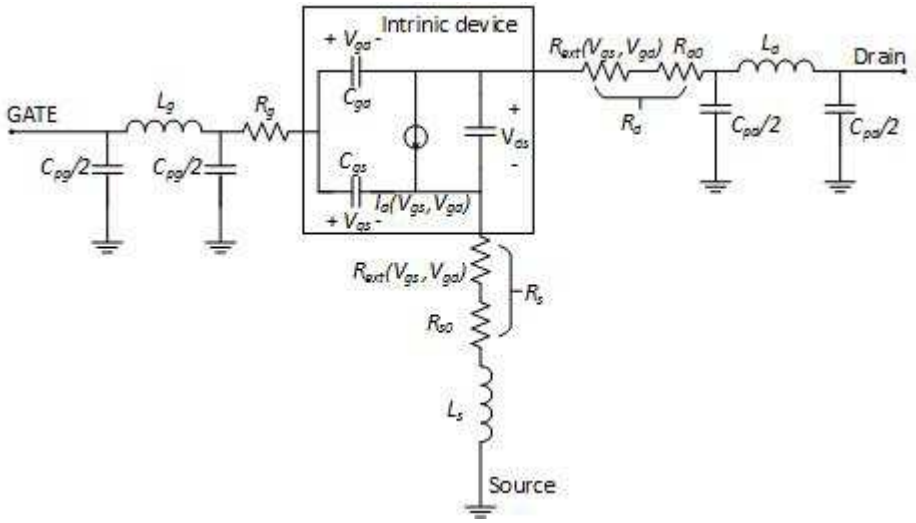


Fig.2 The equivalent circuit topology of GFET

$$I_{\mathrm{ds}} = q\frac{W}{L}\int_0^L n(x)v_{drift}(x)dx \tag{1}$$

$$R_s = R_{so} + R_{ext}(V_{gs}, V_{gd}) \tag{2}$$

where $n(x)$, $v_{drift}(x)$, L, W, R_{s0}, V_{gs}, V_{gd} and R_{ext} represent the carrier density, the carrier velocity, the channel length, the channel width, the intrinsic source resistor, the gate-to-source voltage, the gate-to-drain voltage, and a carrier-dependent term of source resistor, respectively.

To insure the model available for practical circuit design, the above GFET model is realized by Verilog-A language. By this way, the analog behavioral of GFET can be encapsulated as an acceptable description by common analog circuit electronic design automation software. Specifically, the input/output port names and attribute, the variables, the constant expressions, and the nodes are first defined. Then according to the characteristic equation, the electrical behavior descriptions are used to explain the operating principle of the device in an "*analog begin…end*" module [8]. For an example, firstly the I_{ds} is obtained through integration by substitution of the current microscopic equation, and then this physical expression is embedded into the circuit condition by the descriptor "*I(N3,N4) <+ I_{ds};*" in which *N3* and *N4* are two terminals of the channel current. Through above process, the circuit model of GFET is setup, which can be used in HSPICE and ADS directly.

Fig. 3 gives the verification of the Verilog-A GFET circuit model. In it, the dot data is from the analytic equations in [5], and the line is the prediction of our Verilog-A model. From it one can see, our model achieves perfect accuracy under different terminal voltages.

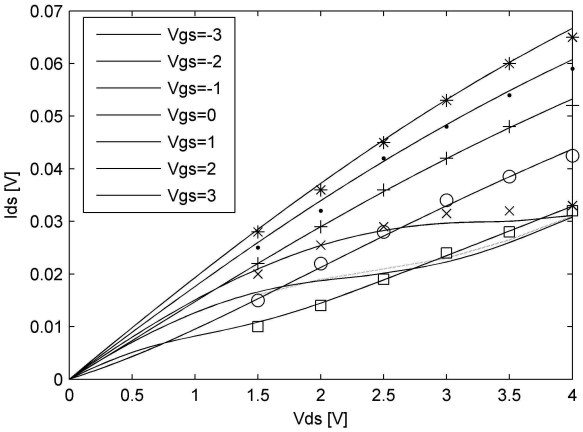


Fig.3 GFET circuit model verification

RF circuit application analysis

Due to extremely high intrinsic carrier mobility and high carrier saturadion velocity, GFET is considered a promising device for high-frequency application. Moreover, its ambipolar transportation characteristics enable GFET to refresh radio frequency circuit structure. In this section, two typical radio frequency circuits reconstructed by GFET are discussed to explore GFET's application foreground.

1. GFET frequency multiplier

Due to the ambipolar transport characteristics, GFET can simplify frequency multiplier. Assuming the transfer characteristic of GFET is perfect symmetrical and can be expressed as a function of V_{GS} as follows [9],

$$\begin{aligned} I_{DS} &= a_0 + a_2\left(V_{GS} - V_{GS,min}\right)^2 + a_4\left(V_{GS} - V_{GS,min}\right)^4 + \cdots \\ &= a_0 + a_2\left(V_{GS,min} + A\cos(\omega t) - V_{GS,min}\right)^2 + a_4\left(V_{GS,min} + A\cos(\omega t) - V_{GS,min}\right)^4 + \cdots \\ &= a_0 + a_2 A^2\cos^2(\omega t) + a_4 A^4\cos^4(\omega t) + \cdots \end{aligned} \tag{3}$$

where $V_{GS,min}$ is the gate-source voltage on the minimum conduction, and a_0, a_2, a_4…are the constants related to the drain-source voltage.

According to eq. 3, if a_2 is much larger than the coefficients of high-order items, GFET's anbipolar transport shows a very significant quadratic component, which is the desired frequency multiply function. But since the high-order items exist, it can be predicted that high-frequency harmonic components will appear in the output drain current of GFET.

Following this rule, the GFET frequency multiplier can be designed as shown in Fig.4. When the gate of a GFET is dc biased at the minimum conduction point and a sinusoidal RF signal is superimposed on that DC bias, the output drain current is carried by electron during the first half period while during the second half period it is carried by holes. (as the signal waves shown in Fig. 4).Thus this circuit realizes the frequency-doubling function and makes the frequency multiplier circuit much more compact than the conventional CMOS doubling circuits. Because of the existence

of high-frequency harmonic waves, the output waveform is not a perfect one. Considering the circuit is very simple, this flaw is understandable, but a filter network is needed.

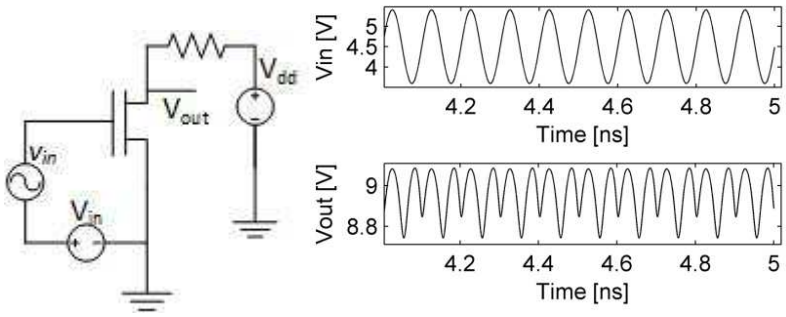


Fig.4 GFET frequency multiplier and its function

Table 1 The Amplitude Ratio of Second Harmonic Component and First Harmonic Component When V_{in} is 4.5V and V_{dd} is 12V

Fvin / Vin	10G Hz	15G Hz	20G Hz
0.5V	1.45	1.16	0.942
0.6V	1.81	1.33	1.04
0.7V	2.02	1.41	1.07
0.8V	2.09	1.42	1.06
0.9V	2.08	1.39	1.03
1.0V	2.02	1.35	0.994
1.1V	1.95	1.30	0.949

To analyze the circuit's performance deeply, using the Fourier transform to deal with the output drain current, and list the ratio of second harmonic component and first harmonic component in tab.1. From it one can see, this ratio is relatively stable on the same input frequency with the changed input signal amplitude, which means the presented GFET frequency multiplier has a large input dynamic range. The ratio decreases with the increase of frequency, which indicates that its amplitude-frequency response degrades with the increase of frequency. It mentions that when the application frequency is quite high, the gain of GFET multiplier should be noticed.

2. GFET frequency mixer

Since the coefficients a_0, a_2, a_4… in eq.3 are related to the drain-source voltage, change the configuration of GFET's drain terminal, the function of the above multiplier can be extended. If a RF signal is applied on the drain of a GFET while a LO signal is superimposed on the gate, the function of frequency-doubled are modulated and thus the output drain current contains the mixed frequencies of gate and drain inputs. Specifically, the sum frequency ($f_{RF}+2f_{LO}$), and the difference frequency ($2f_{LO}-f_{RF}$, also called the intermediate frequency f_{IF}) of the input frequencies generate. This structure is a subharmonic mixer. Normally, in order to extract the intermediate frequency, a low filter is needed, as shown in Fig. 5. It is worth to be mentioned that in the circuit, a small capacitance is added in the drain to prevent intermediate frequency leaking from that terminal.

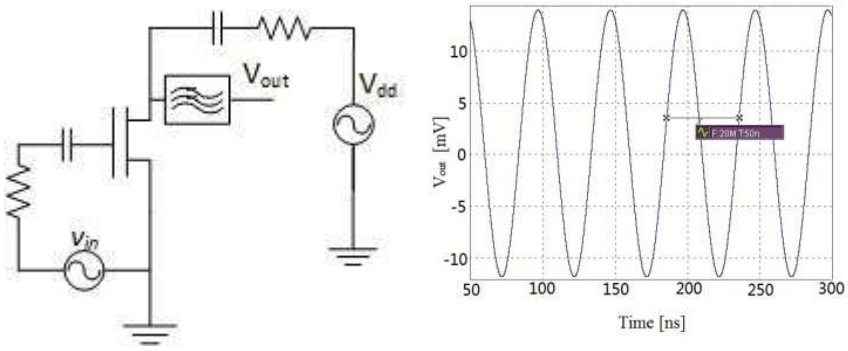


Fig.5 GFET mixer and its function

This circuit can output a perfect mixed intermediate frequency as shown in Fig.5. (In this case a 20M Hz signal is got from a 40G Hz RF signal and a 20.01G Hz LO signal)

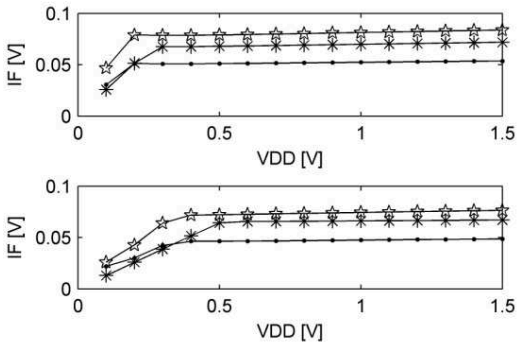


Fig.6 The IF (intermediate frequency) output of GFET mixer under different conditions

Fig.6 illustrates the tests under different RF frequencies (20G Hz and 40G Hz) and different local oscillator frequencies (IF=20M Hz, 40M Hz, 60M Hz), respectively. Form it one can see, the presented GFET mixer works stable on all conditions. That means it has a wide application range.

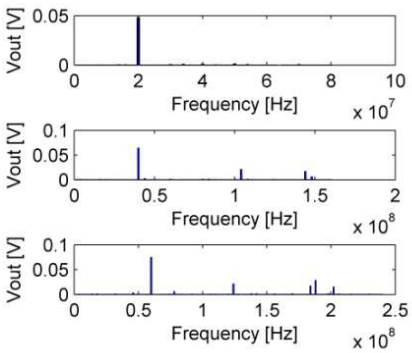


Fig.7 Spectrum analysis of GFET's IF output

Furthermore, the output signal's integrity is discussed in Fig.7 by the spectrum analysis. In all three cases (20M Hz, 40M Hz and 60M Hz IF outputs), the high frequency noise are small comparing with

the desired intermediate frequency signals, which indicates the GFET mixer can output a perfect signal. With the increase of frequency, the harmonic components increase slightly, which will decide the GFET mixer's limit.

From the above analysis of two typical radio frequency circuits, it can be drawn that by the virtue of ambipolar transportation, GFET can realize circuit function by a simpler structure. The more symmetry the GFET's ambipolar transportation characteristics are, the better performance the GFET's circuit has. To get a much more ideal output result, the bigger transconductance is anticipated. In the area of radio frequency application, these rules give the goal of both GFET device improvement and circuit structure innovation.

Summary

In this paper, a circuit model of GFET is presented accurately by Verilog-A language. By taking advantage of the model, novel GFET-based radio frequency circuits, such as GFET frequency multiplier circuit and GFET subharmonic mixer circuit, are deeply analyzed, and relative device and circuit development rules are concluded.

Acknowledgments

This work was supported by the National Natural Science Foundation of China (grant no 61204096 and 61404094), the Science Foundation of Jiangsu Province, China, (grant no BK20141218), the China Postdoctoral Science Foundation (grant no 2012T50688), and the Fundamental Research Funds for the Central Universities, Wuhan University (grant no 2042014kf0238).

References

[1] K.S. Novoselov, A.K. Geim, S.V. Morozov, Electric field effect in atomically thin carbon films, Science. 306 (2004) 666-669.

[2] S. Chang, Y. Zhang, Q.G. Huang, H. Wang, Effects of vacancy defects on graphene nanoribbon field effect transistor, Micro & Nano Letters. IET. 8 (2013) 816-821.

[3] Y.M. Lin, A. Valdes-Garcia, S.J. Han, Wafer-scale graphene integrated circuit, Science. 332 (2011) 1294-1297.

[4] J.S. Moon, H. -C. Seo, M. Antcliffe, Graphene FETs for zero-bias linear resistive FET mixers, IEEE Electron Dev. Lett. 34 (2013) 465-467.

[5] O. Habibpour, J. Vukusic, J. Stake, A large-signal graphene FET model, IEEE Trans. Electron Dev. 59 (2012) 968-975.

[6] G.J. Coram, How to (and how not to) write a compact model in Verilog-A, BMAS 2004. Proceedings of the 2004 IEEE International. IEEE. 21-22 Oct. 2004, San Jose, CA, USA. (2004) 97-106.

[7] Z. X. Wang, Z.Y. Zhang, L.M. Peng, Graphene-based ambipolar electronics for radio frequency applications, Chin. Sci. Bull. 57 (2012) 2956-2970.

[8] X. Deng, S. Chang, G. Wang, Verilog-A Model for Graphene Field Effect Transistors, Micronanoelectronic Technology. 49 (2012) 493-497,533.

[9] H. Wang, A. Hsu, J. Wu, Graphene-based ambipolar RF mixers, IEEE Electron Dev. Lett. 31(2010) 906-908.

Key Engineering Materials Vols 645-646 (2015) pp 145-150
© (2015) Trans Tech Publications, Switzerland
doi:10.4028/www.scientific.net/KEM.645-646.145

Submitted: 2015-01-09
Accepted: 2015-01-13

Synthesis and dispersity of YBCO powder produced by oxalic acid precipitation method

Wang Aiqin[1,*], Han Huihui[1], Li Min[1], Xie Jingpei[1], Wu Qingjie[2], Ma Douqin[2]

[1]College of Material Science, Henan University of Science and Technology, Luoyang 471003, Henan, China

[2]School of Physical Engineering, Zhengzhou University, Zhengzhou, Henan, 450001, China)

[1,*]aiqin_wang888@163.com

Keywords: YBCO powder; oxalic acid precipitation method; agglomeration; dispersity

Abstract. The YBCO powder was prepared by oxalic acid precipitation method and consequent annealing. The correlation between pH values of oxalic acid solution and the precipitation percentage of precursors were analysed based on thermodynamics analysis. The differential scanning calorimetryanalysis (DSC) was used to confirm the synthetic technological parameter. The phases of powder in each process were investigated by XRD. The microstructures of each powder were tested by SEM and TEM. The mean grain size was calculated by the scherrer's equation. The test results indicated that the YBCO powder with high purity, less impurities, smaller particle, but severe agglomeration, was Y123 when annealing at 900℃. However, adding dispersants could effectively solve the severe agglomeration. The size of YBCO particles was nano-sized and coincided with the calculation.

Introduction

Superconductor has Zero resistance effect and Meissner effect (diamagnetic effect completely), and it mainly applies to cable of electricity transmission, high field magnet, bearing of EDS maglev, energy storage flywheel, maglev transportation system, superconducting motor, permanent magnet and so on[1-5]. YBCO as the second generation of high-temperature superconducting material is favored by all research scholars due to its excellent properties. YBCO precursor powders with single-phase, tiny and uniformity particle is not only the foundation of preparation of superconductor YBCO of large size and high performance, but also widely used in the preparation of superconducting device, superconducting film material, single-phase and melt texture block material. YBCO powders were mainly produced by solid reaction process, sol-gel method, coprecipitation method and oxalic acid precipitation method. Solid reaction process, which has a long process cycle, imports impurities easily, particle size was not uniformity and beyond 1μm. YBCO powders made by coprecipitation method and sol-gel method could obtain superfine powder due to reaction at the molecular level[6-8]. While these methods cause the severe agglomeration phenomenon of powders easily and the particle size needs to be further reduced. In this paper, oxalic acid precipitation method was selected to synthesis nano-sized YBCO powder, the temperature of phase formation and reaction process were studied and solved the severe agglomeration phenomenon of powders.

Experimental

Mix yttrium nitrate, barium nitrate and copper nitrate according to the molar ratio of Y^{3+}:Ba^{2+}:Cu^{2+}=1:2:3, and then added excess oxalic acid solution to the mixed solution. Ammonia was added in the solution after Y^{3+}, Ba^{2+}, Cu^{2+} precipitation completely to adjust pH value between 4 and 5. The solution was oxalate coprecipitation solution of yttrium ions, barium ions and copper ions. Filtered and dried the precipitated powder at 80 ℃ for 15h. The precursor was the mixture of $Y_2(C_2O_4)_3 \cdot 9H_2O$, $BaC_2O_4 \cdot 2H_2O$, $CuC_2O_4 \cdot 2H_2O$. The precursor was put in a box type resistance furnace for sintering reaction, finally black YBCO powder was obtained.

The differential scanning calorimetryanalysis (DSC) was used to confirm the synthetic technological parameter. The phase and grain size of YBCO power were investigated by XRD. The microstructure of powder was tested by SEM and TEM.

Theoretical basis of synthesis of YBCO nanopowder

Theoretical calculation of the correlation between pH values and the precipitation percentage of YBCO precursors In the process of using oxalic acid precipitation method, if the metal ion precipitation is not complete, the single-phase YBCO powder may cannot obtained. So the proportion of Y^{3+}, Ba^{2+} and Cu^{2+} must be controlled strictly, to facilitate the preparation of YBCO[9-14]. The chemical reaction in the oxalate precursor solution and the corresponding equilibrium were showed in Tab. 1[8].

In the solution system of Y^{3+}, Ba^{2+}, Cu^{2+}, $C_2O_4^{2-}$, and H_2O, $[Y^{3+}]_T$, $[Ba^{2+}]_T$, $[Cu^{2+}]_T$, $[C]_T$ were respectively used to stand for the total concentration of Yttrium, barium and copper ions and oxalate ions. The following equations were obtained according to the chemical reaction balance and mass balance.

$$[C]_T=[C_2O_4^{2-}]+[HC_2O_4^{-}]+[H_2C_2O_4]=[C_2O_4^{2-}]\{1+10^{4.27-PH}+10^{5.51-2PH}\}=[C_2O_4^{2-}]\times\Phi_C \quad (1)$$

$$\lg[Y^{3+}]_T=\lg(\Phi_C/[C]_T)^{3/2}-14.14+\lg B \quad (2)$$

$$\lg[Ba^{2+}]_T=\lg(\Phi_C/[C]_T)-6.8+\lg A \quad (3)$$

$$\lg[Cu^{2+}]_T=\lg(\Phi_C/[C]_T)-9.36+\lg C \quad (4)$$

where A, B, C, and ΦC are a function of PH.

$$A=1+10^{PH-13.4}+10^{2PH-24.41} \quad (5)$$

$$B=1+10^{PH-9}+10^{3PH-19.9} \quad (6)$$

$$C=1+10^{4PH-37.5}+10^{2PH-8.34}+10^{PH-7}+10^{3PH-25} \quad (7)$$

$$\Phi_C=1+10^{4.27-PH}+10^{5.51-2PH} \quad (8)$$

The concentration of metal ions in the solution under different pH were obtained by means of the above equation and the concentration oxalic acid was $[C]_T$ =0.1mol/L (Fig. 1). Theoretically, completely precipitated could happen when the concentration of metal ions less than 10^{-5}mol/L. According to this theory, metal ion precipitate completely can be obtained when the pH value of Y is 1-9.18, Ba is 3.64-12.5, and Cu is 1.3-5.79. Synthesizes each kind of situation, the pH value range was from 3.64 to 5.79. To obtain YBCO powder with high purity due to the completely precipitate of the metal ions, the test pH value range was from 4 to 5 when the concentration of oxalic acid experiment was 0.1mol/L.

Sintering parameters according to the differential thermal analysis Fig. 2 was TG-DTA curve of the precipitation. It's obvious that the reaction process was mainly divided into three stages: the first stage was before 278 ℃, the quality of the powder decreased significantly due to the crystal water loss of $Y_2(C_2O_4)_3\cdot 9H_2O$, $BaC_2O_4\cdot 2H_2O$, $CuC_2O_4\cdot 2H_2O$; the second stage was from 278 ℃ to 620 ℃,

Table.1 The chemical reactions in solution and their equilibrium constants

Sequence number	The chemical reactions	lgK	Sequence number	The chemical reactions	lgK
1	$H_2C_2O_4 \rightleftharpoons HC_2O_4^{-}+H^{+}$	-1.25	8	$Cu(OH)_2 \rightleftharpoons Cu^{2+}+2OH^{-}$	-19.66
2	$HC_2O_4^{-} \rightleftharpoons C_2O_4^{2-}+H^{+}$	-4.27	9	$Cu(OH)_4^{2-} \rightleftharpoons Cu^{2+}+4OH^{-}$	-18.5
3	$Ba^{2+}+C_2O_4^{2-} \rightleftharpoons Ba_2C_2O_4\downarrow$	6.8	10	$Cu(OH)_3^{-} \rightleftharpoons Cu^{2+}+3OH^{-}$	-17
4	$Cu^{2+}+C_2O_4^{2-} \rightleftharpoons CuC2O4\downarrow$	9.36	11	$CuOH^{+} \rightleftharpoons Cu^{2+}+OH^{-}$	-7
5	$2Y^{3+}+3C_2O_4^{2-} \rightleftharpoons Y_2(C_2O_4)_3\downarrow$	28.28	12	$Y(OH)_3 \rightleftharpoons Y^{3+}+3OH^{-}$	-22.1
6	$BaOH^{-} \rightleftharpoons Ba^{2+}+OH^{-}$	-0.6	13	$YOH^{2+} \rightleftharpoons Y^{3+}+OH^{-}$	-5
7	$Ba(OH)_2 \rightleftharpoons Ba^{2+}+2OH^{-}$	-3.59			

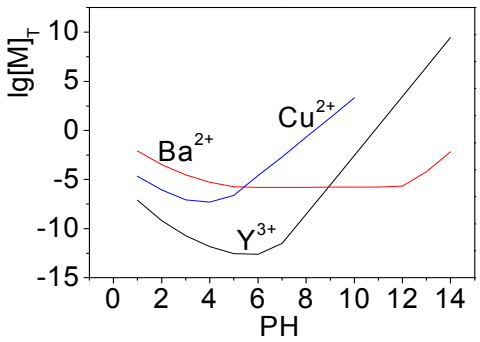


Fig.1 The curves of concentration of metal ions vs pH values

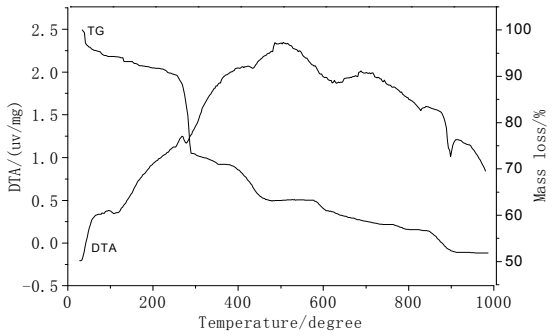


Fig.2 The TG-DTA curve of precursors

the mainly reaction were the decomposition of $Y_2(C_2O_4)_3$, BaC_2O_4 and CuC_2O_4, the powder released a lot of heat at the temperature of 312 ℃, 370 ℃ and 312 ℃, which was considered as the decomposition rate of CuC_2O_4, $Y_2(C_2O_4)_3$ and BaC_2O_4 achieved to maximum, and agree with the results of Feng Jianqing et al [5]; the third stage was from 620 ℃ to 915 ℃, there was an obvious heat absorption process at 900 ℃due to the formation of YBCO. Preliminary determine the sintering temperature was about 900℃.

Characterization of YBCO nanopowders

XRD analysis In order to confirm the final phase formation temperature and the phase of powder, high temperature calcination was performed at 860 ℃, 880 ℃ and 880 ℃, and the powder after calcination was studied by XRD. Fig.3 showed YBCO diffraction peak was more obvious in 860 ℃, showing that precursor has formed YBCO phase, but there were also other phases, such as Ba_2CuO_3, Y_2O_3 and CuO, Ba_2CuO_3 was generated by the barium carbonate and copper oxide reaction. The diffraction peaks of the mixed phase Ba_2CuO_3 was almost disappeared at 880℃, and the diffraction peak intensity of Y_2O_3 and CuO was weaken. When the temperature reach to 900℃, the diffraction peak intensity of YBCO reached the maximum, the diffraction peak of mixed phase was almost entirely disappeared, indicated that phase transformation finished completely.

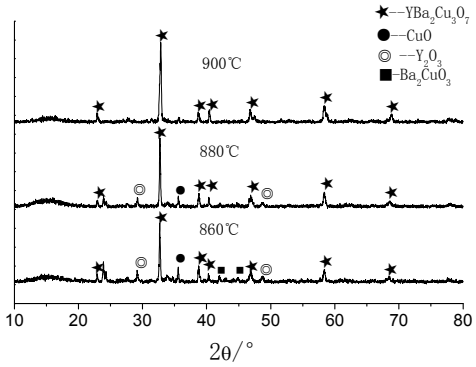


Fig.3 XRD patterns of YBCO powder calcined at different temperatures

Particle size of powder can be calculated according to the Scherrer formula as follows [15]:

$$D=K\lambda/(\beta\cos\theta) \quad (9)$$

Where D is the size of the perpendicular to the surface hkl, K is the Scherrer constant (K = 0.9 for half high width, K = 1 for integral width), λ is the incident X-ray wavelength, the wavelength of Cu target is 0.1541 nm, β is the half high width of the diffraction peak, θ is the Bragg diffraction Angle. The sizes of YBCO particles by calculating under different temperature were shown in Tab. 2. With the increase of temperature, the particle size decreased, but all within 100 nm due to a large number of CO_2 gas emission in the process of the final phase[5]. The releasing gases prevent the accumulation and growth of YBCO grains. So the particle size of YBCO decreased due to the more obvious blocking effect caused by the more CO_2 with the increasing of temperature.

Table. 2 Average grain size of YBCO powders calcined at different temperatures

Calcining temperature/℃	860	880	900
Average grain size/nm	49.0	42.9	32.7

Microstructure characterization of YBCO powders Fig. 4 showed the microstructure of YBCO powders. The grain size of the powder was not uniform. While some particles below microns level, agglomeration phenomenon was serious. In order to further observe the microstructure of powder, TEM analysis was used. TEM morphology was shown in Fig. 5, the particle size of YBCO was about 100 nm, which have a slight difference with the calculated results in Tab. 2. Because the grain shape was irregular, and the surface was not smooth, and there was a lot of small particles on the surface of large particles, which form a larger particles, resulted in the phenomenon of agglomeration.

Dispersion of YBCO powder According to related reports[15-17], the reasons for agglomeration phenomenon of powder were as follows: 1: after grain refining to the nanometer level, the surfaces of particles had a large number of positive and negative charges, as well as the shape of the particles highly irregular. These would cause the accumulation of charges, and lead to the agglomeration for the instability of the particles. 2: Nano-particles had big specific surface area and high surface energy. So in order to reduce the specific surface energy of particles, they would gather each other that leading to a reunion. 3: It would attract each other between the particles and make them gathering to grow up and forming together, by the effect of van der Waals force, hydrogen bond and chemical bond among the particles. In order to solve the problem of agglomeration, surface active agent was added in the

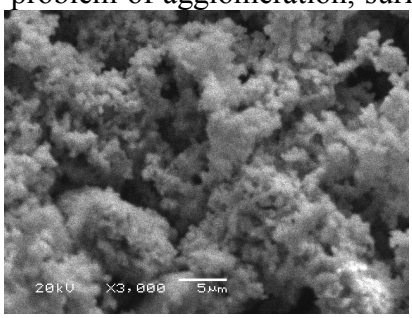


Fig.4 SEM micrographs of YBCO powder

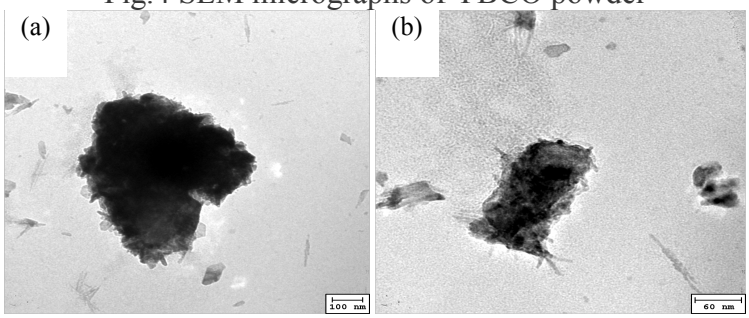


Fig.5 TEM micrographs of YBCO powder

process of reacting solution. That made the surface absorbing active molecules when colloidal particles once formed. So once forming a protective layer on the surface of particles, it prevented particles get together, and improved the dispersion and uniformity of the particles.

Polyethylene glycol was added to solution reaction on the basis of oxalic acid salt precipitation reactions. The calcination temperature of precursor powder was 900 ℃ and the other parameters were constant.The TEM morphology and diffraction spots of preparing YBCO powder were shown in Fig. 6. It could be found that the particles were round, smooth surface, not covered with other small particles, and only a slight connection between particles. The size of the particles was under 60 nm. It shown that dispersant can not only eliminate the agglomeration phenomenon, but also refine the powder particles. The particles size of YBCO nanometer powder after dispersion fit well with calculation.

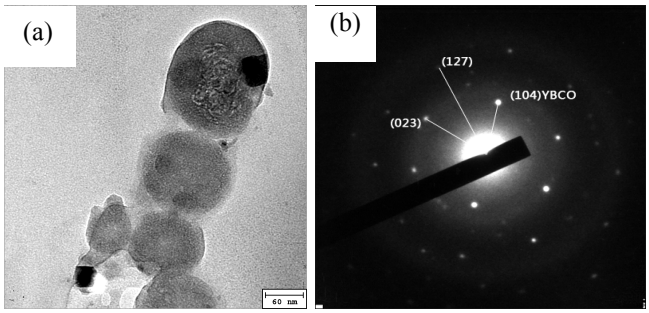


Fig.6 TEM micrographs and diffraction pattern of YBCO powders added dispersant

Summary

(1) Metal ion precipitation completely when the pH was between 3.64 and 5.79 and oxalic acid concentration was 0.1mol/L. The best phase formation temperature was 900℃. The purity of YBCO powder maed by oxalic acid precipitation method was high, but agglomeration phenomenon was quite serious.

(2) The agglomeration phenomenon of YBCO powder was solved efficiently by adding polyethylene glycol as dispersing agent. The grain was refined and achieved nanoscale.

References

[1] Y.X. Guo. Preparation and characterization of YBCO high temperature superconducting materials[D].Changchun: Changchun University of Science and Technology.(2005)1-3.

[2] Z.S. Peng, Z.Q. Hua, B.C. Yang, X.H. Wang, Z.X. Zhao, B. Yin, Y.J. Hao. Preparation and Superconductivity of the Ho Substitution YBCO Thin Film,J. Journal of the Chinese Rare Earth Society. 16(1998) 139-142.

[3] H.W. Gu, J. Yang, H.Z. Liu, F. Qu, H. Zhang. Development of Coated Conductor YBa2Cu307-x Tapes,J. Journal of the Chinese Rare Earth Society. 24(2006) 257-268.

[4] L.Xiao, H.T. Ren, Y.L. Wang. Fabrication and Maglev Properties of Large Bulk Melt-Textured-Growth(MTG) YBC0 uperconductor,J. Journal of the Chinese Rare Earth Society. 14(1996)224-228.

[5] J.Q. Feng, X.Y. Xu, X.M. Xiong, G.Q. Liu ,J. Chinese Journal of Low Temperature Physics, 31 (2009) 241-244.

[6] D.L.Yang, J. Mo, H.X.Lu. Studies on Oxygen Characteristics of YBa2Cu3O7-x and Its Applications to Air Separation and Gas Purification,J. Journal of Rare Earths. 23(2005) 112-115.

[7] X.X. Guan, J. Sun, L. Zhang, J.H. Liu, Z.L. Zhu, Z.T. Huang, D.Q. Zeng, J.P. Huang.Study on Φ100mm YBCO High Tenperature Superconductive Materials and Its Application,J. Journal of the Chinese Rare Earth Society. 20(2002)101-103.

[8] H.C. Li, B. Fu. Chemistry Handbook[M].Beijing:Industry Publisher.2006,349-370

[9] X.M, Cui, B.W. Tao, Y.R. Li. Effects of precursor solution concentration on the properties and morphology of YBCO films deposited by TFA-MOD method. Journal of Rare Earths. 24(2005) 272-276.
[10] W.J. Feng，S.Zhang，Q.J. Guo et al. The influence of PH value on YBCO nanopowder preparation craft and performance,J. Superconductivity. 37(2009)28-30.
[11] Lynn,David M,Amiji, Mansoor M,Langer Robert.pH-responsive polymer microspheres: Rapid release of encapsulated material within the range of intracellular Ph,J Angewandte Chemie – International Edition. 40(2001) 1707-1710
[12] J.L. Tang, M.K. Zhu, C. Chen, Y.D. Hou, H. Jing, H. Yan. Effect of pH Value on the Phase Composition， Properties and Morphology of the Pb(Scl/2Nbl/2)O3 Powders obtained by Precipitation,J. Rare Metal Materials and Engineering. 36(2007) 32-35.
[13] W.Xiang, Y.W. Tang, Y.Yan, B.H.Zhong, W.M.Fang, H.Liu, X.D.Guo. Influence of pH value and chelating reagent on performance of Li3V2(PO4)3/C cathode material,J. Transactions of Nonferrous Metals Society of China (English Edition),J.23(2013) 1395-1402.
[14] J. Hagberg, A. Uusimaeki, J. Levoska, S. Leppaevuori. Preparation of Bi-Pb-Sr-Ca-Cu-O high Tc superconducting material via oxalate route at various pH values,J.Physica C: Superconductivity and its Applications. 160(1989) 369-374.
[15] M.T. Wang, M. Li, Z.G.Liu, Y.H.Hu. Mechanism and Characterization and Countermeasures of Agglomeration of Ultrafine Particles ,J. China Powder Science and Technology. 14(2008) 46-51.
[16] H.M. Cun, H.Liu, J.Y.Wang,et al. Agglomeration and Disperasion of nano-scale Powders,J. Materials for Mechanical Engineering.28(2004)38-41.
[17] W.J.Yuan, Y.M. Zhou. Reasons for Aggregation of Nanoparticles and Solutions ,J. Materials Review.22(2008):59-61.

Key Engineering Materials Vols 645-646 (2015) pp 151-156
© (2015) Trans Tech Publications, Switzerland
doi:10.4028/www.scientific.net/KEM.645-646.151

Submitted: 2015-01-13
Accepted: 2015-01-15

Influence of Defects on the Young's Modulus of [110] Silicon Nanowires with Different Cross Sections

Fang Gu[1,a], Jiahong Zhang[2,3,b], Min Li[2], Linyan Liu[1] and Jing Su[1]

[1]School of Physics & Optoelectronic Engineering, Nanjing University of Information Science & Technology, Nanjing, China

[2]Jiangsu Collaborative Innovation Center on Atmospheric Environment and Equipment Technology, Nanjing University of Information Science and Technology, Nanjing 210044, China

[3]Jiangsu Key Laboratory of Meteorological Observation and Information Processing, Nanjing University of Information Science & Technology, Nanjing, China

[a]gfnuist@163.com, [b]zjhnuist@163.com

Keywords: silicon nanowires, defects, Young's modulus, cross section, molecular dynamics

Abstract. The size dependence becomes more significant as the devices scale down from micro- to nano-dimensions, which is generally attributed to surface effects due to the very high surface-to-bulk ratios in nanoscale structures. However, significant discrepancies between experimental measurements and computational studies indicate that there could be other influences besides surface effects, such as the influences of native oxide layer, fabrication-induced defects and boundary conditions. In this paper, our purpose is to investigate mainly the influence of fabrication-induced defects on the elasticity of [110] silicon nanowires (SiNWs) with different cross sections. We accomplish this by using the molecular dynamics (MD) simulation. Our MD results show that the H-passivated [110] SiNWs without surface defects is slightly elastically softer than bulk, which is in good agreement with other literature MD values. However, the effective Young's modulus of SiNWs with surface defects can significantly decreases as the defects increase. This softening behavior of [110] SiNWs is severe, which indicates the importance of surface defects. It is noted that the influence of defects on the Young's Modulus of SiNWs strongly depended on the distribution and morphology of defects as well as the cross-sectional shapes of SiNWs. It is observed that the influence of defects on square SiNWs is significantly different from those of hexagonal and triangle SiNWs. Our work reveals that fabrication-induced surface defects could be one of the important origins of the reduced effective Young's modulus experimentally observed in ultra-thin SiNWs. Therefore, the effect of defects on the characterization of the mechanical properties of nanowire must be carefully considered.

Introduction

SiNWs hold promise for a wide diversity of device applications, such as transistors, probes, resonators, sensors and actuators in biotechnology and nanoelectromechanical systems (NEMS). Their mechanical properties are very important for applying them in NEMS, which are known to be different from those of their macroscopic counterparts and size-dependent, mainly arising from the low dimensionality and surface effects. In past two decades, this size-dependent mechanical properties of SiNWs has been extensively investigated via experimental measurements [1-5] and theoretical studies, including first-principle density functional theory [6,7], molecular dynamics[8,9] and modifications to continuum theory [10,11]. However, the comparison between theoretical

results and experimental measurements demonstrates that, although surface effects influence the effective Young's modulus of SiNWs to some extent, they alone are insufficient to explain the experimentally observed trends and why the effective Young's modulus decreases prematurely. For example, the experimental results of [110] SiNWs report the observed size dependence at about 100nm, while the computational investigations predict this to occur at a characteristic size of less than 10nm[3]. The considerable discrepancies between experimental measurements and computational investigations show that there could be other influences besides surface effects, such as the influences of native oxide layer [5], fabrication-induced defects [3,7] and boundary conditions [11]. Noted that it was observed that the fabrication-induced defects abruptly increased when the silicon nanostructure was thinned to below 100nm, and these defects became visible as pinholes during HF-etching [3]. Thus, the nanowires are not defect-free and these can influence the experimentally measured data. Based on this phenomenon, Sadeghian et al. have recently utilized MD method to study the impact of defects on the elasticity of silicon nanocantilevers, and found that the fabrication-induced defects significantly influence the behavior of Young's modulus[8].

In this paper, we will focus on the influence of fabrication-induced defects on the elasticity of [110] SiNWs and study the origin of the strong size dependence of the effective Young's modulus in ultra-thin SiNWs. In addition, less attention has been devoted to understanding the effect of cross-sectional shape on the mechanical properties of SiNWs, in spite of the SiNWs with different cross-sectional shapes (square, hexagonal, triangle, etc.) have been fabricated by using the bottom-up method or the top-down technique. Therefore, it is another objective of the current work.

Model and MD calculation details

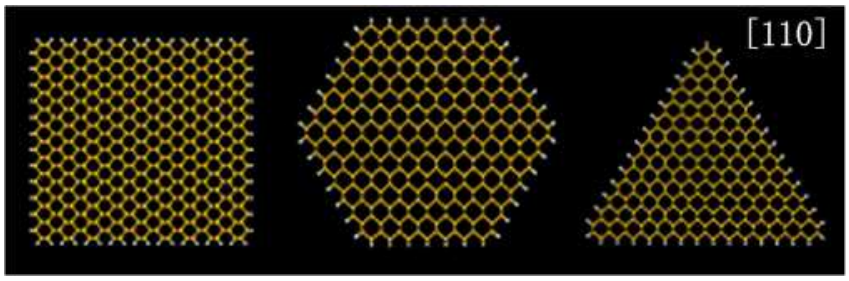


Fig. 1 Cross-sections of the optimized structures of SiNWs along the [110] direction. Yellow and white balls represent Si and H atoms, respectively.

The starting three-dimensional configurations of the SiNWs were cut from a bulk silicon crystal and were bounded by the low-index lateral surfaces using the Materials Visualizer module within Material Studio 4.0 software. In order to investigate the effect of representative cross-sectional shape on the mechanical properties of SiNWs, as shown in Fig. 1, the prototypes of study are the SiNWs with square, hexagonal and triangle cross sections, respectively. For the NEMS sensors, researchers typically select the [110] crystallographic orientation as the sensing direction, thus, we choose the SiNWs along the [110] crystallographic orientation. On the other hand, to generate the appearance of defects in the [110] SiNWs, the defects with the hole shape of different sizes are created by removing the atoms at the surface or edges of the SiNWs. As an example, the atomic configurations of [110] SiNWs with 2.5% defects are plotted in Fig. 2. It is noted that the SiNWs may contain several defects for large defect concentration and the size of the defects varied. Periodic boundary condition is applied along the x (i.e., the length) direction, leaving hydrogenated surfaces along the y and z directions. A sufficiently large vacuum region is built onto the lateral surfaces, so that the starting simulation cells do not interact with each other, and can be fully relaxed and optimized to a minimum energy state at zero Kelvin by using MD simulations in

NPT ensemble up to 50ps simulation times. In this paper, atomistic MD simulations have been performed with the Forcite package in conjunction with the COMPASS force-field mathematical model.

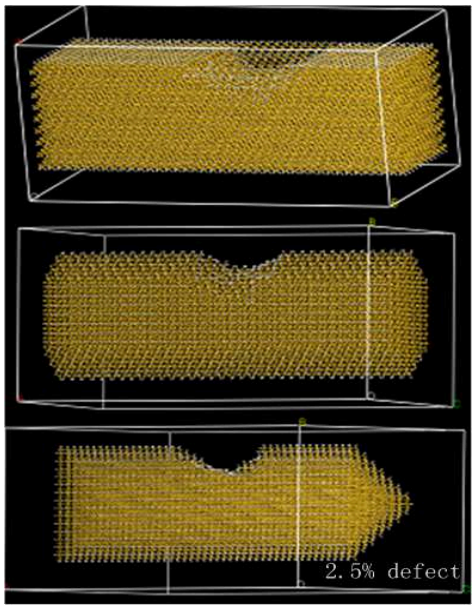


Fig. 2 A schematic diagram of SiNWs with 2.5% defect and different cross-sections. The dig-off parts of SiNWs represent defects.

After reaching equilibrium configurations, the SiNWs are subjected to a quasi-static loading along the *x* direction. The strains ε_x are fixed and imposed along the *x* direction in the range of [-1%, 1%], while the hydrogenated free surfaces facilitate relaxations along the *y* and *z* directions. For each ε_x, the atomic positions are again fully relaxed using the NVT method. The total energy of the nanowire is a function of the strains ε_x, as shown in the Fig. 3.

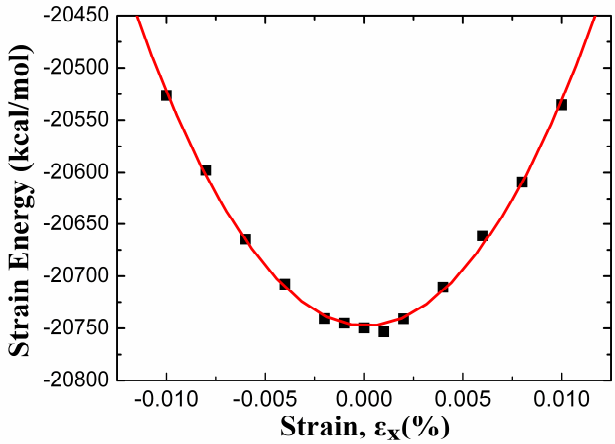


Fig. 3 Strain energy as a function of ε_x for the square SiNW with the thickness of 5.4 nm. Young's modulus is the second-order derivative of the energy with respect to strain ε_x.

The corresponding energy–strain relationship $E(\varepsilon_x)$ gives the effective Young's modulus according to the following formula:

$$Y_x = \frac{1}{V_0}\frac{d^2E(\varepsilon_x)}{d\varepsilon_x^2} . \quad (1)$$

Where V_0 is the volume of the SiNWs in fully relaxed zero-strain configuration (undeformed configuration). In the following sections, a series of MD simulations for different cross-sectional SiNWs have been performed with the concentration of defects ranging from 2 % to 10.5% and the size maintaining invariable.

Results and discussion

Fig. 4 displays the Young's moduli of the SiNWs with different cross sections (square, hexagonal, triangle) as a function of the concentration of defects. In the MD calculation, the length and thickness of the SiNWs is about 15.1nm and 5.4nm, respectively. As we can see from fig. 4, the [110] nanowires without surface defects is slightly elastically softer than bulk, which is in good agreement with other literature values of MD for H-passivated [110] SiNWs [9]. However, the effective Young's modulus of the SiNWs with surface defects can significantly decreases as the defects increase. For example, when the concentration of defects is about 10%, the effective Young's modulus of the SiNWs with square, hexagonal, triangle is reduced by 63.1%, 34.2%, 40.2%, respectively. Obviously, the softening behavior of [110] nanowires is severe, which fully reveals the important role of surface defects in characterizing the mechanical properties of the SiNWs. The significant softening effects are primarily from defect-induced bond loss. Interestingly, the influence of defects on the Young's Modulus of SiNWs strongly depends on the distribution and morphology of defects as well as the cross-sectional shapes of SiNWs. For example, as shown in Fig.4, the influence of defects on square SiNWs is significantly different from those of hexagonal and triangle SiNWs. It is observed that the Young's Modulus of square SiNWs decreases monotonically while those of hexagonal and triangle SiNWs exhibit fluctuating trend. The reason is that the defects of square SiNWs are on the center of their surface while those of hexagonal and triangle SiNWs are in their edges and corners. This different distribution and morphology of defects led to different bonding conditions and electron density around the bonds. As we all known that higher electron density and stronger bonding can give rise to larger Young's Modulus. In addition, the SiNWs with different cross-sectional shapes have different surface-to-bulk ratio and surface effect, which also make their Young's modulus show different variation trends.

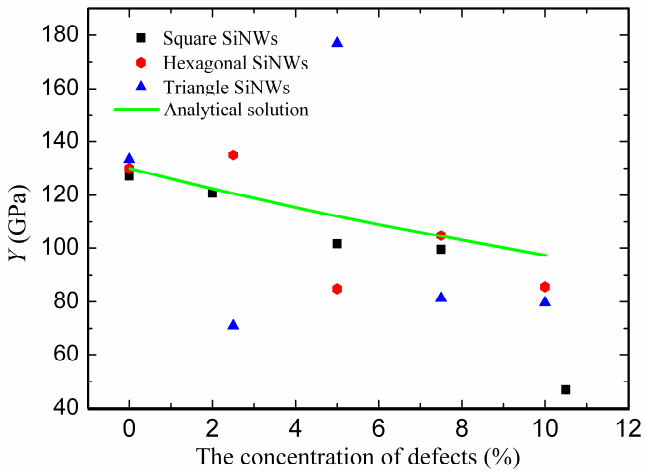


Fig. 4 The Young's modulus of the SiNWs with different cross-sections as a function of the concentration of defects.

In this paper, our MD results are compared with an analytical solution based on continuum theory. In order to approximate the effect of defects on the effective Young's modulus, an analytical solution, described in Ref. [12] is used as

$$Y_d = Y_0(1-\frac{A_d}{A_0}) / (1+2\frac{A_d}{A_0}) . \quad (2)$$

Where Y_d and A_d are the effective Young's modulus of the SiNW with defect and the surface area of defect, and Y_0 and A_0 are the effective Young's modulus and surface area of the SiNW without defect. Eq. (2) relates the relative area of defects with respect to the total area of the SiNW (defect concentration) $\frac{A_d}{A_0}$, to the ratio of the effective Young's modulus with and without defect $\frac{Y_d}{Y_0}$. The result is also shown in Fig. 4, shown as a solid line. Comparison between the MD results and the analytical solution shows a good agreement especially for small defects. Both MD and continuum results indicate that the Y_d can decreases with increasing defect volume fraction. It can be seen from the figure that substantial changes are found when the concentration of the defects is significantly increased. This shows that the defects can be a main contribution to drops in Y of the experimentally tested SiNWs.

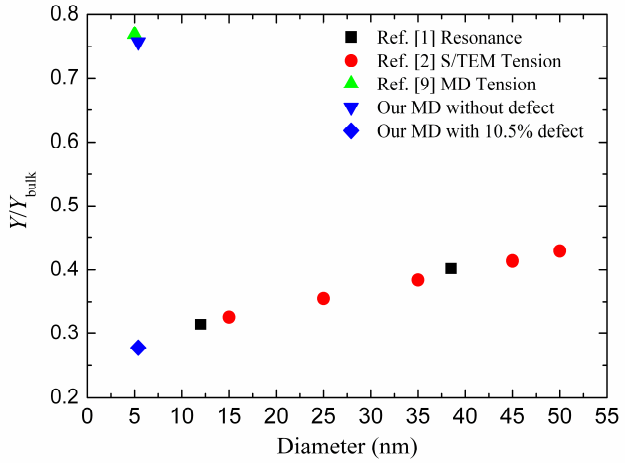


Fig. 5 The normalized experimental and computational (MD simulation without defects and our MD simulation with defects) results for Young's modulus of SiNWs.

Fig.5 presents that normalized experimental [1,2] and computational (MD simulation without considering defects [9] and our MD simulation with defects) results for Young's modulus of square SiNWs. As can be seen, the Young's modulus decreases monotonically with decreasing size, which shows the significant size-dependent elastic properties of the SiNWs. Without surface defects, the [110] SiNWs is elastically softer than bulk, which agrees well with other literature MD values for [110] SiNWs [9]. However, the discrepancy between the calculated result and experimental data [1,2] is significant. When we consider the defects in the nanowires, the discrepancy can be significantly reduced. As shown in fig. 5, our result of MD simulation with 10.5% defects on the surface of the SiNWs is good consistent with the experimental result trend. Thus, our work reveals that fabrication-induced surface defects could be one of the important origins of the reduced effective Young's modulus experimentally observed in ultra-thin SiNWs. In short, our MD simulations show that the effect of defects on the characterization of the mechanical properties of nanowires must be carefully considered.

Summary

In summary, molecular dynamics calculations have been carried out to determine the effects of fabrication-induced defects on the effective Young's modulus of silicon nanowires. The calculations were motivated by a large disparity between the experimental measurements and

theoretical studies of the effective Young's modulus. The conclusion is that the size dependence observed in the SiNWs with different cross-sectional shapes can be explained by a important contribution of fabrication-induced defects. Taking this additional factor into account, the gap between the experimental measurements and computational investigation can be closed and a similar trend was observed in the theory. Moreover, the effect of defects is influenced by the concentration of the defects, which is similar to the analytical solution based on the continuum theory predicts. It is noted that the influence of defects on the Young's Modulus of SiNWs also strongly depends on the distribution and morphology of defects as well as the cross-sectional shapes of SiNWs. Our work reveals that fabrication-induced surface defects could be one of the important origins of the reduced effective Young's modulus experimentally observed in ultra-thin SiNWs. Therefore, the effect of defects on the characterization of the mechanical properties of nanowire must be carefully considered.

Acknowledgement

This Project is supported by the National Natural Science Foundation of China (Nos. 61306138, 61307113), the Natural Science Foundation of Jiangsu Province (No. BK2012460), the National Training Program for Undergraduate on Innovation and Entrepreneurship and Jiangsu Province Practice, Innovation Training Program for College Students (No. 201310300034Z) and the Priority Academic Program Development of Jiangsu Higher Education Institutions. We also acknowledge the support for the computational resources provided by Key Laboratory of MEMS of Ministry of Education of China in Southeast University.

References

[1] X. Li, T. Ono, Y. Wang, M. Esashi, Ultrathin single-crystalline-silicon cantilever resonators: fabrication technology and significant specimen size effect on Young's modulus, Appl. Phys. Lett. 83 (2003) 3081.
[2] X. Han, K. Zheng, Y.F. Zhang, X. Zhang, Z. Zhang, Z.L. Wang, Low-temperature in situ large-strain plasticity of silicon nanowires, Adv. Mater. 19 (2007) 2112
[3] H. Sadeghian, C.K. Yang, J.F.L. Goosen, A. Bossche, U. Staufer, P.J. French, F. Van Keulen, Effects of size and defects on the elasticity of silicon nanocantilevers, J. Micromech. Microeng. 20 (2010) 064012.
[4] Y. Zhu, F. Xu, Q. Qin, W.Y. Fung, W. Lu, Mechanical properties of vapor-liquid-solid synthesized silicon nanowires, Nano Lett. 9 (2009) 3934-3939.
[5] G. Stan, S. Krylyuk, A.V. Davydov, R.F. Cook, Compressive stress effect on the radial elastic modulus of oxidized Si nanowires, Nano Lett. 10 (2010) 2031-2037.
[6] L. Ma, J.G. Wang, J.J. Zhao, G.H. Wang, Anisotropy in stability and Young's modulus of hydrogenated silicon nanowires, Chem. Phys. Lett. 452 (2008) 183-187.
[7] H.S. Park, W. Cai, H.D. Espinosa, H.C. Huang, Mechanics of crystalline nanowires, MRS Bulletin. 34 (2009) 178-183
[8] H. Sadeghian, H. Goosen, A. Bossche, B. Thijsse, F. Van Keulen, On the size-dependent elasticity of silicon nanocantilevers: impact of defects, J. Phys. D: Appl. Phys. 44 (2011) 072001.
[9] K. Kang, W. Cai, Brittle and ductile fracture of semiconductor nanowires-molecular dynamics simulations, Philos. Mag. 87 (2007) 2169 -2189.
[10] F. Gu, J.H. Zhang, L.H. Xu, Q.Q. Liu, M. Li, Influence of surface effects on the elastic properties of silicon nanowires with different cross sections, Chin. Phys. Lett. 28 (2011) 106102
[11]Y.K. Feng,Y.L. Liu, B. Wang, Finite element analysis of resonant properties of silicon nanowires with consideration of surface effects, Acta Mech. 217 (2011) 149-155.
[12]Y. A. Shevlyakov, A. A. Skoblin, Relative stiffness of irregularly perforated plates, J. Math. Sci. 65 (1993) 1389–1395.

Key Engineering Materials Vols 645-646 (2015) pp 157-162
Submitted: 2015-01-27
Accepted: 2015-01-27
© (2015) Trans Tech Publications, Switzerland
doi:10.4028/www.scientific.net/KEM.645-646.157

Sintering Behavior and Electrical Property of Surface Treated Silver Nanoparticle for Electronic Application

Hui. Xie[1, *], Nana Xiong[2], Yuzhen. Zhao[3, *], Yuehui Wang[1, *]

[1] Department of Chemistry and Biology, University of Electronic Science and Technology of China Zhongshan Institute, Zhong Shan，528402, China

[2] State Key Laboratory of Electronic Thin Films and Integrated Devices, School of Microelectronics and Solid-State Electronics, University of Electronic Science and Technology, Cheng Du 610054, China

[3]Department of Materials Science and Engineering, Tsinghua University, Beijing 100084

Corresponding authors: wangzsedu@126.com, zhaoyz@mail.tsinghua.edu.cn, xiehuizsedu@126.com

Keywords: Silver nanoparticle, Sintering Behavior, Surface treatment, Electrical property

Abstract. Large-scale silver nanoparticles with fine dispersion and narrow size distribution were synthesized by reducing silver nitrate with sodium borohydride and sodium citrate and using poly (vinylpyrrolidone) as an adsorption agent in the ethanol solution. The sintering behavior and electrical properties of silver nanoparticles treated with and without glutaric acid were studied. Morphology studies showed that the treated silver nanoparticles obviously agglomerated and began to sinter at 200 ^{0}C and the sintering temperature is higher at least 50 degrees than that of the untreated silver nanoparticles The treated silver nanoparticles as fillers of electronically conductive adhesives (ECAs) is more advantageous to the increase of the conductivity. Otherwise, only in the conditions of the appropriate sintering temperature and loading of silver nanoparticles, the high conductivity of the ECAs was obtained. The effect of the treated silver nanoparticles on the electrical properties contributes to the surface activation and sintering behavior.

1. Introduction

Electronically conductive adhesives (ECAs) has become popular as one of promising candidates for lead-free interconnection solutions in microelectronic packaging application due to their technical advantages such as fine pitch capability, low temperature processing ability, low cost and environmentally-friendly materials and processing, etc. [1-8] To meet the requirements for future fine pitch and high-performance interconnects in advanced packaging, ECAs with nano-materials are attracting more and more interest due to their specific electrical, mechanical, optical, and chemical properties.[4-10] Compared with conventional microparticles, the higher surface area of nanoparticles increases the contact area between the fillers and decreases the percolation threshold, thus, nano-sized silver-filled adhesives can reduce the filler content of the highly expensive silver, the viscosity and the pressure to finally decrease the costs and miniaturize the feature size of the electronic devices. [6-10] However, it also inevitably increases the contact resistance due to interconnection between nanoparticles. So there was no consistent conclusion about the positive or negative effect of nano-sized silver on the conductivity of ECAs. [1-8]

In order to improve the conductivity of ECAs with nano-sized silver fillers, the surface modification of nano-sized silver were introduced into the polymer matrix.[2,4-7] Nano-sized silver surfaces can be chemically modified by the organic monolayers which adsorbed onto the metal surface which form physico-chemical bonds to allow electrons to flow and reduced work-functions, so electrical properties can be improved.

In this paper, silver nanoparticles with fine dispersion and narrow size distribution were synthesized by reducing silver nitrate with sodium borohydride and sodium citrate and using poly (vinylpyrrolidone) as an adsorption agent in the ethanol solution. Microstructure and sintering behavior of silver nanoparticles treated with and without glutaric acid were investigated. Further, the electrical property of silver nanoparticles as fillers of the ECAs were investigated in detail in terms of the content of silver nanoparticles of the total of silver fillers and microstructures.

1. Experimental

Silver nitrate ($AgNO_3$, ≥99.8%) was purchased from Guangdong Guanghua Chemical Reagent Co., Ltd., poly(vinylprrolidone) (PVP, $(C_6H_9NO)n$，K30, M_w≈40000), was purchased from Guoyao Group Chemical Reagent Co., Ltd., sodium borohydride (BH_4Na, ≥98.0%) and sodium citrate ($Na_3C_6H_5O_7$, ≥99.0%) was purchased from Guangdong Chemical Reagent Co., Ltd., glutaric acid ($C_5H_6O_4$, ≥99.0％) was purchased from Shanghai chemical reagent Co., Ltd. Ethanol absolute (CH_3CH_2OH, ≥99.7%) were purchased from Tianjin Yongda chemical Co., Ltd. Diglycidyl ether of bisphenol A (R-128) was purchased from Guangzhou Hongchang Co., Ltd. 4-methylhexahydrophthalic anhydride (MHHPA) and 2-ethyl-4-methylimidazole (2E4MZ) were supplied by Guangtuo Chemical Co., Ltd. Silver flakes (SF1023K, <5 μm) were purchased from Guangdong Fenghua Advanced Technology Group Co., Ltd. Silver nanoparticles were synthesized in our laboratory. All the chemicals were used as received.

Synthesis and Surface Modification of Silver Nanoparticles The experimental process in detail is as follows: 100 mL ethanol solution consisting of 10 mL sodium borohydride (0.26 mol•L^{-1}) and sodium citrate (0.10 mol•L^{-1}) was added into the mixed solution of 50 mL silver nitrate (1.18 mol•L^{-1}) and 50 mL PVP (0.90 mol•L^{-1}) with vigorous stirring at room temperature, then the solution was kept reaction for a further 3 hr while stirring rapidly. Finally, the reaction mixture was washed with acetone, ethanol and deionized water by centrifuging. The PVP on the silver nanoparticles surface can be removed by sonication in ethanol. These colloids could be re-dispersed by either water or ethanol. In this work, the silver colloid was redispersed in ethanol and added to the polymer matrix. The active silver nanoparticles were then treated by sonication for 2hr in an ethanol solution of glutaric acid (0.5 mol•L^{-1}) with 1:1 molar ratio of silver nanoparticles and glutaric acid, and then put 14 hr. The surface treated silver nanoparticles were centrifuged to remove the unreacted glutaric acid, and then were rinsed three times by ethanol. The purchased micro-sized silver flakes were also treated by dicarboxylic acids in the same way.

ECAs Preparation R-128, MHHPA and 2E4MZ with a weight ratio of 1:0.85:0.05 were put in a small beaker, and was sonicated for 30 min. Then, the micro-sized silver flakes were firstly incorporated into the polymer matrix with sonication for another 30 min to make the fillers uniformly dispersed in mixture, and the surface untreated/treated silver nanoparticles were also incorporated into the polymer matrix and were sonicated for more than 60 min to disperse the conductive fillers. Two strips of polyimide tape were applied onto a pre-cleaned glass slide with a gap width of 1 cm. The formulated composite was bladed into the space between the two strips. The polyimide tapes were removed before curing at the desired temperature and time. The thickness of the cured film was controlled by the polyimide tapes.

Characterization Scanning electron microscopy (SEM) images were taken on a JSM-6460. The UV-visible absorption spectrum of silver colloid was obtained using a 760CRT spectrophotometer with quartz cuvettes at room temperature. The resistivity of the ECAs was measured using a DMR-1C four-point probe meter (Nanjing Daming instrument Co., LTD). The resistivity, ρ, was calculated using the following equation (1):

$$\rho = R_L \times \omega \quad (1)$$

where R_L and ω are square resistance and thickness of sample, respectively. The thickness of samples was measured by the micrometer gauge.

2. Results and discussion

Figure 1(a) shows the UV–visible absorption spectrum of the silver colloid, a broad absorption peak centered at 413 nm, attributed to the surface plasma resonance in the nanoparticles, is observed.

Figure 1(a) present the TEM image of the silver nanoparticles. It is found that the shape of these nanoparticles is spherical-like and the range of sizes is 30–50 nm.

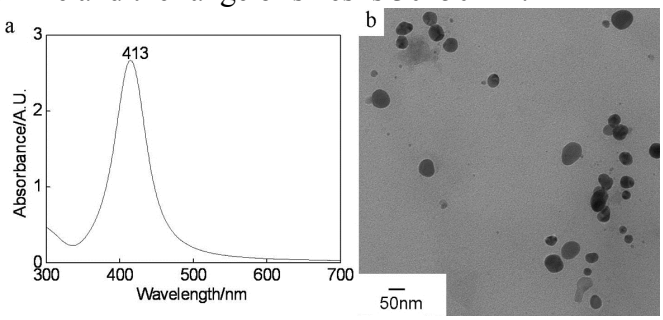


Fig.1 (a) UV-visible of silver colloid and (b) TEM image

Figure 2 shows SEM images of the untreated (Figure 2(a)) and treated (Figure 2(b)) silver nanoparticles. The agglomeration of the glutaric acid treated silver nanoparticles is observed in Figure 2(b) (indicted by arrows) due to the removal of surface adsorption agent.

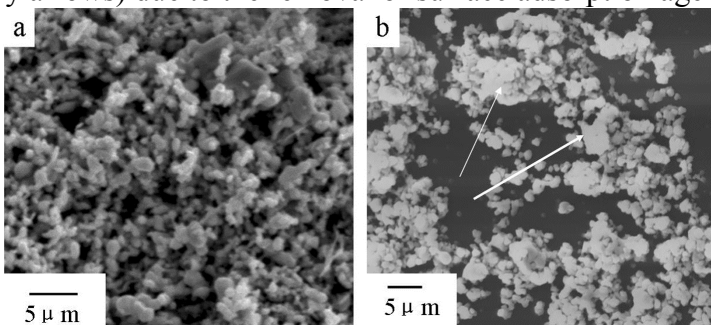


Fig. 2 SEM images of unsurface (a) and surface (b) treated silver nanoparticles

Figure 3 shows SEM images of the untreated (Figure 3(a)) and treated silver nanoparticles (Figure 3(b)) sintered on glass substrates at 180, 200, 250 and 300 °C for 30 min, respectively. The sintering behavior of the treated silver nanoparticles was observed at 200 °C, as shown in Figure 3 (b). At 250 °C, silver nanoparticles were obviously sintered and porously connected between nanoparticles. At 300 °C, the silver nanoparticles formed large chunks and consisted of porous network. However, for the untreated silver nanoparticles the sintering behavior was observed at 250 °C, as shown in Figure 3(a). It is clear that the surface treatment with the glutaric acid may promote sintering because silver nanoparticles treated by glutaric acid can provide fresh surface. [4-7]

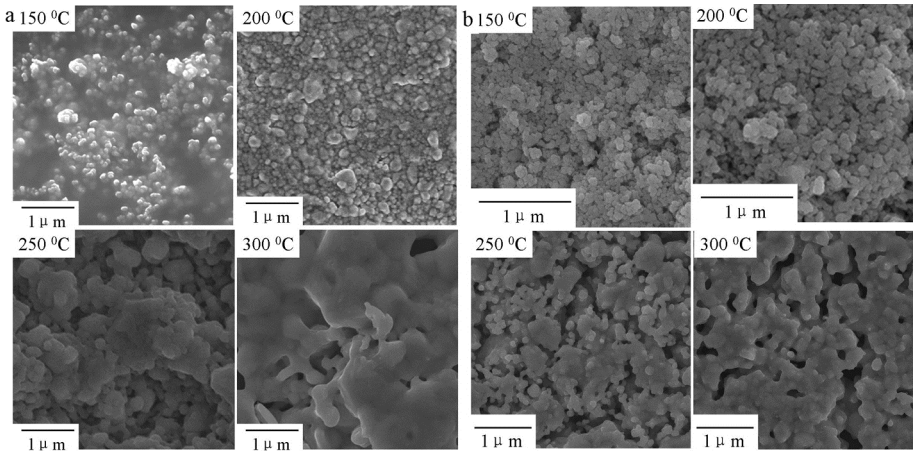


Fig. 3 SEM images of the unsurface (left) and surface (right) treated silver nanoparticles annealed at (a) 150 ^{0}C, (b) 200 ^{0}C, (c) 250 ^{0}C, and (d) 300 ^{0}C

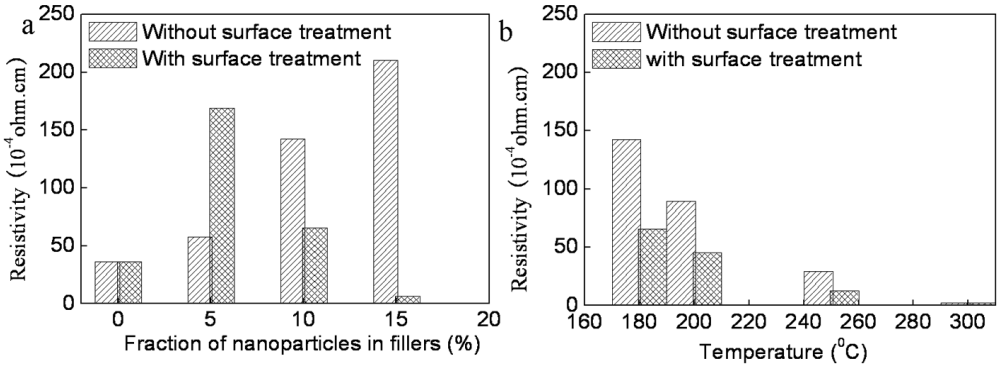


Fig.4 Resistivity of the ECAs filled with micro-sized silver flakes and the untreated/treated silver nanoparticles of different fractions of 60 wt % silver fillers cured at 180 ^{0}C for 60 min (a), and filled with 10% silver nanoparticles of 60 wt% silver fillers cured at 180, 200, 250, and 300 ^{0}C for 60 min (b)

Fig.4 shows the resistivity of the ECAs filled with micro-sized silver flakes and the untreated/treated silver nanoparticles of different fractions of 60 wt % silver fillers cured at 180 ^{0}C for 60 min (Fig.4(a)) and filled with 10% silver nanoparticles of 60 wt% silver fillers cured at 180, 200, 250, and 300 ^{0}C for 60 min (Fig.4 (b)). Seen from Fig.4 (a), the resistivity of the ECAs filled with micro-sized silver flakes and the untreated silver nanoparticles is significantly higher that of the ECAs filled with typical micro-sized silver flakes, and increases with increasing of the content of silver nanoparticles. However, the resistivity of the ECAs filled with micro-sized silver flakes and the treated silver nanoparticles first increases and then decreases with increasing of the content of silver nanoparticles, and the resistivity decreases 6 times when 15% silver nanoparticles of the total of silver fillers were doped into the ECAs. The results above indicated that the addition of the untreated silver nanoparticles brought about increase in resistivity, however, the silver nanoparticles treated by glutaric acid can improve the electrical conductivity in the case of the proper doping amount. Some of the work in the literature mentioned that two types of contact resistance, i.e. restriction resistance due to small contact area and tunneling resistance when nanoparticles are included in the system.[1-5] It is believed that the conductivity of micro-sized Ag particle filled adhesives is dominated by constriction resistance, while that of the nanoparticles-containing conductive adhesives is controlled by tunneling and even thermionic emission.

When silver nanoparticles are introduced into the polyer matrix, the silver nanoparticles inevitably increases the contact resistance, at the same time, they also fill into the gaps among silver flakes to supply junctions for silver flakes-build networks which helps to establish the conductional pathways. It is clear that with the untreated silver nanoparticles as fillers, the overall effect is an increase in resistivity, while, when the glutaric acid treated silver nanoparticles are used fillers, it is likely that because the agglomeration of nanoparticles decreases the distance between the particles. It should be beneficial to the tunneling conductive, so the negative effect on electrical conductivity of the ECAs declines. It has been reported that the organic molecules adhered on the metal surface form physico-chemical bonds, which allow electrons to flow and reduces electrical resistance and enables a high current flow. In addition, for both of the samples cured at different temperature, the resistivity decreases with increasing of the curing temperature, especially the curing temperature at 300 ^{0}C, the resistivities of both of samples are almost same. Based on our results above, we think that the effective dispersion of fillers in the polymer matrix to establish more conductive path is the key factor to obtain the high electrical conductivity.Meanwhile, when the micro-sized silver flakes and nanoparticles are used as hybrid fillers, the conductive networks are established by the synergy of silver flakes and nanoparticles. In most cases, the silver nanoparticles mixed in the silver flakes only play limited and auxiliary effect to form conductive networks. When silver particles in polymer matrix do not connect well enough, the addition of a certain amount of silver nanoparticles helps to build the conductive network and lowers the resistivity of the composite. However, once connected, the addition of nanoparticles seems to maintain balance of the contact resistance and the tunneling conductive effect. As a result, the overall effect is almost no obvious change in resistance.

Fig. 5 shows SEM images of the ECAs filled with micro-sized silver flakes and 5%, 10% and 15% treated silver nanoparticles of 60 wt % silver fillers cured at 180 ^{0}C for 60 min. Seen from Fig. 5, there are lots of the large gaps between the micro-sized silver flakes due to the low fillers loading, and the gaps filled with nanoparticles and nanoparticles adsorbed on the surface of silver flakes can be observed. With increasing the content of silver nanoparticles, a large number of aggregates of the silver nanoparticles fill into the gaps and cover on the surface of silver flakes and distribute in the polymer matrix.

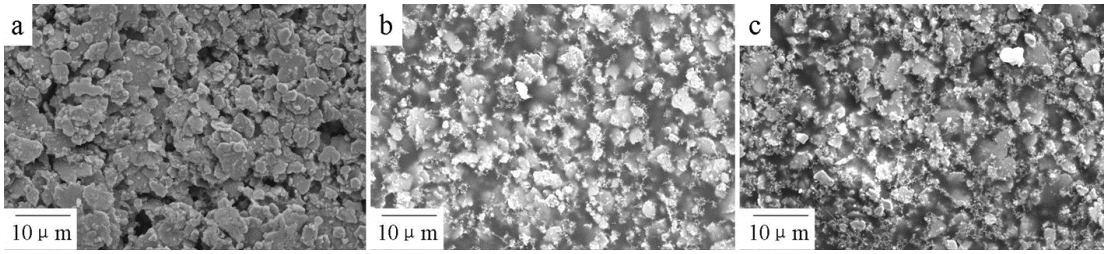


Fig. 5 SEM images of ECAs filled with silver flakes and the treated silver nanoparticles with different fractions of 60 wt% silver fillers cured at 180 ^{0}C for 60 min: (a) 5wt%; (b) 10wt%; (c) 15wt%

Summary

Silver nanoparticles with fine dispersion and narrow size distribution were synthesized by reducing silver nitrate with sodium borohydride and sodium citrate and using poly (vinylpyrrolidone) as an adsorption agent in the ethanol solution. The sintering behavior and electrical properties of silver nanoparticles treated with and without glutaric acid were studied. Morphology studies showed that the treated silver nanoparticles obviously agglomerated and began to sinter at 200 ^{0}C and the sintering temperature is higher at least 50 degrees than that of the untreated silver nanoparticles The treated silver nanoparticles as fillers of electronically conductive adhesives (ECAs) is more advantageous to the increase of the conductivity. Otherwise, only in the conditions of the appropriate sintering temperature and the concent of silver nanoparticles, the high conductivity of the ECAs can be obtained.

Acknowledgements

This work was financially supported by National Science Foundation of China under grants of (61302044, 51302145) and Zhongshan Science and Technology Projects (20123A319) and State Key Laboratory of New Ceramic and Fine Processing (Tsinghua University) and State Key Laboratory of Electronic State Key Laboratory of Electronic Thin Film and Integrate (Zhongshan).

References

[1] H-H. Lee, K-S, Chou, Z-W. Shih. Effect of nano-sized silver particles on the resistivity of polymeric conductive adhesives. Int. J. Adhesives. 2005, 25: 437-441

[2] H. Jiang, K. Moon, Y. Li, C. P. Wong. Surface functionalized silver nanoparticles for ultrahigh condutive polymer composites. Chem. Mater. 2006, 18: 2969-2973

[3] B. Lee, G. Dai. Influence of interfacial modification on the thermal conductivity of polymer composites. J. Mater. Sci. 200, 44: 4848-4855

[4] R. Zhang, W. Lin, K. Moon, C. P. Wong. Fast preparation of printable highly conductive polymer nanocomposites by thermal decomposition of silver caroxylate and sintering of silver nanoparticles. Appl. Mater. & Int.. 2010, 2(9): 2637-3645

[5] Z. X. Zhang, X. Y. Chen, F. Xiao. The sintering behavior of electrically conductive adhesives filled with surface modified silver nanowires. J.adhe. Sci. & Tech. 2011, 25: 1465-1480

[6] H. Dong, K. S. Moon, C. P. Wong. Molecular dynamics study of nanosilver particles for low-temperature lead-free interconnect applications. J. Electron. Mater. 2005, 34: 40-45.

[7] Y. Li, K.S. Moon, C.P. Wong. Monolayer-Protected Silver Nano-Particle-Based Anisotropic Conductive Adhesives: Enhancement of Electrical and Thermal Properties. J. Electron. Mater. 2006; 99: 1573-1578.

[8] H. W. Cui, Q. Fan,D. S. Li. Novel flexible electrically conductive adhesives from functional epoxy, flexibilizers, micro-silver flakes and nano-silver spheres for electronic packaging. Polym.. Int. 2013; 62: 1644-1651.
[9] C. Yang, W. Lin, Z. Y. Li, R. W. Zhang, H. R. Wen, B. Gao, C. P. Wong. Water-Based Isotropically Conductive Adhesives: Towards Green and Low-Cost Flexible Electronics. Adv. Funct. Mater. 2011; 21: 4582-4588.
[10] H. Gao, L. Liu, Y. Y. Luo, D. Jia, F. Wang, K. Liu. Effect of Curing procedures on the Electrical Properties of Epoxy-based Isotropic Conductive Adhesives. Int. J. Polym. Mater. 2011; **60**: 409-427
[11] Inoue M, Muta H, Yamanaka S, Suganuma K. Electrical Properties of Isotropic Conductive AdhesivesComposed of Silicone-Based Elastomer Binders Containing Ag Particles. J. Electron. Mater. 2009; 38: 2013-2022.
[12] H. W. Cui, D. S. Li, Q. Fan. Using a Functional Epoxy, Micron Silver Flakes, Nano Silver Spheres, and Treated Single-Wall Carbon Nanotubes to Prepare High Performance Electrically Conductive Adhesives. Electronic Mater. Lett. 2013; 9: 299-307.
[14] H. P. Wu, X. J. Wu, J. F. Liu, G. Q. Zhang, Y. W. Wang, Y. W. Zeng, J. Z. Jiang. High conductivity of isotropic conductive adhesives filled with silver nanowires. Inter. J. Adhe& Adhes. 2006; 26: 617-621
[15] S. L. Chen, K. H. Liu, Y. F. Luo, D. M. Jia, H. Gao, G. J. Hu, L. Liu. In situ preparation and sintering of silver nanoparticles for low-cost and highly reliable conductive adhesive. Int. J. Adhes & Adhes. 2013; 45: 138-143.
[16] Gao H, Liu L, Liu K H, Luo Y F, Jia D M, Liu J S. Preparation of highly conductive adhesives by in situ generated and sintered silver nanoparticles during curing processJ. Mater. Sci: Mater Electron. 2012; 23: 22-30.

Key Engineering Materials Vols 645-646 (2015) pp 163-168
© (2015) Trans Tech Publications, Switzerland
doi:10.4028/www.scientific.net/KEM.645-646.163
Submitted: 2014-10-28
Accepted: 2014-11-20

Study on the Etching Technique of Non-photosensitive Polyimide

Rui Lei[1.2,a], Weiguo Liu[1,b],Changlong Cai[1,c],Shun Zhou[1.2,d],

Jing Nie[2,e], XuanYang Wang[3,f]

[1]Xi'an Technological University, Xi'an, 710032, China
[2]Science and Technology on Low-Light-Level Night Vision Laboratory, Xi'an, 710065, China
[a]280124564@qq.cm, [b]wgliu@163.com , [c]caichanglong@xatu.edu.cn,
[d]zsemail@126.com , [e]376474610@qq.cm, [f]550848669@qq.cm

Key words:non-photosensitive polyimide; wet etching; dry etching.

Abstract: Polyimide is often used as a sacrificial layer material to make floating structure. Polyimide is also divided into photosensitive and non-photosensitive type; photosensitive polyimide currently has more negative photoresist and poor performance in many ways. Compared with photosensitive polyimide, the non-photosensitive type has low stress, stable performance and other advantages, so non-photosensitive polyimide has been chosen as a sacrificial layer material. To achieve the graphical function and release sacrificial layer, A deeply research was made in this dissertation makes on wet etching and dry etching. By controlling the wet etching process of prebake condition, exposure and developing time, and oxygen dry etching process of etching power, bias voltage and other key process parameters, a good sacrificial layer graph and etching effect have been got. Finally, it can be concluded that when the prebake conditions for 105ºC, 8min and times of exposure and developing were 11s and 29s, the non-photosensitive polyimide wet etching effect is the best; when the etching power is 1000w, an oxygen flux rate is 50sccm, the reaction pressure is 30mTorr, the bias voltage is 140v, oxygen dry etching has a good effect.

Introduction

Bi-material microcantilever arrays based on optical readout infrared thermal deformation imaging technology[1]. It is a new type uncooled infrared thermal imaging technology. This technology uses MEMS manufacturing processes and non-contact optical measurement. Production of infrared focal plane array FPA (Focal Plane Array) which consists of bi-material micro-cantilever structure is the core technology of the whole system. Meanwhile sacrificial layer technology is a key for production of FPA[2]. This paper will focuse on etching process of polyimide sacrificial layer.

The suspended structure is especially critical in the process of making the micro-cantilever devices; it must rely on the sacrificial layer technology, by means of selectively etching the sacrificial layer and the arrangement pattern to get sacrificial layer released and micro-cantilever structure formed. Therefore the suspended structure requires the sacrificial layer material with excellent high temperature resistance, low residual stress, good mechanical property, withstand large strains and satisfy the experiment conditions.

Polyimide is a high molecular material with heat resistance, corrosion resistance, good chemical stability, etc. Meanwhile, PI can usually react with strong alkalis except for becoming stable performance of organic after heating dehydration. A method of O_2 plasma etching is generally used to remove it.

Polyimide is divided into photosensitive and non-photosensitive. Photosensitive polyimide currently is negative photoresist, but the negative photoresist has a poor performance of minimum resolvable feature size, anti-etching ratio, and thermal stability. But non-photosensitive polyimide has low stress, stable performance, etc. Therefore we use the non-photosensitive polyimide as a sacrificial layer material.

2 The etching process of non-photosensitive polyimide sacrificial layer

In the production process of micro-cantilever we use dry etching and wet etching process on the sacrificial layer. The following two processes are studied to find the optimum process parameters.

2.1 Non-photosensitive polyimide sacrificial layer imaging

Shanghai Jiaotong University produced a viscosity of 1000 cps non-photosensitive polyimide PI-5 is used for the preparation of the sacrificial layer. For non-photosensitive polyimide, sacrificial layer imaging must be completed by means of photoresist. We use the positive photoresist EPG533 to obtain the desired sacrificial layer[3] pattern in ways of changing prebake conditions, exposure time and development time and other process parameters.

Sacrificial layer array is 120 × 120, unit size is 6 × 6um. Because the graphic is very small, the process of each step will directly affect the final result. The following are the basic steps of patterning the sacrificial layer:

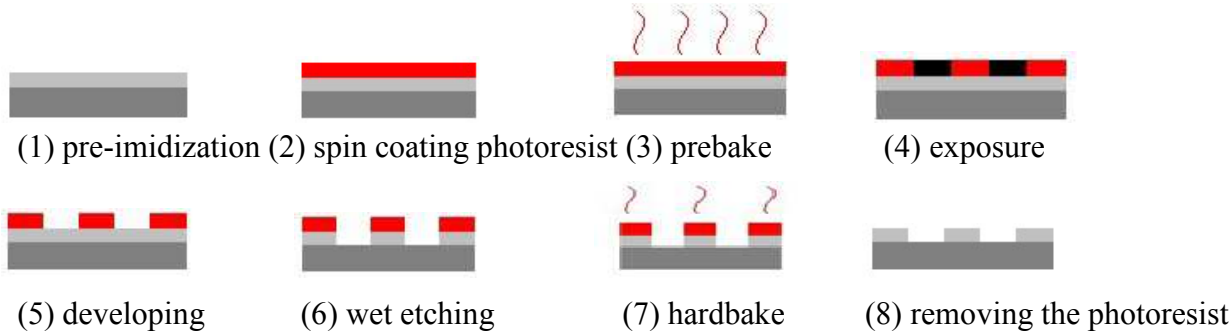


Fig.1 Non-photosensitive polyimide graphical process

2.2 The influencing factors in the wet etching

(1) Effect of surface cleaning on glass substrate in a wet etching

Pinhole phenomenon probabaly occurs when the substrate is not clean. So the glass must be placed in a beaker of acetone, and 5 ~ 10min cleaning in an ultrasonic cleaner, flushing with lots of deionized water, dry with nitrogen gun at last.

(2) Effect of prebake conditions in wet etching

Prebake conditions include pre-baking temperature and pre-baking time. Prebake can remove photoresist solvent, enhance abrasive resistance and adhesion of the photoresist. While heating time too long and too short will cause the exposure of poor sensitivity, precision, and affect graphical effect. So we use a hot plate to prebake. All samples that covered with PI will be pre-imidization treatment for 80 °C, 10min; 120 °C, 20min and then coating photoresist. Observing the effect of prebaking process on the quality of the graphics after prebaking, exposing and other processes, the results are listed in Table 1.

Table 1 Prebaking conditions on the impact of wet etching

PI thickness (um)	Photoresist thickness (um)	Prebakig temperature (ºC)	Prebaking time (min)	Exposure time (s)	Development time (s)	Graphics quality
3.3	1.90	115	8	10	37	Developing good but the surface is not flat, as shown in figure2
3.3	1.90	115	10	10	35	Underdevelopment, it basically has no hole
2.9	2.12	105	8	11	35	Good developing effect of holes and alignment marks
2.9	2.12	105	10	11	35	Overdevelopment, holes is slightly deformed , as shown in figure3



Fig.2 Uneven surface

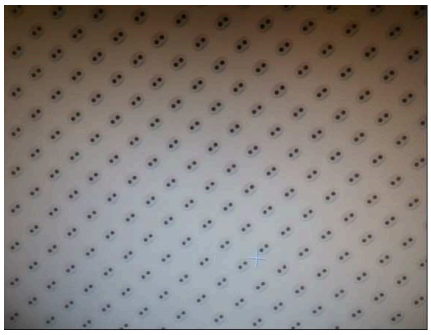


Fig. 3 Overdeveloping

As Table 1 shows that under the pre-baking temperature of 105^{o} C, time of 8min process conditions, pattern is the best.

(3) Effect of exposure time in wet etching

Insufficient exposure time of lithography may lead to the film easy to swell or side etch during developing; Overexposure may cause no vertical sidewalls and hole will residual PI, as shown in figure 4; To get the best graphics, we need to strictly control the exposure time. Observing experimentals results find that the exposure time of 11s is better.

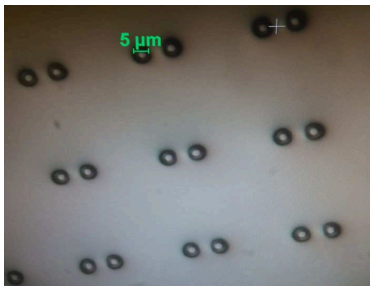


Fig.4 Holes remaining PI

(4)Effect of developing time in wet etching

Polyimide[4] is an organic matter which can react with alkali. Coat the positive photoresist on the imidization polyimide film before expose, then use positive photoresist developer KMP PD238-II to

develop besides wet etching in the polyimide film at the same time, and then the exposed photoresist is developed, and wet etching between the bare polyimide and developing solution. The unexposed photoresist protect lower layer of polyimide, in this way the sacrificial layer pattern is obtained. However, if the wet etching time is too long, the unexposed portion of photoresist and PI is also likely to be etched by developing solution. So the developing time is very important to wet etching. Many experiments we had done are shown in Table 2 to find the best developing time.

Table 2 Effect of developing time on the corrosion

PI thickness (um)	Photoresist thickness (um)	Prebaking temperature and time (ºC, min)	Exposure time (s)	Development time (s)	Effect
2.95	2.1	105ºC 8min	11	25	Alignment mark is good, holes is about 2um and too small, as shown in Figure 5
2.95	2.1	105ºC 8min	11	27	Continuing slightly shaki -ng,underdeveloping ,hol es is about 3-4um
2.95	2.1	105ºC 8min	11	28	Continuing slightly shaki -ng, holes is about 3～ 4um
2.95	2.1	105ºC 8min	11	29	Continuing slightly shaki -ng, good holes effect and the surface is flat, no pinholes and other defects, as show in Figure 6
2.95	2.1	105ºC 8min	11	30	Alignment mark is off, holes is slightly excessive corrosion

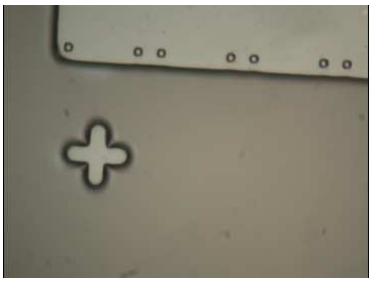


Fig.5 Aligned mark is good but holes is small

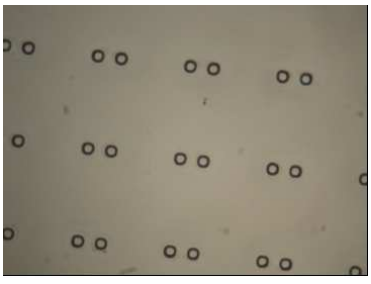


Fig.6 Holes is good

According to the experiments results, when PI film thickness of 2.95um, the exposure time of 11s, developing time of 29s, the best pattern has been obtained. Those problems should also be noted in developing process , as follows:

(1)Middle-baking must be done immediately after exposure that can reduce the standing wave effect and make the edge of graphics distinctive;

(2)Postbaking is very important to the image, it can reduce corrosion of the drill.

(3)Developing solution should be a concentration of 100%, the diluted developer reaction rate is very slow and the effect is not well;
(4)Due to the small size of development of graphics, the magnitude and intensity of shaking have a great impact on the results of corrosion. During a lot of experiments, we found that sustained jiggle is better;
(5)Wet etching is anisotropic, so the most of square holes become circular holes. The sacrificial layer is eventually removed , so circular hole is also well. And to some extent, increasing the hole size is favorable for the formation of a Micro-cantilever structure.

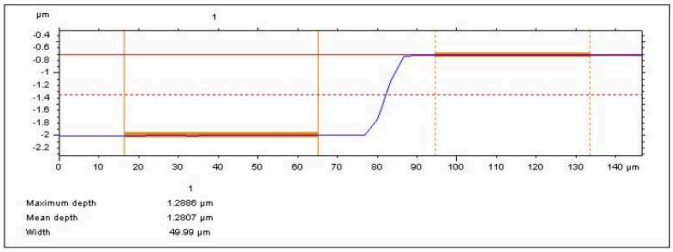
3 Dry etching of Polyimide

Removal technology of the sacrificial layer is a key factor in the sacrificial layer technology. Wet etching easily causes a adhesion phenomenon, and it also introduces etch solution or deionized water and likely leads to a large surface tension. Micro-devices often failed because of adhesion of the substrate and structural layer. Therefore, a method of Oxygen ions dry etching is needed. This method is easy to control, the support layer and the structure layer is almost no damage during etching, and it also has high resolution, no undercutting, the depth and width of the line precision controllable, fast etching rate and other characteristics.
We have a dry etching study on the sacrificial layer after imidization, by using Oxford Instruments produced ICP180 inductively coupled plasma etcher, specific process parameters are shown in Table 3.

Table 3 Etching process parameters

RF power (w)	Reaction pressure (mTorr)	Bias voltage (v)	O_2 flow rate (sccm)	Etching time (s)	Etching effect
500	30	120	50	120	Etching effect is not obvious
1000	30	140	50	120	The surface is flat after etching and the etching rate is 10.3nm / s

Experiments result can be seen in Figure 10 from Talysurf CCI2000 white light interferometer profilometer test, the sacrificial layer has a flat surface after etching and etching effect is good; the etching rate is fast, it about 2min etching 1.24um, etching rate is 10.3nm / s. Therefore, the process parameters in Table 3 can be used to remove the sacrificial layer in a subsequent process.



(a) Etching step height

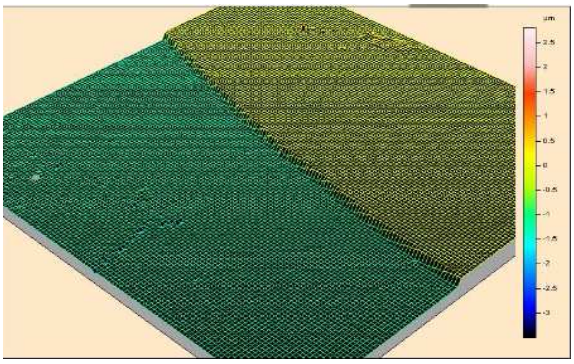


Fig.7 (b) The surface morphology after etching

4 Summary

In the MEMS processes, Polyimide has many advantages as a material of sacrificial layer, such as heat resistance, chemical stability, corrosion resistance, not easily soluble in organic solvents and others. This paper focus on wet etching and dry etching process of the non-photosensitive polyimide sacrificial layer, and finally find the optimum parameters of exposure, developing and etching, at the same time we are having a study on the issues that may arise in those processes and lay the foundation for the realization of the MEMS structure.

Acknowledgement

Project supported by High-end CNC machine tools and basic manufacturing equipment technology major projects(2013ZX04006011); General Armament Department of advanced manufacturing technology projects (51318020109); Shaanxi Provincial Science and Technology Innovation Project co-ordination (2012KTCQ01-33); Xi'an Industrial Technology Innovation Program (CX12161);

References

[1] Dong liang, Uncooled infrared detectors on MEMS Integration, Qinghua University Doctoral Thesis, 2004.
[2] Lliu weiguo, Jin na, Integrated uncooled thermal imaging detector array, first, National Defense Industry Press , BeiJing,2004.
[3] Hsueh H. B., Chen C. Y., Preparation and properties of LDHs/polyimide nanocomposites, Polymer, 2003, 44(4): 1151-1161.
[4] Lee T., Park S. S., Jung Y. I., Han S., Han D., Kim I., Ha C. S., Preparation and characterization of polyimide/mesoporous silica hybrid nanocomposites based on water-soluble poly(amic acid) ammonium salt, European Polymer Journal, 2009, 45(1): 19-29.

Key Engineering Materials Vols 645-646 (2015) pp 169-177
© (2015) Trans Tech Publications, Switzerland
doi:10.4028/www.scientific.net/KEM.645-646.169

Submitted: 2014-10-28
Accepted: 2014-12-23

An Investigation on Resistive Switching Characteristics Induced by HfO_x and Electrode Interfaces

Xiaorong Chen, Jie Feng※

Key Laboratory for Thin Film and Microfabrication of Ministry of Education, Department of Micro/Nano Electronics, Shanghai Jiao Tong University, Shanghai 200240, PR China

email :chenxiaorong@sjtu.edu.cn; ※ jfeng@sjtu.edu.cn (corresponding author)

Key words: interface; resistive switching; HfOx; oxygen vacancy; filament

Abstract

$Pt/HfO_x/Pt$ resistive switching devices with symmetric electrodes were fabricated. Bipolar resistive switching (RS) behaviors and unipolar behaviors were then observed under a positive/negative bias applied to the top electrode (TE). A comparison and analysis of bipolar/unipolar RS behaviors under different voltage polarities was then performed.

The results demonstrated that bipolar RS was achieved via a drift of anion (O^{2-}) under the electric field resulting in the rupture and recovery of filaments at the interface. When the filaments dissolved and formed at the interface near BE, the performance of the bipolar RS devices was better. However, for unipolar RS devices, when filaments dissolved and formed at the interface near TE, the performance was even better. These results indicated that a drift of O^{2-} caused by electric field and a diffusion of O^{2-} induced by Joule heat were the main reasons for unipolar RS. The different characteristics of the bipolar and unipolar devices can be attributed to the existence of a different number of defects at the active interface of the devices. This was where the rupture and recovery of filaments occurred. The results also indicate that the active interface is more important than other interfaces for RRAM performance.

1 Introduction

Resistive random access memory (RRAM) has been cited as the next generation of non-volatile memory. This is due to its fast speed, low power consumption, high data density, longer retention time, high endurance, simple structure and the fact that it is compatible with CMOS[1-6]. Therefore, transition metal oxide (TMO) based RRAM has attracted much attention. TMOs play a vital role in switching between the high resistance state (HRS) and the low resistance state (LRS). Therefore, the use of TMOs as electrolytes has been studied extensively. Examples here include: HfO_x [7-12], TiO_x [13], ZrO_x [14], and TaO_x [15,16]. Among these TMOs, Hafnium oxide (HfO_x) appears to be a promising switching material. HfO_x-based RRAM could offer the advantages of longer retention time, high endurance, scalability and low power consumption [6,11,12].

In most cases, RRAM is switched by the migration of ions and the further dissolution and recovery of filaments [1,2,8-10,13-15,17,18]. Though many researchers have studied filament-type RRAM, many obstacles are yet to be solved. One of these obstacles involves determining the location for the dissolving and recovering of filaments. From the viewpoint of probability, filament ruptures may occur at any site along the entire filament. This causes non-uniformity in the electric parameters. From the viewpoint of technological application, controlling the recovery and dissolution of filaments is of great importance [19,20].In order to recognize the region of filaments which dissolve, some groups have carried out computational simulations and statistics. The results

of these studies indicate that rupture occurred in the middle of filaments [21,22]. However, experimental data has demonstrated that filament dissolution occurred in the region near the anode [13], and even within a localized region of 3-10 nm near the anode [23]. When the film thickness is less than 10 nm, it seems that great fluctuation may still exist in the rupture and recovery site.

To induce dissolution and formation of filaments at the interface between the electrode and matrix, an asymmetrical structure (different metals as top and bottom electrodes) was proposed [10,24].In addition, there was a report on controlling the rupture and recovery of filaments at the interface between layers for a multilayer-electrolyte [25]. However, few reported a symmetrical structure (the same metal as a top and bottom electrode) for their investigation of unipolar and bipolar RS and as a comparison of the two interfaces serving as the active switching region. Here, an HfO_x based resistive switching device with a symmetrical structure was fabricated at room temperature. Bipolar and uniploar behaviors were investigated. It was found that a formation and dissolution of filaments consisting of oxygen vacancies was considered to be an RS mechanism. A different number of defects at the interfaces near TE/BE led to different characteristics.

2 Experiment

The device structure is shown as Fig. 1. We used HfO_x as the electrolyte, and Pt films as the bottom and top electrodes. The fabrication process is detailed below. First, a bi-layer of Ti and Pt, with a thickness of 10 nm and 50 nm, respectively, was deposited by DC magnetron sputtering on an SiO_2/Si substrate at ~20^{o}C. Second, a 10nm film of HfO_x was deposited by reactive DC magnetron sputtering using an Hf target in oxygen and argon gas. Finally, the top electrode Pt with a thickness of 100nm and a 200μm diameter was deposited by DC magnetron sputtering using a shadow mask. A Keithley2400 source meter and an Agilent multi-meter were used during the electrical measurements. As shown in Fig. 1, the DC voltage sweep mode was adopted. Voltage biases were applied to the top electrode (TE) while the bottom electrode (BE) was grounded. In order to protect the devices from breakdown, a compliance current (I_{cc}) of 60μA was used for the bipolar devices. Due to the fact that a larger compliance current was needed to realize resistive switching for the unipolar devices, a larger compliance current of 100μA was used.

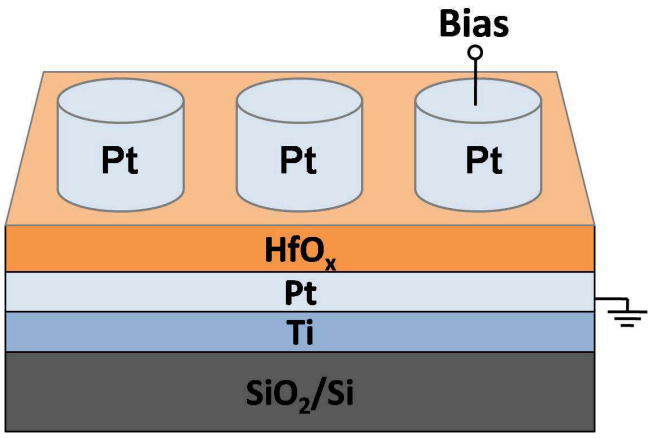


Fig. 1 A schematic view of the Pt/HfO_x /Pt memory device and the electrical measurement configuration

3 Results and discussion

(1) Bipolar resistive switching behavior

To investigate the HfO_x-based device, negative and positive biases were applied to the TE of a device in order to perform an RS measurement. During this investigation, all fresh devices were in a low-resistance state (~100Ω). Sample A was reset into a high resistance state (HRS) under a negative bias. A dc voltage sweep mode was performed with a scanning sequence of: 0→-3.5V,-3.5→0V, 0→6V, 6→0V. Fig. 2(a) shows the current-voltage (I-V) curves from sample A. It can be seen that sample A showed reproducible bipolar RS behavior. Here, the RESET step was switched under a negative voltage (~-2V) with an I_{RESET} of 60mA. Meanwhile a SET step was achieved under a positive voltage (~5V). Sample B was reset into a HRS under a positive bias, and I-V curves were obtained with dc voltage scanning using the sequence of: 0→3.5V, 3.5→0V, 0→-6V, -6→0V. Fig. 2(b) shows the bipolar I-V curves from sample B. The RESET step was achieved with an I_{RESET} of 30mA. However, when compared with sample A, the device parameters of sample B (i.e. V_{SET}, V_{RESET}, I_{cc}, I_{RESET}) were more widely distributed (Fig. 2b).

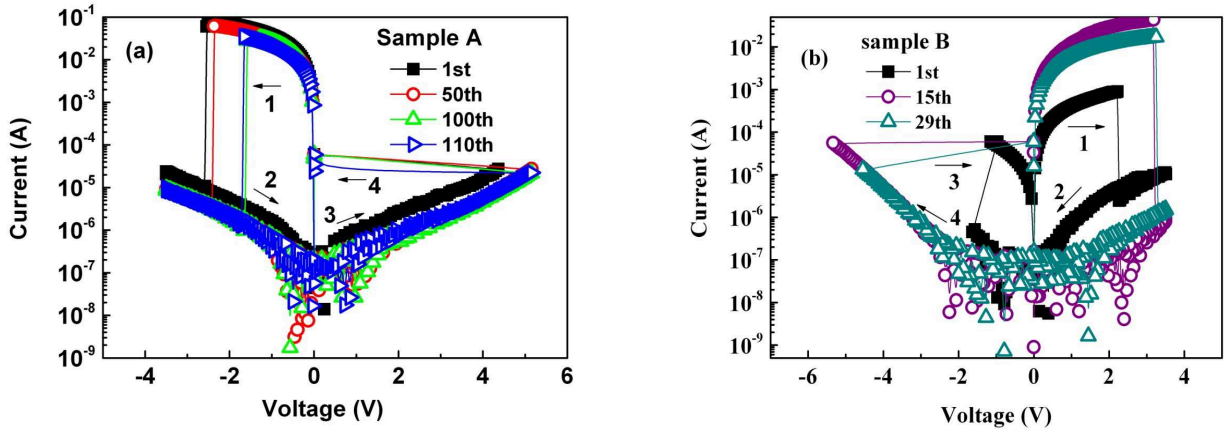


Fig. 2 The I-V curves of bipolar behaviors of Pt/HfO_x/Pt devices. Arrows and figures denote the direction and order of DC sweep, respectively. (a) Sample A, RESET occurring under negative bias first and then SET under positive bias. (b) Sample B, RESET occurring under positive bias first and then SET under negative bias.

Figure 3a shows the distribution of HRS and LRS via a cycle-to-cycle measurement of sample A and sample B. It can be seen that the HRS and LRS of sample A were distributed more tightly. It can also be seen that the R_{off}/R_{on} ratio of sample A was slightly higher. To verify the results from Fig. 3a, 20 bipolar devices, including 10 A-type samples (with the same sweep mode as sample A), and 10 B-type samples (with the same sweep mode as sample B) were employed in order to conduct device-to-device measurements. Figure 3b shows the distribution of HRS and LRS from the 10th cycle of 10 A-type samples and 10 B-type samples. It can be seen that HRS and LRS distribution of A-type samples was narrower, and the R_{off} /R_{on} ratios of the A-type samples were larger than that of the B-type samples.

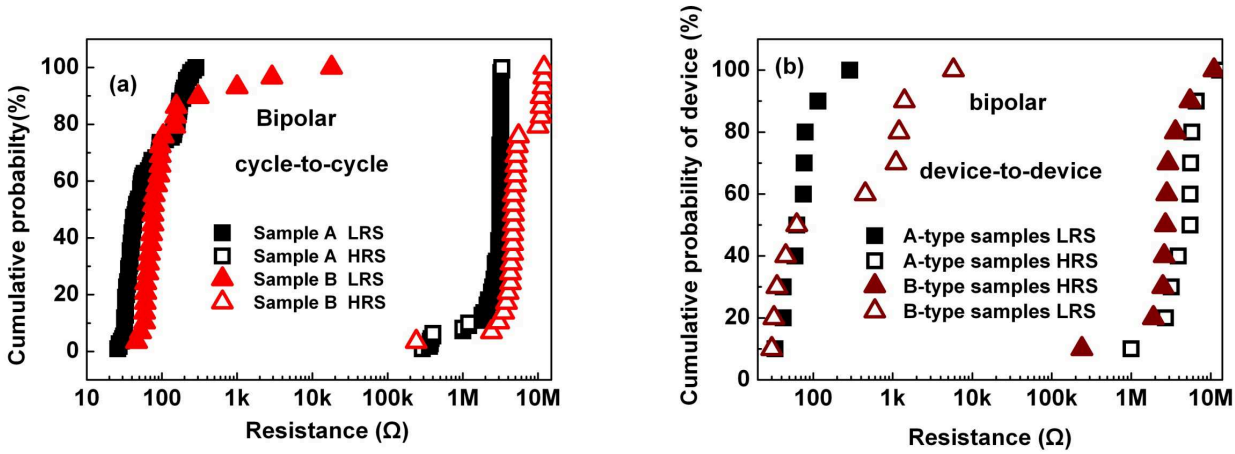


Fig. 3 (a) The distribution of HRS and LRS of cycle-to-cycle measurement of sample A and sample B, (b) the distribution of HRS and LRS of device-to-device measurement of A-type samples and B-type samples.

Although only the converse sequence of voltage scanning for sample A and sample B was employed (Fig. 2), vastly different I-V curves were observed for the two samples. Additionally, the HRS and LRS distribution in sample A was narrower than that of sample B. For a profound insight into the difference, the dispersion of O^{2-}/oxygen vacancy (V_o^{2+}) and the bipolar RS mechanism will be discussed.

In this study, the devices consisted of two electrodes (Pt), an electrolyte (HfO_x), and two interfaces between the electrodes and electrolyte. Due to the symmetrical stack, the inert Pt electrodes, and the random distribution of O^{2-}/V_o^{2+}, it is reasonable to assume that the distribution of O^{2-}/V_o^{2+} inside the HfO_x electrolyte was uniform. However, a few conductive filaments can exist inside all fresh devices due to their initial low-resistance state. Therefore, the differences in the device parameters between sample A and sample B imply that the interfaces of the electrodes and HfO_x played an important role in RS. In this study, BE and HfO_x were deposited successively without breaking the vacuum and the TE was patterned on HfO_x via a metal mask after the exposure of as-deposited HfO_x to air. During this process, it may be possible that oxygen and other foreign impurities were introduced into the interface near the TE. Consequently, more defects existed in the interface near the TE.

A schematic diagram of bipolar RS is shown in Fig. 4. The initial distribution of O^{2-}/V_o^{2+} was uniform, but a few V_o^{2+} connected to form filaments (Fig. 4a). For sample A, when a negative bias was applied to the TE (Fig. 4b), O^{2-} drifted towards the BE under the electric field. When a great deal of O^{2-} piled up at the interface near the BE, the concentration of O^{2-} increased. This led to the dissolution of filaments at the interface near the BE. The device was then reset into HRS from LRS. When the polarity of the applied voltage was reversed, O^{2-} ions were driven back into the HfO_x bulk under the electric field. As a result, filaments consisting of V_o^{2+} were recovered (Fig. 4c), and the device was switched into LRS [10]. For sample B, when a positive bias was applied to the TE, O^{2-} ions drifted towards the TE under the electric field (shown in Fig. 4d). A great deal of O^{2-} accumulated at the interface near the TE. This led to the rupture of filaments at the interface near the TE, and the device was switched into HRS. When the polarity of the applied voltage is reversed, the device can be set into LRS (shown in Fig. 4e).

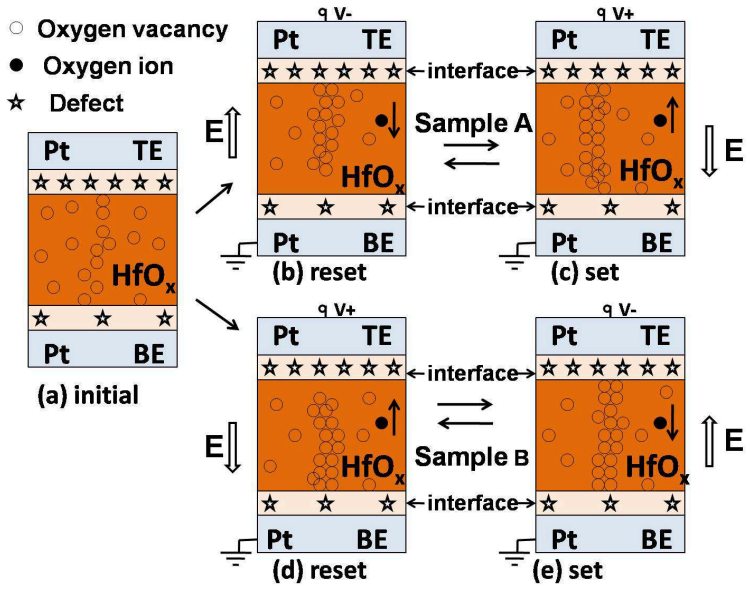


Fig. 4 A schematic diagram of bipolar resistive switching mechanism for Pt/HfO_x/Pt. The solid arrow denoting the direction of O^{2-} movement, the open arrow denoting the direction of electric field, solid circle and open circles denoting $O^{2-}$and Vo^{2+}, respectively, pentacles representing defects at interface, (a) the distribution of oxygen ions and oxygen vacancies of fresh device (b) RESET by a negative bias (c) SET by a positive bias (d) RESET by a positive bias (e) SET by a negative bias

According to the bipolar RS mechanism, the process of transition between HRS and LRS can be divided into two steps. First, O^{2-} drifts under electric field inside the HfO_x and second, filaments dissolve and form at the interface near the TE/BEs. Although the distribution of O^{2-} changed after switching cycles, overall, O^{2-} was distributed uniformly inside the HfO_x [26]. O^{2-} drifting inside HfO_x did not cause the differences between samples A and B. However, parameters of sample B (such as V_{SET}) fluctuated greatly (shown in Fig. 2). Conversely, the parameters of sample A were stable. Furthermore, the distribution of high/low resistance and the R_{off}/R_{on} ratio in sample A were better than those in sample B. Therefore, we believe that only the interfaces near the TE/BE resulted in the different characteristics found in the two samples. It is possible that many defects at the interfaces caused the dissolution of filaments at interfaces near the TE/BE [27]. In this study, the better active interface in sample A led to better device characteristics.

(2) Unipolar resistive switching behavior

A positive/negative bias was applied to the TE in order to perform an RS measurement and investigate the unipolar RS behavior in the devices. The SET and RESET steps for sample C were performed under negative biases on the TE. Meanwhile, the SET and RESET processes for sample D were done under positive voltages. Fig. 5 shows the unipolar I-V curves from sample C and sample D. For sample C, the device was reset into HRS at -1.5—-3V with an I_{RESET} of about 20 mA, while the SET process occurred at ~ -5V under an I_{cc} of 100 μA. Sample D was reset into HRS at -3V with the I_{RESET} of 5 mA and SET was achieved at ~ -5V. Fig. 6a shows the distributions of HRS and LRS via cycle-to-cycle measurements for sample C and sample D. It can be seen that the HRS and LRS distributions for sample D were narrower than those of sample C. It can also be seen that the R_{off} /R_{on} ratio of sample D was larger than that of sample C. These results indicated the RS characteristics of sample D were better than those of sample C.

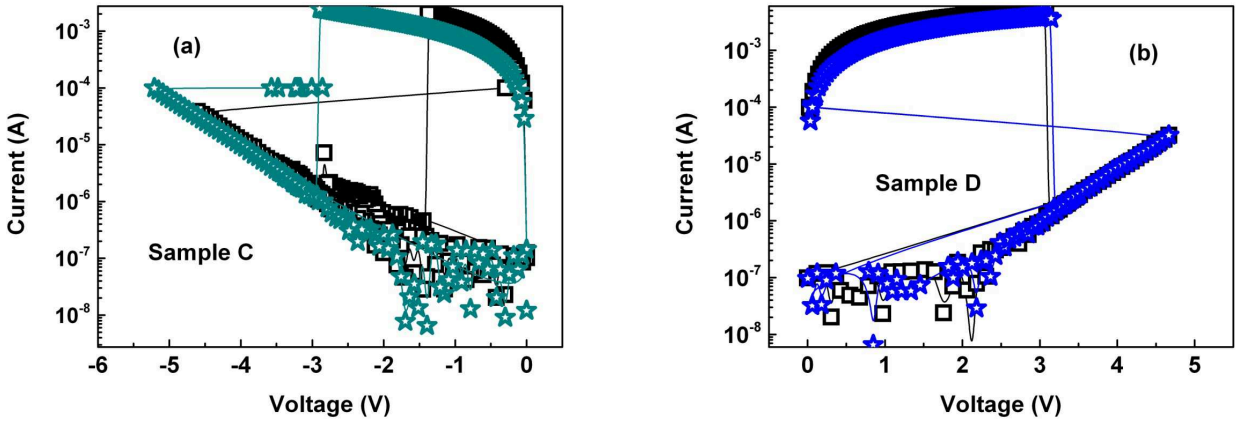


Fig. 5 The unipolar I-V curves of Pt/HfO_x/Pt devices (a) sample C (b) sample D.

To verify the results from Fig. 6a, 20 unipolar devices, including 10 C-type samples (with the same sweep mode as sample C) and 10 D-type samples (with the same sweep mode as sample D) were employed in order to conduct device-to-device measurements. Figure 6b shows distribution of HRS and LRS for the 10th cycle of the 20 unipolar devices. Similar to the results in Fig. 6a, the D-type samples revealed a tighter HRS and LRS distribution and a larger R_{off}/R_{on} ratio than the C-type samples. The transition between HRS and LRS depended on the amplitude of the voltage applied instead of polarity of the voltage for unipolar devices. For a further understanding of the different characteristics between sample C and sample D, analyzing the mechanism and process of unipolar RS will be necessary.

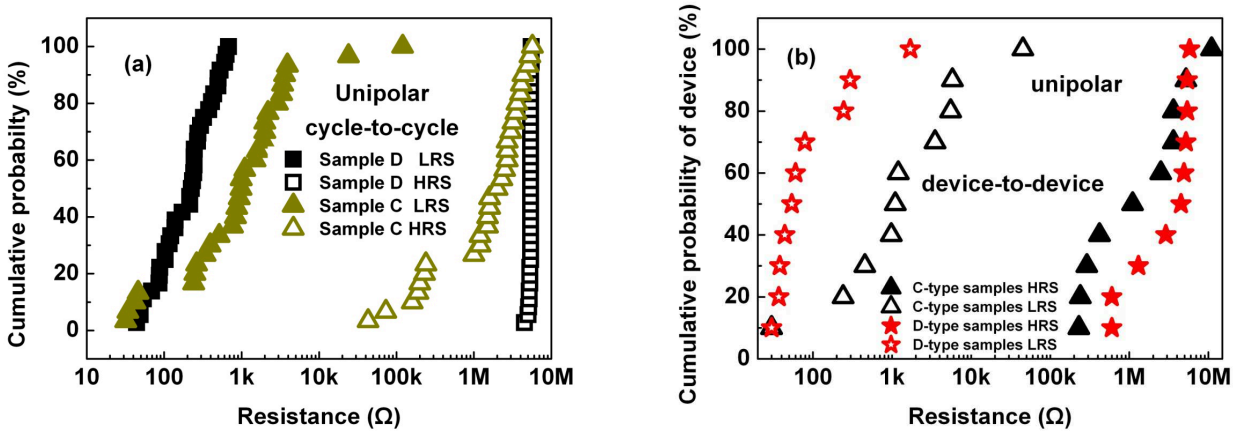


Fig. 6 (a) The distribution of HRS and LRS of cycle-to-cycle measurement of sample C and sample D, (b) the distribution of HRS and LRS of device-to-device measurement of C-type samples and D-type samples.

Figure 7 shows a schematic diagram of the unipolar RS mechanism. The initial distribution of O^{2-}/Vo^{2+} for the as-deposited device was uniform; however, the existence of filaments connected the two electrodes (Fig. 7a). For sample D, when a positive bias was applied, O^{2-} drifted towards the TE under the electric field [28].When more and more O^{2-} accumulated at the interface near the TE,

filaments were dissolved [27]. The device was reset into HRS. When the applied positive voltage was increased further, the SET step was achieved and the device was switched into LRS (Fig. 7e).

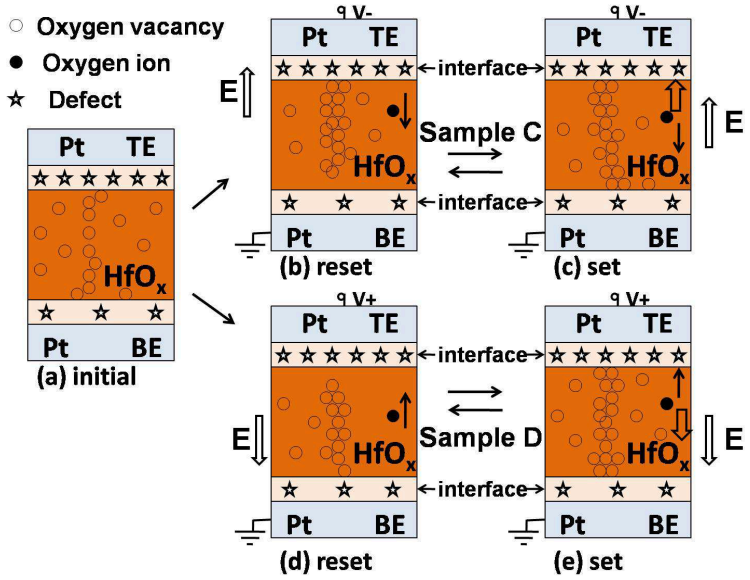


Fig. 7 A schematic diagram of unipolar RS mechanism for Pt/HfOx/Pt, The solid arrow denoting the direction of O^{2-} movement, the open arrows denoting the direction of electric field and the diffusion of O^{2-}, solid circle and open circles denoting $O^{2-}$and Vo^{2+}, respectively , pentacles representing defects at interface, (a) the distribution of O^{2-} and oxygen vacancies of fresh device (b)RESET and (c)SET by a negative bias (d)RESET and (e)SET by a positive bias

O^{2-} anions should drift towards the TE under an increasing positive voltage, so O^{2-} drifting under an electric field doesn't contribute to the SET step. In the HfO_x bulk, O^{2-} anions migrated via drift under the electric field or through diffusion induced by Joule heat and the O^{2-} concentration gradient. In that case, the SET step was achieved via the diffusion of O^{2-} back into the HfO_x bulk induced by the O^{2-} concentration gradient and Joule heat [3,29]. For sample C, with the exception of the opposite polarity of the applied bias and the opposite direction of O^{2-} migration, the SET/RESET steps and driving force were similar to sample D. By a similar analysis to the one that was done with sample A and sample B, we considered that the different characteristics of sample C and sample D were caused by a different number of defects at the interfaces near the TE/BE. Due to the fact that there were more defects at the interface near the TE, the thermal conductivity was lower here [13] and Joule heat dispersion out of the region near the TE was more difficult. For the unipolar device, more Joule heat induced by interfacial defects resulted in a smaller I_{RESET} for sample D (sample C: 20 mA, sample D: 5 mA).

In fact, Joule heat was also generated during switching for samples A and B, but the drift of O^{2-} under the electric field was the main reason for bipolar RS. Moreover, more Joule heat was generated because there were more defects, which would also deteriorate the bipolar devices. Therefore, the parameters of the B-type samples fluctuated greatly, while those of sample A were more stable. This is shown in Figs. 2 and 3. However, for unipolar devices, there was a competition between the drift and the diffusion of O^{2-}. When the diffusion of O^{2-} is stronger than the drift of O^{2-}, it can migrate against the electric field. In other words, Joule heat played a positive role in the diffusion of O^{2-} so as to achieve the SET step in unipolar RS [3,29]. More Joule heat was generated due to the fact that there were more defects at the interface near the TE. In this way, sample D was superior to sample C. Joule heat is beneficial for reducing the reset current for both bipolar devices

and unipolar devices. On the other hand, local thermal conductivity along the length of the filament was lower in the region near the TE [13]. Therefore, larger reset currents were needed to dissolve the filaments near the BE than near the TE. That was why the I_{RESET} of sample A (60 mA) was larger than that for sample B (30 mA), and why the I_{RESET} of sample C (20 mA) was larger than that of sample D (5 mA). Additionally, the smaller I_{RESET} of unipolar devices and the different I_{cc} (unipolar devices: 100 μA, bipolar devices: 60 μA) indicated the role that Joule heat played in the different RS mechanisms within bipolar/unipolar devices.

4 Conclusion

Bipolar resistive switching in Pt/HfO_x/Pt structures was attributed to the drift of O^{2-} under the electric field. This led to the rupture and recovery of filaments (at the interface near the BE for sample A, and at the interface near the TE for sample B). Unipolar resistive switching was achieved by dissolution and formation of filaments (at the interface near the BE for sample C, and at the interface near the TE for sample D) by combining the drift of O^{2-} under the electric field during the RESET step, and by the diffusion of O^{2-} induced by Joule heat during the SET step. For bipolar RS devices, the devices were better when filaments were ruptured and recovered at the interface near the BE. However, for unipolar RS devices, the devices were better when filaments were ruptured and recovered at the interface near the TE. The different number of defects at the interfaces near the TE and the BE (where filaments dissolved and formed) led to the different characteristics in the bipolar and unipolar devices.

Acknowledgement: This research was supported by Samsung Electronics Co., Ltd.

Reference

[1] D.S.Jeong, R.Thomas, R.S.Katiyar, J.F.Scott, H.Kohlstedt, A.Petraru, C.S.Hwang, Reports on Progress in Physics **75**(2012)076502.

[2] R. Waser, M. Aono, Nature Materials. **6**(2007)833-840

[3] H.S.P. Wong, H.-Y. Lee, S. Yu, Y.-S. Chen, Y. Wu, P.-S. Chen, B. Lee, F.T. Chen, M.-J. Tsai, Proceedings of the IEEE **100** (2012)1951.

[4] R. Waser, R. Dittmann, G. Staikov, K. Szot, Advanced Materials **21** (2009)2632.

[5] H. Lee, P. Chen, T. Wu, Y. Chen, C. Wang, P. Tzeng, C. Lin, F. Chen, C. Lien, M.-J. Tsai, IEDM 2008. IEEE International, 2008.

[6] B. Govoreanu, G.S. Kar, Y.Y. Chen, V. Paraschiv, S. Kubicek, A. Fantini, I.P. Radu, L. Goux, S. Clima, R. Degraeve, N. Jossart, O. Richard, T. Vandeweyer, K. Seo, P. Hendrickx, G. Pourtois, H. Bender, L. Altimime, D.J. Wouters, J.A. Kittl, M. Jurczak, IEEE International Electron Devices Meeting (IEDM) Location: Washington, DC Date: DEC 05-07, 2011.

[7] S.Long, X.Lian, T.Ye, C.Cagli, L.Perniola, E.Miranda, M.Liu, J. Sune, IEEE Electron Device Letters. **34** (2013)623.

[8] P.-S. Chen, Y.-S. Chen, H.-Y. Lee, T.-Y. Wu, K.-H. Tsai, P.-Y. Gu, W.-S. Chen, C.-H. Tsai, F. Chen, M.-J. Tsai, Microelectronic Engineering **105** (2013) 40.

[9] Y.S. Chen, B. Chen, B. Gao, L.F. Liu, X.Y. Liu, J.F. Kang, Journal of Applied Physics **113** (2013) 64507.

[10] Y.S. Lin, F. Zeng, S.G. Tang, H.Y. Liu, C. Chen, S. Gao, Y.G. Wang, F. Pan, Journal of Applied Physics **113**,064510 (2013).

[11] Y.Y.Chen, L.Goux, S.Clima, B.Govereanu, R.Degraeve, G.Sankar, A.Fantini, G.Groeseneken, J.Wouters, M.Jurczak, IEEE Transactions on Electron Devices **60** (3)(2013)1114.

[12] Y.Y. Chen, B. Govoreanu, L. Goux, R. Degraeve, A. Fantini, G.S. Kar, D.J. Wouters, G. Groeseneken, J.A. Kittl, M. Jurczak, L. Altimime, IEEE Transactions on Electron Devices **59** (2012)3243.
[13] K.M. Kim, B.J. Choi, C.S. Hwang, Applied Physics Letters **90**(2007)242906.
[14] M.-C. Wu, W.-Y. Jang, C.-H. Lin, T.-Y. Tseng, Semiconductor Science and Technology **27**(2012) 065010.
[15] M.-J. Lee, C.B. Lee, D. Lee, S.R. Lee, M. Chang, J.H. Hur, Y.-B. Kim, C.-J. Kim, D.H. Seo, S. Seo, U.I. Chung, I.-K. Yoo, K. Kim, Nature Materials **10** (2011)625.
[16] T. Liu, M. Verma, Y. Kang, M.K. Orlowski, ECS Solid State Letters **1** (2012)Q11.
[17] K.J. Yoon, M.H. Lee, G.H. Kim, S.J. Song, J.Y. Seok, S. Han, J.H. Yoon, K.M. Kim, C.S. Hwang, Nanotechnology **23** (2012)185202.
[18] W. Lu, K.-H. Kim, T. Chang, S. Gaba, 2011 16th Asia and South Pacific Design Automation Conference. 2011.
[19] P. Jubong, J. Seungjae, L. Joonmyoung, L. Wootae, K. Seonghyun, S. Jungho, H. Hyunsang, Microelectronic Engineering **88** (2011)1136.
[20] X.-J. Zhu, J. Shang, R.-W. Li, Frontiers of Materials Science **6**(2012) 183.
[21] U. Russo, D. Ielmini, C. Cagli, A.L. Lacaita, S. Spiga, C. Wiemer, M. Perego, M. Fanciulli, IEDM 2007. IEEE International, 775(2007).
[22] D.S. Jeong, B.J. Choi, C.S. Hwang, Journal of Applied Physics **100** (2006)**113724**.
[23] K.M. Kim, B.J. Choi, Y.C. Shin, S. Choi, C.S. Hwang, Applied Physics Letters **91** (2007)012907.
[24] X.P. Wang, Z. Fang, Z.X. Chen, A.R. Kamath, L.J. Tang, G.Q. Lo, D.L. Kwong, IEEE Electron Device Letters **34** (2013)508
[25] J.Kim, I.-S.Mok, Y.Kim, K.Lee, D.-H.Ko, Journal of Vacuum Science & Technology B **31**(2013) 032206.
[26] C. Yoshida, K. Kinoshita, T. Yamasaki, Y. Sugiyama, Applied Physics Letters **93**(2008)042106.
[27] R.W. Schwartz, T. Schneller, R. Waser, Comptes Rendus Chimie **7** (2004)433.
[28] D. Ielmini, F. Nardi, C. Cagli, IEEE Transactions on Electron Devices **58** (2011)3246.
[29] S. Yu, B. Lee, H.-S.P. Wong, n *Functional Metal Oxide Nanostructures* (Springer, 2012), pp. 303-335.

Key Engineering Materials Vols 645-646 (2015) pp 178-183
© (2015) Trans Tech Publications, Switzerland
doi:10.4028/www.scientific.net/KEM.645-646.178

Submitted: 2014-11-04
Accepted: 2014-12-23

Study on internal stress in micro-electroformed layer

DU Liqun[1,2,a *],TAN Zhicheng[1,b],SONG Chang[1,c],ZHAO Zhong[1,d],LI Qingfeng[1,e], YIN Penghe[1,2,f]

[1]key Laboratory for Precision & non-traditional Machining Technology of Ministry of Education, Dalian University of Technology, Dalian, Liaoning, China

[2]key Laboratory for Micro/Nano Technology and System of Liaoning Province, Dalian University of Technology, Dalian, Liaoning, China

[a]duliqun@dlut.edu.cn

Keywords: Internal stress, Ultrasonic, Micro electroforming, Compressive stress, MEMS

Abstract. Micro electroforming technology is widely used in fabrication of multilayer or moveable metal micro devices. The fabrication of these devices is usually suffered from high internal stress in micro-electroformed layers which seriously restricts the application and development of micro electroforming technology. Therefore, to control the internal stress is very important for improving the quality and performance of micro-electroformed layer. However, published studies on internal stress in the electroforming layer were mostly based on additive-free solution. According to additive solution, the effect of ultrasonic and current density on compressive stress occurring in the electroforming layer is investigated in this paper. The results indicate that the compressive stress keeps increasing with current density within range from 0.2 to 2 A/dm^2. Meanwhile, the compressive stress in ultrasonic solution decreases by 73.4 MPa averagely comparing to that in ultrasonic-free solution, and the compressive stress also keeps decreasing with the ultrasonic power which gets the lowest value at 200W. Moreover, the mechanisms of additive-induced compressive stress and ultrasonic relieving compressive stress are discussed. This research work will complement the ultrasonic-stress reduction theory and may contribute to the development of micro electroforming technology.

Introduction

Micro electroforming is developed from traditional electroforming. It has the advantages of simple, accurate and easy achieving complicated structure, and is widely used in the fabrication of multilayer or moveable micro devices such as micro molds, micro sensors, micro actuators, etc. However, the fabrication of micro electroforming devices is limited by internal stress in the electroforming layer. Meanwhile, the internal stress reduces the interfacial bond strength between substrate and electroforming layer or between the electroforming layers [1]. High tensile stress can easily result in electroforming layer cracking. While large compressive stress can result in blistering and delamination. These phenomena are aggravated as the electroforming layer goes thicker. High internal stress has become one of the major problems which restricts the application and development of micro electroforming technology.

To solve this problem, researchers have done some studies on the electroforming process parameters in the traditional electroforming field, such as bath types, pH values, current density, etc. As a major influencing factor of internal stress, current density was studied by researchers. Tong [2] studied the influence of direct current on internal stress in additive-free solution, and indicated that the internal stress increased linearly with the current density. Zhao et al [3] studied the influence of pulse current on internal stress in additive-free solution. The experiment results showed that internal stress changed from compressive stress to tensile stress as increasing of the current density and reached the lowest value within range from 7 to 9 A/dm^2. Besides, some researches show that ultrasonic has a marked effect on reducing the tensile stress in the electroforming layers. Vausdevan et al [4] proposed the method to solve the problems of coating cracking, embrittlement and high tensile stress by ultrasonic. The results show that ultrasonic could reduce tensile stress during the electroplating process. Prasad et.al. [5] presented an assumption that ultrasonic reduced the tensile

stress because of inducing a compressive stress. Fang [6] also pointed out that ultrasonic could reduce the tensile stress and analyzed the reason of internal stress reduction with thermodynamic theory. In summary, the existing studies about the internal stress in the electroforming layer are mainly based on additive-free solution system, and the tensile stress in the electroforming layer could be reduced by ultrasonic electrodeposition. Meanwhile, in the micro electroforming area, electroforming micro structures have often high aspect ratio. In order to obtain the electroforming layer with good performance (for example, high filling power, smooth surface, brightness and high hardness), some complementary additives are usually used in micro electroforming technology. However, there are few studies on relieving the compressive stress in the electroforming layer with ultrasonic micro electroforming based on additive solution system. Therefore, it is necessary to study the impact of current density on internal stress in additive solution and the methods by which the internal stress can be reduced.

Internal stress measurement

Measurement principle. According to Bragg′s law $2d\sin\theta=n\lambda$ and elastic theory, the stress measurement formula can be deduced as:

$$\sigma = \frac{-E}{2(1+\upsilon)} \cot\theta_0 \frac{\pi}{180} \cdot \frac{\partial 2\theta}{\partial \sin^2\psi} \quad . \tag{1}$$

Where, E, υ, θ_0 represent the elastic modulus of material, the Poisson ratio and the Bragg angle in non-stress mode. ψ is the angle between material surface normal and crystal surface normal, and 2θ signify the measurement value of diffraction angle corresponding to ψ angle. $M=\partial 2\theta/\partial \sin^2\psi$, is the slope of 2θ corresponding to $\sin^2\psi$, σ is value of internal stress.

Results processing. In the experiments, Ni <111> plane was selected as diffraction surface. At the same time, 0°, 25°, 35° and 45° were selected as inclination angle ψ. Side-inclination fixed ψ method was adopted in the measurement process. Measurement data were smoothed and fitted by origin data analysis software in calculative process. The line slope M can be obtained by linear fitting, and then the value of stress can be obtained by (1) finally.

Experiments

Experimental equipment. In order to build the micro electroforming system of nickel-sulfamate-based solution with additive, a self-developed ultrasonic micro electroforming equipment was applied. Fig.1 presents the experimental set-up. The frequency of direct pulse power is 1000 Hz and the duty ratio is 0.2. KQ-250DB ultrasonic cleaner was applied as ultrasonic vibration equipment. The frequency is 40 kHz, the power can be hanged from 0 to 250 W, and the temperature range is from 10 to 80 ºC.



Fig. 1 The experimental set-up



Fig. 2 Sample after micro electroforming

Micro electroforming. Copper plates were used as substrates. The roughness of the substrates was lower than 0.1μm and measured by a profilometer (Surfcorder ET4000M, Kosaka Laboratory Ltd.Japan) after polishing process. The main experiment conditions were as follows: the cathode reciprocation was used for agitation. The composition of electroforming bath was as below: Ni $(NH_2SO_3)_2$•$4H_2O$ (550 g/L), $NiCl_2$ (10 g/L), Sodium dodecyl sulfate (0.6 g/L), H_3BO_3 (30 g/L). The bath temperature was 50°C and the bath pH value was 4.0.

Stress measurement. The electroforming samples are shown in Fig. 2. A Bruker D8 Discover X-ray diffractometry is used to measure the internal stress, Inductance micrometer is used to measure the thickness of electroforming layer and a tool microscope (MX40F, Olympus Corporation, Japan) is used to observe the surface morphology of electroforming layer.

Analysis and discussion

The impact of current density on internal stress. The value of internal stress is the average of three times respectively. The internal stress was plotted against current density, as shown in Fig. 3 (negative sign denotes compressive stress). It indicates that the internal stress in the electroforming layer is compressive stress within range from -280 to -410 MPa, and the compressive stress keeps increasing with current density. Furthermore, the compressive stress increases faster when the current density is less than 0.4 A/dm^2. And the trend becomes slower when the current density is between 0.4 A/dm^2 and 2.0 A/dm^2.

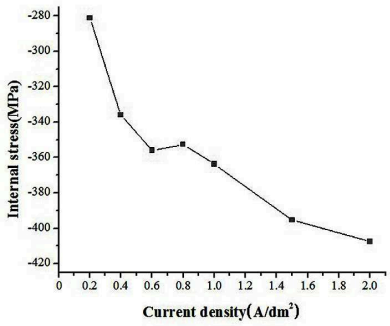


Fig. 3 Relationship of current density with compressive stress

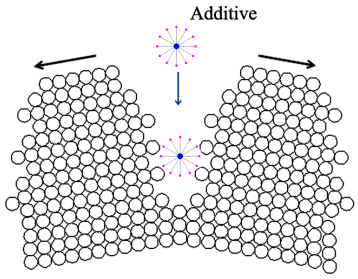


Fig. 4 Illustration of additive incorporated into the electrochemical activity points during film growth

The compressive stress observed during deposition under a low current density or an additive sulfamate bath [7,8]. Our experimental datas are consistent with those results. According to the kinetic trapping model [9,10], the insertion of extra atoms at surface defects and grain boundaries induce the compressive stress. In the process of deposition with additive solution, there are many electrochemical activity points at the coalescence point of two opposite-signed atomic steps. And these electrochemical activity points include grain boundaries, gap, dislocations, surface defects etc. As an additive, sodium dodecyl sulfate (SDS) is an anionic surfactant, which can turn into a spherical micelle in the solution when it works. According to Gibbs adsorption law, SDS can easily be adsorbed at the electrochemical activity point, as show in Fig.4. When the next nickel electroforming layer over-grows the trapped molecular cluster, the electrochemical activity points then essentially become a bulk interstitial that can induce the compressive stress. The steady-state trapping only needs to occur approximately once per 1000 surface lattice sites to reach 100 MPa compressive stress observed in typical metal films [11]. Therefore, the additive incorporated into the electrochemical activity points could be the main reason for the compressive stress in the nickel-sulfamate-based solution with additive. The deposition of nickel atoms will speed up when the current density increases. It will exacerbate the concentration polarization of electroforming solution (Eq. 2) and produce more electrochemical activity points for the adsorption of SDS.

$$\frac{C_{M^+}}{\overline{C}_{M^+}} = e^{\frac{(\alpha-1)zF}{RT}\eta}\frac{i}{2i_0} + e^{-\frac{zF}{RT}\eta} \quad . \tag{2}$$

Where, C_{M^+}, $\overline{C}_{M^+}$ represent solution concentration of metal ion in reality and in balance, i, i_0 represent polarization current and exchange current, T , η represent temperature and overpotential, α, z, F, R represent corresponding coefficient.

As a result, the fraction of SDS incorporated into electrochemical activity points actually increases when the growth rate increases, which links with the larger compressive stress. Meanwhile, diffusion of hydrogen into the Ni electroforming layer occurs during deposition. The incorporation of atomic hydrogen and other impurities are trapped by electrochemical activity points, which results in the lattice to expand and leads to compressive stress. We observed that the faradic current efficiency is far less than 100%, as shown in Fig. 5. The faradic current efficiency keeps decreasing with the current density, which means the lower faradic current efficiency linking with the higher compressive stress. Therefore, it is possible that the incorporation of atomic hydrogen produces part of compressive stress.The increasing of current density will also exacerbate hydrogen evolution reaction. More hydrogen atoms [12] and impurities [13] will generate and spread toward the electrochemical activity points, which may also result in a larger compressive stress in the electroforming layer.

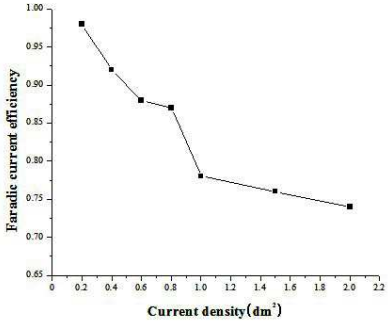


Fig. 5 Faradic current efficiency under different current density

The impact of ultrasonic on internal stress. The internal stress results corresponding to the ultrasonic electroforming experiments were shown in Table. 1.

Table. 1 Internal stress of nickel electroforming layer

	Group 1 [MPa]	Group 2 [MPa]	Group 3 [MPa]	Average stress [MPa]
Ultrasonic-free	-235.9	-293.8	-247.3	-259.0
Ultrasonic	-109.3	-227.8	-219.8	-185.6

Table. 1 shows that the compressive stress in the electroforming layer with ultrasonic agitation is less than that with ultrasonic-free. The compressive stess decreases by 73.4 MPa averagely by ultrasonic. This indicates that introducing ultrasonic in the micro electroforming process has a marked effect on stress reduction. The mechanism of ultrasonic relieving compressive stress can be explained from two aspects. On the one hand, the high-speed micro jets generated by ultrasonic strengthen the stirring capacity of solution. The ion transport capability is enhanced, which reduces the thickness of the diffusion layer and concentration polarization. Nickel atoms are supplied adequately and less electrochemical active points are formed, which make micro electroforming process becomes smoother and continuous. It can be reflected from preferred orientation of nickel, as show in Fig.6. The film has strong (111) fiber texture(40.8%) in an ultrasonic-free solution(Fig.6a), The preferred orientation was reduced in ultrasonic solution(Fig.6b). As a result, the fraction of SDS incorporated into electrochemical activity points actually decreases under ultrasonic, which links

with the lower compressive stress. Meanwhile, hydrogen evolution reaction is greatly influenced by ultrasonic vibration and the hydrogen is rapidly removed by vacuum bubbles.

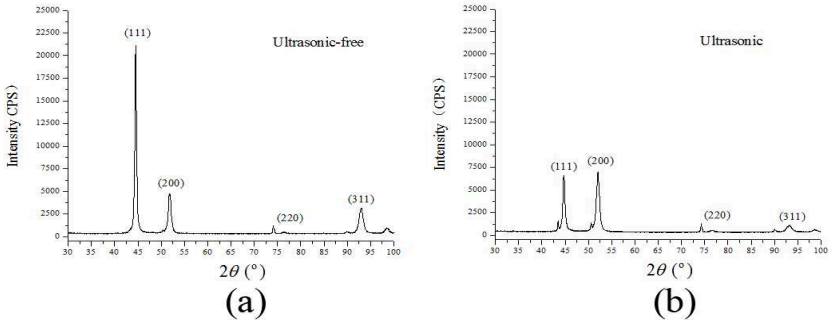


Fig. 6 XRD diffraction peak of electroforming layer

This is the reason for a smooth electroforming layer to be obtained under ultrasonic solution, as show in Fig.7. Fig. 7(a) is the surface topography of ultrasonic-free sample and Fig. 7(b) is the ultrasonic one. From Fig. 7, the electroforming layer with ultrasonic agitation shows a smoother surface and less pitting comparing to ultrasonic-free one.

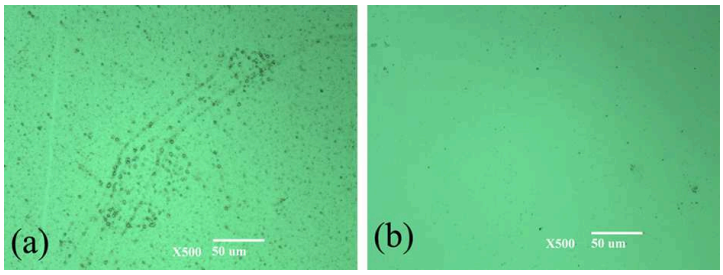


Fig. 7 Surface morphology of samples: (a) Ultrasonic-free, (b) Ultrasonic

A lower incorporation of atomic hydrogen has been linked with the lower compressive stress. On the other hand, ultrasonic produce will be a great vapor pressure around the collapse sites in the electroforming solution, which is due to cavitation bubbles collapsing along with the vibration and nucleation of micro-bubble under ultrasonic. The bubbles under the vapor pressure continuously wash and strike the electrode surface, which makes SDS hard to be adsorbed in the electrochemical activity points. Meanwhile, hydrogen atoms and other impurities are also hardly adsorbed in the electrode surface. Less hydrogen atoms and impurities incorporation link with the lower compressive stress. To further confirm the stress removal with ultrasonic, we performed a series of micro-electroforming experiments at the ultrasonic power of 0W, 100W, 150W, 200W, 250W. The result is showed in Fig. 8. The compressive stress keeps decreasing with the ultrasonic power and gets the lowest value at 200W.

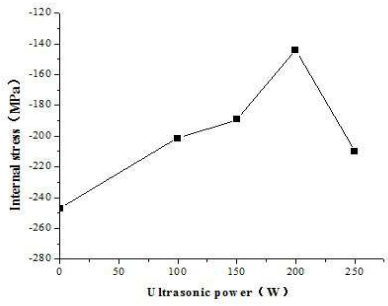


Fig. 8 Relationship of ultrasonic power with compressive stress.

Summary

In this paper, micro electroforming experiments have been carried out in a nickel-sulfamate-based solution micro electroforming system with additive. The impacts of current density and ultrasonic on internal stress are discussed. The results indicate that compressive stress keeps increasing non-linearly with current density within range from 0.2 to 2 A/dm^2. Ultrasonic has a remarkable effect on compressive stress, and the average compressive stress decreases by 73.4 MPa comparing to the ultrasonic-free one. The compressive stress keeps decreasing with the ultrasonic power and it gets the lowest value at 200W. We propose that additive is the main reason for producing compressive stress in the electroforming layer. The additive trapped by electrochemical activity points may be the main reason for the compressive stress generation. The atomic hydrogen and impurities also contribute some compressive stress. Ultrasonic can decrease the comprehensive influence, and then reduce the compressive stress.

Ultrasonic can greatly improve the electroforming condition without the change of the electroforming solution formulation. It has greatly effect on high-performance micro electroforming layer with lower stress. Therefore, it is remarkably promising to introduce ultrasonic into micro electroforming process. The optimization of process parameters and the development of a stable high-performance ultrasonic electroforming device should be studied next.

Acknowledgment

This work was supported by the National Natural Science Foundation of China (No: 51375077) and the National High Technology Research and Development Program of China (863 Program, No: 2012AA040406).

References

[1] K.L. Mittal, Adhesion measurement of thin films,J. Electrocomp. Sci. Tech. 3 (1976) 21-24.
[2] X.Q. Tong, Influence of process parameters on internal stress in nickel plating in sulfamate bath, J. Mater. Prot. 20 (1987) 23-26 (in chinese).
[3] J.F. Zhao, D. Zhu, Effect of pulse current on internal stress of nickel electroformed layer, J. Aeronaut. Manuf.Technol. 22 (1997) 5-7 (in chinese).
[4] R. Vasudevan, R. Devanathan, K.G. Chidambaram, Effect of ultrasonic agitation during electroplating of nickel and copper at room temperature, J. Metal. Finish. 90 (1992) 23-26.
[5] P.B.S.N.V. Prasad, R. Vasudevan, S.K. Seshadri, Residual stresses of nickel electrodeposits with ultrasonically agitated bath, J. Mater. Sci. Lett. 11 (1992) 1424-1425.
[6] X.H. Fang, Study on technique and mechanism of ultrasonic-assisted electroplating of nickel-based diamond bit, Dissertation, 2008, China University of Geosciences, China.
[7] N. Pangarov, R. Pangarov, Stress in electrodeposited metals general thermodynamic theory, J. Electroanal. Chem. 91 (1978) 173-188.
[8] A. Bhandari, S.J. Hearne, B.W. Sheldon, et al, Microstructural origins of saccharin-induced stress reduction in electrodeposited Ni, J. Electrochem. Soc. 156 (2009) 279-282.
[9] E. Chason, B.W. Sheldon, L.B. Freund, et al, Origin of Compressive Residual stress in polycrystalline thin films, J. Phys. Rev. Lett. 88 (2002) 156103(1)-156103(4).
[10] J.K. Heuer, P.R. Okamoto1, N.Q.Lam, et al, Relationship between segregation-induced intergranular fracture and melting in the nickel–sulfur system, J. Appl. Phys. Lett. 76(2000) 3403-3405.
[11] B.W. Sheldon, R. Beresford, J. Rankin, Intrinsic compressive stress in polycrystalline films with negligible grain boundary diffusion, J. Appl. Phys. 94(2003) 948-957.
[12] S. Armyanov, G. Sotirova, Diffusion-elastic phenomena in nickel and cobalt electrodeposits plated on to strip cathodes, J. Surf. Coat. Technol. 34(1988) 441-454.
[13] P.M. Alexander, R.W. Hoffman, Effect of impurities on intrinsic stress in thin Ni films, J. Vac. Sci. Technol. 13(1976) 96-98.

Key Engineering Materials Vols 645-646 (2015) pp 184-189
Submitted: 2014-11-06
© (2015) Trans Tech Publications, Switzerland
Accepted: 2014-12-23
doi:10.4028/www.scientific.net/KEM.645-646.184

Low Temperature Eutectic Alloy Bonding used in MEMS-based Solid Propellant Microthrusters Array

Chengbo RU[1,a], Yinghua YE[2,*,b], Jianbing Xu[3,c], Zhenyou ZOU[4,d], Ji DAI[5,e], Peng ZHU[6,f] and Ruiqi SHEN[7,g]

[1-7]School of Chemical Engineering, Nanjing University of Science and Technology, Nanjing, CHINA

[a]ruchengbo2014@hotmail.com, [*,b] yyinghua@njust.edu.cn (corresponding author)

[c] xujianbing1991@163.com, [d] 771977641@qq.com, [e] 17507207@qq.com

[f] zhupeng05@hotmail.com, [g] rqshen@njust.edu.cn

Keywords: eutectic bonding, eutectic alloy, Ansys simulation, MEMS-based Solid Propellant Microthrusters,

Abstract. Considering the safety of the charge filled in the chambers and the operational reliability, a low temperature eutectic alloy bonding was preferred for the final assembling process of MEMS-based solid propellant microthrusters (SPM) array with top-side igniters. The optimum conditions of the alloy coating are the pH value of the solution is 0.5, the base metal layer is composed of Ti (60nm)/Cu (500nm) deposited by magnetron sputtering. The bonding process was conducted in an oven with air and the bonding temperature is 70°C. To predict the performance of bonding layer, the temperature distributions of eutectic alloy layer were simulated by ANSYS software when the chamber is full of high temperature reactants. The simulation results demonstrated the bonding strength wouldn't cut down since the heat transfer induced by the combustion of charge. The assembled MEMS-SPM array was tested under constant voltage, the results indicated that the eutectic solder bonding procedure meet the requirements of the MEMS-SPM assembling.

Introduction

MEMS-based solid propellant microthrusters(SPM) array is a potential candidate propulsion system for micro/nanosatellite or cubesat[1-3]. It can be used to precise attitude controlling, station keeping and orbit adjustment of the microspacecraft. In general, SPM is composed of three parts: a nozzle, an igniter and a combustion chamber. The SPM can be divided into two classic types: the planar structure and the vertical structure. The vertical SPM is more suitable for the integration of thrusters to fit the demand of the propulsion system used in the microspacecraft.Fig.1 shows the vertical structure of SPM with top-side igniter, from top to bottom is the silicon nozzles integrated with poly-silicon igniters (layer I), the ignition charge chambers (layer II) and the propellant chambers (layer III). The operation principle of SPM is that the charge stored in the combustion chamber is ignited when a setting current load into the igniter, then high temperature products generated by the combustion flow through the nozzle and output thrust.

With the developing of the microelectromechanical system (MEMS), different bonding schemes were researched to meet special requirements of different MEMS products[4]. According to the existence of intermediate layer, bonding techniques could be divided into direct bonding and intermediate layer bonding. The direct bonding techniques include silicon-to-silicon fusion bonding, anodic bonding and room temperature silicon-to-silicon bonding[5], while the intermediate layer bonding mainly contains glass frit bonding, BCB bonding[6], adhesive bonding, solder bonding and eutectic bonding. Although strong and hermetic bonds between two silicon substrates can be achieved after the direct bonding process, it needs very flat substrate surfaces, high temperature, high voltage filed or special substrate surface treatments. To some extent, the intermediate layer bonding process can tolerate some particles, contaminations or structure on the surface of the substrates in lower temperature.

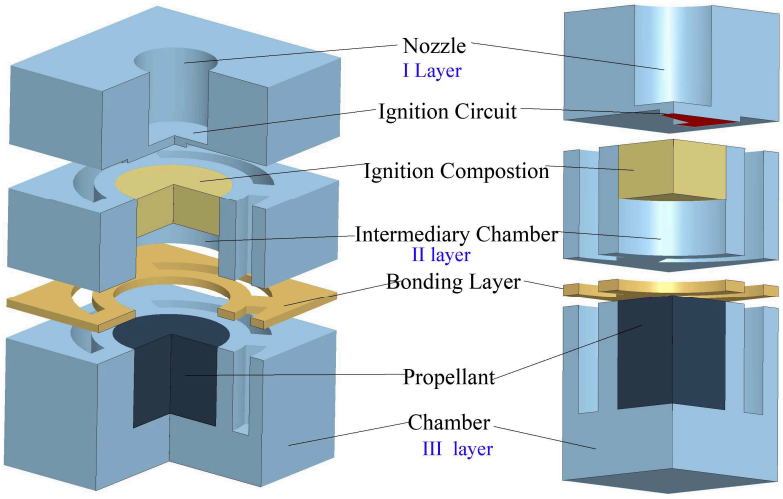


Figure 1. Structure of MEMS-SPM with a top igniter

Two bonding processes will be carried out to obtain a SPM array. Firstly, (the layer I) and the (layer II) are bonded together (the first assembly procedure). Following is the (layer II) and the (layer III) are filled with ignition charge and solid propellant respectively. Secondly, assembling is followed by bonding the propellant chambers (layer III) and the intermediary chambers (layer II) together (the final assembly procedure).

BCB bonding (the bonding temperature is about 220°C) is an adequate scheme for the mission of the first assembly procedure. While glass frit bonding may cause the ignition circuit failure, because the bonding temperature (440°C) is so high that cause the Poly-Si igniter and the gold lead to alloying reaction. Eutectic bonding and solder bonding are also not inappropriately for the electrical contact between two substrates.

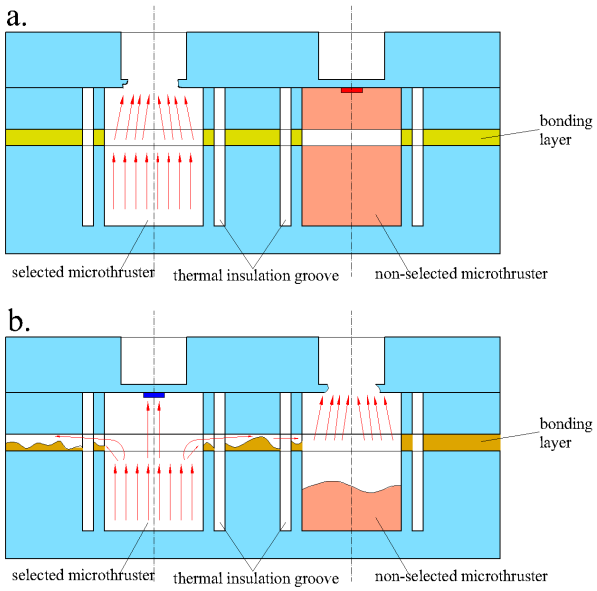


Figure 2. The importance of bonding quality, a. shows ideal bonding, the selected microthruster works without any leakage; b. shows with unreliable bonding layer, the selected microthruster will cause undesired combustion of neighbor unit.

Some limits may impede the final assembly procedure. The surface of chamber layers may be polluted by the charge contaminations when the chamber is filled with charge that will lower the bonding strength. The bonding temperature should be low enough to avoid accidental combustion of charge (for the nano-Al/CuO, the bonding temperature should be lower than 150°C). And the hermetic bonding requirements, when the selected SPM unit is ignited, high temperature and high pressure reaction products may flow to neighbor units through narrow channels caused by unreliable bonding and may induce accidental ignition. Fig.2 illustrates the importance of bonding quality. In

conclusion, the direct bonding techniques and most of intermediate layer bonding processes are not suitable for the final assembly procedure. In this paper, considering the safety of the charge filled in the chambers and the operational reliability, a low temperature eutectic alloy bonding technique is preferred for the assembling process of SPMs array.

Eutectic bonding procedure

Eutectic bonding is evolved by the solder bonding. In this paper, a low bonding temperature eutectic bonding was chosen as the final bonding techniques which is composed of Bi-Pb-Sn-Cd-In (117# Indalloy, Indium Corporation), the melting point is only 47°C, the main parameters of the alloy are shown in Table1. The eutectic alloy bonding process involved the submerging the chamber array into the molten alloy. The eutectic alloy is held within Ethylene glycol (EG) and hydrochloric acid (HCl) solution. Ethylene glycol (EG) was used as the self-assembly fluid, and hydrochloric acid (HCl) was used for removing the oxide in the surface (the oxide in the surface will prevent the alloy wet the base metal layer). According to references [7, 8], the pH of the solution should be 3 and the base metal is a four-layer film (composed of 10, 100, 50 and 100nm thick films of Cr/Pt/Au/Cu). But in our experiments, it's difficult to coat the base metal layer by eutectic alloy when the pH in the range within 1 to 3 and the fabrication of the base metal layer is costly. The optimum conditions of the solder coating were investigated through orthogonal test, which are the pH value of the solution is 0.5, the base metal layer is composed of Ti (60nm) film and Cu (500nm) film deposited by magnetron sputtering, the temperature of the solution is 70°C to keep the alloy in liquid phase during the bonding process.

Table 1. Parameters of indalloy 117# eutectic alloy

Material	*Density /kg·m^{-3}*	*Specific Heat (Solid) /J· kg^{-1}·K^{-1}*	*Specific Heat (Liquid) /J· kg^{-1}·K^{-1}*	*Thermal Conductivity /J·m^{-1}·K^{-1}*	*Melting Point /°C*	*Latent Heat of Fusion /J·kg^{-1}*
117# Indalloy	9.16×10^3	163	197	15	47	3.68×10^4

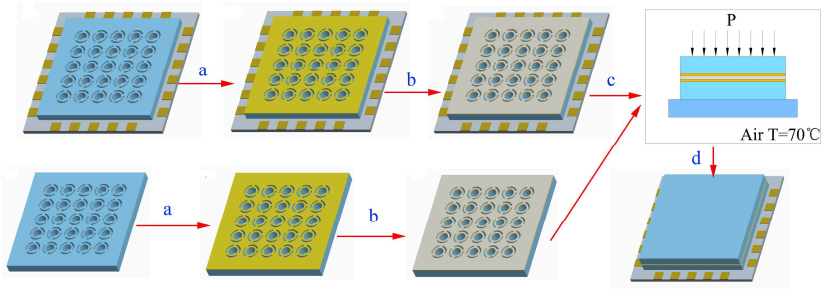


Figure 3. The Assembly Process: a. the base metal layer (Ti/Cu) was deposited on the surface by magnetron sputtering; b. alloy coating in the EG solution; c. bonding in an oven, bonding temperature is 70°C in the air; d. the assembled SPM array.

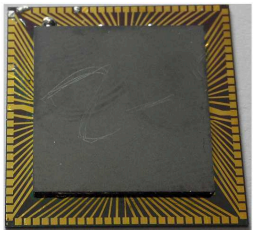


Figure 4. The assembled SPM array.

The eutectic bonding process is shown in Fig 3. Firstly, base metal layer were deposited 50nm/500nm thick films of Ti/Cu on the both surfaces of the chamber layers (layer II and layer III) by magnetron sputtering respectively. After filling process, the surfaces of layer II and layer III was coated by the

uniform alloy films when the chamber parts were submerged in the solution. Finally, the two parts were aligned and brought into contacted, the contacted parts were heated until the alloy became molten in an oven under air atmosphere at 70°C. The assembled SPM array is shown in Fig 4.

Computation of Heat Conduction

When the selected SPM unit works, the temperature of the bonding layer will rise because of the heat conduction between the high temperature products and the eutectic alloy. The decline in bonding strength when the temperature of the bonding layer is higher than 47°C will lead to bonding failure and give rise to accident ignitions. To predict the performance of bonding layer, the temperature distributions of bonding layer was computed by finite-element modeling software Ansys. Ansys was preferred for the simulation because of its enhanced features and functionality in multi-physics problems.

Table 2. Parameters of charges used in MEMS-SPM

Reactant	*adiabatic reaction tempreature/K with phase changes*	*g of gas per g*	*Density, ρTMD /kg·m-3*
Al/CuO	2843	0.3431	5109
NC(12%N)	2840	1	1660

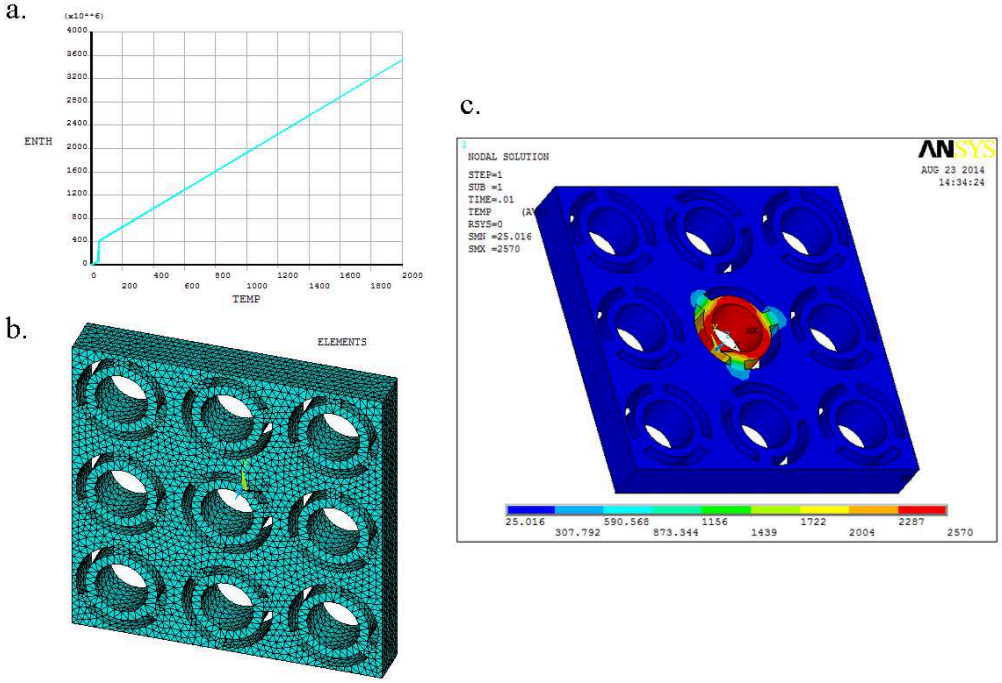


Figure 5.Computation of heat conduction by Ansys. a. shows the enthalpy of the eutectic alloy; b. shows the meshed model (consists of 9 SPM units, and the center unit is selected as the work unit) c. shows temperature distributions of bonding layer on the surface of chamber array after the selected chamber is full of high temperature reactants.

Because of the complex 3-D structure and thermal transfer process, some assumptions were conducted to reduce computational complexity and obtain accurate results. Firstly, the temperature distributions are studied by transient heat transfer analysis. In the submillimeter scale structures, heat conduction is considered as the only form of thermal transfer. Secondly, ignore the influence of silicon substrates. The dimensions of the bonding layer were same as the microchambers, the diameter of chamber is 0.7mm, thermal insulation grooves around the chambers. The matrix dimension size is 3×3, and the center unit is set as the work unit, meshed model is shown in Fig 5.b. And the last one is that applied load was set as temperature (2570°C) on the inner surfaces of the selected chamber, load time is 10ms (0.01s), and the mesh size is 1×10^{-4}. The adiabatic reaction temperature of nano-Al/CuO and NC is 2843K and 2840K respectively, as shown in Table 2. The

combustion process of the charge last less than 5 ms, the temperature of products wouldn't reach 2570°C (2843K) because incomplete combustion and heat loss.
As indicated by the temperature cloud-chart shown in Fig 5.c, the temperature of eutectic alloy around the worked unit wouldn't up to 47°C above. So, the bonding strength wouldn't cut down because of the combustion of charge.

The Ignition Tests

The assembly array was tested under constant voltage to estimate the ignition characteristics and the bonding reliability. The test stand as shown in Fig 6, consists of high speed camera, SPM array, computer and constant voltage source. The selected SPM was ignited under 10V constant voltage supplied by the constant voltage source, the working process was recorded at the rate of 20 000 fps by the camera, these data were collected by the computer.

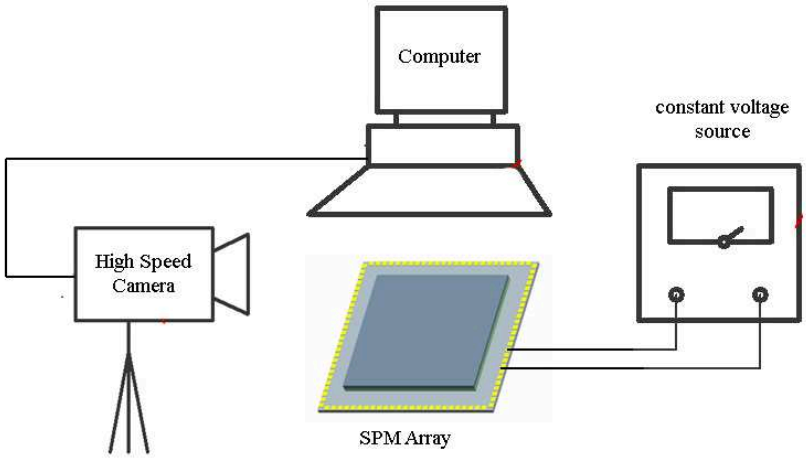


Figure 6.Ignition test stand, includes high speed camera (record the combustion process, the record rate is 20 000fps), constant voltage source, SPM array and computer.

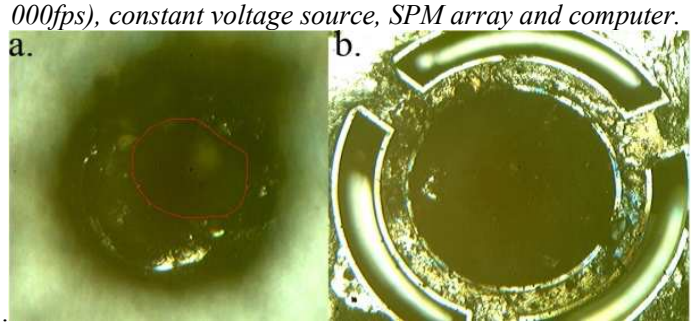


Figure 7.The ignited SPM. a. shows the diaphragm was broken (the red line zone). b. shows the structure of the propellant chamber was not broken down by reaction products (checked without any damage of the SPM array).

The selected SPM units were ignited successfully under 10V constant voltage. The high temperature combustion products broke down the diaphragm (shown as Fig 7.a) and flow through the nozzle, the duration of the combustion process below 5ms, shown as Fig 8. The propellant chamber layer didn't fall off from the ignition chamber layer, and selected SPM worked independently without any accidental ignition occurred.

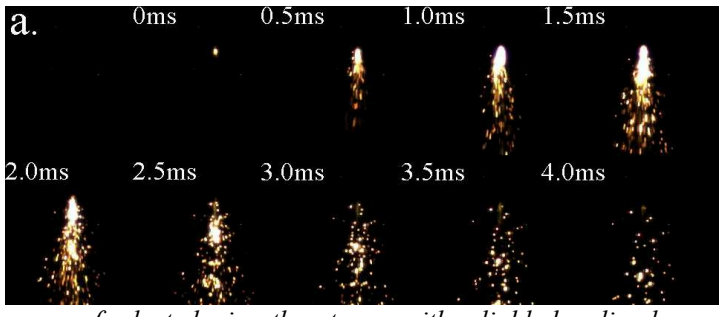


Figure 8.Combustion process of selected microthruster. a. with reliable bonding layer, the combustion process without any leakage of reaction products. The combustion process last 4.0ms.

This eutectic bonding based on the 117# Indalloy can be used to nondestructive testing of SPM array after ignited. Heat the tested SPM array to above the melting point of the eutectic alloy (47°C), the propellant chamber layer could be apart from the ignition chamber easily without any destruction. The structure of ignition chamber was observed after combustion, see Fig 7.b.

Conclusions and Perspectives

In this paper, low temperature eutectic alloy bonding technique was chosen to complete the final bonding process of the SPM array. The optimum conditions of the solder coating are the pH value of the solution is 0.5, the base metal is composed of Ti (60nm)/Cu (500nm) deposited by magnetron sputtering. After alloy coating, the two parts were bonded in an oven in air atmosphere at 70°C.

To predict the performance of bonding layer, Ansys simulation results showed that the bonding strength wouldn't be cut down because of the combustion of charge. The temperature distributions of eutectic alloy layer were simulated by ANSYS software when the chamber is full of high temperature reactants. The simulation results demonstrated the bonding strength wouldn't cut down since the heat transfer induced by the combustion of charge.

The assembled MEMS-SPM array was tested under constant voltage. The selected SPM unit worked independently and no accidental ignition was induced. The results indicate that the eutectic alloy bonding procedure meets the requirements of the MEMS-SPM assembling.

The eutectic bonding will be invalid in the space, the operation temperature of the SPM array in the orbit range from -70°C to 70°C. To avoid this problem, others eutectic alloy like 1# Indalloy composed of In (52.0 wt %) and Sn (48.0 wt %), can meet the requirements of work environment.

* Corresponding Author: Yinghua YE, School of Chemical Engineering, Nanjing University of Science and Technology, Tel: 86-25-84315855, FAX: 86-25-84315855, email: yyinghua@mail.njust.edu.cn.

References

[1] C. Rossi, D. Briand, M. Dumonteuil, et al. Matrix of 10×10 addressed solid propellant microthrusters: Review of the technologies, J, Sens. and Actu. A, Phys., 126(2006),241 -252.

[2] D. H. Lewis Jr., S. W. Janson , R. B. Cohen et al. Digital micropropulsion, J. Sens. and Actu. A, Phys., 80(2000) 143 -154.

[3] C. Rossi, B. Larangot, D. Lagrange, et al. Final characterizations of MEMS-based pyrotechnical microthrusters, J. Sens. and Actu. A, Phys., 121(2005) 508 -514.

[4] F. Niklaus, G.Stemme, J.-Q.Lu, et al. Adhesive wafer bonding, J. J. Appl. Phys. 99(2006) 031101-28.

[5] R. Tong Q Y, Cha G, Gafiteanu R, et al. Low temperature wafer direct bonding, J. Journal of Microelectromechanical Systems, 3(1994) 29-35.

[6] R. Blanco F J, Agirregabiria M, Garcia J, et al. Novel three-dimensional embedded SU-8 microchannels fabricated using a low temperature full wafer adhesive bonding, J. Journal of Micromechanics and Microengineering, 14(2004) 1047-.

[7] C.J. Morris, B.A. Parviz. J. Micro-scale metal contacts for capillary force-driven self-assembly, J. Journal of micromechnical and microengineering, 18(2008) 15022-10.

[8] C.J. Morris, S.A.Stauth, B.A. Parviz. Self-assembly for micro and nano scale packaging: step towards self-packaging, J. IEEE Trans. Adv. Package. 28(2005)600-11.

Key Engineering Materials Vols 645-646 (2015) pp 190-194
© (2015) Trans Tech Publications, Switzerland
doi:10.4028/www.scientific.net/KEM.645-646.190

Submitted: 2014-11-13
Accepted: 2014-12-23

Simulation and Test of Through Silicon Vias Impacted by Large Current Pulse

Ding Xuran[1, a], Wang Yabin[1], Lou Wenzhong[1, b], Liu Fangyi[1]

[1]National Key Laboratory of Electro-mechanics Engineering and Control, School of Mechanical-electronic Engineering, Beijing Institute of Technology, Beijing, China, 100081

[a]xheron9413@163.com, (corresponding author) [b]louwz@bit.edu.cn

Keywords: Micro/Nano systems; TSV; multi-physics; electrostatic discharge

Abstract. The failure mechanism of through silicon vias impacted by large current pulse is reported. A theoretical model has been built to describe how TSVs fails when impacted by large current pulse. The theoretical model is then solved by applying COMSOL Multiphysics and the weak points of the TSV have been pointed out. By applying the large current pulse generating and testing system, an experiment has been done to verify the theoretical model. The results show that although the TSVs may be broken down when impacted by large current pulse, it can still be function by using several TSVs in parallel.

Introduction

The through silicon via (TSV) is the fourth generation of chip packaging, TSV provides advanced vertical inter-connects and system-in-package (SiP) solutions. The TSV has been applied in MEMS devices since it can shorten interconnection length, increase signal speed, reduce power consumption, reduce power dissipation and simplify the assembly of some MEMS devices. Additionally, the TSV can be applied in some MEMS actuators requiring specific assembly position. [1] In some applications, the large current pulse up to several amperes [2] is required to drive the actuator of the device, MEMS igniter like semiconductor bridge (SCB) or metal bridge foil (MBF), for example. Also, the device may be impacted by electrostatic discharge (ESD) [3]. Some theoretical analysis and calculations on mechanical and electrical properties of the TSV have been carried out. [4, 5] However, few researches have been reported on how the TSV works when a large current pulse is applied to it. A copper-filled TSV with a diameter of 50 um and an aspect ratio of 5:1 is introduced in this paper. Fig. 1 shows the TSV chip that we used in this paper. Additionally, this paper also reports the failure mechanisms of the TSV which is impacted by a large current pulse.

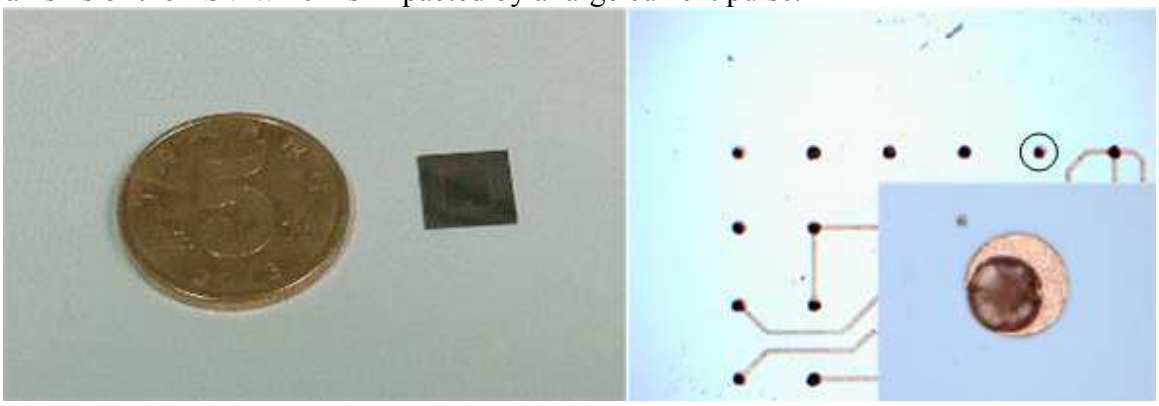


Fig. 1 Copper filled TSV

Firstly, a theoretical model has been built to describe the process how a TSV fails when impacted by a large current pulse. As the mainly failure mechanism of TSV is breakdown of the dielectric isolation layer, according to the state of dielectric isolation layer (SiO_2), the process comes into 5 steps. The phase of SiO_2 changes from solid to gas leading to the potential failure of TSV.
Secondly, a numeral model of the TSV has been analyzed by applying COMSOL Multiphysics to verify the theoretical model.. Then a wafer level experiment has been carried out to verify the

solutions of simulations. A large current pulse is generated by a capacitor discharge circuit and applied to the TSV. By comparing the value of the TSV resistor before and after the current pulse impacting, we can infer if the TSV fails.

Theoretical Model

The copper filled TSV researched in this paper are formed by deep reactive-ion etching (DRIE) and provided by Peking University. The diameter is 50um with an aspect ratio of 5:1. A 1-um thick dielectric isolation layer is deposited covering the vias and the substrate. Then the barrier/adhesion layer is deposited on the dielectric isolation layer. To simplify the theoretical model and reduce the computation, the final model in this paper doesn't include the barrier/adhesion layer. The cross section view of 2D model of such TSVs is illustrated in Fig.2.

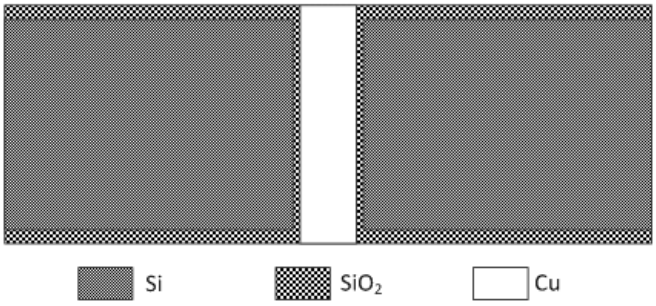


Fig. 2 2D model of TSVs

In MEMS ignitors, the large current pulse comes from a capacitor discharge circuits. So we compute the numeral model under three states: 33uF with the charging voltage 10V, 10uF with the charging voltage 5V and 33uF with the charging voltage 30V. Yet we assumed that the mainly failure mechanism of TSVs impacted by large current pulse results from the breaking down of the dielectric isolation layer.

When the current pulse generated by current pulse generating circuits flows through the TSV, the electro-explosion takes place generating the hot plasma [6-10].

The following sequence describes the operation of the TSV.

(1) The capacitor in current pulse generating circuits is charged to its respective voltages

(2) The trigger between the capacitor and the TSV is closed.

(3) The capacitor discharges resulting in the following.

a) The current density through the TSV effectively heat and vaporize some weak areas of the TSV at the interface between the copper via and the dielectric isolation layer of the TSV.

b) The exploding copper results in plasma burst that, impacted by heat and mechanical shock, the dielectric isolation layer breaks down.

(4) The resulting breakdown of the dielectric isolation layer changes the resistance of TSV.

The failure process can be described in 5 steps. At the very beginning, the dielectric isolation layer is in solid state. Because the heat transfer is not balance, some points are heated rapidly, the weak points will appear. As with the temperature reaches the melting point of the dielectric isolation layer, at some weak points, the SiO_2 begins to melt and becomes into a mixture of solid and liquid. Then the temperature keeps rising, at the weak points the SiO_2 is in liquid state. When the temperature reaches the boiling point of SiO_2, it begins to evaporate. Finally, at the weak points, the SiO_2 becomes into gaseous. The whole process can be described as Eq.1.

$$H=\begin{cases} c_s\left(T-T_0\right),\ T<T_{\mathrm{mp}} \\ c_s\left(T_{mp}-T_0\right)+\dfrac{T-T_{mp}}{T_{tl}-T_{mp}}L_{sl},\ T_{mp}\le T\le T_{tl} \\ c_s\left(T_{mp}-T_0\right)+L_{sl}+c_l\left(T-T_{tl}\right),\ T_{tl}<T<T_{vp} \\ c_s\left(T_{mp}-T_0\right)+L_{sl}+c_l\left(T_{vp}-T_{tl}\right)+\dfrac{T-T_{vp}}{T_{tg}-T_{vp}}L_{\mathrm{lg}},\ T_{vp}\le T\le T_{tg} \\ c_s\left(T_{mp}-T_0\right)+L_{sl}+c_l\left(T_{vp}-T_{tl}\right)+L_{\mathrm{lg}}+W,\ T_{tg}<T \end{cases} \quad (1)$$

where H is enthalpy of SiO_2, c_s is the heat capacity of solid SiO_2, T_{mp} is the melting point of SiO_2, T_{tl} is the temperature where the SiO_2 is totally liquid, c_l is the heat capacity of liquid SiO_2, T_{vp} is the boiling point of SiO_2, T_g is the temperature where the SiO_2 is in totally gaseous state, L_{sl} is solid-liquid latent heat, L_{lg} is liquid-gaseous latent heat.

Simulation based on multi-physics of TSVs impacted by large current pulse

By applying COMSOL Multiphysics, the weak points of TSV have been found, and the temperature field of the TSV when impacted by a large current pulse is illustrated. Fig.3 shows the weak points of the TSV.

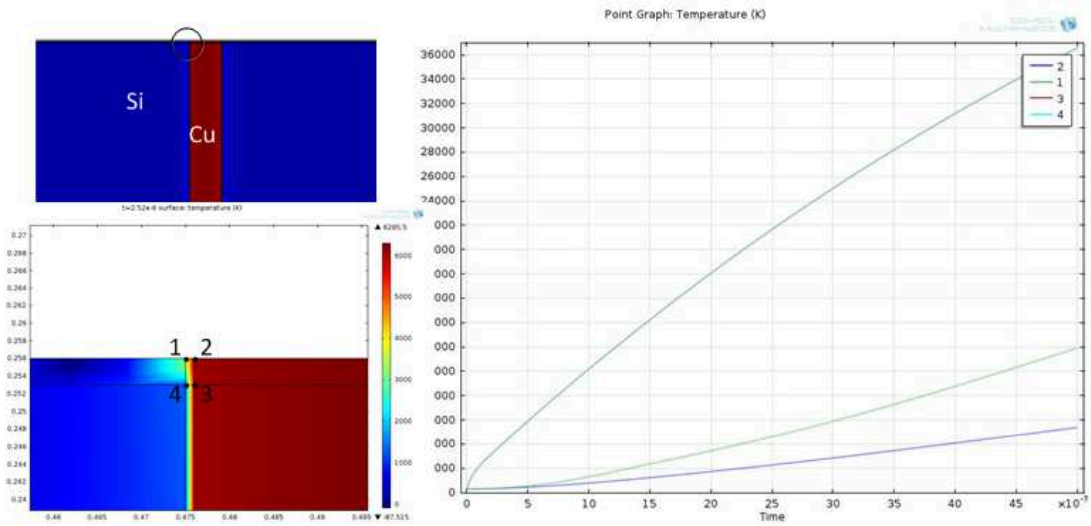


Fig. 3 Weak points of TSV impacted by large current pulse

The discharging condition of Fig. 3 is 33uF with the charging voltage 10V. The weak point is point number 2. At the weak point the temperature rises more rapidly than other points. Fig. 4 shows the temperature-time curve of the weak point under three conditions.

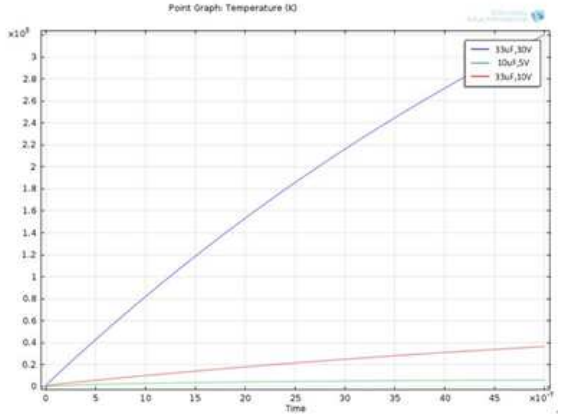


Fig. 4 Temperature-time curve of the weak point under three conditions

The results show that areas of the dielectric isolation layer that attached the TSV will be broken down under all these three conditions. The SiO_2 reaches its boiling point at 0.012us (33uF, 30V), 0.098us (33uF, 10V), 0.57us (10uF, 5V), respectively.

Experimental results

Fig. 5 shows the test system for wafer level testing on micro/nano systems.

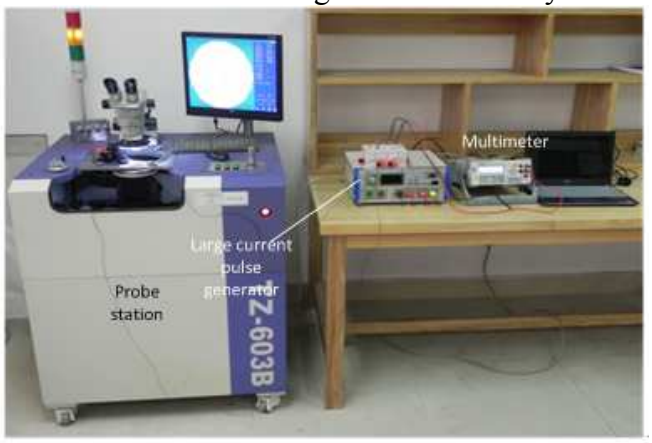
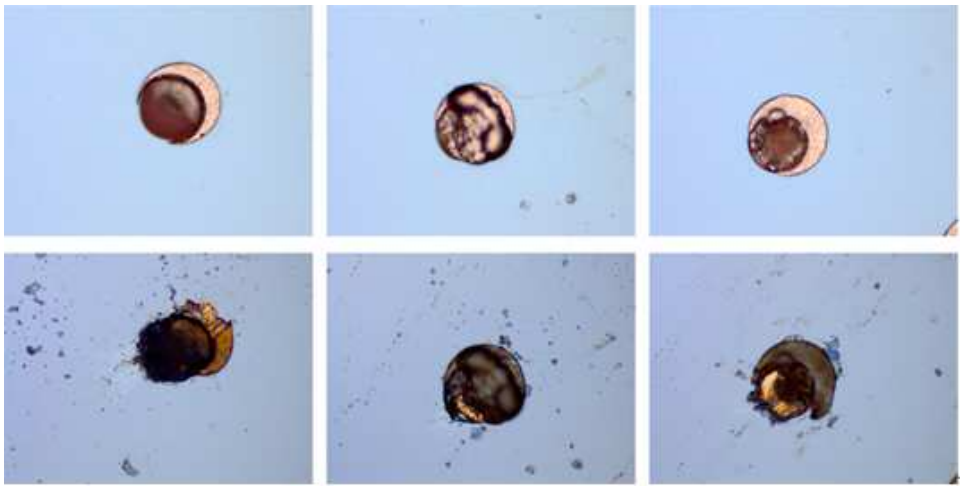


Fig. 5 Test system for wafer level testing on micro/nano systems

The large current pulse generator can generate large current pulse by a capacitor discharge circuits. Fig. 6 shows the TSV before and after the large current pulse applied to it. The discharging condition is the same as the simulation.



33uF, 30V 33uF, 10V 10uF, 5V

Fig. 6 TSV before (top) and after(down) the impact

By mesuring the resistance of the TSV before and after the test, it is confirmed that the TSV have been broken down.

Shinning sparks have been observed and the noise have also been heard when the large current pulse flows though TSVs. Thus, the TSVs may generate hot plasma when impacted. Fig. 6 also shows the broken down areas the same with the simulation results.

Summary

This paper introduces a kind of failure mechanisms of the TSV which is impacted by a large current pulse. Both simulation and experiment results show the weak point appears at the SiO_2 surface between the copper via and the dielectric isolation layer. One single TSV may fail under the discharging conditions that this paper have reported above, however, by using several TSVs in parallel connection simultaneously may help the TSVs to survive from such a harsh discharging condition.

Acknowledgement

The research is supported and funded by National Project (9140A05050313BQ1014) and (9140C360602120C36138).

References

[1] Ogawa S, Yuasa T, Fujii Y, et al. Millimeter-wave transmission line with through-silicon via for RF-MEMS devices, IEICE Electronics Express, 2013.

[2] Zhao Y, Lou W, Li D. Study of a novel bi-stable and easy integrated MEMS ETBS. 7th IEEE International Conference on Nano/Micro Engineered and Molecular Systems (NEMS), 2012, pp. 257-260.

[3] Yoon S W, Yang D W, Koo J H, et al. 3D TSV processes and its assembly/packaging technology. 3D System Integration, 2009, pp: 1-5.

[4] Gong X, Chen J, Lee J H. FEM Simulation of the Thermo-Mechanical Behavior of TSV 3D MEMS Structure. Key Engineering Materials, 2013, pp: 108-113.

[5] Katti G, Stucchi M, De Meyer K, et al. Electrical modeling and characterization of through silicon via for three-dimensional ICs. IEEE Transactions on Electron Devices, 2010, pp: 256-262.

[6] L.E. Hollander Jr., "Semiconductor explosive igniter," US Patent 3366055, Jan. 30, 1969.

[7] D.A. Benson, M.E. Larsen, A.M. Renfund, W.M. Trott, and R.W. Bickes Jr., "Semiconductor bridge: A plasma generator for the ignition of explosives" Journal of Applied Physics, vol. 62, no. 5, pp. 1622-1632, May. 1987.

[8] B.A.M. Tovar, "Electrothermal transients in highly doped phosphorous diffused silicon-on-sapphire semiconductor bridge under high current density conditions," PhD dissertation, University of New Mexico, 1993.

[9] J. U. Kim, C. O. Park, M. I. Park, S.H. Kim, and J. B. Lee, "Characteristics of semiconductor bridge (SCB) plasma generated in a micro-electro-mechanical system (MEMS)," Physics letters A, vol. 305, no. 6, pp. 413-418, 2002.

[10] T. A. Baginski, and K. A. Thomas, "A Robust One-Shot Switch for High Power Pulse Applications," NDIA 52th Annual Fuze Conference, Sparks, NV. 2008.

Key Engineering Materials Vols 645-646 (2015) pp 195-200
© (2015) Trans Tech Publications, Switzerland
doi:10.4028/www.scientific.net/KEM.645-646.195

Submitted: 2014-11-13
Accepted: 2014-12-23

Preparation of Strongly Hydrophobic Film with Large Area and Flexibility Based on Micro Fabrication

Yi-bo Zeng[a], Ting-ting Wang , Jian-yan Wang and Hang Guo [b*]

Pen-Tung Sah Institute of Micro-Nano Science and Technology of Xiamen University, China

[a]zyb2005@xmu.edu.cn, [b*] hangguo@xmu.edu.cn (corresponding author)

Keywords: Micro fabrication Hydrophobic Large area Flexible film Micro molding

Abstract. In order to gain strongly hydrophobic film with large area and flexibility conveniently and effectively, how to prepare film with combination of technologies including micro fabrication, chemical grafting and micro molding is discussed. Firstly, micro channel arrays that the width is 5μm on the silicon wafer are prepared by micro fabrication. Then after spraying PVDF (Polyvinylidene Fluoride) lotion and pouring PDMS (Polydimethylsiloxane) glue solution onto the silicon wafer as the mould successively, the mixture need to be precured, which constructs rough structures in micro and nano scale on the low surface energy film. Finally chemical grafting for film is carried out under the condition of O_2 and 130℃ so that the modification layer easy to adhesive on the boundary between PVDF and PDMS can be formed. Through the above technical routes, the strongly hydrophobic film that the general contact angle exceeds above 145º, the area is 180mm×64mm, the thickness is 0.9mm and the composite layer is firmly combined is gained. Compared to other hydrophobic materials the film is available in large area and has an advantage of flexibility. Meanwhile, the way that the film prepared by micro molding and in virtue of the silicon wafer with micro channel arrays as the mould contributes to large scale production.

1. Introduction

Strongly hydrophobic surface is defined as surface contact angle exceeding 140º. Lotus leaf surface on which water contact angle is 161.0±2.7° has strongly hydrophobic performance. Self-cleaning effect on the surface is produced by strongly hydrophobic performance. Therefore water drops can be easily rolled down the surface to remove automatically dirty matters from the surface. This performance is so-called the "lotus leaf effect". Based on this effect, strongly hydrophobic surface can be obtained through lower surface energy materials with reasonable surface roughness in micro and nano scale. Similar hydrophobic films have a broad application prospect on anti-icing of cable [1, 2], self-cleaning of fabric [3, 4] and anti-sticking layer of micro machine [5, 6].

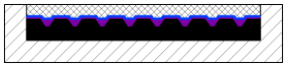
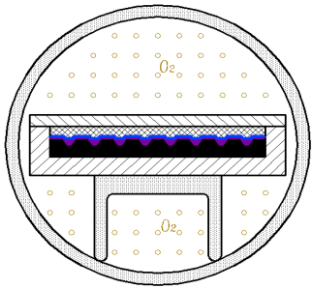
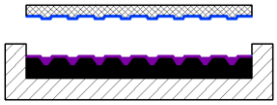
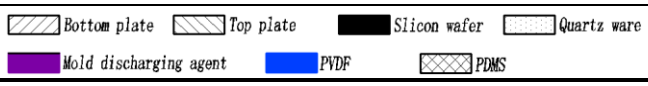
There are two ways to fabricate strongly hydrophobic materials. The one is that the rough structures in micro and nano scale are constructed on the lower energy surface material. For instance, super hydrophobic film of PDMS with nano pattern holes or poles is prepared by nanoimprint, which contact angle exceeds 150º [7, 8]. And the other way is to decorate substrate of rough structures in micro and nano scale with low surface energy material. For example, nano porous aluminum by anodic oxidation is sputtered with C_4F_6, then forming strongly hydrophobic materials of contact angle exceeding 150º [9].

Based on the above two prepartation thesis combined with micro fabrication processes, there are abundant in related prepartion ways of strongly hydrophobic material, especially in small area. However there are some technical issues whether or not strongly hydrophobic materials could be large area employed, available for industrial products of different shapes and materials, and fabrication processes could be suitable for large scale production are to be further researched and resolved. Therefore in this paper micro fabrication as the base combined with precesion maching, micro molding and chemical grafting is adopted to try to achieve strongly hydrophobic film with large area and flexiblity avaible for industrial products. In addtion, related fabrication technologies are expected to be suitable for large scale production.

2. Preparation process of film

Preparation of hydrophobic flexible film is based on the thesis that rough structures in micro and nano scale are constructed on the lower energy surface material. Detail fabrication processes are shown in Tab.1. Firstly, micro channel arrays on the silicon wafer are prepared by micro fabrication, and the same three pieces of diced wafer are assembled into the bottom plate of mould. Secondly, after spraying PVDF lotion and pouring PDMS glue solution onto the silicon wafers as the mould successively, the mixture need to be precured. Through micro molding, micro channel arrays are transferred from silicon to PVDF surface so as to construct rough structures in micro and nano scale on the low surface energy film. Finally chemical grafting for the mixture is carried out under the condition of O_2 and 130℃ so that the modification layer easy to adhesive on the boundary between PVDF and PDMS can be formed. Through the above technical routes hydrophobic flexible film which the area is 180mm×64mm is gained.

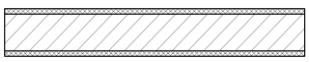
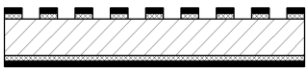
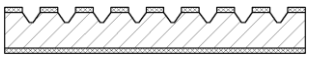
Tab.1 Preparation of hydrophobic flexible film

No.	Graphic	Illustration
1		Micro channel arrays on the silicon wafer are prepared by micro fabrication
2		The three pieces of dicied wafer after are assembled into bottom plate. Then after spraying PVDF lotion and pouring PDMS glue solution successively, the mixture need to be precured
3		Chemical grafting at the condition of O_2 and 130℃
4		Extraction from the mould
Remark		

3. Micro fabrication of silicon wafer with micro channel arrays

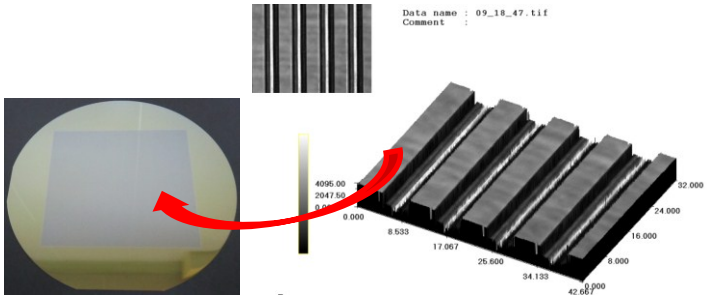
The way that the film is prepared by micro molding with micro channel arrays silicon wafer as the mould not only aims to constructing rough structures in micro and nano scale on the low surface energy materials but also contributes to large scale production because of the micro molding advantages including high efficiency, high precision and low cost.

Tab.2 Preparation of silicon wafer with micro channel arrays

No.	Graphic	Illustration
1		SiO_2 that the thickness is 1μm is deposited by thermal oxidation
2		Lithography for micro channel arrays that the separation distance and width are all 5μm, and SiO_2 etching
3		Removal of photoresist, V-shape micro channel arrays that the depth is 3.5μm are made by anisotropy wet etching
4		Removal of SiO_2
Remark		

The V-shape micro channel arrays that the seperation distance is 5μm, the width is 5μm, the lengthen is 60mm, the depth is 3.5μm are made on the P<100> silicon wafer that the diameter is 100mm with micro fabrication including oxidation, lithography, and anisotropy wet etching, detail fabrication processes and final morphology of the wafer shown in Tab.2 and Fig.1. After that, with wire-electrode cutting the bottom and top of plate of the mould are made for assembly with the same three pieces of diced wafer that the outline dimension is 60mm×64mm, shown in Fig.2. The integral mould that is composite of wafers

and plates is available for filling with the low surface energy materials and micro molding for hydrophobic film. In the mould, the size of cavity for filling is 180mm×64mm×0.9mm.



(a)Silicon wafer (b)Micro channel arrays on silicon wafer

Fig.1 Silicon wafer with micro channel arrays

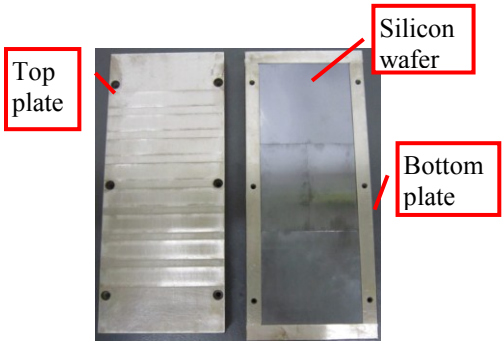


Fig.2 The diced wafers are assembled into the bottom plate

4. Selection for the materials of composite layer

Macromolecule polymer should be selected for the film to be flexible. Compared to rigid materials including Si, Al and Cu, macromolecule polymer has excellent elasticity. Hence rough structures in micro and nano scale are to be constructed in polymer as the base.

In the field of micro fabrication, PDMS is a new kind of macromolecule polymer, and widely used in micro molding. PDMS glue solution consists of base and curing agent in liquid state. After the two ones uniformly mixed, mixture need to be cured with curing temperature ranging from 80℃～120℃. Eventually the mixture could be changed from glue to block. PDMS has certain merits including low cost, good safety performance and high chemical stability, and it's simple and convenient to shape micro channel arrays on PDMS base with pouring practice and micro molding. Fig.3 shows with micro molding micro channel arrays are transferred from silicon base to PDMS base. Fig.4 illustrates that contact angle of PDMS surface with micro channel arrays only reaches about 120°. Compared to intrinsic contact angle (88°～90°), the one with micro channel arrays is significantly enhanced; however there is some distance for PDMS substrate with micro channel arrays to strongly hydrophobic performance。

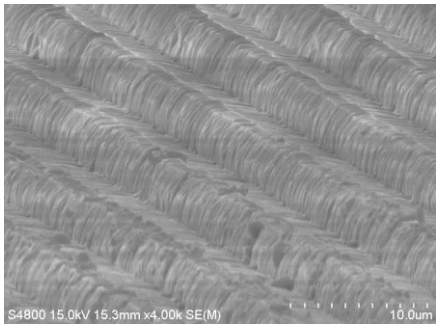
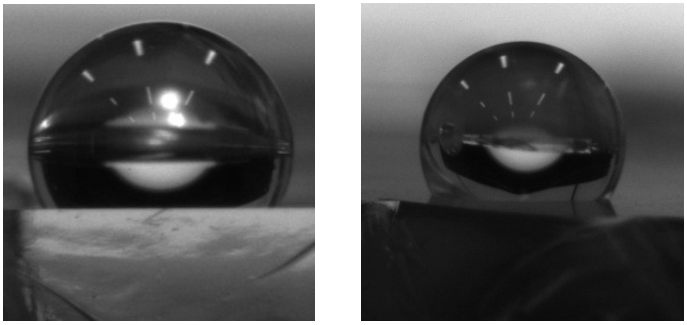


Fig.3 Micro channel arrays are constructed on PDMS substrate



(a)Smooth surface, 88°～90° (b)Micro channel arrays, 118°～121°

Fig.4 The test of contact angle on PDMS substrate

PVDF is also commonly used macromolecule polymer in the field of mciro fabrication which intrinsic contact angle is 108°～110°, and belong to low surface energy material. Molecular formula shown in Fig.5. For pouring practice and micro molding, solid particls of PVDF are heated to high temperature exceeding over 420℃ in the virtue of injection molding machine. By contrast, PVDF lotion (Kynar Aquatec® PVDF) can be completely cured at the temperature of 130℃ for 10mins to meet pouring practice, which is compatiable with curing temperature of PDMS. However PVDF lotion can be only sprayed on existing substrate to form hydrophobic coating. Once the thickness of cured PVDF coating exceeds 100μm, there exists full of cracks and

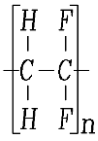


Fig.5 Molecular formula of PVDF

fibrosis. Therefore, it's unavailable for PVDF as only one substrate to gain hydrophobic flexible film with a certain of thickness and mechnical strengthen.

In consideration of characteristics of PDMS and PVDF, the composite layer between PVDF lotion and PDMS substrate is selected and blended to form the hydrophobic flexible film. Through blending of the two ones, on the one hand rough structures in micro and nano scale are constructed on the PVDF of low surface energy substrate to gain strongly hydrophobic performance, on the other hand, based on PDMS substrate as support layer that the thickness is over 800μm, make sure that the film has a certain of mechanical strengthen.

5. Chemical grafting

5.1 Pretreatment

It is necessary for blending lotion to be pretreatment. Fig.7 shows different surface morphology of film with different pretreatment. The experiment results show that in order to gain the strongly hydrophobic film that has favorable apparent surface and mechanical strengthen, it is indispensable for blending lotion to be vacuum and precure. In the process of spraying glue, there exist compressed air bubbles in glue. Bubbles could be removed from glue with vacuum which avoids thermal expansion of bubbles to destroy integral apparent surface of film and reduce mechanical strengthen of one.



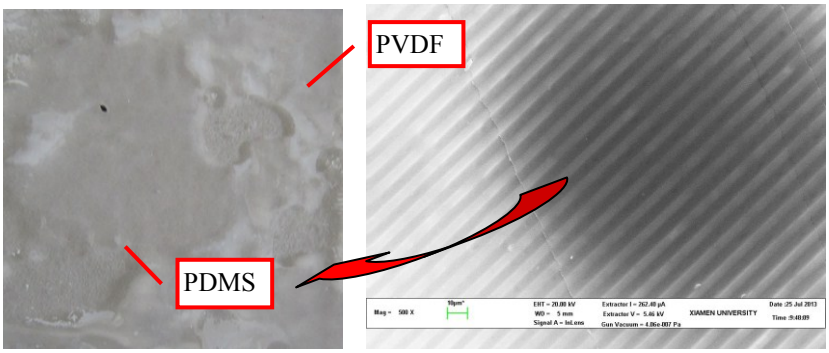
(a)Non vacuum and non precure (b)Vacuum and non precure (c)Vacuum and precure

Fig.7 Different surface morphology of film with different pretreatment

After precured PDMS layer keeps soft state at the temperature of 60℃ for 15mins, which prevents some bubbles of modification air for chemical grafting from entering PDMS layer and avoid air pores left in the film surface, thus make sure that modification air could be transported to the boundary between PDMS and PVDF to be chemical grafting. Fig.7(c) shows a large amount of air pores existing in the film surface could be effectively reduced by vacuum and precure ahead of chemical grafting, thereby to improve adhesive performance between PVDF and PDMS and enhance mechanical strengthen of film.

5.2 Chemical grafting

Macromolecule polymer containing fluorine has some certain characteristics that consist of highly inert surface, low surface energy and critical surface tension ranging from 31～34×10^{-5}N/cm. After blending lotion is fully cured, it is very difficult for PVDF and PDMS to be complete fusion because of low surface energy of PVDF. Without chemical grafting there is only littler PVDF adhesion on PDMS substrate after film has been already cured, as shown in Fig.8. Therefore, chemical grafting needs to be adopted, in an attempt to



(a)Bad adhesion performance (b)Micro channels residues in PVDF surface

Fig.8 The only littler PVDF adhesion on PDMS substrate

improve polarity of boundary between PVDF and PDMS and to enhance the adhesive capacity of the two kinds of macromolecule polymer.

The chemical grafting is employed to introduce hydrophilic groups including C-O, C-O-H, C-O-Si and so on onto the boundary when precured blending mixture is placed at the condition of O_2 and 130℃. Consequently, the modification layer easy to adhesive on the boundary between PVDF and PDMS can be formed in virtue of gas thermal oxidation. Fig.9 presents that after the film has already been chemical grafting, the adhesive capacity of composite layer accompanied by rougher PVDF surface with micro channel arrays and larger adhesive superficial area is significantly enhanced.

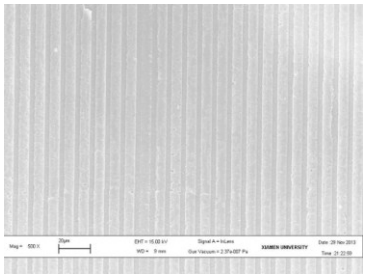


Fig.9 PVDF with micro channel arrays after chemical

6. Experiment results

The processes parameters of film preparation are shown in Tab.3, and the film that has not yet extracted from the mould in shown Fig.10. Fig.11 illustrates the extracted flexible film that the area is 180mm×64mm, the thickness is 0.9mm and the composite layer is firmly combined. With micro molding, the micro channel arrays are transferred to PVDF surface, and the hydrophobic flexible film that general contact angle exceeds above 145º is gained, which aims at strongly hydrophobic performance.

Tab3. Process parameters of fabrication for film

NO.	Process	Parameters
1	Vaccumm	1h
2	Pretreatment	60℃，0.5h
3	Chemical grafting	135℃，0.5h，O_2 flow rate of 10sscm

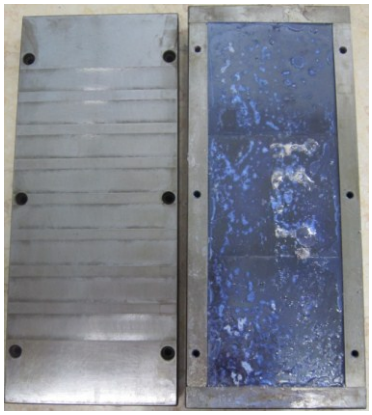
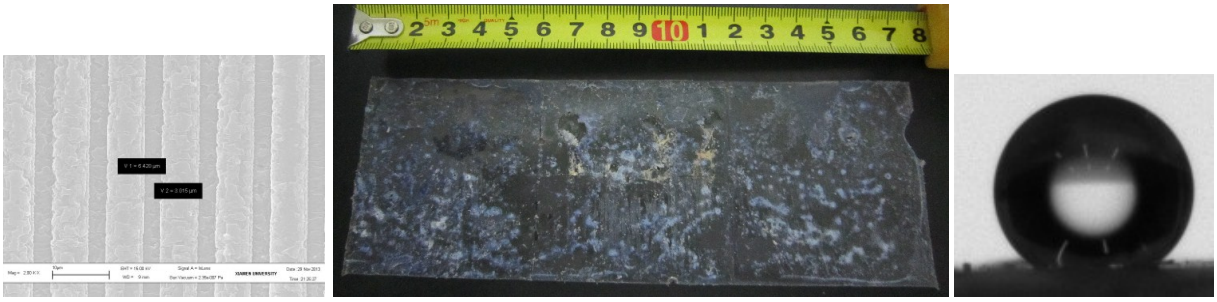


Fig.10 Film that has not yet extracted from the mould



(a)Micro channel arrays on the film (b) Film (c)Contact angle, 145 º

Fig.11 Strongly hydrophobic film with large area and flexibility

Cassie-Baxter equation [10] is usually adopted to analyze and determine wetting characteristic of surface with structure in micro and nano scale, as shown equation (1).

$$\cos\theta^c = f\cos\theta - (1-f) \tag{1}$$

In the equation (1), f stands for solid phase fraction of surface, θ^c is apparent contact angle, and θ is Young's contact angle. Cassie-Baxter equation has shown how a rougher surface can influence the apparent contact angle at the boundary between the liquid and the surface. According to the equation, for hydrophobic materials with fluorine, the rougher surface, the closer to zero for f, and the closer to 180° for θ^c, thus surface presents strongly hydrophobic.

According to micro morphology of film surface, shown in Fig. 11(a), θ^c is calculated to be 140.5º, relevant parameters illustrated on Tab.4. The side wall of micro channel arrays on the silicon wafer prepared by anisotropy wet etching is not yet

Tab.4 Theoretical contact angle calculated by Cassie-Baxter equation

Parameter	Value
f	0.33
θ	PVDF，108 º
θ^c	140.5 º

smooth surface, but orange peel surface, shown in Fig.(12). PVDF surface becomes rougher because of transfer of orange peel surface and chemical grafting, therefore, actual measurement of contact angle is higher than theoretical calculation of the one.

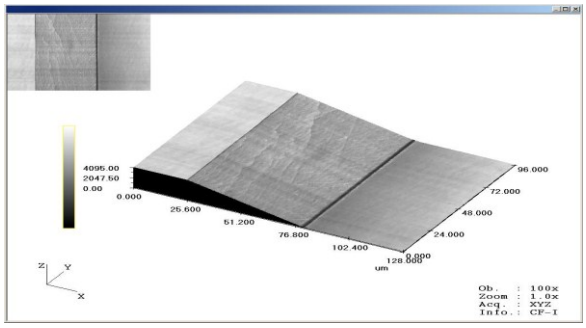


Fig.12 Side wall of micro channel on slicon wafer, Rq value for surface roughness of 0.169μm

7. Summary

Compared to other strongly hydrophobic materials the strongly hydrophobic film prepared by combination of technologies including micro fabrication, chemical grafting and micro molding is available in large area and has an advantage of flexibility. Meanwhile, the way that the film prepared by micro molding and in virtue of the silicon wafer with micro channel arrays as the mould contributes to large scale production. Because of good flexibility of film, film with gum will be affixed to the substrate of any shape. The process parameters of preparation for film will be further optimized in the follow-up experiment to enhance the mechanical strengthen of film, which will satisfy performance requirement of certain industrial products finally.

Acknowledgements

This work is financially supported by the New Century Talent Support Plan of the Ministry of Education of China (2007NCET-07-0723)，the Scientific Research and Development Program of City of Xiamen (3502Z20124036) and Aviation Science Foundation of China (2008ZH68002).

References

[1] L. L. Cao, A. K. Jones, V. K. Sikka, et al., Anti-Icing Superhydrophobic Coatings, American Chemical Society. 25 (2000) 12444-12448.
[2] S. Farhadi, M. Farzaneh, S.A. Kulinich, Anti-icing performance of superhydrophobic surfaces, American Chemical Society. 257 (2011) 6264-6269.
[3] I. P. Parkin and R. G. Palgrave, Self-cleaning coatings, Journal of Materials Chemistry. 15 (2005) 1689-1695.
[4] X. Jiang, X. Tian, J. Gu, et al., Cotton fabric coated with nano TiO_2-acrylate copolymer for photocatalytic self-cleaning by in-situ suspension polymerization, Applied Surface Science. 257 (2011) 8451-8456.
[5] Z. H. Yang, C. Y. Chiu, J. T. Yang, et al., Investigation and application of an ultrahydrophobic hybrid-structured surface with anti-sticking character, Journal of Micromechanics and Microengineering. 19 (2009) 1-11.
[6] M. Nosonovsky, B. Bhushan, Superhydrophobic surfaces and emerging applications: Non-adhesion, energy, green engineering, Current Opinion in Colloid & Interface Science. 14 (2009) 270-280.
[7] M. Kim, K. Kim, N. Y. Lee, et al.. A simple fabrication route to a highly transparent super-hydrophobic surface with a poly(dimethylsiloxane) coated flexible mold, Chemical Communications, 22 (2007) 2237-2239
[8] J. Hwang, S.H. Hong, H. Lee, Mimicking the Nanostructure of Bamboo Leaves (Backside) for Hydrophobicity Using Polydimethylsiloxane Moulding and Nano-Imprint Lithography Journal of Nanoscience and Nanotechnology, 9 (2009) 3644-3647
[9] D. A. Brevnov, M. J. Barela, M. J. Brooks, et al. Fabrication of Anisotropic Super Hydrophobic Hydrophilic Nanoporous Membranes by Plasma Polymerization of C_4F_8 on Anodic Aluminum Oxide, Journal of The Electrochemical Society, 151(2004) 484-489
[10] A. B. D. Cassie, S. Baxter, Wettability of porous surfaces, Transactions of the Faraday Society, 40(1944) 546-551

Key Engineering Materials Vols 645-646 (2015) pp 201-207
© (2015) Trans Tech Publications, Switzerland
doi:10.4028/www.scientific.net/KEM.645-646.201

Submitted: 2014-11-14
Accepted: 2014-12-23

Preparation of TiO_2 Nano-film by Anodic Oxidation Method and Its Hydrophobic Modification

Feng Bin Liu[1,a]; Bao Jing[2,b,*]

[1, 2]College of Mechanical and Electric Engineering, North China University of Technology，Beijing, 100144, China

[a:] fbliu@ncut.edu.cn

[b:] huanmie1002@126.com

Key words: TiO_2 nano-tube; anodic oxidation; hydrophobic nano-film

Abstract: TiO_2 nano-films with different morphology were prepared by anodic oxidation method by changing the electrolyte concentration, anodization voltage, anodization time and anode-cathode distance. The surface of the nano-film was modified by a kind of solution which consists of lauric acid and hexadecane. And this article find a proper electrolytic time, a medium voltage, a proper anode-cathode distance and a lower electrolyte concentration are beneficial to the hydrophobicity of the nano-film.

Introduction

Hydrophobic surface has a very broad application in various fields, such as anti-corrosion, anti-pollution, anti-ice, bacterial adhesion reduction and so on[1]. It is known that the hydrophobic surface could be prepared by using two methods: one is to build the rough structure on the surface of the hydrophobic materials; the other is to modify materials with low surface energy on the rough surface[2].

TiO_2 nano-tube arrays have a rough surface which is very suitable for hydrophobic modification. Besides that the tubular structure is also beneficial to the improvement of the hydrophobicity of the modified surface[3]. Compared with other methods, anodic oxidation method is simple to operate, cost-effective. TiO_2 nano-tube arrays can be prepared directly on the surface of titanium or titanium alloy，and are easy to recycle[4]. Previous literatures investigated the effects of preparation parameters on the surface morphologies of the TiO2 nano-tube arrays by using anodic oxidation method. It is found that the surface structures are significantly dependent on the electrolyte concentration, the voltage, the oxidation time and the anode-cathode distance. Concerning the surface hydrophobicity of the TiO2 nano-tube arrays, various hydrophobic coatings were achieved by means of surface chemical modification [5,6]. However the fluoroalkyl silanes as the modifier is widely used, while the study on the lauric acid as surface modifier for TiO_2 nano-tube arrays is few. In addition, to our knowledge, the study on the detailed effects of the preparation parameters on the hydrophobic property of TiO_2 nano-film is rarely reported.

In this paper, TiO_2 nano-films with various morphologies were prepared in anodic oxidation method on the surface of titanium. The morphology of the nono-films was detected by scanning electron microscopy (SEM). Lauric acid was used as hydrophobic modifier on the surface of the TiO_2 nano-film. The hydrophobicity of the film was tested with contact angle measurement instrument. Finally, the effects of the preparation parameters on the hydrophobic property of TiO_2 nano-film are discussed.

Experimental

The titanium foils(purity 99.5%, thickness 0.5cm)ware polished in sequence by 400#,800#,1500#,2000# sandpaper till the surfaces of the foils are free of scratches. Then the foils were ultrasonicaly cleaned with acetone and deionized water repeatedly. The anodic oxidation was performed at a constant voltage in a HF solution, a graphite electrode was used as cathode and the foils were used as anode. Experiments were conducted in a anodic oxidation tank. Many scholars, at home or abroad, have studied how the electrolyte concentration, the voltage, the oxidation time and the anode-cathode distance effect the length, the diameter, the thickness of the TiO_2 nano-tube[7-10]. By adjusting technological conditions, the length, diameter and wall thickness of TiO_2 nanotube array can be controlled. Detailed preparation parameters of TiO_2 nanotube arrays in anodic oxidation method were listed in Table 1.

Table 1 The No. of samples and experiment parameter

	No. of samples	Electrolyte concentration	Anodization voltage	Anode-cathode distance	Anodization time
Ⅰ	1-1	1%	20V	5cm	1h
	1-2	0.75%	20V	5cm	1h
	1-3	0.25%	20V	5cm	1h
Ⅱ	2-1	0.5%	10V	5cm	1h
	2-2	0.5%	25V	5cm	1h
	2-3	0.5%	30V	5cm	1h
Ⅲ	3-1	0.5%	20V	5cm	0.5h
	3-2	0.5%	20V	5cm	1.5h
	3-3	0.5%	20V	5cm	2h
Ⅳ	4-1	0.5%	20V	3cm	1h
	4-2	0.5%	20V	10cm	1h
	4-3	0.5%	20V	12cm	1h

The prepared TiO_2 nano-films were immersed in a mixture of lauric acid and hexadecane (volume ratio:1:100) at 25 ℃ for 24 hours. The lauric acid is the solute, the hexadecane is the solvent and the concentration of the mixture solution is 5×10^{-3}mol/L. Then the TiO_2 foils were ultrasonically cleaned and stored in the air.

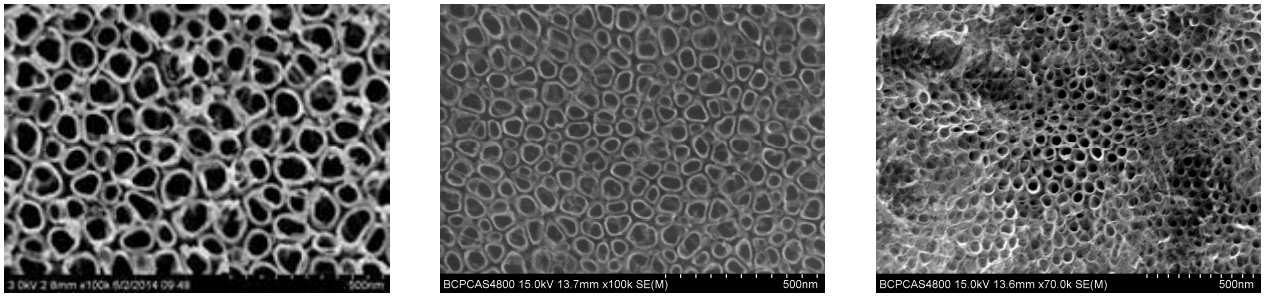
The microstructure and the morphology of the foils before and after modifying were observed with SEM, the elementary composition of the foils before and after modifying were analyzed with EDS, and the contact angle was measured when a water drop on the surface of the foil with optical contact angle measuring device.

Results and discussion

1 Preparation and characterization of the TiO_2 nano-tube arrays

Fig. 1 (a), (b) and (c) show the images of the prepared TiO2 nano-tube arrays under the HF elecytrolyte of 1%, 0.75% and 0.25%, respectively. It indicated that the diameter of the nano-tube will become smaller and smaller as the electrolyte concentration decreases. The results are quite consistent with the literature [11] and [12], which can be attributed to the corrosion pits appeared on the substate surface at the early stage of the anodic oxidation. The nano-tubes grow at the edge of

the pit. The corrosion pit becomes bigger with the increase of the HF concentration, which leads to the enlargement of the nano-tube diameter.

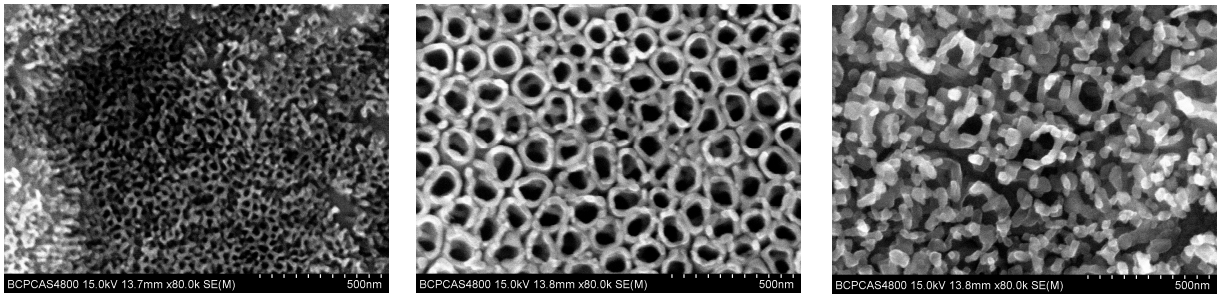


(a) (b) (c)

Fig. 1 SEM top-view images of the foil(the concentration of HF:(a)1%,(b)0.75% and(c)0.25%)

Notes that the shape of the nano-tube becomes irregular and disorderly when the concentration of the electrolyte is too low. The nano-tube arrays obtained under the concentration of 0.25% exhibit high surface roughness, as revealed in Fig. 1. It is known that the growth of the nano-tube is associated with H^+ and F^-[13]. When the concentration of HF is too low, the nano-tube would not appear or form at some location where lack of H^+ and F^-. While the concentration of the electrolyte arrives at 0.75% and 1%, the nano-tube arrays are more regular.

The images of the prepared TiO2 nano-tube arrays under the anodic voltage of 10V, 25V and 30V are shown in Fig 2 (a), (b) and (c), respectively.

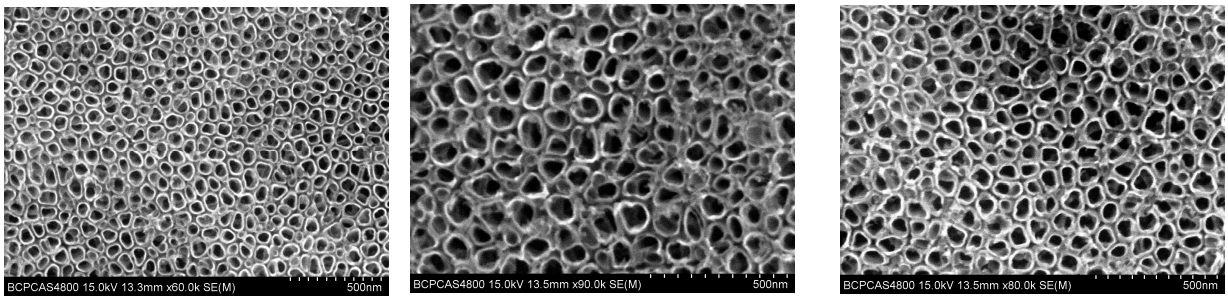


(a) (b) (c)

Fig. 2 SEM top-view images of the foil(the anodization voltage:(a)10V,(b) 25V and (c) 30V)

When the anodization voltage is 10V, many nano-microporous form on the surface of the foil but not nano-tube arrays. The sample surface is very rough as shown in Fig. 2 (a). When the anodization voltage increases to 30V, the tubular structure is destroyed and there are many incomplete nano-tubes with different heights on the surface of the sample (Fig. 2 (c)). In contrast there would be highly ordered nano-tube arrays formed on the sample surface when the anodization voltage is 25V, as shown in Fig. 2 (b). Li Peng et al[14] prepared TiO_2 nano-tube arrays in HF at different voltage from 20V to 25V. Thus it can be seen that the anodic oxidation voltage is an important factor influence the formation and growth of the TiO_2 nano-tube.

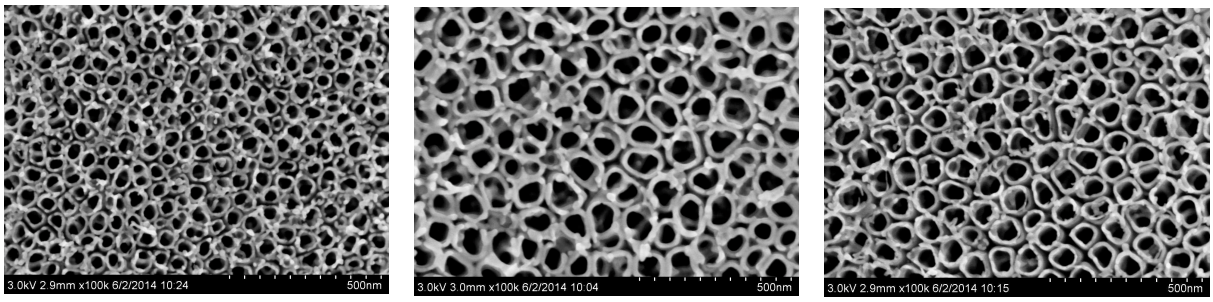
When the voltage is too low, the electric field intensity is also very low, the TiO_2 nano-tube would be dissolved before the tubular structure grows up[15]. Therefore, there appear many nano-microporous on the sample surface. The dissolution rate of the TiO_2 nano-tubes will be in line with the growth rate as the increase of the anodization voltage, there would form highly ordered nano-tube arrays on the sample surface. However, if the voltage increases too high, the wall of the grown TiO_2 nano-tube would dissolve for the huge electric field intensity. Then the tubular structure is destroyed and many incomplete nano-tubes with different height appear.



(a) (b) (c)

Fig. 3 SEM top-view images of the foils (the anodization time:(a)0.5h,(b)1.5h and (c)2h)

Fig. 3 (a) ,(b) and (c) show the top-view of the samples prepared during different time. It revealed that the surface topography of the samples is insensitive to the anodization time. All the three sample surfaces exhibit highly ordered nano-tube arrays during different anodization times when the anodization voltage, the concentration of the electrolyte and the anode-cathode distance are all appropriate.



(a) (b) (c)

Fig. 4 SEM top-view images of the foil(the anode-cathode distance:j3cm,k10cm and n12cm)

When the anode-cathode distance is too small, the diameter of the nano-tube is small and irregular, the surface of the sample is a little rougher relatively. When the anode-cathode distance is 10cm and 12cm, the morphology of the surface of the samples are similar. High ordered nano-tube arrays will be formed on the surface of the foil.

2 Surface modification of the TiO_2 nano-film

Chemical decoration with low surface energy on the rough surface is a better way to prepare a hydrophobic surface, which proven by many experiments[7]. Lauric acid(chemically pure) ws used to modify the surface of TiO_2 nano-film in this article and the hexadecane was used as solvent. When the samples are chemically decorated by lauric acid, the surface morphologies are kept intact. However, the surface components alter after chemical decoration, which is reflected by EDS results (Fig. 5). Compared with that of the original sample surface, the oxygen content increases slightly and the carbon characteristic peak for the decorated sample surface. It followed that the modification layer contains oxygen and carbon, which originate from lauric acid.

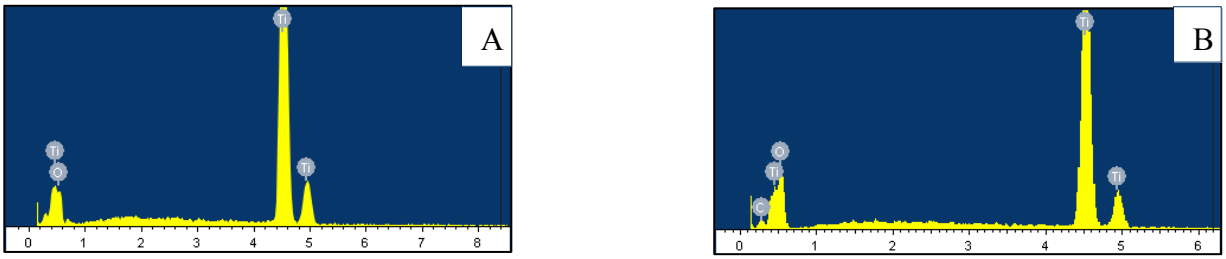


Fig. 5 The EDS of 1-3 before(A) and after(B) modified

The water contact angles of all the samples are listed in Table 2. It can be found from the first 3 sets of data, the hydrophobicity will be much better while the sample has a much rougher surface. Li Songmei find the rougher surface would have a better hydrophobicity too [16].From 2-1 to 2-3, it can be seen that the surface with tubular structure will have a better hydrophobicity. From the last 6 sets of data, it can be found that the surface with similar morphology may have the similar contact angle with water.

Sample 2-1 has the worst hydrophobicity in all these samples. There is few tubular structure on the surface of sample 2-1, while others are all covered with nano-tubes. Therefore, the conclusion can be drown that the tubular structure beneficial to the hydrophobicity. Sample 1-3 both has the roughest surface and the biggest water contact angle, a conclusion can be reached that the roughness has a great influence on the hydrophobicity. The water contact angles of other samples are similar, this shows that the hydorphobicity almost has nothing to do with the nano-tube diameter and the regularity. Therefore, a surface with a better hydrophobicity can be prepared under the appropriate process parameters. It includes a proper electrolytic time, a medium voltage, a proper anode-cathode distance and a lower electrolyte concentration.

Table 2 The contact angle with water of each sample

No.	1-1	1-2	1-3	2-1	2-2	2-3	3-1	3-2	3-3	4-1	4-2	4-3
Contact angle	136.9	130.5	142.1°	108.1°	129.3°	121.9°	125.1°	129.2°	137.5°	127.5°	126.1°	124.6°

The biggest contact angle with water is the sample 1-3 which is detected by contact angle meter. The biggest contact angle is 142.1°, as shown in Fig. 6, and the surface of 1-3 almost super-hydrophobic surface. The contact angle with water of the other samples is more than 110° all. So this paper made all the samples hydrophobic successfully.

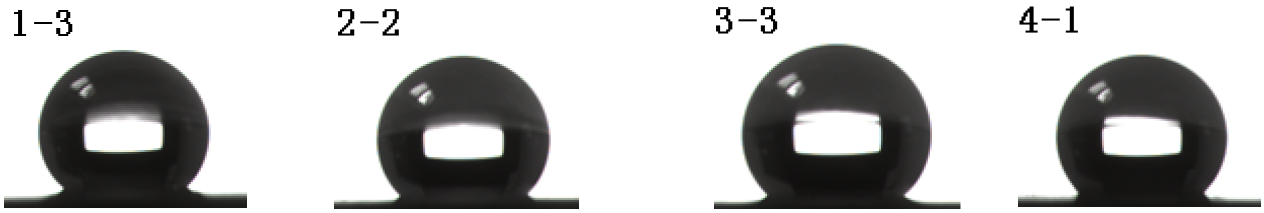


Fig. 6 The contact angle with water of sample 1-3,2-2,3-3 and 4-1 after modifying

The contact surface of TiO_2 nano-tube arrays with water contains gas, because of the exist of nano-tube and the water can't contact with the basal across the nano-tube. According to the theory of Wenzel[17] and the theory of Cassie-Baxter, when the discontinuous contact occurs on the contact surface of solid surface with water drop, this kind of contact form belongs to Cassie-Baxter model. In this case, the contact angle satisfy the following equation:

$$COS\theta_r=f_1COS\theta-f_2$$

The θ_r and θ means the contact angle of water with rough solid surface(apparent contact angle) and the smooth solid surface(eigen contact angle) respectively under the equilibrium state. The f_1 and f_2 means the ratio of raised areas on the solid surface and the ratio of air respectively ($f_1+f_2=1$)[18]. The apparent contact angle will be bigger when the f_2 is bigger. It means that the apparent contact angle will be bigger when the ratio of the contact surface of water with air is bigger.

The sample 1-3 has the biggest contact angle with water maybe because of its more rough surface than other samples. There are many bumps and potholes on the surface of sample 1-3, when the water drop can't go into some small pits, the water will contact with the air in the pits, this

means the f_2 in the equation will bigger than other samples. In this case the ratio of the contact surface of water with air is bigger so that the apparent contact angle is bigger.

Conclusions

(1) The electrolyte concentration and the voltage have a significant impact on the surface roughness of the TiO_2 nano-tube arrays which is prepared by anodic oxidation. And the anodization time and the anode-cathode distance have little effect on surface roughness.

(2) A kind of solution consists of lauric acid and hexadecane can modify the TiO_2 nano-film successfully.

(3) A surface with a better hydrophobicity can be prepared under the appropriate process parameters. It includes a proper electrolytic time, a medium voltage, a proper anode-cathode distance and a lower electrolyte concentration. And the surface hydrophobicity after modifying is almost super-hydrophobic.

References

[1]Wei Li, Yalou Li,Xingwei Wang: 'Nano-TiO2 Modified Super-hydrophobic Surface Coating for Anti-ice and Anti-flashover of Insulating Layer '[J],IEEE,(2010)

[2[Jiang Lei: 'Nanostructured Material swith Superhydrophobic Surface from Nature to Biomimesis' [J],Chemical Industry and Engineering Procress,12(2003) 1258-1264

[3] Bao Yan, Zhang Xiaoyan: 'Construction of super hydrophobic surface and its developing trend' , Dyeing & Finishing, 9(2014) 50-52

[4]Guan Dongsheng，Fang Haitao:'Preparation and Doping of Anodic TiO2 Nanotube Array' , Progressin Chemistry,20(2008),1868-1879.

[5]Hu Yawei, Liu Shan, Huang Siya, Pan Wei: 'Preparation and Effect Factors of TiO2 Super hydrophobic Coating ' , Rare metal materials and engineering,40(2011),469-471

[6]Xue Chaorui, Dong Lihua: 'Preparation and anticorrosion Performance of super hydrophobic TiO2 Nanotube arrays on Pure Ti' , Corrosion Science and Protection Technology, 24,(2012),37-40

[7]Li Jian，Luo Jia:'Preparation and Characterization of TiO_2 Nanotube Arrays by Anodic Oxidation Method' , Journal of Inorganic Materials, 25(2010),490-494

[8]S.C.Han, J.M.Doh: 'Highly Ordered Self-Organized TiO_2 Nanotube Arrays Prepared by a Multi-Step Anodic Oxidation Process' , Met Mater Int,3,(2009),493-499

[9]Mirghasem Hosseini, Mohamad Mohsen Momeni: 'Prapation and Characterisation of TiO_2 Nanotubular Arrays for Electro-Oxidation of Opganic Compounds: Effect of Immobilization of the Noble Metal Particles', Intertional Journal of Modern Physics:Conference Series,5(2012),41-48

[10]Jian Hou, Min Zhang: 'Photocatalytic Activity and Photocurrent Properties of TiO_2 Nanotubule Arrays Influenced by Calcination Temperature and Tube Length',Surface Review and Letters,3(2012),1250023(8 pages)

[11]Guo Zhijun, Zhou Bin: 'Influences of Anodization Processing Factors on The Morphology and Property of TiO_2 Nano-tube Arrays' , Journal of Functional Materials,6(2014),06111-06116

[12]Li He, Yao Suwei: 'TiO_2 Nanotube Arrays Electrode Prepared by Anodic Oxidation and Its Photoelectrochemical Properties' , Journal of Inorganic Materials,22(2007),349-353

[13]Li Hong-Yi, Wang Jin-Shu: 'Preparation of TiO_2 Nano-tube Array Thin Films and Their Growth Mechanism' , Chinese Journal of Inorganic Chemistry, 26(2010),217-222

[14]Li Peng, Zhao Kunyu: ‘Factors and Mechanism for Transition of TiO_2 from Nanopores to Nanotubes’ , Journal of Materials Engineering,1(2014),58-74
[15]Hong Chunyan, Ye Yun: ‘Fabrication and Field Emission Characteristics of TiO_2 Nanotube Arrays’ , Chinese Journal of Vacuum Science and Technology,33(2013),141-145
[16]Li Songmei, Zhou Sizhuo: ‘Fabrication and Anti-corrosion property of Insitu Self-Assembled Super-hydrophobic Films on Aluminum Alloys’ , Acta Physico-Chimica Sinica, 25(2009),2581-2589
[17]Wang R, Hashimoto K, Fujishima A: ‘Light-induced amphiphilic surfaces’ , Nature, 31(1997),388-431
[18]MCHALE G: ‘Cassie and Wenzel: Were They Really so Wrong? ’ , Langmuir, 23(2007), 8200-8205

Key Engineering Materials Vols 645-646 (2015) pp 208-215
Submitted: 2014-11-17
Accepted: 2014-12-23
© (2015) Trans Tech Publications, Switzerland
doi:10.4028/www.scientific.net/KEM.645-646.208

Fabrication and thermal performance of copper pillars modified micro heat pipe (MHP)

Liang-Liang Zou[1], Yi Luo[1]*, Ji-Guang Liu[1], Bei-Ke Yu[1], Qing Shan[1], Xiao-Dong Wang[1]

[1]Key Laboratory for Precision and Non-traditional Machining Technology of Ministry of Education, Dalian University of Technology, Dalian, China

*Corresponding author: luoy@dlut.edu.cn

Keywords: Copper pillars; MHPs; Vapor chamber; Contact angle; Thermal behavior

Abstract. With the excellent thermal conductivity and the compatibility to micro electromechanical systems technology, silicon is widely used in micro heat pipes (MHPs). Copper shows higher heat transfer capability and capillary traction than silicon. Copper pillars modified microgrooves were fabricated on the silicon wafer using electroforming technique in this paper. Water contact angle measurements and thermal behavior tests were employed to the fabricated microgrooves and MHPs. Under the input power of 4 W, how the working fluid flowed in the microgrooves and steam chamber was easily observed by digital camera. The experiments demonstrated the working fluid flowed via copper pillars instead of the silicon microgrooves due to the adhesive force between working fluid and copper pillars were larger than that between working fluid and silicon microgrooves. This work showed copper pillars had a better capillary traction than the silicon microgrooves, and could make the MHP work as a vapor chamber.

Introduction

In recent years, how to reduce the high-power light emitting diode's (HP LED) thermal resistance, junction temperature and hot spot influence have been studied by different research groups in passive and active cooling mechanism. There are several aspects having been studied in heat dissipation, such as package design [1-4], thermal interface material [5], low thermal resistance heat sink material [6-9], and cooling systems [10-14]. The best-known devices for effective heat transfer or heat spreading with the lowest thermal resistance are heat pipes with vapor chambers which are two-phase heat transfer devices with excellent heat spreading and heat transfer characteristics [15, 16].

Micro heat pipe (MHP) was selected as an important device for the heat dissipation for high power electronic devices because it's competitive volume which matches the dimension of the HP LED modules. Many researchers did a lot of work on MHPs. Ye H [17] fabricated a fluid channel by wet etching and wafer bonding with silicon and glass. The phase transition of coolant allowed the package temperature to remain below 115 ^{o}C with LED power up to 2.8 W. A MHP consisted of two layers was introduced by Liu X. W [18]. The bottom layer was Si. Its V-shaped grooves were developed by bulk Si technology. Glass was the up layer, which served as a chamber connecting the vapor phase of all the grooves. The size of the long MHP was 14 mm ×34 mm and the short one was 14 mm×24 mm. Liu W. T [19] fabricated the MHP array in the plate composed of 17 parallel triangular pipes. Nine of the pipes were 371 μm wide and 20 mm long, and the other eight smaller pipes, which served as arteries between every neighbor MHPs, were 268 μm wide and 20 mm long. Ethanol was selected as the working fluid. The working temperature range of MHP was 37.3 ^{o}C - 44.1 ^{o}C.

Vapor chamber was different with the traditional MHP. When heat was added to the evaporator, the liquid vaporized and moved to the condenser from which the heat was removed. The vapor subsequently condensed back into evaporator through wick structure and wick column, and the

cycle was repeated. Wang J. C. [20] took copper-, aluminum- and the packing pure water of a bronze vapor chamber-based plate as the single four LED chips to make thermal analysis. The results showed that the thermal performance of the LED vapor chamber-based plate is better than that of the LED copper-based plate with an input power above 5W. And the experimental thermal resistance values of LED copper- and vapor chamber-based plate are 0.41 °C/W and 0.38 °C/W at 6W respectively. Tsai M. C. [21] designed a prototype vapor chamber heat spreader was built and tested for its thermal performance. The chamber had dimensions of 90 mm × 90 mm × 3.5 mm. It was sandwiched between a heater block and a water cooled plate. Heat was added to the bottom part of the vapor chamber heat spreader by a cartridge heater inserted in an aluminum block. The effective heating area was 12.7 mm × 8.9 mm. The spreader upper surface was attached to an aluminum block, which was compressed against a copper water cold plate from which the heat was removed. The power input varied from 5 W to 50 W. Test results demonstrated that spreading resistance played a vital role in the total thermal resistance. Meng K. [22] identified that Metallic surfaces with high surface free energy were intrinsically hydrophilic, and the performance of MHP could benefit from enhanced wettability. Copper had excellent thermal conductivity and was usually used as heat exchanger materials, and could modify the surface property partially and generally [23-25].

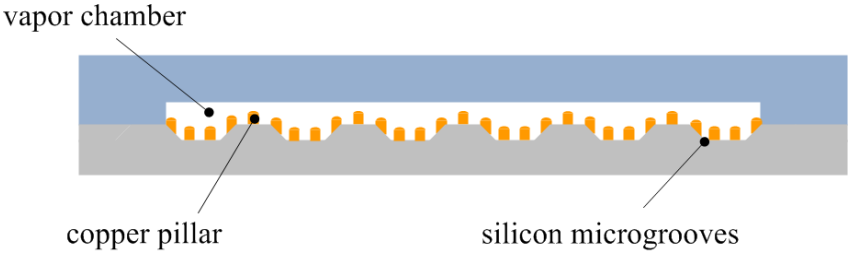
Literature and the experiments prove that copper could increase the surface hydrophilicity of the silicon microgrooves. In this paper, copper pillars were electroformed on the silicon microgrooves of the MHP. The thermal behavior of both copper pillars modified MHP and unmodified MHPs were tested.

Fabrication of the MHP and copper pillars modified MHP

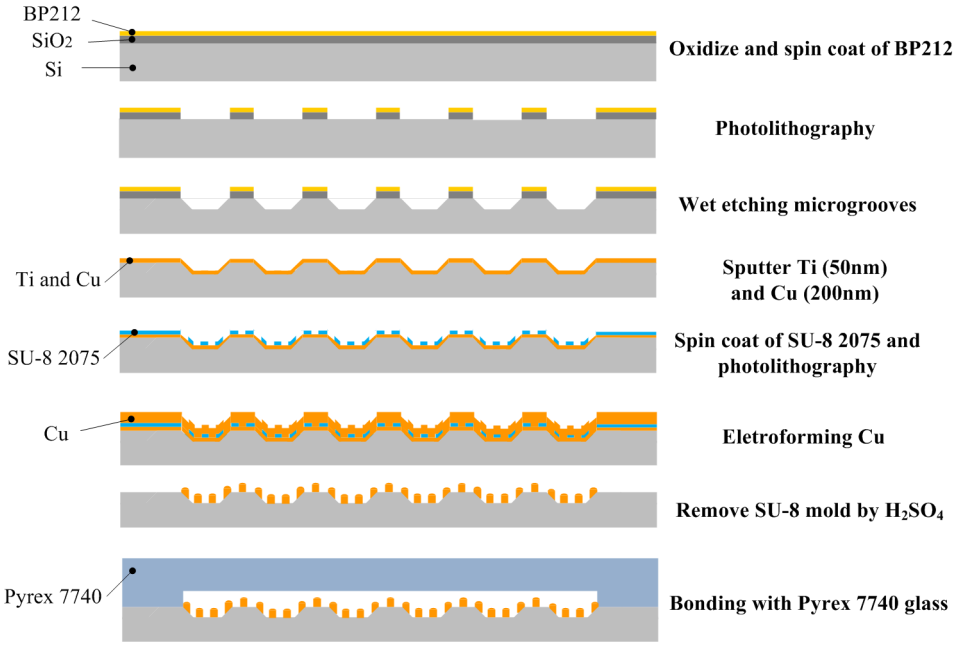
The dimension of the MHPs was designed to suit for 10 W LED module heat dissipation. The length and width of LED module were both 16mm. Considering the three section of the MHP, the overall dimension of MHP was 45 mm (length) ×16 mm (width) ×1.5 mm (thickness). The working area was 35 mm×10 mm, including condenser, adiabatic and evaporation section. The microgrooves were fabricated on the silicon wafer, which was bonded to Pyrex 7740 glass cover plate with a steam chamber. According to the previous study, the steam chamber enhanced the thermal behavior of MHPs compared with the MHPs without the steam chamber [26].Meanwhile, the Pyrex 7740 glass was used to achieve the visualization of how the working fluid was moving. The dimension and space of the silicon microgrooves were both 100 μm. The structure of the copper pillars modified MHP and the manufacturing process were showed in Figure. 1.

Anisotropic wet etching was used to fabricate silicon microgrooves on the n-type silicon (100) wafer. The depth of the microgrooves was about 36 μm. The Pyrex 7740 was wet etched to form a steam chamber with the depth of 200 μm. The silicon wafer and the Pyrex 7740 were bonded using anodic bonding technique at the temperature of 450 ^{o}C and the voltage of 1200 V.

The structure and dimension of the copper pillars modified MHP were the same with those of the silicon MHP. The copper pillars were fabricated using electroforming technique on the surface of the silicon grooves.



(a)



(b)

Figure 1. Copper pillars modified MHP (a) Structure (b) manufacturing process

Electroforming process was used to fabricate copper pillars on the n-type silicon (100) wafer after fabricating the silicon microgrooves. The designed width and space of the copper pillars were both 50 μm. The depth of the copper pillars was about 30 μm. In the electroforming process, the current density was 1A/dm^2 in the first ten minutes and 2A/dm^2 at other time, and electroforming solution was mixed by the mix of $CuSO_4$ (70 g/l), H_2SO_4 (200 g/l), bright plating additive (0.1 ml/l) and leveling agent (2 ml/l). The whole process was under the condition of 24^{o}C. Finally, the fabricated copper micro-grooved silicon wafer and Pyrex 7740 glass were enveloped using sealant (Loctite 326 structural adhesive).

Vacuum charge method was used for the MHP's charging and sealing after the microgrooves were fabricated. This method has been detailed in another paper [27]. The working fluid was degassed DI water, and the filling ratio was 30 %. The fabricated traditional MHP and copper pillars modified MHP were shown in Figure 2.

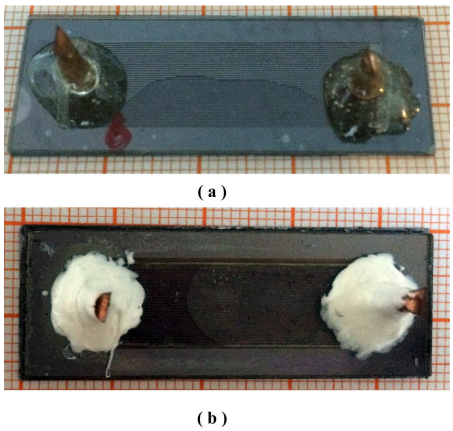


Figure 2.The fabricated MHPs with (a) silicon microgrooves (b) copper pillar modified microgrooves

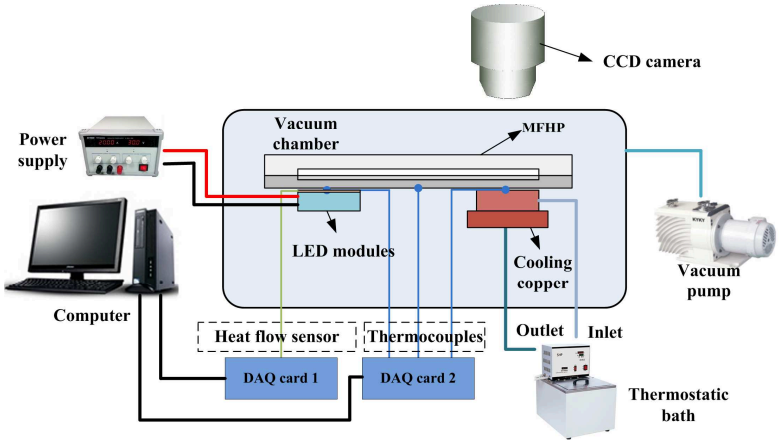
Test of the MHP and copper pillars modified MHP

The thermal performance of the MHPs can be evaluated by the equivalent thermal conductivity which is calculated as follows:

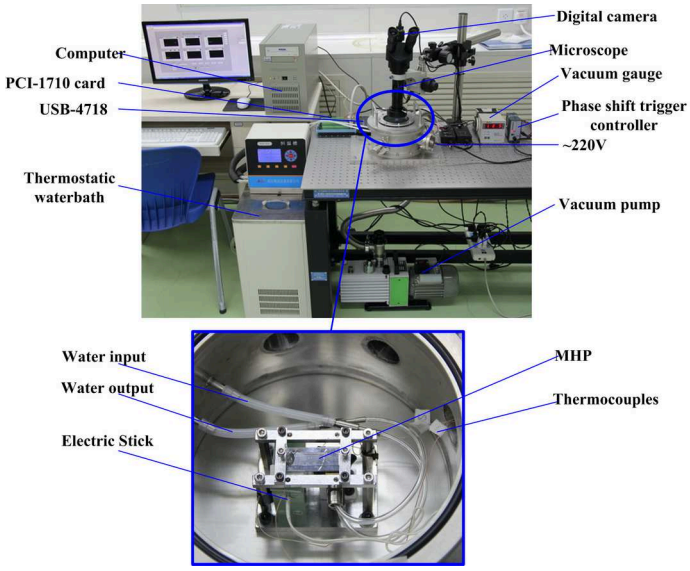
$$K = \frac{Q_{in}}{T_1 - T_2} \times \frac{L}{A_c}. \quad (1)$$

where Q_{in} was the heat input, T_1 and T_2 were the temperatures of the evaporation part and the condensation part, respectively, L was the length between evaporation part and condensation part, and A_c was the cross sectional area of the MHPs.

The thermal behavior testing system was described in another paper [28]. In this system, Two K type thermocouples (Chal-0005, OMEGA Company, USA) were used to test the temperature at the evaporation and condensation section, respectively. A heat flux sensors (HFS-3, OMEGA Company, USA) was used to record the input power of the MHPs. The schematic drawing and physical structure of the system were shown in Figure 3.



(a)



(b)

Figure 3. Thermal behavior testing system (a) schematic drawing (b) physical structure

The accuracy grade of the thermocouple instrument (Testo 735, Germany) was ±0.3 ^{o}C. Calibration of the thermocouples was conducted by measuring the temperature change of thermocouples upon the temperature change inside a well-controlled oven. The 10W LED module was placed as the heat source of the MHP. The input power was 4 W. The temperature rising curves of the two thermocouples at the evaporation and condensation section are shown in Figure 4.

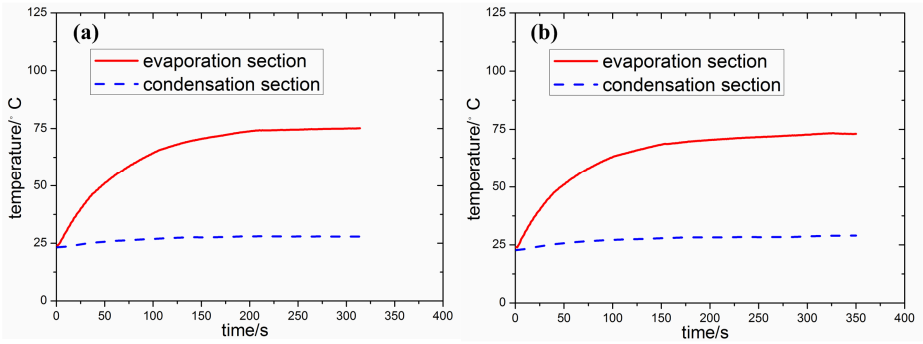


Figure 4.The temperature curve of the MHPs. (a) the temperature curves of the silicon MHP (b) and the copper pillar modified MHP

To better show how the working fluid flowed in the microgrooves and steam chamber, the pictures described the working fluid condition in the MHP and copper pillars modified MHP by digital camera were shown in Figure 5.

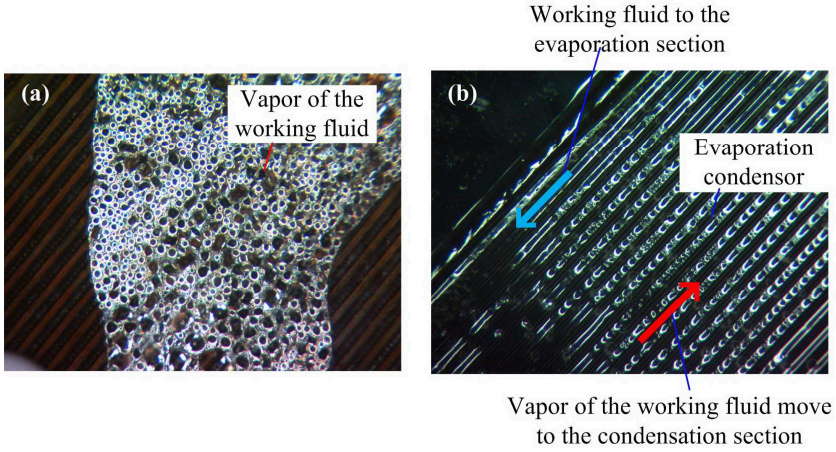


Figure 5. The working picture of the MHP (a) copper - modified MHP (b) silicon - grooved MHP

Results and discussion

With the data shown in Figure 4, the equivalent temperature at the evaporation section of the copper pillar modified MHP and the silicon - grooved one were almost the same. However, the start - up time was reduced from 210 s to 150 s, indicating that the hydrophilic of the copper pillar enhanced the working fluid dispensing and re-arrangement, thus the start - up time can be shorten.
With Equation (1) and the data shown in Figure 4, the equivalent thermal conductivities of the MHPs were calculated and listed in Table 1.

Table 2 The equivalent thermal conductivity

MHP	K^a [$W/\mathrm{K}\cdot\mathrm{m}$]
Silicon microgrooves	198.67
Copper pillars modified microgrooves	212.68

[a] K is the equivalent thermal conductivity of MHPs and Si wafer.

According to the effective thermal conductivity calculated by Equation 1, the copper pillars modified MHP has almost the same value with the silicon-grooved MHP. From Figure 5, copper pillars changed the working style of the MHP. Part of the working fluid flowed via the copper

pillars to the steam chamber instead of flow to the condenser section of the silicon microgrooves, as shown in (a). This effect weakened the heat transfer ability. However, the working fluid vapor cooled down to liquid phase and grown up, when it reached grooves at the evaporation part, this working fluid directly working again instead of flow back to evaporation. Thus for this phenomenon, the heat transfer ability is enhanced. With the combination of these two effects, the effective thermal conductivity of the copper pillars modified MHP was almost same with the silicon-grooved MHP.

Conclusions

Copper pillars modified silicon microgrooves of MHP was introduced in this paper. Copper pillars changed the flow regime of gas-liquid two phase flow of the working fluid, which resulted in the change of the heat transform conductivity. Present experiments indicated start - up time of MHP was shortened but the thermal conductivity didn't appear much different. Future study may focus on improving the thermal conductivity of MHP by selectively increasing the capillary force of the condensation section and droplet reflux ratio of the evaporation section.

The temperature curves in the thermal behavior test also showed the electroformed copper pillars didn't improve the thermal behavior of the silicon-grooved MHP.

With the digital camera of the thermal behavior, it was discovered that the copper pillars modified MHP couldn't work efficiently as designed. The working fluid flowed via the copper pillars instead of the silicon microgrooves. Since the adhesive force between the working fluid to copper pillar was larger than that to silicon microgrooves. The copper pillars made the silicon-grooved MHP work as a vapor chamber.

Moreover, future work will be focused on working limit between the MHP and the vapor chamber. And the designed vapor chamber could also be used for the heat dissipation of the high power LEDs.

Acknowledgments

The authors wish to gratefully acknowledge the financial support provided for this study by the State Key Development Program for Basic Research of China (Grant No. 2011CB013105).

References

[1] Cheng T, Luo X. B, Huang S, Liu S: Thermal analysis and optimization of multiple LED packaging based on a general solution. International Journal of Thermal Sciences 2010,49:196-201

[2] Juntunen E, Tapaninen O, Sitomaniemi A, Heikkinen Ve: Effect of phosphor encapsulant on the thermal resistance of a high-power COB LED module. Transactions on Components, Packaging and Manufacturing Technology2013, 3:148-1154

[3] Luo X.B, Fu X, Chen F, Zheng H: Phosphor self-heating in phosphor converted light emitting diode packaging. International Journal of Heat and Mass Transfer2013, 58:276-281

[4] Hu R, Luo X.B, Zheng H: Hotspot location shift in the high power phosphor converted white light-emitting diode package. Japanese Journal of Applied Physics2012, 51: 09MK05(1-4)

[5] Liou B.H, Chen C.H, Horng R.H, Chiang Y.C, Wuu D.S: Improvement of thermal management of high-power GaN-based light-emitting diodes. Microelectronics Reliability2012,52:861-865

[6] Sim J.K, Ashok K, Ra Y.H, Im H.C, Baek B.J, Lee C.R: Characteristic enhancement of white LED lamp using low temperature co-fired ceramic-chip on board package. Current Applied Physics2012, 12: 494-498

[7] Kang M, Kang S: Influence of Al_2O_3 additions on the crystallization mechanism and properties of diopside/anorthite hybrid glass-ceramics for LED packaging materials. Journal of Crystal Growth2011, 326:124-127

[8] Zhou W, Qi S, Li H, Shao S: Study on insulating thermal conductive BN/HDPE composites. Thermochimica Acta2007, 452:36-42

[9] Luo X, Mao Z: Thermal modeling and design for microchannel cold plate with high temperature uniformity subjected to multiple heat sources. Int. Commun. Heat Mass Transf2012, 39:781-785

[10] Kim L, Choi J.H, Jang S.H, Shin M.W: Thermal analysis of LED array system with heat pipe. Thermochimica acta2007, 455: 21-25

[11] Lu X. Y, Hua T.C, Wang Y. P: Thermal analysis of high power LED package with heat pipe heat sink. Microelectronics Journal2011, 42:1257-1262

[12] Wan Z. M, Liu J, Su K. L, Hu X.H, M S.S: Flow and heat transfer in porous micro heat sink for thermal management of high power LEDs. Microelectronics Journal2011, 42:632-637

[13] Liu S, Yang J.H, Gan Z.Y, Luo X.B: Structural optimization of a microjet based cooling system for high power LEDs. International Journal of Thermal Sciences2008, 47:1086-1095

[14] Anithambigai P, Dinashi K, Mutharasu D, Shanmugan S, Lim C.K: Thermal analysis of power LED employing dual interface method and water flow as a cooling system. Thermochimica Acta2011, 523: 237-244

[15] Kosakabe T, Mochizuki M, Mashiko K, Saito Y, Kiyooka F, Horiuchi Y, Cabusao G, Nguyen T: Heat spreader technology for silicon chip. CPMT Symposium Japan 2010:1-4

[16] Hirachan A, Agonafer D: Removing the hot-spots in high power devices using the thermoelectric cooler and micro heat pipe. Proceedings of the ASME 2012 International Mechanical Engineering Congress & Exposition (IMECE 2012) 2012, 9:1189-1195

[17] Ye H, Mihailovic M, Wong C.K.Y, Zeijl H.W, Gielen A.W.J, Zhang G. Q: Two-phase cooling of light emitting diode for higher light output and increased efficiency. Applied thermal Engineering2013, 55:353-359

[18] Liu X. W, Wang C, Wang L. W, Han T: Design and fabrication of flat heat pipes with different length. Optoelectronics and Microelectronics Technology (AISOMT) 2011:279-282

[19] Liu W, Kang J, Fu X, Stefanini C, Dario P: Analysis on heat resistance of the micro heat pipe with arteries. Microelectronic Engineering2011, 88: 2255-2258

[20] Wang J. C: Thermal investigations on LED vapor chamber-based plates. International Communications in Heat and Mass Transfer2011, 38: 1206-1212

[21] Tsai M. C, Kang S. W, Paiva de K. V: Experimental studies of thermal resistance in a vapor chamber heat spreader. Applied Thermal Engineering 2013,56: 38-44

[22] Meng K, Y, Jiang Z, Lian J, Jiang Q: Cu surfaces with controlled structure: From intrinsically hydrophilic to apparently superhydrophobic. Applied Surface Science2014, 290: 320-326

[23] Zhang Q. Y, Chen Z. M, Qi M. L: Study of hydrophilic films on copper tube. Advanced Materials Research2012, 581-582: 491-494

[24] Min J.C, Wu X.M, Shen L.F, Gao F: Hydrophilic treatment and performance evaluation of copper finned tube evaporators. Applied Thermal Engineering2011, 31: 2936-2942

[25] Nam Y.S, Sharratt S, Cha G, Ju Y. S: Characterization and modeling of the heat transfer performance of nanostructured Cu micropost wicks. Journal of Heat Transfer2011, 133: 101502(1-7)

[26] Luo Y, Liu G, Zou L.L, Yang Y.X, Wang X.D: Experimental investigation of micro heat pipes for high-power light-emitting diode modules. Micro & Nano Letters2013, 8(10): 646-649

[27] Wang X. D, Zou L.L, Liu G, Luo Y: Vacuum Fluid Charging and Packaging Technique for Micro Heat Pipes. Proceedings of 14th International Conference on Electronic Packaging Technology (ICEPT 2013), Dalian, China, 11-14 August 2013: 46-49

[28] Luo Y, Liu G, Zou L.L, Wang X.D: Experimental investigation of micro silicon-Pyrex heat pipe for high-power LEDs. 15th Annual Conference of the Chinese Society of Micro/Nano Technology (CSMNT 2013) 2013:30418

Key Engineering Materials Vols 645-646 (2015) pp 216-220
© (2015) Trans Tech Publications, Switzerland
doi:10.4028/www.scientific.net/KEM.645-646.216

Submitted: 2014-12-03
Accepted: 2014-12-23

Research on TSV Dry Etching Technology

Guoqing Jiang[1,a], Lei Kuang[1], Jian Zhu[1,2]

[1]Nanjing Electronic Devices Institute, Nanjing China 210016
[2]National Key Laboratory of Monolithic Integrated Circuits and Modules, Nanjing 210016, China
[a]email: gq__jiang@126.com

Keywords:TSV technology, dry etching, ICP

Abstract. TSV is a new technology to make interconnections between chips by creating vertical wafer-to-wafer vias. The application of ICP (inductively coupled plasma) dry etching to make TSV is discussed in this paper. Starting with hardware conditions of the equipment, a large number of experiments were conducted to test the process parameters combining with the fundamentals of dry etching. By constantly modifying the parameters to optimize the process, a final result of TSV with the width of 2.62um, depth of 63.5um, verticality of 89.8°and scallop of 70.3nm was realized in this paper.

Introduction

3D packaging using TSV (through silicon via) technique has become a mainstream process for packaging. By making vertical wafer-to-wafer vias to create interconnection between chips, TSV technology can achieve the largest 3-dimensional density and lowest cost to greatly improve the speed of chips and low-power consumption performance[1,2]. TSV technology consists of three key processes, namely via formation, Cu electroplating and wafer thinning. There are four ways to create vias: dry etching, wet etching, laser drilling and photo-assisted electrochemical etching[3]. The application of ICP (inductively coupled plasma) etching in TSV dry etching is discussed in this paper. By experimentally modifying the process parameters, a relatively satisfying result of TSV dry etching process is obtained.

Fundamental of dry etching

ICP etching includes physical bombardment and chemical etching[4]. As a supporting role in the process, physical bombardment can break chemical bonds, cause lattice damage, increase adhesiveness, accelerate the desorption of reactants and promote chemical etching on the substrate surface. In the process of chemical etching, the etching gas is glow-discharged by inductively coupling to produce active free radicals and metastable particles, then those active particles interact with the surface of the substrate. ICP etching consists of three steps: 1) the absorption of etching gas; 2) the forming of volatile products; 3) the desorption of reactants. Deposition and etching take place alternately to get good anisotropy and high aspect ratio when the process is precisely controlled[5,6].

The principle of ICP etching based on Bosch gas-switching is the alternate effect of C_4F_8 and SF_6[7]. The first step is shown in Eq. 1 and Eq. 2. A film of polymer is deposited on the sidewall. C4F8 is decomposed into ionic radicals like CF^+_x, CF^-_x, and F^- when in plasma state. CF^+_x and CF^-_x can react with the silicon surface to produce a layer of macromolecule film nCF_2. The second step is demonstrated in Eq. 3 to Eq. 5. Under the condition of high-frequency glow discharge, SF_6 is added to produce active F^- free radicals, which will firstly etch the nCF_2 film to produce a volatile gas

called CF_2, then react with the silicon. After continuous cycles of deposition and etching, the required depth will be obtained. The theory of etching is shown in Fig. 1.

$$C_4F_8 + e^- \rightarrow CF_x^+ + CF_x^- + F^- + e^- \quad . \tag{1}$$

$$CF_x^- \rightarrow nCF_2 \quad . \tag{2}$$

$$nCF_2^+ + F^- \rightarrow CF_x^- \rightarrow CF_2 \uparrow . \tag{3}$$

$$SF_6 + e^- \rightarrow S_xF_y^+ + S_xF_y^- + F^- + e^- \quad . \tag{4}$$

$$Si + F^- \rightarrow SiF_x \quad . \tag{5}$$

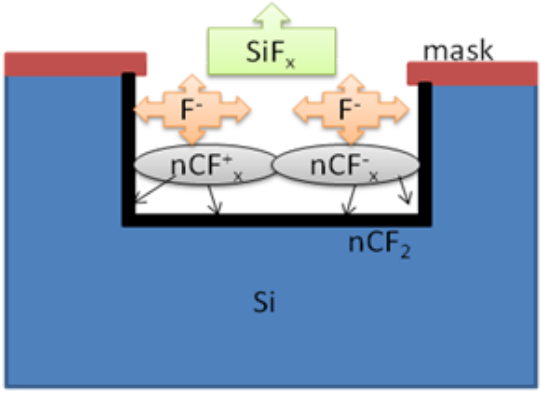


Fig. 1 Schematic of Etching

The etching system used in this paper is Pegasus manufactured by British company STS. This equipment has two 13.56MHz RF power sources, one of which is connected with the induction coil outside of the vacuum reaction chamber to ionize the process gas, and the other one is connected with the platen under the chamber to control the energy and bias of the plasma, as shown in Fig. 2. The main parameters are demonstrated in Table 1. The sample used in this paper is a 100mm single-polished n-type <100> wafer with the thickness of 475μm and the resistivity of 10.3～13.6Ω.cm.

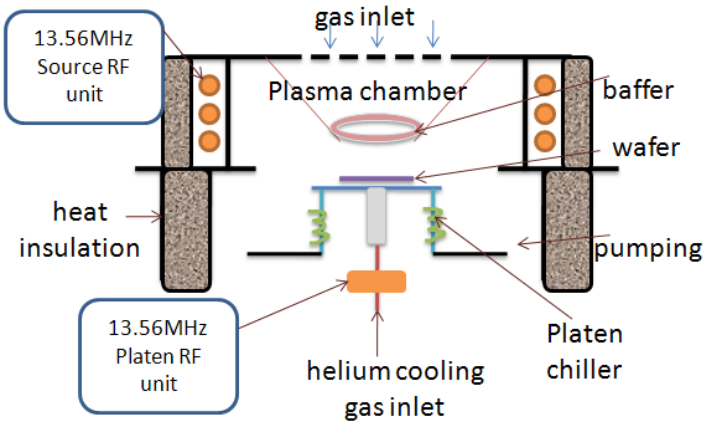


Fig. 2 Structure of the Chamber of Pegasus

Table 1 The Main Parameters of Pegasus Equipment

Planten Chiller[℃]	Inner Heater [℃]	Chamber Heater[℃]	Magnetic Confinement Heater[℃]	Plenum Heater[℃]
15	140	120	120	120

Experiment and discussion of etching

One problem of ICP etching based on Bosch gas-switching is that as the depth increases, the density of the active F^- radicals at the bottom will be slowly reduced, thus the etch rate will decrease. This imbalance of etching and deposition can affect the roughness and verticality of the sidewall. Meanwhile, if the flow of SF_6 is excessive, the F^- radicals at the bottom will be overdosed and the etch rate will increase, causing serious undercutting and poor verticality.

At the beginning the parameters demonstrated in Table 2 were applied in the experiment. After the dissection of the wafer, a severe deformation was found at the bottom of the hole when a certain hole-depth was reached. The etching gas had completely no effect on the sidewall, and the platen power was too weak to carry out the physical bombardment, as shown in Fig. 3.

Table 2 Parameters of Process Procedure

Cycle	Source power[W]	Platen power[W]	Pressure [mTorr]	Gas flow[sccm]		Time[s]
				SF_6	C_4F_8	
Etching	2400	30	60	300	0	6
Deposition	2000	0	25	0	200	3

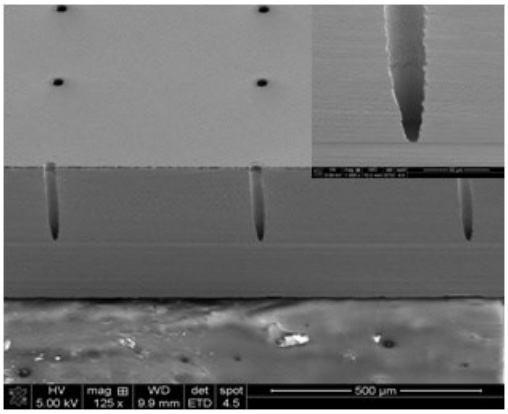


Fig. 3 SEM of poor verticality of TSV

In the process of etching, the width of the bottom of TSV will decrease as the depth increases, therefore high aspect-ratio will be seriously affected. There are many ways to amend this situation, such as increasing the platen power to enhance the bombardment energy of ions, or raising the pressure of etching gas to improve the etching at the bottom.

Another experiment is increasing the platen power and etching gas flow to enhance the effect of etching. The procedure is shown in Table 3. It is indicated that increasing the platen power will enhance the energy of ions but also form negative electric potential with the ions on the sidewall at the same time. Because of the negative electric potential, the ions in the hole deviate from their original paths to boost the etching of the sidewall, causing bowing phenomenon and greatly affecting the roughness of the sidewall, as shown in Fig. 4.

Table 3 Parameters of Process Procedure

Cycle	Source power[W]	Platen power[W]	Pressure [mTorr]	Gas flow[sccm]		Time[s]
				SF_6	C_4F_8	
Etching	2400	30	60	330	0	6
Deposition	2200	0	25	0	200	3

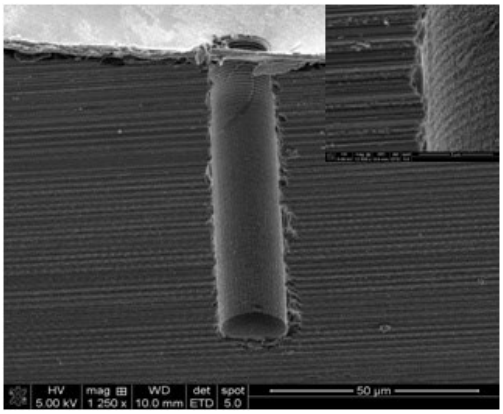


Fig. 4 SEM of poor roughness of TSV

To ensure that the number of ions at the bottom will not reduce as the depth increases and the verticality meets the requirements, the process parameters were adjusted though trial and error. Based on an abundance of experiments, a satisfying procedure shown in Table 4 was achieved by precisely modulating the pressure of the etching gas flow. The result is demonstrated in Fig. 5.

Table 4 Parameters of Process Procedure

Cycle	Source power[W]	Platen power[W]	Pressure [mTorr]	Gas flow[sccm]		Time[s]
				SF_6	C_4F_8	
Etching	2400	30	25>>60	330	0	1.5>>5
Deposition	2200	0	25	0	200	3

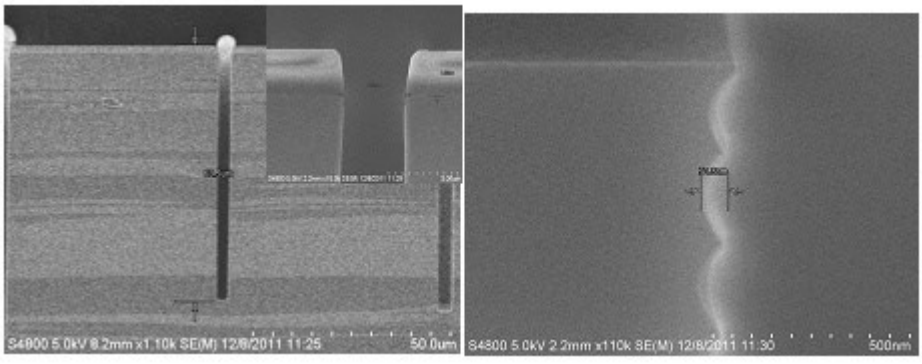


Fig. 5 SEM of better profile of TSV

Summary

TSV technology has been extensively used in the field of computer memory, image sensor and power amplifier. Because of its good selectivity, high control accuracy and fine verticality, ICP dry etching plays an important role in TSV etching and can achieve a far better result than wet etching, laser drilling and photo-assisted electrochemical etching. In this paper a final result of TSV with the width of 2.62um, depth of 63.5um, verticality of 89.8° and scallop of 70.3nm was realized.

Acknowledgement

This work was supported by the International Science & Technology Cooperation Program of China (2013DFB10300).

References

[1] Tong Zhiyi, 3D IC Stacking with TSV Interconnect, J. Package and Test. 170(2009) 27-34.
[2] John H. Lau, Raleigh Convention Center, J. Raleigh-USA. 232(2010) 46-50.
[3] Huang Bo, TSV Technology Research, J. Scientific Practice. 12(2013)301-302.
[4] Liao Ke, Wang Zhiyuan, Application of Inductively Coupled Plasma Etching Technique in 808 nm Laser, J. Chinese Materials Science Technology & Equipment. 5(2007) 101-103.
[5] Chen Shaojun, Li Yigui, Parameter Optimization Based on High-Aspect Ratio Si Dry Etching, J. Micronanoelectronic Technology. 46(2009) 750-754.
[6] Zhuo Min, Jia Shixing, Zhu Jian, ICP Process in Fabrication of Micro-Inertial Devices, J. Journal of Transduction Technology. 19(2006) 45-47.
[7] Xu Gaobing, Huang Hua, Zhan Minghao, Huang Xiaoli, et al. Experimental Evaluation of Inductively Coupled Plasma Deep Silicon Etching, J. Journal of Vacuum Science and Technology. 33(2013) 832-835.

Key Engineering Materials Vols 645-646 (2015) pp 221-225
© (2015) Trans Tech Publications, Switzerland
doi:10.4028/www.scientific.net/KEM.645-646.221

Submitted: 2014-12-04
Accepted: 2014-12-23

Research on Microstructure and Wear Resistance of Cast-Penetrated Layer Strengthened by Nano-Sized TiN Intermediate Alloy

Xie Jing-pei[1, a *], Shao Xing-hai[2], Liu Shu[1], Wang Feng-mei[1], Wang Ai-qin[1], Ma Dou-qin[3]

[1]College of Material Science, Henan University of Science and Technology, Luoyang 471003, Henan, China;

[2] Process materials research institute, the First Tractor Company Limited, Luoyang 471003, Henan, China;

[3] School of Physical Engineering, Zhengzhou University, Zhengzhou450001, Henan, China

[a]xiejp@haust.edu.cn

Key words：nano-sized TiN; intermediate alloy; microstructure; wear resistance.

Abstract. High-Cr cast-penetrated layer contained nanometer ceramic particles was formed on the surface of the medium carbon steel ZG250-470 by adding nano-TiN intermediate alloy powder to cast-penetrated agent. Microstructure and wear resistance of the strengthened cast-penetrated layer were studied. The results showed that: compared with not adding intermediate alloy, there were finer and more uniform microstructure and better high temperature and high speed wear performance of strengthened cast-penetrated layer strengthened by nano-TiN intermediate alloy. Strengthening effect would be best by adding the intermediate alloy containing rare earth. By adding intermediate alloy containing Ni, the best high temperature wear resistance of cast-penetrated layer could be obtained.

Introduction

Ceramic materials have high hardness and stability. They can improve the mechanical properties and wear resistance of metallic matrix by adding as hard phase, and get composite materials with metal powder sintering. Nanometer ceramic powder has higher hardness than micron powder. There is a significant dispersion strengthening effect after adding it to the matrix. So it has the very good research prospect [1,2]. Furthermore, nanometer powder has high surface energy for low temperature sintering densification, but graingrowth will emerge very probably in the sintering process. Casting-infiltration technology is combined casting technology with metallurgical strengthening technology, and can be regarded as a shorter sintering process for using casting solidification heat realizing melting, decomposition and diffusion of needing elements. So, it can make full use of the characteristics of nano-particles and effectively inhibit nanometer grain growing up by adding nanometer ceramic particles to cast-penetrated layer. This method is an important attempt for the solution of sintering incomplete and low penetration capacity of liquid metal in the cast infiltration process. And it also can further improve the surface wear-resisting performance of alloy[3-5]. In this study, different nano-TiN intermediate alloy powder was used as adding material, high carbon Cr-Fe powder as infiltration material. High Cr cast iron layer enhanced by TiN nano-particles was obtained by casting middle carbon steel ZG250-370. Microstructure and wear-resisting performance of cast-penetrated layer were also studied.

Experimental

Preparation of enhanced cast-penetrated layer of nano-sized TiN intermediate alloy. Fine iron powder, TiN nano-particles, and other materials were mixed and then extruded into pieces, broken into intermediate alloy particles by a special technology. TiN nano-particles were distributed evenly

Tab.1 Composition of nanometer intermediate alloy

Intermediate alloy	Nano TiN[wt. %]	Enhanced elements		Others
		Ni[wt. %]	Rare earth [wt .%]	Fe and others [wt. %]
TiN intermediate alloy No.1	15	2	Slight	85
TiN intermediate alloy No.2	15			83
TiN intermediate alloy No.3	15			85

in the intermediate alloy particles. The particles size of nano-TiN was 30-60 nm. And the particles were processed by surface modification. There were kinds of intermediate alloy used in this paper, which were shown in Tab. 1. The penetration alloy powder is high carbon Cr-Fe powder, whose main components were Cr-Fe carbide, Ni-Cr alloy and Ni-Si alloy.

The quality percentage of nano-particles in the cast-penetrated agent was 1%. The adding amount of nanometer intermediate alloy should be 6.67%，due to the mass fraction of nano-particle was 15% in the alloy. There were three steps for preparing cast-penetrated layer: 1) grinding the three kinds of nanometer intermediate alloy powder into fine powder with mortar, taking fine powder (weight of 16.67g) to the high carbon Cr-Fe powder (weight of 233.33g), respectively, mixing them in the blender, adding the right amount of borax, phenolic resin and alcohol to prepare the agent of cast-penetrated slurry; 2) coating the slurry in the fixed position of inner wall of the sand mold to form the prefabrication coating. The thickness of the coating was about 3-5 mm. Choosing CO2 sodium silicate sand, numbering the prefabricated layers after fire drying. Then preheating the sand and coating to about 200 ℃; 3) It used the 1600 ℃ ZG250-370 casting molten steel for casting moulding ，and prepared three different nanometer intermediate alloy with reinforced high Cr cast-penetrated layer on the surface.

High Cr cast iron materials with cast-penetrated layer reinforced by adding not nano-TiN were used in this paper. The preparation method was to mix 250g high carbon Cr-Fe powder in the blender, and make into cast-penetrated agent pulp by adding suitable amount of borax, phenolic resin, and alcohol. The rest preparation process is the same as high Cr cast iron with cast-penetrated layer reinforced by nanometer intermediate alloy.

Experimental methods. The castings were processed into square samples (size of 10 mm×10 mm×10 mm) and wafer samples (size of 10 mm×10 mm×0.5 mm) by wire-cutting. The square samples were corroded in the aqua regia after grinded on the sand paper and polished, then the characterization of cast-penetrated layer were by means of JSM-5610LV scanning electron microscope with EDS. Put the samples (size of Φ3mm×50μm) into ion Polishing System Gatan691, then observe the microstructure of cast-penetrated layer by high resolution transmission electron microscopy (TEM) JEM - 2100.

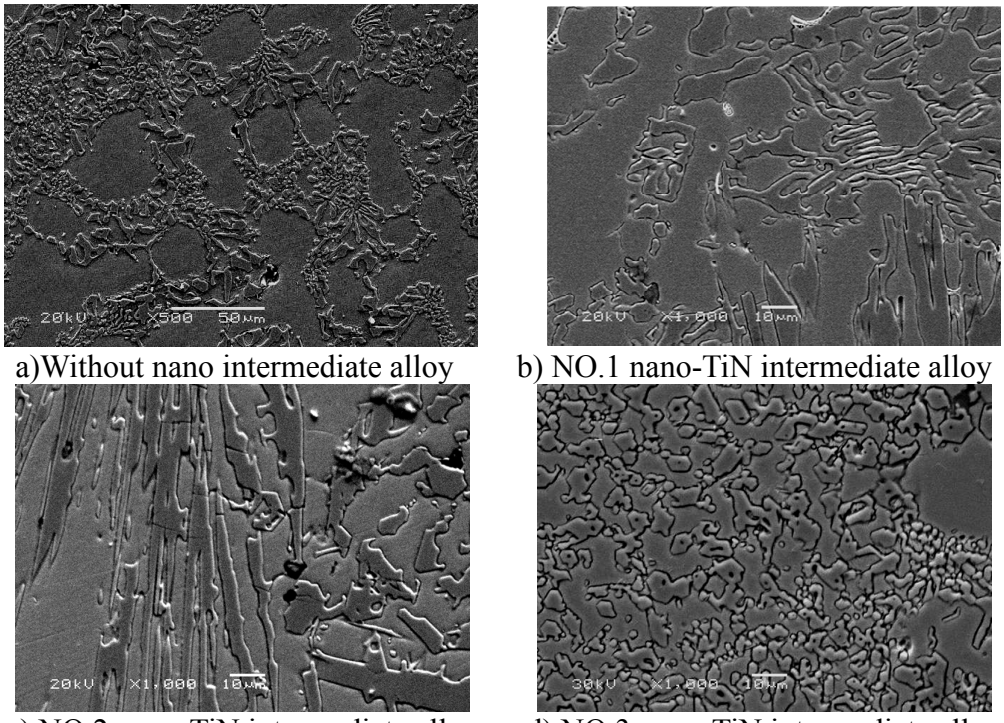
The high temperature wear performance were tested at a high speed and temperature vacuum wear testing machine of MMU-5GA after cutting the castings into Φ 4 mm × 7 mm pin shape samples by wire-cutting. Taking three samples of the same material in each group, and the pair of material was carbon steel casting ZG270-500. Changing to new friction pairs after the test of each group. The experiments were conducted under the environment of 200 ℃ and 500 ℃, and the loading conditions were 0.20 MPa and 2.00 MPa respectively. The friction speed and time were10m/s and 5min.Weighting the quality of the samples before and after the friction experiment of each group. Calculating the wear weightlessness and making it as the index of high temperature wear resistance of cast-penetrated layer.

Results and analysis

Microstructure of cast-penetrated layer enhanced by nano TiN. Fig. 1 is the SEM images of four kind of cast-penetrated layer. From the images, it can be found that, when adding not intermediate alloy, the carbide distributes as the net-like and less quantity in the cast-penetrated layer (Fig. 1-a). The carbides appear independent uniform distribution with the form of granular, bar or layer sheet when nano ceramic particles joined in the form of intermediate alloy (Fig. 1 b - d). NO.3 nano intermediate alloy (containing little rare earth) has the most obvious effect for the optimization of carbide which appears as small granular and uniform dispersion distribution in the matrix. It suggests that cast-penetrated layer has the best microstructure by adding nanometer TiN in the form of NO.3 intermediate alloy: high hardness carbides uniform set in austenite, protect the matrix, and thus improve the performance of penetrated layer.

Fig. 2 shows the TEM images and EDS analysis of strengthened carbide cast-penetrated layer with nano-TiN NO. 3 intermediate alloy. Fig. 3 shows the TEM images and EDS analysis of strengthened carbide cast-penetrated layer with nano-TiN power. It can be found that there are only a few Ti contenting at the interface when nano-particles added as the form of intermediate alloy. This suggests that nano-particles distribute rarely at the interface, and TiN mainly disperse in matrix in the form of nano-sized particles. The document [3] found that, nano-particles have the aggregation of trend to combine at the interface, and the Ti content was twice times as in the matrix after directly adding the nano ceramic powder to the impregnation agent. It can be concluded that, as the liquid steel to permeate prefabricated layer and dilution of alloy liquid, nano-TiN enter into the low carbon Cr steel liquid aside with nano intermediate alloy during the cast-penetrated process. And scatter in austenite after the final solidification, only a few spread to the interface with other elements.

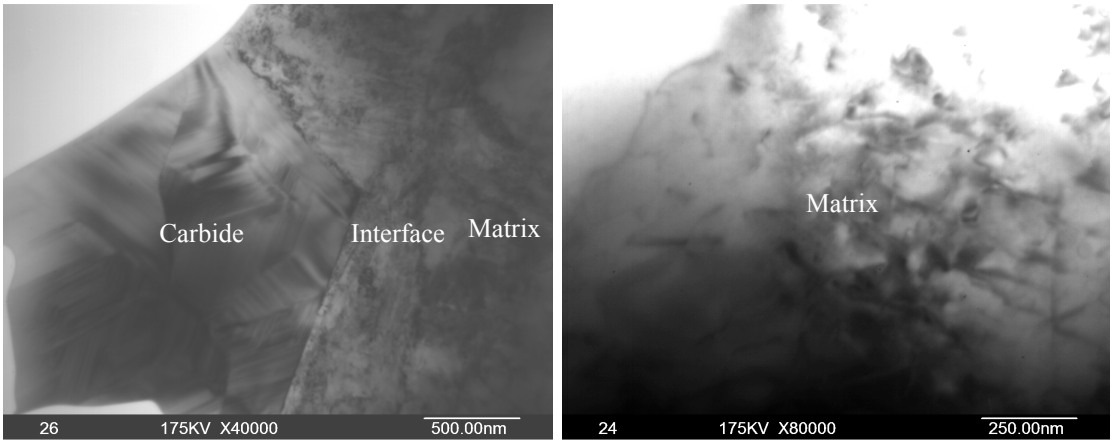
So it can prevent the nano-particles gathering to the interface through the method of adding the nano-particles in the form of intermediate alloy. This method allows more nano-particles diffusing in the matrix for strengthening effect .Thus the effect of optimization of high chromium cast iron alloy microstructure is more significant by nano intermediate alloy. At the same time, the modificator contains a small amount of rare earth or nickel metal, which makes the microstructure further optimized.



a)Without nano intermediate alloy b) NO.1 nano-TiN intermediate alloy

c) NO.2 nano-TiN intermediate alloy d) NO.3 nano-TiN intermediate alloy

Fig. 1 SEM images of strengthened cast-penetrated layer of nano intermediate alloy



EDS analysis of the interface

element	weight percentage	atomic percentage
Ti K	0.08	0.09
Cr K	12.47	13.28
Fe K	85.76	85.03
Ni K	1.69	1.60
Ti K	0.08	0.09
total	100.00	

EDS analysis of the matrix

element	weight percentage	atomic percentage
Si K	0.67	1.32
Ti K	0.27	0.31
Cr K	11.83	12.52
Fe K	85.16	83.91
Ni K	2.07	1.94
total	100.00	

Fig. 2 TEM images and EDS analysis of bonding interface of the matrix and the strengthened carbide cast-penetrated layer with NO.3 nano-TiN intermediate alloy

High temperature and speed wear resistance of nano-TiN enhanced cast-penetrated layer. The high temperature wear performance at a high speed of the cast-penetrated layer was test. The experimental parameters set two temperatures of 200 ℃ and 500 ℃, two loads of 0.20 MPa and 2.0 MPa while the high-speed is fixed at 10 m/s for 5 min. The results are shown in Fig. 3.

As Fig.3 shown, comparing with directly adding nano-TiN powder, it can improve high temperature wear resistance of cast-penetrated layer of the high Cr cast iron by adding nano intermediate alloy. It is most significant to the improvement of wear resistance by adding a small amount of rare earth nano-TiN intermediate alloy NO.3 and nickel nano-TiN intermediate alloy NO. 2. And adding nano-TiN intermediate alloy NO.1 is just after the effect. For the wear resistance of cast-penetrated layer, adding nano-TiN intermediate alloy NO.2 is close to adding nano TiN intermediate alloy NO.3 under the condition of 500 ℃. It shows that, under the condition of high temperature, it is more significant to improve the high temperature wear resistance of cast-penetrated layer by adding Ni nano intermediate alloy.

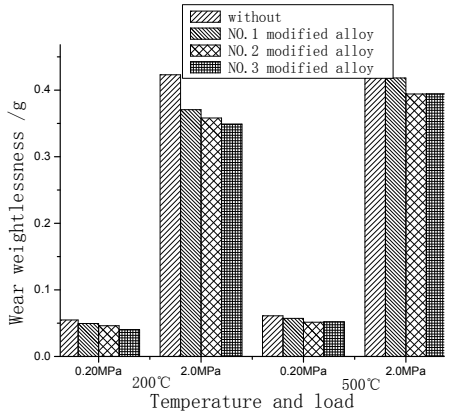


Fig. 3 Test of high temperature wear performance at a high speed

Ni is infinite solid soluble in austenite. It improves the matrix strength and resistance performance to high temperature oxidation corrosion, and reduces the carbide loss in the matrix without reducing the toughness. It is beneficial to thermal fatigue wear from this perspective.

Conclusions

(1). Compared with adding not nano-TiN intermediate alloy, it is better to add nano intermediate alloy into cast-penetrated agent. That can further optimize the microstructure of cast-penetrated layer, promote grain refinement, and make carbide evenly distributed in the form of granular, rods, and layered structure. It has the best effect by adding rare earth to nanometer intermediate alloy.
(2). It can improve the enrichment of the nano-particles near the carbide by adding nano-TiN intermediate alloy (when directly adding nano-TiN powder), more nano-particles dispersed in the matrix due to the heterogeneous nucleation effect by adding nano-particles in the form of nano intermediate alloy.
(3). It can improve the wear resistance of penetrated layer by adding nano intermediate alloy into cast-penetrated agent. The penetrated layer will have the best wear resistance when joining nanometer TiN intermediate alloy containing slight amount of rare earth.
(4).The cast-penetrated layer has good high temperature wear resistance, when adding nano TiN intermediate alloy (containing Ni).

References

[1]. SUN Jian-rong，SUN Yang-shan. Oxidation resistance of TiC particulate reinforced 1 Cr18Ni9 matrix composites prepared by in-situ reaction [J]. MATERIALS SCIENCE＆TECHNOLOGY, 2001，9(4): 393-396.
[2]. XU Kai-hong, LI Kun-da. TiC dispersion strengthening 440C stainless steel prepared by mechanical alloying [J]. Materials Science and Engineering of Powder Metallurgy, 2008, 13(2): 91-96.
[3]. SHAO Xing-hai, XIE Jing-pei, YANG Yu-jiang etc. Study on Wear Resistance of High-Cr Cast Iron Cast-Infiltrated Layer Strengthened by Nano TiN [J]. China Foundry, 2013，3: 52-56.
[4]. XIE Jing-pei, GUO Zheng, SHAO Xing-hai etc. Investigation on Microstructure of Cast Layer in Guide Plate Strengthened by Nanometer TiN [J]. Journal of Henan University of Science and Technology, 2012，33(5): 1-3.
[5]. YU Hui-wu, WANG Wen-yan, XIE Jing-pei etc. Research on the Microstructure and Mechanical Properties of ZGMn18Cr2 Strengthen by Modified TiN Nano-Powders[J]. China Foundry, 2012，(5): 15-18.

Key Engineering Materials Vols 645-646 (2015) pp 226-231
© (2015) Trans Tech Publications, Switzerland
doi:10.4028/www.scientific.net/KEM.645-646.226
Submitted: 2014-12-05
Accepted: 2014-12-23

Research on delamination of plastic packaging device during reflow soldering

Peisheng Liu[1,2, a], Ying Lu[1], Jinxin Huang[1] and Longlong Yang[1]

[1]Jiangsu Key Laboratory of ASIC Design, Nantong University, Nantong 226019, China

[2]Nantong Fujistu Microelectronics Co., Ltd,Nantong 226006, China

[a]psliu@ntu.edu.cn

Keywords: plastic packaging; reliability; reflow soldering; delamination; moisture

Abstract. Due to the application of lead-free solders, the quality and reliability of plastic packaging device are influenced by the increase of reflow temperature. In this paper, a low-profile quad flat package (LQFP) is chosen to illustrate the interface deformation during reflow soldering. The stress analysis theory and the finite element analysis (FEM) simulation are introduced in this paper. By means of finite element software, the distribution of hygrostress, thermal stress and the deformation of device on the printed circuit board (PCB) are analyzed and calculated under different temperature. The relationship between delamination length and deformation is given. The simulation results show that the warping phenomenon is found at the apex angle of the device; delamination is easily produced in the interfaces between different materials by thermal stress, and possibly leads to the device failure.

Introduction

In the packaging industry, plastic packaging integrated circuit (IC) is widely used, because it has many advantages in the side of size, quality, cost, performance and service life. During the printed circuit board (PCB) mounting process, the package is subject to Pb-free soldering shock temperatures between 250℃ and 260℃ [1,2]. At such high temperatures, the package will face with great challenge of thermal reliability. The interfaces between the different materials of IC package may delaminate under the action of thermal stresses caused by the coefficient of thermal expansion (CTE) mismatch. At the same time, if the molding compound (MC) has absorbed moisture, a hygrostress or vapor pressure will build up in the delaminated gap. Once these stresses are more than any of the yield strength or fracture strength of materials, the package crack propagates to the edge of the MC, known as the “popcorn effect” [3]. Fukuzawa et al. [4] were the first to propose a mechanism for this phenomenon.

Delamination refers to the package internal interfaces between different materials appearing tiny stripping or separation, this is a kind of internal latent stress problems of package. It can cause device failure and life greatly reduced [5]. The delamination of plastic packaging device has become more and more serious and complicated [6]. The main factors of the delamination are thermal stress, hygrostress and vapor pressure. For small cracks, the thermal stress is the dominant component, and for large cracks, the vapor pressure is significant [7]. In this paper, a Low-profile Quad Flat Package (LQFP) is chosen to analyze the hygrostress, thermal stress, and the delamination.

Theoretical Analysis

Micro-voids and micro-cracks are formed at the interfaces between different materials during fabrication of plastic packaging ICs, and the MC based on polymer materials is hydrophilic and porous, so it's easy to absorb moisture when exposed to humid ambient condition [8,9]. Moisture diffuses from the package's exterior surfaces into the MC. Fick's second law can be applied to describe the moisture diffusion process in polymer materials [10]. For the isotropic material,

$$\partial C/\partial t=D\ (\partial^2 C/\partial x^2+\partial^2 C/\partial y^2+\partial^2 C/\partial z^2) \quad (1)$$

Where D is the diffusion coefficient, C is the moisture concentration, x, y and z is Cartesian coordinates, and t is the time.

Due to the temperature diffusion conforming to the Fick diffusion law, the moisture diffusion can be analyzed through the heat conduction module of the finite element software (FEM). Since the moisture concentration C is discontinued, Wong et al. [11] proposed a new field variable, relative wetness. That is,

$$w=C/C_{\text{sat}} \quad (2)$$

Where C_{sat} is saturated moisture concentration. When w=1, the material has reached to saturated concentration; when w=0, the material is totally dry. The "wetness" thermal-moisture analogy scheme for finite element implementation is presented in Table 1 [11].

Table 1. FEA "wetness" Implementation Scheme

Properties	Thermal	Moisture
Field variable	Temperature, T [℃]	Wetness, w
Density	ρ [kg/m^3]	1
Conductivity	K [W/(m•℃)]	D•C_{sat} [kg/(s•m)]
Specific capacity	c [J/(kg•℃)]	C_{sat} (kg/m^3)

During the reflow soldering, the outer surface of the plastic device expose to thermal load, then the heat conducts to the internal. A one-dimensional heat conduction of the solid internal follows the Fourier's law, its expression is:

$$q = - k A_{\text{c}}\, \mathrm{d}T/\mathrm{d}x \quad (3)$$

Where q is the heat flow density; k is the thermal conductivity on the heat flow direction; A_c is the cross sectional area on the heat flow direction; dT/dx is the gradient of temperature.

Due to the different CTE (α) of different materials, the thermal stress will occur in the heat transfer process. If the α is constant, the formula of thermal stress is:

$$\varepsilon=\alpha\,\Delta T \quad (4)$$

Failure Analysis

A. Determination of moisture diffusion parameter. Before the solder reflow process, the package is subjected to moisture soaking at a particular temperature/humidity condition. The material properties needed for moisture diffusion study are D and C_{sat}. In the present work the material properties are shown in Table 2 [12].

Table 2. Material Properties for Moisture Diffusion

Material	30℃/RH60%		60℃/RH60%	
	C_{sat} [kg/m^3]	D [mm^2/s]	C_{sat} [kg/m^3]	D [mm^2/s]
Silicon	1×10^{-6}	1×10^{-6}	1×10^{-6}	1×10^{-6}
Die attach	1.47×10^{-5}	9.39×10^{-8}	2.75×10^{-5}	4.81×10^{-7}
Copper	1×10^{-6}	1×10^{-6}	1×10^{-6}	1×10^{-6}
EMC	7.81×10^{-6}	3.13×10^{-7}	1.34×10^{-5}	1.14×10^{-6}

B. Finite-element model and boundary conditions loading. A LQFP is selected as analysis object. According to the JESD51-3 standard, the matched PCB is established. Its size is 76.2mm×114.3mm，thickness is 1.57mm，and material is FR-4. The package is mainly composed of silicon die, conductive adhesive, lead frame and encapsulation materials, but some materials such as gold wires are ignored. Due to symmetry, only a quarter of three-dimensional finite element model needs to be analyzed, as shown in Fig. 1.

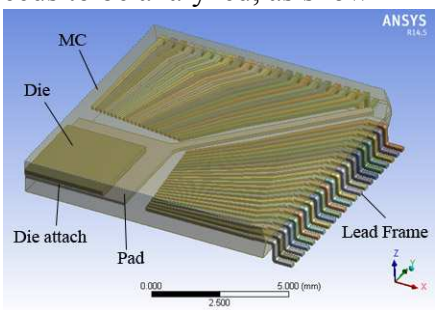


Fig.1 A quarter of three-dimensional finite element model

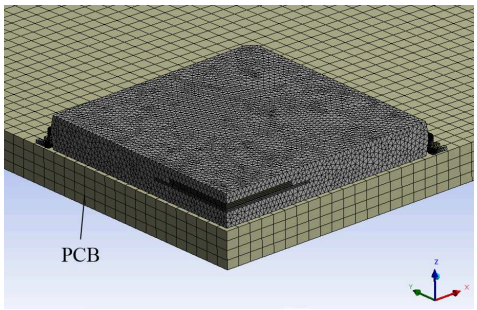


Fig.2 LQFP meshing model

In the sub-modeling technique, a global mesh model is established, as shown in Fig. 2. In order to focus on the analysis of the package, the meshing element size of package is smaller than PCB's.

Using the structure of the transient thermal analysis and steady-state analysis in ANSYS finite element analysis software, the hygrostress, thermal stress and deformation of devices could be analyzed and calculated. According to the moisture diffusion parameters, the moisture absorption processes of different conditions before the reflow soldering are simulated. According to the temperature cure of the lead-free reflow soldering, the boundary conditions of temperature are defined as Table III. Then load the boundary conditions to the model to analyze the thermal stress distribution during the reflow soldering.

Table 3. The Step of Temperature Loading

Steps	Time[s]	Temperature[℃]
1	0	25
1	60	150
2	150	150
3	180	260
4	190	260
5	240	100

Results and Discussion

A. **Moisture absorption process.** Loading the two groups of humidity conditions (30℃/RH60%, 60℃/RH60% for 168h), the results of moisture absorption process are shown in Fig. 3 and Fig. 4.

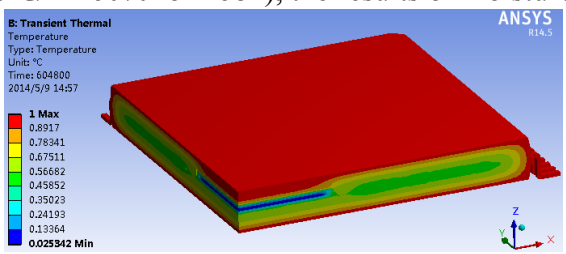


Fig.3 Moisture distribution inside LQFP after 168h soaking in 30℃/RH60%

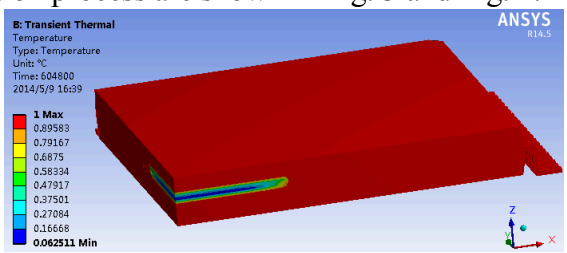


Fig.4 Moisture distribution inside LQFP after 168h soaking in 60℃/RH60%

After 168h soaking in 30℃/RH60%, the package is not completely wet, and the die is still dry. But after 168h soaking in 60℃/RH60%, the EMC is almost completely wet, and the die absorbs little moisture. The moisture absorption speed of die is slower than the EMC's. These results accord with the material properties for moisture diffusion (Table 2).

According to the results of moisture absorption, the hygrostress distributions are solved by structural module, as shown in Fig. 5 and Fig. 6. Comparing to Fig. 5 and Fig. 6, the equivalent stress is changed from 37.6Mpa to 68.1Mpa. The equivalent stress is equal to the hygrostress. The hygrostress is increased with the temperature increasing. So the environment temperature is important to the reliability of the package. And the maximal stress is located at the top corner of die.

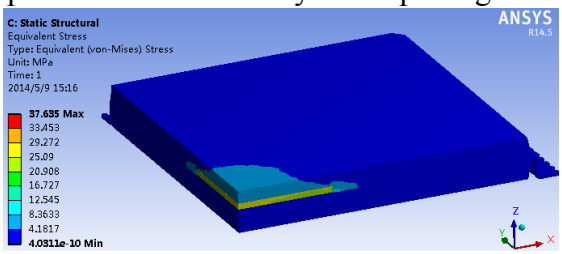


Fig. 5 Equivalent stress results of LQFP subjected to moisture soaking at 30℃/RH60% for 168h

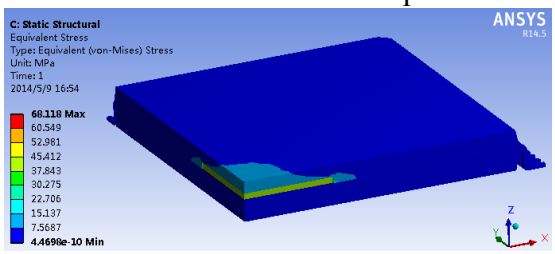


Fig. 6 Equivalent stress results of LQFP subjected to moisture soaking at 60℃/RH60% for 168h

B. Reflow soldering process. Next, according to the temperature cure of the lead-free reflow soldering, the thermal stress analysis is also obtained through FEM simulation. The total deformation and equivalent stress results at the reflow peak temperature of 260℃ are shown in Fig. 7 and Fig. 9. And the total deformation and equivalent stress results at the end of reflow soldering of 100℃ are shown in Fig. 8 and Fig. 10.

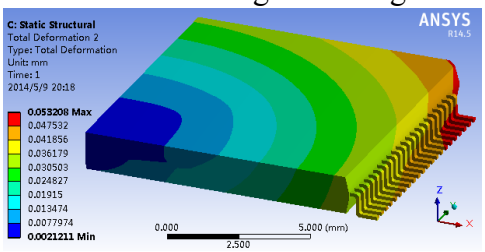


Fig.7 Total deformation results at 260℃

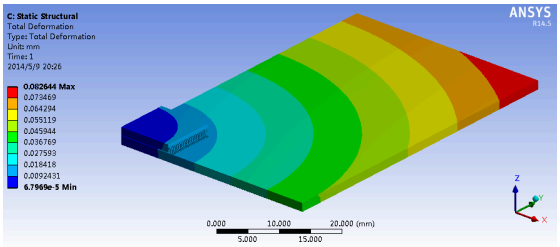
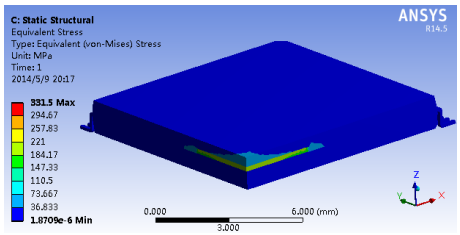
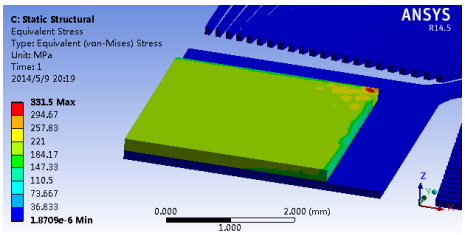


Fig.8 Total deformation results at 100℃

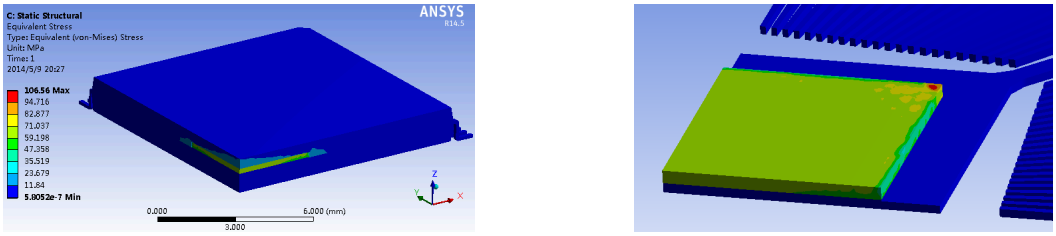




(a)The equivalent stress of package at 260℃ (b)The equivalent stress of die at 260℃

Fig.9 Equivalent stress results at 260℃

The top corners of PCB and package have maximal deformation seeing from Fig. 7 and Fig. 8, so it easy to occur to warping phenomenon. Fig. 9 and Fig. 10 show that the maximal stress of 260℃ is 331.5Mpa, and the maximal stress of 100℃ is 106.56Mpa. The die corner's stress is also the largest. So the die/MC interface is easy cracked and occurs to delamination under the highest temperature about 260℃. It is found that the thermal stress distribution is similar to the hygrostress's, but the value of thermal stress is larger. The thermal stress has greater influence on the delamination of package.



(a)The equivalent stress of package at 100℃ (b)The equivalent stress of die at 100℃

Fig.10 Equivalent stress results at 100℃

According to the characteristics of the reflow soldering temperature curve, time of 30s, 50s, 100s, 150s, 180s, 190s, 200s, 220s and 240s are selected to analyze the deformation and the thermal stress, as shown in Fig. 11 and Fig. 12. The change in the deformation and the thermal stress with respect to temperature are all linear elastic behavior. In the 180s to 190s, they all reach the max. At the same time, there are some other stresses such as hygrostress or vapor pressure. The top corners of die are easy to be cracked under these stresses. Therefore the die/MC interface may delaminate.

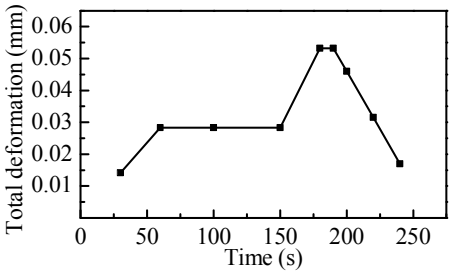


Fig.11Total deformation versus time

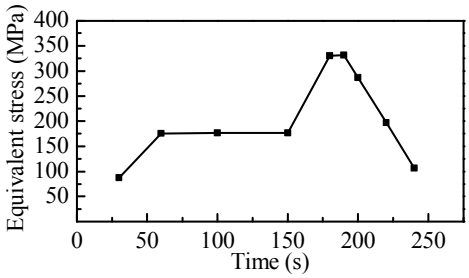


Fig.12 Equivalent stress versus time

C. Delamination simulation. An initial delamination is modeled at the die top corner to discuss the relationship between delamination length, deformation and equivalent stress.

Increasing the delamination length, the deformation will increase as well as the equivalent stress, as shown in Fig. 13. When the deformation reaches to a critical value, the die will be broken, and the package will could not be used. Therefore, the delamination seriously affects the using life and reliability of package. The solution of the delamination problem will greatly improve the development of plastic packaging.

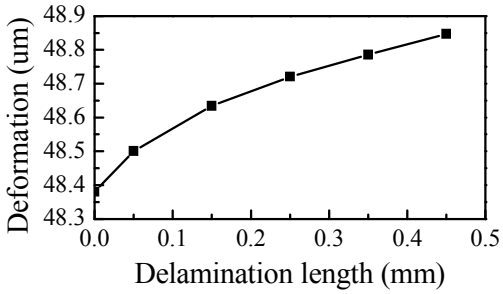


Fig.13 Deformation versus delamination length

Summary

In this study, a finite element model of LQFP is built, material properties for moisture diffusion are defined and boundary conditions are loaded. The moisture absorption and reflow soldering process are analyzed. The hygrostress and thermal stress are calculated by FEA software. The results show that thermal stress is the principal factor of delamination during the reflow soldering. Furthermore, the delamination at the die/MC interface is simulated, and the relationship between delamination length, deformation and equivalent stress is obtained through numerical simulation. It could be used to predict delamination failures, and further study on this method will be carried out in future.

Acknowledgement

This work was financially supported by the Key Natural Science Foundation of the Jiangsu Higher Education Institutions of China (Grant No. 10KJA140043).

References

[1] P. Alpern and K.C. Lee, A simple model for the mode II popcorn effect in thin plastic IC packages, 2003 41st IEEE International Reliability Physics Symposium Proceedings, (2003) 452-457.

[2] C. Yuan and L. Ping, The "popcorn effect" of plastic encapsulated microelectronic devices and the typical cases study, 2011 International Conference on Quality, Reliability, Risk, Maintenance, and Safety Engineering, Xi'an, Shanxi, China, (2011) 482-485.

[3] P. Alpern and C.L. Kheng, Moisture-Induced Delamination in Plastic Encapsulated Microelectronic Devices: A Physics of Failure Approach, IEEE Transactions on Device and Materials Reliability, vol. 8, (2008) 478-483.

[4] I. Fukuzawa, S. Ishiguro and S. Nanbu, Moisture Resistance Degradation of Plastic LSIs by Reflow Soldering, 1985 23rd Annual Reliability Physics Symposium, Orlando, FL, USA, (1985) 192-197.

[5] L. Yumin, L. Yong, S. Belani, and J. Oseob, Investigation of interface delamination in a SO8 package under reflow, 2012 13th International Conference on Thermal, Mechanical and Multi-Physics Simulation and Experiments in Microelectronics and Microsystems, Cascais, (2012) 1-6.

[6] A. Yadur, P. Gromala, S. Green, and K. Mat Daud, Investigation of interface delamination of EMC-copper interfaces in molded electronic packages, 2013 14th International Conference on Thermal, Mechanical and Multi-Physics Simulation and Experiments in Microelectronics and Microsystems, Wroclaw, (2013) 1-6.

[7] A.A.O. Tay, Modeling of delamination in IC packages, 2012 13th International Conference on Electronic Packaging Technology and High Density Packaging, Guilin, Guangxi, China, (2012) 854-860.

[8] A.A.O. Tay, Modeling of interfacial delamination in plastic IC packages under hygrothermal loading, Journal of Electronic Packaging, vol. 127, (2005) 268-275.

[9] J.E. Galloway and B.M. Miles, Moisture absorption and desorption predictions for plastic ball grid array packages, IEEE Transactions on Components, Packaging, and Manufacturing Technology, Part A, vol. 20, (1997) 274-279.

[10] H. Guojun, R. Rossi, L. Jing-En, and X. Baraton, Interface delamination analysis of TQFP package during solder reflow, Microelectronics Reliability, vol. 50, (2010) 1014-1020.

[11] E.H. Wong, S.W. Koh, K.H. Lee, and R. Rajoo, Advanced moisture diffusion modeling and characterisation for electronic packaging, 2002 52nd Electronic Components and Technology Conference Proceedings, (2002) 1297-1303.

[12] T.F. Lam, FEA simulation on moisture absorption in PBGA packages under various moisture pre-conditioning, 2000 50th Electronic Components & Technology Conference Proceedings, Las Vegas, NV, (2000) 1078-1082.

Key Engineering Materials Vols 645-646 (2015) pp 232-237
© (2015) Trans Tech Publications, Switzerland
doi:10.4028/www.scientific.net/KEM.645-646.232

Submitted: 2014-12-21
Accepted: 2014-12-29

Preparation of Nano α-Fe_2O_3 powders and characterization of their photo-catalysis capacities

Zhang Nanyangsheng[1, a], Zen Yanan[1,b*], Wang Shuangbao[1,c], Zhu Bing[1,d]

[1]School of optics and electronic information, Huazhong University of Science & Technology, Wuhan 430074, P.R. China

[a]nyzhang@hust.edu.cn, [b]zya401@126.com(corresponding author), [c]sb_wang@126.com, [d]hust_zhubing@qq.com

Keywords: Nano α-Fe_2O_3, Photo-catalysis, Sol-gel

Abstract. The hematite α-Fe_2O_3 is considered as low cost-effective semiconductor for photo-catalysis recently. We have prepared high quality α-Fe_2O_3 nano powder by sol-gel method, as shown by XRD diffraction, we could find that the powder are as small as 5-10nm. We also characterize the photo-catalysis properties on such magnets, which show unique photo-induced catalysis capacity.

Introduction

Recently, with a continuous reduction of fossil fuels, the photoelectrochemical (PEC) system to convert solar energy into chemical energy becomes one of significant approach to utilizing solar energy. The core of PEC system is a semiconductor electrode used as either photoanode or photocathode. In order to search a suitable electrode, metal oxides such as TiO_2, ZnO, Cu_2O, $SrTiO_3$, Fe_2O_3 [1-3], etc. have been studied. Among various candidate materials, α-Fe2O3 whose bandgap is approximately 2.2 eV has been considered as a potential candidate due to its low cost, chemical stability, widespread availability, and high absorbance (about 40% of the visible solar spectra). In fact, solar UV light reaching the earth surface is relatively small (ca. 3–5%). The band-gap energy of α-Fe_2O_3 is 2.2 eV [4] and can be activated with visible light (<560 nm). Fe_2O_3 photo-electrode is a solar energy conversion material [5]. Here, we report the results on preparation of the hematite and its photo-catalysis capacity. The hematite α-Fe_2O_3 is one of the corundum structures and is an active catalyst for many important reactions like the dehydrogenation of ethyl benzene to styrene [6]. Recently, it has been considered as low cost-effective semiconductor for photo-catalysis [6-7].

In choosing Fe_2O_3 as basic material for researching, the hematite has received considerable attention for the solar energy conversion due to its high resistivity to corrosion and moderate gap. It can capture 40 wt% of the solar light. In addition, α-Fe_2O_3 is by far most attractive from an ecological aspect as well as an economical standpoint. On the other hand, it is worth noting that although the physical properties were actively studied, the photo-electrochemistry has not yet been fully explored.

Experimental

Preparation of nano α-Fe_2O_3. All chemicals were of analytical grade and used without further purification. The starting chemicals used were ferric chloride, SDBS, ammonia without further purification, and the distilled water was used as solvent. Precursor powders were synthesized using the following method: 0.1 mole ferric nitrate was dissolved in 150 ml of distilled water and mixed it with 100 ml aqueous solution of 0.1 mole SDBS. The resulting mixture was stirred for 1 hr at room temperature using a magnetic stirrer. A dark brown fluffy precursor was formed when this mixture was evaporated on a hot plate. Precursor powder prepared by this method will be referred hereafter as "Precursor-2".α-Fe_2O_3 nanometer powders were obtained by grinding the precursor powders, followed by calcinations in air for 2h at different temperatures ranging from 200 to 400 °C.

0.5g ferric chloride were dissolved in a 25 ml (0.1mol/L) solution beaker, then to be made a 25ml of 0.1 mol/L solution; 5ml of ammonia water was filled into a corresponding measuring cylinder and diluted by distilled water by 25 ml of 0.1mol/L solution; agitated until a homogeneous mixture; using

a 25 ml beaker filled with 5 ml distilled water with 0.03g SDBS and agitated into homogeneity. We modify PH value of the solution by dilution hydrochloric acid at room temperature. Using two acidic- and alkaline burettes to drop $FeCl_3$ solution and the ammonia into the beaker with the prepared matrix solution simultaneously, after titrating with the $FeCl_3$ solution, the titrating of ammonia was also stopped, magnetic stirring for 20 min then a sol-gel solution was obtained; (4) stewing for days and sediment was formed from the solution, the sediment was moved out and dried out, finally the dried sediments were ground into super-fine powders.

Common characterization. TG and DSC analyses of the precursors were conducted using DTG–60 and DSC–60 instruments from Shimadzu, Japan respectively. The experiments were conducted under air flow between room temperature and 550 °C at a scanning rate of 20 °C/min. The sample pans were in aluminum in both cases. The crystalline phases present in the materials calcined at various temperatures were identified by XRD using a Powder X-Ray Diffractometer (Rigaku, Japan) with Cu Kα radiation. Scans were recorded in the (2θ) range of 0° to 95° with a scan rate of 2° /min. The particle size for the calcined powder was determined using a Scherr equation and FEI HRTEM (Tecnai G2 30STwin) at an accelerating voltage of 300 kV.

Photo-catalysis measurement. Here, an evaluation platform was set up by ourselves: a quartz cuvette (in a size of 10×10×120mm), OPS-100 fiber spectroscopy, high voltage mercury lamp were used for this goal to evaluate the photo-catalysis capacity. Before the measurement, such chemical regents: α-Fe_2O_3 powders, methyl orange dilute solution and distilled water were mixed and filled into the quartz cuvette. While light from the light source goes through the quartz cuvette, filled with methyl orange, there absorption occurs. The out light was received by CCD spectroscopy(SPEC-100) that is also connected to PC via a USB series port. By using a Lamb-Beer law we could analysis the relationship between the methyl orange concentration and the photo-catalysis capacity of nano α-Fe_2O_3.

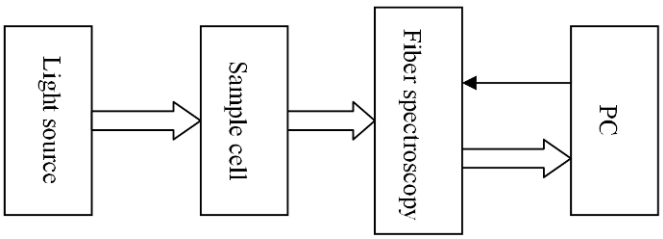


Fig. 1 A measurement system on photo-catalysis of nano-α-Fe_2O_3

Firstly it is to prepare a methyl orange solution of 6.1×10^{-5}M and use it as goal degradation matter. Then we put 25ml of the solution into a 25ml volumetric flask and fill the volumetric flask with 0.05g α-Fe_2O_3 powder. Finally the volumetric flask was irradiated with a high voltage mercury lamp (250W). After each 2 hours' period a part of the solution was moved out and centrifuged, and then the clean top solution was used as the candidate for measurement in the spectroscopy. Moreover, from the calculation of the change in those absorption peaks of the solutions, the photo-catalysis capacity of the nano α-Fe_2O_3 could be expressed.

Results and discussions

Common tests. XRD results show that the as-prepared powder is amorphous like diffraction spectra. The high resolution TEM images (no show) reflect that the grain size is larger than 5 μm. many papers also report that the grain are agglomerate into larger size instead of dispersed into smaller grain size[1,7]. We obtain larger particles. The results reveal that we have rapider reaction between $FeCl_3$ and ammonia water, the sediment forms quickly and the agglomeration occurs as rapid as the reaction. Referencing to this phenomenon, we modify the preparation procedure and parameters step by step to make fine and homogeneous powder.

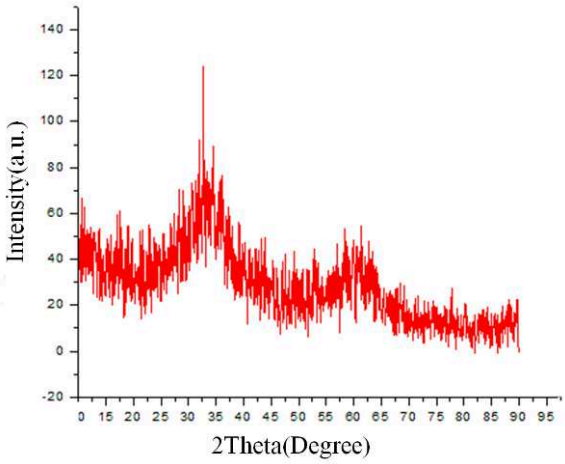


Fig.2 The XRD spectrum of the α-Fe_2O_3 powder prepared

We change the dropping ammonia water instead of using magnet stirring while the dropping was performed. The sediments become slowly and the sediments seem homogeneous and superfine. We use these powders for XRD measurement. The results were shown in Fig.2, which it could be found that the powder is also amorphous-like. Then a series of annealing were carried out on these samples, kept in an oven for 2h at 200℃ and 300℃, respectively.

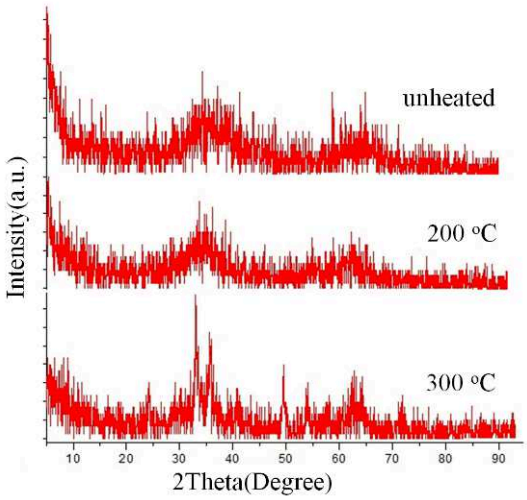


Fig.3 The XRD spectra of the samples annealed at various temperatures

From the XRD results, we could see that the as-prepared sample and the heat-treated sample show any change in the diffraction spectra. While annealing temperature is kept below 300℃, there is small change in the diffraction spectrum. However, above 300℃, the diffraction spectrum show a change in the pattern and there are apparently some peaks corresponding to α-Fe_2O_3. It is understood that the powder shows a grain forming proceeding from amorphous iron oxide.

Photo-catalysis study. In fact, methyl orange belongs a kind of azo dyes [7], which solution shows an absorption in visible light wavelength. Hence, we design a measurement system for evaluation of its photo-catalysis capacity. A 3W white light SLED was used as light source, and a fiber spectroscopy was used as check out appliance. Between them we design a sample cell with quartz materials that had a little absorption in visible wavelength. Based on this measurement system, we could obtain any information on the absorption degree and the concentration change of methyl orange. Due to the photon absorption and the concentration of methyl orang also were in inverse ratio to the degradation velocity of methyl orange. Therefore, a new concept is introduced that the decolorization rate [8] was used for an evaluation the degradation effect of photo-catalysis, and the equation on the decolorization rate was described as followed:

$$D = [(A_0 - A) / A_0] \times 100\% \quad (1)$$

D is the decolorization rate. A_0 is the absorption value before the methyl orang degradation, and A is the absorption value after the methyl orang degradation. Therefore, while the degradation velocity is decreased, the decolorization rate is improved. We could also use the decolorization rate to express the effect of photo-catalysis, thus is more directly.

From the figure we could know that the spectra peak decreases versus an improvement in methyl orang concentration. However, it is clearly that curve isn't linear relationship. Therefore, firstly to obtain an absorption curve of the standard solution, then seeking for the largest absorption peak and calculate the maximum absorption. From these results, we could find that when the concentration ranges from 0.001g/L to 0.009g/L, the corresponding largest absorption degree indicate that their distances are similar equal. In the other words, the absorption degree is almost liner to the methyl orange concentration.

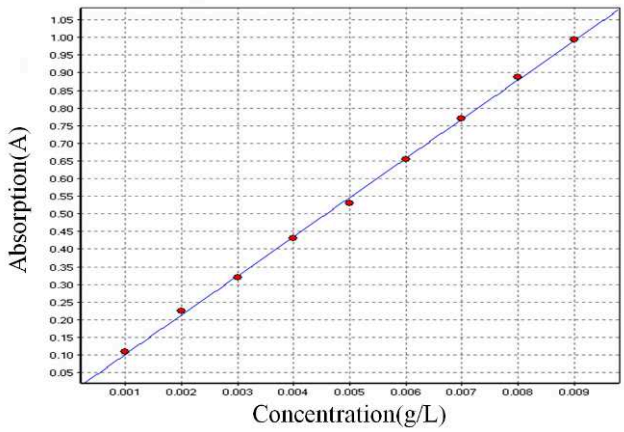


Fig.4 The standard curve on the absorption degree methyl orange at different concentrations

From the Fig.4 we could find that the 9 points corresponding to the standard solution with various methyl orange concentrations. The blue line is the fitting result by these red points. It is clear that the linear degree is high and the slope is about 111.005 and the intercept on the absorption degree axis is -0.008656g/L. Basing on two values, we could calculate all unknown methyl orange concentration in later proceeding.

In order to verify the accuracy, we make a confirmed methyl orange concentration of 0.02g/L solution. Then the measurement system gives out the absorption degree curve. We find that the maximum absorption value is 2.1834. Using the absorption value to calculate the concentration and we obtain that the methyl orange concentration and the difference between the experiment and the calculation is very small, only is 0.0003, it is neglect-able.

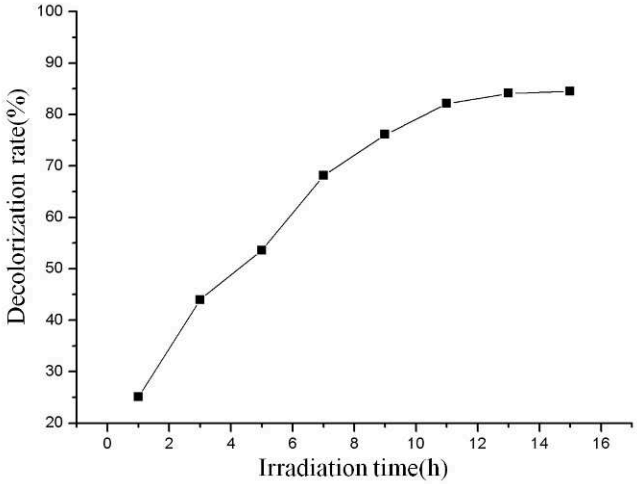


Fig. 5 The change of the decolorization rate versus irradiation time

The photo-catalysis effect of α-Fe_2O_3. 0.02g/L of methyl orange solution without α-Fe2O3 powder was irradiated under 250W high voltage mercury lamp, after each 2 hours to obtain a water sample and measure it and calculate the decolorization rate. The experimental result is shown in Fig.5.

When light irradiation proceeds by 5 hours the decolorization rate achieves 15.2%. And the decolorization rate increase versus time from 1h to 5h the decolorization rate improves by 2 times. However, the methyl orange solution degrades a little under light irradiation without α-Fe_2O_3.

Fig.5 shows that the absorption degree and concentration also decrease while the time is increased in α-Fe_2O_3 case, but the decolorization rate increases. This means that the photo-catalysis capacity of α-Fe_2O_3 on methyl orange increases versus the irradiation time. However, after 15 h irradiation, the decolorization rate changes slightly.

From the Fig.5 it is apparently that the decolorization rate increases rapidly in former time periods. In the later irradiation periods, the velocity decreases (especially from 11h to 15h, it is similar a line). This means that the photo-catalysis of α-Fe_2O_3 on methyl orange is rapid and the concentration of methyl orange decreases much, and then the concentration of methyl orange decreases slowly. From 11h to 15h, the concentration of methyl orange only decreases from 0.0034mg/L by 0.003mg/L, the change is only 0.0004mg/L. This velocity is only the 1/50 of the beginning degradation velocity. The reason for this phenomenon is that at the beginning the concentration is larger and the methyl orange could be easily absorbed onto the surface of α-Fe_2O_3 so that the methyl orange is easy to capture Hydroxyl group. In the later periods, the concentration decreases much. Therefore, the methyl orange captured on the α-Fe_2O_3 surface is less, and they have little chance to capture Hydroxyl group so that the photo-catalysis velocity decreases.

According to the results and analysis above, the nano α-Fe_2O_3 powder own good photo-catalysis ability. It shows that α-Fe_2O_3 is a potential solar sunlight photo-catalysis and an absorber in methyl orange solution also. While using mercury lamp to irradiation, α-Fe_2O_3 absorbs photon to produce electron-hole pair upon the dissolved oxygen and water, and induce active groups [9-10], such as Hydroxyl group. Hydroxyl groups own extremely strong oxidation capacity and can react with many organ matters by oxidation, reduction, displacement, electron capture or loss reaction, which make the organ matter degradation. In fact, photo-catalysis proceeding is an action on the surface. The α-Fe_2O_3 owns larger surface and could absorb methyl orange onto its surface, so photo-catalysis could be preceded and methyl orange could be degraded.

Conclusions

We prepared nano α-Fe_2O_3 by sol-gel route and study its photocatalysis capacity under a home-made optical measurement system. The standard methyl orange solution was used as base curve, and then we also carried out the accurate evaluation on this standard base curve. The photocatalysis property of α-Fe_2O_3 powder on methyl orange solution was also studied here. The experiments show that the as-prepared α-Fe_2O_3 powder is a good photocatalysis semiconductor. The methyl orange solution was degraded well under high voltage mercury lamp irradiation. With the increasing irradiation time, the degradation velocity improves. After 15h irradiation, the decolorization rate achieves 84.5%.

References

Reference an article:
[1] Mazellier P., Bolte M., Heterogeneous light-induced transformation of 2, 6-dimethylphenol in aqueous suspensions containing goethite, Journal of Photochemistry and Photobiology A: Chemistry. 132(2000) 129-135.
[2] Bandara J., Tennakone K., Kiwi J., Surface mechanism of molecular recognition between aminophenols and iron oxide surfaces, Langmuir. 17(2001) 3964-3969.
[3] Andreozzi R., Caprio V., Marotta R., Iron (III)(hydr) oxide-mediated photooxidation of 2-aminophenol in aqueous solution: a kinetic study, Water research. 37(2003)3682-3688.
[4] Bandara J., Mielczarski J. A., Lopez A., et al., Sensitized degradation of chlorophenols on iron oxides induced by visible light: Comparison with titanium oxide, Applied Catalysis B: Environmental. 34(2001) 321-333.
[5] Sun Z. Y., Du J. H., Chen H. S., et al., FTIR study of nano-iron oxyhydroxides' decoloration on the azo dye, Spectroscopy and Spectral Analysis. 26(2006)1226-1229.

[6] Chandra N., Leland J. K., Bard A. J., Semiconductor Electrodes LXI. Photoelectrochemistry of in Aqueous Solutions, Journal of The Electrochemical Society. 134(1987)76-80.
[7] Zhang S., Preparation of Cu2+/TiO2 Photocatalysts and their Application in Degradation of Methyl Orange, Xiangtan University, Xiangtan, 2004.
[8] Lou X., Wang T., Liu S., et al., Study on the photocatalytic degradation of reactive dyes by Fe2O3, Techniques and Equipment for Environmental Pollution Control. 7(2006)97-99.
[9] Liu G., Wu T., Zhao J., et al., Photoassisted degradation of dye pollutants. 8. Irreversible degradation of alizarin red under visible light radiation in air-equilibrated aqueous TiO2 dispersions, Environmental science & technology. 33(1999)2081-2087.
[10] He J., Chen F., Zhao J., et al., Adsorption model of ethyl ester of fluorescein on colloidal TiO2 and the mechanism of the interfacial electron transfer, Colloids and Surfaces A: Physicochemical and Engineering Aspects. 142(1998)49-57.

Key Engineering Materials Vols 645-646 (2015) pp 238-245
© (2015) Trans Tech Publications, Switzerland
doi:10.4028/www.scientific.net/KEM.645-646.238

Submitted: 2014-12-25
Accepted: 2014-12-31

Research on the preparation of nanoporous copper using Taguchi method

Kecheng Li[1, a], Xiaogang Liu[1, b], Yong Chen[1, c], and Mingxiang Chen[1, d *]

[1] School of Mechanical Science & Engineering, Huazhong University of Science & Technology, Wuhan , China, 430074

[a]kclee@hust.edu.cn, [b]xgliu@hust.edu.cn, [c]hbcy147@163.com, [d]chimish@163.com

Keywords: preparation process; nanoporous copper; pore size; process parameters; Taguchi method

Abstract. In this work, the influences of process parameters including electroplating time, annealing temperature, etchant concentration and dealloying time on the microstructures of nanoporous copper (NPC) were quantitatively evaluated in terms of pore size. Taguchi method was utilized to reduce the number of experiments required for the evaluation. The effect of each parameter variable on the characterization length scale of NPC was quantified and discussed. It was found that the annealing temperature was the most dominant factor influencing the microstructure of NPC and the dealloying time, electroplating time and etchant concentration contributed sequentially weakly to that of NPC.

Introduction

Due to high surface area and low density, nanoporous metals (NPMs) show some novel properties, such as high chemical activity and robust mechanical strength, which have attracted more and more attention as a kind of brand new functional materials. Additionally, they have been successfully applied to catalysts [1], sensors [2], actuators [3] and other fields. Currently, there are two mainstream approaches for fabricating NPMs, i.e., the template method and the dealloying method. In general, the template method is used for producing NPMs by replicating the porous anodic aluminum, however, it cannot change the pore size and the distribution unless the template structures are adjusted. By contrast, the dealloying method can readily control the pore size and distribution of NPMs through adjusting corrosion and post-annealing process. Hence, the dealloying method is widely utilized for fabricating NPMs.

Dealloying is a process during which the more electrochemically active element is selectively dissolved from the alloy, leaving behind porous structures composed almost entirely of the more noble alloy constituent. A.J. Forty *et al.* first studied the morphology of the microstructures in detail after immersing the Ag-Au alloy in nitric acid [4]. From the results of transmission electron microscopy (TEM), they figured out how the Ag-Au alloy eventually transformed into bi-continuous metal-void structures through surface diffusion during the selective corrosion process. Until 2001, J. Erlebacher *et al.* proposed a phase separation mechanism based on the percolation theory which was well accepted by world-wide researchers and established a continuum model which was fully consistent with the experiments and theoretical simulations [5]. Since the outstanding work of J. Erlebacher *et al.* that basically describes how the nanoporosity evolves during the alloy dissolution, much attention has been devoted to the fabrication of NPMs by dealloying. For instance, nanoporous platinum with a pore size of approximately 3.4 nm was attained through dealloying of $Cu_{0.75}Pt_{0.25}$ alloy in 1 M H_2SO_4 [6]. C. C. Zhao *et al.* developed a new Mg-Cu system to produce nanoporous copper (NPC) ribbons and bulk NPC by chemical dealloying [7].

For most researches on fabrication of NPMs, considerable attention has been paid to exploring new systems of precursors including Au-Ag [8], Zn-Au [9], Mn-Cu [10], and so forth. Nevertheless, systematical studies of effects of process parameters on microstructures of NPMs have been seldom reported. In this work, Cu-Zn alloy films on silicon substrate were prepared and a series of experiments using Taguchi method were conducted to investigate the influences of differing process parameters including electroplating time, annealing temperature, etchant concentration and dealloying time upon the microstructures of NPC.

Experimental

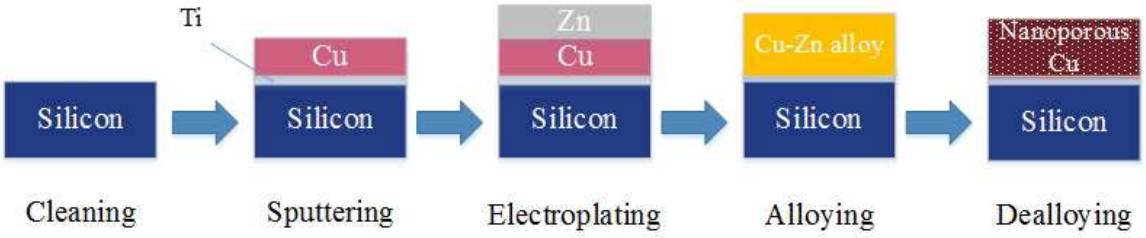


Fig. 1 Process flow of fabrication of NPC

Fig. 1 shows the schematic diagram of the process flow. Firstly, single-side polished n-type (111) standard bare silicon wafers with thickness of 500 μm were ultrasonically cleaned in acetone, ethanol and deionized water for 10 min each, respectively, and then followed by drying with nitrogen gas. After that, 200 nm Ti adhesion layer and 2 μm Cu layer were magnetron sputtered on the unpolished side of silicon substrates, in sequence. Next, electrodeposition of Zn was performed using a commercial Zn plating solution, composed of 60 g/L $ZnCl_2$, 200 g/L KCl, 25 g/L H_3BO_3, and 20 mL/L LuZn-8 additive. During electroplating, a constant current was utilized and the current density was kept at 20 mA/cm^2. After plating, the sample was rinsed by deionized water to remove the residual plating solution, then dried by nitrogen gas and then transferred immediately to a vacuum oven to prepare Cu-Zn alloy under thermal annealing for 2 h. At last, the samples were immersed in hydrochloric acid to fabricate nanostructured copper under free corrosion. Morphologies and microstructures of the as-dealloyed samples were characterized by scanning electron microscopy (SEM) and their components before and after dealloying were examined by X-ray fluorescence (XRF) and energy dispersive spectrometer (EDS), respectively. The detailed process parameters are listed in Table 1.

Table 1. Process parameters and conditions for fabrication of NPC

Process parameters	Conditions		
Electroplating time [min]	1	3	5
Annealing temperature [℃]	100	160	220
Etchant concentration [wt%]	5	15	38
Dealloying time [h]	0.5	5	20

It is well known that both physical and chemical properties of NPMs are greatly affected by their characterization length (pore size/ligament width). For example, studies of Young's modulus of nanoporous gold (NPG) were reported by A. Mathur and J. Erlebacher, and they found that with decreasing ligament size of NPG, their Young's modulus tended to increase [11]. H. J. Jiang *et al.* discovered that the melting point depression occurred when the size of tin particles were below 30 nm [12]. Therefore, the influences of process parameters on microstructures of NPC were evaluated in terms of pore size.

Results and Discussions

We investigated the pore size of the as-dealloyed samples of twelve differing cases (Table 1), comprised of three different conditions for each of the four process parameters, including electroplating time, annealing temperature, etchant concentration and dealloying time. With Taguchi method, 81 possible experiments were reduced to only 9 cases (Table 2) by utilizing $L_9(3^4)$ orthogonal array.

Table 2. Nine experiments for fabricating NPC and results

Exp. No.	Conditions				Pore Size [nm]
	Electroplating Time [min]	Annealing Temperature [℃]	Etchant Concentration [wt%]	Dealloying Time [h]	
1	1	100	5	0.5	14
2	1	160	15	5	37
3	1	220	38	20	0
4	3	100	15	20	17
5	3	160	38	0.5	38
6	3	220	5	5	34
7	5	100	38	5	18
8	5	160	5	20	30
9	5	220	15	0.5	39
K1	17	16.33	26	30.33	
K2	29.67	35	31	29.67	
K3	29	24.33	18.67	15.67	
R	12.67	18.67	12.33	14.66	
CR	21.7%	32.1%	21.1%	25.1%	
Notability	/	*	/	/	

Table 2 summarizes the pore sizes obtained from measuring the SEM images and the pore sizes of the as-dealloyed samples are ranged from 0 nm to 39 nm. By means of the range analysis method, the contribution rate (CR) of every process variables on target index (pore size) is determined as listed in Table 2. The results show that the influence factors from primary to secondary are annealing temperature, dealloying time, electroplating time and etchant concentration. Additionally, the relationship between each of the process variables and the pore size is also identified as plotted in Fig. 2.

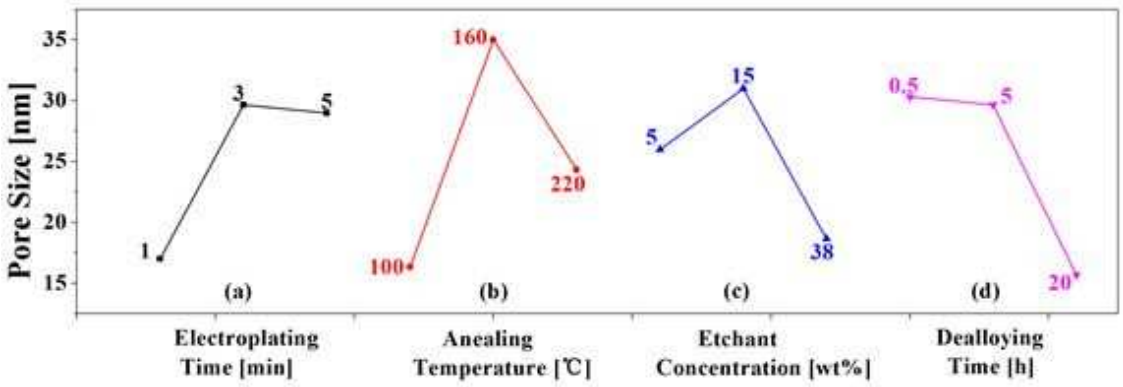


Fig. 2 Influences of process parameters on the pore size of NPC

The influence of electroplating time. From Fig. 2, it could be seen that with increasing electroplating time, the pore size of NPC increased at the initial stage while after 3 min electrodeposition, the pore size did not show noticeable changes. The results obtained in this work were well agreed with the previous research by Falong Jia *et al*. [13]. They observed the similar phenomenon that with an increase of the Zn layers' thickness from 2 μm to 4 μm, the resultant nanostructured Cu did not change remarkably. In other words, the pore size of NPC was kept in a relatively stable state. It was further found that there was a concentration limitation for Zn to form Cu-Zn alloy under a certain annealing temperature, i.e., within the concentration limitation Zn can form alloy while the excess Zn will exist in the unalloyed status. In this paper, the Zn content exceeded the concentration limitation for Zn to form Cu-Zn alloy due to the excessive

electrodeposition (3 min/5 min), which led to the formation of similar highly porous structures, as shown in Fig. 3.

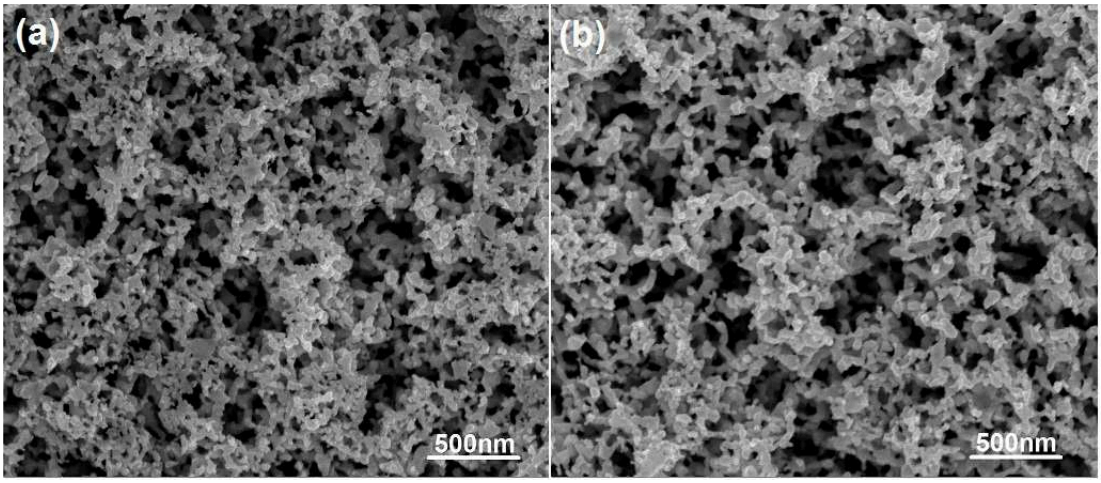


Fig. 3 SEM images of similar nanoporous architectures prepared under different conditions: (a) immersion in 5 wt% HCl solution for 5 h; (b) immersion in 15 wt% HCl solution for 0.5 h. Both of (a) and (b) were thermally alloyed at 220℃for 2 h. The electroplating time was 3 min in (a) and 5 min in (b), respectively

The influence of annealing temperature. Fig. 4(a) shows the SEM image of incompletely dealloyed samples with plenty of cracks, which resulted in the formation of dense island-like structures. On closer investigation, as Fig. 4(b) shown, there were no porous structures emerging on the sample surface and it was confirmed by analyzing the Zn content in Cu-Zn alloy before (Fig. 5a) and after (Fig. 5b) dealloying that the sample was barely corroded.

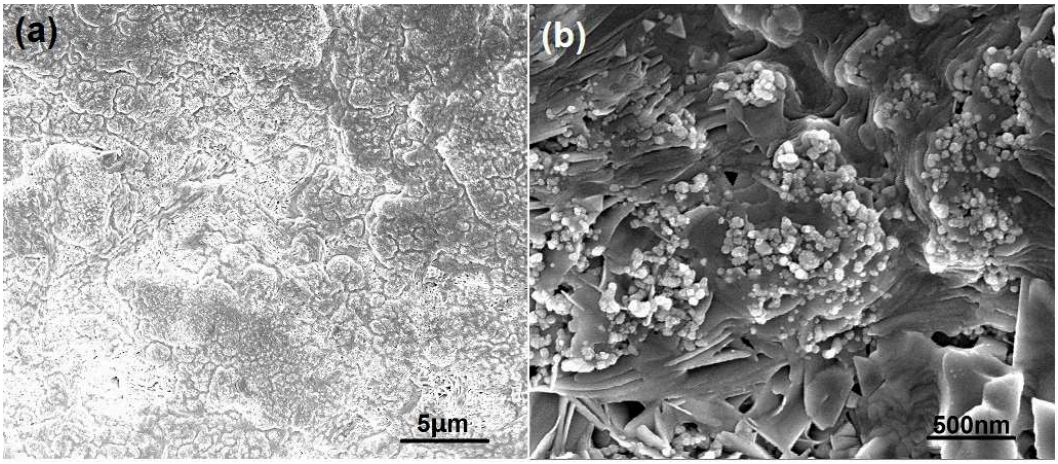


Fig. 4 SEM images of the incompletely dealloyed sample. Electroplating time = 1 min; Annealing temperature = 100℃; Etchant concentration = 5 wt%; Dealloying time = 0.5 h. Image (b) is a local magnified picture of (a)

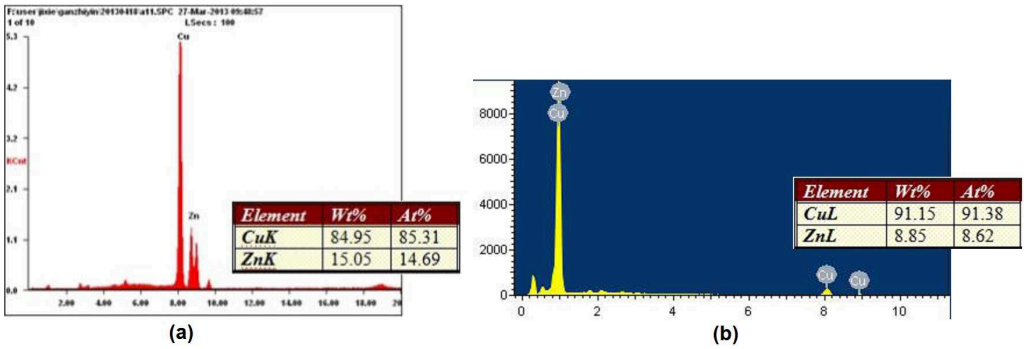


Fig. 5 XRF and EDS analysis of the sample in Fig. 4 before (a) and after (b) dealloying, respectively

Interestingly, similar phenomena were observed in different samples, as shown in Fig. 6. Furthermore, it was worth mentioning that all these samples surfaces displaying microscopically flat were thermally alloyed at 100℃. It could therefore be concluded that annealing temperature had great impacts on the formation of NPC and obviously, 100℃ did not meet the requirement. Meanwhile, it was noticed that there was no NPC formed during the dealloying process even though the electroplating time, etchant concentration or dealloying time were increased, as exemplified by Figs. 4 and 6.

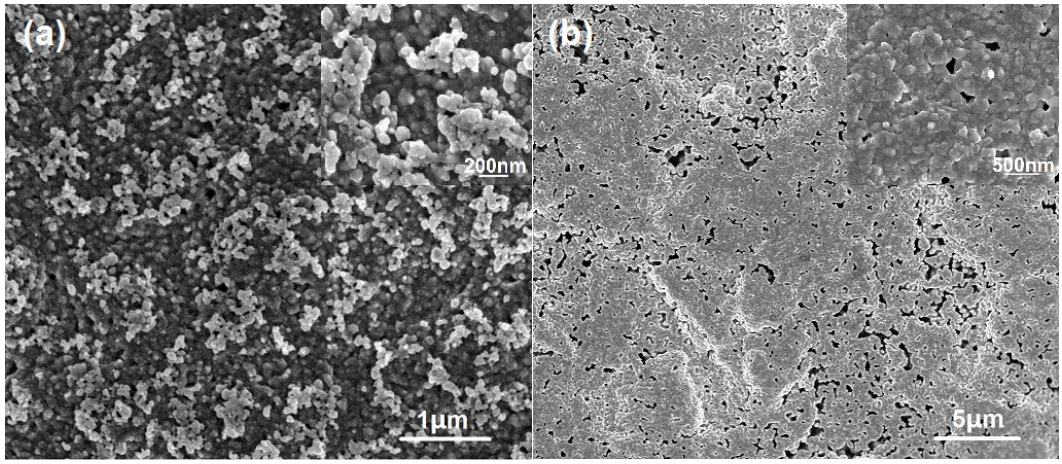


Fig. 6 SEM images of the incompletely dealloyed samples treated under different conditions: (a) Electroplating time = 3 min; Etchant concentration = 15 wt%; Dealloying time = 20 h. (b) Electroplating time = 5 min; Etchant concentration = 38 wt%; Dealloying time = 5 h. Both of (a) and (b) were thermally alloyed at 100℃ for 2 h. Insets are high magnification SEM images of (a) and (b), respectively

However, a drastic change happened to the sample surface when the annealing temperature was increased from 100℃ to 160℃. As Fig. 7 shown, there were homogeneous bi-continuous three-dimensional porous structures generated on the sample surface with a pore size of 37 nm, implying that the sample was fully dealloyed. In effect, such abovementioned phenomena could be well interpreted by the percolation theory [14]. For binary alloys, according to the percolation theory, there were full of less noble atoms comprising dissolution path distributed in the interior of the alloy after the concentration of less noble atoms exceeding the percolation threshold, which facilitated penetration of the electrolyte, resulting in the formation of bi-continuous and highly porous structures. However, the alloy would keep in a passive state and the surface would show a relatively flat morphology if the concentration of less noble atoms was below the percolation threshold. In the light of the percolation theory, it was reasonable to assume that the formation of NPC was substantially dominated by the annealing temperature due to the fact that alloying degree was highly dependent on the annealing temperature for solid state diffusion, which controlled the Zn content in Cu-Zn alloy, therefore determining whether the alloy can be dealloyed entirely or not.

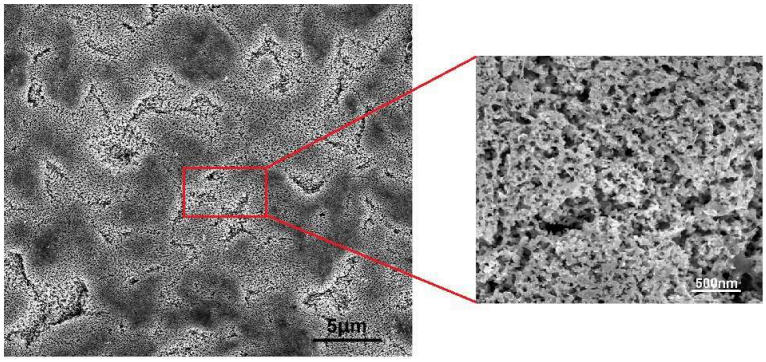


Fig. 7 SEM images of the fully dealloyed sample. Electroplating time = 1 min; Annealing temperature = 160℃; Etchant concentration = 15 wt%; Dealloying time = 5 h. Inserted image shows more details of NPC at higher magnification

In these experiments, it was startling to discover that NPC on some samples surfaces collapsed during the dealloying process, leaving behind nothing else but bare silicon, which was examined by means of EDS, as shown in Fig. 8. In addition, it was observed that numerous cracks even fractures occurred on the silicon substrate, indicating that high stresses were produced in the interior of thin films and between thin films and substrates. The possible reason was that the residual thermal stresses in samples were greatly increased as the annealing temperature was raised up to 220℃. Another possible reason was that high etchant concentration, like 38 wt% HCl solution we used, resulted in high stresses in samples too. In fact, such assumptions were firmly demonstrated by the investigation on the mechanical properties of thin films, which was proposed by W.D. Nix *et al.* [15]. They found that the mechanical stresses in the thin films on substrates were usually high up to several hundred MPa after processing. In this work, it could be therefore assumed that high annealing temperature together with the high etchant concentration utilized in the experiments led to the high internal stresses in NPC films, resulting in collapse of the thin films composed of NPC, by which the dramatic drop in pore size of NPC as shown in Fig. 2(b) could be well explained. Based on the aforementioned discussions, we could naturally draw the conclusion that incomplete alloying of samples could be attributed to the low annealing temperature (100℃) we used, which exhibited high resistant to corrosion, ultimately resulting in the formation of relatively flat surfaces, however, high thermal mechanical stresses would be generated arising from the coefficient of thermal expansion (CTE) mismatch between thin films and substrates under high annealing temperature (220℃), by which the mechanical properties and adhesive strength of thin films were substantially affected. Hence, the appropriate annealing temperature was 160℃ in this work, which was high enough for alloying the Cu-Zn completely without producing high thermal stresses.

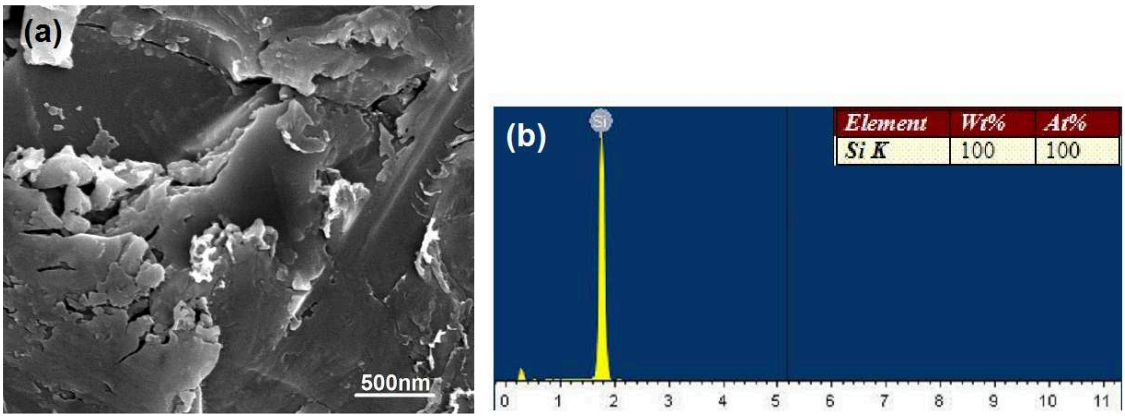


Fig. 8 (a) SEM image showing fractured sample surface prepared under conditions: Electroplating time = 1 min; Annealing temperature = 220℃; Etchant concentration = 38 wt%; Dealloying time = 20 h. (b) EDS analysis of the sample in (a)

The influences of etchant concentration and dealloying time. Fig. 2(c) shows that the pore size of NPC increased with an increase of the etchant concentration from 5 wt% to 15 wt%. However, as the concentration reached up to 38 wt%, the pore size decreased steeply. The possible reason was that the etchant concentration within 15 wt% could enhance the mobility of copper, exposing more zinc for dissolution, which led to an increase of the pore size while the concentration over 15 wt% would degrade that of copper, resulting in a decrease of the pore size. In fact, earlier in 2001, the evolution of nanoporosity in dealloying was intensively studied by J. Erlebacher *et al.* and they revealed that nanoporosity in metals was due to an intrinsic dynamical pattern formation process but the factors that control the length scale of the porosity remained unclear [5]. In this work, we boldly assumed that the changes of pore size can be ascribed to the mobility of more noble atoms associated with the etchant concentration. As for the influence of dealloying time on the characterization length scale, it was clearly observed that the pore size continued to decrease over dealloying time, which was not in agreement with the previous research where significant coarsening occurred by immersing the nanoporous gold leaf in concentrated nitric acid for an extended times and the porosity may be adjusted from less than 10 nm up to the macroscopic scale [16]. Until now, the factors that control the

length scale of the porosity have not been figured out and the underlying physical mechanism of the dealloying process has remained obscure [17]. Although great effort has been paid to this field by world-wide researchers, it's still necessary to make a further study of it.

Summary

In this work, Taguchi method was used to reduce the number of experiments required for the evaluation of the characteristics of NPC. The influences of different process parameters including electroplating time, annealing temperature, etchant concentration and dealloying time on the microstructures of NPC were studied intensively. It was found that similar highly porous structures occurred when the Zn content exceeded the concentration limitation due to the excessive electroplating time. In addition, it was concluded that annealing temperature was the most dominant factor affecting the microstructures of NPC using the range analysis method, on which was our emphasis placed. Specifically, low annealing temperature will result in incomplete alloying, leading to high resistant to corrosion while high thermal stresses would be generated owing to the high annealing temperature, which would lead to the thin films delaminating from the substrate. Therefore, the appropriate annealing temperature was 160℃ in this case. For the etchant concentration, we speculated that the variations of pore size could be attributed to the mobility of copper under a certain etchant concentration. Furthermore, it was worth mentioning that the opposite phenomenon compared with the previous research by Y. Ding *et al.* was observed that the pore size of NPC decreased with an extended dealloying time. As J. Erlebacher *et al.* pointed out, currently, the single most important unresolved issue pertains to identifying the factor(s) that controls the length scale of the porosity [17]. Hence, much more investigations should be undertaken to explore the underlying physical mechanism of the dealloying process and the evolution of nanoporosity.

Acknowledgment

This work was supported by the Nature Science Foundation of China (NSFC) under grant number 51275194 and State Key Laboratory of Advanced Technology for Materials Synthesis and Processing (Wuhan University of Technology, No: 2014-KF-11).

References

[1] D.W. Li, Y. Zhu, H. Wang and Yi Ding, Nanoporous gold as an active low temperature catalyst toward CO oxidation in hydrogen-rich stream, Sci. Rep. 3 (2013).

[2] T. You, O. Niwa, M. Tomita, and S. Hirono, Characterization of platinum nanoparticle-embedded carbon film electrode and its detection of hydrogen peroxide, Anal. Chem. 75 (2003) 2080-2085.

[3] J. Weissmueller, R.N. Viswanath, D. Kramer, P. Zimmer, R. Wuerschum, and H. Gleiter, Charge-induced reversible strain in a metal, Science, 300 (2003) 312-315.

[4] A.J. Forty, P. Durkin, A micromorphological study of the dissolution of silver-gold alloys in nitric acid, Philos. Mag. A, 42 (1980) 295-318.

[5] J. Erlebacher, M.J. Aziz, A. Karma, N. Dimitrov, and K. Sieradzki, Evolution of nanoporosity in dealloying, Nature, 410 (2001) 450-453.

[6] D.V. Pugh, A. Dursun, and S.G. Corcoran, Formation of nanoporous platinum by selective dissolution of Cu from $Cu_{0.75}Pt_{0.25}$, J. Mater. Res. 18 (2003) 216-221.

[7] C. Zhao, Z. Qi, X. Wang, and Z.H. Zhang, Fabrication and characterization of monolithic nanoporous copper through chemical dealloying of Mg-Cu alloys, Corros. Sci. 51 (2009) 2120-2125.

[8] X. Lu, T.J. Balk, R. Spolenak, E. Arzt, Dealloying of Au-Ag thin films with a composition gradient: influence on morphology of nanoporous Au, Thin Solid Films, 515 (2007) 7122-7126.

[9] J.F. Huang, I.W. Sun. Fabrication and surface functionalization of nanoporous gold by electrochemical alloying/dealloying of Au-Zn in an ionic liquid, and the self-assembly of L-cysteine monolayers, Adv. Funct. Mater. 15 (2005) 989-994.
[10] J.R. Hayes, A.M. Hodge, J. Biener, and A.V. Hamza, Monolithic nanoporous copper by dealloying Mn-Cu, J. Mater. Res. 21 (2006) 2611-2616.
[11] A. Mathur, and J. Erlebacher, Size dependence of effective Young's modulus of nanoporous gold, Appl. Phys. Lett. 90 (2007) 061910.
[12] H.J. Jiang, K.S. Moon, H. Dong, F. Hua, and C.P. Wong, Size-dependent melting properties of tin nanoparticles, Chem. Phys. Lett. 429 (2006) 492-496.
[13] F.L. Jia, C.F. Yu, K.J. Deng, and L.Z. Zhang, Nanoporous metal (Cu, Ag, Au) films with high surface area: general fabrication and preliminary electrochemical performance, J. Phys. Chem. C, 111 (2007) 8424-8431.
[14] K. Sieradzki, Curvature effects in alloy dissolution, J. Electrochem. Soc. 140 (1993) 2868-2872.
[15] W.D. Nix, Mechanical properties of thin films, Mater. Trans. A, 20 (1989) 2217-2245.
[16] Y. Ding, Y.J. Kim, and J. Erlebacher, Nanoporous gold leaf: "Ancient technology," Adv. Mater. 16 (2004) 1897-1990.
[17] J. Erlebacher, K. Sieradzki, Pattern formation during dealloying, Scripta Mater. 49 (2003) 991-996.

Key Engineering Materials Vols 645-646 (2015) pp 246-251
© (2015) Trans Tech Publications, Switzerland
doi:10.4028/www.scientific.net/KEM.645-646.246

Submitted: 2015-01-12
Accepted: 2015-01-15

Preparation of Mn-Zn Ferrite Flake Absorbent by Self-reactive Spray Forming Technology

Gao haitao[a*], Wang jianjiang[b], Lou hongfei[c], Cai xudong[d], Hou yongshen[e]

Mechanical Engineering College, Advanced Material Institute, Shijiazhuang, 050003, China

[a]gaohaitao12y1034@163.com, [b]JJWang63@heinfo.net, [c]behond2@qq.com,
[d]caixudong87@qq.com, [e]hys-sor@qq.com

Keywords: self-reactive spray forming technology. Mn-Zn ferrite. flake absorbent.

Abstract. Fe+MnO_2+Fe_2O_3+ZnO reaction system was used to prepare Mn-Zn ferrite flake absorbent by self-reactive spray forming technology. Extrinsic enthalpy (H) and adiabatic temperature (Tad) of system were calculated. The formation mechanism and electromagnetic properties of Mn-Zn ferrite flake absorbent were analyzed. The results show that T_{ad} exceeded 1998K, self-propagation reaction can be ignited and products can be melted. The droplets impacted onto copperplate to achieve flake shape. SEM and XRD were used to characterize the morphology and phase of samples. The results show that most of flake absorbent are at 100μm wide and 10μm thick, and they are constituted by pure $Mn_{0.5}Zn_{0.5}Fe_2O_4$ phase with spinel crystal structure. Absorption test show that the absorbent has two absorption peaks, the minimum value of reflectivity is at -27dB and the bandwidth lower than -10dB reaches to 3.5GHz. The Mn-Zn ferrite flake absorbent provides with preferable properties, which is potential in the further investigations.

Introduction

In recent years, microwave absorbing materials were widely used in military technology including electronic warfare and industrial production labor protection, and they had draw increasing attentions in microwave devices and equipment around the world[1]. The particle size, shape, content and aggregation state of absorbent would affect its absorption properties[2]. Absorbent particles mainly have three shapes including spherical, needle and flake, and the flake absorbent had a large surface so as to produce a large dipole moment, a high loss tangent and high magnetic equivalent anisotropy field, which were helpful to improve microwave absorption properties[3].

Mn-Zn ferrite with spinel structure is a class of applications historic coating absorbing material which provides with ferrous magnetic and dielectric properties[4]. When electromagnetic waves pass through it, magnetic loss and dielectric loss would take place. The current methods for producing Mn-Zn ferrite absorbent are plentiful such as high-energy ball milling method, self-propagating combustion synthesis, chemical co-precipitation method, hydrothermal method, sol-gel method[5-7], and so on. However, some problems appeared in the methods mentioned above , such as high cost, inconvenience process control, the presence of impurities, and reunite phenomenons, etc. And it was difficult for them to prepare flake absorbent. In addition, methods for preparing Mn-Zn ferrite flake absorbent have been few reported.

Self-reactive spray forming technology[8] was integrating SHS(self-propagating high-temperature synthesis), spray forming technology, flame-spraying technology and rapid solidification technology, it was a low-cost and near-net-shape forming technology for preparing new high-performance structural ceramic materials. Low-cost raw materials and simple equipment were needed to prepare ingredients adjustable, size controllable, structure variable and high-performance materials. Currently, self-reactive spray forming technology is mainly used to prepare ceramic matrix composite materials[9], while it was applied for preparing Mn-Zn ferrite flake absorbent by our group, hoping to find a new way to prepare flake absorbent. And it was investigated to provide guidance and reference for the future development of flake absorbent preparation methods.

Experimental

Materials. Reagent raw materials of Fe powders, MnO_2 powders, ZnO powders, Fe_2O_3 powders, sucrose (carbonization agent), epoxy resin (cross-linking agent) were selected as respectively. Then adhesive precursor method[10] was used to prepare agglomerate powder as the following processes. The stoichiometric ratio of the ingredients was shown in Eq(1) , then put the raw materials in a ball mill jar. Ethanol was used as milling media to mill for 6h, and then agglomerate powders with the particle size of 60-105μm were obtained for spraying, by means of stirring, drying, crushing, sieving and other processes .

$$2Fe+MnO_2+Fe_2O_3+ZnO+O_2 \rightarrow 2Mn_{0.5}Zn_{0.5}Fe_2O_4 \quad (1)$$

Agglomerate powders were sprayed onto the rotating copperplate through the CP-DⅢ type flame spraying gun. And then they were cooled down. Distilled water was used as a cooling medium to wash the copperplate. Finally, the flake absorbent was obtained after filtration and drying processes.

Principle. Figure 1 shows the preparation diagram of the flake absorbent. As shown in the figure, aggregate powders were sprayed into the flame field by the traditional flame-spraying gun, and the temperature of the powders increases gradually. When reaching the ignition temperature, the SHS reaction taken place, and combustion temperature exceeds the melt point of ferrite. So ferrite droplets are generated. The droplets crashed on the substrate collision and transmute to flake. The crystallization process of the droplets was controlled by solidification. Then, the composition adjustable and size alterable flake ferrite absorbents were obtained.

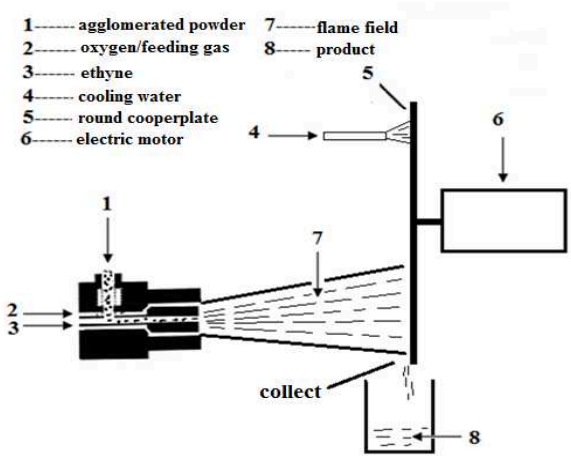


Fig.1 The preparation Principle diagram of flake absorbent

Dual oxygen bottles were used in the experiment, one bottle of oxygen gas at pressure of 0.5MPa was powder feeding gas and another bottle of oxygen and acetylene composited oxyacetylene flame, the pressure was 0.6MPa and 0.11MPa. Spray distance was 180mm. The radius of the circle copperplate was 150mm, and the speed is 200r/min.

Characterization Test. The morphology of products was detected by scanning electron microscope (JSM-7600F type). The phase composition of the products was studied by X-ray diffraction analyzer (D2ADVANCE). The products and paraffin were equably mixed at the ratio of 1:1, and then pressed into ring specimens by molding method. The testing specimens have a toroidal shape with outer diameter of 7mm, the inner diameter of 3mm and the height of 2.5mm. The electromagnetic parameters of products were measured by vector network analyzer (Agilent-8721ET-type) in 0.5-18GHz range. Then, Matlab was applied to calculate the reflection loss curve.

Results and discussion

Thermodynamic Analysis and Formation Mechanism. The amount of heat released during the reaction determines whether the SHS reaction can occur by itself or not. The system adiabatic combustion temperature T_{ad}[11] needs to be calculated in order to determine whether SHS reactions can occur or not and whether they can self-sustains. In addition, the phase composition and the reaction mechanism are also greatly effected by the adiabatic temperature, and the formation of flake absorbent also needs the products at the status of droplets. Thus, calculating the adiabatic temperature of the system is very important in the analysis. There are heat exchange effects such as convective heat transfer and heat conduction during the combustion synthesis of agglomerate powder. But the reaction time is very short, and it can be defined as an adiabatic combustion process. According to the manual[12], MnO_2 will decompose and produce MnO and O_2 at high temperatures.

Therefore Eq. (1) can be decomposed into the following reactions:

$$MnO_2 \longrightarrow MnO+0.5O_2 \quad (2)$$

$$2Fe+1.5O_2 \longrightarrow Fe_2O_3 \quad (3)$$

$$MnO+Fe_2O_3 \longrightarrow MnFe_2O_4 \quad (4)$$

$$ZnO+Fe_2O_3 \longrightarrow ZnFe_2O_4 \quad (5)$$

$$MnFe_2O_4+ZnFe_2O_4 \longrightarrow 2Mn_{0.5}Zn_{0.5}Fe_2O_4 \quad (6)$$

For a self-reactive flame spray synthesis system, the enthalpy was determined by the initial enthalpy of the reaction system and enthalpy of oxyacetylene flame. The system enthalpy determined the adiabatic combustion temperature and the phase balance of the system under this temperature. If the initial reaction system temperature T_0 = 298 K, the adiabatic temperature T_{ad} is less than the product of melting point T_m, there are the following balance equation:

$$H_{in} + \Delta H_{298}^0 + \sum n_i \left(H_T^0 - H_{298}^0\right)_{i,resul\tan t} = 0 \quad (7)$$

H_{in} is extrinsic enthalpy of the oxyacetylene flame. According to the formula given by the literature[13], it can be calculated at 5.2×10^4J/mol. ΔH_{298}^0 is the molar standard generate heat of material at normal temperature, which equals formation heat difference of all the resultants and reactants. $\left(H_T^0 - H_{298}^0\right)_i$ is relative enthalpy of the resultants at the temperature of T, n_i is the molar coefficients of the resultants. Relative enthalpy change of a substance at the temperature of T can be expressed as

$$H_T^0 - H_{298}^0 = \int_{298}^{T} C_p dT \quad (8)$$

The adiabatic combustion temperature of the system can be calculated, and the required thermodynamic parameters of the material are detected by the thermodynamic manual[14]. The adiabatic combustion temperature (T_{ad}) of system was calculated by 1998K. Since T_{ad} ≧1800K, which meets the basic condition for SHS reaction[15]. At this temperature, Fe_2O_3 (T_m = 1863K) is liquid, MnO and ZnO (T_m = 2243K) are solid.

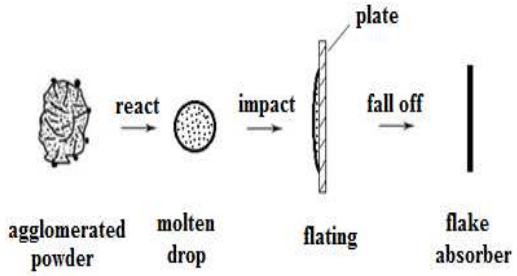


Fig.2 The formation mechanism of flake absorbent

According to the above conditions, the preparation mechanism of flake absorbent can be analyzed, which is shown in Figure 2. The self-propagating reaction occured when original agglomerate powders heated to burn. The Fe_2O_3 melt droplet formed and wrapped MnO and ZnO particles, and constantly wetted and dissolved MnO and ZnO particles, until completely mixed by dissolving-precipitating mechanism. Droplet flies forward under pressure of powder feeding gas, then impacted on the substrate and cooled, solidified and flatted. And after flushed by cooling water, Mn-Zn ferrite fell off and flake absorbent was shaped.

Characterization Analysis of the Flake Absorbent. The XRD patterns of flake absorbent prepared by self-reactive spray forming technology is shown in Figure 3. From the figure, it can be seen that the peaks of Mn-Zn ferrite absorbent was corresponding to characteristic diffraction peaks of $Mn_{0.5}Zn_{0.5}Fe_2O_4$, which means that Eq. (1) can take place smoothly. In addition, single phase peak takes place and no impurity appears in the figure. It can be concluded that self-propagating reaction occurred adequately. The substrate of the diffraction peak is low and the peak intensity is high, which indicates that the droplets were cooled sufficiently to form crystals after impacted on the round copperplate. This indicated that the cooling condition of the copperplate was preferably.

Figure 4 is the SEM photograph of the absorbent. According to Figure 4(a), it can be seen that most of the absorbents prepared by self-reactive spray forming technology were flake with the size

of 100μm wide and 10μm thick. The flake absorbent particles are successfully prepared by self-reactive spray forming technology. However, there are several massive and spherical particles. It could be explained that the particles locating in the edge of the field of flame are hard to impacted on circle copperplate to mold under a weak impact force. And agglomerate powders on the edge of the flame field are less heated and cooled fast, which resulted that the temperature of agglomerate powders is not high enough and reacts inadequately. Moreover, a moiety of the droplets were divided into several tiny drops, the impact strength become smaller. Therefore, the tiny droplets were easily moving to the edge, and finally formed spherical particles. Enlarged photo of one flake absorbent is shown in Figure 4(b). It can be seen that the surface of absorbent is relatively smooth though there are some bulges on it. It is mainly caused by the rough surface of the copperplate. Fine original agglomerate powders are screened by the shale shaker with the mesh size from 150 to 240, and the particles mainly distribute between 60 and 105μm. In other words, the flake absorbent was basically formed from a single droplet, the particle size of absorbent can be controlled by the size of the agglomerate powder.

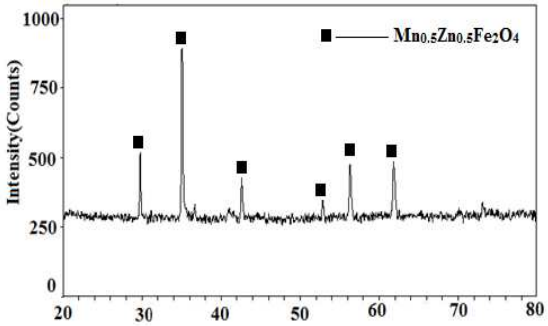


Fig.3 The XRD pattern of Mn-Zn ferrite flake absorber

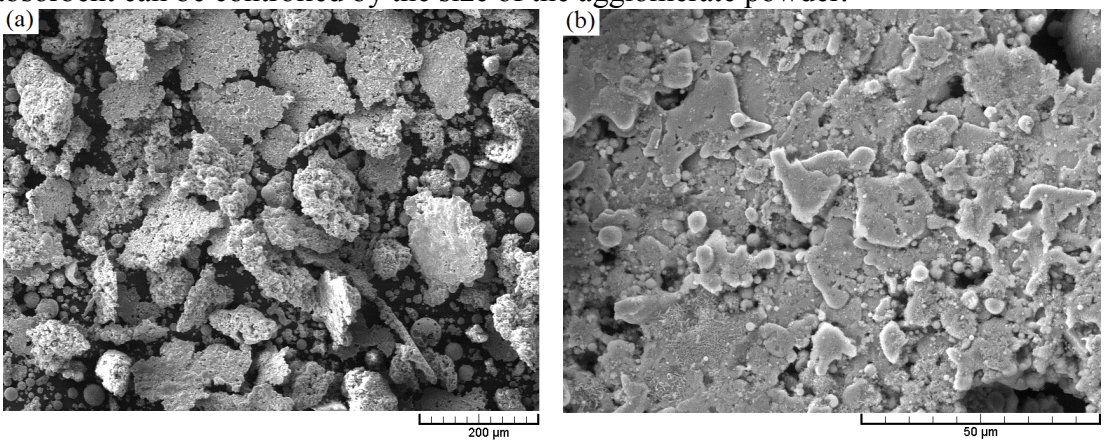


Fig.4 The SEM photographs of Mn-Zn ferrite flake absorbent

Absorption Properties and Theory of the Flake Absorbent. Figure 5 is the diagram of electromagnetic parameters of the flake absorbent. In 0.5-18GHz , the real part of permittivity (ε') of absorbent changed little in the vicinity range of 4, but a downtrend peak emerged at 14GHz. While the imaginary part of permittivity (ε") of absorbent ascended lentamente in 0.5-18GHz, and an uptrend peak appeared at 14GHz, which indicated that a dielectric absorption peak occurs at 14GHz. The presence of the dielectric absorption peak can effectively reduce the skin effect of the material match the electromagnetic impedance in wider frequency range. The real part of permeability (μ') of absorbent decreased from 1.4 to 1.0 in 0.5-18GHz. The imaginary part (μ") was floating at 0.15 befo--re 8GHz, and then slowly declined to 0.1. According to the pictures, the Mn-Zn ferrite materials provided certain dielectric properties and magnetic properties. Meanwhile, the complex permittivity and permeability of the flake absorbent would increase with the width-thickness ratio[16]. The effect of the shapes and sizes guaranteed a better electromagnetic wave absorption characteristics.

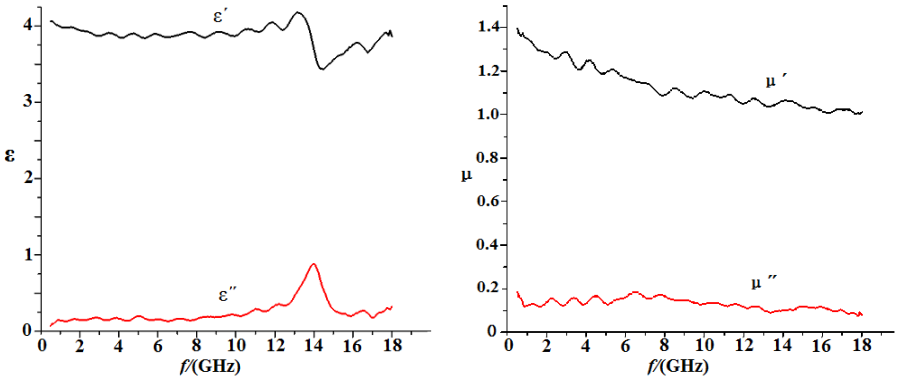


Fig.5 Permittivity and permeability of Mn-Zn ferrite flake absorbent

Figure 6 is the reflectivity curve of flake absorbent. Two absorption peaks can be seen from the figure. The minimum reflectivity was -27dB (at 14GHz) and bandwidth less than -10dB reached 3.5GHz (12.5-16GHz). Electro- magnetic waves was absorbing in ferrites by natural resonance in the condition of impedance match. The complex permeability and complex permittivity of absorbent can express as the formulas: $\tilde{\varepsilon} = \varepsilon_0(\varepsilon' - j\varepsilon'')$ $\tilde{\mu} = \mu_0(\mu' - j\mu'')$.

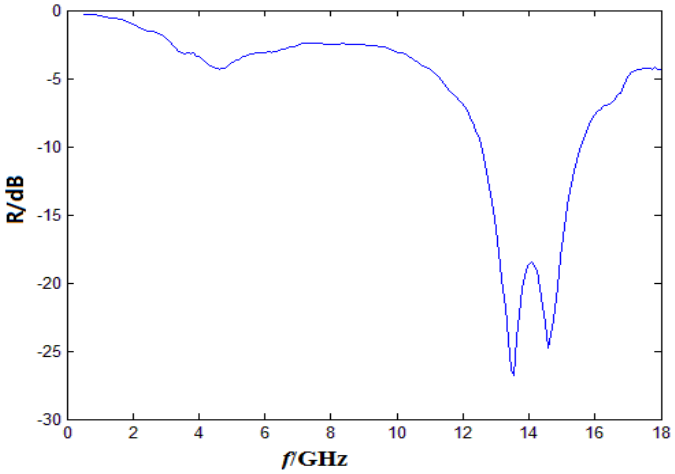


Fig.6 Reflection loss of Mn-Zn ferrite flake absorbent

The condition of impedance match is $\tilde{\mu} = \tilde{\varepsilon}$. A better absorption of electromagnetic wave will occurs if the above condition is matched in a certain bandwidth. In this experiment, the increasing of ε'' of the absorbent at 14GHz made it easily to match the impedance. Thus great absorption properties near 14GHz were obtained, and two absorption peaks appeared. Compared with previous hollow microspheres prepared by our team using self-propagating quenching technology[17], Mn-Zn ferrite flake absorbent prepared in this experiment had been improved on the absorption peak and absorption bandwidth. Therefore, the absorption properties of flake absorbent were better than hollow microspheres. As a result, flake absorbent prepared by self-reactive spray forming technology provided with good absorption properties , which was of great applications and worth being further investigated.

Summary

1. Fe+MnO_2+Fe_2O_3+ZnO reaction system was used to prepare Mn-Zn ferrite flake absorbent by self-reactive spray forming technology. Most of flake absorbent were 100μm wide and 10μm thick, and they were constituted by pure $Mn_{0.5}Zn_{0.5}Fe_2O_4$ phase with spinel crystal structure.

2. The thermodynamic parameters of SHS system was analyzed, the adiabatic combustion temperature(Tad) of the system was calculated by 1998K, meeting the condition for SHS reaction. At that temperature, Fe_2O_3 melt is constantly wetting and dissolved MnO and ZnO, until completely mixed by dissolving-precipitating mechanism, eventually $Mn_{0.5}Zn_{0.5}Fe_2O_4$ was synthesized.

3. The flake absorbent were provided with good absorption properties, two absorption peaks appeared near 14GHz. The minimum reflectivity was -27dB (at 14GHz) and bandwidth less than -10dB reached 3.5GHz(12.5-16GHz). Therefore, the flake absorbent prepared by self-reactive spray forming technology was of great applications and worth being further investigated.

Acknowledgement

Supported by the Natural Science Foundation of China(51172282) and Weapon Equipment Research Foundation (9140A12040211JB34).

References

[1] Y B Feng, T Qiu, C Y Shen. Absorbing properties and structural design of microwave absorbers based on carbonyl iron and barium ferrite.J. Magn Magn Mater, 318 (2007) 8-10.

[2] S F Zheng, G X Xiong, H Q Huang, et al. Study on relation of Morphplogy, properties and preparation of ferrites. Mater Rev, 23(2009): 26-29.

[3] D Y Zhang, W Q Zhang, J Cai, Fabrication and electromagnetic properties of flake ferrite particles based on diatomite. J. Magn Magn Mater ,2011 (323): 2305-2309.

[4] Y F Cui, X Wang, Y F Jiang,et al.Study on Sintering Process of Mn-Zn Ferrite Nanopowders and Its Sintered Properties.J. Synth Cryst,35(2006) 790-794.

[5] C F Zhang, H Y Yu, X C Zhong,et al. Study on Preparation of Mn-Zn Ferrite Materials by High-energy Ball Milling Method. Mater Rev,23(2009) 8-10.

[6] S Y Sun, Y L Fang, Y K Fang,et al. Soft Magnetic Mn-Zn Ferrite Nanoparticles Prepared by Sol-Gel Auto-combustion. Magn Mater Dev, 35(2004) 21-26.

[7] G S Luo, G W Jiang, J D Li, et al. Effect of Heat Treatment on Structure and Magnetic Properties of Mn-Zn Ferrite. J. Nanchang Univ, 32(2010) 78-81.

[8] E J Lavernia, J Grantn. Spray deposition of materials: a review . J. Mater Sci Eng, 98(1988) 381-388.

[9] W Chen, Z Y Wang. The prospective of development trend about self-propagating thermal pressing technique. Mech Eng. 3(2005) 14-16.

[10] X D Cai. Study on the controllable preparation and microwave electromagnetism property of hollow ceramic micro-spheres. Shijiazhuang, 2012.

[11] J X Jiang, Y Li, X D Hao, et al. The combustion synthesis of Mn-Zn ferrite powders. J. Harbin Inst. Univ, 1(2004) 32-36.

[12] D G Xian, B S Lu, H K W. The principle and technology of manufacturing soft magnetic ferrite, Shanxi Sci.and Tech Publishing Inc,2010.

[13] C S Liu, Y H Liu, S Yin. Inflience of extrinsic enthalpy on flame spray synthesis of TiC-Fe coating. J.Met, 36(2000) 1209-1212.

[14] D L Ye, J H Hu. Practical Handbook of the thermodynamic data for inorganic substances, Met Ind Publishing Inc,2002.

[15] A G Merzhanov. Solid Flames:Discoveries,Concepts and Horizons of Cognition. J.Combust. Sci.and Tech,98(1994)307-336.

[16] K H Liu, Investigation on preparation and electromagnetic properties of microwave absorbers filled with flakes, Beijing,2010.

[17] H F Lou, J J Wang, B C Xu,et al. Preparation by self-reactive quenching technology and microwave absorption property of hollow multiphase ceramic microspheres.J. Synth Cryst, 5(2012) 174-180.

Key Engineering Materials Vols 645-646 (2015) pp 252-258
Submitted: 2015-01-14
© (2015) Trans Tech Publications, Switzerland
Accepted: 2015-01-15
doi:10.4028/www.scientific.net/KEM.645-646.252

Intermolecular-interaction and mechanical properties of MNs-plasticizer modified 2,4,6-trinitrotoluene/1,3,5-trinitrohexahydro-1,3,5-triazine molten-energetic-composite(MEC)

Qing Ma[1,2,a], Maoping Wen[2,b], Baohui Zheng[2,c], Hengjian Huang[2,d], Dabin Liu[1,e*], Jinshan Li[2,f*]

[1] School of Chemical Engineering, Nanjing University of Science and Technology, Nanjing 210094, China

[2] Institute of Chemical Materials, China Academy of Engineering Physics, Mianyang 621900, China

[a]qing_ma@foxmail.com, [b]wenmaoping@caep.cn, [c]zhengbaohui@caep.cn, [d]huanghengjian@caep.cn, [e*]liudabin@mail.njust.edu.cn, [f*]lijinshan@caep.cn

Keywords: Quantum-chemical (QC) method, Molecular dynamics (MD), mononitrotoluenes (MNs)-plasticizer, Intermolecular interaction, TNT, RDX

Abstract. Intermolecular interaction of mononitrotoluenes (MNs) plasticizer with 2,4,6-trinitrotoluene (TNT) and 1,3,5-trinitrohexahydro-1,3,5-triazine (RDX) was experimentally and theoretically investigated. The basis set superposition error (BSSE) and interaction energy of TNT, RDX and plasticizers were computed at MP2/6-311++G** levels. Compared with the weak E_{inter} between RDX and TNT (−1.586 kJ/mol), E_{inter} between the o-nitrotoluene and TNT and RDX can increase to −131.557 kJ/mol and −48.487 kJ/mol, indicating there is strong intermolecular-interaction. SEM imagines also show that mononitrotoluene could form layered deposits in TNT and closely surround RDX crystalline. MD simulation results indicate that tensile modulus of (100) TNT and (100) RDX increases when introducing mononitrotoluene plasticizers separately, which agree with the experimental phenomenon of Brazilian disk test.

Introduction

2,4,6-trinitrotoluene (TNT) with its excellent enthermal stability makes it suitable as a carrier for melt-loading more powerful explosives (eg. RDX, HMX, CL-20). Despite candidates have been developed such as DNAN, TNAZ, DNTF, MTNI, and DNP [1−5], TNT is still used widely in military because of its mature process and low manufacturing cost. As a carrier, TNT has its own problems. TNT based molten-energetic-composites (MECs) exhibit poor mechanical properties, and show undesirable defects such as cracks, voids, irreversible growth and brittleness, which have negative effects on sensitivity and safety of munitions based on melt-cast loaded explosives [6−7]. D.L Smith *et al*. [8] found that there were cracks in the formulation of RDX and TNT through SEM technology. Niu and Zhang *et al*. [9] testified that weak H-bonds interaction existed between TNT and RDX by DFT investigations. Mononitrotoluenes (MNs) were composed of o-nitrotoluene (*o*-NT) and p-nitrotoluene (*p*-NT). Kegler [10] found that MNs had positive effect on reducing the cracks of TNT. Wang *et al*. [11] improved the modification effect of MNs through the introduction of MNs with another polymer and controlled the irreversible growth. However, the modification mechanism of MNs has not been discussed before. In the present work, MNs were incorporated into TNT and RDX (35:65) for modification experiments. Scanning electronic microscopy (SEM) was used for observing the interfacial-interaction and the Brazilian disk test was employed for obtaining the mechanical properties of unmodified and modified formulations. Moreover, quantum-chemical (QC) method was carried out to investigate the intermolecular-interaction between plasticizers and TNT together with RDX. Molecular dynamics (MD) simulation was used for acquiring the elastic constants. The experimental phenomenon can be further explained by computational results.

Experimental section

Materials. TNT (purity 99%, laminar particles) was provided by Liaoning Qingyang Chemical Industry Co., Ltd. RDX (purity 99%, fine crystal with particle size of 20–45μm, coarse crystal with particle size of 245–350μm) was supplied by Gansu Yinguang Chemical Industry Co., Ltd. *o*-nitrotoluene (*o*-NT) and *p*-nitrotoluene (*p*-NT) (purity 99%) were provided by Shanghai Puzhen Technology Co., Ltd..

Specimen preparation. TNT raw materials were first melted at 90–100°C with steam in a jacketed vessel. Subsequently, RDX with fine and coarse particle sizes was successively added into TNT slurry in two steps, and lastly the plasticizers were added (*o*-NT and *p*-NT, respectively). Keeping the temperature of 90–100°C, the mixtures were sufficiently stirred until RDX and elastomeric particles dispersed homogeneously in melted TNT. The blends were subsequently concentrated in vacuum (approximately 0.5 MPa) to remove air bubbles, and poured into pre-heated moulds curing for 1h at ambient temperature.

Characterization. The morphologies for the tensile fracture surface of the samples were examined by scanning electronic microscope (SEM; TM-1000, Hitachi, Japan) at an accelerating voltage of 12kV. The prepared surfaces were coated with platinum/palladium in order to prevent charge build up on the specimen surfaces. Brazilian disk test was conducted using a Universal Testing Machine (Instron® 5582, UK) following the Chinese Military Standard [12].

Computational details

Quantum Chemical Computation. Computations were performed with Gaussian 09 package [13] at MP2 method with 6-311++G** basis set [14−15]. The geometric parameters were optimized and no constraints were imposed on molecular structure during optimization process.

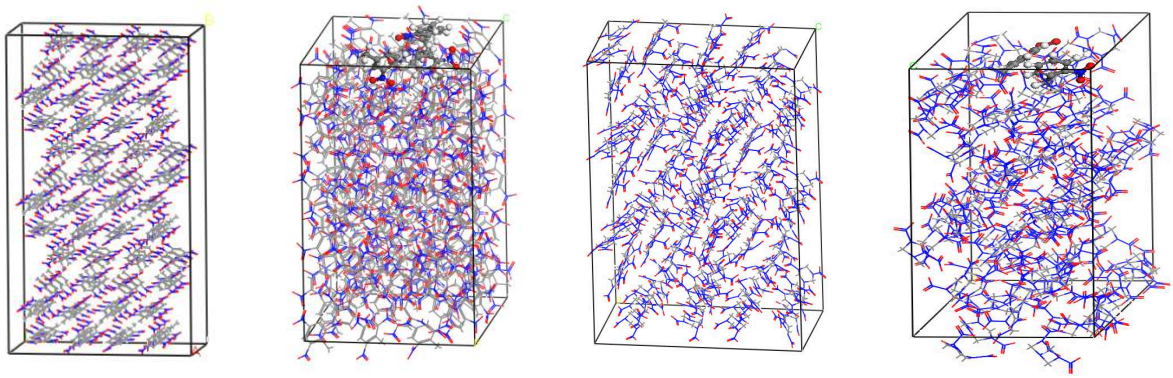
The interaction energies (ΔE) of the dimers were calculated by the supermolecule approach using the Eq.1:

$$\Delta E = E_{\mathrm{dim}er} - (E_{mol1} + E_{mol2}) \quad (1)$$

where E_{dimer}, E_{mol1} and E_{mol2} are energies of the stacked/paried dimer, energy of the molecule1 and energy of the molecule2 respectively. The interaction energies were corrected for basis set superposition error (BSSE) using Boys and Bernardi's counterpoise (CP) method [16].

Molecular Dynamics Simulation. Molecular dynamics simulation was performed with COMPASS force field [17]. The MD computations in this work were carried out using the software program Materials Studio from Accelrys Inc. (San Diego, CA, USA) [18]. Periodic simulation cells of TNT and RDX crystal, containing 144 TNT and 144 RDX molecules respectively, were selected for simulation model. 2×3×3 box of unit cells was cleaved along the crystalline surface (1 0 0). It is reported that (100) crystal-facets of TNT and RDX have comparatively stronger interaction with modifiers than the others [19−21].

The above models established for the (100) TNT, (100) RDX, and their blends with mononitrotoluenes, were allowed to evolve dynamically in isothermal-isobaric (NPT) ensembles with Andersen temperature control [22] using stochastic collision method and Parrinello-Rahman pressure control [23] fully relaxing all cell parameters at atmospheric pressure (0.0001GPa) and temperature (298K). Figure 1 shows the (100) TNT, (100) RDX, (100) TNT/MNs, and (100) RDX/MNs periodic simulation cells.



TNT (1 0 0) TNT (1 0 0)/MNs RDX (1 0 0) RDX (1 0 0)/MNs

Fig.1 (100) TNT, (100) RDX, (100) TNT/MNs, and (100) RDX/MNs periodic simulation cells

Results and discussion

SEM analysis. Scanning electronic microscopy (SEM) was employed for analyzing the interfacial interactions between explosives and plasticizers. Figure 2 shows the SEM images of regular formula RDX/TNT and the modified formula RDX/TNT/MNs, respectively. It is obviously that many crossing cracks in the fracture surface of TNT/RDX regular formula, while in TNT/RDX/MNs formula there are layer-deposits in TNT and closely surround RDX crystalline, suggesting the presence of strong intermolecular-interaction between TNT and MNs. From the 3D structures of TNT, o-NT and p-NT, it is seen that not only H-bonds but also strong π-π interaction exist, which may lead to the formation of eutectic compounds among these poly/mononitrotoluenes.

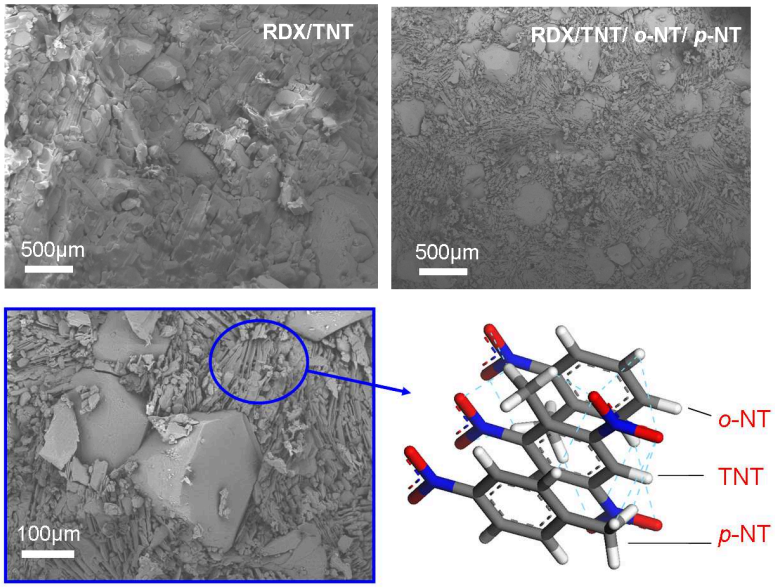
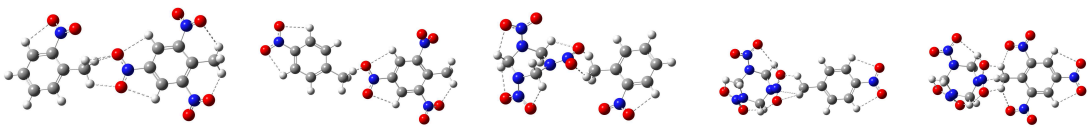


Fig.2 SEM photographs of RDX/TNT and RDX/TNT/MNs fractured surface: (a) RDX/TNT:65/35, (b) RDX/TNT/o-NT/p-NT: 65/35/1.5.

Intermolecular interaction analysis. In order to investigate further the intermolecular-interaction between MNs and Comp B, the interaction energy was computed at MP2/6-311++G** level. The optimized structures of TNT/MNs and RDX/MNs dimers are presented in Figure 3. BSSE and interaction energies of those dimers are listed in Table 2. It is obviously that weak interaction presents in TNT and RDX, the interaction energy is only −1.586 kJ/mol, which agree with the view of Niu and Zhang *et al* [9]. The interaction energies of TNT/o-NT and TNT/p-NT are −131.557 and −95.640 kJ/mol, respectively, while those of RDX/o-NT and RDX/p-NT are individually −48.487 and −4.620 kJ/mol. The results indicate that MNs and TNT have the stronger interac-

tion than that of MNs and RDX, both of which are more vigorous than that of TNT and RDX. The phenomenon can be attributed to the presence of H-bonds and π-π interaction together between TNT and MNs plasticizers, and only H-bonds interaction exists between RDX and MNs plasticizers.



TNT/o-NT TNT/p-NT RDX/o-NT RDX/p-NT RDX/TNT

Fig.3 Optimized geometries of TNT/RDX, TNT/o-NT, TNT/m-NT, TNT/p-NT, RDX/o-NT, RDX/p-NT, and RDX/m-NT with hydrogen bond (N, O and C atom as donor) at MP2/6-311++G** level

Tab.1 Interaction energies for dimers of TNT/RDX, TNT/o-NT, TNT/p-NT, RDX/o-NT, and RDX/p-NT

Dimer structures	BSSE [kJ mol^{-1}]	Interaction energy [kJ mol^{-1}]
TNT−RDX	80.979	−1.586
TNT−o-NT	48.518	−131.557
TNT−p-NT	85.544	−95.640
RDX−o-NT	211.840	−48.487
RDX−p-NT	127.178	−4.620

Elastic-mechanical properties. Elastic parameters were obtained by MD simulation, which were presented in the Table 2. Results show that tensile modulus, bulk modulus and shear modulus of (100) TNT increase after the introduction of MNs, the same as (100) RDX. These indicate that MNs can contribute to the increase of mechanical properties of TNT and RDX. Cauchy pressure (C_{12}−C_{44}) [24] and K/G[25] are related to the brittleness and ductibility of composites. The Cauchy pressure is higher, and the materials are more ductile. From the results in Table 2, it is found that (100) TNT is brittle and the (100) TNT/MNs shows the ductibility, and (100) RDX has slight enhancement after modification which agrees with the results of interaction-energy calculated. The trends of K/G values are little different from the Cauchy pressure since the quotient K/G empirically indicates the extent of the plastic range of a material, which is related to the manufacture performance of a material. Though K/G value of (100) TNT/MNs increases, that of (100) RDX/MNs presents a small decrease, which may suggest the (100) RDX/MNs could show brittleness compared with (100) RDX.

Tab.2 Tensile modulus (E), Poisson's ratio (γ), bulk modulus (K), shear modulus (G), Cauchy pressure (C_{12}−C_{44}) for (100) TNT, (100) RDX), (100) TNT/MNs, and (100) RDX/MNs. Unit for E, K, G, C_{12}−C_{44} is GPa.

	(100)TNT	(100)TNT/MNs	(100)RDX	(100)RDX/MNs
C_{11}	10.44	14.29	10.77	15.43
C_{22}	8.46	13.58	10.68	13.34
C_{33}	5.74	11.14	9.75	12.69
C_{44}	5.71	6.24	3.56	3.69
C_{55}	1.04	2.97	3.05	2.60
C_{66}	2.72	2.77	1.64	3.30
C_{12}	5.75	9.58	6.44	6.59
C_{13}	1.64	4.94	5.82	6.10
C_{23}	3.58	7.14	4.52	7.40
E	5.85	7.83	6.57	9.44

γ	0.31	0.35	0.34	0.32
K	5.18	9.15	7.14	9.07
G	2.23	2.88	2.44	3.55
K/G	2.32	3.17	2.92	2.55
$C_{12}-C_{44}$	0.04	3.34	2.88	2.90

Brazilian Disk Test. Brazilian disk test is a kind of indirect tensile test [26−28], which is suitable for characterizing the tensile mechanical performance of explosives since it is more secure than the direct-tensile test. The testing results show that tensile elastic modulus increases from 4.86 GPa to 6.14 GPa when the MNs plasticizers are incorporated into TNT and RDX blends. Comparing with the big enhancement in modulus, the breaking strength only has a small increase from 0.82 to 0.90 MPa, suggesting that the MNs plasticizers mainly contribute to the reduction of cracks in TNT but lack of the crosslinking properties as elastomeric binders.

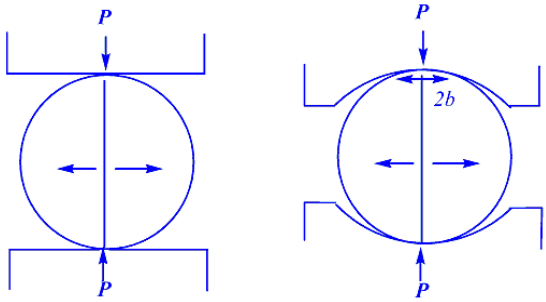


Fig.4 Shematic diagram of the Brazilian disk test

Tab.3 Mechanical properties of TNT/RDX, TNT/RDX/mononitrotoluene and TNT/RDX/mononitrotoluene/resin under the Brazilian disk test

Formula	Breaking strength /MPa	Strain /%	Tensile elastic modulus/GPa	Maximun loading/N
TNT/RDX-35:65	0.82	0.024	4.86	171
TNT/RDX/MNs-35:65:1.5	0.90	0.034	6.14	170

Conclusions

In this work, mononitrotoluene plasticizers were introduced into composition B for experimental and theoretical investigations. Compared with weak intermolecular-interaction between RDX and TNT (−1.586 kJ/mol), interaction energy of TNT/*o*-NT and TNT/*p*-NT was enhanced to −131.557 and −95.640 kJ/mol, respectively. Besides, molecular dynamics simulation results show that tensile modulus of (100) TNT/MNs increases by 33.8 % compared with (100) TNT, and that of (100) RDX/MNs increases by 43.6 %. As is evident, the Brazilian disk test testifies that the tensile elastic modulus of TNT/RDX/MNs (6.14 GPa) increases compared with the regular formula TNT/RDX (4.86 GPa), which agree with the trends of MD simulation results. This study provides a method of investigating small-molecule plasticizers modified MECs by combining microscopy, mechanical test and computational simulations.

Acknowledgments

The authors wish to express their gratitude to the NSAF Foundation of National Natural Science Foundation of China and China Academy of Engineering Physics (Grant No. 11076002) and the NSFC Foundation of National Natural Science Foundation of China (Grant No. 51373159) for financial support.

References

[1] J. W. A. M. Janssen, H. J. Koeners, C. G. Kruse, and C. L. Habraken. Pyrazoles. XII. The preparation of 3(5)-Nitropyrazoles by Thermal Rearrangement of N-Nitropyrazoles, J.Org. Chem. 38 (1978) 1777−1782.

[2] S. Nicolich, J. Niles, P. Ferlazzo, D. Doll, P. Braithwaite, N. Rausmussen, M. Ray, M. Gunger and A. Spencer. Recent developments in reduced sensitivity melt pour explosives. 34th International Annual Conference of ICT, Karlsruhe, Germany, June 24–27, 2003, p135.

[3] D. S. Watt, M. D. Cliff. Evaluation of 1, 3, 3 trinitro azetidine (TNAZ)- A High Performance Melt-Castable Explosive. Defence Science and Technology Organisation, Adelaide, Australia, DSTO-TR-1000. (2000)

[4] F. Zhao, P. Chen, R. Hu, Y. Luo, Z. Zhang, Y. Zhou, X. Yang, Y. Gao, S. Gao, Q. Shi. Thermochemical Propertiesnand Non-Isothermal Decomposition Reaction Kinetics of 3,4-Dinitrofurazanfuroxan (DNTF), J. Hazard. Mater. A113 (2004) 67–71 .

[5] S. Singh, R. Damavarapu, R. Surapaneni, P. Samuel. An insensitive melt-cast energetic material: 1-methyl-2,4,5-trinitroimidazole: MTNI. 38th International Annual Conference of ICT, Karlsruhe, Germany, June 30-July 3, 2007, p147.

[6] Q. Ma, Y. J. Shu, G. Luo, L. Chen, B. Zheng, H. Li. Toughening and elasticizing route of TNT based melt-cast explosives, Chin.J.Energ.Mater. 20 (2012) 618–629.

[7] P. Ravi, D. M. Badgujar, G. M. Gore, S. P. Tewari, A. K. Sikder. Review on Melt Cast Explosives, Propellants, Explos., Pyrotech. 36 (2011) 393–403.

[8] D. L. Smith, B. W. Thorpe. Fracture in the high explosive RDX/TNT, J.Mate.Sci. 8 (1973) 757−759.

[9] X.Q. Niu, J.G. Zhang, X.J. Feng, P.W. Chen, T.L. Zhang, S.Y. Wang, S.W. Zhang, Z.N. Zhou, L. Yang. Theoretical investigation on intermolecular interactions between the ingredients TNT and RDX of composition B. Acta Chim. Sinica 69(2011) 1627−1638.

[10] W. Kegler. Einige Betrachtungen über die Herstellung Von TNT-RDX-giesslingen. Explosivstoffe 8 (1960) 1−4.

[11] Y. Wang, X. Tang. Study on modification of cast TNT-RDX charges. Chin. J. Energ. Mater. 2 (1994) 7−11.

[12] National Military Standard of China. Experimental methods of sensitivity and safety GJB/772A-97. (1997)

[13] M.J. Frisch, G.W. Trucks, H. B. Schlegel, G.E. Scuseria. Gaussian 09 C.01, Gaussian, Inc. (2010)

[14] A.D. Becke, J. Chem. Phys. 97 (1992) 9173.

[15] A.D. Becke, J. Chem. Phys. 98 (1993) 5648.

[16] S.F. Boys, F. Bernardi, Mol. Phys. 19 (1970) 533.

[17] H. Sun, COMPASS: an ab initio force-field optimized for condensed-phase Overview with details on alkane and benzene compounds, J. Phys. Chem. B 102 (1998) 7338.

[18] Accelrys Software Inc. Materials studio release notes, release 6.0. Accelrys Software, San Diego. (2011)

[19] W. Qian, Y. Shu, H. Li, Q. Ma, S. Wang. Simulation Study on the GAP-based comb-like ployurethane modifier used for TNT-based composite explosives. Proceedings of the 17th Seminar on New Trends in Research of Energetic Materials, Pardubice, April 9–11, 2014, 390-399.

[20] W. Qian, Y. Shu, H. Li, Q. Ma. The effect of HNS on the reinforcement of TNT crystal: a molecular simulation study. J. Mol. Model. 20 (2014) 2461.

[21] J.J. Xiao, S.Y. Li, J. Chen, G.F. Ji, W. Zhu, F. Zhao, Q. Wu, H.M. Xiao. Molecular dynamics study on the correlation between structure and sensitivity for defective RDX crystals and their PBXs. J. Mol. Model. 19 (2013) 803−809.

[22] H.C. Andersen. Molecular dynamics simulations at constant pressure and/or temperature. J. Chem. Phys. 72 (1980) 2384−2393.

[23] M. Parrinello, A. Rahman. Polymorphic transitions in single crystals: A new molecular dynamics method. J. Appl. Phys. 52 (1981) 7182−7190.

[24] D.G. Pettifor. Theoretical predictions of structure and related properties of intermetallics. Mater. Sci. Technol. 8 (1992) 345−349.
[25] S.F. Pugh. Relations between the elastic moduli and the plastic properties of polycrystalline pure metals. Philos. Mag. A 45 (1954) 823−843.
[26] J. Ye, F.Q. Wu, J.Z. Sun. Estimation of the tensile elastic modulus using Brazilian disc by applying diametrically opposed concentrated loads. Int. J. Rock Mech. & Mining Sci. 46 (2009) 568−576.
[27] H. Ren, M. Fang, J. He. Experimental study of acoustic emission activity of alumina under compression. Chin. J. Mater. Eng. 2 (2012) 30−34.
[28] J.H. Ye, F.Q. Wu, Y. Zhang, H.G. Ji. Estimation of the bi-modulus of materials through deformation measurement in a Brazilian disk test. Int. J. Rock Mech. & Mining Sci. 52 (2012) 122−131.

Key Engineering Materials Vols 645-646 (2015) pp 259-264
© (2015) Trans Tech Publications, Switzerland
doi:10.4028/www.scientific.net/KEM.645-646.259

Submitted: 2014-10-30
Accepted: 2014-12-23

Research Survey of Electroformed nickel material properties used in MEMS

Guozhong Li[1, a], Gengchen Shi[1, b], Li Sui[1, c], Futing Yi[2, d], Bo Wang[2, e]

[1]Beijing Institute of Technology, Beijing, P.R.CHINA

[2]Institute of High Energy Physics Chinese Academy of Sciences, Beijing, P.R.CHINA

[a]ringup-lgz@163.com, [b]shigengchen@bit.edu.cn, [c]bit_suili@bit.edu.cn (corresponding author), [d]yift@ihep.ac.cn, [e]wangbo@ihep.ac.cn

Keywords: MEMS, Electroformed nickel, Fuze, Material properties

Abstract. As one of the significant structural materials used in safe and arming system of MEMS fuze, the research on micro-electroforming process technologies and micro-electroforming nickel's properties have been a popular field for MEMS area. This paper surveys present domestic and overseas research status of mechanical characterization of electroformed nickel, summarizes and analyzes that changes of the microstructure led by parameters of micro-electroforming process and the external environment make great effects.

Introduction

With physical properties, chemical stability, excellent machining and mechanical properties, products of electroformed nickel are high-precision. For nickel fine crystals and the mechanical characterization could be improved and strengthen [1], nickel is one of the most important metals in electroforming. With outstanding Strength, toughness, corrosion resistance, weakly magnetic, small internal stress in deposition process and excellent micro- dispersion capability of Electroformed nickel solution, nickel electroforming can produce many complex products. And it has proved to be one of the most important structural layer materials used in MEMS devices.

Currently, the research results show that there is a diffusion performance with the mechanical characterization of electroformed nickel. Sharpe [2], Using tensile method, measured Young modulus ranging from 158GPa to 181GPa and yield strength ranging from 330MPa to 420MPa. And the similar method was taken by Cho [3] to get the Young modulus ranging 163±14GPa and yield strength ranging 370±16MPa. J. K. Luo [4] discovered that the Young modulus of electroformed nickel films vary as the change of electroforming temperature and current density by bending method and ranging from 85GPa to 210GPa. Using tensile and indentation methods, Professor Shi Gengchen [5] got the Young modulus 207GPa and yield strength 1047MPa of electroformed nickel of LIGA process. With homemade stretch platform and image method, Liu Rui [6-8] tested the Young's modulus of 32Gpa and 95Gpa, a tensile strength of 750Mpa. Under the condition of 20mA/cm^2 of the current density, Zhang Duanqin [9] got the Young modulus of electroformed nickel films 86±6Gpa with UV-LIGA process.

The fundamental reason of the diffusion performance with the mechanical characterization of electroformed nickel is that changes in microstructure of electroformed nickel leading to differences in micro-mechanism of plastic deformation and fracture of it and then causing variety of macroscopic mechanical properties of electroformed nickel [9]. Currently, the research mainly

focuses on changes of the microstructure led by parameters of electroforming process and the working environment.

The effect of electroformed nickel on MEMS fuze

As one of the significant structural materials used in safe and arming system of MEMS fuze, electroformed nickel has a great effect on mechanical components of MEMS fuze, especially on elastic components. For the effects of micro-electroforming process parameters, environments of high and low temperature and high impact-high strain rate, the change of material properties will changes the properties of mechanical components, therefore affects the normal operation of MEMS fuze. Thus, the change rule of electroformed nickel will be needed to investigate and survey, and provide reference for the mechanical components' design.

Process parameter

With different electroforming process parameters, electroformed nickel presents variety of microstructure leading to different macroscopic mechanical properties. As shown in Fig. 1 and Fig. 2, Research shows that high density electroformed nickel will be formed with Low current density in electroforming process. And with smaller crystal size, it has higher yield strength [10]. Shen and Gu [11-12] had prepared wide grain size distribution of electroformed nickel with different mechanical characterization. L. K. Luo [13] has revealed the law that temperature and current density of electroforming influenced on Young modulus. As shown in Fig. 3, if the electroforming temperature is below 40℃, Young's modulus increases with temperature. But, if the temperature is higher than 40℃, Young's modulus decreases with increasing temperature。Moreover, Young's modulus decreases linearly with increasing plating current density, shown in Fig. 4.



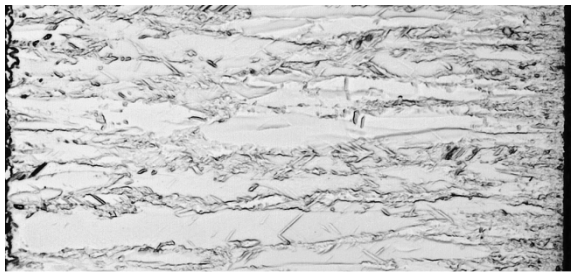


Fig. 1 Microstructure with electroforming current density at 20mA/cm^2

Fig. 2 Microstructure with electroforming current density at 80mA/cm^2

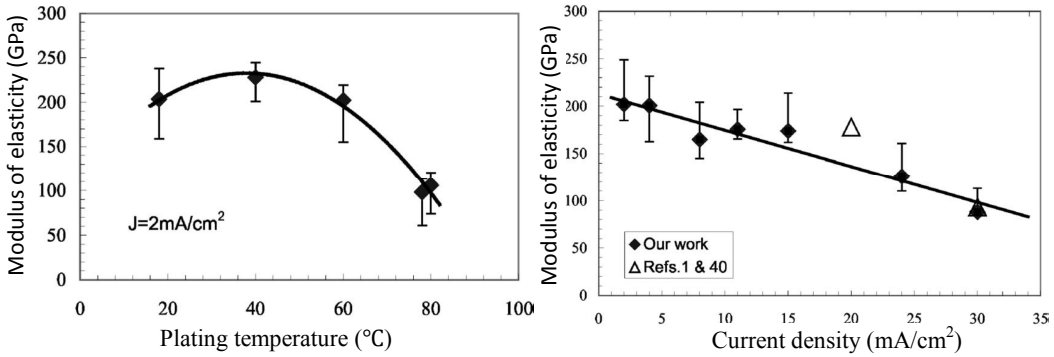


Fig. 3 Modulus of elasticity as a function of plating temperature

Fig. 4, Modulus of elasticity as a function of plating current density, It linearly decreases with increasing current density

Qin Liyuan [14] from Jilin University prepared different crystal size electric electroformed nickel, which were 2μm, 258 nm, 93 nm and 16 nm, throw adjusting plating solution saccharin content, shown in Fig. 5.

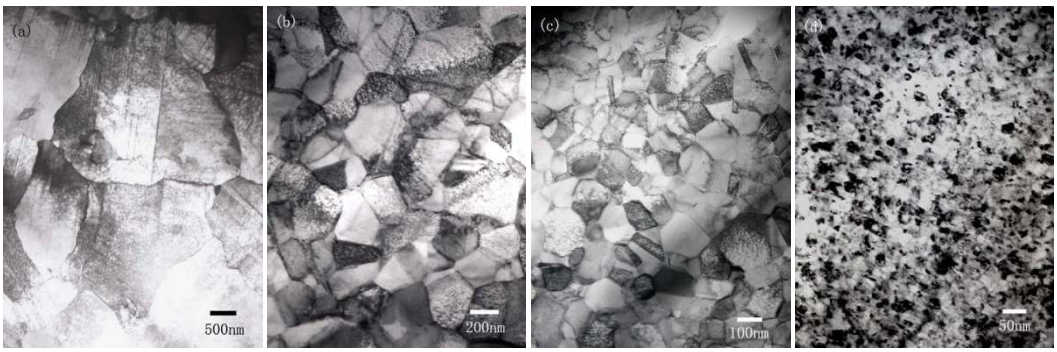


Fig. 5 TEM picture of different crystal size electric electroformed nickel, 2μm, 258 nm, 93 nm and 16 nm

Shen Chunxi [15] tensile fractured and observed the situation of crystal size of 2μm, 95nm, 28nm and 22nm of electroformed nickel at room temperature, shown in Fig. 6.

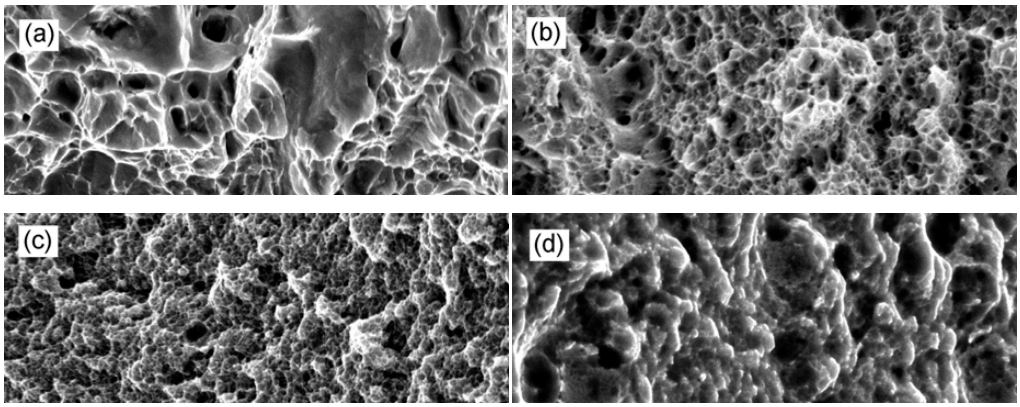


Fig. 6 The fracture surface of different grain size of electroformed nickel (a) 2μm, (b) 95nm, (c) 28nm, (d) 22 nm

By observing the fracture morphology of different grain sizes of electroformed nickel, analyzing the microscopic fracture mechanism, the mechanical characterization of electroformed nickel is proved to be influenced by grain sizes. (1) The coarse grain nickel of 2μm shows open dimple structure with ranging from 1μm to 5μm. In the drawing process from generating micro-pore within the material and the formation of aggregates grow [16]. (2)The 95nm and 28nm samples show a typical small dimple structure which is ten times of the grain size. 28nm sample for example, the size of dimple structure ranges from 100nm to 700nm, which indicates nanocrystalline materials fracture may involve collective grain activities. (3) However, 22nm Ni shows not dimple structure but typical brittle fracture surface features with circular ridges, which is caused by deformation along the grain boundary fracture [17]. All above indicates that the deformation behavior and mechanical characterization of electroformed nickel are affected by grain sizes.

Working conditions

Strain rate. The existing researches show that material properties of electroformed nickel have a close correlation with the strain rate of material. Shen Chunxi [15] tensile fractured and got the stress-strain curve of the same batch of electroformed nickel samples under different strain rate ($1.35s^{-1}$~$1.35\times10^{-6}s^{-1}$) at room temperature shown in Fig. 7. The yield strength ranges from 880MPa to 1320MPa under the condition of strain rate ($1.35s^{-1}$~$1.35\times10^{-6}s^{-1}$), but the young's modulus unchanged.

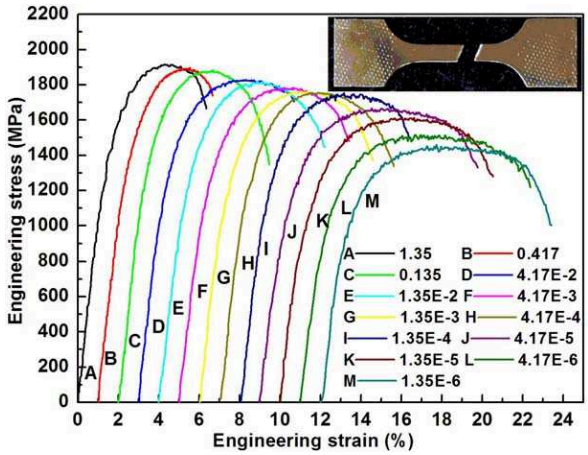


Fig 7 Stress-strain curve of electroformed nickel samples under different strain rate ($1.35s^{-1}$~$1.35\times10^{-6}s^{-1}$)

Strain rate dependency of material properties can be explained by observing the fracture morphology, microstructure and microscopic fracture mechanism of electroformed nickel samples shown in Fig. 8 (a, b, c, d).

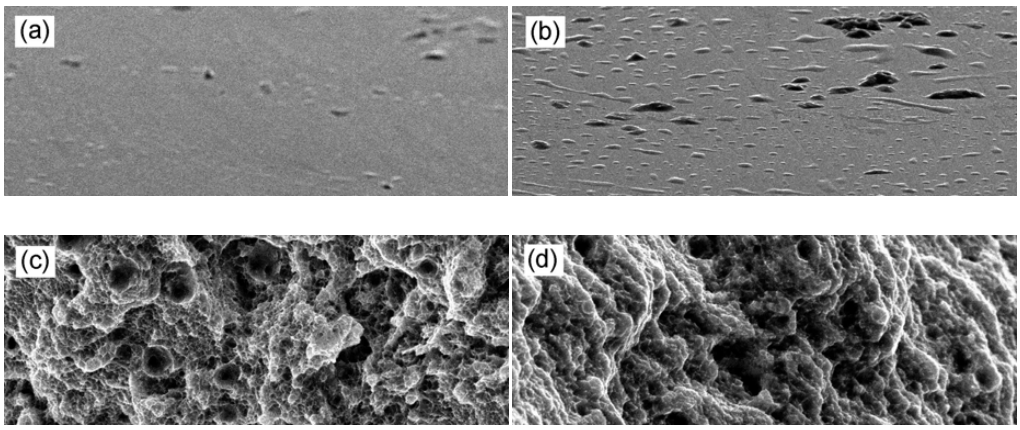


Fig. 8 The Fracture surface morphology under different strain rate. a, c relate high rate(1.35s-1) and b, d relate low rate(1.35×10-6s-1)

As shown in Fig. 8, the fracture of nanocrystalline metal grain may be a collective activity, forming shear planes crossing many grains, and necking and fracture occurred finally [17]. A lot of big bulge, shown in Fig. 8-b, present on the fracture surface under low strain rate, which is not as flat at high strain rate and dimple structure is not obvious. This deformation and fracture surface morphology changes with strain rate further illustrate the fracture mechanism of electroformed nickel changes with strain rate: for short time and the limitation of atomic diffusion and grain boundary sliding, crystal dislocation deformation, as the main deformation mechanism under high strain rate, cause stress concentration at the grain boundaries and grain boundary cracks appear finally. The atomic diffusion and grain boundary sliding will release the stress which is concentrated at grain boundary caused by crystal dislocation, and leading to big bulge on the fracture surface.

Temperature. The existing researches show that the material properties of electroformed nickel will change after heat treatment [18]. As shown in Fig. 9, the microstructure of electroformed nickel presents variety and differences between the stress-strain curves after heat treatment at different temperatures, leading to different mechanical properties of materials. Tensile test results shown in Fig. 10 present stress-strain curve of single crysta nickel at different temperature field performed by Yu Huichen [19] from Beihang University. And as temperature increased, they discovered that the deformation mechanism from original linear dislocation and single slip to Variety of slip and dislocation shown in Fig. 11.

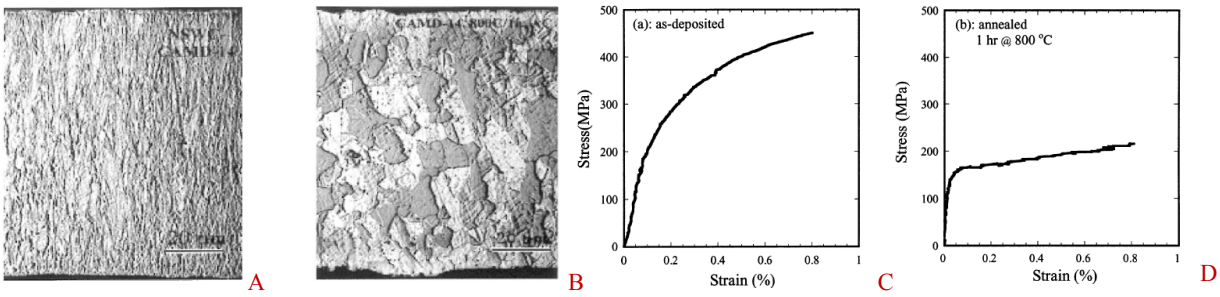
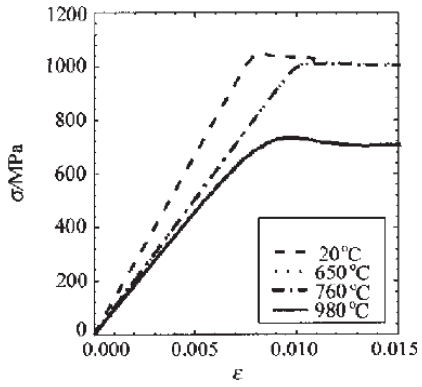


Fig. 9 A and C show the microstructure and tensile test result of electroformed nickel at room temperature. B and D present the microstructure and tensile test result after heat treatment at 800℃ for an hour



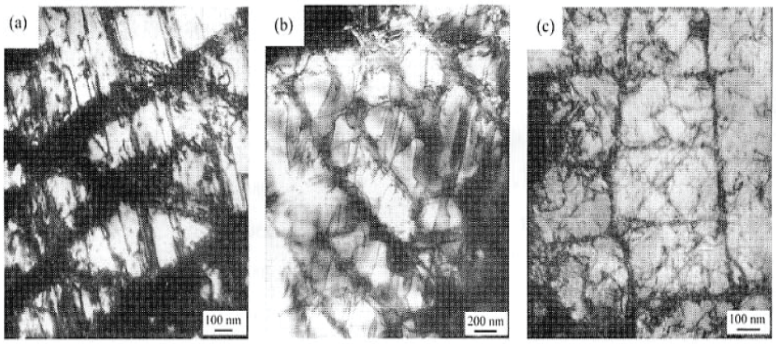


Fig. 10 Fig. 11

Fig. 10 Stress-strain curve of single crystal nickel at different temperature field

Fig. 11 As the temperature increases, the deformation mechanism changes from original linear dislocation and single slip to Variety slip and dislocation

Conclusion

As one of the significant structural materials used in safe and arming system of MEMS fuze, the research on micro-electroforming process technologies and micro-electroforming nickel's properties have been a popular field in MEMS filed. For the changes of electroforming nickel microstructure will cause mechanical properties changes, more research will be needed on it. Especially in environments of alternating temperature and high impact-high strain rate, and acquired correspondence between the mechanical properties and microstructure of electroformed nickel. Therefore provide reference for improving mechanical properties of electroformed nickel material, avoiding the failure of metal micro components in complex environments, and finally designing and applying electroformed nickel components used in fuze.

References

[1] Liu Renzhi, Practical electroforming technology, Chemical Industry Press, Beijing, 2006, pp. 242-246.

[2] SHARPEWN, MCALEAVEYA, Tensile Properties of LIGA nickel, SPIE conference on materials and device characterization in micro machining, Bellingham. (1998) 130-137.

[3] CHOH S, H E,MKER K J, LIAN K, et al. Measured mechanical Properties of LIGA Ni structures, Sensors and Actuators A-Phys, 3 (2003) 59—3.

[4] LUO J K, FLEWITT A J, SPEARING S M, et al., Young's modulus of electro Plated Ni thin film for MEMS applications, Materials Letters. 58 (2004) 2306-2309.

[5] ZHENG Li-bing, SHI Gengchen, HAN Li. Material characteristic of LIGA. Journal of Functional Materials and Devices, 2010 16 (3) 222-226.

[6] Liu Rui, WANG Hong, Li XuePing, et al., A micro-tensile method for measuring mechanical Properties of MEMS materials, Journal of Micromechanics and Micro engineering. 18 (2008) 065002

[7] Liu Rui, Study Of Mechanical Properties of Micro-Scale Materials by Micro-Tensile System and Method, Shanghai Jiao Tong University, 2009.

[8] Wang Hong, TA NG Jun, Liu Rui, Integrated uniaxial tensile test system for measuring mechanical properties of MEMS materials, Optics and Precision Engineering. 18 (2010) 1204-1211.

[9] Zhang Duanqin. Mechanical Properties Characterization of Micro-scale Material through Micro-tensile Testing Method, Dalian University of Technology, 2010.

[10] BUCHHEIT T E, LAVAN D A, MICHAEL J R, et al. Micro structural and mechanical Properties investigation of electrodeposited and annealed LIGA nickel, Metallurgical and Materials Transactions A. 33 (2002) 539-55.

[11] GU C, LIAN J, JIANG Z, JIANG Q. Enhanced tensile ductility in an electrodeposited nanocrystalline Ni, Scripta Materialia. 54 (2006) 579-584.

[12] Shen X, Lian J, Jlang Z, Jiang Q. High strength and high ductility of electrodeposited nanocrystalline Ni with a broad grain size distribution, Materials Science and Engineering: A. 487 (2008) 410-416.

[13] J. K. Luo, M. Pritschow, A. J. Flewitt., Effects of Process Conditions on Properties of Electroplated Ni Thin Films for Micro-system Applications. Journal of Electrochemical Society. 153 (2006) 155-161.

[14] Qin Liyuan. Microstructures and properties characteristic of electrodeposited nanocrystalline Ni and Ni-Co alloys, Jilin University, 2010.

[15] Shen Chunxi, Microstructure and mechanical behavior of electrodeposited bulk nanocrysitalline Ni and Ni-Co alloys, Jilin University, 2009.

[16] Li H Q, EBRAHIMI F. Transition of deformation and fracture behaviors in nanostructured face-centered-cubic metals. Appl. Phys. Lett. 84 (2004) 4307-4309.

[17] HASNAOUI A, VAN SWYGENHOVEN H, DERLET P M. Dimples on nanocrystalline fracture surfaces as evidence for shear plane formation, Science. 300 (2003) 1550-1552.

[18] K.J Hemker, H Last, Microsample tensile testing of LIGA nickel for MEMS applications. Materials Science and Engineering: A, Volumes 319–321 (2001) 882-886.

[19] Yu Huichen, Li Ying, LI Cheng, Tensile behavior of a single crystal Ni-base superalloy at different temperatures, Journal of Aerospace Power. 06 (2005) 958-963.

Key Engineering Materials Vols 645-646 (2015) pp 265-268
Submitted: 2014-11-04
© (2015) Trans Tech Publications, Switzerland
Accepted: 2014-12-23
doi:10.4028/www.scientific.net/KEM.645-646.265

The effect of thermal accumulation to the field emission properties of the carbon nanotubes

Fei Yan[1, a *], Nannan Li[1, 2, b], Lei Chen[1, c], Dazhi Jin[1, d] and Wei Xiang[1, e]

[1]Institute of Electronic Engineering, Chinese Academy of Engineering Physics, Mianyang 621900, China

[2]National Key Laboratory of Science and Technology on Vacuum Electronics, School of Physical Electronics, University of Electronic Science and Technology of China, Chengdu 610054, China

[a]376174148@qq.com (corresponding author), [b]317621169@qq.com, [c]l.chen03@gmail.com, [d]jindazhi@sohu.com, [e]xiangwei-iee@qq.com

Keywords: carbon nanotubes; field emission; thermal accumulation

Abstract: In this paper, we report a recent experimental observation of the effect of thermal accumulation to the field emission properties of the carbon nanotubes. The carbon nanotubes are grown on Ni by CVD. We compare the field emission characteristics of carbon nanotubes cathodes under DC and pulse mode. Our research shows that the higher current and higher current density could be acquired by suppressing the thermal accumulation. The Fowler-Nordheim plot shows a good linear fit, indicating that the emission current of carbon nanotubes follows Fowler-Nordheim behavior.

Introduction

The discovery of carbon nanotubes in 1991[1] has not only opened a rich field in fundamental science but also given a scope of potential technological applications, especially in field emission[2,3]. In 1995, Rinzler's group reported the field emission properties of the carbon nanotubes[4]. As a kind of cold electron emitters[5], carbon nannotubes have been used in a variety of devices, such as flat panel displays[6], high brightness sources for electron microscopes[7], microwave amplifiers, gas discharge tubes[8] and x-ray tubes[9]. While flat panel displays based on carbon nanotubes may one day claim a share of a very large market, other applications are just as promising.

One of the key problems for industrial viability of the devices is the restricted current and current density of the cathodes which could be partly due to the thermal accumulation while electron emit from the carbon nannotubes cathodes to the anode. In this paper, we report a recent experimental observation of the effect of thermal accumulation to the field emission properties of the carbon nanotubes.

Experiments

The carbon nanotubes of diameter about 100 nm we used in the experimental are grown on Ni by CVD. Carbon nanotubes emitters with an area of about 1×1 mm^2 is measured. The effective emission area is not equal to the entire geometrical area of the carbon nanotubes.

A system described in Fig. 1 is used to perform field emission measurements for the carbon nanotubes under different kinds of applied voltage sources, for example, DC voltage soure and pulse voltage sources with different pulse duration and repetition rate. The properties are measured using diode structure at room temperature. The anode is made by copper. The sample lays on the cathode. The anode is maintained at a constant distance of about 250 μm from the cathode, which can be varied with a precision of 10 μm. The experiments are performed in a vacuum chamber below 5×10^{-5} Pa pressure. The high vacuum is obtained by a mechanical pump and a molecular pump. The oscilloscope is used to display the voltage and current curves.

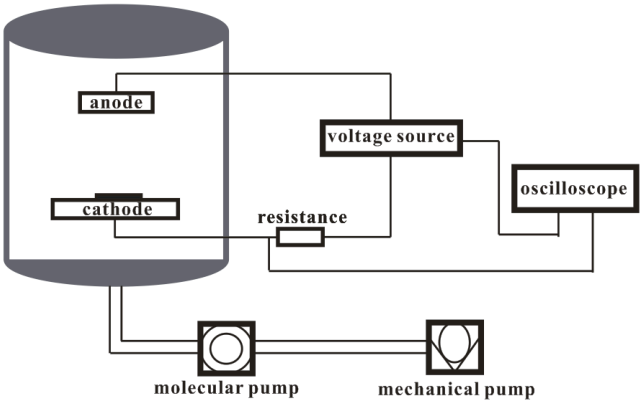


Fig. 1 Schematic diagram of field emission test system.

Results and discussion

Fowler and Nordheim first derived a semiclassical theory of field emission currents from cold metals in 1928[10]. In this theory, the system is simplified as a one-dimensional structure along the direction of the external field. The emission tip is modeled as a semi-infinite quantum well with the work function Φ, and the local electric field E approximated as a linear potential.

By employing the WKB approximation, the following F-N equation was obtained:

$$J = 6.2\times10^{-6}\frac{\mu^{1/2}}{(\phi+\mu)^{1/2}\Phi^{1/2}}E^2\exp(-2.1\times10^{8}\Phi^{3/2}/E) \quad (1)$$

where J is in amperes per square centimeter of emitting surface, μ and Φ are in volts, and E in volts per centimeter. Recordering the equation gives the F-N plot as follows:

$$\log(I/V^2) = a - b/V \quad (2)$$

where V is the applied voltage which is proportional to the local electric field E, I is the current. This equation shows that the field emission's F-N plot should be a good linear fit.

Fig. 2 shows the field emission I-V characteristics acquired with a DC voltage source. The inset inside the figure shows F-N plot. It shows a good linear fit, indicating that the emission current of carbon nanotubes follows F-N behavior. The maximum emission current obtained in this measurement is 1.4 mA when the DC voltage is 800 V. It is not a big value. The spark appear when we try to increase the value of the DC voltage to obtain a bigger current. And carbon nanotubes was partly burned. We suspect the reason of the small current value is partly due to the thermal accumulation.

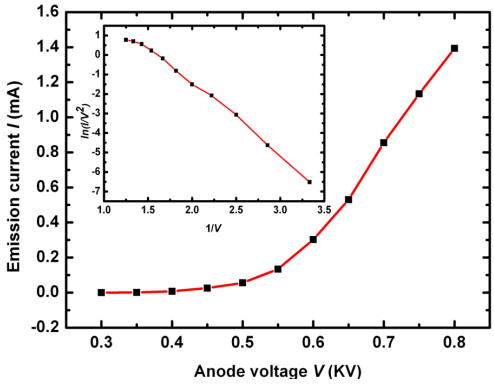


Fig. 2 Field emission characteristic under DC testing. The inset shows F-N plot.

To demonstration this idea, we use a pulse voltage source which is employed to provide voltage with 50 μs pulse duration and 100 Hz repetition rate in Fig. 3. The duty ratio of this pulse voltage is 5%, which would has less thermal accumulation than DC voltage during the electron emit. Compared with the former, the maximum emission current is increased significantly, the value is up to 10.2 mA when the voltage is 1.7 kV.

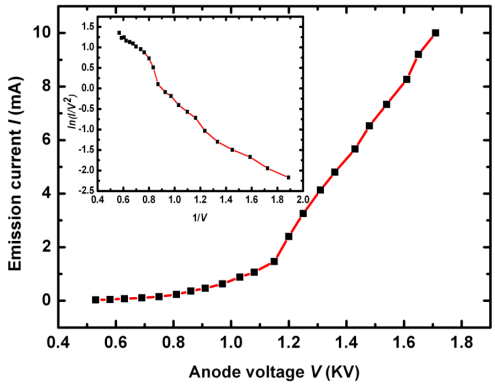


Fig. 3 Field emission characteristic under pulse voltage(50 μs, 100Hz) testing. The inset shows F-N plot.

It can be explained briefly as follows. The temperature of the anode would rise under the bombardment of electron. Then the gas releasing from the anode will lead to local vaccum changing rapidly. After that, the bombardment of electron makes gas ionization to produce ions. Ions bombard the carbon nanotubes under the action of electric field. The spark which bring about the field emission current and current density cannot increase further. Less thermal accumulation would due smaller temperature increase.

In order to confirm the conjecture further, we use oil to cool the anode while the electron emit. Thermal accumulation could be reduced by this way. The thermometer is used to measure the oil's temperature. We obtain 14.4 mA emission current in Fig. 4 which is bigger than the formers. The maximum voltage is 2.4 kV. The temperature of the oil rise from 17^0C to 36^0C. It can be seen that suppressing thermal accumulation and controlling the rise of the temperature would do good for higher current and higher current density.

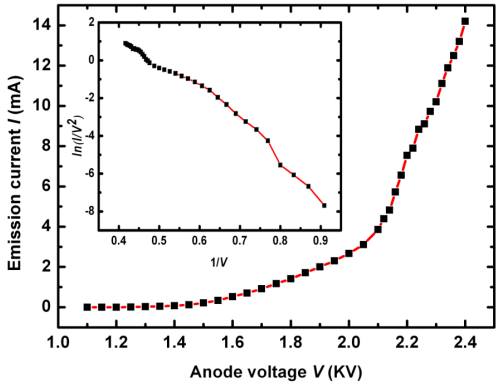


Fig. 4 Field emission characteristic under pulse voltage(50 μs, 100 Hz) testing with the anode cooling by oil. The inset shows F-N plot.

Fig. 5 shows the field emission characteristics acquired with a pulse voltage which has a lower repetition rate (10 Hz). We also use oil to cool the anode at the same time. The bigger emission current 21.56 mA has been got. Less thermal accumulation would due higher-current and higher-current density.

In these figures, especially in Fig. 3 and Fig. 4, the field emission *I-V* curves obtained in the measurement are not very smooth. It's normal. When the voltage is small, the field current is mainly offered by the electron emission from the longer carbon nanotubes. The electron emission from the shorter carbon nanotubes is few. Along with the increase of the voltage, the local electric field and the field current increase. The longer carbon nanotubes become short and smooth, so the quantity of their electron emission decrease. However, the field current from the shorter carbon nanotubes is bigger and bigger. The interaction result in the perturbation of the field emission curves.

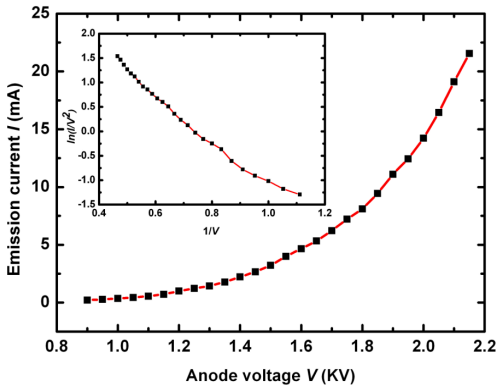


Fig. 5 Field emission characteristic under pulse voltage(50 μs, 10 Hz) testing. The inset shows F-N plot.

Summary

We tested the field emission properties of the carbon nanotubes in different conditions. The research shows that it is beneficial for getting higher current and higher current density by suppressing the thermal accumulation. It can be explained briefly as follows: the temperature of the anode would rise under the bombardment of electron. Then the gas releasing from the anode will lead to local vaccum changing rapidly. The sparks occur on the carbon nanotubes which bring about the field emission current and current density cannot increase further. Suppressing the thermal accumulation could control the increasing of the temperature effectively. It's good for obtaining higher-current and higher-current density.

Acknowledgement

This work was supported by the National Science Foundation of China under the grant No. 11375155, the CAEP THz Science and Technology Foundation under the Grant No. T2013-07-0305 and Laboratory of Precision Manufacturing Technology, CAEP (Grant 426010402).

References

[1] S. Iijima, Helical microtubules of graphitic carbon, Nature. 354 (1991) 56-58.
[2] W. A. de Heer, A. Chatelain, D. Ugarte, A carbon nanotubes field emission electron source, Science, 270 (1995) 1179-1180.
[3] W. B. Choi, D.S. Chung, J.H. Kang, et al, Fully sealed, high-brightness carbon-nanotube field emission display, Appl. Phys. Lett., 75(1999) 3129-3132.
[4] A. G. Rinzler, J.H. Hafner, P. Nilolaev, et al, Unraveling nanotubes: field emission from an atomic wire, Science, 269 (1995) 1550-1553.
[5] J. M. Bonard, H. Kind, T. Stockli, et al, Solid State Electron, 45 (2001) 893-914.
[6] Q. H. Wang, A.A. Setlur, J.M. Lauerhaas, et al, A nanotube-based field emission flat pannel display, Appl. Phys. Lett., 72 (1998) 1912-1913.
[7] N. de Jonge, Y. Lamy, K. Schoots, et al, High brightness electron beam from a muti-walled carbon nanotube, Nature, 420 (2002) 393-395.
[8] R. Rosen, W. Simendinger, C. Debbault, et al, Application of carbon nanotubes as electrodes in gas discharge tubes, Appl. Phys. Lett., 76 (2000) 1668-1670.
[9] G. Z. Yue, Q. Qiu, B. Gao, et al, Generation of continuous and pulsed diagnostic imaging X-ray radition using a carbon-nanotube-based field emission cathode, Appl. Phys. Lett., 81 (2002) 355-357.
[10] R. H. Folwer and L. Nordheim, Electron emission in intense electric fields, Proc. R. Soc. London, 119 (1928) 173-181.

Key Engineering Materials Vols 645-646 (2015) pp 269-274
© (2015) Trans Tech Publications, Switzerland
doi:10.4028/www.scientific.net/KEM.645-646.269

Submitted: 2015-01-19
Accepted: 2015-01-21

Effect of ammonia as an inert solvent on structure and separation performance for oil/water mixtures of PVDF porous membranes

Wei Wei Cui [a *], Jing Qiang Liu [b], Li Zhu Liu[c], Wen Hua Xu[d], Yuan Yuan Li[e] and Zhan Qiang Gao[f]

College of Materials Science and Engineering, Harbin University of Science and Technology, Harbin, Heilongjiang Province, CHINA

[a]cuiww@hrbust.edu.cn, [b]hlgxiaoqiang@163.com, [c]mrliulizhu@163.com, [d]xuwenhuayi@163.com,[e]liyuanyuan1216@126.com and [f]gaozhanqiangcl@163.com

Keywords: PVDF membrane, ammonia, separation, morphology.

Abstract. Porous polyvinylidene fluoride (PVDF) membranes were prepared from PVDF and N-methyl-2-pyrrolidone (NMP) solution system using immersion precipitation phase inversion technique with ammonia as an inert solvent additive. The effects of ammonia amount on pore size, surface morphology, crystallinity, hydrophobic property, oil uptake and water-oil separation performance of the membranes were investigated. It was found that all membranes had an interpenetrating porous structure. The increase of ammonia amount led to significant variations in morphology. Lots of tiny apophysis formed on the membrane surface, pore size deceased, and pore density increased with the increase of ammonia amount. The crystallinity decreased with increasing ammonia amount, and hydrophobic property was improved. The membrane showed high oil uptake and effective separation function of oil-water mixture.

Introduction

Water pollution is becoming a serious social problem in all over the world. Because of its high separation efficiency, easy operation, low energy consumption and no secondary pollution, membrane separation technique has been proven as an effective method for water purification [1–3]. In the filtration processes, the surface morphology of the membrane influences the separation efficiency. Immersion precipitation phase inversion process is a versatile and simple technique used for the preparation of polymeric membranes with different morphologies [4,5]. The membrane morphology can be affected by several parameters such as compositions of casting solution and coagulation bath, temperature and post-treatment of the prepared membranes.

Polytetrafluoroethylene (PTFE), polypropylene (PP) and polyvinylidenefluoride (PVDF) are widely used polymeric materials for the preparation of porous hydrophobic membranes. Due to its good solubility in many common organic solvents such as N,N-dimethylacetamide (DMA), N,N-dimethylformamide (DMF), N-methyl-2-pyrrolidone (NMP) and dimethylsulfoxide (DMSO), PVDF can be used for the preparation of membranes by immersion precipitation phase inversion process[6,7]. Fontananova [8] discussed the effect of pore-forming additives, LiCl and PVP, on the membranes morphology and transport properties. Rahimpour [4] investigated the effects of hot air and hot water treatment on morphology and performance of flat sheet asymmetric polyethersulfone (PES) and PVDF membranes, they found that a dense and smooth surface with thick skin layer was established after treatment, and the milk permeation flux of membranes were increased.

In this study, ammonia as an inert solvent additive was added into the PVDF and NMP solution system. The introduction of ammonia is expect to help forming localized microphase separation of PVDF molecular chain, preventing the crystallization of PVDF chain, and further changing the morphology and crystallization behaviors of PVDF membrane in order to improve the absorbability for oil of membranes. The effects of ammonia amount on the morphology, structure and the separation performance for oil/water mixtures of PVDF porous membranes were investigated.

Experimental

Membrane preparation. PVDF (KYNAR 761, ARKEMA) was dried at 110 ^{o}C for 12 h before use in order to remove moisture content. The casting solution was prepared by dissolving 1.5 g PVDF in 18.5 ml NMP by stirring at room-temperature for several hours. Ammonia water (with 0.1 g or 0.2 g) was then added to the above solution, and stirred for 6 h to form transparent solutions. The casting solutions were obtained after being stand for 12 hour to be degassed. The homogeneous casting solutions were spread into liquid film on a glass plate with an automatic Film Applicator (AFA-Ⅱ, Shanghai Pushen Chemical Machinery Co., ltd.) with a knife gap of 250 μm, and then the solution films were immediately immersed in a coagulation bath of water (25 ^{o}C). The formed membranes were peeled off and subsequently immersed in water to remove residual solvent. After being thoroughly dried at 30 ^{o}C, the membranes were used for structure and property characterizations.
Membrane characterizations. The surface morphologies of prepared membranes were inspected by scanning electron microscopy (Sirion FE-SEM, FEI) after being coated with gold. Fourier Transform Infrared Spectroscopy (WQF-310, Bruker Daltonic Inc.) was used to characterize the membrane in terms of its chemical structure. The crystallinity of the membranes were measured on a differential scanning calorimeter (Pyris Diamond DSC, Perkin Elmer Co.,Ltd.) with a heating rate of 10 ^{o}C/min over the temperature of 40 to 250 ^{o}C under argon atmosphere. The hydrophobic properties were evaluated through observing the change of water contact angles on the surface of the membranes with time. The oil uptake was measured by soaking the membranes in the oil and weighting it after removing the excess liquid electrolyte by wiping it with tissue paper. The oil uptake was calculated using the following equation (Eq. (1)):

$$\eta(\%) = \left({M - M_0} \Big/ {M_0} \right) \times 100 \tag{1}$$

Where η is the uptake of the oil, M_0 is the mass of the membrane, and M is the mass of the membrane after being soaked in the oil. The oil-water mixture for evaluating the separation function of membranes was prepared by mixing water and petroleum ether in 1/9(V/V) and sonicated for 100 min to produce a white and milky solution. The as-prepared PVDF membrane was sealed in a cylinder, and the prepared oil-water mixture was poured into the cylinder, and then the pressure was put on the cylinder to make the water to be filtered from the membrane, finally the separation effect was evaluated through directly observing the original oil-water mixture through the optical microscopy (GX71-6230A) and corresponding collected filtrates and comparing the UV-visible absorption spectrum of them. The UV-visible absorption spectrum was obtained on the UV-VIS Spectrophotometers (TU-1901, Beijing Purkinje General Instrument Co., Ltd.).

Results and discussion

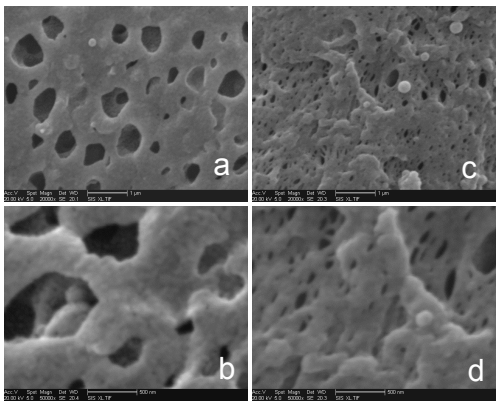


Figure 1 SEM images of PVDF porous membranes added 0.1 g ammonia (a ×20000, b ×50000) and 0.2 g ammonia (c ×20000, d ×50000)

Figure 1 shows the surface morphology of the prepared PVDF membrane with different amount of added ammonia. It can be seen that the membranes showed typical foamy porous structures and

porous were interpenetrating. The average pore size was 0.52 μm when the amount of ammonia was 0.1 g, and the surface of the membrane was smooth. When the amount of ammonia increased to 0.2 g, the average pore size decreased to 0.14 μm, the number of pores in per area was high, the surface of the membrane was rough, and lots of apophysis distributed on the surface. The reason to generate such surface morphology may be due to the function of ammonia as an inert solvent additive. The solvent transferred from good solvent for PVDF chain to poor solvent with the increase of ammonia, which led to the advance aggregation of PVDF chain before phase inversion process, and lots of tiny apophysis formed on the surface.

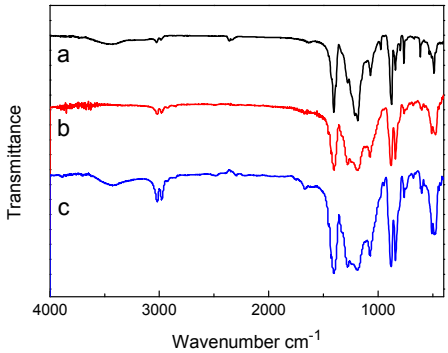


Figure 2 FTIR spectra of PVDF power (a), PVDF porous membranes added 0.1g ammonia (b), and 0.2g ammonia (c)

The FTIR spectra of PVDF power and membranes were shown in figure 2. It can be seen the membranes with different ammonia amount showed similar curves, but they were different with the power's. For curve (a), some typical characteristic peaks of the crystalline α-phase were observed at 974, 796, 764, 613, 532 and 489 cm^{-1}[9,10]. These absorption peaks were attributed to CH out of plane deformation vibration, CH_2 rocking vibration, CF_2 rocking vibration, a mixed mode of CF_2 bending and C-C skeletal vibration, CF_2 bending vibration, bending and wagging vibrations of the CF_2 group ascribed to the α-PVDF polymorph, respectively. The characteristic peaks of the crystalline β-phase were also observed at 1278 and 842 cm^{-1}[11], which was related to CF out of plane deformation and CH_2 rocking vibration, respectively. The intensity of α-phase characteristic peaks is obviously higher than β-phase in curve (a). So we can conclude that the α-phase give priority in PVDF power. For the membranes, the intensity of β-phase characteristic peaks distinguished increase, and the intensity of α-phase characteristic peaks decrease obviously. These indicated that the crystallization of PVDF transfer from α-phase to β-phase during the phase inversion process.

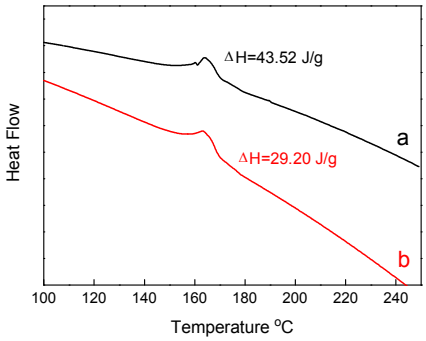


Figure 3 Differential scanning calorimeter curves of PVDF porous membranes added 0.1g ammonia (a) and 0.2g ammonia (b)

The effect of added ammonia on the crystallinity of PVdF membrane was analyzed by measurement of the melting heat during the crystal melting transition of PVdF using DSC as shown in figure 3. The curves had similar shapes with an endothermic peak. The melting temperature (T_m) is noted as the temperature at the maximum value of the melting peak. It can be seen that the melting temperature of membranes are all about 164 °C. The addition of ammonia barely influences the melting temperature of membranes, but there is a considerable decrease of the melting enthalpy. The crystallinity (χ_c) can be calculated from the melting enthalpy from DSC curves by the following equation [12]:

$$\chi_c(\%) = \triangle H_f / \triangle H_f^* \times 100 \quad (2)$$

Where ΔH_f^* is the crystalline melting enthalpy of perfectly crystalline PVdF (104.7 Jg^{-1}) [13]. ΔH_f is the melting enthalpy of the membranes. The crystallinity of the PVdF membrane added 0.1 g ammonia was 41.45%. By increasing the amount of ammonia to 0.2 g, there was a considerable decrease of melting enthalpy, which corresponded to a crystallinity of 27.81%. This observation confirmed that the addition of ammonia inhibited the crystallization process of PVdF and the ratio of amorphous phase increased. These results could be explained that the increase of ammonia made the solution capability of the solvent for PVDF to be decrease, PVDF molecular chain aggregated irregularly and the regular arrangement of PVDF molecular chain was inhabited, which led to the decrease of crystallinity. The irregular aggregation grew up to form apophysis during the phase inversion process.

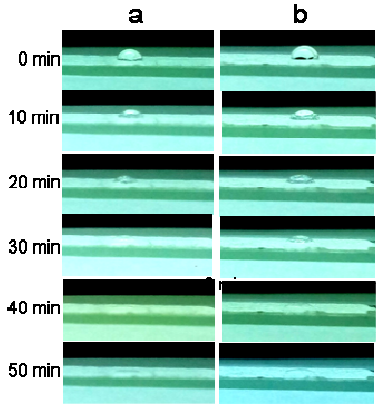


Figure 4 Water droplet images on the surface of PVDF porous membranes added 0.1g ammonia (a) and 0.2g ammonia (b) under different time

The optical photos of water contact angles on the surface of the membranes at different time interval were given in figure 4. It can be seen that the water contact angles were all big at the original time for the membranes with different amounts of ammonia. The water drop permeated slowly into the membranes, while the velocity of permeability was different. The water drop permeated thoroughly into the membrane within 40 min for the membrane with 0.1 g ammonia, while the water drop still partly remained on the membrane with 0.2 g ammonia after 40 min and permeate thoroughly after 50 min. Combined the results of SEM, it can be concluded that the high amount of ammonia enhanced the hydrophobicity of membrane because of abundant apophysis structure on the surface.

Table 1 Oil uptake of PVDF porous membranes added different ammonia amount

	PVDF porous membranes added 0.1g ammonia	PVDF porous membranes added 0.2g ammonia
0 min	0%	0%
10 min	433%	500%
20 min	466%	525%
30 min	460%	525%
40 min	466%	520%
50 min	466%	525%
60 min	466%	525%

The results of the oil uptake of the membranes were listed in table 1. It can be seen that the oil uptake was up to 400%-500% for all membranes. The high oil uptake benefits from the porous structure of the membranes and the excellent affinity of PVDF with oil. The different ammonia amount also affected the oil uptake. The oil uptake is 466% for the membrane with 0.1 g ammonia, then it increased to 525% when the amount of ammonia rose up to 0.2 g. The oil uptake was enhanced by about 60%. The improved uptake capability was mainly due to the increase of amorphous phase of PVDF membrane. For the membrane with 0.2 g ammonia, the average pore size was smaller than the membrane with 0.1 g, but the pore density in per area was more than that one, and more important, the increase of ammonia amount decreased the crystallinity and improved the ratio of amorphous phase,

oil permeated easier into amorphous phase than into crystallization phase. More amorphous phase absorbed more oil.

Figure 5 shows the contrastive optical photos of as-prepared oil-water mixture and its corresponding collected filtrate. The optical microscope images of the mixture and the filtrate are given in Figure 6. It can be seen from figure 5 that the oil-water mixture was milky and not transparent before filtration. The oil droplet distributed uniformly in the water as shown in figure 6. After filtration, the filtrate changed to a colorless and transparent liquid (as shown in figure 5), and not a single droplet was observed in microscope image. These results indicated the effectiveness of the PVDF membranes for separating the oil-water mixture.

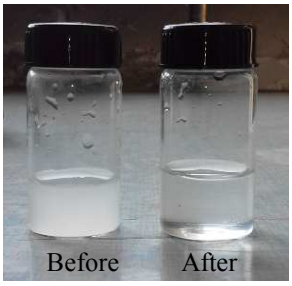


Figure 5 Optical photos of oil-water mixtures before and after filtration

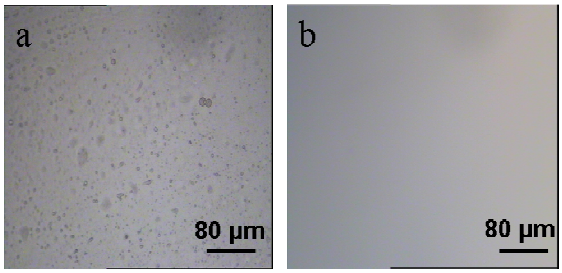


Figure 6 Optical microscopy images of oil-water mixtures before (a) and after (b) filtration

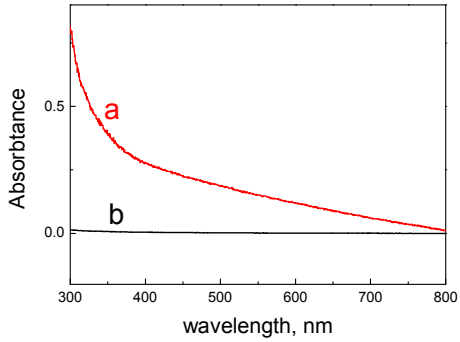


Figure 7 Ultraviolet-visible absorption spectra of the oil/water mixture before (a) and after (b) filtration

To further confirm the separation effect of the PVDF membrane, the ultraviolet-visible absorption spectra of the oil/water mixture before and after filtration were measured and the results showed in figure 7. As shown in figure 7(a), the visible light was absorbed partly in the oil/water mixture, while it can totally pass through the filtrate. These results further confirmed the effectiveness of the PVDF membranes.

Conclusion

Porous PVDF membranes were synthesized using the immersion precipitation phase inversion process. The addition of different ammonia amount exhibited obvious affects on the membrane morphology including pore size, pore number and crystal formation of PVDF membranes. The membrane with high ammonia amount had higher hydrophobicity and the oil uptake capability than that one with low ammonia amount, which was attributed to the apophysis structure formed on the

surface and the decreased crystallinity. The porous PVDF membranes have been demonstrated to have excellent separation function for the oil-water mixture.

Acknowledgement
This work was supported by College Students' Innovative Entrepreneurial Training Plan Program of Harbin University of Science and Technology (No.201310214043), Heilongjiang Provincial Department of Education Science and Technology Research (No.12541113), and Natural Science Foundation of Heilongjiang Province (No.QC2014C051).

References

[1] J. F. Hester, P. Banerjee, and A. M. Mayes, Preparation of Protein-Resistant Surfaces on Poly(vinylidene fluoride) Membranes via Surface Segregation, Macromolecules. 32(1999) 1643-1650.

[2] A. L. Ahmad, N. Ideris, B. S. Ooi, Synthesis of Polyvinylidene Fluoride (PVDF) Membranes for Protein Binding: Effect of Casting Thickness, J. Appl. Polym. Sci. 128(2013) 3438-3445.

[3] W. Zhang, Z. Shi, F. Zhang, Superhydrophobic and Superoleophilic PVDF Membranes for Effective Separation of Water-in-Oil Emulsions with High Flux, Adv. Mater. 25(2013) 2071- 2076.

[4] A. Rahimpour, S.S. Madaeni, M. Amirinejad, The effect of heat treatment of PES and PVDF ultrafiltration membranes on morphology and performance for milk filtration, J. Membr. Sci. 330 (2009) 189-204.

[5] A. Gugliuzza, E. Drioli, PVDF and HYFLON AD membranes: Ideal interfaces for contactor applications, J. Membr. Sci. 300 (2007) 51-62.

[6] T. Ishigami, K. Nakatsuka, Y. Ohmukai, Solidification characteristics of polymer solution during polyvinylidene fluoride membrane preparation by nonsolvent- induced phase separation, J. Membr. Sci. 438(2013) 77-82.

[7] N.J. Lin, H.S. Yang, Y. Chang, Surface Self-Assembled PEGylation of Fluoro- Based PVDF Membranes via Hydrophobic-Driven Copolymer Anchoring for Ultra-Stable Biofouling Resistance, Langmuir. 29(2013) 10183-10193.

[8] E. Fontananova, J.C. Jansen, A. Cristiano, Effect of additives in the casting solution on the formation of PVDF membranes, Desalination. 192 (2006) 190-197.

[9] Z. Yuan, X. Dan-Li, Porous PVDF/TPU blends asymmetric hollow fiber membranes prepared with the use of hydrophilic additive PVP (K30), Desalination. 223(2008) 438-447.

[10] S. Hajibabania, A. Antony, G. Leslie, Relative impact of fouling and cleaning on PVDF membrane hydraulic performances, Sep. Purif. Technol. 90 (2012) 204-212.

[11] L. Yan, Y.S. Li, C.B. Xiang, Effect of nano-sized Al_2O_3-particle addition on PVDF ultrafiltration membrane performance, J. Membr. Sci. 276 (2006) 162-167.

[12] P. Wang, J. Ma, Z. Wang, Enhanced Separation Performance of PVDF/PVP-g-MMT Nanocomposite Ultrafiltration Membrane Based on the NVP-Grafted Polymerization Modification of Montmorillonite (MMT), Langmuir. 28(2012) 4776-4786.

[13] F. Zhang, W. Zhang, Y. Yu, Sol–gel preparation of PAA-g-PVDF/TiO_2 nanocomposite hollow fiber membranes with extremely high water flux and improved antifouling property, J. Membr. Sci. 432 (2013) 25-32.

Key Engineering Materials Vols 645-646 (2015) pp 275-280
© (2015) Trans Tech Publications, Switzerland
doi:10.4028/www.scientific.net/KEM.645-646.275

Submitted: 2015-01-16
Accepted: 2015-01-21

Size Effect of Piezoelectricity in ZnO Nanowires: A First-Principles Study

Chuanqiong Qin[1, a], Yousong Gu[1,b], Xu Sun[1], Chen Li[1], Yue Zhang[1]

[1]Department of Materials Physics and Chemistry, University of Science and Technology Beijing, Beijing 100083, China

[a]qinshujiu101@126.com, [b]yousongu@mater.ustb.edu.cn

Keywords: ZnO Nanowires, Density Functional Theory, Piezoelectricity, Size Effects

Abstract. Piezoelectric properties of ZnO nanowires orientated along [0001] are investigated via density functional theory (DFT). A new method to calculate the volume of nanowires was proposed, which is crucial to the value of piezoelectric coefficients. Results show that the axial effective piezoelectric coefficients are 29.99 Cm^{-2}, 25.93 Cm^{-2}, 22.82 Cm^{-2} for ZnO nanowires with diameters of about 0.6 nm, 1.2 nm, 1.8 nm, which are considerably larger than that of the bulk (20.19 Cm^{-2}). It is found that the change in volume during the strain played a dominated role in size effects. This work helps to gain a deeper understanding of the piezoelectric size effects in ZnO nanowires.

Intorduction

Piezoelectric nanostructures show their distinctions for the following reasons: external mechanical energy is sufficient to actuate small piezoelectric materials; it's easy to prepare mono-crystal nanostructures [1,2] which don't easily failure [3] with applied high strains; novel features such as size effects may become observable when it comes to nanoscale. Most recently, there is an increasing interest in ZnO piezoelectric nano-devices, such as piezoelectric FET [4], strain sensors [5] and nanogenerators [6]. Wang assembled ZnO nanogenerators [7] and introduced the concept of piezo-phototronics [8].

Several theoretical works of the piezoelectric coefficients of ZnO nanowires have been carried out, but they don't seem to reach a conformity in terms of size effects. Xiang [9] concluded that the effective piezoelectric coefficients of ZnO nanowries thinner than 2.8 nm are about 26-39% higher than the bulk value, while Agrawal [10] suggested that nearly 2 orders of magnitude enhancement can be attained when the diameter is less than 1nm. Korir [11] obtained the core region's effective piezoelectric coefficients of two different nanowries which are 1.19 Cm^{-2} and 1.21 Cm^{-2}, very close to the DFT bulk piezoelectric coefficient of 1.28 Cm^{-2} [12].

There are two causes responsible for the above inconformity. The chief one is that different "effective piezoelectric coefficients" were defined in previous works due to the complex atomic relaxation of a nanowire. The second aspect is the method to define the volume of a nanowire, which is very crucial for the value of effective piezoelectric coefficients [11].

In this paper, we propose a new method to calculate the volume of nanowires for reasonable results. Density functional theory (DFT) is employed to study the piezoelectric properties of [0001] oriented ZnO nanowires. The calculated nanowire's effective piezoelectric coefficient is found to increase as the diameter decreases. Through the study for the mechanism of piezoelectric size effects, the change of nanowire's volume during the strain is found to play the dominated role.

Computational Methods

The DFT calculations were perform by the SIESTA [13] code. Generalized gradient approximation in the form of Perdew-Burke-Ernzerhof (GGA-PBE) was adopted for the exchange correlation functional. Double-ζ polarization (DZP) numerical atomic orbitals were chosen as basis sets. Norm conserving pseudopotentials are generated from the Troullier-Martins scheme [14] with core-valence interactions. Mesh cutoff was 400 Ry, and the force tolerance on each atom was less than 0.02 $eVÅ^{-1}$. 1×1×9 Monkhorst-Pack grids were employed after convergence study of k-points. Effective Piezoelectric coefficients are calculated utilizing the Berry Phase [15] method.

Hexagonal supercells were adopted with the same c axis, and with large lateral vacumn distance between the periodic nanowires. After geometry relaxation, cross sections of the ZnO nanowires are shown in Fig. 1. We call them sample A, B, C, with diameters of about 0.6 nm, 1.2 nm, 1.8 nm.

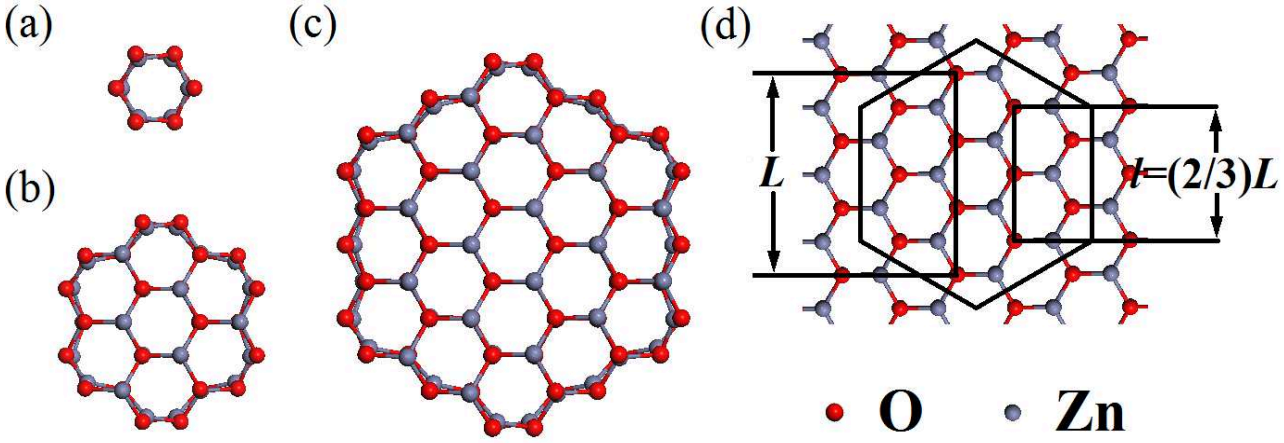


Fig 1. (a,b,c) Cross sections of ZnO nanowires with different sizes. (d) Schematic diagram illustrating the method to estimate the cross sectional area of nanowire B. The cross-section area is specified by a hexagon with black edge, and the lengths of L and l are indicated in the figure.

Regarding the complex atomic movements in a nanowire, it is hard to study the piezoelectric coefficient e_{33}, which is not well defined. Here the pragmatic effective piezoelectric coefficient $e_{33\text{eff}}$, which is different from e_{33},is defined as reported in previous work [10]

$$e_{33\text{eff}} = \partial P_3/\partial \epsilon_3 = \partial (p_3/V)/\partial \epsilon_3 \quad (1)$$

where P_3 and p_3 are the macroscopic polarization and dipole moment along the c axis, and the strain ϵ_3 is defined as change ratio of the lattice constant c, and V represents the volume of certain structure. All the atoms of nanowires are free to move during the strain to minimized the total energy.
Volume occupied by ZnO atoms in the bulk is a well-defined quantity, and the definition of the volume of nanowires can be made in a similar way. A hexagonal zinc oxide nanowire can be abstracted in the wurtzite crystal as shown in Fig. 1 (d), where the nanowire B is located by a regular hexagon, and one can get the nanowire's volume expression for every supercell

$$V = Sc \quad (2)$$

where S is the cross sectional area, and c is the lattice constant. Six edges of the hexagon cut the Zn-O bonds at the middle. Therefore, we can obtain S by figuring out the area of the black regular hexagon as shown in Fig. 1 (d), where L is the lateral length along a axis, and l is the edge length of the hexagon. From geometry consideration, it is found that:

$$l = (n/(2n\text{-}1))L \quad (3)$$

where n is the shell number of a nanowire. Thus Eq. 2 can finally be presented as

$$V = (3*3^{1/2}/2)l^2 c = (3*3^{1/2}/2)(n/(2n\text{-}1))^2 L^2 c \quad (4)$$

One should notice that after atomic relaxation, Zn atoms move inwards much more than O atoms, so the lateral length L should be treated as the average value of both Zn and O atoms.

Results and Discussions

ZnO Bulk Results.

After geometry relaxation, the structural parameters were calculated and shown in Table 1. Bulk lattice parameters in our work are in good agreement with the previous experiment results [16]. To evaluate the bulk piezoelectric coefficient e_{33}, every value of polarization at certain strain is calculated by changing the lattice constant c and keeping lattice constant a fixed. Polarization along the [0001] direction was plotted as a function of strain in Fig. 2 (a), the slope of which yields the value of e_{33}. The obtained result is also very close to that of previous work [12].

Table 1. Lattice parameters (a, c), fractional coordinate (u), and piezoelectric coefficient (e_{33}) of ZnO bulk.

	a[Å]	c[Å]	u	e_{33}[Cm^{-2}]
this work	3.249	5.220	0.380	1.26
reference data	3.249 [16]	5.205 [16]	0.382 [16]	1.28 [12]

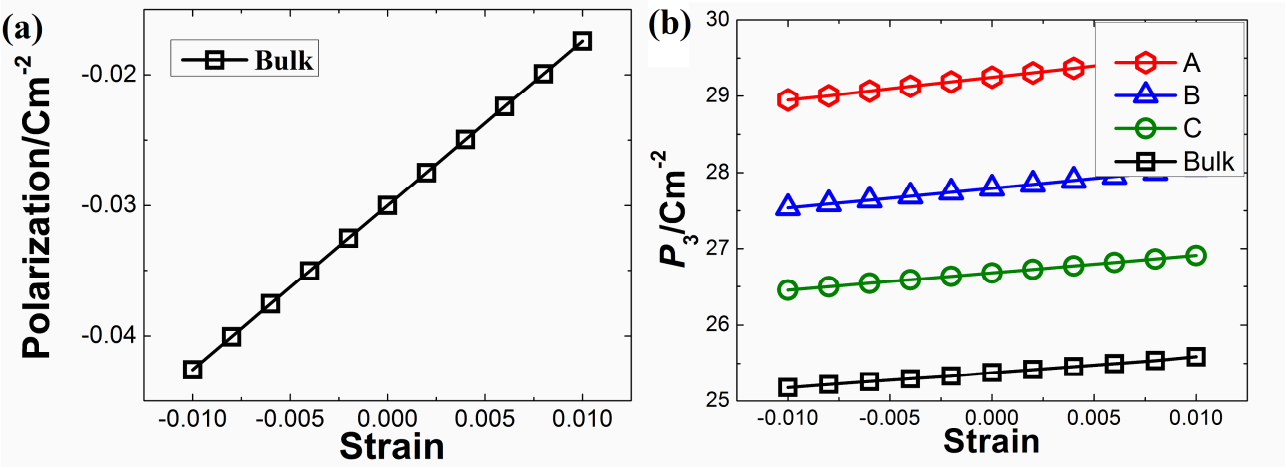


Fig. 2. (a) Polarization along the c axis as a function of strain for calculating the e_{33} of bulk ZnO (lattice constant c is changed and a is fixed). (b) Macroscopic polarization along the c axis (P_3) as a function of strain for ZnO nanowires.

Piezoelectric Size Effects in ZnO Nanowires.

First of all, geometry relaxations were performed and the structural parameters of the nanowires were listed in Table 2. It is clear that lattice constant c increases as the nanowire gets thin, and the atoms in the core region don't move a lot while the surface atoms are relaxation as shown in Fig. 1 (a-c).

Table 2. Information for the relaxed ZnO nanowires: unrelaxed lateral length (L_0), relaxed lateral length (L), relaxed lattice constant (c), average volume (V_a), Poisson ratio (v) surface atom ratio (η) and effective piezoelectric coefficient (e_{33eff}).

sample	L_0[Å]	L[Å]	c[Å]	V_a[Å^{-3}]	v	η	e_{33eff} [Cm^{-2}]
A	3.249	2.979	5.375	20.648	0.474	1.00	29.985
B	9.747	9.201	5.302	21.600	0.427	0.75	25.756
C	16.245	15.685	5.269	22.454	0.391	0.56	22.735
bulk			5.220	23.861	0.372	0.00	20.189

A series of strains from -1% to 1% at an increment of 0.2% were applied along the c axis, and the structures are fully relaxed. One should not directly compare the e_{33eff} of nanowires with the bulk's e_{33}. To calculate the bulk e_{33eff}, lateral contract must be taken into account, and a Poisson ratio of 0.37 was implemented as calculate in our previous work [17].

Values of P_3 at different strains were calculated and plotted in Fig. 2 (b). The result clearly reveals that, P_3 at any given strain is larger than that of bulk. The obtained coefficients are shown in Table 2, from which we finally come to the size effects that $e_{33\text{eff}}$ of a nanowire is considerably larger than the bulk value, and it decreases as the diameter increases. The coefficients are in the same order of magnitude, which is different to the giant size effects in Agrawal's work [10]. Moreover, the difference of $e_{33\text{eff}}$ between nanowire C and bulk is very small, suggesting that a pure and fully relaxed nanowire thicker than 1.8 nm will have almost the same piezoelectricity to that of bulk.

Mechanism of Piezoelectric Size Effects.

Previous works [9,10,11] about the piezoelectric size effects just yield rough explanations, so this section proceeds to elaborate the study of mechanism. Among different nanowires, it's worthless to make a comparison of p_3 or V_3, both of which multiply as the diameter increases. But we overcome the problem by introducing p_{3a} and V_a, the average macroscopic dipole moment and averge volume for every Zn-O pair. Thus Eq. 1 can be written as

$$e_{33\text{eff}} = \partial(p_3/V)/\partial\epsilon_3 = \partial(p_{3a}/V_a)/\partial\epsilon_3 = (\partial p_{3a}/\partial\epsilon_3)V_a^{-1} + p_{3a}(\partial V_a^{-1}/\partial\epsilon_3) \quad (5)$$

where p_{3a} and V_a are the average macroscopic dipole moment and volume for every Zn-O pair. It is clear that there are four variables $\partial p_{3a}/\partial\epsilon_3$, V_a^{-1}, p_{3a}, $\partial V_a^{-1}/\partial\epsilon_3$ determining $e_{33\text{eff}}$ at certain strain. p_{3a} and V_a^{-1} are both plotted as a function of strain in Fig. 3. It's evident that at any degree of strain, the variable quantity V_a^{-1} shows a slowly descending trend as the nanowire grows thick.

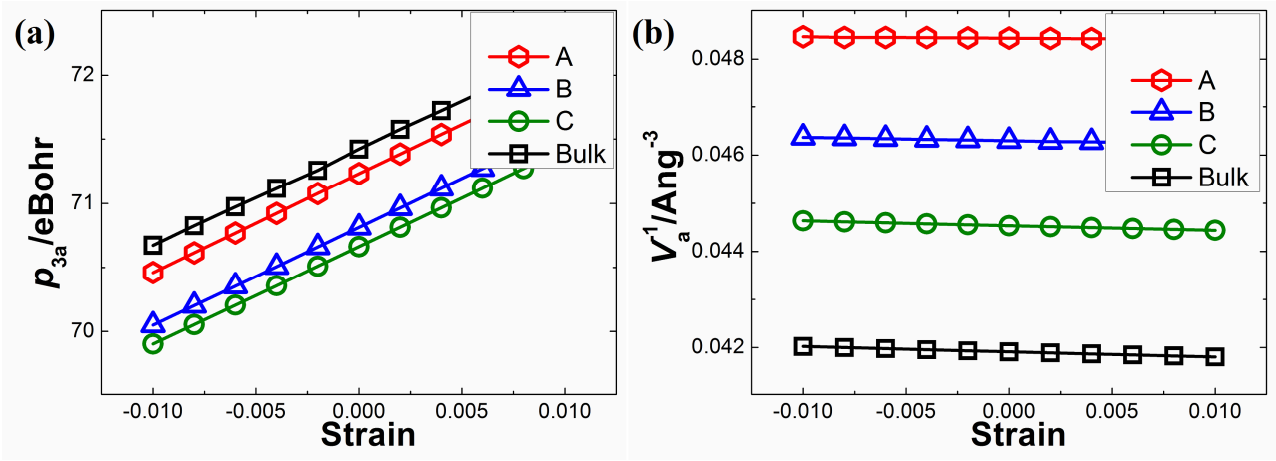


Fig. 3. (a) Averaged electric dipole moment along the c axis. (b) Reciprocal of averaged volume as a function of strain for ZnO nanowires.

The numerical results for the above four variables and the effective piezoelectric coefficients with the condition of ϵ_3=0 are shown in Table 3. Table 3 clearly indicates tiny differences for the terms of $\partial p_{3a}/\partial\epsilon_3$, V_a^{-1}, and p_{3a}, while $\partial V_a^{-1}/\partial\epsilon_3$ varies tremendously in different configurations, which can observed directly in Fig. 4 (a). For nanowire A, a very large variation proportion (nearly 80%) of $\partial V_a^{-1}/\partial\epsilon_3$ to that of bulk is revealed, while that value of V_a^{-1} is just below 20%. Therefore, as $\partial p_{3a}/\partial\epsilon_3$ pertains to the same order of magnitude as p_{3a} at any row of the table, one can distinguish the negligible contribution of V_a^{-1} from the major impact of $\partial V_a^{-1}/\partial\epsilon_3$ to the value of $e_{33\text{eff}}$.

Table 3. The four terms in Eq. 5 without any strain for nanowires and bulk.

Sample	$\partial p_{3a}/\partial\epsilon_3\|\epsilon_3$=0 [eBohr]	$V_a^{-1}\|\epsilon_3$=0 [Å^{-3}]	$p_{3a}\|\epsilon_3$=0 [eBohr]	$\partial V_a^{-1}/\partial\epsilon_3\|\epsilon_3$=0 [Å^{-3}]	$e_{33\text{eff}}\|\epsilon_3$=0 [Cm^{-2}]
A	76.544	0.04843	71.231	-0.00239	29.986
B	76.307	0.04587	70.812	-0.00665	25.752
C	76.031	0.04412	70.662	-0.00974	22.733
bulk	75.389	0.04191	71.421	-0.0109	20.187

Therefore this section indicates the past fallacy in those previous works [9,10] that, the reduction of average volume with respect to bulk, essentially causes the enhancement in effective piezoelectric coefficients. Our researches demonstrate a truth that, the change of average volume in the process of strain dominates the piezoelectric size effects in this set of ZnO nanowires. A value of $\partial V_a^{-1}/\partial\epsilon_3$ close to 0, which means low change rate of the volume, can lead to a large e_{33eff} for nanowires.

A very brief parameter characterzing $\partial V_a^{-1}/\partial\epsilon_3$ is the Poisson ratio v. For nanowire A, $\partial V_a^{-1}/\partial\epsilon_3$ is relatively close to 0, which means a high v, while the value of a thicker nanowire is lower. One can also obtain the regularity in Fig. 4 (b), where the Poisson ratio v of any structure grows up as the size gets smaller. So here we can generally evaluate e_{33eff} by v, and that is, a higher Poisson ratio usually helps to yield a higher e_{33eff} .

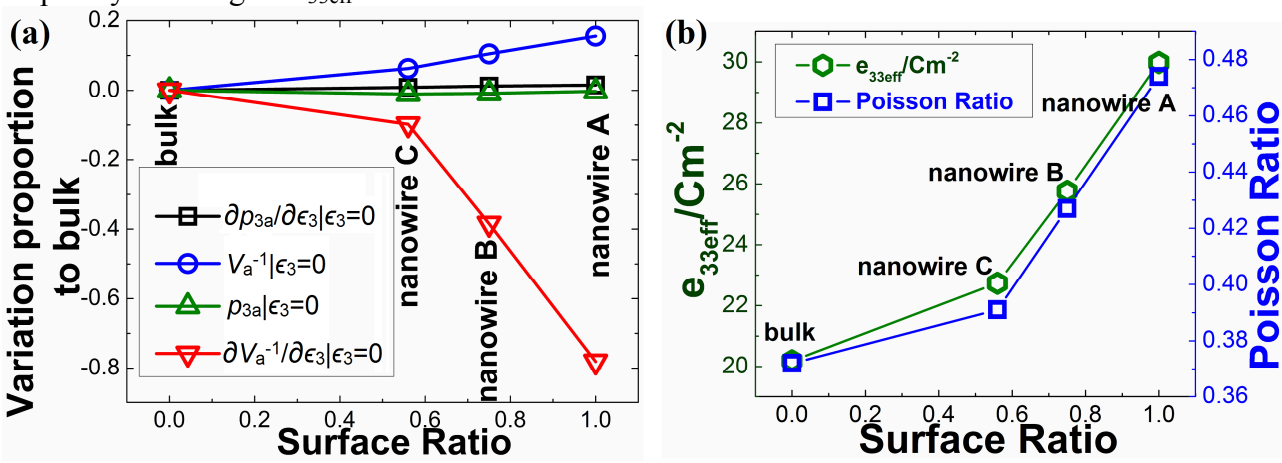


Fig. 4. (a) The variation proportion to bulk at different diameters for four terms of $\partial p_{3a}/\partial\epsilon_3$, V_a^{-1}, p_{3a}, $\partial V_a^{-1}/\partial\epsilon_3$ without any strain. (b) Effective piezoelectric coefficiets and Poisson Ration of different structures as functions of surface ratio.

This inference may be a good suggestion to the research of piezoelectricity, because recent works have showed extensively dispersed Poisson ratios for various ZnO materials. Pant [18] prepared epitaxial ZnO films through a two-step growth method at series of low temperatures, which leads to abnormal Poisson's ratios ranging from 0.08 to 0.54. For single-walled ZnO nanotubes, Mirnezhad [19] has demonstrated a changing values from 0.2 to 0.61 with different patterns of hydrogen adsorption. Qing [20] has obtained a high Poisson ratio of 0.667 for graphene-like hexagonal ZnO monolayer.

Summary

To summarize, first-principles calculations for effective piezoelectric coefficients e_{33eff} in ZnO nanowires and the analysis of size effectis are carried out. The nanowire's value of e_{33eff} falls down as a result of diameter increment. The gradient of the averaged volume's reciprocal $\partial V_a^{-1}/\partial\epsilon_3$ shows a noteworthy diversity in different nanowires, and thus leads to remarkably different values of e_{33eff}. Our study may suggest new search directions for piezoelectric effects in nanostructures.

Acknowledgement

This work was supported by the National Major Research Program of China (No. 2013CB932600), the National Natural Science Foundation of China (51452001, 51172022), the Major Project of International Cooperation and Exchanges (2012DFA50990), the Research Fund of Co-construction Program from Beijing Municipal Commission of Education, the Fundamental Research Funds for the Central Universities, Program for Changjiang Scholars and Innovative Research Team in University.

References

[1] Kong YC, Yu DP, Zhang B, Ultraviolet-emitting ZnO nanowires synthesized by a physical vapor deposition approach, Appl Phys Lett. 78 (2001) 407-409.

[2] Dai Y, Zhang Y, Li QK, Synthesis and optical properties of tetrapod-like zinc oxide nanorods, Chem Phys Lett. 358 (2002) 83-86.

[3] Li P, Liao Q, Yang S, In situ transmission electron microscopy investigation on fatigue behavior of single ZnO wires under high-cycle strain, Nano letters. 14 (2014) 480-485.

[4] Ya Y, Junjie Q, Wen G, Transverse piezoelectric field-effect transistor based on single ZnO nanobelts, Phys Chem Chem Phys. 39 (2010) 12415-12419.

[5] Yang Y, Qi JJ, Gu YS, Piezotronic strain sensor based on single bridged ZnO wires, Physica Status Solidi (RRL). 3 (2009) 269-271.

[6] Hu CJ, Lin YH, Tang CW, ZnO-Coated Carbon Nanotubes: Flexible Piezoelectric Generators, Adv Mater. 23 (2011) 2941-2945.

[7] Song JH, Zhou J, Wang ZL, Piezoelectric and semiconducting coupled power generating process of a single ZnO belt/wire, Nano Lett. 6 (2006) 1656-1662.

[8] Zhong Lin W. Piezopotential gated nanowire devices: Piezotronics and piezo-phototronics, Nano Today. 5 (2010) 540-542.

[9] Xiang HJ, Yang J, Hou JG, Piezoelectricity in ZnO nanowires: A first-principles study, Appl Phys Lett. 89 (2006) 223111-1-3.

[10] Agrawal R, Espinosa HD, Giant piezoelectric size effects in zinc oxide and gallium nitride nanowires, A first principles investigation, Nano Lett. 11 (2011) 786-790.

[11] Korir KK, Cicero G, Catellani A, Piezoelectric properties of zinc oxide nanowires: an ab initio study, Nanotechnology. 24 (2013) 475401-1-5.

[12] Wu X, Vanderbilt D, Hamann D, Systematic treatment of displacements, strains, and electric fields in density-functional perturbation theory, Phys Rev B. 72 (2005) 35105-1-13.

[13] Soler JM, Artacho E, Gale JD, The SIESTA method for ab initio order-N materials simulation, J Phys-Condes Matter. 14 (2002) 2745-2779.

[14] Troullier N, Martins JL, Efficient pseudopotentials for plane-wave calculations, Phys Rev B. 43 (1991) 1993-2006.

[15] King-Smith RD, Vanderbilt D, Theory of polarization of crystalline solids, Phys Rev B. 47 (1993) 1651-1654.

[16] Yoshio K, Onodera A, Satoh H, Crystal structure of ZnO: Li at 293 K and 19 K by X-ray diffraction, Ferroelectrics. 264 (2001) 133-138.

[17] Huang YH, Zhang Y, Wang XQ, Size Independence and Doping Dependence of Bending Modulus in ZnO Nanowires, Cryst Growth Des. 9 (2009) 1640-1642.

[18] Pant P, Budai JD, Aggarwal R, Structural characterization of two-step growth of epitaxial ZnO films on sapphire substrates at low temperatures, Jour Phys D: Appl Phys. 24 (2009) 105409-1-8.

[19] Mirnezhad M, Ansari R, Rouhi H, Effects of hydrogen adsorption on mechanical properties of chiral single-walled zinc oxide nanotubes, Jour Appl Phys. 111 (2012) 014308-1-11.

[20] Peng Q, Liang C, Ji W, A first principles investigation of the mechanical properties of g-ZnO: The graphene-like hexagonal zinc oxide monolayer, Comp Mater Sci. 68 (2013) 320-324.

Key Engineering Materials Vols 645-646 (2015) pp 281-286
© (2015) Trans Tech Publications, Switzerland
doi:10.4028/www.scientific.net/KEM.645-646.281

Submitted: 2015-01-08
Accepted: 2015-01-15

Ejection and Motion Behaviors Simulation for Multi-Jet Electrospinning

Wenwang Li[1,2,a], Zhiwei Luo[1,2,b], Xiang Wang[1,2,c], Jianyi Zheng[2,d], Gaofeng Zheng[2,e*], Daoheng Sun[2,f]

[1.] Department of Mechanical and Electrical Engineering, Xiamen University of Technology, China, 361024

[2.] Department of Mechanical and Electrical Engineering, Xiamen University, China, 361005

[a] xmlww@xmut.edu.cn, [b] zwluo@xmut.edu.cn, [c] 93862712@qq.com, [d] zjy@xmu.edu.cn, [e]zheng_gf@xmu.edu.cn(corresponding author), [f] sundh@xmu.edu.cn

Keywords: Electrospinning, Multi-Jet, Charged Jet, Motion Simulation, Ultrafine Nanofiber

Abstract: Multi-jet ejection is the key factor to promote the industrial application of electrospinning technology. Simulation model based on Maxwell theory was built up to investigate the ejection and motion behaviors of multi charged jets. The charge Coulomb repulsive force among adjacent jet was introduced into the simulation model, which enhanced the instability motion and promoted the stretching process of charged jets. The stretching ratio of charged jet increased with the increasing of injection distance, applied voltage, distance between spinneret and collector. But stretching ratio of charged jet decreased with the increasing of distance between charged jets. Stretching ratio in multi-jet electrospinning was larger than that in single-jet electrospinning. The maximal stretching ratio of charged jet was larger than 9000 in the nine jets electrospinning mode. This work provided a good method to investigate the controlling technology of multi-jet electrospinning.

1 Introduction

Electrospinning utilized electrostatic field to stretch viscoelastic solution, by which nanofiber with diameter of 1~1000nm can be fabricated. With the advantages of small diameter, high surface to volume ratio and low cost[1], electrospinning nanofibers have displayed great potential applications in the fields of filtration[2], sensor[3], bio medical[4], electronic devices[5, 6] and micro/nano energy[7]. Promoting nanofiber throughput and decreasing the nanofiber diameter become the keys for the application researching of electrospinning technology. Multi-jet ejection is the important way to increase the ejection efficiency. At present, there are several methods to realize the multi-jet electrospinning, such as circular cylindrical electrode[8], probe-tip drawing[9], spiral coil spinnerets[10], and ... et al.

As liquid jets ejected from the tip of Taylor cone, which carried away the free charges accumulated on the surface of spinneret and Taylor cone. The charged jet would step into spiral and whipping instability process after a short straight stable stage. The charge Coulomb force plays a great role on the motion and rheology behaviors of charged jets[11]. The instability motion that stemmed from charge Coulomb force promoted the stretching process, decreased the diameter of charged jets and improve the uniformity of electrospun nanofiber[12]. During the multi-jet electrospinning process, the charge Coulomb force among difference charged jets would enhance the instability motion of charged jet, which provides an excess factor to decrease the diameter and increase the uniformity of

electrospun nanofiber. The ejection and motion behaviors investigation of charged jets is a great role to optimize the process controlling of multi-jet electrospinning. The ejection and motion behaviors of charged jets in the multi-jet ejection mode are different form that in the single-jet ejection model. Attribute to the fine diameter and high motion speed, charged jet in the multi-jet mode can't be observed and recorded clearly. Based on the viscoelastic dynamical model, the theoretical and simulation researching has provided an important aspect to investigate the motion and ejection behaviors of electrospinning charged jets [13, 14].

In this work, a simulation model has been built up to analyze the ejection and motion process for multi-jet electrospinning. The motion behaviors and stretching ratio of charged jet are investigated, and then the effects of process parameters on the motion process are also studied.

2 Multi-Jet Electrospinning

Multi nozzles electrospinning method was utilized in this work to realized the multi-jet ejection and fabricate ultrafine nanofiber directly, as shown in Fig. 1. According to the electrospinning theory, liquid jet would carry away free charges from the spinneret. The electrical field force and Coulomb repulsive force were the main factors that define the stretching and motion behaviors of charged liquid jets. The inside Coulomb repulsive force induced charged jet step into instability motion process, which promote the stretching ratio of jet and decrease the diameter of nanofiber[15]. Then, during multi-jet electrospinning process, the Coulomb repulsive force among charged jets would enhance the instability motion of charged jets. Under the same experimental condition, nanofiber electrospun from multi-jet electrospinning process with smaller diameter than that electrospun from single nozzle electrospinning. The ejection and motion behaviors investigations were the key to increase the controlling technology of multi-jet electrospinning [16].

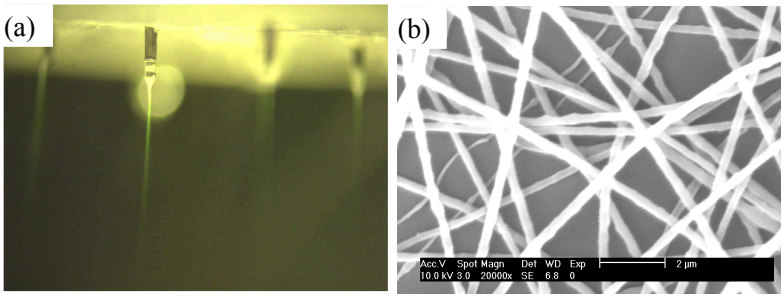


Fig. 1. Multi-jet electrospinning, (a) multi electrospinning charged jets; (b) ultrafine nanofiber electrospun from multi-jet electrospinning. Polymer solution concentration, distance between spinneret and collector, flow rate and applied voltage is 12wt%, 9cm, 1900μl/hr and 11kV, respectively.

3 Computational Modeling

Liquid electrospinning jet displayed viscous and elastic characteristics under electrical field, then the Maxwell model had become an excellent way to describe the motion and rheology behaviors of electrospinning charged jet [16, 17]. Based on the simulation model of single charged jet, multi-jet model of three jets and nine jets were built up to analyze the multi-jet stretching process, as shown in Fig. 2. The charged jet composed charged bead and viscoelastic Maxwell element. The viscoelastic Maxwell element was used to connect two adjacent beads. In this simulation model, all of the mass and charge gathered on the beads.

The electrical field force and charge Coulomb repulsive force define the motion and stretching process of charged jet, as shown in Fig. 3(a). The viscoelastic stress inside jet block the stretching process and promote jet shrinking, as shown in Fig. 3(b). During multi-jet electrospinning process, the adjacent charged jets would also impose repulsive force on each other, which would stretch jet into finer ones, as shown in Fig. 3(c).

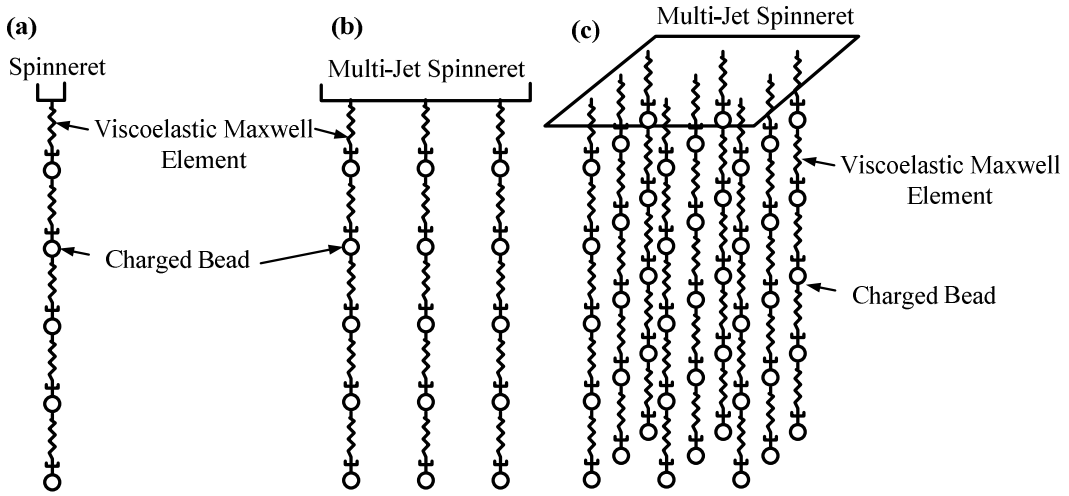


Fig. 2. The diagram of computational simulation model of charged jet ejection process. (a)Single jet; (b) Three jets; (c) Nine jets.

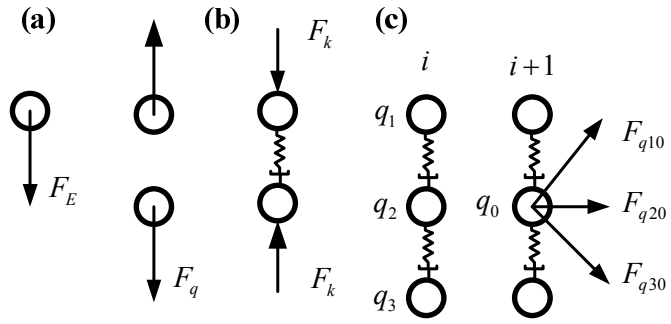


Fig. 3. The diagram of force analysis imposed on the charged jet. (a) Electrical field force and charge Coulomb repulsive force; (b) Viscoelastic stress inside jet; (c) Charge Coulomb repulsive force from adjacent charged jet.

4 Motion Behaviors and Stretching Ratio of Charge Jet

Based on the simulation model, the ejection and motion process of charged jets can be gained, as shown in Fig. 4. As ejected from the tip of Taylor cone, charged jet moved in a straight and stable track. And then, charged jet would step into spiral instability motion attribute to the charge Coulomb repulsive force and uniform electrical field. The instability motion was a key process to stretch the charged jet and decrease its diameter.

In order to describe the stretching process of charged jet, the stretching ratio λ was defined as:

$$\lambda = \frac{l_k}{l_{k0}} = \frac{\sqrt{(x_k - x_{k-1})^2 + (y_k - y_{k-1})^2 + (z_k - z_{k-1})^2}}{l_{k0}} \tag{1}$$

Here, l_{k0} was the original length between two adjacent beads**;** ($x_{k\text{-}1}$, $y_{k\text{-}1}$, $z_{k\text{-}1}$) and (x_k, y_k, z_k) were the location of k-1 and k bead, respectively.

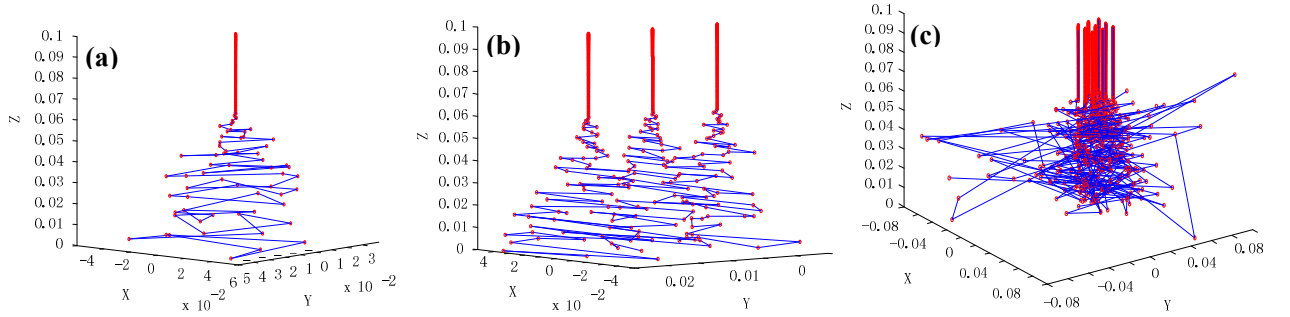


Fig. 4. The simulation results of charged jet motion. (a) Ejection simulation of single jet; (b) Ejection simulation of three jets; (c) Ejection simulation of nine jets.

The original volume of liquid jet between two adjacent beads can be written as:

$$V_0 = \frac{1}{4}\pi D^2 l_0 \tag{2}$$

Here, V_0 was the original volume of liquid jet between two adjacent beads; D was the diameter of liquid jet. During the ejection simulation of charged jet, the volume of liquid jet between two adjacent beads was supposed to stay the same. So, the stretching ratio was an important role to reflect the diameter evolvement of liquid jet. Under the electrical field force, charge jet would move toward collector in an accelerated process. The diameter of liquid jet decreased with the increasing of injection distance, and then the stretching ratio increased with the increasing of injection distance, as shown in Fig. 5.

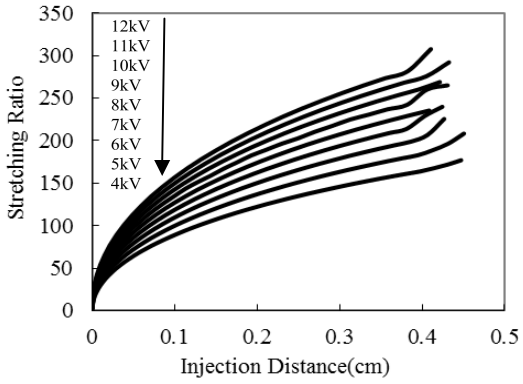


Fig. 5. The relationship between stretching ratio and injection distance in the electrospinning process of single jet. The distance between spinneret and collector is 10cm.

Then, the affects of process parameters on rheology process of charged jet were investigated further. The stretching ratio of liquid jet increased with the increasing of the distance between spinneret and collector, as shown in Fig. 6(a). Higher applied voltage leaded to higher charge density and larger electrical field force, the stretching ratio increased with the increasing of applied voltage, as shown in Fig. 6(b). During the multi-jet electrospinning process, smaller distance between charged jets would increase the charge Coulomb repulsive force and enhance the instability motion of liquid jets. So, the stretching ratio decreased with the increasing of distance between charged jets, as shown in Fig. 6(c).

Simulation results showed that the stretching ratio in multi-jet electrospinning mode was larger than that in the single-jet electrospinning. Then, the stretching ratio in nine jet electrospinning process was larger than that in three jet electrospinning. The maximal stretching ratio of charged jet was larger than 9000 in the nine jets electrospinning.

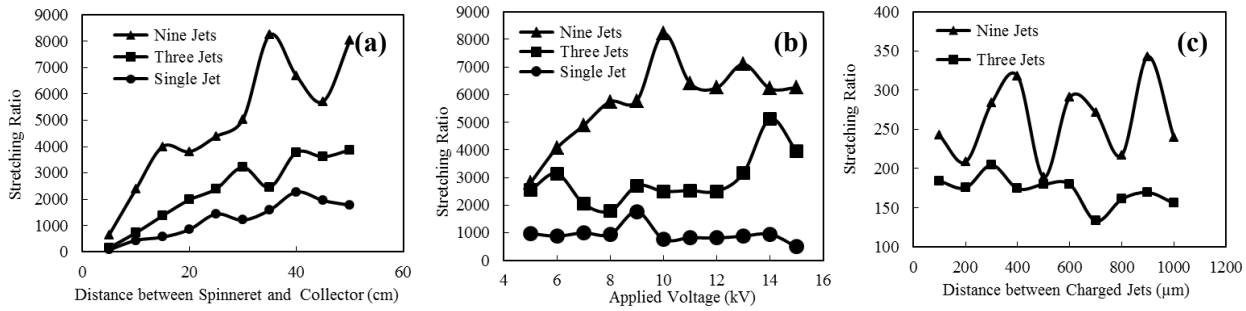


Fig. 6. The effects of process parameters on the stretching ratio. (a) Relationship between stretching ratio and distance between spinneret and collector, the applied voltage and distance between charged jets in multi-jet electrospinning was 8kV and 100μm, respectively; (b) Relationship between stretching ratio and applied voltage, the distance between spinneret and collector and distance between charged jets in multi-jet electrospinning was 10cm and 100μm, respectively; (c) Relationship between stretching ratio and distance between charged jets, the applied voltage and the distance between spinneret and collector was 8kV and 10cm, respectively.

6 Conclusions

Multi-jet electrospinning is a key factor to increase the production efficiency of electrospinning nanofiber, and promote the industrial application of electrospinning technology. During the multi-jet electrospinning, the charge Coulomb repulsive force between different charged jets would enhance the instability motion and decreased the diameter of charged jets. A multi-jet electrospinning simulation model was built up to analyze the motion and rheology process of charged jet. Simulation results showed that the stretching ratio of charged jet increased with the increasing of injection distance, applied voltage, distance between spinneret and collector. But stretching ratio of charged jet decreased with the increasing of distance between charged jets. The stretching ratio in multi-jet electrospinning was larger than that in single-jet electrospinning. The maximal stretching ratio of charged jet was larger than 9000 in the nine jets electrospinning.

This work investigated the ejection and motion behaviors of multi charged jets in multi-jet electrospinning, which would promote the controlling and application of electrospinning technology.

Acknowledge

This work is supported by the National Natural Science Foundation of China (No. 51305373), Major Science and Technology Projects of Fujian Province of China (No. 2012H6022, 2012H0041), Xiamen Municipal Science and Technology Project (No. 3502Z20143033).

* This work is supported by the National Natural Science Foundation of China (No. 51305373), Major Science and Technology Projects of Fujian Province of China (No. 2012H6022, 2012H0041), Xiamen Municipal Science and Technology Project (No. 3502Z20143033)
Corresponding Author: Gaofeng Zheng zheng_gf@xmu.edu.cn

References

[1] J. Anu Bhushani, C. Anandharamakrishnan. Electrospinning and electrospraying techniques: Potential food based applications. Trends in Food Science & Technology, 38(2014), 21-33.

[2] H. Wang, G. Zheng, D. Sun. Air filtration performance of nanofibers membranes electrospuned with difference nanofiber diameters. Journal of functional materials and device, 14(2007), 153-157.

[3] G. Zheng, G. He, H. Liu, J. Zheng, W. Li, D. Sun. Electrospun Zinc Oxide Nanofibrous Gas Sensors for Alcohol and Acetone. Optics and Precision Engineering, 22(2014), 1555-1561.

[4] D. Li, T. Wu, N. He, J. Wang, W. Chen, L. He, C. Huang, H. A. Ei-Hamshary, S. S. Al-Deyab, Q. Ke, X. Mo. Three-dimensional polycaprolactone scaffold via needleless electrospinning promotes cell proliferation and infiltration. Colloids and Surfaces B: Biointerfaces, 121(2014), 432-443.

[5] G. F. Zheng, Y. B. Pei, X. Wang, J. Y. Zheng, D. H. Sun. Electrohydrodynamic direct-writing of conductor-insulator-conductor multi-layer interconnection. Chinese Physics B, 23(2014), 066102.

[6] X. Wang, G. Zheng, G. He, J. Wei, H. Liu, Y. Lin, J. Zheng, D. Sun. Electrohydrodynamic direct-writing ZnO nanofibers for device applications. Materials Letters, 109(2013), 58-61.

[7] P. S. Kumar, J. Sundaramurthy, S. Sundarrajan, V. J. Babu, G. Singh, S. I. Allakhverdiev, S. Ramakrishna. Hierarchical electrospun nanofibers for energy harvesting, production and environmental remediation. Energy & Environmental Science, 7(2014), 3192-3222.

[8] D. Z. Wu, X. P. Huang, X. T. Lai, D. H. Sun, L. W. Lin. High Throughput Tip-Less Electrospinning via a Circular Cylindrical Electrode. Journal of Nanoscience and Nanotechnology, 10(2010), 4221-4226.

[9] X. Hu, X. Huang, D. Sun, D. Wu. Electrospinning via mechanically single probe-tip drawing for massive production. Proceedings of the Institution of Mechanical Engineers, Part N: Journal of Nanoengineering and Nanosystems, 226(2012), 27-30.

[10] X. Wang, H. Niu, X. Wang, T. Lin. Needleless electrospinning of uniform nanofibers using spiral coil spinnerets. Journal of Nanomaterials, 2012(2012), 785920.

[11] H. Sugiyama, H. Ogura, T. Shiojima, Y. Otsubo. Simulation of Electrohydrodynamic Jet Flow in Dielectric Fluids. Journal of Applied Fluid Mechanics, 6(2013), 405-412.

[12] J. A. Fang, H. X. Wang, H. T. Niu, T. Lin, X. G. Wang. Evolution of fiber morphology during electrospinning. Journal of Applied Polymer Science, 118(2010), 2553-2561.

[13] T. A. Kowalewski, S. Barral, T. Kowalczyk. Modeling electrospinning of nanofibers, in: R. Pyrz, J. C. Rauhe (Eds.), Iutam Symposium on Modelling Nanomaterials and Nanosystems, Neu-Isenburg, Spinger, 2009, pp. 279-292.

[14] Y. C. Zeng, Y. F. Sun, X. H. Wang. Numerical approach to modeling fiber motion during melt blowing. Journal of Applied Polymer Science, 119(2011), 2112-2123.

[15] W. Li, G. Zheng, X. Wang, Y. Zhang, L. Li, L. Wang, H. Wang, D. Sun. Directly electrospun ultrafine nanofibres with Cu grid spinneret. Journal of Physics D-Applied Physics, 44(2011), 135502.

[16] S. Rafiei, S. Maghsoodloo, B. Noroozi, V. Mottaghitalab, A. Haghi. Mathematical modeling in electrospinning process of nanofibers: a detailed review. Cellul Chem Technol, 47(2013), 323-338.

[17] J. Jirsák, F. Moučka, I. Nezbeda. Insight into Electrospinning via Molecular Simulations. Industrial & Engineering Chemistry Research, 53(2014), 8257-8264.

Key Engineering Materials Vols 645-646 (2015) pp 287-290
© (2015) Trans Tech Publications, Switzerland
doi:10.4028/www.scientific.net/KEM.645-646.287

Submitted: 2014-12-31
Accepted: 2015-01-12

Measurement on the Mechanical Properties of SiC Thin Films Based on Square Thin Films Theory

Chen Yaomin[1,a*], Dong Peitao[2,b],Wu Xuezong[3,c], Wu Yulie[4,d]

[1,2,3,4]College of Mechatronics Engineering and Automation, National University of Defense Technology, Changsha, 410073, CHINA

[a]yaoming19892008@126.com

[b]peitaodong@gmail.com

Keywords: Square Thin Films, Mechanical Property, SiC, AFM

Abstract. SiC films made of different methods may have different mechanical properties, so their mechanical properties need to be determined by mechanical property measurement [1]. Since SiC films have stable chemical properties, it's very difficult to be etched [2]. This paper introduce a method for SiC films mechanical property testing without processing SiC. Moreover, in view of the lack of square SiC films' mechanical properties research, this paper also do simulation on it.

Introduction

Different type of SiC may have different mechanical properties, but at present, there is no a unified mechanical property parameter of SiC thin films. The same type of SiC films that made of different methods may have different mechanical properties, so their mechanical properties need to be measured before they are used. There are many method to measure the microstructure's mechanical properties of SiC thin films ,but most of the methods need to machining the samples. Since SiC has a very stable chemical property, it's very different to machining it through wet etching. Nano indentation can measure the microstructure's mechanical properties without machining samples, but it can't get fracture strength of the samples. In this paper, we get the mechanical property of SiC thin films through measuring the mechanical property of four fixed-edges SiC thin films. This method doesn't need to machining the SiC, and it can measure its mechanical property rapidly.

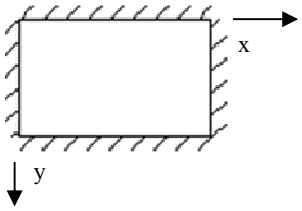


Figure1.Four fixed-edges square thin film

As shown in figure. 1, the SiC thin film is a square thin film with four fixed edges. While applying a vertical force P on the midpoint of the film, its deflection w is

$$w=\sum_{m=1}^{\infty}\sum_{n=1}^{\infty}\frac{48P\left(1-u^2\right)}{\pi^4 abEt^3\left(\frac{3m^4}{a^4}+\frac{2m^2n^2}{a^2b^2}+\frac{3n^4}{b^4}\right)}\times\sin^2\left(\frac{m\pi}{2}\right)\times\sin^2\left(\frac{n\pi}{2}\right) \quad (1)$$

where a is the length of the short edge, b is the length of long edge, t is the film's thickness, E is the Young's modulus, u is the Poisson's ratio. According to equation (1), the maximum stress is in the top surface and bottom surface of midpoint of the film. It depends on the ratio of length to

width, while have no correlation with the absolute length of the edges. Let k be the ratio of length to width. The maximum stress of the thin film is shown as equation (2)[3].

$$\begin{cases} \sigma^{m}{}_{x} = \dfrac{48P}{k\pi^2 t^2} \sum\limits_{m=1}^{\infty} \sum\limits_{n=1}^{\infty} \dfrac{1}{\left(\dfrac{3m^4}{k^4} + \dfrac{2m^2n^2}{k^2} + 3n^4 \right)} \times \left(\left(\dfrac{m}{k} \right)^2 + un^2 \right) \\ \sigma^{m}{}_{x} = \dfrac{48P}{k\pi^2 t^2} \sum\limits_{m=1}^{\infty} \sum\limits_{n=1}^{\infty} \dfrac{1}{\left(\dfrac{3m^4}{k^4} + \dfrac{2m^2n^2}{k^2} + 3n^4 \right)} \times \left(u\left(\dfrac{m}{k} \right)^2 + n^2 \right) \\ \tau^{m}{}_{xy} = 0 \end{cases} \tag{2}$$

FRABRICATION

The technological process is shown in Figure. 2. The 3C-SiC layer is grown on the (100) crystal plane of Si. A square thin film can been obtained with the etching Si on the another side, which width is a and length is b. The profile of the structure is shown in Figure. 3. The thickness of the SiC layer is 5.96um.

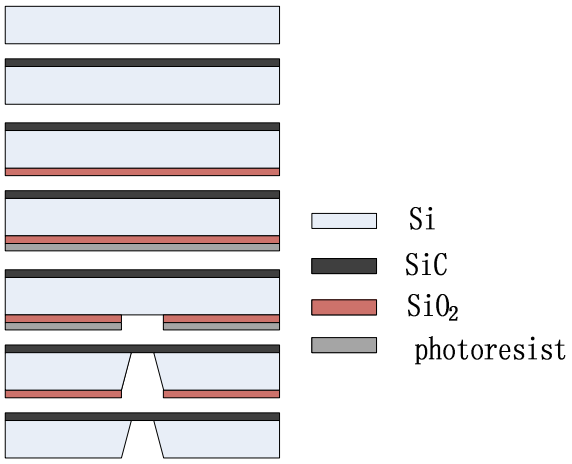


Figure 2. The process of processing SiC square thin films

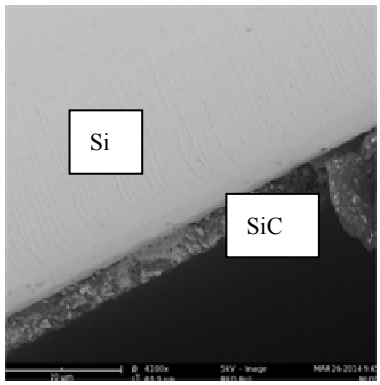


Figure 3. The side section of SiC film

METHOD

Measurement of Young modulus: The Poisson's ratio u has little effect to the measurement result of Young modulus, so it can be supposed to be 0.142.As the equation (1) shows, the midpoint ’ s elastic coefficient is directly proportional to the young modulus while the dimension of the square is constant. As shown in figure 4, the elastic coefficient of middle point can be figured out by equation (3)[4].And then the Young modulus can be figured out according to equation (1).

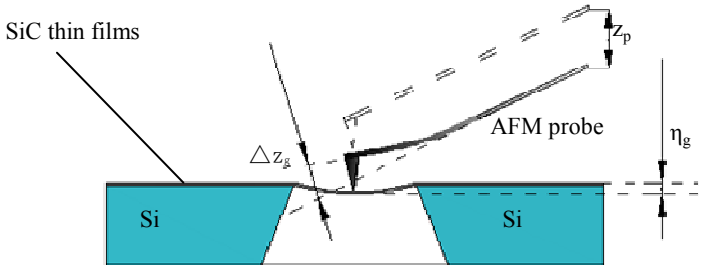


Figure 4. The schematic diagram of measurement measured by AFM

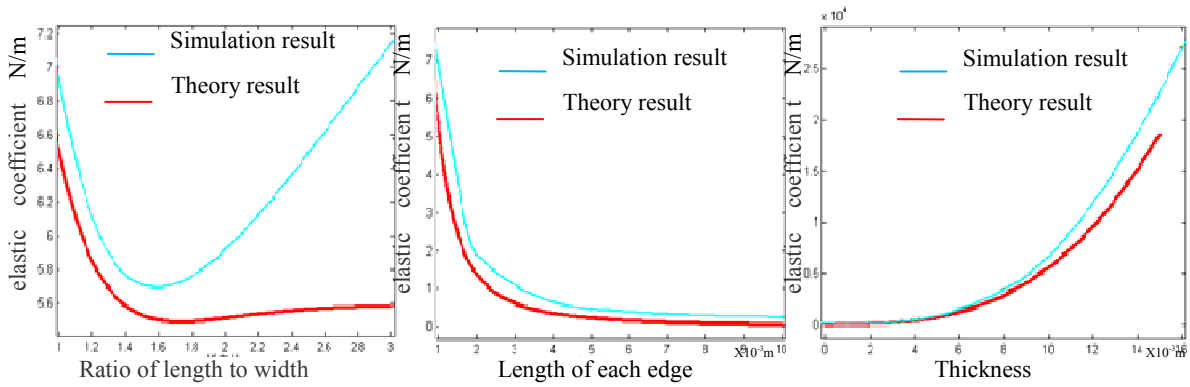
$$k = \frac{k_{AFM} \bullet \Delta z_g}{\left(z_p - \Delta z_g\right)} \tag{3}$$

;

Measurement of fracture strength: Keep increasing the force applying on the film until the film is broken, meanwhile, record the force P. The fracture strength can be figured out according to P and equation (2).

EMULATION

This paper also simulated the midpoint’ s elastic coefficient of four fixed-edge square film with different length-width ratios, areas, thickness while the other parameters were the same. And then compared the simulation results with the theoretical results (as shown as Figure 5). It can be seen from Figure 5 (b) and Figure 5 (c) that the simulation results are similar with the theoretical results, which means the theoretics can describe the actual phenomena well and the young modulus can be gotten through this method. Figure 5 (a) shows that when the length-width ratio is getting larger, the simulation results are running away from the theoretical results, it is probably because of the type of the simulation table.



(a) (b) (c)

Figure 5. The result of simulation

SUMMARY

This paper describes an experimental method for the measurement of the mechanical properties of SiC thin films. This method can measure the Young modulus and fracture strength of SiC thin films without wet etching on the SiC. It can also research the mechanical properties of square thin films. As the emulation result of four fixed-edge square film shows, the elastic coefficient of middle point of square film decreases while length of each edge increases, increases while the thickness of the film increase, and get minimum while the ratio of length to width is about 1.5.

References

[1] Ma Xiangfeng, WuYanqing, NiuLisha, Shi Huiji, Measurement and Analysis on the Mechanical Properties of Silicon Carbide Film, Journal of Experimental Mechanics, 2007, 22(1), PP:49-57.

[2] Li Kunming, JiaLuyu, BaoYiwang, Sun Li,Evaluating Mechanical Properties of SiC Hard Coating by Depth-sensing Indentation Method,Bulletin of The China Society, 2010, 29(2) PP:272-277.

[3] Liu Xiaobo, AnLong, ZhangFengpeng, Analysis on Roof Stability of Gob Area Based on Thin Plate Theory, Journal of Northeastern University, 2012,33(11), PP：1629-1632.

[4] I.W.Frank, D.M.Tanenbaum, A.M.van der Zande, P.L.McEuen, Mechanical properties of suspended frahpene sheets, Microelectronics and Nanometer Structures[J], 2007,25(6):2558-2561.

Key Engineering Materials Vols 645-646 (2015) pp 291-296
© (2015) Trans Tech Publications, Switzerland
doi:10.4028/www.scientific.net/KEM.645-646.291

Submitted: 2014-12-28
Accepted: 2015-01-05

Optimization of Chemical Mechanical Planarization Process of High Enrichment Slurry Under Low Pressure

Yan Li[1,a]; Yuling Liu[1,b*]; Hongbo Li[1,2,c]; Aochen Wang[1,d]; Weijuan Liu[1,e]; Jiao Hong[1,f]

([1] Institute of Microelectronic, Hebei University of Technology, Tianjin, 300130, China)

([2] College of Information Engineering of Hebei United University, Hebei, Tangshan, 063000, China)

[a]email: Liyan424424@126.com, [b]email: Lyl@hebut.edu.cn, [c]email: Hongboli999@sina.com, [d]email: 155322612@qq.com, [e]email:269227849@qq.com, [f]email: 295149378@qq.com

Keywords: high enrichment; chemical mechanical planarization; consistency of polishing rate; step height; surface roughness

Abstract: The polishing process was optimized according to the polishing rate and its consistency of HE slurry with different dilution multiple on the copper wafers, it can be confirmed that: the best pressure value of HE1, HE10, HE20, HE50 type slurries was 6890Pa, the best flow rate value of the preceding three slurries was 300ml/min, the best value of the HE50 slurry was 400ml/min. Through the planarization effects of the slurries with different dilution multiple, it can be obtained that: the initial dishing and erosion heights of the samples were both 1270nm and -500nm, and the two values respectively changed to 539.3nm, -75.7nm and 796.3nm, -191.3nm after being treated by HE1 and HE10 slurries, the step height of the wafer changed from 117nm to 72nm after being treated by HE20 slurry, the step height of the wafer changed from 88nm to 71nm after being treated by HE50 slurry. It was concluded that: the HE slurry shows strong ability for step removal when the slurry is diluted by 1 times and 10 times, the HE slurry also owns high planarization ability when the slurry is diluted by 20 times and 50 times.

1 Introduction

Chemical mechanical planarization technology as the important process in microelectronic field gets more and more attention. In recent years, research and related reports on the surface friction of metal materials are emerging[1]. The copper wafer CMP technology is different from the conventional metal surface treatment technology, its machining precision is need to reach nanometer level. With the wafer size increasing quickly, in order to achieve the global copper wafer planarization, domestic and foreign researchers are faced with great challenges. In order to achieve high removal rate consistency of wafer surface in different units, the best planarization process is further explored, finally, the step height values of each wafer surface units reach the minimum values[2]. In order to control polishing endpoint of copper film more accurately, copper CMP process is divided into two stages named as rough polishing (P1) and fine polishing (P2). The main purpose of rough polishing stage is removing a thick layer of copper, the main purpose of fine polishing stage is effectively removing remaining copper film and controlling the dishing height[3]. Therefore, removal rate of slurry for fine polishing on the wafer is lower than that of slurry for rough polishing. Generally, parameters of slurry contain polishing rate, surface consistency and planarization efficiency. In addition, degree of enrichment is an important index which shows the performance of slurry[4]. The degree of enrichment is higher, the dilution multiple is greater, at the same time, the production cost is lower. In order to protect the low K (dielectric constant) medium

in the wafer, working pressure of the CMP process must be as low as possible. In view of the above problems, this paper developed a kind of slurry with high enrichment based on the previous work, and achieved high rate consistency in low pressure conditions, in this condition, the step heights in the rough polishing and fine polishing stage can be modified effectively[5].

2 Experimental details

2.1 Instrument and materials. AlpsitecE460E type CMP system; Agilent5600LS type atomic force microscopy; AmbiosXP300 type step profiler; Φ300mmblanket copper wafer; Φ300mm copper wiring wafer; two kinds of high enrichment (HE) slurry named as CuI and CuII slurry; HE slurry diluted 1 times, 10times, 20time and 50times are respectively called HE1, HE10, HE20 and HE50 slurry.

2.2 Method. The removal height of film was measured by step profiler, the step height and surface roughness were measured by atomic force microscopy. Calculation method of polishing rate(PR) can be expressed as:

$$PR = SH_{pre} - SH_{post} / t \quad (1),$$

where SH_{pre} is the film thickness before CMP, SH_{post} is the film thickness after CMP, t is the polishing time. Calculation method of consistency of Polishing Rate(COPR) can be written as:

$$COPR = 1\text{-}M_R / \overline{M}\ , M_R = \left[\sum_{i=1}^{n} \left(M_i - \overline{M} \right)^2 \Big/ (n-1) \right]^{1/2}, \overline{M} = \sum_{i=1}^{n} M_i \Big/ n,$$

where M_i is the polishing rate of corresponding test point[6].

3 Results and discussion

3.1 Planarization process optimization of different positions on the wafer surface. Other things being equal, effects of working pressure and flow rate on the PR and COPR of the HE1 and HE10 slurries are respectively shown in Fig.1, Fig.2, Fig.3 and Fig.4. As shown in Fig.1 and Fig.3, PR of HE1 and HE10 slurries increase continuously with the increase of working pressure, but the COPR of the two slurries show a downward trend. The Preston Equation can be written as:

$$RR_1 = KPV \quad (1),$$

where RR_1 is the material removal rate, K is the mechanical friction constant, P is the contact pressure between materials, V is the the relative friction speed between the materials[7]. Eq.1 indicates that the mechanical friction between wafer and polishing pad will increase with the increase of working pressure, and than the PR will increase accordingly. In addition, the friction process between the wafer and polishing pad belongs to sliding friction behavior, according to the law of conservation of energy, the internal energy of the system will continue to increase, leading to a rising contact temperature of materials. The law of mass action can be expressed as:

$$RR_2 = kC_1C_2 \quad (2),$$

where RR_2 is the chemical reaction rate, k is the rate constant of chemical reaction, C_1 and C_2 represent the concentration of each reactants[8]. Generally speaking, the chemical reaction rate

constant *k* is an increasing function of temperature, so the chemical reaction rate will increase with the increase of temperature. The increase of mechanical removal rate and chemical reaction rate lead to the increasing PR of HE1 and HE10 slurries. Figure.1 and Figure.3 also show that COPR of HE1 and HE10 slurries decrease continuously with the increase of working pressure. This phenomenon can be explained as that increasing work pressure may reduce the flow space of slurry between the wafer and polishing pad where microchannels on the polishing pad surface have become the main channels for slurry, and than different contact probability between the wafer and microchannels lead to the apparent rate difference. To sum up, according to the effect of pressure on the PR and COPR, the best working pressure of HE1 and HE10 slurries is 6890 Pa.

It can be seen from Fig.2, PR of HE1 slurry reach the maximum value (678.1nm/min) when the flow rate is 300ml/L, but COPR of HE1 slurry reach the minimum value(94.8%) when the flow rate is 350ml/L. In a certain range, the concentration of reactants will increase with the increase of flow rate, when the flow rate is too large, the mass transfer effect of the system is too strong resulting in unnecessary waste of the unreacted slurry, so PR will reach a maximum value at a certain flow rate. Similarly, unreacted slurry also leads to the apparent rate difference, so COPR will reach a minimum value at a certain flow rate. The increase of COPR in the final stage can be explained as that the chemical reaction rates of convex and concave positions both fail to react completely[9]. Figure.4 shows PR of HE10 slurry increase with the increase of flow rate, COPR experiences a process of first increasing and than decreasing. Reactant concentration of HE10 slurry is lower than that of HE1 slurry, so the mass transfer effect becomes more important. The increase of flow rate will greatly enhance the mass transfer effect, so PR of HE10 slurry will increase accordingly. According to the effect of flow rate on the PR and COPR, the best flow rate of HE1 and HE10 slurries is 300ml/min.

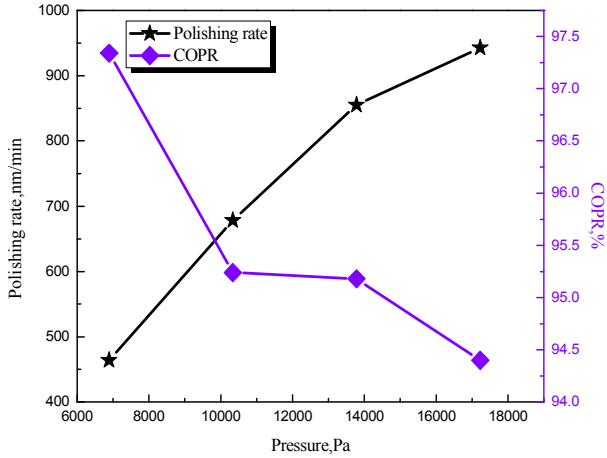


Fig.1 Effect of pressure on PR and COPR of HE1 slurry

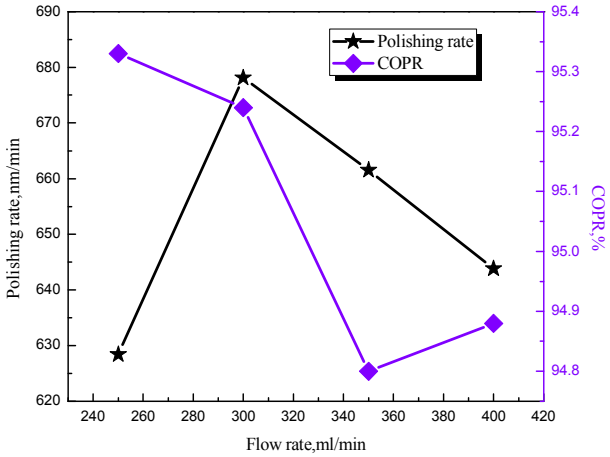


Fig.2 Effect of pressure on PR and COPR of HE1 slurry

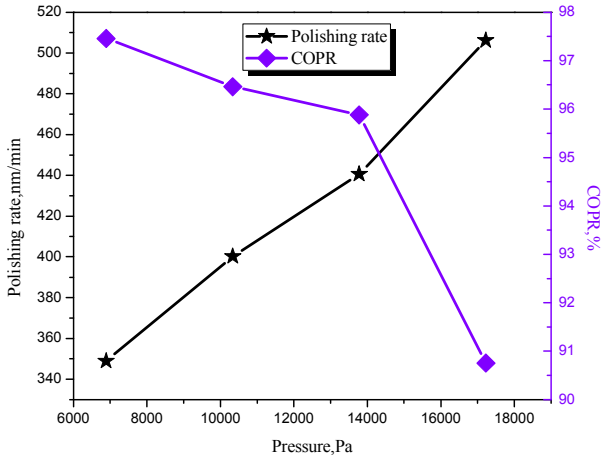


Fig.3 Effect of pressure on PR and COPR of HE10 slurry

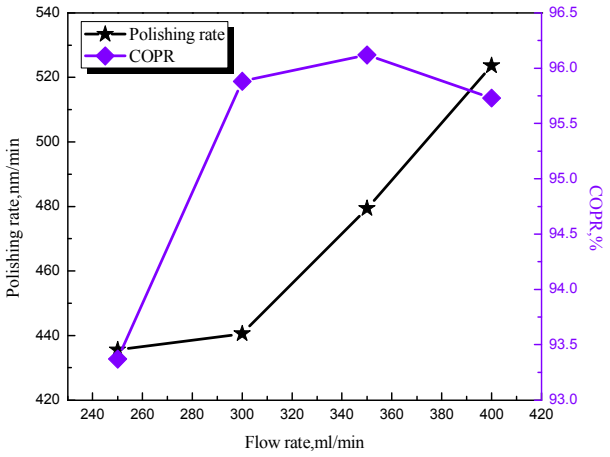


Fig.4 Effect of pressure on PR and COPR of HE10 slurry

Other things being equal, effects of working pressure and flow rate on the PR and COPR of the HE20 and HE50 slurries are respectively shown in Fig.5, Fig.6, Fig.7 and Fig.8. As shown in Fig.5 and Fig.7, PR of HE20 and HE50 increase continuously with the increase of working pressure, but the COPR of the two slurries show a downward trend. The phenomenon is in accord with Fig.1 and Fig.3, related explanations are similar to the text mentioned above. According to the effect of pressure on the PR and COPR, the best working pressure of HE20 and HE50 slurries is 6890 Pa. In addition, change regulation shown in Fig.8 is similar to Fig.4, related explanations are also omitted. Particularly, PR curve of HE20 slurry shown in Fig.6 shows a wave type trend which is different from other PR curves. Flow model of slurry in the microchannels had been explored thoroughly in a previous study, and the microchannel flow equation had been established. It can be described as:

$$V_{ave} = \left[6.33\left(W + \omega^2 R^2/2\right)\rho^{0.5} d^{1.25} g\mu^{-0.25} l^{-1}\right]^{8/7} \quad (3),$$

where V_{ave}, ρ and μ respectively represent the average velocity, density and apparent viscosity of slurry in microchannel, d and l respectively represent the width and length of the microchannel, ω and R respectively represent the rotating speed and radius of polishing pad, W is the work done by the polishing pad whose value will change with the increase of flow rate. Eq.3 shows that the average velocity of slurry in microchannel will change with the increase of flow rate, leading to a wave type trend of PR curve. To sum up, according to the effect of flow rate on the PR and COPR, the best flow rate of HE20 slurry is 300ml/min, the best flow rate of HE50 slurry is 400ml/min.

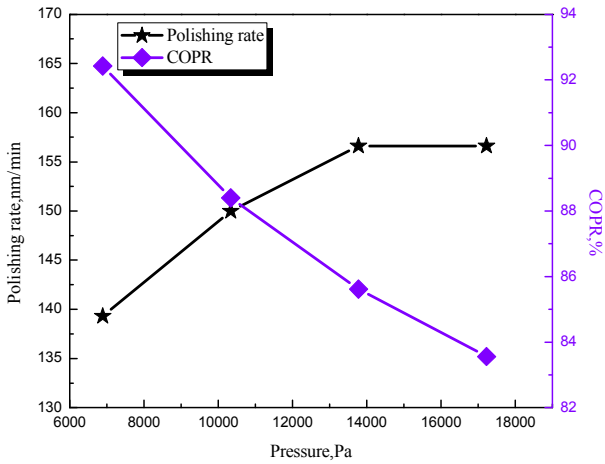


Fig.5 Effect of pressure on PR and COPR of HE20 slurry

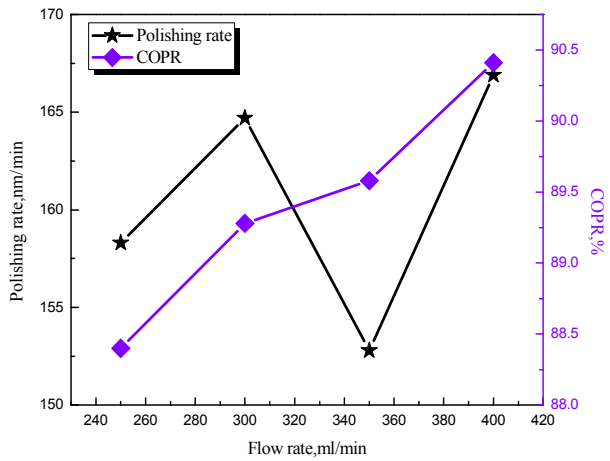


Fig.6 Effect of flow rate on PR and COPR of HE20 slurry

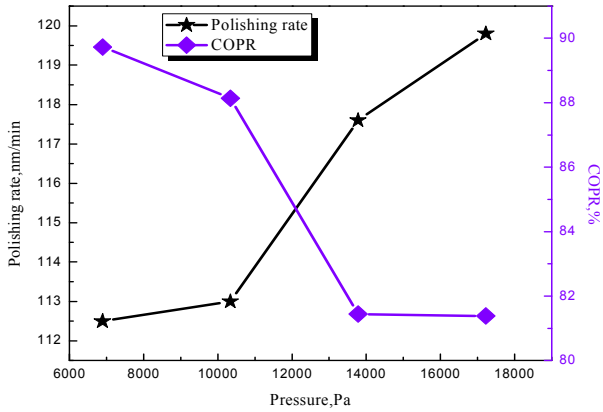


Fig.7 Effect of pressure on PR and COPR of HE50 slurry

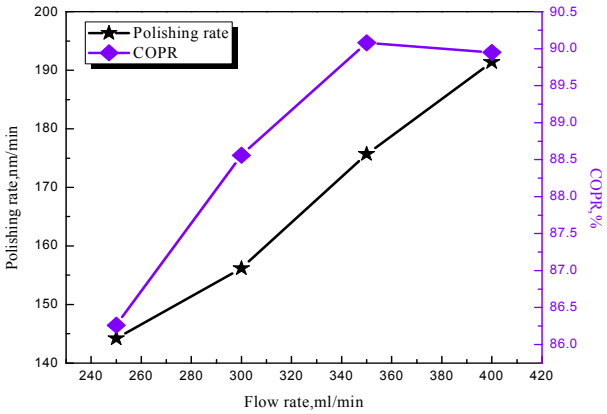


Fig.8 Effect of flow rate on PR and COPR of HE50 slurry

3.2 Planarization process of the same position on the wafer surface. CMP process was conducted on the same wafer, effects of polishing time on the dishing and erosion are shown in Fig.9 and Fig.10. From the figures, the initial heights of dishing and erosion are 1270nm and -5000nm, the heights of dishing and erosion are 539.3nm and -75.7nm after polishing using HE1 slurry, the heights of dishing and erosion are 796.3nm and -191.3nm after polishing using HE10 slurry. It indicates that HE1 and HE10 slurries have a good ability to eliminate steps.

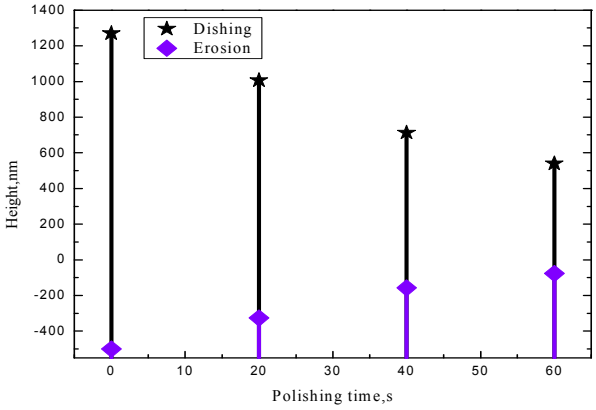


Fig.9 Effect of HE1 slurry on dishing and erosion

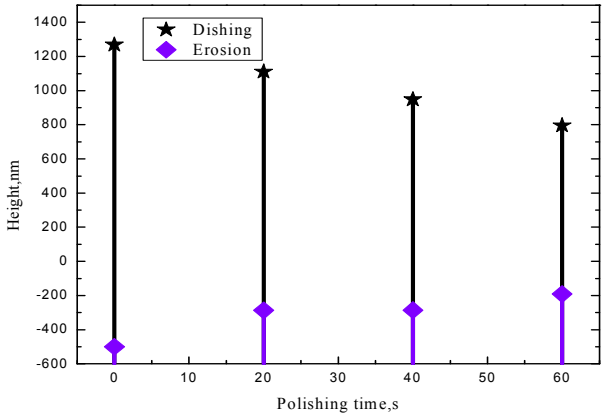


Fig.10 Effect of HE10 slurry on dishing and erosion

CMP process was conducted on the same wafer, step heights of the wafers before and after CMP are shown in Fig.11. From Fig.11, step height changes from 117nm to 72nm after polishing using HE20 slurry, step height changes from 88nm to 71nm after polishing using HE50 slurry. It indicate that HE slurry owns high planarization ability after being diluted by 20 and 50 times.

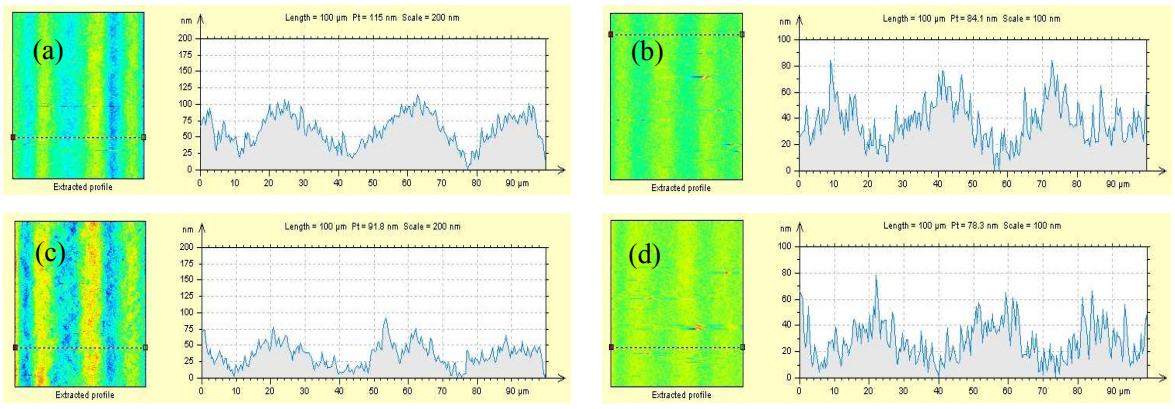


Fig.11 Step heights of wafers.(a): Pre-CMP, HE20. (b): Post-CMP, HE20. (c): Pre-CMP, HE50. (d): Post-CMP, HE50.

4 Conclusion

The best working pressure of HE1, HE10, HE20 and HE50 slurries is 6890 Pa, the best flow rate of HE1, HE10 and HE20 slurries is 300ml/min, the best flow rate of HE50 slurry is 400ml/min. HE slurry owns high planarization ability after being diluted by 1, 10, 20 and 50 times.

Reference

[1]Li Y, Liu Y L, Niu X H, Bu X F, Li H B, Tang J Y, Fan S Y. Application of a macromolecular chelating agent in chemical mechanical polishing of copper film under the condition of low pressure and low abrasive concentration[J]. Journal of Semiconductors, 2014, 35(1)016001: 1-5.
[2]Oh S, Seok J. An Integrated Material Removal Model for Silicon Dioxide Layers in Chemical Mechanical Polishing Processes[J]. Wear. 2009, 266(7-8): 839-849.
[3]Hu Y, Liu Y L, Liu X Y, Wang L R, He Y G. Effect of copper slurry on polishing characteristics[J]. Journal of Semiconductors, 2011, 32(11)116001: 1-5.
[4]Hu Y, Liu Y L, Liu X Y, He Y G, Wang L R, Zhang B G. Effect of alkaline slurry on the electric character of the pattern Cu wafer[J]. Journal of Semiconductors, 2011, 32(7)076002: 1-3.
[5]Noh K, Saka N, Chun J H. Effect of Slurry Selectivity on Dielectric Erosion and Copper Dishing in Copper Chemical-Mechanical Polishing[J]. CIRP Annals-Manufacturing Technology, 2004, 53(1): 463-466.
[6]Wang C W, Ma S H, Liu Y L, Chen R,Cao Y. CMP process optimization using alkaline bulk copper slurry on a 300mm Applied Materials Reflexion LK system[J]. Journal of Semiconductors, 2013,34(12)126001: 1-3.
[7]Wang S L, Yin K D, Li X, Yue H W, Liu Y L. Planarization mechanism of alkaline copper CMP slurry based on chemical mechanical kinetics[J]. Journal of Semiconductors, 2013, 34(8)086003: 1-4.
[8]Yin K D, Wang S L, Liu Y L, Wang C W, Li X. Evaluation of planarization capability of copper slurry in the CMP process[J]. Journal of Semiconductors, 2013, 34(3)036002: 1-4.
[9]Lei H, Luo J J. CMP of hard disk substrate using a colloidal SiO_2 slurry: preliminary experimental investigation[J]. Wear, 2004, 257(5-6): 461-470.

Key Engineering Materials Vols 645-646 (2015) pp 297-302
Submitted: 2014-12-18
© (2015) Trans Tech Publications, Switzerland
Accepted: 2014-12-23
doi:10.4028/www.scientific.net/KEM.645-646.297

Effect of Reaction Inhibitors on Synthesized Silver Nanostructures via Solvothermal Method

Hui. Xie[1,*], Nana Xiong[2], Jianzhuang Liu[1], Yuzhen. Zhao[3,*], Yuehui Wang[1,*]

[1] Department of Chemistry and Biology, University of Electronic Science and Technology of China Zhongshan Institute, Zhong Shan，528402, China

[2] State Key Laboratory of Electronic Thin Films and Integrated Devices, School of Microelectronics and Solid-State Electronics, University of Electronic Science and Technology, Cheng Du 610054, China

[3]Department of Materials Science and Engineering, Tsinghua University, Beijing 100084

Corresponding authors: wangzsedu@126.com, zhaoyz@mail.tsinghua.edu.cn, xiehuizsedu@126.com

Keywords: Silver nanoparticle, Sintering Behavior, Surface treatment, Electrical property

Abstract. In this paper, silver nanostructures were synthesized via a solvothermal method by reducing silver nitrate with ethylene glycol in the presence of poly (vinylpyrrolidone) and using NaCl, $MgCl_2$, $AlCl_3$, $FeCl_3$, $Fe_2(SO_4)_3$, NaOH, NaBr and Na_2S as reaction inhibitor, respectively. Characteristics of the as-prepared silver nanostructures were studied by scanning electron microscopy (SEM), X-ray diffraction (XRD) and UV-visible (UV-vis) absorption spectrum. It is found that the mixture of nanoparticles and nanorods and nanowires can be observed in the $AlCl_3$ and NaOH systems, the nanorods as main products can be obtained in the $MgCl_2$ and NaCl and $Fe_2(SO_4)_3$ systems, the large scale silver nanowires as main products can be obtained in the $FeCl_3$ and Na_2S systems, especially in the Na_2S system, silver nanowires are very long and curved. The results indicated the reasons of the effect of the reaction inhibitors on the morphologies of silver nanostructures depend on the solubility product constant of silver salt which formed with silver ion and inhibitor anion ion in the initial stage and the properties of metal cationic ion of inhibitor. The smaller solubility product constant of silver salt or the presence of Fe^{3+} or low valence metal ion greatly facilitate the formation of one-dimensional silver nanostructures, especially to nanowires.

1. Introduction

In recent years, silver nanowires have attracted a great many of attentions in various fields, because of their unique electrical, optical, thermal, chemical and physical properties.[1-9] In particular, silver nanowires networks are emerging as promising substitutes for conventional transparent conductive oxide films on optoelectronic devices due to their superb optical and electrical performances, mechanical robustness, and comparatively low material costs.[1, 2] Therefore, much effort has been undertaken to the synthesis of AgNWs with the controlled morphology and the high yields.

Until now, many strategies have been reported for the synthesis of silver nanowires.[3,4] The most widely used method is polyol reduction method, because it can not only avoid the post-treatment necessary for template assisted method, [5] but also omit the use of hash chemicals applied in other synthesis methods.[6] Several experimental parameters like temperature, reaction time, concentration of the reactant the exotic agents of salts as inhibitors in polyol reduction process are important factors that affect the affect the final products. Especially, [7,8] as has been reported, the shape and yield of silver nanowires significantly depended on the nature and concentration of the exotic agents of salts, which always playing pivotal role in the formation of the final products by forming Ag_xA_y (A is the anions in the added salts) with different release rates of Ag^+ ions to the solutions. [9-13] Therefore, the

exotic agent of salt is called "reaction inhibitor". For example, Wiley et al.[12]synthesized AgNWs by the polyol reduction of $AgNO_3$ with Fe(II) and Fe(III)- containing salts as the reaction Inhibitors, respectively. These Fe-containing salts were found to facilitate the growth of Ag nanowires. Korte et al. [11] reported the polyol reduction method of AgNWs with copper (I) or copper (II) chloride as the reaction Inhibitors, respectively, and they found that the morphology and composition of the final products significantly depended on the nature and concentration of these additives. To the best of our knowledge, there is still no report systemically investigates the effects of the exotic agent of salt the morphology of the final products. In this paper, we systemically investigated the effects of the exotic agents of salts on the morphology of the final products and discussed the reaction mechanism of the formation of silver nanostructure with different inhibitors.

1. Experimental

Silver nitrate ($AgNO_3$, ≥99.8%) was purchased from Guangdong Guanghua Chemical Reagent Co., Ltd., poly(vinylprrolidone) (PVP, C_6H_9NO)n, K30, Mw≈40000), was purchased from Guoyao Group Chemical Reagent Co., Ltd., Sodium sulfide (Na_2S, ≥98.0%) , ferric chloride ($FeCl_3$•$6H_2O$, ≥99.0%), sodium chloride （NaCl, ≥99.5%）, sodium hydroxide (NaOH, ≥96.0%), sodium bromide，(NaBr, ≥99.0%), magnesium chloride hexahydrate ($MgCl_2 \cdot 6H_2O$, ≥98.0%, aluminum chloride anhydrous ($AlCl_3$, ≥99.0%), ferric sulphate ($Fe_2(SO_4)_3$, 21.0%~23.0%), ethylene glycol (EG, $(HOCH_2)_2$, ≥99.7%), and ethanol absolute (CH_3CH_2OH，≥99.7%) were purchased from Tianjin Yongda chemical Co., Ltd.

The synthesis of AgNWs in detail is as follows: A 40 mL EG solution of 0.1 mmol·L^{-1} $FeCl_3$ was vigorously stirred after the addition of 0.16 mol·L^{-1} PVP. 40 mL $AgNO_3$ (0.1 mol·L^{-1}) was injected drop by drop using a syringe into the above mixed solution in a minute, and stirred 15 min. Afterwards, the solution was put into a 100 mL Teflon-lined autoclave tube. This tube was sealed and maintained at 160 ^{0}C for 2.5 h, followed by natural cooling to room temperature. Finally, the reaction mixture was washed with acetone, ethanol and deionized water by centrifuging at 4500 rpm . In other exotic agents of salts systems, the $FeCl_3$ was replaced by NaCl (0.3 mmol·L^{-1}), $MgCl_2$ (0.15 mmol·L^{-1}), $AlCl_3$ (0.1 mmol·L^{-1}), NaOH (0.3 mmol·L^{-1}), NaBr (0.3 mmol·L^{-1}), $Fe_2(SO_4)_3$ (0.1 mmol·L^{-1}), and Na_2S (0.3 mmol·L^{-1}), and all the other procedures were the same.

All scanning electron microscopy (SEM) images were taken on a MERLIN VP COMPACT (JSM-6460). The phase structures were determined by X-ray diffraction (XRD) (Rigaku2500 X-Ray DIFFRRACTOMETER) on a scintage diffractometer with $Cu_{k\alpha 1}$ radiation (λ= 1.54060 Å) at a scanning rate of 2˚/min in the 2θ range from 20 to 90°. The UV-visible (UV-vis) absorption spectrum was obtained using a 760CRT spectrophotometer with quartz cuvettes at room temperature.

2. Results and discussion

Fig.1shows the SEM images (Fig.1(a)) and the corresponding UV-vis spectra (Fig.1(b)) of the silver nanostructures synthesized with $FeCl_3$, $AlCl_3$, $MgCl_2$ and NaCl as inhibitors, respectively. As Fig.1 (a), there are large numbers of silver nanowires in the $FeCl_3$ system, and only a few silver nanoparticles are dispersed among these nanowires. The products are mainly the mixture of nanoparticles and nanorods and nanowires in the $AlCl_3$ system. The final products are mainly the mixture of nanoparticles and nanorods in the $MgCl_2$ and NaCl used as inhibitors, respectively, and much less silver nanowires can be observed in both of systems. But the NaCl system produced more silver nanorods comparing with that of the $MgCl_2$ system. The above experimental results indicate that the introduction of Fe(III) into the solution greatly facilitates the formation of silver nanowires, and the nature of cation also affect on the morphology and composition of the final products. [2,12] With the decrease of the charge number of the cation (excluding $FeCl_3$) the silver nanostructures tend to grow in the direction of one dimension. Seen the corresponding UV-vis in Fig. 1(b), when the $FeCl_3$ is used as the reaction inhibitor, two peaks at ~354 nm and ~426 nm and wide absorption band in the long wave range can be observed. The weaker peak appearing at ~350 nm is attributable to the quadrupole resonance excitation of nanwires, the maximal peak at ~426 nm corresponds to the transverse plamon resonance of nanowires, and the wide absorption band in the long wave range suggests that the size of nanowires is long and there are some nanoparticles in the solution. When $AlCl_3$, $MgCl_2$ and NaCl is used as the reaction inhibitor, respectively, the peak position at~354 nm

remains unchanged, there is a blue shift in the maximum absorption of the spectrum. It has been known that the peak maximum shifts to a shorter wavelength when the size becomes small.

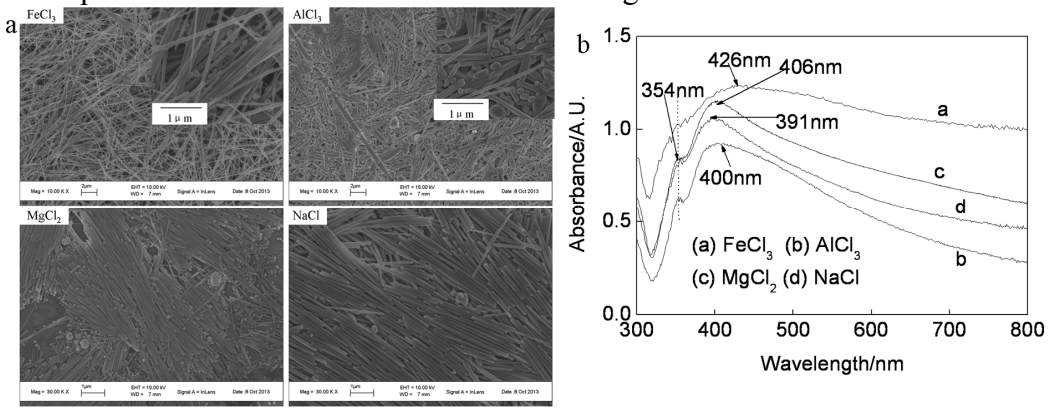


Fig.1(a) SEM images and (b) UV-visible of silver nanostructures synthesized with $FeCl_3$, $AlCl_3$, $MgCl_2$ and NaCl as inhibitor, respectively. The insets inFig.1 (a) are the local amplification

Fig.2 shows the SEM images (Fig.2(a)) and the corresponding XRD pattern (Fig.2(b)) of the silver nanostructures synthesized with NaOH, $Fe_2(SO_4)_3$, NaBr and Na_2S as inhibitors, respectively. Seen from Fig.2, it can be seen clearly that lots of silver nanoparticles and a few nanowires, the mixture of nanoparticles and nanorods are obtained with NaOH and $Fe_2(SO_4)_3$ as the reaction inhibitor, respectively. However, the main products are nanorods and nanowires in the presence of NaBr and Na_2S system, respectively. As shown in Fig.2, the NaBr system produced more nanorods comparing with that of the NaOH system.These phenomenon indicates that anion has also effect on the morphology of the final products. The corresponding XRD patterns of the samples synthesized are shown in Fig. 2(b). Five fraction peaks can be observed and indexed to the (111), (200), (220), and (311) planes of pure face-centered-cubic (fcc) silver crystals (JCPDS file No. 04-0783). The XRD results show that the product are the pure silver nanostructure, and the nanorods and nanowires grow along the (111) direction. The addition of coordination reagent such as polymer and coordination compound is one important factor to control the morphology of silver nanostructure by selective adsorption and desorption on different surfaces to govern the subsequent growth. In our experimental system, PVP is used as an adsorption agent. The PVP molecule is coordinated to the silver surface through the nonbonding electrons of the oxygen atom in carboxyl (C=O). [14] Meanwhile, as we know, PVP can interact more strongly with the (100) plane than with the (111) plane ends due to the lowest surface-energy of (111) plane, which may result in no adsorption of carbon-based polymer. The addition of silver atoms to the (111) plane yielded the anisotropic growth of the material to wire or rod.

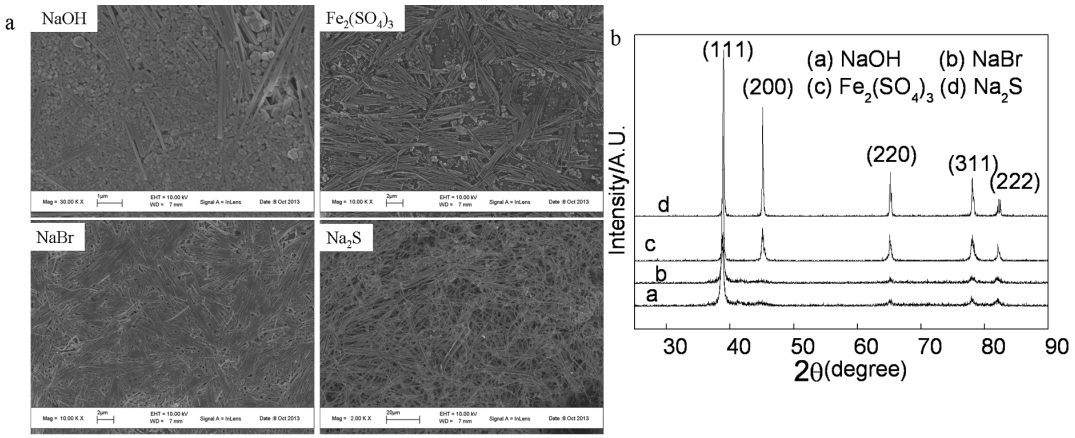


Fig.2 (a) SEM images and (b) XRD pattern of silver nanostructures synthesized with NaOH, NaBr, $Fe_2(SO_4)_3$ and Na_2S as inhibitor, respectively

On the basis of the above results, it is obvious that the exotic agents of salts have the strong effects on the final morphology of the silver nanostructures. The silver nanowires as the main product can be obtained only in $FeCl_3$ and Na_2S systems. As has been demonstrated by Suber et al.[15], the anisotropic

growth rate of silver nanostructure should be slow enough to form silver nanowires. The high concentration of dissociative Ag^+ ion in the reaction solution will lead to a quick reduction rate of Ag^+ ion to Ag atom, it is impossible to the anisotropic growth of silver nanostructure. According to the literature, the addition of the ions, such as Cl^-, S^{2-} and Br^- in the reaction dramatically reduce the free Ag^+ ions in the reaction system by forming amounts of Ag_xA_y colloids in the initial stage.[9,16] The slow reaction is suitable for the formation of the thermodynamically more stable multiply twinned silver seeds required for wire growth. With the process of reaction, the free Ag^+ ions in the solution decreased because they are reduced to Ag atom by EG, so the Ag^+ ions release from Ag_xA_y colloids to the solution for maintaining the equilibrium concentrations of soluble salts. These are the role of the anions in the polyol synthesis of silver nanostructures. The reduction rate from Ag^+ ion to Ag atom is positively correlated with the Ag^+ ion concentration in the system which depends on the Ag^+ ion dissolution rates from different Ag_xA_y that are correlated with their different solubility product constants at the same conditions. As we all known, the solubility product constant of the five Ag_xA_y compounds in our experiment hold the order as follows:[17] K_{sp} (Ag_2SO_4, 1.20×10^{-5}) > K_{sp} (AgOH, 2.0×10^{-8}) > > K_{sp} (AgCl, 1.77×10^{-10} > K_{sp} (AgBr, 5.35×10^{-13}) > >K_{sp} (Ag_2S, 6.3×10^{-50}). It is clear that the initial Ag^+ ion concentrations and the Ag^+ ion dissolution rates in the reaction systems hold same order as the solubility product constant of the five Ag_xA_y compounds. It seems that the low solubility product constant of the Ag_xA_y compound is suitable for the formation of one dimension silver nanostructure, which because of the low initial Ag^+ ion concentrations and the low Ag^+ ion dissolution rate in the reaction system.

It is well documented that O_2 can adsorb and dissociate on silver surfaces. In a polyol synthesis, the adsorbed atomic oxygen could contribute to some degree of oxidative etching, but more importantly, could block the (111) reactive sites from adding Ag atoms efficiently. So Fe ions are necessary for silver nanowires growth because the Fe(II)-added directly to the synthesis or generated in situ from the reduction of Fe(III) by EG, which was an effective oxygen scavenger capable of removing adsorbed oxygen from the surface of twinned silver nanoparticles and thus preventing their dissolution by oxidative etching. The multiply twinned silver seeds can grow into nanowires with the assistance of PVP during the Ostwald ripening process. This is the reason that large-scale silver nanowires can be obtained in the case of $FeCl_3$ as the reaction inhibitor although the solubility product constant of the AgCl is larger than that of AgBr. In the Na_2S system, Ag^+ ions combine with S^{2-} to form AgS whose solubility product constant is the lowest in all of five Ag_xA_y compounds. In this case, the concentration of free Ag^+ ions in the initial is very lower and the Ag^+ ion dissolution rate from AgS is very slower compare with those of others systems. This leads to a reduction in the rate of formation of Ag^0 in the initial stage which is favored to the formation of silver nanowires. In additions, it is interesting to note that the morphology of silver nanowires in the $FeCl_3$ system is different to that of the silver nanowires in Na_2S system (Fig.3).The former is straight and short and thin, while, the latter is curved and long and heavy. This observation enlightens us to consider the affecting factors on the formation of silver nanowires. Two factors, the reaction rate and oxygen scavenger, have important effects on the formation of silver nanowires. We think that control the reaction rate is more advantageous to obtain large size silver nanowires, only relatively.

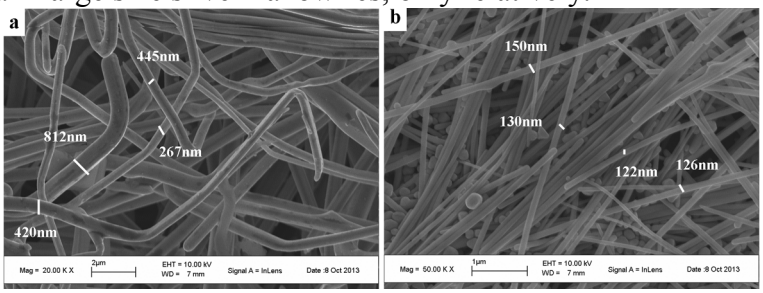


Fig. 3 SEM images of silver nanowires synthesized with (a) Na_2S and (b) $FeCl_3$ as inhibitor, respectively

Comparing to the synthesis of silver nanostructures, chloride salts added the reaction system can reduce drastically the free Ag^+ concentration by forming AgCl in the initial stage, but the final product is very different from each other even if the initial Ag^+ concentrations are kept the same. The

results demonstrate that the final morphology is also related to the nature of cation added in these exotic salts, which have different electrons. We have investigated the effect of cation on the morphology and stability of silver nanoparticles. It was found that the high valence cation can lead to silver nanoparticles to aggregate. [18] In the synthesis system, we think cation can supply electrons to Ag atom adsorbed on its surface and leads to an increase in the rate of formation of Ag^0 in the initial stage which is bad to the formation of silver nanowires. Based on the above results, we propose a mechanism of the silver nanowires formation in the solvothermal process as shown in Fig. 4. It is obvious that it is a convenient and effective method for synthesizing silver nanostructure with different morphologies by introducing the different exotic agents of salts

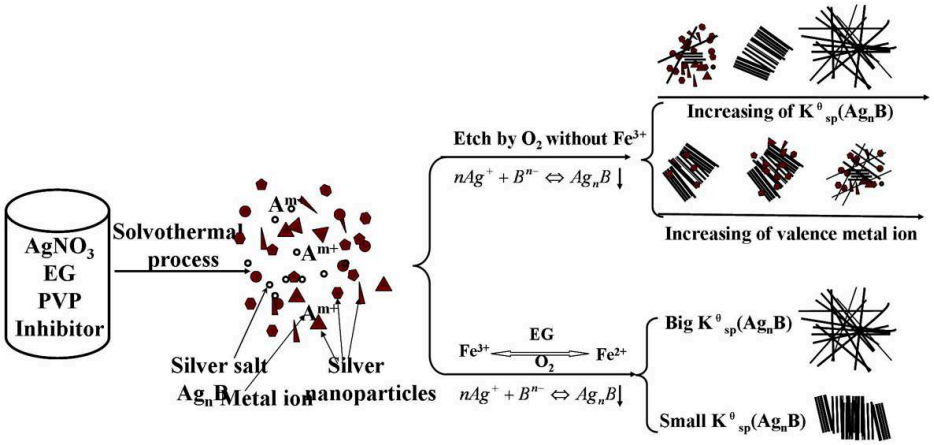


Fig.4 Schematic illustration of the reaction mechanism of formation of silver nanostructure with different inhibitors

Summary

Silver nanostructures were synthesized via a solvothermal method by reducing silver nitrate with ethylene glycol in the presence of poly (vinylpyrrolidone) and using NaCl, $MgCl_2$, $AlCl_3$, $FeCl_3$, $Fe_2(SO_4)_3$, NaOH, NaBr and Na_2S as reaction inhibitor, respectively. Characteristics of the as-prepared silver nanostructures were studied by scanning electron microscopy (SEM), X-ray diffraction (XRD) and UV-visible (UV-vis) absorption spectrum. It is found that the mixture of nanoparticles and nanorods and nanowires can be observed in the $AlCl_3$ and NaOH systems, the nanorods as main products can be obtained in the $MgCl_2$ and NaCl and $Fe_2(SO_4)_3$ systems, the large scale silver nanowires as main products can be obtained in the $FeCl_3$ and Na_2S systems, especially in the Na_2S system, silver nanowires is long and heave and curve. The results indicate that the nature of the exotic agents of salts affect on the morphology of the final products. The introduction of Fe(III), as oxygen scavenger, into the solution greatly facilitates the formation of silver nanowires. The exotic agent of salt, as the reaction inhibitor, whose anion can combine with Ag^+ to form Ag_xA_y colloid in the initial stage facilitates the silver nanostructures to grow in the direction of one dimension, but the lower the solubility product constants of Ag_xA_y is, the more the formation of silver nanowires are.With the decrease of the charge number of the cation of chloride salt s(excluding $FeCl_3$), the silver nanostructures tend to grow in the direction of one dimension. It is obvious that it is a convenient and effective method for synthesizing silver nanostructure with different morphologies by introducing the different exotic agents of salts

Acknowledgements

This work was financially supported by National Science Foundation of China under grants of (61302044, 51302145) and Zhongshan Science and Technology Projects (20123A319, 2014A2FC312) and State Key Laboratory of New Ceramic and Fine Processing (Tsinghua University) and State Key Laboratory of Electronic State Key Laboratory of Electronic Thin Film and Integrate (Zhongshan)

References

[1] J. Lee, F. Sun, J. Lee. Fabrication of large area flexible and highly transparent film by a simple Ag nanowire alignment. J. Exp. Nanosci. 2013, 8: 130–137

[2] B. Wiley, Y. Sun, B. Mayers,Y. Xia.Shape-Controlled Synthesis of Metal Nanostructures: The Case of Silver. Chemistry - A European Journal. 2005, 11(2): 454–463

[3] C. J. Murphy, N. R. Jana. Controlling the aspect ratio of inorganic nanorods and nanowires. Adv. Mater. 2002, 14: 80–82

[4] Y. Sun, B. Gates, B. Mayers, Y. Xia. Crystalline silver nanowires by soft solution processing. Nano. Lett. 2002, 2(2): 165–168

[5] L.F. Gou, M. Chipara, J.M. Zaleski.Convenient, rapid synthesis of Ag nanowires. Chem. Mater. 2007, 19(7): 1755–1760.

[6] Y.J. Han, J.M. Kim, G.D. Stucky.Preparation of Noble Metal Nanowires Using Hexagonal Mesoporous Silica SBA-15. Chem. Mater. 2000, 12: 2068–2069.

[7] Y. Sun, B. Mayers, T. Herricks, Y. Xia. Polyol synthesis of uniform silver nanowires: a plausible growth mechanism and the supporting evidence. Nano. Lett. 2003, 3: 955–960

[8] J. Nishino, Y. Kanno. An Influence of Concentration of Polyvinylpyrrolidone on the Morphology of Silver Metal Formed from $AgNO_3$ Aqueous Solution. J. Nanomater. 2008, 2008: 1–5

[9] C. L. Tang, W. Sun,J.Lu, W. Yan. Role of the anions in the hydrothermally formed silver nanowires and their antibacterial property. J. Colloid Interface Sci. 2014, 416: 86–94

[10] A. Amirjani,P. Marashi, D. H. Fatmehsari. The effects of physicochemical parameters on the synthesis of silver nanowires via polyol method. Int Nano Lett. 2014, 4: 108-113

[11] K. E. Korte, S.E. Skrabalak, Y. Xia. Rapid synthesis of silver nanowires through a $CuCl^-$ or $CuCl_2$-mediated polyol process. J. Mater. Chem. 2008, 18: 437-441

[12] B. Wiley, Y. Sun, Y. Xia. Synthesis of silver nanostructures with controlled shapes and properties. Acc. Chem. Res. 2007, 40: 1067-1076

[13] A. Amirjani, P.Marashi, , D. F. Haghshenas. Effect of $AgNO_3$ addition rate on aspect ratio of $CuCl_2$-mediated synthesized silver nanowires using response surface methodology. Colloids. Surf. A Physicochem. Eng. Asp 2014, 444: 33-39

[14] Y. Gao, P. Jiang, D. F. Liu, .Evidence for the Monolayer Assembly of Poly(vinylpyrrolidone) on the Surfaces of Silver Nanowires. J. Phys. Chem. B. 2004, 108: 12877-12881

[15] L. Suber, I. Sondi, E. Matijevic, D.V. Goia, Preparation and the mechanisms of formation of silver particles of different morphologies in homogeneous solutions**.** J. Colloid Interface Sci. 2005, 288: 489-495.

[16] R. Joerger, T. Klaus, C. G. Granqvist, Biologically produced silver-carbon composite materials for optically functional thin-film coatings. Adv. Mater. 2000, 12, 407-409

[17] H. X.Yang, Z.Ling, X. R. Yan. Inorganic Chemistry, Inorganic Chemistry Teaching and Research Section of Tianjin University,Higher Education Press.2004

[18] Y. H. Wang, T. Wang, J. Zhou. Effect of Silver Nanoparticles on the Spectroscopy Properties of $[Ru(bpy)_3]^{2+}$ and Electrolyte Effect. Acta Phys. -Chim. Sin., 2010, 26(6): 1607-1616

Key Engineering Materials Vols 645-646 (2015) pp 303-312
© (2015) Trans Tech Publications, Switzerland
doi:10.4028/www.scientific.net/KEM.645-646.303

Submitted: 2014-12-16
Accepted: 2014-12-23

Effects of NaOH concentration on section structures of oxide films based on TC4 by anodic oxidation process[1]

YAN Ji-kang[1, 2, a], YANG Gang [1,b,*],SHI Zhe[3], TANG Wan-xia[1, 2], and WU Yun-feng[1]

[1] Kunming Metallurgical research institute, Kunming 650031, P.R. China

[2] Faculty of Materials Science and Engineering, Kunming University of Science and Technology, Kunming 650093, P.R. China

[3] Faculty of Metallurgical and Energy Engineering, Kunming University of Science and Technology, Kunming 650093, P.R. China

[a] scyjk@sina.com, [b]782245313@sina.com

Author：Yan Ji-Kang(1972-）,E-mail: scyjk@sina.com

Corresponding author ：Yang Gang（1959-）,E-mail: 782245313@sina.com

Keywords: TC4 Titanium alloy; Anodic oxidation; NaOH; structure of oxide film

Abstract. The section structure and growth mechanism of oxide films on titanium alloys Ti-6Al-4V (TC4) in the oxalate, silicate and phosphate hybrid electrolyte system by anodic oxidation method were investigated. Using TC4 as anodic, stainless steel as cathode, oxide films on the surface of TC4 titanium alloy were prepared by anodic oxidation process. X-ray diffract meter, spiral-micrometer, eddy current thickness meter and scanning electron microscope were used to measure the crystal structure, thickness, microstructure and chemical composition of the film . The experimental results indicate that NaOH concentration has almost no effects on the crystal structure of oxide films which are amorphous state. The oxide films on TC4 grow through three stages. At anodic oxidation primary stage, a thicker TiO_2 films on TC4 are able to form due to an abundant oxygen atmosphere. At anodic oxidation middle stage, a middle $TiO_{1.5}$ films form due to a not enough oxygen atmosphere. At anodic oxidation latest stage, a thin $TiO_{1.5}$ films form due to a heavily insufficient oxygen atmosphere. With NaOH concentration increasing, the ingrowth velocity (V_{OA}) of the interface between TC4 and oxide film is faster than dissolution rate (V_{AD}) of the surface oxide film resulting in a slight oxide film growth. The thickness of oxide film no longer varies when V_{OA} is equal to V_{AD}.

Intorduction

All Titanium alloy Ti-6Al-4V (TC4) is a kind of good biocompatibility, high specific strength, good corrosion resistance and widely used in hard tissue repair materials [1].The Al and V elements in TC4 can cause side effects because its long-term contact with tissue fluid, it is required for preparation of bioactive ceramic film on surface of TC4 implants because TC4 itself does not have biological activity and its high elastic modulus will cause the obvious stress shielding effect [2].

Titanium anode oxidation is the surface treatment technology of the porous titanium oxide film on titanium alloy under the electrolyte and a certain voltage. Anodic oxidation formation mechanism of oxide film can be summarized as: the dissolution of titanium, formation of titanium

oxide film and dissolution of titanium oxide film and film internal grow into the matrix. Titanium alloy anodic oxidation is a complex process of physical, chemical and electrochemical; the electrolyte are mainly acidic or alkaline electrolyte in water solvent and organic electrolyte, electrolyte concentration is the main factor [3-7]. The electrolyte quality concentration affects the uniformity and continuity of the film, thickness of the film is directly proportional to oxidation time, but when arriving at the time limit, the film thickness will not increase with increasing of time [8].

At present, the voltage and electrolyte concentration are the most important influencing factors. TaoHaiJun *et al.* researched the uneven surface structure formed by different anodic oxidation corrosion speed on TC4 surface riched with Al α phase and V β phase with DC constant voltage. The six-party α phase and cubic β phase of titanium alloy have different corrosion resistance ability, the β phase has stronger corrosion resistance ability in the same electrolyte, thus can form non-uniform microstructure of anodic oxidation film[9]. Also, the same phase composition titanium alloy have different film structure due to the vary grain size [10]. To achieve good modification effect generally require a oxide film with certain thickness and structure, thus the research of titanium oxide film growth mechanism and thickness dynamics under the condition of a given voltage and electrolyte is very important. Film growth kinetics and thermodynamics about aluminum alloy of the anodic oxide film have been deep researched [11-12], but growth kinetics of titanium alloy anodic oxidation surface film is relatively few. B. J. HWANG, *et al.* studied the dynamic model of the titanium alloy anodized film in sulfate electrolyte, the results showed that the change of oxygen control in the entire film formation process and the structure of the film in the anodic oxidation process [13].Gemelli.E *et al.* studied isothermal oxidation kinetics of pure titanium under different temperatures; the results showed that at the beginning of the oxidation, titanium oxidated fast and became slower later because of the protection of passivation film, the passivation film begin transform into the anatase structure at 276 ℃ ,and anatase structure begin transform into rutile at 444 ℃ and the passivation film all transformed into the structure of rutile at 718 ℃ , between 444 ℃ ~ 718 ℃,the passivation film consisted of anatase and rutile [14].

In this paper, effects of different NaOH concentrations to TC4 surface anodic oxidation film section structure and growth mechanism are preliminary studied to provide the theory basis for preparation of TC4 surface oxide film controlled in alkaline electrolyte pulse anodic oxidation process.

1 the experiment process

Anode are titanium alloy TC4 cylindrical (φ20mm×5mm), a square stainless steel(100mm×100mm× 2 mm) as the cathode, electrolytic cell is a 3.5 L glass box and the electrolyte composition is 20 g/L sodium oxalate ($Na_2C_2O_4$), 10 g/L sodium silicate with nine water (Na_2SiO_3-9 H_2O) and 9.25 g/L sodium dihydrogen phosphate (NaH_2PO_4) and (0-4) g/L sodium hydroxide (NaOH).Firstly, Pretreatment of TC4 matrix surface, including: chemical degreasing and washing, burnishing with 120 #, 400 #, 600 #, 800 #, 1000 # and 1200 # sand paper and then pickling and activation, washing by water. WHD - 30 type micro-arc oxidation power provides constant pressure and the forward voltage is 10V-120V, the vreverse voltage is 0, the pulse number is 1, the frequency is 200 Hz, the positive and negative duty ratio is 50%, oxidation time is 50 min and electrolyte temperature is room temperature. In 100 ℃boiled deionized water, 30 min hole sealing post-processing for anodic oxide film. After washing and drying, thickness of the post-processing and anodized TC4 sample was detected by CEM. DT-156

vortex, roughness of the sample was detected by TR200 portable roughness meter and thickness of the TC4 sample before and after the anodic oxidation was detected by the spiral micrometer with accuracy of 0.001 mm, film phase composition was detected by Bruker D8-Advance X-ray diffraction, microscopic structure and chemical composition of surface and cross-section was detected by Philip ESEM X30 and EDS spectrometer.

2 Results and discussion

2.1 phase analysis

Figure 1 is the XRD spectrum of TC4 titanium alloy anodic oxidation for 50 min in 20 g/L $Na_2C_2O_4$, 10 g/L of Na_2SiO_3-$9H_2O$, 9.25 g/L of NaH_2PO_4 and 0~4 g/L NaOH electrolyte under 60V constant voltage at room temperature, after cleaning and drying by deionized water. It can be seen from the figure 1, the main crystal phase of anodic oxidation TC4 titanium alloy are α structure (PDF44-1294) and β structure (PDF44-1288) of titanium alloy substrate, but priority to α structure. XRD of TC4 surface oxidation film is not very clear, the anatase and rutile TiO_2 are not detected out, only when the 2-theta is close to 40 ° ,there are amorphous peaks, which may be the amorphous titanium oxide film formed by anodic oxidation on the surface of TC4.
Concentration of NaOH has no effect on the phase of TC4 surface film. TC4 anodic oxidation is carried out at room temperature, under the joint action of the electrolyte and the electric field, a series amorphous titanium oxide TiOx (x = 1-2) can be generated on the TC4 surface . Titanium anode oxidation generates the amorphous titanium oxide passivation film first, and then the passivation film gradually transformed into the structure of anatase and rutile TiO_2 under the action of electrolyte and oxidation voltage. Studies show that a higher DC voltage or pulse voltage, high concentration of acidic electrolyte and the longer oxidation time are all beneficial to all kinds of intermediate state oxide transfer into stability TiO_2, and form the titanium alloy surface oxidation film with main crystal phase of anatase and rutile [3, 4]. The titanium oxide film cannot crystal into anatase and rutile, probably because of the low concentration of alkaline electrolyte can't reach the thermodynamics transition conditions of the reaction system from amorphous to crystalline.

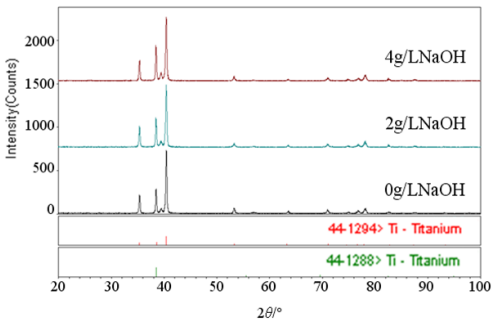


Fig. 1 XRD patterns of TC4 by anode oxidation at different NaOH concentratione

2.2 Growth mechanism of microstructure titanium oxide film

Figure 2 is the microstructure and chemical composition of fracture surface on TC4 anodic oxidation film under the oxidation voltage of 80V. Figure 2 (a) shows that, higher contrast of the back scattered electrons on the left side is the TC4 matrix with high average atomic number, middle low contrast is the oxide film with low average atomic number and right is the zero contrast vacuum.

Thickness of the oxide film was detected 6.31 microns in the back scattered electron. In order to study chemical composition distribution of fracture surface on TC4 anodic oxidation film, cross- section composition analysis was carried on along the line of ab. Line analysis results show that: from point a to point b, O content began to increase and Ti content began to decline, content of O and Ti gradually achieve to stable, content change of Al, V and P is not obvious, but Si content has a evident increase in the film surface, and this is equal to surface chemical composition analysis of existing silicon oxide, the oxide film thickness is 6.22μm when measured through the line analysis, which consistent with the film thickness measured by microscopic. For further analysis of cross-section, data processing for Ti and O atom percentage got by the spectral line was analysised, and we got the average atomic percentage content of Ti and O, atom ratio of O and Ti , and average atom ratio of O and Ti, the result is shown in figure 2 (b). From figure 2 (b),we can see that point A is the interface of TC4 matrix and oxide film, point D is interface of oxide film and the vacuum, so thickness of the oxide film is line AD, and the length is 6.22 microns. By O/Ti ratio, TC4 anodized film can be divided into three layers. When the O/Ti ratio is less than 1, point A¢ is interface O/Ti ratio of titanium alloy film, point B¢ is O/Ti = 1, the AB oxide layer closest to the TC4 matrix is formed between interface A¢A and B¢B interface, and the O content is low and titanium and oxide is inadequate at this time, this is mainly due to the O_2 molecules, or O^{2-} and OH^- ions have a long route to spread into TC4 internal , so the O content is low. When the O/Ti is between 1 and 2, and O/Ti ratio of point G is 1.5, O/Ti ratio of point C¢ is 2, the O/Ti ratio rise up from point B¢ to point C¢, and BC oxide layer formed between the interface B¢B and interface C¢C, at this time O content continues rising to form a series of titanium oxide TiOx (x = 1-2). When O/Ti ratio is greater than 2 ,the O/Ti ratios are all greater than 2, then O content of CD oxide layer formed between interface C¢C and interface D¢D is greater than the O content in TiO_2, that is to say, O in CD oxide film are not all titanium oxide, also including O in oxides of Al, V, and Si and other elements .We noticed that chemical composition and thickness of layer AB, layer BC and layer CD are different, the O content and thickness increases from TC4 matrix to the vacuum and this have obvious relationship with the formation process of anodic oxidation film. At the beginning of the anodic oxidation, O content is relatively sufficient and porous, TiO_2 film formed by violent reaction. Along with formation of the oxide film, O will spread from the oxide layer to the matrix surface to form titanium oxide, then the O is insufficient and generate TiOx (x = 1-2) film. Near interface of titanium alloy, Ti and O may form Ti - O solid solution in the process of anodic [12], O will form titanium oxide on surface of the titanium alloy only when O spread in the Ti - O solid solution, and diffusion coefficient of O in the oxide film is much bigger than it in the Ti - O solid solution, thus the generated TiO film is very thin [13].

Actually because of the difference of oxygen atmosphere, anodic oxidation of titanium alloy will form different valence state of titanium oxide, after anodic oxidation, the surface film mainly contain TiO_2 and there also have Ti_2O_3, TiO and even elemental Ti in the internal film [14].

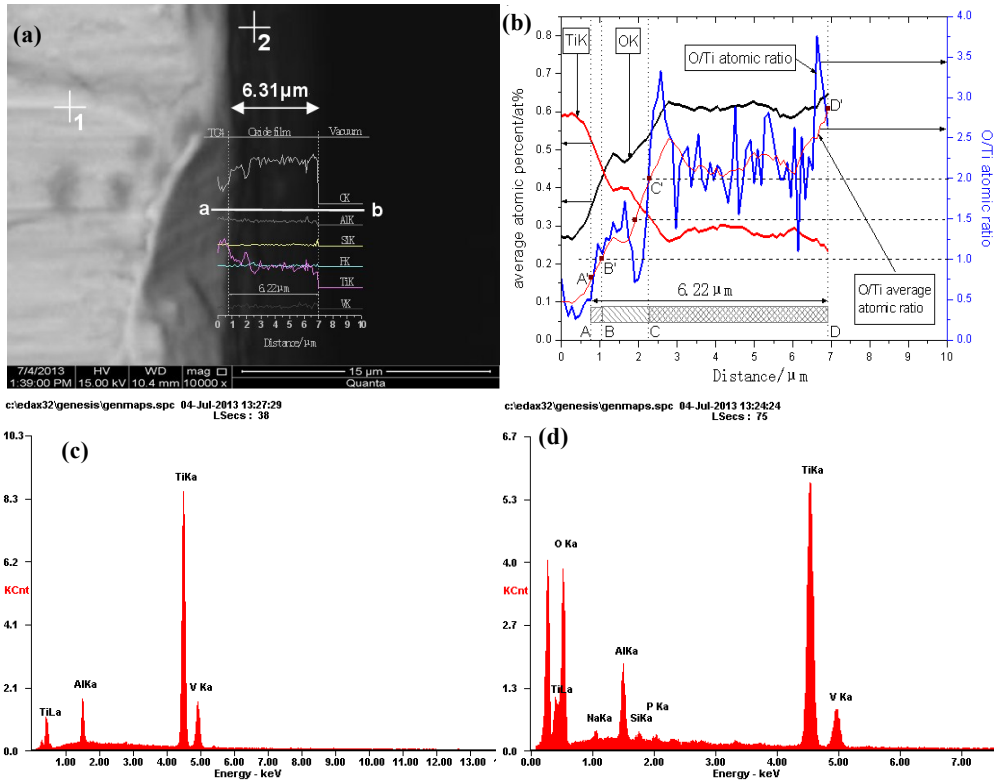


Fig.2 Microstructure and chemical composition of cross-section for oxide films on titanium alloy TC4 by anode oxidation at oxidation voltage 80V: (a) backscattered electron image and line analysis positions of EDS, (b)Ti and O chemical composition,(c)EDS of TC4 substrate and (d) EDS of oxide titanium film

From the backscattered electron figure 2 (a), we can see that contrast gradually reduces to 0 from TC4 / oxide film layer interface to the vacuum, , it shows that titanium content of the film is reducing or the oxygen content is increasing all the time. Point analysises of TC4 titanium alloy matrix and oxide film are shown as points 1 and 2 in figure 2 (a). The TC4 titanium alloy matrix spectrum is shown as point 1 in figure 2 (c), it shows that TC4 matrix is only composed of Ti, Al and V. Oxide film of point 2 in figure 2 (a) is shown in figure 2 (d), and this shows that O content of the surface oxidation film is higher, in addition to the Ti, Al and V, there also exist Si, Na, and P. The elements and their atomic percentage in figure 2(c) and figure 2 (d) are shown in table 1. Table 1 shows that there is no O in TC4 matrix, and O content in the oxide film is 60.73at %, and the content of titanium is 32.09 at %, O/Ti ratio of the oxide film is close to 2. Because in the process of anodizing, the O content is not always meet the stoichiometric of TiO_2, and there also exist other oxides, including: Al_2O_3, V_2O_5, SiO_2, Na_2O and P_2O_5 in the oxide film, so we cannot say oxide in the oxide film are all made up of TiO_2 only because the O/Ti ratio is close to 2. Thus calculate oxide stoichiometric in the oxide film according to Al_2O_3, V_2O_5, SiO_2, Na_2O and P_2O_5, and consider the oxygen content of the titanium oxide TiOx (x = 1-2) as different x values.

Table 1 shows that when x of point 2 in figure 8 (a)in the titanium oxide film TiOx is 1, O content of oxide film should match as 42.955at%, which is lower than the actual O content 60.73 at %;When the titanium oxide in the film is TiOx (x = 1.5), O content of oxide film should match as 59 at %, and the actual O content is 60.73 at %; When the titanium oxide in the film is TiOx (x = 2),O content of oxide film should match as 75.045 at %, which is higher than the actual O content 60.73at % . Therefore, titanium oxide of point 2 in figure 2 (a) is $TiO_{1.5}$, namely Ti_2O_3, this is mainly caused by insufficient oxygen of anodic oxidation at the medium time. Structure of titanium anode oxidation has a similar structure with the surface oxidation of titanium alloy in air.

In air, oxidation film of titanium alloy surface has three-layer structure; the film directly contacted with titanium alloy is TiO, the middle layer is Ti_2O_3, and the outer layer contacted with the environment is TiO_2 anatase structure. This shows that the anodic oxidation have a similar structure with oxidation film oxidated in air.

Table 1 Chemical composition of cross-section for oxide films on TC4 by anode oxidation at 80V

chemical composition of point 1 and 2 in fig.2(a)			Alternative TiO_x（x=1-2）film layer corresponding point 2 in fig.2(a)								
Element	TC4	oxide films	x=1 in TiO_x			x=1.5 in TiO_x			x=2 in TiO_x		
OK		**60.73**	MOn oxides	n values in MOn	O atomic percent matched with MOn	MOn oxides	n values in MOn	O atomic percent matched with MOn	MOn oxides	n values in MOn	O atomic percent matched with MOn
AlK	9.26	4.97	$AlO_{1.5}$	1.5	7.455	$AlO_{1.5}$	1.5	7.455	$AlO_{1.5}$	1.5	7.455
TiK	85.44	32.09	TiO	1	32.09	$TiO_{1.5}$	1.5	48.135	TiO_2	2	64.18
VK	5.29	0.5	$VO_{2.5}$	2.5	1.25	$VO_{2.5}$	2.5	1.25	$VO_{2.5}$	2.5	1.25
SiK		0.44	SiO_2	2	0.88	SiO_2	2	0.88	SiO_2	2	0.88
NaK		0.96	$NaO_{0.5}$	0.5	0.48	$NaO_{0.5}$	0.5	0.48	$NaO_{0.5}$	0.5	0.48
PK		0.32	$PO_{2.5}$	2.5	0.8	$PO_{2.5}$	2.5	0.8	$PO_{2.5}$	2.5	0.8
total O atomic percent matched with MOn					**42.955**			**59**			**75.045**

2.2 growth mechanism of titanium oxide film layer

Figure 3 is the sketch for titanium oxide formed in the process of anodic oxidation. In figure 3, the interface O¢O is the surface of titanium alloy before anodic oxidation, that is the interface of titanium alloy and electrolyte, A¢A is the interface of titanium alloy with oxide film after anodic oxidation and D¢D is the interface of titanium oxide film with the electrolyte after anodic oxidation. Anodic oxidation is general divided into three stages.

Titanium alloy plays the role of anode electrode at the beginning of the anodic oxidation, the current density in the electrolyte is large, and due to the strong electrolysis of water, many small air bubbles appear near the anode, which means there are more O_2 near the anode, and the titanium alloy substrate reaction with O_2 on titanium alloy surface and nucleate to generate dotted TiO_2, as shown in figure 3 (a). The dotted TiO_2 nuclear gradually grow extensionally towards internal, electrolyte and the titanium alloy surface to form a porous passivation titanium oxide film with random pore structure; β phase region with a stronger corrosion resistance can form convex particles with Na, Si and P elements in electrolyte, as shown in figure 3 (b).

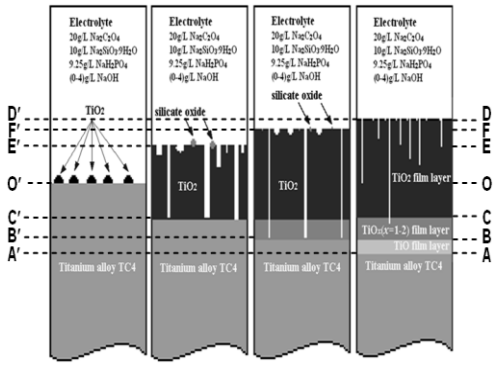


Fig.3 Schematic diagram for formation of oxide films on TC4 by anode oxidation:(a) nucleation and growth of TiO_2;(b) formation of porous TiO_2 films;(c)middle and (d) latest stages of anode xidation

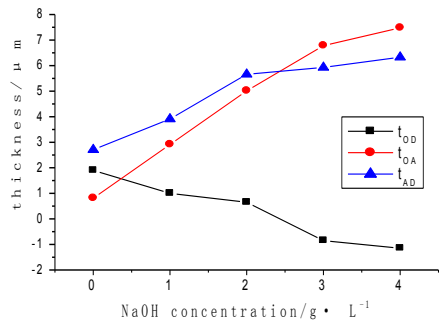


Fig.4 Thickness of films on TC4 by anode oxidation at different NaOH concentratione:t_{OD}-total thickness variation of samples, t_{OA}-solution thickness of titanium alloy,t_{AD}- thickness of oxide films

Then interface of TC4 O′O indentation to the matrix internal as interface of C′C，E′E is the interface of passivation film and the electrolyte, and thickness of the porous film is distance

between the interface C′C and interface E′E, namely, t_{CE}. The surface of titanium alloy contact directly with the electrolyte, and there are many ions dissolved in the electrolyte, the titanium ions react with OH^- can generate TiO_2 on the porous passivation surface. At the beginning of the anodic oxidation, speed of porous titanium oxide film grow fast, and have large aperture, the porous structure of the titanium alloy substrate created the material transport channel for further oxidation of titanium oxide film . In the middle of the anodic oxidation, the surface of titanium alloy TC4 already has a porous titanium dioxide film layer,the resistance increase greatly, the current density of electrolyte greatly reduce, the electrolysis of water rate is low, and a small amount of O_2 produce on the oxide film surface,through spreading to the titanium alloy substrate surface to form the titanium oxide TiOx (x = 1-2), as a result, the titanium alloy directly react with O_2 to produce titanium dioxide is not the main film-forming mechanism of oxide film at the middle time. In the middle of the anodic oxidation, titanium oxide TiOx (x = 1-2) generated mainly due to the reaction of titanium ions with OH^- in the electrolyte. These titanium oxide film generally cannot generate TiO_2 due to inadequate oxygen , they based on the porous structure of titanium dioxide film generated in the early of the anodic oxidation surface or the inner surface of the aperture, then the titanium oxide film grow towards the direction of the electrolyte or make aperture of the porous structure smaller . Due to the effect of sustained oscillation of the anodic oxidation voltage, the early formation anodic oxidation titanium dioxide film will dissolve, and at the same time β phase bump particles rich in V on the titanium dioxide film will also be corroded and dissolved, making the titanium dioxide film surface more smooth and flat. In the middle of the anodic oxidation, growth and dissolution of titanium oxide film layer lead size of the early formed titanium dioxide pores become smaller, the bump particles disappear, surface flatness increases and the roughness reduce, as shown in figure 3 (c). Then the TC4 matrix interface C′C indentation internal as interface B′B, F′F is the interface of film and electrolyte, thickness of the porous film is the distance between interface B′B and F′F, namely the t_{BF}. Pore size of the titanium oxide film formed in the middle of the anodic oxidation is small, and the thickness is smaller. Late in the anodic oxidation, the surface of titanium alloy TC4 already have two porous titanium dioxide film, the resistance further increase, the electrolytic current density is lower and oxygen produced by water electrolysis is very little, not only that, titanium ions dissolved in the electrolyte are few left, on the surface of titanium oxide film, speed of titanium oxide TiOx (x = 1-2) generated by reacting of titanium ions and OH^- is slow. It needs oxygen ions , oxygen molecules or hydroxyl ions to through two titanium oxide layer and spread to the titanium alloy surface to form new titanium oxide film, the titanium oxide film is short of oxygen seriously, and generally form TiO , and due to the speed of forming film is very slow, the film layer is very thin, but the density is high, and this further reduce the formation speed of TiO film, so generally at the later stage of anodic oxidation, the overall structure of the oxide film become basically stable and the thickness change is steady, as shown in figure 3 (d). At this time, the TC4 interface is AA', and D′D is interface of the film and the electrolyte, thickness of the porous film is the distance between interface A′A and D′D, namely t_{AD}. Table 2 is the physical and chemical process and related chemical reaction equations for three stages of titanium alloy anodic oxidation. From table 2: at the beginning of the anodic oxidation, titanium alloy is anode, and the current density is large, titanium prone to occur electrochemical corrosion and then dissolve in the electrolyte, such as the formula (1).

Plenty OH^- in alkaline electrolyte, that's can precipitate O_2 on the surface of titanium alloy, also can directly oxidation Ti into TiO_2, O_2 separated on titanium alloy surface can also directly react with Ti in situ to generate TiO_2, such as formula (2) ~(4).

Under the influence of negative pulse, the TiO_2 film will dissolve, such as formula (5). In the middle of the anodic oxidation, a layer of oxide film generated on surface of titanium, current density decreases greatly, and titanium dissolving capacity greatly reduce, O_2, OH^- and H_2O spread to the titanium alloy interface to generate Ti_2O_3 and will gradually transform into TiO_2, such as fromula (6-10). Late in the anodic oxidation, titanium solubility decreases, O_2, OH^- and H_2O diffusion to the titanium alloy interface will generate TiO, and will gradually form Ti_2O_3, such as formula (11-15). With the extension of oxidation time, speed of the surface TiO_2 oxide dissolution rate will consistent with speed of internal TiO formation, TiO will change: $TiO \rightarrow Ti_2O_3 \rightarrow TiO_2$ to maintain the state of relative balance dynamic growth of overall film structure.

Table 2 Chemical reaction and stages of titanium alloy anode oxidation

Stage of anodizing	physical-chemical processes	chemical reactions	Sequence Number
the initial stage of anodizing	Titanium dissolve in the electrolyte:	$Ti \rightarrow Ti^{4+} + 4e^-$	(1)
	Oxygen precipitate out from the anode titanium alloy:	$4OH^- \rightarrow 2H_2O+O_2\uparrow+4e^-$	(2)
	Formation of TiO_2 film:	$2Ti+8OH^- \rightarrow 2TiO_2+4H_2O+8e^-$	(3)
	Formation of TiO_2 film:	$Ti+O_2 \rightarrow TiO_2$	(4)
	Dissolve fo TiO_2 film:	$TiO_2+4H^++4e^- \rightarrow Ti+2H_2O$	(5)
the middle stage of anodizing	Titanium dissolve in the electrolyte:	$Ti \rightarrow Ti^{3+}+3e^-$	(6)
	Formation of Ti_2O_3 film:	$2Ti+6OH^- \rightarrow Ti_2O_3+3H_2O+6e^-$	(7)
	Formation of Ti_2O_3 film:	$Ti+3/2O_2 \rightarrow Ti_2O_3$	(8)
	Ti_2O_3 film transform into TiO_2film:	$Ti_2O_3+H_2O \rightarrow 2\ TiO_2+2H^++2e^-$	(9)
	Ti_2O_3 film transform into TiO_2film:	$Ti_2O_3+1/2O_2 \rightarrow 2\ TiO_2$	(10)
the later stage of anodizing	Titanium dissolve in the electrolyte:	$Ti \rightarrow Ti^{2+}+2e^-$	(11)
	Formation of TiO film:	$Ti+1/2O_2 \rightarrow 2TiO$	(12)
	Formation of TiO film:	$2Ti+2OH^- \rightarrow TiO+H_2O+2e^-$	(13)
	TiO film transform into Ti_2O_3film:	$2TiO+H_2O \rightarrow Ti_2O_3+2H^++2e^-$	(14)
	TiO film transform into Ti_2O_3film:	$2TiO+1/2O_2 \rightarrow Ti_2O_3$	(15)

Figure 4 is thickness of anodic oxidation film under different NaOH electrolyte concentrations on the TC4 surface. In figure 4, the t_{AD} is the distance between interface A′A and D′D, that's the total thickness of oxide film measured by the eddy current meter; t_{OD} is the distance between the interface O′O and interface D′D, it is the increased thickness through spiral micrometer measured and calculated of the TC4 after anodic oxidation than before, t_{OD} with a positive value indicates the total thickness of the sample increase and t_{OD} with a negative value indicates the total thickness of the samples decrease; t_{OA} is the distance between interface O′O and A′A, namely the distance of titanium alloy surface indentation into the matrix after anodic oxidation. From figure 3: $t_{AD} = t_{OA} + t_{OD}$, namely the oxide film thickness is equal to the diastance of titanium alloy surface indentation into the matrix and distance of the total thickness increased of the sample. Figure 4 shows that different NaOH concentrations has obviously influence on the thickness of the coating.

With the increase of NaOH concentration, rise trends of oxidation film thickness t_{AD} decrease and leveling off; the increasing rate of the total thickness t_{OD} is reduce, and when NaOH concentration is 3 g/L, the total sample thickness decreases, namely $t_{OD} < 0$. Titanium alloy surface indentation into the internal t_{OA} is increasing all the time, and so as the titanium alloy dissolution rate. With the increase of NaOH concentration, dissolve rate of the surface gradually increase, lead thickness of the total sample decreases, dissolution rate of the titanium alloy is

greater than the dissolution rate of sample surface film, so thickness of the oxide film increases can reach a steady state. This shows that with the increase of NaOH concentration, corrosion rate of the film gradually accelerates, leading holes occur on the sample surface, the appearance of pores lead the further oxidation of Ti atoms on the surface of the sample, so that the oxide film gradually becomes thicker.

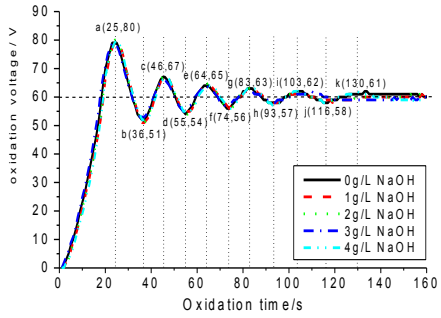


Fig.5 Voltage-time curve of electrolyte with different NaOH concentratione

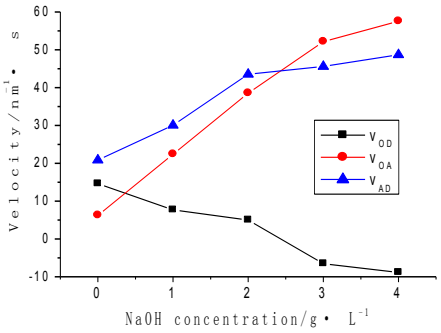


Fig.6 Growth velocity of films on TC4 by anode oxidation at different NaOH concentratione:v_{OD}-total thickness variation velocity of samples, t_{OA}-solution velocity of titanium alloy,t_{AD}- growth velocity of oxide films

Figure 5 is the curves of anodic oxidation in electrolyte for 50 min with the instantaneous voltage of 60V under different NaOH concentrations, that's 0 g/L, 1 g/L, 2 g/L, 3 g/L and 4 g/L, respectively.

As shown in figure 5, with the change of NaOH concentration, curves of voltage and time are remain unchanged, the addition of NaOH amount has little influence on the time curves. With increasing of time, the voltage rise rapidly from 0V to 80V in 25s, that's the point a (25, 80), then drop to 51V at 36 s by the voltage limit of constant voltage 60V, namely point b (36, 51). Then, the voltage reaches point c, d, e, f, g, h, I, j and k in turn. After point k (130, 61), the voltage is nearly 60V and almost remains the same, it can be judged that dissolution and generation of the oxidation film speed has achieve a dynamic balance. Figure 6 shows that, with the increase of NaOH concentration, the average growth rate of the oxide film V_{AD} and the dissolution rate of TC4 interface V_{AD} are all increase. And change speed of the total thickness decreases and finally achieves a stable oxidation film thickness.

3 Conclusions

NaOH concentration has little effect on the phase composition of surface film, and the oxide film is amorphous.

(1) The growth of the film on the TC4 surface experiences three stages and form three different film structure of O/Ti in the initial, middle and later stage. Initial anodic oxidation form the thickest layer of TiO_2,and in the middle stage form the middle tier of $TiO_{1.5}$, and the later stage generate thin oxide film layer of TiO.

(2) With increasing of NaOH concentration, dissolution speed of the TC4 interface with film layer is greater than the dissolution speed of oxide film on surface, which can lead to trace increases of oxide film,when growth speed of the oxide film and the dissolution rate is equal and the film thickness stops changing.

Fund project：Major science and technology projects in yunnan province（2012ZE008），The national natural science fund project（51362017）

References:

[1] R. Van Noort. Titanium: the implant material of today. J Mater Sci,1987,22(11): 3801~3811.

[2] Wang Qiang,Yang Min, Xu Zhujun. J Clin Rehab Tissue Eng Res, 2009, 13(4):739~742.

[3] Qian Jiangang, Li Di,Guo Baolan. J Aviat Mater, 2005, 25 (4):53~58.

[4] Deng Shuhao, Yi Danqing, Lin Shuangpin et al. Plat Surf Finish, 2006, 28 (5):15~20.

[5] Yi Xiaohong, Fan Zhanguo, Zhang Jinglei et al. Mater Eng, 2010, (3):38~41.

[6] Deng Shuhao, Yi Danqing, Lou Jia et al. Plat Surf Finish, 2006, 25 (2):32~36.

[7] Cai Jianping, Liu Minghui, Zhang Xiaoyun. J Mater Prot, 2009, and (3):15~17.

[8] Wen Qiang, Cao Fahe, Zhang Zhao et al. Corros Sci Prot Technol, 2009, 21 (2):182~184.

[9] Wu Songlin, Liu Minghui, Yi Junlan et al. Mater Eng, 2013, (1):6~12.

[10] Zhu Yongming, Hu Huili, Tu Zhenmi et al. Plat Surf Finish, 2009, 31(6):35~38.

[11] Tao Haijun, Tao Jie, Wang Ling et al. J Nanjing University of Aeronautics & Astronautics,2005(5): 597~602.

[12] Li qiang,Yu Jingyuan, Sun Xudong. Rare Metal Mater Eng,2010,33(7) 6:1270~1275.

[13] Pouilleau J, Devilliers D, Garrido F, Durand-Vidal S., Mahea E. Structure and composition of passive titanium oxide films, Mater Sci Eng, 1997, B47:235~243,.

[14] Chen Jingyun, Liu Zongjian, Zhou Huan et al. Zhejiang Chem Ind, 2012,3 (9) : 22~25.

Key Engineering Materials Vols 645-646 (2015) pp 313-318
© (2015) Trans Tech Publications, Switzerland
doi:10.4028/www.scientific.net/KEM.645-646.313

Submitted: 2014-12-05
Accepted: 2014-12-23

A Novel High Precision Analytic Potential Function for diatomic Molecules

YU Chang-feng

(Dept. of physics, College of Science, Xi'an Polytechnic University , Xi'an 710048 China)

Keywords: spectroscopic parameters of molecules; diatomic molecules and ions; analytical potential energy function; RKR method

Abstract: A new analytical potential energy functions is presented, the potential energy function is examined by 13 examples of different diatomic molecules or ions——homonuclear ground-state for neutral diatomic molecules $Na_2-X^1\Sigma_g^+$, heternuclear ground-state for charged diatomic molecular ion $(CS)^+-X^2\Sigma^+$, heternuclear excitation-state neutral diatomic molecules $PbS-A^1\Sigma^+$, heternuclear excited-state for charged diatomic molecular ion $(CS)^+-A^2\Pi$, homonuclear excited-state for neutral diatomic molecule $K_2-B^1\Pi_u$, homonuclear excited-state for charged diatomic molecule $O_2^+-A^2\Pi_u$ etc.. as a consequence, the theoretical values of the vibrational energy level of molecules calculated by the potential energy function are in high-precision consistent with RKR data（Rydberg-Klein-Rees）or experimental data.

0 Introduction

Analytical potential energy functions are of great significance in the study of material science, molecular spectrum, reaction dynamics of atoms and molecules, vibrational and rotational energy-level structures of molecules, interactions between laser and matter, photoionization etc.[1-3]. It is also the basis for studying multi-atomic molecules, ions and clusters. In addtion, chemical reaction, molecular collision and many other problems need precise analytical potential energy functions[4].In this paper, A high precision analytical potential energy function with six parameters is given.The potential energy function is compared with Murrell-Sorbie potential which is extensive used in atomic and molecular physics at present, it shows that the computational precision on the vibrational energy level of molecules calculated by this potential function is superior to that of Murrell-Sorbie potential .

1 The New analytic potential function

The New analytic potential functions are given as follows

$$V(r)=\frac{2D_e}{1+6a+10b+14c}\left\{\frac{1}{2}\left(\frac{R_e}{r}\right)^2+a\left(\frac{R_e}{r}\right)^4+b\left(\frac{R_e}{r}\right)^6+c\left(\frac{R_e}{r}\right)^8-(1+4a+6b+8c)\frac{R_e}{r}\right\}. \quad (1)$$

$$V(r)=\frac{16D_e}{19+112a+144b+176c}\left\{\frac{1}{2}\left(\frac{R_e}{r}\right)^2+\frac{1}{8}\left(\frac{R_e}{r}\right)^4+\frac{1}{16}\left(\frac{R_e}{r}\right)^6+a\left(\frac{R_e}{r}\right)^8+b\left(\frac{R_e}{r}\right)^{10}+c\left(\frac{R_e}{r}\right)^{12}-\left(\frac{15}{8}+8a+10b+12c\right)\frac{R_e}{r}\right\}. \quad (2)$$

where R_e and D_e are the equilibrium internuclear distance and the dissociation energy of a molecule respectively. The undetermined parameters a, b, c can be determined with the experimental spectroscopic parameters (ω_e, $\omega_e\chi_e$, α_e B_e).

Examinations show that the Eq.(1) or Eq.(2) can accurately describe the interaction behaviours of diatomic molecules at a larger range of equilibrium internuclear distance in calculating the vibrational energy level of molecules, but there is a definite deviation between the long-range attractive branch of the potential curve and RKR data or experimental data. So in order to further ameliorating the qualities of the long-range attractive branch, it is necessary to improve the

potential energy function. In this paper, we adopt piecewise-function method to obtain a potential function which can describe the behaviours of whole range of the potential curve. The potential function is

$$V_m(r)=\frac{1}{2}\left(1+\frac{r_0-r}{|r_0-r|}\right)\left(V_1(a,b,c,r)+De\right)+\frac{1}{2}\left(1+\frac{r-r_0}{|r-r_0|}\right)\left(V_2(a_0,b_0,c_0,r)+De\right). \tag{3}$$

Eq.(3) is the analytical potential energy function that is required, which includes six potential parameters a, b, c and a_0,b_0,c_0. Here, the first term on the right side of Eq.(3) is the main part of the potential function, the second is the correction term for improving the long-range attractive branch of the potential function. In Eq. (3), the two potential $V_1(a,b,c,r)$ and $V_2(a_0,b_0,c_0,r)$ choose exactly the same function, which can be selected from one of Eq.(1) and Eq.(2). The potential parameters a, b, c (see table 2) can be determined by experimental spectroscopic parameters. a_0,b_0,c_0 can be obtained by solving the following equations

$$V_1(a,b,c,r_0)=V_2(a_0,b_0,c_0,r_0),\ \left(\mathrm{d}V_1/\mathrm{d}r\right)_{r=r_0}=\left(\mathrm{d}V_2/\mathrm{d}r\right)_{r=r_0},\ V_2(a_0,b_0,c_0,r)\big|_{r=8R_e}=De,\ r_0=\left(\left(R_e+r_m\right)/2\right)\cdot\delta. \tag{4}$$

where r_m is the value of internuclear distance r when $V_1(a,b,c,r)+De=De$. δ is a adjusting parameter for precision.

2 Using experimental spectroscopic parameters to determine a, b, c

The undetermined parameters a, b, c can be determined with the experimental spectroscopic parameters (ω_e, $\omega_e\chi_e$, α_e B_e) of diatomic molecules or ions. The principle of this method is, according to the relationship between undetermined parameters and force constants to obtain a, b, c. The relationships between force constants and spectroscopic parameters are as follows

$$f_2=4\pi^2\mu\omega_e^2c^2=\frac{hc\omega_e^2}{2R_e^2B_e},\ f_3=-\frac{3f_2}{R_e}\left(1+\frac{\alpha_e\omega_e}{6B_e^2}\right),\ f_4=\frac{f_2}{R_e^{\,2}}\left[15\left(1+\frac{\alpha_e\omega_e}{6B_e^2}\right)^2-\frac{8\omega_e\chi_e}{B_e}\right]. \tag{5}$$

where the force constants at the equilibrium internuclear distance can be given by

$$f_m=\left(\frac{\mathrm{d}^mV}{\mathrm{d}r^m}\right)_{r=R_e}\qquad (m=2,\ 3,\ 4). \tag{6}$$

From Eq.(1), Eq.(2), Eqs.(5) and Eq.(6), the undetermined parameters a, b, c can be deter mined.So far, oneof the best and most extensively used analytical potential energy function is Murrel-Sorbie (M-S) potential[3] which is applied to most of diatomic molecules. Murrell-Sorbie potential is as follows

$$V(r)=-D_e\left[1+a_1\left(r-R_e\right)+a_2\left(r-R_e\right)^2+a_3\left(r-R_e\right)^3\right]\exp\left[-a_1\left(r-R_e\right)\right]. \tag{7}$$

The relations between undetermined parameters a_1, a_2, a_3 and force constants are as follows

$$D_e(a_1^2-2a_2)=f_2,\quad 2D_e(3a_1a_2-3a_3-a_1^3)=f_3,\quad D_e(3a_1^4-12a_1^2a_2+24a_1a_3)=f_4. \tag{8}$$

3 Examinations for the analytical potential energy function

For examining potential energy function Eq.(3), 13 kinds of neutral diatomic molecules and charged diatomic molecular ions have ever been investigated and the values of the vibrational energy level of molecules calculated by the potential energy function are compared with RKR （Rydberg-Klein-Rees[5]） data, M-S potential or experimental data. The experimental data on spectroscopic parameters as well as potential paramters of only 13 diatomic molecules are listed in Table 1,2. The potential parameters r_0, a_0, b_0, c_0 calculated by Eqs.(4) are listed in Table 3.

The vibrational energy levels of diatomic molecules $BaO-A^1\Sigma$ is listed in Table 4. Limited to the length, other molecules are omitted. The potential curves of four diatomic molecules plotted with Origin 6.0 by using potential Eq.(3), RKR data, and M-S potential are showed in fig.1.

In order to examine the calculation precision of Eq.(3), the root-mean-square-errors（RMSE）and relative root-mean-errors（RRMSE）between the potential values of 13 kinds of electronic states and RKR data or experimental data are showed in table 5. RMSE and RRMSE are given by the following formulas

$$\mathrm{RMSE}=\sqrt{\frac{1}{N}\sum_{i=1}^{N}\left(U_{\mathrm{RKR}}(i)-U_{\mathrm{CAL}}(i)\right)^2}\ . \qquad (9)$$

$$\mathrm{RRMSE}=\sqrt{\frac{1}{N}\sum_{i=1}^{N}\left(\frac{U_{\mathrm{RKR}}(i)-U_{\mathrm{CAL}}(i)}{U_{\mathrm{RKR}}(i)}\right)^2}\ . \qquad (10)$$

Table 1 Experimental spectroscopic parameters of diatomic molecules

States	$\omega_e/\mathrm{cm}^{-1}$	$\omega_e\chi_e/\mathrm{cm}^{-1}$	B_e/cm^{-1}	$\alpha_e/\mathrm{cm}^{-1}$	R_e/nm	D_e/cm^{-1}	refs.
$Na_2-X^1\Sigma_g^+$	159.120	0.72600	0.15470	0.000874	0.30790	5886.50	[6]
$Li2-X^1\Sigma_g^+$	351.400	2.61000	0.67260	0.00704	0.26730	8518.50	[7]
$He_2^+-X^2\Sigma_u^+$	1698.52	35.30	7.2110	0.2240	0.1080	19963.0	[8]
$(CS)^+-X^2\Sigma^+$	1376.60	7.80000	0.86730	0.00650	0.14925	52147.5	[9]
$AlO-X^2\Sigma^+$	978.20	7.120	0.64148	0.00575	0.16176	42669.2	[10]
$BC^--X^3\Pi$	1301.40	9.82000	1.41800	0.01550	0.14450	45073.0	[11]
$K_2-B^1\Pi_u$	75.0000	0.38760	0.04824	0.000235	0.42350	4183.40	[12]
$N_2^+-B^2\Sigma_u^+$	2419.84	23.1900	2.08300	0.01950	0.10750	71572.0	[12]
$O_2^+-A^2\Pi_u$	900.000	13.4000	1.06170	0.01906	0.14089	14195.4	[13]
$(CS)^+-A^2\Pi$	1013.79	6.78000	0.71840	0.00650	0.16399	39475.9	[9]
$PbS-A^1\Sigma^+$	261.090	0.36500	0.08560	0.000296	0.26650	38040.7	[12]
$BaO-A^1\Sigma$	498.800	1.50000	0.25820	0.00110	0.21340	38159.3	[12]
$AsCl-{}^1\Delta$	436.075	1.38106	0.153766	0.0007099	0.21443	35746.9	[14]

Note :the relation between zero-point dissociation energy D_e and ground-state dissociation energy D_0 given by refs.[12] is $D_e=D_0+\omega_e/2-\omega_e\chi_e/4$

Table2 Potential paramters of diatomic molecules

		This Work			Murrel-Sorbie potential		
states	Eq.	a	b	c	a_1/nm^{-1}	a_2/nm^{-2}	a_3/nm^{-3}
$Na_2-X^1\Sigma_g^+$	(1)	–0.30853	0.09280	–0.01096	19.8311	123.357	315.123
$Li2-X^1\Sigma_g^+$	(1)	–0.33924	0.11979	–0.01816	19.0886	106.818	259.491
$He_2^+-X^2\Sigma_u^+$	(1)	–0.31341	0.08985	–0.01104	32.5478	100.364	596.149
$(CS)^+-X^2\Sigma^+$	(2)	–0.57179	0.41097	–0.09318	41.1945	378.505	1682.30
$AlO-X^2\Sigma^+$	(2)	–0.487425	0.2811056	–0.049149	21.3192	–106.628	1263.112
$BC^--X^3\Pi$	(1)	–0.22101	0.00689	0.00701	27.8925	71.8962	635.581
$K_2-B^1\Pi_u$	(2)	–0.64720	0.47938	–0.10634	12.2985	27.0619	–79.8024
$N_2^+-B^2\Sigma_u^+$	(2)	–0.46214	0.245002	–0.030347	10.0782	–798.592	13832.93
$O_2^+-A^2\Pi_u$	(2)	–0.413374	0.213576	–0.032766	41.8334	198.500	881.264
$(CS)^+-A^2\Pi$	(2)	–0.56856	0.39898	–0.08949	29.3005	92.5409	749.213
$PbS-A^1\Sigma^+$	(1)	–0.37401	0.16266	–0.03536	19.5478	117.409	567.400
$BaO-A^1\Sigma$	(1)	–0.27014	0.052685	–0.002106	14.6159	–31.7396	35.1670
$AsCl-{}^1\Delta$	(1)	–0.151102	–0.039429	0.0093085	24.9992	124.4496	693.665

Table 3 Potential parameters r_0, a_0, b_0, c_0 of the electronic states

states	Eq.	δ	D_e/cm^{-1}	R_e / nm	r_m / nm	r_0 / nm	a_0	b_0	c_0
$Na_2 - X^1\Sigma_u^+$	(1)	1.00	5886.50	0.30790	0.53336	0.42063	–1.87580	1.99240	–0.67404
$Li2 - X^1\Sigma_g^+$	(1)	0.95	8518.50	0.26730	0.51465	0.37143	–2.50605	2.82587	–0.98416
$He_2^+ - X^2\Sigma_u^+$	(1)	0.88	19963.0	0.1080	0.24150	0.1538	–5.93738	7.14578	–2.50926
$(CS)^+ - X^2\Sigma^+$	(2)	1.00	52147.5	0.14925	0.27116	0.21021	95.9105	–161.080	70.1419
$AlO - X^2\Sigma^+$	(2)	0.68	42669.2	0.16176	0.42562	0.19971	1.06735	–2.16973	0.945525
$BC^- - X^3\Pi$	(1)	0.80	45073.0	0.14450	0.30537	0.17995	–6.41106	6.98762	–2.15391
$K_2 - B^1\Pi_u$	(2)	0.80	4183.40	0.42350	1.02440	0.57916	2.96700	–5.58805	2.52769
$N_2^+ - B^2\Sigma_u^+$	(1)	0.85	71572.0	0.10750	0.2155	0.13728	5.61393	–9.4614	3.99083
$O_2^+ - A^2\Pi_u$	(2)	0.99	14195.4	0.14089	0.24312	0.1901	–429.95	694.01	–291.854
$(CS)^+ - A^2\Pi$	(2)	0.95	39475.9	0.16399	0.35506	0.24655	14.3093	–25.2129	11.3202
$PbS - A^1\Sigma^+$	(1)	1.00	38040.7	0.26650	0.57830	0.42240	–3.06280	3.71761	–1.37473
$BaO - A^1\Sigma$	(1)	0.90	38159.3	0.21340	0.42452	0.28710	–2.90527	3.18764	–1.05600
$AsCl - {}^1\Delta$	(1)	0.80	35746.9	0.21443	0.42089	0.25413	–3.32356	3.25193	–0.89515

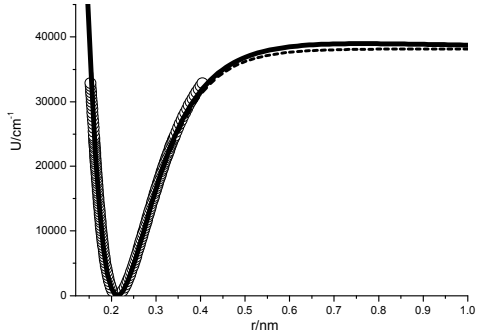
Table 4 The vibrational energy levels of heteronuclear excited-state for neutral diatomic molecule $BaO - A^1\Sigma$

	RKR			this work		Murrel-Sorbies potential	
v	U / cm^{-1}	r_{min} / nm	r_{max} / nm	$U(r_{min})/cm^{-1}$	$U(r_{max})/cm^{-1}$	$U(r_{min})/cm^{-1}$	$U(r_{max})/cm^{-1}$
0	249.025	0.206787	0.220537	248.917	248.873	248.927	248.866
1	744.825	0.202251	0.226127	744.429	744.488	744.566	744.347
2	1237.63	0.199268	0.230169	1236.84	1237.12	1237.32	1236.60
3	1727.43	0.196923	0.233579	1726.27	1726.98	1727.35	1725.76
4	2214.23	0.194951	0.236622	2212.67	2214.08	2214.67	2211.76
5	2698.03	0.193231	0.239418	2696.01	2698.24	2699.29	2694.38
6	3178.83	0.191695	0.242037	3176.50	3179.94	3181.41	3174.05
7	3656.63	0.190302	0.244518	3653.82	3658.63	3660.77	3650.17
8	4131.43	0.189023	0.246892	4128.23	4134.86	4137.63	4123.24
9	4603.23	0.187838	0.249177	4599.70	4608.21	4612.00	4592.81
10	5072.03	0.186732	0.251390	5068.32	5079.20	5083.96	5059.29
11	5537.83	0.185694	0.253541	5533.93	5547.34	5553.40	5522.37
12	6000.63	0.184715	0.255640	5996.57	6013.07	6020.35	5982.23
13	6460.43	0.183787	0.257693	6456.68	6476.07	6485.26	6438.61
14	6917.23	0.182906	0.259707	6913.34	6936.59	6947.23	6891.72
15	7371.03	0.182065	0.261687	7367.69	7394.69	7407.40	7341.58
16	7821.83	0.181261	0.263636	7819.19	7850.11	7865.26	7787.92
17	8269.63	0.180491	0.265559	8267.60	8303.21	8320.56	8231.06
18	8714.43	0.179751	0.267459	8713.54	8754.01	8773.93	8671.00
19	9156.23	0.179039	0.269337	9156.72	9202.17	9225.09	9107.32
20	9595.03	0.178352	0.271197	9597.64	9648.00	9674.57	9540.43

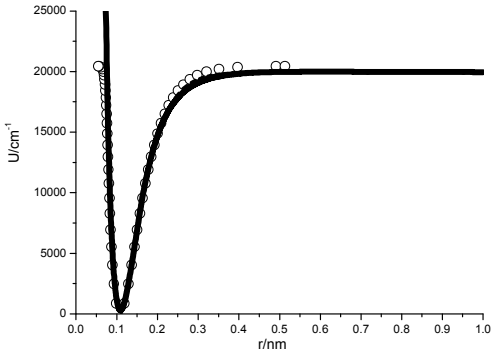
Table 5 The root-mean-square-errors and relative root-mean-errors between the values of potentials and RKR

states	N	This Work				Murrel-Sorbies potential			
		repulsive branch		attractive branch		repulsive branch		attractive branch	
		RMSE/cm^{-1}	RRMSE/%	RMSE/cm^{-1}	RRMSE/%	RMSE/cm^{-1}	RRMSE/%	RMSE/cm^{-1}	RRMSE/%
$Na_2 - X^1\Sigma_g^+$	46	219.5	4.33	15.52	0.50	443.5	9.10	172.9	4.00
$Li2 - X^1\Sigma_g^+$	26	363.2	5.86	16.90	0.39	134.7	2.23	112.4	2.00
$He_2^+ - X^2\Sigma_u^+$	13	774.8	5.33	106.4	0.85	753.8	5.21	82.88	0.63
$(CS)^+ - X^2\Sigma^+$	20	492.2	2.43	114.8	0.62	235.8	1.18	188.0	0.93

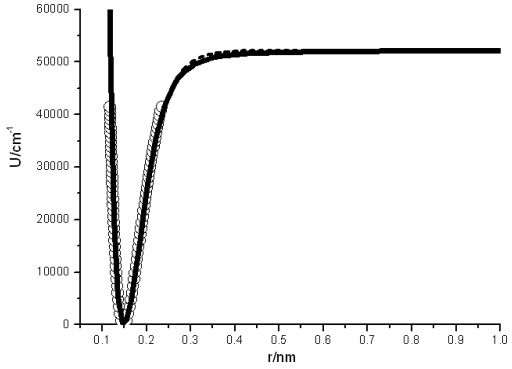
$AlO-X^2\Sigma^+$	23	440.0	2.68	42.28	0.33	549.7	3.39	117.7	0.79
$BC^- - X^3\prod$	26	206.1	0.82	121.8	0.55	489.8	2.20	102.1	0.43
$K_2 - B^1\prod_u$	36	254.0	12.8	4.372	0.26	203.0	17.6	429.0	31.9
$N_2^+ - B^2\Sigma_u^+$	13	69.99	0.29	180.09	0.77	1142.0	4.92	2003.4	8.55
$O_2^+ - A^2\prod_u$	19	1119	10.0	82.09	0.93	1278	11.5	198.4	1.91
$(CS)^+ - A^2\prod$	26	772.8	4.00	30.28	0.22	367.2	1.90	51.13	0.26
$PbS - A^1\Sigma^+$	36	143.6	1.92	24.12	0.33	223.6	3.03	91.12	1.27
$BaO - A^1\Sigma$	61	264.5	1.12	102.8	0.63	639.1	2.82	247.6	1.14
$AlCl - X^1\Sigma^+$	20	33.69	0.47	20.62	0.31	106.1	1.47	134.0	1.82
Mean		396.4	4.00	66.30	0.51	503.1	5.12	302.3	4.28



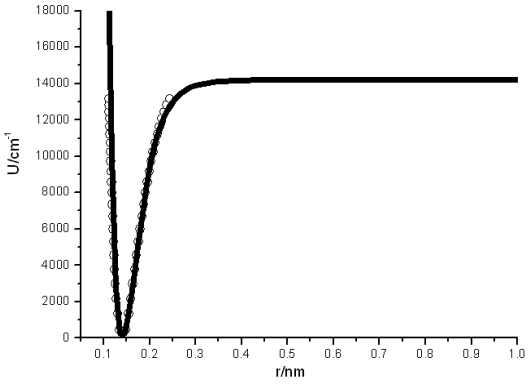
(a) heternuclear excited-state potential curve for neutral diatomic molecule $BaO - A^1\Sigma$



（b）homonuclear ground-state potential curve for charged diatomic molecular ion $He_2^+ - X^2\Sigma_u^+$



（c）heternuclear ground-state potential curve for charged diatomic molecular ion $(CS)^+ - X^2\Sigma^+$



（d）homonuclear excited-state potential curve for charged diatomic molecular ion $O_2^+ - A^2\prod_u$

Fig.1 Pototential energy curves of diatomic molecules(○=RKR; solid line=this work; dash line=Murrel-Sorbie)

4 Conclusions

A new analytic potential energy function which is used to describe diatomic molecules and ions is presented , and good results are obtained. This potential functions has two merits：(1) Seen from Table 6, as concerning the computational precision, this potential function is superior to M-S potential.(2) Attractive branch of a potential function especially the long-range of it is very important in studying chemical reactions, molecular collision etc.,they all need precise potential functions, Seen from Table 6, all the RMSE of the attractive branch of the potential function Eq.(3) are far more smaller than the “chemical precision” that is usually required[4](chemical precision=1.0Kcal/mo l = 0.043295eV $= 349.216\text{cm}^{-1}$), the RRMSE of them are 0.51% or so.

Foundation Item: This work was supported by the National Natural Science Key Foundation of China (No. 61405151)
This work was financially supported by special foundation item of the key academic subjects development of Shaanxi province [Shaanxi education Supporting (2008)169].
Biography:Yu Changfeng (1962-), male, professor, major in theoretical physics. Email: yuh55@126.com

References

[1] Alexandra Yiannopoulou, Gwang-Hi Jeung, Su Jin Park, Hyo Sug Lee,Yoon Sup Lee.Undulation of the Potential Energy Curves for Highly Excited Electronic States in Diatomic Molecules Related to the Atomic Orbital Undulations[J]. *Physical Review A*, 1999,**59**(2): 1178.
[2] Xie Ruihua, Gong Jiangbin. A Simple Three-Parameter Model Potential for Diatomic systems: From Weakly and Strong to Metastable Molecular Ions[J].*Phys Rev Lett*. 2005, **95:**263202.
[3] Murrel J N, Sorbie K S. New AnalyticFrom for the Potential Energy Curves of Stable Diatomic State[J]. *J Chem.,Soc., Faraday Trans*, *II,* 1974, **70**: 1552.
[4] Aguado A, Paniagua M A New Functional form to Obtain Analytical Potentials of Triatomic Molecules. 1992 *J.Chem. Phys*.**96:** 1265
[5] A. L. G. REES. The Calculation of Potential-Energy Curves from Band-Spectroscopic Data[J].*Proc. Phys Soc*.,1947,**59:**998-1008
[6] Yu Benhai, Dai Qirun,,Shi Deheng, *et al* . Investigations on Spectroscopic Parameters, Vibrational Levels, Classical Turning Points and Internal Rotation and Centrifugal Distortion Constant for the $X^1\Sigma_g^+$ States of Sodium Dimer[J] *Chinese Physics,* 2007 ,**16**(10):2962
[7] Shi De-Heng, Sun Jin-Feng, Zhu Zun-Lue, Ma Heng, Yang Xiang-Dong. Investigation on Vibrational levels, Inertial Rotation and Centrifugal Distotion Constants of $^7Li2(X^1\Sigma_g^+)$ [J].*Acta Phys. Sinica.* 2008, 57(1):165.
[8] Haberland H, Issendorff B V, Frochtenicht R, *et al.* Absorption Spectroscopy and Photodissociation Dynamics of Small Helium Cluster Ions[J] *J. Chem. Phys*., 1995,102(22):8773-8779.
[9] Liu Hui, Xing Wei, Shi De-Heng, Zhu Zun-Lue, Sun Jin-Feng. Study on spectroscopic parameters and molecular constants of $CS^+(X^2\Sigma^+)$ and $CS^+(A^2\Pi)$ by MRCI[J]. *Acta Phys. Sin.*2011,**60(4)**: 043102（in Chinese）
[10] Kou Suha, Liu Yan, Lang Jianghua,et al. Theoretical Study on the Potential Energy Curve for the Ground States of AlO Molecule[J].*Journal of Henan normal University (Natural Science Edition).*2013,41(03):68-70
[11] Tzeli D, Mavridis A. Continuing Our Study on the Electronic Structure of the Carbides BC and AlC[J]. *J.Phys.Chem*.A , 2001,**105** 1175.
[12] Herzberg G. Molecular Spectra and Molecular Structure (I. Spectra of Diatomic Molecules*)*[M].Beijing: *Science Press*,1983: 69, 394
[13] CHEN Hong-li,SUN Wei-guo, LIU Guo-yue, *at al.* Studies on the potential energy curves of homonuclear diatomic molecular ions using energy consistent method[J]. *Journal of Atomic Molecular Physics,* 2006,**23(1)**:27-32.
[14] Zhu Zun-Lue, Lang Jian-Hua, Qiao-Hao. Study on Spectroscopic Properties and Molecular Constants of the Ground and Excited States of AsCl Free-radical[J]. *Acta Phys. Sinica.* 2013, 62（11）: 113103-1-113103-7

Key Engineering Materials Vols 645-646 (2015) pp 319-324
© (2015) Trans Tech Publications, Switzerland
doi:10.4028/www.scientific.net/KEM.645-646.319

Submitted: 2014-12-05
Accepted: 2014-12-23

The simulation and analysis of current crowding and Joule heat in flip chip solder bumps

Peisheng Liu[1,2,a] , Longlong Yang[1], Jinxin Hang[1], Ying Lu[1]

[1]Nantong University, Jiangsu Key Laboratory of ASIC Design, Nantong 226019, China

[2]Nantong Fujistu Microelectronics Co., Ltd,Nantong 226006, China

[a]psliu@ntu.edu.cn

Key words: reliability; flip chip; current density; joule heat; finite element analysis

Abstract. Electro-migration has become a critical reliability issue for high density solder joints in flip chip technology, especially for current crowding and joule heat. Electro-migration force and mean time to failure of flip chip are introduced in this paper. This study employs two-dimensional simulation to investigate the distribution of current density and Joule heating in the flip chip joint. It is found that current crowding and Joule heat effect are very serious in the solder bump. The Joule heat may play important role in the void formation and thermo-migration in solder bump. And the factors that impact the distribution of current density and Joule heat are studied. The results show that the thickness of Al and UBM has great influence on the distribution of current density and Joule heat.

Introduction

Because of high I/O density, short interconnects, self-alignment better heat dissipation through the back of the die, smaller footprint, lower profile, and high throughput etc, flip chip has became one of the most attracting techniques in modern electronic packaging. Electro-migration (EM) in Flip chip solder joints is not considered as a serious concern simply because of their much larger dimensions and corresponding low current density. However, in the recent years, with the increase of electronic packaging density and the future miniaturization of the electronic products, the diameter of solder bump and the space between bumps are getting smaller. This results in the sustained growth of current density in the solder joints[1]. When the current density exceeding 10^4A/cm^2, EM will happen in the internal of solder joints, and at the same time a series of interconnect reliability problems appear[2-4]. So the EM of flip chip solder joints becomes an important reliability issue, especially owing to the effects of current crowding or Joule heat[5].

Flip chip interconnection structure consists of three parts, under bump metallization (UBM), solder bump and bond pad. The UBM formed on the Al pad on the chip usually has three layers of structure, Diffusion barrier/adhesive layer, wetting layer, ani-oxidation layer. The solder bump formed on the UBM will form interconnects with Cu pad which is plated with Ni/Au on the substrate. EM easily is originated in the interface of interconnection, UBM, solder bump and Pad[6]. The performance of EM has two aspects[5]: One is the dissolution of UBM metal thin film layer, and another is the enrichment of inter-metallic compounds (IMC) in the area of solder bump near the welding plate.

Theoretical analysis

EM is the phenomenon that metal atoms migrate in the direction of the electronic movement when conductive metal materials are under the large current density[7]. When the large current density through the interconnection solder joint, electrostatic field force drive electronics from cathode to anode. High speed electronics exchange impulse with metal atoms, and atomics are subjected to violent electrons impact which is called electronic wind F_{wd} in EM theory, Actually, the metal atom is also affected by electrostatic force F_{ei}, as shown in Fig.1:

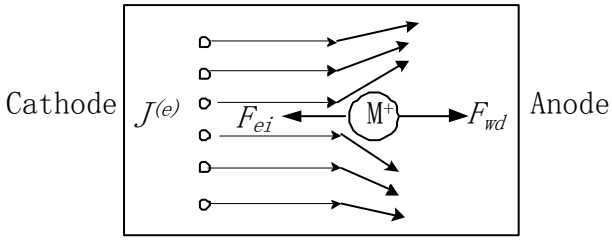


Fig.1 EM effect diagram

So the EM driving force can be represented by the formula:

$$F_{em} = F_{wd} + F_{ei} = Z^* e\rho j \tag{1}$$

$$Z^* = Z_{wd} + Z_{ei} \tag{2}$$

Where F_{wd} is electronic wind, F_{ei} is electrostatic field force, Z^*e is effective charge, ρ is Resistivity, j is current density, Z_{wd} is the effective charge constant of the electronic wind, Z_{ei} is the effective charge constant of electrostatic field force.

This results in the accumulation of atoms on the anode end and vacancies on the cathode end of flip chip interconnection. Such behavior can lead to hillock and void formation, which can become short and open failure, respectively[6].

Mean-time-to-failure usually is used to describe the failure introduced by EM, as described by Black’ s equation[8]:

$$MTTF = \frac{A}{j^n}\exp(\frac{Q}{kT}) \tag{3}$$

Where A is constant associated with conductive material, j is the current density, n is a model parameter for current density, Q is the active energy, k is the Boltzmann’s constant, and T is the average bump temperature.

Nevertheless, it is noticed that the predicted lifetimes did not match well with the measured ones, particularly under a higher current density[8]. As a result, it is suggested that the model should be modified to include the effect of current crowding and Joule heating. A modified Black’s equation was proposed by inserting a multiplying factor(c) of the current density and a temperature increment (ΔT) into Black’s equation[5,9]:

$$MTTF = A\frac{1}{(cj)^n}\exp\left[\frac{Q}{k(T+\Delta T)}\right] \tag{4}$$

In Eq.(4), if we keep both n and Q constant, we see that the effect of both c and ΔT is to reduce $MTTF$. Both of them should depend on the applied current density.

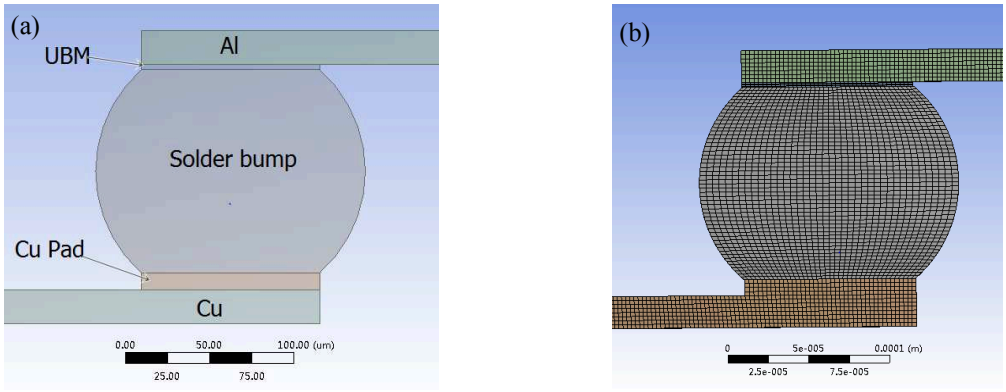
In this study, two-dimensional (2-D) simulation was carried out by finite element analysis to show the detailed current density and joule heat distribution in solder bump. This research provides a deeper understanding on the distribution of the current density and joule heat in the solder bump and the influence factors.

The finite element model

This study investigates current crowding and Joule heating in a single 2-D solder bump. The simplified 2-D model is established by ANSYS Workbench, the structure is shown in Fig.2 (a). To simplify the analysis, the UBM is treated as a single piece of nickel, and the inter-metallic compound (IMC) generated between solder bump and UBM and Cu pad during reflow soldering are all ignored. The total height is 173μm. The dimension of the Al trace is 20μm in thickness and 240μm in length, and the Cu line on the substrate side is also 20μm in thickness and 240μm in length. A simplified thin UBM structure of 3μm is adopted for the chip side and a Cu pad with the thickness of 10μm is

used on the substrate side. The material of solder bump is 63Sn37Pb with the height of 120μm and diameter of 160μm.

The parameters used in the present simulation are listed in table1. This is the basic structure for analysis. The structures used to analyze the influence factors are based on the structure to change. The finite element model is shown in Fig.2 (b). In order to improve the quality of the grid, increase the mesh density and make the simulation results and the actual situation closer, so the relevance is set to 100 and the method of map division is used in solder bump. When the results difference of the further improvement of the grid density is within 1%, the results will be convergent. The number of grid is about 9000 in this model.



(a) 2D model of solder joint (b) The finite element mesh

Fig.2 2D model and FEM net division of solder joint

TABLE 1.Parameters used in the two-dimensional current distribution simulation

Materials	Resistivity (μΩ-cm)	Thermal conductivity (W/m℃)	Dimensions （μm）
Al	2.74	238	20 thick
UBM	7	91	3 thick
63Sn37Pb	11	50	120 high, 160 wide
Cu	1.7	393	20 thick
Cu Pad	1.7	393	10 thick

Result and discussion

According to previous research[10], there is a very large current density change at the contact between the solder bump and the line. Since electric current will take the lowest resistance path, electrons will jam at the entrance into the solder bump, resulting in current crowding. Consequently, electro-migration damage in a flip chip solder joint occurs near the cathode contact on the chip side. The damage begins near the entrance point of the electric current, and propagates across the contact. So the research will be focused on the cathode of the solder bump.

The distribution of current density and Joule heat in flip chip joint. The design rule of packaging requires the each bump is going to carry 0.2 to 0.4 ampere[10]. So in this study, a current of 0.3 ampere is applied. We assume that the electric current flows from the bottom trace (Cu) to the top trace (Al) so that electrons flow in the opposite direction, and the simulated current density distribution is show in Fig.3 (a). As show, due to the special line-to-bump geometry of the flip chip solder joints, instead of flowing through the whole solder bump uniformly, the current flow is actually concentrated at the upper-right corner of the cathode of the solder bump, which is the entrance of the electron flow from the metal line to the solder bump, and the lower-left corner of the anode of solder bump. And the experimental results agree with the results in literature [10].

Fig.3 (b) features a typical vector plot of current densities on the solder bump. For solder bump, tilted current flows can be observed. Orientations of the current flows may correspond to the alignment of microstructures within the solder bump in an electro-migration scenario[11]. The current density along the line between A and B in Fig.3 (b) is plot in Fig.3 (c). Fig.3 (c) shows that the maximum current density in solder bump is about 5 times higher than the min current density in the middle of the solder bump. From the point of view of electro-migration failure, the solder bump could be the weak-link in the very-large-scale-integration of interconnects in a device due to the current crowding. It is proposed that this local high current density was responsible to the initial void formation due to flux divergence.

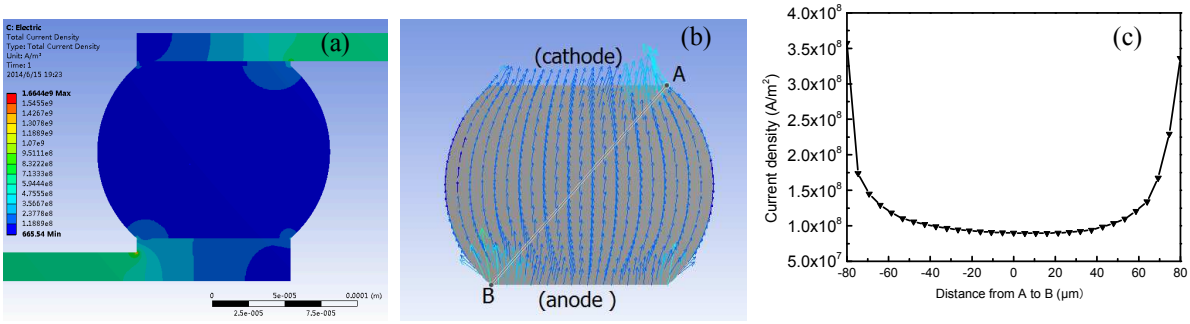


Fig.3 The distribution of current density in flip chip joint (a) the cloud picture of the distribution of current density. (b) The vector diagram of current density in solder bump. (c) the current density between A and B in (b)

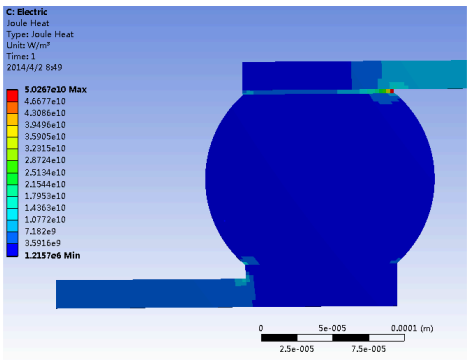


Fig.4 The distribution of Joule heat in flip chip joint

Joule heating effect is a phenomenon produced by current. Usually, the heating power, P, is described by the Joule heating relationship as[6]

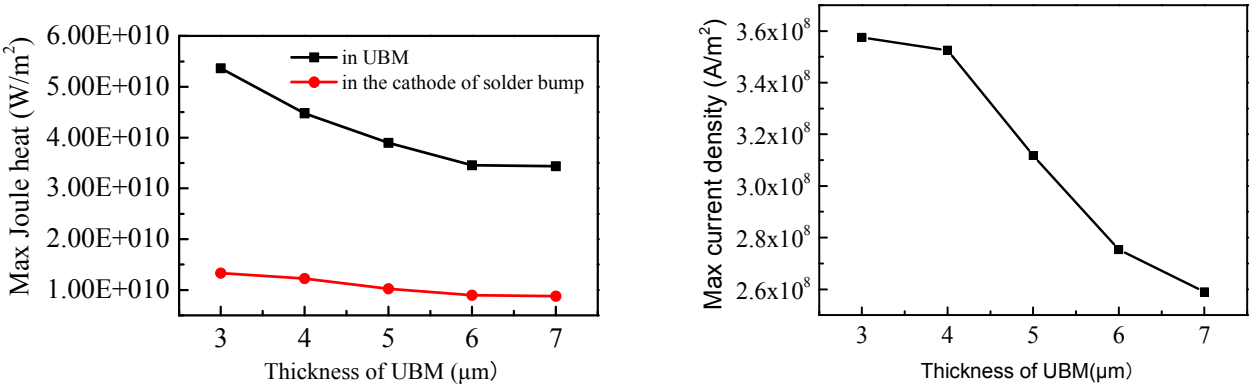
$$P = I^2 R = j^2 \rho V \tag{5}$$

I is the applied current, and $I/A=j$. where A is the cross-sectional area of the conductor, R is the resistance of the entire conductor and $R=\rho l/A$, l is the length of the conductor. Thus, $P=I^2R$ is the Joule heating per unit time of the entire conductor, and $j^2\rho$ is the Joule heating per unit volume per unit time of the conductor.

The Joule heat is proportional to the square of the current density. In our simulation model, the resistance of UBM is higher than the resistance of Cu, so the UBM generates most of the heat causing the side of the solder bump at the chip side to be hotter than that on the substrate side.

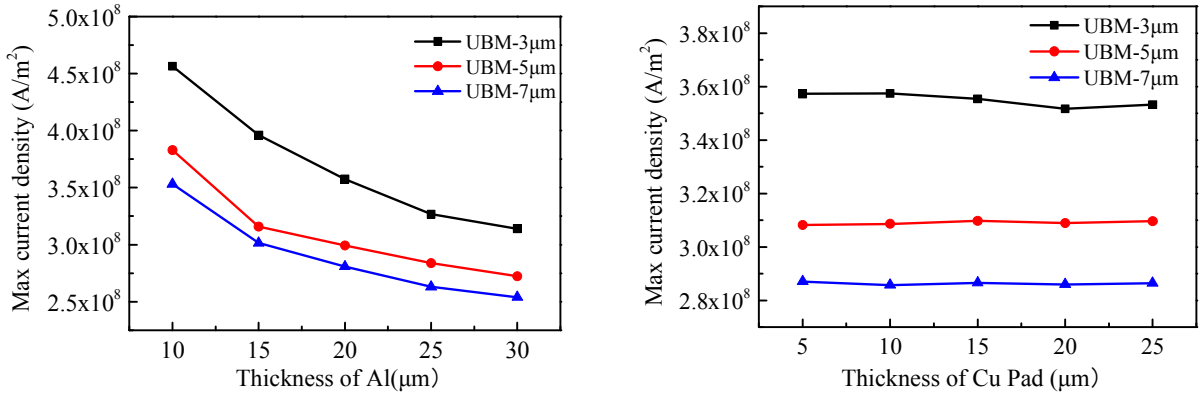
In the study of electro-migration in solder bump, due to the particularity of its structure, current will gather where the electrons flow into the solder bump, so the Joule heating effect is more significant. Finite element simulation shows that the distribution of the Joule heat is also uneven in electro-migration experiment, as shown in Fig.4. Comparing Fig.3 (a) and Fig.4, the distribution of Joule heat is also not uniform like the current density, the more serious the current crowding is, the more obvious the Joule heat is, and the maximum Joule heat generated at the UBM. In other parts Joule heat is more uniform.

Factors that affecting the Joule heat and current density in solder bump. In order to study the effect of the thickness of the UBM on EM, solder bumps with different thickness of the UBM are simulated under constant current, and the results show that the thickness of the UBM has a great influence on the size and distribution of current density and Joule heat. So with the increase of the thickness of the UBM, the biggest Joule heat in the UBM and the cathode of solder bump decreases gradually and finally tends to be constant. And the maximum current density in the cathode of solder bump decreases quickly, as shown in Fig.5 (b). So increasing the thickness of the UBM appropriately can effectively relieve the current crowding effect inside the solder bump and control EM.



(a) (b)

Fig.5 Max current density and max Joule heat changing with the thickness of UBM (a) maximum Joule heat in UBM and the cathode of solder bump changing with the thickness of UBM. (b) max current density in the cathode of solder bump changing with the thickness of UBM.



(a) (b)

Fig.6 The max current density in the cathode of solder bump changing with the thickness of Al and Cu Pad under different thickness of UBM. (a) max current density in the cathode of solder bump changing with the thickness of Al under different thickness of UBM. (b) max current density in the cathode of solder bump changing with the thickness of Cu Pad under different thickness of UBM

The effect that the thickness of Al affects the current density in the cathode of solder bump is also analyzed. Under different thickness of UBM, changing the thickness of Al shows that when the thickness of UBM is certain, with the increase of the thickness of Al, the maximum current density in the cathode of solder bump also decrease, and with the increase of the thickness of UBM, the tend of the decrease of the maximum current density decrease, as shown in Fig.6 (a). That is to say, the thicker the UBM is, the smaller the effect of the thickness of Al affecting the current density is. But changing the thickness of Cu Pad shows that the thickness of Cu Pad has little impact on the size of the maximum current density in the cathode of solder bump, as shown in Fig.6 (b).

Summary

In this study, the theory of atomic diffusion diving force is analyzed, such as electronic wind. Voids are generated in the cathode of the solder bump, so the current density in the cathode of the solder bump is analyzed emphatically. The simulation of current crowding and Joule heating includes the distribution of current density and Joule heat in solder bump and the factors that affect the distribution and size of current density and Joule heat, such as the thickness of UBM, Al and Cu pad. Finally, the regulars that these factors affect the current density and Joule heat are concluded. These results of simulation provide a basis for optimizing the structure of solder bump in producing reliable flip chip package in the process.

Acknowledgement

This work was financially supported by the Key Natural Science Foundation of the Jiangsu Higher Education Institutions of China (Grant No. 10KJA140043), “333 high level talents training project” in Jiangsu province, and the first “Enterprise Doctor Concentration Plan” of Jiangsu Province.

Reference

[1] H.M. TONG, LAI Y S, C.P. WONG. Advanced flip chip package. USA,2013.

[2] J. W. Nah, J. O. Suh, K, W. Paik. Effects of current density on electromigration-induced failure in flip chip composite solder joints at room temperature. IEEE Advanced Packaging Materials: Processes, Properties and Interfaces. (2005)50-53.

[3] Y. M. Lin, C. J. Zhan, J. Y. Juang. Electromigration in Ni/Sn Intermetallic Micro Bump Joint for 3D IC Chip Stacking. Electronic Components and Technology Conference, Lake Buena Vista, (2011)351-357.

[4] M.H. Lu, R. Rosenberg. Electromigration kinetics and critical current of Pb-free interconnects. Applied Physics Letters,(2014).

[5] Y.C. Chan, D. Yang. Failure mechanisms of solder interconnects under current stressing in advanced electronic packages . Progress in Materials Science. (2010)428-475.

[6] C. Chen, H. M. Tong, and K. N. Tu. Electromigration and Thermomigraion in Pb-Free Flip-Chip Solder Joints. Annual Review of Materials Research, (2010)531-555.

[7] B. Buszewski, E. Dziubakiewicz, M. Szumski. Electromigration Techniques. Springer, (2013).

[8] S. H. Chiu, S. W. Liang and C. Chen. Joule Heating Effect under Accelerated Electromigration in Flip-chip Solder Joints. Electronic Components and Technology Conference, San Diego, CA, (2006).

[8] W.J. Choi, E.C.C. Yeh, K.N. Tu. Mean-time-to-failure of flip chip solder joints on Cu/Ni(V)/Al thin-film under-bump-metallization. Journal of Applied Physics,94 (2003)5665-5671.

[9] K.N. Chiang, C.C. Lee, K.M. Chen. Current crowding-induced electromigration in $SnAg_{3.0}Cu_{0.5}$ microbumps. Applied Physics Letters,88 (2006)072102-1-3.

[10] S.W. Liang, T.L. Shao, and C. Chen. 3-D Simulation on Current Density Distribution in Flip-Chip Solder Joints with Thick Cu UBM under Current Stressing. Electronic Components and Technology Conference, Lake Buena Vista, (2005).

[11] Y. S. Lai, C.L. Kao. Characteristics of current crowding in flip-chip solder bumps. Microelectronics Reliability, (2006) 915-922.

Key Engineering Materials Vols 645-646 (2015) pp 325-329
© (2015) Trans Tech Publications, Switzerland
doi:10.4028/www.scientific.net/KEM.645-646.325

Submitted: 2014-11-26
Accepted: 2014-12-23

Effects of *n*-type dopants on electronic properties in 4H-SiC

Jinlong Tang *, Junnan Zhong, Cai Wen

School of Science, Southwest University of Science and Technology, Mianyang 621010, China

* jinlongtang@126.com

Keywords: 4H-SiC; impurity levels; density of states; electronic structures

Abstract. Based on first-principles calculations, we have investigated atomic and electronic structures of 4H-SiC crystal doped by N, P and As elements as n-type dopants. We have obtained the bond lengths of the optimization system, as well as the impurity levels, the band structure and the density of states. The results show that the higher impurity level above the Fermi level is observed when 4H-SiC doped by N with concentration as 6.25% in these dopants, and the band gap of 4H-SiC decreases while the doping concentration or the atomic number of dopant increases.

1 Intorduction

As large band gap semiconductor, 4H-SiC has received much attention for possible application in high power electronic devices as well as in high temperature and high pressure or high frequency instruments due to its stronger breakdown electric field and the advantages of high thermal conductivity and so on [1-3]. Recently, Hao Chen et. al. has growth homogeneous epitaxial to fabricate MESFETS [4, 5] with the whole structure on a substrate of 4H-SiC. Under different temperature, Zh. L. Liu has got many SiC thin films on 4H-SiC substrates by homogeneous epitaxial growing, and then, he has also analyzed the quality of these thin films structure and crystallization [6]. Ping Wang has investigated the electronic transport characteristics of multi-particle by monte cello method on 4H-SiC doped with N atoms, and he has found that 4H-SiC electronic transport properties are greatly influenced by the neutral impurity scattering; 4H-SiC electrons' mobility is small with anisotropy with the high doping concentrate under low temperature [7]. Xiao-wei Guo and others have examined the electronic structure of the 4H-SiC doped by N. Their study has shown that the energy band gap varies with the changing of doping concentration, and they have also found the reason from the electron density of states [8].

However, few researchers focus on n-type 4H-SiC semiconductor neither perform the system researches on V-type dopants in 4H-SiC. Hence, we perform a series study on n-type semiconductor of 4H-SiC doped by N, P and As elements. In the present paper, we study the atomic structure of 4H-SiC crystal with and without dopants. In addition, series models will be configured for 4H-SiC crystal by different concentration using supercell-methods. Finally, band structures and electronic quantum of states in a conduction band will be calculated for the influence of dopants in 4H-SiC.

2 Model and computational details

As well known, 4H-SiC is a typical wurtzite structure, which is belong to the hexagonal system with the P63mc space group (186), closely packed with 4 layer Si-C atoms. We configured the archetypal structure of 4H-SiC, and optimized it before investigating the doping system, using the geometry optimization technology of density functional theory (DFT) method [9,10]. In self-consistent total energy calculation under the framework of DFT by utilizing the Vanderbilt ultra soft-pseudo potential scheme[11], the valence of electrons is configured with $2s^2 2p^2$ for C and $3s^2 3p^2$ for Si in 4H-SiC, and $4s^2 4p^3$ for As, $2s^2 2p^3$ for N and $3s^2 3p^3$ for P in doping models. To expand the electron wave functions, the plane-wave basis set is with the cutoff energy of 25 Ry, which is sufficient to obtain well converged results in the present model. The effects of exchange and correlation are treated within the Local Density Approximation scheme [12,13]. For configuring 4H-SiC *n*-type doping, impurity atom replaces C atoms. Based on the supercell-model, three different size models have been employed by

using the configuration of 2 ×1×1, 2× 2×1 and 2×2×2 supercells for the different concentration of 4H-SiC *n*-type semiconductor structures.

3 Results and discussion

3.1 Atomic and electronic structure of intrinsic 4H-SiC. After our DFT geometry optimization calculating, the crystal cell constant of 4H-SiC structure is obtained as 3.041 Å for *a*, 9.952 Å for *c* respectively, which is in good agreement with experiment [14]. The reliable band structure and density of states of 4H-SiC crystal are also found similar to the report in Ref [15], as showed in Fig. 1. The maximum valence band exists at Γ point, while the bottom of the conduction band locates in different k points M, which reveals that 4H-SiC is indirect band gap semiconductor [see Fig. 1 (a)]. We found that the top of the valence band and the bottom of the conduction band is mainly composed form the states $3p^3$ (the solid line) of Si and atoms by decomposing the electron density of states as Fig. 1 (b-c) display.

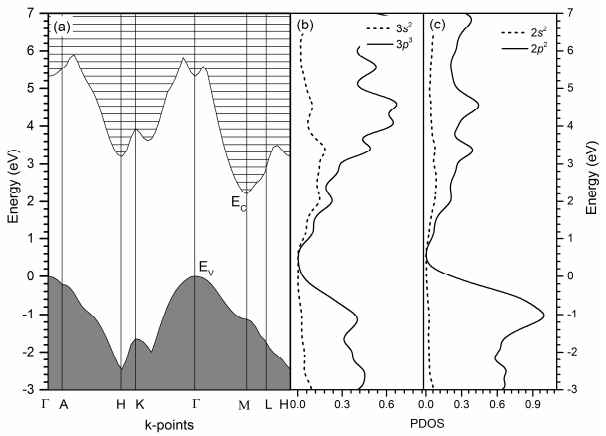


Fig. 1 Band structure (a) and PDOS (b for Si, c for C) of intrinsic 4H-SiC.

3.2 Atomic structure of doped 4H-SiC by *n*-type impurities. Doped 4H-SiC crystal model with *n*-type impurities is optimized as described in section 2. Our results shown that the length of R-Si bond will increases, when doped *n*-type elements concentration increases, as listed in Table 1. And these values are little big than the C-Si bond length of 1.871 Å in the 4H-SiC crystal without dopants. Interestingly, the length of R-Si increases as atomic number increases, for the size of atom growth.

Table 1. Optimized bond length of $Si_{1-x}R_xC$ (R=N, P, As; x=0.03125, 0.0625, 0.125) supper cell (Å)

x		3.125%	6.25%	12.5%
$Si_{1-x}N_xC$	N-Si1	1.902	1.960	1.973
	N-Si2	1.842	1.850	1.854
	N-Si3	1.897	1.897	1.902
	N-Si4	1.897	1.897	1.902
$Si_{1-x}P_xC$	P-Si1	2.136	2.148	2.157
	P-Si2	2.129	2.137	2.148
	P-Si3	2.128	2.137	2.142
	P-Si4	2.128	2.137	2.143
$Si_{1-x}As_xC$	As-Si1	2.194	2.201	2.227
	As-Si2	2.172	2.181	2.209
	As-Si3	2.172	2.181	2.182
	As-Si4	2.172	2.181	2.185

3.3 Band structure of doped 4H-SiC by *n*-type impurities. For the importance of energy levels near the energy gap of semiconductors, the energy band structures near the gap are investigated as shown in Fig. 2. And it gives the part of the energy curve near the Fermi level with doping concentration of 12.5% to analyze the changes in the band structure of the *n*-type doping. In this figure, it can be found that all doped *n*-type elements can lead to a donor level near the bottom of the conduction band (E_C), which means that the impurity level is a donor level. With the atomic number of impurities increases, the impurity level becomes more far away from the E_C. However, at the same

time, the impurity level of N, P, As doped system has crossed the Fermi level with a different degree. The impurity level fills with half full, which lead electrons will be transported to the conduction band easily.

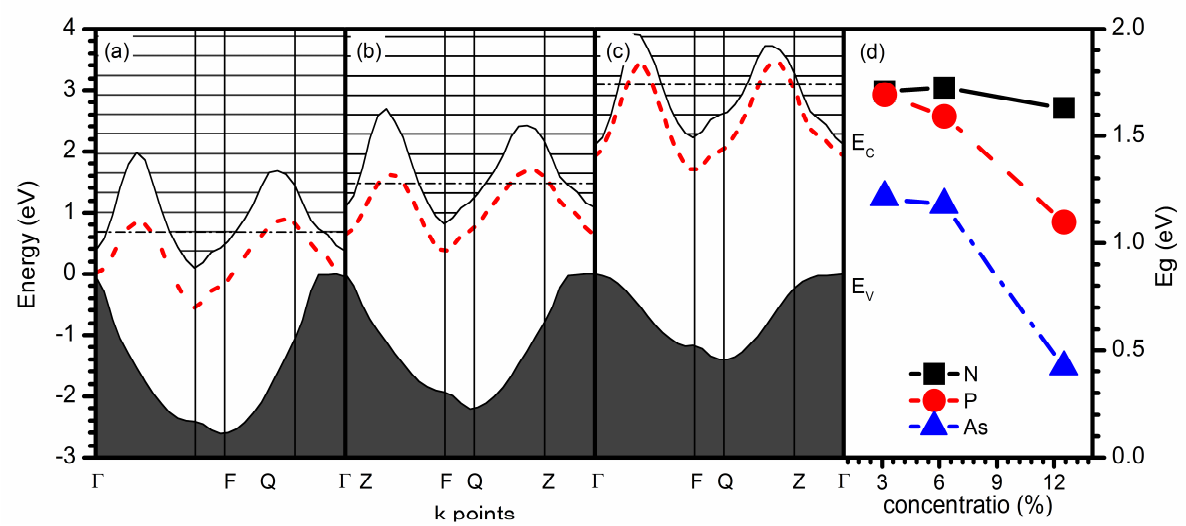


Fig. 2 Band structure of As (a), P (b), N (c) doped 4H-SiC by impurities of 12.5% , and Band gap of $Si_{1-x}R_xC$ (R=N, P, As; x=0.03125, 0.0625, 0.125)

To analyze the energy band gap (E_g) of *n*-type doped system change with doping concentrations increasing, energy gap (E_g) has been investigated as shown in Fig. 2 (d). Obviously, with the same kind of *n*-type impurity elements, E_g of doped 4H-SiC decreases, while the doping atom concentration increases. Under the same doping concentration, E_g decreases as the doping elements of atomic number increases. In addition, the change of E_g for doped 4H-SiC due to the movement of the conduction band and valence band to low-energy zone with different degrees.

3.4 Density of states for doped 4H-SiC by N type impurities. In order to reveal the E_g changes of 4H-SiC doped by *n*-type atoms, the density of states in the models has been systemic investigated (see Fig. 3). For simplifying the analysis, we focus on the impurity atoms with doping concentration by12.5%. Comparing with Fig. 1 and Fig. 3, we found that the contribution of Si atoms' 3*p* and C atoms' 2*s* states for the 4H-SiC in for E_C and E_V has been replaced by 2*p* and 2*s* states of N atoms, and Fermi level entered the conduction band, when one of C atoms in 4H-SiC was replaced by the given dopants. With the change of electronic states near the energy gap, E_g becomes smaller as shown in Fig. 2.(d).

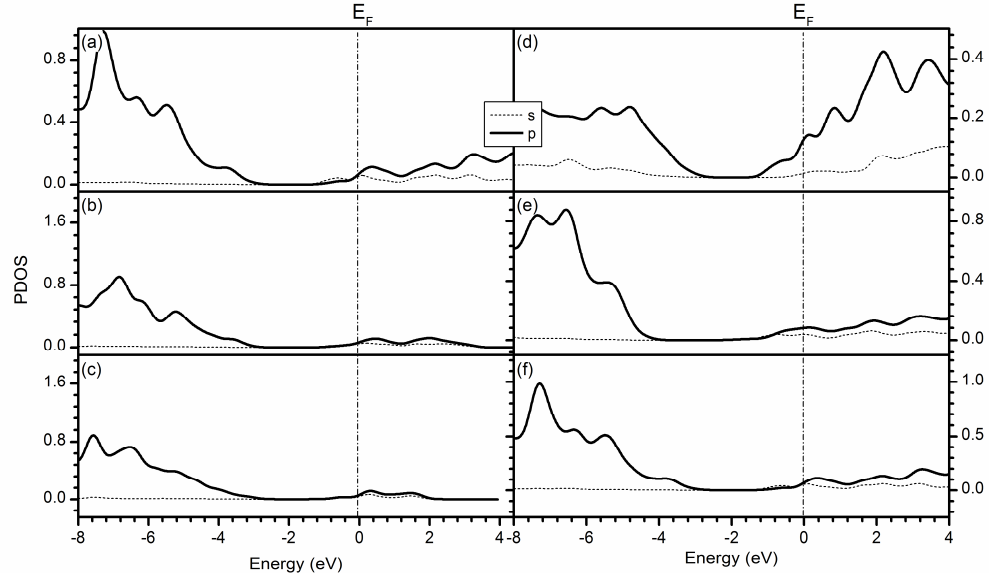


Fig. 3 PDOS of 4H-SiC doped by N atom with 12.5%, (a-c) for PDOS of Si, C, N atom respectively, as well as doped by 12.5% (d), 6.35% (e) and 3.125% (f).

As seen in Fig. 3, the electronic states of the impurity lead little change on the level of E_V, while the 2*p* states of the N atoms have influenced the level of E_C, which is important for electron transporting in semiconductors. The top of valence band has been below under Fermi level at 3.097 eV, 2.8619 eV and 2.7364 eV, with doping concentration is 12.5%, 6.25% and 3.125% respectively. These reveal that the doped 4H-SiC becomes more conductive with the increase of doping concentration. These phenomenons illustrate Eg change as shown in Fig. 2 (d). In the *n*-type doping, the degree of impurity level cross the Fermi level more than others with N by the concentration as 6.25%.

We also studied P and As atoms doping system, and the results show that the large atomic number means large atom size and weak bonding ability. Therefore, N atom can lead the larger change of doped 4H-SiC system compared to P and As atoms, as been shown in tables and figures given above.

4 Summary

To sum up, we have performed a comprehensive calculation of atomic and electronic structure for 4H-SiC with and without *n*-type dopants in the present research, using density functional theory method. It shows that 4H-SiC lattice constant increases as the concentration of *n*-type atoms increase; and the bond length increases with the growth of doping concentration or the doping atomic number. In addition, the impurity level of N, P and As atom in 4H-SiC is typical *n*-type; and the impurity level will be far away from the E_C under the increasing of atomic number with the same doping concentration. In the N atom doping situation for 4H-SiC, the impurity level will cross the Fermi level at the deepest level with the concentration of 6.25%.

Acknowledgement

This work has been supported by National Science Foundation of Young Scientists of China (11204250 and 11104226) and the Doctor Foundation of Southwest University of Science and Technology (08zx7116).

References

[1] W. Ching, Y.-N. Xu, P. Rulis, L. Ouyang, The electronic structure and spectroscopic properties of 3C, 2H, 4H, 6H, 15R and 21R polymorphs of SiC. Materials Science and Engineering: A 422 (2006) 147-156.

[2] E. Konstantinova, M. Bell, V. Anjos, Ab initio calculations of some electronic and elastic properties for SiC polytypes. Intermetallics 16 (2008) 1040-1042.

[3] H. Morkoc, S. Strite, G. Gao, M. Lin, B. Sverdlov, M. Burns, Large-band-gap SiC, III-V nitride, and II-VI ZnSe-based semiconductor device technologies. Journal of Applied Physics 76 (1994) 1363-1398.

[4] H. Chen, Q. Shang, J. Hao, G. Qi, Y. Huo, K. Yang, Device Development and MESFET Epitaxy Growth on Domestic 4H-SiC SI Substrate. Semiconductor Technology (in Chinese) 33 (2008) 1007-1010.

[5] A. Ellison, B. Magnusson, C. Hemmingsson, W. Magnusson, T. Iakimov, L. Storasta, A. Henry, N. Henelius, E. Janzén, in MRS Proceedings, vol. 640, pp. H1. 2.

[6] L. Zhong-liang, K. Chao-yang, T. Jun, X. Peng-shou, Homoepitaxial Growth of SiC Thin Film on 4H-SiC Substrate. Journal of Synthetic Crystals (in Chinese) 41 (2012) 106-109.

[7] P. Wang, Y. Yang, Y. T. Yang, H. Z. Qu, Z. D. Cui, J. X. Fu, An Ensemble Monte Carlo Study of Electron Transport in Nitrogen-Doped 4H-SiC. Acta Electronica Sinica (in Chinese) 8 (2005) 036.

[8] X. W. Guo, R. H. Luo, C. Zhang, X. L. Liu, G. Y. Chu, Y. F. Huo, The impact of doping nitrogen on the electronic structure of 4H-SiC. Laser Journal (in Chinese) 32 (2012) 20-22.

[9] B. G. Pfrommer, M. Côté, S. G. Louie, M. L. Cohen, Relaxation of crystals with the quasi-Newton method. Journal of Computational Physics 131 (1997) 233-240.

[10] P. Hohenberg, W. Kohn, Inhomogeneous electron gas. Physical review 136 (1964) B864.

[11] D. Vanderbilt, Soft self-consistent pseudopotentials in a generalized eigenvalue formalism. Physical Review B 41 (1990) 7892.

[12] D. M. Ceperley, B. Alder, Ground state of the electron gas by a stochastic method. Physical Review Letters 45 (1980) 566.

[13] J. P. Perdew, A. Zunger, Self-interaction correction to density-functional approximations for many-electron systems. Physical Review B 23 (1981) 5048.

[14] N. W. Thibault, Morphological and structural crystallography and optical properties of silicon carbide. (University of MICHIGAN, 1944).

[15]C. Park, B.-H. Cheong, K.-H. Lee, K. Chang, Structural and electronic properties of cubic, 2H, 4H, and 6H SiC. Physical Review B 49 (1994) 4485.

Key Engineering Materials Vols 645-646 (2015) pp 330-334
Submitted: 2014-11-07
© (2015) Trans Tech Publications, Switzerland
Accepted: 2014-12-23
doi:10.4028/www.scientific.net/KEM.645-646.330

Fabrication of Ultrasmooth Polymer Films by Concentration Control and Spin Speed Adjustment

Yan Guo[1,2,a], Weiguo Liu[1,b] *, Huan liu[2,c], Shun Zhou[1,d], Lei Wu[1,e], Fei Li[1,f],

[1]Micro-optoelectrical System Laboratory, Xi'an Technological University, Xi'an, Shaanxi, 710021, China

[2]Science and Technology on Low-light-level Night Vision Laboratory, Xi'an, Shaanxi, 710065, China

[a]gyfly_100@163.com, [b]wgliu@163.com, [c]liuhuan360@163.com, [d]zsemail@126.com,

[e]wulei5521@163.com, [f]lf15229369679@sohu.com

Keywords: Sacrificial Layer, Surface Roughness, Planarization

Abstract. In order to obtain ultrasmooth polymer films, in combination with sacrificial layer a variety of impending structures in MEMS devices can be easily prepared. Two methods using polymer concentration control and spin speed adjustment to planarize polymer surface are presented. The influence of polymer concentration and spin speed on the effect of photoresist planarization is studied on. Through a large number of experiments, optimized process parameters are collected. It is found that the roughness was reduced effectively when the spin high speed was 5000rpm for 50 seconds under the condition of volume dilution ratio of 1:5. This process is able to produce a smooth surface structure.

Introduction

Ultrasmooth polymer films are of great importance in a large body of technical fields, for instance, optical coatings, high reflectance waveguides, and Micro-electromechanical Systems (MEMS). Now MEMS devices are increasingly miniature and complicated. Many of them contain impending and movable mechanical structure such as cantilever beams, resonant beams and so on. To realize these structures, high aspect ratio processing and bulk processing are commonly used. However, those processing methods are complex, difficult to form a structure with a variety of materials (such as silicon and metals), and equipment is expensive. If the specific height and flatness of the hanging structure can be controlled via photoresist sacrificial layer simultaneously, it can greatly simplify the procedure, reduce costs, and improve process reliability. However, there are some dents and bumps often on the sacrificial layer surface. These defects will have adverse effect on the performance of a component so that cannot meet the requirements of surface roughness and flatness of some micro devices. Thus, in preparing the sacrificial layer, it is necessary to planarize it[1]. The sacrificial materials commonly used comprise photoresist, polyimide, and other organic polymer material, silica, porous silicon and some inorganic materials. Compared to the inorganic material, a sacrificial layer's preparation of the organic polymer material is relatively simple, low processing temperature, easy to achieve compatibility with the subsequent process.

As a kind of sacrificial layer material, photoresist plays a very important role in MEMS. Using photosensitive characteristics to transfer patterns and form a mask or sacrificial layer for various microstructures. Surface roughness of spin-coated photoresist films typically originates during processing steps. It is dependent on the experimental parameters used. However, when studying smoothing phenomena, the presence of the underlying substrate may be undesirable. Actually, correlated substrate roughness and contamination can complicate measurements. In general, polymer film smoothing mechanism is a very complicated process which affected by many factors[2]. This paper has described two planarizing methods, studied the main factors and optimized the process parameters.

Experiments

Theory and Methods. To obtain smooth surfaces, we use two ways which are capable of smoothing polymer surface: Concentration control and spin speed regulation. Spin coating method is a basic way of preparing liquid film, which is widely used in the semiconductor and microelectronics industries. Photoresist coating is a deposition process. Coating method commonly used of photoresist films is spin coating by a spin coater[3]. Its working principle is shown in Fig. 1.

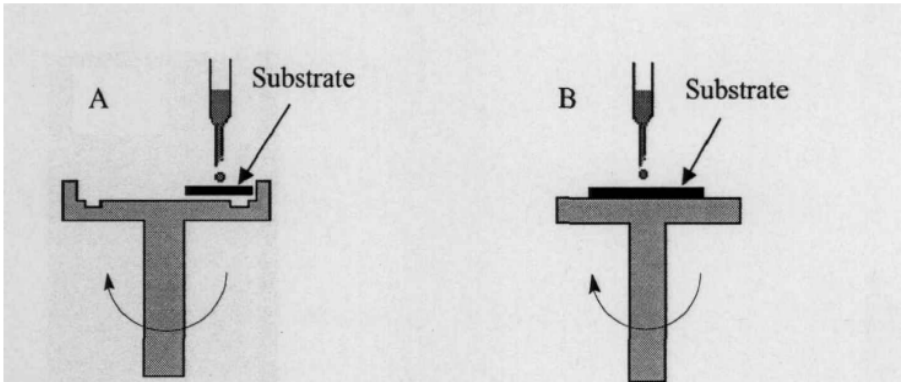


Fig. 1 Spin coating principle

A wafer substrate is disposed on the vacuum chuck which is connected to a spindle. The chuck can firmly suck the substrate. Make the liquid photoresist uniformly distribute on the surface of the component, the centrifugal force generated during the rotation drives the resist to spread to the entire surface and get rid of the excess photoresist, then the substrate will be covered with a uniform layer of photoresist[4]. For different kind of photoresists, the spin coating conditions are not same, need to select the appropriate coating conditions based on the photoresist properties. Spin coating is divided into two stages: The first is the low speed stage. In this stage, the rotation time can be adjusted in the range of 3 to 18 seconds so that photoresist is uniformly distributed throughout the substrate; the second is high speed stage. During this stage, the thickness of the photoresist film will be controlled by the spin speed which can be changed in the range of 1000 to 8000 rpm. Rotation time is adjustable within 10 to 60 seconds.

Photoresist is characterized by large viscosity and poor fluidity. After placed in the air for a long period of time, as the solvent evaporating, the photoresist will gradually become increasingly hard, the surface morphology of the film is not easy to change. The solvent of photoresist is capable of dissolving the polymer and photosensitizer, making them suspend in the liquid photoresist. PGMEA is a kind of solvent of positive photoresists. It has small viscosity, strong liquidity, and large surface tension. Diluted the photoresist with the solvent by a certain volume ratio, the concentration and viscosity of the resist will be reduced, but the film liquidity and the surface tension will increase, surface morphology of the film is easy to change.

Results and Discussion. Choose EPG533 type photoresist, diluted by PGMEA solvent with a certain volume ratio (set the photoresist's volume as 1) to reduce the concentration of photoresist. Change spin coating high speed, then conduct experiments to study the effects of concentration and spin coating speed on the roughness of the photoresist film simultaneously. Use the optical surfaces of polished quartz as the substrate, the initial root mean square roughness Rq is 1.7nm. Process parameters are as follows: Low speed of spin coating is 600rpm for 12 seconds. High speeds of spin coating are 2500, 3000, 3500, 4000, 4500, 5000, 5500, 6000(unit: rpm) for 50 seconds respectively. Then softbaking on a hot plate, the baking temperature is 105℃ for 10 minutes. Use white light interferometer Taylor Surf CCI2000 produced by Taylor Hobson Company to measure the surface roughness. Measurement procedures and parameters are as follows: 1. Adjust the position of the tested surface until the interference fringes appear. 2. Level the initial interferogram. 3. Set material radio range from 0.5% to 99.5%. 4. Select filter type as Gaussian filter, roughness surface: cut-off 0.08mm, waviness surface: cut surface edges. 5. Collect and record surface roughness Rq data. Experimental results are shown in Tab. 1 and Fig. 2.

Tab. 1 Relationship between roughness and concentration, spin speed

Spin speed [rpm]	Roughness of photoresist film of different dilution ratio[nm]					
	Undiluted	1:1	1:2	1:3	1:4	1:5
2500	1.47	1.18	3.19	1.84	1.55	1.24
3000	1.26	3.65	7.48	2.61	2.13	1.51
3500	5.09	6.42	3.90	1.75	1.33	1.79
4000	1.43	4.05	7.98	3.51	1.55	1.25
4500	1.73	1.51	5.06	2.09	1.55	1.09
5000	2.81	1.53	2.72	2.13	1.52	1.03
5500	1.63	1.73	2.29	2.21	2.00	1.07
6000	1.36	8.31	3.99	1.54	1.29	1.26

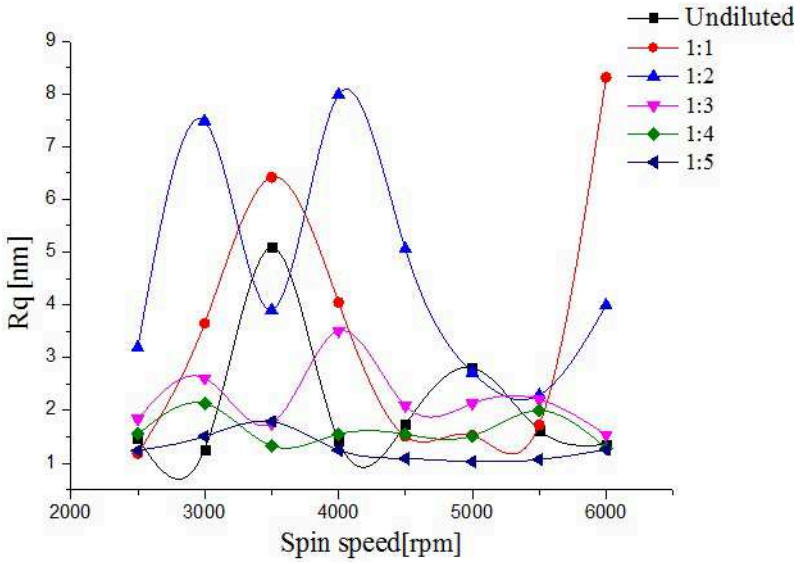


Fig. 2 Effect of spin speed and concentration on roughness

With the increase of the spin speed, the surface roughness of the photoresist hasn't a monotonously increasing or decreasing tendency, but fluctuation, the effect of spin coating speed on the surface roughness is not irregular. Since the spin coating is carried on in the air, rather than in vacuum environment, in the coating process, the substrate is at high speed rotation state, which will result in the surrounding air flow, the air also contains dust and particles which may contaminate the film and increase roughness. What's more, the centrifugal force generated during the spin coating throws redundant photoresist to the vessel wall and these droplets bounce back. These causal factors have an impact on the film roughness. This is why the roughness curves have larger fluctuation at some points. According to the overall trend of these curves, as the dilution ratio increasing and the concentration decreasing, the roughness is decreasing. The roughness curve is lowest in the dilution ratio of 1:5, and this curve has the minimum value in the high speed of 5000rpm. Meanwhile, in order to produce uniform and small film thickness and save time of subsequent process, the high speed of spin coating is set to 5000rpm for the time of 50 seconds.

On the basis of the above experiments, with the concentration of photoresist decreasing, the film surface roughness had declined under the condition of high concentrates. Now, continue to reduce the concentration of photoresist by increasing solvent proportion under the same conditions. Explore the relationship between the surface roughness and concentration at low concentrations. Experimental results are shown in Tab. 2 and Fig. 3.

Tab. 2 Relationship between roughness and concentration

Dilution ratio	1:6	1:7	1:8	1:9	1:10
Rq[nm]	1.06	1.11	1.14	1.19	1.16

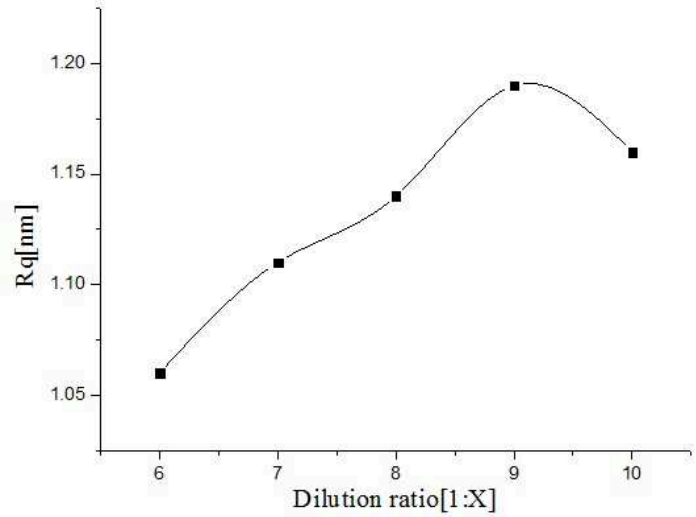


Fig. 3 Effect of concentration on roughness

As the solvent volume increasing, the concentration of mixed solution descended and the film thickness became more and more thin. Surface roughness of the film would exhibit an ascent tendency. The possible reason for this phenomenon is that the undiluted photoresist has greater viscosity, large film thickness and better quality, the formed film is not easily affected by surrounding environment, it can also planarize the rough surface of substrate and reduce surface roughness at the same time. As the solvent being added continuously, the surface roughness first decrease at high concentrations and then increases at low concentrations, it is closest to the minimum in the dilution ratio of 1:5 and 1:6. There are two reasons for the increase of the roughness. On one hand, because of the too small film thickness, the negative effect of surface defects of the underlying substrate on the film morphology may enhance. On the other hand, on account of low viscosity and enhanced liquidity, this film is vulnerable to the outside influence. Finally, the roughness of the polymer film would rise.

Summary

From all above, for the spin coating experiment, the concentration and spin coating speed have great impact on surface roughness and thickness of the photoresist film. These factors will exert a good or bad effect on roughness. Through a lot of experiments, smooth surface can be obtained on the conditions that the spin coating low speed is 600rpm for 12 seconds and high speed is 5000rpm for 50 seconds. Appropriate selection of the process parameters optimized by a large number of experiments can improve film surface morphology and reduce roughness. As an important application in the field of MEMS, planarizing technology of sacrificial layer can greatly simplify the process, reduce costs, and improve process reliability.

Acknowledgement

Thank my teachers for their attention and time to this research. Thanks for the laboratory and fund supporting from “High-end CNC machine tools and basic manufacturing equipment technology major projects” (2013ZX04006011), “Advanced manufacturing technology projects of General Armament Department” (51318020109), “Fund of the Key Laboratory of Science and Technology on Low-light-level Night Vision” (No.J20130203), “Shaanxi province science and technology innovation project” (2012KTCQ01-33). “Xi'an industrial technology innovation program” (CX12161).

References

[1] Ao Yugui, Photoresist Reflow Technology, J. Microelectronics. 22(6), 54-56 (1992).
[2] Zheng Jinhong, The development and application of Photoresist, J. Fine and Specialty Chamicals, 14(16) 24-30 (2006).
[3] Hong xiao, Introduction to Semiconductor Manufacturing Technology, 2nd ed., Electronic Industry Press, Beijing, 2013.
[4] Fu Yongqi, Zhao Jingli, Analysis on influence factors of film thickness uniformity of centrifugal coated, J. Optics and precision engineering, 4(2) 94-97 (1996).

Key Engineering Materials Vols 645-646 (2015) pp 335-340
© (2015) Trans Tech Publications, Switzerland
doi:10.4028/www.scientific.net/KEM.645-646.335

Submitted: 2014-11-05
Accepted: 2014-12-23

Nano-pore in C-S-H Gel Stability Analysis of Hardened Cement Pastes

Lang Wu[1,a], Na Xiong[2,b], Fangyan Yu[2,c]

[1] College of Architecture and Civil Engineering, Jiangxi Science and Normal University, Nanchang 330013

[2] College of Architecture and Civil Engineering, Nanchang Institute of Technology, Nanchang 330044

[a]wulang19812005@126.com, [b]289610964@qq.com, [c]45336603@qq.com

Keywords: cement hydration; capillary pore; stability analysis

Abstract: Based on capillary tension, surface free energy and elasticity theory, a collapse model of nano-pore in C-S-H gel was created in hardened cement pastes. The stability of pore was analyzed by Gibbs free energy theory. The results show that, the capillary is more stable while the capillary is grater and rounder in the case of the aperture changing in the nanometer scope. When the aperture is changing in the scope of micrometer, the collapse possibility of the capillary is tiny. If the capillary size is fixed, the capillary is more stable while the elastic modulus of hydrated products is higher.

1 Introduction

Macroscopic properties of cement-based materials mainly depends on the compositions and their structural characteristics at their micro-level, inquiring into the pore structure evolution of hardening cement paste from the micro perspective is one of the research focus at home and abroad in recent years[1]. The hardening cement paste is generally composed of unhydrated cement particles, C-S-H gel, portlandite and capillary holes, and its microstructure changed due to the chemical composition of cement, water-cement ratio and admixture. Abroad, the study of Gao Peiwei, etc.[2]found that adequate dosage of phosphorus slag powder can increase the content of C-S-H gel, reducing the formation of harmful micro-holes (the aperture is greater than 100nm), thereby improving the microstructure and durability of cement paste. Studies of Pietro, etc.[3] have shown that lowering the relative humidity will promote the formation of pores hole, thus affecting the microstructure of cement paste, reducing the durability of concrete. Through the MIP method and BSE observation, S.Igarashi[4]found that with the hydration reaction, big pores under the condition of low water cement ratio will be divided into a plurality of small holes, and the small pores disappear gradually, and big pores under the condition of high water cement ratio remain in the cement slurry, thus resulting in lower strength. Zhang Guofang, etc.[5] has studied the incorporation of vinyl redispersible polymer (VRP) effects on cement hydration products, and the results show that the VRP can significantly delay the formation of C-S-H gel and affect its structure.

The above are test observations mostly based on the cement paste internal pore structure during the hydration process. The observation results obtained that along with the proceeding of hydration reaction, hydration products piled up and squeezed around capillary hole, so that the hole volume decreases, and the paste volume contraction. At the same time, researchers[6]observed in the early drying cycle process, found the capillary holes of hydration products without the cement paste disappeared, but they failed to make further analysis on why it disappeared, so we speculate that due to the low density and elastic modulus of external hydration product, the pores hole occur instability collapse and disappear. Since the collapse of pores hole will cause shrinkage of cement

paste, and thus the purpose of this study is to explore the mechanism of capillary hole collapse, which has important theoretical significance for further study on the shrinkage mechanism of cement paste.

Figure.1 shows microscopic images of cement paste in hydration process under a scanning electron microscope. Needed for analysis, it is simplified to the model shown in Figure.2, the red part represents unhydrated cement particles, the yellow areas indicate the hydration products, the blue area indicates capillary.

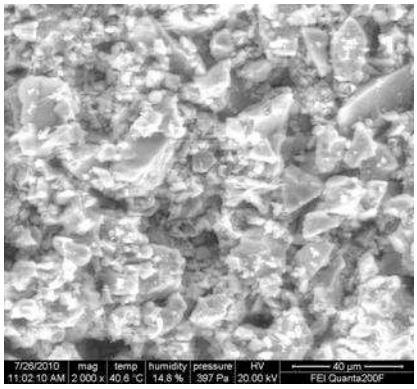


Fig. 1. Cement hydration ESEM photo(2000×)

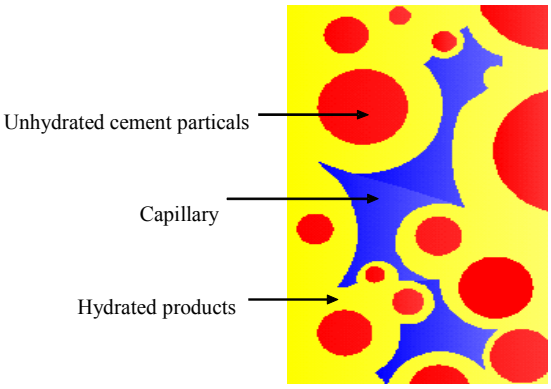


Fig. 2. 2D cement hydration model

2 Elasticity Solution to Infinite Objects with a Elliptical Pore.

To simplify the calculation, we assuming that capillary pores for the elliptical shape, surrounded by an infinite elastic body C-S-H gel, and the pore is filled with water, the liquid surface radius r, the contact angle of liquid surface is the upper tiny area without water, shown in Fig.3. Thus the whole pores suffer negative pressure, and it is simplified to a uniformly distributed load q, so that the problem will be converted into a 2D plane strain case of capillary instability, mechanical model as shown in Figure.4,elliptic pore of an infinite elastic plane containing long and short axis a and b, the surrounding of pores effect the uniform distributed load q, by the conformal mapping function.

Mapping z planar elliptical pore to the central unit circle of the ζ plane, in which $\zeta = \xi + i\eta$, as shown in Figure 4, can be used as:

$$R = \frac{a+b}{2}, m = \frac{a-b}{a+b} \tag{1}$$

The surface force component is,

$$\begin{cases} \overline{f_x} = q(N,x) = lq \\ \overline{f_y} = q(N,y) = mq \end{cases} \tag{2}$$

So, the surface force vector is:

$$\overline{f_x} + i\overline{f_y} = q(l + im) \tag{3}$$

As the surface force is balance state($\overline{F_x} = \overline{F_y} = 0$),And only when the orifice suffer from surface force, the surface force far from the orifice tends to zero, scilicet $B = B' = C' = 0$,then f_0 can be expressed as:

$$f_0 = i\int \left(\overline{f_x} + i\overline{f_y}\right)ds = q\int dz = qz = qR(\frac{1}{\zeta} + m\zeta) \tag{4}$$

On the border with $\rho = 1$,thus $\zeta = \rho e^{i\theta} = e^{i\theta}$,Reference mark $\sigma = e^{i\theta}$，then equation(4) can converted into:

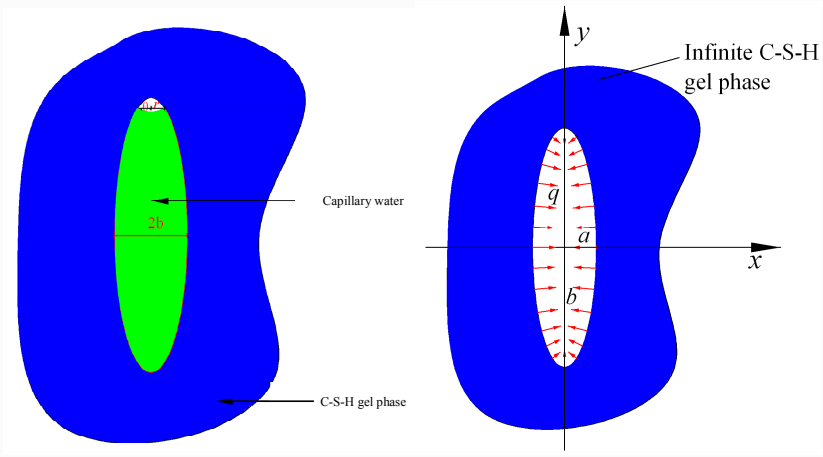


Fig. 3 Capillary pores model in the water saturation condition

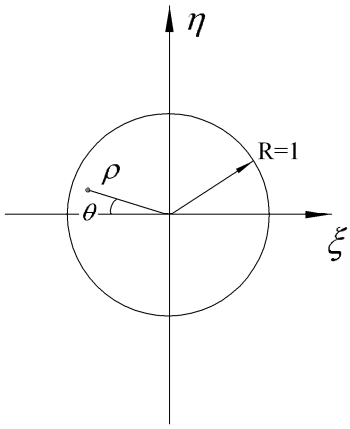


Fig.4 Mechanics model of capillary pores

$$f_0 = qR(\frac{1}{\sigma} + m\sigma) \tag{5}$$

Thus ,function $\varphi_0(\zeta)$, $\psi_0(\zeta)$ can be expressed as,

$$\begin{cases} \varphi_0(\zeta) = \dfrac{1}{2\pi i}\int_\sigma \dfrac{f_0 d\sigma}{\sigma - \zeta} = \varphi(\zeta) = qRm\zeta \\ \psi_0(\zeta) = \psi(\zeta) = qR(1+m^2)\dfrac{\zeta}{1-m\zeta^2} \end{cases} \tag{6}$$

Pay attention to $\overline{\zeta} = \rho^2/\zeta$, then equation (6) can be obtained,

$$\begin{cases} \varphi'(\zeta) = qRm \\ \psi'(\zeta) = qR(1+m^2)\dfrac{1+2m\zeta^2}{(1-m\zeta^2)^2} \end{cases} \tag{7}$$

So,

$$\begin{cases} \Phi(\zeta) = \dfrac{\varphi'(\zeta)}{\omega'(\zeta)} = -\dfrac{qm\zeta^2}{1-m\zeta^2} \\ \Psi(\zeta) = \dfrac{\psi'(\zeta)}{\omega'(\zeta)} = -\dfrac{qm(1+m^2)\zeta^2(1+2m\zeta^2)}{(1-m\zeta^2)^3} \end{cases} \tag{8}$$

3 Stability Analysis of Nanopore in C-S-H gel in the Two-dimensional Water Saturation Condition

free energy of systematic Gibbs can be represented as,

$$G = U + W + \gamma L + qS \tag{9}$$

In the equation: U represented as matrix deformation energy, $U = \frac{1}{2}\int_{\partial u} \underline{t}\underline{u}ds = \frac{1}{2}\int \sigma\varepsilon dV$, W represented as potential energy of pore surface force, $W = -\int_{\partial u} \underline{t}\underline{u}ds = -\int \sigma\varepsilon dV$, γL represented as Pore surface free energy, qS represented as pore compression potential energy.

In the equation: $\underline{t}$, $\underline{u}$ are displacement vector and the surface force vector on the boundary, γ represented as water's surface free energy ,L represented as the elliptical ring volume of unit thickness, S represented as the elliptic cylinder volume of unit thickness.

$$U + W = \frac{1}{2}\int \sigma\varepsilon dV - \int \sigma\varepsilon ds = -\frac{1}{2}\int \mathrm{Re}[(\overline{f_x} - i\overline{f_y})(u_x + iu_y)]ds \tag{10}$$

$$\frac{E}{1+\mu}(u_x+iu_y)=\frac{3-\mu}{1+\mu}\varphi(\zeta)-\frac{\omega(\zeta)}{\overline{\omega'(\zeta)}}\overline{\varphi'(\zeta)}-\overline{\psi(\zeta)} \tag{11}$$

$$\left(\overline{f_x}-i\overline{f_y}\right)ds=q(l-im)dsiq(dx-idy)=iqd\bar{z} \tag{12}$$

Among them $\bar{z}=\overline{\omega(\zeta)}$,put equation (7)(8) into equation (11)(12),and pay attention to the boundary conditions $\rho=1$,and work out,

$$\mathrm{Re}(\overline{f_x}-i\overline{f_y})(u_x+iu_y)=\frac{q^2R^2(1+\mu)}{E}\times\left\{\begin{matrix}(\mu-3)(m^2-m\sin 2\theta)+(m^3-m^2)\sin 2\theta\\-2m^2+m^2\sin 4\theta+(1+m^2)(m^2\sin 2\theta-m)\end{matrix}\right\} \tag{13}$$

As $R=\dfrac{a}{1+m}$， then equation (10) can be converted into

$$U+W=\frac{q^2b^2(1+\mu)\pi}{E}\left[\frac{(3-\mu)m^2}{(1+m)^2}+\frac{m}{2}\right] \tag{14}$$

the perimeter equation of ellipse is:

$$L=4a\int_0^{\frac{\pi}{2}}\sqrt{1-e^2\sin^2 t}\,dt \tag{15}$$

Where e is the elliptical eccentricity, $e=\dfrac{c}{a}=\dfrac{\sqrt{a^2-b^2}}{a}$,Taylor expansion the formula, and neglecting the higher-order terms, get an approximate perimeter equation of ellipse:

$$L=\pi(a+b)\left(1+\frac{m^2}{4}+\frac{m^4}{64}\right)=\frac{2\pi a}{1+m}\left(1+\frac{m^2}{4}+\frac{m^4}{64}\right) \tag{16}$$

Then equation (10) further converted into:

$$G=\frac{q^2a^2(1+\mu)\pi}{E}\left[\frac{(3-\mu)m^2}{(1+m)^2}+\frac{m}{2}\right]+\frac{2\pi\gamma a}{1+m}\left(1+\frac{m^2}{4}+\frac{m^4}{64}\right)+\frac{q\pi a^2(1-m)}{1+m} \tag{17}$$

The function G (m, a) is about the shape parameter a and m on a binary function.

4 Parametric Analysis

As shown in Figure.3, assume that the diameter of pore water level is r, make $k=b/r$, According to the reference [7],obtain that capillary tension of liquid surface q is

$$q=\frac{2\gamma}{r\cos\theta}=\frac{2k\gamma}{r\cos\theta}(1<k<1000) \tag{18}$$

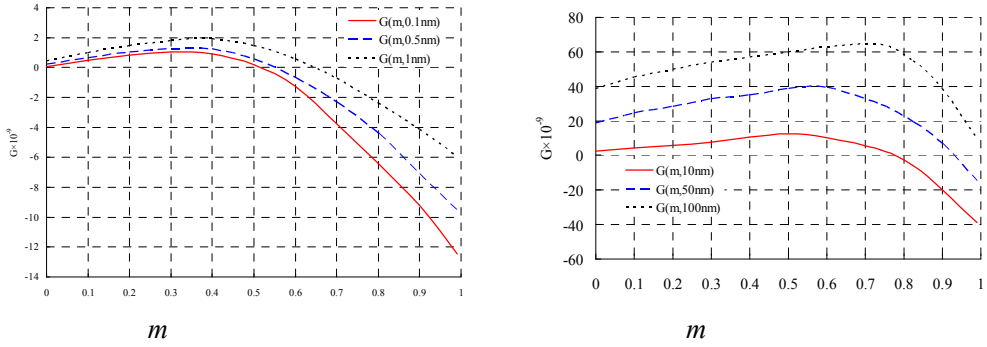
According to the reference[8], modulus of elasticity for water products E=22.4GPa, $\gamma=72.28mN/m$, $\mu=0.3$, k =100(that is the pore water tends to saturated state),the range of θ is ($4.7^0\le\theta\le13.4^0$),in order to simplify the calculation, here we take $\theta=10^0$.

4.1 Evolution of Gibbs free energy with the long axis *a*

Separately take a=0.1nm,0.5nm，1nm，10nm，50nm，100nm,the changeable curve of Gibbs free energy in pores making curve with the shape parameter m (0 <m <1) is shown in Figure.5.

Seen from Figure 5, G (m, a) free energy curve is divided into up and down segments. In the rising segments, G (m, a) free energy curve is stable, but over the extreme point, G (m, a) is unstable and pores prone to instability collapse. When a = 0.1nm,0.5nm,1nm,10nm,50nm,100nm, G(m, a) obtain the maximum value corresponding to the m values were 0.3,0.35,0.4,0.5,0.6, 0.7.When aperture increases within a certain range, the shape parameter m which is most prone to instability collapse also increased. That is, the aperture is larger, the less it is prone to collapse. This

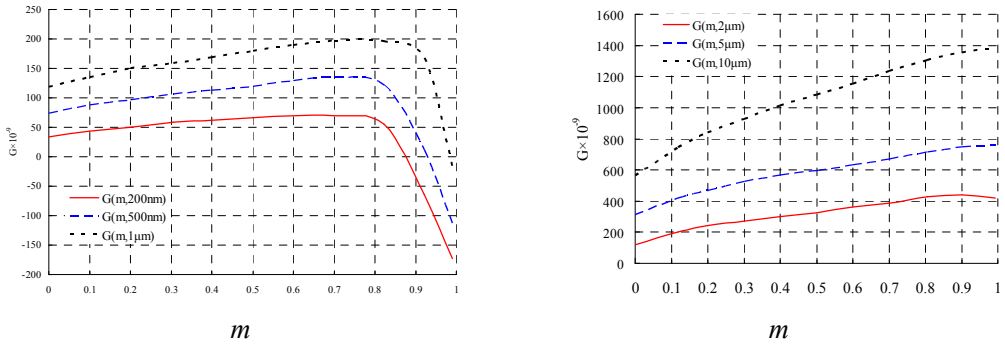
is because the collapse mechanism of pores in certain aperture is associated with a and m, the smaller the pores, the smaller the water's surface free energy and the water potential of pores, when a <0.1nm, the size of the surface free energy and the water potential can be negligible, then the Gibbs free energy is dominant. With the increase of aperture, its collapse shape transferred from round to crack shape gradually.



(a) (a=0.1nm，0.5nm，1nm) (b) (a=10nm，50nm，100nm)

Fig. 5 Evolution of $G(m,a)$ with the parameter m

Then separately take a=200nm,500nm,1μm,2μm,5μm,10μm,the changeable curve of Gibbs free energy in pores making curve with the shape parameter m (0 <m <1) is shown in Figure.6.



(a) (a=200nm，500nm，1μm) (b) (a=2μm，5μm，10μm)

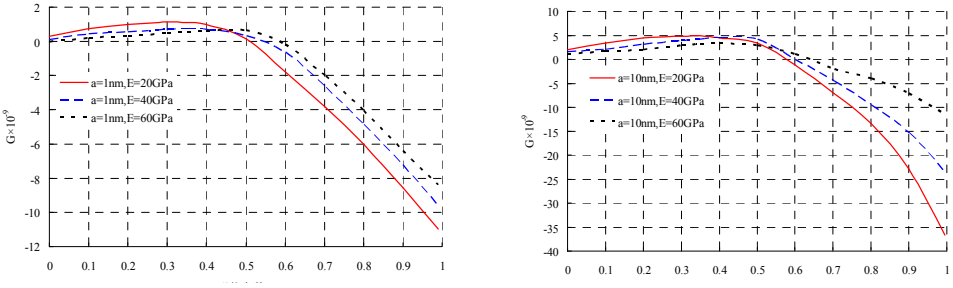
Fig. 6 Evolution of $G(m,a)$ with the parameter m

Seen from Figure 6,when a increase to more than 100 nm, the parameter collapse shape increases to more than 0.8,and after a increases to μm magnitude, as the surface free energy of water increases, the Gibbs free energy is relatively small, it requires large energy to make the pores collapse, its shape parameter is close to 1,that is the state of crack. After pores enlarge entering μm magnitude, the possibility of its collapse is very small.

4.2 Evolution of Gibbs free energy with hydration products elastic modulus *E*

During the hydration process, the hydration products elastic modulus would increase with the hydration degree increase, respectively take E as 20GPa, 40GPa, 60GPa, the changeable curve of G versus m in case of a=1nm and 10nm, as shown in figure.7.

Seen from Figure.7,when a=1nm，E=20Gpa, 40Gpa, 60GPa,$G(m, a)$ *o*btain maximum value corresponding to the value of m are 0.3,0.35,0.4.When a=10nm，E=20Gpa, 40GPa，60GPa，$G(m，a)$ *o*btain maximum value corresponding to the value of m are 0.4,0.45,0.5.That is, when aperture is certain, the greater the hydration products of the elastic modulus, the more difficult to collapse. This is because the increase of hydration products elastic modulus will decreased the Gibbs free energy of pores, and the free energy of the water surface and pore water potential has not changed.



(a) (a=1nm) (b) (a=10nm)

Fig. 7 Evolution of $G(m,a)$ with different elastic modulus

5 Summary

(1) When aperture increases in a certain range (nm level), the shape parameter m of the most prone to instability collapse is also increased. That is, the larger the pores are, the less it is prone to collapse, after the pores increase to μm magnitude, and its collapse is unlikely.

(2) When the aperture is certain, increase the elastic modulus of the hydration products will reduce the Gibbs free energy of pores , but can not change the water's surface free energy and the potential energy of the pore water, the greater the elasticity modulus of hydration products pores are, the less the pores prone to collapse.

Acknowledgments

This research was supported by Jiangxi Province Science and Technology Project(20143BBM26112) and Youth Scientist Foundation of Jiangxi Educational Committee (GJJ13556), Jiangxi science and Technology Normal University Key Laboratory (breeding research base), which is gratefully acknowledged.

References

[1] Wu L, Song G Q, Lei B. Elastic modulus prediction of hardened cement paste[J]. Journal of Building Materials,2011,11(6):819-823.

[2] GAO P W, Lu X L, Yang C X, etal. Microstructure and pore structure of concrete mixed with superfine phosphorous slag and superplasticizer[J]. Construction and Building Materials, 2008, 22 (5): 837-840.

[3] LURA P, JENSEN O.M, BREUGEL K.V. Autogenous shrinkage in high-performance cement paste: An evaluation of basic mechanisms[J]. Cement and Concrete Research, 2003, 33(2): 223-232.

[4] IGARASHI S, KAWAMURA M, WATANABE A. Analysis of cement pastes and mortars by a combination of backscatter-based SEM image analysis and calculations based on the Powers model [J].Cement and Concrete Composites 2004,26(8) :977-985.

[5] ZHANG G F , WANG P M. Effects of Vinyl Redispersible Polymer on Cement Hydration Products[J]. Journal of building materials,2010,13(2):143-149.

[6] JENNINGS H.M, THOMAS J, GEVREBIV J.S, etal. A multi-technique investigation of the nanoporosity of cement paste [J]. Cement and Concrete Research,2007,37 (3) :329-336.

[7] PICHLER C, LACKNER R, MANG H.A. A multiscale micromechanics model for the autogenous- shrinkage deformation of early-age cement-based materials [J]. Engineering Fracture Mechanics,2007,74 (2) : 34-58.

[8] BERNARD O, ULM F.J, LEMARCHAND E. A multiscale micromechanics-hydration model for the early-age elastic properties of cement-based materials [J]. Cement and Concrete Research, 2003, 33 (9): 1293-1309.

Key Engineering Materials Vols 645-646 (2015) pp 341-346
© (2015) Trans Tech Publications, Switzerland
doi:10.4028/www.scientific.net/KEM.645-646.341

Submitted: 2014-11-03
Accepted: 2014-12-23

Simulation and typical application of multi-step diffusion method for MEMS device layers

Lingyun Wang[1, a], Ruhai Zhou[1], Yifang Liu[1], Cheng Zheng[1], Jianfa Cai[1], Yong He[1]

[1]Dept. of Mechanical and Electrical Engineering, Xiamen Univ., Xiamen, China

[a]email: wangly@xmu.edu.cn (corresponding author)

Keywords: heavily boron doped layers; multi-step diffusion method; boron etch-stop technique

Abstract

In MEMS device, heavily boron doped layers are widely used as structural layers. For the manufacture of the thick heavily boron doped layer (boron concentration $\geq 5\times10^{19}$ cm^{-3}), conventional two-step method exposes disadvantages of low efficiency and high energy consumption. Hence, multi-step method is introduced to improve the energy efficiency. In our study, simulation of diffusion in silicon is carried out to compare multi-step method with conventional method. The simulation reveals that multi-step method obtains more quantity of boron dopants and shows better potential to fabricate thick heavily boron doped layers, compared to conventional method within the same total diffusion time. As a typical application of the multi-step method, a butterfly-shape resonant is fabricated.

Introduction

In MEMS device, heavily boron doped layers are widely used as structural layers in many applications, such as pressure sensor resonator, conductive diaphragm, AFM probe tips and optical switches [1-3]. Using a common alkaline etchant, solution of KOH, single-crystal silicon layers having boron concentration greater than 5×10^{19} cm^{-3}(p++ silicon), shows a significant lower etching rate as compared to undoped silicon[4]. This unique etch-stop property of p++ silicon makes it possible to fabricate silicon films with designed shape and thickness by controlling the boron doping in silicon [4].

The universal method in thermal diffusion process is two-step diffusion, in which pre-deposition and driven-in are performed only once. To get a thicker heavily boron-doped layer, the conventional solution is to either elevate diffusion temperature or elongate diffusion duration. This will obviously lead to high energy consumption and low efficiency. In addition, it is well known that borosilicate glass layer, as byproduct of boron pre-deposition, must be removed before follow-up process. However, longer pre-diffusion duration will make the borosilicate glass layer become very compact and finally difficult to be removed, which is the obvious obstacle for fabricating heavily boron doped layer with complex architecture.

In order to overcome the shortcomings in conventional two-step diffusion method, multi-step diffusion method is introduced in our previous work [6]. As illustrated in Fig. 1, multi-step diffusion process divides conventional two-step diffusion process into several periods, while the total diffusion time is kept the same. Each period includes relatively short pre-deposition and drive-in. According to Fick's law, the current density is proportional to dopant concentration gradient. During the initial stage of pre-deposition, current density is large that a great quantity of boron dopants can easily swarm into silicon substrate, due to sheer concentration gradient. Then it falls with the proceeding of pre-deposition, because the gradual increase of dopant concentration near the surface drops the gradient between the boron source and the silicon substrate. Hence, it is meaningful to cut a long pre-deposition into several relatively short pre-deposition followed by short driven-in.

In our study, diffusion simulation of boron in silicon is carried out in Athena to compare multi-step method with conventional two-step method. Then, a butterfly-shape structure is fabricated successfully based on multi-step diffusion method.

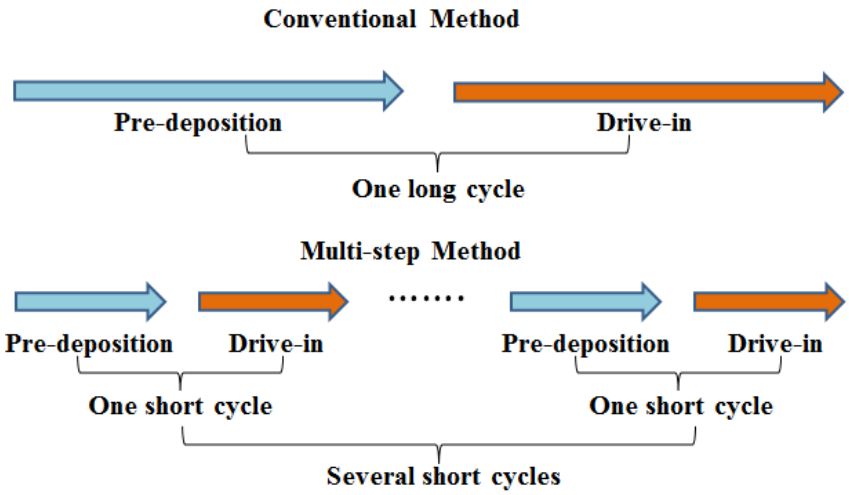


Fig. 1 Schematic diagram of multi-step method vs conventional method

Simulation of multi-step method and conventional two-step method

Athena provided by Silvaco TCAD is a convenient platform for simulation processes in semiconductor industry, such as diffusion and ion implantation. In order to compare multi-step method with conventional two-step method, diffusion simulation is done to estimate the profile of boron concentration. Although simulation is not expected to provide the precise profile of boron concentration, the trend it provides is absolutely correct. Following our process carried out in 4470 tube furnace, the simulation parameters are set to be accordance with experiment. This means the temperature in pre-deposition and drive-in were both set to be 1100 °C both in conventional diffusion process and multi-step diffusion process. In multi-step diffusion simulation, four diffusion periods were performed. Each diffusion period includes 4 h pre-deposition and 8 h drive-in. While in conventional diffusion simulation, only one diffusion period was executed including 16 h pre-deposition and 32 h drive-in. The silicon used is a p-type silicon oriented in <100> with resistivity about 2 Ω•cm. The main diffusion simulation parameters are shown in Tab 1.

Tab 1 Thermal diffusion parameters

Diffusion Method	Substrate	Dopant Concentration in Atmosphere[cm^{-3}]	Pre-deposition Temperature[℃]	Drive-in termerature[℃]	Number of periods	Pre-deposition time[h]	Driv-in time[h]
Multi-step Method	P-type Silicon	5×10^{21}	1100	1100	4	4	8
Conven-tional Method	P-type Silicon	5×10^{21}	1100	1100	1	16	32

In general, the profile of boron concentration in multi-step diffusion process is higher than that in conventional diffusion process under same total diffusion time, as presented in Fig. 3. The starting concentration in multi-step diffusion is 5.6×10^{19} cm^{-3}, while the starting concentration in conventional diffusion only reaches the value of 1.1×10^{19} cm^{-3}. And the two curves intersect at the depth of 11.6 μm with concentration of 6.5×10^{19} cm^{-3}. The highest concentration in multi-step diffusion is 1.6×10^{20} cm^{-3}, however that in conventional diffusion is only $8.8\times10^{19}cm^{-3}$. Moreover, profile of multi-step diffusion has a depth of 8.75 μm with boron concentration more than 1×10^{20} cm^{-3}. By calculating integration of the curves, it is found that the total dopant attained in multi-step process is 52% more than that in conventional two-step process.

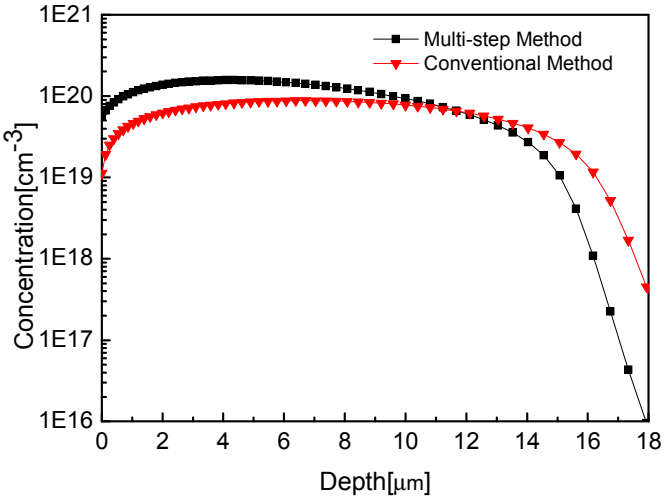


Fig. 2 Profile of boron concentration both in two-step process and multi-step process

With the assist of Athena, the 16h pre-deposition in conventional diffusion is divided into four relatively short 4h pre-deposition, and then the dopants quantity of every 4h pre-deposition brings to the silicon substrate is calculated. It is also very convenient to calculate the quantity of dopants attained after every 4h pre-deposition in multi-step diffusion. This is done to analyze how multi-step process brings 52% more dopants as compared to conventional process. Tab 2 shows the quantity of dopants obtained during every 4h pre-deposition both in conventional two-step process and multi-step process. It can be seen that the two different processes bring in the same quantity of dopants in the 1st 4h pre-deposition duration. Compared to the 1st 4h pre-deposition process, the quantity of dopants obtained by multi-step diffusion process decreases by 25.8% in the 2nd process, 35.3% in the 3rd, 40.7% in the 4th, while the quantity of dopants obtained by conventional diffusion process falls by 58.2%%, 68.0% and 73.0%, respectively.

Tab 2 The quantity of dopants obtained during pre-deposition

Diffusion Method	The quantity of dopants obtained during pre-deposition				Final [cm^{-3}μm]
	1st 4h [cm^{-3}μm]	2nd 4h [cm^{-3}μm]	3rd 4h [cm^{-3}μm]	4th 4h [cm^{-3}μm]	
Conventional Method	7.59×10^{20}	3.17×10^{20}	2.43×10^{20}	2.05×10^{20}	1.06×10^{21}
Multi-step Method	7.59×10^{20}	5.63×10^{20}	4.91×10^{20}	4.50×10^{20}	1.61×10^{21}

Detail of the profile of boron concentration in a multi-step diffusion process with two periods is shown in Fig. 3. This provides a vivid image of how multi-step method brings more dopants into silicon substrate. During the 4 h pre-deposition, a great quantity of boron dopants can easily swarm into silicon substrate, due to sheer concentration gradient. Then an 8 h drive-in is performed to drive the dopants deeper into silicon substrate. This also increases the concentration gradient between the boron source and the silicon substrate, therefore the efficiency of the next 4 h pre-deposition is elevated. And followed is another 8 h drive-in. In this way, multi-step diffusion method can obtain more dopants and higher surface concentration as compared to conventional diffusion method within the same total diffusion time.

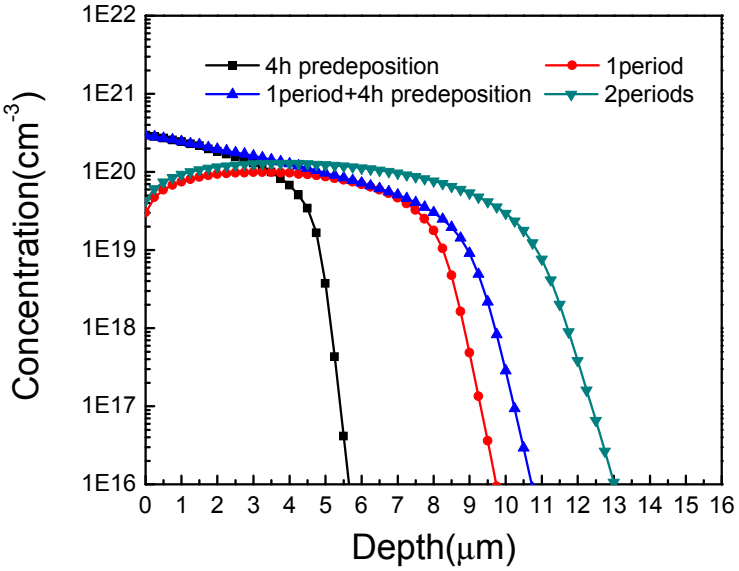


Fig. 3 Details of boron concentration profile during 4 steps thermal diffusion

Under ideal conditions of the constant-surface-concentration diffusion, the total amount of diffused dopants can be computed as function of diffusion time, as listed below:

$$Q = 2N_s\sqrt{\frac{Dt}{\pi}} = 1.13N_s\sqrt{Dt} \quad (1)$$

In function (1), 'Q' is for the total amount of dopants per unit area, 'N_s' is for surface concentration of dopants, 'D' is diffusion coefficient and 't' is for diffusion time. Ignoring the small influence of boron concentration on diffusion coefficient, 'D' is regarded as a constant. And pre-deposition in thermal diffusion is supposed to be constant-surface-concentration diffusion. According to the partial derivative of 'Q' with respect to 't', the term '$\frac{\partial Q}{\partial t}$' is proportion to the term '$\frac{1}{\sqrt{t}}$', suggesting that '$\frac{\partial Q}{\partial t}$' deceases with increasing the 't'. Substitute the't' in Eq. (1) with 4, 8, 12, and 16, theoretically, compared to the 1st 4h pre-deposition process, the quantity of dopants obtained by conventional diffusion process decreases by 58.6% in the 2nd process, 68.3% in the 3rd, 73.2% in the 4th . This calculation result is highly consistent with simulation result above and validates our simulation.

Typical application of multi-step method for a butterfly resonantor

As the analysis above, multi-step diffusion method has shown great advantages over conventional diffusion method to get a thick heavily boron doped layer. As a typical application, multi-step diffusion method is adopted for the fabricating of a butterfly-shape resonant structure for resonant pressure sensor, as shown in Fig. 4. The butterfly resonator is supported by two silicon isolations, and the silicon isolations are on the bottom diaphragm. To simplify the fabrication, boron diffusion and boron etch-stop technique are adopted so that resonator, silicon isolation, and the diaphragm could be fabricated on single silicon wafer. The diaphragm and butterfly-shaped resonator are heavily boron diffused layers released by boron etch-stop technique.

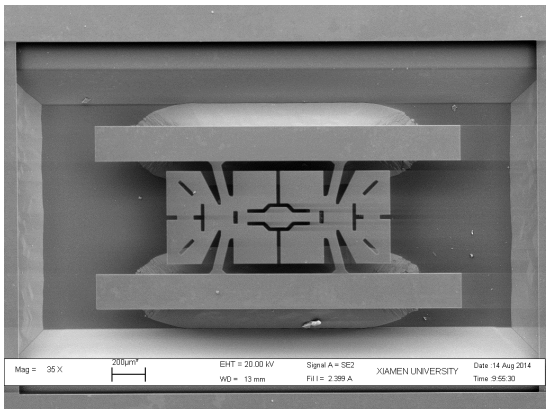


Fig. 4 SEM photograph of the butterfly-shape resonant structure

BH-NT boron nitride diffusion source from Saint-Gobain is used. Thermal boron diffusion with four periods is carried out in 4470 quartz furnace. Every period includes one 4 h pre-deposition and one 8 h drive-in. Parameters of the multi-step diffusion process are shown in Tab 3. After four diffusion periods, another 4h pre-deposition is added to enhance the etch-stop property of the front side of the resonator. Anisotropy wet etching is executed after diffusion. The etchant is 15% KOH solution saturated with IPA. Detail parameters of the etching process are listed in Tab 4.

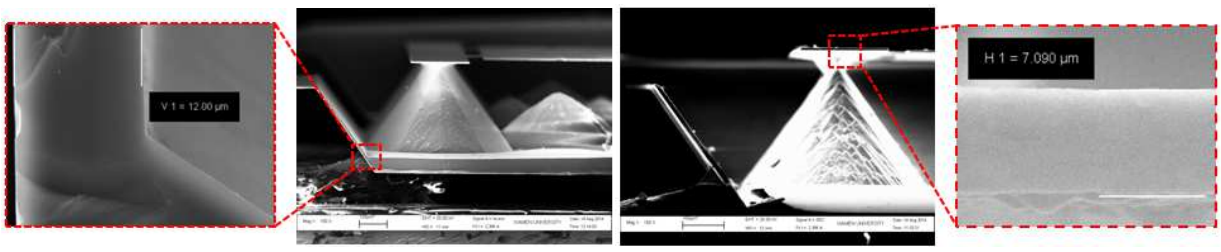
Tab 3 Thermal diffusion parameters of everyl diffusion period

Process	Equipment	Temperature [°C]	Time [h]
Pre-deposition	4470 quartz furnace	1100	4
Drive-in	4470 quartz furnace	1100	8

Tab 4 Wet etching parameters

Solution	Concentration	Temperature [℃]	Time [h]	Additive	Stirring rate [rpm]
KOH	15%	65	33h	Isopropanol	600

After 17h etching, the (111) sidewall of the window intersects the (111) silicon isolation, as shown in Fig. 5(a). It means that the undoped bulk silicon is etched down to the bottom, so 300μm silicon is removed and the etching rate of undoped silicon is 17.647μm/h. At this moment, the thickness of heavily doped silicon at the bottom of the (111) sidewall is 12.00μm. This value is regarded as the thickness of heavily boron doped layer, because the etching rate of the heavily boron doped (111) sidewall is very close to zero. After 33h etching, the bulk undoped silicon beneath the butterfly-shaped resonator is completely removed, as shown in Fig. 5(b). With the help of scanning electron microscope (SEM), the thickness of the resonator is measured to be 7.09μm. As the resonator is etched from the front side and the other side, the nominal etching time is taken as 66h. So the average etching rate of heavily boron doped resonator is calculated to be 0.074μm/h. Therefore, the etching selectivity of 238 between heavily boron doped silicon and undoped silicon is obtained.



(a)17h etching down to the bottom (b) 33h etching to release the resonator completely

Fig. 5 SEM photograph of fabricated butterfly-shape resonant structure

Conclusion

Compared to conventional method in the same total diffusion time, multi-step method obtains more boron dopants and higher boron concentration, which results in higher etching selectivity and thus better etching stop effect. As a typical application of multi-step diffusion method, a butterfly-shape resonator for pressure sensor is fabricated. A 12μm heavily boron doped layer is obtained, and a very high selectivity of 238 between heavily boron doped silicon and undoped silicon is realized.

Acknowledgement

This work funding was supported by China Aviation produce-learn-research projects (cxy2011XD25), National Natural Science Foundation of China (NO 61404111) and Fundamental Research Funds for Central Universities (NO.20720140517).

References

[1] Wang J, Chen D, Liu L, et al. A micromachined resonant pressure sensor with DETFs resonator and differential structure[C]//Sensors, 2009 IEEE. IEEE, 2009: 1321-1324.

[2] Cho I J, Park E C, Yoon E. AFM probe tips using heavily boron-doped silicon cantilevers realized in a< 110> bulk silicon wafer[C]. Microprocesses and Nanotechnology Conference, 2000 International. IEEE, 2000: 230-231.

[3] Seo K S, Cho Y H, Youn S K. A bulk-micromachined silicon micromirror for tunable optical switch applications[C]. Emerging Technologies and Factory Automation, 1996. EFTA'96. Proceedings., 1996 IEEE Conference on. IEEE, 1996, 2: 404-407.

[4] Ning X J. Distribution of residual stresses in boron doped p+ silicon films[J]. Journal of the Electrochemical Society, 143(1996) 3389-3393.

[5] Bassous E, Lamberti A C. Highly selective KOH-based etchant for boron-doped silicon structures[J]. Microelectronic Engineering, 9(1989) 167-170.

[6] Daoheng Sun, Haoer Zhang, Zhan Zhan, Jie He, Xiaohui Du, Lingyun Wang. A Heavily Boron-Doping Method for Fabrication of Thick MEMS Structural Layer [J]. Nanotechnology and Precision Engineering，11(2013) 314-319.

[7] Vick G L, Whittle K M. Solid solubility and diffusion coefficients of boron in silicon[J]. Journal of the Electrochemical Society, 116(1969) 1142-1144

[8] Bagratishvili G D, Dzhanelidze R B, Jishiashvili D A, et al. Boron diffusion from a reactively sputtered glass source in Si and SiO2[J]. physica status solidi (a), 56(1979) 27-35.

Key Engineering Materials Vols 645-646 (2015) pp 347-351
© (2015) Trans Tech Publications, Switzerland
doi:10.4028/www.scientific.net/KEM.645-646.347

Submitted: 2014-10-30
Accepted: 2014-12-23

Synthesis of nano-Al with Fe_2O_3 nanowires to realize core-shell composite materials arrays based on colloidal templates

Simin He[a], Jin Chen[b], Kuang Fang[c], Zhiqiang Qiao[d] and Jinshan Li[e*]

Institute of Chemical Materials, China Academy of Engineering Physics, Mianyang 621900, China

[a]smhe302@163.com, [b]cjyeying@sina.cn, [c]k.fang.z@gmail.com, [d]qzq_zju@163.com, [e]ljshan245@163.com

Keywords: Al/Fe_2O_3; nanowires arrays; silicon substrate; colloidal templates

Abstract. Controlled composite materials arrays have been widely applied for their unique physical and chemical properties, with the aim of developing nanodevices functionality. Nanosphere lithography is a successful technique for fabricating highly ordered arrays of various materials. In this work, the polystyrene colloidal crystal template in large area on Si substrate was obtained via dipping method. The thickness of the single layer template fabricated can be precisely controlling the particle concentration and the film formation speed. The ordered arrays of Fe_2O_3 nanowires were obtained via convenient spin method on this template and heat treatment subsequently. Finally, the uniform Al/Fe_2O_3 arrays were produced by magnetron sputtering method. These periodic composite arrays cover large area substrates (of dimensions > 1 cm × 1 cm) and are uniform in terms of nanowire height and density. The arrays thickness and gaps between nanowires are easily controlled by either the diameter of colloidal crystal or the parameters of magnetron sputtering.

Introduction

There is currently a great deal of interest in composite materials arrays with the aim of improving nanodevices functionality [1-3]. The structure, size, and composition of these particles can be easily altered in a controllable way to tailor their magnetic, optical, mechanical, thermal, electrical, electro-optical, and catalytic properties [4]. The composite material based on arrays with uniform size and easier integration into microsystems. Strong control the morphologies of arrays produced for this purpose is required. Many methods have been introduced to synthesize composite materials including physical mixing, sol-gel [5], aero-gel, and others. However, these methods just control the whole materials ratio, random distribution of the particles.

This control over array morphology can be simply achieved using nanosphere lithography (NSL) [6] and there are many examples in the literature of well ordered, periodical arrays of metal oxide nanowires/nanodots grown via the use of NSL [7-9].

Silicon (Si) is a basic material for microelectronics and microelectromechanical systems. Fe_2O_3 is a kind of important function material and widely studied in powders, particle arrays and 3D porous stuctures [10,11].

In this paper, the polystyrene colloidal crystal monolayer template in large area on Si substrate was obtained via dipping method. The ordered arrays of Fe_2O_3 nanowires were obtained via convenient spin method on this template and heat treatment subsequently, the uniform Al/Fe_2O_3 arrays were produced by magnetron sputtering method. Furthermore, this method provides a foundation for the preparation of different kinds of composite materials based on arrays/nanowires/films.

Materials and methods

Polystyrene (PS) monodisperse latex spheres suspensions (1 micron diameter, 2.5 wt% dispersion in water, standard deviation of the diameter is less than 5%) and $Fe(NO_3)_3 \cdot 9H_2O$ were purchased from Alfa Aesar Company. OP-10 and ethanol were analytically pure obtained from Tianjin kemiou

chemical reagent Co. Ltd. Deionized water was obtained from a Millipore Milli-Q system. Al sheet (99.99 % in purity), with 55 mm in diameter and 5 mm thick, was purchased from Beijing Xing Yuan Technology Co., Ltd. Argon (Ar) with the purity of 99.9999 % was purchased from ChengDu Tai Yu industrial gases Co., Ltd.

Si substrates were ultrasonically cleaned with acetone and hydrogen peroxide/sulfuric acid solution (1:5) for 15 min, respectively, followed by cleaning with deionized water, to remove any organic impurities.

The PS solution was mixed with OT-10 and ethanol in a 1000:1:1 ratio under ultrasonication for 10 min at room temperature. After the Si substrate was immersed in the mixed solution for 5 min, the substrate was drawn upward vertically at a speed of 1μm s^{-1}. Then the sample was then immediately placed into an oven at 80 °C for 5 min for further drying.

The fabrication of Fe_2O_3 nanowires on Si substrate used a chemical process [12,13]. The precursor solution was prepared using $Fe(NO_3)_3 \cdot 9H_2O$ (1mol L^{-1}), which was dissolved in deionized water with continuous magnetic stirring for 30 min. A droplet of the solution (10 μL) was applied to the colloial monolayer with a quantitative pipette, adjusting the custom-built spin-coater spin speed with 5000 min^{-1} for 30 s. This process was then repeated once more in order to ensure that the PS template was fully infiltrated. The sample was place into an oven at 30 °C for 24h and then was heated in a muffle furnace. The temperature was raised at a rate of 1°C min^{-1} to 450 °C and was held steady for 3h under ambient conditions, and then cooled down naturally to 25 °C. During the heating, the latex spheres burn away and Fe^{3+} converted into Fe_2O_3.

Al is deposited by magnetron sputtering onto the substrate with Fe_2O_3 nanowires. Magnetron sputtering was selected over other metal deposition techniques, because it provided enhanced conformal coating, resulting in a uniform nanostructure [14]. The magnetron sputtering process parameters were shown in Table 1. During the deposition, the substrate temperature was maintained at 30 °C.

Table 1 Deposition conditions of the fluorocarbon thin films.

Power (W)	Base pressure (Pa)	Argon pressure (Pa)	Flow rate (sccm)	Time (min)
50	1.0×10^{-4}	0.55	55	20

The particle sizes and morphologies of PS monolayer arrays, Fe_2O_3 arrays and Al/Fe_2O_3 arrays were visualized by field emission scanning electron microscopy (FESEM, Apollo 300) and atomic force microscope (AFM, SPI3800N) operated under a tapping mode. The chemical structures of the arrays were studied via a PHI ESCA 5700 X-ray photoelectron spectroscope (XPS) with a take-off angle of 75°.

Results and discussion

The morphology of the template is characterized by SEM, as is shown in Fig. 1. Substrate is coated with a regular hexagonally close-packed monolayer of PS nanospheres. Each 1 μm sphere is surrounding by six others in one plane formed face-centered cubic structure. Just single layer of the PS sphere can be seen in the cross-section view in Fig. 1b. The height and density of subsequently metal oxide nanowire growing across these areas are easily controlled by the diameter of PS sphere. Damien point out a regular porous medium, its pore space, and the associated fluid motion, which are analyzed in the hexagonally closed-packed sphere arrays [15]. The template assembly processing is an evaporation-driven creeping flow process. The key factors of monolayer arrays are stability of the growing particle interface and the draw velocity of the substrate pate match array growth rate [16].

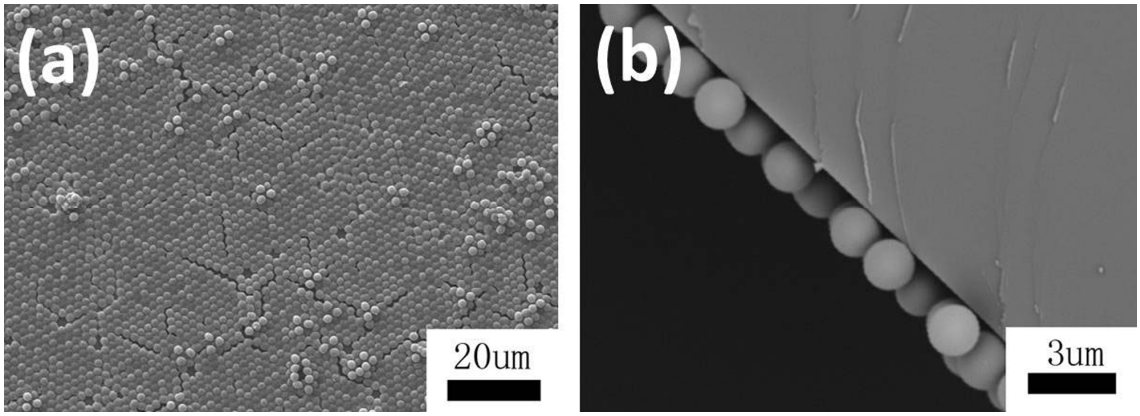


Fig. 1 SEM images of colloidal crystal monolayer template (a) top view, (b) cross-section view.

Fig. 2a shows SEM image of the Fe_2O_3 arrays before Al deposition, Fe_2O_3 arrays grow and PS spheres decompose after annealing, which is consistent with the PS sphere template. The morphology and surface coverage density of the Fe_2O_3 arrays can be easily tuned by varying the diameter of PS spheres. Fig. 2b is a SEM image of the arrays after Al deposition, Al/Fe_2O_3 arrays growth over the entire substrate (of dimensions > 1 cm × 1 cm). In the well-defined periodic structure, nano-Al is uniformly integrated around the Fe_2O_3 nanowires, thus enhancing the interfacial contact and the reactivity. These arrays have several advantages such as enhancing contacts, reducing impurities, tailored dimensions, and easier integration into microsystem.

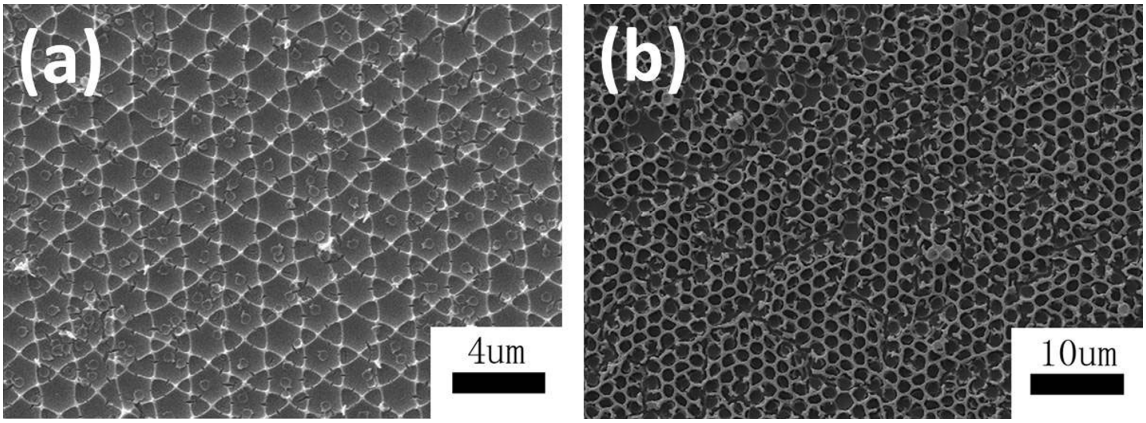


Fig. 2 SEM images of (a) Fe_2O_3 ordered arrays, (b) as-obtained Al/Fe_2O_3 arrays, respectively.

In order to further confirm the case, the fine morphologies are studied by AFM. AFM is employed in a more conventional manner to provide a good assessment of the surface topography of sample [17]. Fig. 3 shows the two-dimensional and three-dimensional surface morphologies of as-synthesized arrays. As it can be seen, the arrays are compact and the average diameter of the nanowires is about 800 nm. Al is not only integrated with the Fe_2O_3 nanowires to form a core-shell nanostructure but also deposited onto the film under the nanowires to form a layered structure. The deposited thickness (on average across the sample) of Al can be easily tuned by varying the sputtering time.

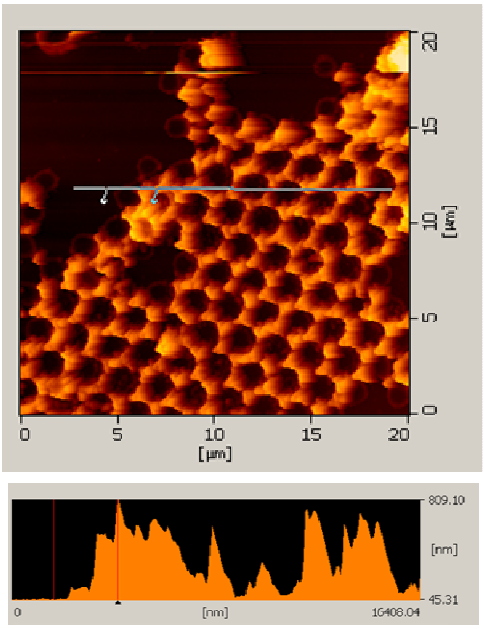


Fig. 3 AFM images of Al/Fe_2O_3 arrays.

For the further investigation of the change in element, XPS analysis is conducted on the arrays in Fig. 4. The characteristic peaks at the binding energies of 285.6 and 532.4 eV correspond to C1s and O1s, respectively (Fig. 4a). It shows that the template is composed of carbon and oxygen, and the peak at the binding energy of 104.2 eV corresponds to silicon substrate. After magnetron sputtering process, two new peaks at the binding energies of 72.2 and 710 eV correspond to Al2p and Fe2p (Fig. 4b), others still exit except carbon element, indicated the sample are composed of iron, aluminium and oxygen.

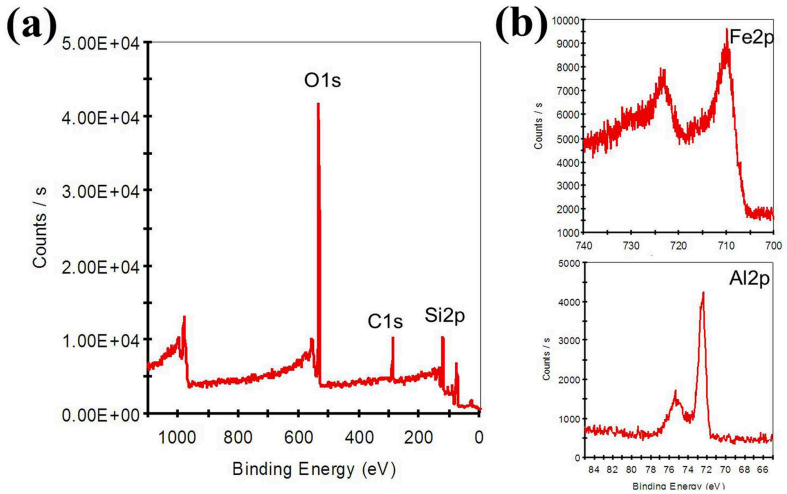


Fig. 4 XPS spectra of as-abtained sample on Si substrate: (a) colloidal crystal monolayer template, (b) the new elements after magnetron sputtering process.

Conclusion

In summary, we have presented a procedure for producing well ordered arrays of Al/Fe_2O_3 on Si substrates. This method provides an efficient way to produce nano/micrometer structure which can be generally applied to fabricate various types of composite materials with large-scale periodic nanowires for the applications in sensor arrays, photonic crystals, piezoelectric antenna arrays and optoelectronic devices.

Acknowledgments

This work is financially supported by National Natural Science Foundation of China (11372288).

References

[1] Xueqin Liu, Zhen Li, Qiang Zhang, Fei Li, Tao Kong, Preparation of CuO/C core-shell nanowires and its application in lithium ion batteries, Mater. Lett. 80 (2012) 37-39.
[2] Kaili Zhang, Carole Rossi, and G. A. Ardila Rodriguez, Development of a nano-Al/CuO based energetic material on silicon substrate, Appl. Phys. Lett. 91 (2007) 113117.
[3] Kaili Zhang, Carole Rossi, Christophe Tenailleau, Pierre Alphonse, and Jean-Yves Chane-Ching, Synthesis of large-area and aligned copper oxide nanowires from copper thin film on silicon substrate, Nanotechnology 18 (2007) 275607.
[4] By Cuikun Lin, Yinyan Li, Min Yu, Piaoping Yang, Jun Lin, A facile synthesis and characterization of monodisperse spherical pigment particles with a core/shell structure, Adv. Funct. Mater. 17 (2007) 1459-1465.
[5] M. Yu, J. Lin, Z. Wang, J. Fu, S. Wang, H. J. Zhang, and Y. C. Han, Fabrication, patterning, and optical properties of nanocrystalline YVO_4 : A (A=Eu^{3+}, Dy^{3+}, Sm^{3+}, Er^{3+}) phosphor films via sol-gel soft lithography, Chem. Mater. 14 (2002) 2224-2231.
[6] Zhengfei Dai, Yue Li, Guotao Duan, Lichao Jia, and Weiping Cai, Phase Diagram, design of monolayer binary colloidal crystals, and their fabrication based on ethanol-assisted self-assembly at the air/water interface, ACS nano 6 (2012) 6706-6716.
[7] S. Garry, E. McCarthy, J.P. Mosnier, E. McGlynn, Control of ZnO nanowire arrays by nanosphere lithography (NSL) on laser-produced ZnO substrates, Appl. Surf. Sci. 257 (2011) 5159-5162.
[8] Yue Li, Weiping Cai, Guotao Duan, Bingqiang Cao, Fengqiang Sun, Fang Lu, Superhydrophobicity of 2D ZnO ordered pore arrays formed by solution-dipping template method, J. Colloid Interface Sci. 287 (2005) 634-639.
[9] Yue Li, Naoto Koshizaki, Weiping Cai, Periodic one-dimensional nanostructured arrays based on colloidal templates, applications, and devices, Coord. Chem. Rev. 255 (2011) 357-373.
[10] Fu Su Yen, Wei Chien Chen, Janne Min Yang, and Chen Tsung Hong, Crystallite size variations of nanosized Fe_2O_3 powders during γ- to α-phase transformation, Nano Lett. 2 (2002) 245-252.
[11] Yue Li, Weiping Cai, Bingqiang Cao, Guotao Duan, Fengqiang Sun, Fabrication of the periodic nanopillar arrays by heat-induced deformation of 2D polymer colloidal monolayer, Polymer 46 (2005) 12033-12036.
[12] Yanguang Li, Bing Tan, and Yiying Wu, Freestanding mesoporous quasi-single-crystalline Co_3O_4 nanowire arrays, J. Am. Chem. Soc, 128 (2006) 14258-14259.
[13] Daguo Xu, Yang Yang, Hua Cheng, Yang Yang Li, Kaili Zhang, Integration of nano-Al with Co_3O_4 nanorods to realize high-exothermic core-shell nanoenergetic materials on a silicon substrate, Combust. Flame 159 (2012) 2202-2209.
[14] Yuma Ohkura, Shih-Yu Liu, Pratap M.Rao, Xiaolin Zheng, Synthesis and ignition of energetic CuO/Al core/shell nanowires, Proceedings of the combustion institute 33 (2011) 1909-1915.
[15] Damien D. Brewer, Joshua Allen, Michael R. Miller, et al, Mechanistic principles of colloidal crystal growth by evaporation-induced convective steering, Langmuir 24 (2008) 13683-13693.
[16] Antony S. Dimitrov, Kuniaki Nagayama, Continuous convective assembling of fine particles into two-dimensional arrays on solid surface, Langmuir 12 (1996) 1303-1311.
[17] Mahalia Miller, Christopher Bobko, Matthieu Vandamme, Franz-Josef Ulm, Surface roughness criteria for cement paste nanoindentation, Cement and Concrete Research 38 (2008) 467-476.

Key Engineering Materials Vols 645-646 (2015) pp 352-355
© (2015) Trans Tech Publications, Switzerland
doi:10.4028/www.scientific.net/KEM.645-646.352

Submitted: 2014-10-30
Accepted: 2014-12-23

Evaluation of the stability on the new alkaline copper bulk slurry

Wang Juan[1,a]，Wang Ru[1,b]and Chen Guodong[1,c]

[1]School of Electrical Information Engineering, Hebei University of Technology, Tianjin, 300130, China

[a]xruyue@hebut.edu.cn (corresponding author), [b]wangru@hebut.edu.cn, [c]cgd@163.com

Keywords: alkalinity, copper bulk slurry, stability

Abstract. At present, the chemical mechanical polishing is the only means for global planarization of an integrated circuit. After the node of the integrated circuit processing comes into 45nm, the diameter of wafer is 300mm, and the copper interconnect layer is above the 10 layer. In the same time the new low dielectric constant materials are used to the integrated circuit processing. That requires the property of the slurry used in the chemical mechanical polishing stricter. So the domestic and international companies carry out a series research works. Based on investigation and research for many years, the new alkaline copper rough slurry has been developed by the teachers and students in the Hebei University of Technology. The slurry has advantages as disadvantages. The composition of cost-effective slurry is simple and the effect of chemical mechanical polishing is good. But its stability is poor. In order to improve the stability, the compositions of the slurry need to adjust.

The new alkaline copper rough slurry composed by abrasive, surface, chelating agent, oxidizing agent and deionized water. Experiments investigate the influence rule of copper polishing rate by the concentration of abrasive, the content of surface, the content of oxidizing agent and the content of chelating agent. The conclusion is arrived. When the concentration of abrasive is 4%, the content of surfactant is 10ml/l, the content of chelating agent is 10ml/l and the content of oxidizing agent is 5ml/l, the copper polishing rate keep 5000 Å /min.

Introduction

With the shrinking of IC feature size and the increasing of metal wiring layer, copper has replaced the aluminum into silicon multilayer materials. Chemical mechanical polishing (CMP) technology, which is a primary planarization method to manufacture semiconductor chips, has gained extensive attention [1]. The evaluation of polishing is connected with polishing machine, pad and slurry[2-4]. In general, polishing machine is fixed after purchased. The slurry and pad are the important consumables. They are closely related with effect of polishing. At present, copper slurry is acidic, which contain benzotriazole[5]. The researchers are devoted themselves to study slurry without benzotriazole. Copper slurry includes the copper bulk slurry and copper fine slurry. With the country special project support, Hebei University of Technology research and develop the copper slurry without benzotriazole. It contains abrasive, surfactant, chelating agent, oxidizing agent and deionized water. The composition of cost-effective slurry is simple and the effect of chemical mechanical polishing is good. But its stability is poor. In order to improve the stability, the compositions of the slurry need to adjust. In this paper the evaluation of the concentration of abrasive, surfactant, chelating agent and oxidizing agent are studied to the pH value and the polishing rate of copper.

1 Experiment

1.1 Experimental materials and instrumentation:

Abrasive, surfactant, chelating agent, oxidizing agent, deionized water, copper wafer(3 inches), E460E polishing machine made in France Alpsitec, IC1000-A2 pad made in USA, TOLEDO 320 pH value measurement made in Mettler company, beaker, measuring cylinder, glass bar and so on.

Experimental conditions:

All the experiments are carried out in the ultra clean laboratory. The room temperature is 25±3℃. The IC1000-A2 pad made in America is used in the polishing experiments. The polishing time is 180s. The process pressure is 13.79Kpa. The rotate speed is 55rpm/60rpm. The flow rate is 50%. The slurry used in experiments is prepared by us.

1.2 Preparation of slurry:

During the chemical mechanical polishing process, slurry plays a dual role. It not only affects the mechanical action of CMP, also affects the chemical action of CMP. So the slurry is the key in the CMP. The component of slurry decides the process and product in the CMP.

When the slurry is preparated, the principle should be followed. The slurry should be no poison, easy to clean, good fluidity, stable.

When the cientific experiments are conducted, the deionized water should be added into the stirring silica sols in the first. Then the chelating agent and surfactant (10ml/l) is poured into the stirring solution respectively. Because the oxidizing agent is volatile, it is added before experiments. Then the slurry is prepareted. The pH value is tested three times. The average value is the pH value of slurry.

1.3 Polishing experiments:

The technological parameter must be setted in the polishing machine before experiments. The copper wafer which is three inch is installed to the polishing head. The polishing experiments are carried out. Then the stability of polishing rate can be analysed.

2 Results and discussion

2.1 Abrasive concentration

In copper CMP, the abrasives in the slurry remove the copper oxide film to help the chemical dissolution induced by the synergy effects between an oxidizer and a chelating agent. After the copper reacts with the hydrogen peroxide to form a porous copper oxide passivation film, the oxidized copper film is hydrolyzed easily, and then is removed by the friction which is mechanically generated between the polishing pad and abrasives. The concentration of colloidal silica in Cu CMP slurry determines the number of abrasive. Thus, the concentration of abrasives in the slurry has an effect on CMP results, such as material removal and WIWNU. In this experiment, the effect of colloidal silica concentrations in the copper CMP slurry was considered. The copper slurry used is similar besides the silica concentrations. The constituent and pH of copper slurry are showed in table 1. Fig. 1 shows the RR with abrasive concentration.

Table 1 The effect of silica concentrations

silica concentration (wt%)	chelating agent (ml/L)	surfactant (ml/L)	Oxidizer (ml/L)	pH
4	10	10	5	10.19
8	10	10	5	10.31
12	10	10	5	10.38
16	10	10	5	10.44
20	10	10	5	10.48

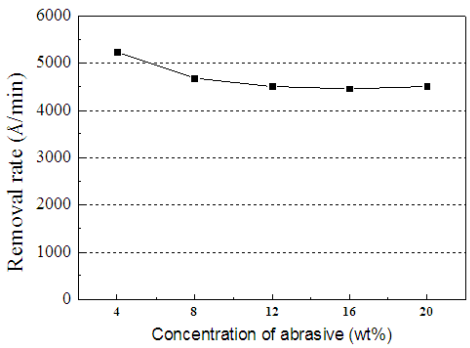


Fig.1 The RR with abrasive concentration

As shown in Fig. 1, the removal rate of wafer was reduced with the increase of abrasive concentration. However, the removal rate of wafer was not changed significantly when the abrasive concentration reached the certain value. In the case of 4wt% abrasive concentration, the removal rate of wafer was higher. These results showed that the copper was dominantly abraded by mechanical removal with abrasives. It is because the abrasives help the removal of the copper oxide film at wafer edge and accelerate chemical dissolution. However, it seems that the abrasive concentration has the optimal value, which is 4%.

2.2 Chelating agent

Theoretical studies of the reaction mechanisms suggest that the chelating agent in Cu CMP usually accelerates Cu oxide dissolution, which enhances the polishing rate of Cu oxide. The role of the chelating agent in the CMP process, which usually has an amine group in its molecular structure, has been the subject of much research. These chemicals have different chemical reaction pathways for Cu in various environments even though they have similar functional groups. In the experiment the new chelating agent was used. It was compounded by Hebei University of Technology. The constituent and pH of copper slurry are showed in table 2. Fig. 2 shows the RR with chelating agent concentration.

Table 2 The effect of chelating agent concentrations

silica concentration (wt%)	chelating agent (ml/L)	surfactant (ml/L)	Oxidizer (ml/L)	pH
4	5	10	5	10.19
4	10	10	5	10.19
4	15	10	5	10.11
4	20	10	5	10.08
4	25	10	5	10.10
4	30	10	5	10.13
4	50	10	5	10.06
4	70	10	5	10.03

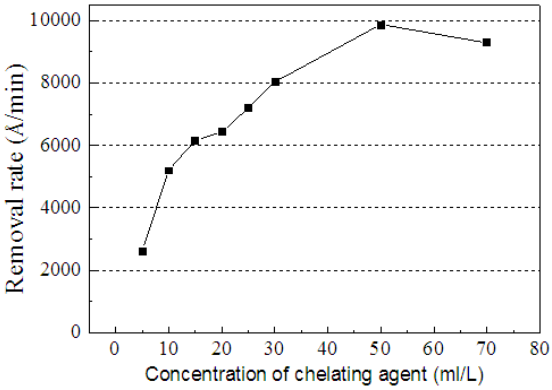


Fig.2 The RR with chelating agent concentration

As shown in Fig. 2, the removal rate of wafer was increased with the increase of chelating agent concentration. The new chelating agent accelerated Cu oxide dissolution, which enhanced the polishing rate of Cu oxide. Because the removal rate of copper needn't to be too fast. So it seems that the chelating agent concentration has the optimal value, which is 10ml/l.

2.3 Oxidizer

It is reported that the polishing rate and surface roughness of copper film were highly dependent on the concentration of H_2O_2 and inhibitor. The differential rate of formation of copper oxide film is owing to the interaction of H_2O_2 with copper and its subsequent dissolution. So the H_2O_2 was used in experiment. The constituent and pH of copper slurry are showed in table 3. Fig. 3 shows the RR with H_2O_2 concentration.

Table 3 The effect of oxidizer concentrations

silica concentration (wt%)	chelating agent (ml/L)	surfactant (ml/L)	Oxidizer (ml/L)	pH
4	10	10	5	10.19
4	10	10	10	10.15
4	10	10	30	9.96

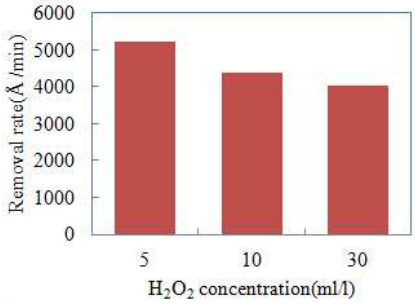


Fig.3 The RR with oxidizer concentration

As shown in Fig. 3, the removal rate of wafer was reduced with the increase of oxidizer concentration. It is consistent that the oxidizer increasing concentration of decreases the chemical–mechanical polishing rate of copper due to dynamic repassivation. So it seems that the H_2O_2 concentration has the optimal value, which is 10ml/l.

Summary

In this research, the component in the copper slurry and its effect on remove rate was intensively studied. The slurry was alkaline, that is different with frequently-used slurry. It was studied by Hebei University of Technology. To improve its property, the experiments were done. After analyzing the results, the conclusion is arrived. When the concentration of abrasive is 4%, the content of surfactant is 10ml/l, the content of chelating agent is 10ml/l and the content of oxidizing agent is 5ml/l, the copper polishing rate keep 5000 Å /min.

Acknowledgement

The work was supported by the Natural Science Foundation for the Youth of Hebei Province (No. F2012202094), Foundation of Hebei Educational Committee (No. QN2014208), and Outstanding youth science and Technology Innovation Fund of Hebei University of Technology (Project name. The research on copper alkaline slurry in low polishing pressure for GLSI.)

References

[1]Hyunseop Lee, Boumyoung Park, Haedo Jeong, Mechanical effect of process condition and abrasive concentration on material removal rate profile in copper chemical mechanical planarization, journal of materials processing technology. 209(2009)1729-1735.

[2]Min Cheol Kang, Yung Jun Kim, Hyo-Chol Koo, Local Corrosion of the Oxide Passivation Layer during Cu Chemical Mechanical Polishing, Electrochemical and Solid-State Letters. 12(2009) H433-H436.

[3] S. Seal, S.C. Kuiry, B. Heinmen, Effect of glycine and hydrogen peroxide on chemical mechanical planarization of copper, Thin Solid Films 423 (2003) 243–251.

[4] Y. Ein-Eli, E. Abelev, E. Rabkin, and D. Starosvetsky, The Compatibility of Copper CMP Slurries with CMP Requirements, Journal of The Electrochemical Society, 150 (2003) C646-C652.

[5] Gilss V, Pen C,Hubin A, Electropolishing of copper:in Ex situ and in situ optical characterization, Journal of the Electrochemical Society. 154(2007) C175-C180.

Key Engineering Materials Vols 645-646 (2015) pp 356-361
© (2015) Trans Tech Publications, Switzerland
doi:10.4028/www.scientific.net/KEM.645-646.356

Submitted: 2014-10-28
Accepted: 2014-12-23

Research on Low Temperature Anodic Bonding Based on Interface Pretreatment of Dielectric Barrier Discharge Plasma

Pan Mingqiang[1,2, a], Sun Linning[1,2,b], Wang Yangjun[1,2,c], Liu Jizhu[1,2], Chen Tao[1,2], Liu Huicong[1,2],and Chen Liguo[1,2]

[1] College of Mechanical and Electrical Engineering & Collaborative Innovation Center of Suzhou Nano Science and Technology, Soochow University, Suzhou 215123, China
[2] Jiangsu Key Laboratory for Advanced Robotics Technology, Soochow University, Suzhou, China

[a]pmqwl@163.com, [b]lnsun@hit.edu.cn, [c]Wangyangjun@suda.edu.cn (corresponding author)

Keywords: Composite anodic bonding; Interface pretreatment; Dielectric barrier discharge; Plasma activation

Abstract. A simple composite bonding that combines dielectric barrier discharge (DBD) plasma activation with anodic bonding has been developed to achieve strong silicon/glass bonding at low temperature. The realization of low temperature bonding is attributed to enhance the hydrophilicity and smooth of silicon and glass surfaces and form lots of free radical after the DBD plasma (including -OH, -H, O, and heat) reacts with the interfaces. And these further reduce the difficulty of chemical bond switching, and improve the speed of the intimate contact formation. The experimental result show that the bonding temperature strongly decreased 100℃ by using composite anodic bonding with DBD pretreatment which strength kept constant, and 10MPa bonding strength was obtained at 250℃/900V after the bonding interface was treated for 10s under the conditions of AC1.5KV/25KHz and the clearance 100μm.

Introduction

The surface bonding technology is an essential technology for MEMS packaging. The anodic surface bonding technology using static electricity can bond glass and metal, alloy or semiconductor together without any adhesive, and thus is widely used in the field of MEMS [1-2]. Compared with other bonding, anodic bonding has lots of advantages with the simple process, little demanding the bonding interface, better bonding strength, good sealing and stability, etc. Therefore, it has become one of the basic technologies in the MEMS field, and is one of the critical technologies during production, assembly, packaging process in many MEMS devices such as sensors.

However, the conventional anodic bonding process cannot meet the requirement for high performance package of MEMS device, because of the existing problems such as bubbles, bonding stress, deformation, metal ion penetration induced by the high temperature process. Lowering bonding temperature or shortening bonding time is an important method to solve these problems. Some scholar experimental results showed that the interface pretreatment is a good approach to realize low temperature and short bonding time. Howlader etc. has successfully obtained the bonding of 30MPa strength under the conditions of 10min and 200℃, because the bonding interface had lots of –OH, -H, O after the activation pretreatment process with complex oxygen plasma and nitrogen plasma [3]. Duck-Jung Lee etc. has achieved 5in silicon/glass bonding at 300℃ after the bonding interface was treated to obtain lots of –H and -OH by strict activation pretreatment process with the hydrogen peroxide and the ammonia [4]. Wang Duoxiao investigated the bonding process with interface pretreatment of the wet chemical activation, and developed the low temperature bonding process at 250℃ that the bonding interface was treated rigorously by several wet chemical activation [5]. These studies show that the interface pretreatment process can effectively reduce the bonding temperature. Therefore the interface pretreatment technology has become an important method to solve the problem of the anodic bonding heat effect, and has aroused widespread concern. The above anodic bonding process with the interfacial activation pretreatment is restricted wide application for

MEMS field, due to the shortcomings of the complex process and poor controllability. These are caused by the strict environmental conditions, the expensive equipment of the plasma activation pretreatment, the strict process conditions and the complex process of the wet chemical activation pretreatment. Based on the previous discussion, this paper proposes a composite anodic bonding process method, which integrates the interface pretreatment process based on dielectric barrier discharge (DBD) and anodic bonding process in one work place. And this composite anodic bonding is cheap, simple, stable and controllable.

Principle and System of Composite Anodic Bonding Based on DBD Plasma

Dielectric barrier discharge

Dielectric barrier discharge is an important non-thermal plasma source and widely used in discharge plasma processing. It has received much attention in recent years due to its generation of non-equilibrium plasma in an economic and reliable way. This has led to many important applications, such as ozone generation and surface modification, etc. [6-7]

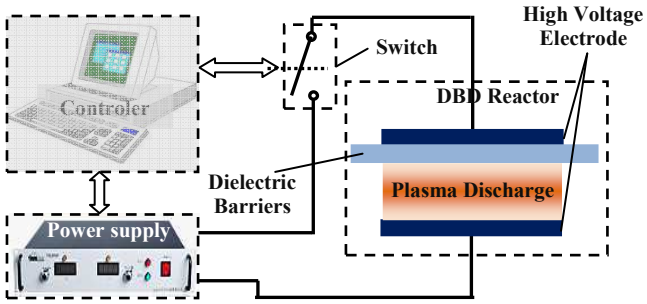


Fig. 1. Schematic of dielectric barrier discharge principle

As shown in Fig.1, the physical phenomenon is well known that the DBD is formed in a narrow discharge gap under high voltage electric field. When an AC or RF voltage is applied to an electrode system with one or both electrodes covered by a dielectric layer, the insulating medium inhibits high–voltage breakdown current. Typical materials used for the dielectric layer are glass, quartz, ceramics and polymer coatings. A voltage of 1to100kV with frequencies of 50Hz to1MHz is necessary to sustain these discharges. According to the gas properties, operating parameters, and boundary conditions, DBD can exhibit pronounced filamentary characteristics, self-organized regular-discharge patterns, or completely diffuse appearance [8-10]. Because of the pronounced advantages of DBD plasma, its application has received attention in the semiconductor field, and the some researches have been conducted on silicon surface [11-12]. This indicates that the DBD can be used to treat Si and glass surface for the anodic bonding.

Composite anodic bonding

The composite anodic process integrates the interface pretreatment process based on dielectric barrier discharge (DBD) and anodic bonding process in one work place, because their process requirements are similar. During the composite anodic bonding process, the DBD plasma (including -OH, -H, O, and heat) reacts with the bonding interface (including Si and glass) to improve silicon and glass surface active, and then, silicon and glass are bonded. And these processes are performed automatically.

As shown in Fig.2, the composite anodic bonding is composed of controller, DBD power supply, anodic bonding power supply and reactor. The gap for DBD is formed by shifting the movable electrode and the high voltage electric field between the two electrodes is generated by DBD power supply. The plasma generated by DBD in the gap will react with the interface surface of silicon and glass. After the interface pretreatment process, the silicon substrate attached on the movable electrode is shifted downward to get in touch with the glass substrate. And DC high voltage generated by anodic bonding power supply is applied to the two electrodes, just as an ordinary silicon–glass anodic bonding.

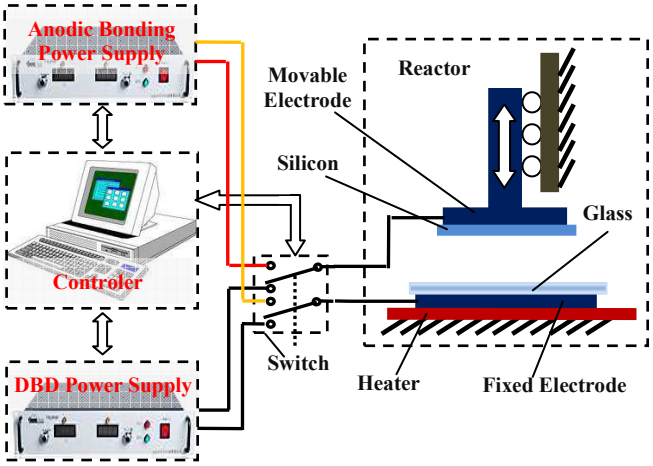


Fig. 2. Schematic of composite anodic bonding

Experiment Details

The double-side polished standard bare wafers of silicon and BF33 glass dices were prepared for the bonding experiments. The 4-inch silicon wafer with the thickness of 500μm was cut into 3mm×3mm square-shaped dice using a diamond cutter. The glass dices are ring type with inner diameter of 2.5mm, outer diameter of 6.2mm, and thickness of 0.5mm. The surface roughness of silicon and glass dices are Ra<5nm. After ultrasonic cleaning in standard solutions at temperature of 80℃, the silicon dice were then rinsed with deionized water and dried by pure N_2. And the glass dices were ultrasonically cleaned by acetone followed by alcohol and deionized water, then purged by pure N_2. As shown in Fig.3, the composite anodic bonding system consists of a DBD power supply with frequency of 10-30kHz and sine output voltage of 0.1-5kV, an anodic bonding power supply with DC output voltage of 0.5-2kV, a heater with temperature varying from 100 to 600℃, and a reactor with motion accuracy of 2μm and range of 0-15mm. By varying the pretreatment parameters including frequency, voltage and discharge time of DBD, effects of different interface pretreatment were achieved. The influence of the bond temperature on the bonding adhesive strength was analyzed for bonding time of 60s, bonding voltage of 900V and contact force of 50gf.

The bonding strength is a very important factor relating to bond quality and reliability. The adhesive strength measurement was carried on after the composite anodic bonding by using the strength testing equipment (as Fig.3 shown). The bonding strength is defined as the maximum pressure of the bonded pairs could withstand divided by the bonded area. The bonding pairs were fixed and sealed with movable clamp and fixed clamp of testing head, and the glass hole was filled with pressure. When the bonding area was divided, the pressure is represented by the bonding strength. To maintain the consistency and stability of the experiments, the three samples were tested and the bonding strength was the average of the three for each bonding condition.

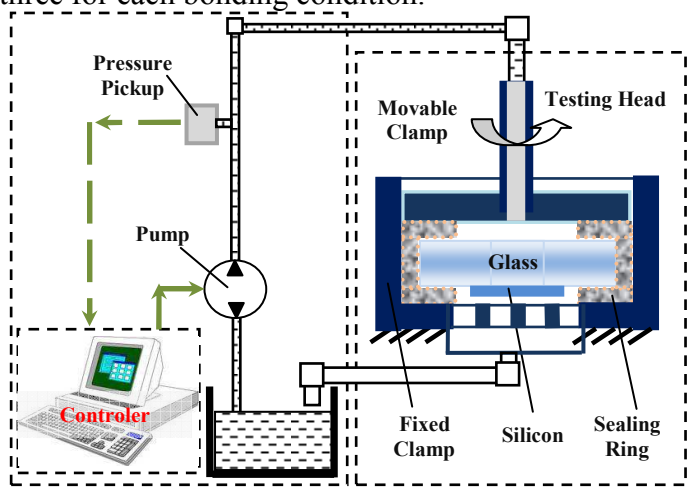


Fig. 3. Schematic of the bonding strength testing system using pressure

Result and discussion

Temperature effect of anodic bonding

Through causes some problems such as bubbles, bonding stress, deformation, etc., the bonding temperature is always a necessary condition to be considered during anodic bonding. It directly affects the other bonding parameters such as voltage and surface roughness of bonding pairs. Fig.4 shows the anodic bonding current varying for 60s at 250℃, 300℃, 350℃, 400℃with an applied voltage of 900V and contact force of 50gf by conventional anodic bonding process. The bonding was failed at 250℃, and the bonding strength was 10.15, 11.57 and 13.68Mpa at 300℃, 350℃ and 400℃, respectively. It is known to all that, the mobility of the alkaline cations in the glass surface and anions in the silicon surface is the key to anodic bonding formation, and the cations and anions activation increases with the temperature in silicon and glass. These determine the bonding current varying curve with the time during anodic bonding. In the meantime, the energy of silicon or glass surface increase with the temperature, and the energy is the key to break chemical bond of Si-Si in silicon and Si-O-Si in glass and to generate lots of free bond on the bond interface. Therefore, increasing the temperature is conducive to the intimate contact formation.

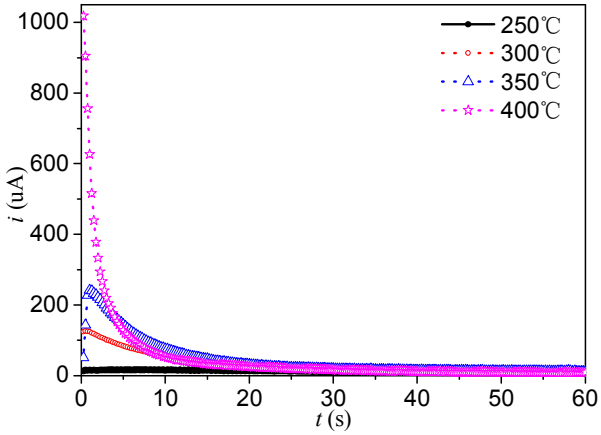


Fig. 4. Current curve with time during conventional anodic bonding process

Influence discharge pretreatment on the bonding temperature

Fig.5 (A) and (B) shows the current curve at 250℃ and 300℃ with conventional anodic bonding process and composite process using the same anodic bonding parameters, respectively. Before anodic bonding process for composite process, the silicon/glass interface is treated by DBD with AC1.5KV/25KHz and the clearance 100μm, and then the silicon and glass were bonded by above conventional process parameters. Compared with the conventional process, the bonding current using composite anodic bonding process is smaller, and its variation is slow. The bonding at 250℃ using conventional process is failed but is successful by using composite process with strength of 10MPa, which is similar to conventional process at 300℃. And the bonding strength at 300℃ increases from 10.47MPa using conventional process to 13.8MPa using composite process.

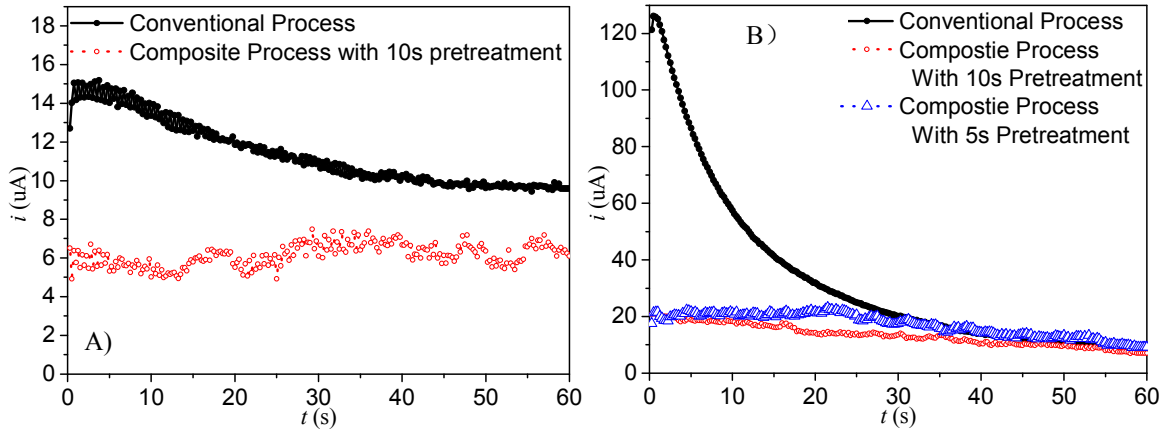


Fig. 5. Curve of bonding current using conventional process and composite process

The anodic bonding principle is using the chemical bond of silicon and glass switch on bonding interface. And the chemical bond in inner of silicon and glass break and new chemical bond forms between silicon and glass under action of temperature field and electric field, when the surface of silicon and glass is smooth enough. And the temperature field and electric field enhance the energy of silicon or glass surface and increasing the electron energy, which easily break chemical bond of Si-Si in silicon and Si-O-Si in glass and generate lots of free bond on the bond interface. And then, the new chemical bond forms easily.

According to Brandenburg et al.[13] and Choi et al.[14] by analyzing the spectral lines, O_2 is ionized by the direct electronic collision ionization in dielectric barrier discharge plasma. And the silicon surface is oxidized during DBD process according to Changquan Wang et al.[15]. During composite anodic bonding process, the silicon/glass interface was treated by the DBD plasma before anodic bonding and the reactions in air plasma are the following:

$$e + O_2 \rightarrow O + O + e \quad (1)$$

$$O + O_2 \rightarrow O_3 \quad (2)$$

$$e + H_2O + O \rightarrow 2HO^- \quad (3)$$

$$O + Si \rightarrow [Si - O-] \quad (4)$$

$$HO^- + Si \rightarrow Si - OH \quad (5)$$

$$HO^- + SiO_2 \rightarrow [SiO - O - OH]^- \quad (6)$$

Silicon and monox on bonding interface react with -OH, -H and O generated during DBD, which generate lots of free radical, such as Si-OH, Si-O-, SiO-O-OH- on bonding interface. Because of these free radical on the interface, new chemical bonds are formed successfully at lower temperature using composite process than using conventional process. At the same time activate silicon and glass surface, the discharge plasma reduces the surface contaminations and smoothen surface. These further reduce the difficulty of chemical bond formation, and improve the speed of the intimate contact formation. Because the intimate contact limits the cations and anions movement, the anodic bonding current curve is different (shown in Fig.5) when using conventional and composite process.

Conclusions

The reliable anodic bonding at low-temperature has been achieved by using the interface pretreatment based on DBD plasma. The ordinary silicon/glass anodic bonding cannot be realized at low temperature due to the presence of surface contaminations and absence of bonding sites. A simple plasma pretreatment process with DBD strongly improves the free radical number, and free radical increase is to ensure intimate contact forming without high temperature. And the same time, the intimate contact limits the bonding peak current, because the speed of intimate contact formation increases. Therefore, the bonding temperature strongly decreased 100℃ by using composite anodic bonding with DBD pretreatment which strength kept constant, and 10MPa bonding strength was obtained at 250℃/900V after the bonding interface was treated for 10s under the conditions of AC1.5KV/25KHz and the clearance 100μm.

Acknowledgments

This work is supported by National Natural Science Foundation of China (the Grant Number 61106110) and Specialized Research Fund for the Doctoral Program of Higher Education (the Grant Number 20133201130003).

References

[1] Wallis G, Daniel I, Pomerant Z. Field Assisted Glass-Metal Sealing, Journal of Applied Physics, 40(1969)3946-3949.

[2] Enikov T E, Boyd J G, A thermodynamic field theory for anodic bonding of micro electro-mechanical systems (MEMS). International Journal of Engineering Science. 38 (2000)135- 158.

[3] M.M.R. Howlader, M.G. Kibria, F. Zhang, M.J. Kim, Hybrid plasma bonding for void-free strong bonded interface of silicon/glass at 200℃.Talanta, 82(2010) 508-515.

[4] Duck-Jung Lee, Byeong-Kwon Ju, Jin Jang, et al., Effects of a hydrophilic surface in anodic bonding. Journal of Micromechanics and microengineering, 9(1999) 313-318.

[5] WANG Duo-xiao, WU YU-ting, CHU Jia-ru, Research on low temperature anodic bonding technique. Journal of Transducer Technology, 24(2005) 37-39.

[6] U. Kogelschatz, "Dielectric-barrier discharge: their history, discharge physics, and industrial applications", Plasma Chem. Plasma Process. Vol. 23, pp.1-46, 2003.

[7] Z. Fang, X. Xie, J. Li, H. Yang, Y. Qiu, E. Kuffel, Comparison of surface modification of polypropylene film by filamentary DBD at atmospheric pressure and homogeneous DBD at medium pressure in air. J. Phys. D: Appl. Phys., 42(2009) 085204-085212.

[8] De Geyter, N., Morent, R. and Leys, C, Penetration of a dielectric barrier discharge plasma into textile structure at medium pressure. Plasma Sources Sci. Technol., 15(2006) 78-84.

[9] Ráhel, J., Sherman, D.M., The transition from a filamentary dielectric barrier discharge to a diffuse barrier discharge in air at atmospheric pressure. J. Phys. D: Appl. Phys., 38(2005) 547-554.

[10] Lee, D., Park, J.M., Hong, et al., Numerical simulation on mode transition of atmospheric dielectric barrier discharge in helium–oxygen mixture. IEEE Trans. Plasma Sci., 33(2005) 949-957.

[11] M.G. Meise, H. Langhoff, Homogeneous high-pressure gas discharge using semiconductor electrodes. Appl. Phys. B: Lasers Optics, 64(1997)41-50.

[12] B.G. Salamov, S. Ellialtioglu, B.G. Akinoglu,et al., Spatial stabilization of Townsend and glow discharges with a semiconducting cathode. J. Phys. D: Appl. Phys. 29(1996) 628-637.

[13] R. Brandenburg, K.V. Kozlov, A.M.Morozov, et al., Behaviour of dielectric barrier discharges in nitrogen/oxygen mixtures. in Germany, vol. 4 Proceedings of the 26th International Conference on Phenomena in Ionized Gases, Greifswald, 2003, pp. 43-49

[14] J.H. Choi, T.I. Lee, I. Han, H.K.et al., Investigation of the transition between glow and streamer discharges in atmospheric air. Plasma Sources Sci. Technol., 15(2006) 416-425.

[15] Changquan Wang, Guixin Zhang, Xiangning He, Effect of dielectric barrier discharge on semiconductor Si electrode surface. Applied Surface Science, 256(2010) 6047-6052.

Key Engineering Materials Vols 645-646 (2015) pp 362-367
© (2015) Trans Tech Publications, Switzerland
doi:10.4028/www.scientific.net/KEM.645-646.362

Submitted: 2014-10-28
Accepted: 2014-12-01

The Study on the Selectivity Ratio of SiC/Epoxy resin Based on ICP Etching

Jiang Hu[1,a], Shun Zhou[1.2,b],Changlong Cai[1,c],

Yufeng Zhu[2,d], Shuai Hu[3,e] , Weiguo Liu[1,f]

[1]Xi'an Technological University, Xi'an, 710032, China
[2]Science and Technology on Low-Light-Level Night Vision Laboratory, Xi'an, 710065, China
[3]Xi'an Electronic Engineering Research Institute, Xi'an, 710048, China
[a]hujiang080212521@126.cm, [b]zsemail@126.com,[c]caichanglong@xatu.edu.cn,
[d]yufengzhou205@126.com,[e]hushuai206@163.com, [f]wgliu@163.com

Keywords: SiC; epoxy resin; Inductively Coupled Plasma; selectivity ratio

Abstract. SiC molds have excellent performance for high-temperature molding optical lenses. The stable physical and chemical properties of SiC results in the difficulty of manufacture high precision SiC molds. Using etching method can manufacture SiC molds apace and accurately, which is used for Micro-embossing needs to study the suitable selectivity ratio of SiC and the anti-etch layer-epoxy resin. The etching gas is SF_6 and O_2. Under different ICP power, bias voltage, the gas mixing ratio and other parameters, it has studied the influence of various factors on the etching ratio, the etching rate and the etching quality. Experiments show that under the parameters of SF_6 flow of 80sccm, O_2 flow of 5sccm, ICP power of 1200w, bias power of 70w, temperature of 30 ℃, and pressure of 30mTorr, the SiC etching rate is 246.44nm/min, and the epoxy etching rate is 616nm/min. The SiC/epoxy resin etching ratio is stable at 1:2.5. The roughness of SiC is 1.2nm （Sa= 1.2nm）. The anisotropic of etching is good.

Introduction

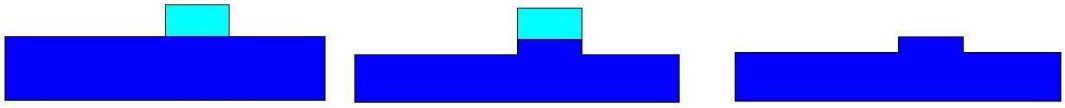
SiC molds have the advantages of high hardness, high temperature resistance, long life, and no adhesions with Infrared Glass, etc. Therefore, SiC molds are very suitable for molding. Using ICP etching method can manufacture the high-precision SiC molds apace and low-costly. First, make the continuous contour diffractive microstructures anti-etch epoxy layer on the SiC wafer. And then etch this SiC wafer with suitable etching selectivity ratio. In this way the microstructures will transfer to SiC substrate. The size of microstructures is according to the etching selectivity ratio. SiC molds are done after these program completed. So it's necessary to focus on researching the etching selectivity ratio of SiC and epoxy. Due to the high hardness and chemical stability of SiC material, wet etching can not achieve the requirements. Currently SiC etching methods are mostly dry etching.Inductively coupled plasma etching system has the advantages of high plasma energy, plasma density, and high quality etching uniformity. And this system can achieve high etch rate at lower substrate bias voltage. Oxford Plasmalabsystem100 ICP-180 etcher used in experiments has the following advantages: 1 Actively cooled electrode for maintaining sample temperature during the etching process. 2 High power ICP source for producing high density plasmas.3 Magnetic spacer for enhancing ion control and uniformity.4 High conductance pumping system.5 Reliable hardware and ease of serviceability for excellent uptime. The inside etching uniformity of wafer is less than ±3%. And the etching uniformity between different wafers is less than ±5%.

Experiment

The 2 inches research-grade double-sided polishing thickness of 330μm single-crystal 4H-SiC wafers used in experiments are obtained from Tianke Heda. The etching machine used in experiments is Oxford Plasmalabsystem100 ICP-180 etcher. The etching gas is SF_6 + O_2. The variational range of ICP power is 500 ~ 1000W. The bias power is 20 ~ 50W. The SF_6 flow rate is 18 ~ 60sccm. The O_2 flow rate is 3 ~ 20sccm. The reaction chamber pressure is 30mTorr. Talysurf CCI profiler is used to measure the step height and roughness measurements after etching.

1 SiC samples prepared

The SiC wafers were cut into 1cm × 1cm as samples to be etched. After cleaning the surface of SiC samples, dropped a glob of PDMS and cured as a masking layer. After completing the etching, peeled off the PDMS layer and got the etching step which was formed by the etched part and the part PDMS protected. Measured the step height and divided the step height data by the etching time used. In this way, the etching rate of SiC was gotten. The results were as shown below.



1 before etching 2 etching finished 3 step hight

Figure 1 Etching step process

2 Epoxy Samples prepared

The Si samples were cuted into pieces about 3cm × 3cm. After the regular cleaning, made up the liquid epoxy resin (bisphenol A type resin body: curing agent = 2:1)and put it into vacuum to eliminate air bubbles. After the liquid epoxy resin vacuum defoaming, dropped globs of epoxy resin on the Si wafer, and let it flow to be a level surface. Heated it to 80 ℃ on a hot plate and kept 30min to solidify. After the epoxy resin solidified，drop a glob of PDMS as a mask. After completing the etching, peeled off the PDMS layer and got the etching step which was formed by the etched part and the part PDMS protected. Measured the step height and divided the step height data by the etching time used. In this way, the etching rate of epoxy resin was gotten.

3 Experimental procedures

An experimental group consisted of a SiC samples and an epoxy resin samples. Pasted the sample group on the chip carrier by the silicone grease and squeezed air bubbles. Put the chip carrier on the arm of transfer chamber. The arm will transfer the chip carrier to the etching chamber. After the etching program finished, the data were obtained. There are 12 groups' data under different parameters in the following table.

Table 1 Etching data sheet

No.	SF_6 flow rate (sccm)	O_2 flow rate (sccm)	ICP Power (W)	RF Power (W)	T (℃)	SiC etching rate (nm/min)	Epoxy etching rate (nm/min)	SiC/epoxy etching ratio
1	18	3	1000	50	30	50	150	1：3.00
2	20	20	700	25	30	36	300	1：8.30
3	30	3	700	30	30	77	200	1：2.60

4	30	5	700	25	42	68.5	195	1：2.96
5	30	10	700	25	30	70	200	1：2.85
6	40	3	500	30	30	43	145	1：3.37
7	45	5	700	30	30	69	259	1：3.76
8	60	0	700	25	30	60	165	1：2.75
9	60	2	1000	40	30	118.67	333.33	1：2.80
10	60	5	700	30	30	67.5	212.5	1：3.14
11	60	18	800	30	30	75	205	1：2.73
12	80	5	1200	70	30	246.44	616	1：2.50

Results and data analysis

1 Data Analysis

1.1The experimental data of Group 8 shows that in pure SF_6 gas plasma environment epoxy removal rate remains about 165nm/min. Epoxy reacts with SF_6 gas plasma mildly. It can be seen that under this etching process parameters the removal of epoxy achieved mainly by Physical etching. And the physical etching removal rate is still relatively high.

1.2 Compared Group 1 with Group 9, it shows that under other consistent parameters, the increasing flow rate of SF_6 gas can increase the etching rate of SiC and epoxy resin. The increasing reaction gas flow rate can increase the chemical etching and physical etching effect at the same time. The more reaction gas product more plasma and increase the density of the plasma. The higher density of plasma can get faster etching rate. Results of compared tests shows that under the same flow of oxygen and the increased SF6 gas flow rate, the growth rate of epoxy resin etching is faster than SiC etching.

1.3 Compared Group 3 with Group 4, it shows that under other consistent parameters, keep the same flow rate of SF_6 but reduce the relative concentration, the etching rate of SiC is lower. It means that not only the reaction gas flow rate but also the relative concentration of reaction gas impacts the etching rate.

1.4 Compared Group 8 with Group 11, it shows that under other consistent parameters, the increasing relative concentration of O_2 not only increase the etching rate of epoxy resin but also increase the etching rate of SiC. The reason is that the increasing relative concentration of O_2 can increase the Chemical etching rate of epoxy resin. When the etching gas of the oxygen gas flow rate increases, oxygen will react with C in the SiC generate CO, CO_2 and other gases, so that the etching solution of the product of the adsorption process is enhanced, and the etching rate increases. When the oxygen content increase continuously, the etching rate decreases with the ratio of the gas mixture increases. Because the oxygen content is relatively high, SiOx which can not be removed is generated on the etched surface and hinder further etching. Furthermore, the increasing oxygen content in the reaction chamber can result in reducing the concentration of SF_6, thereby reducing the etching rate of the chemical reaction.

1.5 Compared Group 8 with Group 9, it shows that under other consistent parameters, increasing ICP power and bias power can improve the etching rate of SiC. As the increasing ICP power increases the plasma density of ions and neutral radicals, the rate of chemical reactions and physical sputtering effect of ions of the etched surface increase, and the etching rate of SiC increases. While the etching rate increases with the increase of the bias power, the enhanced bias voltage can increase ion directivity, to attract ions strike the sample surface with a faster rate, and enhance the physical sputtering of the surface of the ion and the chemical reaction rate. However, with the

further increasing of bias voltage, the increase of etching rate has leveled off. And the physical sputtering plasma velocity continues to increase with the increasing speed. Reactive ion sputtering is too fast to pump by vacuum system before reaction, and results in the non-increasing etching rate [4]. It also can be seen that due to the material properties, the increase amplitude of epoxy etching rate is faster than SiC. It means that the 1:1 etching rate ratio of SiC and epoxy does not exist. It can only be achieved by using a different material as the masking layer.

2 The Selectivity Ratio and roughness

The horizontal axis of Figure 2 is the gas mixing ratio of SF6 and O2. The longitudinal axis of Figure 2 is the etching ratio of epoxy and SiC. As the figure shown, when the radio of SF6 gas flow rate and O2 gas flow rate is 1:1, the selectivity ratio of SiC and Epoxy resin is 1:8.3. In order to achieve a lower etching rate, the O2 flow rate needs to be reduced. The above analysis shows that when the proportion of SF6 gas increases, the etching rate of SiC can be reinforced and the surface quality can be better. However, with the increasing of SF6, the selectivity ratio becomes stable gradually. The etching ratio is stable at around 1:2.5. The reason is that the higher SF6 gas in the proportion of reaction, the increasing rate of chemical etching rate is lower and stable. But the epoxy physical bombardment by high-energy plasma etching effect is significantly growing quickly. So a stable etching selectivity radio of SiC and epoxy was gotten finally.

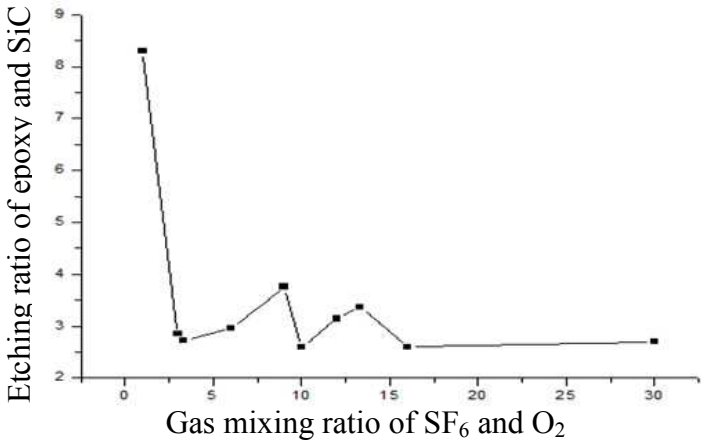


Figure 2 Selectivity Ratio trend

Use etching method to make a SiC mold，it should be considered about not only the faster etching rate, suitable selectivity ratio but also the roughness of etched surface and other factors. Taking into account the performance of the machine and epoxy, it is determined that the etching parameters are SF_6 gas flow of 80sccm, O_2 gas flow of 5sccm, ICP power of 1200w, bias power of 70w, pressure of 30mTorr and temperature of 30 ℃. Under these parameters, SiC etched 369.69nm in 90s, and the etching rate is 246.44nm/min. Epoxy etched 924.17nm in 90s, and the etching rate is 616nm/min. The roughness of SiC is 0.8nm before etching, while the roughness is 1.2nm after etching.

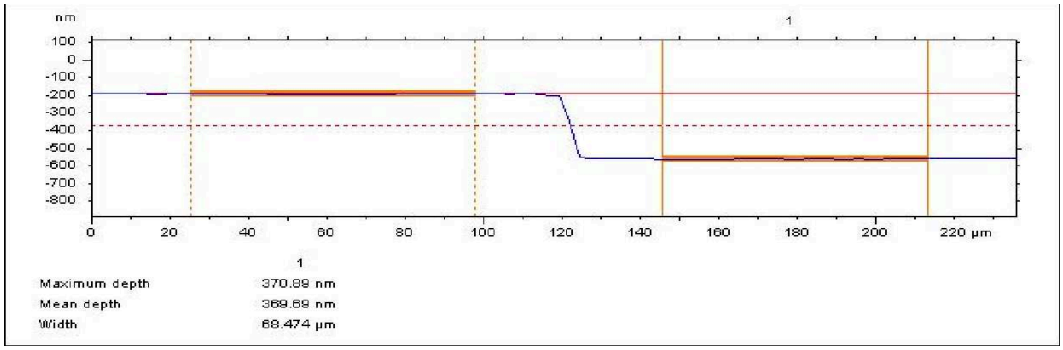


Figure 3 SiC step height

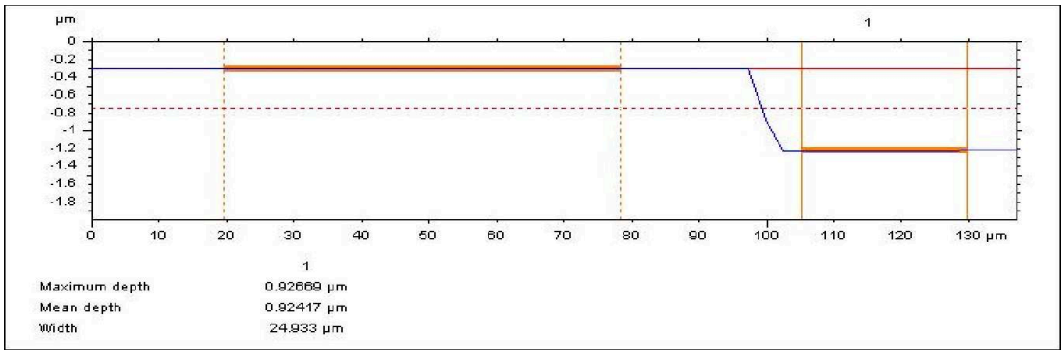


Figure 4 Epoxy step height

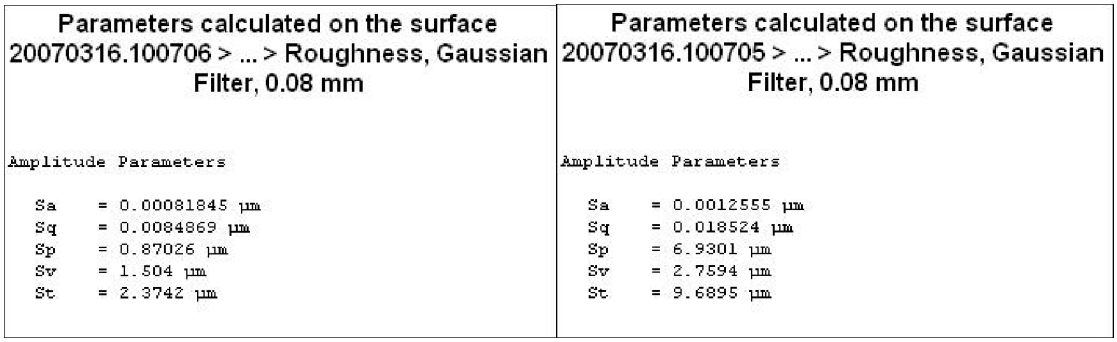


Figure 5 SiC roughness before etching

Figure 6 SiC roughness after etching

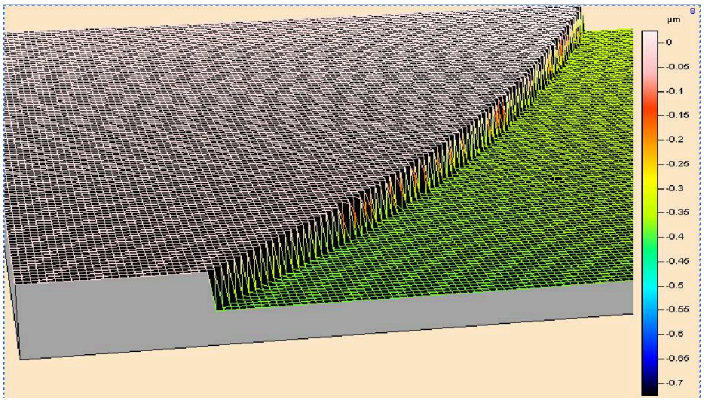


Figure 7 SiC step three-dimensional map

Summarizes

The analysis of experimental data determined that under the parameters of SF_6 gas flow of 80sccm, O_2 gas flow of 5sccm, ICP power of 1200w, bias power of 70w, temperature of 30 ℃, and pressure of 30mTorr, the etching rate of SiC is 246.44nm/min, and the etching rate of epoxy is 616nm/min.

Best etching selectivity ratio of SiC and bisphenol A epoxy resin is about 1:2.5. Under these etching parameters, it can guarantee roughness about 1.3nm or less and good step verticality after etching.

Acknowledgement
Project supported by High-end CNC machine tools and basic manufacturing equipment technology major projects(2013ZX04006011); General Armament Department of advanced manufacturing technology projects (51318020109); Shaanxi Provincial Science and Technology Innovation Project co-ordination (2012KTCQ01-33); Xi'an Industrial Technology Innovation Program (CX12161);

References

[1] HU Jiang; CAI Changlong; LIU Weiguo; GONG Yan-long; Technical Study on Selection ratio of Si /PMMA Based on ICP Etching[J]. Mircoprocessor, 2014, 01:9-11+14.
[2] Leerungnawarat P, Lee K P, Pearton S J, et al. Comparison of F2plasma chemistries for deep etching of SiC [J].J Electron Mater,2001,30(3):202-206.
[3] Kim D W, Lee HY, Park B J, et a l. High rate etching of 6H-SiC in SF6-based magnetically-enhanced inductively coupled plasmas [J]. Thin Solid Films, 2004, 447-448: 100-104.
[4] DING Ruixue, YANG Yintang, HAN Ru. The Etching of Single Crystal 6H-SiC in Inductively Coupled SF6/O2 Plasma [J].Research & Progress of SSE, 2009, 03:343-346.

Key Engineering Materials Vols 645-646 (2015) pp 368-374
© (2015) Trans Tech Publications, Switzerland
doi:10.4028/www.scientific.net/KEM.645-646.368

Submitted: 2014-11-02
Accepted: 2014-12-23

High-Efficiency Preparation of N-Doped Titania with High Visible Light Photocatalytic Activity Using Composite N Precursor

Yulong Hu[1, a], Xiaodong Zhang[2,b], Hongfang Liu[3,c] and Xingpeng Guo[3,d]

[1]College of Science, Naval University of Engineering, Wuhan 430033, China

[2]Office of Research & Department, Naval University of Engineering, Wuhan 430033, China

[3]School of Chemistry and Chemical Engineering, Huazhong University of Science and Technology, Wuhan 430074, China

[a]huyl0702@hotmail.com (corresponding author), [b]zxd2013@vip.sina.com, [c]hongf_liu@163.com, [d]guoxp@mail.hust.edu.cn

Keywords: N-doped TiO_2, high-efficiency preparation, composite N precursor, annealing treatment.

Abstract. N-doped TiO_2 nanoparticle powders were prepared efficiently by the sol-gel method using triethylamine and ammonium hydroxide as composite N precursor. The as-prepared N-doped TiO_2 precursor powders were calcined at 300°C in air for 3 h and subsequently annealed at 300°C in air for 2.5 h. The samples were characterized by X-ray diffraction, transmission electron microscopy, Fourier transform infrared spectroscopy, thermo-gravimetric analysis, and X-ray photoelectron spectroscopy. The visible light photocatalytic activities of as-prepared samples were evaluated by photodecomposition of methyl orange (MO). The results show that the as-prepared samples have high visible light photocatalytic activities. Triethylamine produces the N-species doped in TiO_2 lattice responsible for the high visible light photocatalytic activity. Ammonium hydroxide makes the gel of the TiO_2 nanoparticles nitrided by triethylamine gelate further and facilitates significantly the centrifugation of the gel. An annealing treatment can eliminate effectively the outer N species caused by ammonium hydroxide and the surface organic residues, improve effectively crystallinity, and retain the N species caused by triethylamine.

1. Introduction

Nonmetal-doped TiO_2 nanomaterials are often regarded as promising third generation photocatalysts, and various nonmetal-doped TiO_2 nanomaterials have been widely studied for their visible light photocatalytic activities. [1] Among the various forms of nonmetal-doped TiO_2, N-doped TiO_2 has received the most attention from scientists and engineers. N-doped TiO_2 nanomaterials have been prepared by many methods, [2] such as sol-gel methods, sputtering and implantation techniques, hydrothermal/solvothermal methods, thermal treatment of TiN, high temperature sintering of TiO_2 under N-containing atmosphere. [3] Among these synthesis methods, N-doped TiO_2 nanoparticles are most commonly obtained through the sol-gel method because it can provide a reliable production route of N-doped TiO_2 nanoparticles with low costs and afford simplicity in controlling the N doping level and particle size by simple variations in experimental conditions, such as hydrolysis rate, solution pH and solvent systems. [4] Our previous study [2] and Burda *et al.*'s results [5] show that triethylamine is a good N precursor to prepare N-doped TiO_2 nanoparticles by the sol-gel method, but the preparation efficiency of N-doped TiO_2 nanoparticles through this approach is low. However, it is very difficult to find an N precursor to prepare efficiently N-doped TiO_2 nanoparticles with high visible light photocatalytic activity. The employment of composite N precursor may be an effective way to overcome the problem. In this paper, we use triethylamine and ammonium hydroxide as composite N precursor to prepare N-doped TiO_2 nanocrystalline powders by the sol-gel process. Our study shows that N-doped TiO_2 nanoparticle powders with high visible light photocatalytic activity can be prepared efficiently by the sol-gel method using triethylamine and ammonium hydroxide as fundamental and auxiliary N precursor, respectively, and an annealing treatment is essential for the preparation of high-quality N-doped TiO_2 photocatalysts.

2. Experimental Details

Preparation of N-Doped TiO_2 Nanocrystalline Powders Using Composite N Precursor. The preparation of N-doped TiO_2 nanocrystalline powders was carried out in two steps. First, TiO_2 nanoparticles sol was prepared by controlled hydrolysis of titanium tetraisopropoxide (TTIP, Aldrich, 97 %) in distilled water under controlled pH. Then, the sol was nitrided with N precursor and transformed into gel. The detailed preparation process of N-doped TiO_2 was as follows: 10 mL of TTIP was dissolved in 90 mL of absolute ethanol, and this TTIP solution was then added dropwise into an ethanol mixture solution containing 50 mL of absolute ethanol and 150 ml of distilled water (1 °C) at a given acidity (around pH=1) adjusted with HNO_3. After continuous vigorous stirring of the reaction mixture for 12 h or longer, the solution became transparent and a TiO_2 nanoparticles sol was formed. An excess of triethylamine was added dropwise into the sol to form a suspension of the nitrided TiO_2 nanoparticle gel. In order to facilitate centrifugation of the gel, an adequacy of ammonium hydroxide was added dropwise into the suspension to gelate further. The resulting gel was centrifuged and dried at 65 ºC upon vacuum for 12 h until the formation of xerogel, then the xerogel was grounded into fine powder. The as-obtained N-doped TiO_2 precursor powders were calcined in air at 300 ºC for 3 h and 5.5 h, respectively. The as-obtained powders were designated correspondingly as NT-TA and NT-TA-5.5h, respectively. The powder NT-TA was then annealed in air at 300 ºC for 2.5 h, and the as-obtained powder was designated as NT-TA-An. We also prepared the powders using triethylamine and ammonium hydroxide as single precursor which were calcined in air at 300 ºC for 3 h and designated correspondingly as NT-T and NT-A, respectively.

Characterization. X-ray diffraction (XRD) patterns for N-doped TiO_2 samples were obtained using an X'Pert PRO X-ray diffractometer with Cu Kα radiation. The transmission electron micrographs were obtained using a JEOL JEM-2100F transmission electron microscope (TEM). Fourier transform infrared (FTIR) spectra were measured with a Bruker Equinox 55 spectrometer to analyze the organic residues on the samples. The thermal decomposition behavior of NT-TA was investigated with a thermo-gravimetric (TG) technique using a Cahn TherMax 500 TGA system. The chemical nature of N and the N doping level in TiO_2 were studied by X-ray photoelectron spectroscopy (XPS). The XPS measurements were performed using a VG Multilab 2000 spectrometer. Al Kα X-ray radiation (hv = 1486.6 eV) was used to acquire the core level spectra (O 1s, N 1s, Ti 2p, and C 1s). Linear type background subtraction was utilized to evaluate the XPS data.

Photocatalytic Activity Evaluation. The photocatalytic activities of the N-doped TiO_2 samples were evaluated by the decomposition of methyl orange (MO) under visible light irradiation as described in the previous publication. [2]

3. Results and Discussions

Fig. 1 shows the XRD patterns of the as-prepared N-doped TiO_2 samples. It can be concluded from Fig. 1 that the pure anatase phase was obtained for all samples, but the degrees of crystallization among samples are different. The crystallinities of NT-T and NT-TA are obviously lower than those of NT-A, NT-TA-5.5h and NT-TA-An. The XRD patterns indicate that the increase of calcination time and the annealing treatment at the calcination temperature all improve the crystallization of samples. The average nanocrystal size can be estimated using the Debye-Scherer equation. The sizes calculated from the (101) peak are 7.88, 8.82, and 10.60 nm for NT-TA-An, NT-TA-5.5h, and NT-A, respectively.

Fig. 2 displays the TEM micrographs for the N-doped TiO_2 samples. The agglomeration among the TiO_2 nanocrystals occurred in all as-prepared samples, and larger secondary agglomerated mesoporous particles were formed. Also, Fig.2 shows that the nanocrystal sizes of NT-TA-An is obviously smaller than those of NT-A, larger than those of NT-T. The above results show that the agglomeration of TiO_2 nanoparticle precursor sols caused by ammonium hydroxide is more serious than that caused by triethylamine and the effect of composite N precursor on the agglomeration of TiO_2 nanoparticle precursor sols is between ammonium hydroxide and triethylamine. The TEM

micrographs also show that the annealing treatment at the calcination temperature improves significantly the crystallization of samples.

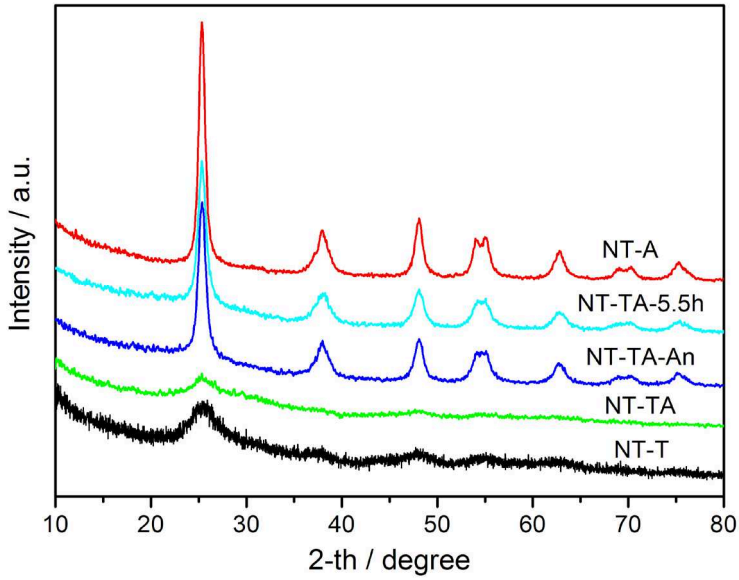


Fig. 1 XRD spectra of serial N-doped TiO_2 samples.

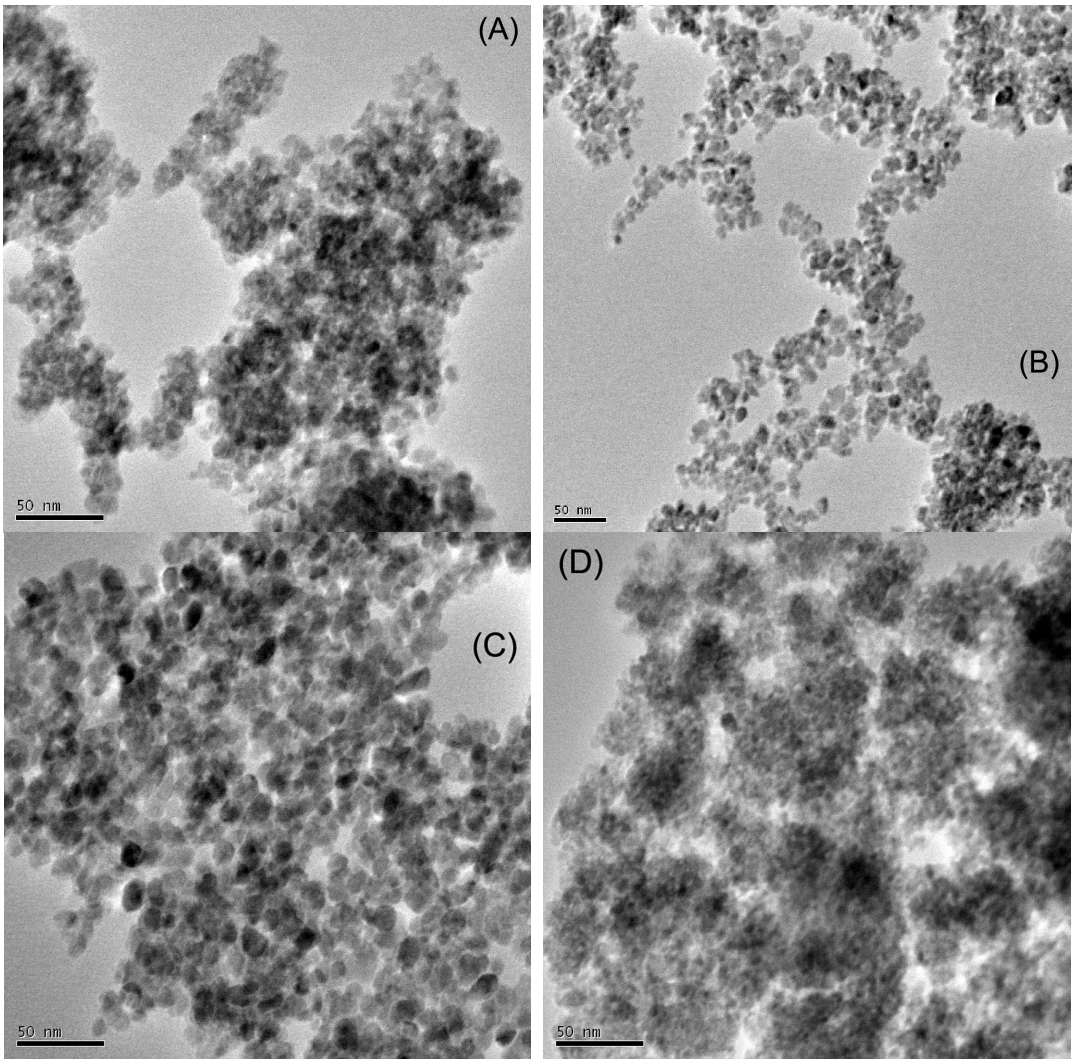


Fig. 2 TEM images of serial N-doped TiO_2 samples: (A) NT-TA , (B) NT-TA-An, (C) NT-A, and (D) NT-T.

The FTIR spectra of N-doped TiO_2 samples are shown in Fig. 3. Three absorption peaks appear in almost all the FTIR spectra, at ~3400, ~1620, and ~1405 cm^{-1}, respectively. The ~1620 cm^{-1} peak is the characteristic bend vibration of N-H, and the ~3400 cm^{-1} peak may be the characteristic stretch vibration of N-H. The ~1620 cm^{-1} peak also may be the characteristic stretch vibration of C=O. The above evidence indicates that the NH group has been doped into the lattice or attached to the N-doped TiO_2 nanoparticles. The ~1405 cm^{-1} peak is the characteristic -O-H bend vibration of adsorbed water molecules, which may come from KBr. The ~1540 cm^{-1} peak, which is also the characteristic bend vibration mode of –N-H, appears in the FTIR spectrum of NT-T and NT-TA, and this may be due to the higher level of NH group in NT-T and NT-TA. The peak at ~1445 cm^{-1}, which is the characteristic deformation vibration mode of $-CH_2-$ or $-CH_3$, appears in the FTIR spectra of NT-T and NT-TA, this indicates that there are more organic residues left on NT-T and NT-TA.

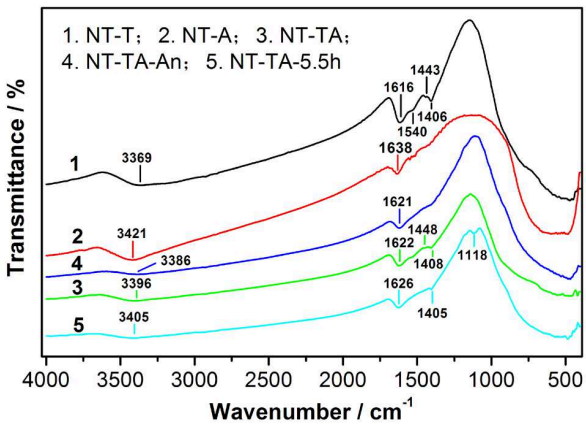


Fig. 3 FTIR spectra of serial N-doped TiO_2 samples.

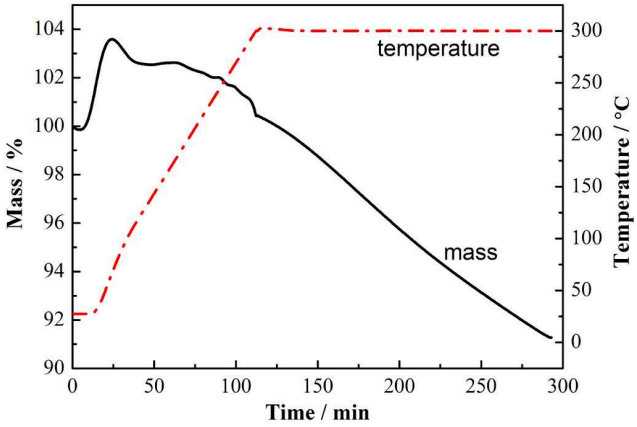


Fig. 4 The TG curve of NT-TA

The thermal behavior of the NT-TA was investigated with a TG technique from room temperature to 300 ºC. The TG curve of NT-TA is shown in Fig. 4. The mass loss is about 8.8%, which is attributed to the loss of organic substances. This illuminates that annealing treatment can eliminate the surface organic residues on the samples effectively.

We have examined four areas of the XPS spectrum: the Ti 2 p region near 460 eV, the O 1s region near 530 eV, the N 1s region near 400 eV, and the C 1s region near 285 eV. The C1s spectra, O1s spectra, Ti2p spectra, and the peak fits of N 1s spectra are shown in Fig. 5. The binding energy of the peaks and the content of elements measured by XPS are listed in Table 1. According to the FTIR results, several studies in the literature [6], and our previous study [2], we assign the N 1s peak at 399-400 eV in the samples to N-H species located in interstitial sites of TiO_2 lattice, which is the active N species responsible for the visible light photocatalytic activity. The content of the doped N species decreases in the order NT-T, NT-TA, NT-TA-An, NT-TA-5.5h, and NT-A. This indicates that long-time calcination can result in the serious loss of the doped N and annealing treatment can retain more doped N. It is known that NO and NO_2 species appear above 400 eV, hence the N 1s peak above 400 eV in the samples can be assigned to the oxidized N, which may be molecularly adsorbed on the samples.

Fig. 6 shows the concentration changes of the MO solution during visible light photocatalytic decomposition over various N-doped TiO_2 samples. The results show that the visible light photocatalytic activity decreases in the order NT-TA-An, NT-TA-5.5h, NT-T, NT-TA, and NT-A while the visible light irradiation time is shorter than 3 h, but the visible light photocatalytic activity of NT-T becomes higher than that of NT-TA-5.5h while the irradiation time is longer than 3 h. The reversal of photocatalytic activity of NT-T and NT-TA-5.5h may be due to photocatalytic decomposition of the surface organic residues on NT-T. The visible light photocatalytic activity of NT-A is very low, and the visible light photocatalytic activity of NT-TA-An is clearly higher than that of NT-T and NT-TA-5.5h.

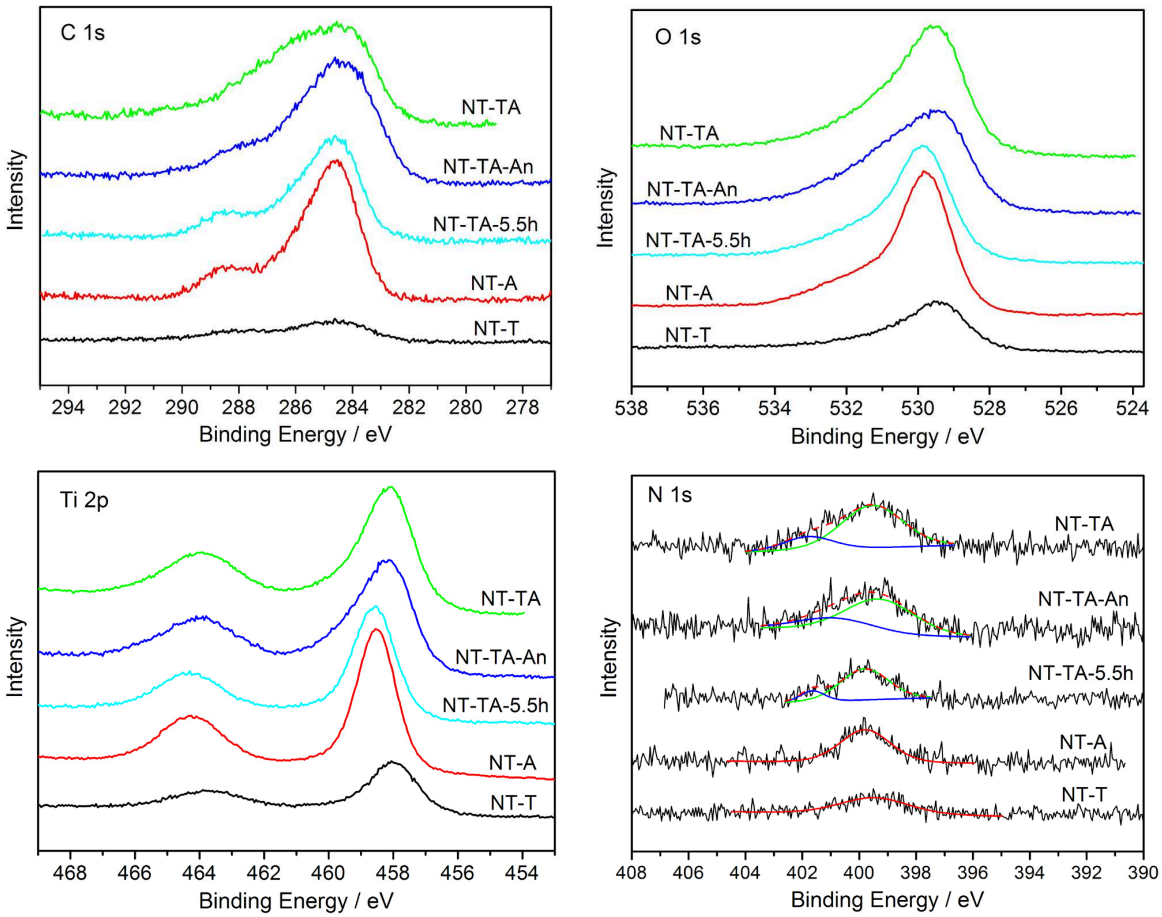


Fig. 5 XPS spectra of serial N-doped TiO_2 samples

Table 1 Positions of the peaks in XPS spectra of serial N-doped TiO_2 samples and quantitative data measured by XPS.

Sample	Ti 2p		O 1s		N 1s	
	Peak, eV	At. %	Peak, eV	At. %	Peak, eV	At. %
NT-T	458.03	20.06	529.48	60.83	399.50	1.40
NT-A	458.50	15.15	529.79	49.77	399.90	0.65
NT-TA	458.12	14.23	529.43	40.46	399.54	1.05
					401.78	0.27
NT-TA-An	458.19	13.6	529.36	36.48	399.27	0.98
					400.86	0.33
NT-TA-5.5h	458.56	14.53	529.85	52.76	399.81	0.80
					401.64	0.14

The visible light photocatalytic activity of N-doped TiO_2 is related to the N doping level, nanocrystal size, surface organic residues, and crystallinity. Although the N-doping level of NT-TA-An and NT-TA-5.5h are lower than that of NT-TA, NT-TA-An and NT-TA-5.5h have higher crystallinity and fewer surface organic residues, which results in that the visible light photocatalytic activity of NT-TA-An and NT-TA-5.5h both are higher than that of NT-TA. The higher N doping level and smaller nanocrystal size result in that the visible light photocatalytic activity of NT-TA-An is significantly higher than that of NT-TA-5.5h. Compared with NT-TA-An, although NT-T has smaller nanoparticle size and higher N doping level, NT-T has more surface organic residues and its

crystallinity is very low. The integrated effect of N doping level, nanoparticle size, surface organic residues, and crystallinity results in the visible light photocatalytic activity of NT-TA-An is significantly higher than that of NT-T.

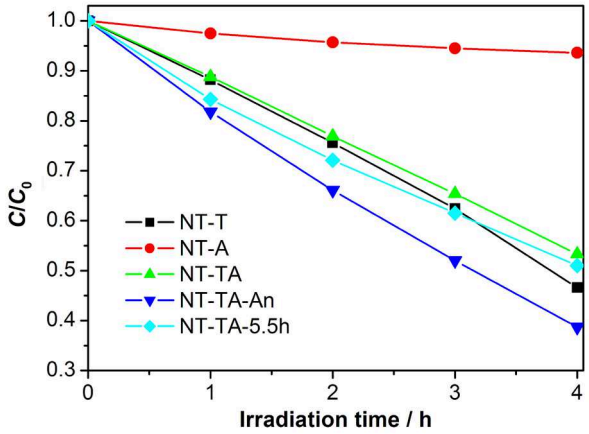


Fig. 6 Concentration changes of MO solution during visible light photocatalytic decomposition over serial N-doped TiO_2 samples.

The above results illuminate that the N-doped TiO_2 nanoparticle powder with high visible light photocatalytic activity can be prepared efficiently using triethylamine and ammonium hydroxide as composite N precursor. The effect of N precursor on the gel process of the TiO_2 nanoparticle precursor sol is different and the agglomerations of TiO_2 nanoparticle precursor sols caused by various N precursors are different. Triethylamine shows a medium alkalinity and causes the residual alkoxy groups of TiO_2 nanoparticle precursor sol to be partially substituted by amine groups and partially substituted by hydroxyl groups, which results in the formation of a loosely agglomerated gel and makes the gel be difficult to be centrifuged. Ammonium hydroxide have strong alkalinity and causes the residual alkoxy group of TiO_2 nanoparticle precursor sol to be primarily substituted by hydroxyl groups, which results in the formation of a closely agglomerated gel and makes the gel be easy to be centrifuged. The difference of N precursor in the gel process results in the difference in the productivity of the TiO_2 nanoparticle powder. The productivity of the TiO_2 nanoparticle powder using ammonium hydroxide as N precursor is significantly higher than that using triethylamine as N precursor. But the visible light photocatalytic activity of the sample prepared using ammonium hydroxide is very low. Different N precursor forms different N species doped in TiO_2 lattice. The N species formed by triethylamine have high visible light photocatalytic activity, but the activity of the N species formed by ammonium hydroxide triethylamine is very low. Therefore, the N species doped in TiO_2 lattice should mainly be formed by triethylamine in order to obtain the sample with high visible light photocatalytic activity. We propose the scheme of gelation using triethylamine and ammonium hydroxide as composite N precursor (Fig. 7). Ammonium hydroxide can make the residual alkoxy group of the nitrided TiO_2 nanoparticle gel by triethylamine be substituted by hydroxyl groups and make the nitrided gel gelate further, which can facilitate obviously the centrifugation of the gel. Undergoing the calcination process of N-doped TiO_2 precursor, there are the N species caused by triethylamine and ammonium hydroxide both existing on the sample. Annealing treatment can eliminate effectively the outer N species caused by ammonium hydroxide and the surface organic residues, improve effectively crystallinity, and retain the N species caused by triethylamine. Long-time calcination also can eliminate effectively the outer N species caused by ammonium hydroxide and the surface organic residues, improve effectively crystallinity, but results in the serious loss of N species caused by triethylamine. We think the above evidence is the main reason why the visible light photocatalytic activity of NT-TA-An is obviously higher than that of NT-TA-5.5h significantly.

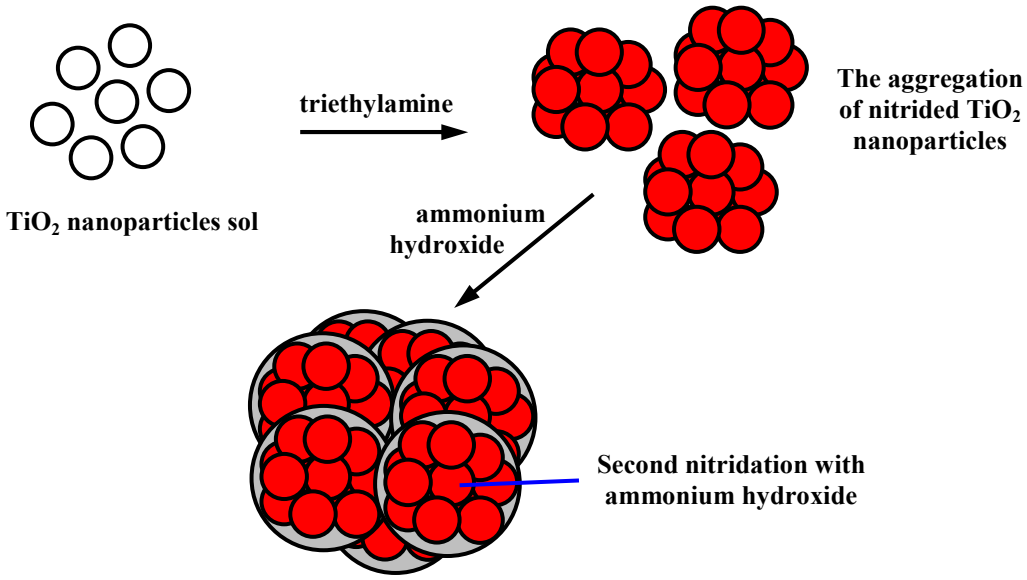


Fig. 7 Simplified scheme of gelation using triethylamine and ammonium hydroxide as composite N precursor

4. Conclusions

Combining with an annealing treatment, N-doped TiO_2 nanoparticle powders with high visible light photocatalytic activity have been prepared efficiently by a sol-gel method using triethylamine and ammonium hydroxide as composite N precursor. As the fundamental N precursor of N-doped TiO_2 nanoparticles, triethylamine makes the TiO_2 nanoparticle sol nitride and gelate, which produces the N-species doped in TiO_2 lattice responsible for the high visible light photocatalytic activity. As the auxiliary N precursor, ammonium hydroxide makes the gel of the TiO_2 nanoparticles nitrided by triethylamine gelate further and facilitates significantly the centrifugation of the gel. The as-prepared N-doped TiO_2 nanoparticle powders were calcined at 300°C in air for 3 h and subsequently annealed at 300°C in air for 2.5 h. An annealing treatment can eliminate effectively the outer N species caused by ammonium hydroxide and the surface organic residues, improve effectively crystallinity, and retain the N species caused by triethylamine. Therefore, an annealing treatment is essential for the preparation of high-quality N-doped TiO_2 photocatalysts.

References

[1] X. Chen, S.S. Mao, Titanium dioxide nanomaterials: Synthesis, properties, modifications, and applications, Chem. Rev. 107 (2007) 2891-2959.

[2] Y. Hu, H. Liu, Q. Rao, X. Kong, W. Sun, X. Guo, Effects of N precursor on the agglomeration and visible light photocatalytic activity of N-doped TiO_2 nanocrystalline powder, J. Nanosci. Nanotechnol. 11 (2011) 3434-3444.

[3] A. Kachina, E. Puzenat, S. Ould-Chikh, C. Geantet, P. Delichere, P. Afanasiev, A new approach to the preparation of nitrogen-doped titania visible light photocatalyst, Chem. Mater. 24 (2012) 636-642.

[4] X. Qiu, C. Burda, Chemically synthesized nitrogen-doped metal oxide nanoparticles, Chem. Phys. 339 (2007) 1-10.

[5] C. Burda, Y. Lou, X. Chen, A.C.S. Samia, J. Stout, J.L. Gole, Enhanced nitrogen doping in TiO_2 nanoparticles, Nano Lett. 3 (2003) 1049-1051.

[6] A. Fujishima, X. Zhang, D. A. Tryk, TiO_2 photocatalysis and related surface phenomena, Surf. Sci. Rep. 63 (2008) 515-582.

Key Engineering Materials Vols 645-646 (2015) pp 375-380
© (2015) Trans Tech Publications, Switzerland
doi:10.4028/www.scientific.net/KEM.645-646.375

Submitted: 2014-11-02
Accepted: 2014-12-23

UV Photocatalytic Digestion Utilizing TiO_2 Nano-fiber for the Determination of Total Phosphorus

Qiang Zhang[1,2], Jianhua Tong[1], Chao Bian[1], Shanhong Xia[1, *]

[1] State Key Laboratory of Transducer Technology, Institute of Electronics, Chinese Academy of Sciences, Beijing, CHINA

[2] Graduate University of Chinese Academy of Sciences, Beijing, CHINA

[*]Corresponding author: Email shxia@mail.ie.ac.cn

Keywords: Electro-Spinning, Nano-TiO_2 Fiber, Ultraviolet Photocatalytic Oxidation, Total Phosphorus

Abstract: This paper describes the fabrication, characterization and the application of the photocatalytic TiO_2 nano-fiber as the photocatalyst for the digestion of total phosphorus (TP). The nano-TiO_2 fibers were fabricated by the electro-spinning technique on silicon substrate. Under the conditions of room temperature(25 degrees Celsius) and humidity less than 40%, the TiO_2 fabricated by the electro-spinning presents a silky coagulation appearance, which can be converted to the nano-fiber appearance by annealed in the muffle furnace at 450 degrees Celsius for 10 hours. X-ray diffraction (XRD) examination shows that the silky coagulation can be converted to anatase-type TiO_2. The absorbance values of different phosphate concentrations after exposure in UV light at the intensity of 7000μW/cm^2 were tested in this paper. Sodium tripolyphosphate solutions serve as the water sample of TP, and five standard concentrations (by weight of P) are 0.0mg/L, 1.0mg/L, 2.0mg/L,3.0mg/L and 4.0mg/L, respectively. The digestion rate exhibits satisfied linearity ranges from 0.0mg/L to 4.0mg/L with acceptable linearity R^2 of calibration curve, in both digestion temperature of 25 degrees Celsius and 50 degrees Celsius.

Introduction

Phosphorus is one of the essential elements of biological growth, but the content of phosphorus in water (if more than 0.1mg/L), can cause overgrowth of algae and accelerate the degree of eutrophication[1]. To protect water quality and control hazards, the detection of TP has been one of the most important parameters of environmental monitoring. A digestion pretreatment procedure of the water sample will be conducted before the determination of TP, to convert various types of phosphorus to phosphate. Compared with traditional digestion method of high temperature oxidation, photocatalysis has the merits of relatively high efficiency, low power consuming, secondary pollution free, and chemically stability [2-5].The high specific surface area of nano-fiber leads to an increase in surface energy and photocatalytic activity, thus TiO_2 nano-fiber has been proposed for the elimination of organic pollutants.

Electro-spinning utilizes static electricity to prepare polymer fibers. In preparing one-dimensional nano-materials, electro-spinning has the merits of relatively simple experimental conditions, easy to operate, and less preparation steps. Electro-spinning equipment mainly includes three parts: a micro syringe pump, a high-voltage statitron and a receptor, as shown in figure 1[6]. The micro syringe pump pushes polymer solution to eject from the syringe needle; the high-voltage statitron provides a DC voltage as high as 1kV ~ 30kV; the receptor is generally a metal plate, which is grounded. During the electro-spinning process, the high voltage power is connected with the polymer solution via a high voltage electrode, and is connected to ground via collector electrode.

The UV digestion method makes the use of ultraviolet oxidation to digest total phosphorus. The photocatalytic process at semiconductors is initiated by the photogeneration of hole/electron pairs (e^-/h^+) by absorption of UV-light with energy equal to or higher than the corresponding band gap (3.2 eV for anatase (TiO_2)). This digestion method can be used to oxidize many organic pollutants that a single oxidant can not break down [7]. Among many kinds of photo catalyst, titanium dioxide (TiO_2) has often been proposed for the elimination of organic pollutants, due to the merits of relatively inexpensive, safe, chemically stable and high photocatalytic activity[8-11].

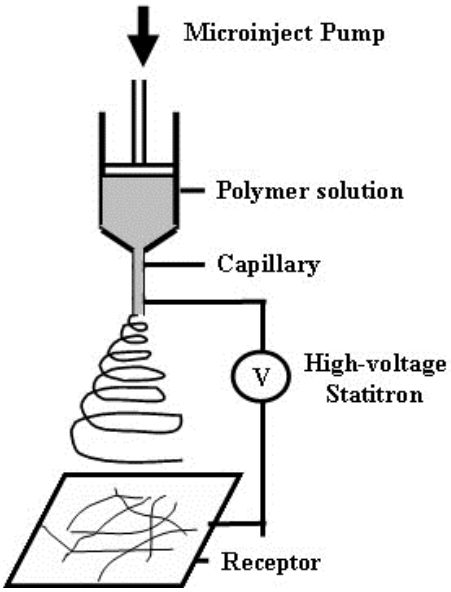


Fig. 1 Schematic diagram of electro-spinning

2 Experimental

2.1 Materials and equipments. Tetrahydrofuran (C_4H_8O) and N, N-dimethylformamide [HCON (CH_3) $_2$] were blended to dissolve polystyrene (C_6H_5). After blended, butyl titanate [$Ti(OC_4H_9)_4$] and acetic acid (CH_3COOH) are added to the PS solution. All chemical regents are from Beijing Chemical Reagent Company, China.

The receptor of electro-spinning is a 2-inch wafer (Electronics Technology Group, China) attached to the aluminum foil; a micro srpinge pump (LSP01-2A, from Lange, China) pushes the polymer solution; The high-voltage equipment is a high voltage power supply (DW-P303-1AC from Eastman high voltage power company, China); a syringe (Beijing Kepujia Instrument Co., China) contains polymer solution; a magnetic stirrer (SH-4, Jinbeide Company, China) is used to blend solutions.

The Sodium tripolyphosphate ($Na_5P_3O_{10}$, Beijing Chemical Reagent Company, China) is used to construct the calibration curves, and the concentrations of the test solutions were 0.0, 1.0, 2.0, 3.0 and 4.0 mg/L (by weight of P). Ascorbic acid ($C_6H_8O_6$), ammonium molybdate [$(NH_4)_6Mo_7O_{24}\cdot 4H_2O$], potassium antimony tartrate ($KSbC_4H_4O_7\cdot 1/2H_2O$) and H_2SO_4 (Beijing Chemical Reagent Company, China) were used to prepare the color reagent for the digested water samples. The solutions were all used without pH adjustment [12].

The UV light was supplied by a middle-pressure lamp (SB-100P/F/J from Brightstars Corporation, China); a hot plate (KW-4AH from Chemat Technology Corporation, China) was used as the heating equipment; Ultraviolet spectrophotometer (Biospec-nano from Shimadiu Corporation, Japan) was employed to measure the concentration of orthophosphate.

2.2 Preparation of TiO_2. Firstly, a amount of Butyl titanate [$Ti(OC_4H_9)_4$]was placed in a stoppered conical flask, followed by the slow (dropwise) addition of acetic acid to the flask, and stirred with a

magnetic stirrer until the TiO_2 precursor solution was yellow and transparent; then polystyrene (C_6H_5) was dissolved in the mixed solution of tetrahydrofuran (C_4H_8O) and N, N-dimethylformamide [HCON $(CH_3)_2$], added the precursor solution, stirred until the mixed polymer solution was transparent; next, the polymer solution was sucked into a glass syringe, followed by adjusting injection rate, output of the high voltage power supply and the distance of the capillary and the receptor, so that the polymer solution ejected from the capillary and amorphous TiO_2 gel fibers fell on the wafer[13-17]; last of all, the fibers were put in a muffle furnace at 450 degrees Celsius for 10 hours, and cool naturally.

2.3 Measurement. The digestion process of water sample was started by immersing the TiO_2 nanofibers-attached silicon chip into the cylinder reactor, and then turned on the UV light and heater. Five reactors (one for blank control, the others for the water samples) were placed on the heater, under the UV lamp. The radiated power of UV light (365nm) on the surface of the chip was 7000 $\mu W/cm^2$, lasting for 120 minutes. The temperature of the reaction was controlled by the heater. When digestion finished, the solutions need to be cooled for 10 minutes, and then 1 ml ascorbic acid solution and 1 ml ammonium molybdate solution were added into the digested solution in order. This mixed solution was kept in stable for 15 minutes after mixed thoroughly. The orthophosphate concentration (weight by P) of the digested solution was measured by the ultraviolet spectrophotometer at the wavelength of 700 nm against a reagent blank. The supported TiO_2 was used repetitively and the silicon wafers was swashed with ultra-pure water for 2 minutes after each digestion process.

3 Results and discussion

3.1 Fabrication results. The SEM image of nano-TiO_2 on the surface of silicon wafer is shown in figure 2. As shown in the image, the TiO_2 nano-fibers were intertwined, and the average diameter of the fiber was about 250nm.

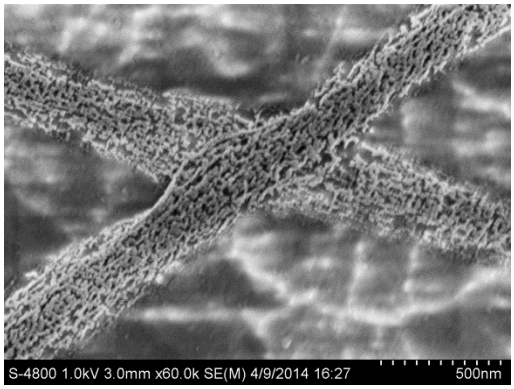


Fig. 2 SEM image of nano-TiO_2 fibers on silicon wafer surface

3.2 Measurement result. Figure 3 shows the calibration curve of the absorbance values and the concentration of phosphate (by weight of P).The obtained photocatalytic TiO2 nano-fiber exhibited acceptable digestion rate when the water sample exposed in UV at the intensity of 7000$\mu W/cm^2$ in the room temperature (25 degrees Celsius) and 50 degrees Celsius for 120 minutes, as shown in figure 4 and figure 5.

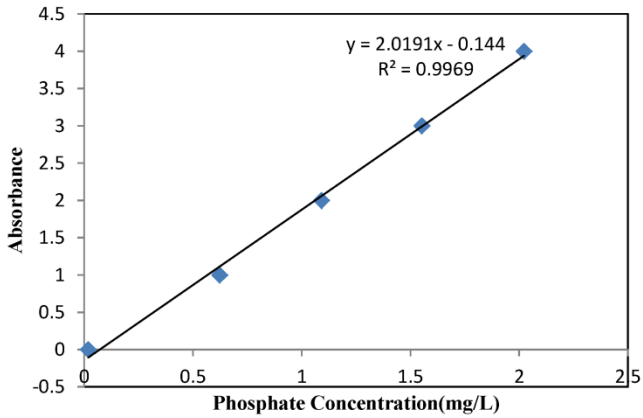


Fig. 3 Calibration curve of the absorbance values and the concentration of phosphate (by weight of P)

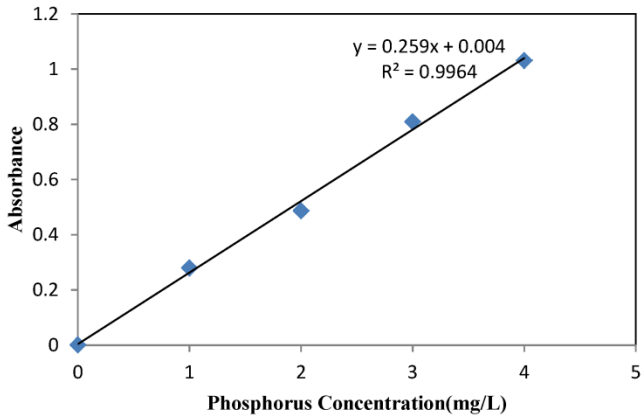


Fig. 4 The absorbance at different phosphorus concentrations after exposure in UV at the intensity of 7000μW/cm^2 at 25 degrees Celsius for 2 hours.

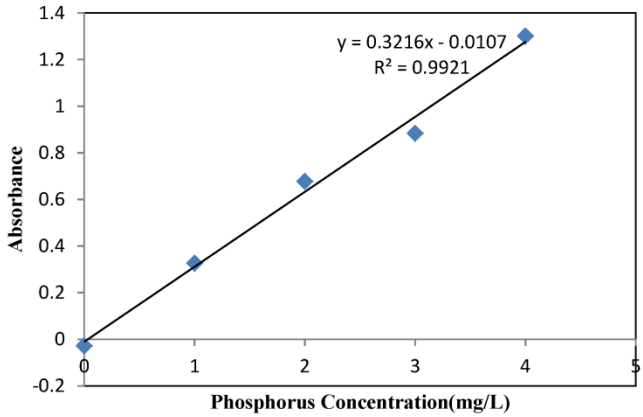


Fig. 5 The absorbance at different phosphorus concentrations after exposure in UV at the intensity of 7000μW/cm^2 at 50degrees Celsius for 2 hours.

4. Conclusion

This work presents the fabrication, characterization and the application of the TiO_2 nano-fiber photocatalyst for total phosphorus (TP) digestion. The nano-TiO_2 fibers were fabricated by the electro-spinning technique on silicon substrate, and annealed in muffle furnace. The absorbance values of different phosphate concentrations after exposure in UV light at the intensity of 7000μW/cm^2 were tested in this paper, and the digestion rate exhibits satisfied linearity ranges from

0.0mg/L to 4.0mg/L with acceptable linearity R^2 of calibration curve, in both digestion temperature of 25 degrees Celsius and 50 degrees Celsius. Compared with traditional digestion method of high temperature oxidation, photocatalytic oxidation has the merits of relatively high efficiency, low power consuming, secondary pollution free, and chemical stability. The high specific surface area of nano-fiber leads to an increase in surface energy and photocatalytic activity, thus the application of TiO_2 nano-fiber will tremendously contribute to the degradation of organic component.

5. Acknowledgements

The authors express our deep gratitude to the staff at the State Key Laboratory of Transducers Technology at the Institute of Electronics, Chinese Academy of Sciences for clean room and micro fabrication support. We acknowledge financial support from the National Natural Science Foundation (No. 61372053), and the National High Technology Research and Development Program (863 Program, No. 2012AA040506).

References

[1] Alfons J. P. Smolders, E. C. H. E. T. L., Roland Bobbink, Jan G. M. Roelofs, Leon P. M. Lamers. How nitrate leaching from agricultural lands provokes phosphate eutrophication in groundwater fed wetlands: the sulphur bridge. Biogeochemistry, 98(1-3), 1-7. doi: 10.1007/s10533-009-9387-8.

[2] J.-M. Lee, M.-S.Kim, B.-W. Kim, Water Res. 38 (2004), pp. 3605.

[3] Sylvie Lacombe‼ HYPERLINK "http://link.springer.com/article/10.1007/s11356-014-3192-1/fulltext.html" \l "ContactOfAuthor1" ¶ ⊥, Fernando Fresno and Urška Lavrenčič Štangar, ‼ HYPERLINK "http://link.springer.com/article/10.1007/s11356-014-3192-1/fulltext.html" \l "ContactOfAuthor3" ¶ ⊥ Photocatalysis: new highlights from JEP 2013. Environmental Science and Pollution Research,10.1007/s11356-014-3192-1.

[4] Malgorzata Wojtoniszak, D. D., Antoni Morawski, Ewa Mijowska. Carbon-modified TiO2 for photocatalysis. Nanoscale Research Letters. doi: 10.1186/1556-276X-7-235.

[5] Xu J, Xiao X, Ren F, Wu W, Dai Z, Cai G, Zhang S, Zhou J, Mei F, Jiang C.Enhanced photocatalysis by coupling of anatase TiO2 film to triangular Ag nanoparticle island. ‼ HYPERLINK "http://www.ncbi.nlm.nih.gov/pubmed/22548875" \o "Nanoscale research letters." ¶ Nanoscale Res Lett.⊥ 2012 May 2;7(1):239. doi: 10.1186/1556-276X-7-239.

[6] G. I. Taylor,Electrically driven jets, Proc. Roy. Soc. Lond,1969, 3 13, 453.

[7] Gabriel L. Kreft, Otoniel C. de Braga. Analytical electrochemistry of vitamin B12 on a bismuth-film electrode surface. Electrochimica Acta. 2012,83:125.

[8] Daniela Daniel, Ivano G.R. Grutz, Microfluidic cell with a TiO2- modified gold electrode irradiated by an UV-LED for in situ photocatalytic decomposition of organic matter and its potentiality for voltammetric analysis of metal ions, Electrochemistry Communications 9 (2007) 522-528.

[9] Mehdi Shirzad Siboni, Mohammad-Taghi Samadi, Jae-Kyu Yang, Seung-MokLee, Photocatalytic removal of Cr(VI) and Ni(II) by UV/TiO2: kinetic study, Desalination and Water Treatment 40 (2012) 77–83.

[10] Mehmet Uğurlu, M. Hamdi Karaoğlu, Removal of AOX, total nitrogen and chlorinated lignin from bleached Krsft mill effluents by UV oxidation in the presence of hydrogen peroxide utilizing TiO2 as photocatalyst, Environmental Science and Pollution Research 16 (2009): 265-273.

[11] J.C. Garcia, J.L. Oliveira, A.E.C. Silva, C.C. Oliveira, J. Nozaki, N.E. de Souza, Comparative study of the degradation of real textile effluents by photocatalytic reactions involving UV/TiO2/H2O2 and UV/Fe2+/H2O2 systems, Journal of Hazardous Materials 147 (2007) 105-110.

[12] Tian Dong, Jian Hua Tong, Chao Bian, Jizhou Sun Sun, Shan Hong Xia,Thermal-assisted UV digestion utilizing nano-TiO2 photocatalyst for the detection of total phosphorous, Nanomaterials 6 (2014) 964-969.

[13] Nguyen Thuy Ba Linh,Kap-Ho Lee, Byong-Taek Lee. Fabrication of photocatalytic PVA–TiO2 nano-fibrous hybrid. J Mater Sci (2011) 46:5615–5620 DOI 10.1007/s10853-011-5511-y.

[14]Allahbakhsh Javid, S. N., Alireza Mesdaghinia, Amir hossein Mahvi, Mahmood Alimohammadi, Rouhollah Mehdinavaz Aghdam, Noshin Rastkari. Performance of photocatalytic oxidation of tetracycline in aqueous solution by TiO2 nanofibers. Journal of Environmental Health Science and Engineering. doi: 10.1186/2052-336X-11-24.

[15] Mario Boehme, W. E. Mixed Phase Anatase/rutile Titanium Dioxide Nanotubes for Enhanced Photocatalytic Degradation of Methylene-blue. Nano-Micro Letters, 3(4), 236-241 doi: 10.1007/BF03353678.

[16] ‼ HYPERLINK "http://www.sciencedirect.com/science/article/pii/S0167577X08006885" ¶ C. Tekmen⊥ , , ‼ HYPERLINK "http://www.sciencedirect.com/science/article/pii/S0167577X08006885" ¶ A. Suslu⊥ , ‼ HYPERLINK "http://www.sciencedirect.com/science/article/pii/S0167577X08006885" ¶ U. Cocen⊥ ,Titania Nanofibers Prepared by Electrospinning. Materials Letters,Volume 62, Issue 29, 30 November 2008, Pages 4470–4472.

[17] Katsuhiro Onozuka, Bin Ding, Yosuke Tsuge, Takayuki Naka, Michiyo Yamazaki, Shinichiro Sugi, Shingo Ohno, Masato Yoshikawa and Seimei Shiratori, Electrospinning processed nanofibrous TiO2 membranes for photovoltaic applications. Nanotechnology, doi:10.1088/0957-4484/17/4/030.

Key Engineering Materials Vols 645-646 (2015) pp 381-387
© (2015) Trans Tech Publications, Switzerland
doi:10.4028/www.scientific.net/KEM.645-646.381
Submitted: 2014-11-03
Accepted: 2014-12-23

Research of thin film for laser polarization beam splitter

Fu Xiuhua Pan Yonggang Liu Dongmei ZHang Jing
and Wang Xiaojuan

College of Opto-Electronic Engineering，Changchun University of Science and Technology，
Changchun，Jilin 130022，China

Key words: Thin film; polarizing beam-splitting film; laser damage threshold; ion assisted deposition; adhesion

Abstract： Based on the design theory of film stack,H4 and SiO2 were selected as the high and low refractive index materials respectively. Through optimization by Macleod and TFCalc software, plus considering the internal electric field intensity distribution of film and laser induced damage threshold as well,the beam-splitting film with Tp=65±5% and Ts=30±5% in the 600-700 band in condition of 45 °± 3 ° incident angle has been achieved. Adopting electron beam ion assisted deposition system to development, the deposition parameters of materials has been optimized via orthogonal matrix experiment. The fabrication of thin film for laser polarization beam splitter has been succeeded. Its optical properties, mechanical properties and resistance to environmental test of the film have been approved to meet all using requirements.

1.Introduction

With the rapid development of laser technology, laser have been used for various kinds of applications, such as aerospace remote sensing , metallurgy, communication, medical science and every daily life. It has become an important part in modern photoelectric instrumentation systems. However, the stability of optical thin film devices plays a crucial role on the performance of laser system, which makes it particularly important to research on thin film for laser polarization beam splitter. At present, the research are mainly done by some European-American countries ,which realize Tp high transmittance ,Ts high reflectivity and high extinction ratio, but there is seldom related reports on specific research of thin film for laser polarization beam splitter[1-5]. This article mainly focus on optical performance in 600-700 band, and high layer intensity, little absorption and small amount of drift are preferred.

2 Selection of film materials:

For laser film, not only the transparent region shall be concerned ,but also absorption, the matching performance between layers, layer and substrate material, and the laser damage threshold of material as well. ZrO2, Ta2O5 and H4 are common used as material of high refractive index, MgF2 and SiO2 of low refractive index in visible band.

The refractive index of material ZrO2 is significantly lower than Ta2O5 and H4, and the ZrO2 film in atmosphere will absorb vapor when heated by e-beam gun evaporation[6], so the ZrO2 multilayer film spectral curve will change, the spectral would lose its stability. Experiments show that the laser damage threshold of Ta2O5 is lower than the H4 . Finally[7-8], H4 was chosen as the material of high refractive index.

The laser damage threshold of MgF2 and SiO2 are both high，and MgF2 will create spray during the deposition process, and it has large tension stress. Thus, when the thickness of MgF2 monolayer film is over 2um, there would be caused stripping phenomenon easily[9]. Therefore, SiO2 is chosen as the material of low refractive index.

3 .Determination of process parameters and refractive index of materials:

Process parameters will affect the film properties directly, so optimization of process parameters for preparation of optical thin film acts as an important step. Once the process parameters being fixed, the optical constants of the material can be took into calculations as reliable.

3.1 Study on the process parameters

Adopting the orthogonal matrix method to optimize the process parameters, by analyzing the experiment data, appropriate optimization parameters have been obtained. This method greatly reduced the number of experiments, shorten the research cycle. The specific, orthogonal experiment data are shown in Table 1, the specific parameters of orthogonal table are shown in Table 2.

Table1 Date of orthogonal matrix tests

Sample No.	Deposition rate	Substrate temperature	vacuum	Ion beam Intensity	Refractive index of H4 (λ=550nm)	Refractive indexofSiO2 (λ=550nm)
1#	1	1	1	1	1.941	1.472
2#	1	2	2	2	1.952	1.475
3#	1	3	3	3	2.004	1.478
4#	2	1	2	3	1.963	1.474
5#	2	2	3	1	1.957	1.476
6#	2	3	1	2	1.948	1.474
7#	3	1	3	2	1.946	1.473
8#	3	2	1	3	1.965	1.476
9#	3	3	2	1	1.938	1.474

Table2 Specific parameters of orthogonal matrix

Sample No.	Deposition Rate of H_4 (nm/s)	Deposition Rate of SiO_2 (nm/s)	Substrate temperature(℃)	vacuum（Pa）	Ion beam Intensity (mA)
1	0.2	0.5	260	5.0x10-3	50
2	0.3	0.7	280	4.0x10-3	60
3	0.6	0.9	310	3.0x10-3	70

From the table, it has been concluded that, in a certain range, with the increase of deposition rate or substrate temperature, vacuum degree, either ion beam density of ion source, the refractive index of H4 and SiO2 will be increased too[10-11]. The reason is that proper increase of deposition rate, substrate temperature ,vacuum degree and ion beam density of ion source can enhance the rate of film-forming particles at the surface of film ,compact the coating, enhance the refractive index of materials.

Observing these 9 groups of test pieces by atomic force microscope, it has been found that, in group 3#, 4#, 8# ,films have larger dimension ? of surface roughness than the other groups, it is because of a higher density by the ion beam assistance, resulting in serious surface etching of film; in addition, too large kinetic energy of particles and the obvious shading effect on the film surface, which were both main reasons lead to surface roughness amplifications.

It was observed that the film has obvious absorption while the deposition rate of H4 is 0.6nm/s in the process. According to experimental verification, it was due to the high deposition rate,

resulting in loss of oxygen of H4. By reducing deposition rate and filling proper amount of high purity oxygen into the vacuum chamber, the absorption phenomenon can be diminish dramatically to nearly zero. According to the research and analysis above, the final parameters have been got as shown in Table 3, Table 4.

Table3 The process parameters of practical preparation

	Deposition rate （nm/s）	Substrate temperature （℃）	vacuum （Pa）	Flow of O_2 （sccm）
H_4	0.3	290	$9.0x10^{-3}$	10
SiO_2	0.7	290	$6.0x10^{-3}$	6

Table4 The parameters of ion source

Plate Voltage/V	Accelerating Voltage/V	Anode Voltage/V	Neutralize Current/A	Cathode Current/mA	Ion beam /mA
420	350	55	20	15	60

3.2 Determination of refractive index of the materials.

As the refractive index of thin film materials behaviors chromatic dispersion distribution，we need to get the real refractive index chromatic dispersion distribution of materials under the conditions above. By depositing a certain thickness coating and measuring its spectral curve, we can obtain the refractive index of materials using Cauthy formula: n（λ）=An+Bn/λ2. (In this formula ,An and Bn represent the fitting parameters） Fig.1 shows the refractive index dispersion curves of H4 and SiO2 obtained in the experiment.

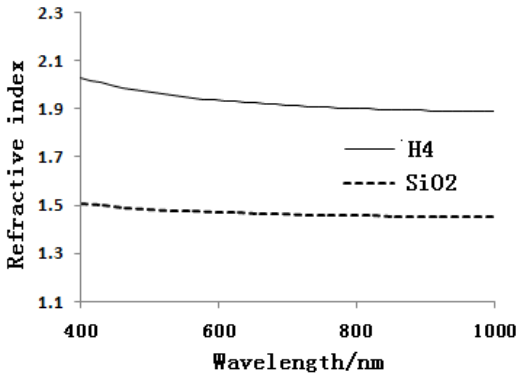


Fig1 The refractive index dispersion curves of H4 and SiO2

4 .Coating design

Based on the analysis of standing wave theory, the amount of film loss is determined by the intensity distribution of light inside the film ,the damage of polarization film depends on the maximum electric field intensity of S-light, P-light in the film. Therefore, we have to consider the distribution of the electric field intensity in the film when we design plate polarized film with high threshold. At the same time, the optical properties and the electric field distribution inside the film should also be considered during the design.

Comparing with the simulation of many optimization methods, it was found that the Optimax optimization method is reasonable, through the repeated simulation optimization by using the Optimax method , we conclude that optimal weights of P and S light, has little influence on the

optical performance of film, but much influence on the distribution of electric field inside the film greatly.

Combined with technical requirements, Sub|2L (HL) ^s 2H|Air is used as the basic coating structure of beam splitting film ,Sub represents the substrate, H and L represent SiO2.Based on the film design software to optimize the basic coating structure. Specific parameters: optimization band is 550nm~750nm;incident angle is 45 °;deviation is 0.5;optimization goal of P-light is 65%; S-light is 30%; using different weights to optimize, among them, two groups of weight are reasonable in repeated experiments. Group 1: P light weight is 0.5, S light weight is 0.5.Group 2 P light weight is 1, S weight is 0.5.Fig 3 shows the theoretical spectral curve of two group weights obtained.

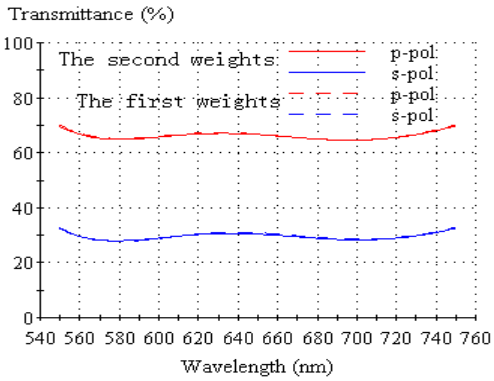


Fig2 Theory spectral curve

From the figure, there are two theoretical design curves coincide basically when adopting two groups of weight to optimize .However, the electric field distribution inside the film are different. The specific distribution were plotted over in Fig.4.

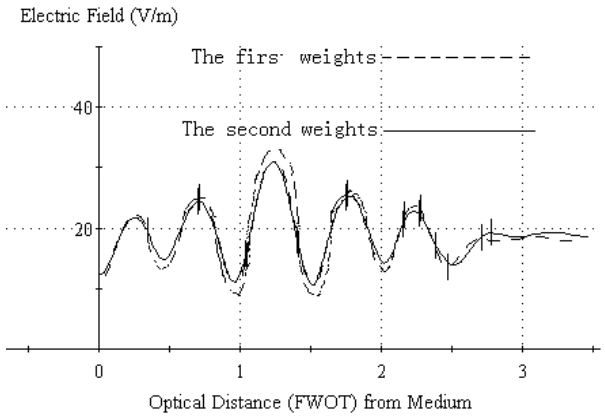


Fig3 The *e*lectric field distribution strength in the film layer

From the figure, we can see that the internal electric field intensity is smaller than that what we got from optimization while adopting the weight in group 2 ,it can reduce the internal damage of layer, and it is beneficial to improve the laser-induced damage threshold of film. Thus, the weight in group 2 was adopted to have the coating structure optimized as Sub|0.6833L 0.3918H 0.1164L 0.1178H 0.4029L 0.3417H 0.3627L 0.3387H 0.3620L 0.3423H|Air. Figure 5 is the spectral curves of 45 °± 3 °theoretical design.

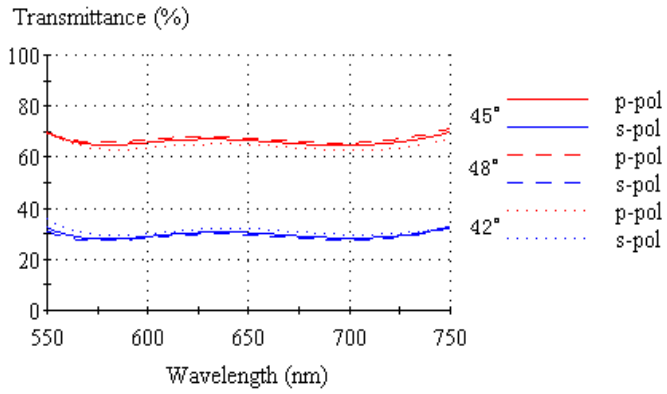


Fig4 The spectral curves of 45 °± 3 °theoretical design.

From the figure4,the P light average transmittance is 65.3%，the S light average transmittance is 30.5%.

5.Preparation process

The experiments were performed in the 900 vacuum deposition apparatus, which has been equipped with two electron gun, double-probe IC/5 quartz crystal film thickness control instrument and Kaufman source[12-13] .

Before the coating process, the substrates were cleaned with acetone, and then by mixed liquid with 3:1 of anhydrous alcohol and anhydrous ether. When the vacuum degree got close to 4×10^{-3}, the ion source was applied for pre-cleaning of the substrates(last for 10 minutes),which can remove the second pollution, activate the surface of substrate, and form pretense diffusion layer at the surface of substrate, enhance the bonding force between the film and substrate, enhance the film stability of anti-laser damage[14-15].

6.Testing results and analysis

6.1 optical properties of film and analysis

SHIMADZU UV-3150 spectrophotometer was used to measure the optical properties of the films. By adding a polarizer in the testing process, S light and P light can be tested respectively. The testing spectral transmittance curves were showed in Fig.5 and Fig.6.

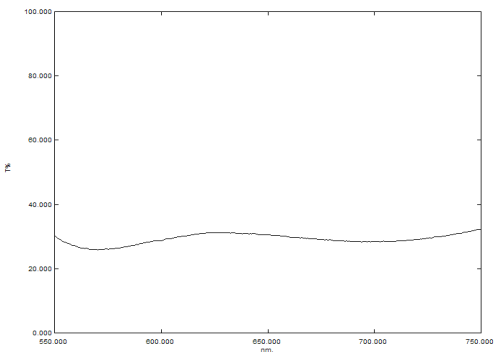


Fig5 Measured spectral transmittance curve of S light

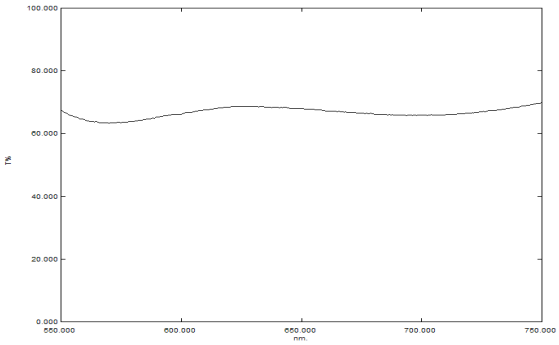


Fig6 Measured spectral transmittance curve of P light

The data comparison table of theory and actual showed intable5

Table5 The data comparison table of theory and actual

	theoretical design		actual preparation	
	average	632.8	average	632.8nm
P	65.3%	67.0%	66.1%	67.5%
S	29.5%	30.5%	30.2%	31.0%

From the table，we can see the spectrum characteristics of film prepared can meet the given requirements, and there are still differences between the theoretical design and actual results. The root cause is that, technological parameters in actual preparation process change slightly and there are random errors in quartz crystal film thickness control instrument, which is difficult to be eliminated.

6.2 Film strength test

A, high and low temperature test: put the sample into the cold box. Decrease temperature from room temperature to -50 ℃,and hold for 2 hours; then set the sample into high temperature box, from room temperature to 70 ℃,for 2 hours also, the film didn't not change obviously.

B, adhesion test: Attach to the film surface with GB/T2407-1992 top tape, pull the tape up from the vertical direction of the edge fast, no falling film.

c, anti laser damage threshold: use laser radiation with half a pulse width of 15 ns, 1064 nm wavelength, peak density 500 MW / cm2 to hit the film, no damage.

D, drift test: put the sample into lukewarm water for 24 hours,then measure the sample,through the comparison of spectral transmittance curve before and after, we find that the spectral curve drifts 1-2nm towards long wavelength after soaking. It basically achieves the process of polarized beam splitting preparation without drift .Although ion source can improve the compactness of the film, certain gaps still exist inside the film, and absorb vapor, resulting in spectral curve's drift towards long wavelength , but has no effects on use.

7.Conclusion

H4 and SiO2 were selected as materials of high and low refractive index, the relationship between the distribution of electric field intensity of film and laser damage threshold is taken into account in coating design,thus improve the damage threshold of the film; by adopting orthogonal matrix method to process the parameters of deposition, the number of experiments has been decreased, and research cycle got shortened; Through ion source assisted deposition, by optimizing the parameters of the ion source, the film firmness got enhanced; thin film for laser polarization beam splitter was prepared successfully aimed at meeting the requirements for use. How to improve the laser damage threshold would be the emphasis of research in the future.

References：

[1] J.H.Campbell.Status of the National Ignition Facility: an optics perspective.in Optical Interference Coating，OSA Technical Digest Series, 2004, paperWF1

[2] Wang Ying. Study and preparation of mid-infrared laser films[D]. Zhejiang University

[3] X. Ya,Q. Liu,M. Gong et al..High-repetition-rate high-beam-quality 43 W ultraviolet laser with extra-cavity thirdharmonicgeneration[J].Appl.Phys.B,2009,95(2):323～328

[4] B. Li,J. Yao,X. Ding et al..High efficiency generation of 355 nm radiation by extra-cavity frequency conversion[J].Opt. Commun.,2010,283(18):3497～3499

[5] Hong DongMei,Yue Wei,Research of optical film for middle infrared lasers[J].Laser and Infrared, 2006,36(12)1157~1159

[6] Zhong Disheng. Vacuum Coating [M].Shenyang: Liaoning University Press,2001. 181~191

[7] Liu Chunling, Wang Chunwu, Wang Guangde et al.. Process investigation of H4 thin film prepared by electron beam evaporation and application on laser diodes cavity coating [J].Chinese J.Laser, 2010,37(12):3141~3144
[8] Tang Jinfa ,Gupeifu, Liu Xu et al .. Modern Optical Thin Film Technology[M]. Hangzhou: Zhejiang University Press,2006.43~48,338~343
[9] Zhong Disheng. Vacuum Coating [M].Shenyang: Liaoning University Press,2001. 278~288
[10] Yang Yongliang, Fu Xiuhua, Liu Guojun et al ..Study and Fabrication of Multi-Wavelength Laser Antireflection Film Using New Mixed Material[J]. Chinese J.Laser.201138(10): 1007002-1-1007002-6
[11] Wang Li, Cheng Xinbin,Wang Zhanshan et al . . Ion-assisted deposition technique[J].Infared and laser engineering 2007 36 （6）896~898
[12] Kaufman HR,Robinson R S.J.VAC.Sci.Tecnol.A5(4)Jul/Aug.1987:2081-2084
[13] Kaufman H R.AIAA J.V23 N1,1985,1:78-87 679-68
[14]Pan Yonggang，Liu Dongmei，Zhang Jing et al . . Research of three-wave-band filters used in free space communication system[J].Laser&optoelectroninc Progress，2012,49:013101-1~013101-6
[15] Anton R,Hagedorn H,Schnel lbugel A.Ion—assisted deposition of high quality [J]]．Thorium free anti—reflection coatings,1994,10(2):288-296

Key Engineering Materials Vols 645-646 (2015) pp 388-393
© (2015) Trans Tech Publications, Switzerland
doi:10.4028/www.scientific.net/KEM.645-646.388

Submitted: 2014-11-25
Accepted: 2014-12-23

Micro laser joining between dissimilar materials of 200μm thick TiNi Alloy and stainless steel and the joint's electrochemical behavior

Yuhua Chen[1,2, a*], Jilin Xie[1,b] and Weihuai Gong [1,c]

[1] School of Aerospace Manufacturing Engineering, Nanchang Hangkong University, Nanchang, Jiangxi, China

[2] State Key Laboratory of Advanced Welding and Joining, Harbin Institute of Technology, Harbin 150001, China

[a] ch.yu.hu@163.com(corresponding author), [b]294235585@qq.com, [c]542079006@qq.com

Keywords: Micro laser welding, TiNi shape memory alloy, dissimilar materials, welded joint, electrochemical behavior.

Abstract. Dissimilar materials between TiNi shape memory alloy (SMA) and stainless steel of 200μm mm thick were butt welded by micro impulse laser and the electrochemical behavior of the weld joints was studied. The results show that the crack sensitivity of the welded joint is very high and good joining between TiNi SMA and stainless steel can be realized with pure Ni wire as filler material presented between TiNi SMA and stainless steel. The tensile strength of the welded joint with pure Ni wire as filler material is 580MPa. The electrochemical tests of the welded joints in different concentrations of NaCl solutions and different pH value solutions show that, the maximum of the corrosion potential Ecorr in the three typical corrosion systems (0.9%NaCl, pH=7.3; 3.5%NaCl, pH=7.3; 0.9%NaCl, pH=4) is the weld seam, which indicates that the corrosion tendency of the weld is smaller than that of TiNi alloy and stainless steel in the three corrosion systems. The pitting corrosion potential of TiNi alloy, stainless steel and the weld gradually decreased with the increase of Cl-concentration; the pitting corrosion potential decreased with the increase of H+ concentration, while TiNi alloy decreased faster than that of the weld and stainless steel, the surface stability of TiNi alloy is low when pH value dropped below 7.

Introduction

TiNi shape memory alloy (SMA) is a new kind of functional material and is used in many fields such as aviation, medical device, atomic energy, instruments, space-flight and ocean development in the last decades due to its unique shape memory effect, pseudo-elasticity and excellent corrosion properties [1]. However, successful applications of any new material not only hinge on its inherent characteristics, but also depend on solving problems of joining technologies and improving the properties of the joint [2]. The dissimilar welded joint between TiNi alloy and stainless steel has broad application prospects in medical devices and space-flight because of its mechanical properties, workability, low cost and corrosion resistance [3]. But large differences in physical and chemical properties between the two materials make the dissimilar welding complex and difficult, especially when the thickness of the materials is micron level.

At present, successful fusion welding, particularly laser welding, of TiNi alloy to itself has been well established [4-6]. However, several have been conducted on welding TiNi alloy to stainless steel. It has been reported that the weld microstructures and joint properties can be improved by using AgCu interlayer in transient liquid phase diffusion bonding [7, 8], silver based fillers in laser brazing [9] and brazing [10], and Ni interlayer in friction welding [11]. In these works, mechanical properties and shape memory effect of the joints were studied. The accomplishment of sound joints is very challenging, since it is not limited to the joint strength, shape memory effect and pseudo-elasticity but also comprises corrosion resistance especially for the application of medical devices.

The present work investigates effects of Ni wire as filler material on the weld crack sensitivity and joint strength of laser-welded joints of 200μm mm thick TiNi SMA and stainless steel, the electrochemical behavior of the welded joints was tested also. Its objective was to evaluate the laser

weldability of TiNi alloy to stainless steel and to provide some foundation for improving the mechanical properties and corrosion resistance of the dissimilar joints.

Experimental procedure

0.3mm thick TiNi SMA and 0.2mm thick stainless steel were used as the base metal in this investigation, the chemical composition of base metal is shown in table 1. The TiNi sheets were produced by coldrolling with a thickness reduction of about 22%. In order to remove the surface layer of oxidem produced during the coldrolling process, the TiNi sheets were degreased with were propanone and soaked 15 minute in the mixture solution of hydrofluoric acid and nitric acid, and then washed with clear water and weathered. After these treatments, the thickness of the sheets was 0.2 mm. The dimensions of the welding specimens were 0.20mm×40mm×60 mm.

Table 1 Chemical composition of base metal (mass fraction，%)

Element	Ti	Ni	Fe	C	Cr	Mn	Si	P	S
TiNi Alloy	44.34	55.66	--	--	--	--	--	--	--
Stainless steel	0.54	9.72	Bal.	0.08	18.07	2	1.0	0.035	0.03

The welding process was carried out using a Nd:YAG laser source(SL-80, made in Italia, average power is 80 W). In order to protect the welding zone, a special clamping fixture was built to protect both frontal surface and back surface of the welded joint. The welding process was carried out using the following parameters: spot diameter = 0.3 mm; welding rate = 0.3mm/s; laser power = 6.4~12W; impulse frequency = 6~12 Hz; impulse width = 4.2~5.6 ms; argon flow rate = 5L/min.

After welding, tensile samples were made by spark cutting and tensile property of welded joints was test on tensile testing machine (INSTRON 5540). Metallographic specimen was made along cross direction of the welded joint and etched by mixture acid solution of (HF:HNO3:H2O=1:4:5). The microstructure and element distribution were studied by metallographic microscope (4XB-TV) and scanning electronic microscope (Quanta2000).

Polarization curve and corrosion rate of the weld, the heat-affected zone on both sides and the two kinds of parent materials in different concentrations of NaCl solutions and different PH value solutions were tested on Autolab PGSTAT30 made by Eco Chemie Company.

Results and discussion

Sensitivity and control measure of Welding crack. Because there is large differences in physical and chemical properties between TiNi alloy and stainless steel, and Ti, Fe elements in the weld forming intermetallic compounds which embrittles the weld, so the crack sensitivity of the welded joint is very high. There are many cracks in the weld seam (as shown in Fig.1) and the cracks can't be avoided only by changing the laser welding parameters. In order to dilute the content of Fe, Ti in the weld seam and cut off the forming of Ti-Fe intermetallic compounds during the welding and avoids the cracks, pure Ni wire as filler material was preseted between TiNi SMA and stainless steel before welding (as shown in Fig.2).

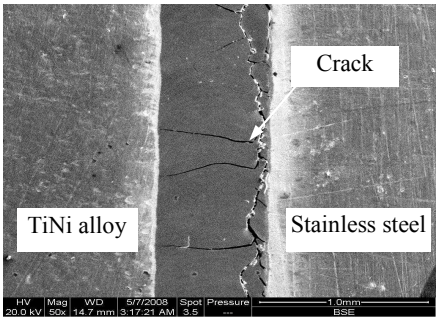


Fig.1 The Cracks on the laser welded joint of TiNi Alloy/Stainless Steel

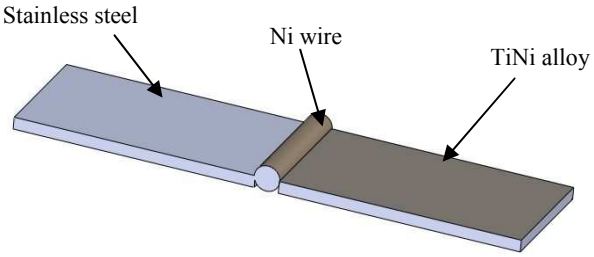


Fig.2 The assembly schemes of welding paste and filling material in order to avoid cracks

Good joining between TiNi SMA and stainless steel can be realized when pure nickel wire was added into the butt joint, the surface appearance and cross-section appearance of the welded joint were shown in Fig.3. There are no obvious cracks in the weld seam and the tensile strength of the welded joint with pure Ni wire as filler material is 580MPa.

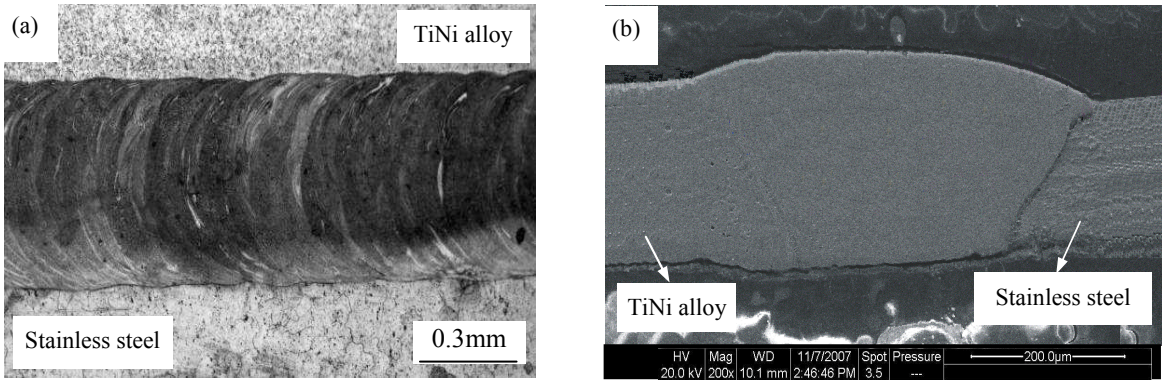


Fig.3 Macrograph of the welded joint: (a) surface appearance (b) cross-section appearance

Electrochemical behavior of the welded joints. The polarization curves of the weld seam with different heat input in the 0.9%NaCl solution (pH=7.3; 3.5%NaCl, pH=7.3; T=37℃) are shown in Fig. 4. It can be seen that the trend of the polarization curves are basically identical. Three groups of data are selected to discuss among the experiment results. The weld seam corrosion potentials Ecorr (respectively -0.21, -0.20 and -0.18)in the polarization curves almost no difference means that the weld seam with different heat input have the same corrosion resistance property and change welding process parameters has no influence on weld seam corrosion resistance property. Therefore, in this paper, the corrosion resistance property of weld seam made by the optimum process parameter was analyzed to find the corrosion law and with stainless steel and TiNi base metals for comparative studies. Fig. 5 shows the polarization curves of weld seam, TiNi and stainless steel base metals in 0.9%NaCl solution (pH=7.3, T=37℃). Fig. 5 shows that the start of the polarization curves trend is almost identical with the current density decline, TiNi and stainless steel base metals decrease faster than that of weld seam. At this time, cathodic polarization protects the electrode surface. When the potential increased, passivation regions are formed in TiNi and stainless steel, and passivation in TiNi with a range from -0.35V to 0.4V is larger than that of stainless steel vary from -0.3V to 0.2V. While the passivation region in weld seam is not obvious, and the current density improved faster as the potential increased. As can be seen from Fig. 1, the self-corrosion potential in weld seam is -0.2V bigger than those of base metals with -0.38V and -0.33V, and the pitting sensitive of weld seam in solution with $Cl^-$is bad. Based on the above descriptions, weld seam have better corrosion resistance over base metals in 0.9％NaCl solution.

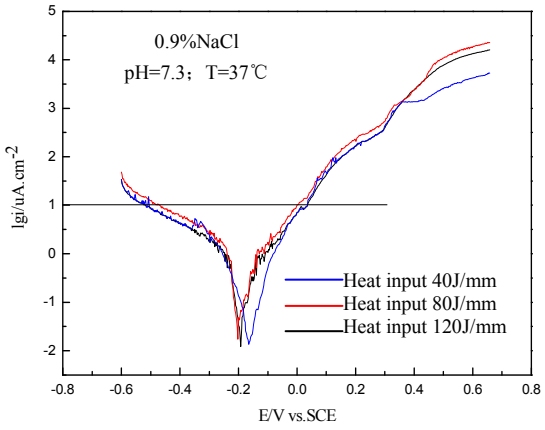


Fig.4 Polarization curve of different welded joints in 0.9%NaCl solution (PH=7.3)

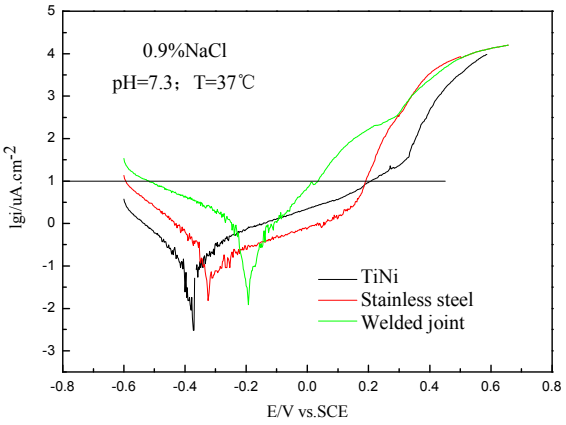


Fig.5 Polarization curve of welded joints and base metal in 0.9%NaCl solution (pH=7.3)

Table 2 The corrosion potential E_{corr} (V)

solution / material	0.9%NaCl	3.5%NaCl	0.9%NaCl PH=4
TiNi alloy	-0.38	-0.56	-0.41
Stainless steel	-0.33	-0.40	-0.36
Welded joint	-0.20	-0.34	-0.23

Table 3 The pitting corrosion potential E_b(V)

solution / material	0.9%NaCl	3.5%NaCl	0.9%NaCl PH=4
TiNi alloy	-0.38	-0.56	-0.41
Stainless steel	-0.33	-0.40	-0.36
Welded joint	-0.20	-0.34	-0.23

Fig. 6 shows the polarization curves of weld seam, TiNi and stainless steel base metals in 3.5%NaCl solution (37℃). The polarization curves in 3.5% NaCl solution show the same trend as that in 0.9%NaCl solution. The current densities are decreased at the start stage of the curves and TiNi current density increased after the corrosion potential of -0.55V, firstly. Passiviation regiones are observed obviously in both TiNi and stainless steel curves. The passiviation region in TiNi is from -0.4V to -0.1V, the passive current density is at the range of -10uA/cm^2 and 0uA/cm^2, and the transfer to the negative side of passivation region compared with that in 0.9%NaCl solution indicates the corrosion resistance property decline. Stainless steel with a passiviation region of -0.35V to 0.09V and the passive current density between -5uA/cm^2 and 7uA/cm^2 shows decreasing in corrosion resistance property. Based on the principles of metal electrochemical corrosion, I_p is indicative for velocity of metals pass through the oxied film. At the beginning of the anodic polarization oxide films on the base metals are stable in media of 3.5%NaCl solution. When corrosion potential keeps growing, the oxide film broken and the current density increase rapidly. Oxide film solution rate is slower than that of oxide film repairing consequently pitting formed at the electrode surface. As shown in Tab. 2, the weld seam pitting potential is the least; the potentials are decrease in TiNi from 0.21V to 0.19V and in stainless steel from 0.08V to 0.05V. The weld seam passivation region in 3.5%NaCl solution is not obvious and the current density growing rate is the fast and with a small platform formed at the end. It is the bi-direction of corrosion process and the increased corrosion products that affect further corrosion, consequently, the current density growth slowdown. The overall comparison shows that weld seam corrosion resistance is better than those of base metals.

It can be seen from Fig. 5 and Fig. 6 that the increase of Cl^- concentration reduces the corrosion resistance properties in weld seam and base metals. The self corrosion potentials are also decline as

shown in Tab. 1. TiNi decreased from -0.38V to -0.56V, stainless steel dropped from -0.33V to -0.34V and weld seam dropped from -0.2V to -0.34V, respectively. The Cl^- reduces the passivation film of protection, makes the electrochemical performance unstable thus the corrosion resistance properties decline.

The polarization curves of weld seam, TiNi alloy and stainless steel in 0.9%NaCl solution(pH=4；T=37℃) are shown in Fig. 7. The trend at the begging of the polarization curves is basically identical with decreased slowly increased after self-corrosion potential. A short passivation region is formed in all three curves, TiNi is from -0.36V to 0.04V, stainless steel 321 is between -0.35V and -0.17V, weld seam is at the range of -0.18V to 0.05V. The passivation region of weld seam is larger than those of base metals. The passive current density I_p of TiNi is 10~13 μA /cm2 and that of stainless steel is 5~8 μA /cm2, weld seam is 10~12 μA /cm2. The I_p of TiNi is the highest one indicates the lowest surface stability. The self corrosion potential of TiNi is the least of -0.14V and weld seam is the biggest of -0.23V. As shown in Tab. 2, the TiNi pitting potential ranks the last with -0.33V, stainless steel ranks the first with -0.1V, and weld seam falls in between. It can be seen from above that in solution of pH=4, the surface stadbility of TiNi is decreased while it is more stable than weld seam and stainless steel.

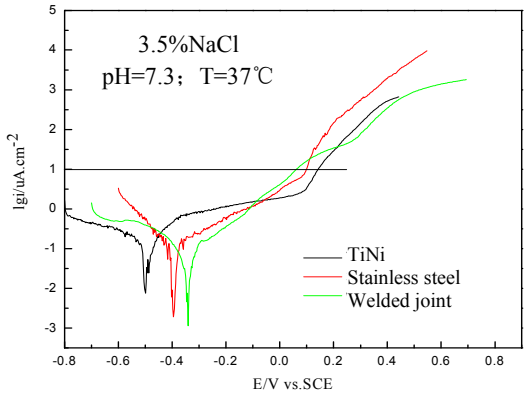


Fig.6 Polarization curve of welded joints in 3.5%NaCl solution (pH=7.3)

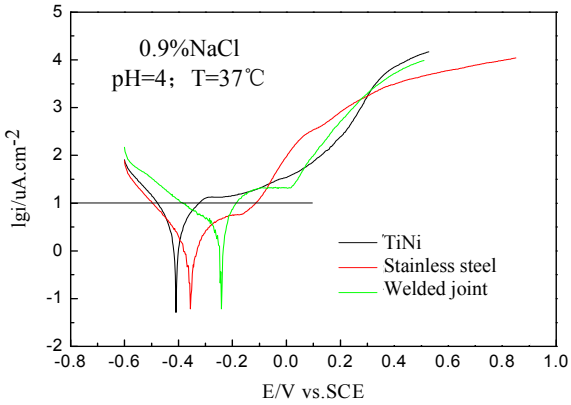


Fig.7 Polarization curve of welded joints in 0.9%NaCl solution (pH=4)

It can be seen from Fig. 4 and Fig. 7 that the corrosion resistance of weld seam and base metals are changed, the passivation region reduced and the pitting sensitive increased as PH value varied. Tab. 1 show that the corrosion potentials of TiNi base metal is decreased from -0.38V to -0.41V, the stainless steal is decreased from -0.33V to -0.36V, and the weld seam is decrease from -0.2V to -0.23V. The increment of H^+ concentration leads to the electrode surface stability and corrosion resistance decline. All specimens corrosion resistance are decreased in solution with pH=4.

The weld seam corrosion potential E_{corr} is higher than those of TiNi alloy and stainless steel base metals indicated that weld seam has excellent corrosion resistance property over base metals. Once corrosion taken place, sharply increasing current density indicates that the rate of the corrosion is higher in weld seam. The increase of Cl^- concentration reduces the surface oxide film stablity on base metals and weld seam then corrosion take place. Also the pH value can change the activity of the active ions then accelerated corrosion.

Summary

The dissimilar materials complex structure of TiNi alloy and stainless steel has broad application prospects in medical devices and space-flight because of its mechanical properties, workability, low cost and corrosion resistance. But it is difficult to obtain good welded joints because of large differences in physical and chemical properties between the two materials. Especially when the thickness of the materials is micron level, the crack sensitivity of the welded joint is very high and the cracks can’t be avoided only by changing the laser welding parameters. Good joining between TiNi

SMA and stainless steel can be realized with pure Ni wire as filler material and the tensile strength of the welded joint with pure Ni wire as filler material is 580MPa.
The corrosion potential Ecorr of the weld seam in the three typical corrosion systems (0.9%NaCl, pH=7.3; 3.5%NaCl, pH=7.3; 0.9%NaCl, pH=4) is larger than base metal, which indicates that the corrosion tendency of the weld is smaller than that of TiNi alloy and stainless steel in the three corrosion systems. The pitting corrosion potential of TiNi alloy, stainless steel and the weld gradually decreased with the increase of Cl^- concentration; the pitting corrosion potential decreased with the increase of H^+ concentration, while TiNi alloy decreased faster than that of the weld and stainless steel, the surface stability of TiNi alloy is low when pH value dropped below 7.

Acknowledgments

This work was supported by Science and Technology Planning Project of Jiangxi Province (20133BBE50021), Shanghai Aerospace Science and Technology Innovation Fund (SAST201209), Frontier Science Research Project of Educational Commission of Jiangxi Province (KJLD14055) and The State Key Lab of Advanced Welding & Joining, Harbin Institute of Technology (AWJ-M15-03).

References

[1] Predki W, Knopik A, Bauer B, Engineering applications of NiTi shape memory alloys, Materials Science and Engineering A, 481(2008) 482-598.
[2] Gugel H, Schuermann A, Theisen W, Laser welding of NiTi wires , Materials Science and Engineering A, 482(2008)668-671.
[3] H.M. Li, D.Q. Sun, X.L. Cai, P. Dong, W.Q. Wang, Laser welding of TiNi shape memory alloy and stainless steel using Ni interlayer, Materials and Design, 39 (2012) 285-293.
[4] Gong W H, Chen Y H, Ke L M. Microstructure and properties of laser micro welded joint of TiNi shape memory alloy, Transactions of Nonferrous Metals Society of China, 21(2011)2044-2048.
[5] Song YG, Li WS, Li L, Zheng YF, The influence of laser welding parameters on the Microstructure and mechanical property of the as-jointed NiTi alloy wires, Material Letter, 62(2008)2325-2328.
[6] YAN Xiao-jun, YANG Da-zhi, LIU Li-ming, Microstructures and properties of laser spot-welded joint of superelastic NiTi alloy wire, The Chinese Joumal of Nonferrous Metals, 15(2005)19-23.
[7] Wang Y L, Li H, Li Z X, Feng J C, Research on transient liquid phase diffusion bonding process of TiNi shape memory alloy to stainless steel, Journal of Material Engineering, (2008)48-51.
[8] Li H, Li ZX, Wang YL, Feng JC. Transient liquid phase diffusion bonding of TiNi shape memory alloy and stainless steel. Rare Metal Materials and Engineering, 40(2011)1382-1386.
[9] Li M G, Sun D Q, Qiu X M, Liu J B, Miao K, Wu W C, Effects of silver based filler metals on microstructure and properties of laser brazed joints between TiNi shape memory alloy and stainless steel, Science & Technology of Welding and Joining, 12(2007)183-188.
[10] Seki M, Nojiri M, Uenishi K, Kobayashi K F, Brazing of Ti-Ni shape memory alloy with stainless steel, Journal of Japan Institue of Metals, 64(2000)632-640.
[11] Fukumoto S, Inoue T, Mizuno S, Okita K, Tomita T, Yamamoto A, Friction welding of TiNi alloy to stainless steel using Ni interlayer, Science & Technology of Welding and Joining, 15(2010)124-130.

Key Engineering Materials Vols 645-646 (2015) pp 394-399
© (2015) Trans Tech Publications, Switzerland
doi:10.4028/www.scientific.net/KEM.645-646.394

Submitted: 2014-10-28
Accepted: 2014-12-10

Electrokinetic research on the dispersion behavior of nano-ceria particles in concentrated suspensions

Wei Gao[1, a], Qilong Wei[1, b], Ling Ding[2], Xiaoyuan Li[1],
Chao Wang[1], Guangping Tang[1], Jianguo He[1]

[1]Institute of Machinery Manufacturing Technology, China Academy of Engeering Physics, Mianyang, China

[2]Institute of Chemical Materials, China Academy of Engeering Physics, Mianyang, China

[a]gaowei906@qq.com, [b]weiqilong2004@126.com (Corresponding author)

Keywords: nanoparticles, ceria, zeta potential, dispersion behavior, rheological properties.

Abstract. A multi-scale method was developed, which utilized intrinsic relationships among zeta potential of particles, rheological properties of suspensions and particle size distribution (PSD), to analyze dispersion behavior of nanoparticles in concentrated suspensions. It was found that PSD of a kind of nano-ceria particles by dynamic light scattering (DLS) method in solution A with concentration 5 wt% accorded well with that by direct TEM analysis, which meant the particles had been dispersed well. However, there had a significant difference when the concentration was increased to 20 wt%. When particles concentration increased from 5 wt% to 20 wt%, zeta potential in solution A changed from -150 mV to -100 mV, while zeta potential in solution B changed from -35mV to -45 mV. Variations of zeta potential of particles accorded well with rheological properties of suspensions too, from phenomenological models. When the suspensions composed by solution A and the nano-particles with concentration about 20 wt% was diluted with its original solution to 5 wt%, the PSD of nano-ceria could be measured indirectly, which accorded well with both that of a suspension prepared directly with near concentration and that from TEM images. Then a method to measure PSD of nanoparticles in concentrated suspension was brought forward.

Intorduction

Ceria has important application as a main slurry component in ultra-precision polishing industry such as chemical mechanical polishing (CMP) and optical finishing, due to its much higher removal rate and surface quality, derived from physical and chemical interactions between ceria-based slurry and workpiece surface during finishing process[1-3]. In most cases, nanoparticles with a narrow size distribution need to be dispersed well in slurries so that it can utilize nano-scale effect thoroughly, which can obtain polishing results of high-precision and high surface quality.

However, due to their small size, nano-ceria particles have so high specific surface area, high specific surface energy that they have great tendency to aggregate. Nano-ceria particles have to be properly dispersed and stabilized in suspension through appropriate technologies in order to reduce and eliminate surface defects caused by the aggregates, and improve surface quality. So far there was no efficient method to characterize dispersion behavior of nanoparticles in concentrated suspensions directly, which severely restricted their applications.

Interactions between nanoparticles can be classified as attractive forces (including van der Waals, hydrophobic, bridging, and depletion,) and repulsive forces (including electrostatic repulsive, steric, hydration, and structural)[4]. Generally, dispersibility of particles is significantly impacted by van der Waals attraction, electrical double layer (EDL) and steric repulsion. According to the extended DLVO theory, zeta potential determines EDL interaction, which provides repulsive forces between particles to overcome van der Waals attraction and keep particles dispersed. Therefore, zeta potential is a strong indication of the stability of the colloid suspension. The general critical value between stable and unstable suspensions is ±30 mV. Particles with zeta potentials more positive than +30 mV or more negative than -30 mV are normally considered stable and not form agglomerates due to their

strong similar charges. For lower values of zeta potential, agglomeration may occur, causing the suspension to become unstable [5].

Kosmulski *et al.* [6] studied the change law of electrokinetic potentials of titania in the suspensions with variation electrolytes. Edita *et al.* [7] considered the effect of silica concentration on zeta potential and particle size for both types of stabilizer and found that the type of stabilizer has crucial effect on silica concentration dependence of the zeta potential. Recently, many researchers [8-10] investigated the correlativity between zeta potentials of particles and rheological behavior of suspensions, dispersibility of particles and PSD. So far, considerable interest in zeta potential focused on experimental investigation of pH titration, by examining variation of zeta potential and particle size vary as a function of pH [11-14].

In fact, the nanoparticles suspensions in actual usages have relatively high concentrations, which caused interparticle spacing become smaller. The increase of interactions among particles leads the particles frequently collisions each other, and makes usual method for dilute suspensions not suitable anymore. In this research, the dispersion behavior was investigated via zeta potential, rheological properties and PSD analysis.

Experimental

A nano-ceria powder with average particle size of 100-200nm was used in research, where two solutions were used as dispersing media. Solution A contained complex polyelectrolytes including sodium hexametaphosphate (SHP) and sodium carboxymethyl cellulose (NaCMC), and solution B contained NaCMC and sodium nitrite. All suspensions were dispersed by an ultrasonic probe device. After stabilized about 24 hours at room temperature, zeta potential and PSD of particles, rheological properties of suspensions were measured respectively.

Morphology and particle size of nano-ceria particles were observed and characterized by TEM (JEOL JEM-100CX). Composition and crystal structure of them were identified by X ray diffraction (DX-1000). Zeta potential was measured with a Colloidal Dynamic's ZetaProbe. Rheological properties of solutions and suspensions were measured by viscometer (Brookfield LV DV II+). The Dynamic Light Scattering (DLS, Horiba LB550) instrument was used to analyze the PSD of particles. All suspensions were shook well before measurement.

Results and discussion

The angular particles characteristic was irregular polyhedral clearly seen in the TEM image shown in Fig.1(a). The average diameter of the ceria particles was 100-200nm. The particles were validated as ceria by comparing the XRD spectrum (shown by Fig.1(b)) with those from some literatures [15, 16].

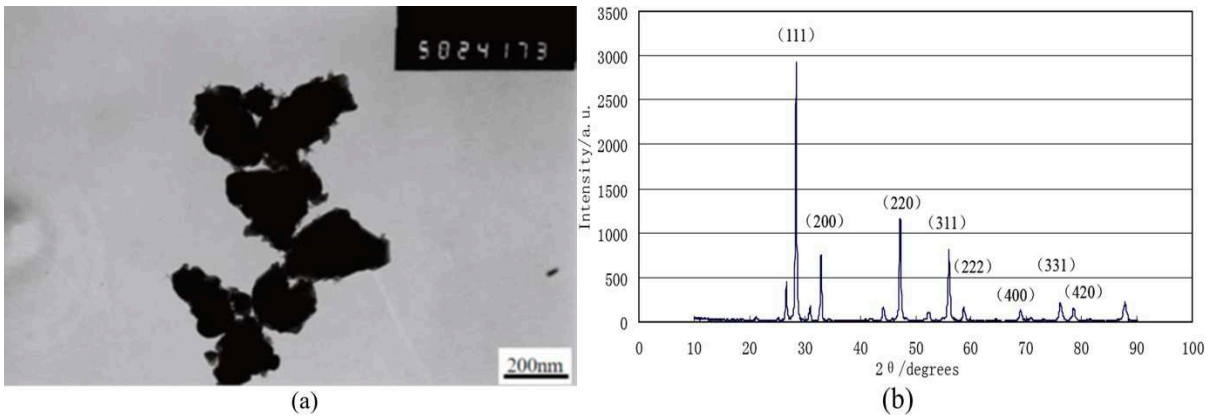


Fig.1. TEM image (a) and (b) XRD spectrum of the nano-ceria particles

The PSD by dynamic light scattering (DLS) method wsa shown Fig.2. PSD of nano-ceria in solution A with concentration 5 wt% accorded well with that by direct TEM analysis, which meant the particles had been dispersed well. However, there had a significant difference when the

concentration was increased to 20 wt%, which was thought to relate to multiple lights scattering during the measurment, or agglomerated particles. The PSD of nano-ceria in solution B with both concentrations did not accord well with that by TEM.

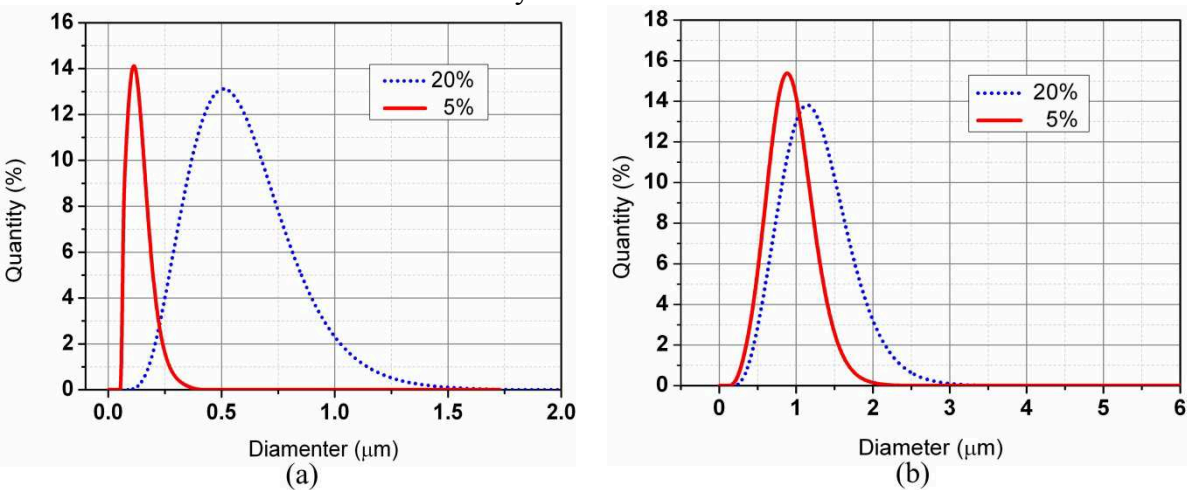


Fig.2. PSD of nano-ceria particles in (a) solution A, (b) solution B

PSD of concentrated suspensions was difficult to measure directly with DLS and laser diffraction method, so the dispersions behavior of particles cannot analyze just according to the PSD. Therefore, based on electrokinetic conditions, it was necessary for developing an effective method to indirectly measure the PSD of concentrated suspensions.

The zeta potential examines the EDL forces between particles in suspension, as both the potential and charge density are dependent on pH and ionic strength. Here, the effects of solid concentration on particles surface potential were examined at a constant pH. The zeta potentials measured by electroacoustic method, across particles concentration range of 5 wt% to 25 wt% (or 20 wt%).

Fig.3 (a) and (b) shows variation of zeta potential with particles concentration in solution A and solution B, respectively. As shown in Fig.3, when particles concentration increased from 5 wt% to 20 wt%, zeta potential in solution A changed from -150 mV to -100 mV, while zeta potential in solution B changed from -35 mV to -45 mV. The zeta potential values in solution A maintain approximately 100 mV with concentration from 25 wt% to 20 wt%. However, its value increased sharply until particles concentration were reduced to about 17.5 wt%, and then the absolute values maintain approximately 150 mV with concentration from 17.5 wt% to 5 wt%.

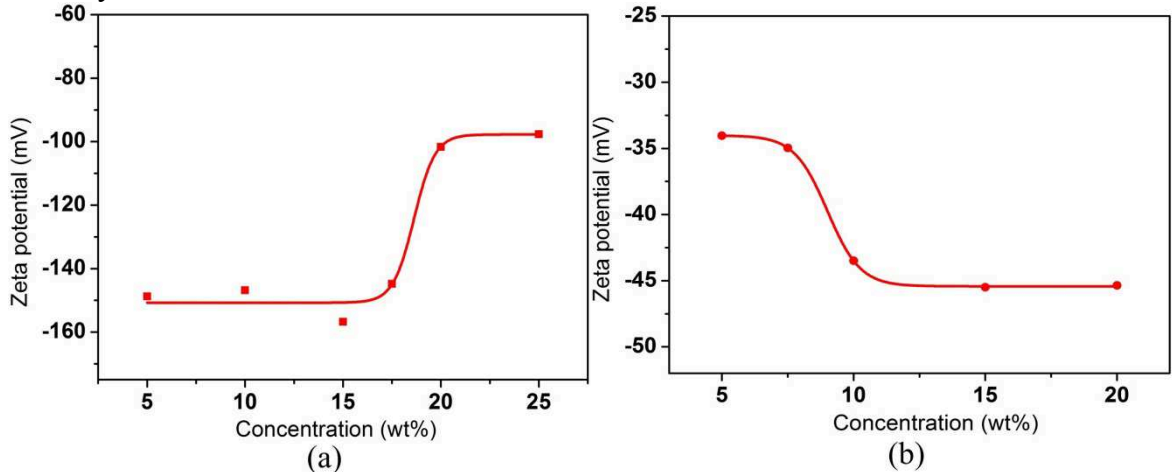


Fig.3. Zeta potential of nano-ceria particles in suspensions with (a) solution A, (b) solution B

Based on these results it could be deduced that when suspensions composed by solution A and nano-ceria with concentration 20~25 wt% was diluted to lower concentration such as 5 wt% with solution A, the EDL repulsive force between particles would change little as zeta potential as high as 100 mV, which was much higher than 30 mV. So, it was feasible to measure PSD in concentrated suspensions with solution A by diluting with its original solution.

However, the zeta potential in solution B had an opposite tendency compared with A. In solution B, the zeta potential always remained about -45 mV when particles concentration varied from 20 wt% to 10 wt%. When particles concentration was decreased from 7.5 wt% to 5 wt%, however, the zeta potential was about -35 mV, which approached to the critical value -30 mV. It was found that when suspensions composed solution B and the nano-ceria particles with concentration 20 wt% was diluted to 5 wt% with solution B, zeta potential would profoundly decreased to critical value and the interparticles EDL repulsive force vanished. So, it was infeasible to measure PSD of the nano-ceria concentrated suspensions with solution B by diluting method.

Variation of shear stress and viscosity with shear rate for ceria suspensions of 5 wt% was shown Fig.4, and viscosities of suspensions were almost not changed with shear rate, which meant that they were both Newtonian fluids. According to Bingham model shear stress of suspensions were calculated from using the follow formulas [17]:

$$\tau = \eta_B \dot{\gamma} + \tau_B \quad (1)$$

Where τ and $\dot{\gamma}$ is shear stress and shear rate, η_B and τ_B is Bingham viscosity and shear yield stress.

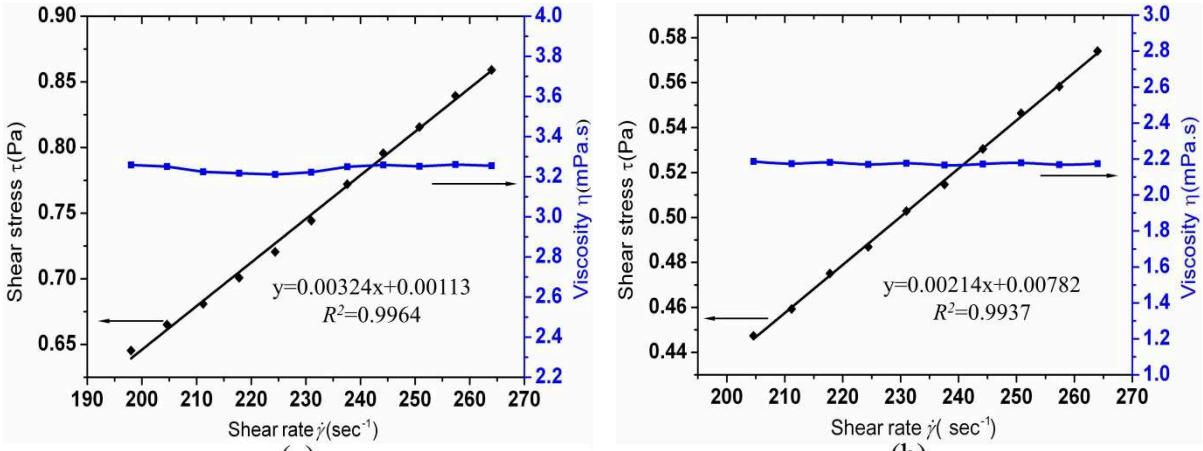


Fig.4. Rheological properties of 5 wt% suspension with (a) solution A, and (b) solution B

Fitted results of rheological properties for all suspensions by Bingham equation were shown table 1 and 2. According to them, yield stress of all suspension with solution B was greater than those of suspension with solution A at the same particles concentration. Yield stress of suspensions with solution A increased monotonically with increased particle concentration, with the maximal percentage about 100%. And yield stress of suspensions with solution B increased about 400% when concentration increased from 5 wt% to 10 wt% but increased not anymore when concentration was higher than 10%. Besides, relative viscosity of all suspensions increased with increased particle concentration, and there was no markedly difference in relative viscosity of suspensions with the same concentrations.

Table 1. Rheological properties of suspensions with solution A

wt%	Fitted equation	R^2	τ_B [mPa]	η_r
5	y=0.00324x+0.00113	0.9664	1.13	1.08
10	y=0.00345x+0.00128	0.9923	1.28	1.18
20	y=0.00364x+0.00247	0.9984	2.47	1.26
25	y=0.00372x+0.00251	0.9942	2.51	1.34

Table 2. Rheological properties of suspensions with solution B

wt%	Fitted equation	R^2	τ_B [mPa]	η_r
5	y=0.00214x+0.00782	0.9937	7.82	1.06
10	y=0.00200x+0.03940	0.9973	39.4	1.13
20	y=0.00201x+0.03261	0.9971	32.61	1.20
25	y=0.00207x+0.03798	0.9920	37.98	1.39

There existed a model to describe relationship between yield stress of suspension and interaction among particles [18]:

$$\tau_y \approx \frac{\phi^2}{a}\left(\frac{A_H}{12D_0^{\,2}} - 2\pi\varepsilon_0\varepsilon\zeta^2\frac{\kappa e^{-\kappa D_0}}{(1+e^{-\kappa D_0})}\right) \quad (2)$$

Where ϕ is the volume fraction of solid particles, a is the particle radius, A_H is the Hamaker constant of the particle in water, D_0 is the surface separation distance between the interacting particles, ε is the dielectric constant in solution, ε_o is the permittivity of free space, ζ is the zeta potential and κ is the Debye parameter.

And many models have been proposed to describe dependence of relative viscosity of concentrated suspensions on concentration of particles. One of the most useful expressions is the semiempirical equation of Krieger and Dougherty for monodisperse suspensions [4]:

$$\eta_r = \left(1 - \frac{\phi}{\phi_{max}}\right)^{-2} \quad (3)$$

Where ϕ_{max} is the maximum packing fraction of particles.

According to above results, when particles concentration in suspensions with solution A increased from 5 wt% to 10 wt%, as zeta potential changed little, yield stress of suspensions increased. And when particles concentration increased from 10 wt% to 20 wt%, as value of zeta potential decreased about 1/3, then yield stress increased markedly. While when concentration increased from 20 wt% to 25 wt%, as value of zeta potential changed little, yield stress increased to some extent.

While for suspensions with solution B, as value of zeta potential was just a litter higher than the critical one, dispersion of particles was not preferred due to much less EDL interactions, and their effective volume percentages were much higher than designed ones. Then it was difficult to analyze dispersion behavior of particles in detail. However, the regularity of yield stress of suspensions with solution B was bad, because those had much lower zeta potential value and particles had not been dispersed well. While relative viscosity of all suspensions increased with the increase of the volume fraction of particles and they almost didn't changed with solution type at the same particles concentration, which might be related to different corresponding relationship between relative viscosity and volume fraction of particles.

Conclusions

The suspensions of particles concentration of 5 wt%~25 wt% whatever using solution A or solution B are Newtonian fluids under tested shear rate (<300 sec^{-1}), which can be described by the Bingham plasticity model.

Zeta potential was crucial in determining the dispersion behavior of particles in aqueous suspensions, thus affecting the rheological properties of suspensions and PSD. Therefore, the particles dispersions in concentrated suspensions can be characterized based on electrokinetic analysis of suspensions, along with analysis method of rheological properties and particle size distribution. By this multi-scale method, dispersion behaviorof nanoparticles in concentrated suspensions could be researched effectively and thoroughly.

When zeta potential of a suspension has extremely high value, the PSD of concentrated suspensions can be characterized by DLS via a dilution method with original solution. If zeta

potential values were relatively lower (e.g. indifference with 30 mV), however, the method will be failure.

Acknowledgment

This research was supported by the Major National Science and Technology Project of China (No.2013ZX04006011), National Natural Science Foundation of China (No.51202228), Laboratory of Precision Manufacturing Technology of CAEP (K859-13-JCZ), and Foundation Research Program of Defense of China.

References

[1] L.M. Cook, Chemical processes in glass polishing, J. Non-Cryst. Solids 120 (1990) 152-171.
[2] D.C. Harris, History of magnetorheological finishing, Proc. SPIE. 6 (2011) 1-22.
[3] T. Hoshino, Y. Kurata, Y. Terasaki, K. Susa, Mechanism of polishing of SiO_2 films by CeO_2 particles, J. Non-Cryst. Solids 283 (2001) 129-136.
[4] D.B. Genovese, Shear rheology of hard-sphere, dispersed, and aggregated suspensions, and filler-matrix composites, Adv. Colloid Interfac. 171-172 (2012)1-16.
[5] J.D. Nelson, J.A. Drucker, A.A. Haefnera, R.A. Wiederholda. Varying electro-kinetic interactions to achieve predictable removal rates and smooth surfaces on ZnS, Proc. SPIE. 3 (2009) 1-10.
[6] M. Kosmulski, Electroacoustic study of titania at high concentrations of 1-2, 2-1 and 2-2 electrolytes, Colloid Surface A 345 (2009) 106-111.
[7] Edita, Determination of particle shape and size distribution of model types of nanomaterials, J. Electr. Eng. 5 (2010) 302-304.
[8] L.M. Zhang, M. Tian, J.L. Yang, Y. Huang, Rheological behavior of alumina suspensions, 5 (2004) 1145-1150.
[9] X.L. Song, G.Z. Qiu, P. Qu, Z.H. Yang, Dispersion behaviors of CeO_2 nanoparticles in water suspension, J. Rare Metals 2 (2005) 167-172.
[10] H. Jun, Y.W. Zhu. C.H. Zhu, Y.F. Liu, Dispersion characteristics of mirco diamond particle in aqueous system, Diam. Abrasives Eng. 3 (2011) 15-18.
[11] M. Kosmulski, P. Prochniak, J.B. Rosenholm, Control of the zeta potential in semiconcentrated dispersions of Titania in polar organic solvents, J. Phys. Chem. C. 113 (2009) 12806-12810.
[12] E.J. Teh, Y.K. Leong,Y. Liu, B.C. Ong, C.C. Berndt, S.B. Chen, Yield stress and zeta potential of washed and highly spherical oxide dispersions-critical zeta potential and Hamaker constant, Powder Technol. 198 (2010) 114-119.
[13] A. Otsuki, S. Barry, D. Fornasiero, Rheological studies of nickel oxide and quartz/hematite mixture systems, Adv. Powder Technol. 22 (2011) 471-475.
[14] R. Lamy, E. Zunic, R. Steding, A. Aamodt. Preparation of stable slurries of spherically shaped silica for coatings. Prog. Org. Coat. 72 (2011) 96-101.
[15] L.P. Alençon, P. Barboux, J.P. Boilot, Synthesis and acid functionalization of cerium oxide nanoparticles. J. Sol-Gel Sci. Technol. 39 (2006) 261-267.
[16] Y.H. Kim, S.K. Kim, N. Kim, et al, Crystalline structure of ceria particles controlled by the oxygen partial pressure and STI CMP performances, Ultramicroscopy 108 (2008) 1292-1296.
[17] R.J. Hunter, Foundations of Colloids Science, second ed., Oxford University Press, Oxford, UK, 2001, pp. 749-760.
[18] R. Goh, Y.K. Leong, B. Lehane, Bentonite slurries-zeta potential, yield stress, adsorbed additive and time-dependent behavior, Rheol. Acta. 50 (2011) 29-38.

Key Engineering Materials Vols 645-646 (2015) pp 400-404
Submitted: 2014-10-30
© (2015) Trans Tech Publications, Switzerland
Accepted: 2014-12-23
doi:10.4028/www.scientific.net/KEM.645-646.400

Study of SiC's Mechanical Property Variance Caused by Film Thickness

Jiao Zonglei[1,a*], Zhu Jian[1,2, b]

([1]NanJing Electronic Devices Institute, Nanjing 210016, China)
（[2]National Key Laboratory of Monolithic Integrated Circuits and Modules, Nanjing 210016,China）
[a]E-mail：scientistjzl@163.com
[b]E-mail：wnmb@nedi.cn

Keywords: SiC, Mechanical Properties, Nanoindentation, Thin films

Abstract

The mechanical properties of SiC thin films deposited by chemical vapor deposition process on silicon substrate are studied using nanoindentation techniques. The SiC thin films are of three different thicknesses: 1.6μm, 4.5μm, 9μm. In this study, nanoindentation method is preferred due to its reliability and accuracy on determining mechanical properties from indentation load-displacement data. The mechanical properties of elastic modulus and hardness are characterized. 1.6μm SiC thin film has the following values: E=345.73Gpa, H=33.71Gpa; 4.5μm SiC thin film has the following values: E=170.18Gpa, H=10.33Gpa; 9μm SiC thin film: E=167.96Gpa, H=9.48Gpa;

Introduction

MEMS device based on SiC has good mechanical properties, such as high hardness, excellent thermal stability and good corrosion resistance [1]. These properties make SiC promising for the fabrication of sensors and actuators operating in high temperature and harsh environment. SiC based devices have been widely used in pressure sensors operating at high temperatures, micromachined components for gas turbine engines, high-g accelerometers [2] and corrosion-resistant microfluidic devices.

Mechanical properties are essential for the design and fabrication of MEMS. There are various methods used in determining the mechanical properties of thin films, including nanoindentation [3], micro-beam bending, bulge test, etc. In this paper nanoindentation is used to characterize the mechanical properties of SiC films. The advantages of the nanoindentation method include its simplicity in the preparation of the testing specimen and the versatility of the testing result. This method has been widely used to characterize the mechanical properties of thin films and microstructures.

In this study, SiC films were deposited onto a silicon substrate by low pressure chemical vapor deposition [4]. In order to improve the SiC films quality we optimized the deposition conditions, including reacting chambers temperature and pressure, the ratio of carbide source and hydrogen source. By controlling the deposition time, different thickness films were obtains. Research of the nanoindentation process of these films was conducted and the elastic modulus and hardness were determined [5.6].

Analysis

The most commonly used method for measuring hardness and elastic modulus is nanoindentation method. First, a small indentation in the film to be tested, then pressure is loaded while indentation load P, and displacement h are recorded. One measurement cycle stops once the pressure or the displacement reaches the set maximum value. After that, the load-displacement

curve is obtained based on indentation load-displacement data .Figure 1 shows a typical load-displacement curve, where p_{max} is the maximum indentation load, h_{max} is the indenter displacement at maximum load, h_f is the final depth of the contact impression after unloading.

Stiffness of the contact between the indenter and the films being tested is required to determine

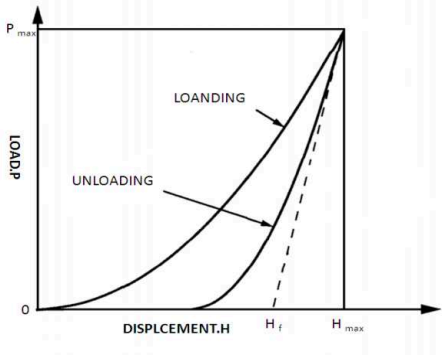


Fig.1 Load-Displacement curve for indentation experiment

mechanical properties of interest. The stiffness, S, is determined from the initial slope of the unloading curve, S=dp/dh. Once the stiffness is measured, the reduced modulus can be determined as:

$$E_r = \frac{\sqrt{\pi}}{2}\frac{S}{\sqrt{A}} \tag{1}$$

where A is the projected area of the elastic contact, E_r is the reduced modulus. Once the reduced modulus is calculated, the actual modulus can be determined as:

$$\frac{1}{E_r} = \frac{1-\upsilon_{sample}^2}{E_{sample}} + \frac{1-\upsilon_{tip}^2}{E_{tip}} \tag{2}$$

where E_{tip}=1140 GPa and υ_{tip}=0.2 are the elastic modulus and Possion's ratio for the diamond tip, respectively. The hardness of materials can be calculated using the equation 3:

$$H = \frac{P_{max}}{A} \tag{3}$$

where p_{max} is the maximum indentation load, A is the projected area of the elastic contact.

Experimental

Materials

SiC films were deposited onto a silicon substrate by low pressure chemical vapor deposition. The reacting gas is SiH_4 and C_3H_8, and the deposition temperature is about 1350℃. The SiC thin films were fabricated with three different thicknesses: 1.6μm, 4.5μm, 9μm by controlling the deposition time.

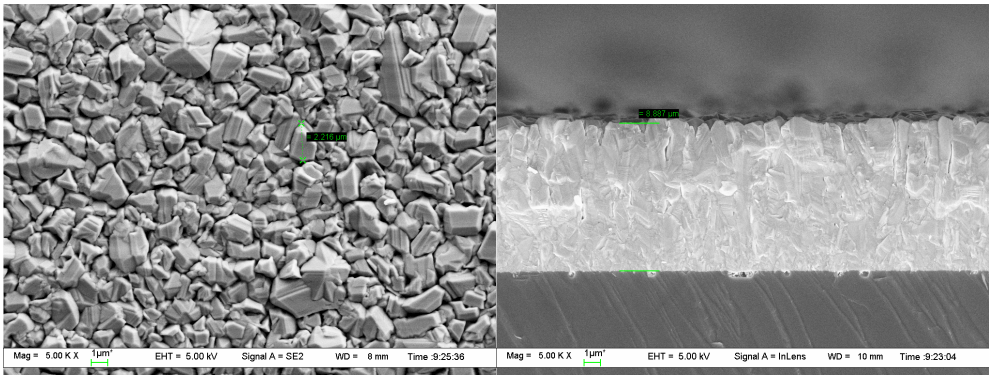


Fig.2 SEM pictures of SiC films with the thickness of 9μm

As shown in figure 2, surface of the film has many grains. However, no obvious defect exists on the films. XRD result show that the SiC deposited on silicon substrate is polycrystalline 3C-SiC. The deposited SiC wafer is then cut into 20 mm by 20 mm sized pieces.

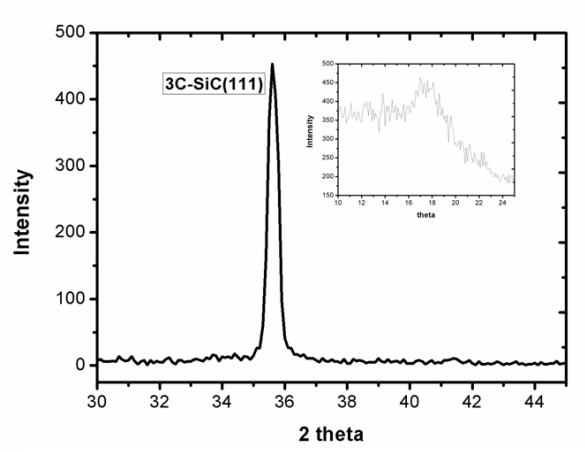


Fig.3 XRD spectrum of 9μm SiC film

Nanoindentation

All experiments are performed using NanoTest indentation tester from Micro Materials Corporation. Load controlled method is used in this study with four different indenter depths [7]: 150nm, 200nm, 250nm, 300nm. Each indentation was done in five different regions in a piece, with the purpose of decreasing the effect of testing regions. But, because of the substrate effect: when the load depths are larger than the films, the test result may be influenced by the substrate. For the piece with the thickness of 1.6μm, only one indentation had been done with the load depth of 150nm. In addition, a single crystal SiC substrate whose material properties have been known was also tested to verify the accuracy of the test.

Results and discussions

Table 1 is the test result of the films with the thickness of 9μm. As is shown, the hardness and elastic modulus almost have no relationship with the peak displacement. The peak displacement been chosen for test is in the appropriate range. So, only one group data of each piece would be drawn into load-displacement curves.

Table 1 Test result of the films with the thickness of 9μm

Peak displacement	Hardness[GPa]	Elastic modulus[GPa]
150[nm]	9.780829	179.09646
	9.967258	176.92491
	10.018723	180.99206
200[nm]	9.098733	159.94133
	5.727434	133.50069
	9.920753	175.81488
250[nm]	9.810507	170.62193
	9.620536	172.7885
	12.2747	176.88744
300[nm]	9.787311	160.29523
	7.123415	160.81005
	9.671608	155.85085

As shown in the load-displacement figures, the result data is scattered, so we take the average value as the test result. SiC thin films with the thickness of 1.6μm has the following values: E=345.73Gpa,H=33.71Gpa; SiC thin films with the thickness of

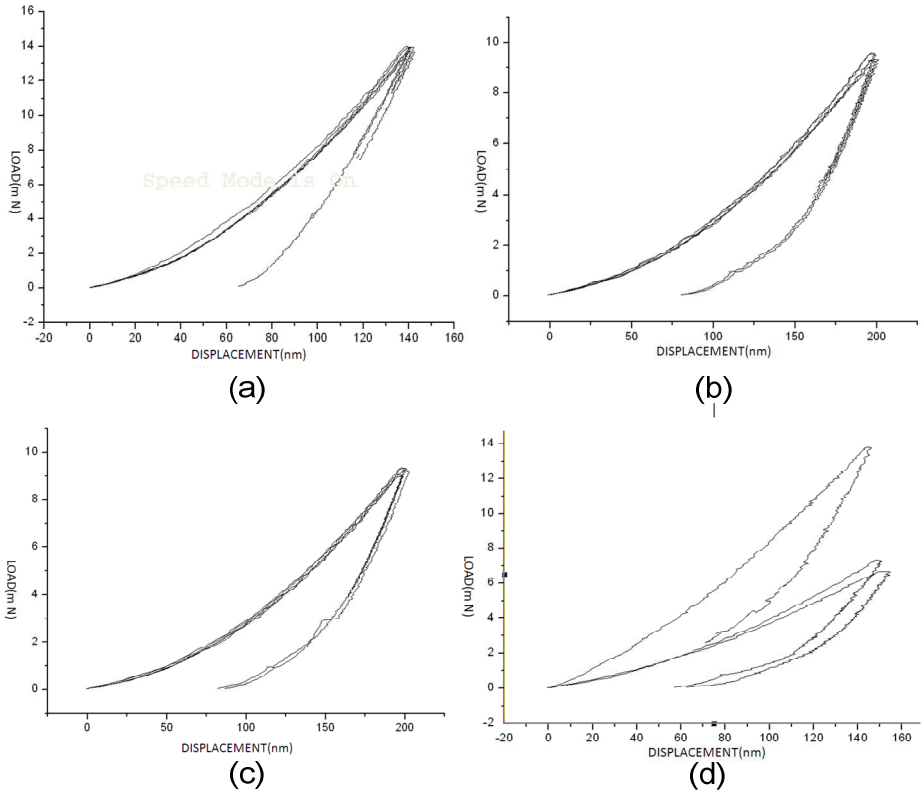


Fig.4 Load-Displacement curves for (a) SiC substrate (b) SiC films with the thickness of 1.6μm (c) SiC films with the thickness of 4.5μm (d) SiC films with the thickness of 9μm

4.5μm has the following values: E=170.18Gpa,H=10.33Gpa; SiC thin films with the thickness of 9μm has the following values: E=167.96Gpa,H=9.48Gpa; SiC substrate has the following values: E=448Gpa,H=30Gpa.The values of SiC substrate is almost the same as the known values. It proved that the test result is accurate. When the thickness of SiC thin films increases, the hardness and elastic modulus become smaller.

There are 20% lattice mismatch between silicon and SiC. When depositing SiC on silicon substrate, there are many defects exist in the interface. The number of defects increases as the thickness of SiC thin films increase, and the grain size of surface becoming larger. As is shown in figure 2, the average diameter of grains is about 2μm, but the grain's diameter of SiC films with the thickness of 1.6μm is about 320.5nm. Large grain size loosens the films, and the values of hardness and elastic modulus decreases.

Acknowledgements

Special thanks must be given to South East University for supplying test instrument, and thanks for Li Yun and Zhao Zhifei of National Key Laboratory of Monolithic Integrated Circuits and Modules for supplying materials. This research was conducted under International Science & Technology Cooperation Program of China grant number 2013DFB10300.

References

[1] W. J. Choyke and G. Pensl, Physical Properties of SiC, MRS Bull,1997,22[3] 25-9.

[2] A.R.Atell, R.S.Okojie, K.T.Kornegay, S.L.Roberson, Simulation, fabrication and testing of bulk micromachined 6H-SiC high-g piezoresistive accelerometers, Sens. Actuator A, Phys,2003,1.4,1,11-18.

[3] Nagasawa,H and Yamaguchi,Y, Thin Solid Films,J.1993,225,191-234.

[4] Li X D,B Hu Shan, A review of nanoindentation continues stiffness measurement technique and its application[J],Materials Characterization, 2002,48(1):11-36.

[5] G.M.Pharr and W.C.Oliver, Measurement of Thin-Film Mechanical Properties Using Nanoindentation, MRS Bull,1992,17[7]28-33.

[6] W.C.Oliver and G.M.Pharr, An Improved Technique for Determining Hardness and Elastic Modulus Using load and Displacement Sensing Indentation Experiments, Mater.Res, J.1993,7[6] 1564-83

[7] J.H.Kim, H.K.Lee, J.Y.Park, Mechanical Properties of Chemical-Vapor-Deposited Silicon Carbide using a Nanoindentation Technique, Journal of the Korean Ceramic Society,2008,45,9,218-523.

Key Engineering Materials Vols 645-646 (2015) pp 405-410
Submitted: 2014-11-04
© (2015) Trans Tech Publications, Switzerland
Accepted: 2014-12-23
doi:10.4028/www.scientific.net/KEM.645-646.405

Experimental study on the relationship between dislocation density and internal stress in micro electroforming layer

Chang SONG[1,a], Liqun DU[1,2,b*], Tong YANG[1,c], Lei LUO[1,d], Yousheng TAO[1,e], Xi ZHANG[1,2,f]

[1] Key Laboratory for Precision & Non-traditional Machining Technology of Ministry of Education, Dalian University of Technology, Dalian, Liaoning, China

[2] Key Laboratory for Micro/Nano Technology and System of Liaoning Province, Dalian University of Technology, Dalian, Liaoning, China

[b]duliqun@dlut.edu.cn

[*] Corresponding Author：Liqun Du, Professor, Key Laboratory for Micro/Nano Technology and System of Liaoning Province, Dalian University of Technology ,
Tel: 86-411-84707713-2121, FAX: 86-411-84707940, email: duliqun@dlut.edu.cn

Keywords: Internal stress, Ultrasonic, Dislocation theory ,Dislocation density

Abstract. In the micro electroforming process, the existence of electroforming layer defects caused by macro internal stress seriously limits the application and development of the micro electroforming technology. Currently, some studies have shown that ultrasonic can reduce the internal stress. But the formation process of the internal stress and the mechanism of ultrasonic stress relief in micro electroforming layer are still unclear now. In this paper, the relationship between dislocation density and internal stress under ultrasonic was studied. The results show that the ultrasonic can make the dislocation density increase and the compressive stress decrease. When the ultrasonic power is 200W, the dislocation density and the compressive stress culminate $3.8\times10^{-15}m^{-2}$ and -144.4MPa, respectively. The ultrasonic can excite the movement of dislocation proliferation, pile-up and opening, which leads to a micro plastic deformation in the crystal, and thereby releases the internal stress.

Introduction

With the rapid development of MEMS, micro electroforming technology has been widely used in micro structure forming, complicated structure forming and mass production. However, the existence of the internal stress in the micro electroforming process is an inevitable phenomenon. High internal stress may cause the electroforming layer cracking, blistering, delamination, etc. These defects seriously affect the dimensional accuracy, make the mechanical properties degradation and result in the decrease of forming rate[1].

Recently years, some scholars have made a great progress. Prasad et al.[2] found that ultrasonic electroplating could reduce the internal stress in nickel coating and improve the hardness and fatigue strength of coating. Fang [3] and Wang [4] also pointed out that ultrasonic could reduce the tensile stress. From the research above, the ultrasonic electrodeposition is an effective way to reduce the internal stress. But, the mechanism of ultrasonic stress relief is still limited to the cavitation effect of ultrasonic. Meanwhile, the essence of micro electroforming is the growth

process of crystal atoms in metal. So a further investigation about the effect of ultrasonic on crystal structure can essentially explain the formation of the internal stress. So far, there have been some referenced research results about the mechanism of VSR (vibratory stress relief). They show that the essence of VSR was the result of the configuration of dislocations and the change of dislocation density in the crystal. The ultrasonic could excite the plastic deformation and increase the dislocation density in the crystal, then homogenized or reduced the internal stress[5,6]. In conclusion, it has been accepted to use the dislocation theory to explain the mechanism of VSR. But, the mechanism of the internal stress in the elecroforming layer is different from the residual stress. In this paper, the relationship between dislocation density and internal stress under ultrasonic was investigated based on the dislocation theory.

The measurement principle of dislocation density

Up to now, X-ray diffraction line profile analysis is a unique non-destructive experimental technique to study the evolution of some important statistical parameters of dislocation systems. X-ray diffraction line broadening contains information about microstructural parameters, such as the lattice microstrain ε and the sizes of domains D. Dislocation is the main lattice defect in the micro electroforming layer. In the experiments, Ni<111>plane was selected as diffraction surface. The dislocation density was calculated by the method of single-line Voigt function analysis of X-ray diffraction patterns. The Voigt function is defined by the following equation[7]:

$$I(x) = \mathrm{Re}\left\{ \beta_C I_C(0) I_G(0) \psi \left[\frac{\sqrt{\pi} x}{\beta_G} + ik \right] \right\}. \tag{1}$$

Where β_C and β_G are the integral breadths of the Cauchy and Gaussian functions, respectively. The measured line profile *h(x)* is the convolution of an instrumental profile *g(x)* with the intrinsic profile *f(x)*.

$$\mathrm{h(x)} = \mathrm{g}(x) * f(x). \tag{2}$$

Ni<111>diffraction peaks corresponding to different ultrasonic power are shown in Fig.1. If the *h(x)*, *g(x)* and *f(x)* are assumed to be Voigt functions, the pure-specimen integral breadths are given by:

$$\beta_C^f = \beta_C^h - \beta_C^g. \tag{3}$$

$$\left(\beta_G^f\right)^2 = \left(\beta_G^h\right)^2 - \left(\beta_G^g\right)^2. \tag{4}$$

Where the intrinsic Cauchy component β_C^f is only due to size effect and the Gaussian component β_G^f is only due to microstrains. According to this approach, the apparent crystallite or domain size D perpendicular to the diffraction planes is:

$$D = \frac{K\lambda}{\beta_C^{\mathrm{f}} \cos\theta}. \tag{5}$$

And the microstrain ε is:

$$\varepsilon = \frac{\beta_G^f}{4\tan\theta}. \tag{6}$$

Where K is a constant, θ is the diffraction angle, λ is the X-ray wavelength.

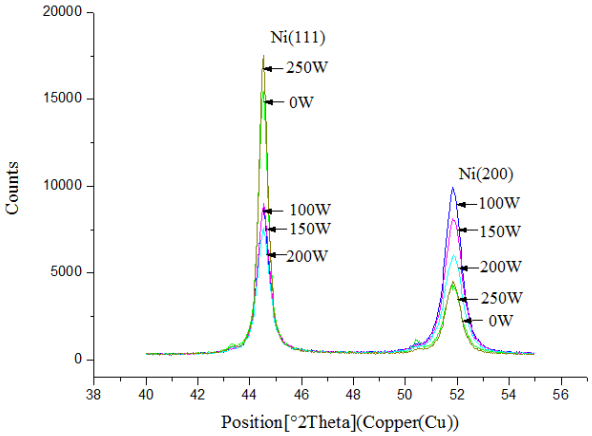


Fig.1 Ni<111>diffraction peaks corresponding to different ultrasonic power

Because the dislocations are completely disordered in the crystal, according to the dislocation distribution model proposed by Wagner[8], the dislocation on the boundary in the crystal and the microstrain in the subgrain can be characterized with the same dislocation density. The formula of the average dislocation density ρ is:

$$\rho = \left[\rho_p \cdot \rho_s\right]^{\frac{1}{2}} . \tag{7}$$

$$\rho_p = \frac{3}{D^2} \quad . \tag{8}$$

$$\rho_S = \frac{K\left\langle \varepsilon_L^2 \right\rangle}{\bar{b}^2} \quad . \tag{9}$$

Where D is crystallite size, $\left\langle \varepsilon_L^2 \right\rangle$ is the mean square strain. $\bar{b}$ is the Burgers vector of dislocations. For nickel, $\bar{b} = 2.4924 \times 10^{-10} m^{-1}$. $K \approx 6\pi$ for Gaussian strain distribution. The releationship between the microstrain and the mean square strain is defined:

$$\varepsilon = 1.25\sqrt{\left\langle \varepsilon^2 \right\rangle} \quad . \tag{10}$$

Thus, the formula of the average dislocation density in the crystal is deduced:

$$\rho = \frac{3\sqrt{2\pi}\varepsilon}{1.25\bar{D}b} \quad . \tag{11}$$

Experimental details

Micro electroforming. Copper plates with the size 50mm×30mm×3mm was used as substrates after a series polishing process. Each sample with a nickel layer electroformed on cooper substrate was obtained under different ultrasonic powers. The ultrasonic powers were 0W, 100W, 150W, 200W, 250W, respectively. The surface size of electroformed layer was 19mm×13mm. The thickness of electroformed layer was near 20μm. The ultrasonic frequency was 40 KHz. In the experiments, the electroforming solution agitation was carried out by the cycle linear movement of the cathode. The composition of electroforming solution was as below: $Ni(NH_2SO_3)4H_2O$(550g/L), $NiCl_2$(10g/L), sodium dodecyl sulfate(0.6g/L), H_3BO_3(30g/L), wetting agent(0.1g/L). The bath temperature was 50℃, the current density was 1.5A/dm^2, the electroforming time was 1.5h and the bath pH value was 4.0. The electroforming sample was shown in Fig.2(a).

Dislocation measurement. A Empyrean X-ray diffractometry was used to measure the dislocation density. There were five samples total, each sample had three measurement position A, B and C, as shown in Fig.2(b). The Ni<111> plane diffraction spectrum was obtained by XRD text. The pure-specimen integral breadths β_C^f and β_G^f were obtained by single-line Voigt analysis based on Equ. (8) and (9). Then through the Equ.(10) and (11), the crystallite size D and the microstrain ε could be calculated. Substituting the above parameters into Equ.(5), the average dislocation density ρ could be calculated. The average dislocation density ρ was the average of ρ_A, ρ_B and ρ_C, where ρ_A, ρ_B, ρ_C were the values corresponding to measurement position A, B, C, respectively. The average dislocation density corresponding to the different ultrasonic power in electroforming experiments were shown in Table 1.

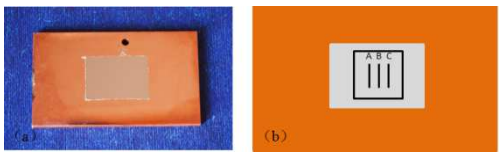


Fig.2 Sample and XRD test.(a) Sample after micro electroforming(b) Surface areas of XRD test

Stress measurement. A Bruker D8 Discover X-ray diffractometry was used to measure the internal stress. The scan mode was side-inclination mode, the scanning speed was 0.6 °/min. The measurement positions were the same with the dislocation measure. In the experiments, Ni<111>plane was selected as diffraction surface, 0 °, 25 °, 35 °, and 45 ° were selected as inclination angle ψ. Diffraction peaks corresponding to different ψ angles were shown in Fig.3. The internal stress value was calculated by the internal stress formulas[9] after the XRD data processing. The internal stress was the average of σ_A, σ_B and σ_C, where σ_A, σ_B, σ_C were the values corresponding to position A, B, C, respectively. The results were shown in Table 1.

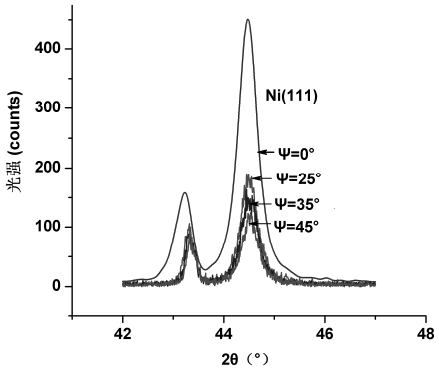


Fig.3 Diffraction peaks corresponding to different ψ angles.

Table 1. The results of the average dislocation density and the internal stress

Ultrasonic power [W]	0	100	150	200	250
Dislocation density average[$10^{15}m^{-2}$]	2.01	3.40	3.20	3.80	2.27
Compressive stress average[MPa]	-259.0	-201.4	-189.2	-144.4	-209.8

Analysis and discussion

(1) The impact of ultrasonic on dislocation density

A relationship curve between the ultrasonic power and the dislocation density is shown in Fig.4. When the ultrasonic power increases from 0W to 200W, the dislocation density increases from

$2.01\times10^{15}m^{-2}$ to $3.8\times10^{15}m^{-2}$ rapidly. At 200W, the dislocation density reaches the maximum value and increases by 88.6%. Then the dislocation density becomes decreased. However, the dislocation density is still $0.21\times10^{15}m^{-2}$ and higher than ultrasonic-free at 250W. Under the ultrasonic, the speed of electrodepositing increases obviously. The speed is more faster, the dislocation density is more higher.

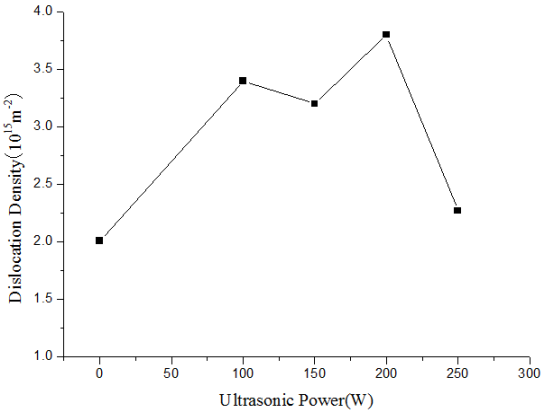


Fig.4 Relationship of ultrasonic power with dislocation density

(2) The impact of ultrasonic on internal stress

Table 1 shows that the internal stress is compressive stress in this experiments, and the compressive stress with ultrasonic is less than that with ultrasonic-free. The compressive stress decreases from 37.2MPa to 102.6MPa. The results of the compressive stress under different ultrasonic power are shown in Fig.5. When the ultrasonic power increases from 0W to 200W, the compressive stress decreses by 114.6MPa from -259MPa to -144.4MPa.The compressive stress keeps decreasing with the ultrasonic power and gets the lowest value at 200W. The stress relief ratio is 44% at this time. This result reflects that the ultrasonic can effectively reduce the internal stress in the electroforming layer.

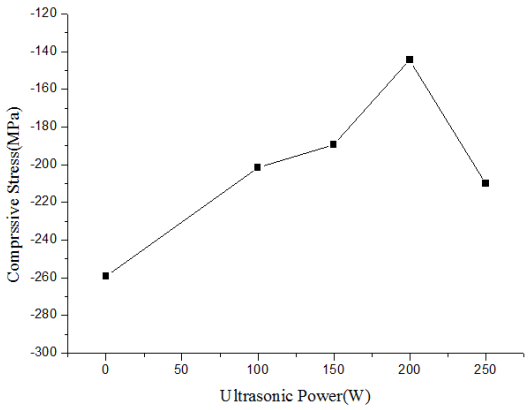


Fig.5 Relationship of ultrasonic power with compressive stress.

From Fig.4 and Fig.5, the change trend of dislocation density and internal stress is opposite under the same ultrasonic power. Dislocation is the main lattice defects in metal crystal. The emergence of lattice defects will destroy the balance between atoms. These defects can make the lattice disorder, deformation, and leads to the lattice distortion in the crystal. The lattice distortion can change the stress field and energy distribution in the crystal, which results in the internal stress increasing. The ultrasonic in the electroforming process can excite the initiation, proliferation,

pile-up and opening of dislocations. The movement of dislocations inspires the micro plastic deformation in the crystal and increases the dislocation density, the increase of dislocation density increases the movement resistance of dislocations and thereby releases the internal stress.

Summary

In this paper, according to the dislocation distribution model, a theoretical formula of the average dislocation density was deduced by X-ray diffraction line profile analysis method. The relationship between dislocation density and internal stress under different ultrasonic power was studied. The experimental results show that the dislocation movement can change the internal stress. The ultrasonic can make the dislocation density increase, and reduce the internal stress. The lattice distortion caused by dislocation may be the main reason for the increased internal stress. This conclusion proves that the dislocation theory can be used to explain the formation of internal stress and the mechanism of ultrasonic stress relief in the micro electroforming layer. It has a practical significance for developing the micro electroforming technology.

Acknowledgement

Authors wishing to acknowledge financial support from the National Natural Science Foundation of China (No:51375077) and the National High Technology Research and Development Program of China (863 Program, No: 2012AA040406).

References

[1] Lei Weining, Zhu Di. Research on microstructure of nanocrystalling nickel electroforming layers, J. China Mech. Engin.. 15(2004) 1283-1286.(in Chinese)

[2] Prasad P B S N V, Vasudevan R, Seshadri S K. The effect of ultrasonic vibration on nickel electrodeposition, J. Mater. Lett.. 17(1993) 357-359.

[3] Fang Xiaohong. Study on technique and mechanism of ultrasonic-assisted electroplating of nickel-based diamond bit, D. China University of Geosciences. 2008. (in Chinese)

[4] Wang Xiuzhi, Yu Aibing. Influence of ultrasonic on hardness of electroplated nickel coating, J. Plating and Finishing. 29(2007) 18-20. (in Chinese)

[5] Jung-Chunghuang, Chih-chia Lin. Investigations on the material property changes of ultrasonic-vibration assisted aluminum alloy up setting, J. Mater. & Design. 45(2013) 412-420.

[6] Rao V V S, Kannan E, Prakash R V, et al. Observation of two stage dislocation dynamics from nonlinear ultrasonic response during the plastic deformation of AA7175-T7351 aluminum alloy, J. Mater. Sci. and Engin. : A. 512 (2009) 92-99.

[7] F.Brunet, P. Germi, M. Pernet. Microstructural study of boron doped diamond films by X-ray diffraction profiles analysis, J. Thin solid films. 322(1998) 143-147.

[8] Lifeng Gui, Rujun Tang. Handbook of Materials Testing for Mechanical Engineering: Physical Metallurgical Volume,1nd ed., Macmillan, The Sci. and Tech. Press of Liaoning, 1999, pp. 433-440. (in Chinese)

[9] Du Liqun, Song Lei, Wang Qijia, et al. Experiments on ultrasonic stress relief used in micro electrodeposited coating, J. Nanotech. and Precis. Engin.. 8(2010) 143–148.

Key Engineering Materials Vols 645-646 (2015) pp 411-415
© (2015) Trans Tech Publications, Switzerland
doi:10.4028/www.scientific.net/KEM.645-646.411

Submitted: 2014-10-29
Accepted: 2014-12-23

Influence of hybrid fibers on flexural properties of Ultra High Toughness Cementitous Composites with nano-SiO_2

Xiang Gao[a], Qinghua Li[b,*] and Shilang Xu[c]

Institute of Advanced Engineering Structures and Materials, Zhejiang University, 310058, Hangzhou, China

[a]tmgcgaoxiang@zju.edu.cn, [b,*]liqinghua@zju.edu.cn (corresponding author), [c]slxu@zju.edu.cn

Keywords: Nano-SiO_2, Hybrid fibers, UHTCC, Flexural properties

Abstract. Ultra High Toughness Cementitous Composites (UHTCC) is a unique class of the ultra-ductile fiber reinforced cementitious composites. To meet the increasingly high requirements for materials in the construction, nano-SiO_2, polyvinyl alcohol (PVA) and steel (ST) fibers were added into UHTCC to improve the mechanical property and control the crack width. Multiple effects of nano-silica and hybrid fibers on the flexural properties of UHTCC under three-point bending are evaluated. The results show that nano-SiO_2 can increase flexural strength of UHTCC while equivalent deformability is guaranteed. When the addition of nano-SiO_2 is 5%, the highest flexural strength is 15.77MPa. Moreover, hybrid steel-PVA fibers effectively mitigate negative influence from nano-SiO_2 which induce the wider cracks of UHTCC as the stronger matrix. Comparing with mono fiber composites, hybrid fibers composites exhibit remarkably higher flexural strength and slightly lower deformation. The best performance are 24.85MPa and 2.34% at maximum volume of hybrid fibers.

Introduction

Ultra high toughness cementitious composites (UHTCC) is one type of polyvinyl alcohol fiber-reinforced cementitious composites designed with micromechanical principles [1]. High-volume fly ash and other minerals are applied into UHTCC to replace part of the cement. UHTCC exhibits excellent pseudo–strain-hardening and multiple-cracking behaviors under bending or tensile forces [2]. Due to the low activity and large volume additions, fly ash inevitably has adverse effects on the strength and microstructure of UHTCC, which will retard the strength development and diminishes the durability of composites as a result of the porous microstructure it engenders [3]. Hence, to satisfy the increasingly strict requirement for the materials in different kinds of construction such as high-rise buildings and nuclear power plant, better performance of the matrix and fibers in the mechanical properties are significantly desired.

Nanotechnology is the extremely hot research field in civil engineering. Many researches [4-6] added nano-SiO_2 at loadings from 0.5 to 4% by weight into cement-based materials and found that the SiO_2 could refine the microstructure, improve the mechanical properties, accelerate the pozzolanic reaction, and react with calcium hydroxide to produce plenty of hydrated calcium silicate (C-S-H) [7]. Moreover, as fibers can effectively bridge the cracks and increase the deformability of materials, different fibers have also been added in the cementitious composites. Short fibers can be expert in bridging the microcracks while the long fibers are more efficient in preventing the development of macro-cracks [8]. Ahmed found that Polyethylene (PE) fibers can improve the tensile strain capacity of composites whereas steel fibers contributed on the improvement of ultimate tensile strength [9]. In four-point bending test, the Steel–PE hybrid composites exhibited lower flexural strength but higher deflection capacity than steel–PVA hybrid composites [10].

In this study, nano-SiO_2 with extremely high specific surface area and steel fibers with excellent strength and modulus, are both added into UHTCC together with PVA fibers to control crack width and furtherly enhance the mechanical properties. It is the first time to apply nano-SiO_2 and hybrid fibers together into this kind of ultra-high ductile cementitious composites. Different additions of nano-SiO_2 and hybrid fibers are evaluated on the three-point bending test.

Materials and experimental methods

Materials and Specimen preparation. In the present research, UHTCC was prepared with cementitious binders containing nano-SiO_2, ultra-fine sand, steel fiber and PVA fiber. The physical properties of nano-SiO_2 and hybrid fibers are shown in Table.1 and Table.2. The binder replacement of nano-SiO_2 is 0, 1%, 3% and 5%. The volume fraction of PVA fiber and steel fiber was 2.0%, 2.5% and 1.0%, 1.2% and 1.4% respectively.

The procedure of mixing was conducted with the Hobart mixer in planetary rotating. First of all, cementitious binders, ultra-fine sand and nano-SiO_2 were put into the mixer together, mixing 4 minutes in dry state. In order to disperse the nano-SiO_2 particles uniformly and keep their activity, Hobart mixer was kept at highest rate, and one superplasticizer of the polycarboxylate type was utilized. Then the rest of water, steel fiber and PVA fiber were added and stirred at high speed for another 10 minutes. The best condition of the mixtures was that the fresh UHTCC were extremely viscous and felt no fiber balls.

The fresh UHTCC was cast into the molds needed in the tests. The dimension of three-point bending specimens was 40mm×40mm×160mm, which were all cast in 2 layers and each layer was tamped by the vibration table for about 30 seconds to decrease the quantity of air bulbs. When the cast completed, all of the specimens were covered with plastic sheets to prevent water from evaporating. The specimens were demolded in 24 hours and put into the standard curing room at 20 centigrade and 95% humidity.

Experimental methods. The specimens in the three points bending test were carried out by a 250kN Instron testing machine with the span of 120mm under displacement control at 0.2mm/min as shown in Fig.1. In the three points bending test, the data of load and displacement were recorded by the force sensor and LVDT respectively and collected in the IMC data acquisition system simultaneously. Finally there were many stress-strain curves of composites obtained. All of the specimens mentioned above were tested at the curing age of 28d and every result of the test was the average of three specimens.

Table.1 Physical properties of nano-SiO_2

Physical properties	Particle diameter	Specific surface area	Bulk density	Purity
Nano-SiO_2	20nm	640m^2/g	<0.1g/cm^3	≥99.7%

Table.2 Physical properties of hybrid fibers

Physical properties	Diameter	Length	Nominal strength	Modulus	Density
PVA fiber	40um	12mm	1600MPa	40GPa	1.3g/cm^3
Steel fiber	220um	13mm	2850MPa	206GPa	7.8g/cm^3

Results and discussion

Three-point bending test. It is feasible to obtain the stress-strain curves of UHTCC in the test. The ultimate flexural stress σ and strain ε at different conditions can be calculated with the equation (1) and equation (2).

$$\sigma=\frac{3FL}{2bh^2} \quad (1) \qquad \varepsilon=\frac{6hf}{L^2} \quad (2)$$

Where, F is the corresponding load. f is the corresponding deflection. L is the span of the specimens which is 120mm. b and h is the width and height of the specimens which are both 40mm.

(a) Effect of nano-SiO_2 on the flexural properties.

Four series composites were evaluated with 0, 1.0, 3.0 and 5.0 wt.% nano-SiO_2. The volume fraction of PVA fibers was 2.0%. Table.3 shows that the flexural stress of composites incorporated with nano-SiO_2 are much higher than that of N0 with the increasing proportion of nano-SiO_2. The maximum initial and ultimate stress are 9.18MPa and 15.77 MPa respectively in N5. It reveals that nano-SiO_2 has active influence on the flexural strength of UHTCC. Nevertheless, the flexural

deflection and nano-SiO_2 do not have positive correlation. The initial and ultimate strain decrease first and then increase along with nano-SiO_2. Comparing N0 with N5, nano-SiO_2 could improve the initial strain of UHTCC and guarantee the nearly equivalent deformability. Excellent pseudo–strain-hardening of UHTCC is more obvious as shown in Fig.2. As the higher matrix strength of N5, more than one failure crack appeared on the specimens, and the crack width became much larger (about 0.1mm) as PVA fibers cannot fully control the development of the macro-cracks due to its low strength and modulus, which are shown in Fig.3.

The active influence of nano-SiO_2 on the flexural properties can be attributed to improving the microstructure of UHTCC. Since nano-SiO_2 can increase the assumption of $Ca(OH)_2$ formed from the hydration of cement and accelerate the hydration of binders. Quantity of C-S-H gel produced by the pozzolanic reaction fills the micropores, and synergistic effect between the matrix and fibers is modified. Hence, the flexural properties are improved.

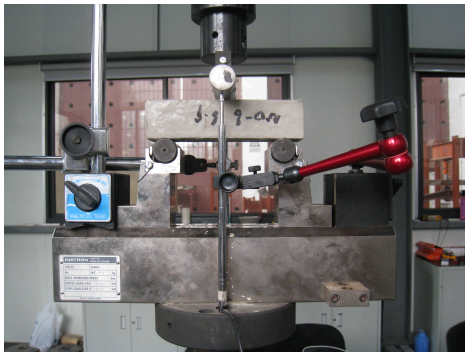


Fig.1 Image of three-point bending test

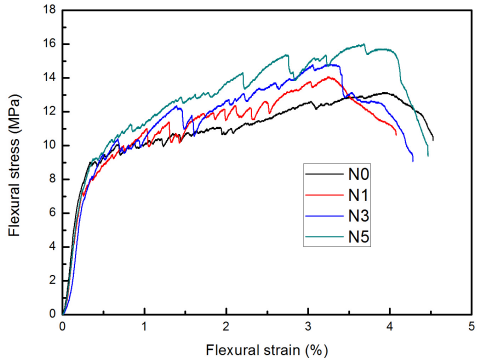
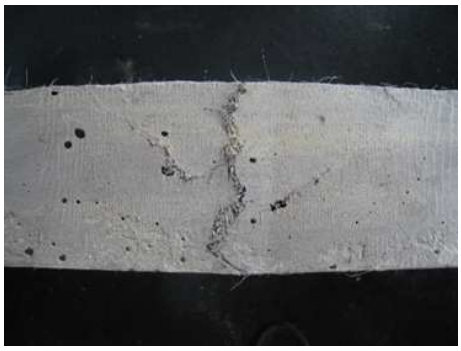
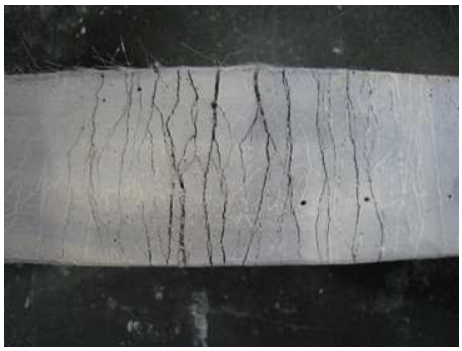


Fig.2 Stress-strain curves with nano-SiO_2



(a) N0



(b) N5

Fig.3 Failure cracks of composites

Table.3 Flexural properties of UHTCC incorporated nano-SiO_2

Sample	Nano-SiO_2 (%)	PVA (%)	σ_{fc} (MPa)	ε_{fc} (%)	σ_u (MPa)	ε_u (%)
N0	0	2.0	6.98	0.279	13.13	3.89
N1	1	2.0	7.29	0.242	14.06	3.26
N3	3	2.0	7.99	0.334	14.79	3.34
N5	5	2.0	9.18	0.351	15.77	3.83

Notes: σ_{fc} and ε_{fc} is the flexural strength and flexural strain when first crack appears on the specimens; σ_u and ε_u is the flexural strength and flexural strain when the load reaches the ultimate value.

(b) Effect of hybrid fibers on the flexural properties.

As N5 exhibits the best performance in the test, it is acted as the basic proportion to study the different fractions of steel fibers and PVA fibers as shown in Table.4. The flexural properties of UHTCC with hybrid fibers was depicted in Fig.4. It reveals that the addition of steel fibers could apparently improve the ultimate flexural strength. For instance, the ultimate flexural strength of T3

with steel fibers (1.4%) was 24.71MPa, which was clearly larger than T1 and T2 (19.44MPa and 22.40MPa respectively). On the contrary, when the volume fraction of PVA fibers was 2.0%, the initial flexural properties and ultimate strain decreased when increasing the volume fraction of steel fibers. However, larger volume fraction of PVA fibers (2.5%) contributed to reflecting the positive influence of steel fibers on the flexural properties.

These results are related to the different roles which hybrid fibers played in the composites according to their own properties. The low strength and modulus fibers (PVA) can effectively restrict the development of the micro-cracks, so deformation of composites are enhanced. The high strength and modulus fibers (ST) can hinder the generation of the macro-cracks, so flexural strength of composites are increased. Furthermore, there is an optimum proportion of hybrid fibers, which leads to the mutual effects between PVA fibers and steel fibers. Fig. 5 illustrates the failure-crack images of the samples with hybrid fibers. Due to high strength of steel fibers, macro cracks have been successfully controlled and crack width has been reduced to 0.04mm almost the same with UHTCC, mitigating the drawback of nano-SiO_2 addition.

Table.4 Flexural properties of UHTCC with hybrid fibers

Sample	Nano-SiO_2 (%)	PVA (%)	ST(%)	σ_{fc} (MPa)	ε_{fc} (%)	σ_u (MPa)	ε_u (%)
T1	5	2.0	1.0	14.39	0.529	19.44	2.10
T2	5	2.0	1.2	13.02	0.371	22.40	1.98
T3	5	2.0	1.4	13.39	0.318	24.71	1.55
T4	5	2.5	1.0	9.93	0.292	20.37	2.19
T5	5	2.5	1.2	10.58	0.221	22.95	2.06
T6	5	2.5	1.4	18.96	0.524	24.85	2.34

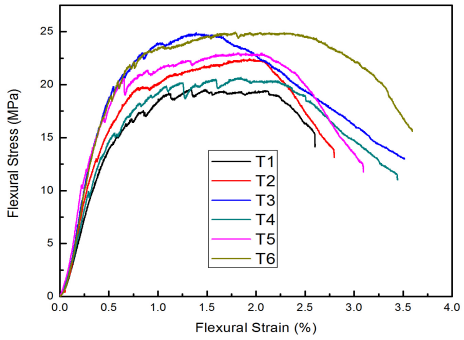


Fig.4 Stress-strain curves with nano-SiO_2



Fig.5 Failure cracks of hybrid fibers composites

Conclusions

(a) Nano-SiO_2 can remarkably improve the flexural properties of UHTCC and modify synergistic effect between the matrix and fibers. With the increase of nano-SiO_2, flexural stress and strain of samples are both enhanced. The maximum values are 15.77MPa and 3.83% in N5.

(b) PVA fibers can effectively restrict the development of the micro-cracks and ST fibers can hinder the generation of the macro-cracks. The optimum proportion of hybrid fibers is T6, whose ultimate flexural stress and strain are 24.85MPa and 2.34% respectively.

Acknowledgements

The authors would like to acknowledge the financial supports provided by National Key Technology Research and Development Program of the Ministry of Science and Technology of China with grant No.2012BAJ13B04.

References

[1] Li VC, and Leung CKY, Steady state and multiple cracking of short random fiber composites, Journal of Engineering Mechanics, J. Eng. Mech. ASCE, 1992, 188(11):2246-2264.

[2] Shilang Xu, Qinghua Li, Basic Application of ultra high toughness cementitious composites in advanced engineering structures, Science Press, Beijing, 2010.

[3] Mustafa, Sahmaran, V.C. Li, Durability properties of micro-cracked ECC containing high volumes fly ash, Cement Concrete Res. 39 (2009) 1033-1043.

[4] Ali Nazari, ShadiRiahi, The Effects of SiO_2 nanoparticles on physical and mechanical properties of high strength compacting concrete, Composites: Part B. 42(2011) 570-578.

[5] Gengying Li, Properties of high-volume fly ash concrete incorporating nano-SiO_2, Cement Concrete Res. 34(2004) 1043-1049.

[6] I.Zyganitidis, M.Stefanidou, Nanomechanical characterization of cement-Based pastes enriched with SiO_2 nanoparticles, Mater. Sci. Eng. B. 176(2011) 1580-1584.

[7] L.Lam, Y.L. Wong, C.S. Poon, Degree of hydration and gel/space ratio of high-volume fly ash/cement systems, Cement Concrete Res. 30(2000) 747-756.

[8] R.Yu, P.Tang, P.Spiesz, H.J.H.Brouwers, A study of multiple effects of nano-silica and hybrid fibers on the properties of ultra-high performance fiber reinforced concrete (UHPFRC) incorporating waste bottom ash (WBA), Con. Building. Mater. 60(2014) 98-110.

[9] S.Ahmed, Analytical model for tensile strain hardening and multiple cracking behavior of hybrid fiber-engineered cementitious composites, J.Mater.Civ.Eng. 19(2007) 527-539.

[10] S.Ahmed, Flexural responses of hybrid steel-polyethylene fiber reinforced cement composites containing high volume fly ash, Constr.Build.Mater. 21(2007) 1088-1097.

Key Engineering Materials Vols 645-646 (2015) pp 416-420
Submitted: 2015-01-15
© (2015) Trans Tech Publications, Switzerland
Accepted: 2015-01-21
doi:10.4028/www.scientific.net/KEM.645-646.416

The Influence of Polyhedral Oligomeric Silsesquioxane on Heat Resistance and Curing Kinetics of Potting Materials

Fan Jinghui[a*], Jing Hua[b], Wu Juying[c]

（Institute of System Engineering, CAEP, Mianyang 621900, China）

[a]fanjh@caep.cn, [b]jingh@caep.cn, [c]wujy@caep.cn

Keywords: polyhedral oligomeric silsesquioxane； heat resistance； curing kinetics

Abstract. The influence of polyhedral oligomeric silsesquioxane on heat resistance and curing kinetics of potting materials were studied. The results showed that POSS can promote the cure, but did not change the potting materials curing mechanism. The research results have important significance for improving the performance of potting materials in electronic products.

Introduction

In order to prevent invasion of moisture, dust and harmful gases, external damage and to improve stability and reliability of components, the electronic components often need to be potted. Especially in navigation and missile, electronic products usually require less thermal release when the potting material is cured, and can withstand the test of temperature over load after curing. Therefore requires potting materials with superior properties. Addition of liquid silicone rubber (abbreviated as LTV) does not produce by-products during vulcanization, and has small linear shrinkage and dimensional stability under high and low temperatures. It would have a broad application prospect in the field of missile electronic products while the curing temperature can be reduced and the heat resistance can be improved.

Polyhedral oligomeric silsesquioxane (abbreviated as POSS) is a kind of organic-inorganic hybrid materials. Because organic and inorganic phases are combined at the nano- or submicron even molecular level, it is different from traditional organic - inorganic phase filler system(shown in Fig.1).

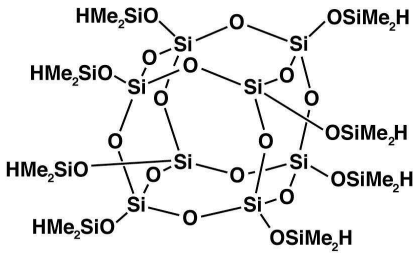


Fig.1 The structure of POSS

In this paper, the mechanism of the heat resistance enhancement of the POSS/LTV composite was studied, by analysis of the thermogravimetric curves and the molecular structure at 298K~968K. The reaction kinetics equation was obtained by investigation the curing kinetics of the POSS/LTV composites using non-isothermal DSC, and by calculation the activation energy and the curing reaction order with Crane equation. The results showed that POSS could promote the cure,

but could not change the curing mechanism. The research results have important significance for improving the performance of potting materials in electronic products.

1. Experimental

1.1 Materials

Octamethyl cyclotetrasiloxane (99%, D4) was supplied by Shin-Etsu Chemical Co. Ltd., Japan. Tetravinyl tetramethylcyelo tetrasiloxane (97%, V4), divinyl tetramethyl disiloxane (96%) and tetramethylammonium hydroxide (98%) were supplied by Alfa Chemical Reagent Co. Ltd., America. Silicone oil with active hydrogen mass fraction of 0.4%~1.2%, MQ resin with M/Q ratio of 0.8 and inhibitor were supplied by GE Toshiba Silicones Chemical Company. Platinum complex and POSS were synthesized with the methods revealed in the references 2. Hexane was supplied by Guanghua Chemical Factory Co. Ltd.

1.2 Preparation of LTV

1.2.1 Synthesis of Raw Vinyl Silicone Rubber

The D4, V4 and divinyl tetramethyl disiloxane were added in the three-necked flask at a mass ratio of 100: 0.96: 0.09 and heated to 358K, dehydrated for 1 hour under vacuum condition. The catalyst tetramethyl ammonium hydroxide was added with the vacuum released, heated to 393K and stirred for 2 hours. Heated to 453K, the reaction was continued 2 hours. And then the appearance of colorless transparent vinyl terminated raw vinyl silicone rubber with viscosity of about 3000 mPa·s, ethylene group molar fraction of 0.8% was got.

1.2.2 Preparation of M Component

The raw vinyl silicone rubber and platinum complex (mass fraction of 3.0×10-5) were mixed evenly. Under vacuum condition, M component with viscosity of 2500~3000 mPa·s was got and packaged.

1.2.3 Preparation of N Component

The raw vinyl silicone rubber, hydrogen containing silicone oil and MQ resin were mixed evenly at a mass ratio of 100: 8: 10, and next the inhibitor was added at a mass fraction of 2.0×10-3.After defoamedunder vacuum condition,N component with viscosity of 2500~3000 mPa·s was got and packaged.

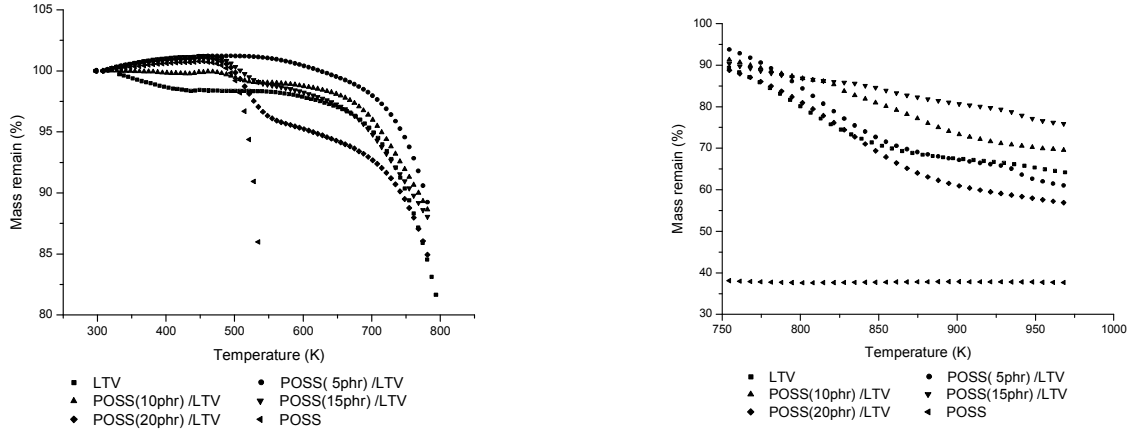
1.3 Preparation of POSS/LTV Composites

According to the formula, the M component of LTV was dissolved in hexane, and the solution was added POSS. Mixing the solution until the solution became clear and uniform. And then it was put in 333K oven, dried until a constant mass is reached. After that, it was mixed with the N component of LTV under vacuum condition, and then vulcanized in an oven under conditions of 353K and 4 hours.As the formula , POSS were added into 100 phr LTV, which contain M and N components of 50 phr each by 5, 10, 15 and 20 phr.

2. Results

2.1 Heat Resistance of POSS/LTV Composites

Thermogravimetric analysis of the composites with different POSS content were proceeded by the thermal analyzer (STA 449 C) obtained from NETZSCH company at 298K~968K and N2 environment with the heating rate 10 K/min(shown in Fig.2).



(a) (b)

Fig.2 TGA curves of POSS/LTV composites at 298K~788K(a) , at 788K~968 K(b)with different POSS content

Fig.2(a) shows that the sample with the 20 phr POSS content lost weight near 473K firstly, and had a lowest mass retention rate. The reason is that the excessive POSS either crystallized or agglomerated, which destroyed the integrity of the polymer and resulted in the thermal stability of the composite. The rest POSS content composites showed that the less the POSS content, the higher the mass retention rate. This shows that the thermal weight loss before 788K is mainly the loss of organic radical, and because the ratio of organic group outside the POSS cage is large, the more the POSS content, the lower the mass retention rate. Thus one of the ways to improve the thermal stability of composites is to choose the POSS with low molecular weight side radicals outside the cage.

Contrary to Fig.2(a), the trend shown in Fig.2(b) is that the more the POSS content, the higher the mass retention rate, which illustrates that the thermal degradation mechanism is different. At high temperature, the weight loss of the composites is mainly due to the main chain degradation.

For cage structure with higher stability, the more the POSS content, the higher the mass retention rate. Therefore, the second way to improve the thermo stability of composites is to add as much POSS as possible as long as the POSS is not excessive.

2.2 Curing Kinetics of POSS/LTV Composites

The curing kinetics study was conducted by using differential scanning calorimeter (DSC) tracking the curing reaction process. The instrument was corrected with high purity indium. The N_2 flow rate was 20 ml/min. The temperature scan range was from room temperature to 423K.The heating rate were 5K/min, 10K/min, 15K/min and 20K/min, respectively.

2.2.1 The Curing Reaction Activation Energy

According to the second law of thermal dynamics, the kinetic parameters of POSS/LTV system can be calculated as follows:

$$\Delta T = \frac{Q}{\Delta S} = \frac{\Delta H}{\Delta S} \tag{1}$$

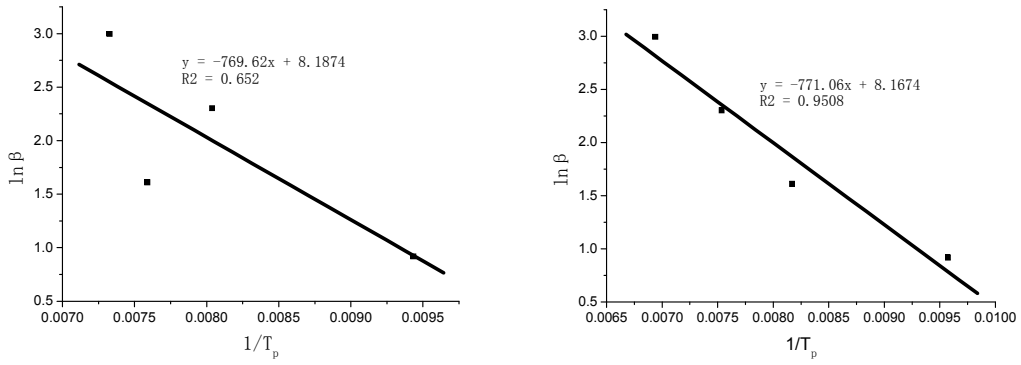
Where △T is the temperature change of the system, △S is the entropy change of the system,△H is the enthalpy change of the system, and Q is the caloric of the system.

The Doyle-Ozawa equation:

$$\frac{d[\ln \beta]}{d[1/T_p]} = -1.052\frac{E}{R} \tag{2}$$

Where β is the heating rate (℃/min), Tp is the peak temperature of the DSC curve (K), E is the apparent activation energy (J/mol) and R is the ideal gas constant and it value is 8.3144J/mol • K.

According to Doyle-Ozawa equation, linear regression of lnβ was for (1/Tp) and the results showed in Fig.3. The slope of the linear regression straight line of Doyle-Ozawa equation was k=d[lnβ]/d(1/Tp)=-1.052E/R, and E=-1.052k×R. The linear correlation of sample a and b were 0.652 and 0.9508, respectively.



(a) LTV (b) POSS/LTV composite

Fig.3 Linear regression of Doyle-Ozawa equation of LTV and POSS/LTV composites

2.2.2 Curing Reaction Order

The reaction order of curing reaction was obtained from the Crane empirical equation. The Crane equation:

$$\frac{d[\ln \beta]}{d[1/T]} = -(\frac{E}{nR} + 2T_p) \tag{3}$$

Where β is the constant heating rate (K/min), Tp is the peak temperature (K), n is the curing reaction order, R is the ideal gas constant(kJ/mol) and E is the apparent activation energy (kJ/mol). When the E/nR is far greater than 2Tp, 2Tp can be omitted and the follow equation can be obtained:

$$\frac{d[\ln \beta]}{d[1/T]} = -\frac{E}{nR} \tag{4}$$

Linear regression was for lnβ～(1/Tp) curve. The reaction order n=-E/(k×R). The reaction order of two specimens calculated by the Doyle-Ozawa method were as follows: sample a n=1.052, sample b n=1.052.

2.2.3 Curing Reaction Kinetics Equation

The curing reaction process of POSS/LTV composite follows the law of conservation of mass.

$$\frac{d\alpha}{dt} = k(1-\alpha)^n \tag{5}$$

Where k is the curing reaction rate constant (K/min) which can be calculated by Arrhenius formula, α is the curing reaction conversion rate. Arrhennius formula:

$$k = Ae^{-E/RT} \tag{6}$$

$$A = \frac{\beta E \exp(E/RT_p)}{RT_p^2} \tag{7}$$

In formula (6) and (7), A is the apparent frequency factor (min-1), Tp is the reaction peak temperature (K), E is the reaction activation energy (kJ/mol), β is the heating rate (K/min).

When the heating rate was 10K/min, ka=2.03×103e-810/T, kb=2.47×103e-811/T. The reaction kinetics equation of the samples were calculated as follows:

sample a

$$\frac{d\alpha}{dt} = 2.03\times10^{3}e^{-810}(1-\alpha)^{1.052} \tag{8}$$

sample b

$$\frac{d\alpha}{dt} = 2.47\times10^{3}e^{-811/T}(1-\alpha)^{1.052} \tag{9}$$

3. DISCUSSION

Through the analysis of the TGA curves and the molecular structure of the POSS/LTV composite materials, the mechanism of the heat resistance enhancement of the composite was studied. The reaction kinetic equation was obtained by investigation the curing kinetics of the POSS/LTV composites using non-isothermal DSC, and by calculation the activation energy and the curing reaction order with Crane equation. The results showed that POSS can promote the cure, but did not change the LTV curing mechanism. The research results have important significance for improving the performance of potting materials in electronic products.

Acknowledgement

This work was supported by NSAF (Grant No. U1330122).

References

[1] Xing Songmin, Wang Yilu. Synthesis and application of organic silicone[M]. Beijing: Chemical Industry Press, 2000: 536-566.

[2] Hasegawa I , Motojima S. Organometallic Chem, 1992, 441 (3):373-380.

[3] Fan Jinghui, Zhang Kai, Wu Juying. Silicone Material, 2011, 25 (5): 318-322.

Key Engineering Materials Vols 645-646 (2015) pp 421-426
© (2015) Trans Tech Publications, Switzerland
doi:10.4028/www.scientific.net/KEM.645-646.421

Submitted: 2014-10-28
Accepted: 2014-12-23

Study on Mechanism of Phase Forming in Ni^+ Implantation into Ti6Al4V at Elevated Temperature

Wang Yuan[1,2a]; Yu Xiaohua[2,b]; Yang Hailong[1,c]

[1]School of Mechanics and Transportation, Southwest Forestry University, Kunming 650224, China

[2]School of Materials Science and Engineering, Kunming University of Science and Technology, Kunming, 650093, China

[a]wyuan88@126.com (corresponding author), [b]xiaohua_y@163.com, [c]274828235@qq.com

Key words: Ni^+ implantation; Ti4Al6V; Mechanism of phase forming; Effective heat of formation

Abstract: Recently, due to the prediction of the forming phase only focuses on the case which a simple metal ion implants into a single metal matrix, we will study that a simple metal ion is implanted into alloy matrix in this paper. The forming phases in Ni^+ implantation into Ti6Al4V at elevated temperature will be predicted by the effective heat of formation (EHF) model. The results show that the prediction is consistent with the experimental findings, the first-phase is TiNi with the most negative EHF, the second-phase is Ti_2Ni which component concentrations of Ni limited element is lower and locates on the left in the Ti-Ni binary alloy phase diagram, and the $TiNi_3$ phase is not found in the experiment. Simultaneously, we explain correctly why the Ni-Al or Ni-V phases don't generate in Ni^+ implantation into Ti6Al4V at elevated temperature.

Introduction

Ion implantation is a special mass transfer process with "implanting + simultaneously diffusing", and this process not only determines the equilibrium distribution of the implanted ions in the matrix, but also determines the forming phase in the implanted layer. Some scholars have built the analytical and numerical models [1] to simulate this special mass transfer process, but the analytical models have been rarely used due to their rigorous employing conditions. The numerical model has described the relative theories about the mass process of ion implantation, but it hasn't gave the relative mechanisms on the process of metal ion implantation into matrix materials at elevated temperature, so it can only predict and simulate the relationship between the concentration and the depth of implanted ion, not to mention the forming phases. During the mechanisms of mass transfer on metal ion implantation at elevated temperature were studied, the Walser-Bene rule[2], the silicide formation criteria[3] and the single-phase growth theory on implanted layer[4] have been proposed to predict the forming phases in metal ion implantation into metal matrix at elevated temperature, these rules have succeed to explain some compound phases formation in binary film, but they have never used the thermodynamic data such as the entropy, enthalpy and heat of formation and so on. Scholars have always been argued whether the thermodynamic data can be used to predict the forming phases in the process of ion implantation, until Pretorius gave the effective heat of formation (EHF) and predicted of aluminide and silicide formation with these data [5], the thermodynamic data were really used. Later, scholars added concentration limits to the EHF model and successfully predicted the forming phases in some metal-Al binary alloy system[6]. However, the theories basically concentrated on the prediction of the forming phases in a simple metal ion implantation into a single metal matrix, hardly dealt with a simple metal ion implantation into alloy matrix. Therefore, we will use the EHF model to predict the forming phases in Ni^+

implantation into Ti6Al4V at elevated temperature in order to inspect whether the EHF model can be used to predict the forming phases in a simple metal ion implantation into alloy matrix.

1 The EHF Model

The EHF (ΔH_f) is the actual exothermic heat at interface in solid-solid reaction system. The calculation equation of the EHF in the non-equilibrium solid state reaction which metal A ion is implanted into metal B matrix to form the intermetallics A_xB_y will be given in the following, the schematic diagram of A_xB_y formation in this process is as shown in Fig1.

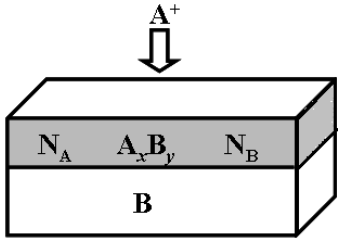


Fig.1 Schematic diagram of A_xB_y formation at interface in metal A^+ implanting metal B matrix

It is assumed that the reaction between atom A and atom B at solid-solid system interface in the process of formation A_xB_y is:

$$z(x\mathrm{A}+y\mathrm{B})=z(\mathrm{A}_x\mathrm{B}_y) \tag{1}$$

In the above equation, the x and y are that of the number of atom A and B actually reacted respectively, the z is that of the number of formation A_xB_y. If the N is that of the total number of atoms at reaction interface, then:

$$N=N_\mathrm{A}+N_\mathrm{B} \tag{2}$$

If the M is that of the number of actually consuming atoms in the process of formation A_xB_y, then:

$$M=zx+zy=M_\mathrm{A}+M_\mathrm{B} \tag{3}$$

The M_A and M_B are that of the number of actually reacted atom A and B, respectively. The effective concentrations of atom A and B can be expressed as the following:

$$C_e^A=\frac{N_A}{N};\quad C_e^B=\frac{N_B}{N} \tag{4}$$

The component concentrations of atom A and B in A_xB_y can be expressed, respectively:

$$C_c^A=\frac{x}{x+y};\quad C_c^B=\frac{y}{x+y} \tag{5}$$

If atom A is completely consumed and B has the surplus in the reaction of formation A_xB_y, atom A is the limited element, then:

$$M_A=N_A=C_e^A(N_A+N_B)=C_e^AN \tag{6}$$

We can also obtain the following formula:

$$\frac{M}{N}=\frac{M_A+M_B}{N_A+N_B}=\frac{C_e^A}{C_c^A} \tag{7}$$

The standard heat of formation (ΔH_0) is the exothermic heat when all the N atoms are completely consumed in the process of formation A_xB_y. If using $\mathrm{kJ\cdot(mol\cdot at)^{-1}}$ as a dimension of ΔH_0, the exothermic heat is $\frac{M}{N}\Delta H_0$ kJ when the M atoms are just consumed in the process of formation

A_xB_y, then a mole atoms consumed in the reaction will release the heat of ΔH_f, it can be expressed as:

$$\Delta H_f = \frac{M}{N}\Delta H_0 = \Delta H_0 \frac{C_e^A}{C_c^A} \tag{8}$$

The ΔH_f is named as the EHF. Obviously, the limited element in the reaction will be determined by the scale of the effective concentration and the component concentration of this atom in the intermetallics, moreover, the EHF can be expressed as the following general formula:

$$\Delta H_f = \begin{cases} \Delta H_0 \dfrac{C_e^A}{C_c^A} & C_e^A < C_c^A \\ \Delta H_0 & C_e^A = C_c^A \\ \Delta H_0 \dfrac{C_e^B}{C_c^B} & C_e^A > C_c^A \end{cases} \tag{9}$$

A new phase in the solid-solid binary system easily form near to the lowest eutectic temperature or liquidus area in the phase diagram, and the atom concentration at interface presenting "metallic glass" state[7], so the previous studies regarded the eutectic composition or the liquid composition at the lowest temperature in the phase diagram as the effective concentration of binary system[8-10].

2 Prediction of the Forming Phases for Ni^+ Implantation into Ti4Al6V

The phase diagram of Ti-Ni binary alloy system is as shown in Fig2. According to the phase diagram, we can know that three kinds of intermetallics such as Ti_2Ni, TiNi and $TiNi_3$ existing in the phase diagram and the lowest eutectic temperature of this system is 942 ℃ with the reaction of L→Ti(β)+Ti_2Ni. Depending on the selection criterion of the effective concentration, the deepest eutectic concentration of Ni with 24at% at the lowest eutectic temperature 942℃ is regarded as the minimum effective concentration in calculating the EHF. Among the three kinds of intermetallics of Ti-Ni binary system, the component concentrations of Ni are all higher than 24at%, therefore Ni is just the limited element at reaction interface.

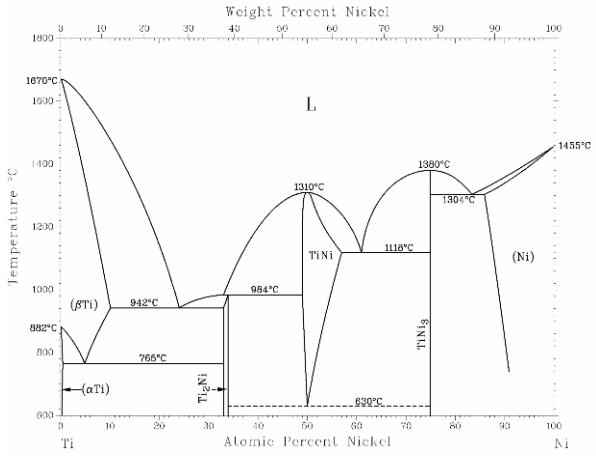


Fig.2 Phase diagram of Ti-Ni binary alloy system

In the experiment, the temperature when Ni^+ is implanted into Ti4Al6V is about 1200K and at the same temperature for 3 hours, so the standard heat of formation ΔH_0[11] at 1200K are selected to calculate the EHF of three kinds of intermetallics in Ti-Ni binary alloy system, and the calculated data are listed in Table1.

Table1 Thermodynamic parameters in Ti-Ni binary alloy system

Intermetallics	Component concentration	Effective concentration of Ni/ at%	ΔH_0 /kJ·(mol·at)$^{-1}$	ΔH_f /kJ·(mol·at)$^{-1}$
Ti_2Ni	$Ti_{0.667}Ni_{0.333}$	24~33.3	–2.18	–1.57
TiNi	$Ti_{0.5}Ni_{0.5}$	24~50	–7.13	–3.42
$TiNi_3$	$Ti_{0.25}Ni_{0.75}$	24~75	–8.78	–2.81

In the range of the common component concentration of the limited element Ni with 33.3at%, the EHF of TiNi is the most negative, the EHF of Ti_2Ni comes second and the EHF of $TiNi_3$ is the minimum, as shown in shading area of Fig3. That is to say, TiNi most easily forms in Ni^+ implantation into Ti6Al4V at about 1200K and Ti_2Ni follows to form, the prediction is consist with the experimental findings of studies of plasma ion alloying on Ti6Al4V surface by Wang Yingqin[12] and Cai Yiping et al[13] and the XRD pattern of the Ni-Ti6Al4V alloyed layers in their experiments are as shown in Fig4(a) and (b). If an element is still residual after the first-phase forming in binary system, the next forming phase should be the intermetallics which contain the unreacted element with higher concentration[14]. In the process of Ni^+ being implanted into Ti6Al4V, Ni is both the implanted element and the limited element, Ni and Ti element are still residual after the first-phase forming, and the effective concentration of the rest of Ni will move forward to the left of the Ti-Ni binary alloy phase diagram, i.e., the orientation of lower Ni concentration, therefore the second-phase is Ti_2Ni which locates on the left of TiNi in the phase diagram, but $TiNi_3$ can't form which contains more high Ni concentration and locates on the right of TiNi. $TiNi_3$ isn't also found in the experimental findings in Wang Yingqin and Cai Yiping's studies.

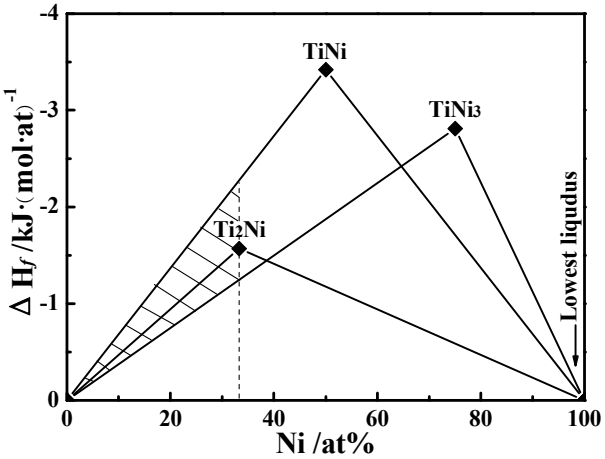
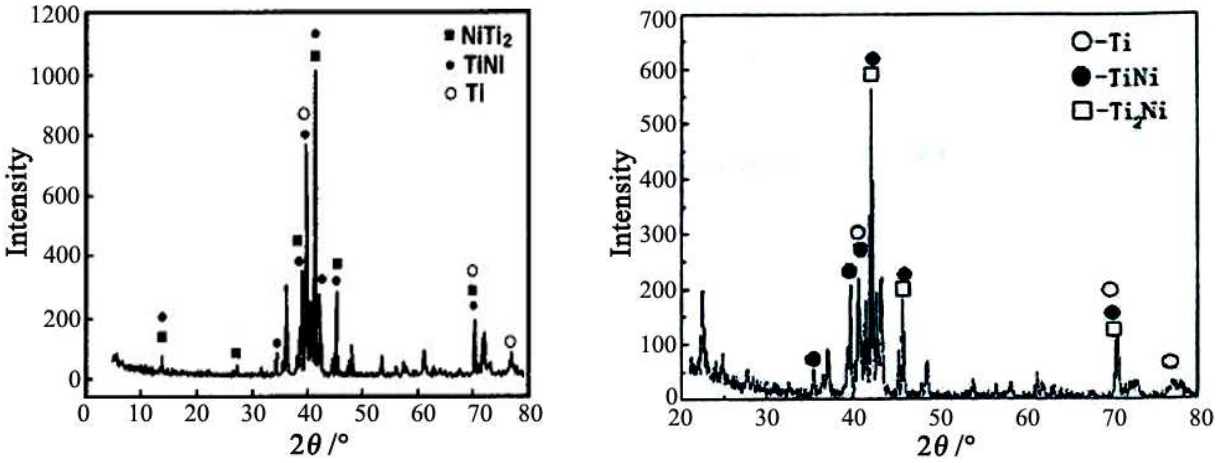


Fig.3 Effective heat of formation diagram of Ti-Ni binary alloy system

The relative phases of Ni-Al and Ni-V haven't been also found in the experimental findings in Fig4(a) and (b) because the major Al and V adding element in Ti6Al4V exist in intermetallics forms in itself. When Ni^+ is being implanted into Ti6Al4V at elevated temperature, the energy of implanted ion is too high to break bond strength of the Ti-Al and Ti-V intermetallics, so the implanted Ni^+ has priority to react with Ti in the state of simple substance and forms Ti-Ni intermetallics.



(a) Wang Yingqin's experimental result (b) Cai Yiping's experimental result

Fig4 XRD pattern of layer with Ni^+ implanted into Ti6Al4V

3 Summary

The forming phases in Ni^+ implantation into Ti6Al4V at elevated temperature were successfully predicted by the EHF model, i.e. the prediction is consistent with the experimental findings. At the same time, the theory that the forming phases in ion implantation will be predicted by the EHF model is extended to the case that a simple metal ion is implanted into an alloy matrix at elevated temperature. Moreover, we explain correctly why the Ni-Al or Ni-V phases don't generate in Ni^+ implantation into Ti6Al4V at elevated temperature.

Acknowledgement

The authors would like to acknowledge the financial support provided by the National Nature Science Foundation of China (Grant No.51301144).

References

[1] P Sigmod. Mechanism and theory of physical sputtering by particle impact [J]. Nucl Instrum Method, 27(1987) 1-20

[2] S Parascandola, W Moller. The nitrogen transport in austenitic stainless steel at moderate temperatures [J]. Appl. Phys.Lett, 79(2000) 2194-2197.

[3] B.Y Tsaur, S.S Lau, J.W Mayer, et al. Sequence of phase formation in planar metal-Si reaction couples [J]. Appl Phys Lett, 38(1981) 922-924.

[4] R.W Bene. First nucleation rule for solid-state nucleation in metal-metal thin-film systems [J]. Appl Phys Lett, 41(1982) 529-531.

[5] G Majni, C Nobili, G.G Ottaviani, et al. Gold-aluminum thin-film interactions and compound formation [J]. J. Appl. Phys, 52(1981) 4047-4055.

[6] Chen Tao, Chang Haiwei, Lei Mingkai. Surface alloying of Al ion implantation into Fe target at elevated temperature [J]. Acta Metallurgica Sinica, 41(2005) 417-420.

[7] Lu Xuechao, Liao Yihuan. Prediction of the first formation at interface in the U-Al binary system by effective heat of formation model [J]. Rare Materials and Engineering, 41(2012) 90-92.

[8] B.Y Tsaur, S.S Lau, J.W Mayer, et al. Sequence of phase formation in planar metal-Si reaction couples [J]. Appl. Phys.Lett, 38(1981) 922-924.

[9] M Ronay. Reinvestigation of first phase nucleation in planar metal-Si reaction couples [J]. Appl. Phys.Lett, 42(1983) 577-579.
[10] R.M Walser, R.W Bene. First phase nucleation in silicon-transition-metal planar interface [J]. Appl. Phys.Lett, 28(1976) 624-625.
[11] Liang Yingjiao, Che Yinchang. Handbook of Thermodynamics Parameters on Inorganics [M]. Dongbei University Press, Shenyang, 1994.
[12] Wang Yingqin, He Zhiyong, Wang Zhenxia, et al. Surface Ni-Ti co-diffusion of Ti6Al4V by plasma surface alloying technology [J]. Journal of Functional Materials, 41(2010) 466-472.
[13] Cai Yiping. Cu-Ni plasma alloying on the surface of Titanium alloy [S]. Taiyuan University of Technology, 2013.
[14] Chang Haiwei. Surface alloying mechanism during metal ion implantation into metal at elevated temperatures [D]. Dalian University of Technology, 2005.

Key Engineering Materials Vols 645-646 (2015) pp 427-434
Submitted: 2015-01-20
© (2015) Trans Tech Publications, Switzerland
Accepted: 2015-01-21
doi:10.4028/www.scientific.net/KEM.645-646.427

Preparation and Mechanical Properties of Ultra-fine Grain Medium-carbon Steel Based on Equal-channel Angular Pressing

Jianmin Wang[1]*, Wentao Hou[1] , Lin Lu[1]

[1]School of Material Science and Engineering , Jiangsu University, Zhenjiang，Jiangsu，China

*Corresponding author, email:jmwang1959@126.com

Keywords: Equal-channel Angular Pressing(ECAP), Martensite Phase Transformation, Ultra-fine Grain, Severe Plastic deformation, Zener-Holloman Parameter

Abstract: A new technology of preparing submicron medium-carbon steel quickly using martensitic steel by equal-channel angular pressing is developed. The technology combines martensite phase transformation with severe plastic deformation. In this research, martensitic steel is heated to 923K quickly and held for appropriate time, then equal-channel angular pressing is implemented. Supersaturated ferrites of average grain size within 0.5μm are obtained by the interaction of dislocation intersection, dynamic recrystallization and strain-induced phase transformation. At the same time, strain-induced phase transformation leads to dispersive precipitation of supersaturated carbon particles in the form of carbide inside grains or in grain boundaries. The optimal size of ferrite grains and the optimal distribution of carbides are acquired by controlling tempering temperature and time. The results show that ultra-fine grained materials prepared by this technology possess superior thermal stability.

0 Introduction

The ways to improve the strength of carbon structural steel include martensite phase transformation, grain refinement,etc, but the toughness will decrease dramatically when martensite phase transformation improves the strength. According to the Hall-Petch equation, grain refinement is the only effective way to strengthen steel, of which the value of brittle vector is negative. It decreases the ductile-brittle transition temperature of steel while improving the strength of steel. Just because the ultra-fine grain (UFG) steel possesses comprehensive performance which includes high strength, high plasticity and high strain rate super-plasticity at low temperature, research interests of UFG steel are aroused in various countries.

Severe plastic deformation (SPD) is the most effective way to refine grains, perfect the microstructure and improve the comprehensive performance of materials. [1-5] But only on the condition of great deformation degree can submicron ultra-fine grains be acquired.[6] During SPD, due to factors such as crystal structure of steel, deformation mode, etc., plastic deformation mechanism is different, and thus the plasticity performance and the process of grain refinement are affected. Realising maximum degree of grain refinement with minimum degree of deformation during SPD is a target that people pursue all the time. According to the relevant literatures at present, a new technology with the most promising industrialization prospect in SPD of steel materials is equal-channel angular pressing (ECAP), of which the research field is only within low-carbon steel. In this paper, the technology combining phase transformation with deformation, namely the combination of martensite phase transformation and ECAP, is proposed for the first time. The technology realizes maximum degree of grain refinement with minimum degree of deformation.

The size of ferrite grains in carbon steel is refined to submicron level quickly and uniform distribution of carbides in ferritic matrix is realized.

1 Test material and method

1.1 Test material

The hot-rolled steel 1045 bar was chosen as the test material, of which the size was φ10 mm×100mm. Fig. 1 shows the SEM image of microstructure of original 1045 steel purchased in the market.

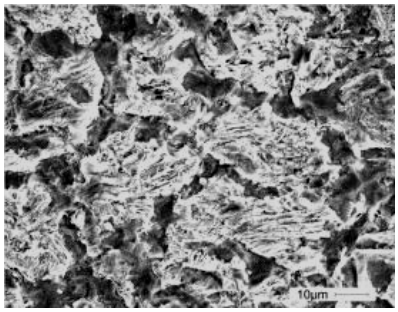


Fig. 1 SEM image of microstructure of hot-rolled 1045

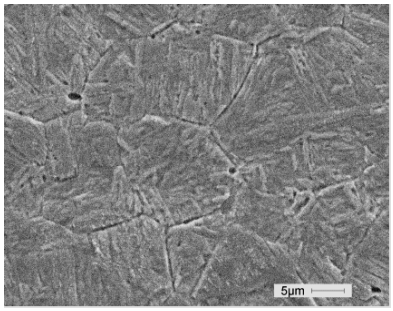


Fig. 2 SEM image of microstructure of quenched 1045

1.2 Test method

In order to realise composition homogenization, and fully exploit potentials of the material, the technology combining phase transformation with deformation was adopted. At first, 1045 steel was quenched to acquire martensite, as shown in Fig. 2. The process was that 1045 steel was heated at 1113K and held for 40 minutes, then quenched quickly in water. Afterwards, the quenched steel was heated quickly to a certain temperature and held for appreciate time then hot ECAP was implemented immediately. With observing structure performance, the optimal process of grain refinement was concluded to provide theoretical basis for practical production.

1.3 Die parameters

Fig. 3 shows the principle diagram of ECAP. When the sample is extruded from one channel to another channel with the action of the plunger, the plastic deformation of pure shear is produced in the corner of the intersection of the two channels. The crossing angle φ of the two channels affects the deformation degree. In this test, 10 mm was chosen as the channel diameter and the crossing angle φ was 110°. In order to facilitate the flow of material, circular arc transition was adopted where the intersectant exterior angle ψ was 30° and circular arc transition of which the radius was 8mm was adopted in the inner side of the intersection of the two channels.[6] Fig. 4 shows extrusion process and extruded samples acquired by adopting the above ECAP die parameters.

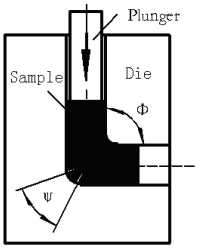


Fig. 3 Experimental set-up for ECAP

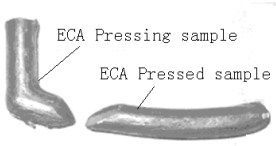


Fig. 4 ECAP extrusion process and extruded samples

2 Test results and discussions

Fig. 2 shows martensite microstructure of quenched 1045 steel. In order to carry out ECAP of the material, tempering treatment of quenched samples was implemented at first to determine the temperature of hot ECAP and how much time to hold before hot ECAP, not only ensuring that the material had sufficient plasticity, but also enabling rapid refinement of grains. The test results show that after rapid tempering at 673 ~ 923 K, implementing the warm extrusion immediately, the quenched medium-carbon steel has much higher plasticity than that of annealed steel.[7] Taking into accout that in the ECAP process, due to the different difficulty levels of metal flow in the interior angle Φ and the exterior angle ψ.When material plasticity is insufficient, cracks will occur in the area of interior angle Φ, as shown in Fig. 5.



Fig.5 Cracks caused by insufficient plasticity

In order to ensure sufficient plasticity for plastic deformation and make dynamic recrystallization occur during deformation in the ECAP process, which realises grain refinement quickly, ECAP warm extrusion tests were conducted at 773 K and 923 K respectively and microstructure evolution processes were observed. And ECAP warm extrusions were carried out at 923 K on the condition of different holding time, then microstructure evolution processes were observed to identify the mechanism of grain refinement and the optimum parameters, providing theoretical basis for practical application.

2.1 Influence of tempering temperature and time on the mechanism of grain refinement

Due to the fact that recrystallization process is a thermal activation process[8], the combined effect of deformation temperature, deformation degree, deformation rate, material original structure, grain size, etc. determines whether dynamic recrystallization will occur and the size of steady-state structure after dynamic recrystallization. The deformation rate factor of temperature compensation, namely the Zener-Hollomon Parameter (Z Parameter), is usually used to determine whether dynamic recrystallization will occur, namely

$$Z = \dot{\varepsilon} \exp(Q / RT) = A\sigma_m^n \qquad \text{Eq.1}$$

In the equation, $\dot{\varepsilon}$ is the deformation rate, Q is the deformation activation energy, of which the value is approximately equal to the self-diffusion activation deformation temperat- ure, A is a constant, n is the stress exponent, σ_m is the peak stress energy, R is the gas constant, T is the absolute.Providing that deformation degree keep constant, dynamic recrystallization can not occur when the value of Z is above a certain value, and the certain value of Z is the critical value Z_c. The Z_c is related to original grains, and the finer the original grains are, the higher the Z_c is. Usually the finer the original grains are, the lower the value of Z is, the higher the critical value Z_c is, and the more easily dynamic recrystallization will occur. Generally with the rise of temperature, stacking fault energy of ferrites increases and, dislocation climb and cross-slip occurs more easily, which produces a large number of sub-structures to increase the critical value Z_c. However, if the deformation temperature is too high, the value of Z will reduce excessively, which in turn makes the obtained steady-state recrystallized grains grow up.[9] In terms of the deformation of the quenched medium-carbon steel, when deformation temperature and holding time is appropriate, the ferrites

still maintain a certain degree of supersaturation. The second phase structures, namely the carbides, precipitate in the shape of tiny particles, grains are relatively fine, grain boundaries account for a relatively large proportion, deformation energy is easily stored in structures during the deforming process. As the deformation goes on, relatively numerous high distortion energy areas are formed around the precipitated carbides. If heating temperature is relatively high or holding time is too long, carbides will precipitate completely from the supersaturated ferrites and grow up with the ferrite grains. Fig. 6 shows the SEM images of transverse and longitudinal microstructures of quenched steel 1045 which wss quickly extruded by warm ECAP after tempered at 773K for 10 min,the structure of quenched steel 1045 extruded by ECAP after held at 773K for 10 min is still tetragonal structure. The degree of supersaturation is still high, lattice distortion energy is relatively high and plastic deformation are mainly in the ways of twinning and dislocation motion. As the deformation goes on, a large amount of deformation energy accumulates in grains, but because of high deformation rate, relatively low deformation temperature, high deformation activation energy value of Q, and relatively high value of Z, recrystallization can not occur.

However, at the moment, imbalanced supersaturated ferrite structures transform into stable ferrite structures and part of supersaturated carbons precipitate in the form of tiny carbides. Thus the degree supersaturation of ferrites becomes moderate, strength and hardness decreases somewhat, and plasticity is considerably improved. But the speed, in which dislocation and twinning produces work hardening, is much faster than that of carbide precipitation, so grain refinement is mainly in the way of dislocation intercrossing. As can be seen from the transverse section microstructure in Fig. 6(a) that the grains of original lath martensites parallel to each another（as shown in Fig. 2） move mutually and rotate by twinning and dislocation intercrossing in the ECAP process，which leads to deformation and fragmentation of martensites and so the laths are no longer parallel to each other. And the emergence of a large number of dislocations makes grains divide into more and tinier sub-grains and the strain-induced fine carbide particles precipitate inside grains and in grain boundaries.

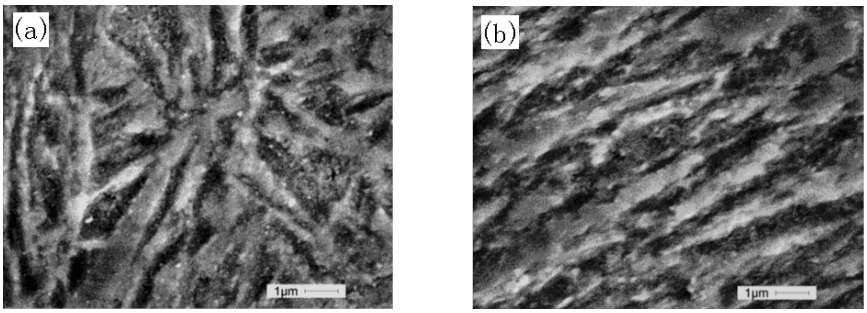


Fig.6 SEM images of microstructures of quenched steel 1045 extruded by ECAP after tempered at 773K for 10 min

(a) transverse section; (*b) longitudinal section*

As can be seen from the longitudinal section in Fig. 6(b), grains are elongated along the axial direction, namely in the deformation direction, and directional structures occur after deformation, which clearly demonstrates that after quenched steel 1045 is tempered at 773 K for 10min, the material possesses certain plasticity and is suitable for ECAP. However, at this temperature which is relatively low for deformation temperature, the increase of dislocation energy caused by the deformation and lattice distortion energy caused by the martensite phase transformation is not sufficient to generate dynamic recrystallization during deformation.

Fig. 7 shows the SEM images of the transverse and longitudinal microstructures of quenched steel 1045 which was quickly extruded by warm ECAP after tempered at 923K for 10 min. After quenched steel 1045 is tempered at 923 K for 10 min, the matrix still maintains a certain degree of

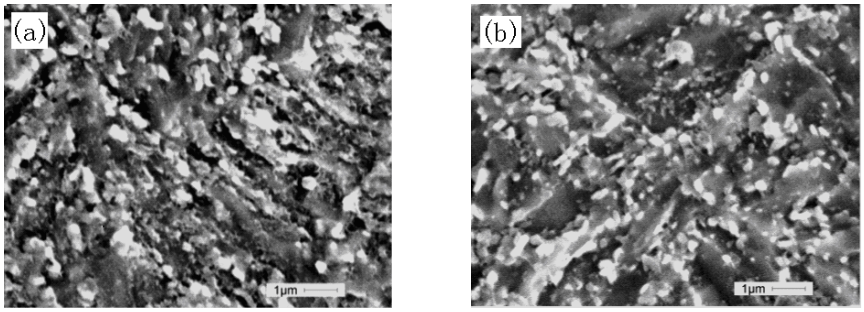


Fig.7 SEM images of microstructures of quedched steel 1045 extruded by ECAP after tempered at 923K for 10 min

(a) transverse section; (b) longitudinal section

supersaturation and retains the original morphology of lath martensites. The tetragonality of crystal structure decreases, the strength and the hardness decreases somewhat and the stacking fault energy increases, which are conducive to motion and cross-slip of dislocations, but the flow stress and the value of Z are relatively high. However, the deformation storage energy which is proportional to the square of the flow stress, the tiny supersaturated structure with certain internal energy and the deformation temperature provides the atomic diffusion movement with the impetus, increasing Zc significantly. As can be seen from the transverse section in Fig. 7(a), lath martensites move mutually by dislocation during ECAP and grain boundaries are splitted, cut off, bent, broken and rotated. Meanwhile, the combined action of the energy accumulated by deformation and the lattice distortion energy transforms the supersaturated ferrites of unstable structures into the stable structures. During deformation, the higher the dislocation density is and the severer the lattice distortion is, the more the locations of carbide precipitation nucleation there are, and the more dispersive the precipitation is. If deformation produces sub-grains and the carbides precipitate in the sub-grains, the carbide distribution is more dispersive. Meanwhile, the carbide precipitation hinders the dislocation motion which makes a large number of dislocations accumulate here or in grain boundaries, and finally dynamic recrystallization occurs, obtaining uniform and tiny microstructures of which average size is less than 0.5μm. According to the comparison between the longitudinal sections in Fig. 7(b) and Fig. 6(b), it can be clearly seen that the microstructures after deformation are equiaxial grains without directionality. There are still part of dislocations inside grains and in grain boundaries, which proves that the ECAP implemented with Z of relatively high value is a discontinuous recrystallization process. After ECAP, the microhardness was 345HV and the tensile strength was equivalent to 1080 MP.

Fig. 8 shows the SEM images of the transverse and longitudinal microstructures of quenched steel 1045 which was extruded by warm ECAP quickly after tempered at 923K for 20 min respectively. As shown in the figure, the microstructures are the equiaxial grains after warm ECAP, which demonstrates that dynamic recrystallization occurs during deformation on this condition. What differ from the above are that the size of ferrite grains and the size of carbide particles increase somewhat and the hardness decreases after ECAP. The micro-hardness was about 254HV and the tensile strength was equivalent to 805MP. It can be concluded that, with the prolongation of tempering time at the same temperature, considerable part of carbon atoms precipitate in the form of cementites from supersaturated ferrites, accumulate and grow up in grain boundaries. As

time goes on, ferrites grow up along with cementites, which leads to the reduction of internal energy of the entire system and the decrease of the critical value Zc. During ECAP, due to the growth of original grains and the reduction of flow stress, the energy of relatively coarse grains stored by deformation is much lower than that of fine grains by deformation. Also the reduction of solute content in ferrites, namely carbon content, leads to the sharp decrease of storage energy. On the condition of the same deformation, the recrystallization nucleation rate decreases and the size of steady-state grains after recrystallization increases somewhat, of which average size is about 1μm.

Fig.9 shows the SEM images of the transverse and longitudinal microstructures of quenched steel 1045 which was quickly extruded by warm ECAP after tempered at 923K for 30 min. After tempering at 923 K for 30 min, carbons have completely precipitated from the supersaturated ferrites. The structures have become the stable two-phase structure of ferrites and cementites and grow up as

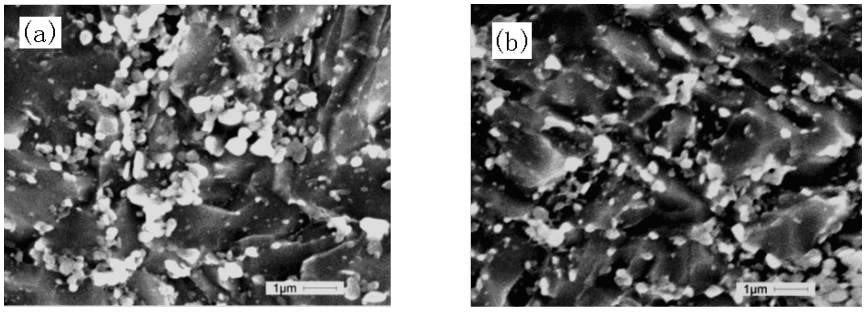


Fig.8 SEM images of microstructures of quedched steel 1045 extruded by ECAP after tempered at 923K for 20 min

(a) transverse section; (b) longitudinal section

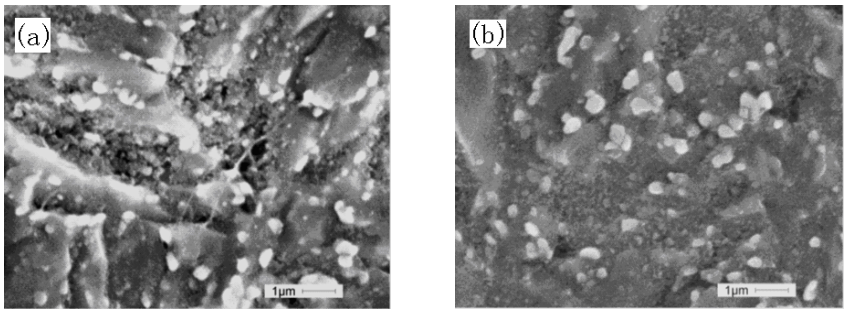


Fig.9 SEM images of microstructures of quedched steel 1045 extruded by ECAP after tempered at 923K for 30min

(a) transverse section ;(b)longitudinal section

time goes on, which makes the internal energy of entire system decrease. At the same time, the reduction of flow stress also leads to the sharp decrease of deformation storage energy and the reduction of Z_c, so that recrystallization becomes difficult. Therefore, on this condition, recrystallization nucleation occurs rarely, the grain size that is about 1.5～2 μm is much larger than that of the above two conditions and there are a large number of dislocations in grain boundaries, as shown in Fig. 9. After deformation, the microhardness was about 301HV and the tensile strength was equivalent to 1010MP.

2.2 Thethermal stability of the microstructure after ECAP

Fig. 10(a) and 10(b) respectively shows the SEM images of the microstructures of quenched steel 1045 annealed at 773K and 853K for 30 min, which was extruded by warm ECAP quickly after tempered at 923K for 10 min. As shown in Fig. 7, dynamic recrystallization occurs when the Z value is relatively high and it is a discontinuous process.[9] After deformation, there are still considerable dense dislocations and a large number of fine carbides distributing inside grains and grain boundaries. During high-temperature annealing, static recrystallization of the fine grains with certain dislocation density occurs and they grow up. But during deformation, fine carbide particles precipitating inside grains and in grain boundaries significantly reduce boundary activity and hinder diffusion and movement of grain boundaries, so that the material has relatively high thermal stability. As shown in Fig. 10, after annealed at 853 K for 30 min, the grain size still remained around 0.5 μm.

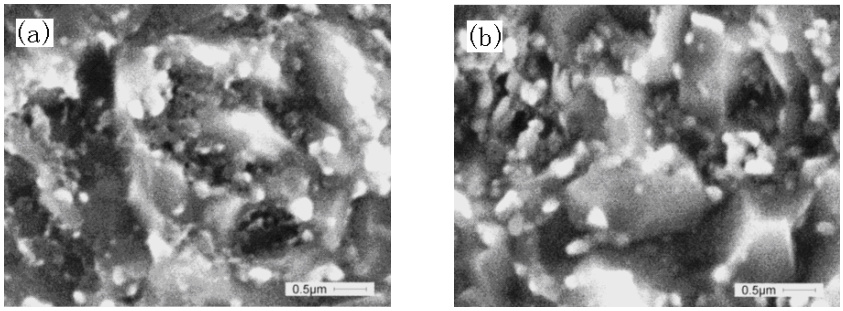


Fig.10 SEM images of microstructures of quenched steel 1045 annealed at *(a)773K* and *(b)853K* for 30 min after tempered at 923K for 10min and warm ECAP

3 Conclusion

1) Ultra-fine grain medium-carbon steel can be prepared quickly by the technology which combines phase transformation with equal-channel angular pressing.

2) Increasing the deformation storage energy and the value of Z appropriately is an important way to refine the dynamically recrystallized grains.

3) By controlling the tempering temperatu- re and time of the quenched steel, grain refinement in accordance with the composite mechanism of dislocation cross-slip, dynamic recrystallization and strain-induced carbide precipitation, etc. can be realised by ECAP using ferrites with certain tetragonality, and the second phase structures which distribute dispersively in the fine ferritic matrix are obtained, of which grain size is about 0.5μm.

4) The precipitated phase of dispersive distribution can effectively prevent and hinder the growth of ferrite grains and such ultra-fine grain structures have good thermal stability.

References

[1] Valiev R Z,Mukherjee A K,Scripta Materialia, 2001, **44(8-9)**, 1747-1750.
[2] Suji N T, Ueji R, Minamino Y, et al, Scripta Materialia, 2005， **46(4)**， 305-310.
[3] Ueji R, Tsuji N, Minamino Y，et al，2004, **5(1/2)**, 153-162.
[4] Huang Y D, Yang W Y and Sun Z Q ,Journal of materials processing Technology，2003，**134(1)**, 19-25.
[5] Song R, Ponge D and Raabe D, Acta Materialia, 2005，**53(18)**, 4881-4892.
[6] Wang Jian-min. Lu Jin. Xu Xiao-jing .et al, China Mechanical Engineering, 2006, **17 (S2)**, 384-387.

[7] Wang Jian-min. Zhou Kong-kang. LU Jin .et al, China Mechanical Engineering, 2006, **17(24)**, 2618-2621, 2627.
[8] Yang Wang-yue, HU An-min, SUN Zu-qing, Acta Metallrugica Sinica, 2000, **36(11)**, 1192-1196.
[9] Li Long-fei, Yang Wang-yue, Sun Zu-qing, Acta Metallrugica Sinica, 2004, **40(2)**, 141-147.
[10] He Yi-zhu, Chen Da-hong, Lei Ting-quan, et al, Journal of Iron and steel research , 2000, **12(1)**, 26.

CHAPTER 2:

Micro/Nanofluids Research and Technologies

Key Engineering Materials Vols 645-646 (2015) pp 437-443
Submitted: 2014-10-29
© (2015) Trans Tech Publications, Switzerland
Accepted: 2014-12-23
doi:10.4028/www.scientific.net/KEM.645-646.437

Tribological Properities of Oil-Based ZnO Nanofluids

Xu Ran[a*] , Xueying Yu[b], Yong Wang, Zhe Xiao

Key Laboratory of Advanced Structural Materials, Ministry of Education,

Changchun University of Technology, Changchun 130012, China

[a*]Corresponding author:Tel:+8615526853785;E-mail:ranxu@mail.ccut.edu.cn

[b]Corresponding author:Tel:+8615543644562;E-mail: a1101075964@126.com

Key words: ZnO nanoparticles; Nanofluids; Oleic acid; Tribological properities

Abstract: In this research, the friction and wear characteristics of nanofluids were studied through experimental investigation by dispersing ZnO nanoparticles into 60SN base oil. Oleic acid was used as a surfactant for the improved dispersibility and stability of nanofluids. Nanoparticles were dispersed using a magnetic stirring apparatus and ultrasonic bath. The micro/nano mechanics comprehensive test system UNMT- 1 wear testing machine was used to evaluate the friction properties. The wear track was measured by a Zeiss laser confocal microscope and scanning electron microscope (SEM). The effect of ZnO nanoparticles on the friction and wear performance of the nanofluids was investigated, and the optimal ratio between the surfactant and particle concentration was studied. The results showed that oil-based nanofluids with ZnO nanoparticles could reduce friction and wear under certain conditions. The optimally stable concentration of the fluids was that the oleic acid adding quantity was 5wt%～10wt% and ZnO nano-particles was 0.2wt%～0.7wt%. And when the oleic acid adding quantity was 10wt% and ZnO nanoparticles was 0.2 wt%, the nanofluids had best friction-reducing and anti-wear properties.

Introduction

In recent years, with the rapid development of nanotechnology research, the thermal properties of nanofluids has been studied ever since due to their unique characteristics, most nanofluid researches have showed that fluids with nanoparticles dispersed in them could improved heat transfer properties compared with the base fluid. But the study of nanofluids for tribological properties has been slow, with problems encountered in dispersing and stabilizing when nanoparticles used as additives in lubricants.

The issue of preparing stable and well-dispersed solutions has been the major problem with this new classification of the fluid. Because nanoparticles in lubricants tend to agglomerate to some much larger particles than intended and agglomeration can lead to inaccurate and non-reproducible data. However, agglomeration can be prevented by using different surfactants, surface modifications and dispersion techniques. Using ligands as a surface coating for nanoparticles was investigated by Mulvihill et al, [1]. They found that nanoparticles coated with long chained ligands (eleven carbons) showed superior stability than the shorter chained ligands tested. Available surface area for coating and ligand length were concluded to be the major factors in stabilizing cadmium selenide nanoparticles. Amstad et al., [2] investigated surface functionalizing iron oxide nanoparticles for magnetic resonance imaging application. They created a custom surfactant by using a polyethylene glycol hydrocarbon and gallol molecule. This research resulted in improved particle stability due to the high affinity between the surfactant and nanoparticles.

The friction and wear characteristics of nanofluids have also been studied recently. Some papers have reported that nanoparticles as additives in lubricant are effective in anti-friction and anti-wear. Several studies have been carried out to determine the tribological properties of different types of nanoparticles. Pure metals, metal oxides, lamellar structures and nanotubes have all been examined by research teams. And the concentration, size and shape of nanoparticles have primarily been investigated in lubrication studies. But the tribological performance of metal oxide nanoparticles added into lubricant has recently been studied. It was reported that the addition of metal oxide nanoparticles to lubricant has improved the friction and wear performance. Oxide nanoparticles scattered in lubricant could decrease the friction coefficient up to 32% and wear depth up to 78.8% in reciprocating sliding block-on-ring tests (Hernandez Battez, et al. [3], [4]; Wu, et al.[5]; Kao and Lin [6]; Chang, et al. [7]; Qiu, et al. [8]; Palacioand Bhushan [9]; Wang, et al. [10]); Nanoparticles such as ZnO have been shown to significantly increase thermal conductivity in oil and in EG. But in the study of tribological properities, ZnO nanoparticles have not achieved significant results. Some paper has reported that ZnO nanoparticles could reduce friction, but does not affect wear significantly in water. In this paper, the tribological proprieties of oil-based ZnO nanofluids were mainly investigated.

Experimental

Test Materials

The ball samples were made of 52100 steel with a diameter of 4 mm, hardness of HRC 64–66. The disk samples were made of 4140 steel with a cuboid which its length and width were 25mm and the height was 10mm and hardness of HRC 41-45. The final surface roughness of the samples was verified by testing the samples with a Zeiss laser confocal microscope. Solutions of 0.2wt%, 0.5wt%, 0.7wt% and 1wt% by weight ZnO were mixed. Commercially available ZnO nanoparticles were used as lubricant additives. ZnO particles size ranged between 10nm and 30nm with an elongated morphology. Commercially available Oleic acid with a purity of >97% was used as a surfactant to keep the nanoparticles stable in solution. Control fluids consisted of base oil with only surfactant added; the tribological performance of the ZnO nanofluids were compared to these control fluids. The base oil was a 60SN with a viscosity of 12 cSt at 40℃ and specific gravity of 0.9.

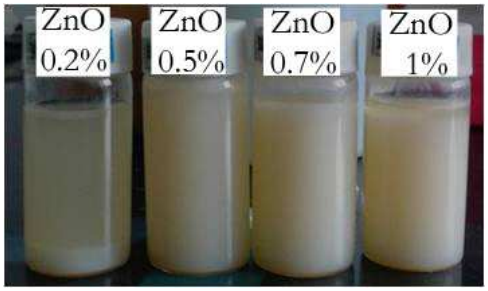
Test Procedures

Before each test, all beakers, scoops, vials, balls and disks were first cleaned with acetone. ZnO nanoparticles, Oleic acid and 60SN base oil were massed precisely and then added to a clean 40mL vial slowly under magnetic stirring. After all components were added, the vial would be stirring continuously for 10 minutes and then placed into an ultrasonic bath for 30 minutes in order to further disperse ZnO nanoparticles and homogenize the solutions. Finally, the fluid should sit for different period of time prior to running friction tests.

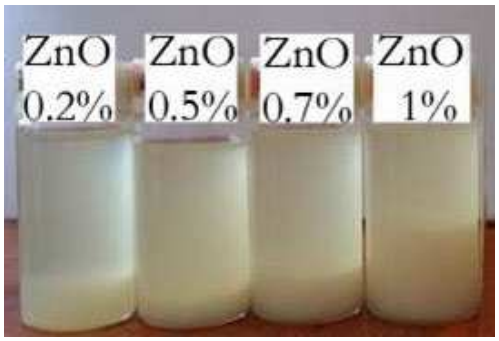
The friction tests were performed on a micro/nano mechanics comprehensive test system (UNMT-1, CETR, USA) under the test conditions of 5 N normal force, 10 mm/s sliding velocity and the experimental time of each test being controlled in 10 minutes. The data of the coefficient of friction was collected automatically by the data acquisition. Three tests were repeated for each test condition and the average value was calculated. All tests were run at room temperature. After each test, the disk and ball samples were cleaned ultrasonically with acetone for further analysis. The wear track was measured using scanning electron microscope (SEM) and the surface roughness were measured using a Zeiss laser confocal microscope

Results and Discussion

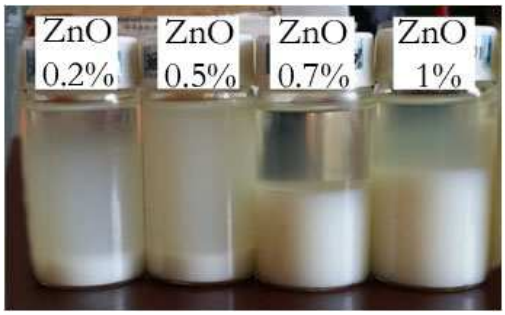
Nanoparticle and Surfactant Concentration on Stability



5wt% oleic acid



10wt% oleic acid



15wt% oleic acid

Fig1 Shows the stability at different ratios of oleic acid and nanoparticles after a two day time duration.

Effect of the ratio between oleic acid and nanoparticles on the stability of nanofluids was investigated by visually examining the sedimentation process over time. Four different ZnO concentrations were chosen in this study (0.2, 0.5, 0.7 and 1wt%) and were stabilized with three different oleic acid concentrations (5, 10, and 15wt%). Each sample was mixed in accordance to the preparation order study.

Fig1 showed the stability at different ratios of oleic acid and ZnO nanoparticles after a two day time duration. It was evident that the concentration of oleic acid was critical to creating stable solutions. The optimally stable concentration of the fluids was that the oleic acid adding quantity was 5wt%～10wt% and ZnO nano-particles was 0.2wt%～0.7wt%. Some studies must be carried out to further seek the best ratio.

Coefficient of Friction

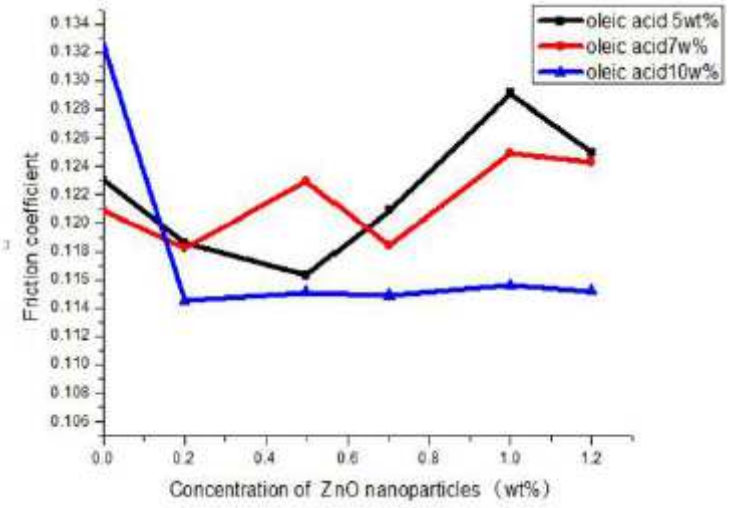


Fig2 Friction coefficient over concentration of ZnO nanoparticles graph for 5wt%, 7wt% and 10wt% oleic acid

Fig2 showed the results of the average friction coefficient for ZnO nanofluids which sit for 2 days. For this test, the concentrations of oleic acid were controlled at 5wt%, 7wt% and 10wt% and the concentrations of ZnO nanoparticles were controlled at 0, 0.2wt%, 0.5wt%, 0.7wt% and 1wt%. The figure showed that the oil with 5wt%, 7wt% oleic acid performed the worst and the curves were volatile compared with 10wt% oleic acid which had the lowest friction coefficient data for the majority of the test. Some results could be obtained from Fig2: ZnO nanoparticles as additives in base oil resulted in a friction reduction. With ZnO nanoparticles percentage increasing, COF was not constantly low decreasing first and then increasing. When the concentration of oleic acid was 10wt% and ZnO nanoparticle was 0.2wt%, there was best anti-friction effect.

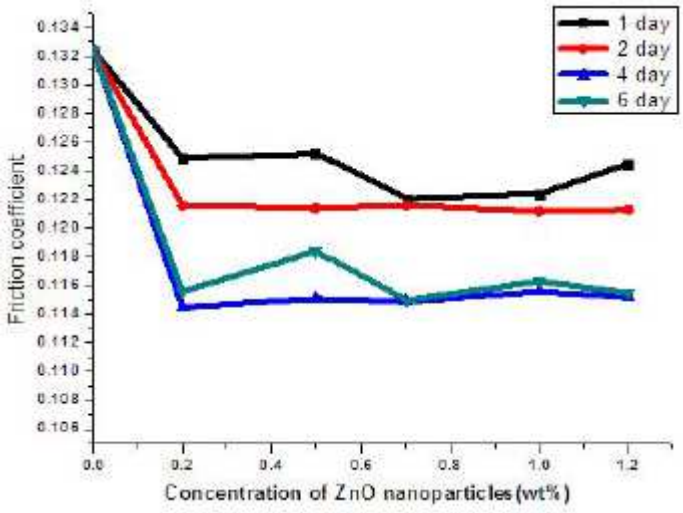


Fig3 Friction coefficient over concentration of ZnO nanoparticles graph with 10wt% oleic acid for different days

And then the effect of different sit time on the anti-friction properties of the nanofluids with 10wt% oleic acid was further investigated. Fig3 showed the result that the average friction coefficient for ZnO nanofluids at different concentrations which sit for different days. In four days, similar trend can be seen obviously from those curves. With extension of sit time, the friction coefficient decreased. And more than four days, the friction coefficient reached steady conditions slightly. The result can be obtained that the optimal sit time in this study was four days.

Wear Track on the Disk

Fig4 showed SEM images on 42CrMo steel sample for a wear track measured by scanning electron microscope (SEM). For this test, oleic acid adding quantity was 10wt% and ZnO nanoparticles ranged from 0 to 1wt%. Fig4 showed that the average grinding crack width of the fluids with different concentrations of ZnO nanoparticles were narrower than the fluid adding only 10wt% oleic acid. And theirs grinding crack boundaries were more gentle. This phenomenon illustrated that ZnO nanoparticles as additives in lubricant had a good anti-wear performance; Comparing (b), (c) and (d), with the concentration of ZnO nanoparticles increasing, the average grinding crack width decreased and grinding crack boundary was more gentle. But when the concentration added up to 1wt%, the average grinding crack width increased sharply and the boundary was irregular.

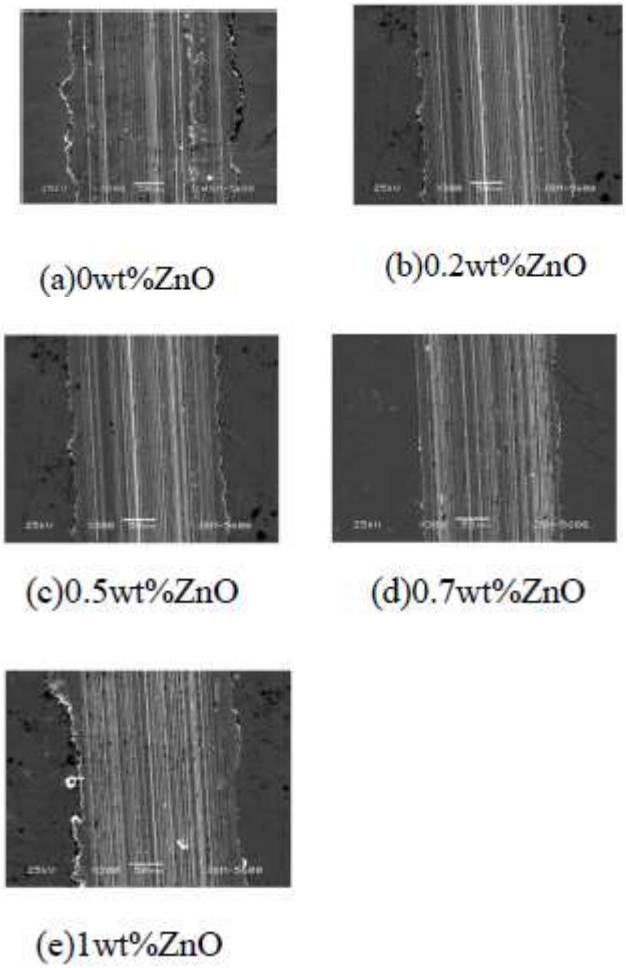


Fig4 SEM images on steel sample for a weartrack at 10wt% oleic acid

Fig5 showed the surface roughness graphs on 42CrMo steel sample for a wear track generated by the different concentrations of ZnO nanofluids for 10wt% oleic acid. It can be seen in Fig5 that with addition of ZnO nanoparticles into based oil, the average surface rough increased compared with the fluid with only oleic acid; and with the concentration of ZnO nanoparticles increasing, the average surface rough was larger and larger. There was no detailed explanation for this result and further investigation was needed for a better understanding of the phenomenon.

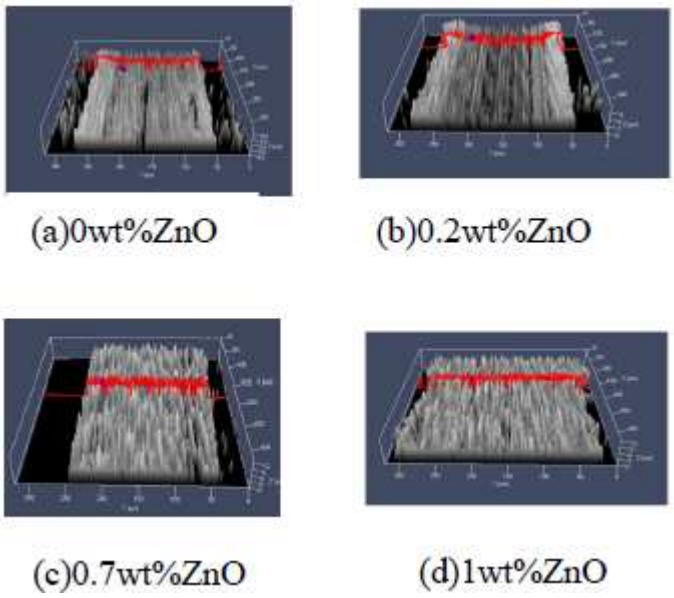


Fig5 The surface roughness graphs on steel sample for a wear track at 10wt% oleic acid.

Wear Volume

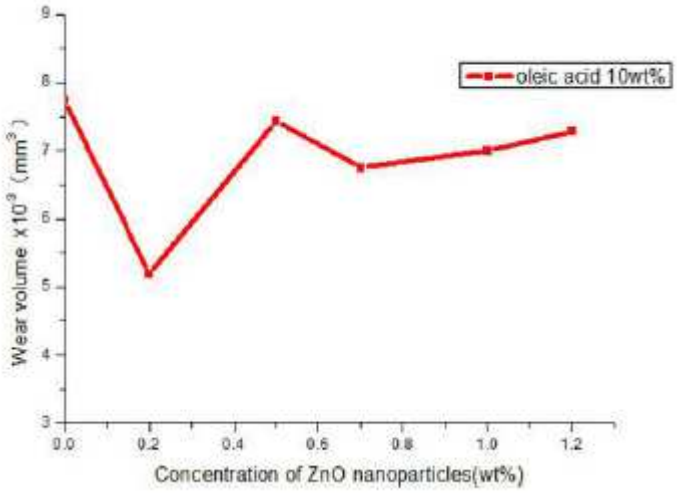


Fig 6 Wear volume over concentration of ZnO nanoparticles graph for 10wt% oleic acid

Fig6 showed the wear volume on the sample disk when 10wt% oleic acid and the different concentrations of ZnO nanoparticles added in base oil. It can be seen from fig6 that the nanoparticles could reduce friction between the surfaces, they did also reduce wear under the same test conditions in this study. The wear volume of the disk lubricanted by ZnO nanofluids was lower than the fluid without ZnO nanoparticles. And when the concentration of oleic acid was 10wt% and ZnO was 0.2wt%, there was also best anti-wear performance.

The main reason for above results might be that ZnO nanoparticles added in base oil can flow into the grooves between the friction pairs, changing the the sliding friction into rolling friction, thus reducing the friction coefficient and wear. When ZnO nanoparticles adding quantity was small, ZnO can reduce the friction and wear to a certain extent, but the effect was not obvious for nanoparticles can't completely fill grooves. With the concentration of ZnO nanoparticles added to the degree that it was fully capable of filling grooves, the fluids had best anti-wear and anti-friction effect and achieve the minimum friction coefficient. But with the concentration of ZnO nanoparticles increasing, nanoparticles tend to agglomerate to much larger particles than intended, scratching the surface of the friction pair, increasing the friction coefficient and causing larger grinding crack diameter and irregular boundary.

Conclusions

The tribological properities of ZnO nanoparticles as aaditives in lubricant were thoroughly studied. Under the test conditions used in this study, the following conclusions can be drawn:

The optimally stable concentration of the fluids was that the oleic acid adding quantity was 5wt%～10wt% and ZnO nano-particles was 0.2wt%～0.7wt%.

Oil-based nanofluids with ZnO nanoparticles could reduce friction and wear under certain conditions. And when the oleic acid adding quantity was 10wt% and ZnO nanoparticles was 0.2wt%, the nanofluids had best friction-reducing and anti-wear properties.

In friction tests, with the extension of sit time, the friction coefficient decreased until kept constant slightly. The optimal sit time was four days.

The contribution of nanoparticles to friction reduction and anti-wear might be because these particles acted as nanosize bearings. Further investigation was needed to better understand the mechanism of friction reduction and anti-wear.

References

[1] M. J. Mulvihill, S. E. Habas, I. Jen-La Plante, J. Wan, and T. Mokari, Influence of size, shape and surface coating on the stability of aqueous suspensions of CdSe nanoparticles, Chemistry of Materials, vol. 22, no. 18, pp. 5251–5257, 2010.

[2] E. Amstad, S. Zurcher, A. Mashaghi, J. Y. Wong, M. Textor, and E. Reimhult, Surface functionalization of single superparamagnetic iron oxide nanoparticles for targeted Magnetic resonance imaging, Small, vol. 5, no. 11, pp. 1334–1342, 2009.

[3] Battez A.H., Gonzalez R., Viesca J.L., Fernandez J.E., et al., “CuO,ZrO2 and ZnO nanoparticles as antiwear additive in oil lubricants,” Wear 265(3-4):422-428, 2008.

[4] Luan Gara, Qian Zou, Friction and wear characteristics of water-based ZnO and Al2O3 nanofluids, Tribology Transactions, 55:3, (2012) 345-35

[5] Yu W., Xie H., Chen L., and Li Y., Investigation of thermal conductivity and viscosity of ethylene glycol based ZnO nanofluid, Thermochim.Acta 491(1-2):92-96, 2009.

[6] Lee S., Choi S., Li S., and Eastman J., Measuring thermal conductivity of fluids containing oxide nanoparticles, J.Heat Transf.-Trans. ASME 121(2):280-289, 1999.

[7] Saidur R., Leong K.Y., and Mohammad H.A., A review onapplications and challenges of nanofluids, Renew.Sust.Energ.Rev.15 (3):1646-1668, 2011.

[8] Colangelo G., Favale E., De Risi A., and Laforgia D., Results of experimental investigations on the heat conductivity of nanofluids based on diathermic oil for high temperature applications, Appl. Energy 97(0):828-833, 2012.

[9] Lee K., Hwang Y., Cheong S., Choi Y., et al., Understanding the Role of Nanoparticles in Nano-oil Lubrication, Tribol. Lett. 35(2):127-131, 2009.

[10] Hwang Y., Lee J., Lee J., Jeong Y., et al., Production and dispersion stability of nanoparticles in nanofluids, Powder Technol 186(2): 145-153, 2008.

[11] Hernandez Battez, A., Gonzalez, R., Viesca, J. L., Fernandez, J. E., Diaz Fernandez, J. M., Machado, A., Chou, R., and Riba, J, CuO, ZrO2and ZnO Nanoparticles as Antiwear Additive in Oil Lubricants," Wear, 265(3–4), pp 422–428,2008

[12] Wu, Y. Y., Tsui, W. C., and Liu, T. C., Experimental Analysis of Tribological Properties of Lubricating Oils with Nanoparticle Additives, Wear, 262(7–8), pp819–825,2007.

[13] Gara, L. and Zou, Q. (2012), Friction and Wear Characteristics of Water-Based ZnO and Al2O3Nanofluids, Tribology Transactions, 55(3), pp 345–350.

[14] Yu, H.-L., Xu, Y., Shi, P.-J., Xu, B.-S., Wang, X.-L., and Liu, Q. (2008),Tribological Properties and Lubricating Mechanisms of Cu Nanoparticles in Lubricant, Transactions of Nonferrous Metals Society of China(EnglishEdition), 18(3), pp 636–641.

[15] Kao, M.-J. and Lin, C.-R. (2009), Evaluating the Role of Spherical Titanium Oxide Nanoparticles in Reducing Friction between Two Pieces of Cast Iron, Journal of Alloys and Compounds, 483(1–2), pp 456–459.

Key Engineering Materials Vols 645-646 (2015) pp 444-448
© (2015) Trans Tech Publications, Switzerland
doi:10.4028/www.scientific.net/KEM.645-646.444
Submitted: 2014-11-20
Accepted: 2014-12-23

Performance Investigation of TiO_2 Nanofluid Coolant for Automobile Cooling Applications

Jinmao Chen[1, a *], Xiaoying Sun[1, b], Guanjun Leng[1, c], Jingheng Feng[1, d]

[1]POL Research Institute of General Logistics Department, Beijing, China

[a] cjm830@sina.com, [b] yingxs1993@126.com, [c] bjflt@aliyun.com, [d] 5784079@qq.com

Keywords: Nanofluid, Automobile, Engine coolant, Evaluation.

Abstract. This study focused on the evaluation of TiO_2 nanofluid coolant for automobile engine cooling applications. It was observed that, about 3% of thermal conductivity enhancement and above 10% convective heat transfer enhancement could be achieved with the usage of 1.0 wt.% TiO_2 nanofluid coolant compared to base coolant without nanoparticles. More importantly, corrosion-inhibiting properties of TiO_2 nanofluid coolant were investigated, which indicated that the nanofluid coolant possess the characteristics of a qualified engine coolant should have. The evaluation results showed that the nanofluid coolant could be a promising engine coolant for automobiles.

Introduction

Nanofluids are nanotechnology-based heat transfer fluids by dispersing nanometer-sized solid particles in a conventional heat transfer fluids at low particle concentrations. Choi and his team [1-3] showed that nanofluids have the potential of being recognized as a new generation of coolants for vehicle thermal management due to their higher thermal conductivities than the base fluids. Leong et al. [4] applied nanofluids in engine cooling and found that overall heat transfer coefficient increased with the usage of nanofluids in engine cooling compared to ethylene glycol (i.e. basefluids).

At present, there are few researches in the problems especially metal corrosion with the actual usage of nanofluid. In order for the enhanced thermal conductivity to be utilized it must be shown that nanofluid has no damage to the metal materials of cooling system. If nanofluids result in excessive erosive wear, they cannot be used. A qualified nanofluid engine coolant requires not only effective heat transfer performance but also good metal corrosion protection abilities.

In this paper, we prepared a TiO_2 nanofluid coolant. Besides heat transfer property, the performance of metal corrosion protection was evaluated according to ASTM D 3306[5], standard specification for glycol base engine coolant for automobile and light-duty service1, which is the authoritative standard in the field of engine coolant study.

Experimental

Preparation of TiO_2 nanofluid engine coolant. Titanium dioxide colloidal was synthesized by a sol-gel and hydrothermal techniques. The obtained TiO_2 colloidal was then added to a mixture of ethylene glycol and deionized water to produce a 1.0 wt.% TiO_2 dispersion. After stirred for 30 min, about 5 wt.% corrosion inhibitors were added to form the nanofluid engine coolant.

Measurements. Particle size distribution of TiO_2 nanoparticles dispersed in base fluid was measured by a Malvern Nanosizer (Malvern Instrument, UK).

The thermal conductivity measurements were taken on a thermal conductivity apparatus (Xi' an Xiatech Electronic Technology Co., Ltd., XIA-TC-THW-S-02).

The convective heat transfer performance was measured by a convective heat transfer measurement device. The experimental system consists of a flow loop, a heating unit, a cooling system, and a measure and control unit as shown in Fig. 1. The flow loop consisted of a pump, a test section, a flow meter, and a reservoir. A straight copper tube was used as flowing channel, which the length is 2 meters and the inner diameter is 12 mm. A pump with controlled speed and flow rate was employed to adjust the flow rates. An electric micro-coil heater was used to obtain a constant wall

heat-flux boundary condition. In order to minimize the heat loss, the entire test section was thermally insulated by asbestos. Eight thermocouples were mounted on the sets section at various axial positions from the inlet of the test section to measure the wall temperature distribution. Two thermocouples were further mounted at the inlet and exit of the channel to measure the bulk fluid temperature.

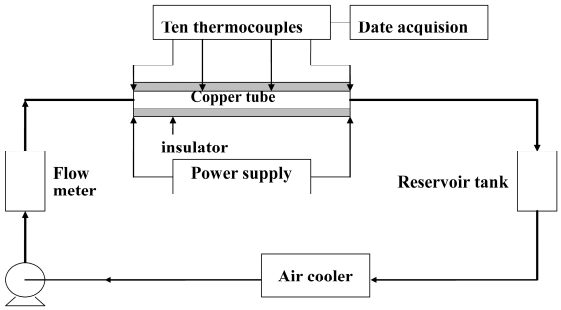


Figure 1 Schematic diagram of convective heat transfer measurement device.

ASTM D 2570 [6] standard test method evaluates the effect of a circulating engine coolant on metal test specimens and automotive cooling system components under controlled, essentially isothermal laboratory conditions. An engine coolant is circulated for 1064 h at 88°C in a flow loop consisting of a metal reservoir, an automotive coolant pump, an automotive radiator, and connecting rubber hoses. Test specimens representative of engine cooling system metals are mounted inside the reservoir, which simulates an engine cylinder block. At the end of the test period, the corrosion-inhibiting properties of the coolant are determined by measuring the mass losses of the test specimens.

Cavitation corrosion test was used to study whether the nanoparticles in fluid lead to pump damage. The test method is according to ASTM D 2809 [7], standard test method for cavitation corrosion and erosion-corrosion characteristics of aluminum pumps with engine coolant. This test method covers the evaluation of the cavitation corrosion and erosion-corrosion characteristics of aluminum automotive water pumps with coolants. This test method consists of pumping an aqueous coolant solution at 113°C through a pressurized 103-kPa simulated automotive coolant system. An aluminum automotive water pump, driven at 4600 r/min by an electric motor, is used to pump the solution and to serve as the object specimen in evaluating the cavitation erosion corrosion effect of the coolant under test. The pump is examined to determine the extent of cavitation erosion corrosion damage and is rated according to the system given in standard.

Results and discussion

Particle size analysis. Generally, the particle size and its size distribution are important for obtaining a stable dispersion system, while particles of smaller sizes with narrow size distribution is favorable. Fig. 2 shows the particle size distributions of titanium dioxide nanoparticles dispersed in ethylene glycol based nanofluid, which was measured by a Malvern Nanosizer (Malvern Instrument, UK).

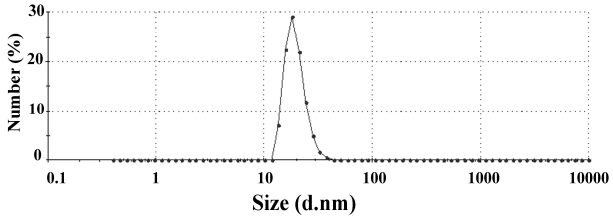


Figure 2 Particle size distribution of TiO_2 nanofluid coolant.

As shown in Table 1, the average particle size is of ca. 18 nm with a narrow size distribution. The small sizes and narrow size distribution of TiO_2 particles indicates that the nanofluid could have good distribution stability.

Table1. Size distribution of TiO_2 nanoparticles in nanofluid coolant.

d [nm]	13.54	15.69	18.17	21.04	24.36	28.21
number [%]	7.1	22.5	29.1	22.0	11.9	5.1

Thermal conductivity measurement. A major interest of the research on nanofluids coolant is focused on the enhanced thermal conductivity of the fluids.The temperature was set to ca. 100 °C, which is similar to the actual operation temperature of engine coolant, and the results are shown in Table 2.

Table 2. Thermal conductivities of base coolant and TiO2 nanofluid coolant.

sample	Thermal conductivity, 100°C [w/m.K]
Base coolant	0.2775
Nanofluid coolant	0.2860

As clearly shown, it was found that the addition of TiO_2 nanoparticles in nanofluid coolant leads to 3% increment in thermal conductivity as compared to its parent base coolant, which should be benefit for enhancing the heat-spreading capability of the engine.

Convective heat transfer analysis. Compared to the experimental and theoretical study of the thermal conductivity of nanofluids, up to now the study on the heat transfer convection is relatively limited.

The forced convective heat transfer is much more complicated than thermal conduction in microscopically static conditions due to the involvement of fluid hydrodynamics, macroscopic motion of particles and nanofluid-wall interactions.

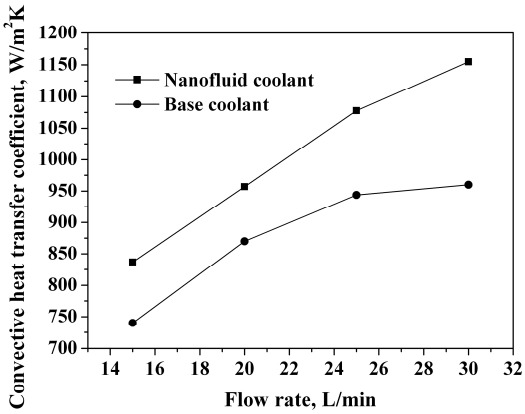


Figure 3 Effect of TiO_2 nanofluid on convective heat transfer coefficient.

Fig. 3 depicts the effect of TiO_2 nanofluid on convective heat transfer performance of coolant. The rising curves show that the convective heat transfer coefficient increases with the increase of the fluid velocity. Interestingly, we found that the addition of TiO_2 nanoparticles in nanofluid coolant leads to above 10% increment in the convective heat transfer coefficient as compared to the coolant without nanoparticles. With the increasing of flow rate, the enhancement was more obviously.

The improvement of the convective heat transfer is ascribed to the addition of TiO_2 nanoparticles in nanofluid coolant. Firstly, the presence of nanoparticles optimized the thermal-physical properties of fluid, increased thermal conductivity; Secondly, the interaction and collision among nanoparticles, fluid and the flow passage surfaces were intensified; Thirdly, the fluid's mixing fluctuation and turbulence were strengthened.

Corrosion-inhibiting properties. Automobile engine cooling system is composed of different metal components, typically including copper, solder, brass, steel, cast iron, cast aluminum etc. Since the metal corrosion will cause the damage of engine, the protection of metals from corrosion is very important factor to characterize a coolant. The corrosion test were carried out by circulating the nanofluid coolant according to ASTM D 2570 standard test method for simulated service corrosion testing of engine coolant.

The nanofluid coolant flows through and collides the surface of metal specimen. In some cases, it is difficult to observe the corrosion or erosion phenomenon of metal pieces before and after the test.

So we apply the value of weight loss of specimen to study the effect of nanofluid on metal specimen, which is also the evaluation method of ASTM D 2570 standard. The corrosion-inhibiting capacity of the nanofluid coolant was determined by measuring the mass losses of metals after circulating coolant for 1064 h, and the results are listed in Table 3.

Table 3. Result of simulated service corrosion test of nanofluid coolant.

Property	Specific Values	Result	ASTM Test Method
Simulated service test			
Weight loss, [mg/specimen]			
copper	20 max	+1	D 2570
solder	60 max	-1	
brass	20 max	-1	
steel	20 max	+1	
Cast iron	20 max	0	
alumimum	60 max	+3	

From Table 3, we found that the average weight changes of copper, solder, brass, steel, cast iron, aluminum were +1, -1, -1, +1, 0, +3 respectively. In all the cases, the value of average weight change for each metal specimen is much lower than the corresponding standard, which clearly indicates that the nanofluid coolant has good corrosion-inhibition capability under the circulating conditions.

Erosion effect on aluminum pump. The solid particles suspended in fluid may cause damage of pump blades due to their continually impact in a closed loop state, which will further accelerate the cavitation corrosion of the pump and shortened the lifetime of the coolant pump. Therefore, the test of determining weather the use of nanofluid coolant result in erosive damage to coolant pump is necessary.

Cavitation corrosion test was used to study whether the nanoparticles in fluid lead to pump damage according to ASTM D 2809.

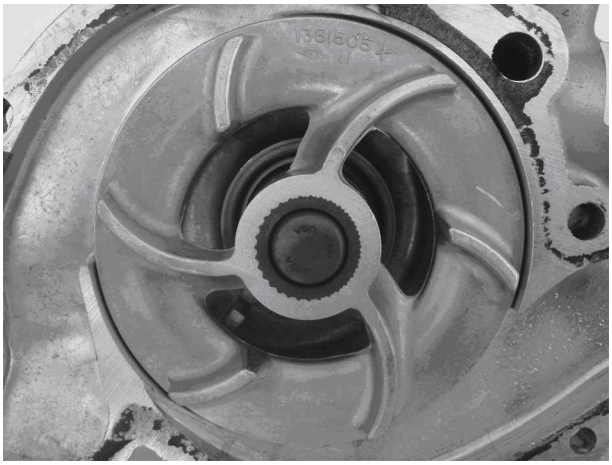


Figure 4 View of a aluminum pump after cavitation corrosion test of nanofluid coolant.

A photograph of aluminum pump after testing was shown in Fig. 4, no visible erosion was observed and no metal loss was detected. According to standard rating system, the extent of corrosion damage of pump was rating 10, which represented the highest level of protection, described as “No corrosion or erosion present, no metal loss. No change from original casting configuration, Staining permitted”.This result indicates that the nanofluid coolant has no damage to the pump under the circulation condition, which was due to the small size, monodisperse state and moderate hardness of TiO_2 nanoparticles.

Conclusions

In this article, experimental heat transfer and corrosion protection performance of TiO_2 nanofluid coolant have been studied, and the following conclusions could be drawn.

1. The heat transfer performance of TiO_2 nanofluid coolant significantly improved compared to the base coolant without nanoparticles. The thermal conductivity enhancement of 3% and convective heat transfer enhancement of above 10% were obtained at the concentration of 1.0 wt.%.

2. The nanofluid coolant in this study has good metal corrosion protection capacity and the nanoparticles in fluid have no damage to aluminum pump in the circulation condition, which indicates that it is a promising automobile engine coolant.

Acknowledgements

The authors gratefully acknowledge the financial support of this work provided by The General Logistics Department, Beijing.

References

[1] S. U. S. Choi, W. Yu, J. R. Hull, Z. G. Zhang, F. E. Lockwood, Nanofluids for vehicle thermal management, SAE technical paper 2001-01-1706.

[2] S. U. S. Choi, Nanofluids: from vision to reality through research, Journal of Heat Transfer 131/033106 (2009) 1-9.

[3] F. E. Lockwood, Z. G. Zhang, T. R. Forbus, S. U. S. Choi, Y. Yang, E. A. Grulke, The current development of nanofluid research, SAE technical paper 2005-01-1929.

[4] K.Y. Leong, R. Saidur, S.N. Kazi, A.H. Mamun, Performance investigation of an automotive car radiator operated with nanofluid-based coolants (nanofluid as a coolant in a radiator), Applied Thermal Engineering 30 (2010) 2685-2692.

[5] Standard Specification for Glycol Base Engine Coolant for Automobile and Light-Duty Service, ASTM Standard D 3306–10, Annual Book of ASTM Standards 2010, Section 15, Vol 15.05

[6] Standard test method for simulated service corrosion testing of engine coolants, ASTM Standard D 2570–09, Annual Book of ASTM Standards 2010, Section 15, Vol 15.05

[7] Standard test method for cavitation corrosion and erosion-corrosion characteristics of aluminum pumps with engine coolants, ASTM Standard D 2809–09, Annual Book of ASTM Standards 2010, Section 15, Vol 15.05

Key Engineering Materials Vols 645-646 (2015) pp 449-454
© (2015) Trans Tech Publications, Switzerland
doi:10.4028/www.scientific.net/KEM.645-646.449

Submitted: 2014-12-04
Accepted: 2014-12-23

The simulation and experimental analysis of hydrodynamic focusing effect inside a rectangular microchannel

Shuaijie Feng[1, a], Xinqun Shi[1,b] , Jing Zeng[1] , Yan Peng[1,c] and Mei Liu[1, 2,d *]

[1] The School of Mechatronics Engineering and Automation, Shanghai University 200072, China

[2] State Key Laboratory of Transducer Technology, Shanghai Institute of Microsystem and Information Technology, Chinese Academy of Sciences, Shanghai 200050 ,China

[a]shfz4418259@163.com, [b]915868345@qq.com, [c]pengyan@shu.edu.cn, [d] mliu@shu.edu.cn

Keywords: Three-dimensional hydrodynamic focusing**;** micro-fluidic chip; COMSOL

Abstract: This paper models the hydrodynamic focusing performance of a micro-fluidic chip with rectangular cross-sections, and the relationships between the aspect ratio, flow rate ratio of sheath flows to the sample flow, and dimensions and position of the focused sample flow are obtained. The simulation results are consistent with theoretical outcomes. And preliminary experiments were carried out to prove the simulation results.

Introduction

Hydrodynamic focusing is a widely applied micro-fluidic technology, which can be used for materials fabrication, such as micro-particles or droplets [1, 2], hollow or composite fibers [3], or for selective deposition of protein [4] or nanowires [5], and can also be used as flow cytometry [6] or micro-mixers [7].

Though hydrodynamic focusing has been investigated both theoretically and experimentally, the research on three dimensional hydrodynamic focusing is still quite limited. This paper modeled three-dimensional hydrodynamic focusing effect by COMSOL, verified the theoretical conclusions, and experimentally testified some simulation results.

Simulation and analysis of three-dimensional hydrodynamic focusing within a rectangular micro-channel

A. Modeling of a rectangular micro-channel with COMSOL

The model of the micro-channel here firstly focuses the sample flow in the vertical direction and then in the horizontal direction. As shown in Figure 1(a), inlets A and C are for sheath flows in the vertical direction, inlet B is for the sample flow, inlets D and E are for sheath flows in the horizontal direction. All the flows are set to be water, and the pressure at the outlet is set zero.

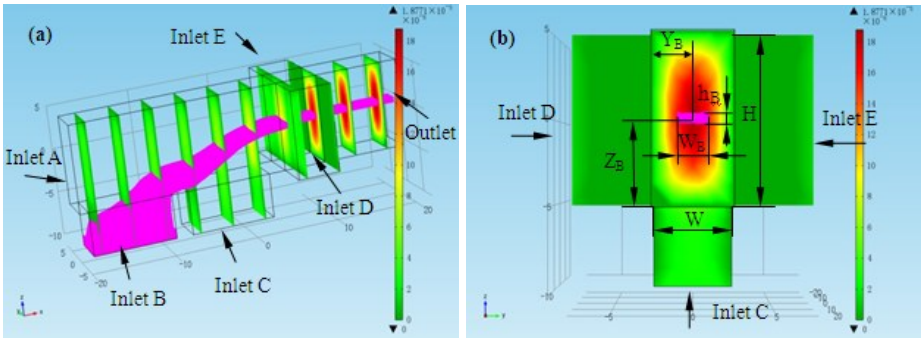


Figure 1. (a) The COMSOL model of hydrodynamic focusing in three-dimensional microchannels, (b) The right side view of the model.

Focusing in the vertical direction is accomplished by squeezing sample flow B with sheath flows A and C, and focusing in the horizontal direction is accomplished by squeezing sample B with sheath flows D and E. As shown in Figure 1, the pink part represents the sample flow, while colors in cross sections represent the velocities at each point. The volume flow rates of the five inlets are respectively defined as: Q_A, Q_B, Q_C, Q_D, Q_E, and the flow velocities are respectively v_A, v_B, v_C, v_D, v_E, velocity

ratios are defined as $i_A = v_A/v_B$, $i_C = v_C/v_B$, $i_D = v_D/v_B$, $i_E = v_E/v_B$. Figure 1(b) is the right side view of the model, where H and W are respectively height and width of the micro-channel, h_B and w_B are respectively height and width of the focused sample flow, Z_B and Y_B are respectively the vertical and horizontal position of the sample flow. The flows in the channel are assumed to be Newtonian fluids, and the velocity is stable and there is no slip on the channel walls.

B. Analysis of symmetric hydrodynamic focusing

The effect of different aspect ratios ε on symmetric hydrodynamic focusing is firstly discussed here. The definitions of the simulation are: $v_B = 5 \times 10^{-7} m/s$, $v_D = v_E = 0$, $v_A = v_C$. Accordingly, the sample flow will be confined at the middle of the micro-channel. On those conditions, the normalized vertical height h_B/H decreases with i_A increasing. In addition, the smaller the ε, the faster h_B/H decrease, and the better the vertically focusing. These results are in consistency with theoretical analysis, and relevant curves can be found in [8, 9]

In three-dimensional hydrodynamic focusing, i.e. $v_D = v_E \neq 0$, the normalized horizontal width w_B/W as a function of $i_D (= i_E)$ is shown in Figure 2(a)-(b). Figure 2(a) illustrates that w_B/W decreases with i_D increasing at a certain ε, which is in accordance with theoretical analysis[9]; with a certain i_D, the sample flow is focused narrower with i_A decreasing, which is because a flow will occupy more space as its relative velocity increases. Figure 2(b) illustrates that with a given i_A, the higher the ε, the faster w_B/W decreases, and the better the horizontally focusing, which is opposite to vertical focusing.

In addition to the horizontal sheath flows, the vertical sheath flows also affect w_B/W. Fig. 2(c) shows that when i_D is constant, the increasing of i_A will lead to the increasing of w_B/W, which means the increase of vertical sheath flow velocity will lead to the widening of horizontally focused sample flow. And the focusing performances of microchannels with different ε are also different, as shown in Fig. 2(d).

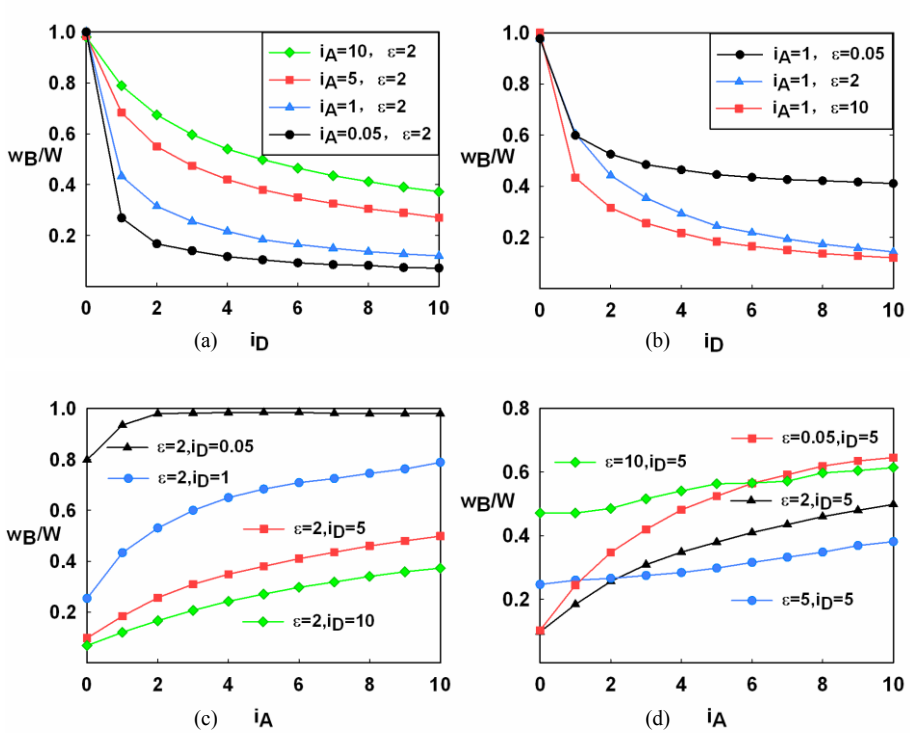


Figure 2. (a) Normalized horizontal width of the sample flow w_B/W versus horizontal focusing velocity ratio i_D with different vertical focusing velocity ratio i_A, (b) Normalized horizontal width of the sample flow w_B/W versus horizontal focusing velocity ratio i_D with different aspect ratio ε, (c) Normalized horizontal width of the sample flow w_B/W versus vertical focusing velocity ratio i_A with different horizontal focusing velocity ratio i_D, (d) Normalized horizontal width of the sample flow w_B/W versus vertical focusing velocity ratio i_A with different aspect ratio ε.

C. Analysis of asymmetric hydrodynamic focusing

Asymmetric hydrodynamic focusing, i.e.,$v_A \neq v_C$, $v_D \neq v_E$, changes the position of the sample flow by altering the velocity of the inlet flows. Actually symmetric hydrodynamic focusing is a special case of asymmetric hydrodynamic focusing.

Similarly, vertical focusing is firstly discussed. The definitions of the simulation are: $v_B = 5 \times 10^{-7} m/s$, $i_D = 5$, $i_E = 6$, based on which the relationship between Z_B/H and i_C was obtained as shown in Figure 3(a). As seen in the figure, Z_B/H increases as i_C increases, i.e., as the sheath flow C increases, the space it occupies also increases, thus the position of the sample flow shifts farer away from the bottom of the channel. It also can be seen that Z_B/H decreases as i_A increases, which is because the increasing i_A will lead to more space occupied by sheath flow A, and the sample flow will shift to the bottom of the channel.

Now horizontal focusing is taken into consideration. The same with symmetric hydrodynamic focusing, when the vertical sheath flow rates are set, the width of focused sample flow in asymmetric hydrodynamic focusing will be controlled by velocities of the horizontal sheath flows. Figure 3(b) shows the relation between Y_B/W and i_E, where the simulation conditions are set to be $v_B = 5 \times 10^{-7} m/s$, $i_A = 5$, $i_C = 6$. As shown in the figure, Y_B/W decreases as i_E increases, and the position of sample flow will get closer to side D. As i_D increase, the space occupied by sheath flow D will increase, and the position of sample flow will be driven away from the side D, i.e., Y_B/W increases.

According to the three-dimensional hydrodynamic focusing theory, when $Q_B \ll Q_A$, Q_C,Q_D,Q_E, the normalized vertical position $\frac{Z_B}{H}$ is closely linearly dependent on the vertical volume flow rate $\frac{Q_C}{Q_C+Q_A}$, and similarly the normalized horizontal position $\frac{Y_B}{W}$ is closely linearly dependent on the vertical volume flow rate $\frac{Q_D}{Q_D+Q_E}$[9]. As simulation conditions are set as $v_B = 5 \times 10^{-7} m/s$, $i_D = 5$, $i_E = 6$, and all the inlets hold the same cross-section, $\frac{Z_B}{H}$ is nearly linearly dependent on $\frac{v_C}{v_C+v_A}$, as shown in Figure 4(a). As simulation conditions are set as $v_B = 5 \times 10^{-7} m/s$, $i_A = 5$, $i_c = 6$, $\frac{Y_B}{H}$ is found to be nearly linearly dependent on $\frac{v_D}{v_D+v_E}$, as shown in Figure 4(b), which is consistent with the theoretical outcomes.

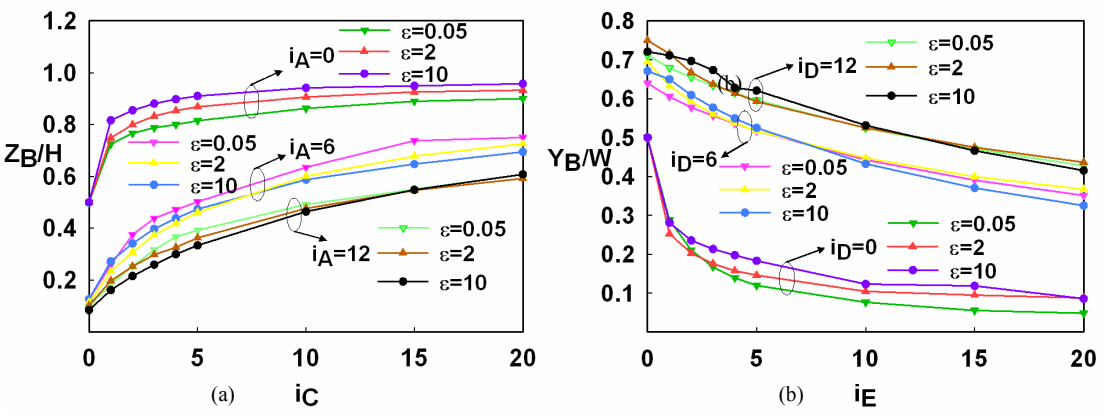


Figure 3. (a) Normalized vertical position Z_B/H as a function of inlet velocity ratio i_C. (b) Normalized horizontal position Y_B/W as a function of inlet velocity ratio i_E.

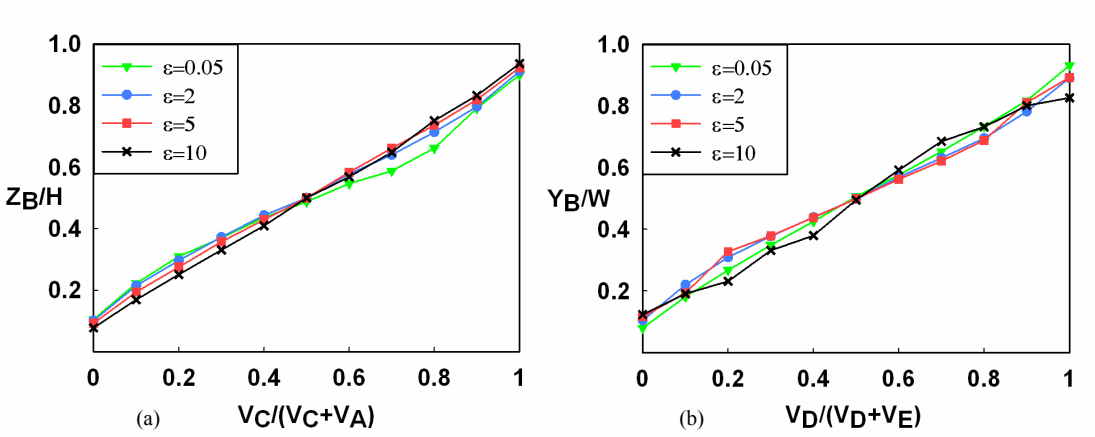


Figure 4. (a) Normalized vertical position of the sample flow Z_B/H as a function of the velocity ratio $v_C/(v_C+ v_A)$. (b) Normalized horizontal position of the sample flow Y_B/W as a function of the velocity ratio $v_D/(v_D+ v_E)$.

Experiments

Here simulation results of two dimensional horizontal hydrodynamic focusing, i.e., $v_A = v_C = 0$, was experimentally testified. The experimental platform is consisting of syringe pumps, a micro-fluidic chip, a microscope, a video camera and a computer. The micro-fluidic chip was fabricated by soft lithography. Red ink solution was used as the sample flow and de-ionized water as the sheath flows. Injection speeds of flows were adjusted by the syringe pumps, while the focusing process was recorded by the the computer.

A. Experiment symmetrical hydrodynamic focusing

The volume flow rate of the sample flow Q_B was fixed at 0.24mL/h, and the volume flow rate ratio of the sheath flows to the sample flow increased from 1 to 10. As a result, the relationship between $\frac{w_B}{W}$ and $\frac{Q_D}{Q_B}$(i) was obtained, as shown in Figure 5, which suggests that the normalized width of sample flow decreases as the flow rate ratio increases, agreeing with the simulation results.

B. Experiments of asymmetric hydrodynamic focusing

The velocity of the sample flow Q_B was still fixed at 0.24mL/h. Four sets of data of normalized width and position of the sample flow were sampled, corresponding to cases of $\frac{Q_D}{Q_B} = 0、3、6、10$ and $\frac{Q_E}{Q_B}$ increasing from 0 to 10. The relationship between $\frac{w_B}{W}$ and $\frac{Q_D}{Q_B} + \frac{Q_E}{Q_B}$, and the relationship between $\frac{Y_B}{W}$ and $\frac{Q_D}{Q_B} + \frac{Q_E}{Q_B}$ were obtained, as shown in Figure 6, both of which are consistent with simulation results. It can be seen from the figure that the increase of $\frac{Q_D}{Q_B}$ will cause the sample flow to shift right, while $\frac{Q_E}{Q_B}$ functions oppositely. So by adjusting $\frac{Q_D}{Q_B}$ and $\frac{Q_E}{Q_B}$, the sample flow can be positioned at various locations within the micro-channel.

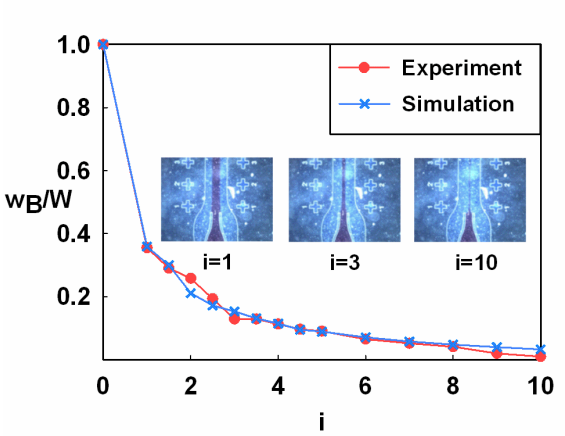


Figure 5. Experimental and simulation relationshipe of w_B/w and i.

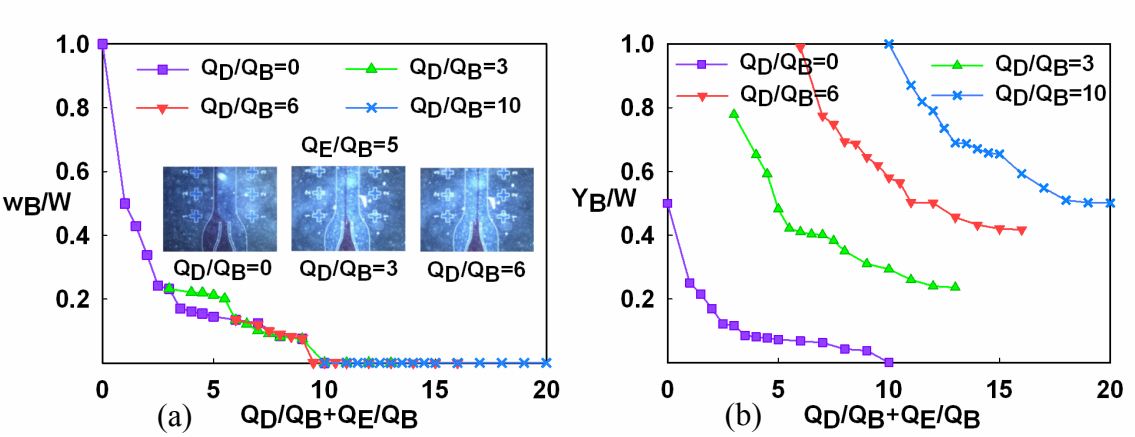


Fig. 6 (a) Normalized width of the sample flow w_B/W as a function of $Q_D/Q_B+ Q_E/Q_B$, (b) Normalized position of the sample flow Y_B/W as a function of $Q_D/Q_B+ Q_E/ Q_B$.

Discussions

In order to guarantee the convergence of computing process, the simulations in this paper was constructed with numerous simplifications and assumptions. Only limited cases are included, where the effect of horizontal sheath flows on vertically focusing and the effect of vertical sheath flows on horizontal focusing are not thoroughly covered and discussed. More work is still needed to get a thorough description of the three-dimensional hydrodynamic focusing phenomenon.

In the experiment, the velocity of sample flow was chosen as 0.24mL/h for two reasons. One is to avoid the pulsatile flow phenomenon typical when flow rates are very low, the other is to ensure more comprehensive data collection. If the sample flow rate is too high, the scope of the sheath flow rate will be greatly reduced in order to avoid burst of the micro-fluidic chip.

The aspect ratio of the microchannel in experiment is around 0.025, which is much smaller than 1, so the flow is parabolic across the microchannel. This is why the four curves in Figure 6(a) nearly coincide with each other.

Conclusion

This paper analyzed the performance of three-dimensional hydrodynamic focusing within a micro-fluidic chip by COMSOL. The simulation results are in good accordance with theoretical conclusions. The two-dimensional hydrodynamic focusing simulation results were experimentally testified. The simulation indicates that aspect ratio has a great influence on the focusing performance: the higher the aspect ratio, the better the horizontal focusing; the lower the aspect ratio, the better the vertical focusing. In short, this paper provides a useful reference for optimization of rectangular micro-channel design and theoretical support for its future applications.

References

[1] R. Karnik, F. Gu, P. Basto, C. Cannizzaro, L. Dean, W. Kyei-Manu, R. Langer, and O. C. Farokhzad, "Microfluidic Platform for Controlled Synthesis of Polymeric Nanoparticles," *Nano Lett.*, vol. 8, no.9, pp. 2906-2912. (2008)

[2] C. Yeh and Y. Lin, "Using a cross-flow microfluidic chip for monodisperse UV-photopolymerized microparticles," *Microfluid. Nanofluid.*, vol. 6, no.2, pp. 277-283. (2009)

[3] Y. Srivastava, C. Rhodes, M. Marquez, and T. Thorsen, "Electrospinning hollow and core/sheath nanofibers using hydrodynamic fluid focusing," *Microfluid. Nanofluid.*, vol. 5, no.4, pp. 455-458. (2008)

[4] A. Bransky, N. Korin and S. Levenberg, "Experimental and theoretical study of selective protein deposition using focused micro laminar flows," *Biomed. Microdevices*, vol. 10, no.3, pp. 421-428. (2008)

[5] M. Liu, Y. Chen, Q. Guo, R. Li, X. Sun, and J. Yang, "An Economic Method for Large-Scale Patterning and Electric Measurement of Nanowires," *J. Nanoelectron. Optoe.*, vol. 6, no.2, pp. 144-151. (2011)
[6] M. Chabert and J. Viovy, "Microfluidic high-throughput encapsulation and hydrodynamic self-sorting of single cells," *P. Natl. Acad. Sci. USA*, vol. 105, no.9, pp. 3191-3196. (2008)
[7] H. Y. Park, X. Qiu, E. Rhoades, J. Korlach, L. W. Kwok, W. R. Zipfel, W. W. Webb, and L. Pollack, "Achieving Uniform Mixing in a Microfluidic Device: Hydrodynamic Focusing Prior to Mixing," *Anal. Chem.*, vol. 78, no.13, pp. 4465-4473. (2006)
[8] G. B. Lee, C. C. Chang, S. B. Huang, and R. J. Yang, "The hydrodynamic focusing effect inside rectangular microchannels," *J. Micromech. Microeng.*, vol. 16, pp. 1024-1032. (2006)
[9] L. F. Zhou, J. Zeng, Y. Peng and M. Liu, "Investigation into 3-D Hydrodynamic Focusing Effect in Rectangular Microchannels," *Microelectron.*, vol. 43, no.5, pp. 698-703. (2013)

Key Engineering Materials Vols 645-646 (2015) pp 455-461
© (2015) Trans Tech Publications, Switzerland
doi:10.4028/www.scientific.net/KEM.645-646.455
Submitted: 2014-12-24
Accepted: 2014-12-31

Threshold Model of Micro-Fluidic Inertial Switch Based on Orthogonal Regression Design

Tingting Liu[1,2,3,a*], Wei Su[2,b], Chao Wang[2,c] and Tao Yang[1,d]

[1]Robot Technology Used for Special Environment Key Laboratory of Sichuan Province, Southwest University of Science and Technology, Mianyang, China

[2]Institute of Electronic Engineering, China Academy of Engineering Physics, Mianyang, China

[3]School of Physical Sciences, University of Science and Technology of China, Hefei, China

[a]ljttlf@163.com, [b]weisu@caep.ac.cn, [c]wchao.lzms@gmail.com, [d]yangtao@swust.edu.cn

Keywords: MEMS; micro-fluidic inertial switch; semi-analytical regression model; micromachining; centripetal test

Abstract. The micro-fluidic inertial switch with liquid metal droplet moving under the action of acceleration has overcome the disadvantages of contact bounce, arcing and welding, as are found in the traditional inertial switch. Micro-fluidic inertial switches have no moving parts, a small contact resistance, a long service life and a large current capability. In this paper, we present a micro-fluidic inertial switch that is composed of two-stage micro-valves. This design facilitates tuning of the threshold by adjusting the mercury volume, and so provides better switching performance. Numerical simulation of an orthogonal experiment is used to identify the semi-analytical model of the switch threshold. Results show that the identified model is in accordance with simulation results. Switch prototypes are fabricated by micro-machining techniques including ICP dry etching, sputtering technology and anodic bonding. Centripetal test results show that the switch threshold can be tuned by the careful adjustment of mercury volume.

Introduction

The inertial sensor based on MEMS(Micro-Electro-Mechanical System) technology has the advantages of small size, low fabrication cost, high reliability and high sensitivity. There has been much recent interest to develop a micro-inertial switch that closes at a predetermined acceleration threshold [1]. The micro-fluidic inertial switch is a new type of micro-acceleration switch, that uses mercury droplet as the sensitive element, thus replacing the traditional elastic solid electrode. The micro-fluidic switch avoids the problems associated with solid-solid switch contacts, such as contact bounce, arcing and welding [2]. The micro-fluidic inertial switch presented in this paper is built from two-stage micro valves. An orthogonal experiment against a semi-analytical model of acceleration gives the switch threshold. Switch prototypes are fabricated by such micro-machining techniques as ICP dry etching, sputtering technology and anodic bonding. Centripetal tests were conducted to investigate prototype threshold characteristics. Finally, these test results are compared with the simulation results and analytical results.

Principle of micro-fluidic inertial switch with tunable threshold

The design of the micro-fluidic inertial switch incorporates a two-stage. A tuning hole, a tuning channel, a central micro-channel, an air duct and a reservoir are etched into a silicon substrate. Anodic bonding binds the silicon substrate to a glass cover. The direction of the sensitive axis is illustrated with an arrow in Fig.1. The mercury droplet can be injected into the central micro-channel through the tuning hole and tuning channel. The first-stage micro-valve ensures that the mercury droplet in the central micro-channel will not flow back to the tuning hole. The second-stage micro-valve is formed from the central micro-channel with varying rectangular cross section, and the air duct that is linked to the central micro-channel, with a reservoir being used to reduce air

resistance. The signal electrodes deposited on the glass cover should be extended to the proper position within the reservoir. With an increase of acceleration, the mercury droplet just breaks through the second-stage micro-valve to close signal electrodes. The acceleration of the moment is described as the acceleration threshold. When the inertial acceleration is less than the acceleration threshold, the mercury droplets cannot close the signal electrodes and the switch is in the "off" position. When the inertial acceleration is increased to the threshold, the switch completes the "off" to "on" position conversion. While the inertial acceleration continues to grow, the mercury droplet remains in the reservoir and close the signal electrodes reliably. The acceleration threshold is determined by the central micro-channel structural parameters and the mercury droplet volume.

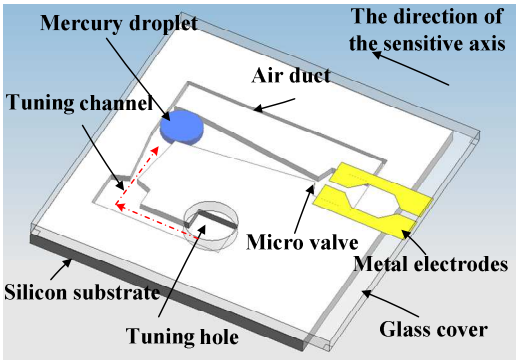


Fig.1 Schematic of the micro-fluidic inertial switch

Identification of acceleration threshold semi-analytical model based on orthogonal experiment

When the mercury droplet moves to the second-stage micro-valve, a pressure difference is present on the advancing and receding mercury meniscus. Thus, motion of the mercury droplet is blocked at the second-stage micro-valve. Our semi-analytical model takes into account a few assumptions. As liquids are free of shear forces under static conditions, we assume that there is no tangential interaction between the middle mercury column (the shadow section in Fig.2) and the neighboring liquid.

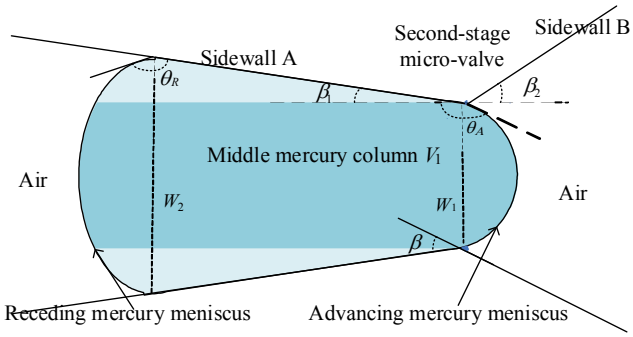


Fig.2 The state of the mercury droplets through the second-stage micro-valve

Applying the Young-Laplace equation to an advancing and receding mercury meniscus, the semi-analytical model of acceleration threshold deduced in [3] is given by Eq.(1).

$$\alpha_{th} = \frac{2\gamma C W_1 h}{\rho V_1}\left[\frac{\cos\theta_I}{W_1} + \frac{\cos\theta_{A1} + \cos\theta_{A2}}{2h} - \frac{\cos\theta_R}{W_2} - \frac{\cos\theta_{R1} + \cos\theta_{R2}}{2h}\right] \quad (1)$$

where ρ is the mercury droplet density; γ is the surface tension between mercury and air; h is the depth of micro-channel; C is the surface roughness coefficient; W_1 is the second-stage micro-valve width; W_2 is the receding meniscus width; where the middle mercury column volume

$V_1=2V_2W_1/(W_1+W_2)$, and V_2 is whole mercury volume; θ_I is within the range of $\min\{\theta_{A1}+\beta,\ 180°\}$; β is the expansion angle; θ_R is the receding contact angle between mercury and sidewall A; θ_{A1} and θ_{R1} are the advancing contact angle and receding contact angle between mercury and silicon wafer, respectively; and θ_{A2} and θ_{R2} are the advancing contact angle and receding contact angle between mercury and glass cover, respectively.

Among physical considerations is the advancing and receding contact angle, which is affected by surface roughness. As the mercury droplet is in a closed environment, it is hard to measure the advancing and receding contact angle. In the Equation (1), the advancing and contact angle quoted in reference [4]. Thus, there is divergence between test values and theoretic values from semi-analytical model. In this paper, multiple linear regression is employed to process the data of orthogonal experiments and so identify the semi-analytical model of the acceleration threshold.

Determination of orthogonal test factors and levels. The target acceleration threshold of our micro-fluidic inertial switch is 10g within an accuracy of 5%. From the semi-analytical model, we see that the acceleration threshold analytical value is 10g when the second-stage micro-valve width W_1, central micro-channel depth h and expansion angle β_1 of sidewall A are 220μm, 240μm and 7° respectively. These parameters are defined as the initial structure parameters.

A piecewise fitting is employed to identify the acceleration threshold model. To improve the accuracy of fitting, the range of W_1 is divided into two intervals: 190-220μm and 220-250μm. Table 1 shows the three factors and three levels in two intervals of W_1.

Table 1. The table of factors and levels

	Interval of W_1:190-220μm			Interval of W_1:220-250μm		
Level Factor	W_1(μm)	h(μm)	β_1(°)	W_1(μm)	h(μm)	β_1(°)
1	190	170	5	220	170	5
2	205	240	7	235	240	7
3	220	310	9	250	310	9

In an orthogonal experiment design, the setting of parameters involves allocating levels within an orthogonal array [5]. The interaction of factors are not considered. According to the orthogonal test of 3 factors and 3 levels discussed above, the experiments are performed in terms of L9 orthogonal array. The orthogonal experiments according to orthogonal array are conducted to obtain the full factorial experiment with fewer numbers of experiment.

Establishment of acceleration threshold semi-analytical regression model. The key structural parameters of the central micro-channel are the second-stage micro-valve width W_1, central micro-channel depth h and expansion angle β_1; these three factors are independent.

The semi-analytical model discussed above, can be rewritten as:

$$\hat{y} = b_0 + b_1X_1 + b_2X_2 + b_3X_3 \qquad (2)$$

where,

$$X_1 = \frac{2\gamma Ch\cos\theta_I}{\rho V_1}$$

$$X_2 = \frac{2\gamma CW_1}{\rho V_1}\left(\frac{\cos\theta_{A1}+\cos\theta_{A2}}{2} - \frac{\cos\theta_{R1}+\cos\theta_{R2}}{2}\right)$$

$$X_3 = -\frac{2\gamma C W_1 h \cos\theta_R}{\rho V_1 W_2}$$

The function *regress* in statistics toolbox of Matlab is used to realize multiple linear regressions. A total of eighteen numerical simulation tests have been carried out. Based on the simulation results, the multiple linear regression equation that we obtain is:

$$\hat{y} = \begin{cases} 4.3962 - 0.0593X_1 - 0.0092X_2 - 0.0324X_3 & 190\mu m \le W_1 \le 220\mu m \\ -0.2184 - 0.0747X_1 - 0.1289X_2 + 0.0051X_3 & 220\mu m \le W_1 \le 250\mu m \end{cases} \quad (3)$$

The results of numerical simulation and segmentation fitting are shown in Table 2. Results show that the fitted results are in accordance with the simulation results and verifies the effectiveness of the regression equation.

Table 2. The results of numerical simulation and segmentation fitting

No.	Interval of W_1:190-220μm					No.	Interval of W_1:220-250μm				
	W_1(μm)	h(μm)	β_1(°)	Simulation results(g)	Fitted results(g)		W_1(μm)	h(μm)	β_1(°)	Simulation results (g)	Fitted results (g)
1	190	170	5	9.20	9.1560	**10**	220	170	5	7.90	7.8472
2	190	240	7	10.90	10.8343	**11**	220	240	7	10.10	10.0358
3	190	310	9	12.60	12.6851	**12**	220	310	9	12.30	12.3572
4	205	170	7	9.50	9.5264	**13**	235	170	7	8.40	8.4379
5	205	240	9	11.20	11.1950	**14**	235	240	9	10.60	10.5761
6	205	310	5	10.70	10.7055	**15**	235	310	5	9.90	9.9394
7	220	170	9	9.80	9.8051	**16**	250	170	9	8.90	8.9070
8	220	240	5	9.40	9.5296	**17**	250	240	5	8.40	8.4686
9	220	310	7	11.20	11.1023	**18**	250	310	7	10.60	10.4901

Micromachining processes of micro fluidic inertial switch

Vertical processing control and depth uniformity control of micro-channel is achieved by ICP etching SOI. By analyzing materials compatibility, Cr/Au-Cr composite metal electrodes are designed, and tuning hole and tuning channel are designed to adjust mercury droplet volume. Batch production of micro-fluidic inertial switch is achieved by wafer level package (WLP) processing. The fabrication processes of micro-fluidic inertial switch are shown in Fig.3.

SEM photo of micro-fluidic inertial switch is shown in Fig.4. A prototype of micro-fluidic inertial switch with mercury droplet is shown in Fig.5. Mercury droplet is put into the initial position by tuning hole and tuning channel.

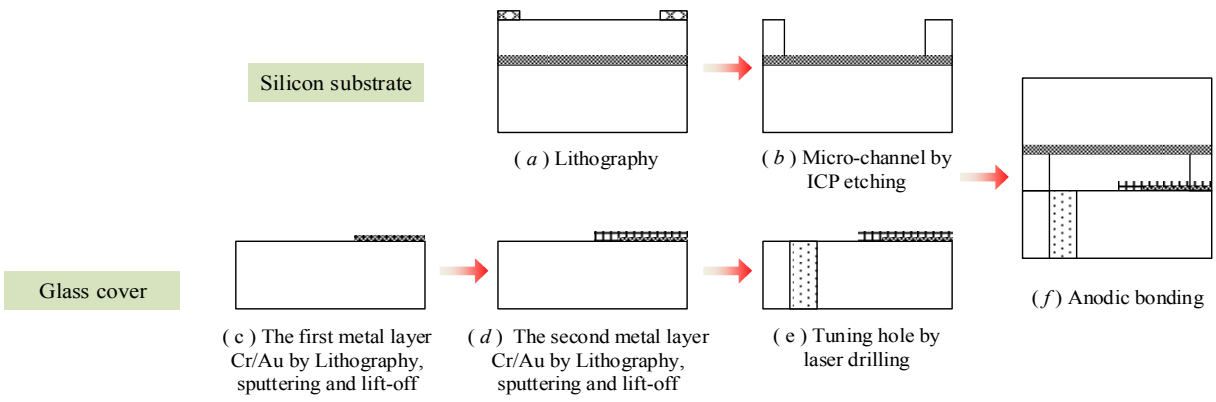


Fig.3 The fabrication processes of micro-fluidic inertial switch includes two parts: the silicon substrate and glass cover.

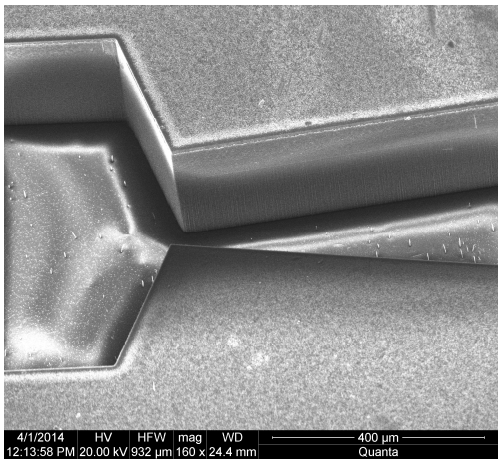


Fig.4 SEM photo of micro-fluidic inertial switch

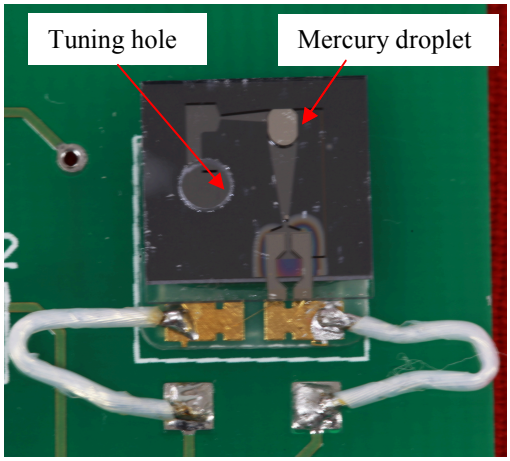


Fig.5 A prototype of switch with mercury droplet with the size of 9mm×9mm×0.8mm

Test of micro-fluidic inertial switch

The acceleration threshold is tested by a precision centripetal turntable to produce centripetal acceleration. The prototype is set on the turnable, and connected with DC power supply and current limiting resistor. High-speed data acquisition synchronously gathers the acceleration signal, as tested by standard accelerometer and the on-off signal of the switch. The acceleration threshold can be obtained by analyzing the acquired data.

Put a mercury droplet on the solid surface, the droplet mercury volume is calculated by contact angle and droplet diameter. We inject the mercury droplet with proper volume into the switch by tuning hole and tuning channel.The acceleration threshold test results are shown in Table 3. Positive values indicate the switch is shifted from "off" to "on" and negative values are just the opposite. Range method is used to evaluate performance stability. The relative error of mercury droplet volume is about 8%.

Table 3. Test results of acceleration threshold

No.	Acceleration threshold		Acceleration threshold		Average value after adjusting the droplet volume (Positive) (g)	Range after adjusting the droplet volume (Positive) (g)
	Positive(g)	Negative(g)	Positive(g)	Negative(g)		
1#	14.16	>25	10.29	9.42	10.22	0.26
	16.31	>25	10.06	8.84		
	15.51	>25	10.32	9.39		
	Droplet volume: 265.24nL		Droplet volume: 306.58nL		Reservoir volume: 291.68nL	
2#	13.16	>25	9.54	7.91	9.59	0.37
	14.28	>25	9.80	8.22		

	15.60	>25	9.43	8.74		
	Droplet volume: 254.32nL		Droplet volume: 313.69nL		Reservoir volume: 291.68nL	
3#	17.58	>25	9.61	6.83		
	14.28	>25	9.22	6.69	9.44	0.39
	15.67	>25	9.48	6.66		
	Droplet volume: 258.46nL		Droplet volume: 324.87nL		Reservoir volume: 291.68nL	

As shown in Table 3, before adjusting the droplet volume, the positive threshold are both larger than the theoretical results. The reason may be the actual surface is rough and surface roughness seriously affects the advancing and receding contact angle. From Equation (1), with a higher droplet volume, the threshold can be decreased. Thus, to achieve the target threshold the more droplet should be injected into the switch. After adjusting the droplet volume, the positive threshold are both decreased and the average positive value of the 1# prototype is closer to the target threshold of 10g. The range of the 1# prototype is minimum and the stability is best of all. Since the droplet volumes are larger than the reservoir volume and cannot completely enter into the reservoir, the negative threshold of prototypes are less than the negative threshold before the adjustment of droplet volume. The increased reservoir volume results in increased negative threshold without affecting the positive threshold. Table 4 show the comparison between average test results, simulation results and theoretical results. These test results are in agreement with simulation results and analytical.

Table 4. Comparison between average test results, simulation results and theoretical results

No.	1#	2#	3#
Average test results(g)	10.22	9.59	9.44
Simulation results(g)	9.70	9.50	9.40
Analytical results(g)	9.66	9.55	9.38

Conclusions

To reduce such disadvantages as contact bounce, arcing and welding, that are so common to traditional micro-mechanical inertial switches, liquid metal substitutes for the solid-solid contact, which improves contact stability. The micro-fluidic inertial switch based on liquid metal utilizes a moving mercury droplet to close the switch under the action of acceleration.

This paper presents the structure of a micro-fluidic inertial switch this is designed from a two-stage micro-valve, that has a tunable acceleration threshold and this structure provides better threshold switching characteristics. Based on numerical simulation results, the orthogonal experiment method is used to identify the semi-analytical model of acceleration threshold. Results show that the identified model is in accordance with simulation results. Switch prototypes are fabricated by micro-machining techniques such as ICP dry etching, sputtering and anodic bonding. Since the contact angle hysteresis caused by surface roughness is greater than the settings in simulation values, the average test results of acceleration thresholds are larger than are theoretical results. Centripetal test results show that the acceleration threshold of our micro-fluidic switch can be tuned by mercury volume adjustment.

Acknowledgement

This work is supported by NSAF under Grant No.11076024, Open Fund of Robot Technology Used for Special Environment Key Laboratory of Sichuan Province under Grant No.13zxtk06 and Major Project of Education Department in Sichuan under Grant No.11ZA216.

References

[1] H.Kim, Y.H.Jang, Y.K.Kim, J.M.Kim, MEMS acceleration switch with bi-directionally tunable threshold. *Sens. Actuators A.Phys*. 208(2014)120-129.
[2] P.Sen, C.J.Kim, A fast liquid-metal droplet microswitch using EWOD-driven contact-line sliding. *J.Microelectromech.Syst.* 18(2009)174-185.
[3] L.Yi, Y.Tao, L.Tingting, C.Guangyan, Analysis and simulation of micro-fluidic inertiaswitch. *Key Eng. Mater.* 503(2012)348–353.
[4] K.Yoo, U.Park, J.Kim, Development and characterization of a novel configurable MEMS inertial switch using a microscale liquid-metal droplet in a microstructured channel. *Sens. Actuators A.Phys*. 166(2011)234-240.
[5] C.Ying, Z.Jiafan, Y.Canjun, N.Bin, The workspace mapping with deficient-DOF space for the PUMA 560 robot and its exoskeleton arm by using orthogonal experiment design method. *Robot Cim-Int Manuf*. 23(2007)478–487.

Key Engineering Materials Vols 645-646 (2015) pp 462-468
© (2015) Trans Tech Publications, Switzerland
doi:10.4028/www.scientific.net/KEM.645-646.462

Submitted: 2014-12-27
Accepted: 2014-12-31

Effect of Flow Rate of Slurry in Micro-channels on The Consistency of Polishing Rate

Yan Li[a]; Ming Sun[b]; Yuling Liu*[,c]; Aochen Wang[d];Jiying Tang[e]; Shiyan Fan[f]

(Institute of Microelectronic, Hebei University of Technology, Tianjin, 300130, China)

[a]email: Liyan424424@126.com, [b]email: 120278175@qq.com, [c]email: Lyl@hebut.edu.cn,

[d]email: 155322612@qq.com, [e]email: 191659302@qq.com, [f]email: 494866895@qq.com

Keywords: chemical mechanical planarization; Bernoulli equation; heterogeneity of polishing rate; heterogeneity of step height difference; central composite experimental method

Abstract: According to the Bernoulli equation and Darcy formula, the flow model of slurry in micro-channels was established, it indicated that slurry viscosity is the main factor affecting the slurry mean velocity. According to the characteristics that liquid viscosity is mainly determined by the liquid temperature and the property that mechanical friction can improve the liquid temperature, the effects of slurry temperature, working pressure and polishing speed on the heterogeneity of polishing rate were investigated. The results showed that the effect of removal rate of each parameter on the central part of the copper film can be described as: slurry temperature > working pressure > polishing speed. In order to obtain the best planarization process, through the central composite experimental method, the technological parameters were optimized regarding the heterogeneity of polishing rate as response value. It was finally concluded that: when the slurry temperature was 21.60℃, the working pressure was 8.83kpa, the system speed was 43.92rpm, the predicted minimum value of the heterogeneity of polishing rate (HOPR) was 0.0574.

1 Introduction

With the rapid development of microelectronics industry, copper CMP (chemical mechanical planarization) technology accompanied by dual damascene process has been widely concerned with growing maturity[1]. A set of theory system with comprehensive range and strong applicability of CMP is still unable to formed due to a wide variety of subjects with large span. For several years, reports on the CMP process are too numerous to be enumerated, but it is difficult to achieve widespread applications due to the lack of corresponding supporting mechanism[2]. The CMP mechanisms were studied in some papers, but most of these mechanisms were aimed at planarization effect on certain locations of wafer surface which were listed in the category of local planarization. With the increase of wafer size, in order to achieve the global planarization of the wafer, the planarization effect of each position on the wafer must be systematic researched, which indicate that the heterogeneity of step height difference of each position on the wafer achieve the best value[3]. Based on the issue listed above this paper regards the velocity of slurry in micro-channels as the breakthrough point, propose the concept of heterogeneity of the step height difference, establish the model of the slurry flow in micro-channels, finally achieve the extremely low heterogeneity of polishing rate through the optimization of the process parameters[4].

2 Slurry flow model in micro-channels

The flow process of slurry in the micro-channel on the surface of the polishing pad comply with the Bernoulli equation, so

$$p + \rho v^2/2 + \rho g h = C_1 \quad (1),$$

the slurry always keep the horizontal flow, Eq.1 can be described as

$$p + \rho v^2/2 = C_2 \quad (2), \quad p\Delta V + \Delta V \rho v^2/2 = C_2 \Delta V = C \quad (3)$$

can be acquired by multiplying both sides of Eq.2 at the same time by the volume variable (ΔV), Eq.3 is equivalent to

$$FS + mv^2/2 = C \quad (4),$$

which shows that the value of pressure potential energy and kinetic energy is a constant. Pressure potential energy is the energy of particle(Δm) due to the deformation in the pressure field F[5]. In the CMP process, the polishing head is pressed on the polishing pad, the grooves on the polishing pad surface becomes closed channels. The slurry with the centrifugal movement trend along the tangential direction of the circular motion can not flow in a circle by centripetal force. Assuming the slurry flow from the **a** cross-section to the **b** cross-section,

$$F_a S + m v_a^2/2 = F_b S + m v_b^2/2 \quad (5)$$

can be obtained using Eq.4 in the **a** section and **b** section. The slurry flow process will cause the loss of mechanical energy, at the same time, the polishing head and polishing pad will do work on the slurry, therefore Eq.5 should be more accurately expressed as

$$F_a S + m v_a^2/2 = F_b S + m v_b^2/2 + h_f - W \quad (6),$$

where h_f is the frictional head loss of slurry, W is the work done by the system on the slurry. The Darcy WeisBach formula can be written as

$$h_f = \lambda l v_{ave}^2 d^{-1} g^{-1}/2 \quad (7),$$

where l is the pipe range, d is the pipe diameter, V_{ave} is the average velocity of liquid in the pipes, $v_{ave}^2 g^{-1}/2$ is the velocity head[6]. According to the Blasius formula, then

$$\lambda = 0.316 Re^{-0.25} \quad (8),$$

where Re whose calculation method is

$$Re = \rho v_{ave} d r^{-1} \quad (9)$$

is the Reynolds number, so

$$\lambda = 0.316(\rho v_{ave} d r^{-1})^{-0.25} \quad (10),$$

where ρ is the slurry density, r is the coefficient of kinematic viscosity of slurry, then

$$h_f = 0.158\rho^{-0.25}v^{1.75}r^{0.25}ld^{-1.25}g^{-1} \tag{11}$$

can be further obtained. The polishing pad is hard and the polishing head pressure can keep constant, so

$$F_aS = F_bS \tag{12},$$

$$W = m(v_b{}^2 - v_a{}^2)/2 + h_f \tag{13}$$

can be further acquired. Assuming the **a** section is the edge position of the polishing pad and the **b** section is the center position of the polishing pad, the polishing pad speed is so large that the speed in the normal direction at the **a** section can be ignored. So Eq.13 can be expressed as

$$W = -m\omega^2R^2/2 + 0.158\rho^{-0.25}v_{ave}{}^{1.75}r^{0.25}ld^{-1.25}g^{-1} \tag{14},$$

then

$$v_{ave} = \left[6.33\left(W + \omega^2R^2/2\right)\rho^{0.25}d^{1.25}gr^{-0.25}l^{-1}\right]^{8/7} \tag{15},$$

Because

$$r = \mu/\rho \tag{16},$$

then

$$v_{ave} = \left[6.33\left(W + \omega^2R^2/2\right)\rho^{0.5}d^{1.25}g\mu^{-0.25}l^{-1}\right]^{8/7} \tag{17}.$$

l and d are the polishing pad intrinsic value, when the slurry composition is fixed, ρ is a fixed value. Then the average velocity of slurry is determined by the viscosity and the speed as shown in Eq.17. Liquid viscosity is mainly decided by the temperature, but the increase of polishing pressure and polishing speed can aggravate the friction effect between the wafer and polishing pad, friction energy can be further converted to internal energy resulting in the increase of slurry temperature, thus affecting the slurry viscosity. In summary, the slurry mean velocity is mainly determined by the slurry temperature, polishing pressure and polishing speed. Slurry mean velocity is faster, the polishing rate of the central part on the wafer is faster and vice versa[7].

3 Experimental details

Experimental apparatus and materials: AlpsitecE460E type polishing machine, Agilent5600LS type atomic force microscope, AMBIOSXP-300 step profiler, Φ300mmblanket copper wafer and MIT854 copper wafer. Experimental method: The film thickness(FT) removal was measured by step profiler. The film step height(SH) was measured by atomic force microscopy. The polishing rate(PR) is calculated as

$PR = FT_{pre} - FT_{post}/t$,

where the FT_{pre} and FT_{post} are respectively the film thickness before and after CMP, t is the time of the CMP process. The heterogeneity of polishing rates(HOPR) is calculated as

$$HOPR = PR_{RMS}/\overline{PR}, \quad PR_{RMS} = \left[\sum_{i=1}^{n}\left(PR_i - \overline{PR}\right)^2 \Big/ (n-1)\right]^{1/2}, \quad \overline{PR} = \sum_{i=1}^{n} PR_i \Big/ n.$$

4 Results and discussion

4.1 Effect of process parameters on the removal rates of each position on the wafer. All else being equal, the effects of slurry temperature, polishing pressure and polishing speed on the removal rate of each position on the wafer in unit time are shown in Fig.1,2 and 3. All the fitting curves are shown in Fig.4. From the figures, when the polishing process parameters are 20*1.5*60 (which means the slurry temperature is 20℃, the working pressure is 1.5psi, the polishing speed is 60rpm, the same below), 20*1*60 and 20*2*40, the removal rate of the central position is smaller than that of the edge position. According to the text mentioned above, increase of the slurry temperature, the work pressure and the polishing speed can reduce the slurry viscosity further leading to the increase of the removal rate of the central part on the wafer. When the process parameters are 25*1.5*60 and 20*2*60, the removal rates of the central part on the wafer begin to exceed the remove rates of the edge part. When the process parameters are 35*1.5*60, 20*4*60 and 20*2*100, the removal rates of the central part on the wafer reach the maximum values under each condition. Figure.4 shows the effects of each parameter on the removal rate of the central part of the wafer can be described as slurry temperature>working pressure>polishing speed. So removal rates of each position on the wafer can be regulated by changing the parameters, which lead to the same film thickness after CMP. To sum up, the improvements of the slurry temperature, working pressure and polishing speed can promote the removal of copper film, and the increase rate of the central part of the copper film is larger than that of the edge part.

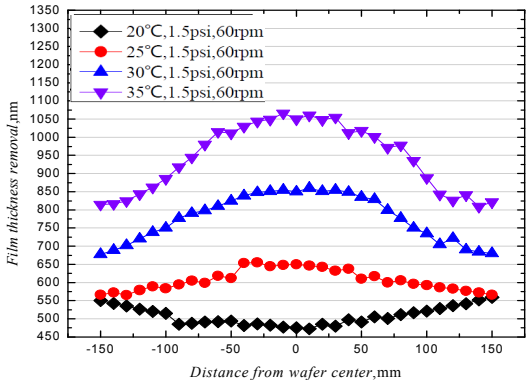


Fig.1 Effect of slurry temperature on the FT removal

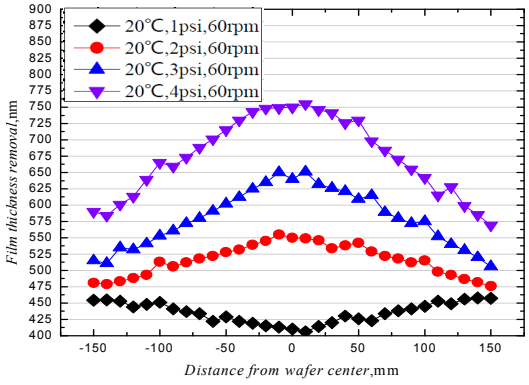


Fig.2 Effect of pressure on the FT removal

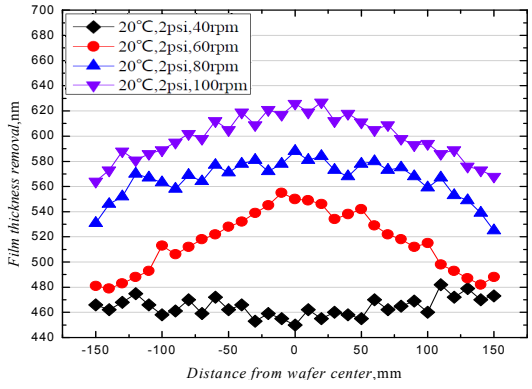


Fig.3 Effect of polishing speed on the FT removal

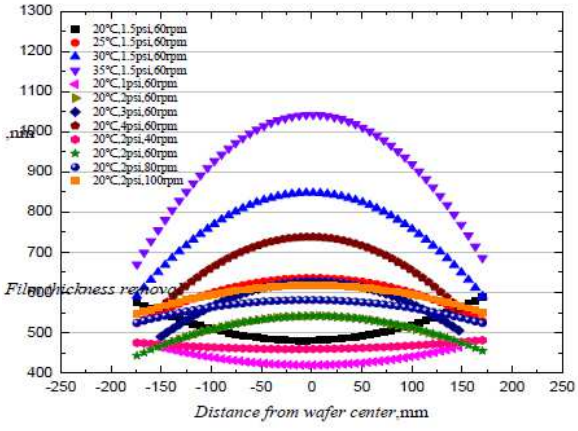


Fig.4 Fitting curves of the curves in Fig.1,2,3

4.2 Optimization of process parameters. To realize the consistent removals of the step heights of each positions on the wafer, the slurry flow rates of each positions on the wafer must be consistent. The consistency of the slurry flow rates of each positions can be characterized by the heterogeneity of polishing rate(HOPR). The HOPR is smaller, the consistency of the slurry flow rates of different positions on the wafer is better, which can realize the consistent removals of the step heights and the planarization of the whole wafer. According to the experimental results mentioned above, process parameter is set to the intermediate values between 20*1.5*60 and 25*1.5*60(22.5*1.5*60 and 25*1*60), removal rates of each positions on the blanket copper wafer after CMP are shown in Fig.5. It can be seen from the fitting curves in Fig.5, when the process parameters are 22.5*1.5*60, the consistency of polishing rate of each position on the wafer is relatively good, the value of HOPR is very low; when the process parameters are 25*1*60, the consistency of polishing rate of each position on the wafer is relatively bad, the value of HOPR is very high, which indicate that the effects of slurry temperature and working pressure on the HOPR are so large that the tiny difference can lead to a great deviation of the HOPR. The central composite experimental design is conducted regarding the slurry temperature, working pressure (in order to achieve more accurate process optimization, pressure unit hereinafter mentioned is kpa), polishing speed and HOPR respectively as the experimental factors A, B, C and the response value. Design details of experiment and the corresponding results of the analysis of variance(ANOVA) are shown in Table.1. The polynomial regression equation according to the experimental results shown in Table.1 can be written as:

$$HOPR=0.42057-0.031342A-2.92201E-3B-5.27750E-4C+1.29011E-5AB+1.11111E-6AC-3.95098E-5BC+7.21384E-4A^2+2.47497E-4B^2+9.73115E-6C^2 \quad (18)$$

"Prob>F" values of A, B, A^2, B^2 shown in Table.1 are less than 0.05, which indicate that A, B, A^2, B^2 are the significant items of the model and the fitting effect between Eq.18 and the experimental results is so well. The response surface analysis results of the corresponding factors are shown in Fig.6, 7, 8. From the figures, The values of HOPR decrease along with the decrease values of each factor. In order to obtain the minimum value of the HOPR, the values of A and B are respectively limited in the range of 20-29 and 8-19 shown in Fig.6, the values of A and C are respectively limited in the range of 20-27 and 45-70 shown in Fig.7, the values of B and C are respectively limited in the range of 8-16 and 45-80 shown in Fig.8, which indicate that the value scopes of A, B, C are respectively 20-27, 8-16, 45-70. The optimal values of predicted probability and HOPR fitted by Eq.18 are shown in Fig.9 and 10. From the figures, when the A, B, C values are respectively 21.60, 8.83, 43.92, the predicted minimum value of HOPR is 0.0574, the predicted desirability is 0.943, the corresponding 95% confidence interval(CI) is 0.0147-0.1, the 95% prediction interval(PI) is 0.0245-0.139, the mean standard error is 0.0191, the predicted standard error is 0.0368. For any given combination of $A_0*B_0*C_0$ of variables A, B, C, the estimation interval of average value of HOPR is 0.0147-0.1. For any given combination of $A_0*B_0*C_0$ of variables A, B, C, the estimation interval of individual value of HOPR is 0.0245-0.139. When the average standard error is counted, the average range of HOPR is 0.0383-0.0765, the range is the proper subset of the 95% CI, which indicate that the range of HOPR mean values caused by the optimized values of the three factors is always in the 95% CI. When the predicted standard error is counted, the predicted range of HOPR is 0.0206-0.0942, the range is not the proper subset of the 95% PI and the value of the excess part is 0.0039. According to the predicted desirability whose value is 0.943 mentioned above, the expected proportion of 0.0039 is 0.057, which shows that the value of the error range is 0.0684 when the desired probability is 100%. Then the upper limit value and the lower limit value of the HOPR real range is respectively 0.1258 and 0, which indicate that when the values of A, B, C are respectively

21.60, 8.83, 43.92 and the experiment is repeated enough times, the average value of HOPR will appear in the interval of 0.0147-0.1 with a 95% probability, in this interval the probability of HOPR optimal value(0.0574) is 94.3%, even if the three factors simultaneously achieve their worst levels, the HOPR value is always lower than 0.1258.

Table.1 The results of experiment design and ANOVA

Design details				ANOVA					
T(°C)	P(kpa)	S(rpm)	HOPR	Source	Sum of Squares	df	Mean Square	F Value	p-value Prob > F
35.00	6.89	40.00	0.22	Model	0.10	9	0.012	11.80	0.0003
20.00	6.89	100.00	0.12	A-T	0.057	1	0.057	57.98	<0.0001
35.00	27.56	40.00	0.288	B-P	0.015	1	0.015	15.06	0.0031
20.00	27.56	40.00	0.145	C-S	4.189E-4	1	4.189E-4	0.42	0.5296
20.00	6.89	40.00	0.09	AB	8.000E-6	1	8.000E-6	8.100E-3	0.9301
20.00	27.56	100.00	0.135	AC	5.000E-7	1	5.000E-7	5.062E-4	0.9825
40.11	17.22	70.00	0.29	BC	1.201E-3	1	1.201E-3	1.22	0.2961
35.00	6.89	100.00	0.26	A^2	0.024	1	0.024	24.03	0.0006
27.50	17.22	19.55	0.09	B^2	0.010	1	0.010	10.20	0.0096
27.50	17.22	70.00	0.1	C^2	1.105E-3	1	1.105E-3	1.12	0.3150
27.50	0.16	70.00	0.06	Residual	9.877E-3	10	9.877E-4		
27.50	17.22	120.45	0.11	Lack of Fit	9.877E-3	5	1.975E-3		
35.00	27.56	100.00	0.27	Pure Error	0.000	5	0.000		
14.89	17.22	70.00	0.09	Cor Total	0.11	19			
27.50	34.61	70.00	0.24						

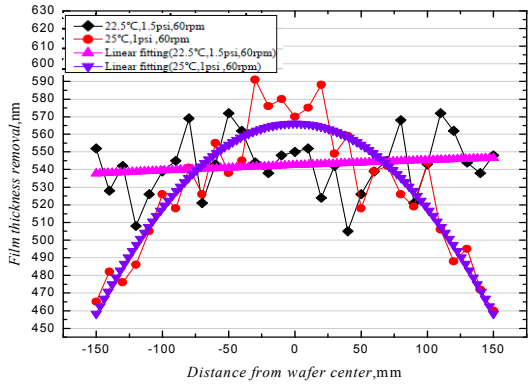


Fig.5 FT removal of each position on the wafer

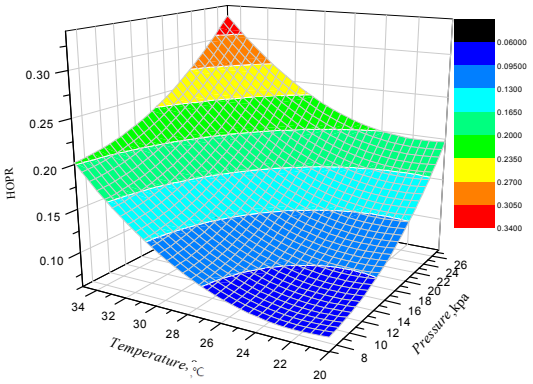


Fig.6 Response surface graph of A and B factors

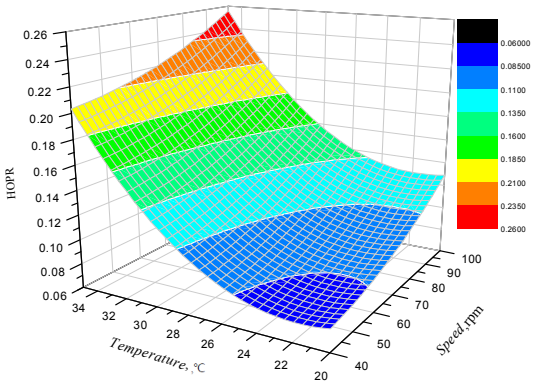


Fig.7 Response surface graph of A and C factors

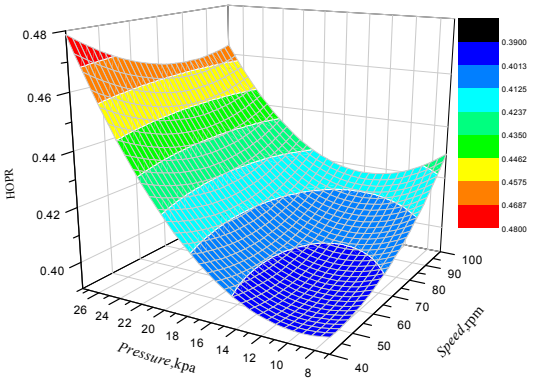


Fig.8 Response surface graph of B and C factors

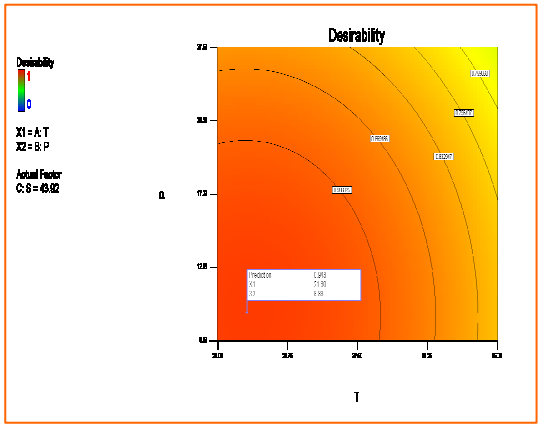


Fig.9 The fitting optimal value of desirability

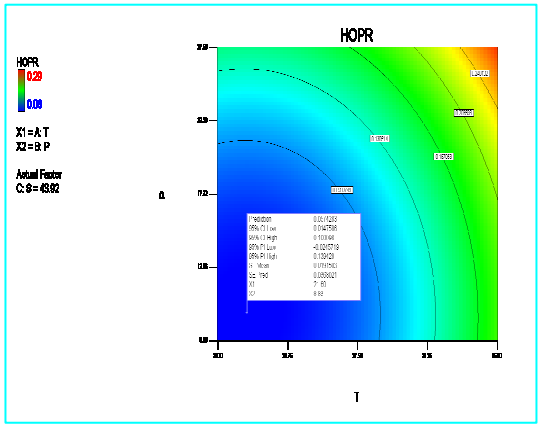


Fig.10 The fitting optimal value of HOPR

5 Conclusion

The fluid flow model in micro-channels is established. It indicate that the liquid viscosity is the main factor affecting the liquid mean velocity. Through the optimization of the CMP process parameters, it is finally concluded that: when the slurry temperature is 21.60℃, the working pressure is 8.83kpa, the system speed is 43.92rpm, the predicted minimum value of HOPR is 0.0574.

Reference

[1]Li Y,Liu Y L,Niu X H,Bu X F,Li H B,Tang J Y,Fan S Y.Application of a macromolecular chelating agent in chemical mechanical polishing of copper film under the condition of low pressure and low abrasive concentration[J].Journal of Semiconductors,2014,35(1)016001:1-5.

[2]Hu Y,Liu Y L,Liu X Y,Wang L R,He Y G.Effect of copper slurry on polishing characteristics[J].Journal of Semiconductors,2011,32(11)116001:1-5.

[3]Hu Y,Liu Y L,Liu X Y,He Y G,Wang L R,Zhang B G.Effect of alkaline slurry on the electric character of the pattern Cu wafer[J].Journal of Semiconductors,2011,32(7)076002:1-3.

[4]Zheng J P,Roy D.Electrochemical examination of surface films formed during chemical mechanical planarization of copper in acetic acid and dodecyl sulfate solutions[J].Thin Solid Films,2009,517(16):4587-4592.

[5]Wang S L,Yin K D,Li X,Yue H W,Liu Y L.Planarization mechanism of alkaline copper CMP slurry based on chemical mechanical kinetics[J].Journal of Semiconductors, 2013,34(8)086003:1-4.

[6]Yin K D,Wang S L,Liu Y L,Wang C W,Li X.Evaluation of planarization capability of copper slurry in the CMP process[J].Journal of Semiconductors, 2013,34(3)036002:1-4.

[7]Wang C W,Ma S H,Liu Y L,Chen R,Cao Y.CMP process optimization using alkaline bulk copper slurry on a 300mm Applied Materials Reflexion LK system[J].Journal of Semiconductors, 2013,34(12)126001:1-3.

Key Engineering Materials Vols 645-646 (2015) pp 469-473
Submitted: 2015-01-19
© (2015) Trans Tech Publications, Switzerland
Accepted: 2015-01-21
doi:10.4028/www.scientific.net/KEM.645-646.469

Discrimination of low-grade oil from edible oil by a microfluidic device

Mei Liu[1, 2, a *], Shuaijie Feng[1, b], Xinqun Shi[1, c], Yan Peng[1, d], Zhizheng Wu[1]

[1] The School of Mechatronics Engineering and Automation, Shanghai University 200072, China

[2] State Key Laboratory of Transducer Technology, Shanghai Institute of Microsystem and Information Technology, Chinese Academy of Sciences, Shanghai 200050 ,China

[a]mliu@shu.edu.cn [b]shfz4418259@163.com, [c]915868345@qq.com, [d]pengyan@shu.edu.cn

Keywords: Low-grade oil, edible oil, discrimination, microfluidic device

Abstract. Illegal cooked oil is a serious food safety issue in China, while an effective authentication method is still lacking. In this paper, a microfluidic device was applied for the discrimination of low-grade oil from edible oil, by creating water droplets of different sizes in different oils.

Introduction

Recycled cooking oil, or gutter oil, has emerged as a serious food safety issue that challenges government authorities and consumers in China. Gutter oil is refined from kitchen waste, gutters, sewer drains, and slaughterhouse waste, as well as oils that have been repeatedly used to fry foods. By a series of simple processes, including collection, preliminary filtration and boiling, refining, and the removal of adulterants, illegal gutter oil can be cleaned up enough to meet the sanitation standards of cooking oil and resold as a cheaper alternative to normal cooking oil, to make huge profits. It is even estimated that up to 1/10 of the edible oil consumed in China is gutter oil.

Because of the same major chemical compositions of gutter oil and normal cooking oil, and lacking of typical chemical markers with strong characteristics and high accuracy, it is extremely challenging to identify gutter oil. Till now numerous detection methods appear for gutter oil [1]: (1) sensory test, (2) physicochemical inspection, (3) instrumental methods. Sensory tests preliminarily estimate the oil by its color, transparency and odor, which are intuitive and fast, but limited and suffer from low precision. Traditional physicochemical inspections use the quantitative difference of feasible parameters between gutter oil and normal cooking oil to inspect, e.g., acid value, refractive index, peroxide number, iodine value, carbonyl value and polar components. In addition, researchers also explored the application of numerous analytical instruments for screening gutter oil, including chromatography, mass spectrometry [2], spectroscopic methodology [3], nuclear magnetic resonance spectroscopy [4-6], Raman spectroscopy [7], and so on, which usually distinguish gutter oil from normal oil based on specific components, characteristic peak, and characteristic spectrum.

In this paper a microfluidic device capable of generating monodispersed droplets was applied to distinguish low-grade oil from edible oil, which is easy to use, portable and economic, and only consumes little sample oil.

Concepts and principles

Droplet formation, which provides an appealing way to produce emulsions with excellent uniformity, could be studied in various microgeometries, such as microchannel arrays, T-sections, hydrodynamic focusing, and concentric injection. In this paper it is studied in a symmetric microfluidic hydrodynamic focusing device, which consists of four microchannels with identical heights.

Hydrodynamic focusing is a common phenomenon that when one fluid flows into another immiscible fluid at certain flow rates, an instability would occur that the inner fluid was split by the

outer one, forming dispersed droplets, which is usually used for the production of micro-droplets [8], bubbles [9] and microparticles [10].

In this study, hydrodynamic focusing is applied to generate water droplets in different oils. According to previous research, sizes of the droplets will depend on the width of microchannel, the flow rates, the geometry, and the property of the oil and water. So with the other conditions remain constant, the difference in sizes of the droplet will reflect the difference in properties of the oil, which could be able to distinguish low-grade oil.

Experimental procedures

A. Materials and devices

Three types of oil are used in experiment, as shown in Figure 1(a). Oil A, the edible oil, is bought at the supermarket (Jinlongyu rapeseed oil), which is dark yellow compared with the others. Oil C is bought at a street stall, which is very cheap and almost colorless-apparently a type of low-grade oil. Oil B, also a type of low-grade oil, is the mixture of Oil A and Oil C (0.5:0.5), which is light yellow. Oil B must be shaken by a vortex mixer for 5min for thorough mixing of the two types of oil.

The microfluidic devices were fabricated using poly(dimethyl)siloxane (PDMS) and a silicon wafer by soft lithography. Briefly, a glass mask was designed and fabricated. The master structures of 29μm high SU-8 photoresist were prepared by mask photolithography on a silicon wafer. A mixture of PDMS prepolymer and curing agent (Sylgard 184, Dow Corning) was poured on the positive master structure on the wafer. After heat curing, the negative PDMS relief was peeled off. Holes were punched at the center of the reservoir areas and the relief was sealed onto a silicon wafer to form a closed channel, as shown in Figure 1(b).

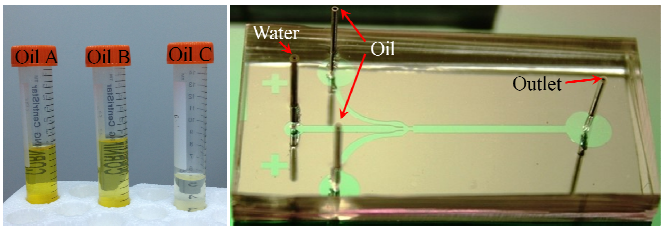


Figure 1 (a) Three different oil samples; (b) The microfluidic device.

B. Establishment of the experimental system

The microfluidic device was connected to the oil and water sources on syringe pumps by plastic tubing. The microscope, video camera and computer recorded the experimental process when it reached stable, as shown in Figure 2.

C. Experimental process

In this experiment, oil was used as the continuous phase, while deionized water was used as the dispersed phase. Oil was injected into the two sheath flow inlets, and deionized water was injected into the middle sample inlet. Each sheath flow was set as 0.2mL/h, while the water flow was adjusted from 0.05mL/h to 0.4mL/h. After each adjustment step, the flow is allowed 3min to get stable before taking images.

Three types of oil were in turn injected into the microfluidic chip with water. Based on the above conditions, and with the combining effect of inner viscous forces and interfacial tensions between water and oil, the water flow will go through the cap displacement, cap squeezing, pinching, tail stretching and completely breaking up process[11], and be split into dispersed droplets by the continuous oil phase, as shown in Figure 3.

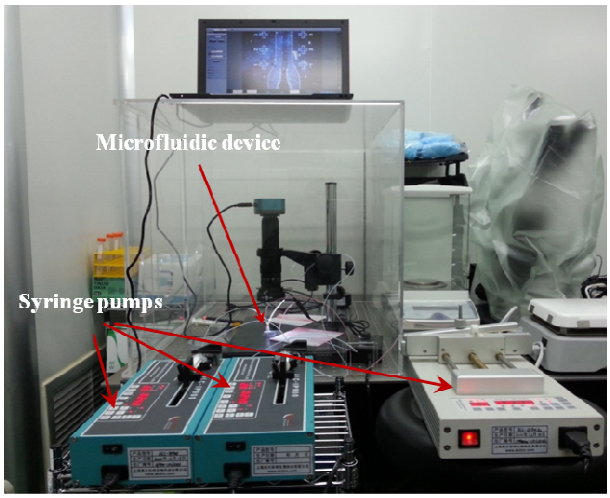


Figure 2 The experimental system

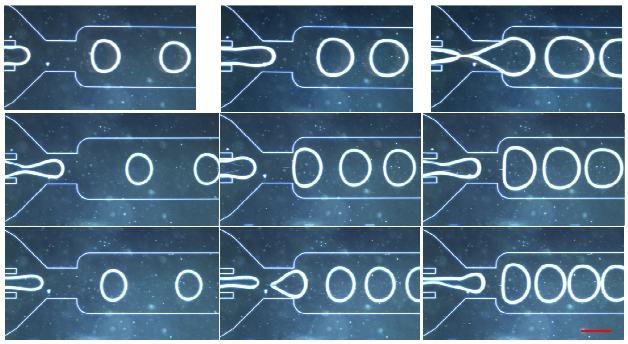


Figure 3. The water-in-oil droplets formed on different conditions. The scale bar in the figure is 0.5mm. (a) The continuous phase is Oil A; (b) The continuous phase is Oil B; (c) The continuous phase is Oil C. The flow rate of oil is set as 0.2mL/h, the flow rates of water are: 0.05mL/h, 0.2mL/h, 0.4mL/h from left to right.

Discussions

A. Formation of water-in-oil droplets

A wide range of instabilities would arise when streams of immiscible fluids get in touch. The various dynamic instabilities depend on the thermodynamic properties of the fluids, the driving stresses, and the flow geometries. In our case, the surface tensions drive an interfacial instability, ultimately overcoming viscosity to cause the water thread to break up into droplets. The size of the droplet strongly depends on the geometry of the microchannel, the flow rates, and viscosity of the oil and water.

One of the advantages of this approach is that, it does not need surface treatment on the microchannel walls, i.e., the microfluidic device could be used as fabricated. And it could be reused as long as it is cleaned before each step and remains intact.

B. Discrimination of oil by droplet sizes

As seen in Figure 3, the oil flow rate is constant, as the water flow rate increases, the droplet will become larger in dimensions, and its distribution density will increase as well. As the sheath flow changes from oil A to oil C, the size of the droplet will also be different. The relationship between the normalized size of the droplet and the flow ratio of water to oil was summarized in Figure 4, where the normalized size of the droplet is the ratio of the size of the droplet to the width of the enveloping microchannel (1mm); the size of the droplet is the average of the length and width of the rightmost droplet in each figure. It is defined this way because the droplets did not evolve into a perfect round shape throughout the imaging zone.

From Figure 4 it can be seen that, the droplet will enlarge as the flow rate ratio of water to oil increases; and with the same flow rates, as the oil is different, the dispersed droplet size will also be distinctly different. Computation results implicate that the difference of droplet sizes for Oil A and

Oil C of the same flow condition could be up to 30%, which means, the microfluidic droplet-generating approach could be a feasible way to distinguish different oil.

Setting Oil A as a reference, Oil B and Oil C could be distinguished. However, a quantitative standard is required, the resolution, linear characteristic, reliability of this approach needs to be identified. What is more, the compositions and sources of oil are very complex and variable, our current work only covers two types of common oil. Further work needs to be done to testify this approach for widespread oil discrimination.

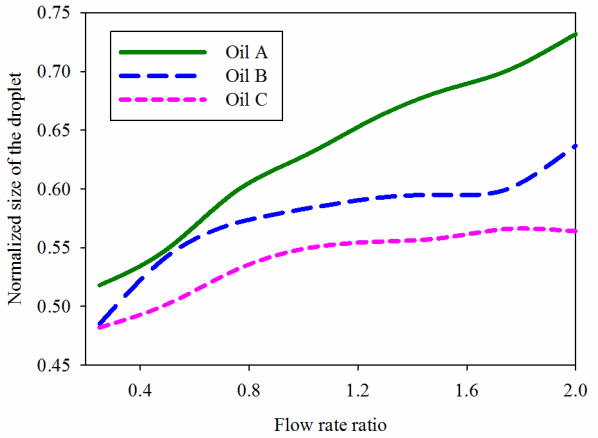


Figure 4 Normalized size of the water droplet vs. the flow rate ratio of water to oil.

C. Selection of flow model and rates

The syringe pumps used in the experiment are mechanical pumps, which often suffer from pulsatile flow, i.e., the flow is not smooth, and changes abruptly, which will in turn cause the droplets to suddenly enlarge or shrink. In the contrary, the microfluidic device will burst if the flow rate is too high. Combining those concerns, the oil flow rate is set as 0.2mL/h (Its minimal programmable flow rate is 0.025mL/h).

For the same reason, water-in-oil mode was selected rather than oil-in-water mode, since the latter one requires a quite high flow rate to happen.

Conclusion

A microfluidic hydrodynamic focusing device was implemented to generate water-in-oil droplets, and by the sizes of the droplets, oil of different grades could be distinguished. Completely different with common spectroscopy methods, this approach is beneficial since it is economic and could be portable and disposable. Future work could be the establishment of reference standards for special type of oil.

Acknowledgement

Research was supported by the National Natural Science Foundation of China (No. 51205245), SRF for ROCS, SEM, the Joint Specialized Research Fund for the Doctoral Program of Higher Education, and Innovation Program of Shanghai Municipal Education Commission (No. 12YZ022).

References

[1] H. Y. Lu, X. Wang, T. T. Zhao, and B. L. Liu, "Research progress on the common detection methods and LF-NMR of illegal cooked oil," *J. of Food Safety and Quality,* vol. 4, no. 5, pp. 1428-1436, 2013.

[2] L. Vaclavik, T. Cajka, V. Hrbek, and J. Hajslova, "Ambient mass spectrometry employing direct analysis in real time (DART) ion source for olive oil quality and authenticity assessment," *Anal. Chim. Acta,* vol. 645, pp. 56-63, 2009.

[3] H. Y. Xu, L. Cheng, D. F. Wang, S. Q. Zeng, Y. C. Xu and Z. P. Yin, "Discerning of swill-cooked dirty oil by FTIR with heating headspace," *China Oils and Fats,* vol. 38, no.6, pp. 64-66, 2013.

[4] R. Shi, X. Wang, B. L. Liu, T. T. Zhao, H. Y. Lu and P. Q. Yang, "Determination of Oil Quality by LF-NMR: Optimization of Measurement Parameters," *J. of Instru. Anal.,* vol. 31, no.11, pp. 1365-1372, 2012.

[5] P. Dais and E. Hatzakis, "Quality assessment and authentication of virgin olive oil by NMR spectroscopy: A critical review," *Anal. Chim. Acta,* vol. 765, pp. 1-27, 2013.

[6] D. I. Ellis, V. L. Brewster, W. B. Dunn, J. W. Allwood, A. P. Golovanov, and R. Goodacre, "Fingerprinting food: current technologies for the detection of food adulteration and contamination," *Chem. Soc. Rev.,* vol. 41, pp. 5706-5727, 2012.

[7] S. F. Graham, S. A. Haughey, R. M. Ervin, E. Cancouet, S. Bell, and C. T. Elliott, "The application of near-infrared (NIR) and Raman spectroscopy to detect adulteration of oil used in animal feed production," *Food Chem.,* vol. 132, pp. 1614-1619, 2012.

[8] C. Yeh and Y. Lin, "Use of an adjustable microfluidic droplet generator to produce uniform emulsions with different concentrations," *J. of Micromech. Microeng.,* vol. 23, no.12, pp. 125025, 2013.

[9] P. Garstecki, I. Gitlin, W. DiLuzio, G. M. Whitesides, E. Kumacheva, and H. A. Stone, "Formation of monodisperse bubbles in a microfluidic flow-focusing device," *Appl. Phys. Lett.,* vol. 85, no.13, pp. 2649-2651, 2004.

[10] L. Martin-Banderas, M. Flores-Mosquera, P. Riesco-Chueca, A. Rodriguez-Gil, A. Cebolla, S. Chavez, and A. M. Ganan-Calvo, "Flow focusing: A versatile technology to produce size-controlled and specific-morphology microparticles," *SMALL,* vol. 1, no.7, pp. 688-692, 2005.

[11] T. Cubaud and T. G. Mason, "Capillary threads and viscous droplets in square microchannels," *Phys. Fluids,* vol. 20, no.5, pp. 053302, 2008.

Key Engineering Materials Vols 645-646 (2015) pp 474-479
© (2015) Trans Tech Publications, Switzerland
doi:10.4028/www.scientific.net/KEM.645-646.474

Submitted: 2014-11-03
Accepted: 2014-12-23

Effect of Elliptical Dimples on Hydrodynamic Lubrication

Jinghu Ji [1,a], Hao Wang[1,2,b] and Yonghong Fu[1,c]

[1]School of Mechanical Engineering, Jiangsu University, Zhenjiang, Jiangsu Province, China

[2]Intellectual Property Research Center of Jiangsu Province, Jiangsu University, Zhenjiang, Jiangsu Province, China

[a]jijinghu@ujs.edu.cn (corresponding author), [b]wanghaozl@126.com, [c]fyh@ujs.edu.cn,

Keywords: hydrodynamic lubrication, surface texturing, elliptical dimple, slender ratio, inclination angle

Abstract. This paper develops an analytical model to investigate the effect of elliptical dimples on hydrodynamic lubrication of surface contact. The hydrodynamic pressure generated by elliptical dimples is solved by the multi-grid method. The evaluation criterion of hydrodynamic effect of dimensionless average pressure is calculated and presented with the variation of elliptical dimple depth, area density, slender ratio and inclination angle. The results indicate that geometrical parameters of elliptical dimples have an obvious influence on the hydrodynamic pressure. The hydrodynamic lubrication performance can be ameliorated by optimizing the geometrical parameters of elliptical dimples according to the operating parameters of the mechanical components.

Introduction

It has been proved that surface texturing can improve tribological performance in mechanical components. [1]. Theoretical and experimental studies have indicated that the geometrical parameters of textures are the most important factors to optimize texturing benefits [2,3]. Therefore, it is of great importance to optimize the design of the surface texture and gain the best surface texture [4]. Yu et al. examined the effect of different geometric structures of dimples on the hydrodynamic lubrication [5]. It was found that the dimple shape, orientation and size affect the hydrodynamic lubrication significantly. Unfortunately, researchers only took the interaction between adjacent dimples along the movement direction with a single cell dimple as the research object, but failed to take the interaction perpendicular to the movement direction into consideration. Therefore, this paper is to investigate the effect of elliptical dimples on hydrodynamic lubrication. Special attention is paid to the orientation angle and major axis radius over minor axis radius ratio of elliptical dimples. Besides, the end effects of parallel and normal to the sliding direction are discussed.

Analytical Model

A schematic description of a surface contacting model is displayed in Fig. 1 and Fig. 2. The lower slider is fixed and fabricated with elliptical dimples, and the upper slider is smooth and moves with a relative speed of U and a clearance of h_0 to the lower slider. Here l_x is the slider length, and l_y is the width of slider. The dimples are evenly distributed on the surface with an area density S_p. Each dimple with major axis radius a, minor axis radius b, depth h_p, and inclination angle θ, is located in the imaginary rectangular cell of sides $2r_1 \times 2r_1$, as shown in Fig. 2b, where

$$r_1 = \frac{1}{2}\sqrt{\pi ab / S_p} \tag{1}$$

The slender ratio of the dimple, representing major axis radius over minor axis radius ratio, is defined as follows

$$\gamma = a/b \tag{2}$$

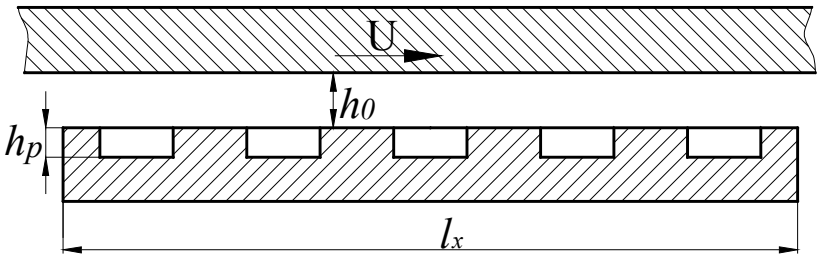
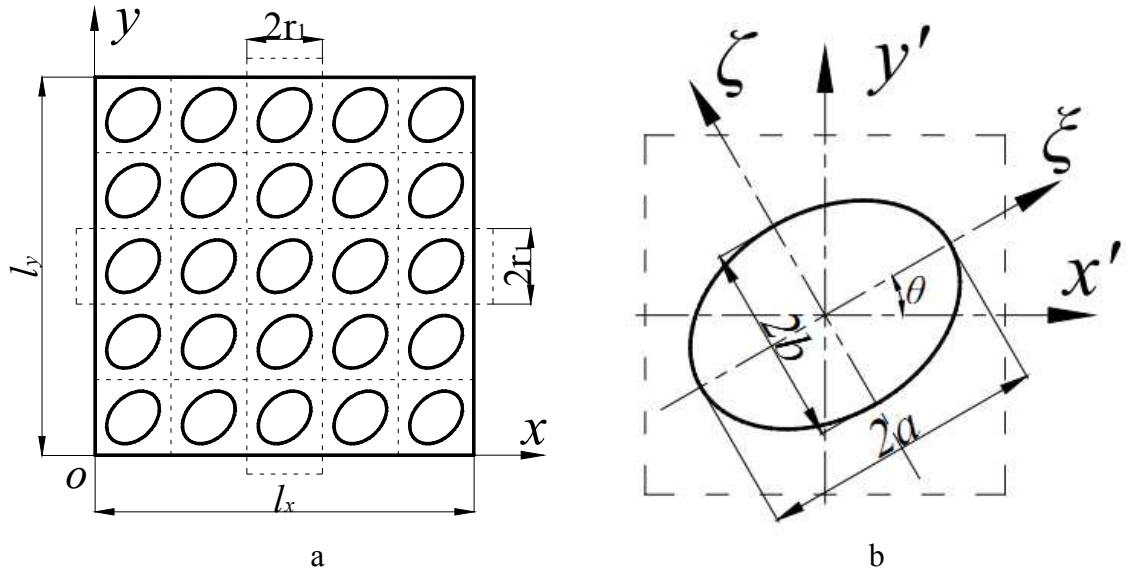


Fig. 1 Schematic of a textured slider.



a b

Fig. 2 A geometrical model of a textured surface: a. dimples distribution and b. individual cell with a single dimple.

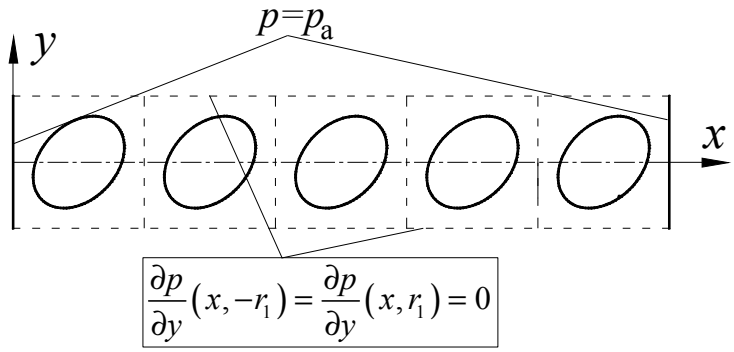


Fig. 3 Longitudinal dimples column with its system of coordinates and boundary conditions.

Assuming the length and width of slider surfaces are sufficient, the end effects can be neglected. Therefore, it is sufficient to consider a longitudinal dimples column with a period equal to the imaginary cell size $2r_1$, as shown in Fig.3. The hydrodynamic pressure distribution over a single dimple column is obtained from the dimensionless Reynolds equation

$$\frac{\partial}{\partial X}\left(H^3\frac{\partial P}{\partial X}\right)+\frac{\partial}{\partial Y}\left(H^3\frac{\partial P}{\partial Y}\right)=\Lambda\frac{\partial H}{\partial X} \tag{3}$$

where the dimensionless parameters are:

$$P=\frac{p-p_a}{p_a},\ x=\frac{x}{r_p},\ y=\frac{y}{r_p},\ H=\frac{h}{h_0},\ X'=\frac{x'}{r_p},\ Y'=\frac{y'}{r_p},\ \bar{\xi}=\frac{\xi}{r_p},\ \bar{\zeta}=\frac{\zeta}{r_p}. \tag{4}$$

where x' and y' are local coordinates with their origin at the center of a single dimple cell, $\Lambda=6U\eta r_p/h_0^2 p_a$, $r_p=\sqrt{ab}$ in the case of circular dimple when $\gamma=1$, p_a is the ambient pressure.

The transformation from $\left(\bar{\xi},\bar{\zeta}\right)$ to (X',Y') is given by

$$\begin{aligned}\bar{\xi} &= X'\cos\theta + Y'\sin\theta \\ \bar{\zeta} &= Y'\cos\theta - X'\sin\theta\end{aligned} \tag{5}$$

And the dimensionless film thickness at a specific point of the textured surface can be given by

$$H(X,Y) = \begin{cases} 1, & \dfrac{\bar{\xi}^2}{A^2} + \dfrac{\bar{\zeta}^2}{B^2} > 1 \\ 1+\delta, & \dfrac{\bar{\xi}^2}{A^2} + \dfrac{\bar{\zeta}^2}{B^2} \le 1 \end{cases} \tag{6}$$

where δ is the dimensionless dimple depth, $\delta = h_p/h_0$; A and B are the dimensionless major and minor axis radius, and $A = a/r_p$, $B = b/r_p$, respectively.

The Reynolds equation with its appropriate boundary conditions is solved by a multi-grid method using a uniform grid in the computational field. More detailed discussions regarding this issue are included in Ji et al. [3].

Results and Discussions

This paper mainly aims at the geometric parameters of elliptical dimple effect on hydrodynamic lubrication. Therefore, the dimples used in this paper have the same areas, s = πab. The pressure distribution is computed under the conditions given in Table1.

Table1 Conditions assumed in hydrodynamic lubrication analysis of surface contact

Nomenclature	Value	Units
r_p	50×10^{-6}	m
s	7.854×10^{-9}	m^2
U	5	m/s
η	0.03	$N\cdot s/m^2$
p_a	1.013×10^5	N/m^2
h_0	5×10^{-6}	m

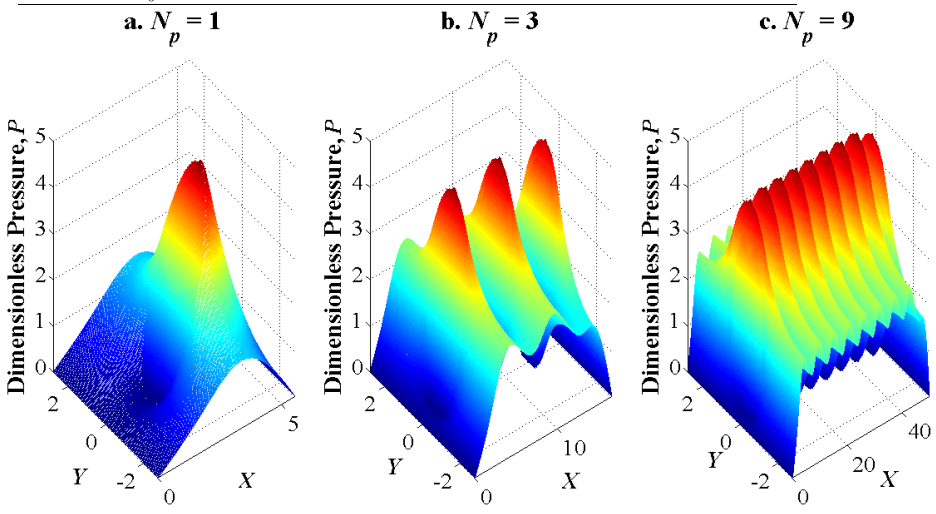


Fig. 4 Dimensionless pressure over a longitudinal dimples column (S_p = 0.10, δ = 1, γ = 1).

Fig.4 shows dimensionless pressure distributions over a longitudinal dimples column with a different number of dimples. As can be seen, the effect of two ends on the pressure distribution decreases with the increasing number of dimples. That proves the interaction between neighboring dimples parallel and perpendicular to the sliding direction has significant effect on the pressure distribution.

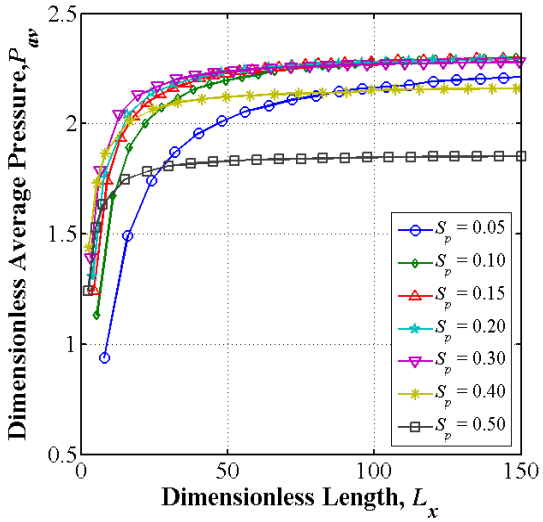


Fig. 5 Dimensionless average pressure, P_{av}, vs. dimensionless slider length, L_x. ($\delta = 1$, $\gamma = 1$).

According to Eq. (1) and the relation $L = 2R_1 \cdot N_p$, it can be concluded that the number of dimples at a given L increases with S_p. Hence, the range affected by the ends effect in hydrodynamic lubrication may be a reasonable analysis by the length of a dimples column. Fig. 5 presents the effect of the dimensionless slider length, L_x, on the dimensionless average pressure. The results in Fig. 5 are presented for a wide range of S_p values. The dimensionless average pressure increases sharply with increasing length when L_x is shorter. However, the rate of increase of P_{av} diminishes with increasing L_x. As can be seen, the dimensionless average pressure is not sensitive to variations in L_x in the range of $L_x > 50$. Therefore, it is recommended to analyze the effect of surface texturing on hydrodynamic lubrication with dimensionless length of 50 in the following analysis.

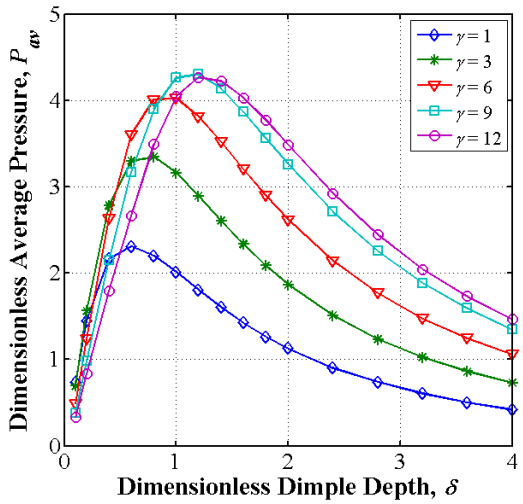


Fig. 6 Dimensionless average pressure, P_{av}, vs. dimensionless dimple depth, δ ($S_p = 0.05$, $\gamma = 1$, $\theta = 0$).

The effect of the dimensionless dimple depth on the dimensionless average pressure, P_{av}, is presented in Fig. 6 for several values of slender ratio, γ. It can be seen from Fig. 6 that there is an optimum value for dimple depth to maximize the average pressure at any given slender ratio. The optimum value of dimple depth ranges from about 0.5 to 1.2 as γ ranges from 1 to 12.

To reveal the effect of slender ratio of elliptical dimples on hydrodynamic lubrication, in Fig. 7, θ is set as 0 and the dimensionless average pressure is set at a wide range of slender ratio, γ, for different values of area density. It is noted that there exists an optimum slender ratio to maximize the hydrodynamic effect at any given value of S_p. The value of optimum slender ratio increases with decreasing area density. When the major axis radius increases in the sliding direction, the flow distance of fluid in the dimples becomes longer, which makes the fluid cumulative effect stronger. In the mean time, the convergence in the sides of the dimples to direct flows towards the region of high hydrodynamic effect and it increases hydrodynamic pressure correspondingly.

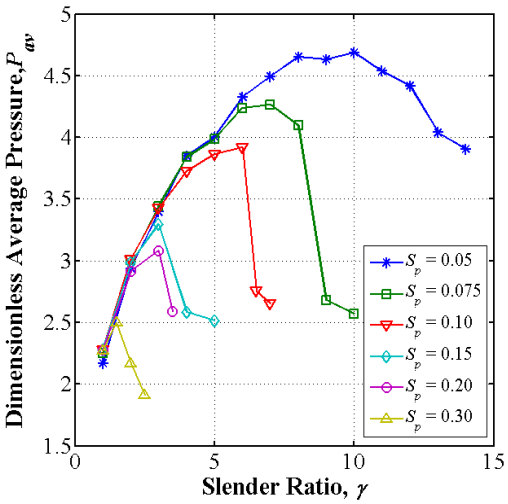


Fig. 7 Dimensionless average pressure, P_{av}, vs. slender ratio, γ, for various area density, S_p ($\theta = 0$ and $\delta = 1$).

Fig. 8 presents the effect of inclination angle at various slender ratio values on the dimensionless average pressure, P_{av}. It can be seen that inclination angle has significant effect on hydrodynamic lubrication. The dimensionless average pressure decreases monotonically with increasing inclination angle. It can also be seen that the influence of slender ratio on the dimensionless average pressure diminishes with increasing inclination angle. That may be caused by the fact the flow distance of fluid in the dimples becomes shorter as the inclination angle increases.

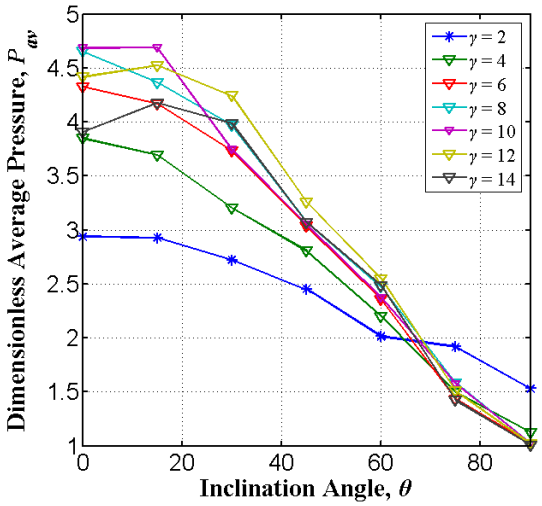


Fig.8 Dimensionless average pressure, P_{av}, vs. inclination angle, θ, for various slender ratio, γ (S_p = 0.05).

Conclusion

A theoretical model is developed to explore the effect of elliptical dimples on hydrodynamic lubrication of surface contact. Elliptical dimples with a wide range of slender ratios and inclination angles are analyzed and the dimensionless average pressure is calculated as a function of the main evaluation criterion. It is indicated that the interaction between adjacent dimples should be considered in parallel or perpendicular to the sliding direction. It is also indicated that both the slender ratio and orientation of ellipse dimples have significant effect on the average pressure. There is an optimum value of slender ratio, at any given area density, to maximize the hydrodynamic effect. The dimensionless average pressure decreases monotonically with increasing inclination angle. Besides, the effect of dimple depth is very significant and there exists an optimum value of dimple depth at any given slender ratio.

Acknowledgement

This paper was financially supported by the National Natural Science Foundation of China (51175233, 51305168), the Natural Science Foundation of Jiangsu Province (BK20130524) and the Research Foundation for Advanced Talents of Jiangsu University (13JDG090).

References

[1] W.J. Zhao, L.P. Wang, Q.J. Xue, Development and research progress of surface texturing on improving tribological performance of surface, Tribology, 30(2011) 622-631.

[2] H.L. Costa, I.M. Hutchings, Hydrodynamic lubrication of textured steel surfaces under reciprocating sliding conditions, Tribology International, 40(2007) 1227-1238.

[3] J.H. J, Y.H. Fu, Q.S. Bi, The influence of partially textured slider with orientation ellipse dimples on the behavior of hydrodynamic lubrication. Industrial Lubrication and Tribology, 66(2014) 161-167.

[4] D. Zhu, T. Nanbu, N. Ren, Yasuda, Q.J. Wang, Model-based virtual surface texturing for concentrated conformal-contact lubrication, J. Engineering Tribology, 224(2010) 685-696.

[5] H.W. Yu, X.L. Wang, F. Zhou, Geometrical shape effects of surface texture on the generation of hydrodynamic pressure between conformal contacting surfaces, Tribology Letters, 37(2010) 123-130.

CHAPTER 3:

Measurements, Sensors and MEMS

Key Engineering Materials Vols 645-646 (2015) pp 483-487
© (2015) Trans Tech Publications, Switzerland
doi:10.4028/www.scientific.net/KEM.645-646.483

Submitted: 2014-10-28
Accepted: 2014-11-13

Study of Bandwidth Expansion Based on Electrochemical Vibration Sensor

Zhengyu Zhang[1, a], Junbo Wang[1, b *], Deyong Chen[1, c], Yinan Li[1, d]

[1]State Key Laboratory of Transducer Technology, Institute of Electronics, University of Chinese Academy of Sciences, No. 19 Beisihuanxi Road, Beijing, China

[a]zzyib163@163.com, [b]jbwang@mail.ie.ac.cn, [c]dychen@mail.ie.ac.cn, [d]yzngb@163.com

Keywords: Bandwidth expansion, electrochemical vibration sensor, MEMS, frequency compensation.

Abstract. A vibration sensor based on electrochemical principle can be widely used in the field of seismology. For its instinctive bandwidth is limited, compensation by circuit is essential to expand the bandwidth. This article presents a method of frequency compensation by circuit based on the original amplitude-frequency characteristic of the electrochemical vibration sensor. The bandwidth is broadened obviously from 2s-10Hz to 25s-20Hz. The noise performance of the final output compared to the CME6011 is also presented.

Introduction

Vibration sensors based on electrochemistry have found wide application in the field of seismology, due to its wide-band and low-noise [1]. Instead of a solid inertial proof mass mostly used in conventional vibration sensors, the electrochemical vibration sensor uses a liquid proof mass combined with elastic membranes as inertial mass [2], which results in low mechanical noise, making it have a high signal to noise ratio. Recording low-frequency seismic signals correctly is crucial in seismology and it happens to correspond to the characteristics of the electrochemical vibration sensor, which is preferred at low frequency. Besides, extremely low power consumptions and the simplicity of the circuitry involved are also their special advantages.

The research on vibration sensors based on electrochemical began in 1960s and R. M. Hurd et al. introduced the basic principles of the electrochemical approach [3]. V. A. Kozlov et al. proposed a completed structure of convective accelerometer [4], which had bad performances in consistency resulted from that net-weaving fabrication methods could not properly align the electrode and spacer layers in their fabrication methodology.

MEMS based approaches were proposed to deal with the problem of consistency and the results were satisfying. Different structures of sensing element in the vibration sensors were presented by our group. Guangbei Li et al. introduced symmetric interdigital electrodes and the anodes and cathodes are coplanar [5], which solved the misalignment problem, but its low sensitivity were unsatisfied. Wentao He et al. proposed a structure that electrodes with square pores and spacers being stacked together, which results in high sensitivity and good consistency [6], but the noise of the sensor and the possibility of extending band width through the circuit has not been studied on so far.

In the field of seismology, the width of band and the level of noise directly matters with the application of the vibration sensor. Therefore, the problem of investigating and reducing the vibration sensor's self-noise and the possibility of extending bandwidth by circuit's frequency compensation is of current interest. In this study, the circuit was designed to broaden the bandwidth by means of compensating the output of sensor and the experimental results verifies the comparable performance.

Structure and Principle

The electrochemical vibration sensor's core component is diagramed by Fig 1. Similar to the previous studies [7], the core component comprises four electrodes which is configured as anode-cathode-cathode-anode (ACCA) and separated by silicon dioxide dielectric spacers. The core

component is located in a plexiglass tube filled with a concentrated electrolyte solution and sealed by elastic membranes. Usually the iodine-iodide electrolyte is used. A small potential drop (0.3V) is applied to the electrodes and reversible electrochemical reactions occur at the anodes and the cathodes are and , respectively [8]. When an external velocity pointing to the right is applied to the sensor, an inertial driving force pointing to the left makes the electrolyte move to the left along the channel. Correspondingly, the ions move to one place to another, resulting in a change of ion concentration around each electrode, hence producing a voltage output after current-voltage conversion and differential circuit.

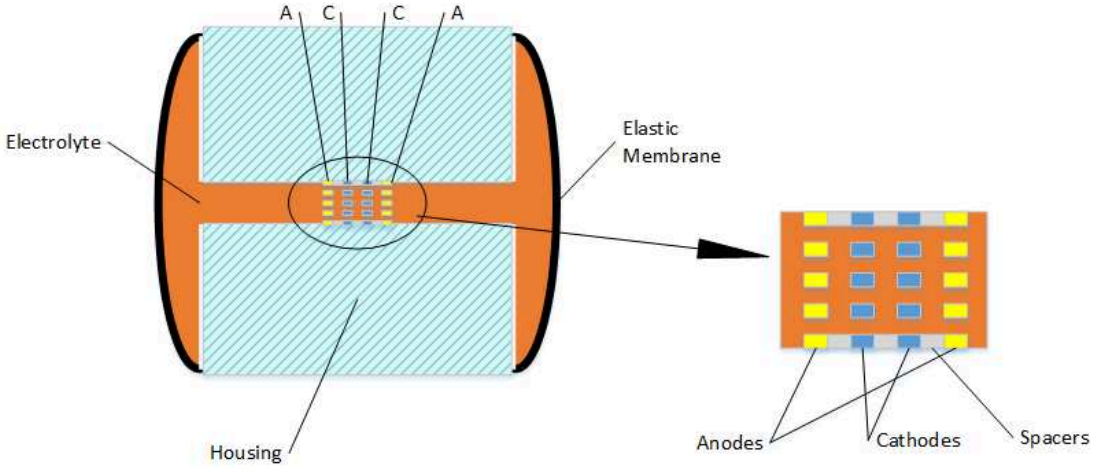


Fig 1. Schematic of the electrochemical vibration sensor

Frequency Compensation to Extend the Bandwidth

The amplitude-frequency characteristic of the electrochemical vibration sensor's original output is diagramed by Fig 2. The curve of amplitude-frequency does not have a flat section so that the bandwidth of 3dB is limited to 2s-10Hz. The bandwidth can be extended by circuit mainly consists of operational amplifier and the block diagram of signal-processing circuit is shown in Fig 3. The core component of the circuit is the frequency compensation module, which is the key of the bandwidth expansion. The circuit of frequency compensation module is detailed in Fig 4.

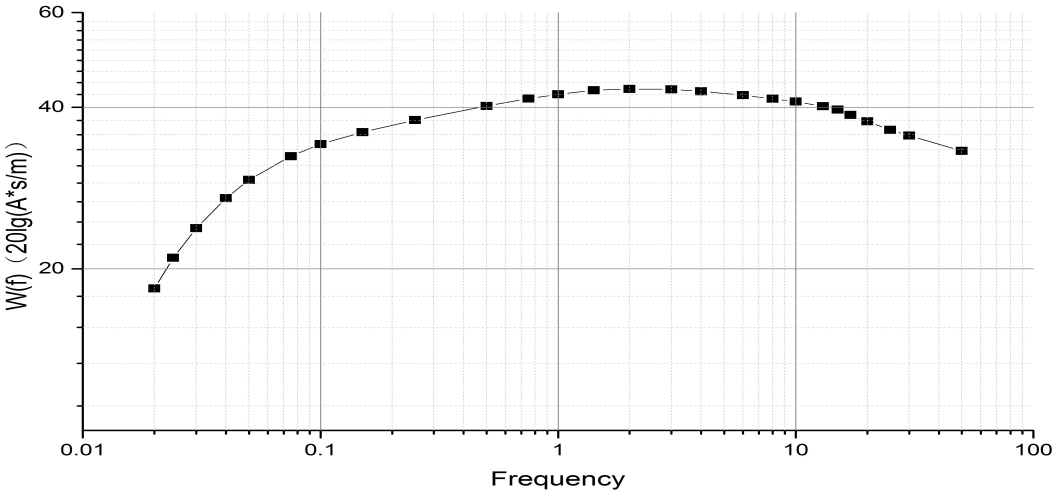


Fig 2. The amplitude-frequency characteristic of the electrochemical vibration sensor's original output

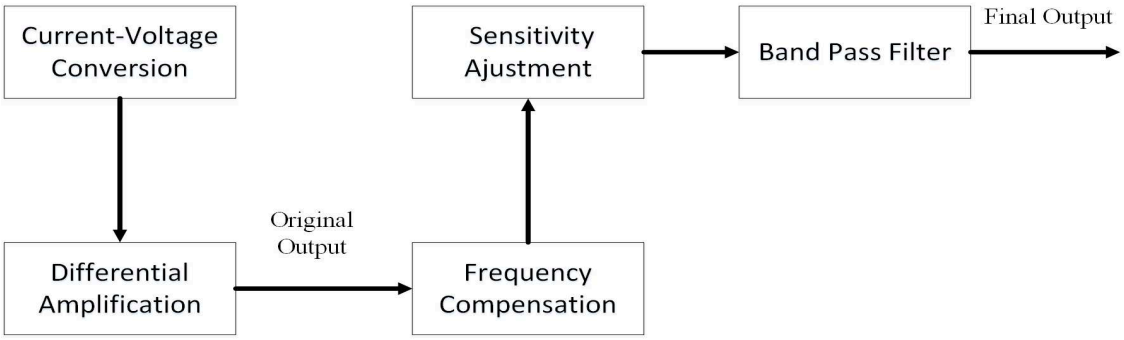


Fig 3. The block diagram of signal-processing circuit

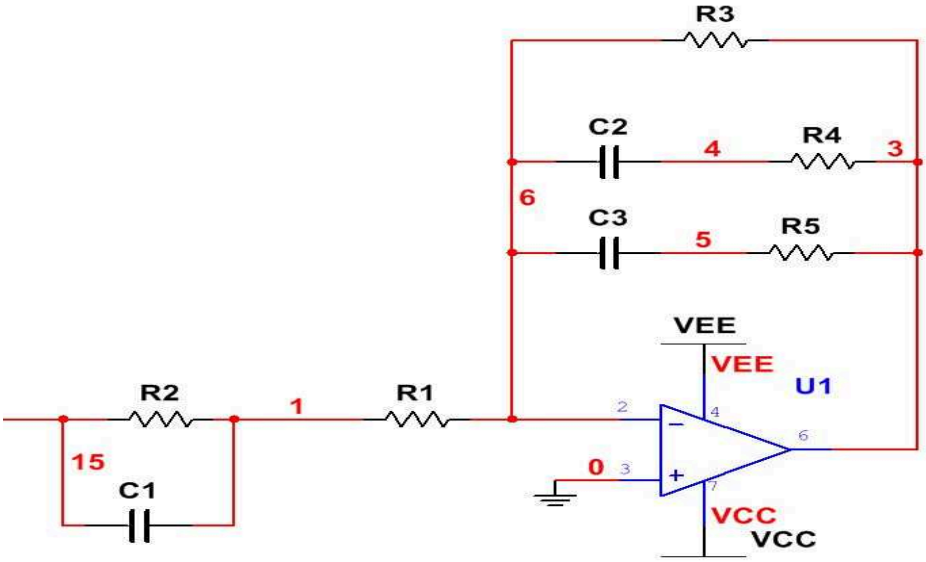


Fig 4. The circuit of frequency compensation module

Manipulated by the frequency compensation, the sensitivity adjustment and the band-pass filter, the original output is changed into the final output and its amplitude-frequency characteristic is shown in Fig 5. The final output's bandwidth of 3dB is 25s-20Hz, which is obviously broader than the original output's bandwidth: 2s-10Hz.

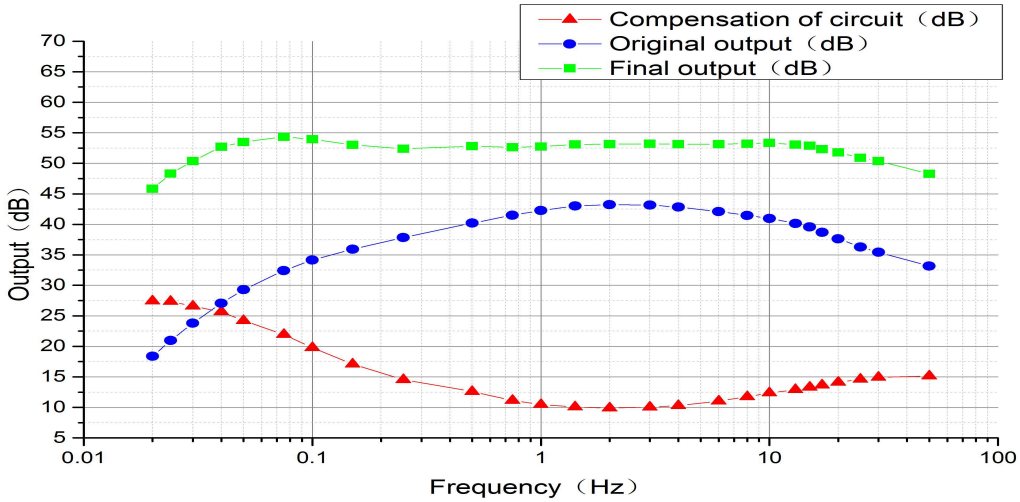


Fig 5. The electrochemical sensor's original output and final output

Noise Testing of the Sensor

Fig 6 shows the measured noise spectrum from our electrochemical vibration's original output and final output which is measured in the laboratory at 2:00am. It can be seen that the noise of the final output is inevitably elevated in the low-frequency section as the result of compensation of circuit in order to make the curve of amplitude-frequency characteristic flat, but the amount of elevation is

acceptable. Besides, the high-frequency section of the final output is brought down in comparison with the original output.

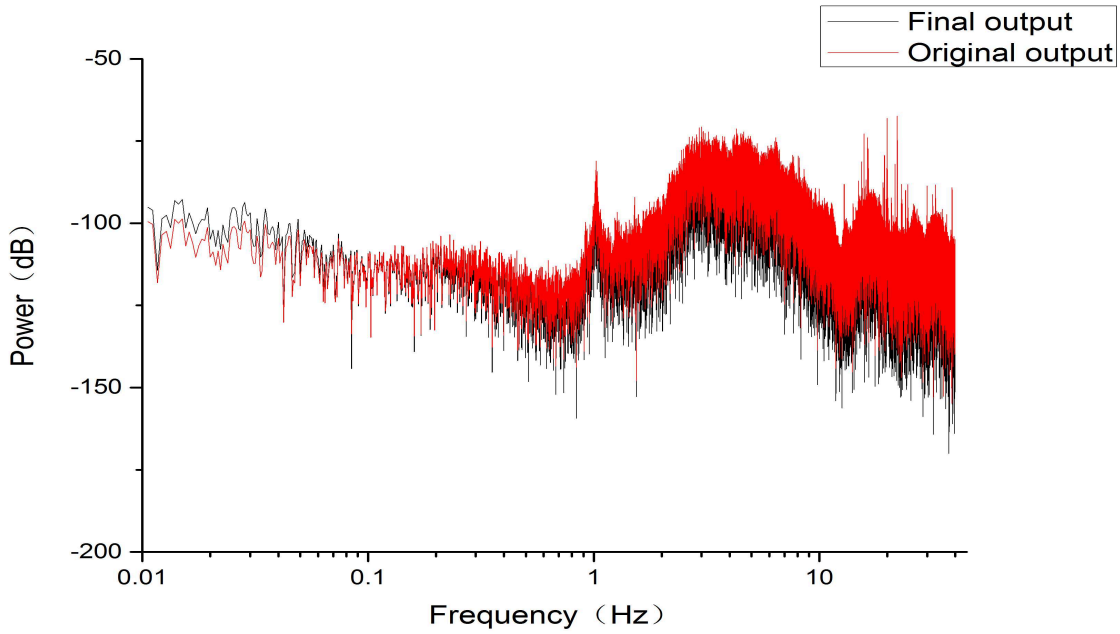


Fig 6. The measured noise spectrum from our electrochemical vibration's original output and final output

Fig 7 shows the measured noise spectrum from our electrochemical vibration sensor's final output in comparison with a commercial broadband vibration sensor CME6011 which is measured in the laboratory at 2:00am. The noise performance of our sensor is very similar with the CME6011 up to periods of 25s. The noise of our electrochemical vibration sensor's final output is lower than that of the CME6011 when the frequency is above 0.15Hz.

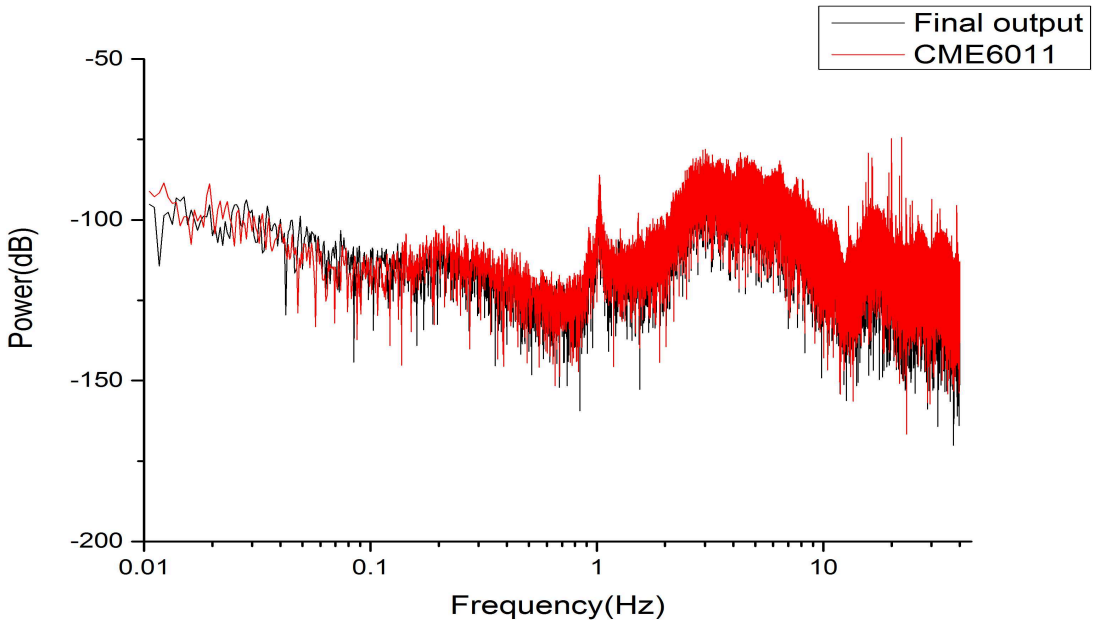


Figure 7. Noise spectrum of our vibration sensor in comparison with CME6011

Summary

Through compensation circuit, the final output of the electrochemical vibration sensor has obviously broader bandwidth (25s-20Hz) than the original output (2s-10Hz). The noise of final output compared

with CME6011 is measured and the noise of our electrochemical vibration sensor's final output is lower than that of the CME6011 when the frequency is above 0.15Hz.

References

[1] Abramovich, I., et al., Development of seismic sensors based on novel technological principles (molecular electronics), Seism. 1999, Prib.

[2] Levchenko, D., et al., Experience in seismic signal recording using broadband electrochemical seismic sensors. Seismic Instruments, 2010. 46(3): p. 250-264.

[3] Hurd, R. and W. Jordan Jr, The principles of the solion. Platinum Metals Review, 1960. 4(2): p. 42-47.

[4] Agafonov, V.M. and V.A. Kozlov, Convective accelerometer. 2009, Google Patents.

[5] Li, G.B., et al., Micro-machined electrochemical seismic sensors with interdigital electrodes. Key Engineering Materials, 2012. 503: p. 61-66.

[6] He, W.T., et al., Low frequency electrochemical accelerometer with low noise based on MEMS. Key Engineering Materials, 2012. 503: p. 75-80.

[7] Deng, T., et al. A MEMS based electrochemical seismic sensor. in Solid-State Sensors, Actuators and Microsystems (TRANSDUCERS & EUROSENSORS XXVII), 2013 Transducers & Eurosensors XXVII: The 17th International Conference on. 2013. IEEE.

[8] Newson, J. and A. Riddiford, The kinetics of the iodine redox process at platinum electrodes. Journal of the Electrochemical Society, 1961. 108(7): p. 699-706.

Key Engineering Materials Vols 645-646 (2015) pp 488-491
© (2015) Trans Tech Publications, Switzerland
doi:10.4028/www.scientific.net/KEM.645-646.488

Submitted: 2014-10-28
Accepted: 2014-12-23

A novel micro-machined out-of-plane resonant accelerometer with differential structure of different-height resonant beams

Shuming Zhao[1, a], Yunfeng Liu[2,b] and Jingxin Dong[3,c]

[1, 2, 3] Department of Precision Instruments, Tsinghua University, 100084, Beijing,

[a]zhaosm10@mails.tsinghua.edu.cn, [b]yfliu@mail.tsinghua.edu.cn, [c]dongjx@mail.tsinghua.edu.cn

Keywords: out-of-plane accelerometer， different-height resonant beams， silicon-on-glass， multi-layer mask etching process

Abstract. A novel micro-machined out-of-plane resonant accelerometer with a differential structure is presented. The micro-machined accelerometer consists of two identical torsional structures with asymmetric mass distribution, torsion beam and two different-height resonant beams. Due to the asymmetric mass distribution, the two mirror-symmetrical-placed torsional structures turn an angle under an out-of-plane acceleration, which makes the different-height resonant beam connected to the structures bear different axial stresses, outputting a differential resonant frequency shift. A multi-layer mask etching process based on silicon-on-glass micro-machined technology was employed to fabricate the differential structure and the different-height resonant beams. Primary experiment shows the differential sensitivity of out-of-plane acceleration is 32Hz/g at the resonant frequency of 21.41 kHz.

Introduction

Micro-machined accelerometer plays an increasingly important role in the field of navigation with the development of the micro mechanical processing technology [1]. Compared with other micro-machined accelerometer, the micro-machined resonant accelerometer has the advantage of high precision, wide range and quasi-digital output. According to relationship between the sensitive axis and the machining plane, the resonant accelerometer structures fall into two types, which are in-plane and out-of-plane resonant accelerometer. In-plane resonant accelerometer developed since 1990s, and achieved a significant progress of long-time stability of 1μg in Draper laboratory in 2006[2].

For out-of-plane resonant accelerometer, the first design was presented in 1995, which was fabricated with double-diffusion electrochemical etch stop process, leading to the sensitive structure suffers from the residual stress [3]. To address this issue， new structures fabricated by silicon-on-insulator MEMS technology were reported by Chinese Academy of Sciences in 2011 and 2012, both shows vary high differential sensitivity[4][5]. And at the same time, as a result of the asymmetry of the designed sensitive structure, the experiments indicate at least 8% disparity of sensitivity between the two resonant beams, which may affect device performance.

In this paper, we will demonstrate a novel out-of-plane resonant accelerometer based on silicon-on-glass micro-machined technology. With the symmetrical structure of accelerometer, the sensitivities of the two different-height resonant beams are uniform. A complete set of the fabrication and primary experiments on the accelerometer will be presented in the following.

Device Structure and Operation theory

The micro-machined accelerometer consists of two identical torsional structures with asymmetric mass distribution, as shown in Fig 1(a). Mass 1 and Mass 2 are supported by two torsion beam respectively. Two different-height resonant beams connect to the different parts of the two torsional structures. While beam 1 connects the top part of the two torsional structures, beam 2 connects the bottom.

Due to the asymmetric mass distribution, the two mirror-symmetrical torsional structures turn an angle under an out-of-plane acceleration, which makes the different-height resonant beam connected to the torsional structures bear different axial stresses, outputting a differential resonant frequency

shift. Since the whole structure is symmetrical about y-axis, the left-side of the y-axis analysis is used instead of the whole analysis. The schematic diagram with design parameters is illustrated in Fig 1b.

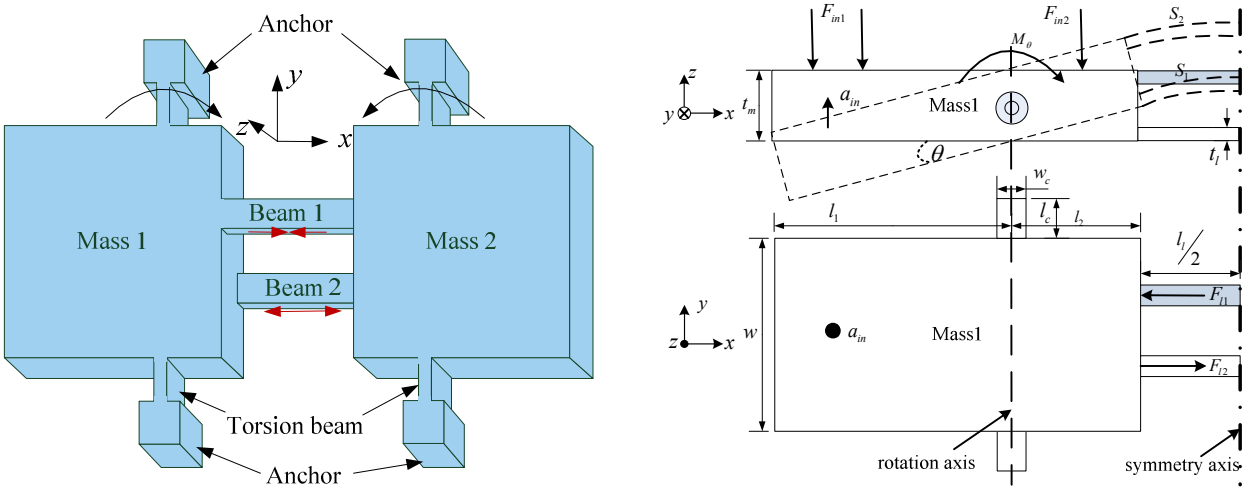


Fig1 (a) Schematic diagram of micro-machined out-of-plane resonant accelerometer (b) Simplified modal and force analysis of the micro-machined out-of-plane resonant accelerometer. F_{in1} and F_{in2} represent the inertial force of asymmetric mass caused by the input acceleration a_{in}, F_{l1} and F_{l2} represent the axis force of the resonant beams

FEM analysis result of the accelerometer under a 1-g positive acceleration is shown in Fig. 2(a). Known from the mechanical modal analysis[6], axial force of the resonant beams exerted by acceleration changed with the thickness of the beams, leading to the variation of the accelerometer sensitivity. The FEM analysis result of sensitivity versus thickness ratio of beams and masses t_l/t_m is shown in Fig 2b.

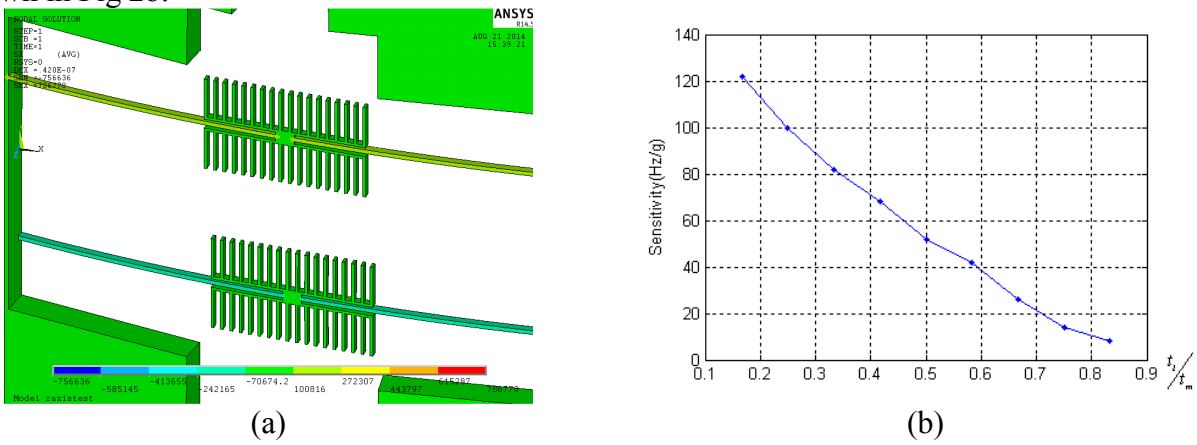


Fig. 2 FEM analysis of the out-of-plane accelerometer (a) Stress distribution of the resonant beams when under a 1-g positive out-of-plane acceleration. Top beam bear a tension stress while bottom beam bear a compression stress ; (b) Sensitivity of the out-of-plane accelerometer with 60μm-thick mass decrease when t_l/t_m increase.($0 < t_l/t_m < 1$)

Fabrication Process

To achieve the different-height resonant beam structure and the different thicknesses of resonant beam and torsional mass, a double sided and multilayer mask etching of silicon-on-glass fabrication technology was used [7]. A 10-μm-thickness-difference is achieved while the mass thickness we designed is 30μm while the beam is 20μm. The fabrication procedure is briefly shown in Fig. 3.

Firstly we prepared a glass substrate with sputtering of metal wire (Fig. 3a), and then formed a layer of SiO_2 by thermally oxidation on the bottom of a monocrystalline silicon wafer and patterned it for anchor areas (Fig. 3b). A second mask layer of photoresist was patterned on the top of the first mask layer (Fig. 3c), and was used to etched the silicon to get a groove of 10μm (Fig. 3d). After removing the photoresist mask layer, we used the patterned SiO_2 layer as a mask to etch the silicon for anchors and deep the groove for 20μm (Fig. 3e). After the removal of SiO_2, we bonded the etched silicon to the glass substrate (Fig. 3f), and thinned the silicon wafer to about 50μm by KOH etching

for structure layer (Fig. 3g). And then a layer of SiO_2 was grown on the top surface of the bonded silicon by PECVD, patterned as the first mask layer of top surface (Fig. 3h). A patterned photoresist layer was formed on top of SiO_2 layer as a second mask layer of top surface (Fig. 3i). By etching the silicon about 18μm depth with the photoresist mask layer, we get an almost released structure (Fig. 3j). Then the photoresist mask was removed and the structure was etched another 10μm with the SiO_2 mask layer (Fig. 3k). This step not only releases the structure but also get a thinned bottom beam. After removing the mask layer, we achieved the different-height resonant beam structure (Fig. 3l).

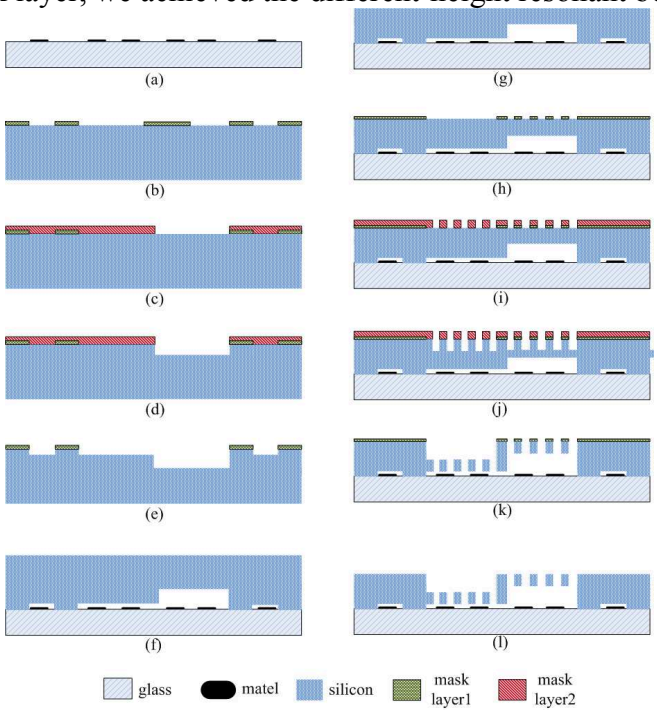
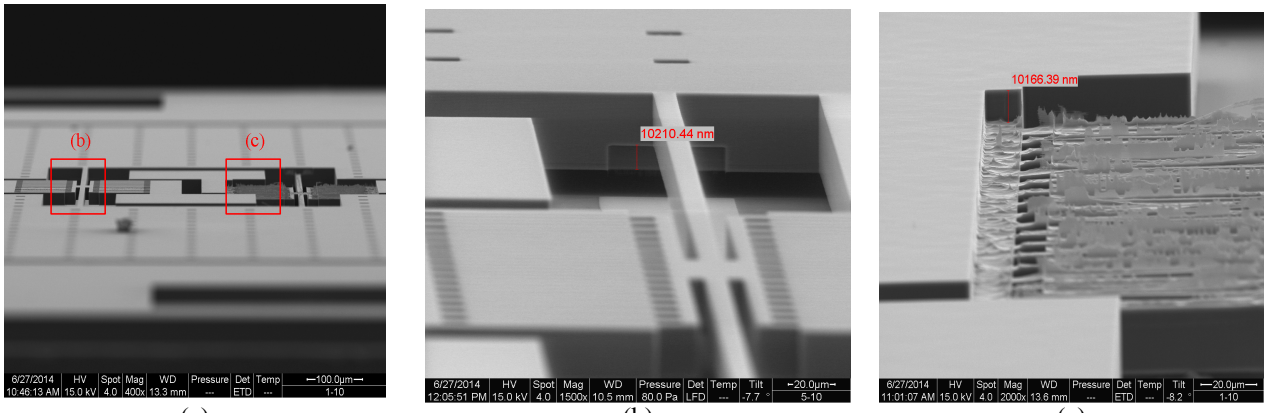


Fig. 3 Fabrication process of the out-of-plane accelerometer

A fabricated out-of-plane accelerometer with different-height resonant beams is shown in Fig. 4. Coarse measurement of the grooves was taken with SEM ruler, as shown in Fig. 4b and c.



(a) (b) (c)

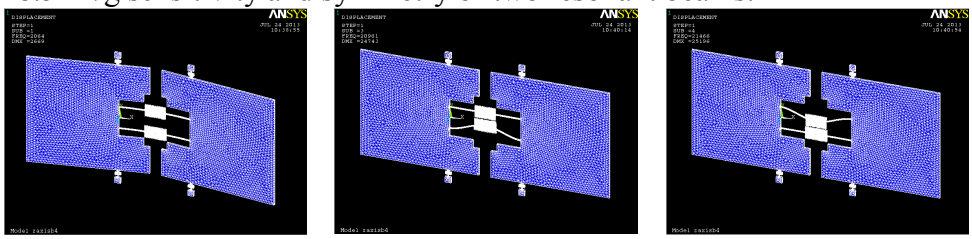
Fig. 4 SEM of a fabricated device. (a) SEM of the different-height resonant beam; (b) coarse measurement of bottom groove with SEM ruler; (b) coarse measurement of top groove with SEM ruler

Primary Experiment

Driving and sensing electrode was designed beside the resonant beams to drive and detect the working mode of the resonant beams and output the frequency shift. The beams vibrate in the structure plane, as FEM analysis results shown in Fig. 5b and c.

The primary tests of the accelerometer's function were carried out by rolling experiment in the field of gravity. The device was packaged under 1000Pa and connected to a dynamic signal analyzer Agilent 35670A. For 30μm-thick torsional mass structure, different-thick resonant beams as 20μm-thick and 22μm-thick were fabricated to test the relationship between the thickness differences

with accelerometer sensitivity. The test results of the 22-thick resonant beams are shown in Fig. 6, indicating a 28.5Hz/g sensitivity and symmetry of two resonant beams.



(a) (b) (c)

Fig. 5 The main modes designed of the out-of-plane accelerometer

(a)shows the working mode of the torsional structures; (b)shows the resonant mode of the beam 2; (c)shows the resonant mode of beam1

Experimental results and FEM analysis shown in Fig. 7 indicate that the fabricated device is consistent with design. The 20μm-thick resonant beams accelerometer achieved the sensitivity of 35Hz/g. Performance testing of the out-of-plane accelerometer will be carried out with close-loop circuit later. Furthermore, to extend the present work to get a higher sensitivity, a double-side-buried-oxide-SOI material could be used in the future.

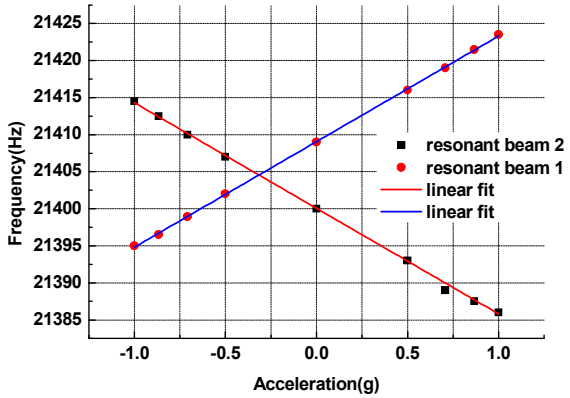


Fig. 6 Rolling experiment of the out-of-plane accelerometer in the field of gravity

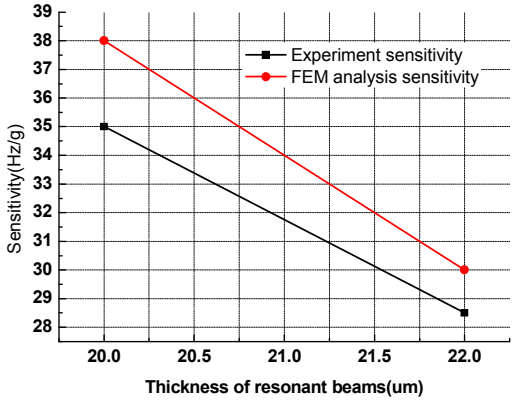


Fig. 7 Sensitivity of different-thick resonant beams in out-of-plane accelerometer

Conclusion

In this paper, we proposed a novel out-of-plane resonant accelerometer based on silicon-on-glass micro-machined technology. The accelerometer consists of two torsional mass and two different-height resonant beams connected to the torsional mass. To achieve the designed structure, a double sided and multilayer mask etching of silicon-on-glass fabrication technology was used. Besides, the fabrication process used is compatible with the processing technology of the typical in-plane micro-machined resonant accelerometer, making it possible to integrate multi-axis machining. Test results of the fabricated different-height verified the feasibility of the design, and a uniform sensitivity was achieved because of the symmetrical and differential structure designed. The fabricated 20μm-thick resonant beams accelerometer achieved the sensitivity of 35Hz/g.

References

[1] George T.Schmidt, INS/GPS Technology Trends, (2011)

[2] Ralph Hopkins, Joseph Miola, Roy Setterlund, et al. The Silicon Oscillating Acclerometer: A high-performance MEMS accelerometer for precision navigation and strategic guidance applications, Draper Technology Degist, 10 (2006), 6-15

[3] Burrer C., Esteve J, A novel resonant silicon accelerometer in bulk-micromachining technology, Sens. Actuators A,46-47 (1995), 185-189

[4] Junbo Wang, Yanlong Shang, Jian Chen, et al. Micro & Nano Letters,7 (2012), 1230-1233

[5] Shang Y.L, Wang J.B, Tu S, Liu L, Chen D.Y: 'Z-axis differential silicon-on-insulator resonant accelerometer with high sensitivity', Micro Nano Letter, 6 (2011), 519-522

[6] Dong jingxin, Micro-inerial instrument----Micro-accelerometers, Tsinghua University Publishing Co., (2003)

[7] X.S. Liu, Z.C. Yang, X.Z. Chi, et al. A doubly decoupled lateral axis micromachined gyroscope, Sensors and Actuators A, 154 (2009) 218-223

Key Engineering Materials Vols 645-646 (2015) pp 492-497
© (2015) Trans Tech Publications, Switzerland
doi:10.4028/www.scientific.net/KEM.645-646.492
Submitted: 2014-10-28
Accepted: 2014-12-23

The Research of Turn-on time for Silicon Micromechanical Gyroscope On A Chip

BIAN YOU[1, a], SHI QIN[2,b] , XIA GUO MING[3,c]

[1] Nanjing University of Science and Technology, Xiaolingwei NO.200, Nanjing, China

[2] Nanjing University of Science and Technology, Xiaolingwei NO.200, Nanjing, China

[3] Nanjing University of Science and Technology, Xiaolingwei NO.200, Nanjing, China

[a] 847612570@qq.com, [b]sqinhy@njust.edu.cn, [c]xgmseu@gmail.com

Keywords: The boot process; Turn-on time; Silicon micromechanical gyroscope on a chip; Compensation method.

Abstract: On the basis of analyzing the boot process of silicon micromechanical gyroscope on a chip at room temperature, -40 ℃ and 60 ℃ constant temperature environment, for the character that the gyroscope can realize the compensation function and possess temperature-sensitive output model, This paper analyzes the relationship between the bias and temperature meter, and presents compensation method of the initial bias so as to reduce different turn-on time caused by the variation with the temperature of working environment. Experimental results demonstrate the method can effectively reduce turn-on time at the variation with temperature of working environment.

Intorduction

For the MIMU, the time interval between the application of power and the presence of a usable output of the gyro needs to be as short as possible. For example, the turn-on time of missile inertial navigation system is usuallynot greater than 5 min. In the paper, Silicon micromechanical gyroscope on a chip has been developed by our team and CETC. It used the analog-digital-hybrid ASIC circuit Etc. For the Silicon micromechanical gyroscope on a chip, the Closed-loop drive base on phase-locked loop and the closed-loop detectingissigma-delta. Ultimately the Gyro output is digitized. Detection circuit using the polynomial compensation is able to achieve a temperature compensation system. This system can make the compensation model that is proposed by the temperature testenter the microprocessor of Silicon micromechanical gyroscope on a chip.This characteristic makes the gyroeasy tocontrol. Silicon micromechanical gyroscope on a chip has temperature sensor digital readout. The gyro generally taking a few minutes from cold to hot stability makes it difficult to apply in the place what needs the shortest turn-on time. As the above example, the period of time from cold to hot stability is called the turn-on time. The turn-on time is the time interval between the application of power and the presence of a usable output of the gyro.
There are two aspects that the variation with the temperature of working environment causes the change of the gyro performance.

The first on the one hand, the performance of Silicon micromechanical gyro equipment material is sensitive to temperature. In the second, the temperature field has effect on the working position of Silicon micromechanical gyro. Whether the different ambient temperatures has the same effect on the boot process of silicon micromechanical gyroscope on a chipor not, and how the

regular works are quite important for reducing the turn-on time of Silicon micromechanical gyroscope on a chip. Researching how the initial drift of gyroworks has an important significance.

EXPERIMENTS

Turn-on time at room temperature

After the gyro is the application of power, the power consumption of electronic components on the circuit board lead to the operating temperature of gyro rising rapidly. It leads to taking a long time to achieve the balance. For the engineering application of Silicon micromechanical gyroscope on a chip, the time interval between the application of power and the presence of usable output of the gyro is the less the better, it is the best that the gyro receives the presence of a usable output, when the gyro power on starting to work. Fig.1, the temperature of Circuit board rose quickly within 3 min at turn-on time, at the same time the bias of Silicon micromechanical gyroscope on a chip fallen fast too. In the following 2 min, the heat caused by the Circuit board reached equilibrium with the heat that lost to the environment, at the same time, the header of silicon micromechanical gyroscope on a chip hasn't reached the temperature balance. After 10 min, Silicon micromechanical gyroscope on a chip completed heat exchange with the outside world system up to the temperature balance. The performance of gyro tended to be stable, the bias range reduced, bias stability comparing with the application of power of the gyro increased to five times. If the gyro was warmed up for a period of time, the performance of bias would be better.

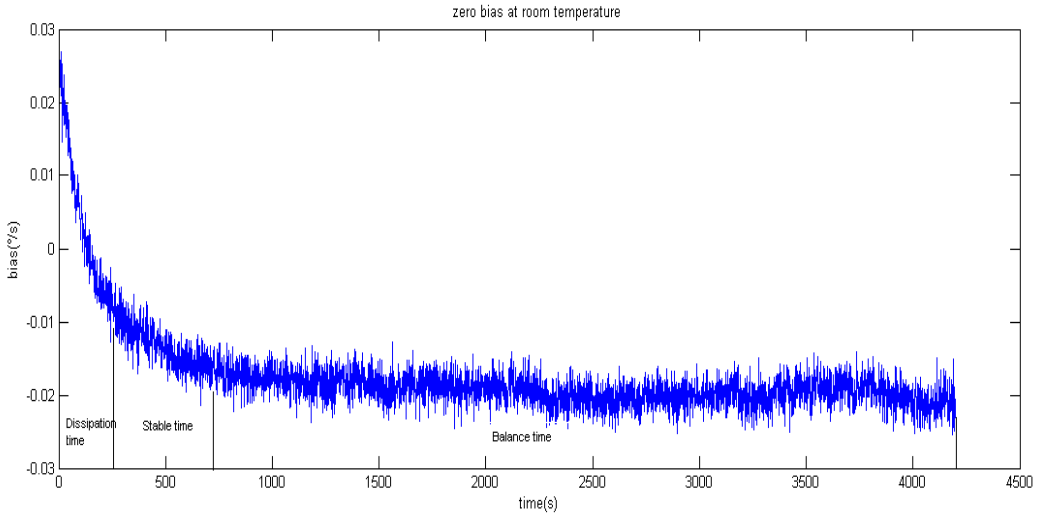


Fig1. Bias at room temperature

Turn-on time test at constant temperature

Mount the gyro in a temperature-controlled chamber. For the first time, stabilized the non-operating gyro temperature for 1 hour with the temperature-controlled chamber setting at -40℃. Measured and recorded the gyro output for 70 min. Repeated these measurements with the temperature-controlled chamber set at the following temperatures: 60℃and room temperature.

Fig.2 showed the experimental results. The improvement of boot process was not obvious comparing -40℃with room temperature. Room temperature Stable time was significant less than -40℃. At the end, bias stability changed from 16.64 ° / h to 10.35 ° / h. It proved that the heat dissipation of circuit board decreased at room temperature.

The improvement of boot process was obvious comparing room temperature with 60℃. Bias stability changed from 10.35 ° / h to 5.23° / h.

Dissipation time and stable time obviously decreased. It showed that stabilizing the non-operating gyro temperature for 1 hour with the temperature-controlled chamber set at 60℃usefully warmed up the header and circuits of silicon micromechanical gyroscope on a chip.

By researching the boot process of silicon micromechanical gyroscope on a chip at room temperature, -40℃ and 60℃, taking temperature control measures and keeping the gyro working near 60℃ temperature are useful to reduce the turn-on time of the gyro. However, we still don't give a kind of ideal model that can describe the relationship between the turn-on time and the environment temperature.

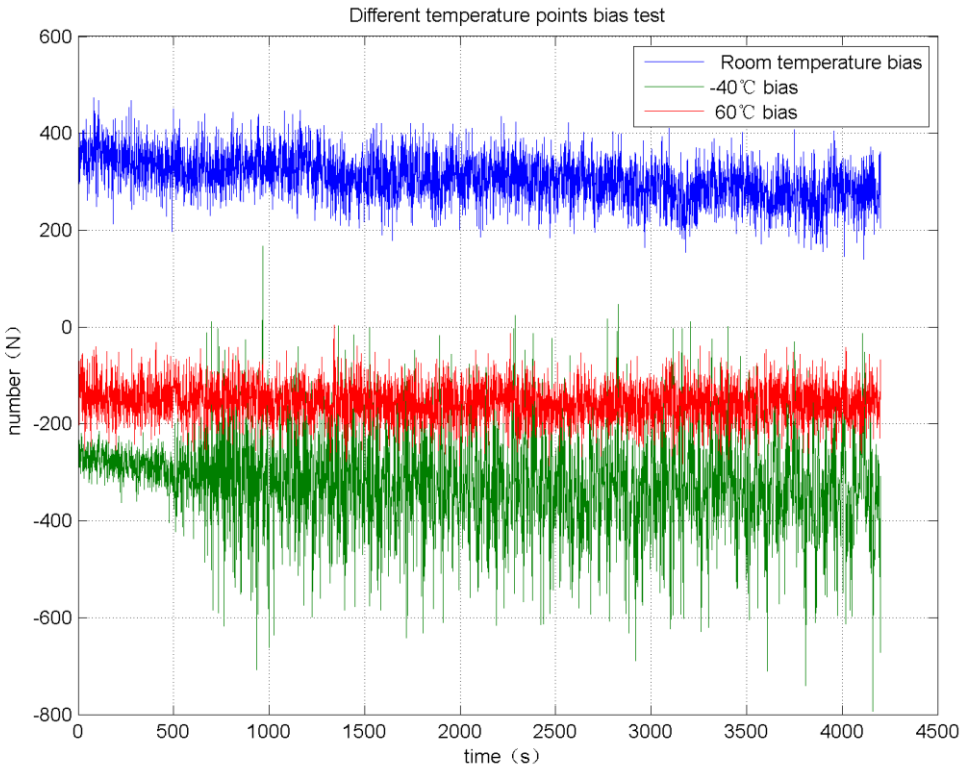


Fig2. Different temperature points bias test

In order to reduce the turn-on time of gyro further, our team self-developedsilicon micromechanical gyroscope on a chip is integrated with temperature sensordigital readout. The gyro output the bias of digital signals at the same time recording the internal temperature data of the gyro header. This can record how the temperature of the gyro header changes during the boot process. Fig.3 showed how the temperature sensordigital readout changed with the time when the gyro was turned on at room temperature. The temperature sensor digital readout of Fig.3 corresponds with the bias digital output of Fig.1.

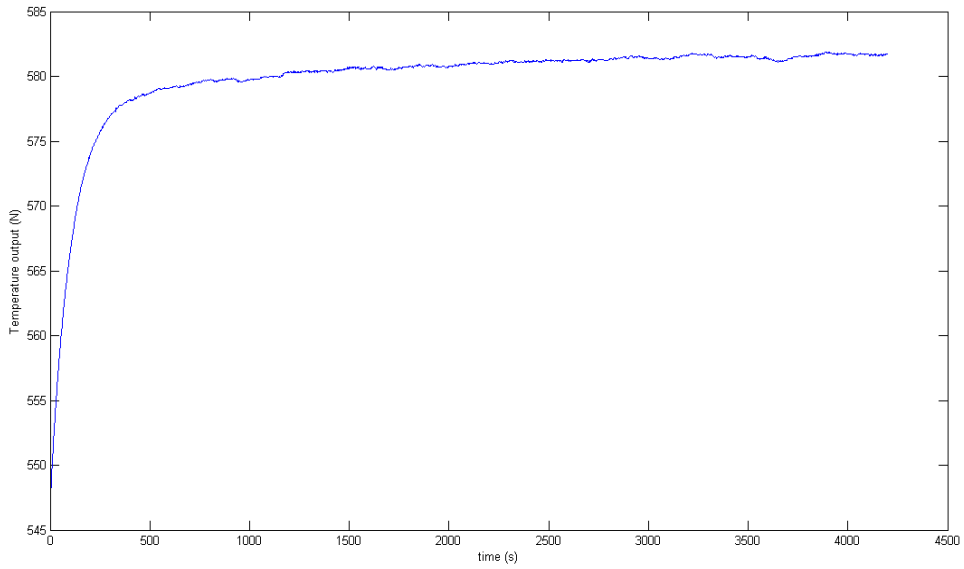


Fig3.Temperature sensordigital readout

In order to find the relationship between temperature sensordigital readout and bias, draw the Corresponding relation curve of temperature sensor digital readout and bias, using temperature sensor digital readout as the X axis and bias output as the Y axis. Fig.4 is it.

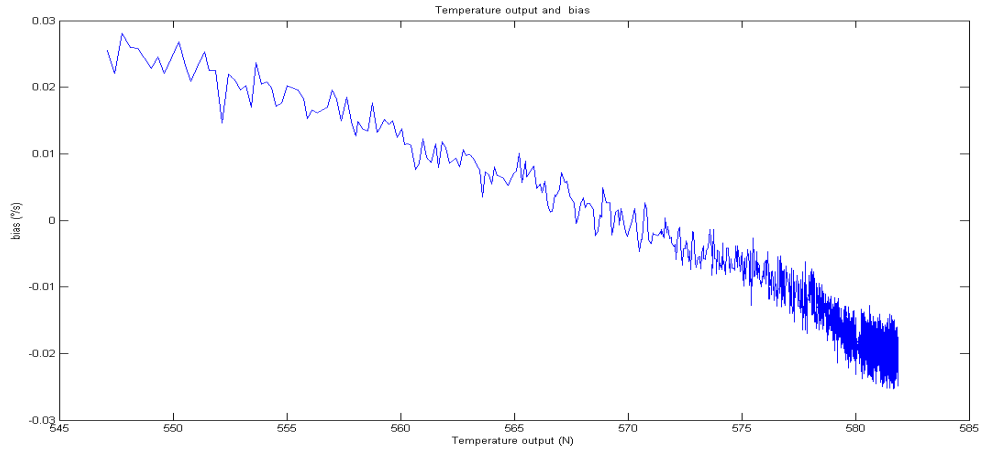


Fig4. Temperature output and bias

Fig.4 showed a kind of approximate polynomial relationship. Using the least square method conducts linear polynomial, quadratic polynomial, and cubic polynomial. Polynomial coefficients keep five significant figures. The temperature and bias can be approximated as:

$$\text{Bias} = 0.80875 - 0.0016191 \times T. \quad (1)$$

$$\text{Bias} = -0.000021291 \times T^2 + 0.022733 \times T - 6.0404. \quad (2)$$

$$\text{Bias} = (-4.5682e\text{-}7) \times T^3 + 0.00075792 \times T^2 - 0.42022 \times T + 77.875. \quad (3)$$

Bias is the bias output, and T is the temperature sensordigital readout.

To compensate the initial bias through the above model, Fig.5, Fig.6, and Fig.7 showed the result.

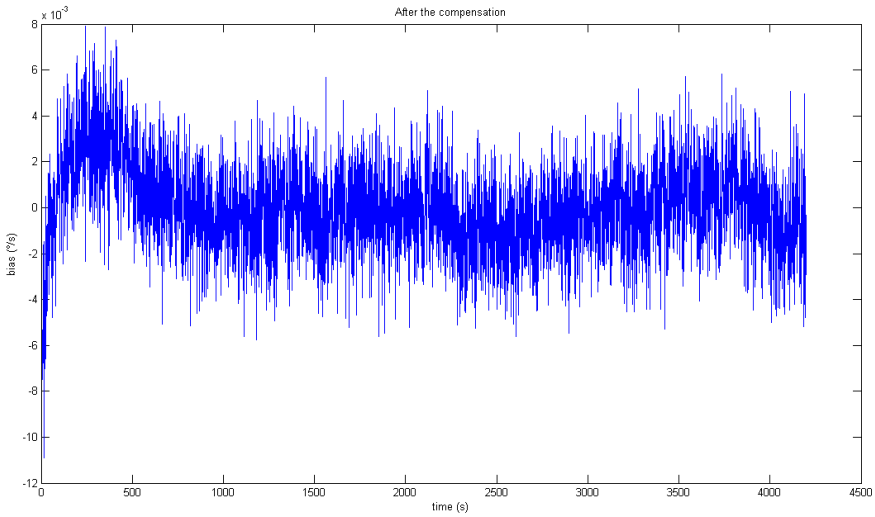


Fig5. Linear compensation

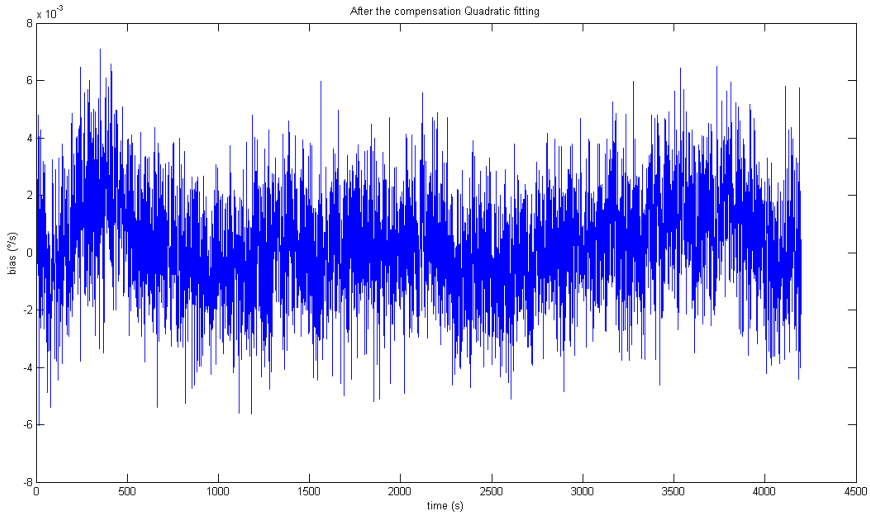


Fig6. Secondary compensation

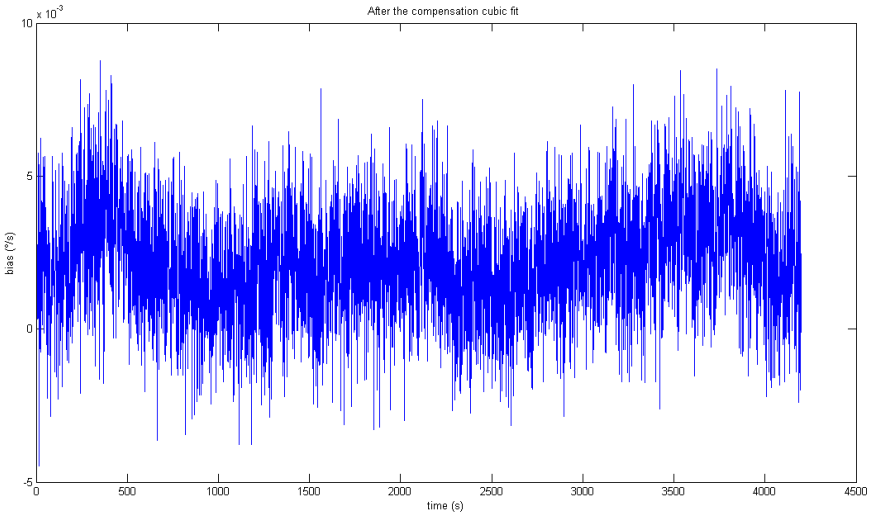


Fig7. Three fitting compensation

Table1. Bias stability after compensation

Order	0	1	2	3
Bias stability	0.0065	0.0021	0.0019	0.0019

Fig.5, Fig.6, and Fig.7 proved that turn-on time of the gyro that was compensated significantly reduced. Table.1 showed the bias stability promoting three times at most, and it is ok to adopt the linear compensation. The model can be used to compensatethe boot process of the gyro being powered on before 5 min. This makes the gyro fast into the stable working condition.

The compensation mode of silicon micromechanical gyroscope on a chip can be thought of as a temperature compensation system. This system can make the compensation model that is proposed by the temperature testenter the microprocessor of Silicon micromechanical gyroscope on a chip. By measuring the gyro working environment temperature at the different timeto calculate the corresponding compensation value, this enables the compensation to real-time tracking the change of header temperature, thereby the turn-on time of silicon micromechanical gyroscope can be reduced.

References.

[1] H.Chen,R.Zhang and B.Zhou,"Micro machined gyroscope temperature characteristics and compensation algorithm," Sensor technology,vol.23,Oct. 2004, pp.24-26

[2] J.Li, H.H.Hong and W.Zhang," Research on Calibration Techniques for MEMS2Micro Inertial Measurement Unit,"Sensor Technology, vol.21,Jul.2008,pp.1170-1173

[3] P.F.Zhang,Y.Wang,X.W.Long and J.X.Tang,G.Li and G.M.Xu," Accelerometer Temperature Compensation Model," Sensor Technology,vol.20,May.2007,pp.1012-1015

[4] Dachuan Liu, Xiaozhu Chi, Jian Cui, Longtao Lin and Qiancheng Zhao, 3rd International Conference on Sensing Technology IEEE, vol.23, Oct. 2007,pp. 273-277

[5] El-Diasty, M.El-Rabbany, and A.Pagiatakis, S, Measurement Science and Technology,vol.18, 2007,pp. 3321-3328

Key Engineering Materials Vols 645-646 (2015) pp 498-503
Submitted: 2014-10-28
© (2015) Trans Tech Publications, Switzerland
Accepted: 2014-12-23
doi:10.4028/www.scientific.net/KEM.645-646.498

3D indoor positioning system based on MEMS sensors

Jinlin Zhu[1, 2, a], Bing Mo[1, 2, b*], Chaodong Ling[1, 2], Wenyuan Fu[1, 2]

[1] Department of Electrical Engineering, Huaqiao University, Xiamen 361021, China
[2] ASIC Key Lab of Xiamen, Xiamen 361021, China
[a]zhu457823@163.com, [b*]mobing@hqu.edu.cn

Keywords: 3D indoor positioning system, sensor data fusion, extended kalman filter, integral drift, heading drift

Abstract. Nowadays, most of scholar study the 2D indoor positioning system based inertial sensors. But in some case, the information of 3D space about person is very important, such as mine accident, fire rescue, and so on. In this paper, we focus on designing and implementing a 3D indoor positioning system based on MEMS sensors and barometer sensor. The MEMS sensors including a three-axis accelerometer, a three-axis gyroscope, and a three-axis magnetometer is used for acquiring information of human movement. Barometer sensor is used to measure the height of the person where he is. Then the collected raw data is sent to a PC by a MCU wirelessly. Thus the performance of the 3D indoor positioning system is optimized by moving data post processing to a PC. In a 3D indoor positioning system, the integral drift and the heading drift are the main sources of the errors. Therefore, a method which is the combination of the zero velocity updates and the sensor data fusion based on an extended Kalman filter is proposed. Further improvement on the accuracy of positioning can be achieved by removing the static biases. A novel method including compensating the sensor biases based on experiment is presented. These methods have been carefully investigated through theoretical study and simulation. The simulation results indicate 3D indoor positioning is achievable through the application of the presented methods.

Introduction

As we all know, GPS can be used to pedestrian navigation and positioning by utilizing its signals for position computation, but GPS signals can be not used in indoor environments [1], [2]. So we focus on study indoor navigation and positioning without GPS. There are two ways to realize indoor positioning. One is based on beacon, such as using ultrasound, Wi-Fi [3], and Bluetooth, but in some cases beacon-free solutions are preferable since they do not depend on an infrastructure or network.

Several beacon-free methods have been presented for accurate person's position estimation based on inertial sensors [6]. These methods, integrate step lengths and orientation estimations at every detected step, in order to calculate the absolute position and orientation of a person [5]. The accuracy of indoor positioning depend on the algorithm optimized and the particular inertial sensor technology development.

With development of Micro-Electro-Mechanical systems allows for integrating multiple sensors into a chip, including accelerometers, gyroscopes, magnetometers and even barometer sensors [8]. Because the function and size of an inertial sensor are linearly dependent parameters, inertial sensors based on MEMS technology have smaller size and lower performance. MEMS sensors have a significant bias and therefore suffer large drifts after integration.

This paper describes, design, and implements a 3D indoor positioning system based on MEMS sensors and barometer sensor. MEMS sensors contain a three-axis accelerometer, a three-axis gyroscope, and a three-axis magnetometer used for acquiring human movement information. Barometer sensor can measure atmospheric pressure used for calculating the height of human by international barometric formula. So we can implement the function of indoor positioning in 3D space. It is significance in some rescue case, such as mine accident, fire rescue, and so on.

Design of 3D indoor positioning system

In this paper, we designed a 3D indoor positioning system based on MEMS sensors and barometer sensor. We used a 9-axis MEMS sensors, MPU-9150 from InvenSense Inc. We used a barometer sensor, BMP085 from Bosch Sensor Tec.

The MPU-9150 is a system in Package (SiP) that combines two chips: the MPU-6050, which contains a 3-axis gyroscope, a 3-axis accelerometer; and the AK8975, the market leading 3-axis digital compass. The BMP085 is a new generation of high precision digital pressure sensor for consumer applications. The ultra-low power, low voltage electronics of BMP085 is optimized in mobile phones, PDAs, navigation and positioning devices and outdoor equipment. The performance of sensors that we used are summarized in table 1.

Table 1 Specification of the sensors

Sensor Type	Full-Scale range	Sensitivity	Maximum sampling rate	Digital resolution
Accelerometer	±16g	0.02% of FS	1000Hz	16bit
Gyroscope	±2000dps	0.04% of FS	8000Hz	16bit
Magnetometer AK8975	±1200μT	0.3μT	100Hz	13bit
Barometer BMP085	10000hPa	0.06hPa	222Hz	16bit

The structure of 3D indoor positioning system is shown in Fig.1. The design of our hardware is shown in Fig. 2. The STM32F103RBT6 microcontroller is interfaced to the MPU9150, and BMP085 via the I^2C protocol. The hardware is attached to the right foot using the shoe's laces. So MEMS sensors can capture the person's movement information. STM32F103RBT6 microcontroller reading the digital sensors data via I^2C interface, and sending raw data with wireless UART. The PC receive the raw data with wireless UART and process raw data, realize the function of indoor positioning.

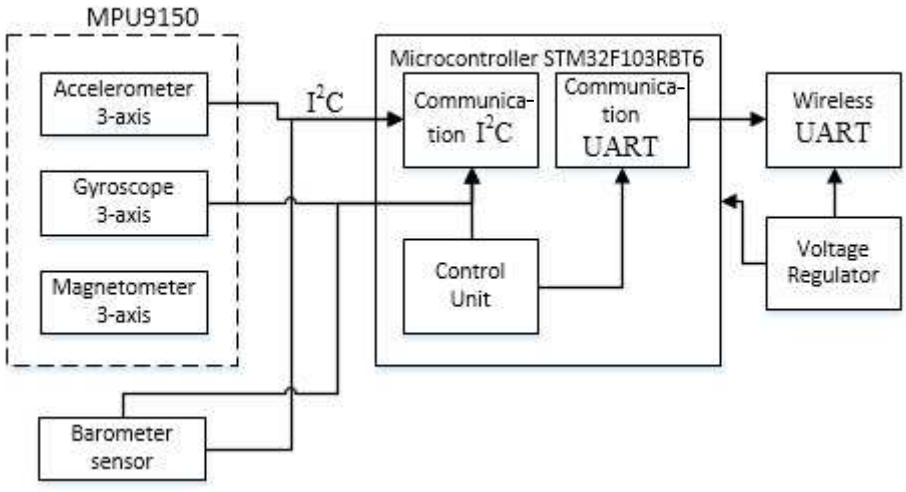


Fig. 1 Block diagram of 3D indoor positioning system



Fig. 2 3D indoor positioning system top view

The indoor positioning algorithm based on Kalman

E. Foxlin et al. has been presented the indoor positioning algorithm based on the Kalman filter in 2005 [6]. The method is to use an Extended Kalman Filter (EKF) to estimate the errors of an indoor positioning system, which accumulate due to the MEMS sensors and barometer sensor's bias. The EKF is update when human in stance phase. In an indoor positioning system, integral drift and heading drift are the main sources of the errors. We can use the method of zero velocity updates compensate the integral drift, and we can use magnetometer calculate heading orientation compensate the heading drift because of gyroscope bias. Figure 3 shows the main blocks in the 3D indoor positioning algorithm.

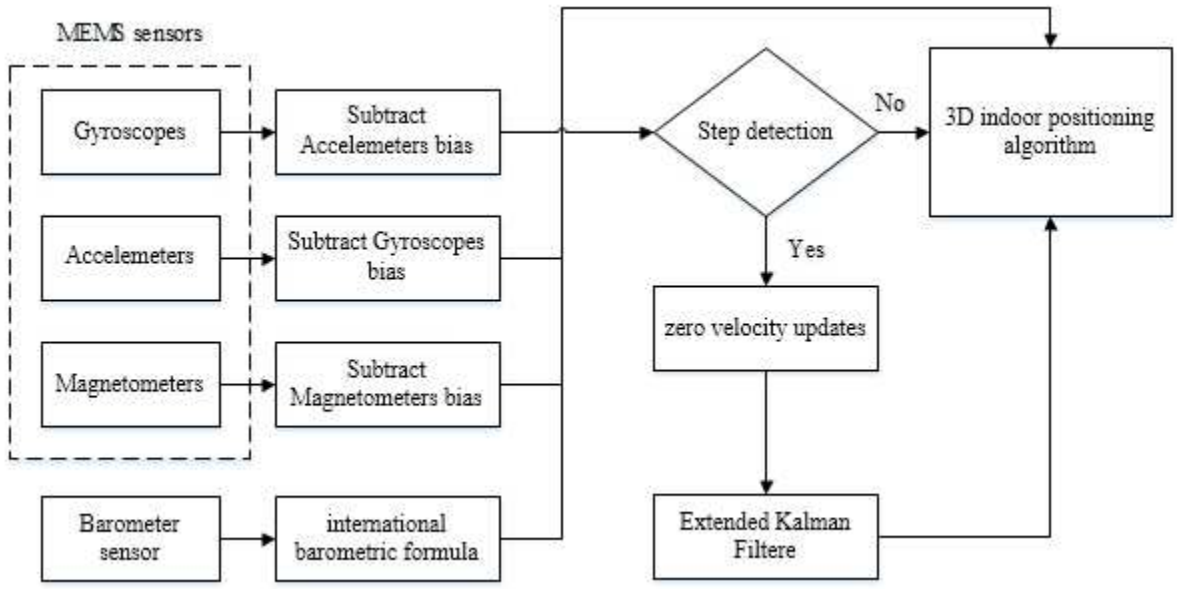


Fig.3 The solution of 3D indoor positioning system

The indoor positioning algorithm uses the accelerometer and gyroscope reading, in the sensor body frame of reference which are taken at every sample interval at discrete sampling times. Firstly, we calculate the quaternion $Q=[q_0,\ q_1,\ q_2,\ q_3]$ by using angular rate of gyroscope based on Quaternion Differential Equations. Then we can get attitude angle (yaw, pitch, and roll) using the

relationship quaternion and attitude angle at equation (1) – (3). Secondly, in order to calculate the velocity and distance, we need to project the acceleration vector $a^b(t)=\left[a_x^b(t),\ a_y^b(t),\ a_z^b(t)\right]^T$ in the sensor body of reference into acceleration vector $a^n(t)=\left[a_x^n(t),\ a_y^n(t),\ a_z^n(t)\right]^T$ in the navigation coordinate (represent east, north, and up) using equation (4). Thirdly, we subtract the acceleration of gravity and then integrate acceleration to obtain velocity and distance in navigation coordinate. Lastly, we combine of attitude angle, velocity, height information from barometer sensor, and distance can implement 3D position.

$$\text{yaw} = \sin^{-1} 2\left(q_2q_3 + q_0q_1\right) \tag{1}$$

$$\text{pitch} = \tan^{-1}\left(\frac{2\left(q_0q_3 - q_1q_2\right)}{q_2^2 - q_3^2 + q_0^2 - q_1^2}\right) \tag{2}$$

$$\text{roll} = \tan^{-1}\left(\frac{2\left(q_0q_2 - q_1q_3\right)}{q_3^2 - q_2^2 - q_1^2 + q_0^2}\right) \tag{3}$$

$$\begin{bmatrix} a_x^n \\ a_y^n \\ a_z^n \end{bmatrix} = \begin{bmatrix} q_1^2 + q_0^2 - q_3^2 - q_2^2 & 2\left(q_1q_2 - q_0q_3\right) & 2\left(q_0q_2 + q_1q_3\right) \\ 2\left(q_1q_2 + q_0q_3\right) & q_2^2 - q_3^2 + q_0^2 - q_1^2 & 2\left(q_2q_3 - q_0q_1\right) \\ 2\left(q_1q_3 - q_0q_2\right) & 2\left(q_2q_3 + q_0q_1\right) & q_3^2 - q_2^2 - q_1^2 + q_0^2 \end{bmatrix} \begin{bmatrix} a_x^b \\ a_y^b \\ a_z^b \end{bmatrix} \tag{4}$$

In order to improvement performance of the 3D positioning system, we get the static bias of the sensors via experiments [7]. It can be used for compensating the raw reading of sensors. In order to improve accuracy of positioning, we can adopt multi sensors data fusion algorithm based on Extended Kalman Filter.

Because the EKF is update when human in stance phase, it is important to exactly detect the step. The algorithm of step detection rely on basic data processing techniques. Most of researchers use the raw data of gyroscope [4] or accelerometer [9]. But we found that step detection based on the raw data of gyroscope is more simper and exactly by the experiment. We set a threshold value at 1rad/s, when we detect angular rate readings at series sampling times less than the threshold value, and we can detect step. Walking tests were done to evaluate the performance of step detection based on angular rate of gyroscope. Figure 3 shows the raw data captured in a walking test, 27 meters long that require required 44 steps. The performance of the step detection algorithm is shown in table 2.

Table 2 Performance of step detection based on gyroscope

Number of tests	Real number of steps	Number of steps failed	Percentage of errors
1	444	10	2.25%
2	444	13	2.92%
3	444	9	2.02%

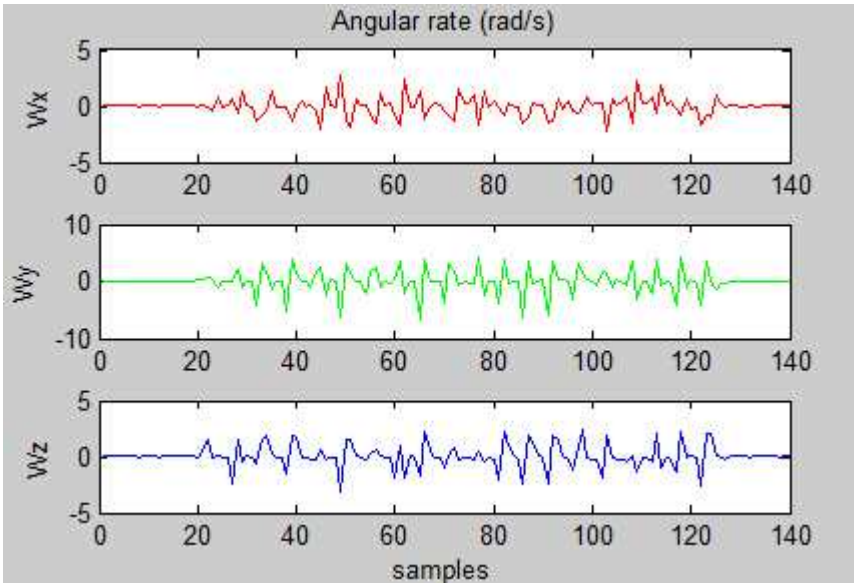


Fig.3 Raw sensor data for a test 27 meters walking in one direction

It is necessary to calculate the stride length at every detected step in order to compute the total travelled distance of a person. The stride length based on zero velocity updates is considered as most reliable method [5]. The foot at floor the velocity is known to be zero, so the idea is to correct the linear velocities obtained after integrating the accelerometer. This is a good way to compensate the integral drift because of double integrated.

When stride length is calculated, we need to know the orientation of the heading. We can use raw readings of gyroscope to calculate attitude angle (yaw, pitch, and roll). The yaw is the orientation of heading. Because gyroscope can't work normally when person's foot at floor. We use magnetometer calculate the yaw at every step to compensate the gyroscope's heading drift. Barometer sensor can measure barometric pressure, the measured barometric pressure p and the pressure at sea level p_0, and the altitude in meters can be calculated with the international barometric formula:

$$\text{altitude} = 44330 * \left(1 - \left(\frac{p}{p_0} \right)^{\frac{1}{5.255}} \right) \tag{5}$$

So we can realize a 3D indoor positioning system based on MPU-9150 and BMP085. We can tracking person movement trajectories in 3D space. In some case, 3D position information is very important, such as emergency services with an immediate view of where building users at any time.

Conclusion

We have described, designed and implemented a 3D indoor positioning system based on MEMS sensors and barometer sensor. The simulation results shown that 3D indoor positioning algorithm based on Extended Kalman Filter is feasible. The emphasis of indoor positioning is cancel out the integral drift and heading drift. Future work will be focused to implemented the algorithm of stride length and optimize the algorithm for improving the accuracy of located in 3D space.

Acknowledgement

The authors would like to thank the financial support of experiments are "the National Natural Science Foundation of China" (Grant No.61204122), "the Science and Technology Project of Quanzhou" (Grant No.2012Z98), "the Fundamental Research Funds for the Central Universities" (Grant No.JB-ZR1206), and all their colleagues in the department of electrical engineering.

References

[1] W.Q. Feng, H.B. Zhao, Integration of GPS and low cost INS for pedestrian navigation aided by building layout [J], Chinese Journal of Aeronautics, 2013,vol. 26, no. 5, pp. 1293-1289.

[2] A. Noureldin, T. B. Karamat, Performance enhancement of MEMS-based INS/GPS integration for low-cost navigation applications [J], IEEE Transactions on vehicular technology, 2009, vol. 58, no. 3, pp. 1077-1096.

[3] L.N. Chen, B.H. Li, An improved algorithm to generate a Wi-Fi fingerprint database for indoor positioning [J], Sensors 2013, vol. 13, no. 8, pp. 11085-11096.

[4] C. L. Huang, Z. Y. Liao, L. Zhao, Synergism of INS and PDR in self-contained pedestrian tracking with a miniature sensor module [J], IEEE sensors journal, 2010, vol. 10, no. 8, pp. 1349-1359.

[5] A.R. Jimenez, F. Seco, C. Prieto and J. Guevara, A Comparison of Pedestrian Dead-Reckoning Algorithms using a Low-Cost MEMS IMU, In 6th IEEE International Symposium on Intelligent Signal Processing,26-28 August, Budapest, Hungary, 2009, pp. 37-42.

[6] E. Foxlin, Pedestrian tracking with shoe-mounted inertial sensors [J], IEEE Computer graphics and Applications, 2005, vol. 1, pp. 38-46.

[7] Hoflinger, F. Albert-Ludwigs Univ. of Freiburg, Freiburg, Germany, Muller, J. ; Rui Zhang ; Reindl, L.M. ; Burgard, W.A wireless micro inertial measurement unit [J], IEEE Transactions on instrumentation and measurement, 2013, vol. 62, no. 9, pp. 2583-2595.

[8] R. Harle, A survey of indoor inertial positioning systems for pedestrians [J], IEEE communications surveys & tutorial, 2013, vol. 15, no. 3, pp. 1281-1293.

[9] A.R. Jimenez, F. Seco, Accurate pedestrian indoor navigation by tightly coupling foot-mounted IMU and RFID measurements [J], IEEE Transactions on instrumentation and measurement, 2012, vol. 61, no. 1, pp. 178-189.

[10] R. Zhang, L. Reindl, Inertial sensor based indoor localization and monitoring system for emergency responders [J], IEEE sensor journal, 2013, vol. 13,no. 2, pp. 838-848.

Key Engineering Materials Vols 645-646 (2015) pp 504-508
© (2015) Trans Tech Publications, Switzerland
doi:10.4028/www.scientific.net/KEM.645-646.504

Submitted: 2014-10-29
Accepted: 2014-12-23

Analysis Temperature Characteristics of Atmosphere Pressure Sensor Caused by Residual Gas

Lidong Du [1, a *], Zhan Zhao [1,b], Shaohua Wu [1] and Zhen Fang [1]

[1] State Key Laboratory of Transducer Technology, Institute of Electronics, Chinese Academy of Sciences, Beijing, CHINA

[a]lddu@mail.ie.ac.cn(corresponding author), [b]zhaozhan@mail.ie.ac.cn

Keywords: Temperature Characteristic, Atmosphere pressure sensor, residual gas, Eutectic bonding

Abstract.
In this paper, temperature characteristic of a previous developed nickel-chromium (Ni-Cr) thin film atmosphere pressure sensor is analyzed caused by residual gas. As expected, the output signal of the previous fabricated sensor increases with atmosphere pressures. But when pressure load is fixed, the voltage-temperature characteristic is nonlinear. One factor of this effect is residual gas. Based on the pressure-displacement equation of membrane, the gas balance equation and Provided that the deformation of membrane is spherical crown, the relationship equation of relative change of piezoresistor is defined. Studying the First order derivative and second order derivative of relationship equation of relative change of piezoresistor, it is proved that the residual gas will affect the temperature characteristic of previous designed sensor.

Introduction

Today, silicon piezoresistive atmosphere pressure sensors which fabricated by micro electro mechanical systems (MEMS) technology have prevailed in the commercial market for several decades. Usually, silicon piezoresistive atmosphere pressure sensors has high temperature coefficient because its piezoresistive coefficient is seriously depended on temperature [1]. Many researchers have do a lots work to change the situation and ameliorate the temperature coefficient. Recently, our group has done some work and developed a nickel-chromium (Ni-Cr) thin film atmosphere pressure sensor based on MEMS technology [2]. Thank to the low temperature coefficient of nickel-chromium (Ni-Cr) thin film, temperature coefficient of pressure sensor is reduced. But, the output of our developed pressure sensor is still complex with temperature variation. Also, we have done some works on why it is. We analyzed the complex temperature characteristics based on theory of thermal mismatch in different strain detecting materials [3]. However, there are many factors which can induce complex temperature characteristics. Residual gas in pressure cavity is the significant one. In this paper, we analyze the temperature characteristics in the angle of residual gas for future enhancing the performance of developed device.

Sensor fabrication and experimental

The model of previous developed sensor is showed in Fig. 1. The thickness of membrane is 40 μm and the side length of the membrane is 3000 μm. The main fabrication processes including dry thermal oxidation, 0.2 μm Si_3N_4 double-sided deposited, KOH etching to form patterned shape and membrane, nickel-chromium alloy deposited and eutectic bonding. In order to enhance the stability of nickel-chromium alloy we design an annealing method: 300^oC annealing 10 minutes in N_2 environment then 150^oC annealing 24 hours in air. In order to complete eutectic bonding step, a 0.2 μm thick Au layer was sputtered as the seed layer on the silicon wafer and glass wafer. Finally, the eutectic bonding step is finished with a load of 0.0013MPa on a vacuum hot plate—by pumping to a surrounding pressure of 10^{-4} Pa, then heated in ramp to 230^oC and maintaining it for 10 minutes.

During the development, the nickel-chromium alloy electrodes should cover a reasonable area of the membrane to utilize more strain with a suitable resistance. So, sensor is finished and shown in Fig. 2.

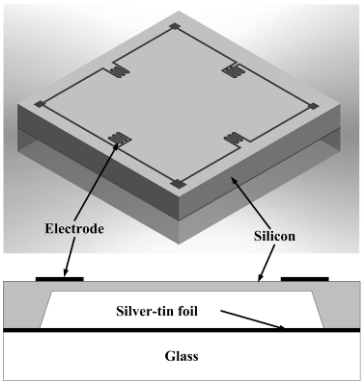


Figure 1. The model of developed sensor

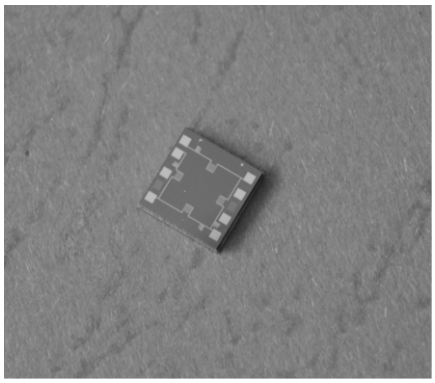


Figure 2. Diced chip of fabricated pressure sensor

We have detailed the eutectic bonding experiment and Ni-Cr thin film experiment in previous work [2]. It is proved that the best bonding quality is obtained when temperature 230°C and bonding pressure no more than 0.0078MPa and stable Ni-Cr thin film resistors can be fabricated in a method 300°C annealing for 10 min in a high purity nitrogen environment then 150°C annealing 24 h in air.

Sensor performance

When the sensor is supplied with a voltage of 5V as an input, typical performances of the pressure sensors are showed in Fig. 3. And the typical temperature curve of the pressure sensors is showed in Fig. 4. It is obvious shown in typical temperature curve that with temperature increase under fixed pressure the output curve of sensor is nonlinear. It will hard to calibrate the pressure sensor.

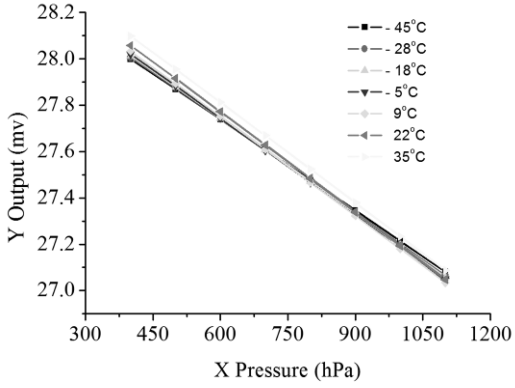


Figure 3. Typical performances of the sensor.

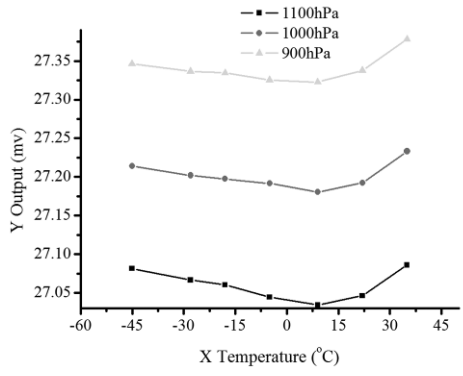


Figure 4. Output-temperature curve under fixed pressure

Usually, the change of maximum membrane strain is proportional to the temperature [1]. After detecting the strain with Wheatstone bridge, we will get a theoretical linearity line between the temperature and bridge output. However, in the previous designed sensor it is not.

In this paper, we will discuss temperature characteristics in the angle of residual gas. On the condition large deflection, the pressure-displacement equation of membrane [1] expressed as:

$$q(w_0)=\frac{2\pi^4}{3}\frac{Eh^3}{(1-\mu^2)L^4}w_0+\frac{\pi^4}{4}\frac{(7-2\mu)(5+4\mu)}{32}\frac{Eh}{(1-\mu^2)L^4}w_0^3 \tag{1}$$

Where, L is half of the membrane, E is young's modulus, μ is the Poisson's ratio, h is the thickness of membrane, and w_0 is the center deflection of membrane. In the fabrication processes, there maybe

have residual air gas in pressure cavity. When temperature changed the residual gas will expanse or contract, then the pressure will change, finally the deflection of membrane will change. The gas balance equation will be

$$\frac{P_1V_1}{T_1}=\frac{P_1V_2}{T_2}=\frac{P_2\left(V_1+\Delta V\right)}{T_1+\Delta T}\Rightarrow P_2=\frac{P_1V_1}{T_1}\frac{T_1+\Delta T}{V_1+\Delta V} \tag{2}$$

Where T_1 is initial room temperature (set 300K), P_1 is initial cavity pressure, and V_1 is initial volume of vacuum cavity; T_2 is the changed temperature, P_2 is the changed cavity pressure, and ΔV is the change of cavity volume. When the membrane pressure is equilibrium, the change of cavity pressure Δq can be calculated by

$$\Delta q=P_2-P_1=\frac{P_1V_1}{T_1}\frac{T_1+\Delta T}{V_1+\Delta V}-P_1=A\frac{T_1+\Delta T}{V_1+\Delta V}-P_1 \tag{3}$$

Also, according to equation (1), the change of cavity pressure Δq can be calculated by

$$\begin{aligned}\Delta q&=q(w_0+\Delta w_0)-q(w_0)\\&=\frac{2\pi^4}{3}\frac{Eh^3}{(1-\mu^2)L^4}\Delta w_0+\frac{\pi^4}{4}\frac{(7-2\mu)(5+4\mu)}{32}\frac{Eh}{(1-\mu^2)L^4}\left(\Delta w_0^3+3w_0\Delta w_0^2+3w_0^2\Delta w_0\right)\\&\approx\frac{2\pi^4}{3}\frac{Eh^3}{(1-\mu^2)L^4}\Delta w_0+\frac{\pi^4}{4}\frac{(7-2\mu)(5+4\mu)}{32}\frac{Eh}{(1-\mu^2)L^4}3w_0^2\Delta w_0\\&=\left(B+3Cw_0^2\right)\Delta w_0\end{aligned} \tag{4}$$

Thus, from equation (3) and (4) we get

$$\left(T_1+\Delta T\right)A\frac{1}{V_1+\Delta V}-P_1=\left(B+3Cw_0^2\right)\Delta w_0 \tag{5}$$

Where, Δw_0 is the change of membrane center deflection. Provided that the deformation of membrane is spherical crown, volume of spherical crown V can be calculated by

$$V=\frac{1}{6}\pi w_0\left(3L^2+w_0^2\right)\approx\frac{\pi L^2w_0}{2}\qquad w_0\ll L \tag{6}$$

If the center deflection changed the change of volume of spherical crown ΔV can be denoted by

$$\Delta V\approx\frac{\pi L^2\Delta w_0}{2} \tag{7}$$

Thus, equation (5) is rewrote as

$$\left(V_1+\frac{\pi L^2\Delta w_0}{2}\right)\left(3Cw_0^2\Delta w_0+B\Delta w_0+P_1\right)-\left(T_1+\Delta T\right)A=0 \tag{8}$$

From equation (8), the relationship between Δw_0 and ΔT will be

$$\Delta w_0=-\frac{\left(P_1\pi L^2+2V_1B+6CV_1w_0^2\right)}{2\pi L^2\left(B+3Cw_0^2\right)}+\sqrt{\left(\frac{P_1\pi L^2+2V_1B+6CV_1w_0^2}{2\pi L^2\left(B+3Cw_0^2\right)}\right)^2+\frac{4A\Delta T}{\pi L^2\left(B+3Cw_0^2\right)}} \tag{9}$$

Relative change of piezoresistor, caused by strain, can be expressed by

$$\frac{\Delta R}{R}=K\varepsilon \tag{10}$$

Strain ε can be calculated by [2]

$$\begin{aligned}\varepsilon_x&=-w_0\frac{L^2}{H^3}\left(\frac{x^2}{L^2}-1\right)\left(\frac{y^2}{L^2}-1\right)^2x\\\varepsilon_y&=-w_0\frac{L^2}{H^3}\left(\frac{y^2}{L^2}-1\right)\left(\frac{x^2}{L^2}-1\right)^2y\end{aligned} \tag{11}$$

When the location x, y of piezoresistor is fixed, strain is proportional to membrane center deflection, strain ε is expressed by

$$\varepsilon=K_1w_0\qquad K_1<0 \tag{12}$$

When membrane center deflection is changed, equation (10) is rewrote as

$$\frac{\Delta R}{R} = K_2\left(w_0 + \Delta w_0\right) \tag{13}$$

Relative change of piezoresistor, caused by change of temperature, can be expressed by

$$\frac{\Delta R}{R} = \alpha\left(T + \Delta T\right) \tag{14}$$

Thus, total relative change of piezoresistor is denoted by

$$\frac{\Delta R}{R} = \alpha\left(T + \Delta T\right) + K_2\left(w_0 + \Delta w_0\right) \tag{15}$$

First order derivative of equation (15) is listed by

$$\begin{aligned}\left(\frac{\Delta R}{R}\right)' &= \alpha + K_2\frac{d\Delta w_0}{d\Delta T} \\ &= \alpha + K_2\frac{2A}{\pi L^2\left(B+3Cw_0^2\right)}\left[\left(\frac{P_1\pi L^2 + 2V_1B + 6CV_1w_0^2}{2\pi L^2\left(B+3Cw_0^2\right)}\right)^2 + \frac{4A\Delta T}{\pi L^2\left(B+3Cw_0^2\right)}\right]^{-1/2}\end{aligned} \tag{16}$$

From equation (16), we know that there is zero point of first order derivative of equation (15). Second order derivative of equation (15) is listed by

$$\left(\frac{\Delta R}{R}\right)'' = -K_2\left(\frac{2A}{\pi L^2\left(B+3Cw_0^2\right)}\right)^2\left[\left(\frac{P_1\pi L^2 + 2V_1B + 6CV_1w_0^2}{2\pi L^2\left(B+3Cw_0^2\right)}\right)^2 + \frac{4A\Delta T}{\pi L^2\left(B+3Cw_0^2\right)}\right]^{-3/2} > 0 \tag{17}$$

From equation (17), we know that second order derivative of equation (15) is more than zero. Thus, total relative change of piezoresistor has minimum value. So, the residual gas will affect the temperature characteristic of designed sensor.

Summary

In previous work, a nickel-chromium (Ni-Cr) thin film atmosphere pressure sensor is developed. In it, nickel-chromium (Ni-Cr) alloy (80:20 wt%) is used as the strain detecting material with a smaller but acceptable sensitivity and simpler processes; silver-tin (Ag-Sn) alloy, which is 3.5%wt Ag and 20um thickness, is used as an alternative and easy bonding choice to complete the vacuum package. The test results suggest that a precision within 0.3% in square fitting and a temperature coefficient offset (TCO) 620 ppm/(^{o}C FSO). As expected, the output signal of the previous fabricated sensor increases with atmosphere pressures. But when pressure load is fixed, the voltage-temperature characteristic is nonlinear. One factor of this effect is residual gas. In this paper, the analysis is started from the pressure-displacement equation of membrane. Then, based on the gas balance equation we obtain the relationship between the change of cavity pressure Δq and the change of membrane center deflection Δw_0. Provided that the deformation of membrane is spherical crown, the relationship is defined between the change of membrane center deflection Δw_0 and the change of temperature ΔT. Finally, the relationship equation of relative change of piezoresistor is obtained. Studying the First order derivative and second order derivative of relationship equation of relative change of piezoresistor, we found that there is zero point of first order derivative and second order derivative is more than zero. Thus, total relative change of piezoresistor has minimum value. It is proved that the residual gas will affect the temperature characteristic of previous designed sensor.

Acknowledgement

This work has been supported by the National Natural Science Foundation of China (Grant No. 51305423), the National Basic Research Programme (2011CB302104), State 863 Programme (2012AA040502), State 863 Programme (2012AA040504) and Special Fund for Public Welfare (GYHY201004004) of China.

References

[1] S.D. Senturia, Microsystem design, 2nd ed., Kluwer Academic Publishers, 2001.

Reference an article:
[2] L.D Du, Z. Zhao, L. Xiao etc., Nickel–chromium alloy piezoresistive pressure sensor using eutectic bonding, Micro & Nano Letters, 12(7) (2012) 1184–1188.

[3] L.D Du, L. Xiao, Z. Zhao, Temperature characteristic of Platinum Piezoresistive Pressure Sensor, Key Engineering Materials, 483 (2011) 180-184.

Key Engineering Materials Vols 645-646 (2015) pp 509-512
© (2015) Trans Tech Publications, Switzerland
doi:10.4028/www.scientific.net/KEM.645-646.509

Submitted: 2014-10-29
Accepted: 2014-11-20

Q-factor Improving of Film Bulk Acoustic Wave Resonator for Chip-scale Atomic Clocks

Zhongshan ZHANG[1,a], Liang TANG[2,b] and Lei JI[1,c]

[1]School of Electronic and Information Engineering, Soochow University, Suzhou, Jiangsu, China

[2]Institute of Acoustics, Chinese Academy of Sciences, Beijing, China

[a]zhangzhongshan@mail.iggcas.ac.cn, [b]tangliang@mail.ioa.ac.cn(corresponding author),

[c]jileisuda@163.com

Keywords: Q-factor, Film bulk acoustic wave resonator, Chip-scale atomic clocks, SiO_2 film

Abstract. Film bulk acoustic wave resonators(FBARs) with relatively high Q-factor are considered good candidates to be used in the RF module of chip-scale atomic clocks(CSACs). In order to simulate and analyze the resonant properties, the Mason equivalent circuit of the FBAR device is introduced, which consists of five parts including top electrode layer, low temperature silicon oxide layer, piezoelectric layer, bottom electrode layer and a composite support structure layer. With the practical processing conditions considered, the piezoelectric layer with a reasonable thickness of 1.30um is selected to achieve a FBAR device with resonant frequency 4.60GHz and Q-factor 278 by the simulation and analysis. In order to further improve the Q-factor, SiO_2 thin films with thicknesses from 0.10um to 0.50um placed between the top electrode and piezoelectric layer are introduced. However, as the SiO_2 thin film is introduced, the resonant frequency of the FBAR device will drop. In order to keep the resonant frequency fixed to 4.60GHz, the thickness of the piezoelectric layer is adjusted. Finally, the FBAR device resonating at 4.60GHz with Q-factor 627 is achieved, the thicknesses of the SiO_2 film and piezoelectric layer of which are 0.20um and 0.69um respectively. The Q-factor of the FBAR device improves about 350, and the FBAR device is expected to be used in CSACs.

Introduction

Chip-scale atomic clocks(CSACs) possess advantages of low power consumption and small size, which are good candidates to be applied in the fields of geophysical survey and military equipments. CSACs consist of three parts including physics package, control loop and RF module, and the power consumption of each part is limited to 10mW in order to meet the 30mW power consumption requirement of CSACs[1]. Traditionally, the RF frequency synthesizer based on crystal oscillator is used to build the RF module, and the power consumption of the RF module is about 60mW, which is much bigger than the spec[2]. An alternative way is using a high-Q resonator to build the RF module. Film bulk acoustic wave resonators(FBARs) have advantages of high frequency, high Q-factor and small size[3], which are considered good candidates to be used in the RF module of CSACs. In this paper, FBAR devices with resonant frequency 4.60GHz for the Cs CSACs are designed, and SiO_2 thin films are introduced to further improve the Q-factor of FBAR devices.

The Mason equivalent circuit

The structure of FBAR device(as shown in Fig. 1) consists of five parts including top electrode layer(TE), low temperature silicon oxide layer(LTO), piezoelectric layer(PE), bottom electrode layer(BE) and a composite support layer(Si_xN_y-SiO_2-Si_xN_y). The material of piezoelectric layer(PE) is Aluminum Nitride(AlN). The materials of the top electrode(TE) and bottom electrode(BE) are both Molybdenum(Mo), and the thicknesses of the TE and BE are fixed to 0.20um. Si_xN_y or SiO_2 thin film is usually used as the supporting material. In our previous work, it was found that the residual stress of a single Si_xN_y or SiO_2 diaphragm often caused wrinkling in the released support diaphragm, which degraded the Q-factor dramatically. Therefore, a composite support layer made up of 0.50um Si_xN_y,

0.20um SiO_2 and 0.50um Si_xN_y is selected herein. The effective diameter of the device is 400um. As for the structure in Fig. 1, the 1-D Mason equivalent circuit is shown in Fig. 2.

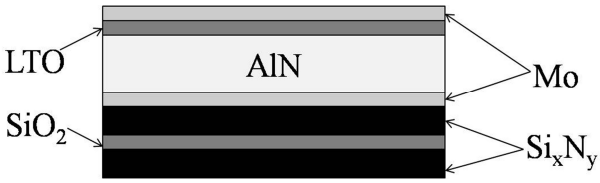


Fig. 1 Structure of the FBAR device

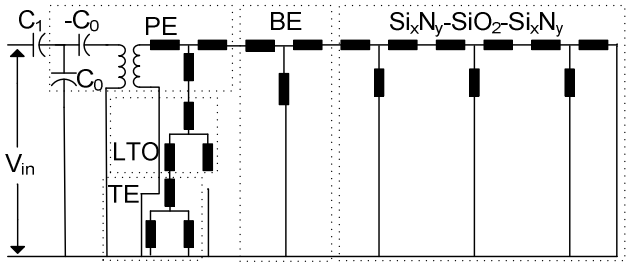


Fig. 2 Mason equivalent circuit of the FBAR device

All parameters used in the simulation are given in Table 1. As for the Fig. 1, each of the mechanical layers can be equivalent to a T-type network, which is shown in Fig. 3. In Fig. 3, Z stands for the acoustic impedance, k is the number of longitudinal wave in the thickness direction of this layer, d stands for the thickness of this layer. As the acoustic loss of the material is considered, k is a plural which is given in Eq. 1,

$$k = k_r - j\alpha \,. \tag{1}$$

In Eq. 1, $k_r = 2\pi f / V$, α is loss coefficient which is proportional to the square of f, f is frequency, V is the velocity of longitudinal wave in the thickness direction. As for Fig. 2, the input impedance is derived by the method of ABCD network, and the Q-factor can be derived by Eq. 2,

$$Q_s = \frac{f}{2}\frac{d\angle Z_{in}}{df}\,|\,f_s \,. \tag{2}$$

Table 1. Material parameters used in the simulation

Material	Acoustic Impedance [$(kg/m^2s)\times10^4$]	Acoustic Velocity [m/s]	Acoustic Attenuation [dB/m@1GHz]	K_t^2	ε
AlN [4]	3600	11050	800	0.065	10.50
Mo [5]	6380	6213	500	/	/
Si_xN_y [4,6]	3590	11000	1200	/	7.60
SiO_2 [4,6]	1460	5500	1400	/	4.00

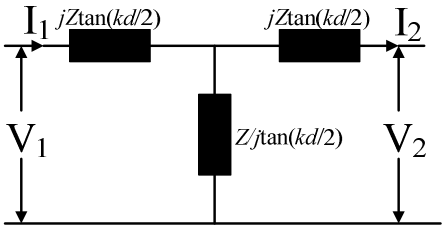


Fig. 3 Equivalent circuit of each mechanical layer of the FBAR device

Simulation and Results

Using the method mentioned above, resonant properties of FBAR devices are simulated with different piezoelectric layer thicknesses to achieve the 4.60GHz resonant frequency with a relatively high Q-factor. With the practical processing conditions considered, the thickness of the AlN piezoelectric layer is restricted to the range from 0.50um to 2.00um. If the thickness of AlN piezoelectric film were thinner than 0.50um, the piezoelectric performance would degrade. On the other hand, as the deposition of AlN piezoelectric thin film is very slow, If the thickness of AlN

piezoelectric film were thicker than 2.00um, the deposition time would be unbearable. Meanwhile, the piezoelectric performance of the AlN piezoelectric film with the thickness thicker than 2.00um would also degrade dramatically due to the large residual stress. Table. 2 shows the possible FBAR devices with a 4.60GHz resonance. The FBAR device with a fundamental resonant frequency of 4.60GHz has the PE thickness thinner than 1.00nm, which is unreasonable. The FBAR device with a second harmonic resonant frequency of 4.60GHz or a fourth harmonic resonant frequency of 4.60GHz has the PE thickness out of the range from 0.50um to 2.00um, which is also unreasonable. Only the FBAR device with a third harmonic resonance frequency of 4.60GHz has the PE thickness of 1.30um, which is within the limits. The Q-factor of such a FBAR device is 278 at the 4.60GHz resonant frequency. Fig. 4 shows the input impedance of the FBAR device versus frequency, and Fig. 5 shows the Q-factor of the FBAR device versus frequency.

Table 2. Q-factor and PE thickness of FBAR devices with a 4.60GHz resonance

f_{s1}[GHz]	Q_{s1}	f_{s2}[GHz]	Q_{s2}	f_{s3}[GHz]	Q_{s3}	f_{s4}[GHz]	Q_{s4}	PE thickness
4.60	~							<1.00[nm]
		4.60	695					0.11[um]
				4.60	278			1.30[um]
						4.60	~	>2.00[um]

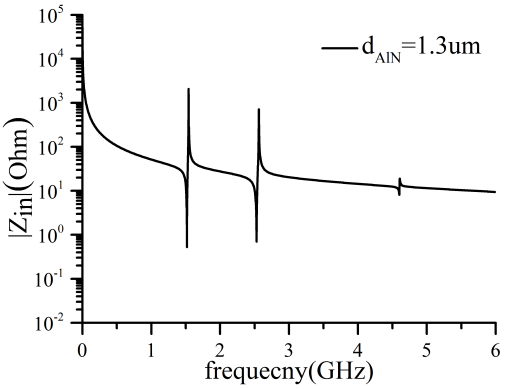


Fig. 4 The input impedance of the FBAR device versus frequency

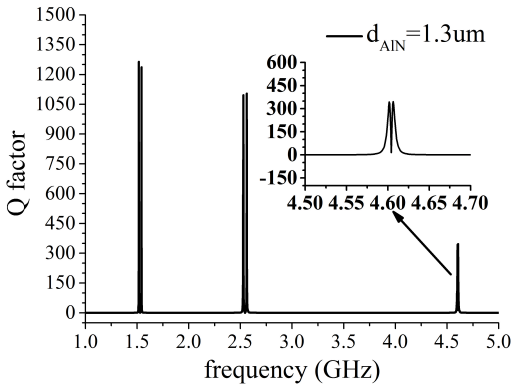


Fig. 5 Q-factor of the FBAR device versus frequency

In order to further improve the Q-factor of the FBAR device mentioned above, SiO_2 film is introduced into the structure of the FBAR between the top electrode and piezoelectric layer. With the practical processing conditions considered, the thickness of the SiO_2 film is restricted to the range from 0.10um to 0.50um. If the thickness of the SiO_2 film were thinner than 0.10um, pinholes would appear in the SiO_2 film and short the top electrode and piezoelectric layer. On the other hand, If the thickness of the SiO_2 film were thicker than 0.50um, large residual stress would appear in the SiO_2 film and further crack the structure of the FBAR device. The resonant characteristics of FBAR devices with different thicknesses of SiO_2 films from 0.10um to 0.50um are simulated. As the SiO_2 thin film is introduced, the resonant frequency of FBAR device will drop. In order to keep the resonant frequency fixed to 4.60GHz, the thickness of piezoelectric layer is adjusted. Simulation results show that the Q-factor increases first and then decreases as the thickness of the SiO_2 film increases from 0.10um to 0.50um(as shown in Table. 3). The FBAR device resonating at 4.60GHz with a biggest Q-factor 627 is achieved, the thicknesses of the SiO_2 film and piezoelectric layer of which are 0.20um and 0.69um respectively. Fig. 6 shows the input impedance of the FBAR device including a SiO_2 film with the thickness of 0.20um versus frequency, and Fig. 7 shows the Q-factor of the FBAR device including a SiO_2 film with the thickness of 0.20um versus frequency. The Q-factor of the FBAR device improves about 350, and the FBAR device is expected to be used in CSACs.

Table 3. Q-factor and PE thickness of FBAR devices with different thicknesses of SiO_2 films

SiO_2 thickness[um]	PE thickness[um]	f_{s3}[GHz]	Q_{s3}
0.10	0.89	4.60	534
0.20	0.69	4.60	627
0.30	0.61	4.60	617
0.40	0.51	4.60	606
0.50	0.39	4.60	573

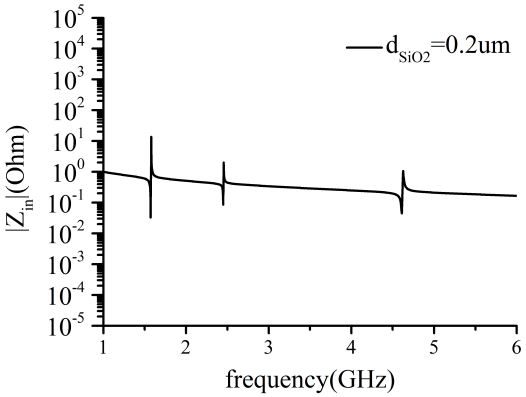


Fig. 6 The input impedance of the FBAR device including a SiO_2 film with the thickness of 0.20um versus frequency

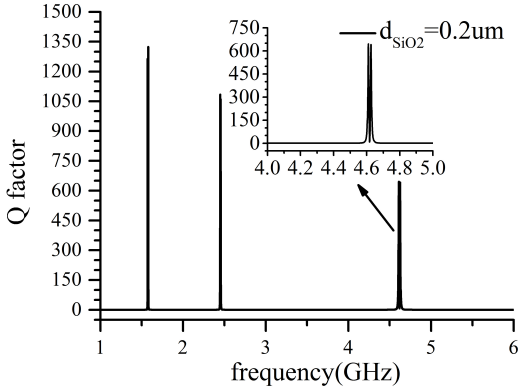


Fig. 7 The Q-factor of the FBAR device including a SiO_2 film with the thickness of 0.20um versus frequency

Summary

With the practical processing conditions considered, the piezoelectric layer with a reasonable thickness of 1.30um is selected to achieve a FBAR device with resonant frequency 4.60GHz and Q-factor 278 by the simulation and analysis. In order to further improve the Q-factor, SiO_2 thin films with thicknesses from 0.10um to 0.50um placed between the top electrode and piezoelectric layer are introduced. Finally, the FBAR device resonating at 4.60GHz with Q-factor 627 is achieved, the thicknesses of the SiO_2 film and piezoelectric layer of which are 0.20um and 0.69um respectively. The Q-factor of the FBAR device improves about 350, and the FBAR device is expected to be used in CSACs.

Acknowledgement

This work is supported by the National Natural Science Foundation of China (Grant No.11104313) and Sinoprobe-09-02-03.

References

[1] S. Romisch, R. Lutwak, Low-power 4.6-GHz stable oscillator for CSAC, IEEE International Frequency Control Symposium and Exposition. (2006)448-451.

[2] R. Lutwak, The chip-scale atomic clock-recent developments, Frequency Control Symposium Joint with the 22nd European Frequency and Time Forum. (2009)573-577.

[3] L. Tang, Z.H. Hao, D.H. Qiao, et al., Development and analysis of a ZnO film bulk acoustic resonator, J. Piezoelectectrics and Acoustooptics. 30(2008)387-389.

[4] W. Pang, H. Zhang, et al., Analytical and experimental study on second harmonic response of FBAR for oscillator applications above 2GHz, IEEE Ultrasonics Symp. 4(2005)2136-2139.

[5] W. Pang, H. Zhang, et al., Analytical and experimental study on the second harmonic mode response of a bulk acoustic wave resonator, J. Micromech. Microeng. 20(2010) 115015-115024.

[6] Y.R. Kang, S.C. Kang, et al., Air-gap type film bulk acoustic resonator using flexible thin substrate, J. Sensors and Actuators. 117(2005)62-70.

Key Engineering Materials Vols 645-646 (2015) pp 513-516
© (2015) Trans Tech Publications, Switzerland
doi:10.4028/www.scientific.net/KEM.645-646.513

Submitted: 2014-10-31
Accepted: 2014-12-23

Study on a Planar Interdigitated MEMS Supercapacitor Using Modeling and Simulation Method

Keren Dai[1,a] , Xiaofeng Wang[2,b*] , Wushuang Lv[3,c] , Zheng You[4,d]

[1]State Key Laboratory of Precision Measurement Technology and Instruments, Department of Precision Instruments, Tsinghua University, Beijing, 100084, P. R. China

[a]daikr1991@qq.com, [b]xfw@tsinghua.edu.cn

Keywords: Interdigitated MEMS Supercapacitor Simulation

Abstract: In this paper, a modeling and simulation method for planar interdigitated ruthenium oxide MEMS supercapacitor was proposed based on the electrochemical reaction mechanism of supercapacitor. The study simulated the planar interdigitated ruthenium oxide MEMS super capacitor using Comsol software. The highly accurate charge and discharge curves of the super capacitor, electric potential distribution graph and the concentration distribution graph were got through simulation. The effects of two structure-parameters were discussed in the research.

Introduction:

Supercapacitor is a research focus in the micro-energy field. Many researchers are interested in the dynamic modeling for supercapacitor. Dynamics modeling of super capacitor, is building a mathematical model by a set of partial differential equations and corresponding boundary conditions, according to the electrochemical mechanism of supercapacitor.

In 1999, Chuan Lin put forward a one-dimensional mathematical model of ruthenium oxide super capacitor, considering both the effect of electric double layer and Faraday reaction in dynamic modeling for the first time [1]. During 2007 ~ 2011, Hossein Farsi and Fereydoon Gobal, completed further simulation for layers of the same structure, using the model of Chuan Lin [2]. They studied how the ruthenium oxide lattice constant, discharge current, exchange current density and other factors affect the property of super capacitor discharge.

However, this model is only applicable to one-dimensional structures that have differences in only one dimension. This model is unable to simulate multidimensional structures, such as two-dimensional planar interdigitated structure and three-dimensional micro column structure. Therefore, there are few researches on the dynamics modeling and simulation of planar interdigitated MEMS super capacitor.

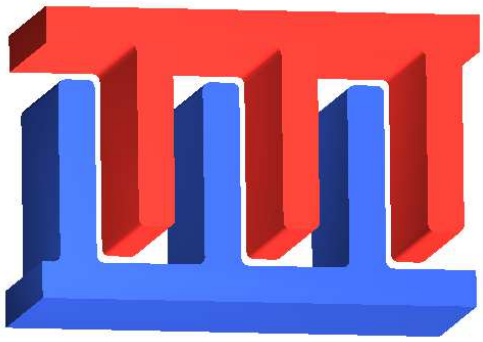


Figure1 Planar interdigitated structure

Tsinghua University, Xiaofeng Wang proposed a two-field coupling model which includes both the potential field and the concentration field, on the basis of Chuan Lin's research. This new model describes electrochemical reaction mechanism of supercapacitor accurately.
This two-field coupling modeling theory is the base of the research. Using comsol software platform, this simulation displayed highly accurate charge and discharge curves of the super capacitor, electric potential distribution graph and the concentration distribution graph. The paper also discussed that how the structure parameters affect the charge and discharge performance of supercapacitor. Finally, the study pointed out the direction to improving the performance of supercapacitor.

Mathematical Model:
According to Xiaofeng Wang's two-field coupling model of supercapacitor, potential equation and the concentration equation are given both in the electrode and the spacer of supercapacitor. These equations describe the mechanism of electrochemical double-layer effects and Faraday reactions.

Table1 Two-field coupling model of supercapacitor

area	electrode	spacer
Potential field	$\nabla\left(-\sigma\nabla\Phi_1\right)=i_F+i_{DL}$ $\nabla\left(\sigma_p\nabla\Phi_2\right)=i_F+i_{DL}$	$\nabla\left(\sigma_S\nabla\Phi_2\right)=0$
Concentration field	$\frac{\partial c}{\partial t}+\nabla(-D_s\nabla c)=\frac{i_F}{F}$	$\frac{\partial c}{\partial t}+\nabla(-D_l\nabla c)=0$

In this table, i_F represents the current density of Faraday reactions. i_{DL} represents the current density of double-layer effects. σ, σ_p and σ_S are the Conductivity of matrix phase, electrolyte phase in the electrode, electrolyte phase in the spacer. Φ_1 and Φ_2 represent the potential of matrix phase and electrolyte phase. Ds and Dl represent the proton diffusion rate of matrix phase and electrolyte phase. F, c, t represent Faraday constant, concentration of the proton and time variable.
The relation between these two fields can be described by associated equations.
By Faraday reaction,

$$i_F = a_v j_{loc}$$

a_v represents the specific surface area of electrode. j_{loc} represents Faraday transfer current density.
By double-layer effects

$$i_{DL} = a_v C_{dl} \frac{\partial(\Phi_1 - \Phi_2)}{\partial t}$$

C_{dl} represents the capacitor of double layers.
By Butler-Volmer equation

$$j_{loc} = i_0 \left\{ \exp\left[\alpha_a f\left(\Phi_1 - \Phi_2 - U_{\mathrm{OC}}\right)\right] - \exp\left[-\alpha_c f\left(\Phi_1 - \Phi_2 - U_{\mathrm{OC}}\right)\right] \right\}$$

i_0 represents Faraday exchange current density, which may be affected by the impedance. α_a and α_c represent transfer coefficient of the anode and cathode. f=F/RT, R is universal gas constant and T is Kelvin degree.

U_{OC} means the open-circuit potential of Faraday reaction.

Anode: $U_{OC} = 0.5(1+\theta)$

Cathode: $U_{OC} = 0.5\theta$

Such mathematical model realizes dynamic modeling of supercapacitor. Using comsol software as calculation tool, the model can realize the dynamic simulation of planar interdigitated ruthenium oxide MEMS supercapacitor.

Simulation results:

Proton concentration distribution and electric potential distribution inside the supercapacitor have important influence on the performance of the capacitor. In the study, simulation shows the electric potential distribution graph, the concentration distribution graph, and concentration gradient distribution graph. These results achieved the basic purpose of dynamic simulation.

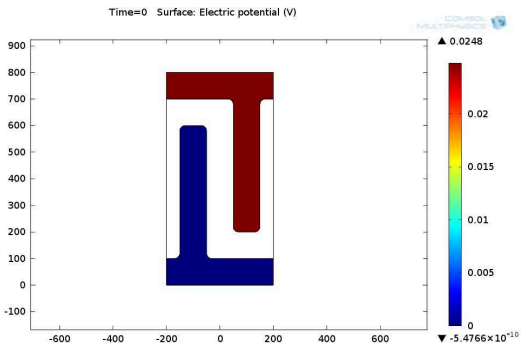


Figure2 Electric potential distribution graph

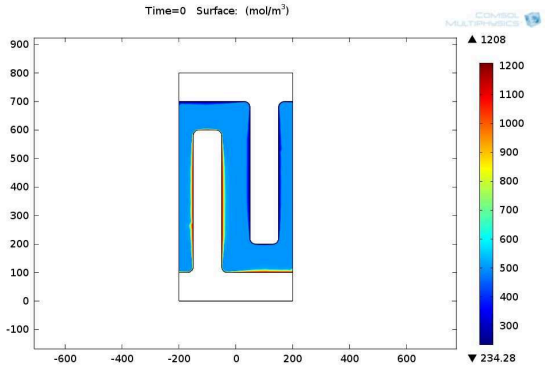


Figure3 Concentration distribution graph

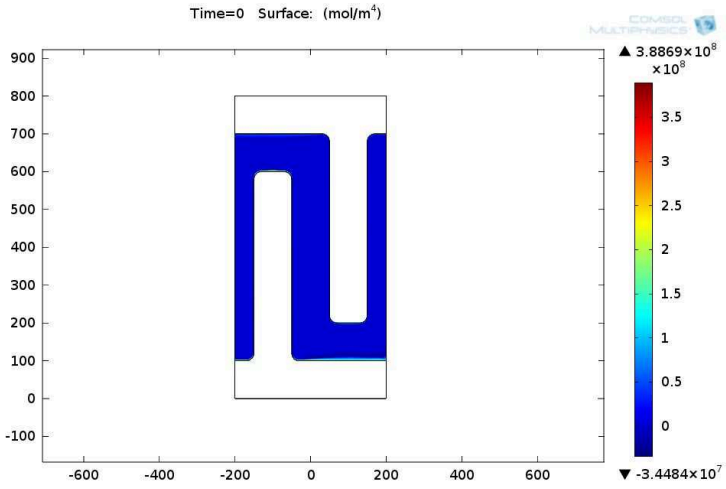


Figure4 Concentration gradient distribution graph

The aspect ratio and clearance ratio are two important parameters of the planar interdigitated structure. The charge and discharge performance of supercapacitor changes as these two parameters change. The study shows discharge curve graphs under different aspect ratios and clearance ratios.

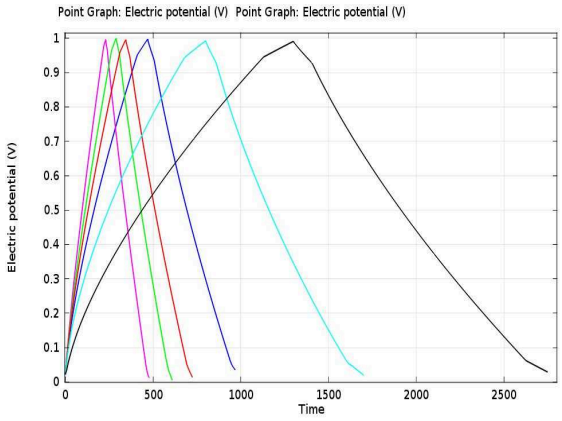


Figure5 Discharge curve graphs under different aspect ratios

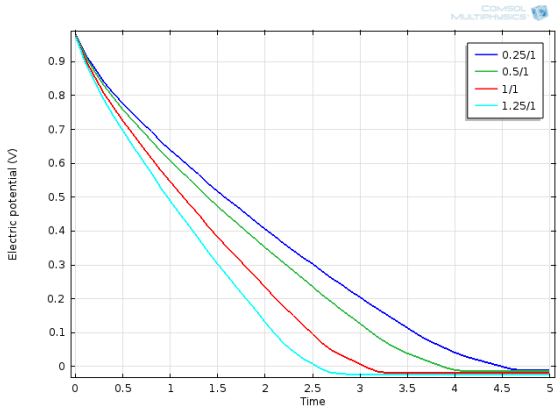


Figure6 Discharge curve graphs under different clearance ratios

Simulation results illustrate that the larger the aspect ratio, the longer the super capacitor charge and discharge time, and the smaller the clearance ratio, the longer the charge and discharge time, too. The two key conclusions are important for planar interdigitated structure design and optimization.

Conclusions:

To sum up, the study established the simulation platform, on the basis of MEMS super capacitor two fields coupling model. The research simulated the planar interdigitated MEMS super capacitor dynamically and discussed the effects of structural parameters on the capacitor performance. The results of the research point out the direction to improving the property of capacitor.

References

[1] Lin C, Ritter J A, Popov B N, et al. A Mathematical Model of an Electrochemical Capacitor with Double-Layer and Faradaic Processes[J]. Journal of the Electrochemical Society, 1999, 146(9): 3168-3175.

[2] Farsi H, Gobal F. A mathematical model of nanoparticulate mixed oxide pseudocapacitors; part I: model description and particle size effects[J]. Journal of Solid State Electrochemistry, 2009, 13(3): 433-443.

Key Engineering Materials Vols 645-646 (2015) pp 517-521
© (2015) Trans Tech Publications, Switzerland
doi:10.4028/www.scientific.net/KEM.645-646.517

Submitted: 2014-11-02
Accepted: 2014-12-23

Passive Acoustic localization based on MEMS microphone Arrays

Dai Ximing[1,a],Lou Wenzhong[1,b],Guo Mingru[1,c],Wang Fufu [1,d],Jin xin[1,e]

[1] National Key Laboratory of Mechatronics Engineering and Control, Beijing Institute of Technology, Beijing, CHINA,100081

[a]shandongximing@163.com(corresponding author), [b]louwz@bit.edu.cn,[c]jiaoluo@bit.edu.cn,

[d]wangfufu2004@sina.com, [e]jinx0798@qq.com

Keywords: MEMS microphone; TDOA; GCC; passive acoustic localization;

Abstract. In this paper we used the MEMS microphone to detect the sound position. A four–microphone array was constructed to localize sound source with Time Difference of Arrival (TDoA) measurements based on hyperbola model. The time delay was calculated using Generalized Cross Correlation (GCC) algorithm. A practical test system was built to confirm the feasibility of the hyperbola model and GCC algorithm using MEMS microphone. Data were collected in field experiments and calculated on PC by matlab. The results show that the method instructed in this paper is feasible in localizing the sound position with MEMS microphone.

Introduction

MEMS microphone has many advantages than traditional ECM (Electret Condenser Microphone). MEMS microphone has smaller size, higher temperature endurance, better stability, lower power consumption and suitable for STM (Surface Mounted Technology). All of these advantages make MEMS microphone acquire quick development. So far MEMS microphones are mainly used in mobile equipment such as smart phones and Tablet PC. With the development of internet of things technology and the arising of intelligent home, MEMS microphones will have a larger space for application.

In civilian areas passive acoustic localization technology can be used in smart conference video system, helping people who has ear problems and so on. In military areas it can be used in sniper and artillery position detection. In industry areas it can be used to find out the position of mechanical failure especially in cars and machine tools.

In this paper, we try to use MEMS microphones to detect the position of sound. Based on the results of experiments we can say that MEMS microphones combined with the method of this paper have high quality in acoustic localization.

1. Geometric Model Description

The four microphone sensors are settled as shown in figure 1.

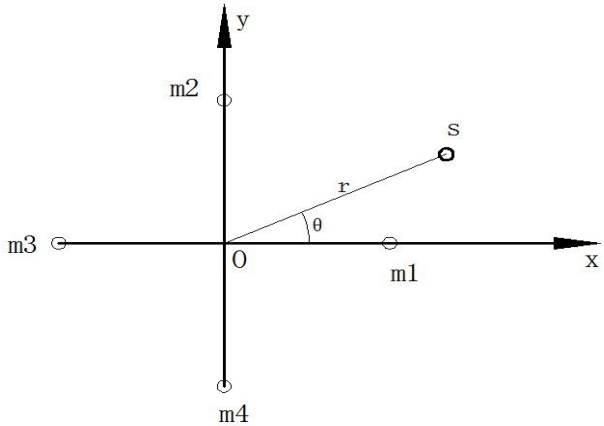


Fig 1. Position of four stationary sensors

These four sensors are symmetrically distributed on axis. m1,m2,m3,m4 are microphones with positions m1(d,0), m2(0,d), m3(-d,0), m4(0,-d) and s is sound emitter with position (r,θ). The four sensors are divided into two groups. m1 and m3 compose the first group and m2 and m3 compose the second. Take the first group for example to explain how the method works.

The distances between s and m1, m3 are r1, r3. At a time the difference of distances between s and m1, m3 is a fix value. Based on the theory of math， sound emitter is located on the hyperbola whose focuses are made up of m1 and m3. So we can get the function as follows.

$$\frac{(r\cos\theta)^2}{\left(\frac{\Delta tc}{2}\right)^2}-\frac{(r\sin\theta)^2}{d^2-\left(\frac{\Delta tc}{2}\right)^2}=1 \tag{1}$$

Where $\Delta t=\frac{r_3}{c}-\frac{r_1}{c}$, c=343.2m/s is the speed of sound in dry air at 20℃.[1]

In function (1) there are three unknown various r,θ and Δt. Since Δt can be got by GCC algorithm in section 2, we can consider Δt as known.

Change the form of equation (1) we can get another equation as follows:

$$\frac{(\cos\theta)^2}{(\Delta tc)^2}-\frac{(\sin\theta)^2}{4d^2-(\Delta tc)^2}=\frac{1}{4r^2} \tag{2}$$

In actual situation the distance d is very short compared to the sound distance r, that is d<<r. so we can consider the right part of equation (2) as zero. Then we can get the result as follows:

$$\cos\theta=\frac{\Delta tc}{2d} \tag{3}$$

Further, we get $\theta=\cos^{-1}\left(\frac{\Delta t\cdot c}{2d}\right)$ (4)

From function (4) we know that the azimuth can be calculated after the time difference Δt was get in section 2.

In this way, two groups of sensors can calculate two independent azimuth. We can combine the two to obtain an accurate result of measurement.

2. Time delay calculate algorithm

From the function (4) we know that the measurement of time delay Δt is critic to the measurement of azimuth. The accuracy of azimuth estimation will be directly depend on the accuracy of time delay measurement.

In this paper, we used the GCC algorithm to calculate the time delay. First, we need to calculate the cross-power spectrum of the signals received by two microphones and weight the result to inhibit environmental noise. Then take inverse Fourier transform to get correlation function which is in time-domain. The coordinate of the peak of correlation function is the time delay Δt.

$$x_1(t)=\alpha_1 s(t)+n_1(t) \tag{5}$$

$$x_2(t)=\alpha_2 s(t-\tau)+n_2(t) \tag{6}$$

Where $x_1(t), x_2(t)$ are signals received by two different microphones at the same time. $s(t)$ presents the sound source, α_1, α_2 are sound attenuation coefficient, $n_1(t), n_2(t)$ are two non-associative white Gaussian noise. Figure 2 shows the calculation process of time delay Δt with GCC algorithm. Because the signal we get from the microphone is sampled signal which is discrete-time signal-sequence, we displace t by n.

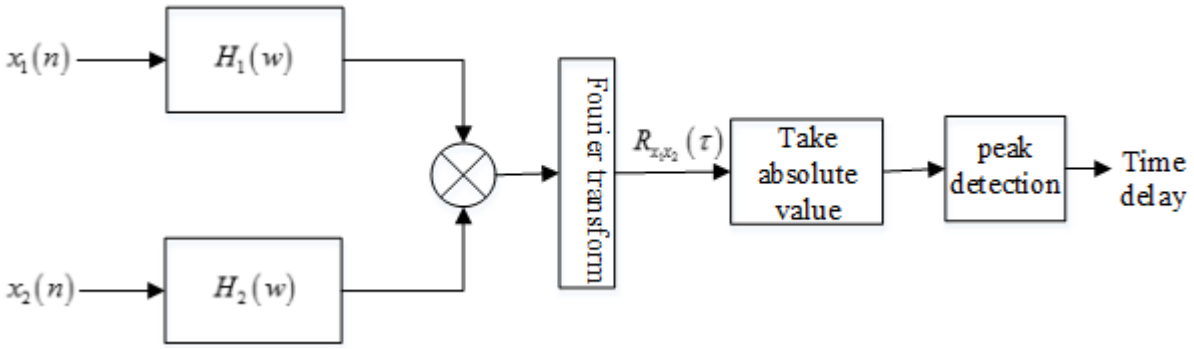


Fig 2 Calculation process of GCC

We take $X_1(\omega)$ and $X_2(\omega)$ as the Fourier transform results of $x_1(n)$ and $x_2(n)$. $H_1(\omega)$ and $H_2(\omega)$ are filter coefficients. The cross correlation function of two channels signal is $R_{x_1x_2}(\tau)$.

$$R_{x_1x_2}(\tau)=\int_0^{\pi}\psi_{12}(\omega)X_1(\omega)X_2^*(\omega)e^{-j\omega\tau}d\omega=\int_0^{\pi}\psi_{12}(\omega)G_{x_1x_2}(\omega)e^{-j\omega\tau}d\omega$$

Where $\psi_{12}(\omega)$ is the generalized cross correlation weighted function. $\psi_{12}(\omega)=H_1(\omega)H_2^*(\omega)$, * is the denotation of conjugation. $G_{x_1x_2}(\omega)$ denotes cross power spectrum. $\psi_{12}(\omega)G_{x_1x_2}(\omega)$ is the generalized cross power spectrum. The key issue is choose a proper cross correlation weighted function $\psi_{12}(\omega)$ to make the peak of $R_{x_1x_2}(\tau)$ more obvious.

The most common cross correlation weighted functions are showed in table 1.

Table 1 Cross correlation weighted functions

Name	$\psi_{12}(\omega)$
Basic cross correlation	$\psi_{12}(\omega)=1$
Roth	$\psi_{12}(\omega)=\frac{1}{G_{x_1x_2}(\omega)}$
SCOT	$\psi_{12}(\omega)=\frac{1}{\sqrt{G_{x_1x_1}(\omega)G_{x_2x_2}(\omega)}}$
CSP	$\psi_{12}(\omega)=\frac{1}{\lvert G_{x_1x_2}(\omega)\rvert}$
Eckart	$\psi_{12}(\omega)=\frac{G_{ss}(\omega)}{\lvert G_{x_1x_2}(\omega)G_{x_1x_2}(\omega)\rvert}$
ML	$\psi_{12}(\omega)=\frac{\lvert\gamma(\omega)\rvert^2}{\lvert G_{x_1x_2}(\omega)\rvert\left(1-\lvert\gamma(\omega)\rvert^2\right)}$
HB weight	$\psi_{12}(\omega)=\frac{\lvert G_{x_1x_2}(\omega)\rvert}{G_{x_1x_1}(\omega)G_{x_2x_2}(\omega)}$
WP weight	$\psi_{12}(\omega)=\frac{\lvert G_{x_1x_2}(\omega)\rvert^2}{G_{x_1x_1}(\omega)G_{x_2x_2}(\omega)}$

$G_{x_1x_1}(\omega)$ and $G_{x_2x_2}(\omega)$ denote self-power-spectrum of signal $x_1(n)$ and $x_2(n)$.

$|\gamma(\omega)|^2 = \frac{|G_{x_1x_2}(\omega)|^2}{G_{x_1x_1}(\omega)G_{x_2x_2}(\omega)}$.[2][3][4][5]

3. Field test system

Figure 3 is the test system with four MEMS microphones and a signal receiver.



Fig 3 Field test system

Figure 4 and 5 is two field experiments. In two experiments we put sound source at three positions A,B,C as showed in figure 4 and 5. We collect signals twice at every position. The calculation results is showed in table 2 and table 3.

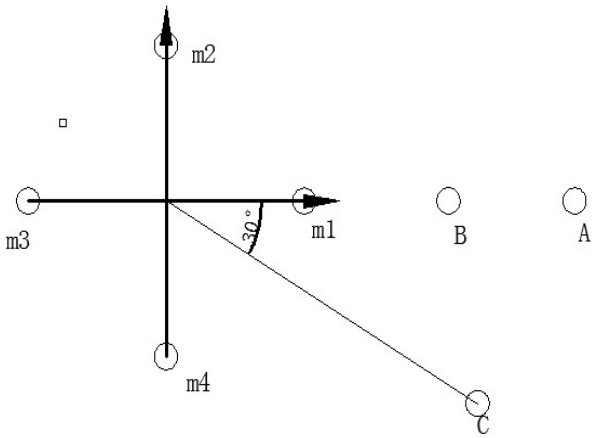


Fig 4 First test sound source position

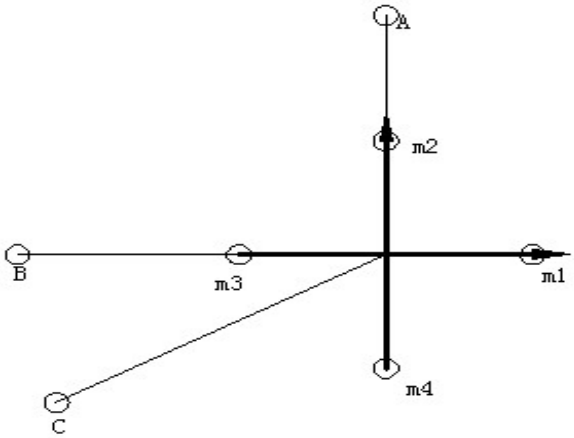


Fig 5 Second test sound source position

Table 2. First test results: $\theta \in [0,360]$, sample rate 51200Hz

position	Sample NO.	Distance [m]	practice value	θ [degree]	Absolute difference
A	1	7	0	1.6022	1.6022
	2	7	0	0.8010	0.8010
B	1	3.5	0	0.8010	0.8010
	2	3.5	0	0	0
C	1	7	330	328.8507	1.1493
	2	7	330	328.8517	1.1483

Table 3. Second test results: $\theta \in [0,360]$, sample rate 6000Hz

position	Sample NO.	Distance [m]	practice value	θ [degree]	Absolute difference
A	1	7	90	90.4785	0.4785
	2	7	90	88.9747	1.0253
B	1	15	180	180	0
	2	15	180	178.6424	1.3576
C	1	7	210	214.4773	4.4773
	2	7	210	214.5978	4.5978

From the results we can see that the absolute difference range from 0 to 4.5978 which shows that the MEMS microphone arrays can realize preliminary sound source localization.

4. Summary

In this paper we build a test system with four MEMS microphones to localize the sound source based on Time Difference of Arrival measurements. Hyperbolic model was used to calculate the azimuth of sound location combining data fusion algorithm. The tests results show that the system build in this paper has high precision relatively in detecting the azimuth of sound source, which is a good reference to further study. In future more tests are needed to find out the pattern about how the distance, sound position, environment condition and uncorrelated noises affect the detection results. And make the method more robust and can detect particular sound.

Acknowledgements

The research is supported by National Project (00404010601) and (20120246110).

References

[1] Christian Steffes, Lisa Meyer “Evaluation of a TDoA based Acoustic Localization System”, Sensor Data Fusion: Trends, Solutions, Applications (SDF), 2013 Workshop on.
[2] WANG Minqing, SONG Daike, XING Xiaoliang “Research on Speaker Tracking in the Smart Conference System” , Audio Engineering, 2007,vol .31.
[3]Ju Tailiang, “Research on speech source localization Methods based on Microphone Arrays”, university of electronic science and technology of china, 2006.
[4] Alexander Sutin, Barry Bunin, Alexander Sedunov, “Stevens Passive Acoustic System for Underwater Surveillance”, Waterside Security Conference (WSS), 2010 International.
[5] LOU Wenzhong, QIAO Jie, “Noise Test and Simulation of Military Aircraft”, transactions of Beijing Institute of Technology, 2007, 27(4):295-298.

Key Engineering Materials Vols 645-646 (2015) pp 522-527
© (2015) Trans Tech Publications, Switzerland
doi:10.4028/www.scientific.net/KEM.645-646.522
Submitted: 2014-11-02
Accepted: 2014-12-23

An Electromagnetic Vibrating Ring Gyroscope Using SOI-MEMS Technology

Yuxin Li[1], Deyong Chen[2], Gang Huang[1], Qi Li[1]

[1]China Astronaut Research and Training Center, Beijing, China

[2]State Key Laboratory of Transducer Technology, Institute of Electronics, Chinese Academy of Sciences, Beijing, China

[a]liyuxin_85@126.com, [b]dychen@mail.ie.ac.cn, [c]huanggang1971@sina.com

Keywords: Vibrating ring gyroscope, Control system, SOI- MEMS, Lag and Footing effects

Abstract. This paper presents the design, fabrication and tests of an electro-magnetic vibrating ring gyroscope based on a control system and SOI-MEMS technology. The control system, including variable gain control (VGC), drive-frequency control and regulation module, is designed to improve mode matching. In device fabrication, and buffered hydrofluoric acid (BHF) solution is used to remove the buried oxide layer and release the suspended spring. Meanwhile, a compensate disk and negative photo resist (AZ303) coated on the backside of the wafer are employed to weaken the Lag and Footing effects during through-wafer etching process. The design of the gyroscope is optimized by FEA simulation and the fabricated devices show a rather good performance.

Introduction

MEMS gyroscope shows high growth potential in automobile electronics, consumer electronics, and defense industry due to small volume, light weight, low power consumption, strong ability of resisting overload and low price. Among different types of MEMS gyroscopes, MEMS resonant gyroscopes prevail in the commercial market due to their advantages of high sensitivity, low power consumption and excellent long-term stability. Many countries have seen MEMS resonant gyroscope as one of priority technologies must be focused[1-3].

Frequency matching is an important factor for MEMS vibrating ring gyroscopes. There exists a $\cos 2\theta$ defference when a ring gyroscope follows a degenerate pair of vibration modes at a mutual angle of 45°. The vibration modes are called drive mode and sense mode. For ideal vibrating ring gyroscope, the resonance frequencies of drive mode and sense mode are equal, however, frequency split between the two modes usually occurs due to the fabrication deviations. Experiments show that the frequency split should be less than 3 dB bandwidth to obtain a superior sensitivity of vibrating ring gyroscope.

According to different excitation and detection mechanisms, there are two kinds of MEMS vibrating ring gyroscopes: electrostatic and electromagnetic[4]. For electrostatic gyroscope, resonantor is packaged in vacuum, which can achieve higher Q-factor and lower frequency split. Compared to electrostatic gyroscope, electromagnetic gyroscope can operate at atmospheric pressure, which achieves lower cost and more simple fabrication process, but relatively larger frequency split for its larger raw sense mode output and lower operating voltage.

In this paper, we present an electromagnetic vibrating ring gyroscope structure with relatively low initial frequency split and an effective control system to obtain superior drive-mode amplitude stability, suitable drive-frequency set-up and electronic trimming capability.

Structure design

The schematic diagram of the electromagnetic vibrating ring gyroscope is shown in Fig.1.The resonant element consists of a vibrating ring (4,000μm radius, 40μm width and 100μm thickness), eight pairs of symmetric crab-leg suspension springs (15μm width and 100μm thickness), and Si3N4

film is formed on the surface as insulation using LPCVD, on which Au is deposited and patterned to form the electrodes.

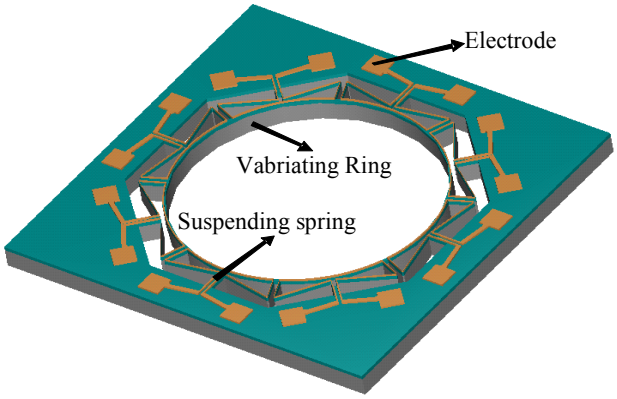


Fig. 1 Schematic of gyroscope

The ring structure is designed using the ANSYS finite-element package and FEA (Finite element modeling) simulation. When analyzing the structure using ANSYS, the vibrating ring is initially defined using solid modeling techniques. The key dimensions were parameterized, enabling the rapid simulation of design modifications and the high-efficiency optimization routine, and the simulated frequencies of drive mode and sense mode are both 6596 Hz according to the parameters of the structure in Fig.1. When subjected to a rotation, deformation of the ring caused by Coriolis force makes the sense mode located 45° apart from the drive mode, causing amplitude to build up proportionally in the sense mode, making the energy transferred from the drive mode to the sense mode, shown in Fig.2. Fig.3 gives the plot of the degenerate drive mode and sense mode with a rotation rate Ω_z simulated by FEA simulation.

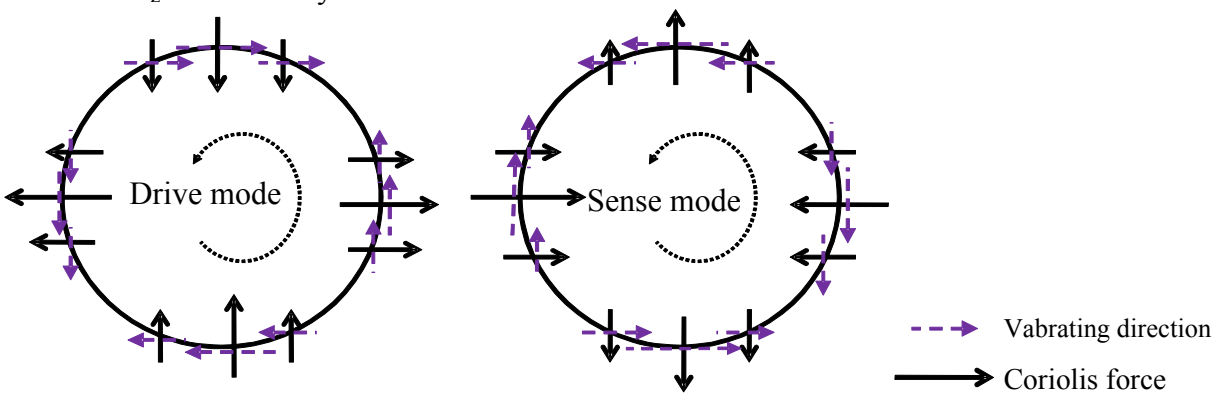


Fig.2 Vabrating ring with Coriolis force

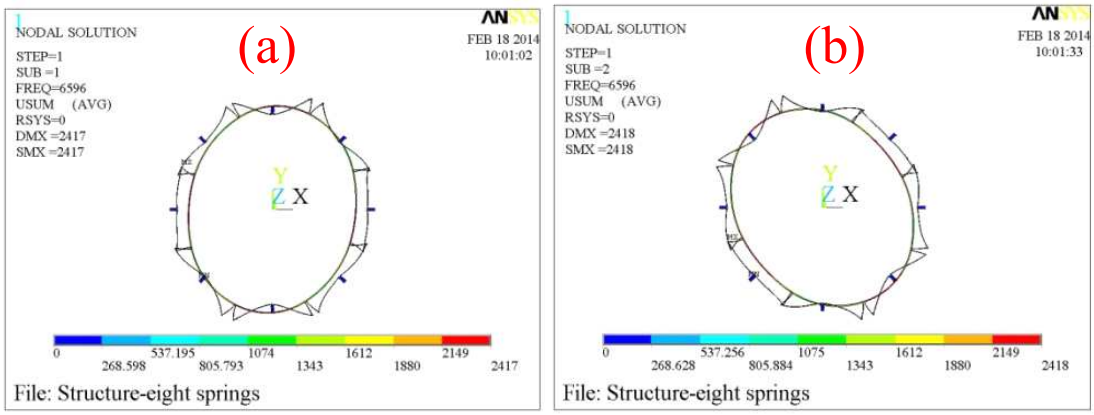


Fig.3 Plot of the degenerate drive mode and sense mode

Set the driving force as $F=F_0 \sin w_f t$, and the amplitude of drive mode can be expressed as:

$$A_d=\frac{F_0}{K_d\sqrt{\left(2\xi_d\frac{w_f}{w_d}\right)^2+\left[1-\left(\frac{w_f}{w_d}\right)^2\right]^2}} \tag{1}$$

Where, w_f is the frequency of the drive force F, w_d is the frequency of the drive mode, ξ_d is the damping coefficients of drive mode, and K_d is the effective stiffness of drive mode. When $w_f=w_d\sqrt{1-2\xi_d^2}$, w_d can be seen as the fundamental frequency of the drive mode, and A_d can be written as:

$$A_d=Q_d\frac{F_0}{K_d} \tag{2}$$

where $Q_d=\frac{1}{2\xi_d}$ is the Q-factor of the drive mode. By the formula of energy transferring and Eq. 1, the amplitude of drive mode can be written as:

$$A_s=\frac{2F_0Q_d\lambda\Omega_z}{K_sw_d}\frac{1}{\sqrt{\left(\frac{w_d}{Q_sw_s}\right)^2+\left[1-\left(\frac{w_d}{w_s}\right)^2\right]^2}} \tag{3}$$

Where w_s is the frequency of sense mode, Q_s is the Q-factor of sense mode, Ω_z is angular velocity. By Eq.3, we can see Ω_z can be obtained by A_s. A_s increases with the increase of Q_s, and decreases with the increase of frequency split, which will be maximal when frequency split is 0($w_d=w_s$)[5-6].

Fabrication

Reducing frequency split of resonant frequencies of the drive and sense mode is an available way to improve the performance of gyroscopes, and the mass and mechanical-spring imbalances are responsible for frequency split. To reduce mass and mechanical-spring imbalances, the vibrating ring should be over 100μm thick, and the thickness of substrate should be no less than 300μm according to FEA simulations. The structure is hard to be achieved by single crystal silicon wafer, so SOI wafer is chosen as the fabrication material of gyroscope, which can easily achieve the 100μm thick gyroscope structure with less residual stresses using simple fabrication processes. FEA simulations indicate that a uniform circular ring fabricated by (100) silicon commonly has an approximately 30 Hz frequency split, while no frequency split occurs in theory according to the ring fabricated by (111) silicon for the Young's modulus is isotropy. Thus, the device layer of the SOI wafer is chosen as the (111) silicon.

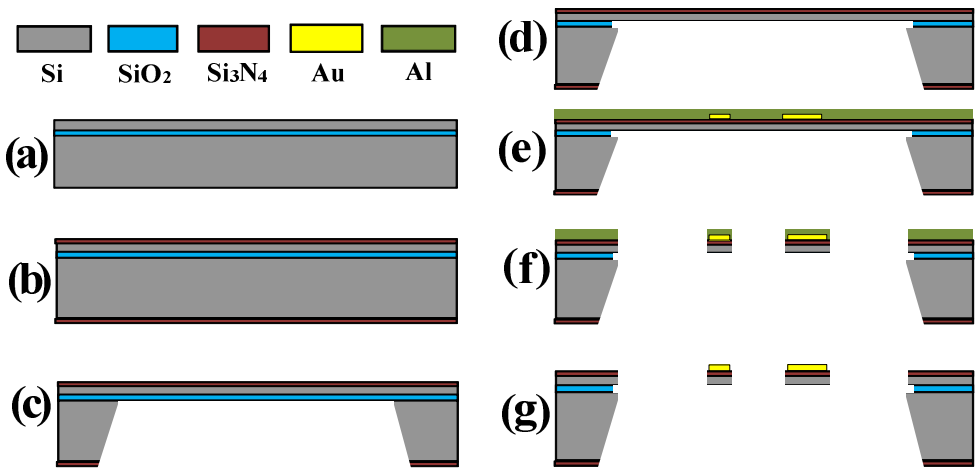


Fig. 4 The fabrication procedure for the MEMS gyroscope, relying on SOI-MEMS fabrication processes: (a) SOI wafer; (b) Si_3N_4 deposition; (c)patterning and wet etching for diaphragm area; (d) etching and releasing of the SiO_2 layer (e)patterning the Au electrodes and sputtering of the Aluminum thin film as mask layer; (f) patterning and DRIE for the ring; (g) removing the Aluminum mask layer.

The MEMS gyroscope is fabricated by MEMS bulk-silicon technologies, including deep reactive ion etching (DRIE), photo lithography and sacrificial layer release. 4 inch SOI wafer composed by (111) silicon with 100 μm thick device layer and (100) silicon with 380 μm handle layer is used as the fabricating material. The fabrication process is shown in fig.4. Through etching is the key factor according to the fabricating process: the portion of the handle wafer underneath the suspending structures is removed by the potassium hydroxide (KOH) solution from the backside; the 2 μm thick sacrificial layer serves as the self-stopped etching layer is removed by the buffer hydrofluoric acid (BHF) solution, which also ensures the equal thickness of the gyroscope structure since these wet-etching processes introduce no destruction to the device; the gyroscope structure is performed by DRIE.

Through-wafer etching processing error comes mainly from the lag effects and footing effects in silicon DRIE. Area inside of the ring is through etched to the bottom in the DRIE whereas the area outside of the ring is still connected due to the lag effect, which will affect the performance of the device greatly. Excessive etching causes the incoming ions deflected due to charge build-up at the surface of the tray and result in the footing effect. Lag and footing effects will destroy the balances of mass and the flatness of mechanical spring structure, shown in Fig 5(a).

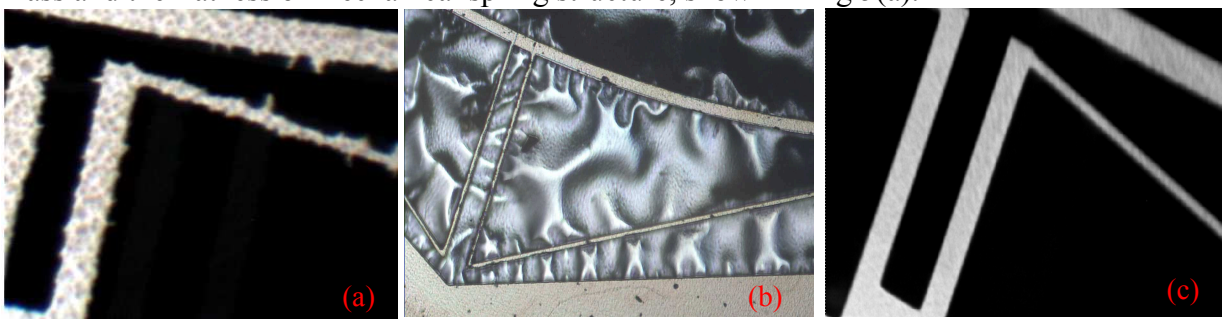


Fig.5 (a) Damage caused by Lag and Footing effects; (b) DIRE process with photo risist mask; (c) Bottom surface of the gyroscope after DIRE with no significant ion damage

To address this issue, a compensate disk is set inside of the ring to weaken the lag effect and negative photo resist AZ303 is coated at the bottom surface of the device layer before DRIE to prevent the footing effect[7-8], shown in Fig. 5(b). Fig. 5(c) shows no significant ion damage at the bottom surface of the gyroscope, demonstrating a significant improvement compared to that shown in Fig. 5(a). After using the solution, it took effect to release the vabriating ring, see Fig.6.

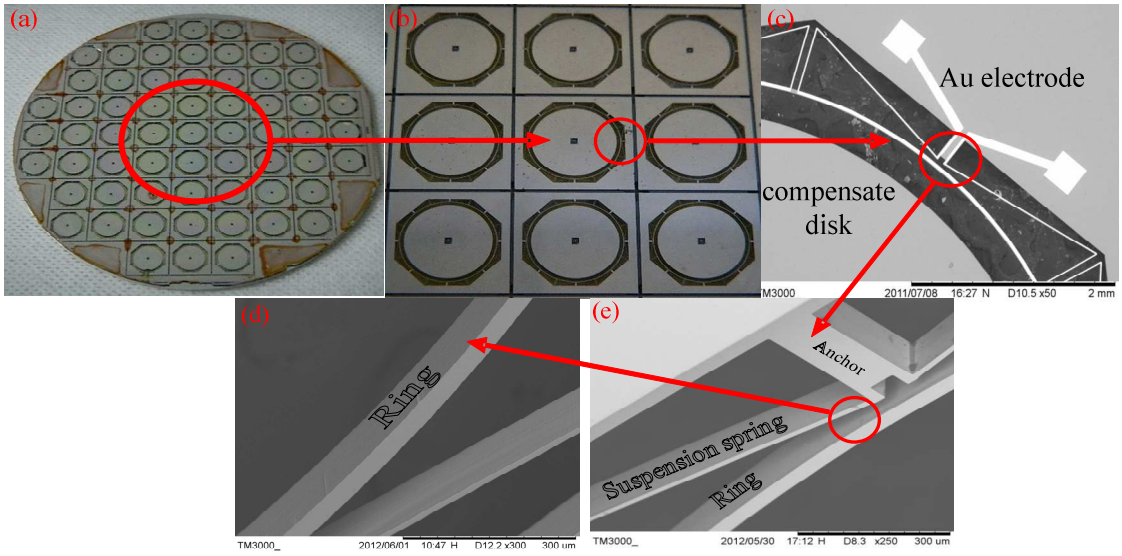


Fig. 6 Pictures of fabrication result: (a-b) photos of SOI wafer die after fabrication processes; (c-e) characteristics of fabricated gyroscope

Control circuit and testing results

Metal substrates (such as kovar, copper) offer the highest reliability characteristics; they are commonly used in resonant pressure sensor package. The package of the sensor is preceded on a kovar substrate. The gyroscope die is mounted to the metal package by fixing the die through a circular permanent magnet with WD3620epoxy resin, shown in fig.7.

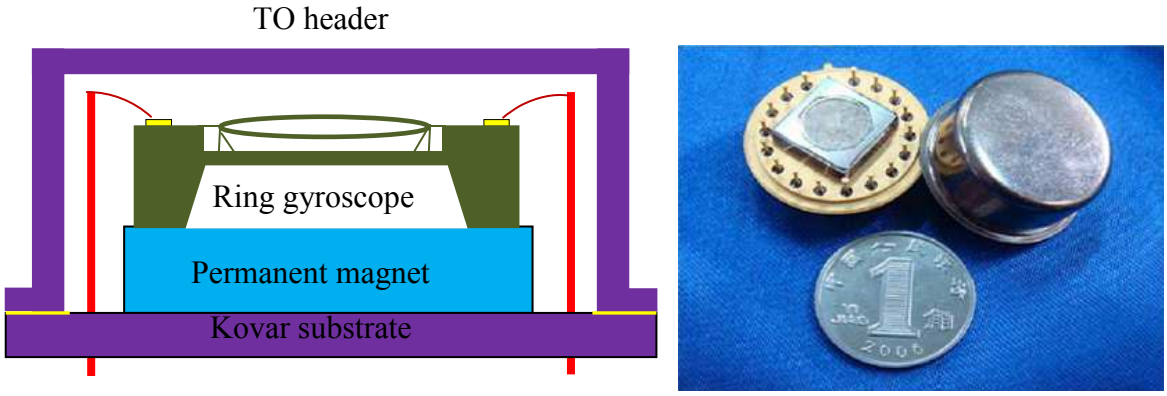


Fig.7 View and Photo of packeged gyroscope

The control system, shown in, including variable gain control (VGC), drive-frequency control and regulation module, is reduce frequency split. The control circuit can regulate parameter such as the Q-factor and the frequency split of the electromagnetic vibrating ring gyroscope efficiently. Fig. 8(b) shows a vibrating ring at work.

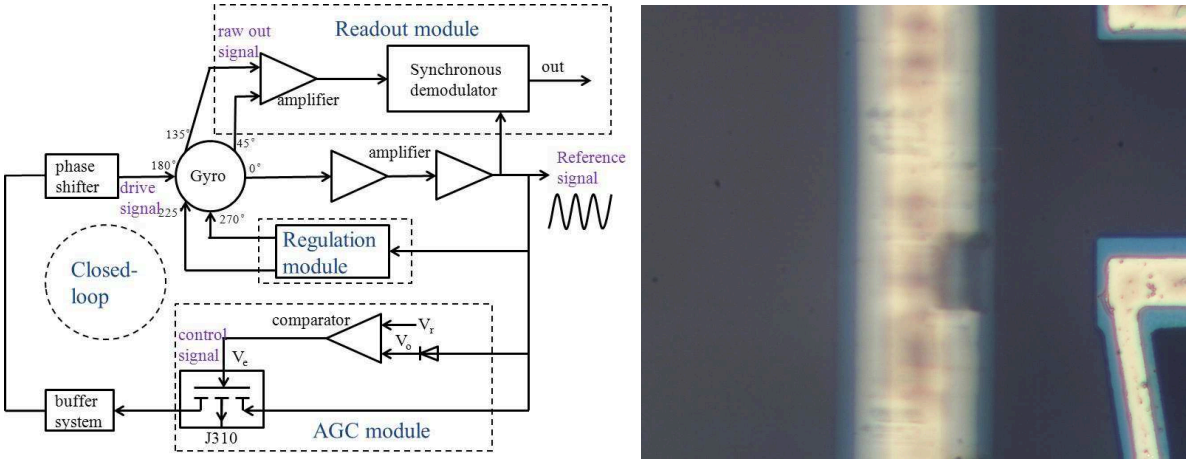


Fig.8 Schematic of control system and a photo of vibrating ring

Fig.9 shows the plot of static behaviors of the the sensors with control system. Measured output frequency shift of the gyroscope show that the initial frequency split is only 0.5 Hz and the sensitivity of the gyroscope is 0.1146μV/°/s.

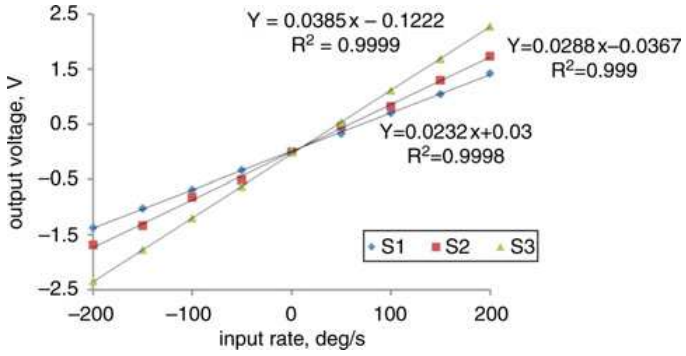


Fig.9 Plot of output with control system

Summary

Detailed fabrication and control circuit experiments have been presented for electro-magnetic vibrating ring gyroscope, which shows that the fabrication process is an effective low cost technique. MEMS bulk silicon processes based on an SOI wafer is used to simplify the fabrications. A modified DIRE process is employed to reduce lag effects and footing effects, which improves the symmetry of the gyroscope a lot. A control system consists of variable gain control (VGC), drive-frequency control and regulation module is adopted to reduce frequency split. Under this control system, better stability of the drive-mode amplitude and more suitable set-up of the drive-frequency are obtained, the frequency split by 6.4 Hz, and Q-factor in the air can be improved from 611 to 908. Testing results show that the gyroscope devices process a rather good performance.

Acknowledgement

This work is sponsored by NSFC (Natural Science Foundation of China) with project NO.21175121.

References

[1] Chen Li, Chen De-yong, Wang Jun-bo et al., High performance electromagnetic micro-machined ring vibration gyroscope, Optics and Precision Engineering. 17(2009)1915-1921.

[2] Li Chen, Deyong Chen, Junbo Wang, The design and analysis of a robust micro-machined vibrating ring gyroscope. Proceeding of SPIE. 71590D(2008) 1-8.

[3] Boxenhorn B, Greiff P, A vibratory micromechanical gyroscope, AIAA Guidance and Controls Conference, Minnesota. (1988)1033-1040.

[4] Maenaka K, Ioku S and Sawai N, Design, fabrication and operation of MEMS gimbal gyroscope, Sensors and Actuators A. 121(2005) 6-15.

[5] Maenaka K, Kohara H, Nishimura M, et al. Novel solid micro-gyroscope, Proceedings of the 19th IEEE International Conference on Micro Electro Mechanical Systems, Istanbul, Turkey. (2006) 634-637.

[6] Eik Arnold, Franz Nuscheler, Compensation methods for a silicon tuning fork gyroscope, Microsyst.Technol. 14 (2008) 623-628.

[7] Said Emre Alper, Kivanc Azgin, Tayfun Akin, A high-performance silicon-on-insulator MEMS gyroscope operating at atmospheric pressure, Sensors and Actuators A.135(2007) 34-42.

[8] Jili Liu, Deyong Chen, Junbo Wang. Regulating parameters of electromagnetic micro-machined vibrating ring gyroscope by feedback control [J], Micro & Nano Letters. 7(2012) 1234-1236.

Key Engineering Materials Vols 645-646 (2015) pp 528-532
© (2015) Trans Tech Publications, Switzerland
doi:10.4028/www.scientific.net/KEM.645-646.528

Submitted: 2014-11-04
Accepted: 2014-12-23

The research on MEMS micro capacitance sensor detection based on MS3110

Huijun Yu [1,a], Ziqiao Ding [1,b], Xiaoping He[2,c], Lianming Du[2,d], Hao Qu [1,e], Wu Zhou [1,f] and Bei Peng [1,g*]

[1]Department of Mechatronics Engineering, University of Electronic Science and Technology of China, Chengdu 611731, P.R. China

[2]Institute of Electronic Engineering, China Academy of Engineering Physics, Mianyang 621900, China

[a]hjyu@uestc.edu.cn, [b]dzquestc@126.com, [c]hexpiee@263.net, [d]13508107238@139.com, [e]708382@163.com, [f]zhouwu916@163.com, [g]beipeng@uestc.edu.cn

Keywords: MEMS capacitance sensor; universal capacitive readout integrated circuit; MS3110; equivalent electric model

Abstract. A universal capacitive readout integrated circuit MS3110 is used to measure capacitances in micro capacitance sensor. The configuration, operating principle and process of MS3110 are introduced and a method of programming the inner register on-chip with STM32 is presented with the control block diagram. Performance of MS3110 has been tested by the inner adjust capacitance. A comb micro accelerometer is designed and manufactured. A tentative equivalent electric model of accelerometer is built according to a series of capacitance tests, and the influence of parasitic capacitance in accelerometer system is discussed.

Introduction

Because of the influence of layout and technological factors, a series of non-ideal parasitic capacitances will produce in the structure of MEMS capacitive sensor, and it will lead to differences between actual distribution of the capacitance and the ideal situation, which may affect the whole performance of the sensor system. In order to analyze and solve problems existing in the high precision sensor, the capacitance between each pin should be measured accurately to build the accurate electric model of the sensor structure. The size of the MEMS devices have a very small size, which means the capacitance in the structure is rather small, usually at sub-pF level, To meet the requirements of high resolution and high precision, the general-purpose programmable capacitive readout IC MS3110 is wildly used, MS3110 using CMOS technology, it has a low noise, low power consumption, single +5V power supply and the resolution can be achieved 4.0aF/Hz1/2 [1,2]. Using MS3110 can greatly reduce the detection circuit and avoid circuit noise, thus it could meet the requirement of high-performance capacitance detection.

Operating principle

The schematic of MS3110 is shown in Figure1. MS3110 use the modulation and demodulation way to read capacitance value [2,3], it contain an internal programmable capacitor array, a charge integrator amplifier circuit, a S/H circuit, a low-pass filter and a amplifier. The output of MS3110 is DC signal, and the output voltage is proportional to the measured capacitance value [1,4]. MS3110 has a high versatility, its internal feedback capacitance, compensation capacitor, gain, filter bandwidth and other parameters can be set by external programming signal.

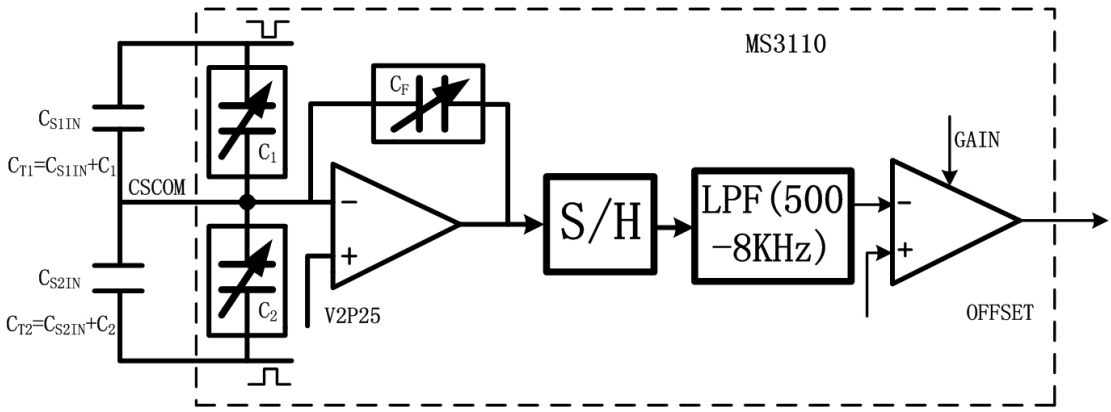


Fig.1 Internal circuit schematic of MS3110

Theoretical transfer function of MS3110 just as formula (1), VOFF is the bias voltage, it can be set at 0.5V or 2.25V, C_F is the feedback capacitance, the value of C_F is range from 0 to 19.44pF, C_T is the total of compensation capacitance and external capacitance, the compensation capacitor C_1 can be set by programming from 0 to 9.709pF and C_2 can be set from 0 to 1.197pF, the trim step of internal capacitance is 19fF.

$$V_o = \frac{GAIN \bullet 2.565 \bullet (C_{T2} - C_{T1})}{C_F} + VOFF \tag{1}$$

GAIN can be set as 2 or 4 by programming. The programmable parameters make the system can satisfy test under different conditions.

Performance test

Before testing the micro accelerometer, in order to guarantee the accuracy of the test, the performance of MS3110 should be tested. During the performance test the internal capacitor array has been changed gradually, by detecting and fitting the output, C/V curves can be obtained and shows in Figure2. In the test, parameter GAIN=2, C_F=10.26pF, VOFF=0.5V. If take these parameters into formula (1), the theoretical Input/output function can be expression as:

$$V_o = 0.5(C_{T2} - C_{T1}) + 0.5 \tag{2}$$

Through the experimental data fitting, the actual Input/output function can be expression as:

$$V_o = 0.4987(C_{T2} - C_{T1}) + 0.46 \tag{3}$$

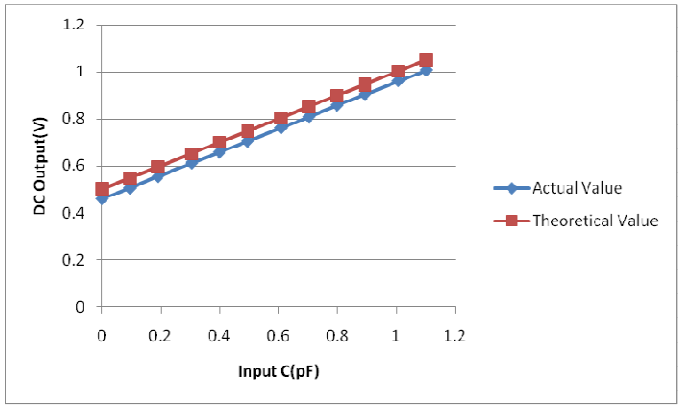


Fig.2 Input-output relationship curve of MS3110

Results show that MS3110 have a good linearity. Compare the real and theoretical curve, the measurement resolution is very close to the theoretical value, the zero error of the output is about 0.04V. Zero error is caused by the interface parasitic capacitance, through calculating its value is about 80fF. During the accelerometer test, the interface parasitic capacitance can be matched by compensation capacitance to decrease zero error. Through the performance test, we have reason to believe that the MS3110 could meet the requirements of high-performance test.

On chip registers programming

There are two ways to change these parameters, write the EEPROM or write the on-chip register, to operate EEPROM requires additional 16V DC voltage supply [4]. Therefore, in the debugging process write register is a better way. Parameters of MS3110 could be changed by the data in register and these data could through a serial manner write into the register, it's very convenient. The reading and writing control block diagram of MS3110 test system is shown in Figure3.

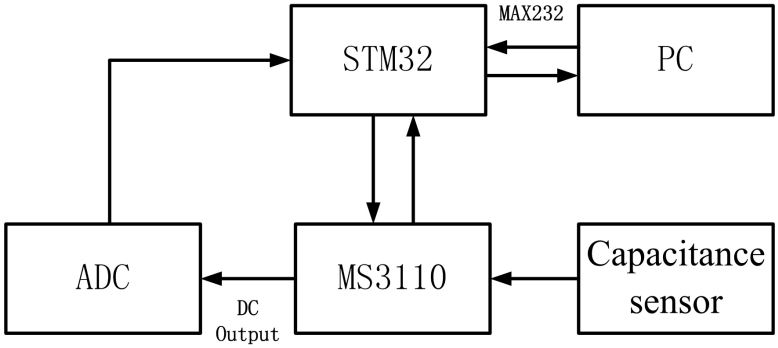


Fig.3 The control block diagram of MS3110 test system

STM32ARM controller is used in debugging, it send program data to the register to change chip parameters. STM32 is connected to the computer through the RS232 serial communication protocol and accept the computer programming data, then STM32 will send the corresponding programming instructions to the MS3110, at last the output of the MS3110 will be read by AD converter and the results will send to the computer through serial communication.

Accelerometer chip testing and modeling

Typical structure of comb capacitive accelerometer is shown in Figure.4. In order to pick good performance accelerometer and analyze various factors that influence on sensor performance, detect the capacitance in the structure and set up a equivalent model is very necessary [5,6,7].

The capacitance in the structure is taken as C_x. A series of detection have done to a group of MEMS accelerometer the result is recorded in Table 1.

In the structure comb capacitance (C_{x1} C_{x2} C_{x3} C_{x4}) are effective capacitance, they will affect the zero offset voltage, linearity and sensitivity of the system. Comb structure in the design is symmetrical, they should have a capacitance value of the same, but in fact their capacitance value due to the effects of process factors will have different, these tests can help us to pick structure of good symmetry. Capacitance between anchors (C_{x5} C_{x6} C_{x7}) are parasitic capacitance, its change value is small under the condition of the same process.

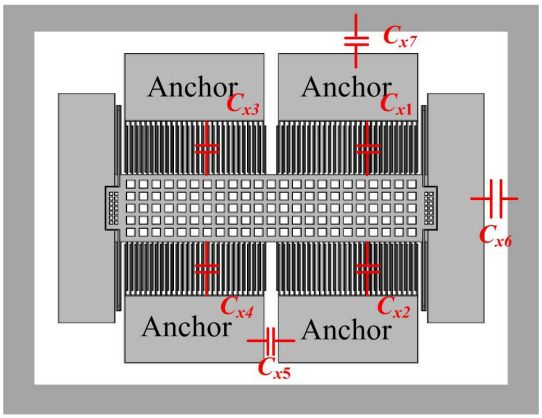


Fig.4 Typical structure of comb capacitive accelerometer

In the simple analysis usually ignore the influence of the parasitic capacitance, but in fact these parasitic capacitances will deteriorate the system noise and lower the system resolution, thus the accurate value of parasitic capacitance is also an important parameter in the accelerometer system.

Table 1 Capacitance in different accelerometer

	C_{x1} [pF]	C_{x2} [pF]	C_{x3} [pF]	C_{x4} [pF]	C_{x5} [pF]	C_{x6} [pF]	C_{x7} [pF]
#1.	1.7714	2.0112	1.8510	1.7448	0.0858	2.2708	0.7354
#2.	1.9122	1.8825	2.1037	1.9652	0.0910	2.2938	0.7326
#3.	1.8332	1.9334	1.7655	2.0122	0.0936	2.2562	0.7014
#4.	1.9656	1.9265	1.9823	1.8355	0.0885	2.2666	0.6966
#5.	2.0036	1.8722	2.0019	1.9210	0.0874	2.2853	0.7276
#6.	1.9324	1.7998	1.8653	1.8995	0.1012	2.2916	0.6898
#7.	1.7628	1.9622	1.9986	1.8206	0.0998	2.3025	0.7155
#8.	1.8836	1.8566	1.8726	1.9832	0.0962	2.2410	0.7088
#9.	2.1026	1.8222	2.0334	1.9916	0.0837	2.2616	0.7334

In an acceleration sensor system, the comb capacitive accelerometer is always regarded as a symmetric differential capacitance. It's hard to analyze in this ideal condition, thus an equivalent electric model that close to the actual situation should be built to analyze the acceleration sensor system. A equivalent electric model include comb capacitance, parasitic capacitance and structural resistance can be built.

Capacitances in the equivalent electric model are detected by MS3110, structural resistance could be detected by high precision digital multimeter.

Conclusion

MS3110 is a general-purpose programmable capacitive readout IC, its operation principle and configuration are introduced in this paper. A programming method through register on-chip is proposed. Through MS3110, capacitance in the structure is detected and a equivalent electric model that close to the actual situation is built, it provides a basis for further study of the acceleration sensor system.

Acknowledgments

This research was partially supported by National Natural Science Foundation of China (Grant No. 51175437 and 91123023), Fundamental Research Funds for the Central Universities (Grant No. ZYGX2013J097)

References

[1] P. Xu, Y. ZHANG, Z. HOU, Research on Detection of Differential Capacitance Based on MS3110 and EMC Design, J. Instrument Technique and Sensor. 5 (2008) 022.

[2] M.J. LIU, Y.F. LIU, J.X. DONG, C.D. ZHAO, MEMS accelerometer based on capacitive readout IC MS3110, J. Journal of Chinese Inertial Technology. 2 (2010) 022.

[3] L. LIN, W.Y. CHEN, K. LI, X.B. JIANG, Study on Structure and Detecting Technique of Micro-accelerometer, J. Instrument Technique and Sensor. 8 (2008).

[4] MS3110- Data Sheet REV, Datasheet USA: Irvine Sensors Corporation 2012.

[5] T. Veijola, H. Kuisma, J. Lahdenpera, T. Ryhanen, Equivalent-circuit model of the squeezed gas film in a silicon accelerometer, J. Sensors and Actuators A. 48(1995) 239-248.

[6] M.G. Kim, B.H. Lee, T.Y. Yun, Equivalent-Circuit Model for High-Capacitance MLCC Based on Transmission-Line Theory. Components, J. Packaging and Manufacturing Technology, IEEE Transactions on 2.6 (2012) 1012-1020.

[7] R.L. Spyker, R.M. Nelms, Classical equivalent circuit parameters for a double-layer capacitor, J. Aerospace and Electronic Systems, IEEE Transactions on 2000 36(3) 829-836.

Key Engineering Materials Vols 645-646 (2015) pp 533-537
© (2015) Trans Tech Publications, Switzerland
doi:10.4028/www.scientific.net/KEM.645-646.533

Submitted: 2014-11-04
Accepted: 2014-12-23

The Influence of Die-attach Adhesives on the Packaging of MEMS Accelerometer

Peng Peng[1, a], He Xiaoping[2, b], Du Lianming[2, c], Zhou Wu[1, d], HuiJun Yu[1, e] and Bei Peng[1, f *]

[1]Department of Mechatronics Engineering, University of Electronic Science and Technology of China, Chengdu 611731, P.R. China

[2]Institute of Electronic Engineering, China Academy of Engineering Physics, Mianyang 621900, China

[a]ppuestc@163.com, [b]hexpiee@263.net, [c]13508107238@139.com, [d]zhouwu916@163.com,[e]276979244@qq.com, [f]beipeng@uestc.edu.cn

Keywords: MEMS accelerometer, Die-attach Adhesives, Stress, Deformation, Finite element analysis

Abstract. The attachment of the micromechanical silicon die to the substrate is one of the most critical steps in the packaging of highly accurate MEMS (microelectro-mechanical systems) accelerometer. The stress and strains, induced during die-attach process because of TCE (thermal coefficient of expansion) mismatches between different materials, will adversely affect the output characteristics of the accelerometer sensor. In this paper, three different materials: OE138, DG-3S and H70E are selected as the die-attach adhesives of a MEMS comb capacitive accelerometer. The stress and deformation of the silicon die, after the accelerometer model is cured from 80 °C to 20 °C, are evaluated with the aid of finite element analysis (FEA). As the results show, Young's modulus and the thickness of the adhesives are the most significant factors influencing the stress and deformation of the silicon die. Soft adhesive material (OE138) have better stress absorption, and the stress and deformation of the silicon die decrease with the increasing thickness of the adhesive. Consequently, a soft and thick adhesive is recommended for the die-attach packaging of MEMS accelerometer.

Introduction

MEMS technology integrates mechanical elements and electronics onto a common substrate by the technology of microfabrication [1]. Over the years, MEMS devices have become smaller, cheaper, more functional, and reliable to use. Packaging of the MEMS devices and systems, however, still faces lots of challenges [2]. A major concern regarding MEMS packaging is the process of die attach. Presently, adhesive materials have been widely used for attaching die onto the substrate because of their primary advantages, including high processing flexibility, low curing temperature and low cost [3]. The temperature variation, required for die attach curing process, will cause undesirable stress and deformation in micromachined structures due to thermal mismatch between the materials used in MEMS devices. The stress and deformation adversely influence the performance of the packaged component. Understanding the influence of the die-attach adhesives on the thermal stress and deformation induced in MEMS sensitive element is, therefore, critical for successful device design [4].

Several investigations have showed that the material properties of adhesives significantly affect the stress and strains of MEMS device sensitive element when cooled from cure temperature to room temperature. Zongyang Zhang et al. [5] analyzed the influence of single parameter of the adhesive on the silicon piezoresistive pressure sensor's output characteristics, the results showed that the thicker die-attaching adhesives with a lower Young's modulus generated lower residual stress and smaller zero offset as well as smaller temperature drift to the sensor. A. Morrissey et al. [6] discussed the selection of materials applicable to the 3D packaging of any microsystem, they found that adhesives

which had lower Young's modulus and cured at a relatively low temperature were better selections for the materials of die attach components. I. Sadaba et al. [7] found the Young's modulus of adhesive Epotek360 increased from 0.9GPa to 1GPa after curing completion, the ''ageing'' process of polymer influenced the long-term output characteristics of MEMS gyroscope. In this paper, three different materials: OE138, DG-3S and H70E are selected as the die-attach adhesives of a MEMS comb capacitance accelerometer. Finite element analysis (FEA) is used to investigate the influence of Young's modulus and the thickness of the adhesives on the stress and deformation of the sensor.

Modeling and Simulation

In this study, a quarter symmetry 3-D capacitive accelerometer is constructed with the aid of ABAQUS finite element analysis software. As shown in Fig. 1, the accelerometer silicon die is sputtered onto the glass, and the glass is attached onto the ceramic substrate with adhesive. Symmetry boundary conditions are confined in the symmetric faces. At the shrinkage node, no displacements occur in all three directions (i.e., Ux =0, Uy =0, Uz =0). Three materials: OE138, DG-3S and H70E are selected as the die-attach adhesives, and the model in this simulation is performed with heating at 80°C followed by cooling down at 20°C to evaluate the package curing process. After cured, the stress in the model and the displacement are considered to study the influence of different die-attach adhesives on the sensor. The meshing result of the quarter symmetry 3-D model is shown in Fig. 2. The material properties for simulation is shown in Table .1.

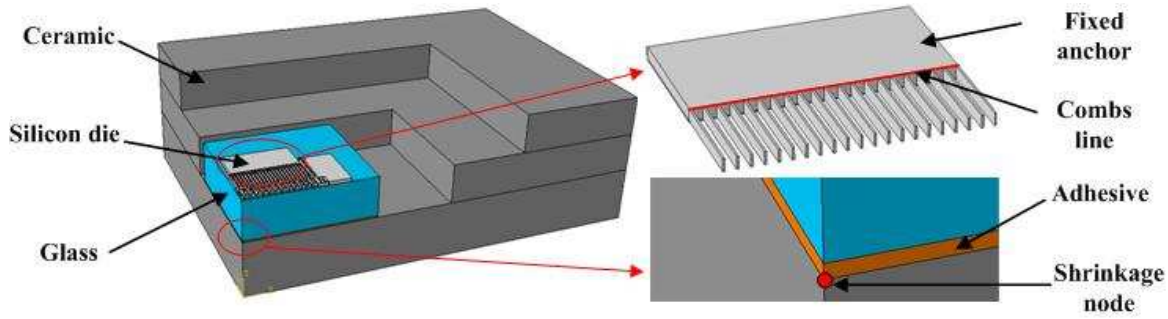


Fig .1 Geometry of the quarter symmetry 3-D model used in the simulation

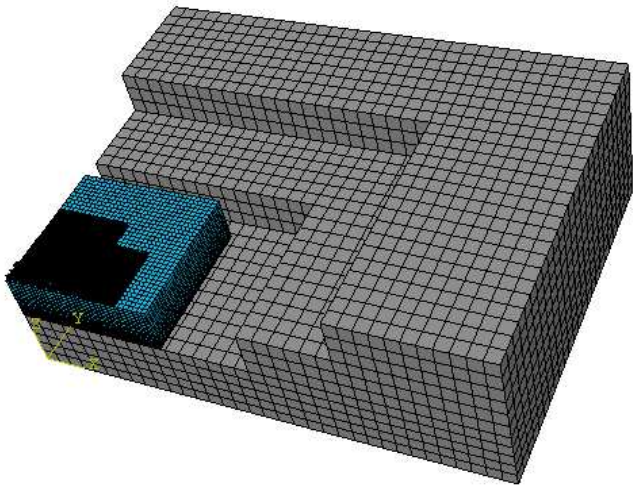


Fig .2 Meshing result of the quarter symmetry 3-D model

Table .1 Material properties for simulation

Material	Young' s modulus (GPa)	Poisson ratio	TCE
OE138	2.7	0.37	2.1×10^{-5}
DG-3S	4	0.37	6×10^{-5}
H70E	5.4	0.37	1.5×10^{-5}
Silicon	160	0.22	2.6×10^{-6}
Glass	62.7	0.2	3.25×10^{-6}
Ceramic	360	0.22	6.5×10^{-6}

Results and Discussion

The pressure distribution of the model with the adhesive of OE138 is shown in Fig .3, the thickness of OE138 in this simulation is 20um. The maximum stress areas are located in the attaching interface between OE138 and ceramic because of the maximum mismatch of TCE.

Fig .4 shows the displacement of the combs line (Fig .1) with different adhesives and different thickness. As the results show, the displacement of the combs shows a rising trend when the Young's modulus of the adhesive increases, which indicates that softer adhesive material (OE138) have better stress absorption. Fig .5 shows the displacement of the combs line for the adhesive OE138 with different thickness. The deformation of the fixed anchor is smaller when the thickness is 30um than the thickness is 20um. The Maximum tresca in the model with different adhesive and different thickness is also studied. As shown in Fig .6, the Maximum tresca in the model decreases with the increasing Young's modulus and the thickness of the adhesives. The results indicates that a soft and thick adhesive is less influential on the stress and deformation of the sensor.

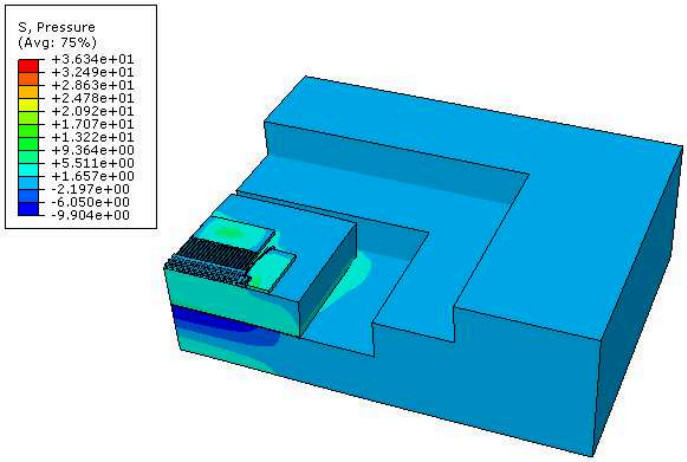
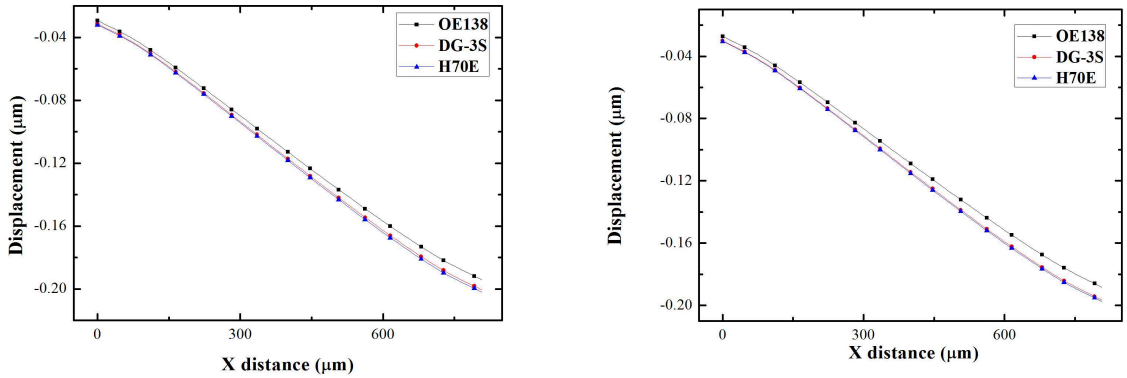


Fig .3 Pressure distribution of the model with the adhesive of OE138



(a) 20μm (b) 30μm

Fig .4 The displacement of the combs with different adhesive material and different thickness

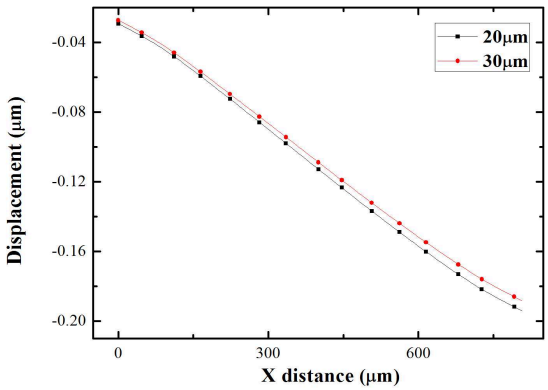


Fig .5 The displacement of the combs with thickness of the adhesive OE138

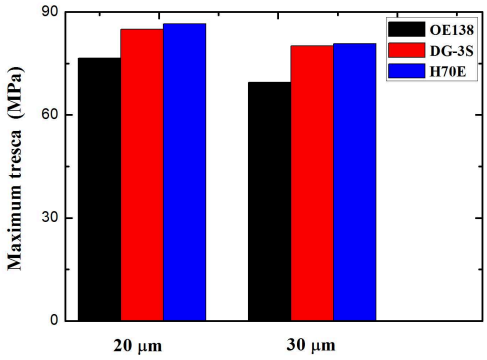


Fig .6 The Maximum tresca with different adhesive and different thickness

Conclusion

In this paper, we evaluated three kinds of adhesive materials for packaging of MEMS accelerometer. According to the simulation results, Young's modulus and the thickness of adhesive material are the critical parameters for controlling the curing stress in the sensor. Soft (OE138) and thick (30um) adhesive material provide lower stress in the simulation model. Consequently, a soft and thick adhesive material is better for packaging of MEMS devices, such as accelerometer, microphones, and so on.

Acknowledgment

This research was partially supported by National Natural Science Foundation of China (Grant No. 51175437 and 91123023), Fundamental Research Funds for the Central Universities (Grant No. ZYGX2013J097).

References

[1] S.M. Spearing, Materials issues in microelectromechanical systems, Acta Mater. 48 (2000) 179-196.

[2] S.S. Walwadkar, P.W. Farrell, L.E. Felton, J. Cho, Effect of die-attach adhesives on the stress evolution in MEMS packaging, Proc. 36th Int. Symp. Microeletron, Boston, MA. 48 (2003) 847-852.

[3] T. Tuhus, A. Bjorneklett, Thermal cycling reliability of die bonding adhesives, 10th Annu Pro Reliability Physics Symposium. (1993) 204-208.

[4] M. Lishchynska, C. O'Mahony, O. Slattery, O. Wittler, H. Walter, Evaluation of packaging effect on MEMS performance: simulation and experimental study, IEEE T Adv Packaging. 30 (2007) 51-59.

[5] Z. Zhang, Z. Wan, C. Liu, G. Cao, Y. Lu, S. Liu, Effects of adhesive material on the output characteristics of pressure sensor, ICEPT-HDP. 163 (2010) 657-660.

[6] A. Morrissey, G. Kelly, J. Alderman, Selection of materials for reduced stress packaging of a microsystem, Sensor Actuat A-Phys. 74 (1999) 178-181.

[7] I. Sadaba, C.H.J. Fox, S. McWilliam, A Study of Residual Stress Effects due to Adhesive Bonding of MEMS Components, AMM. 163 (2000) 51-59.

Key Engineering Materials Vols 645-646 (2015) pp 538-542
© (2015) Trans Tech Publications, Switzerland
doi:10.4028/www.scientific.net/KEM.645-646.538

Submitted: 2014-11-04
Accepted: 2014-12-23

High Resolution Micro-Displacement Sensing Circuit for Rotor Micro-Gyroscope

Mingyuan Ren[1, 2, a], Xiaowei Liu[1,b], Haifeng Zhang[1,c] and Zhigang Mao[1,d]

[1]MEMS Center, Harbin Institute of Technology, Harbin, Heilongjiang Province, China

[2]School of Software, Harbin University of Science and Technology, Harbin, Heilongjiang

[a]rmy2000@126.com (corresponding author), [b]lxw@hit.edu.cn, [c]moonzhf@163.com, [d]mao@hope.hit.edu.cn

Keywords: Gyroscope, Suspended rotor, Capacitance detection, CMOS integrated circuit

Abstract. A novel CMOS interface circuit with high resolution is designed and realized to achieve the integration of interface circuit for liquid suspended rotor micro-gyroscope. The detecting circuit adopts continuous-time current sensing circuit for capacitance measurement. The equivalent output noise power spectral density of phase-sensitive demodulation is 120 nV/Hz$^{1/2}$. The whole circuitry is realized with 0.5 μm 2P2M CMOS process and its testing results show the circuit has a relative capacitance resolution of 1×10^{-8}, in which the power supply is 18 V and the power consumption is 30 mW. The area of the chip is merely 18.5 mm^2.

Intorduction

In MEMS capacitive gyroscope, the rotation-induced capacitance change on sub-aF (10^{-18}F) level always needs to be resolved by readout circuits, which poses a challenge to the high resolusion micro-displacement sensing circuits design.

As shown in Fig. 1, several methods have been reported for detecting weak capacitance, including switched-capacitor (SC) circuit, continuous-time voltage sensing (CTV), and continuous-time current sensing (CTC).

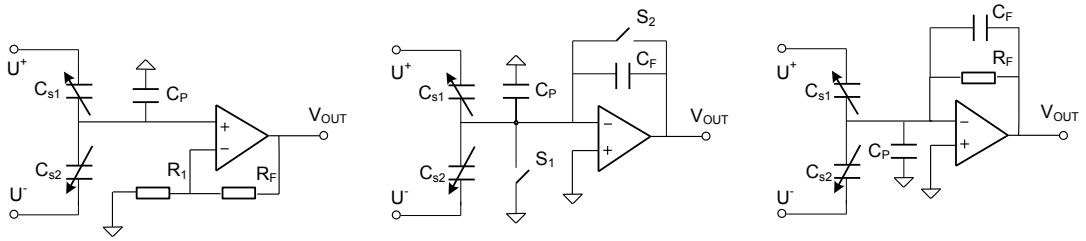


Fig. 1 Several methods for detecting weak capacitance
(a) continuous-time voltage sensing; (b) switched-capacitor circuit; (c) continuous-time

Fig. 1(a) shows the CTV circuit, which use a high input impedance operational amplifier to detect the variable capacitor by open-loop architecture. However, capacitive sensing generates an AM signal that needs to be sampled or demodulated, and noise folding may be introduced during this process. CTV circuits with chopper-stabilized technology were used for reducing low-frequency noise in CMOS technology and removing offset.

SC architecture is shown in Fig. 1(b), which is typical implementations of discrete-time readout circuit for capacitive sensors. It takes the samples from the sensors at periodical time and output it for further processing. The correlate-double-sampling (CDS) is applied on the SC method to reduce the 1/f noise and sampling noise, however, CDS brings about aliasing noise due to the sampling. Its signal to noise ratio (SNR) is about 3 to 5 times lower than CTV's.

As shown in Fig. 1(c), transimpedance amplifiers (TIA) that use a resistor for CTC are described. When the feedback resistor is large, equivalent input noise is small.

In this paper, we present a high resolution and low noise pick-off circuit of micro-gyroscopes which utilizes CTC circuit architectures. Firstly, several methods of readout circuit for capacitive sensor are introduced and their features are analyzed. Secondly, the structures of liquid suspended rotor micro-gyroscopes are described. Thirdly, the developed integrated interface circuit is presented. Then, the implementation and measurement results of interface circuit are reported. Lastly, conclusions is given.

Structure of rotor gyroscope

The structure of proposed rotor gyroscope described in this paper is shown in Fig. 2. The gyroscope is consisted of a stator, 12 driving coils, a closed cavity, a rotor and two sets of capacitance detecting electrodes. The materials of stator are silicon steel sheet as a coil core, and provide support to the cavity structure. Driving current flows through the driving coil and turns into a rotary magnetic field, which drives the rotor. Sensitive to both x-axial and y-axial rotation, the eight capacitance electrodes are grouped into two pairs of differential capacitors. The rotor is regarded as a middle electrode of the differential capacitance.

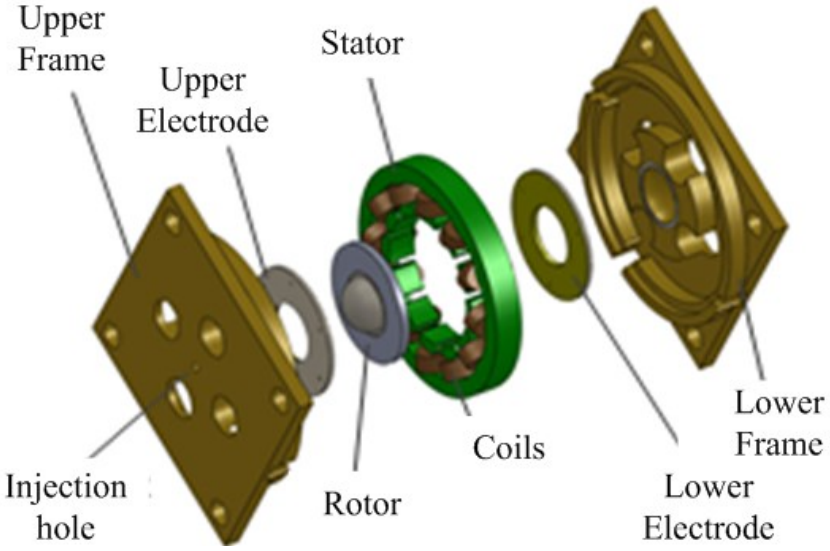


Fig. 2 Structure of liquid floated micro-gyroscope

Design and implementation of capacitance detection circuit

A schematic diagram of the displacement sensing circuit is shown in Fig. 3, which consists of the charge amplifier, differential amplifier, phase-sensitive demodulation, and low-pass filter. The signals from sensing electrode pair are applied to a low-noise preamplifier with feedback capacitor C_F, which converts the differential capacitance between the top and bottom plates into a differential voltage ΔV. It is clear that ΔV is amplitude modulated by the variation in the sensor capacitances. The small ac signal from the readout circuit is then amplified by a low-noise wideband differential amplifying stage before being applied to the demodulation circuit. Phase-sensitive demodulation (PSD) consists of multiplying the modulated signal by a reference voltage Vsin in phase with ΔV using a multiplier and then filtering the resulted signal with a sixth-order low-pass filter.

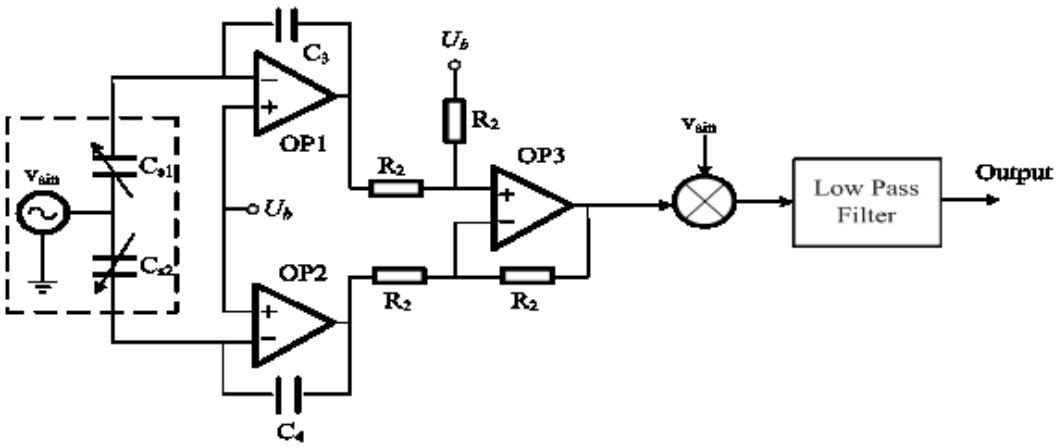


Fig. 3 Schematic diagram of the displacement sensing circuit

Fig. 4 gives the schematic of the charge amplifier using a T-network of resistors. The T-networks consists of M_{17}, M_{18}, M_{19}, R_1, and R_2. M_{18} is a long Channel MOS transistor with small width to length ratio, which gets a smaller gate-source voltage by adjusting M_{17} and M_{19}, since the transistors M_{18} and M_{19} have a same gate-source voltage. In this case, M_{18} is equivalent to a high value resistor of more than $10^6\,\Omega$, and because it is mirrored through the current mirror, it is proportional to the resistor R_0, and resistive to time and temperature influence. Feedback capacitance C_F is to improve the stability of the charge amplifier. Further, the input offset voltage (V_{OFF}) of the op-amp can be canceled by connecting to R_1, as is demonstrated in the schematic. Based on the above using the T-type network structure. The equivalent resistance is

$$R_{eq} = R_M(1+\frac{R_2}{R_1}) + R_2 \tag{1}$$

where R_M is the equivalent resistance transistor. When the $R_M >> R_1$, $R_M >> R_2$, and $R_M > 10^6\Omega$, resistance R_M is the main noise source of charge amplifier.

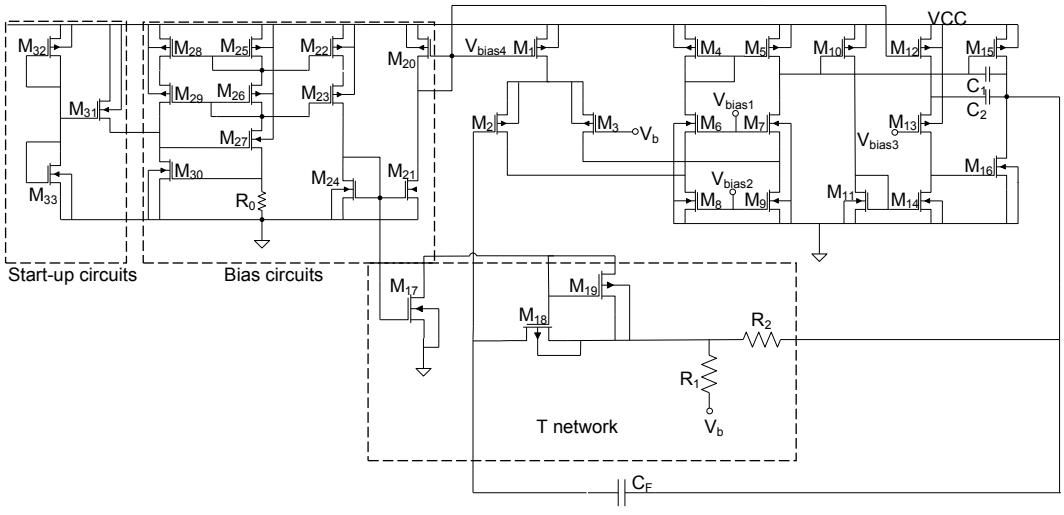


Fig. 4 Transimpedance amplifier schematic

The architecture of TIA circuit adopts three stage folded cascode amplifier configuration. The amplifier equivalent input noise density is

$$V_{n-amp}^2 = \frac{16kT}{3}\left(\frac{1}{g_{m2}} + \frac{g_{m5}+g_{m8}}{g_{m2}^2}\right) \tag{2}$$

The noise of charge amplifier output is

$$V_{n_out}^2 = \frac{16kT}{3}\left(\frac{1}{g_{m2}} + \frac{g_{m5}+g_{m8}}{g_{m2}^2}\right) \times \frac{(\frac{C_S C_{com}}{C_S + C_{com}} + C_P + C_F + C_m)^2}{C_F^2} + \frac{4kT}{R_F \omega^2 C_F^2} \tag{3}$$

TIA output signal to noise ratio at this time is

$$SNR = \sqrt{\frac{I_{IN}^2 R_{eq}}{4KT(R_2/R_1+1)}} \approx \sqrt{\frac{I_{IN}^2 R_M}{4KT}} \tag{4}$$

where, I_{IN} is the input current of the TIA, and its expression is

$$I_{IN} = \frac{\partial C}{\partial t} V_b = C_0 V_b \omega \sin \omega t \tag{5}$$

where C_0 is maximum change of sensitive capacitance, V_b is transimpedance amplifier forward bias voltage, ω is resonant frequency.

By Eq. (4) and (5), it is known that increasing both resistance R_M and the bias voltage V_b can improve signal to noise ratio (SNR) of the detection circuit. When the bias voltage V_b is 5 V, the resonant frequency is 10 kHz, the transimpedance amplifier can detect less than 1 aF/sqrt (Hz) change in capacitance.

The layout of micro-displacement sensing interface circuit is shown in Fig. 5, which is fabricated by 0.5μm 2P2M CMOS process. The entire area of the chip is 18.5 mm^2.

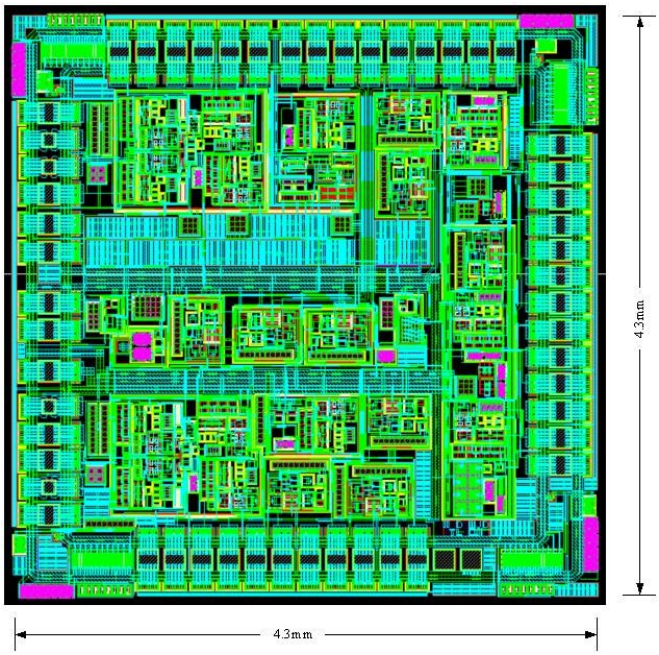


Fig. 5 Layout of micro-displacement sensing interface circuit

The measured open-loop gain is at least 120 dB at 0.5 Hz, which is close to the dc operating point. The flicker noise corner frequency is 4 kHz. The equivalent thermal noise floor of the charge amplifier was calculated to be about 15 nV/Hz.

The equivalent output noise power spectral density of phase-sensitive demodulation is 120 $nV/Hz^{1/2}$ using Dynamic Signal Analyzer (HP35670). By making division between this output noise PSD and the loop gain of charge amplifier, the equivalent input PSD of the charge amplifier is calculated as 15 $nV/Hz^{1/2}$. By calculation, the relative capacitance resolution of the system is 1×10^{-8}.

Summary

In this paper an interface circuit of liquid suspended micro-gyroscope was proposed, which reduced the floor of noise and improved the resolution of capacitor. The readout circuit adopts continuous-time current sensing circuit for capacitance measurement. The proposed interface circuit was obtained in 0.5 μm 2P2M CMOS process. The experimental results of the CMOS chip show that, the power voltage supply is 18 V, the system has a consumption power of 30 mW, relative capacitance resolution of the system is 1×10^{-8}, areas of the chip is 18.5 mm^2. The interface ASIC has higher resolution of capacitor than other recently published papers. The ASIC is suitable for high accuracy requirement in liquid suspended MEMS Micro-gyroscope.

Acknowledgement

This research is supported by National Basic Research program of China (No. 2012CB934104), National Science Foundation of China(No. 61474034), Natural Science Foundation of Heilongjiang Province of China, and Fundamental Research Funds for the Central Universities (No. HIT.NSRIF.2014040).

References

[1] F. Wu, G.K. Fedde, and L.R. Carley, IEEE J. Solid.-State Circuits, 39(2004)722-730 .
[2] B.V. Amini, R. Abdolvand, and F. Ayazi, IEEE J. Solid.-State Circuits, 41(2006) 2983-2991, .
[3] H. Kulah, J. Chae, and K. Najafi, IEEE J. Solid.-State Circuits, 41(2006) 352-361.
[4] C.D. Ezekwe and B.E. Boser, IEEE J. Solid.-State Circuits, 43(2008) 3039-3048.
[5] L. Aaltonen and K. Halonen, Sens. Actuators A, Phys., 154(2009) 46-56.

Key Engineering Materials Vols 645-646 (2015) pp 543-547
© (2015) Trans Tech Publications, Switzerland
doi:10.4028/www.scientific.net/KEM.645-646.543

Submitted: 2014-11-05
Accepted: 2014-12-23

Simulation and Experimental Verification of Silicon Microgyroscope's Closed-Loop Driving Circuits Based on Cadence

Weifeng Tang [1,a], Guoming Xia[2,b] , Anping Qiu[3,c], Yan Su [4,d]

[1] Nanjing University of Science and Technology, Xiaolingwei NO.200, Nanjing, China

[2] Nanjing University of Science and Technology, Xiaolingwei NO.200, Nanjing, China

[3] Nanjing University of Science and Technology, Xiaolingwei NO.200, Nanjing, China

[4] Nanjing University of Science and Technology, Xiaolingwei NO.200, Nanjing, China

[a]547394983@qq.com, [b]apqiu@mail.njust.edu.cn, [c]xgmseu@gmail.com, [d]suyan@mail.njust.edu.cn

Keywords: Silicon microgyroscope; Closed-loop driving; Simulation; RLC

Abstract: The output-current of silicon microgyroscope is at the level of 10^{-7}A, so the requirements for circuits' SNR are very high. This paper conducts the simulation of closed-loop driving circuits in Cadence on the basis of a RLC series resonant circuit. It turns out that experimental results fit the simulation which has a great significance for improving the property of circuits. First of all, the operating principle of silicon microgyroscope is introduced. Secondly, a RLC series resonant circuit is established by measuring Q value and driving frequency. Then the overall simulation is conducted in Cadence combined with chips' models offered by the manufacturers. Finally, the accuracy of simulation is verified by experiments. Experimental results show that, the relative error of driving sense signal's value is 0.5%, for stability time the value is 0.6% and for driving frequency the value is 38ppm. Experimental results agree well with the simulation, which confirms simulation's accuracy. This has a great significance for improving the property of circuits.

Introduction

As a typical inertial measurement device, silicon microgyroscope has following advantages[1,2]: its device dimension is in millimeter and weight is in gram by using silicon processing technology like integrated circuits. It can effectively prevent the effects of external environmental factors and so on.

Silicon microgyroscope's property is improved at home and abroad year by year. The most high-precision silicon microgyroscope's bias stability has been close to $0.1\,°/h$ at the level of tactical accuracy. The output-current of silicon microgyroscope is at the level of 10^{-7}A, so it is very easy to be interfered by large signals and the influence of chips' noise can't be ignored. This means that the requirements of circuits are very high. To improve the property, the simulation of closed-loop driving circuits is very necessary.

This paper analyzes the dual-mass silicon mcrogyroscope and did the following works. Firstly, its fundamental principle is introduced. Secondly, a RLC series resonant circuit is established based on measurement of Q value and driving frequency. Then overall simulation is conducted in Cadence combined with chips' models offered by the manufacturers. Finally, we verify simulation's accuracy by experimental data. This has a great significance for improving the property of circuits Fundamental Principle of Silicon Microgyroscope.

Fundamental Principle

Structure of Silicon Microgyroscope

The structure[3] of dual-mass silicon microgyroscope is shown in Fig.1. It senses the Z-Axis input angular rate by Coriolis effect. X-Axis is the driving direction and the electrostatic force produced by combs 16 drives two masses move to each other along X-Axis. This is the driving mode of silicon

microgyroscope. Y-Axis is the sense direction and the Z-Axis input angular rate is sensed by the capacitance variation of combs 15.

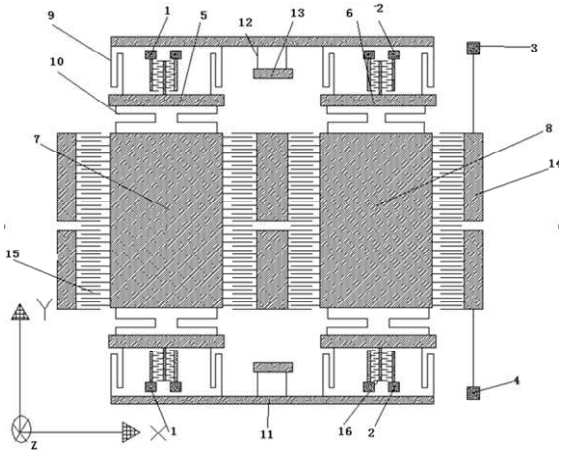


Fig.1 Schematic of silicon microgyroscope

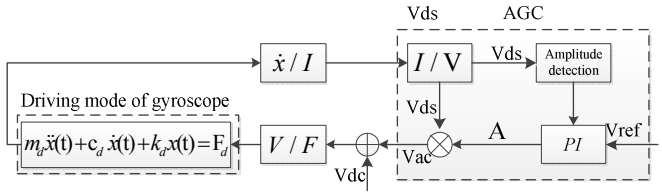


Fig.2 Schematic of the driving circuits of silicon microgyroscope

Principle of Driving Circuits

Silicon microgyroscope is driving by self-excited oscillation circuits with AGC[4](automatic gain control) which is shown in Fig.2. The driving-sense combs convert the movement speed into the current and the transimpedance amplifier converts the current into the voltage. At the same time, the drive combs convert the voltage into the force. The closed loop will achieve self-excited oscillation when the amplitude and the phase condition of transfer function are satisfied.

Modeling of Silicon Microgyroscope

The dynamical model of silicon microgyroscope is the second order oscillation system of "mass-spring-damp". So we can use a RLC series resonant circuit to represent the structure of silicon microgyroscope.

The transfer function from driving voltage V to driving sense current I which are as Fig.2 shown can be written as

$$\frac{I}{V}=K_1K_2\frac{s}{m_ds^2+2m_d\omega_d\xi_ds+m_d\omega_d{}^2}. \tag{1}$$

Where K_1 is the coefficient of V/F which is shown in Fig.2. K_2 is the coefficient of $\dot{x}/I$. m_d is the mass. ω_d is the driving angular frequency. ξ_d is the damping ratio which can be calculated by Eq.2 which is

$$Q=\frac{1}{2\xi_d}. \tag{2}$$

Where Q is the quality factor of the driving modal.

Meanwhile, the transfer function of the RLC series resonant circuit can be written as

$$H=\frac{I}{V}=\frac{s/L}{s^2+Rs/L+1/LC}. \tag{3}$$

We can get the calculation formulas of R, L, C by comparing Eq.1 with Eq.3 which can be written as

$$R = {m_d \omega_d}/{2QK_1K_2} \tag{4}$$

$$L = {m_d}/{2K_1K_2} \tag{5}$$

$$C = {2K_1K_2}/{m_d \omega_d^2}. \tag{6}$$

In order to get the value of R, L, C, the Q value and ω_d need to be measured. As for m_d, we adopt the design value.

The attenuation of Vds (voltage of driving sense) when breaking the closed-loop driving circuits is shown in Fig.3. According to mechanical vibration theory[5], the attenuation amplitude is limited to the curve of $\pm Ae^{-\frac{1}{2Q}\omega_d t}$. So we can get the Q value from the envelope line in Fig.3. And ω_d is measured by a multimeter.

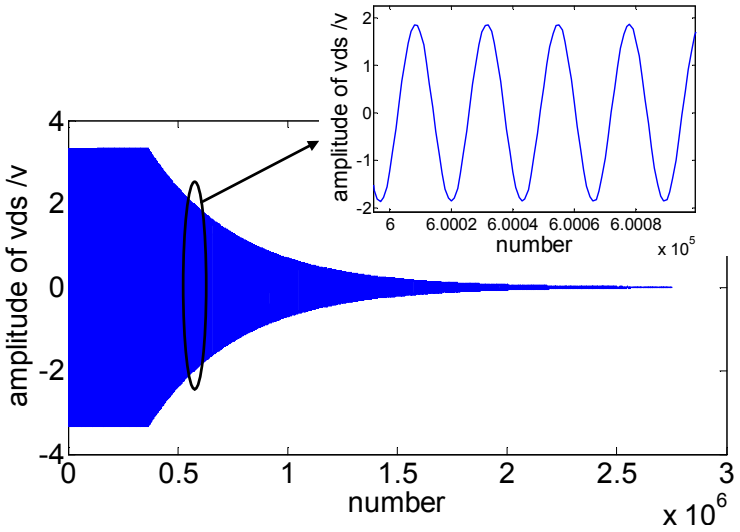


Fig.3 Schematic of the measurement of Q value

Parameters of the RLC series resonant circuit list in Tab.1.

Table.1 Parameters of the RLC series resonant circuit

parameter	value
K_1	1.606e6
K_2	3.303e6
Q	55939
f[hz]	4327.6
m_d[kg]	1.073e-6
R[Ω]	1.606e6
L[H]	3.303e6
C[f]	4.0945e-15

Driving Circuits

The chips' Pspice models are eastablished in Model Editor of Cadence based on the Lib files offered by manufacturers[6]. The closed-loop simulation is set up by combining the driving circuits with the RLC series resonant circuit which is shown in Fig.4.

Cadence has the advantage that the chips' models include their own noise, which makes the simulation's results close to the experiment. In this way, the influence of the amplifiers and multipliers on circuits can be assessed to improve the property.

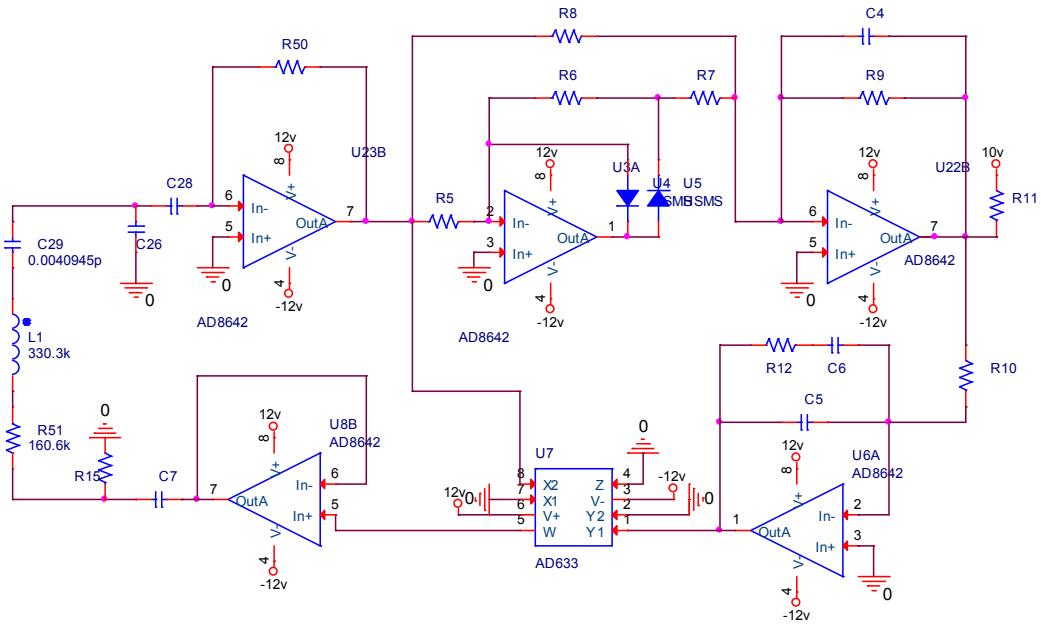


Fig.4 Schematic of simulation of closed-loop driving circuits

Simulation and Experimental data

Time domain simulation of closed-loop driving circuits is performed in the condition that the step size is set as 0.2us to get the high precision simulation results.

Vds represents the movement of the mass in silicon microgyroscope. It should be a sinusoidal signal with a constant amplitude when gyroscope works. It is the main parameter to verify the accuracy of the simulation.

Vds signal in simulation results is shown in Fig.5.

The experimental Vds acquired by high-speed data acquisition cards is shown in Fig.6.

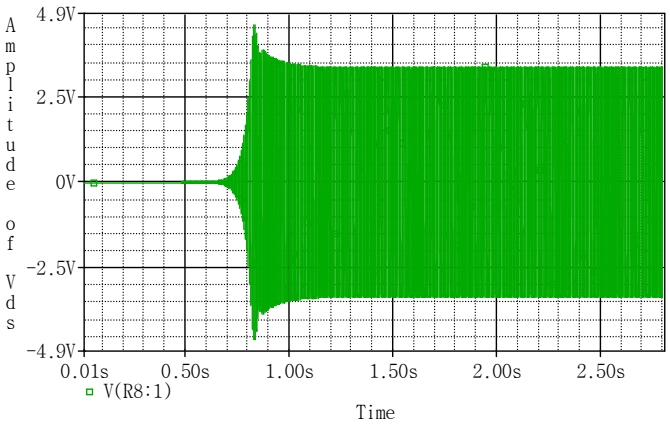


Fig.5 The simulation of Vds when power on

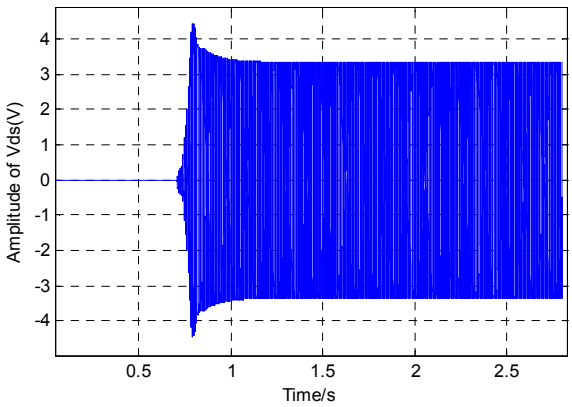


Fig.6 The experimental Vds when power on

The data's comparison between simulation and experiment list in Tab.2. Where the stability time of Vds means the time which is spent when the overshoot within 1% for the first time.

Table.2 The comparison of Vds

	Simulation value	Experimental value	Relative error
Value of Vds	3.3543[V]	3.3380[V]	0.5%
Stability time of Vds	1.405[s]	1.397[s]	0.6%
Frequency of Vds	4327.4[hz]	4327.6[hz]	38ppm

From Tab.2, we know that the simulation values are very close to the experimental values where the largest relative error is less than 1%. This confirms the simulation's accuracy.

Conclusion

This paper measures the parameters of dual-mass silicon microgyroscope and uses a RLC series resonant circuit to represent the second order oscillation system of "mass-spring-damp". Secondly, the driving circuits are established in Cadence based on chips' models. Then, time-domain simulation of closed-loop driving circuits is performed. Finally, the experimental data are used to verify the simulation's accuracy. It turns out that the relative error of Vds's value is 0.5%, for stability time the value is 0.6% and for driving frequency the value is 38ppm. Experimental results agree well with the simulation, which confirms simulation's accuracy. This has a great significance for improving the property of circuits.

Acknowledgements

This work was financially supported by The National Natural Foundation (No.61301214) and Defense Basic Research Program (A2620133002).

References

[1] Jun Liu, Yunbo Shi, Jie Li: submitted to Journal of Micro-inertial Technology. 2005.
[2] Qin Shi: Study on Key Technologies of Silicon Microgyroscopes for Improving Performance[D]. 2005. (in Chinses)
[3] Anping Qiu, Qin Shi, Yan Su: China ZL200710133223.5[P]. 2008-03-05. (in Chinses)
[4] Jinming Li: Research on High Signal-Noise Ratio of Capacitive Micromechanical Gyroscope[D]. 2005,29-31.(in Chinese)
[5] Yiming Zhang. Mechanical vibration[M].Tsinghua university press, 2012, p25.(in Chinses)
[6] Analog Devices. http://www.analog.com[OL].

Key Engineering Materials Vols 645-646 (2015) pp 548-554
© (2015) Trans Tech Publications, Switzerland
doi:10.4028/www.scientific.net/KEM.645-646.548

Submitted: 2014-11-10
Accepted: 2014-12-23

DESIGN OF 16 BIT 200KHZ FEEDFORWARD SIGMA-DELTA ADC APPLIED IN SILICON GYROSCOPE

A. Fuxiang Huang[1,a] B. Zhiqiang Gao[1] C.Xiaowei Liu[1]

[1] MEMS Center, Harbin Institute of Technology, Harbin, Heilongjiang, China
[a] fox2738@163.com(corresponding author)

Keywords: Sigma-Delta, multi-bit quantization, ADC, silicon gyroscope

Abstract. Due to the huge potential applications in military and civil fields, silicon micro mechanical gyro has become the most popular research direction in MEMS field today. Therefore, the corresponding interface circuit of silicon gyroscope has also become a hot topic at home and abroad. Now, integration, digitalization and intelligence has become the focus of future research directions of silicon gyroscope, so the research of analog to digital conversion circuit for gyroscope has become a research priority. Therefore, the conduct of Sigma Delta ADCs research for silicon gyro interface circuit has a very important significance and application prospects.

This topic briefly introduces the working principle of Sigma Delta ADC. Based on the requirements of the modulator design, Sigma Delta modulator structures are carefully analyzed and also carried on the comparison and optimization. Hereby, a three order three bits quantization in single-loop with partial feedback of feed-forward summation system structure for modulator is designed in this paper, and then the ideal model of modulator system in Matlab is simulated. In addition, the focus of this topic is mainly on the nonlinear factors analysis and modeling, and the Data Weighted Average (DWA) technique used in multi-bit quantization is introduced as well as modeling in system level. Then, the non-ideal modeling of system is simulated in Matlab.
In system level design, this paper adopts feed-forward summation and multi-bit quantization structure to reduce the output of the integrator, increase the noise performance of the modulator, and make it easier for the system stability. Furthermore, the use of partial feedback in the structure for zero-point optimization improves the noise shaping ability in signal bandwidth of modulator. This topic employs the single-loop third-order three-bit quantization structure, with the sampling rate 64, signal bandwidth 200 K Hz and the sampling clock frequency 25.6 MHz. For the ideal modeling, the Signal-to-Noise Ratio (SNR) is 125dB, and the Effective Number of Bits (ENOB) is 20.48. When in consideration of modulator's nonlinear factors, the nonlinear systems Simulink simulation results obtained SNR of 104dB, and the ENOB is 16.98.
In order to reduce the harmonic distortion of the modulator, transistor level is implemented by fully-differential switch capacitor circuit. The structure at all levels of the integrator was optimized. To reduce the influence of flicker noise, the integrator adopts Correlated Double Sampling (CDS) technology, and is improved by the partial feedback circuit. The fully-differential operational amplifier with high slew-rate and high bandwidth is designed, and uses switch capacitor circuit as common-mode feedback. Dynamic comparator and multi-bit quantizer are designed to improve the speed of the quantizer and reduce power consumption. The design the nonlinear compensation feedback DAC module--DWA module circuit--realizes noise shaping of capacitance matching error. The overall circuit was simulated in Cadence by 0.6um process. Transistor-level simulation result shows that the SNR is 101.3dB, and the effective number of bits is 16.54bits. The simulation results

are consistent with the established non-ideal model of modulator, which verifies the correction of system level design method.

Introduction

In recent years, Sigma-Delta ADC is the most popular analog to digital conversion techniques, particular in the low-speed and high performance requirements of the field . While obtaining a high signal to noise ratio, as compared with the conventional data conversion technology, Sigma Delta ADC analog device does not require high match rate, and has low power consumption, is fully compatible with CMOS integrated circuit process, and has become main technology of the realization of low-speed, high-accuracy ADC, widely used in speech coding, digital audio and other fields[1]. Although Sigma-Delta ADC has the above advantages, there are few high-performance products available on the domestic, far behind other countries. The design of the system structure and nonlinear factors Sigma-Delta ADC conducted in-depth research, completed a multi-bit Sigma-Delta modulator design, Sigma-Delta ADC on domestic development work has some positive significance.

The purpose of this project is to design a 200KHz bandwidth and can reach 16 single-precision feed-forward loop several Sigma-Delta ADC, which also serves a foundation as the center of the future development of MEMS in the field of data conversion.

System Architecture of Sigma Delta Modulator

The Sigma Delta ADC in this work is used as a part in silicon gyro interface circuit, and therefore the selection of the Sigma Delta modulator structure needs to consider adaptation issues of gyro sensitive structure. A single ring modulator is a better selection, for it is not sensitive to the non-linear of the circuit.Higher-order structure of a single ring modulator, to get a better signal to noise ratio (SNR), select feed-forward structure with zero optimization technology is the best choice, so the design will be selected as the basic structure of the structure using CRFF .The third-order system with multi-quantization is easy to obtain the stability, and it can help to reduce the dependence of quantization-gain to the amplitude of the input signal. The power consumption under the same conditions will be smaller, while simplifying the operational amplifier and an integrating design. Thus this design used third-order three-quantization structure .

Without considering the case of nonlinear factors, according to the system parameters obtained using Simulink in the system ideal type model, build system shown in Figure 1.

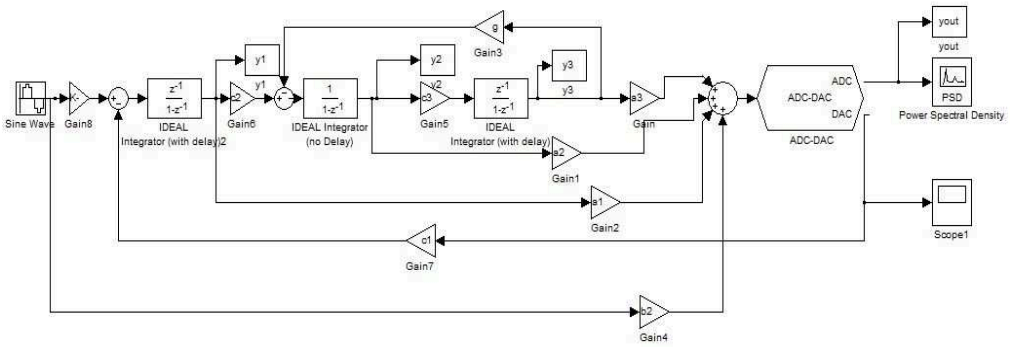


Figure 1 The ideal model of Sigma Delta Modulator

As the result shown in Figure 2, the system SNR reached 125dB, effective number of bits reached 20.48, the ideal model fully meet the design requirements.

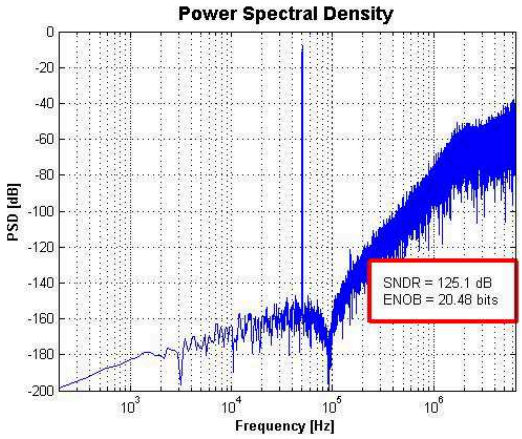


Figure 2 The output power spectral density of the ideal model of Modulator .

Analysis and modeling of non-ideal factors

a.Clock jitter model

Clock jitter is due to the inaccurate of switching time in the sampling process, which leads to the input signal sampling uneven, and ultimately makes the quantization noise energy increase [35].The resulting error due to clock jitter can be expressed as:

$$x(t+\delta)-x(t)=2\pi f_{in}\delta A\cos(2\pi f_{in}t)=\delta\frac{d}{dt}x(t) \tag{1}$$

According to equation (1), the model of the clock jitter can be built as show in Figure 3 .

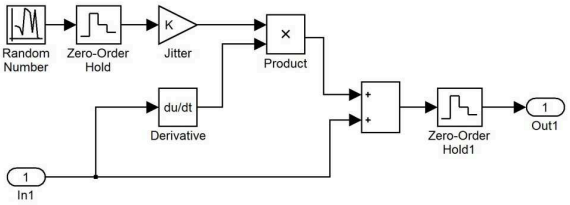


Figure 3 The model of clock jitter

b.Non-ideal model of the integrator

The ideal transfer function of the integrator is:

$$H(z)=\frac{c_s}{c_f}\frac{z^{-1}}{1-z^{-1}} \tag{2}$$

This equation is due to the ideal op amp which DC gain is infinite. The actual DC gain of op amp is limited.The transfer function of the integrator can be modified to

$$H(z)=\frac{c_s}{c_f}\frac{\alpha z^{-1}}{1-\beta z^{-1}} \tag{3}$$

The real op amp has limited slew rate and gain bandwidth, which will also bring some integrator gain error and harmonic distortion.

Considering the case of non-ideal various factors of the integrator , non-ideal integrator model is shown in Figure 4.

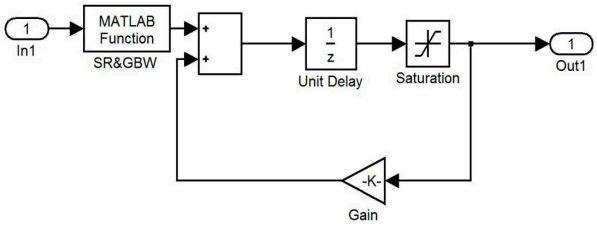


Figure 4 The model of Non-ideal integrator

c.Nonlinear of feedback DAC and Compensation Model

The structure with multi-quantization has several advantages compared to the one with single-quantization:1 it can reduce the quantization error and improve the conversion accuracy modulator. 2 levels due to the integrator output swing is reduced, reducing the design requirements for the op amp. 3 Because the signal transfer process to a lesser extent, the non-ideal factors caused by nonlinear of circuit reduced .

The structure of Multi-quantify will bring very serious nonlinear problems.Therefore, during system design, there is the need feedback to compensate for non-linear DAC.The most common method of compensation of DAC nonlinearity error is dynamic element matching (DEM).This design uses the Data weighted average technique(DWA) technology for nonlinear compensation.The structure of DWA is as Figure 5.

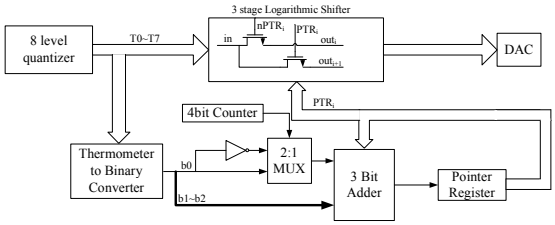


Figure 5 The structure of DWA

As mentioned above ,Figure 6 shows the model of non-ideal system.

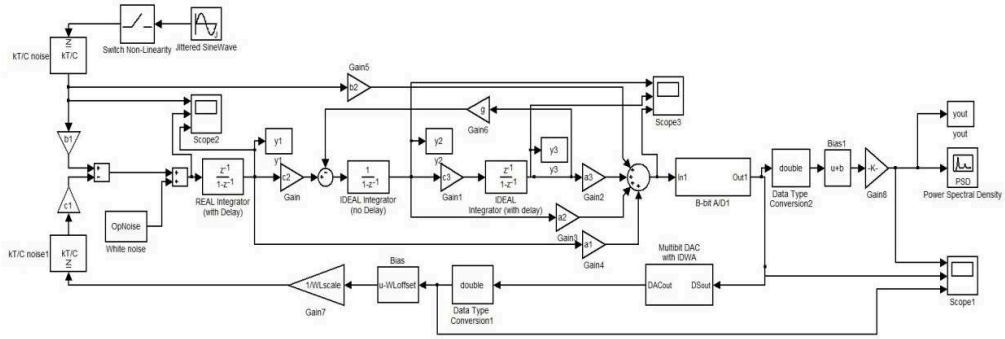


Figure 6 The model of non-ideal system

Simulation results of the non-ideal model show that, the system output signal to noise ratio dropped to 104dB, effective number of bits for 16.98.

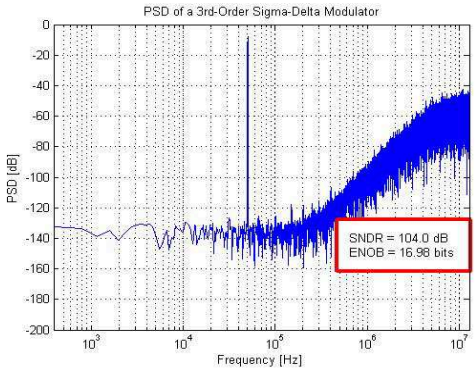


Figure 7 The spectrum of the non-ideal system

Integrator

In this circuit CRFF structure, Sigma Delta Modulator has latency integrator and non-delayed integrator. And because there are zero local feedback circuit optimized at all levels ,therefore integrators are designed separately to meet system requirements.

As described hereinbefore, the noise performance of the input stage of the integrator determines the noise performance of the modulator system. So the first stage integrator needs to be related to the optimization design to reduce circuit noise impact for the system [39]. Because there are no non-ideal factors for modeling flicker noise, so there need to be optimized to reduce flicker noise.

The design uses a correlated double sampling techniques to reduce flicker noise impact.The circuit is a collection of correlated double sampling technique and the feedback DAC structure.The structure of the first stage integrator is shown in Figure 8.

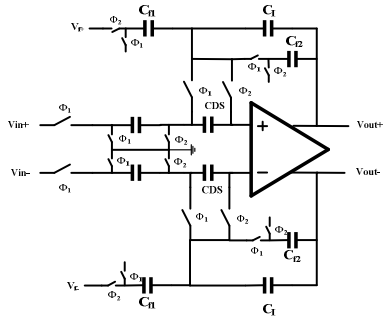


Figure 8 The structure of the first grade integrator

The second stage uses a non-delayed integrator.This structure is shown in Figure 9, still using the correlated double sampling capacitor to reduce flicker noise and op amp disorders.

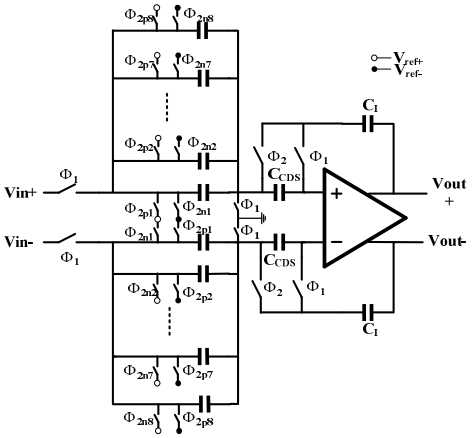


Figure 9 The structure of the second grade integrator

Feedback principle is shown in Eq.4:

$$V_{out} = \frac{C_s}{C_{f2}+C_I} \cdot \frac{z^{-1}}{1-z^{-1}} \cdot V_{in} - \frac{C_{f1}}{C_I+C_{f2}} \cdot \frac{C_{f2}}{C_I} \cdot \frac{z^{-1}}{1-z^{-1}} \cdot V_f \quad (4)$$

Operational Amplifier

Designing a high-performance op amps has a significant role to improve the SNR of the modulator. Due to the high clock frequency, the operational amplifier need a high-speed. The gain of the operational amplifier has tobe large enough to ensure the linearity gain integrator, reducing the non-linear effect on the modulator performance [3].

Since the amplifier requires a high slew rate, high gain-bandwidth product and less noise, so the design and the actual design is based on experience, the final choice fully differential op amp current mirror symmetric, the circuit structure shown in Figure 10, using switched-capacitor CMFB structure neglected.

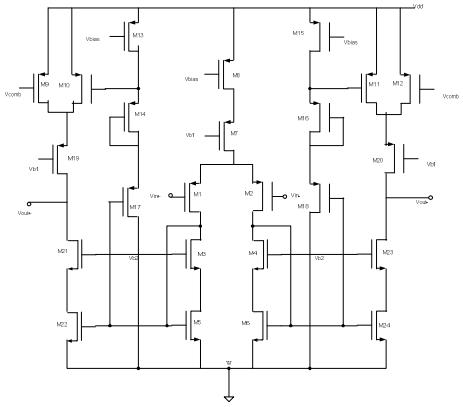


Figure 10 Fully differential op amp

The simulation results of the op amp is given in Table 1, and the performance meet the design specifications.

Table 1 The parameter of the operational amplifier

Parameter	Expect value	Simulate result
A_V	>75dB	100dB
GBW	>100MHz	103MHz
PM	>60°	61°
SR	>100V/μs	130V/μs
ICMR	>0.8Vpp	0.2~4.9V
C_L	2pF	2pF
Noise	50μVrms	57.4μVrms

Result and Conclusion

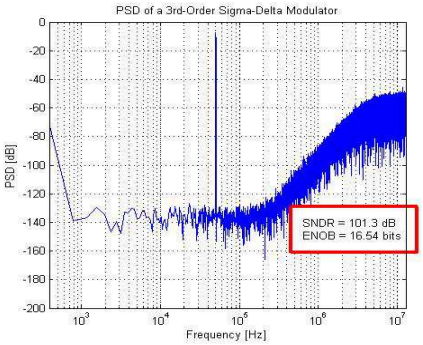


Figure 11 The output power spectral density

The overall circuit was simulated in Cadence by 0.6um process.Transistor-level simulation result in Figure 11 shows that the SNR is 101.3dB, and the effective number of bits is 16.54bits. The simulation results are consistent with the established non-ideal model of modulator, which verifies the correction of system level design method. This work is supported by 2013AA041107.

References

[1] H. Rodjegard, D. Sandstrom, P. Pelin, et al. A digitally controlled MEMS gyroscope with 3.2 deg/hr stability[C]. Solid-State Sensors, Actuators and Microsystems. Digest of Technical Papers. TRANSDUCERS '05. The 13th International Conference on, 2005. 1:535~538.

[2] S. Jaganathan, S. Krishnan, D. Mensa et al. An 18GHz continuous-time Σ-Δ analog-digital converter implemented in InP-transferred substrate HBT technology[J]. IEEE Journal of Solid-State Circuits, 2001, 36: 1343-1350.

[3] J. Deveugele, G. Vander Plas, M. Steyaert et al. A 1V 140μW 88-dB Audio Sigma-Delta Modulator in 90-nm CMOS[J]. IEEE Journal of Solid-State Circuits, 2004, 39:1809-1818.

Key Engineering Materials Vols 645-646 (2015) pp 555-560
© (2015) Trans Tech Publications, Switzerland
doi:10.4028/www.scientific.net/KEM.645-646.555

Submitted: 2014-11-13
Accepted: 2014-12-23

Advancements in micro-structure with multiple stress concentration region for bionic vector hydrophone

Zhang Guojun[1,2,a],Zhao Peng[1,2,b],Zhang Wendong[1,2,c],

([1] School of Marine Science and Technology ,Northwestern Polytechnical University, Xi'an, Shanxi 710072, China;

[2] Science and Technology on Electronic Test & Measurement Laboratory, North University of China, Taiyuan, Shanxi 030051, China)

[a] zhaopeng.08@163.com, [b]910218632@qq.com, [c]wdzhang@nuc.edu.cn (Zhang Guojun)

Keywords: vector hydrophone; MEMS; stress concentration; ANSYS

Abstract. The method of Multiple Stress Concentration Regions(MSCRs) on the surface of MEMS Silicon micro-structure is introduced in order to enhance the sensibility of the hair vector hydrophone without reducing the working bandwidth. The MSCRs with the thickness and width smaller than the rest of the cantilever can produce localized stress concentration when constant force is applied on the structure. ANSYS software has been used as a tool to analyze the effect of different shapes and dimensions on the performance of the micro-structure. The optimum MSCR has been obtained. Results show that compared with the ordinary structure, the sensitivity of the micro-structure with MSCR can be increased by 1.5 times, and the upper limit of bandwidth can be improved from $337Hz$ to $500Hz$. This paper provides a new method to resolve contradiction between the sensitivity and working bandwidth.

Introduction

Recent MEMS technology has a wide range of applications such as biotechnology, military and communication areas and so on, and it is making its way into the field of acoustic sensors. The MEMS bionic vector hydrophone developed by North University of China has the advantages of low frequency, miniaturization, high sensitivity, etc[1-3], which has been caught scholars' eyes at home and abroad for a long time. However, the main factor which hinders the MEMS hydrophone's further engineering application is the discrepancy in that the sensibility and working bandwidth of the MEMS hydrophone can't be improved simultaneously. Guan and Zhang [4] devised a T-shape vector hydrophone to solve the problems above, nevertheless, it had the shortcoming in that the detecting space of hydrophone scaled down from 2D to 1D. Hence, the purpose of this research is to optimize the micro-structure in hydrophone in order to enhance the sensibility of the bionic vector hydrophone without reducing the working bandwidth.

In order to solve this problem, the method of Multiple Stress Concentration Regions(MSCRs) on the surface of MEMS Silicon micro-structure is introduced. The "Multiple Stress Concentration Regions" is that two or more factors in stress concentration makes the localized stress more higher. R. Bashir[5], S.M.Firdau[6-7], MEI Deqing[8], and WANG Guanglong[9] et al. completed similar studies, however, all the researches above introduced only single factor in stress concentration that couldn't improve the sensitivity effectively. This paper proposes that the MSCRs with the thickness and width smaller than the cantilever thickness can produce localized stress concentration. The proposed MSCR designs were analyzed by using ANSYS to predict the parameters of the

design, then discussed in detail the effect of different shapes and dimensions on the performance of the micro-structure. This research provides a new method to resolve the contradiction between the sensitivity and working bandwidth of the hydrophone.

1 Working principle[10-11]

The microstructure of the bionic vector hydrophone, as shown in Fig.1, consists of two parts: the four-beams microstructure and a rigid plastic cylinder. When the cilium responds to the acoustic particle motion, the center block will have a horizontal displacement and an angular rotation, and then the slim cantilever will be subject to deformation. A full-active Wheatstone bridge is logically formed by locating piezoresistors that are implanted into the sensor beams. When there is incentive direct current, the change of the Wheatstone bridge will be detected. Therefore, the vector underwater acoustic signal will be detected.

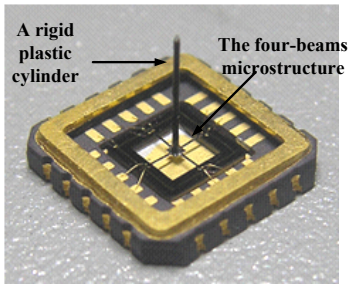


Fig.1 The micro-structure of cilium type

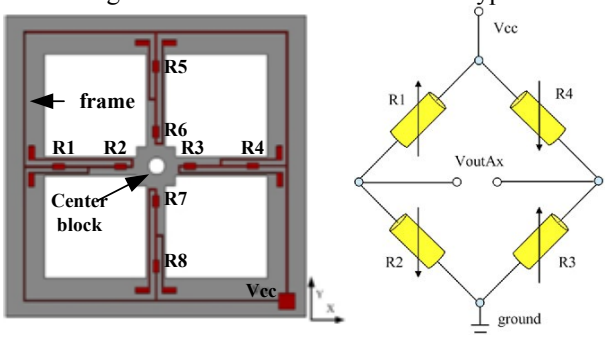


Fig.2 Wheatstone bridge

The Wheatstone bridge in MEMS chip is shown in Fig.2, and the simplified equation of the output voltage is expressed in Eq.(1):

$$U_{out} = \frac{2(\Delta R / R + \Delta R^* / R)}{4 - (\Delta R / R - \Delta R^* / R)^2} U_{in} \tag{1}$$

In the Eq.(1), U_{in} is the power-supply voltage, and U_{out} is the output voltage. Suppose that the resistance values are same, $R_1 = R_2 = R_3 = R_4 = R$. When there is acceleration acting on the microstructure, the change of the piezoresistors which are closed to the frame is $\Delta R_1 = \Delta R_4 = \Delta R$, and The change of the piezoresistors which are closed to the center block is $\Delta R_2 = \Delta R_3 = \Delta R^*$.

Ignoring the transverse stress, the relationship between $\Delta R / R$ (or $\Delta R^* / R$) and the stress on the piezoresistor can be approximated as,

$$\frac{\Delta R}{R} = \pi_l \sigma_l \quad \text{or} \quad \frac{\Delta R^*}{R} = \pi_l \sigma_l^* \tag{2}$$

In this equation, σ_l , σ_l^* are respectively the longitudinal stress along the micro-cantilever where the piezoresistors are implanted, and both of the values are positive. π_l is the longitudinal piezoresistive coefficient. Substituting Eq.(2) into Eq.(1), U_{out} can be expressed as

$$U_{out} = \frac{2\pi_l(\sigma_l + \sigma_l^*)}{4 - \pi_l(\sigma_l - \sigma_l^*)^2} U_{in} \tag{3}$$

Eq.(3) shows that increasing the power-supply voltage or enhancing the stress can increase the output voltage so that the sensitivity is improved. However, increasing the power-supply voltage will result in the increase of the system's electronic noise which should be restrained. So, enhancing the longitudinal stress seems to be the most suitable approach in increasing the sensitivity of piezoresistive sensor. Thus, we need to introduce multiple stress concentration region in order to improve the sensitivity of MEMS vector hydrophone further.

2 Structural design and simulation

In this paper, the FEA software, ANSYS, was used to design different MEMS devices with MSCR and conduct stress analysis or modal analysis. The advantages of ANSYS enable the behavior of the MEMS devices to be predicted quickly, and the parameters of the MEMS devices can be obtained conveniently. The structural material for four-beams and center block is silicon, which has 190GPa as its Young's modulus, 0.27 as its Poison's ratio and $2.33g/cm^3$ as its density. The material for rigid cylinder is plastic, which has 74GPa as its Young's modulus, 0.17 as its Poison's ratio and $2.32g/cm^3$ as its density. In this research, the element type of coarse mesh is SOLID187.

2.1 The MEMS cantilever with MSCR design

Optimizing the micro-cantilever plays a major role in improving the performance of the four-beams sensitive chip. So we analyze firstly the effect of various MSCR shape design on the sensitivity of single cantilever in order to select the MSCR design that has the highest stress. Fig.3 shows that the cantilevers with different MSCRs. In the design, the grooves for stress concentration are etched in the {100} crystal plane of a silicon wafer. There is a 54 degree angle at the edge of those grooves due to the wet etching course. Basically, all beams have $1000\mu m$ length, $120\mu m$ width, $20\mu m$ thickness, and all grooves have $5\mu m$ depth and $50\mu m$ length. Static analysis was performed to simulate the stress on the surface of MSCR when a $1\mu N$ load in the negative z direction was applied at the right end of the cantilevers, and the constraint was selected at the left end of the beams where have MSCRs.

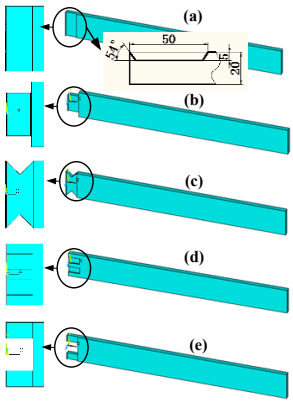


Fig.3 The cantilevers with different MSCRs

When comparing micro-cantilevers with different shapes' MSCR, the higher the mean stress is, the lower the first order modal frequency is. The results show that the design (e) has the highest stress, but considering that the problem about arrangement of wire and lack of technology, among all the designs, design(b) could easily be achieved. Thus, the design(b) is selected for further studying.

2.2 The MEMS cantilever with MSCR design

The MSCR on the four-beams micro-structure is introduced as shown in Fig.4.

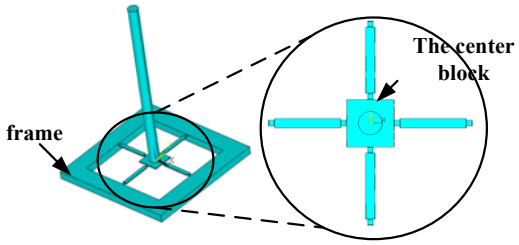


Fig.4 The model of cilium micro-structure with MSCR

To simplify the process of modeling, the constraint was applied at the fixed end instead of the frame as shown in Fig.4. The material for micro-structure was the same as above. Three kinds of structure model were established. The length and width of all cantilevers are respectively $1000\mu m$ and $120\mu m$. The dimension of center block is $600\times600\mu m$ ($length\times width$), and all rigid plastic cylinders have $150\mu m$ radius and $5mm$ length. Both the structure 1 and the structure 2 are ordinary structure without MSCR, and the thickness of their cantilevers is $10\mu m$ and $20\mu m$ respectively. MSCRs are added to structure 3 whose basic beams are $20\mu m$. Length, width and depth of the MSCR are $80\mu m$, $70\mu m$ and $10\mu m$ respectively. Static analysis and modal analysis of these three structures were conducted by ANSYS respectively. After the static analysis, when a $1Pa$ load in the negative y direction is applied on the upper surfaces of the plastic cylinder, the pictures of the stress distribution on those structures along the central axes on the surface of Y-oriented beams are shown in Fig.5 and Fig.6 respectively. The curves of stress distribution along the beams on the positive y-axis obtained by path extraction are shown in Fig.7. Figure 8 shows the first modal vibration types of the three structures.

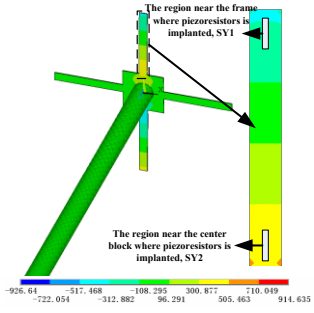


Fig.5 The stress nephogram on the ordinary cantilever of which thickness is $10\mu m$

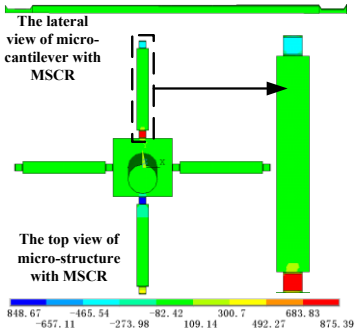


Fig.6 The stress nephogram on the cantilever with MSCR

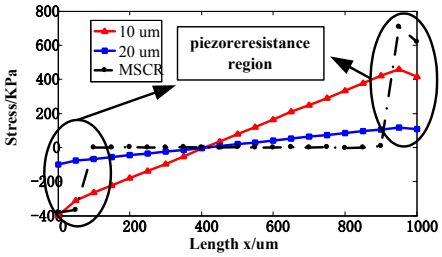


Fig.7 The curves of stress distribution along the beams on the positive y-axis

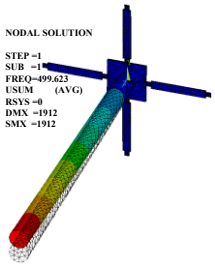


Fig.8 The first-order vibration shape of structure 3

Figure 5 show that the stress on the beams without MSCR is dispersed along the whole beam, and the change of the stress on the beams is slow. Figure 6 shows that the stress can be localized in the stress concentration regions, as compared to the rest of the cantilevers, because the stress from the rest of the cantilever region is displaced and concentrated within the MSCRs. In the analysis, the curves of stress distribution along the path on the upper surface of beams from the frame to the center block were plotted, which show that structure 3 with MSCR has the highest maximum stress. Besides, comparing structure 1 with structure 2, the results show that the thinner beams have the higher stress.

The mean stress in the region where the piezoresistors are implanted is calculated via path analysis in ANSYS, then the sensitivity of the MEMS chip can be obtained by substituting the mean stress into Eq. (3). By comparison, in the region closed to the frame, the mean stress of structure 3 is 1.07 times higher than structure 1 and 3.11 times higher than structure 2. In the region closed to the center block, the mean stress of structure 3 is 1.68 times higher than structure 1 and 6.47 times higher than structure 2. The output sensitivity using structure 3 is increased by 1.5 times compared to structure 1, when compared to structure 2, the magnification is 4.9 times. Figure 9 shows that the first modes of three structures are alike. When comparing the resonant frequencies between the structure with MSCR and the structures without MSCR, the resonant frequency of the structure 3 is $500Hz$, lower than that of the structure 2, $934Hz$, but higher than that of the structure 1, $337Hz$.

2.3 the optimization of MSCR

The dimension of MSCR can have great effect on the performance of the microstructure, thus, the structure with MSCR should be designed further to obtain the best structure.

As table 1 shown, when comparing design (a) with design (b), it obtains that the stress in the concentration region will be higher if the groove on the beam is narrower. In view of the space required for layout of a Wheatstone bridge, $70\mu m$ is selected for the width of the groove for stress concentration. The result in chapter 2.2 has been shown that the thinner beams have the higher stress, so $10\mu m$ is selected for the depth of the groove. Here, we only concern about the influence of the length on stress sensitivity. Fig.9 is a schematic diagram of the cantilever with MSCR. The curves of mean stress and resonant frequency as length of the groove changed are shown in Fig.10 and Fig.11 respectively.

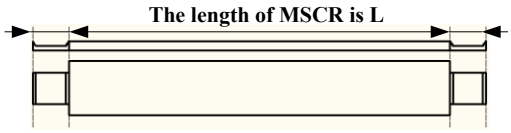


Fig.9 A schematic diagram of the cantilever with MSCR

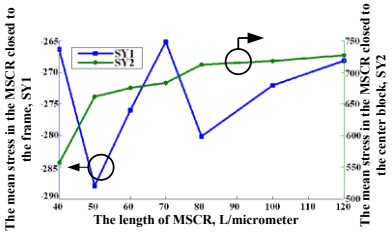


Fig.10 The curves of mean stress as length of the groove changed

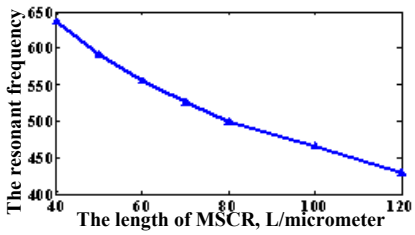


Fig.11 The curves of resonant frequency as length of the groove changed

As can be noted from Fig.10, the curve of the mean stress in the MSCR closed to the frame is irregular as the length of the groove changed, and the maximum difference is less than 23KPa. However, the curve of the mean stress in the MSCR closed to the center block is on the increase as the growing of the length of the groove. The mean stress increases rapidly when the length is from $40\mu m$ to $80\mu m$. When the length continues to increase, the mean stress increases slowly. Besides, Fig.11 shows that the resonant frequency decreases as length of the groove increased. In order to balance the stress sensitivity with the working bandwidth, $80\mu m$ is selected for the length of the groove for stress concentration.

3 Conclusion

In order to improve the sensitivity of MEMS bionic vector hydrophone and broaden the working bandwidth simultaneously, stress concentration was introduced to the microstructure, namely, the grooves were corroded by the wet etching, which makes a beam thinner locally, and the shapes of MSCR were made by the dry etching, which makes a beam narrower locally. The influence of the dimension of MSCR on the performance of the microstructure was analyzed by the finite element software ANSYS, the size of MSCR was obtained finally, $80\times70\times10\mu m$ （$length\times width\times depth$）. Results show that compared with ordinary micro-structure, the sensitivity of the vector hydrophone's micro-structure with MSCR can be increased by 1.5 times, and the upper limit of bandwidth can be improved from $337Hz$ to $500Hz$. This research provides a new method to resolve contradiction between the sensitivity and working bandwidth.

4 References

[1] XUE Chenyang, CHEN Shang, ZHANG Wendong, et al. Design, Fabrication, and Preliminary Characterization of a Novel MEMS Bionic Vector Hydrophone, J. Micro- electronics Journal. 38(2007) 1021-1026.

[2] Binzhen Zhang, Hui Qiao, Shang Chen, et al. Modeling and characterization of a micromachined artificial hair cell vector hydrophone, J. Microsyst Technol.14(2008)821-828.

[3] Linggang Guan, Chenyang Xue, Guojun Zhang, et al. Advancements in technology and design of NEMS vector hydrophone, J. Microsyst Technol.17(2011) 459-467.

[4] Linggang Guan, Guojun Zhang, Jiao Xu, et al. Design of T-shape vector hydrophone based on MEMS, J. Sensors and Actuators A:Physical.188(2012) 35-40.

[5] R Bashir, A Gupta, G W Neudeck, et al. On the design of piezoresistive silicon cantilevers with stress concentration regions for scanning probe microscopy applications, J. Micromech Microeng.10(2000) 483-491.

[6] S.M.Firdaus, I.A.Azid, O.Sidek, et al. Enhancing the sensitivity of a mass-based piezoresistive micro-electro-mechanical systems cantilever sensor, J. Micro & Nano Letters.5(2009) 85-90.

[7] S.M.Firdaus, I.A.Azid, O.Sidek, et al. Half Cut Stress Concentration(HCSC)Region Design on MEMS Piezoresistive Cantilever for Sensitivity Enhancement[C]//33rd International Electronic Manufacturing Technology (IEMT)Conference, 2008.

[8] MEI Deqing, WANG Yancheng, CHEN Ziche. Design of piezoresistive micro-cantilever with stress concentration region, J. Nano-technology and Precision Engineering.5(2007)227-280.

[9] LI Qichang, WANG Guanglong, GAO Fengqi. Design simulation of micro-cantilever with high sensitive SCR. Transducer and Microsystem Technologies.32(2013) 95-98.

[10] CHEN Shang. Research of MEMS bionic vector hydrophone based on silicon, D. Taiyuan: North University of China, 2008.

[11] XU Jiao, ZHANG Guojun, SHI Guixiong, et al. Advancements in encapsulation of hair vector hydrophone, J. Chinese Journal of Sensors and Actuators.24(2011) 517-520.

Key Engineering Materials Vols 645-646 (2015) pp 561-565
© (2015) Trans Tech Publications, Switzerland
doi:10.4028/www.scientific.net/KEM.645-646.561

Submitted: 2014-11-14
Accepted: 2014-12-23

High-precision Quadrature Signal Generator for Digital Demodulation of MEMS Gyroscope

Danhua Chen[1,2], Li Chen[1,2,a *], Hui Zhou[1,2] and Ying Tian[1,2]

[1]Key Disciplines Lab of Novel Micro-nano Devices and System Technology (Chongqing University), Chongqing, CHINA

[2]Key Laboratory of Optoelectronic Technology & Systems (Chongqing University), Ministry of Education, Chongqing, CHINA

[a]Email:CL2009@cqu.edu.cn

Keywords: Quadrature Signal Generator; Direct Digital Synthesis; Digital Demodulation.

Abstract. A new quadrature signal generator based on Direct Digital Synthesis (DDS) algorithm for digital demodulation of MEMS gyroscope was proposed in this paper. To avoid quantization error, the dual-accumulator with signal-ROM structure was adopted. This signal generator was realized in FPGA chip, which could be quit compact to realize all digital demodulation in one chip. Simulations and tests of the generator were carried out. The test results demonstrate that the signal generator achieves high stability. The standard deviation of the frequency is 0.075Hz and the standard deviation of the amplitude is 0.037mV.

Introduction

Tremendous attention has been attracted by MEMS gyroscopes due to their booming market's need, especially in automotive industry, inertial navigation systems and even tactical grade applications[1]. For the past decades, MEMS gyroscopes have got rapid development. To further improve the performance of MEMS gyroscopes, it is badly in need of high-precision, high-stability readout circuits. Traditional analog circuits have been studied for decades and had got much improvement. But due to the susceptible of the analog devices, it is difficult to meet the demand of high-precision, high-stability readout circuits. With many significant advantages such as high integration, robustness, and easy to upgrade, digital readout circuits for MEMS gyroscopes put much more emphasis than ever before to make the gyroscopes possess better performance and the adaptability for environmental parameters' variation[2-4]. As one of the most important part of the readout system, the study on demodulation can not be too overemphasized.

The outputs of most MEMS gyroscopes are amplitude-modulated signals. Therefore, a commonly used approach to obtain the angular velocity information is utilizing quadrature demodulation, which requires a pair of high-precision quadrature reference signals. Many literatures have reported various ways to generate reference signals. In [5,6], fully digital self-oscillating pulse width modulation (PWM) signal generation technique was presented. In that study, a 1st-order PWM signal generator was described, and a simple 2nd-order PWM signal generator with proportional integral (PI) compensation was discussed. In [7,8], the reference generator using the digital signal processor (DSP) and C programming language was introduced. Digital pulse signal generator were described in [9,10]. These devices are mainly implemented by complex programmable logic device (CPLD). In [11-13], a field programmable gate array (FPGA) based signal generator has been designed and tested. In these papers, FPGA was used as the main chip to control the whole system.

In this paper, a new quadrature signal generator based on DDS algorithm and FPGA for digital demodulation of MEMS gyroscope was introduced. In order to obtain rigid orthogonal signals and avoiding the quantization error, the dual-accumulator with single-ROM structure was adopted. This generator was realized in FPGA chip, which could be integrated with the digital demodulator to realize all digital demodulation in one chip.

System Composition and Methodology

Fig. 1 shows the principle of the quadrature demodulation. Firstly, the signal to be demodulated was multiplied by the quadrature signals and two signals can be attained. When the two signals go through the LPFs (Low Pass Filters) respectively, two signals which contain the information of the amplitude and the phase were obtained. By calculating the outputs of the LPFs, the value of the amplitude and the phase were figured out.

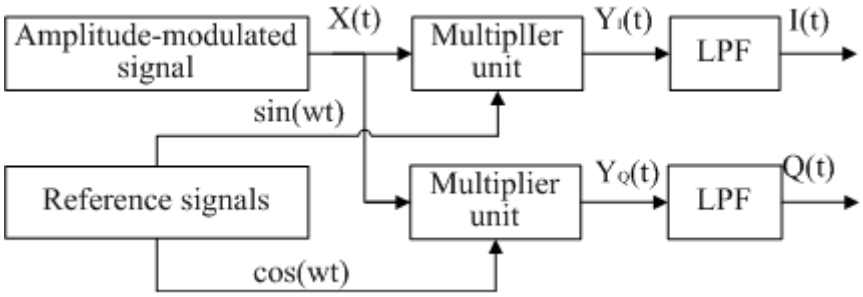


Fig. 1 Structure diagram of quadrature demodulation

Assuming that the signal to be demodulated is depicted by

$$X(t) = A\sin(wt + \varphi) + n(t) \tag{1}$$

Where A is the amplitude of the signal, w is the frequency of the signal, ϕ is the initial phase and $n(t)$ is the noise.

The outputs of the multiplier unit include second harmonic, fundamental harmonic and direct current signal. When they get through the LPFs, direct current signals were obtained which can be written as

$$I(t) = \frac{A}{2}\cos\varphi \tag{2}$$

$$Q(t) = \frac{A}{2}\sin\varphi \tag{3}$$

And then, the exact value of the amplitude and phase can be calculated as follows:

$$A = 2\sqrt{I^2(t) + Q^2(t)} \tag{4}$$

$$\varphi = \arctan(\frac{Q(t)}{I(t)}). \tag{5}$$

From the Fig. 1, we know that a pair of reference signals are highly in need to demodulate the original signal. The reference signals must be high-precision, high-stability and must differ in phase by 90 degrees. In this paper, the DDS algorithm was used to generate the quadrature reference signals.

Fig. 2 shows the structure of the DDS algorithm. The frequency control word K and the clock signal *clk* are sent to the phase accumulator. The phase accumulator, the most important part of DDS, is used to increase the value of frequency control word K on the rising edge of the clock *clk*. The output value of the phase accumulator is used as address into a waveform data table stored in memory. For each input phase value, one waveform data can be read out from the ROM. By this way, arbitrary waveforms can be generated as long as there is corresponding waveform data in the ROM. The frequency of the output waveform f_{out} is dependent on the clock frequency f_{clk}, the length in bits of the phase accumulator N and the frequency control word K. The relationship is shown in equation (6). Equation (7) shows the frequency resolution.

$$f_{out} = \frac{f_{clk}K}{2^N} \tag{6}$$

$$\Delta f = \frac{f_{clk}}{2^N} \tag{7}$$

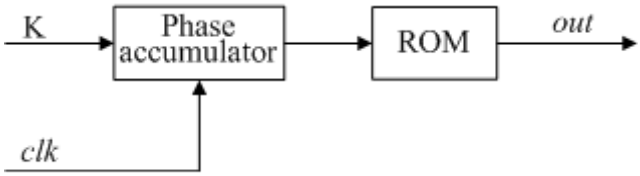


Fig. 2 Structure diagram of DDS

According to the working principle, in order to generate quadrature signals, usually two independent ROMs are adopted, as shown in Fig. 3. One of them stored the sine curve data and the other stored the cosine curve data. The frequency control word K and the clock signal *clk* are given to both of the ROMs synchronously. For each input phase value, disparate waveform data can be read out from the independent ROMs. And then, a pair of quadrature signals can be generated.

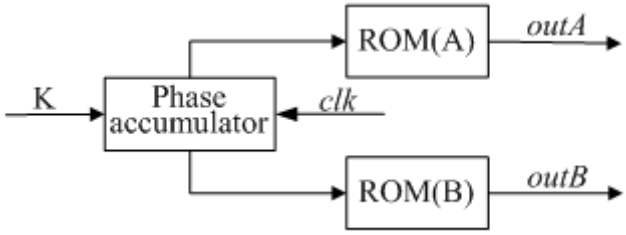


Fig. 3 General quadrature signal generator based on DDS

A new structure is proposed in this paper, as shown in Fig. 4. There are two independent phase accumulators but just one ROM been used in this generator, and the sine curve data is stored in ROM in advance. As long as the output value of the two phase accumulators differs in phase by one quarter of a cycle, two quadrature signals will be generated when both phase accumulators address at the same time. Not only can this new structure simplify the constitution but also it can avoid the quantization error caused by using two independent ROMs.

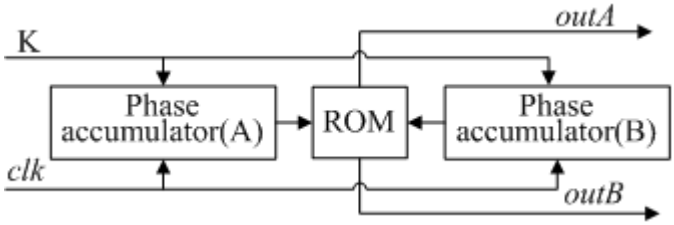


Fig. 4 Improved quadrature signal generator based on DDS

Experiment and Results

Calculation of the important parameter

In the experiment, the frequency of the output signal is 14039Hz and the clock frequency f_{clk} is 2MHz. By multiplying $\frac{2^N}{f_{clk}}$ to solve the equation (6), we obtain

$$K = f_{out} \times \frac{2^N}{f_{clk}}. \tag{8}$$

Where N is defined as 32. Substituting the values of the f_{out} and f_{clk} into equation (8) yields that the K is 30148523.

Simulation of the design

According to the DDS algorithm, we realize the generator using Verilog HDL. In order to verify the function, the simulation was carried out with Modelsim. The simulation result is shown as Fig. 5. The wave upper is a sine curve and the under is exactly right a cosine curve, so they are mutually orthogonal.

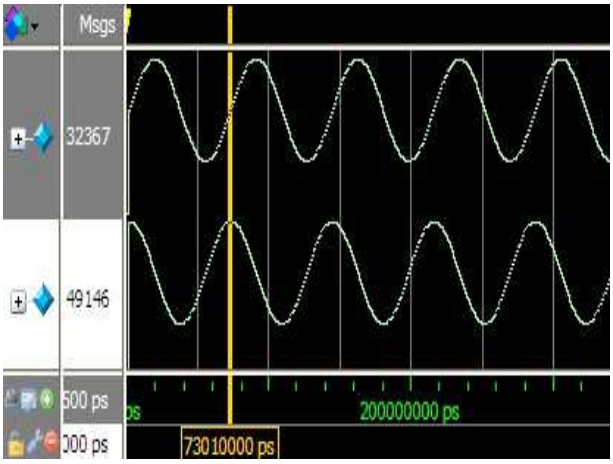


Fig.5 Simulation result of the quadrature signals

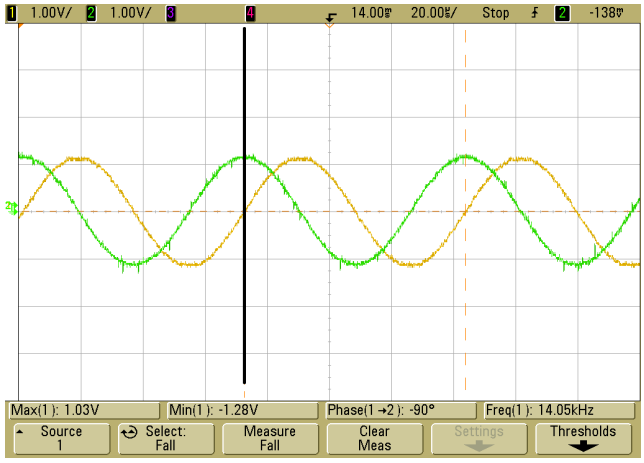


Fig.6 The analog waves of quadrature signals

Test results

In order to test the quality of the signals, a high-speed D/A (Digital to Analog) converter is adopted to convert the digital signals to analog waves, as shown in Fig. 6. The phase difference between the two sinusoidal waveforms is 90 degrees.

The Agilent 34401A digital multimeter was used to test the stability of the signals. The test result of frequency stability is shown in Fig. 7, which reveals that the frequency is about 14041.1Hz and the standard deviation is 0.075Hz. Because of the inaccuracy of the system frequency f_{clk}, the frequency measured differs from the theoretical value. The test result of amplitude stability is shown in Fig. 8, which reveals that the amplitude is about 1.65675V and the standard deviation is 0.037mV.

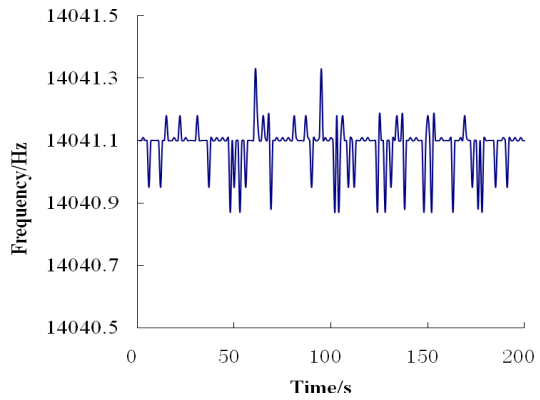


Fig.7 Test result of the frequency stability

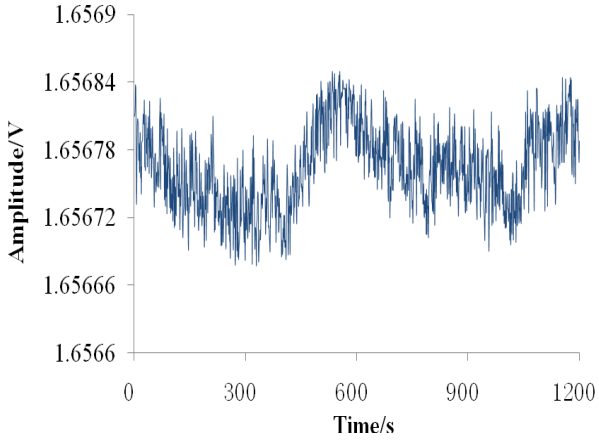


Fig.8 Test result of the amplitude stability

Conclusion

This paper proposed a new quadrature signal generator based on DDS algorithm for digital demodulation of MEMS gyroscope. In order to obtain rigid orthogonal signals, the dual-accumulator with single-ROM structure was adopted. This generator was realized in FPGA. The test results show

that the standard deviation of the frequency is 0.075Hz and the standard deviation of the amplitude is 0.037mV. This generator can be used to high-precision quadrature demodulation of MEMS gyroscope.

Acknowledgment

This work was supported by Research Fund for the Doctoral Program of Higher Education of China (No. 20120191120022), Natural Science Foundation Project of CQ CSTC (No. CSTC2012jjA40010).

References

[1] J Cui, X Z Chi, H T Ding, Transient response and stability of the AGC-PI closed-loop controlled MEMS vibratory gyroscopes, J. JOURNAL OF MICROMECHANICS AND MICROENGINEERING. 19(2009) 125015(17pp).

[2] Gaiber A, Geiger W, Link T, New digital readout electronics for capacitive sensors by the example of micro-machined gyroscopes, J. Sensors Actuators A. 97(2002) 557-562.

[3] Saukoski M, Aaltone L, Halonen K, Integrated readout and control electronics for a microelectromechanical angular velocity sensor, C. 32nd European Solid-State Circuits Conf. (Montreux, Switzerland, 18-22 September 2006), pp. 243-246.

[4] Guomign Xia, Bo Yang, Shourong Wang, New digital drive phase control for improving bias stability of silicon MEMS gyroscope, J. Journal of Southeast University (English Edition). 27(2001) 47-51.

[5] W. Li, Y. Orino, M. K. Kurosawa, Conversion of a single-bit signal into a PWM signal, C. Proc. IEEE TENCON. (Chiang Mai, Thailand, 21-24 November 2004), pp. 519-522.

[6] Weibo Li, Yuichiro Orino, Shinnosuke Hirata, Design of a self-oscillating PWM signal generator with a double integration loop, J. IEEE TRANSACTION ON CIRCUITS AND SYSTEMS-I:REGULAR PAPERS. 60(2013) 2064-2073.

[7] LU Mingcheng, SUN Jingrui, WU Jingcheng, Application and design of signal generator based on DDS chip, J. Journal of Tianjin Normal University (Natural Science Edition). 28(2008) 66-68.

[8] Byung-Moon Han, Byong-Yeul Bae, Seppo J. Ovaska, Reference signal generator for active power filters using improved adaptive predictive filter, J. IEEE TRANSACTIONS ON INDUSTRIAL ELECTRONICS. 52(2005) 576-584.

[9] Fan Duosheng, Shi Shaohua, Ren Ye, Design of multi-channel digital pulse signal generator, C. The 11th IEEE International Conference on Electronic Measurement & Instruments. (2013), pp. 356-360.

[10] WANG CH, HUO ZH J, YANG T D, Design of radar pulse generator based on CPLD, J. Computer Engineering and Design, 28(2007) 3172-3181.

[11] Song Jie, Yuan Hang, Guan Chengbin, Design and implementation of signal generator and real-time analysis system, C. The 25th Chinese Control and Decision Conference. (2013), pp. 4517-4520.

[12] Liu Wenli, Lin Jianying, DDS waveform generator implemented with microcontroller and FPGA, J. Foreign Electronic Measurement Technology, 26(2007) 26-29.

[13] Zhang Xiao, Song Jie, Ding Hao, Simple digital signal transmission performance analyzer based on FPGA, J. Electronic Measurement Technology, 35(2012) 78-81.

Key Engineering Materials Vols 645-646 (2015) pp 566-571
© (2015) Trans Tech Publications, Switzerland
doi:10.4028/www.scientific.net/KEM.645-646.566
Submitted: 2014-11-18
Accepted: 2014-12-23

Study of thin film pressure sensor by magnetron sputtering

[1,a]Hu Dongping, [2,b]Wang Xiaolong

[12]China Academy of Engineering Physics, Institute of system engineering, Mianyang 621900, Peoples R China

[a]Hud1969@163.com, [b]Wxiaolong@caep.ac.cn

Keywords: NiCr alloy; magnetron sputtering; thin film pressure sensor

Abstract. The use of sensors made of thin films has several advantages over wire or foil sensors. Thin film pressure sensors can be used in high temperature, vibration and other special environment with small volume, high sensitivity and stability. Thin film pressure sensors can be made by magnetron sputtering. In this paper the thin film pressure sensors are prepared by elastic Element polishing, growth of dielectric film, NiCr alloy and Ni films with magnetron sputtering, the process and results are analyzed.

1 Introduction

The use of sensors made of thin films has several advantages over wire or foil sensors. Thin film pressure sensors can be used in high temperature, vibration and other special environment with small volume, high sensitivity and stability. In 1977, thin film pressure sensors appeared for the first time, and developed promptly with ion beam sputtering technology [1]. At present, the Senstronics co. in Britain and Bell Howell in America have made thin film pressure sensors in mass production. In China, there are some companies such as Weist Zhonghang that have manufactured this kind of sensor [2]. Thin film pressure sensors can be made by evaporation coating, magnetron sputtering, and ion beam sputtering, etc [3-5]. The key problems of thin film pressure sensors preparation are how to achieve high quality alloy films, strong adhesion between films and substrates, high stability electricity insulation between alloy films and metal substrates. But As yet the quality of alloy films are not consistent, the electricity insulation between alloy films and metal substrates are not stable, the cause of these accidents is not clear [6,7]. In this paper the thin film pressure sensors are prepared by magnetron sputtering, the analysis of process and results are depicted.

2 Experiments

2.1 Elastic Elements

The image of the elastic Element is shown in Fig.1. The thickness of the circular flat diaphragm is 1mm, the diameter is 3.5mm. The material of the elastic Element is 17-4PH, which is a kind of stainless steel. The end Face was polished by diamond aqueous Suspensions, the surface roughness decreased to 0.1μm.

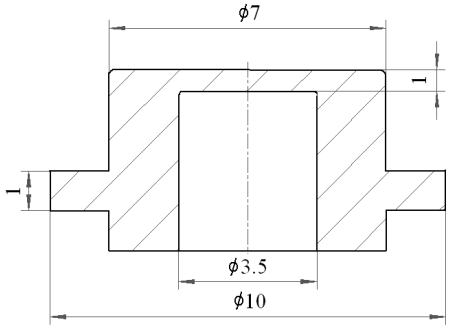


Fig.1 Image of the elastic Element

2.2 Equipment

The magnetron sputtering equipment was fabricated by Shenyang Scientific Instrumentation Co. The schematic is shown in Fig.2. The equipment comprises 5 parts those are vacuum system, powers, sample bolster, targets and gas flow facility. The vacuum system consists of vacuum pump,

turbo molecular pump, valve and pipes. There are 2 DC powers and 1 RF power for vacuum sputtering, and the powers can be switched on one to another of the 5 targets. The sample stages can be heated by coils to 300℃, and rotate while sputtering,. The flow meters are used to control the gas flows.

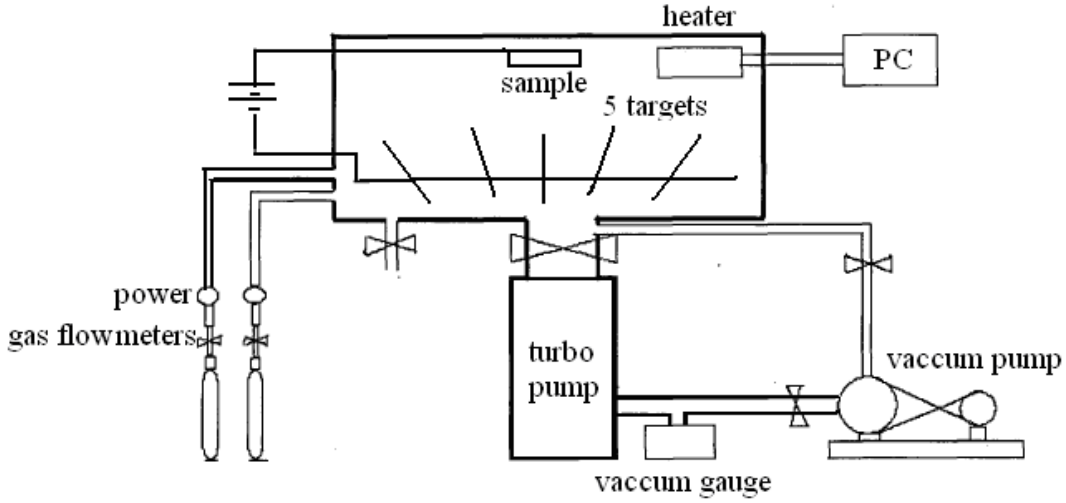


Fig.2 Schematic of the magnetron sputtering equipment

2.3 Preparation of dielectric membrane

2.3.1 SiO_2 membrane

The stainless steel elastic Element were grinded, polished and cleaned to be the substrate, the Cr film of 20 nm thick was deposited on the substrate by DC sputtering to be the transition layer. By RF sputtering, with the target of fused silica, the 1μm thick SiO_2 membrane was prepared. Table 1 shows the parameters of the process, the sputtering time was 3h.

Table Magnetron sputtering process parameters of SiO_2 membrane

working pressure[Pa]	RF voltage [V]	RF current [mA]	flux of Ar[[m3/h]
0.4	750	150	2.4×10^{-4}
bios voltage[V]	incident power[W]	Reflective power [W]	Sample temperature[℃]
-370V	90	1.5	450

2.3.2 Composite membrane

After the 1μm thickness SiO_2 film was prepared, SiO_2 and Ta_2O_5 film were deposited alternately for 8 cycles of 15min. The parameters of the process are shown in Table 2, the thickness of a single layer was presumed about 80 nm based on experience.

Table 2 Magnetron sputtering process parameters off Ta_2O_5 membrane

working pressure[Pa]	RF voltage [V]	RF current [mA]	flux of Ar[m3/h]
0.4	700	140	2.4×10^{-4}
bios voltage[V]	incident power[W]	Reflective power [W]	Sample temperature[℃]
-380V	90	1.5	450

2.4 Preparation of NiCr alloy and Ni films

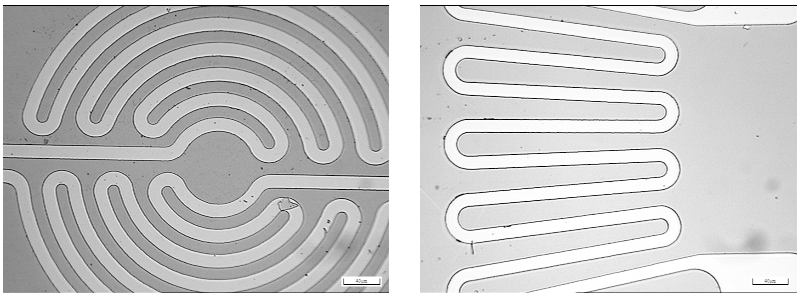
The NiCr alloy film was deposited on the dielectric film with pure Cr and Ni targets by DC co-sputtering, the substrate was heated to 200℃ when sputtering. The parameters of the process are shown in Table 3. On the NiCr alloy film, the Ni film of 1μm thickness was deposited as the electrode layer.

Table 3 Magnetron sputtering process parameters of Ni-Cr alloy film

working pressure [Pa]	Sample rotation[r/min]	Ar flow[m^3/h]	Sputtering time [s]
0.5	9	2.8×10^{-4}	2062
Ni target I/V[A/V]	Cr target I/V [A/V]	Cr sample temperature[℃]	Ni sample temperature[℃]
0.12/340	0.3/280	200	200

2.5 Pattering

By Photolithography, the NiCr alloy and Ni films was wet etched to be the patterns of electric bridge circuit and electrodes. The iron chloride solution was used to etch the Ni film, and the solution of sulfureted cerium, ammonium nitrate and nitric acid was used to etch the NiCr alloy film. The electric bridge circuit consists of 2 inner and 2 external resistors, as shown in Fig 3, Fig 4.



(a) Inner resistors **(b) External resistors**

Fig.3 Patterns of resistors

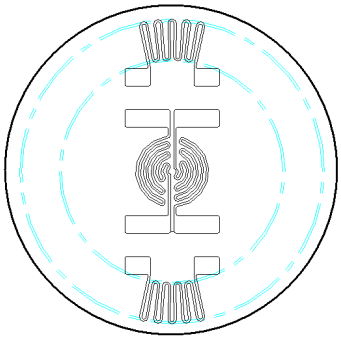


Fig 4 Patterns of electric bridge circuit

2.6 Performance measurement of the sensitive devices

By laser welding, the sensitive devices were fixed on the stainless steel transmission tube. The pressure of special values was put on the sensitive devices with a pressure controller. The response of the circuit to pressure varying signal will be studied using the adjustable DC power and the intelligent data voltmeter. There were 3 samples (1#, 2#, 3#) to be tested. The pattern of the circuit is shown in Fig 5.

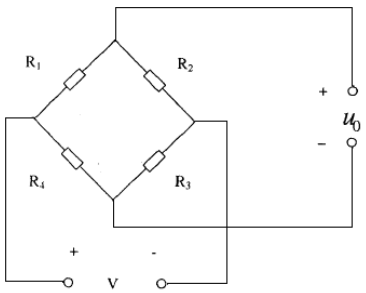


Fig 5 Pattern of the circuit of performance measurement

3 Results and Discussion

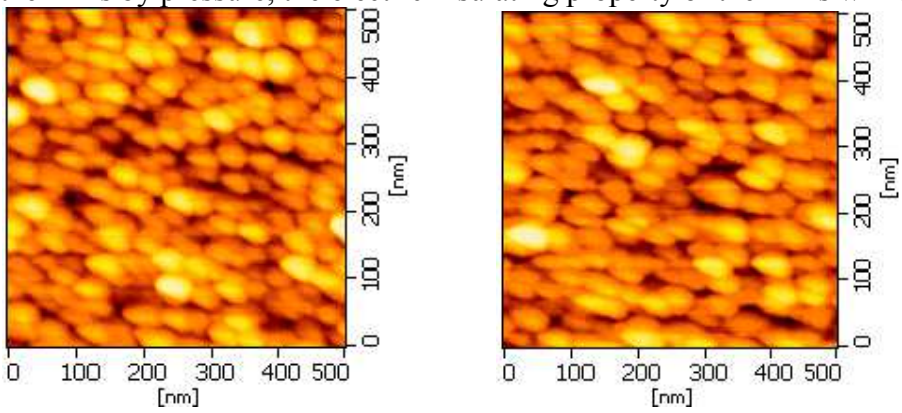
3.1 The dielectric membrane

The 1μm thickness SiO_2 film was test by DC100V, the resistance was no more than 1 MΩ. The electric insulating property of the SiO_2 membrane did not meet the demand. And the resistance value of the composite membrane was more than 500 MΩ, met the demand of sensors.

Mono component SiO_2 membrane prepared by magnetron sputtering can not be the nice insulating layer between the substrate and the alloy film. At the present, SiO_2 films are prepared by magnetron sputtering [9,10], ion beam sputtering [11], chemical vapor deposition [12,13], thermal oxidation method [14], and sol-gel [15,16], etc. Of these ways, the magnetron sputtering is widely applied because of the high precision control and the high quality film deposited. But while magnetron sputtering, the sputtered ions would adsorb the gas when traverse the plasma agglomerate, cause more defects in the membrane because of the impurity and the instability of thermo dynamic, so the insulation strength of the SiO_2 membranes decease. On the other hand, when alloy films sputtered, the metal atoms beat the SiO_2 membranes and impenetrate the SiO_2 membrane at the defects, it cause the conductive connection between the substrate and the alloy film. The composite membrane has the better insulating property because of the interface block out the perforation of the membrane when beat by metal atoms. By magnetron sputtering, the composite should be prepared membrane to meet the demand of sensors.

3.2 The NiCr alloy film

The morphology of the samples were studied by AFM, the results are shown in Fig 7. The results shows that Ni-Cr alloy films were formed by about 20nm～40nm grains. The grains grow after heat treated, the size is about 30nm～60nm. The electrical characteristics of thin films are particular [17,18]. Thin film electric transmission can be divided into two parts: one is the inside the grains; the other is between grains. The transmission inside the grains can be thought as a continuous metal transmission, the transmission between grains will activate the tunneling transmission. Electrons move from a neutral island to another neutral island, the island would be charged, the electronic transmission between electrical islands and neutral islands are a tunneling effect, so the distance between the islands influence tunneling effect mostly. When strain engendered in the films by pressure, the electric insulating property of the films will change.



(a) Deposited NiCr alloy thin films **(b) Annealed NiCr alloy thin films**

Fig 7 Morphology of the samples by AFM

3.3 Capability Test of the sensitive devices

The test results are shown in Table 4. When the pressures were in 0～30MPa，there was a highly linear output.

Table 4 Signal output of the sensitive devices

Sample 1#	Pressures（MPa）	0	5	10	15	20	25	30
	Signal output (mV)	0	0.097	0.185	0.270	0.359	0.442	0.53
	Pressures（MPa）	30	25	20	15	10	5	0
	Signal output (mV)	0.53	0.445	0.359	0.274	0.191	0.104	0.018
Sample 2#	Pressures（MPa）	0	5	10	15	20	25	30
	Signal output (mV)	0	0.090	0.181	0.269	0.351	0.441	0.530

	Pressures（MPa）	30	25	20	15	10	5	0
	Signal output (mV)	0.53	0.443	0.359	0.270	0.183	0.094	0.012
Sample 3#	Pressures（MPa）	0	5	10	15	20	25	30
	Signal output (mV)	0	0.103	0.189	0.276	0.368	0.455	0.545
	Pressures（MPa）	30	25	20	15	10	5	0
	Signal output (mV)	0.545	0.456	0.368	0.282	0.200	0.111	0.026

By the relationship:

$$V = \kappa U\varepsilon) \tag{1}$$

The strain value was calculated by the model of the membrane with Fixed Edge. The sensitive coefficient of the alloy film is:

$$\kappa = \frac{U\varepsilon}{V} = \frac{5 \times 0.000190}{0.000545} = 1.75 \tag{2}$$

It is close to the value reported in some papers [19]. The result shows that the alloy films prepared by magnetron sputtering meet the demand of pressure sensors.

4 Conclusions

(1) Mono component SiO_2 membrane prepared by magnetron sputtering can not be the nice insulating layer between the substrate and the alloy film because that the metal atoms will impenetrate the SiO_2 membrane and cause the conductive connection between the substrate and the alloy film. On the 1μm thickness SiO_2 film, SiO_2 and Ta_2O_5 film were deposited alternately for 8 cycles, then composite membrane was prepared, the composite membrane met the demand of sensors.

(2) The Ni-Cr alloy films were formed by about 20nm～40nm grains, the grains grow after heat treated, the size is about 30nm～60nm. When strain engendered in the films by pressure, the electric insulating property of the films will change because of the distance between the grains changing.

(3) When the pressures were in 0～30MPa，there was a highly linear output results of the sensitive devices tests. So the film pressure sensors can be prepared by magnetron sputtering.

Foundation item: supported by Scientific Special Funds of Institute of system engineering, CAEP (No.2013KJZ)

References

[1] Chang Zengpo, Tang Baisen. Dynamic characteristics of ion beam sputtered thin-film pr essure transducer [J]. Journal of Transducer Technology, 2001, 20(6): 15-17.

[2] Li Rong. The current situation and development trend of pressure sensors [J]. Journal of Xian Technological University, 2002, 22(3): 241 -243.

[3] Alonso A, Garcia E, Castanl, et al. Strain sensitivity and temperature influence on sputtered thin films for Piezoresistive sensors [J]. Sensors and Actuators A, 1993 37-38: 784-789.

[4] Angadi M A, Whiting R. Longitudinal and transverse strain sensitivity of nichrome films [J], Mater. Sci. Eng. B, 1990, L1-L4: 7-11.

[5] Kazi Imam H, Wild P M, Moore T N, et al. The electromechanical behavior of nichrome(80/20wt.%) film [J], Thin Solid Films, 2003, 433:337-343.

[6] Klokhoim E, Berry B S. Intrinsic stress in evaporated metal films [J]. Journal of Elect rochem. Soc., 1968, 115: 823.

[7] Qu Xixin, Yang Bangzhao, Jiang Jiejian. Electronic thin film materials [M]. Beijing, Science Press, 1990, 112 -113.

[8] He Yinghui，Research on the Performance of thin film pressure sensor and Soft Ware Compensation [D], Changsha: Zhongnan University, 2004。

[9] Gong Jianhua, Wang Yating, Jia Qingyun. Discussion on film damage mechanism of large areas of SiO_2 thin film deposited by intermediate frequency sputtering [J].Vacuum, 2003, (4)29-31.

[10] Xu Sheng, Hou Xiaobo, Fan Chuizhen. On-line continuous deposition of SiO2 by medium frequency reactive sputtering and ITO by direct current sputtering [J]. Vacuum, 2002, (5):15-18.
[11] Akimori Tabata, Noriaki Matsuno, Yasuo Suzuoki. Optical properties and structure of SiO_2 films prepared by ion-beam sputtering [J]. Thin Solid Films, 1996, 289: 84-89.
[12] Zhang Jinsong, Ren Zhaoxing, Liang Rongqing. Influence of RF substrate bias on SiO_2 films prepared by ECR PECVD [J].Nuclear Fusion and Plasma Physics，2001, (1)59-64.
[13] Jiang Nan, Hugon M C, Agius B, et al. High quality SiO_2 films deposited by distributed electron cyclotron resonance plasma enhanced chemical vapor deposition [J]. Vacuum Science and Technology, 1998, (3):161-169.
[14] Markwitz A, Trompetter W J, White G V, et al. Ion microscope investigations of non-uniform surfaces of thin SiO2 films produced by high-temperature nitridation experiments [J], Nuclear Instruments and Methods in Physics Research B, 2001, 181: 354-359.
[15] Knoblich B, Gerber T. Aggregation in SiO_2 sols from sodium silicate solutions [J], Journal of Non-Crystalline Solids, 2001, 283:109-113.
[16] Wu Guangming Wang Jue, Shen Jun, et al. Effect of experimental conditions on the structure and properties of nano-porous silica films. Chin. Phys. Soc., 2001, (1):175-18.
[17] Wang Zhendong, Miyamoto Iku, electro thermal alloy [M], chemical industry press, 2006, 1-10.
[18] Fan Ping. Temperature coefficient of resistivity of metallic films [J], Journal of Shenzhen University, 2000, 17(4):33-40.

Key Engineering Materials Vols 645-646 (2015) pp 572-576
© (2015) Trans Tech Publications, Switzerland
doi:10.4028/www.scientific.net/KEM.645-646.572

Submitted: 2014-11-24
Accepted: 2014-12-23

FPGA-based Test Equipment for System-Level MEMS Switch Series

Liu Peng [1, a], Lou Wenzhong [2,b], Lu Yufei [3,c], Feng Xinyu [4,d]

[1,2,3]School of Mechatronical Engineering, Beijing Institute of Technology, Beijing 100081, P.R.China

[4]School of Electrical and Control Engineering, Heilongjiang University of Science and Technology, Harbin 150022, P.R.China

[a]leopardliupeng@126.com(corresponding), [b]louwz@1bit.edu.cn, [c] wslyf66@163.com

Keywords: MEMS Switch Series; FPGA; Test Equipment System; Testing Algorithms

Abstract. A high-performance, low-cost test equipment system for characterization of MEMS switch is to be proposed in this paper, and the purpose is set to master the fundament of the embedded algorithms of the wafer and system production testing. The team has implemented the real-time analysis for MEMS switch, proving the feasibility of the design, based on the original data collected during the dedicated tests, applying the microsystem hardware designed and assembled by the research team, as well as the embedded software. At the end, the framework of the system platform in the future is described.

Introduction

Automatic chip test equipment system is an enabling technology with the potential of solving complex reliability problems caused by design defects and technical disadvantages of microchips in microelectronics and MEMS that have manifested due to complexity in design, manufacturing, maintenance and the sensitivity of the material and structure [1]. And as some sensitive and complex microsystems have to endure severely harsh environment, it's practical and necessary to apply the dedicated chip and system level testing method to realize the high quality and robustness, without mature solution existing, comparatively. The microsystems can contain the MEMS switches and microelectronic chip as shown in Fig. 1.

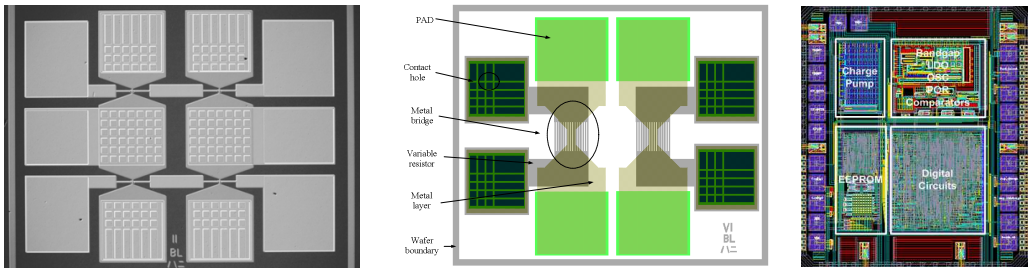


Fig. 1 MEMS & chip to be tested

Research Motivation

As the critical size gradually decreases, the chip test equipment system has become the common implementation in the microchip manufacturing process and the developing flow. And the research of automatic chip test equipment system for the industrial and military applications are in progress, which projects are normally organized by leading research units, such as IBM, DARPA, and so on. For example, the Chip-scale atomic clocks (CSAC) is part of the Positioning, Navigation and Timing (Micro-PNT) program, which embodies the breakthroughs in MEMS and microfabrication techniques, and will ultimately be provided with an integrated automatic chip test equipment system that monitors verification and delivers advanced on-chip diagnosis while an module is tactically deployed in high-dynamic applications, or in storage of hash environment.

As the time domain microchip application amount greatly grows, and more and more complex and sensitive mechanical and electric components are applied, the cost-efficiency of test, the vulnerability, and inspection of the chips becomes definitely crucial. So not only the automatic real-time measuring instruments of the technique process are needed, but also the self-calibrating modules and methods are in demand, thereby enabling more accurate devices..

Novel equipment system and automatic testing algorithms for time domain microchips are the core technology for microsystems during the entire high-dynamic and hash life cycle. And from the standpoint of added cost, space, data collected, and intelligent-decision making of such a system, it is simply feasible to utilize the most optimal algorithms in built-in software with advanced MCU and FPGA platforms, coupled with testing algorithms for parts and system availability management. The targeted system is comprised of three thrust areas: measuring instruments, embedded software, and microscale integration. Each area is made up of various efforts exploring new techniques, deep integration, and on-chip optimization, which go hand-in-hand with the development of automatic architectures.

The developments consider a number of operational scenarios, ranging from the time domain microchips and key MEMS switches, which used in modern munitions and pyrotechnic modules[2]. And the research of multifunctional test equipment system for the military chips is in progress worldwide, which is organized by global leading semiconductor and apparatus manufactures. The automatic chip test system initiatives seek to increase the dynamic range of measuring instruments, reduce testing cycle and complexity, and to develop miniature embedded system providing verification, error location, and correcting information [3].

Test Equipment System

Automatic test equipment (ATE) system is the ultimate design objective, and the corresponding instruments are essential as well. Signal generator, regulated power supply, highly accurate multimeter, and logic analyzer are indispensable in the basic testing system, as shown in Fig. 2. And some optional accessories include test clip, IC puller, pin probe, IC test clips socket adapter, chip carrier, programmer EPROM emulator, chips sucker pickup solder tool, and so on.



Fig. 2. Picture of FPGA-based Test Equipment for Integrated MEMS Switch

Generation Algorithm

Regularly, testing mode relies on either exhaustive, pseudoexhaustive, or pseudorandom testing and the most relevant approaches use LFSRs for test pattern generation. According to the preceding surveys on relative algorithms, one of the key features of pattern generation technology is the ability to obtain a holistic view of a system function as well as to isolate and focus on component-specific reliability issues, incorporating statistical and probability theory in addition to data processing,

dimensionality reduction by compression and transformations, and feature extraction.The signals of the transducer element are analyzed and recorded as shown in Fig. 3 and Fig. 4.

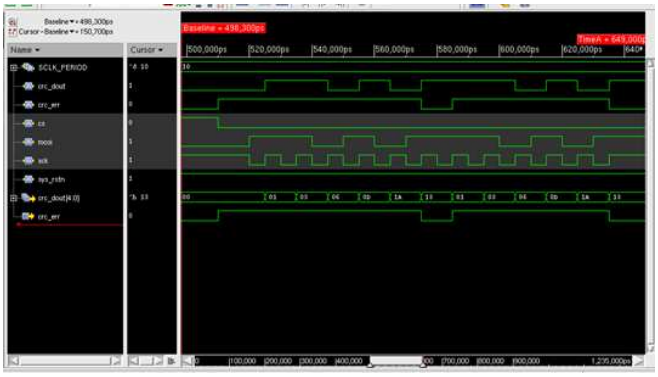


Fig. 3. View of Sequence Signal Testing

Generation algorithms can provide autonomous testing down to the component level have significant application potential, using available and historical information to statistically and probabilistically derive decisions, estimates, and predictions about the correction and reliability of electronic systems. Mainly due to the simplicity and fairly structural regularity of the LFSR. Test pattern generation and proper pseudorandom can be obtained much easier. The characteristic polynomial G(x) is

$$G(x)= g_n \times x^n + \cdots + g_1 \times x^1 + g_0; \quad (1)$$

where x^n is the observed data and g_n denotes a binary constant and if $g_n = 1$ then there is a feedback. The sequence signal testing can been treated as forms of functional testing, and can be used for detecting fatal errors that might occur during the whole chip lifetime, due to aging and fatigue, environment and other factors.

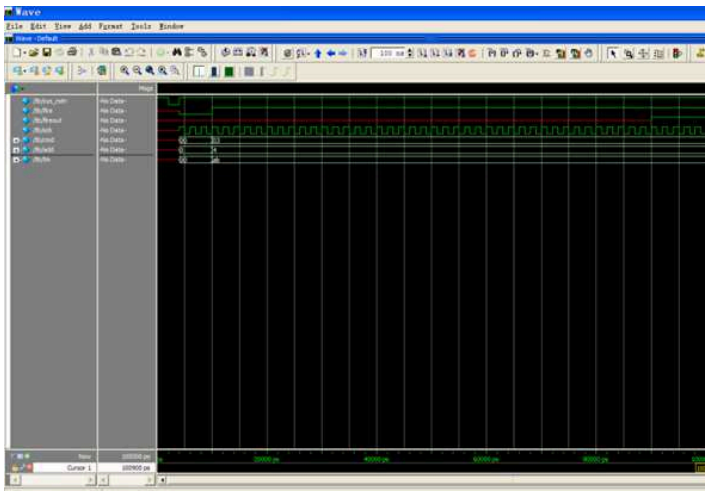


Fig. 4. View of Performance Testing

The total test cost of the hybrid BIST, C_{TOTAL}, can therefore be defined as:

$$C_{TOTAL} = C_{GEN} + C_{MEM} \approx \alpha L + \beta S \quad (2)$$

where C_{GEN} denotes the cost related to the effort for generating L pseudorandom test patterns, and C_{MEM} is related to the memory cost for storing S pre-computed test patterns to improve the pseudorandom test set α and β, which are constants to calculate the test length and memory space to the costs of the test solutions.

With the available and historical information stored in host processor, feature extractions of data from the structure like Fig. 5 can be conducted. Several data-driven prognostic algorithms can use available and historical information to statistically and probabilistically derive decisions, estimates, and predictions about the Status of the system-level heterogeneous MEMS switch systems [4].

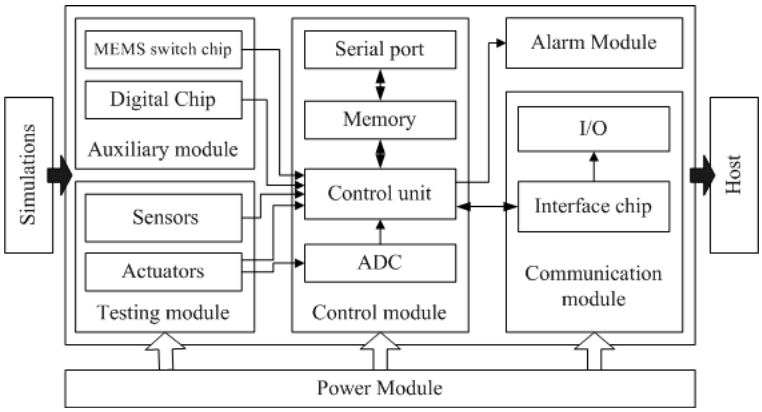


Fig. 5. Schematic of Board-Level Testing Smart System Architecture.

After the comparison of different algorithms, the features of each method will be gained, it's useful during the software developing as the algorithm choosing is the key point. And as the computing rate, data volume and the information complexity required by each algorithm are different, the choosing of the mode can be flexible to meet the needs of cost avoidance and the efficiency [5].

All testing approaches are essentially the extrapolation of trends of the applying scenarios. So the basic system containing the probe platform is shown in Fig. 6



Fig. 6. Picture of Test Equipment with Extended Probe Platform

And the work flow is shown in Fig. 7. As the different design structure produce specific signal characteristics, the working status of the chips can be determined firstly, and then after the computation with the database, the potential defects can be located. With FPGA applied, the algorithms can be altered specifically, with improvement being executed in this way.

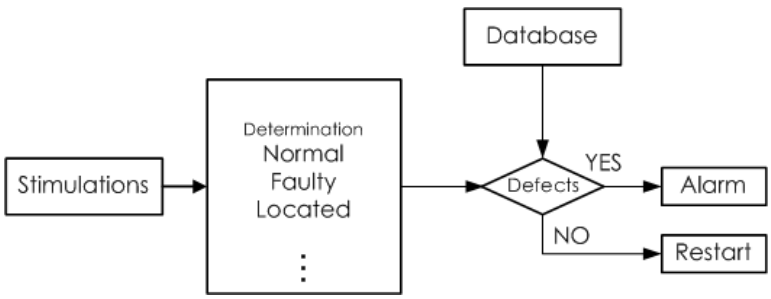


Fig. 7. The Work Flow of the System Logic

The testing conditions of the observation points are listed by Table 1.

Table 1. Scenarios of Test Environment.

Group No.	**Test Environment**	
	Chip Condition	*Observation Point*
Group 1	Normal condition	I / II
Group 2	Faults detected	III / IV
Group 3	Located and identified	V / VI

CONLUSION

Being an economical way, a testing microsystem is presented to implement the embedded testing algorithms for MEMS Switch Series and other key time domain microchip applications. And as the computing rate, data volume and the information complexity required by each algorithm are different, the choosing of the hardware and the embedded algorithms can be flexible to meet the needs of cost avoidance. With the available and historical information stored in host processor, critical extractions of data are conducted.

ACKNOWLEDGMENT

This research is funded by a grant from the National Project (No. 9140A05050313BQ1014& No. 9140c360602120c36138). The author would like to thank Wan Peiyuan from Beijing Embedded System Key Lab for supporting..

REFERENCES

[1]Hudec, B., Paskaleva, A., Jancovic, P., Resistive switching in TiO_2- based metal-insulator-metal structures with Al_2O_3 barrier layer at the metal/dielectric interface, Thin solid films, 563: 10-14, 2014.
[2]Wang Y., Lou W.Z., Zhao Y., High Impact-induced Failure of a Novel Solid MEMS Switch, 8th Annual IEEE International Conference on Nano/Micro Engineered and Molecular Systems (NEMS), 755-758, 2013.
[3]Qiu, W.B., Yu, Y.Y., An FPGA-Based Open Platform for Ultrasound Biomicroscopy, IEEE transactions on ultrasonics ferroelectrics and frequency control, 1432-1442, 2012.
[4] Saury, L., Parametric defect localization on integrated circuits - From static laser stimulation to real-time variation mapping (RTVM), Workshop on Reliability of Compound Semiconductors (ROCS), 366- 373, 2014.
[5] Chuang C.H., Ker M.D., On-Chip Transient Voltage Suppressor Integrated With Silicon-Based Transceiver IC for System-Level ESD Protection, IEEE transactions on industrial electronics, 61(10), 5615- 5621, 2014.

Key Engineering Materials Vols 645-646 (2015) pp 577-582
© (2015) Trans Tech Publications, Switzerland
doi:10.4028/www.scientific.net/KEM.645-646.577

Submitted: 2014-11-27
Accepted: 2014-12-23

Design and Analysis of Capacitive Micromachined Ultrasonic Transducers Based on SU-8

Li Yuping[1,2], He Changde[1,2], Zhang Juanting[1], Song Jinlong[1], Zhang Wendong[1,2], Xue Chenyang[1,2*]

([1.]Key Laboratory of Instrumentation Science & Dynamic Measurement, Ministry of Education, North University of China, Taiyuan 030051, China;

[2.] Key Laboratory of Science and Technology on Electronic Test & Measurement, North University of China, Taiyuan 030051, China;)

Xuechenyang@nuc.edu.cn

Keyword: SU-8, CMUT, finite element method, capacitive membrane.

Abstract：In this paper, a new capacitive micromachined ultrasonic transducer (CMUT) is designed by using SU-8 material, and the theory of elastic thin plate is used to deduce the relationship between the pressure and capacitance of the structure. Simulation has been done about SU-8 CMUT by finite element method software ANSYS. The deformation of CMUT under acoustic pressure, the relationship between frequency, thickness and sensitivity, as well as the acoustic impedance and reflection coefficient of SU-8 material also have been studied through the simulation. The results turn out that SU-8 has the advantages of big dynamic range, high sensitivity and small acoustic impedance, so it has broad application in the ultrasonic field.

Introduction

Capacitive micromachined ultrasonic transducer (CMUT) has advantage of small size, high sensitivity, ease of integration etc., so it has been widely applied in the underwater imaging, medical imaging, nondestructive testing and other fields[1-3]. Most CMUTs are fabricated with silicon nitride material, which has the drawbacks of difficult in fabricating, high cost and stiffness, thus its use in some areas has been limited[4-6]. At present, there are some research institutions using polymer materials to fabricate CMUT and have made some progress. Polymer materials have the characters of good elasticity, not easy to break and large dynamic range etc.. CMUT based on polymer material exhibits abroad application prospects on the underwater acoustic imaging field. The silicon nitride material has a relatively larger impedance difference with water, so the receive efficiency is low. While the CMUT made of polymer material has a smaller impedance difference with the water, the efficiency is also improved[7]. This paper designed a new CMUT by using SU-8 photoresist based on its features of small Young's modulus and Poisson's ratio. The relationship between sound intensity and deformation, resonance frequency and film thickness, as well as the dynamic response characteristics are analyzed, which will provide the basis for the future design and process of CMUT.

1 Design and Working Principles

1.1 Structural Design

CMUT is a two-dimensional array which is composed of many sensitive cells integrated on a silicon wafer. Brief fabricating process of CMUT is: a metal film is plated on the silicon wafer to form the bottom electrode and wires by coating photoresist, exposure and chemical etch, then a protective layer is grown to protect the bottom electrode in the process of membrane releasing. Another metal layer is grown on the protective layer used as sacrificial layer, the areas except which above the bottom electrode is etched, then SU-8 photoresist is prepared by spin-coated method and fully exposed; A metal layer is coated on the SU-8 layer to form the top electrode and wires by coating,

exposure and etching. Finally, etching holes are formed at each corner by using reactive ion etching(RIE), which will allow the chemical solution in to remove the sacrificial metal layer, then a SU-8 layer is coated by spin-coated method, only the area of etching holes is exposured and the rest area is removed, then the ultrasonic transducer is completed.

Fig.1 is the configuration diagram of the designed sensitive cell. The sensitive cell is a square shape with a side length of 140um, middle part of the cell is cavity, the material of top electrode is aluminum with a thickness of 0.5um, and the four corners of the electrode are removed. The layer under the top electrode is the membrane made of SU-8, with the designed thickness of 3, 4, 5, 6, 7, 8um, each of the four corners has a hole for removing the sacrificial layer, the diameter of the hole is 10um.

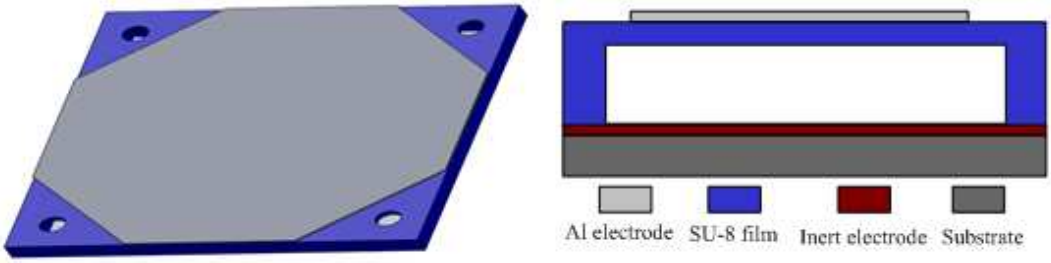


Fig.1Structure diagram of the capacitor plate

1.2 Principles and capacitor deformation model

In the case of no external force applied, the distance between the two electrodes is unchanged, so the capacitance value is constant. When an acoustic signal is applied on the capacitor, the film will have a deformation, thus the capacitance value is changed. In the practical applications, the capacitor plate under the acoustic pressure is a curved deformation instead of a whole downward movement, so there is nonlinear relationship between the capacitor and sound pressure. For better designing and analyzing CMUT based on SU-8 material, the paper establishes a model which is much more consistent with the actual model, and the relationships between the parameters of CMUT are also analyzed.

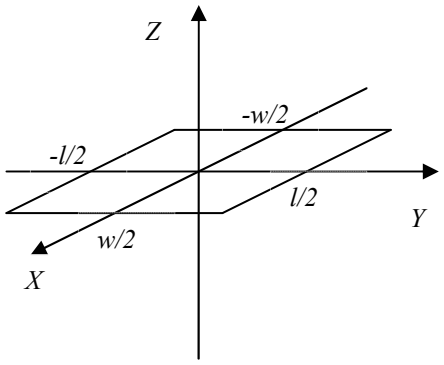


Fig.2 Coordinate of the thin plate

Three explanations should be described firstly: 1.Assuming that the rectangular capacitor film is a stiffness plate and the sound intensity p is distributed uniformly in the capacitor plate. 2. Computation shows for a 10V DC bias there is a small electrostatic force between two capacitors, so it can be ignored in the analysis. 3. All of the analysis is done in the linear region of the material, the nonlinear region will not be considered. Length of the rectangular plate is *l*, width is w and thickness is h, four sides are fixed and the displacement is zero, the coordinate system is shown in Fig.2, the deformation equation of capacitor plate can be obtained according to the analysis of the elastic plate[8]:

$$(\frac{\partial^4}{\partial x^4}+2\frac{\partial^4}{\partial x^2\partial y^2}+\frac{\partial^4}{\partial y^4})\omega-\frac{p}{D}=0 \qquad (1)$$

Where $\omega=\omega(x,y)$ is the variation function, $D=Eh^3/[12(1+\mu^2)]$ is the flexural rigidity of the plate. μ, E and h is Poisson's ratio, Young's modulus and thickness. The boundary conditions are

established as: at $x=-l/2$ and $x=l/2$, $\omega=0$, $\frac{\partial\omega}{\partial x}=0$; at $y=-w/2$ and $y=w/2$, $\omega=0$, $\frac{\partial\omega}{\partial y}=0$. It's known from literature (5) that the expression of ω is:

$$\omega=\frac{7p}{8D[l^4+\frac{4}{7}l^2w^2+w^4]}(x^2-\frac{l^2}{4})^2\bullet(y^2-\frac{w^2}{4})^2 \quad (2)$$

The distance of capacitor plate is d, and $d=d_1+d_2-\omega$, d_1 is the thickness of film, d_2 is the height of air gap. The capacitance can be obtained by doing integral of $\Delta C=\Delta S\varepsilon_1\varepsilon_2/4\pi k[d_1\varepsilon_1+(d_2-w)\varepsilon_2]$ in the region of $x\in(-l/2,l/2)$ and $y\in(-w/2,w/2)$:

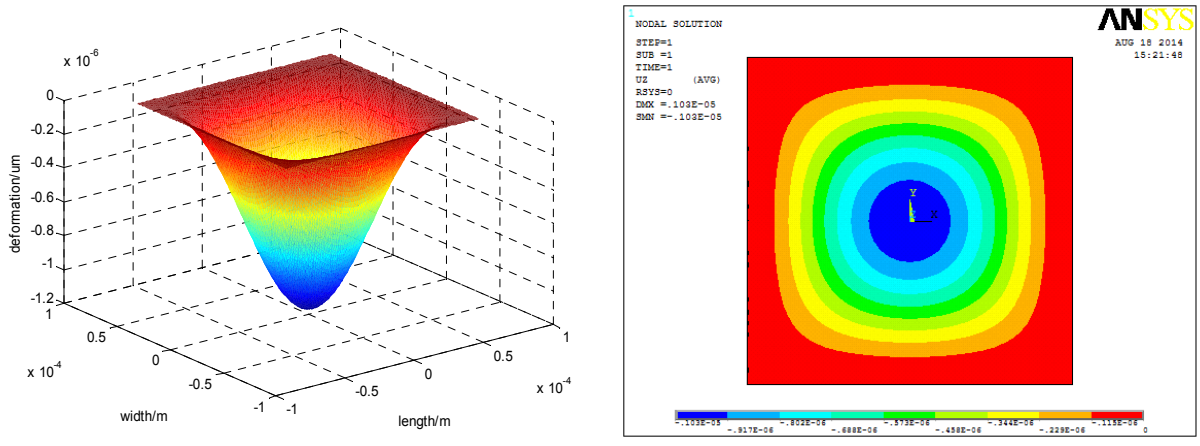
$$C=\int_{-l/2}^{l/2}\int_{-w/2}^{w/2}\frac{\varepsilon_1\varepsilon_2}{4\pi k[d_1\varepsilon_1+(d_2-\omega)\varepsilon_2]}dxdy \quad (3)$$

The capacitance can be calculated by the above equation when it has a non-uniform deformation under the sound pressure, and then the relationship between sensitivity and electric power can be analyzed.

2 Simulation and Analysis

2.1 Static Analysis

The reliability of the simulation model should be verified at first. The relationship between deformation and coordinates has been given above. It can be known that the deformation is approximate to a linear property when it is very small, thus equation (2) is feasible. The relationship between the static pressure and deformation of the capacitor plate with 5um thickness is calculated by MATLAB, as shown in Fig.3(a). The deformation is also simulated by ANSYS. The element type is SOLID92 and element mesh size is 5um; Poisson's ratio and Young's modulus of SU-8 material is 0.22 and 4.41e9, respectively. The simulation result is shown in Fig.3(b), where UZ represents the deformation of the capacitor plate.



(a) (b)

Fig.3 The deformation of 5um thin plate under 100kpa
(a) Calculation results by MATLAB (b) Simulation results by ANSYS

The theoretical result is in accordance with the simulation result, so the feasibility of the structure model established above is proved. It is reliable for using equation (2) to estimate deformation. The relationship between capacitance and pressure is calculated by equation (3), and the result of the 5um capacitor plate is shown in Fig.4.

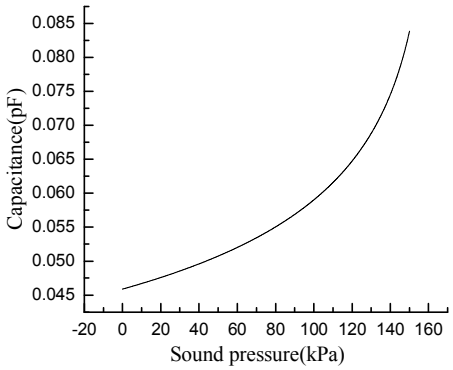


Fig.4 The relationship between capacitance and sound pressure

As known from the calculated results, the slope of capacitance change increases with the increment of the sound pressure. The capacitance value increases twice when the pressure increases from 0Pa to 150kPa, and the measurement accuracy are greatly improved compared with other materials with a large Young's modulus, so CMUT based on SU-8 material is more sensitive.

2.2 Modal Analysis

In this paper, the relationship between resonant frequency and film thickness is analyzed by ANSYS, which will provide the basis for the designing and fabricating process of actual chip structure. On the premise of the distance between the two electrodes is kept unchanged of 9um, several different thickness of SU-8 film, with the value of 3um, 4um, 5um, 6um, 7um is designed. A 0.5um aluminum layer is deposited on the SU-8 film. Poisson's ratio of AL is 0.33 and Young's Modulus is 6.67e10, respectively. Fig.5 shows the simulation results under the load of 100kPa.

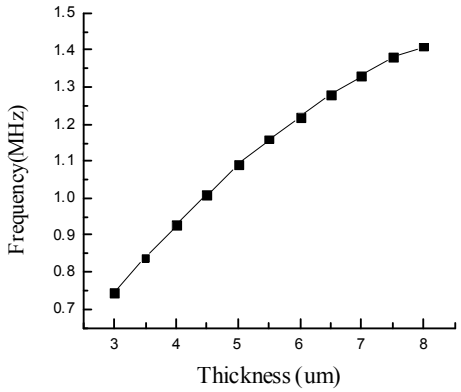


Fig.5 The relationship between resonant frequency and film thickness

The simulation results show that the capacitive transducer based on SU-8 can achieve a higher resonant frequency. The resonant frequency increases but the change rate decreases with the increase of film thickness.

2.3 Harmonic Response Analysis

Harmonic response to the acoustic waves with different frequencies of the SU-8 capacitive transducer is also analyzed, that is the relationship between the vibration amplitude in the vertical direction of the film and frequency, and then the results are compared with the CMUT based on silicon nitride. The structure for simulating is the same as the designed structure, only changing the thickness. Fig.6 is the simulation result of different thicknesses at different frequencies, and the three curves separately represent the thickness of 7um, 5um, 3um. Fig.7 shows the deformation comparison of the transducers respectively based on SU-8 material and silicon nitride material at the same resonant frequency.

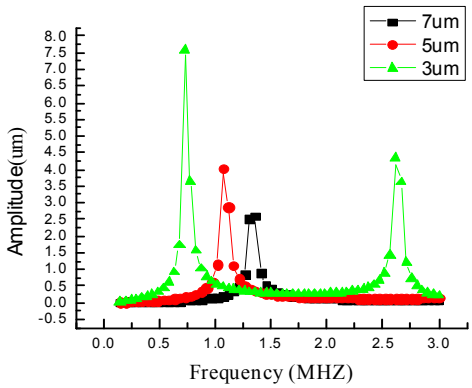


Fig.6 The relationship between frequency and amplitude

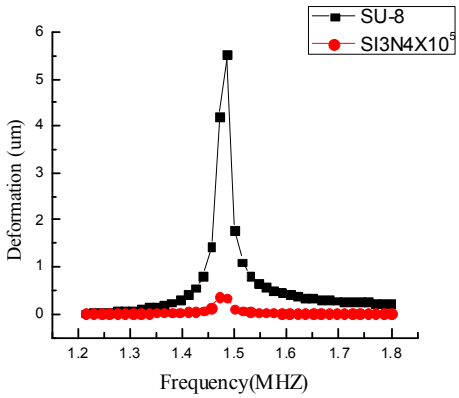


Fig.7 Deformation of silicon nitride and SU-8 film

The simulation results in Fig.6 show that when the frequency of acoustic waves is the same with the natural frequency of the transducers, the capacitor plate can obtain the largest deformation, thus the maximum sensitivity is achieved. The maximum deformation of capacitor plate is decreasing with the increase of film thickness, and the sensitivity is reduced accordingly. Fig.7 shows the deformation after magnifying 10^5 times of the transducers based on silicon nitride material compared with the transducers based on SU-8 material at the same frequency. The response to sound pressure of the former is higher by 6 orders of magnitude than the latter. Although the distance between the capacitor plates is reduced with the increase of film thickness, thus reducing the capacitance value, the sensitivity is still much higher than the transducers based on silicon nitride.

2.4 Analysis of the acoustic properties

Table 1 shows Young's modulus, density, velocity, acoustic impedance and reflection coefficient of the materials used in the acoustic transducer[9], where the intrinsic acoustic impedance and reflection coefficient can be calculated by formula[10]. As can be seen from table 1, SU-8 material has a small impedance difference with water, while piezoelectric ceramic, Si3N4 and Al materials have a relatively larger impedance difference. Conventional material always with a large impedance, thus the reflection coefficient and accept efficiency is low. The capacitive transducers based on Si_3N_4 is failed to achieve the desired sensitivity due to the same reason with piezoelectric ceramic transducer. SU-8 has a smaller reflection coefficient than that of other materials, and the acceptance rate is much higher, so it is an ideal material for capacitive acoustic transducers.

Table1 Parameters of some common materials using in acoustic transducer

	Water	SU-8	Piezoelectric ceramics	Si_3N_4	Al
Young's modulus (MPa)	~	4410	76500	290000	66700
Density (kg)	1000	1400	7500	3200	2700
Sound velocity (m/s)	1540	1775	3190	9520	4970
Impedance(MRayl)	1.54	2.48	23.9	30.5	13.4
Reflection coefficient in water	~	0.234	0.879	0.904	0.794

Summary

Design and simulation of capacitive acoustic transducer based on SU-8 material has been done in this paper, aiming at to theoretically analyze the properties of CMUT based on SU-8 material. The simulation and numerical results under static force show that the simulation results are basically same as that obtained by formula calculation, so we can estimate the deformation by formula (2), and then calculate the relationship between capacitance and sound intensity. Both of the formulas and simulation results show that CMUT based on SU-8 materials has characteristics of high sensitivity and large dynamic range. Compared with other acoustic transducer material, SU-8 material have a small impedance with water, low reflection coefficient and high receiving efficiency, so SU-8 polymer material has broad application prospects in ultrasonic transducers and will become the future research direction of MEMS ultrasonic transducers.

Acknowledgement

The work has been financially supported by the Subsidized Program of 863 Project (2011AA040404), the National Natural Science Funds of China (61127008).

References

[1] Zhang Hui, Song Guangde, Li Dachao, Desigh of Capacitive Micromachined Ultrasonic Transducers[J]. Journal of Tianjin University, 2008, 41(1):17-20.

[2]Ladabauml I, Jin X C, Soh H T, *et a1*. Surface Micromachined Capacitive Ultrasonic Transducers [J]. IEEE Trans on Ultrasonics，Ferroelectrics and Frequency Control. 1998,45(3):678-690.

[3] Ergun A S, Yaralioslu GG, Khuri-Yakub B T,*et a1*. Capacitive Micromachined Ultrasonic Transducers：Theory and technology[J]. Journal of Aerospace Engineering，2003,16(2):76-84.

[4] Igal Ladabaum, Xuecheng Jin, Hyongsk T.Soh, *et al*. Surface Micromachined Capacitive Ultrasonic Transducers[J]. IEEE Transactions on Ultrasonics, Ferroelectrics and frequency Control, 1998,45(3):678-690.

[5] Ömer Oralkan, A.Sanh Ergun, Jeremy A.Johnson, *et al*. Capacitive Micromachined Ultrasonic Transducers: Next-Generation Arrays for Acoustic Imaging[J]. IEEE Transactions on Ultrasonics, Ferroelectrics and frequency Control, 2002,49(11):1596-1610.

[6] Xuecheng Jin, Igal Ladabaum, F.Levent Degertekin, *et al*. Fabrication and Characterization of Surface Micromachined Capacitive Ultrasonic Immersion Transducers[J]. IEEE Journal of Microelectromechanical Systems,1999,8(1):100-113.

[7] Gary P. Scavone, Julius O. Smith. A stable acoustic impedance model of the clarinet using digital waveguides[C]. Proc. of the 9th Int. Conference on Digital Audio Effects (DAFx-06), Montreal, Canada, September 18-20, 2006.

[8] Liu Wei, Wang Hui. Meshless solution for thin plate bending problems[J].Journal of Lanzhou University of technology, 2008,34(6):169-172.

[9] X Zhuang, A Nikoozadeh, M A Beasley, G G Yaralioglu1, B T Khuri-Yakub, B L Pruitt. Biocompatible coatings for CMUTs in a harsh, aqueous environment[J]. Journal of micromechanics and microengineering, 2007,17:994–1001.

[10] Shi Yong, Zhu Xi, Li Yongqing, Li Haitao. The Acoustic Design of Acromolecule Absorbing Material under Water[J]. Noise and Vibration control, 2006.12(6):87-89.

Key Engineering Materials Vols 645-646 (2015) pp 583-588
© (2015) Trans Tech Publications, Switzerland
doi:10.4028/www.scientific.net/KEM.645-646.583
Submitted: 2014-11-30
Accepted: 2014-12-23

Passive Wireless Multi-parameter Sensor System for Hermetic Environment Monitoring

Dan Tang[a], Li-Feng Wang[b], Qing-An Huang[c *]

Key Laboratory of MEMS of the Ministry of Education, Southeast University, Nanjing, China

[a]td_seu@163.com, [b]wanglifeng@seu.edu.cn, [c]hqa@seu.edu.cn (corresponding author)

Keywords: passive, wireless, multi-parameter, coupling inductors, relaxation oscillator, time division multiplexing, load modulation, asynchronous communication.

Abstract. This paper presents a passive wireless multi-parameter sensor system, which is suitable for monitoring the environment in hermetic space like industrial painting room, coal mine, and so on. The system consists of two subsystems: the primary system and the secondary system. The primary system transmits power and receives modulated data through a coupled transformer composed of primary and secondary inductors printed in their subsystems, respectively. The secondary system comprises micro capacitive temperature, pressure and relative humidity sensors and uses a relaxation oscillator to convert capacitance to frequency. Using time division multiplexing unit, it can simultaneously measure multiple sensors. The converted frequency signal is used to vary the amplitude of the waveforms on the coupling inductors. The modulating signal is recovered from the carrier using the envelope detection unit. The measurement results indicate that the pressure, temperature, and relative humidity sensitivities of the passive wireless multi-parameter sensor system are 5.6 fF/hPa, 250fF/°C and 71.4 fF/%RH, respectively. Three sensors linearly response to the change of the environment and the system has good consistency.

Introduction

In the last decades, the radio frequency identification (RFID) has moved from obscurity into mainstream applications that bring convenience to our life. RFID is used for thousands of applications such as gaining entrance to buildings, tracking goods, collecting tolls without stopping and etc.[1]. As the development of the wireless communication technology, integrated circuit technology and circuit design technology, the implement and application of wireless RFID tag chip has become mature. In recent years, wireless data and power gathering has been widely researched. Integrating the RFID technology with sensors and actuators opens a variety of applications in industry [2], health care [3-5] and agriculture [6].

Low power design is a key point when integrating sensors with remotely powered systems in order to maximize the wireless range. It is well known that the capacitive sensors have advantages of the low power consumption, low temperature drift and good long-term stability [7]. The readout circuit of the sensor has several implement methods, such as circuit made in CMOS technology [8] and LC resonance [9,10] etc.

For wireless monitoring systems, an increasing number of applications require the simultaneous measurement of multiple parameters. During spraying process, the coating quality is influenced by the temperature, humidity, air pressure of the spraying shops. It's essential to monitor the environment of the spraying shops. As the spraying shops are sealed, this monitoring problem can be solved through a network of passive transponders that can be distributed across the fields and use the time division multiplexing (TDM) [11] technology to simultaneously measure the multiple sensors.

System Overview

This paper presents a passive wireless multi-parameter sensor system, which is composed of two subsystems: the primary system and the secondary system. Fig. 1 is the block diagram of the system. The primary system transmits power and receives modulated data through a coupled transformer composed of primary and secondary inductors printed in their respectively subsystems. The power

and data transfer work at the same time. The secondary system consumes power obtained from the secondary inductor from which the voltage is rectified and regulated. The secondary system comprises three micro capacitive temperature, pressure, and relative humidity sensors and uses a relaxation oscillator to convert capacitance to frequency. Using time division multiplexing unit, the secondary system can simultaneously measure multiple sensors. Use the converted signal to vary the amplitude of the waveform on the coupling inductors. Thus, the waveform on the primary inductor is load modulated. Use the diode envelope detection circuit to recover the frequency signal which contained the sensors' measurement results. Use the RC filter to smooth and the amplifier to standardize the frequency signal. Then, use digital circuit to sample and count the signal. Finally, every sensor's measurement result can be distinguished from it.

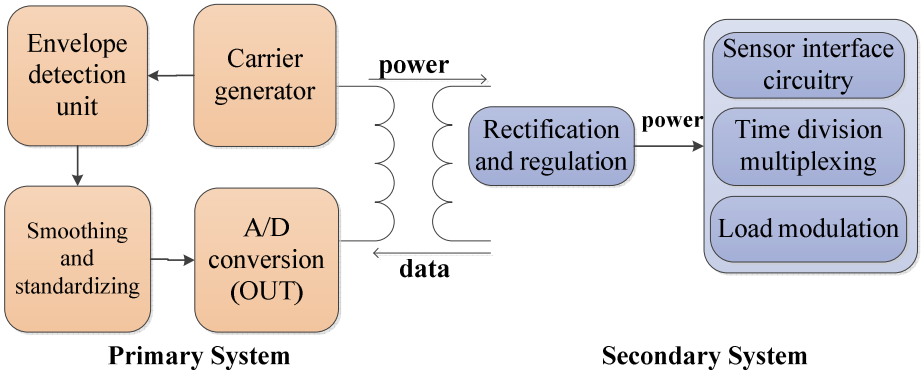


Fig. 1 Block diagram of the system

Design of The System

The primary system comprises carrier generator, envelope detection unit, filtering and standardizing unit and A/D conversion unit. In the primary circuitry, a class-E power amplifier generates 3MHz carrier providing power to the secondary system through coupling inductors. The envelope detection unit recovers the modulating signal from the waveform on the primary inductor. Before A/D conversion, the signal is filtered and standardized. After sampling and counting the modulating signal, we can distinguish three sensors' measurement results and output the digital data to the terminal.

The secondary system is composed of rectification and regulation unit, sensor interface circuitry, time division multiplexing unit and load modulation unit. The secondary inductor is configured as an LC oscillator from which the carrier is rectified and regulated to provide a DC voltage source for the whole secondary circuit. The DC voltage generated from regulation is 5V. The transducer interface unit utilizes the relaxation oscillator to convert the capacitance of sensors to frequency. Through the time division multiplexing, three sensors can be measured simultaneously and the measured signal is used as the modulating signal to vary the amplitude of the waveforms on the coupling inductors. It can be noted that, the power coupling and data transfer operate at the same time.

When design and simulation was done, the system has been implemented on PCB boards as shown in Fig. 2.

Put the system into the sealed test chamber and use the control variate method to carry out the experiments. Fig. 3 shows the photograph of the test chamber OMEGA205 and the pressure test chamber.

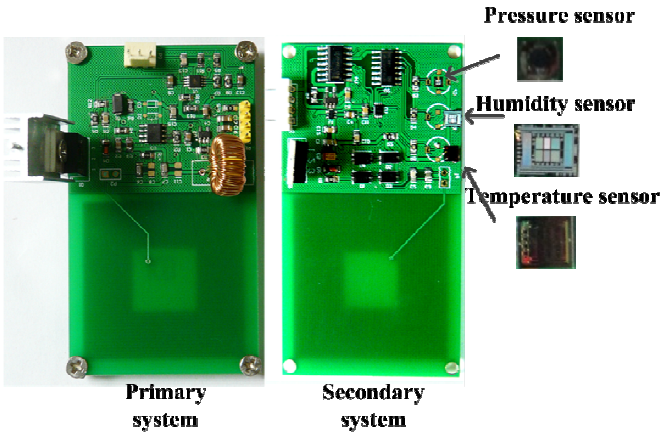


Fig. 2 Photograph of the system



Fig. 3 Test chambers

Sensor interface circuitry. There are three micro sensors implemented in the secondary system. The capacitive pressure sensor is a commercial product VTI SCB10H which is a silicon absolute pressure sensor. The bending of the diaphragm changes with the outer pressure, thus the capacitance changes as well. The sensitive material of the capacitive humidity sensor is graphene oxide. The relative dielectric constant of the graphene oxide would change as a function of humidity，resulting in the change of capacitance. The comb electrodes of the capacitive temperature sensor were fabricated by the SOG (Silicon-On-Glass) process. The sensitive material of the capacitive temperature sensor is PDMS and the relative dielectric constant of the PDMS would change as a response to temperature. Use the Schmitt trigger to form a relaxation oscillator.

The relaxation oscillator converts the capacitance of the sensor to frequency. The correspondence between the capacitance and the frequency is shown as Fig. 4.

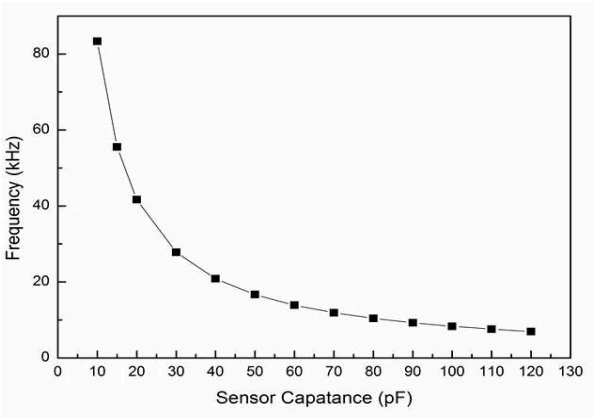


Fig. 4 Capacitance vs frequency

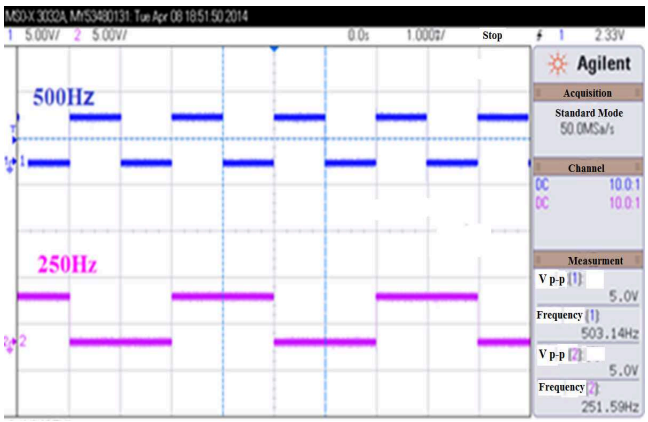


Fig. 5 Control signals of analogy switch

Time Division Multiplexing Unit. The TDM unit is composed of a clock generator, a frequency divider and an analog switch multiplexer.

First, use a silicon oscillator LTC6900 to generate a 1kHz clock signal. Use two D flip-flops to divide the clock signal twice, generating a 500Hz signal and a 250Hz signal. The test result is shown in Fig. 5.

These two signals are used to control the analog switch TS5A3359, so the measurement results of three sensors can be sequentially output from TS5A3359's COM pin during one period 4ms (as shown in Fig. 6). Then the signal from the COM pin is used to control a MOSFET switch, lead to the amplitude varying of the waveform on the coupling inductors. Fig. 7 shows the modulated waveforms on the primary inductor and the secondary inductor. The upper one is the waveform on the primary inductor, the bottom one is the waveform one the secondary inductor. In one period there are four channels among which there is a spare channel. The modulation depth affects the power provided for the secondary system and the complexity of the demodulation. Thus it has a compromise.

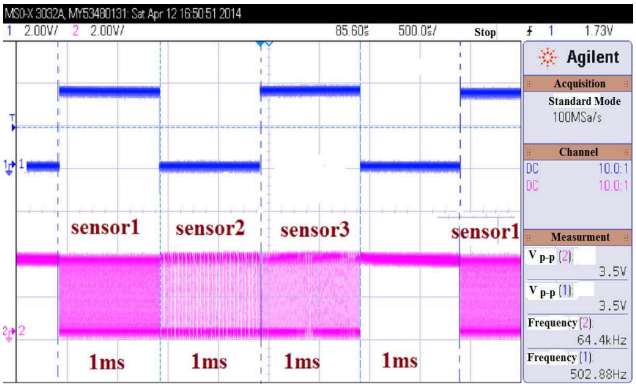


Fig. 6 Modulating signal

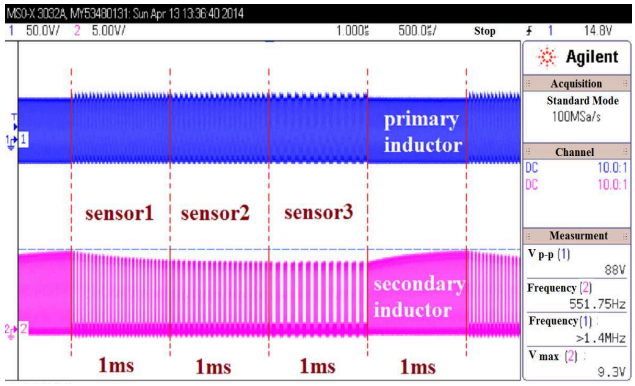


Fig. 7 Modulated waveforms on the coupling inductors

Demodulation, Smoothing and Standardizing. The modulating signal can be easily extracted from the modulated waveform used a diode demodulator. Then, use a RC filter to smoothing the recovered signal. Before digitizing the signal, it should be standardized.

The output signal is shown as the following Fig. 8. The upper one is the modulating signal tested in the secondary system, and the bottom one is output from the primary system which has been standardized. The low level is 0V and the high lever is 5V. However, the signal has ripple wave. Before further processing, it should be digitized.

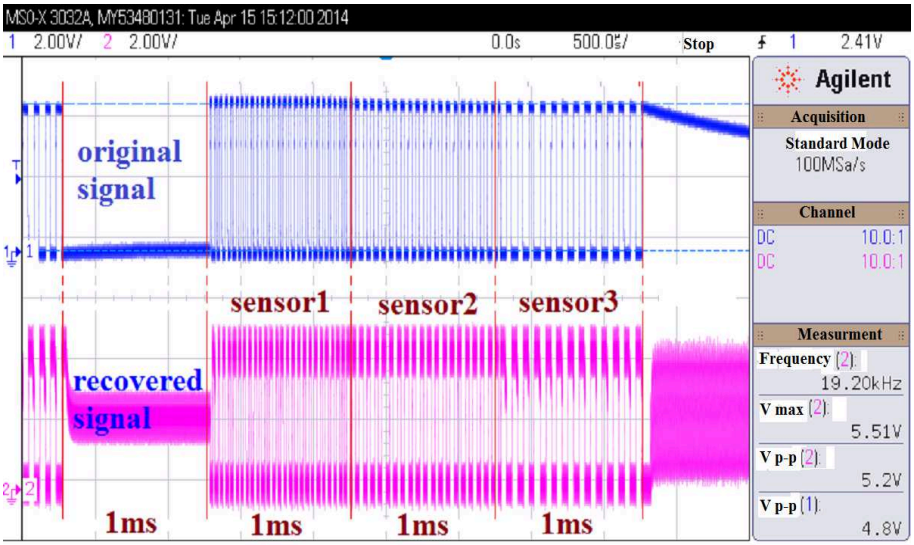


Fig. 8 Original signal vs. recovered signal

Measurement Results

Put the system into the sealed test chambers and use the control variate method to carry out the experiments. A temperature and humidity test chamber OMEGA205 was used to test the temperature and humidity respectively. During the temperature and humidity test, a portable pressure control box which can be placed in the chamber is used to keep the pressure unchanged. When test the pressure, the pressure test chamber can keep the temperature and humidity unchanged.

For temperature response, the frequency changed from 25kHz to 55kHz when the temperature increased from 20°C to 80°C. The relative humidity kept constant at 50%RH and the pressure was maintained at 1000hPa. Vary the pressure from 100hPa to 1000hPa and keep the temperature and humidity unchanged, the response frequency decreased from 53kHz to 39kHz. For humidity response, the relative humidity ranged from 20%RH to 90%RH with a step of 10%RH while the temperature was kept at 25°C and the pressure was 100kPa. The response frequency decreased from 79kHz to 70kHz. As shown in Fig. 9, every variable has been tested both in ascending order and descending

order and the two curves tested in different orders almost completely overlapped. It means that the system has excellent reliability and consistency.

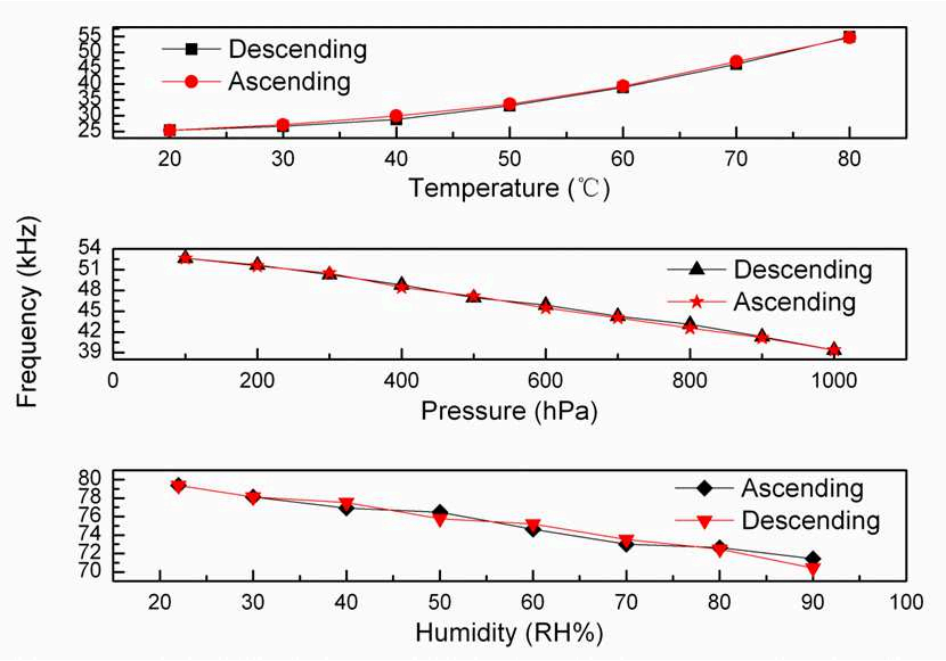


Fig. 9 Test curve of temperature, pressure and relative humidity

Summary

This paper has reported the design and test results of a passive wireless multi-sensor system for measuring pressure, temperature, and relative humidity. The wireless system is assembled on two PCB boards and transmits power and data through coupling inductors. The pressure, temperature, and relative humidity sensitivities of the passive wireless multi-sensor system are 5.6 fF/hPa, 250fF/°C and 71.4 fF/%RH, respectively. The passive wireless system is very suitable for monitoring the hermetic environment.

Acknowledgement

This work is supported by the National Natural Science Foundation of China (Grant NO. 61136006) and the National High Technology Research and Development Program of China (Grant NO. 2013AA041101) and the new teacher start-up fund of Southeast University (Grant NO.1106007111).

References

[1] J. Landt, The history of RFID, Potentials, IEEE, 24 (2005) 8-11.
[2] M Merenda, C Felini, F G Della Corte, Battery-less smart RFID tag with sensor capabilities, RFID-Technologies and Applications, IEEE International Conference, (2012) 160-164.
[3] Q Huang, M Oberle, A 0.5-mW passive telemetry IC for biomedical applications, Solid-State Circuits, IEEE, 33.7(1998)937-946.
[4] T Akin, K Najafi, R M Bradley, A wireless implantable multichannel digital neural recording system for a micromachined sieve electrode, Solid-State Circuits, IEEE, 33.1(1998) 109-118.
[5] B. D. Farnsworth, R. J.Triolo, D. J.Young, Wireless implantable EMG sensing microsystem, IEEE. (2008) 1245-1248.
[6] K E Kunkel, Operational soil moisture estimation for the midwestern United States, Journal of Applied Meteorology, 29.11(1990)1158-1166.
[7] R. Puers, Capacitive sensors when and how to use them, Sens. Actuators A, Phys., 37-38(1993)93-105.

[8] D Cirmirakis, A Demosthenous, N Saeidi, et al. Humidity-to-frequency sensor in CMOS technology with wireless readout, Sensors Journal, IEEE, 13.3(2013) 900-908.
[9] T Salpavaara, J Verho, P Kumpulainen, et al. Readout methods for an inductively coupled resonance sensor used in pressure garment application, Sensors and Actuators A: Physical, 172.1(2011)109-116.
[10] Y Wang, Y Jia, Q Chen, et al. A passive wireless temperature sensor for harsh environment applications, Sensors, 8.12(2008)7982-7995.
[11] A D DeHennis, K D Wise. A wireless microsystem for the remote sensing of pressure, temperature, and relative humidity, Microelectromechanical Systems, 14.1(2005)12-22.

Key Engineering Materials Vols 645-646 (2015) pp 589-594
© (2015) Trans Tech Publications, Switzerland
doi:10.4028/www.scientific.net/KEM.645-646.589

Submitted: 2014-12-14
Accepted: 2014-12-23

Statistical Analysis and Yield Enhancement of MEMS Devices by Considering Multi-Process Variations

Lili Gao[1, a *], Wei-Hua Li[2, b] and Qing-An Huang[3, c]

[1-3] Key Laboratory of MEMS of the Ministry of Education, Southeast University, Nanjing 210096, China

[a]LilyGaoChina@gmail.com, [b]liwh@seu.edu.cn, [c]hqa@seu.edu.cn

Keywords: MEMS devices, process variation, statistical analysis, yield enhancement, Monte Carlo method.

Abstract. A methodology is developed statistically to make MEMS devices robust to process variations to improve manufacturability and yield. Two approaches are applied to discuss the effects of multi-process variations. Comparisons have been made between the proposed method and Monte Carlo simulations, which confirm the robustness of the proposed one with performance error less than 4%. Experiments on beams and comb-drive resonator verified the effectiveness of the methodology and it is useful for practical device designs to be more robust to process variations and yield enhancement realization.

Introduction

Micro-electro-mechanical systems (MEMS) have been used in widespread sensing and actuation application such as micro-switches, gyroscopes, accelerometers, etc.. However, while the potential of such devices is widely recognized, MEMS devices are typically developed via VLSI-tuned processes, leading to a number of tolerance related issues. Rapid and reliable design of these devices is still a challenging issue. Various physical fields, such as electrical, mechanical and fluidic, are required to accurately model their interactions for such devices. Advances in numerical simulations and underlying multi-fields understanding have greatly improved the pace of devices modeling [1-2]. Unfortunately, assumptions have been made in these works that properties of the devices are all deterministic. On contrary, significant uncertainties exist from low-cost process, residual stresses, uneven topography, contaminations, etc. [3]. The uncertainties are mainly caused by variations in materials properties, like Young's modulus, geometrical features, like dimensions and gaps, operating environment and boundary conditions.

Process deviations during fabrication of MEMS devices will bring in variations between design and fabrication results, tuning into property variations like stiffness, frequency or switching characteristics. Eventually, they are the causes for low yield and systematic unstability or device failure. To obtain a compliant one, designers may choose to minimize the size of the device empirically or by analyzing huge number of samples which is economically burdensome and wasteful. All these limit the industrialization of most MEMS devices. Actual device performance variation is always dependent on the geometric variations [4], and MEMS devices benefit especially from the smaller size. Attempts to evaluate the system statistically and analytically have been proved to be valid [5,6]. Stochastic variations in various design parameters shall be considered during the development of numerical models. By quantifying the effect of manufacture variations on performance parameters and determining the uncertain quantification to identify critical design parameters, efficient MEMS device design with desired yield is available.

A methodology is statistically developed here to make MEMS devices robust to process variations, in order to improve manufacturability or yield and reduce sensitivity to the variations. The design criteria throughout this work are mainly spring constant and resonant frequency. Two approaches have been applied to discuss the effects of minimum geometries and material property, in the form of single and multiple. Comparisons have been made between the proposed method and Monte Carlo

simulations, which confirm the robustness of the proposed one with performance error less than 4%. Process models used here are Uniform, Exponential or Gaussian in nature. Experiments on beams and comb drive resonator verified the effectiveness of the proposed methodology and it is efficiently useful for practical device designs to be more robust to process variations and yield enhancement realization.

Yield

At different steps of process fabrication, yield can be defined uniformly as:

$$\text{Yield} = \frac{\text{working products}}{\text{fabricated products}}. \quad (1)$$

In reality, we are usually confused that we just had 2000 devices manufactured, but 1076 of them didn't meet the specifications. They are actually destroied by the monster, yield loss. The two pricipal kinds of defects casing the monster are catastrophic defects and parametric defects. By yield optimization, more products shall be effectively useful. Fig. 1 reveals the difference between yield optimization and doing nothing. With parameters deviations caused by yield loss, performance range may switch to the edge of the whole distribution. Statistically, we've easily got that even the same variation range length, the part falling to the edge is much worser than the part in the center. The yield of the latter one may be over 20 times higher.

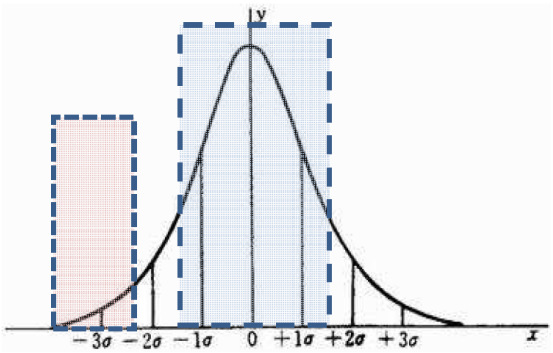


Fig 1: The effectiveness of yield optimization: the red shadow=doing nothing, the yield is less than 2%, the blue shadow=yield optimization, the yield is about 90%.

Statistical optimization

Integrating all the concerns, the so-called cost function is appropriate to reveal the effectiveness of the design. Thus, much attention should be paid to the careful initial point choice. Fig. 2 tells the significance that the lowest cost function point seems to be the best, but variations between acceptable range may bring the design to be unacceptable. Therefore, small deviation from the lowest should be considered. Although higher price than the lowest point, all are in contrl of the acceptable range.

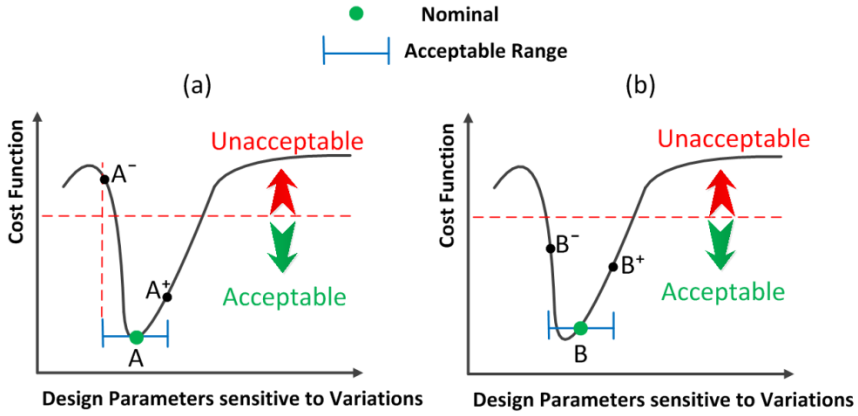


Fig 2: The effect of different choice of initial design point, the lower the cost function, the better design

In this paper, we try to treat the uncertainties in two ways, independent and dependent, which decides the probability density function (*pdf*). With the expressions of pdfs and boundary conditions, the yield is solvable. With the initial design point, we consider the key geometric factors.

Single-parameter variation

Fixed-fixed beam

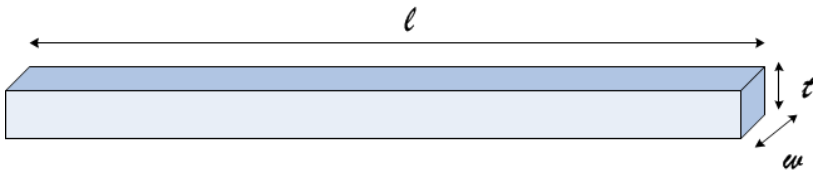


Fig 3: Fixed-fixed beam

Starting with the fixed-fixed beam, we know that the frequency can be represented as (taking the beam mass into account):

$$f_n = \frac{k_n}{2\pi}\sqrt{\frac{EIg}{wl^4}} \tag{2}$$

Considering $k_1 = 22.4$,

$$f_1 = \frac{5.6t}{\pi l^2}\sqrt{\frac{E}{3\rho}} \propto \frac{t}{l^2} \tag{3}$$

while $\frac{\Delta l}{l} \ll \frac{\Delta t}{t}$, for example $l = 200, \Delta l = 1; t = 2, \Delta t = 1$, the length effect could be ignored campared with the thickness's. It is normal in most devices. Fig. 4 explains it intuitively that smaller size variation results in larger target parameter fluctation.

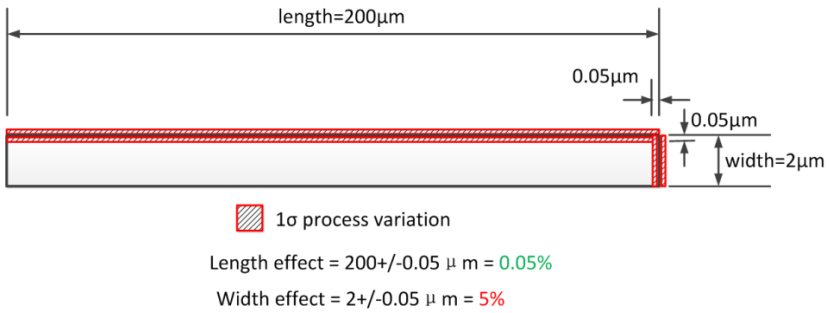


Fig 4: The effect of smaller geometric variation

Comb-drive resonator

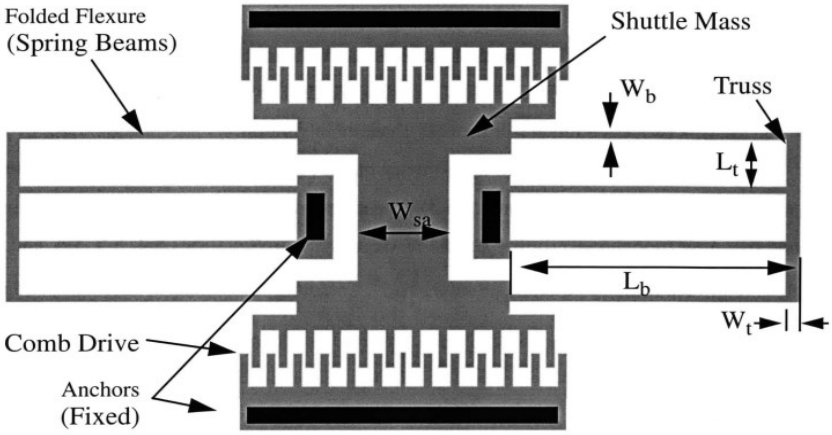


Fig 5: Comb-drive resonator

As for comb-drive resonator, the mass system model can be represented as (refered to Fig. 5):

$$m_x = m_{\text{shuttle}} + m_{\text{truss,effective}} + m_{\text{beams,effective}} \tag{4}$$

Furthermore, with some calculations, the sysmatic effective spring constant is represented as:

$$k_x = \frac{2Etw_b^3}{L_b^3} \cdot \frac{L_t^2 + 14\alpha L_t L_b + 36\alpha^2 L_b^2}{4L_t^2 + 41\alpha L_t L_b + 36\alpha^2 L_b^2} \tag{5}$$

Easily, we could see,

$$k_x \propto \frac{w_b^3}{L_b^3} \tag{6}$$

Similarly, the smaller size is the main factor during geometric variations.

Multi-parameter variations

Evidently, when focusing on frequency related questions, we could ignore the length variation caused by fabrication. How about the two other geometric variations' influences? As it shows in Fig. 6, given specific performance parameter error range, like 5%, the width variation play a more serious part. Even doubling the error, devices yields much lower for the width variation.

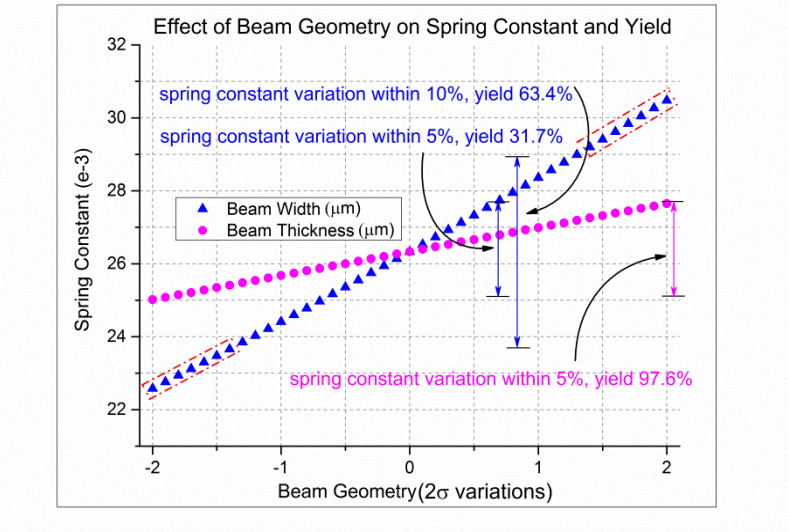


Fig 6: Effect of beam geometry on spring constant and yiedl: red dot=beam width, blue star=beam thickness.

Enlarging the size of width, its negtive effects would be lower or even ignored like the length factor. However, there are boundaries for the sizes of width. Device area is the leading one. Appropriate size of width ends up both in target factor variation reduction and device area saving, referring to Fig. 7.

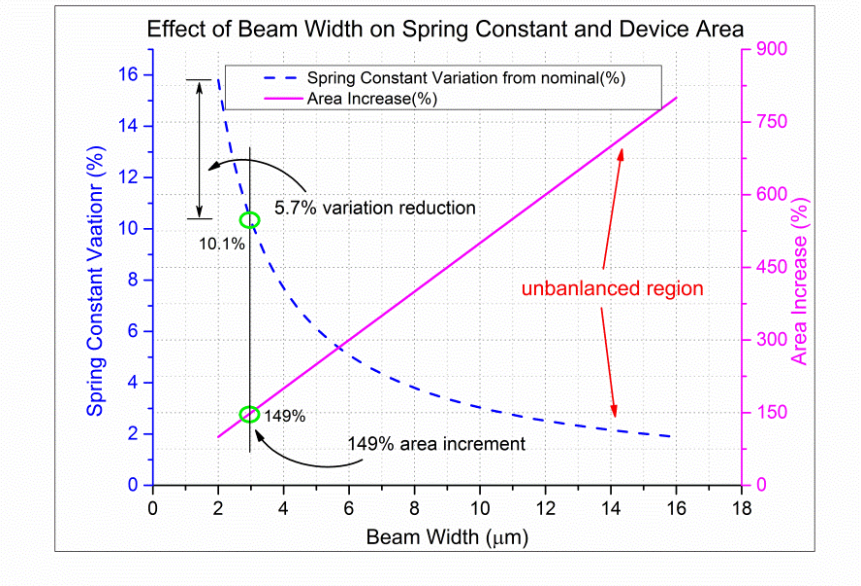


Fig 7: Effect of beam width on spring constant and device area.

When beam width is larger than 9μm, the device area is severely affected. Also, too narrow the width, great deviation would occur to the performance parameter, spring constant. Only by careful choice, both the performance parameter and device area would benefit, foe example, choosing width 2.8μm, compared with seemingly much better 2μm, there would be 5.7% variation reduction for the spring constant and only 49% area increment for the device area.

As a fundamental property of the underlying process, variation in thickness is difficult to control so we treat it as independent from the others. For multivariates, corelevance is of great significance for the choice of operational regions. Fig. 8 explains the corelevance of variates concerned, parameters here are lineraly related, and the shadow region represents the operational one. For unlinearly situation, the shadow would be nearly oval-shaped.

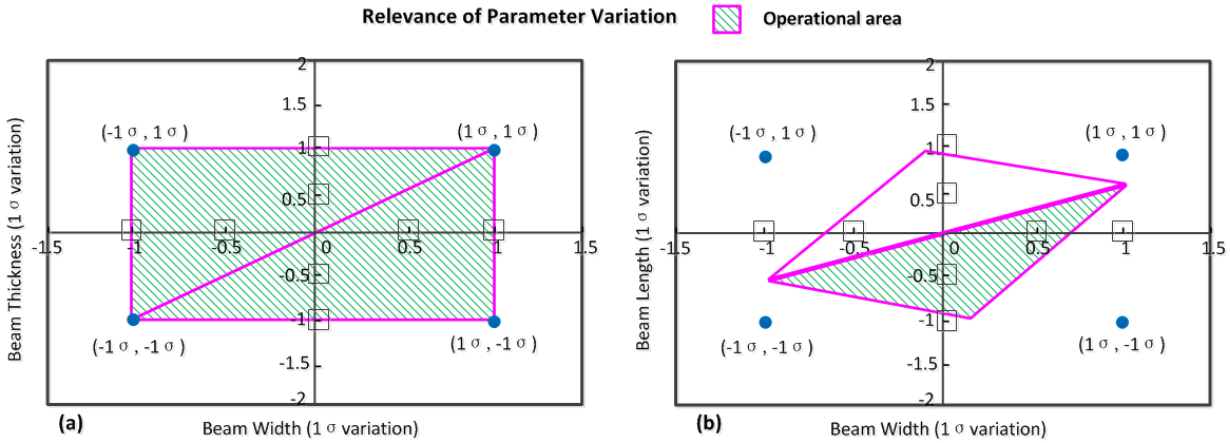


Fig 8: Relevance of parameters within 1σvariation: (a) uncorrelated, (b) correlated. The shadow is the operational region.

Summary

Given specific performance parameter error ranges, interval symmetricity, parameter variations and synchronicities all shape the final yield and systematic stability inordinately. Compared with the results of Monte Carlo simulations, the proposed method predict devices performance with error

range less than 4%. Here, we assume the distribution Gaussian, Uniform and Exponential separately. Accordingly, suggestions for parametric design tolerance and further device design are available with desired device yield.
In the future work, we would like to focus on variations of material properties and performance under multi-physics, like coupled mechanical-electrical questions.

References

[1] S. D. Senturia, N. R. Aluru, and J. White, Simulating the behavior of MEMS devices: Computational methods and needs, IEEE Comput. Sci. Eng., vol. 4, no. 1, (1993)30-43

[2] S.K. De and N. R. Aluru, Full-Lagrangian schemes for dynamics analysis of electrostatic MEMS, J. Micromech. Microeng., vol. 16, no. 8, (2006)1705-1719

[3] M. Liu, K. Maute, and D. M. Frangopol, Multi-objective design optimization of electrostatically actuated microbeam resonators with and without parameter uncertainty, Reliab. Eng. Syst. Saf., vol. 92, no. 10, (2007)1333-1343

[4] Vudathu, S. P., K. K. Duganapalli, Yield analysis via induction of process into the design of MEMS and other microsystem, MICROSYST. TECHNOL., vol. 13, nr. 11-12, (2007)1545-1551

[5] Dewey, A., H. Ren, Behavioral modeling of microelectromechanical system (MEMS) with statistical performance-variability reduction and sensitivity analysis, IEEE T. CIRCUITS-I, vol. 47, nr. 2, (2000)105-113

[6] Shavezipur, M., K. Ponnambalam, Fabrication uncertainties and yield optimization in MEMS tunable capacitors, Sensors and Actuators a-Physical, vol. 147, nr. 2, (2008)613-622.

Key Engineering Materials Vols 645-646 (2015) pp 595-599
© (2015) Trans Tech Publications, Switzerland
doi:10.4028/www.scientific.net/KEM.645-646.595

Submitted: 2014-12-15
Accepted: 2014-12-23

Effects of Hall Output Probes Shape on Magnetic Characterization of Hall Magnetic Field Sensor based on MOSFET

ZHAO Xiao Feng[1,2a], LIN Qian Ru[1], MU Ai Lin[1], WEN Dian Zhong[1,b], ZHANG Hong Quan[1]

[1]Key Laboratory of Electronics Engineering, College of Heilongjiang Province, Heilongjiang University, Harbin, China
[2]The 49th Research Institute of China Electronics Technology Group Corporation, Harbin, China
[a]zhaoxiaofeng@hlju.edu.cn, [b]wendianzhong@hlju.edu.cn (corresponding author)

Keywords. Hall output probe shape；Hall effect；magnetic fileld sensor；magnetic sensitivity；

Abstract. This paper presents the effects of Hall output probes shape on the magnetic characteristic of magnetic field sensors with Hall output probes, which is based on metal-oxide-semiconductor field effect transistor (MOSFET). The Hall sensor chips are fabricated on <100> silicon substrates with high resistivity by using CMOS technology. Experiment results show that, when drain-source voltage V_{DS}=5.0 V, the magnetic sensitivity of the magnetic field sensor with the concave Hall output probes and channel length-width ratios of 160 μm/80 μm, 320 μm/80 μm and 480 μm/80 μm are 53.3 mV/T, 32.54 mV/T and 20.32 mV/T, respectively. At the same condition, the magnetic sensitivity of the magnetic field sensor with convex Hall output probes and the channel length-width ratio of 160 μm/80 μm is 76.8 mV/T.

Introduction

Since 1879, the Hall Effect discovered by Dr. Edwin Hall has been utilized to detect external magnetic field. Hall magnetic field sensors are used extensively in many applications, such as positioning and controlling. Fields like medicine or industrial process control take advantage of Hall magnetic field sensors[1]. If the sensitivity of these sensors can be improved, they will be applied more and more, and the research in this field will be actively.

During the last years, many sensor proposals have been published[2-4]. In 2012, Leonid Dolgiy et al. designed and optimized a MOSFET Hall sensor on SOI structure. It shows that when the thickness of gate dielectric decreases from 50 nm to 30 nm, the electric characteristic of the structure improves[5]. In 2013, Jana Sentkerestiova et al. fabricated a metal Hall sensor based on copper. The experiment results show a good correspondence between sensitivities and theoretical values, and remained constant in ITER expected temperature range from 100-250°C[6]. In 2013, A Grose et al. manufactured Planar Hall effect sensors with subnanotesla resolution, have decreased the sensor 1/f noise drastically and improved its resolution at low frequencies[7].

In this paper, the Hall magnetic field sensor was made on <100> orientation silicon by using CMOS technology. And compare the magnetic sensitivity of Hall magnetic field sensor of concave and convex hall output.

Basic structure and working principle

Basic structure. Figure.1 (a), (b) show a plan view and a cross-sectional view of magnetic field sensor with concave Hall output probes, respectively. Figure.2 (a), (b) show a plan view and a cross-sectional view of magnetic field sensor with convex Hall output probes, respectively. Both of the magnetic field sensor contain the source (S), drain (D), gate (G) and the ohm-contact Hall output probes (V_{H1} and V_{H2}) on both sides of the channel. The channel width (W) of the magnetic field sensor is 80 μm. The length (L) are 160 μm, 320 μm and 480 μm, respectively. And the width (d) of the Hall output probes is 18 μm.

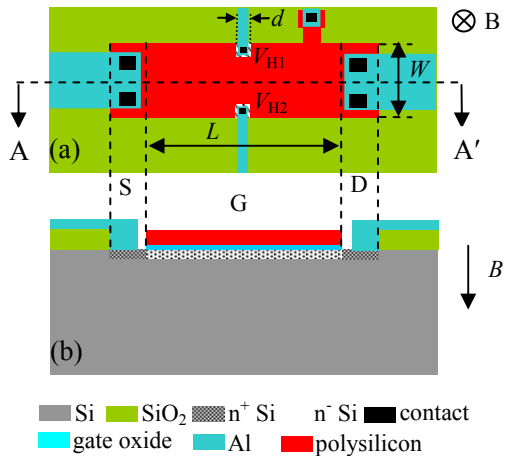


Figure 1 Basic structure of Hall magnetic field sensors with concave Hall output probes. (a) top-view (b) cross-section

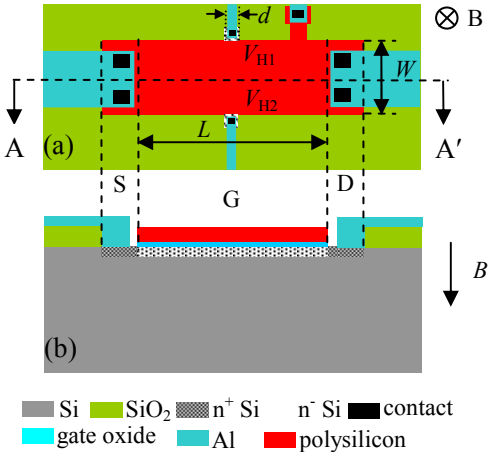


Figure 2 Basic structure of Hall magnetic field sensors with convex Hall output probes. (a) top-view (b) cross-section

Working principle. According to the working principle of MOSFET and Hall effect, the magnetic field sensor with convex Hall output probes is used as an example to show the working principle of magnetic field sensor[8]. As shown in Fig.3 (a), when external magnetic field B is 0 T, the channel carriers don't deflect and drain current equally distributed. Under ideal condition, the Hall output voltage (V_H) can be expressed as:

$$V_H = V_{H1} - V_{H2} = 0 . \quad (1)$$

Defined the magnetic field direction inward perpendicular to the paper as $B>0$ T, outward perpendicular to the paper as $B<0$ T. As shown in Fig.3 (b) and (c), when an external magnetic field $\boldsymbol{B}$ is applied perpendicularly to the magnetic field sensor channel layers, channel carriers will deflect due to the action of Lorentz force, and the V_H changes with the variation of external magnetic field $\boldsymbol{B}$. Taking the geometrical correction factor into account, the V_H is:

$$V_H = V_{H1} - V_{H2} = f_H \cdot \mu_n \cdot \frac{W}{L} \cdot V_{DS} \cdot B , \quad (2)$$

where f_H is a geometrical correction factor, V_{DS} is the drain-source voltage, μ_n is the electron mobility.

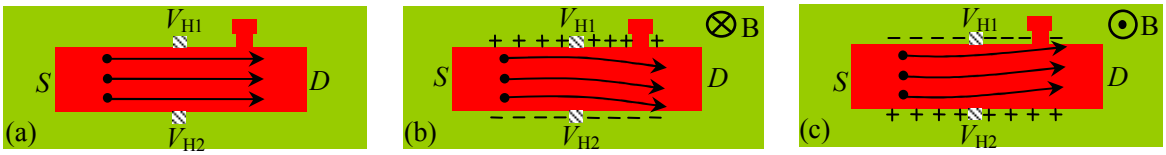


Figure 3 Working principle of Hall magnetic field sensors with concave Hall output probes. (a) B=0 T (b) B>0 T (c) B<0 T

Fabrication technology of the sensor chip

The Hall magnetic field sensor was fabricated on <100> silicon substrates with high resistivity by using CMOS technology. The main processing steps are shown in Figure.4, as follows: a) <100> orientation high resistivity silicon; b) growing SiO_2 layer on the top side of the silicon substrate by thermal oxidation, patterning SiO_2 layer by the first lithography to form active region; c) using an ion implantation machine to inject P type ions; d) growing SiO_2 layer (with thickness of 50 nm) to form gate oxide; e) depositing polysilicon by using low pressure chemical vapor deposition (LPCVD) system, patterning polysilicon layer by the second lithography to form polysilicon gate; using an ion implantation machine to form source, drain and Hall output probes by injecting P^+ type ions; f) patterning SiO_2 layer by the third lithography to form contact holes, evaporating Al on the top side and patterned it by the fourth lithography to create electrode geometry, metalizing at 420 ℃ for 30 min to achieve ohmic contacts of source, drain, Hall output probes and gate. Figure.5 (a), (b) show the photographs of concave and convex Hall output probes, respectively.

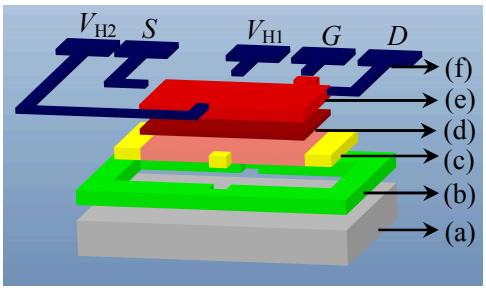


Figure 4 Fabrication technology process of the Hall magnetic field sensor.

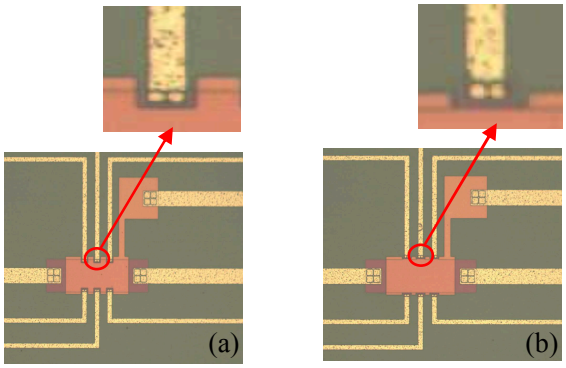


Figure 5 Chip photographs of the sensors.
(a) concave Hall output probes (b) convex Hall output probes

Experimental results and discussion

In this paper, the magnetic characteristics of the magnetic field sensors were measured at room temperature by magnetic field generator system (CH-100) and multimeter (Agilent 34401A), where the external magnetic field B ranges from 0 T to 0.6 T with the step of 50 mT, the supply voltage ranging from 0 V to 5.0 V with the step of 1.0 V.

Figure 6 (a), (b) and (c) show the input-output characteristic curves of the proposed sensor with concave Hall output probes, where the length-width ratios of channel are 160 μm/80 μm, 320 μm/80 μm and 480 μm/80 μm, respectively. The experiment results show that, the Hall output voltage increases linearly with external magnetic field when the supply voltage is fixed, and is proportional to supply voltage V_{DD} when the external magnetic field is constant. Under the same supplied voltage

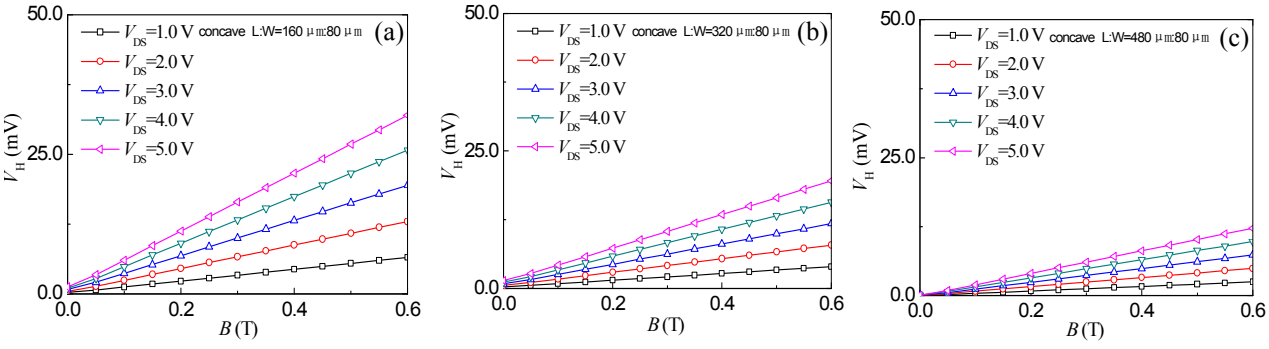


Figure 6 Input-output characteristic curves of the magnetic field sensor based on MOSFET with concave Hall output probes.
(a) L/W =160 μm/80 μm (b) L/W=320 μm/80 μm (c) L/W=480 μm/80 μm

and external magnetic field, the Hall output voltage decreases with the increasing of channel length. When drain-source voltage V_{DS}=5.0 V and channel length-width ratio is 160 μm/80 μm, the magnetic sensitivity is 53.3 mV/T.

Figure 7 (a), (b) and (c) show the input-output characteristic curves of the proposed sensor with convex Hall output probes, where the channel length-width ratios are 160 μm/80 μm, 320 μm/80 μm and 480 μm/80 μm, respectively. According to the experiment results, the Hall output voltage of the magnetic field sensors that changes with supply voltage, external magnetic field and channel sizes is the same as concave ones. But the Hall output voltage of the magnetic field sensor with convex Hall output probes is significantly higher than that of concave ones, when the supply voltage, external magnetic field, channel sizes and fabrication process are the same. When V_{DS}=5.0 V and channel length-width ratio is 160 μm/80 μm, the magnetic sensitivity is 76.8 mV/T. It shows that the magnetic sensitivity of the magnetic field sensor with convex Hall output probes is 1.44 times as the concave ones.

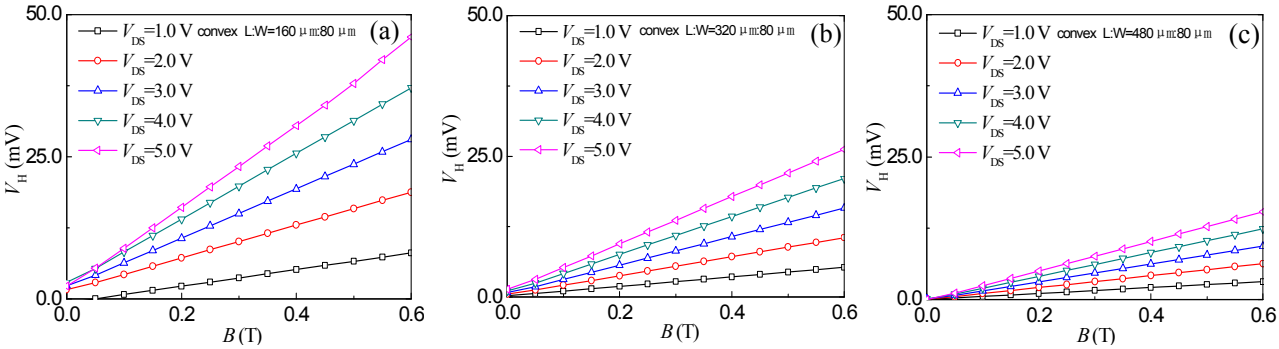


Figure 7 Input-output characteristic curves of the magnetic field sensor based on MOSFET with convex Hall output probes.
(a) L/W =160 μm/80 μm (b) L/W=320 μm/80 μm (c) L/W=480 μm/80 μm

Summary

A MOSFET magnetic field sensor with Hall output probes is proposed in this paper. The sensor chip was designed and fabricated on <100> silicon substrates with high resistivity by using CMOS technology. We studied the effects of Hall output probes shape and channel length on magnetic characterization of Hall magnetic field sensor. The experiment results show that, the magnetic sensitivity of the magnetic field sensor with convex Hall output probes is higher than that of concave ones, when the other conditions are the same. The magnetic sensitivity is reduced with the increasing of channel length when the channel width is constant. When the supplied voltage is 5.0 V and channel length-width ratio is 160 μm/80 μm, the magnetic sensitivity of the magnetic field sensor with convex Hall output probes can reach 76.8 mV/T. This conclusion will lay the foundation for the optimal design and application in 2-dimensional and 3-dimensional magnetic field of the MOSFET Hall magnetic field sensor.

Acknowledgements

This work is supported by the National Natural Science Foundation of China (Grant No. 61471159, 61006057), the China Postdoctoral Science Foundation (Grant No. 2013M530163), the Heilongjiang Province Natural Science Foundation of China (Grant No. F201433), the Special Funds for Science and Technology Innovation Talents of Harbin in China (Grant No. 2014RFQXJ007), the Modern Sensor Technology Innovation Team for College of Heilongjiang Province in China (Grant No.2012TD007).

References:

[1] Leonid Dolgiy, Ivan Lovshenko, Vladislav Nelayev, et al. Technology and device design and optimization for the MOSFET Hall sensor on SOI structure[C]. International Conference on Mixed Design of Integrated Circuits and Systems, 19 (2012),pp.398-400.
[2] Jana Sentkerestiova, Ivan Duran, Karel Kovarik, et al. Performance of metal Hall sensors based on copper[J]. Fusion Engineering and Design, 88 (2013),pp.1310-1314.
[3] A.Grosz, V.Mor, E.Paperno, S.Amrusi, et al. Planar Hall effect sensors with subnanotesla resolution[J]. IEEE Magnetic Letters, 4 (2013)6500104(1-4).
[4] Zhao Xiaofeng, Wen Dianzhong, Zhuang Cuicui, et al. High sensitivity magnetic field sensors based on nano-polysilicon thin-film transistors[J]. Chinese Physics Letters, 29 (2012)118501(1-4).
[5] Zhao Xiaofeng, Wen Dianzhong, Zhuang Cuicui, et al. Fabrication and characteristics of the magnetic field sensors based on nano-polysilicon thin-film transistors[J].Journal of Semiconductors, 34(2013)036001(1-6).
[6] Leonid Dolgiy, Ivan Lovshenko, Vladislav Nelayev, et al. Technology and Device Design and Optimization for the MOSFET Hall Sensor on SOI Structure[C]. International Conference on Mixed Design of Integrated Circuits and Systems, 19 (2012),pp.398-400.
[7] Jana Sentkerestiova, Ivan Duran, Karel Kovarik, et al. Performance of metal Hall sensors based on copper[J]. Fusion Engineering and Design, 88 (2013),pp.1310-1314.
[8] Zhao Xiaofeng, Wen Dianzhong, Lü Meiwei, et al. Fabrication and characterization of the MAGFET based on the nano-polysilicon thin-film transistors[J]. Journal of Semiconductors, 35(2014)094004(1-6).

Key Engineering Materials Vols 645-646 (2015) pp 600-604
Submitted: 2014-12-19
Accepted: 2014-12-23
© (2015) Trans Tech Publications, Switzerland
doi:10.4028/www.scientific.net/KEM.645-646.600

Chip-Level Active Temperature control for Improving Temperature Robust of a micro-gyroscope

Zhihua Chen[a], Lele Liu[b *], Dingbang Xiao[c], Hongjuan Cui, Xinghua Wang

College of Mechatronics Engineering and Automation, National University of Defense Technology, Changsha, Hunan, CHINA, 410073

[a]13873145827@163.com, [b]liullning@163.com, [c]dingbangxiao@nudts.edu.cn

Keywords: butterfly gyroscope.temperature control. zero-rate output.

Abstract. Silicon micro-fabricated gyroscope are very sensitive to ambient temperature, this paper conducted a novel active temperature controlling system. Combined with the PTC thermistor to detect internal temperature and the inserted TEC to control the temperature, encapsulation condition inside the gyroscope was kept in a stable situation. Experimental results showed that it greatly improved the performance of the micro-gyroscope.

Introduction

In many micro-electro-mechanical systems (MEMS), the ambient environment temperature variation and fluctuation are of great concern since they can directly affect the performance of these devices. Silicon micro-fabricated gyroscope, as a typical MEMS sensor, is widely used in various applications. However, they are very fragile and sensitive to ambient temperature. The resonant frequency, scale factor and zero drift caused by temperature fluctuation have become a big roadblock and barrier for manufacturing high precision gyroscopes. Lots of studies have been done to evaluate and decrease the influence of temperature on micro gyroscopes [1,2], including temperature compensation, thermal isolation, heater package, etc. However, these methods cannot basically solve the temperature problem and few attentions have been focused on the active controlling of the on-chip temperature of the micro gyroscopes by both heating and cooling.

Experimental work

In this abstract, we mainly proposed a novel active temperature control system for improving the temperature robustness of a micro-fabricated butterfly gyroscope which has been introduced in our previous work [3]. The schematic view of the control system is shown in Figure 1. The system consists of thermistor, temperature-control board and a Peltier thermo-electric cooler (TEC) module. Due to the system, thermal feedback from the package inside is compared to the set-point temperature, an instrumentation amplifier and a high precision integrator amplifier are supplied to create a PID controller to directly control the TEC by the H-bridge. If the temperature is deviated from the set-point temperature, Thermal feedback from the Thermistor is compared to the set-point voltage to generate the TEC current control signal. The temperature-control board controls TEC current to accurately regulate temperature. Stability of the temperature could be highly effectively controlled which can greatly improve the performance of the micro-gyroscope.

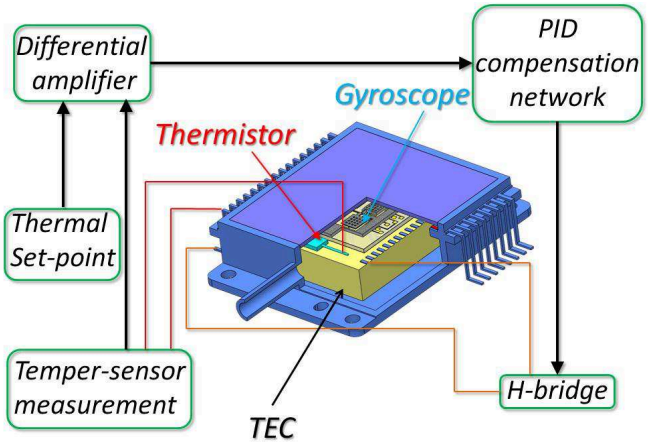


Figure 1. Schematic view of the temperature-control system

The resonant frequency of the drive mode changes with the temperature's variation, paper have shown that drive mode resonant frequency is proportional linearly to the temperature [4]. In order to validate this linearity, temperature experiments were performed using a temperature control chamber. The power supply, control signal and output signal were connected to the chamber. The temperature was raised up from -40°*C* to 60°*C* at 10°*C* intervals and each temperature point was maintained for 1h. The frequency responses of the drive mode were tested and recorded by a frequency response analyzer (NF FRA5087). As can be seen in Figure 2, the experiment result was recorded and the temperature coefficient of the resonance frequency (TCF) was linear fitted to be 67.5*ppm*/°*C*.

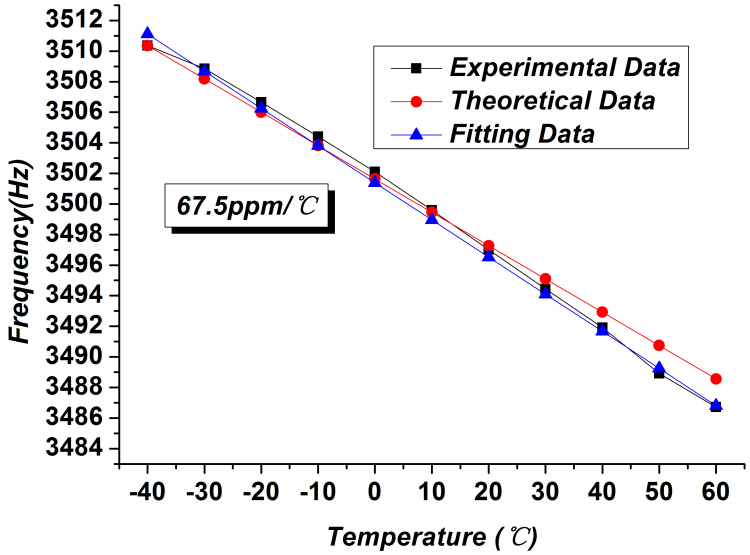


Figure 2. Temperature coefficients of the resonant frequency of the drive mode

Due to the manufacture imperfections and the electro-circuit error, the zero-rate output of the micro gyroscope is not basically zero. In order to evaluate the actual impacts of temperature on the micro-gyroscope, relevant experiments are carried out. The gyroscope's zero drift was measured under the same condition, and the zero-rate output of the gyroscope variation with the temperature was shown in the Figure 3, which indicates that zero drift of the gyroscope changes 58.48*mV* varieties with the temperature.

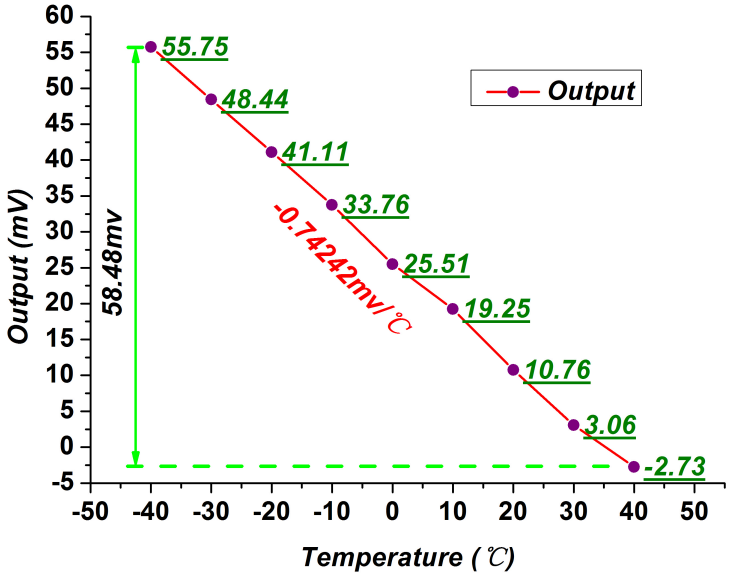


Figure 3. Trend of zero output change with temperature

Experimental result

When the temperature-control loop was constructed, test without the gyroscope has been implemented. By means of the Labview multi-channel data acquisition card, test results were shown in Figure 4 that set-point voltage (equivalent temperature) was set in 0.769V (or 40°C) while the actual tracing output are nearly between 0.7691V~0.7692V (or 0.01°C).

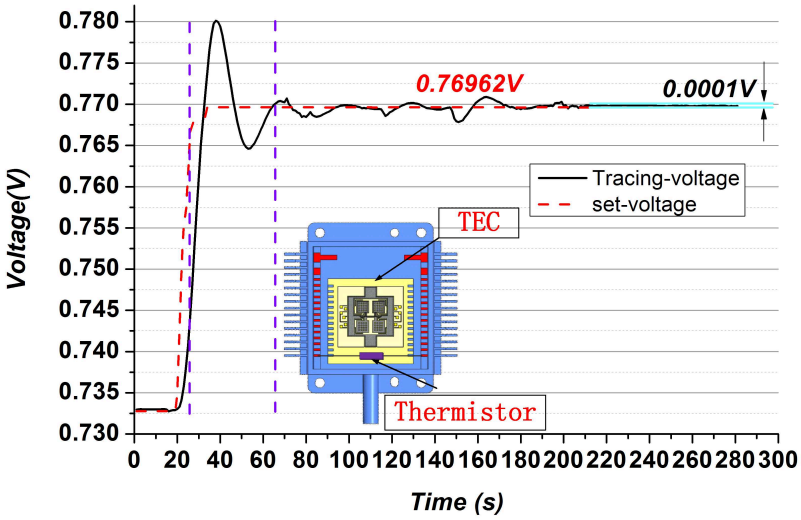


Figure 4. Ability of the temperature-control system

After the test, the drive frequency and the zero-rate output drift were monitored when the temperature increased from −40°C to 60°C at 10°C intervals. And the measured results was shown in Figure 5, due to the active temperature controlling system, the changing trends of gyroscope's resonant frequency with temperature has been reduced to 2.49ppm/°C from 67.5ppm/°C. While the bias variation of the micro-gyroscope with temperature-controlling decreased to 36.27mV in Figure 6. The experiment results indicated that this chip level integrated active system for gyroscope could effectively improve the micro-gyroscope's performance under the severe ambient environment temperature changes.

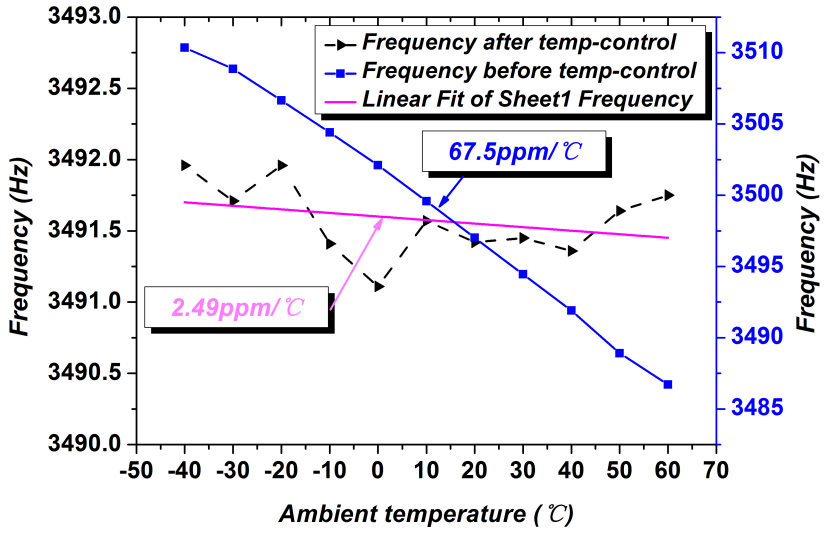


Figure 5. Comparison of the drive mode frequency after tem-control

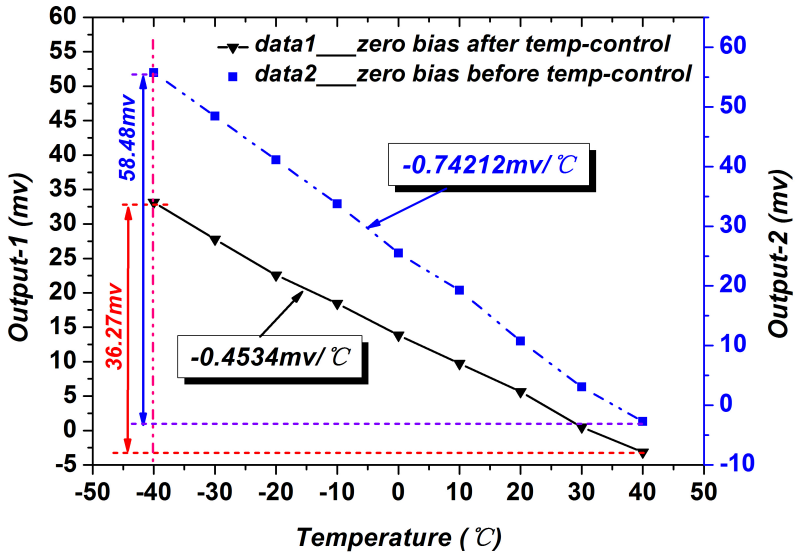


Figure 6. Comparison of the zero bias after tem-control

Summary

In this work, a novel active temperature control system for improving the temperature robustness of a micro-fabricated butterfly gyroscope is presented. The resonant frequency of the drive mode and the zero-rate output of the micro gyroscope are both changed with the temperature's variation. When the temperature increased from $-40°C$ to $60°C$ at $10°C$ intervals, with the effect of the active temperature control system, the changing trends of gyroscope's resonant frequency with temperature has been reduced to $2.49ppm/°C$ from $67.5ppm/°C$, while the bias variation of the micro-gyroscope with temperature-controlling decreased to $36.27mV$ from $58.48mV$. The demonstrated active temperature-control system may provide a path for Silicon micro-fabricated gyroscope to operate in stability. The experiment results indicated that this chip level integrated active system for gyroscope could effectively improve the micro-gyroscope's performance under the severe ambient environment temperature changes

Acknowledgement

The work described in this paper was carried out at the Microsystem Laboratory, College of Mechanical Engineering and Automation, National University of Defense Technology. The authors are grateful to Qiang Xu, Xuanhui Meng, Zhanqiang Hou, Qingsong Li and Shijie Cao for their help in device design, fabrication, analysis and test. The authors especially thank Jing Yang for the device encapsulation.

References

[1] Xia. D, Chen. S, Wang. S, Li. H, Microgyroscope Temperature Effects and Compensation-Control Methods, Sensors, 9 (2009), 8349-8376.

[2] S.-H. Lee, S. W. Lee, and K. Najafi. A Generic Environment-Resistant Packaging Technology for MEMS, the 14th international conference on solid-state sensors, actuators and microsystems, Lyon, France, June 10-14, 2007.

[3] Xiao Dingbang, A Study on Key Technologies of a Novel Butterfly Micromachined Gyroscope, [D] National University of Defense Technology, Changsha, 2009.

[4] Man Haiou, Xiao Dingbang, Research on Temperature Characteristic of Mode Frequency of Silicon Micro-Gyroscope, CHINESE JOURNAL OF SENSORS AND ACTUATORS, 22 (2009), 1117-1121.

Key Engineering Materials Vols 645-646 (2015) pp 605-609
© (2015) Trans Tech Publications, Switzerland
doi:10.4028/www.scientific.net/KEM.645-646.605

Submitted: 2014-12-19
Accepted: 2014-12-23

A 16 Bits 500 kHz Sigma-Delta DAC for Silicon Micro Gyroscope

Zhao Yingkai[1], Yin Liang[1,2,a], Liu Zhaotong[1], Chen Weiping[1,2],Liu Xiaowei[1,2]

[1]MEMS Center, Harbin Institute of Technology, Harbin, Heilongjiang, China
[2] Key Laboratory of Micro-Systems and Micro-Structures Manufacturing, Ministry of Education, China
[a]yinliang2003@126.com

Keywords: Silicon Gyroscope, Interface Circuit, Sigma-Delta, DAC

Abstract. In this paper, a 16 Bits 500 kHz Sigma-Delta DAC for Silicon Micro Gyroscope is proposedin order to enhance the precision of the digital to analog converter level.The interpolation filterhas achieved 64 times interpolation function,using three cascaded manner, it employs three level cascaded of FIR filterstructure. It achieves a 64 times oversampling feature. The signalbandwidth of the designs interpolation filter is 100 kHz, SNR reach 106dB. Fifth -order single-loop structure CIFB achieve noise shaping modulator function to verify the stability of the system, after the completion of CSD coefficient coding, signal to noise ratio reached 119.7dB, effective bits reached 19.59. The switched capacitor technology actualize analog reconstruction filter module, and using a typically switched capacitor DAC achieved high jump "0, 1" digital signal is converted into an analog signal, the digital-analog conversion achieved.

1 Introduction

MEMS micro-machined gyroscope has been widely used in the field of aerospace, automotive, military equipment and electronic products for its advantages of integration, miniaturization, intelligent, low power consumption,high reliability, etc[1]. Technologically advanced human societies require specialized tools and equipment to enable their diverse and mobile activities, which means the increasingly high requirements for the performance, size andportable degrees of gyroscope. Therefore, further digitization of silicon micro-machined gyroscope becomes extremely important, which can significantly improve its performance[2].

In silicon gyroscope interface circuit, the precision of the digital to analog converter level has a significant influence on system performance[3]. This topic mainly aimed at the research of silicon gyroscope DAC interface circuit,a16 bits 500 KHz Sigma-Delta (ΣΔ) DAC for silicon micro gyroscope is proposed. Including three important module of interpolation filter, the sigma-delta modulator,and low DAC analog reconstruction filter.

2 SIGMA DELTA DAC Overall Design In Silicon Gyroscope

The inertial sensor readout circuit is often an open-loop circuit in the past, It needs in terms of resolution and better performance, lower sensitivity of temperature and vibration of the object in the future market[4]. Temperature has a great influence on the quality factor of the sensor, therefore, it also have a great influence on the dynamic properties of sensitive factors.

Oversampling D/A converter consists of four modules, including up-sampling filter, delta-sigma modulator structure, a bit DAC and switched-capacitor filters. Its block diagram shown in Figure 1:

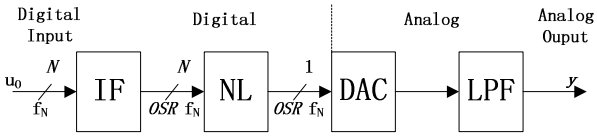


Fig.1Sigma-Delta DAC block diagram

In order to meet Nyquist sampling theorem, input signal u0 thatthe sampling rate is f_N, N-bit digital signal. After sampling filter modulethe input signal u0 digits unchanged, but oversampling rate increases, and improves the OSR times, and the sampling filter system also has a feature that can filter out most of the the band signals, avoids entering noise shaping loop. After increasing the sampling rate of the digital signal, flowinginto delta-sigma modulator, the signal is truncated word length, the number of bits from the N-bit transformed into one, but the signal to noise ratio will not change significantly, the sampling rate of the signal unchanged. DAC is within the 1 bitDAC, which converts the digital signal into an analog signal. Analog signalfilter out unwanted noise bandthrough an analog low-pass filter (LPF) module, and reconstructed analog signal.

3 Designing of Interpolation Filter

The interpolation filter is a vital part ofdelta-sigmaDAC, which is located in the front of the system, which is provide data tosigma-delta modulator[5]. It has two main effects. Firstly, improving the oversampling ratio, noise shaping function to achieve, secondly, interpolation points of filtered signal are on the image, thereby reducing noise entering the shapingloop band noise[6].

Enter oversampling modulator signal is sampled 64 times over a digital signal, so we use three series ofFIR filter to achieve interpolation digital filter. The first stage is relatively steep transition, preferably linearity half-band filter, to achieve two times interpolation function. The first stage of the half-band filter for the performance of the digital interpolation filter plays a decisive role, to more than a degree in design parameters. Half of half-band filter coefficient is 0 and the coefficient symmetry, so only half-band filter coefficients can take a little more appropriate, in order to improve the filter transition length, passband ripple, stopband attenuation performance, but nota substantial impact on the hardware resources ; the second stage is 1/4 band filter, to achieve four times the interpolation function. This filterstage does not require a large number of coefficients that can ensure the accuracy of the interpolation filter because of the front half band filter substantially determines the performance of the filter,which is also relatively easy to control the hardware resources; the third stage is 8 times sample and hold circuit which using the clock frequency to achieve the interpolation function, having simple structure, and the hardware resource consumption will be lower.

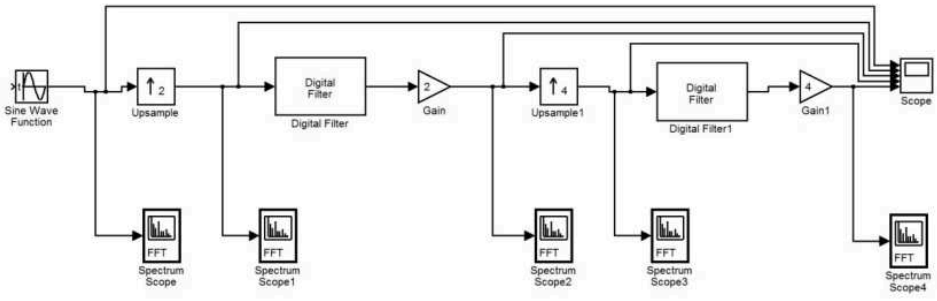


Fig.2The model of the interpolation filter

System validation is to test the performance of the filter and the filter performances parameters are quantified weathersatisfy the design requirements. Specific model interpolation filter shown in Figure 2, wherein the*upsample* module is inserted two adjacent zero data signals; *filter* in front of the filter is designed to use this tool FDAtool filter coefficients quantized parameter is not floating point type coefficient; sine wave is a signal source. As shown in Figure 3can be seen that the interpolation filter model achieved a data interpolation function by observing the output signal waveform scope window, the waveform is gentle, which is satisfied the design requirements.

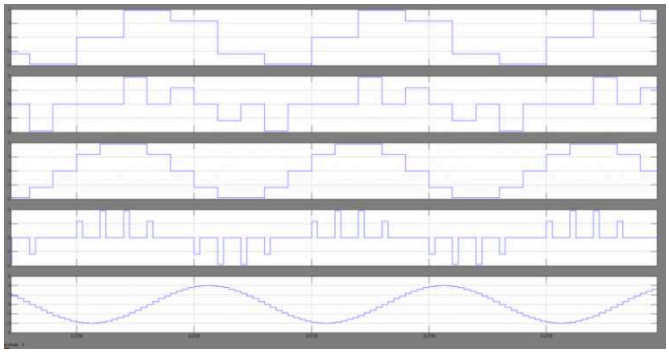


Fig.3The simulation frequency of the symmetrical folded system

In this Pape, filter uses three cascaded manner, detailed description on the design processfor each level of the FIR filter. The first stage uses a half-band filter to achieve twotimes interpolation function,designed a 58-order half-band filterthrough FDAtool tool, because the first stage filter plays a decisive rolefor digital interpolation filter , so stay in the parameters of the design more than a certain degree. The second stage uses a 1/4 band filter to achieve four times interpolation function, designed a 33-order interpolation filter. Finally, one for the sample and hold circuit, using the clock frequency to achieve 8x interpolation function. CSD filter coefficients coding circuit to saves resources and facilitate hardware implementation.

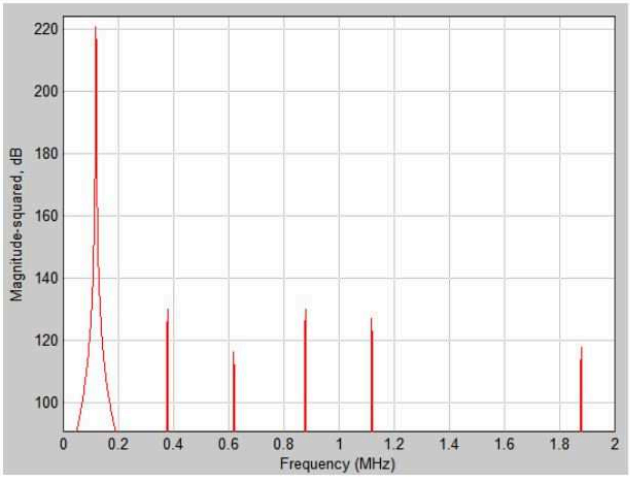


Fig.4 Symmetrical folding system 100 KHZ simulation spectrum

Use simulink simulation, verification filters meet the design requirements, sampling fold symmetrical structure of the simulation system, saving the number using the multiplier. Design 64 times oversampling interpolation filter signal bandwidth is 100KHz, SNR reach 106dB, which is meet the needs of digital silicon gyroscope.

4 The Modulator Design of SIGMA-DELTA

This paper uses CIFB (Cascade of Integrators, Feedback form) framework to design the5-order sigma-delta modulator, and this is obtained using the Matlab function of the signal transmission system STF, the noise transfer function NTF, SNR, and the correlation coefficient[7]. After 5 NTF order to simplify the derivation j CIFB sigma-delta modulator system framework shown in Figure 4-3, find the signal transfer function and the noise transfer function STF get:

$$NTF=\frac{V}{E}=\frac{(z-1)^5}{(z-1)^5+(z-1)^4 c_5a_5+(z-1)^3 c_5c_4a_4+(z-1)^2 c_5c_4c_3a_3+(z-1)c_5c_4c_3c_2a_2+(z-1)^4 c_5c_4c_3c_2c_1a_1} \quad (1)$$

Curing parameters on CIFB chart, gets the system model for system simulation in simulink,

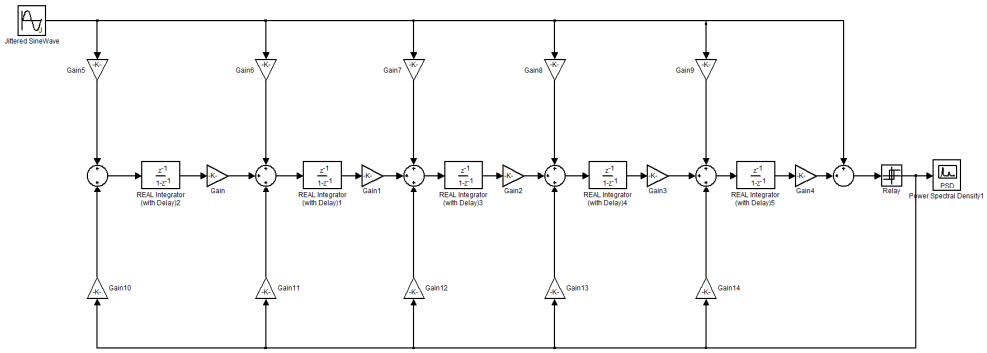


Fig5. The hardware modules of fifth -order structure CIFBmodulator

Which simulink hardware module shown in Figure 4-6, the power spectral density of the simulation results shown in Figure 4-10: modulator SNR 119.7dB, effective number of bits ENOB is 19.59bits, considering that many irrational factors, effective for 16 bits is adequate to meet the requirements of the silicon gyroscope interface circuit.

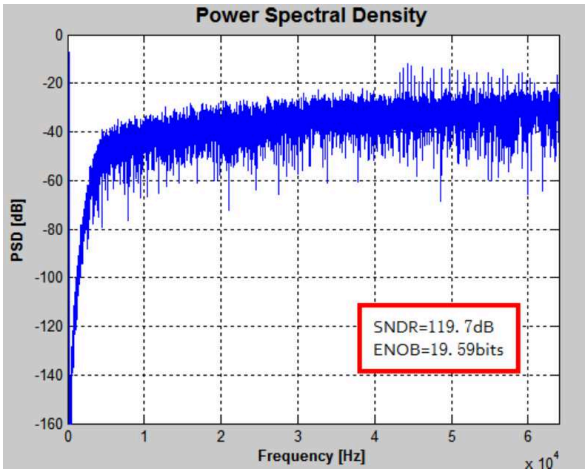


Fig6. The modulator output power spectral density

In determining the modulator parameters, selects the oversampling rate of 64 fifth-order noise shaping CIFB structure to achieve the function, and then CIFB modulator structure specific analysis derived NTF and STF relation. With these foundations after conducted in matlab specific design, the use of sigma-delta modulator dedicated software package that implements a silicon gyroscope to meet the digital interface circuit DAC modulator module, and decodingCSD for the coefficientmodulator, which is convenient for hardware implementation of follow-up and FPGA verification. Facilitate subsequent FPGA hardware implementation and verification. Simulation, the modulator in simulink SNR 119.7dB, effective number of bits reached 19.59bits, better meet the needs of the system.

5 Conclusion

A 16 Bits 500 kHz Sigma-Delta DAC for Silicon Micro Gyroscope is proposed in this paper.The entire circuits are implemented with 0.5μm CMOS process. The interpolation filter has achieved 64 times interpolation function, using three cascaded manner, it employs three level cascaded of FIR filter structure. It achieves a 64 times oversampling feature. The signal bandwidth of the designs interpolation filter is 100 kHz, SNR reach 106 dB. Fifth -order single-loop structure CIFB achieve noise shaping modulator function to verify the stability of the system, after the

completion of CSD coefficient coding, signal to noise ratio reached 119.7dB, effective bits reached 19.59.

Acknowledgment

1. This work is supported by "The Fundamental Research Funds for the Central Universities"(Great No.HIT.NSRIF.2013 040)

2. This work is supported by "National Basic Research Program of China"， (No. 2012CB934104)

References

[1] E. Mounier and J. Baron. Changes in the way MEMS are Manufactured are Primarily being Driven by Volume Consumer MEMS Markets. Solid State Technology Mag., Vol. 55, Issue 6, July 2012.

[2] J. Shah, H. Johari, A. Sharma, et al. CMOS ASIC for MHz Silicon BAW Gyroscope. Circuits and Systems, vol. 8, 2008: 2458-2461

[3] I. Fujimori, T. Sugimoto. A1.5 V,4.1mW Dual-channel Audio Delta-sigma D/A Converter. IEEE Journal of Solid-State Circuits, 1998.33(12):1863-1870.

[4] S. Bandyopadhyay and A. P. Chandrakasan. Platform Architecture for Solar, Thermal, and Vibration Energy Combining with MEMS and Single Inductor. Solid-State Circuits, IEEE Journal, Vol. 47, Issue 9. Sept. 2012: 2199-2215.

[5] J. W. Weigold, K. Najifi, S. W. Pang. Design and Fabrication of Sub micrometer, Single Crystal Si Accelerometer. IEEE Journal of Micro electro mechanical Systems, 2001, 10(4): 518-524

[6] Robert H. Walden. Analog-to-Digital Converter Survey and Analysis. Journal on Selected Areas in Communications, vol. 17, 1999: 164-176.

[7] A. Kulygin, C. Kirsch, P. Schwarz, et al. Decoupled surface micro-machined gyroscope with single-point suspension. Journal of micro-electro-mechnical system. 21(1), 2012.02:206-216.

Key Engineering Materials Vols 645-646 (2015) pp 610-615
© (2015) Trans Tech Publications, Switzerland
doi:10.4028/www.scientific.net/KEM.645-646.610

Submitted: 2014-12-21
Accepted: 2014-12-29

An Integrated Pressure and Magnetic Field Sensor Based on Piezoresistance Effect

Tong Wu[1,a], Xiaofeng Zhao[1,2,b], Xianghong Yang[1], Dianzhong Wen[1,c], and Gang Li[1]

[1]Key Laboratory of Electronics Engineering, College of Heilongjiang Province, Heilongjiang University, Harbin, China

[2]The 49th Research Institute of China Electronics Technology Group Corporation, Harbin, China

[a]wutong890929@126.com, [b]zhaoxiaofeng@hlju.edu.cn(corresponding author), [c]wendianzhong@hlju.edu.cn

Keywords: integrated sensor; pressure sensor; magnetic field sensor; piezoresistance effect; MEMS technology.

Abstract. An integrated pressure and magnetic field sensor based on piezoresistance effect is proposed in this paper. The integrated sensor is composed of a C-type silicon cup, ferromagnetic material and Wheatstone bridge constructed by four metal oxide semiconductor field effect transistors (MOSFETs) channel resistances as piezoresistances. Based on the piezoresistance effect of channel resistances, the measurement to the external pressure ***P*** and magnetic field ***B*** can be achieved by the sensor. Through using complementary metal oxide semiconductor (CMOS) technology and microelectromechnical system (MEMS) technology, the sensor chip was designed and fabricated on <100> orientation silicon substrates, locating the ferromagnetic material on its squared silicon membrane center. The experimental results show that when supply voltage of the sensor is 2.0 V, the pressure sensitivity of sensor is 0.39 mV/kPa (***B***=0 T), and the magnetic field sensitivity of sensor is 1.48 mV/T (***P***=0 kPa).

Introduction

In 1954, C.S.Smith proposed piezoresistive effect in germanium and silicon[1]. Since then, the piezoresistive effect has been widely used in the information technology industry. In 1988, Henry P.Baltes et al. reported integrated semiconductor magnetic field sensors which reviewed a variety of integrated semiconductor magnetic field sensors and described the development of integrated sensors based on piezoresistive effect[2]. Presently, integrated sensors are being increasingly developed for a variety of applications by integrating sensitive elements on the same semiconductor chip. For instance, Ch. Roumenin et al. designed and fabricated a new type of multi-sensors for magnetic field and temperature based on the diode Hall effect in 2000, which can achieve simultaneous and independent measurement to the strength and the direction of magnetic field and temperature[3]. In 2007, Liu Jian et al. reported detailed design and study of a piezoresisive microcantilever magnetic field sensor with on-chip self-calibration function integrated, resulting in the piezoresistive sensitivity as 1.06×10^{-4}/mT[4]. In 2010, Z. Xu et al. designed a dual mode humidity and pressure MEMS sensor with an integrated temperature function[5]. In 2013, Clifton L.Roozeboom et al. designed and fabricated an integrated multifunctional environmental sensor, which can achieve simultaneous monitoring of ten multiple environmental parameters on one silicon chip[6].

In order to realize the measurement to the sensitive characteristics of external pressure and magnetic field, an integrated pressure and magnetic field sensor based on the piezoresistance effect is presented in this paper, where Wheatstone bridge constructed by four p-MOSFETs is used as the sensing element of sensor. Through CMOS technology and MEMS technology, the sensor chip is fabricated. For the further development of sensor, the influence of external pressure and magnetic field on the characteristics of sensor is studied.

Basic structure and operating principle

Basic Structure. Figure 1 shows the basic structure of integrated sensor consisted of a C-type silicon cup, ferromagnetic material and Wheatstone bridge[7,8]. The Wheatstone bridge composed of four MOSFET channel resistances (R_1, R_2, R_3 and R_4) locating on the every edge center of squared silicon membrane is used as an insensitive element of sensor, and the MOSFET channel resistances locating on the regions of maximum stresses are used as piezoresistances. Ferromagnetic material is adhered to the backside of surface center of squared silicon membrane by adhesive.

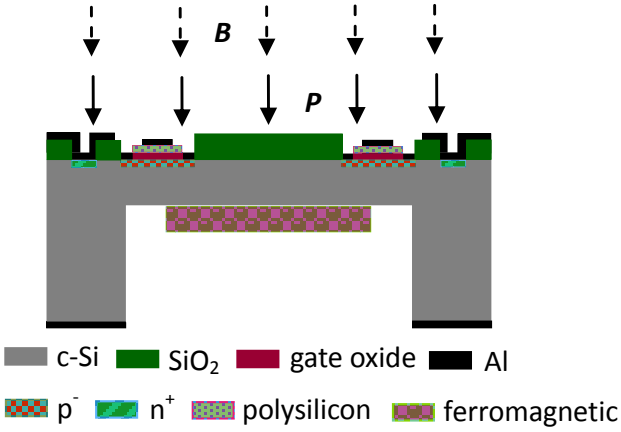


Fig. 1: Basic structure of the integrated pressure and magnetic field sensor.

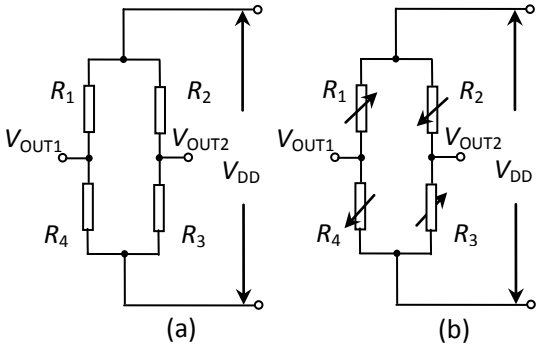


Fig. 2: Equivalent circuit of the integrated pressure and magnetic field sensor: (a) ***B***=0 T and ***P***=0 kPa (b) ***B***≠0 T or ***P***≠0 kPa

Operating principle. The equivalent circuit of the proposed sensor is shown in Fig.2. As shown in Fig.2(a), when external pressure ***P***=0 kPa and additional magnetic field ***B***=0 T, under ideal conditions, $R_1 = R_2 = R_3 = R_4$, the output voltage (V_{OUT}) of the Wheatstone bridge is zero. It can be expressed as:

$$V_{\mathrm{OUT}} = V_{\mathrm{OUT2}} - V_{\mathrm{OUT1}} = 0, \tag{1}$$

As shown in Fig.2(b), when external pressure ***P***≠0 kPa and additional magnetic field ***B***=0 T, the silicon membrane is bended by the action of the external pressure ***P*** and four channel resistances change. The V_{OUT} of the Wheatstone bridge changes with the external pressure ***P***:

$$V_{\mathrm{OUT}} = V_{\mathrm{OUT2}} - V_{\mathrm{OUT1}} = \frac{\Delta R}{R_0} V_{\mathrm{DD}}, \tag{2}$$

where R_0 is channel resistance of the MOSFET at ***P***=0 kPa and ***B***=0 T, ΔR is the variation of channel resistance at ***P***≠0 kPa and ***B***=0 T. The measurement of external pressure can be achieved.

When external pressure ***P***=0 kPa and additional magnetic field ***B***≠0 T, the magnetic force induced by the interaction between the ferromagnetic material and the additional magnetic field ***B***, can cause the bend of the silicon membrane and the changes of R_1, R_2, R_3 and R_4. The magnetic force ***F*** is[9,10]:

$$F = \frac{1}{2\mu_0} B^2 S, \tag{3}$$

where μ_0 is the permeability of free space, $\mu_0 = 4\pi \times 10^{-7}\mathrm{N/A}^2$ and S is the interaction area between the additional magnetic field and the ferromagnetic material. The V_{OUT} of the Wheatstone bridge

changes due to additional magnetic field, and can be expressed as equation (2), where ΔR is the variation of the channel resistance at $\boldsymbol{P}$=0 kPa and $\boldsymbol{B}\neq 0$ T. The measurement of additional magnetic field can be realized.

Fabrication technology

The proposed integrated sensor was fabricated on <100> orientation n-type silicon wafers with high resistivity by CMOS technology and MEMS technology. The main fabrication process of the sensor is shown in Fig.3: (a) the <100> orientation n-type silicon substrates with high resistivity (ρ>2000 Ω ·cm) were prepared; (b) first oxidation, growing SiO_2 layer; (c) first lithography, etching SiO_2 layer to form active region windows and using an ion implantation machine to inject boron ions; (d) second oxidation, growing gate SiO_2 layer and polysilicon thin films by low pressure chemical vapor deposition (LPCVD); (e) second lithography, etching polysilicon thin films to form gate electrode; (f) third lithography to form contact hole openings and injecting phosphorus ions to form n-type doping region; (g) growing aluminum eletrodes, etching aluminum, metalizing at 420 °C for 30 min to achieve ohmic contacts of source (S), drain (D) and gate (G); (h) fourth lithography, etching aluminum to form C-type cup window; (i) fifth lithography, inductively coupled plasma (ICP) deep etching the backside of the silicon wafer to realize silicon membrane; (j) fabricating ferromagnetic material on the center of C-type silicon cup backside. Figure 4 shows the packaging photograph of integrated pressure and magnetic field sensor chip.

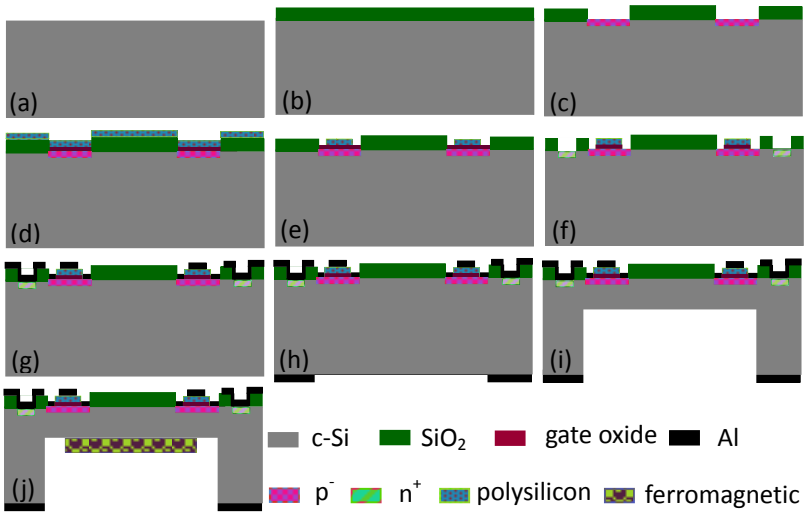


Fig. 3: Fabrication technology process of the integrated pressure and magnetic field sensor.

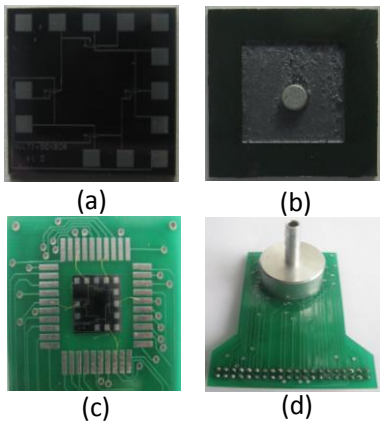


Fig. 4: The photograph of the integrated pressure and magnetic field sensor. (a) top-view (b) back-view (c) bonding chip (d) packaging chip with tube socket

Results and Discussion

At room temperature, the characteristics of the integrated pressure and magnetic field sensors were measured by using multi-meter (Agilent 34401A), power supply (RIGOL DP832A), magnetic field generator (CH-100) and pressure calibration system (FLUKE 719 100G).

The external pressure $\boldsymbol{P}$ ranged from 0 kPa to 20 kPa with a pressure step of 2 kPa, and the experiments were repeated for three time cycles. Figure 5 shows the input-output characteristics fitting beelines and experimental curves of the pressure sensor. As shown in Fig.5, it is observed that V_{OUT} of

the pressure sensor increases with external pressure ***P***. When the supply voltage is 2.0 V, the full range (20 kPa) V_{OUT} is 8.05 mV, the linearity of the pressure sensor is 4.20% F.S., the pressure sensitivity of integrated sensor is 0.39 mV/kPa. Figure 6 and Figure 7 show the repeatability experimental curves and the hysteresis experimental curves of the pressure sensor, respectively. When the supply voltage is 2.0 V, the repeatability of the pressure sensor is 2.04% F.S. and the hysteresis of the pressure sensor is 2.14% F.S..

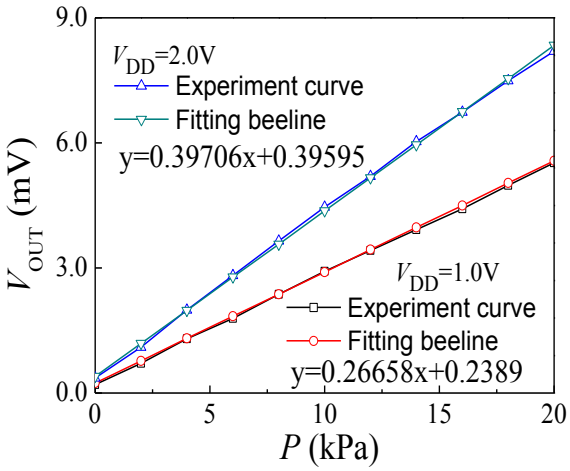


Fig. 5: Input-output characteristics fitting beelines and experimental curves of the pressure sensor.

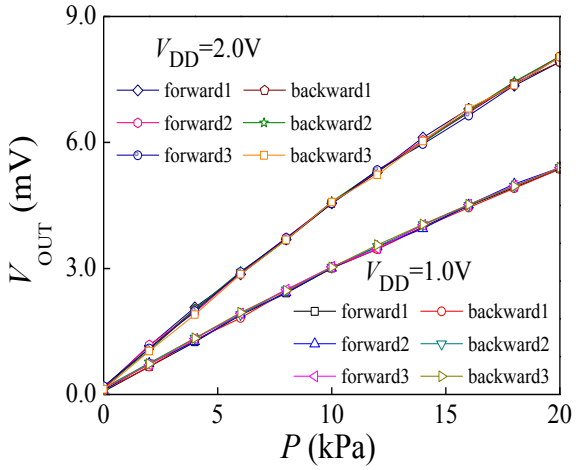


Fig. 6: Repeatability experimental curves of the pressure sensor.

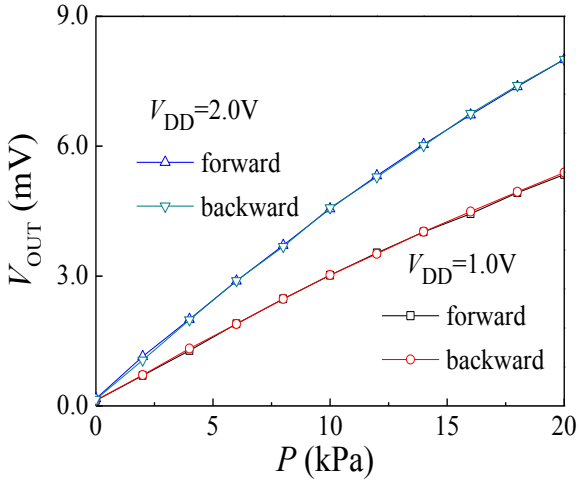


Fig. 7: Hystereses experimental curves of the pressure sensor.

The additional magnetic field ***B*** ranged from 0 mT to 600 mT with a magnetic field step of 50 mT, and the experiments were repeated for three time cycles. Figure 8 shows the input-output characteristics fitting beelines and experimental curves of the magnetic field sensor. As shown in Fig.8, it is observed that V_{OUT} of the magnetic field sensor increases with additional magnetic field ***B***. When the supply voltage is 2.0 V, the linearity of the magnetic field sensor is 1.27% F.S., the full range (600 mT) V_{OUT} is 2.49 mV, the magnetic sensitivity of integrated sensor is 1.48 mV/T. Figure 9 and Figure 10 show the repeatability experimental curves and the hysteresis experimental curves of the magnetic field sensor, respectively. When the supply voltage is 2.0 V, the repeatability of the magnetic field sensor is 13.80% F.S. and the hysteresis of the magnetic field sensor is 7.11% F.S..

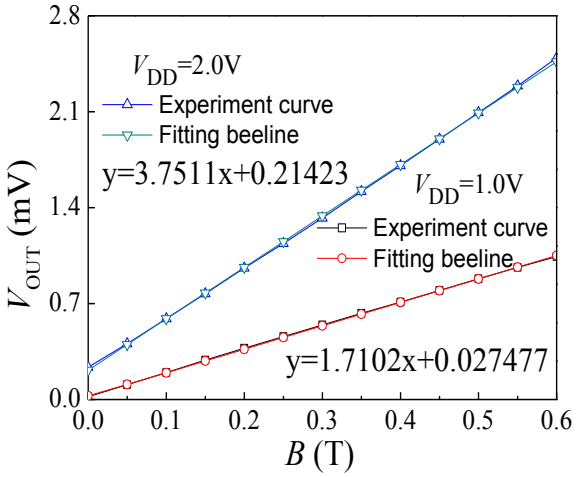


Fig. 8: Input-output characteristics fitting beelines and experimental curves of the magnetic field sensor.

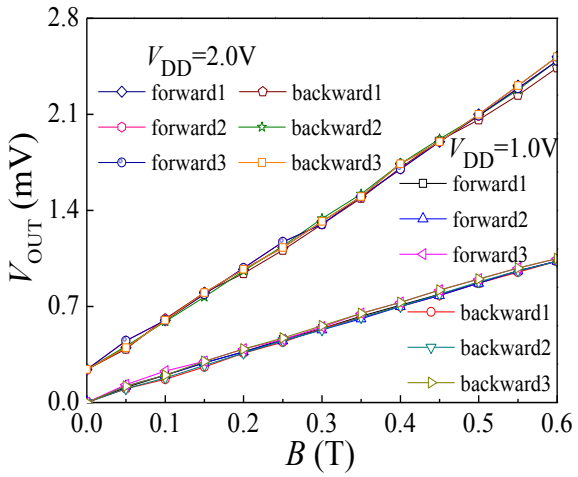


Fig. 9: Repeatability experimental curves of the magnetic field sensor.

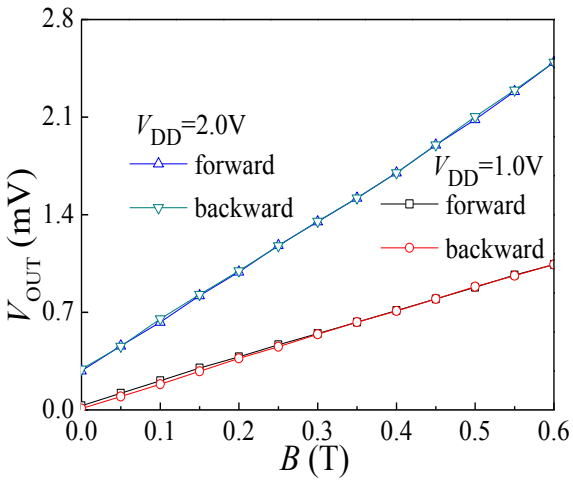


Fig. 10: Hystereses experimental curves of the magnetic field sensor.

Conclusion

Based on piezoresistive effect, through analyzing the influence of external pressure ***P*** and additional magnetic field ***B*** on the elastic deformation of square silicon membrane, the MOSFETs channel resistances were adopted as piezoresisitances, where the four MOSFETs were placed on C-type cup surface to form Wheatstone bridge. The results of theoretical analysis show that the proposed sensor can realize the measurement to the external pressure ***P*** and additional magnetic field ***B***. Based on that, the sensor chip was designed and fabricated on <100> direction silicon wafers by CMOS technology and MEMS technology in this paper. Through researching the sensitivity characteristics of sensor, the experiment results indicate that the proposed sensor can not only achieve the measurement of external pressure ***P*** (***B***=0 T) and additional magnetic field ***B*** (***P***=0 kPa) but also give a preferable characteristics, it is important to the integration research of pressure and magnetic field sensor.

Acknowledgements

This work is supported by the National Natural Science Foundation of China (Grant No. 61471159, 61006057), the China Postdoctoral Science Foundation (Grant No. 2013M530163), the Heilongjiang

Province Natural Science Foundation of China (Grant No. F201433), the Special Funds for Science and Technology Innovation Talents of Harbin in China (Grant No. 2014RFQXJ007), the Modern Sensor Technology Innovation Team for College of Heilongjiang Province in China (Grant No. 2012TD007), the Postgraduate Innovation Project of Heilongjiang University in China (Grant No. YJSCX2014-023HLJU).

References

[1] C.S.Smith. Piezoresistance effect in germanium and silicon [J]. Physics Review. Vol. 94 (1954), p. 42-49.

[2] S. Kordić. Integrated silicon magnetic-field sensors [J]. Sensors and Actuators A. Vol. 10 (1986), p.347-378.

[3] Ch. Roumenin, A. Ivanov, P. Nikolova. A new class of multisensors for magnetic field and temperature based on the diode Hall effect [J]. Sensors and Actuators A. Vol.85 (2000), p.163-168.

[4] Liu Jian, Li Xinxin. A piezoresistive microcantilever magnetic field sensor with on-chip self-calibration function integrated [J]. Microelectronics Journal. Vol.38 (2007), p.210-215.

[5] Z. Xu, D. Koltsov, A. Richardson, et al. Design and simulation of a multi-function MEMS sensor for health and usage monitoring [C]. 2010 Prognostics & System Health Management Conference.2010, p.1-7.

[6] C.L. Roozeboom, M.A. Hopcroft, W. S. Smith, et al. Integrated multifunctional environmental sensors [J]. Journal of Microelectromechanical Systems. Vol.22 (2013), p.779-793.

[7] Zhao Xiaofeng, Wen Dianzhong, Li Gang. Fabrication and characteristics of an nc-Si/c-Si heterojunction MOSFETs pressure sensor [J]. Sensors. Vol.12 (2012), p.6369-6379.

[8] Zhao Xiaofeng, Wu Tong, Cao Jingya, et al. Fabrication and characteristics of silicon bridge magnetic sensor based on nano-polysilicon TFTs [J]. Key Engineering Materials. Vol.609-610 (2014), p.1100-1105.

[9] Du Guangtao, Chen Xiangdong, Lin Qibin, et al. MEMS magnetic field sensor based on silicon bridge structure [J]. Journal of Semiconductors. Vol. 31 (2010), p.104011(1-6).

[10] Du Guangtao, Chen Xiangdong, Lin Qibin. Micromechanical magnetic sensor based on cylindrical ferromagnets [J]. IEEE Sensors Journal. Vol.11 (2011), p.2973-2979.

Key Engineering Materials Vols 645-646 (2015) pp 616-623
© (2015) Trans Tech Publications, Switzerland
doi:10.4028/www.scientific.net/KEM.645-646.616

Submitted: 2014-12-25
Accepted: 2014-12-31

The SOI micro-accelerometer fabricated by sacrificial process

Zhaoyun Zhang[1,2,a], Wei Su[1,2,b], Zhigui Shi[1,2,c], Bin Tang[1,2,d], Zhuang Xiong[1,2,e],Yinhui Chen[1,2,f]and Bo Peng[1,2,g *]

[1] Institute of Electronic Engineering, China Academy of Engineering Physics, Mianyang 621999, China;

[2] Laboratory of Precision Manufacturing Technology, China Academy of Engineering Physics, Mianyang 621999, China;

[a]zzy_caep@163.com, [b] weisu@caep.cn, [c] shicxf@sina.com, [d] john46311@hotmail.com, [e]machoxiong@gmail.com, [f] chenyh09@163.com, [g] peng670@163.com

Keywords: MEMS; SOI; Micro-accelerometer; sacrificial process.

Abstract. This paper presents the fabrication of SOI micro-accelerometer by using the sacrificial process. The structure of the SOI micro-accelerometer is designed and analyzed by the finite element modeling. As for the fabrication issue, the problem of electrode metal layer to stand against HF etching is first studied. Second, to prevent the over-etching of the BOX layer during structure releasing process, the etching rate of the BOX layer is carefully investigated and an optimal etching duration is obtained. Third, the adhesion phenomenon between comb fingers during releasing process is studied and optimized finger geometry is proposed to solve such problem. Devices based on the sacrificial process is carried out successfully, the measurement results show that the sensitivity of the accelerometer is about 35 mV/g, with a maximal measurement error of 12mg, and a maximal nonlinear error of 0.41% within 50g.

Introduction

In recent years, the SOI (silicon on insulator) having a monocrystalline structure layer material has been paid widespread attention in the study of the micro-mechanical devices. Depending on the production process and application purposes, the SOI material structure thickness can be from 20 nm to several hundred microns. The thick layer of structure can be able to achieve high aspect ratio structures, large inertial mass and detection capacitance, so SOI material has an advantage in the development of high-performance inertial devices[1-4]. The ADI Company has achieved the integrated accelerometer using SOI material [2]. Amini [3] has developed successfully the SOI accelerometer using back cavity to release the structure. The Peking University Mao Xu also fabricated the SOI micro-accelerometer using DRIE(Deep Reactive Ion Etching)from the backside of the substrate to release the structure[5].Their process using DRIE to release the structure avoid adhesion problem, but the process is complexity. The process named sacrificial process is using HF solution to release the SOI micro-structure from structure side by wet etching buried silicon dioxide (BOX) is relatively simple, but there are several problems are hard to solve, so the SOI micro-accelerometer fabricated by this process is rarely reported.

This paper discusses the SOI micro-accelerometer fabricated by sacrificial process. Fist the structure of the SOI micro-accelerometer is designed and is analyzed by the finite element simulation. Then the problems of metal electrode corrosion, oxide layer etching time and micro-structure adhesion is discussed. And at last, the SOI micro-accelerometer is obtained with nice performance.

1. Structure Design.

In this paper we want to obtain a SOI micro-accelerometer with maximal measurement accelerometer of 50g. The structure sectional view of the SOI micro-accelerometer is shown in Fig. 1 and the parameter is shown in the table 1. Use the parameter, the resonant frequency can be calculated.

$$k = \frac{2Ehw^3}{l^3} = 34 \tag{1}$$

$$f = \frac{1}{2\pi}\sqrt{\frac{k}{m}} = 3.6\text{KHz} \tag{2}$$

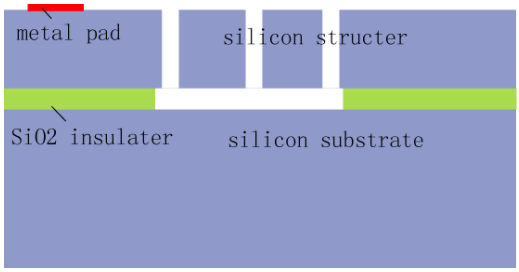


Figure 1. The structure sectional view of SOI micro-accelerometer.

Table 1. The parameter of SOI micro-accelerometer.

Parameter	value/ μm
Structure thickness	40
Beam length	440
Beam width	6
Comb electrode length	320
Comb electrode width	6
Capacitive gap	3
Proof mass length	1720
Proof mass width	420

The finite element simulation is used to validate the parameter of SOI micro-accelerometer. The accelerometer's finite element simulation model is shown in Fig. 2. With 50g acceleration applied to the measurement direction Y, the accelerometer's structure stress and displacement can be obtained, as shown in Fig. 3 and Fig. 4. The maximal stress is 11.6 Mpa, and the maximal displacement is 1.5 less than the capacitive gap. In static state, the gravity is applied on the accelerometer, and the maximal stress is 0.019 Mpa, and the maximal displacement is 0.0004μm, as shown in the Fig. 5 and Fig.6. By the finite element simulation, the accelerometer structure parameter is validated properly.

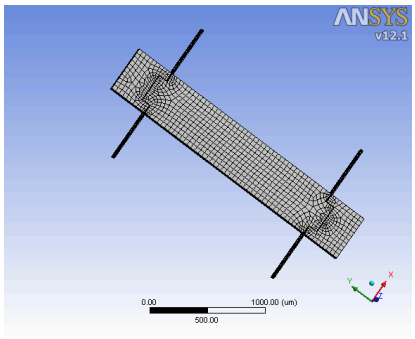


Figure 2. Finite element simulation model.

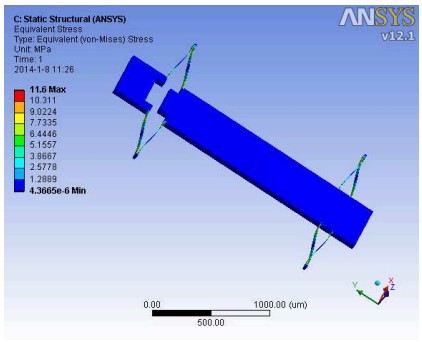


Figure 3. Equivalent stress contours in Y direction.

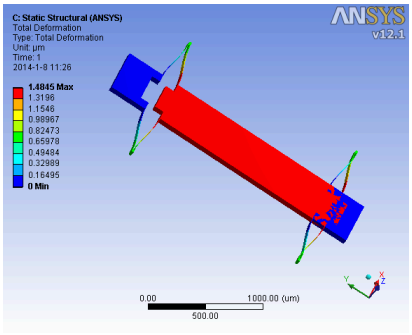


Figure 4. Displacement distribution in Y direction.

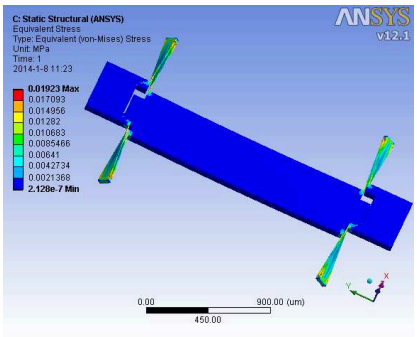


Figure 5. Equivalent stress contours in Z direction.

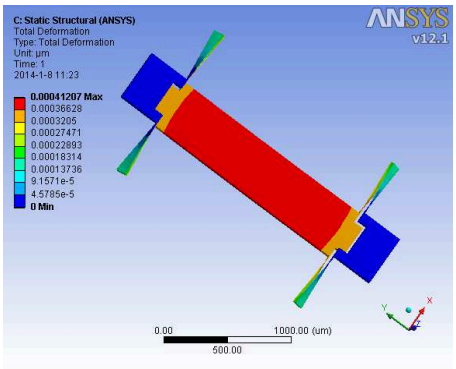


Figure 6. Displacement distribution in Z direction.

By the finite element simulation, the accelerometer's mode is analyzed, as shown in table 2. From the table 2, the accelerometer's fist mode is 3430Hz and is consistent with theoretical calculation. The first mode is accelerometer's fundamental mode, and the first on-axis spurious mode is ten times the fundamental, so the cross-axis coupling can be restrained.

Table 2. Modal analysis results.

Mode	frequency/Hz	Mode	frequency /Hz
1order	3430	4order	32722
2order	25277	5order	42632
3order	29625	6order	55949

2. Fabrication Process

The main fabrication process flow of SOI sacrificial process is shown in Figure 7. The structural layer is patterned with a 3um thick positive photoresist, followed by sputtering metal film on the front side for interconnection. After stripping the photoresist by acetone solvent, the metal electrode is obtained(Fig.7(a)).By ashing in oxygen plasma to remove the remaining organic residues, the structural layer is patterned with a 3um thick positive photoresist and etched in DRIE down to the oxide layer to define the device features, release holes(Fig. 7(b)). After DRIE, the structures are released by wet etching the buried SiO2 layer using HF solution(Fig.7 (c)).

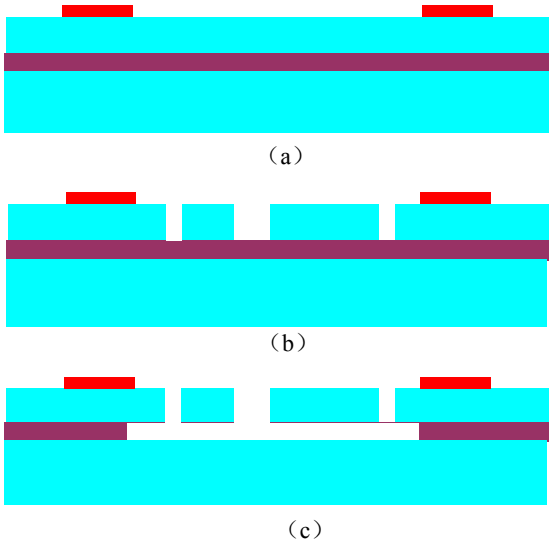


Figure 7. The process flow of front release process:(a) metal film sputtering, (b) DRIE down to the buried silicon dioxide,(c) etching of the buried silicon dioxide underneath the proof mass.

3. Fabrication Results and Issues

The process is simple, but there are some key steps should be settled, for example, when using HF solution to release the micro-structure, the metal electrode is eroded. These key steps are discussed in detail as follows.

3.1 The Fabrication of Metal Electrode

The process requires metal electrode was fabricated on the structure layer before the release of the micro-structure using HF solution. But during the etching of SiO2 layer, the metal electrode was corrupted by HF acid. Through experiments, found that there are pinholes on the metal electrode etched a certain time in the HF solution. As the etching time increases, the number of pinholes increase. When the time is further extended, some electrode partly shedding, and some electrode completely shedding, as shown in Fig.8.



Figure 8. The phenomenon of electrode pinholes and shedding [6].

In order to design a metal electrode of high ability of anti-HF acid corrosion, the metal electrode corrosion property was studied from the metal material, the metal thickness, the metal layer number, the solution property and corrupt temperature, and so on the other condition. Through the study, we obtain the following conclusions[6]: with different materials as the primer material, the corrosion resistance of the metal electrode is not the same, Tiw as a primer material the corrosion resistance of the metal electrode can be better than Cr, Mo as a primer material. Appropriately to reduce the thickness of the primer metal layer, electrode corrosion resistance is better. When increase the temperature of the etching solution, the metal electrode corrosion resistance time becomes shorter.

In order to prolong the metal electrode corrosion resistance time, the metal pad can be protected using a protection layer covering the metal pad and preventing the etchant from reaching the metal pad. There are two protection layers can be used, one is silicon nitride and the other is photoresist. The silicon nitride can be deposited at 300℃ without damaging the metal pad. However, this complicates processing considerably. To allow selective removal of the silicon nitride layer over the mechanical structure for DRIE the structure, one extra deposition and one extra masks are needed. Furthermore, PECVD nitride shows many mechanical defects in the form of pinholes, through which the etchant could reach the metal pad and ruin the metal pad. The second possible layer that can be used to protect the metal pad is photoresist[7-8]. However, photoresist is not as strong as silicon nitride and during etching several problems arise. One is the etch rate of the photoresist in 40% HF is of the order of 50 nm min-1 when the photoresist is not baked completely to remove all the solvent present in the resist, leaving it relatively soft and porous. To prolong the resist etch time, the resist need a complete postbake to remove all solvents. The other problem is the adhesion of the photoresist layer to the surface of the structure. A weak bond can cause the resist to separate from the surface, allowing etchant to seep underneath and attack the under laying metal pad. To improve the adhesion, the wafer are dehydrated by a short bake before the resist is deposited and the some adhesion promoter can be used. The photoresist layer can use structure DRIE mask layer and can be removed afterwards, without danger of damaging the mechanical structures of the metal pad. So, we use the photoresist to prolong the metal etching time.

At last, one metal electrode of Tiw/Au with the Tiw thickness 20nm and Au thickness 200nm is designed. When the metal is covered by photoresist, and the photoresist is hardened, at normal temperature, the metal is good after one hour corrupting in the 40% HF solution.

3.2. The Etching of Oxide Layer

The movable structure of SOI micro-accelerometer is obtained by etching oxide layer use HF solution. However, the corrosion characteristics of the silicon dioxide changes in a microscopic. When the etching time is over, the oxide layer of the connector area is etched and the structure is shedding from the connector area, as shown in Fig.9. In order to control the etching time, the etching rate of SOI oxide layer should be obtained.

Factors like wafer temperature, size of the release holes, and the thickness and amount of BOX layer to be etched determine the lateral etch rate, which was experimentally determined by measuring the undercut in the BOX layer after a certain amount of etching time. In the experiment, we use 40% concentration HF solution, and the temperature is 20$^{\circ}C$. The undercut length was measured after 10 min of etching, for the BOX layer thickness 2um, the measurement values of undercut length are

8.30um, 7.80um, 8.04um, 8.10um, 8.00um after five measurement. So the average lateral etch rate was calculated as 0.8048um/min. Use the same method, for the BOX layer thickness 5um, the average lateral etch rate was 1.875um/min.



Figure 9. The oxide layer of the connector area is over etched.

The difference of corrosion rate largely depends on the difference SiO2 area of the etching front[8-10].The silicon surface is hydrophobic, due to the influence of surface tension, HF solution is difficult to reach etching front in 2um thick oxide layer SOI chip. So that there will be serious diffusion limiting, causing a decline in the concentration of etching front, the corrosion rate becomes low. However, for 5um thick oxide layer SOI chip, the etching front SiO2 area is larger, the influence of surface tension is smaller, the impact of the diffusion limiting is reduced, so that the decline of the concentration of etching front is smaller, the corrosion rate of the silicon oxide is fast.

3.3 The Release of Structure

The 40% HF etchant is used to etch oxide layer underlying the structure layer. However, rinse-drying of wet surface micro structures results in their permanent adhesion with the substrate due to capillary forces unless the structure is sufficiently stiff. It was found that when the micro-structure released through the HF acid etching oxide layer, combfingers adhere tightly together(Fig.10).By destructive experiment, found that not only combfingers adhere together, the mass also adhere to the substrate tightly. Through the test structure, found that, the combfingers width and length of the same case, when combfingers one end fixed, the combfingers not adhere together. It shows that, the occurrence of adhesion between the combfingers is the comprehensive results of the beam and the combfingers. Increases the stiffness of the beam, reducing the combfingers length, increasing combfingers width and the gap can reduce adhesion. Methods to prevent adhesion are on the one hand the appropriate choice of oxide etchants rendering the surface of the MEMS structure rough or hydrophobic. On the other hand, dedicated rinse-drying procedures were successfully applied: drying from low-surface tension alcohols, freeze-drying (sublimation drying using water-methanol, supercritical point CO2 drying, and the immersion in solidifying liquids that can finally be dry-etched). (1)

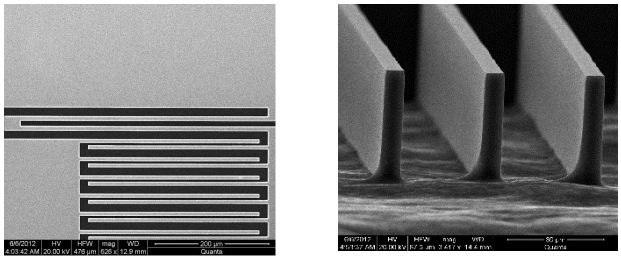
In order to prevent the adhesion between the combfingers, we produced in each combfingers on one end protrusion, and supercritical point CO2 drying was used, the adhesion problem was successfully solved.



Figure 10. Combfigures stick together.

4. Measurement and Results

Through above studies, the devices of SOI micro-accelerometer are obtained successfully. Fig.11 is a SEM image of a part SOI accelerometer. From this figure, can be seen that this process can obtain good surface micro-structure, and with small footing effect.



（a） （b）

Figure 11. SEM images of a part SOI accelerometer: (a） Positive diagram，（b）Back diagram of combfingers.

The fabricated devices are mounted on a printed circuit board（PCB）designed for measurement purposes. By centrifugal rotational platform test with less than 50g applied acceleration, the accelerometer's capacitive sensitivity is 35 mV/g, the maximal measurement error is 12mg, the maximal nonlinear error is 0.41%, as shown in Fig. 12.

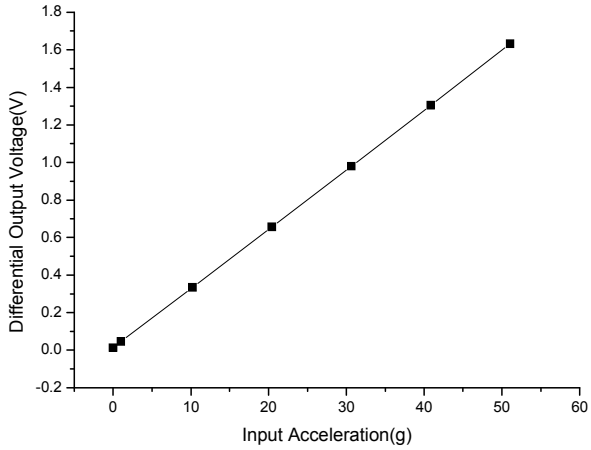


Figure 12. Open-loop centrifugal rotational platform test of the accelerometer.

5. Conclusions

The paper discusses the SOI micro-accelerometer fabricated by sacrificial process in details, including the choice of electrode method layer, the etching of BOX layer and the adhesion problem of comb fingers during releasing process. The fabricated devices have good surface quality and with small footing effect. By centrifugal rotational platform measurement, the sensitivity of the accelerometer is about 35 mV/g, the maximal measurement error is 12mg, and the maximal nonlinear error is 0.41% within 50g.

Acknowledgments

This work was supported by the Laboratory of Precision Manufacturing Technology of CAEPunder Grant No. ZZ14007 and ZZ1204.

References

[1] Yoshiyuki Watanabe;Toshiaki Mitsui;Takashi Mineta,etal. SOI micromachined 5-axis motion sensor using resonant electrostatic drive and non-resonant capacitive detection mode. Sensors and Actuators A: Physical，130 /131(2006),116-123.

[2] Chen T D;Kelly T W;Collins D,et al. The next generation integrated MEMS and CMOS process on SOI wafers for overdamped accelerometers.The 13th International Conference on Solid-State Sensors，Actuators and Microsystems. Seoul，Korea，2005;pp. 1123-1125.

[3] Amini B V;Pourkamali S;Ayazi F. A high resolution,stictionless,CMOS compatible SOI accelerometer with alow noise,low power，0.25 μm CMOS interface.Proceedings of 17th IEEE International Conference on MEMS. 2004, 572-575.

[4] Qu X D;Xie H K. Process development for CMOS MEMS sensors with robust electrically isolated bulk silicon microstructures. IEEE J Microelectromechanical Sys，2007，4, 1152-1161.

[5] MAO Xu, YANG Z C, et al. SOI Micro-accelerometer fabrication with anti-footing technique.Nanotechnology and Precision Engineering, 2010, 4, 330-334.

[6] Zhang Zhaoyun; Shi Zhigui; GaoYang,et al. Study of the Corrosive Property of Metal Electrode.Chinese Journal of Sensors and Actuators，2012，3, 326-328.

[7] C.Linder and N.J.deRooij. Investigation on free-standing polysilicon beams in view of their application as transducers, sensors and actuators A,1990,21-A23, 1053-1059.

[8] K.S.J.Pister. Hinged polysiliconstructures with integrated CMOS TFT'S. Proc.IEEE Solid-State Sensor and Actuator Workshop,Hiton Head Island, SC,USA,22-25 June,1992,136-139.

Key Engineering Materials Vols 645-646 (2015) pp 624-629
© (2015) Trans Tech Publications, Switzerland
doi:10.4028/www.scientific.net/KEM.645-646.624

Submitted: 2014-12-28
Accepted: 2015-01-05

Noise Analysis of Silicon Microgyroscope's Transimpedance Amplifier Interface Circuit

Weifeng Tang [1,a], Anping Qiu [2,b], Guoming Xia [3,c], Yan Su [4,d]

[1] Nanjing University of Science and Technology, Xiaolingwei NO.200, Nanjing, China

[2] Nanjing University of Science and Technology, Xiaolingwei NO.200, Nanjing, China

[3] Nanjing University of Science and Technology, Xiaolingwei NO.200, Nanjing, China

[4] Nanjing University of Science and Technology, Xiaolingwei NO.200, Nanjing, China

[a]547394983@qq.com, [b]apqiu@mail.njust.edu.cn, [c]xgmseu@gmail.com, [d]suyan@mail.njust.edu.cn

Keywords: Silicon microgyroscope; Transimpedance; Interface circuit; Noise analysis

Abstract: The output-current of silicon microgyroscope is at the level of 10^{-7}A. So the requirements for circuits' SNR are very high. This paper proposes a method to improve transimpedance amplifier interface circuit's SNR. First of all, the operating principles of silicon microgyroscope and transimpedance amplifier interface circuit are introduced. Secondly, resistor thermal noise, amplifier's current and voltage noise are analyzed. Then noise density in a certain frequency range is calculated based on Matlab. Besides, a method to improve SNR is proposed, namely, increasing the value of DC offset resistance. Finally, simulation based on Cadence is operated to verify the method. Simulation results fit well with the theoretical analysis. That means the method to improve the SNR is feasible.

Introduction

As a typical inertial measurement device, silicon microgyroscope has following advantages[1,2]: its device dimension is in millimeter and weight is in gram by using silicon processing technology like integrated circuits. It can effectively prevent the effects of external environmental factors and so on.

Silicon microgyroscope's property is improved at home and abroad year by year. The most high-precision silicon microgyroscope's bias stability has been close to $0.1°/h$ at the level of tactical accuracy. The output-current of silicon microgyroscope is at the level of 10^{-7}A. So it is very easy to be interfered by large signals. Besides the influence of resistor thermal noise and amplifer's noise can't be ignored. This means that the requirements for circuits are very high. In order to improve the property of silicon microgyroscope, low noise interface circuit's design is very necessary.

This paper analyzes the transimpedance amplifier interface circuit and did the following works to improve the property. Firstly, the fundamental principle is introduced. Secondly, the formulas of resistor thermal noise and amplifier's noise are derived. Then a method to improve SNR is proposed based on theoretical analysis. Finally, this paper uses simulation based on Cadence to verify the method.

Fundamental Principle

Structure of Silicon Microgyroscope

The structure[3] of dual-mass silicon microgyroscope is shown in Fig.1. It senses the Z-Axis input angular rate by Coriolis effect. X-Axis is the driving direction and the electrostatic force produced by combs 16 drives two masses move to each other along X-Axis. This is the driving mode of silicon microgyroscope. Y-Axis is the sense direction and the Z-Axis input angular rate is sensed by the capacitance variation of combs 15.

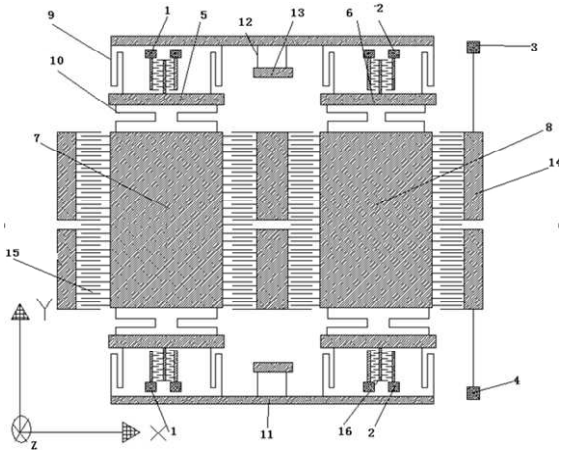


Fig.1 Schematic of silicon microgyroscope

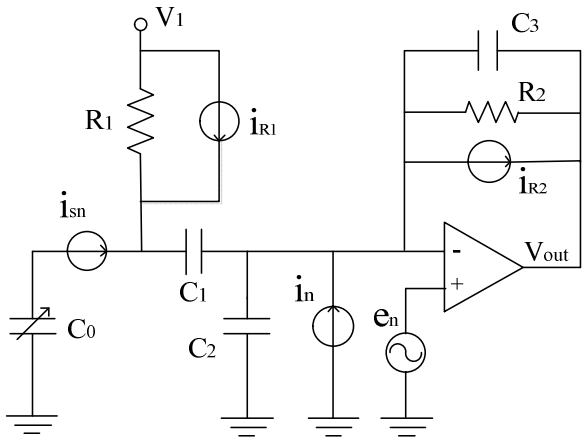


Fig.2 Schematic of transimpedance amplifier interface circuit

Principle of interface circuit

From the structure of silicon microgyroscope, we know that the movement of masses is realized and sensed by combs, namely the variable capacitance. So the input of interface circuit can be represented by the variable capacitance.

The interface circuit of silicon microgyroscope is shown in Fig.2. Where C_0 is the variable capacitance. R_1 is the DC offset resistance. V_1 is the DC offset voltage. C_1 is the decoupling capacitance. R_2 is the gain resistance. C_3 is the parasitic capacitance. Other parameters in Fig.2 are used to analyze the noise. They well be introduced in following chapters.

Variable current i_{sn} is generated by C_0 in the condition of DC offset voltage. Then the transimpedance amplifier converts i_{sn} into the output voltage V_{out}. The transfer function of interface circuit can be written as

$$A = \frac{V_{out}}{i_{sn}} = \frac{R_2}{1 + R_2 C_3 s}. \tag{1}$$

The amplitude-frequency response curve and phase-frequency response curve are shown in Fig.3. Silicon microgyroscope's working frequency is about 4khz. From Fig.3, we know that the gain is the value of R_2 and the phase shift is about zero.

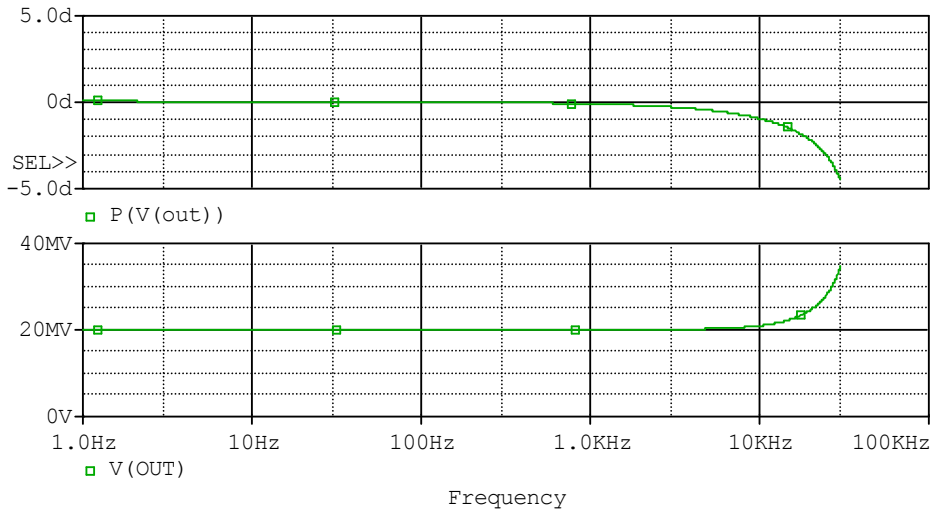


Fig.3 Amplitude and phase frequency response curve of interface circuit

Noise Analysis

Interface circuit's noise consists of resistor thermal noise, amplifier's current and voltage noise. The noise is evaluated by noise density in output. The amplifier chip is AD8642.

(1) Noise of R_1

The formula of R_1 noise density can be written as

$$e_{R1} = \sqrt{\frac{4kT}{R_1}} \cdot \frac{R_2}{1 + R_2 C_3 s} \quad (2)$$

Where e_{R1} is the R_1 noise density in output. k is the Boltzmann constant. T is the environment temperature.

(2) Noise of R_2

The formula of R_2 noise density can be written as

$$e_{R2} = \sqrt{\frac{4kT}{R_2}} \cdot \frac{R_2}{1 + R_2 C_3 s} \quad (3)$$

Where e_{R2} is the R_2 noise density in output.

(3) Amplifier's current noise

The formula of amplifier's current noise density in output can be written as

$$e_i = \frac{R_2}{1 + R_2 C_3 s} \cdot i_n \quad (4)$$

Where e_i is amplifier's current noise density in output. i_n is the amplifier's current noise density which is offered by manufacturer[4]. For AD8642, i_n is 5e-16 A/$\sqrt{hz}$.

(4) Amplifier's voltage noise

The formula of amplifier's voltage noise density can be written as

$$e_{AD} = \frac{1 + R_2 (C_2 + C_3) s}{1 + R_2 C_3 s} \cdot e_n . \quad (5)$$

Where e_{AD} is amplifier's voltage noise density in output. C_3 is the amplifier's output capacitance. e_n is the amplifier's voltage noise density which is offered by manufacturer[4]. For AD8642, e_n's amplitude-frequency response curve is shown in Fig.4.

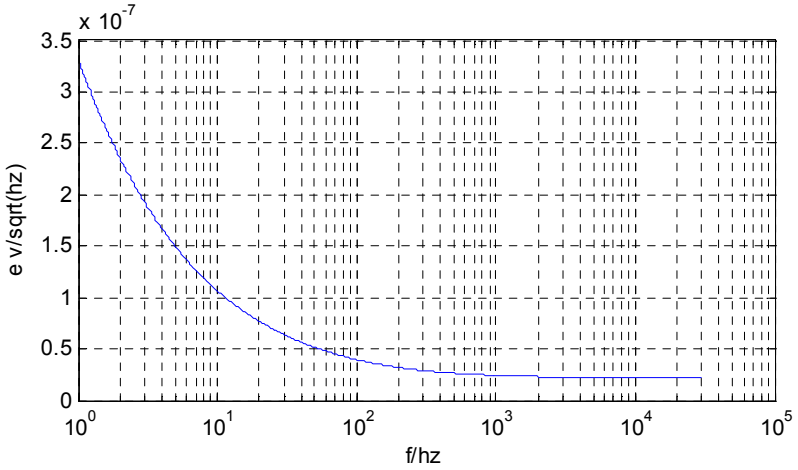


Fig.4 Amplitude-frequency response curve of e_n for AD8642

Theoretical Analysis

The total equivalent noise density in output can be calculated by superposition of power[5]. The formula can be written as

$$e_{equ} = \sqrt{e_{R1}^{\ 2} + e_{R2}^{\ 2} + e_i^{\ 2} + e_{AD}^{\ 2}} \ . \tag{6}$$

Where e_{equ} is the total equivalent noise density in output.

The parameters' values in Fig.2 list in Tab.1. The all kinds of noise density are calculated in the range of 0hz to 30khz according to formula (2) - (6) based on Matlab. The results are shown in Fig.5.

Table.1 Values of parameters in interface circuit

Parameter	Value
R_1	1e6[Ω]
R_2	2e7[Ω]
C_1	1e-7[f]
C_2	2e-11[f]
C_3	4e-13[f]
i_n	5e-16[A/$\sqrt{hz}$]

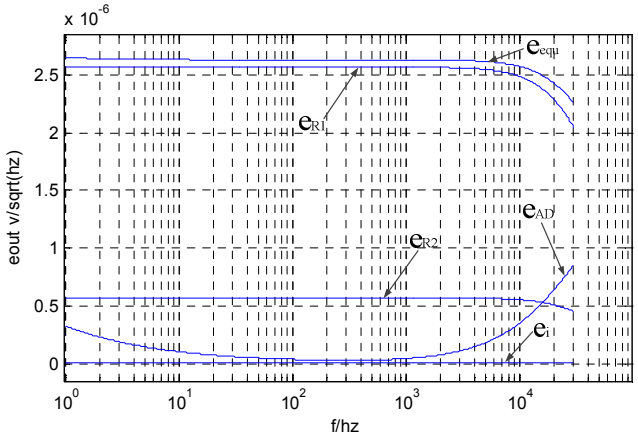


Fig.5 All kinds of noise density when R_1 is 1e6Ω

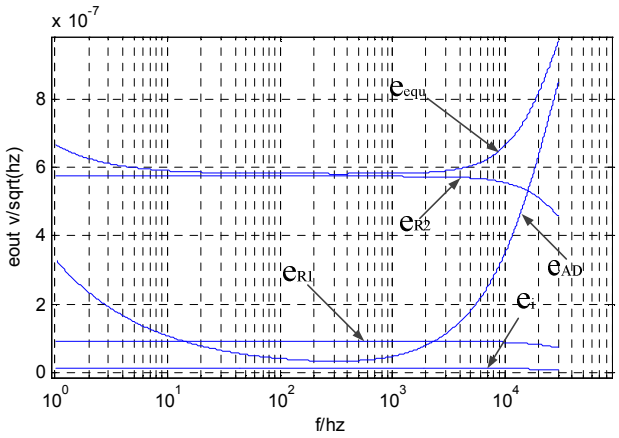


Fig.6 All kinds of noise density when R_1 is 8e8Ω

From Fig.5, we know that e_{R1} is noise's main component. The noise density in the range of low and medium frequency is about 2.5e-6$V/\sqrt{hz}$. From formula (2), we know that the larger the value of R_1, the lower e_{R1} is. So we increase the value of R_1 to 8e8Ω. Meanwhile the other parameters are as same as Tab.1.

The all kinds of noise density is shown in Fig.6 when R_1 is 8e8Ω. From Fig.6, we know that e_{R2} is noise's main component in the range of low and medium frequency. The noise density is about 6e-7 $V/\sqrt{hz}$. It reduces by 76% comparing with the noise density when R_1 is 1e6Ω.

From Fig.3, we know that interface circuit's gain is the value of R_2. While the value of R_2 in Fig.5 is as same as in Fig.6. So we can draw a conclusion that increasing the value of R_1 is a method to improve interface circuit's SNR.

Simulation

The comparison between calculation and simulation is shown in Fig.7. The simulation is operated in Cadence using AC sweep type simulation including noise analysis function.

Where e_{simu_1M} means simulation results of total equivalent noise density in output when R_1 is 1e6Ω. e_{cal_1M} means calculation results when R_1 is 1e6Ω. In the same way, e_{simu_800M} means simulation results when R_1 is 8e8Ω. e_{cal_800M} means calculation results when R_1 is 8e8Ω.

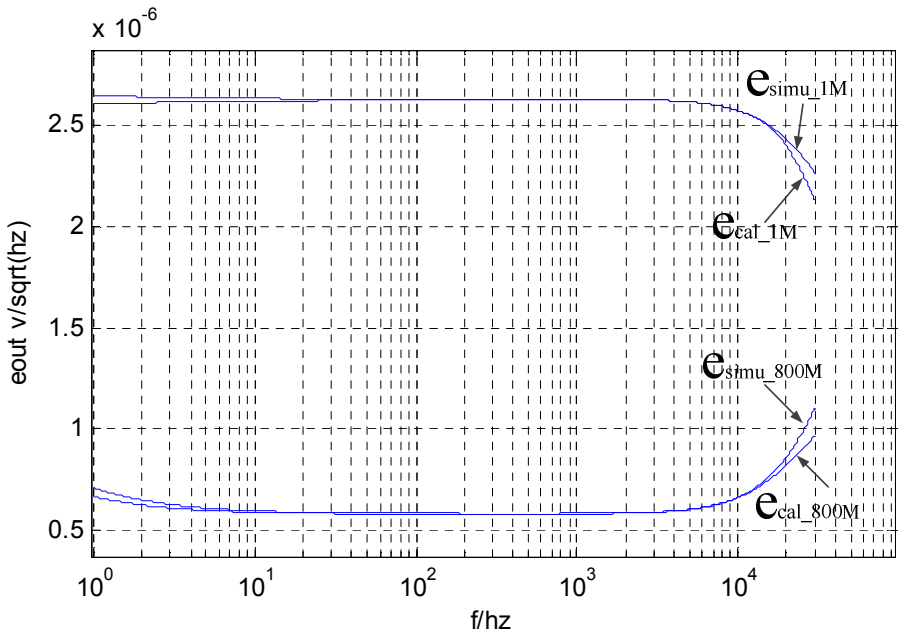


Fig.7 Comparison between calculation and simulation

From Fig.7, we know that simulation results fit well with the theoretical analysis. That means the method to improve SNR is feasible.

Conclusion

In order to improve transimpedance amplifier interface circuit's SNR, this paper analyzes interface circuit's noise in detail. Firstly, the fundamental principle of silicon microgyroscope is introduced. Secondly, the formulas of resistor thermal noise and amplifier's noise are derived. Then all kinds of noise density in output are calculated in Matlab. On the basis of calculation results, a method to improve SNR is proposed, namely increasing the value of DC offset resistance R_1. Finally, simulation in Cadence is operated to verify the method. The simulation results fit well with the theoretical analysis. That means increasing the value of R_1 is a feasible method to improve interface circuit's SNR.

Acknowledgements

This work was financially supported by The National Natural Foundation (No.61301214) and Defense Basic Research Program (A2620133002).

References

[1] Jun Liu, Yunbo Shi, Jie Li: submitted to Journal of Micro-inertial Technology. 2005.
[2] Qin Shi: Study on Key Technologies of Silicon Microgyroscopes for Improving Performance[D]. 2005. (in Chinses)
[3] Anping Qiu, Qin Shi, Yan Su: China ZL200710133223.5[P]. 2008-03-05. (in Chinses)
[4] Analog Devices. http://www.analog.com[OL].
[5] Jinzhan Gao: Detection of weak signals[M]. *Tsinghua university press*, 2004, p56. (in Chinese)

Key Engineering Materials Vols 645-646 (2015) pp 630-635
© (2015) Trans Tech Publications, Switzerland
doi:10.4028/www.scientific.net/KEM.645-646.630

Submitted: 2015-01-08
Accepted: 2015-01-15

Micromachined tri-axis capacitive accelerometer based on the single mass

Fei Yuan[1,a], Liguo Chen[1,2,b*], Tao Chen[1], Lining Sun[1,2]

[1]Jiangsu Provincial Key Laboratory of Advanced Robotics, Soochow University, Suzhou 215021, People's Republic of China

[2]Collaborative Innovation Center of Suzhou Nano Science and Technology, Soochow University, Suzhou 215123, People's Republic of China

[a]20124229031@suda.edu.cn, [b]chenliguo@suda.edu.cn [1]

Keywords: MEMS; Single proof mass; Tri-axis accelerometer; Differential capacitance; Cross sensitivity; Thermomechanical stress

Abstract: A novel micromachined tri-axis capacitive accelerometer based on the single mass is proposed in this paper. The presented accelerometer contains a single proof mass acting as the sensitive element which is suspended by two flexible beams above the substrate, and an array of movable and fixed electrodes is utilized. To match the sensitivity design requirement, the differential capacitive detection is utilized, and the cross-sensitivity problem of three orthogonal axes is avoided ideally. The accelerometer structure is based on the EPI-poly process to realize the 18 microns thickness. Thus the detection capacitance, sensitivity and reliability are improved, the mechanical noise is decreased. To reduce the thermomechanical stress' effect on the offset, a special anchor-middle structure is designed. Simulation results show that the offset is insensitive to the thermomechanical stresses and the sensor has a good consistency in three axes which has been validated by the testing results.

Introduction

Microelectromechanical systems (MEMS) sensor products have conquered the market in the last decades occupied by conventionally fabricated sensors due to their smaller size, excellent technical features and reliability. As a representative of MEMS sensor, micromachined accelerometer is used in numerous applications such as navigation, biomedical activity monitoring, seismology, safety systems in automobiles, and consumer electronics [1-3].

Due to its excellent characters such as lower temperature effect, higher sensitivity, higher linearity and simple structure, the capacitive accelerometer has become the mainstream of research and products [4-5]. To a large extent, single axis accelerometer could match the requirements in the use of air bag, pedometer, etc. Most recently, the consumer electronics marketplace has demanded 3-axis sensors and at a much lower cost than most of the previous devices could support. Christian Wenzel et al proposed a 3-axis accelerometer micromachined by the UV-LIGA process, which was composed of three independent masses on the same chip utilizing to detect the acceleration along the three orthogonal directions respectively [6]. This accelerometer minimized the quadrature error in three axes, and its fabrication process was simple. However, the structure increased the die dimension to location the three masses, it is disadvantage to miniaturize the device. Nonomura Y and Omura Y et al proposed a single mass accelerometer which utilized the differential capacitor to detect the displacements in three axes induced by the accelerations [7]. This accelerometer used the special structure of Zigzag-Shaped Z-electrode to ensure the same gap between two Z-axis capacitor plates in different locations, and this structure improved the sensitivity and reliability with the weakness of complex process. As a consequence, 3-axis consumer sensors require a significantly smaller die, production with simple or commodity process, low cost package and higher performance [8].

Capacitive accelerometers which utilize displacement measurement have a full-scale range from a few tens of nanometers to angstroms. Due to this high sensitivity, the output signal may deviate from the initial null point due to the thermomechanical stresses induced by the plastic packaging assembly process and external loads applied during subsequent use in the field. It is thus essential to

understand and qualify the stresses for optimal sensor performance and reliability. Meanwhile, a structure which is insensitive to the stresses should be utilized.

In this paper, a novel micromachined tri-axis capacitive accelerometer based on the single mass is proposed. To reduce the die dimension, this accelerometer utilizes a single proof mass to detect accelerations in the three orthogonal directions. To match the sensitivity design requirement, the differential capacitive detection is utilized, and the cross-sensitivity problem of three orthogonal axes is avoided theoretically. The special anchor-middle structure makes the sensor is less sensitive to the external stresses.

Design and Principle

Fig.1 illustrates the schematic structure and detection principle of the proposed accelerometer. The overall dimension of the structure is 668μm × 475μm × 18μm. The structure consists of a seismic mass integrated by a polysilicon plate with an array of holes, and the mass is supported by two polysilicon beams (283μm × 2.8μm × 18μm).

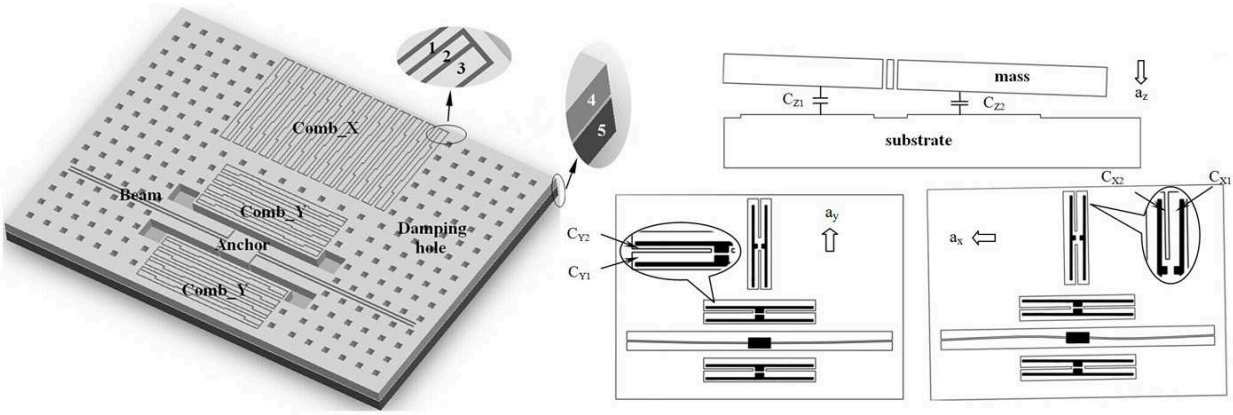


Fig.1 Schematic structure and detection principle of tri-axis accelerometer
1: Movable electrode **2**: Fixed electrode_1 **3**: Fixed electrode_2 **4**: Mass **5**: Substrate

As shown in Fig.1, 1 is the movable electrode which is a part of the mass, 2 and 3 are fixed electrodes with different potentials. In this structure, an array of 1, 2 and 3 is utilized to compose the detecting capacitors in the two orthogonal X and Y directions, labeled as Comb_X and Comb_Y. The separation gap between the movable and the fixed electrodes is 2μm. In Comb_X, each movable electrode array is formed by 12 electrodes (175μm × 4μm × 18μm), each fixed electrode array is integrated by 13 electrodes (171μm). In Comb_Y, each movable electrode array is formed by 8 electrodes (217.5μm × 4μm × 18μm), each fixed electrode array is integrated by 8 electrodes (213μm).4 is the seismic mass and 5 is the substrate, the mass and substrate can detect capacitance variation caused by accelerations forces exerted to the Z direction. The separation gap between the mass and substrate is 2μm.

In all the three orthogonal X, Y and Z directions, to improve the sensitivity and reduce the sensitivity coupling, the differential capacitive detection is utilized to sense the displacements induced by accelerations.

MEMS capacitive accelerometers detect the capacitance variation to estimate the acceleration impacted on the sensors. In this design, when separation gap changes, the capacitance changes. Fig.1 illustrates the detection principle of the accelerometer.

Due to the eccentric mass, the separation gap between mass and substrate will change when accelerations in Z direction force on the sensor. As shown in Fig.1, the capacitance C_{z1} decreases, and the capacitance C_{z2} increases. Then the difference value of C_{z1} and C_{z2} will be outputted. However, C_{Y1} and C_{Y2} will decrease at the same time as well as C_{x1} and C_{x2}, the output signals in X and Y axes will be zero.

When accelerations in Y direction force on the sensor, the mass will undergo a translational motion as shown in Fig.1. The separation gaps between movable and fixed electrodes will change. The capacitance C_{y1} decreases, and the capacitance C_{y2} increases. Then the difference value of C_{y1} and C_{y2} will be outputted. However, the separation gaps between mass and substrate do not change, C_{z1} and C_{z2} remain the same as well as C_{x1} and C_{x2}, the output signals in X and Z axes will be zero.

When accelerations in X direction force on the sensor, the mass will have a rotation around the anchor as shown in Fig.1. The capacitance C_{x1} decreases, and the capacitance C_{x2} increases. Then the difference value of C_{x1} and C_{x2} will be outputted. However, the separation gaps between mass and substrate do not change, C_{z1} and C_{z2} remain the same as well as C_{y1} and C_{y2}, the output signals in Y and Z axes will be zero.

For three-axis accelerometer, how to reduce or eliminate the cross-sensitivity between the axes is very important, it is also a focus of current research. As discussed above, with the comb structure design, the output of each axis has nothing to do with the inputs of the other axes.

Finite element analysis of thermomechanical stress

Due to its high sensitivity, the sensor's output signal may deviate from the initial null point due to the thermomechanical stresses induced by the plastic packaging assembly process and external loads applied during subsequent use in the field. To reduce the influence of thermomechanical stress, a structure with only one anchor is designed, and the anchor is located in the middle of the substrate. Meanwhile, the influence of thermomechanical stress on this structure is estimated with finite element analysis.

Fig.2 shows the model of this analysis. As is shown, the model is made up of two parts, one is the sensor structure – the smaller one, and the other is substrate – the bigger one. In particular, there are bonding glue and metal electrodes between sensor layer and substrate layer. To simplify the analysis, the bonding glue, metal electrodes and substrate are simplified as one plate with 300μm thickness. The dimension of sensor structure is the same as the designed one.

In this analysis, all degrees of freedom of four vertices of substrate bottom are restrained as shown in Fig.2 (a), and the substrate is under the circumstances of thermomechanical stress which value is 20Mpa.

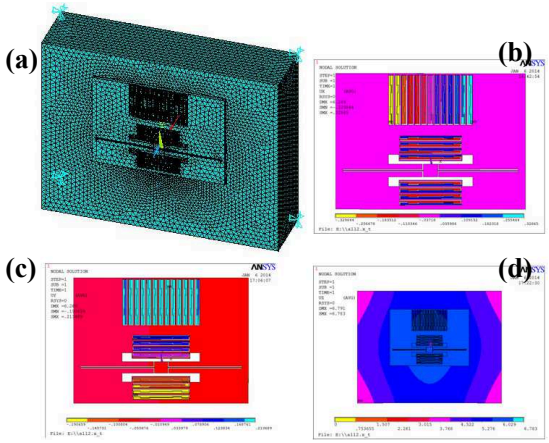


Fig.2 Model and results of finite element analysis (b) Deformation of sensor in X direction (c) Deformation of sensor in Y direction (d) Deformation of sensor in z direction

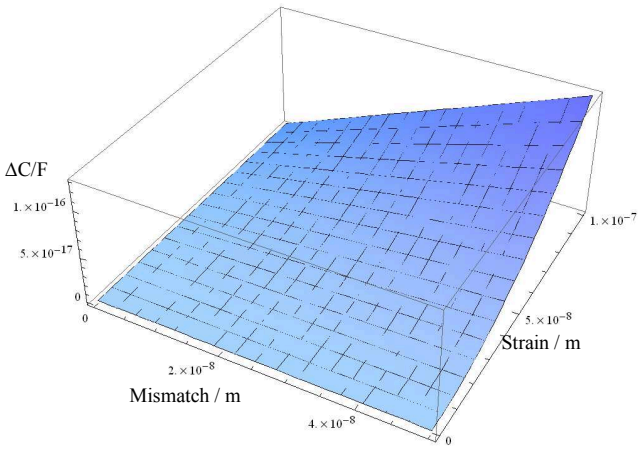


Fig.3 The capacitance change of Y direction against the mismatch and strain

Fig.2 (b), (c) and (d) show the results of analysis. Under the circumstances, when checking the deformation in X direction, it can be found the mass has a uniform deformation and the electrodes of Comb_Y also has a uniform deformation as shown in Fig.2 (b). That means in X direction, the output signals of Y and Z axes are zero. The same result can be found in Fig.2 (c) and Fig.2 (d). These results prove that cross-sensitivity among three axes is reduced.

In this model, the separation gaps between movable and fixed electrodes are 2μm, when suffering from the thermomechanical stress, the gaps change. Depending on the simulation results, the

calculation values can be got that thermomechanical stress causes the capacitance change of 0.274fF in X direction, 0.0352fF in Y direction and 0 in Z direction.

However, the processing error may cause the mismatch between the gaps. Fig.3 shows the capacitance change of Y direction against the mismatch and stress (or strain). When the mismatch and strain amplify, the capacitance change will amplify, and it tends to amplify quickly.

Fabrication

Fig.4 shows the fabrication process flow of the accelerometer. (A) 2-2.5μm oxide is generated as insulating layer on the polishing wafer, then a polycrystalline silicon layer is deposited and etched, used to transfer potential and capacitance signal to an external device, (B) another 2μm oxide layer is deposited next, used as sacrificial layer, (C-D) a polysilicon seed layer is deposited on the oxide layer by LPCVD process, and then etched to form an anchor zone of polycrystalline silicon devices, (E) a structure layer is generated with the thickness of 20μm using the polycrystalline silicon epitaxial process, (F) a aluminum layer is deposited and patterned as the pad and the bonded area on the polished structure layer, (G) the structure layer is etched till the first oxide layer by the deep reactive ion etching process to form the designed structure, (H) sacrificial layers are removed by the VHF steam to release the designed structure.

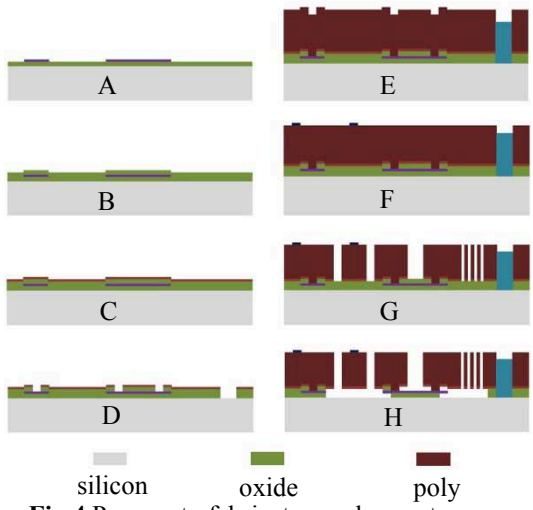


Fig.4 Process to fabricate accelerometer

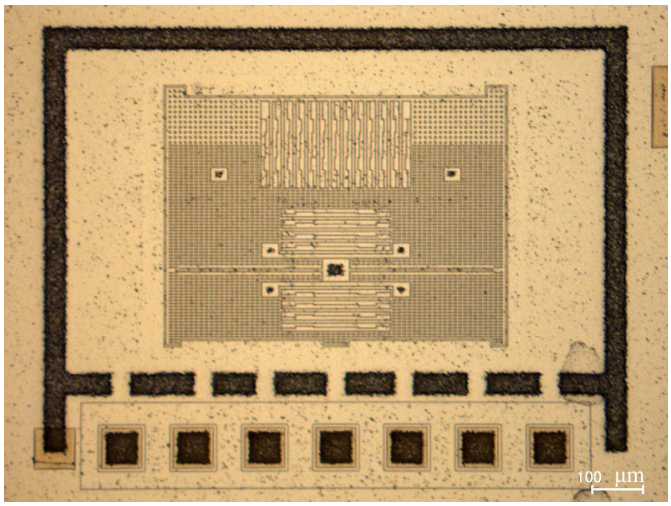


Fig.5 Optical microscope images of accelerometer

Experiments results

Fig.6 shows the test results of sensitivity. The curves from top to bottom are outputs of ±1G in X, Y, Z directions respectively. Depending on the relationship between ASIC and sensor capacitance (1.2fF/g to X, Y axes and 1.5fF/g to Z axis), the sensitivity of each axis is shown in table.1.

As shown in Table.1, device outputs at +1g acceleration are in value with the outputs at -1g acceleration, the maximum error is only 4%. The sensitivities of three axes are 1.44fF/g, 1.47fF/g and 1.65fF/g respectively, the consistency of sensitivity along three axes has been proved.

Table.1 Sensitivity of each axis

Axis	*+1g Output / mg*	*-1g Output / mg*	*Sensitivity fF/g*
X	*1200*	*-1200*	*1.44*
Y	*1200*	*-1250*	*1.47*
Z	*1100*	*-1100*	*1.65*

As shown in Fig.6, external acceleration applied to each axis has no effect on other axial outputs. For example, when the output of Z is 1 g acceleration, output values of the X, Y axis are zero (when X, Y axes are under acceleration, outputs of Z axis are stability, that means it is caused by zero bias, we can adjust offset to eliminate it).

Table.2 shows the testing results and calculated ones of static capacitance. The testing instrument works at the frequency of 100 KHz.

Table.2 Static capacitance of each axis

Capacitance /pF	*X*	*Y*	*Z*
Testing	*0.239*	*0.192*	*0.268*
Calculation	*0.225*	*0.185*	*0.247*

As shown in table.2, testing values are slightly bigger than calculated ones. The difference comes from two aspects, one is the parasitic capacitance, the other is fabrication error. An undercut from 0.3 micrometer to 0.5 micrometer will be made in fabrication process, and this is the dominant factor which causes the difference.

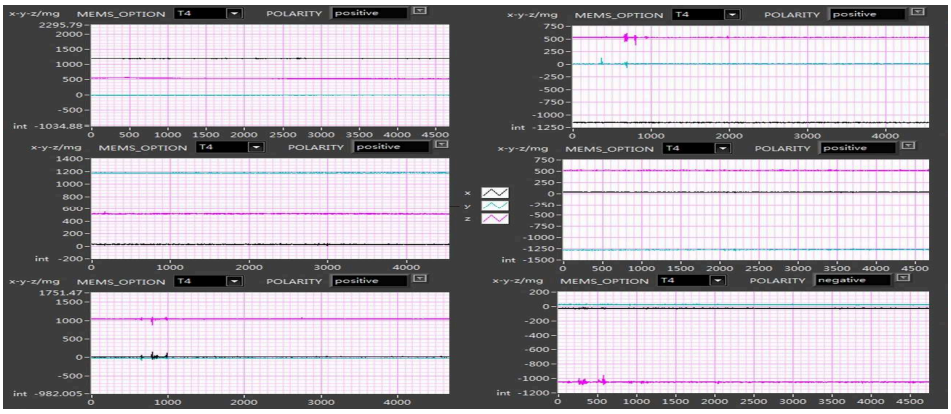


Fig.6 Test results of sensitivity

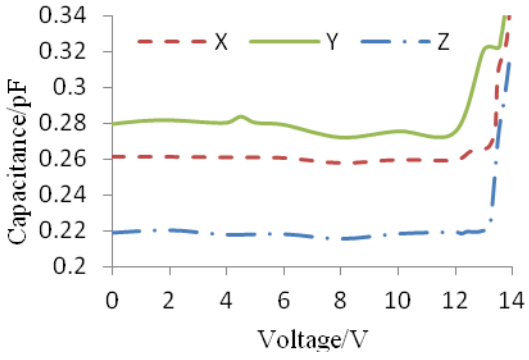


Fig.7 Pull-in voltages of each axis

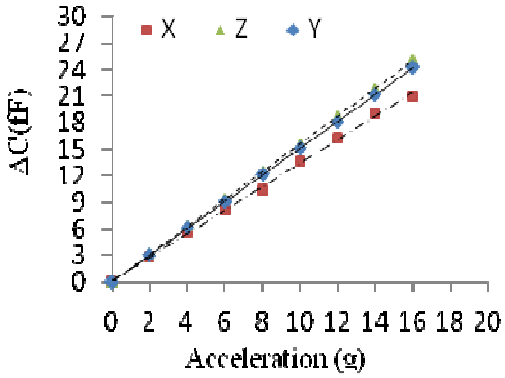


Fig.8 Capacitance variation against g

Fig.7 shows the pull-in voltages of each axis. With the increase of driving voltage, the gap between movable electrode and fixed electrode becomes smaller. The capacitance variation caused by tiny displacement is little, so the curve is stable except small fluctuations in the former period. When the voltage increases to a certain value, the system reached a tipping point, the movable electrode and fixed electrode will paste together, and the capacitance will change sharply after this point. The voltage at this point is called pull-in voltage. As shown in Fig.9, the pull-in voltages of three axes are 13.5V, 12.5V and 13.5V respectively.

The measuring rang of this proposed accelerometer is -16g – +16g. Changing the external acceleration variation from 0 to 16 g, then the nonlinearity is got. As shown in Fig.8, the capacitance variations against the g values of three axis are basically linear, the nonlinear error is about 2.16% FS.

Summary

This paper proposes a novel micromachined tri-axis capacitive accelerometer based on the single mass. To match the sensitivity design requirement, the differential capacitive detection is utilized, and the sensitivity coupling problem of three orthogonal axes is avoided theoretically. Finite elements analysis shows that the special anchor-middle structure makes the sensor less sensitive to the thermomechanical stresses. The capacitance changes caused by thermomechanical stresses are 0.274fF in X direction, 0.0352fF in Y direction and 0 in Z direction. The accelerometer structure is based on the EPI-poly process to realize the 18 micrometer thickness. Thus the detection capacitance, sensitivity and reliability are improved, the mechanical noise is decreased. Experiments results show

that the sensitivities of three axes are 1.44fF/g, 1.47fF/g and 1.65fF/g respectively and the nonlinear error is about 2.16% FS. Thanks for the simple structure and fabrication process, this presented single-mass tri-axis capacitive accelerometer can be widely used in Consumer Electronics applications.

[I] Project funds: State 863 projects (2011AA040404); Specialized Research Fund for the Doctoral Program of Higher Education (20133201110009). New Century Excellent Talents in University （NCET-13-0923）

References

[1] Kuehnel W. Modelling of the mechanical behaviour of a differential capacitor acceleration sensor[J]. Sensors and Actuators A: Physical, 1995, 48(2): 101-108.

[2] Zhang X, Park S, Judy M W. Accurate assessment of packaging stress effects on mems sensors by measurement and sensor–package interaction simulations[J]. Microelectromechanical Systems, Journal of, 2007, 16(3): 639-649.

[3] Serrano-Vázquez F X, Herrera-May A L, Bandala-Sánchez M. Design and modeling of a single-mass biaxial capacitive accelerometer based on the SUMMiT V process[J]. Microsystem technologies, 2013, 19(12): 1997-2009.

[4] Li B, Lu D, Wang W. Micromachined accelerometer with area-changed capacitance[J]. Mechatronics, 2001, 11(7): 811-819.

[5] Xie J, Agarwal R, Liu Y, et al. A three-axis SOI accelerometer sensing with both in-plane and vertical comb electrodes[J]. Microsystem technologies, 2012, 18(3): 325-332.

[6] Qu W, Wenzel C, Gerlach G. Fabrication of a 3D differential-capacitive acceleration sensor by UV-LIGA[J]. Sensors and Actuators A: Physical, 1999, 77(1): 14-20.

[7] Nonomura Y, Omura Y, Funabashi H, et al. Chip-Level Warp Control of SOI 3-Axis Accelerometer with the Zigzag-Shaped Z-Electrode [J]. Procedia Engineering, 2012, 47: 546-549.

[8] Hollocher D, Zhang X, Sparks A, et al. A very low cost 3-axis MEMS accelerometer for consumer applications[C]. Sensors 2009 IEEE, 2009: 953-957.

Key Engineering Materials Vols 645-646 (2015) pp 636-639
© (2015) Trans Tech Publications, Switzerland
doi:10.4028/www.scientific.net/KEM.645-646.636

Submitted: 2015-01-09
Accepted: 2015-01-15

Multi-chip Module Design of a MEMS Air Pressure Sensor

Guang-Xiu Yao[1, a], Han-Yu Du[2, b], Qing-An Huang [3, c] and Meng Nie[4, d]

[1,3,4] Key Laboratory of MEMS of the Ministry of Education, Southeast University, Nanjing, China

[2]The 28th Research Institute of China Electronics Technology Group Corporation, Nanjing, China

[a]gx_yao@163.com, [b] bbcdashu@hotmail.com, [d*]m_nie@seu.edu.cn

Keywords: MEMS, Multi-chip module, Pizeoresistive pressure sensor

Abstract. A MEMS air pressure sensor system is proposed in the paper, which can monitor the air pressure by means of measuring the discharge time of the sensor. The system contains two parts: the MEMS air pressure sensor and the data acquisition system. The MEMS air pressure sensor is an enhanced pizeoresistive pressure sensor. The data acquisition system contains a time-to-digital part, which measures time interval by using of the propagation delays of logical gates. The time-to-digital part can measure the resistors' discharge time and turn it into digital output, when the resistors on the air pressure sensor are connected to a capacitor which is full of charge. The discharge time is only related to the resistor, and then the pressure measurement is changed to time measurement. The digital output is shown through a liquid crystal display screen.

Intorduction

MEMS air pressure sensors have been widely used in industrial area, especially in the automatic weather station, radiosonde observation, and so on [1~4]. MEMS air pressure sensors are classified into piezoresistive sensors and capacitive sensors depending on the pressure sensing mechanism. The piezoresistive pressure sensor is a mature technology and has been widely used in air pressure sensor industry [5]. Fig.1 is the structure of the MEMS air pressure sensor. One air pressure sensor contains four resistors, two of which are fixed and the other two are variable. The variable resistors vary with the pressure. The variation of the resistance represents the variation of the air pressure.

The traditional method to measure the variation of stresses applied on the sensor is applying a fixed voltage to the resistor and measures the current through the resistor. The disadvantage of this method is that the resolution is limited by the power source. A novel system is proposed in this paper. As shown in Fig.2, a fixed capacitor is connected to the resistors through analog switches, which are controlled by the Micro Controller Unit (MCU). The MCU turns on and off the analog switches one by one and measures four discharge time intervals. For a 5k ohm resistor and a 34nF capacitor, the discharge time is about 100 microseconds. The resolution of the time-to-digital part is about 10 picoseconds. The resolution can be 80000 peak-peak divisions with noise consideration.

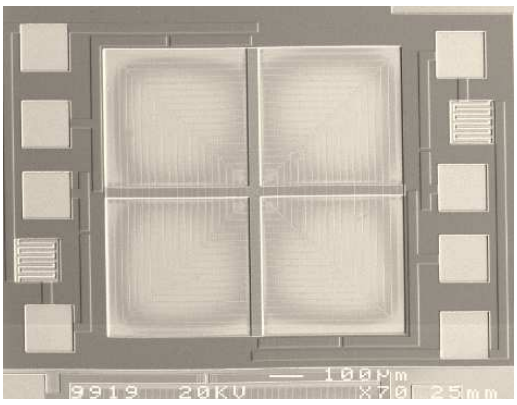


Fig. 1 Structure of air pressure sensor

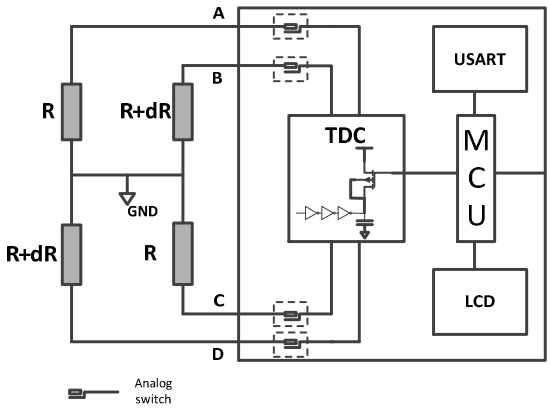


Fig. 2 Readout circuit

Theory and design

Measuring strain gages is one of the big challenges for sensor technology, especially in the air pressure sensor industry field. For the variation of the resistance is very small, and the high resolution request, the resistors must be measured with very high precision. Generally, the Wheatstone bridge is used to do the job. The classical Wheatstone bridge is shown in Fig.3. Eq. 1 shows the relationship between the Wheatstone bridge's output and the resistors.

$$output = \frac{dR}{2R + dR} V_{in} \tag{1}$$

As we can see from the Eq. 1, the drawbacks of the Wheatstone bridge measuring method is that the precision is limited by the power source, and the output is not linear with the variation of the resistors unless the variation is much smaller compared with the fixed resistance. The power source with high precision often has big volume, which is unacceptable in MEMS package.

The measuring method presented in this paper overcomes the drawbacks of the traditional way. With the development of CMOS technology, the fabrication of the time-based signal processing chips has come true. Time based signal processing is a novel approach to change the voltage and current variables into corresponding time differences. And the time differences are usually transformed into digital signals, which can be widely used in digital products. The design of the readout circuit is based on the time-based signal processing chips. Fig.4 shows the simplified schematic of the readout circuit. The sensor's resistors which working with a capacitor act as low-pass filters. The capacitor, charged to Vcc, will discharge through the sensor's resistors when the analog switch is turned on by the MCU. The discharge time is precisely measured by a Time-to-Digital Converter.

The discharge time is given by Eq. 2:

$$t = kRC \tag{2}$$

where k is a constant coefficient.

With the different discharge times, the MCU does not export the discharge times, but the relationship among them. The output of the chip is given by Eq. 3,

$$output = \frac{(t_B - t_A) + (t_D - t_C)}{(t_A + t_B) + (t_C + t_D)} \tag{3}$$

From Eq. 3, Eq. 4 can be obtained,

$$output = \frac{dR}{2R} \tag{4}$$

From the Eq. 4, it can be seen that the output has nothing to do with the power supply, and the output is linear with the variation of the resistors. Besides, the power consumption in this way is much smaller than the power consumption in the traditional way.

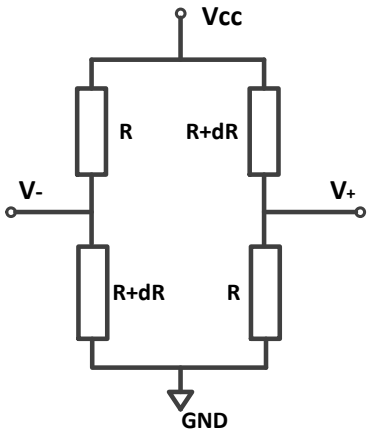


Fig. 3 Classical Wheatstone bridge

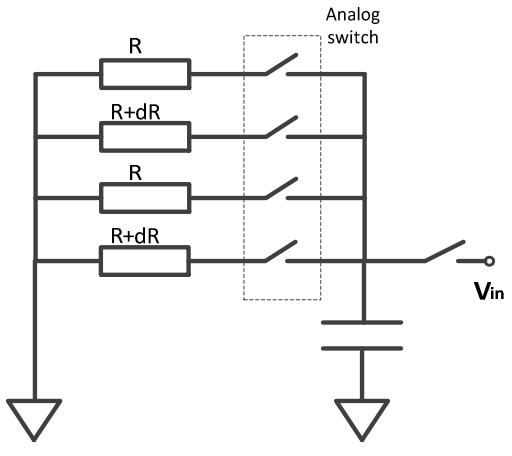


Fig. 4 Simplified schematic of the readout circuit

Results and analysis

An air pressure gauge with a standard barometer is used to test the readout circuit. The air pressure sensor is put into the sealed test chamber, and connected to the readout circuit through an air plug, which can ensure the test chamber to be sealed. The digital output is shown through a liquid crystal display screen.The range of the test pressure is from 100hPa to1000hPa, at the room temperture. Both ascending order and descending order are adopted in the test. Through the test, a set of data has been obtained and is given in Fig.5, where the abscissa values represent the pressure and the ordinate values represent the output results of the chip.

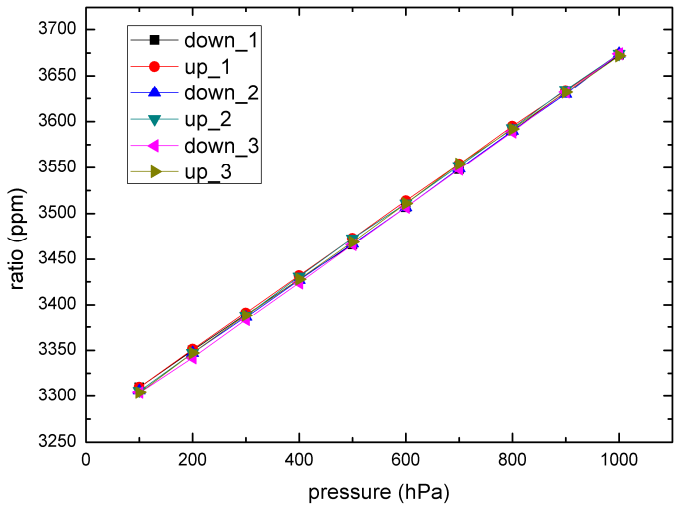


Fig.5 Test curve of pressure uncompensated

As we can see in Fig.5, when air pressure varies from 100hPa to 1000hPa, the output of the readout circuit varies from 3300 to 3670. The test repeated six times. The six curves in the figure are nearly overlapped, which means that the system has excellent consistency and repeatability.

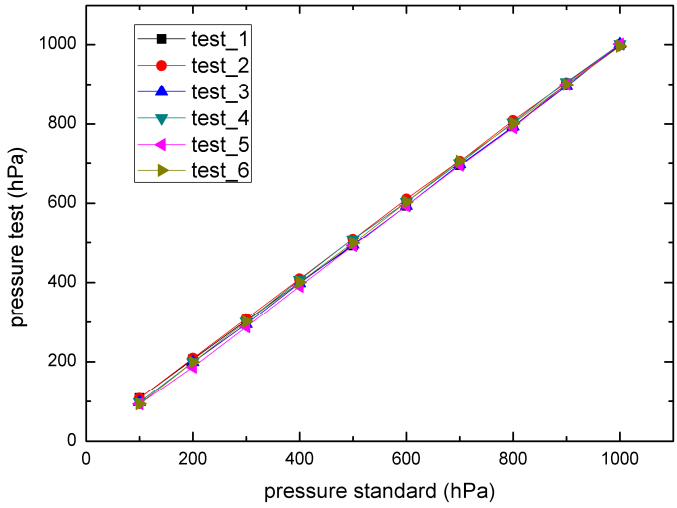


Fig.6 Test curve of pressure after compensation

Fig.6 shows the test result after compensation. After compensation, the output value of the readout circuit is transformed to pressure, which is much easier for observation. The output results are much closed to the standard pressure values.

Summary

Based on the time mode signal processing principle, a novel method to measure the air pressure is studied in this paper. The variations of the resistors are transformed to time differences. The precision of the readout circuit has nothing to do with the power supply, and the output of the readout circuit is only linear to the resistance.

Acknowledgement

The research was sponsored by Shenzhen strategic emerging industry development funds (JCYJ20120821162230172) and (JCYJ20140418100633634).

References

[1] H. Dudaicevs, M. Kandler, Y. Manoli, W. Mokwa, and E. Spiegel, Surface micro-machined pressure sensors with integrated CMOS read-out electronics, Sens. Actuators A, vol. 2, (1994) 157-163.

[2] Zhen Fang, Zhan Zhao, Lidong. Du, Jiangang Zhang, Cheng Pang and Daoqu Geng, A New portable micro weather station, Nano/Micro Engineered and Molecular System, (2010) 379-382.

[3] A. D. DeHennis and K. D. Wise, A wireless microsystem for the remote sensing of pressure, temperature, and relative humidity. Microelectromechanical Systems, Journal of 14, (2005) 12-22.

[4] Suja K J, Mathew S, Komaragiri R. Optimized design of a stacked diaphragm MEMS pressure sensor for Tsunami warning system. Global Humanitarian Technology Conference: South Asia Satellite (GHTC-SAS), IEEE, (2013) 346-351.

[5] J. C. Suhling and R. C. Jaeger, Silicon piezoresistive stress sensors and their application in electronic packaging, IEEE Sensors J., vol. 1, no. 1, (2001) 14-30.

Key Engineering Materials Vols 645-646 (2015) pp 640-645
© (2015) Trans Tech Publications, Switzerland
doi:10.4028/www.scientific.net/KEM.645-646.640

Submitted: 2015-01-09
Accepted: 2015-01-19

A Modulated Feedback Approach to Improve Closed Loop MEMS Accelerometer Bias Instability

Mingjun Ma[1,a], Zhonghe Jin[1,b*] and Yidong Liu[1,c]

[1]Micro-satellite Research Center, Zhejiang University, Hangzhou, P.R. China

[a]edward-ma@zju.edu.cn, [b*]jinzh@zju.edu.cn(corresponding author), [c]ydliu@zju.edu.cn

Keywords: Allan Variance, Modulated feedback, Bias instability, Closed-loop MEMS accelerometer

Abstract.

Bias instability serves as one important performance specification for MEMS accelerometer. The bias instability is affected by 1/*f* noise. Conventional operation adopts the correlated double sampling (CDS) to reduce the 1/*f* noise, but is only feasible with switch capacitors. The paper proposes a novel and universal modulated feedback approach to improve the bias instability of closed loop MEMS capacitive accelerometer. The modulated feedback method is utilized to isolate the 1/*f* noise the electronic interface brings to the system. The comparison experiments are set up and the Allan Variance show significant improvement for the bias instability. We achieve the bias instability around 8μg after applying modulated feedback approach, making the closed loop MEMS accelerometer being able to enter high precision inertial sensor level.

Introduction

Bias instability is one of the most important specifications on evaluating the performance of inertial sensors. Typically, it indicates the drift of certain inertial sensor. For conventional inertial sensors like quartz accelerometer, the bias instability can achieve less than 1 micro-g, with Allan Variance (AV) used as the judgment criterion. In recently years, MEMS accelerometer evolved as the promising sensors that are replacing old-fashioned heavy and power-consuming ones. However, the drift property is quite inferior in front of traditional mechanical sensors. This is due to the drift of electronic system and sensor element. The cutting-edge research has achieved the bias instability less than 10μg [1], [2], [3] and [4], whereas the averaging level stagnated on the 10~100μg level.

Up-to-the-date some literatures are reported to improve the bias instability and long term drift. It is mentioned in [1] and [2] that the closed-loop benefits the reduction of bias instability, and a careful design on the sensor element should be taken enough attention [2]. However, more researches are waiting to find the dominant factors that determine the bias instability when referring to the specific blocks of systems. Under such context and background, we conducted research on the improvement of bias instability with analysis in depth to find the most likely reasons in the system, and achieved an improvement of more than 20μg with the novel modulated feedback approach.

Table I Specifications of MEMS capacitive accelerometer

Parameters	Value
Proof Mass	3milli-gram
Quality Factor	160
Resonant Frequency	780Hz
Static Sensitivity	0.1pF/g

Allan variance

Allan Variance is taken as the primary evaluation approach for performance. In literatures such as [5], [6], and [7], the shape of AV has unique meaning at each stage of the fitted line corresponding to

different noise existed in the system. This concept is illustrated in Fig. 2 and more detailed meaning can be found in [6] and [7]. In fact, the 1/*f* noise determines the lowest point of AV curve referred as bias instability. The quantization noise often occupies as the high frequency noise and the velocity random walk is the noise with frequency between that of quantization noise and 1/*f* noise. The Acceleration Random Walk (ARW) and Acceleration Ramp (AR) are the components with even lower frequency, which meaning the fluctuation periods can be minutes or hours. The quantization noise and velocity random walk (VRW) are modeled as white noise. The origin of these two noises as well as the 1/*f* noise mainly comes from the electronic interfaces.

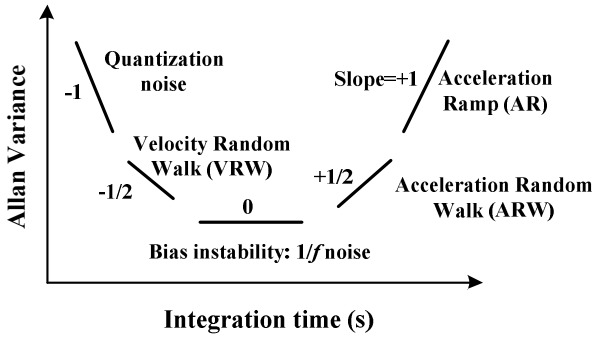


Fig.1 Allan Variance curve with analysis results.

1/*f* Noise isolation

For a common closed loop diagram as depicted in Fig.1, the dominant noise sources come from electronic noises. Brownian noise of the accelerometer is calculated as small as 0.02μg/√Hz to be neglected. The feedback approach in Fig. 1 is named as direct feedback approach (DFA) in this paper, which applies the differential feedback voltage $V_{bias}\pm V_{fb}$ on differential feedback electrodes of the accelerometer to form the differential electrostatic force. The net electrostatic force can counteract the inertial force generated by input acceleration a_{ext}.

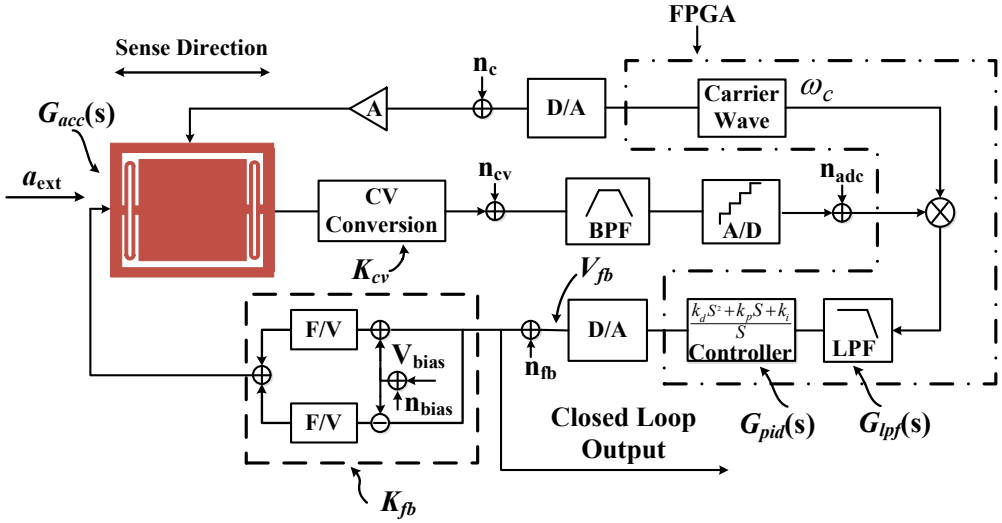


Fig. 1 The original continuous time MEMS capacitive accelerometer closed loop diagram.

Typically, the noises from CV circuit named as n_{cv}, A/D module as n_{adc}, and carrier circuit as n_c are concerned only in the vicinity of carrier wave at sense direction. Whereas the noises from feedback DAC circuit as n_{fb}, bias voltage in feedback path as n_{bias} are modeled as 1/*f* noise in low frequencies. The feedback voltage, the feedback bias and the net electrostatic force containing noise are expressed in the followings:

$$F_{e,x_fb}=\frac{1}{2}\frac{\partial C}{\partial x}[((V_{bias}+n_{bias})+(V_{fb}+n_{fb}))^2-((V_{bias}+n_{bias})-(V_{fb}+n_{fb}))^2] \quad (1)$$

The simplified Eq.1 is yielded as Eq. 2:

$$F_{e,x_fb} = 2\frac{\partial C}{\partial x}[V_{bias}V_{fb} + V_{bias}n_{fb} + V_{fb}n_{bias} + n_{bias}n_{fb}] \quad (2)$$

The net electrostatic force F_{e,x_fb} direct affects the accelerometer motion with the 1/*f* noise n_{bias} and n_{fb}. Different from the conventional correlated double sampling (CDS) technique that requires discrete time operation on switch capacitors, we developed modulated feedback approach (MFA) for the closed loop. The concept simply modulates the original V_{bias} and V_{fb} signals on a another carrier wave with frequency ω_d before the D/A module with only additional high pass filters to filter away low frequency noise. Therefore, the 1/*f* noise the original signal V_{bias} and V_{fb} take is isolated. The similar method was reported previously in [8] for the coupling elimination of gyroscope closed loop system, and this approach is even more suitable for the 1/*f* noise reduction in accelerometer system. The implementation of such method is presented in Fig. 2.

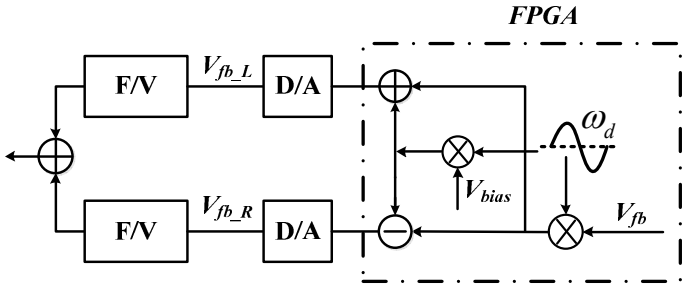


Fig. 2 Modulated feedback approach schematic for replacing the original direct feedback approach in closed-loop system.

The differential feedback voltages for left and right feedback electrodes are labeled as V_{fb_L} and V_{fb_R}, as written in Eq. 3 and Eq.4. The total electrostatic force generated by the feedback voltages are expressed in Eq. 5:

$$V_{fb_L} = V_{bias}\cos(\omega_d t + \theta) + V_{fb}\cos(\omega_d t + \varphi) \quad (3)$$

$$V_{fb_R} = V_{bias}\cos(\omega_d t + \theta) - V_{fb}\cos(\omega_d t + \varphi) \quad (4)$$

$$F_{e,x_fb} = \frac{1}{2}\frac{\partial C}{\partial x}(V_{fb_L}{}^2 - V_{fb_R}{}^2) \quad (5)$$

Where ω_d is the frequency of feedback carrier wave, θ and φ are the phase of modulated bias and feedback signals, F_{e,x_fb} is the total restoring electrostatic force. The previous n_{bias} and n_{fb} do not exist in the process because they are the low frequencies noises.

Substitute Eq.3 and Eq.4 into Eq.5 yielding Eq.6:

$$F_{e,x_fb} = \frac{\partial C}{\partial x}V_{bias}V_{fb}[\cos(\theta - \varphi) + \cos(2\omega_d t + \theta + \varphi)] \quad (6)$$

The higher frequency part is filtered by the mechanical element of accelerometer, and the left DC part is the feedback force to counteract the input acceleration.

Experiments

With updated closed loop configuration, we conducted experiments regarding the closed loop with DFA and MFA for comparison. The closed loop output signal is measured in HP 89441A vector signal analyzer. With previous DFA, the closed loop output spectrum is displayed in Fig. 3. At frequencies lower than 50Hz, there is obvious 1/*f* noise profile. The feedback voltage is the DC voltage. When measuring the loop with MFA, the closed loop output spectrum should shift to the modulation carrier frequency. Here we adopt the frequency ω_d as 6KHz. The measured spectrum is shown in Fig. 4. The feedback voltage is modulated on 6KHz frequency, and the closed loop output noise is the noise around 6KHz. Fig. 4 shows that in the 25Hz range near 6KHz, the profile of noise is still flat. The closed loop scale factor with DFA is 2.5V/g, and the loop with MFA is about 15V/g. Therefore, by calculating the noise equivalent acceleration, the loop DFA achieved 3.2μg/√Hz, and

the loop with MFA achieved 1.3μg/√Hz. Fig. 5 shows the spectrum of loop with MFA at low frequencies. The range of spectrum in Fig. 5 does not contain the feedback voltage V_{fb}, but it can show that there is also no distinct 1/*f* noise profile in the low frequencies. Therefore, the 1/*f* noise in the loop with MFA is alleviated through comparison.

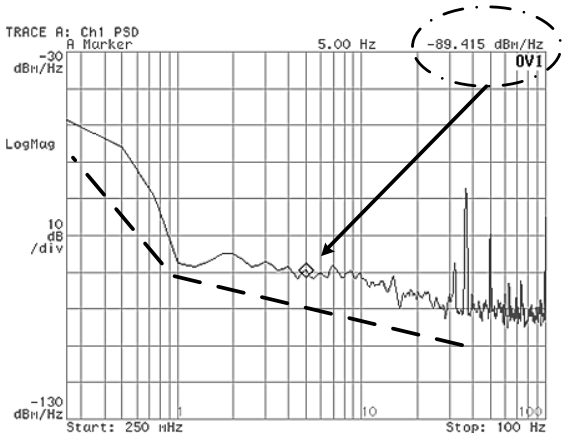


Fig. 3 The loop output with DFA in low frequencies.

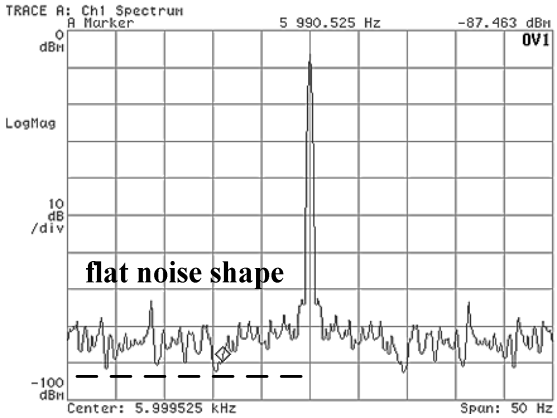


Fig. 4 The loop output with MFA at modulation frequency 6KHz.

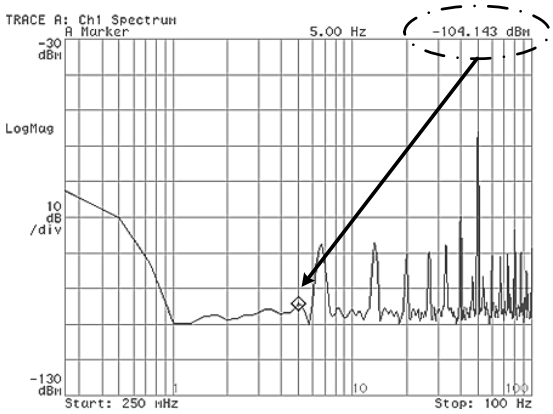


Fig. 5 The loop output with MFA at low frequencies.

One hour stability test is carried out between loop with DFA and loop with MFA. The time domain results and corresponding Allan Variance results are demonstrated in Fig. 6 and Fig. 7. The sampled bandwidth is 10Hz. The bias instability of the loop with DFA reaches 30μg, but the bias instability of loop with MFA is only 8μg. Such comparison confirms that the 1/*f* noise is minimized after applying the MFA.

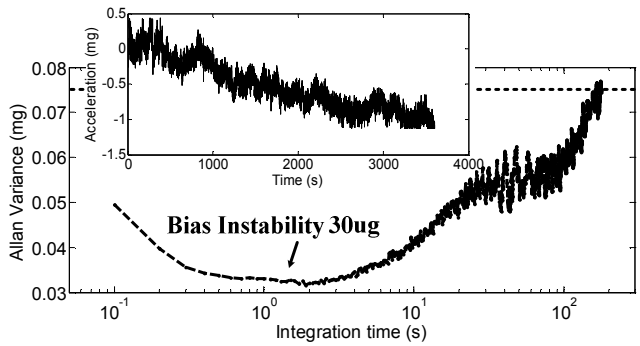


Fig. 6 One hour stability test with DFA.

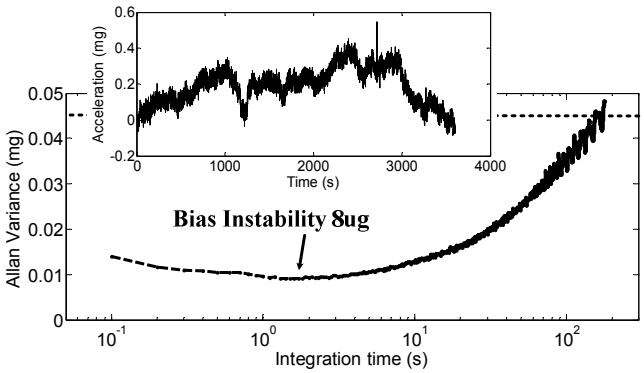


Fig. 7 One hour stability test with MFA.

Besides from bias instability, the long term drift at integration time 100s is also improved by observing Fig. 6 and Fig. 7. The drift at integration time 100s is around 75μg with DFA, and is reduced to 32μg with MFA. The alleviation of long term drift may be due to the isolation of even low frequencies interference and the improvement of loop noise.

Discussion

The comparison experiments suggest that the 1/*f* noise stem from electronics directly contributes to the bias instability. The isolation of 1/*f* noise through modulation successfully reduces the low frequencies noise and interference that exerted on accelerometer, which could be confirmed from the noise spectrum and bias instability test. Our experiments with Allan Variance plots suggest that the closed loop MEMS accelerometer system can achieve bias instability as low as 8μg, which is among the high precision level in the MEMS accelerometer community. The additional cost for this approach lies in the added D/A module and the signal synthesizer for producing modulation carrier at ω_d. For massive IC production, this novel approach can be considered as alternative choice.

Conclusion

We developed a novel and universal modulated feedback approach to improve the bias instability. The 1/*f* noise is significantly reduced by the modulated feedback method and the bias instability reaches as less as 8μg. The long term drift at integration time 100s are also improved with modulated feedback method. This modulated feedback approach is proved to be effective and renders the closed loop MEMS capacitive accelerometer entering the high precision inertial sensors level.

Acknowledgement

The authors would like to thank researchers in the Micro-satellite Research Center of Zhejiang University for their kind assistant and advice.

References

[1] B.V. Amini, R. Abdolvand, F. Ayazi, A 4.5-mW Closed-Loop Delta-Sigma Micro-Gravity CMOS SOI Accelerometer, IEEE Journal of Solid-State Circuits, 41(2006) 2983-2991.

[2] P. Zwahlen, Y. Dong, A-M. Nguyen, et.al, Breakthrough in High Performance Inertial Navigation Grade Sigma-Delta MEMS Accelerometer. Position Location and Navigation Symposium (PLANS), 2012 IEEE/ION, 15-19.

[3] S. Seok, H. Kim, K. Chun, An Inertial-grade Laterally-driven MEMS Differential Resonant Accelerometer. Sensors, 2004, Proceedings of IEEE, 24-27 Oct. 2004, 654-657.

[4] A.A. Trusov, S.A. Zotov, B.R. Simon, A.M. Shkel, Silicon Accelerometer with Differential Frequency Modulation and Continuous Self-Calibration. Micro Electro Mechanical Systems (MEMS), 2013 IEEE 26th International Conference, 20-24 Jan. 2013, 29-32.

[5] N. EI-Sheimy, H. Hou, X. Niu, Analysis and Modeling of Inertial Sensors Using Allan Variance, IEEE Transactions on Instrumentation and Measurement, 57(2008), 140-149.

[6] IEEE Standard Specification Format Guide and Test Procedure for Linear Single-Axis, Nongyroscopic Accelerometers, IEEE Std 1293^{TM}-1998 (R2008).

[7] IEEE Standard Specification Format Guide and Test Procedure for Single-Axis Interferometric Fiber Optic Gyros, IEEE Std 952^{TM}-1997 (R2008).

[8] J. Cui, Z.Y. Guo, Z.C. Yang, Y.L. Hao and G.Z. Yan, Electrical coupling suppression and transient response improvement for a microgyroscope using ascending frequency drive with a 2-DOF PID controller, J. Micromech. Microeng. 21(2011) 095020, 1-11.

[9] O. Aydin, T. Akin, A Bulk-Micromachined Fully Differential MEMS Accelerometer With Split Interdigitated Fingers. IEEE sensors journal, 13(2013), 2914-2921.

Key Engineering Materials Vols 645-646 (2015) pp 646-652
© (2015) Trans Tech Publications, Switzerland
doi:10.4028/www.scientific.net/KEM.645-646.646

Submitted: 2015-01-14
Accepted: 2015-01-20

A Second Differential Bandpass Filter with Tuning Center Frequency and Constant *Q*

Yanxiao Zhao*, Wanrong Zhang, Hongyun Xie, Xin Huang, Lianghao Zhang

College of Electronic Information and Control Engineering, Beijing University of Technology, Beijing, 100124, China

*yanxiao1977@163.com

Keywords: *Q*-enhancement, Multi-regulated Cascode, Tunable active resistor, Tuning center frequency, *Q*-compensation

Abstract: A second order differential filter with *Q*-enhancement and tunable active inductor is presented. The design technique for a tunable *Q*-enhancement SiGe HBT active inductor operating in the wide RF-band for the filter is described. Multi-regulated Cascode circuit is employed to enhance the quality factor *Q* by increasing the output impedance. Tunable active resistor is introduced to boost the tuning ability of the active inductor. Employing the proposed active inductor, the center frequency of the filter is tuned in the frequency of 1.05~2.45GHz by adjusting the bias current, *Q* reducing with different bias current can be compensated via tuning the feedback effective resistance of the active inductor, and *Q* has almost constant value of 209~225 at the frequency of 2.15GHz.

Introduction

RF bandpass filters are used extensively in wireless communications. The main drawbacks of the traditional bandpass filters with spiral inductors are the low center frequency, the high insertion loss and large chip area[1,2]. That can be improved by employing active inductor instead of spiral inductor, which offers wide center frequency tuning ability and high *Q* under small chip area[3,4]. The filter with active inductor exhibits a number of attractive characteristics including a high bandpass center frequency, a large center frequency tuning range, a large and constant quality factor *Q* subsequently a low insertion loss, and a low silicon consumption.

In this paper, the design technique for a tunable *Q*-enhancement SiGe HBT active inductor operating in the wide RF-band is described, and it is followed by the analysis of *Q*-enhancement and tuning ability improvement. Then, the design of a second differential bandpass filter with active inductor is presented, and the simulated results are also addressed.

1. SiGe HBT active inductor

A series of synthesized active inductors are conventional combined a gyrator and capacitor. A common feature of these active inductor topologies is that they all employ transistors back-to-back to emulate the inductive impedance[5,6]. Two kinds of simple topologies combined with common base-common emitter or common collector-common emitter amplifiers are shown in Fig.1[7,8]. We found that the active inductor in Fig.1(a) is also current reuse structure, consequently lower power consumption, but its tuning ability is limited due to only one tunable current resource. The active inductor in Fig.1(b) has slightly more power than that in Fig.1(a) but its tuning ability is more flexible. The active inductor in Fig.1(c) not only offers flexible tuning ability but also increase effective inductance. In our design, the active inductor is based on Fig1(c). Considering the high-frequency

small-signal model of Q_1 and Q_2 is generally chosen and depicted including base-emitter junction capacitance C_{be}, transconductance g_m and collector-emitter resistor r_{ce}, the active inductor can be behaved as an active inductor with its parasitic resistance R_p, capacitance C_p and resistance R_s, as shown in Fig.2, and herein R_p, C_p and R_s can be expressed as follows:

$$R_p = r_{ce1} // (1/g_{m1}) \tag{1}$$

$$C_p = C_{be2} \tag{2}$$

$$L_s = \frac{C_{be1}[R_f / r_{ce2} + 1]}{g_{m1} g_{m2}} \tag{3}$$

$$R_s = \frac{1}{r_{ce2} g_{m1} g_{m2}} \tag{4}$$

herein "//" represents two resistors in parallel with each other.

The quality factor Q can be expressed by

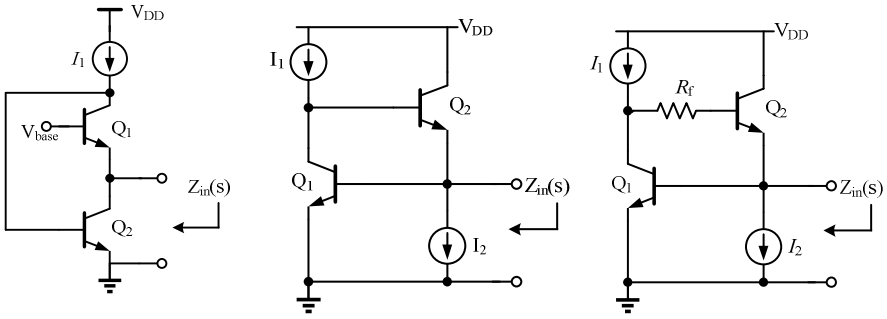
$$Q = \frac{\mathrm{Im}[Z_{in}]}{\mathrm{Re}[Z_{in}]} \approx \frac{\omega L_s}{R_s} = \omega C_{be1}(R_f + r_{ce2}) \tag{5}$$

The resonant frequency of the equivalent RLC networks of the active inductor is given by

$$\omega_n \approx \frac{1}{\sqrt{L_s C_p}} = \sqrt{\frac{g_{m1} g_{m2}}{C_{be1} C_{be2} (R_f / r_{ce2} + 1)}} \tag{6}$$

The frequency f_{max} at which Q is maximized is

$$f_{max} \approx \frac{1}{2\pi L_s g_{m1} \sqrt{g_{m2} r_{ce2}}} = \frac{\sqrt{g_{m2} r_{ce2}}}{2\pi C_{be1}(R_f + r_{ce2})} \tag{7}$$



(a) (b) (c)

Fig.1 Basic circuit topology of active inductor

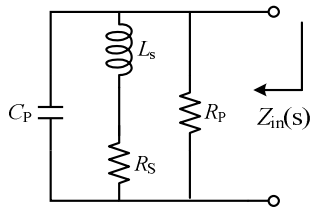


Fig.2 RLC equivalent network

From the expression (3)~(7), it is concluded that the effective inductance L_s, quality factor Q of the active inductor are tunable with changing the bias current of the transistor Q_1 or Q_2, so as to resonant frequency ω_n and frequency f_{max}. As can be seen from the expression (5), quality factor Q can be enhanced by increasing C_{be1}, R_f or r_{ce2}. Q enhanced by increasing C_{be1} or R_f is actually via increasing L_s. It is preferable to reduce ohmic loss for active inductor with excellent performance. That can be realized by increasing r_{ce2}, g_{m1} or g_{m2} from expression (4), but increasing g_{m1} or g_{m2} will also affect L_s. In our design, Multi-regulated Cascode(MRC) circuit performs the common-emitter transistor Q_2 to reduce ohmic loss R_s. On the other hand, the active inductor may be unstable with the bias current of the transistor Q_1 or Q_2 excessively changing. The tunable active resistor(TAR) acting as the feedback resistor can provide another way to tune the effective inductance L_s, as can be seen from expression (3). That offers a new method to reconfigure the active inductor and enhance its tuning ability. The active inductor with MRC and TAR is presented as shown in Fig.3.The DC bias currents of Q_1, Q_2, Q_3, Q_4, Q_5 are provided by M_1, M_2, M_3 which operate in saturation.

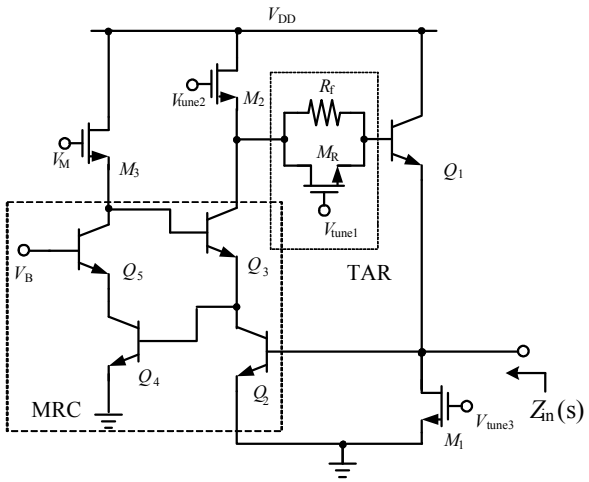


Fig.3 Topology of MRC active inductor with TAR feedback

As shown in Fig.3, MRC circuit is a Cascode amplifier (Q_2 and Q_3) with a feedback network employing a Cascade amplifier itself (Q_4 and Q_5). That the gain of the Cascade amplifier is regulated by the Cascode feedback amplifier is namely MRC. As we all know, the signal equivalent model of the Cascode circuit is equal to that of common-emitter transistor except the output impedance[9,10]. The output impedance of the Cascade amplifier is much larger than the common-emitter amplifier, and the output impedance of the Cascade amplifier multiplied by the gain of the Cascode feedback amplifier, so the output impedance of MRC can be expressed by:

$$R_{o_MRC} = A_{Cascode} R_{o_Cascode} = [g_{m3} r_{ce4} g_{m4} (r_{ce3} // r_{be4})] r_{ce2} g_{m2} (r_{ce1} // r_{be2}) \quad (8)$$

wherein $A_{Cascode}$ is the gain of the Cascode amplifier, $R_{o_Cascode}$ is the output impedance of the Cascode amplifier. It is concluded that the output impedance of MRC is much larger than that of common-emitter configured. In addition, the output impedance is controlled by the gain of the feedback Cascode amplifier which can be tuned by changing V_M or V_B. The signal does not pass through the feedback Cascode amplifier, so the equivalent transconductance of MRC is equal to that of Cascode amplifier as well as common-emitter amplifier. It can be considered that the signal equivalent model of MRC is same as that of common-emitter transistor except for the output impedance much more increased, and Q can be enhanced and independently tuned.

TAR is implemented with the passive resistor R_f in parallel to the transistor M_R as shown in Fig.3, and it can be equivalent to tunable resistor R_g which is controlled by the gate-source voltages V_{tune1} as shown in Fig.4. Fig.5 shows R_g varies with frequency and tuning voltage when R_f =1KΩ. It can be

observed that R_g decreases with the V_{tune1} increasing, and when V_{tune1} is $0V$, R_g reaches maximum. It can be concluded that L_s of the active inductor can be tuned via changing only V_{tune1}, and the tuning ability is more flexible.

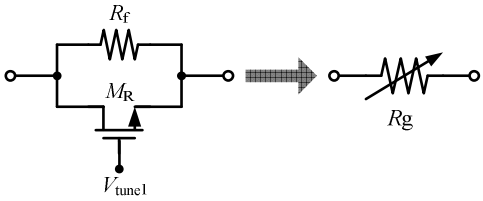


Fig.4 TAR topology

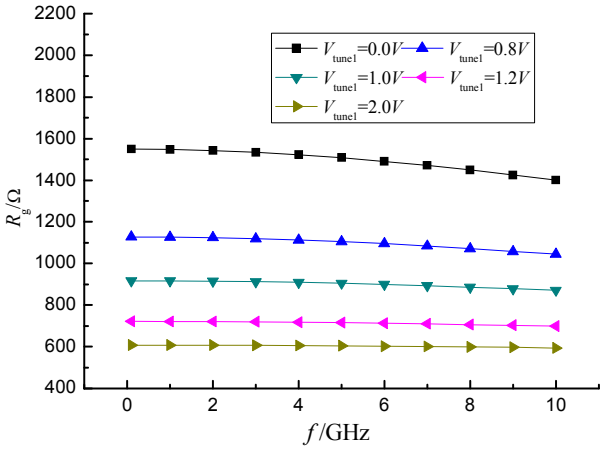


Fig.5 R_g changing with V_{tune1}

In conclusion, the active inductor with MRC and TAR proposed in Fig.3 provides high-Q and flexible tuning ability. The effective inductance L_s and resonant frequency ω_n can be tuned by adjusting V_{tune1}, V_{tune2} or V_{tune3}, and quality factor Q can be compensated by adjusting V_M or V_{tune1}. It can be reconfigurable for communication systems employing the active inductor.

2. Second differential bandpass filter based on active inductor

Applying the high-Q active inductor with flexible tuning ability in Fig.3, a second differential bandpass filter is implemented with Spectre of Cadence's EDA using TSMC 0.35μm SiGe BiCMOS process design kit (PDK), as shown in Fig.6. The second differential bandpass filter consists of differential input stage, two improved active inductors, negative resistor network and differential output stage. V_{in}^+ and V_{in}^- are two differential input ports, V_{out}^+ and V_{out}^- are two differential output ports, the gates and drains of MOS transistors M_{11} and M_{12} are cross connected to realize a negative resistor.

The center frequency of the filter can be expressed by:

$$\omega_C \approx \frac{1}{\sqrt{L_s C_P}} = \sqrt{\frac{g_{m1}g_{m2}}{C_{be2}C_{be1}(R_g/R_{o_MRC}+1)}} \tag{9}$$

Considering R_g<<R_{O_MRC}, the above expression can be simplified by:

$$\omega_C \approx \sqrt{\frac{g_{m1}g_{m2}}{C_{be2}C_{be1}}} \tag{10}$$

It is concluded that the center frequency of the filter can be shifted by changing g_{m1} or g_{m2}, which can be realized by varying V_{tune3} or V_{tune2}. Fig.7 shows the center frequency is shifted from 1.05 GHz to 2.45 GHz with V_{tune2} varying from $2.50V$ to $2.62V$.

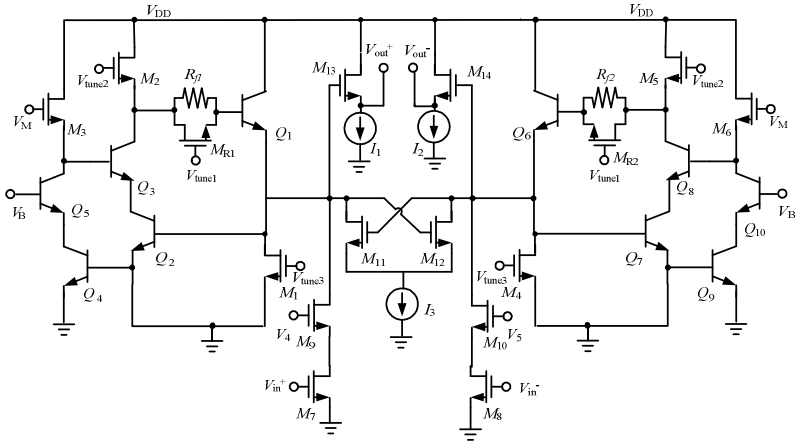


Fig.6 Second differential bandpass filter

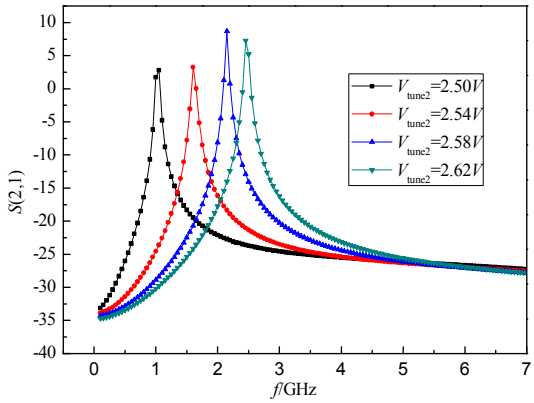


Fig.7 S_{21} of the filter versus frequency with different V_{tune2}

According to expression (5), the quality factor Q of the filter can be given by

$$Q = \omega C_{be1}(R_g + R_{o_MRC}) \tag{11}$$

It is seen from the above expression that the tunable R_g can enhance Q. Table 1 is the quality factor Q of the filter under different V_{tune1} at the frequency of 2.15GHz, According to the table1, adjusting V_{tune1} can compensate the reducing of quality factor Q of the filter due to the change of V_{tune2}.

Table1 Quality factor Q under different V_{tune1}

V_{tune1}	Q
0.9	340
1.2	300
1.5	226
1.8	128

Fig.8 exhibits quality factor Q compensated via tuning V_{tune2} in comparison with no compensation. The compensated Q has a value of 209~225 at the frequency of 2.15GHz, and it almost maintains constant.

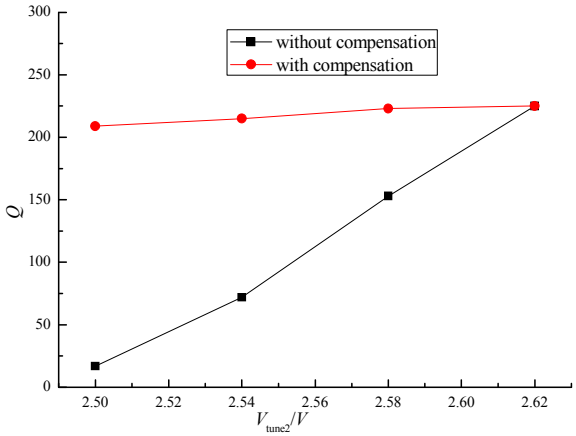


Fig.8 Compensated quality factor Q in comparison with no compensation

3. Conclusions

The design of the tunable filter with constant Q in TSMC 0.35μm SiGe BiCMOS process design kit (PDK) has been introduced and verified. It has been demonstrated that it achieves almost constant Q of 209~225, a large tuning range from 1.05 to 2.45GHz. Furthermore, the center frequency shifting is independent of Q in multiband frequency. The proposed filter with small consumption, low cost, enhanced tunability and good integration can be applied to multiband wireless system.

4. Acknowledgements

This work was supported by Beijing Municipal Natural Science Foundation, (Contract Nos. 4142007, 4122014, 4143059).

5. References

[1] Kacar F, Yesil A. Novel grounded parallel inductance simulators realization using a minimum number of active and passive components [J]. Microelectronics Journal, 2010(41): 632–638.

[2] CaoYu, Robert A. Groves, Xuejue Huang, et al. Frequency-independent equivalent-circuit model for on-chip spiral inductors[J]. IEEE Journal of Solid-State Circuits, 2003, 38(3): 419-426.

[3] Andersson S, Svensson C. An active recursive RF filter in 0.35μm BiCMOS [J]. Analog Integrated Circuits and Signal Processing, 2005, 12: 213-218.

[4] Cristian A, Liviu G. On the tuning possibilities of an RF bandpass filter with simulated inductor[C]. Proceedings of the International Semiconductor Conference, CAS. Sinaia, Romania, 2007: 489-492.

[5] Bakken T, Choma J. Gyrator-Based synthesis of active on-chip inductances [J]. Analog Integrated Circuits and Signal Processing, 2003, 34(3): 171-181.

[6] Thanachayanont A. CMOS transistor-only active inductor for IF/RF applications [C]//International Conference on Industrial Technology. Bankok, Thailand, 2002, 12: 1909-1912.

[7] Y. Wu, M. Ismail, H. Olsson. CMOS VHF/RF CCO based on active inductors[J]. IEEE Electronics Letters, 2001, 37(8): 472–473.

[8] C. Hsiao, C.Kuo, C. Ho, Y. Chan. Improved quality factor of 0.18μm CMOS active inductor by a feedback resistance design [J]. IEEE Microwave and Wireless Components Letters, 2002, 12(2): 467–469.

[9] Palr.Gray, Paulj.Hurst, Stephevh.Lewis, et al. Ayalysis and design of analog integrated circuits [M]. Higher Education Press, 2005: 194-197.

[10] Yuan F. CMOS current-mode circuits for data communications. New York: Springer Science-t-Business Media. 2007.

Key Engineering Materials Vols 645-646 (2015) pp 653-656
© (2015) Trans Tech Publications, Switzerland
doi:10.4028/www.scientific.net/KEM.645-646.653
Submitted: 2015-01-19
Accepted: 2015-01-21

Trajectory Guidance Law For MAV Based On MEMS Sensor / GPS

Cai Yu [1,a], Xiong Wei [2,b], Cao Xiaotang[3,c], Zhaoying Zhou[4,d]

[1,4]State Kay Laboratory of Precision Measurement Technology and Instruments, Tsinghua University, Beijing, China
[2]Collaborative Innovation Center of Advanced Nuclear Energy Technology Tsinghua University, Beijing, China
[3]State Key Laboratory of Instrumentation Science & Dynamic Measurement, North University of China, Taiyuan, China
[a]caiyu@mails.tsinghua.edu.cn,[b]xwthu@mail.tsinghua.edu.cn,[c]caoxiaotang@163.com
[d]zhouzy@mail.tsinghua.edu.cn,

Key Words: Micro Air Vehicle (MAV); lateral control law; guidance logic; micro-electro mechanical system (MEMS).

Abstract
This paper studies a new trajectory guidance logic system for Bank-To-Turn fixed-wing (BTT) micro air vehicle (MAV) based on MEMS sensor / GPS , and introduce the method of estimating the navigation information from MEMS sensors and GPS. a nonlinear guided logic based on literature is utilized to get the desired roll angle , and a total energy controller is utilized in the longitudinal loop. Based on the kinematic model of the coordinated turning of MAV, the system can ensure that the aircraft stably track a flight plan segment. Flight tests on MAV prove the feasibility of the trajectory guidance logic system.

1 Introduction

With the widely use of micro air vehicle (MAV), it need to track the designed trajectory precisely and ensure its stability when performing a specific flight mission. Hence, requirement of developing a highly efficient trajectory guidance system is vigorous growth. There are varieties of trajectory guidance systems that have been proposed for MAV. Traditionally, Nelson[1] described an approach using vector fields to represent desired ground track headings. Moreover, the trajectory tracking[2] showed apparent delay, and was susceptible to wind. Sanghyuk Park[3,4] presented a nonlinear acceleration guidance logic, which had performed excellently in guiding MAV on curved trajectories, in order to make up for the insufficiency of traditional guidance logic. The logic contains an element of anticipatory control that takes into account the limit of the input, current state and output of navigation part. Meanwhile, it adopts the inertial speed change which affects the flight trajectory tracking, and it can't eliminate the steady-state error of the trajectory tracking when following a straight line path.

This paper studies a new trajectory guidance logic system for MAV, Micro Measurement and Flight Control System based on MEMS sensor and GPS, whose installation precision and attitude angle measurement accuracy are not very high. Based on the kinematic model, the paper puts forward a lateral control law to eliminate the influence and satisfy the accuracy in navigation information. Then, the paper proposes the longitudinal control law[5] mainly. The controller in longitudinal loop is used to solve the coupling problem between longitude flight path control and flight speed control. The overall trajectory guidance logic can reduce the magnitude of the cross-track error and lessen the trajectory tracking steady-state error. In this case, a number of modern control design techniques can be applied, such as receding horizon[6], differential flatness[7,8], and neural network based adaptive controls. At last, flight tests prove the feasibility of the trajectory guidance system.

2 Overall plan

The overall plan of trajectory tracking scheme is MAV obtaining desired flight trajectory from ground station. When flying autonomously, MAV gains current position, trajectory deflection angle

and other control parameters by navigation information block, and then transmits them to guidance link, and sequentially obtains the deviation between MAV and desired trajectory. The guidance link generates desired guidance order according to the deviation. Then, flight control link provides aileron and rudder's control value, and eliminates deviation by Bank-To-Turn (BTT), and consequently makes MAV fly along desired trajectory precisely.

3 Estimation of Navigation Information from MEMS sensor and GPS for MAV

The basic task of the MAV navigation information estimate block is to give real-time control measurement parameters for the guidance link. For trajectory tracking, it needs to provide some parameters, such as horizontal position(X, Y), trajectory deviation angle χ from GPS receiver. The following section will give the kinematics model of the MAV, and then introduce the method of estimating the Navigation Information from MEMS sensors and GPS for the MAV. When the MAV flies autonomously, the speed is relatively slow. It is considered to be in coordinated turning[9] state and to have smaller pitch attitude angle and pneumatic angle. Therefore, when the MAV is in coordinated turning state, its lift force L, roll angle ϕ, and horizontal overload az have similar relation[10] as follows:

$$ma_Z = L\sin\phi \tag{1}$$

In vertical direction, the component of lift force and gravity are approximately equal,

$$mg = L\cos\phi \tag{2}$$

In geographic coordinate system, the rate of change of trajectory deviation angle $\dot{\chi}$, horizontal overload a_z and ground velocity V_g satisfy:

$$\dot{\chi} = a_Z / V_g(t) \tag{3}$$

From(1)-(3), we can get the following equation:

$$\dot{\chi} = g \cdot \tan\phi / V_g \tag{4}$$

When MAV is in geographic coordinate system, its east displacement X, north displacement Y, and ground velocity V_g and trajectory deviation angle χ have such relations[11]:

$$\begin{cases} \dot{X} = V_g \cos\chi \\ \dot{Y} = V_g \sin\chi \end{cases} \tag{5}$$

Then, the navigation information N=[X, Y, χ] is regarded as the output $\vec{Z}$ of the Kalman filter. The state measurement equations are formulated as follows:

$$\begin{aligned} \dot{N} &= [\dot{X},\ \dot{Y},\ \dot{\chi}] \\ Z &= N + R \end{aligned} \tag{6}$$

Where R is the measurement noise, then, the state vector N can be estimated by using an Extended-Kalman-Filter.

4 Trajectory guidance law

The paper mainly presents the outer loop control law. It separates the vehicle guidance problems into lateral control law and longitudinal control law.

4.1 Lateral control law design: for the MAV keep following the desired trace, a nonlinear guided logic based on [11] gives the desired roll angle ϕ_d to complete the trajectory following. The lateral guided logic works by selecting a reference point on the desired trajectory, at a predefined distance D from the MAV. Based on the angle η between the MAV velocity vector and a line from the MAV to the reference point, as a bank-to-turn vehicle, a lateral roll command, and yaw rate command p_d are calculated as:

$$\begin{aligned} \phi_d &= \arctan\left(2\frac{V^2}{g \cdot D}\sin\eta\right) \\ p_d &= \frac{g \cdot tg\phi_d}{V} \end{aligned} \tag{7}$$

Then, there is a yaw rate controller and an attitude controller to complete the coordinate turn by an aileron deflection ς_{AIL}^{p} .

4.2 Longitudinal control law design: in the longitude loop of MAV, the coupling feature of elevator and throttle is based on SISO controller design method, which can't realize individual control of flight speed and altitude. For MAV's longitudinal loop, the common style is to change height when keeping certain flight speed. Because of the lack of the coordination of control surface and throttle, the coupling effect is very apparent between altitude and speed. In order to solve the coupling problem between longitude flight path control and flight speed control, the paper adopts MAV total energy control technology to design longitudinal guidance law.

The paper introduces flight altitude deviation h_e and flight speed deviation v_e to eliminate longitudinal steady-state error. When MAV is in a small track angle, the paper defines MAV's total energy change rate $\dot{E}$ and total distribution rate $\dot{L}$ as follows:

$$\begin{aligned} \dot{E} &= \frac{\dot{v}_e}{g} + K_v^E \cdot v_e + \frac{\dot{h}_e}{v} + K_h^E \cdot \frac{h_e}{v} \\ \dot{L} &= \frac{\dot{v}_e}{g} + K_v^L \cdot v_e - \frac{\dot{h}_e}{v} - K_v^L \cdot \frac{h_e}{v} \end{aligned} \tag{8}$$

Where, h_e and v_e denote the flight altitude deviation and flight speed deviation, $\dot{h}_e$, $\dot{v}_e$, $\dot{E}$ and $\dot{L}$ denote flight altitude deviation change rate, flight speed deviation change rata, total energy change rate and total distribution rate. K_v^E, K_h^E, K_v^L, K_v^L are proportional coefficient.

According to the option of total energy change rate $\dot{E}$ and total energy distribution rate $\dot{L}$, using PI controller, longitudinal guidance law can be gained as

$$\begin{aligned} \Delta\delta_T^H &= K_{Tp}^H \cdot \dot{E} + \frac{K_{Ti}^H}{s} \cdot \dot{E} \\ \theta_d &= K_{\theta p}^H \cdot \dot{L} + \frac{K_{\theta i}^H}{s} \cdot \dot{L} \end{aligned} \tag{9}$$

Where, K_{Tp}^H, K_{Ti}^H, $K_{\theta p}^H$, $K_{\theta i}^H$ are proportional coefficient, $\dot{E}$ and $\dot{L}$ denote total energy change rate and total energy distribution rate.

5. Flight test and result analysis

The control law was tested with TMAV-380, shown in Fig.1. and a MEMS sensor based micro-autopilot in the MAV. As shown in Fig.2, micro-autopilot integrates MEMS sensors, such as tri-axial gyroscope ADIS-16100, tri-axial accelerometer ADXL345, and tri-axial magnetometer HMC5843. The MAV has a wing span of 380 mm and total weight of 0.25 kg. In the test, the flight velocity is about 16 m/s, GPS time delay is about 0.4 s, and the output frequency of navigation information estimate module is 4 Hz. The trajectory guidance law makes it follow the desired path given by four way points, as shown in Fig.3. The data of roll angle is shown in Fig.4.

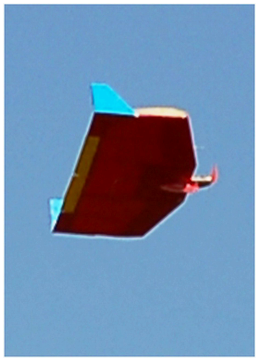


Fig. 1 TMAV-380

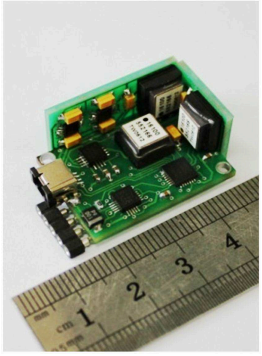


Fig. 2 Micro-Autopilot

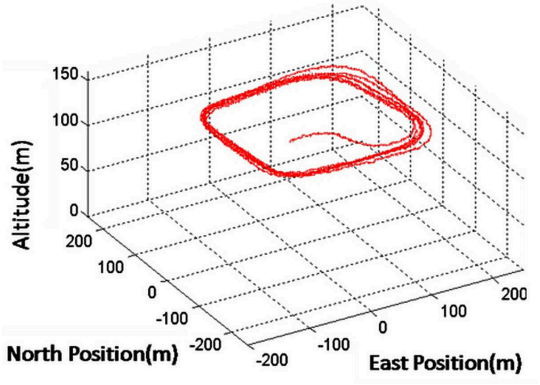


Fig.3 Trajectory guidance result

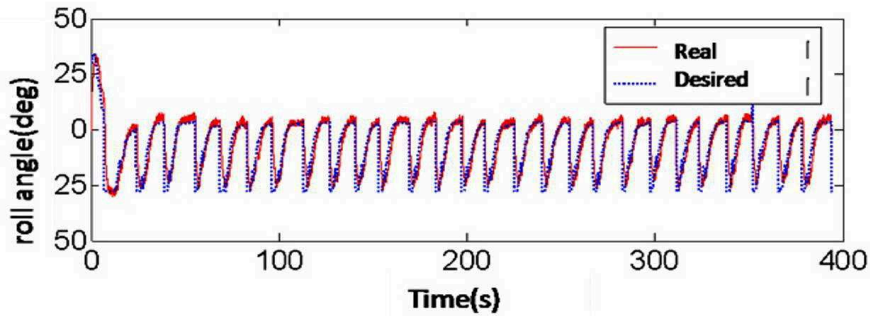


Fig. 4 The record data of roll angle

6. Conclusion

The paper presents a trajectory guidance logic applied to BTT fixed-wing MAV and MEMS sensor based micro-autopilot, and introduce the method of estimating the navigation information from MEMS sensors and GPS. To let the MAV keep following the desired trace, a nonlinear guided logic based on literature is utilized to get the desired roll angle , and a total energy controller is utilized in the longitudinal loop. The flight results indicate this logic can guide MAV to complete desired trajectory tracking.

References

[1] Y. Oshman, M. Isakow, Mini-UAV attitude estimation using an inertially stabilized payload, IEEE Transactions on Aerospace and Electronic Systems 35 (1999) 1191–1203.

[2] Rong Zhu, Dong Sun, Zhaoying Zhou, in: Integrated Design of Trajectory Planning and Control for Micro Air Vehicles, Mechatronics. Vol.17 (2007), p. 245-253

[3] Sanghyuk P, John D, Jonathan P. Performance and Lyapunov Stability of a Nonlinear Path-Following Guidance Method [J]. Journal of guidance, control, and dynamics. Vol.30(6), (2007), p.1718 – 1724.

[4] Sanghyuk P, John D, Jonathan P. How. A new nonlinear guidance logic for trajectory tracking[R]. (2004), AIAA 2004-4900.

[5] QUYaohong, YAN Jianguo, LU Jingchao. Study on kalman filter in GPS/Radio/DR integrated navigation system of an MAV [J]. Systems Engineering and Electronics. Vol.126(19), (2004), p.1239-1242.

[6] Zhu R, Sun D, Zhou ZY, et al. A linear fusion algorithm for attitude determination using low cost MEMS-based sensors. Measurement 40 (3) (2007), 322-328

[7] Fulghum D A. Miniature air vehicles fly into army's future [J]. Aviation Week & Space Technology, (1998), Vol. 11, p.37-38

[8] Deptula DA. Firing for Effect: Change in the Nature of Warfare [M].USA:Aerospace Education Foundation, (1995).

[9] Amidi,O., Thorpe,C., Integrated Mobile Robot Control[J]. Proceedings of SPIE: the international society for optical engineering, (1991), Vol.1388, p.505-523.

[10] Ollero,A., Heredia,G., Stability Analysis of Mobil Robot Path Tracking[C], Proceeding of the Institute of electrical and electronics engineers/robotics society of Japan international conference on robot and systems (1995), p.461-466

[11] John J. Deyst, Jonathan P. How Lyapunov Stability of a Nonlinear Guidance Low for MAVs [R]. (2005), AIAA 2005 -6230.

Key Engineering Materials Vols 645-646 (2015) pp 657-661
© (2015) Trans Tech Publications, Switzerland
doi:10.4028/www.scientific.net/KEM.645-646.657

Submitted: 2015-01-20
Accepted: 2015-01-21

A Feed-forward Sigma-delta Modulator Applied in Silicon Gyroscope

Shao Qi[1], Lv Qiuye[1],Meng Hao[1],Fu Qiang[1,a],Liu Xiaowei[1]

[1]MEMS Center, Harbin Institute of Technology, Harbin, Heilongjiang, China

[a]shaoqi0401@163.com

Keywords: Modulator, Sigma-delta, Micro-Gyroscope, DWA

Abstract: Aiming to be applied in silicon gyroscope, a three-order single loop feedforward modulator with three-bit quantizer and local feedback is designed in this paper. Signal band is 200 KHz, sampling rate is 25.6 MHz, OSR is 64. Ideal modulator is then designed and simulated in MATLAB, getting SNR 125dB. Non-ideal factors are also added to ideal model, DWA technology is adopted to restrain the nonlinearity of multi-bit quantizer, getting SNR 104dB. Finally, transistor-level full-difference modulator is designed and simulated in Cadence, fetting SNR 101.3dB.

Introduce

Micro-inertia sensors bear the advantages of small volume, low cost, low power consume and compatible with CMOS technology. Research of micro-inertia sensors is becoming more and more popular[1], of which Sigma-delta modulator is the key technology. Research of high-precision Sigma-delta applied in silicon gyroscope is meaningful.

In the second section, working principles and structure of Sigma-delta ADC is analyzed and a three-order single-loop modulator with three-bit quantizer is designed[2] and simulated in MATLAB. In the third section, Non-ideal factors are analyzed and DWA model is set up. In the fourth section, transistor-level modulator is designed and simulated using 0.6 μ m CMOS technology. In the last section a conclusion.

Analysis of working principles

Modulator designed in this paper is majorly applied in ADC of silicon gyroscope interface, requiring input signal band 20KHz, OSR 64, SNR larger than 96dB. In order to realize a stable system, a three-order three-bit modulator is chosen. This structure can also reduce the dependence between quantizer gain and amplitude of input signal, the power consume of which is also smaller.

Modulator is designed using SD Toolbox, getting noise transfer function as follows:

$$NTF(z)=\frac{(z-1)[(z^2-1.999z+1]}{(z-0.3657)(z^2-0.7924z+0.2623)} \tag{1}$$

Based on analysis above, ideal model is constructed as Fig,1. Simulation is then processed, PSD result is shown in Fig.2.

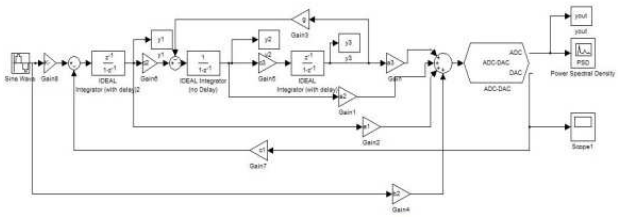


Fig.1 Ideal model of Sigma Delta modulator

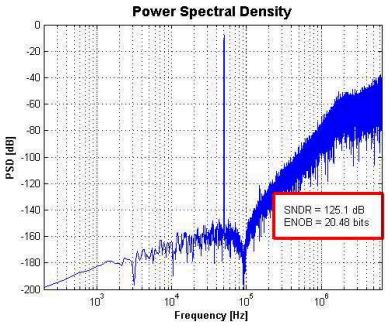


Fig.2 PSD of ideal modulator

As is shown in Fig.2, SNR of ideal system is 125dB and ENOB is 20.48 bits.

Non-ideal model

There are lots of non-ideal factors in actual circuit, such as clock jitter[3], finitude gain of operational amplifier, thermal noise brought about by switched capacity integrator, nonlinearity of feedback DAC. Because multi-bit quantizer is adopted in this paper, harmonic distortion resulted from feedback DAC nonlinearity affected precision of the modulator a lot. When designing modulator, nonlinearity of feedback DAC must be compensated[4].

Multi-bit feedback DAC usually accomplished by parallel DAC shown in Fig.3, M-bit quantizer is accomplished by $2^M - 1$ feedback units controlled by strobe switches. Because of fabrication error, all feedback units can't match with each other totally, leading to feedback non-linearity. In order to compensate non-linearity, Date Weighted Average (DWA) technic is adopted.

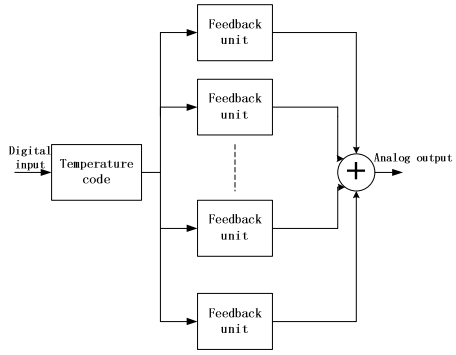


Fig.3 Structure of feedback DAC

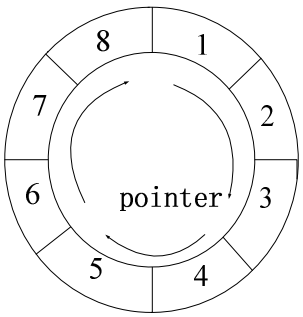


Fig.4 Working principle diagram of DWA

Basic idea of DWA is shown in Fig.4, feedback units are recycled repeatedly and DAC feedback capacities are periodically gated according to signal amplitude. As the sampling time is long enough, the total capacity error can be seen as zero, thus shaping the noise, making the harmonic white noise distributed in the frequency band equally.

Model the feedback DAC based on analysis given above, as is shown in Fig.5.

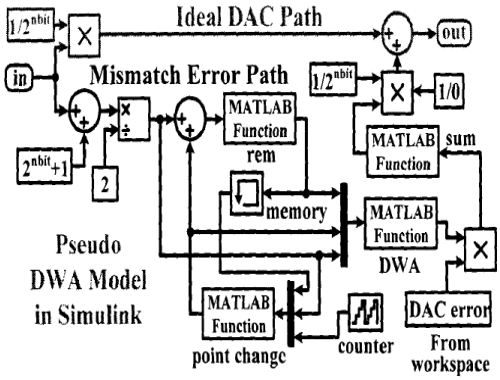


Fig.5 DWA model of DAC non-linearity compensating circuit

Adding non-ideal factors given above to the modulator, a model of non-ideal modulator is achieved and is shown in Fig.6, the simulation result of which is shown in Fig.7.

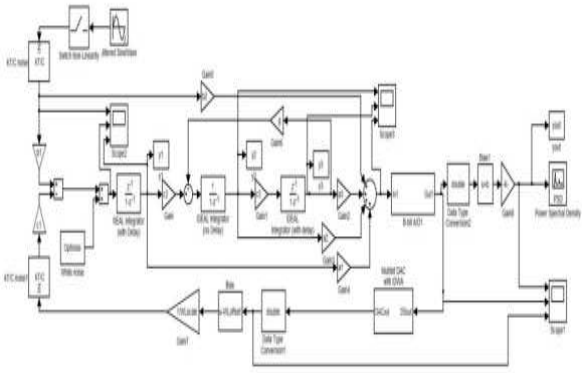


Fig.6 Simulink model of non-ideal system

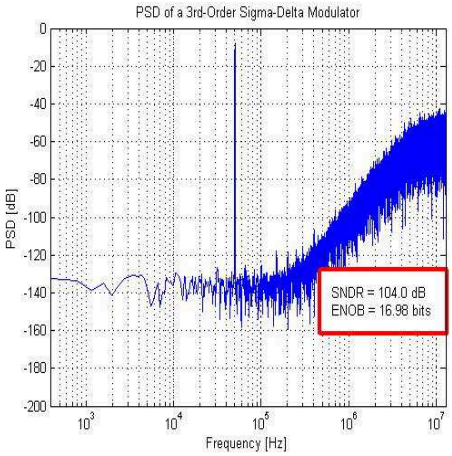


Fig.7 SNR of non-ideal system

It can be seen from Fig.7 that when non-ideal factors are added to modulator, SNR of system output decreases to 104dB, ENOB is 16.98 bits.

Transistor-level design

In this section, transistor-level design of three-order three-bit feedforward Sigma-delta modulator is processed. In order to get high precision, full differential switch capacitor circuit is adopted to implement the whole circuit. ALL module of modulator, such as integrator, operational amplifier, clock generation circuit, comparator and multi-bit quantizer and DWA module, are designed and simulated. In the end, the whole circuit is simulated.

The design of integrator

Integrator is the key component of modulator, circuit implementation is shown in Fig.8, Fig.8(a) is a delay integrator, conducted as input-level integrator, the noise performance of which determines the noise performance of the whole modulator, Correlated Double Sampling technology (CDS) is adopted to reduce the impact of flicker noise. The second integrator is an non-delay one with zero-optimization technology to improve the SNR, which is implemented by introducing local feedback.

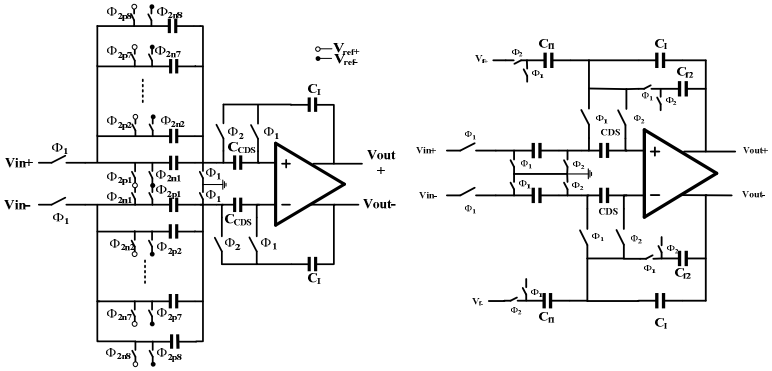


Fig.8 (a)structure of the first-stage integrator (b)structure of the second-stage integrator

Design of operational amplifier

Because of the high clock frequency, a high-speed, high-gain operational amplifier is designed in this paper[5], a high slew rate is also needed to drive the large load. A full differentially symmetrical current mirror op-amp is adopted and the structure of which is shown in Fig.9, the common-mode feedback (CMFB) is implemented by switched capacitor circuit.

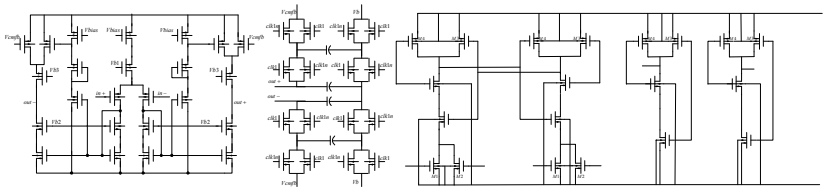


Fig.9 Circuit of full differential op-amp Fig.10 Circuit of comparator

Simulation of the op-amp shows that, the gain of op-amp is 100dB, bandwidth is 103MHz, slew rate is 130V/ μs .

Design of comparator and multi-bit quantizer

Comparator is the key component of quantizer, of which a high resolution ratio is needed. Comparator used in this paper is shown in Fig.10, the resolution ratio of which is 5mV.

The multi-bit quantizer is then be designed, as is shown in Fig.11, a full differential FLASH ADC is designed for the purpose of easy implementation and high speed.

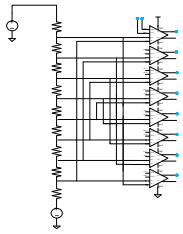


Fig.11 Circuit diagram of FLASH ADC

Design of two-phase non-overlapping clock

Switched capacitor circuit is controlled by clock signal, in order to decrease the charge injection and clock feedthrough, two-phase non-overlapping clock is designed in this paper[6], as is shown in Fig.12.

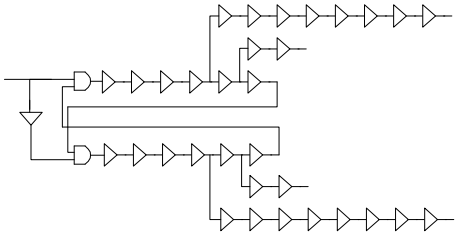


Fig.12 Circuit of two-phase non-overlapping clock

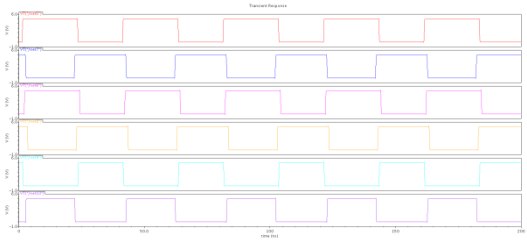


Fig.13 Simulation waveform of clock

Design of DWA

Design of DWA module is shown in Fig.14, consisting of three-bit full adder, three-bit logarithmic shift register, pointer register, transcoder, etc. Matching error is noise-shaped when DWA technology is applied.

Simulation results

The whole circuit is simulated in Cadence Spectre and the simulation result is then imported into MATLAB and FFT is processed, getting a PSD diagram of modulator output, as is shown in Fig.15. It can be seen that SNR of modulator is 101.3dB and ENOB is 16.54 bits.

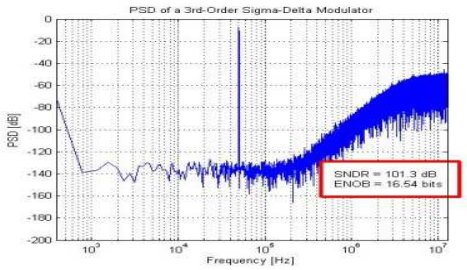


Fig.15 PSD diagram of modulator output

Conclusion

A three-order feedforward sigma-delta modulator with multi-bit quantizer is designed in this paper taking requirement of silicon gyroscope interface into account. Non-ideal factors are then modeled, non-linearity compensation, local feedback optimization are also designed and simulated, getting SNR 104dB. In the end, transistor-level design is processed, CDS technology is adopted to reduce the impact of flicker noise, when simulated using 0.6um technology, a SNR 101.3dB is achieved.

References

[1] K.S.Kundert. Introduction to RF simulation and its application[J]. IEEE Journal of Solid State Circuits 1999.1:298~319.

[2] Vijay Dhanasekaran. et al. A Continuous Time Multi-Bit AI ADC Using Time DomainQuantizer and Feedback Element[J]. IEEE J. Solid-State Circuits. 2011, 46: 639-659.

[3] H. Z. Hoseini, I. Kale, O. Shoaei. Modeling of Switched-Capacitor Delta-Sigma Modulators in SIMULINK.IEEE Trans.on Instrumentation and Measurement. 2005, 54(4): 1646~1654

[4] Steven R. Norsworthy, Richard Schreier and Gabor C. Temes, Delta-Sigma Data Converters Theory, Design, and Simulation. Piscataway USA: IEEE, Circuits & SystemsSociety, 1996.

[5] J. Deveugele, G. Vander Plas, M. Steyaert et al. A 1V 140μW 88-dB Audio Sigma-Delta Modulator in 90-nm CMOS[J]. IEEE Journal of Solid-State Circuits, 2004, 39:1809-1818.

[6] T. Hayashi, Y. Inabe, K. Uchimua. A multistage delta-sigma modulator without double integration loop[C]. ISSCC Dig. Tech Pap, Feb 1985: 182-183.

Key Engineering Materials Vols 645-646 (2015) pp 662-669
© (2015) Trans Tech Publications, Switzerland
doi:10.4028/www.scientific.net/KEM.645-646.662

Submitted: 2015-01-29
Accepted: 2015-01-29

A novel capacitive temperature sensor for real-time monitoring of temperature in the silicone oil fan clutch

Qing-Ying Ren, Li-Feng Wang, Jian-Qiu Huang, and Qing-An Huang[a]

Key Laboratory of MEMS of the Ministry of Education, Southeast University, Nanjing 210096, China

[a]Electronic mail：hqa@seu.edu.cn

This paper presents a novel capacitive sensor for real-time monitoring of temperature in the silicone oil fan clutch. The structure of the temperature sensor is designed and fabricated by the Silicon-On-Glass (SOG) process based on the bonding technology. The silicone oil is designed as the temperature sensing materials in the capacitive sensor. The capacitance of the embedded sensor is changing with respect to temperature of the silicone oil fan clutch. Experimental results show that the sensor provides a sensitivity of 27.3fF/℃ in the -30 to 40℃ range, 58.2fF/℃ in the 50 to 110℃ rang. It is also demonstrated that the temperature sensitive capacitor can be integrated with a copper inductance antenna and tests as a passive wireless temperature sensor. The resonant frequency of the inductor-capacitor (LC) resonator changes with respect to the changing capacitance. Then temperature changes can be remotely determined towards a frequency spectrum study. Experimental results show that the LC type passive wireless sensor provides a sensitivity of 6.35kHz/℃ in the -30 to 110℃ range.

I. INTRODUCTION

There are various automobile sensors play very important role in the efficient operation of vehicles. One of demanded topics for automobiles refers to the requirement of miniaturization in those sensors. However, micro electro-mechanical systems (MEMS) technology, evolved from the integrated circuit industry, has long been applied to the fabrication of various electronic devices from which some have already been in use for several years. [1],[2],[3] MEMS sensors offer significant advantages over their macroscopic counterparts, they offer higher sensitivity, lower noise and lower production costs, and MEMS sensors have a high potential of making a new field of applications for automobiles. [4],[5]

The viscous fan clutch, which is effective in large vehicles such as commercial trucks, has been introduced 50 years ago to reduce fan power and the noise level. [6],[7] Fan clutch functions when the surrounding temperature rises, the bimetal strip opens the valve and the fluid moves into the labyrinth groove between the clutch plate, the cover housing creating torque which in turn operates the fan [Fig. 1(a)]. The bimetal strip fluid cooling fan works by sensing the temperature of the hood under the engine.

The major drawback of the fan clutch is that the speed of the fan cannot be controlled from the outside, and overheating can easily occur with the danger of flames. There are generally equipped the fan clutch device with on-board computers, and predict and control the vehicle dynamics in real time by changes in the MPU. Implementation of this system requires good theoretical models that are capable of accurately predicting torque transfer as a function of the actuator signal at any given operating condition.[8] In order to obtain good agreement with experimental data, it is necessary to include an appropriate thermal model where temperature should be taken seriously. [9] It is necessary to monitoring the temperature of the fan clutch in real-time.

In this paper, a novel capacitive temperature sensor for real-time monitoring of temperature in the silicone oil fan clutch is introduced [Fig. 1(b)]. The capacitive-type temperature sensors are regarded the mostly preferred ones since their lower power consumption and fabrication costs. [10] The sensing capacitance of this kind of sensors can be given by[11],[12],[13]

$$C_s = \frac{\varepsilon_0 \varepsilon_s A}{d}. \quad (1)$$

where ε_s represents the dielectric constant of the silicone oil with temperature, meanwhile, vacuum dielectric constant ε_0, capacitor sensing area A and the distance between the capacitor plates d are the constants in Eq. 1. Hence, the sensing capacitance C_s is only determined by ε_s, [14] the dielectric constant of silicone oil can be used as the sensing parameter.

We also connected capacitive temperature sensor with a fixed planar spiral copper inductor to form an integrated inductor-capacitor (LC) resonator structure [Fig. 1(c)]. In this passive wireless sensor, a spiral inductor L_s is connected in series with a sensing capacitor C_s, temperature changing monitored by the capacitive temperature sensor which shifts the resonance frequency of the inductor-capacitor (LC) resonator structure. The resonance frequency of the LC-type passive wireless sensor is given by[15]

$$f_s = \frac{1}{2\pi} \frac{1}{\sqrt{L_s C_s}}. \quad (2)$$

The resonance frequency shifts with the changing temperature, therefore, temperature can be monitored remotely using the LC-type passive wireless temperature sensor. [16],[17] In the following sections, we will describe the design, fabrication, and testing of the temperature sensor.

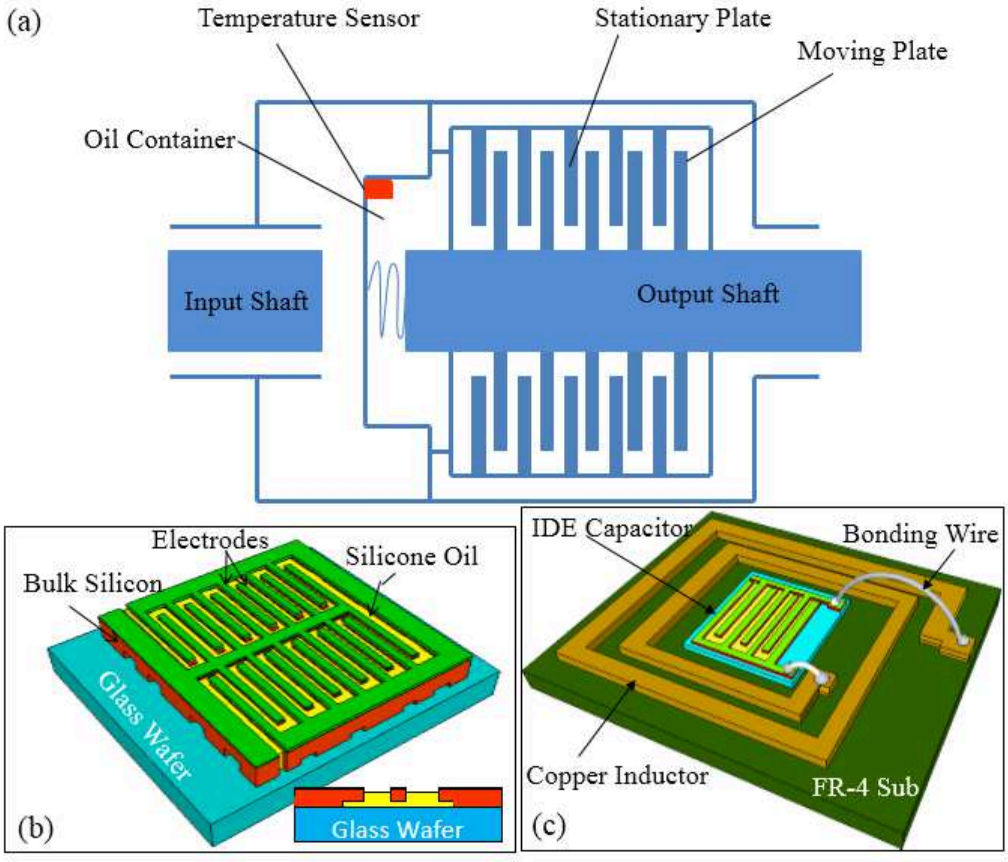


FIG. 1. The silicone oil fan clutch device with temperature monitor system. (a) The principle figure of the fan clutch with the temperature sensor. (b) Configuration of the interdigital capacitive temperature sensor. (c) Configuration of the LC-type passive wireless temperature sensor.

II. STRUCTURE AND FABRICATION

A. Capacitive temperature sensor

The novel temperature sensor is fabricated with bulk micromachining technology. The basic structure design of the temperature sensor is shown in Fig. 1(b). The capacitive-type temperature

sensor mainly consists of two parts, the temperature sensing material and the interdigital electrodes. The silicone oil (Dow Corning Co., Ltd., PMX200) is used in the fan clutch device, and acts as the temperature sensing material. Table I shows the properties of the silicone oil. The fixed interdigital electrodes of the capacitor are fabricated on a glass wafer. The gap between the electrodes is 10μm, the thickness of the electrodes is 50μm and the length of the overlap segment of the electrode plate is 600μm, and the depth of the rectangular grooves under the interdigital electrodes is 10μm. The size of the whole structure is 3.6mm×3.9 mm.

The fabrication process of the bulk silicon interdigital capacitive temperature sensor is shown in Fig. 2. Firstly, the silicon wafer is patterned by reactive ion etching (RIE) process [Fig. 2(a)]. Secondly, the silicon wafer is flip-chipped, and bonded onto the Pyrex7740 glass wafer by anodic bonding process, and the bonded wafer is thinned to about 60μm from the silicon side [Fig. 2(b)]. Thirdly, a 500nm aluminum film is evaporated[Fig. 2(c)], and the capacitor electrodes is created by the patterned aluminum film[Fig. 2(d)]. Fourthly, the inductively coupled plasma (ICP) etching process is used to create a deep trench [Fig.2(e)]. Finally, the silicone oil is dropped into the trench [Fig. 2(f)]. Fig. 3 shows photographs of the interdigital capacitive structures.

TABLE I. Properties of Silicone Oil (25℃)

Property	*Unit*	*Silicone Oil PMX200*
Specific gravity	-	0.934
Kinematic viscosity	[cSt]	10
Service temperature high	[℃]	200
Service temperature low	[℃]	-40
Relative permittivity	-	2.70
Volume resistivity	[Ωcm]	>1014
Thermal conductivity	[W/(m^2•K)]	0.134
Surface tension	[mN/m]	20.1

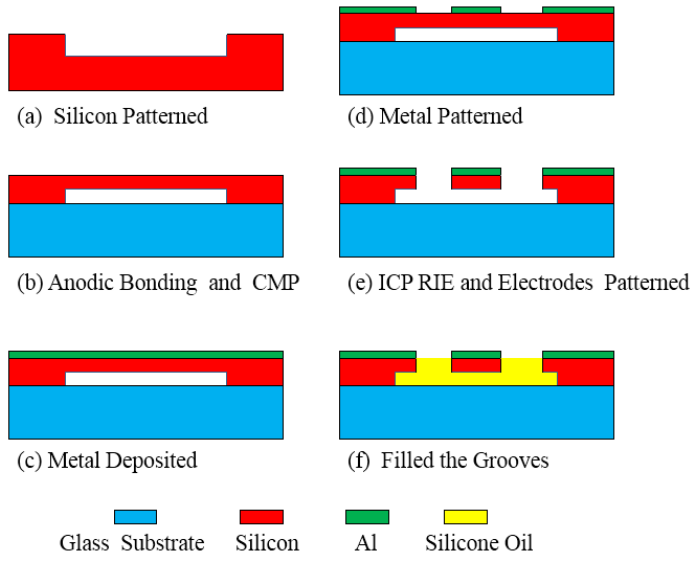


FIG. 2. Fabrication process of the interdigital capacitive temperature sensor

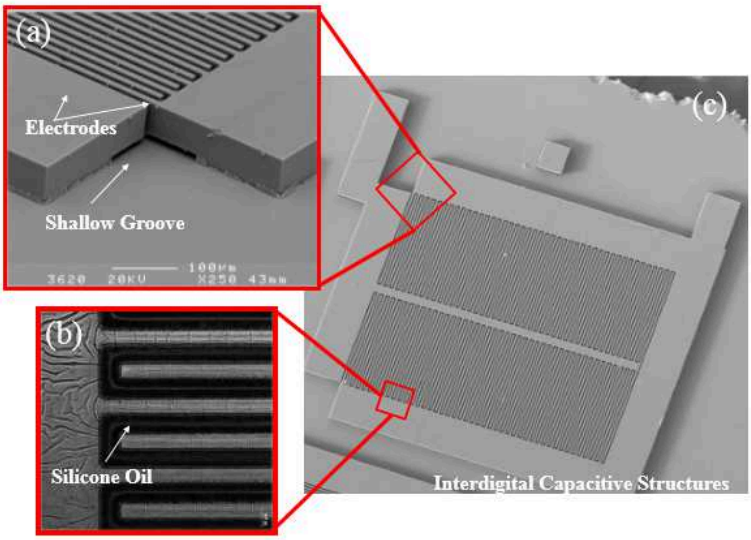


FIG. 3. Photographs of the interdigital capacitive temperature sensor.(a) SEM photograph of the shallow grooves under the interdigital capacitive structure.(b) DHM photograph of the front part of interdigital capacitive structures after the filled of silicon oil.(c) Top view of the whole interdigital capacitive structures

B. LC-type passive wireless temperature sensor

The capacitive temperature sensor, which introduced above, can be connected with a fixed planar spiral copper inductor to form an integrated inductor-capacitor (LC) resonator structure. The capacitive temperature sensing die is attached to the PCB substrate with the adhesive layer, and the temperature sensing capacitor is wire bonded with a single layer planar spiral copper inductor to form the LC tank circuit as the passive-telemetry front end. The fabrication process is shown in Fig. 4.

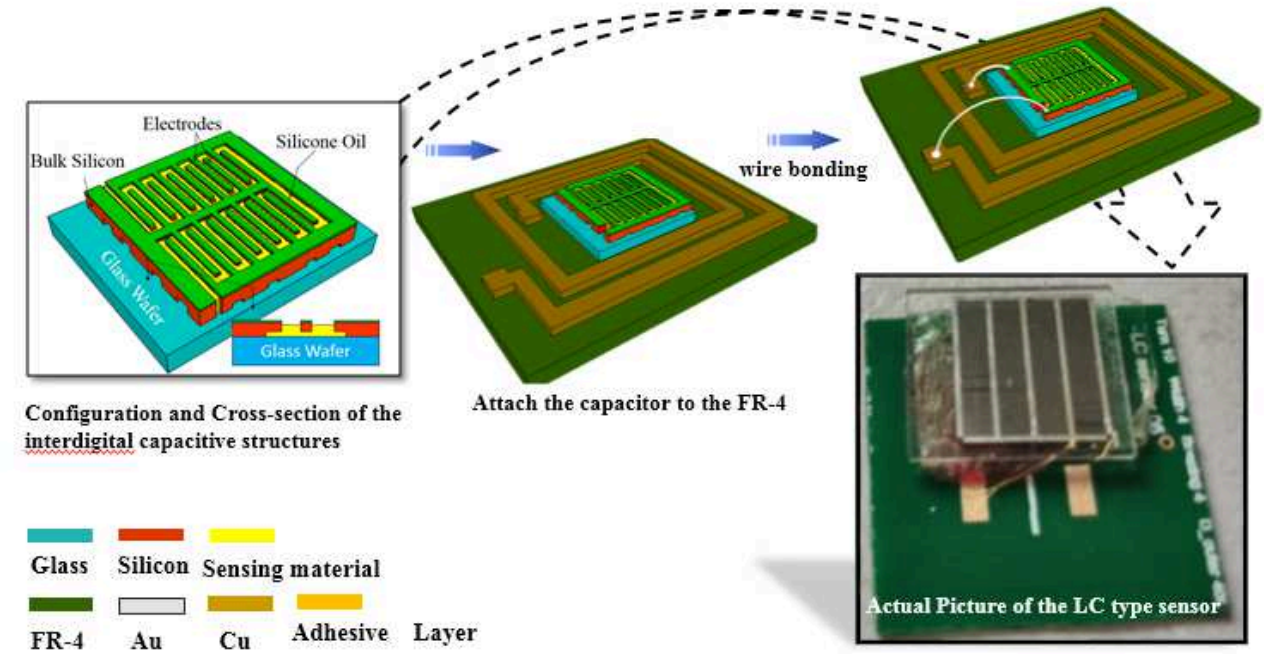


FIG. 4. Fabrication process of the passive wireless temperature sensor.

III. RESULTS AND DISCUSSION

The two type of temperature sensors are tested inside an environmental chamber. The humidity of the chamber is fixed at 65%RH, and the temperature is changed from -30 ^{o}C to 110 ^{o}C range. The deviation of the temperature and the humidity during measurement is ±0.5^{o}C and ±3%RH, respectively.

A. Capacitive temperature sensor

The temperature of the environment chamber is raised from -30℃ to 110℃ with the steps of 10℃. The temperature capacitance sensor is detected by AD7745 (Analog Device), a 24-bit capacitance-to-digital converter. Test results are presented below.

Sensitivity. The sensor sensitivity(S) is defined as the slope of a least square linear-fit line of capacitance(pf) versus temperature(℃) characteristic. Fig. 5 gives the sensing capacitance as a function of temperature. The change of sensing capacitance is best linear in a 50-110℃ range with a sensitivity of 58.2fF /℃. In the range of -30-40℃, the sensitivity is 27.3fF/℃.

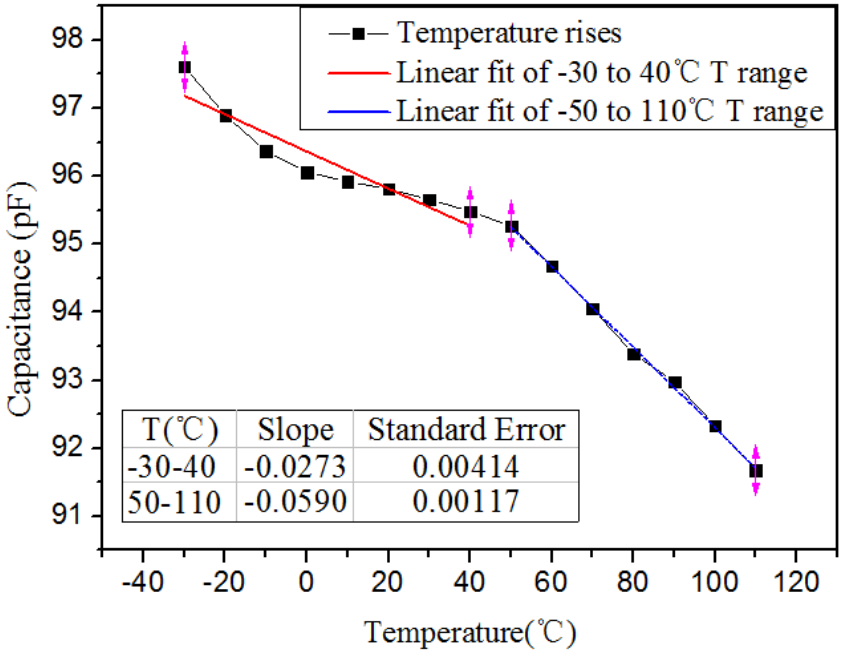


FIG. 5. Sensitivity measurement of the temperature sensor of the capacitive temperature sensor.

Hysteresis. Test is also performed to investigate the hysteresis behavior of the sensor. Fig. 6 shows a typical hysteresis measurement. At the beginning of the measurement, the temperature of chamber is kept at 110℃. The capacitance of the sensor is recorded when temperature of the environment chamber is lowered from 110℃ to -30℃with a step of 10℃, and then temperature is raised from -30℃ to 110℃ with a step of 10℃. The chamber temperature is shown on x-axis. The capacitance of the sensor is shown on y-axis. The maximum hysteresis is 0.89pF at 80℃.

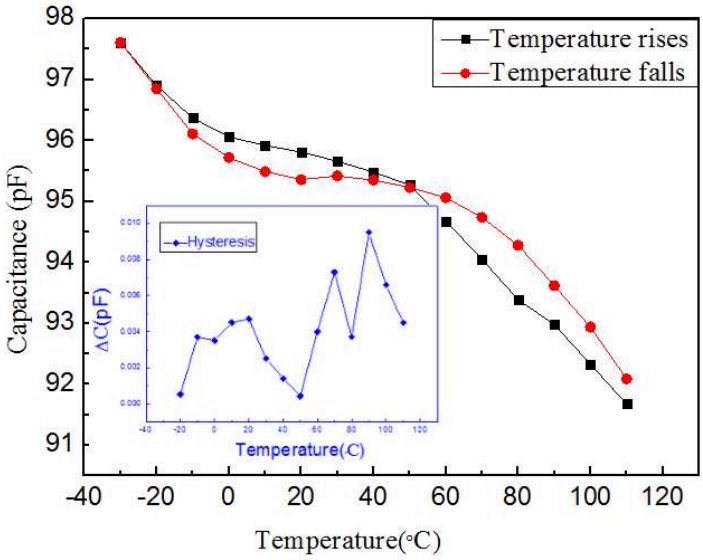


FIG. 6. A typical hysteresis measurement of the temperature sensor

Stability. The sensor is tested at the temperature of -30℃ and 110 ℃ for 24 hours, respectively. Fig. 7 presents the test results of the capacitance versus temperature so as to study the short-term stability measurement. The sensing capacitance varies in a range of 0.30 p*f* at -30℃ and 0.26 p*f* at 110 ℃ .

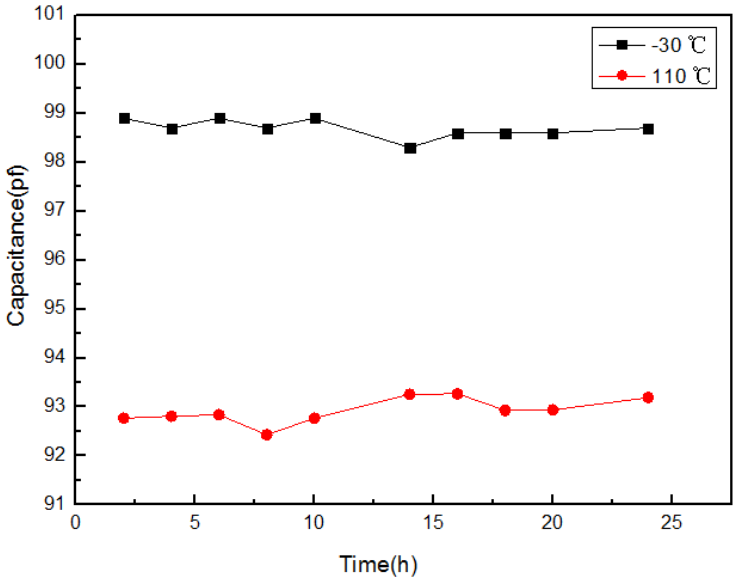


FIG. 7. Short-term stability measurement of the temperature sensor.

LC-type Passive Wireless Temperature Sensor. A vector impedance antenna analyzer connected with a readout coil is used as the telemetric unit to measure the LC-type passive wireless temperature sensor. The resonant frequency for the sensor changes with the capacitance due to environmental temperature. The temperature of the chamber is controlled to range from -30℃ to 110℃ at 20℃ intervals. The changes in the resonant frequency of the impedance is remotely monitored through a wireless link. The sensitivity of the LC-type passive wireless temperature sensor is defined as the slope of resonant frequency(MHz) versus temperature(℃) characteristic. Fig. 8 presents the measured Re(Z) as a function of resonant frequency for different temperature at 65%RH. As temperature increases, the maximum real part of the impedance shifts monotonically to higher frequencies because the capacitance decreases. The sensitivity of the LC-type passive wireless temperature sensor is about 6.35kHz/℃.

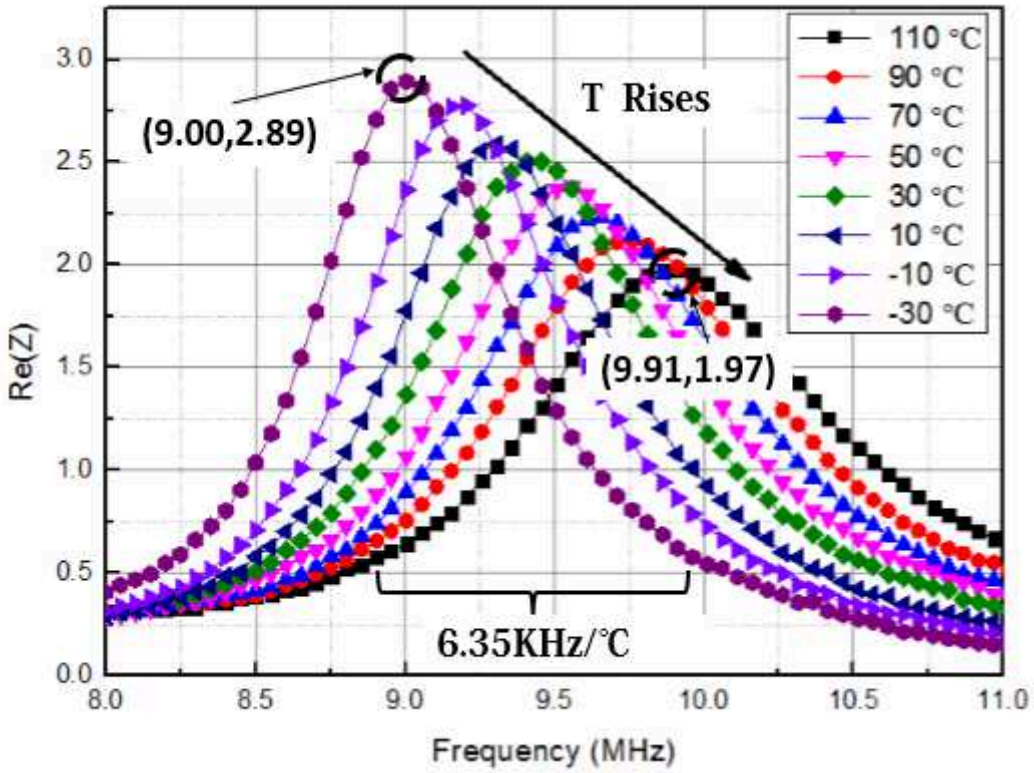


FIG. 8. Measured maximum Re(Z) resonant frequency shift as a function of temperature at 40%RH

IV. CONCLUSIONS

A novel capacitive sensor for real-time monitoring of temperature in the silicone oil fan clutch has been designed and fabricated by MEMS technology process. The silicone oil acts as the sensing dielectric. The novel temperature sensor provides a best sensitivity of 58.2 fF/℃ in the 50-110℃ range. And the measurement results show a good linearity and repeatability performance over the whole testing range. As the form of a LC-type passive wireless sensor, it can provide a sensitivity of 6.35 kHz/℃ at the -30 to 110℃ range for the silicone oil fan clutch.

ACKNOWLEDGMENTS

This work was supported by the National Natural Science Foundation of China (Grant NO. 61136006 and 61401084) and the National High Technology Research and Development Program of China (Grant NO. 2013AA041101) and the new teacher start-up fund of Southeast University (Grant NO.1106007111).

References

[1] D.S. Eddy, D.R. Sparks, Proceedings of the IEEE **86**, 1747(1998).
[2] D.J. Bell, T.J. Lu, N.A. Fleck, J. Micromech. Microeng. **15**, S153(2005).
[3] D. Iverson, S. V. Garimella, Microfluidics and Nanofluidics **5**, 145(2008).
[4] M. Tanaka, Microelectronic Engineering **84**, 1341(2007).
[5] R. Bogue, Sensor Review **27**, 7 (2007).
[6] M.H. Lee, M.K. Kim, H.G. Park, K.S. Lee, H.H. Chun, International J. precision engineering and manufacturing **12**,983(2011).
[7] K.H. Lee, J.H. Lee, B.J. Koo, SAE Paper, 980838(1998).
[8] P. Marklund, R. Maki, R. Larsson, E. Hoglund, M.M. Khonsari, J. Jang, T, Tribology International **40**, 876(2007).
[9] J.Y. Jang, M.M. Khonsari, J. tribology **121**, 610(1999).
[10] Zhao C L, Qin M, Huang Q A, IEEE Sensors J. **11**, 2986(2011).

[11] Y. Lee and G. B. Lee, J. Micromech. Microeng. **5**, 620(2003).
[12] L. T. Chen, C. Y. Lee, and W. H. Cheng, Sens. Actuators A, Phys. **147**, 522(2008).
[13] L. Gu, Q. A. Huang, and M. Qin, Sens. Actuators B, Chem. **99**, 491(2004).
[14] E.B. Baker, A.J. Barry, M.J. Hunter, Industrial and Engineering Chemistry **38**, 1117(1946).
[15] T. J. Harpster, B. Stark, and K. Najafi, Sens. Actuators A, Phys. **95**, 100(2002).
[16] A.D. DeHennis and K.D. Wise, J. Microelectromech. Syst. **14**, 12(2005).
[17] S.Bhadra, D.S.Y Tan, D.J. Thomson, M. S. Freund, and G. E. Bridges, IEEE Sensors J. **13**, 2428(2013).

Key Engineering Materials Vols 645-646 (2015) pp 670-674
© (2015) Trans Tech Publications, Switzerland
doi:10.4028/www.scientific.net/KEM.645-646.670

Submitted: 2014-11-24
Accepted: 2014-12-23

Active disturbance rejection control design for fast AFM

Daixie Chen [1,a], Bohua Yin[1,b], Junbiao Liu[1], Wenping Li[2], Liqiang Wu[2], and Han Li[1,c*]

[1] Department of Micro-nano Fabrication Technology, Institute of Electrical Engineering, Chinese Academy of Scineces, Beijing, 100190, China

[2] Beijing University of Aeronautics and Astronautics, Beijing 100191, China

[a]chendaixie@mail.iee.ac.cn, [b]yinbh@mail.iee.ac.cn, [c]lihan@mail.iee.ac.cn

Keywords: active disturbance rejection control; atomic force microscopy; fast scan

Abstract. Active disturbance rejection control (ADRC) as an alternative to classical PID control to solving control problems, has gained significant traction these years. With its simple tuning method, robustness against process parameter variations and ability of disturbance rejection, we tried it in our homemade fast atomic force microscope (AFM). Experiments are carried out in contact mode on standard optical grating sample with 50Hz line rate. The results show that ADRC can reject external disturbances well, and can reduce system vibrations obviously.

Introduction

Since its invention in 1984, the atomic force microscope (AFM) has been widely used in characterization and manipulation of almost all types of materials[1]. Recently, as an advanced instrument, AFM has proved attractive support for semiconductor industry[2,3]. The working principles of AFM have been shown in Fig.1. In this figure, the signal variation from laser spot movement which is caused by the probe movement or vibration, can be detected by a split photodiode sensor when the cantilever travels over the sample surface. Through a PID feedback loop in Z scanner, this signal variation is collected and imaged by the PC, and atomic resolution can be achieved.

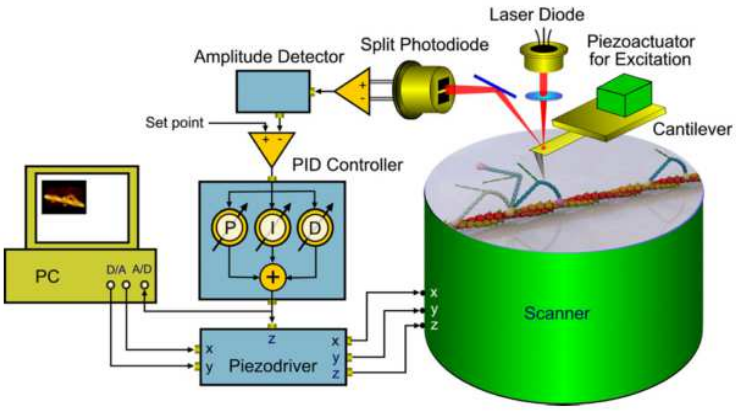


Fig.1 Schematic diagram of AFM operation[4]

The speed of detection as one of the most critical techniques for industrial application, is also a problem faced by AFM, such as for on-line semiconductor detection. Various devices and techniques, such as small cantilevers, high-speed scanners, active damping and feedback control techniques, and electronics have been developed for AFM fast scanning[5].Although through a proof-of-principle stage the technology of fast AFM has reached maturity, when faced with industrial application, the small scan range is still one of the bottleneck problems to be solved. To enlarge the scan range, we built a fast AFM, where the X-Y motion is handled by a flexure stage that moves the sample while the Z motion is handled by a piezo stack moving the cantilever up and down. This homemade fast AFM has up to one hundred micrometers scan range and up to 50Hz line scan rate[6]. When in test processing, we found that with the most popular controller in AFM fast scanning, such as dynamic PI

controller[7], model-based feedback controller[8] and inversion-based iterative controller[9], the Z scanner vibration can not be eliminated ideally.

The nature of fast AFM control problems, in our opinion, is disturbance rejection, and the key question in design is how to deal with it. The PID control strategy, by default, deals with the disturbances in a passive way as it merely reacts to the tracking errors caused by the disturbances. An alternative, and better, solution is to reject the disturbances actively by estimating the disturbance directly and canceling it out, before it affects the system in a significant way, and this is at the core of automatic disturbance rejection controller (ADRC)[10].

ADRC

ADRC technique, initiated by prefessor Han Jinqing, is a practical comprehensive nonlinear synthesis method on control system. It mainly consists of Tracking Differentiator (TD), Extended State Observer(ESO), and Nonlinear State Error Feedback(NSEF). The architecture of ADRC is shown in Fig.2. TD is used to preprocess the input angular signal. ESO is used to estimate state and perturbation of the system respectively. The error caused by uncertain system model is regarded as internal disturbances. The total disturbances consisting of internal disturbances and external disturbances work on the system as a whole. Comprehensive errors are measured directly. NSEF is used to obtain the compensation of disturbances. The efficiency of signal processing is improved by the nonlinearity combination of integral and differential of error signals.[11]

ADRC is practical because it requires very little knowledge about the plant dynamics, which in real systems may be both unknown and non-stationary. In the case of a linear time invariant system, it requires only the knowledge of the relative degree of the system and an estimation of the high frequency gain[12].The disturbances and the plant variations can be estimated and compensated in each control loop. Hence the entire system has strong robustness and ability of disturbance rejection.This control strategy seems very compatible with AFM system.

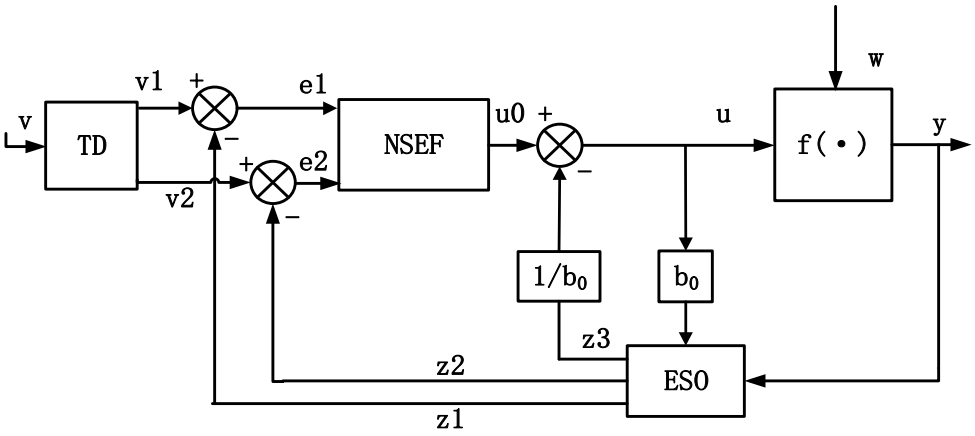


Fig.2 The architecture of the ADRC

Simplified model for fast AFM

The fast AFM system worked in contact mode, where the dynamic parts for feedback control along the vertical positioning axis are Z scanner and tip, can be modeled as a simplified mathematical mass spring system as shown in Fig.3. The derived model is of low order, gives physical insight, and is useful for both process and control design. In Fig.3, the mass m1 is the Z scanner plus the mass of the sample on it, m2 is the mass of tip, which has the effective spring constant k, and the effective damping coefficient can be ignored when keeping the tip contacted with the sample in elastic range. Let the positions of the center of the masses be x1 and x2. Let the drive signal created by ADRC be u. w1 and w2 are noise signals influence m1 and m2 separately.

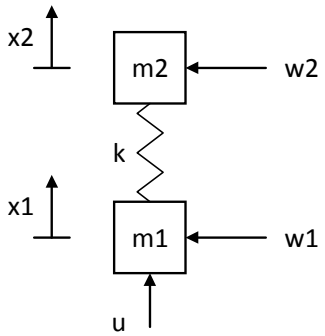


Fig.3 The simplified model for fast AFM

As a result, the fast AFM system can be written as:

$$\begin{cases} \ddot{x}_1(t)+\dfrac{k}{m_1}[x_1(t)-x_2(t)]=\dfrac{u(t)+w_1(t)}{m_1} \\ \ddot{x}_2(t)+\dfrac{k}{m_2}[x_2(t)-x_1(t)]=\dfrac{w_2(t)}{m_1} \end{cases}$$

Taking Laplace transforms and we can get the transfer function G(s) from driving signal U(s) to position of the tip X2(s):

$$G(s)=\frac{k}{s^2(s^2+2k)}$$

Corresponding ADRC design

The equation of a control system can be described as:

$$\mathrm{x}^{(\mathrm{n})}=f\left(x^{(n-1)},\cdots,\dot{x},x,w,t\right)+b(t)u, y=x$$

where y is output, u is the control input, $b(t)$ is a variable, and w represents the external disturbance. The elastic, viscosity and various other nonlinearities in fast AFM system are all simply modeled above as the function $f(\cdot)$. The control objective is to make x tracking the given sampled signal v(t).

Rewrite the control system in state space:

$$\begin{cases} \dot{x_1}=x_2 \\ \vdots \\ \dot{x}_{n-1}=x_n \\ \dot{x_n}=f(x_1,x_2,\cdots,x_n)+b(t)u \\ y=x_1 \end{cases}$$

TD as a feed forward controller can be described as:

$$\begin{cases} \dot{v_1}=v_2 \\ \dot{v_2}=-r^2(v_1-v)-\sqrt{3}rv_2 \end{cases}$$

where v is an input vector, and v_1 is the tracking vector of v, and v_2 is the derivative vector of v_1, and r is a parameter which determines the tracking speed.

The ESO is a unique nonlinear observer to estimate $f(\cdot)$, and it can be described as:

$$\begin{cases} z_1=z_1+h*\left(z_2-\beta_1(z_1-y)\right) \\ z_2=z_2+h*(z_3-\beta_2(z_1-y)+b_0u) \\ z_3=z_3-h*\beta_3(z_1-y) \end{cases}$$

where h is the samping time, β_1,β_2,β_3 are observer gains, b_0 represents the estimated value of b in real time. The estimated state variables of the controlled object are z_1 and z_2. An expanded state z_3 is used to calculate real-time sum of external disturbances and to estimate all uncertain internal disturbances. Because the extended state can track the actual actions of the whole disturbances, the ESO could compensate disturbances well and have high robustness to the variations of the model parameters.

To make the parameters easier to be ajusted, we propose the NSEF as follows:

$$\begin{cases} e_1 = v_1 - z_1 \\ e_2 = v_2 - z_2 \\ u_0 = b_{t1} * e_1 + b_{t2} * e_2 \end{cases}$$

Here, b_{t1} and b_{t2} are setted as linear parameters. As an alternative, they can be setted as nonlinear for better approach[13]. As a result, the control law can be defined as:

$$\mathrm{u} = \frac{u_0 - z_3}{b_0}$$

Results and Discussion

In order to prove the usefulness of ADRC controller in fast AFM, we compared it with PI control in our homemade fast AFM, where DSP is used as the main processor while FPGA as the co-processor.

According to several step response tests, the sampling time can be setted as $\mathrm{h} = 1 * 10^{-6}\mathrm{s}$ while the analog-to-digial conveter(ADC) has 100MSPS output rate. The parameters $\beta_1, \beta_2, \beta_3$ can be given in the range and have the relationships below:

$$\begin{cases} \beta_1 = 10^{5\sim8} \\ \beta_2 = 3(\frac{\beta_1}{3})^2 \\ \beta_2 = (\frac{\beta_1}{3})^3 \end{cases}$$

So the parameters left to be ajusted are only b_{t1} and b_{t2}, just as easy as the P and I parameters in PI controller.

Single line scan tests on standard optical grating in the same lab condition have been compared. While mentioned fast scan in AFM, the scan speed is the most critical indicator, so we tuned PI and ADRC to make them have the same setting time. In practical scanning, we found that when ADC sampling rate was setted a little too high, there would be electrical outliers. We can see in Fig.4 that these external disturbances will be transfered to output through PI controller, but not by ADRC. To further prove the vibration constraint ability of ADRC, the line scan results on standard optical grating are shown in Fig.5, where we can see that with almost the same setting time through ADRC the output amplitude got less vibrations.

Conclusions

This article studied the active disturbance rejection control (ADRC) whose validity and superiority are demonstrated in our homemade fast AFM practically. ADRC is not sensitive to the objects models, it has strong robustness and ability of disturbance rejection. Now we are trying to use ADRC in our dual-scanner fast AFM scanning for further high speed improvements.

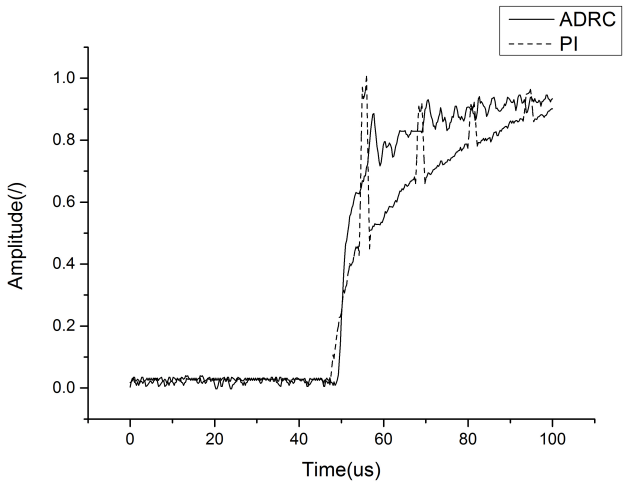


Fig.4 External disturbance rejection results by different controllers

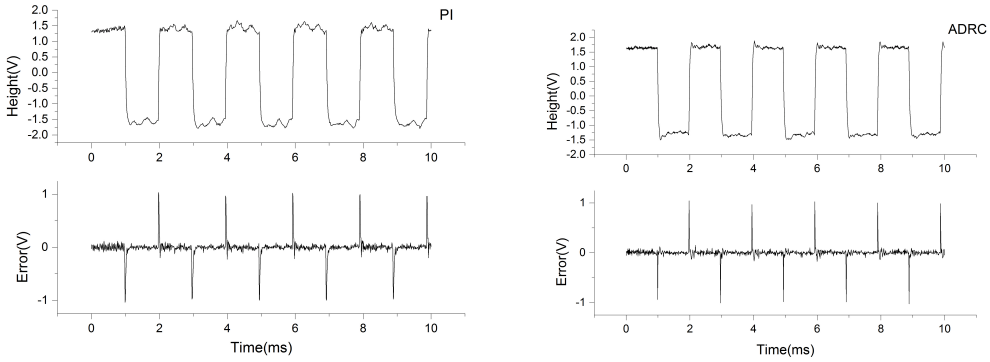


Fig.5 Line scan results on standard optical grating (Line rate:50Hz)

* This work has been supported by the "863 Program" (No.2012AA041204).

References

[1] C. Steffens, F. L. Leite, C. C. Bueno, A. Manzoli, P. Sergio, and D. P. Herrmann, Atomic force microscopy as a tool applied to nano / biosensors, Sensors, 12, 8278 (2012).

[2] C. Shin, K. Kim, J. Kim, W. Ko, Y. Yang, S. Lee, and Y. S. Kim, Fast, exact, and non-destructive diagnoses of contact failures in nano-scale semiconductor device using conductive AFM, Sci. Rep, 3, 2088 (2013).

[3] Y. Hua, C. Buenviaje-Coggins, Y. H. Lee and S. I. Park, High-throughput and non-destructive sidewall roughness measurement using 3-dimensional atomic force microscopy, In SPIE Advanced Lithography, 83240I (2012).

[4] T. Ando, High-speed atomic force microscopy coming of age, Nanotechnology, 23, 06200 (2012).

[5] T. Ando, T. Uchihashi, and N. Kodera, High-speed atomic force microscopy, Japanese Journal of Applied Physics, 51, 1–15 (2012).

[6] Jing Li, Zhifeng Deng, Daixie Chen, Zhuo Ao, Quanmei Sun, Jiantao Feng, Bohua Yin, Li Han and Dong Han. High-speed afm for scanning the architecture of living cells, Nanoscale, 5, 18, 8355-8358 (2013).

[7] A. J. Fleming, Dual-stage vertical feedback for high-speed scanning probe microscopy, IEEE Transactions on Control Systems Technology, 19, 1, 156–165 (2011).

[8] S. Kuiper, and G. Schitter, Model-based feedback controller design for dual actuated atomic force microscopy, Mechatronics, 22, 3, 327–337 (2012).

[9] Y. Yan, H. Wang, and Q. Zou, A decoupled inversion-based iterative control approach to multi-axis precision positioning: 3D nanopositioning example, Automatica, 48, 1, 167–176 (2012).

[10] J. Vincent, D. Morris, N. Usher, Z. Gao, S. Zhao, A. Nicoletti, and Q. Zheng, On active disturbance rejection based control design for superconducting RF cavities, Nuclear Instruments and Methods in Physics Research Section A: Accelerators, Spectrometers, Detectors and Associated Equipment, 643, 1, 11–16 (2011).

[11] L. Q. Wu, J. Q. Han, and Z. G. Hou, A novel control method for a class of cascade nonlinear systems, ICNSC '06, 654-657 (2006).

[12] J. Q. Han, From pid to active disturbance rejection control, IEEE Transactions on Industrial Electronics, 56, 3, (2009).

[13] Y. X. Su, C. H. Zheng, and B. Y. Duan, Automatic disturbances rejection controller for precise motion control of permanent-magnet synchronous motors, Industrial Electronics, 52, 814–822 (2005).

Key Engineering Materials Vols 645-646 (2015) pp 675-680
Submitted: 2014-11-29
© (2015) Trans Tech Publications, Switzerland
Accepted: 2014-12-23
doi:10.4028/www.scientific.net/KEM.645-646.675

Plastic strain effect in progressive multi-cycle nano-indentation measurement

Wei Qilong[a*], Li Xiaoyuan[b], Yue Xiaobin[c], Lei Dajiang[d]

Institute of Machinery Manufacturing Technology, China Academy of Engineering Physics, Mianyang 621900, China

[a*]weiqilong2004@126.com, [b]lxy20056482@126.com, [c]yuexbin@sohu.com, [d]leidajiang@163.com

Keywords: progressive multi-cycle nano-indentation; hardness; plastic strain; second convergence

Abstract. Properties of materials and their variations in depth direction in the same location could be measured directly by progressive multi-cycle (PMC) nano-indentation method. But influences of strain-hardening on measured results in this process haven't been researched thoroughly. Measurements on an austenitic steel sample and a fused silica sample were conducted by PMC nano-indentation and standard nano-indentation methods, and differences of the results by two methods of the two materials were analyzed. It was found that hardness of austenitic steel measured by PMC method decreased monotonously with increased depth, while hardness measured by standard method decreased to stable value with increased depth. And properties of fused silica measured by both methods accorded much well. Based on analysis of plastic strain during indentation process, it was deduced that austenitic steel with high plasticity could introduce second convergence of plastic strain and stress in PMC indentation process, which made measured hardness decrease monotonously with increased depth.

Introduction

Hardness is an important property, which figures the ability of materials to resist plastic deformation under applied forces. The traditional technologies measure hardness through indentation force and area of remnant impressions, which adopt much high indentation force and much big indenter, and produce much large impressions [1, 2]. These technologies have low resolution, which couldn't satisfy high resolution requirements to measure small scale materials such as films and interfaces.

Nano-indentation (instrumented indentation, depth-sensing indentation) technology measures properties of materials with load down to several μN, which could obtain hardness, elastic modulus, fracture toughness, creep, strain-hardening exponent [3-5]. And it could select microscopic regions to measure and gain materials' properties corresponding to microstructures, with the help of optical microscope or atomic force microscope [6, 7]. It could also study variation of properties in depth direction with resolution about several nm [8, 9], which is very important for researching on gradient materials, films, surfaces and interfaces.

Progressive multi-cycle (PMC) indentation method is a kind of nano-indentation, which indents on the same location by a loading, un-loading partially, and re-loading manner, with increasing maximal load [10, 11]. It's hopeful to study variation of properties with depth effectively, especially for samples difficult to prepare.

But as measured locations are indented repeatedly in PMC process, strain-hardening could be produced [12, 13], which would make materials' responding different from those in standard indentation process. And its influences on measured results are important questions, which haven't been researched and analyzed thoroughly. Then a single-phase austenitic steel and a fused silica will be measured by both PMC and standard indentation methods. Measured properties by each method will be compared, and possible reasons for their differences will be analyzed. These studies will provide technological basis for evaluate PMC indentation method and promote its valid applications.

Experiments and Methods

Experiments were conducted on a nano mechanics synthetical measurement system of Swiss CSM Instruments, with Berkovich diamond indenters. Microstructures of samples were observed, and measured locations were chose with its optical video microscope. A fused silica sample was used to calibrate the area function of indenters. PMC indentation and standard indentation were conducted on both an austenitic steel sample and the fused silica standard sample.

Results of Austenitic Steel

Results of austenitic steel by PMC indentation were showed in Fig 1, where the four indented spots were in 2×2 matrix and space in each direction was 30 μm, with the maximal indentation load 40~320 mN, and unloading down to 15 mN between two cycles.

It was found that in Fig 1(a) that remnant impressions were all intact inverse three-edge pyramid, with № 1 and № 2 indents inside a grain about 50 μm×50 μm, and № 2 and № 4 indents near grain boundary. And PMC indentation curves in Fig 1(b) were much regular, with indentation depth increasing with increased load, and the maximal indentation depth about 2500 nm.

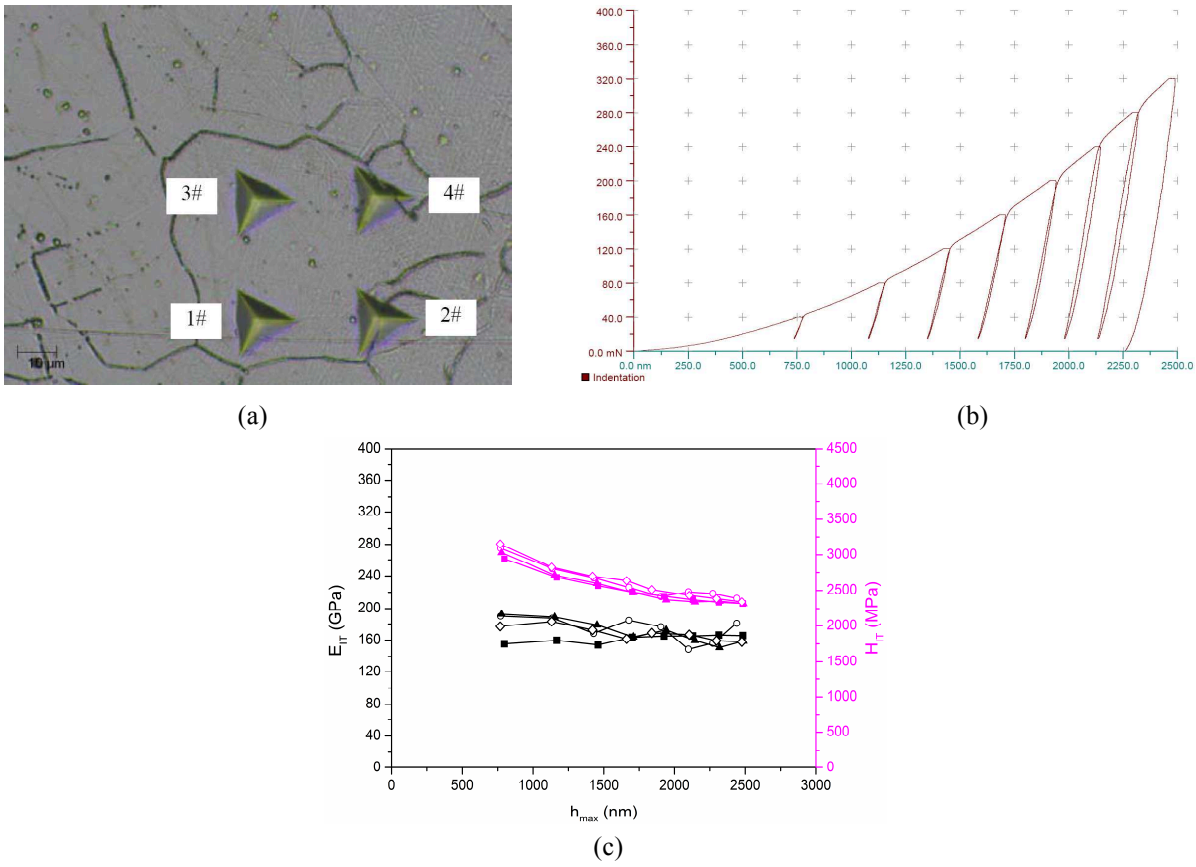


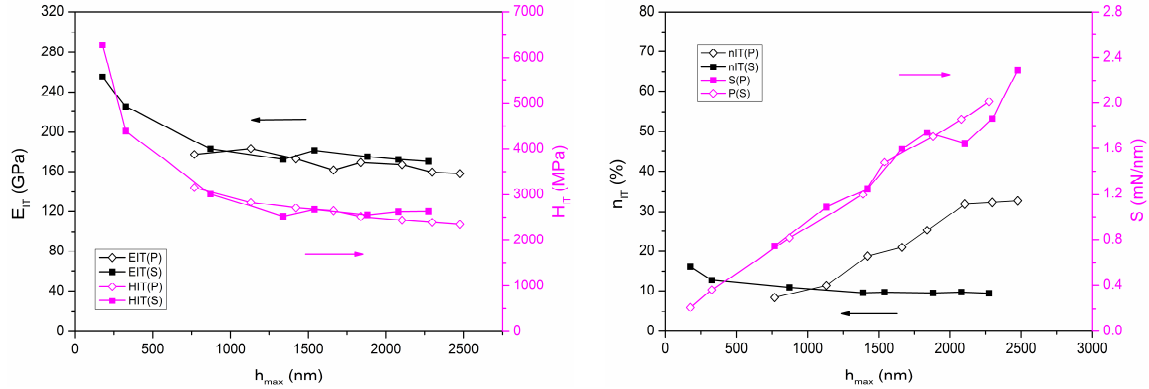
Fig 1. PMC indentation results of austenitic steel. (a) remnant impressions, (b) indentation curve,(c) properties.

In the Fig 1(c), the first points of four modulus curves attributed to № 2, 1, 4, 3 indentations respectively, while the first points of four hardness curves attributed to № 4, 1, 2, 3 indentations respectively. It was found that variation of modulus with depth or load was much complex, while hardness decreased monotonously with increased depth or load, but it can't approach to stable values in experimental conditions. And indentation locations hardly had regular impact on both modulus and hardness.

Results of standard indentations on austenitic steel were showed in Fig 2(a), with icon S, where and the maximal load varied from 4 mN to 300 mN, distance between each indentation was above 30 μm.

And results of a PMC indentation were also showed in Fig 2, with icon P. It was showed that measured hardness and modulus by standard indentation were much higher when the maximal load was small, while measured values decreased when the maximal load increased and they approached to steady values which didn't vary with load any more when the maximal load increased to above 100 mN. Mean hardness of the latter five indentations was 2593.44 MPa with relative deviation 2.31%, and mean modulus of the latter five indentations was 174.06 GPa with relative deviation 2.48%. These were markedly differences between results of standard indentation and those of PMC indentation.

Variation of elastic work ratio and unloading stiffness of the austenitic steel with the maximal loads measured by two methods were showed in Fig 2(b), in which elastic work ratio was the percentage of elastic work in the total work during indentation. It was found that elastic work ratio during standard indentation decreased little with increased maximal load, but it kept between 9% and 10% when the maximal load increased to above 100 mN, while unloading stiffness increased monotonously with increased load. And during PMC indentation, elastic work ratio increased from 8.37% to 32.59% with increased maximal load, and unloading stiffness increased with increased maximal load, with a bizarre point. It could be saw that elastic work rations of the austenitic steel by two kinds of indentation differed greatly, while unloading stiffness accorded much well.

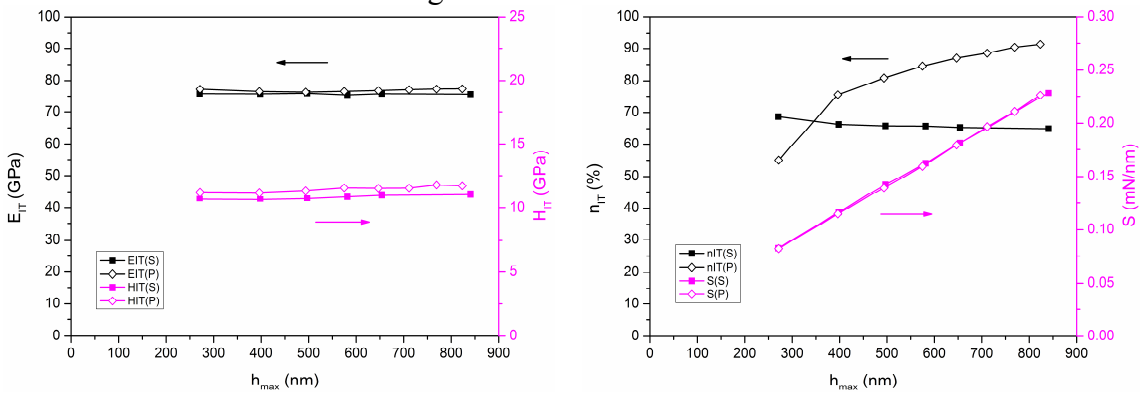


(a) (b)

Fig 2. Measured results of austenitic steel by two methods, (a) properties, (b) other results.

Results of Fused Silica

Variation of properties including modulus and hardness of fused silica with depth by PMC and standard indentations were showed in Fig 3.



(a) (b)

Fig 3. Measured results of fused silica by two methods, (a) properties, (b) other results.

It was found that measured modulus and hardness during PMC indentation changed hardly, with mean values 76.96 GPa and 11.52 GPa respectively, and relative deviations 0.54% and 1.96% respectively. While measured modulus and hardness by standard indentation changed hardly too,

with mean values 75.76 GPa and 10.89 GPa respectively, and relative deviations 0.23% and 1.47% respectively. According to these results, it could be deduced that measured properties of fused silica by these two methods didn't change with indentation depth, which was unlike austenitic steel.

It could be found in Fig 3(b) that unloading stiffness of fused silica by both methods increased with increased depth, and the two curves superposed fully. While elastic work ratio of fused silica reduced little and stabilized at about 65% during standard indentation, but it increased with increased depth during PMC indentation.

Analysis and Discussions

There was indentation size effect (ISE) during nano-indentaion measurement, which meant that measured properties on surfaces were different from those of bulk. The ISE was thought to relate to surface traits of materials, such as oxides, residual stress, strain-hardening, while area function of indenters, elastic and plastic deformation might also produce ISE [14-16]. When indentation load increased and yielded the material below an indenter and made it flow plastically, measured properties didn't change with load and they represent properties of the bulk material. The above law was reflected by data in Fig 2.

During indentation measurement, materials deformed elastically, then deformed plastically, accompanied with indentation work. And during unloading process, materials recovered elastically while plastic deformation was reserved and remnant impressions was formed [17, 18]. There would produce and evolve dislocations, which would bring strain-hardening phenomenon in materials and its amplitude would depend on materials' characteristics.

The austenitic steel in experiment had plastic work ratio more than 90%, which meant that most deformation was plastic during indentation process and it could produce strain-hardening easily. And indentation was made on the same location in PMC process, which would bring accumulative plastic deformation, strain-hardening and ISE, making indentation hardness and plastic work ration decrease gradually.

But the above analysis could not make clear why PMC indentation hardness of the austenitic steel could not stabilize at the standard indentation hardness. It would be analyzed sequentially through stress distribution and strain localization during PMC indentation process.

The mean contact pressure during indentation process, P_m, was determined by the following equation:

$$P_m = P/(\pi a^2). \tag{1}$$

where P was indentation load, and a the radii of contact circle between material and the indenter [19, 20].

At the same time, intensity of pressure in the material below the indenter was determined by the following equation:

$$\sigma_z/P_m = (-3/2)[1-(r^2/a^2)]^{1/2}. \tag{2}$$

where r was the distance from the centre of the contact circle [20].

From these two equations, it could be deduced that intensity of pressure in the central zone of the contact circle in the material was maximal, which meant that deformation of the material was converged in this zone.

According to this deduction, the austenitic steel which had very high plastic work ratio would produce markedly plastic deformation and strain-hardening after partial unloading during PMC indentation process. And when it was indented on the remnant impressions again, the contact area between the indenter and the material would be smaller than that during indentation on initial plane. Then it made real intensity of pressure higher than nominal one, and indentation deformation be converged to tip of the indenter secondly, which meant that nominal resistance of the material to

plastic deformation, namely nominal hardness, decreased. And during the latter loading and unloading process, this mechanism appeared repeatedly, which made nominal hardness decrease repeatedly, even less than stable hardness of bulk measured by standard indentation.

There had great difference in elasticity and plasticity between fused silica and austenitic steel, as the plastic work ratio of fused silica was about one third of that of austenitic steel, and elastic deformation ratio of fused silica was about seven times of that of austenitic steel, where elastic deformation ratio (h%) was calculated by the maximal indentation depth (h_{max}) and the residual indentation depth (h_r) according to the following equation:

$$h\% = [(h_{max}-h_r)/h_{max}] \times 100\%. \quad (3)$$

Then fused silica had much higher elastic recovery than austenitic steel after partial unloading during PMC indentation process, and its second convergence of strain-hardening and corresponding deformation was finite, which had little influence on measured indentation hardness.

It was deduced from above discussions that there would appear obvious second convergence of deformation and strain-hardening to tip of indenters when PMC indentation method was used to measure properties of soft materials such as the austenitic steel, which made measured hardness decrease continuously and couldn't obtain stable values. Then PMC indentation method was thought not suitable for measuring these materials with high plasticity. But it might suitable for measuring materials with low plasticity such as fused silica, which would reduce requirements for preparing samples and improve measurement efficiency.

Summary

Indentation properties of an austenitic steel and a fused silica were measured by both progressive multi-cycle and standard methods, and influences of the two methods on measured results were analyzed. The main conclusions were drew as follows:

1) Measured indentation hardness of austenitic steel by PMC method decreased continuously with indentation depth in experiment conditions, even below measured hardness of bulk material by standard method which had eliminated indentation size effect.

2) Measured indentation hardness and modulus of fused silica by PMC method didn't change with indentation depth in experiment conditions, and accorded well with those by standard method.

3) Based on analysis of stress, strain and plasticity of materials, it was deduced that measured hardness of austenitic steel decreased continuously during PMC indentation process because there appeared second convergence of stress and strain due to its higher plasticity, which reduced effective contact area between the indenter and the material.

Acknowledgement

Financial support of this research work was provided in part by the Major National Science and Technology Special Projects of China (2013ZX04006011)), National Science Foundation of China (51202228), Foundation of CAEP Key Laboratory of Ultra-precise Machining Technologies.

References

[1] G. D. Quinn, P. J. Patel, I. Lloyd, Effect of loading rate upon conventional ceramic microindentation hardness, J. Res. Natl. Inst. Stand. Technol. 107 (2002) 299-306.

[2] H. Sumiya, Thermally activated deformation under Knoop indentations in super-hard directions of high-quality synthetic type-IIa diamond crystals, Diamond. Relat. Materi. 15 (2006) 1576-1579.

[3] C. H. Tsai, S. R. Jian, J. Y. Juang, Berkovich nanoindentation and deformation mechanisms in GaN thin films, Appl. Surf. Sci. 254 (2009) 1997-2002.

[4] O. Sahin, O. Uzun, M. Sopicka-Lizer, H. Gocmezd, U. Kölemen, Dynamic hardness and elastic modulus calculation of porous SiAlON ceramics using depth-sensing indentation technique, J. Euro. Ceram. Soc. 28 (2008) 1235-1242.
[5] L. J. Hu, D. Wang, Z. S. Lu, Y. W. Song, C. M. Song, Correlation between functionated structure and nanomechanical property profiles of silsesquioxane films and bulks, Macromol. Symp. 267 (2008) 79-84.
[6] F. J. Ulm, M. Vandamme, H. M. Jennings, etal, Does microstructure matter for statistical nanoindentation techniques, Cem. Concr. Compos. 32 (2010) 92-99.
[7] A. Veillère, A. Sundaramurthy, J. M. Heintz, etal, Relationship between interphase chemistry and mechanical properties at the scale of micron in Cu–Cr/CF composite, Acta Mater. 59 (2011) 1445-1455.
[8] C. W. Chang and J. D. Liao, Nano-indentation at the surface contact level: applying a harmonic frequency for measuring contact stiffness of self-assembled monolayers adsorbed on Au, Nanotechnol. 19 (2008) 315703.
[9] C. L. Xu, C. H. Zhang, J. J. Li, etal, A HRXRD and nano-indentation study on Ne-implanted 6H–SiC, Nucl. Instr.Meth. Phy. Res. B286 (2012) 129-133.
[10] B. Wolf, A. Richter, V. Weihnacht, Differential and integral hardness -new aspects of quantifying load–depth-data in depth-sensing nanoindentation experiments, Surf. Coat. Technol. 183 (2004) 141-150.
[11] A. Richter, C. P. Daghlian, R. Ries, V. L. Solozhenko, Investigation of novel superhard materials by multi-cycling nanoindentation, Diamond Relat. Mater.15 (2006) 2019-2023.
[12] C. Polizzotto, Strain gradient plasticity, strengthening effects and plastic limit analysis, Int. J. Solids Struct. 47 (2010) 100-112.
[13] Y. Idell, G. Facco, A. Kulovits, etal, Strengthening of austenitic stainless steel by formation of nanocrystalline c-phase through severe plastic deformation during two-dimensional linear plane-strain machining, Scripta Mater. 68 (2012) 667-670.
[14] A. A. Elmustafa, D. S. Stone. Nanoindentation and the indentation size effect: Kinetics of deformation and strain gradient plasticity, J.Mech. Phy. Solids 51 (2003) 357-381.
[15] L. Q. Zheng, A. W. Schmid, J. C. Lambropoulos. Surface effects on Young's modulus and hardness of fused silica by nanoindentation study, J. Mater. Sci. 42 (2007) 191-198.
[16] D. Ye, S. Matsuoka, N. Nagashima. Determination of fatigue mesoscopic mechanical properties of an austenitic stainless steel using depth-sensing indentation (DSI) technique, Mater. Sci. Engin. A456 (2007) 120-129.
[17] C. L. Eriksson, P. L. Larsson, D. J. Rowcliffe. Strain-hardening and residual stress effects in plastic zones around indentations, Mater. Sci. Engin. A340 (2003) 193-203.
[18] D. A. Lucca, K. Herrmann, M. J. Klopfstein. Nanoindentation: Measuring methods and applications, CIRP Annals – Manufac. Technol. 59 (2010) 803-819.
[19] A. Rubin, C. Gauthier, R. Schirrer. The friction coefficient on polycarbonate as a function of the contact pressure and nanoscale roughness, J. Polymer Sci. Part B: Polymer Phy. 50 (20120 580-588.
[20] A. C. Fischer-Cripps. Nanoindentatio, third ed., Springer, New York, 2011.

Key Engineering Materials Vols 645-646 (2015) pp 681-686
© (2015) Trans Tech Publications, Switzerland
doi:10.4028/www.scientific.net/KEM.645-646.681

Submitted: 2015-01-04
Accepted: 2015-01-12

Micro-fabricated Pre-concentrator Filled with Single-Walled Carbon Nanotubes as Adsorbent Material

Xiaofeng Zhu[1,a], Zhanwu Ning[1,a], Jianhai Sun[2,b,*], Tianjun Ma[1,b], Yanni zhang[1,a],Jinhua Liu[1,a]

[1]Beijing Municipal Institute of Labour Protection, Beijing, 100054, China

[2]State key laboratory of transducer technology, Institute of Electronics, Chinese Academy of Sciences , Beijing, 100190, China

[a]zxf_402@163.com, [b]nzwu@163.com,

[c]jhsun@mail.ie.ac.cn (corresponding author),[d]tjma@mail.ie.ac.cn

*Corresponding author: Tel: +86-10-58887183; E-mail:jhsun@mail.ie.ac.cn;

Keywords: Micro Pre-concentrator; Concentration Factor; Carbon Nanotubes; PID system

Abstract:

As concentration of components in environmental gas is very low, and the available analytical instruments are not sufficiently sensitive, so that micro pre-concentrators developed for effectively concentrating components are very important and necessary. Therefore, in this work a micro pre-concentrator was fabricated for concentrating trace gas. The micro pre-concentrator with 4 parallel channels filled with Single-Walled Carbon Nanotubes (SWCNTs) as adsorbent materials was developed for concentrating volatile organic compounds (VOCs). This choice was done on the basis of the consideration: 4 parallel channels ensure that the pre-concentrator can be filled with a sufficient amount of adsorbent materials. Moreover, SWCNTs was acted as adsorbent material owing to their chemical and thermal stability, a high surface-to-volume ratio, and a large affinity to the non-polar compounds. The experimental results show that the micro pre-concentrator effectively concentrated benzene with a concentration factor of 15 and the chromatography peak broadening was also greatly compressed.

1.Introduction

As sample pretreatments occupied in an important position for on-site rapid detection, micro gas sample pretreatment systems received an unprecedented development with development of MEMS technology. Therefore, this research direction has become a research focus, and many famous research teams [1-14] invested a lot of scientific resources on the development of the micro pre-concentrator, such as university of Michigan, university of Virginia, Sandia national laboratories, Westinghouse electric, etc. University of Michigan developed a micro pre-concentrator [1] based on MEMS technology, the chip with a area less than 1 cm x 1 cm can be heated up to 200℃ in less than 1 second, so the micro pre-concentrator demonstrated a transient concentration much higher than traditional tube pre-concentrator. Moreover, the chromatography peak broadening was greatly compressed. B. Alfeeli [2-4] had made a lot of meaningful works on the development of micro pre-concentrator, they developed a micro pre-concentrator with a size of 7 mm × 7 mm × 0.35 mm which can be used for concentrating VOCs in breath gas, leading to monitoring biomarkers of lung cancer in exhaled air that indicate diseases in early stage. I. Voicolescu [5] developed a micro pre-concentrator which can be successfully integrated into a hand-held chemical warfare agents analyzer (monitoring the nerve gas (dimethyl methyl hosphonate)) and a hand-held explosives analyzer (monitoring the explosives (2, 4, 6-trinitrotoluene)), and these integrated analyzers can be widely used in the battlefield as well as public security. Sandia national laboratory [6] developed micro pre-concentrators with several different structures which were integrated into portable FID detector for monitoring industrial gases online.

It is well known that the efficiency of micro pre-concentrator was closely linked to several keys parameters such as the adsorption capacity, desorption heating rate and detection volume. Therefore, in order to improve the concentration factor, a micro pre-concentrator with 4 parallel channels filled with enough adsorbent materials was developed. Moreover, a heater and cooler were respectively integrated on upside and lower-side of the pre-concentrator. In addition, SWCNTs with a larger aspect ratio and higher effective surface area and good chemical and thermal stability, which demonstrated higher adsorption capacity than carbopack X and other traditional adsorption materials, were used as adsorbent material.

2. Experimental details

2.1 The preferred adsorption material

As we can see that the chemical adsorption is known as activated adsorption, and the adsorption was caused by the chemical bond force between the solid surface and the adsorption molecules. One of the most important factors to affect the adsorption capacity is effective surface are of the adsorption materials which is determined by the porosity, pore size and graininess.

With development of technology, there are more adsorption materials that can be available than before. In addition to the traditional adsorption materials were widely used as adsorption material, such as Tenax-TA, carbopack X, activated carbon, etc. Recently some nano materials were developed as adsorption materials, such as carbon nanotubes, molecularly imprinted polymers, nano-particles, etc.

Single-walled carbon nanotubes (SWCNTs) have a lot of advantages, such as large aspect ratio, high effective surface area, chemical and thermal stability, a large affinity to non-polar compounds and higher adsorption capacity than carbopack X. Moreover, SWCNTs can't be dissolved in water and organic solvents. Therefore, SWCNTs were the preferred material used as adsorbent material.

2.2. The fabrication of the micro pre-concentrator

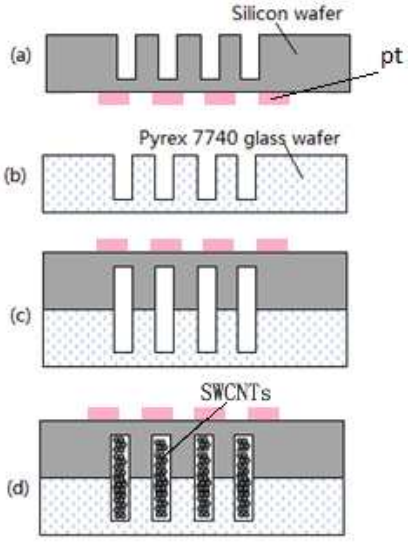


Fig.1. The details of the fabrication process.

Micro pre-concentrator was fabricated based on MEMS technology, and silicon and glass were used as substrate wafers. The fabrication process of the micro pre-concentrator is reported as follows (refer to Fig.1): (1) a layer of 300 nm silicon nitride was deposited by a PECVD technology on the silicon wafer. (2) A micro heater with a resistance of 8 Ω was fabricated as a 20 nm/250 nm Cr/Pt stack deposited by a magnetron sputtering technology and patterned by a lift-off technology. (3) Configuration of the micro pre-concentrator was drawn by AutoCAD software. (4) Micro channels were etched on silicon and glass wafer by laser dicing saw according to the configuration, and the depth and width of the channels was 400 μm and 1000 μm, respectively. (5) The silicon and glass were then polished, respectively. (6) Channels on silicon were aligned and bonded to channels on

glass wafer after cleaning and drying the silicon and glass wafer. In order to increase adsorption capacity as much as possible in adsorption process, a thermoelectric cooler was integrated on upside of the pre-concentrator. Photograph of the fabricated pre-concentrator is shown in Fig.2.

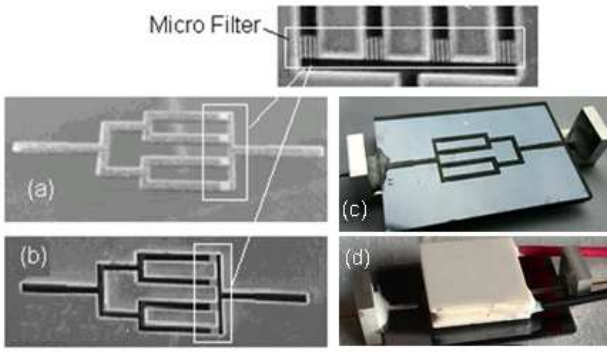


Fig.2. Photograph of the fabricated micro pre-concentrator: (a) channels on glass wafer,(b) channels on silicon wafer, (c) the fabricated pre-concentrator filled with SWCNTs, (d) the pre-concentrator integrated with a thermoelectric cooler.

2.3 Filled with SWCNTs

The details of filling process were reported as follows: (1) SWCNTs were added into TNWDIS solvent for forming suspending agent. (2) One end of the pre-concentrator was connected with a capillary which was emerged into a SWNTs solution, and the other end of the pre-concentrator was connected with a micro-pump. (3) After channels were full of SWNTs solution, nitrogen gas was delivered through it for a few hours to completely evaporate the TNWDIS solvent. (4) The pre-concentrator was put into a temperature programmed oven under a nitrogen flow inside, and temperature of the oven was firstly increased gradually by 5 °C/min until 200°C, then the temperature of the oven was kept at 200°C for 4 hours. (5) Finally, the deposited weight of SWNTs adsorption materials in the channels of the pre-concentrator is 0.15 mg.

2.4 The experimental set-up

In order to evaluate performance of the micro-fabricated pre-concentrator filled with SWCNTs adsorbent material, a portable photoionization detector (PID) [15, 16] was developed to measure its performance. In this set-up, a nozzle with a volume slightly less than the ionization chamber is parallel to the VUV lamp and positioned in the center of the ionization chamber, and thus the volume of the ionization chamber is substantially reduced to 10 μl, decreasing the response time and improving the response sensitivity. Moreover, the collection electrode was shielded by the inner wall of the ionization chamber and the annular accelerating electrode was embedded in the the nozzle groove to shield from vacuum ultraviolet (VUV) light radiation, decreasing background noises. Therefore, the PID demonstrated an ultra low background noise and lower detection limit than its commercial PID counterparts.

The whole characterization set-up is described in Fig. 3. Firstly, the cooler is opened (at working or cooling state), and temperature of the pre-concentrator was rapidly cooled down. Then the sample (50 ppb benzene) was introduced into the proposed pre-concentrator (flow rate of the analyte is 100 ml/min) using a sampling pump, and adsorbed by the SWCNTs. Secondly, the integrated heater is opened (at working state) when the adsorption tends to saturated, and the temperature of the micro pre-concentrator was rapidly increased, rapidly releasing the adsorbed components. Finally, the desorbed analyte from SWCNTs was consequently carried into the portable photoionization detector (PID) by the N_2 carrier gas (with a flow rate of 200 ml/min). The concentrator factor (*CF*) can be calculated by comparing the chromatographic peak area with pre-concentrator (A_f) and without pre-concentrator (A_0).

$$CF = {A_f}/{A_0} \tag{1}$$

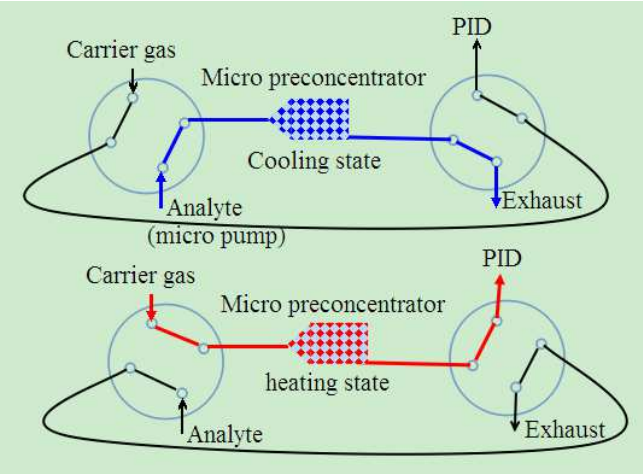


Fig.3. Pre-concentrator characterisation set-up based on PID

2.5. Materials and reagents

In this paper, the sample was detected using the proposed mini-GC-PID system. The pure N_2 was used as carrier gas and sample was composed of benzene with concentration of 5 ppm (provided by the Beijing Hua Yuan Gas Chemical Industry Co., Ltd). SWCNTs were purchased from Chengdu institute of organic chemistry, Chinese academy of sciences. In order to accurately simulate the actual samples, this standard sample was diluted 100 times.

3. The results and discussion

3.1 Temperature characteristic of the Micro pre-concentrator

According to the theory of pre-concentrator, Low temperature is conducive to improve the adsorption capacity of adsorption material. However, in the desorption state, high temperature is conducive to rapidly release the adsorbed components, leading to improving the concentration factor as maximum as possible. To evaluate temperature characteristics of the micro pre-concentrator, a measurement cycle of 200 seconds was considered. Firstly, the cooler is opened, and temperature of the pre-concentrator can be cooled down to 5℃ in less than 100 seconds (refer to Fig.4). Secondly, the cooler is closed and the heater is opened, and the temperature can be rapidly raised up to 180°C after 150 seconds and successively settles to a steady value of 200°C.

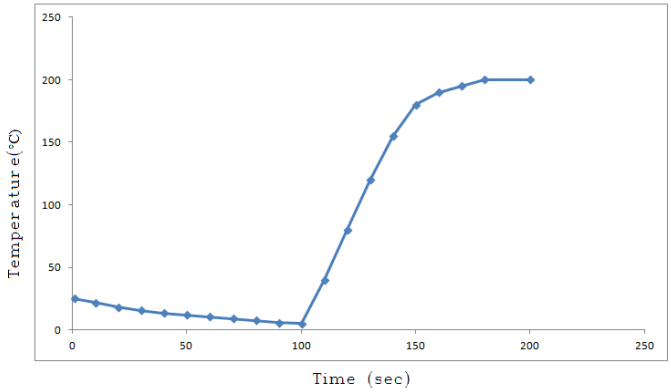


Fig.4. Temperature characteristic of the micro pre-concentrator.

3.2 The characterization of the Micro pre-concentrator filled with SWCNTs

To evaluate the performance of the micro pre-concentrator filled with SWCNTs as adsorbent material, the fabricated pre-concentrator was conducted to concentrate the traces sample of benzene.

The details of the test process are reported as follows: (1) Firstly, the sample of benzene with a concentration of 50 ppb was directly transported into the PID without the pre-concentrator, and the chromatographic signals were obtained (refer to Fig.5). (2) Secondly, the sample was carried into the pre-concentrator without opening the cooler, and the micro pre-concentrator was heated after the adsorption tends to saturated, then the adsorbed aromatic benzene was consequently released and delivered into the PID by carrier gas. (3) Finally, the experiment was performed under the cooler in working state.

Fig.5 indicates the output of chromatographic signals obtained by the PID. The result obviously shows that the fabricated pre-concentrator can effectively concentrate diluted benzene even if there is no thermoelectric cooler. However, compared with the performance of the pre-concentrator with and without the cooler, the value of CF can be improved from 12 to 15 by increasing adsorption capacity in the adsorption stage. Therefore, it's an effective method to improve the CF by integrating a cooler on the pre-concentrator. Moreover, the chromatography peak broadening can also be compressed.

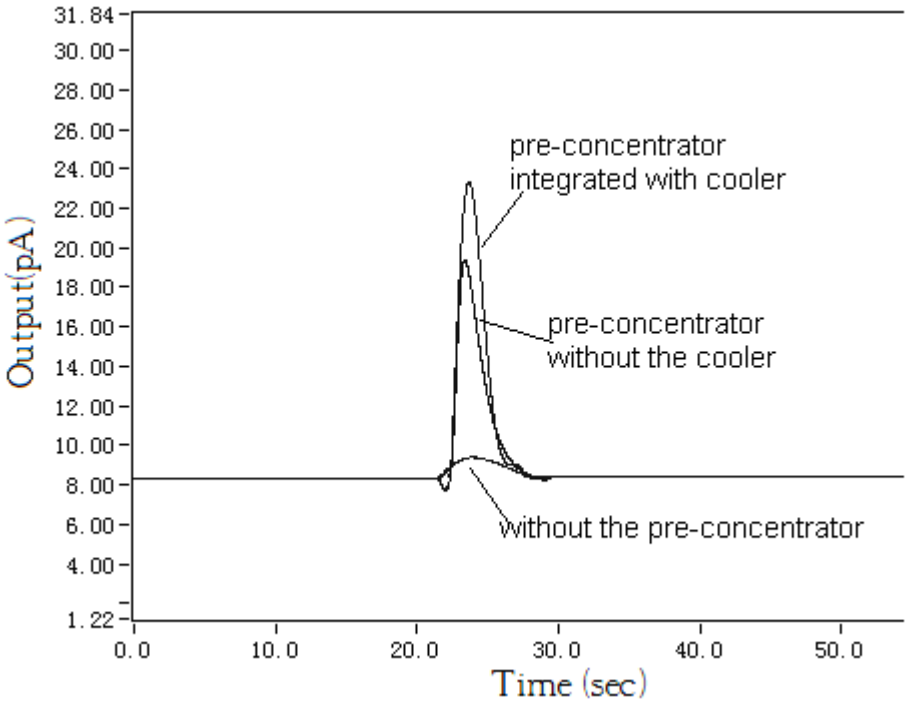


Fig.5. The performance of the fabricated pre-concentrator.

4. Conclusion

The work here demonstrates that it is possible to fabricate a micro pre-concentrator filled with SWNTs as adsorbent material. The experimental results demonstrated the developed pre-concentrator can effectively concentrate the component more than 15 times, and the adsorption capacity can be increased by integrating a cooler on the pre-concentrator in the adsorption stage, thus improving the *CF*.

Acknowledgment

The authors greatly acknowledge the financial support from the Beijing science and technology plan project under Grant number Z141100003414003, 2014 science and technology innovation projects of Beijing Academy of Science and Technology (PXM2014-178304-000001-00130138), 2013 youth backbone project of Beijing Academy of Science and Technology and Natural Science Foundation of China (61176112,60976088).

References

[1] M. Martin, M. Crain, et al., Sensors and Actuators, B: Chemical, 126 (2)(2007)447-454

[2] B. Alfeeli, M. Agah, Proceedings of IEEE Sensors, 2008, 736-739.

[3] B. Alfeeli, M. Agah, IEEE Sensors Journal , art. no. 5928373 (2011) 2756-2762.

[4] B.Alfeeli, H. Vereb, et al., Proceedings of the IEEE International Conference on Micro Electro Mechanical Systems (MEMS), art. No. 5734575(2011) 916-919.

[5] I. Voicolescu, R. A. McGill, et al., IEEE Sensors Journal,6 (5)(2006)1094-1103.

[6] P.R. Lewis, P. Manginell, et al., Sensors Journal, IEEE, 6(3)(2006)784-795

[7] W.C. Tian, S.W. Pang, et al., Journal of Microelectromechanical Systems,12 (3)(2003) 264-272

[8] I. Gr`acia, P. Ivanov, et al., Sensors and Actuators B 132 (2008)149–154

[9]J. Zhao, T. Luo, X.Zhang, et al., Analytical Chemistry,84(15)(2012) 6303-6307.

[10] M. Phillips, R.N. Cataneo, et al., Chest, 123(2003) 2115-2123.

[11]Chen X, Xu FJ, et al., Cancer, 110(4)(2007) 835-844.

[12]S.Takada, T.Nakai, et al., IEEJ Transactions on Sensors and Micromachines, 130 (6)(2010) 207-211.

[13] I.Gràcia, P.Ivanov, F.Blanco, et al., Sensors and Actuators, B: Chemical,132 (1) (2008)149-154.

[14] Jiemin Liu, Lin Li, Chinese Journal of Analytical Chemistry,35(6)(2007)830~834.

[15] J.H. Sun, F.Y. Guan, D.F. Cui, X. Chen, L.L. Zhang, J. Chen, Sensors & Actuators: B. Chemical, 188(2013) 513-518.

[16] J.H. Sun, D.F. Cui, X.Chen，L.L.Zhang, H.Li, J. Chromatogr. A 1291(24)(2013)122–128.

Key Engineering Materials Vols 645-646 (2015) pp 687-692
© (2015) Trans Tech Publications, Switzerland
doi:10.4028/www.scientific.net/KEM.645-646.687

Submitted: 2015-01-08
Accepted: 2015-01-15

Research on Rapid Detection and Accounting of Small Particles in Marine Hydraulic Oil

Lin Zeng[1, a], Hongpeng Zhang[1, b*], Enchen Liu[1, c], Haiquan Chen[1, d], Fangyu Cui[2, e]

[1]Dalian Maritime University, Marine Engineering College, Dalian Liaoning 116026, China

[2] Dalian Chun An Ship Management Co., Ltd, Dalian Liaoning 116001, China

[a]bob666zl@126.com, [b]zhppeter@163.com, [c]574298919@qq.com, [d]chenapec@163.com, [e]494239670@qq.com

Keywords: Marine hydraulic oil; Microfluidic detection chip; detection and counting of small particles; fault diagnosis

Abstract. Hydraulic system is widely used in the ship, when the diameter of tiny particles in hydraulic oil exceeds 20μm it indicates that the abnormal wear occurred and the malfunction may cause. This paper uses the light blockage method, the microfluidic detection chip for hydraulic oil detection has been designed and fabricated, a simple and effective optical detection system is developed with the signal amplification and data collection to achieve the detection of tiny particles, and finally through the JAVA programming to count the number of particles in which the diameter is more than 20μm. The results of rapid detections on iron particles with diameter between 25μm and 38μm show the good performance of the detection system and prove that the method is feasible.

Introduction

Hydraulic system is extensively used on board ship. Compared with other hydraulic systems, marine hydraulic system has the characteristic of high strength, stricter maintenance requirements and more severe working environment [1]. Practice shows that more than 75% of the faults in the hydraulic system are caused by hydraulic oil pollution [2]. During the normal working condition of hydraulic equipment, the abrasive grain in hydraulic oil has a constant concentration and smaller size (usually the size is in the range of 10~20μm). If abnormal wear occurs, the concentration of abrasive grain will increase and the diameter of particles will increase to 50~100μm [3].So the counting detection of small particles in hydraulic oil has important significance.

In recent years, the optical detection is widely used for the counting of small particles with the advantages of high sensitivity, fast detection and can achieve morphology analyze of particles [4, 5], one of the most important optical detection method is the light blockage method, which work on the principle that when the particles pass through the detecting counter the sensor will induct the intensity mutation caused by blocking light of particles [6, 7]. The accuracy of light blockage method depends on the sectional area which is the projective area of particles in the direction of light. The bigger the sectional area the more light is sheltered. Meanwhile, the light blockage method is also one of the main methods of particles detecting based on microfluidic chip thanks to the characteristics and superiorities of optical blockage. The optical detection device based on microfluidic chip is widely used on the research of detection and counting of cells and bacteria as its small volume and light influence caused by external environment [8].

According to the characteristics and advantages of optical detection method and microfluidic detection chip, in this paper, we use the light blockage method which applies to the microfluidic chip to accomplish the detection and counting of tiny particles in marine hydraulic oil. We achieve the quick detection of iron particles (particle size between 20μm and 40μm) through the optical detection

system which based on microfluidic chip that we established during experiment and the counting of particles by the use of JAVA program.

1 Design and fabrication of detection chip and focusing effect simulation

1.1 Design and fabrication of detection chip

The following requirements should be kept during design of detection chip:

(1) The chip should have a good aggregation effect on the oil sample, this allows small particles to pass through the detection zone in single file and ensure single cell level detection.
(2) The designed chip should be easily fabricated and have reliable performance.
(3) The chip can easily control the flow rate of the sample [9].

According to the above design requirements, microfluidic chip structure used in this paper design as shown in Fig. 1.

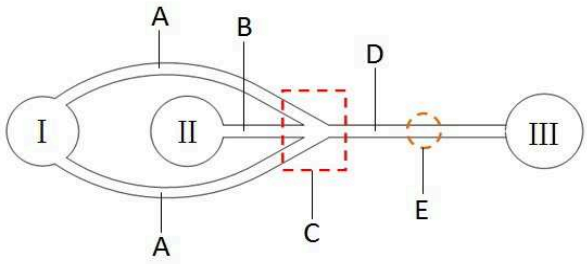


Fig. 1 Design diagram of detection chip

Fig. 1 Structural design drawing of the detection chip. Ⅰ is the sheath fluid pool, Ⅱ is the oil pool, Ⅲ is the effluent pool. Microchannel (A) is a sheath fluid flow channel, microchannel (B) is sample solution flow channel, (C) is the converging zone of sheath fluid and sample solution, microchannel (D) is the detection channel and (E) is detection zone. The width of microchannel (A), (B) and (D) are 100μm, the height of whole microchannel is 100μm, the angle between microchannel (A) and (B) is 30°.

The effluent pool Ⅲ connects with the micro-injection pump (Harvard Apparatus B-85259, American) to provide a negative pressure. Sheath fluid and hydraulic oil reach the microchannel simultaneously powered by the negative pressure, then gather at the converging zone. Here, the hydraulic oil is under the pressure of sheath fluid on both sides, causing its flow diameter to narrowed substantially. This causes an aggregation effect on the hydraulic oil. This aggregation effect allows the small particles in hydraulic oil to pass through the detection area in single file.

Method for making microfluidic chip includes soft lithography, molding method, laser ablation method, etc. In this paper, we use soft lithography method to make detection chip. The detection chip that we have fabricated is shown in Fig. 2.

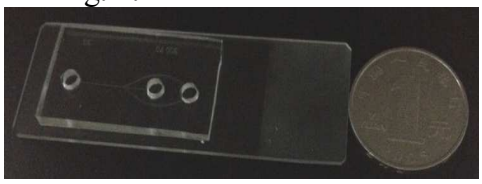


Fig. 2 Picture of detection chip

1.2 Simulation of the focusing effect

In order to test the focusing effect of detection counting chip that we have designed, we use ANSYS CFX to simulate the focusing effect of internal fluid at structure (C) (the converging zone), the main workflow of simulation is shown in Fig. 3.

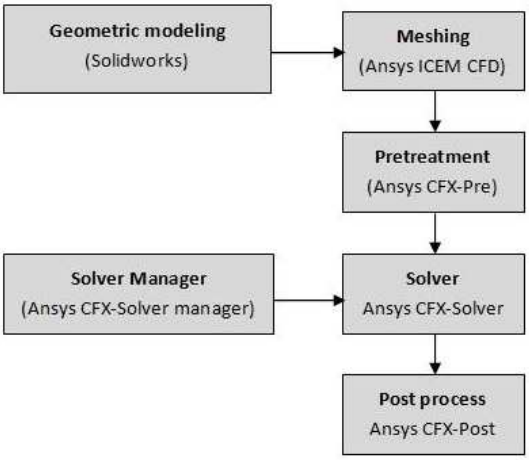


Fig. 3 Flow charts of simulation

During the post process we define the flow rate of oil and sheath fluid as constant for the sake of reflecting the focusing result more directly. Flow trajectories of oil and sheath fluid inside channel are shown in Fig. 4. Within the figure, the mazarine parts indicate sheath fluid and the yellow parts are the hydraulic oil, the flowing direction is from left to right. The figure express that the width of oil after focusing is about 35μm, so the solid particles in the oil also be located within the range of 35μm and the purpose that solid particles in a single row pass through the detection area of flow channel comes true.

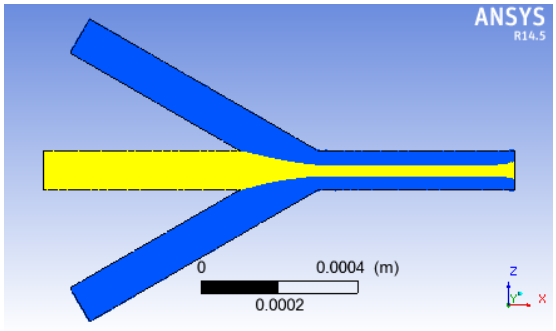


Fig. 4 Trajectory figure of fluid

The above two figures show that the chip structure that we have designed in this paper has an excellent effect on the focus of small particles in oil, it can ensure that particles pass through the detection area one by one rather than side by side or the blocking the microchannel.

2 Detection system setup

The rapid detection and counting system of small solid particles in hydraulic oil that we used in the experiment mainly include: microfluidic detection chip, laser source, photodiode, the micro injection pump, signal amplification circuit and data acquisition board. According to the function of each part and the need of the whole system, we build each part together and finish the building of counting system. System layout is shown in Fig. 5.

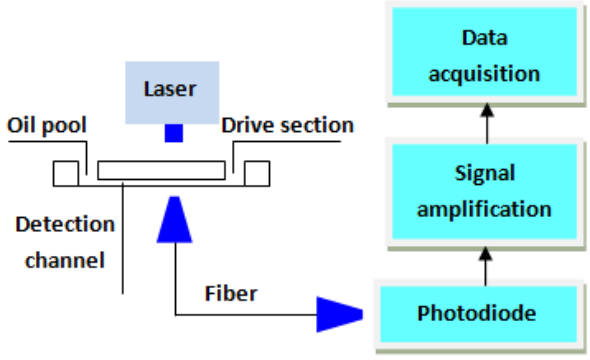


Fig. 5 Detection system diagram

While building up the detection and counting system, we draw the 3D graphics through Solidworks software and print out the laser support bracket, the detection chip pallet with optical fiber jack and the whole optical system with 3D printer. The support which used in this experiment and printed out by 3D printer is shown in Fig. 6.

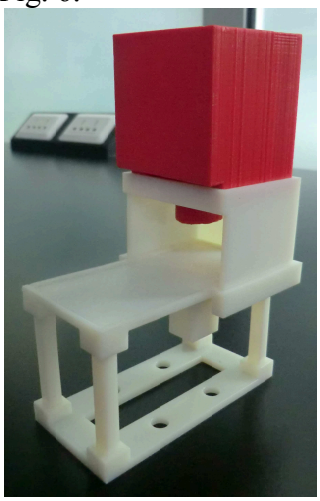


Fig. 6 Optical detection support

3 Detection and counting experiment and data analysis

3.1 Detection and counting experiment

In order to avoid the external light source influent the accuracy, so the experiment is carried out in the dark. The laser is fixed on the bracket, laser center and the optical fiber center plug in the same axis, thus guarantee the optical fiber can receive laser emission. Place the chip on the tray, and move chip forward and back so that the laser transmit light through detection channel. Connecting the micro injection pump and effluent pool through the hose, thus forming negative pressure driven aggregation. Another fiber head face the photodiode's sensing part. Connecting the photodiode to the amplifying circuit, the signal amplifying circuit will transfer the circuit signal which is generated in the photodiode into voltage signal and amplify it to more than 100mv. The amplified voltage signal pass through the data acquisition card and fed into the computer, finally the data is deal, analyzed and displayed by LabVIEW software.

3.2 Detection result and data analysis

In this paper, we mix clean marine hydraulic oil with iron particles (the max size is 38μm) and the mixture is our detection sample. The signal chart we get in this experiment is shown in Fig. 7, Horizontal and vertical coordinate are time(S) and voltage (V), respectively.

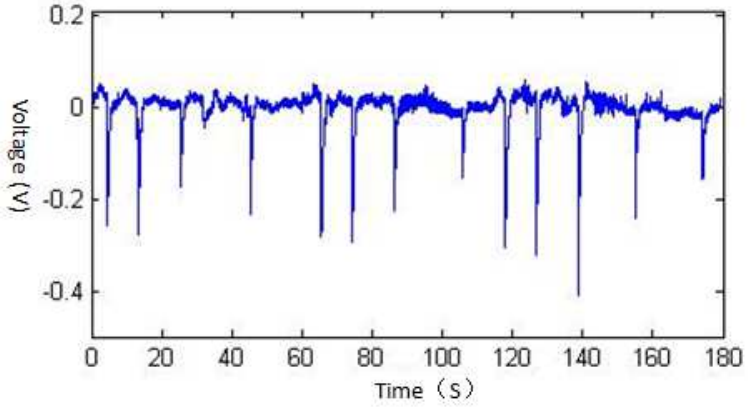


Fig. 7 Detection signal figure

From the signal figure, we can see it clearly that, the maximum amplitude of the signal is about 0.4V, the minimum is about 0.15V. Because the iron particles are screening out with a sieve (400 and 500 meshes per square inch), the maximum diameter of particles is 38μm, meanwhile, there are many particles with diameter less than 38μm and this lead to the difference of the signal amplitude.

When the size of the particle is larger than 20 μm, the abnormal wear is likely to happen in the hydraulic oil. According to solid particles pollution in oil grading standards, it's necessary to count if the particle size larger than 20μm. The quantity of amplitude is equal to the quantity of iron particles in the detection signal figure.

Detection of tiny particles by light blockage detecting method, the relationship between the electrical pulse amplitude of particle size and characterization of light changes are generally showed by the traditional formula [11]:

$$E = \frac{s}{A} E_0 = \frac{E_0}{A} \cdot \frac{\pi d^2}{4} \tag{1}$$

While E represents for the voltage pulse amplitude when the particles go through the detection channel; S represents for the projection area in the beam direction; A is the effective receiving area of the photoelectric sensing element; E_0 is the voltage pulse amplitude when no particles pass through the detection channel. If the particle is spherical, D is the diameter of the particle.

From the signal figure, the signal amplitude of 38 μm particle is about 0.4V, so that can be calculated by the formula (1), the signal amplitude of 20 μm particle is about 0.11V, so this paper chooses the lowest reference signal amplitude of 0.1V, all the signal amplitude were compared with 0.1V, the amplitude of the signal pulse will begin to count more than 0.1V.

In this paper, we use the Java language to program for achieving in all kinds of portable mobile platform to count particles. The program firstly extracted each trough values from signal pulse, and then each trough values were compared with the lowest reference signal amplitude, if more than 0.1V, count +1, and so on, until the program is running, the count number is the number of particles with the size larger than 20μm. The extracted trough value and the result of running the program is shown in Fig. 8.

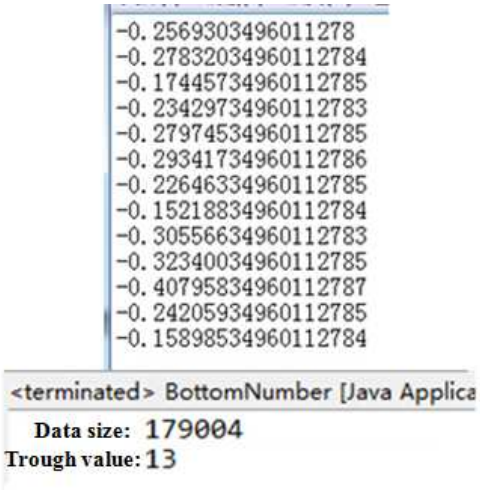


Fig. 8 Program running result

After running the program, the number of the troughs and the effective number of pulse waveform are consistent, meanwhile gives the corresponding pulse amplitude, which proved the feasibility of this program. By using the pulse amplitude can be nearly calculated the size of particles that go through the particle detection channel.

4 Conclusion

In this paper, we use the optical detecting method to achieve the rapid detection and counting of marine hydraulic oil in designed microfluidic chip, the experiments show that, this system can effectively detect the solid particles in hydraulic of which the diameter is larger than 20μm, and count

the particles(larger than 20μm) by Java program. The microfluidic chip that is proposed in this paper has small size, high detection speed and required less oil sample, which achieved the rapid detection of oil in the field, and provides the research foundation and the strong technical support for the development of portable marine hydraulic oil particle counting equipment, at the same time through the detection of small particles can provide important basis for fault diagnosis of hydraulic system on the ship.

Acknowledgement

Support for this work was provided by the following: the Natural Science Foundation of China (51205034), Scientific Research Program of the Ministry of Transport (2013329225260) and the Fundamental Research Funds for the Central Universities (3132014332), the authors wish to thank these financial supports.

References

[1] Ge Wang, Dongfeng Liu, Xinfa Shi. Marine hydraulic oil monitoring technology research status [J].Lubricate oil,2013,04:38-41.

[2] Shiyou Wu, Shufang Wang. The sources and harm of hydraulic oil pollution and its control measures [J]. Equipment Manufacturing Technology, 2008, 03:80-82.

[3] Tucker Je, Galie Tr, Schultz A, et al. Lasernet Fines Optical Wear Debris Monitor a Navy Shipboard Evaluation of Cbm Enabling Technology[C]. 54th Mach Fail Prev Technol Proc, 2000:191.

[4] Xiaoying Zeng, Yunhua Li. Using the image measuring method of oil pollution of online monitoring and prediction [J]. Pneumatic and hydraulic pressure seal.

[5] Yang Li, Zheng Yingna, Wang Renhuang. Experimental Study and the Theoretical Model of Optical Flowmeter of Solid Debris[J]. Mechanical Engineering, 2004,8:160-165

[6] Qian Tian. Window type automatic particle counting method to determine oil pollution in the hydraulic system [J]. Intelligence development of science and technology and economy, 2003(5):109-110.

[7] Huanxiao Wen, Fu Jingye. Light resistance method to measure the oil particle pollution in the study[J]. The space measuring technology, 2002(6):38-41.

[8] Dongqing Li. Microfluidic lab-on-a-chip devices for biomedical applications[J]. Microfluidics Based Microsystems: Fundamentals and Applications. 2010:377-396

[9] Wen Huang. Ship sewage rapid detection method for basic research. Master's thesis. Da Lian Maritime University. 2012.

[10] Bingcheng Lin, Jianhua Qin. Microfluidic chip laboratory[J]. The chromatographic. 2005.09:456-463.

[11] Tao Xu, Yucheng Gao, Xing Wu. For now method in principle analysis of the small particle size of particle detection[J]. Journal of instrument, 2005,01:13-16+22.

Key Engineering Materials Vols 645-646 (2015) pp 693-697
© (2015) Trans Tech Publications, Switzerland
doi:10.4028/www.scientific.net/KEM.645-646.693

Submitted: 2015-01-15
Accepted: 2015-01-20

Dissemination of Micro-gram weights from 500 μg to 50μg Based on Automatic Mass Measuring System

X.P. Ren [1, a], J. Wang [1,b], L. Dong[2,c], Ombati Wilson [3,d]

[1] Mass Lab, Division of Mechanics and Acoustics, National Institute of Metrology, Beijing, CHINA

[2] Shaanxi Institute of Metrology Science, Xi'an, CHINA

[3] Kenya Bureau of Standards, Nairobi, Republic of Kenya

[a]renxp@nim.ac.cn(corresponding author), [b]wjian@nim.ac.cn, [c] dl_721@163.com,

[d] wilombati@gmail.com

Keywords: Micro-gram Weights; Automatic Mass Measuring System; Calibration of Weights; Subdivision Method

Abstract. Microgram weights have a wide range of applications in the mechanical testing of bio-material sensors and nanotechnology market which typically involves the manufacture of objects with dimensions of less than 100 nanometers. Now it is available with a calibration certificate in National Institute of Metrology (China) that customers can be assured of full traceability to the national primary standard of mass, NO.60, which make allow customers with specialized nanotechnology applications to use the weight values range from 0.05 mg to 0.5 mg with standard uncertainty of just 0.3 μg to 0.08μg.

In the paper, an effective method was developed to calibrate weights, along with new methods of calculating uncertainties that would satisfy OIML R111 requirements. This new calibration method involved comparing the weights with the 1 mg standard mass standards using a combination of subdivision and substitution weighing scheme.

Intorduction

The growing and evolving dynamics in mass and force measurements has inevitably necessitated the need for high precision and accurate results. As a result, measurements in micro-gram(s) and nano-Newtons levels have increasingly attracted potential research interests[1]. However, at the moment, such results have no measurement assurance since traceability to the International System of Units (SI) has not yet been developed [2].

An automatic system can reliably and accurately perform the micro-mass measurements without manual intervention. In 2007, Fröhlich and Fehling had used a fully automated mass comparator robot system to calibrate an entire 1 kg – 1 mg weight set against one 1 kg reference by subdivision in less than 1½ days [3]. Zelenka in BEV of Austria developed and realized three handling systems for automatic calibration of weights (1 mg to 10 g) on high-precision mass comparators [4]. In 2009, Chung[10]used an automatic mass comparator to calibrate of microgram weights with direct-comparison method. At the moment, NIM is undertaking research on microgram weights (range: 500 μg to 50 μg)[5]. This paper introduces the installation and operation of a robotic measurement system, and discusses a sub-multiple calibration scheme that has been adopted in calibrating selected microgram weights.

Micro-Mass Standard Measurement System

To meet the stringent requirements of an advanced metrology institute, a measurement robot system, CCR10and its housing unit (shown in Fig. 1), was set up at NIM on June 2013. This system, characterized by high calibration speed, offers efficiency in the determination of mass of weights, OIML Class E1. It consists of the following main parts: built-in mass comparator (and support table),

control unit, robot arm and weights, and magazines (for storage of reference and test weights) (shown in Fig. 2). Besides, we add our air density measurement system into this system, it can measurement the environment parameters when it measures. During the measurement process, measurement results and climate data are recorded synchronously,

Fig.3 shows our self-making micro-weights range from 500 μg to 50 μg, which is made of aluminum material.

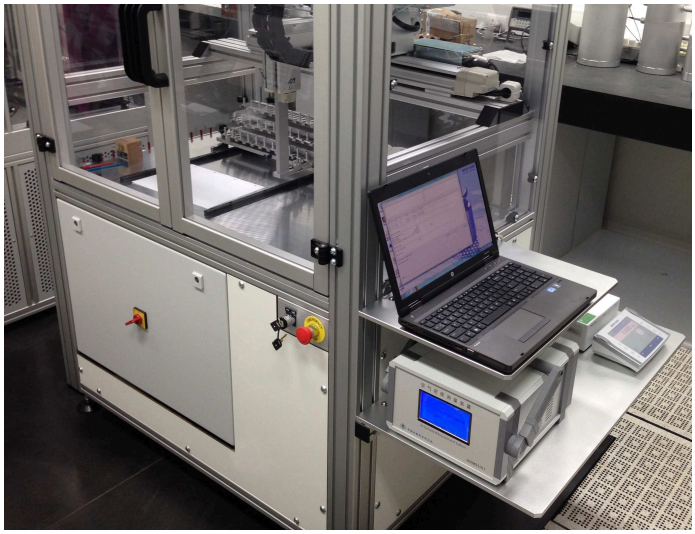


Figure 1. a5 automatic mass comparator

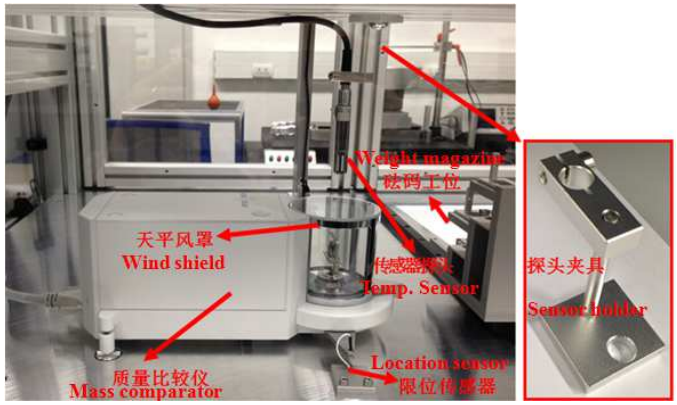


Figure 2. Ambient Sensor and air density measurement



Figure 3 View of Micro-weight from 500 μg to 50 μg

Calibration of weights and Weight sets based on Subdivision Method

Subdivision calibration method using ABBA scheme was used in calibrating weights of nominal mass, 1m g to test weight (500 μ g to 50 μ g). These weights were all E_1 class and placed on magazines. The weight measure scheme of micro-weight is shown in Table1[6][7].

Table 1. Weight Scheme of micro-weight

No.	Standard Weight	Test Weight
1	[1]+Δm_1	[0.5]+[0.5・]
2	[0.5] +Δm_2	[0.5・]
3	[0.5] +Δm_3	[0.2]+[0.2・]+[0.1]
4	[0.2]+ Δm_4	[0.1]+[0.1・]
5	[0.2・]+ Δm_5	[0.1]+[0.1・]
6	[0.1]+ Δm_6	[0.1・]
7	[0.1] +Δm_7	[0.05]+[0.05・]
8	[0.05]+ Δm_8	[0.05・]
9	[0.2]+ Δm_9	[0.2*]
10	[0.2・]+ Δm_{10}	[0.2・*]

From Table 1 above, average mass difference $\overline{\Delta m_i}$ is calculated from the indication differences of the balance in the above equations. The conventional mass of the reference weight, [8] (1mg), is subtracted from results of average mass differences of respective weights under calibration, and then corrections were estimated by the least squares method. And Table2 gives out the final result for standard uncertainty of each test weight. The expanded uncertainty U [9][10]of the mass of test weight is in the last column.

Tab. 2 Combined standard uncertainty of test weight (μg)

Standard uncertainty of test weight	Uncertainty of the reference weight $u(m_r)$	Combined standard uncertainty u_c
$u_{0.5}=\frac{1}{2}\sqrt{u^2(m_r)+u_1^2+u_2^2+2u_1u_2}$	0.45	0.23
$u_{0.5\cdot}=\frac{1}{2}\sqrt{u^2(m_r)+u_1^2+u_2^2+2u_1u_2}$	0.45	0.23
$u_{0.2}=\frac{2}{5}\sqrt{\begin{matrix}u_{0.5}^2+u_3^2+u_4^2+u_5^2+u_6^2+2u_3u_4+2u_3u_5+2u_3u_6\\+2u_4u_5+2u_4u_6+2u_5u_6\end{matrix}}$	0.23	0.12
$u_{0.2\cdot}=\frac{2}{5}\sqrt{\begin{matrix}u_{0.5}^2+u_3^2+u_4^2+u_5^2+u_6^2+2u_3u_4+2u_3u_5+2u_3u_6\\+2u_4u_5+2u_4u_6+2u_5u_6\end{matrix}}$	0.23	0.12
$u_{0.1}=\frac{1}{2}\sqrt{u_{0.2}^2+u_4^2+u_6^2+2u_4u_6}$	0.12	0.07
$u_{0.1\cdot}=\frac{1}{2}\sqrt{u_{0.2}^2+u_4^2+u_6^2+2u_4u_6}$	0.12	0.07
$u_{0.05}=\frac{1}{2}\sqrt{u_{0.1}^2+u_7^2+u_8^2+2u_7u_8}$	0.07	0.06
$u_{0.05\cdot}=\frac{1}{2}\sqrt{u_{0.1}^2+u_7^2+u_8^2+2u_7u_8}$	0.07	0.06
$u_{0.2*}=\sqrt{u_{0.2}^2+u_9^2}$	0.07	0.12
$u_{0.2\cdot*}=\sqrt{u_{0.2\cdot}^2+u_{10}^2}$	0.07	0.12

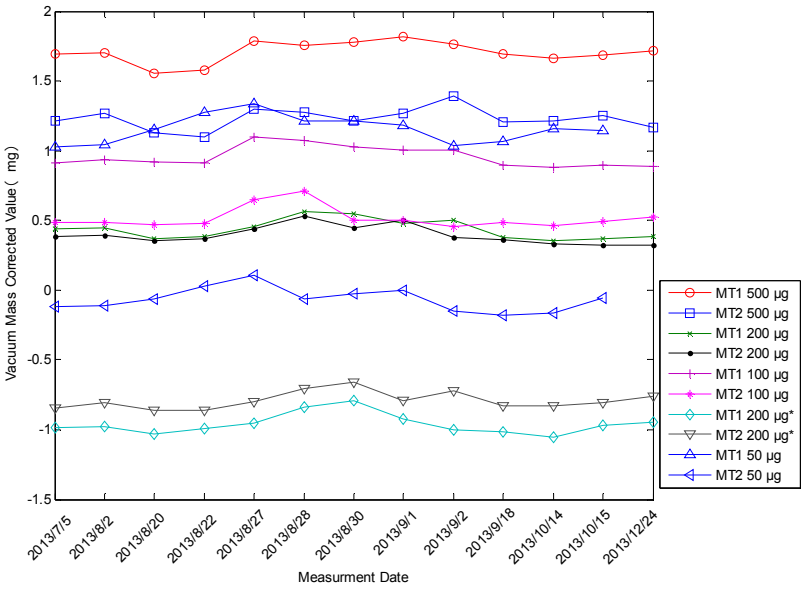


Figure 4. Long-term stability of mass corrected value of micro-weights

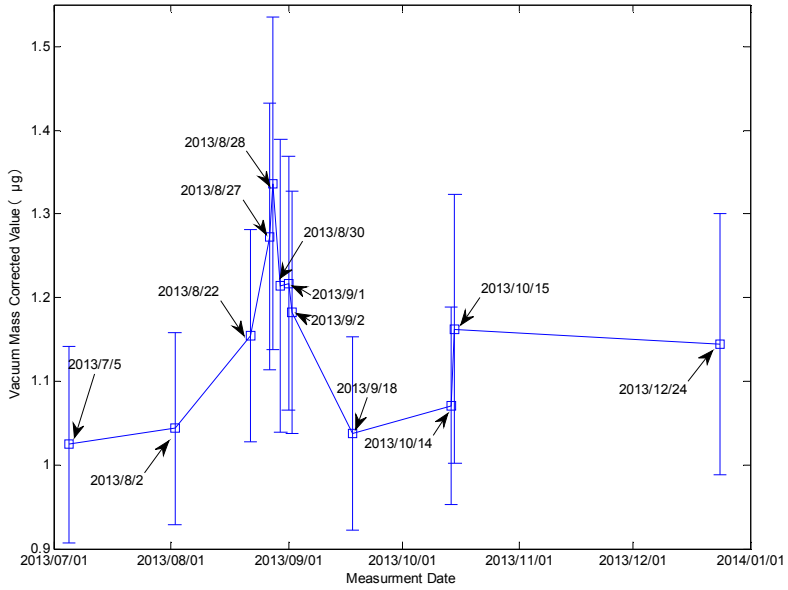


Figure 5. Mass Corrected Value and standard uncertainty of 50 μg Micro-weight

Summary

In the paper, an effective method was developed to calibrate weights, along with new methods of calculating uncertainties that would satisfy OIML R111 requirements[11][12]. This new calibration method involved comparing the weights with the 1 mg standard mass standards using a combination of subdivision and substitution weighing scheme. After the final measurement, we also gave out the long term stability of micro-weight in Fig.4, and the uncertainty evaluation for 50 μg micro-weight is shown in Fig5. Micro-weights values range from 0.05 mg to 0.5 mg with standard uncertainty of just 0.3 μg to 0.08μg.

Acknowledgement

The grants that have been received from the National Natural Science Funds of China(51405459), National Science and Technology Support Program (2011BAK15B06) , Special-Funded Program on National Key Scientific Instruments and Equipment Development (2012YQ090208) are hereby acknowledged with much gratitude.

References

[1]X.P. Ren, J. Wang, R. L. Zhong, et al. Some Issues in Magnetic Measurement of Mass Standards[J]. Advanced Materials Research, 2013(631-632):837-841.

[2]Xiao Ping Ren, Jian Wang, Yue Zhang, Wilson Ombati. Calibration of Weights and Weight Sets Based on Micro-Mass Standard Measurement System. Key Engineering Materials, 2014, (Volumes 609 - 610),1473-1477

[3]M. S. Kim, J. R. Pratt. SI traceability: Current status and future trends for forces below 10 micro-Newtons [J]. Measurement, 2010, 43:169-182.

[4]D.B. Newell, J.A. Kramar, J. R. Pratt, et al. The NIST Microforce Realization and Measurement Project [J]. IEEE Transactions on instrumentation and measurement, 2003, 52(2): 508-511.

[5]T. Madec,G. Mann,P.A. Meury, et al. Micro-mass standards to calibrate the sensitivity of mass comparators[J]. Metrologia, 2007, 44:266-274

[6]T. Madec, M. Gaëlle, P. A. Meury. Extension of dissemination of mass unit between 1 mg and 100 μg [J]. Revue Française de métrologie, 2011(27) 3:29-38.

[7]M. S. Kim, J. H. Choi, Y. K. Park. Test of a microbalance below 1 mg using the electrostatic load and micro weights[C].Proceedings of Asia-Pacific Symposium on Mass, Force and Torque (APMF 2007), 2007, 142-146.

[8]Chung J W, Lee S J, and Kim K P. Establishment of mass standards from 1 mg to 50 μg [C]. Proceedings of Asia-Pacific Symposium on Measurement of Mass, Force, Torque. 2009, 66-70.

[9]X.P. Ren, J.Wang, H. Yao, et al. Review of microgram standards metrology. Journal of Huazhong university of science and technology (nature science edition), 2012, 40(II): 91-97.

[10] YAO Hong, REN Xiao-ping,WANG Jian,Zhong Rui-lin, Ding Jing-an. Recent Research on the Automated Mass Measuring System. International Journal of Modern Physics: Conference Series on Measurement of Mass, Force and Torque (APMF 2013),24,1360003,1-6.

[11] Arthur R. A new mass comparator generation for the automatic calibration of weight sets[C]. Proceedings of the 17th international conference on force, mass, torque and pressure measurements, IMEKO 2001,17-21, 310-319.

[12] Masaaki U., Kazunaga U. Uncertainty evaluation on the fully-automated sub-multiple calibration in the milligram range[C]. Proceedings of SICE annual conference 2007, 17-20, Ibaraki, 2007,24-28.

Key Engineering Materials Vols 645-646 (2015) pp 698-705
© (2015) Trans Tech Publications, Switzerland
doi:10.4028/www.scientific.net/KEM.645-646.698

Submitted: 2015-01-19
Accepted: 2015-01-21

Design and Fabrication of High Vacuum Gauge Based on Micro Hotplate

Fengtian Zhang[1, a*], Yingbin Zhen[1] , Bin Tang[1], Wei Su[1], Zhen'an Tang[2]

[1]Institute of Electronic Engineering, China Academy of Engineering Physics,
Mianyang, Sichuan, 621900. China

[2] Institute of Electronic Science and Technology, Dalian University of Technology,
Dalian, Liaoning, 116024, China

[a]zftstuart@sohu.com(corresponding author)

Keywords: Vacuum gauge; Micro hotplate; Thermal conductivity; Constant current

Abstract

Vacuum gauge based on micro hotplate (MHP) is a kind of promising MEMS vacuum gauge due to its advantages including high sensitivity, wide measurement range, fast response speed and comparably easy fabrication, etc. In this paper, through analyzing various of heat dissipation approaches including solid heat conduction, gas heat conduction, heat radiation, and convection, the sensor output expression of MHP-based vacuum gauge is obtained when keeping electric current of heating resistor constant. With the structure size and material properties, the relationship curve between vacuum gauge output and gas pressure can be obtained. By wet etching silicon under the compound dielectric films with embedded metal film resistor, MHP suspended over silicon substrate is fabricated. Then the sensor chip is assembled and put into vacuum system, and test is conducted when keeping the heating resistor at constant heating current of 5mA. The measurement results show that the sensor measurement range is 5×10^{-3}Pa～10^{3}Pa, which is basically consistent with the theoretical analyzing results.

Introduction

Various kinds of MEMS vacuum gauges have appeared with the development of microfabrication technology, which are based on the principles of piezoresistive [1], capacitive [2], ionization [3], thermal conductivity [4], etc. At the same time, high vacuum gauges are more and more required to be embeded into some devices such as vacuum electronic devices, microwave devices, resonant MEMS devices to monitor their health, in which vacuum pressure level must be higher than a certain value. Piezoresistive and capacitive vacuum gauges are based on the deformation of thin membrane, it is difficult for high vauum measurement due to the difficulty of manufabricating large thin sensitive floating membranes. Ionic and thermal conductivity vacuum gauges use the relationship between gas physical properties and gas pressure, no large deformation happens in the micro structure, so they are main approaches for high vacuum measurement. Compared with ionic vacuum gauges which always need high working voltage and their microfabrication are comparatively complicated, thermal conductivity vacuum microsensors are more attractive for high vacuum measurement. Research by Jin-Shown Shie has shown an example of high vacuum gauge which can measure pressure down to at least 10^{-4}Pa, with a complicated thermoelectric stabilization method [5].

In this paper, we present the design and fabrication of high vacuum gauge based on micro hotplate (MHP), which has large surface for thermal conductance and more gas molecules to join in heat conduction. By analyzing influences of gas pressure and the characteristic length on gas thermal conductance, key points of designing high vacuum gauge are presented. To obtain the relationship between the sensor output voltage and gas pressure, heat transfer characteristics of the MHP are analyzed. Then one MHP-based high vacuum gauge is fabricated with front –side bulk silicon micromachining technology and measurement results with constant current method are shown.

1 Structure design and theoretical analysis

The behaviour of gas thermal conduction as a function of pressure is determined by the Knudsen number:

$$K_n = \frac{\lambda}{d} \tag{1}$$

where λ is the mean free path of the gas and d is the characteristic length involved in the heat transfer. In rarefied gas dynamics,four different regimes can be distinguished[6]:free molecules(K_n>10), transition (10>K_n>0.1), temperature jump (0.1>K_n>0.01) and continuum (K_n<0.01).In the continuum regime, the effective thermal conductivity is pressure independent while in the free molecule regime it depends linearly on pressure. In the temperature jump and transition regimes gas thermal conductivity gets more and more pressure dependent as K_n increases. The thermal conductance G_g of a gas between two parallel plates for all pressure regimes can be approximately expressed by the following formula[7]:

$$G_g = \frac{H}{T_2 - T_1} = \alpha G_{mol} \frac{PP_{tr}}{P + P_{tr}} \tag{2}$$

$$G_{mol} = \frac{(\gamma + 1)}{2(\gamma - 1)} \sqrt{\frac{k}{2\pi m T}} \tag{3}$$

where H is heat transferred per square meter(in W/m^2), T_2 and T_1 are respectively the temperature of two plates, G_{mol} is the free-molecular thermal conductivity, α is the effective accommodation coefficient, γ is the ratio of the specific heat at constant pressure to that at constant volume(γ is approximately 5/3 for monatomic gases,7 /5 for diatomic gases and approaches unity for multiatomic gases), k is Boltzmann's constant (1.3805×10^{-23}), m is molecular mass(in kg),P_{tr} is called transition pressure which can be given by[8]:

$$P_{tr} = \frac{\lambda_{1Pa}}{\alpha d} \frac{9\gamma - 5}{\gamma + 1} \tag{4}$$

where λ_{1Pa} is the mean free path of the gas at 1 Pa for the relevant gas.

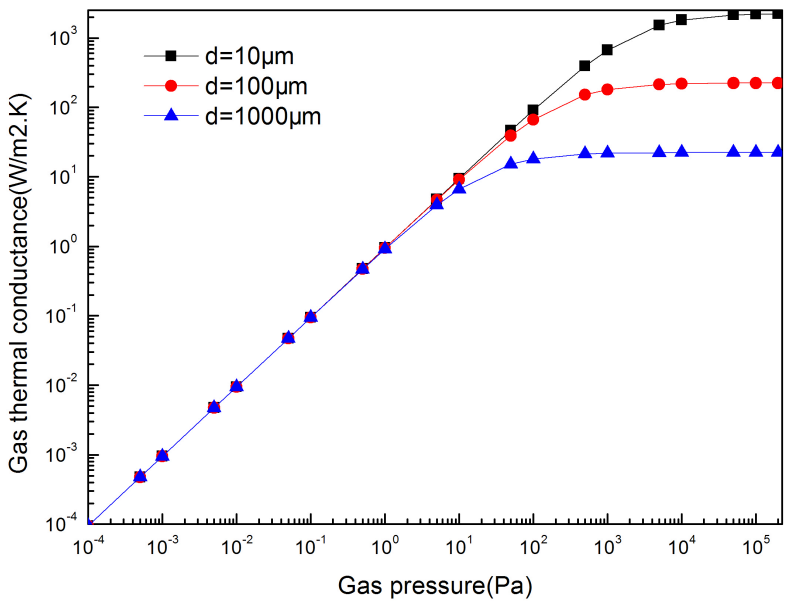


Fig.1 The relationship between gas thermal conductance and gas pressure

According to Eq.2~ Eq.4, the gas thermal conductance variation with gas pressure and the distance between the flat two plates for one microstructure are shown in Fig.1.It can be shown that a bigger gap size decreases the transition pressures and lowers the device's upper operating range and output sensitivity in the atmospheric pressures. In Fig.1,the gas thermal conductance at lower end of the gas pressure range doesn't obviously depend on the gap size. However,according to the research of Kourosh[9]and E. Zaker[10], at the lower end of the pressure range, the bigger gap size leads to larger gas thermal conductance at the same gas pressure, which is mainly because that the bigger gap size leads to a larger number of gas molecules in the gap to join in heat transfer and a higher thermal conductivity. So in order to extend the lower end of pressure measurement range to high vacuum, the gap size of the device has to be increased, although it will decrease the upper operating range.

MHP-based vacuum gauge often consists of one heating area in which the heating resistor is embedded and several supporting beams, and gas heat conduction gap is formed between heating area and the substrate, as shown in Fig.2. When gas pressure in the gap changes, gas heat conduction from the suspended heating area to cold substrate will change. The heating area temperature will change with gas pressure if heating power is constant, and heating power will change with gas pressure if the heating area temperature is kept constant through the constant temperature circuit, so the gas pressure can be measured by measuring the temperature change or heating power to keep the heating area temperature constant.

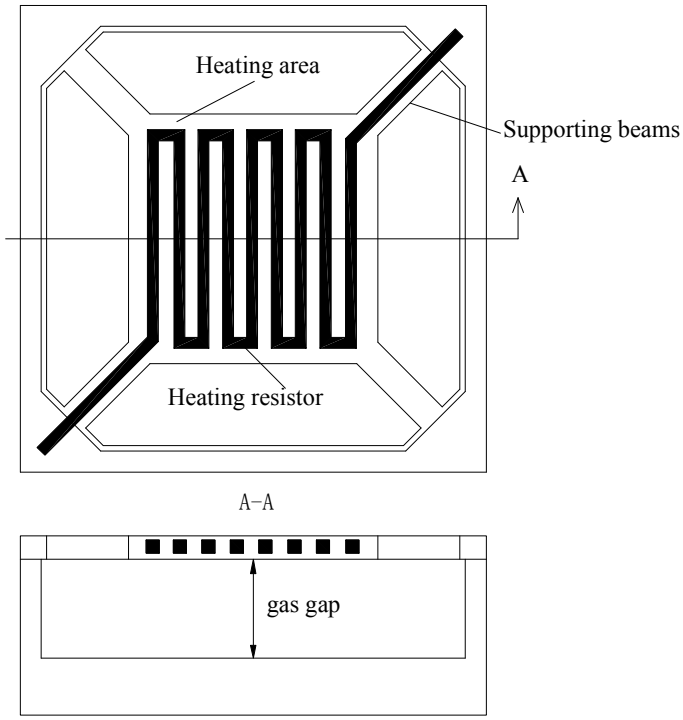


Fig.2 Schematic of MHP-based vacuum gauge

In this paper, the MHP-based vacuum gauge has a 300μm×300μm square MHP supported by four 230μm long and 30μm wide beams. The platinum heating resistor with the total length of about 4380μm is 8μm wide and 0.2μm thick. The gas gap below the MHP is 170μm wide. Heating power(Q_z) on the MHP can dissipate through gas thermal conduction in the gas gap(Q_g), solid thermal conduction of supporting beams(Q_s),gas thermal convection(Q_c), and thermal radiation(Q_r). Due to the small surface area and low operating temperature of the MHP in vacuum gauge, the latter two heat dissipation approaches are neglected. Thus,

$$Q_z = Q_g + Q_s \tag{5}$$

From Eq.2,we can obtain

$$Q_g = \alpha G_{mol} \frac{PP_{tr}}{P + P_{tr}} A_s (T_s - T_a) \tag{6}$$

Where A_s is the area of the MHP,T_s is the average temperature of the MHP, T_a is the ambient temperature.

Assuming that temperature distribution of the MHP is uniform and temperature of the supporting beam end is equal to the ambient temperature T_a, and ignoring the infulence of gas thermal conduction below the supporting beams and heating resistor in the supporting beams on temperature distribution of the supporting beams, heat dissipation through the supporting beams can be expressed by

$$Q_s = \frac{\sum k_i A_i}{L_b} (T_s - T_a) \tag{7}$$

where k_i and A_i are respectively thermal conductivity and cross section area of thin films in the supporting beams,L_b is the length of the supporting beam.

Substituting Eq.6,Eq.7 into Eq.5, we can obtain

$$I_s^2 R_{sa}(1 + \beta(T_s - T_a)) = (\alpha G_{mol} \frac{PP_{tr}}{P + P_{tr}} A_s + \frac{\sum \lambda_i A_i}{L_b})(T_s - T_a) \tag{8}$$

where β is temperature coefficient of the platinum heating resistor, I_s is heating current, R_{sa} is the resistance of heating resistor at ambient temperature.

From Eq.8, we can obtain

$$T_s = \frac{I_s^2 R_{sa}}{\alpha G_{mol} \frac{PP_{tr}}{P + P_{tr}} A_s + \frac{\sum \lambda_i A_i}{L_b} - I_s^2 R_{sa} \beta} + T_a \tag{9}$$

Then output voltage of the vacuum gauge at constant heating current can be expressed by:

$$U_s = I_s R_{sa}(1 + \beta \frac{I_s^2 R_{sa}}{\alpha G_{mol} \frac{PP_{tr}}{P + P_{tr}} A_s + \frac{\sum \lambda_i A_i}{L_b} - I_s^2 R_{sa} \beta}) \tag{10}$$

From Eq.10, for P<<Ptr,

$$\frac{dU_s}{dP} \approx \frac{-\beta I_s^3 R_{sa}^2 \alpha G_{mol} A_s}{(\frac{\sum \lambda_i A_i}{L_b} - I_s^2 R_{sa} \beta)^2} \tag{11}$$

For the designed vacuum gauge, the supporting beams are composed of 1μm PECVD SiO_2 and 1μm PECVD SiN_x. Fig.3 shows the relationship of the sensor output voltage and gas pressure. It can be seen that the sensor output decreases if gas pressure increases and higher sensitivity can be obtained if increase the heating current.Fig.4 shows the sensor output voltage at gas pressure of 10^{-5}Pa～10^{-3}Pa when heating current is 0.7mA.It can be seen that the vacuum gauge is obviously sensitive at least down to 5×10^{-3}Pa. According to Eq.(1), for high vacuum pressure measurement range, increasing heating area, temperature coefficient of heating resistor, heating current, and decreasing solid heat conduction through supporting beams will increase the MHP-based vacuum gauge sensitivity.

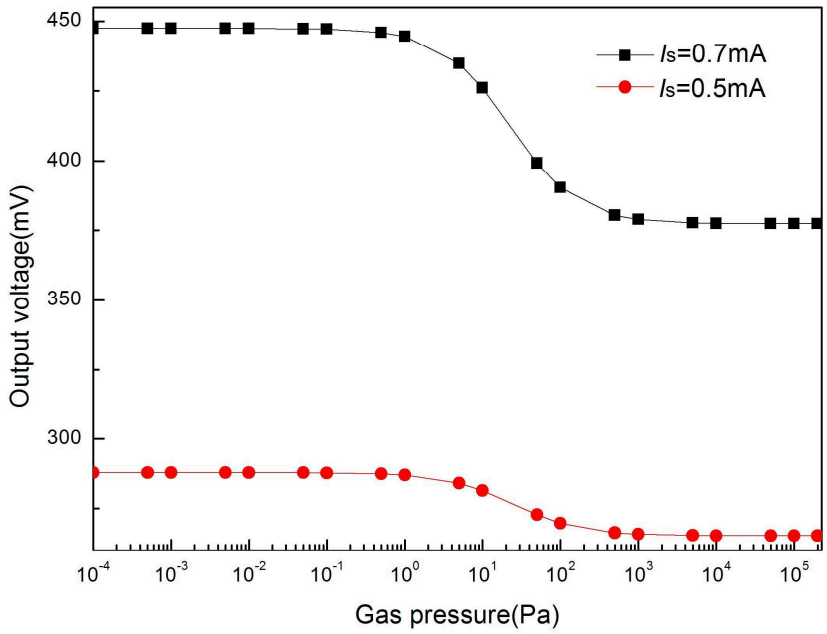


Fig.3 The relationship of the sensor output voltage and gas pressure

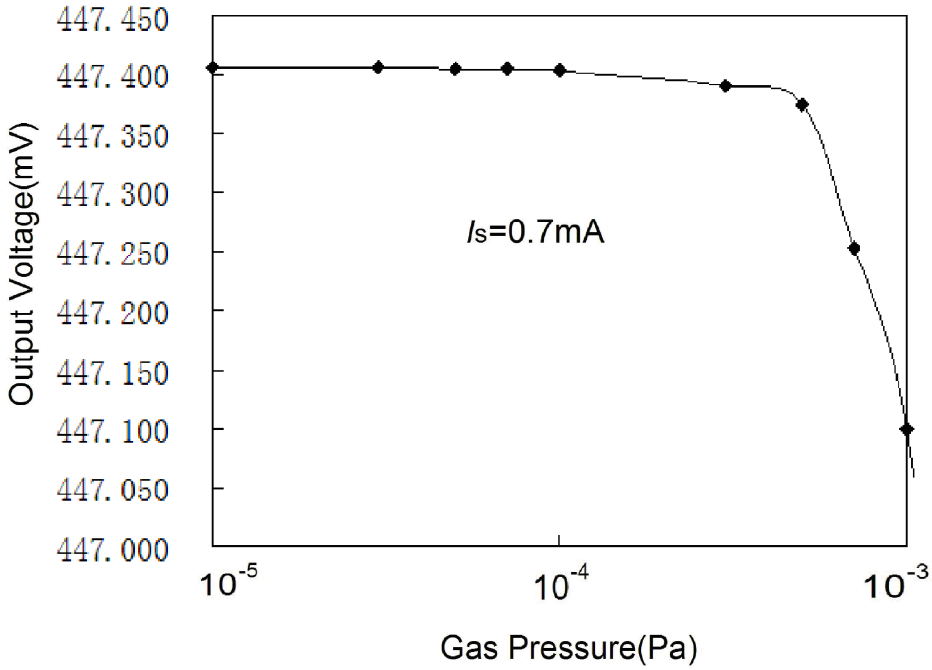


Fig.4 The sensor output voltage at gas pressure of 10^{-5}Pa～10^{-3}Pa

2 Fabrication

Figure 5 shows the fabrication process steps of vacuum gauge. Device fabrication starts by depositing 0.5μm PECVD SiO2 on the back side of a (100) silicon wafer which is used as the masking material in the following wet etching process. Then 0.5μm thick PECVD SiO2,1μm thick PECVD SiNx and 0.5μm thick PECVD SiO2 are deposited on the front side as the MHP structure layer. After that, 20nm thick Cr film as adhesive layer and 200nm thick Platinum film are sputtered and patterned by lift-off with the first mask to form the heating resistor. In order to suspend the MHP,

wet etching windows are opened by etching PECVD SiO2/SiNx/SiO2 layer with the second mask so that silicon substrate can be etched under the MHP. Then, the whole wafer is put into the TMAH etchant which has good etch selectivity between PECVD SiO2/SiNx/SiO2 and silicon until the silicon substrate under the MHP becomes a smooth plane, which forms a gas gap of about 170μm wide. At last the wafer is diced and the dies are packaged and wire bonded in the DIP-8 packages. Figure 6 shows SEM pictures of the vacuum gauge chip.

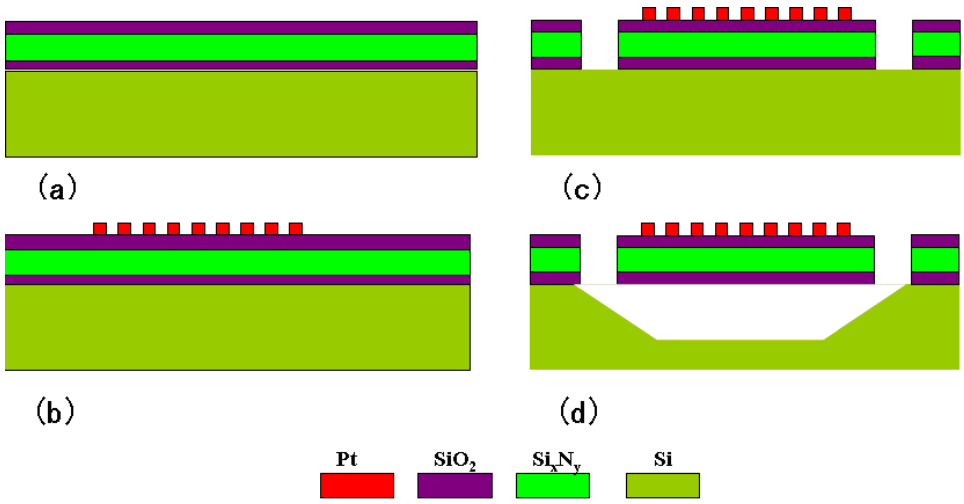


Fig.5 Fabrication process steps：(a)deposition of PECVD SiO2/SiNx,(b)patterned platinum resistor,(c)wet etching window opened,(d)structure release in TMAH**.**

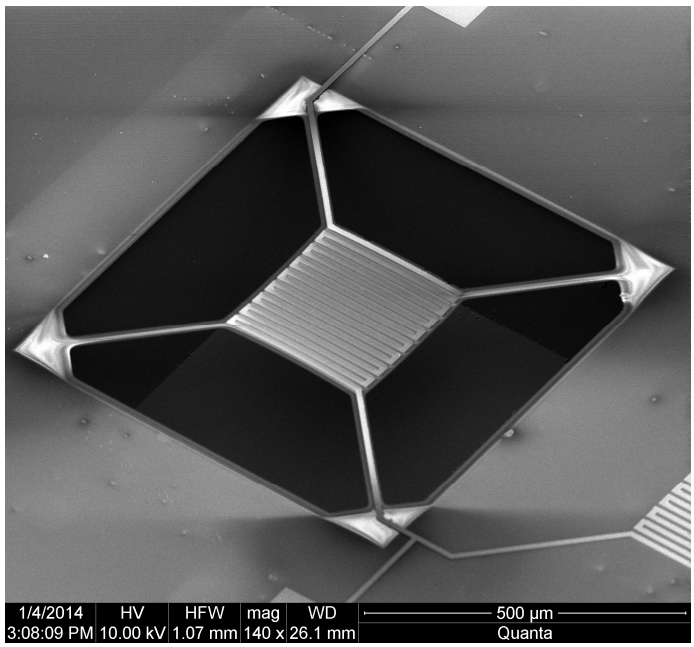


Fig.6 SEM pictures of the vacuum gauge chip

3 Experiment results

The resistance variation with temperature of the platinum resistor in two MHP-based vacuum gauge is shown in Fig.7.It can be seen that platinum resistor shows good linear dependence on temperature, and annealing process can improve the temperature coefficient of platinum resistor. After three hours annealing process at about 770K, the temperature coefficient changes from 1.68‰ to 1.87‰/K.

The packaged MHP-based vacuum gauge is fixed in a vacuum system which can obtain high vacuum down to at least 10^{-3}Pa with molecular pump. Then Keithley 2400C Source is used to

generate 0.5mA heating current for the heating resistor.Figure.8 shows the sensor output voltage varied with gas pressure. Due to the vacuum control difficulty, the curve connecting measurement points are not smooth, but it can be seen clearly that the developed MHP-based vacuum gauge show good sensitivity in the pressure range of 5×10^{-3}Pa～10^{3}Pa.

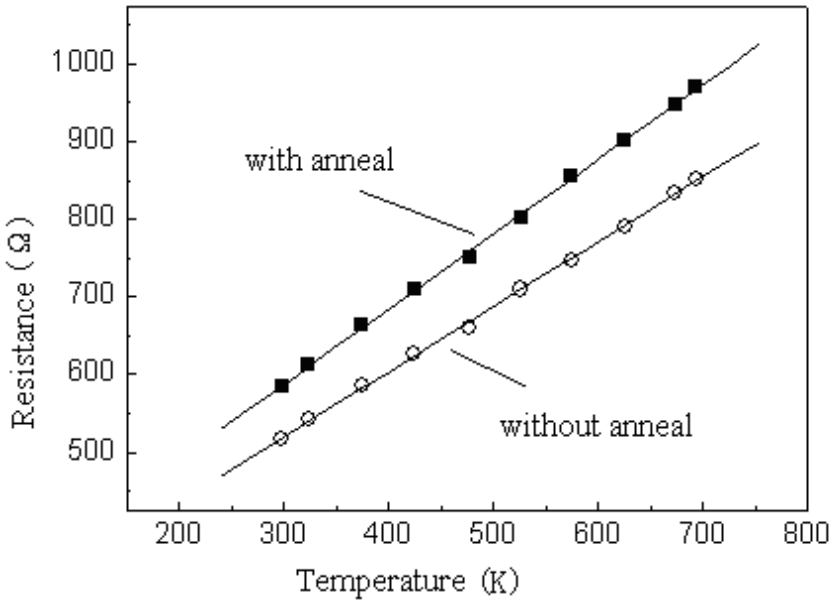


Fig.7 Resistance of platinum resistor variation with temperature

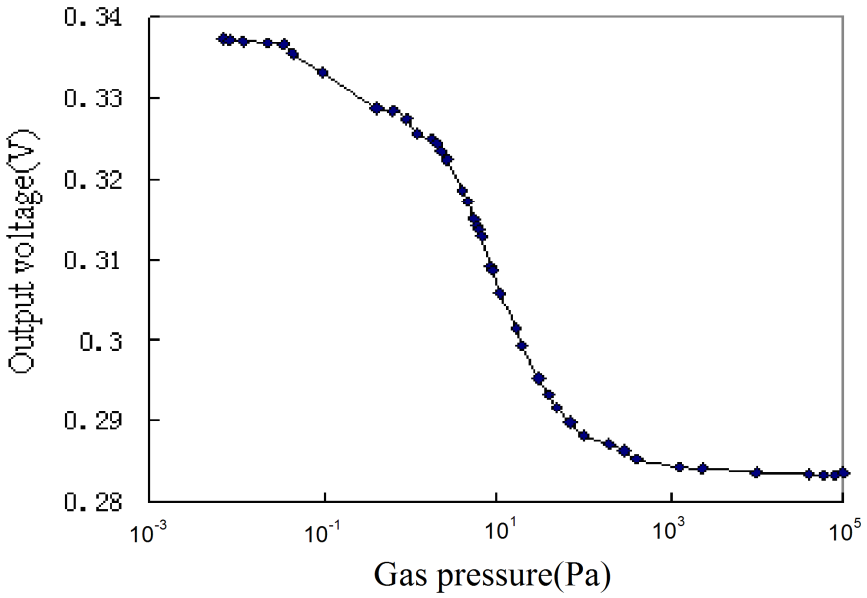


Fig.8 The sensor output voltage varied with gas pressure

Conclusions

A MHP-based high vacuum gauge with heating area of 300μm×300μm was successfully fabricated and tested. The effects that determine the sensor sensitivity were analyzed in theory when the heating current was kept constant. The analyzing results show that increasing heating area, heating current, and decreasing solid heat conduction through supporting beams will increase the MHP-based vacuum gauge sensitivity at high vacuum pressure. The sensor was fabricated with front-side wet etching technology and the gas gap size of 170μm was formed below the MHP.The

device was measured in a vacuum system when heating current was kept at 0.5mA.The measurement results show that the fabricated device is sensitive in the pressure range of 5×10^{-3}Pa～10^{3}Pa.

Acknowledgements

The authors would like to thank many other colleagues for the help in sensor manufabrication. This work is supported by the grant of Science and Technology Development (No.2012A0403018) in China Academy of Engineering Physics.

References

[1] Zhao Xingyu, Wang Xun, Shi Ziguang. A Study of the Piezoresistor Used as Low Vacuum Gauge. Vacuum Science and Technology 1997, 17(5), 330-335.

[2] Rosengren L, Söderkvist J, Smith L. Micromachined sensor structures with linear capactive response. Sensors and Actuators A 1992, 31,200-205.

[3] Williams K R, Muller R S. Micromachined Hot-Filament Ionization Pressure Sensor and Magnetometer. lnternational Conference on Solid-state Sensors and Actuators (TRANSDUCERS'97), 16-19 Jun 1997. Chicago,USA; Volume 2, pp.1249-1252.

[4] Chou B C S, Chen Y-M, Yang M O. A Sensitive Pirani Vacuum gauge and the elcetrothermal SPICE modeling.Sensors and Actuators A. 53(1996)273-277.

[5] Shie J S, Chou B C S, Chen Y M. High performance Pirani vacuum gauge. J.Vac.Sci.Technol. A .13(1995) 2972-2979.

[6] G.S. Springer, Heat Transfer in Rarefied Gases. In Advances in Heat Transfer; J.P. Hartnett, T.F. Irvine,Eds.; Academic Press, New York, USA, 1971;Volume 7, pp.163–218.

[7] A.W. van Herwaarden. Thermal vacuum gauges based on integrated silicon thermopiles. Ph.D. Thesis, Delft University of Technology, Delft, 24, June 1987.

[8] P. Bruschi, M. Piotto, G. Barillaro. Effects of gas type on the sensitivity and transition pressure of integrated thermal flowsensors. Sensors and Actuators A. 132(2006)182–187.

[9] Kourosh Khosraviani and Albert M Leung. The nanogap Pirani—a pressure sensor with superior linearity in an atmospheric pressure range. Journal of Micromechine and Microengineering. (2009)1-8.

[10] E.Zaker, S.Farid, S.K.Selvaraj.etc. Thermal-based MEMS vacuum gauges for measuring pressures from 10-2 Torr to 10-6 Torr. The 25th International Vacuum Nanoelectronics Conference(IVNC), 9-13 July 2012; pp.1-2.

Key Engineering Materials Vols 645-646 (2015) pp 706-718
Submitted: 2015-01-20
© (2015) Trans Tech Publications, Switzerland
Accepted: 2015-01-21
doi:10.4028/www.scientific.net/KEM.645-646.706

Analysis of Impact of Bottom Electrode Position on Dynamic Pull-in Parameters of Microcantilevers

Chang Shuangkai[1,a], Zhang Gaofei[1,b]*, You Zheng[1,c]

[1]State Key Laboratory of Precision Measurement Technology and Instruments

Department of Precision Instruments, Tsinghua University, Beijing,100084, China

[a]changsk12@mais.tsinghua.edu.cn,

[b]zgf@tsinghua.edu.cn(corresponding author),[c] yz-dpi@mail.tsinghua.edu.cn

Keywords: bottom electrode position, electrostatically actuated cantilever, Rayleigh-Ritz Method, Dynamic pull-in parameter

Abstract

The stable range of MEMS electrostatically actuated beam during the pull-in process is crucial to the device performance. Different devices have specific requirements for stable pull-in region based on their applications. In this paper, Rayleigh-Ritz energy method is used to establish dynamic pull-in model of electrostatic cantilever actuated by a step voltage. Modified trial function is derived according to different position of bottom electrode. The model takes into account the effects of fringe capacitance and variable cross-sectional beam. Published numerical methods and experimental data are used to verify the model . The impact of bottom electrode position on pull-in parameters is analyzed in present model. With fitting empirical equations, pull-in parameters can be easily satisfied through the distribution of bottom electrode, which provide an effective reference for the design of MEMS electrostatically actuated beam under given pull-in parameters (138).

1. Introduction

Electrostatic actuated cantilever structures are widely used in MEMS sensors and actuators, such as magnetometers, pressure sensors, microrelays, RF switches and micro mirrors. Due to light weight, small size and low power consumption, these devices have a wide range of applications in the biomedical equipment, aerospace, automatic control and other fields. Generally, operation of the electrostatic driving structure is the result of combination between electrostatic force and the elastic restoring force caused by the stiffness of the beam. After the deformation of the beam reaches a certain position, the electrostatic force will be far greater than the elastic restoring force , so the movable structure snaps down into the lower electrode, which is called the pull-in instability. The specific displacement of movable structure at pull-in position is called pull-in displacement and the corresponding voltage is called pull-in voltage. Pull-in phenomenon can be a double-edged sword according to different occasions. For example, pull-in is essential for material property measurement[1]. And for MEMS electrostatic drive-contact switches and relays, a low driving voltage and high contact force are required, thus a smaller pull-in displacement and lower pull-in voltage are needed. As for MEMS micro mirror or magnetometer, the device is expected to remain stable during the operation, so the greater pull-in displacement is needed. Due to different requirements of specific applications, pull-in phenomenon has become a hot topic of electrostatically actuated MEMS structures, which mainly focuses on two aspects: one is how to

find the pull-in point of different structures, the other is the influence of relevant factors on pull-in parameters, such as material properties, structural geometry and the air gap between the electrodes. Studies have shown that [2,3] the stability of MEMS electrostatic drive beam can be improved through a series capacitor, but often at the expense of the increased pull-in voltage, so this paper mainly approach this topic from aspects of the design of beam structure itself.

Since different damping situations in which different structures work is quite complex, research of pull-in parameters generally considers two extreme situations[4] : dynamic (zero damping) and static (high damping) situations. The pull-in point of the former is called unstable dynamic pull-in point, which is the lower bound for the actual pull-in voltage; the latter corresponding point is called static pull-in point, which means the upper bound. For a one-dimensional electrostatic driven damped mass-spring system, the dynamic voltage is about 91.9 percent of static voltage[5] . Taking into account that MEMS devices generally work in low damping or even vacuum situation and the applied voltage is similar to a step voltage, the paper discusses the dynamic pull-in point of cantilever beam under the step voltage. There are three main ways of solving pull-in point: the first is FEM-based numerical methods, which is most accurate but time-consuming. Besides, due to the presence of large deformation and drastic air compression under dynamic conditions, it becomes very difficult to achieve the solver convergence. Generally the material parameters and solving step length [6] need to be modified discreetly; the second is analytical models: it can be separated into lumped parameter model and PDE model. The former one, which modified the elastic coefficient and capacitance to adapt to the deformation of the beam structure, is a correction of 1D parallel-plate model[7,8]. As for PDE analytical model, PDE (partial differential equations) and boundary conditions are established to describe the deformation of the beam, which converts the problem to the mathematical problem of solving PDE. With the use of strain gradient theory in Elastic Mechanics and some numerical methods such as Galerkin method and Differential Quadrature Method [9,10,11,12], the deformation of every part of beam over time can be solved, but the solving process is cumbersome. Since in the research of pull-in phenomenon only the pull-in point really matters, the information of deformation of beam at other time points would be unnecessary.

The last one, energy method, can be used to simplify the solution of pull-in point. In 1997 Rob Legtenberg et al. [13] built the simplified model based on Rayleigh-Ritz Method to obtain analytical solution of static pull-in parameters, and discussed the relationship between curved electrode and pull-in parameters. From then on, researchers had continually refined and improved this model. In 2006 Neilson and Barbastatis[5] first applied the model to dynamic characteristics of pull-in phenomenon, and concluded that dynamic instabilities may occur below the static pull-in voltage, but the model in their paper was rigid plate, which was not consistent with the actual deformation behavior . In 2008 M.Joglakar et al. [14,15] took into account the impact of the fringing fields of capacitance and linear changes of the beam width, and deduced the empirical formula of pull-in parameters. In 2012, FANG Yuming et al.[16] established Ritz energy-method based dynamic pull-in model for cantilever and clamped-clamped beam, and the influence of ratio of the air gap g to beam width b was discussed.

The impact of beam size on the pull-in parameter has been quite adequately studied as mentioned above. However, in actual design, for the consideration of device performance or

limitation of process capability, the bean size is usually restricted and cannot be set arbitrarily, so it is essential to find a more effective and free way to control the pull-in parameters. This article discusses the impact of location of bottom electrode on dynamic pull-in parameter based on the Rayleigh-Ritz energy method[17]. Fringing field effect and variable cross-sectional beam are taken into account in the model respectively.

2. The Dynamic Pull-in point of microcantilevers

Mainly four kinds of energy can be interconverted in the pull-in course of an electrostatic actuated cantilever beam as follows: the electrostatic energy $E_{injected}$ caused by externally applied voltage, the kinetic energy $E_{kinetic}$, the potential energy $E_{potential}$ of the beam, and the dissipated energy $E_{dissipated}$. Based on energy conservation, their relation can be expressed as,

$$E_{injected} = E_{kinetic} + E_{potential} + E_{dissipated}. \tag{1}$$

For the ideal case in which all damping is neglected, the energy dissipation $E_{dissipated}$ equals to zero, then the system overshoot exists. When the beam reaches the maximum overshoot position, the kinetic energy is zero, then the electrostatic energy $E_{injected}$ is equal to the potential energy storage,

$$E_{injected} = E_{potential}. \tag{2}$$

The Eq. 2 holds for the maximum overshoot position under different driving voltages. Clearly, both sides of the equation are related to the deformation of the beam z, and therefore the relationship between the drive voltage V and the deformation z can be obtained. The pull-in point where drive voltage reaches extreme value can be obtained by taking the derivation of V. The location of that point is corresponding to pull-in displacement, the extreme value V is dynamic pull-in voltage $V_{dynamic}$. Instead of solving PDE, the energy method seeks for the extreme value according to the principle of minimum potential energy, which significantly simplifies the solving process.

A. Rectangular-sectional cantilever beam

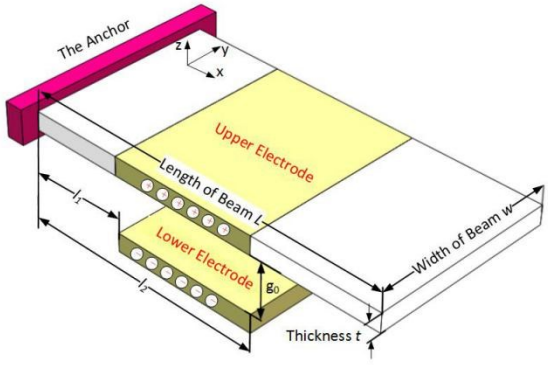


Figure 1 *Schematic of cantilever beam with uniform cross-section*

For a typical Rectangular-sectional cantilever beam, Eq. 3 can be derived as follows from the force and moment equilibrium of cantilever bending vibration in Euler–Bernoulli beam theory,

$$EI\frac{\partial^4 z}{\partial x^4}+c_{damp}\frac{\partial z}{\partial t}+\rho wh\frac{\partial^2 z}{\partial t^2}=F_E. \tag{3}$$

z (x, t) , displacement of the beam is the binary function of the position coordinates x and time t. With the use of separation of variables,

$$z(x,t)=a\phi(x). \tag{4}$$

Wherein, a is a unary function of time t. ϕ(x) is a function of the position coordinates x and can be derived from boundary conditions,

$$\phi(0)=\phi'(0)=\phi''(L)=\phi'''(L)=0. \tag{5}$$

Generally a quartic polynomial is used to approximate the deformation of the beam as shown in Eq. 6, which is called trial function. The trial function is actually the deflection of the beam under uniform force,

$$\phi(x)=x^4-4Lx^3+6L^2x^2. \tag{6}$$

In order to make the results more widely applicable, the following dimensionless quantities are defined,

$$x^*=x/L,\ a^*=a/g_0,\ \alpha=l_1/L,\ \beta=l_2/L. \tag{7}$$

Then Eq. 6 is normalized as,

$$\phi(x^*)=\frac{1}{3}\left(x^{*4}-4x^{*3}+6x^{*2}\right). \tag{8}$$

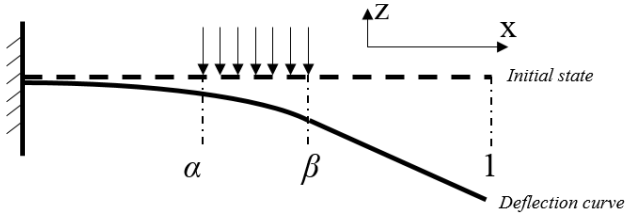


Figure 2 *The deformation of cantilever beam under uniform load from α to β in the x direction (The length is normalized)*

However, for partial electrostatic force as shown in Figure 2, the load merely exists in part of beam, it is necessary to modify the trial function based on the new deflection curve [18],

$$\phi(x)=\begin{cases}\dfrac{2(\beta-\alpha)x^2\left[3(\alpha+\beta)-2x\right]}{\alpha^4-\beta^4+4(\beta^3-\alpha^3)} & x\in[0,\alpha)\\ \dfrac{6(\beta^2-\alpha^2)x^2-4(\beta-\alpha)x^3+(x-\alpha)^4}{\alpha^4-\beta^4+4(\beta^3-\alpha^3)} & x\in[\alpha,\beta)\end{cases}. \tag{9}$$

The normalized potential energy can be written as Eq. 10. It should be noted that there is no potential energy when $x\in[\beta,1)$, because no bending moment exists in this section.

$$\begin{aligned}E_{potential}&=\frac{1}{2}\int_0^L EIa^2\left(\frac{\partial^2\phi(x)}{\partial x^2}\right)^2dx=\frac{EIa^2}{2}\int_0^L\left(\frac{\partial^2\phi(x)}{\partial x^2}\right)^2dx\\&=\frac{EIa^2}{2L^3}\int_0^1\left(\phi''(x^*)\right)^2dx^*=\frac{EIa^{*2}g_0{}^2}{2L^3}\left(\int_0^\alpha\left(\phi''(x^*)\right)^2dx^*+\int_\alpha^\beta\left(\phi''(x^*)\right)^2dx^*\right).\end{aligned} \tag{10}$$

During the dynamic pull-in process, the electrostatic energy is the converted result of total work of electrostatic force. The integration limit [l_1, l_2] represents the location of the lower electrode in the x-direction.

$$\begin{aligned}E_{injected}&=\int_{l_1}^{l_2}\int_0^{a\phi(x)}F_e\,dz\,dx=\int_{l_1}^{l_2}\int_0^{a\phi(x)}\frac{\varepsilon bV^2}{2\left(g_0-z\right)^2}dz\,dx\\&=\frac{\varepsilon bV^2}{2g_0}\int_{l_1}^{l_2}\frac{a\phi(x)}{g_0-a\phi(x)}dx=\frac{\varepsilon bLV^2}{2g_0}\int_\alpha^\beta\frac{a^*\phi\left(x^*\right)}{1-a^*\phi\left(x^*\right)}dx^*.\end{aligned} \tag{11}$$

Then,

$$\begin{aligned}E_{kinetic}&=E_{injected}-E_{potential}\\&=\frac{\varepsilon bLV^2}{2g_0}\int_\alpha^\beta\frac{a^*\phi\left(x^*\right)}{1-a^*\phi\left(x^*\right)}dx^*-\frac{EIa^{*2}g_0{}^2}{2L^3}\left(\begin{array}{l}\int_0^\alpha\left(\phi''(x^*)\right)^2dx^*\\+\int_\alpha^\beta\left(\phi''(x^*)\right)^2dx^*\end{array}\right).\end{aligned} \tag{12}$$

Suppose that $E_{kinetic}{}^*=\dfrac{E_{kinetic}L^3}{EIg_0{}^2}$, $V^*=\sqrt{\dfrac{\varepsilon bL^4V^2}{2EIg_0{}^3}}$, then Eq. 12 can be simplified as,

$$E_{kinetic}{}^{*} = V^{*2}\int_{\alpha}^{\beta}\frac{a^{*}\phi\left(x^{*}\right)}{1-a^{*}\phi\left(x^{*}\right)}dx^{*} - \frac{a^{*2}}{2}\left(\int_{0}^{\alpha}\left(\phi''(x^{*})\right)^{2}dx^{*} + \int_{\alpha}^{\beta}\left(\phi''(x^{*})\right)^{2}dx^{*}\right). \quad (13)$$

Assuming $M = \int_{\alpha}^{\beta}\frac{a^{*}\phi\left(x^{*}\right)}{1-a^{*}\phi\left(x^{*}\right)}dx^{*}$ $N = \frac{a^{*2}}{2}\left(\int_{0}^{\alpha}\left(\phi''(x^{*})\right)^{2}dx^{*} + \int_{\alpha}^{\beta}\left(\phi''(x^{*})\right)^{2}dx^{*}\right)$. The Eq. 14 is always true at the maximum overshoot position,

$$E^{*}_{kinetic} = 0. \quad (14)$$

That is,

$$V^{*2} = \frac{N}{M}. \quad (15)$$

Take the left side of above equation as the function $V^{*}(a^{*})$, then the pull-in point occurs when derivation of $V^{*}(a^{*})$ equals to zero.

$$M'N - N'M = 0. \quad (16)$$

Simplify Eq. 16 as,

$$\int_{\alpha}^{\beta}\frac{\phi}{1-a^{*}\phi}dx^{*} - 0.5\int_{\alpha}^{\beta}\frac{\phi}{\left(1-a^{*}\phi\right)^{2}}dx^{*} = 0. \quad (17)$$

It is difficult to solve such a formula directly. Here Gauss - Legendre numerical integration is used to approximate original equation. The integrating range is mapped to [-1 1] through variable transformation. The integration points and integral coefficient can be found in mathematics handbook [19]. The numerical integral results of these two terms are represented as X and Y severally, then

$$X - 0.5Y = 0. \quad (18)$$

The function $F=(X-0.5Y)^{2}$ equals to zero if and only if the beam reaches dynamic pull-in point. Based on this, the optimization function [20] $f_{minsearch}$ in MATLAB is used to seek for the minimum of function F. The corresponding a^{*} is the pull-in displacement, and then V^{*} can be obtained through Eq. (15).

B. Cantilever beam with fringing field effect

In the case of a narrow and thick beam, that is, the ratio of beam width to air gap b/g is small and the ratio of beam thickness to air gap t/g is large, the impact of fringing field effect cannot be neglected[21],

$$C' = \varepsilon_0[\,b/g - 0.36 + 0.85\left(b/g\right)^{0.24} + 2.5\left(t/g\right)^{0.24}\,]. \tag{19}$$

In this situation, the former Eq. 12 of electrostatic energy is converted into,

$$\begin{aligned} E_{injected} &= \int_{l_1}^{l_2}\int_0^{a\phi(x)} F_e\,dz\,dx = \int_{l_1}^{l_2}\int_0^{a\phi(x)} 0.5V^2\frac{\partial C'}{\partial z}\,dz\,dx \\ &= \frac{\varepsilon bLV^2}{2g_0}\left[\int_\alpha^\beta \left[\begin{array}{l}\left(1-a^*\phi\right)^{-1} - 1 + 0.85c_1^{-0.76}\left(\left(1-a^*\phi\right)^{-0.24} - 1\right) \\ +2.5c_2^{0.24}/c_1\left(\left(1-a^*\phi\right)^{-0.24} - 1\right)\end{array}\right] dx^*\right]. \end{aligned} \tag{20}$$

Wherein, $c_1 = b/g_0$, $c_2 = t/g_0$ .Accordingly, M in Eq. 15 is turned into,

$$M = \int_\alpha^\beta \left[\begin{array}{l}\left(\left(1-a^*\phi\right)^{-1} - 1\right) + 0.85c_1^{-0.76}\left(\left(1-a^*\phi\right)^{-0.24} - 1\right) \\ +2.5c_2^{0.24}/c_1\left(\left(1-a^*\phi\right)^{-0.24} - 1\right)\end{array}\right] dx^* \tag{21}$$

The pull-in point can be solved as the same method in Section 2.A. Actually, the first term of integration in Eq. 21, which has no relation to fringing capacitance, can be converted into the expression of M in Section 2.A exactly.

C. Variable rectangular cross-sectional cantilever beam

In actual design of MEMS devices, cantilever may not appear in uniform cross-section. For example, it is common to increase the contact area to enhance the load capacity of MEMS relay [22], then the width at the end of cantilever beam becomes larger, as shown in Fig. 3.

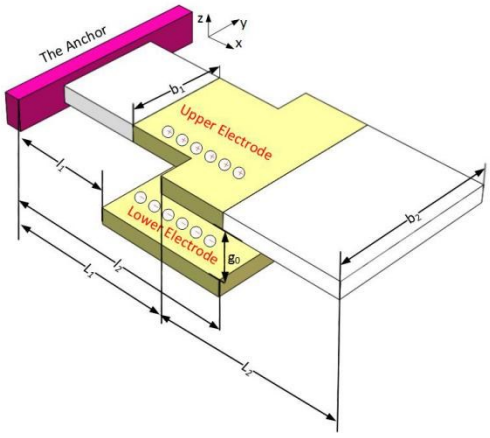


Figure 3 *Schematic of cantilever beam with variable rectangular cross-section*

In variable cross-sectional condition there may be three kinds of locations of low electrode: (1) entirely within the area of width b_1; (2) located within the cross-sectional area; (3) entirely within the area of width b_2. Obviously case (2) is the most complex of the three, which will be analyzed in detail as follows.

Through piecewise integration of different width, the expression of $E_{injected}$ and $E_{potential}$ can be rewritten. Then Eq. 17 is turned into,

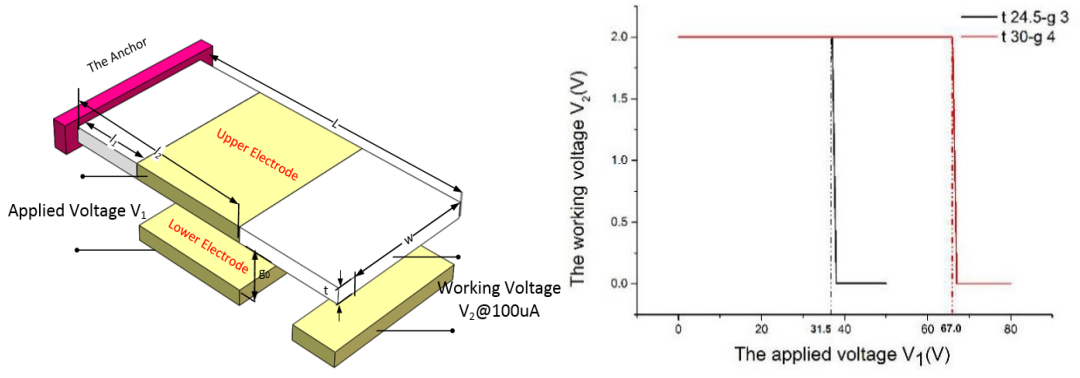
$$\left(\int_{\alpha}^{\gamma}\frac{\phi}{1-a^{*}\phi}dx^{*}+\int_{\gamma}^{\beta}\frac{\left(b_2/b_1\right)\phi}{1-a^{*}\phi}dx^{*}\right)-0.5\left(\int_{\alpha}^{\gamma}\frac{\phi}{\left(1-a^{*}\phi\right)^{2}}dx^{*}+\int_{\gamma}^{\beta}\frac{\left(b_2/b_1\right)\phi}{\left(1-a^{*}\phi\right)^{2}}dx^{*}\right)=0 \tag{22}$$

Wherein, $L=L_1+L_2, \alpha=l_1/\mathrm{L}, \beta=l_2/L, \gamma=L_1/\mathrm{L}$.

When it satisfies the uniform cross-sectional condition that $b_1 = b_2$, the above equation can be converted exactly into (17). If taking into account the impact of the fringing field effect and variable cross-section simultaneously, the integral terms in Eq. 22 should be recalculated based on the expression of fringe capacitance (19), the process of which is the same as Section 2.A and not listed here due to limited space.

3. Model verification

The accuracy of the proposed model is verified for rectangular-sectional and variable cross-sectional beams respectively. A pair of single crystal silicon cantilever switches is selected to verify the present model, as Figure 4(a) shown. The working and control circuits are inserted into two different channels of Agilent B1500A parameter analyzer. The working voltage V_2 under 100μA current source is acquired in real time with the sweep of control voltage V_1. So the V_2-V_1 diagram can be obtained as Figure 4(b) : The pull-in voltages of these two switches are 31.5V and 67.0V respectively. As shown in Table 1, the results of the present model have good agreement with test results.



(a) *(b)*

Figure 4 *Test results of MEMS switches with specific electrode distribution (a)Schematic of MEMS cantilever switch;(b)Test results by parameter analyzer*

Table 1*Comparison of the dynamic pull-in voltage obtained by the present model and experiment*

L[μm]	*w[μm]*	*t[μm]*	*g_0[μm]*	*BottomElectrode [l_1, l_2]*	*Present model*	*Experimental Result*	*Relative Error(%)*
1500	*300*	*30*	*4*	*[200,1100]*	*67*	*66.1*	*1.3*
1500	*300*	*24.5*	*3*	*[200,1100]*	*31.5*	*31.8*	*0.9*

The further validation example is the cantilever beam with variable cross-section and regional electrostatic force simultaneously, which is actually the most common situation of MEMS cantilever devices. Figure 5 shows a variable cross-sectional cantilever beam made up of polysilicon[23], having the lower electrode from l_1 to l_2 in the X direction. The geometric parameters are given in Table **2**.

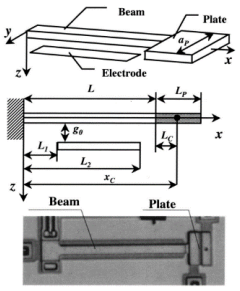


Figure 5 *Variable cross-sectional polysilicon cantilever beam*

Table 2 *The size of polysilicon beam with variable cross-section[23] (Unit: μm)*

Parameter	*Size*	*Parameter*	*Size*
L	*175*	*g0*	*4*
Lp	*26*	*l1*	*0*
ap	*38*	*l2*	*170*
h	*1.5*		

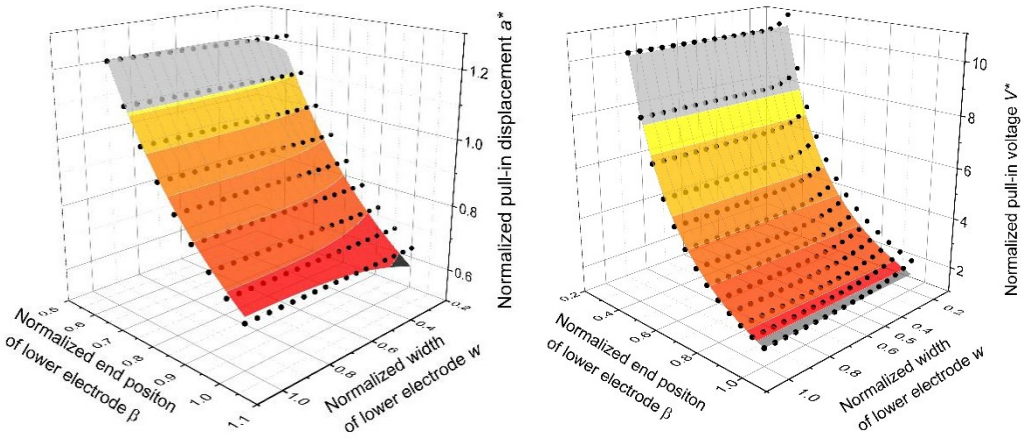
Use the methods in Section 2.B and 2.C to solve dynamic pull-in voltage. As can be seen in Table 3 , the pull-in voltage calculated by the proposed method is close to the numerical solution and experimental data for different beam width. Compared to Galerkin procedure with orthogonal eigenmodes used in [23], without consideration of the complexity of the different eigenmodes and damping effect, the present model is greatly simplified and still has acceptable precision.

Table 3 *Comparison of dynamic pull-in voltage obtained by the presented model and reference*[23]

Parameters	*Dynamic pull-in voltage*	
	b_1=20μm	*b_1=4μm*
The presented model	*29.3*	*25.15*
Numeric method [26]	*29.508*	*25.626*
Experimental Data[26]	*29.44*	**Not mentioned*

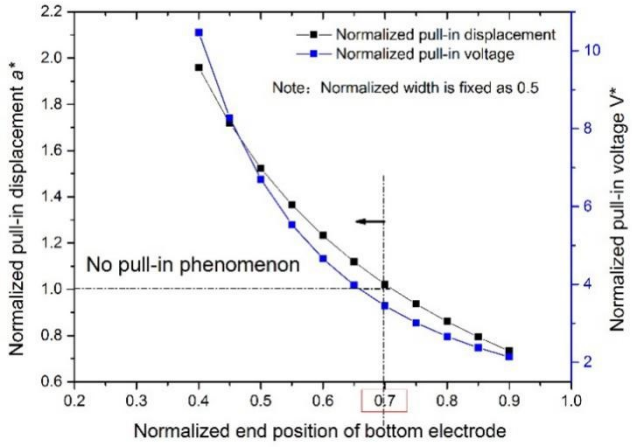
4. Impact of the bottom electrode position on pull-in parameters

Based on above analysis, it can be concluded that common factors that affect the stability of the travel range is geometry parameters of cantilever beam, such as *g/b*, *t/g*, which are relevant to the thickness(Z) direction and usually constrained by MEMS processing technology, but the bottom electrode position is only influenced by the size of the parameter in XY plane, so it can be freely adjusted in the layout design stage, which will not have any impact on the fabrication process.



(a) (b)

(the scatterplot indicates the results calculated by present model, the surface plot indicates the fitting function described below)



(c)

Figure 6 *Impact of the bottom electrode position on pull-in position*

The bottom electrode position is defined by two variables, the end position*β*and the length of electrode *w*, both of which are normalized for the convenience of analysis. Impact of these two parameters on the pull-in position can be expressed as 3D diagram shown in Figure 6 (a)(b). It can be seen that bottom electrode position has a quite large control range of pull-in position. When the end position of lower electrode *β* is less than 0.7, the normalized pull-in displacement is greater than 1 in Figure 6(a), that is, no pull-in phenomenon occurs in all the travel range no matter what the

electrode width *w* is. This has been demonstrated more clearly in Figure 6(c). When the width of bottom electrode *w* is more than 0.5 in Figure 6(b), almost no change can be observed in the pull-in voltage. So the distribution of bottom electrode near the fixed end can increase the pull-in stable region, and oppositely, the bottom electrode near the tip will help reduce the voltage.

In actual design usually both pull-in voltage and displacement need to comply with certain requirement, then it is essential to perform trial calculation so that β and *w* can be set for overall consideration. For convenience of that, use MATLAB Curve Fitting Toolbox [24] to obtain the fitting function of pull-in point. The following function form is selected as a fitting model of pull-in displacement and voltage,

$$F(\beta, w) = \frac{1}{b_1 + b_2 e^{(m_1\beta + m_2 w)}} \tag{23}$$

Table 4 *The fitting results of the function of pull-in point*

Function name	*Function Coefficients*				*Imitative Effect*	
	b1	*b2*	*m1*	*m2*	*R2*	*RMSE*
Pull-in displacement	*-1.475*	*1.494*	*0.7192*	*-0.005193*	*0.9991*	*0.01877*
Pull-in voltage	*-0.1606*	*0.1241*	*1.803*	*-0.007019*	*0.9987*	*0.1716*

Fitting results are shown with desirable imitative effect in Table 4. With these fitting functions, trial calculation can be performed easily and quickly so that pull-in parameters can be satisfied through the distribution of bottom electrode.

5. Conclusion

In order to study the impact of electrode position on stable pull-in range, we use the Rayleigh-Ritz energy method to establish a dynamic drop-in model of the cantilever, and take into account the effect of fringing capacitance and variable cross-section. For narrow and thick cantilever which has a small ratio of *b/g* and large ratio of *t/g*, the pull-in displacement increases and the pull-in voltage decreases because of the fringing capacitance effect. Modified trial function is derived in the case of partially distributed uniform load. Subsection integral is used to solve the pull-in point of variable cross-sectional cantilever, which expands the application scope of the energy method. By comparison with the published numerical model, the present model is more concise, and the deviation from experimental data is admissible.

Due to the processing limitations in the thickness direction of MEMS structures, it is more convenient to control the pull-in stability through the location of the bottom electrode. This paper deduces the fitting function of pull-in parameters, which can offer quantitive references for the design of MEMS devices. It should be pointed out that trial function is vital to the model validity. Because of geometric nonlinear problem and defects in the assumptions of Euler Bernoulli beam, the approximate polynomial this paper uses as trial function could introduce some slight error. In addition, the present model is based on a single eigenmode of model, so it cannot be used to solve the structural frequency response of higher modes.

References

[1].Osterberg P M, Senturia S D.,1997. M-TEST: a test chip for MEMS material property measurement using electrostatically actuated test structures. Microelectromechanical Systems, Journal of, 6(2): 107-118.

[2].Rebeiz G M.,2004. RF MEMS: theory, design, and technology. John Wiley & Sons.

[3].Seeger J I, Crary S B.,1997. Stabilization of electrostatically actuated mechanical devices Proceedings of the 1997 International Conference on Solid-State Sensors and Actuators, p 1133-1136.

[4].Elata D., 2005.On the static and dynamic response of electrostatic actuators. TECHNICAL SCIENCES, 53(4).

[5].Nielson G N, Barbastathis G.,2006. Dynamic pull-in of parallel-plate and torsional electrostatic MEMS actuators. Journal of Microelectromechanical Systems, 15(4): 811-821.

[6].Comsol Model Gallery. http://www.cn.comsol.com/model/pull-in-of-an-rf-mems-switch-16379

[7].Chowdhury S, Ahmadi M, Miller W C.,2005. A closed-form model for the pull-in voltage of electrostatically actuated cantilever beams. Journal of Micromechanics and Microengineering, 15(4): 756.

[8].Pamidighantam S, Puers R, Baert K, et al. ,2002. Pull-in voltage analysis of electrostatically actuated beam structures with fixed–fixed and fixed–free end conditions[J]. Journal of Micromechanics and Microengineering, 12(4): 458.

[9].Lam D C C, Yang F, Chong A C M, et al.,2003. Experiments and theory in strain gradient elasticity. Journal of the Mechanics and Physics of Solids, 51(8): 1477-1508.

[10].Kong S, Zhou S, Nie Z, et al.,2009 Static and dynamic analysis of micro beams based on strain gradient elasticity theory. International Journal of Engineering Science, 47(4): 487-498.

[11].Sedighi H M.,2014. Size-dependent dynamic pull-in instability of vibrating electrically actuated microbeams based on the strain gradient elasticity theory. Acta Astronautica, 95: 111-123.

[12].Sadeghian H, Rezazadeh G, Osterberg P M. ,2007.Application of the generalized differential quadrature method to the study of pull-in phenomena of MEMS switches. Microelectromechanical Systems, Journal of, 16(6): 1334-1340

[13].Legtenberg R, Gilbert J, Senturia S D, et al.,1997. Electrostatic curved electrode actuators. Microelectromechanical Systems, Journal of, 6(3): 257～265

[14].Joglekar M M, Hardikar K Y, Pawaskar D N. ,2008.Analysis of electrostatically actuated narrow microcantilevers using Rayleigh-Ritz energy technique. Second International Conference on Integration and Commercialization of Micro and Nanosystems. American Society of Mechanical Engineers, p. 309-319.

[15].Joglekar M M, Pawaskar D N.,2011. Closed-form empirical relations to predict the dynamic pull-in parameters of electrostatically actuated tapered microcantilevers. Journal of Micromechanics and Microengineering, 21(10): 105014.

[16].Fang Y, Li P. ,2013.A new approach and model for accurate determination of the dynamic pull-in parameters of microbeams actuated by a step voltage. Journal of Micromechanics and Microengineering, 23(4): 045010.

[17].Shames I H.,1985. Energy and finite element methods in structural mechanics. CRC Press

[18].Roark R J, Young W C.,2002.Roark's Formulas for Stress and Strain . 7th ed New York: McGraw-Hill

[19].GUAN Zhi, LU Jinfu.,2010. Fundamentals of Numerical Analysis. 2th ed Beijing: HIGHER EDUCATION PRESS

[20].The MathWorks, Inc. 2012 Optimization toolbox Toolbox™, User's Guide

[21].Batra R C, Porfiri M, Spinello D.,2006. Electromechanical model of electrically actuated narrow microbeams. Microelectromechanical Systems, Journal of, 15(5): 1175-1189.

[22].Schiele Ignaz, Huber Jorg, Evers Christian, et al.,1997. Micromechanical relay with electrostatic actuation. Proceedcings of the 1997 International Conference on Solid-State Sensors and Actuators, ChicagoILUSA, Piscataway: p.1165-1168

[23].Krylov S, Maimon R.,2004. Pull-in dynamics of an elastic beam actuated by continuously distributed electrostatic force[J]. Journal of vibration and acoustics, 126(3): 332-342.

[24].The MathWorks, Inc. 2012 Curve Fitting Toolbox™, User's Guide.

Key Engineering Materials Vols 645-646 (2015) pp 719-723
Submitted: 2014-11-28
© (2015) Trans Tech Publications, Switzerland
Accepted: 2014-12-23
doi:10.4028/www.scientific.net/KEM.645-646.719

Fabrication and formaldehyde-sensing property of quartz crystal microbalance (QCM) coated with PVP-MWCNTs composites

Yingfei He[1,a], Yadong Jiang[1,b], Huiling Tai[1,c*], Guangzhong Xie[1, d]

[1]State Key Laboratory of Electronic Thin Films and Integrated Devices, School of Optoelectronic Information, University of Electronic Science and Technology of China, Chengdu 610054, China

[a]hyfuestc@163.com,[b]Jiangyd@uestc.edu.cn, [c]taitai1980@uestc.edu.cn,[d]gzxie@uestc.edu.cn

Keywords: Quartz crystal microbalance (QCM); Sensors; Polyvinyl pyrrolidone (PVP); Multiwalled carbon nanotubes (MCWNTs); Formaldehyde

Abstract. In this paper, the quartz crystal microbalance (QCM) sensors coated with polyvinyl pyrrolidone (PVP)-multiwalled carbon nanotubes (MCWNTs) nanocomposite thin films were developed by the spray process, which were used for the detection of low concentration formaldehyde at room temperature. The surface morphology and structure of films was analyzed by scanning electron microscope (SEM), UV-Vis absorption spectrometry, respectively, and the formaldehyde-sensing properties of sensors were investigated. The results showed that the prepared QCM gas sensor exhibited the linear characteristic, fast response, good reproducibility to low concentration formaldehyde within 6 ppm, and the poisoning of films was observed when the formaldehyde concentration exceeded 6ppm. Moreover, the sensitivity of the sensor could achieve up to 1Hz/ppm and had the good stability of response values.

Introduction

Formaldehyde (HCHO) is a colorless gas with strong irritative smell, which belongs to one of volatile organic compounds (VOCs) that are widely used in household materials, medical laboratories and a variety of industries [1]. As a major contributing factor to the sick building syndrome (SBS), the human body will feel uncomfortable, headache, pain in the eyes when they prolonged exposure to low concentration of formaldehyde [2]. The transitional analytical methods including the spectrophotometry and gas chromatography are restricted by the relatively expensive and large equipment, slow analytical time and so on [1].

Among various techniques, chemical sensor based on quartz crystal microbalance (QCM) is a very promising system for detection of low concentration formaldehyde [3]. It is well-known that QCM is a low cost, short response times, easy portability, high sensitivity and the capability to operate at room temperature device which could be used for measuring an extremely small mass change on the nanogram scale [4]. Zheng et al. [5] used a PANi/TiO2 nanocomposite as the sensitive layer on a QCM sensor with response times of less than 300s. A series of typical QCM formaldehyde gas sensors had been reported by Bin Ding's group, in which the sensing materials included PEI/TiO2 nanocomposite [6], PEI/PVA nanofibrous membranes [7], PEI/bacterial cellulose (BC) membrane [8]. However, to the best of our knowledge, PVP-MWCNTs nanocomposite has been seldom prepared for the QCM formaldehyde sensor application.

In this study, a novel formaldehyde sensor was developed based on QCM devices coated with PVP-MCWNTs nanocomposite thin films by a simple and easy spray process. The sensing characteristics such as response, reversibility, reproducibility and long-term stability were discussed. The formaldehyde adsorption mechanism was also analyzed. Moreover, the morphology and structure of sensitive films was characterized by scanning electron microscopy (SEM) and UV-Vis absorption spectrometry, respectively.

Experimental

Materials and sensor fabrication. The water-dispersed MWNTs (outer diameter > 50nm ,length10-20*um*) solution (3wt%)was purchased from Chengdu Organic Chemicals Co.Ltd., Chinese Academy of Sciences. 2ml of this solution was diluted to 0.3wt% by 18ml deionized water (18MΩ.cm). Polyvinyl pyrrolidone (PVP) powder with M of 8,000 was purchased from J&K Chemical Ltd. 50mg PVP was added into 10ml deionized water, and then the mixture was sonicated for half an hour to achieve a uniform PVP solution. Afterwards, solution of PVP-MWCNTs composite materials was prepared by mixing 10 ml MWCNTs solution (0.3 wt%) with 10 ml PVP solution, and then was sonicated for one hour.

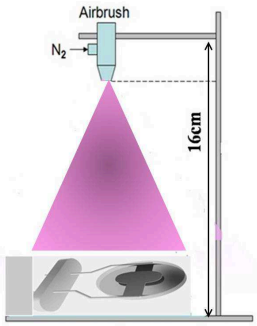


Fig .1. The sketch map of the spraying process

The PVP-MWCNTs solution was sprayed onto the electrode surface of QCM. The spraying process was adopted to fabricate the gas-sensing films, as shown in Fig. 1. Here AT-cut 8MHz quartz crystals with Ag electrodes of 4mm diameter on both sides were purchased from Benyue Technology Ltd., China. The frequency shifts of the QCM after sprayed by PVP-MWCNTs composite flims can be used to estimate the thickness of the composite films according to Sauerbrey equation[9-10] .The QCM coated PVP-MWCNTs nanocomposite films was dried in vacuum under 60℃ for 48h.

The experiments setup of QCM gas sensors. To investigate the sensitive performance of PVP-MWCNTs nanocomposite films for formaldehyde, a schematic diagram of the QCM testing system was exhibited in Fig. 2. The QCM gas sensor was installed in the testing chamber (100mL) which kept at the constant temperature of 25℃.The resonance frequency shifts of QCM sensors due to gas adsorption were measured by the counter and the recorded data were transferred to the computer versus GPIB interface. QCM-5 Oscillator was used to excite the QCM device. The formaldehyde concentration was controlled by a mass flow controller with the flow rate of 100 mL/min. During the measurement, the dry air was first introduced into the test chamber until the baseline frequency was stable, and then the tested gases were allowed to pass through the surface of sensors. The sensor response is defined as the variation in operating frequency of oscillation due to the interaction with the target gas. The response and recovery time is defined as 90% of the time taken for the total frequency shift in the presence of test gas and recover original baseline after desorption, respectively [11].

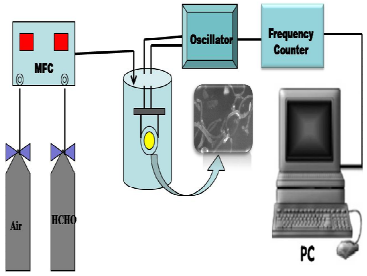


Fig .2. Schematic diagram of the QCM testing system

Results and discussion

Morphological characterization and UV-Vis. The morphologies of PVP-MWCNTs nanocomposite films were observed with a field emission scanning electron microscope (FESEM, S-4800,HITACHI, Japan),as shown in Fig. 3. It is obvious that the PVP film is continuous and the film surface like a bunch of circular morning glory, as shown in Fig. 3(a). It could provide larger amounts of gas channels of the sensor. For the composite films, the sensing surface showed the distribution of PVP-MWCNTs. Most of the carbon nanotubes embedded in the composite films and some CNTs were on the composite films at magnification ratio 50.0K as shown Fig. 3(b). It is difficult to obtain very uniformly and continuously dispersed films by the spraying process.

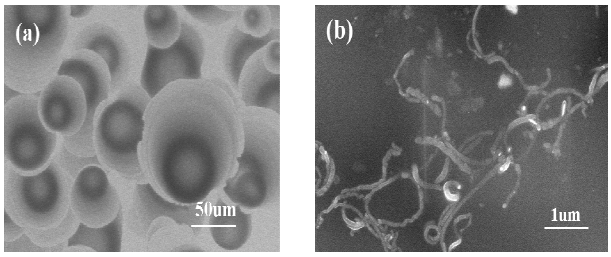


Fig. 3. SEM micrograph of the thin films: (a) the PVP film, (b) the PVP-MWCNTs composite films

Fig. 4 was the UV-Vis absorption spectra of sprayed PVP and PVP/MWCNTs composite thin films on glass. It could be seen that the $\pi \rightarrow \pi^*$ band of MWCNTs was in the 267 nm region, one absorbance peak of pure PVP appeared at 196 nm. It can be noted that the characteristic peaks of PVP and MWCNTs all appear in the PVP-MWCNTs nanocomposite thin films.

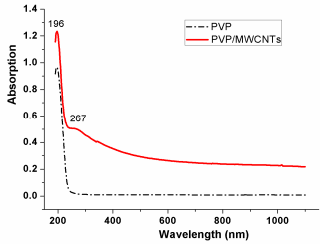
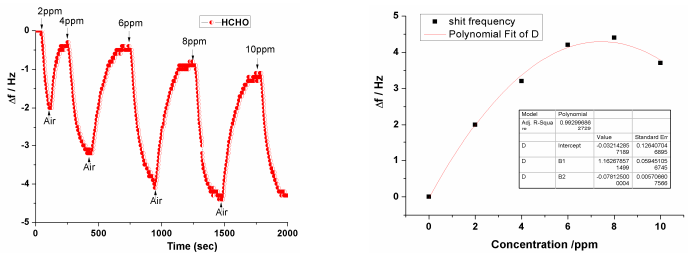


Fig. 4. The thin films were characterized by using ultraviolet-visible absorption spectrometry

Formaldehyde sensing properties. The sensor was first exposed to a formaldehyde gas pulse sequence of 2ppm, 4ppm, 6ppm, 8ppm and 10ppm concentrations. The chamber was purged with dry air between pulses to allow the QCM sensor to recover. The dynamic response to formaldehyde gas concentrations in dry air was shown in Fig. 5 (a). It exhibits good and fast response, meanwhile, the response time and recovery time of the sensor were 180s and 270s at 4 ppm formaldehyde, respectively. Furthermore, the curve of responses vs concentration of formaldehyde was plotted in Fig. 5 (b). It is obvious that as the concentration increased, the frequency shift also increased, while the frequency shift increases nonlinear with the increase of formaldehyde concentrations for 6-10ppm. The sensors reached dynamic equilibrium at 6ppm formaldehyde, the frequency shift attains a stable value. At > 6ppm of formaldehyde, the sensors of the frequency shift descend with the formaldehyde concentration increasing, which can be explained by the surface effect and bulk effect [12].



(a) (b)

Fig. 5. (a) Real-time frequency shift measurement of the QCM-based PVP-MWCNTs sensor, (b) requency shift of the sensor versus 0-10 ppm formaldehyde concentration

Reproducibility of the prepared sensor was observed as indicated in Fig. 6 when the sequential three pulses of 4ppm formaldehyde gas were introduced into the sensor chamber. It was found that the PVP-MWCNTs nanocomposite thin film based sensor produced repeatable responses of the same magnitude with good baseline stability [13].

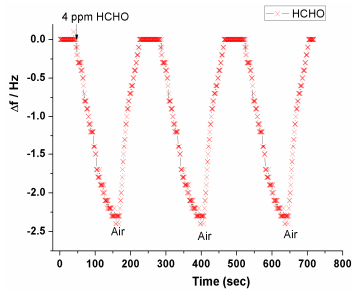


Fig. 6. The repeatability testing of QCM sensors

To test the long-term stability of the sensor, it was exposed to air for 1, 30 and 60 days, respectively, and then the frequency shifts of the sensor exposed to 4ppm formaldehyde were measured, as shown in Fig. 7. The stability performance parameters QCM-based PVP-MWCNTs sensor were calculated and shown in Table 1.

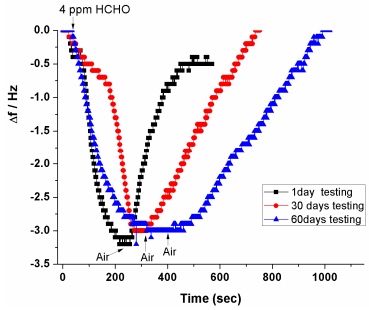


Fig. 7. The response curves of sensors exposed to 4ppm formaldehyde for the long-term stability testing

Table 1 The stability performance parameters of QCM sensor

Days	Frequency shift((Hz)	Response time (s)	Recovery time (s)
1	3.3	180	270
30	3.0	245	451
60	3.0	303	594

It was supposed that, on the one hand, the humidity or solid particles absorbed on the surface of films hinder the diffusion of formaldehyde gas molecules; on the other hand, after entire evaporation of the solvent in nanocomposite thin films, the film tended to be contractive and tight, which strongly influenced the rate of formaldehyde molecules permeating into the composite membrane. However, the further reason and improvement of long-term stability should be performed in the further work.

Conclusions

A formaldehyde gas sensor for QCM based on PVP-MWCNTs by airbrush spray deposition technology was fabricated. The sensor showed good repeatability and long-term stability for formaldehyde gas and a fast response and recovery towards formaldehyde in the concentration range of 0-10ppm at room temperature. Furthermore, Due to the room temperature operation, the prepared QCM formaldehyde sensors may prove to be useful for environmental and industrial applications after further development.

Acknowledgements

This work was supported by the Natural Science Foundation of China (Grant Nos. 61176066, 61101031) and Program for New Century Excellent Talents in University (Grant No. NCET-13-0096).

Reference

[1] P.-R. Chung, C.-T. Tzeng, M.-T. Ke, C.-Y. Lee, Formaldehyde Gas Sensors: A Review, Sensors. 13(2013) 4468-4484.

[2] R.-Q. Xing, L. Xu, Y.-S. Zhu, J. Song, W.-F. Qin, Q.-L. Dai, D.-L. Liu, H.-W. Song, Three-dimensional ordered SnO2 inverse opals for superior formaldehyde gas-sensing performance, Sens. Actuators B. 188(2013) 235-241.

[3] R. Das, S. Biswas, R. Bandyopadhyay, P. Pramanik, Polymerized linseed oil coated quartz crystal microbalance for the detection of volatile organic vapours, Sens. Actuators B. 185 (2013) 293-300.

[4] Y.H. Zhu, H. Li, Q. Zheng, J.Q. Xu, X. X. Li, Amine-functionalized SBA-15 with uniform morphology and well-defined mesostructure for highly sensitive chemosensors to detect formaldehyde vapor, Langmuir. 28 (2012) 7843-7850.

[5] J. Zheng, G. Li, X. Ma, et al, Polyaniline-TiO2 nanocomposite based trimethylamine QCM sensor and its thermal behavior studies, Sens. Actuators B. 133(2008) 374-380.

[6] X.F. Wang, F.H. Cui, J.Y. Lin, B. Ding, J.Y. Yu, S.S. Al-Deyab, Functionalized nanoporous TiO2 fibers on quartz crystal microbalance platform for formaldehyde sensor, Sens. Actuators B. 171-172 (2012) 658-665.

[7] X.F. Wang, B. Ding, M. Sun, J.Y. Yu, G. Sun, Nanofibrous polyethyleneimine membranes as sensitive coatings for quartz crystal microbalance-based formaldehyde sensors, Sens. Actuators B. 144 (2010) 11-17.

[8] W.L. Hu, S.Y. Chen, L.T. Liu, B. Ding, H.P. Wang, Formaldehyde sensors based on nanofibrous polyethyleneimine/bacterial cellulose membranes coated quartz crystal microbalance, Sens. Actuators B. 157 (2011) 554-559.

[9] G. Sauerbrey. Use of quartz vibration for weighing thin films on a microbalance, Zeitschrift für Physik. 155(1959) 206-222.

[10] Z.Ali, Acoustic wave mass sensors, Journal of thermal analysis and calorimetry.55(1999) 397-412.

[11] J.Q. Xu, Y.P. Chen, D.Y. Chen, Hydrothermal synthesis and gas sensing characters, Nano Lett.3(2003) 929-933.

[12] Ping Sun, Yadong Jiang，Guangzhong Xie, Xiaosong Du, Jia Hu, A room temperature supramolecular-based quartz crystal microbalance (QCM) methane gas sensor Sensors and Actuators B. 141(2009) 104-108.

[13] TAI HuiLing, LIAO Jian, DAN WenChao, DUAN Chengli, Li Xian, Preparation of bilayer/three-layer PEO-carbon nanotube composite thin films and their toluene-sensing application, SCIENCE CHINA Technological Sciences. 56(2013) 1124-1128.

Key Engineering Materials Vols 645-646 (2015) pp 724-729
© (2015) Trans Tech Publications, Switzerland
doi:10.4028/www.scientific.net/KEM.645-646.724
Submitted: 2014-10-29
Accepted: 2014-12-23

A micro direct formic acid fuel cell with PDMS fluid flow plates

Tingting Wang[2,1], Yibo Zeng[1,2], Zuguang Zhao[2,1], Hang Guo[1,2*,a]

[1]Pen-Tung Sah Micro-Nano Science and Technology Institute, Xiamen University, China

[2]Department of Mechanical and Electrical Engineering, Xiamen University, China

[a]hangguo@xmu.edu.cn

Keywords: DFAFC; formic acid; PDMS; MEMS

Abstract: Micro direct formic acid fuel cell (DFAFC) is currently one of the promising technologies to power micro/nano devices and systems. Compared with micro direct methanol fuel cell (DMFC), micro (DFAFC) can have higher proton conductivity and energy density, and crossover of formic acid through Nafion membrane is significantly less than methanol. In this paper, a micro DFAFC has been developed. Polydimethylsiloxane (PDMS) is chosen as the material for fluid flow plates in both cathode and anode of the micro DFAFC in order to simplify its structure and improve its packaging performance. The developed micro DFAFC has been tested and results show that its input concentration of formic acid solution can reach up to 10mol/L with its peak power output of 13.6mW/cm^2 and maximum output current of 97.66mA/cm^2.

Introduction

During the past 20 years, MEMS and nano technology have gained great progresses with various kinds of micro/nano devices and systems developed for applications, leading to a fast-growing power demand on micro power technologies. Micro fuel cell is very attractive due to its advantages like high efficiency of energy conversion, environmentally friendly, quick load response and wide range of fuels [1-7]. In different kinds of micro fuel cells, proton exchange membrane fuel cell (PEMFC) is considered to have the most research value and application prospect [8]. Among which, direct methanol fuel (DMFC) is most popular since it has many advantages, such as rich fuel source, convenient storage and transportation, and high reliability. However, it also finds that methanol can easily permeate into Nafion membrane and thus input methanol concentration is very low (1-2 mol/L) [9], resulting in a low power output for DMFC. Meanwhile, direct formic acid fuel (DFAFC) has been more and more popular in recent years. Compared with methanol, formic acid has higher theoretical open circuit potential (1.45V), better electric catalytic oxidation performance and higher proton conductivity. Though the energy density of formic acid is only 2104Wh/L (energy density of methanol is 4900Wh/L), the crossover of formic acid through Nafion membrane is very low. Thus, the concentration of formic acid solution can be much higher to get high power output [10, 11]. In this paper a micro DFAFC has been developed.

Micro fuel cells are generally fabricated by using MEMS technology where silicon is used for fluid flow plates. There are some disadvantages on these silicon-based plates. Besides complex process and long fabrication cycle, silicon wafers are so fragile that fluid flow plates would be broken very easily during packaging. Moreover, it is hard to tight the micro fuel cell with silicon fluid flow plates. In this study, PDMS, instead of silicon, is used as material to fabricate flow fluid plates to solve above issues, and certain techniques are taken for anti-corrosion due to utilization of formic acid. It turns out that packaging of the micro DFAFC with PDMS fluid flow plates is greatly improved and high output power can be achieved.

Principle of DFAFC

As shown in Fig.1, a DFAFC consists of two parts: fluid flow plates and membrane electrode assembly (MEA). Fluid flow plates have two parts, fluid flow plate and cathode fluid flow plate.

MEA is made of proton exchange membrane (PEM), electrode diffusion layer, and electrode catalytic layer, where electrochemical reaction occurs. PEM has the function of transferring proton, stopping electronic transmission and isolation of reactants. Diffusion layer supports the catalytic layer, transferring reactants and conducting electrons. Both anode and cathode fluid flow plates will collect current and distribute reactants.

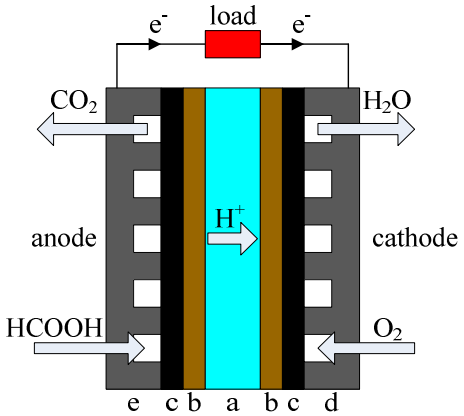


Fig.1. Schematic Diagram of DFAFC
a. PEM; b. electrode diffusion layer; c. electrode catalytic layer;
d. cathode fluid flow plate; e. anode fluid flow plate.

When a DFAFC is in a working condition, formic acid is injected into anode and oxidation reactions occur under the action of catalyst, and protons (H^+), electrons (e^-), and CO_2 are produced. The electrons form the current in external circuit, while the protons transfer to cathode through PEM and react with the O_2 and e^- to form H_2O as reduction reaction. Thus, the circulation of fuel cells is realized.
Oxidation reaction occurs in anode of DFAFC is

$$HCOOH \rightarrow CO_2 + 2H^+ + 2e^-.$$

And reduction reaction occurs in cathode is

$$^1/_2O_2 + 2H^+ + 2e^- \rightarrow H_2O.$$

The overall reaction of the DFAFC can be written as

$$HCOOH + ^1/_2O_2 \rightarrow CO_2 + H_2O.$$

Fig.2 shows the structure of the micro DFAFC in our study, where PDMS instead of silicon is used as the material of fluid flow plates. Generally, micro fuel cells usually use silicon and steel for fluid flow plates. Silicon wafer is fragile and steel is less flexible, and it usually needs damping structures like O-rings for packaging the micro fuel cell. For PDMS, it has suitable strength and toughness. So the damping structures are not needed anymore. The PDMS fluid flow plates not only avoid to be broken into pieces, but also simplify the structure of fuel cells and make it easy to package the micro fuel cell. Fig.2b and Fig.2d show the PDMS cathode fluid flow plate and anode fluid flow plate, respectively.

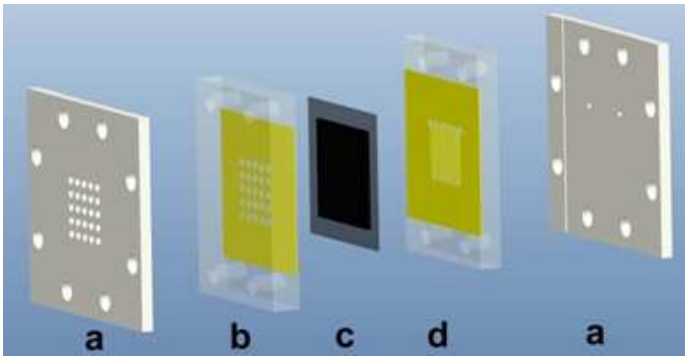
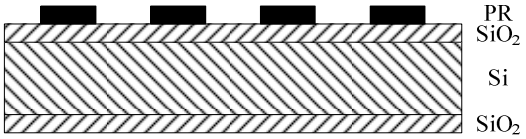
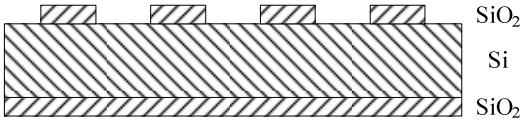
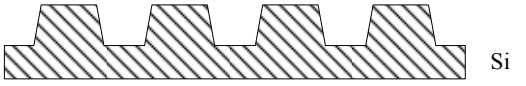
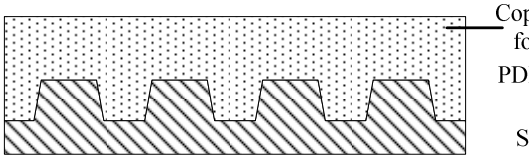
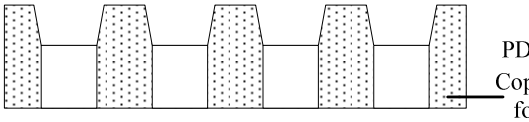
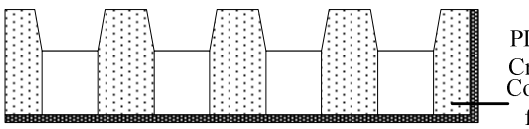


Fig.2. Structure of a DFAFC with PDMS fluid flow plates
a. aluminum plate; b. cathode fluid flow plate; c. PEM; d. anode fluid flow plate.

Microfabrication of DFAFC

Molding method is used for fabrication of PDMS fluid flow plates and its process is shown in Table 1. Microfabrication techniques such as low pressure chemical vapor deposition (LPCVD), photolithography and anisotropic etching are used to get micro channels in silicon substrates, and the microfabricated silicon molds are shown in Fig.3. The PDMS mixed by prepolymer and curing agent in a certain ratio are poured into silicon mold, and then put it into a vacuum oven to solidify the PDMS. After de-molding and punching the initial PDMS fluid flow plates are obtained. A layer of gold is sputtered onto the flow plates to collect the electrons generated from electrochemical reaction. Fig.4 shows the PDMS fluid flow plates, where the effective area of the flow channel is 9.4mm×10mm in the anode fluid flow plate, and the size of the plates is 38mm×36mm. The width of flow channel and distance between every 2 channels are all 400μm, and depth of the channel is 200μm.

Table 1 Fabrication process of PDMS fluid flow plates

Step	Schematic diagram	Fabrication process
1		Oxidation; Photolithography
2		BHF etching; Removing photoresist
3		KOH solution corrosion; Removing SiO_2 layer and forming silicon wafer mold
4		Based on the silicon mold, curing the PDMS to form the basic flow field plates
5		De-molding; Punching to form the air channels
6		Sputtering Cr/Au to collect current

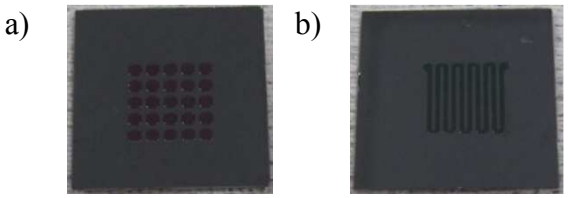


Fig.3. Silicon mold of fluid flow plates
a) cathode mold; b) anode mold

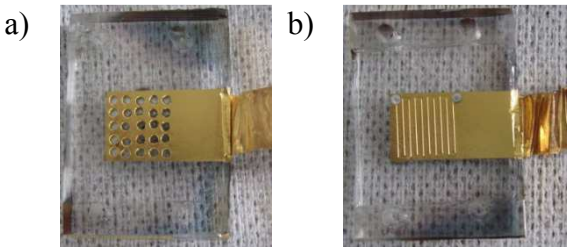


Fig.4. PDMS fluid flow plates
a) cathode plate; b) anode plate

Fig.5 shows a sample of MEA, with an effective area of 10mm×10mm. The Nafion 115 membranes from DuPond company are chosen as PEM. Toray-90 carbon paper is used as diffusion layer after cleaning, carbon powder coating and high-temperature sintering. The anode catalyst is Pt/Ru powder while the cathode catalyst is Pt/C powder, and they are sprayed onto the surface of PEM. In the end, MEA is obtained by hot compressing PEM with two pieces of carbon paper into one piece.

Compared with DMFC, formic acid in DFAFC has stronger corrosion than methanol. Because formic acid solution will corrode copper foil slightly, the copper foil and the fluid flow plate should be made into a one-piece, as shown in step 4 of Table 1. By embedding the copper foil into the uncured PDMS fluid flow plates, the copper foil and the fluid flow plates will be adhered strongly into a one-piece after being solidified. At the same time, in process of metallization, a layer of sputter Cr/Au is sputtered on both fluid flow area and copper foil in order to protect the copper foil from corrosion and ensure that electrical connection is in good condition. The surface of PDMS is hard to be wet since it is hydrophobic. Also it is difficult to form strong adhesion between PDMS and metal layer since PDMS has high crystallinity and weak boundary layer. To solve these issues, the fluid flow plates should be cleaned critically by methylbenzene, and low temperature oxygen plasma is used to activate surface before metallization.

As shown in Fig.6 the fixtures on aluminum plates should be passivated in the concentrated sulfuric acid and then a layer of polytetrafluoroethylene (PTFE) should be sputtered onto aluminum plates to resist corrosion. PTFE is a type of artificial polymer material with characteristics of anti-corrosion from acid, alkali and various organic solvent. The aluminum plates and fixtures sputtered with PTFE can resist the long-term corrosion of formic acid and protect the cells. In the end, the DFAFC is obtained with a size of 38mm×36mm×14mm after packaging.

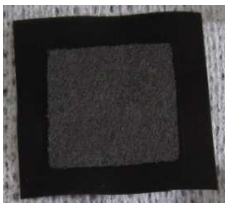


Fig.5. Sample of MEA

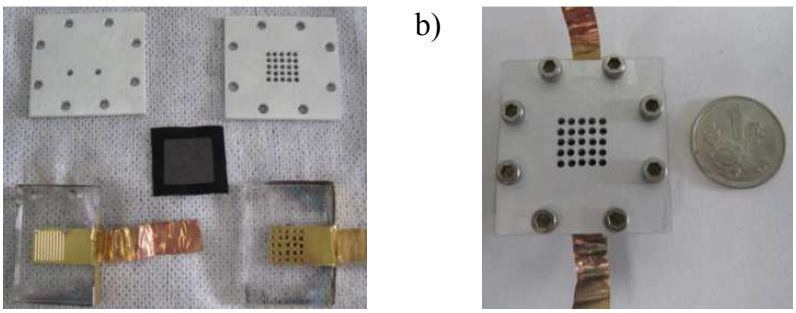


Fig.6. Packaging of DFAFC a) before packaging; b) after packaging

Test and analysis

The DFAFC are tested by using CHI660E electrochemical workstation at an ambient temperature and pressure. The flow rate of the formic acid solution is 0.5ml/min and 1ml/min, respectively, and its concentration is 10mol/L. Under the same conditions, 1mol/L methanol solution is used as fuel to test the DMFC cells. Results are shown in Fig.7. The maximum current density of DFAFC is 97.66mA/cm^2, and its peak power density is 13.61mW/cm^2. The output power of DFAFC increases about 2 times compared with DMFC. Also, the results show that flow rate of formic acid has little influence on the performance of DFAFC and the cells have no leakage during

the test. It turns out our packaging technology for DFAFC is effective and can be applied to other types of micro fuel cells.

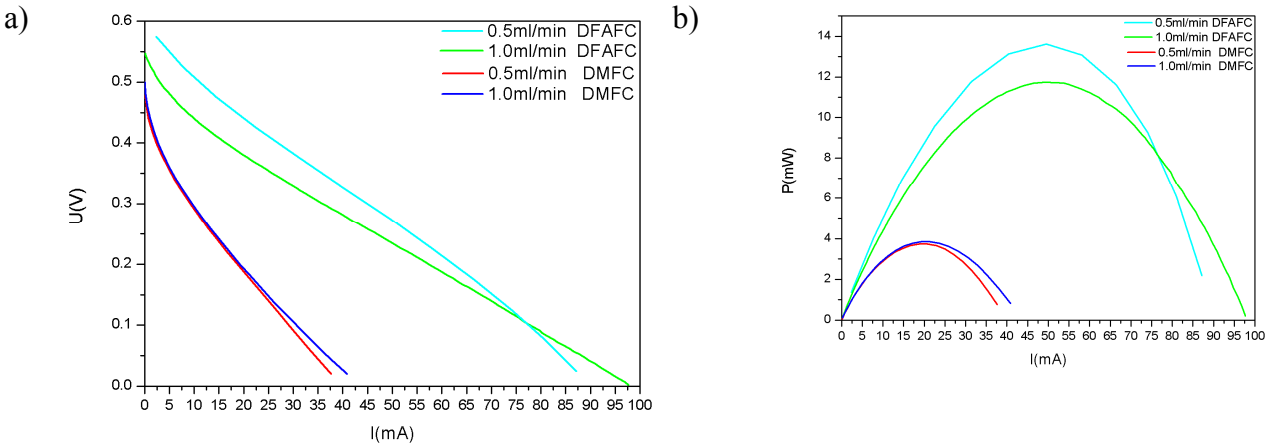


Fig.7. Output tests of the fabricated DFAFC a) I-V test; b) Output power test

Table 2 Output performance of the fabricated DFAFC

Flow rate	DFAFC		DMFC	
	Maximum current density [mA/cm^2]	Peak power density [mW/cm^2]	Maximum current density [mA/cm^2]	Peak power density [mW/cm^2]
0.5ml/min	87.18	13.61	37.64	3.75
1ml/min	97.66	11.74	40.92	3.85

It is noted that since the methanol can easily permeate the Nafion membrane almost 40% methanol will oxidize in cathode, which would generate mixed potential to lower the performance of cells. Thus, 1mol/L methanol was chosen as the input concentration for the test, resulting in that output power of DMFC is very low. On the other hand, formic acid is strong electrolyte and $HCOO^-$ will be created in the solution due to ionization. But they are rejected by the sulfonic acid groups in Nafion membrane [12], resulting in a very low permeability of formic acid in Nafion membrane. Therefore, though energy density of formic acid is lower than that of methanol, input concentration of solution can be much higher to get high output power from DFAFC. In addition, intermediate products produced by electrocatalytic oxidation of methanol will strongly poison the catalyst Pt [13]. Thus, efficiency of oxidation of methanol in anode of DMFC would be lower. But for formic acid, it has good electro-chemical activity and its oxidation peak potential is about 0.2V in Pt/C electrode which is far more less than that of methanol. Overall, the output performance of DFAFC is better than DMFC.

Conclusions

In this paper a micro direct formic acid fuel cell with PDMS fluid flow plates has been developed. The structure of the micro fuel cell is simplified and packaging performance is greatly improved. A technique for anti-corrosions from formic acid is also developed and verified by tests. Compared with DMFC, the output power of DFAFC is nearly doubled since high concentration of formic acid is allowed to input into DFAFC. Study in this paper demonstrates that DFAFC is a very promising technology to power micro/nano devices and systems.

Acknowledgement

This work is financially supported by the New Century Talent Support Plan of the Ministry of Education of China (2007NCET-07-0723), the National Natural Science Foundation of China (60936003) and Aviation Science Foundation of China (2008ZH68002).

Reference

[1] Yun Wanga, Ken S. Chen, Jeffrey Mishler, Sung Chan Cho, Xavier Cordobes Adroher., A review of polymer electrolyte membrane fuel cells: Technology, applications, and needs on fundamental research, Applied Energy. 88 (2011) 981-1007.

[2] Ito T， Kimura K， Kunimatsu M, Characteristics of micro DMFCs array fabricated on flexible polymeric substrate, Electrochem Commun. 8 (2006) 973-976.

[3] Liu Xiaowei, Suo Chunguang, Zhang Yufeng, et al, Novel modification of Nafion R 117 for a MEMS-based micro direct methanol fuel cell (μDMFC), Micromech Microeng. 10 (2006) 226-232.

[4] WOLFGANG S, ARDALAN V, A review of the main parameters influencing long-term performance and durability of PEM fuel cells, Journal of Power Sources. 180 (2008) 1-14.

[5] JACQUES R, DEBORAH J J, Non-fluorinated polymer materials for proton exchange membrane cells, Annual Review Materials Research. 33 (2003) 503-55.

[6] STEELE B C H, HEINZEL A, Materials for fuel-cell technologies, Nature. 414 (2001) 345-352.

[7] RIKUKAWA M, SANUI K, Proton-conducting polymer electrolyte membranes based on hydrocarbon polymers, Progress Polymer Science. 25 (2010) 1463-1502.

[8] Paola Costamagna, Supramaniam Srinivasan, Quantum jumps in the PEMFC science and technology from the 1960s to the year 2000 Part I. Fundamental scientific aspects, Journal of Power Sources. 102(2001) 242-252.

[9] Shuqin Song, Vasiliki Maragou, Panagiotis Tsiakaras, How Far Are Direct Alcohol Fuel Cells From Our Energy Future, Journal of Fuel Cell Science and Technology. 4 (2007) 203-209.

[10] C. Rice, S. Ha, R.I. Masel, P. Waszczuk, A. Wieckowski, Tom Barnard, Direct formic acid fuel cells, Journal of Power Sources. 111 (2002) 83-89.

[11] Xingwen Yu, Peter G. Pickup, Recent advances in direct formic acid fuel cells (DFAFC), Journal of Power Sources. 182 (2008) 124-132.

[12] B.D. Bath, H.S. White, E.R. Scott, Anal. Chem, Electrically Facilitated Molecular Transport. Analysis of the Relative Contributions of Diffusion, Migration, and Electroosmosis to Solute Transport in an Ion-Exchange Membrane, Analytical Chemistry. 72 (2000) 433–442.

[13] Xin Wang, Ji-Ming Hu, I-Ming Hsing, Electrochemical investigation of formic acid electro-oxidation and its crossover through a Nafion membrane, Journal of Electroanalytical Chemistry. 562 (2004) 73-80.

Key Engineering Materials Vols 645-646 (2015) pp 730-735
© (2015) Trans Tech Publications, Switzerland
doi:10.4028/www.scientific.net/KEM.645-646.730

Submitted: 2014-10-31
Accepted: 2014-12-23

A novel microfluidic time gate for controlling flow of liquids

Lu Gan[1,a], Chong Liu[1,2,b] , Jingmin Li[1,c*] , Yahui Ma[1], Lijie Zhou[1], Hao Zhang[1], Tao Li[1], and Lei Wang[1]

[1]Key Laboratory for Micro/Nano Technology and System of Liaoning Province, Dalian University of Technology, Dalian, Liaoning Province, China

[2]Key Laboratory for Precision and Non-traditional Machining Technology of Ministry of Education, Dalian University of Technology, Dalian, Liaoning Province, China

[a]ganludlut@163.com, [b]chongl@dlut.edu.cn,

[c]jingminl@dlut.edu.cn

Keywords: Microfluidic systems, Capillary force, Time gate, Controlling flow time

Abstract. Microfluidic time gates are applied to control accurate flow time of liquids in the autonomous capillary systems, which are critical structures for point-of-care diagnostic and analytical applications. The time gate employs several abruptly changing geometry of the flow path to change the wettability of micro-channels to meet the requirement of delaying flow. However, obtaining desirable flow of liquids in microfluidics is still a limiting factor in the practical implementation. The work demonstrates a novel 2D serial cross-channel time gate and 3D serial cross-channel time gate. They are fabricated in PDMS-based autonomous capillary system. 2D serial cross-channel time gate is comprised of multiple paralleled channels of changeable width with dimensions from 300-800μm. The number of the channels and the width variation of the cross intersections are crucial factors to influence the flow velocity of liquids. Compared with the 2D serial cross-channel time gate, the 3-D structures can eliminate the problem of entrapping air and improve the flow velocity of liquids in the time gate. The controlling time of the flow in 3D serial cross-channel time gate and 2D serial cross-channel time gate are 9~13s and 5s~51s, respectively.

1 Introduction

Microfluidic systems are increasingly required to control the accurate flow time of liquids in chemical and biological analytical applications, especially in point-of-care diagnostic and analytical applications [1,2].

The microfluidic systems, which driving fluid by capillary effect, can avoid the embedment of the external devices and the complex of microfluidic systems [3,4]. Some researchers have demonstrated microfluidic liquid-driving units basing on capillary force [5,6,7]. E. Delamarche et al. [8] have developed an autonomous micro-valve formed by increasing the dimension of semicircular channels connected to each other. Such micro-valve adjusts its capillary force through changing the size of the meniscus of the fluid fronts. They demonstrated that the valve is effective to slow down the velocity of the fluid front to the next micro-channels. In their subsequent studies, other functional units are integrated into such valves for effecting immunoassays with one step [9]. C.H. Ahn et al. [10] have invented a series of micro-channels with cyclic olefin copolymers (COC)-based passive valves located at programmed positions. Abruptly changing cross-sectional area would reduce the capillary force across the passive valves. The passive valves have a round geometry to

avoid any residual solution trapped in the dead corners instead of an abruptly rectangular corner. The passive micro-valves were successfully integrated into the microfluidic system with a disposable smart lab-on-a-chip for point-of-care clinical diagnostics. M.I. Mohammed et al. [11] have presented that a microfluidic delay valve is formed by a main channel split into two channels, one channel ending at a rectangular or arrow stop valve and the other channel ending at the secondary channel combining with the stop valve. The fluids of the stop valve are triggered to migrate into the valve chamber by the fluids of the secondary channel. The valve can have a delay time of approximately 30s, and the controlling time of the valve can be produced by adjusting geometry of the secondary channel. All valves of the above literatures presented are easy to be under the risk of entrapping air. Most of the structures are the channel of single exit which can only allow the limited volumes of fluids to flow the cross section of the channel. Therefore they can't be satisfied to the multiple integrated tests for the follow-up test chamber.

In this paper, a serial cross-channel time gate was designed to be embedded into the microfluidic systems. The fabrication of the microfluidic systems were based on PDMS by UV-LIGA technology using SU-8 molds. Unlike the systems mentioned above, this system demonstrates a time gate that allows a large volume capacity of liquids in the test chamber that has advantages over the multiple integrated tests (Fig.1 (a)) [12,13,14,15]. A liquid pipetted into a loading pad of the systems is actuated into the time gate by the capillary force generated through the micro-pillar arrays. Subsequently, the liquid flowing out of the multiple exits in 2D serial cross-channels can achieve accurately delaying time and the uniformity of the flow velocity of the fluid front in each channel. To minimize the risk of the entrapping air, 3D serial cross-channel time gate having the similar structures with 2D serial cross-channel time gate was performed.

2 Experiments

2.1 Solutions

Goat serum was used as a model liquid in the experiments ignoring its evaporation. Deionized water was used in the rinsing process.

2.2 Design of the serial cross-channel time gate

The microfluidic chip icludes five parts: loading pad, reaction chamber, time gate, test chamber, waste reservoir. Reaction chamber and test chamber are comprised of the micro-pillar arrays designed with the diameter in 50μm. The micro-pillar arrays changing the wettability of the PDMS surface contribute to the flowing liquid to the next zone. Fig.1. (b) shows the structure of 2D serial cross-channel time gate in the top view. 2D serial cross-channel time gate is comprised of multiple paralleled channels with the lateral equidistant distribution in the flow path. There are three cross intersections in each channel. The cross intersection of 2D serial cross-channel time gate employs abruptly changing geometry of the flow path to change the wettability of micro-channels. Here the micro-channel wall changes its direction by the angle 90^0. The number of micro-channels ranges from 2 to 4 with dimensions from 300-800μm in the same area ($2.9\times3.5mm^2$), as shown in Fig.3. As the contrast experiment, the width variation of the cross intersection in 4 channels of 2D serial cross-channel time gate is 100μm, 150μm and 200μm, respectively. The depth of the micro-channels in 2D serial cross-channel time gate is 70μm. 3D time gate has the similar shape with 2D time gate. The difference of 3D structure with 2D structure is the existence of a space gap of 40μm between the top of the serial cross-channel microstructures and the sealing interface in the time gate zone.

2.3 The SU-8 molds fabricated by UV-LIGA technology

The microfluidic chips used for experiments were fabricated in PDMS (Sylgard 184, Dow Corning Corp, USA) using UV-LIGA technology by the lithography machine (MA/BA6, SUSS MicroTec, German) [17]. The UV-LIGA technology was used for three times. Because of the structural characteristics of the micro-pillar arrays in the reaction chamber and test chamber, as shown in Fig.1 (a), the marked patterns are needed for the alignment. The process starts with the fabrication of several micrometers thick positive photoresist (BP212, Kempur Microelectronics, Inc. China) mold on the back of silicon substrate. Then 40μm thick SU-8 photoresist (SU-8 2015, MicroChem Corp, USA) was coated on the top of silicon substrate. The SU-8 photoresist was selectively exposed to UV light by an aluminum mask on quartz. After the post exposure, the 30μm thick SU-8 photoresist was coated and then exposed selectively. Subsequently two layers of the SU-8 photoresist were developed together by SU-8 developer (MicroChem Corp, USA). The developed SU-8 molds were rinsed with ethanol, flushed by deionized water and dried under a stream of N_2.

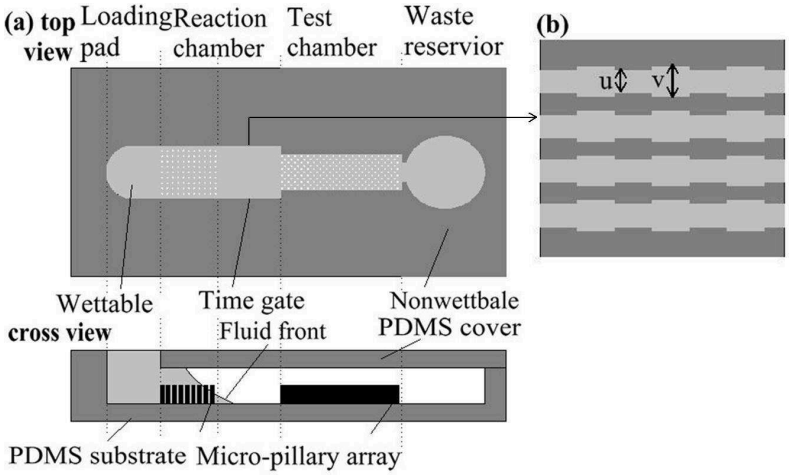


Fig.1 The structures of the microfluidic chip used for experiments and the time gate. (a) The structure of the microfluidic chip. (b) The structure of the serial cross-channel time gate in the top view.

2.4 The fabrication of PDMS microfluidic chips

The PMMA plates were used as the mold of the PDMS cover and the SU-8 molds were used to fabricate the PDMS substrate. A 10:1(w/w) mixture of base PDMS and curing agent was poured in the molds and cured for 2.5h at 65^0C. The PDMS substrates and the flat PDMS sheets were exposed to 5os of the oxygen plasma treatment in the power of 15W by the plasma etching machine (K1050X, Emitech, France) to oxidize the PDMS surface and improve its hydrophilicity. After oxidation, the PDMS microfluidic chips were achieved by sealing the PDMS substrates with the covers.

3 Results and discussions

3.1 Different width variations of the cross intersection in 2D serial cross-channel time gate

The microfluidic chips starts flowing upon pipetting the serum into its loading pad. Then the serum was actuated by the micro-pillar arrays into the time gate. Fig.2 shows the flow behavior of the serum in the 2D serial cross-channel time gate. Each micro-channel has three cross intersections with angle 90^0 variation in the wall direction. Such time gates retard the fluid front by the formation

of the meniscus and thereby reducing the capillary force. The velocity of the fluid front in the cross intersections is slower than the fluid front in the original channels. The menisci of the fluid fronts in Fig.2 (b), (f), (j) move from regions of high capillary force (width of micro-channel 300μm) into regions of reduced capillary force (width of micro-channel 400μm, 450μm, 500μm, respectively) in 4 channels. And the flow behavior of the fluid front repeats again in the next cross intersection. In the end of the time gates, the fluid fronts of all micro-channels form a large meniscus and merge into the test chamber as shown in Fig.2 (c), (g), (l). The structures of two sides in the end of the time gates are designed to control the shape of meniscus and orientation of the fluid fronts. Therefore the appearance of the entrapping air in two sides of the end of the time gates doesn't matter to affect the flow of the whole liquids, as shown in Fig.2 (d), (h).

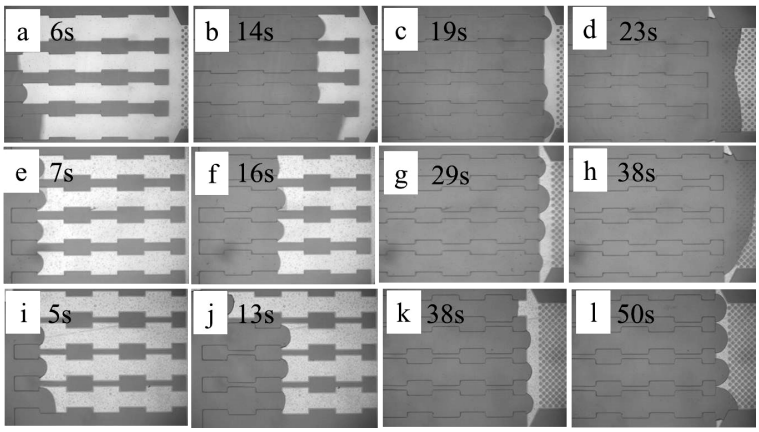


Fig.2 The experimental results of flow control by using 2D serial cross-channel time gate with 4 channels. (a)-(d) show the time series of optical micrographs on 6s, 14s, 19s, 23s, respectively, with characteristic dimensions u=300,v=400. (e)-(h) show the time series of optical micrographs on 7s, 16s, 29s, 38s, respectively, with characteristic dimensions u=300,v=450. (i)-(l) show the time series of optical micrographs on 5s, 13s, 38s, 50s, respectively, with characteristic dimensions u=300,v=500. Serum flows from left to right.

With the increase of the width variation of the cross intersection, the size of the meniscus of the fluid front will be increasing and the delaying time in the time gate will be prolonged. Fig.3 indicates that the reproducibility of the delaying time in the time gate has been controlled in the reasonable range. Through the multiple experiments in the same experimental condition, the calculated mean value of the flow time is 24.4s, 35.8s, 48.6s in the width variation of the cross intersection 100μm, 150μm and 200μm, respectively. If the longer delaying time is needed in some functional microfluidic chips, it's easy to obtain through increasing the number of the cross intersections in each micro-channel.

3.2 Different nuber of channels in 2D serial cross-channel time gate

As a contrast experiment, 2, 3 and 4 channels in 2D serial cross-channel time gate are selected. All of the width variation of the cross intersections are 100μm. As shown in Fig.3, the calculated mean value of the flow time is 5.6s, 13.6s and 24.4s in 2, 3 and 4 channels, respectively. The less of the number of the channels is, the shorter flow time in the time gate can obtain. In 2 channels of the time gate, the velocity of the fluid front of cross intersections has no obvious change. The reason is that the fluid front is quickly actuated forward by the surface-liquid adhesion force before the meniscus of the fluid front doesn't form completely in the relatively small width variation of the cross intersection.

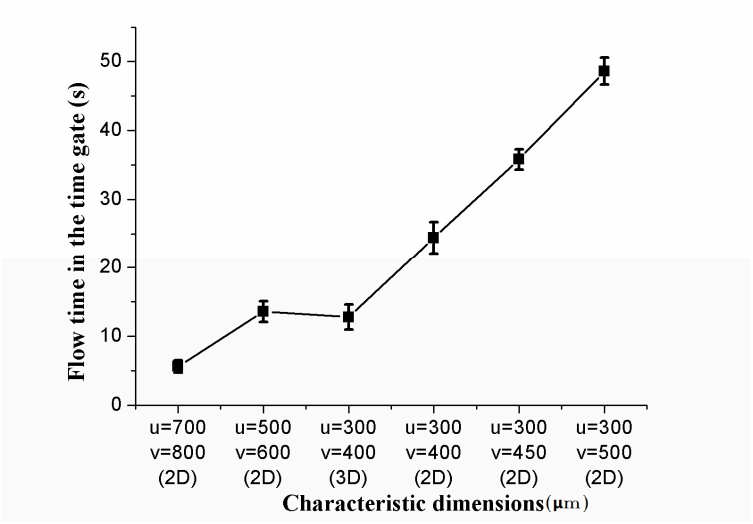


Fig.3 Flow time of the fluid front in the different characteristic dimensions of the serial cross-channel time gate. The mean value and error bar of flow time are also given in the figure.

3.3 Advanced 3D structure in the time gate

In some cases of 2D serial cross-channel time gate with 4 channels, the problem of the entrapping air happened to block the fluid of the intermediate micro-channels moving further. To minimize the risk of the entrapping air, here this part presents a structure of 3D time gate. 3D time gate is modeled as networks of the serial cross-channel structure. There is a space gap of 40μm between the top of the serial cross-channel structure and the sealing interface. Fig. 4 shows the time series of optical micrographs on 8s, 10s, 12s, 15s, respectively. Through the multiple experiments, the velocity of the fluid front remains stable and the mean value of the flow time is 12.8s, as shown in Fig. 3. 3D time gate has comparatively lower flow resistance and increases its volume capacity of the fluid. Moreover, the excellent uniformity of the fluid front sustains until the test chamber, which is beneficial for the accuracy and stability of the test results.

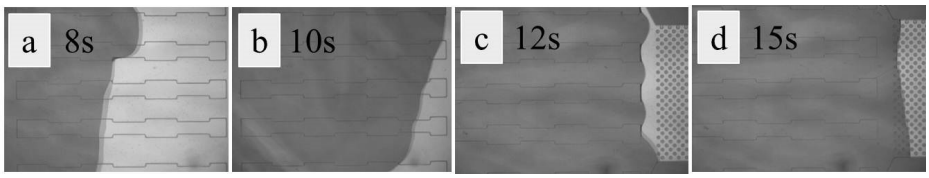


Fig.4 The experimental results of flow control by using 3D time gate. (a)-(d) show the time series of optical micrographs on 8s, 10s, 12s, 15s, respectively. Serum flows from left to right.

4 Conclusions

The microfluidic chips are applied to point-of-care testing in which the controlling time unit is indispensable. The work here presents a serial cross-channel time gate integrated into a microfluidic chip. 2D serial cross-channel time gate obtains the controlling flow time of the fluid front from 5s to 51s. The advanced 3D time gate is successful to avoid the possibility of the entrapping air, with the mean value of the controlling flow time in 12.8s.Two structures of the time gates have a high reproducibility for the controlling flow time of the fluid front in the time gate. The volume capacity of the fluid front is enough to meet the requirement of the multiple integrated tests in the test chamber. Based on the experimental results, the above structures of the time gates can be extended to satisfy the longer controlling flow time through increasing the number of the cross intersections

in each micro-channel. The redesigned time gate can be available to the various point-of-care testing for the required controlling flow time.

Acknowledgements

This work is supported by National Natural Science Foundation of China (51105060; 51375076), the National High-tech R&D Program of China (2012AA040406), the Fundamental Research Funds for the Central Universities (dut12rc(3)71; DUT12ZD212).

References

[1] A. J. DeMello , Control and detection of chemical reactions in microfluidic systems, Nature. 442 (2006) 394-402.

[2] P.S. Dittrich, K. Tachikawa, A. Manz, Micro total analysis systems. Latest advancements and trends, Anal. Chem. 78 (2006) 3887-3907.

[3] K. W. Oh, C. H. Ahn, A review of microvalves, J. Micromench. Microeng. 16 (2006) 13-39.

[4] D. Juncker, H. Schmid, U. Drechsler, et al., Autonomous microfluidic capillary system, Anal. Chem. 74 (2002) 6139–6144.

[5] T.M. Squires, S.R. Quake, Microfluidics: Fluid physics at the nanoliter scale, Rev. Mod. Phys. 77 (2005) 977–1026.

[6] T. Vestad, D. W. M. Marr, J. Oakey, Flow control for capillary-pumped microuidic systems, J. Micromech. Microeng. 14 (2004) 1503-1506.

[7] P. Novo, F. Volpetti, V. Chu, et al., Control of sequential fluid delivery in a fully autonomous capillary microfluidic device, Lab Chip. 13 (2013) 641-645.

[8] M. Zimmmermann, P. Hunziker, E. Delamarche, Valves for autonomous capillary systems, Biomed Microdevices. 11 (2009) 1-8.

[9] M. Zimmmermann, H. Schmid, P. Hunziker, E. Delamarche, Capillary pumps for autonomous capillary systems, Lab Chip. 5 (2007) 119-125.

[10] C.H. Ahn, J.W. Choi, G. Beaucage, et al., Disposable smart lab on a chip for point-of-care clinical diagnostics, Proceedings of the IEEE. 92 (2004) 154-173.

[11] M.I. Mohammed, E. Abraham, M.P.Y. Desmulliez, Rapid laser prototyping of valves for microfluidic autonomous systems, J. Micromech. Microeng. 23 (2013) 1-9.

[12] A. H. C. Ng, U. Uddayasankar, A. R. Wheeler, Immunoassays in microfluidic systems, Anal. Bioanal. Chem. 397 (2010) 991–1007.

[13] J. Hong, J. B. Edel, A. J. Demello, Micro-and nanofluidic systems for high-throughput biological screening, Drug Discovery Today. 14 (2009)134–146.

[14] M. M. Sanchez, S. Miserere, A. Merkoci, Nanomaterials and lab-on-a-chip technologies, Lab Chip. 12 (2012) 1932–1943.

[15] E. Eteshola, D. Leckband, Development and characterization of an ELISA assay in PDMS microfluidic channels, Sens. Actuators, B. 72 (2001) 129–133.

[16] S. C. Tadic, G. Dernick, D. Juncker, et al., High-sensitivity miniaturized immunoassays for tumor necrosis factor α using microfluidic systems, Lab Chip. 4 (2004) 563–569.

[17] P. Novo, D. M. F. Prazeres, V. Chu et al., Microspot-based ELISA in microfluidics: chemiluminescence and colorimetry detection using integrated thin-film hydrogenated amorphous silicon photodiodes, Lab Chip. 11 (2011) 4063–4071.

Key Engineering Materials Vols 645-646 (2015) pp 736-740
© (2015) Trans Tech Publications, Switzerland
doi:10.4028/www.scientific.net/KEM.645-646.736

Submitted: 2014-11-03
Accepted: 2014-12-23

Microfluidic Amperometric Detection Sensor with Integrated Ag/AgCl Reference Electrode

He Zhang[1, a], Xiaowei Liu[1, b], Li Tian[1, c], Xiaowei Han[1, d], Tong Dai[1, e]

[1]Department of Microelectronics, Harbin Institute of Technology, Harbin, Heilongjiang, China

[a]zhanghe.hit@gmail.com, [b]lxw@hit.edu.cn, [c]tianli@hit.edu.cn,

[d]hanxiaowei2017@163.com, [e] daitong@126.com

Keywords: microfluidic; vertical embedded electrodes; composite structure; electro-osmotic

Abstract. In this paper, we presented a novel method for fabricating the integrated electrochemical sensor based on a microfluidic device. The device included: printed circuit board (PCB) substrate with vertical embedded electrodes; polymethyl methacrylate (PMMA) with micro structures; PMMA cover with amperometric detection sensor (ADS). The ADS employed three-electrode sensor system which was composed by two Au electrodes and an Ag/AgCl reference electrode. The polyvinyl chloride (PVC) membrane was used as ion-exchange medium of reference electrode and installed between Au electrodes. Then, the potential changes and the standardization oxidation-reduction experiments were executed to characterize the integrated reference electrode performance. Finally, the ADS system was tested by cyclic voltammetry (CV).

Intorduction

Recent years, many research activities of micro total analysis systems (μTAS) have focused on the developing miniaturized electrochemical sensors [1-3]. Due to precise dimensions, excellent uniformity and high yield, these Micro-electromechanical Systems (MEMS) sensors were generally fabricated by semiconductor-compatible techniques such as screen-printing, ink-jet printing and lithography [4-6]. As a stable electrochemical potential provider, the reference electrodes such as saturated calomel electrode (SEC) and silver-silver chloride electrode (Ag/AgCl) were essential for electrochemical sensors [7-8]. Evidently, the miniaturized and robust reference electrodes are vital to facilitate for the development of electrochemical sensors. However, the integration of such type reference electrodes on the μTAS has remained a major challenge.

Since the mercury in SEC is harmful to environment and human, many researchers focused on Ag/AgCl integration, and fabricated a variety of solid state reference electrodes which were termed quasi reference electrode [9-10]. However, the quasi reference electrodes which were more suitable for construct and integrate, had inevitable problems also. First, due to the finite amount of the KCl presented in the modified membrane, the quasi reference electrode cannot provide stable potentials for a long time. Second, due to efflux or influx from the electrode sensors, the concentration of Cl^- was incessant variation. It is difficult to ensure the measurement accuracy. Finally, the mobility of Cl^- was substantial decline in Solid-state membrane, which could limit the exchange current density and introduce capacitive effects. For the above reasons, integrating the traditional reference electrodes in the μTAS is still very attractive.

In this paper, we presented a novel structure to integrate the traditional Ag/AgCl reference electrodes on a microfluidic device. The chip only had a dimension of 70 (mm) × 40 (mm) × 12 (mm), but included electroosmosis driven separation and electrochemical detection. The reference electrode of ADS was embedded into the PMMA cover slip, this design not only can ensure detection accuracy, but also can replace KCl filling solution easily and extend the life of the chip effectively.

Design and Fabrication

The device included: PCB substrate with vertical embedded electrodes; PMMA middle layer with micro structures; PMMA cover with ADS. The driven electrodes were made by Pt micron wire and soldered vertically on the PCB. Then, the electrodes were connected to the external drive power via the pads on the PCB. PMMA middle layer with microstructures were fabricated by using micro precision engraving machine. The separation microchannel was 5 cm × 300 μm × 300 μm, and in the end of channel was the detection cell. The filling solution pool, the wire cabin and the ADS were all embedded on the cover slip. The polyvinyl chloride (PVC) membrane was used as ion-exchange medium of reference electrode and installed between Au electrodes on the PCB substrate. The device assembly diagram and sensor structure were shown in Fig.1.

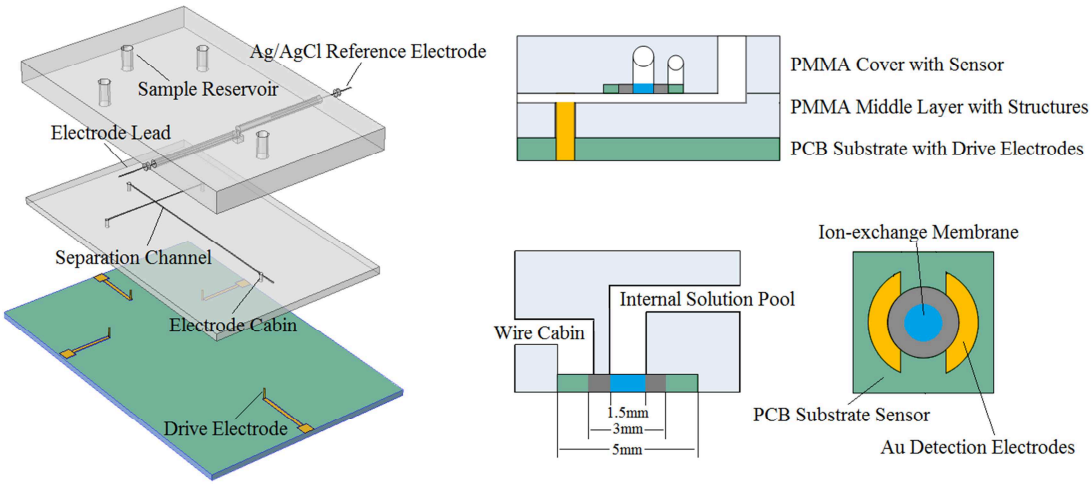


Figure 1. The device assembly diagram and sensor structure

Experimental

The PMMA with microstructures were fabricated by using micro precision engraving machine.Then, the device was bonded by a novel organic solvent fumigation bonding method [11]. The bonding process was described in briefly as follows. Pretreatment before bonding: cleaned substrates by ultrasonic, then protect no-need-bonding side of the cover sheet by polyimide tape; Cover sheet fumigation: put the cover sheet into the chloroform saturated steam and fumigated for 5minutes; Device bonding: remove the polyimide tape and assemble the fumigation cover sheet to the substrate with micro channel by using fixture, then put the fixture and the substrates into the oven, dried at 40 ℃ for 10 minutes. Finally, remove the fixture after dried, the bonding complete. The assembled chip and microscope photograph of channel were shown in Fig.2.

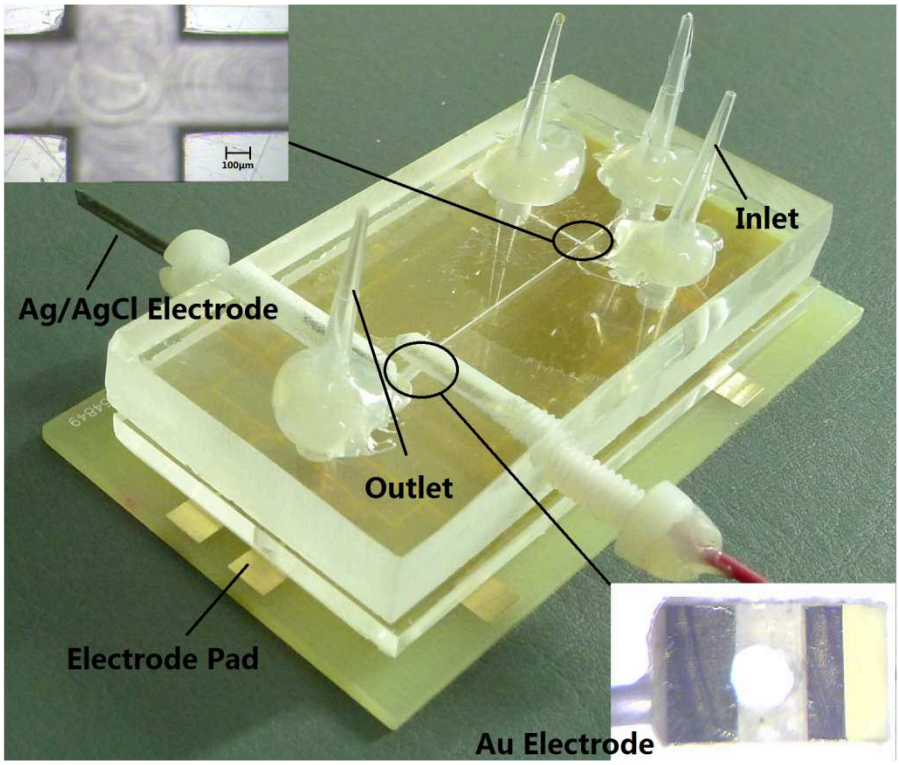


Figure 3.The assembled chip and microscope photograph of channel

Results and Discussion

Before assemble and install on the micro device, a series of tests were executed in the conventional scale electrolytic cell to characterize the ADS performance. The potential change experiment was utilized to the stability of Ag/AgCl reference electrode. The integration electrode was activated for 12 hours in the KCl solution. During activation, reference electrode potential change was measured every hour. Then, the potential changes of three samples were shown in Fig.3. From the Fig.2 we can see that, the potentials of all three sample electrodes were fluctuated in the range of 3.4 (mv)-3.6 (mv). It indicated that, the integration Ag/AgCl reference electrode which was used PVC membrane as ion-exchange medium had good stability.

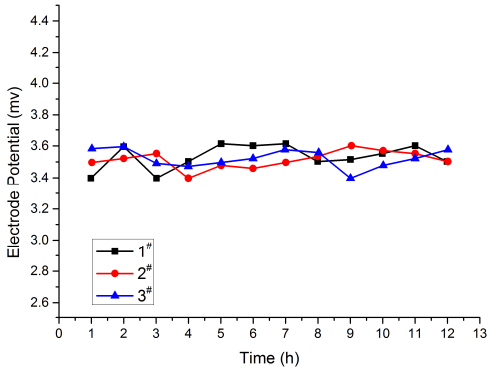


Figure 3. The Potential changes of integration reference electrode in 0.01mol/L KCl for 12h.

In the range of 5°C -80°C, the temperature response of the electrode reference was investigated by using KCl (0.01mol/L). The electrode potential and temperature fitting curve were shown in Fig.4. The curve shown that, the temperature and the electrode potential was a linear relationship.

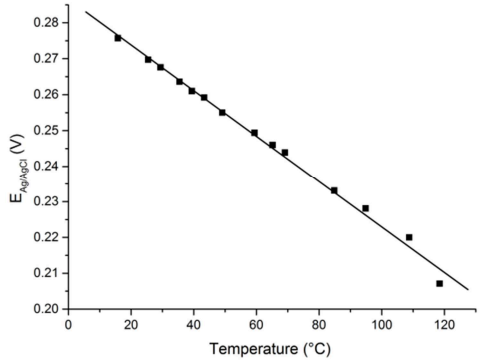


Figure 4. Potentials of the reference electrode at different temperature

In the Fig.5, there were three electrodes redox curves. The blue curve was the standard commercial ORP meter with the slope 0.987; the red was the curve of Pt wire electrode and the Ag/AgCl reference electrode, the slope was 1.065; the black one was the integration ADS, and the slope was 0.976. Slope of all the three curves are close to the theoretical value 1. The result shown that, the integration sensor can represent the redox potential of the solution accurately

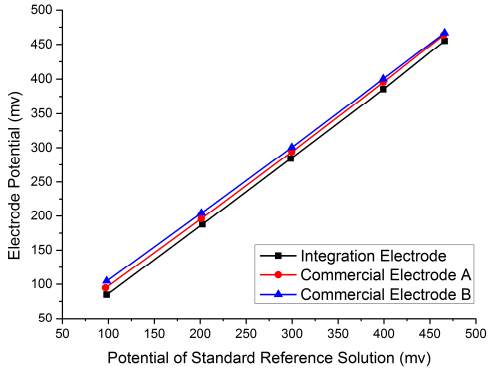


Figure 5. Standardization ORP for the three probes against three standard solutions

Finally, the Cyclic Voltammetry (CV) was used to test electrode performance in the 1×10^{-3} mol /L $K_4Fe(CN)_6$ and 1×10^{-3} mol /L $K_3Fe(CN)_6$. The CV curves were shown in Fig. 6. All the tests show that, the integrated reference electrode has a good reversibility, reproducibility and stability, it can provide an accurate reference potential to the microfluidic amperometric detection sensor.

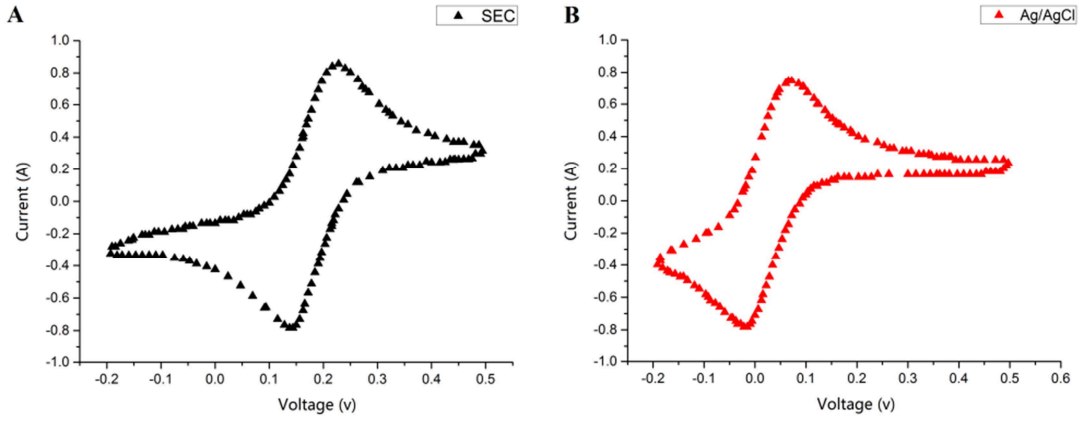


Figure 6. CV curves of the SCE and integrated Ag/AgCl reference electrodes in the 1×10^{-3} mol /L $K_4Fe(CN)_6$, 1×10^{-3} mol /L $K_3Fe(CN)_6$.

Conclusions

In this paper, a novel multilayer microfluidic device with amperometric detection sensor was proposed and validated. This device consists of printed circuit board (PCB) substrate with vertical embedded electrodes, the polymethyl methacrylate (PMMA) with micro structures and PMMA cover with amperometric detection sensor (ADS). The ADS were embedded within the cover, and used the polyvinyl chloride (PVC) membrane incorporating as ion-exchange medium. A series of tests were executed to characterize the ADS performance. The results shown that, the integration reference electrode can provide an accurate reference potential to the microfluidic amperometric detection sensor.

Acknowledgements

This work is supported by Natural Science Foundation of Heilongjiang Province under Grant No.F201007, “the Fundamental Research Funds for the central Universities” (Grant No.HIT.NSRIF. 2010077)

References

[1] Dykstra P H, Roy V, Byrd C, et al. Microfluidic electrochemical sensor array for characterizing protein interactions with various functionalized surfaces[J]. Analytical chemistry, 2011, 83(15): 5920-5927.
[2] Wang J N. A Microfluidic long-period fiber grating sensor platform for chloride ion concentration measurement[J]. Sensors, 2011, 11(9): 8550-8568.
[3] Kim J, Elsnab J, Gehrke C, et al. Microfluidic integrated multi-walled carbon nanotube (MWCNT) sensor for electrochemical nucleic acid concentration measurement[J]. Sensors and Actuators B: Chemical, 2013, 185: 370-376.
[4]Cardenas-Valencia A M, Dlutowski J, Knighton S, et al. Aluminum-anode, silicon-based micro-cells for powering expendable MEMS and lab-on-a-chip devices[J]. Sensors and Actuators B: Chemical, 2007, 122(1): 328-336.
[5] Liu B, Rieck D, Van Wie B J, et al. Bilayer lipid membrane (BLM) based ion selective electrodes at the meso-, micro-, and nano-scales[J]. Biosensors and Bioelectronics, 2009, 24(7): 1843-1849.
[6]Ul Haque A, Rokkam M, De Carlo A R, et al. Design, Fabrication and Characterization of an In Silico Cell Physiology lab for Bio Sensing Applications[C]//Journal of Physics: Conference Series. IOP Publishing, 2006, 34(1): 740.
[7] Shinwari M W, Zhitomirsky D, Deen I A, et al. Microfabricated reference electrodes and their biosensing applications[J]. Sensors, 2010, 10(3): 1679-1715.
[8] Polk B J, Stelzenmuller A, Mijares G, et al. Ag/AgCl microelectrodes with improved stability for microfluidics[J]. Sensors and Actuators B: Chemical, 2006, 114(1): 239-247.
[9] Chen Y P, Zhao Y, Chu J, et al. Fabrication and characterization of an innovative integrated solid-state microelectrode[J]. Electrochimica Acta, 2010, 55(20): 5984-5989.
[10] Zhou J, Ren K, Zheng Y, et al. Fabrication of a microfluidic Ag/AgCl reference electrode and its application for portable and disposable electrochemical microchips[J]. Electrophoresis, 2010, 31(18): 3083-3089.
[11] Zhang H, Liu X W, Tian L, et al. Organic Solvent Fumigation Bonding for Multi-Layer Poly (methyl Methacrylate) Microfluidic Device[J]. Key Engineering Materials, 2014, 609: 654-659.

Key Engineering Materials Vols 645-646 (2015) pp 741-745
© (2015) Trans Tech Publications, Switzerland
doi:10.4028/www.scientific.net/KEM.645-646.741

Submitted: 2014-11-04
Accepted: 2014-12-23

Optimization of Microfluidic Chip Bonding Technology Based on Polydimethylsiloxane

Jing Mao[1,2,a], Wei Chen[1,2,b], Long Zhao[1,2,c], Luxia Yang[1,2,d], Binzhen Zhang[1,2,e*]

[1]Key Laboratory of Instrumentation Science & Dynamic Measurement (North University of China), Ministry of Education, Taiyuan 030051, China

[2]Science and Technology on Electronic Test & Measurement Laboratory (North University of China), Ministry of Education, Taiyuan 030051, China

[a]13546349292@163.com, [b]willenchan@163.com,

[c]18334792157@163.com, [d]ylxfyz328@163.com

[e]zhangbinzhen@nuc.edu.cn(corresponding author)

Keywords： polydimethylsiloxane； Bonding strength； Microfluidic chip

Abstract. This paper introduce a new polydimethylsiloxan(PDMS) microfluidic chip bonding technology. By studying the influence of prepolymer with different curing agents, curing temperatures and curing time to the PDMS-PDMS chip bonding strength，we get the optimal bonding parameters. The experiment results show that when the cover plate of PDMS with ratio 15:1 bond with the substrate whose ratio is 10:1，the largest strength can be reached. The research which was applied to the packing of microfluidic analysis chip has achieved good results.

Introduction

In recent years, microfluidic chips have been extensively applied.They can integr-ate such a se ries of functions as sampling, enrichment, reaction and detection in only a microchip about some sq uare centimeters. Moreover, they consume much less samp-les and reagents and have greatly shorte ned the time of analyzing [1, 2, 3]. Traditional cell apparatus are bulky and expensive in the field of single cell analysis [4, 5], it's feasible and essential to design and manufacture microfluidic chip which based on polymer material, therefore the manufacture of biological microfluidic analytical chip, which is the key part, draws more attention. At present, the main makings of micro fluidic chips is PDMS.As a kind of cured macromolecule organic silicon compounds, it is generally inert, nontoxic and nonflammable. In the meantime, PDMSs have higher optical transparency and better bio-compatibility that they can copy the information of micro fluidic chips with high fidelity [6]. But efficient and rapid bonding of the substrate and the cover plates in PDMS microfluidic chip is needed to do further research.

At present, there are some bonding methods widely used including oxygen plasma surface treatment[7] and the coating of UV-curable adhesive photoresist [8], etc. The former method requires expensive equipment, then the latter can't be used in chips which are consisted of tiny structure. Mark A Eddings mentioned several bonding methods of different proportions in his paper, however he didn't compare the bonding strength of PDMS, which have different proportions [7]. The cover which made up of PDMS of 5:1 proportion is bonded with the substrate with 10:1 matching by Ye Mei Ying. She measured the bonding strength between the substrate and the solidified PDMS of 5:1 proportion in different time, without considering the other ratios of PDMS [9].

The varying curing ratio bonding is based on the principle that molecular of polymers with different concentrations will diffuse and then cross link with each other on their contact surfaces. During this procedure, the Brownian motion of PDMS make the polarity groups of molecular of polymers approximate each other that when the distances between them reach nanoscale, they can attract each other and then bond finally. This method has big advantages, which not only lower the requirement of lab's cleanliness in the process of PDMS-PDMS bonding, but also is suitable for mass production of microfluidic chip.

This paper does a research about the influence on the curing time of PDMS, which comes from the time and the proportions of prepolymer and curing agent. Then analyze the bonding strength after bonding between the cover plates of microfluidic chip, which made of prepolymer and curing agent in different mixing ratios, and the 10:1 PDMS substrate. After comprehensively considering the two factors (different ratios and curing time), the best bonding parameters have been obtained.

Bonding parameter optimizing of PDMS samples

Different ratios of PDMS curing in different temperature. Mix PDMS prepolymer in different proportions with curing agent, then degass it in the chamber evacuation for 10 minutes after stirring sufficiently. In order to make sure for better remove air bubbles in the mixture, let it rest for 30 minutes. After this, cast the mixture in PMMA (polymethyl methacrylate) mould, form 5 mm thick liquid layer, then cure it in the oven under different temperatures. Make a note of the time needed for solidifying of PDMS mixture in different mass ratios.

Under different temperatures, the required curing time for different proportions of PDMS mixture in PMMA moulds is shown in fig. 1.Under the same temperature, the lower the mass ratio of PDMS prepolymer and curing agent, the shorter of the time needed for curing. Under the same ratio, the higher the temperature, the shorter the curing time. It is suggested from the type SYLGARD184 PDMS of the company Dow corning that the mass ratio of prepolymer and curing agent is 10:1, the curing temperature is 50～100℃[9].From the experiment, it is obvious to see that the more the curing agent, after curing, the worse the elasticity. Too low temperature lead to too long curing time and difficulty demoulding. Too high lead to too short curing time and the difficulty of controlling the experimental condition. Therefore, in the subsequent experiments, we choose 75 ℃for the curing temperature.

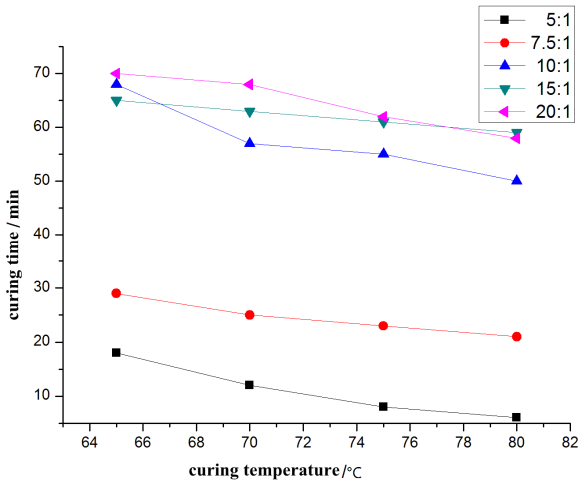


Fig. 1 The impact of curing temperature and ratio of PDMS on curing time.

Test of bonding strength between the cover plates in varying ratios and Substrate in the ratio of 10:1. Four experiments are set in this thesis. Four groups used cover plates , which the ratios are 5:1,10:1,15:1,20:1 respectively, bonding with 10:1 substrate.

Firstly, as shown in table 1, heat and solidify the cover, which has been degassed sufficiently and has taken fully rest, under 75℃ with different time. When it is not completely solidified, peel off the cover from the mold and combine with the completed substrate, then let it rest for 12 hours under 75℃. In order to enhance the bonding strength, some pressure was given to the samples. Then as shown in fig. 2, according to the national standard GB1040, use the electronic tensile testing machine(XLW(L) – PC) and the 12 bonded samples to carry out the bonding strength test. Set the drawing speed to 300 mm/min. Finally, use scanning electron microscope to observe the stripped morphology.

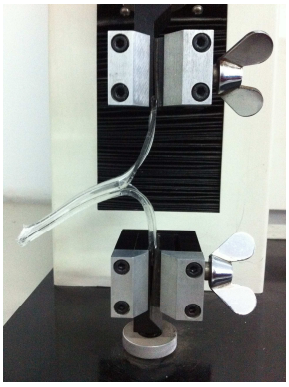


Fig. 2 Stripping plate used by"T"type stripping.

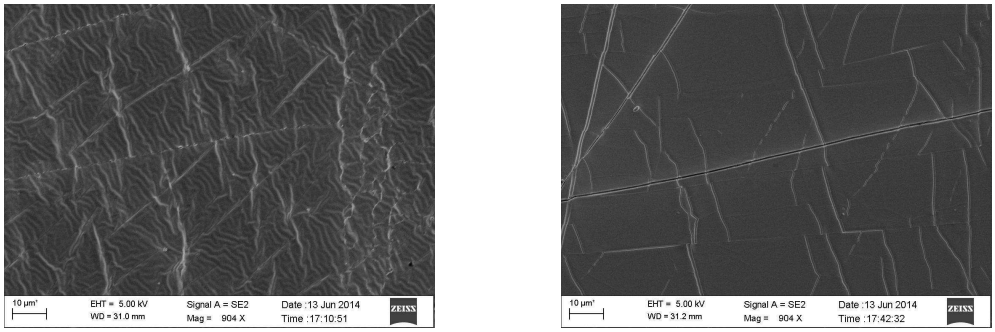
Tab 1 Average strength contrast of different ratios bonding

	Average bonding strength[kpa]	Curing time of cover plate[minute]	Curing time of substrate[minute]
A1	202	10	55
A2	185	15	55
A3	179	17	55
B1	114	35	55
B2	103	40	55
B3	98	45	55
C1	452	40	55
C2	423	45	55
C3	391	50	55
D1	410	55	55
D2	385	60	55
D3	406	65	55

The table1 indicates that the bonding strength is biggest at the ratio of 15:1.The VDW (Van der Waals' force) is induced based on several factors: the greater the density of the uncured prepolymer, the easier to diffuse into the substrate in the ratio of 10:1. The bonding strength of PDMS used for making substrate is although very big in the ratio of 20:1, but the curing time is longer, so this is not the best choice.

After peeling and observing the C1 samples and B3 samples under the electron microscope， we found that the wrinkles is on the peeled surface. (fig. 3) , the wrinkles of C1 samples are

intensive and deep. It is said that the bonding strength is bigger when taking this bonding parameters. It is consistent with the result of table 1.



(a) **(b)**

Fig. 3 SEM comparison of stripped morphology of PDMS.（a）stripped morphology of sample of C1.（b）stripped morphology of sample of B3.

Eventually, by proceeding a series of experiments, we acquire the optimal bonding parameters of PDMS-PDMS, that is, the mass ratio between the prepolymer and curing agent of substrate and cover plate are 10:1 and 15:1 respectively, the curing time under 75℃ is 55 minutes and 40 minutes respectively.

Bonding effect validation of microfluidic chip

Firstly, by using ultraviolet light carving craft to produce SU - 8 microfluidic chip master mould which is consist of both sides of the left and right sheath channel and sample flows channel(fig. 4) . Then cast on the structure with the 10:1 PDMS solution. The microfluidic chips PDMS master mould can be obtained after twice times of moulding (fig. 5) .

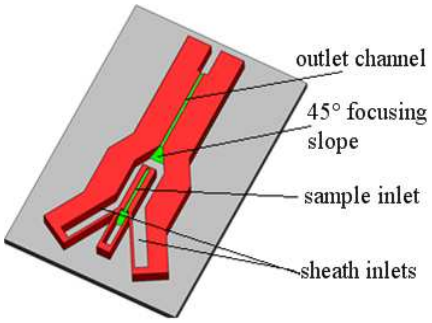


Fig. 4 Structure of microfluidic chip.



Fig. 5 PDMS master mould of microfluidic chip.

Bonding the microfluidic chip by taking use of the optimized parameters. Then inject the red Rhodamine B solution from the sample flows inlet to the chip structure and the colorless buffer solution in both sides. Finally，observe the sealabily and the liquidity.

From the fig. 6, it is obvious to see that it has good sealability when using this proportions for bonding of the chip. Besides, there is no liquid leakage from the side of the micro flow channel. In the meanwhile, there is no channel obstruction after bonding. The Rhodamine B solution can smoothly flow from sample inlet to focusing channel. Finally flow out from the outlet channel. The optimized bonding parameters are proved to be effective and reliable.

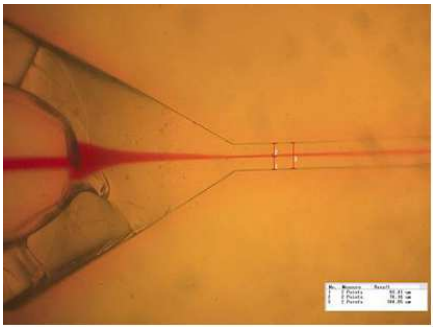


Fig. 6 Focusing effects of PDMS microfluidic channels.

Conclusion

A simple and efficient bonding method of different proportion is mentioned in this article. The strength of bonding of PDMS-PMDS is improved after parameter optimization. With the best parameters of bonding, It is easily to control the craft and realize mass production of microfluidic analytical chip.

Acknowledgement

The research work presented in this paper had been supported by a grant from National Science Foundation of China (Grant#61401405), (Grant#51475438), (Grant#61176115), Basic Research Priorities Program of Shanxi, China (Grant#2014011021-4) and Program for New Century Excellent Talents in University (Grant#130951862).

References

[1]K. Choonee, R.R.A.Syms, M.M.Ahmad, H.Zou, Post processing of microstructures by PDMS spray deposition, Sensor actuat a-phys. 155(2009) 253-262.

[2]Hsih Yin Tan, Weng Keong Loke, Nam-Trung Nguyen, A reliable method for bonding polydimethylsiloxane(PDMS) to polymethylmethylmethacrylate(PMMA) and its application in micropumps, Sensor actuat b-chem. 151(2010) 133-139.

[3]Bjorn Samel, M Kamruzzaman Chowdhury, Goran Stemme, The fabrication of full-wafer adhesive bonding using a poly(dimethylsiloxane)catalyst, J micromech microeng. 17(2007) 1710-1714.

[4]Anthony T.Design of a Microfluidic Chip for Three Dimensional Hydrodynamic Focusing in Cell Cytometry Applications[D].Concordia University, 2011.

[5]Mao X,Lin S C S,Dong C,et al. , Single-layer planar on-chip flow cytometer using microfluidic drifting based three-dimensional(3D)hydrodynamic focusing, Lab chip. 9(2009) 1583-1589.

[6]Cai D,Neyer A, Polydimethylsiloxane(PDMS)based optical interconnect with copper-clad FR4 substrates, Sensor actuat b-chem . 160(2011) 777-783.

[7]Mark A Eddings, Micheal A Johnson, Bruce K Gale, Determining the optimal PDMS–PDMS bonding technique for microfluidic devices, J micromech microeng. 18(2008) 1-4.

[8]Nea Yoon Lee, Bong Hyun Chung, Novel poly(dimethylsiloxane)bonding strategy via room temperature “chemical gluing”,J am chem soc. 25(2009) 3861-3866.

[9]Ye Meiying, Fang Qun, Yin Xuefeng , Fang Zhaolun, Studies On Bonding techniques f or Poly(dimethylsiloxane)Microf luidic Chips,Chem j Chinese u. 23(2002) 2243-2246.

Key Engineering Materials Vols 645-646 (2015) pp 746-755
© (2015) Trans Tech Publications, Switzerland
doi:10.4028/www.scientific.net/KEM.645-646.746

Submitted: 2014-12-23
Accepted: 2014-12-31

Applied Research on Self-sensing Micro-flow Injection Device based on Piezoelectric Ceramics

Jie HUANG [1, a], Liping SHI[2, b], Haimin ZHOU [3,c], Xiwen WEI[4,d], Yanbo WEI [5,e]

[1,2,3,4,5]School of Mechanical and Electrical Engineering, Heilongjiang University, Harbin 150080, China

[a] huangjie1510453@163.com,[b] shlp1971@163.com(corresponding author),
[c]zhouhm0919@163.com,

[d] wxw198806@163.com ,[e] weiyanbobo@163.com

Keywords: Piezoelectric Ceramics, Self-sensing, Micro-flow Injection

Abstract: Experimental research of first inverse, secondary positive piezoelectric effects are performed through the PZT-5 piezoelectric ceramics. Introduce a concept of self-sensing micro-flow injection device based on piezoelectric ceramics. Utilized the characteristic of the first inverse piezoelectric effect which can generate micro-displacement, micro-position and then micro-injection can be realized by the micro-change of piezoelectric ceramic's volume. Self-sensing displacement in micro-injection process can be obtained by utilizing the secondary direct piezoelectric effect. The experimental data: if the external voltages which were applied to the stack are 20V and 40V, the theoretical displacement generated by the first inverse piezoelectric effect are 4μm and 8μm respectively, the actual measured values are 3.57μm and 8.12μm respectively, self-sensing displacement of secondary direct piezoelectric effect are 1.48μm and 2.53μm respectively. It proves that the theoretical and experimental device could sense the displacement of micro-injection and the integration of sensor and actuator can be achieved.

1 Introduction

With the gradual maturity of microelectronics and micro-processing technology, micro-flow control system based on MEMS (Micro Electro Mechanical System) technology has gradually become the central investigated issue in recent years. Micro-actuators and micro-sensors based on piezoelectric, electrostatic and thermoelectric effects are the key components of MEMS [1].

MEMS-based micro-flow system in industrial control, bio-medical, precision electronics manufacturing and pharmacy fields have broad application prospects because of small size, low power consumption, high control accuracy characteristics. The traditional way to micro-flow inject is manual, relying on the operator using both hands to adjust while injecting under a microscope [2,3]. This mode of operation is not only wasting time for operator training, but also the accuracy affected by the experience and skill of the operator's. With the development of science and technology, the trend of micro-flow injection development is automation instead of artificial operation. It makes it easier and more accurate to control the microinjection process [4]. Higher automation, higher precision micro-injection devices are believed to be needed in large quantities because of the rapid development of gene injection, IVF and drug development technologies in the past decade [5-7].

The micro-flow injection system based on MEMS had been studied in this paper. This paper presents a new self-sensing micro-flow injection device which is designed by the principle of the

piezoelectric ceramic's first inverse, secondary positive piezoelectric effects for improving micro-manipulation techniques and tools. As an actuator, this device utilizes the characteristic of the first inverse piezoelectric effect can generate micro-displacement, then micro-position and micro-injection can be realized; as an sensor, self-sensing displacement in microinjection process can be obtained by utilizing the secondary positive piezoelectric effect, then integration of sensor and actuator can be achieved.

2 The principle of self-sensing micro-flow injection device

2.1 The relationship between piezoelectric effect and boundary condition

Only the boundary conditions are determined, it can decide the material's electrical and mechanical state, so it is necessary to determine the boundary conditions in the application of the piezoelectric ceramic. The piezoelectric ceramics can be in different electric boundary conditions (electrical open circuit, electrical short circuit) and mechanical boundary conditions (mechanical freedom, mechanical clamping) [8,9].

The controllable micro-flow injection device with fast response, high control accuracy, high resolution displacement mentioned in this paper is based on the principles of ceramics' first inverse, secondary positive piezoelectric effects. Piezoelectric effect is divided into positive effect and inverse effect: positive piezoelectric effect means that when the crystal is subjected by the external force in a fixed direction, internal polarization charge is generated, while the external force is removed, the crystal has returned to the uncharged state; inverse piezoelectric effect refers to the phenomenon of mechanical deformation of the crystal caused by the alternating electric field applied to the crystal. In order to study the integration of sensor and actuator, it is necessary to know the two-way effect in the same crystals (positive and inverse piezoelectric effect) [10]. Piezoelectric effect boundary conditions include electrical and mechanical boundary conditions, in which the electrical boundary conditions include electrical open circuit and electrical short circuit; mechanical boundary conditions include mechanical freedom and mechanical clamping. The electrical boundary conditions in this experiment: voltage-driven, the internal resistance of the piezoelectric material with respect to the equivalent resistance of the voltage source is very small, it can be seen as the boundary conditions of the piezoelectric body is electrical short-circuit. Mechanical boundary conditions: The prerequisite for piezoelectric material generating a piezoelectric strain applied the external electric field is the piezoelectric material in the mechanical freedom state, in this case, the piezoelectric material can deform freely. Hence, under the premise of freedom in the machinery and short in electricity, the piezoelectric crystals can produce the subsequent piezoelectric effects from the inverse piezoelectric effect.

2.2 The piezoelectric principle of micro-flow injection device

This paper analyzes the first inverse, secondary positive piezoelectric effects from the beginning of first inverse piezoelectric effect. That is to say, in the case of voltage-driven and mechanical freedom condition, if external electric field is E_n^{wai} applied to the piezoelectric crystal and external stress is zero, the piezoelectric effect process is as follows:

External electric field E_n^{wai} $\rightarrow$ Strain $S_i^{(1)}$: The first inverse piezoelectric effect.

Strain $S_i^{(1)}$ $\rightarrow$ Electric displacement $D_m^{(2)}$: The secondary positive piezoelectric effect from the beginning of the first inverse piezoelectric effect.

Applying the case of the first set of piezoelectric equations to analyze the first inverse piezoelectric effect:

$$S_i^{(1)} = d_{ni} E_n^{wai} \tag{1}$$

Where, d_{ni} is piezoelectric strain constant.

It can be obtained from the secondary positive piezoelectric effect and piezoelectric equations:

$$D_m^{(2)} = e_{mi} S_i^{(1)} = e_{mi} d_{ni} E_n \tag{2}$$

Where, e_{mi} is the piezoelectric stress constant.

Therefore, using equation (1), namely, the stroke and injection volume of micro-flow injection device can be controlled by the strain $S_i^{(1)}$ which is generated by the first inverse piezoelectric effect; using equation (2), namely, output displacement of the device can be sensed by the electric displacement $D_m^{(2)}$ which is generated by the secondary positive piezoelectric effect.

3 Experimental study of micro-flow injection device's piezoelectric ceramic

3.1 Laboratory equipment

The main equipments which are used in the experiments are as follows: Integrated precision positioning control system PPC-1CR0150 (BSJM), Piezoelectric ceramic (10*10mm), MDS Series LVDT Micrometer, YE6230T Series Data Acquisition Card and so on.

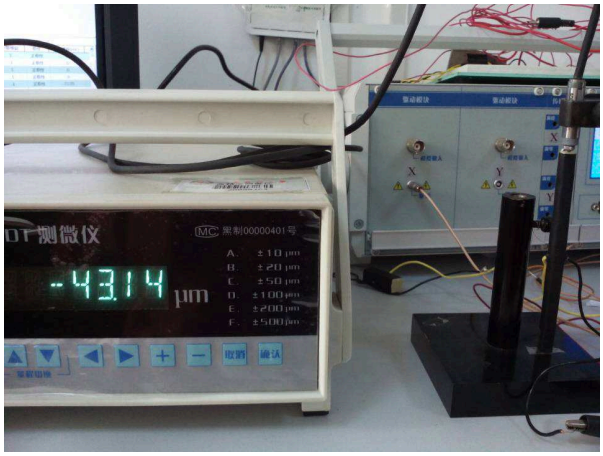


Fig. 1 Picture of laboratory equipment

Table 1 Basic parameters of the piezoelectric ceramic

Type	Piezoelectric constant (10^{-12}C/N)	Size (mm)	Pieces (piece)	Drive voltage (V)	Maximum driving force (N)
10*10	$d_{33} = 800$	$10 \times 10 \times 30.4$	250	0 ~ 100	4000

3.2 Experimental analysis of the first inverse piezoelectric effect

3.2.1 The experimental structure

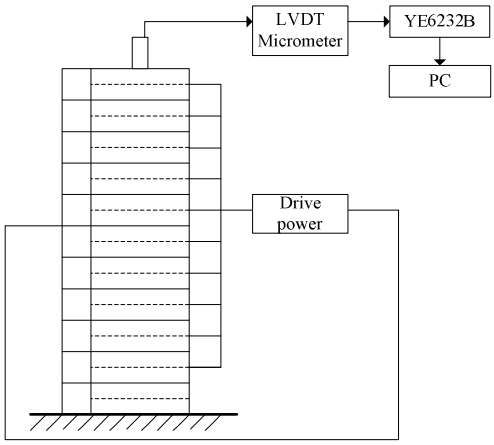


Fig. 2 Experimental structure diagram of the first inverse piezoelectric effect

3.2.2 First inverse piezoelectric effect of the piezoelectric ceramic

In the conditions of mechanical freedom and no external force, external electric field E_n^{wai} applied to the piezoelectric ceramic by using integrated precision positioning control system PPC-1CR0150 (BSJM), applying a range of 0~100V, step is 10V, measuring the displacement of piezoelectric ceramic by LVDT Micrometer, collecting the data by data acquisition card, data is transmitted to the computer for data processing finally.

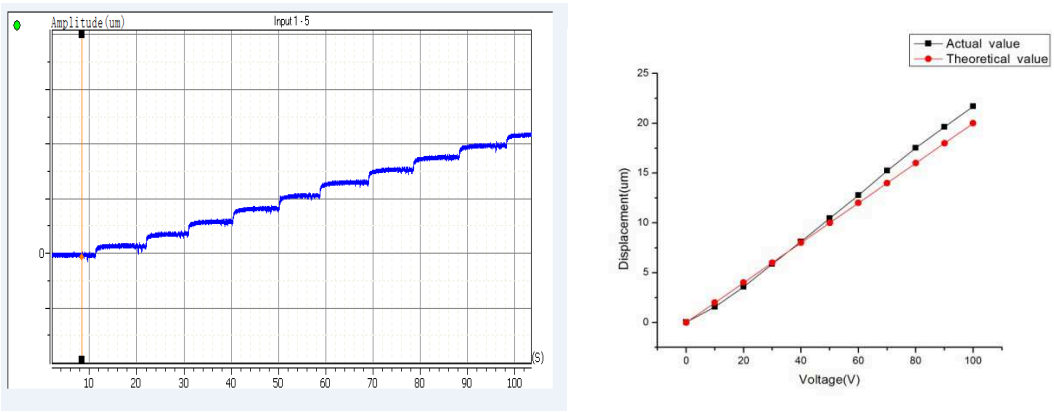


Fig. 3 Experimental data of the first inverse piezoelectric effect

The experiment shows the output displacement of the first inverse piezoelectric effect under external electric field. The theoretical value can be calculated from Eq.3.

$$\delta = nd_{33}V_3 \tag{3}$$

Where, δ is the displacement of the first inverse piezoelectric effect, n is the pieces number of piezoelectric ceramic, d_{33} is piezoelectric constant, V_3 is the driving voltage.

Table 2 The comparison between theoretical and actual displacement of the first inverse piezoelectric effect

Applied voltage (V)	10*10 Ceramic stack	
	Theoretical displacement (μm)	Actual displacement (μm)
0	0	-0.03
10	2	-1.57
20	4	-3.57
30	6	-5.86
40	8	-8.12
50	10	-10.45
60	12	-12.78
70	14	-15.24
80	16	-17.52
90	18	-19.62
100	20	-21.71

3.3 Experimental analysis of the secondary positive piezoelectric effect

3.3.1 The experimental structure

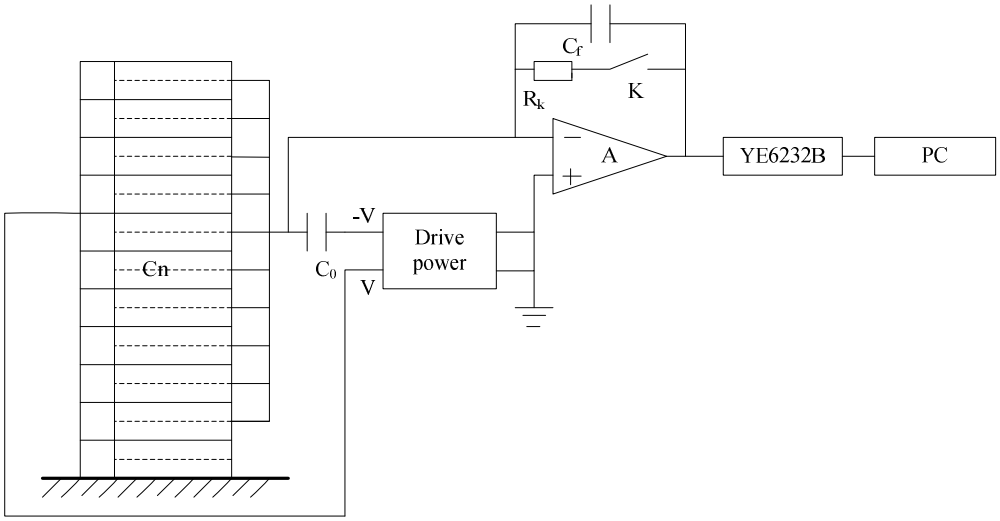


Fig 4 Experimental structure diagram of the secondary positive piezoelectric effect

3.3.2 Secondary positive piezoelectric effect of the piezoelectric ceramic

In the experiment of secondary positive piezoelectric effect, while the condition is mechanical freedom, the piezoelectric can produce displacement of first inverse piezoelectric effect, in addition to this, it also can generate an additional amount of charge of secondary positive piezoelectric effect.

In the experiment, equivalent capacitance of the piezoelectric ceramic Cn consists of two parts: 1. equivalent capacitance of the piezoelectric ceramic itself C_0 (generates charge Q_{C0}); 2.the increased capacitance portion C_2 (generates charge Q_{C2}).The two parts of the charge are separated by the experimental structure of Fig. 4. The charge generated in the capacitor Cn and the charge generated in the capacitor C_0 is equal but opposite. The charge which is collected by the integrator circuit just is Q_{C2} which is generated by the secondary positive piezoelectric effect.

The theoretical voltage of the secondary positive piezoelectric effect can be calculated from Eq.4.

$$V^{(2)} = \frac{Q^{(2)}}{C} = \frac{AD^{(2)}}{C} = \frac{Ae_{33}d_{33}V_3}{Ct} = \frac{Ae_{33}}{Ct}\delta \tag{4}$$

$$e_{33} = d_{33} y_{33} \tag{5}$$

Where, $V^{(2)}$ is the out voltage of secondary positive piezoelectric effect, $Q^{(2)}$ is the out charge of secondary positive piezoelectric effect, C is the equivalent capacitance of piezoelectric ceramics, A is the cross-sectional area of piezoelectric ceramics, e_{33} is the piezoelectric stress constant, d_{33} is the piezoelectric coefficient, t is the chip thickness of piezoelectric ceramics, y_{33} is elasticity.

Substituting the out voltage of secondary positive piezoelectric effect actual measured into Eq.4, by this way, the sensed displacement of secondary positive piezoelectric effect can be deduced.

Table 3 The comparison between self-sensing displacement of secondary positive piezoelectric effect and actual displacement of first inverse piezoelectric effect

Applied voltage（V）	theoretical voltage of secondary positive piezoelectric effect (mV)	actual voltage of secondary positive piezoelectric effect (mV)	self-sensing displacement of secondary direct piezoelectric effect（μm）	actual displacement of first inverse piezoelectric effect （μm）
0	0	0	0	-0.03
10	32.76	10.78	0.66	-1.57
20	65.52	24.27	1.48	-3.57
30	98.28	36.44	2.22	-5.86
40	131.04	41.47	2.53	-8.12
50	163.8	50.35	3.07	-10.45
60	196.56	72.67	4.43	-12.78
70	229.32	84.93	5.18	-15.24
80	262.08	97.16	5.93	-17.52
90	294.84	113.31	6.91	-19.62
100	327.6	125.64	7.66	-21.71

4 The design of microinjection device

4.1 Structural design

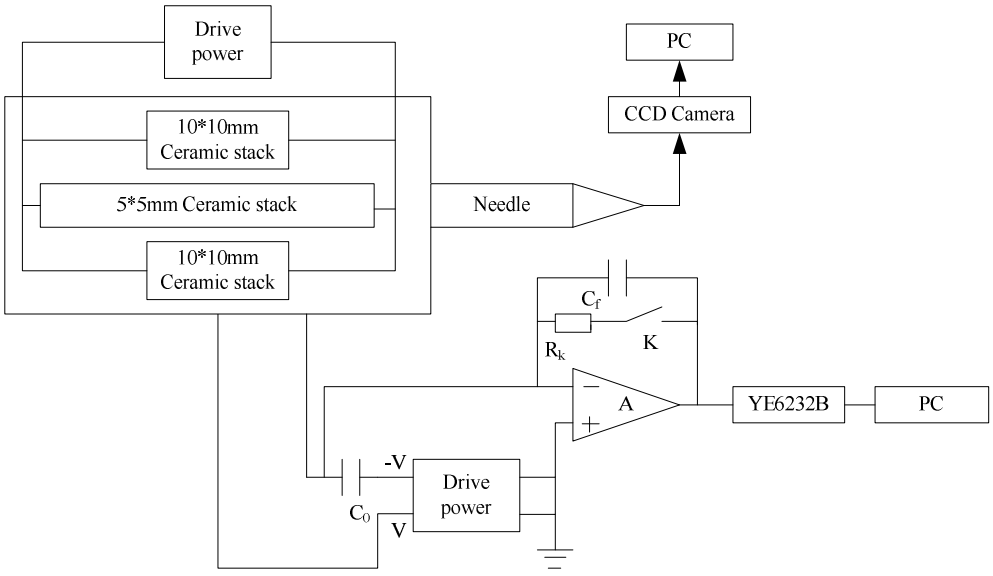


Fig. 5 Diagram of the Micro-flow injection system

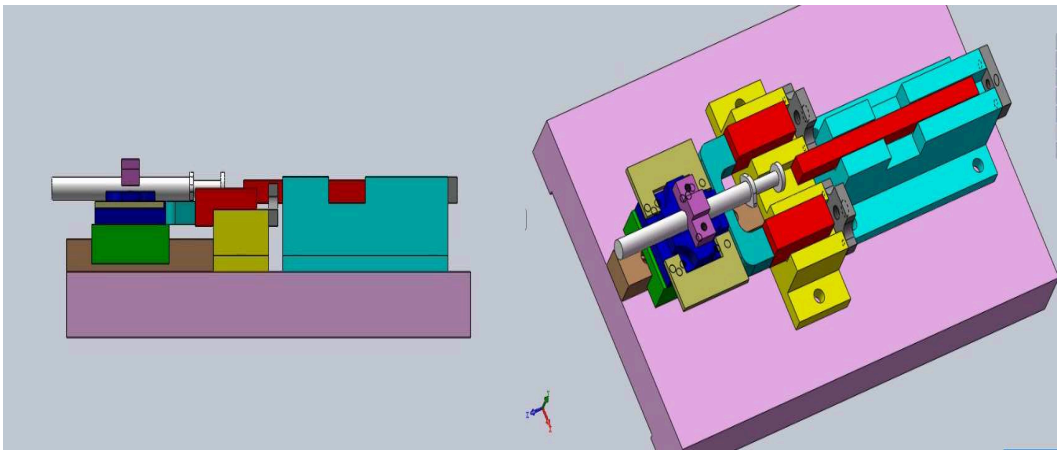


Fig. 6 Diagram of Micro-flow injection device structure

Experimental system including: Drive power, Digital micro flow injection device, Data acquisition card, CCD camera and PC. In these, micro-flow injection device structure is dominated by 5*5mm and 10*10 piezoelectric ceramics, Needle, Rail slider, Couplings and other components.

4.2 Experiment

As shown in Fig. 5 and Fig. 6:

1. Control the voltage which is applied to the 5*5mm piezoelectric ceramic, piezoelectric ceramic producing micro-displacement and then promoting the U-shaped block by the first inverse piezoelectric effect. Therefore, injection positioning is achieved by rail slider (syringe) moving.
2. Under the condition of sucker magnet energized (syringe fixed), control the voltage which is applied to the 10*10mm piezoelectric ceramic, piezoelectric ceramic producing micro-displacement and pushing the needle by the first inverse piezoelectric effect. Therefore, microinjection is achieved.
3. Sense the displacement of first inverse piezoelectric effect by the voltage of secondary positive piezoelectric effect. Therefore, the micro-movement amount of syringe and the micro-injection amount of drug injecting can be sensed.

4.3 Experimental data

The theoretical value can be calculated y substituting basic parameters of piezoelectric ceramic into the above Eq.3 and Eq.4. Experimental data can be measured by the experimental structure of the second part in this paper. As follows:

Table 4 Basic parameters of the piezoelectric ceramic

Type	Piezoelectric constant (10^{-12}C/N)	Size (mm)	Pieces (piece)	Drive voltage (V)	Maximum driving force (N)
10*10	$d_{33} = 800$	$10 \times 10 \times 30.4$	250	0 ~ 100	4000
5*5	$d_{33} = 800$	$5 \times 5 \times 103$	1000	0 ~ 100	1000

Table 5 The comparison between theoretical and actual displacement of the first inverse piezoelectric effect

Applied voltage（V）	10*10 Ceramic stack（1）		10*10 Ceramic stac（2）	5*5 Ceramic stack	
First inverse piezoelectric effect	Theoretical displacement（μm）	Actual displacement（μm）	Actual displacement（μm）	Theoretical displacement（μm）	Actual displacement（μm）
0	0	-0.03	-0.08	0	0.05
10	2	-1.57	-1.67	8	-5.98
20	4	-3.57	-3.88	16	-14.18
30	6	-5.86	-6.07	24	-20.95
40	8	-8.12	-8.96	32	-29.15
50	10	-10.45	-11.25	40	-37.13
60	12	-12.78	-13.06	48	-45.14
70	14	-15.24	-15.11	56	-53.06
80	16	-17.52	-17.34	64	-60.97
90	18	-19.62	-19.76	72	-69.05
100	20	-21.71	-21.85	80	-76.69

Table 6 The comparison between self-sensing displacement of secondary direct piezoelectric effect and actual displacement of first inverse piezoelectric effect

Applied voltage（V）	10*10 Ceramic stack（1）		10*10 Ceramic stac（2）		5*5 Ceramic stack	
	actual displacement of first inverse piezoelectric effect（μm）	self-sensing displacement of secondary direct piezoelectric effect（μm）	actual displacement of first inverse piezoelectric effect（μm）	self-sensing displacement of secondary direct piezoelectric effect（μm）	actual displacement of first inverse piezoelectric effect（μm）	self-sensing displacement of secondary direct piezoelectric effect（μm）
0	-0.03	0	-0.08	0	0.05	0
10	-1.57	0.66	-1.67	0.72	-5.98	2.87
20	-3.57	1.48	-3.88	1.52	-14.18	7.06
30	-5.86	2.22	-6.07	2.39	-20.95	10.33
40	-8.12	2.53	-8.96	3.23	-29.15	15.24
50	-10.45	3.07	-11.25	3.42	-37.13	18.37
60	-12.78	4.43	-13.06	4.84	-45.14	23.02
70	-15.24	5.18	-15.11	5.39	-53.06	27.34
80	-17.52	5.93	-17.34	5.78	-60.97	32.51
90	-19.62	6.91	-19.76	6.81	-69.05	35.28
100	-21.71	7.66	-21.85	7.76	-76.69	39.12

4.4 Analysis and Conclusions

A controlled micro-flow injection device is designed in this paper. This device utilizes the characteristic of the first inverse piezoelectric effect can generate micro-displacement and micro-position and then micro-injection can be realized by the micro-change of piezoelectric ceramic's volume. Self-sensing displacement in microinjection process can be obtained by utilizing the secondary direct piezoelectric effect, then integration of sensor and actuator can be achieved.

1. Under the action of the drive power, the 10*10mm stack can produce maximum displacement 21.7μm, 5*5mm stack can produce maximum displacement 74.69μm. The improved micro-flow injection device can be applied to cell microinjection as is known from the experimental data.

Animal cell diameter is about 20μm, nucleus diameter is about 5μm, Such data is fully capable to pierce the membrane.

2. According to the first inverse piezoelectric effect experimental data, the result generated by the first inverse piezoelectric effect and the applied external voltage are all linear with the external voltage, therefore the quantitative flow injection can be achieved by controlling the input voltage.

3. According to the secondary piezoelectric effect experimental data, the micro-displacement of the first inverse piezoelectric effect can be perceived by measuring the voltage of the secondary piezoelectric effect, therefore the movement amount and the injection amount can be controlled.

Found through Table 6, there are some errors between the values which should be equal. The main reasons are as follows: firstly, piezoelectric ceramic's inherent nonlinearity, hysteresis, creep and other characteristics affect the results; secondly, in the experiment of secondary positive piezoelectric effect, the capacitor C_0 should be equal to the piezoelectric ceramic capacitor in theory, but is not identical in practice, this also influences the results. However, even though there is a large error, self-sensing displacement of secondary direct piezoelectric effect and actual displacement of first inverse piezoelectric effect have proportional relationship. Experimenters can use this relationship to determine the movement amount and injection amount of this device.

5 Conclusions

The research of micro-flow injection device has practical significance, it can solve the problem of target location and flow quantification effectively and it can control the accuracy values of injection volume and the amount of displacement. These are not achieved by any manual operation. Piezoelectric ceramic stack will wear unavoidable due to prolonged be used, the gap between theoretical value and actual value will become increasingly larger, while it is tedious to manual disassemble. Self-sensing mentioned in this paper happens can solve this problem, the actual displacement value can be measured after the wear by self-sensing. On the one hand, all operations are realized by a computer which can reduce labor interference and improve the success rate of the injection; on the other hand, this device is simple to operate, does not require an experienced operator, easily formed to commercialize.

Acknowledgements

This work is supported by Heilongjiang Provincial Department of Education Science and Technology Research Project (12541624).

References

[1] SHI Yan-hua, HE Xiu-li, GAO Xiao-guang. MEMS Hot-film Micro Flow Sensor[J]. Micro and Nano Electronics,2013,50(7) , pp. 434-441.

[2] ZHU Li, HOU Li-ya, ZHANG Wei-yi. The Research of Digital Micro-injection Technology Which Is Based on Piezoelectric Drive[J]. Machine Tool & Hydraulics,2008,36(8) , pp. 17-20.

[3] Yanliang Zhang, Mingli Han, Cheng Yap Shee. Calibration of Piezoelectric Actuator-based Vision Guided Cell. International Conference on Advanced Intelligent Mechatronics, 2008:808-812.

[4] LIU Tian-jun. Piezoelectric-driven Microinjection Instrument[J]. Machine Design and Research, 2009, 25(10):42-44.

[5] Haibo Huang, James K. Mills, Dong Sun. A New Piezo-driven Ultrasonic Cell Microinjection System. International Conference on Ingormation and Automation, 2010:18-23.

[6] HE Si-min, CHE Xiu-ge, ZHAO Xin. Ultrasonic Vibration Microscopic Penetration System Based on Piezoelectric Actuator[J]. Chinese Control Conference, 2012, 6(25):5036-5041.

[7] LI Yang-min, TANG Hui, XU Qing-song. Micromanipulator Technology Development Trend For Biomedical Application [J] ,2011,47(23): 1-13.

[8] WEN J M, MA J J, ZENG P. The production and performance test of piezoelectric rotary actuator[J]. Optics and Precision Engineering, 2013,21(1):131-136.

[9] ZHANG F X, WANG L K. Modern Piezoelectric Study[M]. Beijing: Science Press, 2001.

[10] SHI L P, SUN L N, RONG W B. Application of the First Converse and Secondary Positive Piezoelectric Effect in Self-sensing[J]. Nanotechnology and Precision Engineering. 2010, 8(3):211-214.

[11] HAN Tong-peng, LI Guo-ping, SHEN Jie. The Research of Precise Positioning Technology Which Is Based on Piezoelectric Ceramic Actuator[J]. Sensors and Microsystems, 2010,29(2), pp. 51-53.

Key Engineering Materials Vols 645-646 (2015) pp 756-760
© (2015) Trans Tech Publications, Switzerland
doi:10.4028/www.scientific.net/KEM.645-646.756

Submitted: 2014-12-03
Accepted: 2014-12-23

Iron wear particle content measurements in process liquids using micro channel - inductive method

BO Zhao[1, a], ZHANG Xing-ming[1, b], ZHANG Hong-peng[1, c*], LIU En-chen[1, d], Chen Hai-quan[1, e]

[1]Marine Engineering College, Dalian Maritime University, Dalian Liaoning 116026, China

[a] 15941178340@163.com , [b] zhangxingming1985@163.com ,

[c] zhppeter@163.com (corresponding author), [d] 574298919@qq.com ,[e] chenapec@163.com,

Keywords: micro channel - inductive method, iron wear particle, content, hydraulic oil

Abstract. A detection chip is designed and manufactured to study the relationship between iron wear particle content in hydraulic oil and the detected variation of average inductance, which detects content of iron wear particle by means of micro channel - inductive. Through experiments, we obtained inductive values in the cases. The case is that the sizes of iron wear particle are the same, while the content of iron wear particle are different. Thus the curve between content of iron wear particle content and variation of average inductance was drawn. Experimental results show that the inductance value increases with the increase of the iron wear particle content in hydraulic oil. Experiments prove that the way is feasible for the detection of iron wear particle content in hydraulic oil. This study has an important significance for the realization of iron wear particle content detection in hydraulic oil.

Introduction

Detection of iron wear particle in oil has become the main content of oil detection [1-2]. The current oil detection contains iron spectrum measurement analysis, pollution gravimetric method, microscope comparison method, and particle counting method [3]. Online detection methods can be mainly divided into ultrasonic testing method, capacitance detection method and inductance detection method. Because the micro-inductor has the advantages of high sensitivity, easy integration and modularization, and it is applicable to the measurement of displacement, velocity measurement, angle measurement, nondestructive testing. Therefore, the use of micro-inductor in oil detection has attracted more and more attention [4-6]. In the process of the production, the cutting or wear particle produced by the friction pairs of mechanical equipment, suspended in the oil system, along with the change of time and different wear condition, composition, size, density, shape parameters of them are changing [7]. For the detection of iron wear particle mainly concentrated in the composition and size, while the study of morphology and concentration is rare. Because of the limitation of the sensor precision, only the large iron wear particle will destroy the balance between the inductance sensor coils, so as to achieve the counting of iron wear particle, but for the more micro iron wear particle, counting temporarily unable to realize.

However it also can cause great harm when the tiny particle content reaches a certain degree. Therefore if we can realize the content detection of small iron wear particle, it will be great meaningful in the industrial production. Based on the above reasons, the paper put forward the

micro channel - inductance method which can detect the iron wear particle during the content is different, test and verify the feasibility of this method.

Theoretical Analysis

When the hydraulic oil mixed with iron wear particle flows through the coil, the iron wear particle in the hydraulic oil will change the coil inductance value, so the method by monitoring the coil inductance value and its variation can realize the detection of iron wear particle in hydraulic oil, as shown in figure 1.

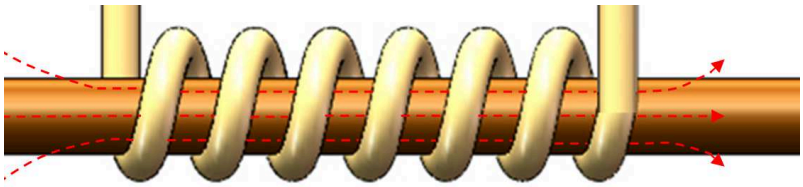


Fig.1 Schematic diagram of the electromagnetic detection

When the iron wear particle flows through the solenoid coil, the inductance will put the metal particle magnetization. The magnetized particle produces new magnetic, which lead to an increase in the total magnetic field intensity. So when the iron wear particle through the coil, we can realize the detection of iron wear particle according to the change of the equivalent inductance value. When the content of tiny iron wear particle reaches a certain degree, it can be equivalent to large iron wear particle, which upset the balance due to inductive worth changes. Through analysis, the larger the content of iron wear particle, the greater the inductance value change. The mathematical expression between the variation of inductance value and particle size is shown in literature [8-10]. Based on the above reasons, the paper put forward the micro channel-inductive method to detect the content of iron wear particle in hydraulic oil.

The fabrication of micro channel detection chip

The experiment uses the optimal micro channel oil detection chip mentioned in the literature [11]. The import of detection channels designed streamlined, so that oil sample flows through the chip area quickly without retention. PDMS is used to forming the flow since its low cost of fabrication and its superior optical properties [12].The micro channel detection chip mainly includes the solenoid type inductance coil, detection channel, oil import and export, and so on. The detection coil is a key element of the whole chip, it undertakes the monitoring and transfer the signal to the monitoring task of particles, the coil performance also determines the sensitivity of detection.

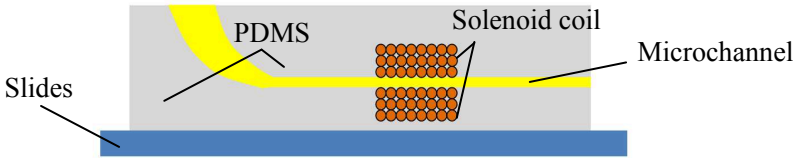


Fig.2 Schematic of microfluidic detection chip

In the experiment, the test chip micro channel - inductance sensor is a solenoid type. The chip is composed of copper wire with diameter of 25 μm and turn around 600 turns (According to the theory of state, the actual manufacturing process and the requirements, we determine the above parameters). Considering the detection sensitivity, machining accuracy and selected particle's continuous flow condition, the micro detected channel diameter is 300 μm.

The configuration of test oil sample

Since the content of iron wear particle in the experiment is low, the Precisa electronic balance is used for the configuration of test oil sample. The oil sample configuration data are listed in the following table 1:

Tab.1 Configuration data of experimental oil sample

Content of metal wear debris[%]	0.1%	0.3%	0.5%	0.7%	0.9%
The quality of metal wear debris[kg]	0.0263	0.1113	0.1037	0.1110	0.1443
The total quality of oil sample[kg]	26.3021	37.1263	20.7417	15.8503	16.0828
The actual content[%]	0.0010	0.0030	0.0050	0.0070	0.0090

Configured oil samples can be used in the experiment for the error of iron wear particle in the allowed range.

The manufacture of detection system

Experimental detection system manufactured in accordance with Figure 3. This system is composed of the syringe pump, microfluidic detection chip, the LCR impedance analyzer (Aglient E4980A, Santa Clara, CA) and the computer. Oil sample to be tested pass through the detection system driven by syringe pump. Two joints of the coil are connected with the LCR impedance analyzer. The signals measured with appropriate frequency being fed into the computer for display and storage. Impedance analyzer provides not only the alternating current into inductive coil, resulting in an alternating magnetic field, but also can record timely the changes in the amount of equivalent inductance in the coil. In view of that the restrictions under the instrument itself and the inductive signal interfered by external environment, the detected signals are of the high frequency interference noise and baseline drift phenomenon. Thus the LabVIEW software is used to signal processing and programming [13-14].

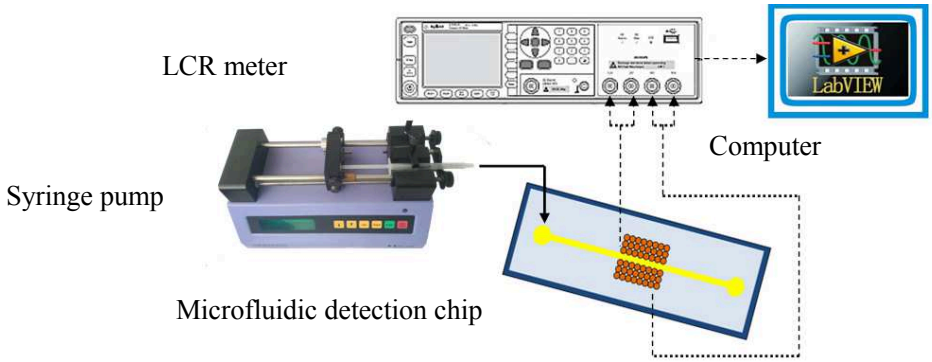


Fig.3 Schematic diagram of the detection system

Experimental procedures

In the experiment, configured oil passes through the detection system descending in accordance with the content of iron particles. Specific experimental procedure is as follows:

1. Measure resistance between two joints of microchannel - inductive chip. The chip is available because the measurement result is 64.6 Ω ;
2. The configured oil should be in the good uniformity;
3. Connect the detection system according to Figure 3;
4. Adjust the frequency of Aglient E4980A to 2MHz, the voltage to 2V and the detection method to series Ls-Rs;

5. The configured oil passes through the detection system descending in accordance with the content of iron particles. The oil flow slowly through the chip at a rate of 0.5mL/min by using syringe pump;
6. Record the detected inductance value, and do some analysis of the data.

Tab.2 Inductance test data of different content oil samples

Content of wear particle [%]	No	0.1	0.3	0.5	0.7	0.9
The average inductance [μH]	85.3816	85.3890	85.3926	85.4034	85.4231	85.4366
Inductance value basis [μH]			85.3816			
The variation of average inductance [nH]		7.4130	11.0115	21.7805	41.4690	54.9870
Error bars [nH]		2.4286	3.5772	4.8460	6.6015	6.8732

Experimental data are shown in table2. Keep the external conditions and the advancing speed consistent during measurement. Five kinds of hydraulic oil with different content pass through the micro channel inductor type detection system and measured respectively. After each oil sample flowing, the pure oil will pass through it to ensure accurate experimental data.

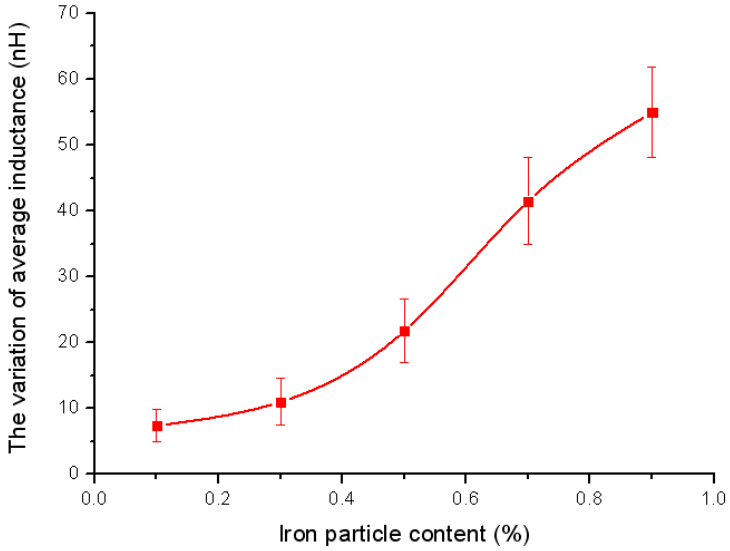


Fig.4 Curve between inductance variation with iron wear particle content

The curve shown in figure 4 indicates the relationship between the variation of average inductance (nH) and the content of iron wear particle which is drawn according to the data gained in the experiment. Experimental results consistent with prior speculation. With the increase of iron wear particle content, the variation of average inductance will increase since that it corresponds to a larger particle.

Conclusions

According to the results, the curve between the variation of average inductance with iron wear particle content can be drawn. As is shown in the figure 4, the variation of average detected inductance increases with the increase of iron wear particle content. The detection method which based on the principle of micro channel-inductance is suitable for the detection of iron wear particle content in hydraulic oil. This method is expected to use in the field of ship hydraulic oil monitor due to its advantage of quick, accurate, and low cost.

Acknowledgement

The experiments were carried out in the microfluidic chip laboratory of Dalian Maritime University. The study is financially supported by the National Natural Science Foundation of China (51205034), Ministry of Transport of the People's Republic of China (2013329225260) and the Fundamental Research Funds for the Central Universities (3132014332).

References

[1] Bozchalooi I S, Liang M. Enhancement of the signals collected by oil debris sensors[C]//American Control Conference, 2008. IEEE, 2008: 2810-2815.

[2] Du L, Zhe J. A high throughput inductive pulse sensor for online oil debris monitoring[J]. Tribology International, 2011, 44(2): 175-179.

[3] Zhang H, Chon C H, Pan X, et al. Methods for counting particles in microfluidic applications[J]. Microfluidics and nanofluidics, 2009, 7(6): 739-749.

[4] Du L, Zhe J. A high throughput inductive pulse sensor for online oil debris monitoring[J]. Tribology International, 2011, 44(2): 175-179.

[5] Zhang H, Huang W, Jin J, et al. Debris Detection in Hydraulic Oil Using a Microfluidic Inductive Pulse Device[C]//ASME 2012 Third International Conference on Micro/Nanoscale Heat and Mass Transfer. American Society of Mechanical Engineers, 2012: 51-57.

[6] FAN H, ZHANG Y, LI Z, et al. Study on magnetic characteristic of ferromagnetic wear debris in inductive wear debris sensor[J]. Tribology, 2009, 29(5): 452-457.

[7] TUCKER J E, GALIE T R, SCHULTZ A, et al. LASERNET fines optical wear debris monitor: a navy shipboard evaluation of CBM enabling technology[C]. 54th Mach Fail Prev Technol Proc ,2000: 191.

[8] Zhang H P, Huang W, Zhang Y D, et al. Design of the microfluidic chip of oil detection[J]. Applied Mechanics and Materials, 2012, 117: 517-520.

[9] YAN H, ZHANG Y. The Design of an On-line Monitoring Sensor of Wear Mental Particals and the Analysis of Its Characteristic[J]. Journal of Transcluction Technology, 2002, 4: 014.

[10] Du L, Zhe J. Parallel sensing of metallic wear debris in lubricants using undersampling data processing[J]. Tribology International, 2012, 53: 28-34.

[11] Zhang X, Zhang H, Sun Y, et al. Research on the Output Characteristics of Microfluidic Inductive Sensor[J]. Journal of Nanomaterials, 2014, 2014.

[12] Gui L, Ren C L. Exploration and evaluation of embedded shape memory alloy (SMA) microvalves for high aspect ratio microchannels[J]. Sensors and Actuators A: Physical, 2011, 168(1): 155-161.

[13] ZHANG H P, ZHANG X M, GUO L. Design of the oil detection microfluidic chip[J]. Chinese Journal of Scientific Instrument, 2013,34(4):762-767

[14] Song Y, Li M, Yang J, et al. Capacitive detection of living microalgae in a microfluidic chip[J]. Sensors and Actuators B: Chemical, 2014, 194: 164-172.

Key Engineering Materials Vols 645-646 (2015) pp 761-765
© (2015) Trans Tech Publications, Switzerland
doi:10.4028/www.scientific.net/KEM.645-646.761

Submitted: 2014-10-29
Accepted: 2014-12-23

Fluid dynamic analysis on solar heating error of radiosonde MEMS humidity measurement

Xiaoli Mao[1, a], Jiahong Zhang[1,b*], Min Li[1], Shaorong Xiao[2,3] and Qingquan Liu[1,2]

[1]School of Electronic and Information Engineering, Nanjing University of Information Science and Technology, Nanjing 210044, China

[2]School of Atmospheric Physics, Nanjing University of Information Science and Technology, Nanjing 210044, China

[3]School of Physics and Optoelectronic Engineering, Nanjing University of Information Science and Technology, Nanjing 210044, China

[a]mxl426@163.com, [b]zjhnuist@163.com

Keywords: MEMS humidity sensor, solar radiation, error correction, computational fluid dynamics

Abstract. The dry bias of MEMS humidity sensor induced by solar radiation heating seriously affects the accuracy of the relative humidity(*RH*) measurement. To solve this problem, this paper presents a novel numerical analysis method for the error correction of *RH* based on computational fluid dynamics(CFD). Firstly, considering the solar radiation, the distribution of temperature field of MEMS humidity sensor is simulated from the ground to 32km altitude by using CFD soft under the boundary condition of fluid-solid coupled heat transfer. Secondly, the numerical analysis model of *RH* is put forward for solar radiation dry bias(SRDB) correction based on the working principle of the MEMS capacitive humidity sensor and the definition of *RH*. The results of numerical analysis show that the error of *RH* caused by solar radiation is nonlinearly increased with the altitude. Meanwhile the errors decrease with the reflectivity of sensor or of solder point increase. The simulation data also indicate that the SRDB can be reduced by improving the reflectivity of sensor or of solder point, adopting the substrate material with high thermal conductivity or choosing the suitable thickness of sensor. However, the SRDB should be corrected, for it still is more than 20% under the low atmospheric pressure. In this paper, the method based on fluid dynamics simulation provides a new way to correct the error of radiosonde MEMS humidity measurement caused by solar radiation heating.

Introduction

In recent years, natural disaster occurred frequently and has seriously affected people's production and daily life. Numerical weather prediction and climate analysis can provide important information for early warning of natural disasters, which strongly rely on the accurate measurement of high-altitude meteorological elements[1-3]. Radiosonde has been early adopted in high-altitude sounding since the 1920s. With the development of technology, meteorological aircraft, meteorological rocket and meteorological satellite was adopted gradually. Nonetheless, radiosonde is the only means of high-altitude sounding for a long time, and still in use, which provides important data self-evidently[4]. At present, high-altitude meteorological elements, such as temperature, wind speed, air pressure, have been measured with high precision. While the measurement precision of humidity is relatively low due to the lack of technology and process, and the influence of environment[5]. However, the accurate measurement of humidity profile is very crucial for precipitation forecast[6,7]. And it is also indispensable for the formation and forecast of fog.

Finland Vaisala company has been committed to study on the upper-air sounding. A new generation of radiosonde RS92 adopts the twin MEMS capacitive humidity sensors(HUMICAPS). In order to remove the measurement error caused by ice and water on the hygrometer, two sensors are alternatively heated. In the case, the SRDB[8,9] can not be ignored. In this paper, taking the humidity sensors of RS92 as the calculation model, we discuss the above problem using the CFD method[10],

and the influencing factors on the solar radiation error include the reflectivity of the MEMS humidity sensors, solder reflectivity, substrate material and the thickness of the sensor. Finally a new method was proposed to correct the error caused by solar radiation heating.

Radiation error correction theory and research methods

As shown in fig. 1, RS92 radiosonde is equipped with twin HUMICAPS designed to remove ice and water on the hygrometer through alternative heating of the two sensors. Due to the lack of radiation shield, solar radiation heating is more likely to occur, resulting in a dry bias to the measured *RH*[11]. So it is necessary to correct the SRDB of *RH* measurement data.

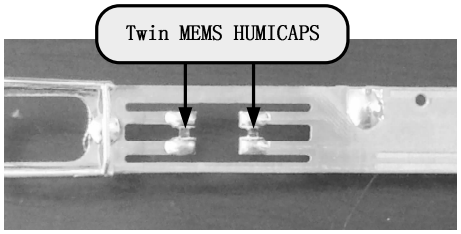


Fig.1. RS92 radiosonde equipped with twin HUMICAPS

The definition of *RH* can be represented as

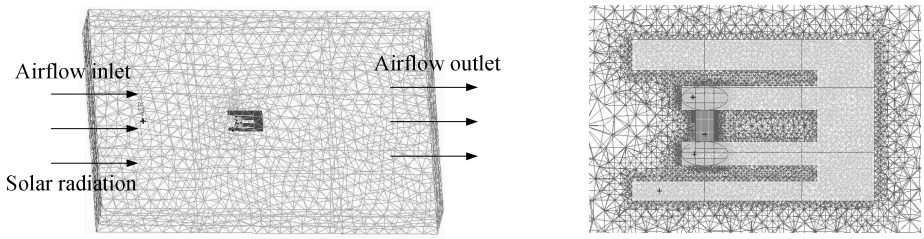
$$RH = e / e_s(T) \tag{1}$$

where e is the vapor pressure and $e_s(T)$ is the saturation vapor pressure at air temperature T. The temperature around the humidity sensing film is higher than the actual environment temperature owing to the solar radiation heating. As a consequence, the *RH* value measured by the humidity sensor is not the right value at the actual environment temperature, which is provided by the temperature sensor on the same radiosonde. Thus, the solar radiation error of measured *RH* data should be corrected. It is assumed that the temperature of air is T at altitude H, and ΔT is a temperature rise around the humidity sensing film due to the solar radiation heating. Using the Goff-Gratch formula, we can obtain the saturation vapor pressure $e_s(T)$ and $e_s(T+\Delta T)$ which are before and after solar radiation heating respectively. If the vapor pressure is e, the relative humidity is $RH_0 = e / e_s(T)$ according to the definition of *RH*. However, the *RH* value provided by HUMICAPS is $RH_1 = e / e_s(T+\Delta T)$. The relative error of RH r can be derived as:

$$r = \frac{RH_1 - RH_0}{RH_0} = \frac{e_s(T+\Delta T) - e_s(T)}{e_s(T)} \tag{2}$$

As can be seen from Eq. (2), the relative error of *RH* r is directly related to air temperature at altitude H and the temperature rise ΔT caused by solar radiation heating. That is to say, the SRDB can be researched by simulating the temperature field distribution of the humidity sensor. By using CFD commercial software package Fluent, we get the temperature error caused by solar radiation heating varying with different influencing factors. Thus, the relations between the SRDB of *RH* measurement and influencing factors are derived from Eq. (2).

Firstly, the calculation model is established by using 3D CAD software Pro/E. After comparison, we find that the simplified model (only a humidity sensor) has no effect on the results of numerical simulation because of the symmetry of two sensors. In view of calculation precision and scale, the size of the air domain generally take 10 times of that of sensor domain. Secondly, the grid division of the model is carried out with software ICEM as shown in fig.2. In fig.2(a), the model of sensor is in middle of calculation domain and airflow is around the sensor. The left is the entrance of airflow while the right is the export. The solar radiation direction is in the same direction of air inlet. In order to accurately capture the physical phenomena in the boundary layer, a boundary layer grid technology is implemented. Fig.2(b) displays the interface of local grid refinement which can improve the calculation accuracy of the simulation.



(a) The entire grids (b) Local refinement grids

Fig.2. The grids of the simplified model and air domain

Finally, the file of the divided mesh is imported to software Ansys Fluent for numerical simulation. Ansys Fluent widely used in various fields is a powerful tool to deal with computational problems of complex flow and heat transfer. The steady state heat transfer model of radiosonde humidity sensor is established with Fluent. Then the convection-solar radiation coupled thermal boundary conditions are adopted in the numerical simulation for analysis of fluid-solid coupled heat transfer. Through Fluent simulation we get the temperature field distribution around the humidity sensor which displays the relation between the temperature of humidity sensor and the altitude. According to Eq.(2) , then we can deduce the relative error of humidity measurement due to temperature change caused by solar radiation.

Fig. 3 displays the distribution of temperature field around the sensor at altitude 20km under certain condition considering solar radiation heating. Obviously, due to the effect of solar radiation heating, the temperature of the humidity sensor is 2 degrees higher than that of the surrounding air. The temperature of wet air exchanging water vapor with the sensing film of humidity sensor is higher than the actual temperature of the surrounding air. Based on radiation error correction theory, it is necessary to correct the SRDB as the measurement value of humidity is obviously less than true value. Next, we focus on investigating the relationships between SRDB and the altitude, the reflectivity of sensor, the reflectivity of solder point and the substrate material.

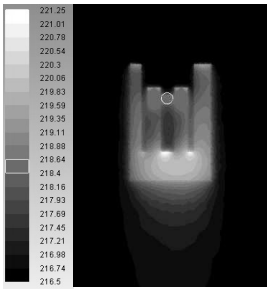


Fig.3. The temperature field distribution of computation domain at altitude 20km

Results and discussion

As we know, the solar radiation dose is related with the solar elevation angle (SEA), and the SEA is closely related to the latitude of the observation location and the solar declination. This paper assumes that Nanjing is the observation location where the latitude is 32 degrees and the date is 21 June (the sun declination is about 23.4 degrees). In the case, the solar radiation dose is calculated combined with the solar constant. The radiosonde rotate round with air flow in the process of balloon rising. Assuming that the sensor rotate at a constant speed, then the effective area to receive the solar radiation can be equivalent to radiation area with a solar incident angle .

Assuming that the sensor material is ceramic (Al_2O_3), Fig. 4 and 5 reveal the influences of the sensor reflectance and solder reflectance on the SRDB, respectively. First of all, two figures show that the relative error of humidity increases with the altitude, which means the SRDB is more significant in the upper air. Fig. 4 indicates that the SRDB decreases obviously with the increase of humidity sensor reflectance. The reason is that the absorption rate of material is lower with its higher reflectivity, leading to the lower temperature rise caused by the solar radiation heating, thus the SRDB decreases. Moreover, the effect of the reflectivity of sensor and solder gradually increases in the low altitude. Above 12 kilometers, the reduction of solar radiation error is in the same ratio to the

increment of the reflectance. Similar to Fig. 4, Fig. 5 demonstrates that the solar radiation error decreases with the solder reflectivity increasing, which is slightly larger than that caused by sensor reflectance increase. This result reveals that the SRDB can be reduced by improving the reflectivity of solder if the sensor reflectivity can't be increased when designing the humidity sensor.

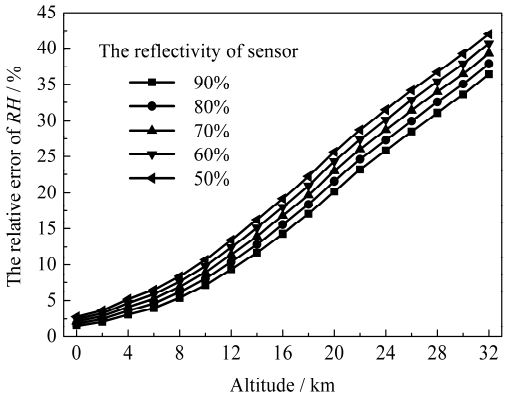


Fig. 4 The effect of humidity sensor reflectivity on the solar radiation error

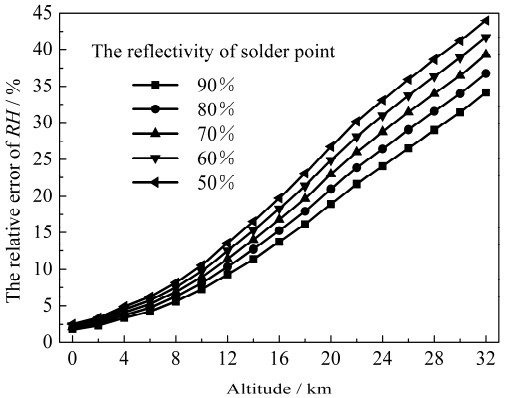


Fig. 5 The effect of solder point reflectivity on the solar radiation error

As we know, the key material of the HUMICAPS is humidity sensing film which has been caught more attention. However, few studies have been reported on the substrate material. The silicon (Si), borosilicate glass (SiO_2) and ceramic (Al_2O_3) are commonly used as the substrate materials of humidity sensor. In order to investigate comparatively the influences of substrate material on SRDB, this paper chooses the three materials mentioned above as substrate. All calculating settings are consistent except substrate materials. Fig. 6 gives the relation curve between the SRDB and the altitude with different substrate materials. It is shown that the SRDB is minimum when using Si as substrate material, while the bias is equal when using SiO_2 and Al_2O_3. The reason is that the heat exchange becomes faster when using the substrate material with the greater thermal conductivity, which can quickly dissipate the absorbed solar radiation through external air. So the SRDB is minimum using Si as the substrate material because its thermal conductivity is largest in three kinds of materials.

In addition to the substrate material, the size and thickness of the sensor are also important aspects for sensor design. International Meteorological Organization (IMO) doesn't provide the standard size of the humidity sensor. The length and the width of RS92 radiosonde humidity sensor in this study are 2.7mm and 1.6mm respectively, and the thickness is 0.45mm. Fig. 7 reveals the relation between the SRDB and the thickness of the sensor such as 0.3mm, 0.45mm and 0.6mm. Relationship between the relative error of *RH* and the sensor thickness is non-monotonic. The relative error is minimum when using 0.3 mm thickness while it is maximum when using 0.45 mm. Therefore, combining with the mechanical properties of the actual sensor structure, it is necessary to consider the influence of sensor thickness on SRDB in the process of optimization design of MEMS humidity sensor.

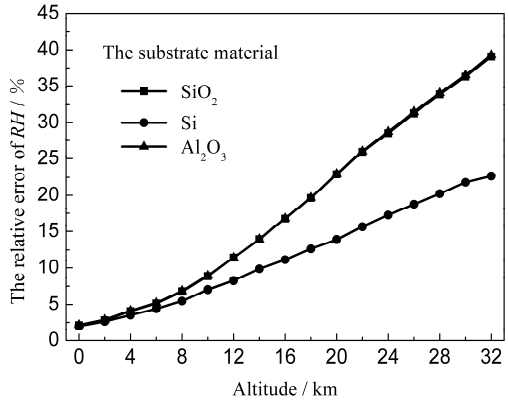


Fig. 6 The effect of the substrate material of the sensor on solar radiation error

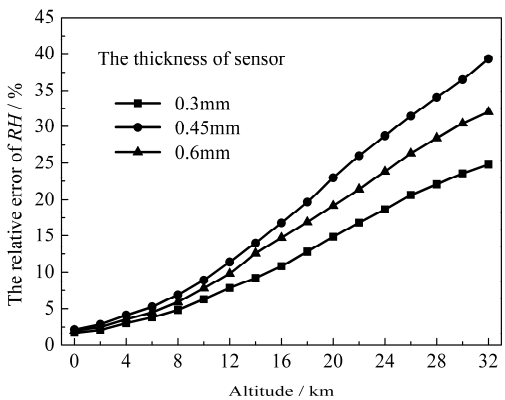


Fig. 7 The effect of the thickness of the sensor on solar radiation error

Summary

The temperature and humidity characteristics of RS92 radiosonde humidity sensor are investigated from sea level to 32 km altitude by computational fluid dynamics (CFD) method. The influences of substrate materials on SRDB of humidity measurement are discussed in detail. Our preliminary researches show the potential of the numerical analysis for the correction of the SRDB. The following conclusions can be obtained.

(1)There are significant influences caused by solar radiation on humidity measurement of radiosonde HUMICAPS.

(2)The SRDB both monotonically increases with the decrease of the reflectivity of the sensor and the solder point. While the effect of solder point reflectivity on the SRDB is slightly larger than that of the sensor reflectivity.

(3)Si, SiO_2 and Al_2O_3 are often used as the substrate material of humidity sensor. Their discrepancies in the SRDB are resulted from their different thermal conductivity, and the SRDB is minimum using Si as the substrate material.

(4)The thickness of the sensor has a significant influence on the SRDB and their relation is non-monotomic. The SRDB is maximum (minimum) for the humidity sensor with 0.45mm (0.3mm).

In short, this paper provides a novel and effective method based on fluid dynamics simulation to correct the error of radiosonde MEMS humidity measurement caused by solar radiation heating.

Acknowledgement

The project is supported by the National Natural Science Foundation of China (Nos. 41275042, 61306138) and Natural Science Foundation of Jiangsu Province (No. BK2012460).

References

[1] G. A. Wick, P. J. Neiman, F. M. Ralph, T. M. Hamill, Evaluation of forecasts of the water vapor signature of atmospheric rivers in operational numerical weather prediction models, Wea.Forecasting, 28(2013)1337-1352.

[2] W. P. Elliott, R. J. Ross, Effects on climate records of changes in national weather service humidity processing procedures, J. Climate, 11(1998)2424-2436.

[3] R. Posada, E. García-Ortega, J. L. Sánchez, L. López, Verification of the MM5 model using radiosonde data from Madrid-Barajas Airport, Atom. Res., 122(2013)174-182.

[4] Z. Z. Liu, M. Li, W. K. Zhong, M. S. Wong, An approach to evaluate the absolute accuracy of WVR water vapor measurements inferred from multiple water vapor techniques, J. Geodrn., 72(2013)86-94.

[5] L. M. Miloshevich, A. Paukkunen, H. Vömel, S. J. Oltmans, Development and validation of a time-lag correction for vaisala radiosonde humidity measurements, J. Atoms. Ocean. Tech., 21(2004)1305-1327.

[6] E. Campmany, J. Bech, J. Rodríguez-Marcos, Y. Sola, J. Lorente, A comparison of total precipitable water measurement from radiosonde and sunphotometers, Atom. Res., 97(2010)385-392.

[7] A. Koulali, D. Ouazar, O. Bock, A. Fadil, Study of seasonal-scale atmospheric water cycle with ground-based GPS receivers, radiosonde and NWP models over Morocco, Atom. Res., 104-105(2012)273-291.

[8] J. H. Wang, L. Y. Zhang, A. G. Dai, Radiation dry bias correction of vaisala RS92 humidity data and its impacts on historical radiosonde data, J. Atmos. Ocean. Tech., 30(2013)197-214.

[9] H. Vömel, H. Selkirk, L. Miloshevich, J. Valverde-Canossa, J. Valdés, E. Kyrö, R. Kivi, W. Stolz, G. Peng, J. A. Diaz, Radiation dry bias of the vaisala RS92 humidity sensor, J. Atmos. Ocean. Tech., 24(2007)953-963.

[10] X. L. Mao, S. R. Xiao, Q. Q. Liu, M. Li, J. H. Zhang. Fluid dynamic analysis on solar heating error of radiosonde humidity measurement, Acta phys. sin., 14(2014)144701.

[11] F. Guichard, D. Parsons, E. Miller, Thermodynamic and radiative impact of the correction of sounding humidity bias in tropics, J. Climate, 13(2000)3611-3624.

Key Engineering Materials Vols 645-646 (2015) pp 766-770
Submitted: 2014-11-23
© (2015) Trans Tech Publications, Switzerland
Accepted: 2014-12-23
doi:10.4028/www.scientific.net/KEM.645-646.766

Experimental study on velocity of flyer based on silicon

Fu Qiu-bo*, Wang Yao, Wang Meng, Qin Wen-zhi, Guo Fei

Institute of chmical materials, china academy of engineering physics Mianyang 621900, China

*email:fumiao1977@163,com

Keywords:silicon flyer, fly velocity, MEMS process, slapper detonator

Abstract. This paper researches the characteristic to the flyer velocity of silicon flyer. The material of flyer is different in comparison to polyimide which is considerde to conditional flyer. It is found that the movement trendency is clearly different of velocity between silicon flyer and polymide flyer, which is resulted by modality change. The silicon flyer velocity decreases gradually with the increase of flyer thickness. The inclusion is also applicable for polyimide flyer. It is clearly that the fatal influence parameter is silicon flyer thickness for slapper detonator based on MEMS fabrication process, which determined the success of explosion.

Introduction

Slapper detonator has been extensively studied because of its high safety, reliability and environmental worthiness, which is applied for explosion systems[1]. MEMS slapper detonator has useful performances in terms of structure miniaturiation, system integrated, intellectualized and low cost, which is the future development trendency. In 2009, Desal[2] et al produced a integrative slapper detonator of putting bridge foil, flyer, and barrel together by depositon and lithography, resulting improving sapce and energy efficiency. O'Brien et al[3] fabricated a exploding foil initiator system. Amish Desai [3]made a process which can realize large-scale fabricaiton. Firstly, magnetron sputtering, lithography and wet etching were used to fabricate the bridge foil and flyer, then the barrel with the SU-8 negetive photolithography by pre-bake, mask, exposure and developing. Zheng Qing-xuan et al[5] prepared a slapper detonator with the micro-electromechanical system. The bridge foil was fabricated by magnetron sputtering, lithography and wet etching on glass substrate. The polyimide flyer was stuck on it, then the barrel with the UV curable epoxy resin was produces. The exploding tests showed that it is credibility. Shi Zhi-gui et al[6] describes a method of fabricationg an integrated slapper detonator based on the MEMS technology, which includes metal bridge, tamper, flyer and barrel. It is found that the HNS-Ⅳ can be exploded.

From the above investigation, it is the main researching focus of flyer and barrel. It is conducted by altering fabricaiton process and material of flyer and barrel by designing an integrated slapper detonator. It is concluded that the material of flyer is commonly polyimide and silicon. The material of barrel can be choosed from metal, epoxy resin and silicon. From the reference by Shi Zhi-gui, the silicon flyer is demonstrated that the slapper detonator successed in exploding HNS-Ⅳ. This conclusion is consistent with researching paper of Guo Fei[7]. Although the silicon flyer have successed in exploding detonator, the exploding energy has the difference between silicon and conditonal polymide flyer.

In this paper, the velocity is investigated of silicon flyer in order to make clear the difference of the two flyer. It will provide a foundation of mechanism researching about the slapper detonator based on silicon. It will make a progress to the MEMS slapper detonator.

2 Experimental process

The silicon integrated slapper detonator is developed on the basis of reference 7. A list of parameters used in slapper detonator is given in table 1.

Table 1 The parameter of slapper detonator based silicon

No.	The dimension of bridge foil /mm	The diameter of barrel /mm	The thickness of flyer /μm
1	0.3×0.3×0.004	Φ 0.5	15
2	0.3×0.3×0.004	Φ 0.45	30
3	0.3×0.3×0.004	Φ 0.5	20
4	0.3×0.3×0.004	Φ 0.45	15

The principle of photonic doppler velocimetry system[8] is shown on Fig.1. In this paper, the velocity of flyer is conducted by PDV system.

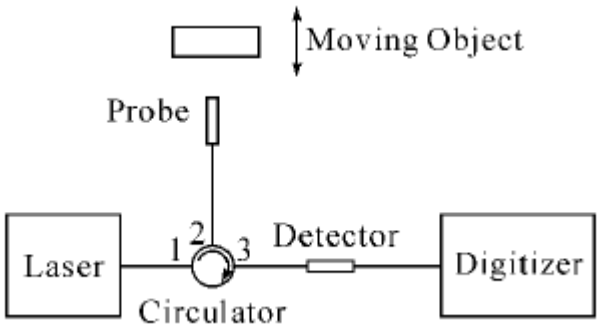
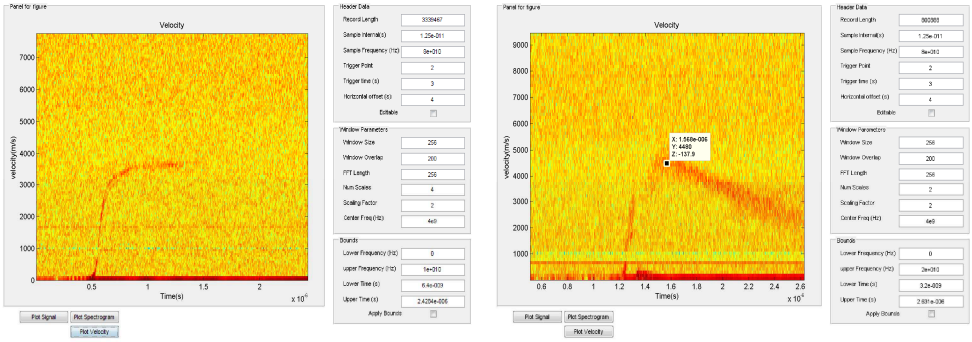


Fig.1 The principle diagram of PDV

3 Result and discussion

The testing curve of flyer velocity are shown on Fig.1. It is clear that the difference exists of flyer trendency between silicon and polyimide flyer. when a high voltage is connected across the metal contacts of the detonator die, the metal bridge is instantaneously vaporized, resulting in the formation of a plasma which is confined by the face plate and which creates a large pressure shock wave effective to shear the flyer at its interface with the back barrel and to send it with high velocity down the barrel and, upon impacting with a secondary explosive. The curve of polyimde flyer shows a increasing trend. When the velocity comes to the peak, the curve keeps mostly constant for sereval times. But the conclusion is not familiar with the silicon flyer. The curve of silicon velocity shows a increasing and decreasing trend. When the velocity of flyer comes to the maximum value, the curve drops mostly. One reason of explaining the phenomena is that the process of decelerating did exist. This explaination shows the exist of air resistance. The phenomena should be found in the process of polymide flyer due to the same pressure shock which resulted from identical dimension bridge foil[9]. Moreover, the resistance of polymide flyer is high compared to silicon flyer because of high velocity. The accerelating cure of polymide flyer keeps constant for several microtimes at peak. So, it is deduced that the air assitance is not the reason of decelerating process.

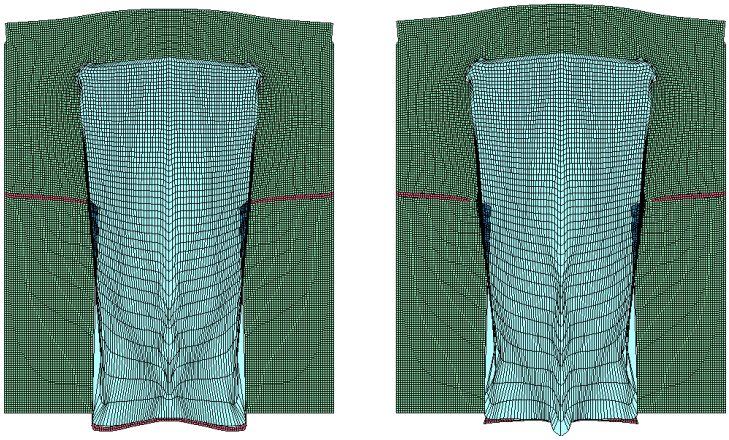


a）polyimide flyer b）silicon flyer

Fig.1 The image of PDV curve

The other reason of explaing the phenomena is that the movement of flyer can not be detected because of modality altering. The full polymide flyer can be found at collector whose distance is far from barrel about 1mm. The same testing for the silicon flyer is conducted. The resulting shows fragile silicon flyer.

Fig. 2 shows the numerical resulting for silicon and polyimide flyer by ansys using JWL state equation of BNCP instead of plasma expansion. The numerical resulting shows the surface roughness of polyimide flyer. Because the polymide flyer belongs to polymer plastic materials which would has a buffer effection for detonation wave. Whenas, when the flyer changed into silicon, the phenomenon is vary from polyimide. The silicon flyer gradually tinned at the center under driving by detonation wave, resulting fragile flyer. So, it is concluded that the silicon would be disintegrated in the process of plasma expansion.



(a) polyimide flyer (b) silicon flyer

Fig.2 The images of numercial resulting for silicon and polyimide flyer

The thoretical maximum velocity of silicon and polyimide flyer should be same according to equationg Gurney. As we know, the velocity keeps same because of identical mass of flyer and dimension of bridge foil. But the difference between theory and practice exist. The PDV curve shows that the maxium velocity comes to 5000m/s for polymide flyer, but the silicon flyer only 4000m/s. The conclusion can be explained by fragile silicon flyer which is consistent with the above reason of modality altering. The PDV system can not detected because of fragile silicon flyer resulting the decelerating process.

From analyse, the difference is that the silicon flyer comes to the modality altering during the flying process between silicon and polyimide flyer. It would be fragile or gesture changing for the modality altering.

The expression of ultimate flyer velocity can be summarized as the following according to Gurney of Tucker and Stanton. According to the equation, the flyer thickness is the only influence parameter on velocity, when the bridge foil and flyer keeps constant.

$$V_f = \sqrt{2kJ_b^{\,n}}\left(\frac{m_f}{m_e}+\frac{1}{3}\right)^{-\frac{1}{2}} \quad (1)$$

Where k and n are the constants of experiment determined, respectively, $k=2.36\times10^{-6}$, n=0.85 for the Cu foil, mf and me are the exploding foil masses per unit area, Jb is the density of exploding current A/cm^{-2}.

Fig.3 hows the practical silicon flyer velocity by PDV and thoretical velocity calculated by equation (1). The curves showing downword trend indicated that the thickness of flyer changed from 30μm to 15μm accompaning with velocity fall. The minimum velocity comes to 3512m/s corresponding to 30μm thickness silicon flyer. In contrary, the maximum velocity comes to 4480m/s corresponding to 15μm. The conclusion is consistent with researching paper by Guo Fei[7] and Wang Yao[10]. The success of initiation explosive is determined by two factors consisted of force P and force duration τ according to the short-duration pulse initiation criterion value for solid heterogeneous explosive by walker and wasley[11]. The researching paper presents that reducing the thickness of flyer would be the efficient way to improve the flyer velocity, resulting improving initiation performance, accompanied by reducing the force duration of τ which is not benefit for initiating explosive. So, It is common to fail to initiate explosive with the thickness of 15μm.

Table 2 The velocity of silicon flyer

No.	The maximum velocity m/s	The flying distance /mm
1	4480	0.137
2	3512	0.132
3	4117	0.134
4	4723	0.128

In summary, it is important to choose the appropriate thickness of flyer for slapper detonator based on MEMS technology. The thickness of silicon flyer should be fixed from 20μm to 30μm.

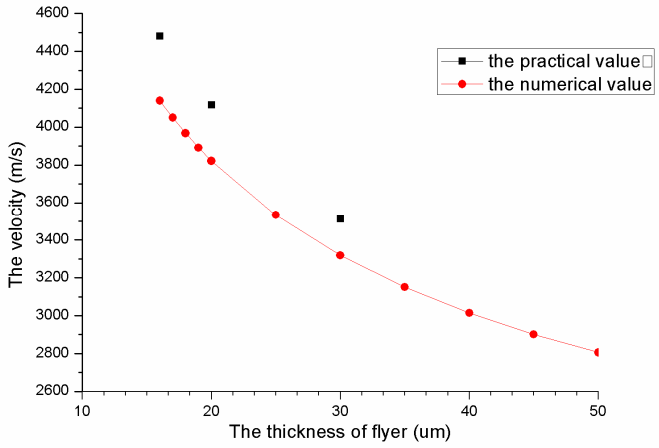


Fig.3 The image of flyer velocity between practical testing and thoretical calculation

4 Conclusions

The slapper detonator based on MEMS technology is fabricated by using lithography and depostion. The flyer materials which is ranged from polymide to silicon is researched by PDV systems and numerical modeling calcuation.

1) The modality altering would be existed of silicon flyer during the flying process, namely, fragile or gesture changing. But it is not influence on the initiation explosives. This conclusion is different from the theory which is that the key point on the success of initiation is keepting the integrity of flyer.

2) The thickness of flyer did have effect on velocity for the silcion and polyimide flyer. The veloctiy variation as a function of thickness of flyer showed the conclusion, which is consistent with experimetal resulting.

3) It is important parameter of flyer thickness on the success of initiation for the slapper detonator based on MEMS technology.

References:

[1] Wang Yu, Wei Chao, Zhang Song, Developing status on new techniques and new energetic materials in insensitive pyrotechnics, Science & Technology Review. 31(2013):74-79.

[2] Desal A., U.S. Patent 0151584. (2009).

[3] O'Brien D W,Druce R L,Johnson G W,Vogtlin G E,Barbee Jr.T W,and Lee R S., U.S. Patent 5731538. 1998.

[4] Amish Desai,Altadena,CA., U.S. Patent 7938065 B2. 2011.

[5] Zheng Qing-xuan, Zheng Zhi-meng, Li Ming-yu, Lu Jun-jun, Research on fabrication method of integrated slapper detonator, Initiarors & Pyrotechnics, 5(2012):1-3.

[6] Shi Zhi-gui, Guo Fei, Xi Shi-wei, Zhang Qian-mei, Wang Ya-jun, A method for fabricating an integrated metal slapper detonator, Initiarors & Pyrotechnics, 3(2010):1-3.

[7] Guo Fei, Shi Zhi-gui, Jiang Xiao-hua, He Bi, Fu Qiu-bo, The test research on the initiation of HNS-Ⅳ by an integrated silicon exploding foil assembly, Initiarors & Pyrotechnics, 12(2009):5-7.

[8] Jian Wang, Chong-qing Wu, Hong-wei Song, Measurement of the velocities in the thansient acceleration process using all-piber photonic Doppler velocimetry[C], SPIE,2011,7753:77536.

[10] Fu Qiu-bo, Jiang Xiao-hua, Guo Fei, Wang Li-ling, Wang Liang, Effect of exploding foil size on flyer velocity, Acta Armamentar Ⅱ, 4(2010):434-436.

[11] Wang Yao，Guo Fei，Fu Qiubo, An optimum matching study on the parameters of slapper detonator based on MEMS technology, Journal of Beijing Institute of Technology, 23(2014):83-86.

[12] Geng Chunyu, Velocity analysis of a plastic flyer accelerated by an electrically exploded metal foil. Energetic Materials, 3(1995):37-42.

Key Engineering Materials Vols 645-646 (2015) pp 771-776
Submitted: 2014-12-09
© (2015) Trans Tech Publications, Switzerland
Accepted: 2014-12-23
doi:10.4028/www.scientific.net/KEM.645-646.771

A New Method of Design and Verification of Digital Silicon Gyroscopes Closed-loop Driving System Based on MicroBlaze

Peng Sun[1,a *], Qi Shao[1,b], Yingyu Liu[1,c] and Weiping Chen[1,d]

[1]MEMS Center, Harbin Institute of Technology, Harbin, Heilongjiang, China

[a]wwwsunpeng_love@126.com, [b]542379859@qq.com, [c]460596141@qq.com, [d]chenwp@hit.edu.cn

Keyword: MicroBlaze; gyroscopes; closed-loop; FFT

Abstract. The article brings out a digital silicon gyroscopes closed-loop driving system using the phase relationship of the input driving signal and the signal of the forced motion of the mass block in sensor structure based on analyzing the working principle and phase characters of digital silicon gyroscopes. We make a low-cost, simple and high precision measurement technique for resonant frequency of silicon micro-machinery gyroscopes by the whole digital locked loop system designed with MicroBlaze method. Dichotomy and Fourier transform spectrometry method constitute the algorithm of the system and the solution precision can be determined by the number of the times of approximation. Under the control of the MicroBlaze softcore, the system realizes the realization of the digital signal, the high speed frequency transformation, the acquisition of mass block response signal and the calculation of phase difference. Lastly, each module of the system and the whole system are simulated, the whole system is approved on the test broad.

Introduction

Resonant frequency is a significant parameter that describes the system driving and sensor modal vibration character of silicon micro-machined gyroscope sensor system. The precise measurement of resonance frequency is necessary in many occasions such as sensor performance test, closed-loop driving control and the principle analysis of error [1-2]. At present, the sweep-frequency method is the main measurement of resonant frequency in silicon micro-machined gyroscope sensor system. The principle of this method is simple and the result is relatively reliable. However, if we need a high accuracy, enough frequency points are required. It relies on the high storage of the measurement platform, leading to the increased test cost and the failure to be applied to some specific occasions [3-4]. Since FPGA adopts hardware technology to process signal and can be repeatedly used in programming, the measurement of resonant frequency based on FPGA technique can combine speed, flexibility, real-time prediction and simulation. This paper designs a digital silicon gyroscopes closed-loop driving system based on the phase relationship between the input driving signal and the forced motion of sensor mass after analyzing the principle and the phase character of digital silicon gyroscope. Thus a MicroBlaze-based full digital frequency locked loop is designed. Compared with the existing measurement, a low-cost, simple to implement and high accuracy measurement of resonant frequency of silicon micro-machined gyroscope is raised.

The definition of the system algorithm

The basic structure of the micro-machined gyroscope is driven comb. Mass block will be forcedly vibrated at the balanced position, since a sinusoidal driving force is forced horizontally on mass block. When the frequency of the driving signal equals to the resonant frequency of the

gyroscope, the phase difference will be 90 degrees. According to this character, this paper designs a Fourier analysis to calculate the phase. It mainly depends on the Fourier analysis of the signal that satisfies the Deliheli criteria to get the fundamental parameters of the input signal. Assume the sinusoidal signal $x(t)$ is following:

$$x(t) = x_0 + \sum_{k=1}^{\infty} x_{km} \sin(k\omega t + \theta_{xk}) \tag{2-1}$$

among them，k =1，2，3，……。In this expression, x_0 is the DC part of the $x(t)$, x_{km} is the harmonics amplitude, θ_{xk} is the phase angle of harmonics signals. The existence of harmonic leads to the distortion of fundamental. To decrease the influence of harmonic, only fundamental is processed. Therefore, $x(t)$ is sampled by the cycle of nT and the sample $x(n)$ of which depth is N is discrete Fourier transformed:

$$\begin{aligned} X(k) &= DFT[x(n)] = \sum_{n=0}^{N-1} x(n) e^{-j\frac{2\pi}{N}kn} \\ &= \sum_{n=0}^{N-1} x(n)[\cos(\frac{2\pi}{N}kn) - j\sin(\frac{2\pi}{N}kn)] = \mathrm{Re}[X(k)] + \mathrm{jIm}[X(k)] \end{aligned} \tag{2-2}$$

Among them，k =0，1，2，3，……$N-1$。

The phase of fundamental signal is:

$$\tan\theta_k = \frac{\mathrm{Im}[X(k)]}{\mathrm{Re}[X(k)]} \tag{2-3}$$

in the expression，$k = \frac{f_0 N}{f_s} + 1$，$f_s$ is the rate of the signal sampling and N is the depth of signal sampling. By extracting fundamental parameters from Fourier transform and then solving angle of the driving signal and response signal, the phase angle difference is gained. Since the parameter N is enormous in this paper, by setting N=2^M，the speed can be increased by more than 200 times with base 2 FFT M butterfly operations. Based on the above analysis, combining Dichotomy and Fourier transform spectral analysis is available to approximate the resonant frequency of the gyroscope. The accuracy can be determined by the number of times of approximation.

Design and simulation of functional modules

Design and simulation of the digital signal generator module DDS

As shown in Figure 1 is the DDS(Direct Digital Synthesizer)design structure. It mainly consists of the phase accumulator, phase truncation module and sine ROM lookup table.

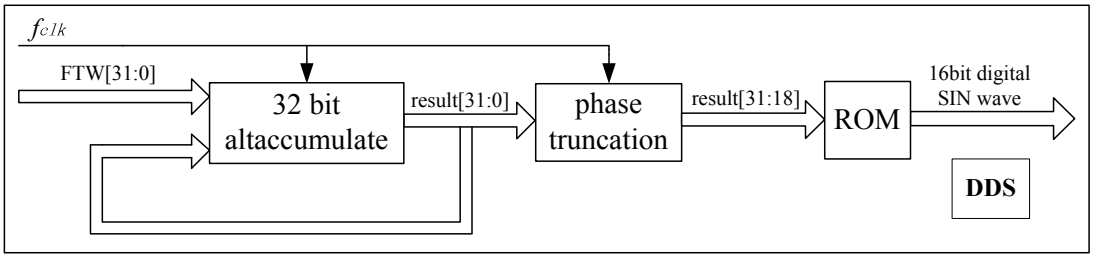


Fig.1 DDS design structure

Phase accumulator is the significant part of the DDS. It should have the function of phase accumulation and its input is the FTW (the frequency tuning word, phase increment) that is set to 32bits in this article. Sine ROM lookup table transfers the phase of the signal to the amplitude and its input is the output of the phase accumulator. In fact, the input of ROM is its address and the output is sent to DAC to be converted into analog signal. To prevent the storage of ROM from being too large, phase truncation module is added between phase accumulator and ROM lookup table, it truncates the high 14-bit data of the output of the phase accumulator as the input of the sine ROM lookup table. Based on the above principles, the output frequency of DDS is following:

$$f_{out} = \frac{B_{\Delta\theta}}{2^N} \cdot f_{clk} \tag{3-1}$$

in the expression, $B_{\triangle\theta}$ is the FTW, f_{clk} is base frequency value，N is both the width of the FTW and the data bandwidth of phase accumulator. The frequency of input signal f_{clk} is set to 1MHZ and the output frequency is set from 2KHZ to 10KHZ. In the simulation, the output signal is set to 4KHZ.According to the expression(3-1), $B_{\triangle\theta} \approx 17179870$。By the simulation with ISE13.3, waveform is shown in Figure 2,the 16-bit digital sine wave output is *dout*.

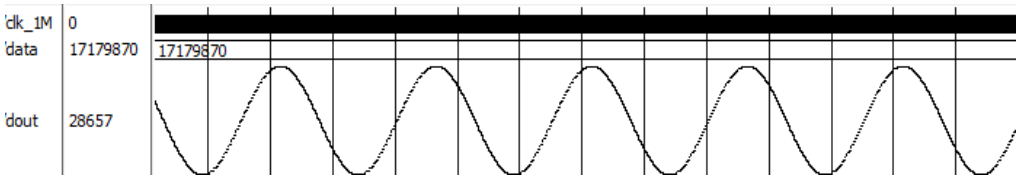


Fig.2 DDS simulation waveform

According to the Nyquist sampling theorem, the highest sampling frequency should be less than half of f_{clk}. After observing the simulation, the waveform of the output sine wave is normal in the range of 2KHZ to 10KHZ without obvious distortion when f_{clk} = 1*MHz*in this design. When $B_{\triangle\theta}$is 1, the minimum frequency of progress is 0.000234HZ. Thus the design meets the requirement of this article absolutely.

Design and simulation of digital signal processing module FFT

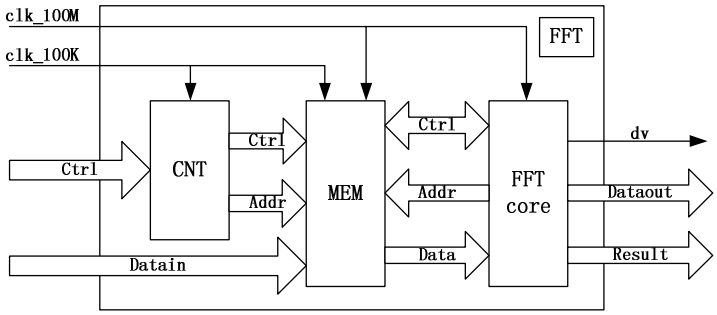


Fig.3 Design structure of FFT

As shown in Figure 3 is the design structure of FFT. It mainly consists of CNT (address counter),MEM(data storage module)and calculation module(FFT core).CNT is controlled by the external signal to enable MEM to store addresses and to provide MEM with storage address. The store address is generated by CNT itself. After MEM finishes storing the data, CNT will inform FFT core of getting values and beginning FFT operation. FFT core is the core of the FFT module which is formed by the FPGA configuration, it is set to dual channel,16 bits data width and 16384calculation depth. Since the port of data in is connected to an external ADC, the frequency(100KHZ) cannot be changed. In order to improve efficiency, this module also adds 100MHZ clock signal to control MEM and FFT core. The entire simulation waveform of FFT is

shown in Figure 4 which costs about 0.17s. Since the clock frequency in the sampling stage is 100KHZ, this procedure takes the majority time. On the other hand, since the clock frequency in calculating and outputting result is 100MHZ, this procedure cost a little part, estimated at 2.6ms.

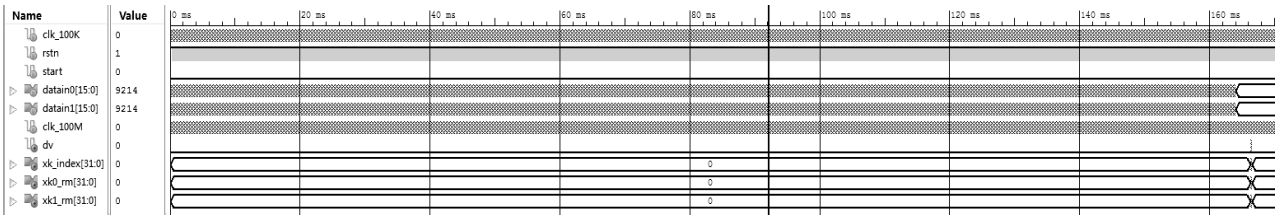


Fig.4 FFT simulation waveform

The establishment of system based on MicroBlaze

The establishment of system hardware platform

The whole MicroBlaze system whose processor can be configured is designed and realized by the widely used EDK (Embedded Development Kit) with Xilinx Virtex-6ML605 as embedded development platform. The custom IP core of this paper is connected to the whole system with the PLB bus. As is shown in Figure 5, fft_mem_cnt_dds_0 module is consisted of DDS module and FFT module. Xps_bram_if_cntlr_rm0_block and xps_bram_if_cntlr_rm1_block are the structures to store operation results, xps_bram_if_cntlr_rm0 and xps_bram_if_cntlr_rm1 are memory controllers.

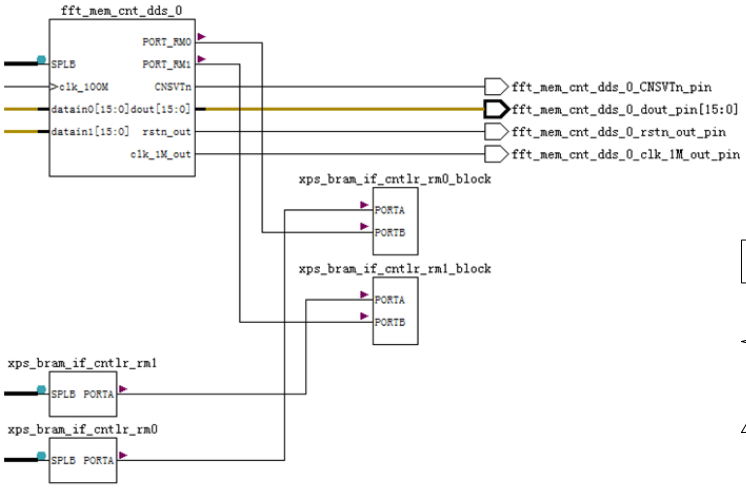


Fig.5 Whole system based on MicroBlaze

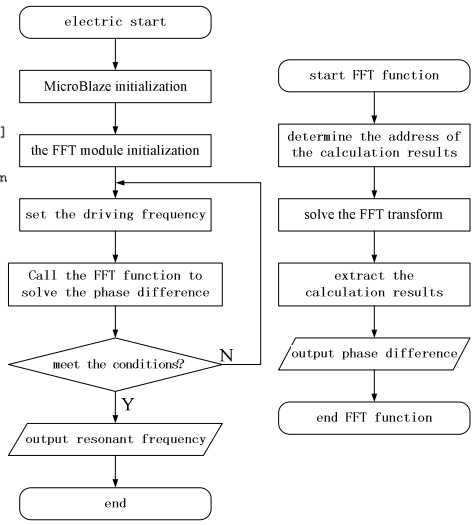


Fig.6 Flowchart of the system

Design and implementation of system software

Timing match should meet requirements strictly when the software programming is configured. It should be fully complied with configuration timing requirements of Virtex-6FPGA, or it may lead to the failure of configuration. The main function of the program which is run on the MicroBlaze processor is to read the data of input ports and control the Fourier transform. It also reads the result from some address and turns it into phase difference by fixed transform. Since the fft_mem_cnt_dds module is already created, we only need to program the main function. After debugging and running the application successfully, an executable file whose suffix name is .elf will be generated. Figure 6 is the main function flowchart of the system and FFT function flowchart.

Board-level verification of the micro-machined gyroscope closed-loop driving system

The verification platform of the micro-machined gyroscope closed-loop driving system is the Xilinx Virtex-6 ML605 which uses the 200M crystal oscillator clock. The frequency divider configured by system can generate 100MHZ, 1MHZ and 100KHZ clock signals to drive the whole system. After adding top-level file in IES13.3, invoking the EDK project and adding ChipScpoe file and constraint files, the final generated bit file can be downloaded to FPGA. Thus the closed-loop driving system can be debugged and verified.

Data printed in the form of UART can test the software code of MicroBlaze. Some significant results should be printed though UART such as the phase difference after using FFT function every time. We build a virtual gyroscope structure on the verification platform which can simulate the characteristics of the resonant frequency of micro-machined gyroscope. Virtual gyroscope can generate two specific frequency signals with a phase difference which can be controlled by the frequency of the signals when be input a FTW according to the formula (3-1). We connect virtual gyroscope with the micro-machined gyroscope closed-loop driving system. By setting the resonant frequency of the virtual gyroscope structure to 4KHZ and setting the maximum frequency error to 0.1HZ in system software code, the main result can be printed though UART port and the whole system verification result is shown in Figure 7.

```
set the driving frequency as 2000.000000Hz, the phase error is 56.309932degree
set the driving frequency as 6000.000000Hz, the phase error is 39.805570degree
set the driving frequency as 10000.000000Hz, the phase error is 64.536655degree
set the driving frequency as 5600.987819Hz, the phase error is 34.453519degree
set the driving frequency as 4423.562103Hz, the phase error is 11.400358degree
set the driving frequency as 4087.250528Hz, the phase error is 2.471329degree
set the driving frequency as 3640.766810Hz, the phase error is 10.673774degree
set the driving frequency as 4024.077117Hz, the phase error is 0.687661degree
set the driving frequency as 3939.556012Hz, the phase error is 1.744336degree
set the driving frequency as 4004.480125Hz, the phase error is 0.128273degree
set the driving frequency as 3991.703834Hz, the phase error is 0.237912degree
set the driving frequency as 4001.833421Hz, the phase error is 0.052510degree
set the driving frequency as 3999.260137Hz, the phase error is 0.021196degree
set the driving frequency as 3999.037977Hz, the phase error is 0.027562degree
set the driving frequency as 4000.130131Hz, the phase error is 0.003726degree
set the driving frequency as 4000.225417Hz, the phase error is 0.006456degree
set the driving frequency as 3999.894028Hz, the phase error is 0.003034degree
set the driving frequency as 3999.971709Hz, the phase error is 0.000809degree
set the driving frequency as 4000.004728Hz, the phase error is 0.000134degree
the number of the loops is 19
the resonant frequency is 3999.971709Hz
the phase error is 0.000809degree
OK
```

Fig.7 The verification result of the overall system

Summary

Virtex6 ML605 is adopted to design the digital silicon gyroscopes closed-loop driving system based on analyzing the working principle and phase characters of digital silicon gyroscopes. The whole algorithm combines Dichotomy and Fourier transform spectrometry method. This paper mainly completed the implementation of the FPGA part of the whole system which mainly consists digital signal generator module DDS and digital signal processing module FFT. The function of DDS is generating digital signal to drive the mass block in the micro-machined gyroscope and the function of FFT is sampling the response signal of the mass block and calculating phase difference by Fourier transform spectrometry method. MicroBlaze softcore control the state of DDS and FFT to make FPGA work normally. Under coordination of the external ADC and DAC, resonant frequency of gyroscope can be locked ultimately. Lastly, each module of the system as well as the overall system are simulated, the whole system is tested successfully on the test board.

References

[1] C. Acar, C. C. Painter, A. R. Schofield, A. M. Shkel. Robust Micromachined Gyroscopes for Automotive Applications. 2005 NSTI Nanotechnology Conference and Trade Show-NSTI Nanotech 2005 Technical Proceedings. San Francisco, United States, 2005:375~378

[2] A. M. Shkel. Micromachined Gyroscopes: Challenges, Design Solutions, and Opportunities. Proceedings of SPIE. San Francisco, United States, 2001, 4334:74-85

[3] T. Veijola, Accelerometer model in APLAC, Tech. Rep. CT-18, Helsinki University of Technology, Circuit Theory Laboratory, 1994: 232-236

[4] T. Veijola, H. Kuisma, J. Lahdenpera. Equivalent circuit model of the squeezed gas film in a silicon accelerometer. Sensors and Actuators A: Physical. 1995, 48: 239-248

Key Engineering Materials Vols 645-646 (2015) pp 777-782
Submitted: 2014-12-24
© (2015) Trans Tech Publications, Switzerland
Accepted: 2014-12-31
doi:10.4028/www.scientific.net/KEM.645-646.777

Design and Fabrication of a SOI Optical Waveguide Sensing Platform for Biochemical Sensor Application

Yujin Liu[a], Ying Dong[b] *, Dengpeng Yuan, and Tianjian Li

Graduate School at Shenzhen, Tsinghua University, Shenzhen, CHINA

[a]liuyj13@mails.tsinghua.edu.cn, [b] dong.ying@sz.tsinghua.edu.cn (corresponding author)

Keywords: Optical Waveguide, Silicon-on-Insulator (SOI), Biochemical Sensor, Geometric Compensation, Photoresist Desquamation

Abstract

A micro biochemical sensor based on a SOI optical waveguide sensing platform is reported in this article. The sensing platform utilizes a Mach-Zehnder Interferometer (MZI) configuration. In order to satisfy the single-mode transmission condition of the waveguide and match the coupling size of standard single-mode fiber, a ridge waveguide structure is adopted to construct the MZI configuration. The key parameters of the waveguide are optimized by FDTD method. A process composed of contact exposure photolithography and Inductively Coupled Plasma (ICP) etching technology has been worked out for the fabrication of the optical waveguide sensing platform on SOI wafer. In the process, only one photolithographic mask is used. The mask is designed to have several patterns including an array of MZI configurations for multiple species sensing, a group of ridge waveguides with different key parameters as test references, and a group of geometric compensation schemes to test the methods of modifying the deviation which may arise during the ICP etching step. Process simulations are conducted to predict the exposure and etching results, which give strong support to the fabrication process control. Lithography problems including photoresist desquamation and line narrowing are solved to achieve the special structure.

Introduction

In recent years, the environment issue has drawn lots of attention and the pollution monitoring technology is becoming a research hotspot. Optical waveguide sensor on the basis of evanescent field sensing principle has the capability of electromagnetic interference resistance and working in tough environment conditions such as high temperature and high pressure, which makes it a possible solution for pollution monitoring [1, 2]. Common materials for optical waveguide include lithium niobate, gallium arsenide, indium phosphide and organic polymer materials etc. Recently, Silicon-on-Insulator (SOI) as material of optical waveguides has attracted a growing interest due to its capability of reducing the radiation loss and the overall size of the waveguide, the IC compatible processing technology, and the potential of opto-electro-mechanical system integration [3]. And the SOI optical waveguide sensor which utilizes a Mach-Zehnder Interferometer (MZI) configuration has both the advantages of SOI and the advantage of high sensitivity of MZI configuration. Several important researches in this field have been done. In article [4], a MZI waveguide interferometer integrated on SOI is fabricated by using KOH anisotropic etching, of which the insertion losses and modulation depths are measured to be 4.81dB and 98%. But the anisotropic etching makes the ridge sidestep shaped, which may affect the device performance. A single-mode photonic wires in SOI with propagation loss as low as 2.4dB which is fabricated with deep ultraviolet lithography and dry etching, is reported in [5].

To satisfy single mode propagation and achieve high sensitivity for biochemical sensor application, the ridge waveguide MZI should have a specially long and thin structure with a very small Y-branch angle, which will bring great difficulty to photolithography and etching process. This paper discusses the parameter design and optimization of the SOI ridge waveguide MZI, introduces the layout design and the fabrication process, and presents the solutions to the problems in the process due to the structure's specialty.

Design and Optimization of the Structure Parameters

Ridge Waveguide. The advantages of SOI optical waveguide is the large refractive index difference that makes the light energy better limited in waveguide layer relative to other materials, so that a small thickness waveguide layer is required to meet the planar single-mode condition. To reduce the coupling loss between the waveguide and standard single-mode fiber, a ridge waveguide structure is adopted [6, 7], as shown in fig.1.

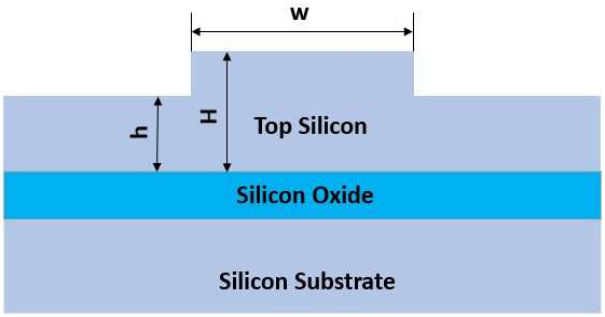


Fig. 1. Schematic of the SOI ridge waveguide

To ensure the single-mode condition, the key parameters of the ridge waveguide must satisfy the conditions [8, 9] below:

$$\frac{h}{H}>0.5-0.5\sigma \quad . \tag{1}$$

$$\frac{w}{H}<(1+\sigma)\frac{(h+\sigma)/(H+\sigma)}{\sqrt{1-[(h+\sigma)/(H+\sigma)]^2}} \quad . \tag{2}$$

For TE mode， $\sigma=\frac{1}{\sqrt{k(n_1^2-n_2^2)}}+\frac{1}{\sqrt{k(n_1^2-n_3^2)}}$, λ is for the wavelength, $k=2\pi/\lambda$ is the number of waves in vacuum.

When designing the key parameters of ridge SOI waveguide, we take both matching the fiber core diameter and reducing fabrication difficulty into consideration. And a FDTD method is adopted to optimize the value of w, H, and h to get the best mode shape, as shown in fig. 2, where H=10 μm， h=6.5 μm， w=6.0 μm.

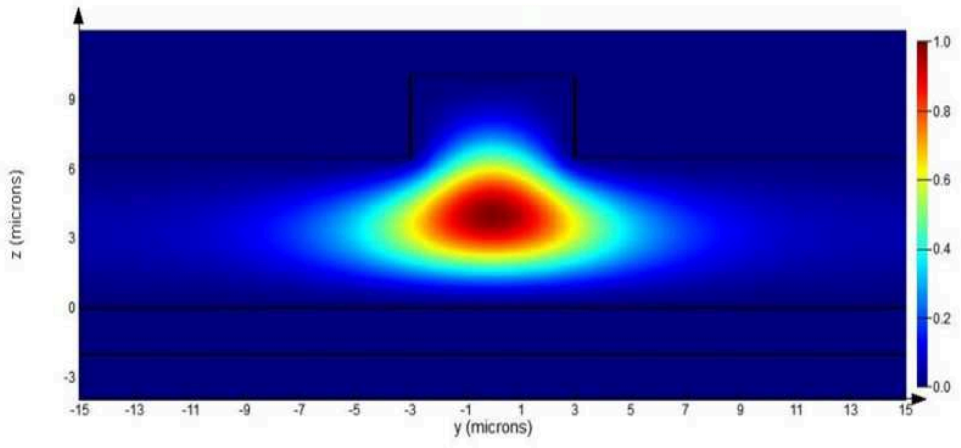


Fig. 2. The best mode shape in the FDTD optimization

MZI structure. The MZI configuration has advantages of high sensitivity and high integration. The key parameters that determine the sensitivity and light transmission losses of the device include D, L and θ, as shown in fig.3.

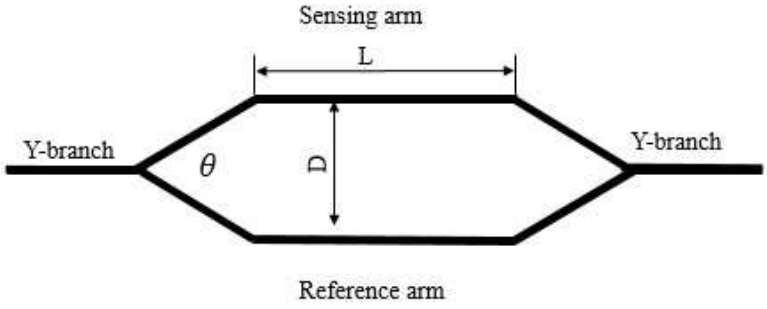


Fig. 3. Schematic of the MZI configuration

According to the power transfer function of MZI structure:

$$\frac{I_{\text{out}}}{I_{\text{in}}} = \left|\frac{E_{\text{out}}}{E_{\text{in}}}\right|^2 = \frac{\eta^4}{2}\,[1+\cos(\Delta\varphi)]\,. \tag{3}$$

$$\Delta\varphi = (2\pi/\lambda)\cdot\Delta NL\,. \tag{4}$$

Here L should be long enough to ensure the sensitivity.

The light transmission losses of MZI mainly include photonic absorption loss, scattering loss, substrate leakage loss and radiation loss, of which the radiation loss at the Y-branch occupy the vast majority [10]. The relation between the radiation loss at the Y-branch and θ can be derived by the follow function:

$$\int_{-\infty}^{+\infty} \mathrm{E_{yo}}\,(x)\mathrm{E_{yo}}\,(x)\cdot\cos[2\beta_0\cdot\tan(\theta/2)\cdot x]dx = \partial_0\frac{2\omega\mu_0}{\beta_0}\,. \tag{5}$$

$$\Gamma = 1-\left|\partial_0\right|^2\,. \tag{6}$$

With the increase of the bending Angle θ, Y-branch radiation will gradually increase. But with the same D when θ is too small, the device will become too long to be fabricated. So taking the transmission losses and the fabrication feasibility into consideration, we set $\theta = 2.6^\circ$.

Mask Design, Simulation and Geometric Compensation

Mask Design. Only one mask is needed to pattern the ridge waveguide structure, which can eliminate the alignment error during the lithography process and largely simplify the fabrication process. When arraying the devices, we put 10 devices equidistantly in a group so that we can deposit 10 different sensitive layers to detect different substance. Because the ridge structures of the device are long and thin lines, etching off the Si all around will make the processing volume huge, so we just etch grooves around the lines to shape the structure. The groove width should satisfy the follow principles: (1) the width should be large enough to ensure there's no coupling phenomenon between device area and the non-device area; (2) the width is suitable for ICP etching. Considering this, we set the groove width to be 50 μm.

Simulation. The small Y-branch angle leads the whole structure to be long and thin. To predict the potential fabrication defection that may cause during lithography and etching, a process simulation is conducted with Intellisuite software. The simulation result shows that the angle area may be expanded and turns out to be rounded angle, as shown in fig. 4, which may increase the radiation loss and affect the device performance.

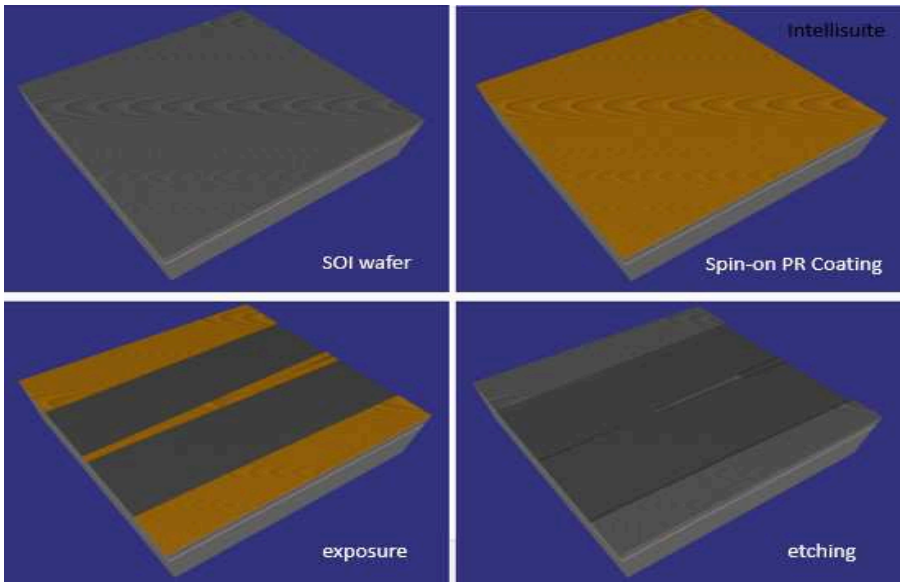


Fig. 4. Results of the process simulation with Intellisuite software which is licensed by the Intellisense co.

Geometric Compensation. The rounded angle is considered to be the result of the extreme small gap of the angle and the limited resolution of lithography and etching process. Four geometric compensation schemes, including rectangle compensation, circle compensation, parallel compensation and angle-decrease compensation, are designed to test the methods of modifying the deviation which may arise during the lithography and ICP etching step, as shown in fig. 5.

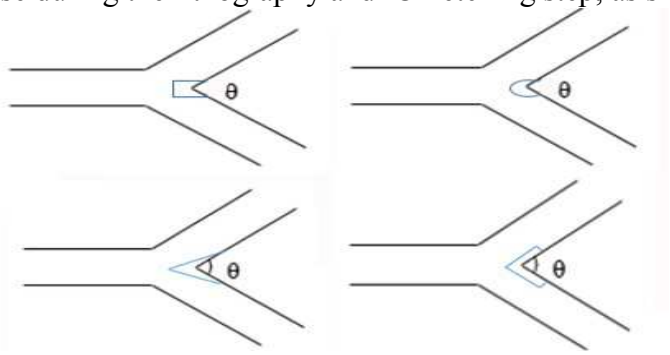


Fig. 5. The four geometric compensation schemes

To test the effects of ICP etching process to the devices with different parameters, a group of different key parameters are set as references. The final mask layout drawn with L-edit is shown in fig. 6.

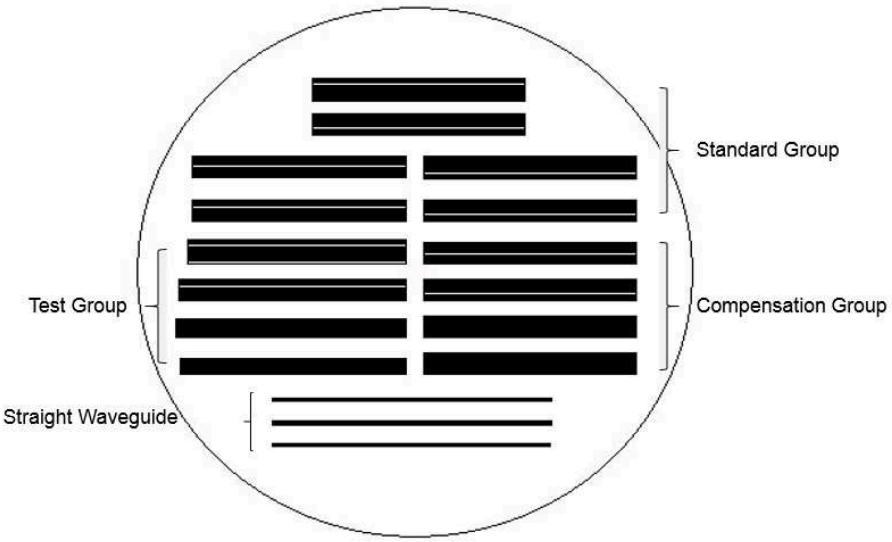


Fig. 6. The layout of the photolithographic mask

Fabrication

The fabrication process includes lithography and ICP etching. To ensure enough exposure resolution, contact exposure is adopted with ultraviolet light source. As discussed before, to reduce the radiation loss a very small banch angle is needed, and for the feasibility of sensitive layer depoisition the distance between the two arms should be wide enough. Therefore the device is inevitable thin and long which brings great difficulty to the practical processing, especially the lithography process.

The whole lithography process includes cleaning, Pre-Baking, Priming, Spin-on PR Coating, Soft Baking, EBR，Edge Bead Removal, Alignment, Exposure, Contact Printing, PEB, Post Exposure Baking, Development, Hard Baking. In order to guarantee the lithography resolution, we chose to use positive photoresist, which leads to the lack of photoresist adhesion. During the process, the photoresist is prone to desquamation, as shown in fig. 7.

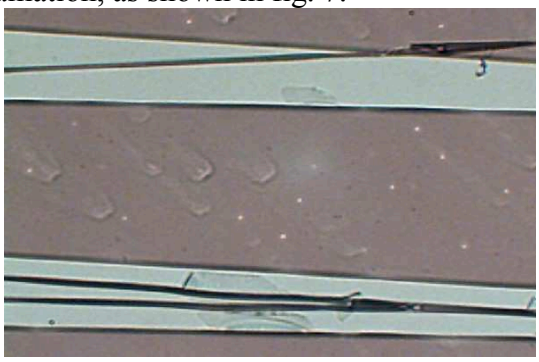


Fig. 7. Photo of the photoresist desquamation

To deal with the photoresist desquamation, we spin coating a layer of tackifier Hexamethyldisilazane (HMDS) 3 minutes earlier before spining the photoresist on the SOI surface. Then, we appropriately increase soft baking temperature from 100 degree centigrade to 110 degree centigrade and increase soft baking time from 1 minute to 3 minute. The photoresist desquamation problem is effectively solved.

As a result of adding the tackifier, the photoresist tends to be underexposed, so the developing time becomes longer. This leads to developed photoresist lines narrowing and shaping into trapezoids, which would seriously affect the precision of lithography. Measures including appropriately increasing the exposure time and improving the developer concentration are taken to reduce the development time, which effectively avoided the problem and guaranteed the line width.

After lithography, photoresist lines are strongly adhered and the line width comply with the design requirements. Fianally, the devices are fabricated with ICP etching. The fabracation result is shown in fig. 8.

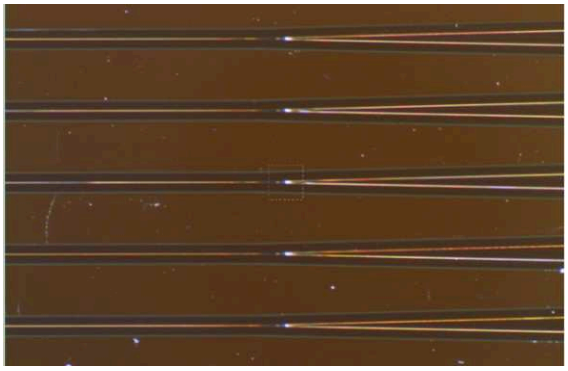


Fig. 8. Photo of the fabrication result

Summary

In this paper the sensing platform, utilized a Mach-Zehnder Interferometer (MZI) configuration, is designed based on the ridge waveguide single-mode condition, and the key parameters of the waveguide are optimized by FDTD method. The most important parameter of the MZI configuration, the Y-branch angle, is designed in consideration of the transmission loss. Process simulations are

conducted to predict the processing results. Lithography problems including photoresist desquamation and line narrowing are solved to achieve the special structure. This fabrication process is a tentative for the development of the biochemical sensor based on SOI ridge waveguide MZI.

Acknowledgement

This work is supported by Shenzhen Science and Technology Research and Development Funds (No： JCYJ20140709145631545)

References

[1] E. A. Mendenz, R. R. Lagune, J. A. A. Lucio, Design and characterization of PH sensor based on sol-gel silica layer on plastic optical fiber, Sensors and Actuators B, 106(2), (2005) 518-522.

[2] D. Adam, D. X. Xu, et al, A Silicon-on-Insulator Photonic Wire Based Evanescent Field Sensor, Photonics Technology Letters, IEEE 18.23 (2006), pp. 2520-2522.

[3] R. A. Soref, Applications of silicon-based optoelectronics, MRS Bull., 23(4), (1998) 20-24.

[4] C. Z. Zhao, G. Z. Li, et al, Silicon on Insulator Mach–Zehnder Waveguide Interferometers Operating at 1.3μm, Applied Physics Letters, 67(1995), pp. 2448-2449.

[5] D. Pieter, et al, Low-loss SOI Photonic Wires and Ring Resonators Fabricated with Deep UV Lithography. IEEE Photonics Technology Letters 16.5 (2004), pp. 1328-1330.

[6] R. A. Soref, J. Schmidtchen, K. Petermann, Large single-mode rib waveguides in GeSi-Si and Si-on-SiO2, IEEE J. Quantum Electronic, 27(8), (1991) 1971-1974.

[7] Y. Du and Y. Dong, Micro Biochemical Sensor Based on SOI Planar Optical Waveguide, Proc. SPIE 2014, pp. 91421Y-91421Y.

[8] S. P. Pogossian, H. E. Gall, J. Gieraltowski, et al., Determination of the parameters of rectangular dielectric waveguides by new effective methods, Journal of Modern Optics, 42(2), (1995) 403-409.

[9] A. Kumar, D. F. Clark, B.Culshaw, Explanation of errors inherent in the effective-index method for analyzing rectangular-core waveguides, Optics Letters, 13(12), (1988) 1129-1131.

[10] F. P. Payne and J. P. R. Lacey, A theoretical analysis of scatting loss from planar optical waveguides, Opt. Quant. Electron., 26(10), (1994) 977-986.

Key Engineering Materials Vols 645-646 (2015) pp 783-789
© (2015) Trans Tech Publications, Switzerland
doi:10.4028/www.scientific.net/KEM.645-646.783

Submitted: 2015-01-08
Accepted: 2015-01-13

The Research on Electroplating Technology used for RF Micro Inductor Coil

Ruike Bi[1, a], Xiuyan Wei[1, b], Jing Wu[1, c], Hang Guo[2, d *]

[1]School of Physics and Mechanical Electrical Engineering, Xiamen University, Xiamen, Fujian, China

[2]Pen-Tung Sah Micro-Nano Technology Institute, Xiamen University, Xiamen, Fujian, China

[a]biruike2009@163.com, [d]hangguo@xmu.edu.cn

Keyword: electroplating; linear sweep voltammetry; citrate copper plating system; micro inductor

Abstract. In this paper, we focus on the electroplating technology used for RF micro inductor coil. The technological parameters in DC electroplating are determined by SEM, linear sweep voltammetry and so on. It turns out that a high quality of plating layer is obtained when the PH value of electrochemical solution is 9, temperature is 45□， current density is 1 A/dm^2, additive is added and stirred slowly. Then the research on pulse electroplating is conducted on the basis of DC electroplating, and the result indicates that the pulse plating layer is of better quality compared with DC plating layer. Afterwards, surface structure and resistance of the copper layer are analyzed, demonstrating the obtained coating layer is good enough to be the main structure of micro inductor coil. In the end, this electroplating technology is applied to micro inductor coil. The simulation, fabrication, package and test of micro inductor coil are introduced briefly.

Introduction

High-performance on-chip micro inductors have been increasingly needed for satisfying advanced demands in modern wireless communication and microwave products [1, 2].In order to improve the performance of micro inductor coil, people reduce the metal resistance by thick gold metallization [3], multiple metal layers in parallel [4], or copper metallization [5]. Considering cost and performance, most RF micro inductor coils use copper as main structure. Compared with PVD, CVD, sputtering and other thin film growth technology, electroplating has the character of low cost and is easy to operate, moreover, the coating has an uniform morphology and broad range for thickness that can be easily controlled. So the copper structure of RF microcoil is fabricated by electroplating usually. Citrate copper plating system is superior to the commonly used cyanide copper plating in industry at present. In citrate solution, copper electrodeposition is highly inhibited and results in a small number of large hemispherical crystals located mainly on top of the solid surface [6], leading the plating layer finer, that means lower resistance coating can be obtained. Therefore, this paper employs citrate copper plating system as electroplating solution. The line width of RF microcoil is in micron level, leading microcoil very sensitive to the defects of fabrication process such as pinhole, crack, hydrogen embrittlement and overlap joint [7], that means the electroplating technology we use must be in high quality. In the fabrication of RF microcoil, electroplating technology is one of the most core technology, electroplating quality directly affects the electrical performance of the micrcoil. However, little attention has been paid to the research on electroplating used for micro coil, so it is very important and necessary to research the

electrochemical behavior and technological parameters of electroplating. The analysis is useful in improving the performance of RF micro coil.

Experiment

The operating principle of electroplating used for micro coil fabrication is shown in Fig.1. The electroplating workbench is set up in the experiment. Plating solution is citrate copper plating system, the electrochemical workstation is Shanghai Chenhua CHI660E, which also serves as the power source. Electrochemical workstation adopts three electrodes system, the reference electrode is saturated calomel electrode (SCE), electroplating cathode is a silicon wafer with sputtered Ti/Cu on it. Test method is linear sweep voltammetry, initial potential is 0V and terminal potential -2.5V, scanning rate 1 mv/s.

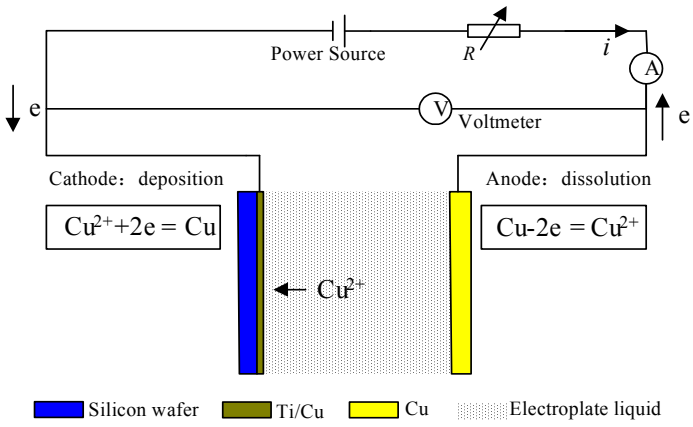


Fig. 1 Operating Principle of Electroplating

Results and Analysis

With the rising of PH value of plating liquid, hydrogen release potential shift negatively [8], weakening the influence of hydrogen release on copper deposition. Also, cathodic polarization increases within a certain range as well. The increase of cathodic polarization makes plating layer finer for the increase of cathode potential and the decrease of reaction rate. However, when PH value is too high, cuprous oxide particles will emerge in the solution, attaching on the surface of cathode. Consequently, side-reaction and adhesion failure between coating and substrate will appear. Shown in Fig.2 is the cathodic polarization curve under different PH value. Here we can see 9 is the best choice for PH value for the strongest cathodic polarization.

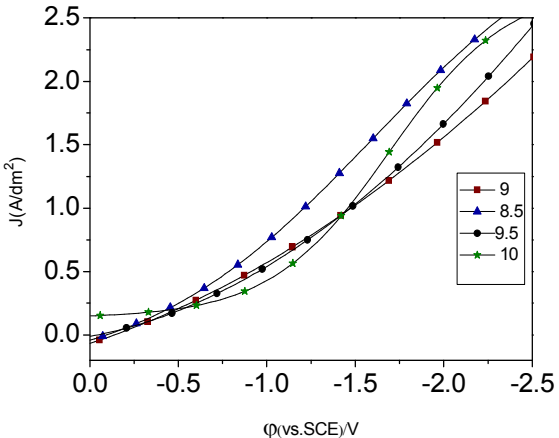


Fig. 2 Cathodic Polarization Curve under Different PH Value

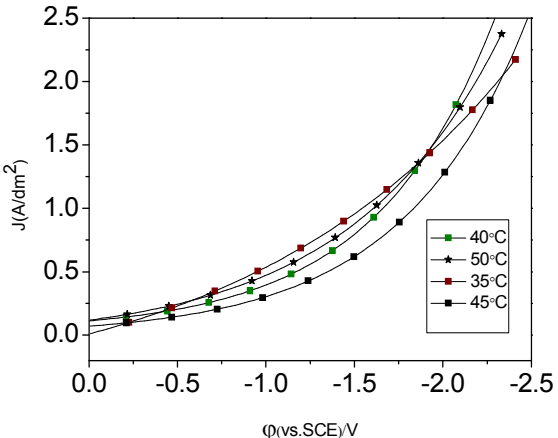


Fig. 3 Cathodic Polarization Curve under Different Temperature

Temperature is another important factors affecting coating quality. Low temperature result in low current efficiency, severe hydrogen release and appearance of pinhole, that decreases the largest current density the solution can bear and raises the internal stress of coating [9]. But if

temperature is too high, replacement reaction will occur on the substrate, worsening the adhesion of coating. As seen in Fig.3, 45℃ should be choosed as solution temperature, when cathodic polarization is the most powerful in the figure.

Stirring reduces the concentration polarization and increase effective current density while improving uniformity of the coating and rising deposition rate when electroplating [10]. Further, stirring also bring the solution oxide, which oxidate Cu^{+} into Cu^{2+}, decreasing the defects of coating. But if stir too rapidly, consumed Cu^{2+} around the cathode can't be supplied in time, the coating will become rougher as the reaction progress. As we can see in Fig.4, the cathodic polarization is strongest when stirring slowly, that indicates the coating is better than others when stir slowly.

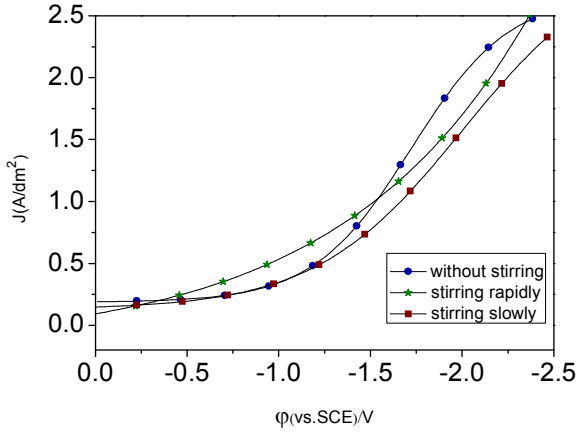


Fig. 4 Cathodic Polarization Curve with Stirring or Not

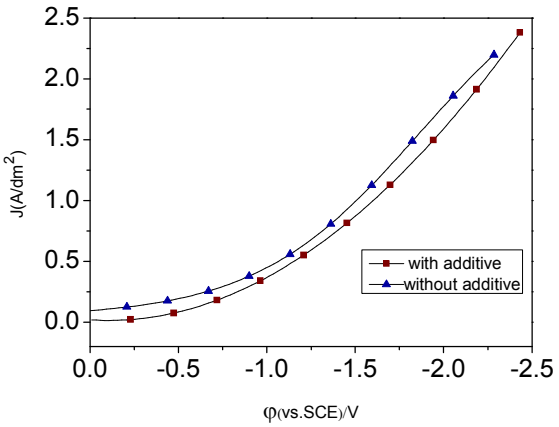


Fig. 5 Cathodic Polarization Curve with addictive or Not

Additive like polyethyleneimine (PEI) in the solution forms a strong adsorption layer on the cathode, and Cu^{2+} must get through this layer to discharge on the cathode, that makes discharge on the cathode become fast reaction and getting through the absorption layer slow reaction while side reaction is inhibited. Consequently, the deposition rate is inhibited, the plating layer is compacted [9]. The coating also shows preferred crystal orientation of (1,1,1) [11]. Fig.5 is the cathodic polarization curve with additive or not, from the figure we can see additive enhances cathodic polarization when electroplating, contributing to obtaining a uniform exquisite coating.

In DC electroplating, cathodic polarization strengthens along with the increase of current density. Low current density generates rough coating surface for large copper particle. The increased reduction potential due to the increased current density is conducive to the production of crystal nucleus, resulting in closer plating layer as well. However, if the current density continues to rise, hydrogen evolution reaction will occur [12]. Fig.6 is the SEM image of plating layer under different current density of 0.5A/dm^2, 1A/ dm^2 and 1.5A/ dm^2, from the figure we know coating morphology is the best when current density is 1A/ dm^2, that implies the most suitable current density for this plating technology is 1A/ dm^2.

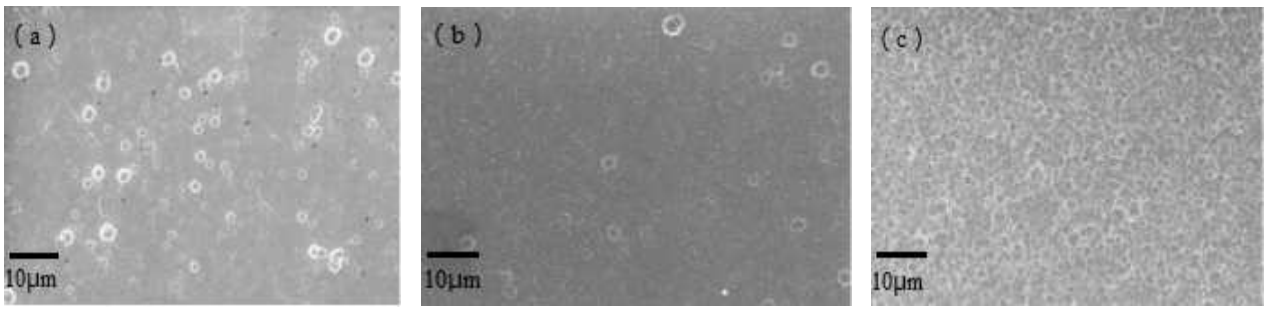


Fig. 6 SEM Image of Coating under Different Current Density.(a) 0.5A/dm^2, (b)1 A/dm^2, (c)1.5 A/dm^2

In DC electroplating, concentration polarization cannot be avoided for the continually deposition of metal iron around the cathode. But in pulse plating, metal iron around the cathode is adequately deposited when current is on, when current is off, the concentration of metal iron around the cathode returns to the original [13]. Off time in every period not only do good to the recovery of the metal iron concentration around the cathode, but also lead to some phenomenon like adsorption-desorption, re-crystallization and so on, optimizing the plating layer. During pulse deposition period, charged particles around the cathode is more than that in DC electroplating for the much higher current density, that increases the nucleation rate, leading to a fine grain structure. Microsecond impulse makes electro deposition for metal iron under high potential and inhibit side effect like hydrogen release, promoting the performance of plating layer. Pulse off time is a very active period. During this period, the cathode growth centre is shield by a certain retarder, forcing the cathode to generate other crystal nucleus when the next pulse comes. Fig.7 and Fig.8 is the SEM image of coating plated in DC current and pulse current. The thickness of them is about 5μm. From the figure we can see the coating plated in pulse current is finer.

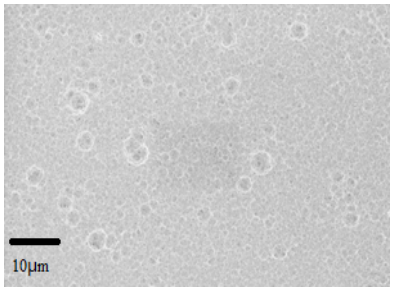


Fig. 7 Coating SEM Image in Pulse Current

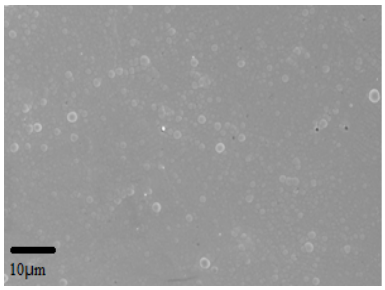


Fig. 8 Coating SEM Image in DC Current.

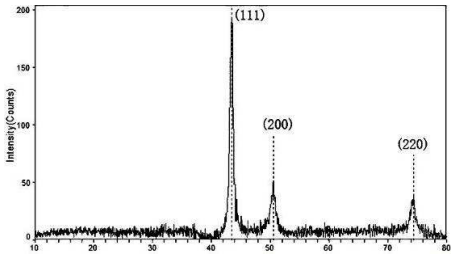


Fig. 9 XRD Diagram of coating

Fig.9 is the XRD diagram of the obtained coating. Compared with standard JCPDS card of copper powder, we can know the coating we obtained under this process is face-centered cubic crystal structure, with the diffraction peaks of (111), (200) and (220), and the planar spacing of all the diffraction peaks are very close to standard copper interplanar space. In addition, no other impurity peaks appear in XRD diagram, that means the quality of obtained coating is superior, without impurities like copper oxide, cuprous oxide.

Coating resistance is tested instantly after plating, and the average coating resistance is 2.03μΩ • cm, which is a little higher compared with the standard copper resistance 1.67μΩ • cm. it is mainly because the oxidation and defects of the coating. Hence, the coating must be protected instantly after plating by anti-oxygenation and packaged in time.

Fabrication and Test

After the determination of technological parameter, the electroplating technology is applied in the manufacture of micro inductor. Fig.10 is the model of micro coil build by electromagnetic field software HFSS. Through simulation result the optimized fabrication parameters are determined on the basis of actual requirement. Fig.11 is the simulated Q value curve obtained by simulation [14].

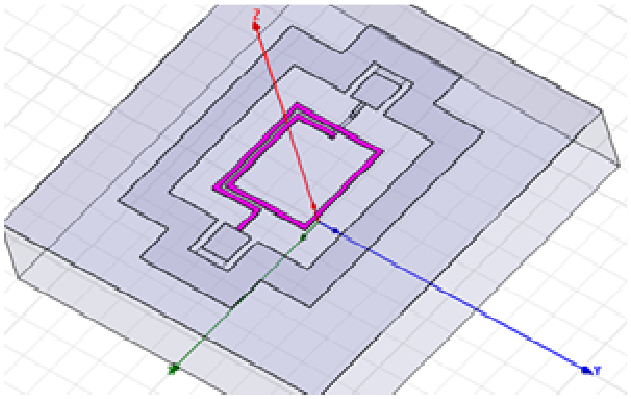


Fig. 10 Model of Microcoil

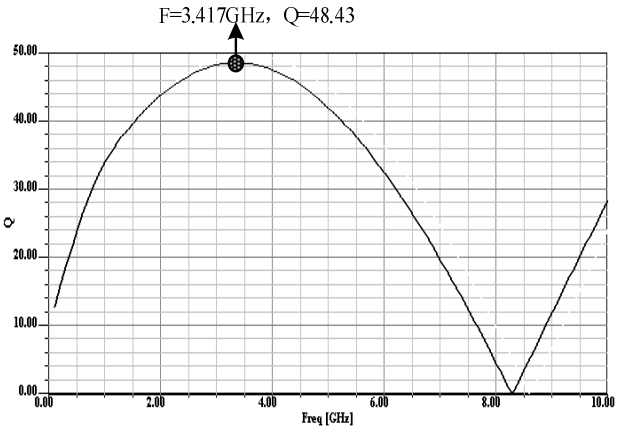


Fig. 11 Q Value Simulated by HFSS

Fig.12 is the micro coil fabrication made up of four parts, the preparation of electroplating cathode, the preparation of electroplating mould, electroplating and the removing of seed layer. Electroplating mould is obtained after a series of processing on silicon wafer, like gluing, photoetching, development and magnetron sputtering. Then the copper is electroplated onto the electroplating mould in previous DC plating technology. Afterwards, the photoresist and seed layer is removed. And we get the microcoils on the silicon wafer finally. Its SEM image is shown in Fig.13.

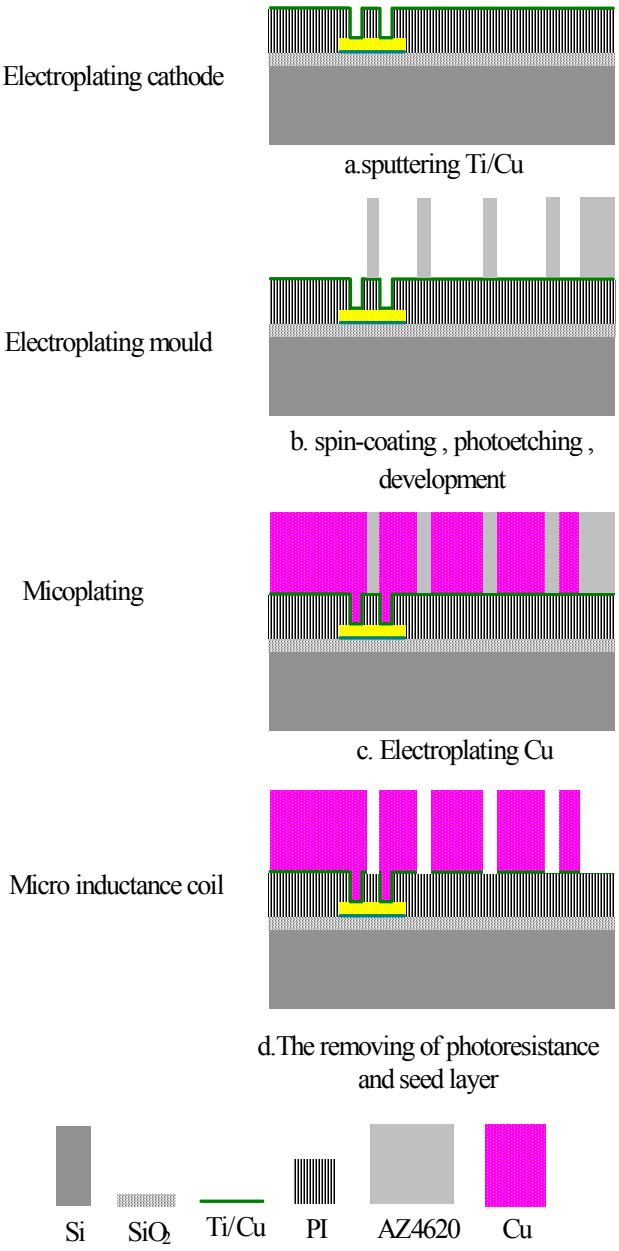


Fig. 12 fabrication flow of RF microcoil

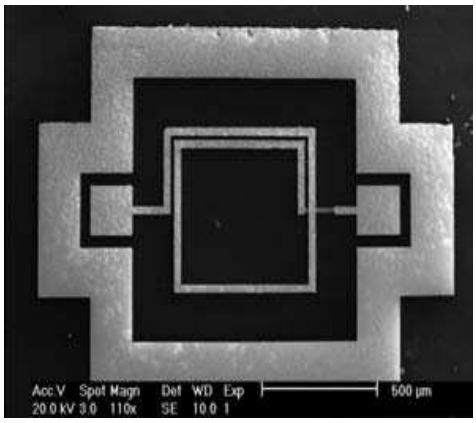


Fig. 13 SEM image

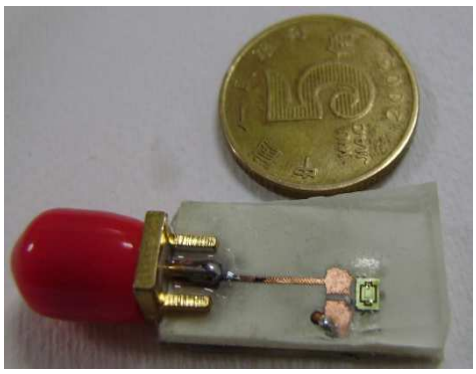


Fig. 14 packaging

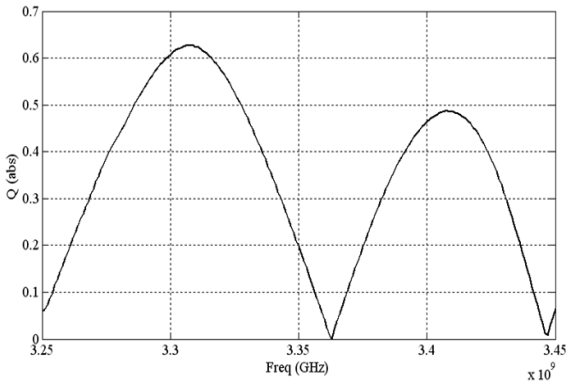


Fig. 15 test Q-value curve

As soon as the fabrication is over, the microcoil is packaged (shown in Fig.14) instantly. Then the device is tested with vector network analyzer. After that the data is analyzed with MATLAB. Fig.15 is the obtained Q value curve of the packaged device, which shows that the micro inductors fabricated with our electroplating technology work effectively.

Summary

The scope of this article lies in the electroplating technology used for RF micro inductor. It determines the main technological parameter of plating and compares DC plating layer with pulse plating layer. Afterwards, the electroplating technology is applied in the fabrication of micro inductor and the test result shows micro inductor works effectively, but its Q value is a little lower, one of the reason is the performance of plating layer, To improve the Q value, pulse plating can be used instead of DC plating layer in the future fabrication.

Acknowledgement

The research is funded by the New Century Talents Supporting Plan of The Education Department of China (project #2007NCET-07-0723), the National Natural Science Foundation of China (60936003) and Aviation Science Foundation of China (2008ZH68002).

References

[1] J.-B. Yoon, C.-H. Han E. Yoon, and C:K. Kim, Monolithic high-Q overhang inductors fabricated onsilicon and glass substrates,IEDM Tech. Dig., 1999, 753-756.

[2] J.-B. Yoon. C.-H. Han. E. Yoon and C.-K. Kim, High performance three-dimensional on-chip inductor fabricated by novel micromachining technology for RF MMIC, 1999 IEEE M7TS Int. Microwave Symp. Dig.,1999,1523-1526.

[3] K. B. Ashby, I. A. Koullias, W. C. Finley, J. J. Bastek ,S. Moinian, High Q inductors for wireless applications in a complementary silicon bipolar process, J. Solid-State Circuits, 31(1996)1-4.

[4] J. N. Burghartz, M. Soyuer, K. A. Jenkins ,M. D. Hulvey, High-Q Inductors in Standard Silicon Interconnect Technology and its Application to an Integrated RF Power Amplifier, IEDMTech. Dig., 1995, 1015-1017.

[5] J. N. Burghartz, D. C. Edelstein, K. A. Jenkins, C. Jahnes, C. Uzoh, E. J. O'Sullivan, K. K. Chan, M. Soyuer, P. Roper, S. Cordes, Monolithic Spiral Inductors Fabricated Using a VLSI Cu-Damascene Interconnect Technology and Low-Loss Substrates, IEDM Tech. Dig., 1996, 99-96.

[6] IVANOV S, TSAKOVA V, Influence of copper anion complexes on the incorporation of metal particles in polyaniline Part I: Copper citrate complex, J.Applied Electrochemistry, 32(2002)701-707.

[7] Wu J, Tang X， Microelectroplation for Soft Magnetic Cantilever of Radio Frequency Microelectromechanical System Switch. J.Journal of shanghai dianji university, 13(20100, 193-196.

[8] Wu W, Yang F, Tian Z, Electrodeposition of Copper in a Citrate Bath and Its Application to a Micro-Electro-Mechanical System, J. Acta Phys. -Chim. Sin., 26(2010):2625-2636.

[9] Wang G, Zhang X. electro plating additive and technology, first ed., Chemical Industry Press, Beijing,2011:91-94.

[10] Zhang Y, Hu R. Electroplating Manual. Second ed. National Defence Industry Press, Beijing,1997:84-86.

[11] Wen Z, Lixin H, Zhi Z, The influence of PEI additive on alkalinity copper electroplating behavior, J.Material Protection, 43(2010)1-3.

[12] Jiang L. Q., Sun W.,Zheng J. W., Material Science and Technology, first ed., Chemical Industry Press,Beijing，2008.

[13] Guopu X. Theory and Tpplication of Pulse Plating, first ed., Tianjin science and technology Press, Tianjin,1990:1-3.

[14] J. Wu, R. Xia, X.Y. Wei, H. Guo, Design and Microfabrication of A Microfabricated 3.417GHz RF Coil for Rubidium Atomic Clock, Proceedings of the 6th Asia-Pacific Conference on Transducers and Micro/Nano Technologies, Nanjing, China, 2012.

Key Engineering Materials Vols 645-646 (2015) pp 790-795
© (2015) Trans Tech Publications, Switzerland
doi:10.4028/www.scientific.net/KEM.645-646.790

Submitted: 2014-12-08
Accepted: 2014-12-23

Study On Magnetization and Detection the Metal Particle in Harmonic Magnetic Field

ZHANG Xing-ming[1,a], ZHANG Hong-peng[1,b] ,BO Zhao[1,c], Chen Hai-quan[1,d], SUN Yu-qing[1,e]

[1]Marine Engineering College, Dalian Maritime University, Dalian Liaoning 116026, China

[a] z_xm01@163.com, [b] zhppeter@163.com (corresponding author), [c]15941178340@163.com, [d]chenapec@163.com, [e] sunyq@dlmu.edu.cn

Keywords: Metal particle; Impedance analyze; Microfluidic chip

Abstract: Inductance detection methods of metal particle in hydraulic oil are generally based on the inductance change detection. With this method, when particles pass through the microchannel, ferromagnetic and non-ferromagnetic metal particle can be distinguished by monitoring inductance. In this study, it was found that not only inductance pulse but also resistance pulse was produced when detecting particle by inductance detection method. The theory of inductance or resistance change caused by particle is presented from the perspective of electromagnetism in this paper. To verify this phenomenon, the oil sample mixed with different metal particles was forced through the detection coil of microfluidic by constant flow rate. Then several sizes of iron and copper particles were measured. Experimental results showed that the resistance pulses caused by iron particles and copper particles were positive. And for copper particle, SNR (Signal Noise Ratio) of copper particles detected in improved effectively by detecting the resistance pulse.

Introduction

Oil detection is significant way to fault diagnosis and state prediction of mechanical equipment. As common method, inductance detection method is usually used to judge the source metal particle [1,2]. Not only can it differentiate ferromagnetic and non-ferromagnetic of metal particle, but also it can judge the wear status of oil by particle counting and particle size measurements [3]. The microfluidic oil detection chip of solenoid and planner coils were designed and manufactured by our research team. Counting of 19 μm iron particle and 50 μm copper particle has been achieved. Nowadays, inductive metal particle detection is based on the inductance analysis of coil. The mechanism of inductance pulse generated and its factors were illustrated in reference [4,5]. Relevant law of the inductance pulse signal to planar inductor is illustrated in [6,7]. The rules and principles of the pulse signal generated by solenoid inductor are demonstrated in [8]. By the existing research, the smallest particle can be identified for non-ferromagnetic metal particle is limited by sensitivity of the inductive measurement unit.

This paper analyzes the mechanism of inductance and resistance pulse generated with simultaneous and experimental study. The properties of particles can be determined by positive and negative performance of two signals. Therefore SNR higher pulse signal can be selected to determining the size of particles. It can improve the detection sensitivity of the metal particles from the principle.

Demonstration of sensing mechanism

Fig. 1 illustrates the inductive sensing principle, which was described in our prior publication [3].The 3D solenoid oil detector chip was fabricated with our prior method [5]. An LCR meter

(Agilent E4980A) connected to a computer is applied across the microfluidic chip, which induces a magnetic field in the micro-inductor, and monitors the impedance change caused by metal particle. For the experiments using iron and copper particles were prepared reducing method. Oil sample was made by 10 mg of metal particles mixed with 50 ml of SAE-5W30 lubrication oil, a syringe forces oil samples flowing through the microchannel. The equivalent diameter was also measured by NIS-Element-D (Nikon, Japan). In all experiments, the excitation signal, which was produced by the LCR meter, was a 2 Vpp, 2 MHz sine wave, and the oil detection chip has a channel with 400μm, and a 3D solenoid coil which is 800 turns wrapped with 35μm diameter varnished wire.

Eleven groups of metal particles(six groups of iron particles and five groups of copper particles) were used in testing, each group has similar particle size. Their approximate sizes are summarized in Table 1. The iron and copper particles are roughly spherical in shape.

According to Maxwell–Faraday equation, When a particle flows through inside the coil (shown in Fig.2(a)), the first, the magnetic flux is enhanced due to the higher permeability, causing an increase magnetic flux density around particle. Second, eddy current density is generated by the alternative magnetic field (the blue arrow in Fig.2(b) and Fig.2(c)), the direction of eddy current(the red arrow in Fig.2(b)) is perpendicular to magnetic field. The current has different phase angle relative to excitation magnetic field which is shown in Fig.2(c). Thus current at different phase inside the metal particle producing a magnetic field has both effects on coil inductance and resistance. Therefore a metal particle generates an inductance pulse and a resistance pulse at same time.

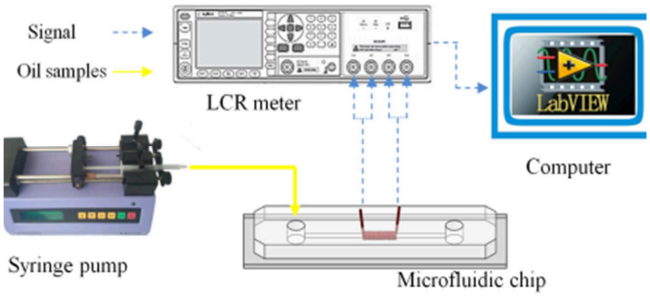


Fig. 1 Oil contamination identification experimental system

Table 1 Metal particles used in testing the device

Iron particles		Copper particles	
Group No.	Diameter(μm)	Group No.	diameter(μm)
f_1	300	c_1	300
f_2	200	c_2	200
f_3	150	c_3	150
f_4	100	c_4	100
f_5	50	c_5	50
f_6	20		

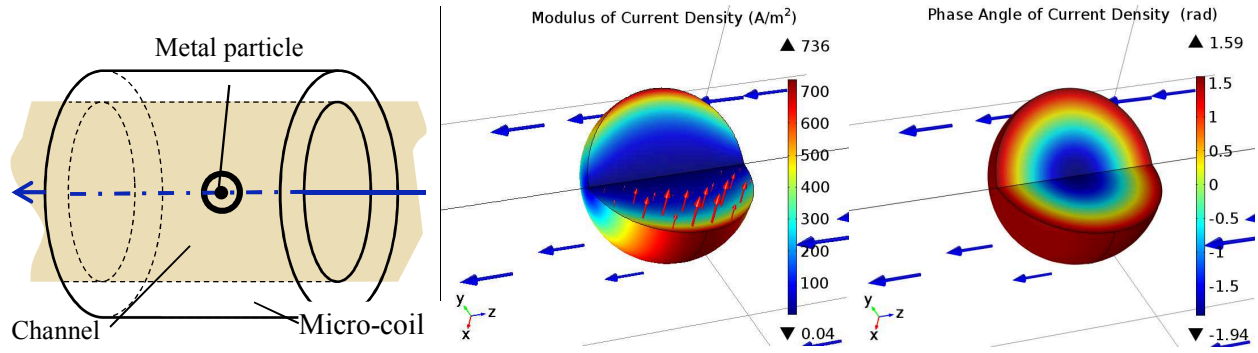
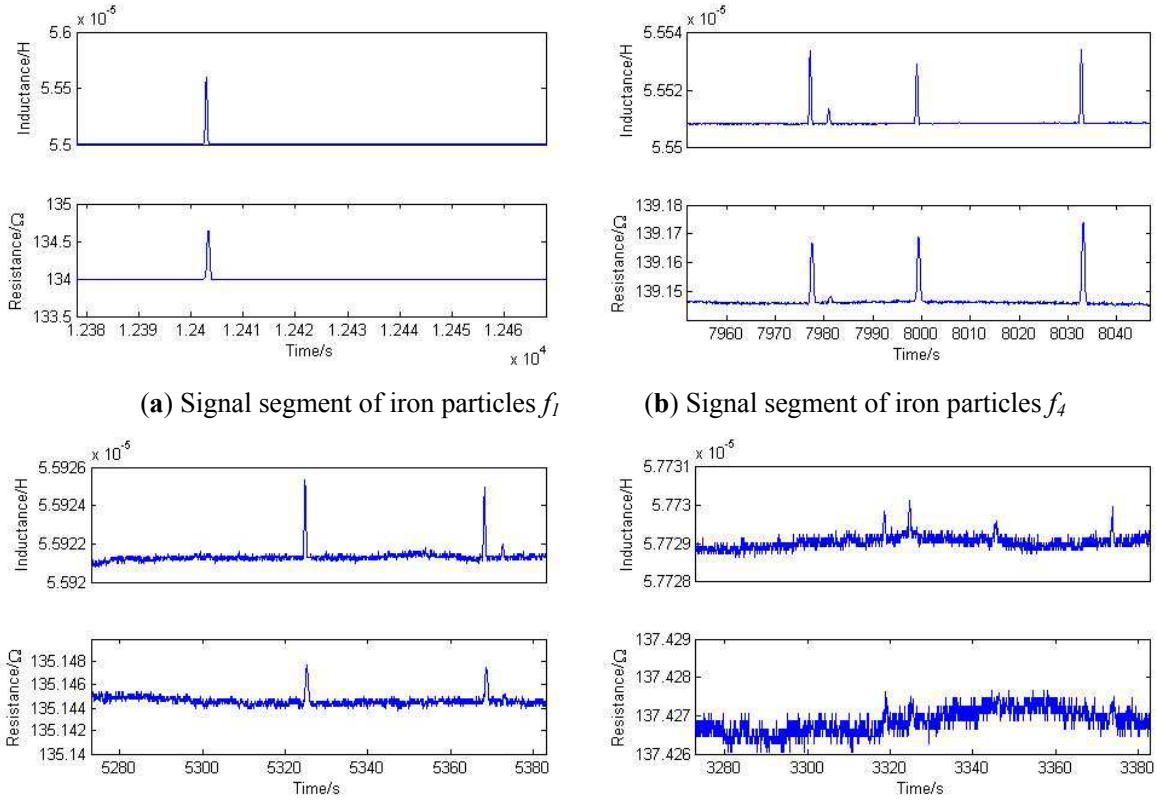


Fig. 2 Sensing principle of a metal particle **a** A metal particles is flowing through the micro-coil, it could be magnetized by harmonic magnetic field. **b** Eddy current inside the particle is generated by harmonic field (the blue arrow). **c** The phase angle of current density.

Experiment and discussion

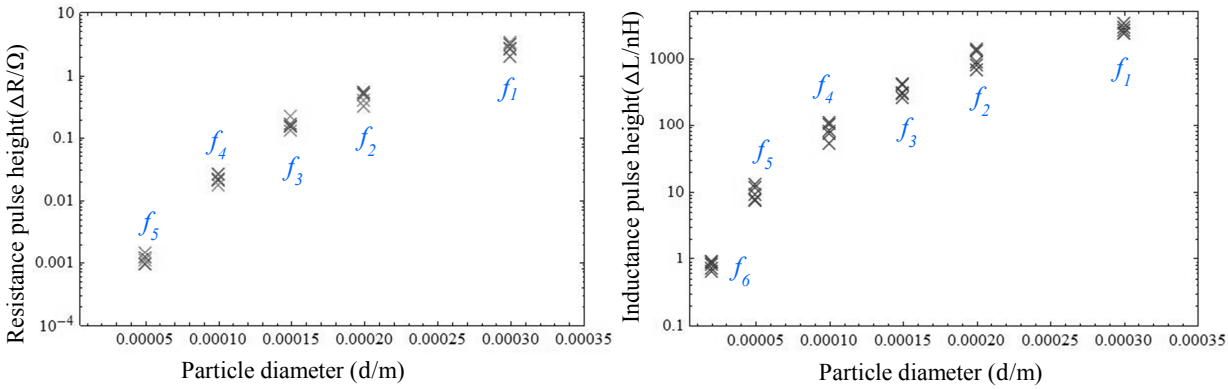
For the first test, six groups of iron particles were used. Their approximate sizes are listed in Table 1. Fig. 3 shows the inductance pulse and resistance pulse caused by different size of particles as they were moved through coil. Fig. 3 (a, b, c, d) were the signal segments generated by iron particle f_1, f_4, f_5 and $f6$ respectively. We note Fig. 3(a-c) that each iron particle produced positive inductance and positive resistance pulse simultaneously. Fig. 3(d) implies that the current setup can detect ferrous particles of smaller size by observing inductance signal. Fig. 4 shows inductance and pulse height generated by different size group, it implies that both two pulse height are monotone increasing functions of iron particle size, and inductance signal contributes to smaller iron particle detection.



(**a**) Signal segment of iron particles f_1 (**b**) Signal segment of iron particles f_4

(**c**) Signal segment of iron particles f_5 (**d**) Signal segment of iron particles f_6

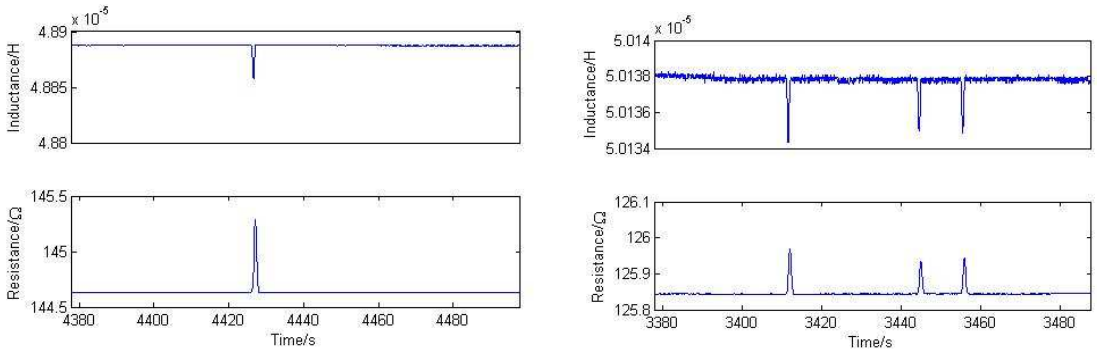
Fig.3 Original inductance and resistance signals are generated by different size of iron particles. (a), (b) and (c) illustrate that iron particle can produce positive inductance and resistance pulses, (d) illustrates that smaller iron particles can be detected from observing inductance signal.



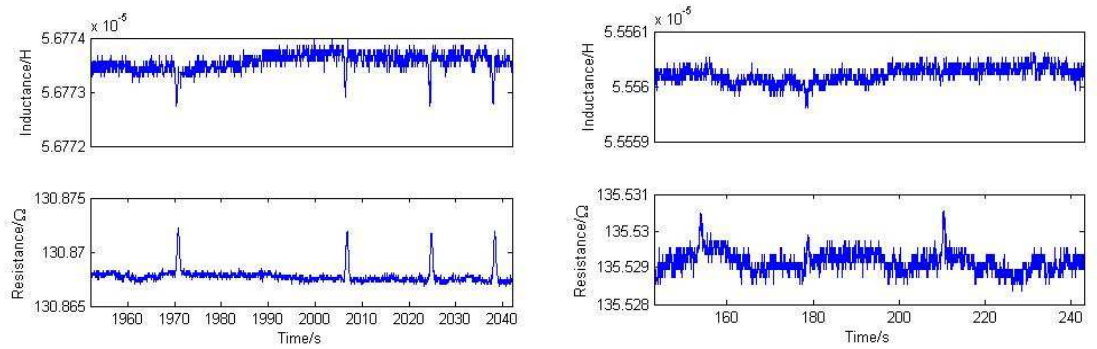
(**a**) (**b**)

Fig. 4 Pulse heights generated by iron particles. (**a**) Resistance pulse heights under iron particle group f_1~f_5. (**b**) Inductance pulse heights under iron particle group f_1~f_6.

For the second test, five groups of copper particles were used. Their approximate sizes are listed in Table 1. Fig. 5 shows the inductance pulse and resistance pulse caused by different size of particles as they were moved through coil. Fig. 5 (a, b, c, d) were the signal segments generated by copper particle c_1, c_3, c_4 and c_5 respectively. We note Fig. 5(a-c) that each copper particle produced negative inductance and positive resistance pulse simultaneously. Fig. 5(d) implies that the current setup can detect nonferrous particles of smaller size by observing inductance signal. Fig. 6 shows inductance and pulse height generated by different size group, it implies that both two pulse height are monotone increasing functions of iron particle size, and resistance signal contributes to smaller copper particle detection.

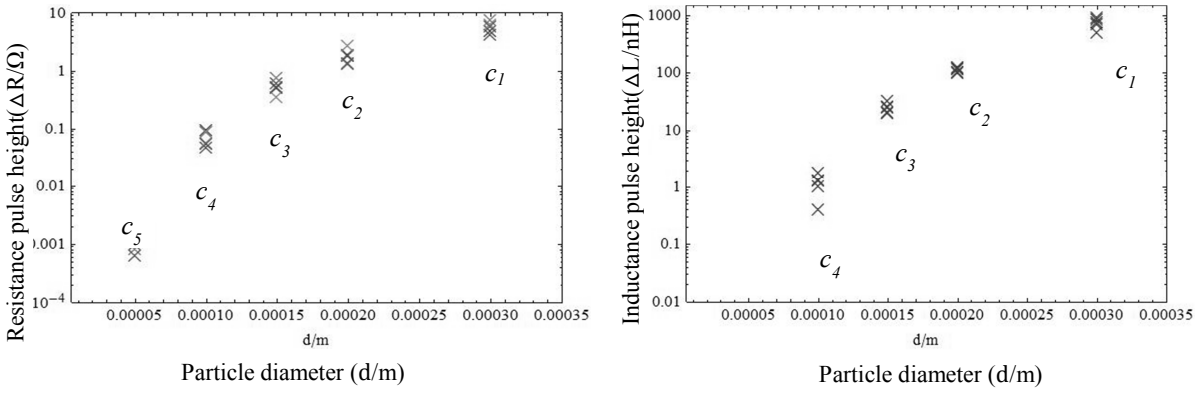


(**a**) Signal segment of copper particles c_2 (**b**) Signal segment of copper particles c_3



(**c**) Signal segment of copper particles c_4 (**d**) Signal segment of copper particles c_5

Fig.5 Original inductance and resistance signals are generated by different size of copper particles. (a), (b) and (c) illustrate that the single copper particle can produce a negative inductance pulse and a positive resistance pulses, (d) illustrates that smaller copper particles can be detected from observing resistance signal.



(**a**) (**b**)

Fig. 6 Pulse heights generated by copper particles. (**a**) Resistance pulse heights under copper particle group c_1~c_5. (**b**) Absolute value of inductance pulse heights under copper particle group c_1~c_4.

Conclusion

Both inductance and resistive pulse signals caused by ferromagnetic and non-ferromagnetic metal particles were detected by LCR meter in this paper. The inductance pulse signal is positive and negative to ferromagnetic and non-ferromagnetic metal particles, respectively. However the resistive pulse signals of them are all positive. Using impedance analysis module, experiments demonstrated that:

1. The SNR of inductance signal is better than the resistance signal for the ferromagnetic metal particles within the size range of the experiment.
2. Inductance detection method can be used to detect smaller ferromagnetic metal particle.
3. The SNR of resistance signal is larger than the inductance signal for the non-ferromagnetic metal particles within the size range of the experiment.
4. Resistance detection method can be used to detect smaller non-ferromagnetic metal particle.

Acknowledgement

The experiments were carried out in the microfluidic chip laboratory of Dalian Maritime University. The study is financially supported by the National Natural Science Foundation of China (51205034), Ministry of Transport of the People's Republic of China (2013329225260) and the Fundamental Research Funds for the Central Universities (3132014332).

References

[1] L. Du, J. Zhe, J. Carletta, et al. Real-time monitoring of wear debris in lubrication oil using a microfluidic inductive coulter counting device. Microfluidics and Nanofluidics, 2010, 9(6):1241-1245.

[2] Y. Li,Y. Zheng,R. Wang. Experimental study and the theoretical model of optical flowmeter of solid debris. chinese journal of mechanical engineering, 2004, 40(8):160-165.

[3] X. M. Zhang, H. P. Zhang, L. Guo. Design of the oil detection microfluidic chip. Chinese Journal of Scientific Instrument, 2013,34(4):762-767

[4] X. M. Zhang, H. P. Zhang,Y. Q. Sun, et al. Research on the output characteristics of microfluidic inductive sensor. Journal of Nanomaterials, 2014, 2014.

[5] X. M. Zhang, H. P. Zhang, H. Q. Chen, et al. Study on the resolution-frequency characteristic of microfluidic oil detection chip, Chinese Journal of Scientific Instrument. 2014,35(2),427-433

[6] H. P. Zhang, W. Huang, Y. D. Zhang, et al. Design of the microfluidic chip of oil detection. Applied Mechanics and Materials, 2012, 117: 517-520.

[7] L. Du, J. Zhe. A high throughput inductive pulse sensor for online oil debris monitoring. Tribology International, 2011, 44(2): 175-179.

[8] J.L. Miller, D. Kitaljevich. In-line oil debris monitor for aircraft engine condition assessment, 2000 IEEE Aerosp. Conf. Proc, 2000: 49-56.

Key Engineering Materials Vols 645-646 (2015) pp 796-799
© (2015) Trans Tech Publications, Switzerland
doi:10.4028/www.scientific.net/KEM.645-646.796

Submitted: 2015-01-19
Accepted: 2015-01-21

The Buckling Simulation of Planar W-form Micro-Spring in MEMS Safety and Arming Device

Wang Fufu[1, a], Lou Wenzhong[1, b], Liu Fangyi[1, c*], Wang Dakui[1, d],
Lu Jun[2, e], Wu Jian[2, f], Guo Xuhong[2, g], Zhang Zhe[2, h]

[1]National Key Laboratory of Electro-mechanics Engineering and Control, School of Mechanical-electronic Engineering, Beijing Institute of technology, Beijing, China, 100081

[2] China North Industries Group Corporation, Changzhi, 046000

[a]wangfufu2004@sina.com, [b]Louwz@bit.edu.cn, [c]lfyhbu@163.com(corresponding author),

[d]wangdakui1987@163.com , [e] 25841301@qq.com, [f] jake2000-wj@163.com,
[g]guoxh.mems@gmail.com,[h] kb235@163.com

Keywords: buckling simulation; W-form micro-spring; MEMS; safety and arming device

Abstract. This paper describes the stability research of MEMS spring used in fuze. The micro-spring in thickness dimension is thin, while the size of axial direction is larger, during compression the micro-spring is prone to suffering buckling and become unstable. In order to consider the extreme environments in launch, this paper aims to carry out buckling simulation in high or low temperature, by using FEM analysis. The effect of temperature load on the micro-spring buckling can be obtained. These researches can provide theory reference for the design applications and reliability analysis of micro-spring, and also lay the foundation for the response characteristics of the micro-scale elastic components under compressive force.

Introduction

Planar micro-spring is an important part of MEMS (Micro-electromechanical Systems) S&A (safety and arming) device, which function is same as the traditional spring. The design and processing quality of micro-spring determines the security of MEMS S&A device at ordinary time and reliability of MEMS S&A device in the arming process. The MEMS S&A device was used in an OICW (Objective Individual Combat Weapon) shown as Fig. 1, including the application of planar W-form micro-spring [1, 2]. The structure of planar W-form micro-spring is shown as Fig. 2.

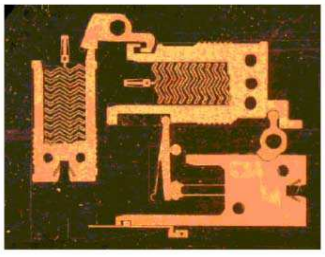


Fig. 1 MEMS S&A device used in OICW

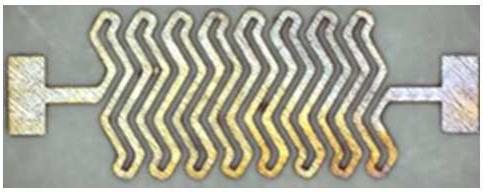


Fig. 2 Structure of planar W-form micro-spring

Micro-spring in thickness dimension is thin, while the size of axial direction is larger, during compression the micro-spring is prone to suffering buckling, and the occurrence of buckling can make the micro-spring lose bearing capacity [3]. While in MEMS S&A device, micro-spring installed between the substrate and the slider, due to the restraint of inner wall of the substrate, the micro-spring can continue to load and stress [4]. Even so, the buckling phenomenon can make large friction between cover plates and micro-spring or between sideway and micro-spring, thus affect the normal movement of slider. Considering the fuze might encounter all kinds of extreme environments in the application, such as high or low temperature, and the change of surrounding temperature can make certain changes in the mechanical properties of materials, so the effect of temperature load on the micro-spring buckling cannot be ignored. In this paper, the eigenvalue buckling analysis of the planar W-form micro-spring is performed using the FEM (finite element method) software ANSYS

Multiphysics. The micro-spring is used in the MEMS S&A device, which is fabricated in our laboratory, shown as Fig. 3.

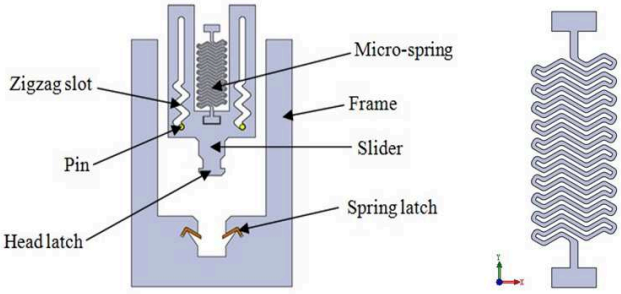


Fig. 3 The diagram of MEMS S&A device and micro-spring

Theoretical Analysis [5] and Material Properties

Initially the bar is totally flat and withstands axial pressure F, shown in Fig.4 (a). If the axial pressure F is greater than its threshold (F_{th}), the equilibrium stable begins to lose, shown in Fig.4 (b). Deflection will continue to expand until it reaches the new equilibrium stable. In this case, the structure instability, also known as buckling.

Assuming there is a slight deflection of the bar, and the differential deflection curve is

$$EI\frac{d^2y}{dx^2}=F(\alpha-y) \tag{1}$$

Where E is elastic modulus, I is the inertia moment of the bar cross-section, F is axial pressure, α is the y displacement at x=m.

Take k2=F/EI, the Equ.1 becomes

$$\frac{d^2y}{dx^2}+k^2y=k^{2}\alpha \tag{2}$$

The general solution of the equation is

$$y=\alpha+A\cos kx+B\sin kx \tag{3}$$

According to the fixed end boundary conditions can be obtained that

$$y=\alpha(1-\cos kx) \tag{4}$$

According to the free end boundary conditions can be obtained that

$$km=(2n-1)\pi/2 \tag{5}$$

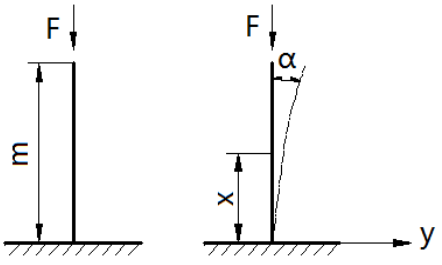
Where m is the length of the bar, n=1, 2, 3…

Take the n=1, the minimum value of k can be obtained, which fit the Equ.5. The corresponding F is the critical load.

$$F_{th}=\frac{\pi^2EI}{4L^2} \tag{6}$$

Where, F_{th} is the minimum critical load, and it is a minimum axial force sufficient to maintain a slight deflection of the bar.

Similar to the bar, the micro-spring can lose stability when subjected to compressive load.



(a) (b)

Fig. 4 The buckling analysis of rod

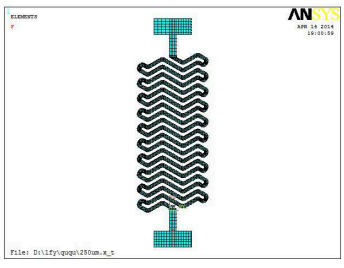


Fig. 5 The finite element model

The material of micro-spring is nickel. The material properties obtained by experiments are summarized in Tab.1.

Table 1 Material properties of Ni

Elastic modulus （GPa）	Tangent modulus （GPa）	Density （kg/m^3）	Poisson ration	Yield strength （GPa）
200	2.15	8.9×10^3	0.31	1.05

Finite Element Analysis

The finite element analysis model of the planar W-form micro-spring is established in ANSYS Mulitiphysics, shown in Fig.5. One end of the micro-spring is fixed and the other is free. The micro-spring is easy to appear the six order buckling mode under the action of axial load. Based on the actual fuze application environment, two extreme temperatures -40℃and +50℃are selected to analysis the influence of temperature on micro-spring. Three groups simulation have been finished: buckling simulation of W-form micro-spring at room temperature, buckling simulation of W-form micro-spring at -40℃ and buckling simulation of W-form micro-spring at +50℃.

Simulation Results. Apply unit axial force to the free end of the spring at room temperature. Through simulation analysis, the critical buckling forces on micro-spring buckling are obtained. Six order modes of micro-spring are shown in Fig. 6-11 and the critical values are shown in Tab. 1.

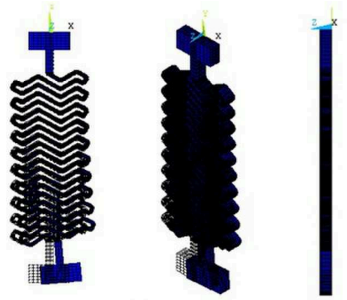


Fig. 6 First-order buckling mode

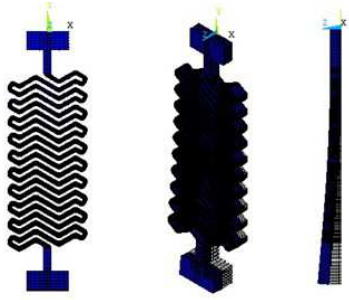


Fig. 7 Second -order buckling mode

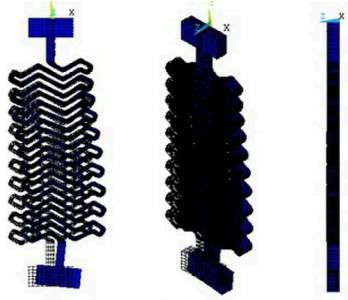


Fig. 8 Third-order buckling mode

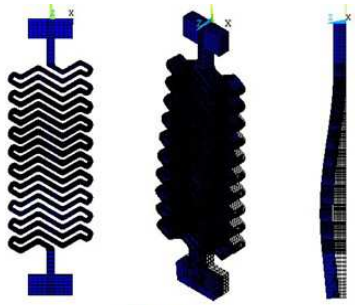


Fig. 9 Fourth-order buckling mode

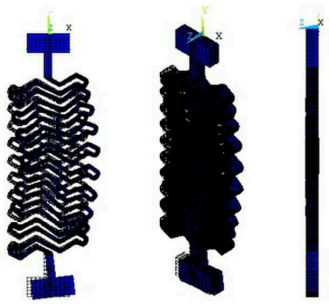


Fig. 10 Fifth-order buckling mode

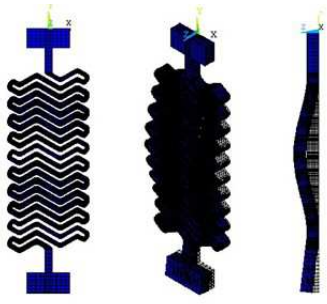


Fig. 11 Sixth-order buckling mode

Table 2 Buckling deformation plane and critical buckling values

Plane	XY Plane			YZ Plane		
Buckling mode	First-order	Third-order	Fifth-order	Second-order	Fourth-order	Sixth-order
Critical buckling forces (N)	0.028657	0.043191	0.27645	0.38593	0.81680	0.99152

Apply unit axial force to the free end of the spring at two extreme temperatures -40℃and +50℃. Each order buckling critical load values at different temperature are shown in Fig.12.

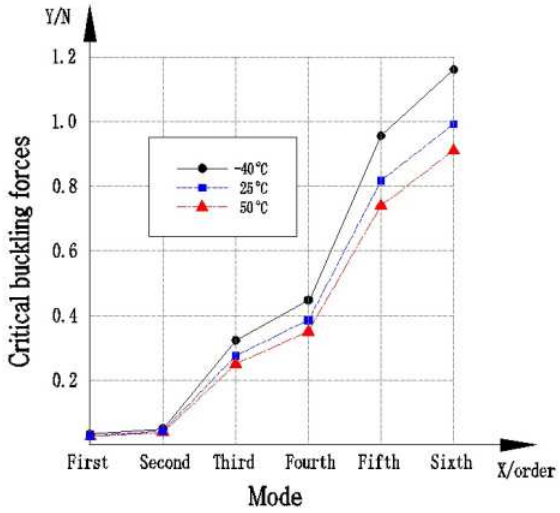


Fig. 12 The critical buckling force of six order modes in different temperature

Simulation Analysis and Conclusions. By comparative analysis, it arrives at the conclusions as follows: firstly, according to the six modes of micro-spring deformation diagram, first-order, third-order, fifth-order buckling occurred in plane (XY plane), second-order, fourth-order, sixth-order buckling occurred in thickness direction (YZ plane); secondly, if there is a first-order buckling occurred, the slider connecting with the micro-spring is likely to deviate and stuck; thirdly, if there is a second-order buckling occurred, the slider breaks away from micro-spring; fourthly, if micro-spring in case of third-order or fifth-order buckling will cause the friction between spring and slide way , which affect the flexibility of slider movement; fifthly, if micro-spring in case of fourth-order or sixth-order buckling will cause the friction between spring and cover plates , which increase the resistance of mechanism motion; sixthly, for the same order buckling, the higher of temperature, the lower of micro-spring critical buckling value, namely the micro-spring more prone to buckling instability.

Summary

This paper has completed the buckling simulation of micro-spring in high, low and room temperature by using FEM simulation analysis, and obtained six buckling modes of micro-spring. The research can provide theory reference for the design applications and reliability analysis of micro-spring. The next step is to do buckling experiments to verify the correctness of the simulation trend.

Acknowledgement

The research was supported by the State Key Laboratory of Mechatronics Engineering and sponsored by the National Project of China (51305060302) and the National Project of China (9140C360602120C36138).

References

[1] James L. Zunino III, Donald R. Skelton, Charles Robinson. Reliability testing & analysis of Safing & Arming devices for Army fuze [J]. Proc. of SPIE, 2008-144. 206. 159. 178.

[2] Robinson C. H. Ultra-miniature, monolithic, mechanical safety-and- arming (S& A) device for projected munitions: USP, 6064013[P], 2001.

[3] Shi Gengchen, Li Hua. MEMS springs of fuze [J]. Journal of Detection &Control, 2008, 30(2):8-12

[4] Sui Li, Shi Gengchen. The assembly research of MEMS fuze mechanism [J]. Journal of Detection &Control, 2008, 30(3): 64-67.

[5] Wang Zhen. Stability analysis and optimization of micro compressed spring [D]. Beijing: Beijing institute of technology, 2014.

Key Engineering Materials Vols 645-646 (2015) pp 800-805
© (2015) Trans Tech Publications, Switzerland
doi:10.4028/www.scientific.net/KEM.645-646.800

Submitted: 2015-02-03
Accepted: 2015-02-03

Design, Optimization and Simulation of an Electric Field Microsensor based on PZT Piezoelectric Interdigitated Cantilevers

Ke Feng[1, 2, a]*, Jianhua Tong[1, b] ,Yu Wang[1, 2, c] and Shanhong Xia[1, d]

[1]State Key Laboratory of Transducer Technology, Institute of Electronics, Chinese Academy of Sciences, Beijing, P.R.China

[2]Graduate University of Chinese Academy of Sciences, Beijing, P.R.China

[a]kingfisher3721@126.com, [b]jhtong@mail.ie.ac.cn, [c]wangyuiecas@163.com, [d]shxia@mail.ie.ac.cn

Keywords: Electric field microsensor, Piezoelectric , PZT driven.

Abstract. In this paper, we demonstrate the design, optimization and simulation of an electric field microsensor based on PZT piezoelectric interdigitated cantilevers driven. The working principle is introduced, and the induced charge ability of the sensitive cantilever structure is simulated and analyzed using finite element analysis (FEA) method. A multilayer compound cantilever structure ($Al/Si_3N_4/Pt/PZT/Pt/Ti/SiO_2/Si$) have been designed as the sensing element and $PbZr_xTi_{(1-x)}O_3$ (PZT) thin film is used as the piezoelectric material to drive the cantilevers vibrating. This microsensor is fabricated based on the simulation results. The electric field microsensor is tested under the direct current electric field with the field intensity from 0 to 45000 v/m, and the output voltage signal of the microsensor showed a good linear response to the intensity of applied electric field.

Introduction

Electric field measurement is very important in the fields of meteorology, aerospace, power grid, industry and so on. Therefore, an increasing prospect has been paid to the research of electric field sensor. At the present time there are a number of methods for electric field measurement, and the miniaturization of electric field sensor has become a trend due to some advantages such as small dimension, light weight, low power consumption, easy to be integrated with other devices and low cost. Accordingly, several electric field microsensors have been developed in past few years which have electrostatic [1], thermal [2], and piezoelectric [3] driving system. However, electrostatic driving system generates noise derived from a relatively high actuation voltage which interferes with the precise measurement of electrostatic field, and thermal driving system is sensitive to temperature variation of the environment. [4] Piezoelectrically actuated sensor exhibits the advantages of high reliability, robustness, low power consumption, and great anti-interference performance, which makes it possible for piezoelectrically driven electric field microsensor.

In this article, we present an electric field microsensor which is fabricated by piezoelectric interdigitated cantilevers with vertical staggered vibration structure. Each cantilever is a multilayer compound structure (elastic substrate (Si/ insulator SiO_2/ bonding layer Ti/ bottom electrode Pt/ piezoelectric material PZT/ top electrode Pt/ bonding layer Ti /insulator Si_3N_4/ sensing electrode Al), and PZT thin film was employed as the actuator. Meanwhile, we also describe the design, working principle, the simulation and test results of the electric field microsensor.

Structure Design and Working Principle

The structure of the electric field microsensor is shown in Figure 1. The enlarged cross-sectional view of the micro-cantilever along A-B broken line in Figure 1 is shown in Figure 2. This microsensor consists of several piezoelectric cantilever beams with vertical staggered vibration structure. The microsensor includes substrate, bonding pad to sensing electrode, bonding pad to top electrode, bonding pad to bottom electrode and piezoelectric cantilever beams. The microsensor is fabricated by MEMS microfabrication technology. The fabrication process mainly involves functional films preparation and pattern, silicon micromachining and structure release. SiO_2 layer

was perpared on a silicon wafer by thermal oxidation process. The layer of 200nm thick SiO_2 was prepared to improve the adhesion of the bottom Ti/Pt electrode to the wafer surface and will act as the insulating layer and the etch mask. The 200nm thick Pt bottom electrode and 500Å thick Ti bonding layer was sputtered on oxide layer. PZT thin film was deposited by sol-gel method. A precursor solution spin-on coated on $Pt/Ti/SiO_2/Si$ substrates at 3000 rpm for 30s, and heated at 280℃ for 5 min, and then the rapid thermal annealing process at 700℃ for 30 min was carried out to obtain the perovskite phase PZT thin film which was about 1μm thick. Top electrode Pt was sputtered and the thickness was 200 nm. The 300 nm thick Si_3N_4 insulating layer was deposited on top electrode layer by a plasma enhanced chemical vapor deposition (PEVCD) method. Finally, a 200nm thick Al sensing electrode was sputtered on the insulating layer (Si_3N_4).

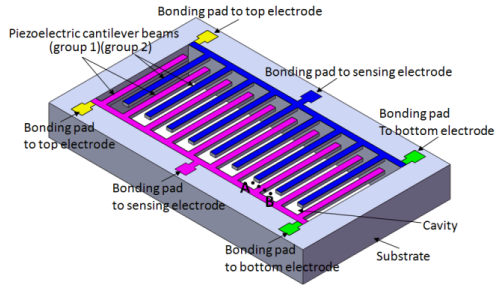


Figure 1. The schematic structure of the sensor.

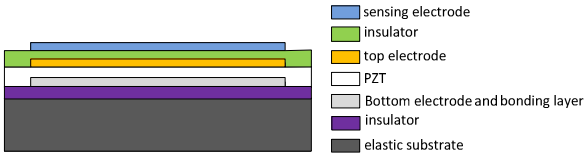


Figure 2. The enlarged cross-sectional view of the micro-cantilever along A-B broken line in figure 1.

The device operates as follows: The initial state of the cantilever beams is at the same level when there is no driving voltage. Piezoelectric cantilever beams group 1 and 2 of the sensor applied opposite polarity driving voltage which causes the piezoelectric material in the cantilever beams to be tensed and compressed. The tensed piezoelectric material tilts the comb structure upward, and the compressed piezoelectric material tilts the comb structure bends downward, as shown in Figure 3(a) and (c). Each piezoelectric cantilever beams can both shield and detect the external electric field. The surface induced charge of the sensing electrode increases because the beams exposed to the external electric field and are higher than the horizontal plane of the initial state, as shown in figure 3(b). The beams tilted upward are regarded as the sensing electrodes and play a role in shielding the external electric field at the same time. When the beams are lower than the initial horizontal plane which shielded by the beams of the tilted upward, the induced charge on the surface of the electrode reduces, as shown in Figure 3(c) and (d).

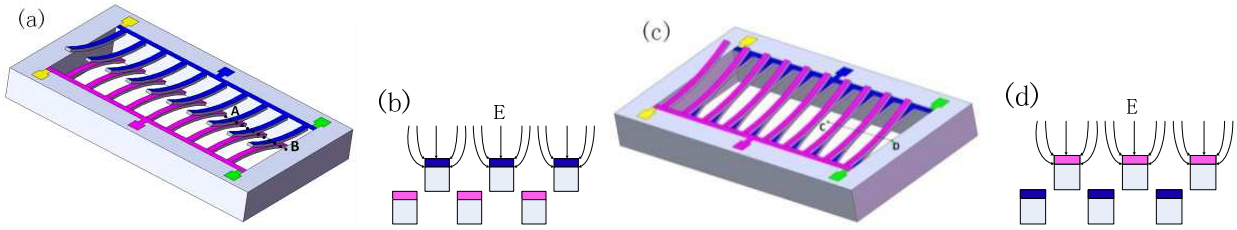


Figure 3 Working principle the proposed PMEFS. (a) and (c):Schematic view of two working state, (b) and (d):enlarged cross-sectional view of the micro-cantilever along A-B and C-D broken line.

Induced Charge Simulation

The Charge Simulation Model. The induced charges of the sensitive structures are simulated and analyzed by using two-dimensional model because the width of a single cantilever is far less than the length of the comb. The simulation model is shown in Figure 4.

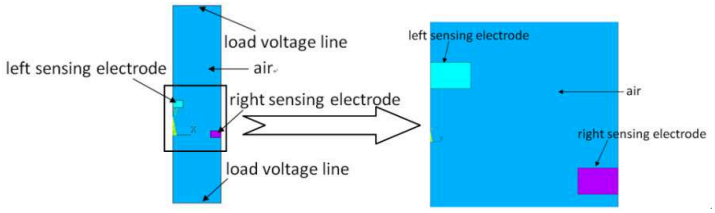


Figure 4.FEA model of electric field sensor

The simulation results and analysis. The simulated induced charge is called the charge line density q/L because a two dimensional model is used in this simulation process. According to the Gauss law the amount of the charge is proportional to exposed area A. The quantity of the induced charge on the surface of the sensing electrode is

$$Q = \xi |E| A \tag{1}$$

The state of the induced charge is described as the ratio of the induced charge variation Δq and the maximum induced charge Q. The width (w) of each cantilever beam is 20 μm and the distance between two adjacent cantilever beam of group 1 or 2 is d which is shown in Figure 5. Δq/Q can be written as:

$$\frac{\Delta q}{Q} = \frac{q/L}{Q/L} = \frac{q/L}{\varepsilon |E| \mathrm{A/L}} = \frac{q/L}{\varepsilon |E| w} \tag{2}$$

The size of the output signal is determined by the difference of the maximum and the minimum induced charges on the two group cantilever beams. According to simulation result in Fig. 6, when the vibration amplitude is 2 times than the gap between cantilever beams, the sensor output is close to 75% of the theoretical maximum value. From Fig. 6, when the y gradually increases, $\Delta q/Q$ is close to 100%.

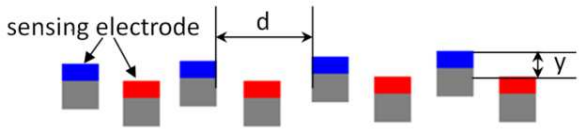


Figure 5. Structure parameter of simulation model

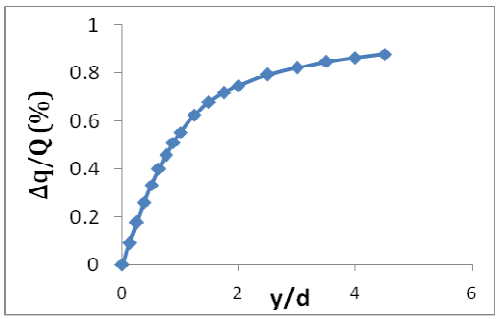


Figure 6. Induced charges state in the deferent amplitude

When the vibration amplitude (y), the width of the beam and the distance (d) between adjacent beams are all constant and the thickness of the beam is incrassation, the induced charge increase as shown in figure 7. So when we designed the sensor, we try our best to enhance the thickness of the beams. But when the thickness of beam increase from 10μm to 70μm, the amount of induced charge improve less than 10%, and driving ability become poor. Micro fabrication technology does not allow too much thick of beams. The reason of induced charge augment is analyzed with more and more thickness of beam. The beam side plays an important role as shielding electric field. The incrassation of the beam makes shielding effect better, which can reduce more induced charge of downbent beams.

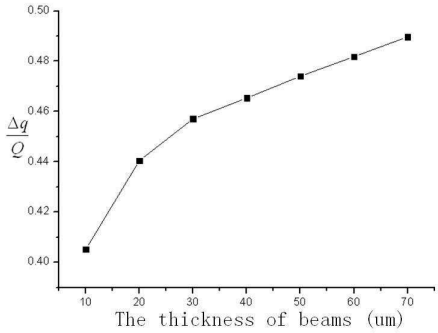


Figure 7 The relationship between the thickness of the beam and the induced charge

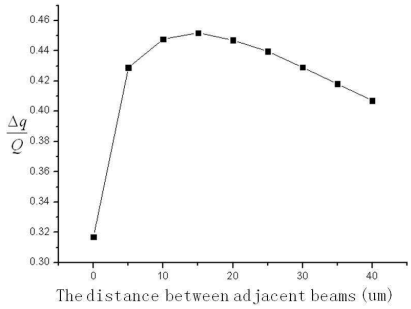


Figure 8 Relationship between the distance between adjacent beams and induced charge

When the vibration amplitude, width and thickness of beam are all constant and the distance between the adjacent beam is changed, the relationship curve is obtained about the induced charge and adjacent beams distance, as shown in figure 8. When the distance of the adjacent beam is augmented, the amount of induced charge rapidly increases, and then slowly decreases. the induced charge variation is maximum between 10μm and 20μm distance of adjacent beams. The reason is that the augmentation of adjacent beam distance makes induction area also increased. While the distance increases to a certain value, the shielding effect is poor, and then the inducted charge variation decreases.

Structure Parameter Optimization

Model. As shown figure 7, when some condition is invariableness and the *y* increases to a certain constant, Δq/Q is close to 100%. So driving ability should be tried to enhance. The driving ability is simulated by using three-dimensional model. In the proposed model we assumes that insulator layer, bonding layer and electrode layer are negligible because elastic substrate and piezoelectric materials layer are much more thickness than other layers. The model is simplified like figure 9. As the material properties of the thin film PZT layer have not yet been determined, and hence the values of the bulk PZT 52/48 are chosen.

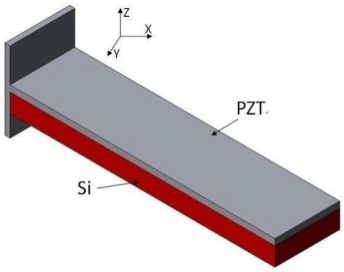


Figure 9 The simplify three-dimensional model.

Simulation results. As shown in figure 10, with the increase of the length , the displacement of the beam end increases. So with permission the length of beam can be designed longer.

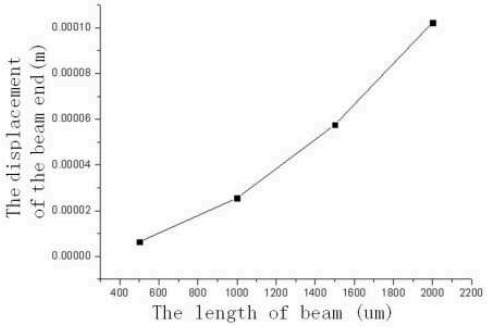


Figure 10 The relation curve of the length of the beam and the displacement of the beam end

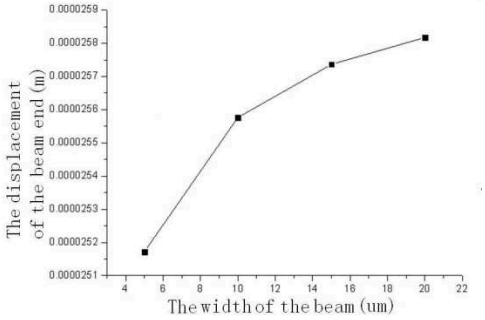


Figure 11 The relation curve of the width of the beam and the displacement of the beam end

Figure 11 shows the relation of the width and the displacement of the beam. When the width of the beam increases, the displacement of the beam end increases very slowly. It is not obvious for the influence of the width.

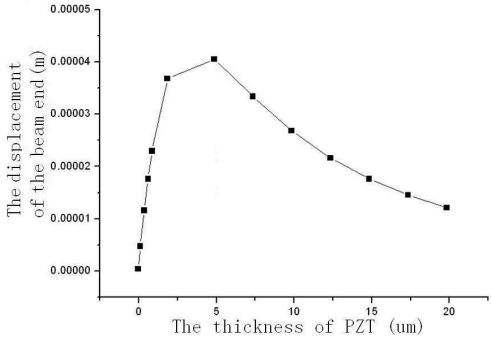


Figure 12 The relation curve of the thickness of PZT and the displacement of the beam end

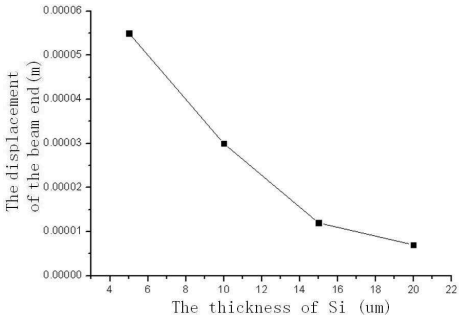


Figure 13 The relation curve of the thickness of Si and the displacement of the beam end

Figure 12 shows the relation curve of the thickness of PZT and the displacement of the beam end. The displacement of the beam end rapidly increases with the increase of the thickness of PZT. But when the thickness of PZT increases to a certain constant, the displacement of the beam end begins to decrease slowly. Figure 13 shows the relation curve of the thickness of Si and the displacement of the beam end. The displacement of the beam end decreases with the increase of the thickness of Si. So with permission the thickness of beam can be designed thinner.

Testing Result

In the design process of the mirosensor, we have comprehensively considerated the micromachining process, driving and inducted charge ability. The mirosensor is fabricated by MEMS technique. Finally after all steps of the process are completed, the scanning electron microscopy (SEM) photograph of the PZT piezoelectric interdigitated cantilevers is shown in Figure 14.

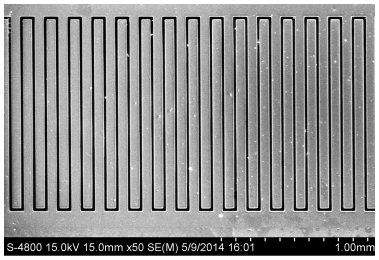


Figure 14. SEM image of the PZT piezoelectric interdigitated cantilevers

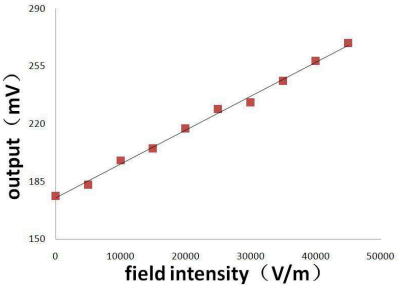


Figure 15. Variation of sensor response with DC field

According to the reported test method, [5] the mirosensor is tested with parallel plate electrode. The electric field intensity is from 0 to 45kV/m on the electrode plates. The testing result is shown in Figure 15. The output voltage signal of the microsensor showed a good linear response to the intensity of applied electric field

Since some of the geometrical parameters are restricted each other. For example, with permission the cantilever can be designed longer and thinner beams, but PZT and Si need be designed thicker. So, in the design of the electric field microsensor we have comprehensively considerated the inducted charge and driving ability, and then the structural parameters of the microsensor are chose by the simulating results. These emulational results can help us to optimize the structure of the beams and performance of the microsensors.

Conclusion

In this paper, we present an electric field microsensor with piezoelectric interdigitated cantilevers beams. The working principle of this electric field microsensor is analyzed, and the structure characteristics of the electric field microsensor were simulated by using the finite element analysis software. The inducted charge and the driving ability were simulated and analyzed. The relationship between the geometrical parameters was obtained. The microsensor was fabricated by MEMS technique, and tested under direct current electric field with the field intensity from 0 to 45000 v/m. The output voltage signal of the microsensor showed a good linear response to the intensity of applied electric field.

References

[1] Gong Chao, Xia Shanhong, Deng Kai, Bai Qiang, Chen Shaofeng. MEMS Device &Technology. Dec 2004, 41-44

[2] Ye Chao, Chen Xianxiang, Peng Chunrong, Tao Hu, Xia Shanhong. Chinese Journal of semiconductors. Sep. 2006, 1672-1675.

[3] Tao Hu, Peng Chunrong, Chen Xianxiang, Bai Qqiang, Xia Shanhong. Technology. CHINESE J ELECT DEVI. Sep. 2006, 639-642.

[4] Takeshi KOBAYASHI, Syoji OYAMA, Masaharu TAKAHASHI, Ryutaro MAEDA, and Toshihiro ITOH, Microelectromechanical Systems-Based Electrostatic Field Sensor Using $Pb(Zr,Ti)O_3$ Thin Films, The Japan Society of Applied Physics, Vol. 47, No. 9, 2008, 7533–7536.

[5] Li Difei, Bi Wu, Zhang mingyuan, WangLi-feng. Calibration Methods of Thundercloud Electric Field Sensors, Forestry machinery & woodworking equipment. Vol 38 No. 2 Feb. 2010.

Key Engineering Materials Vols 645-646 (2015) pp 806-809
© (2015) Trans Tech Publications, Switzerland
doi:10.4028/www.scientific.net/KEM.645-646.806

Submitted: 2014-10-28
Accepted: 2014-12-23

Design and Application of Digitally-Programmable Delay-Time Microchip in Detonating System

Lu Yufei[1, a], Lou Wenzhong[2, b], Ding Xuran[3, c], Wang Yabin[4, d]

[1]National Key Laboratory of Electro-mechanics Engineering and Control, School of Mechanical-electronic Engineering, Beijing Institute of technology, Beijing, China, 100081

[a]wslyf66@163.com (corresponding author), [b]louwz@bit.edu.cn, [c]axheron9413@163.com

Keywords: power and data-translating; digitally-programmable; C-MBUS; delay-time microchip; detonating system;

Abstract. A novel digitally-programmable delay-time microchip is introduced in this paper, which is based on detonating system. In order to make the detonating system more safety and reliability, C-MBUS is proposed in this paper. The programmable delay-time detonator can get power and data from Logger simultaneously. As a conclusion, the programmable delay time of this microchip ranges from 1 millisecond to 10000 milliseconds using the dedicated programming device, and the time programmable increment step can reach 1 millisecond. With its safety and reliability, its accuracy in delay time and its easy use, it will be extensively applicable to complicated blasting engineering of high quality.

Introduction

This paper is based on a detonating system, which contains a Blaster, a Logger and programmable delay-time detonators. This system is designed to provide accurate, flexible and reliable sequencing of both surface and underground blasts. The Logger is used during hook-up to assign the delay sequence and perform testing functions. The Logger reads and stores the unique detonator Identification Number and acquires the delay time. The Blaster is used to conduct final system tests, blast programming and firing. The digitally-programmable delay-time detonator is designed to provide the precise control necessary to produce accurate and consistent blasting results in a variety of blasting applications in the mining, quarrying and construction industries [3]. A digitally-programmable delay-time microchip was used in the delay-time detonator. The programmable delay-time detonator may be programmed in 1-millisecond increments from 1 millisecond to 10000 milliseconds using the dedicated programming device called the Logger. What's more, the programmable delay-time detonator can get power and data from Logger simultaneously.

The digitally-programmable delay-time detonators are fully programmable and have on board digital timing circuit and energy storage enabling them to function independently once the fire signal has been sent. A connecting harness of twin copper wire is used to hook-up the detonators. The harness is connected to a Logger to enable delay assignment and testing during hook up. As each detonator is connected, the Logger checks the detonator, reads the ID of detonator and then writes along with the delay time to its memory. The user is able to edit the assigned delay times stored in the Logger upon review of the delay list. Up to 200 detonators can be logged to a single Logger in delay increments of 1 millisecond from 0 to 10000 milliseconds. The Loggers are connected to the Blaster via a firing line. The blaster communicates with the detonators via the Loggers. Blasters are protected by a firing key to prevent use by unauthorized personnel. The Blaster can fire up to 2000 detonators on 10 Loggers [3].

Design of Digitally-Programmable Delay-Time Microchip

The digitally-programmable delay-time microchip can be used in C-MBUS based application. This microchip can get the power from C-MBUS and translate data with detonator control host. Cooperating with the external components on detonator board, the delay-time microchip can realize

the functions including power management, communicating with host and detonating-control with digitally programmable delay time. The delay-time microchip is implemented in TSMC 0.35μm mixed-signal process and operates at a single power supply of 5V [4]. The digitally-programmable delay-time microchip is shown in Fig.1.

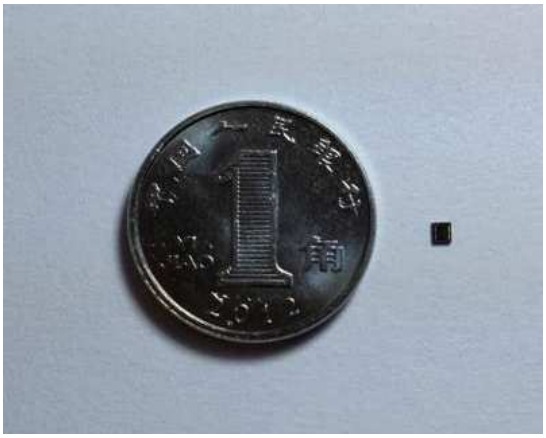


Fig.1 The digitally-programmable delay-time microchip

The block diagram of the digitally-programmable delay-time microchip is shown in Fig.2. Analog part includes bandgap reference circuit, LDO regulator, power-on reset and oscillator, 3 comparators and on-chip 64-bit EEPROM and charge pump. Analog circuit provides stable 3.3V power supply, clock and POR signal to digital parts. 3 comparators are used to detect received data, bridge error and capacitor voltage respectively. On-chip EEPROM is used to save the ID and delay time information, even when the power supply is off. Charge pump provides high voltage to EEPROM to perform the program. Digital circuit processes the data and performs the control function [4].

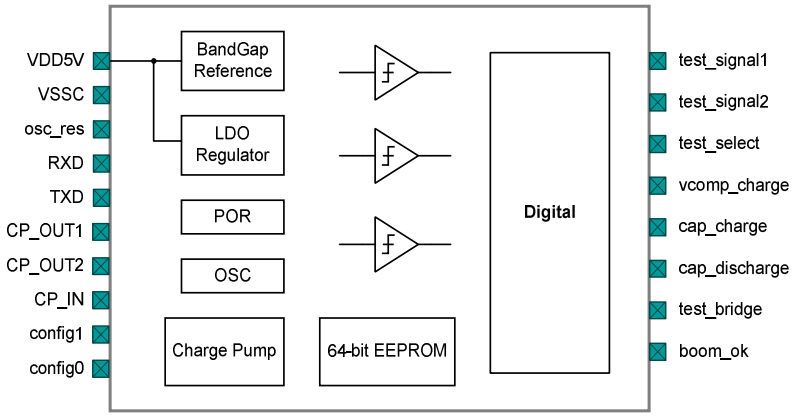


Fig.2 The digitally-programmable delay-time microchip block diagram

The digitally-programmable delay-time microchip can complete power and data-translating shared communication and it is low power consumption and support long programmable time. What's more, it has in-situ error self-detection of bridge wire and on-chip charge pump, on-chip oscillator and EEPROM. The delay-time microchip has 10 function pins and 8 test pins.

Application of Digitally-Programmable Delay-Time Microchip

The digitally-programmable delay-time microchip can be used in C-MBUS based application. For example, the digitally-programmable delay-time microchip can be used in detonating system. The detonating system used C-MBUS (Chinese Meter Bus) as power and data transmission Bus, whose communication speed is high, transmission distance is long and communication capacity is large. The Bus can connect 256 pieces of equipment at the same time. The biggest electric current of this Bus reaches 500mA and the distance of communication is 2000m and can offer the power long-distance. What's more, the C-MBUS is cheaper and its peripheral circuit design is relatively simple.

The detonating system consists of programmable digital detonators and control equipment (Logger and Blaster). The digitally-programmable delay-time microchip is used in the programmable digital detonators. The Logger and Blaster used C-MBUS as power and data transmission Bus. The Logger and Blaster devices use CMT100 control chip produced by ANPE Corporation. The CMT100 control chip is a special-purpose integrated circuit for center communication of C-MBUS. The Logger and Blaster supply the electric power for the whole detonating system by C-MBUS. The Logger and Blaster control the communication module of the detonators by the Meter Bus. Through the Logger and Blaster, the computer can send the command to the Logger and the Logger can transmit the data to the computer. The RXD port and the TXD port of chip connect with microcontroller through the photoelectrical coupler, which make sure the microcontroller will not be damaged by high voltage. The Fig.3 is the transmit module of C-MBUS circuit design diagram.

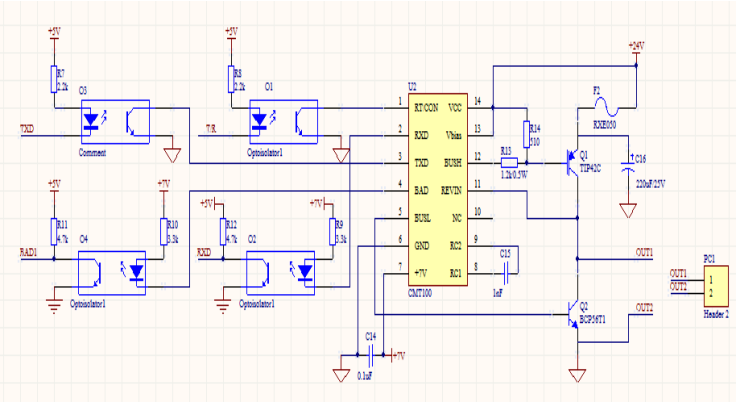


Fig.3 Transmit module of C-MBUS circuit design

The board diagram of digitally-programmable delay-time microchip is shown in Fig.4. The non-polarity 2-line C-MBUS provides power and signal to the digitally-programmable delay-time microchip. The digitally-programmable delay-time microchip operates under a 5-V voltage. Thus, high voltage interface circuits including RX and TX front-end, power management unit with rectify and LDO (or DC_DC), and control circuits are placed on the detonator board. Almost these circuits can be integrated with the digitally-programmable delay-time microchip into one single chip if a high-voltage process will be used. The digitally-programmable delay-time microchip communicates with Logger and controls the detonator switch with programmable delay time. The delay time is set by the Logger.

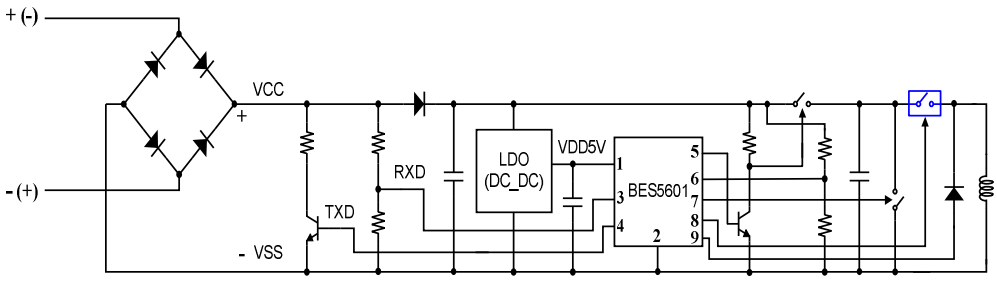


Fig.4 The board diagram of digitally-programmable delay-time microchip

Chip Testing

The function testing of this delay-time microchip is firstly performed with cob (chip on board) packaging. After cob test is done, a SSOP16L or smaller packaging can be used for prototype testing. Firstly, analog circuit of the digitally-programmable delay-time microchip is testing. After that, digital circuit of the microchip is testing through use Logger and Blaster. The program flow chart of the Logger and Blaster is shown in Fig.5. The program flow chart of the digitally-programmable delay-time microchip is shown in Fig.6.

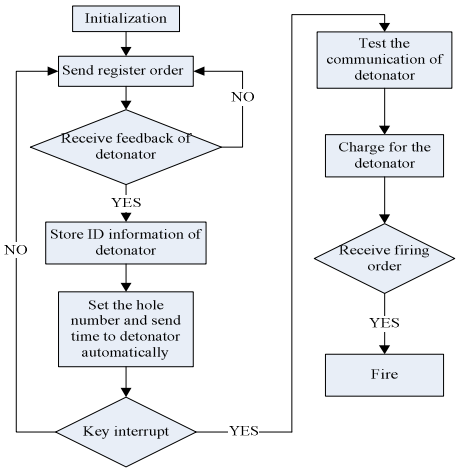


Fig.5 Program flow chart of the Blaster and Logger

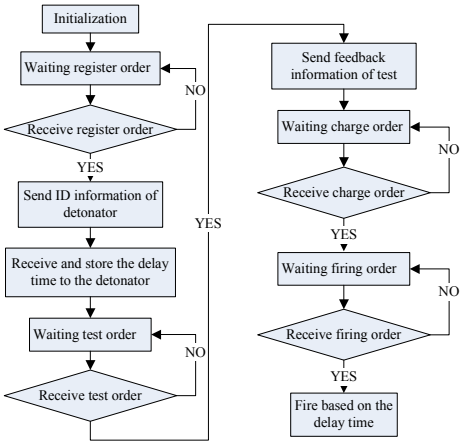


Fig.6 Program flow chart of the delay-time microchip

The testing shows that LDO voltage is 3.2V, Oscillation frequency is 1.1MHz, bandgap voltage is 1.2V, which is in the reasonable range. The digital circuit testing is normal when the delay-time microchip communicates with the Logger and Blaster.

Summary and Future Work

This digitally-programmable delay-time microchip can communicate with the Logger and Blaster and it can provide the precise control necessary to produce accurate and consistent blasting results. More important is that this system is security and reliability through C-MBUS. Except two large charging capacitors, almost all external components can be integrated in one single chip if a high voltage process can be used in future. The external LDO or DC_DC can also be designed on chip. Potentially the digitally-programmable delay-time microchip can be improved further with high integration level.

Acknowledgement

The author would like to thank Wan Peiyuan from Beijing Embedded System Key Lab for supporting. The research is supported by National Project (914A05050313BQ1014) and (No. 00404010601).

References

[1] Li Hongyue, Liu Feng, Yan Shilong, Design of online programming electronic delay detonator, Anhui university of science and technology, 2013.
[2] Qian Weiming, Yin Zejie, Wu Xiaoyi, Application of programmable-delay IC in system timing control, Nuclear electronics & detection technology, 2000.
[3] I-kon TDS digital energy control system, Orica Mining Services, 2006.
[4] Detonator IC with Digitally-Programmable Delay-Time, Beijing Embedded System Key Lab, 2014. V0.2

Key Engineering Materials Vols 645-646 (2015) pp 810-816
© (2015) Trans Tech Publications, Switzerland
doi:10.4028/www.scientific.net/KEM.645-646.810

Submitted: 2014-10-28
Accepted: 2014-12-23

A traceable metrological method with nanometer scale resolution for micro-structure

Bohua Yin[1, a], Daixie Chen[1, b], Hong Xue[1, c], Yunsheng Lin[1, d], Sitian Gao[2, e], Wei Li[2, f], Li Han[1, g]

[1,] （Beijing Key Laboratory of Bioelectromagnetics, Institute of Electrical Engineering, Chinese Academy of Sciences, Beijing，China, 100190）

[2,]（National Institute of Metrology，Beijing，China, 100013）

[a]yinbh@mail.iee.ac.cn, [b]chendaixie@mail.iee.ac.cn, [c]xuehong@mail.iee.ac.cn, lysh@mail.iee.ac.cn, [e]gaost@nim.ac.cn, [f]liwei@nim.ac.cn,

[g]lihan@mail.iee.ac.cn (corresponding author)

Keywords: scanning electron microscope, line width measurement, laser interferometer, image edge detection, flexure stage.

Abstract. Micro-structure dimension metrology is a grand challenge to current metrological methods and tools. In this paper, a retraceable metrological scanning electron microscopy (M-SEM) system with precision stage and laser interferometer is presented in detail. The double stages structure is used to realize both sample positioning in 50mm×50mm range and accuracy imaging in several tens of micron scale. In order to acquiring metrological scanning image, the control system based on digital signal processing (DSP) is constructed. Furthermore, this paper focuses on demonstrating a metrological SEM image edge detection algorithm which is the essential part of the metrological SEM system to realize the traceable metrology of line width.

Intorduction

The semiconductor industry has exploited productivity improvements through aggressive feature size reduction for over four decades [1]. Especially, for international technology roadmap for semiconductor [2], metrology is an important part of integrated circuits manufacturing system. Device feature size has shrunk from the micron to deep sub-micron until the nanometer. Generally, as one of the strong popular microstructure imaging and analysis tools, scanning electron microscope [3] (SEM) is used to watch the surface micro or nanometer scale structure of conductor or semiconductor materials. The SEM has great magnification ability up to several hundred thousand multiple with resolution of 1~2 nm, even to 0.8nm. So, in theory, SEM is very suitable as the nanometer range observation tool. Although the SEM has above advantage characters, it normally could not be considered as the traceable metrology tool relation to standard meter definition. There are several factors which can influence SEM metrological accuracy, such as magnification rate, deflection coils nonlinear, acceleration voltage, work distance, and so on. In order to overcome these difficulties, the researchers in American National Institute of Standards and Technology[4] (NIST) have continued developing M-SEM and seeking for measuring method for many years from one dimension line scanning for standard reference material(SRM-484) to the recent 2-dimension scanning research projects. Physikalisch-Technische Bundesanstalt (PTB) has constructed the electron optical metrology system (EOMS) and made monte carlo simulation [5] with respect to a variation of edge slope angle and e-beam diameter. In this paper, we develop our metrological scanning electron microscopy based on thermal field emission SEM, double stages and laser interferometer [6] measurement system. Special imaging methods based on flexure stage moving and line width roughness are discussed.

Metrological SEM Setup And Metrological Methodology

The structure of the metrological SEM. The whole structure of our M-SEM is shown in Fig. 1.The M-SEM is constructed by three parts: a thermal field emission SEM, double precision stages, and control system. The double precison stages consist of large moving range ultrasonic motor driving stage and short moving range flexure stage [7]. The double precision stage and plane mirror are mounted in the field emission SEM chamber, replacing the SEM original stage. The interferometer is in charge of measuring the displacement of the double stage by monitoring the L-type plane mirror movement. In order to acquiring scanning image with the M-SEM system, the electrical control system is indispensability. The real time control system based on digital signal processing [8] (DSP) is constructed, which is discussed in the next section.

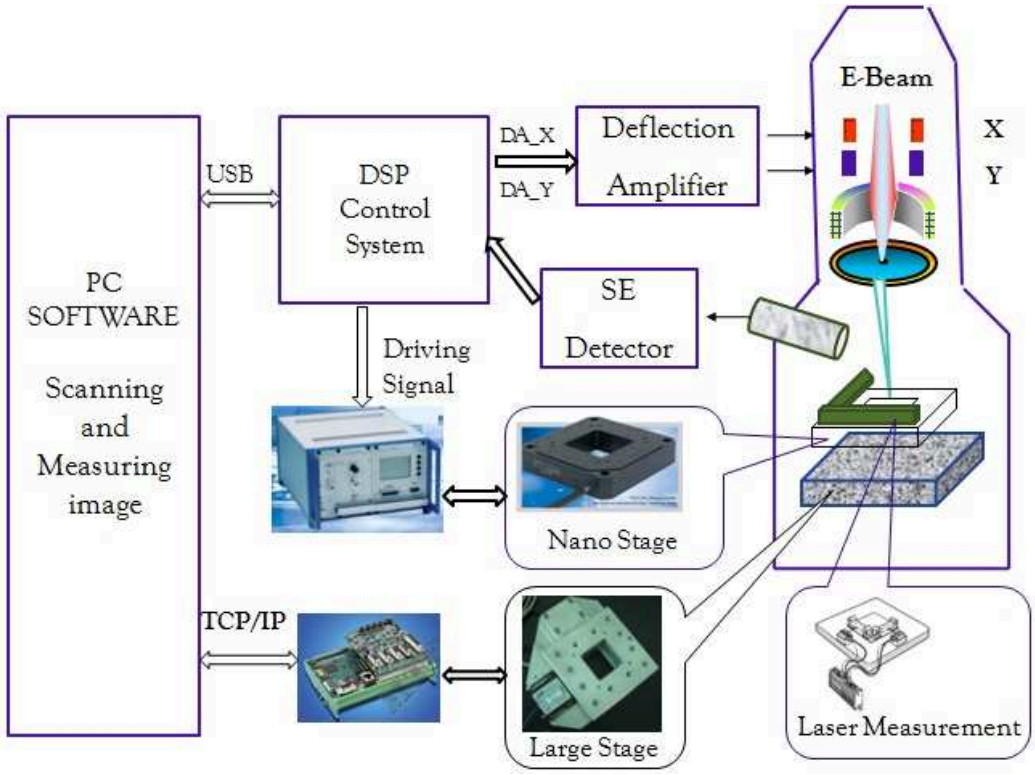


Fig.1 The system design diagram of the metrological SEM

The control system of the metrological SEM. In order to realize the scanning image based on the M-SEM in fig. 1, the electrical control system is designed. The block diagram of control system is shown in fig. 2. For achieving fast calculation and dealing with the laser interferometer measuring data quickly, the digital signal processor of TMS3206713 is used as the core unit of the control system. The USB2.0 interface is designed for image data transport from the DSP unit to PC program. The digital-to-analog units (D/A) produce the driving signal for the flexure stage movement in x and y direction. By TCP/IP protocol and motion control card, the large range stage is driven to the position where the scanning image process will be executed. And the analog-to-digital units (A/D) is used to acquire the secondary electron signal image or the back scatter signal image.

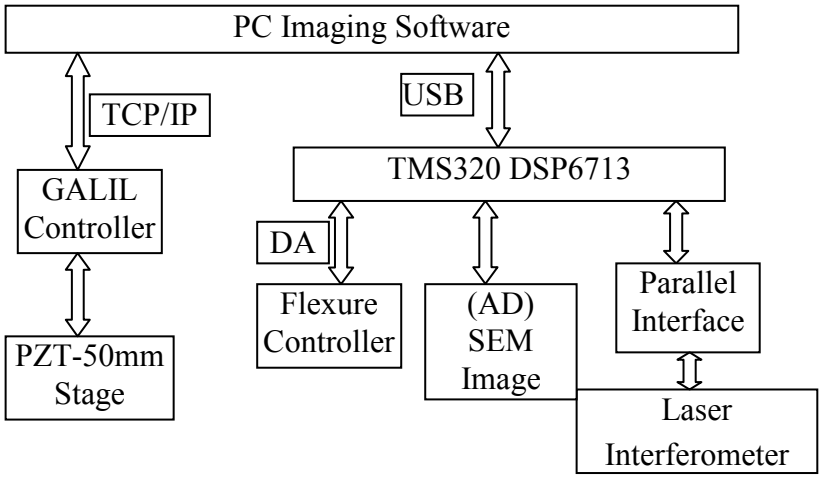
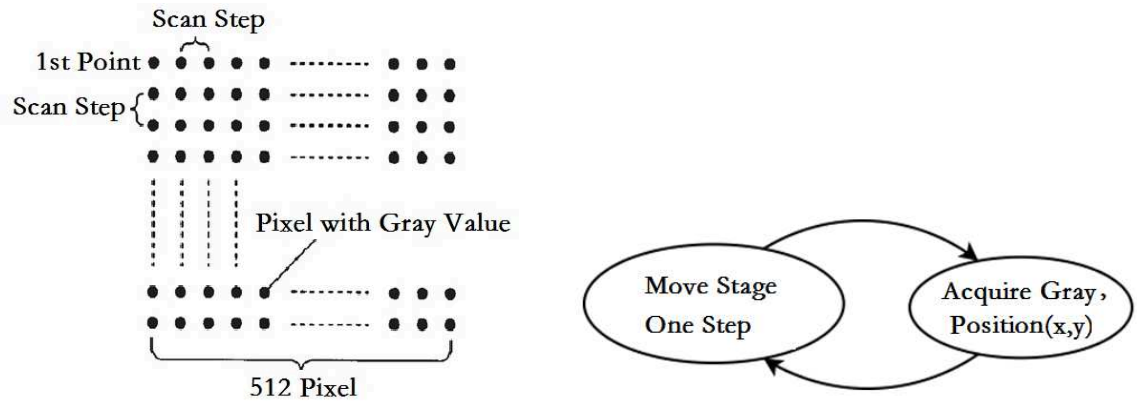


Fig.2 The block diagram of E-SEM control system

Metrological SEM imaging methods. In ordinary SEM mode, the image is acquired by e-beam deflection scanning motion in x and y direction, while the sample stage is maintained stationary. In our metrological SEM system, the image is obtained by the x-y stage scanning motion step by step, while the e-beam is stationary. This imaging method is shown in Fig. 3.

Firstly, the sample is moved to the 1st point by the flexure stage. Then the DSP controller commands the A/D unit to get the gray value of the 1st point by acquiring the secondary electron signal. At the same time, the position coordination(x, y) of the 1st point measured by interferometer are also latched to the DSP memory. Then the flexure stage is driven to move one step to the next point. Repeating the above imaging process, each image pixel point's secondary electron gray value and the position information are attained. Finally, a whole metrological SEM image with position coordination value measured by interferometer is obtained by this stage scanning method. Measuring distance in the M-SEM image is shown in Fig. 4. Because using the laser interferometer as the distance measuring tool, in theory, the measuring results precision can be trace to the define of standard meter.



(a) Acquiring SEM image by stage step (b) Repeat action each step

Fig.3 The scanning image process based on flexure stage moving step by step

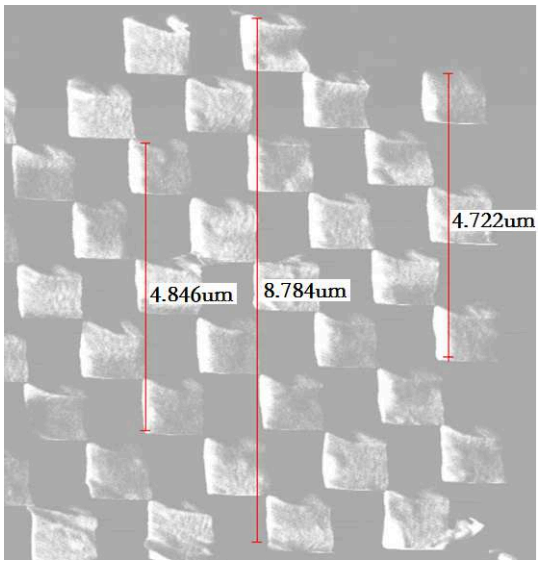


Fig.4 Measuring distance in the metrological SEM image

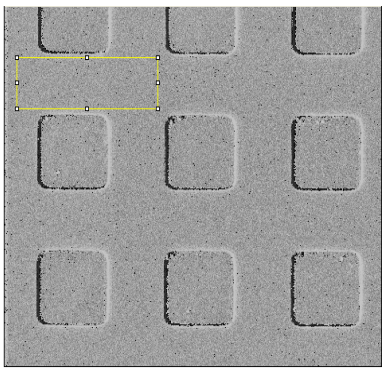
MODELLING

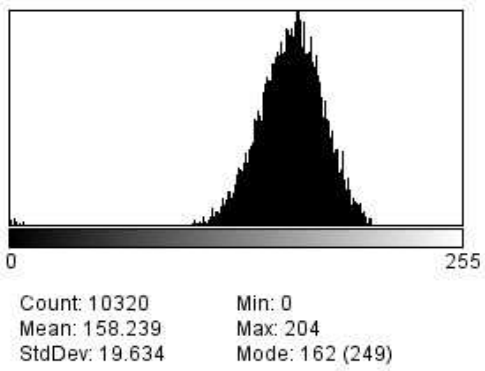
SEM image noise filter model. Although the traceable distance metrological method is gotten in the above section, measuring the width of structure in the M-SEM image is not so easily to complete. In fact, the noise in the SEM image blurs the structure edge. So the noise filter [9] design is important to SEM image measurement and analysis. An SEM image may contain various types of noise. Noise identification problem can be attributed to the judgment of the histogram curve shape. The histogram reflects the relationship between each gray level of the digital image and its frequency.

Firstly, set up the histogram curve formula which is showed in Eq. (1). N is the total number of pixels in the image; n_k is the number of pixels of gray level; r_k represents the k-th gray level.

$$P(r_k) = n_k / N . \tag{1}$$

Then, the detailed process of noise analysis is illustrated as follow. In figure 5(a), choose a region of relatively uniform gray level, and then get its histogram. The noise type is identified by analyzing the histogram curve characteristics. As is shown in figure 5(b), the histogram curve matches with Gaussian noise. A few isolated pixels grayscale is close to pure black points. The histogram shows that the image contains salt and pepper noise and Gaussian noise [10].





(a) Region selected for noise analysis. (b) Histogram of the selected region

Fig. 5 Histogram analysis for the SEM image

Median filter method can be used for reducing salt and pepper noise and preserving the edge information appropriately. Gaussian filter method can be used for reducing Gaussian noise. The Gaussian filter is especially appropriate choice in the field of edge detection. The filter parameters should be set rightly in the Gaussian filter, which is characterized by α, the size of the filter template. The median filter template size can be set as 3×3.Two-dimensional zero-mean discrete Gaussian function is adopted for smoothing filter, the filter equation is:

$$g[i,j] = e^{-\frac{(i^2+j^2)}{2\sigma^2}} \tag{2}$$

The variable α is the filter width, i and j is the row and column of filter matrix. Characteristics of the Gaussian filter function meet the requirements of preserving the image edge properly as well as achieving the purpose of denoising.

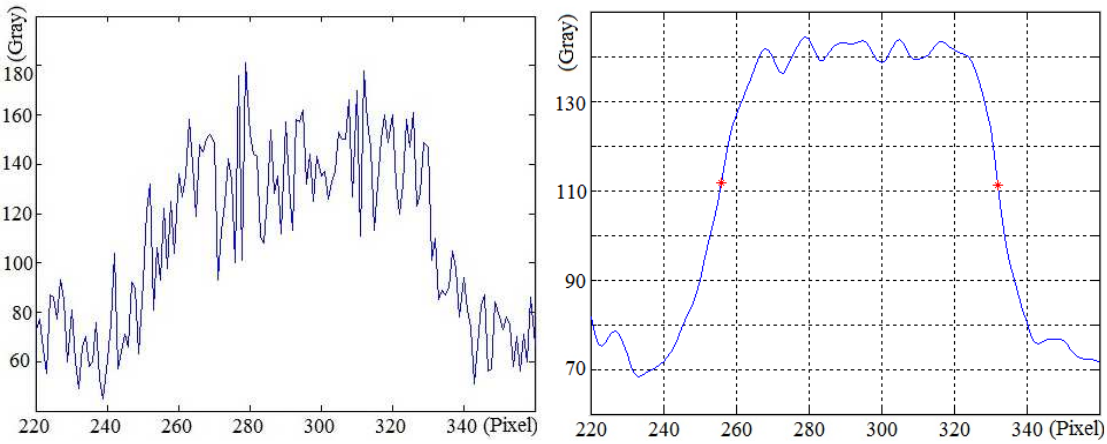
Edge pixel coordinates determination of SEM image. In theory, image edge refers to the part with the most significant grayscale change. In fact the gray change is not instantaneous but across certain width. This special region is called the transition zone between the target and the background.

For image whose edge grayscale has sudden change, the peak-to-peak technique is adopted to determine the edge pixel coordinates. In such case, linewidth is defined as one peak to another. Because the sample's side-wall is often not vertical to the bottom, the linewidth of the image is often characterized with sudden changes in the edges. The definition of such linewidth is still not get acknowledgement by the international standard.

For image whose edge grayscale changes smoothly, the image edge is defined as where the gray level value has the most significant change. In the curve of the pixel value, the edge is detected as where the absolute value of the first derivative is largest and the value of second derivative is zero. In our metrological test, a pair of edges is detected for linewidth measurement. They are defined by the direction of the pixel gray level value change. They are called left edge and right edge respectively.

Results and Discussion

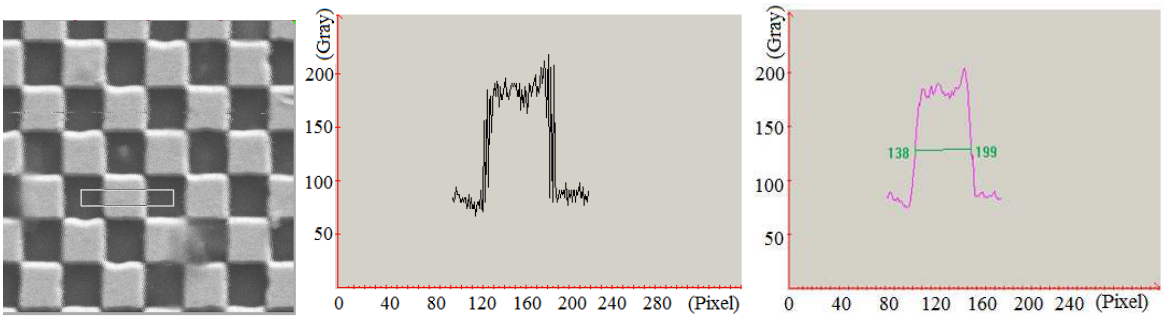
SEM image denoise experiments result. The original pixel information of a specific target is presented in figure 6(a). It is hard to recognize the edges from the curve with much noise. In contrast, after noise reduction, the gray level value change of the edge is distinctly shown in figure 6(b).



(a) Pixel information of original image. (b) Pixel information after noise reduction
Fig. 6 Histogram analysis for the SEM image.

Line edge measuring experiments result. In figure 7(a), the area to be used for detecting the edge is select by the rectangle window. Then, the gray value data of each line is shown in figure 7(b).

In figure 7(c), the final linewidth data is shown clearly after filtering and averaging to the original image data.



(a) Sampling area in SEM image. (b) Acquiring original edge data. (c) Final Edge Data after noise filtering and averaging

Fig. 7 Metrological SEM image edge detection algorithm

Summary

In this paper, the metrological SEM based on thermal field SEM, double precision stage and laser interferometer measurement is set up. The M-SEM can perform measurement function for standard sample used in normal SEM calibration. Furthermore, we discussed the denoising algorithm and metrological SEM image edge detection methods. The experiment results show that the effect of denoising is distinct.

For future work, we will carry out research and analysis on various influence factors to the M-SEM, such as e-beam drift, temperature fluctuations, and vibration. These factors often produce uncertainty which will reduce the measurement precision. The line edge detection algorithm and the line width roughness evaluation method also need more research work to do. After our M-SEM running properly, we want to participate in the metrological comparison among the world metrology institute.

Acknowledgement

This work has been supported by the national nature science foundation of China, NO: 51375470. The authors would like to thank Prof. GAO SI-TIAN, the head of Division of Nano Metrology and Materials Measurement in National Institute of Metrology in China, for his help with developing the metrological SEM structure and experiments suggestion.

References

[1] International Technology Roadmap for Semiconductors, 2013 Edition, Metrology Section
[2] S. Knight et al., “Advanced metrology needs for nanoelectronics lithography, ”C. R. Physique 7 (2006).
[3] F. Meli, T. Klein, E. Buhr, “Traceable size determination of nanoparticles, a comparison among European metrology institutes”, Meas. Sci. Technol. 23 (2012) 125005 (15pp)
[4] J. Fu, M. C. Croarkin, and T. V.Vorburger,” The Measurement and Uncertainty of a Calibration Standard for the Scanning Electron Microscope” J. Res. Natl. Inst. Stand. Technol. 99, 191 (1994)
[5] F.C. Georg; B. Egbert; D. Kai, “CD characterization of nanostructures in SEM metrology”, Meas. Sci. Technol, v 18, n 2, p 510-519, (2007)
[6] T. Hatsuzawa, Y. Tanimura, and K. Toyoda, “A compact laser interferometer with a piezodriven scanner for metrological measurements in regular SEMs. ”Rev. Sci. Instrum. 65, 2510 (1994);

[7] B.H.Yin, D.X.Chen, R.Xia, L.D.Wen, H.Xue, M.Z.Chu, L.Han. Micron and nanometer measuring methods based on metrological scanning electron microscope. Key Engineering Materials, v 609-610, p 1195-1200, (2014).
[8] L.D.Wen, B.H.Yin, J.B.Liu, A design method of signal generator based on DSP6713 and D/A converter. Applied Mechanics and Materials, v 336-338, p 1514-1518, (2013)

[9] D. H. Kim, S. J. Kim, S. K. Oh. “Image improvement with modified scanning waves and noise reduction in a scanning electron microscope,”Nuclear Instrument and Methods in Physics Research,620, 112(2010)
[10] M. Basu, “Gaussian-based edge-detection methods-a survey,” IEEE Trans. Syst., Man, Cybern. C, 32, 252(2002)

Key Engineering Materials Vols 645-646 (2015) pp 817-823
Submitted: 2014-10-29
© (2015) Trans Tech Publications, Switzerland
Accepted: 2014-12-23
doi:10.4028/www.scientific.net/KEM.645-646.817

Accurate and traceable calibration of the stiffness of various AFM cantilevers

Yuwen Zhao, Yunpeng Song,Sen Wu, Xing Fu *

The State Key Laboratory of Precision Measurement Technology & Instruments, Tianjin University, Tianjin, CHINA

yuwenzhao@tju.edu.cn, xingfu@tju.edu.cn (corresponding author)

Keywords: AFM, calibration, cantilever, stiffness

Abstract. Atomic force microscope(AFM) is widely used to measure nano-force in the analysis of nanomechanical and biomechanical properties. As the critical factor in the nano-force measurement, the stiffness of the AFM cantilever must be determined properly. In this paper, an accurate and SI-traceable calibration method is presented to obtain the stiffness of the AFM cantilever in the normal direction. The calibration system consists of a homemade AFM head and an ultra-precision electromagnetic balance. The calibration is based on the Hooke's law i.e. the stiffness is equal to the force divided by the deflection of the cantilever. With this system, three kinds of cantilevers were calibrated. The relative standard deviation is better than 1%. The results of these experiments showed good accuracy and repeatability.

Introduction

Atomic force microscope(AFM) is a member of the scanning probe microscopes with nanometer resolution. It is widely used to measure the nano-force in the analysis of nanomechanical and biomechanical properties [1-6]. The small forces measured with AFM can be obtained by multiplying the known stiffness of a cantilever and its deflection. So the stiffness of the cantilever has a direct impact on the force measurements. However, the stiffness values given by manufacturers have relative large uncertainties as they are calculated according to the geometry and the material of the cantilever. Therefore, a reliable method to acquire the proper stiffness of the cantilever must be proposed. Over the last 20 years, there have been many methods developed to calibrate the stiffness of cantilevers[7]. These methods can be divided into three categories with some overlap: 1) dimensional; 2) dynamic experimental; 3) static experimental[8-10]. The dimensional method needs to know the material and geometrical properties of the cantilever. As cantilevers are not perfectly homogeneous and the thickness may vary, the uncertainty of this method will be between 10%-25%[8]. Dynamic experimental method includes Cleveland method, Sadder method and Thermal noise method, relying on analyzing the resonance response of cantilever. As these methods require the knowledge of cantilever's material and geometrical properties, the calibration result has a high uncertainty between 10% -20%[8, 9, 11]. In static experimental method, the cantilever is bended by a known force, which can be supplied by an added mass, a reference cantilever or an indentation device[7, 9, 10, 12, 13].The stiffness can then be calculated using the force-displacement curve by Hooke's Law.

Comparatively speaking, static method is more accurate and direct than other methods, and it is regardless of cantilever geometry and materials. Another advantage of using a known force is that it is potentially traceable to the Syst`eme International (SI)[14, 15], since the static loading can be obtained by high-precision balance which is SI-traceable as the reference device. In this paper, we demonstrate a reliable and SI-traceable calibration method for obtaining the effective stiffness of the AFM cantilever in the normal direction. The calibration system is mainly made up of a homemade AFM head and the electromagnetic balance. The force acting on the cantilever can be obtained by the balance, while the deflection of the cantilever can be determined by the optical lever integrated in the AFM head. By using this method, we give the calibration results of three kinds of cantilever's normal stiffness . The relative standard deviation is better than 1%.

Calibration System

A schematic diagram of our experiment system is shown in Fig.1. In order to decrease the influence of the temperature, air flow, vibration, electromagnetic and other factors, the calibration system is enclosed by an isolation box and laid on a vibration isolator platform.

As shown in Fig.1, the calibration system consists of a homemade AFM head , an electromagnetic balance and a set of positioning stages. The homemade AFM head is made up of an infinite microscope, a piezo scanner and an optical lever system. The cantilever is held by a commercial probe holder installed in the bottom of the z-axis scanner, of which the incline angle is 12° to the ground. So the measured stiffness is the effective stiffness of this AFM facility. The z-axis scanner is motivated by the piezo blocks, which can position with 6μm range and about 2nm resolution. Better still; a closed loop control of the z-axis scanner is realized in this system, which can ensure every step of the cantilever deflection remains constant. Such procedure can effectively remove the calibration error induced by the limited stiffness of the measurement system.

The measuring laser beam ($635nm$, $4.5mW$) of the optical lever is reflexed by a beam splitter and then converged to the cantilever through the objective of the microscope. Then the laser beam is reflected to the dual-axis position sensitive detector(PSD) from the back of cantilever. Once the cantilever has a deflection or torsion, the position of laser spot on the PSD will have a vertical or horizontal shift. Then the PSD will generate a corresponding output voltage in the appropriate axis. The benefit of this method is that it can directly acquire the deflection of the cantilever, and can remove some hidden uncertainties compared with other systems[4, 16, 17].

The electromagnetic balance (SE2) with compensating type has the resolution of $0.1\mu g$ and the capacity of 2.1g . Therefore, the balance can measure the force in the range of 0- $21mN$ with resolution of $1nN$. A $30mm$ height aluminum column is installed on the weighing pan with a small piece of silicon stuck on its top. It makes the cantilever press the silicon instead of the weighing pan during the calibration and can prevent the cantilever from approaching too close to the balance. In order to make the balance work in its' linear area, the total weight of the aluminum column and the silicon is designed about1.4g , beyond 2/3 of the measurement range of the balance.

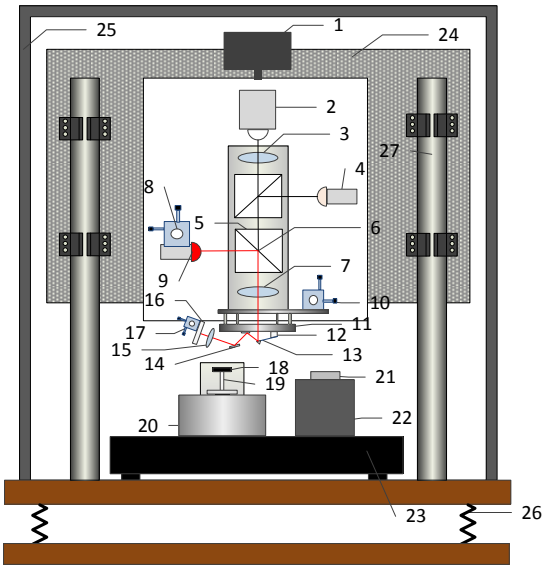


Fig . 1 Schematic of cantilever calibration setup. The numbered components are: 1. Z-axis motor stage; 2.CCD; 3.Tube lens; 4.Illuminator; 5,6.Beam splitters; 7. Objective; 8. Multi-axis kinematic mount; 9. Laser diode; 10,17. Ultra-precision 3D motor stages; 11. Z-scanner; 12. Commercial cantilever-holder; 13. Cantilever; 14. Reflector; 15. Lens; 16. PSD; 18. Silicon piece; 19. Aluminum column; 20. Electromagnetic balance; 21. Sapphire plate; 22. Nano-positioning stage; 23. XY-axes motor stage; 24.Supporting breadboard; 25.Enclosure; 26.Vibration isolator;27.Shore

This stage with closed loop control mode can location in the z-axis over $10\mu m$ with $0.2nm$ resolution.

Calibration Experiment

To verify the feasibility and the reliability of the calibration system, we selected three types of popular used cantilevers with different shapes, functions and stiffness. The characteristic parameters are shown in the Table 1.

Table1. The cantilever characteristic parameters given by manufacturer

Mode	Shape	Dimension			Typical stiffness $k\,(N/m)$	Uncertainty range of $k\,(N/m)$
		L	W	t		
CSG10	Rectangular	225 ± 5	30 ± 3	1.0 ± 0.5	0.11	0.01~0.5
NSG10	Rectangular	125 ± 5	30 ± 3	2.0 ± 0.5	2.1	1.45~15.1
NSG20	V-shaped	90 ± 5	60 ± 3	2.0 ± 0.3	48	28~91

In this paper, the whole calibration process can be divided into two steps. The first step is calibrating the sensitivity of optical lever by using the nano-positioning stage and PSD. The stage mounted under the AFM head can give a known vertical upward displacement to the cantilever in steps. In the meanwhile the voltage signal in the y-axis of PSD will response to the deflection of the cantilever. As the bending of the tip is small enough, the displacement of the cantilever is equal to the movement of the nano-positioning stage. Then the sensitivity of the optical lever S_D can be expressed by the ratio of the voltage change in the PSD y-axis ΔU to the relevant movement of the nano-positioning Δy, as the equation shown below:

$$S_D = \frac{\Delta U}{\Delta y} \quad . \tag{1}$$

The second step is the force calibration. The nano-positioning stage was replaced by the balance. First, the cantilever was positioned down to the motor stage. When the tip of cantilever touched the silicon piece on the balance, the scanner in the AFM head shifted the cantilever to press the balance in steps. This process can be executed by software program automatically. At the same time, the PSD output signals were recorded. As the balance worked in a compensating type, the weighing pan maintains its original position (i.e. The stiffness of the balance is so large enough that guarantee the balance won't have deformation.) all the time. Therefore, the deflection of cantilever can be regarded the same as the displacement of the scanner, which can be represented by the y-axis voltage output ΔU_y from the PSD. What's more, we used a PID loop to control the scanner in this system, which can ensure every step of the cantilever deflection remains constant. Thus, this process can decrease the errors to the deflection of the cantilever. If the output voltage of PSD is U_y, the deflection can be expressed as U_y / S_D. At the same time, the contact force(Δm•g) is measured by the balance. So the normal stiffness can be calculated by the equation below.

$$k = S_D \cdot \frac{\Delta m}{\Delta U_y} \cdot g \quad . \tag{2}$$

Calibration Results and Discussion

Three kinds of cantilevers were calibrated in this paper. As an example, typical calibration results of the cantilever NSG10 are presented in Fig.2. Fig.2(a) shows that the PSD output voltage responds linearly to the cantilever vertical displacement in the optical lever sensitivity calibration. The first two points in the curve indicates that the cantilever tip contacted the sapphire plate from the second point. Then the NSG10 cantilever was pushed by nano-positioning stage ten times with the maximum

deflection of 1μm. From point 2 to 12, a linear polynomial fit was performed. The linearity between the voltage and displacement can also be found in other calibration curves of cantilever. The residuals from the linear fit line were less than 0.6%. In Fig.2(b), a force and displacement curve of cantilever NSG10 is obtained in force calibration. The cantilever was also bent in the same steps as sensitivity calibratrion. As you can see in Fig.2(b), a linear relationship between the force and displacement of cantilever was presented. The residuals from the linear fit were less than 0.4%.

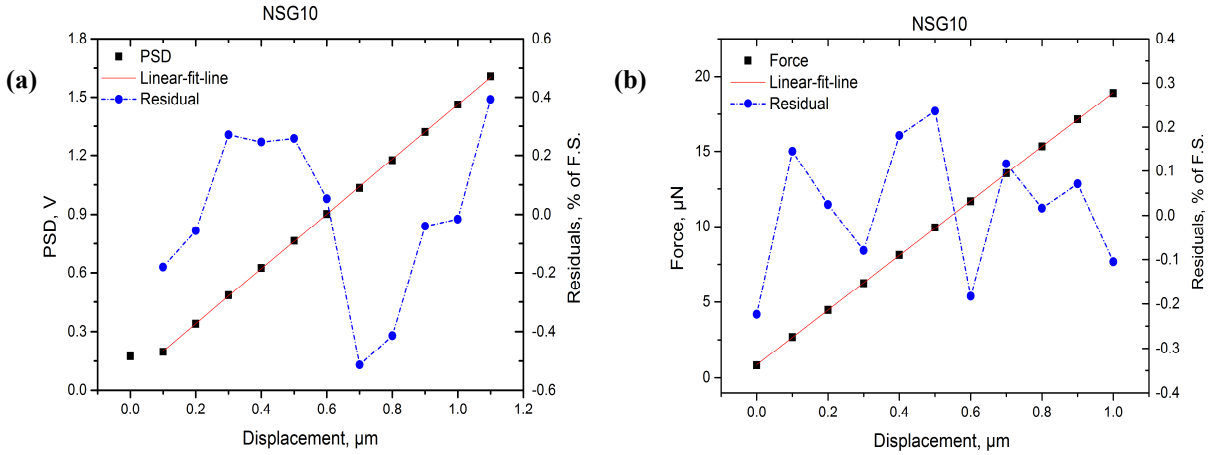


Fig . 2 Typical calibration result of NSG10 **(a)** PSD voltage responding to the cantilever vertical displacement curve in optical lever sensitivity calibration; **(b)** Force and displacement curve obtained in force calibration;

The optical lever sensitivity calibration of each cantilever was repeated for 15 times. Then fifteen slopes of the linear fit lines were obtained. The mean value of these slopes was recorded as the optical lever sensitivity. As shown in the Fig.3(a)(c)(e), the mean optical lever sensitivity of the cantilever CSG10, NSG10, NSG20 are $0.8238V/\mu m$, $1.410V/\mu m$, $2.271V/\mu m$, respectively. The standard deviations of the sensitivity calibration on these cantilevers are $0.0013V/\mu m$ (0.16%), $0.002V/\mu m$ (0.14%), $0.008V/\mu m$ (0.35%), respectively.

The stiffness of each cantilever was calibrated 40 times for force calibrations. The mean value of the slopes of force and displacement curves was taken as the stiffness of the corresponding cantilever. We can see from the Fig.3(b)(d)(f), the stiffness of the cantilever CSG10, NSG10, NSG20 are $0.1894\,N/m$, $18.13\,N/m$, $49.84\,N/m$. And the standard deviations are $0.0004\,N/m$ (0.21%), $0.04\,N/m$ (0.22%), $0.37\,N/m$ (0.74%). The calibration results are summarized in Table2. The standard deviation for each stiffness is small, typically 0.1%–0.8% of the average value, which indicates that our calibration was with great repeatability.

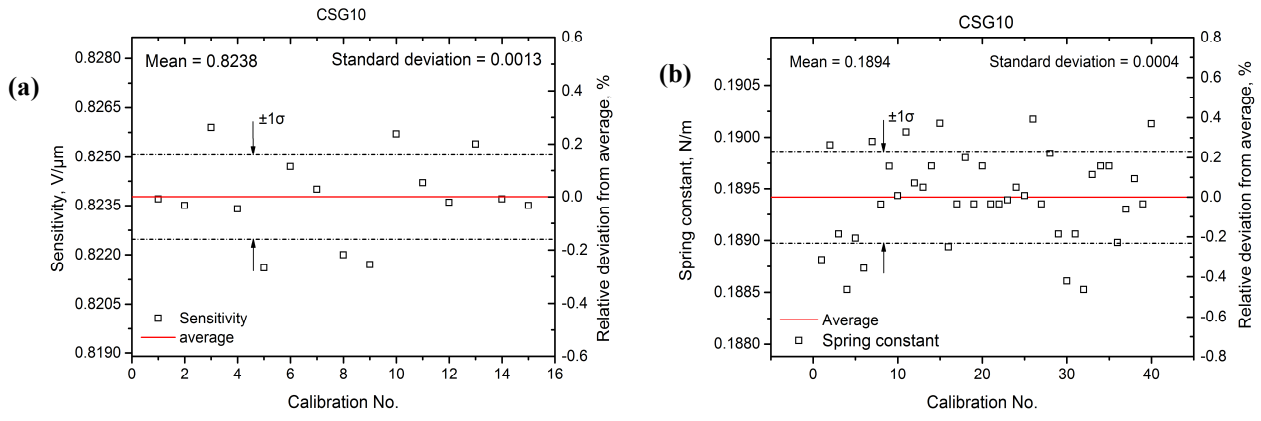


Fig . 3 Calibration results of CSG10,NSG10,NSG20 (a)(c)(e) scatter of the measured sensitivity of the optical lever in 15 times; (b)(d)(f) scatter of the measured effective stiffness of the cantilever in 40 times;

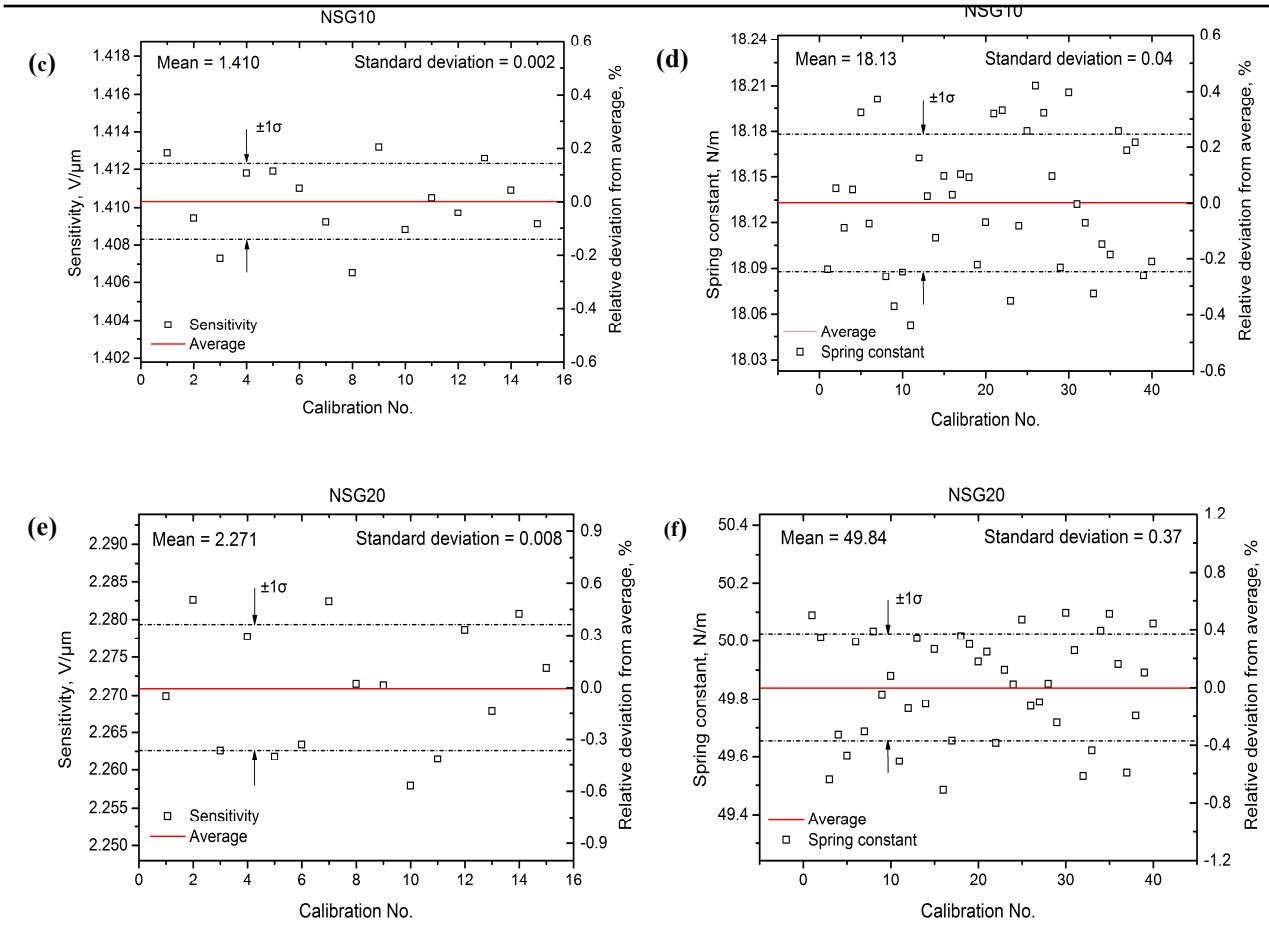


Fig . 3 Calibration results of CSG10,NSG10,NSG20 **(a)(c)(e)** scatter of the measured sensitivity of the optical lever in 15 times; **(b)(d)(f)** scatter of the measured effective stiffness of the cantilever in 40 times;

Table2. Optical lever sensitivity and stiffness calibration result

Cantilever Model	The Optical Lever Sensitivity Calibration		The Stiffness Calibration	
	S ($V/\mu m$)	Standard deviation(%)	k(N/m)	Standard deviation(%)
CSG10	0.8238	0.16	0.1894	0.21
NSG10	1.410	0.14	18.13	0.22
NSG20	2.271	0.35	49.84	0.74

A comparison between this method and the thermal tune method based on the commercial Multimode AFM has been established in this paper. Considering that the incline angle of the cantilever and the tip height were not taken into account in the thermal tune method, the results need to be corrected by dividing $\cos^2\alpha(1-\frac{2D}{L}\tan\alpha)$. Thus we can acquire the effective stiffness of the corresponding cantilever as shown in Table3. Here α and D are the incline angle and the tip height of the cantilever, respectively. We used 12° as α and 15μm as D. The nominal lengths (L)of these cantilevers are listed in Table1.

Table3. Calibration result comparison in different methods

Cantilever Model	Thermal Tune		Balance	Relative Deviation(%) $(k_2-k)/k$
	Multimode AFM k_1 (N/m)	Effective k_2 (N/m)	k(N/m)	
CSG10	0.1668	0.1794	0.1894	-5.1
NSG10	17.17	19.24	18.13	6.1
NSG20	41.13	46.26	49.84	-7.2

From Table3, we can easily find stiffer the cantilevers are, larger the deviation of the two methods are.Because of the thermal vibration amplitude of the stiffer one is not big enough, the thermal vibration would be swallowed up by the mechanical vibration and the circuit noise, which would reduce the accuracy of measurement.

Conclusion

In summary, an accurate and traceable calibration of the stiffness of cantilever is performed in this paper. With this system, we obtained the effective normal stiffness of three types of cantilevers. The relative standard deviation is better than 1%. The calibrated cantilever can be applied to measure the nano-force more precisely in nanometrology applications.

References

[1] P.K. Hansma, V.B. Elings, O. Marti, C.E. Bracker, Scanning tunneling microscopy and atomic force microscopy: application to biology and technology, Science (New York, N.Y.), 242 (1988) 209-216.

[2] A. Alessandrini, P. Facci, AFM: a versatile tool in biophysics, Measurement Science and Technology, 16 (2005) R65-R92.

[3] H.J. Butt, B. Cappella, M. Kappl, Force measurements with the atomic force microscope: Technique, interpretation and applications, Surface Science Reports, 59 (2005) 1-152.

[4] M.-S. Kim, J.R. Pratt, SI traceability: Current status and future trends for forces below 10 microNewtons, Measurement, 43 (2010) 169-182.

[5] C. Serre, A. Perez-Rodriguez, J.R. Morante, P. Gorostiza, J. Esteve, Determination of micromechanical properties of thin films by beam bending measurements with an atomic force microscope, Sensor Actuat a-Phys, 74 (1999) 134-138.

[6] F. Gaboriaud, Y.F. Dufrêne, Atomic force microscopy of microbial cells: Application to nanomechanical properties, surface forces and molecular recognition forces, Colloids and Surfaces B: Biointerfaces, 54 (2007) 10-19.

[7] M.-S. Kim, J.-H. Choi, J.-H. Kim, Y.-K. Park, Accurate determination of spring constant of atomic force microscope cantilevers and comparison with other methods, Measurement, 43 (2010) 520-526.

[8] C.A. Clifford, M.P. Seah, The determination of atomic force microscope cantilever spring constants via dimensional methods for nanomechanical analysis, Nanotechnology, 16 (2005) 1666-1680.

[9] C.T. Gibson, D. Alastair Smith, C.J. Roberts, Calibration of silicon atomic force microscope cantilevers, Nanotechnology, 16 (2005) 234-238.

[10] S. Wu, Q. Chen, Z. Zhang, X. Fu, X. Hu, X. Hu, Calibration of the spring constant of AFM micro-cantilever based on bending method, Yi Qi Yi Biao Xue Bao/Chinese Journal of Scientific Instrument, 33 (2012) 2446-2453.

[11] S.M. Cook, K.M. Lang, K.M. Chynoweth, M. Wigton, R.W. Simmonds, T.E. Schäffer, Practical implementation of dynamic methods for measuring atomic force microscope cantilever spring constants, Nanotechnology, 17 (2006) 2135-2145.

[12] N.A. Burnham, X. Chen, C.S. Hodges, G.A. Matei, E.J. Thoreson, C.J. Roberts, M.C. Davies, S.J.B. Tendler, Comparison of calibration methods for atomic-force microscopy cantilevers, Nanotechnology, 14 (2003) 1-6.

[13] H.-J. Butt, B. Cappella, M. Kappl, Force measurements with the atomic force microscope: Technique, interpretation and applications, Surface Science Reports, 59 (2005) 1-152.

[14] P.J. Cumpson, J. Hedley, Accurate analytical measurements in the atomic force microscope: a microfabricated spring constant standard potentially traceable to the SI, Nanotechnology, 14 (2003) 1279-1288.

[15] J.F. Portoles, P.J. Cumpson, A compact torsional reference device for easy, accurate and traceable AFM piconewton calibration, Nanotechnology, 24 (2013) 15.

[16] M.S. Kim, I.M. Choi, Y.K. Park, D.I. Kang, Atomic force microscope probe calibration by use of a commercial precision balance, Measurement, 40 (2007) 741-745.

[17] M.S. Kim, J.H. Choi, Y.K. Park, Calibration of the spring constants of various AFM cantilevers with the small uncertainty level of 2%, 2006 SICE-ICASE International Joint Conference, Vols 1-13, (2006) 175-180.

[18] E.D. Langlois, G.A. Shaw, J.A. Kramar, J.R. Pratt, D.C. Hurley, Spring constant calibration of atomic force microscopy cantilevers with a piezosensor transfer standard, The Review of scientific instruments, 78 (2007) 093705.

Key Engineering Materials Vols 645-646 (2015) pp 824-829
© (2015) Trans Tech Publications, Switzerland
doi:10.4028/www.scientific.net/KEM.645-646.824

Submitted: 2014-10-29
Accepted: 2014-12-23

Design of Minimal Capacitance Detect Circuit for MEMS Capacitive Sensor

Hao Qu[1,a], Huijun Yu[1,b], Wu Zhou[1,c],Xiaoping He[2,d] Lianming Du[2,e], and Bei Peng[1,f,*]

[1]Department of Mechatronics Engineering, University of Electronic Science and Technology of China, Chengdu 611731, P.R. China

[2]Institute of Electronic Engineering, China Academy of Engineering Physics, Mianyang 621900, P.R.China

[a]708382@163.com, [b]yuhjuestc@126.com, [c]zhouwu916@uestc.edu.cn, [d]hexpiee@263.net, [e]13508107238@139.com, [f]beipeng@uestc.edu.cn (Corresponding Author)

Keywords: MEMS, Comb Accelerometer Sensor, Capacitance measurement

Abstract. The capacitance among the structure of the accelerometer is rather small, usually at sub-pF level. Detection of the capacitance among the sensor's tiny structure and analysis of the variation of these capacitances are necessary to improve the sensor's performance. In this paper, one capacitance detect circuit for minimal capacitance is designed. Simulation and experiment results indicate a good linearity when the circuit is applied to detect capacitance range from 0.5pF to 5pF.

Introduction

Capacitive sensors can transform the other variables into capacitance variation through structure deformation. However, due to the small size of the structure, the capacitance variation is easily affected by the inherent capacitance of the other structures beside the sensing structure. Thus, the measurement of capacitance among the structures and analysis of the variation of these capacitances are necessary to improve the sensor's performance.

Commonly used methods for capacitance measurement includes oscillate circuit approach, AC bridege and charge amplify circuit [1]. Capacitance can set up the resonant frequency or the self-oscillation frequency of the oscillate circuit. Therefore, the capacitance value can be measured through the measurement of the frequency [2]. AC bridge may be balance or imbalance, when a capacitance is connected with it. Since the other components of the AC bridge is known, the capacitance value can be calculated in both situation. Charge amplify circuit is based on the capacitance charge and discharge progress [3]. Oscillate circuit approach need an oscillator to calculate the frequency. The components of the oscillator might be affected by temperature[4], thus, this method could not be used in the situation which require high accuracy. AC bridge has a very high accuracy, however, the circuit is very complex. Charge amplify circuit has a simpler construction, high resolution and low power consumption [5,6,7,8]. In this paper, a capacitance detect circuit based on charge amplifier circuit is designed, it can be used to detect static and variable capacitance. Simulation and experiment results prove a good linearity when the circuit is applied to detect capacitance range from 0.5pF to 5pF.

Principle of the charge amplify circuit

Basic schematic of the charge amplify circuit is shown in Fig. 1.C_x is the unknown capacitance, C_f is the feed back capacitance. S_1, S_2 and S_3 are switches and ϕ_1,ϕ_2 are control signals. ϕ_1 controls S_1 and S_3, ϕ_1 controls S_2. Thus, S_1 and S_3 can synchronously open or close, S_1 and S_2 can asynchronously open or close. When S_1 and S_3 are close, S_2 is open. Non-inverting terminal is connected to ground, V_o is zero, C_x is charged by V_s. The amount of the charge q_x is given by [3]:

$$q_x = V_s C_x \tag{1}$$

When S_2 is close, S_1 and S_3 are open. Left plate of C_x is connected to ground, the charge stored in C_x could not change immediately, thus, the potential of the inverting terminal is negative, and output V_o is positive. Through the feedback capacitance C_f, the potential of the inverting terminal is raised from

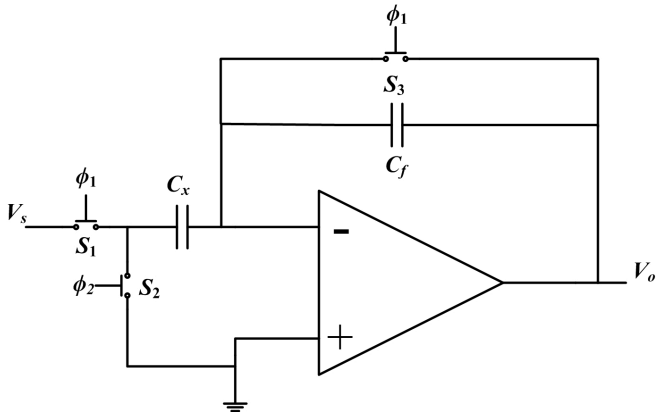


Fig. 1 Basic schematic of the charge amplify circuit

negative to zero, until the discharge process is done [3]. The charge stored in C_x is transformed to C_f. The amount of the charge keeps balance, thus,

$$q_x = V_s C_x = V_o C_f \tag{2}$$

And the relationship between the output V_o and C_x is :

$$V_o = \frac{C_x}{C_f} V_s \tag{3}$$

The value of V_o indicates the capacitance C_x.

Simulation results

Typical structure of comb capacitive accelerometer is shown in Fig. 2. Detection of the capacitance between the structures is necessary for the analysis of the capacitance variation. Thus, the capacitance between the structures is taken as C_x. Before the circuit test, simulation is required to testify the function of the circuit.

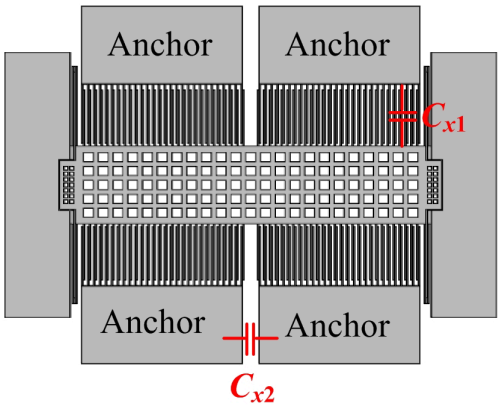


Fig. 2 Structure of comb capacitance accelerometer

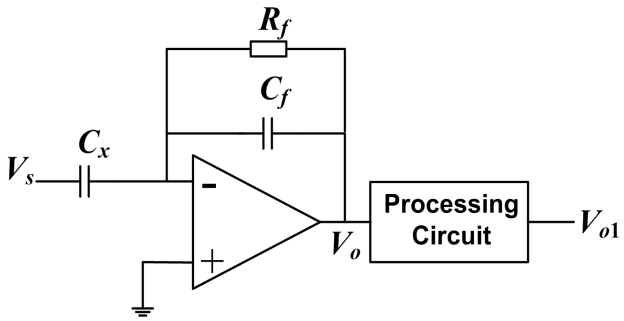


Fig. 3 Simulation schematic

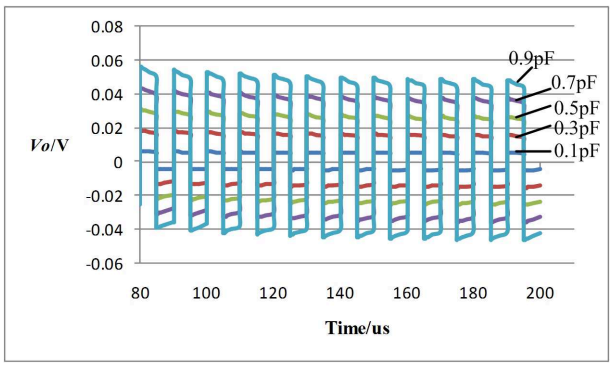
Circuit simulation is carried out by Pspice. Fig. 3 shows the simulation circuit. V_s is square wave, in the first period, C_x is connected to the positive voltage of V_s and charged by positive voltage, when the negative voltage of V_s comes, C_x is discharged and charged by negative voltage. When the next positive voltage comes, C_x is discharged and charged again by positive voltage. Thus, C_x is charged and discharged two times by positive and negative voltage in one period. R_f is the feedback resistance. R_f connect the output of the amplifier to the inverting input. R_f usually has a large value to prevent the charge of C_x from leaking to the output terminal. Output of the amplifier V_o can be derived:

$$V_o = \frac{j\omega C_x}{1 + j\omega R_f C_f} V_s \tag{4}$$

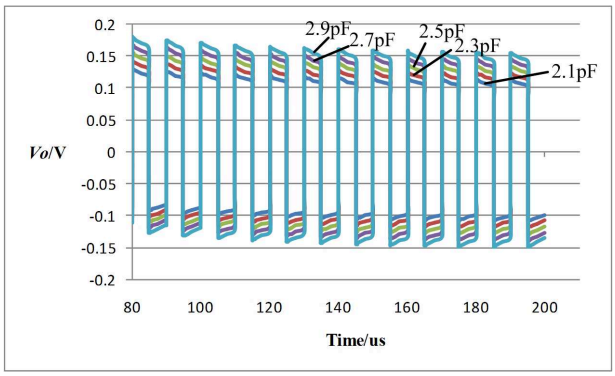
By choosing R_f and C_f, and let the frequency of the circuit carrier wave V_s satisfies $\omega R_f C_f >> 1$, V_o can be approximately written as :

$$V_o = \frac{C_x}{C_f} V_s \tag{5}$$

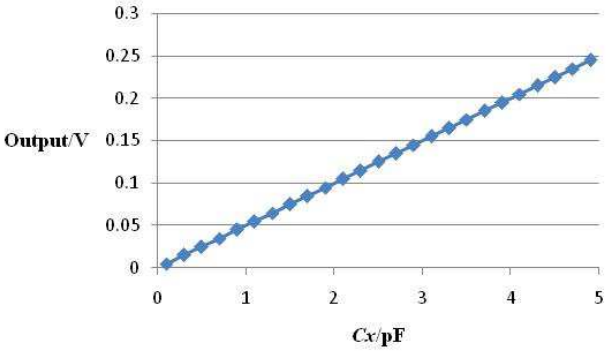
C_x varied from 0.1pF to 5pF, with increment of 0.2pF, amplifier output V_o is shown in Fig. 4. C_f is fixed to 100pF. The period of input signal is set to 10us, with a raise and fall time of 0.1us. output signal V_o is stable after 80 us. V_o with corresponding C_x is taken individually.



(a) small variation C_x with output V_o



(b) relative large variation C_x with output V_o



(c) variation C_x with absolute value of V_o

Fig. 4 Simulation results

Fig. 4(a) shows the results of small detection range, from 0.1pF to 0.9pF, with increment of 0.2pF. Fig. 4(b) shows the results of relative large detection range, from 2.1pF to 2.9pF, with increment of 0.2pF. V_o increases with the increment of C_x. The absolute value of V_o is plotted versus C_x in Fig. 4(c). When C_f is fixed, linear relationship between V_o and C_x is shown in Fig. 4(c), as theoretical analysis results.

Processing circuit

V_o and V_s have same frequency, thus a modulation of V_o is needed to get the DC output. The modulation is performed by a multiplication of V_o and V_s[9][10]. Suppose :

$$V_s = V_n \sin \omega_s t \tag{6}$$

$$V_o = kV_n \sin \omega_s t \tag{7}$$

ω_s is the frequency of V_s, k=C_x/C_f, after the operation of the multiplier,

$$\begin{aligned} V_{o1} &= V_o \bullet V_s \\ &= kV_n^2 \sin^2 \\ &= \frac{kV_n^2}{2}(1-\cos 2\omega_s t) \end{aligned} \tag{8}$$

The high-frequency part could be removed by a low-pass filter, and the constant part of V_{o1} is the final output.

Experiment results

Experiment circuit is based on the theoretical and simulation analysis. The final output V_{o1} in Fig. 3 is recorded in Table 1. Capacitance of 1pF, 2pF, 3pF and 5pF, is nominal and standard. Thus, output voltages of 1pF, 2pF, 3pF, 5pF are directly recorded while these capacitances are connected in the detect circuit as C_x. The other capacitances are obtained by serially connecting the standard capacitances. For example, the serial connection of 1pF and 5pF result in a capacitance of 0.83pF. These serial connection pair is connected to the detection circuit to generate the other experiment results.

Table 1 Experiment and calculation results

C_x（pF）	Experiment results(mV)	Calculation results(mV)
0.5	104.8	143.2
0.67	124.2	167.7
0.75	139.4	179.2
0.83	158.3	190.8
1	213.1	215.4
1.5	224.2	287.6
2	354.5	389.9
2.5	363.3	332.2
3	516.8	504.4
5	788.2	793.4

Based on the output voltages of standard capacitances, a description curve L of V_{o1} versus C_x can be derived, as shown in Fig. 5. The calculation results in Table 1 is calculated through the curve L.

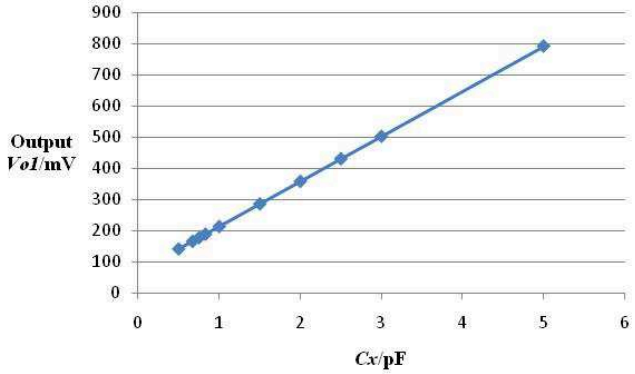


Fig. 5 Variation C_x with output V_{o1}

The divergences between the experiment results and calculated results in Table 1 can be explained by the Equivalent Serial Resistance (ESR) of the ceramic capacitance [11,12,13]. When the standard capacitances is serial connected, the effect of ESR should not be neglected. For example, the serial connection of two 2pF capacitances generates an output of 154.1 mV, which is smaller than the output of 1pF capacitance.

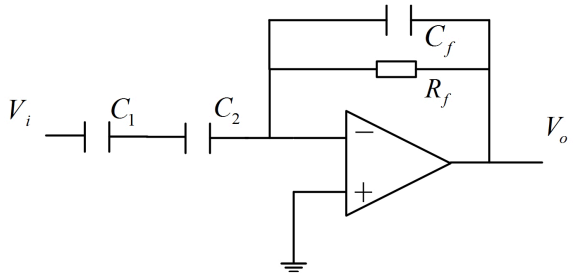


Fig. 6 Capacitance serial connection without ESR

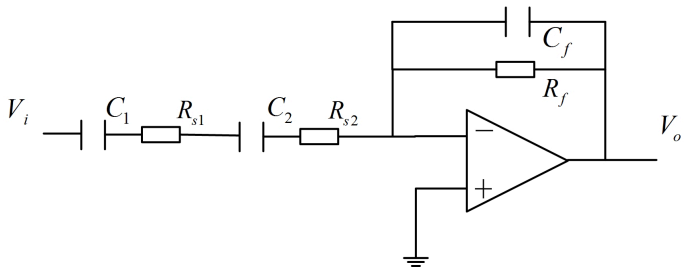


Fig. 7 Capacitance serial connection with ESR

Fig. 6 and Fig. 7 show the circuit without and with ESR. Donate V_o in Fig. 6 as V_{oc} and donate V_o in Fig. 7 as V_{ot}. V_{oc} can be regarded as calculation result and V_{ot} is the experiment result.

$$V_{oc} = -\frac{j\omega R_f}{1+j\omega R_f C_f} \bullet \frac{C_1 C_2}{C_1 + C_2} V_i \tag{9}$$

$$V_{ot} = -\frac{j\omega R_f}{1+j\omega R_f C_f} \bullet \frac{C_1 C_2}{C_1 + C_2 + j\omega C_1 C_2 \left(R_{s1} + R_{s2}\right)} V_i \tag{10}$$

Thus,

$$\frac{V_{ot}}{V_{oc}} = \frac{1}{1+j\omega \dfrac{C_1 C_2}{C_1 + C_2}\left(R_{s1} + R_{s2}\right)} \tag{11}$$

When the same standard capacitance is serial connected, C_1=C_2=C_0, R_{s1}=R_{s2}=R_{s0}.

$$\frac{V_{ot}}{V_{oc}} = \frac{1}{1+j\omega R_{s0} C_0} \tag{12}$$

The calculation results V_{oc} and experiment results V_{ot} of 0.5pF, 1pF, 1.5pF and 2.5pF can be taken into Eq.(12) to estimate the ESR of 1pF, 2pF, 3pF and 5pF. Considering the effect of ESR, the experiment results of 0.67pF, 0.75pF, 0.83pF can be estimated by taking the calculation results of 0.67pF, 0.75pF, 0.83pF in Table 1 into Eq.(11).The errors between the estimated output voltage value and experiment results of 0.67pF, 0.75pF, 0.83pF are 2%, 4% and 9%. The error is tolerable. Thus, the derived curve *L* can be used to calculate the corresponding capacitance from the output voltage, as capacitance ranges from 0.5pF to 5pF.

Conclusion

Capacitance detect circuit in this paper is based on charge amplify circuit. It can linearly transform capacitance to corresponding voltage. Simulation results and experiment results testify the linear characteristic. In terms of detection capacitance value, the detectable capacitance value range is from 0.5pF to 5pF, which is testified by experiment. This detect circuit can be implemented with simple discrete components.

Acknowledgments

This research was partially supported by National Natural Science Foundation of China (Grant No. 51175437 and 91123023), Fundamental Research Funds for the Central Universities (Grant No. ZYGX2013J097).

References

[1] Huang, S. M., et al. Electronic transducers for industrial measurement of low value capacitances, Journal of Physics E: Scientific Instruments on 21.3 (1988): 242.
[2] Shuxiang Song, Dongmei Zhou, High frequency electronic circuit , Peking University press,2010.
[3] Stephen D, Senturia, Microsystem Design, New York, 2001.
[4] Kevin Bull, Methods of Accurately Measuring capacitive RH Sensors (ISHM), 2006 5th Intermational Symposium on Humidity and Moisture, 2006.
[5] Arfah Nurul, A. H. M. Zahirul Alam, and Sheroz Khan, Capacitance-to-voltage converter for capacitance measuring system, Mechatronics (ICOM), 2011 4th International Conference On, IEEE, 2011.
[6]A.H.M.Zahirul Alam, Arfah Nurul, Sheroz Khan, Md. Rafiqul Islam, Design of capacitance to voltage converter for capacitive sensor transducer, American Journal of Applied Sciences on 7.10 (2010): 1353-1357.
[7] Arfah Nurul, A. H. M. Zahirul, Alam, and Sheroz Khan, Design of capacitive measuring systems for high frequency band sensor transducer, Computer and Communication Engineering (ICCCE), 2010 International Conference on, IEEE, 2010.
[8] Joost C.Lötters, Wouter Olthuis, Peter H.Veltink, A sensitive differential capacitance to voltage converter for sensor applications, Instrumentation and Measurement, IEEE Transactions on 48.1 (1999): 89-96.
[9] Ma wenying, The design and research of the detection circuit for a new micromachined capacitive accelerometer, Jilin University, 2007 31-34.
[10] Blair D P, Sydenham P H, Phase sensitive detection as a means to recover signals buried in noise, Journal of Physics E: Scientific Instruments, 1975, 8(8): 621-627.
[11] Kim, Myoung-Gyun, Byoung Hwa Lee, and Tae-Yeoul Yun, Equivalent-circuit model for high-capacitance MLCC based on transmission-Line theory, Components, Packaging and Manufacturing Technology, IEEE Transactions on 2.6 (2012): 1012-1020.
[12] Jeffrey Cain, Parasitic inductance of multilayer ceramic capacitors, Technical Information, AVX corporation.
[13] Yoon, Songhun, Chul Wee Lee, and Seung M. Oh, Characterization of equivalent series resistance of electric double-layer capacitor electrodes using transient analysis, Journal of Power Sources on 195.13 (2010): 4391-4399.

Key Engineering Materials Vols 645-646 (2015) pp 830-835
© (2015) Trans Tech Publications, Switzerland
doi:10.4028/www.scientific.net/KEM.645-646.830

Submitted: 2014-10-30
Accepted: 2014-12-23

Micro-Spring's Variable Stiffness Design and Characteristics Analysis

Guohua Liu[1, a], Li Sui[1, b], Gengchen Shi[1, c], Xuhong Guo[2, d]

[1]Beijing Institute of Technology, Beijing, P.R.CHINA

[2]Huaihai Industry Group co., Ltd, Changzhi, Shanxi Province, P.R.CHINA

[a]2120120171@bit.edu.cn, [b]bit_suili@bit.edu.cn(corresponding author), [c]shigengchen@bit.edu.cn, [d]guoxh.mems@gmail.com

Keywords: micro-spring, Variable stiffness, contact pair, characteristic curve, stiffness increase spring, stiffness convexity spring.

Abstract. The variable stiffness micro-springs' load and deformation have nonlinear relationship, thus they can be used in special occasions. MEMS processing technology can manufacture any complex structures in a plane, using this feature, a variable stiffness design idea for the planar micro-spring is proposed. That is, using one type of structure named contact pairs to achieve stiffness change during the micro-spring's stretching process. Using contact pairs, two types of variable stiffness springs are designed: stiffness increase spring and stiffness convexity spring. Because of the influence of processing precision, the contact pairs' sizes of the first type of variable stiffness spring are different each other, the machining error makes the test results and simulation results various. In order to avoid the above problem of above spring, this paper designs another two variable stiffness micro-springs, test results indicate that the improved variable stiffness springs can realize the variable stiffness' tendency.

Introduction

In a spring's working process, the relationship between load and deformation of the spring is called characteristic curve. The variable stiffness springs' characteristic curves are nonlinear, these springs' load and deformation have nonlinear relationship, and they can be used in special occasions. In recent years, variable stiffness springs have been used in macro field as the elastic connections, especially in vehicle suspension systems [1]. The purpose for vehicles using variable stiffness coil springs is that: to ensure the ride comfort. In MEMS setback arming device, it is also necessary to design variable stiffness micro-spring to improve the fuze's safety and reliability [2]. During fuze service management process, the micro-spring's stiffness should be as rigid as possible, and then the spring's deformation can be as small as possible, so that the mass block moves a short distance and the fuze meet security requirement. During fuze launch process, the micro-spring's stiffness should be flexible, and then the spring's deformation can be large enough to make the mass block's movement in prescribed place and the fuze meet reliability requirement. Currently, there is no information about variable stiffness micro-springs.

Design Idea of Variable Stiffness Micro-spring

Stiffness change method for macro-spring. For coil springs, there are several methods to realize change of spring's stiffness, such as changing spring's pitch, changing spring's mean diameter and changing spring's wire diameter [3-5]. Besides coil springs, disc springs and leaf springs can also change their stiffness during the working process [6, 7].

By analyzing the above springs' stiffness change methods, the following conclusion can be gotten:

1) Using state nonlinear to achieve the change in stiffness. Coil springs achieve variable stiffness by reducing the number of spring's working steps during its deformation process. Essentially, it uses spring's state change to variety spring's stiffness, such as changing the number of working steps or the number of working springs.

2) Most variable stiffness macro-springs are compression springs. In macro field, spring's stiffness change occurs in the process that the spring is compressed. There is no information about a tension spring achieving its stiffness change.

Stiffness change method for micro-spring. Now, most of micro-springs used in micro-systems are tension springs. For this reason, the variable stiffness micro-springs in this paper are tension springs.

When two structures contact each other, their state will change from linear condition to nonlinear condition. For a conical spring, its working steps contact each other during the whole spring is compressed, and this kind of state change make the number of the conical spring's working steps reduce, so that the conical spring's stiffness is variable during working process. Using state nonlinear idea, contact pairs are designed between the two level beams of a linear micro-spring, such as S-shape spring, shown in Fig. 1. The spring marked "1" is S-shape spring, and its characteristic curve is linear, while the spring marked "2" is S-shape spring with six contact pairs and its characteristic curve is nonlinear. Fig. 2(a) is contact pair's partial enlarged drawing, and the two structures are in separate state. In the course of the micro-spring is stretched, contact air's state changes from separate to closed (shown in Fig. 2(b)), so that the stiffness of the spring changes from flexible to rigid.

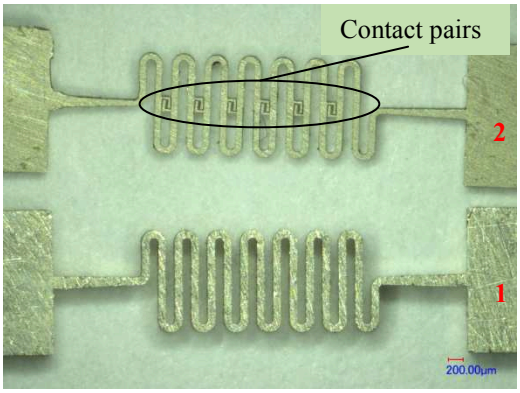


Fig. 1 Linear micro-spring and nonlinear micro-spring

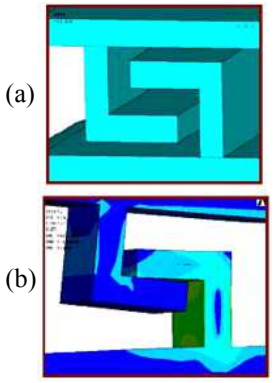


Fig. 2 Two states of contact pair for micro-spring

Simulation and Test results of Variable Stiffness Micro-spring

Using contact pairs method and LIGA process, this paper has designed and fabricated several kinds of variable stiffness micro-springs.

Simulation results. Fig. 3 shows one contact pair's size of spring "2", the contact pair is consisted by two short flexible beams, the beams' line width is 25μm, the overlap of beams is 100μm, and the separation distance between the two short beams is 50μm.

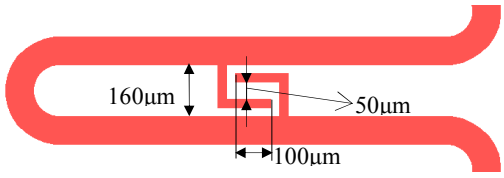
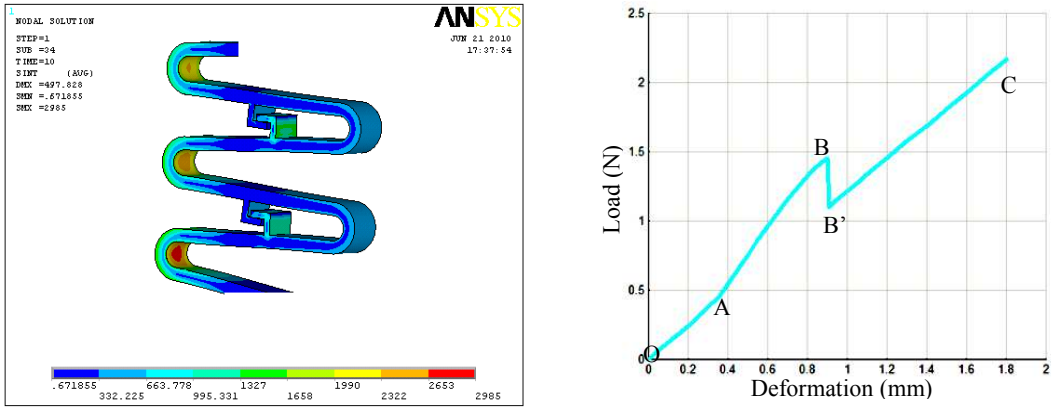


Fig.3 The contact pair's size for micro-spring "2"

Using FEA software ANSYS to complete characteristic analysis for the micro-spring marked "2", and the simulation result is shown in Fig. 4, and where, Fig. 4(a) is SEQV result when six contact pairs closed each other, and Fig. 4(b) is the micro-spring's characteristic curve during the spring's tension process. From the characteristic curve shown in Fig. 4(b), we can see that spring "2" is a stiffness convexity micro-spring. The micro spring's deformation process is following: when the load is less than 0.45N (section OA), the contact pairs are separate each other, and the spring's characteristic curve is same as spring "1"; with the increase of the load (section AB), these contact pairs closed each other, and the spring's stiffness increases significantly; when the load is greater than 1.45N, these contact pairs break away each other (section BB'), and the spring's load bearing is weakened; finally, the spring's stiffness is same as spring "1" (section B'C).

From simulation results, the micro-spring with six smaller contact pairs can realize variation of stiffness, and its characteristic curve is convex.



(a) (b)

Fig. 4 Simulation results of micro-spring "2"

Test results. The simulation result has indicated that spring "2" can realize the stiffness's convexity tendency, but the characteristic test for specimens of spring "2" can't copy the above tendency. Fig. 5 is the characteristic curve of spring "2" gotten by tensile test machine, from the figure, we can find the test curve shows zigzag, but don't like Fig. 4(b). During the micro-spring's tensile test, the contact pairs can't closed and separated at the same time, instead they separated one by one, see Fig. 6.

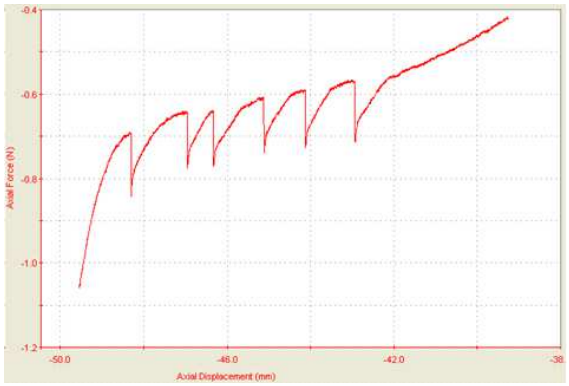


Fig. 5 Test characteristic curve of micro-spring "2"

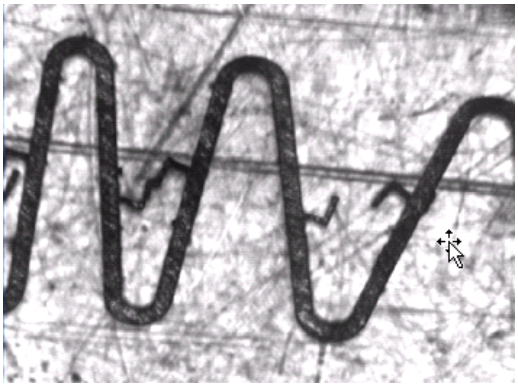


Fig. 6 Contact pairs separated one by one

Comparing the simulation results and the test results, the actual stiffness curve's variation tendency is very different from the ideal condition. In the cause of FEA, the micro-spring's six contact pairs close and separate at the same time, and the curve's variation has a single convexity. But during the test process, the six contact pairs' closing and separating are out of order, and the curve's variation has six convexities. From the test result, the actual variable stiffness micro-spring's load and displacement curve appears multiple bounces.

Table. 1 The contact pairs' actual size

No.	*The distance between short beams (μm)*	*The contact pair's line width (μm)*
1	57	30
2	47	37
3	47	35
4	51	30
5	47	30
6	51	37

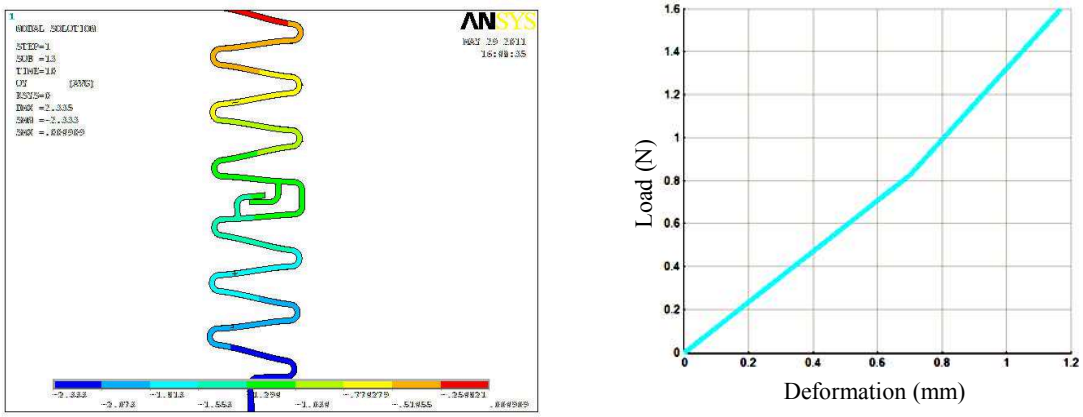
This paper has measured a batch of micro-springs' geometry size, the test results show that the contact pairs' geometry size gotten from the same spring are different each other. The six contact pairs' actual sizes is shown in Tab.1, because of the influence of processing precision, the six contact pairs' sizes are different each other, the line width distributes between 30 μm-37 μm (nominal size is 25 μm), and the distance distributes between 47 μm-57 μm (nominal size is 50 μm). Machining error makes the test results and simulation results various.

Improvement design. In order to avoid the above problem of spring "2", this paper designed another variable stiffness micro-spring, and its structure is shown in Fig. 7. Spring "3" only has one contact pair, so this kind of structure can effectively avoid the size's inconsistent problem caused by machining error.



Fig. 7 One kind of improvement variable stiffness spring

Using ANSYS to complete characteristic analysis for spring "3", and the simulation result is shown in Fig. 8, where, Fig. 8(a) is SEQV result when the contact pair closed each other, and Fig. 8(b) is the micro-spring's characteristic curve during the spring's tension process. From the simulation results, we can see that spring "3" is a stiffness increase micro-spring. From Fig. 8(b), the micro-spring's stiffness is 1178 N/m before its contact pair closed, and its deformation is 710 μm. After the contact pair become closed, the micro-spring's stiffness is 1350 N/m, and the contact pair makes the spring's stiffness increase 14.6%.



(a) (b)

Fig. 8 Simulation results of micro-spring "3"

Due to the structural limitation, this kind of variable stiffness micro-spring's variation is not great. For this kind of structure, relative variation of the micro-spring's stiffness is relative with the number of micro-spring's sections, and the smaller the section number, the greater the relative variation.

Series Variable Stiffness Micro-spring's Design and Analysis

MEMS processing technology can manufacture any complex structures in a plane, so contact pairs can be designed in varied forms. Micro-spring "2" can't realize achieve desired variation because of machining error, and the effect of micro-spring "3" isn't obvious, so this paper designed another two variable stiffness micro-springs using series structure.

Stiffness increase micro-spring. Fig. 9 is stiffness increase micro-spring, and it is micro-spring's nature state. From Fig. 9, we can see the whole spring consists of two sub-springs, two short and rigid beams, and one rigid connector. The rigid beams are static beams, so when the contact pairs consisted by rigid connector and two rigid beams closed each other, they will not separate forever. When

spring's deformation is small, contact pairs are separate and the whole spring is equivalent to two sub-springs in series; when deformation reaches a certain value, contact pairs are closed, therefore sub-spring I don't deform anymore and only sub-spring II deforms continually.

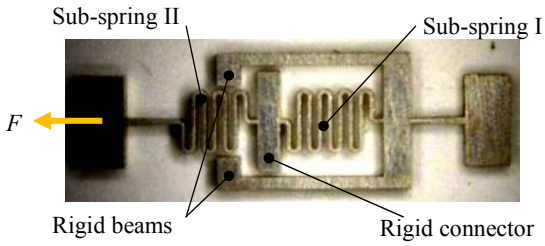


Fig. 9 One kind of series stiffness increase micro-spring

Fig. 10 is stiffness increase micro-spring's characteristic curves, where, the solid line is simulation result, and star line is test result. From the test result, the spring's stiffness is 1295 N/m before the contact pairs closed and the tensile deformation is 640μm; when the contact pairs are closed, the spring's stiffness is 2530 N/m, and the increase is about 95.37%.

The gap's design size between rigid connector and rigid beams are 400 μm, but the actual sizes are smaller than design size because of machining error, such as the sample shown in Fig. 11. Therefore, machining error led to test stiffness is greater than simulation stiffness, and the tensile deformation corresponding to the knee point is smaller than simulation date. According to test result and simulation result, the series stiffness increase micro-spring can realize the expected variable stiffness, and the amplitude of variation is very big.

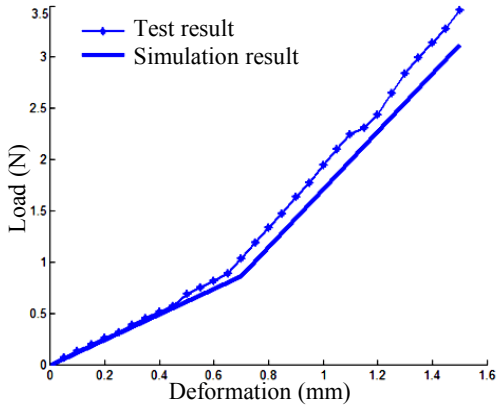


Fig. 10 Series stiffness increase micro-spring's characteristic curve

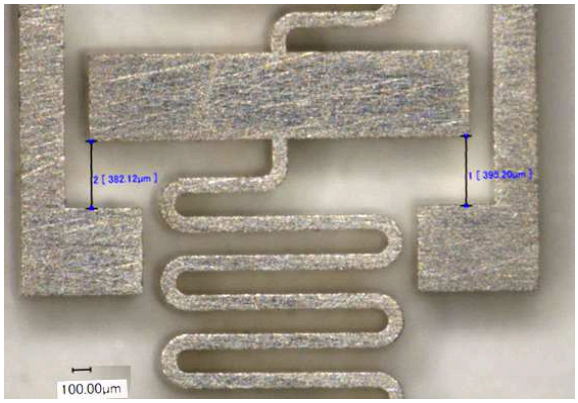
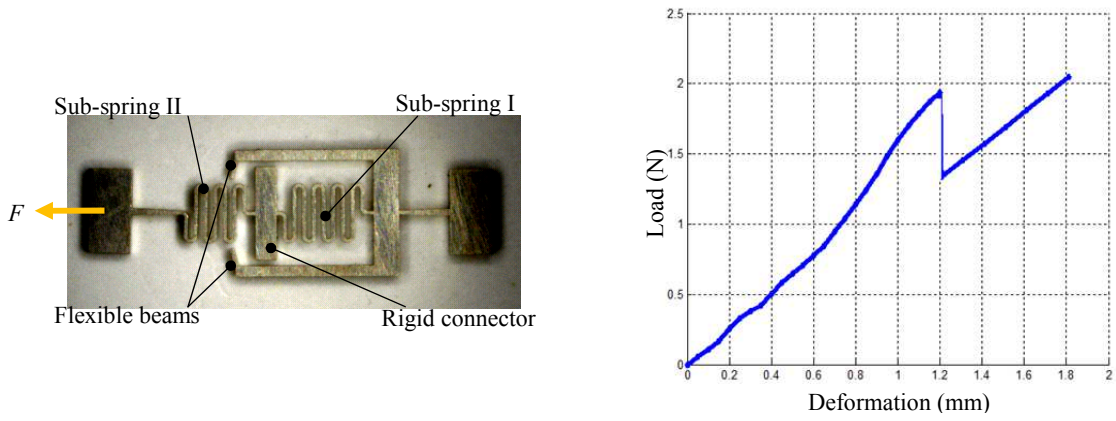


Fig. 11 The gap's actual size

Stiffness convexity micro-spring. Fig. 12(a) is stiffness convexity micro-spring, whose static beams are flexible, and its contact pairs consist of one rigid connector and two flexible beams. When spring's deformation is small, contact pairs are separate and the whole spring is equivalent to two sub-springs in series; when deformation reaches a certain value, contact pairs are closed, therefore sub-spring I don't deform anymore and only sub-spring II deforms continually. When deformation increases continuously, the contact pairs will be separated with the increasing of deformation, so that the two sub-springs deform together again.



(a) (b)

Fig. 12 One kind of series stiffness convexity micro-spring and its characteristic curve

In order to verity the above theoretical analysis, tensile test is performed for the series stiffness convexity spring, and the test result is shown in Fig. 12(b). Fig. 12(b) shows that the spring's characteristic curve is divided into three sections:

1) When the spring's deformation is smaller, the flexible beams and rigid connector are separated, and the spring's stiffness is 1250 N/m.

2) When the spring's deformation is 680 μm, the flexible beams and rigid connector are closed, at that time, the spring's stiffness is 2100 N/m, and the increase is 68%.

3) When the spring's deformation is about 1210 μm, the rigid connector loosens the bonds of the flexible beams, at that time, the spring's stiffness is 1180 N/m and closed to section one.

Conclusion

This paper provides an idea of changing stiffness for MEMS planar spring, and designs two kinds of variable stiffness micro-springs: stiffness convexity micro-spring and stiffness increase micro-spring. The simulation and test results show that:

1) Because of machining error, the micro-spring with six contact pairs can't realize the stiffness's convexity tendency; due to the structural limitation, the stiffness variation of the micro-spring with one contact pair is not great.

2) Series Variable stiffness micro-springs' simulation and test results show that, series micro-springs can achieve greater variation.

References

[1] Hrishikesh Deo, Nam P. Suh, Pneumatic suspension system with independent control of damping, stiffness and ride-height, in Proceedings of the Tony Stockman 4th International Conference, 2006.

[2] Li Sui, Zhen Wang, and Geng-chen Shi, MEMS variable stiffness spring and its application in fuze, Sensors and Transducers. 168 (2014) 101-107.

[3] Shi Peichang, Gong Jiancheng, Vehicle suspension coil springs variable stiffness optimized design, Modern Manufacturing Engineering. 11 (2006) 112-114.

[4] Ling Kaifu, Application research of cone spiral spring on locomotive vehicle, Journal of Zhuzhou Institute of Technology. 15, (2001) 48-51.

[5] Lei Lei, Zuo Shuguang, Yang Xianwu, et al., Study of stiffness calculation and test of barrel-shaped helical spring in suspension of vehicles, Journal of Machine Design. 28 (2011) 15-17.

[6] Enlai Zheng, Fan Jia, Zhisheng Zhang, et al., Modeling and simulation of nonlinear combination disc-spring vibration, Advanced Materials Research. 211-212 (2011) 40-47.

[7] Junho Choi, Seonghun Hong, Woosub Lee, et al., A variable stiffness joint using leaf springs for robot manipulators, in Proceedings of the IEEE International Conference on Robotics and Automation. 1(2009) 4363-4368.

Key Engineering Materials Vols 645-646 (2015) pp 836-840
© (2015) Trans Tech Publications, Switzerland
doi:10.4028/www.scientific.net/KEM.645-646.836

Submitted: 2014-10-31
Accepted: 2014-12-23

Fabrication Process and Electro-Thermal Modeling for the Cathode of the CMOS-Compatible Hot-Filament Vacuum Gauge

Wang Jiaqi [1, a*] and Yu Jun[2,b]

[1] Liaoning IC Technology Key Laboratory, Dalian Institute of Semiconductor Technology, and School of Electronics Science & Technology, Dalian University of Technology, Dalian, LiaoNing, China

[2] Liaoning IC Technology Key Laboratory, School of Electronics Science & Technology, Dalian, LiaoNing, China

[a]wjq@dlut.edu.cn, [b]junyu@dlut.edu.cn

Keywords: Vacuum gauge, hot-filament vacuum gauge, CMOS-compatible, electro-thermal model.

Abstract. The hot-filament vacuum gauge is a traditional gauge for the vacuum measurement below 10^{-1}Pa. It consists of the cathode, grid and anode. The cathode is used to emit the electron to collide with a gaseous molecular to form a pair of ion and electron. The number of these ions is proportional to the gaseous molecule density and the gas pressure. Unlike the traditional gauge with the large dimension, this paper develops a CMOS-compatible hot-filament vacuum gauge. With it, the vacuum gauge and its control circuit can be fabricated monolithically on a chip which will decrease the noise and be easy to use. Besides that, the optimal heating current for the cathode is also considered in this paper. The electro-thermal modeling using COMSOL software is introduced to calculate the heating current for cathode. The results show that for 200μm×5μm×0.2μm tungsten resistor, 200mA current is needed to heat the tungsten resistor to 1800°C to emit the electron.

Introduction

There are different types of vacuum gauge to measure the different ranges of vacuum. The Pirani gauge is usually used to measure the vacuum from 10^{5}Pa to 10^{-1}Pa [1]. The hot-filament vacuum gauge is used for the vacuum measurement below 10^{-1}Pa. It consists of the cathode, grid and anode. Electrons emitted from the filament cathode move several times in back and forth around the grid before finally entering the grid. During these movements, some electrons collide with a gaseous molecular to form a pair of ion and electron (Electron ionization). The number of these ions is proportional to the gaseous molecule density multiplied by the electron current emitted from the filament, and these ions pour into the anode to form an ion current. Since the gaseous molecular density is proportional to the pressure, the gas pressure is estimated by measuring the ion current [2].

The traditional hot-filament vacuum gauge has a relatively large dimension, weight and the high power consumption, so there is a limitation for its application in some special area, such as the space area and micro packaging. Thus, some research groups have developed the silicon-based hot-filament vacuum gauge using MEMS technology. The micro tungsten resistor fabricated by tungsten film deposition and etching process is used as the cathode for the vacuum gauge [3,4]. Their measurement range can reach 10^{-3}Pa. Also, the nanotube is introduced as the material for cathode to decrease the power consumption and the dimension [5,6]. All of these researches decrease the dimension of the gauge to some extent.

In this paper, besides the silicon-based hot-filament vacuum gauge, a CMOS-compatible hot-filament vacuum gauge is developed. With it, the vacuum gauge and its control circuit can be fabricated monolithically on a chip which will decrease the noise and be easy to use. This ion gauge occupies a volume that is orders of magnitude smaller than its conventionally sized counterpart, making the gauge suitable for pressure measurement in, for example, a microchip package.

The optimal heating current for the cathode is also considered in this paper. The electro-thermal modeling for the cathode is introduced to calculate how much current to heat the cathode to emit the electron. The results show that 200mA current is required to heat the cathode to 1800°C to emit the electron.

Basic Theory for Hot-Filament Vacuum Gauge

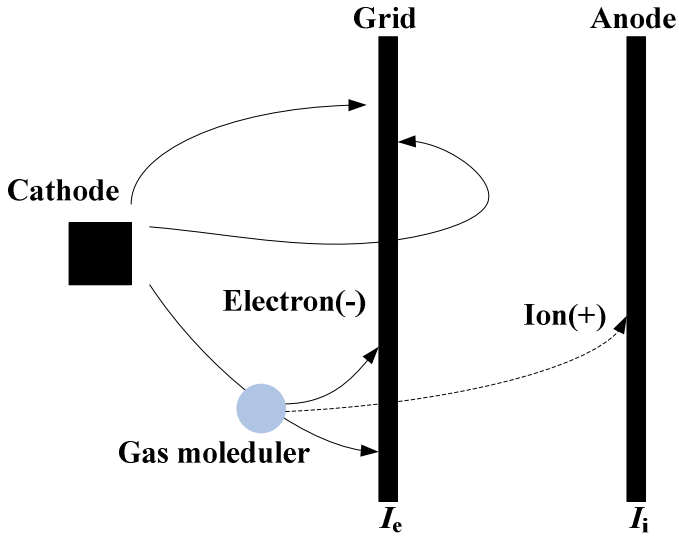


Fig. 1. The operation of the hot-filament vacuum gauge

In operation, the cathode is heated ohmically. Electrons are thermionically emitted and accelerated towards the grid (or electron collector) which has a large positive voltage applied to it, seen in Fig. 1. Electrons that initially miss the grid circle back until they are collected, forming the electron current I_e. If the gas molecules are present, some of the energetic electrons collide with some of the molecules, ionizing them. The ions are collected by the anode, which has the negative potential, forming the ion current I_i. The electrons generated by the ionization are also collected by the grid, adding to I_e. Theoretically, the I_i is proportional to the electron current I_e, the gas pressure p, the ionization rate α of the ambient gas and the electron path L

$$I_i = I_e\, p\alpha L \tag{1}$$

Thus

$$(I_i/I_e)/p=\alpha L \tag{2}$$

The gauge sensitivity can be defined as:

$$S=\alpha L \tag{3}$$

The sensitivity S given in Eq. 3 is a function of α and the average electron-path length L, which depends on the biasing voltage, dimension and the relative position of the cathode, grid and anode [7]. Thus, in our design, two grids are added on both sides of anode to make the electron path longer, seen in Fig. 2.

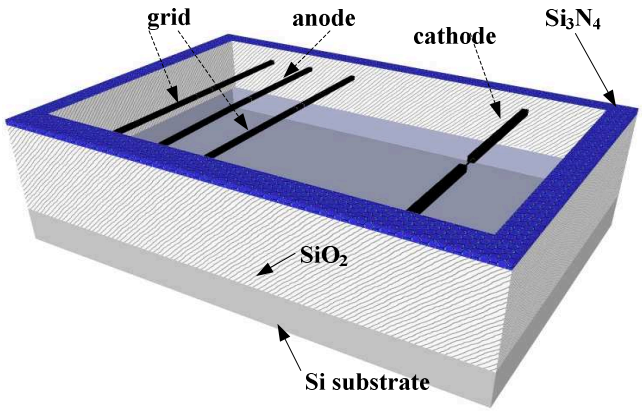


Fig. 2. The structure of the hot-filament vacuum gauge

Fabrication Process

In this paper, a CMOS-compatible hot-filament vacuum gauge is developed. With it, the vacuum gauge and its control circuit can be fabricated monolithically on a chip which will decrease the noise and be easy to use. The feasibility is that the common material for the cathode of the hot-filament vacuum gauge is tungsten which is also used as the plug material in the standard CMOS process [8,9]. In our design, the hot-filament gauge is implemented in 0.5μm CMOS process that features two metal layers (Metal1, Metal2). The main fabrication process consists of CMOS process and Post-CMOS process, as shown in Fig. 3. In CMOS process, the tungsten resistor is fabricated with its anchors connected only to Metal2, leaving the Metal1 unconnected, seen in Fig. 3(a). In the bonding pad opening process, the surface of the tungsten resistor is also exposed by overetching the PSG and Si_3N_4 passivation layer. In post-CMOS process, the Al pad is protected by photoresist and HF is used to remove the PSG below the tungsten resistor, seen in Fig. 3(b). In Fig. 3(c), the Al pad is protected by Au layer and the silicon substrate below the tungsten resistor is etched by KOH to further suspend the tungsten resistor as the cathode of the hot-filament gauge. The SEM picture of the cathode is shown in Fig. 4.

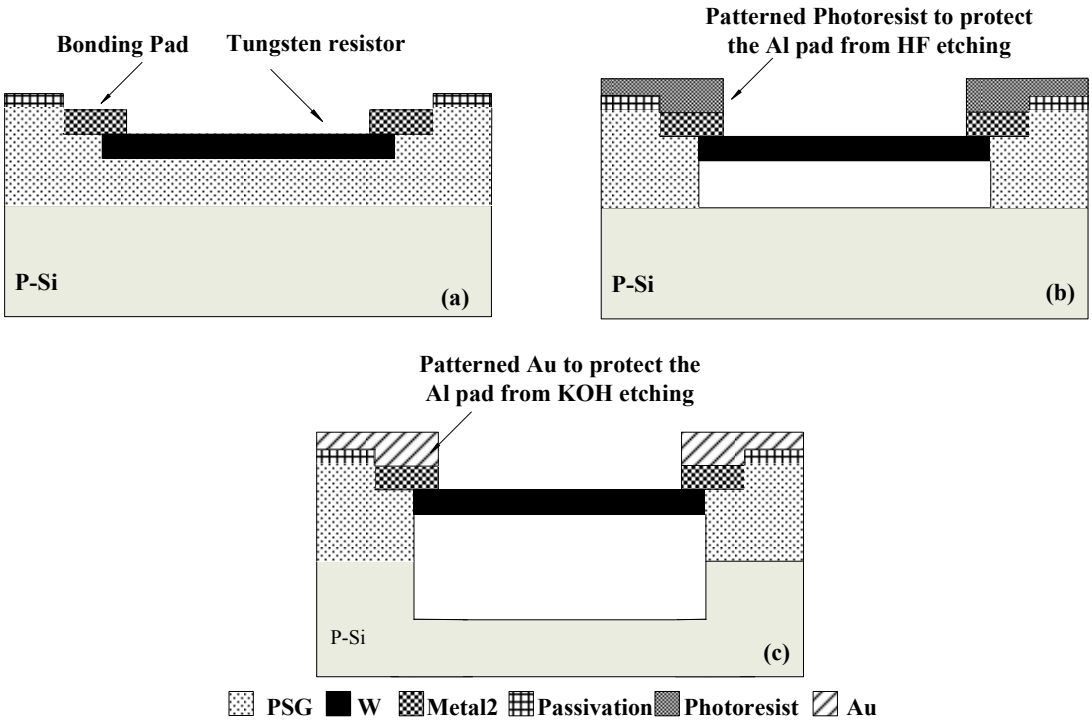


Fig. 3. The fabrication process for the hot-filament vacuum gauge

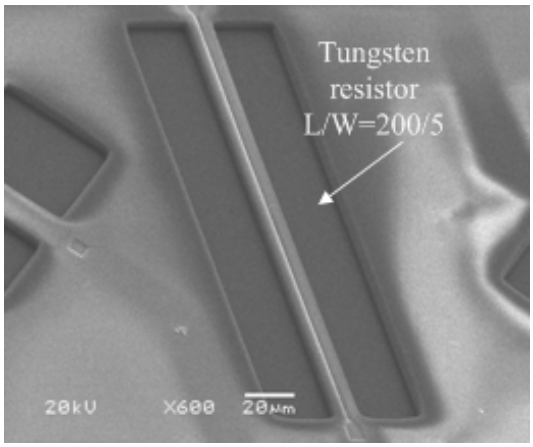


Fig. 4. The SEM picture of the cathode for hot-filament vacuum gauge

Simulation

The heating current for the cathode is the most important parameter for the vacuum gauge design, so the optimal heating current for the cathode is also considered in this paper. The electro-thermal model for the cathode is introduced to calculate how much current to heat the cathode to emit the electron. The model and the simulation result are shown in Fig. 5 using the joule heating module of COMSOL software. The tungsten resistor is 200μm×5μm×0.2μm and 200mA current is needed to heat the tungsten resistor to 1800°C to emit the electron. This model can be used to optimize the vacuum gauge design and guide the vacuum measurement experiment.

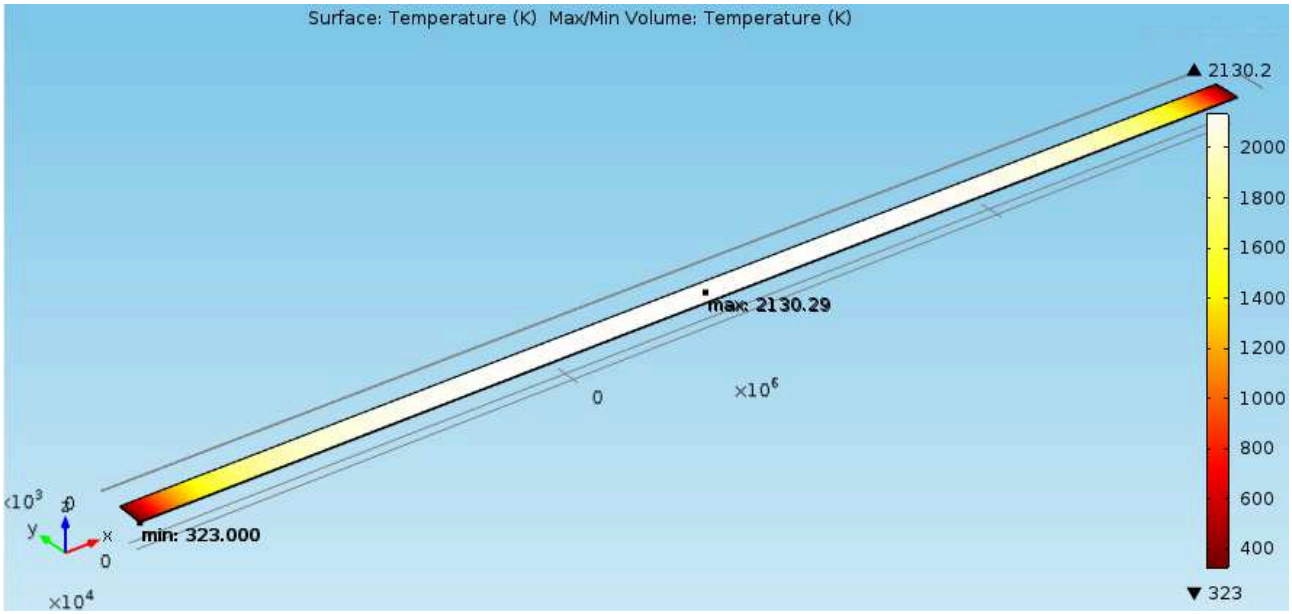


Fig. 5. The model and the simulation result for cathode of hot-filament vacuum gauge

Summary

In this paper, a CMOS-compatible hot-filament vacuum gauge is fabricated with the 0.5μm standard CMOS process. It consists of a cathode, two grids and an anode. The material for cathode is tungsten which is also used in the CMOS process as the via contact material. For the cathode, the tungsten resistor is fabricated with its anchors connected only to one metal layer, instead two metal layers as in CMOS process. The dimension for the cathode is 200μm×5μm×0.2μm. A series of post-CMOS etching process is used to expose the tungsten resistor as the cathode. In order to get the optimal current to heat the cathode to emit the electron, the electro-thermal model using COMSOL software is established. By calculation, the 200mA current is required to heat the tungsten resistor to 1800°C to emit the electron for the 200μm×5μm×0.2μm dimension. The model can also be used to optimize the structure for the vacuum gauge with the magnetic and electrical field model to make the vacuum gauge design more effectively.

Acknowledgement

This work was supported by the National Natural Science Foundation of China (No. 61201035, 61274076).

References

[1] Jiaqi Wang, Zhenan Tang, and Jinfeng Li. Tungsten-Microhotplate-Array-Based Pirani Vacuum Sensor System with On-Chip Digital Front-End Processor. IEEE/ASME Journal of Microelectromechanical Systems, 20(4) (2011) 834-841.

[2] P.J. Abbott, J.P. Looney, P. Mohan. The effect of ambient temperature on the sensitivity of hot-cathode ionization gauges, Vacuum, 77 (2005) 217–222.

[3] Kirt R. Williams and Richard S. Muller. Micromachined Hot-Filament Ionization Pressure Sensor and Magnetometer. 1997 lnternational Conference on Solid-state Sensors and Actuators (Transducers 97'), Chicago, 1997: 1249-1252.

[4] John Liebeskind. Micro High-Vacuum Pressure Sensor. US patent 0186017A1(2002).

[5] Lin Xiao, Liang Liu, Kai-Li Jiang, Shou-Shan Fan. Ionization vacuum gauge. US patent 0278436A1(2009).

[6] Changkun Dong and Ganapati R. Myneni. Carbon nanotube electron source based ionization vacuum gauge, Applied physics letter, 84(26) (2004) 5443-5445.

[7] Kirt R. Williams. Micromachined hot-filament vacuum devices, PhD dissertation, UC Berkeley, 1997.

[8] Wang Jiaqi and Tang Zhenan. Tungsten for CMOS-MEMS Pirani and Ionization Vacuum Gauges, Nanotech 2013, 2(2013), 146-149.

[9] M. Quirk, and J. Serda, Semiconductor Manufacturing Technology. Englewood Cliffs, Prentice Hall, New Jersey, 2001.

Key Engineering Materials Vols 645-646 (2015) pp 841-846
© (2015) Trans Tech Publications, Switzerland
doi:10.4028/www.scientific.net/KEM.645-646.841
Submitted: 2014-10-31
Accepted: 2014-12-23

A new design of a piezoelectric triaxial micro-accelerometer

Jianyan Wang[1, 2], Tingting Wang[1, 2], Hang Guo[2,1*,a]

[1]Department of Mechanical and Electrical Engineering, Xiamen University, Xiamen, China

[2]Pen-Tung Sah Institue of Micro-Nano Science and Technology, Xiamen 361005, China

[a]hangguo@xmu.edu.cn

Keyword: accelerometer, theotetical analysis, simulation, circuit connection

Abstract: Accelerometer in MEMS always is made by capacitive or piezoresistive, whose dynamic response is not good, the operating frequency is narrow, and the cross-axis sensitivity is low. A new type of piezoelectric micro-accelerometer is designed, and its structure is "x" type. The sensing unit is piezoelectric PZT films, which is achieved by sol-gel method. The accelerometer is a triaxial accelerometer. The theoretical and simulation analysis is used to achieve the charge sensitivity and response frequency, and also get the optimal structural parameters. A new circuit connection is proposed to improve the sensitivity and avoid the cross-axis sensitivity. The design achieves the z-axis sensitivity with more than 40 pC/g, x, y-axis sensitivity with more than 8pC/g, and the response frequency is about 3000Hz.

Introduce

Accelerometers is one of the most widespread applications of silicon micro-sensor technology, mainly by its small size, low power consumption, light weight, good reliability and so on. They are widely used in automotive civil aviation and robotics [1-3]. Currently, a variety of accelerometers have been investigated that use different measuring principles, including capacitive, piezo-resistive, resonant, etc. The capacitive and the resistive are usually used in micro-electro mechanical system (MEMS). However, the piezo-resistive accelerometer needs high energy consumption and the capacitive accelerometer not only needs high energy consumption but also require higher electronic design [4]. Instead, piezoelectric accelerometers have a great advantage due to its low power consumption, high sensitivity.

Due to the low cross-axis sensitivity and the presence of crosstalk [5], the triaxial accelerometer has fewer applications. Currently, micro-accelerometers is mainly uniaxial accelerometer which needs three uniaxial accelerometers to detect three directions. This situation will result in a large volume and poor consistency. So this paper presents an application of piezoelectric film (PZT) as triaxial micro-accelerometer, which is aimed to improving the sensitivity and frequency response bandwidth, avoiding crosstalk problems.

The principle of piezoelectric accelerometer

Like Figure 1, when the mass subjected one inertia force, it will move vertically. The piezoelectric film will be deformed with the cantilever. According to the piezoelectric effect, the upper and lower electrodes of the piezoelectric thin film can produce charge. Based on the amount of charge the acceleration will be detected [6]. In order to develop the range of the sensitivity and frequency, this paper proposes a new piezoelectric accelerometer which contains a mass, four cantilever unit and eight piezoelectric films, like Figure 2. The mass and the cantilevers are made by silicon material, while the material of the piezoelectric element is PZT.

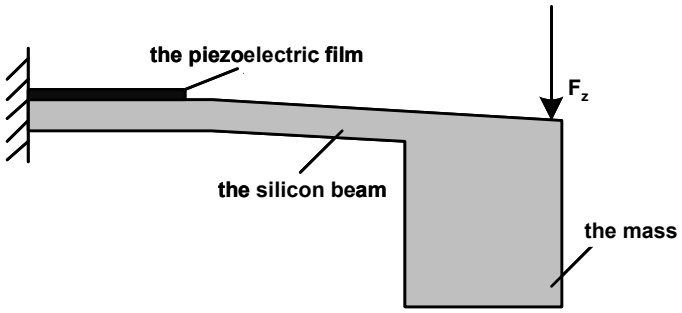


Fig. 1 The principle schematic of piezoelectric accelerometer

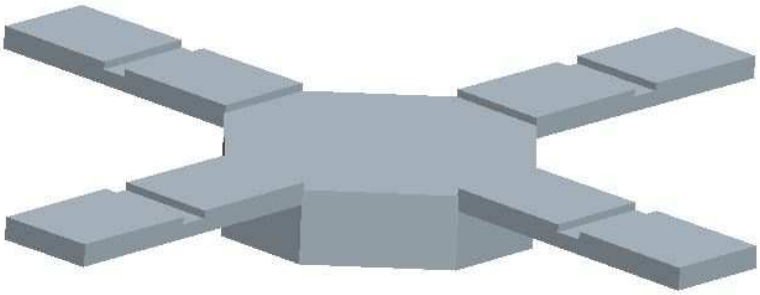


Fig. 2 Schematic diagram of piezoelectric accelerometer

The theoretical analysis of piezoelectric accelerometer

Static analysis

Static analysis of piezoelectric accelerometer is to analyze the vibration when inertial force is on the mass. The charge will generate on the piezoelectric films, the detection methods can be charge or voltage. What the design chooses is the charge. Depending on the mount of the charge, the inertial force will be derived, and then the acceleration will be achieved.

Before analysis, some assumptions will be made: 1. comparing with the mass, the quality of the cantilever is so small, which can be negligible; 2. the mass will be analyzed as a particle since it is rigid; 3. the piezoelectric film PZT and the silicon cantilever is elastic and obey Hooke's law; 4. the thickness of the upper and lower electrodes on the PZT films can be ignored; 5. when the mass is applied with the vertical direction acceleration, the stress along the x- and y-axis is very small, and can be negligible. Since the whole model is symmetrical, a quarter of it is analyzed. The force analysis model is simplified as shown in Figure 3.

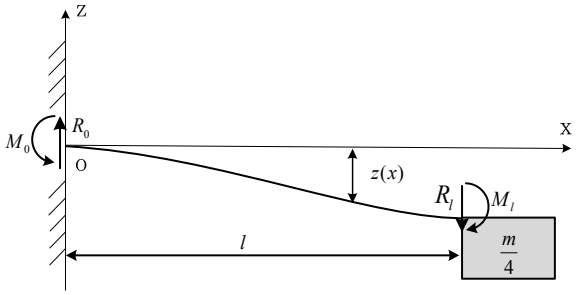


Fig. 3 Analytical model of piezoelectric accelerometer

By symmetry, the simplified of the structure is subjected to external forces R .

$$R = \frac{1}{4}ma_z \tag{1}$$

where m is the quality of the mass, a_z is the acceleration along z-axis. According to the boundary condition and the symmetry, the bending moment of the cantilever $M(x)$ is:

$$M(x) = \frac{1}{4}ma_z(\frac{1}{2}l - x) \tag{2}$$

where l is the length of the cantilever. Since the thickness of the cantilever is less different with the PZT films, the thickness of PZT films will be considered, shown in Figure 4. The strains of the PZT films need to meet the following equation:

$$\varepsilon_1 = \frac{z(x)}{\rho} \tag{3}$$

where ε_1 is the strain, $z(x)$ is displacement in x coordinate, ρ is the radius of curvature of this location. According to the relationship between the stress and the strain, the following equation will be achieved.

$$\delta_i = C_{ij}\varepsilon_j, \quad i,j = 1,\cdots,6 \tag{4}$$

where C_{ij} is the stiffness matrix of the PZT films. Ignoring the other direction stress, this equation transform to the following equation:

$$\delta_1 = C_{11}\varepsilon_1 \tag{5}$$

The C_{11} is written as $E_p = C_{11}$, then $\delta_1 = E_p\varepsilon_1$. Because silicon is isotropic, the stress-strain relationship is written as:

$$\delta_s = \frac{E}{1-\nu^2}\varepsilon_s \tag{6}$$

Where E the Young's modulus of silicon is, ν is the Poisson's ratio of silicon. So $E_S = \frac{E}{1-\nu^2}$, then $\delta_s = E_S\varepsilon_s$.

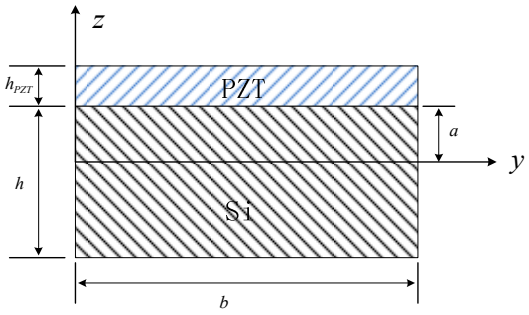


Fig. 4 Sectional view of the accelerometer

Based on the force and moment balance condition in the cantilever, the balance equation is achieved, as following.

$$\int_{-(h-a)}^{a} bE_s\frac{z}{\rho}dz + \int_{a}^{h_{PZT}+a} bE_p\frac{z}{\rho}dz = 0 \qquad \int_{-(h-a)}^{a} bE_s\frac{z}{\rho}zdz + \int_{a}^{h_{PZT}+a} bE_p\frac{z}{\rho}zdz = M(x) \tag{7}$$

where a is the location of the neutral surface. The y-axis is located at neutral surface, as figure 4. b is the width of the cantilever, h is the thickness of the silicon beam, h_{PZT} is the thickness of the PZT films. Solving Equation (7), the result is as following:

$$a = \frac{1}{2}\frac{E_s h^2 - E_p h_{PZT}^2}{E_s h + E_p h_{pzt}} \tag{8}$$

$$\frac{1}{\rho} = \frac{M(x)}{(bE_s/3)(h^3 - 3ah^2 + 3a^2h) + (bE_p/3)(h_{PZT}^3 + 3ah_{PZT}^2 + 3a^2h_{PZT})} \tag{9}$$

So $EI_{eq} = (bE_s/3)(h^3 - 3ah^2 + 3a^2h) + (bE_p/3)(h_{PZT}^3 + 3ah_{PZT}^2 + 3a^2h_{PZT})$, the stress on the silicon beam at arbitrary position is:

$$\delta_1 = \frac{E_p}{\rho}z = \frac{E_p M(x)}{EI_{eq}}z \tag{10}$$

Then the amount of charge generated in the PZT films during vibration is as following equation:

$$Q = \int_0^l p\ Dbdx = \frac{1}{32}d_{31}b\frac{E_p}{EI_{eq}}(h + h_{PZT})ma_z l^2 \tag{11}$$

According to the Equation (11), the charge sensitivity and the voltage sensitivity are achieved. And from the formula (11), the charge sensitivity has noting to do with the width of the beam.

Dynamic analysis

In dynamic analysis, the model is also equivalent to a quarter, at the same time the system can be modeled as a spring-mass system. Rayleigh energy method is used to achieve the natural frequency. Rayleigh energy method is based on the conservation of energy law. In this system, the energy converted to the electric field energy is ignored. When the velocity of the particle is zero, the mechanical energy is completely converted into potential energy; when the deformation is zero, the mechanical energy is completely to kinetic energy [7, 8].

When the accelerometer is vibrating, the displacement of the silicon beam and the mass is meeting the equation $Z(x,t) = z(x)\sin(\omega t)$, so the kinetic energy of the system is:

$$dT = \frac{1}{2} \cdot dm \cdot v^2 = \frac{1}{2} \cdot dm \cdot [\frac{\partial Z(x,t)}{\partial t}]^2 = \frac{1}{2} \cdot dm \cdot [\omega z(x) \cos(\omega t)]^2 \quad (12)$$

When $\cos(\omega t) = 1$, the silicon beam is in the equilibrium position, the maximum kinetic energy of the system is as following:

$$T_{\max} = \int_0^L \rho b H \omega^2 [z(x)]^2 dx \quad (13)$$

Where ρ is density, H is the height value of the integral position. The potential location of the system is meeting the following equation:

$$U = \int_0^L \frac{1}{2} EI \left[\frac{\partial^2 Z(x,t)}{\partial x^2} \right]^2 dx = \int_0^L \frac{1}{2} EI [z''(x)\sin(\omega t)]^2 dx \quad (14)$$

when $\sin(\omega t) = 1$, the silicon beam is has the maximum potential energy, so the potential energy is as following,

$$U_{\max} = \int_0^L \frac{1}{2} EI [z''(x)]^2 dx \quad (15)$$

According to the Rayleigh energy method, $T_{\max} = U_{\max}$, the frequency has achieved.

Simulation analysis

The simulation analysis is made by ansys software. Depending on the manufacturing process, the piezoelectric constant, dielectric constant and the elastic constant of the piezoelectric films have different values. In the simulation those parameters is common values. When the z-axis acceleration is 1g, the stresses along the x-, y-, z-axis in the PZT films is showing in Figure 5. The stresses along y- and z-axis are very small which can be ignored. The stress is mainly provided by the x-axis direction, and the theoretical value is very close to the simulation results. The result also verified the assumption that the mass and the beam are rigid in this model.

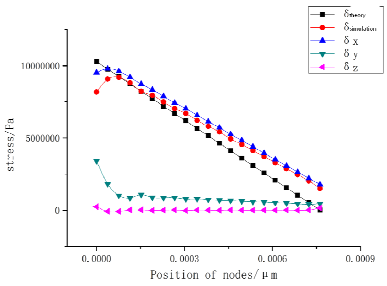


Fig. 5 Stress analysis

From the formula (11), the charge sensitivity is directly related to the thickness, the width, the length of the silicon beam and the thickness of the PZT films. So the influences of those parameters are studied, as shown in Figure 6. From the graphs, the length of beam has greatest impact. The width of the beam has little effect to the charge sensitivity of the accelerometer, which is consistent with the results of formula (11).

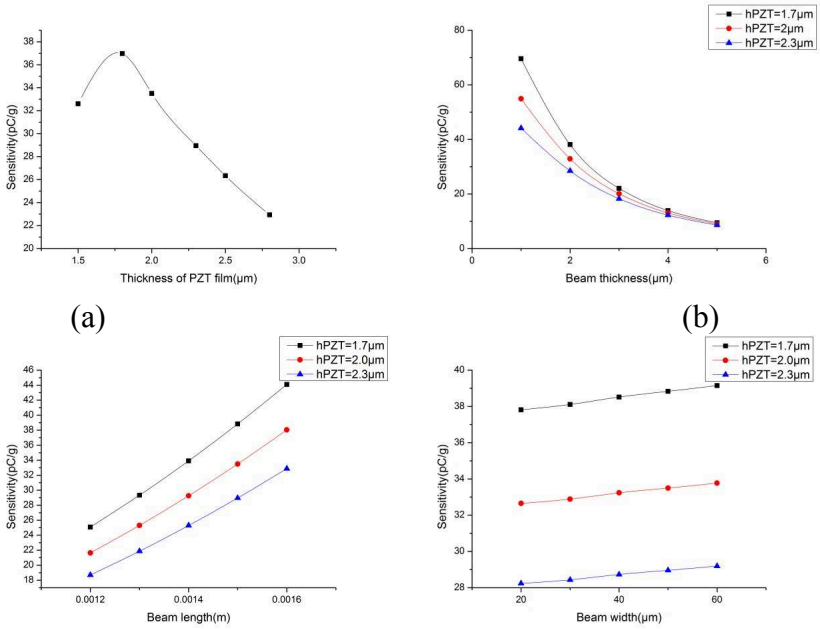


Fig. 6 The effect of the structural parameters to the piezoelectric accelerometer charge sensitivity
(a) the effect of the thickness of PZT films (b) the effect of the thickness of silicon beam
(c) the effect of the length of silicon beam (d) the effect of the width of silicon beam

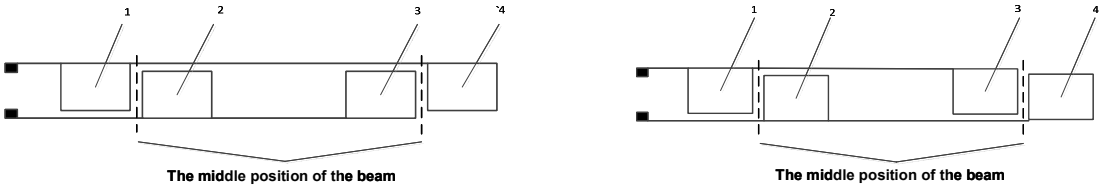
Circuit connections

In order to solve crosstalk in the accelerometer, a new circuit connection is provided, which can not only solve the crosstalk effectively but also improve the charge sensitivity.

There are four piezoelectric films on two opposing beams, numbered 1,2,3,4. The 1 and 4 generate the same charge and are opposite to 2 and 3 when the z-axis direction acceleration is on the mass. The 1 and 3 generate the same charge and are opposite to 2 and 4 when the x- or y-axis direction acceleration is on the mass. So two connections are produced: symmetrical connection and antisymmetric connection, as the Figure 7.

According to the principle, the actual circuit connection is showing in Figure 8. This structure can detect the acceleration coming from x/y/z axis.

According to the principle, the actual circuit connection is showing in Figure8.



(a) z-axis detection connection (b) x- or y-axis detection connection

Fig. 7 The different direction detection circuit connection

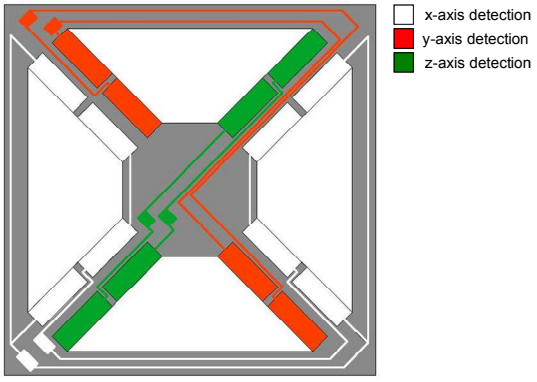


Fig. 8 Accelerometers actual circuit connection

Conclusion

This paper presents piezoelectric film as miniature accelerometer sensing element. The structure is “x” type, and the PZT film is made by sol-gel method. And the z-axis charge sensitivity is more than 40 pC/g, and x-axis and y-axis charge sensitivity is about 8pC/g. The response frequency of the accelerometer is about 2900Hz, higher than the conventional accelerometer. With the new circuit connection the crosstalk can be effectively avoided, which also improve the charge sensitivity. This accelerometer can be used in aviation or others.

Acknowledgement

The research is funded by the New Century Talents Supporting Plan of The Education Department of China (project #2007NCET-07-0723).

Reference

[1] Roger De Reus, Jens Ole Gullov, and Patrick R Scheeper, Fabrication and characterization of a piezoelectric accelerometer, Journal of Micromechanics and Micraengineering. 9(1999) 123-126.

[2] Y.Nemirovsky, A.Nemirovsky, P.Muralt, N.Setter, Design of a novel thin-film piezoelectric accelerometer, Sensors and Actuators. 56(1996) 239-249.

[3] Korbinian Kunz, Peter Enoksson, Goran Stemme, Highly sensitive triaxial silicon accelerometer with integrated PZT thin film detectors, Sensors and Actuators. 92(2001) 156-160.

[4] Han Geun Yu, L.Zou, K. Deng, el, Lead zirconate titanate MEMS accelerometer using interdigitated electrodes. 107(2003)26-34.

[5] Christian Carstensen Hindrichsen, Ninia S. Almind, el, Analytical Model of a PZT Thick-Film Triaxial Accelerometer for Optimum Design, IEEE SENSORS JOURNAL.4(2009)419-429.

[6] J. Hillenbrand, M. Kodejska, el, High-sensitivity Piezoelectret-film Accelerometers, 4(2010)1021-1027.

[7] R.P.van Kampen, R.F.Wolffennbuttel. Modeling the mechanical behavior of bulk-micromachined silicon accelerometers, Sensors and Actuators. 64(1998)117-150.

[8] A.T.Kollias, J.N.Avaritsotis. A study on the performance of bending mode piezoelectric accelerometers [J], Sensors and Actuators, 121(2005)434-442.

Key Engineering Materials Vols 645-646 (2015) pp 847-852
© (2015) Trans Tech Publications, Switzerland
doi:10.4028/www.scientific.net/KEM.645-646.847

Submitted: 2014-11-03
Accepted: 2014-12-23

UVC-thermal coupled digestion without oxidant for the detection of total phosphorus

Long Li[1,2,a], Chao Bian[1,b*], Jianhua Tong[1,c], Heng Li[1,2,d], Shanhong Xia[1,e]

[1] State Key Laboratory of Transducer Technology, Institute of Electronics, Chinese Academy of Sciences, Beijing, CHINA

[2] University of Chinese Academy of Sciences, Beijing, CHINA

[a]lil264@163.com, [b*]cbian@mail.ie.ac.cn, [c]jhtong@mail.ie.ac.cn, [d]lih1212@163.com, [e]shxia@mail.ie.ac.cn

Keywords: total phosphorus (TP) digestion, UVC, oxidant-free

Abstract: In this paper, a catalyst-free and non-oxidant digestion method based on UVC and thermal coupled mechanism was developed for the digestion of total phosphorus (TP). Two kinds of digestion devices, "hamburg-type" and "screw-type", were designed and compared to get higher digestion efficiency. Both of the two devices contain a quartz tube, UV light tubes, a flexible heating unit, UV light reflecting layer, and a temperature meter, etc. UVC light with the wavelength of 254nm is used to produce hydroxyl radicals to degrade TP into phosphate in water. Compared with the "hamburg-type" digestion device, the "screw-type" device exhibited a higher digestion rate. At the condition of 1 hour and 80℃, the digestion rate of 1mg/L (by weight of P) water sample can come to 96% by using the "screw-type" device.

Introduction

Eutrophication has become a serious problem in water environment of China. Total phosphorus as one of the important factors for eutrophication is the sum of all various forms of phosphorus, including orthophosphates, condensed phosphates and organically bound phosphorus [1]. The huge use of chemical fertilizer in agriculture and discharge of urban sewage have largely increased the amount of phosphorus in water environment. Once the water with phosphorus taken orally, the phosphorus will be absorbed in and do harm to human body [2]. So, the detection of TP has become an important part of the environment quality monitoring process.

Before the detection of TP, a digestion pretreatment procedure of the water sample must be proceeded to convert all types of phosphorus to orthophosphate. Subsequently, either electrochemical or optical method is employed to detect the concentration of phosphate, and then complete the detection of TP. The traditional method for TP digestion is oxidation with potassium persulfate as the oxidant at high temperature of 120℃ and at high pressure of 1.1kg/cm^2, which is high power consuming. There are also many other developed methods such as microwave digestion [3] and nano-TiO_2 photocatalysis digestion [4], which are complicated to practice. The using of oxidant and catalyst in the digestion procedure complicates the digestion process and would disturb the subsequent detection of phosphate in either electrochemical or optical method. Therefore it is very important to build up a simple and efficient method for TP digestion. UV photolysis [5] has recently appeared as a new emerging technique for water treatment with the advantages of high

efficiency and environmental friendly and it is studied that UVC has the capability of degrading many kinds of larged molecular organic components [6]. So in this paper, UVC light with the wavelength of 254nm is used to degrade TP into phosphate in water.

UVC and thermal coupled digestion shows high efficiency for TP degradation. There isn't any catalyst or oxidant used in the process of digestion and the volume of sample water for every digest is 1mL in this paper. This greatly simplifies the procedure of TP digestion and would conduce to the achievement of automation and miniaturization for TP detection device.

Experimental

Reagents and equipments. Potassium dihydrogen phosphate solutions (KH_2PO_4, Beijing Chemical Reagent Company, China) with the concentrations of 0.25, 0.5, 1.0, 2.0, 3.0 and 4.0mg/L (by weight of P) were used to construct the calibration curve. Sodium glycerophosphate solutions ($C_3H_7Na_2O_6P$ Beijing Chemical Company, China) as TP sample were used for testing. Ascorbic acid ($C_6H_8O_6$), ammonium molybdate [$(NH_4)_6Mo_7O_{24}\cdot 4H_2O$], potassium antimony tartrate ($KSbC_4H_4O_7\cdot 1/2H_2O$) and H_2SO_4 were obtained from Beijing Chemical Reagent Company, China and were used to prepare the color reagent for the digested water samples. The solutions tested were all used without pH adjustment and the water used for solutions was deionized water in this paper.

Ultrapure Water Polishing System (ULTRAPURE WATER from Millipore, USA) supplied deionized water for the experiment, and Ultraviolet spectrophotometer (Biospec-nano from Shimadiu Corporation, Japan) was employed to measure the concentration of orthophosphate. Some micropumps, microvalves (Bio-Chem Fluidics, USA), rubber hoses and the drive circuit were used for the construction of the digestion system.

Design of the digestion tube. In this paper, two kinds of digestion tubes were designed for TP detection, both of which could contain 1mL sample water. One is plane winding, and the other is helical, as shown in Figure 1. The plane winding digest tube had a 10×5×0.3cm outline dimension and its inner diameter was 1.5mm which could make UV light penetrating through the sample water. The helical digest tube with the outline dimension of 8×2.5×2.5cm was reformed from the plane winding, and its inner diameter was 1.0mm. Quartz which has a high effective transmission of UV light was used as the material for the digestion tube, and the transmission rate of UV light is about 90%.

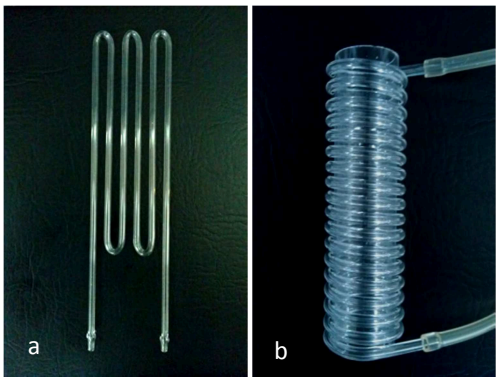


Fig. 1 The entity pictures of the two kinds of digestion tubes,(a)plane winding digestion tube (b)helical digestion tube

Design of the digestion device. Based on the plane winding and the helical digestion tubes, two kinds of digestion devices for TP detection were designed and fabricated. The digestion device with the plane winding digest tube was called the "hamburg-type", as it looks like a hamburg. The

"hamburg-type" digestion device is composed of a plane winding digestion tube, three UV light tubes over the digestion tube, a flexible heating unit under the digestion tube, UV light reflecting layer made of aluminum foil and a temperature meter, etc., as shown in Figure 2. The UV light tube used in this paper was a kind of cold cathode UV lamp with the advantages of long operating life, high luminous flux and low power consumption. The whole device was put in a hermetic plastic box for human safety as UV light can do harm to human body.

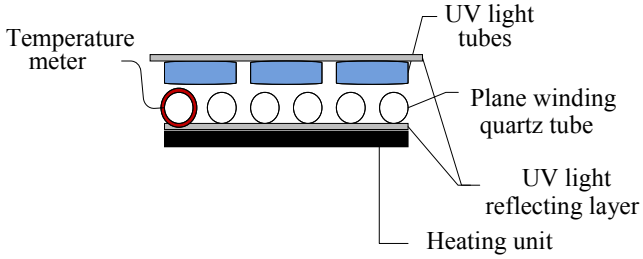


Fig. 2 The sectional drawing of the "hamburg-type" digestion device

The other device with the helical digest tube was called the "screw-type". As shown in Figure 3, it is composed of three UV light tubes, a helical digestion tube around the UV light tubes, a flexible heating unit around the digestion tube, UV light reflecting layer around the flexible heating unit, and a temperature meter.

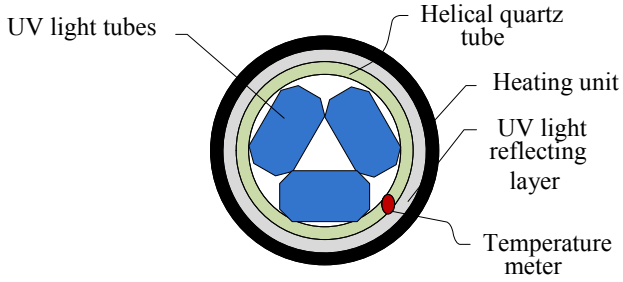


Fig. 3 The sectional drawing of the "screw-type" digestion device

Digestion experiment. Sample water was sent to the digestion tube by micropump firstly. Then the inlet and the outlet of the digestion tube were closed by two microvalves. After that the heating unit started to work. When the temperature of the sample water approached a certain value, the UV light tubes controlled by the drive circuit were turned on and temperature was retained at the certain value to degrade TP in the sample water. After the UV light tubes worked for 5 minutes in which the power of the UV light would become stable, the drive circuit started timing until the setting time. Then the digested sample water was pumped out and mixed with the coloring reagent. After mixed thoroughly, the orthophosphate concentration (weight by P) of the digested solution was measured by the Ultraviolet spectrophotometer at the wavelength of 700 nm against a reagent blank.

Results and discussion

During the digestion process, water was stimulated by photons with energy from the 254nm UV light and decomposed into hydroxyl radicals, which had a strong oxidizing nature. TP in the sample water reacted with the hydroxyl radicals and was degraded to phosphate. More hydroxyl radicals could be produced by improving the temperature of the sample water and a satisfactory digestion

rate was obtained by heating the sample water to 80℃ at the condition of no use of oxidant and catalyst in this paper.

The calibration curve as shown in Figure 4 exhibited a good linearity ranging from 0.0mg/L to 4.0mg/L between the concentration of phosphate and the absorbance value.

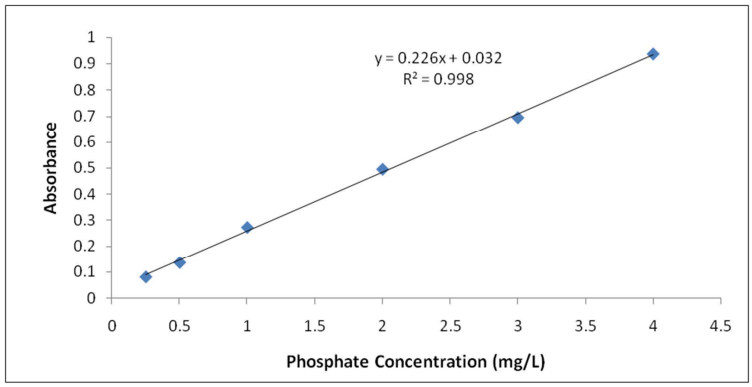


Fig. 4 Calibration curve of the absorbance values and the concentration of phosphate (by weight of P)

0.5mg/L, 1.0mg/L and 2mg/L sodium glycerophosphate solutions (by weight of P) were digested by using the "hamburg-type" and the "screw-type" digestion device at the temperature of 80℃ for 1 hour, respectively. The results are shown in Figure 5. The digestion device of the "screw-type" showed a higher digestion rate compared with the "hamburg-type" due to the possibility of the better distribution of UV light and temperature. The results also indicated that with increasing of the initial concentration of reactant, the digestion rate of TP decreases [7].

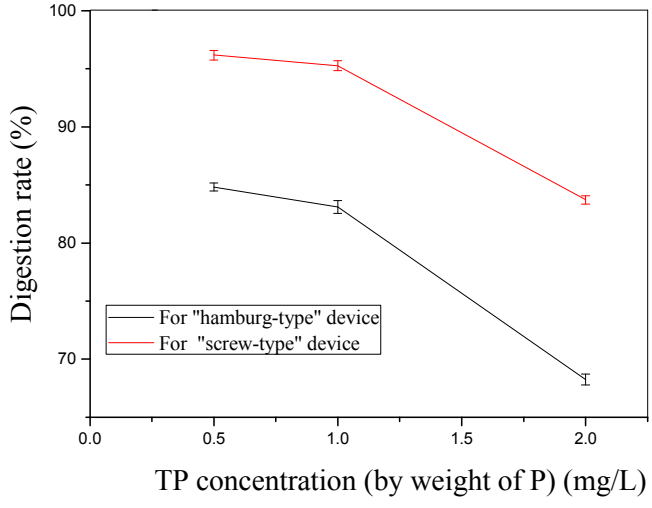


Fig. 5 The digestion rates of the two kinds of digestion devices at 80℃ for 1 hour

To study the influence of temperature to the digestion rate of TP, 0.5mg/L, 1.0mg/L and 2.0mg/L sodium glycerophosphate solutions (by weight of P) were digested by using the "screw-type" digestion device at different temperature for 1 hour in this work. As shown in Figure 6, the digestion rate of TP increases with the increasing of the digest temperature. According to the collision theory, heating can improve the activity of the reagent molecules, and this increased the

chance of reaction between the reagents in the solution. So the digestion rate can be improved by heating, and at the temperature 80℃, the digestion rate of 0.5mg/L and 1.0mg/L sodium glycerophosphate solutions could reach to 96%, almost completely digested.

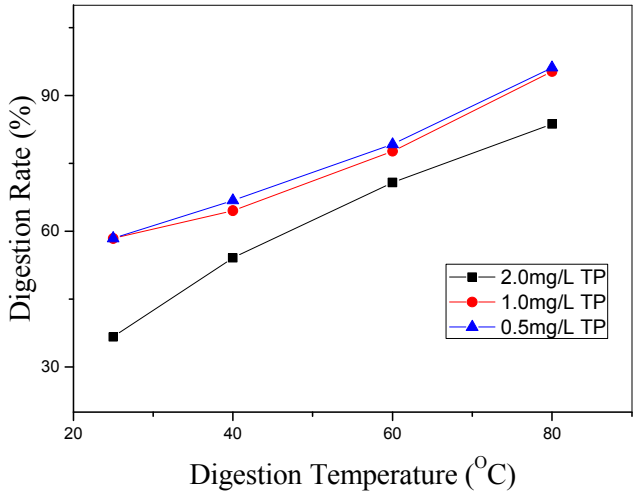


Fig. 6 The digestion rates of the "screw-type" digestion device at different digestion temperature for 1 hour

Conclusion

In this paper, a novel UVC-thermal coupled digestion method without oxidant for the detection of TP was proposed. 254nm UVC light was used as the light source and two kinds of devices were designed for the TP digestion. Compared with the conventional thermal digestion method for TP detection, the UVC-thermal coupled digestion method decreased the temperature under 100℃, which enabled the digestion process work at normal pressure. Due to the no use of catalyst and oxidant in the digestion process, the UVC-thermal coupled digestion device can be integrated with the electrochemical detection device, which could make the detection system of TP automated, miniaturized and portable.

Acknowledgements

The authors gratefully thank the staff at the State Key Laboratory of Transducers Technology at the Institute of Electronics, Chinese Academy of Sciences for clean room and micro fabrication support. This work is supported by the National Natural Science Foundation (No. 61372053), National High Technology Research and Development Program (863 Program, No. 2012AA040506).

References

[1] I.D. McKelvie, D. Peat, P.J. Worsfold, Techniques for the quantification and speciation of phosphorus in natural waters, Analytical Proceedings. 32 (1995) 437-445.

[2] Nollet, Leo M.L, Handbook of Water Analysis, Food Science and Technology, Marcel Dekker, Inc., CRC Press, 2000.

[3] Almeida, Multi-syringe flow injection system with in-line microwave digestion for the determination of phosphorus, Talanta. 64 (2004) 1283-1289.

[4] Mehdi Shirzad Siboni, Mohammad-Taghi Samadi, Jae-Kyu Yang, Seung-MokLee, Photocatalytic removal of Cr(VI) and Ni(II) by UV/TiO2: kinetic study, Desalination and Water Treatment. 40 (2012) 77-83.

[5] Damiano Monticelli, Gabriele Carugati, Alessio Castelletti, Sandro Recchia, Carlo Doss, Design and development of a low cost, high performance UV digester prototype: Application to the determination of trace elements by stripping voltammetry, Microchemical Journal. 95 (2010) 158-163.

[6] Burrows H D, Canle L M, Santaballa J A, etal, Reaction pathways and mechanisms of photodegradation of pesticides, J. Photoch Photobio B. 67 (2002) 71-108.

[7] LI Lei, GAO Nai-yun, YIN Di-di, etal, Modified kinetics model of degradation of mc-lr by advanced oxi-dation Process, Environmental Science. 30 (2009) 1050-1054.

Key Engineering Materials Vols 645-646 (2015) pp 853-858
© (2015) Trans Tech Publications, Switzerland
doi:10.4028/www.scientific.net/KEM.645-646.853

Submitted: 2014-11-04
Accepted: 2014-12-23

Fabrication of SU-8 microneedle based on backside exposure technology

DU Liqun[1,2,a*], WANG Zhongzhou[2], RUAN Xiaopeng[2], CHEN Shengli[2], SHAN Qing[2]

[1]Key Laboratory for Precision & Non Traditional Machining Technology of Ministry of Education, Dalian University of Technology, Dalian, Liaoning, China

[2]Key Laboratory for Micro/Nano Technology and System of Liaoning Province, Dalian University of Technology, Dalian, Liaoning, China

[a]duliqun@dlut.edu.cn

Keywords: microneedle, backside exposure, diffraction, SU-8, Matlab

Abstract. An optimization method for fabricating 3D microneedle arrays with larger cone angles through backside exposure is demonstrated in this paper. A photo mask was designed to fabricate SU-8 microneedle based on diffraction of UV light. A circular hole diffraction was simulated with Matlab to obtain light intensity distribution. The simulation results show that the cone angles and surface profile can be adjusted by changing the thickness of substrate and exposure dose. Based on the simulation results, the microneedles with heights of 265 μm to 380 μm and cone angles in the range of 5.1° to 15.6° were fabricated by the backside exposure technology through one time UV lithography. Compared with previous approaches, the fabrication process in this paper takes advantages of simple, low cost and mass production.

Introduction

Miniaturization, integration and intelligentization are the development trends of technology[1]. MEMS fabrication technology is an important means to achieve it. In the field of bioMEMS, microneedle has become one of the research focus due to its great application potentials. Generally, microneedles are fabricated by silicon materials. However, silicon is not suitable to fabricate batch replication mold because of its brittle feature. Recently, researches of microneedle materials focus on metal and polymer. Among polymer, SU-8 photoresist is an epoxy-based, near-UV, negative tone resist and has become an ideal photoresist material for the fabrication of high aspect ratio structure in MEMS[2,3], which makes it an ideal material for fabricating microneedles. Microneedles can principally be classified into two kinds: in-plane and out-of-plane microneedle[4]. Compared with in-plane microneedle, out-of-plane microneedle has the following features: it is difficult to fabricate microneedles with high aspect ratio and it is more convenient to obtain large arrays of microneedles.

In this paper, an optimization method for fabricating SU-8 out-of-plane microneedle based on backside exposure technology was proposed. The microneedles were obtained with ideal length, good cone angle, small cross-section size and smooth profile. The research work in this paper accumulates experience for further development of backside exposure microneedle molding technology.

The simulation of circular hole diffraction

SU-8 is an epoxy-based negative-tone resist, in the case of UV lithography, the top area of the patterned SU-8 resist is observed to be larger than the bottom area[5]. This phenomenon is especially

obvious in the case of thick layer or high aspect ratio structures and it is difficult to avoid it. Backside exposure technology makes good use of this phenomenon. There are two essential points for successful fabrication of microneedle: The first one is to fabricate a tapered micro structure with a smaller head and a larger bottom. The second one is to control the photoresist surface profile and its height. In order to achieve two goals mentioned above, the theory of scalar diffraction angle spectrum[6] was used to simulate circular hole diffraction. The simplified model of simulation is shown in Fig. 1. In the model, the hole diameter on the diffraction screen and the gap between the diffraction screen on the mask and the observation screen at the bottom of microneedle are variables. After the wavelength of UV, transmittance of quartz glass, the absorption coefficient and transmittance of SU-8[7] were substituted into the simulation program, the light diffraction pattern and the intensity distribution were obtained.

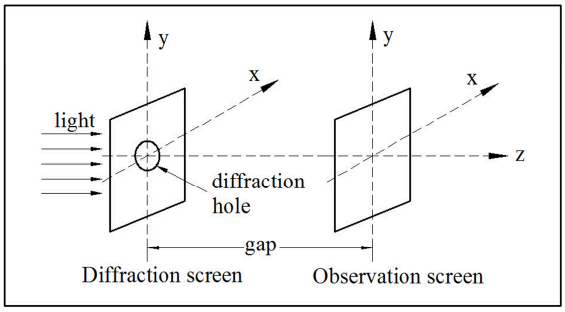


Fig. 1 Circular hole diffraction model

In this paper, 60 μm diameter hole on the mask were taken as an example to calculate the propagation distances. And the propagation distances included 0 μm, 500 μm, 1200 μm and 1500 μm. According to the different propagation distances, the light diffraction pattern and the intensity distribution corresponding to the light diffraction pattern were shown in Fig. 2 and Fig. 3.

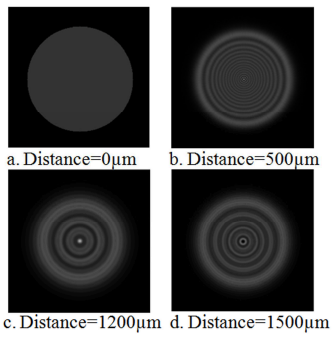


Fig. 2 Light diffraction pattern

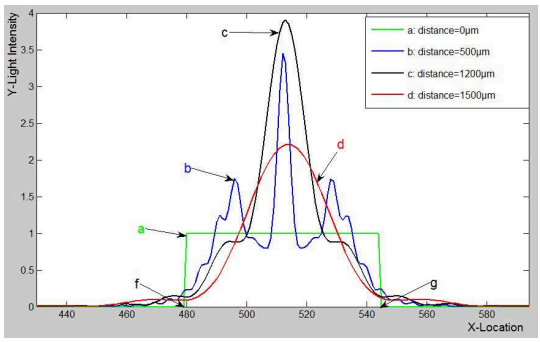


Fig. 3 The intensity distribution

In Fig. 3, the x axis and the y axis represent the spatial position and light intensity, respectively. At the propagation distance of 0 μm, light intensity distribution curve intersects with x-axis at points f and g and the light intensity is a constant between the points. The light intensity in the central region starts to increase and change regularly with the increase of ring radius at the propagation distance of 500 μm. Compared curve c with a, b and d, light intensity of curve c reaches a maximum in the center and it decreases quickly with the increase of ring radius. And the curve is very smooth. At the propagation distance of 1500 μm, light intensity weakens in the center and its decrease speed slows down with the increase of ring radius compared with curve c. The attenuation speed of light intensity determines the height and cone angle of microneedles. The smoothness of the curve has an important effect on surface profile of microneedle. For 60 μm diameter hole, the limited region corresponding to the propagation distance of 1200 μm is an ideal area for fabricating microneedle with sharp tip and smooth profile. Fig. 3 shows that there is a best

propagation distance for a certain diffraction hole. At the propagation distance, the light intensity will reach a maximum in the center. As the distance increases continually, the light intensity weakens fast in the same x position, which is quite obvious in a certain range.

The hole diameter on the mask ranges from 15 μm to 100 μm, and the step is 5μm. A 1000-μm -thick JGS1 quartz glass with 90% transmittance[8] in terms of wavelength of 365 nm UV was chosen in the experiment to verify the best region for fabricating microneedle with mask diameter of 60 μm. 200-μm-thick fully exposed SU-8 photoresist layer and 1000-μm-thick quartz glass were used as a substrate. The reason why chose the fully exposed SU-8 layer lies in three aspects: Firstly, the diffraction distance can be adjusted by the fully exposed SU-8 layer. Secondly, fully exposed SU-8 photoresist can be used as an adhesive layer. Due to the small size of microneedle at the bottom, microneedle can be easily detached from the substrate if it stands directly on the quartz glass. Thirdly, fully exposed SU-8 photoresist can be used to attenuate the light energy. The light intensity needs to be adjusted to a constant before SU-8 is exposed.

Fabrication process flow

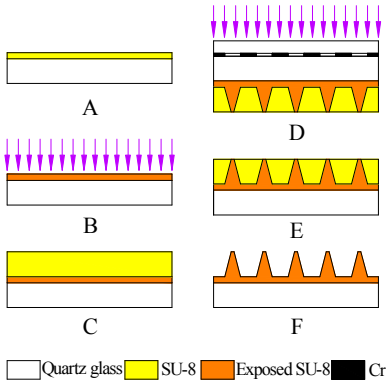


Fig. 4 Diagram of fabrication process of microneedles

Fig. 4 shows the fabrication process flow of SU-8 microneedles. The quartz glass was cleaned by concentrated sulfuric acid, hydrogen peroxide and deionized (DI) water , respectively. A layer of 200-μm-thick SU-8 2075 was spin-coated on 1000-μm-thick transparent quartz glass (Fig. 4A). In order to obtain flat photoresist layer, two steps spin-coating of SU-8 photoresist were applied. For the first spin-coating, SU-8 2075 was spin-coated with 1000 rpm for 30 s, soft-baked at 65°C for 30 minutes and 95°C for 2.5 hours. For the second spin-coating, SU-8 2075 was spin-coated with 1000 rpm for 30 s, soft-baked at 65°C for 30 minutes and 95°C for 3 hours. After soft bake, the SU-8 was exposed with a dose of 150 mJ/cm^2 (Fig. 4B), 95°C was selected as the post-exposure bake (PEB) temperature for 5 minutes. At last, a 1200-μm-thick substrate for fabricating microneedle was obtained.

The continuing steps are similar with mentioned above. 400-μm-thick SU-8 2075 was spin-coated on the fully exposed SU-8 layer (Fig. 4C). To obtain flat and ultra thick photoresist layer, three steps spin-coating of SU-8 photoresist were applied. For the first spin-coating, SU-8 2075 was spin-coated with 1200 rpm for 30 s, soft-baked at 65°C for 30 minutes and 95°C for 2.5 hours. For the second spin-coating, SU-8 2075 was spin-coated with 1200 rpm for 30 s, soft-baked at 65°C for 30 minutes and 95°C for 2.5 hours. For the third spin-coating, SU-8 2075 was spin-coated with 2000 rpm for 30 s, soft-baked at 65°C for 30 minutes and 95°C for 3 hours. 5000 mJ/cm^2 exposure doses were applied to expose the second layer from the backside of the quartz glass (Fig. 4D). 95°C was selected as the PEB temperature for 5 minutes (Fig. 4E). The sample was developed in SU-8 developer for about 40 minutes (Fig. 4F) and was cleaned by absolute ethyl alcohol and DI water. Then the microneedles with different heights, diameters and cone angles were fabricated.

Experiment results and discussions

According to the fabrication process described above, the heights of the microneedles were 380μm, 370 μm, 365 μm, 360 μm, 358 μm, 355 μm, 352 μm, 265 μm, 335 μm and 310 μm when the cone angles were 5.1°, 5.7°, 6.5°, 6.9°, 7.4°, 8.7°, 10.2°, 15.6°, 12.3° and 11.0°, respectively.

The geometry parameters of microneedle, including bottom diameter, top diameter, height and cone angle, are shown in Fig. 5. We define the ratio of the top diameter of microneedle to the hole diameter on the mask as R. R and cone angles are used to evaluate the sharpness of microneedle in the experiments. The larger cone angles and smaller R are, the sharper microneedle is. Table 1 lists the statistical data of three kinds of SU-8 microneedles exposed with the dose of 5000mJ/cm^2 on the same substrate. And it also shows that there is a difference between the top diameter and the bottom diameter. The bottom diameter is much bigger than the hole diameter on the mask, which can obviously make the microneedle more strong and stable. This indicates very sharp microneedles can be fabricated by the method because the top diameter of microneedle is much smaller than the diameter on the mask. So it is possible to fabricate ultra sharp microneedle with tiny tip by designing the mask pattern small enough.

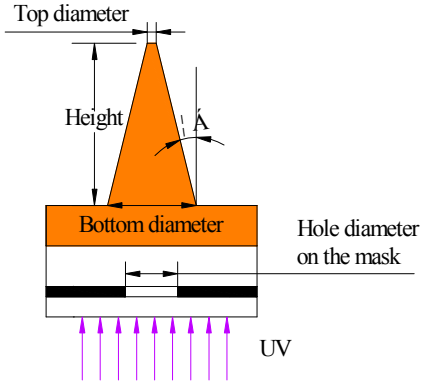


Fig. 5 Schematic diagram of geometry parameters of microneedle

Table 1 Statistical data of three kinds of SU-8 microneedles with exposure dose of 5000mJ/cm^2

Mask diameter	Bottom diameter	Top diameter	Height	Cone angle	R
55μm	140.7μm	9.0μm	337.5μm	11.0°	0.164
60μm	157.2μm	8.7μm	265.2μm	15.6°	0.145
65μm	163.3μm	10.8μm	348.3μm	12.3°	0.166

Some problems encountered in the experiments, such as the tips were not sharp, microneedles broke off due to the impact of SU-8 developer, microneedles were bifurcated at the top, the surface profile was not smooth and SU-8 residues were difficult to remove at the bottom of the microneedles, are analysed as follows.

Microneedles fabricated with mask diameter of 100 μm and diameter of 60 μm are shown in Fig. 6. Compared with microneedles fabricated with mask diameter of 100 μm, the microneedles fabricated with mask diameter of 60 μm have sharper tips and larger cone angles. The limited region corresponding to propagation distance of 1200 μm is the best area for fabricating microneedle with mask diameter of 60 μm rather than 100 μm. These experimental results agreed well with the simulation results. Because the light energy is absorbed by the SU-8 layer by layer, the exposure dose of the microneedle tip is smaller. If SU-8 photoresist exposes insufficiently, the microneedle tip would be removed during the development of the SU-8 and the radii of curvature would increase.

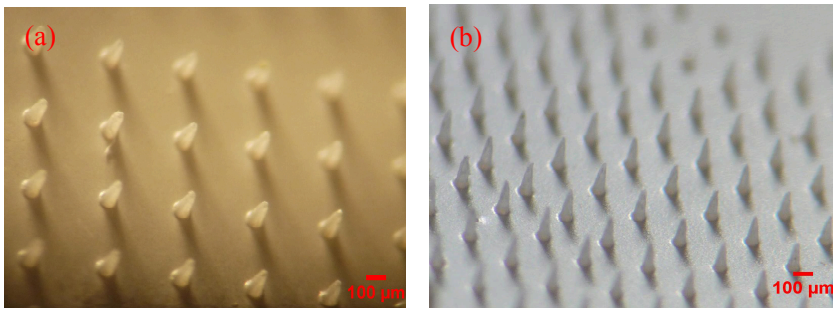


Fig. 6 (a) Microneedles fabricated with mask diameter of 100 μm ; (b) Microneedles fabricated with mask diameter of 60 μm

Bifurcation and breaking off phenomena are shown in Fig. 7(a) and 7(b). The traditional development way accelerates the substrate movement so as to help the removal of non-crosslinked SU-8. The diameter of microneedle at the bottom is only in the range of tens μm to hundreds μm, but the microneedle reaches three hundreds μm in height. Although slight substrate movement is allowed during development of SU-8 in this experiments, there is still a great impact on the microneedles surface and the relatively poor strength of the microneedles will break off**.** Insufficient post-exposure bake and the erosion of the developer result in the bifurcation phenomenon. By the method to fabricate the microneedles on the fully exposed SU-8 layer instead of quartz glass substrate, the microneedles are not easy to detach from substrate during development of SU-8. To avoid the phenomena mentioned above, the methods of double-side post-exposure bake and prolonging development time without slight substrate movement are taken.

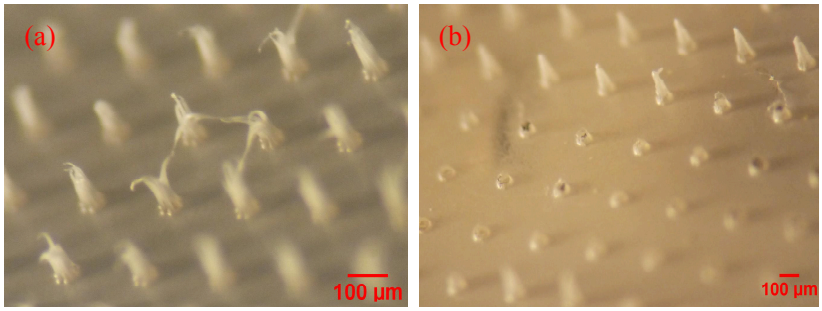


Fig. 7 (a) Bifurcation phenomenon, microneedles fabricated with mask diameter of 35 μm; (b) Breaking off phenomenon, microneedles fabricated with mask diameter of 75 μm

There are always two sides to everything. The way to prolong development time without slight substrate movement reduces breaking off and bifurcation phenomena, but it also introduces some drawbacks. The surface of microneedle are often removed during the development of SU-8 (exposure doses of microneedle surface close to critical exposure doses of SU-8) due to the longer development time. The long development time may cause the surface roughness of microneedle. There is still some residual photoresist at the bottom of microneedle after development, as shown in Fig. 8. To remove residues, the substrate can be alternately placed in SU-8 developer and absolute ethyl alcohol.

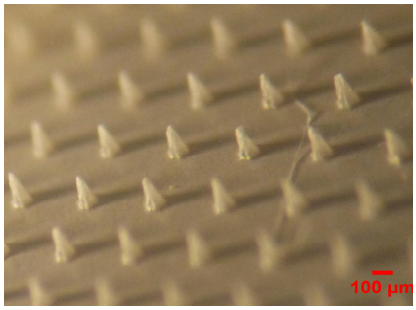


Fig. 8 Microneedles fabricated with mask diameter of 80 μm

Summary and conclusions

A low-cost process for fabricating out-of-plane SU-8 microneedle was developed based on backside exposure in this paper. In order to obtain the light intensity distribution, a circular hole diffraction was simulated with Matlab. 265 μm to 380 μm tall microneedles with cone angles in the range of 5.1° to 15.6° were fabricated by controlling the exposure dose and adjusting the thickness of substrate. Cone angles and the ratio R were used to evaluate the sharpness of microneedles. Compared with other microneedles based on the backside exposure technology, the tip size of the microneedles fabricated in this paper is small and the cone angle increases. The method to fabricate SU-8 microneedle based on backside exposure was optimized. The research work in this paper accumulates experience for the further development of the microneedle process based on backside exposure.

Acknowledgements

This work was supported by National Natural Science Foundation of China (Grant No. 51375077).

References

[1] J. Yang, J. Zhu, H.M. Jiang, Develop of Fabrication and Application of MEMS Micro-needle, Piezoelectrics & Acousto Optics. 32 (2010) 1053-1058. (in Chinese)
[2] J. Zhang, K.L. Tan, H.Q. Gong, Characterization of the Polymerization of SU-8 Photoresist and Its Applications in Micro-Electro-Mechanical Systems (MEMS), Polymer Testing. 20 (2001) 693-701.
[3] H. Yu, R.X. Du, Y.H. Guo, et al., Fabrication of taper hollow metallic microneedle array for portable drug delivery system, in proceedings of the 5th IEEE International Conference on Nano/Micro Engineered and Molecular Systems. (2010) 676-679.
[4] F. Keizo, I. Ayaka, M. Hiromi, et al., Two-layered dissolving microneedles for percutaneous delivery of peptide/protein drugs in rats, Pharm Res. 28 (2001) 7-12.
[5] C. Fu, H. Huang, Different methods for the fabrication of UV-LIGA molds using SU-8 with tapered de-molding angles, Microsystem Technologies. 13 (2007) 293-298. (in Chinese)
[6]F. Wang, X.J. Deng, C.X. Liu, et al., Non-paraxial corrections of scalar diffraction theory, Chinese Journal of Quantμm Electronics. 24 (2007) 17-21.
[7] X.H. Tian, G. Liu, Y.C. Tian, et al., Simulation of pattern transfer accuracy on SU-8 resist, Chinese Journal of Vacuμm Science and Technology. 22 (2002) 417-420. (in Chinese)
[8] K. Kabseog, S.P. Daniel, M.L. Hong, et al., A tapered hollow metallic microneedle array using backside exposure of SU-8, Journal of Micromechanics and Micro engineering. 14 (2004) 597-603.

Key Engineering Materials Vols 645-646 (2015) pp 859-864
© (2015) Trans Tech Publications, Switzerland
doi:10.4028/www.scientific.net/KEM.645-646.859
Submitted: 2014-10-30
Accepted: 2014-12-23

Analysis on the Effect of Machining Error on the Vibration of MEMS Device

Hui Wang, Wei hua Li*, Lili Gao

Key laboratory of MEMS of the Ministry of Education, Southeast University, Nanjing 210096, China
E-mail: 220121245@seu.edu.cn, E-mail: liwh@seu.edu.cn, E-mail: 230129199@seu.edu.cn
Wei hua Li: (1956-) Male, Professor of Southeast University, E-mail: liwh@seu.edu.cn,
Tel: 025-837926328806

Key words: MEMS, geometry size deviation, geometry shape error, frequency, vibration

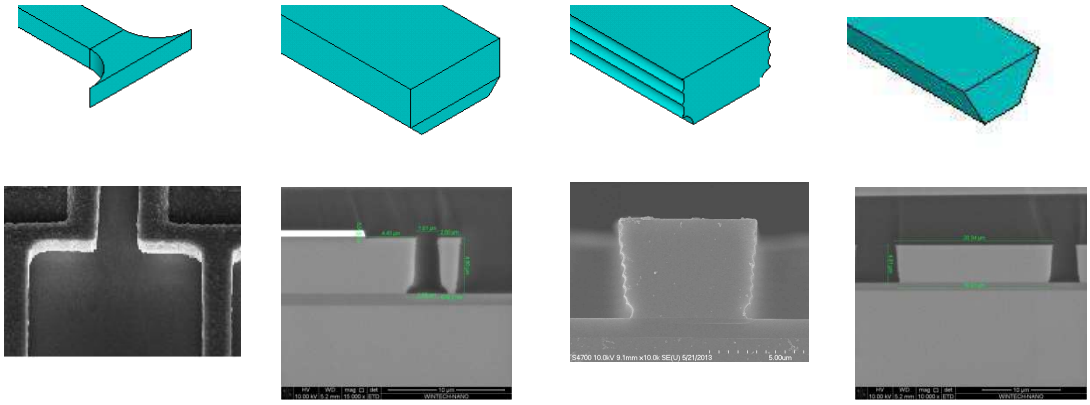
Abstract. With the development of MEMS, more attention has been paid to the uniformity between the performance of the products in practical processing and the expected performance. A case study is conducted here with fixed-fixed beam and comb-drive resonator as the pattern to explore how geometry size deviation and geometry shape error influence the devices. It is discovered that the length, inclining profile and undercutting of the anchor is the key factor which influences the vibration mode of the fixed beam, and the geometry size and corrugating profile mainly affect the comb-drive resonator.

1. Introduction

Design for manufacturability (DFM) in Integrated Circuit (IC) industry has proved to be a mature issue. However, DFM is still a relatively fresh topic in MEMS industry. In addition, it is important to improve product yield via DFM. In order to make MEMS products approach the ideal performance, designers are required to consider the effect of possible error from processing on performance, thus compensatory design can be conducted, making the final products reach or approach the expected performance.

In practical process, some negative factors will appear and influence the device on account of improper operations or inevitable effects. For instance, the variety of geometry size results from lithography or etching, footing effect in SOI structures, corrugated profile shape in DRIE processing, the corner arc in anisotropic etching processing etc. This work mainly focuses on the effect of geometry size deviation, footing effect [1], corrugated profile shape, the rounded corner [2], the inclining profile, and undercutting of the anchor on the frequency and vibration mode of fixed-fixed beam (see Fig. 1). We also investigated how the width of the folded beam and comb, the thickness of the whole device, coupled with footing and inclining effect affect the frequency and vibration mode of the electrostatic comb-drive resonator.

The finite element tool ANSYS is used for the following simulation. To determine the vibration characteristics of a structure, modal analysis is conducted here to calculate natural frequency and mode shapes. The simulation is focused on the first five modes of both the fixed-fixed beam and electrostatic comb-drive resonator.



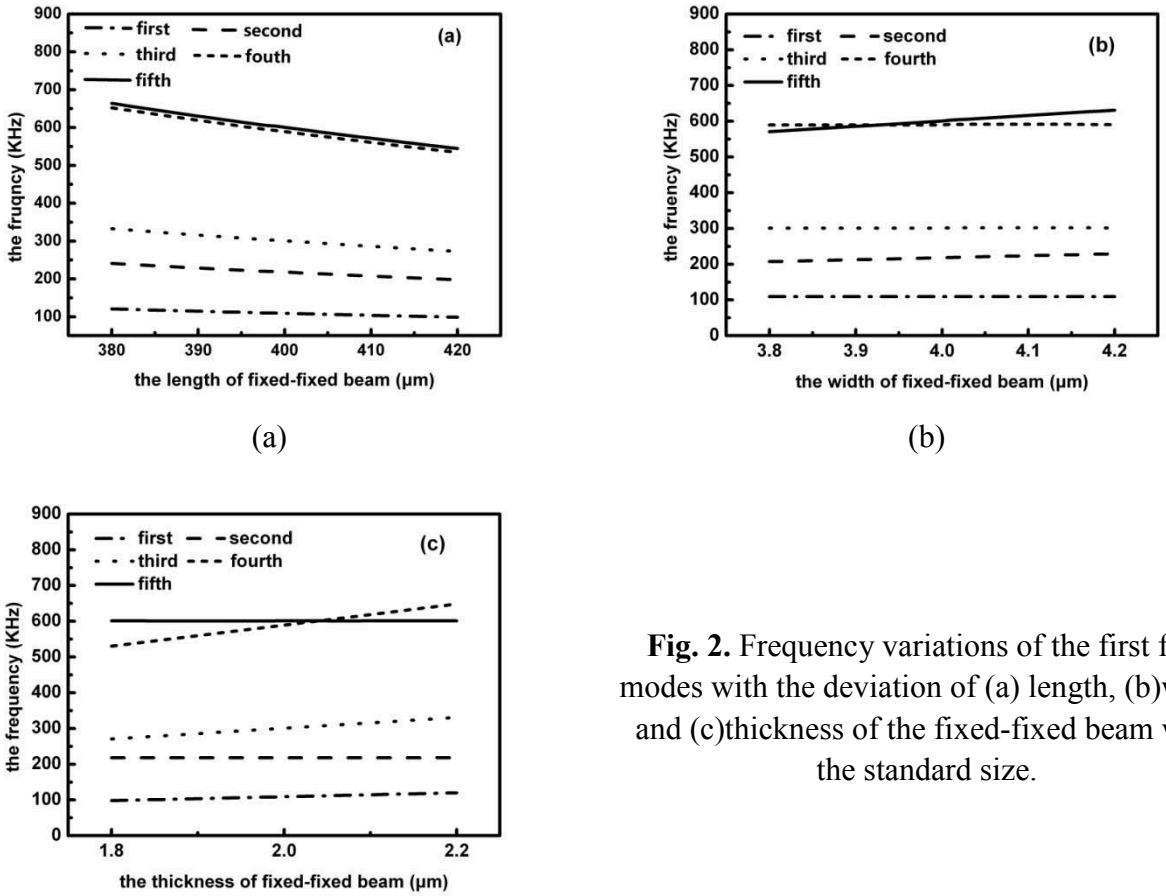
(a) (b) (c) (d)

Fig. 1. The simulation shapes shown in the top and the experiment shapes below of (a) the rounded corner, (b) footing effect, (c) corrugated profile and (d) inclination.

2. Fixed-fixed beam

The fixed-fixed beam is set to be (standard) length 400μm, width 4μm, and thickness 2μm. The first, third and fourth modes vibrate out-of-plane (in xz plate), and the second and fifth modes vibrate in-plane (in xy plate). The frequency of fixed-fixed beam is depicted as [3]:

$$f_n = \frac{k_n}{2\pi}\sqrt{\frac{ET^2}{12\rho g l^4}} \tag{1}$$

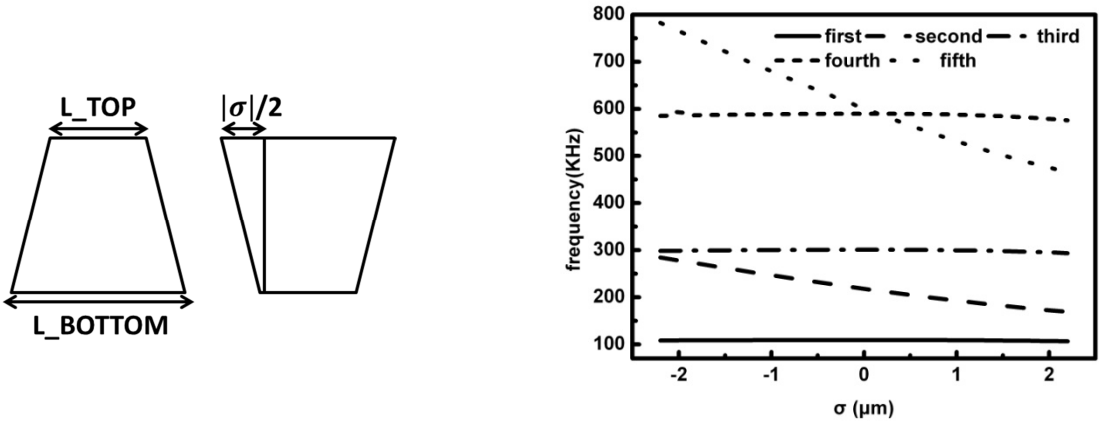


(a) (b) (c)

Fig. 2. Frequency variations of the first five modes with the deviation of (a) length, (b)width and (c)thickness of the fixed-fixed beam with the standard size.

In practical process, the geometry size of the fixed-fixed beam usually doesn't comply with the design value, resulting in 5% error in general. How the length, width and thickness affect the frequency and vibration mode is demonstrated in Fig.2. As is presented clearly in the picture, the frequency of the first five modes all decreases with the length of fixed-fixed beam and increases with the thickness, which is coincident with the results of the formula. However, the frequency is independent from the width according to the formula. It is incompatible with the simulation results that the frequency is increasing with width. Also the frequency of the first, third and fourth modes remains steady with the increase of width, while the frequency of the second and fifth modes is almost constant when the thickness increases. The width mainly affects the in-plane mass, and the thickness impacts the out-of-plane mass. Furthermore, as the neighboring frequency of the fourth and fifth modes, they exchange when the width decreases to 3.92μm and the thickness reaches 2.04μm (All the vibration modes demonstrated in the pictures of this article are arranged by vibration pattern).

In practical process, the concave corner is rounded [4] instead of square as expected and footing effect [1] can't be avoided in SOI structure. In time multiplexed deep etching (TMDE) process, the deposition process and etching process are executed alternately [5], resulting in the corrugated profile. Due to the excessive absorption of photoresist or standing wave effect [6], the profile of the beam will incline. Furthermore, undercutting of the anchor often happens in specified process.



(a) (b)

Fig. 3. (a) the inclining profile and (b) the simulation results of the effect of inclining profile on the fixed-fixed beam, σ=L_TOP-L_BOTTOM.

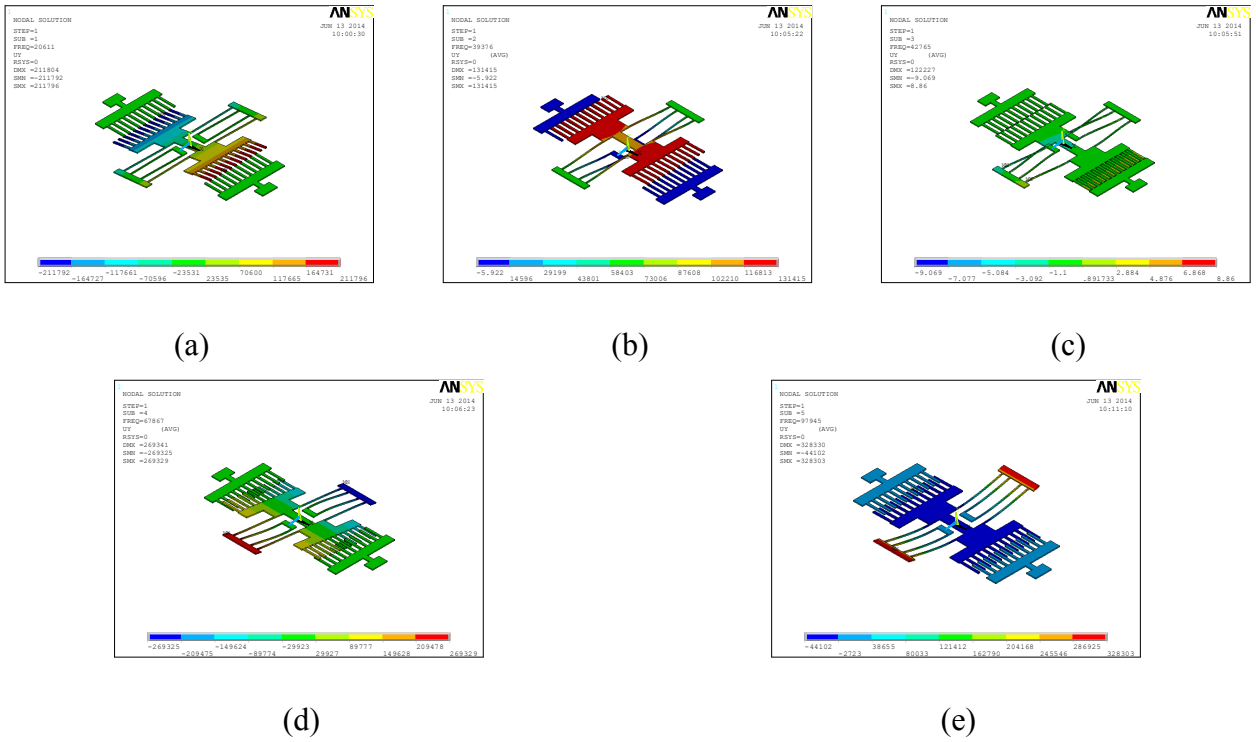
Table 1. The simulation results of the effect of various profiles on the fixed-fixed beam

Profiles	First Mode		Second Mode		Third Mode		Fourth Mode		Fifth Mode	
	f[KHz]	Error	f[KHz]	Error	f[KHz]	Error	f[KHz]	Error	f[KHz]	Error
Standard	109.12		218.10		300.73		589.42		600.71	
Round-corner	109.65	0.48%	220.16	0.94%	302.17	0.48%	592.20	0.47%	606.36	0.94%
Footing	107.03	1.91%	212.77	2.44%	294.99	1.91%	578.15	1.91%	586.05	2.44%
Corrugation	109.03	0.09%	211.80	2.9%	300.49	0.07%	588.92	0.08%	586.01	2.88%
Undercutting	105.60	3.22%	202.20	7.29%	289.59	3.71%	571.40	3.06%	559.55	6.85%

Five models are designed here to express which factor affects the frequency most. The first model is fixed-fixed beam with inclining profile, the second one is rounded concave corner, the third is based on footing effect, the fourth one is corrugated profile caused by TMDE process, and

the last one is modeled after undercutting of the anchor, presented respectively in Figure 3 and Table 1. The $|\sigma|$ in Figure 3 means the difference between the top side and the bottom side, while L_TOP remains 4μm and L_BOTTOM varies. By analyzing Table 1, it is found that the rounded corner scarcely affects the vibration mode, while footing effect, corrugated profile and undercutting effect reduces the frequency a little. Inclination will make the frequency of the beam decrease most. For example, the first five frequency decreases by 0.284%, 13.22%, 0.15%, 0.15%, 13.20% respectively when $|\sigma|$=1μm. What's more, for beams with various profiles, the frequency of the second and fifth modes decreases more than that of the other modes. As mentioned in the previous, the second and fifth modes vibrate in-plate, while the other modes vibrate out-of-plate, so the change of the profile affects the in-plate vibration. The reason is that the width is larger than the thickness, resulting in the larger influence in the in-plane mass. Furthermore, the frequency of the fourth and the fifth modes exchanges in corrugated and undercutting structure. Because the frequency of the fifth mode is larger than that of the fourth mode in standard structure, while it decreases more in practical structure.

3. Comb-drive resonator



(a) (b) (c)

(d) (e)

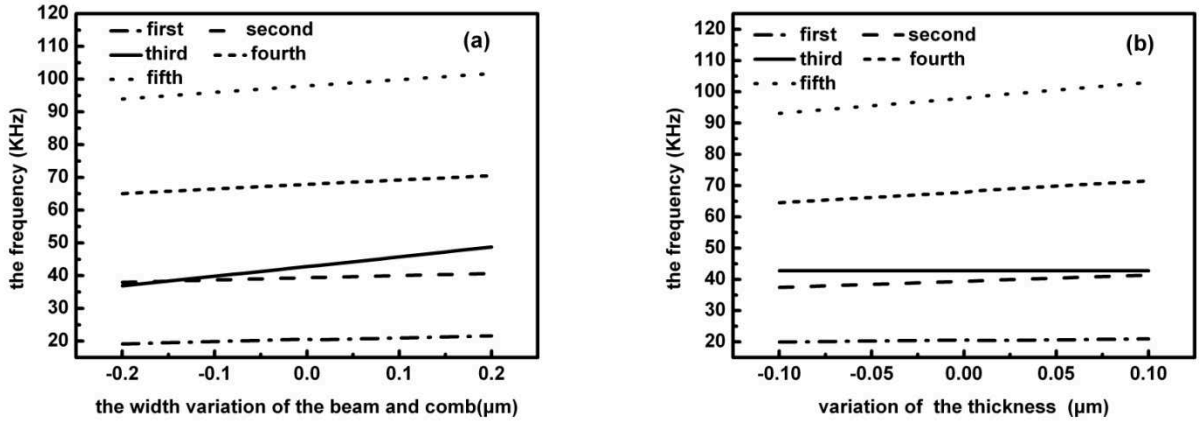
Fig. 4. (a) the first, (b) the second, (c) the third, (d) the fourth and (e)the fifth vibration modes of the comb-drive resonator.

Table 2. The standard size of the comb-drive resonator

Structure parameters	Size [μm]	Structure parameters	Size [μm]
Comb length	40	The length of folded beam	100
Comb width	4	The width of folded beam	2
The gap of combs	2	The length of truss	78
Structure thickness	2	The width of truss	13
The number of combs	12	The movable plate 1	20*140
Initial overlapping length between combs	19.44	The movable plate 2	28.26*60
		The mass	54.9*19.26

Comb-drive resonator is a common resonator that is widely used due to the high quality factor, low power dissipation, small volume and easy integration [7]. The standard size of the electrostatic comb-drive resonator is shown in Table 2. It is revealed in Fig.4 that the resonator of the first mode rotates around y axis, the second mode vibrates along z axis, the third mode (operation mode) vibrates in xy plate, and the fourth and fifth mode rotates around x axis by finite element simulation. When the width of the beam and comb varies in a small range, the frequency of the first five modes increases with the width, of which the frequency of the third mode increases most. The frequency of the first and third modes keeps invariable, while the frequency of the other modes increases with the thickness. Furthermore, when the comb width decreases by 0.16μm or the thickness increases by 0.18μm, the second mode and the third mode exchange. As mentioned earlier, this is because the increasing rate of the frequency of the neighboring modes is different, so the frequency would intersect.

For high-aspect ratio comb-drive resonator, footing effect and corrugation profiles will impact the vibration mode. We increase the thickness of the resonator into 10μm and carry out the simulation process. From Table 3, we can get the conclusion that the second mode of the comb-drive resonator which vibrates out-of-plane is affected most by irregular profiles. What's more, the impact caused by corrugating profile is larger than that caused by footing effect.



(a) (b)

Fig. 5. Frequency variations of the first five modes with the deviation of (a) width and (b) thickness of the comb-drive resonator

Table 3. The simulation results of the effect of various profiles on the comb-drive resonator

Profiles	First Mode		Second Mode		Third Mode		Fourth Mode		Fifth Mode	
	f[KHz]	Error	f[KHz]	Error	f[KHz]	Error	f[KHz]	Error	f[KHz]	Error
Standard	343.89		464.58		798.06		1083.01		1417.64	
Footing	341.00	0.84%	456.21	1.80%	796.39	0.21%	1083.58	0.05%	1398.43	1.36%
Corrugation	333.84	1.80%	424.75	8.9%	803.34	0.76%	1050.35	1.66%	140.04	0.91%

4. Conclusion

The simulation results about the effect of geometry size deviation and various geometry profile shape on the fixed-fixed beam and electrostatic comb-drive resonator are presented. The frequency of the first five modes decreases nearly in the same way with the increase of the length of the fixed beam. With the increase of the beam width, the frequency of the first, third, and fourth modes stays

almost the same, while the frequency of the second and fifth modes is increasing. On the contrary, the frequency of the first, third, and fourth modes increases with the beam thickness, while the frequency of the second and fifth modes keeps unchangeable. It can be summarized that the inclining profile and the undercutting of the anchor make the frequency decrease the most and the frequency of the second and fifth modes has the most change. For the electrostatic comb-drive resonator, with the increase of the width, the frequency of the first five modes increases. The frequency of the first and third modes remains the same, while the frequency of the second, fourth and fifth modes increases with the thickness. Due to footing effect and corrugation profile, the second mode of the comb-drive resonator is affected most and the impact caused by corrugating profile is larger than that caused by footing effect.

Acknowledgement

This work was supported by a grant-in aid for Scientific Research from the major issue (2011ZX02507-001-003).

References

[1] Zhang Jian, ICP etching model available for footing effect simulation, Chinese Journal of Scientific Instrument, vol.28, nr.12, 2007.

[2] Prem Pal, Microstructures with rounded concave and sharp-edged convex corners in a single step wet anisotropic etching, Micro-machining and Micro-fabrication Process Technology XIII, Vol. 6882, 68820F-1~8, 2008.

[3] Chang Liu, Foundations of MEMS, second ed., Beijing, 2013.

[4] Zhang Han, Theoretic Research for MEMS Design in Bulk Silicon Wet Anisotropic Etching Process, Nanjing: Southeast University, 2010.

[5] GMBH B R B. U.S. Pat.4855017, U.S. Pat.4784720, and Germany Pat.4241045CI, 1994.

[6] Michael Quirk, Julian Serda, Semiconductor Manufacturing Technology, Beijing, 2004.

[7] Wang Qiang, Design and Fabrication of the Micromechanical Comb-Drive Resonator, Mianyang: Southeast University of Science and Technology.

Key Engineering Materials Vols 645-646 (2015) pp 865-868
© (2015) Trans Tech Publications, Switzerland
doi:10.4028/www.scientific.net/KEM.645-646.865

Submitted: 2014-11-02
Accepted: 2014-12-23

A Variable Resistor Micro system Based on Electro-explosion

Ding Xuran[1, a], Wang Yabin[1, b], Lou Wenzhong[1, c], Guo Yunlong[1, e]

[1]National Key Laboratory of Electro-mechanics Engineering and Control, School of Mechanical-electronic Engineering, Beijing Institute of Technology, Beijing, China, 100081

[a]xheron9413@163.com, (corresponding author) [c]louwz@bit.edu.cn

Keywords: MEMS; Micro/Nano systems; variable resistor; metal bridge

Abstract. A novel type of variable resistor micro system based on electro-explosion is described and its performance test results are presented. The variable resistor consists of four metallic leads in parallel with different width and length thus different resistances and four one-time shot MEMS solid on-off switches [2-4]. By killing off the metallic lines, the variable resistor varies its resistance. Switching is accomplished by a voltage pulse. The resistor can be driven by external signal and its predicted lifetime is very long. Besides, the resistor has no movable parts, therefore the resistor can be used for long term store systems and harsh environments.

Introduction

In traditional design, variable resistors consist of a resistance track with connections at both ends and a wiper which moves along the track as user turns the spindle. Because of this, its volume is large and cannot be applied in many micro/nano systems. To avoid that, some programmable resistors have been applied. Such programmable resistors have a variable resistor and a heating element. A dielectric material separates the heating element from the variable resistor. The heating element changes the resistance of the resistor by heating the resistor [1] However, such programmable resistors have high power consumption, cost much and may not be used in harsh environment, especially those with large temperature difference.

This paper introduces a novel variable resistor micro system based on electro-explosion and it can only be triggered by a voltage pulse. This state-of-the-art variable resistor micro system has great advantages in the reliability under high dynamic environment or harsh environment. This micro system has some key features such as long-term stability, bi-stable and IC compatible. It also can be used for some systems needed to be stored for a long time. The planar processing is used for variable resistor micro system fabrication. Through theoretical calculations, simulations and production, the micro system has been proved to be feasible and has good performances in less action time and low power consumption.

Theory and Design

This paper introduces a novel type of variable resistor micro system based on electro-explosion (as shown in Fig. 1) which has a structure of six layers.

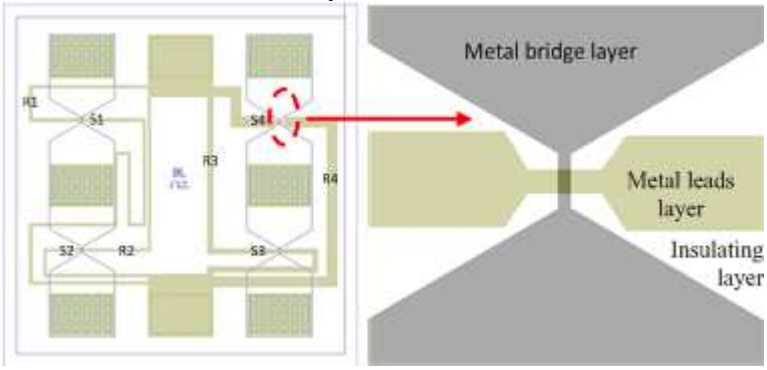


Fig. 1 A variable resistor micro system based on electro-explosion

These layers are bottom insulation layer, MEMS metal film bridge layer, layer of metallic lines with different width and length, middle insulation layer, top insulation layer and metallic pads. There are four metallic lines with different resistance in parallel. Each line is controlled by a solid one-time shot MEMS solid on-off switch so that the resistance of the variable resistor micro system has at most 16 different resistances to choose from. The solid one-time shot MEMS solid on-off switch switches only when a large voltage pulse signal generated by peripheral circuits is applied to it. After the voltage pulse signal pass the switch, the temperature of the switching area increased rapidly until it above the melting point of the material. The switch will explode and mechanically break the metallic line that above it. By controlling different switches to switch, there will be different metallic lines being broken down. After that, the total resistance of the variable resistor micro system varies.
When a voltage pulse is applied to the switch, it is heated rapidly and its phase changes from solid state to liquid state, then gaseous state, finally the hot plasma.
The schematic of the novel variable resistor micro system is described as Fig.2.

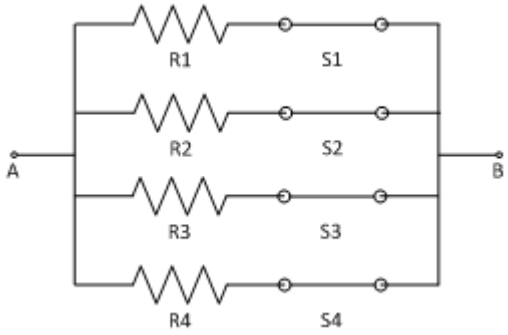


Fig. 2 Schematic of the novel variable resistor micro system

Totally, there are four metallic leads with different resistances, four single use bi-stable MEMS solid on-off switches in parallel. The variable resistor micro system is connected to the peripheral circuits, the resistance between port A and port B can be calculated as Eq.1.

$$R_{AB} = \frac{1}{\sum_{i=1}^{4} \frac{1}{R_i}} \tag{1}$$

Each switch has two states, on and off. Thus, the variable resistor micro system has at most 16 different resistances. By controlling the switch, the resistance R_{AB} varies.

Fabricated and Test

The variable resistor micro system is fabricated with MEMS planar process. This resistor consists of a MEMS metal bridge layer, metallic leads layer and another layers used to insulate or connect different layers or protect single use bi-stable MEMS solid on-off switches and metallic leads. And it was made on a silicon substrate through oxidation, photolithography, CVD, sputtering, and wet etch. The process of fabrication and the layout of die are illustrated in Fig. 3.

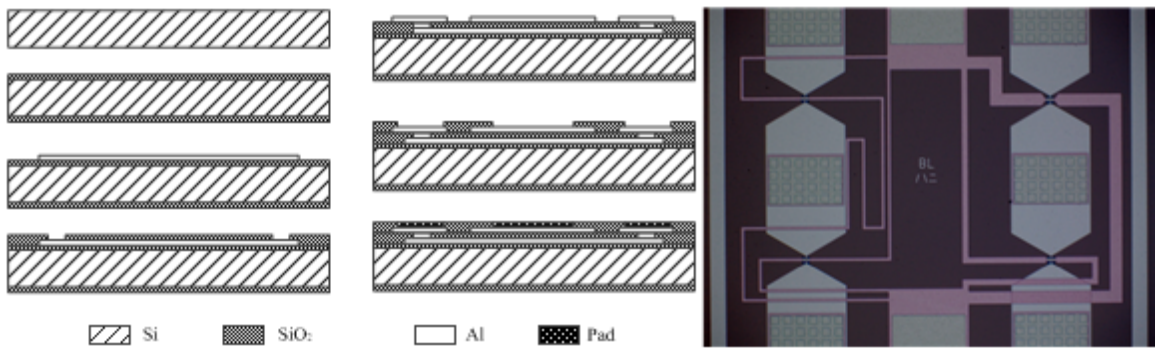


Fig. 3 Process of variable resistor micro system and layout of die

To measure the resistance of the device, a test system for wafer level testing of micro/nano system has been built. Fig. 4 shows the test system.

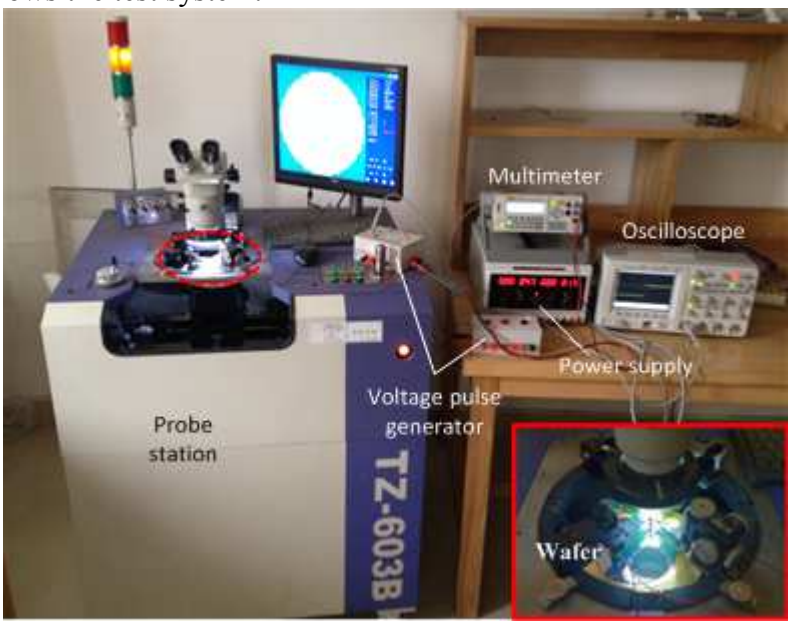


Fig. 4 Working process of OFF-ON switch and the switch after turning on

With the test system illustrated above, many tests have been accomplished. By controlling the MEMS solid on-off switches switch, different metallic lines have been disconnected from the peripheral circuit. The switching time of this micro system is no more than 10us.

Table 1 Results of variable resistor micro system

R1	R2	R3	R4	R_{AB}/ Ω (average value)
○	×	×	×	10.37
×	○	×	×	5.18
×	×	○	×	2.52
×	×	×	○	1.43
○	○	×	×	3.40
○	×	○	×	1.99
○	×	×	○	1.22
×	○	○	×	1.68
×	○	×	○	1.11
×	×	○	○	0.95
×	○	○	○	0.80
○	×	○	○	0.70
○	○	×	○	0.96
○	○	○	×	1.42
○	○	○	○	0.68

We can infer from the table.1 that this kind of variable resistor has at least 5 typical resistances, which are 1 Ω , 2 Ω ,3 Ω ,5 Ω and 10 Ω . To meet different need, the different width of metallic leads may be designed in the future.

Summary

This paper has given a novel type of a variable resistor micro system based on electro-explosion, and its theoretical model has been described and analyzed. Then the design and fabrication of the resistor has been shown, finally the results of test have been given. The resistor has at least 5 typical resistances, which are 1Ω, 2Ω,3Ω,5Ωand 10Ω. The switching time of such a micro system is no more than 10us.

Acknowledgement

The research is supported and funded by National Project (9140A05050313BQ1014) and (9140C360602120C36138).

References

[1] J.C. Chiou, L.C. Chou, Y.L. Lai, S.C. Huang, A novel thermal switch and variable capacitance implement by CMOS MEMS process approaching in micro electrostatic converter, Solid-State Electronics, v77(2012), pp. 56-63.

[2] Y. Zhao, W.Z. Lou, D.G. Li, Study of a novel bi-stable and easy integrated MEMS ETBS, 7th IEEE International Conference on Nano/Micro Engineered and Molecular Systems (NEMS 2012), Kyoto, Japan, pp. 257-60.

[3] Y. Zhao, D.G. Li, W.Z. Lou, L.F. Zhang, J.H. Li, M.B. Fang, Study of a MEMS short-circuit fuse based on electro-thermal theory, Key Engineering Materials, v503(2012), p 277-283.

[4] Y. Zhao, W.Z. Lou, D.G. Li, Research in a novel integrated chip of safe and initiation control, Technical Proceedings of the 2012 NSTI Nanotechnology Conference and Expo, NSTI-Nanotech 2012, pp. 247-250.

Key Engineering Materials Vols 645-646 (2015) pp 869-874
Submitted: 2014-11-05
Accepted: 2014-12-23
© (2015) Trans Tech Publications, Switzerland
doi:10.4028/www.scientific.net/KEM.645-646.869

Design and experimental study of a composite materials micro-deformation measurement device

Ye Yuan*, He Bao, Hong Xu, Zhilai Li

Changchun Institute of Optics, Fine Mechanics and Physics,

Chinese Academy of Sciences, Changchun 130033, PR China

Email:yuanye080888@163.com
*Corresponding author.
E-mail: yuanye080888@163.com

Keywords: Composite materials; Space environments; Measurement device; Micro-deformation

Abstract

In the space environments, the size and weight of composite materials will produce small changes. In order to measure the small changes accurately, a micro-deformation measurement device has been designed. The carbon fiber tube was made from cyanate ester resin or epoxy resin was tested in vacuum and hygrothermal environments. The deformation in the vacuum test is -1.7 to 3.8 microns, in the hygrothermal test, the deformation is -1.3 to -6.4 microns. The same as theoretical analysis, the environmental stability of cyanate ester resin better than epoxy resin.

1.Introduction

Composite materials compared with conventional metallic materials possess a number of attractive features, such as high specific strength, high specific modulus, high temperature resistance, corrosion resistance, fatigue resistance, performance can be designed and so on[1-4]. Composite materials have become one of the four structural materials after aluminum, steel, and titanium. The amount of the composite materials has become one symbol of the advancement of aerospace structures.

The composite materials used in aerospace structures can reduce the weight 20% to 30%, which not only brings considerable economic benefits, but also can increase the mobility of weaponry. In addition, composite materials itself can also make other performance of aerospace structures effectively improved, such as the composite aerodynamic tailoring technology can significantly improve the structural efficiency[5-7]; Integrally molded technology can effectively reduce the connection, improve structural reliability, reduce costs and so on.

In recent years, a large number of composite materials used in aircraft fuselage, the proportion increased year by year. In the field of lightweight, high specific stiffness, dimensional stability and other strict requirements, the composite materials has a wide application[8-15]. However, due to the low density, gas diffusion in composite materials is much easier than in the metallic materials[16]. There are a huge difference in terms of pressure, temperature, humidity between the space environment and the laboratory environment, it will lead to gas and moisture permeate in the composite materials surface, resulting in weight and shape changes.

2. Measurement device design

As shown in Figure 1, the device consists of carbon fiber tube, connector and steel ball. The connector is made of Invar, linear expansion coefficient of this material is zero, the vent is designed in its axial and radial, make sure air can circulate freely inside and outside of the device; The steel ball is made of stainless steel which has high circularity, The carbon fiber tube is divided into two types, one is made from cyanate ester resin and carbon fiber, the other is made from epoxy resin and carbon fiber.

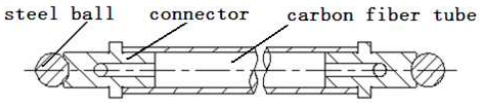


Fig.1 The measurement device model

When the working environment of the composite materials is changed, the cyanate ester resin and epoxy resin will produce expansion or contraction, This will lead to produce micro-deformation of the tube. Because the connector and steel ball are almost free from environmental changes, the micro-deformation of the tube will be directly reflected in the distance between the two steel balls.

3. Experimental

3.1 Materials

Cyanate ester resin, with the trade name AroCy B-10 was supplied by Ciba Specialty Chemicals.
Epoxy resin, with the trade name F-44 was supplied by Shanghai Resin Plant.
Carbon Fiber，with the trade name T700 was supplied by Toray.

3.2 Conditions and methods

Vacuum test:

According to the space environment test standards, vacuum test conditions are as follows:
a) Environmental pressures: not more than 1.0 × 10-4Pa;
b) Test temperature: 20 ± 1 ℃;
c) Hold Time: 72h.

Hygrothermal test:

According to the space environment test standards, hygrothermal test conditions are as follows:
a) Test temperature: high temperature is 35 ℃, low temperature is 2 ℃; Each cycle of high and low temperature stability and maintaining time is 4h;
b) The relative humidity is 80% and 94%;
c) Cycles: 10 cycles, each cycle is 12 hours.

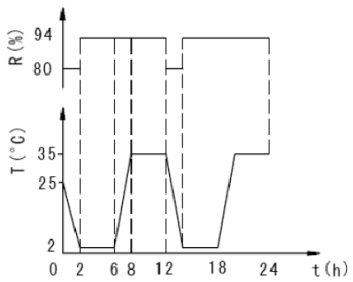


Fig.2 Hygrothermal test conditions

3.3 Methods and instrumentation

The weight gain:
Carbon fiber tubes were stored in a drier for 4 weeks, then the measurement device were stored at the laboratory environment for 4 weeks until a constant weight was obtained. After the moisture of the surface was wiped with filter paper, measure the weight of the measurement device when the test ends. The weight gain was determined by the following equation:

$$\text{Weight gain} = (W_2 - W_1)/W_0 \times 100\% \quad (1)$$

Where W_0 and W_1 denote the weight of carbon fiber tubes and the weight of measurement device before the test, W_2 denote the weight of the measurement device after the test. BSM4100.2 was selected to measure the weight of the measurement device which its accuracy is 10mg.

The micro-deformation:

The Coordinate Measuring Machine of Zeiss (Prismor Navigator) was employed to measure the distance between the two steel balls, which its accuracy is 0.5 microns. The change of the distance can be considered as micro-deformation of the carbon fiber tubes.

4. Results and discussion

4.1 Effects of Vacuum test on weight gain and micro-deformation

As shown in Fig. 3 and Fig. 4 respectively, it is the weight gain and micro-deformation changes of the carbon fiber tubes in nine days after the vacuum test.

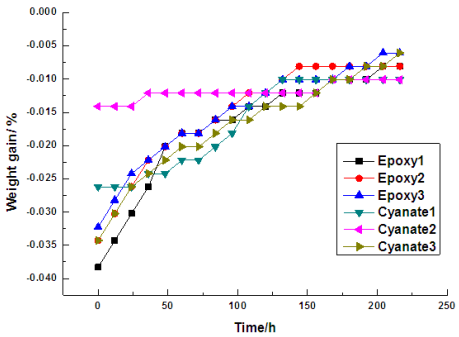


Fig.3 The weight gain after vacuum test

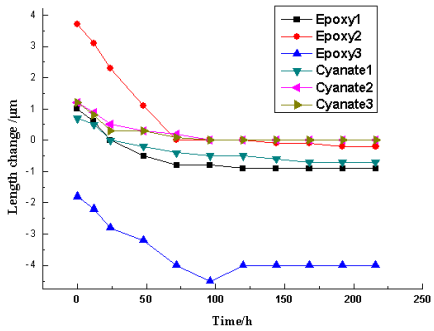


Fig.4 The length change after vacuum test

After the vacuum test, the weight gain of the carbon fiber tubes (cyanate resin) is -0.014% to -0.034%, its deformation is -0.5microns to 0.5 microns; While the weight gain of the carbon fiber tubes (epoxy) is -0.033% to -0.039%, its deformation is -1.7microns to 3.8 microns.

The trends can be seen from the figure, the first two days after the test, the weight gain and micro-deformation of the composite materials changes relatively quickly, the first 3 to 6 days tends to gently, after 6 days the change almost can be ignored.

4.2 Effects of hygrothermal test on weight gain and micro-deformation

As shown in Fig. 5 and Fig. 6 respectively, it is the weight gain and micro-deformation changes of the carbon fiber tubes in nine days after the hygrothermal test.

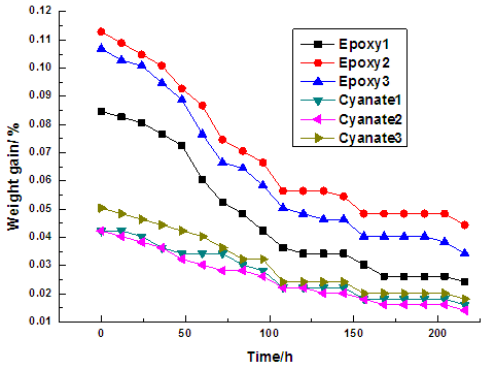


Fig.5 The weight gain after hygrothermal test

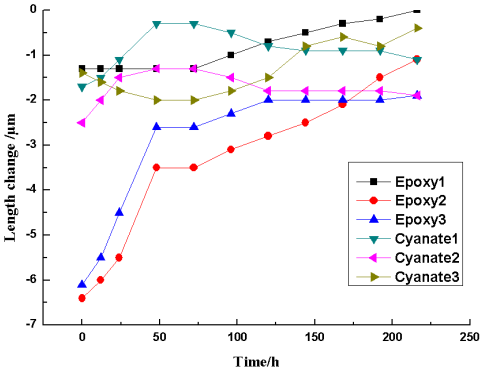


Fig.6 The length change after hygrothermal test

4.3 Discussion

Phenomenon 1: The weight of composite materials produce changes in different environments, there are two reasons:

The density of the composite materials is poor, when stored for long periods under the laboratory environment, the surface of the composite materials will absorb a certain amount of gas and moisture. When the pressure, humidity produce dramatic changes, the gas and moisture will penetrate or escape in the composite materials surface. During the preparation of the polymer matrix, a portion of gas, moisture will dissolve inside the matrix, when the pressure in the vacuum state, the gas will diffuse from the inside to the outside, then release at the interface.

Phenomenon 2: The weight gain of cyanate and epoxy has a clear distinction, it is because:

The weight gain of cyanate lower than epoxy since it contains a number of the intramolecular triazine bicyclophane cage structures. It contributes to the suppression of gas into the interior of the composite materials, so the cyanate has certain environmental insensitivity.

Phenomenon 3: The change of the weight gain and the micro-deformation are synchronized, and the deformation of cyanate smaller than epoxy. This is because:

The expansion coefficient of the composite materials and its weight gain has the following relationships[17]:

$$\alpha_L = \frac{E_{fL}V_f\alpha_f C_f + E_m V_m \alpha_m C_m}{\left(E_{fL}V_f + E_m V_m\right)C} \tag{2}$$

$$\alpha_T = \frac{V_f\alpha_f C_{fm}(1+v_{fLT}) + V_m\alpha_m C_m(1+v_m)}{\left(\rho_f V_f C_{fm} + \rho_m V_m\right)C}\rho \tag{3}$$

α_L is the longitudinal expansion coefficient of the composite materials， α_T is the transverse expansion coefficient of the composite materials.

E, V_f, V_m, v respectively represent modulus of elasticity, the volume percentage of fiber, the volume percentage of matrix and Poisson's ratio.

In the formula:

$$\left.\begin{aligned} C &= \Delta M / M \\ C_f &= \Delta M_f / M_f \\ C_m &= \Delta M_m / M_m \end{aligned}\right\} \tag{4}$$

M， M_f， M_m respectively represent the weight of composite materials, fiber and matrix.

$\Delta M, \Delta M_f$， ΔM_m， respectively represent the weight gain of composite materials, fiber and matrix.

From the above equation, when the other parameters (representing material properties, process parameters) keep constant, the coefficient of expansion is directly related to the weight gain of matrix, so the change of the weight gain and the micro-deformation are synchronized, and the deformation of cyanate smaller than epoxy.

5. Conclusions

1. A composite materials micro-deformation measurement device had been designed, the device can effectively measure the small changes of the deformation and the weight of the composite materials.

2. The environmental stability of cyanate ester resin better than epoxy resin. After the vacuum test, the deformation of the carbon fiber tubes (cyanate resin) is -0.5microns to 0.5 microns; While the deformation of the carbon fiber tubes (epoxy) is -1.7microns to 3.8 microns. After the hygrothermal test, the deformation of the carbon fiber tubes (cyanate resin) is -1.3microns to -2.5 microns, While the deformation of the carbon fiber tubes (epoxy) is -1.2 microns to -6.4 microns.

3. The micro-deformation recovery after test divided into three stages: quick, gentle and stable.

Acknowledgement

The authors gratefully acknowledge the financial support of this work provided by National 863 high-tech Research and Development Program funded projects, PR China, grant No.2009AA7020107.

References

[1] G.W. Meetham, M.H. Van de Voorde, Materials for High Temperature Engineering Applications, Springer, New York, 2000.

[2] R. Schutze. Lightweight Carbon Fiber Rods and Truss Structures. Materials and Design. 1997, 18: 231~238.

[3] JIANG X X, LAURIN D, LEVESQUE D, et al. Design and fabrication of a lightweight laser scanning mirror from metal-matrix composites. SPIE, 2001, 4444:1-8.

[4] AN Yuan, JIA Xue-zhi, ZHANG Lei. Optimizing design of CFRP based main backbone with high stiffness ratio for space camera. Optics and Precision Engineering, 2013, 21 (2) 416-422.

[5] Oshkovr SA, Eshkoor RA, Taher ST, Ariffin AK, Azhari CH. Crash worthiness characteristics investigation of silk/epoxy composite square tubes. Compos Struct 2012;94:2337–42.

[6] Wolff G E. Introduction to the Dimensional Stability of Composite Materials. Lancaster: DE Stech Publications, Inc. 2004: 1-419.

[7] Krenkel, W., and F. Berndt. C/C–SiC composites for space applications and advanced friction systems. Materials Science and Engineering: A 412.1 (2005): 177-181.

[8] Dao B, Hodgkin J, Krstina J, Mardel J, Tian W. Accelerated ageing versus realistic ageing in aerospace composite materials–IV. Hot/wet ageing effects in a low temperature cure epoxy composite. J Appl Polymer Sci 2007;106(6):4264–76.

[9] Fox B, Lowe A, Hodgkin J. Investigation of failure mechanisms in aged aerospace composites. Eng Fail Anal 2004;11(2):235–41.

[10] Bondzic S, Hodgkin J, Krstina J, Mardel J. Chemistry of thermal ageing in aerospace epoxy composites. J Appl Polym Sci 2006;100(3):2210–9.

[11] Yang Nai-bin. Present Status Analysis of Application of Composite Air frame Structure Abroad. Aeronautical Manufacturing Technology. 2002, (9): 21~23.

[12] Zhao Jia-xing. Application of Carbon Composite Materials for Civil Aviation.Hi-Tech Fiber and Application. 2003, 28(3): 1~5.

[13] Jeff W, Yap H, Murray L S. The Analysis of Skin-to-stiffener bonding in composite aerospace structures. Composite Structures. 2002, 57(1): 425~435.

[14] Hoskins and Baker. Composite Materials for Aircraft Structures. New York, American Institute of Aeronautics and Astronautics, Inc,1986, 93~113.

[15] GUO, J., SHAO, M. D., WANG, G. L.,et al. Design of optical-mechanical structure made of CFC in space remote sensing camera, Optics and Precision Engineering, 2012, 20 (3) 571-578.

[16] Lin Y, Chen X. Investigation of moisture diffusion in epoxy system:experiments and molecular dynamics simulations. Chem Phys Lett 2005;412:322–6.

[17] WANG Zhen-ming, Mechanics of composite materials and composite material structural mechanics, Machinery Industry Press,Beijing,1991.

Key Engineering Materials Vols 645-646 (2015) pp 875-880
© (2015) Trans Tech Publications, Switzerland
doi:10.4028/www.scientific.net/KEM.645-646.875
Submitted: 2015-01-09
Accepted: 2015-01-19

A Low-Frequency Filter in Inertial Applications

Li Qiang[1,a], Liu Xiaowei[1,2], Yin Liang[1], Zhou Jiajun[1]

[1]MEMS Center, Harbin Institute of Technology, Harbin, Heilongjiang, China

[2]Key Laboratory of Micro-Systems and Micro-Structures Manufacturing, Ministry of Education, China

[a]lq2518409@sina.com

Keywords: Inertial sensors; Low-frequency filters; Transconductance reduction techniques

Abstract. A fourth-order cascade low-pass transconductance capacitor filter is designed, and the coefficients of the filter are calculated. For the implementation of large-time constants the current shunt technique and the current cancellation technique are employed in the operational transconductance amplifiers. The whole filter is simulated in Hspice, the the cutoff frequency is 150.2Hz and the THD of the filter is 65dB, which meet the technical requirements of the inertial applications.

Introduction

With the inertial sensors be widely applied in aerospace, military, defense and other fields, the design of the inertial sensors is not straightforward, it requirements micro-miniaturization, integration, accuracy and other characteristics. Low-frequency filters are important parts of the inertial sensors, they should be low noise and low distortion to present the demands of the high performance circuits. The filters used in interface circuits of the micro-gyroscope are used to sense the signals of the gyroscope, so the cutoff frequency of them should be several hundred Hz. In this case, a low-pass filter is necessary to meet the design specifications.

The research of Gm-C filter has become a hotspot in analog signal processing research. It can achieve a wide dynamic range and large tuning capabilities, and it is a high integrated continuous-time circuits. In 1983, a fully integrated active filter is proposed in [1]. In 1984, a fully integrated continuous-time transconductance capacitor filter in which OTA is the basic module is presented [2], marking the transconductance capacitor filters become an important part of the fully integrated continuous-time filters. CMOS technology is used to produce the transconductance element in [3]. The use of linearity and temperature compensation technique is presented in [4] to design the CMOS transconductance circuit. The linearity of the transconductance is increased by using the bias transistors [5]. Large cross-coupled transconductance technique has improved the ability to process the large signals [6]. Current addition technique is further enhanced the linearity of the transconductance [7]. In [8], the design use fully symmetrical structure to improve the linearity and signal to noise ratio (SNR). The using of multi-input OTA has improved the ability to process the signals [9] [10]. In numerous OTA linear regulation schemes, the most attractive one is the four transistor CMOS linear transconductance technique [11].

The design of very low-frequency filters for integrated circuit implementations need to realize a large time constants. For example, an implementation of a 100-Hz Gm-C filter needs a transconductances of1 nA/V and capacitors larger than 40 pF. To meet the design requirements, the design of the transconductance amplifier is very important. In this paper, the structure of the transconductance amplifier has used the current shunt technique and the current cancellation technique to realize a very small transconductance value. In this design, a four order cascade implementation is used. In addition, a low-distortion, low-noise transconductor with reduced transconductance using in low frequency applications is proposed. Design guidelines for high-performance implementations this circuit are also given. Finally, the simulation results and conclusion are given in the end of this paper.

1. Analysis of traditional CMOS transconductors

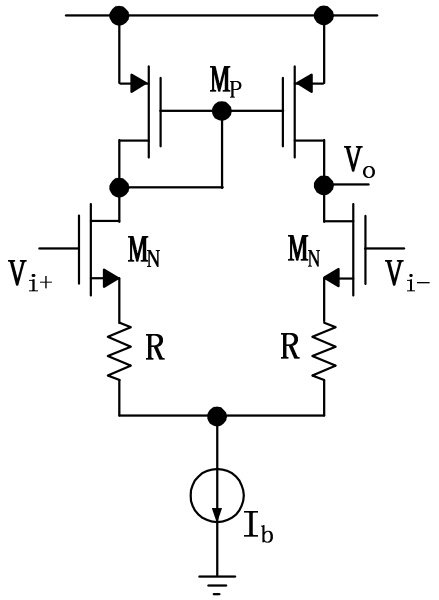


Figure 1. Implementation of a basic differential pair input stage.

Fig. 1 shows the implementation of a basic differential pair input stage. The non-linear output current is given by equation (1) and (2):

$$i_o = v_{id}\sqrt{\frac{2KI_b}{1+N}}\sqrt{1-(\frac{v_{id}}{2(1+N)V_{Dsat}})^2} \tag{1}$$

$$HD_3 = \frac{1}{32}\left(\frac{v_{id}}{(1+N)V_{Dsat}}\right)^2 \tag{2}$$

where $v_{id}=V_{i+}-V_{i-}$, $V_{Dsat}=V_{GS}-V_{thn}$ and $N=g_mR$ is the source degeneration factor. From (1) and (2), it is shown that the output current is degenerated by 1+N and its third harmonic distortion (HD3) is degenerated by $(1+N)^2$. So make the factor N larger can increase the linearity performance of the circuit.

From Fig. 1, we can get the input referred thermal noise power density.

$$v_{in,th}^2 = \left[2\left(1+\frac{g_{mMP}}{g_{nMN}}\right)\right]\frac{8kT}{3g_{mMN}} \tag{3}$$

Over the frequency range of the filter bandwidth BW, the noise level is:

$$v_{\text{int},th}^2 = \int_{BW} v_{in,th}^2 df = 2\left(1+\frac{g_{mMP}}{g_{nMN}}\right)BW\frac{8kT}{3g_m} \tag{4}$$

Considered with the flicker noise, the input referred flicker noise power density is shown as the following equation.

$$v_{in,f}^2 = \frac{I_B}{L^2C_{ox}fg_m^2}\left(K_{Fn}k_n' + K_{Fp}k_p'\right) \tag{5}$$

The noise level over BW is:

$$v_{\text{int},f}^2 = \int_{BW} v_{in,f}^2 df = \left[\frac{I_B}{L^2C_{ox}g_{mMN}^2}\left(K_{Fn}k_n' + K_{Fp}k_p'\right)\right]\ln\frac{1}{BW} \tag{6}$$

Considered with both thermal and flicker noise, the total input referred noise power density is shown as follows.

$$v_{\text{int},t}^2 = 2\left(1+\frac{g_{mMP}}{g_{nMN}}\right)\frac{8kT}{3g_{mMN}}BW + 2\left[\frac{I_B}{L^2C_{ox}g_{mMN}^2}\left(K_{Fn}k_n' + K_{Fp}k_p'\right)\right]\ln\frac{1}{BW} \tag{7}$$

If the frequency is low, the flicker noise is dominant in the total input referred noise. From (7), we can get that if the bias current is very low and both transistors and transconductance gains have a large value, the total noise level can have a huge degeneration.

2. Linearized OTA for low-frequency filter

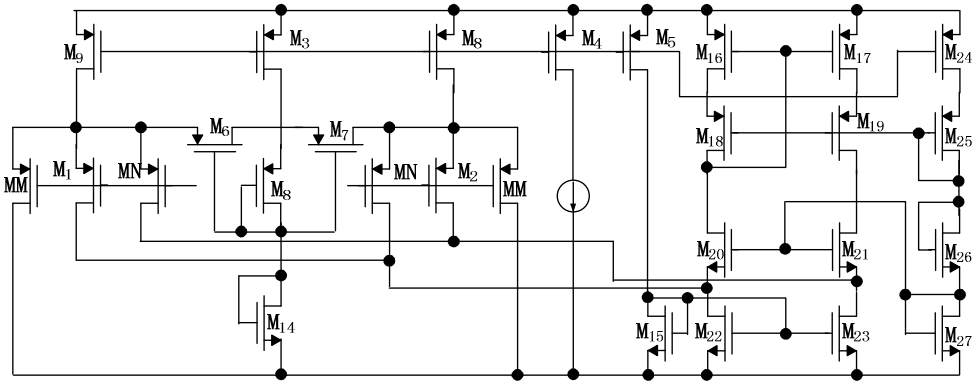


Figure 2. Implementation of the proposed operational transconductance amplifier.

Fig. 2 shows the implementation of the operational transconductance amplifier in this filter. In general, according to the relationship between the cutoff frequency and the transconductance, it requires a very small transconductance values to get a small cut-off frequency. So the bias current of the transconductance should be very small. Furthermore, a small input current will lead to a large noise, so the input current is cannot be very small. So, the current shunt technique and the current cancellation technique are used in this circuit. Specifically, the transistors M_6 and M_7 in the middle of the main circuit are biased in the triode region, so g_{m6} and g_{m7} are sensitive to the common-mode input voltage. Transistors M_6 and M_7 make a convert from the input differential voltage (v_1-v_2) to a current, then the current is shunt by transistors M_M, M_1, M_2, and M_N. The small signal transconductance of M_M is designed larger than others, so the current mostly flow to ground through it. At the same time, a large proportion of the residual currents from M_1 and M_N are also cancelled at the output of the amplifier. As result, the small signal transconductance has a huge reduction.

$$g_m = \frac{N-1}{M+N+1}g_{oM6} \tag{8}$$

$$g_{oM6} = \mu_P C_{ox}\frac{W_{M6}}{L_{M6}}(V_{GSM6} - V_{TH}) \tag{9}$$

From (8) and (9), we can see that if the M and N ratios are adjusted and g_{m6} is reduced, huge degeneration of G_m of the OTA can be obtained.

In the output referred noise density current, transistors M_3, M_6, and M_M have a very small contributions for the noise current of them are degenerated by the current divide. So that transistors M_1, M_N, and M_{14} contribute more noise. If we set M>>1 and g_{mMM}>>g_{mM6}, the output referred noise density voltage is shown as follows.

$$v_{o,th}^2 = 2\left(i_{oM1}^2 + i_{oMN}^2 + i_{oM14}^2\right) \tag{10}$$

From (10), we can get the noise level over BW.

$$v_{\text{int},th}^2 = \int_{BW} v_{in,th}^2 df \approx \frac{16kT}{3G_m}\frac{g_{mM1}+g_{mMN}+g_{mM14}}{G_M}BW \tag{11}$$

Considered with the flicker noise:

$$i_{o,f}^2 \approx \frac{2\frac{I_B}{M}}{C_{ox}^2 L^2 f}\left(k_n' K_{Fn} + 2k_p' K_{Fp}\right) \tag{12}$$

$$v_{\text{int},f}^2 = \int_{BW} v_{in,f}^2 df \approx \frac{2\frac{I_B}{M}}{L^2 C_{ox}^2 G_m^2}\left(k_n' K_{Fn} + 2k_p' K_{Fp}\right)\ln\left[\frac{1}{BW}\right] \tag{13}$$

From (12) and (13), we can see that $M_1$and M_N have the same concernment. Considered with both the thermal and flicker noise, the final input referred noise power density is given by

$$v_{\text{int},t}^2 \approx \frac{16kT}{3G_m}\frac{g_{mM1} + g_{mMN} + g_{mM14}}{G_M} BW + \frac{2\frac{I_B}{M}}{L^2 C_{ox}^2 G_m^2}\left(k_n' K_{Fn} + 2k_p' K_{Fp}\right)\ln\left[\frac{1}{BW}\right] \tag{14}$$

From equation (14), we can get that increasing the length L, reducing I_B and keeping large G_m values can reduce the noise level.

3. Architecture of the Gm-C filter

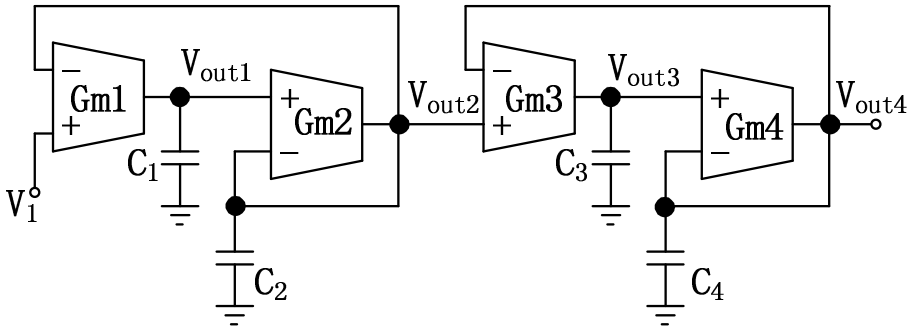


Figure3. Structure of the cascaded Gm-C filter.

A straightforward method to design the architecture of the filters is to connect the OTAs the cascade connection form. There are many advantages for cascade forms, such as the low output impedance of each part eliminates the load effect between them, so that each part can be tuned independently. In this paper, the cascaded connection form is selected to design a low-pass transconductance capacitor filter.

According to the specifications of the filter, the transfer function of the fourth-order low-pass Butterworth system is the optimization. So four-order system is selected.

Fig. 3 is the structure of the cascade fourth-order low-pass filter. The correspondence between the parameters in Fig. 3 is as follows:

$$\begin{cases} (V_1 - V_{out2})\cdot g_{m1}\cdot\dfrac{1}{C_1 s} = V_{out1} \\ (V_{out1} - V_{out2})\cdot g_{m2}\cdot\dfrac{1}{C_2 s} = V_{out2} \\ (V_{out2} - V_{out4})\cdot g_{m3}\cdot\dfrac{1}{C_3 s} = V_{out3} \\ (V_{out3} - V_{out4})\cdot g_{m4}\cdot\dfrac{1}{C_4 s} = V_{out4} \end{cases} \tag{15}$$

The output of the filter is given by:

$$\frac{V_{out4}}{V_1}=\frac{g_{m1}g_{m2}g_{m3}g_{m4}}{(C_1C_2s^2+g_{m2}C_1s+g_{m1}g_{m2})(C_3C_4s^2+g_{m4}C_3s+g_{m3}g_{m4})} \tag{16}$$

Using the normalized form of the fourth-order low-pass Butterworth:

$$H(s)=\frac{1}{\left[\left(\frac{s}{\omega_p}\right)^2+0.76537\left(\frac{s}{\omega_p}\right)+1\right]\left[\left(\frac{s}{\omega_p}\right)^2+1.84776\left(\frac{s}{\omega_p}\right)+1\right]} \tag{17}$$

We can get that:

$$\begin{aligned}
&\frac{C_1C_2C_3C_4}{g_{m1}g_{m2}g_{m3}g_{m4}}=\frac{1}{\omega_p^4}\\
&\frac{C_1C_2C_3}{g_{m1}g_{m2}g_{m3}}+\frac{C_1C_4C_3}{g_{m1}g_{m4}g_{m3}}=\frac{2.61313}{\omega_p^{\ 3}}\\
&\frac{C_1C_2}{g_{m1}g_{m2}}+\frac{C_1C_3}{g_{m1}g_{m1}}+\frac{C_3C_4}{g_{m3}g_{m4}}=\frac{3.4122}{\omega_p^2}\\
&\frac{C_1}{g_{m1}}+\frac{C_3}{g_{m3}}=\frac{2.61313}{\omega_p}
\end{aligned} \tag{18}$$

So, $g_{m1}=g_{m2}=g_{m3}=g_{m4}=3.3\times10\text{-}9$, $C_1=6.4$pF, $C_2=1.9$pF, $C_3=2.7$pF, $C_4=4.6$pF are the final choice.

4. Simulation results

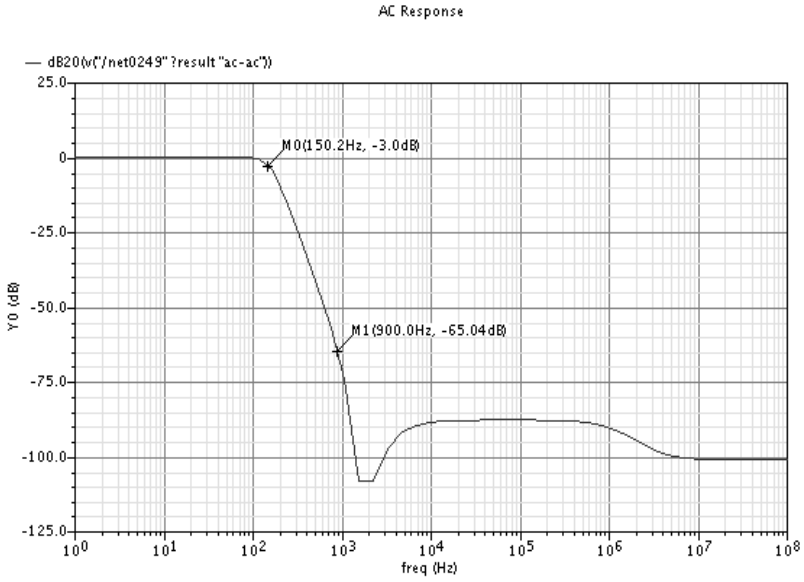


Figure 4. The simulation results of the filter

Fig. 4 is an amplitude-frequency curve of the fourth-order cascade transconductance capacitor filte. It can be seen that when the amplitude is-3dB, the cutoff frequency is 150.2Hz. The THD of the filter is 65dB.

Summary

A method combined with current shunt and current cancellation techniques to reduce the non-linearity of the transconductance under nano-scale technology has been presented for inertial

applications at a very low frequency, which show that high performance low frequency filters can be realized under CMOS technology.

Acknowledgements

This material is based upon work supported by the National Natural Science Foundation of China (NSFC) under grant No. 61204121. The authors are grateful to Dr. Yin Liang for helpful discussions.

References

[1] B. Mihai, T. Yannis. Fully integrated active RC filters in MOS technology. IEEE Journal of Solid-State Circuits. 1983, vol. SC-18: 644-651
[2] K. Haideh, Gray Paul R. High frequency CMOS continuous time filters. IEEE Journal of Solid State Circuits. 1984, vol. 3: 1498-1501.
[3] Nedungadi A., Viswanathan T. R. Design of linear CMOS transconductance Elements. IEEE. Trans on CAS. 1984, vol. CAS-31: 891-894.
[4] Torrance R P. CMOS voltage to current transducers. IEEE Trans on CAS. 1985. 32(11): 1097-1041.
[5] Tsividis Y. MOS transconductors and intergrators with high linearity. Electron Lett. 1986: 245-246.
[6] Czamui Z. Tsividis Y. MOS tunable transconductor. Electron Lett. 1986: 721-722.
[7] Wu P. A . CMOS OTA with improved Linearity based on current addition. IEEE Press ISCAS. 1990: 2296-5599.
[8] Peterson K D. Geiger R L. A fully balanced CMOS OTA for high frequency monolithic filters. Proc 29th Midwes Syrup on CAS. 1987:208-211.
[9] Reed R D. Geiger R L. An operational transconductance amplifier with multiple input and a wide linear range. Proc 29th Midweat Symp on CAS. 1987: 368-371.
[10] Wang Z. Making. CMOS OTA a linear transconductor. Electron Lett. 1990. 26(18): 1418-1449.
[11] Park C S. Schaumann R. A high frequency CMOS linear transconductance Element. IEEE Trans on CAS. 1986. 33(1): 1132-1138.

Key Engineering Materials Vols 645-646 (2015) pp 881-887
© (2015) Trans Tech Publications, Switzerland
doi:10.4028/www.scientific.net/KEM.645-646.881

Submitted: 2015-01-08
Accepted: 2015-01-15

Experimental Investigations on New Characterization Method for Giant Piezoresistance Effect and Silicon Nanowire Piezoresistive Detection

Jiahong Zhang[1,2,3,a], Min Yang[3], Qingquan Liu[1,2,3], Fang Gu[4,b], Min Li[1,3] and Yixian Ge[1, 3]

[1] Jiangsu Key Laboratory of Meteorological Observation and Information Processing, Nanjing University of Information Science & Technology, Nanjing 210044, China

[2]Jiangsu Collaborative Innovation Center on Atmospheric Environment and Equipment Technology, Nanjing University of Information Science and Technology, Nanjing 210044, China

[3] School of Electronic and Information Engineering, Nanjing University of Information Science and Technology, Nanjing 210044, China

[4] School of Physics & Optoelectronic Engineering, Nanjing University of Information Science & Technology, Nanjing 210044, China
[a]zjhnuist@163.com, [b]gfnuist@163.com

Keywords: silicon nanowire, giant piezoresistive effect, the characterization method, piezoresistive detection

Abstract. This paper presents a novel and effective characterization method for giant piezoresistive properties of silicon nanowires by using the reference structures. This contrast detection approach investigates the influences of quantum size effect and surface defects effect on piezoresistive coefficients of silicon nanowires by direct comparison of the resistivity change ratio of silicon wires with nanoscale-to-microscale width under the same applied stress conditions. The characterization experiments based on four-point bending tensile test demonstrate that piezoresistive coefficient of small nano-width silicon nanowire can be significantly increased to about five times higher levels than that of bulk silicon under the same impurity concentration, which indicates that the silicon nanowire can have giant piezoresistive effect. On the other hand, to solve the problem on nanowires pick-up, we proposed a nanowire piezoresistive detection approach, whose validity is confirmed by the dynamic LDV resonance test. Meanwhile, to investigate the influence of undercut arising from the wet chemical release process of the suspended silicon nanowire, a three-dimensional finite element simulation is also carried out for the fundamental resonant frequency using ANSYS software. The numerical and experimental results show that our piezoresistive detection is accurate and effective and the undercut should be carefully considered in the design of the high frequency resonator and mixer. The findings of this paper provide some useful references for the piezoresistive effect measurement and the piezoresistive pick-up in nanoelectromechanical system.

Introduction

In view of the small size and the ultra-high or giant piezoresistance effect [1-4], the silicon nanowire piezoresistive sensing structures have become key building blocks for the highly sensitive nanoelectromechanical system (NEMS) sensors, high frequency resonators and high performance mixers[5,6]. In order to make these NEMS applications reliable, it is essential and critical to investigate the characterization method for giant piezoresistance effect in the silicon nanowire and the piezoresistive detection using the silicon nanowire sensing structures. On the one hand, measurement and evaluation of giant piezoresistive effect of silicon nanostructures at this stage is mainly based on the four-point bending tensile test [1,2] and the cantilever tensile test [3,4]. These experiments need to simultaneously measure the stress of the silicon nanowire and its change rate of resistance, and the experimental apparatus is complicated, and easily affected by many factors. For this reason, this paper presents a contrast detection method for giant piezoresistive properties of silicon nanowires by using the reference structures. This novel and effective approach investigates the influences of size effect and surface effects on piezoresistive coefficients of silicon nanowires by direct comparison of the resistivity change ratio of silicon wires with nanoscale-to-microscale width under the same stress

conditions. On the other hand, optical measurement method has been widely used to detect the vibration of the naostructure, however, when the size of high frequency silicon nanowire resonator and mixer further reduces, the nanowire can not effectively reflect laser light, and in this case we need more expensive and complex testing equipment to complete the optical pick-up. Other pick-up methods, such as capacitive detection, magnetic potential detection and single-electron device detection, require very complicated circuit, very low temperature, strong magnetic field and the vacuum environment. In comparison, the piezoresistive detection, i.e., piezoresistive pick-up by using the silicon nanowire has a certain application advantages due to its high sensitivity, good stability, low-cost and mass-production. In this paper, we confirm the feasibility of nanoscale piezoresistive pick-up by comparing the experimental measurement results of the silicon nanowire piezoresistive detection and optical pick-up based on the laser Doppler vibrometer (LDV) [7].

Experiment on characterization of piezoresistance effect and nanoscale piezoresistive detection

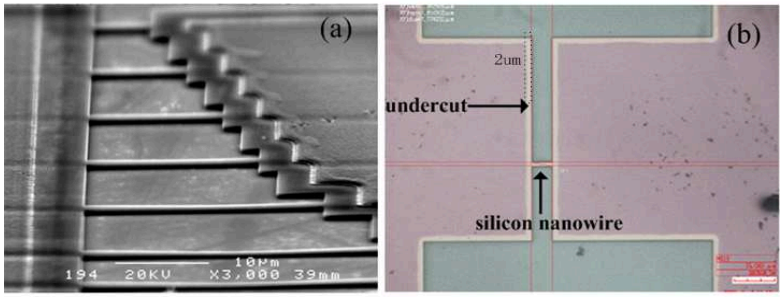


Fig. 1 (a) the SEM image of 200nm thick silicon nanowires with different length, (b) Optical microscope image of the silicon nanowire. The white strip near the base of nanowire indicates the undesired undercut with about 2μm long.

In this paper, silicon nanowires test structures along the [110] crystallographic orientation were fabricated from p-type (100) SOI wafers with a 200nm thick buried oxide (BOX) and a 200nm thick single-crystal silicon surface device layer by using the SMIC 0.18μm CMOS lithography process. The first step of the fabrication process was to selectively dope the wafer by ion implantation. Doping thickness (t) is about 60nm or 200nm, and the formed p-type piezoresistors have a doping level of near $10^{19}cm^{-3}$[8]. Next, we determined the patterns of [110] oriented silicon nanowires of different lengths (l) and widths (w) onto silicon surface device layer by the standard photolithography. After this, reactive ion etchings were used to etch the silicon device layer and the exposed BOX until the silicon substrate. Then heavily doped p-type layer was formed in the anchor region, followed by sputtering 600nm Al metal as the pad. A photoresist was then spinned in the metal pad region in order to prevent corrosion of Al metal in the release process of nanowires. Fig. 1(a) displays the SEM image of 200nm thick silicon nanowire array manufactured by the above CMOS process. These non-suspended silicon nanowires would be applied in the experiment on the characterization of the piezoresistive effect. For the suspended silicon nanowires using for the piezoresistive detection, the BOX underneath nanowires need be etched using a buffered oxide etcher solution and silicon nanowires were then released using critical point drying in liquid carbon dioxide (post-CMOS process), which inevitably generating the undercut of the nanowire clamping. As we can see from fig.1(b), it is noted that the undesired 2μm long undercut will lead to a significant deviation from the linear relation between the fundamental resonance frequency and the inverse length [7]. If we do not consider the effect of the undercut, erroneous conclusions may be obtained.

After the silicon nanowire array test structures were prepared, as shown in the fig. 2(a), we employ a homemade four-point bending tensile device to characterize their enhanced piezoresistive properties. As we known, through four-point bending tensile test, the stress can be applied uniformly on silicon nanowire array chip. To further confirm this fact the stress of chip substrate is uniformly transmitted to each silicon nanowires, a three-dimensional finite element (FE) simulation is carried out for the stress distribution of the device using the commercial software ANSYS. From the mechanical point of view, there is no difference between the young's modulus of 200nm thick silicon

nanowires and bulk silicon value [9,10], so the continuum theory (ANSYS) is still valid. As in the ANSYS input parameters are assumed, the experimental value for the mass density (2330 kg/m^3) is used whereas the Young's modulus (170GPa) and Poisson's ratio (0.064) are taken. Fig. 2(b) illustrates three-dimensional FE simulated *x* direction strain contours of double clamped silicon nanowires with different width in the four-point bending tensile test. It is initially observed that the strain of silicon nanowires with different widths of 50 nm, 100 nm, 250 nm, and 2000nm is the same. Fig. 2(c) further shows the partially enlarged strain contours of the silicon nanowire array. Obviously, the strain values of different locations of different silicon nanowires are basically the same. In addition, as can be seen from Fig. 2(d), the stress contours of the different long and wide silicon nanowires, which are on the same chip substrate, are same with each other. In a word, the ANSYS analysis results show that the substrate stress can be evenly transferred to each silicon nanowires.

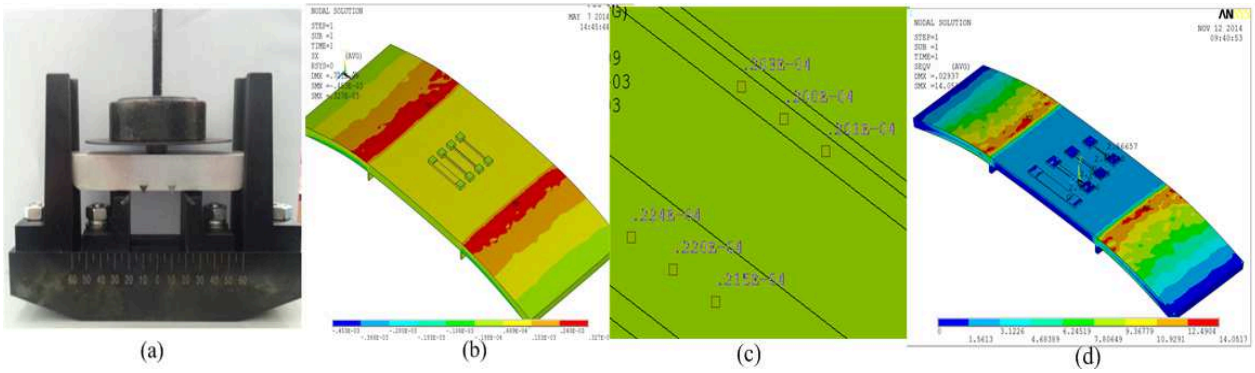


Fig. 2 (a) The picture of four-point bending tensile device, (b) three-dimensional FE simulated *x* direction strain contours of silicon nanowire array chip in the four-point bending tensile test, (c) the partially enlarged straincontours of the double clamped silicon nanowires.(d) three-dimensional FE simulated x direction stress contours of silicon nanowire array with different long and wide.

For a silicon nanowire piezoresistor with area A_R, the resistance change ΔR can be calculated as the function of the longitudinal and transverse stresses as follow:

$$\frac{\Delta R}{R}=\frac{1}{A_R}\int_0^{A_R}\pi_L\sigma_L+\pi_T\sigma_T\partial A \ . \tag{1}$$

Where π_L and π_T are the longitudinal piezoresistive coefficient (for stress applied parallel to the current flow) and transverse piezoresistive coefficient, respectively, while σ_L and σ_T are the longitudinal and transverse stress in the silicon nanowire. The σ_T can be neglected in the four-point bending tensile test so this equation can be simplified and converted to:

$$\pi_L=\frac{\Delta R}{R\cdot\sigma_L} \tag{2}$$

According to Eq. (2) and the above discussion on the stress distribution of silicon nanowire array, a contrast detection method is put forward in order to accurately characterize giant piezoresistive properties of silicon nanowires. The contrast detection method is based on a fundamental principle: in view of the adjacent silicon nanowires on the array chip having the same stress in the four-point bending tensile test, piezoresistive coefficient ratio of silicon nanowires with different widths is equal to the ratio of the rate of resistance change. The specific expression is as follow:

$$\frac{\pi_{L1}}{\pi_{L2}}=\frac{\Delta R_1}{R_1\cdot\sigma_{L1}}\Big/\frac{\Delta R_2}{R_2\cdot\sigma_{L2}}=\frac{\Delta R_1}{R_1}\Big/\frac{\Delta R_2}{R_2} \ . \tag{3}$$

In this case, the giant piezoresistive properties of silicon nanowires can be studied by using the reference test structures and the ratio measurement. Because the narrow and wide nanowires were prepared by using the same process and close to each other, through the ratio measuring the change of piezoresistive coefficient with the nanowire width variation can exclude the impact of many common factors, such as temperature and process condition. Especially when the piezoresistive coefficient of the wide wire itself is same as that of bulk silicon, piezoresistive coefficient of a narrow nanowire can be calculated directly by the ratio of resistance change rate measured by Keithley4200 semiconductor

analyzer[8]. Thus, the contrast detection method can also be applied for investigating the impacts of the size and surface effects on the piezoresistive properties of the nanowires.

On the other hand, the experimental piezoresistive pick-up using the silicon nanowire as sensing element has been performed in this paper. As shown in the fig. (3), the basic principle of nanowire piezoresistive detection is as follow: the silicon nanowire is electrostatically excited to vibration in a given resonant mode, and the periodical bending deformation results in a significant periodical change of the resistance of the piezoresistor integrated in the nanowire due to the high piezoresistive effect. Then, a periodic voltage output signal can be conveniently obtained by using a Wheatstone bridge circuit. It is obvious that the resistance change of the piezoresistor is largest when the nanowire deviates from the equilibrium position furthest. In the case, the amplitude of the periodic variation of the measured voltage signal is also maximized. Therefore, the maximum amplitude of the voltage signal corresponds to the fundamental resonant frequency of the silicon nanowire.

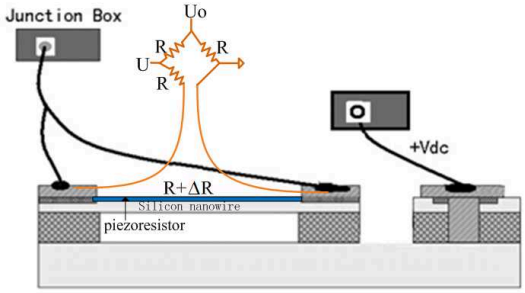


Fig. 3 Schematic plot of piezoresistive pick-up measurement setup by AC and DC excitation, the change in resistance of the nanowire may be readily and accurately measured by a Wheatstone bridge

Results and discussion

In the following sections, we present experimental research results on the characterization method for giant piezoresistance effect of silicon nanowires and the piezoresistive detection utilizing the piezoresistor integrated in the silicon nanowire. In the characterization method, the resistance change rate of non-suspended silicon nanowires of different widths are firstly obtained via four-point bending tensile test. The experiment results are displayed in table 1. As we can see, the resistance change rate of the silicon nanowire piezoresistor ($l \times w \times t$= 18μm×1.50μm×0.06μm) is 1.619%, while that of the silicon nanowire piezoresistor (14μm×0.18μm×0.06μm) is 3.407%. Obviously, the resistance change rate is related to the width of the piezoresistor. Based on a contrast detection method proposed by us, their piezoresistive coefficient can be ultimately calculated and is $115\times10^{-11}Pa^{-1}$ and $242\times10^{-11}Pa^{-1}$, respectively. Thus, it is found that piezoresistive coefficient of silicon nanowire with small nanoscale width can be significantly increased to about five times higher comparing to that of bulk silicon (about $50\times10^{-11}Pa^{-1}$)[11] of the same doped concentration, which indicates that the silicon nanowire can have high or giant piezoresistive effect. This is mainly due to the combined influence of quantum confinement effect in the piezoresistor and surface defects effect at the interface of silicon and native silicon dioxide [4].

Table 1. Resistance change rate of silicon nanowires of different widths and the corresponding piezoresistive coefficient

Piezoresistor size ($10^{19}/cm^3$)	resistance change rate	piezoresistive coefficient ($\times10^{-11}Pa^{-1}$)
14μm×0.18μm×0.06μm	3.407%	242
18μm×1.50μm×0.06μm	1.619%	115
18μm×3.00μm×0.2μm	0.704%	50

In our work, in order to confirm the validity of the nanowire piezoresistive pick-up, the fundamental resonant frequency of the suspended silicon nanowire of 22μm×3μm×0.2μm is measured and compared by the piezoresistive detection and the dynamic LDV resonance test. The silicon nanowire is electrostatically excited to vibrate, and vibration amplitude-frequency relation of

the silicon nanowire obtained by using LDV optical pick-up is plotted in the fig. 4(a), and the relationship between the relative change of output voltage and frequency of the silicon nanowire obtained by using piezoresistive pick-up is shown in the fig. 4(b). As we can see from the fig.(4), the fundamental resonant frequency of silicon nanowire obtained by the piezoresistive pick-up (2.9641MHz) is substantially equal to that of the optical detection (2.9780MHz), and the relative error is 0.47%, which reveals that our piezoresistive detection is accurate and effective. It is worth noting that the undesired 2μm long undercut caused by the post-CMOS process will lead to a significant deviation from the linear relation between the fundamental resonance frequency and the inverse length [7,12]. In other word, the measured fundamental resonance frequency may be not the original design value. Thus, if we do not consider the effect of the undercut, the unwanted and problematic results may be obtained.

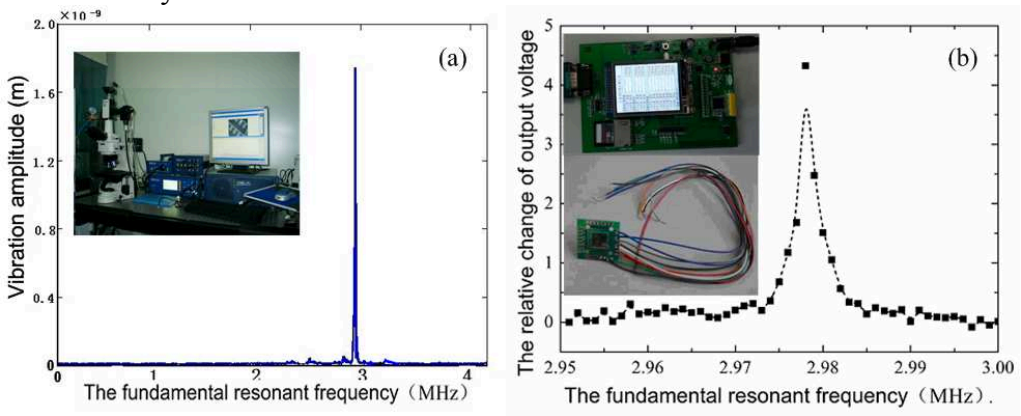


Fig. 4 The silicon nanowire is electrostatically excited to vibration, (a) amplitude-frequency relation of the silicon nanowire obtained by using LDV optical pick-up, illustrations displays the LDV measurement setup, (b) the relative change of output voltage-frequency relation of the silicon nanowire obtained by using piezoresistive pick-up, and illustrations display the silicon nanowires array chip and high-frequency measuring circuit.

In order to investigate the influence of undercut arising from the wet chemical release process of the nanomechanical structure, a three-dimensional FE simulation is carried out for the fundamental resonant frequency using ANSYS. The underetched nanowire is modeled as a stepped beam as illustrated in fig. 5(a). In the specific simulation, the nanowire is attached to the 2μm long and 15μm wide plate. Three lateral edges of the plate are clamped, while the nanowire is attached to the free edge. Moreover, released areas of silicon nanowire and underetched base regions (plate with three clamped lateral edges) are allowed to move freely in the FE simulation. In this case, FE results are uniquely determined. Fig. 5(b) indicates the vibration mode dependence on the stress distribution in close proximity to the clamped end of the nanowire. The simulations show that the stress propagation into the overhang region is significant, which numerically reveals that the undercut inevitably affects the mechanical resonant characteristics of the silicon nanowire.

.

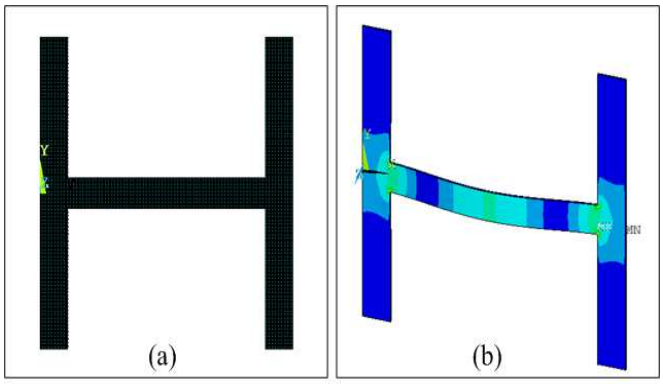


Fig. 5 (a) Three-dimensional FE mesh of the silicon nanowire, (b) FE simulation of the vibration mode dependence on the stress distribution near the double clamped end of the silicon nanowire

Table 2 lists the FE simulated and experimental measured nanowire resonant frequencies. For the silicon nanowire of 22μm×3μm×0.2μm, LDV optical detection is very accurate, thus we use its measurement value as a standard value. It's observed that FE simulation without considering the undercut exhibit overvalued resonant frequency and the relative error is up to 23.57%. This is because that the undercut results in effective length becomes larger, and reduces the resonant frequency. However, FE simulation with considering the 2μm long and 15μm wide plate undercut significantly reduces the error between the simulated value and the actual measured value. It is concluded that the undercut should be carefully considered in the design of the high frequency resonator and mixer. In short, the findings of this paper provide some reference for NEMS piezoresistive effect measurement and piezoresistive pick-up.

Table 2. The resonant frequencies obtained by using various methods and the relative errors compared to the optical detection value.

22μm×3μm×0.2μm	FE simulation	optical detection	piezoresistive detection	FE simulation with undercut
Resonant frequency(MHz)	3.6628	2.9641	2.9780	2.7549
Relative error (%)	+23.57	0	-0.47	-7.06

Summary

In this paper, we firstly present a contrast detection method for giant piezoresistive properties of silicon nanowires by using the reference structures. This novel and effective approach investigates the influences of size effect and surface effects on piezoresistive coefficients of silicon nanowires by direct comparison of the resistivity change ratio of silicon wires with nanoscale-to-microscale width under the same stress conditions. Our characterization experiments display that piezoresistive coefficient of silicon nanowires with small width can be significantly increased comparing to that of bulk silicon of the same doped concentration, which indicates that the silicon nanowire can have high or giant piezoresistive effect. On the other hand, in order to confirm the validity of the nanowire piezoresistive pick-up proposed by us, the fundamental resonant frequency of the suspended silicon nanowire is measured and compared by the piezoresistive detection and the dynamic LDV resonance test. Meanwhile, a three-dimensional FE simulation is also carried out for the fundamental resonant frequency using ANSYS to investigate the influence of undercut arising from the wet chemical release process of the nanomechanical structure. The numerical and experimental results show that our piezoresistive detection is accurate and effective and the undercut should be carefully considered in the design of the high frequency resonator and mixer.

Acknowledgement

The project is supported by the National Natural Science Foundation of China (Nos. 61306138, 61307113, 41275042, 61307061), Natural Science Foundation of Jiangsu Province (No. BK2012460) and the Priority Academic Program Development of Jiangsu Higher Education Institutions. All the authors gratefully acknowledge their support.

References

[1] R.R.He, P.D.Yang, Giant piezoresistance effect in silicon nanowires, Nature, 1(2006)42-46.
[2] K. Reck, J. Richter, O. Hansen, E.V. Thomsen, Piezoresistive effect in top-down fabricated silicon nanowires, Proc. MEMS 2008, (2008)717-720.
[3] A. Lugstein, M. Steinmair, A. Steiger, H. Kosina, E. Bertagnolli, Anamalous piezoresistive effect in ultrastrained silicon nanowires, Nano Lett. 10(2010)3204-3208.
[4] Y.l. Yang, X.X. Li, Giant piezoresistance of p-type nano-thick silicon induced by interface electron trapping instead of 2D quantum confinement, Nanotechnology, 22(2011)015501.
[5] B.W. Soon, P. Neuzil, C.C. Wong, J. Reboud, H.H. Feng, C.K. Lee, Ultrasensitive nanowire pressure sensor makes its debut, Procedia Engineering, 5(2010)1127-1130.

[6] E. Mile, G. Jourdan, I. Bargatin, S. Labarthe, C. Marcoux, P. Andreucci, S. Hentz, C. Kharrat, E. Colinet, L. Duraffourg, In-plane nanoelectromechanical resonators based on silicon nanowire piezoresistive detection, Nanotechnology, 21(2010)165504.
[7] J.H. Zhang, X.L. Mao, Q.Q. Liu, F. Gu, M. Li, H. Liu, Y.X. Ge, Mechanical properties of silicon nanobeams with an undercut evaluated by combining thedynamic resonance test and finite element analysis, Chin. Phys. B, 21 (2012)086101.
[8] J.H. Zhang, Q.Q. Liu, Y.X. Ge, F. Gu, M. Li, X.L. Mao, H.X Cao, Extraction of interface state density and resistivity of suspended p-type silicon nanobridges, Journal of Semiconductors, 34(2013) 052002.
[9] T. Namazu, Y. Isono, T. Tanaka, Evaluation of size effect on mechanical properties of single crystal silicona by nanoscale bending test using AFM, J. Microelectromech. Syst., 9(2000)450-459.
[10] K.R. Virwani, A.P. Malshe, W.F. Schmidt, D.K. Sood, Young's modulus measurements of silicon nanostructures using a scanning probe system: a non-destructive evaluation approach,Smart. Mater. Struct., 12(2003)1028-1032.
[11] J. Richter, J. Pedersen, M. Brandbyge, O. Hansen, E.V. Thomsen, Piezoresistance in p-type silicon revisited, Journal of Applied Physics, 104(2008)023715.
[12] S. Guillon, D. Saya, L. Mazenq, S. Perisanu, P. Vincent, A. Lazarus, O. Thomas, L. Nicu, Effect of non-ideal clamping shape on the resonance frequencies of silicon nanocantilevers, Nanotechnology, 22(2011)245501.

Key Engineering Materials Vols 645-646 (2015) pp 888-895
© (2015) Trans Tech Publications, Switzerland
doi:10.4028/www.scientific.net/KEM.645-646.888

Submitted: 2015-01-06
Accepted: 2015-01-12

Application of magnetic filter technology in improving the precision of a micro attitude reference system

Guangmin Yuan[1, a], Xiaorui Cao[2,b], Yanming Zhao[1,c], Ping Wang[1],Jianbin Xie[1] and Honglong Chang[1]

[1]Key Laboratory of Micro/Nano Systems for Aerospace, Ministry of Education, Northwestern Polytechnical University, Xi'an, 710072, China

[2]China Academy of launch Vehicle Technology R&D Center, Beijing,100076,China

[a]yuangm@nwpu.edu.cn, [b]caoxr1981@163.com, [c]zhaoyanming@mail.nwpu.edu.cn

Keywords: Allan variance, Sage–Husa adaptive filter, three-component magnetic vector, magnetic filter technology, overload interference.

Abstract. A micro attitude reference system is vulnerable to overload interference. To solve this problem, a type of Kalman filter was designed on the basis of a geomagnetic technique. Allan variance analysis was used to improve the Sage–Husa adaptive filter algorithm. Attitude error and gyro drifts were used as state variables for adaptive filtering updates, and a three-component magnetic vector was used for adaptive filtering measurement updates. Experimental results show that the pitch accuracy of the attitude reference system with magnetic filter technology working in 2 g vibrations improves by 4.7 times, the roll accuracy improves by 1.5 times, and the heading accuracy improves by 5.4 times. The proposed method can effectively reduce overload interference and ensure angular accuracy.

Introduction

With the development of the MEMS technology, the application research of micro attitude reference systems based on micro inertial sensors has become an important topic in military and civil areas. At present, the MEMS gyroscope relative to fiber optic gyroscopes and laser gyro accuracy are low, zero drift and random errors exist in the course of work, and a significant integration error is produced during the attitude angular update process. These factors hinder the achievement of practical accuracy requirements. The commonly used methods for solving these problems include the following: measurement of MEMS gyros, MEMS accelerometers, and micro magnetic sensors, use of strap down inertial navigation theory and the Kalman filtering algorithm to achieve attitude angular resolve and information fusion, building of a combined attitude determination system, inhibiting the spread of attitude errors [1, 2].

References [3, 4] used accelerometer output to calculate attitude angles, magnetometer output to calculate heading, gyro output to calculate attitude matrix, discrete Kalman filtering technique to complete information fusion, and a good steady system angular precision. References [5, 6, 7] designed a discrete Kalman filter that uses attitude quaternion and gyro drift as the system status variable and acceleration of gravity and magnetic information as the system measurement variables to achieve the recursion results of estimated attitude angle information. Both methods use the accelerometer output as the Kalman measurements variables. However, the accelerometer cannot distinguish between gravitational acceleration and overload acceleration. Thus, in overload conditions, the accelerometer output will introduce significant system errors and cause system filter divergence.

In response to these conditions, an attitude algorithm based on geomagnetic filtering technologies was designed and used in the sensor information fusion of the micro attitude reference system. Experimental results show that the gyro drift, attitude angular accumulated error, and overload interference of the system are effectively suppressed.

Adaptive filtering algorithm based on Allan variance

In the application of the stochastic dynamic system, the structural parameters and statistic characteristics of noises show a large error, thus decreasing the accuracy of the standard Kalman filter and leading to filtering divergence. To improve usability, the Sage–Husa adaptive filtering algorithm is used to enable the real-time measurement of the statistic characteristic of noises while estimating the state of the system. Therefore, for systems with unknown models, the adaptive filtering algorithm is a good solution to maintain filter accuracy instead of the standard Kalman filter. The Sage–Husa adaptive filter stands out among the alternatives because of its simple principle and great real-time response [8, 9].

Sage–Husa adaptive filtering algorithm. Suppose that the state space model of the linear discrete system can be described as follows:

$$X_k = \Phi_{k/k-1} X_{k-1} + W_{k-1} \tag{1}$$

$$Z_k = H_k X_k + V_k \tag{2}$$

where X_k is the state vector of the system, Z_k is the measurement vector, $\Phi_{k/k-1}$ is the transition matrix of the state from t_{k-1} to t_k, H_k is the measurement matrix, W_k is the excitation noise sequence, and V_k is the measurement noise sequence. W_k and V_k separately represent the n-dimensional and m-dimensional Gauss white noise vector sequence ($W_k \sim WN(q_k, Q_k)$ $V_k \sim WN(r_k, R_k)$). q_k and r_k are the average value of the Gauss white noise vector sequence. q_k and r_k are the covariance matrix of the Gauss white noise vector sequence.

In cases wherein the noise parameters are unknown, the Sage–Husa adaptive filter is given by the following:

Time update formula:

$$\hat{X}_{k/k-1} = \Phi_{k/k-1} \hat{X}_{k-1} + q_{k-1} \tag{3}$$

$$P_{x,k/k-1} = \Phi_{k/k-1} P_{x,k-1} \Phi_{k/k-1}^T + Q_{k-1} \tag{4}$$

Measurement updates formula:

$$\hat{Z}_{k/k-1} = H_k \hat{X}_{k/k-1} + r_k \tag{5}$$

$$P_{z,k/k-1} = H_k P_{x,k/k-1} H_k^T + R_k \tag{6}$$

$$P_{xz,k/k-1} = P_{x,k/k-1} H_k^T \tag{7}$$

$$K_k = P_{xz,k/k-1} P_{z,k/k-1}^{-1} \tag{8}$$

$$\hat{X}_k = \hat{X}_{k/k-1} + K_k (Z_k - \hat{Z}_{k/k-1}) \tag{9}$$

$$P_{x,k} = P_{x,k/k-1} - K_k P_{z,k/k-1} K_k^T \tag{10}$$

Noise parameter estimation:

By processing the estimation of noise parameters with time-weighted average, we obtained the following iterative algorithm on the condition that systematic noise and measurement noise are stationary stochastic:

$$\hat{r}_k = (1-\frac{1}{k})\hat{r}_{k-1} + \frac{1}{k}(Z_k - H_k\hat{X}_{k/k-1}) \tag{11}$$

$$\hat{R}_k = (1-\frac{1}{k})\hat{R}_{k-1} + \frac{1}{k}(e_{z,k/k-1}e_{z,k/k-1}^T - H_k P_{x,k/k-1}H_k^T) \tag{12}$$

$$\hat{q}_{k-1} = (1-\frac{1}{k})\hat{q}_{k-2} + \frac{1}{k}(\hat{X}_k - \Phi_{k/k-1}\hat{X}_{k-1}) \tag{13}$$

$$\hat{Q}_{k-1} = (1-\frac{1}{k})\hat{Q}_{k-2} + \frac{1}{k}(K_k e_{z,k/k-1}e_{z,k/k-1}^T K_k^T + P_{x,k} - \Phi_{k/k-1}P_{x,k-1}\Phi_{k/k-1}^T) \tag{14}$$

where $e_{z,k/k-1} = Z_k - \hat{Z}_{k/k-1}$ is one step forecast error.

Sage–Husa adaptive filtering algorithm based on Allan variance. After the analysis of the Sage–Husa adaptive filtering algorithm process, we found that the instability of the filter is attributed to the connection and interaction between the mode and noise parameter estimation because the SHAKF algorithm we adopted processed both of them in the time domain [10].

$$\hat{R}_k = \left(1-\frac{1}{k-1}\right)\hat{R}_{k-1} + \frac{1}{2(k-1)}(Z_k - Z_{k-1})^2 \tag{15}$$

In this method, measurement noise and Kalman filtering are considered two mutual independence factors such that the system can improve observability and increase stability.

New Sage–Husa filter design based on three-component geomagnetic vector

Mathematical model in micro attitude reference system. System function based on serial inertial navigation system. Despite of location and speed information, a micro attitude reference system only considers the error of an attitude angle. Three attitude angle errors and three gyro drift errors constitutes the following six dimensional state equations:

$$\dot{X}(t) = F(t)X(t) + W(t) \tag{16}$$

where E, N, and U are the east, north, and up coordinates, respectively, ϕ_E, ϕ_N, and ϕ_U are the attitude errors of the system, ε_{rx}, ε_{ry}, ε_{rz} are the three axial direction gyro drifts, i.e., random walk errors and systematic noises.

Geomagnetic Filter measurement equation based on the three-component geomagnetic vector. The tight combination mode of the micro attitude calculating arithmetic based on a geomagnetic filter requires a systematic measurement equation that constitutes inertial sensor data and a three - component geomagnetic vector measured by a three-axis magnetometer. According to the information of local position and time, we obtained the calculated value $B_{igrf}^n = [B_E^n, B_N^n, B_U^n]^T$ in the navigation system with an IGRF magnetic field model. After the coordinate transforming process between the three-component geomagnetic vector ($B_m^b = [B_{mx}^b, B_{my}^b, B_{mz}^b]^T$) and an attitude matrix

$C_b^{n^*}$, the calculated value $B^{n^*}=[B_E^{n^*},B_N^{n^*},B_U^{n^*}]^T$ of the homologous magnetic intensity vector in the actual navigation coordinate system was obtained. The difference between B_{igrf}^n and B^{n^*} was considered the measurement value $Z \triangleq [B_{igrf}^n - B^{n^*}]$. If the measuring error of the magnetometer, magnetic deviation, and other random factors such as geomagnetic anomaly are ignored, the considered attitude angle error will be the only factor influenced by the measurement value. Thereafter, we obtained the relationship between the attitude matrix $C_b^{n^*}$ by the quaternion attitude calculation and the accurate attitude matrix C_b^n from the carrier coordinate to the ideal navigation coordinate.

$$C_b^n = [I_{3\times3} + (\phi\times)]C_b^{n^*} \tag{17}$$

where $(\phi\times)$ is the vector cross product matrix that constitutes an attitude error vector ($\phi=[\phi_E,\phi_N,\phi_U]^T$).
On the basis of the coordinate transformation theory, we obtain the following equations:

$$B_{igrf}^n = C_b^n B_m^b + V_1 \tag{18}$$

$$B^{n^*} = C_b^{n^*} B_m^b + V_2 \tag{19}$$

By combining Eqs. (17), (18) and (19), the following equation is derived:

$$\begin{aligned} Z &= B_{igrf}^n - B^{n^*} \\ &= [\left((-C_b^{n^*} B_m^b)\times\right) \quad 0_{3\times3}][\vec{\phi}^T \quad \varepsilon_r^T]^T + V \\ &\triangleq HX + V \end{aligned} \tag{20}$$

where H is the measurement matrix ($H=[\left((-C_b^{n^*} B_m^b)\times\right) \quad 0_{3\times3}]$) and V is the equivalent measurement noise.

Model discretization. Given that the state space model obtained by Eqs. (16) and (20) are continuous nonlinear and Sage–Husa adaptive, the Kalman filter is only suitable for a linear discrete model. Thus, a dispersion of the system function and measurement equation is needed. The discretization process focused on system function. According to the computation and filtering accuracy, the suitable approximate value of doder ($\phi_{k/k-1}$) is chosen. The filtering cycle was set to $T = t_k - t_{k-1}$. By using linear system theory [11], we can obtain the following,

$$\Phi_{k/k-1} = e^{TF(t_{k-1})} \tag{21}$$

For easy calculation, we used the Maclaurin expansion and conducted a second-order approximation.

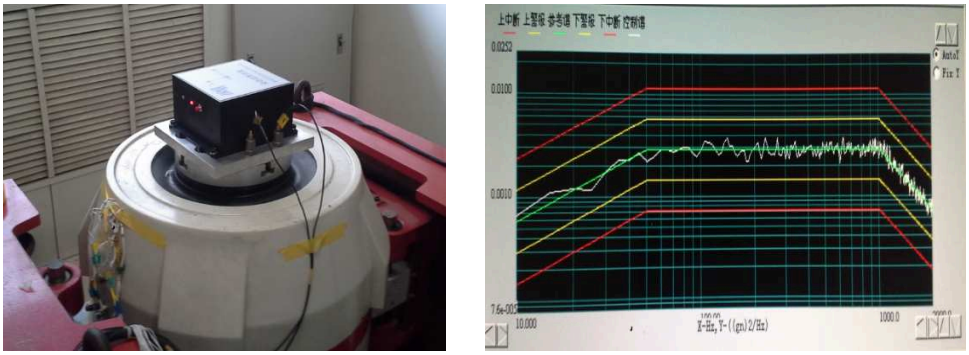
$$\Phi_{k/k-1} \approx I + TF(t_{k-1}) + \frac{T^2}{2!}F^2(t_{k-1}) \tag{22}$$

$$H_k = [\left((-\mathrm{C}_{\mathrm{b}}^{\mathrm{n}^*}\mathrm{B}_m^b)\times\right) \quad 0_{3\times3}]_{t=t_k} \tag{23}$$

In the equation, the relevant parameters of system noise and statistical parameters, namely, q_k, r_k, Q_k, and R_k, are achieved by the adaptive parameter estimation algorithm. After the discretization of the above equation, real-time optimal estimation was established by the Sage–Husa adaptive filter algorithm.

Physical simulation experiment and result analysis

Vibration test and simulation conditions. The designed attitude measurement system is installed vertically on the vibrating table (Fig. 1(a)). In the working condition, the motion parameters and vibration power under random vertical vibration with 2 g acceleration are recorded (Table 1 and Fig. 1(b)). By using the raw data, we implemented a simulation with MATLAB 7.0.



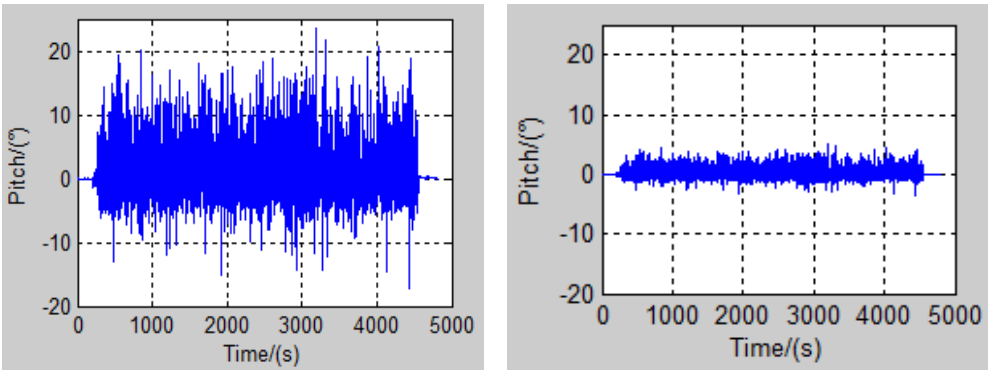
(a) (b)

Fig.1 (a) Vertical random vibration test (b) Power spectrum density waveform of the vibration test

Table.1 Random vibration parameters at 2 g

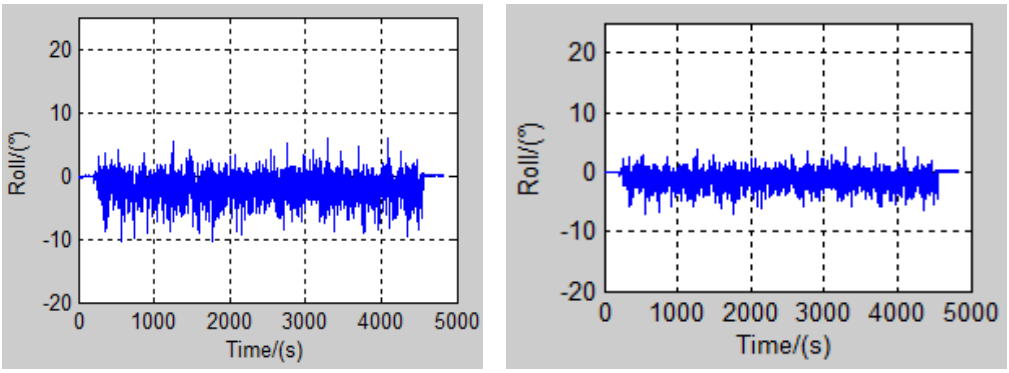
Vibration mode	Frequency range	Power spectral density
Random vibration	10–50Hz	+3 dB/oct
	50–1000Hz	$0.0007(g_n)^2$/Hz
	1000–2000Hz	−6 dB/oct

Experimental results and analysis. Two comparisons (i.e., geomagnetic filter and without geomagnetic filter) were conducted on the attitude angles obtained by the two methods. The results of the two attitude algorithms are shown in Fig. 2 to Fig. 4.



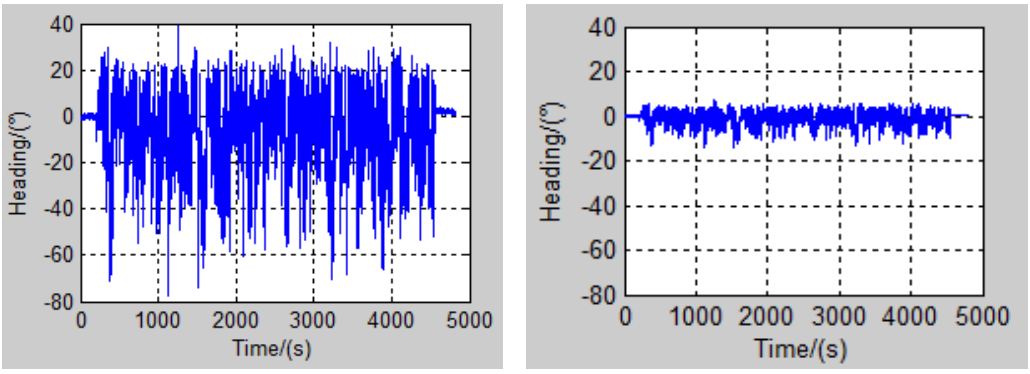
(a) (b)

Fig.2 (a) Curve of pitch without geomagnetic filter (b) Curve of pitch with geomagnetic filter



(a) (b)

Fig.3 (a) Curve of roll without geomagnetic filter (b) Curve of roll with geomagnetic filter



(a) (b)

Fig.4 (a) Curve of heading without geomagnetic filter (b) Curve of heading with geomagnetic filter

Table.2 Comparison of attitude angle error

Algorithm	Error pattern	$\delta\theta$	$\delta\gamma$	$\delta\psi$
Without Geomagnetic filter	MEAN	1.7722°	−1.6090°	−5.7345°
	RMS	4.3293°	2.3319°	17.3036°
	MAX	22.7554°	10.6351°	75.4351°
With Geomagnetic filter	MEAN	0.3558°	−1.0527°	−1.0360°
	RMS	0.9211°	1.5543°	3.2044°
	MAX	5.0624°	6.9540°	14.3244°
Multiple improved		4.7	1.5	5.4

$\delta\theta$, $\delta\gamma$, and $\delta\psi$ are the attitude errors of pitch, roll, and heading, respectively. EAN, RMS, and MAX stand for the mean value, virtual angle, and maximum value of the error parameters.

With an acceleration of 2 g, the system operates erratically (reflected by the large fluctuation bandwidth) because the attitude calculation process lacks the geomagnetic filter technology. The corresponding errors of pitch, roll, and heading are 4.3293°, 2.3319°, and 17.3036°. On the contrary, with magnetic filter technology, the attitude angle error significantly improved to 0.9211°, 1.5543°, and 3.2044° and increased 4.7, 1.5 and 5.4 times.

Conclusion

Aiming at the high precision of micro attitude reference systems in an overload situation, this study designed a new attitude algorithm. The proposed method took advantage of three-component geomagnetic measurements and corrections with adaptive filtering to achieve real-time attitude measurements. This method is valuable for the attitude reference system algorithm design under overload conditions.

Acknowledgments

This research is financially supported by the National Natural Science Foundation of China (Grant NO.51405388), the 111 Preject (Grant No.B13044), and NPU Foundation for Fundamental Research (Grant No. 3102014JCS05001).

References

[1] ZeMin Li, FengYang Duan, ZanPing Li. Design of digital attitude heading reference system based on MEMS sensor. Transducer and Microsystem Technologies.2012,6,pp.94-100.

[2] YuTao Zhai, Qiang Wei, XiaoHao Wang, ZhaoYing Zhou. Micro Attitude Determination System Based on MEMS Inertial Sensors. Nanotechnology and Precision Engineering. 2009,4, pp. 375-379.

[3] XUE Lang, LI Tian-zhi, LI Xiao-ying, CHANG Hong-long. Study of Micro Attitude Determination System Based on MEMS Sensors. Chinese journal of sensors and actuators. 2008, 3, pp. 457-460.

[4] Fang Wang, ShaoHua Zhu, HongJie Lei, Algorithm design of digital strapdown attitude and head reference system based on Kalman filter.2008, 2, pp.208-211.

[5] WEI Ping, HAN Bo, LI Ping. The Design and Realization of AHRS Based S3C44BOX.Mechanical and Electrical Engineering Magazine.2006,.4,pp.17-20.

[6] Du Yaling, Liu Jianye, Li Rongbing, Lai Jizhou. Strapdown Inertia Attitude Heading Reference System Based on DSP. Chinese Journal of Scientific Instrument. 2005,S1,pp.365-376.

[7] Liang Jianhong, Tian Weicheng, Wang Tianmiao. Design of AHRS Based on ARM and Low-cost MEMS Devices. Microcontrollers & Embedded Systems. 2012,5,pp.1-4.

[8] Sage A P, Husa G W. Adaptive Filtering with Unknown Prior Statistics. Proceedings of Joint Automatic Control Conference. Boulder Colorado,1969,pp.760-769.

[9] Qin Longyuan, Zhang Hongyue, Wang Shuhua. Kalman filter and the principle of integrated navigation.Northwestern Polytechnical University : Xi'an, China, 2012.pp.130-134.

[10] Yan Gongmin, Li Sihai, Qin Yongyuan. Test and data analysis of inertial instrument. National Defence Industry : Beijing ,China,2012.pp.245-248.

[11] Callier F M and Desoer C A. Linear system theory. Springer-Verlag: New York, USA. 1991. pp. 85-97.

Key Engineering Materials Vols 645-646 (2015) pp 896-899
© (2015) Trans Tech Publications, Switzerland
doi:10.4028/www.scientific.net/KEM.645-646.896

Submitted: 2014-11-11
Accepted: 2014-12-23

Intelligent Logistics Monitoring Microsystem Based on STM32

Wang Feng[1, a], Lou Wenzhong[2, b], Guo Mingru[3, c] Lu Yufei[4,d]

[1]National Key Laboratory of Electro-mechanics Engineering and Control, School of Mechanical-electronic Engineering, Beijing Institute of technology, Beijing, China, 100081

[a]beiliwangfeng@126.com(corresponding author), [b]louwz@bit.edu.cn ,
[c]jiaoluo@bit.edu.cn,[d]wslyf66@163.com

Keywords: acceleration; temperature/humidity; miniaturization; low power consumption; STM32;

Abstract.A intelligent logistics monitoring microsystem has been designed based on STM32F103T8, which is high ability, low power consumption and low cost. The radio frequency (RF) chip CC1101, the acceleration sensor BMA280 and the temperature and humidity sensor HTU21D are selected to acquire the corresponding data for the intelligent logistics microsystem, which are ultra-low power consumption and ultra-small size. Moreover, in order to further reduce power consumption, the interrupt mode is adopted in the data acquisition module and the sleep mode is used in the MCU module in the software control. On the other hand, in order to further optimize the performance of miniaturization, the SWD (Serial Wire Debug) protocol is used. Meanwhile, the system will alarm the transportation officer once the acquired data met or exceed the threshold, which will help him to take corresponding measures timely, thus reducing the risk of occurrence effectively.

Introduction

Logistics is the process cargo flows from the supply to the consumer, which consists of warehousing, transportation, loading, unloading, handling, carrying, packaging, processing, distribution and information. Among them, transportation occupies a crucial position. A lot of efforts has spared to study the intelligent logistics monitoring microsystem[1][2], however, the performance of miniaturization and low power consumption is not that satisfactory. Therefore, In order to further optimize the performance of miniaturization and low power consumption , the intelligent logistics monitoring microsystem has been designed. As shown in Fig.1, STM32F103T8, the CC1101 chip, the BMA280 and the HTU21D are integrated in the microsystem, which are ultra-low power consumption and ultra-small size.We can predicted, the intelligent logistics monitoring microsystem will promote the development of the logistics industry .

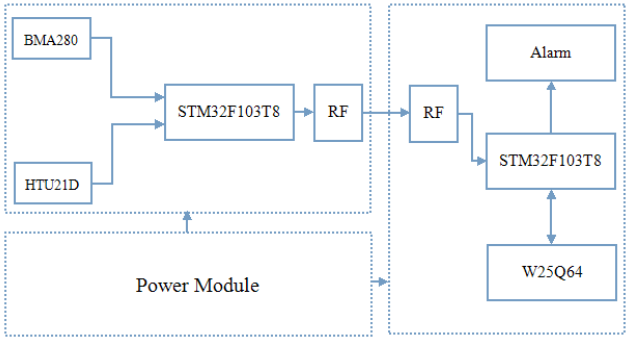


Fig.1 System architecture

MCU Module

STM32F103T8 is chosen for the microsystem's MCU(Micro Control Unit), which is high ability, low power consumption and low cost. Operating at the72 MHz frequency, the MCU allows the system to acquire and process the data rapidly, which improves the real-time character of the system. In harsh environment, the temperature ranging from –40 to +105 °C, the MCU can keep performing excellently. Moreover, a comprehensive set of power-saving modes enable the system to work in a low power mode. Because the MCU consumes the most power, if we want to reduce the system's consumption, we have to reduce the MCU's consumption. Therefore, in the experiment, the sleep mode was applied for the MCU. In sleep mode, only the Cortex-M3 core is stopped and All peripherals continue operating. The sleep mode is entered when receiving the WFE (Wait for Event) or WFI (Wait For Interrupt) instructions. In the experiment, the WFI mode is chosen. If the WFI instruction is used to enter Sleep mode, any peripheral interrupt acknowledged by the NVIC(nested vectored interrupt controller) can wake up the Cortex-M3 core from Sleep mode. In the experiment, when the acquired data met or exceed the threshold, the CC1101 or the acceleration sensor BMA280 will generate the interrupt signal to wake up the MCU, which will highly reduce power consumption. Meanwhile, the MCU will alarm the transportation officer timely. The MCU's application circuit is shown in Fig.2.

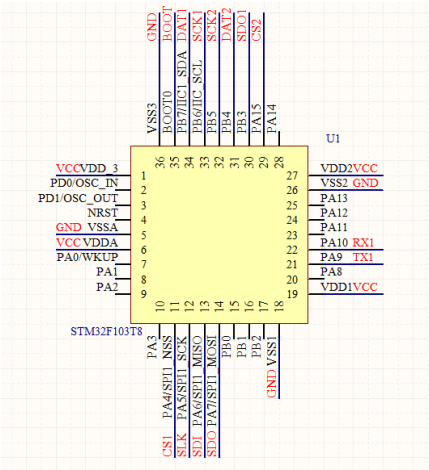


Fig.2 STM32 application circuit

RF Module

Working at 433MHz, the CC1101 chip is a low-cost transceiver designed for very low-power wireless applications[3][4]. The chip supports for sync word detection, address check, flexible packet length, and automatic CRC (Cyclic Redundancy Check) handling. Integrated with a highly configurable modem, the RF transceiver is very small,which helps to further optimize the performance of miniaturization.In the experiment, the RF mode receives and transmits the data acquired by the acceleration sensor BMA280 and the temperature and humidity sensor HTU21D.The data transmission rate of the ship can reach 500kbps and the rate can be flexibly programmed, which improves the real-time character of the system. On the other hand, because of the CRC coding ,the data accuracy can be ensured[5]. Above all, the GDO0 pin can be configured in many modes. In the experiment, the GDO0 pin is configured to set when sync word has been sent/received, and de-asserts at the end of the packet, thus producing a interrupt signal to wake up the MCU, which helps to reduce the consumption of the system.

Acceleration acquisition Module

The acceleration sensor BMA280 has a ultra-small LGA package (footprint 2mm x 2mm, height 0.95mm),and its total supply current in normal mode has reduced to 130uA. Moreover,the BMA280 has six different power modes. In the experiment, low-power mode 2 was selected, in which register access is available at any time and the device is switching between the wake-up state and the sleep state periodically. Above all, the BMA280 has two interrupt pins which can be configured to wake up the MCU easily. Therefore, the power consumption can be reduced in the reasonable range.

The BMA280 provides two serial digital interface protocols for communication:SPI(Serial Peripheral Interface) and Inter-Integrated Circuit IIC(Inter-Integrated Circuit),In the experiment, the SPI protocols is selected, and SPI operates in the standard 4-wire configuration. Its application circuit is shown in Fig.3. The BMA280 allows measurements of acceleration in three perpendicular axes, which can reflect the corresponding tilt in the three perpendicular axes. Once the data acquired met or exceeded the threshold, the BMA280 will produce a interrupt signal to wake up the MCU and the RF module will transmit the data to the MCU and the MCU will alarm the transportation officer timely.

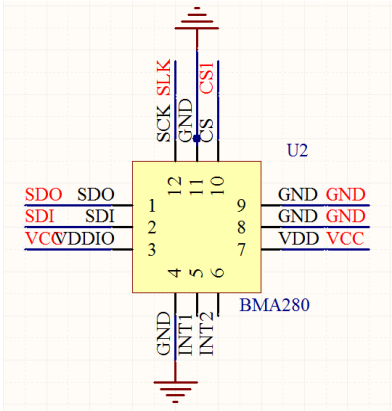


Fig.3 BMA280 application circuit

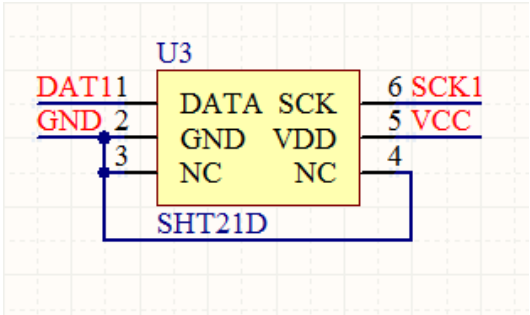


Fig.4 HTU21D application circuit

Temperature and Humidity Acquisition Module

Measuring temperature and humidity simultaneously, the HTU21D has small DFN package(footprint 3mm x 3mm, height1mm) ,which is highly suited for high performance and low cost applications with tight space limitation, and the current consumption has reduced to 450uA in measuring mode.This sensor provides signals in digital in the format of IIC protocol for communication,which makes the control relatively simple and accurate. Its application circuit is shown in Fig.4.

In the experiment, the HTU21D provides real-time monitoring of the temperature and humidity for the microsystem, Once the data acquired met or exceeded the threshold, the data will be transmitted to the MCU by the RF module and the MCU will alarm the transportation officer timely.

SWD Module

In the convenient case, the JTAG mode was adopted. However, the JTAG will occupy as many as 20 pins and the JTAG device has to used, which is much wasteful in the pin and volume aspect. Therefore, in the experiment, the SWD(serial wire Debug) is adopted instead of JTAG. The SWD only occupies 2 pins of the MCU, the SWDIO pin and the SWCLK pin. Meanwhile, the SWD provides equivalent performance. In a word, the SWD mode has further optimized the performance of miniaturization.

Summary and Future Work

Monitoring the real-time logistics status accurately，the system has further optimized the performance of miniaturization and low power consumption, which contributes to reduce the risk of occurrence effectively. the BMA280 sensor can acquire the corresponding angle rapidly and precisely; the HTU21D sensor can reflect the temperature and humidity rapidly and accurately. The experiments prove that the system can operate well in various harsh environments in long term. We can predicted, the intelligent logistics monitoring microsystem will promote the development of the logistics industry. However, the requirement of other practical factor maybe not well considered and further research will be devoted to removing this limitation.

Acknowledgement

The research is supported by National Project (00404010601) .

References

Reference articles:

[1] Chen bo. Liu Kaihua. Hardware Design of RFID Handheld Terminal Based On STM32 [J].Microcontrollers & Embedded Systems,2012,12(4):2

[2] Zu Shaopeng. Guo Mingru. Liu Huichao. Zhang Longfei. Lou Wenzhong. Intelligent Microsystem for Monitoring Logistics of Dangerous Cargo[J]. Chinese Journal of Sensors and Actuators2012, 25(7)

[3] Zhu Yu. Yue Yong. Design and realization of CC1100 wireless server based on ARM [J]. Electronic Design Engineering2013,21(4):1

[4] Zhang Ling .Mei Junjin. Realization of Wireless Communications Based on ATmega48 and CC1100[J]. Journal of Huangshi Institute of Technology,2008,24(5):2

[5] Zheng Wei. Li Zhimin. Luo Dehan.Wireless network design and implementation of intelligent home[J].TV Technology 2013,37(21):2

Key Engineering Materials Vols 645-646 (2015) pp 900-905
© (2015) Trans Tech Publications, Switzerland
doi:10.4028/www.scientific.net/KEM.645-646.900

Submitted: 2014-10-30
Accepted: 2014-12-23

Nondestructive Microscopy Test on Damage of Waterproof Material in Underground Engineering

Qingguo Wang[1,a], Qixin Yang[1,b *], Yajun Jiang[1,c] and Juan Yang[1,d]

[1]Key Laboratory of Transportation Tunnel Engineering, Ministry of Education,
School of Civil Engineering, Southwest Jiaotong University, Chengdu 610031, China

[a]qingguow@126.com, [b]yangqixin113@163.com, [c]yajunjiang@126.com, [d]yangjuan287@126.com

Keywords: spray-on waterproof material; XRM; porosity; connectivity; failure

Abstract. The microstructure changes of acrylate spray-on waterproof material in alkaline groundwater environment were tentatively studied with X-ray microscopy (XRM), and the validity of deciding the failure of the material was explored in paper. Regarded NaOH solution with pH=12 as corrosive medium, after the immersion in the alkaline solution, spray-on waterproof material was scanned with XRM, and the structure was characterized with some indexes such as porosity and pore connectivity. The results show that when the waterproof material is immersed in alkaline solution for some time, the surface of the material becomes uneven, the overall porosity falls and the pore connectivity rises. It is feasible to study on the failure of waterproof material in underground engineering with XRM.

Introduction

With the increasing development of underground space, the durability and service life of the structures will be highlighted in the near future. Groundwater slowly penetrates the structures and causes some degree of corrosion damage to them during the service life. Waterproof material is the first barrier that resists corrosion and damage, so it is necessary that the paper sets to study on the damage and deterioration of waterproof material in groundwater environment [1]. As a new kind of polymer, compared with traditional waterproof material, acrylate spray-on waterproof material has many advantages such as no special requirements for construction environment, good adaptability, uniform mass, no joints, good durability, rapid and convenient construction, high integrity, no poison and taste, no burning, no pollution to the environment, so it has a great prospect [2–4].

For special water environment in underground engineering, it is quite difficult to study the damage and deterioration of spray-on waterproof material. Adopting conventional research methods has many defects and does not reflect the authenticity of the material. Damage research method based on computed tomography (CT) technology is a new approach. It is put forward for eliminating the defects of the existing ones. This paper conducted exploratory research on the damage and deterioration of acrylate spray-on waterproof material in alkaline water environment of underground engineering with CT.

Material and Methods

When spray-on waterproof material was immersed in alkaline solution, it was corroded. Based on the previous macroscopic experiment results, the damage and deterioration were studied with the help of CT. The basic idea was that test groups were divided based on the material being corroded or not, the samples were placed on scanning workbench of CT and scanned respectively, scan images were gained and eventually the damage laws were summarized by processing the images and analyzing the data.

Early macroscopic experiment results [5] limited pH value of alkaline solution in groundwater environment, as shown in Table 1. In the test NaOH solution with pH=12 was used to simulate alkaline water environment in underground engineering.

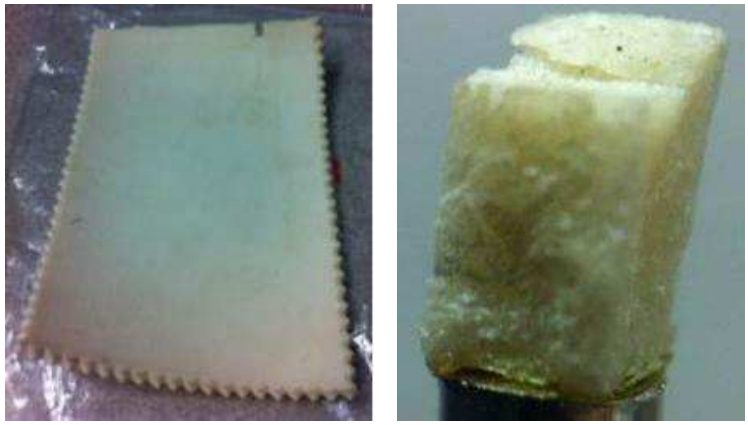
Table 1 pH value limited in groundwater environment

Corrosive medium	pH value
NaOH	12

Sample Preparation

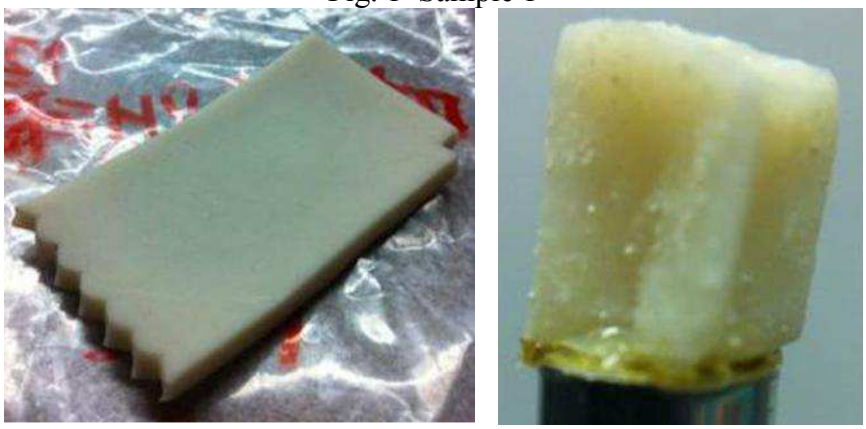
Test Material Preparation. Waterproof membrane was sprayed out by self-developed spraying machine at normal temperature and pressure after oxidizer and reducer were added to A and B primary solutions (acrylate) and they were stirred together respectively. It was about 3 mm thick.

Test Sample Preparation. The waterproof material was immersed in NaOH solution with pH=12 for 12 hours. The original and immersed materials were cut into the smaller samples whose size were 4.5 mm×4.5 mm, as shown in Fig. 1 and Fig. 2. The samples were placed on the workbench and scanned.



(a) Sample location (b) Magnified sample

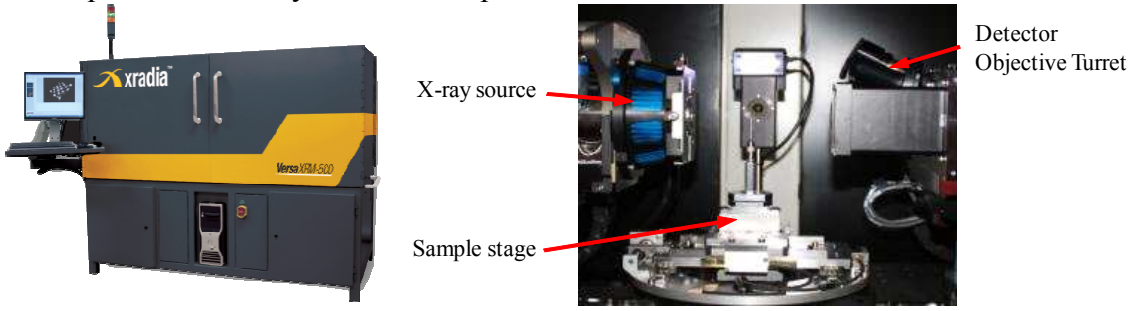
Fig. 1 Sample 1



(a) Sample location (b) Magnified sample

Fig. 2 Sample 2

Scan Equipment. It was the first attempt to research on acrylate spray-on waterproof material with the help of X-ray microscopy (XRM) that Xradia offered, as shown in Fig. 3. The equipment that has the best resolution and highest contrast, can scan the samples flexibly and provide 3D nondestructive images for quantitative analysis and a complete solution for related multi-scale research.



(a) Equipment appearance (b) Key parts

Fig. 3 Equipment used for scanning samples

Different from traditional CT system whose resolution depends on small focus and high geometric magnification, XRM adopts a two-stage amplification technology. First, the sample image is amplified geometrically as traditional CT system. Second, when X-rays reach the screen of the detectors, they are converted into visible light and the image is further amplified by visible light system.

Scan Steps. The working process of XRM mainly includes search with full field and local amplification. Firstly, the whole sample is scanned with search mode, and region of interest (ROI) is distinguished and confirmed with the moderate resolution. Secondly, a virtual sample is taken locally again and the smaller region of interest is scanned with the highest resolution. Parameters of XRM for scanning samples are shown in table 2.

Table 2 Parameters of equipment used for scanning samples

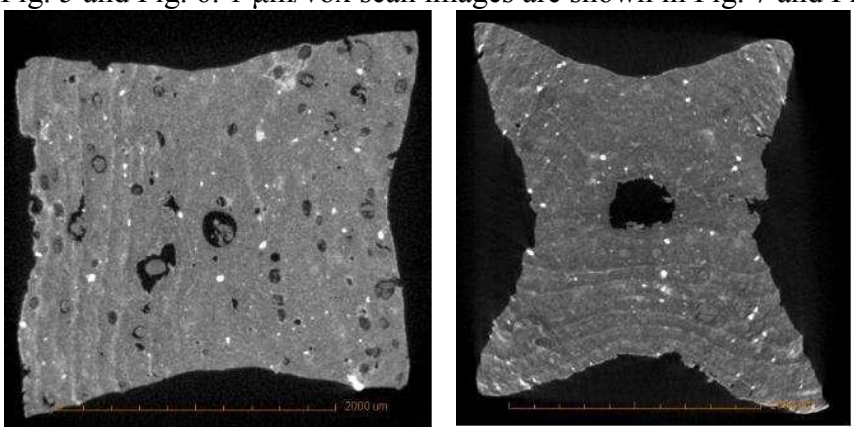
Sample ID	Voxel size (μm)	Field of view (mm)	Energy/Power (kV/w)	Total scan time (Hrs.)
1 and 2	4.5	4.5 mm×4.5 mm	40/3	1
	1	1 mm×1 mm	40/3	5.5

Image Processing. Improving image quality is often necessary to obtain the best results with image analysis. When the samples were scanned with XRM, there were CT artifacts in the images. CT artifacts referred to the difference between reconstruction data and attenuation coefficient that scanning equipment or scanned objects led to, or the case that the scanned objects did not exist but they appeared in the images [6]. CT artifacts affected the image quality seriously. In order to get good analysis data on related indexes to spray-on waterproof material, the artifacts had to be handled [7].

The main procedures for processing images were as follows. First of all, the original RGB images were converted into the gray images, and the noise was weakened or eliminated by filtering and transformation. Secondly, referring to morphology characteristics in previous SEM images and the equalized histograms, different materials and image background segmentation thresholds were gained. Thirdly, according to the thresholds, the whole images were segmented and displayed in different colors respectively. Finally, the volume (area) and percentage of each material in a solid (slice) were calculated. If one pore contacted with another, separation had to be carried out prior to the statistical analysis in order to reduce the errors.

Results and Discussion

After scan image results were processed, high quality images were obtained and then they were analyzed, as shown in Fig. 4, Fig. 5, Fig. 6, Fig. 7 and Fig. 8. Full field of view (FOV) scan images are shown in Fig. 4, Fig. 5 and Fig. 6. 1 μm/vox scan images are shown in Fig. 7 and Fig. 8.

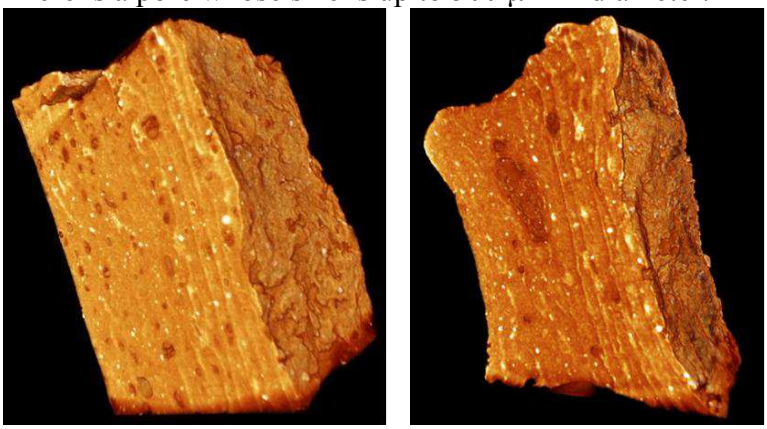


(a) Sample 1 (b) Sample 2

Fig. 4 Slices with an orthogonal direction

Fig. 4 shows slice images in an orthogonal direction. Both orthogonal slices have obvious stripes. There are many white spots which are additive particles in both images. They have higher gravity and density than other compositions. The boundary of sample 1 is the smoother. There are many small

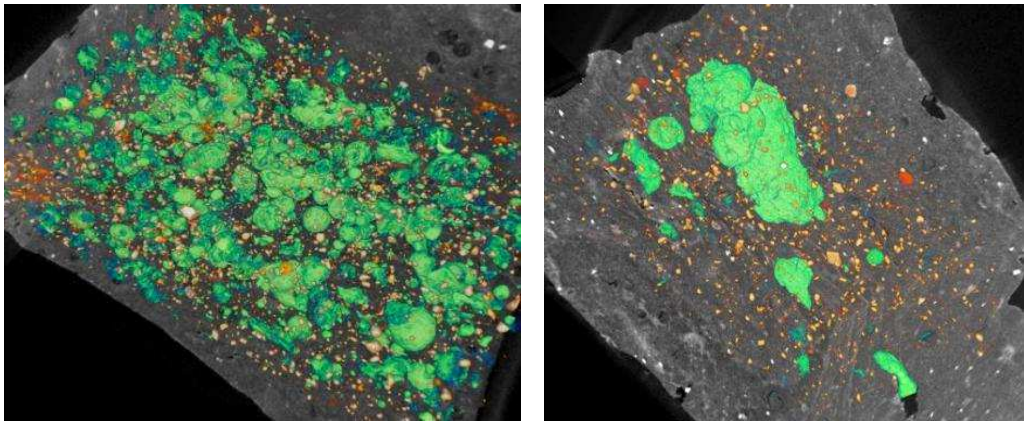
pores and the diameter of the largest pore is only 200 μm in the slice of sample1. But the boundary of sample 2 is uneven. There is a pore whose size is up to 500 μm in diameter.



(a) Sample 1 (b) Sample 2

Fig. 5 3D renderings of the scan images for samples

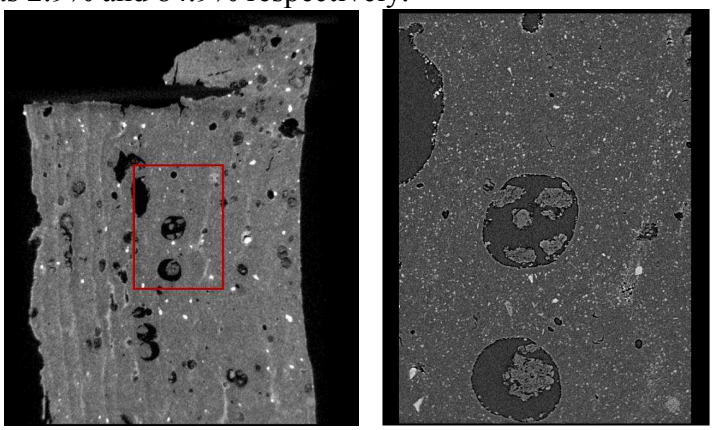
Fig. 5 shows 3D renderings of images for sample 1 and sample 2. The surface morphology of the samples before and after immersion is seen clearly. The brighter the material color is, the higher the density of the material is and the more the absorption of X-rays is. The surface of sample 1 is relatively smooth. But for sample2 the surface becomes wrinkled and uneven due to the corrosion of NaOH solution.



(a) Sample 1 (b) Sample 2

Fig. 6 Images processed with image processing software

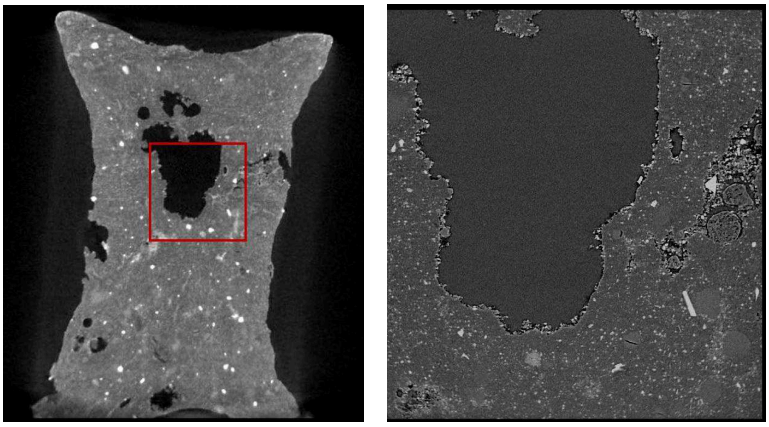
Fig. 6 shows processed images of sample 1 and sample 2. The distribution of each component in both samples is seen directly. There are a large number of small pores in sample 1. The percentage of the porosity and the pore connectivity are high as 6.6% and 6% respectively. But there are a few pores in sample 2 and the size of each single pore is the larger. The percentage of the porosity and the pore connectivity are high as 2.9% and 84.9% respectively.



(a) Full FOV scan (b) 1 μm/vox scan

Fig. 7 Scan images for sample 1

Fig. 7 (a) shows an orthogonal slice image with full FOV of sample 1, Fig. 7 (b) shows zoomed-in view with 1μm/vox of the red box area in Fig. 7 (a). Material structure in the region can be seen from the image with 1μm/vox. No pores basically exist anywhere except for three pores in the upper left corner and the middle. But there are many white additive particles. Their density is high and they are distributed throughout the region. The length of the pore in the upper left corner is about 530 μm. The diameter of the two pores in the middle is both nearly 320 μm and the two pores are partly filled with waterproof material.



(a) Full FOV scan (b) 1μm/vox scan

Fig. 8 Scan images for sample 2

Fig. 8 (a) shows an orthogonal slice image with full FOV of sample 2, Fig. 8 (b) shows zoomed-in view with 1μm/vox of the red box area in Fig. 8 (a). Material structure in the region can be seen from the image with 1μm/vox. There is a very large pore whose size is more than 1200 μm in the middle. There is a weak zone that slants to the upper right in the middle of the right boundary. The weak zone is about 640 μm long in the region.

Through the above analysis, when spray-on waterproof material is immersed in NaOH solution for some time, the sample surface becomes uneven on the whole. Many small pores join together, a small number of large pores form, the porosity of the sample falls and the pore connectivity rises. If the size of the largest pore exceeds a limited value, water molecules will go through waterproof membrane and waterproof material will lose its effectiveness.

Conclusions

The influence on spray-on waterproof material damage that alkaline medium had in groundwater environment was briefly analyzed with XRM.

By using XRM which had the high contrast and best resolution, waterproof material samples were scanned with full FOV and high quality images were obtained. It was easy to identify various structural features in the samples.

After acrylate spray-on waterproof material is immersed, the surface of the material becomes uneven, the overall porosity falls and the pore connectivity rises.

Based on high quality images, 2D or 3D reconstructed models can be obtained with image processing software. The reconstruction results can be imported into numerical computational software and relevant analyses can be carried on. More reasonable calculations can be acquired.

The exploratory experiment verifies that it is feasible to study on the damage of waterproof material in underground engineering with XRM. It is of great significance and can provide microscopic study in the field of waterproof material damage with the reference on methods and tools later.

Acknowledgments

The research was supported by the National Natural Science Foundation of China (Grant No. 51178401, 51108385) and the State Key Development Program for Basic Research of China (973

Project) (Grant No. 2010CB732105). The authors are extremely grateful to the Xradia, Inc. in the United States for the sample test work.

References

[1] Y. Yuan, X. Jiang, C.F. Lee, Tunnel waterproofing practices in China, Tunnelling and Underground Space Technology. 15 (2000) 227-233

[2] O.B. K, Radical approach to waterproofing using spray applied membranes, Concrete. 38 (2004) 45-46

[3] Q.X. Yang, D.M. Liu, C.Y. Sheng, et al, Shotmembrane waterproofing technology for tunnels and underground engineering, Journal of the China Railway Society. 24 (2002) 83-88

[4] Q.X. Yang, B.Y. Chang, D.M. Liu, Experimental research on waterproof performance damage of waterproof membrane under the mechanical circumstance in tunnel, Journal of Building Materials. 13 (2010) 487-491

[5] Q.X. Yang, C.Y. Sheng, X.F. Zhang, Influence of Corrosive environment on the performance and failure of acrylate spray-applied waterproof membrane, Modern Tunnelling Technology. 45 (2008) 39-45

[6] S.S. Lai, R.M. Yang, CT image artifacts and its solution, Journal of Mathematical Medicine. 22 (2009) 206-210

[7] Q.X. Yang, P. X, S.F. Zheng, Experimental study of CT test on the failure of acrylate spray-applied waterproof layer in the groundwater environment, Science China·Technological Sciences. 53 (2010) 512-518

Key Engineering Materials Vols 645-646 (2015) pp 906-911
© (2015) Trans Tech Publications, Switzerland
doi:10.4028/www.scientific.net/KEM.645-646.906

Submitted: 2014-10-30
Accepted: 2014-12-23

A Robust Adaptive Angle Algorithm for Imaging bionic Polarization navigation Sensor

Bin Li[1, a], Le Guan[1,b] , Shiyun Li[1] , Jinkui Chu[2]， Yan Cui[2]

[1]Key Laboratory for Dalian University of Technology Precision & Non-traditional Machining of Ministry of Education, Dalian, Liaoning, CHINA

[2]Key Laboratory for Micro/Nano Technology and System of Liaoning Province, Dalian, CHINA

[a]libin@mail.dlut.edu.cn, [b]haishengtian@mail.dlut.edu.cn (corresponding author)

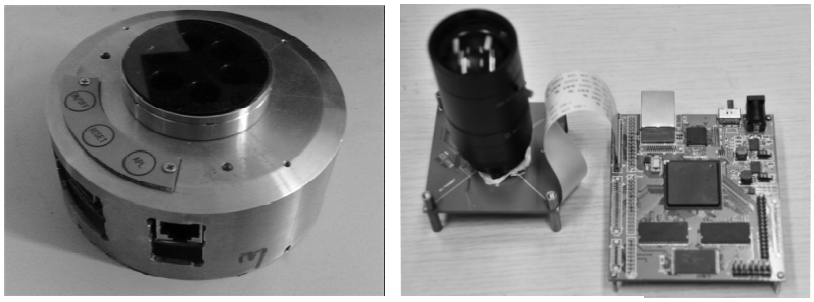
Keywords:. angle measurement, polarization navigation, nanowire polarizer, polarization imaging sensor.

Abstract. This paper presents a precise angular algorithm for the imaging bionic polarization navigation sensor. The algorithm is targeted for a imaging sensor with bilayer nanowire polarizer which is multi-orientated of 0°, 60°, 120° and 90°, 150°, 210°. The algorithm is considered to extract intensity values of pixels in homogeneous regions, eliminate noise contained in image and compensate errors occured in the fabricaiton process of nanowire polarization filters. And the occlusion problem has to be compensated by neighboring pixels. The algorithm considered in this paper is able to solve overdetermined system of linear equations, and give a set of least square solutions of the Stokes parameters and the angle of polarization as output. The performance of the algorithm along with the experimental results of the angle measurement are also presented. Based on the comparison results, the algorithm achieves a best performance for the angle of polarization.

Introduction

Modern biologists found that ants, beetles and other insects can use its polarization vision (a visual organization, organ or nervous system, which is extremely sensitive to the pattern of polarized sky light) to analyze a relatively stable polarization map in the sky for the direction of travel [1]. This celestial compass based on polarized sky light is not affected by the electromagnetic interference, and its error is not accumulated over time.

Combined with nanofabrication technologies and techniques, the bionic micro-nano optical navigation sensor is an important research field of bionic navigation. In preliminary work, our group has designed two kinds of the sensor, polarization multichannel sensor and CMOS polarization imaging sensor [2,3], as shown in Fig. 1. While the polarization imaging sensor is capable of collecting polarization information in the scattering skylight, on this basis, giving the angle of polarization as output, and have properties of highly real time and good robustness.



(a) (b)

Fig. 1. Polarization multichannel sensor (a) and CMOS polarization imaging sensor (b)

The real-time requires the sensor selects an efficient digital signal processor (DSP). The robustness requires the algorithm exclude the interference and give an accurate output. But traditional algorithms of computing angle just consider the intensity value of the filtered light wave with the

direction of 0°, 45°, 90° and 135° polarization filter, but taking no account of the imaging error caused by discrete pulse, salt and pepper noise, and difference of filter transmittance etc [4]. Actually these influence factors will affect the accuracy.

A successful candidate for a algorithm must satisfy four basic criteria. First, the algorithm must be able to extract intensity values of pixels in homogeneous regions as to reduce influence of defect position of filters. Second, the algorithm has to eliminate noise contained in image. Thirdly, the ratio of light transmittance of distinct polarization filters has to be normalized in order to be able to eliminate errors occured in the fabricaiton process of nanowire polarization filters. Finally, the occlusion problem has to be compensated by neighboring pixels. If a filtered light wave is blocked from a pixel, the polarization information is potentially lost.

We sought a algorithm for the polarization imaging sensor that would satisfy the four criteria mentioned above. We hypothesized that high accuracy of the extracted polarization information can be achieved by directly depositing a multi-orientated bi-layered nanowire polarizer on top of the imaging sensor as close as possible to the photosensitive element. In this paper, we present a algorithm,which uses the pixel intensity value of the filtered light wave with 0°, 60°, 120° and 90°, 150°, 210° polarization filter extracted in homogeneous regions.And It is designed to solve overdetermined system of linear equations, give a set of least square solutions of the Stokes parameters and output the angle of polarization.

The remainder of this paper is structured as follows. Section II describes the designed imaging sensor including six polarization sense regions with multi-orientated bi-layered nanowire polarizer. Section III illustrates problems we may encounter and strategies behind the algorithm. Section IV presents the performance of the algorithm along with the experimental results of the measured angles. Section V details the conclusions, and an outline of the future work is presented.

Polarization imaging sensor overview

The polarization imaging sensor mainly consists of DSP and a CMOS imaging sensor with a multi-orientated bi-layered nanowire polarizer. The sensor is able to simulate insects‘ small cornea, crystalline cone, and microvilli etc, which is extremely sensitive to the pattern of polarized sky light. DSP is used to control CMOS imaging sensor‘s clock, trigger image capture, extract intensity values of pixels and finally compute polarization azimuthal angle via I2C interface.

The computing of polarization information needs real-time image datas and data analysis. As the amount of information could be cumbersome, the processing speed should be high. And the computing results should be sent to the host PC in time via a serial port or network. Therefore, for the data processing module, we choose TI company's chip TMS320DM642 as the core. As its calculation speed is high and peripheral is rich.

In the image capture module, we use Aptina company's image sensor MT9M001. The MT9M001 is an SXGA-format with a 1/2-inch CMOS active-pixel digital image sensor. The active imaging pixel array of 1,280H x 1,024V [5]. It is programmable through a simple twowire serial interface. For the data storage module, we choose synchronous dynamic random access memory (SDRAM).The SDRAM‘s data storage area is divided into several banks, allowing the chip to work on several memory access commands at a time, interleaved among the separate banks. This allows higher data access rates.

For the polarizer module, we use a multi-orientated bi-layered nanowire polarizer fabricated in our previous work [6]. The bilayer nanowire polarizers with 200 nm period were fabricated on flexible plastic substrates by nanoimprint lithography, followed by aluminum deposition. The parameters of the polarizers are optimized. The position of the peak transverse magnetic (TM) transmission of the bilayer nanowire polarizer is designed to be around 500nm. This means that the sensor has the highest responsivity near the blue band which is very helpful to the polarization navigation.

Algorithm strategies

Light travels as transverse waves, i.e., waves that vibrate in a direction perpendicular to its direction of propagation. Polarization is the distribution of an electric field in a plane normal to the propagation direction, which is a phenomenon peculiar to transverse waves. In an unpolarized or a randomly polarized light, the orientation of the e-vector changes randomly.

A polarization state describes the time averaged properties of the orientation of the electric field. A common description of light wave is the intensity parametrization of the state in the form of a Stokes vector.

The first Stokes parameter *I* describes the total intensity of the incoming light wave; the second Stokes parameter *Q* describes the intensity value of the 0° orientation component, and the third Stokes parameter *U* describes the intensity value of the 45° orientation component. The fourth Stokes parameter *V* deals with ircularly polarized component.

The polarization state altered by the polarizer can be represented by the MULLER matrix [7]. From the image, we get the intensity value, i.e., the first Stokes parameter *I'* directly. Hence, we just focus on the first line of the matrix:

$$I'(\psi) = \frac{1}{2} K(I + Q\cos 2\psi + U\sin 2\psi) . \quad (1)$$

Extraction of the polarization information from the image means actually computing the first three Stokes parameters *I, Q, U.*

Extracting pixel values. The nanowire polarizer is composed of 0°, 60°, 120° and 90°, 150°, 210° orientated filters, are shown in Figure 2. The left and right distinct filters are offset by 60 degrees. The up and down distinct filters offset by 90 degrees. During the fabrication of the polarizer, restricted by the environment and the operation, some regions would have defects. While imaging, black pixels would occur, and computing results would be influenced. Therefore, we select pixels in homogeneous regions for extracting intensity values.



Fig. 2. The image of nanowire polarizerwhich the orientations are, correspondingly, 0°, 90°, 60°, 150°, 120° and 210°

Image filtering. Sometimes the image may be polluted by the pulse, salt and pepper noise, etc. As an indispensable image preprocessing operation, image filtering is able to reduce noise contained in the target image, and meanwhile preserve details of the image [8]. It helps to improve the validity and reliability of the flowing computing. The median filter is a nonlinear digital filtering technique, often used to remove noise. The main idea of the median filter is to run through the image pixel by pixel, replacing each pixel with the median of neighboring pixels, as described by Eq. 2:

$$Median(O_1, O_2, O_3, O_4, O_5) = \max(\min(O_1, O_2, O_3), \min(O_1, O_2, O_4), ...) . \quad (2)$$

Transmittance normalizing. Influenced by the fabrication parameters, the aperture size,and the incoming light intensity, the light transmittance of distinct filters varies. Therefore, before computing the angle, the ratio of the transmittance has to be revised to make intensity values normalized. The ratios are computed as shown in the linear equations:

$$\begin{bmatrix} 2I_{11} & -I_{12} & -I_{13} & 2I_{14} & -I_{15} & -I_{16} \\ 0 & I_{12} & -I_{13} & 0 & I_{15} & -I_{16} \\ 2I_{21} & -I_{22} & -I_{23} & 2I_{24} & -I_{25} & -I_{26} \\ 0 & I_{22} & -I_{23} & 0 & I_{25} & -I_{26} \\ 2I_{31} & -I_{32} & -I_{33} & 2I_{34} & -I_{35} & -I_{36} \end{bmatrix} * \begin{bmatrix} k_1 \\ k_2 \\ k_3 \\ k_4 \\ k_5 \end{bmatrix} = \begin{bmatrix} I_{16} \\ I_{16} \\ I_{26} \\ I_{26} \\ I_{36} \end{bmatrix} \tag{3}$$

Where *k1, k2* are the nomarlized ratio, I_{mn} is the intensity value of *m th* filter recorded in *n th* time.

Occlusion compensation. When a light wave is blocked from the sensor, the polarization information is potentially lost. While computing the angle, this loss shuould be compensated. In this paper, we just deduce the case of odd number filters. The case of even number ones are the same.

The orientations of filters are given separately, as shown in Eq. 4:

$$\psi = 0, \frac{\pi}{2}, \frac{\pi}{3}, \frac{5\pi}{6}, \frac{2\pi}{3}, \frac{7\pi}{6}. \tag{4}$$

This is then fed into Eq. 1. And the Eq.5, 6, 7 are obtained.

$$I = I_{2m-1} + I_{2m} (m = 1,2,3). \tag{5}$$

$$\Delta = I_{2n''-1} - I_{2n'} (n \neq n' \neq n''). \tag{6}$$

$$I_{2n-1} = \frac{I}{2} - \Delta (n = 1,2,3). \tag{7}$$

Where *I* is the intensity value. Using Eq. 7, we can estimate the intensity value of the blocked odd filter.

Least square method to compute *I, Q, U*. The intensity value is determined by the first three Stokes parameters *I, Q, U* and the orientation of the filter ψ:

$$I_n = f(I, Q, U, \psi). \tag{8}$$

Where *I, Q, U* are the unknown quantities.There are six distinct filters, and we get a system of six linear equations:

To solve the euqations, we make the value of $\sum_{j=1}^{6} (I_j - \sum_{i=1}^{3} a_{ij} x_i)^2$ minimum. The system is modulated as follows:

$$A * \begin{bmatrix} I \\ Q \\ U \end{bmatrix} = \begin{bmatrix} I_1 \\ I_2 \\ I_3 \\ I_4 \\ I_5 \\ I_6 \end{bmatrix} \Rightarrow A^T A * \begin{bmatrix} I \\ Q \\ U \end{bmatrix} = A^T * \begin{bmatrix} I_1 \\ I_2 \\ I_3 \\ I_4 \\ I_5 \\ I_6 \end{bmatrix}, A = \begin{bmatrix} \frac{1}{2} & \frac{1}{2} & 0 \\ \frac{1}{2} & -\frac{1}{2} & 0 \\ \frac{1}{2} & -\frac{1}{4} & \frac{\sqrt{3}}{4} \\ \frac{1}{2} & \frac{1}{4} & -\frac{\sqrt{3}}{4} \\ \frac{1}{2} & -\frac{1}{4} & -\frac{\sqrt{3}}{4} \\ \frac{1}{2} & \frac{1}{4} & \frac{\sqrt{3}}{4} \end{bmatrix} \tag{9}$$

Solving Eq. 9, we get the value of *I, Q, U,* and then feed the value into Eq. 10.

$$\chi = \frac{1}{2}\tan^{-1}\frac{U}{Q}. \tag{10}$$

Finally, we get the angle of polarizatio χ shown in Figure 3

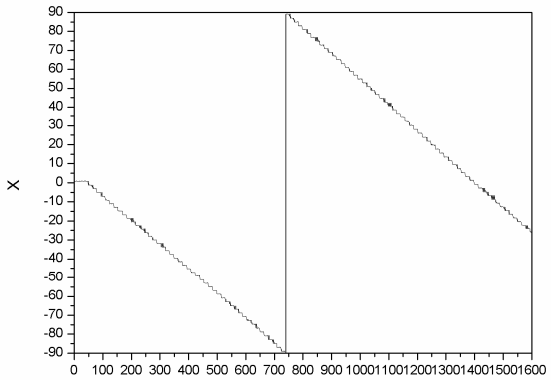


Fig. 3. Measured angle of the sensor, which was set on a rotary table that was rotating at a constant speed. And 1600 angles are record.

Noise simulation and occlusion experiment

Noise simulation. The salt and pepper noise is a form of noise often seen on images. It presents itself as sparsely occurring white and black pixels [9]. Its probability density function *p(x)* are defined as follows

$$p(x) = \begin{cases} a, x = 0 \\ b, x = N-1; a, b \in [0,1); a+b = p \in (0,1) \\ 0, else \end{cases} \tag{11}$$

In Eq. 11, *N* is the number of grayscale.

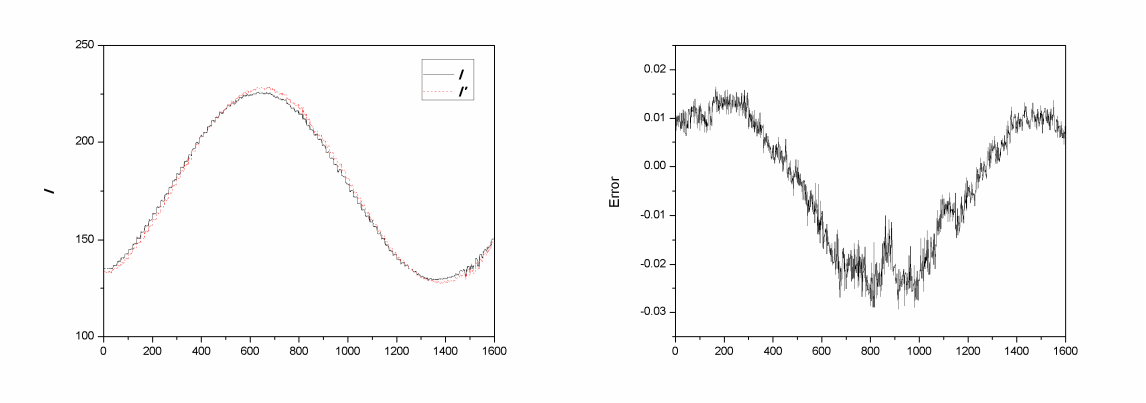
Filtering and performance. We added the salt and pepper noise into the region of the 1st filter of the target image, used the paper's algorithm and the normal algorithm separately, and compared the performance. Based on the simulation, results presented in Table 1:

Table 1. Performance Comparison of Algorithms

	The paper's algorithm	The normal algorithm
Angle [°]	45	45
Initial output [°]	45.1129	45.2028
Noised output [°]	45.1254	39.5205
Standard deviation [°]	0.0331	3.1972

The anti-interference ability of the normal algorithm is poor. When interfered, a significant change occured to the output of the angle. The noised output would deviate from the initial one. While the ability of the paper's algorithm is better. It's able to reduce the noise contained in the image. When interfered, a minor change occured. The output is much more stable and repeatable.

Occlusion experiment. We blocked the linearly polarized light from the region of the 1st filter of the target image and compare the inital measurement *I* and the estimated value *I* `. A minor error has been found in Figure 4.



(a) (b)

Fig. 4. Comparison of the inital measurement *I* and the estimated value *I'* (a) and relative error(*<0.03*) (b)

Conclusion

In this paper, we present a algorithm for the CMOS polarization imaging sensor. The algorithm computes the ratio of the filter transmittance, compensates the data loss, and extracts the polarization information contained in the image. After an series of repeated experiment on the sensor, we find the algorithm is more accurate than the normal one. When interfered, the algorithm performs better and obtains more polarization information of the skylight. And it helps to enhance the robustness of the sensor without substantial increase in computation. The algorithm can satisfy the demand of the real-time navigation task. In future work we plan to optimise its detail and make it more robust and practical.

Acknowledgement

This project is supported by National Natural Science Foundation of China (Grant No. 51305057) and National Basic Research Program of China (Grant No. 2011CB302105).

References

[1] Byrne M, Dacke M, Nordström P, et al. Visual cues used by ball-rolling dung beetles for orientation, J. Journal of Comparative Physiology A, 189.6 (2003): 411-418.
[2] Chu J, Zhao K, Zhang Q, et al. Construction and performance test of a novel polarization sensor for navigation, J. Sensors and Actuators A: Physical, 148.1 (2008):75-82
[3] Li B, Guan L, Liu Q, et al. A novel imaging bionic polarization navigation sensor system based on skylight, J. Key Engineering Materials, Tranducer and Microsystem Technologies, 8(2014): 020.
[4] Sarkar M, San Segundo Bello D, Van Hoof C, et al. Integrated polarization-analyzing CMOS image sensor for detecting the incoming light ray direction, J. Instrumentation and Measurement, IEEE Transactions on, 60.8 (2011): 2759-2767.
[5] 1/2-Inch Megapixel CMOS Digital Image Sensor on http://www.aptina.com.
[6] Wang Z, Chu J, Zhang Y, et al. Design of an integrated polarization band-pass filter, J. Proceedings of the Institution of Mechanical Engineers, Part N: Journal of Nanoengineering and Nanosystems, 227.3(2013): 120-124.
[7] Azzam R M A, Bashara N M. Ellipsometry and polarized light. North-Holland. sole distributors for the USA and Canada, Elsevier Science Publishing Co., Inc., 1987.
[8] Arias-Castro E, Donoho D L. Does median filtering truly preserve edges better than linear filtering? J. The Annals of Statistics (2009): 1172-1206.
[9] Dreyfus S E. An appraisal of some shortest-path algorithms, J. Operations research, 17.3 (1969): 395-412.

Key Engineering Materials Vols 645-646 (2015) pp 912-919
Submitted: 2014-10-24
© (2015) Trans Tech Publications, Switzerland
Accepted: 2014-11-03
doi:10.4028/www.scientific.net/KEM.645-646.912

A Nano-cantilever Bending Method for Interface Cracking in Nanoscale Materials

Xiaoyuan Wang[1,a], Yabin Yan[1,b *]

Institute of Systems Engineering, China Academy of Engineering Physics, Mianyang 621900, China

[a]xjtuwxy@gmail.com, [b]yanyabin@gmail.com

Keywords: Nanoscale, cantilever bending method, interface, cracking, delamination, thin film.

Abstract. A nano-cantilever bending method is developed to investigate the interface cracking in multilayered nanoscale materials basing on the technology of the focused ion beam (FIB) and the transmission electron microscopy (TEM). With FIB, a nano-cantilever specimen consisting of 20-nm-thick copper (Cu) layer and 500-nm-thick silicon nitride (SiN) layer on a silicon (Si) substrate is fabricated from a macroscale multi-layered material (Si/Cu/SiN) with the proposed method. By using a minute loading apparatus, the loading experiment is conducted in TEM, and the crack initiation at the edge of Cu/Si interface in different specimens is in situ observed. The critical stress fields at crack initiation are analyzed with the finite element method, and both normal and shear stresses concentrate at the region of 100 nm from the interface edge in all specimens. In addition, the normal stress is much larger than the shear one. A close observation on stress fields shows that the normal stress field at the area 20 nm – 30 nm away from interface edge produces the local criterion for crack initiation at the edge of Cu/Si interface in nanoscale components.

1. Introduction

Micro- and nano-mechanical systems and electronic devices consist of dissimilar components, of which size is on the nanometer scale. Since intrinsic bi-material interfaces are inevitably introduced into these devices, deformation mismatch between the dissimilar materials induces a stress concentration at the interface. Thus, the interface is one of the potential sites of fracture [1–4]. Since the stress concentration region is proportionally scaled down for the shrinkage of component size, the stress concentration region at the interface edge is confined to the nanoscale in advanced devices [5–7]. The strength for the interface cracking in nano-scale is important in terms of assurance of integrity and reliability.

Different from the traditional experiment methods for macroscale materials, the extremely small volume of nanoscale specimen brings a series of technical difficulties to the experimental study of nano-materials, such as the grip of specimen, applying load to interfaces inside of specimen and precisely measurement of tiny mechanical quantities. Therefore, some experimental methods have been proposed to investigate the interface cracking in multilayered thin films since 1980s [8, 9]. The typical methods include pull test [10], peeling test [11], bulge test [12], scratch test [13], indentation test [14], and bending test [15]. Until now, the cracking behavior and the bonding strength of interfaces in different types of thin films have been widely studied with above experiments. However, it should be noted that only the size along thickness-direction is on nanoscale and others are still on macroscale for thin film specimen. Thus, the specimen adopted in these tests is actually a macroscale material, and the obtained interface strength can only represent the mechanical property of macro-material instead of the nano-materials. In practice, the three-dimensional geometrical sizes of components and structures in micro-systems are all on nanoscale, where the size effect and surface effect strongly make the mechanical properties of nano-materials to be significantly different from macro-materials [7, 16]. So, to precisely evaluate the interface strength of nano-materials, it is necessary to develop a suitable method for performing interface fracture experiments in nanoscale materials and to investigate the criterion for interface cracking due to the nanoscale stress concentration.

In this study, we develop a nano-cantilever method and use it to perform crack initiation experiments for the interface between 20-nm-thick copper (Cu) film and silicon (Si) substrate by using the focused ion beam (FIB) and the transmission electron microscopy (TEM).

2. Experimental procedures

2.1 Tested material

The specimen is manufactured from a multi-layered material, *i.e.* silicon/copper/silicon nitride (Si/Cu/SiN). A Si (100) wafer surface is cleaned by inverse sputtering, and then a Cu layer is deposited up to a thickness of 20 nm by radio-frequency magnetron sputtering. A SiN layer is subsequently deposited up to a thickness of 500 nm with the same method without breaking the vacuum. This study focuses on the interface between Cu and Si, which is referred as the Cu/Si interface below.

2.2 Tested material

Figure 1 shows the schematic illustration of the nano-cantilever specimen used to investigate the cracking at the Cu/Si interface edge in this study. As shown in Fig. 1, the cantilever specimen is consisted of a 20-nm-thick Cu layer, a 500-nm-thick SiN layer and passivation gold (Au) and carbon (C) layers deposited during the subsequent FIB fabrication processes. A minute mechanical loading apparatus is used to apply a force and the behavior of interface fracture is *in situ* observed by TEM. The load is applied to the SiN layer with a diamond loading tip to apply stress to the Cu/Si interface by a bending moment. Three specimens with different size are prepared and their scales are summarized in the table 1.

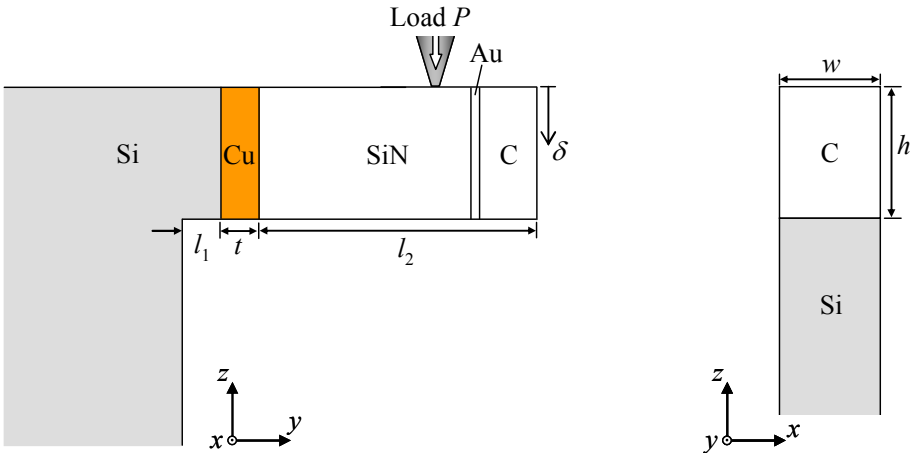


Fig.1 Schematic illustration of a nano-cantilever specimen and its loading scheme

Table 1 Dimensions of nano-cantilever specimens

Specimen	t [nm]	l_1 [nm]	l_2 [nm]	w [nm]	h [nm]
I1	20	220	715	434	250
I2	20	84	480	287	415
I3	20	120	480	220	308

Figure 2 schematically illustrates the fabrication procedure for the nano-cantilever specimen. Prior to the sample fabrication, passivation layers of Au and C are deposited on the SiN layer to prevent the specimen from damage during processing. A cubic block with the side length of about 10 μm is cut from the multi-layered material by a focused ion beam (FIB) (Hitachi, FB2200) (Fig. 2(a)), and then it is picked up by attaching a manipulator of a micro-sampling system embedded in the FIB (Fig. 2(b)) with the block by carbon deposition. After gluing the block to the flat top of an Au wire

with a diameter of 0.25 mm (Fig. 2(c)) by using carbon deposition. Finally, the cantilever part of specimen is made by the ion beam (Fig. 2(d)). During the process, the gallium (Ga) ion beam energy is set to 40 kV and the beam current is altered between 5 pA and 5 nA depending on the fabrication precision.

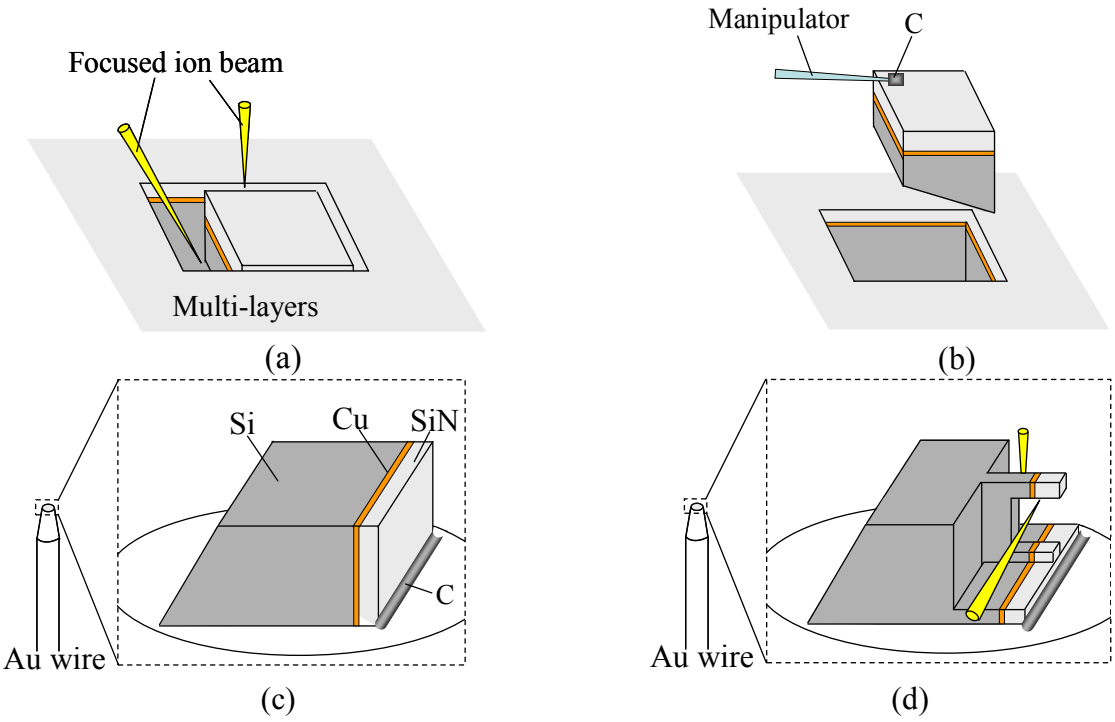


Fig. 2 Schematic illustrations of the procedure for preparing nano-cantilever specimen

Figure 3 shows TEM micrographs of a nano-cantilever specimen. It shows that there is no defect or damage on the Cu/SiN interface edge before the experiment.

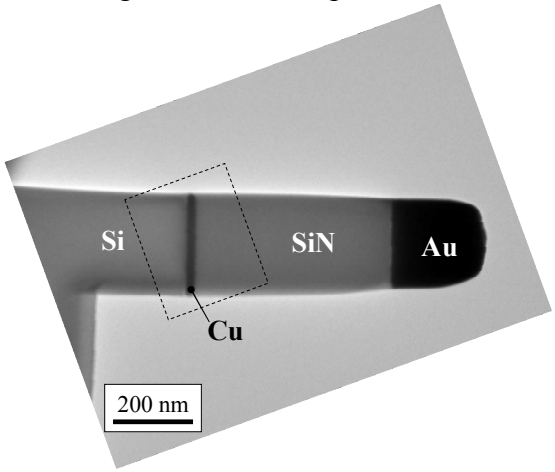


Fig. 3 TEM image of a nano-cantilever specimen (side view)

2.3 Mechanical loading apparatus

The minute mechanical loading apparatus (Nanofactory Instruments AB, SA2000N) used in this study is shown in Fig.4. The apparatus consisting of a movable sample stage and a diamond loading tip with a load sensor is built into a transmission electron microscopy (TEM) holder. The gold wire with a nano-cantilever specimen mounted on top is attached to the sample stage, which is actuated three-dimensionally by a piezoelectric actuator. The load resolution of the sensor is 0.1 μN and the alignment resolution of the piezoelectric actuator in each direction is approximately 1 nm.

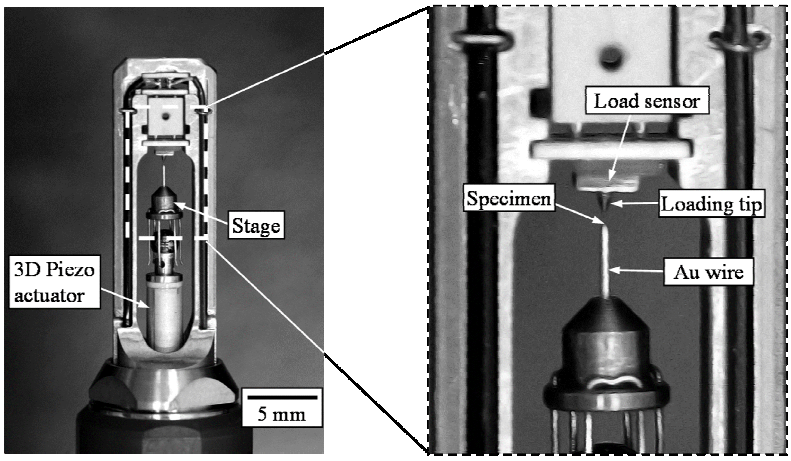


Fig. 4 Mechanical loading apparatus used in the interface cracking experiments of nanoscale specimen

3. Numerical analysis

To obtain the stress distribution along the Cu/Si interface at crack initiation, elasto-plastic analysis is performed by the finite element method (FEM) by using the commercial software, ABAQUS. Figure 5 shows typical finite element meshes for specimen I1. The configuration of the simulation model is reconstructed on the basis of SEM and TEM micrographs of specimens. The area near the free edge of the Cu/Si interface, where the stress concentration is expected, is carefully divided into fine meshes. A perfect constraint condition is imposed on the back and bottom ends.

Since the Si substrate is a single crystal, it was treated as an orthotropic elastic material. The Young's modulus of the SiN layer which affects the stress distribution along the Cu/Si interface is measured by an indentation test. Table 2 lists the elastic constants of the component materials.

Because the yield stress of the Cu layer is much lower than the Si substrate (σ_y > 3.4 GPa [17]) and the SiN layer (σ_y > 8.4 GPa [18]), only the Cu layer is subjected to elasto-plastic deformation during these experiments. The constitutive relation has been experimentally obtained in a previous study [19], and is given by:

$$\sigma = \begin{cases} 129000\varepsilon & \text{for } \sigma \le 765 \text{ MPa} \\ 3316\varepsilon^{0.332} & \text{for } \sigma \ge 765 \text{ MPa} \end{cases}, \tag{1}$$

where σ and ε are the von Mises stress and strain, respectively.

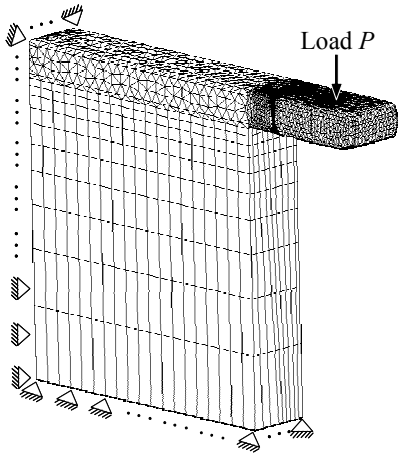


Fig. 5 Typical finite element meshes for numerical analysis of specimen I1

Table 2 Elastic constants of materials

Material	Young's modulus [GPa]		Possion's ratio
Cu	129		0.34
SiN	197		0.27
Au	78		0.44
C	400		0.30
	C_{11} [GPa]	C_{12} [GPa]	C_{44} [GPa]
Si	167.4	65.23	79.57

4. Results and discussions

Figure 6 shows the loading curve (P–t) obtained for specimen I1 and TEM micrographs of the specimen at three specific loading levels (A, B, and C). As shown in Fig. 6(a), after the loading tip hits the SiN layer at point A, the applied load, P, increases monotonically up to a peak magnitude of 16.88 μN (point B), after which it abruptly decreases to zero (point C). Figure 6(b) clarifies that no crack initiation is recognized before the peak load while the specimen has an interface crack after, which indicates that the crack initiates at point B at the top edge of the Cu/Si interface and instantly propagates along the interface. A magnified image of the Cu/Si interface edge after crack initiation (at point C) indicates that no dissimilar material remains on either delaminated surface, which confirms the pure interface cracking. Similar behavior is also observed in the other two specimens. Thus, the peak load for crack initiation, P_C, is defined as the critical load, as listed in Table 2.

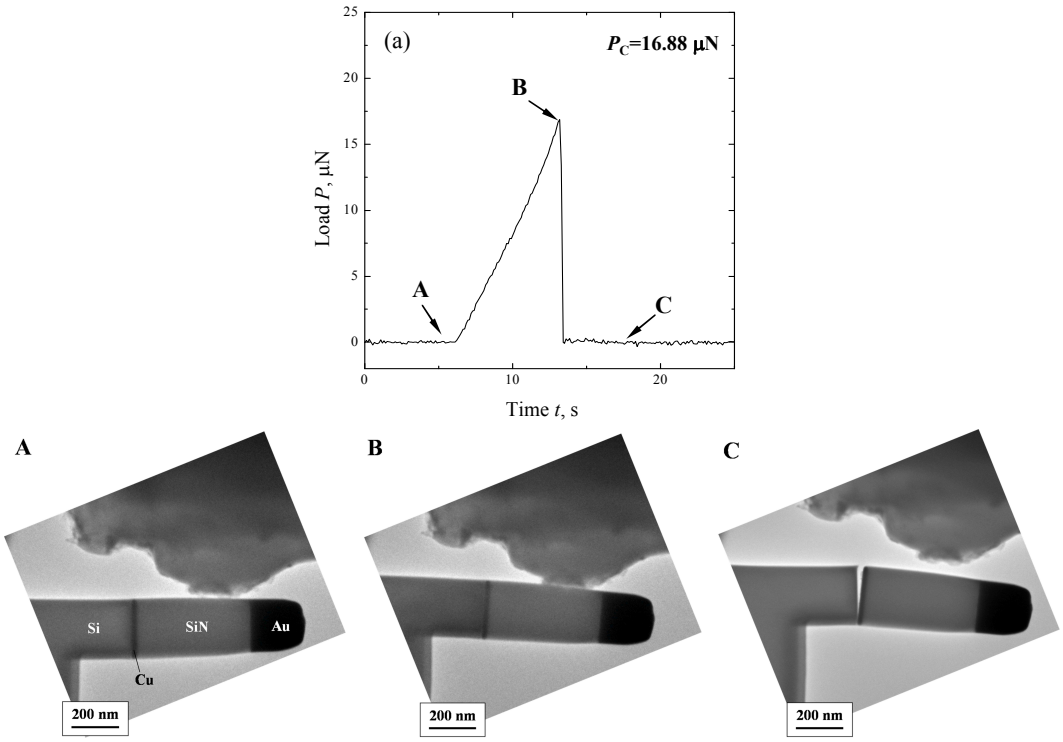
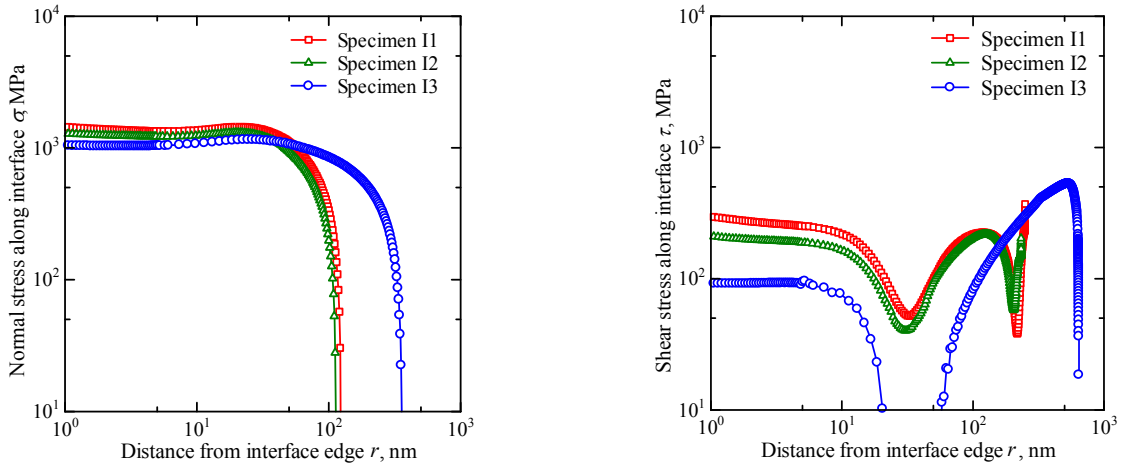


Fig. 6 (a) Load–time curve and (b) *in situ* observations of interfacial cracking of specimen I1

Table 2 Critical loads for crack initiation at interface edge

Specimen	Critical load, P_C [μN]
I1	16.88
I2	85.34
I3	10.37

Figure 7 shows the distributions of (a) normal and (b) shear stresses on the Cu/SiN interface of specimen I1-I3, respectively. Although the stresses away from the edge differ from each other, they show good consistence near the edge of Cu/Si interface, which indicates that crack initiation is governed by the concentrated stress field. The normal stress distribution near the interface edge resulted in a high stress of about 1 GPa, which is much larger than the shear one (≈300 MPa). Thus, the normal stress dominates the crack initiation at the Cu/SiN interface. In addition, the region in which the normal stress distribution agrees is 20 nm – 30 nm away from the free edge of interface, and the stress field in this region can produce local fracture via interface crack initiation.



(a) (b)

Fig. 7 Distribution of critical (a) normal stress and (b) shear stress at crack initiation at the edge of Cu/Si interface

5. Summary

In order to investigate the interface cracking due to the nanoscale stress concentration, we developed a methodology and conducted the fracture experiments using novel nano-cantilever specimens with the interface between a 20-nm-thick Cu layer and a Si substrate basing on the FIB and TEM. The results are summarized below:

(1) By using FIB, a nano-cantilever specimen was successfully fabricated from a macroscale multilayered thin film, and several specimens were prepared.

(2) With a minute mechanical loading apparatus, the load was successfully applied to the interface in nano-materials, and interface cracking experiments were conducted in TEM. The crack initiation at the edge of Cu/Si interface was in situ observed, measured and recorded.

(3) FEM analysis on the critical stress distribution along Cu/Si interface at crack initiation shows that the normal stress dominated the interface cracking, and the normal stress field in the region of 20 nm – 30 nm away from the free edge produced the local fracture via interface crack initiation.

Acknowledgement

This study was supported by the Foundation of President of China Academy of Engineering Physics (Grant No. 2014-1-097), and the Science and Technology Development Foundations of China Academy of Engineering Physics (Grant No. 2013B0302043 and No. 2013B0302044), and the National Natural Science Foundation of China (Grant No. 11302205).

References

[1] D.B. Bogy, Two edge-bonded elastic wedges of different materials and wedge angles under surface tractions, J. Appl. Mech. 38 (1971) 377–386.

[2] P.E.W. Labossiere, M.L. Dunn, Fracture initiation at three-dimensional bimaterial interface corners, J. Mech. Phys. Solids 49 (2001) 609–634.

[3] E.D. Reedy, T.R. Guess, Comparison of butt tensile strength data with interface corner stress intensity factor prediction, Int. J. Solids Strcut. 30 (1993) 2929–2936.

[4] X.J. Fan, H.B. Wang, T.B. Lim, Investigation of the underfill delamination and cracking in flip-chip modules under temperature cyclic loading, IEEE Trans. Compon. Pack. Technol. 24 (2001) 84–91.

[5] T. Kitamura, T. Shibutani, T. Ueno, Crack initiation at free edge of interface between thin films in advanced LSI, Engng. Fract. Mech. 69 (2002) 1289–1299.

[6] T. Kitamura, H. Hirakata, T. Itsuji, Effect of residual stress on delamination from interface edge between nano-films, Engng. Fract. Mech. 70 (2003) 2089–2101.

[7] T.L. Becker Jr., J.M. McNancy, R.M. Cannon, R.O. Ritchie, Limitations on the use of the mixed-mode delaminating beam test specimen: effect of the size of the region of K-dominance, Mech. Matter. 25 (1997) 291–308.

[8] S. Zhang, D. Sun, Y.Q. Fu, H.J. Du, Toughness measurement of thin films: a critical review, Surf. Coat. Technol. 198 (2005) 74—84

[9] A.A. Volinsky, N.R. Moody, W.W. Gerberich, Interfacial toughness measurements for thin films on substrates, Acta Mater. 50 (2002) 441—466

[10] M.P.K. Turunen, P. Marjamaki, M. Paajanen, J. Lahtinen, J.K. Kivilahti, Pull-off test in the assessment of adhesion at printed wiring board metallization/epoxy interface. Microelectron. Reliab. 44 (2004) 993—1007.

[11] Y.G. Wei, J.W. Hutchinson, Interface strength, work of adhesion and plasticity in the peel test, Int. J. of Fract. 93 (1998) 315 – 333.

[12] L.H. Xiao, X.P. Su, J.H. Wang, Y.C. Zhou, A novel blister test to evaluate the interface strength between nickel coating and low carbon steel substrate, Mat. Sci. Engng. A-Struct. 501 (2009) 235—241.

[13] P.A. Steinmann, Y. Tardy, H.E. Hintermann, Adhesion testing by the scratch test method: The influence of intrinsic and extrinsic parameters on the critical load, Thin Solid Films 154 (1987) 333—349.

[14] M.Y. Lu, H.T. Xie, H. Huang, Characterisation of interfacial adhesion of thin film/substrate systems using indentation-induced delamination: A focused review, Key Engng. Mater. 533 (2012) 201—222.

[15] F. Shang, T. Kitamura, H. Hirakata, I. Kanno, H. Kotera, K. Terada, Experimental and theoretical investigations of delamination at free edge of interface between piezoelectric thin films on a substrate, Int. J. Solids Struct. 42 (2005) 1729—1741.

[16] R. Dingreville, J. Qu, M. Cherkaoui, Surface free energy and its effect on the elastic behavior of nano-sized particles, wires and films, J. Mech. Phys. Solids 53 (2005) 1827–1854.

[17] W.D. Nix, Mechanical properties of thin films, Metall. Mater. Trans. 20 (1989) 2217–2245.

[18] K.S. Lee, S. Wuttiphan, X.Z. Hu, S.K. Lee, B.R. Lawn, Contact-induced transverse fractures in brittle layers on soft substrates: a study on silicon nitride bilayers, J. Am. Ceram. Soc. 81 (1998) 571–580.

[19] T. Sumigawa, T. Shishido, T. Murakami, T. Iwasaki, T. Kitamura, Evaluation on plastic deformation property of copper nano-film by nano-scale cantilever specimen, Thin solid films 518 (2010) 6040–6047.

Key Engineering Materials Vols 645-646 (2015) pp 920-925
© (2015) Trans Tech Publications, Switzerland
doi:10.4028/www.scientific.net/KEM.645-646.920

Submitted: 2014-11-01
Accepted: 2014-12-23

The displacement characteristics of piezoelectric ceramic micro actuators evaluated by laser interferometer

Wu Hong[1, a], He Long Biao[2, b *], Zhou Jing Lin[1,c], Yang Ping[2,d]

[1]Beijing University of Chemical Technology, Beijing, 100029, China

[2]National Institute of Metrology, Beijing, 100013, China

[a]wuhong_158@126.com, [b]helb@nim.ac.cn, [c]jinglinzhou@mail.buct.edu.cn, [d]yangp@nim.ac.cn

Key words: Laser interferometer; Displacement characteristic; piezoelectric coefficient d_{33}

Abstract: Understanding and measuring the displacement characteristics of piezoelectric ceramic under electric field exciting are particularly important. The piezoelectric coefficient d_{33} as the indication of its displacement characteristics, is the key parameter of its energy transformation. In this paper, the characteristics of two kinds of piezoelectric ceramics, PZT4 and PZT5 were studied by the laser interferometer measurement. The influence factors of d_{33} were studied, including the frequency and amplitude of the exciting signal, the ways of fixing, and the loading sequence. Then the measurement results of piezoelectric ceramic with laser interferometer and the quasi-static method were compared, the results showed they had consistence and the analysis of the piezoelectric coefficient d_{33} measurement by converse piezoelectric effect and by piezoelectric effect was discussed.

Introduction

The micro actuator is one of the key parts of Micro electromechanical systems (MEMS) [1,2]. The operating range, efficiency, and reliability of actuators determine the performance of the total system. Piezoelectric ceramic can provide high force with relatively low energy loss, now most micro actuators use it as the energy transfer material. Therefore, understanding and measuring the displacement characteristics of piezoelectric ceramic under electric field exciting are particularly important. The piezoelectric coefficient d_{33} as the indication of displacement characteristics, is the key parameter of its energy transformation. The displacement of piezoelectric ceramic under certain electric field exciting can only reach micron level even nano level. Among the micro-displacement measurement techniques, the laser interferometer technology is widely used with its unique advantages of traceable, non-contact, and high resolution[3].

In 1970s V. T. Goloborodko[4] first used laser interferometer to measure the displacement of piezoelectric ceramic. Later, Pan[5] established a high frequency double beam laser interferometer system, the results had good agreement with the values calculated by modified Card equations. With the widely application of the piezoelectric ceramic, the piezoelectric coefficient d_{33} was investigated. Cai[6] developed a laser vibrometer, and the error of d_{33} is about 5%. In order to improve the precision, a new modulation method with the principle of coherent detection was carried out, and its accuracy reached 4%[7]; In order to get the three-dimensional images of d_{33}, a laser scanning interference vibration with the Doppler principle was developed[8]. For d_{33} measurement, simple introductions were given[9,10], while few researches focused on the influence factors of d_{33} measurement. In this paper the influence factors of d_{33} were studied, including the frequency and amplitude of the exciting signal, the ways of fixing, and the loading sequence. And the analysis of the intrinsic link of the piezoelectric coefficient d_{33} with the converse piezoelectric effect and the piezoelectric effect was discussed.

Experimental Principles and Apparatus

When applied electric field on the polarized piezoelectric ceramic, it can produce micro displacement in the thickness direction with the converse piezoelectric effect. According to the piezoelectric equation, the relationship between the strain S and the electric field E as follows:

$$S=s^{E}T+dE \quad (1)$$

Where s^{E} is elastic compliance constant, T is stress, and d is the piezoelectric coefficient. When T is zero,

$$d_{33}=S/E=s/u \quad (2)$$

Where s is the displacement, u is the exciting voltage. Laser heterodyne interferometer is selected to measure the micro-displacement. Set the frequency of the reference beam is f_r, and the measuring beam is f_m. The electric field intensity E_r and E_m reached the surface of the photoelectric detector is.

$$E_r=A_1\,(cos(2\pi f_r t)+\varphi_1) \quad (3)$$

$$E_m=A_2\,(cos(2\pi f_m t)+\varphi_2) \quad (4)$$

Where A_1 and A_2 are the amplitude, φ_1 and φ_2 are the initial phase. The electric field intensity E_t after interfered is.

$$E_t=A_1^{2}+A_2^{2}+2A_1A_2cos\,(cos(2\pi ft)+\varphi) \quad (5)$$

Where: $f=f_r-f_m$, $\varphi=\varphi_1-\varphi_2$

The light intensity is proportional to the square of the amplitude, so

$$i(t)=I_1+I_2+2(I_1I_2)^{1/2}cos(2\pi ft+\varphi) \quad (6)$$

Finally, the displacement s and the piezoelectric coefficient d_{33} could be obtained by signal demodulation.

The laser interferometer systems were established as Fig.1. It included the laser heterodyne interferometer, as well as homodyne interferometer and signal demodulation program developed by ourselves. Two kinds of piezoelectric ceramic, PZT4 and PZT5, were chosen. The diameter is 10 mm, and thickness is 2 mm, 5 mm, 8 mm respectively. The d_{33} of PZT4 is about 280-340 pm/V, and PZT5 is about 400-470 pm/V. It has only about 300 nm with the exciting voltage of 300 V.

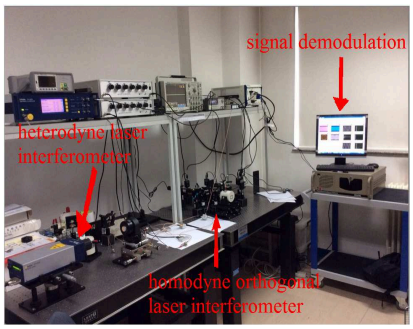


Fig.1 Picture of measurement system

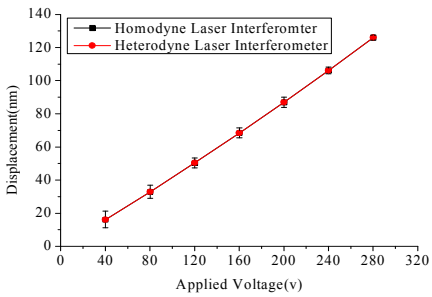


Fig.2 Comparison of homodyne and heterodyne interferometer

The function generator and the amplifier gives an exciting signal to the piezoelectric ceramic, and the Polytec OFV505 sensor head transmits laser and receives the measuring signal reflected from the surface of the PZT, then transfers it to the OFV5000 for signal demodulation. The result is transmitted to NI6251 acquisition card, and the displacement is calculated according to the relationship between velocity and displacement:

$$s=v/2\pi f \quad (7)$$

Comparison of displacement measurement by homodyne and heterodyne interferometer was shown in Fig.2. The homodyne laser interferometer developed ourselves could be controlled in each part, while the commercial heterodyne system could not. The agreement of the measurement results showed that the heterodyne system is accurate for the displacement measurement.

Result and Discussion

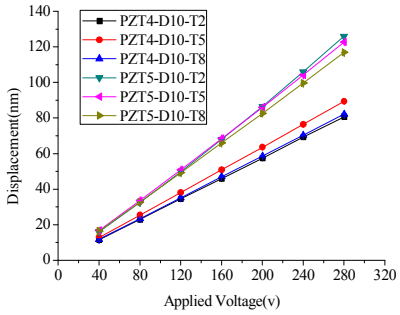
Displacement with Different Applied Voltage

As the micro actuators, piezoelectric ceramics' displacement characteristics under electric field exciting are particularly important. The displacement curve of PZT4 and PZT5 with different exciting voltage is shown in Fig.3. The frequency of the exciting voltage is 1 kHz, *D* means diameter and *T* means thickness.

The displacement of piezoelectric ceramic is only about 20 nm to 130 nm. With the increase of exciting voltage, the displacement of PZT4 and PZT5 increased gradually, and with good linearity. In addition, the slop of PZT5 from 404pm/V to 450 pm/V, is larger than PZT4 from 282 pm/V to 320 pm/V, the measurement results are in good agreement with the piezoelectric coefficient d_{33} of soft PZT5 is larger than hard PZT4 in theory.

Loading Sequence

When piezoelectric ceramic is used in practice, its displacement is likely to change from large to small, as well as possible from small to large, so, the relationship of displacement changes under different loading sequence should also be concerned. Assuming that exciting voltage changes from small to large as positive load, the load sequence of positive, reverse and positive again was chosen to take the measurement, Six times measurements were carried out under each exciting voltages, and the average displacement are shown in Fig.4 and table 1. The diameter of PZT5 is 10 mm and the thickness is 2 mm.



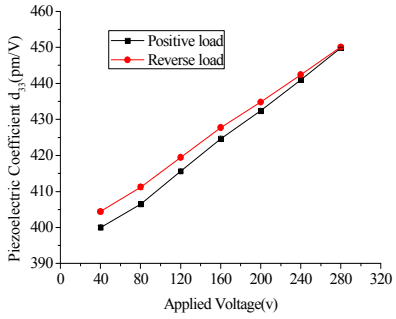


Fig.3 Displacement with different applied voltage *Fig.4. Influence of loading sequence*

Table 1. Displacement measurement in different loading sequence

Voltage[V]	40	80	120	160	200	240	280
Positive[nm]	16.05	32.59	49.92	67.99	86.53	105.89	125.99
Reverse[nm]	16.18	32.94	50.38	68.47	87.01	106.19	126.08
Positive[nm]	16.08	32.55	49.89	67.94	86.62	105.82	125.96

With the increase of exciting voltage in Fig.4, the d_{33} of PZT5 gradually increased, and the d_{33} increased slightly when with the same exciting voltage in the reverse load sequence, which indicated that the initial measurement has brought some deaging or other effects. When applying reverse load, the displacement is slightly larger than the positive load under the same exciting voltage. For example, with 120 V exciting voltage, the displacement by positive loading is 49.92 nm, while with the reverse loading is 50.38 nm, and the change rate is about 0.1%. In addition,

when applying positive load again, the displacement characteristics agreed with the measurement at the first time. It indicated that in a certain range of exciting strength, there was about 0.1% difference in positive and reverse sequence in one loading time, while there were almost no difference between the loading at the second and the first time.

Exciting Field

The d_{33} is the key parameter of piezoelectric ceramic energy transformation, the measurement result of d_{33} change of PZT under different exciting field strength was shown in Fig.5. The d_{33} of PZT5 is larger than PZT4. The d_{33} of PZT4 nearly remains the same value, 320 pm/V under the exciting field from 8 V/mm to 56 V/mm, while the d_{33} of PZT5 increased gradually. In the linear theory of piezoelectric coefficient d_{33} should be a constant, which means that it does not vary with the applied field. The difference may be related to the material compositions and the ways of polarization, Comparing with the hard PZT4, PZT5 belongs to soft piezoelectric ceramic, its performance is unstable relatively, and easily affected by ambient conditions.

Exciting Frequency

The vibration modes of piezoelectric ceramic may be affected by the exciting frequency, so the resonant frequency should be avoided. Considering the work frequency of the quasi static method usually is 100 Hz to 200 Hz, at the same time at higher frequencies the PZT holding issues become more critical, the frequency points at 200 Hz, 400 Hz, 600 Hz, 800 Hz, 1 kHz were selected. The d_{33} change of PZT with different exciting frequency is shown in Fig.6. The d_{33} of PZT5 is larger than PZT4 under the same exciting frequency, and it is almost a constant, about 434pm/V. The d_{33} of PZT4 increased slightly with the increase of exciting frequency. In a certain error range, the results are in good agreement with the d_{33} does not vary with the exciting frequency in theory.

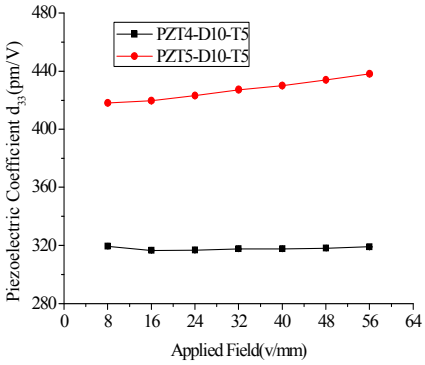


Fig.5 Influence of applied field

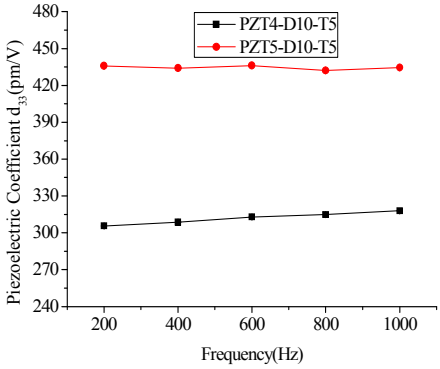


Fig. 6 Influence of exciting frequency

Holding Methods

When measuring piezoelectric ceramic, the holding unit should provide suitable electrical contact to the sample, and apply minimal mechanical constraints. Two methods were used, one is sticking and the other is clamping it at the middle part. Fig.7 showed test results.

With the increase of exciting voltage, the d_{33} of PZT5 increased gradually no matter clamping or sticking, and the measurement results have good linear characteristic. Comparing the two measurement results the sticking method gave higher results consistently, about two times. The disparity between the two holding methods could be attributed to the fact that the clamping method brought a pre-stress to the piezoelectric ceramic when holding the sample, because it is hard to clamp at the middle part exactly. And the pre-stress should have changed the boundary conditions, and it makes the stress of sample increased, finally the d_{33} measurement result became small.

In order to determine the stability of the sticking method, experiments were carried out ten times with the test sample taking off and sticking on the basement. The exciting signal is 240 V at 1 kHz, the result is shown in Fig.8. The d_{33} of PZT5 remained unchanged, which is about 435pm/V, and the maximum deviation is about 0.5%. The result indicated that sticking method should have little influence on the d_{33} measurement.

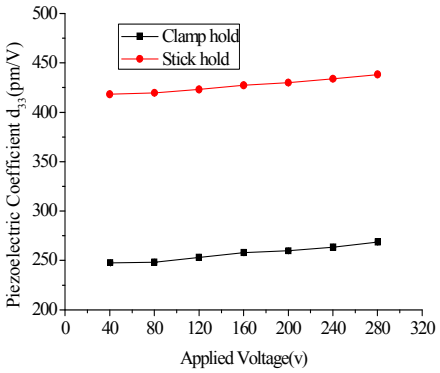


Fig. 7 Influence of holding methods

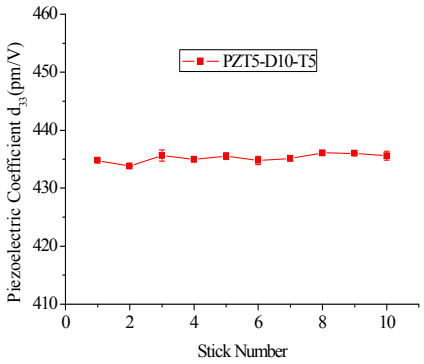


Fig.8 The stability of the sticking method

Comparison with Quasi Static Method

Among the d_{33} measurement methods, quasi static method and laser interferometer method have been used mostly. Table 2 shows the comparison of quasi-static and laser interferometer measurements on PZT material.

Table 2. Comparison of quasi-static and laser interferometer measurements on PZT material

Method	Principle	Reliability	Advantages And Disadvantages
Quasi-static	Piezoelectric effect	Low	Simple; Low accuracy
Laser interferometer	Converse piezoelectric effect	High	High spatial resolution; Frequency restricted

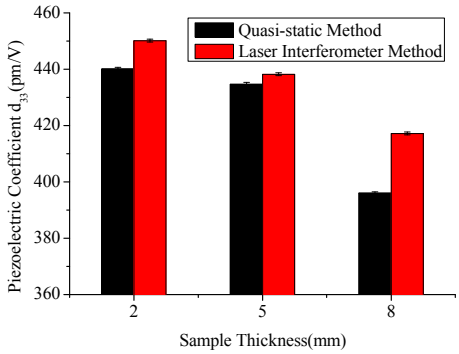


Fig. 9 Comparison of different methods

In order to evaluate the consistency of d_{33} under piezoelectric effect and converse piezoelectric effect, the results measured by quasi static method and laser interference method for different thickness on PZT5 are shown in Fig.9. The d_{33} result of the laser interferometer method was higher than quasi static method. And the trend for the different sample is the same. In a certain error range, the two measurement results have consistency, when the ratio of thickness to diameter is 0.5, the result was almost the same. The difference between the methods could be attributed to the different boundary and stress condition. In the interferometer method, large fields are applied in order to produce more measurable displacement, the sample experienced tensile and compressive stresses with the block sticking on a basement. While in the quasi static method the charge from a small AC

stress can easily be measured, however a 10 N pre stress is needed to hold the sample in place, so the sample is always in compression. The stress *T* in formula (1) is different and not always zero, which leads to the different result with different methods.

Summary

Piezoelectric ceramic can provide high force with relatively low energy loss, and most micro actuators use it in modeling and manufacture. The displacement characteristics and d_{33} of piezoelectric ceramic can be carried out by the laser heterodyne vibrometer. For the soft PZT materials, the value of d_{33} increased gradually with the increase of exciting field strength, but almost remained the same value at different exciting frequencies. While for the hard PZT materials the value of d_{33} was a constant, it did not vary with exciting field. The difference between the two kinds of PZT materials may be related to their components and its nonlinear characteristic. Comparing d_{33} measurement methods by converse piezoelectric effect and by piezoelectric effect, the result of the laser interferometer was always higher than quasi static method. The different stress condition in different methods leads to the difference.

Acknowledgement

This research is supported by NSFC (No. 51205378) and Special Fund for Scientific Research in the Public Interest (201310010).

References

[1] Li L, Wang LD, The new progress of the MEMS research-study of micro system and its development and application, Optics and Precision Engineering. 5 (1997) 67-68.

[2] Zhang L, Study of the micro actuators application. Machine Building & Automation, 2 (2010) 151-153.

[3] Su SJ, Research of theory and key technologies of long-rang displacement measuring with nanometer resolution by grating, National University of Defense Technology. 2001.

[4] V. T. Goloborod'ko, Use of a scanning fabry-perot interferometer with a piezoelectric ceramic at a very low modulation frequency, Journal of Applied Spectroscopy. 10 (1969) 442-443.

[5] Pan. W. Y., et al, Double beam laser interferometer measurements of surface displacements at the resonance frequencies of PZT piezoelectric ceramic resonators, Ferroelectrics. 120 (1991) 231-239.

[6] Chai QD, Piezoelectric coefficient vibrometer, Piezoelectric&Acoustooptics. 5 (1979) 173-176.

[7] Yi YY, Zhou ZB, Study of modulated laser interferometry for piezoelectric characteristic measurement of piezoelectric ceramic, Applied Optics. 25 (2004) 27-32.

[8] Yao, Kui, F. E. Tay, Measurement of longitudinal piezoelectric coefficient of thin films by a laser-scanning vibrometer, Ultrasonics, Ferroelectrics and Frequency Control, *IEEE Transactions on*. 50 (2003) 113-116.

[9] Wang ZH, Measurement of longitudinal piezoelectric coefficient of film with scanning-modulated interferometer, Sensors and Actuators A: Physical. 128 (2006) 327-332.

[10] Stewart. M. Battrick, W. Cain, M G, Measuring piezoelectric d33 coefficients using the direct method, Measurement Good Practice Guide. 44 (2001) 1368-6550.

Key Engineering Materials Vols 645-646 (2015) pp 926-930
© (2015) Trans Tech Publications, Switzerland
doi:10.4028/www.scientific.net/KEM.645-646.926

Submitted: 2014-12-05
Accepted: 2014-12-08

On the temperature-related mechanical properties of UV-LIGA Nickel material

Shuangshi Yuan[a], Guang He[b*], Ming Zhang[c], Guozhong Li[d]

National Key Laboratory on Electromechanical Dynamic Control,

Beijing Institute of Technology, Beijing 100081, China

[a]648692551@qq.com,[b]heguang@bit.edu.cn,

[c]505814374@qq.com,[d]331655701@qq.com

[*] Corresponding author: associate professor, Ph. D., Tel. / fax: +8610-68914151

Keywords: MEMS nickle material; Uniaxial tension; Temperature-related; Mechanical properties.

Abstract:MEMS nickel material is commonly used for structural material in micro devices. In order to study the effect of environmental temperature on its mechanical properties,this paper has built up a experimental system which can measure the temperature-related static mechanical parameters of the UV-LIGA nickel material. By using the system for uniaxial tensile experiments of the micro specimen under different temperature, the stress-strain curves of the micro specimen under different temperature were obtained; the mechanical parameters of the micro specimen such as elastic modulus, yield stress and failure stress under different temperature were also calculated out;Finally, the relationship between temperature and mechanical parameters including elastic modulus, yield stress and failure stress was analyzed.

Introduction

MEMS processing technology is based on the integrated circuit processing technology. With the emergence of the LIGA and UV - LIGA technology, all kinds of metal, ceramic and polymer replacing silicon and silicon compounds have become the commonly used materials in MEMS. Using LIGA electroforming process, varieties of micro device, such as micro elastic element[1], can be processed with metal nickel which is commonly used for LIGA processing. Mechanical properties of nickel material, such as elastic modulus, yield stress and failure stress, etc., determine the performance of nickel electroformed device[2].

To evaluate the mechanical behavior of the micro-scale structure has become the frontier issue in current research[3]. Reliability is one of the important performance index of MEMS devices. With the development of MEMS technology and the extensive applications of the MEMS devices, it is required that the MEMS materials can have good mechanical properties to adapt to the harsh environment. The performance and response characteristics of the electroformed nickel MEMS devices are different under different environments[4], including temperature, humidity, ph, etc. The environmental temperature will affect the mechanical properties of the material, for example,high temperature can make the material soften, low temperature can cause the material harden. Associate professor He Guang from Beijing Institute of Technology has studied the dynamic characteristics of the UV - LIGA nickel material under different temperature and obtained the constitutive relation under different strain rate [5]; the mechanical performance of the electroformed nickel material was also studied under static environment[6]. In order to study static mechanical properties of the UV-LIGA nickel material under different temperature and ensure the nickel electroformed device reliably work under high and low temperature, the static mechanical properties of the UV-LIGA nickel material in high and low temperature environment (-40 ℃ ~50 ℃) are studied.

Experiment System

The experiment system consists of micro material testing system MTS Tytron250 and micro temperature box system.

Micro Material Testing System. As is shown in Fig.1, micro force test system (MTS) is used for tensile experiment. The system is capable of dynamic and static tests for a variety of materials and components. The force sensor and high-precision displacement sensor whose resolution is 0.1 um can real-time record the force-displacement in stretching process.



Fig.1 The Tytron 250 micro force test system(MTS)

The Micro Temperature Box System. The micro temperature box system is used to implement the temperature of -40 ℃ ~ 50 ℃ which is the working temperature of the nickel MEMS devices. Micro temperature box adopts thermoelectric cooling , PTC ceramic heating and its temperature controller as shown in Fig.2. It adopts PID algorithm to control the temperature. Its controllable temperature range is -50 ℃ ~ 70 ℃ and the control precision is ± 0.5 ℃. To ensure the micro temperature box properly works ,the paper used recycled water for cooling on the hot side of the thermoelectric coolers.



Fig.2 The temperature controller of the micro temperature box system

Tensile Experiment

Standard Spline. According to the structural characteristics of MTS Tytron 250 micro force test system, standard splines were processed by the Institute of high energy physics, Chinese academy of sciences.As is shown in Fig.3, its effective length L is 5000 um, line width B is 150 um, thickness H is 300 um.

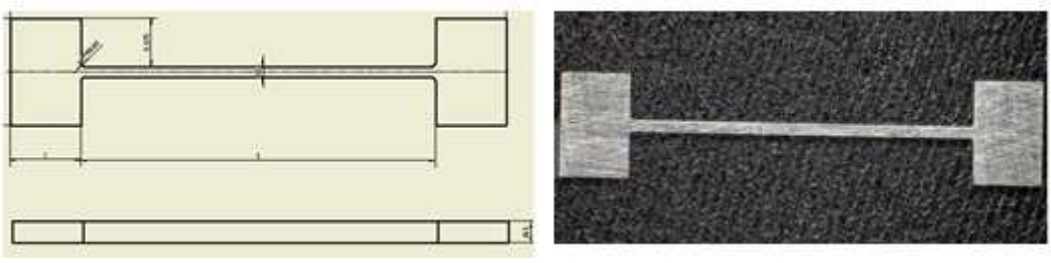


Fig.3 The structure and picture map of UV-LIGA nickel spline

Clamping Device. The clamping of the specimens is the most important part of micro material tensile experiment, the quality of the clamping directly affects the experimental results. As is shown in Fig.4, a dedicated fixture is designed; one end of the fixture with an internal thread is fixed with tensile test machine; the other end opened a through slot for clamping. The clamping blocks which was same as through-slot structure were designed, so that the both sides of the spline are fixed.



Fig.4 Fixture structure for clamping

Dimensional Measurement. In order to obtain the true structural parameters of the spline, the size of each spline was measured. The effective length and the line width were measured by three-dimensional microscopy measurement system, the thickness measured by three-dimensional optics profiler. It is concluded that the effective length dimension error is within 3.6%, line width dimension error within 10.7%, the thickness within 16.7%, which is in line with the requirements of the experiments.

Experimentation. UV-LIGA nickel spline was stretched on the micro tensile system shown in Fig.5. Firstly,the two clamps were fixed on both ends of the tensile tester, then fine tune the knob to keep the clamps at the same level, move the micro temperature box to the left to put the UV-LIGA nickel spline into the clamps, Then put four clamping blocks into the slot to catch the nickle spline.Finally, move the micro temperature box to the right to make nickel spline locate in the middle of the temperature box. The 25 nickel splines were divided into five groups and the tensile tests were done five times at each temperature node (50℃, 25℃, 0℃, -20℃, -40℃).After setting the stretching time 1000s, the stretching displacement 1mm and holding time 30min, the static tensile test began.

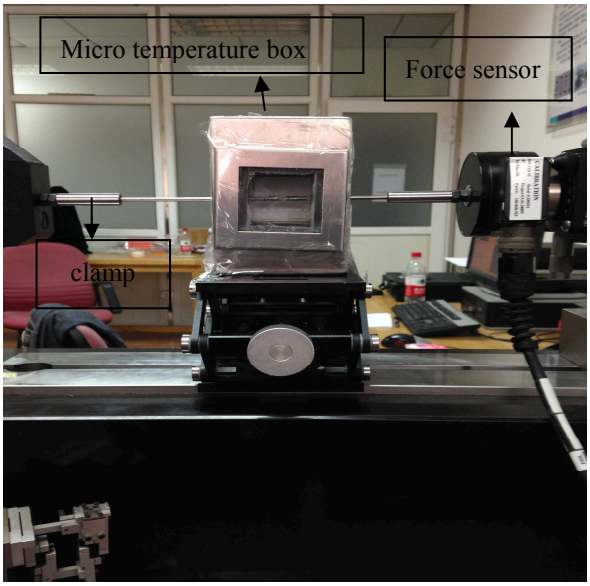


Fig.5 Physical map of micro tensile system

Data Processing and Analysis

The force-displacement date of the nickle spline when stretching was acquired at each temperature node (50℃, 25 ℃, 0℃, -20℃, -40℃). After conversion and filter smoothing, the stress-strain curves were obtained. Figure 6 ~ 10 respectively shows the stress-strain curves of UV-LIGA nickle in the temperature of 50℃, 25℃ ,0 ℃, -20℃ and -40℃.

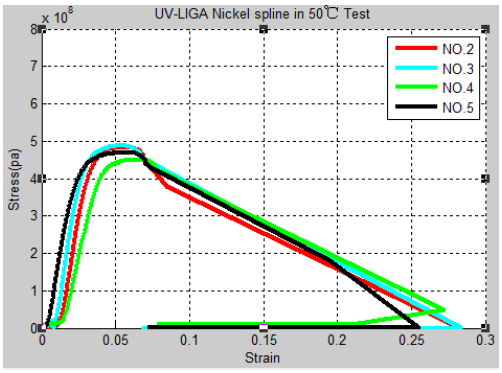


Fig.6 The stress-strain curve in 50 ℃

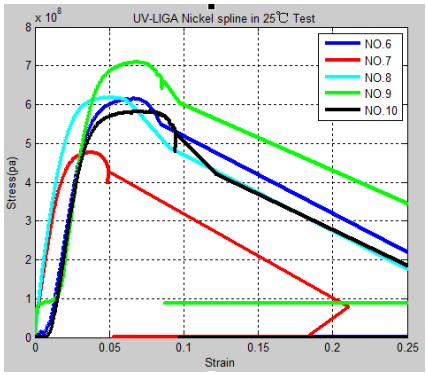


Fig.7 The stress-strain curve in 25 ℃

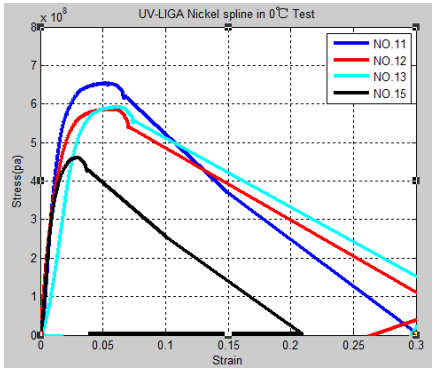


Fig.8 The stress-strain curve in 0 ℃

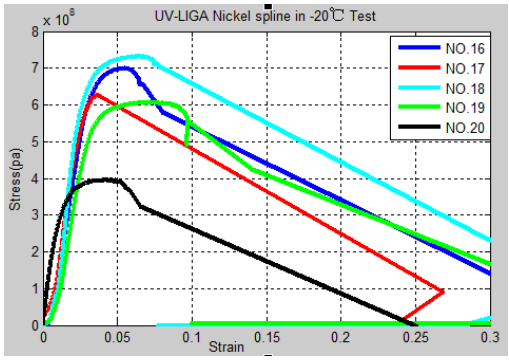


Fig.9 The stress-strain curve in -20 ℃

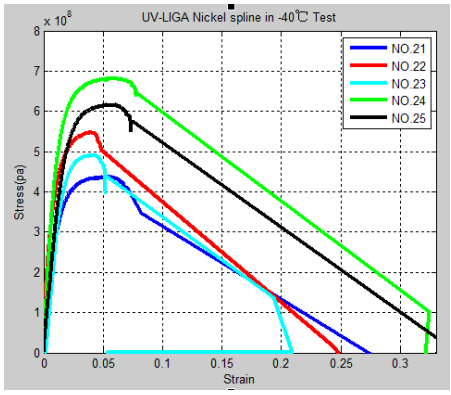


Fig.10 The stress-strain curve in -40℃

As is shown in Fig.11, the stress-strain curves of UV-LIGA nickle were obtained in the temperature of 50℃, 25℃, 0℃, -20℃ and -40℃ after data smoothing processing. And the elastic modulus, yield stress and failure stress shown in table 1 were calculated out.

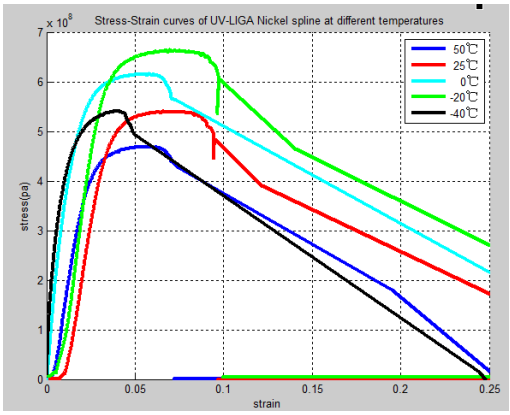


Fig.11 Stress-strain curve of UV-LIGA nickle spline under different temperature

Table1 Mechanical parameters of UV-LIGA nickel material under different temperature

Temperature (℃)	Elastic modulus (GPa)	Yield stress (MPa)	Failure stress (MPa)
50	21.6	399	474
25	24.4	478	559
0	31.3	528	611
-20	33.9	585	666
-40	39.3	483	556

It can be concluded from table2 that the temperature has an influence on the material;the elastic modulus, yield stress and failure stress will reduce with the temperature increases; But the yield stress and failure stress of the material in -40℃ has been reduced compared to -20℃.

Conclusion

The paper has built a experimental system composed of micro material tensile instrument and micro temperature box , which can measure the temperature-related static mechanics parameters of the UV-LIGA Nickel material; the stress-strain curves of the micro spline under different temperature were obtained; and the rule that elastic modulus, yield stress and failure stress changes as temperature varies was summarized. It is concluded that the temperature has an influence on the material;the elastic modulus, yield stress and failure stress will reduce with the temperature increases; But the yield stress and failure stress of the material in -40℃ has been reduced compared to -20℃.Experimental results can provide technical support for reliability analysis and optimization design of MEMS device.

References

[1] Yi Futing, Research of LIGA Technology, Institute of High Energy physics chinese Academy of Science , 2000.

[2]Libing Zheng, Gengchen Shi, Material Properties of LIGA Nickel Based on electroformed processing, Functional Materials and Devices Journal[J], 2010: 222-226.

[3]Bin He, The Development of Micro Tensile Experiment and the Evaluation of the mechanical properties of Micro Structures[D], Harbin Industrial University, 2011

[4]Xiaoke Li, Test technology research on the dynamic characteristics of high-temperature environment of MEMS component[D], Dalian University of Technology, 2009.

[5]Yajun Wang, On the Dynamic Mechanical Characteristics of Typical MEMS Material and Structure in Complex Environment[D], Beijing：Beijing Institute of Technology, 2013.

[6]Guang He, Geng-chen Shi, On the mechanical behavior of LIGA nickel, C. 4th IEEE International Conference on Nano/Micro Engineered and Molecular Systems (IEEE-NEMS 2009), 2009, 758-762.

Key Engineering Materials Vols 645-646 (2015) pp 931-941
© (2015) Trans Tech Publications, Switzerland
doi:10.4028/www.scientific.net/KEM.645-646.931

Submitted: 2015-01-08
Accepted: 2015-01-19

Design and Experiment Research on MEMS Vector Hydrophone Vibration Damping Structure

Nan Guo [1, a *], Guo Jun Zhang [2,b], Wen Dong Zhang [2,c]

[1] Science and Technology on Electronic Test & Measurement Laboratory, North University of China, Taiyuan 030051, China

[2] Key Laboratory of Instrumentation Science & Dynamic Measurement, Ministry of Education , North University of China, Taiyuan 030051, China

[a] guonan0902@163.com, [b] zhangguojun1977nuc@163.com, [c] wdzhang@nuc.edu.cn

Keywords: MEMS vector hydrophone; vibration-isolation; damping material; loss factor; packaging structure

Abstract: A novel vibration damping structure is designed based on the existing package structure of MEMS vector hydrophone. It is desirable that this novel structure can isolate the vibration noise caused by working platform so as to improve the anti-noise ability of hydrophone. This novel structure is made of "dow corning" damping silicone rubber which is manufactured with a certain proportion because of its small Young's Modulus. The hydrophone is fabricated in the form of original packaging structure firstly and then in vibration-isolation packaging structure. Laboratory tests by means of the shaking table test and standing-wave tube test are performed to validate the theoretical results. The test results prove that the vibration damping structure can effectively isolate the interference signal produced by working platform without affecting the sensitivity of hydrophone obviously.

1. Introduction

The MEMS vector hydrophone is a new type of underwater acoustic measurement equipment[1]. When the underwater sound source launches sound waves, they carry on much information. The sound waves together with ambient sea noise, reach the vector hydrophone or hydrophone array; then being converted to electric signals by the vector hydrophone. Processing the sound field information received from the vector hydrophone, it can be determined whether the target exists, its identity and status parameter, etc. Consequently, needed information about the target can be provided. The MEMS vector hydrophone has shown broad application prospects[2]. So far, the study of hydrophone based on MEMS technology has been increasingly mature[3,4].

However, noises, such that ship machinery vibration noise, propeller noise, hydrodynamic noise and flow noise, are inevitable due to the complexity and diversity of working environment and installation platform, and then become the barrier of extraction for useful signal. The existence of noise restricts the performance optimization development of hydrophone, making it limited to practical engineering application. Therefore, it is very necessary to solve the vibration problem of the vector hydrophone packaging structure. Faced with the fact, combined with the vibration damping principle[5], a vibration damping structure of vector hydrophone, which improves the existing packaging structure logically, is designed in this paper, aiming to realize the isolation of interference signal generated by vibration of the installation platform when the vector hydrophone is applied in engineering application.

2. Design and Principle of Vibration Damping Structure

2.1. MEMS vector hydrophone principle

According to the bionic principle[6], the sense- conducting pathway of a fish's lateral line organ can be obtained. Pressure in water will change under external force caused by sound waves, vibration waves and water flow velocity. This pressure travels into the lateral line canal through the lateral line pore, where the force is transferred to the mucus, causing the mucus to flow, which

moves into the neuromast and results in motion of the sensory cupula. The motion of the cupula results in deflection of the kinocilia via the lymphatic mucus flowing into the cupula. The kinocilia is the relevant mechanical stimulus for the hair cells. Thus, the hair cells are stimulated, then the signals are transferred to the medulla oblongata through the sensory nerve fibers and the lateral nerve[7].

According to the bionic principle of a fish's lateral line, previous research has developed one kind of bionic package of MEMS vector hydrophone[8], as shown in Figure 1, Figure 2. When the sound signal is sensed by the cylinder, the piezoresistors located at the beam transform the sound signal into strain and finally into a differential output voltage signal via the Wheatstone Bridge circuit. Thus, the sound signal can be detected[9].

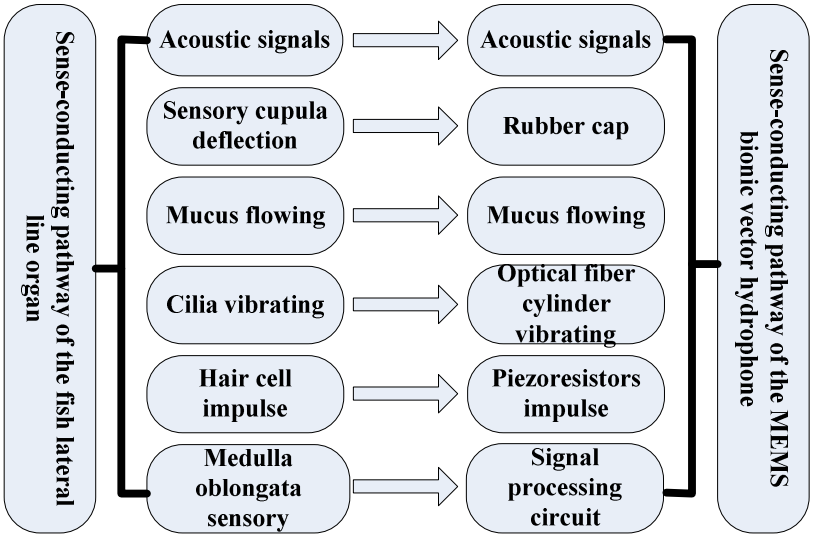


Figure 1. Bionic package principle of the vector hydrophone

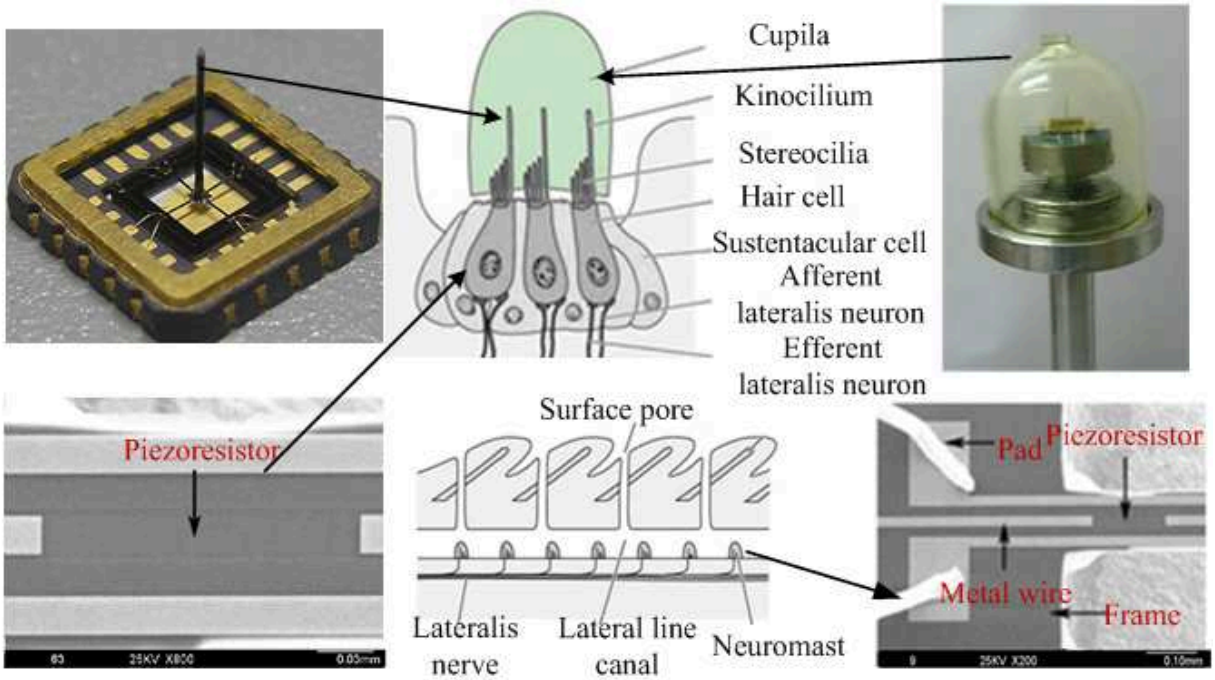


Figure 2. Package of the MEMS bionic vector hydrophone

2.2. Design principle

Polymer damping material is widely used in vibration damping and noise reduction. As polymer has high viscoelasicity, adhering polymer damping material to the surface of subjects can effectively transfer structural vibration into thermal energy[10]. Polymer is a viscoelastic material.

The stress-strain relation of polymer under a periodic driving force can be expressed with complex modulus as follow

$$\sigma = E^* |\varepsilon| \sin \omega t \tag{1}$$

$$E^* = E' + iE'' \tag{2}$$

where σ is the sinusoidal alternative stress; E^* , the complex modulus; ε, the strain; ω, the frequency of external force acting on the sample; t, time. E' is storage modulus, which measures the storage of energy of deformed material, namely resilience, and E'' is loss modulus, which measures the energy dissipation in deformation.

Stress can also be written as

$$\sigma = |E^*||\varepsilon| \sin(\omega t + \delta) \tag{3}$$

$$\tan \delta = E'' / E' \tag{4}$$

$$E' = |E^*| \cos \delta \tag{5}$$

$$E'' = |E^*| \sin \delta \tag{6}$$

where δ is the phase angle between stress and strain, and $tan\delta$ is loss factor, which characterizes the materials' capability of energy dissipation, hence it can also represent the damping property of materials.

Rubber is widely used in many engineering fields to eliminate vibration and noise due to its integrated mechanical properties, which includes adjustable modulus, high intrinsic damping, excellent tolerance of large strain and carry capability under deformation.

Transmissibility characterizes the capability of isolating and attenuating vibration of damper. The definition of vibration transmissibility is the ratio of response amplitude X_o and stimulating amplitude X_i. The load cell of rubber damper is rubber, which functions similarly as a spring. Hence, the standard damper model is a system constituted by a linear spring with stiffness of K and a damper with the damping factor of C. It is acceptable to neglect the uneven force distribution of each supporting points of the device and the coupling among them. Therefore, the mechanical model of the configuration can be simplified as shown in Figure 3. F is the stimulating force from external vibration; M is the mass of the object placed on damper. The displacement impedances of the spring, damper and mass block are K, $j\omega C$, $-\omega^2 M$ respectively, where ω is the angular frequency and $j = \sqrt{-1}$. Take the reciprocal of displacement mobility, then

$$M_{D_1} = \frac{D_1}{F} \tag{7}$$

where D_1 represents the displacement at point 1, which is the sum of the displacements of the damper, D_{KC} , and the mass block, D_M ,

$$M_{D_1} = \frac{K - \omega^2 M + j\omega C}{-\omega^2 M (K + j\omega C)} \tag{8}$$

As shown in Figure 3, the displacement at point 2 is D_2 , which is the same as D_M .

$$D_M = \frac{F}{-\omega^2 M} \tag{9}$$

The transmissibility of this system can be written as

$$\eta = \frac{X_o}{X_i} = \frac{D_2}{D_1} = \frac{K + j\omega C}{K - \omega^2 M + j\omega C} \tag{10}$$

Take absolute value of η,

$$|\eta| = \sqrt{\frac{1+\left(2\xi\frac{\omega}{\omega_A}\right)^2}{\left(1-\frac{\omega^2}{\omega_A{}^2}\right)^2+\left(2\xi\frac{\omega}{\omega_A}\right)^2}} \tag{11}$$

where ω_A is the resonant frequency and ξ is damping ratio $\xi = C/C_0$ (C_0 -the critical damping).

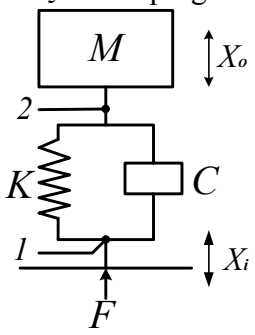


Figure 3. The standard model of single degree of freedom system

As shown in Figure 4, transmissibility is close to 1, when ω is very small. When $\omega = \omega_A$, transmissibility reaches maximum value due to resonance. When $\omega > 1.41\omega_A$, $|\eta| < 1$, and the effect of vibration damping increases with ω.

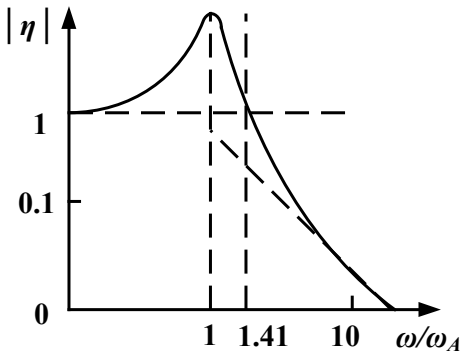


Figure 4. Transmissibility and frequency response curve

It follows that, to enlarge the valid region for vibration damping, it is necessary to minimize ω_A. The stiffness of damper, alternatively the hardness of rubber component, should be chosen carefully. Low hardness may result in excessive compression; high hardness may reduce the valid region for damping. Plug $\omega = \omega_A$ into Equation (11)

$$|\eta| = \sqrt{\frac{1+4\xi^2}{4\xi^2}} \approx \frac{1}{2\xi} = \frac{1}{\tan\delta} \tag{12}$$

Inspection of Equation (12) shows that, the larger ξ is, the smaller $|\eta|$ will be. To improve the function of the damper in resonance region, high damping viscoelastic material should be used. Damping loss factor $\tan\delta$, is often used to measure the capability of vibration damping (at resonant point, $\tan\delta = 2\xi$).

The damping material used in this paper is 'dow corning' silicone rubber. It is a block copolymer consisting of soft segments and hard segments[11]. Among large molecular, especially among hard segments, the electrostatic force is extremely high, and hydrogen bond exits there. Apart from affecting its mechanical properties, these intermolecular forces boost the aggregation of soft segments, and then micro-phase separation structure is produced. Therefore, it has a high damping loss factor. Besides, to increase loss factor, it can be achieved by adjusting the ratio of its two

components or changing damping structure and shape to change the stiffness and damp of the damper, increasing friction among molecular chains.

3. Vibration Damping Structure

3.1. Structural analysis

As shown in Figure 5, the vibration damping structure is composed of the soft bearing as the core device(as shown in Figure 6), the upper support connected on the top of the soft bearing and the lower support connected on the bottom of the soft bearing. The soft bearing is processed of 'dow corning' silicone rubber with features of low cost and easy to process. The stainless steel material processing units can ensure the stability and firmness of the hydrophone packaging structure; the core part of unit-typed vibration isolation device fabricated by 'dow corning' silicone rubber has high capability of vibration isolation. The middle part between the link units and support units is hollowed-out, equipped with buffer units and balance units, which can cushion the vibration delivered from outside working platform; the upper support, namely the installing groove for the microstructure, is used for installing MEMS vector hydrophone chip; the lower support is located between the soft bearing and the outer support; at the bottom of the outer support is installing groove for the circuit board. The soft bearing, upper support, lower support and outer support are all provided with central pylome for the electric cable of MEMS chip to extend into and connect with the circuit board.

The soft bearing, made of 'dow corning' silicone rubber, which has very small Young's Modulus, is the core part of the vector hydrophone's vibration damping packaging structure. The soft bearing is designed with a ring-type elastic element, four supporting columns on the elastomer as buffer units and other four columns as balance units on the below; the two layers are crossed of 45 degrees, corresponding to strain beams fixed at both ends while loaded in the middle. Under stress, the strain beam can be simplified to a rectangular statically indeterminate beams, that is to say the buffer units and balance units can be simplified as a whole into eight statically indeterminate beams. According to the statically indeterminate beams theory, when under concentrated loads, the freedom terminal of the beam only has displacement, no rotation, thus S-shaped deformation formed[12]. In consequence, such designs can guarantee the stability of vector hydrophone's encapsulation structure.

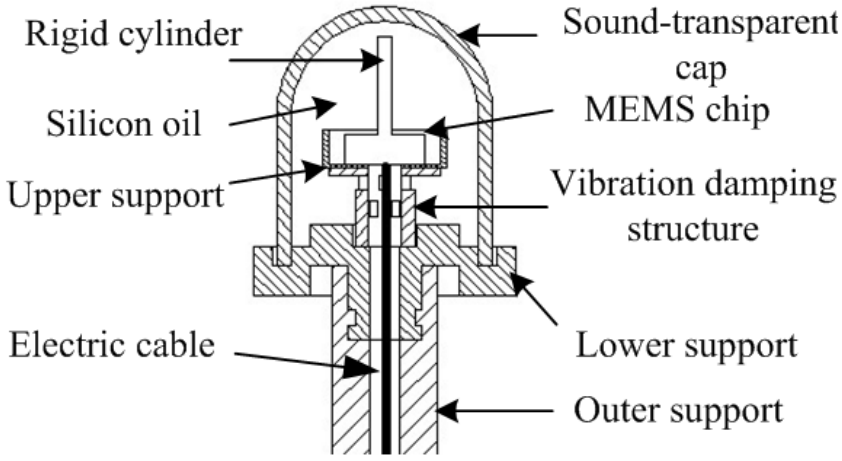
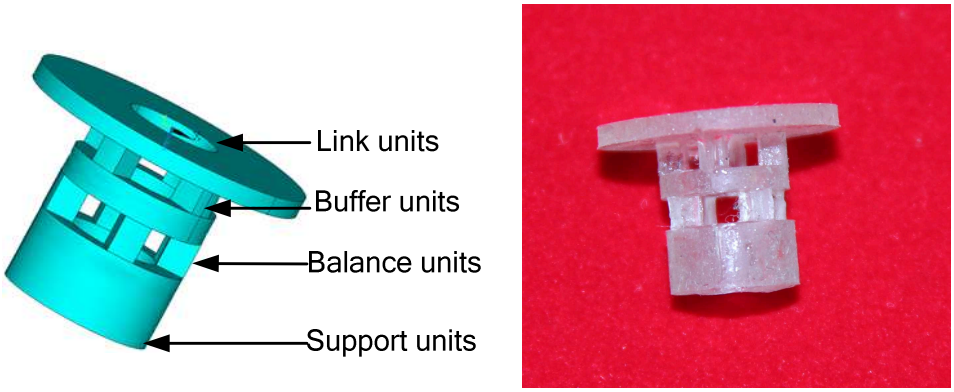


Figure 5. The package structure of MEMS vector hydrophone



(a) (b)

Figure 6. Structure(a) and real subject photo(b) of the soft bearing

The vector hydrophone is connected to the working platform through the outer support. Vibration noise generated by working platform transmits through the support structure towards the MEMS hydrophone chip, and goes through the soft bearing on the route of transmission. Since the soft bearing is like a spring with high loss factor and viscoelasticity, it can increase the damping of the entire system. By adjusting the ratio of rubber components and processing conditions, the soft bearing's loss factor can be further increased to eliminate vibration noise without affecting the normal operation of hydrophone to extract useful signal. Further, the buffer units and balance units are hollowed-out which can be seen as a second-order vibration isolation system. Thus, the vibration noise can be basically eliminated after passing the soft bearing structure, then ensure the sensitive microstructure inside the hydrophone is not affected by the vibration noise of working platform.

In order to verify the correction of our analysis and further optimize vector hydrophone's package system, the design above is simulated by ANSYS 12.0, as shown in Figure 7. The property parameters are given in Table 1.

Table 1. Material property parameters

Material	Young's modulus ($N*m^{-2}$)	Poisson Ration	Density ($kg*m^{-3}$)
Vibration damping rubber	6.25e7	0.42	1040
Cylinder	7.4e10	0.17	2320
Silicon base	1.3e11	0.27	2330

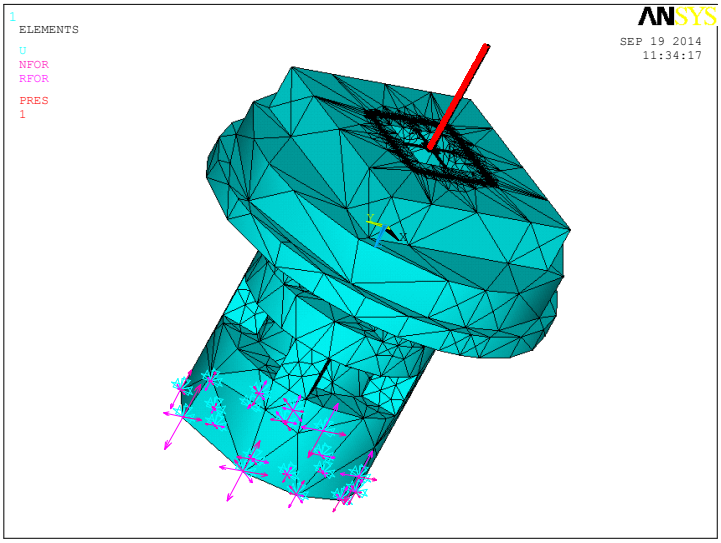
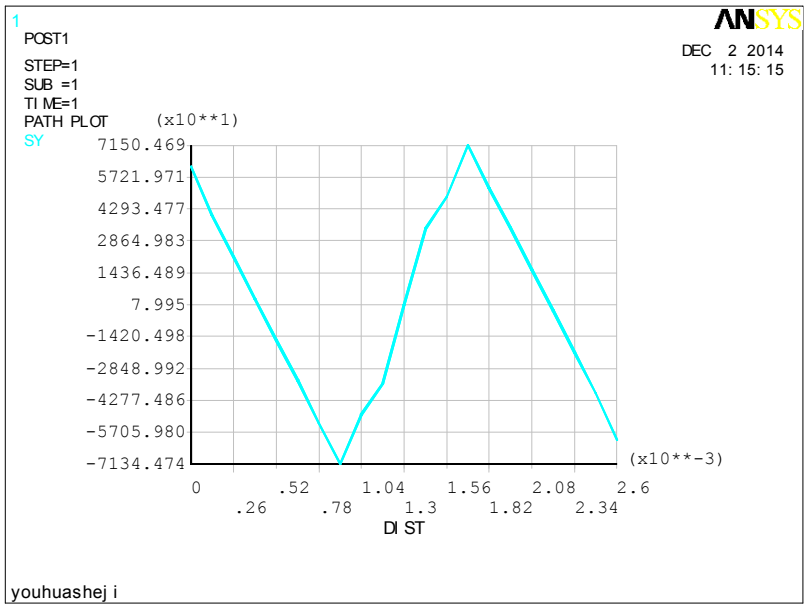
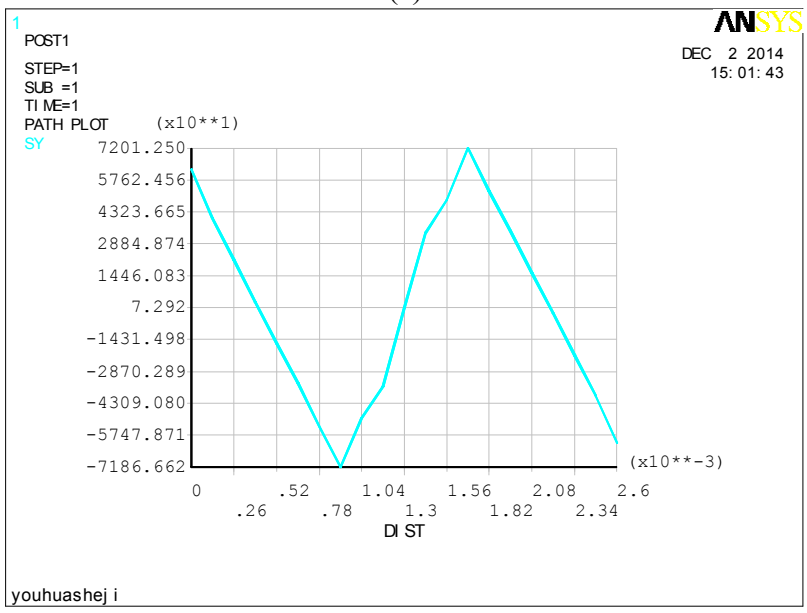


Figure 7. The finite element figure of soft bearing



(a)



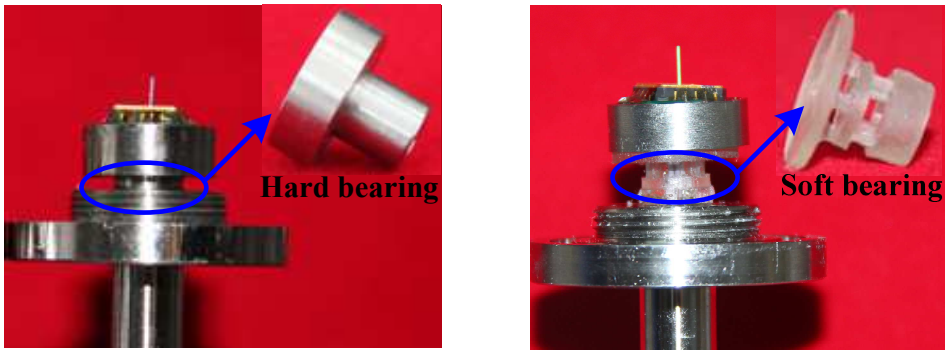
(b)

Figure 8. Simulation results of stress on beams (a) stress on beams of original packaging structure (b) stress on beams of vibration-isolation packaging structure

Figure 8 shows that the stress on beams of original packaged structure and vibration damping packaged structure are nearly equal, 71505Pa and 72013Pa respectively. It proves that the vibration damping structure basically does not affect the acquisition for useful signal of vector hydrophone.

3.2. Calibration tests and results

To verify the performance of the hydrophone with vibration damping packaging structure, the same hydrophone is packaged in original packaged form without vibration damping structure and then in vibration damping packaged form, as shown in Figure 9. The vibration damping test and sensitivity test are conducted in shaking table and standing wave tube with BK3629 sensor calibration system and sensitivity measurement system, as shown in Figure 10, Figure 13, testing results shown in Figure 11, Figure 14. The measurement system includes a function generator, a power amplifier, a calibration tube, data acquisition system, and revolver, as shown in Figure 12.



(a) (b)

Figure 9. (a) original packaging structure. (b)vibration-isolation packaging structure.



Figure 10. Shaking table test

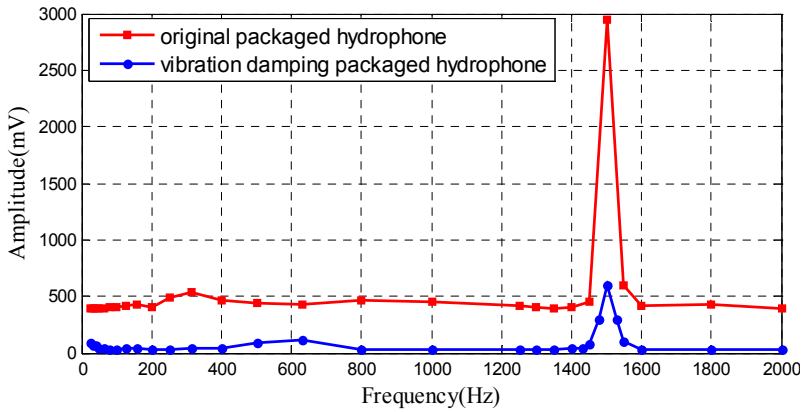


Figure 11. Vibration damping test result

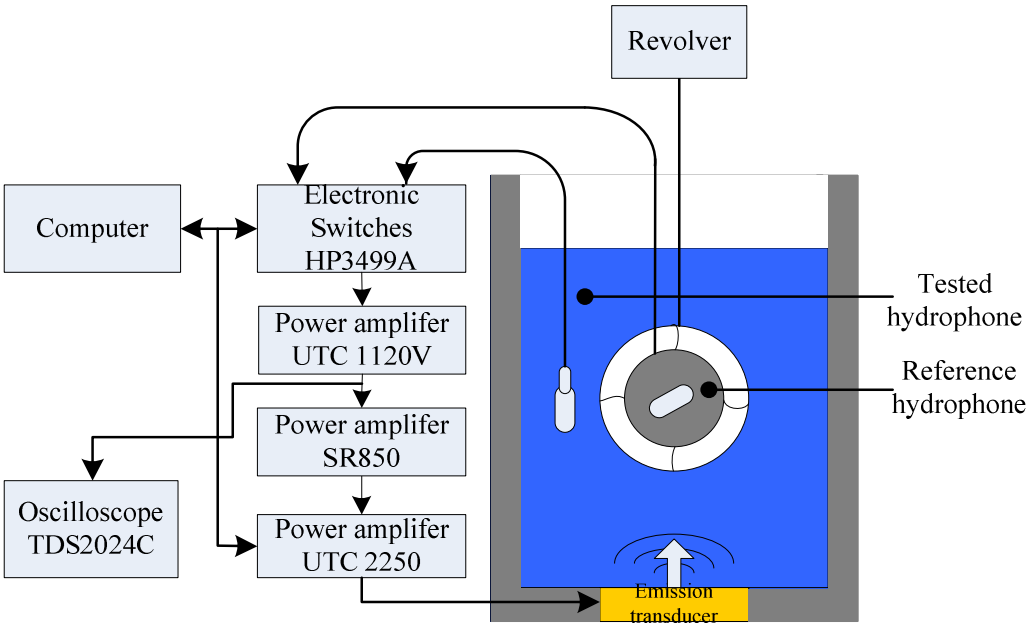


Figure 12. Schematic of the measurement system

The experimental results show that, the output voltage of vibration damping packaged MEMS vector hydrophone is obviously reduced than that of original packaged hydrophone, which proves that the application of vibration damping structure surely plays an important role in eliminating interference signal and the design has a certain effect of vibration reduction. While, the frequency response curves show that the sensitivity of vibration damping packaged hydrophone decrease inconspicuously, that is, basically doesn't affect the acquisition of useful signal for vector hydrophone.

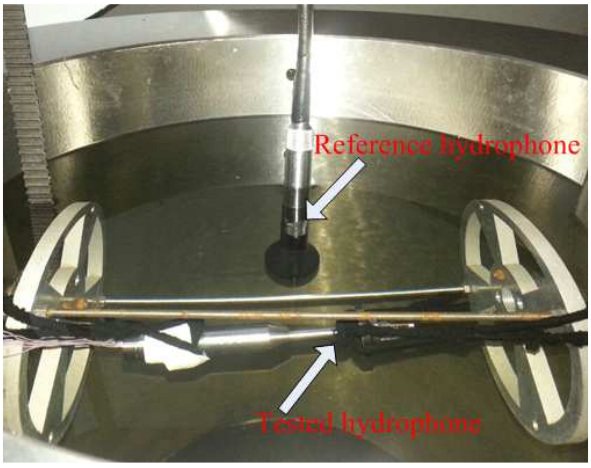


Figure 13. Sensitivity test

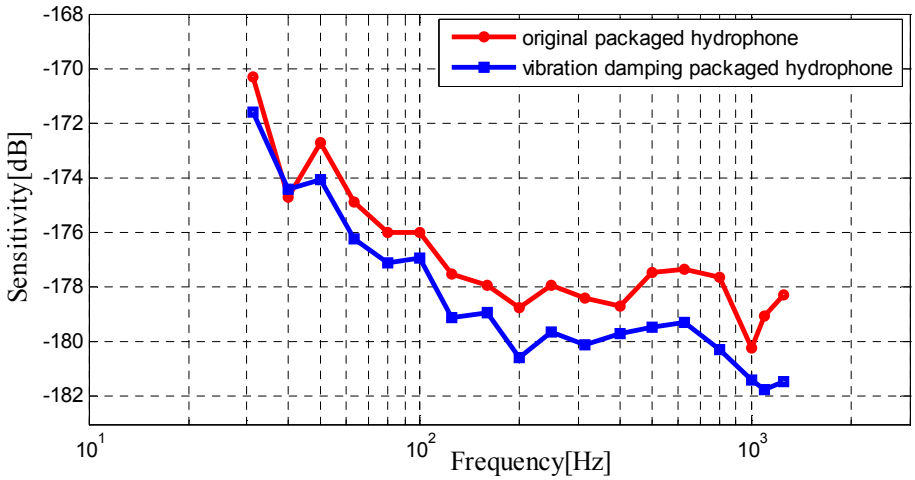


Figure 14. Frequency response curves of two types of package

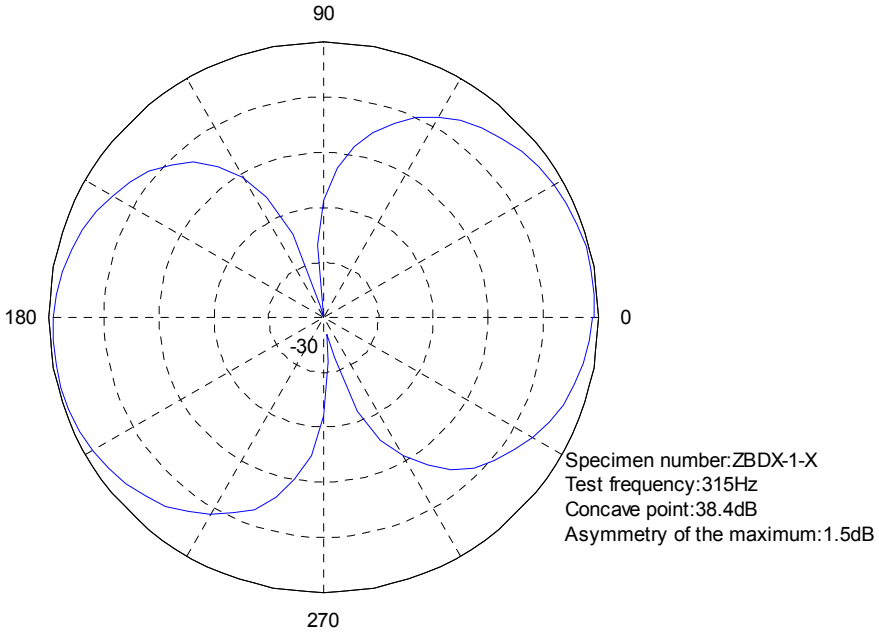


Figure 15. Directivity pattern of vibration damping packaged hydrophone at 315Hz

The directivity pattern of the vibration damping packaged hydrophone at the frequency of 315Hz is depicted in Figure 15, which shows that the hydrophone has a good directional pattern in the form of an "8"shape(dipole directivity) and good symmetry property.

4. Conclusions

Based on MEMS vector hydrophone, a new type of vibration damping packaged structure is designed and fabricated in this paper, aiming to reduce the interference of installation platform's vibration noise on hydrophone in engineering application. The results prove its feasibility, namely that the vibration damping structure designed in this paper can effectively realize isolation of interference signal without affecting the sensitivity of hydrophone obviously. Hence, make it much easier for MEMS vector hydrophone to be adapted into harsh underwater environment.

Acknowledgments

This work has been financially supported by the National Natural Science foundation of China (Grant No. 61127008, 51205374).

Author Contributions

G.J.Z conceived and designed the experiments; W.D.Z contributed materials tools; N.G. has contributed substantially to the work reported.

Conflicts of Interest

The authors declare no conflict of interest.

References and Notes

[1]. Xue, C.Y.; Chen, S.; Zhang, W.D. Design, Fabrication, and Preliminary Characterization of A Novel MEMS Bionic Vector Hydrophone, J. *Microelectronics.* **2007**, *38*, 1021-1026.

[2]. Leslie C B. Hydrophone for Measuring Particle Velocity, J. *Journal of the Acoustical Society of America*. **1956**, *04*, 711-715.

[3]. Chen, L.J.; Zhang, P.; Xu, X.Y. Overview of Vector Hydrophone, J. *Transducer and Microsystem Technologies*. **2006**, *25*(6), 5-8.

[4]. CHEN Li-jie; YANG Shi-e. The Design of Piezoresisive Vector Hydrophone[C].Harbin: The 4th International Symposium on Acoustic Engineering and Technology, 2005, 29-30.
[5]. ZHANG Guo-jun; CHEN Shang; XUE Chen-yang, et al. Bionic Encapsulation of a Hair Cell Vector Hydrophone Based on MEMS, J. *Nanotechnology and Precision Eingineering*. **2009**,7(3), 221-226.
[6]. W.K.Metcalfe; C.B.Kimmel; E.Schabtach. Anatomy of the Posterior Lateral Line System in Young Larvae of the Zebrafish. Comparat, Neurol, 1985; vol.233, no.3, pp. 377-389.
[7]. Fan Z; Chen J; Zou J, et al. Design and Fabrication of Artificial Lateral-line Flow Sensors, J. *Journal of Micromechanics and Microengineering*, **2002**, 12(5), 655-661.
[8]. CHEN Shang; XUE Chen-yang; ZHANG Bin-zhen, et al. A Novel MEMS Single Vector Hydrophone, J. *ACTA ARMAMENTARII*. **2008**, 29(6), 673-677.
[9]. Wen Dong Zhang; Ling Gang Guan, et al. Research of DOA Estimation Based on Single MEMS Vector Hydrophone, J. *Sensors*, **2009**, 9, 6823-6834.
[10]. James H M; Guth E. Theory of Elastic Properties of Rubber, J. *Journal of Chemical Physics*, **1943**, 11, 455-481.
[11]. Flory P J; Rehner J. Statistical Mechanics of Cross-linked Polymer Networks I: Rubber Elasticity, J. *Journal of Chemical Physics*, **1943**, 11, 512-520.
[12]. YU Changan; LI Ping; WANG Lou. Design of Elastic Component of Three-Component Strain Gauge Sensor, J. *Chinese Journal of Sensors and Actuators*, **2012**, 25(3), 333-336.

Key Engineering Materials Vols 645-646 (2015) pp 942-947
© (2015) Trans Tech Publications, Switzerland
doi:10.4028/www.scientific.net/KEM.645-646.942

Submitted: 2014-11-02
Accepted: 2014-12-23

The Test and Simulation Modeling of Micro Scale Solid Particles Fuel Cloud Dispersal under High Dynamic

Jin Xin[1, a]，Lou Wenzhong[1,b]，Guo mingru[1,c]，Dai Ximing[1,d]

[1] National Key Laboratory of Electro-mechanics Engineering and Control, School of Mechanical-electronic Engineering, Beijing Institute of technology, Beijing, China, 100081

[a]jinx0798@qq.com, [b]louwz@bit.edu.cn, [c]jiaoluo@bit.edu.cn (corresponding author), [d]shandongximing@163.com

Keywords: fuel-air-explosive; simulation modeling; test; solid fuel dispersion; cloud; experiment; micro scale; MEMS sensor

Abstract. Cloud forming by solid explosive dispersal plays a decisive factor for twice-detonating FAE. The study of the flow field of internal cloud field can be more intuitive to understand the whole process of the formation of cloud diffusion, and it also has an important role to the delay time setting of secondary detonating fuze. Internal parameters of spreading cloud are difficult to obtain even through by the experiment method, but numerical analysis and simulations method can get the parameter. In this paper, we use experimental and simulation methods to study fuel dispersal process, aims to establish an effective and reliable mathematical models of cloud dispersal, and get the model data coinciding with the real situation.

Introduction

Fuel-air explosives (FAE) is a kind of high-energy fuel, it does not contain oxygen. Under certain conditions, FAE reacts with oxygen in the air, and then form clouds detonation, FAE has different explosive properties with conventional explosives[1]. The dispersal of fuel and the formation of FAE are the main contents of cloud detonation technology research, it is an important way to improve the power of FAE weapon.

After explosive dispersal, fuel forms explosive cloud, it is a complex issue. In this paper, we use high-speed motion analysis system to record the growth of fuel cloud, provide some of the important parameters and necessary experimental data for numerical calculations. On this basis, we establish cloud dispersion model, study on regularity of dispersal, and get some important conclusions.

Experimental Design

Test equipment. Experimental high speed analysis system contains high-speed camera (Fig. 1) and data-processing system. During test, high speed camera adopts the frame rate for 1000f/s, explosion process stores in the computer with the form of pictures (Fig.2). After experiment, we use DIC method to process image, observe the whole process of detailed FAE cloud formation accurately. In this test, missile body is cylinder, explosion forms a pie-shaped fuel cloud, expand cloud cover as much as possible.



Fig.1 High-speed video camera module

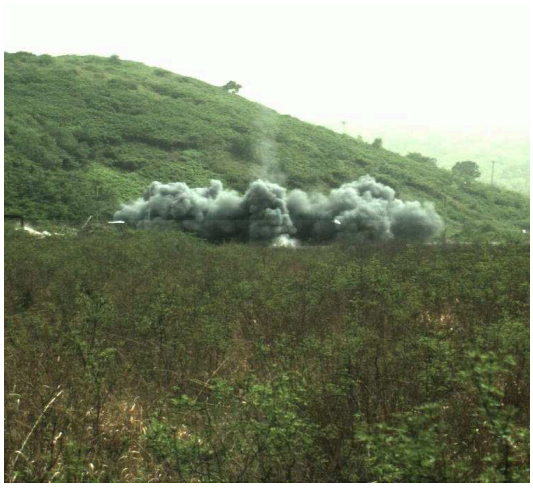


Fig.2 Picture of cloud explosion test

Test arrangement. Three high-speed video cameras emplace in a secure area, about 100m from the explosion source position, and observe the clouds grow from three directions. One camera locates on the mountain observation points, the other two locate in the same horizontal plane with explosion source, and three cameras film the explosion directly. Through the analysis of images acquired from different angles, we can have a more comprehensive understanding about the process of explosive dispersal.

At the same time, we place Mems electric field sensors (Figure 3) with the distance of 3m, 5m and 7m near explosive source, detect the situation of cloud proliferation when the first explosion, record the time when the cloud arrive at sensor and sensor voltage amplitude variation.

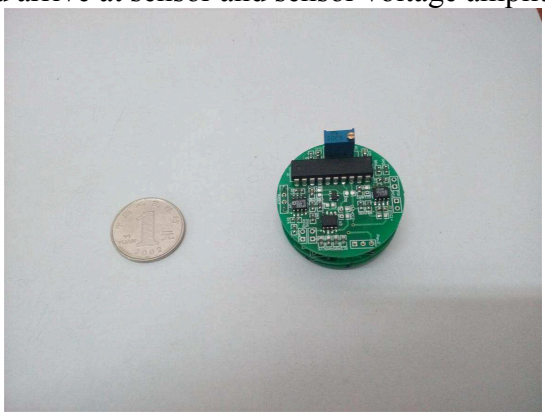


Fig.3 Electric field sensor circuit

Data processing. Sensor data can be obtained by empirical mode decomposition method, processed data shows in Fig.4 and Fig.5.

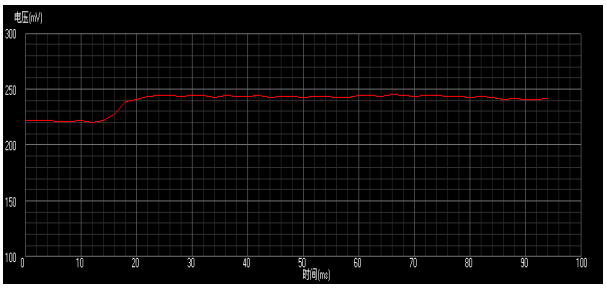


Fig. 4 Continuous peak change of the first test equipment

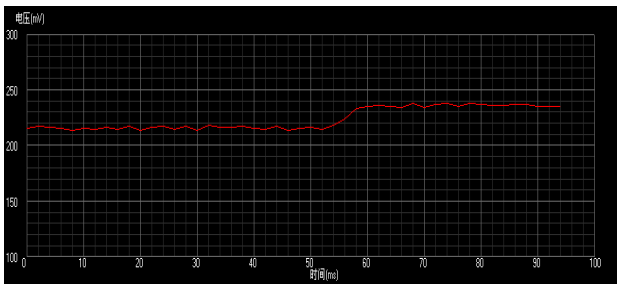


Fig.5 Continuous peak change of the third test equipment

We can see from the figures, after the FAE detonate 12ms, clouds spread to the position at 3m distance from the explosion source, at the time of detonation after 52ms, clouds spread to the position at 7m from the explosion source. Assuming clouds do uniform motion in the distance between 0m~3m and 3m~7m, , we can figure out, in 0m~3m, clouds diffusion speed is 250m/s, and in 3m~7m, clouds diffusion speed is 100m/s. It can be concluded that clouds dispersal process in the first few milliseconds after the explosion, explosive plays a dominant role for an accelerated process, and after some time, aerodynamic drag plays a leading role, rate fell sharply.

Numerical Simulation of Solid Fuel Dispersion

In the experiment, we select aluminum as solid fuel, cloud dispersal model chosen in this article is based on gas-solid flow diffusion model. Aluminum dust diffusion model supposes: flow field is one-dimensional unsteady, aluminum particles distribute in the gas uniformly, they have same initial diameter. The inner temperature of the particles is uniformly distributed; interaction between the particles and the role between the solid particles and the wall can be ignored.[2] Since only considering the first diffusion, without chemical change, there has no heat of reaction.

Research of solid-fuel near-field acceleration stage. The first initiation is equivalent to the situation of one-dimensional transient detonation. Since the detonation occurred in the air, detonation products start flying and interact with the surrounding air, form shock waves in air, meanwhile, reflect the sparse wave to the internal product. Research on near-field acceleration phase is to calculate the cloud diffusion radius during the acceleration phase. Assume that at the moment $t_0 = 0$, high explosive detonates instantaneously, its detonation products in constant region satisfy Eq. 1[3]:

$$\begin{cases} a^2 = \overline{a^2{}_H} = \dfrac{3}{8}D^2 \\ p = \overline{p_H} = \dfrac{1}{8}\rho_0 D^2 \\ \rho = \overline{\rho_H} = \rho_0 \\ u = \overline{u_H} = 0 \end{cases} \tag{1}$$

where $\overline{\rho_H}$, $\overline{p_H}$, $\overline{u_H}$, $\overline{a_H}$ are bomb densities, detonation pressure and detonation velocity and detonation acceleration when the products begin spreading after instantaneous detonation.

When the first initiation in FAE, blast field pressure is high (more than 2000kg/cm2), gas-solid two-phase flow is equal to entropy flux. But with the expansion product proliferation, pressure decreases, isentropic assumption failure (adiabatic index also changes). In order to estimate the flying range, we use the following method:

(1)Ammunition is cylindrical, select instant detonation state, initial state satisfies Eq.1;

(2)Assumes that the proliferation is piecewise constant entropy, selected critical pressure Pc as decomposition basis, $p_c = 2000kg/cm^2$;

(3)The volume of explosives is v0, due to the instantaneous detonation, the initial volume v=v0;

When p≥Pc: $pv^k = const = \overline{p_H} v_0{}^k = p_c v_c{}^k$

When p≤Pc: $pv^\gamma = const = p_c v_c{}^\gamma$

where k≈3， $\gamma = \dfrac{5}{4} \sim \dfrac{7}{5}$

(4)Based on the above assumptions, according to the average pressure, from the overall perspective, we can estimate the maximum volume of product diffusion expansion. That is, when the product of the pressure p=pa, the product of the maximum volume $v_{\max} = (\frac{\overline{p_H}}{p_c})^{\frac{1}{k}} (\frac{p_c}{p_a})^{\frac{1}{\gamma}} v_0$;

(5)Assume for a certain type of high explosive dynamite, its parameter index for the following data: $\rho_0 = 1.72\mathrm{g}/cm^3, D = 8300m/s, p_a = 1kg/cm^2$;

when $\gamma = \frac{5}{4}$, $v_{\max} = 1836v_0$, Since the drug is columnar, so the radius of the product is installed 42 times the volume of drug radius;

when $\gamma = \frac{7}{5}$, $v_{\max} = 957v_0$, Since the drug is columnar, so the radius of the product is installed 31 times the volume of drug radius;

When the detonation products reach the maximum volume vmax, the product does not immediately stop due to inertia, but continues outward movement until the border product speed is zero, this process makes possible volume 30%~40% larger than vmax. Final cloud radius estimates of 42 to 56 times the cylinder charge. In the accelerating expansion of the proliferation phase, cloud size is 31 to 42 times the radius of the cylinder charge.

Research of solid-fuel far-field acceleration stage.When the blast field pressure is equal to the critical pressure, the acceleration phase ends, solid fuel go into a far-field slowdown phase. Based on near-field modeling of FAE fuel, the maximum speed is obtained at the end of the fuel acceleration phase[4]:

$$V = \sqrt{\frac{r_0^2}{2k_{21}}\left[1-\left(\frac{r_0}{r_k}\right)^4\right] + \frac{r_0^2}{0.4k_{22}}\left[\left(\frac{r_0}{r_k}\right)^{0.8} - \left(\frac{r_0}{r}\right)^{0.8}\right]} \tag{2}$$

where $k_{21} = \frac{1}{2}\left(R_0^2 - r_0^2\right)\rho_0 / p_0, k_{22} = \frac{1}{2}\left(R_0^2 - r_0^2\right)\rho_0 / \left(2\times10^8 \times \left(p_0/\left(2\times10^8\right)\right)^{\frac{2.8}{6}}\right)$, r_0 is the initial radius of high explosive in the center pipe, R_0 is the radius of FAE device column, r_k is the radius of explosion gas cavity when $p = 2\times10^8 Pa$, $p_0 = \frac{1}{8}\rho_0 D_e^2$, ρ_0, D_e are the density and detonation speed of the high explosive in center pipe respectively.

Using the method in "research of solid-fuel near-field acceleration stage",we can estimate the cloud radius r, then we put r into Eq.2 to calculate the maximum velocity $V = v_{\max}$.

In the deceleration phase, we research the speed relaxation phenomenon of particle group as a single particle speed relaxation phenomena, derive solid fuel particles deceleration movement model in a multi-force and obtain the dispersal distance in far-field.

Particles in fluids are pulled in multiple directions, including longitudinal and lateral forces and other forces. This article looks at the horizontal motion of the particle, therefore does not consider the effect of lateral forces on the particle motion. The force balance equation acting on the particle is Eq.3 (d is the diameter of the particle, ρ is density, ρ_c is fluid density, μ is fluid dynamic viscosity coefficient, v is fluid motion viscosity coefficient, g is gravitational acceleration, g_x is g on the direction of x component)[5]:

Inertial force + Added mass force + Resistance + Pressure + Gravity=0 (3)

where $\text{Inertial force} = -\frac{1}{6}\pi d^3 \rho_p \frac{\mathrm{d}u_p}{\mathrm{d}t}$. $\text{Added mass force} = -\frac{1}{12}\pi d^3 \rho_c \varepsilon$, where $\varepsilon = \frac{\mathrm{d}u_p}{\mathrm{d}t} - \frac{\mathrm{d}u_c}{\mathrm{d}t}$. $\text{Resistance} = \frac{1}{8}\pi C_D d^2 \rho_c \left|u_c - u_p\right|\left(u_c - u_p\right)$, where CD is the drag coefficient. When Re is not too large, $C_D = \frac{24}{\mathrm{Re}} f(\mathrm{Re})$, where $\mathrm{Re} = \frac{\rho_c d\left|u_c - u_p\right|}{\mu}$, in this paper, $f(\mathrm{Re})$ use Stokes resistance formula: $f(\mathrm{Re}) = 1$. $\text{Pressure} = -\frac{1}{6}\pi d^3 \frac{\mathrm{d}p}{\mathrm{d}x}$, where $\frac{\mathrm{d}p}{\mathrm{d}x}$ is pressure gradient; if this pressure gradient is caused by the gravity of the fluid, x-axis vertically upward, so $-\frac{\mathrm{d}p}{\mathrm{d}x} = \rho_c g$. $\text{Gravity} = \frac{1}{6}\pi d^3 \rho_p g_x$.

We integrate the above equation to Eq.3:

$$-\frac{1}{6}\pi d^3 \rho_p \frac{\mathrm{d}u_p}{\mathrm{d}t} - \frac{1}{12}\pi d^3 \rho_c \left(\frac{\mathrm{d}u_p}{\mathrm{d}t} - \frac{\mathrm{d}u_c}{\mathrm{d}t}\right) + \frac{1}{8}\pi \frac{24}{\frac{\rho_c d\left|u_c - u_p\right|}{\mu}} f(\mathrm{Re}) d^2 \rho_c \left|u_c - u_p\right|\left(u_c - u_p\right) + \frac{1}{6}\pi d^3 \rho_p g_x - \frac{1}{6}\pi d^3 \frac{\mathrm{d}p}{\mathrm{d}x} = 0 \tag{4}$$

Consolidation equation:

$$\frac{\mathrm{d}u_p}{\mathrm{d}t} = \frac{\left(u_c - u_p\right)}{\frac{\rho_p d^2}{18\mu f(\mathrm{Re})}} + g_x - \frac{1}{2}\frac{\rho_c}{\rho_p}\left(\frac{\mathrm{d}u_p}{\mathrm{d}t} - \frac{\mathrm{d}u_c}{\mathrm{d}t}\right) - \frac{1}{\rho_p}\frac{\mathrm{d}p}{\mathrm{d}x} \tag{5}$$

Velocity relaxation time is $\tau_v = \tau_{v,0} / f(\mathrm{Re})$, where $\tau_{v,0} = \frac{\rho_p d^2}{18\mu}$ is the velocity relaxation time corresponding to the Stokes resistance. Using the equations of fluid motion: $\frac{\mathrm{d}u_c}{\mathrm{d}t} \approx g_x - \frac{1}{\rho_p}\frac{\mathrm{d}p}{\mathrm{d}x}$ to eliminate pressure gradients, we can get the last equation of particle motion:

$$\frac{\mathrm{d}u_p}{\mathrm{d}t} = \frac{\left(u_c - u_p\right)}{\varepsilon_2 \tau_v} + \frac{\varepsilon_1}{\varepsilon_2} g_x + \frac{\varepsilon_2 - \varepsilon_1}{\varepsilon_2}\frac{\mathrm{d}u_c}{\mathrm{d}t} \tag{6}$$

Where $\varepsilon_1 \equiv 1 - \frac{\rho_c}{\rho_p}$, $\varepsilon_2 \equiv 1 + \frac{1}{2}\frac{\rho_c}{\rho_p}$.

Because the fluid is a gas, $\frac{\rho_c}{\rho_p} << 1$, $\varepsilon_1 \approx \varepsilon_2 \approx 1$, particles move in the flow field where air velocity is zero, and there is no other forces in the flow direction. The equation of particle motion is:

$$\frac{\mathrm{d}u_p}{\mathrm{d}t} = \frac{u_c - u_p}{\tau_v} \tag{7}$$

Through Eq.7, we can get the speed of the particles in the far field and particle dispersion radius. We assume that maximum speed at the end of the near field is 1, then we use Eq.7 to get the velocity relaxation process(Fig.6).

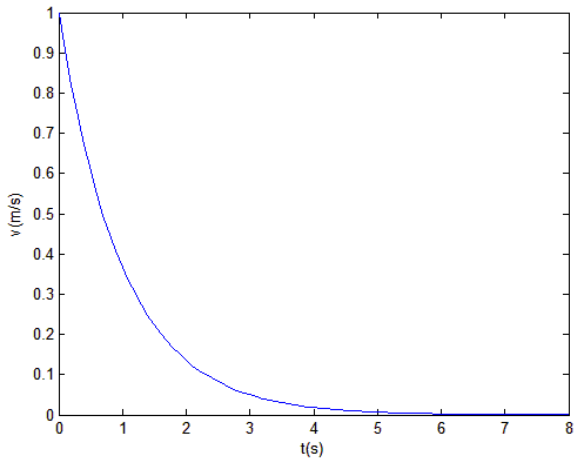


Fig.6 Picture of the velocity relaxation process

Summary

The study of the flow field of internal cloud field can be more intuitive to understand the whole process of formation of cloud diffusion, and also has an important role to the delay time setting of secondary detonating fuze. Internal parameters of spreading cloud are difficult to obtain even through by the experiment method, but numerical analysis and simulations method can get the parameter.In this paper, we use experimental and simulation methods to study fuel dispersal process.

In test phase, we successfully use sensors detected the real-time information of the situation of clouds spread, provide effective data for modeling.

In mathematical modeling stage, through basic knowledge of two-phase flow, we set up the model of cloud dispersion in the near-field and far-field, calculate the final radius and speed changes in the process of Cloud diffusion.At last, we get a more complete model.

Acknowledgement

The research is supported by National Project (No.00404010601).

References

[1] SUN Ye-bin, HUI Jun-ming, CAO Xinmao. Military composite explosives [M]. Beijing: Ordnance Industry Press, 1995.

[2] HONG Tao, QIN Chengsen. Numerical modeling of detonation in gas-fuel droplets system [J]. Explosions and Shock Waves, 2004.24(3):193-199

[3] Lv Hongsheng, Zeng Xinwu. Continuum mechanics-fluid mechanics and mechanics of explosion [M] .Chang sha: National Defence Science and Technology University Publishing Ho use, 1999. 365 - 366. (in Chinese)

[4] Zhang Qi, Bai Chunhua, Liu Qingming, et al. Near-field dispersal researching for fuel-air-ex plosive [J]. Journal o f Beijing Institute of Technology, 1999, 8(3) : 121- 130.

[5] Liu Dayou. Fluid dynamics of two-phase systems[M]. Beijing : Higher Education Pr ess, 1993. 26 -35. (in Chinese)

CHAPTER 4:

Micro Actuators and Devices

Key Engineering Materials Vols 645-646 (2015) pp 951-956
© (2015) Trans Tech Publications, Switzerland
doi:10.4028/www.scientific.net/KEM.645-646.951

Submitted: 2014-10-29
Accepted: 2014-12-23

Performance-enhanced heat converter used in FPA utilizing a SiOx/Al corrugated micro-cantilever actuator

Kong Yanmei[1, 2,a] Liu Ruiwen [1,b], Jiao Binbin[1,c] , Lu dike [1,d], Zhu Encheng[2,e], Fu Qiangsheng[2,f], Chen Dapeng[1,g]

[1]Integrated Circuit Advanced Process Center, Key lab of Microelectronics Device and Integration Technology, Institute of Microelectronics, Chinese Academy of Sciences, Beijing, CHINA

[2]Kunshan MicroOptica Electronic Co.Ltd, Jiangsu, CHINA

[a] kongyanmei@ime.ac.cn(corresponding author) [b] liuruiwen@ime.ac.cn

[c] jiaobinb@ime.ac.cn [d] ludike@ime.ac.cn [e] 873675873@qq.com

[f] ztefuqiangsheng@sina.com [g] dpchen@ime.ac.cn

Keywords: bi-material micro-cantilever; corrugation; temperature response sensitivity; stiffness factor; Finite Element Method (FEM)

Abstract:

This paper proposes a performance-enhanced SiO*x*/Al corrugated micro-cantilever structure, which transfers heat to mechanical deformation. Analytical simulations are carried out using the Finite Element Method (FEM), compared to the traditional straight bi-material structure(TSBMS) with same length *L*, the corrugated bi-material structures(CBMS) have higher temperature response sensitivity S_T and lower stiffness factor K. Furthermore, two types of cantilever was fabricated, and the test result verifies the change of the stiffness factor *K*. Finally, the thermal-mechanical uncooled infrared focal plane array (FPA) with CBMS was fabricated, and the test results show that the bending response of the CBMS is about 2 times greater than TSBMS with same length. The CBMS proposed in this paper could be used widely in MEMS apparatus field based on bimaterial microcantilever.

1. Introduction

With the development of micro-electromechanical system（MEMS）technology, bi-material micro-cantilever has been used as micro-actuators for many applications, such as biosensor[1], flow sensor[2], micro-mirror array[3,4], uncooled thermal-mechanical IR detector[5],et al. The principle of bi-material cantilever is that it will deform when an external physical quantity is applied on the cantilever and then the deformation is transferred to detectable electrical or optical signals, the scale of the deformation is proportional to the intensity of the measured external physical quantity. Therefore, the deformation of cantilever should be further enhanced in order to improve the response sensitivity. This paper proposes a performance-enhanced SiO*x*/Al CBMS, which transfers heat to mechanical deformation. Analytical simulations are carried out using the FEM, which has great value in the IR Focal Plane Array (FPA) and other MEMS apparatus field based on bi-material micro-cantilever.

2. Design and Simulation

The design of the corrugated micro-cantilever heat converter, shown in Fig.1 and Table 1, is to get the highest temperature response sensitivity (S_T).In order to be used in the IR-FPA, the total length L and width is fixed to 42μm and 1.5μm respectively, corresponding to the pixel dimension. t_1, t_2 and h is 0.5μm,0.3μm and 3μm respectively, various CBMS could be obtained by changing other variable parameters, shown in Table2.

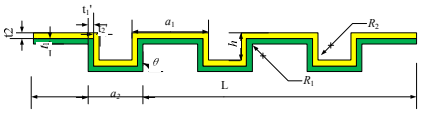
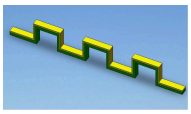
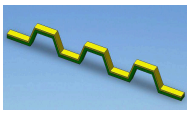
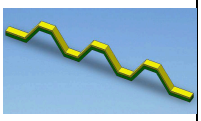
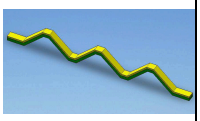
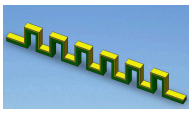
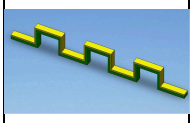
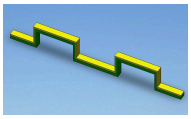
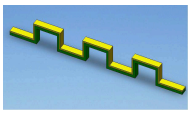
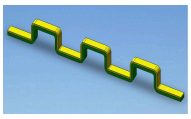
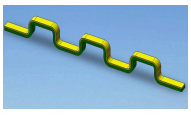
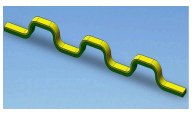
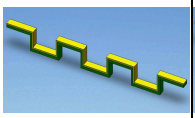
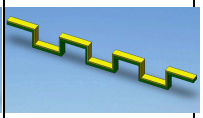
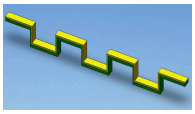
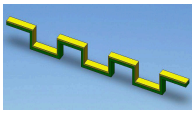
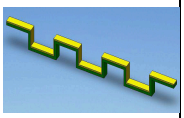
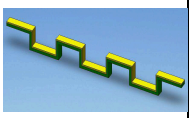


Fig.1 The corrugated micro-cantilever structure

material	Parameters			
	Young's modulus (MPa)	*Poisson ratio*	*Coefficient of thermal expansion (1/K)*	*Density ($10^3Kg/m^3$)*
SiO*x*	7000	0.25	$0.5*10^{-6}$	2.2
Al	7000	0.35	$23.1*10^{-6}$	2.7

Table 2.Bi-material micro-corrugated cantilever structures with different parameters 1-5 inclination angle θ 6-8corrugation number n 9-12 curvature R 13-18 step coverage rate t'/t

1: traditional	**2:** θ=90°, R_1=R_2=0	**3:** θ=60°, R_1=R_2=0	**4:** θ=45°, R_1=R_2=0	**5:** θ=30°, R_1=R_2=0	**6:** θ=90°,a_1=a_2=3μm
					
7: θ=90°, a_1=a_2=6μm	**8:** θ=90°, a_1=a_2=10μm	**9:** θ=90°, R_1=R_2=0μm	**10:** θ=90°, R_1=R_2=0.5μm	**11:** θ=90°, R_1=R_2=1μm	**12:** θ=90°, R_1=R_2=1.5μm
					
13: θ=90°, R_1=R_2=0μm, t_1'=0.4μm, t_2'=0.3μm	**14:** θ=90°, R_1=R_2=0μm, t_1'=0.3μm, t_2'=0.3μm	**15:** θ=90°, R_1=R_2=0μm, t_1'=0.2μ, t_2'=0.3μm	**16:** θ=90°, R_1=R_2=0μm, t_1'=0.5μm, t_2'=0.25μm	**17:** θ=90°, R_1=R_2=0μm, t_1'=0.5μm, t_2'==0.2μm	**18:** θ=90°, R_1=R_2=0μm, t_1'=0.5μm, t_2'=0.15μm
					

The influence of incline angle θ, the number of corrugations n, radius at the corrugation R and step coverage rate t'/t on the characterization of corrugated micro-cantilever are discussed, respectively, using the software ANSYS. The micro-cantilever is composed of SiO*x* and Al, the parameters of material used are shown in table 2. The initial ambient temperature is set T_0=22 ℃, the tip-deflection ΔZ is obtained by imposing a temperature T_1 which is different from the ambient temperature on the corrugated micro-cantilever, as shown in Fig. 2.

2.1 the inclination angle θ *(structures1-5)*

Fig. 3 shows the temperature response of cantilever with different inclination angle θ under different temperature conditions. It shows that the temperature response of corrugated cantilever is also linear to the variation of the temperature. As we know, temperature response sensitivity S_T is calculated by the expression: $S_T=\Delta Z/(T_1-T_0)$. Similarly, the effective stiffness factor of corrugated micro-cantilever K is obtained by the expression: $K=\Delta N/\Delta Z$, where ΔZ is the tip-deflection when a pressure ΔN is put on the tip of corrugated micro-cantilever, So the slope of the line stands for the S_T. Compared with the traditional straight cantilever, corrugated cantilevers have higher S_T regardless of the size of the inclination angle θ, and S_T improves with the increase of inclination angle θ, it reaches to the maximum when θ=90°. Namely, the right-angle corrugated cantilever has the maximum S_T.

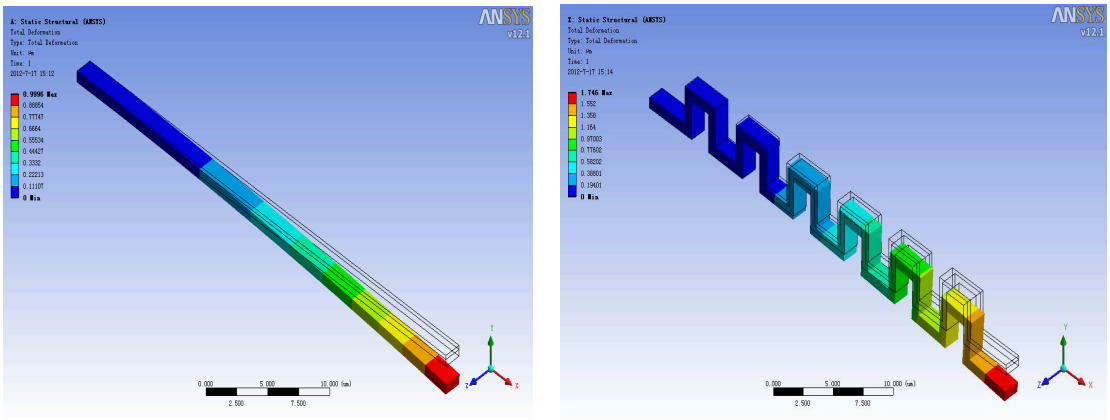
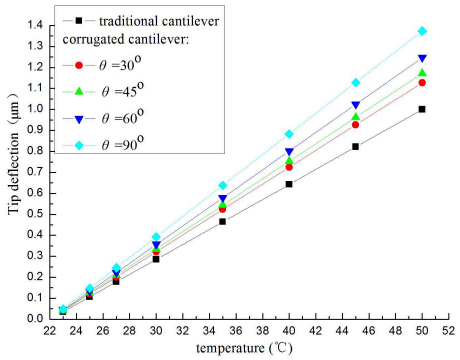


Fig. 2. The temperature response of micro-cantilever（T_1=50 ℃，T_0=22 ℃）
(a) Traditional straight micro-cantilever (b) Corrugated micro-cantilever

2.2 The number of corrugation *n (structures6-8)*

Fig. 4 shows the temperature response of bimaterial microcantilever with different number of corrugations in the same length. S_T improves with the increase of n, when a_1=a_2=3μm, S_T of traditional straight and corrugated micro-cantilever are 0.0357 μm/K and 0.053639 μm/K respectively. That's, S_T of corrugated micro-cantilever is improved by 1.5 times compared to traditional straight micro-cantilever. Therefore, in order to improve S_T, micro-cantilever in same end-to-end length L should be reasonable fabricated with as much corrugations as possible.



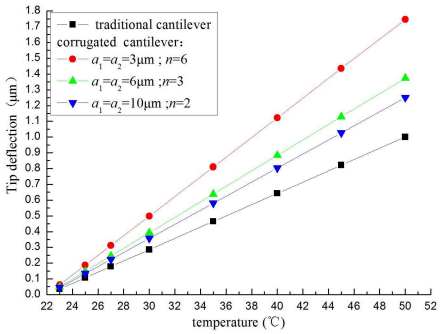


Fig.3 Tip deflection of micro-cantilever with T &θ

Fig. 4. Tip deflection of micro-cantilever with T & n

2.3 the influence of radius of curvature *R(structures9-12)*

Actually, it is very difficult to obtain perfect right-angle at the junction of ridges and trenches in corrugation in fabrication process, a circular arc will be generated. Fig. 5 shows the influence of radius of curvature of the circular arc R_1, R_2 on the S_T. It is worthy to note that S_T improves with the decrease of radius of curvature R_1, R_2, and reaches to the maximum when R_1,=R_2 =0. Therefore, R_1, R_2 should be decreased to the reasonable minimum in actual fabrication process.

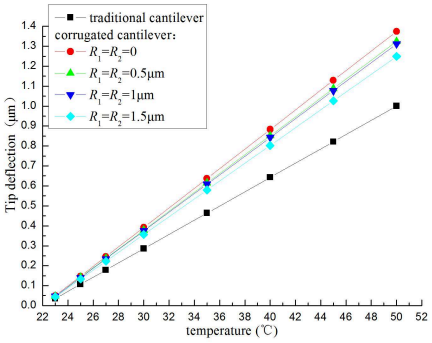


Fig.5 Tip deflection of micro-cantilever with T & R

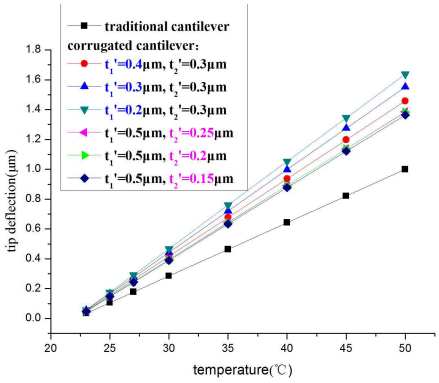


Fig. 6 Tip deflection of micro-cantilever with T & t'

2.4 the step coverage rate *t'/t (structures13-18)*

In addition, the step coverage rate t'/t of two films could not be same, that's the step coverage rate of two films could not be 100% in actual fabrication process, here, the thickness of the films is fixed, so the influence of step coverage rate could be represented by the variation of t_1', t_2'. As shown in Fig. 6, the simulation shows that S_T increases with the decrease of step coverage rate of lower coefficient of thermal expansion (CTE) material layer t_1', and decreases but not evidently with the reduction of step coverage rate of higher CTE material layer t_2' in bi-material micro-cantilever.

In conclusion, S_T of bi-material corrugated micro-cantilever is enhanced due to two factors:

First, as shown in Fig.8, the trend of the response sensitivity S_T is same to the equivalent length L' of the thermal bi-material cantilever except the area labeled in red, it's noted , in the area labeled in red, the change of S_T is due to the variety of step coverage rate of two films, though L' is invariant. So, the bi-material corrugated micro-cantilever enforces an increase in its actual equivalent length without changing its end-to-end length, which results in a greater bending response sensitivity.

Second, the stiffness K of the corrugated structure reduces in the direction of deflection of bimaterial microcantilever. Stiffness K，namely effective spring constant was evaluated from the FEA model by applying the Newton force of 1 μN on the tip of the corrugated microcantilever, and recording the resulting tip-deflection of the microcantileverΔZ. The force of 1μN resulted in the displacement of ΔZμm. Hence, the stiffness factor is K= 1μN /ΔZμm, so, the variation of the K is opposite to S_T.

3. Fabrication

From the above discussed forms of the corrugated micro-cantilever, it's noted that the right angle corrugated micro-cantilever has the highest temperature response sensitivity, which is increased by almost 2 times, compared with the traditional straight micro-cantilever with the same end-to-end length. Therefore, the right angle corrugated micro-cantilever was demonstrated and the basic fabrication process is shown in Fig.8.

(1) It starts from a 4 inch single side polished Si wafer with a thickness of 430μm. 0.2μm SiO_x film is deposited by plasma enhanced chemical vapor deposition (PECVD). And, then SiO_x film is patterned using photo etching and etching processes, as shown in Fig.8 (a)

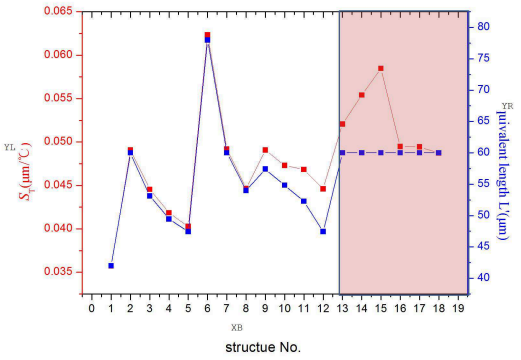


Fig.7 The temperature response and equivalent length of corrugated micro-cantilevers

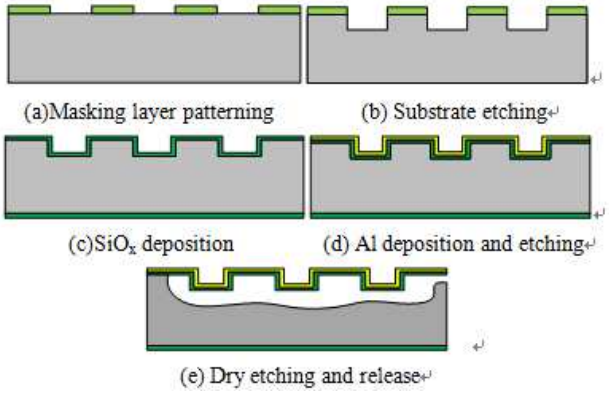


Fig.8. Fabrication process of right angle corrugated micro-cantilever

(2) Si substrate is etched anisotropically to obtain the expected trench, shown in Fig. 8(b), then SiO_x film is cleared away by BOE.

(3) SiO_x film of 0.5μm in thickness is deposited on both sides by low pressure chemical vapor deposition(LPCVD) process, then 0.3μm Al film is deposited by electron beam evaporation process, shown in Fig. 8(c)and (d), then Al film and SiO_x films are patterned respectively by using photoetching and etching processes.

(4) Finally, the bi-material corrugated micro-cantilever structure is released from the Si substrate by using XeF_2 dry etching process, shown in Fig. 8(e).

Fig.9 shows the SEM image of fabricated corrugated microcantilevers with different structural parameters. The corrugated microcantilever and the traditional straight microcantilever with the same end-to-end length were interval fabricated.

The initial deformation of the cantilever depends on the parameters such as the inclination angle, number of corrugation in unit length, step coverage rate, et al. It's noted that the corrugated microcantilever has greater initial deformation compared with traditional straight micro-cantilever due to the same residual stress. The structures labeled in 1, 2, 3 represents micro-cantilever of the traditional, six and fifteen corrugations respectively, the SEM image shows that the initial tip deflection of corrugated micro-cantilever 3 is larger than that of 2, and the tip deflection of corrugated micro-cantilever 2 is larger than that of the traditional straight micro-cantilever with the same end-to-end length and the same residual stress, which verifies that the stiffness K is undoubtedly decreased compared to the traditional cantilevers, due to the increase of the equivalent length .

4. Application in IR-FPA

The designed corrugated bi-material cantilever could be used in many sensors or structures based on the thermal-converter, here it was successfully used into the thermal-mechanical uncooled IR- FPA, whose deformation could be further read by the optical readout and compared to the straight micro-cantilever, it indeed improved the response sensitivity of the infrared detector. Fig. 10 shows the microscope pictures of the fabricated FPA both with and without corrugated cantilever structures. It is noted that the initial deformation of FPA with corrugated cantilever is larger than that of TSBMS with the same structure parameters and under the same fabrication process, so the corrugated one is low brightness with large deflection. The initial distortion angular of FPA both

with and without corrugated cantilever is about 37° and 22° respectively, which verifies that the stiffness K is reduced 1.61 times (sin37° / sin22°) compared with the structure of traditional straight cantilever with the same bi-material residual stress, thus the temperature sensitivity improved corresponding the reduce of the stiffness. And the performance of the FPA would be improved.

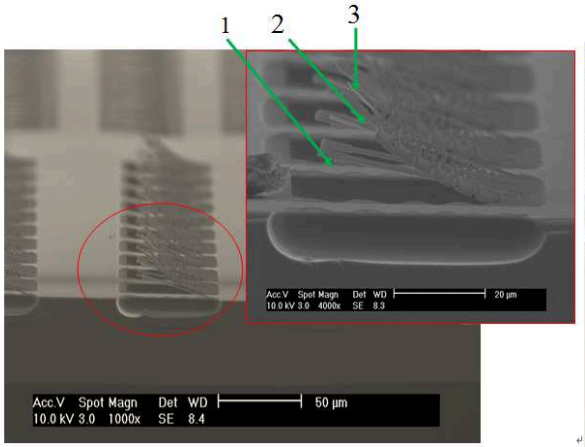


Fig.9 SEM picture of bi-material micro-cantilevers

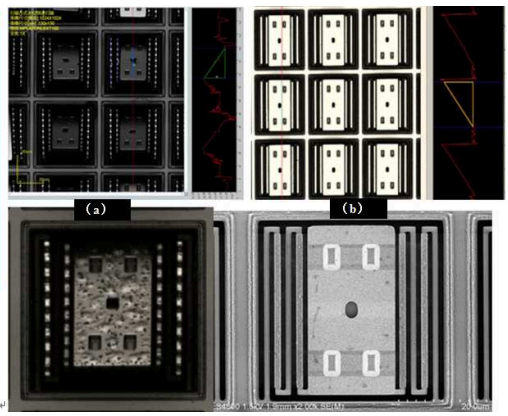


Fig.10 (a) FPA with CBMS (b) FPA with TSBMS

5. Summary

A type of corrugated micro-cantilever was designed, simulated and fabricated, and the simulated result shows that the corrugated micro-cantilever structures have higher temperature response sensitivity S_T and lower stiffness factor K compared with traditional straight bi-material cantilever structure with the same end-to-end length, then the experimental result shows that the initial deformation is different compared with that of traditional one with the same residual stress, which verifies K of the corrugated micro-cantilever is changed compared with traditional straight micro-cantilever. The designed corrugated micro-cantilever was successfully applied to the thermal-mechanical uncooled IR-FPA, and the K is reduced 1.61 times compared to the traditional cantilever. The designed corrugated micro-cantilever has a good prospect in MEMS component based on micro-cantilever.

Acknowledgement

This program is supported by Natural Science Foundation of JiangSu Province(BK2012219), and theNational High Technology Research and Development Program of China (863 Program:2013AA041109)

References

[1]. Gajendra Shekhawat, Soo-Hyun Tark, Vinayak P. Dravid. *Science.* 311(2006) 1592-1595.
[2]. A Ezkerra, L J Fernandez, K Mayora and J M Ruano-Lopez. *J. Micromech. Microeng.*17(2007) 2264–2271.
[3]. Yu-Hsiang Wang, Chia-Yen Lee, and Che-Ming Chiang. *Sensors* 7(2007) 2389-2401.
[4]. D. Grbovic, N. V. Lavrik, P. G. Datskos, *et al. Appl. Phys. Lett.* 89(2006) 073118-1-3.
[5]. Binbin Jiao, Chaobo Li, Dapeng Chen, *et al Infrared Physics & Technology.* 51(2007). 67-69.

Key Engineering Materials Vols 645-646 (2015) pp 957-962
© (2015) Trans Tech Publications, Switzerland
doi:10.4028/www.scientific.net/KEM.645-646.957

Submitted: 2014-10-29
Accepted: 2014-12-23

Modeling of hysteresis in piezoelectric actuator using linear play operator adaptive filter

Rui Xiong[1, a*], Xiangdong Liu[2,b] and Fengmin Shan[3,c]

[1 , 2 , 3] Key laboratory for Intelligent Control & Decision of Complex Systems, Beijing,China

[1,2 , 3] Automation College, Beijing Institute of Technology, Beijing,China

[a] xiongrui_2418@sina.com (corresponding author), [b] xdliu@bit.edu.cn, [c]2120120967@bit.edu.cn

Keywords: Modeling; hysteresis; piezoelectric actuator; LPO; adaptive filter

Abstract. Piezoelectric actuator(PEA) is widely applied in micro/nano positioning system. However, its inherent hysteresis limits its application. Modeling of hysteresis plays an important role in solving this problem. Linear play operators (LPO) adaptive hysteresis model is introduced in this paper. LPO operators are used to replace delay operators of adaptive transversal filter to compose a new serial structure of adaptive transversal filter model, and LMS (Least Mean Square) algorithm is used to adjust the weight values. As hysteresis loop of piezoelectric actuator is asymmetric and LPO operator is symmetric, a modified LPO （MLPO）adaptive filter is proposed for asymmetric hysteresis effect. At last, the two LPO filters are applied to model hysteresis characteristic of Piezoelectric actuator, and the modeling effect is verified via a micro-positioning system experiment platform based on Piezoelectric actuator. Experimental results show that the modified LPO filters can achieve better accurate hysteresis modeling.

Intorduction

Piezoelectric actuators have been widely used in micro/nano positioning systems due to their characteristics of simple institution, small size, high displacement resolution and high frequency response. However, its inherent hysteresis limits its application, since it can seriously affect the performance of the system and reduce the precision of positioning control. So modeling of hysteresis in piezoelectric actuator is the key issue to be resolved in high-accuracy positioning system.

Many efforts have been made on models that can describe hysteresis phenomenon of piezoelectric actuator. These models are classified into two types[1]: (1) differential-based models which use differential equation to characterize hysteresis; (2)operator-based models which use operators to characterize hysteresis. The Bouc-Wen model[2,3], Duhem model[4] belong to the first category. They are expressed by means of a nonlinear differential equation. The advantages of the differential-based models are simplicity and analyzability. But the numbers of parameters constituting its governing equation are limited. Therefore, it's hard to obtain a high accuracy. Amid various operator-based models, preisach model[5] is one of the most popular operator-based model to characterize the hysteresis behavior in nonlinear systems. However, it contains quadratic integral which leads to complex computation. What's more, it's hard to be used in real-time compensation. The Prandtl-Ishlinskii (PI)model[6,7] is the subclass of preisach model. This model is simpler to realize and its inverse can be computed analytically. PI model exploits two essential operators: stop operator and play operator.

B.Widrow[8] proposed the adaptive modeling method. An adaptive transversal filter is used to model nonlinear phenomenon. This kind of model has advantages of simple structure and easy computer simulation. However, it has unsatisfactory accuracy when describing nonlinear object. In order to solve this problem, preisach operator based and Backlash operator based adaptive traversal filters are proposed in [9], the effectiveness of modeling on piezoelectric actuator are verified. In this paper，Linear play operators are used to replace delay operators of adaptive transversal filter to compose a new serial structure of adaptive transversal filter model. However, linear play operator is

symmetric while hysteresis loop of piezoelectric actuator is asymmetric. Therefore, A modified LPO adaptive transversal filter is introduced for asymmetric effect.

The structure of LPO adaptive filter

LPO operator. The linear play operator is the basic hysteresis operator with symmetric property. The graphical representation of LPO operator used in this paper is shown in Fig. 1.

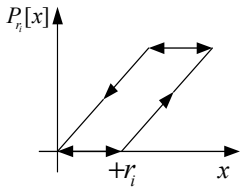


Fig. 1 The transfer characteristic

The transfer of LPO is defined as follow:

$$y(t) = P_{r_i}[x(t)] = \max\{x(t) - r_i, \min\{x(t), x(t-T)\}\} \tag{1}$$

Where $x(t)$ is the input of the operator, $y(t)$ is the output of the operator, r_i is the threshold of input control, T is the sampling time.

LPO operator satisfies the following discrete transfer function:

$$P_{r_i}[x(k)] = \begin{cases} x(k) - r_i & x(k) > x(k-1) \,\&\, P_{r_i}[x(k-1)] \le x(k-1) - r_i \\ x(k) & x(k) < x(k-1) \,\&\, P_{r_i}[x(k-1)] \ge x(k-1) \\ P_{r_i}[x(k-1)] & \text{others} \end{cases} \tag{2}$$

The LPO adaptive model. To approach the hysteresis in the PEA, we replace the delay module with the LPO operators of the same threshold width to compose a novel LPO adaptive filter. Fig. 2 shows the structure of LPO /MLPO adaptive filter. The LPO adaptive filter has the same structure as delay adaptive filter, so it has the advantages of delay adaptive filter. And it's a nonlinear filter which has good performance on approximating nonlinear system. All the linear play operators of the filter have the same threshold width, avoiding the trouble to decide different widths. Since the LPO is symmetric while hysteresis loop is asymmetric, a modified LPO(MLPO) filter is produced by adding rectangular box part to LPO filter for asymmetric effect.

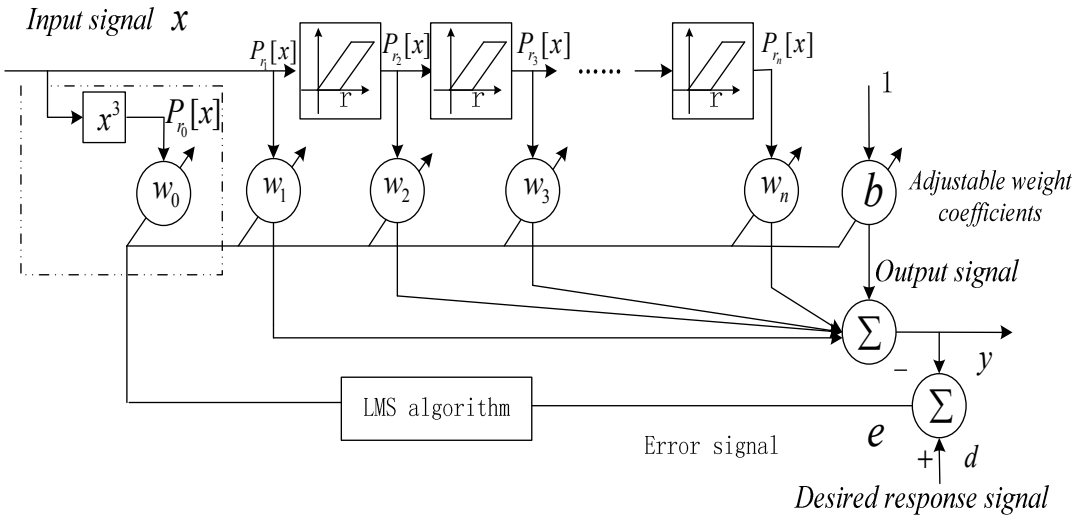


Fig. 2 The structure of the proposed LPO/MLPO adaptive filter

In fig.2, x is the input of the model, y is the output of the model, $P_{r_i}[x]$ is the output of each LPO. b is the bias of the model. d is the desired output response signal. e is the error between desired response signal and model output signal.

The model output y can be described as follow:

$$Y[x(k)] = W^T \cdot P_r[x(k)] \tag{3}$$

Where $W = [w_1, w_2, \cdots, w_n]$ is the vector of the adjustable weight coefficient; $P_r[x(k)] = [P_{r_1}[x(k)], P_{r_2}[x(k)], \cdots, P_{r_n}[x(k)]]$. In the case of modified LPO adaptive filter, $W = [w_0, w_1, w_2, \cdots, w_n]$, $P_r[x(k)] = [P_{r_0}[x(k)], P_{r_1}[x(k)], P_{r_2}[x(k)], \cdots, P_{r_n}[x(k)]]$.

Hysteresis modeling based on LMS algorithm adaptive filter

LMS algorithm is used to identify the weights of LPO/MLPO adaptive filter. The LMS algorithm is based on gradient search. The mean square error can be obtained through calculating the variance of each step in the iterative process.

Eq.3 is the expression of e ,

$$e(k) = d(k) - y(k), k = 1, 2, \cdots, Q \tag{3}$$

Where $e(k), d(k), y(k)$ represent the value of at time k . Q is the number of sample time.

The mean square error of model is measured as eq.4:

$$mse = \frac{1}{Q}\sum_{k=1}^{Q} e^2(k) = \frac{1}{Q}\sum_{k=1}^{Q} (d(k) - y(k))^2 \tag{4}$$

The derivatives of $e(k)$ with respect to w_j , b are as follow:

$$\frac{\partial e^2(k)}{\partial w_j} = 2e(k)\frac{\partial e(k)}{\partial w_j} \tag{5}$$

$$\frac{\partial e^2(k)}{\partial b} = 2e(k)\frac{\partial e(k)}{\partial b} \tag{6}$$

Substitute eq.3, we have:

$$\frac{\partial e(k)}{\partial w_j} = \frac{\partial [d(k) - y(k)]}{\partial w_j} = \frac{\partial [d(k) - \sum_{i=0}^{n} w_i \cdot P_{r_i}(k) - b]}{\partial w_j} = -x_i \tag{7}$$

$$\frac{\partial e(k)}{\partial w_j} = \frac{\partial [d(k) - y(k)]}{\partial w_j} = \frac{\partial [d(k) - \sum_{i=0}^{n} w_i \cdot P_{r_i}(k) - b]}{\partial b} = -1 \tag{8}$$

The variations of the weights and bias vectors can be obtained:

$2\mu e(k)x(k)$, $2\mu e(k)$

μ is the learning rate.

So the weight and bias update formula of the step adjustment are as eq.9:

$$W(k+1)=W(k)+2\mu e(k)(\frac{\partial e(k)}{\partial W(k)})^T \tag{9.1}$$

$$b(k+1)=b(k)+2\mu e(k) \tag{9.2}$$

Experimental validation

Experimental devices. The effectiveness of such LPO adaptive filter is verified on a micro-positioning system which is based on piezoelectric actuator of PST150 (Displacement Resolution: 0.01μm, open loop working status<0.002%F.S., close loop working status<0.02%F.S.; Withstand-voltage range: -30~150V; Maximum output displacement: 0~12μm; Stiffness: 25N/μm; Electrostatic capacitance: 3.60μF). The HPV series of piezoelectric actuator driving power and TI's TMS320LF2407 control devices are chosen. Digital-analog and analog-digital conversion chips are 16-bit AD669 and AD976, and serial port is used to pass the data from the controller to the host computer. The devices are shown in fig.3.

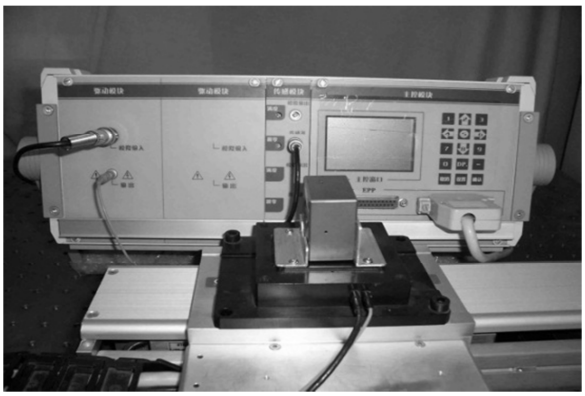


Fig. 3 Experimental devices

Modeling experiment of LPO and Modified adaptive filter. In the experiments, the actual dynamic responses of the piezoelectric actuator are compared with the outputs of the LPO adaptive filter models. In addition, the effectiveness of modified LPO adaptive filter model for asymmetric effect is also shown in contrast to LPO adaptive filter. Two kinds of excitation signals are employed in this experiment. The input-output hysteresis loops under excitation signals with uniform amplitude triangular wave are shown in fig.4. The input-output hysteresis loops under excitation signals with attenuation triangular wave are shown in fig.5.

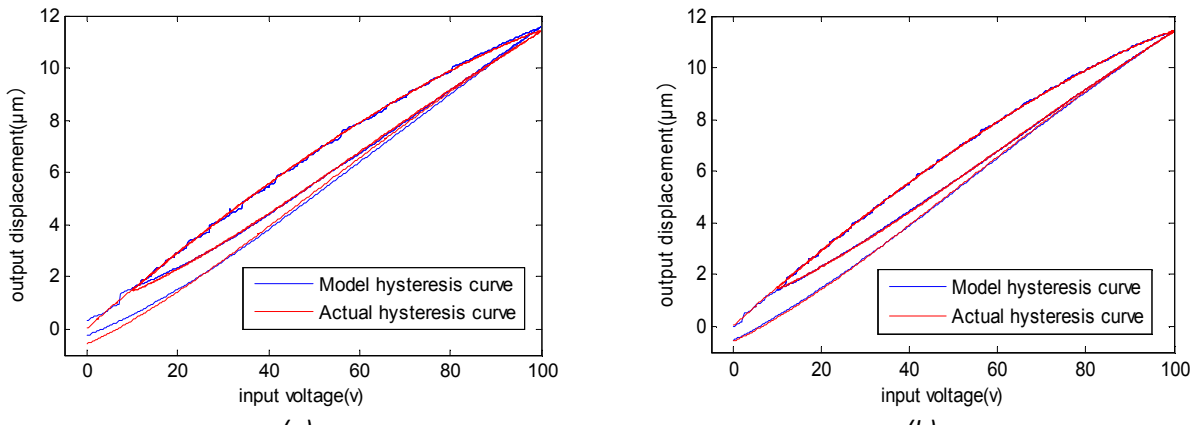
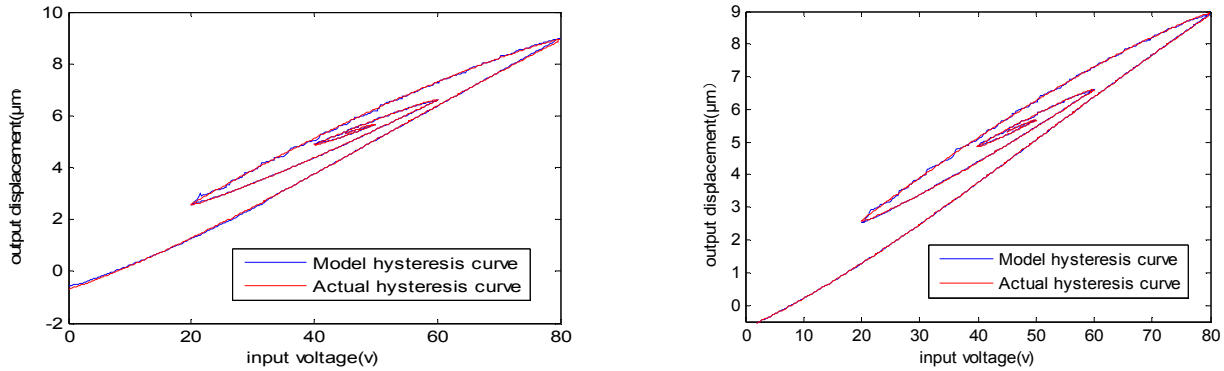


Fig.4. The input (V)-output (μm) curves of model.(a) LPO adaptive filter model (b) MLPO adaptive filter model.



(a) *(b)*

Fig.5. The input (V)-output (μm) curves of model.(a) LPO adaptive filter model(b) (b) MLPO adaptive filter model.

Table1 shows modeling errors of LPO adaptive filter model and modified LPO(MLPO)adaptive filter with different excitation signals. We can see that this LPO adaptive filter hysteresis model can characterize hysteresis of piezoelectric actuator well. Considering asymmetric property, the modified LPO filter significantly reduces the modeling error.

Table1 Modeling errors in different excitation signals

		LPO filter	MLPO filter
Attenuation triangle signal	$\|e\|_{ave}$(μm)	0.0235	0.0131
	MSE(μm2)	0.0011	3.9475e-004
Triangle signal	$\|e\|_{ave}$(μm)	0.0268	0.0187
	MSE(μm2)	0.0012	7.0893e-004

Summary

Linear play operator adaptive hysteresis model is proposed on the basis of adaptive transversal filter in this paper. LPO operators are used to replace delay operators of adaptive transversal filter, and LMS (Least Mean Square) algorithm is used to adjust the weight values. As hysteresis loop of piezoelectric actuator is asymmetric and LPO operator is symmetric, a modified LPO （MLPO） adaptive filter is proposed for asymmetric hysteresis effect. Experimental results show the accuracy of the proposed modeling methods. The LPO adaptive filter model can achieve an accurate hysteresis modeling , the modified LPO adaptive filter model can further decrease the modeling error one times.

Foundation

This research was supported by Natural Science Funds of Beijing(No. 4122066).

References

[1]V. Hassani, T. Tjahjowidodo, T.N.Do. A survey on hysteresis modeling, identification and control. Mechanical systems and signal processing. 49(1-2):209-233.2014

[2] J.E. Hurtado and A.H. Barba. Equivalent linearization of the Bouc-Wen hysteretic model.English structures.22(9):1121-1132.2000

[3]M.Ishmail,F.lkhouane and J.Rodellar. The hysteresis Bouc-Wen model,a suvey. 16(2):161-188.2009.

[4]Ying Feng,Camille Alain Rabbath, Tianyou Chai, C.Y.Su. Robust adaptive control of systems with hysteretic nonlinearities:a duhem hysteresis modeling approach, in:Proceedings of the IEEE AFRICON,2009.

[5]H.Hu, R Ben Mrad. On the classical Preisach model for hysteresis in piezoceramic actuators.Mechatronics.13(2):85–94.2003.

[6]Guo-Ying Gu,Li-Min Zhu, Chun-Yi Su. Modeling and compensation of asymmetric hysteresis nonlinearity for piezoceramic actuators with a modified prandtl-ishlinskii model. IEEE transactions on industrial electronics. 61(3):1583-1595.

[7]Guo-Ying Gu, Mei-Ju Yang, and Li-Min Zhu. Real-time inverse hysteresis compensation of piezoelectric actuators with a modified Prandtl-Ishlinskii model. Review of Scientific Instruments.83,065106,2012.

[8]Bernard Widow, Eugene Walach, Adaptive inverse control, Xi'an:Xi'an Jiaotiong University Press,2000.

[9]Xiangdong Liu, Ying Wang, Jie Geng, Zhen Chen. Modeling of hysteresis in piezoelectric actuator based on adaptive filter. Sensors and actuators A-physical, 189:420-428.

Key Engineering Materials Vols 645-646 (2015) pp 963-967
© (2015) Trans Tech Publications, Switzerland
doi:10.4028/www.scientific.net/KEM.645-646.963

Submitted: 2014-10-30
Accepted: 2014-12-23

The Dynamic Characteristics Research of MEMS V-shaped SiO_2/Al Electrothermal Actuator

Yueyue Shen[1,a*], Rongchang Song[1,b], Haimi Tang[1,c], Qingsen Chen[1,d], and Ping Guan[1,e]

[1] National Key Laboratory of Science and Technology on Electro-mechanical Dynamical Control, Beijing Institute of Technology, Beijing, CHINA, 100081

[a]shenyueyue.cool@163.com (corresponding author), [b]bit_src@bit.edu.cn , [c]tanghaimi@163.com, [d]1990chs@163.com, [e]752591599@qq.com

Keywords: V-shaped electrothermal actuator, dynamic characteristics, surface silicon process, multiphysics simulation.

Abstract: Traditional MEMS V-shaped electrothermal actuator is always fabricated with doping polysilicon, which always need a big voltage due to high resistivity of material. A new structure of actuator is proposed, which embeds heating layer, AL, into structural layer, SiO_2. Using the surface silicon technology, the fabrication process of new actuator is built and verified by simulation in Coventorware. Besides, through multiphysics dynamic simulation in Comsol Multiphysics, which takes some material property change with temperature into consideration, effect of structure parameter and input voltage on displacement is studied. The result proves that the new actuator structure can obtain a big displacement under a lower voltage in short time.

Intorduction

The micro actuator is the indispensable part in the microsystem and kinds of actuators have been studied, designed, and applied in the many occasions, such as fixing of fiber optics [1], positioning system [2], micropump [3] and so on. Because electrothermal actuator can obtain a bigger actuating force and overcome the dependence on distance compared with electric, magnetic actuator, it's applied in the more environments. The V-shaped electrothermal actuator can generate a perfect plane displacement, and the common structure material is polysilicon, which generate a displacement due to thermal expansion under Joule effect.

In 2007, Mohammad Mayyas has studied a microgripper where V-shaped thermal actuator is applied. The dynamic response measurement is made, which includes DC input voltage vs. deflection, the measured deflection responses under square excitation signals and with several frequencies [4]. In 2008, Zhang Wenyue analyzed how the direct current power and alternating current power affect the steady state displacement [5]. And Zhang Yongyu made research on the steady state characteristics of the V-shaped electrothermal actuator, which mainly includes the effects of angle of tilt, beam length and beam numbers on the maximum displacement [6]. In 2009, Mu Xiaojing studied the actuator's angle of tilt and obtain the most appropriate angle applied in Optical Coherence Tomography [7]. In 2012, Alex Man Ho Kwan changed the uniform beam cross shape and beam length, which improve actuator's performance [8].

In this paper, the finite element method (FEM) is used to analyze the dynamic characteristics of V-shaped actuator. Firstly, the structure of actuator is different from the traditional. The heater layer is AL, embedded into structure layer, SiO_2. Secondly, the fabrication process of this model will be discussed based on surface silicon process. Lastly, comparing FEM simulations of different structure device, the effects of structure parameter of actuator on displacement will be obtained.

The Modeling of Actuator and the Design of Fabrication Process

The Model of Actuator. The traditional model of electrothermal V-shaped actuator is built with polysilicon, which is also used as heating layer through the doping technology decreasing its

resistivity. Due to the limitation of the doping polysilicon resistivity, the efficiency is not satisfactory. So the way that the metal is chosen to embed into structural layer as heating layer, is proposed. The new model and displacement-time curve is showed as Fig. 1, and the structure parameters are listed in Table 1. The materials of structural and heating layer are Silicon Dioxide (SiO_2) and Aluminum (AL).

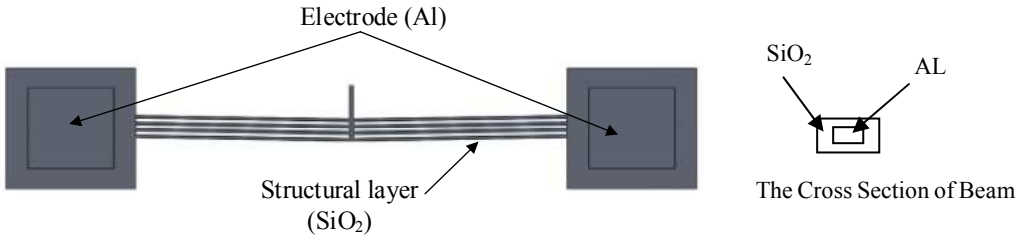


Figure 1. The Model of V-shaped Electrothermal Actuator and the Cross Section of Beam

Table1 The Structure Parameter of New Actuator Model

The beam length [um]	The beam width [um]	The beam thickness [um]	Interval of each group of beam [um]	The angle of tilt [°]	The group number of beam	Pads [um×um]
1000	5	3.5	10	1	4	200 × 200

While electrodes are applied with a voltage, the temperature will increase due to Joule effect, but be controlled within the melting points of materials. Then thermal expansion of beams generate a plane displacement. Fig. 2 shows the deformation of an actuator with 4 group of beams and 1 degree angle of tilt applied with a voltage of 1V. The maximum temperature is about 599K and the displacement is about 18um at 1ms after applying a 1V voltage.

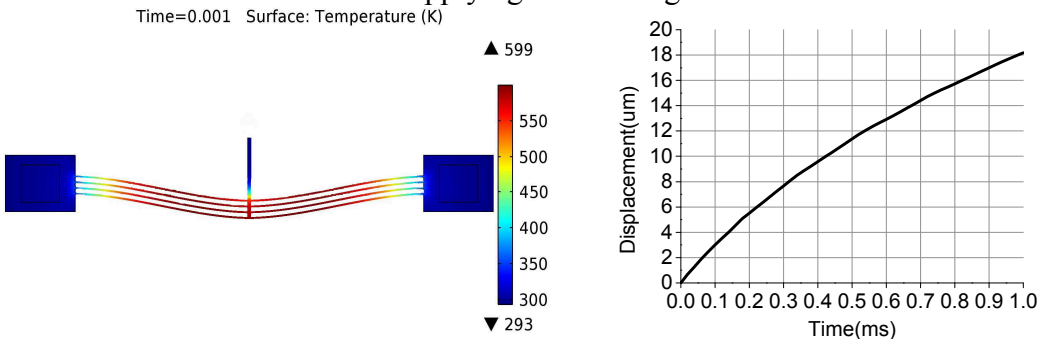


Fig. 2 The Deformation of V-shaped Thermal Actuator and Displacement-time Curve

The Fabrication Process. The new actuator model is fabricated based on the Surface Silicon Fabrication Technology [9]. And the whole process is showed in Fig. 3, consisting of the following six steps: (a) deposit 1.5um SiO_2 on silicon wafer; (b) sputter 0.01um Ti and 0.5um AL; (c) etch Ti and AL to form the heater layer shape; (d) deposit 1.5um SiO_2;(e) etch SiO_2 from actuator;(f) etch silicon substrate with XeF_2 to release actuator.

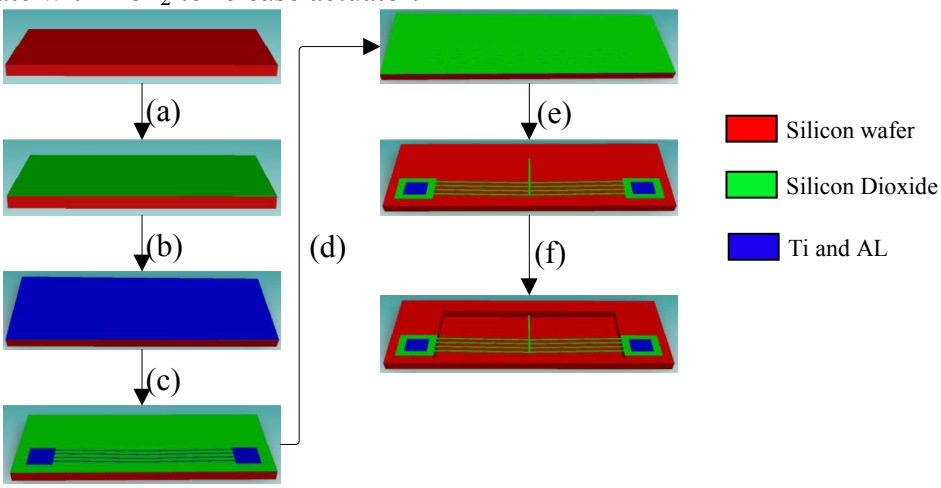


Fig. 3 The Surface Silicon Process of V-shaped Thermal Actuator

The Multiphysics Dynamic Simulation of Electrothermal Actuator

In the movement of actuator, there are two processes of energy conversion. Firstly, the electric energy is transformed into thermal energy and then transformed into mechanical energy. Therefore, the multiphysics simulation based on Comsol Multiphysics software can be used to analyze the characteristics of actuator.

The steady characteristics of traditional V-shaped polysilicon thermal actuator was already studied. But the heating material of the studying model is AL, whose resistivity is much less than doped polysilicon, the response characteristics of displacement with time is important in case the actuator will be damaged due to high temperature caused by Joule Effect.

The necessary material parameters of AL and SiO_2 are listed in the Table 2. With temperature increasing, some material properties are also changing and the varying coefficients are also seen in Table 2.

Table 2 The Necessary Materials Parameters of Actuator

	Coefficient of thermal expansion α [1/K]	$\frac{d\alpha}{dT}$ [$1/K^2$]	Heat capacity C [J/(kg*K)]	Density ρ [kg/m^3]	Thermal conductivity k[W/(m*K)]	$\frac{dk}{dT}$ [$W/(m*K^2)$]
AL	23.1e-6 (20℃)	2.3e-8	904	2700	237(20℃)	0
SiO_2	0.5e-6(20℃)	0	730	2200	1.4(20℃)	1.5e-3

	Young's modulus E [Pa]	$\frac{dE}{dT}$ [Pa/K]	Poisson's ratio σ	Resistivity ρ_1[Ω*m]	$\frac{d\rho_1}{dT}$ [Ω*m/K]	Relative permittivity ε
AL	70e9(20℃)	-0.06e9	0.35	0.28e-7(20℃)	0.12e-9	1
SiO_2	70e9(20℃)	0.014e9	0.17	0	-	-

To insure that the temperature is always within the allowed value, the voltage is 0.5V and studying time is 1ms. The coefficient of heat convection on the whole surface exposed in air (20℃) is 12 $W/(m^2*K)$. For studying the effects of structural size on displacement, the following simulations are conducted.

Different Beam Length. There are two actuators of different beam length, 0.5mm and 1mm. The displacement with time curves are showed in Fig. 4.

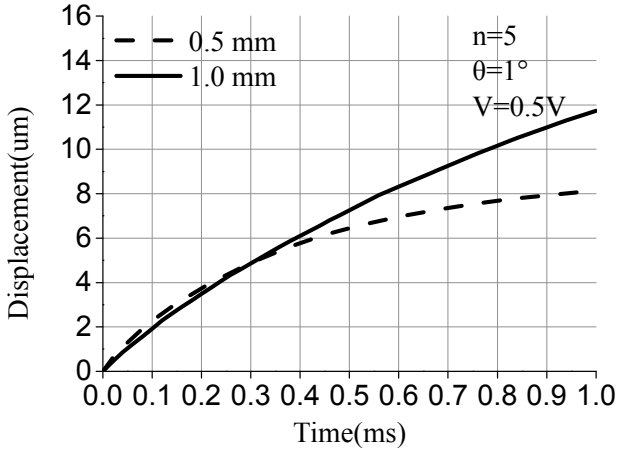


Fig. 4 The Displacement-time Curves of Different Beam Length of Actuators: n is the beam group number, V is the voltage and θ is the beam angle of tilt.

From Fig.4, it is known that the maximum deformation displacement are 12um and 8um when the beam length are 1mm and 0.5mm. Obviously, the displacement is proportional to the beam length. But the big beam length may cause the actuator unsteady.

Different Beam Group Number. Fig. 5 shows the contrast figure of different beam group number effects on displacement. From it, it is concluded that however many beam group number is, it

mostly has no difference on displacement, about 18um at 1ms. Since the increasing number of beam group is helpful to stability of actuator itself, it is a good measure to eliminate the instability caused by the overlong beam length through increasing the beam group number.

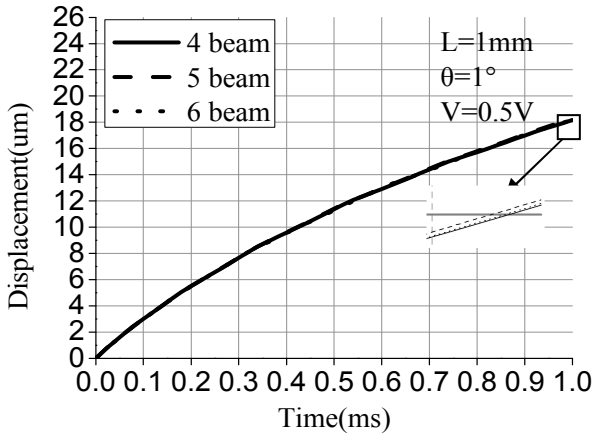


Fig. 5 The Displacement-time Curves of Different Beam Group Number of Actuators: L is the beam length.

Different Angle of Tilt. Fig. 6 shows the effect of angle of tilt on displacement. This result shows that the displacement range from 5um to 18um when the angle of tilt decreases from 4 degree to 1 degree and it means that the less angle can generate a bigger displacement.

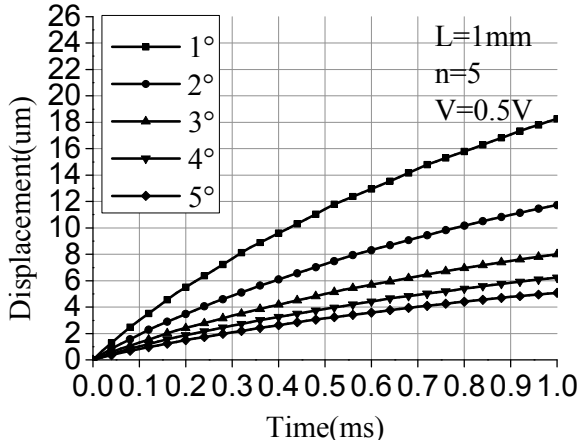


Fig. 6 The Displacement-time Curves of Different Angle of Tilt of Actuators

Different Input Voltage. The deformation energy and heat energy is the output of actuator, and the electric energy is the input. Obviously, output is proportional to input, as displacement-time curves showed in Fig. 7. When voltage is 0.1V, 0.3V, and 0.5V, the maximum displacement is 1um, 8um and 18um.

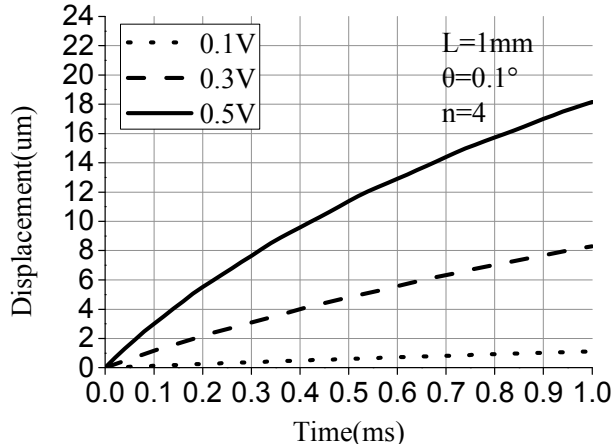


Fig. 7 The Displacement-time Curves of Actuators under Different Voltages

Conclusion

A new model of V-shaped electrothermal actuator is proposed, which consists of SiO_2 structural layer and AL heating layer. Compared with traditional polysilicon actuator, it can obtain 18um displacement in 1ms, which is highly efficient. And through multiphysics dynamic simulations, the effect of beam length, beam group number, angle of tilt and input voltage on displacement is known, which can give a good advice to researcher.

References

[1] A. Unamuno, J. Yao, and D, Alignment and Fixing of Fiber Optics Based on Electrothermal MEMS Actuators[J], ,IEEE Photonics Technology Letters, 2005, 17(4), pp.816-818.

[2] Sahil Oak, Sandesh Rawool, Ganapathy Sivakumar, Egbert J. Hendrikse, Jr.,Daniel Buscarello, and Tim Dallas, Development and Testing of a Multilevel Chevron Actuator-Based Positioning System [J], Journal of Microelectromechanical Systems, 2001, 20(6), pp.1298-1309.

[3] Saket Karajgikar, Smitha Rao, Jeongsik Sin, Dereje Agonafer, Jung-Chih Chiao,Dan Popa, and Harry Stephanou, Electro-Thermal Analysis of In-Plane Micropump [J], IEEE Transactions on Components and Packaging Technologies, 2010, 33(2), pp.329-339.

[4] Mohammad Mayyas, Ping Zhang, Woo H. Lee, Panos Shiakolas, and Dan Popa, Design Tradeoffs for Electrothermal Microgrippers [C], IEEE International Conference on Robotics and Automation, 2007, pp.907-912.

[5] Wenyue Zhang, Markus Gnerlich, Jonathan J Paly, and etc, A polymer V-shaped electrothermal actuator array for biological applications [J], J. Micromech. Microeng, 2008, 18(7): 075020(8pp).

[6] Yongyu Zhang, Performance of V-Shaped Electrothermal Silicon Microactuator and Its Application [D]. Shanghai: Shanghai University, 2008.

[7] Xiaojing Mu, Guangya Zhou, Hongbin Yu, and etc, Compact MEMS-driven pyramidal polygon reflector for circumferential scanned endoscopic imaging probe [J], Optics Express, 20(6), 2009, pp.6323-6339.

[8] Alex Man Ho Kwan, Sichao Song, Xing Lu, and etc, Compact MEMS-driven pyramidal polygon reflector for circumferential scanned endoscopic imaging probe,Journal of Microelectromechanical Systems [J], 21(3), 2012, pp.586-595.

[9] Xiaoming Liu, Zhonggan Zhu, MEMS Design and Manufacture [M]. Beijing: National Defense Industry Press, 2006, pp.70-138, pp.180-201.

Key Engineering Materials Vols 645-646 (2015) pp 968-971
© (2015) Trans Tech Publications, Switzerland
doi:10.4028/www.scientific.net/KEM.645-646.968

Submitted: 2014-11-02
Accepted: 2014-12-23

The Parametric Analysis of the Threshold Value Judging Mechanism in MEMS Safety and Arming Device

Wang Fufu[1, a *], Lou Wenzhong[1,b], Liu Fangyi [1,c], Wang Dakui[1,d], Zhang Mingrong[2, e], Xu Chenggang[2, f]

[1]School of Mechatronical Engineering, Beijing Institute of Technology, Beijing, China, 100081

[2] Changan Industry, Chongqing, 401120

[a]wangfufu2004@sina.com, [b]louwz@bit.edu.cn, [c]lfyhbu@163.com, [d]wangdakui1987@163.com, [e] zhangmr@163.com, [f] 13896053015@139.com

Keywords: Threshold Value Judging Mechanism; MEMS; Safety and Arming Device

Abstract. In this paper, a mechanical MEMS S&A device has been proposed. The size of the device is 10mm×13mm×0.5mm. The role of the threshold value judging mechanism is to determine the environment suffered by centrifugal force and control the sub-centrifugal slider not movement under the threshold, so as to effectively guarantee the time of long-distance arming. Through establishing the three-dimensional model of threshold value judging mechanism, establishing the force and the parameters of locking-releasing mechanism, deriving the mathematical model according to the rigid dynamic mechanics theory and establishing the finite element model by using ANSYS/LS-DYNA, appropriate threshold value judging mechanism is designed to meet two items, one item is the deformation of threshold value rod is not enough to release sub-centrifugal slider when the speed is less than 60000r/min; the other item is deformation of threshold value rod can release sub-centrifugal slider when the speed is more than 60000r/min.

Introduction

Along with the fuze used in OICW (Objective Individual Combat Weapon) becoming smarter and smaller, MEMS (Micro-electromechanical Systems) is becoming increasingly important. Since 1990s, the superiority and approaches of MEMS fuze have been introduced [1]. The miniaturization of S&A (Safety and Arming) device takes priority over other tasks. Battlefield is a complex electromagnetic environment, so it may affect the reliable work of MEMS S&A device relying on electric insurance. However, this kind of MEMS S&A device is the most common currently, as shown in Fig.1 [2-5]. Our term (National Key Laboratory of Mechatronics Engineering and Control) puts forwards a mechanical MEMS S&A device innovatively, the concrete structure as shown in Fig.2. This device includes main centrifugal slider, sub-centrifugal slider, lock-releasing mechanism, threshold-value judging mechanism, elastic-beam delaying mechanism and so on. And the size of the device is 10mm×13mm×0.5mm

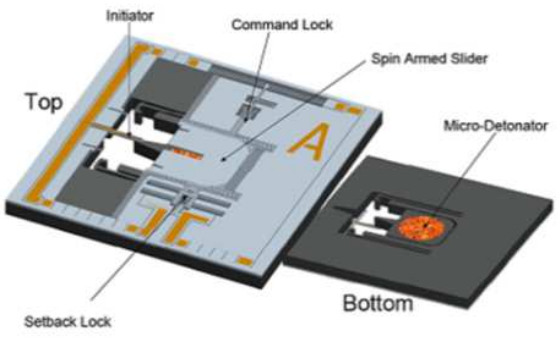


Fig. 1 The MEMS S&A device

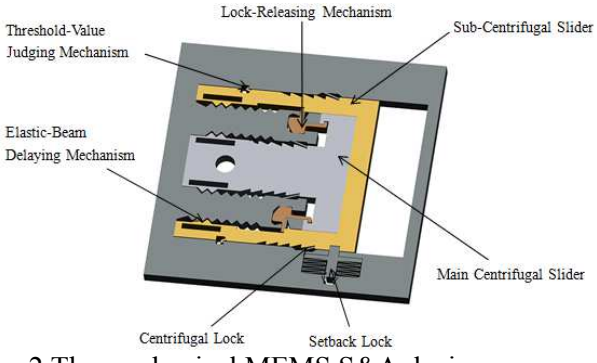


Fig. 2 The mechanical MEMS S&A device

Among them, the role of the threshold value judging mechanism is to determine the environment suffered by centrifugal force and control the sub-centrifugal slider not movement under the threshold,

so as to effectively guarantee the time of long-distance arming. Fig.3 shows that the threshold value judging mechanism is composed of positioning block， threshold value rod and accomodated groove. The mechanism is designed to meet two items, one item is the deformation of threshold value rod is not enough to release sub-centrifugal slider when the speed is less than 60000r/min; the other item is deformation of threshold value rod can release sub-centrifugal slider when the speed is more than 60000r/min.

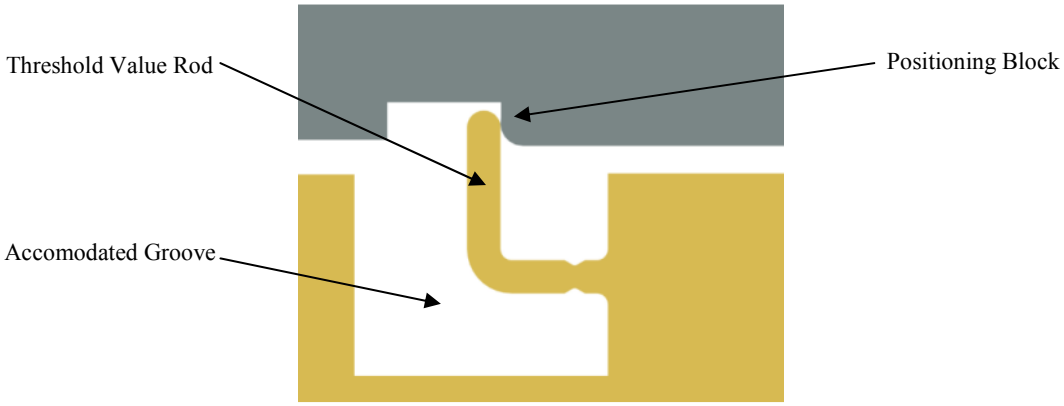


Fig. 3 The threshold value judging mechanism

Model and Theoretical Analysis

The center of gravity, rotation center and stroke of the sub-centrifugal slider are shown in Fig.4. The parameters of threshold value judging mechanism are shown in Fig.5.

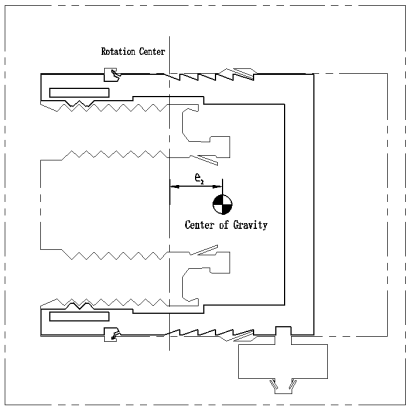


Fig. 4 The center of gravity, rotation center and stroke of the sub-centrifugal slider

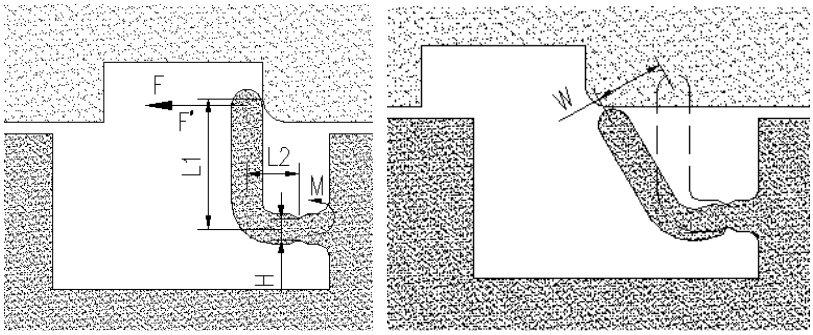


Fig. 5 The parameters of threshold value judging mechanism

According to the Fig.4, we can get the initial acceleration

$$a_0 = e_2\omega^2 \tag{1}$$

Where, e_2 is the initial eccentricity of sub-centrifugal slider; ω is the angular velocity of the device.

So, we can get the initial force

$$F = ma_0 \tag{2}$$

The relative length

$$L = \sqrt{L_1^2 + L_2^2} \tag{3}$$

Where, L_1 is the vertical component of the length; L_2 is the horizontal component of the length.

So, we can get the relative component of the initial force

$$F' = F \times \frac{L_1}{L} \tag{4}$$

Applied cantilever deflection curve equation to analysis the threshold value judging mechanism, as shown in Fig.6.

So

$$W = -\frac{\mathrm{F'L}^3}{3EI} \tag{5}$$

Combining equation (1) ~ (4), we can get

$$W = \frac{\mathrm{me}\omega^2 L_1\left(L_1^2 + L_2^2\right)}{3EI} \tag{6}$$

Where, W is the deflection of the threshold value rod; E is the elastic modulus of the threshold value rod; I is the moment of inertia of the threshold value rod.

$$I = b \cdot h^3 / 12 \tag{7}$$

Where, b=0.5mm; h is the width of the threshold value rod.

According to the design criteria: $W = 0.09$ mm, combining equation (6) and (7), we can get

$$h = 0.0244\,\mathrm{mm} \tag{8}$$

Eventually, we get *h*=0.025mm.

Simulation Analysis and Conclusions

The launch overload curve shown in Fig.7 is obtained in the launch process.

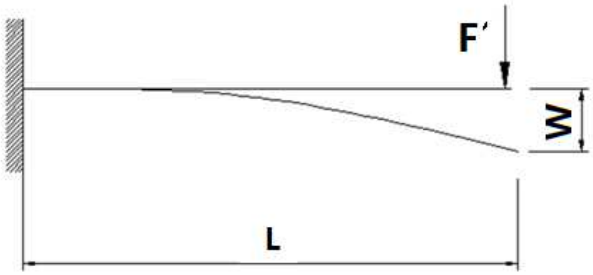


Fig. 6 The deflection of the threshold value rod

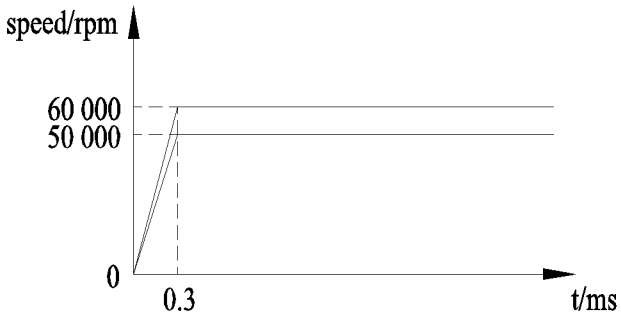


Fig. 7 The launch overload curve

According to the result (h=0.025mm), establishing the finite element model, setting different step length, searching different rotational speed and observing the release situation of the sub-centrifugal slider, as shown in Table I . According to the Table I , loading the different launch overload curves(Fig.7), making nonlinear dynamic mechanics simulation by using ANSYS/LS-DYNA, different displacement(Fig.8) and speed curves(Fig.9) are obtained.

Table I Search step and the corresponding release conditions

Step length （r/min）	Rotational speed （r/min）	Whether or not the sub-centrifugal slider releases (Y/N)
10000	50 000	N
	60 000	Y
3000	55 000	N
	58 000	Y
1000	56 000	N
	57 000	N

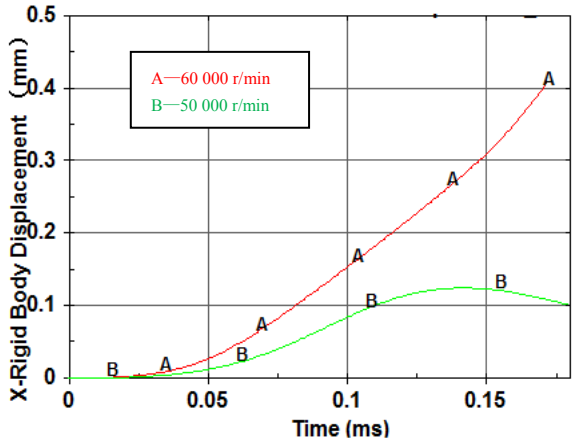


Fig. 8 The displacement curve

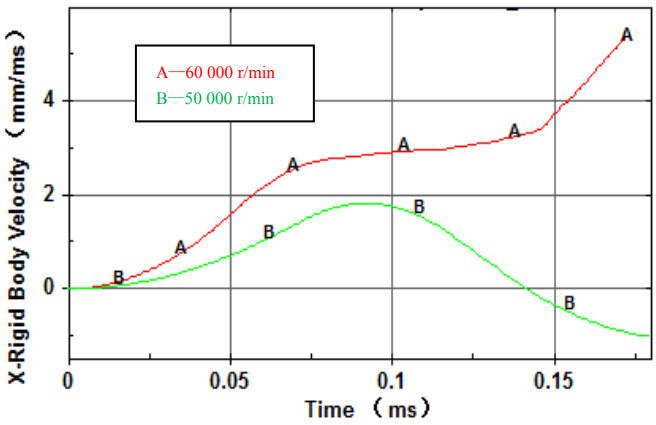


Fig. 9 The velocity curve

Through analyzing the Fig.8 and Fig.9, it arrives at the conclusions as follows.

1) The threshold value judging mechanism can judge the rotational speed of the S&A device and the threshold value of the designed mechanism is 57 000 r/min according to table I , the Fig.8 and Fig.9.

2) The mathematical model is verified through analyzing different displacement and speed curves.

3) In reality, the critical rotational speed may be relatively larger because of the friction.

4) The feasibility of the above research is confirmed.

Next

The MEMS S&A device with the threshold value judging mechanism is being fabricated and the Centrifugal test will be tested to verify the validity of the threshold value judging mechanism.

Acknowledgment

The research was supported by the State Key Laboratory of Mechatronics Engineering and sponsored by the National Project of China (Z092014B001) and the National Project of China (914A05050313BQ1014).

References

[1]Robinson, C. H., Wood, R. H. and Hoang, T. Q., “Development of Inexpensive, Ultra-Miniature MEMSBased Safety Andarming (S&A) Device for SmallCaliber Munition Fuzes,” Proceedings of 23rd ArmyScience Conference, pp. 111-116 (2002).

[2]Renaud Lafont. Micro-machined or micro-engraved safety and arming device [P]. US Patent No.0205526A1,2009.

[3]Chopin Hua. High-g MEMS Fuzes [R]. Baltimore, USA: 56TH ANNUAL FUZE CONFERENCE, 2012

[4]David A. Olson. Microelectromechanical Systems Ignition Safety Device [P]. US Patent No.7971532A1,2011.

[5]Wang Fufu, Lou Wenzhong, Wang Ying. Design and analysis of a novel locking mechanism of MEMS safety and arming device [J]. p 856-859, 2014, Micro-Nano Technology XV

Key Engineering Materials Vols 645-646 (2015) pp 972-979
© (2015) Trans Tech Publications, Switzerland
doi:10.4028/www.scientific.net/KEM.645-646.972

Submitted: 2014-11-15
Accepted: 2014-12-23

The error analysis of micro-flow self-sensing actuator

Yanbo WEI [1,a], Liping SHI [2*,b], Haimin ZHOU [3,c]

[1,2,3]School of Mechanical and Electrical Engineering, Heilongjiang University, Harbin 150080, China

[1]Harbin Institute of Petroleum, Harbin 150027, China

[a] weiyanbobo@163.com, [b] shlp1971@163.com(corresponding author), [c]zhouhm0919@163.com

Key words: micro-flow injection; self-sensing actuator; error analysis; nonlinearity; hysteresis

Abstract: In this article the micro flow self-sensing actuator has carried on the theoretical analysis and experimental research. Using output micro-displacement generated by the first inverse piezoelectric effect to realize cell micro flow injection, using output voltage generated by secondary direct piezoelectric effect of piezoelectric ceramic to self-sensing the output displacement in the process of the micro flow injection. The experimental results show that the micro-displacement of micro-flow self-sensing actuator has nonlinear error, error is 5.03%. The error between measured micro-displacement and self-sensing micro-displacement is 63.13%. In this paper, the error causes analysis of micro-flow self-sensing actuator is from non-linearity and hysteresis, external factors, it lay the foundation for the further study of micro-flow self-sensing actuator.

1 Introduction

After decades of development, in the field of MEMS, the application of integration of piezoelectric sensors and actuators become more mature. In recent years, in the field of biomedical, the actuator based on piezoelectric effect become the hot topic which the domestic and foreign scholars research, especially the research of cell micro flow injection technology, promote the development of the automation process which requires cell micro operations, such as cell clone, hybridization, chromosome and embryo transfer [1-2].

Currently, domestic and overseas scholars have extensive research in the operation of cell injection, and put forward the method of cell micro-flow injection with the piezoelectric drive power supply. For instance, mechanical structure and control system of cell drug micro-injection is composed of piezoelectric-driven micro injection platform and motor-driven micro-cell stage; micro-flow injection method is used impact type inertial force generated by low-frequency vibration of piezoelectric ceramic to overcome micro-feed force generated by friction[3-5]. These methods are based on the first inverse effect of piezoelectric ceramic, on this basis, the design on the basis of the principle of secondary piezoelectric effect of the micro flow self-sensing actuator was proposed, its basic principle is: using micro-displacement of piezoelectric ceramic due to its first inverse piezoelectric effect to achieve cell micro-flow injection. Using the charge due to the secondary direct piezoelectric effect to detect the force and displacement in the injection by itself [6-7] .

2 The theoretical analysis of micro-flow self-sensing actuator

The micro-flow self-sensing actuator is based on the first inverse and the secondary direct piezoelectric effect in this paper.

In mechanical free boundary conditions, the external electric field E_n is applied to piezoelectric ceramic stack, external stress is zero, then piezoelectric strain $S_i^{(1)}$ is generated through first inverse piezoelectric effect, Eq.1 can be obtained from the first class piezoelectric equations.

$$S_i^{(1)} = d_{ni} E_n \tag{1}$$

where d_{ni} is piezoelectric strain constant.

At the same time, $S_i^{(1)}$ will produce an additional electric displacement $D_m^{(2)}$ through the secondary piezoelectric effect, Eq.2 can be obtained from the first class and second class piezoelectric equations.

$$D_m^{(2)} = e_{mi} S_i^{(1)} = e_{mi} d_{ni} E_n \tag{2}$$

where e_{mi} is piezoelectric stress constant.

From Eq. 1 and Eq.2, it can be seen that strain $S_i^{(1)}$, displacement $D_m^{(2)}$ and external electric field E_n are correspondence relationship, therefore, by changing the applied electric field, using strain $S_i^{(1)}$ generated by the first inverse piezoelectric effect to achieve actuator function of micro-flow self-sensing actuator, cells flow injection can be performed. Using displacement $D_m^{(2)}$ generated by the secondary direct piezoelectric effect to achieve sensor function, self-sensing the feed amount of micro-flow self-sensing actuator.

3 Experimental study of micro-flow self-sensing actuator

In experimental study of micro-flow self-sensing actuator, there are the output voltage $V^{(2)}$ of secondary direct piezoelectric effect and $S_3^{(1)}$ micro-displacement of first inverse piezoelectric effect. They are measured with the piezoelectric ceramic stack under the external voltage.

The output voltage $V^{(2)}$ of secondary direct piezoelectric effect can be gained through electric displacement $D_m^{(2)}$, which is shown in Eq.3.

$$V^{(2)} = \frac{Q^{(2)}}{C} = \frac{AD^{(2)}}{C} = \frac{Ae_{33}d_{33}V_3}{Ct} = \frac{Ae_{33}}{Ct} \cdot \delta \tag{3}$$

where $V^{(2)}$ is the output voltage of secondary direct piezoelectric effect, $Q^{(2)}$ is output charge of secondary direct piezoelectric effect, A is cross-sectional area of ceramics stack, e_{33} is piezoelectric stress constant, C is equivalent capacitance of the piezoelectric ceramic stack, t is monolithic thickness of piezoelectric ceramic stack.

δ is the output displacement of first inverse piezoelectric effect.

Micro-displacement δ of first inverse piezoelectric effect and the output voltage $V^{(2)}$ of secondary direct piezoelectric effect can be measured by circuit, which is shown in Fig.1. DF1743003C provide driving voltage from 0 V to 60 V to equivalent capacitance C_0, step is 10V. LVDT micrometer is used to measure micro-displacement. Two channel of YE6230T-16 data acquisition device can collect the displacement generated by the first inverse piezoelectric effect and the output voltage by self-sensing circuit.

The theoretical displacement of the first inverse piezoelectric effect and theoretical voltage of the secondary direct piezoelectric effect of piezoelectric micro-flow self-sensing actuator can be calculated by the Eq.1 and Eq.3, measured value can be gained in the experiment. By means of the measured voltage in the secondary direct piezoelectric effect, we can calculated the displacement of secondary piezoelectric effect from the first converse secondary piezoelectric effect, shown in Table1.

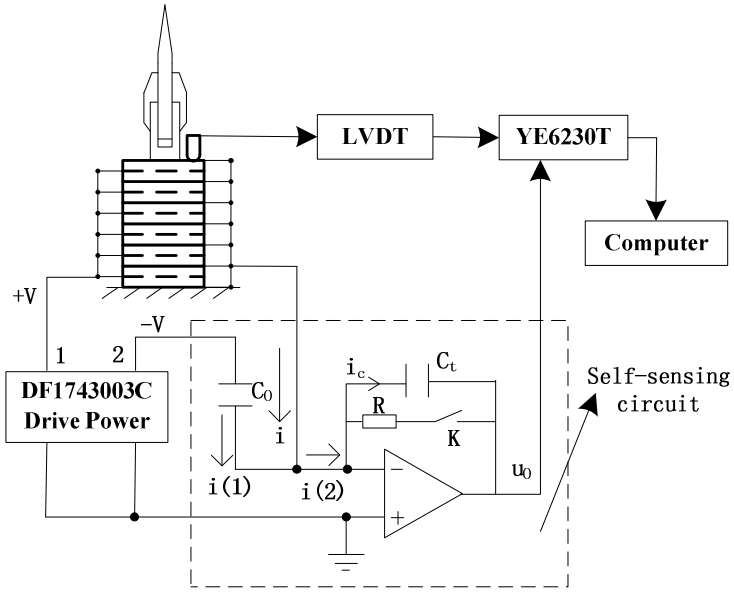


Fig.1 The experimental structure of micro-flow self-sensing actuator

Table 1 The experimental data of micro-flow self-sensing actuator

External voltage (V)	The theoretical displacement of the first inverse piezoelectric effect (μm)	The measured displacement of the first inverse piezoelectric effect (μm)	The theoretical voltage of the secondary direct piezoelectric effect (mV)	The measured voltage of the secondary direct piezoelectric effect (mV)	The self-sensing displacement of the secondary direct piezoelectric effect (mV)
0	0	0	0	0	0
10	2	1.43	32.75	10.30	0.63
20	4	3.37	65.50	23.26	1.42
30	6	5.51	98.25	36.31	2.22
40	8	7.82	131	50.12	3.06
50	10	10.15	163.75	63.11	3.85
60	12	12.53	196.5	75.74	4.62

Fig.2 is the compared curve of micro-flow self-sensing actuator between measured displacement and self-sensing displacement. The graph shows linearity of measure displacement generated by the first inverse piezoelectric effect is good, while there is error in it. The linearity of self-sensing

displacement is well, but there is large error compared with the measured value of the first inverse piezoelectric effect. So it's necessary to analyze the causes of error to avoid the occurrence of error and design correction methods to improve the performance of micro-flow self-sensing actuator, lay the foundation for the subsequent studies and practical application.

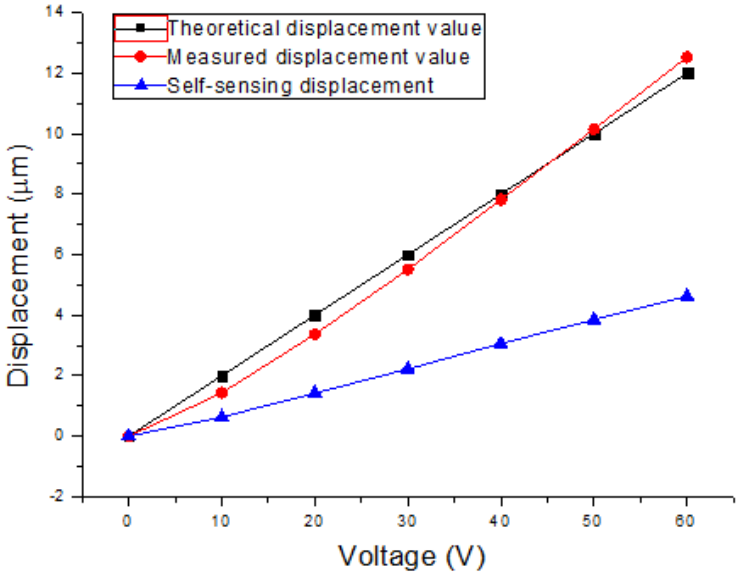


Fig.2 The comparison between self-sensing displacement and measured displacement of micro-flow self-sensing actuator

4 The error analysis of micro-flow self-sensing actuator

There are many occurrences of error in micro-flow self-sensing actuator, for instance, the nonlinearity, hysteresis characteristics and creep property of the micro-flow self-sensing actuator. These are the major factors of the occurrence of error. Besides, the influences of interfering noise of external environment and operational amplifier to measuring circuit are the significant factors to occurrences of error in micro-flow self-sensing actuator.

4.1 The error analysis of the nonlinearity

The error of nonlinearity in micro-flow self-sensing actuator can be concluded from the aspects of higher-order effects, multi-piezoelectric effect, electrostrictive effect [8]. In this paper, the influence of electrostrictive effect to self-sensing actuator is the major consideration.

The piezoelectric ceramic stack is applied by the electric field E_0, shown in Fig.3, electric charge density on polar plate $\pm\sigma_0$, charge density after poled on the surface of piezoelectric ceramic $\pm\sigma'$, the dielectric constant of piezoelectric ceramic ε. The charge σ_0 of the dielectric medium producing the electric field is equivalent to dipole, which is stressed under external electric field [9]:

$$F = QE_0 \tag{4}$$

The charge is the sum of the charge after poled on the surface of piezoelectric ceramic and the residua charge after poled of piezoelectric ceramic:

$$Q = Q' + Q_r \tag{5}$$

On account of piezoelectric ceramic is equivalent to elastomer, it satisfies Hooke's law:

$$F = k \cdot \Delta L \tag{6}$$

Eq.7 can be obtained from Eq. 4 and Eq. 6:

$$QE_0 = k \cdot \Delta L \tag{7}$$

Because

$$Q' = \sigma' \cdot S = \frac{\varepsilon - \varepsilon_0}{\varepsilon} \cdot -\sigma_0 \sigma_0 \cdot S = \frac{\varepsilon - \varepsilon_0}{\varepsilon} \cdot E_0 \cdot \varepsilon_0 \cdot S \tag{8}$$

We can conclude:

$$E_0 = \frac{Q'\varepsilon}{\varepsilon_0 S(\varepsilon - \varepsilon_0)} \tag{9}$$

Where S is the area of polar plate, ε_0 is the dielectric constant of vacuum.

Put the Eq. (5) and Eq. (9) into Eq. (7), concluding:

$$\Delta L = (Q' + Q_r) \cdot \frac{Q'\varepsilon}{\varepsilon_0 S(\varepsilon - \varepsilon_0)} \tag{10}$$

For the dielectric constant ε of piezoelectric ceramic greater than the dielectric constant ε_0 of vacuum, Eq. (7) can be simplified:

$$\Delta L = \frac{Q'}{\varepsilon_0 Sk}(Q' + Q_r) = \frac{1}{\varepsilon_0 k}(E^2 \varepsilon^2 S + E\varepsilon Q_r) \tag{11}$$

ΔL is the displacement of piezoelectric ceramic under external electric field. When $Q_r = 0$ the part of it is caused by electrostrictive effect:

$$\Delta L == \frac{\varepsilon^2 S}{\varepsilon_0 k} \cdot E^2 \tag{12}$$

In the Eq.11, we can find the displacement S of micro-flow self-sensing actuator and the electric field intensity E are co-linear. That's why the nonlinearity in micro-flow self-sensing actuator.

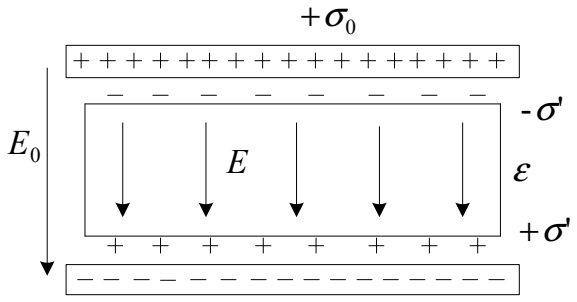


Fig. 3 The electric charge distribution diagram of Piezoelectric ceramic in the electric field

4.2 The analysis of hysteresis characteristics

Ferroelectric crystal is always divided into some small region called electric domain in the process of the spontaneous polarization, the polarization direction of the electric domains vary, external electric field offsetting because of the different Electric domains polarization direction, thus the entire crystal is not present electric field.

Piezoelectric ceramics have isotropic electric domains structure, similar to the spherical in the structure, electric domains presented chaotically distributed and have different polarization directions,offsetting polarization effects inside the crystal, leading to the crystal intensity of polarization is zero, so the crystal does not exhibit piezoelectric effect. Placed Piezoelectric ceramic materials into the strengthening DC field, the internal electric domain of ceramic will be rearranged and its polarization direction will orientation again, piezoelectric ceramic presents the macroscopic residual polarization [10]. The process of piezoelectric polarization is shown in Fig.4.

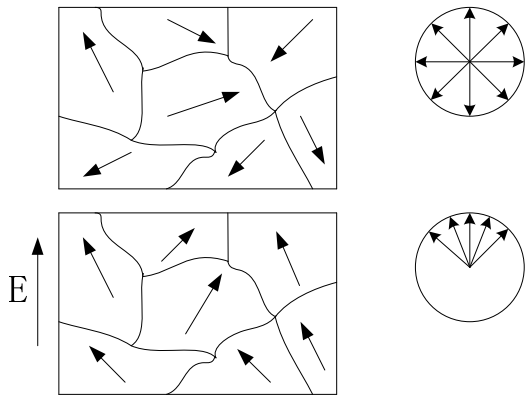


Fig. 4 The polarization process diagram of piezoelectric ceramic

After the polarization treatment, subjected to the external electric field, piezoelectric ceramics will produce displacement. Assume that the polarization axis length of I-th electric domains is l_i, the angle of electric domain direction and the electric field direction is α_{ie}, shown in Fig.5. Therefore, under the electric field, the strain of I-th electric domain is:

$$S_i = l_i \cos\alpha_{ie} - l_i \cos\alpha_{i0} \tag{13}$$

Thus, the total strain produced in the piezoelectric ceramic can be obtained as follows:

$$S = \sum_{i=1}^{n} l_i (\cos\alpha_{ie} - \cos\alpha_{i0}) \tag{14}$$

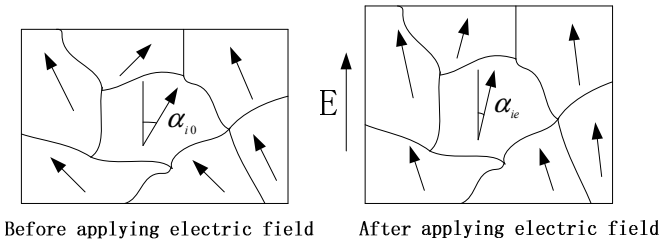


Fig. 5 Displacement generation process of piezoelectric ceramic under the external voltage

Because after pre polarization of the piezoelectric ceramic, the direction of the electric domain and spontaneous polarization axial length has been determined, so Eq.14, α_{i0} and l_i can be as constants, Therefore, the size of the deformation of the piezoelectric ceramic is proportional to the cosine of the steering angle, which is the main cause of the hysteresis error of micro-flow self-sensing actuator.

4.3 The analysis of external factors measurement error

In the theoretical voltage value calculation of the secondary piezoelectric effect, The integrated amplifier is equivalent to an ideal operational amplifier, open-loop gain and input impedance is infinite, input resistance and wiring resistance is approximately zero, while the actual measurement is not the case, the output voltage depends on these parameters of the amplifier. Therefore, there must error between the actual working condition and ideal analysis, called calculation error. These errors can't be eliminated only by selecting the device to minimize the error.

In addition, the measuring physical quantities of experiment, whether it is a micro-displacement generated by the first inverse piezoelectric effect of, or voltage generated by the secondary direct piezoelectric effect, is a very weak signal. Power supply fluctuation, temperature fluctuations, drifting and component aging of detection circuit is the source of the error [11]. Interference noise source power is much greater than the useful signal power of measured circuit, after coupling path, the noise power is greatly diminished, but relative to the weak useful signal, it is still very strong interference. The size of the environmental interference noise influence on measurement results is closely related to the layout and structure of measurement circuit, its characteristic is depends on the characteristics of interference sources, and depends on the characteristics of the coupling way.

5 Conclusions

This paper has theoretical analysis and experimental research of the micro-flow self-sensing actuator based on piezoelectric ceramic. The experimental results show that the displacement of first inverse piezoelectric effect self-sensing through the secondary direct piezoelectric effect has a good linear relationship, but compared with the theoretical value, there is still a certain error. From the internal aspects, analyzes the impact of errors caused by inherent characteristics of piezoelectric ceramic stack, such as non-linearity and hysteresis, from the external aspects, analyzes the impact of errors caused circuit and environmental interference. Error analysis of micro-flow self-sensing actuator can lay the foundation for the design of error correction device and achieve precision measurements and precise positioning.

Acknowledgement

This work is supported by Heilongjiang Provincial Department of Education Science and Technology Research Project (No.12541624).

Reference

[1] Tang Zhaojun. The device fabrication and micro-injection of Automated cell microinjection[D]. Nanjing: Nanjing university of science and technology, 2011: 1-4.

[2] Chen Wei. The research and development of cell micro injection system implementing device[D]. Jilin: Northeastern university, 2010: 1-8.

[3] Nagaki A, Miyazaki A, Tomida Y, et al. Anionic polymerization of alkyl methacrylates using flow microreactor systems[J]. Chemical Engineering Journal, 2010, 7413:1-8.

[4] Yu Xie, Dong Sun, Senior Member,IEEE, Chong Liu.Penetration Force Measurement and Control in Robotic Cell Microinjection[C].The 2009 IEEE/RSJ International Conference on Intelligent Robots and Systems. USA, 2009: 4701-4706.

[5] Xiao Xianqiang, Li Xinxin, et al. Research on the device of cell medicine microinjection based on piezoelectric actuator[J]. Machinery Design & Manufacture, 2005, 12: 29-31.

[6] Shi Liping, Sun Lining, Rong Weibin. Application of the first inverse and the secondary direct piezoelectric effect to self-sensing actuators[J]. Nanotechnology and precision engineering, 2010, 8(3): 211-214.

[7] Wei Yanbo, Shi Liping, Wei Xiwen. Research on Micro-flow Self-sensing Actuators based on Piezoelectric Ceramic Stack[J]. Journal of Harbin Institute of Technology (New Series), 2014,2(21): 99-103.

[8] Shi Liping, Wei Xiwen, Wei Yanbo. Investigation on Nonlinear Analysis and Correction Method of Piezoelectric Sensors and Actuators [J]. 2012 International Conference on Measurement, Information and Control (MIC). 2012, 912-916.

[9] Zhang Tao, Sun Lining. The basic characteristic research on piezoelectric ceramic[J]. Optics and Precision Engineering, 1998,10(6): 26-32.

[10] Shi Liping, Wei Yanbo, Wei Xiwen. The origin and correction of hysteresis nonlinearity on piezoelelctric ceramic[J]. Journal of Heilongjiang Hydraulic Engineering College, 2013,4(2): 103-112.

[11] Zhang Jiawei, Liu Fang. The circuit design and error analysis of high precision strain detection[J]. Process automation instrumentation. 2011,32(6): 83-86.

Key Engineering Materials Vols 645-646 (2015) pp 980-985
© (2015) Trans Tech Publications, Switzerland
doi:10.4028/www.scientific.net/KEM.645-646.980

Submitted: 2014-11-24
Accepted: 2014-12-23

Analysis of Harmonic Distortion of Sigma-Delta Modulator

Dong Yan[1], WenNing Jiang[1], Siqi Tao[1], Jian Yang[1], liang Yin[1,a], Xiaowei Liu[1,2]

[1]MEMS Center, Harbin Institute of Technology, Harbin, Heilongjiang, China

[2]Key Laboratory of Micro-systems and Micro-structures Manufacturing (Harbin Institute of Technology), Ministry of Education, Harbin, Heilongjiang, China

[a]hit2010yd@163.com

Keywords: Sigma-Delta modulator, Single-loop, THD, Non-linearity

Abstract: In this paper, the harmonic distortion of fourth-order sigma-delta modulator is analyzed. Based on the analysis non-ideal models are established and simulation results demonstrated the validity of these models. The non-linear capacitors introduce harmonic distortion and the non-linear on-resistance nearly only introduce second order harmonic distortion. The non-ideal integrators can increase the noise floor of the modulator.The fully-differential topology can be adopted to eliminate even order harmonic distortion and the operational amplifier with high performance can also be used to decrease noise floor of the modulator.

Introduction

With the development of the VLSI (Very Large Scale Integrated) circuit, the digital circuit has made great progress. Compared with the analog circuit, the digital circuit has many advantages such as high resolution, high reliability, low power and so on [1]. ADC (Analog to Digital Converter) is the connection between analog and digital world and is widely used in processing digital audio. Nearly all analog signals such as temperature, light, electricity must be transformed into digital signals through ADC and then be processed by digital circuit [2]. The computer's ability in digital signal processing is improving, so high resolution and high speed converters are needed [3-4]. The sigma-delta ADC has these advantages. As the harmonic distortion in the output of the sigma-delta modulator can decrease the performance of Sigma-Delta ADC, it is essential to eliminate the harmonic distortion. The sources of the harmonic distortion are mainly the nonlinear circuits in the system. In this paper the sources of distortion will be analyzed and modeled in Simulink. Therefore an effective method to design high performance Sigma-Delta ADC will be presented.

Analysis of the non-idealities of sigma-delta modulator

In this paper the topology of modulator is the forth-order, single-loop, single-bit sigma-delta modulator which is shown in Fig.1. a_1, a_2, a_3, a_4 are the feed-forward coefficients of the modulator and b_1, b_2, b_3, b_4 are the coefficients of the integrators. The noise and signal transfer functions are:

$$STF(z) = 1 \tag{1}$$

$$NTF(z) = \frac{(z-1)^4}{(z-1)^4 + a_1 b_1 (z-1)^3 + a_2 b_1 b_2 (z-1)^2 + a_3 b_1 b_2 b_3 (z-1) + a_4 b_1 b_2 b_3 b_4} \tag{2}$$

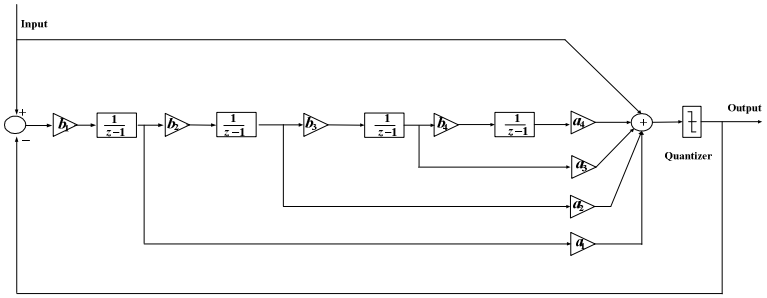


Fig.1 Fourth-order, single-loop, single-bit sigma-delta modulator architecture

From the two equations above it is obvious that the signal transfer function is unity, and it can not be affected by non-idealities of the building blocks in the system. The eight coefficients in the system can only change the noise transfer function. Therefore, the noise shaping ability and stability can be optimized by changing coefficients without considering the signal transfer function. In the above topology, the output swings of integrators are smaller than classical topology and there is only one feed-back signal to the first integrator which is easier for the design on circuit-level.

Distortion due to the non-linear capacitors. The sigma-delta modulator is realized by switched capacitor circuit on circuit-level. The capacitors in the switched capacitor circuit are often made of poly-silicon or metal. They play important role in storing and transforming charge in the integrator. However, their values are affected by the stored voltage. This relationship is commonly expressed with a Taylor expansion as

$$C(v)=C_0(1+a_1v+a_2v^2+...) \tag{3}$$

Where C_0 reprents the value of capacitor when it is discharged and a_1, a_2 … are non-linear coefficients of the capacitor。

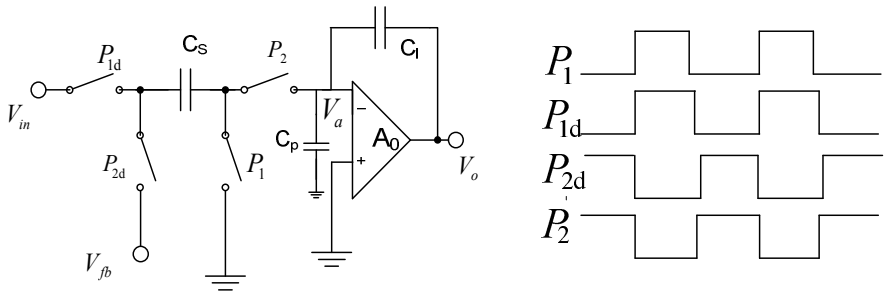


Fig.2 Switched capacitor integrator and clock

The distortion introduced by a non-linear capacitor is strongly dependent on the placement of the capacitor in the modulator [5]. Consider the parasitic-insensitive switched capacitor integrator shown in Fig.2. The switch P_{1d} is shut down later than P_1 which can reduce the charge injection in the circuit. One branch is connected to the input of the modulator, the other branch feeds the output of the modulator back ($V_{fb,n}=-y_nV_{ref}$). The sampling and integratoring capacitors are non-linear. The main distortion source is introduced by the sampling capacitor C_s. In this case the output of the integrator can be expressed:

$$v_{o,nT_s+T_s} \cong v_{o,nT_s}+\frac{C_s}{C_I}v_{\text{in},nT_s}(1+\frac{a_1}{2}v_{\text{in},nT_s}+\frac{a_2}{3}v^2_{\text{in},nT_s}) \tag{4}$$

In this paper 0.5um CMOS processing is adopted, and the equation illustrating the non-linear capacitor is

$$C(v)=C_1\bullet\text{area}\bullet(1+a_1v+a_2v^2+...) \tag{5}$$

This equation consits with equation (3). Where $a_1=1.594\times10^{-4}$, $a_2=2.1\times10^{-5}$. From the analysis above the non-linear capacitor model is established in Simulink which is shown in Fig.3

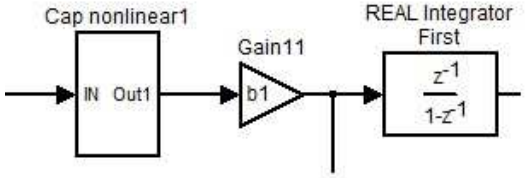


Fig.3 Non-linear capacitor model

Distortion due to the switch non-linear on-resistance. The distortion introduced by the non-linear on-resistance will be analyzed in this part. The CMOS switches is widely used in order to reduce the effect of non-linear on-resistance[6]. Considering that the NMOS and PMOS transistor operate in the linear region and the equivalent resistance of CMOS switch is

$$R_{on}=R_{onp}//R_{onn}=\frac{1}{\mu_n C_{ox}(\frac{W}{L})_n(V_{DD}-V_{thn})-\mu_p C_{ox}(\frac{W}{L})_p(|V_{thp}|)-\alpha V_{in}} \tag{6}$$

Where $\alpha=\mu_n C_{ox}(\frac{W}{L})_n-\mu_p C_{ox}(\frac{W}{L})_p$. In theory, when $\alpha=0$, the on-resistance R_{on} is indenpended on the input signal. As is shown in Fig.4 the on-resistances of PMOS, NMOS and CMOS switches versus the input signal. It is obvious that only the CMOS switch is indenpended on the input signal

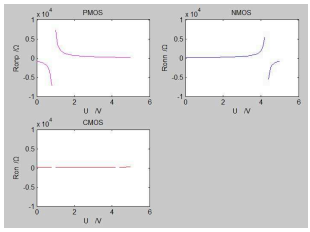


Fig.4 On-resistance versus the input signal

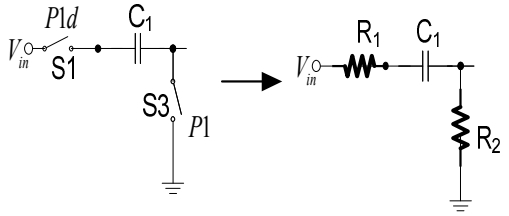


Fig.5 Equivalent resistance when switch is on

However, it cannot be guaranteed that α equals zero and CMOS switches are also dependent on the input signal in practice. During the sampling phase, when the switch is on, its equivalent circuit in the integrator is shown in Fig.5. After analyzing the function of the circuit it can be concluded that R_2 has less to do with the system when compared with R_1. Therefore, it is only necessary to analyze the non-linear on-resistance of R_1. Considering the sample phase in the circuit, the input signal goes through R_1C_1, it can be assummed that

$$A=\mu_n C_{ox}(\frac{W}{L})_n(V_{DD}-V_{thn})-\mu_p C_{ox}(\frac{W}{L})_p(|V_{thp}|) \tag{7}$$

So the on- resistance can be expressed

$$R_{on}(\mathrm{s})=\frac{1}{A-\alpha V_{in}(\mathrm{s})} \tag{8}$$

In the real circuit if it satisfies $A \gg \alpha$, R_{on} can be approximated

$$R_{on}(\mathrm{s})=\frac{1}{A}[1+\frac{\alpha}{A}V_{in}(\mathrm{s})]=R \tag{9}$$

In this case the output of the integrator can be expressed

$$V_{\mathrm{int}}(z)=V_{out}(z)H_{int}(z)\approx\frac{C_S}{C_I}\frac{1}{z-1}V_{in}(z)-\frac{\alpha}{T_S A^2}\frac{C_S^2}{C_I}V_{in}^2(z) \tag{10}$$

Where T_s is the period of clock. The first part of equation(10) is the output of ideal integrator, and the second part is the error introduced by the non-linear on- resistance. The non-linear on-resistance model is established in Simulink which is shown in Fig.6.

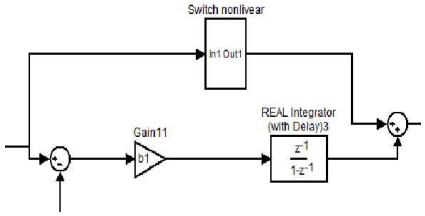


Fig.6 Non-linear on-resistance model

Distortion due to the amplifier non-linear gain. As the gain, bandwidth, slew rate of operational amplifier are finite, the non-linear gian of the operation amplifer in the integrator is analyzed firstly. The dc-gain of the integrator affects the position of the dominant pole and the integrator's gian. Distortion introduced by the integrator's dc-gain non-linearity results from its dependence on the

output voltage which is illustrated in Fig.7. The operation amplifier's gain can be approximated by the polynomial

$$A(V_o)=A_0 \bullet (1+b_2V_o^2+b_4V_o^4+b_6V_o^6...) \tag{11}$$

Where b_i (i=2,4,6,…) are nonlinear coefficients, A_0 is the maximum dc gain when V_0 is in the neighborhood of 0V. Compared with the second and fourth order coefficients, other higher order coefficients can be neglected. The expression of b_2 and b_4 are expressed [7-8]

$$\begin{aligned} b_2 &= -9(\frac{A_0^{0.01}}{(1+V_{os})^{2.6}})^2 \\ b_4 &= -6(\frac{A_0^{0.0001}}{(1+V_{os})^{0.83}})^4 \end{aligned} \tag{12}$$

Where V_{os} is the maximum output swing of the integrator.

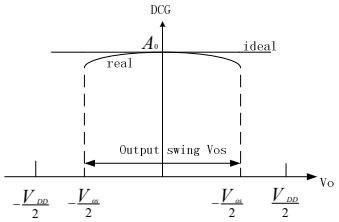


Fig.7 DC-gain curve versus output voltage

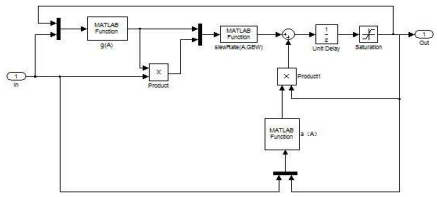


Fig.8 Non-ideal integrator model

When the non-idealities of operational amplifier are considered, the transfer function of the integrator shown in Fig.2 can be illustrated

$$H(z)=\frac{C_s}{C_I} \bullet g(A) \bullet \frac{z^{-1}}{1-a(A)z^{-1}} \tag{13}$$

where： $K_s=\frac{C_s}{C_I}$， $K_p=\frac{C_p}{C_I}$， $g(A)=\frac{A}{A+1+K_S+K_P}$， $a(A)=1-K_S/A$ .Analyze the sampling and integrating phases. With the help of charge conservation law the output of the integrator is

$$V_o(nT_s)=V_o(nT_s-T_s)+K_sV_{in}(nT_s-T_s)-\frac{1+K_s+K_P}{A_{nT_s}}V_o(nT_s)+\frac{1+K_P}{A_{nT_s-T_s}}V_o(nT_s-T_s) \tag{14}$$

With the help of equation (14) it is easy to establish non-linear gain model in Simulink.

Effect of the operational amplifier finite gain-bandwidth and slew rate. When analyze the finite gain-bandwidth and slew rate of the operational amplifier, the output of the integrator in Fig.2 during integrating phase [9-12]

$$V_o(nT_s-\frac{T_s}{2}+t)=V_n(t)=V_o(nT_s-T_s)+K_sV`_{in}(1-e^{-t/\tau}) \tag{15}$$

Where $V`_{in}=V_{in}(nT_s-\frac{T_s}{2})=V_{in}(nT_s-T_s)$， $0\le t\le T_s/2$， $\tau=1/(2\pi GBW)$ ， GBW is the unite gain bandwidth of the operational amplifier.

There are two cases in the analysis:

a. If $K_s\frac{|V`_{in}|}{\tau}\ge|SR|$， the output of the intgration can be expressed：

$$\begin{cases} V_o(nT_s)=V_n(\frac{T_s}{2})=V_o(nT_s-T_s)+\frac{1}{2}SRT_s, \frac{T_s}{2}\le t_0 \\ V_o(nT_s)=V_n(\frac{T_s}{2})=V_o(nT_s-T_s)+K_sV`_{in}-SR\tau e^{-(\frac{T_s}{2}-t_0)/\tau}, \frac{T_s}{2}>t_0 \end{cases} \tag{16}$$

Where $t_0 = K_s \frac{|V`_{in}|}{|SR|} - \tau$,

b. If $K_s \frac{|V`_{in}|}{\tau} \le |SR|$, the output of the intgration can be expressed:

$$V_o(nT_s) = V_n(\frac{T_s}{2}) = V_o(nT_s - T_s) + K_s V`_{in}(1 - e^{-\frac{T_s}{2\tau}}) \tag{17}$$

Simulation results of the proposed model

Considering the non-idealities discussed above non-ideal models in the modulator system are established which is shown in Fig.9. The output swings of the four integrators are shown in Fig10 (a). It's easy to get the output PSD (power spectral density) of the modulator after introducing non-ideal models. As is shown in Fig10 (b), the nonlinear capacitors increase second harmonic distortion by 80dB, and third harmonic distortion by 18dB. Fig10(c) indicates that the nonlinear on-resistances increase second harmonic distortion by 50dB, and has little to do with third harmonic distortion. The non-ideal integrators increase noise floor by about 70dB which is shown in Fig10 (d). After analyzing Fig10 (e) it is easy to infer that these non-idealities are nearly irrelevant and can be added in the whole system.

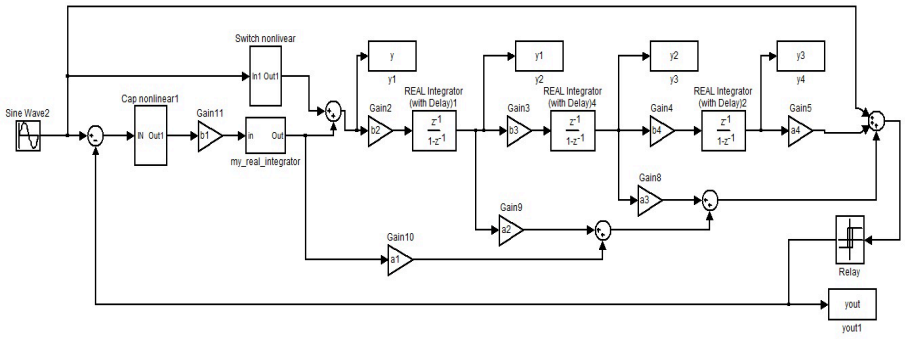
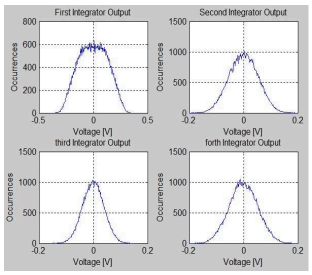
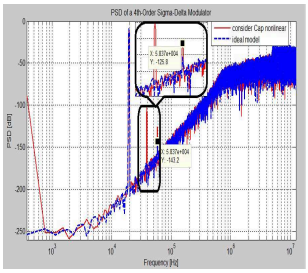


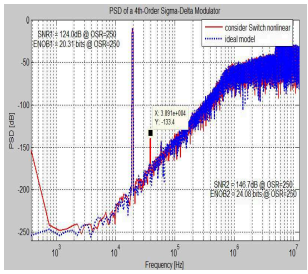
Fig.9 All non-ideal models in the Simulink



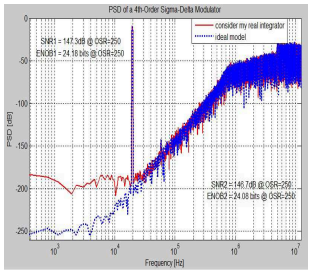
(a) output swings of integrators



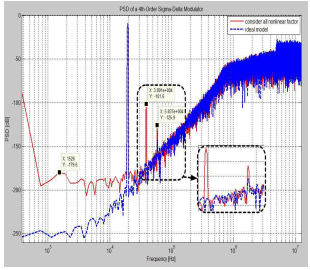
(b) PSD of nonlinear capacitors



(c) PSD of nonlinear on-resistance



(d) PSD of nonideal integrator



(e) PSD of all nonideal models

Fig.10 Simulation results

Conclusion

In this paper the harmonic distortions of sigma-delta modulator are analyzed and proposed model are established to verify the analysis. In this modulator topology the output swings of the integrators are small compared with classical topologies which can ease the difficulties in designing circuit and reducing harmonic distortion introduced by nonlinear capacitors. In order to decrease the noise floor of the modulator the operational amplifier with high bandwidth and slew rate are needed. But the bandwidth should not be too large because it may increase noise floor because of noise aliasing. The second harmonic distortion is mainly introduced by the nonlinear capacitors and nonlinear on-resistamces, and full-differential topology can be adopted to eliminate even order harmonic distortion. The third harmonic distortion is mainly introduced by the nonlinear capacitors which are dependent on the process level. Therefore in order to eliminate the odd order harmonic distortion introduced by nonlinear capacitors advanced process or special circuit architecture are needed.

Acknowledgement

This work is supported by National Basic Research Program of China (NO.2012CB934104) and National Hi-Tech Research and Development Program of China (863 Program) (Grant No. 2013AA041107)

References

[1] Van De Plassche. Integrated analog-to-digital and digital-to-analog converters[M]. Norwell MA: Kluwer Academic Publisher, 1994.

[2] Xu Jian, Analysis of high resolution and high performance of ΣΔ modulator [D]. ZheJiang University, HangZhou, ZheJiang. 2012

[3] J. C. Candy and G. C. Temes. Oversampling delta-sigma data converters, theory, design and simulation[M]. New York: IEEE Press, 1992.

[4] S. R. Norsworthy, R. Schreier, and G. C. Temes. Sigma Data Converters Theory, Design, and Simulation[M]. New York: IEEE Press, 1997.

[5] B. Brandt, P.F. Ferguson, and M. Rebeschini, "Analog Circuit Design of sigma-delta ADCs", Chapter 11 in Delta-Sigma Data Converters: Theory, Design and Simulation (S.R. Norsworthy, R. Schreier, and G.C. Temes, Editors). IEEE Press, 1997.

[6] Behzad Razavi. Design of Analog CMOS Integrated Circuits[M]. Xian Jiaotong University Press. 2011:337-340.

[7] Fu-Chuang Chen and Chih-Lung Hsieh. Modeling Harmonic Distortions Caused by Nonlinear Op-Amp DC Gain for Switched-Capacitor Sigma–Delta Modulators [J]. IEEE transactions on circuits and systems—II: express briefs, 2009, 56(9):694-698.

[8] Hashem Zare-Hoseini, Izzet Kale, and Omid Shoaei. Modeling of Switched- Capacitor Delta–Sigma Modulators in SIMULINK[J]. IEEE transactions on instrumnetation and measurement,vol. 54, pp. 1646-1654, August 2005.

[9] W.M.C. Sansen, H. Qiuting, and K.A.I. Halonen, Transient Analysis of Charge Transfer in SC Filters-Gain Error and Distortion[J]. IEEE Journal of Solid-State Circuits, vol. 22, pp. 268-276, April 1987.

[10] V.F. Dias, G. Palmisano, P. O'Leary, and F. Maloberti, Fundamental Limitations of Switched-Capacitor Sigma-Delta Modulators[J]. IEEE Proceedings-G, vol. 139, pp. 27-32, February 1992.

[11] L.A. Williams and B.A. Wooley, A Third-Order Sigma-Delta Modulator with Extended Dynamic Range[J]. IEEE Journal of Solid-State Circuits, vol. 29, pp. 193-202, March 1994.

[12] F. Medeiro, B. Pérez-Verdú, and A.Rodríguez-Vázquez, Top-Down Design of High-Performance Modulators[M]. Kluwer Academic Publishers, 1999.

Key Engineering Materials Vols 645-646 (2015) pp 986-989
© (2015) Trans Tech Publications, Switzerland
doi:10.4028/www.scientific.net/KEM.645-646.986

Submitted: 2015-01-12
Accepted: 2015-01-13

The Parametric Analysis of the Lock-Releasing Mechanism in MEMS Safety and Arming Device

Wang Fufu[1, a], Lou Wenzhong[1, b], Liu Fangyi[1, c], Wang Dakui[1, d], Lu Jun[2, e], Wu Jian[2, f], Guo Xuhong[2, g], Zhang Zhe[2, h]

[1]National Key Laboratory of Electro-mechanics Engineering and Control, School of Mechanical-electronic Engineering, Beijing Institute of technology, Beijing, China, 100081
[2]China North Industries Group Corporation, Changzhi, 046000

[a]wangfufu2004@sina.com(corresponding author), [b]Louwz@bit.edu.cn, [c]lfyhbu@163.com, [d]wangdakui1987@163.com , [e] 25841301@qq.com, [f]jake2000-wj@163.com,

[g] guoxh.mems@gmail.com,[h]kb235@163.com

Keywords: lock-releasing mechanism; MEMS; safety and arming device

Abstract. In this paper, a mechanical MEMS S&A device has been proposed. The size of the device is 10mm×13mm×0.5mm. The role of the lock-releasing mechanism is to amplify the moving distance of two times, so as to effectively guarantee the time of long-distance arming. Through establishing the three-dimensional model of without optimized lock-releasing mechanism, establishing the force and the parameters of locking-releasing mechanism, deriving the mathematical model according to the rigid dynamic mechanics theory and establishing the finite element model by using ANSYS/LS-DYNA, appropriate lock-releasing mechanism is designed to meet two items, one item is that the lock-releasing rod locks the main centrifugal slider before sub-centrifugal slider movement in place; the other item is that sub-centrifugal slider will hit the lock-releasing rod when it movement in place, so the lock-releasing rod rotates around rotational positioning block and releases the main centrifugal slider.

Introduction

In order to meet the challenge of modern war, the fuze, as "the brain" of ammunition, shows a particular tendency of miniaturization, intelligent and facility [1-2]. The miniaturization of S&A (Safety and Arming) device takes priority over other tasks. Battlefield is a complex electromagnetic environment, so it may affect the reliable work of MEMS S&A device relying on electric insurance. However, this kind of MEMS S&A device used in the large-caliber grenade is the most common currently, as shown in Fig.1 [3-5]. Our term (National Key Laboratory of Mechatronics Engineering and Control) puts forwards a mechanical MEMS S&A device innovatively, the concrete structure as shown in Fig.2. This device includes main centrifugal slider, sub-centrifugal slider, lock-releasing mechanism, threshold-value judging mechanism, elastic-beam delaying mechanism and so on. And the size of the device is 10mm×13mm×0.5mm.

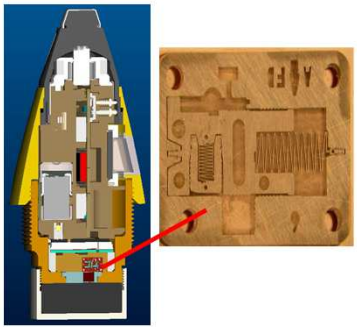


Fig. 1 The MEMS S&A device used in the large-caliber grenade

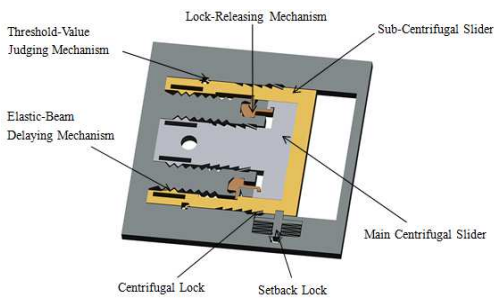
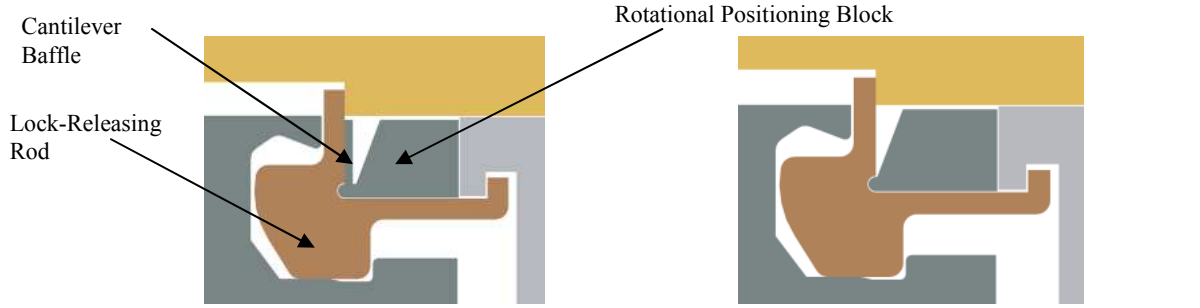


Fig. 2 The mechanical MEMS S&A device

Among them, the role of the lock-releasing mechanism is to amplify the moving distance of two times, so as to effectively guarantee the time of long-distance arming. The lock-releasing mechanism can be used in large-caliber grenade or small-caliber bullet. Fig 3a shows that the lock-releasing mechanism is composed of lock-releasing rod and rotational positioning block. The mechanism is designed to meet two items, one item is that the lock-releasing rod locks the main centrifugal slider before sub-centrifugal slider movement in place; the other item is that sub-centrifugal slider will hit the lock-releasing rod when it movement in place, so the lock-releasing rod rotates around rotational positioning block and releases the main centrifugal slider.



a) Optimized lock-releasing mechanism b) Without optimized lock-releasing mechanism

Fig. 3 The locking-releasing mechanism

Model and Theoretical Analysis

The center of gravity, rotation center and stroke of the sub-centrifugal slider are shown in Fig.4. The parameters and force of locking-releasing mechanism are shown in Fig.5.

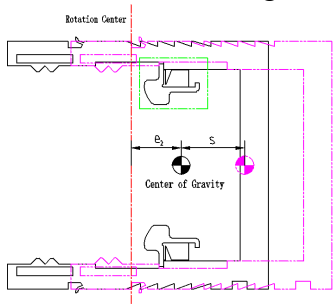


Fig. 4 The center of gravity, rotation center and stroke of the sub-centrifugal slider

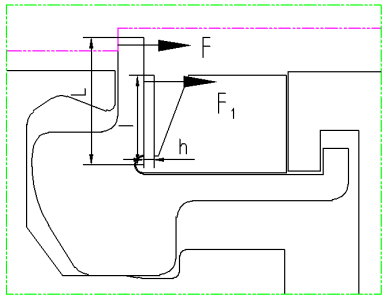


Fig. 5 The parameters and force of locking-releasing mechanism

We have some hypotheses:

1.Not consider the impact of the elastic-beam delaying mechanism, when calculating the speed of the sub-centrifugal slider;

2.The velocity of the sub-centrifugal slider from v_{max} to 0 is a uniform deceleration process, when sub-centrifugal slider hits the locking-releasing mechanism.

According to the Fig. 4, we can get the initial acceleration

$$a_0 = e_2\omega^2 \tag{1}$$

Where, e_2 is the initial eccentricity of sub-centrifugal slider; ω is the angular velocity of the device. S is the displacement of sub-centrifugal slider before hitting the cantilever baffle, S is divided into n portions, each portion is $\Delta S = S/n$

According to

$$v_t^2 = v_0^2 + 2aS \tag{2}$$

For the first portion , we can get

$$v_1^2 = 2a_1\Delta S = 2(e_{20} + \Delta S)\omega^2\Delta S \tag{3}$$

For the second portion , we can get

$$v_2^2 = v_1^2 + 2a_2\Delta S = v_1^2 + 2(e_{20} + 2\Delta S)\omega^2\Delta S \tag{4}$$

.....

For the n portion , we can get

$$v_n^2 = v_{n-1}^2 + 2a_n\Delta S = v_{n-1}^2 + 2(e_{20} + n\Delta S)\omega^2\Delta S \tag{5}$$

So, we can get

$$v_n^2 = 2a_1\Delta S + 2a_2\Delta S + \cdots + 2a_n\Delta S = 2\left[n\cdot e_{20} + (1+2+\cdots n)\Delta S\right]\omega^2\Delta S \approx 2\omega^2 S\left[e_{20} + \frac{S}{2}\right] \tag{6}$$

Because the velocity of the sub-centrifugal slider is a uniform deceleration process, when sub-centrifugal slider hits the locking-releasing mechanism. According to kinetic energy theorem, we can get

$$F = \frac{mv_n^2}{2S_2} \tag{7}$$

Where, F is the force of sub-centrifugal slider after hitting the cantilever baffle; m is the mass of sub-centrifugal slider; S_2 is the displacement of sub-centrifugal slider after hitting the cantilever baffle.

So

$$FL = F_1 l \tag{8}$$

Applied cantilever deflection curve equation to analysis the cantilever baffle, as shown in Fig. 6.

So

$$W = -\frac{F_1 l^3}{3EI} \tag{9}$$

Combining equation (6) and (7), we can get

$$W = \frac{m\omega^2 S\left[e_2 + \frac{S}{2}\right]\cdot L\cdot l^2}{3S_2 EI} \tag{10}$$

Where, W is the deflection of the cantilever baffle; E is the elastic modulus of the cantilever baffle; I is the moment of inertia of the cantilever baffle.

$$I = b\cdot h^3 / 12 \tag{11}$$

Where, b=0.5mm; h is the width of the cantilever baffle.

According to the design criteria: $W \geq 0.17mm$,combining equation (10) and (11), we can get

$$h \leq 0.13mm \tag{12}$$

Due to limitation of the size of the rotational positioning block, eventually, we get h=0.05mm.

Simulation Analysis and Conclusions

The launch overload curve shown in Fig. 7 is obtained in the launch process.

In order to obtain the lock release function shown in Fig.3a, a three-dimensional model of without optimized lock-releasing mechanism is established, as shown in Fig.3b.

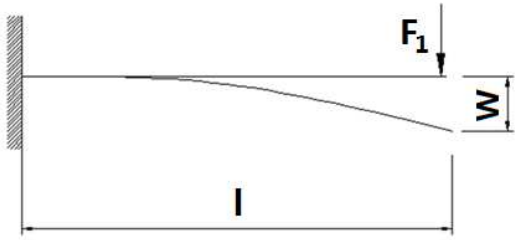


Fig. 6 The deflection of the cantilever baffle schematic

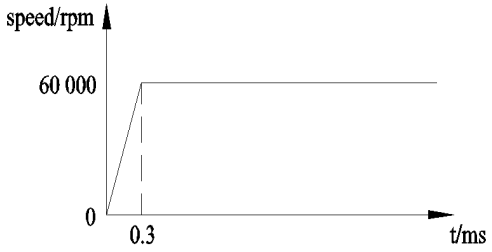
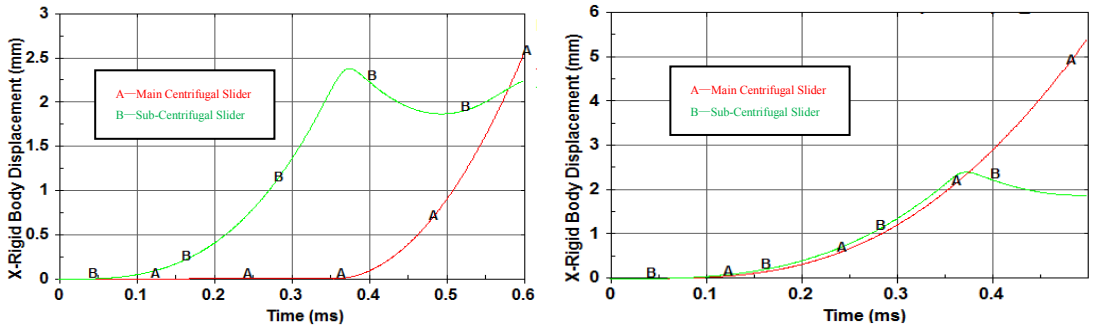


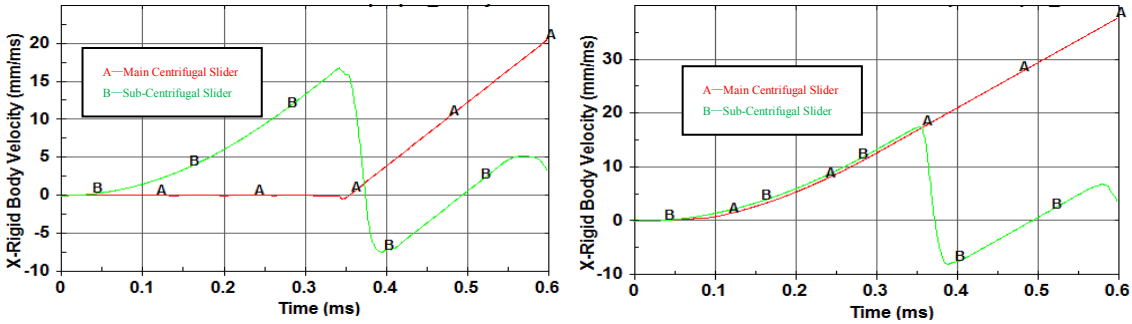
Fig. 7 The launch overload curve

After establishing the infinite model, loading the same launch overload curve (Fig. 7), making nonlinear dynamic mechanics simulation by using ANSYS/LS-DYNA, different displacement (Fig. 8) and velocity curves (Fig.9) are obtained.



a) Optimized lock-releasing mechanism b) Without optimized lock-releasing mechanism

Fig. 8 The displacement curve



a) Optimized lock-releasing mechanism b) Without optimized lock-releasing mechanism

Fig 9 The velocity curve

Through analyzing the Fig.8 and Fig.9, it arrives at the conclusions as follows. 1) The main centrifugal slider is released prematurely through the main centrifugal slider gives a disturbance to lock-releasing rod, as shown in Fig.3b. 2) The cantilever baffle is added to rotational positioning, as shown in Fig.3a, and it can resist the centrifugal force of the main centrifugal slider. At the same time, sub-centrifugal slider will hit the cantilever baffle, which causes the cantilever baffle deflection and the main centrifugal slider release. 3) The mathematical model is verified through analyzing different displacement and speed curves. 4) The feasibility of the above research is confirmed.

Next

The MEMS S&A device with the lock-releasing mechanism is being fabricated and the Centrifugal test will be tested to verify the validity of the lock-releasing mechanism.

Acknowledgment:

The research was supported by the State Key Laboratory of Mechatronics Engineering and sponsored by the National Project of China (51305060302) and the National Project of China (914A05050313BQ1014).

References

[1] Robinson, C. H., Wood, R. H. and Hoang, T. Q., “Development of Inexpensive, Ultra-Miniature MEMSBased Safety Andarming (S&A) Device for SmallCaliber Munition Fuzes,” Proceedings of 23rd ArmyScience Conference, pp. 111-116 (2002).

[2] Pezous, H., Rossi, C., Sanchez, M., Mathieu, “Integration of a MEMS Based Safe Arm and Fire Device,” Sensors and Actuators: A Physical, Vol. 159, No. 2, pp.157-167 (2010).

[3] Chopin Hua. High-g MEMS Fuzes [R]. Baltimore, USA: 56TH ANNUAL FUZE CONFERENCE, 2012

[4] David A. Olson. Microelectromechanical Systems Ignition Safety Device [P]. US Patent No.7971532A1,2011.

[5] Wang Fufu, Lou Wenzhong, Wang Ying. Design and analysis of a novel locking mechanism of MEMS safety and arming device [J]. p 856-859, 2014, Micro-Nano Technology XV

Key Engineering Materials Vols 645-646 (2015) pp 990-994
© (2015) Trans Tech Publications, Switzerland
doi:10.4028/www.scientific.net/KEM.645-646.990

Submitted: 2015-01-19
Accepted: 2015-01-21

Theoretical investigation of the electronic properties in BN nanowires

Cuicui Zhuang[1, a], Ling Li[1*, b], Sidi Fan[1, c], Chuncheng Ban[1], Xiaowei Liu[1]

[1]MEMS Center, Harbin Institute of Technology, Harbin 150001, China

[a]zhuangcuicui@126.com [c]fansidicity@163.com [b]linglimems@hit.edu.cn (corresponding author)

Keywords: BN nanowires, Electronic properties, First principles

Abstract. Theoretical investigation of BN nanowires have been performed by density functional theory (DFT). The energy gap and electronic properties of BN nanowires (BNNWs) in the direction of growth [001] and [111] have been calculated. The calculations show that both nanowires exhibit a wide band gap at center of Brillouin zone, and the calculated band gaps are 1.90eV and 2.40eV, respectively. Noticeably, in the absence of any bias voltage, the transmission spectrum exhibit a region of zero transmission and a step-like behavior.

Introduction

Low-dimensional (1D) nanostructure materials exhibit peculiar electronic and optical properties due to structural quantum-mechanical confinement effects, and have attracted great attention over the past years[1-5]. Boron nitride (BN), as an important wide-gap semiconductor, possesses many outstanding physical and chemical properties, such as prominent electrical and thermal properties, high mechanical strength, high melting point, and outstanding oxidation resistance[6,7]. In recent years, BN low-dimensional quantum structures, such as nanotube[8-10], nanoribbon[11-13] and nanowire[14,15], have been intensively studied for their potential applications in optical and electronic devices[16,17], sensors[18,19] and biological probes[20]. Many theoretical investigations of BNNTs and BNNRs have been carried out. For example, the mechanism for and the methods of achieving a tuning of the electronic properties of the BNNTs have been widely studied[21-25]. Also, the effect of defects on the electronic properties of the BNNRs have been investigated[26,27]. However, very little has been reported on the electrical properties of the BN nanowires (BNNWs). Thus, theoretical investigation of the BNNWs, is remarkably important for better utilizing BNNWs in the optical and electric devices, and sensors.

In this work, the first-principle calculations have been used to investigate the structure and electronic properties of BNNWs in the direction of growth [111] and [001]. Generalized gradient approximation (GGA) was used to describe the exchange–correlation potential. The energy gap and their dependence on growth direction, as well as the density of states, have been illustrated.

Computational model and method

The geometry optimizations and property calculations were performed by means of the first-principle calculations. BNNWs in the direction of growth [111] and [001] were extracted from the relaxed bulk BN supercell. And then the geometry optimization was performed using ultrasoft pseudopotentials, in which density functional theory is implemented based on the GGA with the Perdew-Burke-Enzerhof (PBE). All the structural relaxation were achieved until the residual force on each atom was less than 0.03 eV/Å. A large supercell was used to constructed the periodic boundary condition, and a 1×1×6 Monkhorst–Pack special k-point was applied for the Brillouin zone integration. These conditions give continuity along the BNNW axis and large repeat distances along the two other axes. This large cell guarantees no interaction between neighboring nanowires. The cutoff energy for the plane-wave basis set is 280 eV to ensure the convergence in the calculations. Figure 1 shows the optimized BNNWs in the direction of growth [111] and [001], in which the blue and pink balls denote nitrogen and boron atoms.

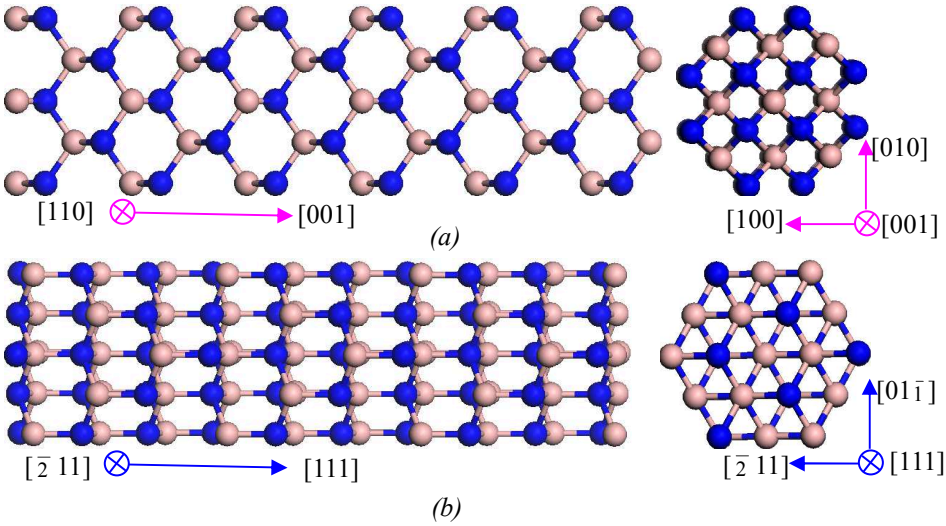


Figure 1. The side view and top view of BN nanowires in the direction of growth [001](a) and [111](b)

To study the electron transport properties of BNNWs, a two-probe model was adopted, which consists of a central region, a left electrode and a right electrode. Atoms in both the electrodes include parts of the semi-infinite bulk electrodes, which interact with the atoms of the central region. The conductance calculations were performed at zero bias using a non-equilibrium Green's function technique based on the GGA-PBE with double-zeta polarized (DZP) numerical basis set. The k-points sampling and cutoff energy is 1×1×100 and 100 Hartree, respectively. The convergence criterion for the total energy is 10^{-5} via the mixture of the Hamiltonian.

Results and discussion

In this paper, the electronic band structures for the BNNWs with similar radical and length in the direction of growth [111] and [001], are investigated. Figure 2(a) and 2(b) show the energy bands for the BNNWs in the direction of growth [001] and [111], respectively. It can be indicated that for the BNNWs in the direction of growth [111], the conduction band minimum and the valence band

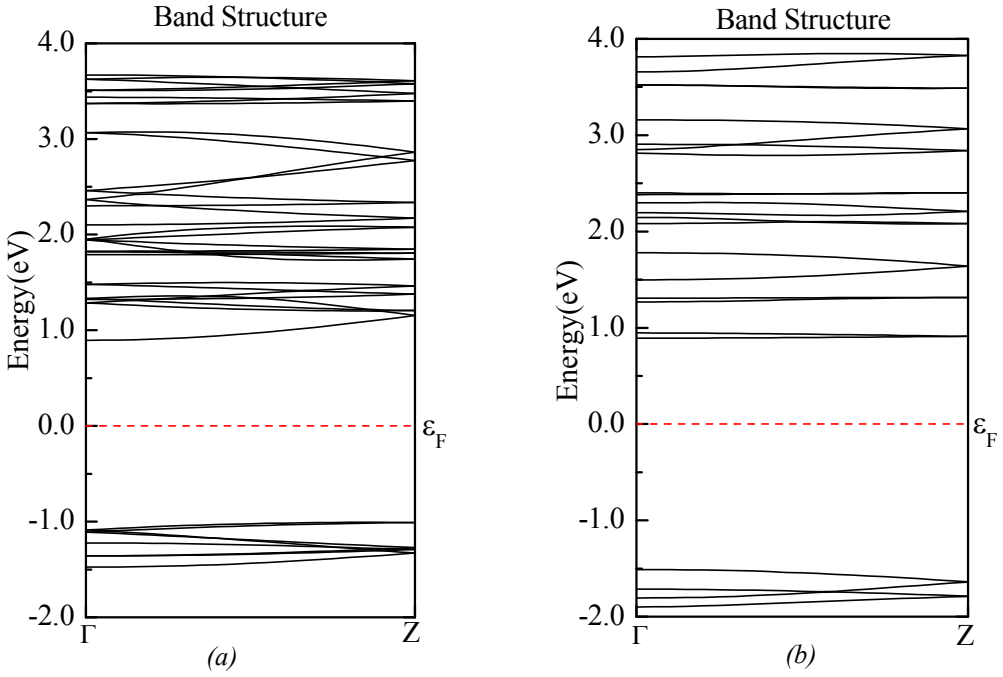
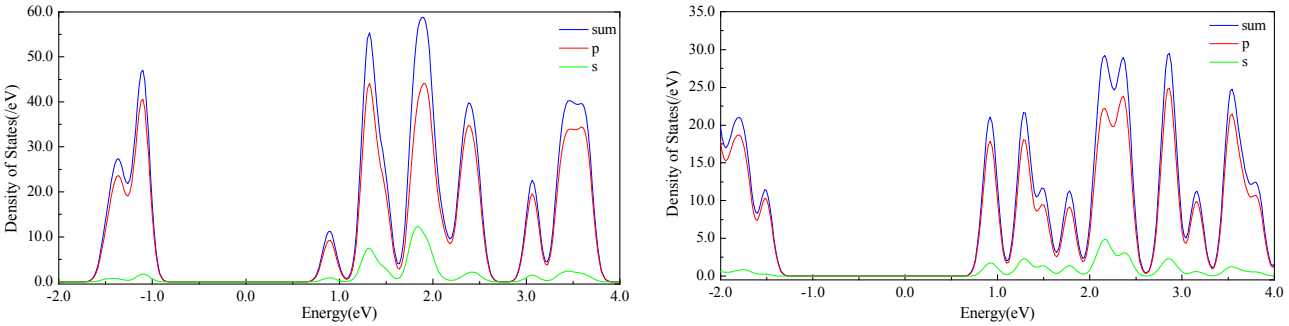


Figure 2. Energy bands for BN nanowires in the direction of growth [001](a) and [111](b)

maximum are all located at the Γ point, indicating that they have a direct band gap, and the calculated band gaps are 2.40eV. However, the BNNWs in the direction of growth [001] have a indirect band gap with 1.90eV. These results show that electronic property has a little dependence of growth direction.

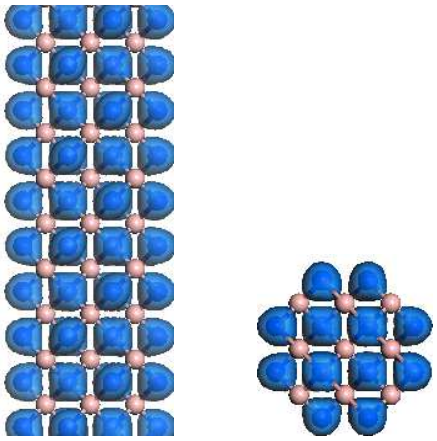
We have calculated the total density of states (TDOS) and partial density of states (PDOS) for both BNNWs, as shown in Fig. 3. In the figures, the energy zero is set at the Fermi level. These results show that the DOS at the Fermi level is zero, and the Strong effect of 2p orbital can be observed on the densities of states. And in both kinds of BNNWs, the conduction band edge near the Brillouin zone center is primarily formed by p states, the contribution of s states being negligible.



(a) *(b)*

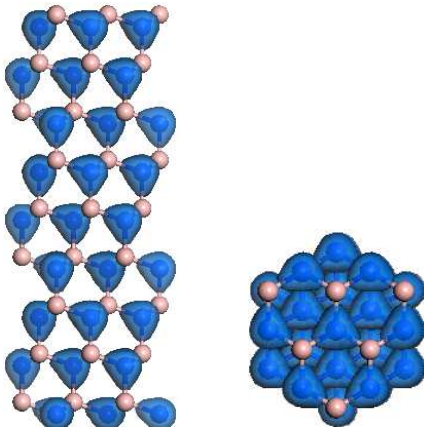
Figure 3. Density of states for BN nanowires in the direction of growth [001](a) and [111](b)

Figure 4 and Figure 5 show the isosurface plots of electron density distributions for the BNNWs along [001] and [111] direction, respectively. A significant fact can be seen from the Fig.4 and Fig.5, that the electron density is strongly accumulated around the N atoms, which are due to the fact that these N has higher electronegativities than B, meaning that the B atoms would transfer most of their charge to these other atoms. Therefore, it can be predicted that there mainly are B states in the conduction band.



(a) Longitudinal view *(b) cross sectional view*

Figure 4. The isosurface plots of electron density distributions for the BNNWs along [001] direction



(a) Longitudinal view *(b) cross sectional view*

Figure 5. The isosurface plots of electron density distributions for the BNNWs along [111] direction

The computed transmission coefficients for both BNNWs are plotted in Fig. 6 as a function of energy. The Fermi level has been set to zero for simplicity. Transmission spectra show that, for both kinds of BNNWs, there is a region of zero transmission which is symmetrically distributed on both sides of the Fermi level. The width of the zero transmission region for (001) and (111) BNNWs is 2.29eV. This indicates BNNWs exhibit semiconducting behavior. Moreover, a step-like behavior is observed, which is related to the available conductance channels from bands.

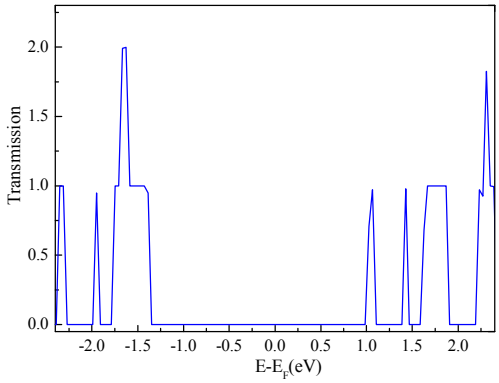


Figure 7. The transmission spectrum for the [111] BNNWs

Summary

In conclusion, the calculated band gaps of BNNWs in the direction of growth [111] and [001] are 2.40eV and 1.90eV, respectively, exhibiting a little dependence on the orientation. The computed transmission spectra, band structures, and DOS spectra show that in the absence of any bias voltage, the transmission probability for both BNNWs devices reaches to zero exhibiting semiconducting behavior. BNNWs with wide band gap are promising candidates for optoelectronics applications such as light emitting devices and photodetectors.

Acknowledgements

This work is financially supported by the National Natural Science Funds of China (Grant No. 61404036) and the National Basic Research Program of China (2012CB934104).

References

[1] Javey A., Guo J., Farmer D., et al, Self-Aligned Ballistic Molecular Transistors and Electrically Parallel Nanotube Arrays, Nano Lett. 4 (2004) 1319–1322.

[2] Huang Y., Duan X. F., Cui Y., et al, Gallium Nitride Nanowire Nano devices, Nano Lett. 2 (2002) 101–104.

[3] Duan X. F., Huang Y., Cui Y., et al, Indium Phosphide Nanowires as blocks for Nanoscale Electronic and Optoelectronic Devices, Nature. 409 (2001) 66–69.

[4] Barrelet C. J., Greytak A. B., Lieber C. M, Nanowire Photonic Circuit Elements, Nano Lett. 4 (2004) 1981–1985.

[5] H. Pan, Y. P. Feng, Semiconductor Nanowires and Nanotubes: Effects of Size and Surface-to-Volume Ratio, ACS NANO. 2 (2008) 2410-2414.

[6] Chen Y. J., Tong Z. F., Luo L. J., Boron Nitride Nanowires Produced on Commercial Stainless Steel foil, Chin. J. Chem. Eng. 16 (2008) 485-487.

[7] Chen Y. J., Chi B., D. C Mahon, An effective approach to grow boron nitride nanowires directly on stainless-steel substrates, Nanotechnology. 17 (2006) 2942-2946.

[8] Li L.，Li L.H., Chen Y., et al, Mechanically activated catalyst mixing for high-yield boron nitride nanotube growth, Nanoscale Research Letters. 7 (2012) 417.

[9] Li L.H., et al. High yield BNNTs synthesis by promotion effect of milling-assisted precursor, Microelectronic Engineering. 110 (2013) 256-259.

[10] Liu X. W., Li L., J. Dai, et al. Synthesis of High Density Boron Nitride Nanotube Film, Key Engineering Materials. 562-565 (2013) 926-929.

[11] Li L.，Li L.H., Chen Y., et al, High Quality Boron Nitride Nanoribbons: Unzipping during Nanotube Synthesis, Angewandte Chemie-International Edition. 52 (2013) 4212-4216.

[12] Nag. A., Raidongia. K., Hembram. K. P. S. S., Graphene Analogues of BN: Novel Synthesis and Properties, ACS Nano. 4 (2010) 1539−1544.

[13] Zeng H. B., Zhi C.Y., Zhang Z.H., et al. "White Graphenes": Boron Nitride Nanoribbons via Boron Nitride Nanotube Unwrapping, Nano Lett. 10 (2010) 5049–5055.

[14] Li L.H., Li C.P., Chen Y., Synthesis of boron nitride nanotubes, bamboos and nanowires, Physica E. 40 (2008) 2513-2516.

[15] Huo K. F., Hu Z., Chen F., et al, Synthesis of boron nitride nanowires, Appl. Phys. Lett. 80 (2002) 3611-3613.

[16] C. Attaccalite, L. Wirtz, A. Marini, et al, Efficient Gate-tunable light-emitting device made of defective boron nitride nanotubes: from ultraviolet to the visible, Scientific Reports. 3 (2013) 2698-1-2698-7.

[17] Augustinus M. Goossens, Stefanie C. M. Driessen, Tim A. Baart, et al. Gate-Defined Confinement in Bilayer Graphene-Hexagonal Boron Nitride Hybrid Devices, Nano Lett. 12 (2012) 4656−4660.

[18] Yu Y.L., Chen H., Liu Y., et al. Humidity sensing properties of single Au-decorated boron nitride nanotubes, Electrochemistry Communications. 30 (2013) 29–33.

[19] Huang, Q., Bando, Y., Zhao, L. P., et al, pH Sensor Based on Boron Nitride Nanotube, Nanotechnology. 20 (2009) 415501.

[20] Wu J.M., Yin L.W., Platinum Nanoparticle Modified Polyaniline-Functionalized Boron Nitride Nanotubes for Amperometric Glucose Enzyme Biosensor, ACS Appl. Mater. Interfaces. 3 (2011) 4354–4362.

[21] Chen C. W., Lee M. H., Clark, S. J, Band Gap Modification of Single-Walled Carbon Nanotube and Boron Nitride Nanotube under a Transverse Electric Field, Nanotechnology. 15 (2004) 1837.

[22] Cho, Y. J., Kim, C. H., Kim, H. S., et al, Electronic Structure of Si-Doped BN Nanotubes Using X-ray Photoelectron Spectroscopy and First Principles Calculations, Chem. Mater. 21 (2009) 136–143.

[23] Li Y. F., Zhou Z., Golberg D., et al, Stone-Wales Defects in Single-Walled Boron Nitride Nanotubes: Formation Energies, Electronic Structures, and Reactivity, J. Phys. Chem. C. 112 (2008) 1365–1370.

[24] Wang Z. G., Li Z., Cheng D. M, Effects of Uniaxial Strain on the Band Structure of Boron Nitride Nanotubes: A First Principle Study, Eur. Phys. J. 69 (2009) 20601.

[25] Wang R. X., Zhu R. X., Zhang D. J, Adsorption of Fomaldehyde Molecule on the Pristine and Silicon Doped Boron Nitride Nanotubes, Chem. Phys. Lett. 467 (2008) 131–135.

[26] Chen W., Li Y.F., Yu G. T., et al, Electronic Structure and Reactivity of Boron Nitride Nanoribbons with Stone-Wales Defects, J. Chem. Theory Comput. 5 (2009) 3088–3095.

[27] Tang P. Z., Zou X. L., Wang S. Y., et al, Electronic and magnetic properties of boron nitride nanoribbons with topological line defects, RSC Adv. 2 (2012) 6192-6199.

Key Engineering Materials Vols 645-646 (2015) pp 995-1003
Submitted: 2014-12-19
© (2015) Trans Tech Publications, Switzerland
Accepted: 2014-12-23
doi:10.4028/www.scientific.net/KEM.645-646.995

Dynamic Modeling and Output Characteristic Analysis of a Micro Bistable Piezoelectric Generator

Xinhua Mao[1, a *], Qing He[1,b] and Tingting Huang[2,c]

[1] School of Energy Power and Mechanical Engineering, North China Electric Power University, Beijing 102206, P.R. China

[2] Beijing Chonglee Machinery Engineering Co., Ltd, Beijing 101111, P.R. China

[a]maoxinhuadamao@163.com, [b]hqng@163.com, [c] 409918089@qq.coml

Keywords: energy harvesting; bistable; nonlinear vibration; piezoelectric generator; Mathematical Modeling; Output characteristics

Abstract. For effectively harvesting the broadband and low-frequency vibration energies in real environment, a micro bistable piezoelectric generator, without containing magnet, is designed. On the basis of analysis the nonlinear behavior of the stiffness, damping and the electromechanical coupling coefficient about the bistable vibration system, a precise mechanical-electric transfer model is built. The output characteristic of the piezoelectric generator is simulated and tested. The results showed that the piezoelectric generator can effectively harvest the broadband and low frequency vibration energies. And the output voltage can meet the electricity demand of a wireless sensor network node. The structure of the piezoelectric generator does not contain magnets, and it is easy to realize miniaturization and integration.

1. Introduction

A distributed wireless sensor network has an important application value in the field of the equipment condition monitoring and environmental health monitoring. However there are still many problems about power supply of wireless sensor network nodes. For example, the fuel cell and chemical battery have brought pollution, and their supply power time is not persistent. Sometimes it is difficult to replace these batteries on special occasions[1–5]. In order to fundamentally solve the power supply problem of a wireless sensor network node, many scholars have been trying to extract energy from the environment and convert it into electricity. The vibration energy almost exists everywhere in the real environment, and is not easily affected by the weather and seasonal changes .So the vibration energy has become hot of micro energy using. The vibration energy collecting converter is based on the piezoelectric effect as the preferred transducer equipment. It`s coupling coefficient is higher, and it`s energy density is larger. It is beneficial to miniaturization and integration[6–11].

The cantilever piezoelectric stator based on the theory of linear piezoelectric equation, has advantages of the simple structure and high output voltage .And it becomes the first choice device of the vibration energy collector. However, Research shows that it also has obvious limitations in practice. The frequencies of many vibration sources in the real environment are lower, with the strong randomness and large volatility. The cantilever piezoelectric vibrator has a high resonance frequency and the narrow resonant bandwidth, and not applies to the low frequency environment. It cannot supply power under a low-frequency weak signal in real environment. The bistable stochastic resonance is a special kind of nonlinear vibration. It is not necessary that the vibration source frequency is equal to the natural frequency of a piezoelectric vibration generator. And the larger output amplitude can be obtained[12–17]. Currently, the nonlinear force for the bistable piezoelectric generator is provided by the magnet in many literatures, a bistable harvester is designed with two magnets for the repulsive force[18–21]. In the harvester two NdFeB permanent magnets are held in plastic holders and spanned at a distance. By adjusting the distance between the two magnets, a bistable stochastic resonance phenomenon will be produced. It can increase the deformation of the

cantilever beam and improve the energy conversion efficiency of a piezoelectric generator. A magnetic attraction harvester is designed by Erturk A and so on[22-24]. In the harvester two magnets with the same polarity produce the nonlinear force for developing a bistable stochastic vibration. It can improve the resonance performance and energy conversion efficiency of a piezoelectric vibration generator. In the above research, the vibration energy harvesting structures all contain the magnets. It makes the harvesting structure complex. So it is not easily to do miniaturization and integration.

According to the above problem, a bistable piezoelectric generator without containing magnets is designed in this paper. It can produce bistable stochastic resonance phenomenon based on the elastic beam bending deformation. The machine-electrical conversion model of the piezoelectric generator is established in this paper. The output characteristics with the low frequency and broadband incentives have respectively carried on the simulation analysis. Above simulation results have been verified by experiments.

2. The structure and model of a micro bistable generator

2.1 Transduction structure device and the output charge analysis

To achieve the objectives of this work， we consider a buckling piezoelectric beam which one end is clamped, the other is scalable at axial direction. Transduction structure of the bistable piezoelectric generator is shown in Fig 1. The structures are made up of a metal framework, thin elastic beam with length $2l$ and two PVDF piezoelectric films. When the axial load P is greater than the critical buckling load, the piezoelectric beam occurs the buckling and presents a bistable state. The piezoelectric generator will constantly transform between two steady states, produce the continuous electricity.

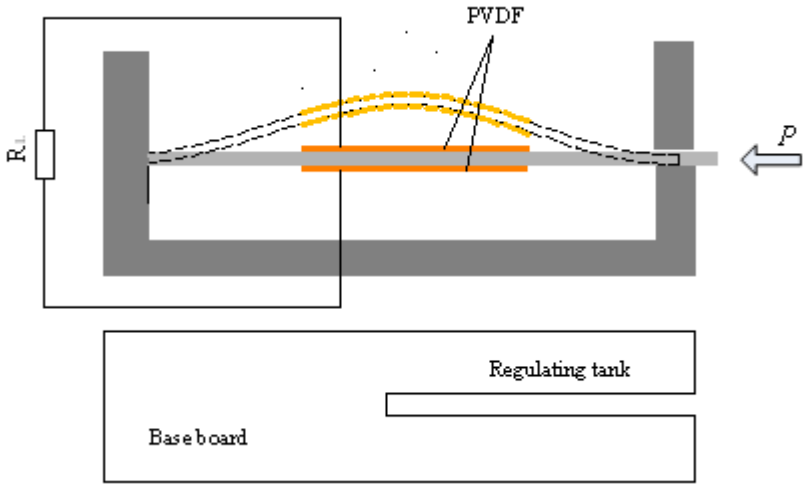


Fig. 1 Transduction structure of the micro piezoelectric generator

According to the piezoelectric effect, the output charge sizes of a piezoelectric generator have something to do with stress distribution of the piezoelectric material. When the piezoelectric beam moves in a different position, the surface stress distributions of the piezoelectric beam present different situations. When the piezoelectric beam moves to the middle equilibrium position in Fig.2 (a), the upper surface and the lower surface of the piezoelectric beam have the same surface stress distributions. The output charges of two PVDF piezoelectric films also are equal. When the piezoelectric beam moves to the above in Fig.2 (b), the upper surface stress is greater than the lower surface stress. At the moment, the piezoelectric film located in the upper surface supplies the major output charges. When the piezoelectric beam moves to the lower in Fig.2 (c), the lower surface stress is greater than the upper surface stress. At the moment, the piezoelectric film located in the lower surface supplies the major output charges.

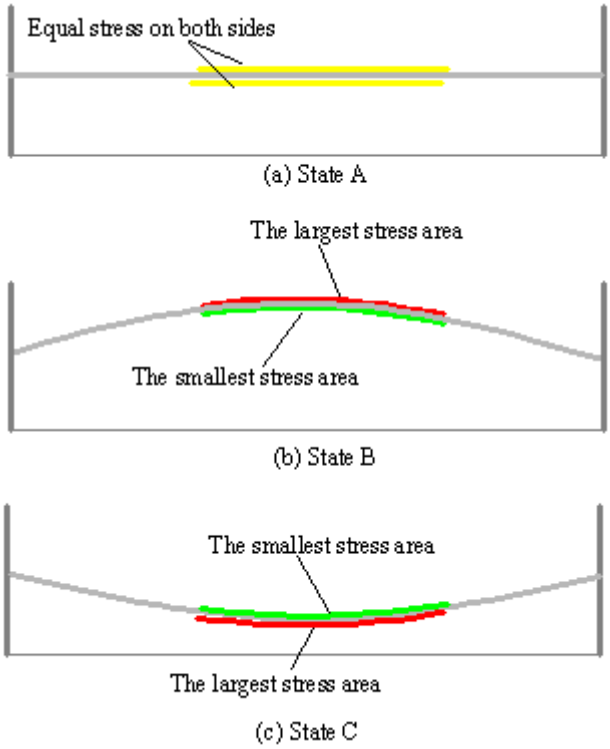


Fig.2 Analysis of output charges with different motion state

2.2 Mechanical-electric transfer model

The micro bistable piezoelectric generator system is a complex vibration system. It is made up of the quality system, the stiffness system, the damping system, and the mechanical & electrical combination system [25–27]. It is shown in Fig 3. The quality of the equivalent lumped parameters is m .The stiffness of two slant springs with the initial length L is k_h . The micro piezoelectric generator system presents the negative stiffness characteristics under the action of two slant springs. The resultant force of two slant springs on the vibration direction can be expressed as follows [28].

$$F_X = k_h(2X - \frac{2LX}{\sqrt{l^2 + X^2}}) \quad (1)$$

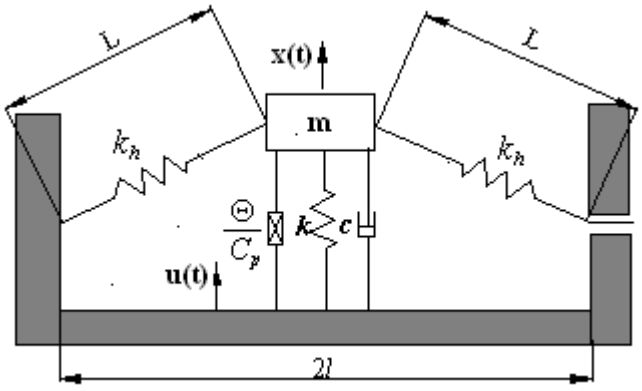


Fig. 3 Lumped parameter model of the micro piezoelectric generator

Because of the micro vibration generator being subjected to initial preloading pressure, the piezoelectric beam occur a buckling-jump phenomenon in the vibration process. And the piezoelectric beam has a large geometric deformation. There are obviously nonlinear characteristics in the deformation process. So the stiffness coefficient and the damping coefficient, the electromechanical coupling coefficient are no longer a constant terms. They will take place change with the size of the displacement. According to the literature [29], these coefficients are approximated as follows:

$$k \approx k_1 + k_2 X^2 \quad (2)$$

$$c \approx c_1 + c_2 \left| \dot{X} \right| \quad (3)$$

$$\Theta \approx d_1 + d_2 \sqrt{|X|} \quad (4)$$

where, k represents the nonlinear stiffness coefficient. c represents the nonlinear damping coefficient. Θ represents the electromechanical coupling coefficient.

According to the Newton's law, dynamics equation of the micro piezoelectric generator system is as follows:

$$m\ddot{X} + c\dot{X} + kX + F_X - \Theta \frac{Q}{C_p} = -m\ddot{u} \quad (5)$$

where, X represents the relative displacement of the mass. $u = A\sin(\omega t + \phi)$, u represents the basis excitation displacement.

According to Eq. (1), Eq. (2), Eq. (3), and Eq. (4), Eq. (5) can be written as follows.

$$m\ddot{X} + (c_1 + c_2 \left| \dot{X} \right|)\dot{X} + (k_1 + k_2 X^2)X + k_h (2X - \frac{2LX}{\sqrt{l^2 + X^2}}) - (d_1 + d_2 \sqrt{|X|}) \frac{Q}{C_p} = -m\ddot{u} \quad (6)$$

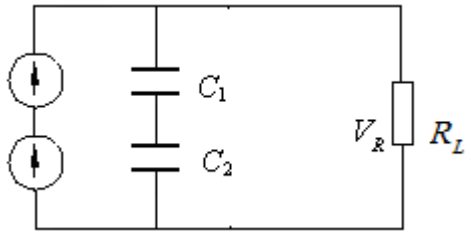


Fig.4 Equivalent circuit diagram of the bistable generator

The micro piezoelectric vibration generator has the two groups of PVDF piezoelectric patches. Piezoelectric films connect in series. We can assume the load to be purely resistance. Its equivalent circuit diagram is shown in Fig 4. According to the Kirchhoff law, the electrical equations of the micro piezoelectric generator system are established as follows:

$$R_L \dot{Q} + \frac{\Theta \dot{X}}{C_p} - \frac{Q}{C_p} = 0 \quad (7)$$

$$C_p = \frac{C_1 C_2}{C_1 + C_2} \quad (8)$$

where, C_p represents the piezoelectric layer internal total capacitance. C_1, C_2 respectively represents the internal capacitance of two piezoelectric films.

The above Eq. (6) and Eq. (7) is the machine-electrical conversion model of the bistable piezoelectric generator system.

3. The output characteristic of the micro bistable piezoelectric generator

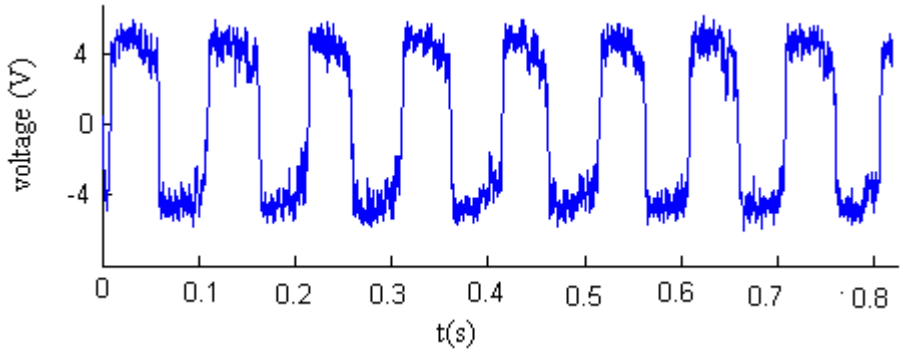
3.1 Output performance under the low frequency environment

According to the Eq. (6), Eq. (7) and model parameters of a bistable piezoelectric generator (such as table 1), adopting the fourth rank Rounge-Kutta calculable method, output voltages of the micro piezoelectric generator under the low frequency excitation can be achieved by computer simulation. Simulation results are shown in Fig5.

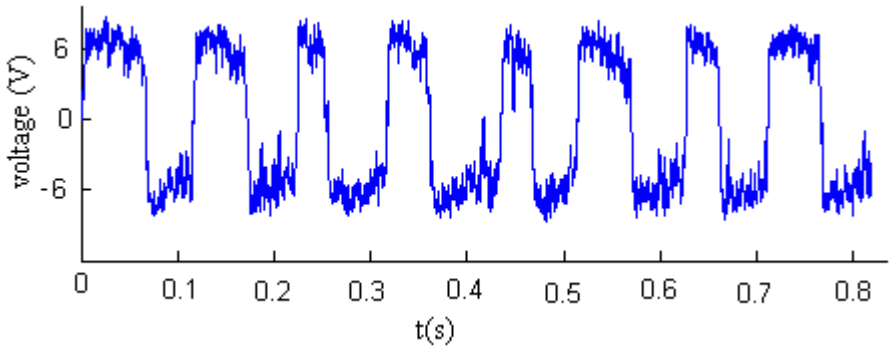
Table 1.Model parameters of the bistable piezoelectric generator

Parameter type	Parameter values	Units
Equivalent mass M	0.0867	Kg
Stiffness coefficient k_1, k_2	1660 , 9.78×10^7	N/m
elastic coefficient k_h	6.77×10^6	N/m

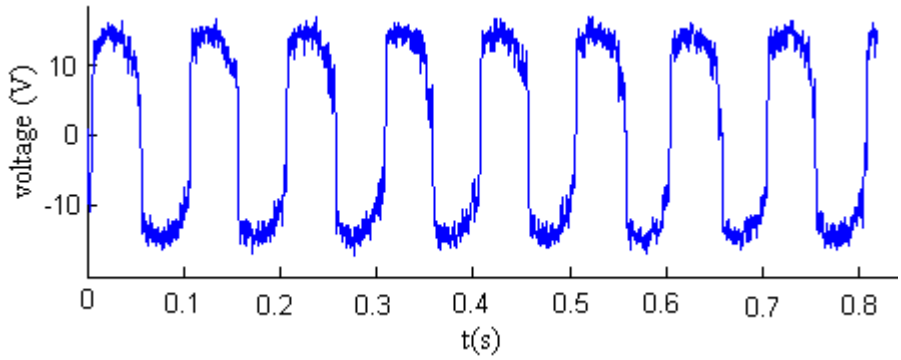
Damping coefficient c_1, c_2	2.3, 3.4	N/s
Electromechanical coupling coefficient d_1, d_2	0.0047, 0.084	N/V
Equivalent capacitance C_p	1.4×10^{-7}	F
Equivalent resistance R_L	47.5	Ω
Exciting frequency	0～100	Hz



(a) $a_{rms} = 2m/s^2$



(b) $a_{rms} = 4m/s^2$



(c) $a_{rms} = 8m/s^2$

Fig.5 Output voltages of the micro piezoelectric generator when $\omega = 10Hz$

Simulation results show that under the low frequency vibration source excitation, the output voltages of the micro bistable piezoelectric generator are basically stability. It can meet the electricity demand of a wireless sensor network node. And, with the increase of the source of vibration acceleration, output voltages will be increased dramatically.

3.2 Output performance simulation under the broadband frequency environment

The vibration source frequency not only has the low-frequency characteristics, but a wide frequency band in real environment. When the vibration source frequency is continuously adjusted from 0 Hz to100 Hz, output voltages of the micro piezoelectric generator can be obtained by computer simulation. The results are shown in Fig6. Results show that under the broadband frequency excitation, the micro bistable piezoelectric vibration generator generates the stable sine wave voltage.

And the output voltage value exceeds 3V when the excitation frequency is from 10Hz to 60Hz. It shows that the micro bistable piezoelectric vibration generator has the larger working bandwidth.

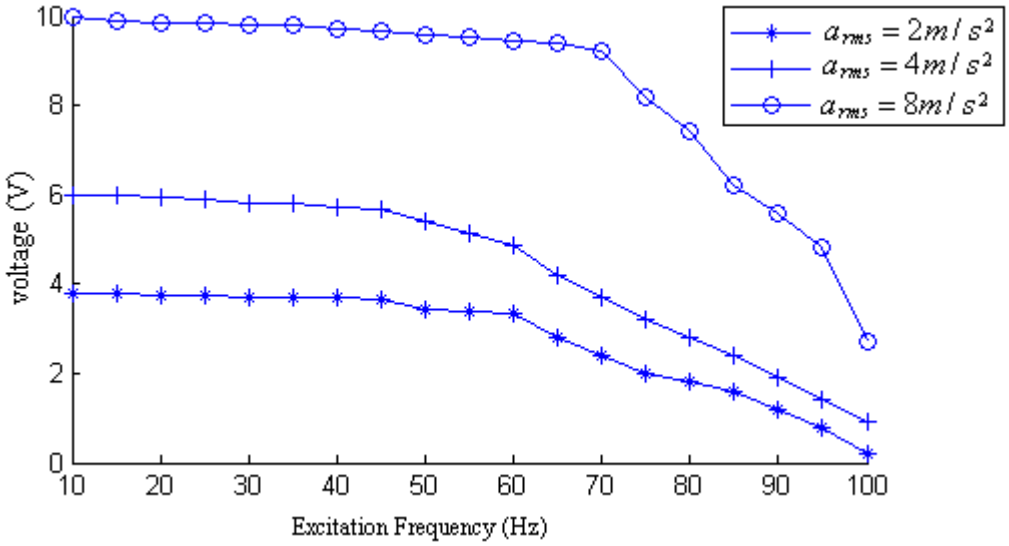


Fig. 6 Output voltages of the micro piezoelectric generator under the broadband frequency excitation

4. Experiment and analysis

To verify the theoretical analysis results, a micro bistable piezoelectric generator is made based on the parameters in table 1 and Fig 1. Because of the good elastic, the PVDF piezoelectric film is used for piezoelectric material. The stainless steel material is used for the body of the piezoelectric generator. The piezoelectric beam is made of the spring steel material. The experimental test system is shown in Fig 7.

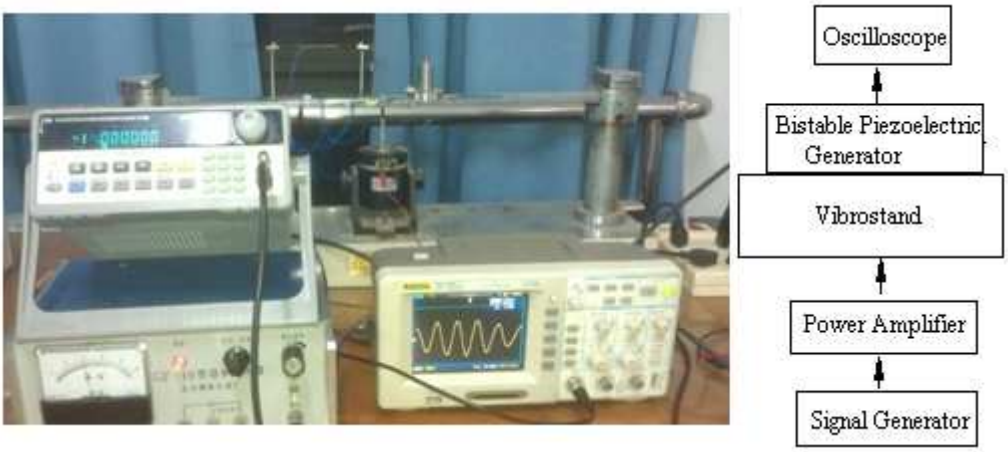


Fig.7 Test system of the micro bistable piezoelectric generator

The signal generator will generate a series of signal with frequencies 1~100 Hz. A broadband and low-frequency vibration source has been formed after signals are magnified by the power amplifier. The bistable piezoelectric generator will generate the electric energy under the vibration source excitation. The experimental results are shown in Fig 8.

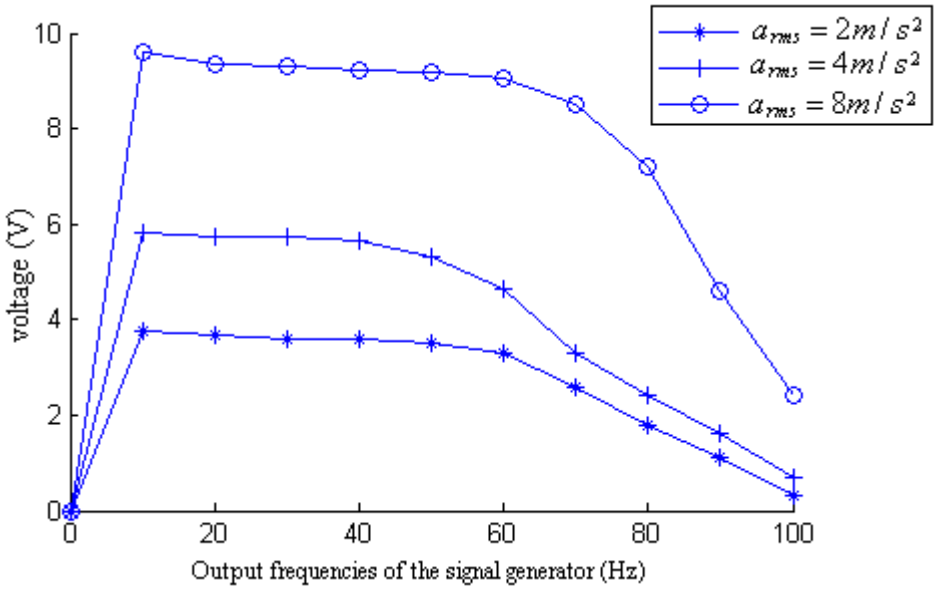


Fig. 8 The experimental testing result

According to the experimental results, we know that the piezoelectric vibration generator, without containing magnets, can not only collect the low frequency vibration energy, but has a larger resonance bandwidth. When the vibration source frequency is about from 8 to75 Hz, output voltages of the piezoelectric vibration generator are more than 3 V. It can meet the electricity demand of a wireless sensor network node. And with the increase of the vibration acceleration of an excitation source, the output voltages also gradually increase. Experimental results verified output characteristic of the bistable piezoelectric generator. However, it is not exactly the same with the simulation result. This is because of modeling errors in the modeling process and approximation errors caused by the numerical computation.

5. Conclusion

A micro bistable piezoelectric vibration generator, without containing any a magnet, is designed in this paper. The structure analysis and stress analysis have been carried out. The precise machine-electrical conversion model of the bistable piezoelectric generator has been built in this paper. Output characteristics of the piezoelectric vibration generator is simulated by computer and verified by experimentation. It is proved from theory and experiment that the micro piezoelectric vibration generator, without containing magnets, can not only collect the low frequency vibration energy, but has a larger resonance bandwidth. Because of not containing magnets, it is easy for the micro piezoelectric generator to realize miniaturization and integration.

Acknowledgement

The work was supported by the Fundamental Research Funds for the Central Universities of China. The grant number is 13XS13.

References

[1] YAN Zhen, HE Qing. Performance Analysis on Incentive Environment of Micro Cantilever Piezoelectric Vibration Generator [J]. Proceedings of the CSEE, 2011, 31(30):140-145.

[2]YANG Jin, WEN Yumei, LI Ping,et al. A new Magnetoelectric Broadband Vibration Energy Harvester [J]. Chinese Journal of Scientific Instrument, 2012, 33(12):2863-2868.

[3]ZHU Liya, CHEN Renwen, LEI Xia. Current Status and Development Trends of Vibration-based Piezoelectric Generator [J]. China Mechanical Engineering, 2011.22(24):3016-3022.

[4] ZHAO Zhigang, DING Xusheng, LIU Fugui, et al. Structural Design and Simulation of Micro Electromagnetic Vibration Energy Harvester [J]. Transactions of China Electrotechnical Society, 2012, 27(8):255-260.

[5]HOU Zhiwei, CHEN Renwen, LIU Jianxiang. Optimization Design of Multi-direction Piezoelectric Vibration Energy Harvester [J]. Journal of Vibration and Shock, 2012, 31(16):33-37.

[6] JEFFREY L. KAUFFMAN AND GEORGE A. LESIEUTRE. A Low-order Model for the Design of Piezoelectric Energy Harvesting Devices [J]. Journal of Intelligent Material Systems and Structures, 2009, 20(5):495-503.

[7] Kanwar Bharat Singh, Vishwas Bedekar, Saied Taheri, et al. Piezoelectric Vibration Energy Harvesting System With an Adaptive Frequency Tuning Mechanism for Intelligent Tires[J]. Mechatronics, 2012, (22):970-988.

[8] ZOU Yuwei, HUNG Xueliang, TAN Linlin. First-order Resonance Frequency and Power Output of a Cantilever Piezoelectric Generator [J]. Journal of Southeast University (Natural Science Edition), 2011, 41(6):1177-1181.

[9] Cuong P Le, Einar Halvorsen, Oddvar Søra°sen, et al. Microscale Electrostatic Energy Harvester Using Internal Impacts [J]. Journal of Intelligent Material Systems and Structures, 2012, 23(13):1409-1421.

[10] David A. W. Barton, Stephen G. Burrow, Lindsay R. Clare. Energy Harvesting From Vibrations with a Nonlinear Oscillator [J]. Journal of Vibration and Acoustics, 2010, 132(6): 1-7.

[11] B.P. Mann, N.D.Sims. Energy Harvesting From the Nonlinear Oscillations of Magnetic Levitation [J]. Journal of Sound and Vibration, 2009, (319):515-530.

[12] Mohamed M.R. El-Hebear, Mustafa H. Arafa, Said M. Megahed. Modeling and Experimental Verification of Multi-modal Vibration Energy Harvesting From Plate Structures [J]. Sensors and Actuators A, 2013, (193):35-47.

[13] I.N. Ayala-Garcia, P.D. Mitcheson, E.M. Yeatman,et al. Magnetic Tuning of a Kinetic Energy Harvester Using Variable Reluctance [J]. Sensors and Actuators A, 2013, (189):266-275.

[14] Po-Cheng Huang, Tung-Hsiang Tsai, Yao-Joe Yang. Wide-bandwidth Piezoelectric Energy Harvester Integrated with Parylene-C Beam Structures [J]. Microelectronic Engineering, 2013, (111):214-219.

[15] FrancescoDiMonaco, MaryamGhandchiTehrani, StephenJ.Elliott, et al. Energy Harvesting Using Semi-active Control [J]. Journal of Sound and Vibration, 2013, (332):6033-6043.

[16] Jedol Dayou, W.Y.H.Liew, Man-SangChow. Increasing the Bandwidth of the Width-split Piezoelectric Energy Harvester [J]. Microelectronics Journal, 2012, (43):484-491.

[17] Roszaidi Ramlan, Michael J Brennan, Brian R Mace, et al. On the Performance of a Dual-mode Non-linear Vibration Energy Harvesting Device [J]. Journal of Intelligent Material Systems and Structures, 2012, 23(13):1423-1432.

[18] Lihua Tang, Yaowen Yang and Chee-Kiong Soh. Improving Functionality of Vibration Energy Harvesters Using Magnets [J]. Journal of Intelligent Material Systems and Structures, 2012, 23(13):1433-1449.

[19] M.A. Acar, C. Yilmaz. Design of an Adaptive–passive Dynamic Vibration Absorber Composed of a String–mass System Equipped with Negative Stiffness Tension Adjusting Mechanism [J]. Journal of Sound and Vibration, 2013, (332):231-245.

[20]W Q Liu, A Badel, F Formosa, et al. Novel Piezoelectric Bistable Oscillator Architecture for Wideband Vibration Energy Harvesting [J]. Smart Materials and Structures, 2013, (22):1-11.

[21] Einar Halvorsen. Fundamental Issues in Nonlinear Wideband-vibration Energy Harvesting [J]. Physical Review, 2013, (87): 0421291-6.

[22]Erturk A and Inman D J .Broadband Piezoelectric Power Generation on High-energy Orbits of the Bistable Duffing Oscillator with Electromechanical Coupling[J]. Journal of Sound and Vibration, 2011,330 2339–53.

[23] M.N. Fakhzan, Asan G.A. Muthalif. Harvesting Vibration Energy Using Piezoelectric Material: Modeling, Simulation and Experimental Verifications [J]. Mechatronics, 2013, (23):61-66.

[24] Özge Zorlu, Haluk Külah. A MEMS-based Energy Harvester for Generating Energy From Non-resonant Environmental Vibrations [J]. Sensors and Actuators A, 2013, (202):124-134.

[25]ZHAO Jian.A Study on Threshold Acceleration Switches Based on Bistable Characteristic[D].Xian: Xidian University, 2008.

[26]CHEN Zhongsheng, YANG Yongming. Stochastic Resonance Mechanism for Wideband and low Frequency Vibration Energy Harvesting Based on Piezoelectric Cantilever Beams [J].Acta Physica Sinica, 2011, 60(7):074301-074306.

[27]SUN Shu, CAO Shuqian. Dynamic Modeling and Analysis of a Bistable Piezoelectric Cantilever power generation System [J].Acta Physica Sinica, 2012, 61(21): 2105051-21050511.

[28]Bin Tang , M.J.Brennan. On the shock performance of a nonlinear vibration isolator with high-static-low-dynamic-stiffness [J]. International Journal of Mechanical Sciences, 2014, (81): 207-214

[29] Waleed Al-Ashtari, Matthias Hunstig, Tobias Hemsel, et al. Enhanced energy harvesting using multiple piezoelectric elements: Theory and experiments [J]. Sensors and Actuators A, 2013, (200): 138-146.

[30] M. Ferrari, V. Ferrari, M. Guizzetti et al. A Single-magnet Nonlinear Piezoelectric Converter for Enhanced Energy Harvesting from Random Vibrations [J]. Procedia Engineering, 2010, (5): 1156-1159.

Key Engineering Materials Vols 645-646 (2015) pp 1004-1008
© (2015) Trans Tech Publications, Switzerland
doi:10.4028/www.scientific.net/KEM.645-646.1004
Submitted: 2014-12-25
Accepted: 2014-12-31

Impact of Cross-Section and Size on Vibration of Silicon Nanowires

Zhang Peng[1], Chen Hong Bo[2]and Yu Hong[*]

Key Lab of MEMS of Ministry of Education, Nanjing, Jiangsu, 210096, China

h_yu@seu.edu.cn (corresponding author)

Keywords: Silicon nanowire, vibration frequency, molecular dynamics, cross-section and size

Abstract: In this article, impact of cross-section and size on vibration of silicon nanowires is simulated by the molecular dynamics method based on molecular dynamics software Material Studio. The comparison of fundamental frequencies of the silicon nanowires with triangle, diamond, and hexagon cross sections is carried out. The orientations of these silicon nanowires are all in {111}direction. Then we change the length and the width of silicon nanowires to investigate the impact of size on vibration of silicon nanowires. The results show that with the influence of surface effect, the vibration frequency of silicon nanowires strongly depends on cross-section and size.

Introduction

NEMS [1] is a new concept put forward at the 20th century, and its feature size is at the range of 1-100nm.With the recent development of semiconductor technology [2], process line width decreases from micrometer to nanometer. Because of size effect, surface effect and quantum effect [3,4,5], the properties of nano-scale material are known to be different from those of their macroscopic analogs, which are difficult to explain by continuous theories. Therefore, new methods to study the nanometer material are needed. According to the research on the silicon nanowires [6,7,8], many applications such as nano-resonator and nano-oscillator are based on the variation of high frequency characteristics and resonant characteristics of nanowires. So the high frequency characteristics and its influence factors will determine the accuracy of the detection and the sensitivity of detection system. For example，We can use the high frequency characteristics of silicon nanowires to detect the chemical composition of biological sample.

Affected by the prepared process, the cross sections of the silicon nanowires are not shaped in perfect circular or rectangle. They may be shaped in hexagon or other shapes. This generates different surface to volume ratio (SVR) even for the nanowires which have the same lengths. At the same time, the length and the width of silicon nanowires will also affect its SVR.As a result, the vibration behavior of these nanowires will be different from each other and will give out different detection sensitivity and accuracy when they are used to detect tiny mass and forces. An investigation of effects of the cross section on vibration frequency of the silicon nanowire is carried out based on molecular dynamics method [9].

Simulation Model

The prototypes in this paper are doubly-clamped silicon nanowires with cross sections in triangle, rhombus, and hexagon shape, respectively, and the orientations of these silicon nanowires are all in {111} direction, as shown as in Figure 1. The vibration behavior of the silicon nanowire is simulated in detailed. The simulation software based on molecular dynamics is Forcite module from Material Studio, which is a commercial software and has been used extensively to study characteristics of nano scale materials. To enable the nanowire to vibrate, an aluminum AFM probe is built above the nanowire, which is denoted by red atoms. Because of the Van der Waals force between the AFM and the nanowire, the silicon nanowire is bended as shown as in Figure 2. It will vibrate freely after the AFM is removed. Compass (Condensed-phase Optimized Molecular Potential for Atomistic Simulation Studies) force-field is selected when the simulation is performed.

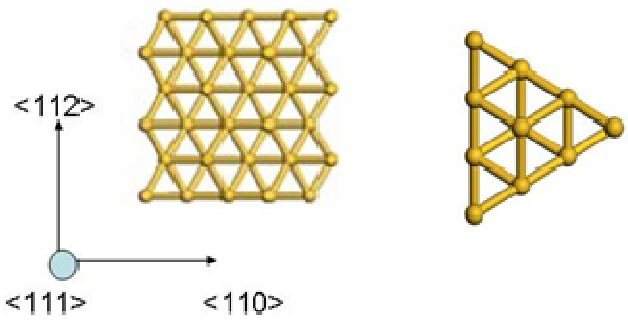


Figure 1.Cross section of{111} silicon nanowire

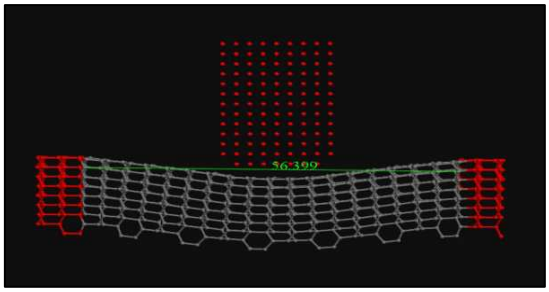


Figure 2. Silicon nanowire and AFM after structure optimization

Simulation Results and Discussion

Figure 3 shows the four kinds of energy (kinetic energy, potential energy, non-bond energy and total energy) of the silicon nanowire when the nanowire is vibrating, where the non-bond energy is non-bond interactions, which contains Van der Waals energy, electrostatic energy and or hydrogen bonding energy .And it does not change significantly in the process of simulation. It can be seen that after undergoing very short transient oscillations, the kinetic energy and potential energy start oscillating almost in one uniform period. At the maximum point of the kinetic energy, the potential energy reaches to the minimum, and vice versa while the total energy almost keeps one value. It means that exchange between the kinetic energy and the potential energy occurs during one period. The frequency response of the silicon nanowire can be obtained by performing FFT of the kinetic energy or the potential energy.

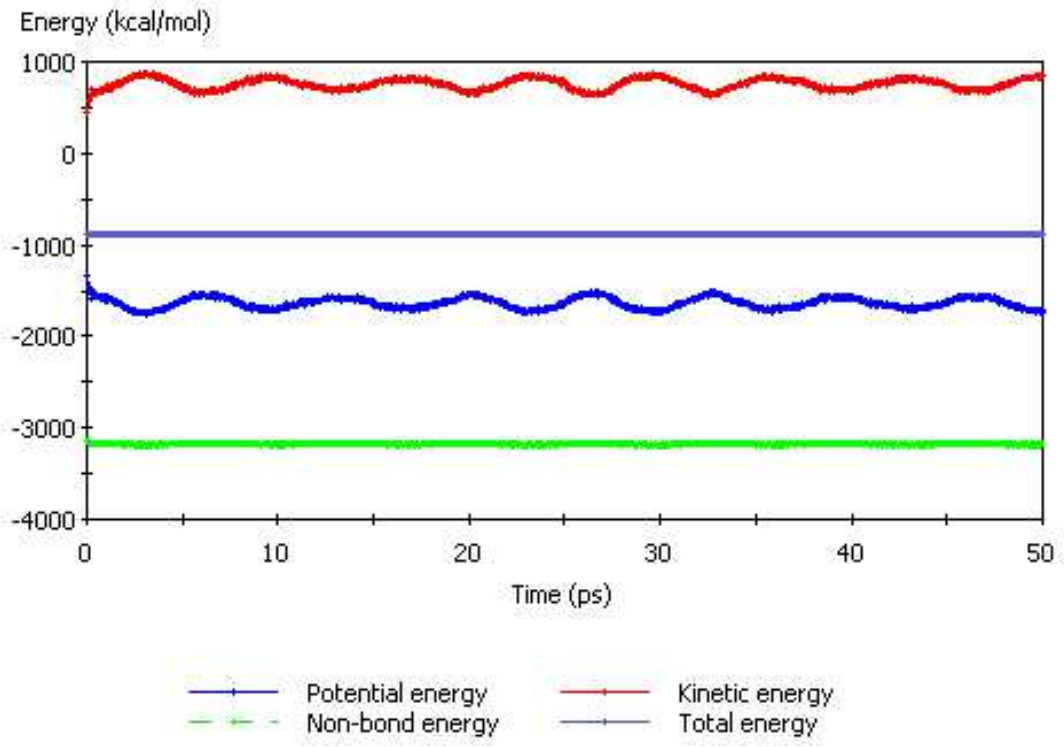


Figure 3. The different energy when the silicon nanowire vibrates.

The vibration frequency responses of the silicon nanowires with the triangle cross section are shown in Figure4, Figure5 and Figure6.

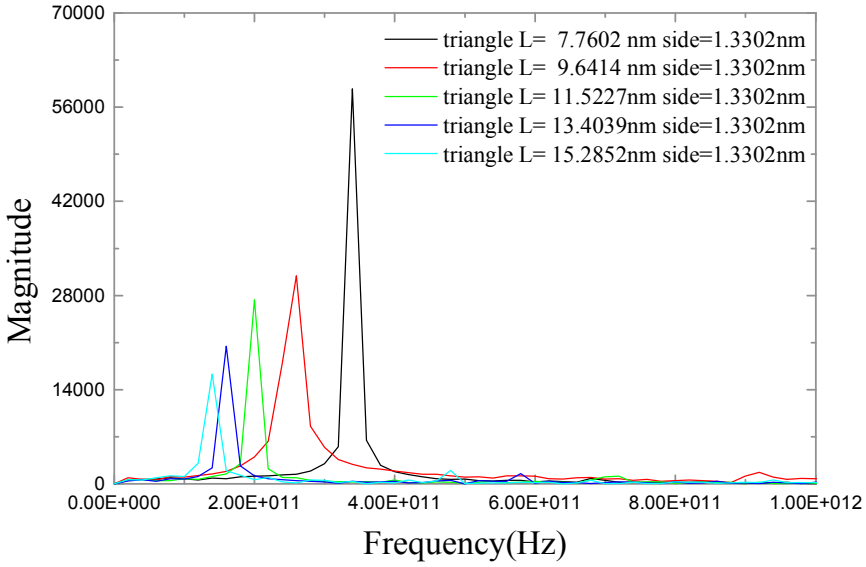


Figure 4. Frequency response of silicon nanowires with triangle cross section.

The vibration frequencies of doubly clamped silicon nanowires with different lengths are studied in figure 4. The lengths of the triangle vary from 7.7602nm to 15.2852nm while the nanowire keeps a width of 1.3302nm. We can see with the variation of length, its vibration frequency has a significant change. With the decrease of length, the vibration frequency will increase, and the increase ratio becomes larger .This is also similar with the result of silicon nanowires in [10].

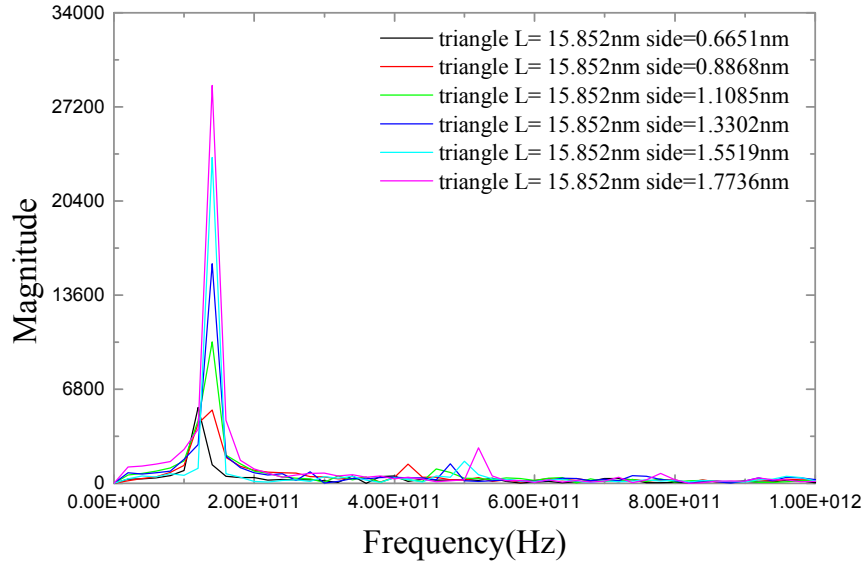


Figure 5. Frequency response of silicon nanowires with triangle cross section.

The vibration frequencies of doubly clamped silicon nanowires with different lengths are studied in figure 4. The lengths of the triangle vary from 7.7602nm to 15.2852nm while the nanowire keeps a width of 1.3302nm. We can see with the variation of length, its vibration frequency has a significant change. With the decrease of length, the vibration frequency will increase, and the increase ratio becomes larger .This is also similar with the result of silicon nanowires in [10].

Figure 5 shows the impact of the width of triangle cross-section on its vibration frequency. The side of the triangle varies from 0.6651nm to 1.7736nm while the nanowires keep a length of 15.582nm. When the width is changed, the frequency response of the nanowire only has a slight change.

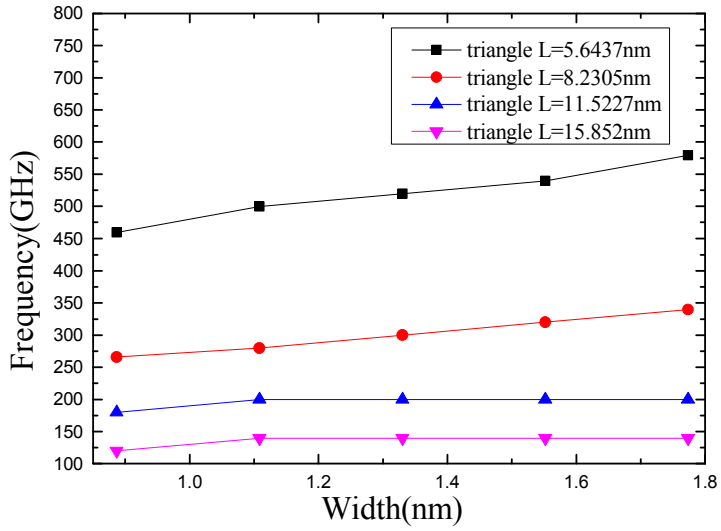


Figure 6. Frequency response of four silicon nanowires with triangle cross section.

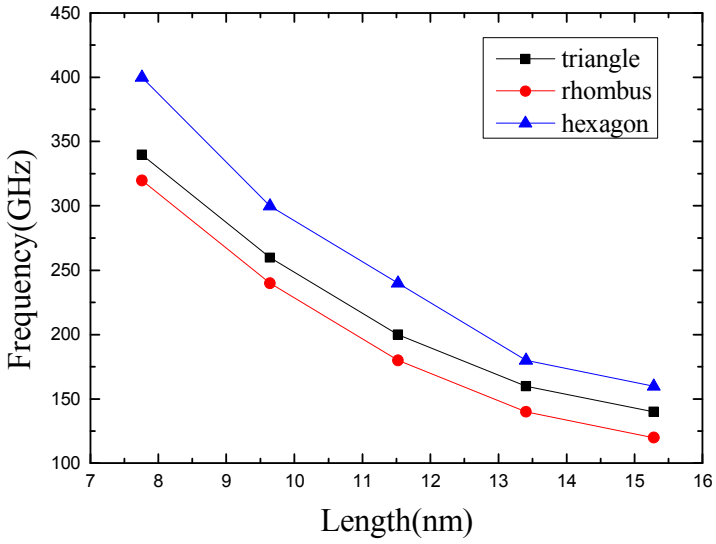


Figure 7. The vibration frequency of three silicon nanowires.Their cross-section are triangle, rhombus, and hexagon respectively.

In order to study the impact of width on vibration of silicon nanowires further. Figure 6 gives the frequency of four triangle cross-section silicon nanowires, their lengths are 5.6437nm, 8.2305nm, 11.5227nm and 15.8552nm. Their width varies from 0.6651nm to 1.7736nm. We can see that with the decrease of length, the impact of width on vibration frequency of silicon wires is becoming more and more obvious.

To investigate the effect of cross section on the vibration frequency of the silicon nanowire, we calculate the frequency of three silicon nanowires, as show in Figure 7. Their cross-sections are

triangle, rhombus, and hexagon respectively, and their lengths vary from 7.7602nm to 15.2852nm while the nanowires keep a width of 1.3302nm. According to the simulation results we can see with the decrease of length of three cross-sections nanowires, their vibration frequency become bigger and the increase ratio gets larger. For the three cross-section nanowires, when both of their length and width are the same, the biggest surface to volume ratio is triangle, than is the rhombus and the last is hexagon. So just thinking of surface effect, their vibration frequency will decrease in turn, but the simulation results is not so. On the basis of continuum theory, we can find that the thickness of the nanowires also affects the vibration frequency of the nanowires, and with the increase of thickness the vibration frequency will increase too. Although both of their length and width are the same, the thickness of hexagon is the biggest. The combined effect of thickness and surface effect led to the vibration frequency of hexagonal silicon nanowire is the biggest then triangular silicon nanowire, and the last is rhombic silicon nanowire.

Conclusion

Based on the molecular dynamics method, the effect of the cross-section and size on the vibration of the silicon nanowire is studied in detailed. Surface effect and size effect generate great impact on vibration frequency. With the decrease of length, the vibration frequency will increase, the increase ratio becomes larger. The impact of width on vibration frequency of the silicon nanowire is becoming more and more obvious with the decrease of length. For different shapes of cross sections both of their length and width are the same, the vibration frequency of hexagonal silicon nanowire is the biggest, and then is triangular silicon nanowire, and the last is rhombic silicon nanowire.

Acknowledgement

This research is support by the Natural Science Foundation of Jiang Su Province China (Grant Nos.SBK201320668).

References

[1] Craighead H G, Nano-electro mechanical systems, J. Science. 290 (2002) 1532-1535.
[2] Scavennec, A. Sokolich, M. Baeyens, Semiconductor technologies for higher frequencies, J. IEEE microwave magazine. 10 (2009) 154-158.
[3] Ausain H, Hone J, Postma H W C, et al.,Nanowire-based very-high-frequency electromechanical resonator, J. Appl. Phys. Lett. 83 (2003) 1240-1242.
[4] Toiyama T, Funai D, Sugiyama S, Piezoresistance measurement on single crystal silicon nanowires, J. Journal of Applied Physics. 93 (2003) 561-565.
[5] Ma D D D, Lee C S, Au F C K, et al., Small-Diameter Silicon Nanowire Surfaces, J. Science. 299 (2003) 1874-1877.
[6] H. B. Peng, C.W. Chang, S. Aloni, T. D. Yuzvinsky, and A. Zettl, Ultrahigh Frequency Nanotube Resonators, J. Phys. Rev. Lett. 97 (2006) 087203.
[7] Cui Y, Wei Q Q, Park H k, et al., Nanowire nanosensors for highly sensitive and selective detection of biological and chemical species, J. Science. 293 (2001) 1289-1292.
[8] Zhou X T, Hu J Q, Li C P, et al., Silicon nanowires as chemical sensors, J. Chem. Phys. Lett. 369 (2003) 220-224.
[9] E. T. Gawlinski and J. D. Gunton, Molecular-dynamics simulation of molecular-beam epitaxial growth of the silicon (100) surface, J. Phys. Rev. B. 36 (1987) 4774-4781.
[10] H. Yu, W. W. Zhang, S. Y. Lei, L. B. Lu, C. Sun, and Q. A. Huang, “Study on vibration behavior of doubly-clamped silicon nanowires by molecular dynamics”, Journal of Nano-materials, vol. 2012: Article ID 342329, 5 pages, 2012

Key Engineering Materials Vols 645-646 (2015) pp 1009-1015
Submitted: 2015-01-08
© (2015) Trans Tech Publications, Switzerland
Accepted: 2015-01-19
doi:10.4028/www.scientific.net/KEM.645-646.1009

Controlled encapsulation of micron-sized beads in a droplet based on pulse inertia force driving of micro-fluids

Hongcheng Wang [1, a], Lijun Yang[2, b], Jia Liu[2, c], Zhendong Dai [1,d]

[1] Institute of Bio-inspired Structure and Surface Engineering, Nanjing University of Aeronautics and Astromautics, Nanjing, Jiangsu, China;

[2]School of Mechanical Engineering, Nanjing University of Science and Technology, Nanjing, Jiangsu, China

[a]whch31@163.com (corresponding author), [b]fulisayang@163.com, [c]njustliujia@gmail.com, [d]zddai@nuaa.edu.cn

Keywords: bead encapsulation; droplet microfluidics; piezoelectric actuator; micro-nozzle

Abstract

Loading drops with discrete objects, such as particles and cells, is often necessary when performing chemical and biological assays in microfluidic devices. The vast majority of reported encapsulating methods of particles into monodisperse picolitre droplets are based on micro-fluidic chip using the standard soft lithography technique are necessary. This paper presents a new approach, not based on micro-fluidic chip, for encapsulating particles into droplets actuated by microfluidic pulse inertia force. The polystyrene bead suspension can be ejected out of a tapered glass capillary in mineral oil drop by drop actuated by an enough pulse inertia force which is produced by a hollow PZT stack. The polystyrene beads will be randomly encapsulated in monodisperse picolitre droplets. The tapered glass capillary has the advantages of good chemical resistance, low friction, easy to manufacture and low cost and is suitable for chemical and biological analysis. The minimum size of the spherical droplets can reach 12 μm in diameter and about 1 picolitre in volume. The percentage of the droplets with single 5 μm-diameter polystyrene bead can reach 40% when the droplet size is 40 μm and the concentration of the bead suspension is 1×10^7 beads per milliliter. The experiment result can be applied in droplet-based single cell encapsulating and analyzing.

Introduction

Droplet-based microfluidics offers a wider range of application over conventional or continuous analytical techniques [1-2]. By encapsulating reagents in droplets, advanced control of reaction kinetics can be obtained and physical and chemical isolation of droplets eliminate the risk of cross-contamination with a higher concentration of products generated confined in the droplets[3-4]. Droplets of reagents can be transported faster or more precisely than conventional microfluidic devices with controlled contents. These merits result in the increase of areas of applications of cell dynamic behavior [5], directed evolution of enzymes [6], protein crystallization [7], polymerase chain reaction [8] and gene detection and expression of single cells [9].

However, in order to further utilize droplet microfluidics, stable generation of ultrasmall droplets with a predetermined size should be first established. The vast majority of reported encapsulating methods of particles into monodisperse picolitre droplets are based on micro-fluidic chip. In the micro-fluidic chips, T-junction [10] and flow-focusing configuration [11] are frequently adopted, the shearing force of one flowing fluid against another is used and droplets are

continuously generated utilizing the oil-aqueous interface instability. In the above two shear-flow-driven droplet generators, microfluidic devices (or microfluidic chips) usually fabricated with polydimethylsiloxane (PDMS) using the standard soft lithography technique are necessary [12]. The fluids are usually driven by syringe pumps and the sizes of the particle droplets can be changed by altering the fluid flow rates, the channel widths, or by changing the relative viscosity between the aqueous phase and oil phase [13]. Despite their great potential, studies of single-beads in drops suffer from an intrinsic limitation; because the process of loading beads into drops is purely random, the distribution is dictated by Poisson statistics [14]. For example, only 36.8% of all droplets will contain one bead if the mathematical expectations of Poisson distribution $\lambda=1$ by adjusting bead suspension concentration and droplet size. To control the number of beads in droplets, Edd et al. designed a flow-focusing microfluidic chip with high aspect-ratio microchannels to controllably load beads into drops because the high aspect-ratio microchannels can cause beads to self-organize into two evenly-spaced streams [15]. Another reported encapsulating method is droplet assembling technique and has high controllability on the compositions and volumes of droplets in the nanoliter to picoliter range [16-17]. This method is not based on micro-fluidic chip and using a capillary sampling probe and array of horizontally positioned micro-sample vials with a slot fabricated on the bottom of each vial. The bead suspension and the oil are in different vials, into which the capillary sampling probe dips successively.

In our previous work, based on microfluidic pulse inertia force we have developed a drop-on-demand droplet generator for ejecting droplets of low viscosity liquid in gaseous environment [18] and applied it to fabrication of mcropellistor [19]. The droplet size can be precisely controlled. Herein, based on microfluidic pulse inertia force, we developed another bead encapsulating approach without using micro-fluidic chips. The droplets of bead suspension are ejected from a tapered glass capillary actuated by a hollow PZT stack, without the need of special microchannel networks or external devices.

Experiment

Fig.1 shows the assembly of the picoliter droplet generator based on microfluidic pulse inertia force to generate bead suspension droplets in oil phase. The structure of the generator consists of five main parts: (1) tapered glass capillary (usually referred as micro-nozzle), (2) capillary holder, (3) hollow PZT stack actuator, (4) connector A and (5) connector B. The micro-nozzle clamped by the nozzle holder, which is fixed with the right face of the hollow PZT stack actuator (WTYDCR, CETC) through connector A while the left face is fixed with body frame and kept stationary through connector B. There are neither micro pumps nor micro valves, which have either micro moving parts or embedded micro electric circuits, therefore significantly simplifying the structure, and decreasing the difficultness in manufacturing and the cost of the generator.

The hollow PZT stack actuator is constructed of several disc-shaped piezoelectric ceramic pieces, the thickness of which is in the range of 0.02 mm to 1 mm. There is an approximate linearity between applied voltage amplitude and the right face displacement of the actuator. So, the actuator will cause a larger displacement instantaneously and consequently provide a greater pulse inertia force for tapered glass capillary and bead suspension inside when being applied a higher pulse driving voltage.

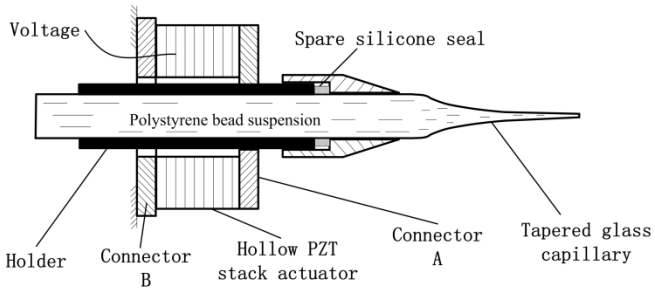


Fig.1 Sketch of the picoliter droplet generator based on microfluidic pulse inertia force

Glass material was chosed to make the tapered glass capillary because of several merits, such as good chemical resistance, low friction, easy to manufacture and low cost. The raw material is borosilicate glass capillary (Beijing Zhengtianyi Scientific And Trading Co., Ltd.). The dimensions of glass capillary are 1.6 mm, 1.0 mm and 100 mm in external diameter, internal diameter and length, respectively. Glass heating process was adopted to fabricate the micro-nozzle without complicated microfabrication technologyd can be divided into two steps: (1) pulling a capillary to form a micro-nozzle with straight outlet and (2) forging the straight outlet to form a shrinkage one. The detail fabrication process for the micro-nozzle was presented in literature [19]. The micro-nozzles with different outlet diameters can be obtained by varying the control parameters of the voltage amplitude and balance weights. The minimum outlet diameter of the fabricated micro-nozzle can reach as small as 10 μm. The fabricated micro-nozzle with outlet diameter of 40 μm is shown in Fig.2.

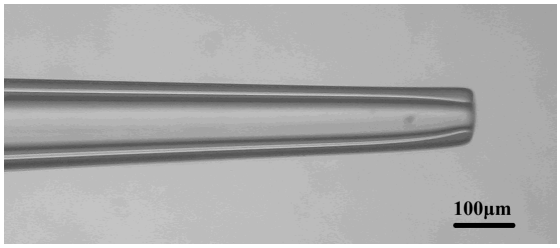


Fig.2 Micrograph of a tapered glass capillary with outlet diameter of 40 μm

The bead suspension liquid driving principle of the droplet generator based on microfluidic pulse inertia force is shown in Fig.3. When being applied with a pulse voltage, the PZT actuator stretches and exerts a driving force F_1 on the solid wall of the tapered micro-nozzle. In consequence, the glass solid wall and the boundary flow obtains a movement along with the nozzle axis. Then the viscous force V_1 within the fluids transfers the movement and the microfluidic body obtains a velocity υ. When the applied pulse voltage decreases rapidly to zero in magnitude, the PZT actuator contracts and the liquid inside the micro-nozzle obtains a pulse inertia force F_2 relative to the micro-nozzle. When the inertia force F_2 is small in magnitude, the viscous forces V_2 within the liquid is greater than the inertia force F_2, the liquid will move along with the nozzle, while, when the inertia force F_2 is larger enough in magnitude, the inertia force F_2 exceeds the viscous force V_2, a droplet of the liquids will be thrown out of the micro-nozzle drop by drop in the direction of the inertia force F_2. In the process of the bead droplet formation, the droplet size can be easily changed by changing any one of the micro-nozzle outlet diameter and the shape, frequency, amplitude of the applied pulse voltage. Consequently, the bead suspension will be ejected out of the micro-nozzle drop by drop in aid of the shear force from the oil phase liquid. The droplets will encapsulate beads in it and the number of the beads is stochastic.

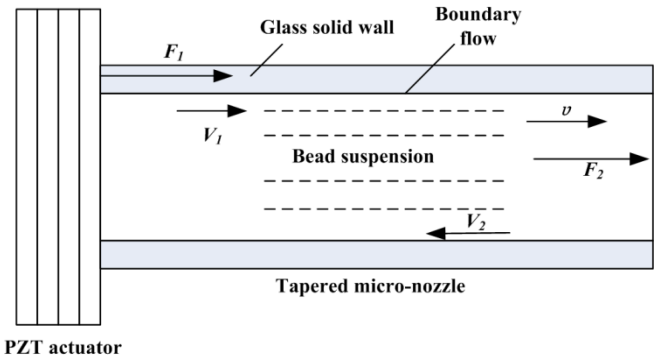


Fig.3 Bead suspension driving principle of the droplet generator based on microfluidic pulse inertia force

As is shown in Fig. 4, an apparatus for encapsulating micron-sized beads in mineral oil based on microfluidic pulse inertia force was established. The droplet generator is fixed on a three-dimension adjusting frame through the connector B and make the micro-nozzle inhaled a certain amount of aqueous phase liquid by a small negative pressure in the micro-nozzle produced by a pressure regulator. The micro-nozzle orifice is immersed in the mineral oil in a watch glass, which is placed on the stage of a chatelier-type microscope (TS-100, Nikon).

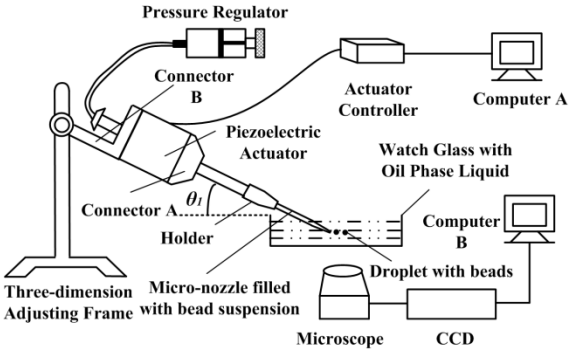


Fig.4 Sketch of the experimental apparatus for encapsulating micron-sized beads in an oil environment

Results and discussion

In the experiment, the polystyrene beads with average diameters of 5 μm are purchased from Tianjin Bay Point Chromatography Technology Development Center and the mineral oil (M5904) were purchased from American Sigma-Aldrich Company. Span 80 were purchased from Tianjin Hengxing Chemical Preparation Co., Ltd. The 5 μm-diameter polystyrene beads are shown in Fig.5. Mineral oil was added with 10% span 80, a kind of surfactant, to prevent the generated deionized water droplets or bead droplets from being fused.

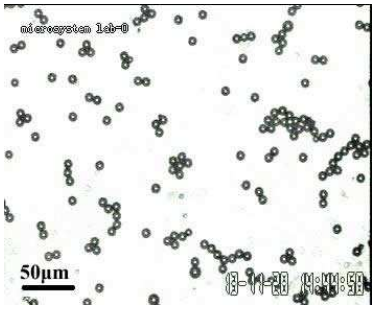


Fig.5 Micrograph of monodisperse polystyrene beads before being capsulated

The experiment of deionized water droplets jetting process and the size control methods was researched firstly. The experiment result showed that the pulse inertia force of microfluids can be used as active force to generate deionized water droplets in an oil environment. Fig.6 (a) shows the jetting process of deionized water droplets from a micro-nozzle in the mineral oil. The dependence of deionized water droplet size on voltage amplitude for different diameters of nozzle outlet is shown in Fig.6 (b). The frequency of the applied voltage is set as a lower value of 2 Hz. Each data point is an average of ten measurements. The hollow PZT stack actuator causes a larger displacement instantaneously and consequently provides a greater pulse inertia force for the micro-nozzle and aqueous phase liquid inside when being applied a higher driving voltage. So, deionized water droplets will be ejected and the droplet size increased with the increase of voltage amplitude. If the voltage is lower in magnitude, deionized water droplets won't be ejected when the micro-nozzle size is relatively small. For instance, the minimum voltage to eject droplets is 30 V and 20 V for nozzle orifice diameters of 10 μm and 20 μm respectively. On the other hand, when the voltage amplitude is relatively high, the inertia force was big enough to eject more mass of aqueous phase liquid, thus forming satellite droplets. For instance, the maximum voltage to stably eject droplets without satellite droplets is 50 V when the nozzle orifice diameter is 60 μm.

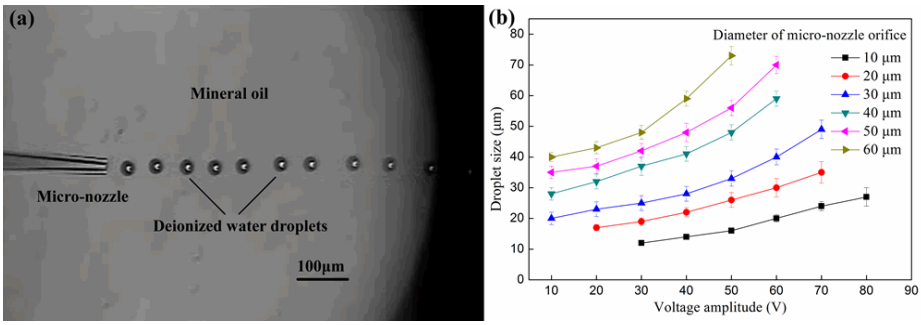


Fig.6 The jetting process of deionized water droplets from a micro-nozzle in mineral oil: (a) Micrograph and (b) dependence of deionized water droplet size on voltage amplitude for different diameters of nozzle outlet

The number of the beads encapsulated in droplets is random. It is the concentration of the bead suspension determined the average number of beads in a droplet as well as the droplet size. Fig.7 shows the variation of single bead droplet percentage with concentration of the bead suspension for different droplet sizes. Each presented data point represents an analysis of 200 droplets observed by a chatelier-type microscope. If the bead density of the suspension is relatively low (below 6×10^6 beads per milliliter), the fraction of droplets with single bead decreases with the increase of the droplet size and the fraction is relatively low (below 25%), because the number of the c beads is too small and a large number of the droplets encapsulating no bead s.

If the bead density of the suspension is relatively high (above 6×10^6 beads per milliliter), the fraction of droplets with single bead has a maximum point. For instance, when the bead density is 1×10^7 beads/mL and if the droplet size is too small (below 40 μm) there will be a large number of droplet encapsulating two, three or four beads and the fraction of single bead droplet is not large enough. Fig.8 (a) shows the process of encapsulating beads into droplets in mineral oil environment when the concentration of the bead suspension is 4×10^6 beads per milliliter and the droplet size is about 40 μm. When the droplet size is 40 μm with the concentration of the bead suspension being 1×10^7 beads per milliliter, the fraction of droplets with single bead obtains the maximum value of 0.4.

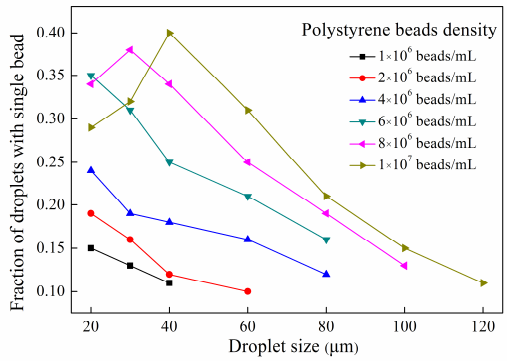


Fig.7 Variation of single bead droplet percentage with concentration of the bead suspension for different droplet sizes.

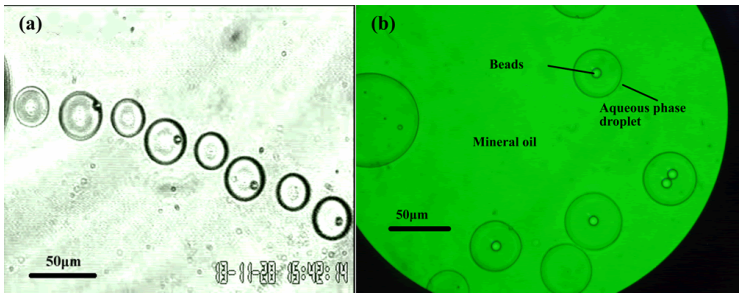


Fig.8 Micrograph of the picolitre droplets encapsulated with polystyrene beads in mineral oil environment: (a) the droplet ejecting process and (b) bead counts in droplets

Conclusions

This paper presents a new approach for encapsulating particles into droplets actuated by microfluidic pulse inertia force without using micro-fluidic chips. The polystyrene bead suspension can be ejected out of a tapered glass capillary into an oil environment actuated by an enough pulse inertia force which is produced by a hollow PZT stack. The polystyrene beads will be randomly encapsulated in monodisperse picolitre droplets. In the process of the bead encapsulation, the droplet size can be easily changed by changing the micro-nozzle outlet diameter and the shape amplitude of the applied pulse voltage. The minimum size of the spherical droplets can reach 12 μm in diameter and about 1 picolitre in volume. The number of the beads encapsulated in droplets is random. It is the concentration of the bead suspension determined the average number of beads in a droplet as well as the droplet size. The percentage of the droplets with single 5 μm-diameter polystyrene bead can reach 40% when the droplet size is 40 μm and the concentration of the bead suspension is 1×10^7 beads per milliliter. The experiment result can be applied in droplet-based single cell encapsulating and analyzing.

Acknowledgement

The work was supported by Postdoctoral Science Foundation of China (no. 2014M551584) and Jiangsu Planned Projects for Postdoctoral Research Funds (no. 1402006B)

References

[1] O.D. Velev, B.G. Prevo, K.H. Bhatt, On-chip manipulation of free droplets, Nature 426 (6966) (2003) 515–516.
[2] S.-Y. Teh, R. Lin, L.-H. Hung, A.P. Lee, Droplet microfluidics, Lab Chip 8 (2) (2008) 198.
[3] Y. Matsubara, K. Kerman, M. Kobayashi, S. Yamamura, Y. Morita, Y. Takamura, E. Tamiya, On-chip nanoliter-volume multiplex TaqMan polymerase chain reaction from a single copy based on counting fluorescence released microchambers, Anal. Chem. 76 (21) (2004) 6434-6439.

[4] H. Ding, S. Sadeghi, G.J. Shah, S. Chen, P.Y. Keng, C.J. Kim, R.M. Van Dam, Accurate dispensing of volatile reagents on demand for chemical reactions in EWOD chips, Lab Chip-Miniaturisation Chem. Biol. 12 (18) (2012) 3331-3340.
[5] M.A. Khorshidi, P.K.P. Rajeswari, C.Wählby, H.N. Joensson, H.A. Svahn. Automated analysis of dynamic behavior of single cells in picoliter droplets, Lab Chip 14 (2014) 931-937.
[6] S.L. Sjostrom, Y.P. Bai, M.T. Huang, Z.H. Liu, J. Nielsen, H.N. Joensson, H.A. Svahn, High-throughput screening for industrial enzyme production hosts by droplet microfluidics, Lab Chip, 14(2014) 806-813.
[7] S. Guha, S.L. Perry, A.S. Pawate, P.J.A. Kenis. Sens. Actuators B, Fabrication of X-ray compatible microfluidic platforms for protein crystallization 174(2012) 1-9.
[8] D.Y. Liu, G.T. Liang, X.X. Lei, B. Chen, W.Wang, X.M. Zhou, Highly efficient capillary polymerase chain reaction using an oscillation droplet microreactor, Anal. Chim. Acta 718(2012) 58-63.
[9] T.D. Rane, H.C. Zec, C.Puleo, A.P. Lee, T.H. Wang., Droplet microfluidics for amplification-free genetic detection of single cells, Lab chip, 12(2012) 3341-3347.
[10] T. Thorsen, R.W. Robert, F.H. Arnold, S.R. Quake, Dynamic pattern formation in a vesicle-generating microfluidic device, Phys. Rev. Lett. 86(2001) 4163-4166.
[11] A.Gupta, H.S. Matharoo, D. Makkar, R. Kumar, Droplet formation via squeezing mechanism in a microfluidic flow-focusing device, Computers & Fluids 100(2014) 218-226.
[12] A. Kang, J. Park, J. Ju, G.S. Jeong, S.H. Lee, Cell encapsulation via microtechnologies, Biomaterials 35(2014) 2651-2663.
[13] Y. Shi, G.H. Tang, H.H. Xia,Lattice Boltzmann simulation of droplet formation in T-junction and flow focusing devices, Computers & Fluids 90(2014) 155-163.
[14] A.R. Abate, C.H. Chen, J.J. Agresti, D.A. Weitz, Beating Poisson encapsulation statistics using close-packed ordering, Lab Chip 9(2009) 2628-2631.
[15] J.F. Edd, D.D. Carlo, K.J. Humphry, S. Koster, D. Irimia, D.A. Weitz, M. Toner, Controlled encapsulation of single-cells into monodisperse picolitre drops, Lab Chip 8(2008) 1262-1264.
[16] S.Q. Gu, Y.X. Zhang, Y. Zhu, W.B. Du, B. Yao, Q. Fang, Multifunctional picoliter droplet manipulation platform and its application in single cell analysis, Anal. Chem. 83(2011) 7570-7576.
[17] W.B. Du, M. Sun, S.Q. Gu, Y. Zhu, Q. Fang, Automated microfluidic screening assay platform based on dropLab, Anal.Chem. 82(2010) 9941-9947.
[18] W.Y. Zhang, L.Y. Hou, Method, apparatus and application of affecting fluid flow,China: ZL03152948.8 (2006) (in Chinese).
[19] H.C. Wang, L.Y. Hou, W.Y. Zhang, A drop-on-demand droplet generator for coating catalytic materials onmicrohotplates of micropellistor Sens. Actuators B, 183(2013) 342-349.

Key Engineering Materials Vols 645-646 (2015) pp 1016-1023
© (2015) Trans Tech Publications, Switzerland
doi:10.4028/www.scientific.net/KEM.645-646.1016

Submitted: 2015-01-13
Accepted: 2015-01-15

Interference Fit Assembly of Micro-parts Based on Microscopic Vision and Force

Juan Zhang[1, a], Wenrong Wu[1, b], Fei Shen[1, 2, c], Yongjun Deng[1, d]

[1]Laser Fusion Research Center, China Academy of Engineering Physics, Mianyang, China

[2]Institute of Automation, Chinese Academy of Sciences, Beijing, China

[a]lgdzhangjuan@163.com, [b]rongwwr@163.com, [c]fei.shen@ia.ac.cn, [d]deng6352818@163.com

Keywords: interference fit, microscopic vision, force control, control strategy, micro-assembly

Abstract. To assemble easily damaged micro-parts safely in interference fit way, the assembly process is designed and the interaction force in assembly process is analyzed. The pose of micro-parts is aligned based on calibration of three microscopic vision systems from different directions. In addition, a control strategy based on feedback of vision and force is proposed to assemble safely. In the case of two micro-parts just contact, position of micro-part is adjusted based on force information to compensate pose alignment error and keep force in safe range. When micro-part is deformed as increased contact force, position of micro-part is adjusted based on force in the interference fit process and deformation of micro-part. Experimental results demonstrate the effectiveness of proposed methods.

1. Introduction

Micro-assembly technology is used widely in MEMS (Micro-Electro-Mechanical System) production process. Vision and force sensor are used widely in micro-assembly system [1-3]. However, there are some limitations when using these sensors. For micro-assembly based on vision, vision detection process fails when visual occlusion occurs during assembly process. The subsequent assembly process can't be monitored [4, 5]. Furthermore, vision detection accuracy is limited by hardware devices. Micro-assembly only based on visual guidance is easier damage micro-parts in assembly process as vision detection accuracy is limited.

Micro-assembly based on force always requires precise calibration of the relationship between contact force and position to achieve assembly process control, while the calibration process is always complex [6, 7]. In addition, assembly based on force is only applicable to the situation when two micro-parts contact, it can't monitor the entire assembly process.

Compose vision and force information together to guide micro-assembly is an effective way to solve the above problems. In the field, related technologies have been studied and some research results have been made [8-10]. However, research on interference fit assembly of easily damaged micro-parts is less involved. As easily damaged micro-parts always have thin, brittle quality, interference fit assembly process deform these micro parts easily, or even damage them in assembly process. To solve the problem, we propose a strategy based on vision and force feedback to assemble easily damaged micro-parts safely in interference fit way. The assembly process is continuous monitored by vision and force. As micro-part deformed as contact force, the contact force of micro-parts and deformation amount of micro-part are both detected in real-time, the position of micro-part is adjusted according to the detection results. The strategy ensures that easily damaged micro-parts are safely in assembly process.

2 Assembly process design and analysis

2.1 Assembly process design

The structures of two easily damaged micro-parts are shown in Fig.1. Fig.1 (a) is the structure of one micro-part named silicon arm, which is made of silicon. The overall structure of silicon arm is sheet structure, while the end is arc structure. The end of silicon arm is distributed with 16 elastic

claws uniformly. The claws open different amount according to the amount of interference fit in assembly process. Fig.1 (b) is the structure of the other micro-part named sleeve, which is made of aluminum. The overall structure of sleeve is columnar structure. There is chamfer in the entrance of sleeve. The claws of silicon arm will open slowly in the effect of chamfer, until the claws contact with the outside wall of sleeve. Fig.1 (c) is the assembled structure of silicon arm and sleeve.



(a) Silicon arm (b) Sleeve (c) Components

Fig. 1 The structure of micro-parts

The thickness of silicon arm is about 0.5mm, and the length is about 70mm. The arc diameter of silicon arm end is about 16mm, and the inner diameter of the end is about 5.35mm. The height of the sleeve is about 5.9mm, and the outside diameter of it is about 5.37mm.

To assemble silicon arm and sleeve, firstly, realize pose alignment of the two micro-parts. Secondly, control sleeve movement in vertical direction until the claws of silicon arm is contact with the chamfer of sleeve. Thirdly, control sleeve movement slowly to make sure the claws of silicon arm open safely until the claws contact with the outside wall of sleeve. Lastly, control silicon arm movement in the vertical direction until arrive the ideal position.

2.2 Force analysis in assembly process

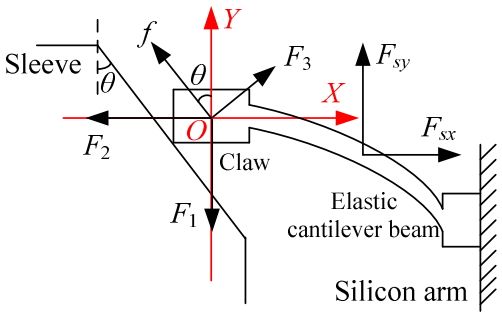


Fig.2 Force analysis of a claw

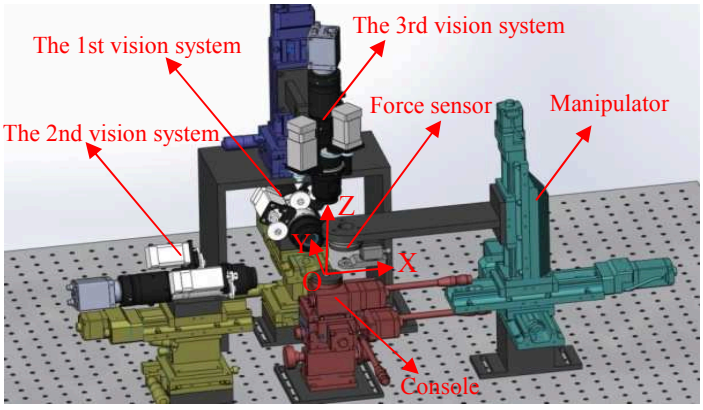


Fig.3 The configuration of assembly system

In interference fit assembly process, the force of a claw is shown in Fig.2, that is, the downward pulling force F_1 and the forward pushing force F_2 coming from elastic cantilever beam, the supporting force F_3 coming from sleeve, and the friction force f coming from sleeve surface.

OXY coordinate system is established at the center of claw, as shown in Fig.2. The horizontal direction force F_x and the vertical direction force F_y of a claw are calculated by formula (1), where θ is the chamfer size of sleeve.

$$\begin{cases} F_x = F_3\cos\theta - f\sin\theta - F_2 \\ F_y = f\cos\theta + F_3\sin\theta - F_1 \end{cases} \tag{1}$$

When the claw in uniform motion, the sliding frictional force $f=\mu F_3$, where μ is the coefficient of sliding friction. Thus, force of elastic cantilever beam in the horizontal direction F_{sx} and in the vertical direction F_{sy} are calculated by formula (2).

$$\begin{cases} F_{sx} = F_3\cos\theta - \mu F_3\sin\theta \\ F_{sy} = \mu F_3\cos\theta + F_3\sin\theta \end{cases} \tag{2}$$

The scale factor k of F_{sx} and F_{sy} is calculated by formula (3).

$$k = \frac{F_{sx}}{F_{sy}} = \frac{\cos\theta - \mu\sin\theta}{\sin\theta + \mu\cos\theta} \tag{3}$$

Order $\sin\alpha = \mu/\sqrt{1+\mu^2}$, $\cos\alpha = 1/\sqrt{1+\mu^2}$, the scale factor k is calculated by formula (4).

$$k = \frac{\cos\theta\cos\alpha - \sin\theta\sin\alpha}{\sin\theta\cos\alpha + \sin\alpha\cos\theta} = \cot(\theta+\alpha) \tag{4}$$

From equation (4), we can see that the scale factor k and chamfer size θ are cotangent relationship. As the chamfer size decreases, the scale factor increases.

As the elastic cantilever beam has strong stretchability in the horizontal direction, while has weak stretchability in the vertical direction. Therefore, in order to enhance security of the elastic cantilever beam in the assembly process, we should decrease the force of elastic cantilever beam in the vertical direction. As shown in formula (4), in the premise of satisfying micro-part processing, we should decrease θ as far as possible to decrease force in the vertical direction.

3 Micro-parts pose alignment

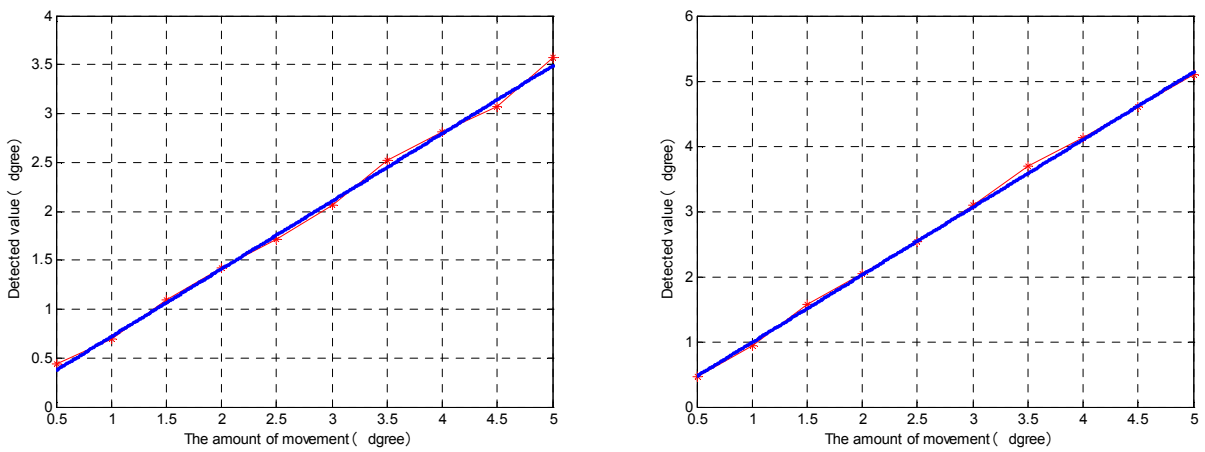
3.1 Micro-assembly system

The configuration of assembly system is shown in Fig.3. The system includes three microscopic vision systems, which are named 1st, 2nd, and 3rd microscopic vision system, respectively. The three vision systems are arranged orthogonal to each other in space. In addition, the system includes a manipulator and a console, while the manipulator has three freedom of translational movement, and the console has three rotational freedoms and one translational freedom in the vertical direction. The end of the manipulator connects with a force sensor, which feedback the contact force between silicon arm and sleeve in the assembly process. The force sensor is connected with silicon arm gripper, which grips silicon arm by vacuum suction way. The sleeve is set on the top of the console by a sleeve gripper.

The X-axis and Y-axis of manipulation movement coordinate are parallel with the X-axis and Y-axis of console movement coordinate. The optical axis of 1st microscopic vision system is parallel with Y-axis of console movement coordinate, and the optical axis of 2st microscopic vision system is parallel with X-axis of console movement coordinate.

3.2 Pose alignment method

As short depth of field of microscopic vision system, it's only sensitive to two translational freedoms vertical to optical axis, and one rotational freedom along the optical axis. Therefore, detect angle deviation $\Delta\theta_y$ based on 1st visual system, detect angle deviation $\Delta\theta_x$ based on 2nd visual system, and detect position deviation ΔT_x, ΔT_y, and angle deviation $\Delta\theta_z$ based on 3rd vision system. The pose of silicon arm and sleeve are adjusted according to detection results, to achieve pose alignment.



(a) Before error compensation (b) After error compensation

Fig.4 Calibration results of vision system

As system installation error exists, the optical axis of microscopic vision system may not parallel with motion axes. In the case of not parallel, there will be big visual detection error, and the two micro-parts can't be aligned precisely. To solve the problem, we compensate vision detection error by calibrating the relationship of detected amount of movement and actual amount of movement by control micro-parts movement.

Fig.4 (a) is the relationship of detected movement amount and actual movement amount in the guide of 2nd microscopic vision system. We can see that the detection amount does not correspond to actual movement amount. Using least-squares fitting algorithm to fit the straight line of detection results, we can see that the slope of line is 0.69, and the intercept is 0.04. Compensate detection error by calibrated result. Fig.4 (b) is the relationship of detected movement amount and actual movement amount after error compensation. Using least-squares fitting algorithm to fit the straight line of detection results, the slope of line is 1.04, and the intercept is -0.03. The detection values correspond to actual movement values well.

4 Control strategy of interference fit assembly

As pose alignment error and processing error of micro-parts, the 16 claws of silicon arm have different size of force at the same time in assembly process. Consequently, the claws open different amount at the same time. The single claw is easily damaged when force is bigger than the maximum force. To solve the problem, an assembly control strategy based on force and vision is proposed to achieve safe assembly.

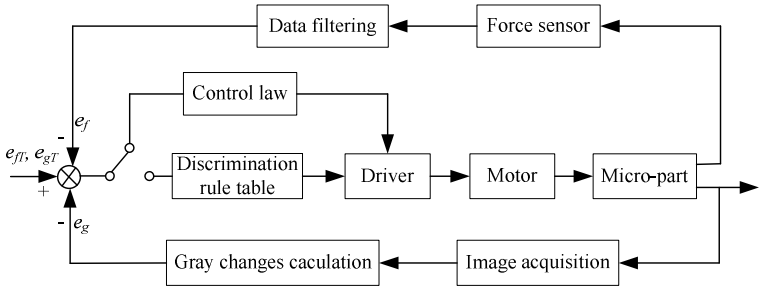


Fig. 5 The block diagram of control strategy

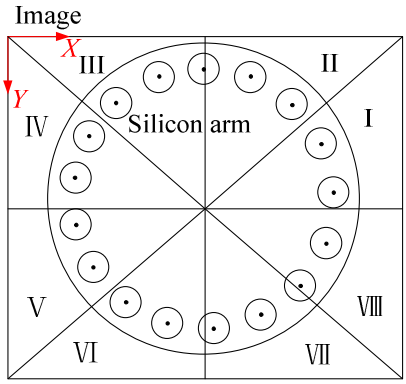


Fig.6 Schematic of image partition

Fig.5 is the block diagram of control strategy, where e_f is the force feedback in real-time, e_g is the gray variation in image, e_{fT} is the threshold used to determine whether the force is in a safe range, e_{gT} is the threshold used to determine whether the elastic cantilever beam has big deformation. As silicon arm and sleeve just contact, the deformation of elastic cantilever beam is small, control assembly process by force. As deformation amount of elastic cantilever beam is bigger than e_{gT}, control assembly process by force and vision.

4.1 Closed-loop control based on force

At the stage of silicon arm claws just contact with sleeve chamfer, as contact force are small, the claws don't have significant deformation. So open the closed-loop control based on force to compensate the pose alignment error and keep force in safe range.

$$\Delta u_x(k) = \begin{cases} L_{Sx}, & \mathrm{e}_{fx}(k) \geq \mathrm{e}_{fTx} \\ 0, & |\mathrm{e}_{fx}(k)| < \mathrm{e}_{fTx} \\ -L_{Sx}, & \mathrm{e}_{fx}(k) \leq -\mathrm{e}_{fTx} \end{cases} \tag{5}$$

The movement control law of silicon arm is shown by formula (5), e_{fx} is the force of silicon arm in the X-axis direction, e_{fTx} is the given threshold, when the force of silicon arm in the X-axis direction is smaller than e_{fTx}, the silicon arm is regarded as safely in the X-axis direction, L_{Sx} is the movement distance of silicon arm in the X-axis direction, Δu_x is the control value, k is the number of control cycle. The movement control law in Y-axis is similar as control law in X-axis.

With the downward movement of silicon arm, the elastic cantilever beam deforms as contact force increases. To prevent damage to the claws, close closed-loop control based on force, open closed-loop control based on vision and force. The gray variation in the image is used to measure claw deformation. Via detecting force and gray variation in image in real-time to control position adjustment of silicon arm in assembly process.

4.2 Closed-loop control based on vision and force

When the contact force of silicon arm and sleeve is in the safe range, the deformation of single elastic cantilever is measured to control assembly process. When the contact force of silicon arm and sleeve is out of the safe range, the assembly process is stopped to avoid micro-part damaged.

The deformation of elastic cantilever is measured by detecting gray variation in image. As shown in Fig.6, the image is divided into four quadrants, and each quadrant is divided into two regions. The amount of gray variation in different regions is calculated, respectively.

The calculation of gray variation in single region is shown in formula (6), $F(i,j)$ is the gray value at position (i,j) in current image， $B(i,j)$ is the gray value at position (i,j) in last image, V is the value of gray variation. If V is bigger than a given threshold, it's regard as an effective result.

Compare effective results from different regions, the region that maximum value belongs to is regarded as the effective control region. The movement control rules of silicon arm are listed in Table 1, where s is the given movement distance.

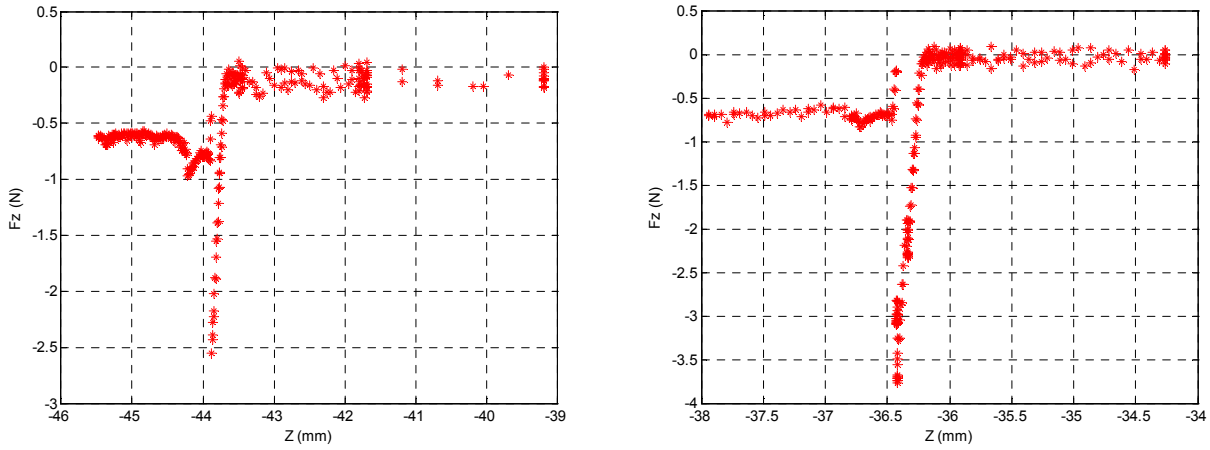
$$V = \sum_{i=m}^{n} \sum_{j=p(i)}^{q(i)} [F(i,j) - B(i,j)] \tag{6}$$

Table 1 Movement control rules

Effective control region	Movement direction			
	X+	X-	Y+	Y-
I	s		1/2s	
II	1/2s		s	
III		1/2s	s	
IV		s	1/2 s	
V		s		1/2 s
VI		1/2s		s
VII	1/2s			s
VIII	s			1/2s

5 Experiment and results

5.1 Experiment results of force analysis



(a) 30 degree chamfer (b) 60 degree chamfer

Fig.7 The force of silicon arm in vertical direction with different chamfer size

As described in section 1.2, the force of elastic cantilever beam in the horizontal direction has cotangent relationship with the force in the vertical direction. To decrease the force of elastic cantilever in the vertical direction, we should decrease the chamfer size.

To prove the theoretical derivation results, the force of sleeve with different chamfer size in interference fit assembly process is detected. Fig.7 is vertical force of silicon arm with different chamfer size in the assembly process. Fig.7 (a) is the result with 30 degree chamfer, the max force in assembly process is about 2.6N, and Fig.7 (b) is the result with 60 degree chamfer. The max force in Fig.7 (b) is 3.8N. Compare results, we can see that the max force of silicon arm with 30 degree chamfer is the minimum.

Table 2 Experiment results with different chamfer size

Number	Max force (N)	
	30 degree	60 degree
1	3.01	3.68
2	2.56	3.77
3	3.32	3.55
4	2.44	2.71
5	2.58	3.04
Average	2.78	3.35

In addition, the repeated experiments are performed to validate the result of theoretical analysis. Table 2 shows the results of five repeated experiments with 30 degree chamfer and 60 degree chamfer, respectively. The average force with 30 degree chamfer is 2.78N, while the average force with 60 degree chamfer is 3.35N. It proves that theoretical analysis and experimental results are consistent.

5.2 Experiment results of assembly control

Base on force and vision guidance, silicon arm and sleeve were assembled. Fig.8 is the images in assembly process. Fig.8 (a) is the image after micro-parts pose alignment, Fig.8 (b) is the image in interference fit assembly process, Fig.8 (c) is the image after assembly, and Fig.8 (d) is the image after silicon arm was released by the gripper. Claws of silicon arm were safely in assembly process.



(a) Pose alignment (b) Interference fit assembly process

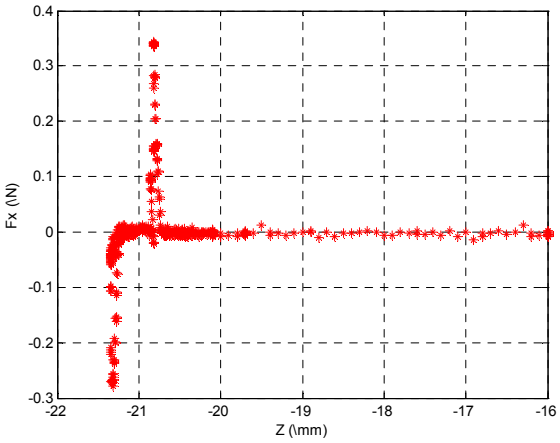


(c) Complete assembly (d) Release of silicon arm

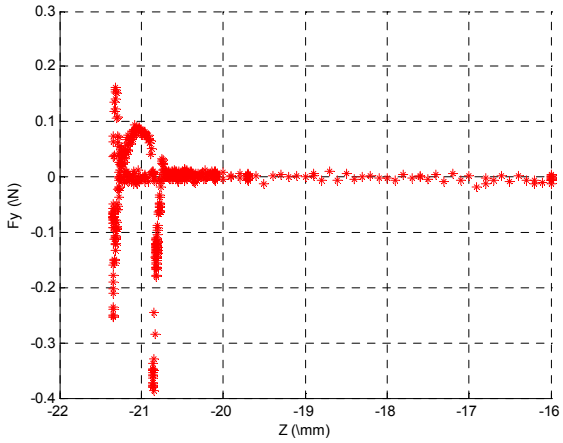
Fig.8 Images in assembly process

Fig.9 is the force of silicon arm in assembly process. The amount of interference between silicon arm and sleeve is 13μm. Fig.9 (a) is the force in X-axis direction, Fig. 9(b) is the force in Y-axis direction, and Fig.9(c) is the force in Z-axis direction. With the movement of silicon arm in the Z-axis direction, silicon arm is contact with sleeve. As pose alignment error and interference amount, the force of silicon arm is increased, via control position of silicon arm in X-axis and Y-axis, keep force

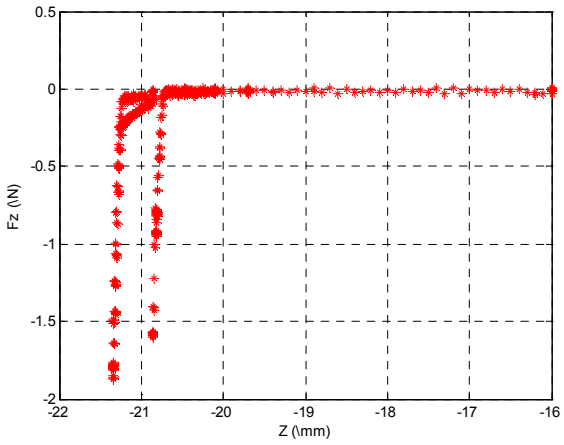
of silicon arm in the safe range. With the further movement of silicon arm, the elastic cantilever beam of claw is deformed as increased interference amount. Open closed-loop control based on vision and force. Based on detect force and gray variation in different image region, control silicon arm movement in the X-axis and Y-axis direction, until silicon arm arrive the ideal position.



(a) Force in X-axis direction



(b) Force in Y-axis direction



(c) Force in Z-axis direction

Fig.9 Force in assembly process

6 Conclusion

In this paper, the problem of interference fit assembly of easily damaged micro-parts is studied. For special micro-parts, the assembly process is designed based on structure qualities of micro-parts, and the force in assembly process is analyzed. Based on calibration of microscopic vision system, the relative pose of micro-parts can be detected, and the two micro-parts are aligned. For interference fit assembly safely, a control strategy based on vision and force was proposed in the paper. In the case of two micro-parts just contact, the position of micro-part is adjusted by contact force detection, to compensate pose alignment error and keep contact force in safe range. In the case of micro-part is deformed as gradually increased contact force, control micro-part movement via deformation detection of micro-part and the contact force between two micro-parts. Experimental results have proved the effectiveness of the strategy.

Acknowledge

This research is partially supported by Foundation of Laboratory of Precision Manufacturing Technology CAEP under Grant ZZ14003, Development Fund of CAEP (2014B0403066), and China Postdoctoral Science Foundation.

References

[1] Y. Zhao, C. C. Cheah. Vision-based neural network control for constrained robots with constraint uncertainty. IET Control Theory and Applications, 2008, 10(2): 906-916.

[2] K. Rabenorosoa, C. Clevy, P. Lutz. Active force control for robotic micro-assembly: application to guiding tasks. In Proceedings of the IEEE International Conference on Robotics and Automation, Anchorage, USA, 2010, pp: 2137-2142.

[3] R. K. Jain, S. Majumder, A. Dutta. SCARA based peg-in-hole assembly using compliant IPMC micro gripper. Robotics and Autonomous Systems, 2013, 61: 297-311.

[4] L. D. Wang, L. Ren, J. K. Mills, et al. Automated 3-D micrograsping tasks performed by vision-based control. IEEE Transactions on Automation Science and Engineering, 2010, 7(3): 417-426.

[5] B. Tamadazte, N. L. Piat, E. Marchand. A direct visual servoing scheme for automatic nanopositioning. IEEE Transactions on Mechatronics, 2012, 17(4): 728-736.

[6] Y. Xu, J. Zhu. The analysis and optimum design on compliant microgripper with micro-force sensor. International Congress on Image and Signal Processing, 2009, pp: 1-5.

[7] J. Choi, S. Hong, W. Lee, et al. A robot joint with variable stiffness using leaf springs. IEEE Transactions on Robotics, 2011, 27(2): 229-238.

[8] R. Saeidpourazar, N. Jalili. Towards fused vision and force robust feedback control of nanorobotic-based manipulation and grasping. Mechatronics, 2008, 18: 566-577.

[9] K. Rabenorosoa, C. Clevy, P. Lutz. Hybrid force/position control applied to automated guiding tasks at the microscale. In Proceedings of the IEEE/RSJ International Conference on Intelligent Robots and Systems, Taipei, Taiwan, China, 2010, pp: 4366-4371.

[10] Juan Zhang, De Xu, Zhengtao Zhang, Wensheng Zhang. Position/Force hybrid control system for high precision aligning of small gripper to ring object. International Journal of Automation and Computing, 2013, 10(4): 360-367.

Key Engineering Materials Vols 645-646 (2015) pp 1024-1031
© (2015) Trans Tech Publications, Switzerland
doi:10.4028/www.scientific.net/KEM.645-646.1024

Submitted: 2015-01-09
Accepted: 2015-01-15

Scalable Electrical Model and Performance Analysis of a Novel Bar TSV Structure

Zhensong Li[1, 2, a], Min Miao[1, b], Shaochun Yang[1] and Dacheng Yang[2]

[1] Beijing Information Science and Technology University, #35, Beisihuan Middle Road, Chaoyang District, Beijing, China

[2] Beijing University of Posts and Telecommunications, #10, Xitucheng Road, Haidian District, Beijing, China

[a]lizhensong@bistu.edu.cn, [b]miaomin@bistu.edu.cn

Keywords: through silicon via(TSV); scalable Model; three dimensional system in package(3D SIP)

Abstract. A novel Bar TSV(B-TSV) structure, formed by two semi-cylinders combining with a quadrangular is studied in this paper. This B-TSV structure extends the TSV design options by introducing new design parameters. The scalable electrical model of B-TSV is proposed and the effects of design parameters, such as the side length of quadrangular and the minimum distance between TSVs are investigated and concluded by a 3D electromagnetic solver. Performance comparison between B-TSV and the traditional cylindrical one is also provided by simulation under the Ground-Signal-Ground configuration. Simulation results show that B-TSV has better performance than the traditional one, and can be used to increase the TSV array density without degrading the electrical performance of TSV system.

Introduction

Through Silicon Via (TSV) technology is the most promising technology enabling a vertical electrical connectivity for the three dimensional system in package (3D SIP). This vertical interconnect significantly shortens signal paths and reduces electrical latency thus achieves higher system performance. According to the reports of International Technology Roadmap for Semiconductors(ITRS) [1], high density of I/O ports, large depth-to-width ratio of TSV array, are the key characteristics of future 3D SIP. Under this situation, the interconnection density and complexity will reach a high level.

For the traditional cylindrical TSV structure, the geometric parameters are just two, diameter of TSV and pitch between TSVs. As the characteristic dimension of semiconductor technology steadily decreasing, the main vertical interconnect structure, TSV, is forced to reduce structure size and increase array density which brings huge challenge in TSV design and fabrication. Furthermore, the chip stacking fashion is converting from interposer staking into direct active chip stacking. When it comes to direct active chip stacking, the TSV structure has to be processed in the mature active chips without destructing the original functional circuit. So the TSV processing is facing space limitation. In this situation, the traditional cylindrical TSV structure may not be the best choice and some novel TSV structures are required[2].

In this paper, we propose a B-TSV structure and investigate the impacts of B-TSV geometries on its electrical characteristics. We also explore the equivalent circuit elements(RLCG) analytical calculations. Moreover, the electrical performance comparison of B-TSV and traditional TSV is given by simulations done by a 3D electromagnetic solver.

Scalable modeling of the B-TSV structure

The B-TSV structure, as shown in Fig.1 (a), is formed by two semi-cylinders combining with a quadrangular. The diameter of the cylinder cross section is d_B, the two side lengths of the quadrangular cross section are d_B and l_B, respectively. Obviously, when l_B =0, the B-TSV structure reduces to cylindrical TSV structure, which means the traditional cylindrical TSV is the special case of B-TSV. For the B-TSV structure, d_B and l_B can be flexibly adjusted to fit particular requirement for the pitch p_B and the minimum distance $d_{B,\min}$ between TSVs.

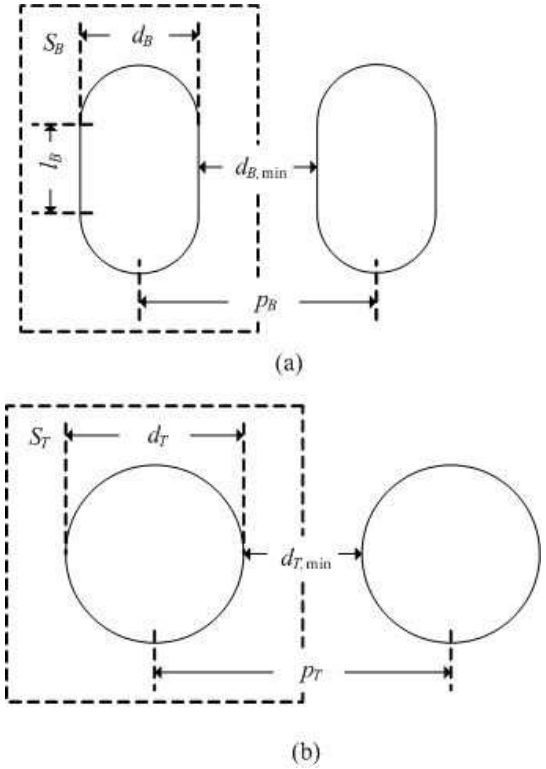


Fig.1 Top view of (a) B-TSV and (b) Traditional cylindrical TSV

3D modeling of B-TSV structure is performed using Ansoft's High Frequency Structure Simulation (HFSS) to verify the validity of the scalable model. This model, shown in Fig. 2 is using the Ground Signal Ground (GSG) configuration[3] and the modeling parameters are listed in Table 1.

Table 1 Simulation parameters of the GSG configuration with B-TSV structure

Parameter	Symbol	Value
B-TSV diameter[μm]	d_B	10
TSV quadrangular side length[μm]	l_B	7.85
TSV height[μm]	h_{TSV}	100
Bump height[μm]	h_{Bump}	10
TSV-to-TSV pitch [μm]	p_{TSV}	25
Insulator thickness[μm]	t_{ox}	1
Resistivity of TSV [$Q \cdot m$]	ρ_{TSV}	$1.7*10^{-8}$
Conductivity of silicon substrate[S/m]	σ_{Si}	10
Relative permittivity of silicon substrate	$\varepsilon_{r,Si}$	11.9
Relative permittivity of insulator	$\varepsilon_{r,Insulator}$	4
Relative permeability of TSV	$\mu_{r,TSV}$	1

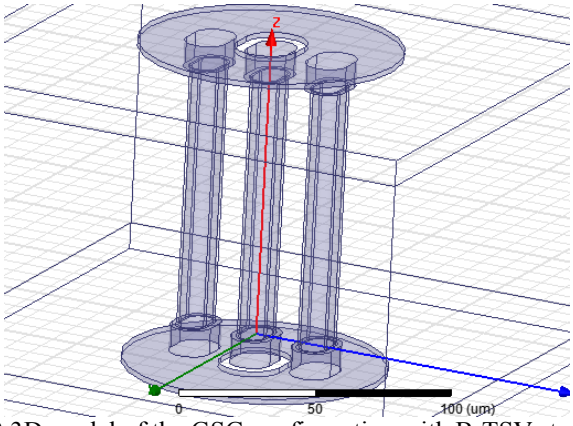


Fig. 2 3D model of the GSG configuration with B-TSV structure

With the 3D model given in Fig. 2, the high-frequency scalable electrical model of B-TSV is proposed as show in Fig. 3. The analytic RLCG equations are derived from the physical configuration with the design parameters[4,5].

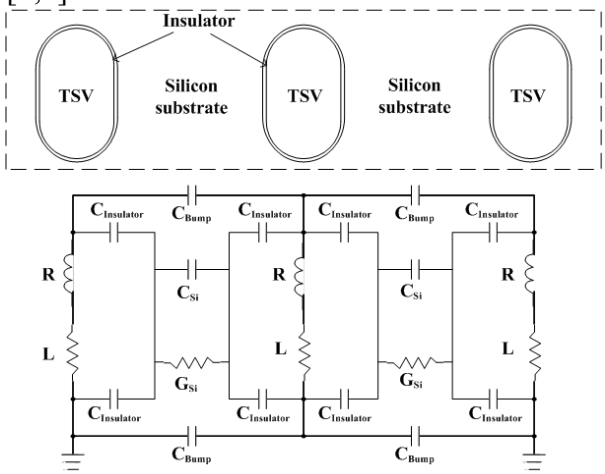


Fig. 3 Top view and scalable electrical model of GSG configuration with B-TSV structure

The resistance of B-TSV is given as

$$R = \sqrt{R_{dc}^2 + R_{ac}^2}[\Omega] \tag{1}$$

Here, R_{dc} and R_{ac} are direct-current resistance and alternating-current resistance, respectively. Taking the structure parameters of B-TSV into consideration, R_{dc} can be expressed as

$$R_{dc} = \rho_{TSV} \times \frac{h_{TSV}}{\pi(d_B/2)^2 + d_B l_B}[\Omega] \tag{2}$$

High-frequency current flows close to the surface of TSV conductor due to the "skin effect", so the skin depth has to be determined to calculate AC resistance of TSV[6].

$$\delta_{skin} = \frac{1}{\sqrt{\pi f \mu_{TSV} \sigma_{TSV}}}[\mathrm{m}] \tag{3}$$

Suppose the alternating-current uniformly distributes around the surface of B-TSV conductor and R_{ac} can be presented as

$$R_{ac} = k_p \left(\rho_{TSV} \times \frac{h_{TSV}}{(\pi d_B + 2l_B)\delta_{skin} - \pi\delta_{skin}^2} \right)[\Omega] \tag{4}$$

The proximity factor k_p is introduced here to describe the "proximity effect" which induces current flow nonuniformly on the inside-facing surfaces of the conductors. If other TSVs are located near the single-ended signal TSV, then this effect does not have to be considered, and the factor should be omitted.

Considering the specific geometric structure of B-TSV, the capacitance and inductance parameters are difficult to be precisely calculated. In order to simplified the analysis, the B-TSV structure is

replaced by elliptic cylinder structure with equivalent parameters, as show in Fig. 4. Using the conformal transformation[7], this elliptic cylinder structure can be transformed into cylinder structure, and then the coaxial-cable capacitance model and the loop inductance model between two parallel conduction wires can be used to deduce the capacitance and inductance parameters in the B-TSV structure[8].

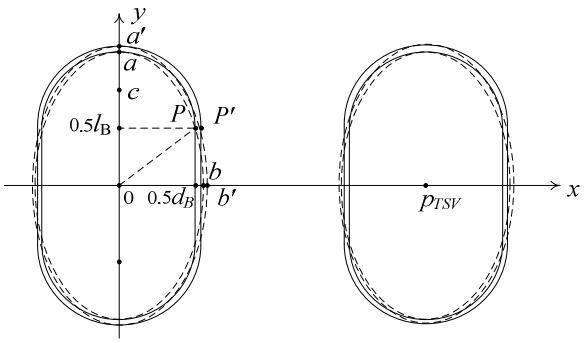


Fig. 4 Equivalent model of the B-TSV structure

The inner elliptic equation in Fig. 4 is

$$\left(\frac{y}{a}\right)^2+\left(\frac{x}{b}\right)^2=1 \tag{5}$$

Obviously, the semi major axis a=0.5(d_B +l_B). The unique coordinate of point P is (0.5d_B, 0.5l_B) according to the geometric structure shown in Fig. 4. Substituting these conditions into Eq.5, the semi minor axis b can be calculated as

$$b=\frac{0.5(d_B+l_B)}{\sqrt{1+2l_B/d_B}} \tag{6}$$

For the outer elliptic cylinder containing the insulator layer, a'= a+t_{ox} =0.5(d_B +l_B)+t_{ox}. And using the same analyzing method, the semi minor axis b' is calculated as

$$b'=\frac{0.5d_B(d_B+l_B+0.5t_{ox})}{\sqrt{d_B^2+2d_Bl_B+0.5t_{ox}(d_B+l_B+0.5t_{ox})}} \tag{7}$$

Using the conformal transformation[7], the equation of $C_{\text{insulator}}$ is expressed as

$$C_{\text{Insulator}}=\frac{1}{2}\left\{2\pi\times\varepsilon_0\varepsilon_{r,\text{Insulator}}\times\frac{h_{\text{TSV}}}{\ln\left((a'+b')/(a+b)\right)}\right\}[\text{F}] \tag{8}$$

The capacitance of bump and silicon are given as Eq.9 and Eq.10, respectively.

$$C_{\text{Bump}}=\pi\times\varepsilon_0\varepsilon_{r,\text{Bump}}\times\frac{h_{\text{Bump}}}{\cosh^{-1}\left(p_{\text{TSV}}/(a+b)\right)}[\text{F}] \tag{9}$$

$$C_{\text{Si}}=\frac{\pi\varepsilon_0\varepsilon_{r,\text{Si}}h_{\text{TSV}}}{\cosh^{-1}\left(p_{TSV}/(a'+b')\right)}[\text{F}] \tag{10}$$

Considering the dielectric losses in high frequency region, the relationship between capacitance and conductance is given in Eq.11[3].

$$\frac{C_{\text{Si}}}{G_{\text{Si}}}=\frac{\varepsilon_{\text{Si}}}{\sigma_{\text{Si}}} \tag{11}$$

So the conductance of silicon substrate is

$$G_{\text{Si}}=\frac{\pi\sigma_{\text{Si}}h_{\text{TSV}}}{\cosh^{-1}\left(p_{TSV}/(a'+b')\right)}[S] \tag{12}$$

The inductance of TSV is expressed as

$$L=\frac{1}{2}\left\{\frac{\mu_0\mu_{r,\text{TSV}}}{2\pi}\times h_{\text{TSV}}\times\ln\left(2p_{TSV}/(a+b)\right)\right\}[\text{H}] \tag{13}$$

Using the above formulas, the values of circuit elements showed in Fig.3 can be calculated. Then the scalable electrical model is performed using advanced design system (ADS), shown in Fig.5. The simulation frequency range is set from 100MHz to 20GHz.

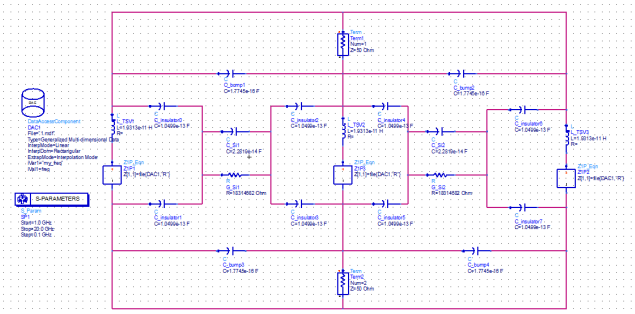


Fig.5. Scalable electrical model of GSG configuration with B-TSV in ADS

Fig.6 illustrates the S21 performance simulated by HFSS and ADS. From the simulation result, the scalable electrical model has the same variation tendency with the 3D model and the margin of error is acceptable, which means the scalable electrical model is verified and can be used to analysis the characteristic performance of systems formed by B-TSV structure.

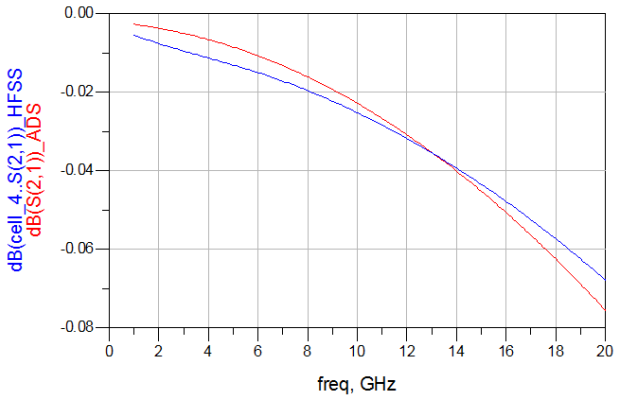


Fig.6. S21 performance for the verification of the proposed scalable model and 3D model in HFSS and ADS

Electrical characteristics analysis of the B-TSV structure

Some of the design parameters, such as d_{TSV}, l_B, p_{TSV} and t_{ox}, are swept to analysis the electrical characteristics of the B-TSV structure. The other parameters in the scalable electrical model are fixed as shown in Table 1.

The S21 performance is demonstrated in Fig. 7(a) as parameter l_B varies from 0, which represent traditional TSV, to 5πμm under the condition $\pi d_{TSV}+2l_B$=constant, namely the surface area per unit of B-TSV is constant. The result shows that the electrical performance improves as l_B increases. It is because when l_B increases, the minimum distance between TSVs increases, and causes insertion loss decreasing.

When the sum of d_{TSV} and l_B is constant, the S21 performance improves as l_B increases, as shown in Fig. 7(b). Under this condition, the section area of B-TSV decreases as l_B increases, so the effective area where TSV faces the silicon substrate through the insulation layer decreases, leading to the insertion loss decreasing. And the minimum distance between TSVs increases as l_B increases when the pitch is fixed. This is the main reason that the B-TSV structure has better performance than the traditional one.

As shown in Fig. 7(c), as p_{TSV} increases from 25μm to 75μm, the S21 magnitude increases from miners 0.09dB to about miners 0.01dB at the frequency of 20GHz. This result indicates that p_{TSV} is the main factor which influences the electrical performance of TSV system under the high TSV array density situation.

The result of variation of the insulator thickness t_{ox} is presented in Fig. 7(d). It can be seen that the S21 performance improves a little as t_{ox} increases from 0.5μm to 1.5μm. It means that the electrical performance is not sensitive with the variation of t_{ox} when t_{ox} is bigger than 0.5μm.

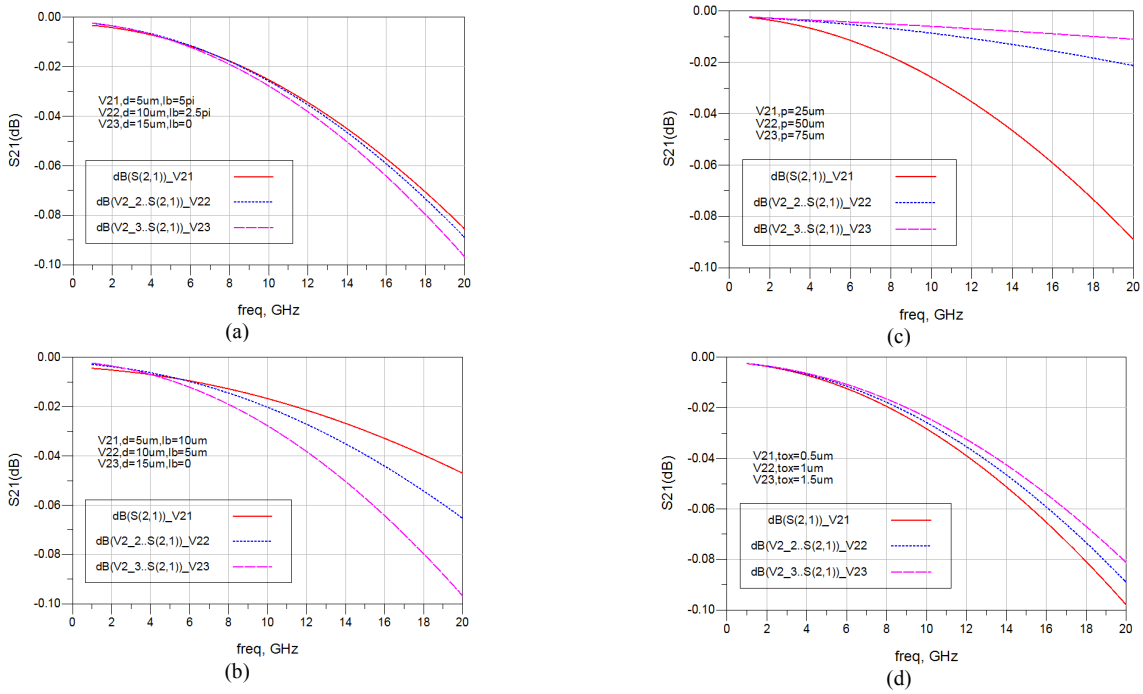


Fig. 7 S21 performance from the proposed scalable model of B-TSV with (a) l_B variation when $\pi d_{TSV}+2l_B$=constant, (b) l_B variation when $d_{TSV}+l_B$=constant, (c) TSV-to-TSV pitch variation, and (d) insulator thickness variation.

Simulation analysis of GSG configuration with different TSV structures

For electrical performance comparison, five cases of GSG configuration with different TSV structures and parameters, as shown in Fig. 8, are modeled and simulated by HFSS.

The GSG pattern in case (a) is formed by traditional cylindrical TSVs, in case (c) and (e) are formed by B-TSVs, and case (b) and (d) are the hybrid GSG pattern, using cylindrical TSV as signal TSV and B-TSVs as ground TSVs.

The diameter of traditional TSVs is d_T=15μm and d_B=10μm, respectively, which means d_T=1.5d_B. The parameter l_B in B-TSV is set to be l_B=0.5π(d_T-d_B)=7.85μm, making sure that the two kinds of TSVs have the same surface area per unit. For case (a), (b), (c), the pitch between TSVs is equal, namely p_{TSV}=25μm, and for case (a), (d), (e), the minimum distance d_{min} between TSVs is the same, namely d_{min}=10um. Other structure and material parameters are fixed as listed on Table 1.

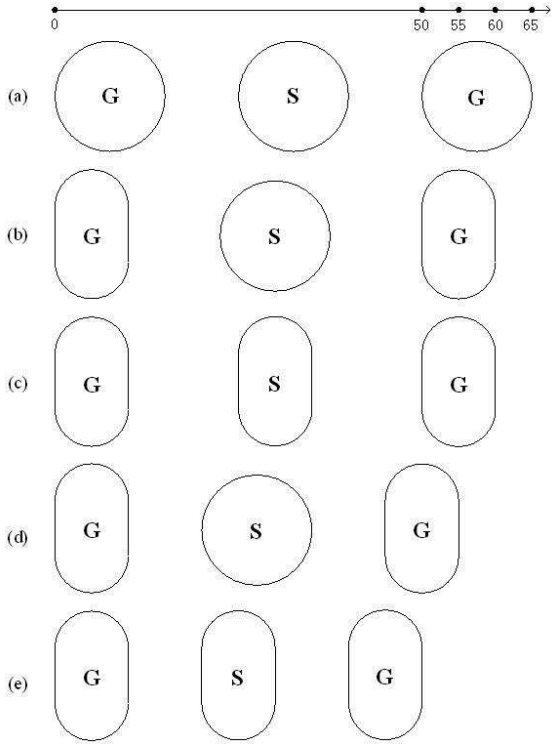


Fig. 8 Top view of GSG configuration with different TSV structures

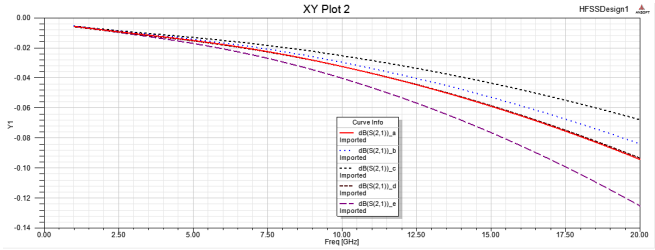


Fig. 9 S21 performance of the five GSG configuration models with different TSV structures

The simulation result is illustrated in Fig.9. This simulation result illustrates that case (c) achieves the best S21 performance, followed by case (b), (d), (a), and case (e) gets the worst performance. Comparison of case (a), (b) and (c) as these three cases have the same pitch between TSVs shows that the performance sequence from good to bad is case(c), (b) and (a). This can be explained that using B-TSV obtains larger minimum distance between TSVs when the pitch is fixed, which reduces the insertion loss and improves transmission performance.

Comparing case (a), (d) and (e) as these three cases have the same minimum distance between TSVs, case (d) gets almost the same performance of case (a) and overcomes case (e). This means the hybrid TSV structure can achieve higher TSV array density while without reduce the transmission performance. If the chip margin for processing TSVs is limited, the hybrid TSV structure will be surely a better choice than the traditional one.

Case (e) gets the worst performance because this case has the minimum pitch between TSVs, which significantly enhance the insertion loss. Another factor should be noticed here is the direct facing area between TSVs. The direct facing area between B-TSVs is bigger than that between cylindrical TSVs, which is a shortage of the B-TSV structure. Considering the excellent performance in case (c), the direct facing area between TSVs plays smaller role than the minimum distance between TSVs and it can be get rid of by using the hybrid TSV pattern as shown in case (d).

Over all, the main factor costing for the transmission performance degradation of TSV are the minimum distance between TSVs. The smaller the minimum distance is, the worse the transmission performance will be. The second factor that influences transmission performance is the direct facing area between TSVs. The performance declines when the direct facing area between TSVs increases. Using the B-TSV structure can improve transmission performance under the same pitch condition, or

reduce occupation area of TSV, namely increase TSV array density without degrading the electrical performance. This proves that the B-TSV structure has better performance than the traditional one.

Summary

A novel B-TSV structure is studied in this paper. 3D model and scalable electrical model of B-TSV are proposed by carefully analysis of the structure characteristic. The scalable electrical model is developed with analytic RLCG equations which are derived from the physical configuration. These models are validated by simulation using the 3D electromagnetic solver HFSS and EDA software ADS. Based on the proposed scalable model of B-TSV, we analyzed the electrical characteristics from S21 with design parameter variations. Simulations about GSG configuration with different TSV structures have been done to investigate the effects of design parameters. The simulation results show that the minimum distance and direct facing area between TSVs are the main factors which affect transmission performance of TSV structure. The B-TSV structure achieves better performance than the traditional one by obtaining bigger minimum distance as pitch between TSVs fixed. And the hybrid TSV structure gets higher TSV array density than the traditional one under a fixed minimum distance between TSVs.

Acknowledgement

The work presented here has been funded by National Natural Science Foundation of China (Project No.61176102, 60976083 and 60501007), Beijing National Science Foundation (Project No.3102014) China. In addition, research funding from National S&T Major Project with the contract No.2009ZX02038 is greatly acknowledged.

References

[1] The International Technology Roadmap for Semiconductors (ITRS), 2012 Edition. Information from http://www.itrs.net.

[2] Zheng Xu, Jian-Qiang Lu, Three-Dimensional Coaxial Through-Silicon-Via (TSV) Design, *IEEE Electron Device Letters*, vol. 33, No. 10, 2012.

[3] Lei Liang, Min Miao, Zhensong Li, Shufang Xu, Yuexia Zhang, Xiaoqing Zhang, "3D Modeling and Electrical Characteristics of Through-Silicon-Via (TSV) in 3D Integrated Circuits," *2011 International Conference on Electronic Packaging Technology & High Density Packaging*. pp:471-475.

[4] Kim, J., rt al., High-Frequency Scalable Electrical Model and Analysis of a Through Silicon Via (TSV). *Components, Packaging and Manufacturing Technology. 2011. IEEE Transactions on*, 2011.1(2): p. 181-195.

[5] Kim, J., rt al., High-Frequency Scalable Modeling and Analysis of a Differential Signal Through-Silicon Via. *Components, Packaging and Manufacturing Technology. 2014. IEEE Transactions on*, 2014.4(4): p. 697-707.

[6] S. H.Hall, High Speed digital System Design, New York: Wiley.

[7] Das, B. N., Das, B. N., Parida, D.. Capacitance of transmission line of parallel cylinders with variable radial width, *Electromegnetic Compatibility*. 1998,Vol 40, pp.325-330.

[8] I. Savidis and E. G. Friedman, Closed-form expressions of 3-D via resistance, inductance, and capacitance. *IEEE Trans. Electron, Devices*, vol. 56, No. 9, pp: 1873-1881, 2009.

Key Engineering Materials Vols 645-646 (2015) pp 1032-1037
© (2015) Trans Tech Publications, Switzerland
doi:10.4028/www.scientific.net/KEM.645-646.1032

Submitted: 2015-01-08
Accepted: 2015-01-19

Experimental investigation of thermal conduction performance on silicon-based micro flat heat pipe

Congming Li[1,a], Yi Luo[1,2,b*], Chuanpeng Zhou[1,c],

Liangliang Zou[1,d], Xiaodong Wang[1,2,e], Qing Shan[1,f]

[1]Key Laboratory for Micro/Nano Technology and System of Liaoning Province, Dalian University of Technology, Dalian, Liaoning, China

[2]Key Laboratory for Precision and Non-traditional Machining of Ministry of Education, Dalian University of Technology, Dalian, Liaoning, China

[a]email: lcm123lcm525@163.com, [b*]email(corresponding author): luoy@dlut.edu.cn,

[c]email: 576045988@qq.com, [d]email: 604672054@qq.com,

[e]email: xdwang@dlut.edu.cn, [f]email: shq@dlut.edu.cn

Keywords: Micro flat heat pipe; Thermal conduction; Filling ratio; Effective thermal conductivity

Abstract. There are several factors that affect heat transfer of heat pipe, for example, structure dimension, filling ratio and vacuum degree of charging. This paper studied the thermal conductivity of micro flat heat pipes (MFHPs) with different structure dimension and with different filling ratio, when the charging vacuum degree of MFHP was decided. When electric power was 2W or 4W, MFHPs with parallel grooves and nonparallel grooves, charged by working fluid with different filling ratio, were carried out. And the filling ratio is 30%, 40% and 50%, respectively. The better thermal performance of MFHP can be evaluated by lower thermal resistance and higher effective thermal conductivity. The experiment results show that MFHP has the highest effective thermal conductivity when the filling ratio is 40%; and the thermal performance of MFHP with nonparallel structure in axial direction is better than that of MFHP with parallel structure.

Introduction

Micro heat pipe, which is proposed by Cotter et al.[1] for the first time under the background of electronic cooling applications, is mainly used to heat-sink cooling and enhancing heat transfer. Whereafter, many scholars began to research something about micro heat pipe, for example, rectangle and triangle cross section grooves. K. N. Shukla[2] conducted a study on the transport capability of micro heat pipe depended on the vapor continuum limitation ,capillary limitation and the gravity. By using wet anisotropic etching, S. Launay et al. [3] fabricated micro heat pipes of triangular cross-section and with liquid arteries. Compared to silicon, the effective thermal conductivity of micro heat pipe increased sharply. In ref.[4], it was implied that the bent heat pipe is more sensitive to the change of the inclination angle than the straight in terms of the thermal response time and the heat flux of the condenser. Shwinchung Wong et al. [5] performed an experiment on thermal resistance testing to evaluate the thermal performance, and micro heat pipes were charged with water, alcohol and acetone, respectively. Then micro heat pipe charged with water accommodated larger thermal load. A novel study on full visualization and startup

performances of pulsating heat pipe using ammonia as working fluid were experimented in Ref.[6]. Kuan-Ting Lin et al.[7] studied the performance degradation of flattened heat pipes experimentally. The efficient and rapid heat dissipation has been a problem, because of the sharp increasing of electric device's watt density. With the advantages of good thermal uniformity, high thermal conductivity and the reversibility of heat transfer, heat pipe becomes one of main heat-dissipation device. Compared to traditional heat pipe, micro heat pipe owns smaller dimensions and can transfer heat more efficiently. However, development time of micro heat pipe is so shorter in terms of structure design, technology process and packaging that its thermal performance does not show the best. By now, there are few of studies on micro heat pipe which is applied in heat dissipation of LED device. Therefore, in this paper, the study of micro flat heat pipe for LED device primarily is based on the charging ratio of working fluid.

According to the testing system setup before, as shown in Fig.1, this paper performed the testing study for both parallel and nonparallel structure MFHPs on the filling ratio of working fluid. MFHP with parallel structure has the uniform cross section, while MFHP with nonparallel structure can be divided into two parts and each part has the uniform cross section. Under the condition that input watt is 2W or 4W, the thermal performance of both kinds of MFHPs is evaluated, when the filling ratio is 30%, 40% and 50%.

Experimental setup and fabrication of MFHP

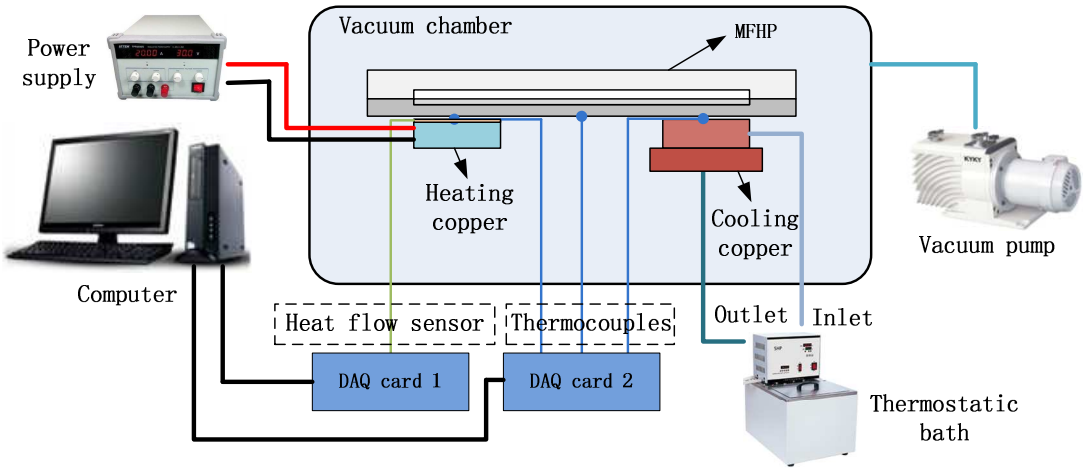
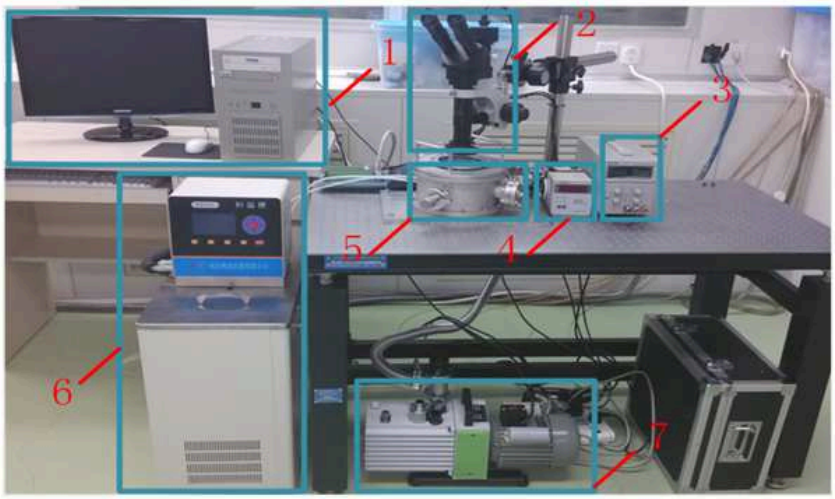


Fig. 1 Schematic diagram of thermal performance testing system for MFHP

Experimental setup. The experiment testing system is shown in Fig.1, and the heating source is supplied by heating copper and the output electric power can be adjusted by power supply. There are a heat flow sensor (CAPtec HS-10 with 0.946μv/(W/m^2) sensitivity) and a thermocouple (OMEGA TT-K-36 with ±1.05℃ accuracy) fixed between the MFHP and the heating copper, which are used to acquired the heat flux *q* input to MFHP and the temperature *Te* of evaporation section of MFHP. In addition, the insulation section and the condensation section of MFHP are installed two thermocouples, and the temperatures are *Ta* and *Tc*, respectively. In order to reduce the interface thermal resistance, silicon grease (thermal resistance<2K/W) is coated between the surfaces of heat flow sensor and heating copper and between the surfaces of heat flow sensor and evaporation section. In a similar way, between the condensation and the cooling copper is also coated with silicon grease. It is important that the thermal testing experiment is conducted in a vacuum chamber (vacuum degree about 10Pa) to avoid heat transfer by means of convection and radiation.



1. Computer 2. CCD Camera 3. Power Supply 4. Vacuum Gauge 5. Vacuum Chamber
6. Thermostatic Bath 7.Vacuum Pump

Fig.2 The photo graph of testing system for MFHP

Fabrication of MFHP. In this paper, microgrooves on the n-type silicon (100) wafer were obtained by anisotropic wet etching, and the depth of the microgrooves was about 150 μm. In order to make visualization, the silicon wafer and the Pyrex 7740 with a 200 μm steam chamber were bonded with each other using anodic bonding technique at the temperature of 450 ℃ and voltage of 1200 V[8][9]. The length, width and thickness of MFHP are 45mm, 16mm and 0.5mm, respectively. Internal channel region has length of 35mm, width of 10mm, and thickness of 0.15mm.The detailed dimension of MFHP is shown in Table 1.

Table 1. Structure size of MFHPs

ID	Shape of channels	width-to-space ratio of channels[μm]		Depth of channels[μm]	Height of steam chamber [μm]
NO.1	parallel	150/50		150	200
NO.2	non-parallel	230/70	180/120	150	200

The detailed process of the charging of MFHPs is shown in Fig.3. Firstly, MFHPs were pumped until the vacuum degree reached to 3-4Pa, and then cold welding 1 was performed. Secondly, deionized water, as working fluid, was charged into MFHPs with different filling ratio 30%, 40% and 50% by using micro syringe with 1μl accuracy. The charging percentage of working fluid was calculated according to the total internal volume of MFHPs. Finally, cold welding 2 was carried out.

Results and discussion

Under the condition that input watt is 2W or 4W, the thermal performance of both kinds of MFHPs is evaluated, when the filling ratio is 30%, 40% and 50%.The effective thermal conductivity can be obtained from Eq.1, which is suggested by Y.J. Youn et al.[10][11].

$$K_{eff} = \frac{Q \times L_{eff}}{A_c \times (T_e - T_c)}. \quad (1)$$

Where Q is the input watt; $Leff$ is the effective length of MFHP; Ac is the cross section of MFHP; Te and Tc represent the temperatures of evaporation section and condensation section of MFHP, respectively.

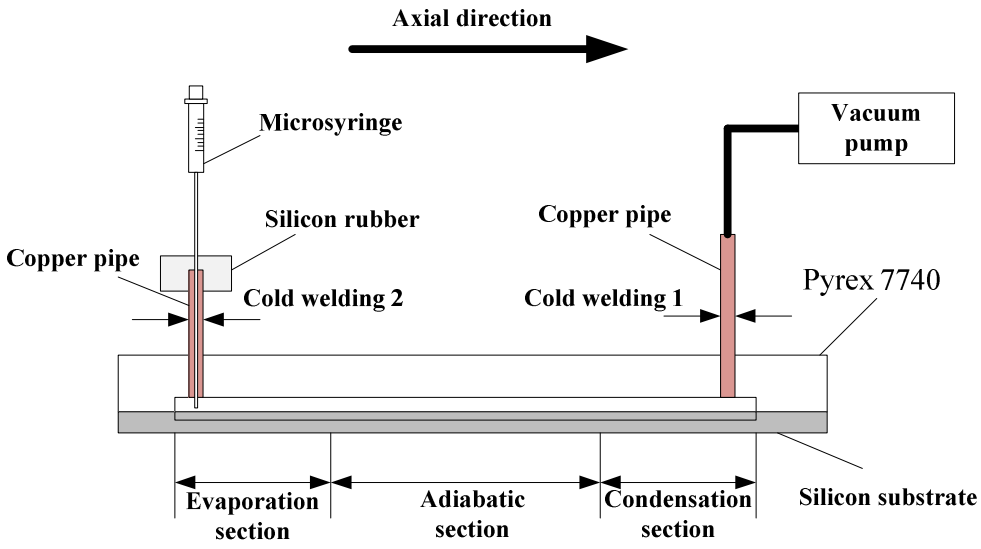


Fig. 3 Schematic diagram of charging system

$$L_{eff} = \frac{L_e + L_c}{2} + L_a \tag{2}$$

Where L_e and L_c are the length of evaporation and condensation, respectively, and L_a means the length of adiabatic section.

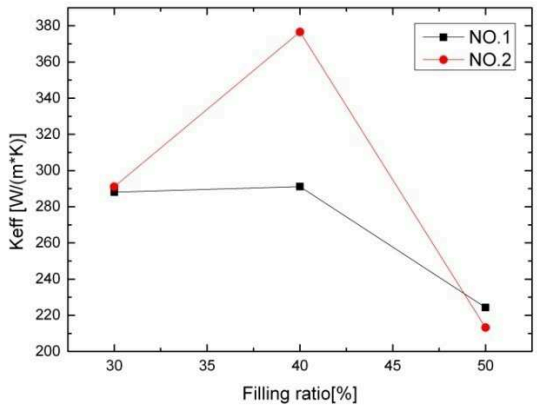


Fig. 4 Effective thermal conductivity with different filling ratio when input watt is 2W

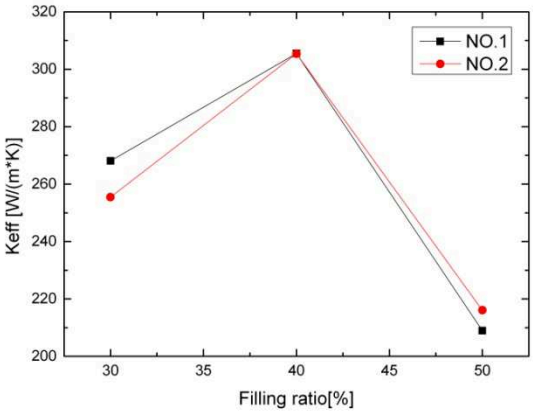


Fig. 5 Effective thermal conductivity with different filling ratio when input watt is 4W

As can be seen from Fig. 4, when filling ratio is 30% or 50%, the effective thermal conductivities of both parallel and nonparallel MFHP, numbered as *NO.1* and *NO.2* respectively, have no significant difference. And the effective thermal conductivity of *NO.1* MFHP is 290W/(m·K) while *NO.2* MFHP is 220 W/(m·K). When filling ratio is equal to 40%, *NO.2* MFHP has the highest effective thermal conductivity with the value of 360 W/(m·K). However, the effective thermal conductivity has almost no changes, when filling ratios are 30% and 40%.

When input watt is changed to 4W, the difference of the effective thermal conductivities of the two structure MFHPs is very small, as shown in Fig.5. When filling ratio is 30%, the effective thermal conductivity of *NO.1* MFHP is slightly larger than that of *NO.2* MFHP. When filling ratio is 40%, the effective thermal conductivities of both MFHPs are equal to each other. When filling ratio increases to 50%, the effective thermal conductivity of *NO.1* MFHP is a little less than that of *NO.2* MFHP.

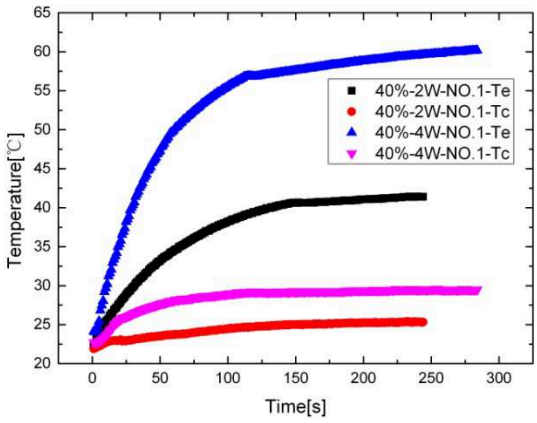


Fig.6 Temperature changing curve of NO.1 MFHP under different input watt

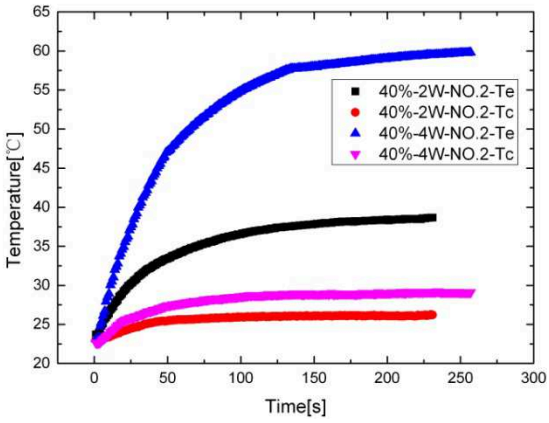


Fig.7 Temperature changing curve of NO.2 MFHP under different input watt

In Fig.6 and Fig.7, when reaching to a steady state of heat transfer, both *NO.1* and *NO.2* have similar steady temperature curves when input watt is 4W. If the input watt is 2W, the steady temperature of *NO.2* is slightly lower than that of *NO.1* in evaporation section.

The results of testing experiment imply that the thermal performance of nonparallel structure MFHP is much better. Especially, when filling ratio is 40%, the effective thermal conductivity of nonparallel MFHP is larger than that of parallel MFHP about 90 W/(m·K). This is because that there is no dryout phenomenon happened in evaporation section so that vapor can return to condensation section and condense effectively; In the mean time, nonparallel structure can strengthen the capillarity and promotes working fluid returning to evaporation section quickly. To some extent, the efficiency of phase change heat transfer increases sharply. However, an obvious decline of the heat transfer of both kinds of MFHPs appears when filling ratio is 50% and the thermal resistance reaches to above 14K/W. The reason is that too much working fluid in MFHP results in that part of vapor and liquid cannot participate in phase change, which is negative to efficient heat transfer.

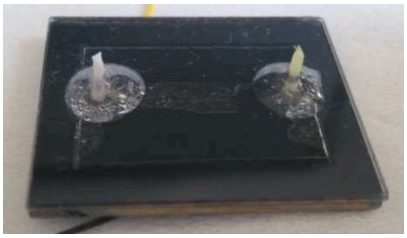


Fig.8 Graph of MFHP with the dimension of 20mm*26mm

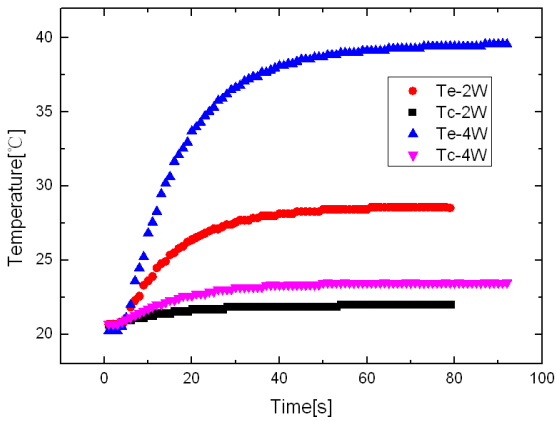


Fig.9 Temperature changing curve of evaporation and condensation sections

This paper also studied the thermal performance of smaller MFHP, which has only the length of 26mm, the width of 20mm, and thickness of 1.5mm. It is called SMFHP in this paper, and the width-to-space ratio of channels is 150[μm]/50[μm]. As show in Fig.8, the phase change area of the MFHP is 20mm*13.5mm, and the inner height is 0.3mm. In order to make a comparison with two kinds of MFHPs mentioned above, SMFHP also be charged into 40% of working fluid.

According to Fig.6, Fig.7 and Fig.9, whether input power is 2W or 4W, SMFHP can reach a steady status. It is obvious that the temperatures of SMFHP on evaporation and condensation are much lower than that of both kinds of MFHPs above. The temperatures of evaporation are lower about 20℃ and 10-15℃, respectively, when input power is 2W and 4W; while the temperatures of condensation are lower about 2℃ and 4℃, respectively. The experiment result implies that shorter length of MFHP in axis direction can accelerate phase change by decreasing the distance of flowing. In the process of heat transfer, vapor can travel to condensation quickly and liquid can also flow back to evaporation immediately.

Conclusions

Under the condition of different filling ratio, the heat transfer test of MFHPs with nonparallel structure and parallel structure were conducted. When the filling ratio is 40%, effective phase change cycle in MFHP can be formed, and the biggest effective thermal conductivity can be obtained. Meanwhile, the nonparallel grooves can promote capillarity and accelerate heat transfer of phase change, which results in that the temperature difference between evaporation section and condensation section is very small. Under similar condition, SMFHP shows better with smaller temperature difference and higher effective thermal conductivity.

Acknowledgement

Thanks are due to the financial support provided for this study by the State Key Development Program for Basic Research of China (Grant No. 2011CB013105).

References

[1] Cotter, T. P., Principles and Prospects of the Micro Heat Pipes, Proceedings of the Eighth Heat Pipe Conference, 1984, pp. 328–335.

[2] K. N. Shukla, Heat Transfer Limitation of a Micro Heat Pipe, Journal of Electronic Packaging, 131(2009) 024502/1–024502/3.

[3] S. Launay, V. Sartre, M. Lallemand, Experimental study on silicon micro-heat pipe arrays, Applied Thermal Engineering, 24 (2004) 233–243.

[4] Junye Wang, Experimental investigation of the transient thermal performance of a bent heat pipe with grooved surface, Applied Energy, 86 (2009) 2030–2037.

[5] Shwinchung Wong, Yuchung Lin, Jhan-Hong Liou, Visualization and evaporator resistance measurement in heat pipes charged with water, methanol or acetone, International Journal of Thermal Sciences, 52 (2012) 154-160.

[6] Zhihu Xue, Wei Qun, Minghui Xie, Full visualization and startup performance of an ammonia pulsating heat pipe, Propulsion and Power Research, 4 (2013) 2:263–268.

[7] Kuan-Ting Lin, Shwin-Chung Wong, Performance degradation of flattened heat pipes, Applied Thermal Engineering, 50 (2013) 46-54.

[8] Xiaodong Wang, Gang Liu, Liangliang Zou, Yi Luo, Vacuum fluid charging and packaging technique for micro heat pipes, 14th International Conference on Electronic Packaging Technology (ICEPT), Dalian, China, Piscataway, NJ, USA IEEE press (2013) 46-49.

[9] Yi Luo, Gang Liu, Liang-liang Zou, Yan-xia Yang, Xiao-dong Wang, Experimental investigation of micro heat pipes for high-power light-emitting diode modules, Micro &Nano Letters 2013, 8(10): 646-649

[10] Y.J. Youn, S.J. Kim, Fabrication and evaluation of a slicon-based micro pulsating heat spreader, Sens. Actuators A: Phys. (2011), doi:10.1016/j.sna.2011.12.006.

[11] Xiang-you Lu, Tse-Chao Hua, Mei-jing Liu. Thermal analysis of loop heat pipe used for high-power LED, Thermochimica Acta, 2009, 493: 25–29.

Key Engineering Materials Vols 645-646 (2015) pp 1038-1042
© (2015) Trans Tech Publications, Switzerland
doi:10.4028/www.scientific.net/KEM.645-646.1038

Submitted: 2014-12-04
Accepted: 2014-12-23

Analysis of Effective Field Emitting Angle for Spindt Cathode

Nannan Li[1, 2, a], Shucai Pang[2, b], Fei Yan[2, c], Dazhi Jin[2, d], Wei Xiang[2, e], De Zhang[2, f], Jingyi Dai[2] and Baoqing Zeng[1, g]

[1]National Key Laboratory of Science and Technology on Vacuum Electronics, School of Physical Electronics, University of Electronic Science and Technology of China, Chengdu 610054, China

[2]Institute of Electronic Engineering, Chinese Academy of Engineering Physics, Mianyang 621900, China

[a]317621169@qq.com, [b]hbpsc@126.com, [c]376174148@qq.com, [d]jindazhi@sohu.com, [e]xiangwei-iee@qq.com, [f]zhangdey@189.cn, [g]bqzeng@uestc.edu.cn (corresponding author)

Keywords: Spindt cathode, effective field emitting angle, field emission

Abstract. Effective field emitting angle plays an important role when investigating field emission characters. In this work, effective field emitting angle is introduced for Spindt-type emitter to relate spatial variation of current density along tip's surface to emission current. The effects of various parameters on effective field emitting angle are analyzed. The results show that effective field emitting angle decreases exponentially as half angle increases, decreases quadratically as radius of gate aperture increases, but increases logarithmically as gate voltage increases linearly. It is also found that effective field emitting angle increases first and then decreases with emitter's height increasing. Similar trends can be also found with insulator height. Grid thickness nearly has no effect on the effective field emitting angle.

Introduction

Spindt cathode has attracted much attention since it was developed by Spindt and his co-workers [1] because of its excellent electrical properties, such as high available current density, low power dissipation, and instant turn on [2-5]. Effective field emitting angle plays an important role when investigating field emission characters since emission current from an emitter is often calculated by the electric field at the apex and the effective field emitting angle. It has been proposed that effective field emitting angle of Spindt-type emitter can be defined by the angle where the field has dropped by 10% [6]. However, conventional method of estimating emission current from Spindt-type emitter usually considers the effective emitting angle as constant [7-9].

In this work, the symbol θ_{eff} is introduced as effective field emitting angle for Spindt-type emitter to relate spatial variation of current density along tip surface to emission current. The characteristic that current density varies on the tip surface is considered into the factor θ_{eff}. The main purpose of this work, therefore, is to investigate the effects various parameters of Spindt cathode have on effective field emitting angle.

Simulation

Spindt cathodes are simulated in 3D simulation method of finite integration technique (FIT) [10]. The local electric field E at each grid point can be obtained by simulation. The corresponding current density J will be obtained according to Fowler-Nordheim (FN) equation [11]. Total current from the emitter's surface should be obtained through integration of current density over cap surface. When effective field emitting angle θ_{eff} is introduced to calculate emission current, the characteristic that current density varies on the emitter's surface is considered into the factor θ_{eff}. Thus effective field emitting angle θ_{eff} can be expressed as

$$\cos\theta_{eff} = 1 - \frac{\int J(\theta)dS}{2\pi r^2 J(0)}, \quad (1)$$

where r is tip's curvature radius, $J(\theta)$ is the emission current at the polar angle θ and $J(0)$ is the emission current density at the apex.

Figure 1 shows the schematic of the simulated model of Spindt cathode. Simulations have been done on Spindt cathode with one variable parameter at a time. θ_{eff} of Spindt cathode with different conditions is calculated. The effects of various parameters on θ_{eff} are analyzed.

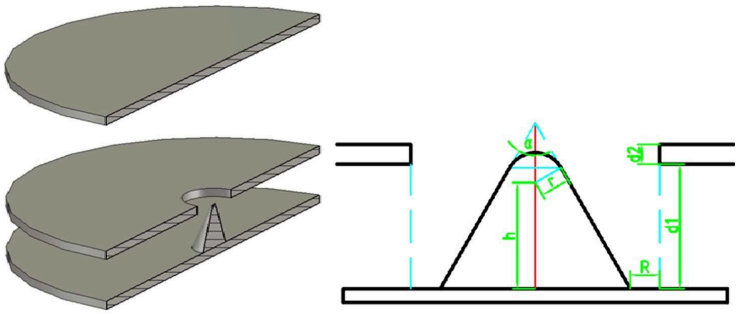


Fig. 1 Schematic of the simulated model of Spindt cathode.

Results and discussion

The Potential contours distribution and emitted electron trajectory are shown in Fig. 2 when r = 0.03 μm, h = 0.5 μm, α = 10 degrees, R = 0.2 μm, d_1 = 0.5 μm, d_2 = 0.1 μm, distance between grid and anode d_3 = 1 μm, v_g = 80 V and v_a = 500 V. It can be found that the potential changes largely near the brim of the emitter while changes little above grid electrode. The phenomenon should be contributed to that the conductivity of emitter is great and the tip curvature radius is very small, a strong electric field arises at the top. It can be also found that the aperture in an accelerating grid electrode will limit the focusing degree of the electron beam.

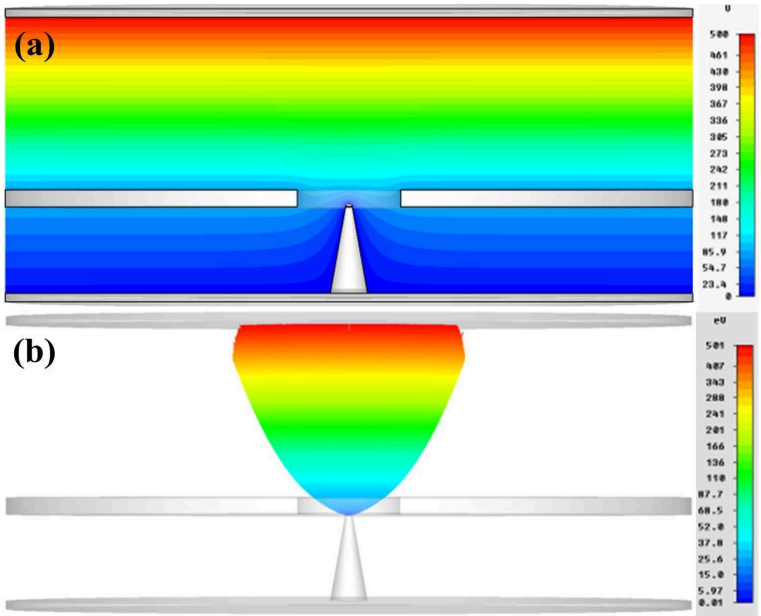


Fig. 2 View of potential contours distribution and emitted electron trajectory.

Field distributions on tip surface have been investigated for Spindt cathode with one variable parameter at a time. Normalized field distributions $E(\theta)/E(0)$ along cap surface with different half angle α, tip center height h, grid hole increment R, insulator height d_1, grid thickness d_2 and grid voltage v_g are shown respectively in Fig. 3. It shows that electric field on tip surface decreases regularly with polar angle increasing and half angle has greatest effect on the field distribution. Figure 3(a) shows the electric field on tip surface drops off more quickly when half angle α is larger. Figure

3(b) shows $E(\theta)/E(0)$ increases as h increases and the increasing degree is smaller and smaller. The field distribution trend on the tip surface will not change any more when h is larger than insulator height d_1. Figure 3(c) shows the electric field on tip surface drops off more quickly with polar angle when insulator height d_1 is larger. The field distribution trend on the tip surface will not change any more when emitter is much lower or higher than grid electrode. Figure 3(d) and (e) show d_2 and R have less effect on the field distribution trend. Figure 3(f) shows grid voltage vg has no effect on the field distribution trend.

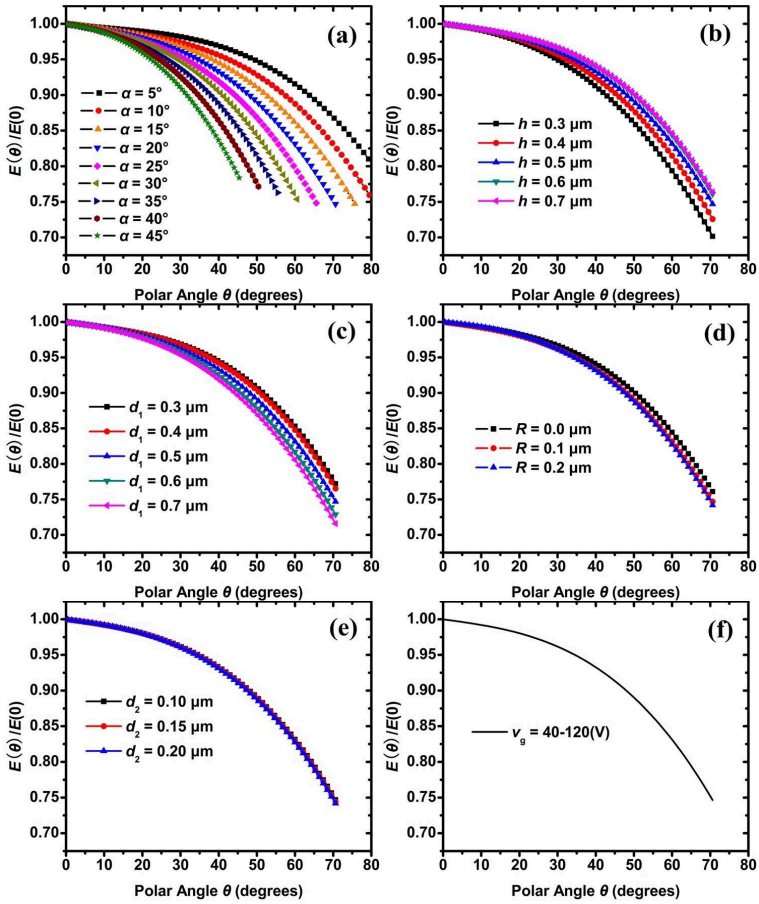


Fig. 3 Normalized field distributions $E(\theta)/E(0)$ along cap surface with different (a) half angle α, (b) tip center height h, (c) grid hole increment R, (d) insulator height d_1, (e) grid thickness d_2 and (f)grid voltage v_g.

Local electric field at the apex $E(0)$ at variable α, h, R, d_1, d_2 and v_g are shown respectively in Fig. 4. Figure 4(a) shows that the local electric field at the apex decreases linearly with half angle increasing. When half angle increases one degree, the local electric field strength will decrease by about 3%. Figure 4(b) shows that the field at the apex increases first and then decreases with h increasing. It can be noticed that the closer the distance between cone's height $h + r$ and insulator height d_1 is the lager the field at the apex will be. Similar trends can be also found in Fig. 4(c). Figure 4(d) shows the field at the apex decreases rapidly with R increasing. It is attributed to that the macroscopic field is sensitive to R when grid voltage is certain. Figure 4(e) shows the field at the apex changes slightly with grid thickness d_2. Figure 4(f) shows the field at the apex will increase linearly with vg increasing.

The distribution of current density $J(\theta)$ can be obtained according to FN equation since the local electric filed $E(\theta)$ has been obtained by simulation. According to Eq. (1), the effective field emitting angle θ_{eff} of Spindt cathode can be obtained.

The dots shown in Fig. 5 are the calculated effective field emitting angles θ_{eff} according to simulated field distributions and Eq. (1). The red solid lines are corresponding fitting functions. Figure 5(a) shows the relationship between θ_{eff} and half angle α. Mean deviation between simulation results and the fitting function is about 2.4%. Figure 5(b) shows the relationship between θ_{eff} and tip center height h. The effective field emitting angle increases first and then decreases with h increasing.

The maximum deviation is about 0.76% at $h = 0.5$ μm. Figure 5(c) shows d_1 has similar effect with h on the effective field emitting angle. The effective field emitting angle increases first and then decreases linearly with d_1 increasing. The relationship between θ_{eff} and grid hole increment R is shown in Fig. 5(d). The maximum deviation is about 0.43% at $R = 0.1$ μm. Figure 5(e) shows that grid thickness d_2 has little effects on the effective field emitting angle. The mean deviation between simulation results and fitting function shown in Fig. 5(e) is about 0.36%. Figure 5(f) shows the relationship between θ_{eff} and grid voltage v_g.

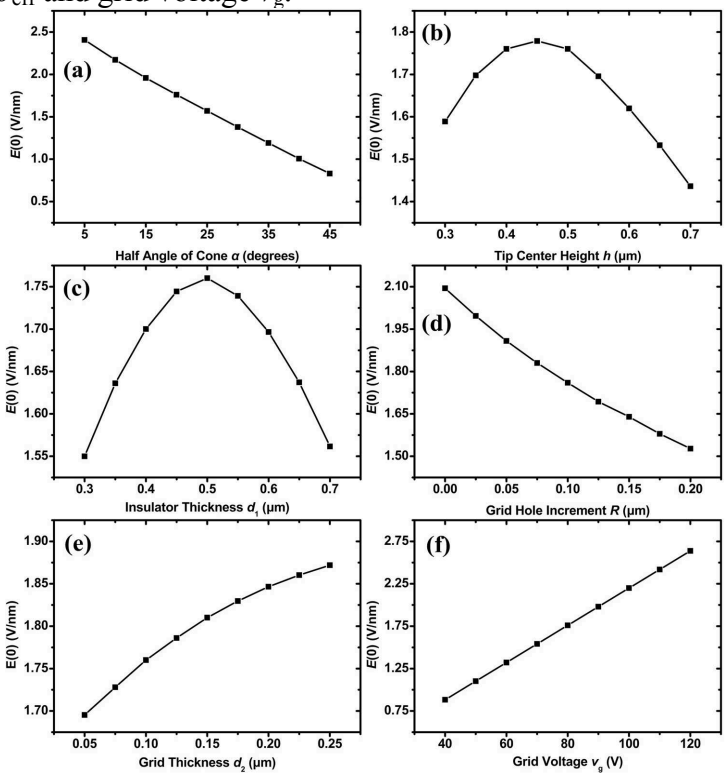


Fig. 4 Local electric field strength at the apex $E(0)$ with different geometrical parameters.

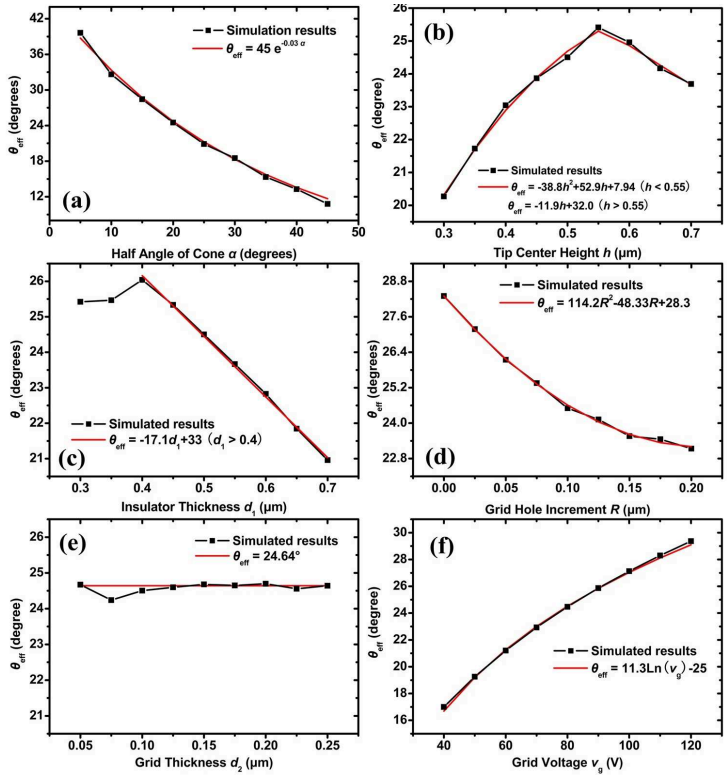


Fig. 5 Distributions of effective field emitting angles θ_{eff}. The calculated results are shown as dots. The red solid lines are according to fit function.

Summary

In summary, effective field emitting angle θ_{eff} is introduced for Spindt cathode and demonstrated to be depended on the grid voltage and geometrical parameters. The 3D simulation method FIT has been successfully used to investigate the electric field distribution for Spindt cathode with different parameters. The effective field emitting angles θ_{eff} of Spindt cathode with different parameters have been obtained. It can be found that θ_{eff} decreases exponentially as half angle increases linearly, decreases quadratically as gate hole radius increases linearly, but increases logarithmically as gate voltage increases linearly. It can be also found effective field emitting angle increases first and then decreases linearly with h increasing. Similar results can be also found with d_1. Grid thickness d_2 nearly has no effect on the effective field emitting angle.

Acknowledgement

This work is supported by the CAEP THZ Science and Technology Foundation (Grant T2013-07-0305), Laboratory of Precision Manufacturing Technology, CAEP (Grant 426010402).

References

[1] C. A. Spindt, J. Appl. Phys. 39 (1968) 3504.
[2] C. A. Spindt, C. E. Holland, P. R. Schwoebel, and I. Brodie, J. Vac. Sci. Technol. B 16 (1998) 758.
[3] Q. H. Wang, M. Yan, and R. P. H. Chang, Appl. Phys. Lett 78 (2001) 1294.
[4] D. R. Whaley, B. M. Gannon, C. R. Smith, C. M. Armstrong, and C. A. Spindt, IEEE Trans. Plasma Sci. 28 (2002) 727.
[5] C. A. Spindt, I. Brodie, L. Humphrey, and E. R. Westerberg, J. Appl. Phys. 47 (2009) 5248.
[6] C. A. Spindt et al., J. Appl. Phys. 47 (1976) 5248.
[7] J. Q. Liu and J. M. Zhan, Acta Phys. Sin. 54 (2005) 3439-3443.
[8] H. C. Lee and R. S. Huang, IEEE Electron Device Letters. 11 (1990) 579-581.
[9] Jun Cai et al., 4th International Conference on Microwave and Millimeter Wave Technology Proceedings, 2004, pp. 527-530.
[10] T. Weiland, Electronics and Communications AEU, 31 (1977) 116.
[11] E. L. Murphy and R. H. Good, Phys. Rev. 102 (1956) 1464.

Key Engineering Materials Vols 645-646 (2015) pp 1043-1048
Submitted: 2014-10-29
Accepted: 2014-12-01
© (2015) Trans Tech Publications, Switzerland
doi:10.4028/www.scientific.net/KEM.645-646.1043

Fabrication of Convex Plate-shaped Micro Tool Electrode and its Application in Micro hole Machining by ECM

Zhiwei He[1a], Minghuan Wang[2b*], Li Zhang[3c], Wei Peng[4d]

(Key Laboratory of Special Purpose Equipment and Advanced Processing Technology of Ministry of Education, Zhejiang University of Technology, Hangzhou, 310014, Zhejiang, China)

[a]hezhiwei135@163.com, [b]wangmh@zjut.edu.cn(corresponding author), [c]574986712@qq.com, [d]pengwei@zjut.edu.cn

Keywords: Electrochemical micromachining, convex plate-shaped micro electrode, machining locality, hole taper

Abstract: A method of fabricating convex plate-shaped micro electrode was proposed based on the electrochemical etching principle. The square sectional electrodes were prepared in advanced using wire-EDM, The micro cylindrical electrode was fabricated firstly by using the eletrochechemical etching method. Then the top end was insulated to protect it from etching. Then the convex plate-shaped micro electrode was obtained in subsequent etching. Comparative experiments in drilling micro-hole in stainless steel with the thickness of 1mm were done by using the cylindrical and convex plate-shaped micro electrode. Results shows that the better locality, smaller side-gap and hole taper could be obtain by using convex plate-shaped micro electrode.

Introduction

With the development of science and technology, precision has become a tendency both in military industrial and civil use. Micro holes and components are necessary in this process [1,2]. The advantages of electrochemical micromachining(EMM) over other non-traditional machining such as no tool wear, stress-free, smooth surfaces, regardless of workpiece hardness and high tension, makes it a vital part in micromachining[3-5]. In EMM, tool fabrication is a difficult problem, especially in 3D microstructure machining. Tool fabrication is limited to some simple shape by now.

In the machining of micro holes by EMM, the small side gap makes the electrolyte difficult to renew, which would led to short-circuit, especially in machining micro hole with high aspect ratio. In order to solve these problems, many attempts have been done. Y.P. Xie et al [6] fabricated the inverted cone-shaped micro electrode using electrochemical machining (ECM) With the top end insulated. Y.Liu et al [8] processed micro hole with negligible taper by using the spherical end shape electrode. V. Rathod et al.[8] fabricated disk microelectrode by using the ECM with the cathode insulated. Using micro EDM, B. H. Kim et al.[9] machined the disk-tape electrode, with which they reduced the micro hole taper. M.H.Wang et al.[10] using a high-speed rotating spiral electrode to renew the electrolyte in the machining region and get a good result. B. J. Park et al.[11,12] reduced the hole taper by insulating the side wall.

In this paper, the method of fabricating convex plate-shaped micro electrode was introduced. The method is based on the ECM principle [10]. Under the protection of insulation, the top end size could be kept and the shank diameter tends to thinner and thinner. A convex plate-shaped micro

electrode was well fabricated, through the experiment study on the machining on the 304 stainless steel using both cylindrical and convex plate-shaped micro electrode, proved that the convex plate-shaped micro electrode has more advantages.

Experimental system

As shown in fig.1, the experimental system for micro ECM mainly includes the electrochemical power supply system, the motion control system and the electrolyte system. The motion part of X, Y, and Z axes are driven by servo motors, which are controlled by a computer. The motion part of the Z-axis is equipped with the rotating precision spindle. The precise sensors, which are used to detect current, voltage and other electric signals, were applied in the power supply system. The power will turn off as soon as the computer captures signals from the sensor to protect the electric circuit. The electrolyte system consists of the electrolyte tank, small pump, filter and so on.

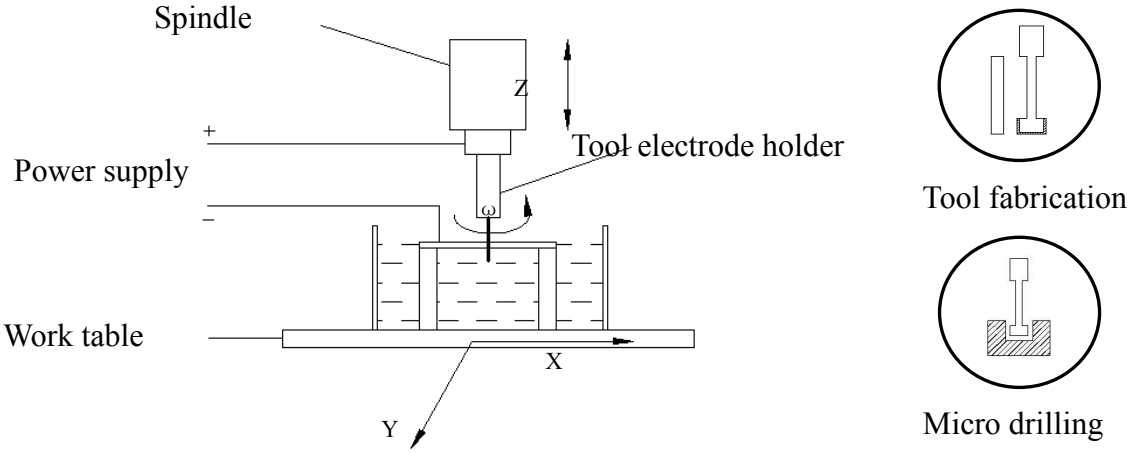


Fig.1 Sketch of experimental system

Fabrication of convex plate-shaped micro tool electrode

The convex plate-shaped micro tool electrode could be prepared after the micro cylindrical electrode were fabricated in advance.

Fabrication of micro cylindrical electrode. In this part, a DC power supply is applied, and NaOH solution is used as the electrolyte, the initial diameter of the tungsten carbide bar is 1mm. The tungsten carbide bar was cleaned in acetone with ultrasonic to remove the impurity substance before etching. Fix the tungsten carbide bar on the spindle and connect it to the positive of the power, turn on the power after the bar is immerged into the electrolyte (room temperature) a certain depth. A stainless steel block as the cathode and connected to the negative terminal of the power supply. Electrochemical reaction occurs as soon as the power is turned on. Table 1 shows the machining conditions of fabricating the cylindrical electrode.

Table 1 Experimental conditions for fabricating cylindrical electrode

Machining voltage, [v]	4V
Electrolyte	2mol/L NaOH
Electrode gap, [mm]	20
Machining time, [min]	150
Electrolyte temperature, [^{o}C]	20
Electrode diameter, [μm]	270

However, the end of the etched electrode was always be taper because of the electric field focus on the sharp edge and the diffusion layer that made this part react faster. In order to fabricate the convex plate-shaped micro tool electrode, the taper tendency was cut off by the EDM.

Fabrication of convex plate-shaped micro tool electrode. When the micro cylindrical electrode is obtained, it should be cleaned ultrasonically again. With the detection by the high speed photography and control by the spindle, the top end of the cylindrical electrode moves down into the light cured resin on demand. The immersion depth determines the height of the convex plate. Then put the electrode with the top end coated with cured resin lighting two minutes by ultraviolet light. Then, the electrode was immersed in dilute NaOH electrolyte solution for desired depth. During etching, material is removed from the uncoated part to gets thinner. Since the top end was insulated, its diameter will be kept and this part was called the convex plate. Table 2 shows the machining conditions of fabricating the convex plate-shaped tool electrode and fig. 2 shows SEM image of the tool electrode.

Table 2 Experimental conditions for fabricating convex plate shaped electrode

Maching voltage	3V
Electrolyte	2mol/L NaOH
Electrode gap, [mm]	10
Machining time, [min]	20
Electrolyte temperature, [^{o}C]	20
Shank diameter, [μm]	110

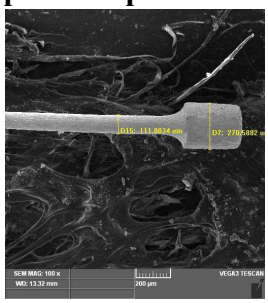


Fig. 2 The convex plate- shaped electrode

Micro hole machining using the convex plate shaped micro tool electrode

Comparative experiments using two different electrodes. If the diameter of the electrode top ends is same, the interelectrode gap would be same no mater the tool electrode is cylindrical or a convex plate-shaped one. Comparing with cylindrical electrode, the convex plate-shaped tool has a thinner neck in the machined region. The electrolyte is easier to renew and this is hopeful to minimize the taper of the micro hole.

A DC power supply is applied while the 5%NaNO3 solution is chosen as the electrolyte. The feed speed is 60μm/min and the initial gap 20μm. As a byproduct produced in the electrochemical reaction, Fe(OH)3 is positively charged and is captured by the tool electrode which is connected to the negative terminal of the power supply. The dilute nitric acid could help to dissolve the Fe(OH)3 sediment and improve the machining stability. SS304 stainless steel with thickness of 1mm is selected as the workpiece. Other machining parameters are shown in table 3.

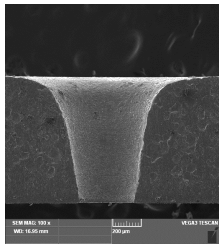
Table 3 Experimental conditions for EMM

Machining voltage,[V]	6
Convex plate diameter, [μm]	270
Shank diameter, [μm]	110
Cylindrical electrode diameter, [μm]	217

By using micro cylindrical electrode, the diameter of the hole is bigger in the inlet than in the outlet because of there is no insulation on the electrode side. Fig.3 shows a taper hole machined by the micro cylindrical electrode. The diameter is about 570μm and 406μm for entry and exit respectively, The taper is almost 0.16. In micro hole drilling by using the fabricated convex plate-shaped micro electrode in ECM, the hole diameters and the taper all diminished. As shown in Fig. 4, the diameter of hole is 533μm and 449μm for inlet and outlet, the taper is nearly 0.08. It will

be seen that the convex plate-shaped micro electrode has better locality and is helpful to reduce the hole taper in micro ECM.

Fig. 3 Micro hole machined by cylindrical electrode



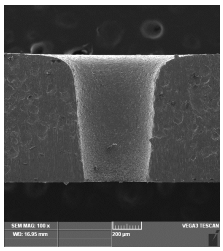


Fig. 4 Micro hole machined by convex plate shaped electrode

Micro ECM using convex plate-shaped micro electrode

During the micro ECM, the diameter and taper of the hole is influenced by many parameters such as the power supply, machining voltage, electrolyte, pulse on time, empty duty and so on.

ECM using different voltage. $NaNO_3$ and $NaClO_3$ solutions with concentration of 5% are applied respectively. The feed rate was 60 μm/min.

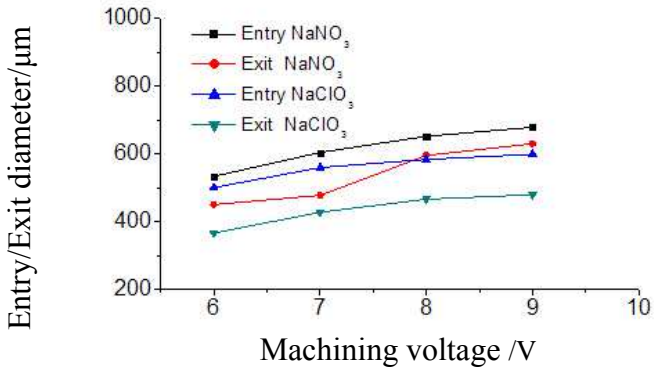
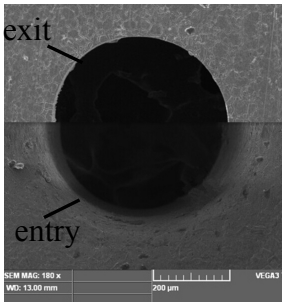
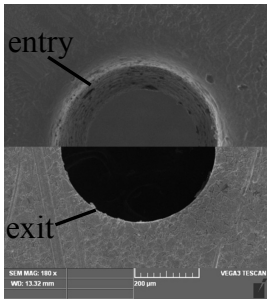


Fig. 5 Influences of the machining voltage on diameters of hole machined

As shown in fig.5, with increasing of the machining voltage, both the entry diameter and the exit diameter increase simultaneously. When the machining voltage is 6V, the hole diameter reduced in a certain degree. Fig. 6 shows the SEM image of the micro hole machined with voltage of 6V using different electrolyte. It also shows that the locality and the size of the micro hole reduce substantially when $NaClO_3$ electrolyte was applied.





(a) $NaNO_3$ electrolyte (b) $NaClO_3$ electrolyte

Fig. 6 Micro hole machined with different electrolyte

ECM with different electrolyte concentration. Based on the experiment above, two doubles of different electrolyte concentration was applied in the following fabrication. The machining voltage was 6V. Results are shown in fig.7, it denotes with the increase of the electrolyte concentration, the hole diameter increases gradually. When the concentration of the electrolyte is 3%, the interelectrode side gap reduced to 90 μm with $NaNO_3$ while it is 63 μm with $NaClO_3$, the hole taper is 0.098 and 0.08, respectively.

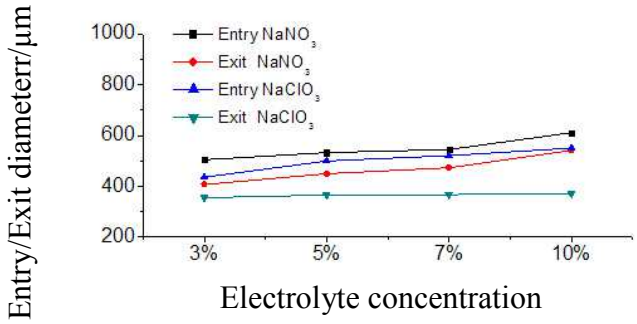


Fig. 7 Influences of the electrolyte concentration on diameters of hole machined

Hole taper influenced by electrolyte concentration. The taper is computed after the experiments (see fig.8). As is shown, the hole taper decreases with the increase of electrolyte concentration by using $NaNO_3$ electrolyte. On the contrary, the taper increases as the concentration increase by using $NaClO_3$ electrolyte. This is because the side gap machined with $NaClO_3$ electrolyte is smaller than that of $NaNO_3$ electrolyte, thus less fresh $NaClO_3$ electrolyte could get to the machining region than the $NaNO_3$ electrolyte. And then the former material remove rate is slower than that of the latter.

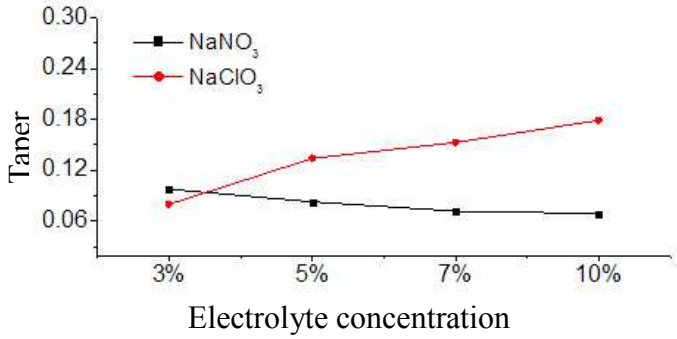
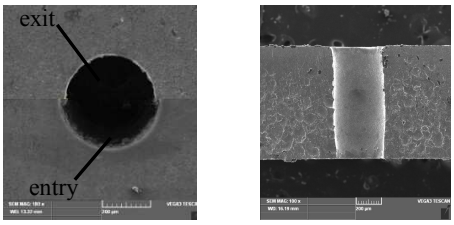


Fig. 8 Influences of the electrolyte concentration on taper of hole machined

In ECM, the pulsed power supply could improve the localization, reduce the side gap and the hole taper. In this study, micro hole drilling was done by using pulse power. The voltage is 9V, pulse frequency is 100KHz, duty ratio is 0.5, feeding speed is 20μm/min, initial gap is 20μm and 3% $NaClO_3$ was selected as the eletroylte. Fig. 9(a) shows the micro hole machined by using the convex plate-shaped electrode and fig. 9(b) shows its cross-sectional view. The entry diameter is about 409μm, and the exit diameter is about 370μm, the taper is 0.04. Evidently, micro ECM using the convex plate-shaped electrode with pulse DC power supply could effectively reduce the hole taper and improve the processing performance.



(a) Entry/exit (b) Cross-sectional view

Fig. 9 Micro hole with little taper

Conclusion

The convex plate-shaped electrode is fabricated by using the electrochemical etching. Then, groups of experiments were carried out to verify the advantages of the convex plate-shaped electrode in micro hole drilling in ECM. The effects of various parameters on micro hole drilling in ECM were studied by using the convex plate-shaped micro tool electrode. Results denote that decreases of the machining voltage or the electrolyte concentration can reduce the hole diameter and side gap. The locality and hole taper could be improved by using the convex plate-shaped micro tool electrode with pulse power supply in micro ECM. However, the hole diameter and the side gap is reduced on different levels.

Acknowledgement

This research was supported by Zhejiang Provincial Natural Science Foundation of China (No. LY13E050019) and National Natural Science Foundation of China (No.51475428).

Reference

[1] B.H. Kim, S.H. Ryu, D.K. Choi, Micro eletrochemical milling, J. Micromech.Microeng. 15 (2005) 124-129.
[2] S.H. Choi, B.H. Kim, H.S. Shin, Analysis of the electrochemical behaviors of WC-Co a lloy for micro ECM, J. Journal of Materials Processing Technology. 213 (2013) 621-630.
[3] S.H. Ryu, Micro fabrication by electrochemical process in citric acid electrolyte, J. Journal of Materials Processing Technology. 209 (2009) 2831-2837.
[4] Z.W. Fan, L.W. Hourng, C.Y. Wang, Fabrication of tungsten microelectrodes using pulsed electrochemical machining, J. Precision Engineering. 34 (2010) 489-496.
[5] V.K.Jain, K. Soubodh, A. Sidpara, Fabricatio n of micro-fe atures and micro-tools using electrochemical micromachining, J. Int J Adv Manuf Technol. 61 (2012) 1175-1183.
[6] Y.Y. Xie, Z. Liu, W. Chen, Experimental Investigation on Fabrication ofInverted Cone-shaped Micro-electrode byUsing Electrochemical Machining, J. ELECTROMACHINING & MOULD. 1 (2011) 18-22.
[7] Y. Liu , D. Zhu, Y. Zeng, H. Yu , Development of micro electrodes for electrochemical micro machining, J. Int. J. Adv. Manuf. Technol. 55 (2011) 195–203.
[8] V. Rathod, B. Doloi, B. Bhattacharyya, Parametric Investigation Into the Fabrication of Disk Microelectrodes by Electrochemical Micromachining, J. Journal of Micro and Nano Ma nufacturing. 1 (2013) 1-11.
[9] B.H. Kim, B.J. Park, C.N. Chu, Fabrication of multiple electrodes by reverse EDM and their application in micro ECM, J. Micromech.Microeng. 16 (2006) 843-850.
[10] M.h. Wang, Study on micro ECM, D. Nanjing University of Aeronautics and Astronautics. (2007).
[11] Y. Liu, R.Q. Hu, Micro electrochemical machining for tapered holes of fuel jet nozzles, J. Procedia CIRP. 6 (2013) 395-400.
[12] B.J.Park, B.H.Kim, C.N.Chu, The Effects of Tool Electrode Size on Characteristics of Micro Electrochemical Machining, J, Annals of CIRP. 55 (2006) 197-200.

Key Engineering Materials Vols 645-646 (2015) pp 1049-1053
© (2015) Trans Tech Publications, Switzerland
doi:10.4028/www.scientific.net/KEM.645-646.1049

Submitted: 2014-11-02
Accepted: 2014-12-23

Design of Micromachining System Based on Nanosecond Pulsed Laser

Dong Xu[1,a], Yao Yao[1,b], Xing Fu[1,c *], Chao Wang[1,d]

[1] State Key Laboratory of Precision Measuring Technology and Instruments, Tianjin University, Tianjin 300072, China

[a] xudongxd@tju.edu.cn, [b] yaoyao714@tju.edu.cn,

[c] xingfu@tju.edu.cn, [d] jwcy@tju.edu.cn

Keywords: Nanosecond Laser; PMAC; Microstructure;

Abstract. In recent years, pulsed laser processing technology is widely used in MEMS device manufacturing, aerospace technology, precision instrument manufacturing and circuit board processing. According to the characteristics of nanosecond laser, this paper designs a novel nanosecond pulsed laser micromachining system with PMAC card as its core unit. The system can achieve automation control of laser parameters and movement pattern of motion system by software, which can easily realize automatic processing of point, line, and plane structure in micron scale. In this paper, several groups of experiments are taken to test the reliability and accuracy of the machining system and find the group to obtain the best processing result.

1. Introduction

The beam from a small pulsed laser can readily be focused on a solid material to cause sufficient heating to give surface evaporation. The process is called laser ablation, and is now widely used in microstructure manufacturing.

Generally, pulsed laser can be divided into femtosecond pulsed laser, picosecond pulsed laser and nanosecond pulsed laser by pulse width. Femtosecond and picosecond laser have relatively high peak power and processing accuracy. However, they have many disadvantages: low repetition rate and average power, more expensive machining equipment and high equipment maintenance charge. Compared with ultra-short pulsed laser, nanosecond laser has high repetition frequency (up to 100 kHz), high processing efficiency, fast processing speed, and low cost [1,2]. Therefore, nanosecond laser can be seen as the combination of quality and efficiency. With the development of laser technology, it has a broader prospect to be an important method of laser research and practical application [3,4,5].The lasers normally used have pulse durations in the range 5–50 ns, and recently ultraviolet lasers have been widely used.

However, laser is not the only key factor to decide processing quality, movtion control system also has great influence on it. A good movtion control system should have faster response speed, more accurate action and higher efficiency.According to such principles, a laser machining system based on nanosecond pulsed laser is established to achive high efficient microsturture processing. Programmable multi-axes controller (PMAC)[6,7] is used as the core of the motion control system. A PC software is developed to control both laser's parameters and mode of motion during processing. A series of expements confirms the stability and efficiency of the system.

2. System design

The system consists of nanosecond pulsed laser, optical path mechanical structure, transmission system, motion control system, software on PC. Nanosecond pulsed UV laser, with 355 nm wavelength and 40ns pulse width, is chosen as the light source. Optical path mechanical structure is

designed to get ideal result of focus of laser beam. Motion control system, which is based on PMAC card, can control the 3-D motion platform completing microstructure processing. The software, which can change the parameters of both laser and motion system, is developed to complete microstructure process. A CCD monitoring system is used to help researchers to get real-time election on the effect of laser beam focusing and processing process. The laser manufacturing process depends on several laser parameters (wavelength, fluence, repetition frequency and pulse duration) and movement pattern.

Fig.1 shows the diagrammatic sketch of micromaching system and relationship between each compoument. The PC software can change the parameters of laser and motion mode during processing, which can ablate differient structures on samples. PMAC can ensure accurate motion, which decreases the deviation into sub micron size.

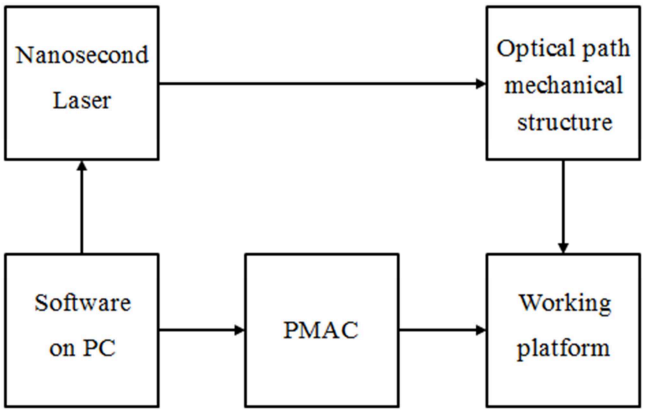


Fig 1 Sketch of micromaching system

2.1 Laser source

The experiment is carried out using a Coherent AVIA 355-3000 frequency-tripled, Q-switched Nd:YAG laser. The length of the resonator is set to an optimal value, to compensate for the thermal lens effect, with the built-in optimization routine called ThermTrack. This provides the highest output power and the best beam quality. Thus the beam diameter and the energy distribution of the beam can be considered independent from the laser source parameters, the pumping current and the pulse repetition frequency. The main parameters of laser described in its manual are showen in Table.1[8].

Table.1 Specifications of AVIA 355-3000

Parameters	Specification
Wavelength	355nm
Average Power@20kHz	3W
Pulse repetition frequency	1~100kHz
Pulse duration	<40ns up in 60kHz
Beam diameter	2.7mm
Pulse stability	<5%rms IN 30kHz
Pulse mode	TEM_{00}
Polarization	>100:1 Horizotional
Beam divergence	<0.3 rad

2.2 Optical path mechanical structure

Optical path mechanical structure is an imptotamt part of the processing system. The focused beam spot decides the mimimum size of the microstruture. The energy loss when laser beam is transmitting in the mechanical structure limits the maxium processing fluence.

Fig.2 shows the optical path. After twice reflection by mirror (reflection rate > 99%), laser beam enters into a collimating lens and is adjusted into parallel beam. After another reflection by spiltting prism, the laser beam is focused on the sample by a 20× objective lens (focus length 20mm). The CCD monitor is set to observe processing effect in real time and help to adjust sample position to ensure that the sample is located on the focal plane. Continuous laser is used to help find focal plane, because pulsed laser is invisible.

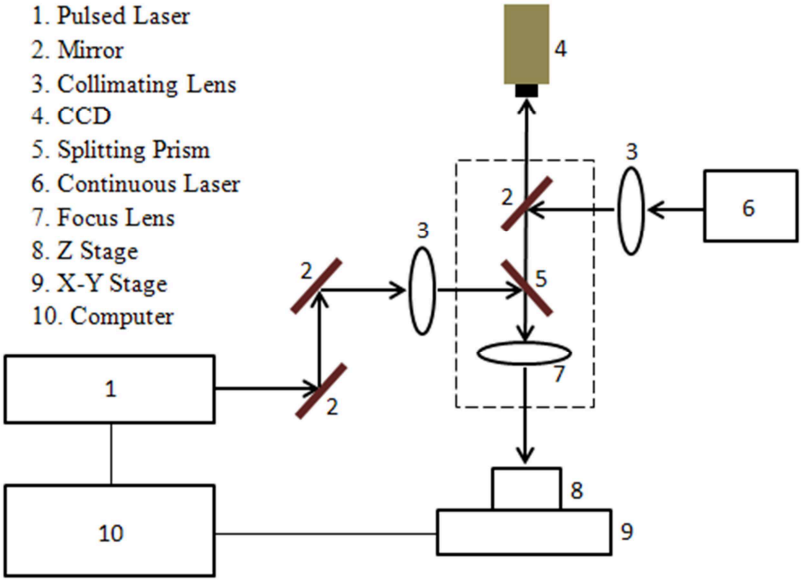


Fig.2 Optical path mechanical structure of the system

2.3 Motion control system and working platform

Motion control system is the most critical component of the whole system. Fig.3 shows the systematic diagram of the system. PMAC controler is the center of the system because it has connection with all other components. PMAC is a high performance open servo motion controller, which is capable of commanding up to eight axes of motion simultaneously. In this system, PMAC is used to control motion mode of working platform and on-off of nanosecond laser. While working, PMAC can communicate with PC: on one hand, PC gives PMAC command to set the position of motion mode of platform, on the other hand, PMAC can feedback the position. This ensures accurate control of sample's pisotion.

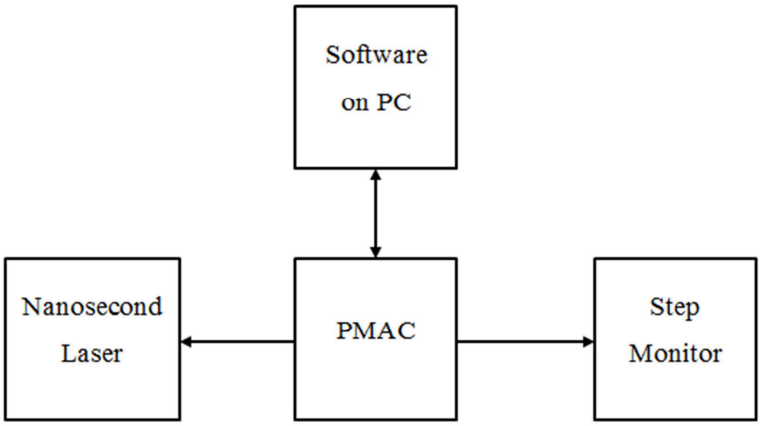


Fig.3 Connection relationship between PMAC and other compoments

2.4 PC software

The software of the pulsed laser micromachining system is mainly made up of PMAC real-time control software, laser paraments adjust software and system management software. PMAC real-time

control software is used to add software function module on the basic PMAC module (mainly including PMAC initialization module, interpolation processing module, processing procedure explanation module, PLC monitoring module, data acquisition and output module) according users' need. Laser paraments adjust software sets laser paraments (including laser energy and repetition frequency) while processing to adjust to differient need. Based on Windows XP operating system , the system management software uses Visual C++6.0 programmable development tool to finish editing and debugging the micromachining control programs, mainly including system initialization, faults diagnosis, parameters setting, status display, dual CPU communication. With the software, the system realizes automatic operation.

3. Experiment results

Based on this processing system, some experiments have done on samples of steel and copper films, and analyzed the results. During the laser pulse micromachining process, the selection of laser parameter and motion mode, like laser energy, pulse repetition frequency and moving speed of work platform, will lead to different machining quality.

3.1 Spot on steel

Fig.4(a) shows spots on a part of steel ring. Parameters are set as follows: repetition frequency 20 kHz, laser pulse energy is 145uJ. The distance between each hole is 100μm. Fig.4(b) is holes made by micro drilling bit. It's easy to see that pulse this system can make microstructure smaller and more precise than traditional machine tools.

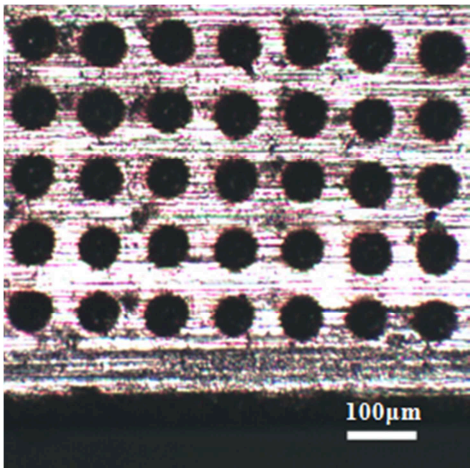


Fig.4(a) Holes on steel by pulsed laser

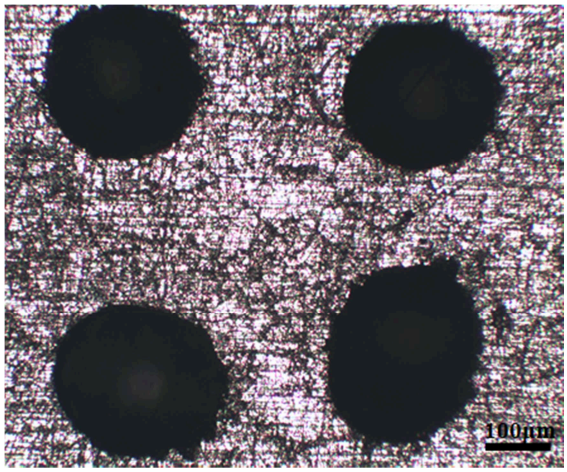


Fig.4(b) Holes on steel by drilling bit

3.2 Laer direct write on copper film

Laser direct write and patterning are general terms that includes modification, subtraction, and addition processes capable of creating patterns of materials directly on substrates without the need for lithography or masks. With a laser source, one can either fix the location of the beam and raster the substrate using motion-control stages, fix the substrate and raster the beam using mirrors, or use a combination of both. For laser direct-write modification (LDWM) or subtraction (LDW), the material of interest is directly irradiated and is either removed (laser micromachining) or modified (melting, sintering, and so on)[9].

With the system in this paper, some LDW experiments on copper film are done. Experiment results are observed by metallographic microscope. The sample is copper film sputtered on glass. The thickness of copper film is 200nm. Experiment results are shown in Fig.5(a) and Fig.5(b). Parameters are set as follows: repetition frequency is 50Hz, moving speed of the working platform is 0.15 mm/s.

Laser pulse energy is 50μJ in Fig.5(a) and 130μJ in Fig.5(b). The sample is located between focus lens and focal plane and is away from focal plane about 50μm in Fig.5(a) and 100μm in Fig.5(b).

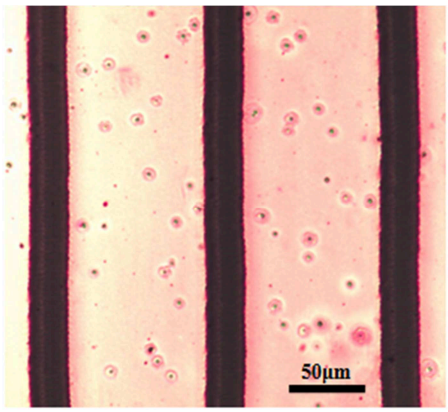


Fig.5(a) lines on copper film by LDW (50μm from focal plane)

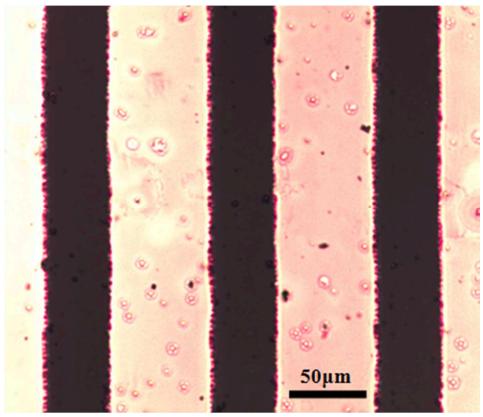


Fig.5(b) lines on copper film by LDW (100μm from focal plane)

Summary

A nanosecond pulsed laser micromachining system based PMAC has been designed. Experiments are operated on metallic and nonmetallic materials, including steel and copper film. Through compiling PMAC's PLC program, PC graphic processing interface and adjusting processing parameters, the system is able to process various microstructures of different materials to meet the increasing demand in laser micromachining field.

References

[1] B. N. Chichkov, C. Momma, S. Nolte, F. von Alvensleben. Femtosecond, picosecond and nano-second laser ablation of solids. Appl. Phys. A, 1996, Vol. 63(2): 109-115.
[2] Chunyang Liu. Design & Research of Nanosecond Pulse Laser Micromachining System. Tianjin, China: Tianjin University, College of Precision Instrument and Opto-electronics Engineering, 2008.
[3] Malcolm Charles Gower. Industrial applications of laser micromachining. Optics Express, 2000, Vol. 7 (2): 56-67.
[4] Tsuneo Kurita, Kazuhisa Komatsuzaki, Mitsuro Hattori. Advanced material processing with nano- and femtosecond pulse laser. International Journal of Machine Tools and Manufacture, 2008, Vol. 48 (2): 220-227.
[5] D.M. Karnakis. High power single-shot laser ablation of silicon with nanosecond 355nm. Applied Surface Science, 2006, Vol. 252 (22): 7823-7825.
[6] DELTA TAU Data System Inc. PMAC user's manual. DELTA TAU Data System Inc, 2004.
[7] DELTA TAU Data System Inc. Accessory 34AA user's manual. DELTA TAU Data System Inc, 2004.
[8] AVIA 355/AVIA 355-X Lasers Operater's Manual. Coherent, Inc.
[9] Dajun Yuan. Laser direct-write microfabrication and patterning. University of Michigan, 2008.

Key Engineering Materials Vols 645-646 (2015) pp 1054-1058
© (2015) Trans Tech Publications, Switzerland
doi:10.4028/www.scientific.net/KEM.645-646.1054

Submitted: 2014-12-04
Accepted: 2014-12-23

Experimental Research on Nanostructure Fabricated by AFM Probe combining with a CW Laser

Lijun Yang[a], Bai Cheng[a] and Yang Wang[b]

School of Mechatronics Engineering, Harbin Institute of Technology, Harbin 150001, China

[a]yljtj@hit.edu.cn, [b]wyyh@hit.edu.cn

Keywords: AFM probe, Laser, Fabrication, Nanostructure

Abstract. Although the nanostructure machining by AFM probe assisted with laser has gain a great progress, few studies has been done on the optical fiber probe guiding the continuous laser to irradiate on AFM probe to machining nanostructure. Using this technology to create nanodot and nano-groove was presented in this paper. The law of how the experiment parameters influenced the results was summarized in the paper. The scale of nanodot is about 450nm, and nano-groove is about 40nm. When the fabrication is completed, the wear of the AFM probe was observed by SEM and drew a conclusion. In the method of nano machining by AFM Probe combining with a CW Laser, there will be a combined field to achieve the fabrication, and the method is better than mechanical characterization with AFM probe.

Introduction

With the development of modern nano science-technology, the manufacturing sector experienced a journey from the traditional to the special processing and then to the nanoscale-manufacturing technology. As a kind of manufacturing technology which can achieve nanoscale, more and more researchers pay their attention to nano-manufacturing techniques. The AFM probe combining with laser, as an efficient tool to machining nanostructure, more and more researchers developed many kinds of methods to create nanostructure based on AFM probe combining with laser.

For this technology, researchers can machine a nanostructure which minimum feature size could reach less than 100nm, some nanostructures even can achieve 10nm scale [1-5]. They used a pulse laser or femtosecond laser to irradiate the AFM probe [4,5], and then the material under the probe tip was processed to be a nanostructure. And many investigators believed that the near field enhancement is the main reason for nanostructure machining [6-7], although there was a thermal expansion on the AFM probe tip, and some other researchers think that it also makes contribution anyway. This ambiguity is worth to move forward to a single step to be clarified.

However, few investigations have been attempted to explore continuous laser combining with AFM probe to create the nanostructure. The purpose of this paper is to investigate the possibilities of this technology and attempt to explain the mechanism of creating a nanostructure with AFM probe assisted by a CW laser. Our study is significant that it provides the basis and reference for using the optical fiber probe guides a low power continuous laser to irradiate on AFM probe to machining nanostructure.

Experimental Setup

The experiment system consists of a Laser Diode (LD, 808nm, 60mW) attached to an AFM (BenYuan CSPM5500). The overall system is illustrated in Figure 1. The AFM is used characterize the sample surface and it also has Vector scanning mode which is specialized for nano-fabrication. The continuous laser gets through the optical fiber probe (aperture: 100nm) to irradiate the AFM probe. The alignment of the AFM probe and optical fiber probe could be controlled by Micro/nano motion and observed from CCD. This system allows the continuous laser to irradiate the AFM probe perfectly and does no influence on the sample surface. The AFM probe tip was sharp silicon probes designed to allow a direct optical view when imaging and the reflex and tip sides were coated with gold. The optical fiber probe was made up of SiO_2 and 80nm layer of Aluminum was applied to the

SiO_2 surface to protect the tip. At last, the sample was polyethylene (PE) which melting point is about 400K.

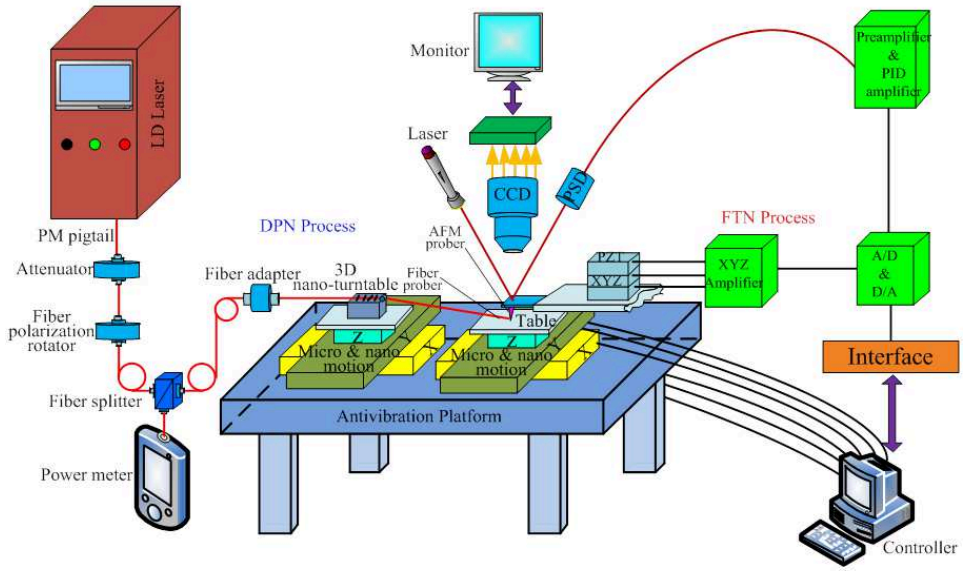


Figure 1. The combining nanofabrication system

Experimental Result and Discussion

Nanodot Fabracation. For this nanostructure, there are three parameters in the experiment: laser energy, machining time, distance between probe tip and sample. The single factor experiment was done with all the parameters.

Influence of Distance between Probe Tip and Sample. The experiment arrangement is in table 1 and the experiment result is showed in Figure 2. From this result, the feature of the nanodot is unsatisfactory. Otherwise, the width and depth could not be recognized clearly. However, it showed a fact that the AFM probe can process the nanostructure when the probe keeps away from the sample. The biggest distance between probe and sample was 1450nm, and the nanostructure was also created. In addition, it proved that the near-field enhancement is the main reason in nano-fabrication because the biggest thermal expansion was just 20nm in simulation.

Table 1. The arrangement of distance

parameter	（laser energy E=60mW, machining time t=15s）
Distance between probe tip and sample L/[nm]	140,290,430,580,730,870,1000,1160,1300,1450

Influence of Machining Time and Laser Energy. The machining time means the duration of laser irradiates the AFM probe. According to the result of influence of distance between probe tip and sample, when the distance L=0, the better nanostructure was gained with laser energy ranged from 1mW to 30mW. Choose the distance zero, other experimental parameters are shown in Table 2, and the experiment results were showed in Figure 3 and Figure 4. These two Figures showed the size of the nanostructure and how the time influenced the results. From Figure 3 we can see that the feature of the nanodot is better than before. Moreover, the size of nanodot was increased as the energy and time grew which was observed in Figure 4.

Table 2. The arrangement of time and laser energy

Parameters	Laser energy E=1mW	Laser energy E= 30mW	Laser energy E= 60mW
Machining time/[s]	1, 2, 4, 6, 8, 10, 12, 15, 20, 25	1, 2, 4, 6, 8, 10, 12, 15, 20, 25	1, 2, 4, 6, 8, 10, 12, 15, 20, 25

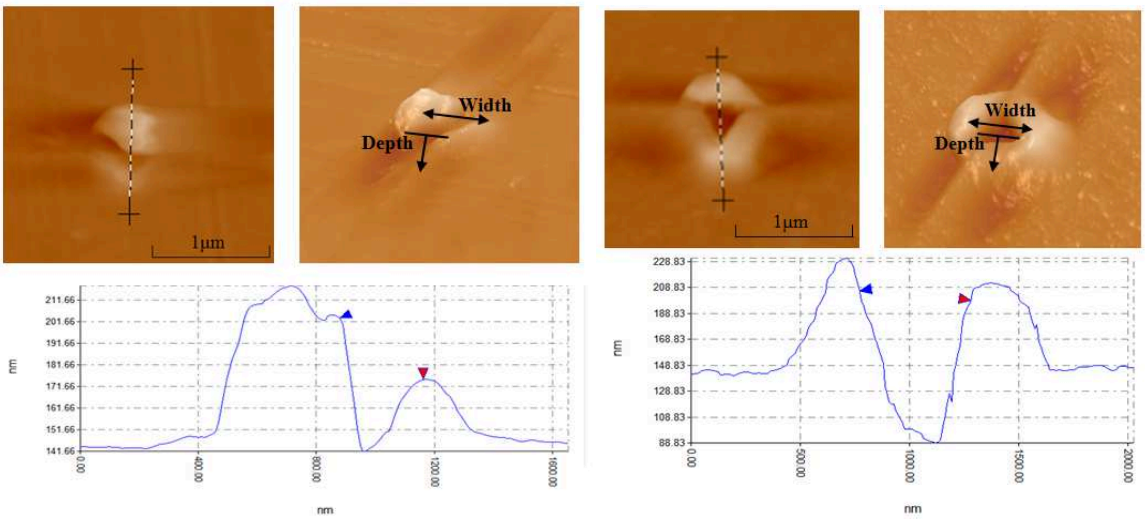


Figure 2. Nanodot structure and size of the laser energy

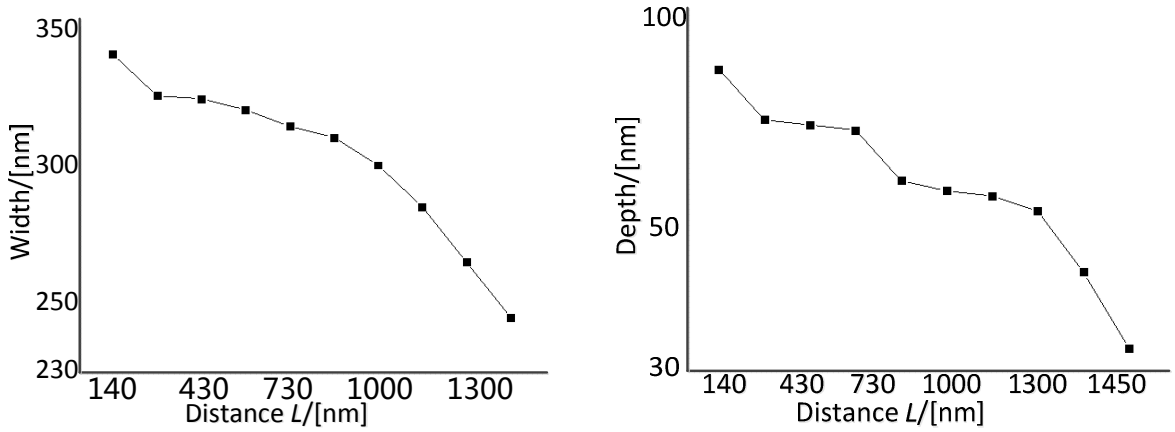


Figure 3. Influence to nanodot size of the distance between probe tip and sample

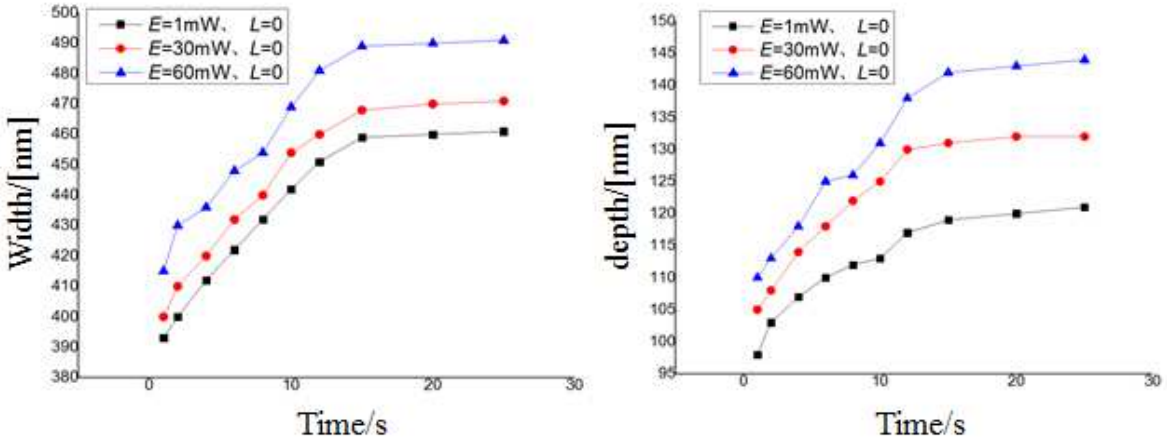


Figure 4. Influence to nanodot size of the machining time and laser energy

Nano-groove Fabrication. In the experiment of nano-groove fabrication, using the vector scanning mode of the AFM to fabricate the groove. And in this mode, the control-force mode is used in the moving sample. The Force means how much the depth of cantilever drops. When the AFM sends a signal to probe going down, the cantilever of probe will drop to insure the AFM probe could apply force to sample. And the Force was represent by voltage because of 1V is equal to 8.09nm. Under the

leading of this knowledge, the nanowire was created. The arrangement of experiment parameters is in table 3, and the experiment result is showed in Figure 5.

Table 3. The arrangement of parameters of nano-groove fabrication

Parameter	Rangement
Laser energy/[mW]	1, 10, 20, 30, 40, 50, 60
Machining time/[s]	1, 2, 4, 6, 8, 10
Force/[V]	0, 0.1, 0.2, 0.3, 0.4, 0.5

As shown in Figure 5, the feature of nano-groove is terrible in the left figure and wonderful in the right figure. The reason of this phenomenon is that the laser energy is higher used in the left than right. So the experiment is done with a low laser energy (E=30mW) and force (F=0V, 0.1V, 0.2V). And the machining time ranges from 1s to 10s, and the experiment result is showed in Figure 6. As shown in the Figure 6, the width and the depth of the groove are increased with machining time increasing.

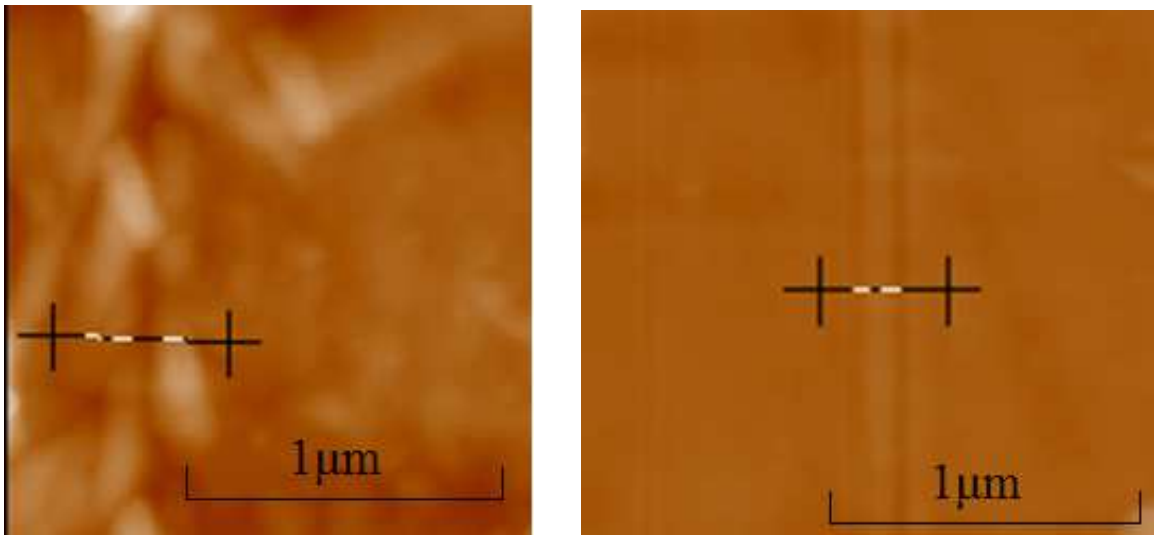


Figure 5. Structure of the nano-groove

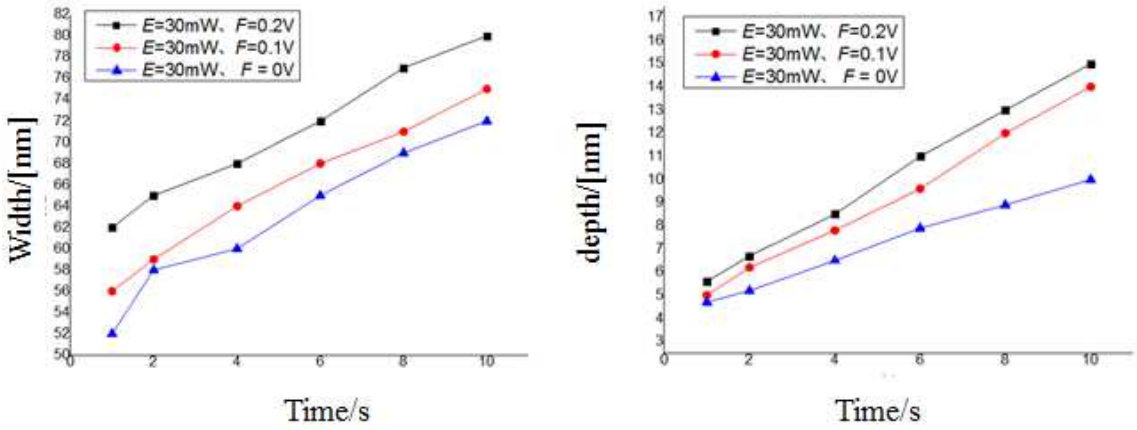
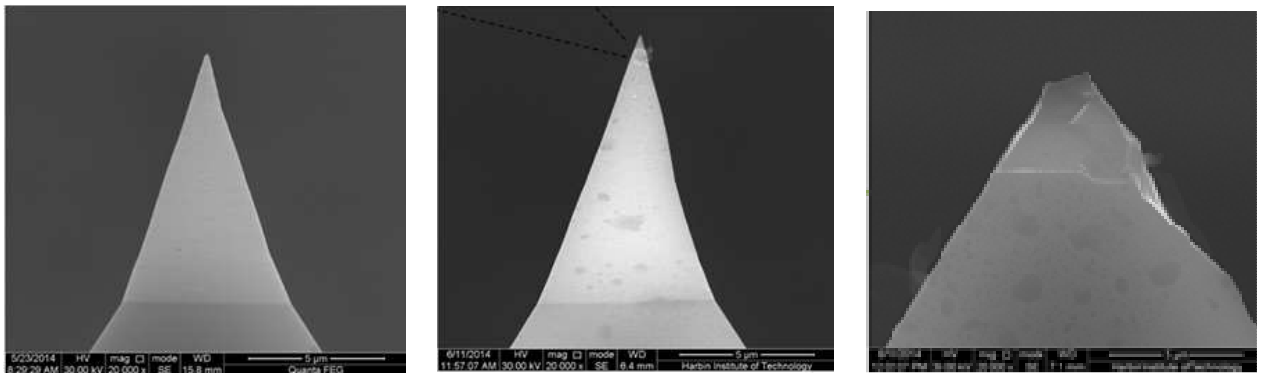


Figure 6. Influence to the size of the nano-groove of machining time

Wear of the probe. After the experiment, the AFM probe was observed under the SEM in Figure 7. The probe tip had scarcely any wear only some pollutant on the probe tip with this combining machining. And the probe tip is strong wear and broken with AFM direct machining without combining a laser, as shown in the figure 3 c). It proved that the AFM probe assisted with laser was an efficient way for nano-fabrication and good for AFM probe life.



a) original probe tip b) probe tip with combining machining c)probe tip with machining

Figure 9. The wear of the AFM probe tip

Summary

The experiment results of nanodot and nano-groove fabrication with AFM combining a CW laser is shown in the paper, it proved that the nanodot and nano-groove can be fabricated by the AFM probe combining a lower energy CW laser through the experiment. It can gain a nanodot which size was 450 nm and a nano-groove which size was 40 nm both with good feature. The size of the nanostructure is increased with the machining time increasing, and decreased with the distance between probe tip and sample increasing. And the laser energy, the location on the tip of laser irradiating, the distance between probe tip and sample is the important factors in this combining machining. With this machining method, the probe tip is not wear in the nano fabrication processing. And the mechanism of this new fabrication method is going to research in the future.

Acknowledgement

This project was supported by the National Natural Science Foundation of China (51275122), the national 863 project (2012AA040210), and the 111 Project of China (B07018). All the authors gratefully acknowledge their support.

References

[1] J. Jersch, K.Dickmann, Nanostructure fabrication using laser field enhancement in the near field of a scanning tunneling microscope tip, App. Phys. Letters. 68(1996) 868-870.

[2] S.M. Huang, M. H. Hong, Y. F. Lu, et al, Pulsed-laser assisted nanopatterning of metallic layers combined with atomic force microscopy, J. app. Physics. 91(2002) 3268-3274.

[3] S.M.Huang, M.H.Hong, B.S.Lukyanchuk, et al, Sub-50nm nanopatterning of metallic layers by green pulsed laser combined with atomic force microscopy, J. Vacu.Sci. & Tech. B.20(2002) 1118-1125.

[4] A.Chimmalgi, D.J.Hwang, C.P.Grigoropoulos, Nanoscale rapid melting and crystallization of semiconductor thin films, Nano letters. 5(2005)1924-1930.

[5] A.Chimmalgi, C.P.Grigoropoulos, K.Komvopoulos, Surface nanostructuring by nano-femto-second laser-assisted scanning force microscopy, J. App. Physics. 97(2005)104319-104319-12.

[6] A.Chimmalgi, T.Y.Choi, C.P.Grigoropoulos, et al, Femtosecond laser aperturless near-field nanomachining of metals assisted by scanning probe microscopy, App. Phys. Letters, 82(2003)1146-1148.

[7] P.I.Geshev, F.Demming, J.Jersch, et al, Calculation of the temperature distribution on laser-illuminated scanning probe tips, App. Phys. B. 70(2000) 91-97.

Key Engineering Materials Vols 645-646 (2015) pp 1059-1063
© (2015) Trans Tech Publications, Switzerland
doi:10.4028/www.scientific.net/KEM.645-646.1059

Submitted: 2014-12-05
Accepted: 2014-12-23

Constructing dual band metamaterial absorbers at mid-infrared by employing multi-resonant structures

Wei Ma, Yongzheng Wen, Rui Zhao and Xiaomei Yu[a]

National Key Laboratory of Science and Technology on Micro/Nano Fabrication, Institute of Microelectronics, Peking University, Beijing 100871, China

[a] yuxm@pku.edu.cn

Keywords: Metamaterials absorber, Dual band, mid-Infrared, Resonantor, Split-ring.

Abstract. In this paper, we present two metamaterial absorbers (MMA) at mid-infrared using multi-resonant structures. The dual band MMAs employ the typical metal/dielectric/metal structure with 80 nm gold ground plane at the bottom, 190 nm SiO_2 dielectric spacer in the middle and periodic gold patterns on top. The top resonant structure in MMA1 consists of a gold cross resonator ringed by four gold split-ring resonators (SRR) at the ends of the cross, while in the unit cell of MMA2, gold SRRs are placed at the four quadrants of the cross resonator. MMA1 shows two absorption peaks of 90.3% and 88.4% at 4.17μm and 4.86μm respectively, and the absorption peaks of MMA2 are observed to be 72.4% at 3.90μm and 48.0% at 5.66μm.

Introduction

The perfect metamaterial absorber is a burgeoning branch of electromagnetic metamaterials, which are arrays of structured subwavelength elements designed to imitate the atoms in natural materials [1]. Since they were first demonstrated by experiment [2], the design and fabrication of metamaterial absorbers have been investigated intensively, finding a vast range of potential applications including selective thermal emitters [3], bolometers [4] and plasmonic sensors [5]. However, the conventional metamaterial absorber with a single absorption band can hardly meet the requirement in some fields such as spectroscopic detection or energy harvesting. So, high absorptivity is not the only pursuit of the metamaterial absorbers, some other favorable features like polarization independence, wide accepted angle, multiband or broad-band absorption are in urgent desires.

In the implementation of the multiband metamaterial absorber, either single resonant structure or multi-resonant structure can be adopted. By exploiting higher order modes of a single resonant structure, multiband response of the metamaterial absorber can be obtained [6]. However for a single resonant structure, the frequency and strength of different resonant modes are closely related by the geometry of the structure, and thus it is difficult to tune them separately. The multi-resonant metamaterial absorbers exhibit a great advantage in manipulating different resonant modes conveniently, since they function almost independently of each other [7]. Moreover in practice, different resonant elements can be arranged in various configurations like nested [7], stacked [8] or planar multiplexed [9], which offer much flexibility in design and applications. In the presented dual band metamaterial absorbers of this work, the multi-resonant structure is constructed by combining the cross resonator and the split ring resonators (SRRs) in two different configurations. We investigated the performance of both metamaterial absorbers experimentally and analyze the mechanism of the dual band absorption.

Design and simulation

The top gold resonators of the two MMAs are fabricated on a 80 nm thick gold ground plane spaced by a 190 nm thick SiO_2 layer and have the same lattice constant of 2 μm, which are schematically shown in Fig. 1. For MMA1 in Fig. 1(a), the dual band resonant structure consists of a cross resonator symmetrically ringed by four split-ring resonators (SRR) at each end. For MMA2 in Fig. 1(b), the SRRs has degraded to broken lines with right angle to fit the four quadrants of the cross

and the four degraded SRRs are in alignment with the cross resonator at the ends. All the geometric parameters of MMA1 and MMA2 are listed is Table 1.

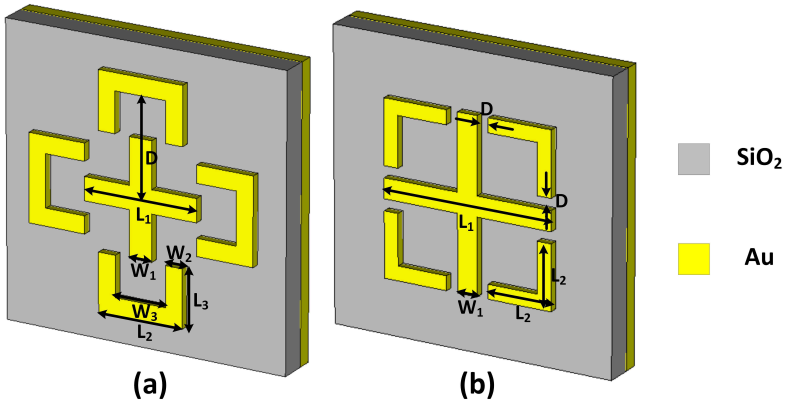


Fig. 1. Schematic diagram of the unit cell of (a) MMA1 and (b) MMA2.

Table 1. Geometric parameters of MMA1 and MMA2

Parameter (nm)	L1	L2	L3	W1	W2	W3	D
MMA1	800	600	400	160	120	360	680
MMA2	1200	450	–	100	–	–	80

The geometric parameters of the two MMAs are optimized by commercial FDTD software CST Microwave Studio. Gold is characterized as Drude metal with a plasma frequency $\omega_p=2\pi\times2175$ THz and collision frequency $\omega_c=2\pi\times6.5$ THz [10]. SiO_2 is modeled with dielectric constant of 4.1 and loss tangent of 0.025. Time domain solver was carried out with appropriate boundary conditions to extract the S parameters, from which the reflection can be obtained by $R(\omega)=|S_{11}(\omega)|^2$. Since transmission is eliminated by the ground plane, which is much thicker than the penetration depth of gold at infrared regime, the calculation of absorption can be simplified to $A(\omega)=1-R(\omega)$.

The simulated absorption of the two dual band MMAs are plotted as the solid lines in Fig. 2(a) and Fig 3(a) respectively with normal incidence and electric field along x axis. For MMA1, two peaks are observed at 4.07 μm and 4.84 μm with the absorption of 97.1% and 96.4% respectively, while for MMA2, the two peaks are 91.35% at 3.58 μm and 99% at 5.55 μm. To investigate the origin of the two absorption peaks, the corresponding single band metamaterial absorber for both MMAs with only a cross resonator and that with only four SRRs in the unit cell are also simulated separately, whose absorption spectra are depicted as the blue-dot and red-dash lines in Fig. 2(a) and Fig. 3(a). The simulated absorptions indicate that the dual band response for both MMAs originates from the mutually independent response of their constituent single band MMAs but with a small red shift, which is caused by the loading effect when the two types of resonators are combined together [7]. The independent functions of the cross resonator and the SRRs are further confirmed by the power loss density at the two absorption peaks in Fig. 2(b), (c) and Fig. 3(b), (c). At a certain resonant frequency for the MMA, either the cross resonator or the SRRs dissipate the majority of the incident energy while the coupling between these two types of resonators is negligible.

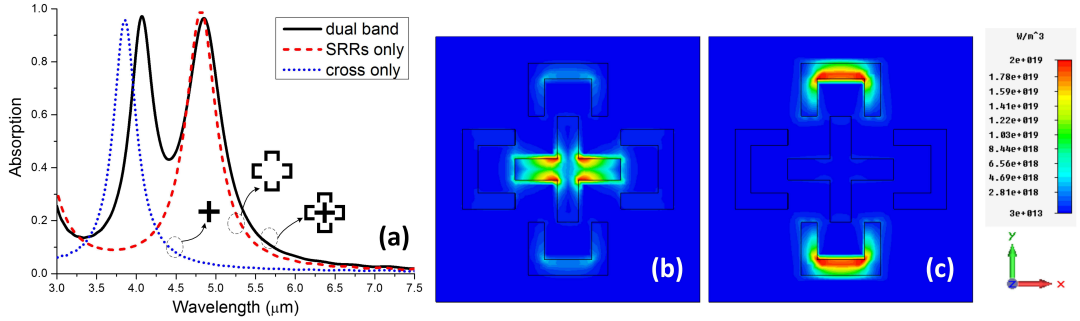


Fig. 2. (a). Simulated absorptions of MMA1 and two constituent single band absorbers. Power loss density at the two absorption peaks of (b) 4.17μm and (c) 4.86μm.

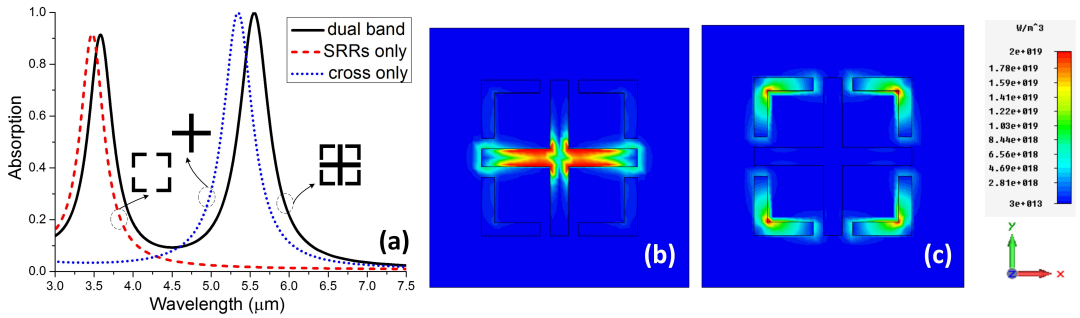


Fig. 3. (a). Simulated absorptions of MMA2 and two constituent single band absorbers. Power loss density at the two absorption peaks of (b) 5.44μm and (c) 3.51μm.

The mechanism of metamaterial absorbers is believed to be the impedance matching between the metamaterial surface and the free space [2]. Wherein the top resonant structure couples strongly to the uniform electric field and the magnetic response is introduced by the presence of the ground plane separated a distance from the top structure. The electric and magnetic property of the metamaterial absorber can thus be tuned independently by either changing the geometry of the top resonant structure or by varying the thickness and dielectric constant of the spacer. To give a detailed discussion on the origin of the absorption peaks, the electric field distribution at the two resonant wavelengths for MMA1 is depicted in Fig. 4(a) and 4(b), where the electric component of the incident wave is 1 V/m. A strongly concentrated electric field is observed at the ends of the cross resonator for the peak at shorter wavelength, and for the peak at longer wavelength most electric filed is around the SRRs. In addition, the two cross sections in Fig. 4(a) and 4(b) (the positions are indicated by the dash line) are taken to reveal the distribution of E_z, the normal component of the electric field, as plotted in Fig. 4(c) and 4(d). Obviously for both absorption peaks, a dipole resonance is stimulated in either the cross resonator or the SRRs, which leads to an intense concentration of the electromagnetic field, and the absorption is caused by the dissipation of electromagnetic energy by both the metal and the lossy dielectric [11].

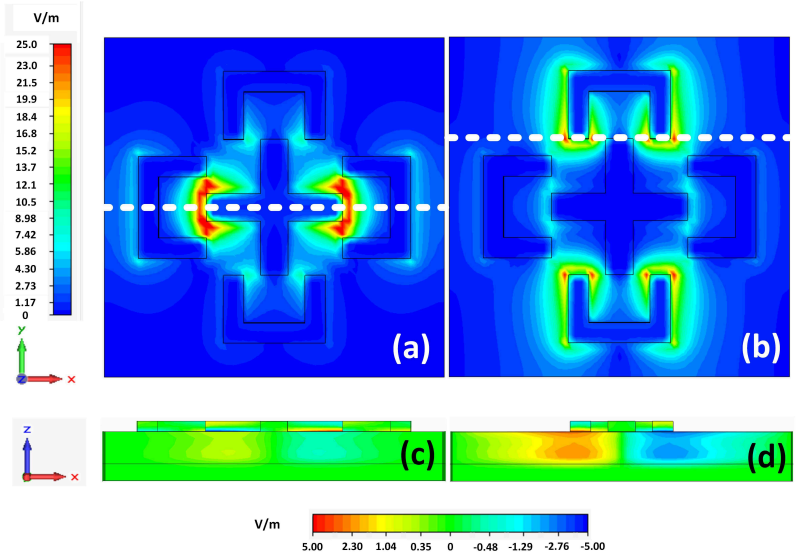


Fig. 4. Top view of the magnitude of electric field strength at the two absorption peaks of (a) 4.07μm and (b) 4.84μm respectively. The normal electric field strength in the cross section of the absorber at (c) 4.07μm and (d) 4.84μm respectively.

Fabrication and experimental results

The fabrication process of the dual band MMAs began with a 525 μm thick polished silicon wafer. First, a 20 nm chromium adhesion layer was sputtered on the substrate followed by an 80 nm gold film, which serves as the ground plane of the metamaterial absorber. Then a 190 nm thick SiO_2 layer was deposited by Plasma Enhanced Chemical Vapor Deposition (PECVD). Next, a layer of e-beam

resist of PMMA was spin coated on the SiO_2 dielectric spacer and e-beam lithography was used to define the pattern of the dual band resonant structure. After development, an adhesion layer of 10 nm titanium and a 50 nm gold film were evaporated onto the patterned resist. Finally, a standard lift-off process was carried out in acetone to remove the resist and the unwanted gold. The total size of the sample is 2 mm × 2 mm. Figure 5 displays the SEM image of the fabricated MMAs and the inset is the zoomed-in pattern of a single unit cell.

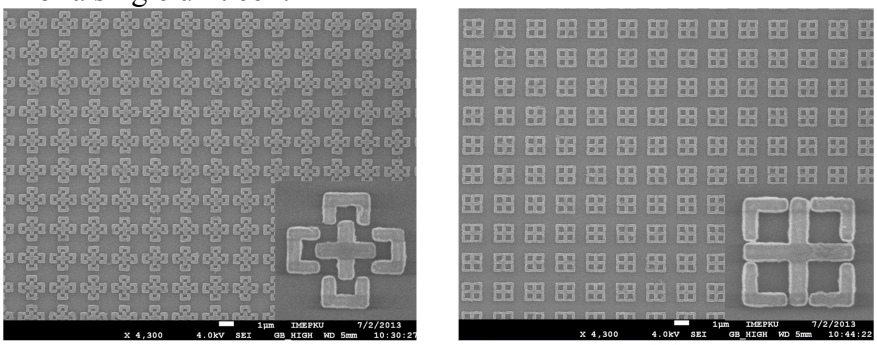


Fig.5. The SEM image of (a) MMA1 and (b) MMA2.

We measured the power reflection of the dual band metamaterial absorber using a microscope coupled Fourier transform infrared (FTIR) spectrometer (magna-IR 750). Gold mirror was taken as the normalization reference to obtain the reflectivity of the sample in percentage, from which the absorption can be calculated. The measured absorption of the fabricated MMAs is depicted in Fig. 6. Two absorption peaks of 90.3% and 88.4% were obtained at 4.17μm and 4.86μm respectively for MMA1, while for MMA2 two absorption peaks of 72.4% and 48.0% were observed at 3.90 μm and 5.66 μm. The experimental results agree with the simulations, but with slight discrepancy. We believe this is attributed to various non-idealities of the fabrication, including the error of line-width in the EBL, the non-uniformity of the dielectric spacer and the surface roughness of the gold pattern, especially the residual gold at the pattern edges after lift-off process.

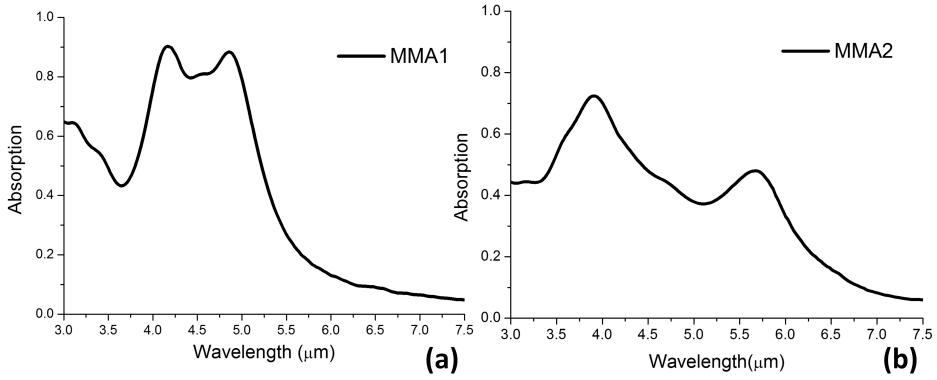


Fig. 6. Measured absorption of (a) MMA1 and (b) MMA2.

Summary

In conclusion, the design, fabrication and theoretical analysis of two dual-band metamaterial absorbers at mid-infrared are demonstrated. Both MMAs employ a cross resonator ringed by four SRRs in a unit cell as the multi-resonant structure, but with different configurations. Each MMA shows two distinct absorption peaks by experiment, which agrees with the simulation. The idea of combining different types of resonators together into one unit cell provides useful guidelines for designing various MMAs. The unique trait of the multiband metamaterial absorber makes it a promising candidate for future applications.

Acknowledgement

This work was funded by the National Natural Science Foundation of China (grants No. 61036006 and 61275104).

References

[1] C. M. Watts, X. Liu, and W. J. Padilla, "Metamaterial electromagnetic wave absorbers," Advanced Materials, vol. 24, pp. OP98-OP120, 2012.
[2] N. Landy, S. Sajuyigbe, J. Mock, D. Smith, and W. Padilla, "Perfect metamaterial absorber," Physical review letters, vol. 100, p. 207402, 2008.
[3] X. Liu, T. Tyler, T. Starr, A. F. Starr, N. M. Jokerst, and W. J. Padilla, "Taming the blackbody with infrared metamaterials as selective thermal emitters," Physical review letters, vol. 107, p. 045901, 2011.
[4] F. Alves, D. Grbovic, B. Kearney, N. V. Lavrik, and G. Karunasiri, "Bi-material terahertz sensors using metamaterial structures," Optics Express, vol. 21, pp. 13256-71, Jun 3 2013.
[5] N. Liu, M. Mesch, T. Weiss, M. Hentschel, and H. Giessen, "Infrared perfect absorber and its application as plasmonic sensor," Nano letters, vol. 10, pp. 2342-2348, 2010.
[6] H. Cheng, S. Chen, H. Yang, J. Li, X. An, C. Gu, et al., "A polarization insensitive and wide-angle dual-band nearly perfect absorber in the infrared regime," Journal of Optics, vol. 14, p. 085102, 2012.
[7] Y. Ma, Q. Chen, J. Grant, S. C. Saha, A. Khalid, and D. R. Cumming, "A terahertz polarization insensitive dual band metamaterial absorber," Optics Letters, vol. 36, pp. 945-947, 2011.
[8] N. Zhang, P. Zhou, D. Cheng, X. Weng, J. Xie, and L. Deng, "Dual-band absorption of mid-infrared metamaterial absorber based on distinct dielectric spacing layers," Optics letters, vol. 38, pp. 1125-1127, 2013.
[9] B. Zhang, J. Hendrickson, and J. Guo, "Multispectral near-perfect metamaterial absorbers using spatially multiplexed plasmon resonance metal square structures," JOSA B, vol. 30, pp. 656-662, 2013.
[10] M. A. Ordal, L. L. Long, R. J. Bell, S. E. Bell, R. R. Bell, J. R. W. Alexander, et al., "Optical properties of the metals Al, Co, Cu, Au, Fe, Pb, Ni, Pd, Pt, Ag, Ti, and W in the infrared and far infrared," Applied Optics, vol. 22, pp. 1099-1119, 1983.
[11] X. Liu, T. Starr, A. F. Starr, and W. J. Padilla, "Infrared spatial and frequency selective metamaterial with near-unity absorbance," Physical review letters, vol. 104, p. 207403, 2010.

Key Engineering Materials Vols 645-646 (2015) pp 1064-1071
© (2015) Trans Tech Publications, Switzerland
doi:10.4028/www.scientific.net/KEM.645-646.1064

Submitted: 2014-12-16
Accepted: 2014-12-23

Structure Design of Large Travel One-arm Bridge Type Z-axis Nano-positioning Stage

[1]FAN Wei [2]LI Zhongshen [3]JIANG Shaoyin

[1]College of Mechanical Engineering and Automation, Huaqiao University, Xiamen 361021
[2]Institute of engineering technology, Huaqiao University, Xiamen 361021
[3]College of Mechanical Engineering and Automation, Huaqiao University, Xiamen 361021
Corresponding author: FAN Wei
E-mail address: fanwei@hqu.edu.cn

Keyword: large travel, one-arm bridge type, nano-positioning stage, Abbe error, structure design

Abstract: In some areas such as micro-mechanical, ultra-precision machining, nano-technology, the high-precision positioning and very fine vertical scanning motion are needed urgently. Therefore, the Z-axis micro-displacement driving control technology has become the key technology in these areas. The piezoelectric ceramics actuator and stepper motor were integrated into hybrid linear actuator in Z-axis nano-positioning stage, and this can simplify the structure of the drive system. By calculating the gravity center of the vertical scanning system, and using single counterweight, a new one-arm bridge type structure was built. Appropriate tension and current sensors were also equipped in order to real-time monitor the drive status. It is feasible to balance the weight with this simplified system structure, and also guarantee the driving control accuracy of nano-positioning stage. Besides, in the structural design, the Abbe error can be reduced greatly by placing the stage center, grating ruler and displacement measurement centerline on the same line with grating reading head. The driving travel of nano-positioning stage is 150mm, and driving resolution is 1nm. The designing method introduced gives a scientific method and practical reference for the development of z-axis driving control system.

1. Introduction

The ultra-precision machining, precision measurement level and production level of large scale integrated circuits have been affected directly by micro-displacement drive technology[1-3]. At the same time, the technical indicators of micro-displacement drive also are important symbol of high technology development in each country. Therefore, how to achieve nano-scale positioning drive control key technologies has become a hotspot and difficulty of current research [4-5].

With the development of technology, the vertical scanning drive has become an important content for micro-electromechanical systems, but the driving precision of Z-axis stage is much lower than x-axis and y-axis planar drive, the precision of entire system will be affected seriously[6-7]. This is mainly due to the uneven driving force in the vertical driving round trip, the counterweight should been added accordingly. The counterweight of existing stage is mostly symmetrical structure with double mass block, it is very difficult to achieve the balance of gravity, an uneven oblique pulling force will apply to the guide rail continuously, the structure of whole system is also complex relatively, and the driving control is difficult to be uniform and smooth. In addition, the Abbe arm of double mass block structure is longer, the larger Abbe error will be introduced [8-10].

For the deficiency of existing Z-axis nano-positioning stage, a new design of one-arm bridge type counterweight structure was built. First of all, the stage center, grating ruler and displacement measurement centerline were placed on the same line with grating reading head, the Abbe error of system can be reduced greatly. By calculating gravity center of the vertical scanning system, using single counterweight, and designing the corresponding position fine adjustment mechanism of the traction rope, so that the boom can pull stage vertically in the gravity center line of the system, to avoid oblique pulling force exert an influence on the guide rail continuously. In addition, the balance of gravity can be ensured through the real-time monitoring with the tension on the traction rope and motor output power, the Z-axis drive system will be the best working condition, in order to achieve nanometer level positioning control precision.

2. Overall system structural design

2.1 Drive system

The driving system utilized macro and micro two-level driving control, the piezoelectric and stepper motor were integrated into hybrid linear actuator. The first-level drive system of large travel was constituted with stepping motor, coupling and screw pair. The effective rail travel length of screw pair mechanism is 260mm, and the size of precision positioning table is 110 × 110mm, the large driving of 150mm can be achieved. The PSt150/5/40VS10 piezoelectric ceramics actuators were used as drive elements in Precision positioning stage, the nominal displacement travel is 40μm, and displacement resolution is 1nm. Figure 1 shows drive system.

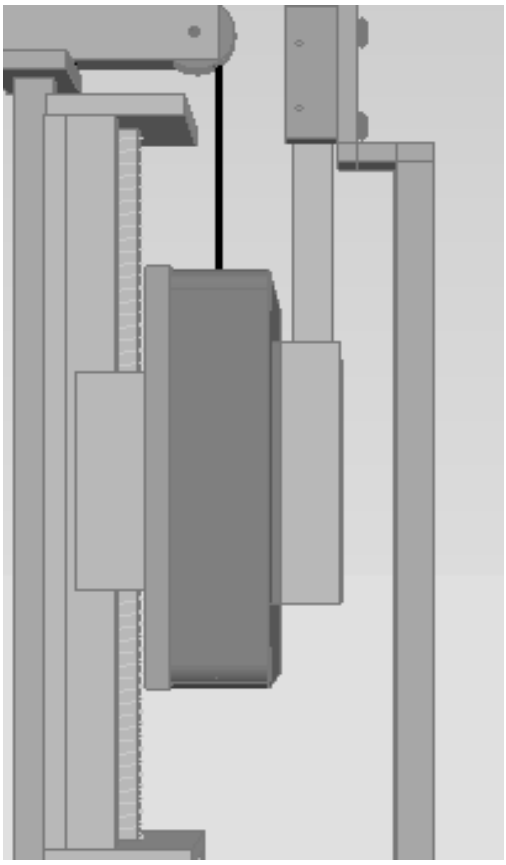


Fig.1 The drive system

2.2 The structure design of Z-axis nano-positioning stage

The measured dimensions and size as a standard should be the same straight line, this is the Abbe principle. The Abbe error would affect the measurement accuracy of driving displacement seriously in driving control with nano-scale. The most important reason of Abbe error is that the measured displacement and reference quantity of measurement instruments is not in the same line

when system mechanic institutions were designed. Therefore, in the structural design of Z-axis nano-positioning stage, the stage center, grating ruler and displacement measurement centerline were placed on the same line with grating reading head, the zero Abbe error can be achieved theoretically. Figure 2 shows the overall structure solid figure of system，and Figure 3 shows setting drawing of overall structure.

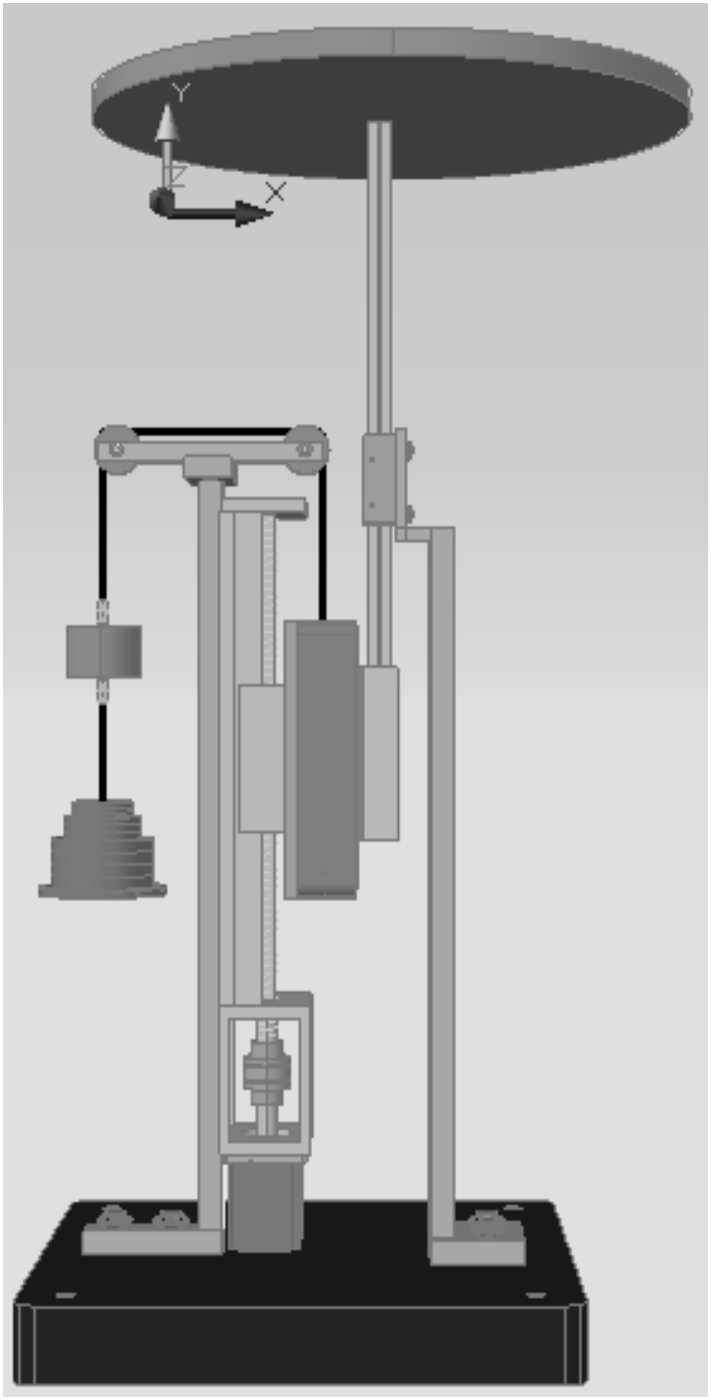


Fig.2 The overall structure solid figure of system

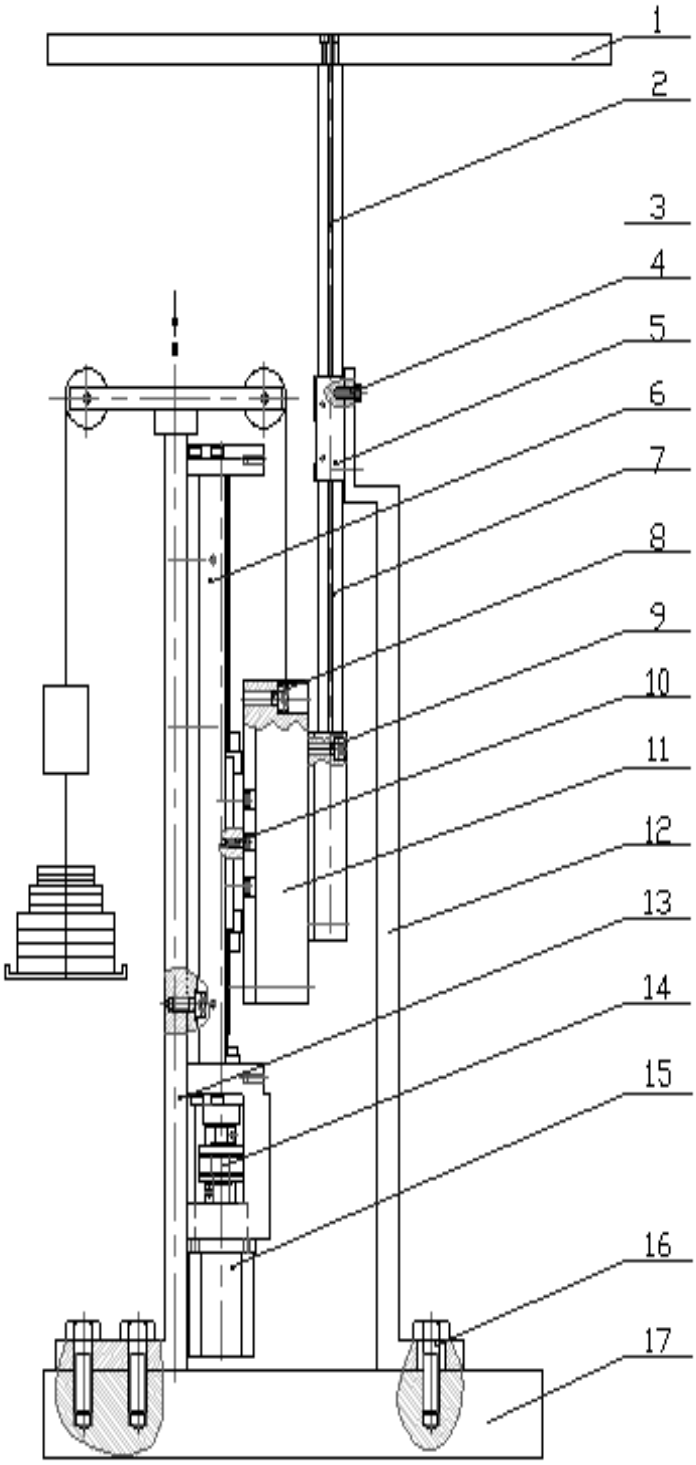


Fig.3 The overall structure setting drawing of system

3. The one-arm bridge type structure design of Z-axis nano-positioning Stage

3.1 The gravity center calculation of system

The combination method was applied to seek gravity center of homogeneous composite body in engineering mechanics, the combination method also is known as segmentation method. The principle of combination method is that a complex combination-type body is divided into a number of simple graphics. First of all, the gravity center of simple graphics should be found, the gravity center of combination-type body can be determined by

$$Xc=\sum \triangle AiXi/ A \quad (1)$$

$$Yc=\sum \triangle AiYi/ A \quad (2)$$

$$Zc=\sum \triangle AiZi/ A \quad (3)$$

Using Auto Cad draws graphics, then connecting the graphics into complex line with pedit command, turning the graphic into surface domain with region command, Using Boolean operation finds different set or union of surface domain, at last, displaying the information of surface domain with massprop command, Writing down the location of gravity center, so that the traction rope can match together with gravity center in vertical direction.

3.2 The counterweight structure of one-arm bridge type

According to the insufficient of existing dual-mass block symmetry structure, a new one-arm bridge type counterweight structure was designed. By calculating the gravity center of the vertical scanning system, and using single counterweight structure, so that the boom can pull stage vertically in the gravity center line of the system.

The weight was adopted as counterweight structure, in order to change the counterweight mass according to the weight of measurement objects on stage. Figure 4 shows the solid figure of one-arm bridge type counterweight structure.

3.3 The design of gravity center fine adjustment mechanism

The gravity center of Z-axis nano-positioning stage can be found by calculating in theory, but there is deviation with the real gravity center. Therefore, the gravity center fine adjustment mechanism should be designed to achieve the around micro distance adjustment of counterweight traction rope, making the traction rope to coincide with the gravity center of the Z-axis nano-positioning stage, thus the optimal driving could be ensured.

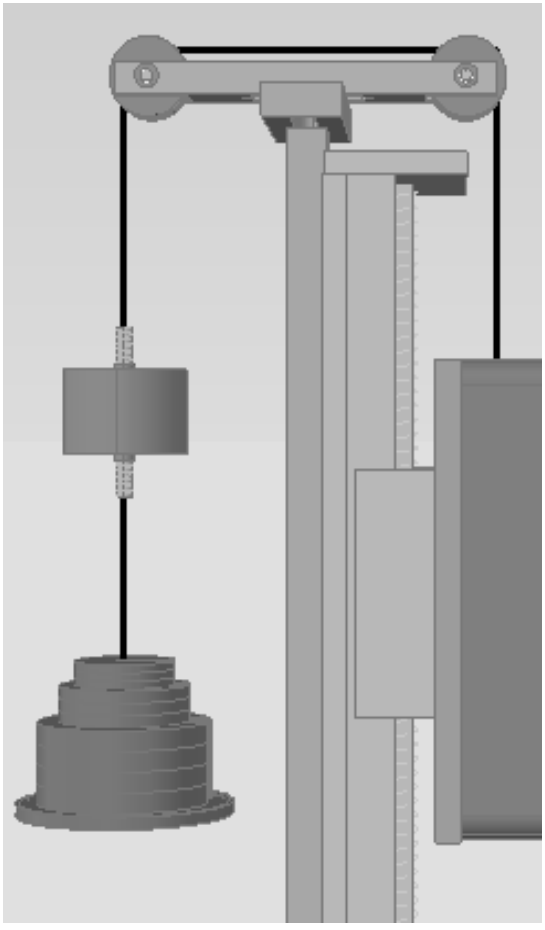


Fig.4 The solid figure of one-arm bridge type counterweight structure

In order to achieve the position adjustment of traction rope, a 5mm thick plate was installed between the fixed pulley bracket and L-bracket of guide rail, Figure 5 shows the fine adjustment mechanism of counterweight traction rope.

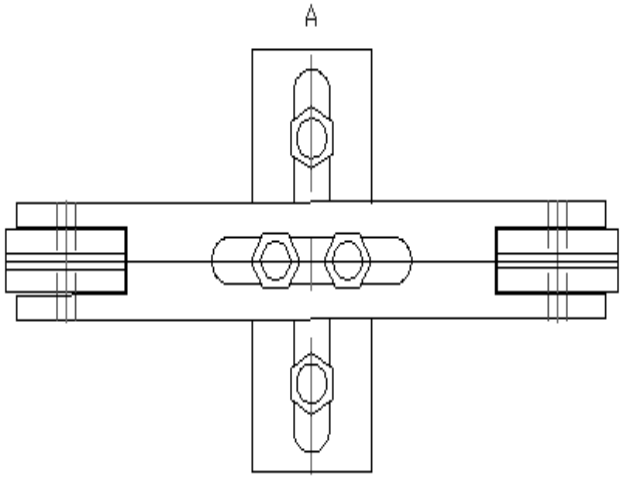


Fig.5 The fine adjustment mechanism structure diagram

The front and rear, right and left movement can be achieved between the fixed pulley bracket and the plate, and thus the position of traction rope will be adjusted to coincide with the gravity center of the Z-axis nano-positioning stage. Figure 6 shows the solid figure of fine adjustment mechanism.

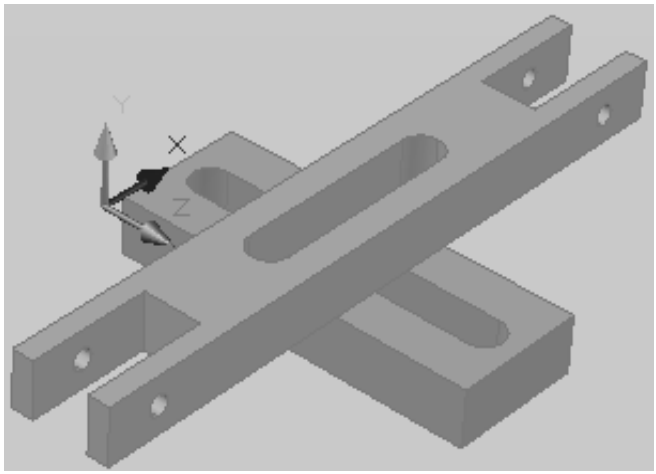


Fig.6 The fine adjustment mechanism solid figure

4. Driving condition monitoring system construction

How to know the position of the counterweight traction rope? If the traction rope coincides with the gravity center of system, the guide rail of stage will not be influenced by an oblique pulling force, and the driving force of round trip also will be more uniform and smooth. Accordingly, the JLBM tension sensor was adopted to monitor the tension of counterweight traction rope. The foil strain gauge was attached to spring-steel in tension sensor, it demonstrates superior characteristics of good seal, long-term operation stability etc. The precision of sensor is 0.03 percent, and it can measure the tension change of 0.015N.

Moreover, a CHB-25NP/SP6 loop current sensor was installed in drive system. The precision of sensor is 0.08 percent, and it can measure 10mA current variation in driving trip. Figure 7 shows the force sensors and current sensors were adopted. The drive voltage of stepper motor is constant, and the output power of the motor can be calculated by

$$P = UI \tag{3}$$

The resistance variation of friction and gravity in driving trip can be obtained by real-time monitoring motor output power. Finally, the gravity balance of the entire system can be achieved through the adjustment mechanism, and the driving state of Z-axis nano-positioning stage in round trip can be uniform and smooth.



Fig.7 Force sensor and current sensor

5. Conclusions

To satisfy the requirements of large travel, high-resolution, and high positioning accuracy simultaneously, the Z-axis nano-positioning stage has the following structural design characteristics.

(1) The zero Abbe error structure. In the structural design, the stage center, grating ruler and displacement measurement centerline were placed on the same line with grating reading head, and the zero Abbe error can be realized in theory.

(2) The one-arm bridge type counterweight structure. By calculating the center of gravity of the vertical scanning system, and using one single counterweight, a new one-arm bridge type structure was built. When there is deviation between the theoretical gravity center and real gravity center, the boom can pull stage vertically in the gravity center line of system by fine adjustment mechanism structure.

(3) Equipped with tension and current sensors. The appropriate tension and current sensors also were equipped in the stage, thus the drive status can be monitored in real time. The tension sensor was adopted to monitor the tension of counterweight traction rope, and the variation of resistance in driving trip also can be obtained by real-time monitoring motor current.

The driving travel of nano-positioning stage is 150mm, and driving resolution is 1nm. The achievements from the stage will build up the scientific methods and practical reference for the development of z-axis driving control system.

ACKNOWLEDGMENTS

This research has been supported by “the Fundamental Research Funds for the Central Universities(The project NO. JB-2R1159)”,2013 Fujian Provincial Natural Science Foundation funded projects (The project NO.21201316), and (The project NO.50420120134)International Cooperation is supported by the National Natural Science Foundation of China (NSFC)

Author Resume: Fan wei(1980-), male（the Han nationality）, Yumen, Gansu Province, Huaqiao University lecturer, Dr. Majoring in Precise Measuring and Testing Technique& Instrument.

Address*:*

College of mechanical engineering and automation

Huaqiao University

Xiamen, Fujian, China

Zip: 361021

Tel: 15805903856

Email: fanwei@hqu.edu.cn

REFERENCES

[1]Yung-Tien Liu, Rong-Fong Fung, Tai-Kun Huang.Dynamic responses of a precision positioning table impacted by a soft-mounted piezoelectric actuator Precision Engineering 28 (2004) 252–260

[2]Kazuhiro Takahashi，Makoto Mita，Hiroyuki Fujita，et al.A high fill-factor comb-driven XY-stage with topological layer switch architecture[J]．IEICE Electronics Express，2006，3（9）：197-202

[3] Gu Lei ，Li Xinxin ，Bao Haifei ，et al. Single-waferprocessed nano-positioning XY-stages with trenchsidewall micromachining technology［J］．J Micromech Microeng， 2006 16（7）：1349-1357

[4]Cox J , Miller L. The first 50 years of electronic watermarking[J].Journal of Applied Signal Processing , 2002 , (2) :126 —132.

[5]Kramar J A.Nanometre resolution metrology with the molecular measuring machine[J].Measurement Science and Technology ,2005 ,16 :212122128.

[6]Gred J , Rainer G, Eberhard M, et al. A nanopositioning and nanomeasuring machine :operation-measured results[J].Nano-technology and Precision Engineering ,2004 ,2 (2) :81284.

[7]Holmes M, Hocken R , Trumper D. The long-range scanning stage, a novel platformfor scanned2probe microscopy[J]. Precision Engineering ,2000 ,24 :1912209.

[8]Tian YL，Shirinzadeh B，ZhangDW. A flexure-based mechanism and control methodology for ultra-precision turning operation [J].Precision Engineering， 2009，33 (2) : 160 - 166.

[9] Canudas W C，Lischinsky P． Adaptive friction compensation with partially known dynamic friction model［J］． International Journal of Adaptive Control Signal Process， 2007，11(1) :65- 80．

[10] Kim H M，Park S H，Han S I． Precise friction control for the nonlinear friction system using the friction state observer and sliding mode control with recurrent fuzzy neural networks ［J］． Mechatronics，2009，19(6) : 805- 815．

Key Engineering Materials Vols 645-646 (2015) pp 1072-1077
© (2015) Trans Tech Publications, Switzerland
doi:10.4028/www.scientific.net/KEM.645-646.1072

Submitted: 2015-01-08
Accepted: 2015-01-19

Effect of Undercut on the Characterization of the Mechanical Properties of Silicon Nanocantilevers with Dynamic and Static Test

Jiahong Zhang[1,2, a], Fang Gu[3, b*], Xianling Zhang[3], Min Li[1], Yixian Ge[1,2] and Xiaoli Mao[1]

[1]Jiangsu Key Laboratory of Meteorological Observation and Information Processing, Nanjing University of Information Science & Technology, Nanjing 210044, China

[2]Jiangsu Collaborative Innovation Center on Atmospheric Environment and Equipment Technology, Nanjing University of Information Science and Technology, Nanjing 210044, China

[3]School of Physics & Optoelectronic Engineering, Nanjing University of Information Science & Technology, Nanjing 210044, China

[a]zjhnuist@163.com, [b]gfnuist@163.com

Keywords: silicon nanocantilevers, undercut, mechanical properties, mechanical testing, finite element method

Abstract. The elastic mechanical properties of silicon nanocantilevers are of prime importance in biotechnology and nanoelectromechanical system (NEMS) applications. In order to make these applications reliable, the exact evaluation of the effect of the undercut on the mechanical properties of silicon nanocantilevers is essential and critical. In this paper, a numerical-experimental method for determining the effect of the undercut on resonant frequencies and Young's modulus of silicon nanocantilevers is proposed by combining finite element (FE) analysis and dynamic frequency response tests by using laser Doppler vibrometer (LDV) as well as static force-displacement curve test by using an atomic force microscope (AFM). Silicon nanocantilevers test structures are fabricated from silicon-on-insulator (SOI) wafers by using the standard complementary metal-oxide-semiconductor (CMOS) lithography process and anisotropic wet-etch release process based on the critical point drying, which inevitably generating the undercut of the nanocantilever clamping. Combining with three-dimensional FE numerical simulations incorporating the geometric undercut, the dynamic resonance tests demonstrate that the undercut obviously reduces resonant frequencies of nanocantilevers due to the fact that the undercut effectively increases the nanocantilever length by a correct value ΔL. According to a least-square fit expression including ΔL, we extract Young's modulus from the measured resonance frequency versus the effective length dependency and find that Young's modulus of a silicon nanocantilever with 200-nm thickness is close to that of bulk silicon. However, when we do not consider the undercut ΔL, the obtained Young's modulus is decreased 39.3%. Based on the linear force-displacement response of 12μm long and 200nm thick silicon nanocantilever obtained by using AFM, our extracted Young's modulus of the [110] nanocantilever with and without undercut is 169.1GPa and 133.0GPa, respectively. This error reaches 21.3%. Our work reveals that the effect of the undercut on the characterization of the mechanical properties of nanocantilevers with dynamic and static test must be carefully considered.

Introduction

Silicon nanocantilevers are the key building blocks for NEMS and biotechnology applications such as high frequency mechanical resonators and ultrasensitive force or mass sensors and actuators [1]. Obviously, reducing the size of the silicon nanocantilevers significantly improves their resonant performance and sensitivity so much that they are able to demonstrate the GHz fundamental resonance frequency, zeptonewton-scale force sensing and zeptogram-scale mass sensing. However, reducing the dimensions of nanocantilevers causes the elastic mechanical behavior to deviate from the bulk values and is strongly size-dependent, mainly arising from the low dimensionality and surface effects. Therefore, in order to make these NEMS applications reliable, the exact evaluation of mechanical properties of silicon nanocantilevers is essential and critical. In past two decades, this

size-dependent mechanical properties of silicon nanocantilevers has been extensively investigated via experimental measurements [2,3] and theoretical studies, including first-principle density functional theory [4], molecular dynamics[5] and modifications to continuum theory [6]. It is noted that most of the previous researches focus on the influences of surface effects on the size-dependent mechanical properties. In fact, there could be other influences besides surface effects, such as the influences of native oxide layer, fabrication-induced defects and fabrication-induced undercut. These factors may significantly affect the elastic properties of silicon nanocantilevers. Unfortunately, the understanding of the effects of fabrication-induced defects and undercut involved in post-CMOS process on the mechanical properties of Si nanostructures is very few at present [7,8]. Therefore, from the perspective of large-scale production, it is necessary and meaningful to study the influences of defects and undercuts involved in the post-CMOS process on the mechanical properties of Si nanostructures.

In the paper, we will focus on the effect of the undercut caused by overetching during final wet release process on the characterization of the mechanical properties of silicon nanocantilevers with dynamic and static Test. It is worth noting that the combined methods which rely on the modeling of the beam geometry by a FE analysis together with experimentally frequency response test have received more and more attention[7-10], and there has been a tendency to determine the resonant frequency and Young's modulus of the nanostructure and the undercut effect by using this combined method. In order to complete our task, a novel and effective numerical-experimental method for determining resonant frequencies and Young's modulus of silicon nanocantilevers is presented by combining FE simulation analysis and dynamic frequency response test based on an electrostatic excitation and visual detection by LDV as well as static force-displacement curve test by using AFM. Because the undercut cannot be avoided in the CMOS-NEMS fabrication process, this work might be useful for evaluating the influence of manufacturing process-induced undercut on mechanical properties of the nanocantilever-based NEMS.

Fabrication of silicon nanocantilevers and correction model for the undercut

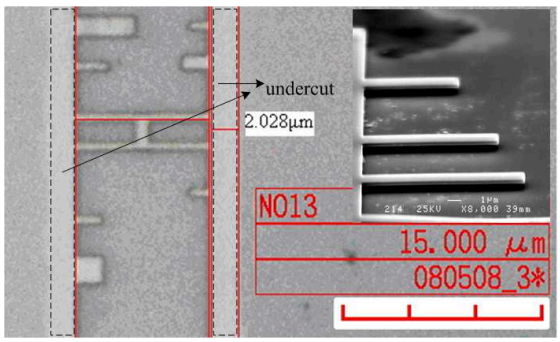


Fig.1 Optical microscope image of silicon nanocantilevers. The white strip near the base of nanocantilevers indicates the undesired undercut with about 2μm long. Inset in Fig.1 shows SEM image of 200nm thick silicon nanocantilevers with different length.

In this paper, silicon nanocantilevers test structures along the [110] crystallographic orientation were fabricated from (100) SOI wafers with a 200-nm thick buried oxide (BOX) and a 200-nm thick single-crystal silicon surface device layer by using the SMIC 0.18μm CMOS lithography process and anisotropic wet-etch release post-CMOS process. The first step of the fabrication process was to determine the patterns of [110] oriented silicon nanocantilevers of different lengths (L) and widths (w) onto silicon surface device layer by the standard photolithography. After this, reactive ion etchings were used to etch the silicon device layer and the exposed BOX until the silicon substrate. Then heavily doped p-type layer was formed in the anchor region, followed by sputtering 600-nm Al metal as the pad. A photoresist was then spinned in the metal pad region in order to prevent corrosion of Al metal in the release process of SiNBs. Finally, the BOX underneath nanocantilevers was etched using a buffered oxide etcher (BOE) solution and silicon nanocantilevers were then released using critical point drying in liquid carbon dioxide (post-CMOS process) [8], which inevitably generating the undercut of the nanocantilever clamping. As we can see from fig.1, the undesired 2.028μm long

undercut will lead to a significant deviation from the linear relation between the resonant frequency (f_0) and the inverse length squared obtained by using LDV(as shown in fig. 2) or the linear relation between the Young's modulus (E) and the length cubed obtained by using AFM. For example, the resonance frequency may be shifted towards lower values because of the increase in effective length of the nanocantilever, which reduces the spring constant. Apparently, the undesired undercut will have an important impact on the assessments of Young's modulus of the nanocantilevers. If we do not consider the effect of the undercut, erroneous results may be obtained.

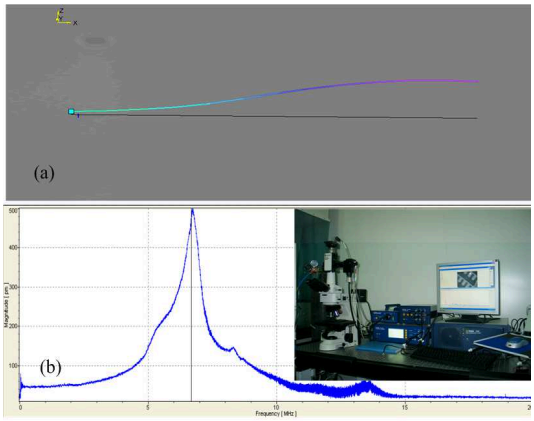


Fig. 2 (a) Vibration pattern of the silicon nanocantilever, (b) amplitude-frequency relation, Inset shows the LDV measurement setup.

In order to accurately extract mechanical properties of silicon nanocantilevers, the effect of undercut should be included into the nanocantilever effective length by adding a correction length ΔL [7-10]. In the case, the effective length of the nanocantilever with undercut is given by $L_{\text{eff}} = L+\Delta L$, where L is the original length and ΔL is the correction length of the undercut. Thus we have:

$$f_0 = \frac{\lambda^2 t}{4\pi L_{\text{eff}}^2}\sqrt{\frac{E}{3\rho}} = \frac{\lambda^2 t}{4\pi(\Delta L + L)^2}\sqrt{\frac{E}{3\rho}} \quad \text{(Based on LDV)} \tag{1}$$

$$E = \frac{4L_{eff}^3}{wt^3}S = \frac{4(L+\Delta L)^3}{wt^3}S \quad \text{(Based on AFM)} \tag{2}$$

Where λ =1.875, ρ is the density of silicon, S is the slope of load force-displacement curve, w and t is the width and thickness of the nanocantilever, respectively. Based on the above correction equations, we can extract the Young's modulus by using the fitting method and research the effect of the undercut.

Results and discussion

In our combined numerical and experimental method, the first step is to detect the fundamental resonant frequencies by a dynamic resonance test and static force-displacement curve by using AFM. Noted that in the LDV measurement setup, in order to accurately observe the amplitude-frequency of the nanocantliever, optimally adjusting the laser spot position to the free end of the nanocantilever as measurement point is also a critical issue. Fig. 2 shows vibration pattern of the silicon nanocantilever and its amplitude-frequency relations measured by using LDV. Then the second step is to model the frequency response of the nanocantilever with and without the undercut. A three-dimensional FE simulation is carried out for the fundamental resonant frequency using ANSYS. As in the ANSYS input parameters are assumed, the experimental value for the mass density (2330 kg/m^3) is used whereas the Young's modulus (170 GPa) and Poisson's ratio (0.064) are taken. In order to investigate the influence of undercut arising from the wet chemical release process of the nanomechanical structure, the underetched nanocantilever is modeled as a stepped cantilever as illustrated in fig. 3(a). In the specific simulation, the nanocantilever is attached to the 2μm long and 15μm wide plate. Three lateral edges of the plate are clamped, while the nanocantilever is attached to the free edge. Moreover, released areas of silicon nanocantilever and underetched base regions (plate with three clamped

lateral edges) are allowed to move freely in the FE simulation. In this case, FE results are uniquely determined. Fig. 3(b) illustrates the vibration mode dependence on the stress distribution in close proximity to the clamped end of the nanocantilever. The simulations show that the stress propagation into the overhang region is significant, which numerically reveals that the undercut inevitably affects the mechanical resonant characteristics of the silicon nanocantilever.

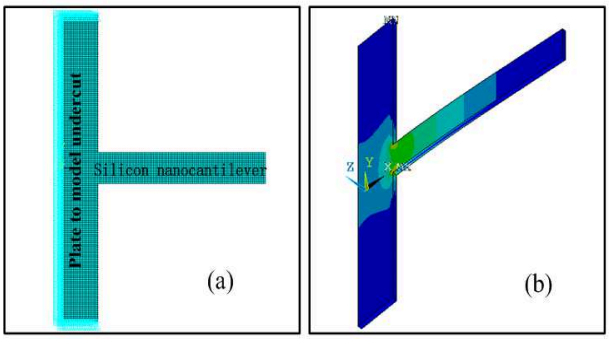


Fig. 3 (a) Three-dimensional FE mesh of the silicon nanocantilever. (b) FE simulation of the vibration mode dependence on the stress distribution near the single clamped end of the silicon nanocantilever.

In the numerical-experimental method, the last step is to compare experimental results in the first step and FE numerical simulation results in the second step to determine the practical Young's modulus. Experimental results by a dynamic resonance test and FE simulation results are presented in fig. 4. As can be seen, FE simulation results with undercut agree well with experimental results, while the resonant frequencies of FE simulation without undercut are larger than those of FE simulation with undercut and LDV measurement, especially for the relatively short silicon nanocantilever. Thus, in conjunction with three-dimensional FE numerical simulations incorporating the geometric undercut, dynamic resonance tests reveal that the undercut significantly decreases resonant frequencies of nanocantilevers due to it effectively increases the nanocantilever length by a correct value ΔL, which is the key parameter that correlates deviations in the resonant frequencies predicted from the ideally Euler-Bernoulli beam theory (Eq.(1)) and experimental measured data.

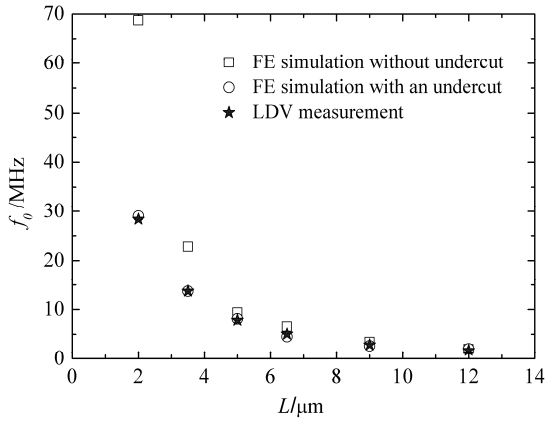


Fig. 4 Comparing the measured and FE simulated resonant frequencies of silicon nanocantilevers with and without undercut.

Based on the corrected Euler-Bernoulli theory, i.e., Eq. (1), once the dimensions L, t, and the fundamental resonance frequencies of bending mode of the nanocantilevers with undercut are experimentally or theoretically determined, by performing a least-square fit through the obtained resonance frequency data with ΔL and E used as free parameters in the fitting routine, one can simultaneously extract the correction length ΔL and the Young's modulus E of the silicon nanocantilevers. The relationship between fundamental resonance frequency of bending mode and $1/ L_{\text{eff}}^2$ is plotted in fig.5. The Young's modulus and the correction length ΔL of silicon nanocantilevers are 171.1GPa (170.6GPa) and 1μm (1μm) for FE numerical simulations with undercut and LDV measurement, respectively. As shown in fig. 5(a) and 5(b), we can clearly see that

the results of FE numerical simulations with undercut are consistent with LDV experimental results, which demonstrates that Young's modulus of silicon nanocantilevers with 200nm thickness is close to that of bulk silicon (169GPa). This result supports that finite size effect due to surface effect does not play a role on mechanical elastic behavior of silicon nanocantilevers with the thickness > 200nm.

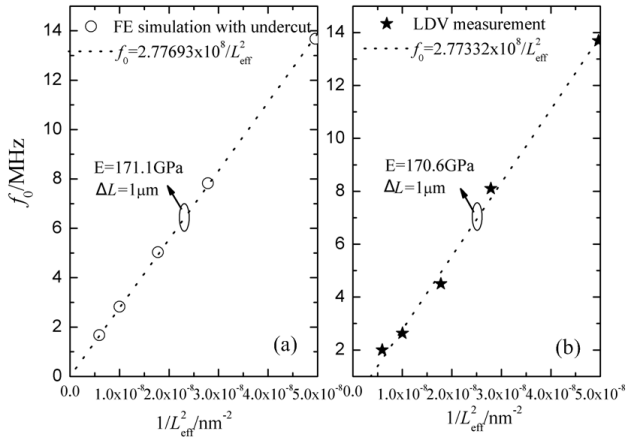


Fig. 5 Young's modulus and the correction length of silicon nanocantilevers were obtained by fitting the resonance frequencies from (a) FE numerical simulations with undercut, (b) LDV measurement. The dashed line shows a fitting straight line.

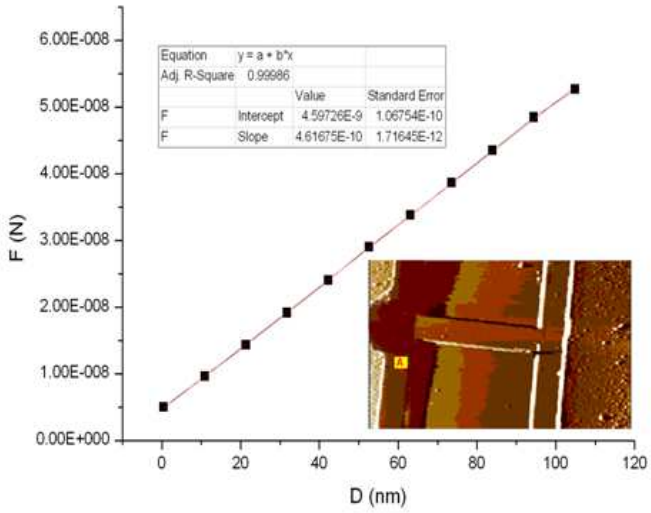


Fig. 6 Force-displacement curve of the silicon nanocantilever obtained by using AFM. Inset shows the AFM image of 200nm thick silicon nanocantilevers

Fig.6 displays linear force-displacement response of 12μm long and 200nm thick silicon nanocantilever obtained by using AFM. Through the Eq.(2), using a least-square fit expression including ΔL, we have finally extracted Young's modulus based on the slope of the measured load force-displacement curve of the silicon nanocantilever obtained by using AFM. Table.1 presents that the calculated Young's modulus of the nanocantilever with and without undercut is 169.1GPa and 133.0GPa, respectively. This error reaches 21.3%. For LDV dynamic test, when we do not consider the undercut ΔL, the obtained Young's modulus is decreased 39.3%. Therefore, our work indicates the effect of undercut on the characterization of the mechanical properties of nanocantilevers with dynamic and static test must be carefully considered.

Table 1. Comparing Young's modulus extracted from measured resonant frequencies and force displacement curve for the silicon nanocantilever with and without undercut respectively.

Dynamic and Static Test	$E_{without}$ (GPa)	$E_{undercut}$ (GPa)	$(E_{undercut} - E_{without}) / E_{undercut}$ %
LDV	103.6	170.6	39.3%
AFM	133.0	169.1	21.3%

Summary

In summary, we presented a novel and effective numerical-experimental method to analyze the resonance properties of silicon nanocantilevers with undercut fabricated by using a CMOS-NEMS process and to determine their Young's modulus. In this combined method, we can simultaneously extract the Young's modulus and the correction length of the nanocantilever with undercut by performing and comparing a least-square fit through the measured frequency response data combined with the FE numerical simulation data. Our work shows that the undercut significantly reduces the resonance frequencies of the silicon nanocantilevers because of the increase in their effective length. In the case, by introducing a correction length, we can obtain reasonable results for the resonant frequency and Young's modulus. Finally, we have also extracted Young's modulus based on the slope of the measured load force-displacement curve of the silicon nanocantilever obtained by using AFM. Our work indicates the effect of undercut on the characterization of the mechanical properties of nanocantilevers with dynamic and static test must be carefully considered, and otherwise erroneous results will be obtained.

Acknowledgement

This Project is supported by the National Natural Science Foundation of China (Nos. 61306138, 61307113, 61307061), Natural Science Foundation of Jiangsu Province (No. BK2012460) and the Priority Academic Program Development of Jiangsu Higher Education Institutions. All the authors gratefully acknowledge their support. We also acknowledge the support for post-CMOS wet etching and laser Doppler vibrometer measurements provided by Key Laboratory of MEMS of Ministry of Education of China in Southeast University.

References

[1] X. L. Feng, R. R. He, P. D. Yang, M. L. Roukes, Very high frequency silicon nanowire electromechanical resonators, Nano Lett. 7 (2007), 1953-1959.
[2] X. Li, T. Ono, Y. Wang, M. Esashi, Ultrathin single-crystalline-silicon cantilever resonators: fabrication technology and significant specimen size effect on Young's modulus, Appl. Phys. Lett. 83 (2003) 3081.
[3] H. Sadeghian, C.K. Yang, J.F.L. Goosen, A. Bossche, U. Staufer, P.J. French, F. Van Keulen, Effects of size and defects on the elasticity of silicon nanocantilevers, J. Micromech. Microeng. 20 (2010) 064012.
[4] B. Lee, R.E. Rudd, First-principles study of the Young's modulus of Si<100> nanowires, Phys. Rev. B, 75(2007) 041305(R).
[5] S. H. Park, J. S. Kim, J. H. Park, J. S. Lee, Y. K. Choi, O. M. Kwon, Molecular dynamics study on size-dependent elastic properties of silicon nanocantilevers, Thin Solid Films, 492 (2005) 285-289.
[6] J. H. Zhang, M. Li, F. Gu, Q.Q. Liu, Influences of surface effects and large deformation on the resonant properties of ultrathin silicon nanocantilevers, Chin. Phys. B, 21 (2012) 016203.
[7] S. Guillon, D. Saya, L. Mazenq, S. Perisanu, P. Vincent, A. Lazarus, O. Thomas, L. Nicu, Effect of non-ideal clamping shape on the resonance frequencies of silicon nanocantilevers, Nanotechnology, 22 (2011), 245501.
[8] J.H. Zhang, X.L. Mao, Q.Q. Liu, F. Gu, M. Li, H. Liu, Y.X. Ge, Mechanical properties of silicon nanobeams with an undercut evaluated by combining the dynamic resonance test and finite element analysis, Chin. Phys. B, 21 (2012) 086101.
[9] B. Ilic, S. Krylov, H.G. Craighead,Young's modulus and density measurements of thin atomic layer deposited films using resonant nanomechanics, J. Appl. Phys.108 (2010) 044317.
[10]K.B. Gavan, E.W.J.M. van der Drift, W.J. Venstra, M.R. Zuiddam, H.S.J. van der Zant, Effect of undercut on the resonant behaviour of silicon nitride cantilevers, J. Micromech.Microeng. 19 (2009) 035003.

Key Engineering Materials Vols 645-646 (2015) pp 1078-1084
Submitted: 2014-11-02
Accepted: 2014-12-23
© (2015) Trans Tech Publications, Switzerland
doi:10.4028/www.scientific.net/KEM.645-646.1078

Implementation of convolutional encoder in Quantum-dot Cellular Automata

Mingliang Zhang*, Li Cai, Xiaokuo Yang, Huanqing Cui and Zhichun Wang

College of Science, Air Force Engineering University, Xi'an 710051, China

zml0818@gmail.com

Keywords: Quantum-dot cellular automata, Convolutional encoder, Majority-based convolutional encoder

Abstract: As a nanoelectronic system, Quantum-dot cellular automata (QCA) is very likely to present high defect and fault rates. Therefore making QCA bits distortion-free is a necessary work. In this paper, we present the QCA based rate-1/2 and memory length-2 convolutional encoders that can generate one kind of error correcting codes from the perspective of information redundancy. Three schemes of layouts are presented and compared, and the majority-based type has the compactest layout and lowest latency. Our simulation results demonstrate that these encoders can all functionally work.

1 Introduction

Quantum-dot cellular automata is a promising nanoscale computing paradigm, in which edge-driven computation can be performed with an array of two-state cells [1-4]. Due to the probabilistic nature of interactions on nanometer scales, the reliability of QCA based circuits may be low. In order to make QCA bits distortion-less, fault-tolerance has been an important and active area of QCA research [5-7]. At present, Some researchers use hardware redundancy technique to improve the robustness of the circuits [8,9]. Their proposed structures commonly consist of the replicated components working in parallel, so that a correct result can be extracted via majority voting despite faults in the underlying hardware. An attendant deficiency is that this technique consumes large layout zone and much energy. In a different way, information redundancy technique creates additional information to the original data to accomplish tolerance. Error correcting codes (ECC) are the usual form to represent redundant information, which are widely used in communications and memory [10]. The use of ECC in QCA can lead to a scheme in which computation takes place in the encoded space, whereby errors are corrected locally. We only need make encoding and decoding at the beginning and the end of the computation, respectively. Thus, implementing the QCA based encoders and decoders of ECC is an interesting and important work.

To our knowledge, few works about this have been reported. Literature [11] proposed a Hamming encoder using QCA basic logic gates. However,the idea that they directly translated existing CMOS design into QCA layout may cause the encoder lowly efficient. Because lots of cascade XOR-gates made it consume large layout and high latency. Literature [12] presented the check node processing element of Low Density Parity Check decoder, and simulated the design by the QCA model written using VHDL language. It can be viewed as an idealistic model because using VHDL language to describe the behavior of QCA basic logic gates has weaken the physical mechanics behind the model.

In this paper, we propose the QCA based convolutional encoders. As a paradigm, we study how to design the rate-1/2 and memory length-2 convolutional encoder (denoted as ***B***(2,1,2)) using QCA technology, since the ***B***(2,1,2) convolutional encoder is an important element in other convolutional encoders.

2 Background Materials

A quantum cell can be symbolized as a square nanostructure of electron wells confining free electrons [1]. Each cell has four quantum dots which can hold a single electron per dot. The four dots are positioned at the corners of the cell and two mobile electrons are injected into the cell. Due to Coulombic repulsion, the two electrons reside in opposite corners so that two polarizations are possible as seen in Fig. 1(a). The two stable polarizations are defined as binary “1” and “0”, respectively. These basic cells can be used to make QCA-based logic gates,such as inverters and majority gate shown in Fig. 1 [2,4]. The majority gate with the inputs A, B, C has the logic function M(A, B, C) = AB + AC + BC. Two-input logic AND and OR gates can be implemented from the majority gate by setting the third input permanently to a "0" or "1".

In QCA, the circuits are usually partitioned into four adjacent quasi-adiabatically switched regions 0, 1, 2 and 3 using four clock signals shown in Fig. 1(d). Each clock signal is phase shifted by 90° and each clock cycle consists of four phases locking, locked, relaxing, and relaxed [3,4]. The four clock phases display the changes in the tunneling barriers of each cell. The locking state means the tunneling barriers are being raised; the locked state means tunneling is entirely restricted by the presence of high barriers and bistable configuration polarizations are formed at this stage; the relaxing state stands for tunneling barriers are being lowered; and the relaxed state stands for tunneling barriers are held very low and the cells are in “NULL” state. The information unidirectionally flows from Region 0 to Region 3 in pipelined fashion as the arrows indicate.

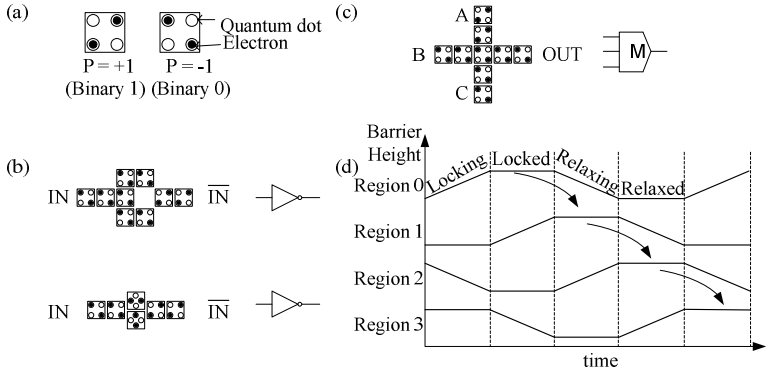


Fig.1. (a) Basic QCA cell and binary encoding, (b) inverters (c) majority gate, and (d) clocking.

3 Convolutional Encoders

Scheme 1: cascade type convolutional encoder A convolutional code is a type of error-correcting code in which each *m*-bit information symbol to be encoded is transformed into an *n*-bit symbol, where *m/n* is the code rate. As a paradigm, we design the ***B***(2,1,2) convolutional encoder for the codes (see Fig. 2(a)), which usually appears in many elementary text on convolutional codes. ***B***(2,1,2) denotes a encoder of which rate is 1/2 and memory length is 2, where ***B*** expresses binary, the former '2' and '1' are the numbers of output and input, respectively, and the latter '2' is the memory length. It consists of two connected delay elements (a shift register) and three modulo-2 adders that equate to three XOR gates. The output of a delay element time *t* is equal

to the input at time t - 1. The time t is integer. Let T be the number of binary symbols that is to be encoded. For the input u_t of the encoder we assume that $u_t \in \{0,1\}$, for $t = 1,2,...,T$. For the outputs b_t^1 and b_t^2 of the encoder we then have that

$$\begin{aligned} b_t^1 &= u_t \oplus u_{t-1} \oplus u_{t-2,} \\ b_t^2 &= u_t \oplus u_{t-2}, \end{aligned} \tag{1}$$

While u_t satisfy $u_0 = 0, u_{-1} = 0$.

In QCA, a wire can play a role of 1-bit shift register, so we can assign corresponding number of clock cycles in each wire according to the number of delay elements. Fig. 2(b) shows the cascade type layout by straightly replacing the delay elements by QCA XOR gates, which has 13/2 clock cycles (CLK).

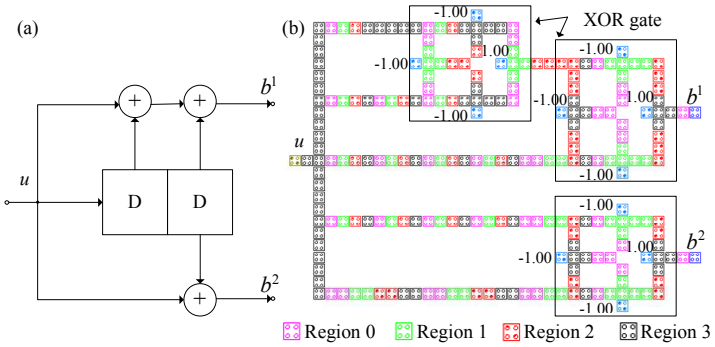


Fig. 2. (a) Block diagram of ***B***(2,1,2) convolutional encoder, and (b) its QCA layout in cascade type.

Scheme 2: parallel type convolutional encoder Obviously, a complex convolutional encoder in cascade type will occupy high latency and large layout. In order to cope with this issue, we can express the logic function of ***B***(2,1,2) convolutional encoder in terms of sum-of -products

$$\begin{aligned} b_t^1 &= u_t u_{t-1} u_{t-2} + \overline{u_t}\,\overline{u_{t-1}} u_{t-2} + u_t \overline{u_{t-1}}\,\overline{u_{t-2}} + \overline{u_t} u_{t-1} \overline{u_{t-2}}, \\ b_t^2 &= \overline{u_t} u_{t-2} + u_t \overline{u_{t-2}}. \end{aligned} \tag{2}$$

Thus, all terms in Eq. 2 can be operated in parallel shown in Fig. 3(a).

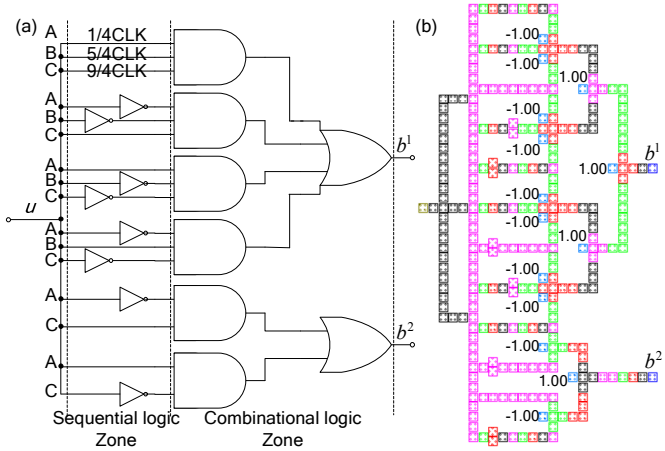


Fig. 3. (a) Logic diagram and (b) layout of the parallel type convolutional encoder.

In Fig. 3(a), there are sequential logic zone (between the leftmost dot line and the middle one) and combinational logic zone (between the middle dot line and the rightmost one). In sequential

logic zone, routines labeled as A, B and C occupy 1/4 CLK, 5/4 CLK and 9/4 CLK, respectively, while all routines in combinational logic zone have the same clock cycles. Besides, these groups of routines labeled A, B and C are cyclo-symmetric, which is helpful to fabricate the layout. The four three-input AND gates shown in Fig. 3(b) [13] can be fabricated end to end. In this way, the layout has 4 CLK.

Scheme 3: Majority-based convolutional encoder Since majority logic is the basic computing in QCA and is more reliable than the three-input AND gates when circuits get larger, we simplify the Eq. 2 with majority reduction [14].

$$b_t^1 = M\left(M\left(\overline{u_t}, u_{t-1}, u_{t-2}\right), M\left(u_t, \overline{u_{t-1}}, u_{t-2}\right), \overline{u_{t-2}}\right),$$
$$b_t^2 = M\left(M\left(\overline{u_t}, u_{t-2}, 0\right), M\left(u_t, \overline{u_{t-2}}, 0\right), 1\right). \tag{3}$$

Figs. 4(a) and (b) are its logic diagram and layout in QCA, respectively. The circuit is also divided into sequential logic zone and combinational logic zone. In the latter, routines labeled as A, B and C have 1/4 CLK, 5/4 CLK and 9/4 CLK, respectively. This design has only six majority gates (AND gate or OR gate is viewed as a majority gate) and four inverter gates, so the layout is more compact and only occupies 7/2 CLK.

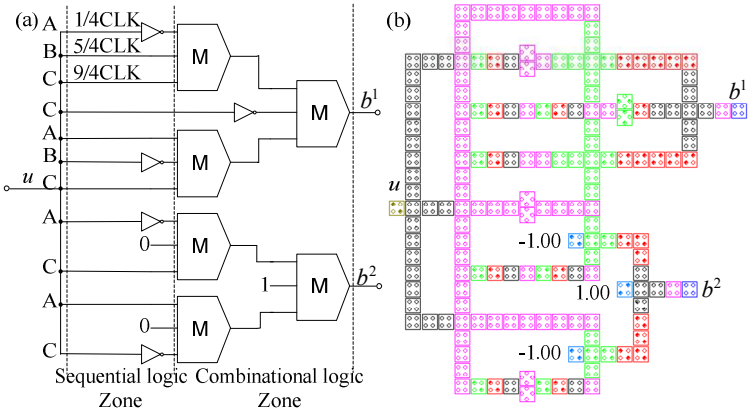


Fig. 4. (a) Logic diagram of majority-based convolutional encoder and (b) its layout in QCA.

Table 1 gives the comparison of the three proposed convolutional encoders on the hands of complexity, area and latency. It is obvious that although cascade type convolutional encoder has the least cells, it has the highest latency. That means it is a low efficient encoder. Parallel type convolutional encoder has the most cells and the largest area, but consumes 5/2 CLK less than the first scheme. Majority-based convolutional encoder consumes almost complexity and area with comparison of the first design, but has the lowest latency which is nearly reduced by 50% than the first design. Besides, Majority-based convolutional encoder has regular clock zones, so it is the optimal scheme among them.

Table 1. Comparison of the three proposed QCA Convolutional encoders

Convolutional encoder	Complexity	Area	Latency
Cascade type convolutional encoder	228 cells	0.34 um^2	13/2 CLK
Parallel type convolutional encoder	378 cells	0.71 um^2	4 CLK
Majority-based convolutional encoder	239 cells	0.34 um^2	7/2 CLK

4 Results

In this paper, we use QCADesigner (version 2.0.3) [15] to check the proposed layouts and their functionalities. The parameters of the layouts and the simulation are all default values in QCADesigner, such as cell size = 18 nm, number of samples = 12800, convergence tolerance =

0.001, radius of effect = 65 nm, and maximum iterations per sample = 100. Fig. 5 shows the simulation results of the third scheme. The other results of the rest schemes are all omitted here for they are similar with these shown in Fig. 5.

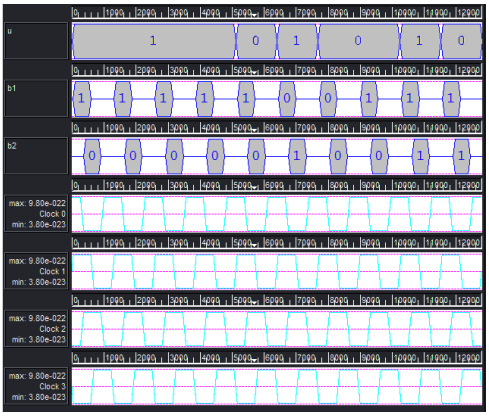


Fig. 5. Simulation results of the majority-based convolutional encoder.

It is worthing to mention that the convolution encoder can normally encode when $t > 2$. In other words, it can't get the following coding words, namely b_1^1, b_1^2, b_2^1 and b_2^2. When $t = 1$, the logic of the rate-1/2 convolutional encoder should be

$$\begin{aligned} b_1^1 &= u_1 \oplus 0 \oplus 0 = u_1, \\ b_1^2 &= u_1 \oplus 0 = u_1. \end{aligned} \tag{4}$$

Similarly when $t = 2$,

$$\begin{aligned} b_2^1 &= u_1 \oplus u_2 \oplus 0 = u_1 \oplus u_2, \\ b_2^2 &= u_2 \oplus 0 = u_2. \end{aligned} \tag{5}$$

However, the four mentioned outputs of the proposed QCA encoder are random outputs, because the initial information bits held in the shift registers are random values. On second thoughts, we let all the shift register in the asynchronous zone hold the first bit of input words. In third design, there are two shift registers in the longest routine of the asynchronous zone. So the first bit of input words should be fed into the encoder three times. In this way, the Eqs. 4 and 5 are substituted into the following equations, respectively:

$$\begin{aligned} b_1^1 &= u_1 \oplus u_1 \oplus u_1 = u_1, \\ b_1^2 &= u_1 \oplus u_1 = 0. \end{aligned} \tag{6}$$

$$\begin{aligned} b_2^1 &= u_1 \oplus u_1 \oplus u_2 = u_2, \\ b_2^2 &= u_1 \oplus u_2. \end{aligned} \tag{7}$$

Obviously, the original output words generated by the Eqs. 4 and 5 can be easily achieved from the Eqs. 6 and 7. There is the comparison of them in Table 2.

Table 2. Comparison of original outputs and existing outputs.

Code words	**Original outputs**		**Existing outputs**	
	$t = 1$	$t = 2$	$t = 1$	$t = 2$
b^1	u_1	$u_1 \oplus u_2$	u_1	u_2
b^2	u_1	u_2	0	$u_1 \oplus u_2$

For example, we intend to encode the information string $u = (1,1,0,1,0,0,1,0,...)$ into the code words in Fig. 5. In the simulation, we feed the leftmost bit 1 into the encoder three times, namely (1,1,1,1,0,1,0,0,1,0). Then the code words are encoded as b^1 = (1,1,0,0,1,1,1,...) and b^2 = (0,0,1,0,0,1,1,...). Further, they can be transformed into the final results b^1 = (1,0,0,0,1,1,1,...) and b^2 = (1,1,1,0,0,1,1,...).

5 Conclusions

In this paper, convolutional encoders implemented in QCA have been studied that can generate a kind of error correct encoding in many communications. Three schemes of ***B***(2,1,2) convolutional encoders are presented and compared on complexity, area and latency of their layouts. Majority-based convolutional encoder is the optimal scheme that much more accords with the QCA characteristics. Majority gate based logic and parallel type makes the layout very compact, regular and easy to be fabricated. In addition, this work can be expanded into other more complex convolutional encoders and even apply to other coding encoders.

Acknowledgment

This work has been supported by the National Natural Science Foundation of China under Grants 61172043 and 61302022, and by the Natural Science Basic Research Plan in Shaanxi Province of China under Grant 2013JQ8010.

References

[1] Craig S. Lent, P. Douglas Tougaw, Wolfgang, and Gary H. Bernstein, Quantum cellular automata, Nanotechnology 4 (1993) 49-57.

[2] P. Douglas Tougaw, Craig S. Lent, Logic devices implemented using quantum cellular automata, J. Appl. Phys. 75 (1994) 1818-1825.

[3] Géza Tóth and Craig S. Lent, Quasiadiabatic switching for metal-island quantum-dot cellular automata, J. Appl. Phys. 85 (1999) 2977-2984.

[4] Douglas Tougaw and Mahfuza Khatun, A scalable signal distribution network for quantum-dot cellular automata, IEEE Trans. Nanotechnol. , 12 (2013) 215-224.

[5] G. A. Anduwan, B. D. Padgett, M. Kuntzman, M. K. Hendrichsen, *et al*, Fault-tolerance and thermal characteristics of quantum-dot cellular automata devices, J. Appl. Phys. 107 (2010) 114306.

[6] M. Khatun, T. Barclay, I Sturzu and P. D. Tougaw, Fault tolerance properties in quantum-dot cellular automata devices, J. Phys. D: Appl. Phys. 39 (2006) 1489-1494.

[7] Xiaojun Ma, Fabrizio Lombardi, Fault Tolerant Schemes for QCA Systems, IEEE Int. Symposium on Defect and Fault Tolerance of VLSI Systems, Boston, MA, 2008, pp. 236-244.

[8] Timothy J. Dysart, Peter M. Kogge, Reliability impact of N-modular redundancy in QCA, IEEE Trans. Nanotechnol. 10 (2011) 1015-1022.

[9] Sanjukta Bhanja, Marco Ottavi, Fabrizio Lombardi, and Salvatore Pontarelli, Novel designs for thermally robust coplanar crossing in QCA, Proc. Conf. on Design, automation and test, Belgium, 2006, pp. 786-791.

[10] Ferdinand Peper, Nanocomputers, Encyclopedia of complexing and systems science, Springer, 2009, pp. 5859-5889.

[11] Mirmansour Ziabari, Ahmad Mohades Kassai, et al, Designing a hamming coder/decoder using QCAs, J. Appl. Sci. 8, (2008) 2569-2576.
[12] Muhammad Awais, Marco Vacca, Mariagrazia Graziano, *et al*, Quantum dot cellular automata check node implementation for LDPC decoders, IEEE Trans. Nanotechnol. 12, (2013) 368-377.
[13] K. Navi, R. Farazkish, S. Sayedsalehi, and M.Rahimi Azghadi, A new quantum-dot cellular automata full-adder, Microelectronics J. 41 (2010) 820-826.
[14] Rumi Zhang, Walus K., Wang Wei, and Jullien G. A., A method of majority logic reduction for quantum cellular automata, IEEE Trans. Nanotechnol. 3, (2004) 443-450.
[15] Konrad Walus, Timothy J. Dysart, Graham A. Jullien, and R. Arief Budiman, QCADesigner: A rapid design and simulation Tool for quantum-dot cellular automata, IEEE Trans. Nanotechnol. 3, (2004) 26-31.

CHAPTER 5:

Optics in the Scale of Micro and Nano

Key Engineering Materials Vols 645-646 (2015) pp 1087-1092
© (2015) Trans Tech Publications, Switzerland
doi:10.4028/www.scientific.net/KEM.645-646.1087

Submitted: 2014-10-31
Accepted: 2014-12-23

Theoretical and experimental studies on microcavity organic light-emitting diodes with different emitters

Cuiyun Peng[1, a], Mengjie Wei[2, b], Rongjuan Huang[2, c], Kunping Guo[2, d], Yuelin Jing[2, e], Tao Xu[2, f] and Bin Wei[2, g, *]

[1] School of Mechanical Engineering and Automation, Shanghai University, 149 Yanchang Road, Shanghai, 200072, P. R. China

[2] Key Laboratory of Advanced Display and System Applications, Ministry of Education, Shanghai University, 149 Yanchang Road, Shanghai, 200072, P. R. China

[a]salience@shu.edu.cn, [b]weimengjie@shu.edu.cn, [c]huangrj822@shu.edu.cn, [d]gkp@shu.edu.cn, [e]jingyuelin@shu.edu.cn, [f]xtld@shu.edu.cn, [g]bwei@shu.edu.cn (corresponding author)

Keywords: microcavity organic light-emitting diodes; distributed Bragg reflector; reflectivity; peak intensity; forward luminance.

Abstract. We have theoretically and experimentally investigated the microcavity organic light-emitting diodes (MOLEDs) that enhanced the emission intensity and narrowed the spectra simultaneously. In this work, MOLEDs with the reflectivities of 70% and 90% have been successfully fabricated. Comparing to non-cavity OLEDs, the maximum forward electroluminescence intensity and the peak luminescence can be improved by 6.8 times and 2.2 times, respectively. The full width at half maximum could be sharply narrowed to 10 nm. The different configurations of MOLEDs with varied emitting layers have also been evaluated which fitted well with the experimental results.

Introduction

In recent years, organic light-emitting diodes (OLEDs) have attracted increasing attention due to their potential advantages in low-power, emissive, flexible, and cost-competitive flat-panel displays [1-3]. Many breakthroughs have led to significant enhancements in the performance of OLEDs, such as the improvement in charge-carrier balance [4,5], the development of low-work function electrode materials [6], the realization of high carrier mobility and high electroluminescence (EL) quantum efficiency in organic light-emitting layers [7], high fluorescence efficiency emitting materials [8-10], and phosphorescence emitting materials [11]. Therefore, the internal quantum efficiency of OLEDs has been optimized gradually close to the theoretical limit [9].

However, its limited external quantum efficiency that arises from the Snell's law; i.e., light generated in a high refractive index layer tends to remain trapped in these materials, still remains to be solved for the practical application [12,13]. Actually, whatever the internal quantum efficiency, the light extraction efficiency of OLEDs constructed is only ca. 20% of the internal efficiency [14,15]. Therefore, much attention has been paid to optical microcavity structures, in which an active layer is placed between top and mirrors to increase light extraction from inner OLED structures [16-21].

Generally, the use of microcavity structures in OLEDs is an effective approach to enhancing extraction efficiency, because a microcavity structure concentrates spontaneous emission photons to be perpendicular to a cavity structure, the emission intensity of a cavity device increases as compared with the non-cavity device [22]. Furthermore, the effect of the reflectivity of the introduced distributed Bragg reflector (DBR) in microcavity OLEDs (MOLEDs) on the opto-electrical characteristics has already been investigated [23].

In this work, a series of studies have been conducted on MOLEDs that can enhance the emission intensity and narrow the spectra simultaneously. The MOLEDs with the reflectivities of 70% and 90% were fabricated for comparison, which was modified by numbers of the pairs of quarter-wave layers (QWL). Employing the two different reflectivities of microcavities, we fabricated devices with different emitters as the light-emitting layer (EML) to investigate the relationship between the

maximum forward EL intensity, the peak luminescence, the full width at half maximum (FWHM) and the reflectivity of the DBR. In addition, the theoretical calculations of the MOLEDs have been simulated by the Mathematica, the theoretical analyses agreed basically with the experimental results.

Experimental

The Design of MOLED. The device structure of the MOLEDs and OLEDs is schematically shown in Fig.1(a). In MOLEDs, a microcavity structure is defined by a metal cathode and a DBR formed on a glass substrate. We used aluminum (Al) layer as the metal cathode and several pairs of SiO_2/TiO_2 QWL as the DBR. To cover the original emission spectra of the emitting materials, the centers of stop band of the dielectric mirrors were designed to be 510 nm. The reflectivities of the dielectric mirrors were estimated to be about 70% and 90% from a classical calculation using the refractive indices. The light generated inside the MOLEDs was emitted through the dielectric mirror and glass substrate.

The theoretical emission spectrum in the forward direction can be calculated by the following equation based on classical optics [24]:

$$E_{cav}(\lambda)^2 = \frac{(1-R_d)[1+R_m+2R_m^{0.5}\cos(\frac{4\pi x}{\lambda})]}{1+R_dR_m-2(R_dR_m)^{0.5}\cos(\frac{4\pi L}{\lambda})} E_n(\lambda)^2, \quad (1)$$

where λ is the emission wavelength, x is the effective distance of the emitting layer from the metal mirror, R_m and R_d are the reflectivities of the metal mirror and dielectric mirror, respectively. L is the total optical length of the microcavity device, and $E_n(\lambda)$ is an original spectrum. The L is expressed, taking into account a substantial penetration depth into the dielectric mirror, by [24]

$$L = \frac{\lambda}{2}(\frac{n_{eff}}{\Delta n}) + \sum_i n_i d_i + \left|\frac{\phi_m}{4\pi}\lambda\right|, \quad (2)$$

where n_{eff} and Δn are the effective refractive index and the index difference between the two layers in the dielectric mirror, n_i and d_i are the refractive index and the thickness of organic layers and indium-tin-oxide (ITO), and Φ_m is the phase change at the metal mirror. Cavity modes are given by the relationship $m\lambda = 2L(\lambda)$, where m is the mode index. The mode index can be adjusted by varying the cavity length $L(\lambda)$.

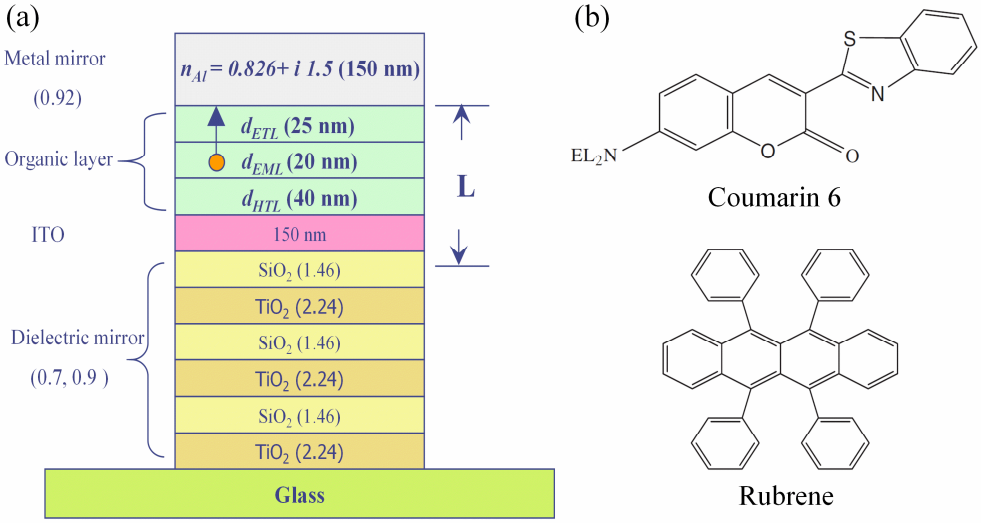


Fig. 1. (a) Configuration of MOLEDs and (b) chemical structures of coumarin 6 and rubrene used as dopant light-emitters.

Devices Fabrication and Measurement. We fabricated a non-cavity device and two kinds of MOLED devices for comparison named Devices A, B and C, and the reflectivities of Devices B and C were 70% and 90% respectively. Firstly, we prepared DBRs consisting of several pairs of SiO_2/TiO_2 and ITO anode on the glass substrates. The DBRs and ITO layers were deposited by electron beam deposition and RF sputtering, respectively. The thicknesses of the SiO_2 and TiO_2 layers were set to be equal to the quarter optical lengths of a center wavelength (510 nm); they were 87.3 nm and 56.9 nm, respectively. The numbers of the SiO_2/TiO_2 pair were 4 and 6 which correspond to Devices B and C. The thickness of the ITO anode was 150 nm for each device. The prepared glass substrate was cleaned with detergent, de-ionized water, acetone, and isopropanol respectively. The substrates were then exposed to a UV-ozone environment for 15 min.

All the devices were fabricated by conventional vacuum deposition, under the pressure lower than 2.0×10^{-4} mbar. Each organic layer consisted of 4,4'-bis[*N*-(1-napthyl)-*N*-phenyl-amino]-biphenyl (α-NPD) as hole transport layer (HTL), tris(8-hydroxyquinoline) aluminum (Alq_3) as electron transport layer (ETL), Alq_3 doped with 0.4-wt % coumarin 6 as EML, lithium fluoride (LiF) as an electron injection layer (EIL), and Al as a cathode. The thicknesses of all layers and molecular structures of the light-emitting materials are shown in Fig. 1. The typical deposition rates of organic material, LiF and Al were 0.6, 0.1 and 5.0 Å/s, respectively. The active area was 2×2 mm^2. The EL spectra were measured, in the forward direction, with a source measure unit (HP4140B, Hewlett-Packard) and a luminance color meter (BM-7, TOPCON). The color meter was placed normal to the test device to measure the front luminance at a solid angle of 1°.

Moreover, we employed different emitters as the EML to simulate the relationship between the parameters and the reflectivity of the DBR, including Alq_3, Alq_3 doped with 0.4-wt % coumarin 6 and Alq_3 doped with 0.4-wt % 5,6,11,12-tetraphenylnaphthacene (rubrene). The configuration of the MOLED is glass/dielectric mirror/ITO/HTL (x nm)/EML (y nm)/ETL (z nm)/LiF (0.3 nm)/Al (300 nm).

Results and Discussion

Visible light emission from the resultant MOLEDs and the reference device were observed at an applied voltage from 0 to 8 V. A remarkable feature in the EL characteristics of these devices was the narrowing of emission spectrum, as shown in Fig. 2(a). These spectra of MOLEDs showed a distinct narrowing comparing to the non-cavity device, especially for Device C. The inset reveals the specific values of the FWHM for three devices, the non-cavity OLED exhibits broad emission spectrum with a half width of 68 nm, whereas the MOLEDs exhibit rather narrow spectra centered at the resonance wavelength (510 nm), the half widths of Devices B and C are 22 nm and 10 nm, respectively.

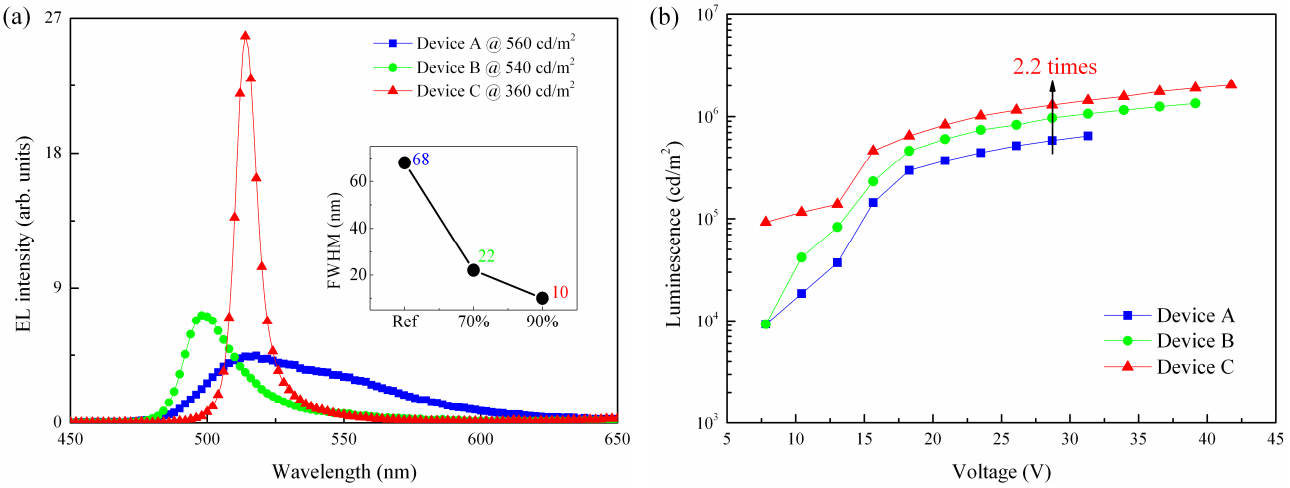


Fig. 2. (a) EL spectra for the Devices A, B and C at the same current density. The inset shows the FWHM of the three devices; (b) the luminescence-voltage (*L*-*V*) characteristics of the three devices.

On the other hand, the enhancement of the emission intensity at the peak wavelength was clearly observed in each MOLED. Here, the enhancement ratio was defined as the emission intensity in the forward direction at the peak wavelength normalized to the emission intensity of the noncavity OLED at the same wavelength [25]. The measured enhancement ratios were 1.6 and 5.8 for Devices B and C.

Comparing the two MOLEDs, the peak of Device C is closer to the resonance wavelength and has a narrower spectrum, that is, Device C has a better performance. The main reason for the phenomenon can be explained as follows: The reflectivity at the center wavelength increases with increasing number of SiO_2/TiO_2 pairs, the DBRs with high reflectivity have a sufficiently broad stop band to confine the entire EL emission except for the cavity resonance wavelength [23].

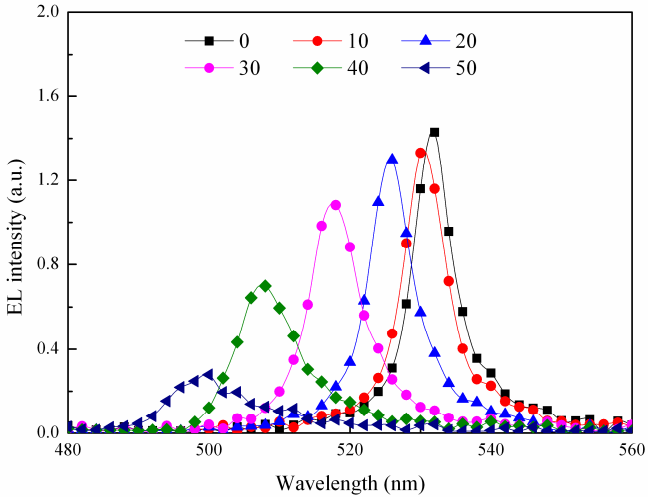


Fig. 3. EL emission spectra measured at different angles for Device B.

Table 1. Theoretical calculations of enhanced intensity for the MOLEDs with Alq_3, coumarin 6 in Alq_3 and rubrene in Alq_3 as EML

Device /Mirror	Device Configuration [nm]			Peak Wavelength [nm]	FWHM [nm]	Forward Intensity Enhancement	Luminance enhancement
70%	50[a]	20[b]	30[c]	520(-10[d])	34	4.1	2.65
	65	20	15	520(-10)	34	4.5	2.79
90%	50	20	30	535(+5)	19	6.0	2.27
	65	20	15	520(-10)	19	6.5	2.38
70%	40	20	30	500(-10)	40	3.0	1.95
	55	20	15	500(-10)	40	3.0	2.05
90%	40	20	30	510(+0)	10	6.3	2.07
	55	20	15	510(+0)	10	6.8	2.18
70%	50	20	45	553(-12)	36	2.8	1.95
	65	20	30	555(-10)	36	3.1	2.10
90%	50	20	45	565(+0)	14	6.1	2.12
	65	20	30	570(+5)	14	6.5	2.28

Captions: a, b and c represent the thicknesses of HTL, EML and ETL, respectively, d represent the deviations of peak wavelength between MOLEDs and the non-cavity device, '+' and '-' represent the red and blue shift respectively.

Additionally, brightness expressed as luminance is significantly important for the practical applications. The *L-V* characteristics of the three devices are shown in Fig. 2(b). The luminance values of these MOLEDs have increased substantially compared to the Device A. As for Device C, it is about 2.2 times larger than the reference device at the same voltage in average.

We also measured the angular dependence of EL spectra from the MOLEDs. Figure 3 shows the EL spectra of Device B with 4-SiO_2/TiO_2-pair DBR, the resonance wavelengths as the angle against normal to the device increases, and peak intensity decreases gradually.

To further investigate the characteristics of different MOLEDs, the parameters for varied configurations with different EMLs of MOLEDs have been calculated by the Mathematica. Table 1 has summarized the calculated peak wavelength, FWHM, peak intensity enhancement and luminance enhancement for the different Alq_3-based MOLEDs. The emission spectra simulated by the software for an optimized MOLED fitted well with the experimental results. From the table we have summed up several conclusions of the simulation.

Firstly, the configurations of the MOLEDs have little impact on the results of simulation in the circumstance where the DBRs for the MOLEDs have the same reflectivity. Secondly, after the holistic comparison of the results, we have found that the devices with a DBR whose reflectivity is 90% have better performance, either on the narrowing the spectrum or enhancing the forward EL intensity and luminance. These phenomena coincide with the experimental results, and the reason is that the higher reflectivity can make the spectrum narrower. Finally, the device with the best performance exhibits about 6.8 times and 2.2 times of the non-cavity OLED in the aspect of forward EL intensity and the peak luminescence. Besides, these conclusions are instructive on the design of DBRs and the configurations of MOLEDs in the future research.

Summary

We have studied the enhancement of the emission intensity and narrowing of the spectra in the OLEDs simultaneously using a microcavity structure. The MOLEDs with reflectivities of 70% and 90% have been successfully fabricated. The results have shown that the spectra and the intensity were strongly modified. Comparing two types of MOLEDs, the one with reflectivity of 90% had better performance, its forward EL intensity has been improved about 5.8 times greater than the reference device and the FWHM can be narrowed as sharply as 10 nm. From a practical point of view, satisfying both the strong directionality and the intensity enhancement is significantly attractive for application to the light sources such as backlights. Moreover, the theoretical calculations for the emission spectra fitted well with the experimental results. On the basis of the results, the MOLEDs employing different DBRs and emitters have also been simulated, the maximum forward EL intensity and the peak luminescence improved about 6.8 times and 2.2 times, respectively. It further proved that the Alq_3-based MOLEDs with reflectivity of 90% performing better.

Acknowledgements

This work was supported by the National Natural Science Foundation of China (61136003, 61275041) and the Project of Science and Technology Commission of Shanghai Municipality, China (Grant No. 14XD1401800).

References

[1] B. Richter, U. Vogel, R. Herold, K. Fehse, S. Brenner, L. Kroker, J. Baumgarten, Bidirectional OLED microdisplay: combining display and image sensor functionality into a monolithic CMOS chip, Solid-State Circuits Conference Digest of Technical Papers (ISSCC), 2011 IEEE International, IEEE2011, pp. 314-316.

[2] O. Prache, Active matrix molecular OLED microdisplays, Displays. 22 (2001) 49-56.

[3] R. Martins, V. Shaoulov, Y. Ha, J. Rolland, A mobile head-worn projection display, Opt. Express. 15 (2007) 14530-14538.

[4] J. Kido, T. Matsumoto, Bright organic electroluminescent devices having a metal-doped electron-injecting layer, Appl. Phys. Lett. 73 (1998) 2866-2868.
[5] L. Hung, C. Tang, M. Mason, Enhanced electron injection in organic electroluminescence devices using an Al/LiF electrode, Appl. Phys. Lett. 70 (1997) 152-154.
[6] I.D. Parker, Carrier tunneling and device characteristics in polymer light‐emitting diodes, J. Appl. Phys. 75 (1994) 1656-1666.
[7] L. Hung, C. Chen, Recent progress of molecular organic electroluminescent materials and devices, Mater. Sci. Eng., R. 39 (2002) 143-222.
[8] C. Tang, S. VanSlyke, C. Chen, Electroluminescence of doped organic thin films, J. Appl. Phys. 65 (1989) 3610-3616.
[9] C. Adachi, M.A. Baldo, M.E. Thompson, S.R. Forrest, Nearly 100% internal phosphorescence efficiency in an organic light-emitting device, J. Appl. Phys. 90 (2001) 5048-5051.
[10] Y. Cao, I.D. Parker, G. Yu, C. Zhang, A.J. Heeger, Improved quantum efficiency for electroluminescence in semiconducting polymers, Nature. 397 (1999) 414-417.
[11] M. Baldo, S. Lamansky, P. Burrows, M. Thompson, S. Forrest, Very high-efficiency green organic light-emitting devices based on electrophosphorescence, Appl. Phys. Lett. 75 (1999) 4-6.
[12] H. Benisty, H. De Neve, C. Weisbuch, Impact of planar microcavity effects on light extraction-Part I: Basic concepts and analytical trends, IEEE J. Quantum Elect. 34 (1998) 1612-1631.
[13] H. Benisty, H.D. Neve, C. Weisbuch, Semiconductor Devices-Impact of Planar Microcavity Effects on Light Extraction--Part II: Selected Exact Simulations and the Role of Photon Recycling, IEEE J. Quantum Elect. 34 (1998) 1632-1643.
[14] T. Miteva, A. Meisel, W. Knoll, H.G. Nothofer, U. Scherf, D. Müller, K. Meerholz, A. Yasuda, D. Neher, Improving the Performance of Polyfluorene‐Based Organic Light‐Emitting Diodes via End‐capping, Adv. Mater. 13 (2001) 565-570.
[15] T. Tsutsui, M. Yahiro, H. Yokogawa, K. Kawano, M. Yokoyama, Doubling Coupling‐Out Efficiency in Organic Light‐Emitting Devices Using a Thin Silica Aerogel Layer, Adv. Mater. 13 (2001) 1149-1152.
[16] S. Dirr, S. Wiese, H.H. Johannes, W. Kowalsky, Organic Electro‐and Photoluminescent Microcavity Devices, Adv. Mater. 10 (1998) 167-171.
[17] S. Han, C. Huang, Z.-H. Lu, Color tunable metal-cavity organic light-emitting diodes with fullerene layer, J. Appl. Phys. 97 (2005) 093102.
[18] C.-L. Lin, H.-W. Lin, C.-C. Wu, Examining microcavity organic light-emitting devices having two metal mirrors, Appl. Phys. Lett. 87 (2005) 021101.
[19] A. Dodabalapur, L.J. Rothberg, T.M. Miller, E.W. Kwock, Microcavity effects in organic semiconductors, Appl. Phys. Lett. 64 (1994) 2486-2488.
[20] A. Dodabalapur, L.J. Rothberg, R.H. Jordan, T.M. Miller, R.E. Slusher, J.M. Phillips, Physics and applications of organic microcavity light emitting diodes, J. Appl. Phys. 80 (1996) 6954-6964.
[21] T. Tsutsui, N. Takada, S. Saito, E. Ogino, Sharply directed emission in organic electroluminescent diodes with an optical‐microcavity structure, Appl. Phys. Lett. 65 (1994) 1868-1870.
[22] K. Neyts, Microcavity effects and the outcoupling of light in displays and lighting applications based on thin emitting films, Appl. Surf. Sci. 244 (2005) 517-523.
[23] T. Fukuda, B. Wei, M. Ohashi, M. Ichikawa, Y. Taniguchi, High Coupling Efficiency of Microcavity Organic Light-Emitting Diode with Optical Fiber for as Light Source for Optical Interconnects, Jpn. J. Appl. Phys. 46 (2007) 642-646.
[24] D. Deppe, C. Lei, C. Lin, D. Huffaker, Spontaneous emission from planar microstructures, J. Mod. Optics. 41 (1994) 325-344.
[25] S. Tokito, T. Tsutsui, Y. Taga, Microcavity organic light-emitting diodes for strongly directed pure red, green, and blue emissions, J. Appl. Phys. 86 (1999) 2407.

Key Engineering Materials Vols 645-646 (2015) pp 1093-1098
© (2015) Trans Tech Publications, Switzerland
doi:10.4028/www.scientific.net/KEM.645-646.1093
Submitted: 2014-11-26
Accepted: 2014-12-23

A Method to Fabricate Thin Micro Silicon Cantilever based on Optical lithography with AZ 1518

Chenzhi TANG[1, a *]

[1]Institute of Chemical Materials, CAEP, Mianyang, Sichuan, 621900, CHINA. P. R.C

[a]czt558@uowmail.edu.au

Keywords: Photo lithography; silicon cantilever; AFM

Abstract: AZ 1518 is a standard thin positive photoresist in AZ1500series which has been widely used in photolithography process, beside this, as a perfect semiconductor material, micro sized silicon cantilevers have been widely used in micro electromechanical systems (MEMS). In This paper, we have presented the process of fabricate micro silicon cantilever, including the selection of the photoresist, developer and substrate, optical lithography method and PLD method. After these, AFM is used to study the cantilever pattern and the angle of inclined planes. The research results show the exposure time and experimental environment can significantly influent the quality of cantilever pattern.

1. Introduction

As a perfect semiconductor material, micro sized silicon cantilevers have been widely used in micro electromechanical systems (MEMS) because of their simplicity and ability to function in small sizes as sensors and actuators. Beside this, AZ 1518 is a standard thin positive photoresist in AZ 1500 series which has been widely used in photolithography process. For micro cantilever fabrication, usually the cantilevers were fabricated from(100)silicon-on-insulator wafers. For thinner cantilevers, the sample wafer was thermally oxidized and etched in HF to reduce the device layer thickness. For thicker cantilevers, single crystalline silicon was grown on the sample wafers by epitaxy [1]. With the development of photolithography technology, many micro and nano-sized patterns can be obtained by this method.

In this paper, we study the process of fabricate micro silicon cantilever by optical lithography method. The paper is organized as follows: the first part describes the fabrication method and preparation process, the second part is the fabrication process, the third part analyzed the quality of pattern based on AFM research. Finally, conclusions and future work on the lithography fabrication are presented.

2. Fabrication Method and Preparations

2.1 Fabrication Method of micro silicon cantilever

The thin micro silicon cantilever includes two parts, namely pedestal and flat. Pedestal like the cantilever holder of an atomic force microscopy and flat is the top layer of pedestal with a silicon cantilever at the top of flat. Because the thickness of silicon cantilever is in the range of micrometer, (1.5μm×15μm×150μm), we propose a method to bond the silicon beam on a silicon pedestal, the procedures has been shows in Figure 1.

Firstly, we need to fabricate the silicon pedestal, Secondly, a very thin silicon film is fabricated with the same length and width with pedestal, but the thickness is as same as silicon cantilever, which is at the top of flat. Finally, bonding the flat with the pedestal to obtain the silicon cantilever with pedestal. Thus, we divide the fabrication process into nine steps, which has been shown as Table 1.

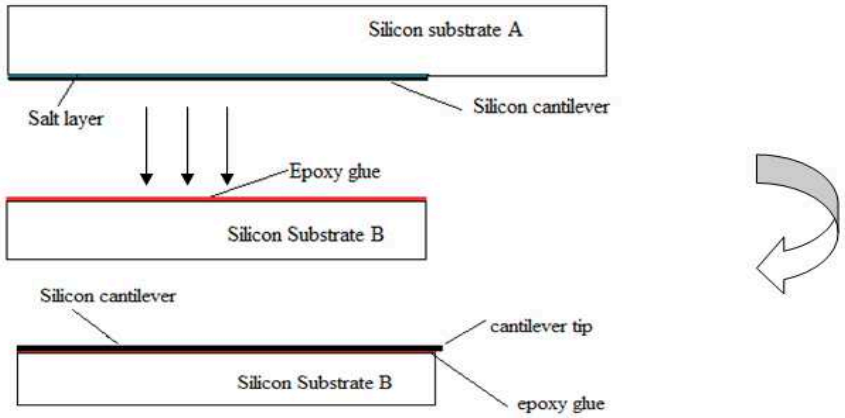


Figure. 1 The process of transferring a micro cantilever to a silicon substrate

Table 1 The process of fabrication micro cantilever by photolithography process,

Step No.	Process
1	Spin photoresist on the substrate
2	Pre-bake (SB).
3	Set the opportune light source at a proper distance to the mask and substrate assembly to expose the photoresist.
4	Post exposure bake (PEB).
5	Remove residual photoresist by developer.
6	Post bake.
7	Pulse laser deposition process.
8	Dissolve the sacrificial layer together with the target material on its surface to obtain silicon flat with cantilever.
9	Bond silicon pedestal with silicon flat use epoxy.

2.2 Preparation of micro silicon cantilever

The photoresist thickness must be greater than the thickness of the final silicon layer because a positive photoresist is used as a sacrificial layer. There must be a discontinuity in the silicon layer to allow the acetone to dissolve the photoresist during the lift-off step [2]. Usually that the ratio between the photoresist thickness and the deposited layer is approximately 1:3 to 1:5 [3-5]. The thickness of the top silicon layer is determined to be the same as the silicon cantilever's. The type of photoresist is AZ 1518, which is a standard thin positive photoresist in AZ1500 series. The spin speed curve of the photoresist is shown in Figure 2.

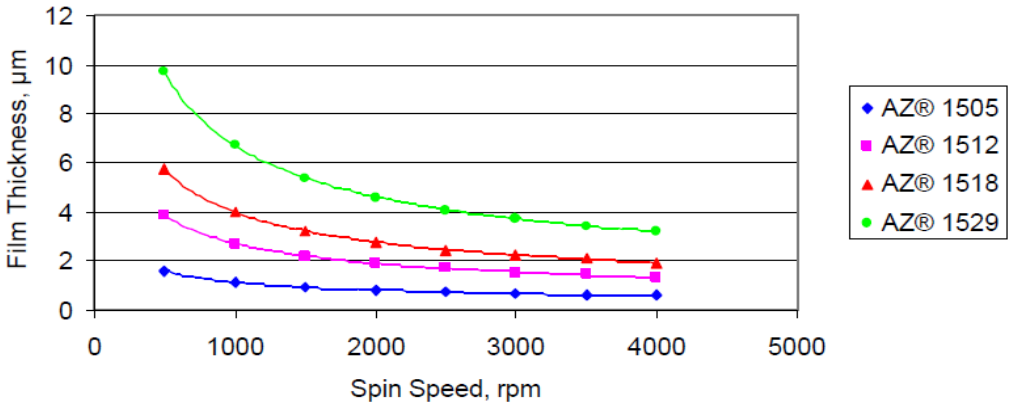
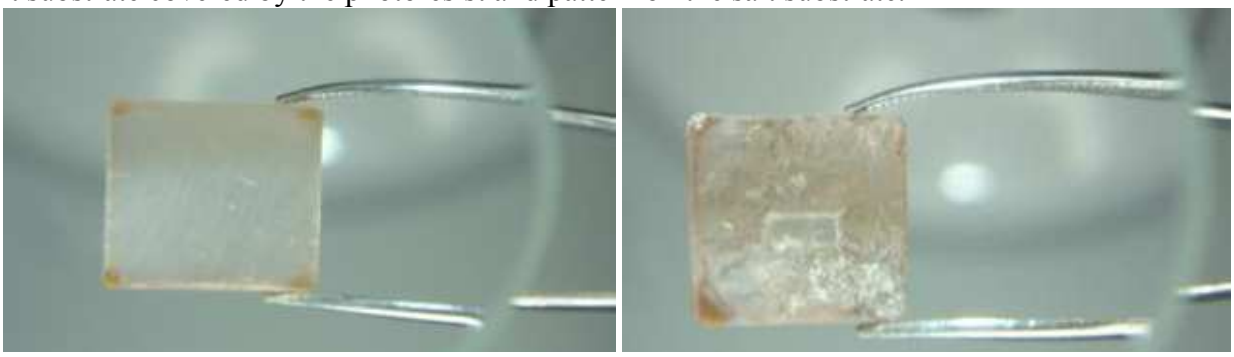


Figure. 2 Spin speed curve for AZ® 1500 Resist Products [6]

In this fabrication process, we need two substrates, substrate A and B. While substrate A is used to fabricate the silicon pedestal, substrate B is used to fabricate silicon flat. At first, a salt substrate was proposed for the substrate B. The reason is that after we use acetone to remove the photoresist and the

target material on its surface, the salt substrate can be easily dissolved in water. Figure 3 shows the salt substrate covered by the photoresist and pattern on the salt substrate.



(A) (B)

Figure. 3 (A) Salt substrate covered with photoresist (B) Pattern on the salt substrate after exposure process.

It can be seen from Figure 3, the salt substrate can be dissolved by the developer. This strongly affects the dimensional accuracy of the pattern. Therefore, the salt substrate is not suitable for this project. This follows that we chose a silicon substrate.

2.3 light source

We define NA is the numerical aperture of the lens as seen from the wafer, which can be defined as:

$$NA = \mathrm{n}\sin\theta \tag{1}$$

where n is index of refraction. n=1 for air. θ is the half-angle of the maximum cone of light that can enter or exit the lens, which can be shown in Figure 4. In our study, θ=15.6.With reference to Eq. 1, we can obtain NA=0.268.

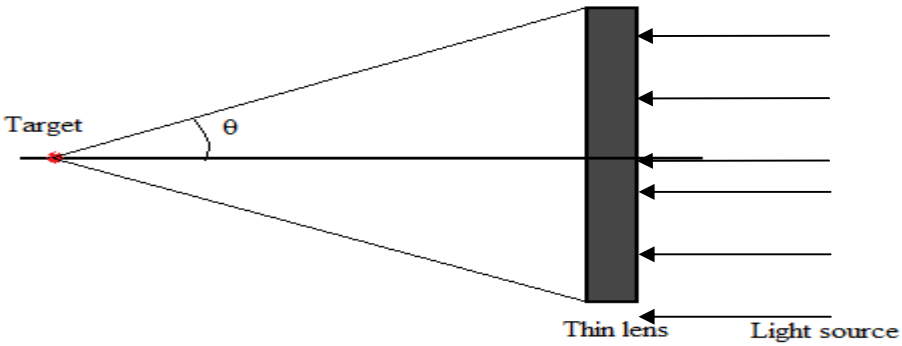


Figure. 4 Numerical aperture of a thin lens

The ability to project a clear image of a small feature onto the wafer is limited by the wavelength of the light and the ability of the reduction lens system to capture enough diffraction orders from the illuminated mask. The minimum feature size is called critical dimensions (CD) that a projection system can print is given approximately by a Rayleigh relation [7]:

$$CD = k_1 \times \frac{\lambda}{NA} \tag{2}$$

And the depth of focus can be expressed as[7]:

$$D_F = k_2 \times \frac{\lambda}{NA^2} \tag{3}$$

where k_1 and k_2 are process-related coefficients, λ is wavelength. k_1 equals 0.4 for production. Based on Eq. 2, we can obtain:

$$CD = k_1 \times \frac{\lambda}{NA} = 651nm \tag{4}$$

We assume $k_2 = 1$, With reference to Eq. 3, we can obtain:

$$D_F = k_2 \times \frac{\lambda}{NA^2} = 7.895\mu m \quad (5)$$

The minimum feature size is about 651nm, it means when the dimension is smaller than 651nm, this projector can not give us a satisfactory results. Beside this, when the Spin speed is smaller than 1000rmp, the photoresist can not form a smooth surface.

3. Fabrication of micro silicon cantilever

We use a projector as the light source, the type of the projector is MT-1030, NEC Company, Japan, which is shown in Figure 5 (A). The wavelength of light, λ=436nm.

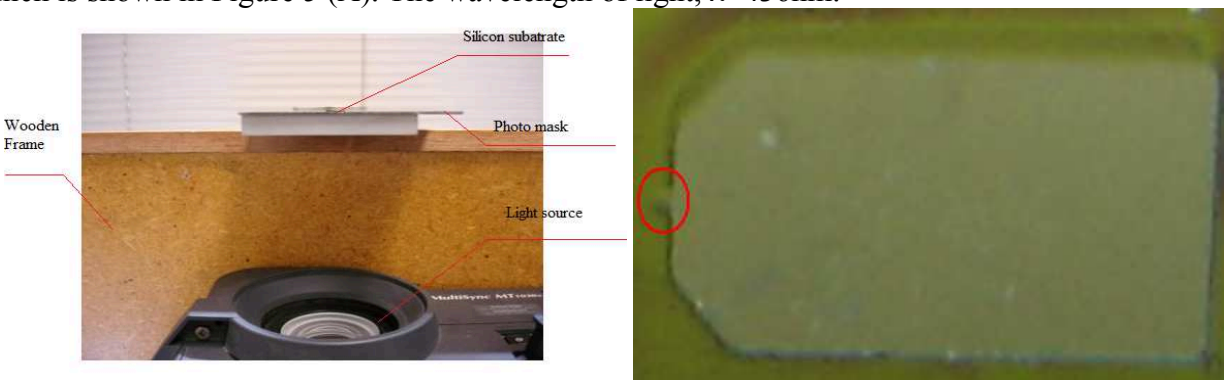


Figure. 5 (A) Exposure system (B) Cantilever Pattern(Red circle)

After exposure, a post exposure bake (PEB) is applied to reduce the standing waves which are produced when a coherent monochromatic light reflected back from a substrate interference with the incident light [8]. Then the substrate is immersed in a developer for 90sec. and is moved into water to wash the residual photoresist. Finally, the pattern is showed as Figure 4(B). The substrate is baked on hot plate at 115°C for 50 sec. The technical specifications of the PLD used in this study are depicted in Figure 6 and Table 2.

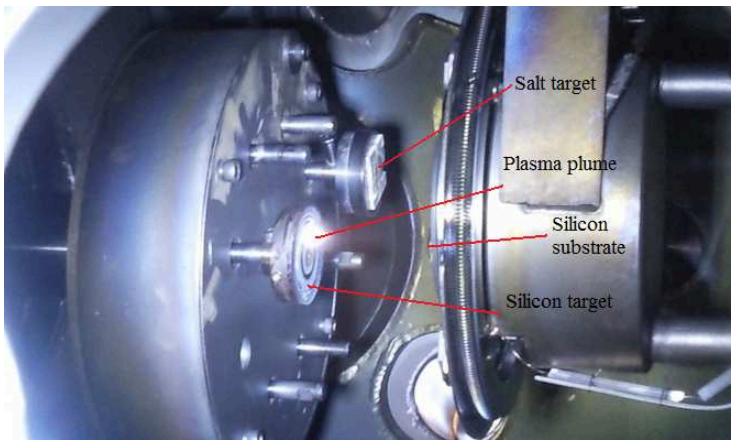


Figure. 6 PLD system and its components

Table 2 Technical specifications of the PLD system

Specifications	Parameter
Laser wavelength	248 nm, KrF excimer laser
Energy	500mJ/pulse
Frequency	10Hz
Target to substrate distance	50mm
target	Silicon single crystal, >99.9% pure
Atmosphere	1x10^-5 Torr vacuum
Deposition time	NaCl: 20 sec, Si: 15 min

After the PLD process, at first acetone is used to remove the residual photoresist and silicon, the silicon flat is finally bonded onto a silicon pedestal with epoxy glue and the salt substrate is dissolved

using water. Then heating at 150 ◦C for 30 min in an oven, the glue layer becomes very thin with no detrimental effect on the bonding process. We can obtain silicon cantilever with pedestal.

4. Analysis of results and discussion

An atomic force microscopy is used to obtain the image of the cantilever pattern on the silicon substrate. Which are shown as Figures 7-8.

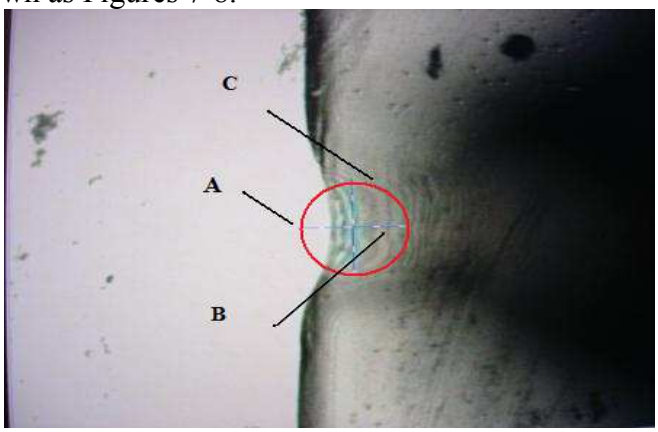


Figure. 7 Cantilever pattern after exposure

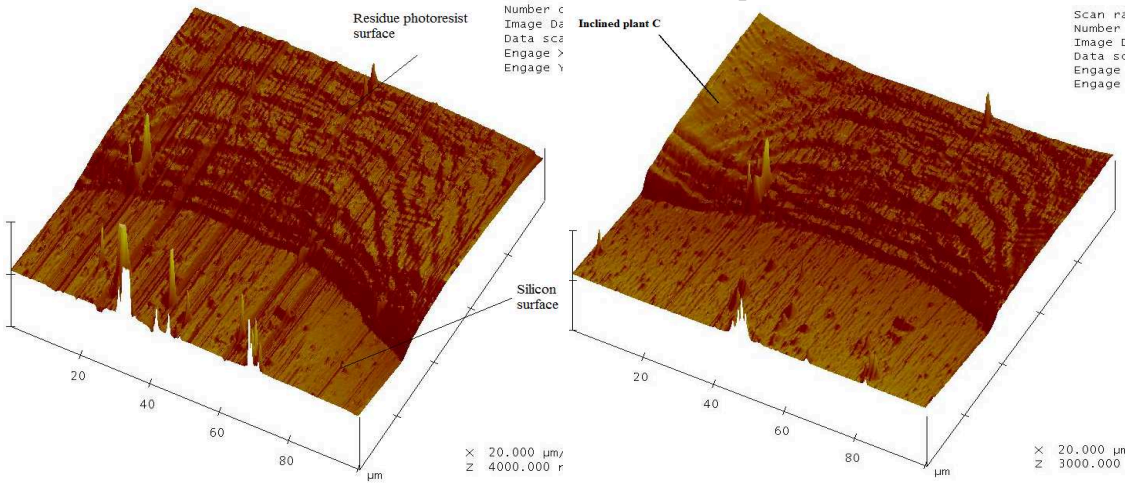
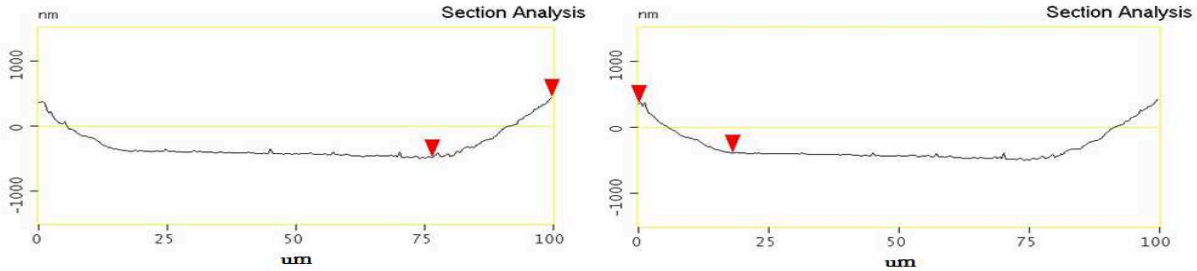


Figure. 8 Cantilever pattern image under the AFM

In the Figure 7, plane B follows the length direction of cantilever, another is the plane C, which is connected with plane B. As shown in Figures 7-8, after lithography process, the cantilever pattern can not form completely, with the distance between photoresist and cantilever flat increase, the thickness of photoresist will increase, finally, it will form two inclined planes.

Besides this, with reference to AFM, while the angle formed by plane B is very small, only 0.359°, the angles formed by plant C are 2.284° (right side) and 2.343° (left side), which are shown as Figure 9.



(A) The section of the inclined plane C (Left side), (B) The section of inclined plane C (Right side).

Figure. 9 The section of the inclined planes

The experimental environment can significantly influent the quality of cantilever pattern. In this study , we just use the projector to propose light source, the wavelength of light can't be measured correctly. Besides this, the humidity, temperature and light from other source also can influence the cantilever pattern.

5. Conclusions

This paper has done some research of the AZ 1518 positive photoresist, and proposes a new method, namely use salt as sacrificial layer to fabricate thin micro cantilever. The process of fabricate micro silicon cantilever, including the selection of the photoresist, developer and substrate, optical lithography method and PLD method, AFM also used to analyzed the cantilever pattern. The research results shown experimental environment and light source can significantly influent the quality of pattern. In the future, this work should be done in a dark room with a light source. This research results can be used in micro and nano-sized derives fabrication and simulation.

6. Acknowledgments

The authors thank Prof. Gursel Alici from the University of Wollongong for sharing his expertise on micro- and Nano cantilever fabrication. This work was supported by an ARC Discovery Project (DP0878931) and an ARC LIEF grant (LE0989804).

References

[1] Benjamin Y. Park, Rabih Zaouk, and Marc J. Madou, "Fabrication of Microelectrodes Using the Lift-Off Technique", Methods in Molecular Biology, vol. 321, (2006), p: 23-26.

[2] H.S. Lee and J.B. Yoon, "A simple and effective lift-off with positive photoresist", Journal of Micro machine and Micro engineering, Vol.15, (2005) p: 2136–2140.

[3] L.L. Sohna, R.L. Willett, "Fabrication of nanostructures using atomic-force-microscope-based lithography", Applied of Physics, Vol. 67, No.11, (1995), 123-126.

[4] J. Jahns and S.J. Walker, "Two-dimensional array of diffractive microlenses fabricated by thin film deposition", Journal of Applied Optics, Vol. 29, No. 7, p: 931-936.

[5] M. Veinguer, A. Feigel, B. Sfez, M. Klebanov, and V. Lyubin, "New application of inorganic chalcogenide photoresists in lift-off photolithography", Journal of Optoelectronics and Advanced Materials, Vol. 5, No. 5, (2003), p: 1361-1364.

[6] J. Golden, H. Miller, D. Nawrocki, and J. Ross, "Optimization of Bi-layer Lift-Off Resist Process", Micro Chemical Corp., 90 Oak St., Newton, MA. 02464, (617) p: 965-5511.

[7] information on www.az-em.com/PDFs/1500/az_1500_photoresist.pdf, access on 10/06/2010.

[8] Jaeger, Richard C. (2002). "Lithography", Introduction to Microelectronic Fabrication, Upper Saddle River: Prentice Hall.

Key Engineering Materials Vols 645-646 (2015) pp 1099-1104
© (2015) Trans Tech Publications, Switzerland
doi:10.4028/www.scientific.net/KEM.645-646.1099

Submitted: 2014-12-19
Accepted: 2014-12-23

Design and Experiment of Phase Laser Ranging System Based on MEMS Mirror for Scanning Detection

Chi Zhang[1,*], Hu Huang[2]

[1]Beijing Institute of Nanoenergy and Nanosystems, Chinese Academy of Sciences, Beijing, China

[2]China Ship Development and Design Center, Wuhan, China

[*]czhang@binn.cas.cn

Keywords: laser ranging, phase-shift method, scanning, space detection

Abstract. A laser ranging system for scanning detection based on phase-shift ranging technology and a MEMS mirror for space detection and measurement is presented in this paper. The laser ranging system is mainly composed of a modulation module, a laser, a MEMS mirror, a photo-electric conversion module and a signal processing module. The phase-shift ranging method is used to measure the relative range to the target. The MEMS mirror is a micro scanner with two DOF, which is used to change the direction of the emitted laser beam. The modulated laser beam is emitted through the MEMS mirror and reflected from the target. The relative range is calculated by the phase shift between the emitted beam and the reflected beam. The experimental results indicate that the measurement accuracy is 0.10 m in static status and 0.17 m in scanning status in the range of 3 m. The differences between the static and the scanning status are analyzed and improvements are proposed.

Introduction

Relative distance between two space objects is an important parameter for space applications. To detect the relative distance to non-cooperative targets such as disabled satellites, space debris and so on, a scanning system which can detect a large region is needed [1, 2]. In this paper, a laser ranging system for scanning detection is presented.

Laser ranging techniques include two main categories: triangulation and time-of-flight (TOF) methods. Triangulation is easy to implement, in which the angle formed by the incident beam and the reflected beam backscattered by the target are measured. But it can only be used in close range measurement and is limited by the shadowing problem [3, 4]. The TOF method measures the round trip time of the laser between the ranging system and the target. It is easier to measure for the farther distance, because of the longer round trip time. So it is suitable for long-distance ranging and this method is selected in this work.

The TOF laser ranging method also includes two categories: the pulse laser ranging method and the sine continuous wave (CW) laser ranging method [5-8]. The time difference between the emitted pulse and the received pulse is measured to calculate the relative range to the target in the pulsed laser ranging method. For the CW laser ranging method, the relative range is calculated by the phase-shift between the emitted beam and the reflected beam. The pulsed laser ranging method is not suitable for laser scanning ranging, for the reason that some scanning detection areas are target areas between the two pulses. Therefore, the CW laser ranging method is adopted in the laser scanning ranging system.

Principle of the CW Ranging Method

A laser beam with intensity modulated is emitted into space and will be reflected when a target is detected. A phase-shift will generate between the emitted beam and the reflected beam. The principle of the CW ranging method is measuring the phase-shift and then calculating the relative range by the equations:

$$D = \frac{\lambda}{2} \cdot \frac{\varphi}{2\pi} = \frac{c}{2f} \cdot \frac{\varphi}{2\pi} \tag{1}$$

where D is the relative range, c is the velocity of light, f is the modulated frequency of the emitted beam and φ is the phase-shift [9].

c is a constant and f is a fixed value after the emitted beam is modulated. D is determined by the value of φ accordingly. Therefore, the measurement of the phase-shift is the key of the laser ranging system.

Compositions of Phase Laser Ranging System

The laser ranging system is mainly composed of a modulation module, a laser, a two-dimensional scanning micro-mirror, a photo-electric conversion module and a signal processing module as shown in Fig. 1.

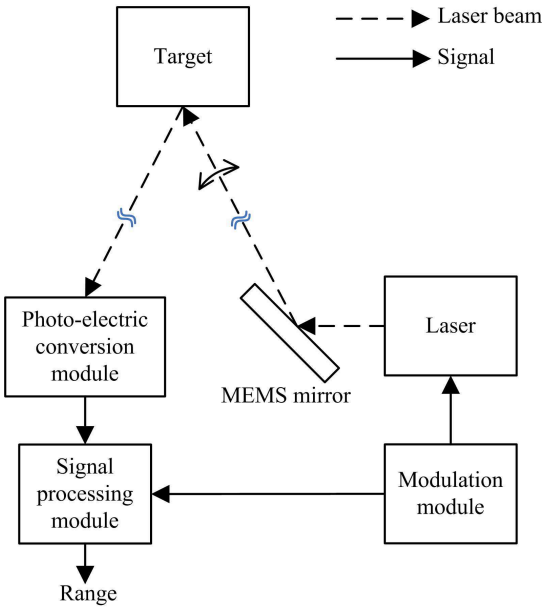


Figure 1. Compositions of Phase Laser Ranging System

The modulation module provides a sine signal with frequency of 2 MHz. The sine signal is sent to the laser and the signal processing module at the same time. The intensity of the laser beam is modulated by the sine signal sent from the modulation module. And another sine signal which is sent to the signal processing module is a reference signal used in the phase-shift detection.

Gas laser, solid, liquid laser and semiconductor laser are commonly used lasers [10-13]. Among them, semiconductor laser has great advantages of small size, low power consumption, long operating life, low price and easy modulation. It is very suitable for micro-satellite. The maximum operating current of the semiconductor laser used in our work is 50mA, the wavelength of the laser is 650nm, the power is 2~5mW, and the size is Φ7mm×20mm.

Compared with common static laser ranging systems, the MEMS mirror is used in the scanning laser ranging system. The MEMS mirror is fabricated by MEMS process technology and has abilities of two-dimensionally and continuously deflection when a voltage is applied [14, 15]. Therefore, it can be used for the direction modulation of the emitted laser beam and space region scanning.

The photo-electric conversion module is used to convert the reflected beam to the electrical signal. Photomultiplier and photodiode are commonly used photo-electric converters. Photomultipliers are usually have bulk mass and should be operated at high voltage. Therefore, they can not be used in micro-system. Photodiodes include avalanche photodiode and PIN photodiode. Compared with avalanche photodiode, PIN photodiode has lower sensitivity without a reverse bias voltage. Therefore, PIN photodiode is used in this work. The sensitivity of the PIN photodiode is 0.55A/W@650nm.

The signal processing module is used to obtain the phase-shift of the reflect signal and the reference signal, and then calculate the relative range. The detail of this module will be introduced in the following part.

Working Principle of the System

The laser beam whose intensity modulated by the modulation module is emitted into space through the MEMS mirror and form a scanning region. When a target is detected, the modulated beam is reflected to the photo-electric receiving module and converted to a sine electrical signal. Then the electrical signal is sent to the signal processing module and the range is calculated, which is shown in Fig.1.

The process of the signal is shown in Fig.2. The signal processing module mainly includes four modules: an amplifier, filter modules, an A/D converter and a MCU. The electrical signal from the photo-electric conversion module is very weak and must be amplified to a suitable voltage. The amplifiers should be high speed, low-noise ones based on a multistage amplifier circuit. The amplified signals include some noises, and filters are absolutely necessary part. For a better filtering effect, the signal should be filtered by a low-pass filter first, and then by a band-pass filter. The filtered signal is sent to an A/D converter and becomes a digital signal. The modulation signal also should be converted to digital signal as a reference signal. Both two digital signals are sent to the MCU. Therefore, the MCU can detect the phase-shift by FFT algorithm and calculate the relative range.

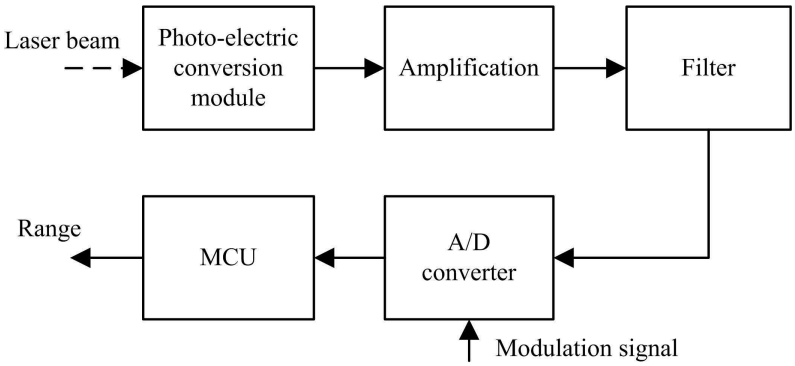
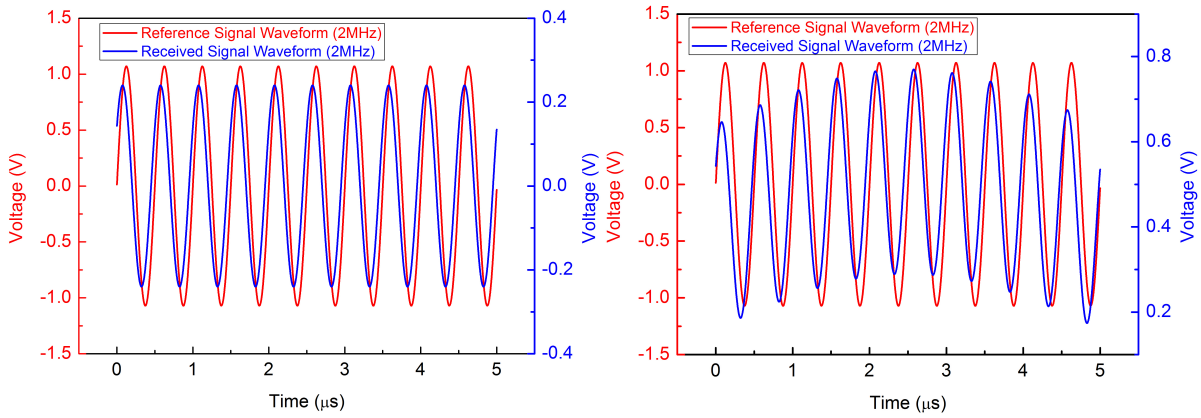


Figure 2. Process of the Signal

Experiment and Analysis

To characterize the laser ranging system, experiments are achieved on a vibration isolation platform. Firstly, the difference between the static ranging and the scanning ranging is measured. The measured electrical signals which have been amplified are shown in Fig.3. The Fig.3 (a) shows the static ranging waveform and the Fig.3 (b) shows the scanning ranging waveform.



(a) Static ranging waveform (b) Scanning ranging waveform

Figure 3. Received Signal Waveform and Reference Signal Waveform

The phase-shift between the receiving signal and the reference signal in the Fig.3 is generated for two reasons: the optical path difference between the emitted beam and the reflected beam, and the phase-shift introduced by the signal processing module. The later is a fixed value, so it will not affect the measuring result and can be eliminated by calibration.

The amplitude of the static ranging waveform is uniform and the wave is continuous, but the scanning ranging waveform is different, for its amplitude is not uniform and the wave can be obtained only when the laser beam is reflected back.

In the scanning status, the intensity of the reflected beam is uniform and the intensity in the center is higher than the edge. The edge of the reflected beam will arrive at the photo-electric conversion module first and then the center, so the amplitude of the scanning ranging waveform increases gradually and then decreases gradually. Two main frequencies are included in the scanning ranging waveform: one is the modulation frequency (2MHz) and the other is the scanning frequency of the micro-mirror (400Hz), which is validated by the crooked blue waveform in Fig.3 (b).

Secondly, the measurement accuracy of the system is measured. A 3m sliding guide with calibration is located on the vibration isolation platform and a simulated target which can reflect laser beam is also located on it. A set of data is measured each time when the distance moving 0.3 m in the static status but 0.4 m in the scanning status for the limitation of the accuracy. The result is the average of this set of data. The maximal measuring distance in scanning status is 1.6 m for the intensity of the reflect beam is too weak to measure when the distance is larger than 1.6 m. While the maximal measuring distance in static status is 3 m. Fig.4 shows the measured curve of the static ranging and Fig.5 shows the measured curve of the scanning ranging.

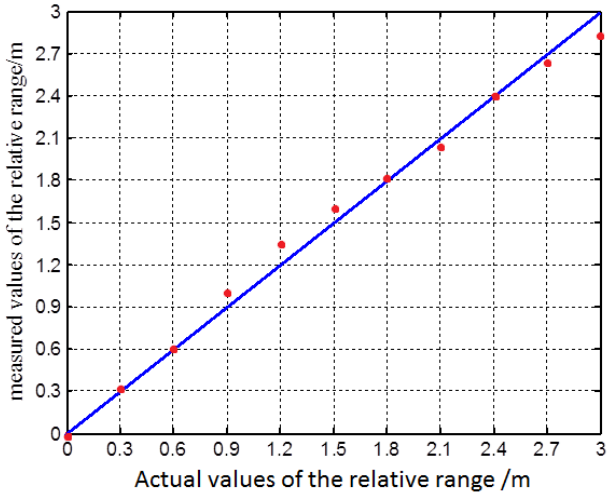


Figure 4. Measured Curve of the Static Ranging

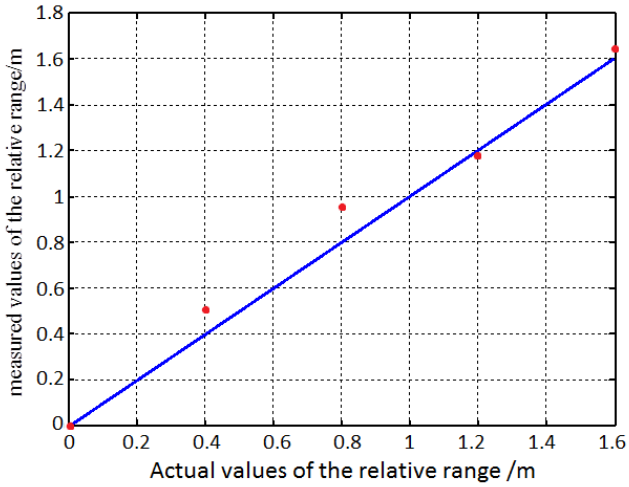


Figure 5. Measured Curve of the Scanning Ranging

The experimental results indicate that the measurement accuracy is 0.10m in static status and 0.17m in scanning status. The reasons of the differences are the ununiformity of the intensity of the received beam and the different response of the photo-electric conversion module to the uneven intensity.

The measurement accuracy is also limited by the modulation frequency of the laser. If a higher frequency laser is used, the same distance will cause more phase shift. In addition, automatic gain control (AGC) can be also applied to the circuit to maintain the amplitude of receive waveforms uniform. It is helpful to improve the measurement accuracy and increase the measurement distance.

Conclusion

A laser ranging system for scanning detection based on phase-shift ranging technology and a MEMS mirror for space detection and measurement is presented in this paper. The relative range is calculated by the phase shift between the emitted beam and the reflected beam. The experimental results indicate that the measurement accuracy is 0.10m in static status and 0.17m in scanning status in the range of 3m. It has great application prospect in space detection and target identification in micro-satellites.

Acknowledgement

The project supported by National Natural Science Foundation of China (No. 51105228).

References

[1] T. Mizuno, M. Mita, T. Takahara, Y. Hamada, N. Takeyama, T. Takahashi and H. Toshiyoshi, “Two dimensional scanning LIDAR for planetary explorer,” Proc. of CANEUS, 11038: 1-6 (2006).

[2] B. Song, W. Zheng. “The research of precision timing measurement in application of TDC_GP2 in laser ranging,” ISPDI 2013-Fifth International Symposium on Photoelectronic Detection and Imaging. International Society for Optics and Photonics, 890523-890523-11(2013).

[3] M. Lescure, C. Ganibal, R. Prajoux, M. Briot. “Compact robotics perception system based on a laser range finder coupled with silicon micromirrors,” Optical Engineering, 42(9): 2653-2658(2003).

[4] T. W. Murphy. “Lunar laser ranging: the millimeter challenge,” Reports on Progress in Physics, 76(7): 076901(2013).

[5] R. Ahola, R. Myllyla. “A time-of-flight laser receiver for moving objects,” IEEE Trans. Instrum. Meas. 35(2): 216–221(1986).

[6] T. Bosch, M. Lescure. “Crosstalk analysis of 1–10 m laser phase shift range-finder,” IEEE Trans. Instrum. Meas. 46(6): 1224–1228(1997).

[7] Y. Liang, J. Huang, M. Ren, et al. “1550-nm time-of-flight ranging system employing laser with multiple repetition rates for reducing the range ambiguity,” Optics express, 22(4): 4662-4670(2014).

[8] J. Huang, M. Ren, Y. Liang, et al. “Photon-counting laser ranging with InGaAs/InP avalanche photodiode in the passively quenched and 1-GHz sinusoidally gated,” Optik-International Journal for Light and Electron Optics, 125(14): 3744-3747(2014).

[9] X. Wang, J. Wang, X. Yang, L. Wang, Z. Wu. “Phase laser rang finding technology and research summarization,” LASER JOURNAL, 27(2): 4-5(2006).

[10] R. L. Ward, R. Fleddermann, S. Francis, et al. “The design and construction of a prototype lateral-transfer retro-reflector for inter-satellite laser ranging,” Classical and Quantum Gravity, 31(9): 095015(2014).

[11] A. K. Dubey, V. Yadava. “Laser beam machining—A review,” International Journal of Machine Tools & Manufacture, 48: 609-628(2008)

[12] R. Gaulton, F. M. Danson, F. A. Ramirez, et al. “The potential of dual-wavelength laser scanning for estimating vegetation moisture content,” Remote Sensing of Environment, 132: 32-39(2013).

[13] Wang Z, Zhang L, Fang T, et al. “A Structure-Aware Global Optimization Method for Reconstructing 3-D Tree Models From Terrestrial Laser Scanning Data,” IEEE T. Geoscience and Remote Sensing, 52(9): 5653-5669(2014).

[14] C. Zhang, G. F. Zhang and Z. You, “Design of space target detection system based on a two-dimensional scanning micro-mirror,” 9th International Conference on Electronic Measurement and Instruments, 2: 718-721 (2009).

[15] C. Zhang, Z. You, H. Huang, G. H. Li. “Study on a Two-dimensional scanning micro-mirror and its application in a MOEMS target detector,” Sensors-Basel, 10(7): 6848-6860 (2010).

Key Engineering Materials Vols 645-646 (2015) pp 1105-1110
© (2015) Trans Tech Publications, Switzerland
doi:10.4028/www.scientific.net/KEM.645-646.1105

Submitted: 2015-01-12
Accepted: 2015-01-15

High-frequency InP-InGaAsP Heterojunction Phototransistor Employing a UTC structure

Zhiyun Jiang[1,a], Hongyun Xie[1,b], Wanrong Zhang[1,c], Lianghao Zhang[1,d]

[1]College of Electronic Information and Control Engineering, Beijing University of Technology, Beijing, 100124, China

[a]jzhiyun@sina.com, [b]xiehongyun@bjut.edu.cn, [c]wrzhang@bjut.edu.cn, [d]zhanglianghaozi@126.com

Keywords: uni-traveling-carrier, double hetero-junction phototransistor, optical responsivity, optical transition frequency

Abstract. In this paper, the working mechanism and high characteristics of an InP/InGaAsP uni-traveling-carrier (UTC) double hetero-junction phototransistor (DHPT) has been analyzed. The UTC-DHPT employs a heavy doping base and two hetero-junctions to realize UTC structure to ease the contract between HPT responsivity and HPT working speed. Optical responsivity and optical transit frequency are analyzed physically through illustrated several kinds of paramistic capacitors in BE junction and BC junction under different electrical bias, optical bias and combined electrical and optical bias in this work. The results show that three-terminal (3T) working mode with combined electrical bias and optical bias in base achieves a highest maxim f_T of 120GHz at collector current of 30mA and keeps the same optical responsivity (37.5A/W) compared with two-terminal (2T) working mode.

Introduction

Recently there has been considerable interest in photo-detectors for optical-fiber communications. P-i-n detectors, which have no gain, are suitable for short distance low-bandwidth transmission, while avalanche photodiodes (APD's), which do provide gain, are necessary for optimum performance wide-bandwidth applications where the sensitivity of the detection systems is limited by the noise of the load resistor-amplifier combination[1,2]. Heterojunction phototransistors (HPT's) are alternatives to the PIN detectors and APD's for they are able to detect, amplify, or mix the microwave or millimeter-wave sub-carrier[3,4]. Hence, they are capable of satisfying the photo-detector requirements of a modern fiber communication system[5,6].

Hetero-junction phototransistor (HPT) as a high performance photo-detector for lightwave communications reported in the past two decades, fabricated using the AlGaAs/GaAs, InGaP/GaAs or InP/InGaAs material structures, and always have one hetero-junction in emitter/base junction and one homo-junction in base/collector junction with base, base/collector depletion region and collector as the absorption area. In the depleted zone between the base and collector, electron–hole pairs are generated and separated. The optic generated holes dismiss/drift slowly from collector to emitter, which limits device high frequency performance and thus the photoelectric response speed[7,8]. In an attempt to overcome these problems, we utilize an uni-traveling-carrier (UTC) structure[9,11], which employs two hetero-junctions at emitter/base junction and base/collector junction separately. In this case, both electrons and holes are generated only in base region to hope to get faster response speed, better dc characteristics and higher optical transit frequency.

This paper is organized as following. In section 2, the device structure and working mechanism of a 6μm×1μm $In_{1-x}Ga_xAs_yP_{1-y}$/InP materials UTC double hetero-junction phototransistor (DHPT) are described first, and the positive influences of UTC structure on UTC-DHPT of high-frequency characteristics performance under different biased conditions (electrical bias, two-terminal working

mode and three-terminal working mode) are analyzed through illustrated several kinds of paramistic capacitors in BE junction and BC junction under those different biased conditions. In section 3, the simulation results of optical responsivity and high-frequency characteristics of a 6μm×1μm UTC-DHPT under different biased conditions are given, which are in good agreement with the analysis in section 2. Finally, the conclusions are given in the last section.

UTC-DHPT device structure and analysis of transition frequency f_T

The device epilayer structure and structure parameters of InP/InGaAsP UTC-DHPT are given in Fig.1 and Table 1 respectively. It consists of the InP substrate up, a 0.5um n^+ InP buffer, a 1um n^+ InGaAsP and 0.4um n^- InGaAsP layer with band energy of 1.12eV as sub-collector and collector respectively, a thin p^- and n^- InGaAsP transition layer for reduce energy gap in collector/base junction, a 0.1um p^+ InGaAsP layer with band energy of 0.80eV as base, a 0.05um n InP layer emitter, a 1.8um n^+ InP cover layer, and a 0.1um n^+ InGaAs ohmic contact layer. The use of medium doping wide-gap emitter and high base doping levels results in a small base-capacitance. This UTC structure forms two hetero-junctions at emitter/base junction and collector/base junction separately, which differs from the conventional single hetero-junction HPT (SHPT) in which the $In_{0.53}Ga_{0.47}As$ always was employed as both base and collector. Thus, in the UTC-DHPT structure, only the highly doping InGaAsP base region is used as optical absorption layer, while the collector is used as collection region with sub-collector together.

Based on the theoretical analysis, an InP/InGaAsP UTC-DHPT is modeled utilizing a numerical device simulator (ATLAS).

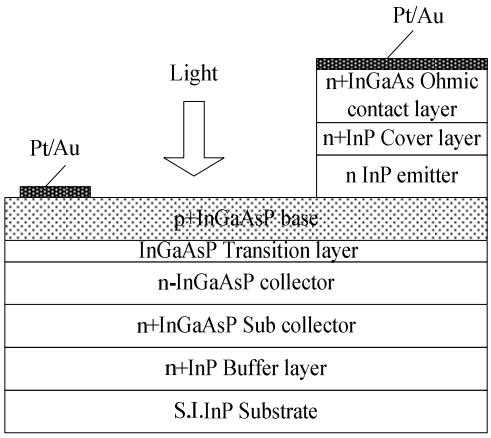


Fig. 1. Device structure of the UTC-DHPT

Table 1. Epitaxial-layer parameters of the UTC-DHPT

layer	material	doping(cm^{-3})	Thickness(um)	Bandgap(eV)
Ohmic contact	n^+:InGaAs	10^{19}	0.1	0.75
Cover layer	n^+:InP	10^{19}	1.8	1.35
emitter	n:InP	10^{17}	0.05	1.35
base	p^+:InGaAsP	10^{18}	0.1	0.80
Transition layer 1	p^-:InGaAsP	10^{15}	0.01	0.80
Transition layer 2	n^-:InGaAsP	10^{15}	0.01	0.88
collector	n^-:InGaAsP	10^{16}	0.4	1.12
sub collector	n^+:InGaAsP	10^{19}	1	1.12
buffer	n^+:InP	10^{19}	0.5	1.35
substrate	n^+:InP	S. I		1.35

As illustrated in Fig.1, the incoming light is injected into the exposed 6um*1um base mesa from an optical window to avoid additional light power loss from emitter layer, cover layer and contact layer absorption. Incident radiation on the UTC-DHPT penetrates through the top surface of the base and is absorbed into the base region. Electron–hole pairs are generated and separated only in the p-doped base region instead of the combined absorption region in conventional SHPT. The energy band diagram of the UTC-DHPT in dark and under light with V_{ce}=2V is shown in Fig.2. The photo-generated electrons diffuse across the p+-InGaAsP absorption layer to the adjacent totally depleted n-InGaAsP collection layer, where they are swept by the reversely enhanced electric field to form the initial electron photocurrent. The photo-generated holes, as the majority carrier in base, meanwhile relax fast toward the emitter and accumulated at the base/emitter hetero-interface and then lower the base-emitter barrier potential, which allows a large amount of electrons to inject from the emitter to collector and amplifies the initial electron photocurrent. A significant amount of photocurrent gain can be achieved by this process. The phototransistor optical responsivity $\gamma_{\mathrm{UTC-DHPT}}$ (A/W) is calculated as:

$$\gamma_{\mathrm{UTC-DHPT}} = I_p / P_{opt} \tag{1}$$

where P_{opt} is the power of the optical beam and I_p is the output current of the UTC-DHPT.

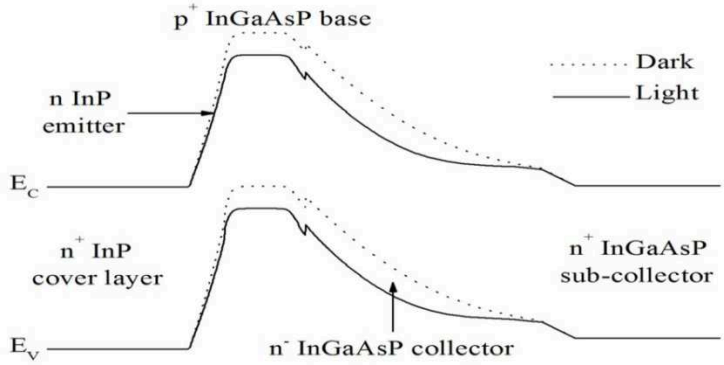


Fig. 2. Energy band diagram of the UTC-DHPT in dark and under light

The UTC-DHPT can operate under two working modes when base is illuminated by CW light, the two-terminal (2T) working with a floating base and three-terminal (3T) working mode with a combined electrical and optical bias in base, and also can operate in dark with electronic bias as double hetero-junction bipolar transistor (DHBT). Note that the HPT is characterized as an HBT with the photocurrent as base bias. The f_T of DHBT at electrical bias and UTC-DHPT at 2T working mode or 3T working mode can all express as follows:

$$f_T = \frac{g_m}{2\pi C} = \frac{1}{2\pi(C_{j,BE} + C_{j,BC} + C_{dn} + C_{sc})} \tag{2}$$

Here, g_m is the transconductance of the device, C is the total capacitance of in our device. $C_{j,BE}$ and $C_{j,BC}$ are the base/emitter junction and base/collector junction capacitance, respectively. C_{dn} is the diffusion capacitance due to electronics inject to the base. C_{sc} is the space charge capacitance caused by electronics inject to the collector depletion region.

For the base uniform doping DHBT and UTC-DHPT, C_{dn} is expressed as:

$$C_{dn} = \frac{qW_B^2 I_C}{2kTD_{nB}} = \frac{W_B^2}{2D_{nB}} \tag{3}$$

where, W_B is the base width, D_{nB} is the elctron diffusion coefficient. Because there is only one carrier (electron) diffuse fast across the base area while the major hole relax fast to emitter/base junction, the high electronic mobility leads to an extremely weak C_{dn} and helps to improve the

DHPT working speed. C_{sc} is expressed as:

$$C_{sc} = \frac{W_{DC}}{2\upsilon_s} g_m \tag{4}$$

where W_{DC} is the width of base/collector depletion layer, υ_s is electronics saturated velocity. C_{sc} depends on the thickness of the depletion region, 1um n^+ InGaAsP and 0.4um n^- InGaAsP layer are used for sub-collector and collector respectively in order to optimize the phototransistor optical responsivity.

$(C_{j,BE} + C_{j,BC})$ which is dominated when DHBT or UTC-DHPT deal with high frequency signals, and can express as equation (5):

$$C_{j,BE} + C_{j,BC} = A_{j,BE}\left[\frac{q\varepsilon}{2(V_{BJ,BE} - V_{A,BE})}\left(\frac{N_{ED}N_{BA}}{N_{ED}+N_{BA}}\right)\right]^{\frac{1}{2}} + A_{j,BC}\left[\frac{q\varepsilon}{2(V_{BJ,BC} - V_{A,CE})}\left(\frac{N_{CD}N_{BA}}{N_{CD}+N_{BA}}\right)\right]^{\frac{1}{2}} \tag{5}$$

where ε is the dielectric constant of the InP/InGaAsP material, $V_{BJ,BE}$ and $V_{BJ,BC}$ are the built-in voltage of base/emitter and base/collector junction, $V_{A,BE}$ and $V_{A,CE}$ are the external voltages of base/emitter and collector/emitter junction, N_{ED}, N_{BA} and N_{CD} are the emitter, base, and collector doping concentration. For a DHBT at electrical bias and UTC-DHPT at 3T working mode, $V_{A,BE}$=1.4V. All the collector bias in those three operating conditions are the same of $V_{A,CE}$=2V. When a DHBT at electrical bias or UTC-DHPT at 2T and 3T working mode, $V_{BJ,BE}$ and $V_{BJ,BC}$ can express as:

$$V_{BJ} = \frac{kT}{q}\ln\frac{n_n p_p}{n_i^2} \tag{6}$$

where n_i is the intrinsic carrier concentration, n_n and p_p are the electronic and hole concentration, respectively. Fig.3 shows the electronic concentration in emitter, base, collector region under these three operating conditions. It is observed that the external voltages of base/emitter can improve n_n in emitter and collector region, and from Eq. (6), DHBT at electrical bias and UTC-DHPT at 3T working mode have higher V_{BJ} than UTC-DHPT at 2T working mode. So we can tell, the optical biasing and combined base electrical biasing in 3T UTC-DHPT can make sure that the UTC-DHPT provides smaller $(C_{j,BE} + C_{j,BC})$ then higher optical cut-off frequency than 2T UTC-DHPT.

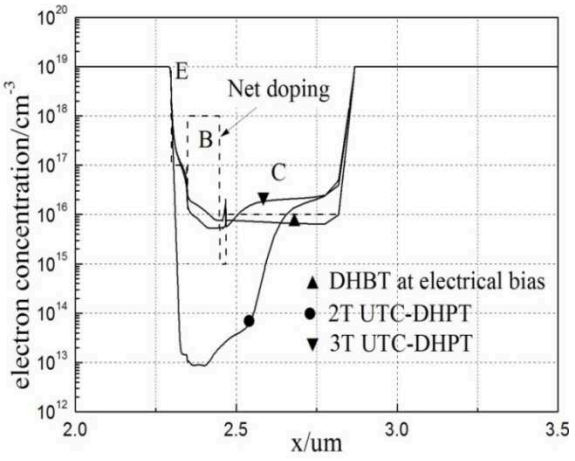


Fig.3 The electronic concentration in emitter, base, collector region for 2T and 3T UTC-DHPT as well as the UTC-DHPT operated at DHBT.

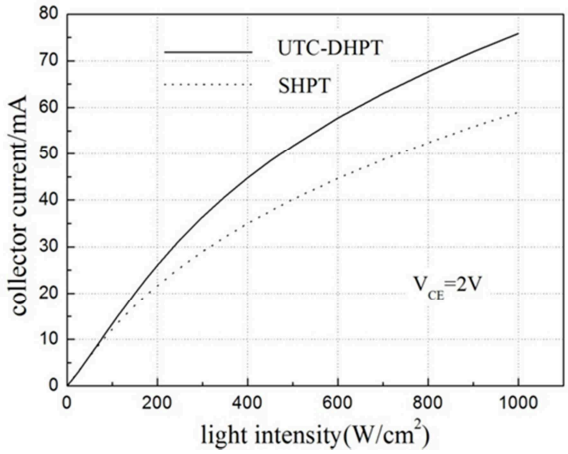
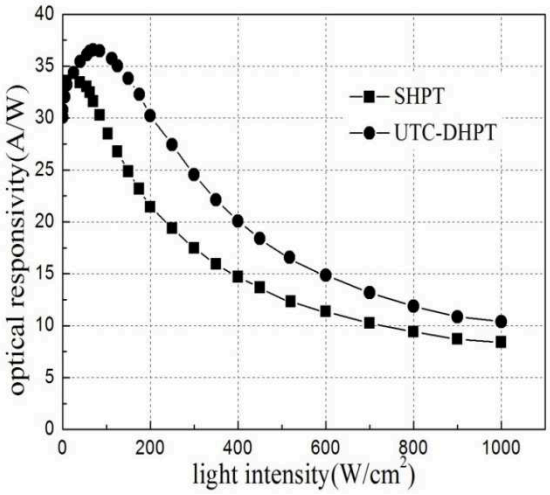


Fig.4 Collector current of the UTC-DHPT as a function of incident light intensity.

Results and discussion

At first, I_c dependence on incident light intensity of both UTC-DHPT and SHPT are shown in Fig. 4. The optical beam having a light intensity from 0 to 1000 W/cm^2 is injected into the base with collector biasing at V_{ce}=2V. It is clear that I_c of UTC-DHPT is larger than that of SHPT at same optical intensity. Fig. 5 shows the optical responsivity $\gamma_{UTC-DHPT}$ of UTC-DHPT and SHPT as a function of incident light intensity. It is observed that the maximum $\gamma_{UTC-DHPT}$ of UTC-DHPT is 37.5A/W and bigger than SHPT optical resposivity of 34.5/W.



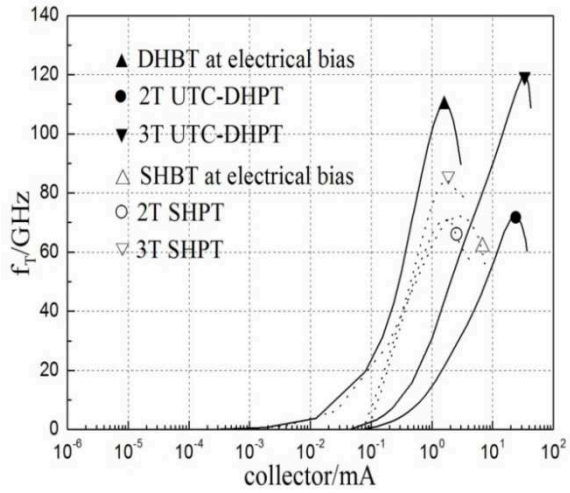


Fig.5The optical responsivity of SHPT and UTC-DHPT as a function of light intensity.

Fig.6f_T dependence on Ic for 2T and 3T UTC-DHPT as well as the UTC-DHPT operated at DHBT.

The dependence of transition frequency f_T on I_c for 2T UTC-DHPT and 3T UTC-DHPT as well as the UTC-DHPT worked as DHBT is shown in Fig.6. Simulations results of the conventional single heterojunction bipolar transistor (SHBT) and SHPT are also shown in Fig.6. It is observed that the UTC-DHPT has excellent transition frequency compare with the conventional SHBT and SHPT because UTC structure breaks the speed limitation from slow hole's mobility.

The transition frequency f_T of DHBT operates at common-emitter configuration reaches maximum value of 115GHz as I_c is about 1.6mA. The UTC-DHPT also operates at common-emitter configuration by biasing c-b junction negatively at V_{ce}=2V with optical injection into the base region. Under 2T UTC-DHPT working mode with base bias is provided only with 1.55um light illumination, maximum optical transition frequency f_T of UTC-DHPT is about 80GHz when I_c is about 24mA. The reason for the attenuation of f_T compared with the electrical biased DHBT is that the optic generated electrons and holes in p-doped base region have big influence on the inner carrier transportation, which lead an increase of $(C_{j,BE} + C_{j,BC})$ as illustrated in section 2. When the UTC-DHPT operates at 3T working mode with combined electrical biasing and optical biasing, maximum optical transition frequency f_T increases to 120GHz at collector biasing current of 30mA. This indicates that the combined base electrical biasing and optical biasing in 3T UTC-DHPT can make sure that the UTC-DHPT provides both high optical cut-off frequency and high optical responsivity.

Conclusions

In this paper, the positive influence of UTC structure on DHPT optical responsivity and high frequency characteristics are analyzed in details through illustrated several kinds of paramistic capacitors in BE junction and BC junction under those different biased conditions. Analytical expressions indicate that the UTC-DHPT can have sufficient optical transit frequency if a voltage source wad applied in base is used. Benefits from the single electron transportation of UTC

structure, optical responsivity of UTC-DHPT reaches at 37.5A/W under 2T working mode and 3T working mode. When the UTC-DHPT operates in 3T working mode with combined electrical and optical biasing, maximum cutoff frequency f_T of about 120 GHz is achieved, which is larger than cutoff frequency f_T of SHBT and proves that 3T UTC-DHPT can achieve both high working speed and high optical responsivity. Therefore the UTC-DHPT designed in this paper exhibits enhanced electrical and optical characteristics compares with the conventional SHPT, and 3T UTC-DHPT paves the way for future high-speed InP-based optoelectronic integrated circuits.

Acknowledgments

This work was supported in part by the National Natural Science Foundation of China (Grant No. 61006044), the Natural Science Foundation of Beijing, China (Grant Nos. 4122014, and 4142007), and Beijing Municipal Education Committee, China (Grant No. KM200910005001).

References

[1] C.L.Ho, M.C.Wu, W.J. Ho, et al. Effectivenessof Metallic Mirror for Promoting the Photoresponse of InGaAs PIN Photodiode, Solid-State Electronics, Vol. 43, pp: 961~967, 1999.

[2] Tan SW, Chen HR, Chen WT, et al. The influence of base bias on the collector photocurrent for InGaP/GaAs heterojunction phototransistors, Applied Physics, Vol. 97, No. 3, pp: 034502 - 034502-7, 2005.

[3] Shangjian Zhang, Yong Liu, Yongzhi Liu, et al. All-optical sampling exploiting nonlinear polarization rotation in a single semiconductor optical amplifier, Optics Communications, Vol. 285, No. 6, pp:1001-1004, 2012.

[4] Shangjian Zhang, Heng Wang, Xinhai Zou, et al. Self-calibrating measurement of high-speed electro-optic phase modulators based on two-tone modulation, Optics Letters, Vol. 39, No. 12, pp:3504-3507, 2014.

[5] John P. Helme, Peter A. Houston, Analytical Modeling of Speed Response of Heterojunction Bipolar Phototransistors, Journal of Lightwave Technology, Vol. 25, NO. 5, pp: 1247-1255, 2007.

[6] Mutsuo Ogura, Sung Woo Choi, Shigenori Furue, et al. Effects of Zn Doped Mesa Sidewall on Gain Enhanced InGaAs/InP Heterobipolar Phototransistor, IEEE Journal of Quantum Electronics, Vol. 46, NO. 2, pp: 214-219, 2010.

[7] Jean-Luc Polleux, Laurent Paszkiewicz, Anne-Laure Billabert, et al. Optimization of InP–InGaAs HPT Gain: Design of an Opto-Microwave Monolithic Amplifier, IEEE Transactions on Microwave Theory and Techniques, Vol. 52, No. 3, pp: 871-881, 2004.

[8] Hassan A. Khan, Ali A. Rezazadeh, Analytical Modeling of the Spectral Response of Heterojunction Phototransistors, IEEE Electron Device Letters, Vol. 30, No. 11, pp: 1158-1160, 2009.

[9] Rangel-Sharp G., Miles R. E., and Lezekiel S., Physical Modeling of Traveling-Wave Heterojunction Phototransistors, Journal of Lightwave Technology, Vol. 26, No. 13-16, pp: 1943-1949, 2008.

[10] J. Kim, S. Kanakaraju, W.B. Johnson, InP/InGaAs uni-travelling carrier heterojunction phototransistors, Electronics Letters, Vol.45, No. 12, pp:649-650, 2009.

[11] Junghwan Kim, S. Kanakaraju, W.B. Johnson, High upconversion gain optoelectronic mixer using uni-travelling carrier phototransistors, Electronics Letters, Vol.48, No 10, pp: 649-650, 2012.

Key Engineering Materials Vols 645-646 (2015) pp 1111-1114
Submitted: 2015-01-13
© (2015) Trans Tech Publications, Switzerland
Accepted: 2015-01-19
doi:10.4028/www.scientific.net/KEM.645-646.1111

A compact Infrared gas sensor based on an asymmetry gas cavity

MING Anjie[1,2]*, REN Yaohui[3], ZHANG Yu[2],ZHANG Le[2], ZHANG Wenbo [2,] TAN Zhenxin [2], OU Wen[1,2] ,TAN Qiulin[3], MAO Haiyang[1,2], XIONG Jijun[3], CHEN Dapeng[1]

[1] Integrated Circuit Advanced Process Center, Key lab of Microelectronics Device and Integration Technology, Institute of Microelectronics, Chinese Academy of Sciences, Beijing 100029, China

[2] Intelligent Sensors Engineering Center, Jiangsu R&D Center for Internet of Things, Wuxi 214135, China

[3] Key Lab of Instrumentation Science and Dynamic Measurement, North University of China, Taiyuan 030051, China

*Email:minganjie@ime.ac.cn

Keywords: MEMS, gas sensor, carbon dioxide, IOT

Abstract

Many gas molecules absorb electromagnetic radiation at characteristic wavelengths in the infrared region. This absorption can be used to identify defined substances like CO2, ammoniac, and so far. This study presents a comparative analysis of parameters of infrared radiation source and detector hardware that are most important for the creation of portable optical nondispersive infrared (NDIR) gas sensors. One of the central issues in the design of this kind of sensors is the geometry of the sensor cell. In this paper we investigate an asymmetry sensor cavity and predict the performance using Tracepro software. Then, the CO2 sensor is made and tested.

Introduction

With the development of internet of things(IOT), more and more intelligent apparatus integrating with different gas sensors emerge used as a assessment method of indoor or local air quality. Continuous carbon dioxide (CO2) releasing into the atmosphere by a sharp acceleration of industrialization causes the greenhouse effect, the main suspect for global warming. Nondispersive infrared (NDIR) optical methods of detection and measurement of gas concentration within the spectrum range 3-5μm(mid IR) are generally implemented in gas sensors that refer to a portable device class and industrial class application. The optical methods of gas sensor are superior in their capability to electrical chemical and catalytically ones used in this device by ensuring high operation speed, selectivity, corrosive medium stability, service long life.

Theoretical model

Optical gas sensors are spectral measurement devices whose operation is based on the well-known Beer-Lambert absorption law relating the intensity of monochromatic radiation(λ) that has passed through a target gas with concentration(C),absorption path length(L,cm) and gas spectral absorption coefficient(α(λ),cm-1)[1,2]

$$I(C, \lambda) = I_0(\lambda) \cdot \exp\left[-\alpha(\lambda) \cdot L \cdot C\right] \quad (1)$$

The optical sensor consists of a radiation source(sometimes with a narrowband spectral filter) in order to form a probing beam I0(λ) in a given spectral interval, a gas cavity and detector of radiation. The target gas attenuates the intensity of the radiation during its passing through the gas cavity of length L. An electric signal U(I0,L,C, λ)depends on the intensity of the probing radiation I0(λ) and contains information on the gas concentration C is formed at the sensor output. This condition may be fulfilled by introducing an additional “reference” channel in which a quantity proportional to I0(λ) is measured. We shall consider the transmittance coefficient of the optical cavity with gas as an output of the optical sensor[1,3]

$$\tau(\mathrm{C},\ \mathrm{L},\ \alpha(\lambda)) = \frac{I(C,\lambda,L)}{I_0(\lambda)} = \frac{U(C,I_0,\lambda,L)}{U_0(I_0,\lambda)} = \exp\left[-\alpha(\lambda)\cdot L\cdot C\right] \quad (2)$$

The transformation(2) that determines the functional dependence of the output quantity of an optical sensor on its input quantity, gas concentration C, is the transfer function of the sensor; it permits estimating the required gas concentration C at the gas sensor input by measuring the value τ(L,C, λ) at its output.

Results of Measurements and discussion

We use a standard two element thermopile detector of type TPD 2T 0625 G2 G20 / 3189 with NEP of 36nV/Hz1/2 and Responsivity of 33V/W as detector and device of type IR715EN as emitter source. Combining the datasheet of the above device and equation (2), we derived the absorption length of optical cavity at L=4.35cm within the maximum measure range of 50000ppm and limit of detection (LOD) of 50ppm.

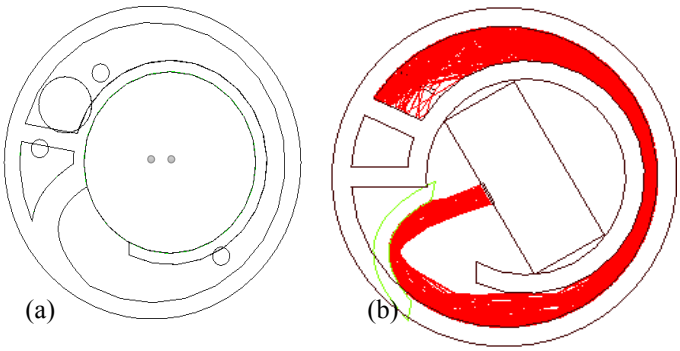


Figure 1. The schematic images of optical cavity(a) and simulation using Tracepro software(b)

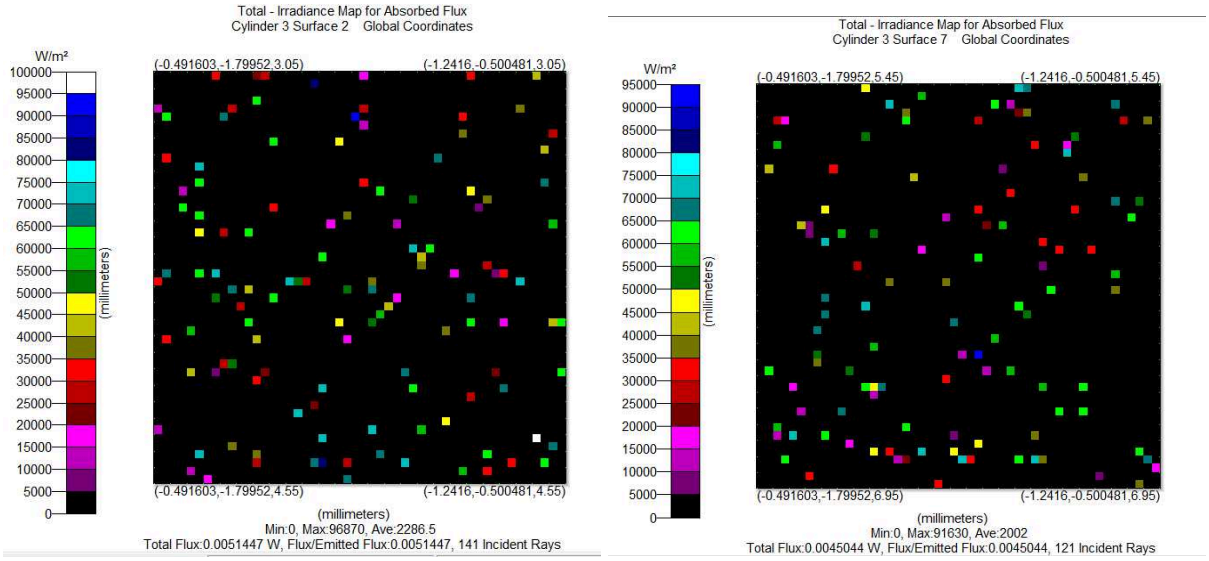


Figure 2. Simulated energy distribution of the reference detector (a) and target detector after optical cavity(b)

The light concentration is generally enhanced by manipulating the optical cavity structure using commercial ray tracing software Tracepro as shown in Fig.1 and we designed the asymmetry gas cavity to reduce the dimension of gas sensor with deviation of the center of inner circle and outer circle[4,5].

The simulated energy distribution of the two channels with 0.45% and 0.51% remaining source energy (Fig.2) show good symmetry indicating optical cavity with high performance using the measured reflectivity of gas cavity coating Au membrane of 500nm thickness. The measured reflectivity which is about 75%~80% with wavelength from 3.0um to 5.0um is shown in Fig.3.

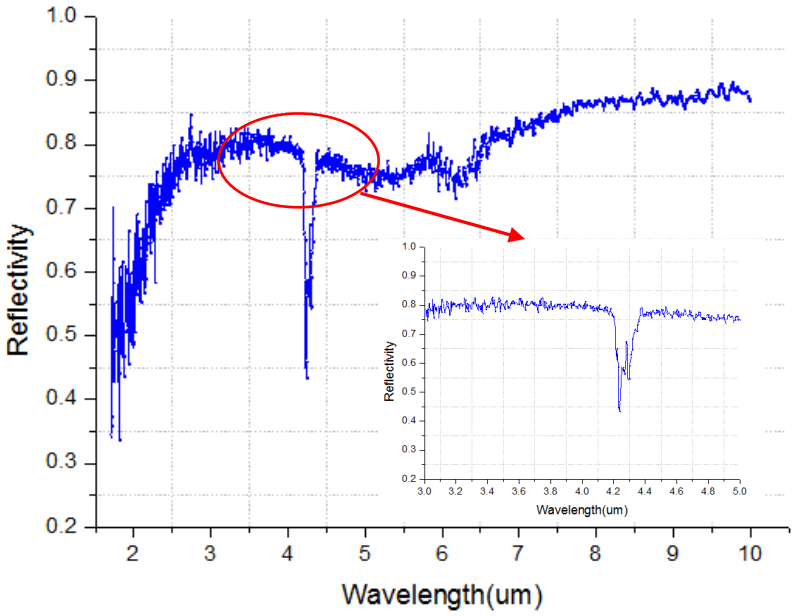


Figure 3. The measured reflectivity of gas cavity coating 500nm Au membrane

It is important to be appropriate the deviation of the center of inner circle and outer circle. It shows the relationship of the deviation of the center of circles and the energy to reach the detectors in Fig.4.

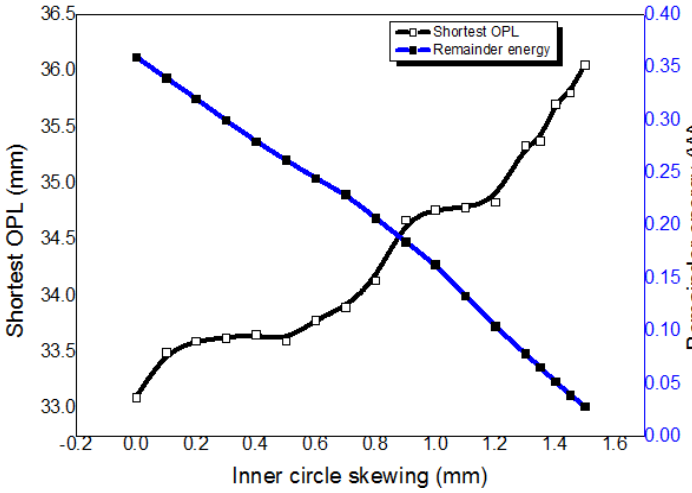


Figure 4. Remaining energy Vs. deviation of the center of two circles

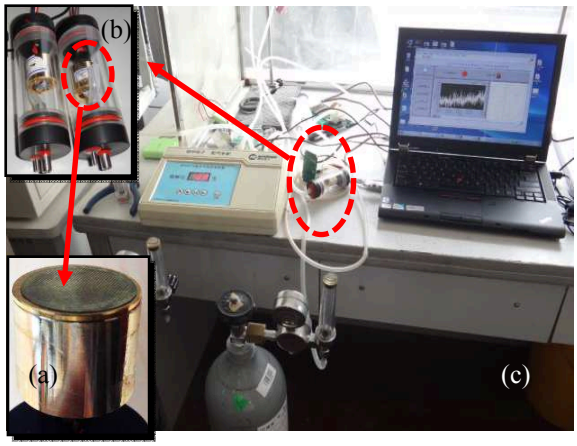


Figure 5. Packaged CO2 gas sensor(a) , mini testing cavity (b) and the whole testing platform(c)

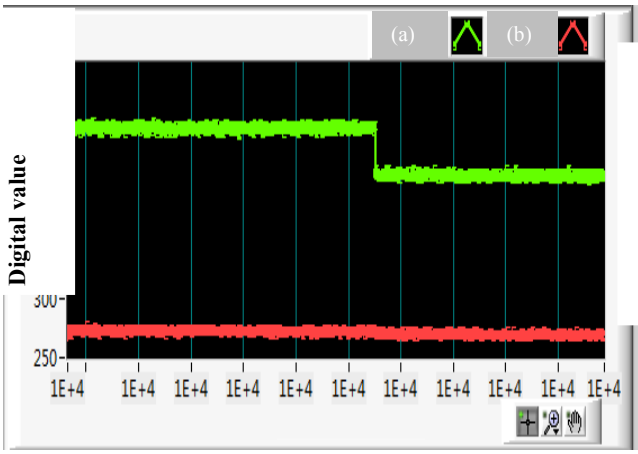


Figure 6.Output digital signal from PCB readout circuit of target channel(a) and reference(b)

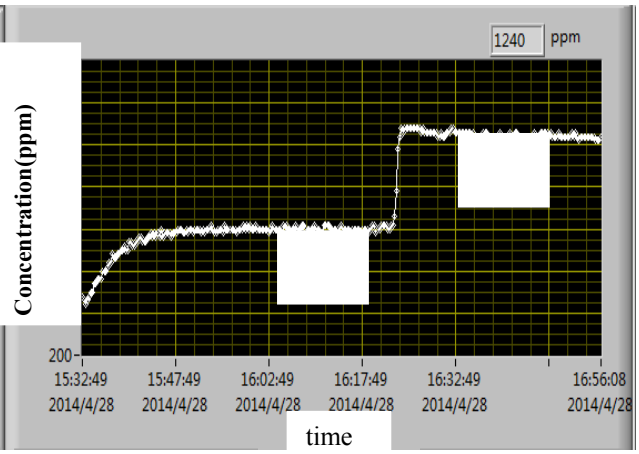


Figure 7. Concentration measurement of CO2 sensor under atmosphere environment (a) and 1200 ppm standard CO2 gas(b)

Then, the packaged gas sensor which consists of asymmetry gas cavity, IR emitter, infrared thermopile, PCB readout circuit is shown and the testing platform is also shown in Fig.5.

After that, the digital signal from PCB readout circuit of reference and target channel derived as shown in Fig.6. At last, Concentration measurement of CO2 sensor under atmosphere environment (a) and 1200 ppm standard CO2 gas(b) is given in Fig.7 and more testing work is under way.

Summary and conclusions

In this paper we investigate the use of statistic ray tracing to predict the efficiency of gas cavity geometries for NDIR gas sensors and we designed the asymmetry gas cavity to reduce the dimension of gas sensor with deviation of the center of inner circle and outer circle. Reflectivity of gas cavity coating Au membrane of 500nm thickness is given. At last, the packaged gas sensor is tested. On the basis of the shown measurement results, we demonstrated that the presented NDIR CO2 sensor system is able to fulfill the requirements of the IOT.

Acknowledgements

The authors acknowledge the financial support from NSFC(61335008,61274119,61306141) and the National High-tech Research and Development Program (2013AA041101).

References

[1]Galina Yu.Sotnikova,Gennadyy A.Gavrilov et al, IEEE sensors Journal,Vol.10,No2,February 2010, pp.225-234.
[2] Jacob Y. Wong, Roy L. Anderson. International Frequency Sensor Association (IFSA) Publishing. 2012.
[3] Pierre Barritault, Mickael Brun & Olivier Lartigue. Sensors and Actuators. 2013(182),pp.565-570.
[4] Robert Frodl, and Thomas Tille, IEEE SENSORS JOURNAL, VOL. 6, NO. 6, DECEMBER 2006,pp.1697-1705.
[5] Johann Mayrwöger, Peter Hauer, Wolfgang Reichl, Reinhard Schwödiauer, Christian Krutzler, and Bernhard Jakoby, IEEE SENSORS JOURNAL, VOL. 10, NO. 11, NOVEMBER 2010,pp.1691-1698.

Key Engineering Materials Vols 645-646 (2015) pp 1115-1119
© (2015) Trans Tech Publications, Switzerland
doi:10.4028/www.scientific.net/KEM.645-646.1115

Submitted: 2015-01-01
Accepted: 2015-01-12

Surface Micromachined Mirror Based on Pre-stress Comb-drive Actuator

Weimin Wang[1, 2, 3, a], Shengmei Yan[4, b], Qiang Wang[1, 2, c], Chuankai Qiu[1, d], Zexiang Chen[2, e], Bin Fan[1, f]

[1]State Key Laboratory of Optical Technologies on Nano-Fabrication and Micro-Engineering, Institute of Optics and Electronics, Chinese Academy of Science, Chengdu 610209, China

[2]School of Optoelectronic Information, University of Electronic Science and Technology of China, Chengdu 610054, China

[3]University of Chinese Academy of Science, Beijing 100049, China

[4]Institute of Electronic Engineering, Chinese Academy of Engineering Physics, Mianyang 621900, China

[a]weiminwang@qq.com, [b]shengmeiyan@yahoo.cn, [c]battery007@163.com, [d]ckqiu@ioe.ac.cn, [e]zxchen@uestc.edu.cn, [f]fanbin@ioe.ac.cn (corresponding author)

Keywords: micromirror; electrostatically actuated; surface micromachined; pre-stress comb-drive actuator(PCA);

Abstract. A micromirror fabricated by surface micromachined process is developed. The developed micromirror contains four pre-stress comb-drive actuators, which support tip/tilt/piston degrees of freedom. Pre-stress comb-drive actuators have the advantage of large displacement and fast response. Prototype is fabricated by a commercially available MEMS surface micromachined process. Experimental results indicate that the device can realize designed function and have the potential in MOEMS applications.

1. Intorduction

Micromirror, which can be used in projection display[1], optical beam scanning[2], adaptive optics[3], etc., is one of the most important devices of MOEMS. Micromirror can modulate the direction of reflection through its uniaxial or biaxial rotation. The characteristics of micromirrors, such as rotation angle and response speed, are mainly determined by the fabrication process and driven method. Due to its low cost, batch fabrication capability and small size, surface micromachined fabrication process has obtained growing interests[4].

Among conventional actuators, electrostatic actuator offers the advantages of fast response, lack of hysteresis and low power consumption[5]. Parallel-plate actuator and comb-drive actuator are two main types of electrostatic actuator[6, 7]. But the driving force of electrostatic actuator is small, result in a high driving voltage. Additional, the range of rotation or piston motion of electrostatic actuator manufactured by surface micromachined, the *stroke*, is small, which heavily limited its applications[8].

For improving the motion range, a micromirror based on novel pre-stress comb-drive actuator (PCA) was proposed in this paper. This paper is organized as follows. In section 2, the structure of micromirror is designed and analyzed. Section 3 shows the fabrication process and Section 4 summarizes the test.

2. Design of structure

PCA was proposed by J. C. Chiou et al. in 2005[9, 10], which exhibits no pull-in and no hysteresis characteristics. Fig. 1(a) shows a classical structure of PCA. For simplicity, it is a vertical comb-drive actuator, and the support beam of movable comb is a composite bilayer beam. Compared with the bottom layer material of the composite beam, the upper layer material of the composite beam has a larger residual tensile stress. Metal, for example chrome, fabricated by megnetron sputtering in general has a large residual tensile stress. After released, the height of free end of composite beam

will be lift by the residual stress, as shown in Fig. 1(b). When a bias voltage is applied between the fixed comb and movable comb, the support beam will be pulled downward to the fixed comb by the electrostatic attractive force, as shown in Fig. 1(c). Due to the large initial lift height, the support beam has a large moving range.

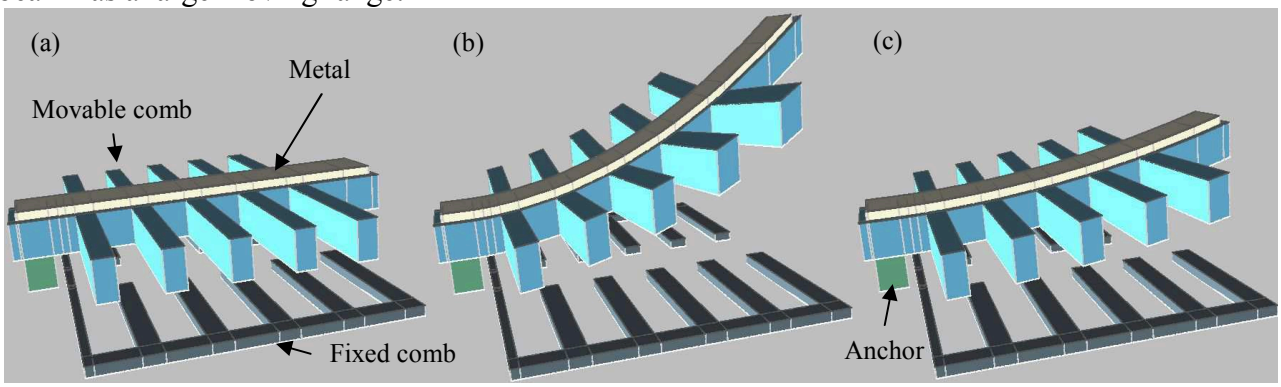


Fig. 1 The PCA at different states; (a)initial state without residual stress, (b)initial state with residual stress and (c)bias voltage state with residual stress.

The structure of the micromirror investigated in this paper is depicted in Fig. 2(a). It contains four PCAs and a square micromirror. After released the micromirror is elevated from the substrate. Different PCAs are actuated will cause three mode of the micromirror: piston mode along Z-axis, tilt modes around X- and Y-axis, as shown in Fig. 2(b), (c) and (d).

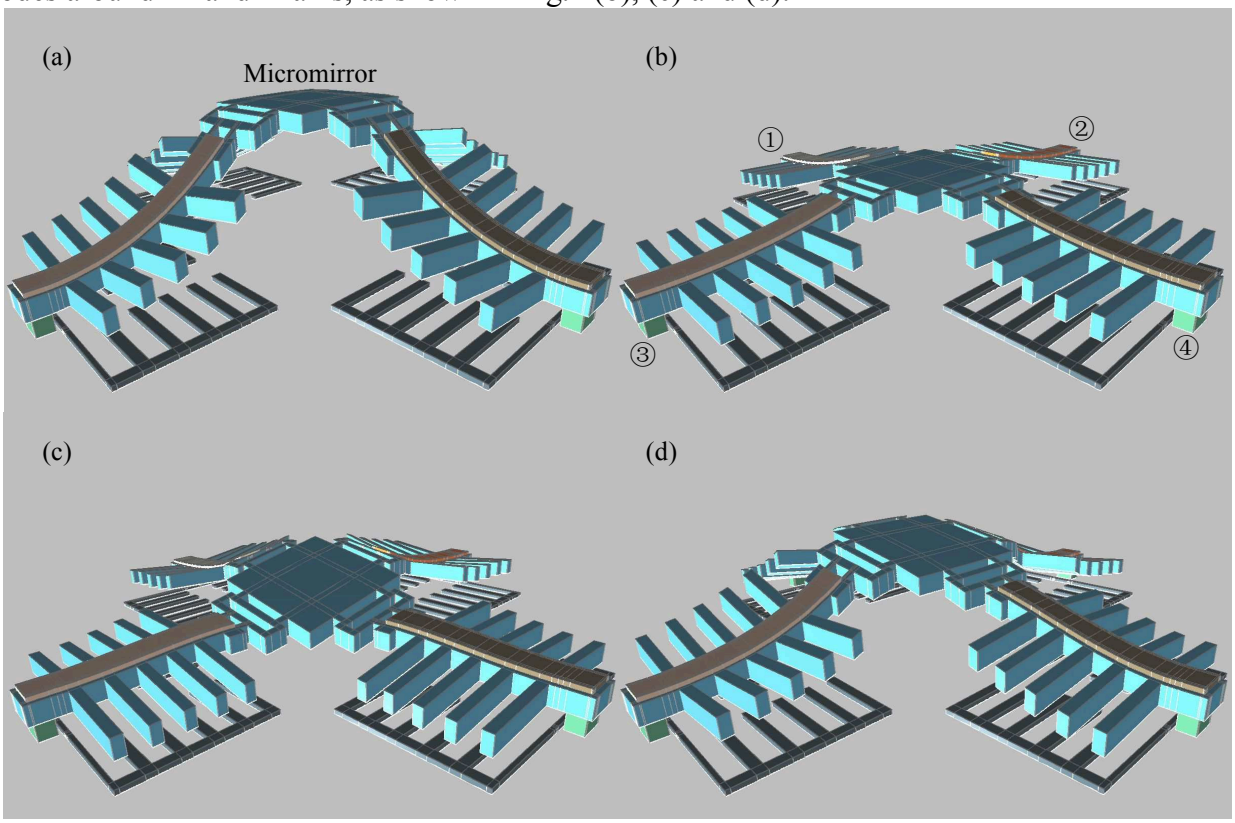
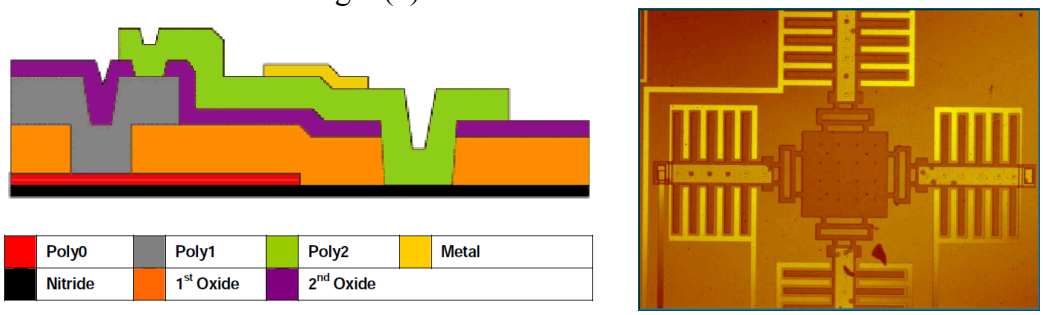


Fig. 2 (a)structure of the micromirror; (b)PCA ①②③④ are all actuated; (c)PCA ③④ are actuated; (d)PCA ④ is actuated.

3. Fabrication of the micromirror

Micromirror prototype is fabricated by PolyMUMPs process[11], a commercially multi-user MEMS surface process. Fig. 3(a) depicts the cross-section of the PolyMUMPs process. It consists of a silicon nitride layer for isolation, three polysilicon layers (Poly0-Poly2) for structure, two phosphosilicon glass layers (1st Oxide and 2nd Oxide) for sacrifice, and a gold layer (Metal) for optical reflection and

electronic connection. At last, HF is used to release the device structure. A micrograph of the fabricated micromirror is shown in Fig. 3(b).



(a) (b)

Fig. 3 (a)cross-section of PolyMUMPs process (not to scale); (b)micrograph of the fabricated micromirror.

4. Experiment

The performance of the micromirror is test using a 3D scanning white light profiler, the Zygo NewView 7300[12]. A 3D profile of the fabricated micromirror is shown in Fig. 4(a).

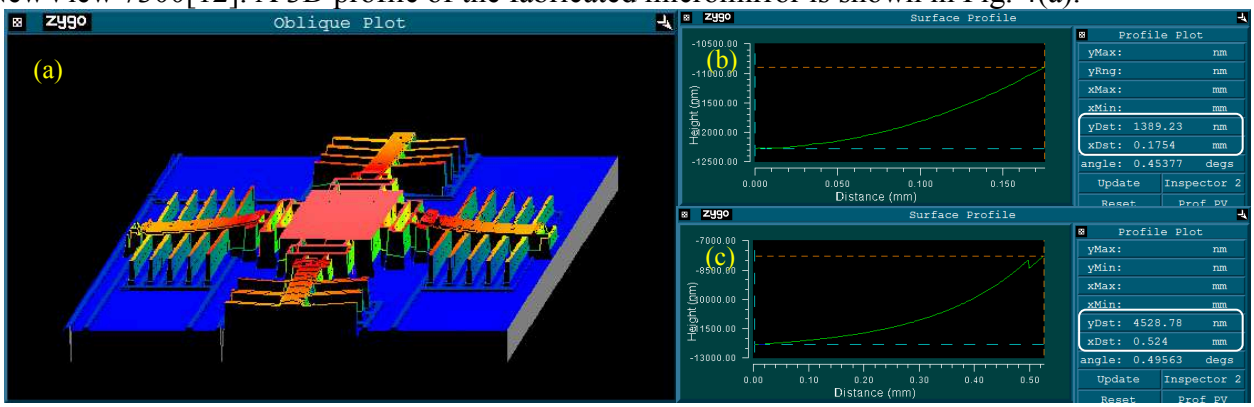


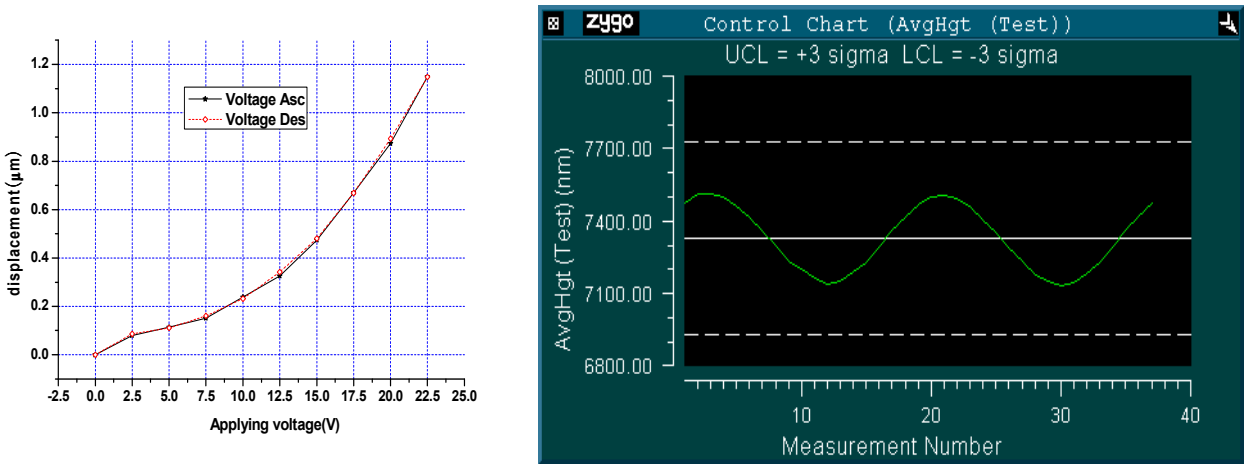
Fig. 4 (a)3D profile of a fabricated micromirror; (b)lift height for a composite beam with length 176um; (c)lift height for a composite beam with length 524um.

A. Lift height

Obviously, as the length of composite beam increase, the lift height will increase too. So different length composite beam is designed, fabricated and test. As shown in the white frame of Fig. 4(b) and (c), the lift height for 176um and 524um length beam is 1.4um and 4.5um respectively.

B. Static performance

The static electromechanical voltage-displacement relationship of piston motion of the micromirror is measured. Fig. 5(a) shows the measured displacement as a function of increasing and decreasing voltage. The result draws no hysteresis and high reversibility, which implies that the micromirror is fit for micro optics applications, as expected for an electrostatic driving system. The maximum displacement is about 1.2um with a 22.5V driving voltage, which is about twice as large as the displacement of micromirror fabricated under the same process but no PCAs.



(a) (b)

Fig. 5 (a)measured displacement as a function of increasing and decreasing voltage; (b)the dynamic performance under a sinusoidal driving voltage for one period.

C. Dynamic performance

Besides reversibility and no hysteresis, fast response is also necessary for micromirror. So a preliminary dynamic result is measured. A sinusoidal driving voltage with a frequency of 430Hz is applied to the micromirror. The dynamic performance is measured for one period as shown in Fig.5(b). The movement of the micromirror is an approximate perfect cosine curve, showing a fast and synchronous response.

5. Summary

In this paper, a surface micromachined mirror based on PCA is proposed and test. Preliminary measurement results show that it has a relative large motion range and fast response time. Potential applications of this device include optical switches, laser display and scanner.

Acknowledgments

This work is supported by the National Natural Science Foundation of China (grant no. 61308064 and 11403029). Weimin Wang wish to extend special thanks to Dr. Jun Yao for helpful instruction. Z. X. Chen's research is supported by the National Science Foundation of China (grant no. 61071027).

References

[1] J. Chong, S. He and R. B. Mrad, Development of a Vector Display System Based on a Surface-Micromachined Micromirror, IEEE Trans Ind Electron. 59(12) (2012) 4863-4870.
[2] K. Jia, S. R. Samuelson and H. Xie, High-Fill-Factor Micromirror Array With Hidden Bimorph Actuators and Tip–Tilt-Piston Capability, J Microelectromech Syst. 20(3) (2011) 573-582.
[3] T. G. Bifano and J. B. Stewart, High-speed wavefront control using MEMS micromirrors, Proc. SPIE. 5895 (2005) 1-9.
[4] H. Yu and H. Chen, Development of a novel micromirror based on surface micromaching technology, Sensors and Actuators A. 125 (2006) 458-462.
[5] D. Hah, S. T.-Y. Huang, J.-C. Tsai, H. Toshiyoshi and M. C. Wu, Low-Voltage, Large-Scan Angle MEMS Analog Micromirror Arrays With Hidden Vertical Comb-Drive Actuators, J Microelectromech Syst. 13(2) (2004) 279-289.
[6] F. R. Hu, J. Yao, C. K. Qiu and H. Ren, A MEMS micromirror driven by electrostatic force, J Electrostat. 68(3) (2010) 237-242.

[7] P. R. Patterson, D. Hah, H. Nguyen, H. Toshiyoshi, R.-M. Chao and M. C. Wu, A SCANNING MICROMIRROR WITH ANGULAR COMB DRIVE ACTUATION, Proc. IEEE. (2002) 544-547.
[8] Q. Sun, K. He and E. Cretu, Optimization designed large-stroke MEMS micromirror for adaptive optics, CHINESE OPTICS LETTERS. 8(12) (2010) 1163-1166.
[9] J. C. Chiou and Y. J. Lin, A novel large displacement electrostatic actuator: pre-stress comb-drive actuator, J Micromech Microeng. 15 (2005) 1641-1648.
[10] J.-C. Chiou, C.-F. Kou and Y.-J. Lin, A Micromirror With Large Static Rotation and Vertical Actuation, IEEE J Sel Topics Quantum Electron. 13(2) (2007) 297-303.
[11] Information on http://www.memscap.com/en_mumps.html.
[12] D. Grigg, E. Felkel, J. Roth, X. C. D. Lega, L. Deck and P. D. Groot, Static and dynamic characterization of MEMS and MOEMS devices using optical interference microscopy, Proc. SPIE. 5455 (2004) 55-61.

Key Engineering Materials Vols 645-646 (2015) pp 1120-1124
Submitted: 2014-10-29
Accepted: 2014-12-16
© (2015) Trans Tech Publications, Switzerland
doi:10.4028/www.scientific.net/KEM.645-646.1120

Design and Simulation of MEMS Mirror Based 3D Shape Measurement System

Chi Zhang*

Beijing Institute of Nanoenergy and Nanosystems, Chinese Academy of Sciences, Beijing, China

*czhang@binn.cas.cn

Keywords: MEMS mirror, phase-shift method, scanning, shape measurement

Abstract. A 3D shape measurement system based on a laser rangefinder and a two-dimensional MEMS mirror is presented in this paper. According to the requirement of surface profile measurement, the 3D shape measurement system is mainly composed of a laser module, a two-dimensional MEMS mirror, a ranging module, an orientation module and an image composition module. Based on the MEMS scanning technology and phase-shift ranging method, the surface profile of the target can be acquired by the measurement system. For the coupled scanning mode, the scanning pattern is simulated in Lissajous figure and the condition of covering all the field of view is analyzed. The simulation results show that the 3D shape measurement system based on the laser rangefinder and the two-dimensional MEMS mirror can realize the measurement the surface profile of the target in all the field of view.

Introduction

3D shape measurement technology is an important method to acquire the surface characteristics and record the morphological characteristics of the object, which has great applications in the fields of industry, scientific research and national defense. With the rapid development of equipment manufacturing industry, complex surface shape measurement for large size objects is always a key technical problem for the online testing in automobile, aerospace and advanced manufacturing industry, and it is also very urgent to realize the 3D shape measurement with high precision, rapid and real-time. In the 3D shape measurement, the technology based on optical measurement principle has great advantages of non-contact, high precision and high resolution. With kinds of high-performance devices, such as semiconductor laser, CCD (charge-coupled device), CMOS (complementary metal oxide semiconductor) image sensor, position sensor devices, optical 3D shape measurement technology has been widely used in CAD/CAE, reverse engineering, online testing and machine vision, which has been a very promising3D shape measurement method [1,2].

For the large size objects, traditional optical 3D shape measurement technology always adopts moving laser, polyhedral prism or galvanometer to realize the 2D scanning, which is large in weight, power and size [3,4]. These methods have low scanning frequency, which are not suitable for the micromation and integration, and cannot satisfy the high standard for rapid and real-time measurement. Recently, with the development of the MEMS (Micro-Electro-Mechanical Systems) technology and photoelectron technology, MOEMS (Micro-Optic-Electro-Mechanical Systems) has been great prompted. As the integration of MEMS and optical technology, MOEMS can integrate the sensor, actuator, microprocessor and other electrical, optical or mechanical parts into a micro space. With the precisely drive and control the parts in MOEMS, information acquisition, process and action are realized, which is widely used in photo-communication, photo switch, optical scanning and image display [5]. 2D MEMS mirror based on MEMS technology is a self-scan key technology and can replace the traditional optical scanning mechanism driven by the motor, which has great advantages of small volume, low power, high integration and high scanning frequency.

In this paper, a 3D shape measurement system based on a laser rangefinder and a two-dimensional MEMS mirror is presented for surface profile measurement, which has great increase the system integration and measuring efficiency, reduce the production cost of optical instruments and satisfy the requirements of rapid and real-time measurement. It is an important research field in target

topography measurement technology and has an important application value in equipment manufacturing industry.

3D Shape Measurement System

According to the mission of surface profile measurement, the 3D shape measurement system has abilities of regional scanning, relative range and orientation measurement, which is mainly composed of a laser module, a two-dimensional MEMS mirror, a ranging module, an orientation module and an image composition module as shown in Fig.1.

In the 3D shape measurement system, each part is started by the signal communication module which commanded by the external computer. The signal-modulated CW laser beam is emitted by the laser module to the two-dimensional scanning micro-mirror. The micro-mirror is fabricated by MEMS technology and actuated by piezoelectricity. It has two DOF and changes the direction of the emitted laser beam for a regional 2D scanning. The scanning angles are detected by piezoresistors which are integrated in the scanning mirror. The beam reflected from the target is received by the ranging module. With the contrast between the emitted beam and the reflected beam, the relative range to the measurement point is calculated by the phase-shift ranging method. With the scanning angles of micro-mirror and the corresponding time of the reflected beam, the relative orientation to the measurement point is calculated by the orientation module, accordingly. Therefore, the relative position of each measurement points are acquired and exported from the signal communication module to image composition module to reconfigure and restore the surface profile.

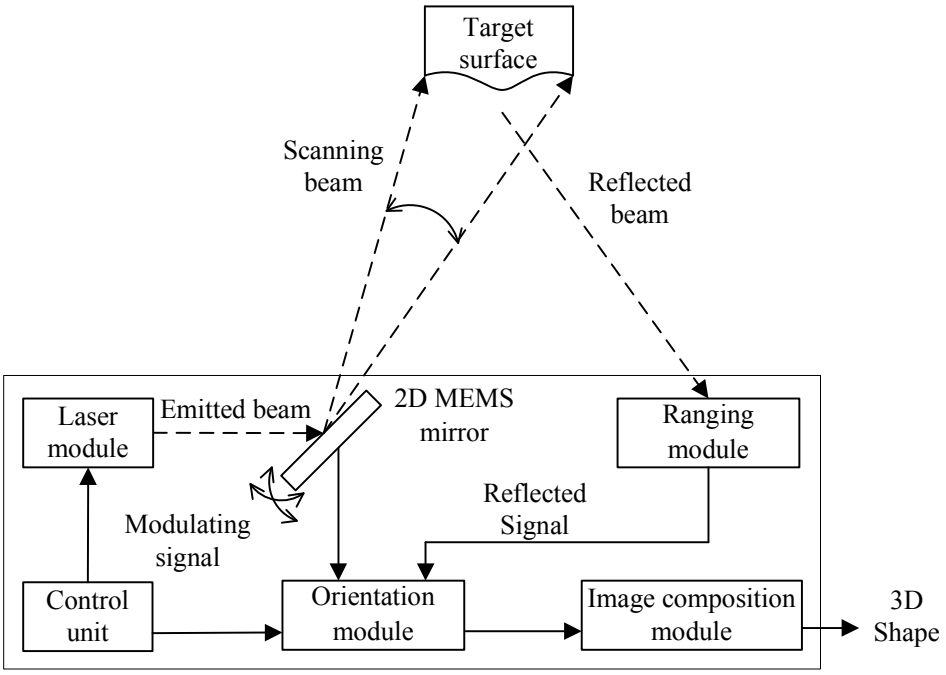


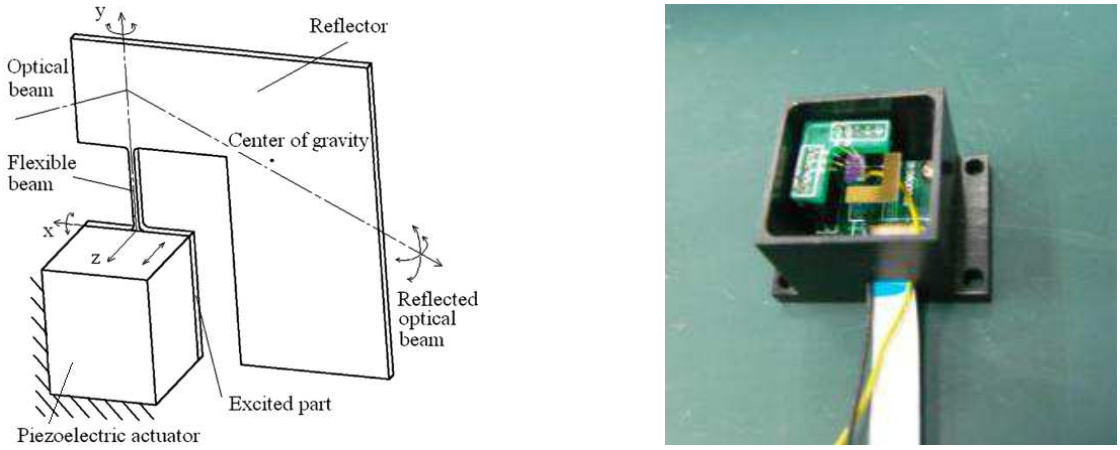
Figure 1. Composition of 3D shape measurement system

2D MEMS Mirror

Si-based MOEMS is the main technology for the scanning micro-mirror and many researches are concentrating on the multidimensional deflection and actuation methods in recent years. By the electrostatic, magnetic, or piezoelectric actuation, etc, the micro-mirror is capable of scanning a light beam multi-dimensionally with large scanning angle and low voltage [6-10]. Therefore, a 2D MEMS mirror with a piezoelectric actuator and piezoresistors is used for the 3D shape measurement system in this paper.

The 2D MEMS mirror with a piezoelectric actuator and piezoresistors is designed as shown in Fig.2(a). The mirror has two vibration modes: bending by x-axis and twisting by y-axis. The 2D

MEMS mirror can be equivalent to a two dimensional vibration system with two different resonant frequencies. Actuating the 2D MEMS mirror at each resonant frequency can make the mirror vibrate with a large deflection angle by each axis. When a resultant voltage including two different resonant frequencies is imposed to the piezoelectric actuator, both vibration modes are excited and the MEMS mirror is capable of scanning a light beam two-dimensionally with large scanning angles by a single driving source.



(a) (b)

Figure 2. Design and package of 2D MEMS mirror device

Scanning Simulation

When the 3D shape measurement system is used to measure the surface profile of the object, the two scanning directions of the 2D MEMS mirror are in the resonant states. Because of the two resonant frequencies are relatively prime, the scanning pattern of the reflect laser beam appears an unstable Lissajous figure, which is simulated as shown in Fig. 3. Therefore, according to the characteristics of the Lissajous figure, the coverage condition of the 2D region for scanning is investigated.

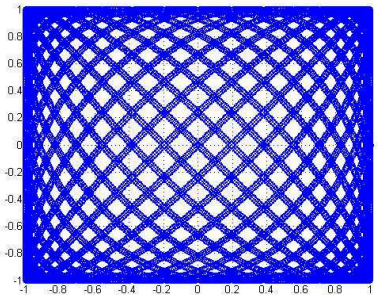


Figure 3. Simulated scanning pattern in Lissajous figure

The Lissajous figure can be considered as a resultant movement composed of two movements, which can be described as follow:

$$\begin{cases} x = a\sin(2\pi f_x t + \varphi_x) \\ y = b\sin(2\pi f_y t + \varphi_y) \end{cases} \tag{1}$$

where a and b are amplitude coefficient, f_x and f_y are the scanning frequencies for each directions, and φ_x and φ_y are the initial phases for each directions.

Considering the Lissajous figure has the scanning blind corners in the scanning process, the divergence angle of the laser beam should be matched to coverage the full field of view. Assume the

maximal scanning angle for each axis is ±θ, the object distance is D, the divergence angle is θ_T, the coverage condition of the 2D region for scanning can be described as below:

$$\tan\theta \cdot D \cdot \delta d = \frac{1}{2} D \tan\theta_T \tag{2}$$

The maximum interval coefficient can be described as below:

$$\delta d = \frac{\pi}{N_d} \tag{3}$$

If the θ_T is considered very small, the condition can be described as below:

$$\theta_T = \frac{2\pi}{N_d} \tan\theta \tag{3}$$

According to designed parameters, θ=10°, N_d=2165 and the minmal divergence angle is 0.01mrad. Therefore, the 3D shape measurement system has successfully covered the 2D scanning region and realizes the measurement of the full surface profile.

Conclusion

To achieve the mission of object surface profile measurement, a 3D shape measurement system based on a laser rangefinder and a two-dimensional MEMS mirror has been developed in this paper. The design of the system including the orientation module and the ranging module are detailed. The two-dimensional MEMS mirror which has the capabilities of 2D regional scanning is presented. Based on the MEMS scanning technology and phase-shift ranging method, the surface profile of the target can be acquired by the measurement system. For the coupled scanning mode, the scanning pattern is simulated in Lissajous figure and the condition of covering all the field of view is analyzed. The simulation results show that the 3D shape measurement system based on the laser rangefinder and the two-dimensional MEMS mirror can realize the measurement the surface profile of the target in all the field of view.

Acknowledgement

The project supported by National Natural Science Foundation of China (No. 51105228).

References

[1] Yoshizawa T, Wakayama T. Three-dimensional profilometry system incorporating a MEMS scanner. Optical Inspection and Metrology for Non-Optics Industries, 2009, Proceedings of SPIE 7432, 74320P.

[2] Xu L, Zhang Z J, Ma H. Real-time 3D profile measurement using structured light. Journal of Physics: Conference Series, 2006, 48: 339-343.

[3] Acosta D, Garcia O, Aponte J. Laser triangulation for shape acquisition in a 3D scanner plus scan. Proceedings of IEEE Conference on Electronics, Robotics and Automotive Mechanics, 2006, 2: 563-572.

[4] Franca J G, Gazziro M A, Ide A N, et al. A 3D scanning system based on laser triangulation and variable field of view. Proceedings of IEEE International Conference on Image Processing, 2005, 1: 425-428.

[5] Legkiy V N, Shumeyko V A, Balasov I Y, et al. Simulation of algorithm for relief profile measurement and recognition of objects in on-board scanning pulsed laser rangefinders. International Conference and Seminar on Micro/Nanotechnologies and Electron Devices (EDM), 2010, Section V: 390-392.

[6] Laszczyk K, Bargiel S, Gorecki C, et al. A two directional electrostatic comb-drive X–Y micro-stage for MOEMS applications. Sensors and Actuators A: Physical, 2010, 163: 255-265.

[7] Koha K H, Kobayashi T, Hsiao F L, et al. Characterization of piezoelectric PZT beam actuators for driving 2D scanning micromirrors. Sensors and Actuators A: Physical, 2010, 162: 336-347.

[8] Schreiber P, Hoefer B, Braeuer A, et al. Laser display with single-mirror MEMS scanner. Journal of the Society for Information Display, 2009, 17(7): 591-595.

[9] Jain A, Xie H. A single-crystal silicon micromirror for large bi-directional 2D scanning applications. Sensors and Actuators: A. Physical, 2006, 130: 454-460.

[10] Yang H A, Tang T L, Lee S T, et al. A novel coilless scanning mirror using eddy current lorentz force and magnetostatic force. Journal of Microelectromechanical Systems, 2007, 16(3): 511-520.

CHAPTER 6:

Energy Harvesting, Power Supply and Technologies for Fuel Cells

Key Engineering Materials Vols 645-646 (2015) pp 1127-1132
© (2015) Trans Tech Publications, Switzerland
doi:10.4028/www.scientific.net/KEM.645-646.1127

Submitted: 2014-10-29
Accepted: 2014-12-23

The Design of an Interface Circuit for Micro-Electrostatic Vibration Energy Harvesters and Super-Capacitor

Si Chen[1,a], Yingxian Lu[1,b] and Xiaohong Wang[1,2,c *]

[1]Tsinghua National Laboratory for Information Science and Technology

[1]Institute of Microelectronics, Tsinghua University, Beijing, 100084, P.R. China

[2]State Key Laboratories of Transducer Technology, Chinese Academy of Sciences, P.R. China

[a]chensi12@mails.tsinghua.edu.cn, [b]yingxianlu@ee.buaa.edu.cn, [c]wxh-ime@tsinghua.edu.cn

Keywords: Interface circuit, micro-electrostatic vibration energy harvester, super-capacitor.

Abstract. This paper presents the design of an interface circuit for storing power generated by low-frequency vibration based electrostatic energy harvesters. The circuit includes a structure of negative voltage converter with an active diode to minimize the forward voltage drop, and it also includes a boost-buck converter to accommodate a wide input voltage. The circuit has also been optimized to perform resistive matching. The maximum voltage of the capacitor in charging reaches about 1.83 V in simulation.

Introduction

With the development of the wireless technology and low power electronics, self-powered electronics have caused attractions over the past decade. Nowadays, the conventional electrochemical batteries are widely used. However, it's tough and even expensive to replace or recharge a battery, because of its limited lifetime in some cases. Harvesting energy from the environment can be an alternative, instead of substitution of the battery as the power supply, or recharging it [1]. Electrostatic vibration energy harvesters have been of great interest and promise for its high efficiency at low frequency and manufacturing in micro-scale. However, the output voltage of electrostatic harvester is alternating and the average power is too small. Generally, it's hard to store the output energy in capacitors directly for intermittent use. Moreover, the output matching impedance is relatively high. Hence, it is challenging to design an efficient interface circuit for electrostatic harvesters.

In conventional interface circuits, AC-DC or DC-DC converters have been used since AC power is generated in vibration-based harvesters [2]-[5]. In order to gain high efficiency under low power output of the harvesters, a gate cross coupled rectifier [6] and a negative voltage converter [7] have been specially designed. There is limited literature on interface circuits for electrostatic harvesters, whilst many electrostatic harvester solutions have been proposed [8]-[10]. The system presented in [11] uses a diode-based charge pump with inductive energy fly-back structure which has ultralow power consumption; however an initial power investment is required to charge the supply capacitor. In [12], a high voltage and low power inductive DC-DC buck converter as the interface of an electrostatic energy harvester is introduced, but its minimum input voltage is limited since the low-frequency output voltage of the electrostatic harvester is relatively low.

This study introduces the design of an interface circuit which concerns all the problems mentioned above. The proposed circuit is designed for high output matching impedance and low power non-resonant electrostatic harvesters. The interface circuit consists of a negative voltage converter with an active diode to minimize the forward voltage drop, and also includes a boost-buck converter to accommodate a wide input voltage, as shown in Fig. 1. The performance of the circuit has been validated in simulation.

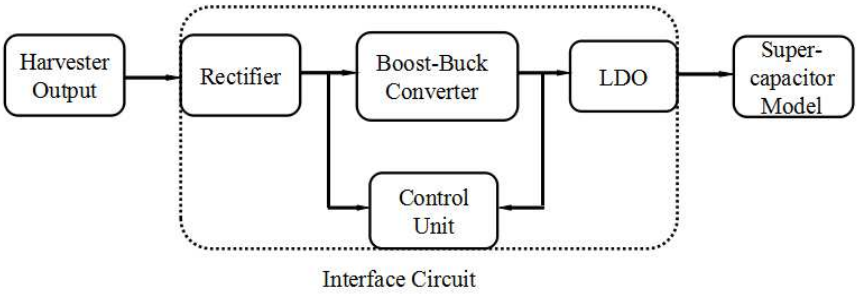


Fig. 1 Schematic of system architecture including micro-electrostatic vibration energy harvester (μEVEH), the design interface circuit and storage unit super-capacitor.

Modeling of the Electrostatic Energy Harvester and the Super-Capacitor

It is a popular way to extract ambient mechanical energy with electrostatic harvester. In order to facilitate resistive matching, it is necessary to establish electric models for both the electrostatic harvester and the super-capacitor.

Modeling of the Electrostatic Energy Harvester. A wideband electrostatic energy harvester, as showed in Fig. 2, is used as the power source. Simulation of transient output voltage of the harvester when it is excited by sinusoidal vibrations is carried out, both with resistive and capacitive loads, and the frequency range is 10 - 80 Hz. The optimal resistive load ranges from 10MΩ to 100MΩ. The result of Fourier spectrum analysis of the transient output voltage shows that the frequency components of the μ-EVEH output majorly include 1st to 4th harmonic components. Thus, the electrostatic harvester can be modeled as a sinusoidal current source including 1st to 4th harmonic components of a capacitance C, a parallel resistance R_p, and a serial resistance R_s, as shown in Fig. 1(b). The current of the load can be given by Eq. 1 .

$$I_L = \frac{I_S}{j\varpi C + 1/(R_S + R_L) + 1/R_P} \cdot \frac{1}{R_S + R_L} \Rightarrow |I_L| = \frac{|I_S|}{(R_S + R_L)\sqrt{\varpi^2 C^2 + (1/(R_S + R_L) + 1/R_P)^2}} \quad (1)$$

Fig. 3 shows the comparison between the fitting curve using Eq. 1 and experimental effective currents under different resistive load at 20Hz, 40Hz, 60Hz, and 80Hz respectively. It can be inferred that the testing results matches well with Eq. 1.

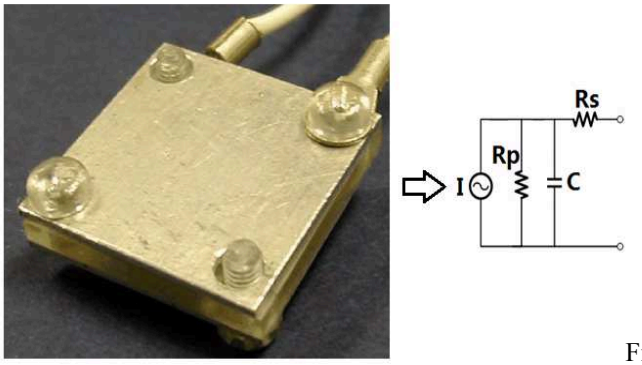


Fig. 2 The electrostatic energy harvester prototype which has a PTFE thin slide inside the PDMS cavities with two electrodes and its equivalent circuit when excited by sinusoidal vibrations.

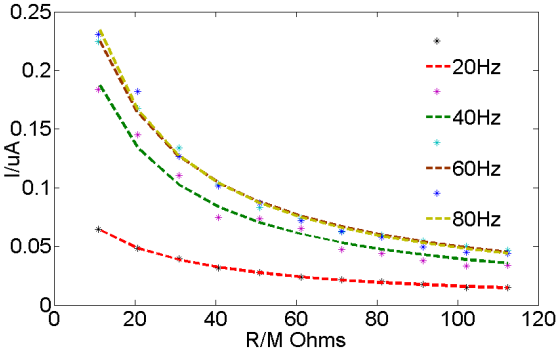
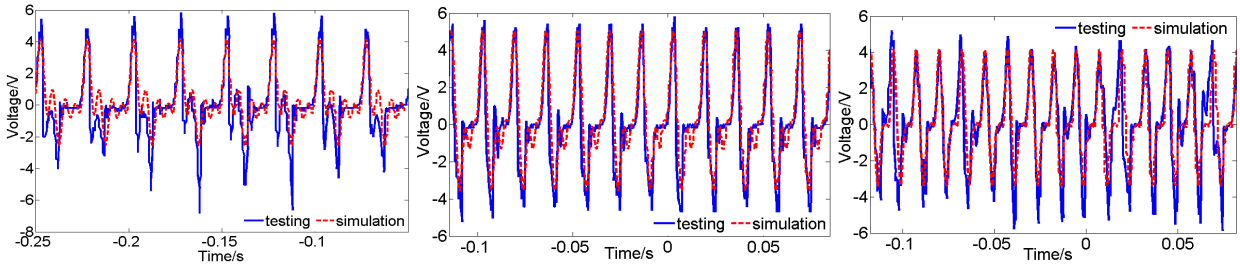


Fig. 3 Comparison of testing effective value of load current and fitting curves using Eq. 1: asterisks(*) represent the testing effective values of load current; dotted lines represent the fitting curves.

The tested output signals of the harvester and the simulated output of the equivalent circuit with same loads at different frequencies are shown in Fig. 4, the frequencies are 40 Hz, 60 Hz and 80 Hz respectively. The tests and the simulations match well with each other. Thus, it is desirable to use the model in simulation of the interface circuit's performance.

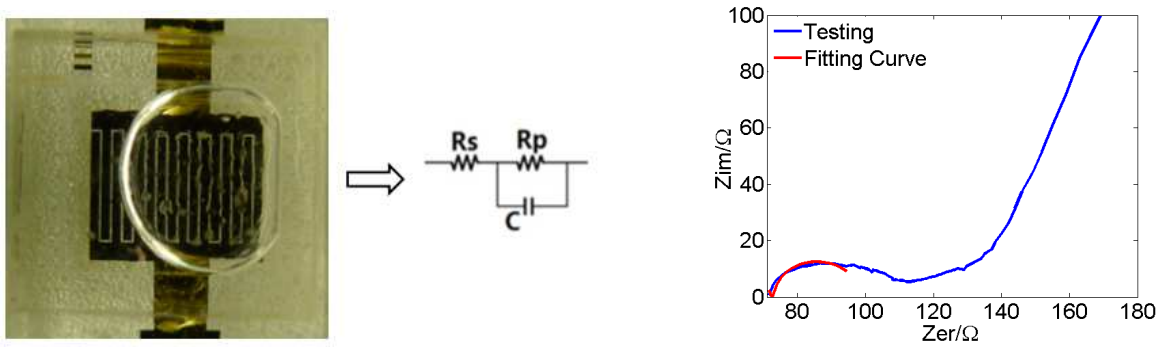


(a) (b) (c)

Fig. 4 Comparison of testing results and simulation results of the harvester under different frequencies with the same load 10.3MΩ: (a) Comparison of simulated and tested voltage under 40Hz vibration; (b) Comparison of simulated and tested voltage under 60Hz vibration; (c) Comparison of simulated and tested voltage under 80Hz vibration .

Modeling of the Super-Capacitor. A simplified super-capacitor, as showed in Fig. 5(a), is used as the energy storage unit of the system. For the super-capacitor, usually a simplified 3RC model was used, which is composed of an RC parallel branch and a resistor R_s to characterize the ohmic loss. The parameters of the 3RC model are obtained from constant current tests and impedance spectroscopy tests, impedance spectroscopy is the blue line, as shown in Fig. 5(b). It is also inferred that when the frequency decreases, the impedance spectroscopy would be a straight line with 45 degrees into the real axis representing Warberg impedance component. In order to obtain the average value of the capacitance, the Eq. 2 is used for fitting curve when the frequency goes to infinity, as the red line shown in Fig. 5(b). The relationship between the real component and the imaginary component can be given by Eq. 2. Results show that the capacitance C, R_p in the RC parallel branch, and Rs of the module are ~0.3 mF, 60 kΩ, 71 Ω respectively.

$$Z = \frac{1}{j\omega C + 1/R_P} + R_S \Rightarrow Z_{IM}^2 + (Z_{RE} - R_S - R_P/2)^2 = (R_P/2)^2 \quad (2)$$



(a) (b)

Fig. 5 (a) The super-capacitor prototype and its 3RC equivalent circuit. (b) Picture of the impedance spectroscopy test with simulation fitting curve when the frequency goes to infinity.

Design and Simulation of the Interface Circuit

Design of the Interface Circuit. Fig. 6 depicts the block diagram of the proposed circuit. The circuit is composed of a rectifier, a boost-buck voltage converter, and an LDO. The rectifier uses the structure of a negative voltage converter to decrease the voltage drop [7], and in order to control the current direction, there is a PMOS as diode which is driven by a comparator, as shown in Fig. 6 (a). The boost-buck converter works under switch mode with feed-forward and feed-back control, as illustrated in Fig. 6 (b). An LDO circuit, shown in Fig. 6 (c), is used to regulate the voltage and to increase the load capacitor, which consists of a feed-back amplifier.

The operation of the boost-buck converter is as follows.

When the input voltage is lower than the voltage needed, the circuit operates at boost mode. Under this mode, as shown in Fig. 6(b) the switch S_2 keeps on so that the inductor L_2 and the

capacitor C_2 will form a filter. When the switch S_1 turns on and the charge is stored on the inductor L_1, and the charge stored in the capacitor C_1 will be the power supply for the follow-up circuit. When S_1 turns off, the charge is stored in C_1 through L_1, stepping up the voltage.

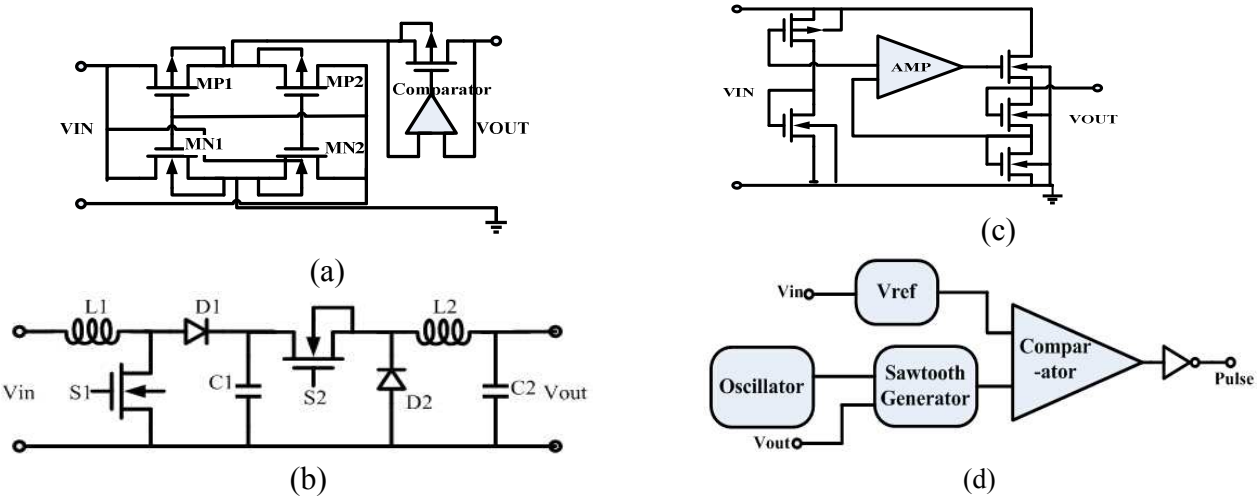


Fig. 6 (a) Schematic of the rectifier with a diode to keep the current direction. (b) Schematic of the boost-buck DC-DC converter. (c) Schematic of the LDO. (d) Schematic of the feedback feed-forward control unit.

When the input voltage exceeds the voltage needed, the circuit operates at buck mode. Under this mode, S_1 keeps off so that the L_1 and C_1 will form the filter. Similarly, when S_2 turns on, the charged is stored in C_2 through L_2. When S_2 turns off, the charge stored in C_2 will be as the supply to step down voltage.

The boost-buck converter has two controlling units, each of which consists of a saw-tooth generator, an oscillator, and a comparator [13], as illustrated in Fig. 6 (d). The principle of operation can be explained as follows. When the reference voltage is higher than the saw-tooth voltage, the output voltage drops, otherwise, it rises. Therefore, the switch will turn on and off, changing the input voltage, namely, the reference voltage.

Simulation of the Interface Circuit. The simulation is done in Cadence Spectre, UMC 180 nm COMS technology. The test setup in simulation is the same as shown in Fig. 1, equivalent circuits of the harvester and the super-capacitor are used as the power source and the storage part, respectively. Frequencies of the input signal range from 20Hz to 80Hz. The capacitors in the model of the super-capacitor are chosen from 0.1mF to 0.5mF. Two external inductors with series resistance are connected with the boost-buck converter.

Results and Discussions

The characteristic signals of the interface circuit are shown in Fig. 7 to observer the functionality of the interface circuit. The input signal is shown in Fig. 4(a). The V_{re} is the signal after rectification, V_{saw} is the output signal of sawtooth generator in the control unit, V_{P1} represents the control signal for S_1, and V_{P2} represents the control signal for S_2. The circuit works in BOOST mode, V_{P2} is nearly 0V. The simulated output voltages of the circuit with different load capacitors are shown in Table 1. The maximum voltage can reach 1.83 V when the voltage of the input signal is 5 V in simulation. It can be seen from the table that when the input voltage varies from 1.1 V to 5 V, the maximum output voltage nearly reaches ~1.7V. Results carry out that a relatively stable voltage can be obtained to be as a supply for lower power- application.

In order to verify the functionality of the DC-DC circuit, the simulations with the input voltage varying from 1 to 5 V has been committed particularly. The output signal of the DC-DC circuit is shown in Fig. 8. It can be inferred that when input voltage exceeds 3 V, the circuit works at buck

mode, the output voltage nearly keeps the same. When the input voltage is lower than 3 V, the circuit operates at boost mode. Results show that the boost-buck DC-DC circuit is functional for a wide voltage.

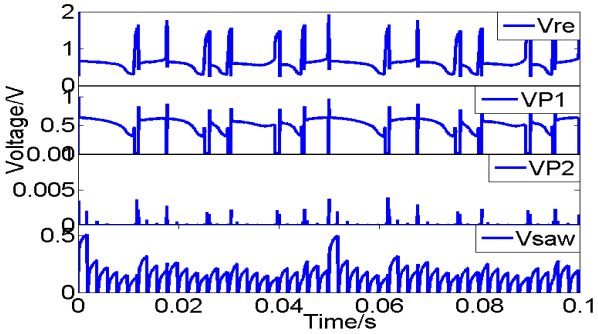


Fig. 7 The characteristic signals of the interface circuit including V_{re} , V_{P1}, V_{P2}, and V_{saw} at 40Hz.

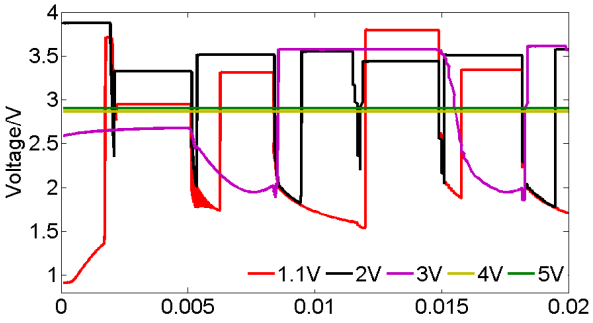


Fig. 8 Simulation results of the DC-DC converter with different input voltage from 1.1 to 5 V.

Table 1. Output voltage and power of different capacitor with different input

Capacitor(mF)	Input (V)	1.1	2	3	4	5
0.1~0.5	Initial Voltage(V)	0.536	1.075	1.71	1.736	1.751
	Maximum Voltage(V)	1.604	1.89	1.847	1.846	1.83

Table 2. Performance comparison with recently reported interface circuits

Ref	Harvesting Mechanism	Impedance Matching Design	Self-powered
[2]	Electromagnetic	No	Yes
[3]	Piezoelectric	No	Yes
[11]	Electrostatic	No	Need Supply
This work		Yes	Yes

Table 2 shows the comparison of the proposed interface circuit with other recently reported interface circuits. The presented circuit considers the output impedance matching of the harvester. The high input impedance of the interface circuit matches with the harvesters. Furthermore, it is self-powered for electrostatic harvester. The circuit can rectify the input signal, boost or buck the voltage to obtain needed voltages, and store electrical energy into super-capacitors effectively.

Summary

In summary, a self-powered interface circuit for low-frequency-vibration-based micro-electrostatic energy harvester is presented. The interface circuit has been evaluated by simulation in Cadence Spectre. The interface circuit was simulated with the capacitor load ranging from 0.1mF to 0.5mF and results show that the maximum voltage of the capacitor in charging reaches ~1.83V. In conclusion, the circuit presented can be a promising way for energy supplication in low power applications.

Acknowledgment

This work is supported by the National Natural Science Foundation of China (No. 60936003), National Basic Research Program (973 Program, No. 2009CB320304), and National High-tech Development Research Program (863 Program, No. 2009AA04Z319) of China.

Reference

[1]P. D. Mitcheson, E. M. Yeatman, G. K. Rao, A. S. Holmes, and T. C. Green, Energy harvesting from human and machine motion for wireless electronic devices, *Proceedings of the IEEE*, 96 (2008)1457-1486.

[2]Husan Ulusan, Kaveh Gharehbaghi, Ozge Zorlu, Ali Muhtaroglu, and Haluk Kulah, An efficient integrated interface electronics for electromagnetic energy harvesting from low voltage sources. Transducers & Eurosensors XXVII, (2013)450-453.

[3]S. Chamanian et al., A self-powered integrated interface circuit for low power piezoelectric energy harvesters, ICEAC, (2013)45-49.

[4]Ying-Khai Teh and Philip K. T. Mok, A piezoelectric energy harvesting interface circuit using one-shot pulse transformer boost converter based on water bucket fountain strategy, ISCAS(2014)1993-1996.

[5]M. Dini, M. Filippi, M. Tartagni, and A. Romani, A nano-power power management IC for piezoelectric energy harvesting applications, PRIME, (2013)269-272.

[6] M. Ghovanloo and K. Najafi, Fully integrated wideband high-current rectifiers for inductively powered devices, *IEEE J. Solid-State Circuits*, 39(2004)1976-1984.

[7]C. Peters et al., A CMOS integrated voltage and power efficient AC/DC converter for energy harvesting applications, J. Micromech. Microeng., 18(2008)104005.

[8]K. Tao, S. W. Liu, J. M. Miao and S. W. Lye, A three- dimensional electrostatic/electrets micro power generator for low acceleration and low frequency vibration energy harvesting, IEEE 27th International Conference on MEMS, (2014)366-369.

[9]Z. Yang, Einar Halvorsen, and T. Dong, Electrostatic energy harvester employing conductive droplet and thin-film electret, Journal of Micro-electro-mechanical Systems, 23(2014)315-323.

[10]Qianyan Fu, and Yuji Suzuki, MEMS vibration electret energy harvester with combined electrodes, IEEE 27th International Conference on MEMS, (2014)409-412.

[11]Asantha Kempitiya, Diana-Andra Borca-Tasciuc, and Mona Mostafa Hella, Low-power ASIC for microwatt electrostatic energy harvesters, IEEE Transactions on Industrial Electronics, 60(2013) 5639-5647.

[12] Stefano Stanzione, Chris van Liempd, Rob van Schaijk, Yasuyuki Naito, Firat Yazicioglu, and Chris Van Hoof, A high voltage self-biased integrated DC-DC buck converter with fully analog MPPT algorithm for electrostatic energy harvesters, IEEE Journal of Solid-State Circuits, 48 (2013)3002-3010.

[13]X. Cao et al., Electromagnetic energy harvesting circuit with feedforward and feedback DC－DC PWM boost converter for vibration power generator system, IEEE Transactions on Power Electronics, 22(2007)679-685.

Key Engineering Materials Vols 645-646 (2015) pp 1133-1138
© (2015) Trans Tech Publications, Switzerland
doi:10.4028/www.scientific.net/KEM.645-646.1133
Submitted: 2014-11-18
Accepted: 2014-12-23

Fabrication of aluminum nitride films by Reactive Pulse DC magnetron sputtering for Vibration Energy Harvester

Zhengguo Shang[1,2, a], Dongling Li[1,2] and Shengqiang Wang[1,2]

[1]National Key Laboratory of Fundamental Science of Micro/Nano-Device and System Technology,Chongqing University, Chongqing, China
[2]Microsystem Research Center of Chongqing University, Chongqing, China
[a]zhengry@cqu.edu.cn

Keywords: Aluminum nitride film, FWHM, peak intensity, preferred orientation, magnetron sputtering.

Abstract: Aluminum nitride(AlN) film as a piezoelectric material has been used widely, particularly in vibration energy harvester due to its unique and enhanced properties such as high temperature resistance and compatibility with CMOS processes. In this work, AlN film with (002) preferred orientation was prepared on silicon wafers by pulse DC reactive magnetron sputtering(RMS), and the properties such as peak intensity, full width at half maximum (FWHM) and surface morphology were investigated by x-ray diffraction (XRD) and scanning electron microscopy (SEM). The preferred orientation was found to be sensitive to deposition conditions such as gas flow rate, power, bottom electrodes materials and substrates temperature. The results shows that the intensity was 1.1×10^5 counts, the FWHM was 1.9ºwhen the temperature was 260℃. The film was used to fabricate the vibrated energy harvester successful and the power density reached about 3000uW/cm^3 at the vibration frequency under 1g acceleration.

1. Introduction

AlN films have been used widely in a variety of sensing, actuating and transduction applications because of their excellent physical and chemical properties in recent years[1, 2]. Now they are increasingly studied in energy harvester applications due to their high-energy density, moderate voltage levels, good electromechanical coupling coefficients, low permittivity especially their compatibility with CMOS processes as opposed to other piezoelectric ceramics such as lead zirconate titanate (PZT) and polycrystalline zinc oxide (ZnO)[3-5].

AlN films have been deposited in several methods including molecular beam epitaxy (MBE)[6, 7], chemical vapor deposition(CVD)[8, 9] and reactive magnetron sputtering(RMS)[10-13]. Among various deposition techniques, MRS has many advantages for thin film growth with the same properties as films obtained though CVD and MBE[11, 14] because of low temperature(as low as 200℃ or even at room temperature), process simplicity and low thermal budget. So the last method is paid more and more attentions. There are radio frequency(RF) MRS and direction current(DC) MRS included in MRS. In this work, the AlN films for vibration energy harvester deposited by reactive pulse DC magnetron is investigated. X-ray diffraction(XRD) and scanning electron microscopy (SEM) are used to character the performance of AlN films such as peak intensity , FWHM and morphology. The results shows that the qualities of AlN film is mainly depended on the bottom materials and process-related factors such as the temperature, the pressure, the power and gas flows rates. The optimized AlN film is successful to fabricate the vibrated energy harvester and obtained perfect results.

2. Experiments

N(100) silicon wafers with resistivity 2–4Ω•cm and thickness 500um were prepared for the deposition of AlN film. Before grown AlN film, 250nm silicon oxide as a dielectric layer was grown by Oxide Diffusion System. All the materials preparing for AlN film depostion including aluminum target(99.999%), argon(99.995%) and nitrogen(99.995%) are in high purity. The base conditions is list in table1, one parameters was changed and kept other ones constant every process. The schematic cross section of AlN films is shown in fig1. AlN films on the silicon oxide as a seed layer enhanced the crystal orientation of Mo(110) as bottom electrode and AlN(002) as a functional layer in fig.1.

Table1. The base conditions for grown AlN films

Vacuum	$5.6\sim2.3\times10^{-3}$mbar
Power	200W~1200W
Ar/N_2 flows	2.8/4sccs~4/24sccm
Electrode materials	Al, Ti, Mo, Cr/Au, Ti/Pt
Temperature	Room～400℃



Fig.1. The schematic cross-section of AlN film growth

3. Results and discussion

All the films are deposited by MS×100 Reactive Magnetic Sputtering (FHR, Germany). The sputtering sequence was set as dielectric layer (SiO_2) →seed layer (AlN)→electrode layer (Mo, Al/Mo, Cr/Au/Mo, Ti/Pt/Mo)→functional layer (AlN). The lattice match of Mo is closest to that of the AlN film[15], so the conditions was optimized firstly for AlN films deposited on Mo layer used as bottom electrode. The fig.2 shows the curve crossing of Mo layer after optimizing conditions of Mo deposition. Taking into account the compatibility of the process for fabricating vibration energy harvester[16, 17], composite electrode materials such as Al/Mo, Cr/Au/Mo and Ti/Pt was used respectively. So based on the optimized Mo parameters, AlN films were deposited on Al/Mo, Cr/Au/Mo and Ti/Pt layers used as bottom electrodes, respectively. It is clearly that AlN film with (002) crystal orientation was obtained when Al/Mo or Ti/Pt as bottom electrodes, but (101) perfected orientation on the Cr/Au/Mo layer from figure3. The piezoelectricity effects of AlN films with (002) orientation crystal is better than other orientation crystal, so it is the fabrication of AlN film with(002) orientation crystal that is focused on. The influence of process parameters such as gas flows rate, power, bottom electrode materials and temperature on the AlN film properties were discussed in the papers.

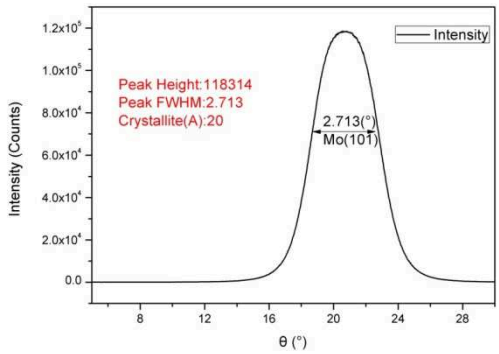


Fig.2 The rocking curve of the optimized Mo(101) film

3.1 Electrode materials

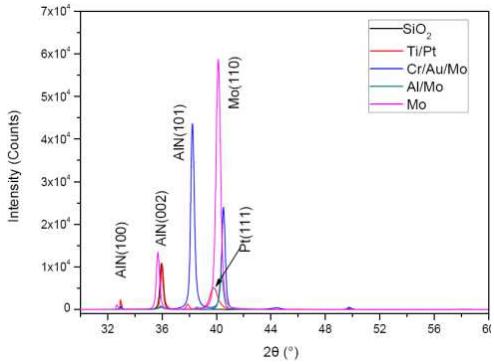


Fig.3 The XRD of AlN films deposited on different electrode materials

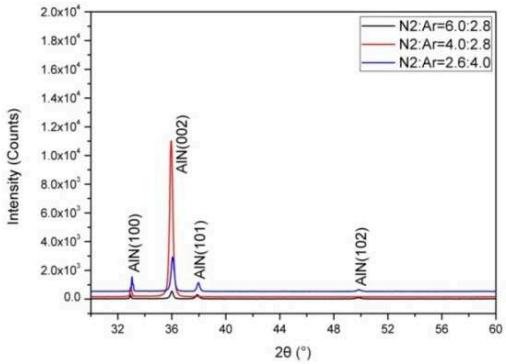


Fig.4 The XRD of AlN film in different flows conditions

As shown in fig.3, the electrode materials influenced on the preferred orientation of AlN film. AlN film with (101) crystal preferred orientation can be achieved when Cr/Au/Mo was used as bottom electrode materials, but AlN film have (002) crystal preferred orientation on other bottom electrode materials. The main reasons are that lattice matching and atomic arrangements are different. Taking accounts for the compatibilities and the properties of AlN film, the Ti/Pt/Mo was used as bottom electrode materials for fabrication of AlN with (002) preferred orientation.

3.2 Gas flow rate

Fig.4 shows 2θ XRD patterns of the AlN films deposited at different gas flow rates. It is shown that the gas flow rate play an important roles on the (002) peak intensity except for the crystal preferred orientations. When the gas flow rate is 4.0/2.8, the atoms of Al and N can be reactive fully, so the (002) peak intensity is higher.

3.3 Power

The mean free path of gas molecules was mainly determined by the power. From the fig.5, a clear conclusion can be drawn that the (002) peak intensity increase as the power increase in the ranges. The reasons are that the power increasing results in weaken the reaction between atomics because of the mean free path deceasing, in the other sides, the power increases, the plasma density increasing enhance reaction between atoms.

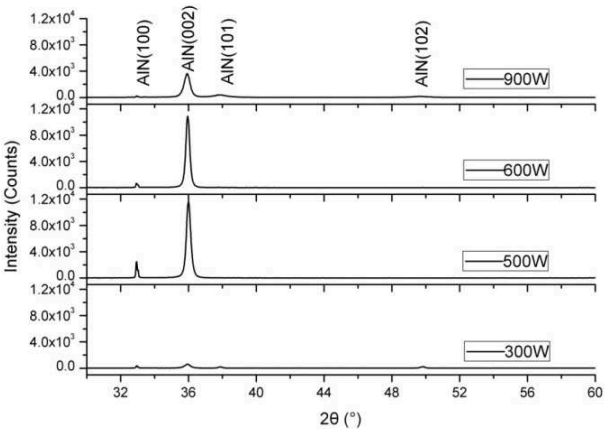


Fig.5 The XRD of AlN film under different power conditions

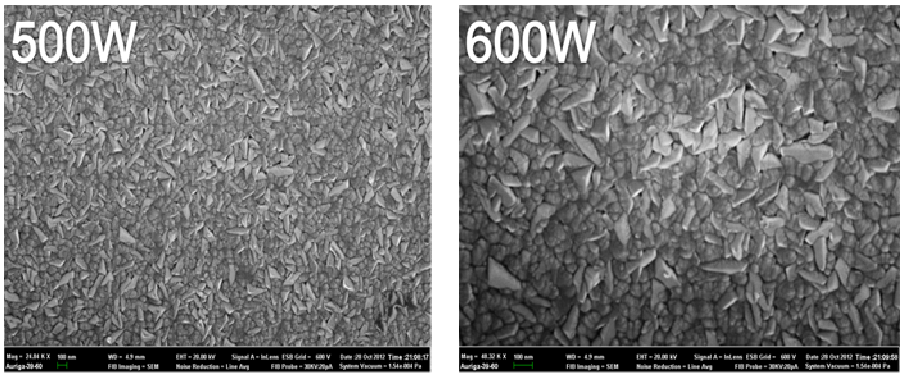


Fig.6 The surface SEM of AlN film at different powers

Fig.6 shows that the surface morphology of AlN films deposited at various powers. Worm-like grains were found in all the deposited films, coinciding with the reference[18]. Difference in surface mobility of adatoms is believed to be responsible for the great changes in morphology.

3.4 Temperature

Fig.7 exhibits the XRD of AlN films prepared by the tuning sputtering substrate temperature. (002) peak intensity increases as the temperature increases when the temperature is no more than 300℃, while the peak intensity will be reduced when the temperature is further increased. The reason is that when the temperature is increased, the atomic kinetic energy increases, (002) peak intensity

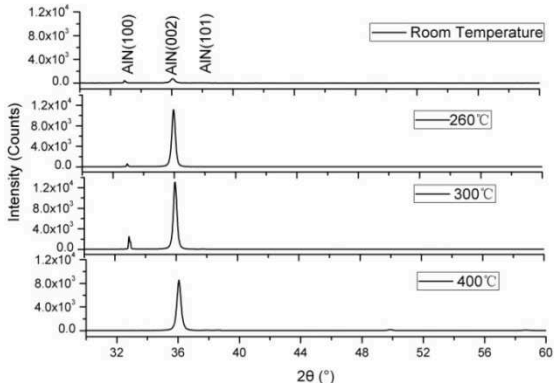


Fig.7 The XRD of AlN film at different temperatures

increases. While the temperature is further increased, physical deposition rate the rate of chemical reaction, the (002) peak intensity reduces.

4. Conclusion

The interaction of gas flow rate, power, temperature and bottom electrode materials must be taken into account in order to prepare AlN film with high performance, the table 2 shows the optimized conditions for grown AlN films. The performance of the AlN film is shown as in fig.8 and fig.9. (002) peak intensity and FWHM 1.1×10^5 counts and 1.9^o, respectively. The film was used to fabricate the vibrated energy harvester successful and the power density reached about 3000uW/cm^3 at the vibration frequency under 1g acceleration.

Table2. The optimized conditions of AlN films

Vacuum	3.0×10^{-3}mbar
Power	600W
Ar/N2 flows	4/24sccm
Electrode materials	Ti/Pt /Mo
Temperature	260℃

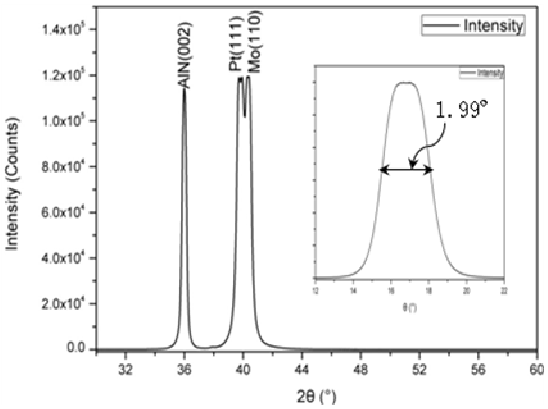


Fig.8 The XRD of AlN film

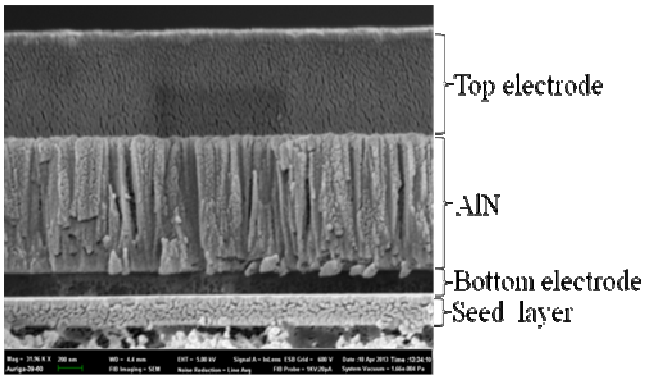


Fig.9 The cross-sectional SEM of AlN film

5.Acknowledgements

This work was supported by the National Natural Science Foundation of China (Grant Nos. 61076106 and 61376116) and the Cultivation Fund of the Key Scientific and Technical Innovation Project of Ministry of Education of China (Grant No. 708072).

Reference

[1] M. Nirschl, A. Rantala, K. Tukkiniemi, et al., Sensors-Basel, 10 (2010) 4180-4193.
[2] W. Pang, H. Zhang, R.C. Ruby, et al., Journal of Micromechanics and Microengineering, 20 (2010) 2316-2319.
[3] A.B. Alamin Dow, H.A. Al-Rubaye, N.P. Kherani, et al., in, IEEE, 2011, pp. 1-4.
[4] Z.G. Shang, D.L. Li, Z.Y. Wen, et al., Key Engineering Materials, 562 (2013) 942-946.
[5] X.-f. He, J. Gao, Microelectron Eng, (2013).
[6] S. Zollner, A. Konkar, R. Gregory, et al., in: MATERIALS RESEARCH SOCIETY SYMPOSIUM PROCEEDINGS, Cambridge Univ Press, 1999, pp. 231-236.
[7] T. Chu, A. Noreika, Solid-state electronics, 10 (1967) 1023-1027.
[8] W. Thomas, L. Sylvia, (1999).

[9] C.-M. Yang, K. Uehara, S.-K. Kim, et al., in: Ultrasonics, 2003 IEEE Symposium on, IEEE, 2003, pp. 170-173.
[10] K.-H. Chiu, J.-H. Chen, H.-R. Chen, et al., Thin Solid Films, 515 (2007) 4819-4825.
[11] J. Cherng, T. Chen, Ferroelectrics, 408 (2010) 41-47.
[12] R. Thapa, B. Saha, S. Goswami, et al., Indian Journal of Physics, 84 (2010) 1347-1354.
[13] G. Piazza, M. Rinaldi, C. Zuniga, in, IEEE, 2010, pp. 2202-2207.
[14] J. Cherng, D. Chang, Vacuum, 84 (2009) 653-656.
[15] J. Cherng, T. Chen, C. Lin, Thin Solid Films, 519 (2011) 6797-6800.
[16] 尚正国, 李东玲, 温志渝, et al., 光学 精密工程, 21 (2013) 3058-3065.
[17] S. Tanner, V. Felmetsger, Journal of Vacuum Science & Technology A: Vacuum, Surfaces, and Films, 28 (2010) 69-76.
[18] H. Cheng, Y. Sun, P. Hing, Thin Solid Films, 434 (2003) 112-120.

Key Engineering Materials Vols 645-646 (2015) pp 1139-1144
© (2015) Trans Tech Publications, Switzerland
doi:10.4028/www.scientific.net/KEM.645-646.1139

Submitted: 2014-11-13
Accepted: 2014-12-23

Novel Wind Energy Harvesting Device for City Building Based on ZnO Films Array

Shaohua Wu[1, a], Lidong Du[1], Zhan Zhao[1, b], Deyi Kong[2], Zhen Fang[1]

[1]State Key Laboratory of Transducer Technology, Institute of Electronics, Chinese Academy of Sciences. Beijing, 100190, China.

[2]University of Chinese Academy of Sciences, Beijing, 100049, China.

[3]State Key Laboratory of Transducer Technology, Institute of Intelligent Machines, Chinese Academy of Sciences. Hefei, Anhui, 230031, China.

[a]randlife_str@163.com, [b]zhaozhan@mail.ie.ac.cn (corresponding author)

Key Words: MEMS, novel wind energy harvesting device, ZnO piezoelectric thin films array.

Abstract: A kind of novel wind energy harvesting device with square ZnO piezoelectric thin films array structure has been investigated in the article. It is designed and fabricated for ambient wind energy on high buildings in city blocks particularly. Ordinary elements of wind energy harvesting are various windmills or turbines, they are usually expensive and noisy, and are not suitable to be used in the crowed city. The novel wind energy harvesting device is fabricated by Micro Electro Mechanical System (MEMS) technology in order to avoid the deficiencies mentioned above. The films array has a multilayer structure with five layers, and has a thickness of about 2.5μm. The maximum open circuit output voltage of the device reaches 2.81V, and its maximum output power density is 23.39nW/cm^2.

Introduction

Wind energy is common in the environment, and it could be collected and storage for energy consumption. Existing wind energy harvesting technology mainly depends on the windmill or turbine structure [1-5], they are usually huge, expensive and complex. These equipments are suitable to be fixed in the open area, while would be difficult to be utilized for wind energy in the crowed city, especially on high buildings. Thus, several kinds of miniaturized wind energy harvesting structure have been developed, such as the cm-scale shrouded wind turbine [6], the wake galloping energy harvesting system [7], piezoelectric reed and resonant cavity device, piezoelectric windmill and piezo-leaf [8-11]. While most of them are manufactured by machining, but the wind energy harvesting on high buildings in city would require large area or great amount. Its cost of duplication would be the obstacles on application of devices mentioned above.

MEMS technology has the advantage of batch fabrication, the produced structures have good consistency as well. This kind of fabrication skills would be employed to solve the difficulties of duplication by machining. Existing MEMS energy harvesting devices are usually used as vibration energy scavenger, the cantilever and film structures are usually adopted [12-14], but seldom energy harvester is designed and fabricated for ambient wind energy on high buildings in city blocks particularly. The MEMS device with ZnO films array structure for wind energy harvesting is designed and fabricated in the article. The wind energy harvesting experiments have been carried

out in wind tunnel to estimate the characteristics of the structure. They could be used to harvest the wind energy on buildings by attaching themselves onto the outside surfaces of the building. The blueprint for the future can be seen in Fig.1.

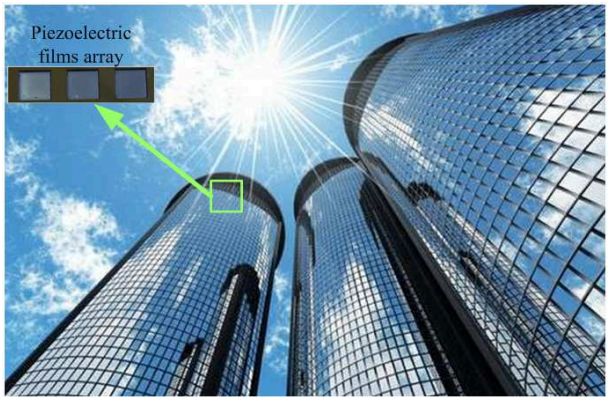
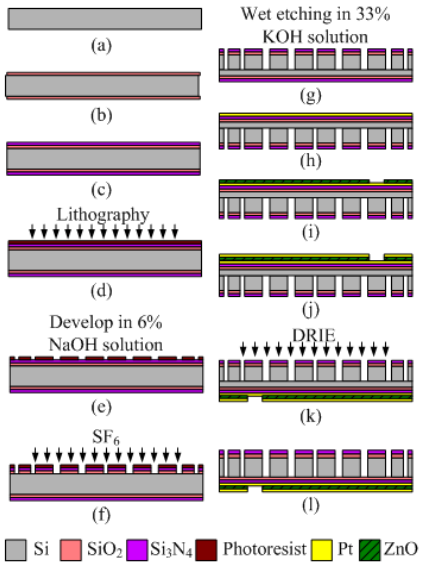


Figure. 1. The imaginary blueprint of the application of ZnO piezoelectric films array

Design and Fabrication

There are many factors that should be considered in the design of the device, for example, robust, sensitive to the wind and energy capacity. The three requirements for the wind energy harvesting element based MEMS technology are mutual restraint. The challenge is fit all factors in design. The principle of energy harvesting is piezoelectric thin film for the device. The large film may have high energy capacity and the thinner film has large flexibility so that it has high sensitivity to the wind. However the device with the large thin film structure has lowered robust. Thus, thin films array structure is suitable to meet the requirements all above. Single film could be small to make sure enough stability, and the silicon between films could also enhance the robust of the device. The total area of the films is able to be increased by films array structure, and that means the power density can be increased effectively.

The film has a multilayer structure, there are total five layers which are respectively SiO_2 layer, Si_3N_4 layer, bottom platinum layer, ZnO layer, and up platinum layer in accordance with the order from the bottom to top. SiO_2 and Si_3N_4 layers are grown on the silicon wafer's surfaces at the beginning of the fabrication, the thickness of the two layers are 200nm and 300nm respectively. This ratio of the two layers can reduce the stress of the film, and two layers can also play a role of insulated layer. Lithography and wet etching processes are carried out to produce square cavity arrays from the backside of the wafer. Afterward a bottom platinum layer with 300nm thickness is sputtered on front of the wafer to be the bottom electrode and pads. The 300nm thickness ZnO layer and the up platinum layer are sputtered onto the bottom platinum layer in sequence. At last, the DRIE process is adopted to remove the residual silicon in the square cavities at the backside to release the films. The fabrication schematics are illustrated in Fig. 2. The picture of the thin films array silicon panel can be seen in Fig. 3.



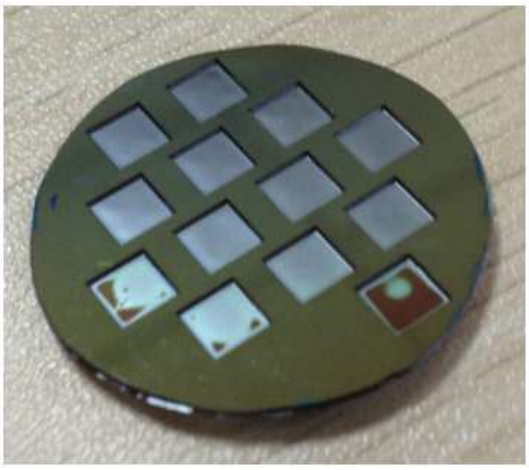


Figure. 2. MEMS fabrication schematics of films array Figure. 3. Picture of films array panel

Experiment and Analysis

The experiment is carried out in self-manufactured small wind tunnel, the Reynolds number of the wind tunnel is larger than 2300 when the wind velocity is larger than 0.799m/s, the equipment is mainly worked in turbulence status [15]. Its picture can be seen in Fig. 4.The wind velocity is measured by anemometer KANOMAX 6004 (FIG. 5), and the wind energy harvesting device is placed above the anemometer shown in Fig. 6.

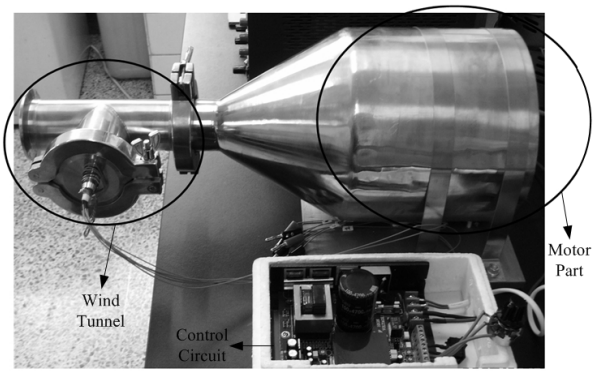
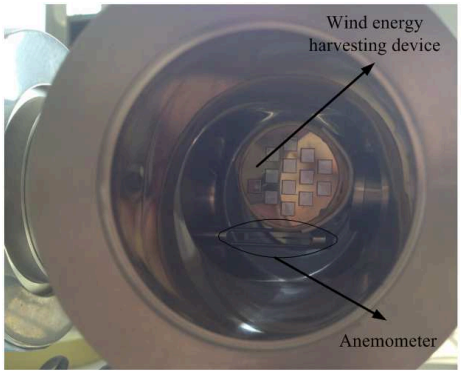




Figure. 4. Picture of self-manufactured small wind tunnel Figure. 5. Anemometer



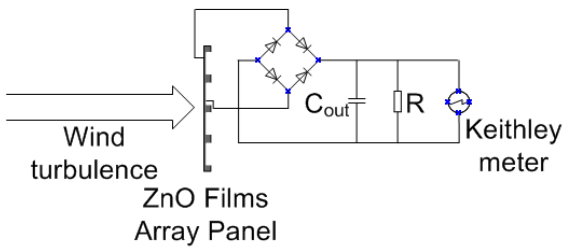


Figure. 6. Wind energy harvesting experiment Figure. 7 Wind energy receiving circuit

The receiving circuit of the wind energy harvesting system is shown in Fig. 7. Wheatstone bridge circuit transfers alternative voltage into direct voltage, it is necessary because there are

complicate vibration of air in the turbulence which causes the vibration of the films. Capacitor is used to store the electric produced by the films array panel, and Keithley meter is applied for voltage monitoring.

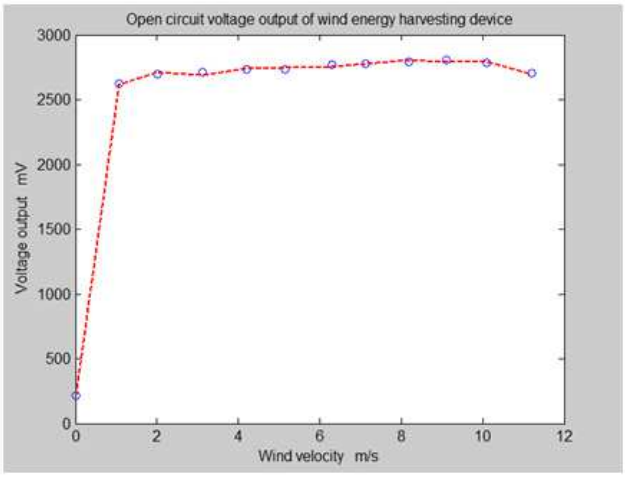


Figure. 8. Open circuit output voltage of the device

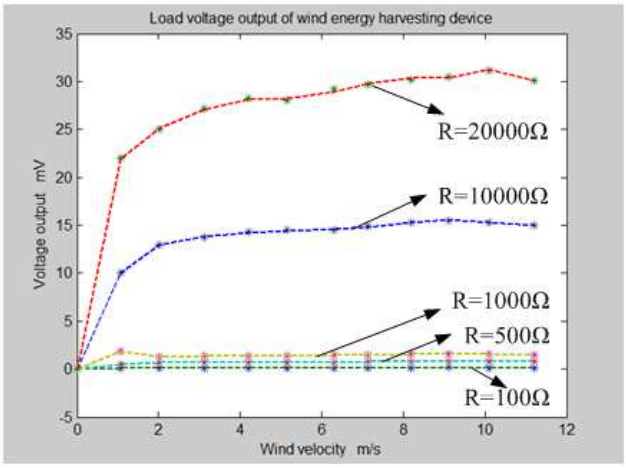


Figure.9. Load voltage of the device

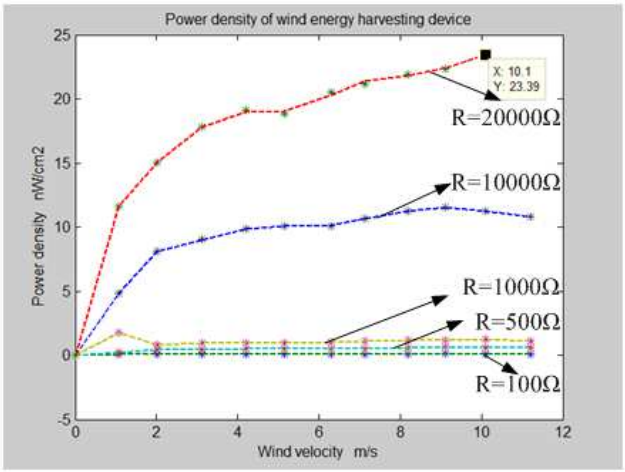


Figure. 10. Output power density of device

The output voltage of the wind energy harvesting device with the MEMS ZnO films array structure is tested at different wind velocity conditions. The experiment results are exhibited in Fig.s 8, 9 and 10. Fig. 8 shows the relationship between wind velocity and open circuit voltage, it reveals

that the maximum open circuit output voltage of the device is about 2.7V when the wind velocity is more than 1m/s, high output voltage is obtained when the films array excited by wind turbulence, and afterwards it rises slowly along with the increase of wind velocity. The circles in Fig. 8 are experiment data and the dash line is the least square curve. Fig. 9 displays the load voltage of device in different wind velocity. The phenomenon can be observed that output voltage increases when the load resist is large. The variable trend of the load voltage is similar with the open circuit voltage when the load resist is selected. The output power density of device with different load resist can be seen in Fig. 10, it shows that higher load resist would be able to gain more power, that means the device has good load capacity. The maximum output power density reaches 23.39nW/cm^2. The stars in Fig. 9 and Fig. 10 are the data measured by Keithley meter, the dash lines are the least square curves. Detailed experiment data are exhibited in Table 1.

Table 1 Detailed voltage data of wind energy harvesting device in wind tunnel

Wind velocity (m/s)	Open circuit voltage (mV)	Load voltage (mV)				
		R=100Ω	R=500Ω	R=1000Ω	R=10000Ω	R=20000Ω
0	212	0	0	0	0	0
1.06	2624	0.10	0.50	1.90	10.0	22.0
2.01	2694	0.12	0.70	1.30	13.0	25.0
3.11	2710	0.13	0.70	1.39	13.7	27.2
4.21	2730	0.14	0.71	1.42	14.3	28.2
5.15	2736	0.14	0.72	1.42	14.5	28.0
6.30	2772	0.14	0.72	1.45	14.5	29.2
7.12	2776	0.14	0.75	1.51	14.9	29.7
8.18	2791	0.15	0.79	1.55	15.3	30.2
9.10	2810	0.16	0.81	1.55	15.5	30.5
10.10	2785	0.15	0.80	1.59	15.3	31.2
11.20	2701	0.15	0.76	1.51	15.0	30.1

The films array vibrates with the resonant frequency in wind turbulence, so the output voltage is high even the wind velocity is low. The formation of the film changes when the wind velocity increase, thus the resonant frequency of the film various because of the formation change. At the same time, the increase of the wind velocity will enlarge the force applied on the film, and as a result increase the flexibility of the film. Both two reasons mentioned above rise up the output voltage slowly. Larger resist may have higher voltage when the inner resist of the device is invariable, so the voltage and the power density increase drastically as one can observe in Fig. 9 and Fig. 10.

Conclusion

The novel wind energy harvesting device based on MEMS square ZnO piezoelectric thin films array structure has been introduced in the article. The design met the requirements of the energy harvesting element that the film is stable even in wind with a high velocity in the experiment. The device is fabricated successfully by MEMS technology. The maximum output power density reaches 23.39nW/cm^2, thicker ZnO layer or material with higher piezoelectric coefficient (like PZT) may enhance the power density effectively. The progress is still primary, and there is a large room to improve the power density. The relevant technology is promising for ambient wind energy harvesting on high buildings in city blocks prospectively.

Acknowledgement

This work is supported by National Basic Research Program of China (No.2011CB302104) and National Natural Science Foundation of China (No.51305423).

Reference

[1] S.K. Salman, and A.L.J. Teo, Power Systems, IEEE Transactions on, **18**, 793 (2003).
[2] M. Chinchilla, S. Arnaltes, and J.C. Burgos, Energy Conversion IEEE Transactions on, **21** ,130 (2006).
[3] Y. Bazilevs, M. C. Hsu, and J. Kiendl, Int J Numer Meth FL, **65** ,236(2011).
[4] B. Boukhezzar, and H. Siguerdidjane, Energ Convers Manage, **50** ,885(2009).
[5] M. Huleihil, J. Appl. Phys. **105**, 104908 (2009).
[6] D. A. Howey, A. Bansal, and A.S. Holmes, Smart Mater. Struct, **20**, 0964(2011).
[7] H. J. Jung, and S. W. Lee, Smart Mater. Struct, **20** ,055022(2011).
[8] J. Ji, F. R. Kong, and L. G. He, Jpn. J. Appl. Phys. **49** ,050204(2010).
[9] S. Priya, C. T. Chen, and D. Fye, Jpn. J. Appl. Phys. **44** ,L104(2005)
[10] S.G. Li, J. P. Yuan, and H. Lipson, J Appl. Phys, **109** ,026104(2011).
[11] S.W. Ibrahim, and W. G. Ali, J Renewable Sustainable Energy, **4**, 062703(2012).
[12] H. C. Liu, C. J. Tay, C. G. Quan, T. Kobayashi, and C. K. Lee, J Microelectro Mech S, **20** ,1131(2011).
[13] H. B. Fang, J. Q. Liu, and Z. Y. Xu, Microelectr J, **37** ,1280 (2006).
[14] D. N Shen, J. H Park, and J. Ajitsaria, J. Micromech. Microeng.**18** ,055017(2008).
[15] L. D. Du, Z. Zhao, and C. Pang, Sensors and Actuators A **151** ,35(2009).

Key Engineering Materials Vols 645-646 (2015) pp 1145-1149
© (2015) Trans Tech Publications, Switzerland
doi:10.4028/www.scientific.net/KEM.645-646.1145

Submitted: 2014-11-03
Accepted: 2014-12-23

VCu_xO_y thin film by magnetron sputtering as cathode material for thin film lithium-ion microbatteries

Lin Jie[a], Guo Jianlai, Liu Chang, Guo Hang[b,*]

Pen-Tung Sah Micro-Nano Science and Technology Institute, Xiamen University, 361005, China
[a]linjie987@163.com, [b]hangguo@xmu.edu.cn

Keywords: VCu_xO_y; thin film; magnetron sputtering; cathode; lithium-ion microbattery

Abstract. A Cu doped V_2O_5 film for lithium-ion batteries is prepared by magnetron sputtered using a vanadium target. Coppers are doped in varying proportions to investigate the effect of doping on the electrochemical properties. In comparison, the surface of doped samples is smooth and uniform. And the results of electrochemical tests indicate that the proper doped films (V: Cu=8: 1 by area) exhibit better cycle performance, wider voltage plateaus and higher capacity than other samples.

Introduction

With the rapid development of Micro electro mechanical system (MEMS) technology, the demand for powering various micro/nano devices and systems is increasing. On chip energy and/or power source devices are under investigation to satisfy this urgent trend [1, 2]. Rechargeable thin film lithium-ion microbatteries hold great attention owing to their high energy density, long lifespan and environmental friendliness, and have a wide application prospect in MEMS or other fields. Many people have found that the electrode materials with doping metal are most desirable to improve the electrochemical performance [3].

Among the potential cathode materials, vanadium pentoxide (V_2O_5) has been extensively studied recently because of its low cost, abundance, ease of synthesis, as well as its high energy efficiency and relatively high theoretical capacity (294 mAh g^{-1}) compared with other commonly used cathode materials [4]. However, due to its poor structural stability, low electrical conductivity and slow electrochemical kinetics, the major problem is the limited cyclic stability [5, 6]. To mitigate this shortcoming, many nanostructure forms of V_2O_5 (nanotubes, nanorods, nanofibers, nanoparticles, and nanowires) are synthesized via various methods [7-11]. Among these methods, magnetron sputtering is a very facile method to prepare smooth thin film and dope metal. It is demonstrated that doping metal (Cu, Ag, Fe, et al) into V_2O_5 film in different proportions can significantly improve the electrochemical properties [12-14]. Herein, we apply this method by magnetron sputtering to fabricate VCu_xO_y thin film. And stable structure, large reversible capacity and excellent rate capability are obtained in the proper doped sample.

Experiment

P-type (100) Si with a resistivity of ~0.0015 Ω cm was used as the substrate. After oxidation, Ti/Au with a thickness of 30/300 nm were magnetron sputtered on the Si substrate, and then a layer of V_2O_5 doped with coppers was deposited by radio frequency (RF) magnetron co-sputtering for 3 h. It was kept in an atmosphere of O_2: Ar = 1: 11, the working pressure was 1 Pa and the sputtering power was 150 W. The structure of the working electrodes is shown in Fig. 1. Undoped V_2O_5 thin film and largely doped sample were also prepared to compare the influence of Cu doping content to the structure and properties. The fabrication parameters are shown in Tab. 1, and the chemical

composition were measured by X-ray Photoelectron Spectroscopy equipment (XPS, PHI Quantum 2000 Scanning ESCA Microprobe).

Tab. 1 Fabrication parameters of VCu_xO_y films.

Sample number	V: Cu (target area)	Thickness (nm)	Atomic radio
A	1:0	201	V_2O_5
B	8:1	210	$VCu_{1.6}O_3$
C	6:1	206	$VCu_{3.55}O_{4.88}$

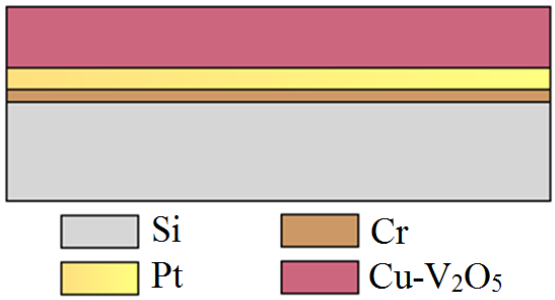


Fig. 1 Structure of VCu_xO_y films.

The coin cells (CR2016) were assembled in a glove box full of argon air with the prepared films as the working electrode, Li metal foils as the counter electrodes, and 1.0 mol/L $LiPF_6$ mixed with EC+EMC+DMC (1:1:1, in volume) as the electrolyte. After the cells were aged for 12 h, the galvanostatic charge/discharge tests were conducted on an Arbin BT-2000 instrument. The voltage range was 1.5~4.0 V, and the current density was 20 μA cm^{-2}. The cyclic voltammetry (CV) tests were performed in a PAR263A potentiostat with a rate of 0.1 mV s^{-1} between 2.0 and 4.0 V. The morphology was examined by field emission scanning electron microscopy (SEM, ZEISS Sigma).

Results and discussion

The SEM images of different samples are shown in Fig. 2. The surface of sample A is uneven and full of flaws. On the contrary, the morphology of doped samples are smooth and uniform, and no obvious clusters are observed. Thus the contact areas between electrode and electrolyte are increased, and the contact resistance is decreased. As a result, the structure of doped samples are more stable which benefit the intercalation/de-intercalation of lithium-ion (Li^+), and lead to an excellent cycle performance.

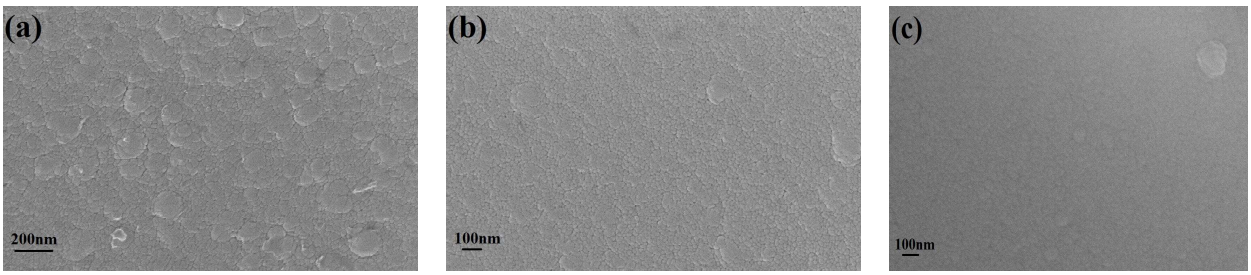


Fig. 2 SEM images of (a) sample A, (b) sample B, (c) sample C.

The cyclic voltammogram curves of the different samples are shown in Fig. 3. As shown in the cures of Fig. 3a, three obvious redox peaks corresponding to the structural phase transitions during the intercalation of Li^+ can be seen. With the increasing of embedded Li^+, the stratified structure of V_2O_5 film turns folded, and the chemical reactions are as below [15]:

$$\alpha\text{-}V_2O_5 + 0.5Li^+ + 0.5e^- \rightleftharpoons \varepsilon\text{-}Li_{0.5}V_2O_5$$

$$\varepsilon\text{-}Li_{0.5}V_2O_5 + 0.5Li^+ + 0.5e^- \rightleftharpoons \delta\text{-}LiV_2O_5$$

$$\delta\text{-}LiV_2O_5 + 0.6Li^+ + 0.6e^- \rightleftharpoons \gamma\text{-}Li_{1.6}V_2O_5$$

If the Li^+ further embed into the film, a new phase of rock salt ω-$Li_3V_2O_5$ will appear [16]. Li^+ can reversibly intercalate/deintercalate the new structure in a form of solid solution, and perform as a slope line in the curves without any plateaus. As shown in Fig. 3b, a big peak appears at ~2.1 V related to the first intercalation of Li^+ irreversibly. Nonetheless, the irreversible peak reduces in the curves of Fig. 3c, acting as a stable pair of redox peak. After cycling for a long time, the stress caused by the irreversible reactions leads to the collapse of structure, and Li^+ is captured in these areas, so that the resistance is increased [17] and the capacity is decreased [18].

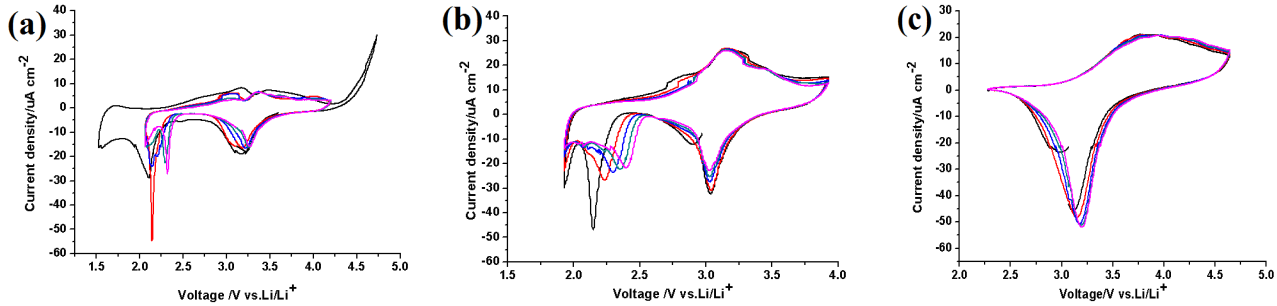


Fig. 3 Cyclic voltammogram curves of (a) sample A, (b) sample B, (c) sample C.

As shown in Fig. 4a, no broad plateaus can be seen in the charge/discharge curves of pure V_2O_5 film, and the discharge capacity is relatively lower than the doped films. With the increasing of doping Cu, the plateaus during discharge become wider and the capacity is improved significantly in Fig. 4b and c. Moreover, the reversibly capacity of sample C in the second cycle reaches up to 350 μAh cm^{-2} $μm^{-1}$, and the plateaus during discharge are distinct compared to sample A and B.

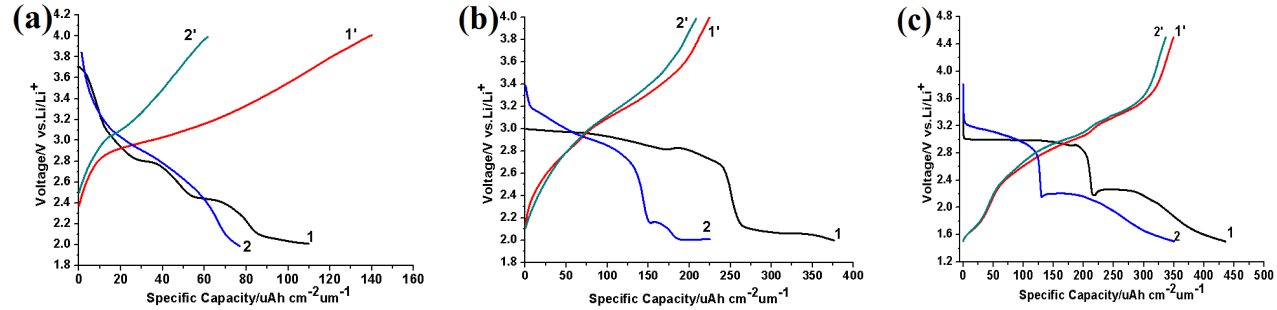


Fig. 4 Charge/Discharge curves of (a) sample A, (b) sample B, (c) sample C.

The discharge capacity of all samples in the first 52 cycles is compared in Fig. 5. Sample A exhibits a continues attenuation capacity with an initial irreversible capacity loss of 44%. The capacity is 30 μAh cm^{-2} $μm^{-1}$ after 50 cycles, which is only 12% of the one in the second cycle. Relatively, the reversible capacity of sample B is close to 270 μAh $cm^{-2}μm^{-1}$ even after 50 cycles, showing an outstanding cyclic stability. Furthermore, the charge/discharge properties of sample C are increased obviously with a capacity of 320 μAh $cm^{-2}μm^{-1}$ even after 50 cycles. In other words, the doping contents should be enough to improve the diffusing kinetics and electronic conductivity.

Fig. 6 shows the cyclic curve and coulombic efficiency of sample C. From the 45th cycle, the charge/discharge capacity begins to decrease, but the coulombic efficiency remains at ~100%. After 100 cycles, the capacity retention radio is 73% compared to the second cycle. The results indicate that the doped coppers enhance the Li^+ storing ability and stabilize the conductive framework.

In order to further research the electrochemical property of sample C, the rate testing was also performed as shown in Fig. 7. With the increasing of current density from 20 μA cm^{-2} to 50 μA cm^{-2}, the discharge capacity gradually decreases. However, at the current density of 50 μA cm^{-2} sample C

keeps a high capacity of 290 μAh cm^{-2} μm^{-1} which is reliable to the reported results [19, 20]. In addition, the capacity returns to 320 μAh cm^{-2} μm^{-1} when the current density is back to 50 μA cm^{-2}. This implies a good rate property of the doping appropriately sample.

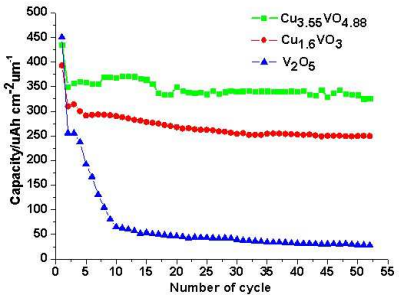


Fig. 5 Cycle performance of all samples.

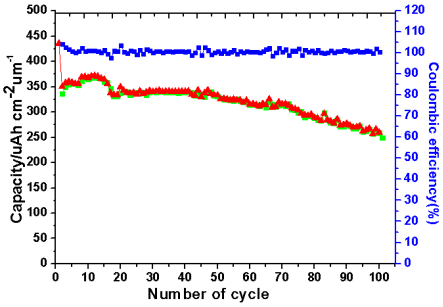


Fig. 6 Cyclic curve and coulombic efficiency of sample C.

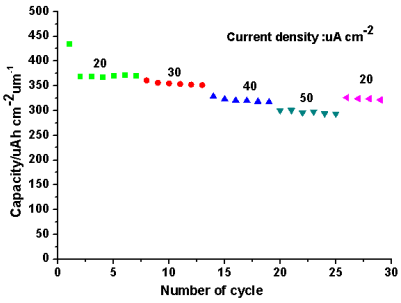


Fig. 7 Rate capability of sample C.

Summary

The Cu doped V_2O_5 thin films are prepared by magnetron sputtering as cathode material for thin film lithium-ion microbatteries. The SEM results show that with the increasing of doping coppers, the V_2O_5 grains became more flat and smooth. The electrochemical properties were studied by CV measurement and galvanostatic charge/discharge tests. As the doping coppers enhance the energy storing ability and stabilize the conductive framework, the $VCu_{3.55}O_{4.88}$ thin film remains a high discharge capacity of 320 μA h cm^{-2} μm^{-1} even after 50 cycles, and exhibits an excellent rate capability. This paper reveals the advantages of doping metal into film for lithium-ion batteries, and provides a guidance to prepare high performance cathode material for thin film microbatteries.

Acknowledgments

This work is financially supported by the New Century Talent Support Plan of the Ministry of Education of China (2007NCET-07-0723), the National Natural Science Foundation of China (60936003) and the Aviation Science Foundation of China (2008ZH68002).

References

[1] K.B. Lee, L.W. Lin, J Microelectromech S, 12 (2003) 840-847.
[2] J.P. Carmo, J.F. Ribeiro, M.F. Silva, L.M. Goncalves, J.H. Correia, J Micromech Microeng, 20 (2010).
[3] L. Wang, S. Kitamura, K. Obata, S. Tanase, T. Sakai, J Power Sources, 141 (2005) 286-292.
[4] A. Benayad, H. Martinez, A. Gies, B. Pecquenard, A. Levasseur, D. Gonbeau, J. Phys. Chem. Solids, 67 (2006) 1320-1324.
[5] S. Chung, N. Chmilenko, A.Y. Borovykov, S. Lee, J Power Sources, 84 (1999) 6-11.
[6] S.Q. Wang, S.R. Li, Y. Sun, X.Y. Feng, C.H. Chen, Energ Environ Sci, 4 (2011) 2854-2857.
[7] V. Mohan, B. Hu, W. Qiu, W. Chen, J Appl Electrochem, 39 (2009) 2001-2006.
[8] R. Ostermann, D. Li, Y. Yin, J.T. McCann, Y. Xia, Nano Lett, 6 (2006) 1297-1302.
[9] D. Yu, C. Chen, S. Xie, Y. Liu, K. Park, X. Zhou, Q. Zhang, J. Li, G. Cao, Energ Environ Sci, 4 (2011) 858-861.
[10] M. Koltypin, V. Pol, A. Gedanken, D. Aurbach, J Electrochem Soc, 154 (2007) A605-A613.
[11] T. Zhai, H. Liu, H. Li, X. Fang, M. Liao, L. Li, H. Zhou, Y. Koide, Y. Bando, D. Golberg, Adv Mater, 22 (2010) 2547-2552.
[12] Y. Wei, C.-W. Ryu, K.-B. Kim, J Power Sources, 165 (2007) 386-392.

[13] F. Coustier, J. Hill, B.B. Owens, S. Passerini, W.H. Smyrl, J Electrochem Soc, 146 (1999) 1355-1360.
[14] M. Sananes-Schulz, F.B. Abdelouahab, G. Hutchings, J. Volta, Journal of Catalysis, 163 (1996) 346-353.
[15] P. Rozier, J.M. Savariault, J. Galy, Solid State Ionics, 98 (1997) 133-144.
[16] C. Delmas, H. Cognac-Auradou, J. Cocciantelli, M. Menetrier, J. Doumerc, Solid State Ionics, 69 (1994) 257-264.
[17] H.-K. Kim, T.-Y. Seong, Y.S. Yoon, Journal of Vacuum Science & Technology B: Microelectronics and Nanometer Structures, 21 (2003) 754-759.
[18] J.G. Zhang, J.M. McGraw, J. Turner, D. Ginley, J Electrochem Soc, 144 (1997) 1630-1634.
[19] L.T. Zhang, J. Song, M.Z. Cai, F.C. Xu, S.T. Wu, Q.F. Dong, Chem J Chinese U, 30 (2009) 971-975.
[20] L.Z. Li Jing, Wu Suntao, Journal of Functional Materials, 36 (2005) 1301-1304.

Key Engineering Materials Vols 645-646 (2015) pp 1150-1155
© (2015) Trans Tech Publications, Switzerland
doi:10.4028/www.scientific.net/KEM.645-646.1150

Submitted: 2014-12-02
Accepted: 2014-12-23

High performance supercapacitor electrode materials based on activated carbon and conducting polypyrrole

Yuan Wentao[1,a], Yang Yajie[1,b], Qiu Yonglong[2,c], Xu Jianhua[1,d]
Yang Wenyao[1,e], Xia Shuang[3,f]

[1]School of Optoelectronic Information, University of Electronic Science and Technology of China, Chengdu, Sichuan, China

[2]Fire-controlling and Technology Center of China Ordnance Group, Chengdu, Sichuan, China

[3]68129 PLA troops, Lanzhou, Gansu, China

[a]kobe371660435@163.com, [b]jj_eagle@163.com(corresponding author),[c]305487956@qq.com, [d]xujh9913@163.com, [e]yang0220@163.com, [f]552018814@qq.com

Keywords: supercapacitor; electrode; polypyrrole; activated carbon; electrochemical.

Abstract. The traditional supercapacitor is made of activated carbon, which shows lower specific capacity and higher resistance. In this paper, we demonstrated preparation of high performance supercapacitor electrode materials based on activated carbon and conducting polymer polypyrrole (ppy). In order to obtain well dispersion of ppy in activated carbon for lower resistance of electrode, a high-speed agate beads milling process was used to mix the ppy and porous carbon powder. By controlling the synergistic effect between ppy and activated carbon, a uniform structure composite electrode was prepared and the performance of this composite based supercapacitor was investigated. Compared with pure activated electrode, the obvious electrochemical performance improvement was achieved in composite electrode after the introduction of ppy. It has been found that electrode based on this composite has a maximum specific capacitance about 159 F/g, which was higher than pure activated carbon, and exhibited low resistance about 3.35 Ohm. The cycle performance results revealed that a 142 F/g (more than 88% of initial capacitance) capacitance was kept in composite electrode after 1000 cycles charge/discharge process. We conclude that the excellent synergistic effect between activated carbon and ppy resulted in superior electrochemical performance of composite electrode. Furthermore, the simple preparing method of composite electrode for supercapacitor assembly has potential commercial applications.

Introduction

It is essential that new, low-cost energy storage systems should be found to meet the needs of modern society and emerging ecological concerns [1]. Supercapacitor (also called electrochemical capacitors and ultracapacitor) are able to store and deliver energy at relatively high rates because the mechanism of energy storage is the simple charge-separation at the electrochemical interface between the electrode and the electrolyte [2]. The advantage of supercapacitors is that they have several orders of magnitude higher energy density than that of conventional dielectric capacitors. Furthermore, supercapacitors have long cycle life and rapid charging and discharging at high power densities [3]. As its outstanding characteristic, supercapacitors have generated wide application in many fields, including smart watch, outdoor switch, electric vehicles, electric utilities, factory power backup and so on.

The common material of commercial supercapacitors is porous carbon. Although porous carbon materials have high specific surface area, the low conductivity and the energy storage mechanism of porous carbon materials limits its application in high specific capacitance supercapacitors. Hence, many studies have focused on the addition of high conductive nanostructured materials, like CNTs, graphene and so on, into activated carbon for improved electrochemical performance [4], However, the disadvantages of these materials are that they are too expensive and the production technology is complicated.

Conducting polymers (CPs) has been a subject of growing interest due to their promising application in supercapacitor. Conducting polymers can afford high specific capacitance due to its pseudo capacitance energy storage process. However, the brittle and weak in mechanical strengths nature makes electrochemical energy storage devices based on pure conducting polymer working unstably during the long cycle charge/discharge process. So, coupling conducting polymer with high stable carbon materials is an effective way to improve electrochemical stability of conducting polymer. Conductive polymer ppy has been tested in electrochemical capacitors applications as pseudocapacitive capacitors [5], which show high gravimetric and volumetric pseudocapacitance in aqueous electrolyte under the operating voltages of 1 V. Moreover, ppy show both cheaper and simple preparation process than other materials and it is promising to introduce ppy into the electrode material for supercapacitor applications. However, when used as bulk materials, ppy also suffer from a limited stability during cycling that reduces the initial performance.

In this paper, in order to improve the activated carbon capacitive performance, the ppy was mixed with activated carbon as composite electrode. We focus on balancing the mass ratios of porous carbon and ppy for optimized electrochemical performance of composite electrode. In order to obtain well dispersion of ppy in activated carbon for lower resistance of electrode, a high-speed agate beads milling process was used to mix the ppy and porous carbon powder. By controlling the synergistic effect between ppy and activated carbon, a uniform structure composite electrode was prepared and the performance of this composite based supercapacitor was investigated.

Experimental Section

Materials. Polypyrrole was purchased from Aldrich. Porous carbon was purchased from Nanjing XF Nano Co., Ltd. The other reagents were used as received without further treatment.

Fabrication of Supercapacitor Electrode. An activated carbon electrode was composed of activate material (activated Carbon, 80wt.%), conductive agent (acetylene Black, 15wt.%) and binder (Teflon, 5wt.%). The other six composite electrodes were composed of ppy and activated carbon electrode, varying with different ppy mass ratio (10%, 20%, 30%, 40%, 60%, 100%) in active material. In order to obtain a good dispersion of ppy into activated carbon, a high-speed agate beads milling process was used to prepare ppy/activated carbon composites. After the thorough mixing of ppy/activated carbon, the Teflon solution was added into composites to get the carbon mixture. Then, the carbon mixture was ground with a pestle at a temperature of 100 °C. The high temperature resulted in a fiber structure of Teflon for better package of ppy on active materials. After this mixing process, the obtained composite powder was compressed into disk electrode with a 24mm×80μm dimension. Finally, this disk sample was compressed on a Ni foam current electrode under a pressure of 20 MPa.

Electrochemical Measurements and Characterization. The morphology of composite electrode was characterized by Scanning Electron Microscope (SEM) with model JSM-6610LV. The electrochemical performance of composite based supercapacitor were studied in a three-electrode system by cyclic voltammetry(CV), electrochemical impedance spectroscopy(EIS) and galvanostatic charge/discharge methods using a electrochemical workstation(CHI660, Shanghai). The cyclic voltammetry (CV) curves of the electrodes were measured at different scan rates varying from 20 mV/s to 100 mV/s. Galvanostatic charge/discharge testing was carried out at potentials between 0 and 1.0 V using a 1mol/L Na_2SO_4 aqueous electrolyte solution. Impedance spectroscopy measurements were carried out at a dc bias of 0 V with sinusoidal signal of 5 mV over the frequency range from 100 kHz to 10 MHz.

Results and Discussion

The three-electrode system was used for these measurements. For a three-electrode system, the voltage potential applied to the working electrode is that shown on the X-axis of the cyclic voltammetry (CV) chart. So it provides the most reliable results of a material's performance for electrochemical capacitors [6]. Three-electrode system consists of a working electrode, a reference electrode, and a counter electrode. The performance of the supercapacitor electrodes are analyzed

using CV, galvanostatic charge/discharge and EIS. The rectangular CV curve indicate an excellent capacitance behavior and low contact resistance of the electrodes, the specific capacitance is calculated from the slope of the charge-discharge curves [7]. The EIS data is analyzed using Nyquist plots. Each data point in Nyquist plot is at a different frequency [8].

Figure 1 shows cyclic voltammetry (CV) curves of activated carbon electrode with various scan rates in the range of 0 to 1V/s. For an ideal capacitor, the rectangular shape of CV curve means the low contact resistance of devices. The CV curves of our devices based on activated carbon electrode are almost rectangular at various scan rates and even at a high scan rate of 100mV/s. This result reveals that an excellent capacitance behavior and low contact resistance are obtained in this capacitor.

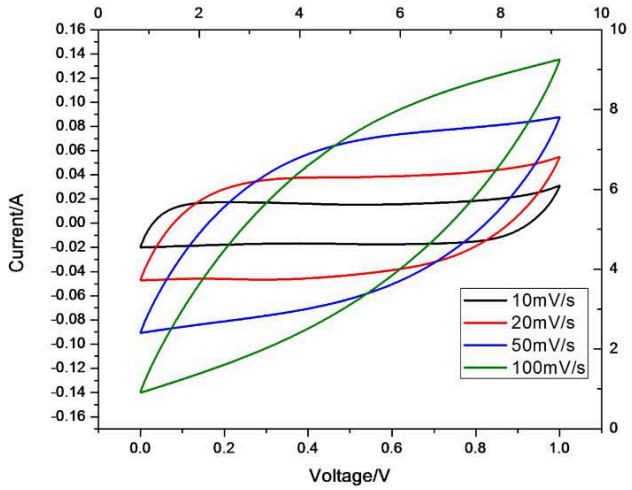


Fig. 1. Cyclic voltammetry (CV) curves of benchmark electrode (BE) at different scan rates

The influence of ppy mass ratio in composite on capacitive performance of electrode was investigated, which is shown in Figure 2. It can be seen that, at a 20mV/s scan rate, the CV curve of different electrode are close to rectangular, indicating the good capacitance property of composite electrode. It also can be seen in Figure 2, with the increase of mass ratio of ppy in composite, the CV curve exhibits irregular rectangular shape due to the irregular CV characteristics of ppy pseudocapacitance. In this composite electrode, the presence of ppy results in irregular part in composite CV curve, and the composite CV curve exhibit more irregular shape with the increasing of ppy mass ratio. Hence, we conclude that the ppy play an important role in capacitive performance of composite electrode.

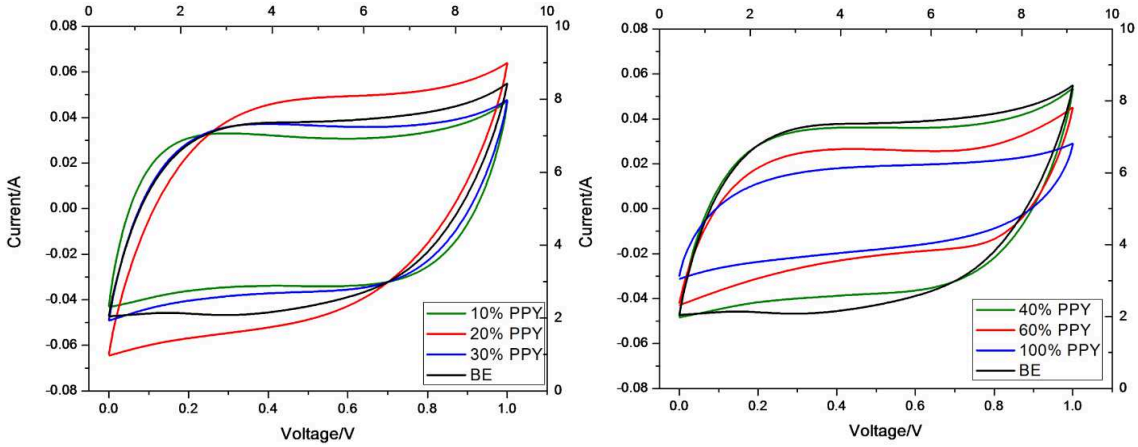


Fig. 2. Cyclic voltammetry (CV) curves of various electrodes at scan rate of 20mV/s

Galvanostatic charge/discharge curve of composite electrodes is performed at a constant current density of 1A/g. As shown in Figure 3, the discharge curves are linear in the total range of potential with constant slopes, indicating nearly perfect capacitive behavior [9]. Furthermore, the galvanostatic charge/discharge curve of composite electrode shows a non-symmetric trend with the increasing of ppy mass ratio, which results from the non-asymmetric CV curve characteristics of ppy during chare/discharge process.

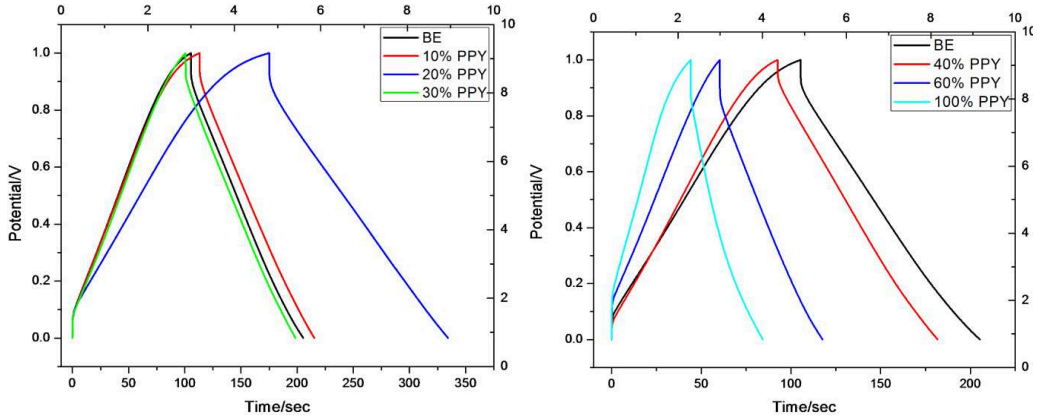


Fig. 3. GC curve of various electrodes at a constant current density of 1A/g

The specific capacitance is evaluated from the slope of the charge-discharge curves according to the following equation:

$$C = I\Delta t/ (m\Delta V) \quad (1)$$

where I is the applied current and m (not including the mass of acetylene black and Teflon) is the mass of each electrode [10]. The specific capacitance of the activated carbon electrode and other electrodes with various ppy mass ratio were calculated, which is shown in Table 1. It can be seen that the electrode containing 20% mass ratio of ppy shows the maximum specific capacitance about 160F/g, and this result is good accordance with the results of cyclic voltammetry.

Table 1. Specific capacitance (F/g) of various electrodes at a constant current density of 1A/g

	BE	10% PPY	20% PPY	30% PPY	40% PPY	60% PPY	100%PPY
SC(F/g)	100	110	159	90	82	60	35

From Figure 3, an IR drop in initial portion of the discharge curve is observed due to the internal resistance of electrode.， ΔV is the voltage drop caused by IR drop.

Table 2. Internal resistance (Ω) of various electrodes

	BE	10%PPY	20% PPY	30% PPY	40% PPY	60% PPY	100%PPY
EIS(Ω)	5.51	3.67	3.35	4.37	4.11	4.21	4.31

We calculate the internal resistance of different electrodes and the results are shown in Table 2. The results indicate that a 20% ppy mass ratio ensures the lowest resistance of composite electrode, and this optimized mass ratio also results in better synergistic effect in composite electrode.

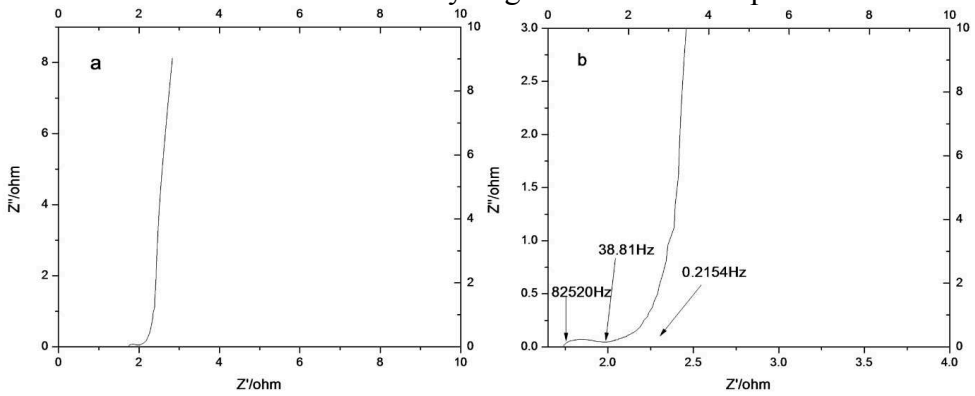


Fig. 4. (a) Nyquist plot for electrode with 20 percents of ppy. (b) Local amplification of Nyquist plot

Figure 4 shows the EIS performance of the composite electrode containing 20% mass ratio of ppy. A straight line in the low-frequency region and an inconspicuous arc in the high frequency region are presented in Nyquist plots. The high frequency curve is related to the electrical resistance between the ppy and porous carbon. The inconspicuous arc in the high frequency region indicates that the electrical resistance between the ppy and porous carbon is very low. The slope of the 45° portion of the curve is called the Warburg resistance and response to frequency dependence of ion diffusion path between electrolyte and electrode surface. The shorter Warburg curve means the shorter diffusion path of electrolyte ion. The vertical curve at lower frequencies indicates a pure capacitive behavior,

representing the fast transportation of the electrolyte ion between opposite electrodes [11]. The more vertical the curve appears at lower frequencies, the more closely the supercapacitor behaves like an ideal capacitor. So, we can conclude that the composite electrode exhibits lower contact resistance and fast ion adsorption-desorption performance after the doping of ppy into activated carbon.

We investigated the influence of morphology on electrochemical performance of composite electrode. As we mentioned above, the composite electrode was baked at high temperature about 100 °C to soften the binder Teflon into the fibrous structure. This fibrous structure ensures better adhesiveness between activated carbon and ppy. Figure 5 shows the cross sectional structure of composite electrode containing 20% mass ratio of ppy. The SEM image indicates that the active material was connected compactly by Teflon fiber, resulting in ideal Nyquist plot of the electrode. Figure 5(b) is the larger magnification SEM image of composite electrode. Uniform distribution of Teflon fiber in the composite electrode is presented, which is benefit for lower internal resistance and rapidly charge-discharge progress of the electrode.

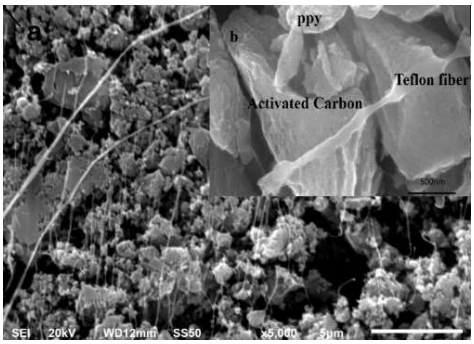


Fig. 5. Cross section SEM image of composite electrode containing 20% ppy

In order to obtain well dispersion of ppy into activated carbon as high performance electrode material, a high-speed agate beads milling process was utilized to mix the ppy and activated carbon. Figure 6 shows morphology change of composite electrode with and without a milling process treatment. As shown in Figure 6 (a), without the milling process, the large aggregation of active materials is observed in composite and clear interface between the active materials is formed. However, after the milling treatment (as shown in Figure 6(b)), the well distribution of ppy into activated carbon is achieved, and the composite exhibits a uniform structure. From the Figure 6 we can conclude that the milling treatment to activated carbon and ppy produce a uniform composite structure as high performance electrode materials.

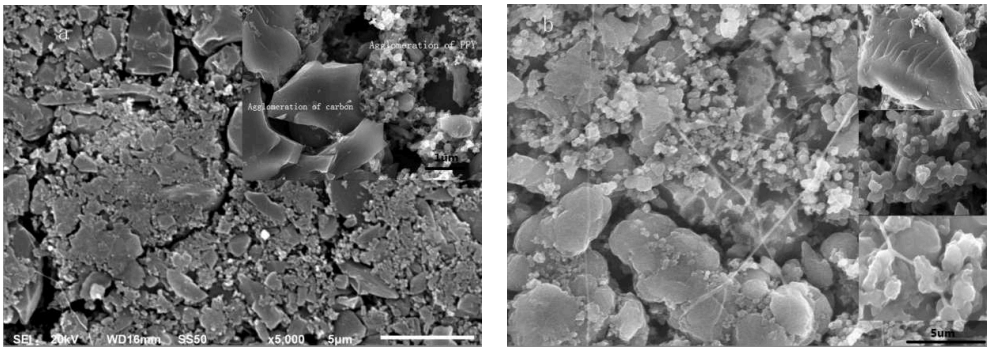


Fig. 6. SEM images of composite electrode containing 20% mass ratio ppy, (a) without a milling treatment, (b) with the milling treatment.

Long cycle life of supercapacitor is important for its practical applications. Figure 7 shows the variation of specific capacitance as a function of cycle number for composite electrode containing 20% mass ratio ppy at a constant current density. For this activated carbon/ppy electrode, the specific capacitance maintained 88% capacitance after 1000 cycles. The result indicates a good cycling ability of the composite electrode. The activated carbon provided a robust support for the conducting polymer ppy during the electrochemical activity, resulting in excellent cycling stability of composite electrode.

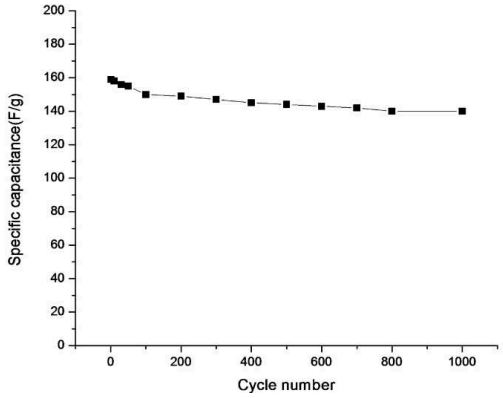


Fig. 7. Specific capacitance change as a function of cycle numbers at a 1 A/g constant current density.

Summary

A high-speed agate beads milling process was utilized to prepare uniform structure of activated carbon and ppy composites. The SEM images showed that the active materials were connected by Teflon fiber effectively. This uniform structure contributes to the lower internal resistance (3.35 Ohm) and rapidly charge-discharge progress of composite electrode. The introduction of ppy in activated carbon obviously improved the capacitive property of electrode, and an optimized mass ratio of ppy in composite results in a high specific capacitance about 159F/g. The excellent synergistic effect between activated carbon and ppy resulted in high stable electrochemical activity of composite electrode during the energy storage process, which shows promising future as real supercapacitor applications.

Acknowledgement

This work was supported by the National Science Foundation of China (NSFC) (No. 61101029 and No. 61204098), A Plan for Supporting the New Century Talents (No.NCET-12-0091).

References

[1] A.S. Arico, P. Bruce, B. Scrosati, J. M. Tarascon, S.W. Van, Nanostructured materials for advanced energy conversion and storage devices, Nat. Mater. 4 (2005) 366-377.

[2] A.G. Pandolfo, A.F. Hollenkamp, Carbon properties and their role in supercapacitors, J. Power Sources. 157 (2006) 11-27.

[3] P. Simon, Y. Gogotsi, Materials for Electrochemical Capacitors, Nat. Mater. 7 (2008) 845-854.

[4] G. Lota, T.A. Centeno, E. Frackowiak, F. Stoeckli, Improvement of the structural and chemical properties of a commercial activated carbon for its application in electrochemical capacitors, Electrochim. Acta. 53 (2008) 2210-2216.

[5] V. Khomenko, E. Frackowiak, F. Beguin, Determination of the Specific Capacitance of Conducting Polymer/Nanotubes Composite Electrodes Using Different Cell Configurations, Electrochim. Acta, 50 (2005) 2499–2506.

[6] S. D. Meryl, P. Sungjin, Z. Yanwu, A. Jinho, R. S. Rodney, Graphene-Based Ultracapacitors, Nano. Lett. 8(2008) 1679-1682.

[7] B. E. Conway, Modern Aspects of Electrochemistry**,** Plenum, New York, 1986.

[8] Y. Z. Wei, B. Fang, S. IWASA, A novel electrode material for electric double-layer capacitors, J. Power Source, 141(2005) 385-391.

[9] A. Burke, Ultracapacitors: why, how, and where is the technology, J. Power Sources 91 (2000) 37-50.

[10] A. Nishino, Capacitors: operating principles, current market and technical trends, J. Power Sources 60(1996) 137-147.

[11] W. C. Chen, T. C. Wen, H. S. Teng, Polyaniline-deposited porous carbon electrode for supercapacitor , Electrochim. Acta. 48 (2003) 641-649.

Key Engineering Materials Vols 645-646 (2015) pp 1156-1162
© (2015) Trans Tech Publications, Switzerland
doi:10.4028/www.scientific.net/KEM.645-646.1156

Submitted: 2015-01-15
Accepted: 2015-01-15

Electrohydrodynamic atomization deposition of fuel cell catalyst-coated membrane with structure and material gradient variation

Dazhi Wang[1, 2, a], Wen Zha[1, b], Xiaohu Zhu[1, c], Yang Li[1, d], Junsheng Liang[1, 2, e], Tongqun Ren[1, 2, f *], Yi Luo[1, 2, g], Xiaodong Wang[1, 2, h] and Chong Liu[1, 2, i]

[1]Key Laboratory for Micro/Nano Technology and System of Liaoning Province, Dalian University of Technology, Dalian, 116024, China

[2]Key Laboratory for Precision and Non-traditional Machining Technology of Ministry of Education, Dalian University of Technology, Dalian, 116024, China

[a]d.wang@dlut.edu.cn, [b] wenz@mail.dlut.edu.cn, [c] zhuxiaohu@mail.dlut.edu.cn, [d]y.li@mail.dlut.edu.cn, [e]jsliang@dlut.edu.cn, [f]ren_tq@dlut.edu.cn, [g]luoy@dlut.edu.cn, [h]xdwang@dlut.edu.cn and [i]chongl@dlut.edu.cn

Keywords: Fuel cell, Catalyst-coated membrtane, Electrohydrodynamic atomization, Film

Abstract. A catalyst-coated membrane (CCM) with structure and material gradient variation was deposited layer-by-layer (LbL) using electrohydrodynamic atomization (EHDA) deposition. This CCM contained 7 layers which is C cathode diffusion layer, Pt/C-C cathode transition layer, Pt/C cathode catalyst layer, Nafion membrane, Pt-Ru/C anode catalyst layer, Pt-Ru/C-C anode transition layer and C anode diffusion layer. The cathode and anode side were named as cathode and anode catalyst-diffusion layers, respectively. It was observed that the cathode and anode catalyst-diffusion layers presented the dendritic structure. Within the cathode and anode catalyst-diffusion layers, the Pt/C-C and Pt-Ru/C-C transition layer was more porous compared to the C layer, Pt/C layer and Pt-Ru/C layer. It was also shown that the EHDA LbL deposited CCM still presented close-packed structure after life test.

Introduction

Direct methanol fuel cells (DMFCs) have received increasing attentions as portable electronic devices due to their high energy density, simple system configuration, low emissions and operating temperature [1,2]. Membrane electron assembly (MEA) is the most important unit in the DMFC, in which the catalyst-coated membrane-based MEA (CCM-based MEA) provides better power density due to an extended catalyst/ionomer interface and improvement of catalyst utilization [3]. MEA is composed of gas diffusion layers (GDLs), catalysis layers (CLs), and a polymer electrolyte membrane (PEM). The GDLs as current collectors have excellent electronic contact with CLs and allow ready access of fuel and oxidant to the anode and cathode catalyst surfaces, respectively [4]. CLs support the efficient electrochemical reaction areas and transport the reactants and reaction products. PEM as a solid polymer electrolyte has high proton conductivity and takes the roles of a separator between the methanol-water mixture on the side of anode and air of cathode [5].

The structure of CLs is significant important in DMFC, which should match the requirement of transporting the reactants of methanol and oxygen to the triple-phase boundary (TPB) [6] and removal of the reaction products. The cathode CL should allow the oxygen to reach the catalyst surface and support the efficient removal of product water to prevent flooding. The anode CL should provide the efficient transport of methanol from the flow field to the catalyst surface and promote the removal of the product of carbon dioxide. Therefore, the CL close to the GDL should be porous in order to transport the reactants. In addition the high content of C and low content of Nafion are required to improve the electron transport and the product removal at the area of CL close to the GDL. The CL close to PEM should has low porosity and high catalyst and Nafion content in order to promote the catalysis action and proton transport [7].

For the MEAs made on traditional methods such as painting [8], catalyst decaling [9] and spraying [10], the structure features including the material distribution and structural porosity are difficult to control due to the thick coating single layer [11]. In addition, the delamination of MEA usually happens during the long-term working process due to the poor binding energy between the CLs and PEM, which can result in the reduction of the catalytic efficiency [12].

In this work, The CCM was prepared by successively electrohydrodynamic atomization (EHDA) deposition of C nano-suspension, Pt/C-C nano-suspension, Pt/C nano-suspension, Nafion solution, Pt-Ru/C nano-suspension, Pt-Ru/C-C nano-suspension and C nano-suspension. Moreover, the structure and performance of the CCM with structure and material gradient variation were examined. EHDA is a promising method to deposit CCM using nano-suspensions and Nafion solution. In EHDA process electrostatic and mechanical forces were applied a liquid, then a liquid jet and atomization were formed [13]. The distinct advantage of this technique for the fabrication of the CCM is its capability of depositing the nano-particles via LbL which is convenient to adjust the structure and the material distribution of the deposited film [14].

Experimental

EHDA deposition of CCM with structure and material gradient variation. This CCM contains a C cathode diffusion layer, a Pt/C-C cathode transition layer, a Pt/C cathode catalyst layer, a Nafion membrane, a Pt-Ru/C anode catalyst layer, a Pt-Ru/C-C anode transition layer and C anode diffusion layer. The cathode and anode side were named as cathode and anode catalyst-diffusion layers, respectively. The components of the suspensions/solution and the atomization parameters during the formation of the CCM are shown in Table 1**.** The preparation procedure of suspensions and Nafion solution were described in our previous work [15].

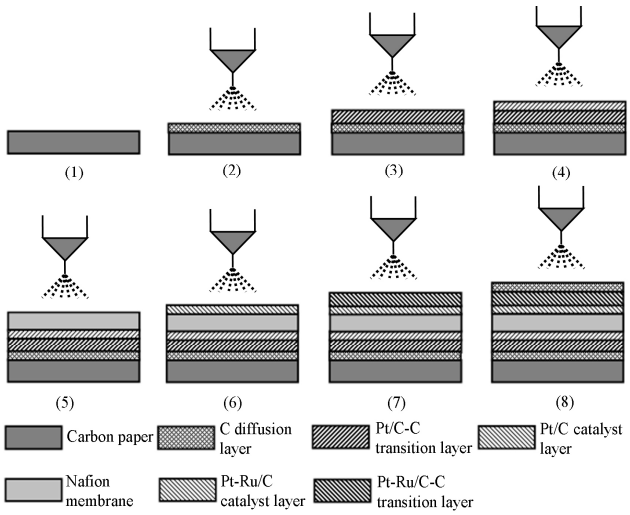


Fig. 1 The fabrication flow chart of the MEA using EHDA deposition.

Fig. 1 shows the fabrication process of the CCM using the EHDA LbL deposition. In this process, the CCM was produced by EHDA deposition of the C, Pt/C-C, Pt/C nano-suspensions, Nafion solution, Pt-Ru/C, Pt-Ru/C-C and C nano-suspensions on a 15 mm × 15 mm carbon paper (15 mm × 15 mmTGP-H-060, Toray Carbon, Japan) in succession. During the EHDA deposition of the diffusion layer, cathode/anode catalyst layers and cathode/anode transition layers, the atomization parameters were varied in order to form graded structure. The details of the EHDA equipment for this deposition were described in our previous work [16].

Single DMFC test. In order to test the performance of the prepared CCM, a single air-breathing DMFC was assembled with the EHDA deposited CCM. This single DMFC was prepared by assembling the CCM, anode GDL, anode and cathode current collectors, anode flow field plate and cathode end plate. The anode GDL of the single cell was carbon paper (TGP-H-060, Toray Carbon, Japan). The anode current collector has a ‘s’ shape methanol flow channel (800 μm in width) and the cathode current collector has air breathing hole arrays (each hole has 800 μm in diameter). The anode flow field plate is polymethyl methacrylate (PMMA) sheets having the same ‘s’ shape corresponding to the anode current collector. During test, methanol solution (3 mol L^{-1}) was supplied in the anode using a syringe pump at a flow rate of 8.3×10^{-10} m^3 s^{-1}. The cathode side was air-breathing mechanism, which absorbed oxygen from the ambient air. The performance of the cell including current density-voltage (I-V) and current density-power density (I-P) at the temperature range from 20 °C to 70 °C was obtained using a DC electronic load. During the test the temperature was controlled using a temperature programmable chamber (Dong Guan Bell Test Equipment Co., Ltd, Guangdong, China).

Results and discussion

Formation of catalyst-diffusion layer. The major advantage of EHDA LbL deposition technique is that it can modify the structure by adjusting the working parameters during the LbL deposition process. In order to improve the contact behavior between the catalyst layer and the diffusion layer, materials transition from the catalyst to diffusion layer were EHDA deposited. In addition, the structure of this catalyst-diffusion layer was varied in order to meet the requirement of the transport the reactant and resultant [7]. Fig. 2a shows the cross-section of cathode catalyst-diffusion layer which presented dendritic structure. It can be seen that the Pt/C-C layer was more porous compared to the C layer and Pt/C layer. It is reported that the catalyst layer close to the diffusion layer with more porous structure compared with that contact with the Nafion membrane can help to improve the transport of reactants and the remove of resultants [7]. Therefore, in this work, the atomization distance for the Pt/C-C layer deposition (7 mm) is higher than that for the C and Pt/C layer deposition (3 mm). The higher working distance can produce more porous structure [17]. The same atomization conditions were applied on the anode side and the structure characteristics were similar to the cathode side, that is more porous Pt-Ru/C-C layer compared with the C and Pt-Ru/C layer (Fig. 3a). Fig. 2b and 3b show the element distribution of the cathode and anode catalyst-diffusion layer, respectively. It can be seen that the content of Pt or Pt-Ru increases from the Pt/C-C or Pt-Ru/C-C layer to Pt/C or Pt-Ru/C layer.

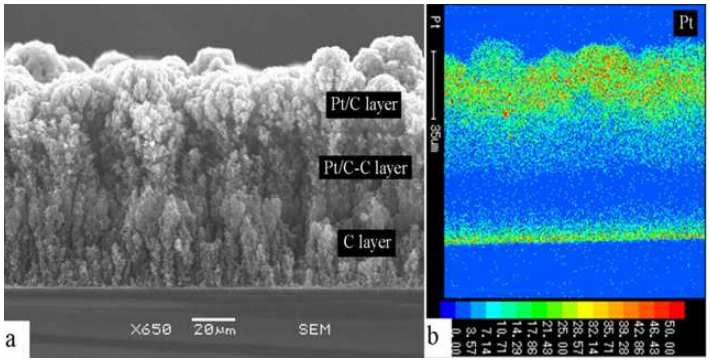


Fig. 2 The cross-section of cathode catalyst-diffsion layer (a) and Pt catalyst distribution inside (b).

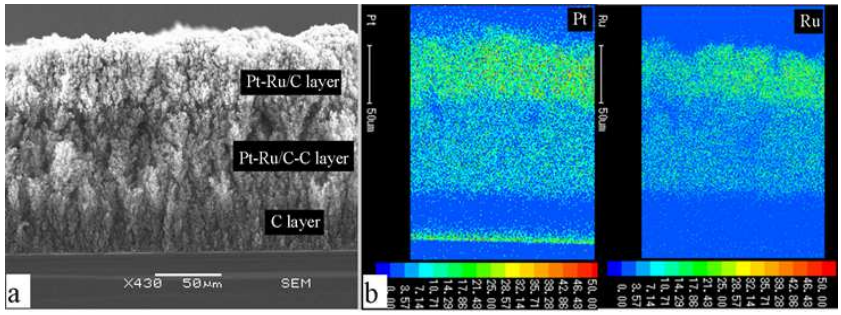


Fig. 3 The cross-section of anode catalyst-diffusion layer (a) and Pt and Ru catalysts distribution inside (b).

Table 1 The components of suspensions/solution and the atomization parameters during the EHDA deposition of the CCM.

Suspension /solution	Components of the suspensions/solution [g]							Atomization parameters		
	C	Pt/C	Pt-Ru/C	Distilled water	Ethanol	Methanol	5wt% Nafion solution	Working distance [mm]	Flow rate [10^{-10}m^{3}s^{-1}]	Voltage [kV]
Pt/C suspension	—	0.05	—	1.5	1.5	—	0.1	3	0.33	2.9
Pt/C-C suspension	0.25	0.05	—	2	9	—	1	7	0.33	3.3
Pt-Ru/C suspension	—	—	0.1	1	2	—	0.15	3	0.33	2.9
Pt-Ru/C-C suspension	0.07	—	0.05	1.5	3	—	0.45	7	0.33	3.3
C suspension	0.05	—	—	—	1.5	—	0.2	3	0.42	2.7
Nafion solution	—	—	—	—	—	1	2	15	2.5	3.5

Deposition of CCM and performance of single DMFC. Fig. 4 shows the cross-section of the CCM produced using the EHDA LbL deposition. This CCM contains cathode catalyst-diffusion layer, Nafion membrane and anode catalyst-diffusion layer. These functional layers were deposited

in succession. The atomization conditions for the cathode catalyst-diffusion and anode catalyst-diffusion layer were the same with that described in section 3.1. The Nafion membrane was deposited at an applied voltage of 3.5 kV, a flow rate of 2.5×10^{-10} m^3 s^{-1} and a working distance of 15 mm. It can be seen that the CCM exhibited close-packed structure. It also can be seen that the anode catalyst layer was more uniform compared with the cathode side. Nafion membrane was EHDA deposited on the cathode CL. During this process the Nafion solution can infiltrate into the pores existing in the cathode CL. In addition the pores can be enlarged by the following evaporation of the solvent process, which resulted in the crack and irregular structure of the cathode CL (Fig. 4). The thickness of the Nafion membrane, cathode catalyst-diffusion and anode catalyst-diffusion layer was approximately 200 μm, 100 μm and 120 μm, respectively. The thicker of the Nafion membrane is to ensure the separation of the cathode catalyst and anode catalyst layer. The catalyst loading was 0.4 mg Pt cm^{-2} and 1 mg Pt-Ru cm^{-2} in the cathode and anode catalyst-diffusion layers, respectively.

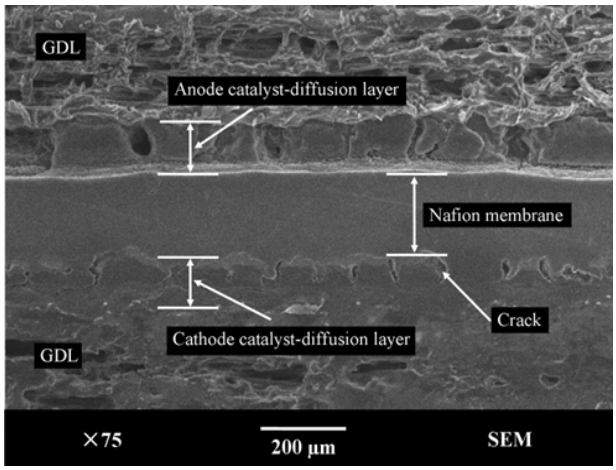


Fig. 4 SEM micrograph showing a typical cross-section of the CCM fabricated using the EHDA LbL deposition.

Fig. 5 illustrates the I-V and I-P behaviour of the DMFC assembled with the EHDA LbL deposited CCM at different temperatures. It can be seen that the cell power density increased with higher temperatures, which is due to the higher activity of gas (O_2) molecule, catalytic reaction and the high efficiency of proton transfer at higher temperature. Between 20 °C and 60 °C, the powder density increased with a level of 0.3 mW cm^{-2} at each 10 °C step. However, when the temperature increased from 60 °C to 70 °C, the cell performance had 0.1 mW cm^{-2} increased which was lower than the temperature range from 20 °C to 60 °C (0.3 mW cm^{-2}). This is because that the larger amount of water will generate at the cathode side when the reaction activity increases with higher temperature, which increase gas-phase transport resistance, thus, decreasing the improvement of the cell performance at higher temperature range from 60 °C to 70 °C.

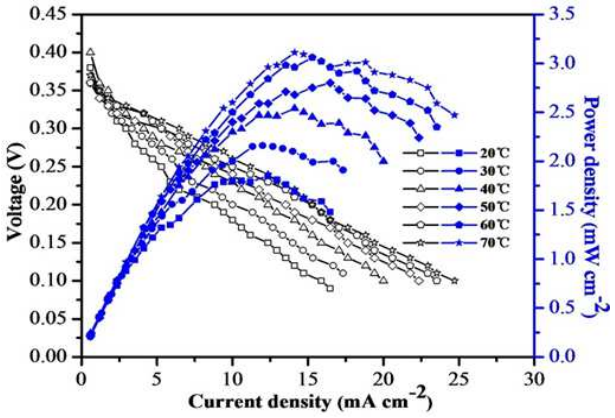


Fig. 5 The polarization curves and power density curves of the DMFC assembled with the EHDA LbL deposited CCM at different temperatures.

The life test was carried out at the temperature of 25 °C. The result of a 48 h life test of the DMFC at 5 mA cm^{-2} is shown in Fig. 6. It was found that after 3 h the cell reached the steady work voltage and the performance of the cell can recover to its initial level within the 42 h duration test. Fig. 7 shows the cross-section of

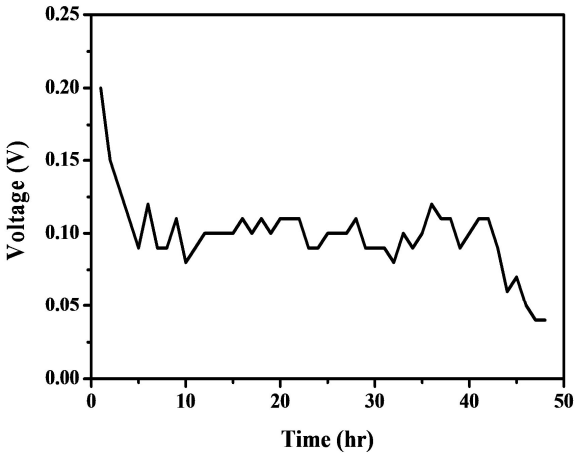


Fig. 6 Life test of the single DMFC assembled with the CCM at the temperature of 25 °C and 5 mA cm^{-2} working current.

the CCM after the 48 h life test. It was observed that the CCM both in the cathode and anode side still remained the compact structure after the life test (Fig. 7). There was no distinct delamination between the GDL, CL and PEM, which was an improvement compared the CCM produced by the heat press, decal method and spray method [18,19,20]. This indicated that the EHDA LbL deposition of CCM with structure and material gradient variation can prevent the delamination and increase the reliability of cell. There are two reasons contribute this reduced delamination behavior. Firstly, the droplet atomized by EHDA process are nanometer in size and thus each function layers are formed by the deposition of nano-structures [21], which can give well-knit contact among each function layers. Secondly, there is a catalyst-diffusion transition layer between catalyst and diffusion layer, which reduces the interface effect between the catalyst and diffusion layer and can help to increase the contact force between them.

Conclusion

The CCM with structure and material gradient variation fabricated using EHDA LbL deposition was aptly demonstrated in this paper. The CCM was prepared by EHDA LbL depositing C nano-suspension, Pt/C-C nano-suspension, Pt/C nano-suspension, Nafion solution, Pt-Ru/C nano-suspension, Pt-Ru/C-C nano-suspension and C nano-suspension, successively. It was found that the cathode and anode catalyst-diffusion layers presented dendritic structure. The Pt/C-C and Pt-Ru/C-C layer was more porous compared to the C layer, Pt/C layer and Pt-Ru/C layer. The content of Pt/Pt-Ru increased from the diffusion layer to the Nafion membrane. It also can be seen that the CCM presented closed-packed structure. The cell performance increased with higher temperature. However, the enhancement level decreased when the temperature higher than 60 °C. After a 48 h life test, it was shown that the functional layers in the CCM still exhibited well compact contact feature. The fabrication of CCM with structure and material gradient variation using EHDA LbL deposition provides a promising manufacturing route for fuel cell device.

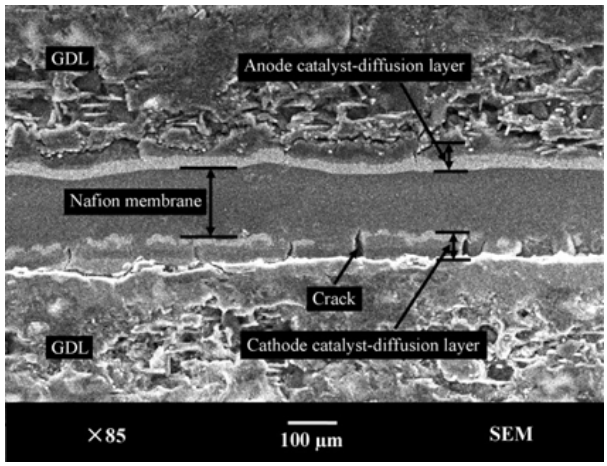


Fig. 7 SEM micrograph showing a typical cross-section of the CCM after 48 h life test.

Acknowledgments

This research is supported by the National Natural Science Foundation of China (No. 51475081, 61340052, 51275076), Science Fund for Creative Research Groups of NSFC (51321004), State Education Ministry and State Key Development Program for Basic Research of China (grant 2011CB013105), Liaoning Provincial Natural Science Foundation of China (2013020051) and Scientific Research Fund of Liaoning Provincial Education Department (L2013036).

References

[1] X. Ren, P. Zelenay, S. Thomas, J. Davey and S. Gottesfeld, Recent advances in direct methanol fuel cells at Los Alamos National Laboratory, J. Power Sources 86 (2000) 111-116.

[2] A. Faghri and Z. Guo, An innovative passive DMFC technology, Appl. Therm. Eng. 28 (2008) 1614-1622.

[3] M. Prasanna, H.Y. Ha, E.A. Cho, S.A. Hong and I.H. Oh, Investigation of oxygen gain in polymer electrolyte membrane fuel cells, J. Power Sources 137 (2004) 1-8.

[4] M.V. Williams, E. Begg, L. Bonville, H.R. Kunz and J.M. Fentona, Characterization of Gas Diffusion Layers for PEMFC, J. Electrochem. Soc. 151 (2004) A1173-A1180.

[5] M. Schuster, T. Rager, A. Noda, K.D. Kreuer and J. Maier, About the choice of the protogenic group in PEM separator materials for intermediate temperature, low humidity operation: a critical comparison of sulfonic acid, phosphonic acid and imidazole functionalized model compounds, Fuel Cells 5 (2005) 355-365.

[6] M.C. Tucker, M. Odgaard, P.B. Lund, S. Yde-Andersen and J.O. Thomas, The Pore Structure of Direct Methanol Fuel Cell Electrodes, J. Electrochem. Soc. 152 (2005) A1844-A1850.

[7] Q.P. Wang, D.T. Song, T. Navessin, S. Holdcroft and Z.S. Liu, A mathematical model and optimization of the cathode catalyst layer structure in PEM fuel cells, Electrochim. Acta 50 (2004) 725-730.

[8] L. Xiong, and A. Manthiram, High performance membrane-electrode assemblies with ultra-low Pt loading for proton exchange membrane fuel cells, Electrochim. Acta 50 (2005) 3200-3204.

[9] T. Suzuki, Y. Tabuchi, S. Tsushima and S. Hirai, Measurement of water content distribution in catalyst coated membranes under water permeation conditions by magnetic resonance imaging, Int. J. Hydrogen Energy 36 (2011) 5479-5486.

[10] K.H. Kim, K.Y. Lee, S.Y. Lee, E. Cho, T.H. Lim, H.J. Kim, S.P. Yoon, S.H. Kim, T.W. Lim and J.H. Jang, The effects of relative humidity on the performances of PEMFC MEAs with various Nafion® ionomer contents, Int. J. Hydrogen Energy 35 (2005) 13104-13110.

[11] D. You, Y. Lee, H. Cho, J.H. Kim and C. Pak, High performance membrane electrode assemblies by optimization of coating process and catalyst layer structure in direct methanol fuel cells, Int. J. Hydrogen Energy 36 (2011) 5096-5103.

[12] J.R. Yu, T. Matsuura, Y. Yoshikawa, M.N. Islam and M. Hori, Lifetime behavior of a PEM fuel cell with low humidification of feed stream, Phys. Chem. Chem. Phys. 7 (2005) 373-378.

[13] A. Jaworek and A. Krupa, Classification of the modes of end spraying, J. Aerosol Sci. 30 (1999) 873-893.

[14] B.Y. Tay, J.R.G. Evans and M.J. Edirisinghe, Electrohyohy-drodynamic Atomization of a Concentrated Nano-Suspension, Int. Mater. Rev. 48 (2003) 341-370.

[15] D. Wang, L. Wang, J.S. Liang and C. Liu, Formation of integrated catalyst coated membrane using EHDA Layer-by-Layer deposition for direct methanol fuel cells, J. Power Source 224 (2012) 202-210.

[16] D. Wang, L. Wang, J.S. Liang and C. Liu, Instrument for layer-by-layer deposition of catalyst layers directly on proton exchange membrane for direct methanol fuel cell, Rev. Sci. Instrum. 83 (2012) 095005-095005-5.

[17] D. Wang and R.A. Dorey, Formation of PZT Thick Film Single Elements Using EHDA Deposition, Mater. Sci. Forum 628-629 (2009) 405–410.

[18] L.H. Jiang, G.Q. Sun, S.L. Wang, G.X. Wang, Q. Xin, Z.H. Zhou and B. Zhou, Electrode catalysts behavior during direct ethanol fuel cell life-time test, Electrochem. Commun. 7 (2005) 663-668.

[19] W.M. Chen, Sun G.Q., J.S. Guo, X.S. Zhao, S.Y. Yan, J. Tian, S.H. Tang, Z.H. Zhou and Q. Xin, Test on the degradation of direct methanol fuel cell, Electrochim. Acta 51 (2006) 2391-2399.

[20] J.G. Liu, Z.H. Zhou, X.S. Zhao, Q. Xin, G.Q. Sun and B.L. Yi, Studies on performance degradation of a direct methanol fuel cell (DMFC) in life test, Phys. Chem. Chem. Phys. 6 (2004) 134-137.

[21] D. Wang, H. Duan, J. Liang and C. Liu, Formation of porous and dense Pt/C catalyst films using electrohydrodynamic atomisation deposition, Micro Nano Lett. 7 (2012) 235-239.

Key Engineering Materials Vols 645-646 (2015) pp 1163-1169
© (2015) Trans Tech Publications, Switzerland
doi:10.4028/www.scientific.net/KEM.645-646.1163

Submitted: 2015-02-02
Accepted: 2015-02-02

Secondary Synthesis of Microporous Heteroatoms Y Zeolite and their Hydrodesulfurization Properties for Model Fuel

HONG Xin , TANG Ke*

School of Chemical and Environmental Engineering, Liaoning University of Technology, Jinzhou, 121001, Liaoning Province, China.

* Corresponding Author: School of Chemical and Environmental Engineering, Liaoning University of Technology, Tel: 86-416-4198019, FAX: 86-416-4198019, email: tangke0001@163.com

Keywords: Gallium, Zeolite, Model Fuels, HDS.

Abstract: Gallium atoms have been introduced into the framework of Y zeolite by treating the zeolite with an aqueous solution of ammonium hexafluoro gallate. The synthesized Y zeolite ([Ga]AlY) was characterized by means of X-Ray Diffraction (XRD), N_2 adsorption, Infrared spectrophotometer (IR) and Inductively Coupled Plasma (ICP). The results indicated that Ga has been substituted into the faujasitic framework. Hydrodesulfurization (HDS) of various model fuels containing about 500 μg/g sulfur has been studied over the [Ga]AlY. The activity of the [Ga]AlY catalysts on HDS reaction is highly affected by the temperature and kind of sulfide in model fuels. The conversion for thiophene, benzothiophene (BT) and dibenzothiophene (DBT) in model fuel 1, 2 or 3 was 81.2%, 60.7% and 37.2% respectively. Compared with the model fuel 1, 2 and 3, the conversion of every sulfide in model fuel 4 was much lower which can be due to the competitive adsorption between between the three of them.

1 introduction

Zeolites are porous crystalline materials formed by corner sharing between tetrahedral SiO_4 and AlO_4 groups, resulting in Si-O-Si and Si-O-Al linkages. Other elements, such as B or Ga, can be substituted into the tetrahedral sites of the lattice and these substitutions also lead to the formation of acidic bridging hydroxyls, such as Si-OH-B and Si-OH-Ga. The differences in acid strength as well as catalytic activities offer the potential to design zeolites for new application[1]. It has been shown that the introduction of different heteroatoms into the framework of zeolites leads to the improvement of acidities, catalytic properties and adsorption properties. Many methods based on hydrothermal crystallization, gas-solid and liquid-solid reactions for heteroatom-substituted zeolites have been developed. The heteroatom zeolite is usually synthesized by using hydrothermal crystallization which has some disadvantages. In 1985, it was first reported that Si atom was incorporated into faujastic framework by applying the isomorphous substitution method using NH_4SiF_6 solution to improve the acidities, adsorption and catalytic properties of the dealuminated products[2]. In recent years, some heteroatoms such as Zr, Ti[3], Ga[4], Te, and Cr[5] have been incorporated into the framework of zeolites by using this secondary synthetic technique.

In recent years, deep desulfurization of transportation fuels has attracted much attention in most countries in that the tolerable sulfur concentration in the product must be reduced to low levels due to environmental concerns. Desulfurization of transportation fuel is actually carried out by HDS in the industry. Many efforts have been made to develop catalysts that are particularly active with respect to the HDS. Some kinds of catalysts have been reported for the removal of sulfur compounds from the diesel fuels, gasoline, jet fuels or model fuels. New kinds of support materials such as mixed oxides[6-9], zirconia[10], titania[11] and zeolite[12,13], novel catalytically active metals such as Co[14], Ru[15], Re, Pt, Pd[16,17] and new kinds of materials such as Mo nitride[18] and carbide [19] are strong candidates for future types of HDS catalysts with high performances.

However, in spite of these catalyst systems can take the sulfur levels down to meet the present legislation, the present catalyst performance is not high enough to meet the future more severe legislative restriction of sulfur content in petroleum products. Development of newly, highly active and selective HDS catalysts is one of the most urgent problems in the petroleum industries. In the present study, the introduction of heteroatom gallium into the framework of a Y zeolite by the isomorphous substitution method is reported and the HDS of model fuel containing 500 μg/g sulfur on the heteroatoms Y zeolite prepared by secondary synthesis has been studied.

2 experimental

2.1 model fuels

In the experiment, the hydrodesulfurization of thiophene, BT or DBT as sulfur compounds in n-nonane containing about 500 μg(S)/g over the synthesized microporous heteroatoms Y zeolite was studied (seen Table 1).

Table 1 Compositions of model fuels

Model fuel No.	Concentration (μg/g)			Sulfur Concent (μg/g)
	Thiophene	BT	DBT	
1	1313	---	---	500
2	---	2093	---	500
3	---	---	2875	500
4	438	698	958	500

2.2 catalyst preparation and characterization

The synthesis of Y and NH_4Y zeolite used in this study could be referred to the literature [20], the synthesis of [Ga]AlY zeolite could be referred to in the literature[21-23]. The NH_4Y zeolite was stirred with ammonium acetate solution (1 mol·L^{-1}). The slurry (5 g zeolite to 50 mL solution) was then heated to the reaction temperature (75 °C) and the solution of gallium nitrate and ammonium fluoride was added over a period of 3-5 h. Then the products were filtered and washed in an ammonium sulphate solution (1.5 mol·L^{-1}) at 80 °C for 1.5 h with a ratio of solid to solution of 1:10. The washing process was repeated to remove the fluoride.

The XRD patterns were acquired on a D/Max-RD type diffractometer system (Rigaku, Tokyo/Japan) equipped with monochromatic CuKα radiation.

The IR was performed on a spectrumTM GX IR spectrometer (Perkin–Elmer, Waresley /Massachusetts/U.S.A.) using the nujol mull or KBr method.

The metal content of [Ga]AlY and NH4Y was measured by a MS X7 type inductively coupled plasma spectrometer (ICP: Thermo Elemental, Wellesley/Massachusetts/U.S.A).

The Sorption isotherms of nitrogen in [Ga]AlY and pore size distribution for NH_4Y and [Ga]AlY were measured by Intelligent Gravimetric Analyser (Hiden Co. Bristol /U. K.).

2.3 catalytic testing

HDS of model fuel over [Ga]AlY catalysts was carried out in a high-pressure fixed-bed continuous-flow reactor at a hydrogen pressure of 5.5 MPa, 30.4 h^{-1} liquid space velocity and several temperatures in the 260-340 °C range. Prior to the reaction, the [Ga]AlY catalysts were dried at 100 °C several hours and calcined at 500 °C for 5 h to remove the adsorbed water and were then sulfided in a 10% H_2S/H_2 flow (75 cm^{-3}/min) at 300 °C for 2 h. The [Ga]AlY catalysts in the test was 3.2 g. The model fuel after treatment were taken periodically and analyzed by using the WK-2D coulombmeter (Jiangfen Electroanalytical Instrument Co., Ltd, Jiangyan/Jiangsu/China) or GC (Perkin-Elmer, Waresley/Massachusetts/U.S.A.; Column: PONA, 50 m×0.2 mm×0.5 μm, Agilent, U. S. A.; Models 355 Sulfur Chemiluminescen-ce Detectors, Agilent , U. S. A.)

3 results and discussion

3.1 catalyst characterization

The cell parameter of [Ga]AlY, determined by XRD using the internal standard method, is 2.4756 nm and that of NH_4Y is 2.4685 nm as a result of replacing Al-O (0.169 nm) with Ga-O (0.172 nm), implying that the Ga atoms have been introduced into the framework of Y zeolite. The XRD pattern of [Ga]AlY agrees well with that of raw material NH_4Y, as shown in Fig. 1, indicating that the crystallinity of [Ga]AlY keeps unchanged. ICP analysis shows that the aluminium content decreased from 11.9% for the NH_4Y to 8.8 % for the [Ga]AlY. The gallium content of [Ga]AlY is 4.32%. The ratio of Ga, Al and Si in the zeolite framework is about 1:2:8. The results of ICP further indicate that Ga has been substituted into the faujasitic framework.

The FT-IR spectra of [Ga]AlY zeolites and NH_4Y were shown in Fig. 2. The internal tetrahedral symmetrical stretching shows a blue shift due to the substitution of Ga for Al[24]. Nitrogen adsorption isotherms were measured on both [Ga]AlY and NH_4Y to evaluate their structural and surface properties (Fig. 3 and 4). The specific surface area was determined according to the standard Brunauer-Emmett-Teller (BET) method in the relative pressure range of 0.04-0.2. The specific surface area of [Ga]AlY is 799.9 m^2/g which is almost equal to that (785.0 m^2/g) of raw material NH_4Y zeolites. This further proves that the crystallinity of [Ga]AlY keeps unchanged. [Ga]AlY has a wide pore distribution (Fig. 4) in the range of 0.45-1.15 nm, compared with NH_4Y, which has a pore distribution in the range of. 0.5-0.95 nm. The results show that the modified zeolite has a wide pore distribution[25]. The small pore is because the salts dispersed inside of zeolite pores and the big pore is due to dealumination of NH_4Y.

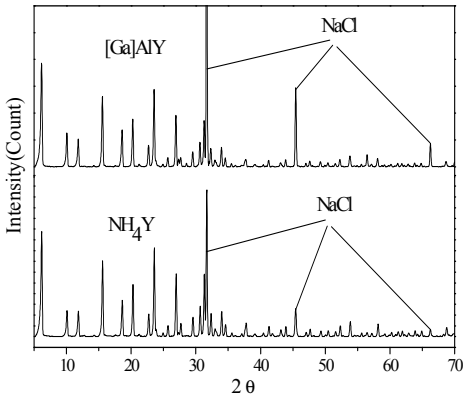


Fig. 1 XRD spectra of [Ga]AlY and NH_4Y zeolites

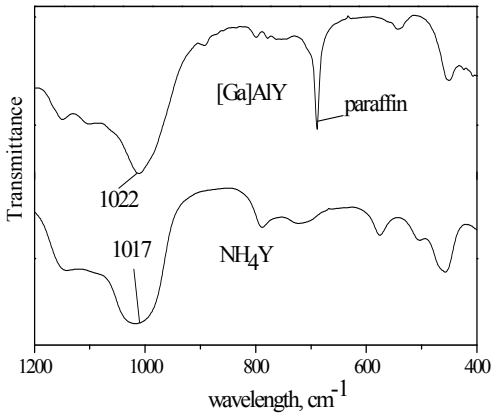


Fig. 2 FT-IR spectra of [Ga]AlY and NH_4Y zeolites

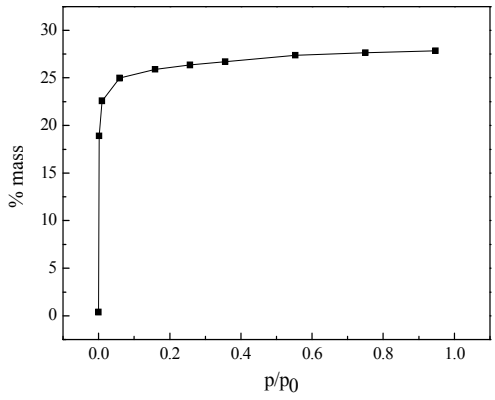


Fig. 3 Sorption isotherms of nitrogen in [Ga]AlY

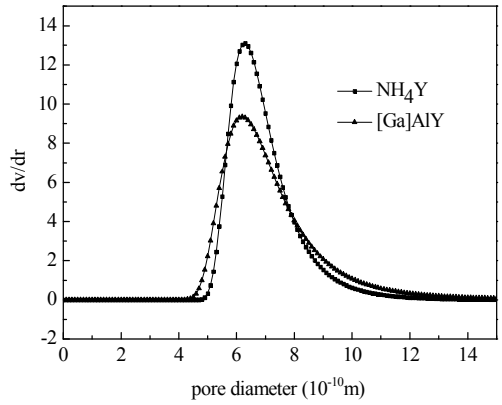


Fig. 4 The pore distribution curve of NH_4Y and [Ga]AlY

3.2 HDS activity measurements

Fig. 5 shows the HDS activities of model fuel 1, 2 and 3 on [Ga]AlY catalysts. As can be seen, The [Ga]AlY catalysts shows the highest activity for the thiophene HDS reaction. The HDS activities of DBT on [Ga]AlY catalysts was very low and medium in that HDS activities of BT. The difference may be due to the kind or molecular structure of sulfide. It has been showed that the HDS activities of DBT on [Ga]AlY catalysts is as following: thiophene>BT>DBT which is the common effect of electric density on sulfur atom and stetric hindrance of benzene. It was also found that the conversion of thiophene and BT increased with increasing temperature from 260 °C to 320 °C and that of DBT from 260 °C to 300 °C. In a word, the optimal temperature of HDS was 320 °C. Under the optimal temperature, the conversion for thiophene, BT and DBT was 81.2%, 60.7% and 37.2% respectively.

In order to research the influence each other of these sulfides on the HDS, the HDS activities of model fuel 4 on [Ga]AlY catalysts are presented in Fig. 6. It was also found that the conversion for thiophene, BT and DBT hydrodesulfurzation over [Ga]AlY catalysts is strongly dependent on the reaction temperature. Compared with the model fuel 1, 2 and 3, the conversion of every sulfide was much lower which can be due to the competitive adsorption between three of sulfides[26].

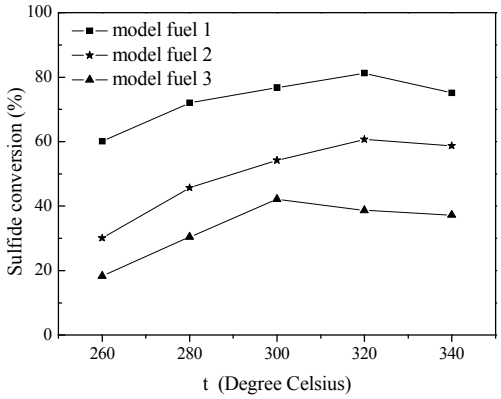


Fig. 5 Sulfide HDS conversion in model fuel 1, 2 and 3 over [Ga]AlY. (Hydrogen pressure: 5.5 MPa, liquid space velocity: 30.4 h^{-1})

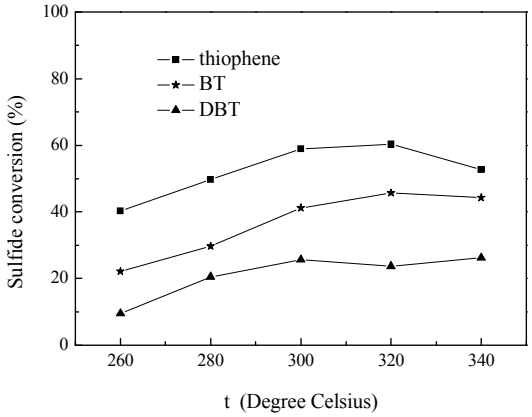


Fig. 6 Sulfide HDS conversion in model fuel 4 over [Ga]AlY. (Hydrogen pressure: 5.5 MPa, liquid space velocity: 30.4 h^{-1})

4 Conclusion

(1) The [Ga]AlY zeolite was synthesized by treating the zeolite with an aqueous solution of ammonium hexafluoro gallate and characterized by means of XRD, N_2 adsorption, IR and ICP. The specific surface area of [Ga]AlY is 799.9 m^2/g which is almost equal to that (785.0 m^2/g) of raw material NH_4Y zeolites. The cell parameter of [Ga]AlY increased from 2.4685 nm of NH4Y to 2.4756 nm. The aluminium content of [Ga]AlY decreased from 11.9% for the NH_4Y to 8.8 % for the [Ga]AlY and the gallium content of [Ga]AlY is 4.32%.

(2) The activity of the [Ga]AlY catalysts on HDS reaction is highly affected by the temperature and kind of sulfide. The conversion for thiophene, BT and DBT in model fuel 1, 2 or 3 was 81.2%, 60.7% and 37.2% respectively. Compared with the model fuel 1, 2 and 3, the conversion of every sulfide in model fuel 4 was much lower which can be due to the competitive adsorption between three of sulfides.

Acknowledgements

We are grateful to Professor SONG Lijuan who works in Key Laboratory of Petrochemical Catalytic Science and Technology of Liaoning Shihua University for measuring the sorption isotherms of nitrogen in [Ga]AlY and NH_4Y.

This work was supported by Program for Liaoning Excellent Talents in University (LJQ2012057) P. R. China, Liaoning Provincial Natural Science Foundation of China (2014020113) and the Priming Scientific Research Foundation for the Teachers of Liaoning University of Technology (X201311).

References

[1] Deka R. C., Tajima N., Hirao K., Influence of isomorphous substitution on acidity of zeolites: ab initio and density functional studies, J. Mol. Struct-Theochem. 535 (2001) 31-38.
[2] Breck D., Skeels G. W., U.S. Patent 4,503,023. (1985)
[3] Tang Y., Xu J. S., Gao Z., Isomorphous substitution of metallic elements for zeolite Y in aqueous solution. Chem. J. Chinese. Universities. 11 (1990) 1317-1321. (In Chinese)
[4] Xu Z. L., Zhang Y. Z., Zheng L. B., The secondary synthesis of zeolites via framework substitution for aluminum Ⅰ preparation and characterization of zeolite Y containing Ga. J. Mol. Catal. (China). 6 (1992) 271-278. (In Chinese)
[5] Dwyer J., Karim K., The incorporation of heteroatoms into faujastic framework by secondary synthesis using aqueous fluoride complexes. J. Chem. Soc. Chem. Commun. 14 (1991) 905-906.
[6] Sergio L., González-Cortés, Comparing the hydrodesulfurization reaction of thiophene on γ-Al_2O_3 supported CoMo, NiMo and NiW sulfide catalysts, React. Kinet. Catal .Lett. 97 (2009) 131-139.
[7] Luděk K., Miroslav Z., Zdeně|k V., Deposition of NiO onto MoO_3/γ-Al_2O_3 extrudates by slurry impregnation method. React. Kinet. Catal. Lett. 97 (2009) 307-313.
[8] Ara CSHM, Development of highly active Co(Ni)Mo catalysts for the hydrodesulfurization of dibenzothiophene compounds. Catal. Surv. Asia. 14 (2010) 64-74.
[9] Palcheva R. A., Spojakina KJ, Kaluza L, Effect of Co on HDS activity of alumina-supported heteropolymolybdate. Cata.l Lett. 137 (2010) 216-223.
[10] Ge H., Li X. K., Qin Z. F., Liang F. X. and Wang J. G., Effects of carbon on the sulfidation and hydrodesulfurization of CoMo hydrating catalysts. Korean. J. Chem. Eng. 26(2009) 576-581.
[11] Takashi F., Highly active HDS catalyst for producing ultra-low sulfur diesel fuels. Top. Catal. 52 (2009) 872-879.
[12] Lilia Y. L., Tatiana EK, SBA-15 modified with Al, Ti, or Zr as supports for highly active NiW catalysts for HDS. J. Mate.r Sci. 44 (2009) 6617-6628.
[13] Shen B. J., Li H. F. and Shen S. K., Tailoring alumina support with crystalline AlPO4-5 for enhancing hydrodesulfurization activity. Catal. Lett. 106 (2006) 55-60.
[14] Masahiko A., Yui M., Kazuo T. and Masayuki S., Cobalt-containing smectite-like mesoporous material as a new type of catalyst for hydrodesulfurization of thiophene. Catal. Lett. 61 (1999) 83-87.
[15] Teh C. H., Hydrodesulfurization with RuS_2 at low hydrogen pressures. Catal. Lett. 89 (2003) 21-25.
[16] Adeline N. R. and Roel P., Infuence of nitrogen-containing components on the hydrodesulfurization of 4,6-dimethyldibenzothiophene over Pt, Pd, and Pt–Pd on alumina catalysts. Top. Catal. 46 (2007) 65-78.
[17] Lu X., Luo L. T. and Chen X. S. Influence of Pd-Ce interaction and chlorine ion on hydrodesulfurization reaction: the Pd-CeO_2/Al_2O_3 catalyst. React. Kinet. Catal. Lett. 94 (2008) 35-46.
[18] Zdeněk V., Daniela G., Luděk K. and Miroslav Z., Effect of support on the synergy in HDS of thiophene and HDN of pyrindine over Mo sulfide catalysts promoted by Rh. React. Kinet. Catal. Lett. 83 (2004) 237-244.
[19] José A. R., Ping L., Yoshiro T., Kenichi N., Francesc V. and Francesc I., Desulfurization reactions on surfaces of metal carbides: photoemission and density–functional studies. Top. Catal. 53 (2010) 393-402.
[20] TANG K., HONG X., ZHAO Y. H., SONG L.J. and SUN Z. L.. Adsorptive desulfurization on a heteroatoms Y zeolite prepared by secondary synthesis. Sci. China Chem. 1(2010) 281-286.

[21] Dwyer J., Karim K., The incorporation of heteroatoms into faujastic framework by secondary synthesis using aqueous fluoride complexes. J. Chem. Soc. Chem. Commun. 14 (1991) 905-906.
[22] David R., Khalid K. and John D. Gallium zeolites. U.S. Patent 5,238,675. (1993)
[23] Tang K., Song L. J., Duan L. H., Li X. Q. , Gui J. Z. and Sun Z. L., Deep desulfurization by selective adsorption on a heteroatoms zeolite prepared by secondary synthesis. Fuel Process. Technol. 89 (2008) 1-6.
[24] Xu R. R., Pang W. Q., Chemistry-zeolites and porous materials. Science Press, Bei Jing, 2004. (In Chinese)
[25] Xiao F. S., Zheng S., Sun J. M., Yu R. B., Qiu S. L. and Xu R. R., Dispersion of inorganic salts into zeolites and their pore modification. J. Catal. 176 (1998) 474-487.
[26] Xiang L., Wang A. J., Wang Y., Chen Y. Y., Liu Y. H. and Hu Y. K., Hydrodesulfurization of dibenzothiophene over Ni-Mo sulfides supported by proton-exchanged siliceous MCM-41. Catal. Lett. 84 (2002) 107-113.

Key Engineering Materials Vols 645-646 (2015) pp 1170-1174
© (2015) Trans Tech Publications, Switzerland
doi:10.4028/www.scientific.net/KEM.645-646.1170

Submitted: 2014-11-10
Accepted: 2014-12-23

A 3D all-solid-state thin film microbattery with inverted pyramid arrays

Lin Jie[a], Guo Jianlai, Liu Chang, Guo Hang[b,*]

Pen-Tung Sah Micro-Nano Science and Technology Institute, Xiamen University, 361005, China
[a]linjie987@163.com, [b]hangguo@xmu.edu.cn

Keywords: 3D thin film microbattery; inverted pyramid; microfabrication; magnetron sputtering

Abstract. A 3D all-solid-state thin film lithium-ion microbattery (TFLM) with inverted pyramid arrays is fabricated by microfabrication technology. Compared with 2D TFLMs, the effective area of this 3D TFLM increases more than 30%. The 3D TFLM prepared by magnetron sputtering is composed of $LiCoO_2$ cathode, LiPON solid electrolyte, and copper doped SnO_x anode. The 3D TFLM is tested by electrochemical measurements, and the results show that it has reliable capacity and excellent performance.

Introduction

Recently, with the rapid development of micro electro mechanical system (MEMS) technology, external power sources can not satisfy the increasing demand of miniaturization and integration. TFLMs are talent showing themselves in micro power sources for its flexible size, safety and high energy density. However, existing all-solid-state TFLMs are limited to plane area [1, 2], and have a low space utilization rate. The 3D TFLMs are attractive as it provides distinct advantages over conventional batteries in significantly miniaturizing the size and weight of power for advanced lithium-ion batteries. The correct frame for comparison of our work is the 2D TFLM fabricated by using microfabrication process [3], which exhibits a initial discharge capacity of 15 nAh.

The structures of present 3D TFLMs are complicated [4, 5] and high technological requirement is needed. Most of the 3D TFLMs use rectangle [6] or columnar [7] structure, that is hard to be combined with microelectronic process for the stacking of photoresist. Moreover, many people only research single electrode [8] or liquid electrolyte is required [9, 10]. So the really miniaturization and solidification has not yet been achieved in 3D TFLMs. Through anisotropic etching of silicon, inverted pyramid arrays are fabricated, and applied to all-solid-state TFLMs. Thus, the effective materials in footprint unit area are increased, and the contact between films is closer. Few people consider the plane design of circuits with TFLMs, leading to the necessary of down-lead wires. The photo mask used in this 3D battery results in the elimination of leading wires in different planes. This paper provides an effective method to improve the structural stability and electrochemical properties of TFLMs.

Microfabrication and Packaging

Firstly, a 4 inch (100) silicon wafer was treated with standard cleaning. Then a 500 nm thick silicon dioxide film was grown by thermal oxidation as an insulating layer (Fig. 1a). After etching the silicon dioxide film in windows by HF solution (2%) (Fig. 1b), the photoresist was removed in acetone. Using the remaining silicon dioxide film as mask layer, anisotropic etching of silicon was processed in 40% (wt %) KOH solution combined with ultrasonic technology (Fig. 1c). Lastly, all the primary dioxide film was removed and a new silicon dioxide film was grown (Fig. 1d). The 3D structure obtained is shown in Fig. 2 and Fig. 3. The width, depth and spacing of the inverted pyramid arrays were 50 μm, 35 μm and 20 μm, thus the effective area of 3D TFLM was 30% more than 2D TFLM with a same footprint area.

All the films of microbatteries were deposited by the JC500-3/D magnetron sputtering system. The photolithography was carried out using a Karlsuss MA6/BA6 mask aligner. The fabrication process of 3D TFLMs is schematically represented in Fig. 1e-h. The prepared 3D silicon substrate was patterned with photoresist (BP212) to define the current collector. After a 10 nm thick Cr adhesion film and a 200 nm thick Pt film were deposited on the photoresist, the Si substrate was then immersed in acetone to remove the photoresist and tear off the excess Cr/Pt film (Fig. 1e). To define the cathode, the wafer was again patterned with photoresist forming square openings with an area of 500 μm × 500 μm on the cathode current collector. A $LiCoO_2$ film was magnetron sputtered over the photoresist, and the substrate was then immersed in acetone to lift off the excess $LiCoO_2$ film (Fig. 1f). In order to decrease lattice strain and enhance the crystallization of as-deposited $LiCoO_2$ film, the substrate was treated with an annealing process at 600°C for 1h in O_2 atmosphere. The substrate was then patterned with photoresist to define the electrolyte and anode film. The solid state electrolyte LiPON was deposited over the cathode electrode with a thickness of ~600 nm. For preventing the breakdown of LiPON in air during lift off, a copper doped SnO_x film was directly deposited following the sputtering of LiPON. Then the substrate was immersed in acetone to lift off the excess LiPON and copper doped SnO_x (Fig. 1g). After the film was patterned with photoresist to define the top current collector, a Cu film was subsequently deposited on the anode film by direct current magnetron sputtering. Finally, the excess Cu was lifted off as mentioned above. The full structure of 3D TFLM was completed (Fig. 1h).

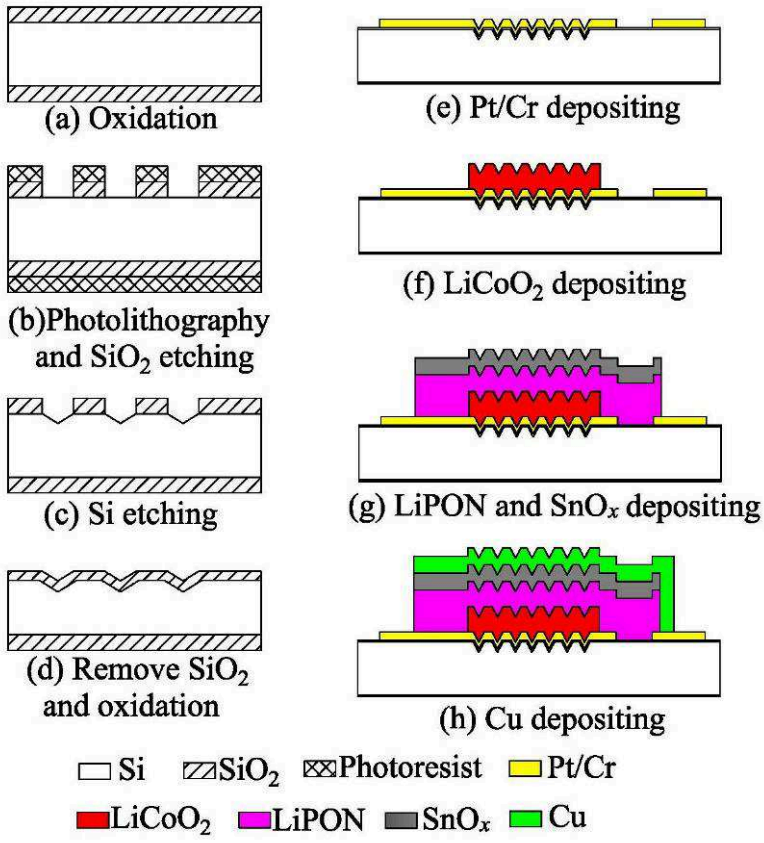


Fig. 1 Fabrication Process of 3D TFLMs.

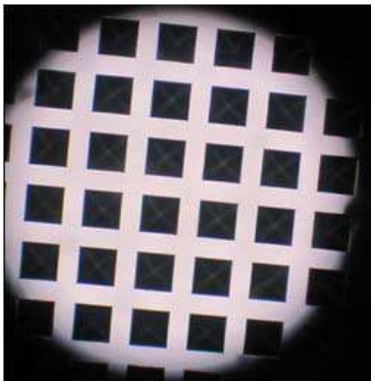


Fig. 2 Metalloscope photo of inverted pyramid arrays.

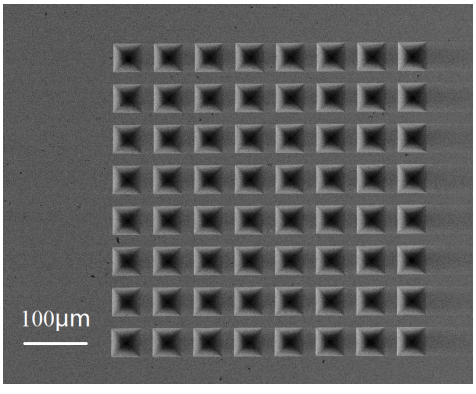


Fig. 3 SEM image of 3D Si substrate.

Following the separation of four batteries per cell by diamond dicing saw, the cells were attached on semiconductor device bases shown in Fig. 4, and then were connected with external circuits using ultrasonic bonding with an aluminum wire. The metallic protective caps were placed over the microbatteries, and the devices were sealed by epoxy in the glovebox as shown in Fig. 5.

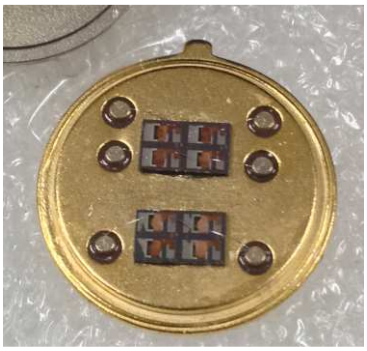


Fig. 4 All-solid-state 3D TFLM cells.

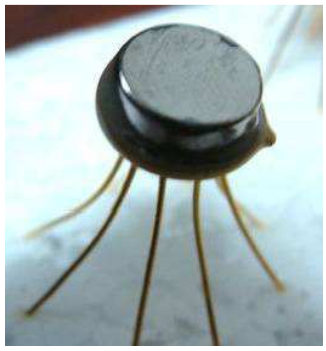


Fig. 5 Sealed 3D TFLM cells.

Test and Discussion

The cells were charged/discharged using an Arbin BT2000 instrument. The electrochemical impedance measurements were conducted with a CHI660E electrochemical workstation. The cross-section of microbatteries was examined by field emission scanning electron microscopy (ZEISS Sigma). The phase identification was carried out by X-ray diffraction equipment (Rigaku Ultima IV). The coin cells (CR2016) were assembled in an Ar-filled glove box using the electrode films deposited on Au/Si substrates, lithium foils as the counter electrodes, and 1M $LiPF_6$ dissolved in a mixture of ethylene carbonate/dimethyl carbonate/diethyl carbonate (EC/DMC/DEC, 1:1:1 in volume) as the electrolyte.

The $LiCoO_2$ film as cathode material was prepared by magnetron sputtering and following annealed in different temperature. The XRD patterns of all samples investigated are shown in Fig. 6. With the increasing of annealing temperature, the films prefer to (003) crystal orientation more obviously. This crystal orientation corresponds to the hierarchical $LiCoO_2$ film, which is in favor of storing Li^+. As a result, the electrochemical properties of annealed samples are better than not annealed. And the sample annealed at 600℃ is the candidate as cathode material for 3D TFLMs.

Fig. 7 lays out the cyclic capacity of SnO_x and copper doped SnO_x films. As shown in the curves, the capacity of doped film is higher than undoped film. When doping coppers, the SnO_x particles on the surface become smaller, and the contact areas between anode and electrolyte increase. This makes the interface resistance smaller and benefits the intercalation/de-intercalation of Li^+. Thus the copper doped SnO_x film is chosen as the anode material for 3D TFLMs.

A Li_3PO_4 target was used to deposit the solid electrolyte LiPON film by magnetron sputtering in pure N_2 atmosphere. A sandwich structure of Al/LiPON/Al was fabricated to measure the ionic conductivity by alternating current impedance method at the same time. The frequency ranges from 1Hz to 1MHz, and the electrochemical impedance spectrum is shown in Fig. 8. A straight line corresponding to the interface resistance of Al-LiPON in high frequency region and a semicircle corresponding to the electrochemical impedance of LiPON film can be seen. The calculated ionic conductivity of LiPON is about 8×10^{-7} S/cm, which is close to the optimal results reported [11, 12].

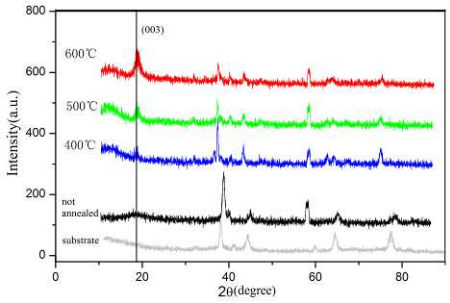


Fig. 6 XRD patterns of $LiCoO_2$ films annealed in different temperature.

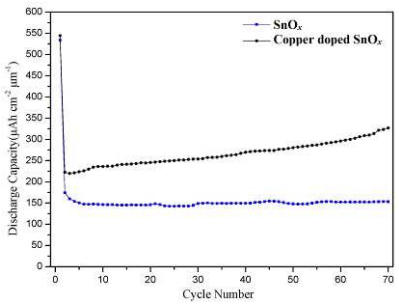


Fig. 7 Cyclic curves of SnO_x and copper doped SnO_x films.

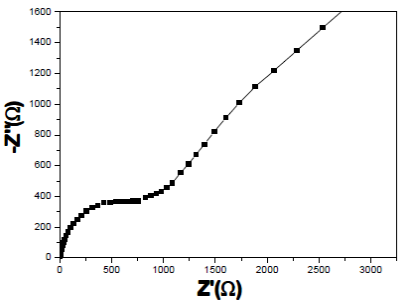


Fig. 8 Nyquist plot of LiPON film.

As shown in Fig. 9, the total thickness of the 3D TFLM is about 1.2 μm. As presented in the picture, the boundary of each layer is obvious and the contact between films is close, as well as the materials grow along a direction vertical to the substrate. The surface and the cross section of 3D microbattery with inverted pyramid arrays are given in Fig. 10 and 11. The inverted pyramid arrays are in alignment, and the deposited films are uniform and smooth without any pinholes or cracks.

The charge/discharge curves of the 3D microbattery are shown in Fig. 12. The plateau during charge is at about 2.5V, which is associated with the extraction of Li^+ from $LiCoO_2$ and then the insertion into SnO_x through LiPON film. On the contrast, a sloping voltage profile instead of a flat discharge curve appears during discharge. This is probably because the internal resistance of the microbattery is large due to the thin films and the low ionic conductivity of the LiPON electrolyte.

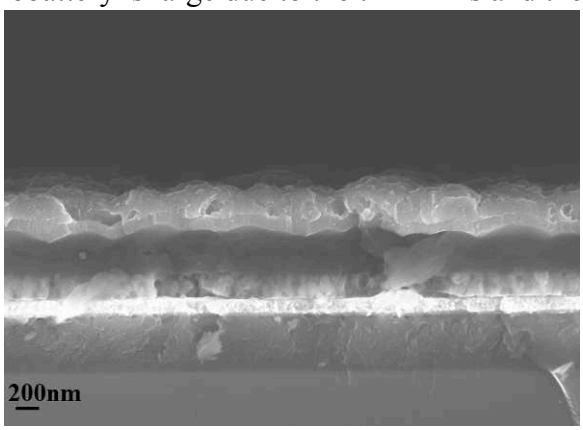


Fig. 9 Cross section SEM image of 3D microbattery.

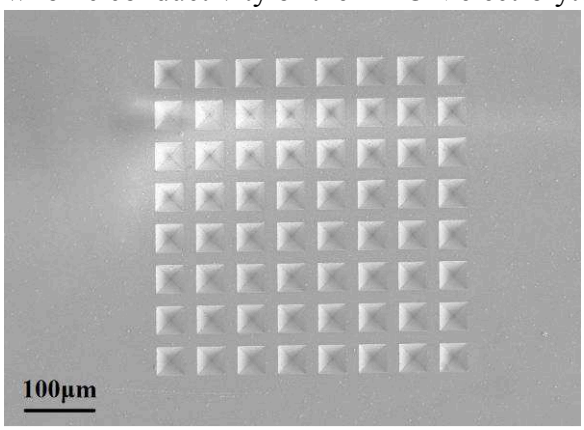


Fig. 10 Surface SEM image of 3D microbattery.

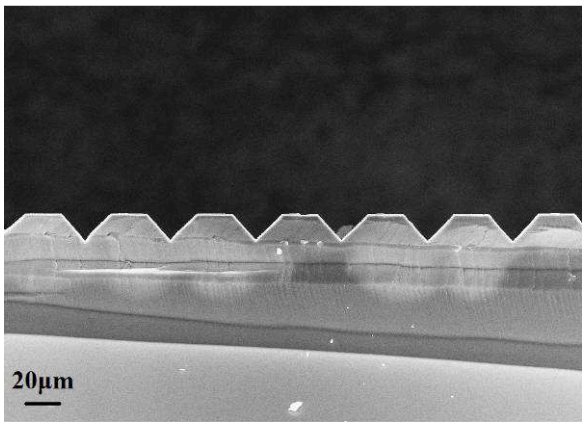


Fig. 11 Cross section SEM image of 3D structure.

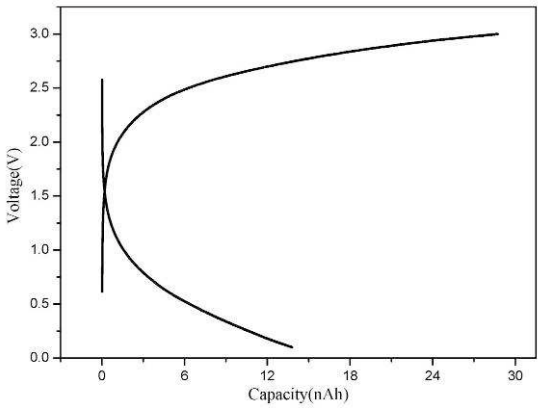


Fig. 12 Charge/Discharge curves of 3D TFLM.

As the capacity of microbattery is limited to the $LiCoO_2$ cathode, the volumetric capacity of $LiCoO_2$ is ~35μAh cm^{-2} μm^{-1} calculated by the results of coin cells, thus the theoretical capacity of a microbattery is ~27nAh. The 3D TFLM delivers a initial discharge capacity of 14nAh, which is comparable to the result reported by Whitacre et al [3] (~15nAh) who used lithium metal as anode, and the TFLM fabricated by pulsed laser deposition with Li_2O-V_2O_5-SiO_2 solid state electrolyte[13] (~15nAh). But it is lower than the theoretical value, and we attribute this difference to the air and water leakage into the protective caps, causing the damage of the 3D microbattery.

Summary

A 3D all-solid-state TFLM with inverted pyramid arrays was fabricated by microfabrication process such as chemical etching, photolithography, and magnetron sputtering. Annealed $LiCoO_2$, amorphous LiPON and copper doped SnO_x film were used as the cathode, electrolyte and anode to improve the properties of the whole 3D microbattery. The effective contact area of the 3D TFLM is 30% bigger than the 2D TFLM with a equal footprint area, and the 3D TFLM delivers a discharge

capacity of 14 nAh in the first cycle. We can expect good performances of 3D TFLMs with further optimization in microfabrication and encapsulation. The micropower systems will be useful for providing energy to on-chip devices or integrated circuits.

Acknowledgments

This work is financially supported by the New Century Talent Support Plan of the Ministry of Education of China (2007NCET-07-0723), the National Natural Science Foundation of China (60936003) and the Aviation Science Foundation of China (2008ZH68002).

References

[1] K.F. Chiu, C.C. Chen, K.M. Lin, H.C. Lin, C.C. Lo, W.H. Ho, C.S. Jiang, Vacuum, 84 (2010) 1296-1301.
[2] B.J. Neudecker, N.J. Dudney, J.B. Bates, J Electrochem Soc, 147 (2000) 517-523.
[3] J.F. Whitacre, W.C. West, B.V. Ratnakumar, J Electrochem Soc, 150 (2003) A1676.
[4] L. Baggetto, R.A.H. Niessen, F. Roozeboom, P.H.L. Notten, Adv Funct Mater, 18 (2008) 1057-1066.
[5] L. Baggetto, H.C.M. Knoops, R.A.H. Niessen, W.M.M. Kessels, P.H.L. Notten, J Mater Chem, 20 (2010) 3703.
[6] M. Kotobuki, Y. Suzuki, H. Munakata, K. Kanamura, Y. Sato, K. Yamamoto, T. Yoshida, J Electrochem Soc, 157 (2010) A493.
[7] D. Golodnitsky, V. Yufit, M. Nathan, I. Shechtman, T. Ripenbein, E. Strauss, S. Menkin, E. Peled, J Power Sources, 153 (2006) 281-287.
[8] P.R. Abel, A.M. Chockla, Y.M. Lin, V.C. Holmberg, J.T. Harris, B.A. Korgel, A. Heller, C.B. Mullins, Acs Nano, 7 (2013) 2249-2257.
[9] K. Yoshima, H. Munakata, K. Kanamura, J Power Sources, 208 (2012) 404-408.
[10] T. Ripenbein, D. Golodnitsky, M. Nathan, E. Peled, Electrochimica Acta, 56 (2010) 37-41.
[11] T. Pichonat, C. Lethien, N. Tiercelin, S. Godey, E. Pichonat, P. Roussel, M. Colmont, P.A. Rolland, Mater. Chem. Phys., 123 (2010) 231-235.
[12] C.S. Nimisha, K.Y. Rao, G. Venkatesh, G.M. Rao, N. Munichandraiah, Thin Solid Films, 519 (2011) 3401-3406.
[13] N. Kuwata, J. Kawamura, K. Toribami, T. Hattori, N. Sata, Electrochem Commun, 6 (2004) 417-421.

Key Engineering Materials Vols 645-646 (2015) pp 1175-1180
© (2015) Trans Tech Publications, Switzerland
doi:10.4028/www.scientific.net/KEM.645-646.1175

Submitted: 2015-01-15
Accepted: 2015-01-20

Formation of membrane electrode assembly for high temperature methanol fuel cells

Dazhi Wang[1, 2, a], Xiaohu Zhu[1, b], Wen Zha[1, c], Tongqun Ren[1, 2, d]*, Mingqiang Li[3, e], Junsheng Liang[1, 2, f] and Chong Liu[1, 2, g]

[1]Key Laboratory for Micro/Nano Technology and System of Liaoning Province, Dalian University of Technology, Dalian, Liaoning, 116024, China

[2]Key Laboratory for Precision and Non-traditional Machining Technology of Ministry of Education, Dalian University of Technology, Dalian, Liaoning, 116024, China

[3]School of Energy and Power Engineering, Dalian University of Technology, Dalian, Liaoning, 116024, China

[a]d.wang@dlut.edu.cn, [b]zhuxiaohu@mail.dlut.edu.cn, [c]wenz@mail.dlut.edu.cn, [d]ren_tq@dlut.edu.cn, [e]limingq@dlut.edu.cn, [f]jsliang@dlut.edu.cn and [g]chongl@dlut.edu.cn

Keywords: High temperature methanol fuel cell (HTMFC), membrane electrode assembly (MEA), high temperature proton exchange membrane (HTPEM), electrohydrodynamic atomization (EHDA)

Abstract. In this work, a quaternized polysulfone/PTFE/H_3PO_4 composite membrane was prepared and used to a high temperature sustainable proton exchange membrane (HTPEM). This HTPEM was prepared based on a porous PTFE membrane, which can sustainable for 200 ºC. Pt/C nano-suspension was prepared and deposited layer-by-layer on the gas diffusion layer (GDL) using electrohydrodynamic atomization (EHDA) deposition technique for the formation of cathode and anode catalyst layers (CLs). The CLs presented well packed and porous features. This EHDA deposited cathode and anode CLs, GDL and HTPEM were assembled to a membrane electrode assembly (MEA) and high temperature methanol fuel cell (HTMFC). The results showed that low concentration and high flow rate of methanol aqueous solution led to the loss of phosphoric acid on HTPEM, which resulted in the decline of the HTPEM. When the concentration and the flow rate of the methanol aqueous solution was increased and reduced, respectively, the cell can work properly at a temperature of 170 ºC.

Introduction

Direct methanol fuel cells (DMFCs) are the electrochemical reaction devices which transform the chemical energy of methanol directly into electrical energy. They have the advantages of high energy density and no pollution [1-3]. DMFCs are the potential power sources for portable electronic devices such as cellular phones, laptops and vehicle applications. As alternatives to low temperature DMFC, high temperature direct methanol fuel cells (HTMFCs) have their advantages of higher electrochemical oxidation, lower cathode polarization, higher conductivity of membrane and the improved ability to resist CO poisoning, which have been paid considerable attentions in recent years [4, 5]. Membrane electrode assembly (MEA) is a key part in HTMFC systems, and it is comprised of high temperature proton exchange membrane (HTPEM), catalyst layers (CLs) and gas diffusion layers (GDLs). In this system HTPEM has the ability to work at a temperature higher than 120 ºC. There are two types of the HTPEM, one is modified on the traditional Nafion membrane by using hydrophilic inorganic or solid acid solution with high boiling point and low volatilization. The other is developed based on a new PEM materials, such as phosphate mixed polybenzimidazole (PBI) membrane and composite membrane with the base of PTFE porous membrane [6, 7]. The

GDLs on either side of the MEA provide a good electrical contact for the CLs [8]. The anode and cathode electrochemical reactions take place within the CLs. During the formation of MEA, the CLs could be coated either onto a GDL (GDL-based MEAs) or onto the PEM (CCM-based MEAs) by spraying [9], painting [10] and catalyst decaling [11] to form cathode and anode electrodes. However, the structure features, including porosity and catalyst dispersity of the CLs are difficult to control using the above fabrication methods, which consequently cannot adequately match the requirement of MEA. EHDA layer-by-layer (LbL) deposition technique has notable advantages of fine and controllable deposition products and the absence of droplets coagulation [12]. This technique has shown great potential in recent years and has been introduced to form micro- and nano-particles [13] and deposit thin films [14].

In this work, a HTPEM of quaternized polysulfone/H_3PO_4 membrane was fabricated. Pt/C nano-suspension was prepared and deposited on the GDL using the EHDA deposition technique for the cathode and anode CLs. The HTMFC was assembled with the deposited CLs and HTPEM. The fabricated HTPEM and the deposited cathode and anode CLs structures were studied, the performance of HTMFC with different methanol feeding conditions were also examined.

Experiment details

Preparation of HTPEM. The quaternized polysulfone (QNPSU)/PTFE/H_3PO_4 membrane was prepared by the following procedures. Firstly, the Chloromethylation polysulfone/PTFE membrane was prepared, the detailed preparation procedures were described in our previous work [15]. Then, the composite membranes (CMPFS/PTFE) were bathed in Trimethylamine (TMA) solution until the membranes became soft. Finally, the QNPSU/PTFE membrane was immersed in phosphoric acid at 150 ºC to make the QNPSU/PTFE/H_3PO_4 membrane. The loading of phosphoric acid was calculated according to the molar ratio between phosphorics acid and the QNPSU. Furthermore, the QNPSU/PTFE/H_3PO_4 membrane was dried at a temperature of 150 ºC for 2 h to remove the water.

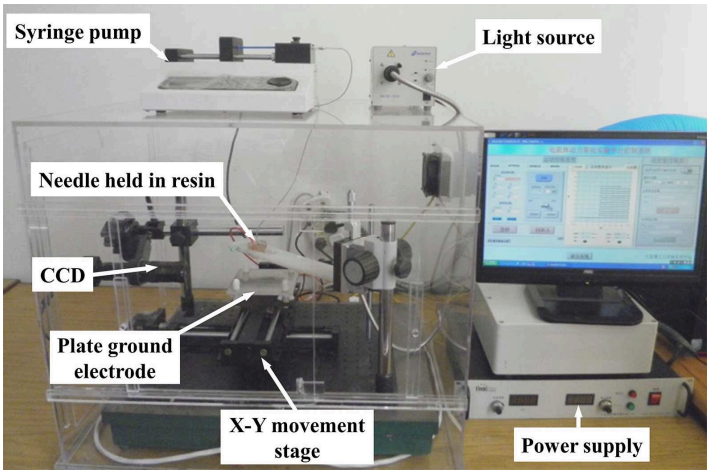


Fig.1 EHDA deposition equipment

Preparation of CLs. The anode and cathode CLs were prepared by EHDA deposition of Pt/C nano-suspensions. The quality of Pt/C nano-powder, distilled water, ethanol and Nafion solution in Pt/C nano-suspension was 0.1 g, 3 g, 3 g and 0.22 g, respectively, the preparation details were described in our previous work [16]. **Figure 1** shows the EHDA deposition equipment, which comprises of an electrohydrodynamic deposition system coupled together with a computer controlled X-Y movement stage and a microscopic vision device. The details of the EHDA deposition equipment were described in our previous

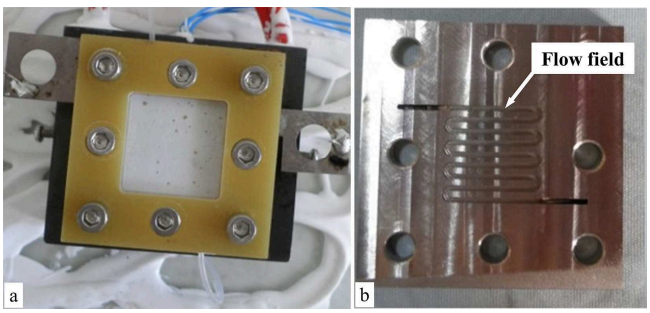


Fig.2 The assembled HTMFC (a) and the flow-field plate (b)

work [17]. **Figure 2a** and **b** show the assembled HTMFC and the flow-field plate. The flow field plate, made of steel plate, had a ‘‘s’’ shape channel with 800 μm in width and 600 μm in depth. The working temperature of the HTFC was controlled by placing the cell in a temperature programmable chamber (Dong Guan Bell Test Equipment Co., Ltd, Guangdong, China).

Results and discussion

Formation and analysis of HTPEM. The preparation of QNPSU/PTFE/H_3PO_4 membrane was based on porous PTFE membrane. The prepared HTPEM is shown in **Figure 3a**. **Figure 3b** is the surface of the porous PTFE membrane. It can be seen that the porous PTFE membrane has a compact structure and a high porosity. **Figure 3c** shows the cross-section of HTPEM, the pores of the PTFE membranes was uniformly filled, which can minimize methanol crossover during the working process. The prepared HTPEM has high mechanical strength and sustainable to a temperature higher than 200 ºC without property decline. In addition, it was measured that the conductivity of the HTPEM was higher than 0.1 S cm^{-1} at the conditions of the relative humidity below 0.5 % and the temperature at 180 ºC.

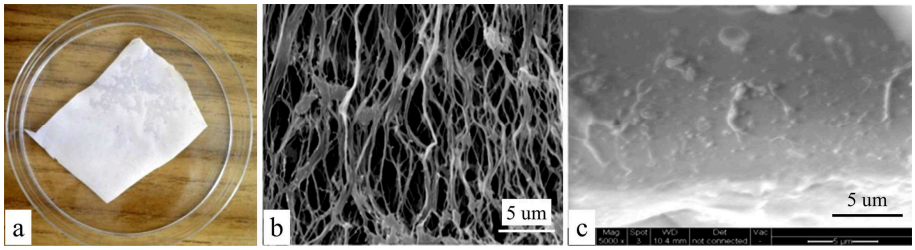


Fig.3 The prepared HTPEM (a), surface of the porous PTFE membrane (b) and cross-section of HTPEM (c)

EHDA deposition of cathode and anode CLs. Figure 4a shows a typical stable cone-jet mode of Pt/C nano-suspension obtained at an applied voltage of 3.5 kV, a flow rate of 3.3×10^{-11} m^3s^{-1} and a working distance (distance between needle outlet and substrate) of 5 mm. The following deposition films were produced under this type of stable cone-jet mode. In this work the CLs were deposited on the GDLs and then assembled with the HTPEM to form MEA. Before deposition of cathode and anode CLs the GDL (carbon paper) was treated by dipping in a 20 wt.% PTFE solution for 1min and coated with carbon ink to form micro-porous layer using painting process. **Figure 4b** shows a typical surface feature of the CL produced by EHDA deposition. During the EHDA deposition of Pt/C nano-suspension, the substrate, GDLs (15 mm × 15 mm) of cathode and anode were scanned with the X-Y movement in the X direction (Y direction step) for one layer and in the Y direction (X direction step) for each alternate layer with a speed of 3.2 mm s^{-1}. The distance between two neighboring parallel paths of deposition was set to 0.4 mm to ensure a degree of overlap between deposited materials. The loading of the anode and cathode CLs after 70 layers EHDA LbL deposition was 0.8 mg Pt cm^{-2}. In **Figure 4b**, it can be seen that the CLs present well packed and porous features. This porous structure was beneficial to the transmission of reactant and product in the process of the electrochemical reaction.

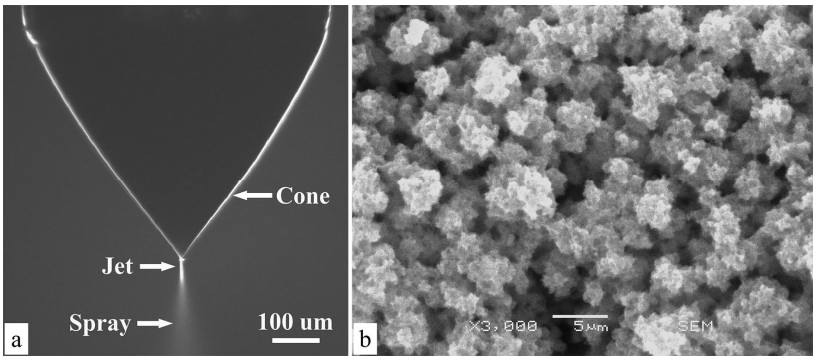


Fig.4 A stable cone-jet mode of Pt/C nano-suspension (a) and surface of CL produced by EHDA deposition (b)

Performance analysis of HTMFC. After deposition of the CLs, the GDLs and CLs were placed on the both sides of the HTPEM (20 mm × 20 mm) for the formation of MEA, then further assembled into HTMFC. HTMFC was heated at 170 ºC for 1 h before the measurement. Initially, 8 mol L^{-1} methanol aqueous solution was pumped into the anode at a flow rate of 1 mL h^{-1} at 170 ºC for the measurement of HTMFC. It was observed that no current was generated. It was found that the PH of the solution flowing from the outlet after reaction is ~4. It means that the solution after reaction contained acid. Therefore, it can be concluded that phosphoric acid on the HTPEM was removed by the flow of methanol-water vapor mixture. This will damage the structure of the HTPEM and affect the protons transfer, thus no current was generated. In order to reduce the affect of the flow of the vapor mixture the concentration and the flow rate of the methanol aqueous solution was increased and reduced, respectively. Then 16 mol L^{-1} methanol aqueous solution was pumped into the anode at a flow rate of 0.5 mL h^{-1} at 170 ºC. It was found that the PH of solution after reaction is ~5, which is higher than that with lower methanol aqueous solution concentration and higher flow rate. It was observed in our experiment that when the relative humidity of methanol-water vapor mixture was high, the phosphoric acid on the HTPEM will be removed, which will reduce the conductivity of proton. The increase of the concentration of methanol aqueous solution can reduce the relative humidity of the vapor mixture. However, it was found that if the concentration of methanol aqueous solution was too high, the permeability of methanol will increase, which will result in the methanol crossover and affect the fuel cell performance. Therefore, only 16 mol L^{-1} methanol aqueous solution was used to test the feasibility of this HTMFC. **Figure 5** shows the current density-voltage and current density-power density curves of the HTMFC. It can be seen that the peak power density of the cell was 1.7 mW cm^{-2}. It should be noted that the performance of the cell is lower than that with the use of H_2 as reactant [18]. The main reason for this lower performance is the flow away of the phosphoric acid on the HTPEM which reduce the property of the HTPEM. In addition, the high methanol concentration will lead to higher methanol crossover and reduce the performance of the fuel cell.

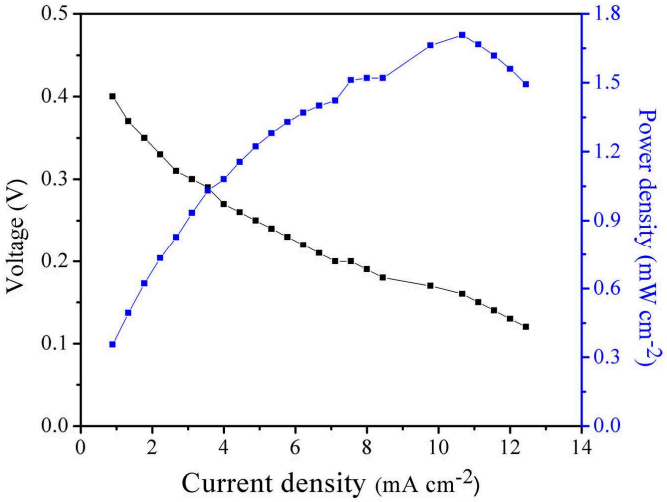


Fig.5 Current density-voltage and current density-power density curves of the HTMFC

Conclusions

The use of the EHDA deposition technique for depositing Pt/C nano-suspension on GDLs and the assembling with HTPEM to form MEA were aptly demonstrated. The deposition of cathode and anode CLs presented porous and well packed features. The HTMFC was tested with the active feed method of methanol-water vapor mixture at a working temperature of 170 ºC. The results showed that low concentration methanol aqueous solution led to the loss of phosphoric acid on HTPEM, which resulted in the decline of the cell. When the concentration and the flow rate of the methanol aqueous solution was increased and reduced, respectively, the HTMFC can work properly at a working temperature of 170 ºC. The performance can be improved further by reinforcing the adhesion behavior of the phosphoric acid on HTPEM and using active oxygen breath instead of passive air breath in the cathode.

Acknowledgements

This research is supported by the National Natural Science Foundation of China (No. 51475081, 61340052, 51275076), State Education Ministry and State Key Development Program for Basic Research of China (grant 2011CB013105), Science Fund for Creative Research Groups of NSFC (51321004), Liaoning Provincial Natural Science Foundation of China (2013020051) and Scientific Research Fund of Liaoning Provincial Education Department (L2013036).

References

[1] X. Ren, P. Zelenay, S. Thomas, J. Davey, S. Gottesfeld, Recent advances in direct methanol fuel cells at Los Alamos National Laboratory, J Power Sources. 86 (2000) 111-116.

[2] A. Faghri, Z. Guo, An innovative passive DMFC technology, Appl Therm Eng. 28 (2008) 1614-1622.

[3] M. Carmoa, V.A. Paganina, J.M. Rosolenb, E.R. Gonzaleza, Alternative supports for the preparation of catalysts for low-temperature fuel cells: the use of carbon nanotubes, J Power Sources. 142 (2005) 169-176.

[4] X.M. Ren, M.S. Wilson, S. Gottesfeld, High Performance Direct Methanol Polymer Electrolyte Fuel Cells, J Electrochem Soc. 143 (1996) 12–15.

[5] P.L. Antonucci, A.S. Aricò, P. Cretì, Investigation of a direct methanol fuel cell based on a composite Nafion-silica electrolyte for high temperature operation, Solid State Ionics. 125 (1999) 431–437.

[6] Z. Florjanczyk, E. Wielgus-Barry, Z. Poltarzewski, Radiation-modified Nafion membranes for methanol fuel cells, Solid State Ionics. 145 (2001) 119–126.

[7] C. Yang, S. Srinivasan, A.S. Aricò, Composition Nafion/zirconium phosphate membranes fordirect methanol fuel cell opration at high temperature, Electrochem Solid St. 4 (2001) 31–34.

[8] S.K. Kamarudin, N. Hashim, Materials, morphologies and structures of MEAs in DMFCs, Renew Sust Energy Rev. 16 (2012) 2494–2515.

[9] Q. Mao, G. Sun, S. Wang, Comparative studies of configurations and preparation methods for direct methanol fuel cell electrodes, Electrochim Acta. 52 (2007) 6763–6770.

[10] L. Xiong, A. Manthiram, High performance membrane electrode assemblies withultra-low Pt loading for proton exchange membrane fuelcells, Electrochim Acta. 50 (2005) 3200–3204.

[11] T. Suzuki, Y. Tabuchi, S. Tsushima, Measurement of water content distribution in catalyst coated membranes under water permeation conditions by magnetic resonance imaging, Int J Hydrogen Energy. 36 (2011) 5479–5486.

[12] A. Jaworek, A.T. Sobczyk, Electrospraying route to nanotechnology: An overview, J Electrostat. 66 (2008) 197–219.

[13] F. Bortolani, R.A. Dorey, Synthesis of spherical lead zirconate titanate (PZT) nanoparticles by electrohydrodynamic atomization, Adv. Appl. Ceram. 108 (2009) 332-337.

[14] N.M. Muhammad, A.M. Naeem, N. Duraisamy, Fabrication of high quality zinc-oxide layers through electrohydrodynamic atomization, Thin Solid Films. 520 (2012) 1751–1756.

[15] M. Li, K. Scottb, A polytetrafluoroethylene/quaternized polysulfone membrane for high temperature polymer electrolyte membrane fuel cells, J Power Sources. 196 (2011) 1894–1898.

[16] D. Wang, L. Wang, J. Liang, Formation of an integrated catalyst-coated membrane using electrohydrodynamic atomization Layer-by-Layer deposition for direct methanol fuel cells, J Power Sources. 224 (2013) 202–210.

[17] D. Wang, H. Duan, J. Liang, Formation of porous and dense Pt/C catalyst films using electrohydrodynamic atomisation deposition, Micro Nano Lett. 7 (2012) 235–239.

[18] S.F. Lu, R.J. Xiu, X. Xu, D.W. Liang, H.N. Wang, Y. Xiang, Polytetrafluoroethylene (PTFE) reinforced poly(ethersulphone)-poly(vinyl pyrrolidone) composite membrane for high temperature proton exchange membrane fuel cells, J Membrane Sci. 464 (2014) 1-7.

Key Engineering Materials Vols 645-646 (2015) pp 1181-1188
© (2015) Trans Tech Publications, Switzerland
doi:10.4028/www.scientific.net/KEM.645-646.1181

Submitted: 2015-01-13
Accepted: 2015-01-19

Asymmetric design of anode and cathode current collectors for micro direct methanol fuel cells

Yufeng Zhang[1, a, *], Shubin Zhang[1, b], ZeZhong Ma[1], Hailong Chen[1, c], Xiaowei Liu[1, 2]

[1]MEMS Center, Harbin Institute of Technology, Harbin 150001, China

[2]Key Laboratory of Micro-Systems and Micro-structures Manufacturing, Ministry of Education, Harbin 150001, China

[a]yufeng_zhang@hit.edu.cn, [b]sobean@126.com, [c]harlen.chen@hit.edu.cn

*Corresponding Author: Yufeng Zhang, Professor, MEMS Center, Harbin Institute of Technology, Tel: 86-451-86413451, FAX: 86-451-86413441

Keywords: micro direct methanol fuel cell (μDMFC); current collectors; mass transport; water crossover

Abstract. This paper studied the combined effect of anode and cathode current collectors on the behavior of water and methanol crossover in micro direct methanol fuel cells (μDMFC). A two-phase, two-dimensional, isothermal model was built to analyze the mass transport behavior in the membrane electrolyte assembly (MEA). The results show that the distribution of methanol exhibits uniform concentration feature over the anode porous area with the asymmetric anode and cathode current collectors. Also, lower water content gradient across the membrane is found. Comparing experiments were conducted to verify the simulation results. Two passive μDMFCs were fabricated and tested. The cells presents almost the same performance at relatively low methanol concentration. However, an increase of 10% cell performance (from 27.5 $mW.cm^{-2}$ for symmetric current collectors to 30.3 $mW.cm^{-2}$ for asymmetric current collectors) at 5 $mol.L^{-1}$ methanol solution was observed. This reveals that the couple of asymmetric current collectors induced the methanol to distribute uniformly and largely suppressed the water and methanol crossover.

Introduction

Over the past decade, the micro direct methanol fuel cell (μDMFC) has been regarded as one of the most promising candidates for portable power supply and huge progress has been achieved towards the commercialization of this fuel cell technology. However, there are still some crucial issues that need to be solved properly, for example, methanol and water crossover [1-4]. Previous work show that the structure of membrane electrolyte assembly (MEA) has a significant impact on water and methanol crossover [5,6]. Properties of the MEA component, like porosity, contact angle, and permeability were discussed by Zhao [7]. The reduction of water and methanol crossover can be achieved by means of reducing the diffusion flux from the anode to the cathode or enhancing the back convection of the water from the cathode to the anode. Xu assembled a highly hydrophobic cathode diffusion layer to build up a hydraulic liquid pressure in the cathode [8]. According to his study, water and methanol crossover is much lower through a thick membrane than through a thin one. The studies [9,10] on the anode porous area show highly hydrophobic anode diffusion layer and micro porous layer could also lower the water crossover flux.

However, little attention was paid on the combined effect of the shape of anode and cathode current collectors on water and methanol crossover. When fabricating a typical μDMFC, the MEA is clamped tightly by the anode and cathode current collectors to bring good ohmic contact, thus the methanol and water crossover is influenced by the shape of current collectors and deformation of

the MEA. Based on these understandings, we believe asymmetric current collectors between anode and cathode will show different cell performance comparing with symmetric ones. This paper presents a numerical and experimental study on the effect of the symmetry of the current collectors of a passive μDMFC.

Simulation

A two-phase, two-dimensional, isothermal model was built to analyze the mass transport behavior in the MEA with the help of the software COMSOL Multiphysics.

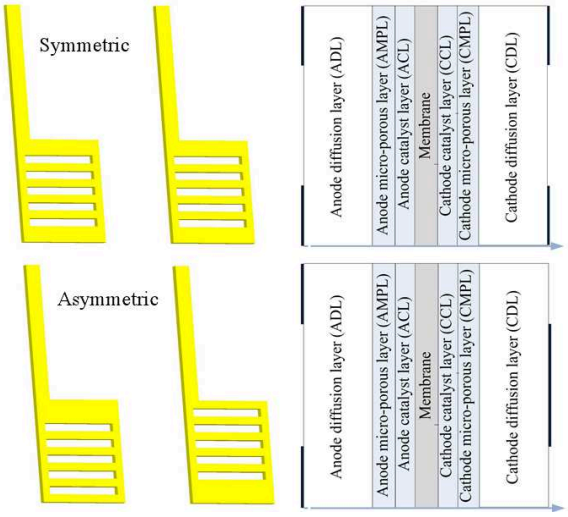


Fig. 1. Schematic of the current collectors and the simulation domain

Fig. 1 shows the schematic of the symmetric and asymmetric current collectors with parallel flow field and the simulation domain of a MEA with the different designs. The flow fields are set to be overlapping and crossing for the symmetric and asymmetric design, respectively. The typical MEA consists of a pair of gas diffusion layers, micro porous layers and catalyst layers on both anode and cathode, and a polymer electrolyte membrane (PEM). The geometry properties of the model is given in Table 1.

Table 1. Properties of the model

Subdomain\Parameter	Permeability K (m^2)	Porosity ε	Thickness δ (m)
Anode Gas Diffusion Layer(AGDL)	1×10^{-12}	0.7	2.5×10^{-4}
Anode Micro Porous Layer (AMPL)	1.5×10^{-14}	0.3	3×10^{-5}
Anode Catalyst Layer(ACL)	1×10^{-14}	0.3	2×10^{-5}
Proton Exchange Membrane (PEM)	1×10^{-18}	-	1.75×10^{-3}
Cathode Catalyst Layer(CCL)	1×10^{-14}	0.3	2×10^{-5}
Cathode Micro Porous Layer(CMPL)	1.5×10^{-14}	0.3	3×10^{-5}
Cathode Gas Diffusion Layer (CGDL)	1×10^{-12}	0.7	2.5×10^{-4}

In this model, there are a total of seven variables involved, namely methanol concentration (C_{M}), anode gas pressure ($p_{\mathrm{g,a}}$), anode liquid pressure ($p_{\mathrm{l,a}}$), oxygen concentration ($C_{\mathrm{O_2}}$), cathode gas pressure ($p_{\mathrm{g,c}}$), cathode liquid pressure ($p_{\mathrm{l,c}}$), and water concentration in the PEM ($C_{\mathrm{W,N}}$).The corresponding governing equations are presented below and the parameters and boundary conditions are listed in Table 2.

$$\nabla\left(-\frac{Kk_{\mathrm{rl}}}{\mu_{\mathrm{l}}/\rho_{\mathrm{l}}}\nabla p_{\mathrm{l,a}}\right)=\dot{m}_{\mathrm{l,a}} \tag{1}$$

$$\nabla\left(-\frac{Kk_{\mathrm{rg}}}{\mu_{\mathrm{l}}/\rho_{\mathrm{g}}}\nabla p_{\mathrm{g,a}}\right)=\dot{m}_{\mathrm{g,a}} \tag{2}$$

$$\nabla\left[\left(-\frac{Kk_{\mathrm{rl}}}{\mu_{\mathrm{l}}}\nabla p_{\mathrm{l,a}}\right)C_{\mathrm{M}}-D_{\mathrm{M}}^{\mathrm{eff}}\nabla C_{\mathrm{M}}\right]=\dot{R}_{\mathrm{M}} \tag{3}$$

$$\nabla\left(-\frac{Kk_{\mathrm{rl}}}{\mu_{\mathrm{l}}/\rho_{\mathrm{l}}}\nabla p_{\mathrm{l,c}}\right)=\dot{m}_{\mathrm{l,c}} \tag{4}$$

$$\nabla\left(-\frac{Kk_{\mathrm{rg}}}{\mu_{\mathrm{l}}/\rho_{\mathrm{g}}}\nabla p_{\mathrm{g,c}}\right)=\dot{m}_{\mathrm{g,c}} \tag{5}$$

$$\nabla\left[\left(-\frac{Kk_{\mathrm{rg}}}{\mu_{\mathrm{g}}}\nabla p_{\mathrm{g,c}}\right)C_{\mathrm{O_2}}-D_{\mathrm{O_2}}^{\mathrm{eff}}\nabla C_{\mathrm{O_2}}\right]=\dot{R}_{\mathrm{O_2}} \tag{6}$$

The pressure difference between liquid and gas is balanced by the capillary pressure as follows:

$$p_{\mathrm{c}}=p_{\mathrm{g}}-p_{\mathrm{l}}=\sigma\cos\theta_{\mathrm{c}}\left(\frac{\varepsilon}{K}\right)^{0.5}J(s) \tag{7}$$

Where σ represents the surface tension coefficient, θ_{c} is the contact angle, ε is the porosity of the porous media and $J(s)$, as the Leverette function, is expressed as:

$$J(s)=\begin{cases}1.417(1-s)-2.120(1-s)^2+1.263(1-s)^3 & 0<\theta_c<90^o\\ 1.417s-2.120s^2+1.263s^3 & 90^o<\theta_c<180^o\end{cases} \tag{8}$$

In the PEM, the water crossover flux and the methanol crossover flux depending on diffusion, electro-osmotic drag and convention can be expressed as:

$$N_{\mathrm{W,cross}}=-D_{\mathrm{W,N}}\nabla C_{\mathrm{W,N}}+n_{\mathrm{d,H_2O}}\frac{I}{F}-\frac{\rho_{\mathrm{l}}}{M_{\mathrm{H_2O}}}\frac{K}{\mu_{\mathrm{l}}}\nabla p_{\mathrm{l}} \tag{9}$$

$$N_{\mathrm{M,cross}}=-D_{\mathrm{M,N}}^{\mathrm{eff}}\nabla C_{\mathrm{M}}+n_{\mathrm{d,M}}\frac{I}{F}-\left(\frac{K}{\mu_{\mathrm{l}}}\nabla p_{\mathrm{l}}\right)C_{\mathrm{M}} \tag{10}$$

Note that the water content (λ) in the PEM is related to the water concentration:

$$\lambda=\frac{EW}{\rho_{\mathrm{dry}}}C_{\mathrm{W,N}} \tag{11}$$

On the anode, the simplified Tafel-like expression is used for the methanol oxidation reaction (MOR) kinetics:

$$j_{\mathrm{a}}=A_{\mathrm{v,a}}j_{\mathrm{m}}^{\mathrm{ref}}\left(\frac{C_{\mathrm{m}}}{C_{\mathrm{m}}^{\mathrm{ref}}}\right)^{\gamma}\exp\left(\frac{\alpha_{\mathrm{a}}F}{RT}\eta_{\mathrm{a}}\right) \tag{12}$$

Where $A_{\mathrm{v,a}}$ is the specific area, $C_{\mathrm{m}}^{\mathrm{ref}}$ and $j_{\mathrm{m}}^{\mathrm{ref}}$ stand for the reference methanol concentration and transfer current density, α_{a} is the anode transfer coefficient, and η_{a} represents the anode over-potential. The reaction order γ is related to the methanol concentration and is assumed to be zero when methanol concentration is higher than a reference value. Otherwise, a first-order reaction is specified.

Similarly, the rate of oxygen reduction reaction (ORR), which takes place on the cathode, is governed by:

$$j_{\mathrm{c}}=A_{\mathrm{v,c}}j_{\mathrm{O_2}}^{\mathrm{ref}}\left(\frac{C_{\mathrm{O_2}}}{C_{\mathrm{O_2}}^{\mathrm{ref}}}\right)\exp\left(-\frac{\alpha_{\mathrm{c}}F}{RT}\eta_{\mathrm{c}}\right) \tag{13}$$

The cell current is measured by the protons and electrons produced by the MOR in the ACL:

$$I_{\mathrm{Cell}} = \int_{\mathrm{ACL}} j_{\mathrm{a}} \mathrm{d}x \tag{14}$$

To account for the effect of methanol crossover, a parasitic current density is calculated as:

$$I_{\mathrm{p}} = 6F \cdot N_{\mathrm{M,cross}} \tag{15}$$

The current density generated by the ORR is:

$$I_{\mathrm{c}} = \int_{\mathrm{CCL}} j_{\mathrm{c}} \mathrm{d}x \tag{16}$$

It is assumed that both the cell current and the parasitic current are entirely consumed by ORR:

$$I_{\mathrm{c}} = I_{\mathrm{p}} + I_{\mathrm{Cell}} \tag{17}$$

Finally, the cell voltage can be determined as:

$$E_{\mathrm{Cell}} = E_0 - \eta_{\mathrm{a}} + \eta_{\mathrm{c}} - I_{\mathrm{Cell}} \left(R_{\mathrm{contact}} + \frac{\kappa_{\mathrm{m}}}{\delta_{\mathrm{mem}}} \right) \tag{18}$$

Where E_0, R_{contact} and κ_{m} denote the thermodynamic equilibrium voltage, the contact resistance and the proton conductivity of the PEM, respectively.

Table 2. Parameters and boundary conditions used in the simulation

Parameters, symbol (unit)	Value	Reference
Faraday constant F (C/mol)	96485	-
Gas constant R (J/mol·K)	8.314	-
Working temperature T (K)	298	-
Electric drag coefficient of H_2O $n_{\mathrm{d,H_2O}}$	$2.5\lambda/22$	[7]
Electric drag coefficient of methanol $n_{\mathrm{d,M}}$	$x_{\mathrm{M}}\ n_{\mathrm{d,H_2O}}$	[7]
Liquid dynamic viscosity μ_{l} (kg/m·s)	4.05×10^{-4}	[7]
Gas dynamic viscosity μ_{g} (kg/m·s)	2.03×10^{-5}	[7]
Methanol diffusion coefficient D_{M} (m^2/s)	$1.58\times10^{-9}e^{0.02623(T-298)}$	[7]
Diffusion coefficient of methanol in Nafion $D_{\mathrm{M,N}}$ (m^2/s)	$4.9\times10^{-10}e^{2436(1/333-1/T)}$	[7]
Diffusion coefficient of H_2O in Nafion $D_{\mathrm{W,N}}$ (m^2/s)	$4.17\times10^{-8}\lambda(161e^{-\lambda}+1)\ e^{-2436/T}$	[7]
Equivalent molar mass of Nafion EW (kg/mol)	1.1	[13]
Density of dry Nafion ρ_{dry} (kg/m^3)	1980	[13]
O_2 diffusion coefficient $D_{\mathrm{O_2}}$ (m^2/s)	$1.775\times10^{-5(T/273)1.823}$	[7]
Electrical conductivity of electronic conductor κ_{s} (S/m)	4000	[14]
Electrical conductivity of PEM κ (S/m)	$7.3e^{1268(1/298-1/T)}\times\lambda/22$	[7]
Proton conductivity of catalyst layer κ_{m} (S/m)	0.14	[14]
Anode reference current density $A_{\mathrm{v,a}}j_{\mathrm{M}}^{\mathrm{ref}}$ (A/m^3)	10^5	[7]
Cathode reference current density $A_{\mathrm{v,c}}j_{\mathrm{O_2}}^{\mathrm{ref}}$ (A/m^3)	1.14×10^3	[7]
Reference methanol concentration $C_{\mathrm{M}}^{\mathrm{ref}}$ (mol/m^3)	100	[7]
Reference O_2 concentration $C_{\mathrm{O_2}}^{\mathrm{ref}}$ (mol/m^3)	0.52	[7]
Transfer coefficient of Anode catalyst layer α_{a}	0.3	[7]

Transfer coefficient of cathode catalyst layer α_c	0.8	[7]
Methanol oxidation reaction equilibrium Potential E_a^{eq} (V)	-1×(131350-408.22×T)/6/F	[7]
Oxygen reduction reaction equilibrium Potential E_c^{eq} (V)	-1×(-285830×3+489.52×T)/6/F	[7]
Thermal equilibrium potential E_0 (V)	1.21	[7]
Contact resistance $R_{contact}$ (Ωm^2)	8×10^{-5}	[7]
Anode inlet O_2 concentration C_M^{in} (mol/m^3)	3000	-
Cathode inlet O_2 concentration $C_{O_2}^{in}$ (mol/m^3)	8.58	-
Anode inlet liquid Saturation s_a^{in}	1	-
Cathode inlet liquid Saturation s_c^{in}	0	-
Anode inlet gas & liquid Pressure p_a^{in} (Pa)	1.013×10^5	-
Cathode inlet gas & liquid Pressure p_c^{in} (Pa)	1.013×10^5	-

Fig. 2 shows the simulation results of the methanol concentration distribution patterned with different current collectors at a cell current density of 80 $mA.cm^{-2}$. An evener distribution of methanol in anode porous area is observed in the cell with the asymmetric current collectors. As shown in Fig. 2a, the methanol concentration decreases from 3 $mol.L^{-1}$ at inlet to 0.755 $mol.L^{-1}$ at the under-rib region in the cell with the symmetric current collectors. The decrease is found to be smaller (from 3 $mol.L^{-1}$ to 0.801 $mol.L^{-1}$) in the cell with the asymmetric current collectors as shown in Fig. 2b. The asymmetric current collectors lead to a longer distance for water and methanol to transport through the MEA. It implies that the water and methanol crossover flux can be reduced and it is easier for the methanol to achieve a uniform distribution in this condition. Accordingly, the reaction rates in both ACL and CCL are uniformly distributed.

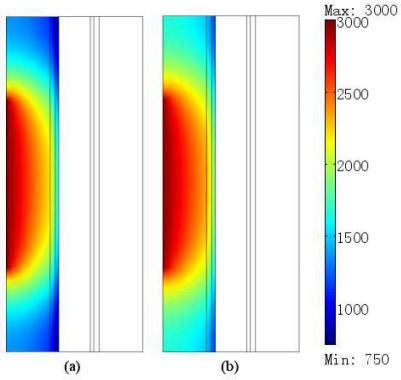


Fig. 2. Simulation results of methanol concentration distribution: (a) symmetric; (b) asymmetric

Another benefit of asymmetric current collectors is the increase of water content in the MEA. Fig. 3 shows the average water content in the PEM from the anode to the cathode at different current densities. Water content is a parameter that measures the total water in the PEM in terms of mole and it plays an important role in proton conduction and water diffusion [11]. As can be seen from both Fig. 3a and Fig. 3b, the water content increases with the increase of current density in the cathode side, but decreases in the anode side. This is mainly due to two facts. First, CO_2 bubbles generated in the anode side reduces the contact area between liquid and the PEM. Second, more water is dragged away from anode to cathode when the current density rises. We can also see that water content distributes more evenly and is higher when using asymmetric current collectors. However, higher water content gradient across the membrane is found in the cell with symmetric current collectors, as shown in Fig. 3a. This unwanted phenomenon can do a huge damage to the

fuel cell. The higher water content gradient drives the water diffusion to the cathode, making the problem of water and methanol crossover become heavier, which is displayed in Fig. 4.

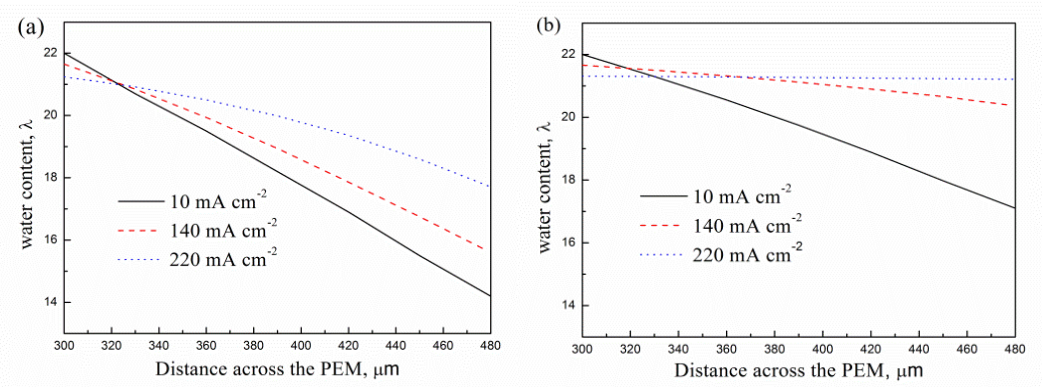


Fig. 3. Simulation results of water content in the PEM: (a) symmetric; (b) asymmetric

The curves in Fig. 4 indicate that water crossover flux increases and methanol crossover flux decreases with increasing current density. Water and methanol crossover depend on three mechanisms, namely diffusion, convection, and electro-osmotic drag. For water, the electro-osmotic drag flux increases when the current density goes up. In the meantime, the diffusion flux decreases and the back convection from the cathode to the anode increases due to lower water content gradient and higher cathode liquid pressure. Overall, the electro-osmotic drag flux dominates the three principles, which makes the total flux of water crossover increases when increasing the current density. On the other hand, the concentration of methanol in the anode side decreases gradually with the increase of current density. This result comes from the fact that more and more methanol gets into the chemical reaction and there is little left to transport through membrane to the CCL. As a consequence, the electro-osmotic drag flux and diffusion flux of methanol both decease with increasing current density. This explains why the methanol crossover flux goes down to almost zero when the current density goes to the maximum. Hence, it can be concluded that water and methanol crossover flux in the MEA with asymmetric current collectors is effectively suppressed.

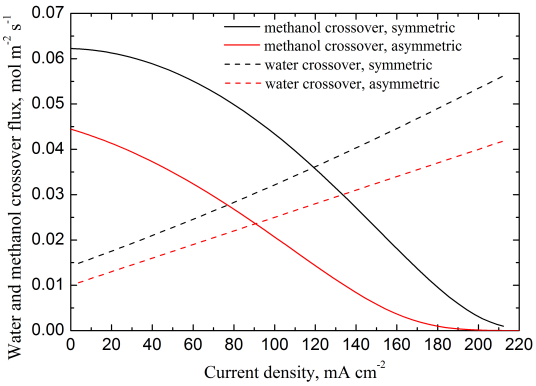


Fig. 4. Simulation results of water and methanol crossover flux

Experimental

Comparing experiments were conducted to verify the simulation results. Two passive μDMFCs with an active area of 1 cm^2 were fabricated, as shown in Fig. 5. The current collectors made of 316L stainless steel with an open ratio of 50% were fabricated using laser-cut technology [12,13]. Au layers were sputtered on the surface to prevent corrosion. Anode gas diffusion electrolyte (GDE) with 4.0 $mg.cm^{-2}$ Pt-Ru/C catalyst and cathode GDE with 2.0 $mg.cm^{-2}$ Pt/C catalyst were adopted. Nafion117 membranes were used as the PEM. These experiments were carried out at room temperature.

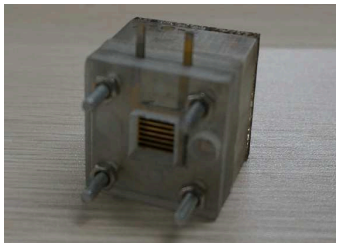


Fig. 5. Picture of the assembled μDMFC

The Data from Fig. 6 depicts the cell performances with different current collectors and different methanol concentration. The maximum power densities are 25.6 $mW.cm^{-2}$ for symmetric current collectors and 25.7 $mW.cm^{-2}$ for asymmetric current collectors with 2.5 $mol.L^{-1}$ methanol solution. We can see that at this relatively low methanol concentration, the two cells exhibit almost the same performance. However, with the increase of methanol concentration, the cell with symmetric current collectors shows lower output power than with the symmetric ones. The maximum power densities reaches 27.5 $mW.cm^{-2}$ for symmetric current collectors and 30.3 $mW.cm^{-2}$ for asymmetric current collectors at 5 $mol.L^{-1}$ methanol solution. The improvement for asymmetric current collectors is mainly obtained from the fact that they induced the methanol to distribute uniformly and effectively suppressed the water and methanol crossover. At this point, the experimental results are in accordance with the simulation results. Therefore, current collectors should be carefully designed for the μDMFCs and avoid to be symmetric because they have an impact not only on the mass transport in anode and cathode porous regions but also on water and methanol crossover.

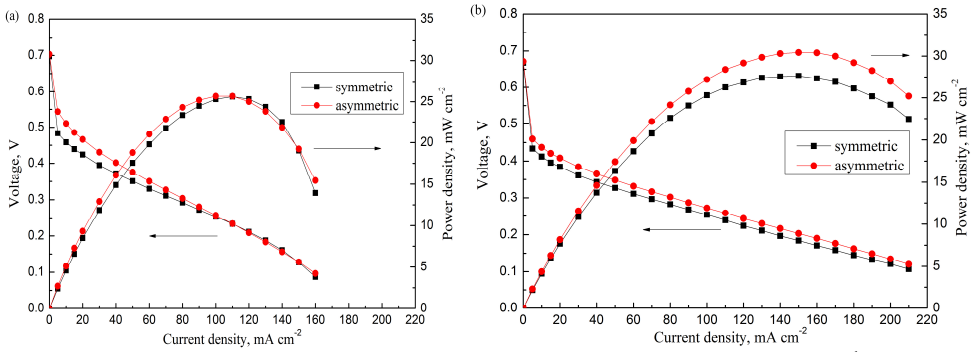


Fig. 6. Performance of the μDMFCs with methanol concentration of: (a) 2.5 $mol.L^{-1}$, (b) 5 $mol.L^{-1}$.

Summary

The combined effect of anode and cathode current collectors on the behavior of water and methanol crossover in μDMFCs has been studied numerically and experimentally in this paper. The simulation results show the asymmetric current collectors lead to a longer distance for water and methanol to transport through the MEA. Therefore, water and methanol crossover flux can be reduced and it is easier for the methanol to achieve a uniform distribution in the entire anode catalyst layer, which is beneficial for the chemical reaction. Two passive μDMFCs with an active area of 1 cm^2 were fabricated to validate the numerical results. An improvement of 10% output power is obtained for asymmetric current collectors when feeding 5 $mol.L^{-1}$ methanol solution. It confirmed that the cell with the asymmetric current collectors can effectively suppress the water and methanol crossover and consequently exhibits better performance.

Acknowledgements

The work described in this paper was supported by the National Natural Science Funds of China (NO.61404037, and NO.61376113).

References

[1] A. Kundu, J.H. Jang, J.H. Gil, C.R. Jung, H.R. Lee, S.H. Kim, B. Ku, Y.S. Oh, Micro-fuel cells - Current development and applications, J. Power Sources 170 (2007) 67-78.

[2] T. Schultz, U. Krewer, T. Vidakovic, M. Pfafferodt, M. Christov, K. Sundmacher, Systematic analysis of the direct methanol fuel cell, J. Appl. Electrochem. 37 (2007) 111-119.

[3] Y.L. He, Z. Miao, T.S. Zhao, W.W. Yang, Numerical study of the effect of the GDL structure on water crossover in a direct methanol fuel cell, Int. J. Hydrogen Energ. 37 (2012) 4422-4438.

[4] F.Q. Liu, G.Q. Lu, C.Y. Wang, Low crossover of methanol and water through thin membranes in direct methanol fuel cells, J. Electrochem. Soc. 153 (2006) 543-553.

[5] K. Kang, G. Lee, G. Gwak, Development of an advanced MEA to use high-concentration methanol fuel in a direct methanol fuel cell system, Int. J. Hydrogen Energ. 37 (2012) 6285-6291.

[6] A. Yamauchi, T. Ito, T. Yamaguchi, Low methanol crossover and high performance of DMFCs achieved with a pore-filling polymer electrolyte, J. Power Sources 174 (2007) 170-175.

[7] W.W. Yang, T.S. Zhao, Numerical Investigations of Effect of Membrane Electrode Assembly Structure on Water Crossover in a Liquid-feed Direct Methanol Fuel Cell, J. Power Sources 188 (2009) 433-446.

[8] C. Xu, T.S. Zhao, A new flow field design for polymer electrolyte-based fuel cells, Electrochem. Commun. 9 (2007) 497-503.

[9] C. Xu, T.S. Zhao, In situ measurements of water crossover through the membrane for direct methanol fuel cells, J. Power Sources 168 (2007) 143-153.

[10] F.Q. Liu, C.Y. Wang, Water and methanol crossover in direct methanol fuel cells - Effect of anode diffusion media, Electrochim. Acta 53 (2008) 5517-5522.

[11] S. Motupally, A.J. Becker, J.W. Weidner, Diffusion of water in Nafion 115 membranes, J. Electrochem. Soc. 147 (2000) 3171-3177.

[12] Y.C. Park, P. Chippar, S.K. Kim, S. Lim, D.H. Jung, H. Ju, Effects of serpentine flow-field designs with different channel and rib widths on the performance of a direct methanol fuel cell, J. Power Sources 205 (2012) 32-47.

[13] C. Xu, T.S. Zhao, W.W. Yang, Modeling of water transport through the membrane electrode assembly for direct methanol fuel cells. J. Power Sources 178 (2008) 291-308.

[14] C.H. Chen, T.K. Yeh, A mathematical model for simulating methanol permeation and the mixed potential effect in a direct methanol fuel cell, J. Power Sources 160 (2006) 1131-1141.

Key Engineering Materials Vols 645-646 (2015) pp 1189-1194
© (2015) Trans Tech Publications, Switzerland
doi:10.4028/www.scientific.net/KEM.645-646.1189

Submitted: 2015-01-08
Accepted: 2015-01-15

Study on the Energy Harvesting Performance of PE Cantilever Beam

Hai-peng LIU[1, a], Shi-qiao GAO [2,b] and Lei JIN [3,c]

[1,2] State Key Laboratory of Explosion Science and Technology, Beijing Institute of Technology, China

[3] School of Mechatronical Engineering, Beijing Institute of Technology, China

[a]lhp@bit.edu.cn(corresponding author), [b]gaoshq@bit.edu.cn, [c]jinlei@bit.edu.cn

Keywords: Energy Harvesting, Piezoelectric, Cantilever Beam, Vibration.

Abstract. Harvesting ambient vibration energy through piezoelectric (PE) means is a popular energy harvesting technique. The merit of applying PE means to supply energy for microelectronic devices is that they can reduce the battery weight and possibly make the device self-powered by harvesting mechanical energy. This investigation will examine the energy generating performance of miniature PE cantilever beam through theoretical modeling, simulation and experiment testing. Through the theoretical analysis of the piezoelectric energy harvesting structure, the expression of open circuit voltage output is obtained. Using ANSYS software, the working performance of piezoelectric cantilever beam is analyzed. On the basis of theoretical analysis and simulation optimization, a set of experimental system is established to test the energy harvesting performance of the piezoelectric cantilever beam. The testing result shows that the harvested energy by the piezoelectric cantilever beam could supply electrical power to some micro electrical devices.

Introduction

In recent years, with the rapid development of MEMS and the advances in the integrated circuits, the wireless sensor network technology has become a hot topic. However, the technical difficulty during the development of the wireless sensor networks is how to ensure long-time energy supply. With the expanding application of MEMS sensors, the energy consumption of many microelectronic devices can be reduced to a few microwatts, which allows the application of energy harvesting from environment to be possible. Harvesting ambient vibration energy using piezoelectric (PE) means is a popular energy harvesting technique that can potentially supply 10 to 100 μW of available power[1-4]. After studying the various ambient energy harvesting methods, some researchers such as Roundy[5], Sodano[6], Mateut[7], Priya[8] point out that the merit of applying PE means to supply energy for microelectronic devices is that they can reduce the battery weight and possibly make the device self-powered by harvesting mechanical energy. According to the recently investigations, the advantages of piezoelectric energy harvester are, no pollution, no electromagnetic interference, easy miniaturization and integration and so on. Many countries in this world had focus on this aspect[9]. This investigation will examine the energy generating performance of miniature PE cantilever beam through the theoretical model, simulation and experiment.

Theoretical Analysis on the Piezoelectric Cantilever Beam

The structure diagram of cantilever piezoelectric energy harvester is shown in Fig. 1, and Fig. 2 shows a physical structure of the cantilever energy harvester. A layer of metal sheet and a layer of piezoelectric sheet which is polarized in the thickness direction are composed of the cantilever beam. The root of the cantilever beam is fixed. A metal block is added at the end of cantilever to adjust resonance frequency and increase the output voltage.

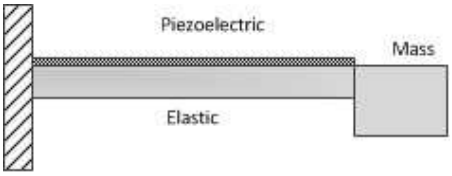


Fig.1 The structure diagram of cantilever

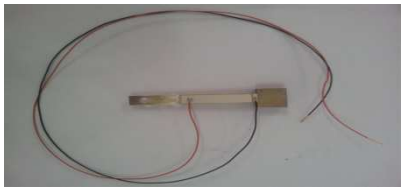


Fig.2 A physical structure of cantilever

The piezoelectric cantilever beam can be equivalent to a lumped parameter model. Fig.3 shows a diagram when a cantilever beam is subjected to an external force. The moment at C-section can be expressed as:

$$M = m_2 a(L-x) + \int_0^{L-x} sqds = m_2 a(L-x) + \frac{m_1 a}{2L}(L-x)^2 \tag{1}$$

Where m_1 is mass of cantilever beam, m_2 is mass of metal block, L is length of cantilever. According to the small deflection bending theory, x and y axes are all coincide with the neutral layer of the cantilever beam. The neutral layer of the cantilever beam is shown in Fig.4. e is the distance between neutral layer and piezoelectric film surface, h is the thickness of cantilever beam, δ is the thickness of PZT.

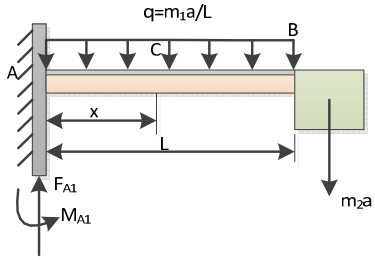


Fig.3 The cantilever beam diagram

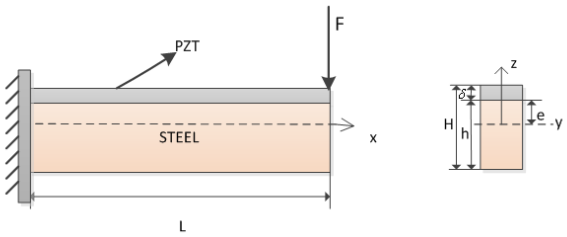


Fig.4 The neutral axis diagram

Let $N = \frac{Y_1}{Y_2}$, $n = \frac{h}{\delta}$. The cantilever beam will deform when it is subjected to an external force. We assume that the composite beam cross-section remains plane after deformation. Then the stress at anywhere of cantilever beam can be given as:

$$T_2 = Y_2 \varepsilon = Y_2 \frac{z_2}{\rho} \tag{2}$$

From equation (1) and the plane assumption:

$$T_1 = Y_1 \frac{z_1}{\rho} - \frac{d_{31}}{s_{11}^E} E_3 \tag{3}$$

Where Y_1 is the Young modulus of piezoelectric material, ε is strain, ρ is the curvature radius of neutral layer, Y_2 is the Young modulus of steel.

The position of neutral axis (shown in Fig.4) can be determined through the following equation,

$$\sum F_x = \int_0^H Tbdz = b\int_e^{e+\delta} (Y_1 \frac{z}{\rho} - \frac{d_{31}}{s_{11}^E} E_3) dz + b\int_{-(h-e)}^{e} Y_2 \frac{z}{\rho} dz = 0 \tag{4}$$

The centric y-coordinate of section A_1 and A_2 are $\overline{y}_1$ and $\overline{y}_2$ respectively,

$$\int_{A_1} \frac{z}{\rho} dA = A_1 \overline{y}_1 = b\delta(e + \frac{\delta}{2}) \tag{5}$$

$$\int_{A_2} \frac{z}{\rho} dA = A_2 \overline{y}_2 = bh(e - \frac{h}{2}) \tag{6}$$

That is:

$$e = \frac{d_{31} V}{s_{11}^E (Y_1 \delta + Y_2 h)} + \frac{Y_2 h^2 - Y_1 \delta^2}{2(\delta Y_1 + h Y_2)} \tag{7}$$

The internal bending moment of the composite beam is equal to the external moment, the relationship is as follows:

$$\begin{aligned} M &= \int_A zTdA = \int_A z(T_1 + T_2)dA \\ &= b\int_e^{e+\delta}\left(Y_1\frac{z^2}{\rho} - \frac{d_{31}}{s_{11}^E}E_3 z\right)dz + b\int_{-(h-e)}^{e} Y_2\frac{z^2}{\rho}dz \\ &= \frac{b}{3\rho}\left[Y_1(3e^2\delta + 3e\delta^2 + \delta^3) + Y_2(3e^2h + 3eh^2 + h^3)\right] - \frac{d_{31}Vb(\delta+2e)}{2s_{11}^E} \end{aligned} \tag{8}$$

That is

$$\frac{1}{\rho} = \frac{3\left(M + \frac{d_{31}Vb(\delta+2e)}{2s_{11}^E}\right)}{b\left[Y_1(3e^2\delta + 3e\delta^2 + \delta^3) + Y_2(3e^2h + 3eh^2 + h^3)\right]} \tag{9}$$

The total charge quantity Q on the piezoelectric sheet is,

$$Q = \int_A D_3 dA = b\int_0^L (d_{31}T_1 + \varepsilon_{33}^T\frac{V}{\delta})dx \tag{10}$$

Where

$$E_3 = \frac{V}{\delta} \tag{11}$$

If the resistance of the external circuit between two electrodes is much greater than that of piezoelectric sheet, the outside circuit is in an open state. And the voltage $V = 0$.

$$e = \frac{\left[Y_2h^2 - Y_1\delta^2\right]}{2(\delta Y_1 + hY_2)} \tag{12}$$

$$\frac{1}{\rho} = \frac{3M}{b\left[Y_1(3e^2\delta + 3e\delta^2 + \delta^3) + Y_2(3e^2h + 3eh^2 + h^3)\right]} \tag{13}$$

Stress at any section of the piezoelectric sheet is:

$$\begin{aligned} T_1 = Y_1\frac{z}{\rho} &= \frac{3MY_1z}{b\left[Y_1(3e^2\delta + 3e\delta^2 + \delta^3) + Y_2(3e^2h + 3eh^2 + h^3)\right]} \\ &= \frac{3\rho Mz}{b\left[(3+3Nn)e^2\delta + (3+3Nn^2)e\ \delta^2 + (1+Nn^3)\delta^3\right]} \end{aligned} \tag{14}$$

The average stress at any section of the piezoelectric sheet is :

$$\begin{aligned} T_1 &= \frac{3M(\frac{\delta}{2}+e)}{b\left[(3+3Nn)e^2\delta + (3+3Nn^2)e\delta^2 + (1+Nn^3)\delta^3\right]} \\ &= \frac{3(\delta+2e)}{2b\left[(3+3Nn)e^2\delta + (3+3Nn^2)e\delta^2 + (1+Nn^3)\delta^3\right]}\left[m_2a(L-x) + \frac{m_1a}{2L}(L-x)^2\right] \end{aligned} \tag{15}$$

If the gravity of piezoelectric cantilever beam and piezoelectric sheet are ignored, we can obtain the following expression:

$$T_1 = \frac{3(\delta+2e)}{2b\left[(3+3Nn)e^2\delta + (3+3Nn^2)e\delta^2 + (1+Nn^3)\delta^3\right]}\left[m_2a(L-x)\right] \tag{16}$$

And the total charge quantity Q on the piezoelectric sheet is,

$$\begin{aligned} Q &= \int_A D_3 dA = b\int_0^L d_{31}T_1 dx \\ &= b\int_0^L \frac{3d_{31}(\delta+2e)}{2b\left[(3+3Nn)e^2\delta + (3+3Nn^2)e\delta^2 + (1+Nn^3)\delta^3\right]}\left[m_2a(L-x) + \frac{m_1a}{2L}(L-x)^2\right]dx \\ &= \frac{d_{31}(\delta+2e)(m_1+3m_2)aL^2}{4\left[(3+3Nn)e^2\delta + (3+3Nn^2)e\delta^2 + (1+Nn^3)\delta^3\right]} \end{aligned} \tag{17}$$

The equivalent capacitance of the piezoelectric element is:

$$C = \frac{\varepsilon A}{\delta} \tag{18}$$

where $\varepsilon = 3\times10^{-8} F/m$, $A = bL$.

The open circuit voltage of PZT from $U = \frac{Q}{C}$ can be given as:

$$U = \frac{d_{31}(\delta + 2e)(m_1 + 3m_2)aL}{4b\varepsilon\left[(3+3Nn)e^2 + (3+3Nn^2)e\delta + (1+Nn^3)\delta^2\right]} \tag{19}$$

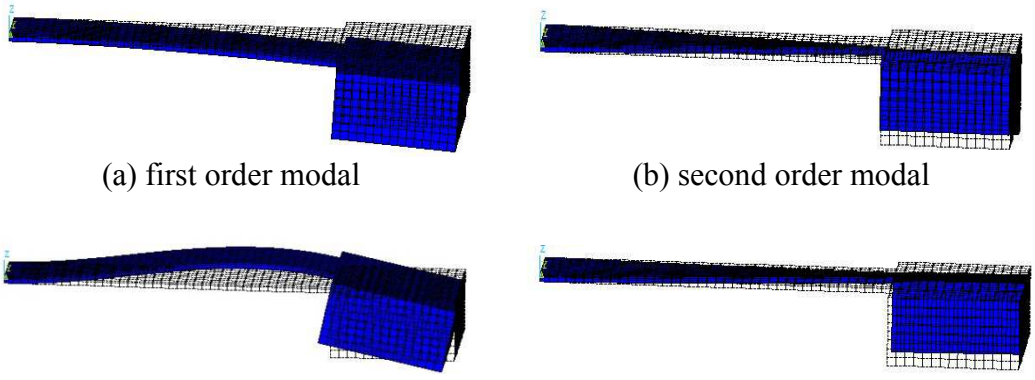
where $a = a_0 \sin\omega t = a_0 \sin 2\pi f$, and the open circuit voltage can be expressed as:

$$U = \frac{d_{31}(\delta + 2e)(m_1 + 3m_2)La_0 \sin 2\pi f}{4b\varepsilon\left[(3+3Nn)e^2 + (3+3Nn^2)e\delta + (1+Nn^3)\delta^2\right]} \tag{20}$$

Where Q is charge quantity, U is open circuit voltage, A is plate area, C is capacitor of PZT, ε is permittivity of PZT.

Simulation Anylasis on the PE Cantilever Beam

In order to better understand the energy harvesting performance of piezoelectric cantilever beam, the working modal of piezoelectric cantilever beam is analyzed by using of ANSYS software. Fig.5 shows the top four order vibration modal of cantilever beam. From the top four order vibration modal, we can find out that the first order modal is the main modal to harvest energy from the vibration environment. The simulation result shows that the simulation on the vibration modal could optimize the design of the piezoelectric cantilever beam.



(a) first order modal (b) second order modal

(c) third order modal (d) forth order modal

Fig.5 The top four order vibration modal of cantilever

Through simulation analysis, the influence of the piezoelectric cantilever beam thickness on the structural vibration frequency is obtained. From Fig.6, we can find out that each order of the structure natural frequency increases gradually with the increasing of the beam thickness.

According to the simulation analysis, the natural frequency of cantilever beam will decrease with the increasing of beam length or the increasing of the metal block mass. Therefore, it is necessary that the length of beam or the mass of metal block can be increased and the width of beam can be decreased in order to obtain a piezoelectric energy harvester working on the low frequency vibration environment.

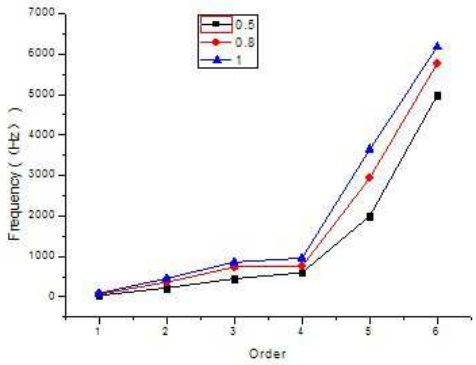


Fig.6 The natural frequency on the diferent beam thickeness



Fig.7 The testing system diqagam

Testing on the Energy Harvesting Performance of PE Cantilever Beam

On the basis of theoretical analysis and simulation optimization, a set of experimental system (shown in Fig.7) including a signal generator, power amplifier, exciter, dynamic signal analyzer, acceleration sensors is established to test the energy harvesting performance of the piezoelectric cantilever beam. Using a self-developed circuit, the energy harvesting ability of piezoelectric cantilever beam is tested. After the frequency sweeping and power spectrum analysis on the acceleration signal, the resonant frequency of piezoelectric cantilever is 57Hz. Using the established testing system, the stable voltage output of the piezoelectric cantilever beam can be obtained when the environmental vibration acceleration is 0.2g (shown in Fig.8). The testing result shows that the harvested energy by the piezoelectric cantilever beam could supply stable electrical power to some microelectrical devices.

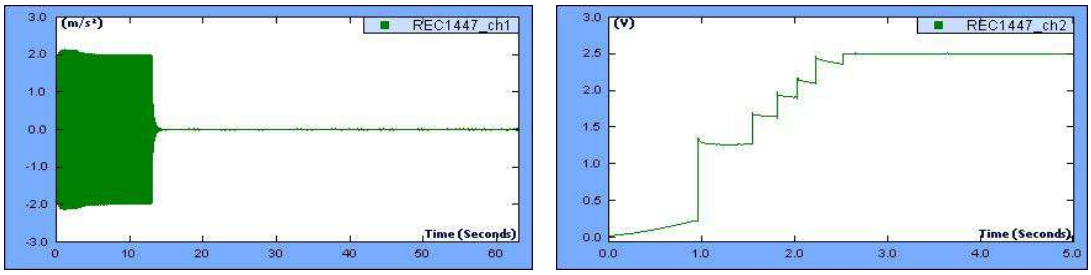


Fig.8 The stable output of PE cantilever beam

Summary

Harvesting ambient vibration energy through piezoelectric (PE) means has beccom a popular energy harvesting technique. Through the theoretical analysis of the piezoelectric energy harvesting structure, the open circuit voltage output expression is obtained. Using ANSYS software, the working performance of piezoelectric cantilever beam is analyzed. The experimental testing result obtained by using a self-developed testing system shows that the piezoelectric cantilever beam can output a stable voltage through the optimization on the various circuit parameters and the piezoelectric cantilever beam structure parameters. If the volume of the energy harvesting structure can be further reduced, it may provide energy for MEMS devices as a self-powered supply device by using the ambient mechanical vibration.

[1] Project supported by the National High Technology Research and Development Program of China (No.2013AA041104)

References

[1] Sand Hills grams. Priya (India), Daniel Yin Man (America), Energy harvesting technology, Southeast University Press, Nanjing, 2011 (in Chinese)
[2] Chen Renwen. New ambient energy collection technology, National Defense Industry Press, Beijing,2011. (in Chinese).
[3] ERTURK A, INMAN J D. A distributed parameter electromechanical model for cantilevered piezoelectric energy harvesters. Journal of Vibration and Acoustics. 130(2008) 041002-1-15.
[4] Roundy, S., On the effectiveness of vibration-based energy harvesting. Journal of Intelligent Material Systems and Structures, 16(2005) 809-823.
[5] Roundy S, Wright P K, Rabaey J, A study of low lever vibrations as power source for wireless sensor nodes, Computer Communications. 26(2003) 1131-1144.
[6] Sodano, H.A., Inman, D.J., and Park, G., Comparison of piezoelectric energy harvesting devices for recharging batteries. Journal of Intelligent Material Systems and Structures. 16(2005)799-807.
[7] Mateu L, Moll E, Review of energy harvesting techniques and applications for microelectronics. Proceeding of SPIE：Conference on VLSI Circuits and Systems II, (2005) 359-373.
[8] PRIYA S. Advances in energy harvesting using low profile piezoelectric transducers, Appl. Phys. Lett. 19(2007)165-182.
[9] Alper Erturk, Renno J M, lnman D J. Modeling of Piezoelectric Energy Harvesting from an L-shaped Beam-mass Structure with an Application to UAVs, Journal of Intelligent Material Systems and Structures. 20(2009)529-544.

Key Engineering Materials Vols 645-646 (2015) pp 1195-1200
© (2015) Trans Tech Publications, Switzerland
doi:10.4028/www.scientific.net/KEM.645-646.1195

Submitted: 2014-11-04
Accepted: 2014-12-23

To Improve Micro-Planar-Magnetic Generator Performance Based on Addition of Magnetic Material

Lin DU[1,a*], Gengchen SHI[1,b], Jingjing ZHAO[1,c]

[1]National lab of Mechatronic Engineering and Control,
Beijing Institute of Technology, Beijing, China

[a]dldulin@163.com(corresponding author)

[b]shigengchen@bit.edu.cn

[c]jing.jing.youxiang@163.com

Keywords: Micro generator, magnetic generator, Power MEMS.

Abstract: By finite element simulation and experiment, this paper compares the performance of generators with magnetic material to generators without magnetic material (Fe) in its coil and analyzes the reason why there is difference between simulation results and experimental results. Experimental results present that under the same rotational speed, output voltage improves 60% with the addition of magnetic material in coil compared to generator without magnetic material in coil. We further discuss the feasibility to add magnetic material in coil, present the existed problems and improvement methods.

Introduction

Research on micro power generations is increasing as wireless sensor networks and wearable devices are becoming smaller and increasingly widely used. Compared with traditional electrochemical batteries, micro magnetic generators have advantages as long-time storage, no need for replacement, ease of maintenance, less pollution, etc. Besides, micro planar magneic generator owns features of short in axial dimension, high power density and high energy effeciency and so on. Hence, research communities have done research to improve performance of micro planar magnetic generators.

C.T. Pan et al [1] fabricated a 5×5×2 mm^3 generator in 4 pole-pairs and the maximum power output reached 0.412 mW at 149.3 Hz. This device had a multi-layer planar coil to increase coil enclosed area. Florian Herrault et al [2] fabricated a generator consisting of a three-phase microfabricated surface-wound copper coil and a multi-pole permanent-magnet rotor of 2 mm in diameter. The generator exhibited up to 6.6 mW of alternating current (AC) electrical power across a resistive load 1.8Ω at a rotation speed of 392 kr/min. They did research on how different magnetic materials and coil enclosed area influence the output performance. In the following year, the same research team [3] fabricated a generator with a laminated magnetic stator core to obtain power of 1.05 W at a rotation speed of 200 kr/min. Sun shao-chun et at [4] presented a three-phase stator coil which delivered 357.3 μW at 10 kr/min with a 0.23 Ω resistor load and showed how the changing rate of magnetic flux impacts the generator performance. R. Cordero1 et al [5] developed a generator composed of commercially available NdFeB permanent magnets and planar coils manufactured by photolithography. The generator was capable of producing 3.2 V and 5.8 mW of output power at a rotation speed of 4 kr/min. They further analyzed the affect of multi-layer coil. Y. J. Chen et al [6] established a generator with the size of 0.761 cm^3 which generated 218.127 mV induced voltage at 1395.34 rad/s. Besides, they did research with different shapes of coil.

According to Faraday's law of electromagnetic induction, the induced voltage can be expressed as Eq.1.

$$U(t) = -\frac{d\Phi(t)}{dt} = -S\frac{dB(t)}{dt} \tag{1}$$

where *U(t)* is the induced voltage, *Φ* represents the magnetic flux through coil, *B* means the magnetic flux density, *S* is the area enclosed by coil

Eq.1 indicates that there are three methods to improve output voltage: (1) To increase the magnetic flux density through the coil, (2) To enlarge the area enclosed by the coil, (3) To improve the change rate of magnetic flux. Generator design also focuses on the above three points.
There are two methods to increase magnetic flux density: (1) To use material with high residual magnetism as the magnet, (2) To add magnetic material in coil. Since NdFeB is widely spread and with high residual magnetism, existed micro magnetic generators usually use NdFeB as magnet, while addition of magnetic material to coil has no practical application so far. Next, we'll analyze the output performance of generator with and without magnetic material (Fe) in its coil by finite element simulation and experiment respectively.

2 Overall design

Main structure of micro-planar-magnetic generator contains a stator multilayer coil and rotor multi-pole magnets on both sides of the coil, as shown in Fig.1. Magnet provides magnetic field as energy source and when the turbine drives the magnets to rotate, they rotate relatively to the coil and magnetic flux through the coil changes and there is electromotive force produced in coil.

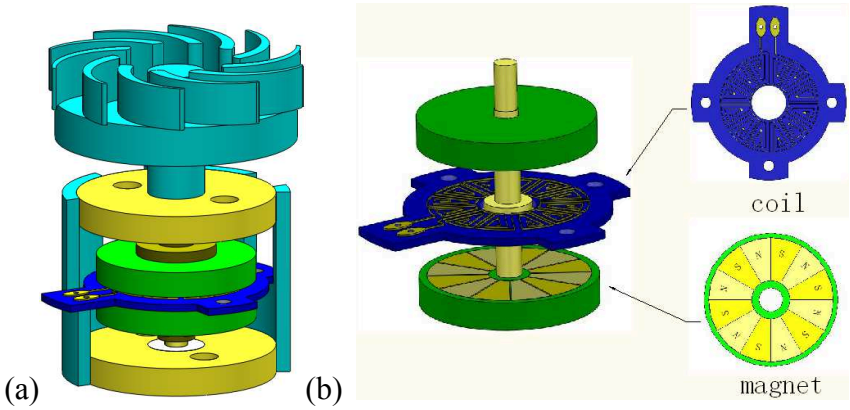


Fig.1 Micro planar magnetic generator (a) overall structure (b) main structure

To compare the performance of generator with magnetic material to generators without magnetic material in its coil, we designed comparison programs as follow,
(1)Add an iron film in the middle of coil and the structure is: coil+ adhesive+ iron film+ adhesive+ coil, as shown in Fig.2(a).
(1)Add paper in the middle of coil which has the same thickness of iron film and the structure is: coil+ adhesive+ paper+ adhesive+ coil, as shown in Fig.2(b).
In this design, coil is double layer and thickness of coil, iron film, adhesive is 0.1mm, 0.3mm, 0.04mm respectively, and the total structure thickness is 0.58mm.

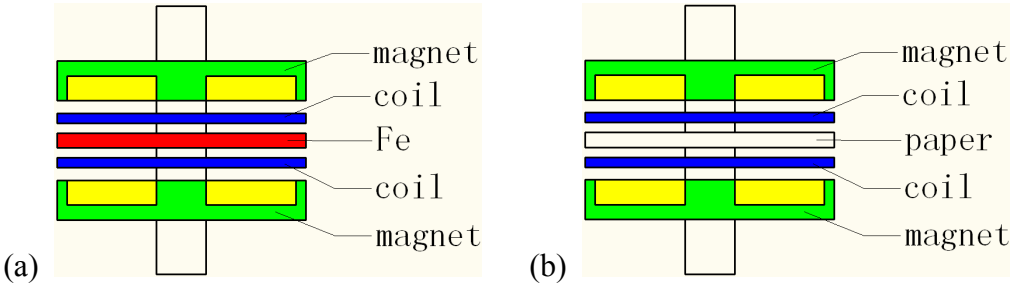


Fig.2 (a) Model with magnetic material in coil (b) Model without magnetic material in coil

Then we compared the performance of generators with magnetic material to generators without magnetic material (Fe) in its coil by finite element simulation and experiment respectively.

3 Finite element analyses

We carry out finite element analysis (FEA) simulations using Ansoft Maxwell software and compare the magnetic distributions of the prototypes with magnetic material to generators without magnetic material in its coil.

3.1 Simulation model

A circumferential cross section in the three-dimensional magnetic structure of the generator is expanded into a plane as a two-dimensional (2D) model, as shown in Fig.3(a). Width of the magnet is defined as the average of outer arc and inner arc of a three-dimensional magnet. After model building, material allocating, boundaries definition, mesh and corresponding post-processing operation, we obtained magnetic flux distribution as shown in Fig.3(b).

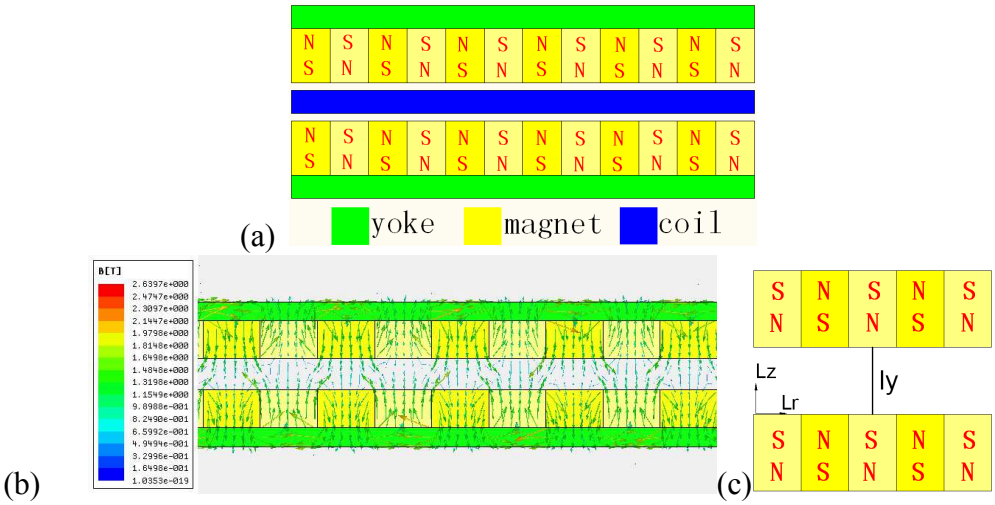


Fig.3 (a)Simulation model (b)Magnetic flux distribution (c)Model coordinate

Fig.3(b) shows that magnetic field in the magnetic gap is not uniform. There is circumferential component Lr besides axial component Lz. Along the middle line ly there is only axial component and no circumferential component. As the distance from ly increases, axial component decreases and circumferential component increases. Axial component is the effective value. Magnetic flux distribution on ly is shown in Fig.4.

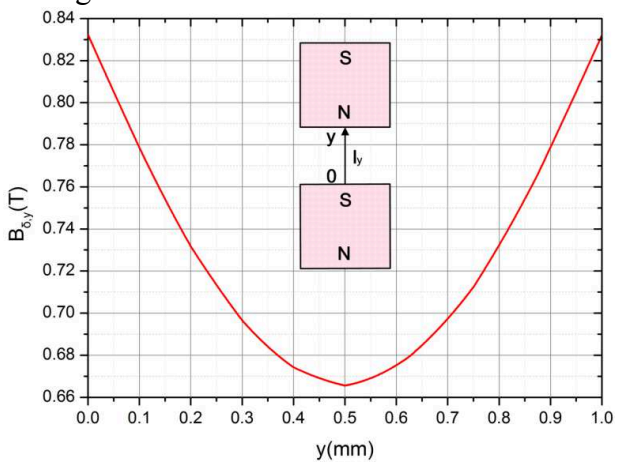


Fig.4 Magnetic flux density distribution along the middle line ly

Fig.4 indicates that magnetic density is the strongest on surface of magnet and weakest in the middle of the gap. We can get magnetic density in the magnetic gap with this simulation method.

3.2 Comparison between magnetic flux distribution of generators with and without magnetic material

According to the simulation method above, we can get the magnetic flux distribution of generator with and without magnetic material in coil, as shown in Fig.5.

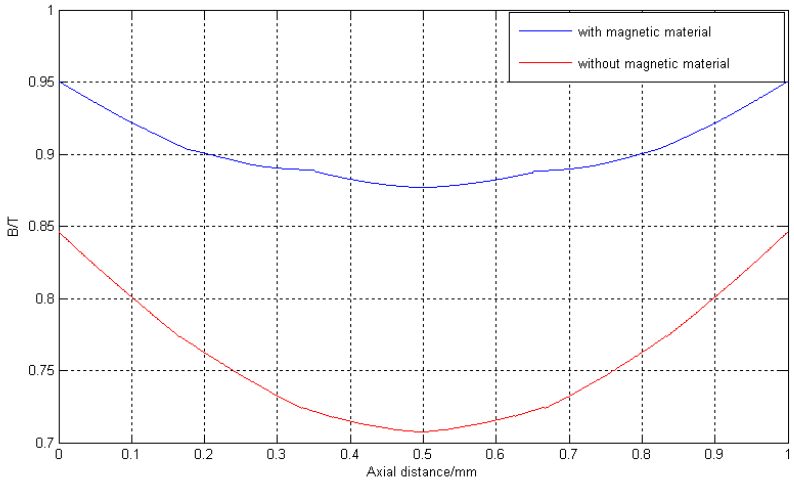


Fig.5 Magnetic flux density distribution of generators with and without magnetic material

Fig.5 shows that addition of magnetic material increases magnetic density in the gap effectively. Thickness of gap is 1mm, coil is double layer. The layers of the upper coil are located at 0.24mm and 0.28mm from the upper magnetic surface. The layers of the lower coil are located at 0.72mm and 0.76mm from the upper magnetic surface. And we can get the magnetic flux density of different layers of coil from Fig.5.

Table.1 Magnetic density at different layers of coil

Location of coil	0.24mm	0.28mm	0.72mm	0.76mm	Magnetic flux density average[T]
Magnetic flux density without magnetic material in coil[T]	0.750203	0.739149	0.739149	0.750207	0.744677
Magnetic flux density with magnetic material in coil [T]	0.895735	0.891489	0.890901	0.895018	0.8932858

Magnetic flux distribution of generators with and without magnetic material in its coil is obtained by finite element method. Then put these values into Eq.1, we can get the output voltage with various rotational speed.

4 Experimental results

In experiment, rotor is driven by motor and output voltage of generators with and without magnetic material in coil is tested. Comparison between experimental results and simulation results is shown in Table.2 and Table.3.

Table.2 Experimental results without magnetic material in coil

No.	Rotational speed [kr/min]	Output voltage [V]	Output voltage / Rotational speed in experiment [V/kr]	Output voltage / Rotational speed in simulation [V/kr]	Simulation error [%]	Simulation error average[%]
1	0.879	0.2	0.228		2.79	
2	1.965	0.42	0.213696		9.48	
3	2.572	0.58	0.225504		3.74	
4	2.629	0.56	0.213024	0.233947	9.82	6.56
5	3.962	0.88	0.222112		5.33	
6	5.507	1.2	0.21792		7.35	
7	5.967	1.3	0.21788		7.37	

Table.3 Experimental results with magnetic material coil

No.	Rotational speed [kr/min]	Output voltage [V]	Output voltage / rotational speed in experiment [V/kr]	Output voltage / rotational speed in simulation [V/kr]	Simulation error [%]	Simulation error average[%]
1	0.779	0.30	0.3852		-27.15	
2	1.238	0.48	0.38784		-27.64	
3	1.754	0.58	0.3306		-15.11	
4	2.439	0.80	0.328	0.280634	-14.44	-19.62
5	2.495	0.82	0.328656		-14.61	
6	3.056	1.08	0.353376		-20.58	
7	4.980	1.70	0.34136		-17.79	

Experimental results present that under the same rotational speed, output voltage improves 59.6% with the addition of magnetic material in coil compared to coil without magnetic material.

When there is no magnetic material in the coil, the error between simulation and experiment is 6.56% which indicates that the simulation method is feasible. While when there is magnetic material added in the coil, error between simulation and experiment is -19.62%. Simulation result is less than experimental result with bigger errors and that's because: (1) Definition of iron material is different with the one used in experiment, (2) In experiment, magnetic material is attracted by the magnets and the coil is on the one side of the gap instead of in the middle as the model in simulation. In the middle of the gap, the magnetic flux density is smallest, so attracted on one side of the gap, the coil is in an area with a bigger magnetic flux density and the output voltage is increased.

However, magnetic material attracted by the magnet and located on one side of the gap increases frictional resistance and incurs difficulty in rotational speed increasing. Meanwhile, there's hysteresis torque and eddy current loss produced between rotating magnets and static magnetic material. Last, since there's negative correlation between magnetic flux density and gap thickness, adding magnetic material increases gap thickness and decreases output voltage. Further we should thinner the magnetic material and that would improve the output performance.

5 Conclusions

Addition of magnetic material in coil increases magnetic flux density in the gap and improves output performance effectively. We further discussed the feasibility to add magnetic material in coil, presented the existed problems and improvement methods. In the future, we will analyze how different magnetic material and shapes influence output performance and solve the problem of frictional resistance caused by addition of magnetic material. Addition of magnetic material improves output performance considerably and deserves further research.

References

[1] C.T.Pan,T.T.Wu. Development of a rotary electromagnetic microgenerator, J. Journal of Micromechanics and Microengineering , 2007, 17: 120–128

[2] Florian Herrault, Chang-Hyeon Ji, and Mark G. Allen. Ultraminiaturized High-Speed Permanent-Magnet Generators for Milliwatt-Level Power Generation, J. Journal of Microelectromechanical Systems,2008,17(6): 1376-1387

[3] Florian Herrault, Bernard C. Yen, Chang-Hyeon Ji, et al. Fabrication and Performance of Silicon-Embedded Permanent-Magnet Microgenerators, J. Journal of Microelectromechanical Systems, 2010,19(1): 4-13

[4] SUN Shaochun, SHI Gengchen. Design and fabrication of micro rotational generators, J. Optics and Precision Engineering,2011.6(19)6:1306-1312

[5] R. Cordero, A. Rivera, M. Neuman, R. Warrington, and E. Romero. Micro-rotational Electromagnetic Generator for High speed Applications, 25th International Conference on Micro Electro Mechanical Systems (MEMS). Paris, France: MEMS 2012:1257-1260

[6] Y. J. Chen , C. T. Pan , Z. H. Liu. Analysis of an in-plane micro-generator with various microcoil shapes, J. Microsyst Technol ,2013,19:43–52

Key Engineering Materials Vols 645-646 (2015) pp 1201-1206
© (2015) Trans Tech Publications, Switzerland
doi:10.4028/www.scientific.net/KEM.645-646.1201

Submitted: 2014-11-04
Accepted: 2014-12-23

Electrospun PVDF/PMMA/SiO_2 Membrane Separators for Rechargeable Lithium-ion Batteries

Xiaolin Wu[1,a], Jie Lin[1,b], Jianyan Wang[2,1,c], Hang Guo[1,2,d*]

[1]Pen-Tung Sah Micro-Nano Science and Technology Institute, Xiamen University, 361005, China
[2]Department of Mechanical and Electrical Engineering, Xiamen University, 361005, China
[a]ahead9alin@163.com, [b]linjie987@163.com, [c]1052566157@qq.com, [d]hangguo@xmu.edu.cn

Key words: PVDF, PMMA, SiO_2, electrospun, polymer separator

ABSTRACT: In this paper composite nanofiber membranes were prepared by electrospinning technology from poly (vinylidene fluoride) (PVDF)-poly (methyl methacrylate) (PMMA)-SiO_2 blend solutions with different PMMA and SiO_2 contents. It was found that the diameter of electrospun nanofibers was greatly increased with the added PMMA content but decreased with the added SiO_2 content, and when both PMMA and SiO_2 were added the diameter of electrospun nanofibers was decreased. With a proper ratio of the PMMA and SiO_2 added, the electrospum nanofiber membrane could have a suitable diameter with high porosity. The XRD results revealed that electrospun nanofiber membranes contained mainly β-phase crystal structure of PVDF, and its crystalline is reduced with the added PMMA and SiO_2 contents due to the inhibited crystallization of the polymer by the inorganic particles and PMMA during the solidification process. These nanofiber membranes exhibited a high electrolyte uptake, around 300%. Moreover, the incorporation of PMMA and SiO_2 into the nanofiber membrane improved the ionic conductivity from 1.7×10^{-3}S/cm to 2.0×10^{-3}S/cm at room temperature. Compared with commercial film PE, their cell cycle and charge and discharge performance were also greatly improved.

Intorduction

Compared to traditional liquid electrolytes, polymer electrolytes with good ambient temperature conductivity and minimum resistance to ion transportation have attracted great interest. Different processing methods such as solvent casting, plasticizer extraction and phase inversion have been adopted for the preparation of porous polymer membranes. However, polymer membranes made by these methods show low-rate capabilities at high discharge rates because of low porosity and poor channel in ionic conduction [1].Recently, the electrospinning technique has been employed to prepare polymer membranes that are composed of ultrafine fibers with micron and submicron diameters. Electrospun polymer membranes from polymers such as poly (vinylidene fluoride) (PVDF) [2, 3], poly (vinylidene fluoride-cohexafluoropropylene) (PVDF-HFP) [4], poly (ethylene oxide) (PEO) [5], poly (methyl methacrylate) (PMMA) [6, 7], Polyvinyl Pyrrolidone (PVP) [8] and polyacrylonitrile (PAN) [9] are particularly suitable as host matrices for polymer electrolytes. PVDF has become a favorable polymer matrix for porous polymer electrolytes due to its high dielectric constant and strongly electro-withdrawing functional groups (–C–F).

But the higher crystallinity of PVDF limits the ion conduction which occurs almost in amorphous region, so the PVDF membranes need to be modified to reduce the crystallinity of PVDF and improve the ability of the ionic conduction of amorphous area, to improve the ionic conductivity. The commonly used methods include copolymerization, the introduction of low crystallinity or

amorphous polymer to blend spinning and adding inorganic nanoparticles to destroy the regularity of the polymer. Yanhuai Ding [10] used electrostatic spinning method to prepare P (VDF-HFP)/PMMA fiber membrane, and studies have shown that PMMA improves the mechanical properties, fluid absorption rate and ionic conductivity. Na Wu [11] prepared the thermoplastic polyurethane and PVDF blending polymer electrolyte membrane by electrostatic spinning, and improved the performance of the film by adding SiO_2 and TiO_2. Youg Jin Kim [12] prepared fiber membranes of PVDF/SiO_2 by electrostatic spinning, and the ionic conductivity could be as high as 4.7×10^{-3} S/cm. Meltem Yanilmaz[13] covered SiO_2 / PVDF fiber membrane on PP film by electrostatic spinning, and its ionic conductivity could be reached 2.6×10^{-3} S/cm.

In the present study, to improve the physical properties and electrolyte affinity, a blend of PVDF /PMMA/ SiO_2 polymer electrolytes were prepared by electrospinning. Using PVDF as polymer skeleton, blending PMMA and SiO_2 could improve the mechanical strength, electrolyte uptake, ionic conductivity and electrode/electrolyte interfacial properties.

Experimental

Membrane preparation.

All the reagents used were analytical grade. PVDF (Mw 400, 000, Arkema), PMMA (Mw 220, 000, 3FNM) and nano SiO_2 (15±5nm, Aladdin) were dissolved in a mixed solvent of N, N-dimethylacetamide (DM Ac) and acetone. The concentration of the mixed solution was 10wt.%. The as-prepared solution was placed in a plastic syringe equipped with a needle-diameter of 0.5mm. The membranes were electrospinning at 18 kV with a high-voltage supply. The distance between the collector and the needle was 15 cm. Fig. 1 shows the electrospinning apparatus. The obtained membranes were placed in vacuum for 24 h at 60℃. The compositions of four different films are shown in the following Table 1.

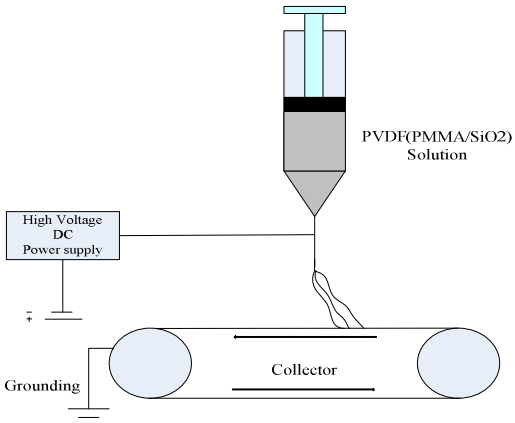


Fig.1. Electrospinning apparatus.

Table 1 Composition of the PVDF/PMMA/SiO_2 polymer film.

Film	PVDF[g]	PMMA[g]	SiO_2[g]	DM Ac[mL]	Acetone[mL]
F1	3	0	0	20	10
F2	2.55	0.45	0	20	10
F3	3	0	0.3	20	10
F4	2.55	0.45	0.3	20	10

Results and discussion

Crystal structure of XRD tests.

X-ray diffraction (XRD) measurements were carried out to characterize the crystalline phase of the nanofiber membranes with an X-ray diffractometer Rigaku Ultima IV. XRD spectra of polymer films are showed in Fig.2. It is seen from Fig. 2 that both two XRD patterns exhibit a sharp peak at around 2Theta=20.5^o, which is a characteristic peak of PVDF β-phase crystalline structure, corresponding to the β(200/110). Other main X-ray diffraction peaks observed include 2Theta=36.1^{o}and 41.6^o, which are ascribed to β(201) and β(111), respectively. This result indicates that β-phase crystal mainly exists in PVDF fibrous membranes. From Fig. 2, it is also seen that with PMMA and nano SiO_2, the diffraction intensities of a peaks decrease. It indicates that the addition of PMMA and nano SiO_2 helps to reduce the crystallinity of the PVDF membrane. And this helps to enhance electrolyte uptake, the ionic conductivity and electrochemical properties of the film.

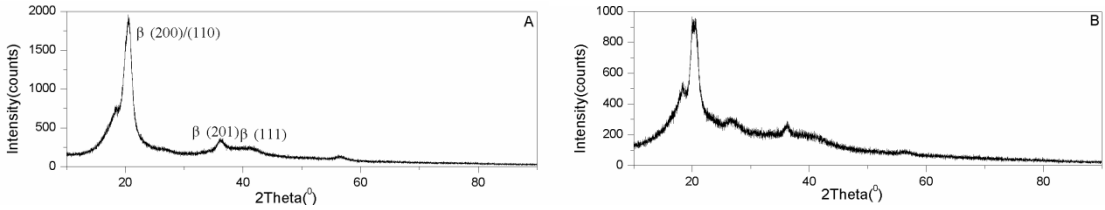


Fig.2. XRD pattern for polymer films, A – film F1, B – film F4.

Morphology of SEM tests.

Fig. 3 presents SEM images of PVDF fibrous membranes (F1, F2, F3 and F4). Table 2 shows the four fibrous membranes' average diameter and diameter range. From the Fig. 3 and Table 2, we can know that compared to F1, the addition of PMMA increases the fibrous membrane's average diameter from 530 nm to 700 nm and diameter range. It is mainly because PVDF and PMMA macromolecular chain overlap and entanglement make spinning fluid viscosity increases, which results in increased fiber diameter. But the addition of SiO_2 decreases the fibrous membrane's average diameter from 530 nm to 360 nm and diameter range. This is because the addition of SiO_2 nano inorganic materials destroys the regularity of the PVDF polymers and reduces the fiber diameter. Mixed with PMMA and SiO_2, F4 film fiber diameter decreases, and is greater than the F3, but less than the F1 and F2. That will improve electrolyte uptake of the F4 film.

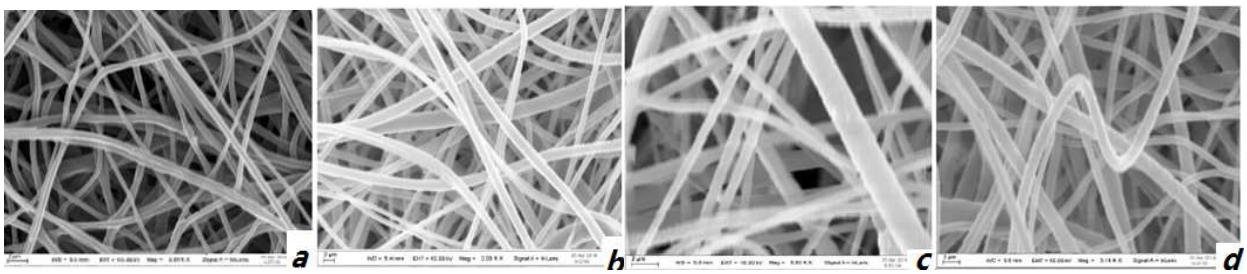


Fig.3. SEM images of polymer films, a- film F1, b- film F2, c- film F3, d- film F4.

Table 2 The fiber diameter distribution.

Film	F1	F2	F3	F4
average diameter[nm]	530	700	360	450
diameter range[nm]	350-700	550-900	300-450	350-550

Porosity and electrolyte uptake.

The results of porosity measurements are presented in Table 3. It is seen that the porosity of electrospun nanofibers was decreased with the added PMMA content, but slightly increased with the added SiO_2 content, and with both PMMA and SiO_2 the porosity of electrospun nanofibers was also slightly increased. The decrease in membrane porosity is mainly caused by the PMMA, because with the added PMMA content there was phase separation in the solution which leaded to denser electrospun nanofibers. However, the use of SiO_2 did not largely affect the porosity of the nanofiber membranes. The porosity of electrospun nanofibers was slightly increased with the both PMMA and SiO_2 content due to the PMMA and SiO_2's effect.

Table 3 also presents a comparison of the electrolyte uptake of the nanofiber membranes. It is found that F2, F3, and F4's electrolyte uptake are higher than that of F1 nanofiber membranes. It is because PMMA has a strong affinity to the electrolyte and the nanofiber membranes with SiO_2 content has smaller average diameter and diameter range.

Table 3 Porosity and electrolyte uptake of the polymer films.

Film	Porosity	Electrolyte uptake
F1	79.4%	172.2%
F2	75.3%	231.4%
F3	80.5%	241.7%
F4	80.1%	293.2%

Ionic conductivity.

The ionic conductivity was measured from AC impedance by sandwiching polymer electrolyte between two stainless steel electrodes. It can be seen from Table 4 and Fig.4 that all fiber membrane ionic conductivity is larger than 10^{-3} s/cm just to meet the requirements of the performance of lithium ion battery separator. The ionic conductivity of F2 and F3 is bigger than F1 and the F4's is larger than the F2 and F3. This is because after absorbing enough electrolytes, PMMA will be swelling to storage electrolyte in the amorphous region of fiber membrane in the form of gel. SiO_2 particles hindered the crystallization of polymer, increased the electrolyte systems of the amorphous region and provided channels for lithium ion migration. So lithium ion migration velocity will increase, the ionic conductivity of the diaphragm will be improved.

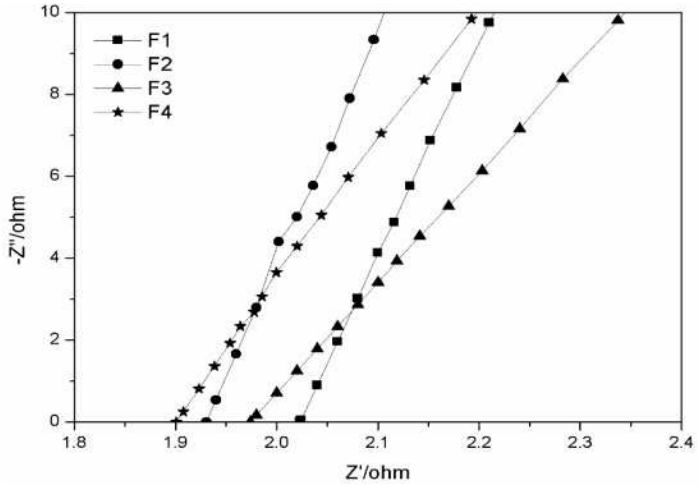


Fig.4. AC impedance spectra of polymer Li-ion battery.

Table 4 Ion conductivity and electrolyte uptake of the polymer films.

Film	Thickness[μm]	Body resistance[Ω]	Ion conductivity[S/cm]	Electrolyte uptake
F1	101	2.02	1.76×10^{-3}	172.2%
F2	105	1.93	1.92×10^{-3}	231.4%
F3	102	1.97	1.83×10^{-3}	241.7%
F4	106	1.90	1.97×10^{-3}	293.2%

Battery performance.

In order to evaluate the feasibility of these fibrous membranes in practical rechargeable Li-ion batteries, Li/$LiFePO_4$ cells using film F4 as the separator were fabricated and evaluated. For comparison, commercial PE separator was also tested. The first-cycle charge/discharge capacity curves at a current density corresponding to 0.2C-rate are showed in Fig. 5. It is seen that the first-cycle charge and discharge capacities of cells containing F4 membranes are 1.712 and 1.708 mAh/cm^2, respectively, which are higher than those (1.468 and 1.457 mAh/cm^2) of cells containing PE separator. F4 membranes have high porosities and interconnected porous structures, so they are able to uptake large amounts of liquid electrolytes and offer effective conduction channels, which in turn lead to high ionic conductivities and increase charge and discharge capacities.

The discharge capacities as a function of cycle number are shown in Fig. 6 for Li/$LiFePO_4$ cells containing commercial PE separator and F4 fibrous membranes. After 30 cycles, the cells using F4 fibrous membranes show a discharge capacity of 1.600 mAh/cm^2, which is significantly higher than that (1.395 mAh/cm^2) of cells using commercial PE separator. The good cycle performance of F4 fibrous membranes could be attributed to their unique porous structure, high liquid electrolyte uptake and high ionic conductivity.

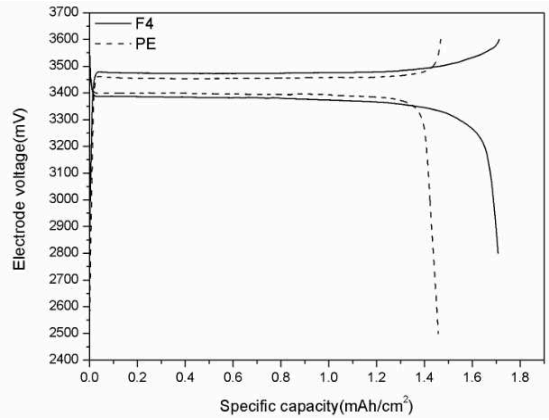


Fig.5. First-cycle charge and discharge capacities of Li/$LiFePO_4$ cells with liquid electrolyte-soaked F4 membrane, PE separator.

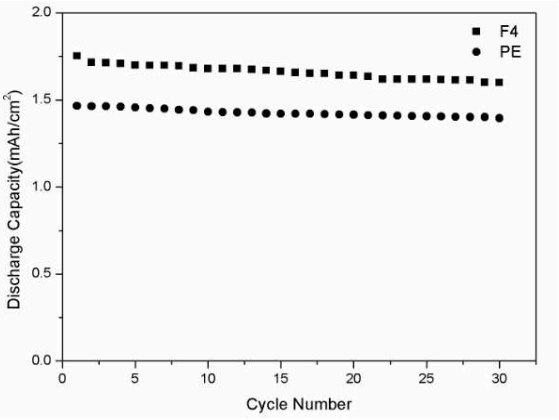


Fig.6. Cycle performance of Li/$LiFePO_4$ cells containing liquid electrolyte-soaked F4 membrane, PE separator.

Conclusion

The electrospinning technique was used to prepare PVDF fibrous membranes. In order to improve its properties, the PVDF fibrous membranes were blended with PMMA or SiO_2. The liquid electrolyte-soaked PVDF/PMMA/SiO_2 fibrous membranes showed a high ionic conductivity of 1.97×10^{-3} S/cm at room temperature, compared with PVDF membranes' 1.76×10^{-3} S/cm. At a 0.2C rate, Li/$LiFePO_4$ cells using PVDF/PMMA/SiO_2 fibrous membranes as the separator showed high first-cycle charge/discharge capacities and stable cycle performance. The PVDF/PMMA /SiO_2 fibrous membranes also have higher porosity and electrolyte uptake, and smaller diameter range.

Acknowledgement

This work is financially supported by the New Century Talent Support Plan of the Ministry of Education of China (2007NCET-07-0723), the National Natural Science Foundation of China (60936003) and the Aviation Science Foundation of China (2008ZH68002).

References

[1] Young Jin Kim, Chang Hyun Ahn, Myung Bok Lee, Myung-Seok Choi, Characteristics of electros pun PVDF/SiO2 composite nanofiber membranes as polymer electrolyte, Materials Chemistry and Physics. 127 (2011) 137–142.

[2] Guodong Kang, Yiming Cao, Application andmodification ofpoly(vinylidene fluoride) (PVDF) membranes – A review, Journal ofMembraneScience.463(2014)145–165.

[3] Fang Chyou Chiu, Ching Chia Chen, Ying-Jing Chen, Binary and ternary nanocomposites based on PVDF, PMMA,and PVDF/PMMA blends: polymorphism, thermal, and rheological properties, J Polym Res. 21(2014)378.

[4] Hui Xie, Zhiyuan Tang, Zhongyan Li, Yanbing He, Yong Liu, Hong Wang, PVDF-HFP composite polymer electrolyte with excellent electrochemical properties for Li-ion batteries, J Solid State Electrochem. 12(2008)1497–1502.

[5] Margaret W. Frey, Lei Li, Electrospinning and Porosity Measurements of Nylon-6/Poly(ethylene oxide) Blended Nonwovens, Journal of Engineered Fibers and Fabrics. Volume 2, Issue 1(2007).

[6] Clarisa Carrizales, Sean Pelfrey, Roman Rincon, et al, Thermal and mechanical properties of electrospun PMMA, PVC, Nylon 6, and Nylon 6, 6, POLYMERS FOR ADVANCED TECHNOLOGIES. 19(2008) 124–130.

[7] Tamer Uyar, Rasmus Havelund, et al, Cyclodextrin functionalized poly(methyl methacrylate) (PMMA) electrospun Nnanofibers for organic vapors waste treatment, Journal of Membrane Science. 365 (2010) 409–417.

[8] Meice Wang, Dawei Fang, Nannan Wang, et al, Preparation of PVDF/PVP coreeshell nanofibers mats via homogeneous electrospinning, Polymer. 55 (2014) 2188-2196.

[9] Kyunghwan Yoon, Kwangsok Kim, Xuefen Wang, et al, High flux ultrafiltration membranes based on electrospun nanofibrous PAN scaffolds and chitosan coating, Polymer. 47 (2006) 2434–2441.

[10] S. S. Choi, Y. S. Lee, C.W. Joo, Electrospun PVDF nanofiber web as polymer electrolyte or separator, J. Electrochemical Acta. 50(2004) 339-343.

[11] Yanhuai Ding, Ping Zhang, Zhilin Long, et al, The ionic conductivity and mechanical property of electrospun P(VdF-HFP)/PMMA membranes for lithium ion batteries, Journal of Power Sources. 329(2009)56-59.

[12] Na Wu, Qi Cao, Xianyou Wang, Sheng Li, Xiaoyun Li, Huayang Deng, In situ ceramic fillers of electrospun thermoplastic polyurethane/poly(vinylidene fluoride) based gel polymer electrolytes for Li-ion batteries, J. of Power Sources. 196(2011)9751-9756.

[13] Meltem Yanilmaz, Chen Chen, Xiangwu Zhang, Fabrication and Characterization of SiO_2/PVDF Composite Nanofiber-Coated PP Nonwoven Separators for Lithium-Ion Batteries, JOURNAL OF POLYMER SCIENCE, PART B: POLYMER PHYSICS. 51(2013) 1719–1726.

Key Engineering Materials Vols 645-646 (2015) pp 1207-1213
© (2015) Trans Tech Publications, Switzerland
doi:10.4028/www.scientific.net/KEM.645-646.1207

Submitted: 2014-11-06
Accepted: 2014-12-23

Electrospun SnO_2−Graphene composite nanofibers as high performance anode for lithium ion batteries

Yuling Wu[1, a], Jie Lin[1, b], Jianyan Wang[2, 1], Hang Guo[1, 2, c*]

[1]Pen-Tung Sah Micro-Nano Science and Technology Institute, Xiamen University, China

[2]Department of Mechanical and Electrical Engineering, Xiamen University, China

[a]moyingyue@yeah.net, [b]linjie987@163.com, [c]hangguo@xmu.edu.cn

Keyword：SnO_2, Graphene, electrospinning

Abstract: A promising anode material for lithium ion batteries is reported in this paper. It is one-dimensional SnO_2-graphene composite nanofibers (SnO_2-G nanofibers) fabricated by using electrospinning technique. In the study, X-ray diffraction (XRD) and scanning electron microscopy (SEM) are used to characterize its structural and morphological properties. Samples with different ratio of SnO_2 to graphene (wt%) are prepared to investigate its electrochemical performance. Galvanostatic charge/discharge tests reveals that Li-insertion/extraction is carried out through a two-phase reaction mechanism that is supported by galvanostatic charge-discharge profiles. It is found that the optimal proportion of SnO_2 to graphene is 8：1 (wt%) for the electrospun composite materials. Furthermore, micro thin film batteries have been fabricated and tested. The results show that initial discharge capacity is 301.86 mA h g^{-1} at current density of 50 μA g^{-1}, and battery can retain 63.3% of reversible capacity after 300 cycles, which is 5 times higher than bare SnO_2.

1. Introduction

Rechargeable lithium-ion batteries are considered as the most power sources in portable electronics in recent years due to their superior properties such as high energy density, long cycle life and good power performance[1]. Most commercial lithium-ion batteries use graphitic materials as anode material. Lithium storage capacities of alloy-type anodes (e.g., silicon, tin, germanium, and their oxides) are much higher than graphite anode. Among different alloy-type anodes, tin oxides (SnO_x, x = 1 and 2) are considered as one of the most promising candidates for next-generation lithium ion batteries because of their high capacity(782 mAh g^{-1}), low cost, high abundance, and environmental friendliness[2, 3]. Unfortunately, the huge volume change (~300%) occurring during the charge-discharge process of SnO_2 poses serious problems[4, 5], which leads to pulverization and loss of electrical contact between particles, resulting in severe capacity fade and poor rate capability. Several strategies have been proposed in the literature to alleviate this problem, such as design and prepare hollow and/or porous nanostructures[6, 7] or introduce a flexible buffering matrix to prevent the pulverization of SnO_2 materials during discharge-charge cycling[3, 8, 9]. For instance, Ding *et al*[6] report the graphitic carbon SnO_2 exhibit higher specific capacity and better cycle performance because the carbon shells can stabilize nanoscale particles and mitigate the physical strains from the volume change during the Li^+ uptake/release process. Recently, a novel two-dimensional carbon matrix, graphene, has attracted more and more attention because of their unique properties like high specific surface area (2630 m^2 g^{-1}), high intrinsic mobility (200 000 cm^2 v^{-1} s^{-1}), high Young's modulus (1.0 TPa), and excellent electrical conductivity[10-12], and is preferable to replace other carbon matrices (e.g. graphite, carbon nanotube) for metal oxides[13-15]. Because the graphene layers not only provide large specific surface area, electronic conductivity and flexibility, but also can accommodate the mechanical

stress induced by the substantial volume expansion and shrinkage of the high-capacity SnO_2 spheres. But, most research[14-16] on SnO_2-Graphene composite only obtain nano-paticles that is difficult to apply to all-solid-state thin film lithium batteries for MEMS power.

Electrospinning is a simple, cost-effective method that enables the synthesis of nanofibers with small diameters (nanofibres) through the action of an external electric field imposed on a polymer solution. Nanofibers produced by electrospinning have high surface area and have found application in fuel cells, dye-sensitized solar cells, lithium-ion batteries and other materials[17-19]. Dong *et al[20]* think that for lithium ion batteries, the key advantage of electrospinning is that it produces macroporous interconnected nanoparticle network of high aspect ratio nanofibers that would provide higher electrode/electrolyte contact surface, better electronic and ionic conductivity and a facile Li^+ diffusion pathway. Zhang *et al[21]* report the synthesis one-dimensional TiO_2-graphene composite nanofiibers by electrospinning for the first time. Their Li/TiO_2-G cell retained 84% of reversible capacity after 300 cycles, which is 25% higher than bare TiO_2 nanofibers under the same test conditions. In the present study, we have fabricated electrospun SnO_2-graphene (SnO_2-G) one-dimensional nanofibers as compared to bare SnO_2 electrospun nanofibers, demonstrating their potential as a prospective anode for high-performance all-solid-state thin film lithium batteries applications.

2. Experimental

The development of various methods for producing graphene has stimulated a vast amount of research in recent years[22]. Here we use a modified Hummers method to synthesize Graphene nanosheets by chemical reduction of exfoliated graphene oxide. First, 2.5 g of $NaNO_3$ was dissolved in 120 mL of concentrated H_2SO_4 in an ice bath. Five grams of commercial graphite powder and 15 g of $KMnO_4$ were slowly added into this mixture, and the temperature was maintained below 20 °C with vigorous stirring for 1 h. The temperature of this mixture was increased to 80 °C and the mixture was stirred at this temperature for 0.5 h to form a brown paste. Deionized water (DI water) (150 mL) was added to the mixture, it was stirred for 0.5 h, and 100 mL of DI water and 20 mL of 30% H_2O_2 were consequently added into the mixture to compete the oxidation process. The color of the mixture changed from brown to yellow. The mixture was washed with 1 M HCl and DI water to remove residual ions and dried at 60 °C under ambient conditions. Exfoliation was carried out by sonicating the graphene oxide (500 mg) in deionized water (100 mL) for 1 h followed by reduction with hydrazine hydrate (1.5 g) for 24 h in an oil bath (90 °C). The solution pH was adjusted in the range of 9-10 using Na_2CO_3 or NaOH. The as prepared graphene was centrifuged and washed with deionized water and dried at 60 °C.

The SnO_2-graphene were synthesized by low-cost and up-scalable hydrothermal method. In brief, 50 mg of graphene was firstly added in 30mL deionized water by ultrasonic dispersion about 30min. 1.5 mmol of stannic chloride ($SnCl_4$) and 0.25 g of NaOH were slowly added into this solution under stirring conditions. Then this solution was transferred into the 50 mL Teflon lined stainless steel autoclaves and heated at 160 °C for 15 h. In the reaction, stannic chloride ($SnCl_4$) is change to stannic oxide as shown in reaction:

$$SnCl_4 \bullet 5H_2O(s) + 4NaOH(s) \rightarrow 4NaCl(s) + 7H_2O(l) + SnO_2(s)$$

The final SnO_2-graphene product was collected by centrifugation, washed with water, and dried at 60 °C in vacuum. Other group SnO_2-graphene composites can be produced by the same method (as shown in table 1).

At last, the high quality and stable composite film was prepared by electrospinning technique. Firstly, composite (40 mg) was sonicated for 0.5 h in 8 ml of methyl alcohol and 2 ml of ethyl

alcohol mixed solvent. Polymer vinyl acetate (PVAc, 2g) was added to the above solution, the mixture was stirred continuously for 4 h to yield homogeneous solution. The prepared homogeneous solution was loaded into plastic syringes (10 mL) and subsequently placed into a electrospinning setup. (Fig. 1 shows a schematic illustration of the basic setup for electrospinning.) A high-voltage power of 20 kV was applied to the needle tip. The flow rate of fluid was set to 6 mL/h. The nanofibers were collected on copper foil tiled in a flat plate placed 20 cm below the needle tip. The electrospun SnO_2-graphene composite nanofibers were then calcined at 300 °C for 1 h in N_2 environment to decompose PVAc. The heating and cooling rate was set to be 3 °C min^{-1}.

Table 1 The proportion of each group's reactant

Group	Graphene[g]	NaOH[g]	$SnCl_4$[g]
A	0.05	0.25	0.39 (1.5 mmol)
B	0.05	0.25	0.26 (1.0 mmol)
C	0.05	0.25	0.16 (0.5 mmol)
D	0.00	0.25	0.26 (1.0 mmol)
E	0.05	0.25	0.00

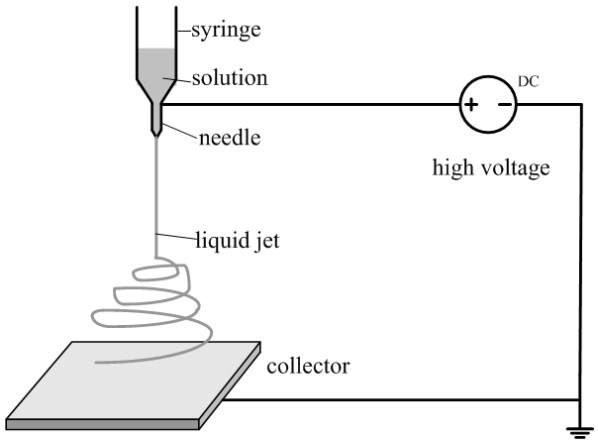


Figure 1 Schematic illustration for electrospinning

3. Results and discussion

The phase purity and crystallinity of the as-prepared SnO_2-Graphene samples were characterized using X-ray diffraction (XRD). Fig. 2 shows the typical XRD patterns of different group's SnO_2-Graphene samples synthesized by hydrothermal method. It can be observed that the position of the characteristic peaks of the A, B, D samples is consistent, whereas the peak intensity differs from one material to the next. Among the XRD patterns, the peak intensity of the the E sample (the pure graphene) is strongest, indicating its highly crystalline structure. The obvious broadening of peaks for the D sample (the pure SnO_2) is owing to the fine grain size and defects along the particle produced in hydrothermal reaction process. A, B, D samples are in excellent accordance with a tetragonal rutile structure (JCPDS 41-1445), which belongs to the space group P42/mnm (number 136). The lattice parameters of the nanowires were a=b=4.738 Å and c=3.188 Å. (Because the proportion of SnO_2 in sample C is much smaller. The sample C isn't in good agreement with the standard values (JCPDS 41-1445)). A single diffraction peak is observed in Sample E at ~26° that can be attributed to the (002) diffraction of graphene, indicating the successfully obtain via a modified Hummers method. However, the (002) peak of graphene may coincide with the (110) peak of SnO_2 in Sample A and B. No peaks from other phases have been detected, indicating that the samples are of SnO_2-Graphene compound.

The morphological features of SnO_2-graphene-PVAc composite nanofibers are studied by a field emission scanning electron microscope (FE-SEM, Hitachi S-4800). The image (Fig. 3 a) clearly indicates the formation of highly interconnected networks of fibers. The PVAc solution resulted in dry fibers with relatively smooth, regular and cylindrical morphology with very little droplets (Fig. 3 b). We can deduce formation of homogeneous solution before spinning. It is obvious that black line in the Si substrate can be observed under scanning electron microscopy,

which implies less sample and short electrospinning time. High magnification SEM image (Fig. 3 d) of SnO_2-graphene-PVAc composite nanofibers reveal that a general view of randomly aligned fibers with diameters between 1.22 μm and 2.85 μm. After heat treatment, a highly porous surface of fibers is obtained with part of PVAc decomposing.

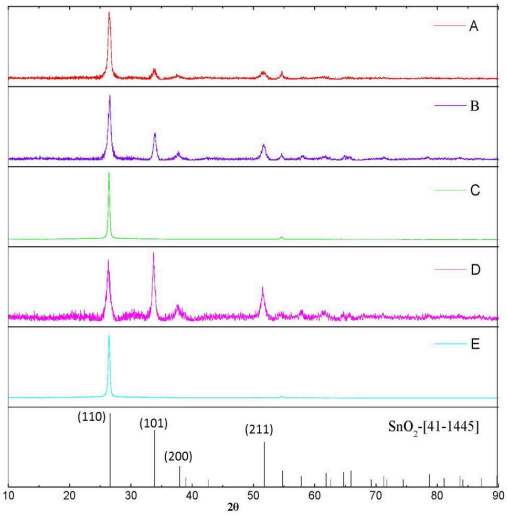


Figure 2 The typical XRD patterns of differrnt group's SnO_2-graphene samples synthesized by hydrothermal method: the optimal proportion of SnO_2 to graphene is 8：1 (a), 5：1 (b), 8：1 (c) (wt%), d) the pure SnO_2, e) the pure graphene

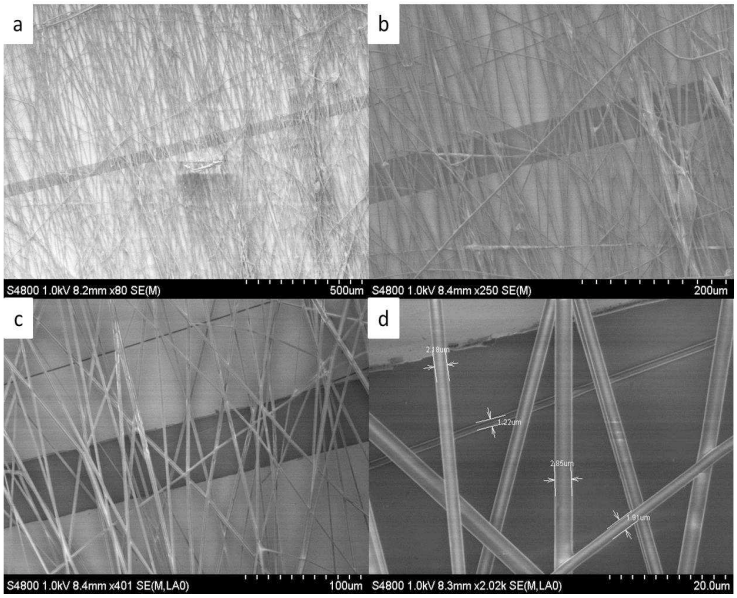


Figure 3 SEM image of SnO_2-graphene-PVAc composite nanofibers under different magnification: a) 80X, b) 250 X, c) 401X, d) 2.02KX

Electrochemical performances of bare and SnO_2-G nanofibers were evaluated in half-cell configuration (Li/SnO_2, Li/G or SnO_2-G) between 0.01 and 3 V in room temperature. Half-cells were subjected to galvanostatic charge/discharge measurement, in which metallic lithium acts as counter and reference electrode, respectively. The anodic performance of different group's SnO_2-Graphene composite nanofibers is presented in figure 4. The curves show the lower plateau during discharge and higher specific capacity of SnO_2-G composite nanofibers than bare SnO_2. Fig. 4 a~e show the first and second cycle charge-discharge voltage profiles for A~E samples. The curves were in good agreement with previous results reported in the literature, indicating the same electrochemical pathway[15, 23, 24].

When the proportion of SnO_2 to graphene is 8: 1 (wt%), the first charge and discharge capacities of SnO_2-G composite nanofibers were 301.86 and 146.88 mAh g^{-1}. When the proportion of SnO_2 to graphene is 5：1 (wt%), the first charge and discharge capacities of SnO_2-G composite nanofibers were 235.62 and 108.82 mAh g^{-1}. When the proportion of SnO_2 to graphene is 3：1 (wt%), the first charge and discharge capacities of SnO_2-G composite nanofibers were 131.92 and 50.90 mAh g^{-1}. It is noteworthy that the lower proportion of SnO_2 to graphene has lower charge and discharge capacities, because the theoretical capacity of SnO_2 (782 mAh g^{-1}) is higher than the theoretical capacity of graphene (744 mAh g^{-1}).The SnO_2 incrpotated graphene is at the cost of decreasing capacity. Notwithstanding, the initial Coulombic efficiency of SnO_2-G (~73%, 46.18%, and 38.58% corresponding to the proportion of SnO_2 to graphene is 8:1, 5:1, and 3:1(wt%)) was still higher than that of bare SnO_2 (19.35%) and bare graphene (19.34%), revealing good cycleability of composite nanofiber. Fig. 4 (f) shows cycling profiles of the group A~E

Li/SnO_2-graphene composite nanofiber cell at the current density of 50μA g^{-1}. SnO_2-G exhibited a higher specific capacity and better cycle performance in comparison with bare SnO_2 and bare graphene. After 300 cycles, the bare SnO_2 and bare graphene samples retained a discharge capacity of 38.48 mAh g^{-1} and 35.50 mAh g^{-1}. Respectively, the SnO_2-G composite nanofibers still retained 190.98 mAh g^{-1} (the proportion of SnO_2 to graphene is 8：1 (wt%)), 131.94 $mAhg^{-1}$ (the proportion of SnO_2 to graphene is 5：1 (wt%)), 61.62 mAh g^{-1} (the proportion of SnO_2 to graphene is 3：1 (wt%)). When the proportion of SnO_2 to graphene is 8：1 (wt%), the button cell retained 63.27% of reversible capacity after 300 cycles, which is 5 times higher than bare SnO_2 and 4 times higher than bare graphene. This outcome is obvious since the electrochemical properties of nanoparticles can be improved by fabrication of porous structure and using carbon as a support, and graphene is one of the best carbon support up to date. Additionally, the graphene nanosheets may effectively buffer the strain from the volume change of particles during cycles and also preserve a high electrical conductivity of the electrode.

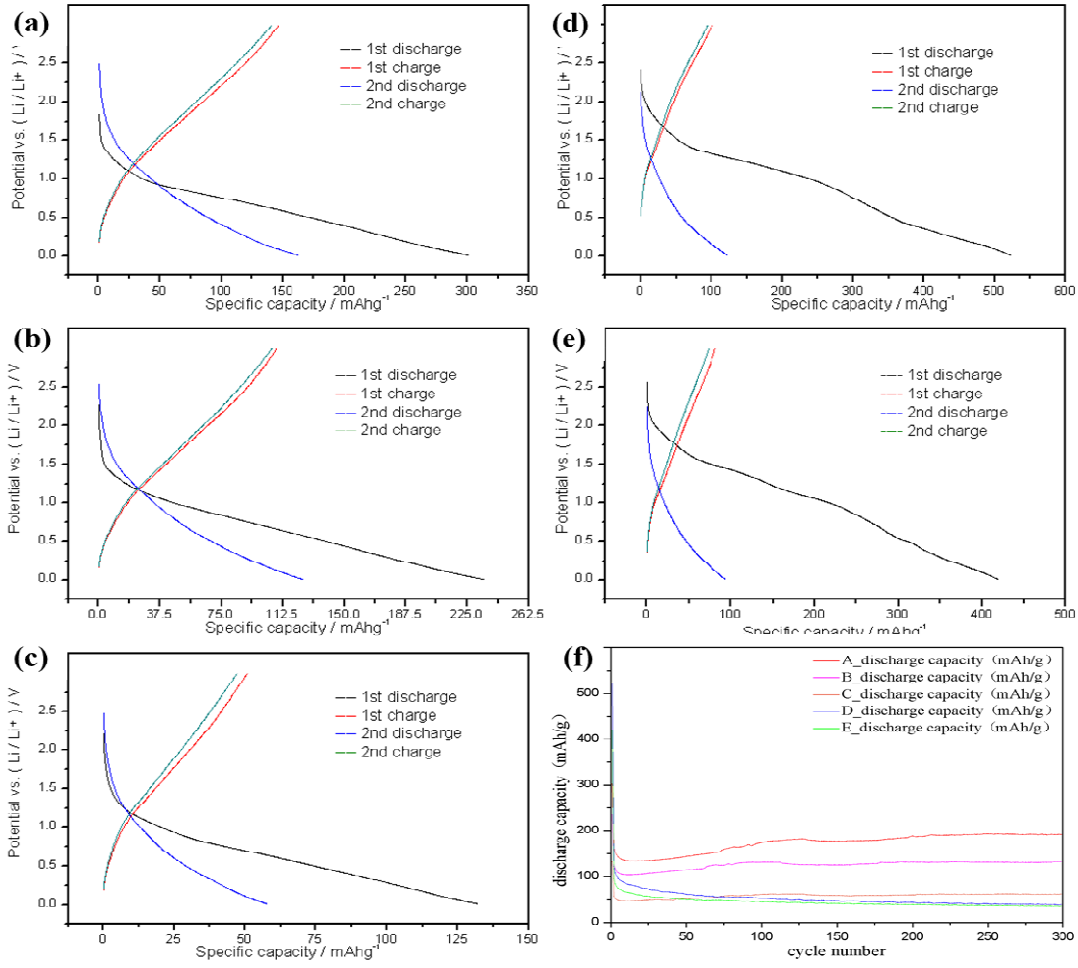


Figure 4 The anodic performance of different group's SnO_2-graphene composite nanofibers: (a) ~ (e) the charge-discharge curves of group A~E Li/SnO_2-graphene composite nanofibers during the 1st and 2nd cycles within the voltage from 0.01 and 3 V at a current density of 50μA g^{-1}, and (f) cycling profiles of the group A~E Li/SnO_2-graphene composite nanofiber cell

4. Conclusion

one-dimensional SnO_2-graphene composite nanofibers (SnO_2-G nanofibers) were synthesized for the first time using a simple electrospinning technique. Subsequent sintering of these fibers at 300 ◦C (3◦C min^{-1}) led to crystallization of SnO_2 nanocrystallitesand removal of polymer precursor,

resulting in a porous nano-particulate interconnected fibrous as high performance anode for lithium ion batteries. Phase formation of anatase SnO_2 and graphene was confirmed by X-ray diffraction measurements. Nanofiber morphology was clearly evident from the SEM. Cyclic voltammetric analysis showed that the Li insertion/extraction takes place by a two phase reaction mechanism and is reflected well in galvanostatic measurements. The SnO_2-G composite nanofibers (the proportion of SnO_2 to graphene is 8：1 (wt%)) can retain 63.3% of reversible capacity after 300 cycles, which is 5 times higher than bare SnO_2. This study clearly showed SnO_2-G composite fibers are one of the prospective anode materials for all-solid-state thin film lithium battery for MEMS power.

Acknowledgments

This work is financially supported by the New Century Talent Support Plan of the Ministry of Education of China (2007NCET-07-0723), the National Natural Science Foundation of China (60936003) and Aviation Science Foundation of China (2008ZH68002).

References

[1] X.W. Zhang, L.W. Ji, O. Toprakci, Y.Z. Liang, M. Alcoutlabi, Polymer Reviews, 51 (2011) 239-264.

[2] F. Han, W.C. Li, M.R. Li, A.H. Lu, J. Mater. Chem., 22 (2012) 9645-9651.

[3] X.W. Guo, X.P. Fang, Y. Sun, L.Y. Shen, Z.X. Wang, L.Q. Chen, Journal of Power Sources, 226 (2013) 75-81.

[4] Y. Wang, J.Y. Lee, H.C. Zeng, Chem. Mat., 17 (2005) 3899-3903.

[5] D. Larcher, S. Beattie, M. Morcrette, K. Edstroem, J.C. Jumas, J.M. Tarascon, J. Mater. Chem., 17 (2007) 3759-3772.

[6] S.J. Ding, J.S. Chen, G.G. Qi, X.N. Duan, Z.Y. Wang, E.P. Giannelis, L.A. Archer, X.W. Lou, Journal of the American Chemical Society, 133 (2011) 21-23.

[7] S.J. Ding, Z.Y. Wang, S. Madhavi, X.W. Lou, J. Mater. Chem., 21 (2011) 13860-13864.

[8] M. Dirican, M. Yanilmaz, K. Fu, Y. Lu, H. Kizil, X.W. Zhang, Journal of Power Sources, 264 (2014) 240-247.

[9] J. Liu, W. Li, A. Manthiram, Chemical Communications, 46 (2010) 1437-1439.

[10] K.S. Novoselov, A.K. Geim, S.V. Morozov, D. Jiang, Y. Zhang, S.V. Dubonos, I.V. Grigorieva, A.A. Firsov, Science, 306 (2004) 666-669.

[11] M.D. Stoller, S.J. Park, Y.W. Zhu, J.H. An, R.S. Ruoff, Nano Lett., 8 (2008) 3498-3502.

[12] K.I. Bolotin, K.J. Sikes, Z. Jiang, M. Klima, G. Fudenberg, J. Hone, P. Kim, H.L. Stormer, Solid State Commun., 146 (2008) 351-355.

[13] W.B. Yue, Z.Z. Lin, S.H. Jiang, X.J. Yang, J. Mater. Chem., 22 (2012) 16318-16323.

[14] S.J. Ding, D.Y. Luan, F.Y.C. Boey, J.S. Chen, X.W. Lou, Chemical Communications, 47 (2011) 7155-7157.

[15] S.M. Paek, E. Yoo, I. Honma, Nano Lett., 9 (2009) 72-75.

[16] S. Li, Y.Z. Wang, C. Lai, J.X. Qiu, M. Ling, W. Martens, H.J. Zhao, S.Q. Zhang, Journal of Materials Chemistry A, 2 (2014) 10211-10217.

[17] D. Li, Y.N. Xia, Adv. Mater., 16 (2004) 1151-1170.

[18] D.Y. Liu, X.W. Yuan, D. Bhattacharyya, J. Mater. Sci., 47 (2012) 3159-3165.

[19] T.P. Mthethwa, M.J. Moloto, A. De Vries, K.P. Matabola, Mater. Res. Bull., 46 (2011) 569-575.

[20] Z. Dong, S.J. Kennedy, Y. Wu, Journal of Power Sources, 196 (2011) 4886-4904.

[21] X. Zhang, P. Suresh Kumar, V. Aravindan, H.H. Liu, J. Sundaramurthy, S.G. Mhaisalkar, H.M. Duong, S. Ramakrishna, S. Madhavi, The Journal of Physical Chemistry C, 116 (2012) 14780-14788.

[22] A.K. Geim, K.S. Novoselov, Nature Materials, 6 (2007) 183-191.

[23] S.J. Han, B.C. Jang, T. Kim, S.M. Oh, T. Hyeon, Advanced Functional Materials, 15 (2005) 1845-1850.

[24] M.S. Park, G.X. Wang, Y.M. Kang, D. Wexler, S.X. Dou, H.K. Liu, Angewandte Chemie, 46 (2007) 750-753.

Key Engineering Materials Vols 645-646 (2015) pp 1214-1222
© (2015) Trans Tech Publications, Switzerland
doi:10.4028/www.scientific.net/KEM.645-646.1214
Submitted: 2014-12-02
Accepted: 2014-12-23

Numerical optimization approach of the gap between the magnet and coil for electromagnetic vibration energy harvesters design

Yiming Lei[1,2,3,a] Zhiyu Wen[1,2,3,b]

[1]Key Laboratory of Fundamental Science on Micro/Nano Device and System Technology, Chongqing University

[2]National Center for International Research of Micro/Nano System and New Material Technology, Chongqing University

[3] Micro system Research Center of Chongqing University, Chongqing, CHINA

[a]cqulym@sohu.com, [b]wzy@cqu.edu.cn

Key words: Vibration energy harvesting, magnetic flux linkage gradient, electromagnetic damping coefficient

Abstract. In the design of the micro electromagnetic vibration harvester, an important goal is maximization of the magnetic flux linkage gradient, which directly determines the induced voltage and output power of the electromagnetic vibration harvester. This paper established a numerical model based on structure of the electromagnetic vibration energy harvester. An analytic expression for the magnetic field of rectangular permanent magnets is used to build up an electromagnetic coupling model. The magnetic field distribution of the rectangular permanent magnet was analyzed. The effects of the gap between the magnet and the coil on the load voltage of the electromagnetic vibration energy harvester were investigated. According to the formula, the magnetic flux linkage and flux gradient were calculated to optimize the geometrical parameter of the magnet and coil. The method and boundary conditions of optimizing the gap between the magnet and coil were presented. The maximum output voltage can be obtained by optimizing the gap between the magnet and the coil. A simple prototype was fabricated and measured to validate the theoretical deducing and the feasibility of method.

1. Introduction

With the growing demand for wireless sensor networks, electronic equipment and micro-actuator, micro energy harvesters have become increasingly significant in recent years. Many researches are interested in developing micro energy harvesters which capture small amounts of energy form the environment, e.g., solar[1], thermal[2], radio frequency[3], or kinetic energy[4]. Vibration energy harvesters are used in many commercial applications since mechanical vibrations are widely existent[1]. There are three well-known transduction mechanisms in vibration-based energy harvesting: electromagnetic, piezoelectric, and electrostatic. An electromagnetic vibration energy harvester normally generates low-voltage and high-current output[5]. For micro electromagnetic vibration energy harvesters, the most works aim at reducing the size whilst increasing the electromechanical conversion efficiency to get the higher output voltage and power[6]-[9].

It is well known that the electromotive force of electromagnetic vibration energy harvesters is determined by the time rate of change of the magnetic flux linkage of that circuit[6]. In a linear vibration energy harvester, assume that the motion between the coil and the magnet is in a single direction, the magnet flux linkage gradient and the velocity are important parameters to determine output voltage of the electromagnetic energy harvester. Moreover, the flux linkage gradient is largely dependent on the permanent magnet which was used to produce field, the area and number of turns for the coil and the relative position of the magnet and the coil[7]. Hence, it is necessary to optimize arrangement of the magnet and the coil for obtaining a higher output voltage or power.

In this paper, a new optimization strategy was proposed to extract maximum output voltage by calculating the magnetic flux gradient directly. Corresponding analytical models were adopted to perform theoretical analysis. In order to obtain the maximum output voltage, the gap between the magnet and the coil was optimized by according to the calculated magnetic flux linkage gradient. The method and boundary conditions of optimizing the gap between the magnet and coil were presented. In order to observe effects of the gap on the output voltage, an experiment was implemented and the theoretical results were verified by experiments.

2. Basic Theory

The operating principle on which almost all electromagnetic vibration harvesters are based is Faraday's law of electromagnetic induction. Figure 1 shows a schematic of electromagnetic vibration harvesters. The relative movement between the magnet and the coil is caused by the vibration and then an induced electromotive force is generated in the coil.

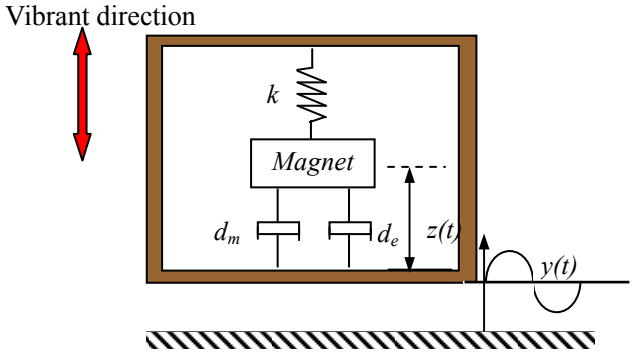


Fig.1. Schematic of an electromagnetic vibration harvester

Micro electromagnetic vibration energy harvesters vibrating at a resonance frequency are conventionally modeled as a second-order mass-spring-damper system[5], which consists of a proof mass m, a spring with constant k, and two dampers d_m and d_e (d_m is parasitic produced damping coefficient and d_e is electrically induce damping coefficient). The system is represented as:

$$m\ddot{z}(t) + (d_m + d_e)\dot{z}(t) + kz(t) = m\omega^2 Y_0 \sin(\omega t) \tag{1}$$

Where z is the relative displacement, ω the resonant frequency in *rad/s*, Y_o is the input vibration amplitude [6]. For a sinusoidal-driven input function, the steady state solution of formula (1) is:

$$z(t) = \frac{Y_o \omega_r}{\sqrt{(1-\omega_r{}^2)^2 + [2(\zeta_m + \zeta_e)\omega_r]^2}} \sin(\omega t - \psi) \tag{2}$$

Where ω_r represents the ratio of input frequency to natural resonant frequency $\omega_r=\omega/\omega_n$. ζ_m and ζ_e is parasitic produced damping ratio and electrically induce damping ratio respectively($\zeta_m=d_m/(2m\omega_n)$, $\zeta_e=d_e/(2m\omega_n)$), and ψ is the phase angle.

The magnitude of the voltage induced across the coil, as described by Faraday's law of induction, is equal to the time rate of change in the magnetic flux[7].

$$V_{emf} = -\frac{d\Phi}{dt} = -\frac{d\Phi}{dz}\frac{dz}{dt} \tag{3}$$

Where V_{emf} is the generated voltage and Φ is the magnetic flux linkage. $d\Phi/dz$ is the gradient of the magnetic flux linkage along the direction of relative motion. dz/dt is the relative velocity between the magnet and the coil.
The velocity is calculated by the first derivative of the steady state amplitude of formula (2):

$$\dot{z} = \frac{dz}{dt} = \frac{\omega Y_o \omega_r^2}{\sqrt{(1-\omega_r{}^2)^2 + [2(\zeta_m + \zeta_e)\omega_r]^2}} \tag{4}$$

The ζ_e is also called electromagnetic damping which is shown in the equation (5):

$$\zeta_e = \frac{1}{2m\omega_n(R_L + R_c + j\omega L_c)} \cdot \left(\frac{d\Phi}{dz}\right)^2 \tag{5}$$

Where R_L and R_c are load and coil resistances, respectively, and L_c is the coil inductance. For operation at resonance ($\omega=\omega_n$), the output voltage can be deduced by formula (3), (4), (5). :

$$V_{load} = \left(\frac{d\Phi}{dz}\right) \cdot \frac{m\omega^2 Y_0 \cdot R_l}{[(d\Phi/dz)^2 + (R_c + R_l + j\omega L_c)d_m]} \tag{6}$$

In order to obtain the maximum output voltage, assuming that the load resistance R_l and the parasitic damping d_m are constants, the first derivative of the formula (6) of $d\Phi/dz$ was calculated and expressed as follow:

$$\dot{V}_{load} = \frac{(R_l + R_c + j\omega L_c)d_m - (d\Phi/dz)^2}{[(d\Phi/dz)^2 + (R_l + R_c + j\omega L_c)d_m]^2} \tag{7}$$

According to the formula (7), the maximum output load voltage appears when the flux linkage gradient square is equal to the produce the impedance of the system and the parasitic damping coefficient. In other words, the magnetic flux linkage gradient can be adjusted to make equal the parasitic mechanical damping and the electrical induce damping corresponding to the maximum output voltage. In such a case, the output voltage and power of electromagnetic vibration harvesters depends on the flux linkage gradient[7].
The output power can be calculated using Joule's law[8].

$$P_{load} = \frac{V_{load}^2}{R_l} \tag{8}$$

According to the formula (6) and (8), we can see that the magnetic flux linkage gradient is an important parameter to determine the output voltage and power of micro electromagnetic vibration energy harvesters.

3. Modeling and Calculation

3.1Modeling

In this paper, we focused on an electromagnetic vibration energy harvester which consists of a rectangular permanent magnet attached on a resonant structure and a wire-wound coil, the motion between the coil and the magnet is in a single direction (*Z-axis*). As the polarization orientation and moving direction of magnet are along the *Z*-axis, the magnetic induction density of the *Z* direction is a function of the coordinate variables. The rectangular coordinates of the permanent magnet are shown in Figure 2. The magnetic flux density B_z to an arbitrary point in space *P* (x, y, z) can be written as[9]:

$$B_z = \frac{\mu_0 J}{4\pi}[-\Psi(b-y,a-x,z)] - \Psi(y,a-x,z) - \Psi(a-x,b-y,z) - \Psi(x,b-y,z)] \\ -\Psi(b-y,x,z) - \Psi(y,x,z) - \Psi(a-x,y,z) - \Psi(x,y,z)]\Big|_0^h \quad (9)$$

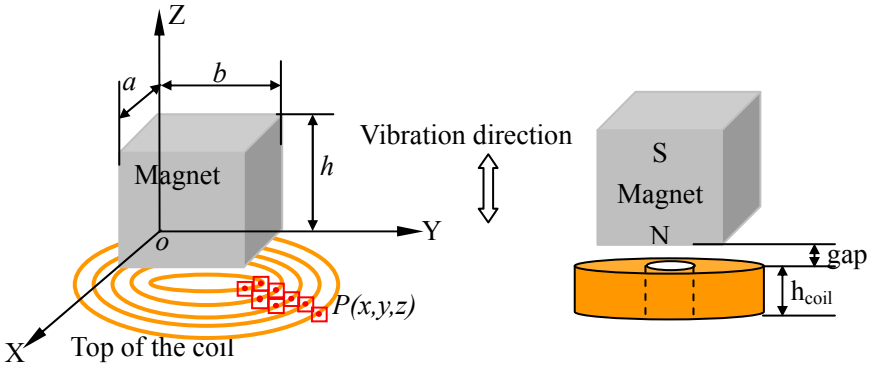


Fig. 2 Coordinates of the rectangular permanent magnet

Where μ_0 is the magnetic permeability in the air and J is current density. a, b and h indicates the length, the width and the height of the magnet. Function Ψ is the expression:

$$\Psi(\psi_1,\psi_2,\psi_3) = arctg\left[\frac{\psi_1}{\psi_2}\frac{(\psi_3 - z_o)}{\sqrt{\psi_1^2 + \psi_2^2 + (\psi_3 - z_o)^2}}\right|_{z_o = 0}^{z_o = h} \quad (10)$$

The flux linkage for a multiple turn coil should be evaluated as the sum of the linkages for the individual turns [2], i.e.

$$\Phi_i = \iint_s B_i ds \quad (11)$$

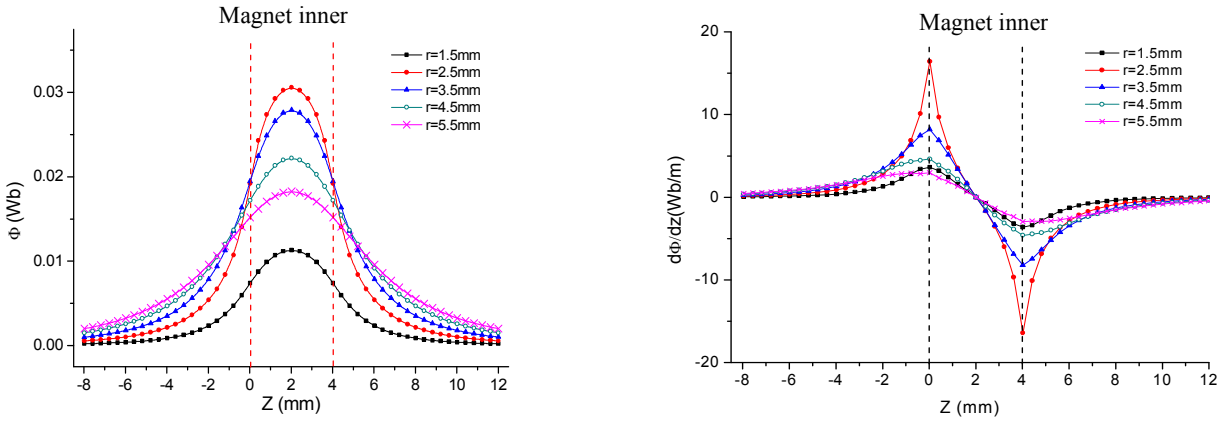
$$k_t = \frac{d\Phi}{dz} = \frac{d}{dz}\cdot\frac{1}{h_{coil}}\int_0^{hcoil}[\sum_i^n \int_{ri}(d\vec{l}\times\vec{B}_{ri})]dz \quad (12)$$

Where S is the area of the ith turn of the coil, B is a summation of the magnetic field flux density corresponding to the ith turn of the coil. The magnetic flux gradient can be expressed as the formula (12). So the calculation of surface integral was transformed to curvilinear integral.

3.2 Calculating

Exemplarily, it shows the specific calculation steps to a rectangle magnet. According to the geometry parameters of the magnetic and coil, in the first step, the area of coil was discretized into N circles with different radius as shown in Figure 2. The magnetic field flux density (B) of each point on the ith ring was calculated. Whilst, the B_i multiplied by a small area that contains the corresponding the point coordinate to get the magnetic flux linkage and the small area is determined by the calculating step length. In the second step, the magnetic flux linkage of each circle was calculated respectively and was sum. The total magnetic flux in the whole coil is a summation of the circles magnetic flux contributions. In the third step, the magnetic flux linkage Φ corresponding to different Z coordinate was calculated and the curve of the magnetic flux versus Z coordinate was obtained. In the forth step, the thickness of wire-wound coil and the number of coil turns were considered. The magnetic flux linkage of the coil is an average of the different position in the range of the height of the coil. In the last step, $d\Phi/dz$ was obtained by calculating the tangential derivative of the curve $\Phi(z)$.

For example, assume that a volume of rectangular (NdFeB) permanent magnet is $4.5\times4.5\times4mm^3$ and the number of turns for a coil is 2000. The changing trend of magnetic flux linkage and flux linkage gradient for different radius of coil with the same height at different position was computed. Results are shown as Figure 3(a) and (b).



(a) (b)

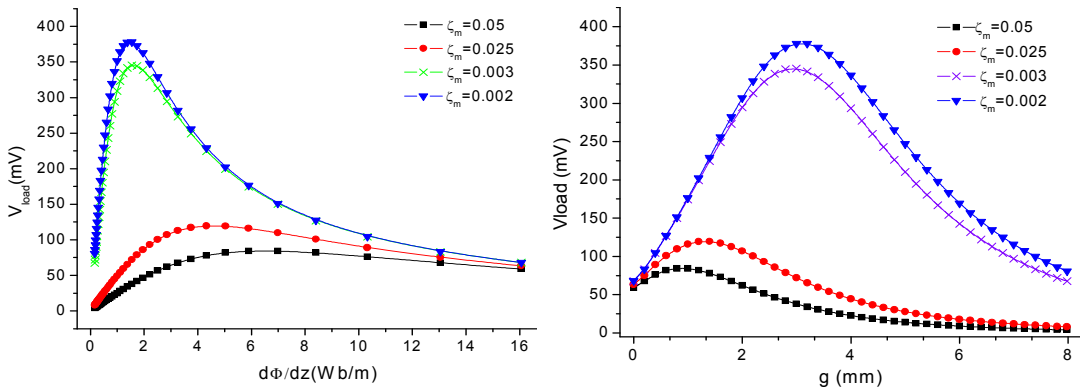
Fig.3 (a) Magnetic flux linkage for different radius of coil at different position (b) Magnetic flux linkage gradient for different radius of coil at different position

Assume that a rectangular magnet oscillates towards a cylindrical coil without immersion. The magnet internal magnetic flux and flux linkage gradient was not considered. As can be seen form Figure 3, the magnetic flux and the flux linkage gradient have symmetry for the geometric center of the magnet. When the magnet and the coil spacing is greater than 4mm, the magnetic flux gradient is very small. It is worth noting that both the magnetic flux linkage and the flux linkage gradient are more sensitive to the coil height. For the wire-wound coil with the height of 4 mm and the radius of 2.5 mm, the magnetic flux of the bottom of the coil is only 11.3% of the top of the coil. Under the same conditions, the magnetic flux linkage gradient of the bottom is about 5.4% of the top. In the case, the height of wire-wound coil must be considered in the calculation. The final curve of the magnetic flux linkage can be obtained by calculating weighted averages of different coordinate in the coil height.

4. Analysis and Optimization

In the model, the output voltage of energy harvester is a function of two variables which are ($d\varphi/dz$) and d_m. Moreover, the magnetic flux linkage gradient ($d\varphi/dz$) depends on the gap between the magnet and the coil. When the parasitic damping of electromagnetic vibration energy harvester is known, a value of the optimum gap for generating the maximal output voltage can be calculated according to the formula (7). In general, the gap which between the magnet and the coil is limited by vibration amplitude and load resistance is adjusted to make the electrical damping equal to the parasitic damping. However, the load resistance remains unchanged and an optimum gap is chosen to extract the maximum output voltage in our work.

When the external excitation, load resistor is a constant and parasitic damping is known, the changing trend of output voltage with the increasing magnetic flux linkage gradient is shown in Figure 4(a):



(a) (b)

Fig. 4 (a) Output voltage versus the magnetic flux linkage gradient and (b) Output voltage versus the gap

Curves of Figure (4) were calculated under conditions of 0.5g acceleration, a rectangular magnet with volume of 4.5×4.5×4mm^3 and a coil with radius of 2.5mm, height of 4mm, load resistance of 500 Ω, and number of turns 2000. In figure 4, the change trend of output voltage which versus the magnetic flux linkage gradient and the gap are steeper corresponding to the smaller parasitic damping of the system. The parasitic damping ratio is expressed ζ_m ($\zeta_m=d_m/(2m\omega_n)$) and limits the output voltage of electromagnetic vibration energy harvester. Figure 4(a) shows a plot of the output voltage for various parasitic damping ratios versus the magnetic flux linkage gradient. The output voltage of electromagnetic vibration energy harvester is not always increase with the increase of magnetic flux linkage gradient. There exists a value of the magnetic flux linkage gradient where the output voltage is maximal and corresponds to a certain position of coil. After passing the optimal magnetic flux linkage gradient, the output voltage will be decreased with increasing the magnetic flux gradient continually. Moreover, the decreasing trend of output voltage is more obvious with a smaller parasitic damping ratio. As shown in Figure4 (b), there is an optimal gap between the magnet and coil for generating the maximal output voltage. The optimized position of the coil will be closer the magnet with increasing the parasitic damping ratio. i.e., the optimized gap decreases with increasing parasitic damping ratio.

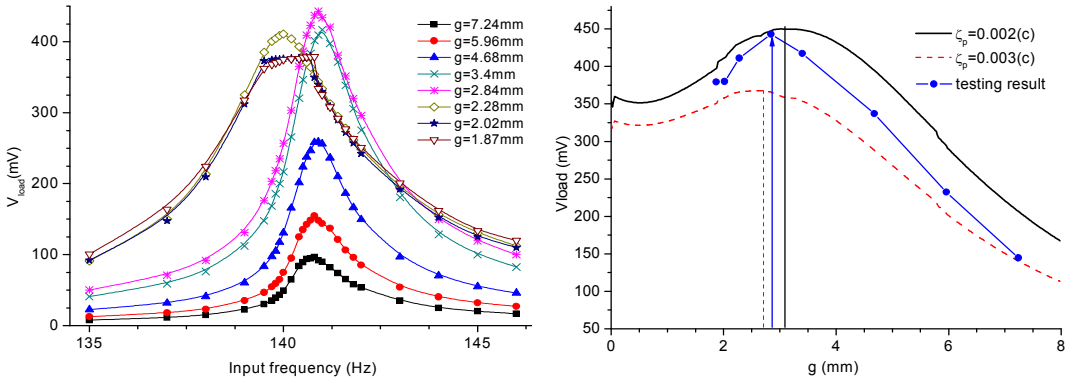
5. Experimental verification

In order to verify the derived conclusion, a macro model was fabricated and tested. The macro energy harvester has a rectangle magnet, a wire-wound coil and a cantilever. A magnet was attached to the end of a copper cantilever and suspended above a copper coil as resonant structure. The coil with inner radius of 0.38mm, outer radius of 4.8mm, height of 1.24mm and the magnet with volume of 4.42×4.52×4 mm^3. Seven plastic gaskets were used to change the gap between the magnet and the coil. There are three gaskets with thickness of 1.22mm, two with thickness of 0.5mm, one of 0.2mm and a gasket with thickness of 0.15mm. The setup consists of an electromagnetic shaker, a signal generator, an accelerometer, a computer and an oscilloscope. The electromagnetic energy harvester was immobilized on the vibration table. The experimental setup is shown in Figure 5.



Fig.5 Photograph of the experimental setup

The electromagnetic vibration energy harvester was tested on a shaker, which drives the beams with an acceleration of constant magnitude of 0.5 g ($g=9.8ms^{-2}$). The load resistance is also a constant with a value of 500 Ω. The parasitic damping ratio of the vibration energy harvester was estimated at between 2‰ to 3‰ without considering the impact of air damping and package factors. In order to decrease the gap between the magnet and the coil, gaskets of different height were sequentially added to the bottom of the coil. Results of measured and calculation were shown as Figure 6.



(a) (b)

Fig. 6 (a) Curve of the output voltage for the different gap between the magnet and the coil (b) Measuring output voltage of electromagnetic vibration energy harvester

Figure 6 (a) is the curve of the output voltage of the frequency response for the various gaps by actual measurement. The output voltage varies with the increase of the gap is decreased until the best gap is reached, and then continues to reduce the gap the output voltage is start to decrease. The star and open-down-triangle on curves in the Figure 6(a) which corresponding to the gap 2.02 mm and 1.87 mm respectively show that: the gap between the magnet and the coil may be less than the vibratory amplitude of the magnet. In this case, the energy harvester exhibits nonlinear may be due to the vibrant amplitude is limited. Figure 6 (b) shows how the gap affects the output voltage of electromagnetic vibration energy harvesters. The dotted-line and solid-line in the Figure 6 (b) shows the output voltage corresponding to the different gap, which are obtained by calculating. The line with circles is the testing result. As can be seen in Figure 6(b), when the parasitic damping ratio is 2‰, the optimizing gap between the magnet and the coil was 3.04mm by calculating and when the parasitic damping ratio is 3‰, the optimizing gap became 2.68mm. By calculation, the gap between the magnet and the coil can be limited to a small range, so as to optimize the gap. Meanwhile, the

best gap is about 2.84mm by testing. The testing results show that: the best spacing between the magnet and coil located in the range of calculating. The actual measurement results are consistent with the theoretical calculation results.

6. Conclusion

In general, a method of adjusting load resistor is adopted to make the coefficient of electrically induce damping equal to the parasitic damping for getting the maximum output power and voltage. However, when the load resistor was determined as a constant for practical application, the method for the optimizing gap needs to be used for getting the maximum output power and voltage. This paper obtains a method for the optimizing gap between the magnet and coil by calculating the permanent magnet magnetic field distribution. A prototype was fabricated to validate this optimizing method. The parasitic damping ratio of the prototype was estimated between 2‰ to 3‰ and the optimizing gap is between 2.68 mm to 3.04mm by calculating. The actual measured value is 2.84 mm and just locates in this range. The feasibility of the method to optimize parameters of the electromagnetic vibration energy harvester was proved by the experiment. However, several conditions must be satisfied for use of this optimizing method. Firstly, the dimension parameters of the magnet and the coil are determined, and the magnetic flux linkage and the magnetic flux gradient can be calculated accurately based on these parameters. Secondly, it is possible to measure or accurately estimate the parasitic damping ratio. Finally, during the process of calculation, the parasitic damping is set to a constant without considering impacts of air damping which increased as the gap reduces in micro structures. This optimized method for electromagnetic vibration energy harvesters which are vacuum-packaged and increased the bandwidth using an amplitude limiter has an important significance. It can provide a method to optimize design key parameters of micro electromagnetic vibration energy harvester.

Acknowledgement

This work was supported by the Higher school specialized research fund for the doctoral program (No. 20090191110009).

References

[1] S.Roundy, P.k. Wright, J. Rabaey, A study of low level vibrations as a power source for wireless sensor nodes, Solar Cells 26(2003) 1131-1144.
[2] Hakan Toreyin, Emre Topal, Haluk Kulah, A multi-source micro power generator employing thermal and vibrtion energy harvesting, Procedia Engineering 5(2010) 1176-1179.
[3] Rashed H. Bhuigyn, Roger A. Dougal and Mohannmod Ali, A miniature energy harvesting device for wireless sensor in elelctric power system, Sensors Journal (2010), Vol. 10, NO.7.
[4] E. Sardini, M. Balsi, An efficient electromagnetic power harvesting device for low-frequency applications, Sensors and Actuators A: Physical 172 (2011) 475-482.
[5] S. P. Beeby, M. J. Tudor, and N. M. White, Energy harvesting vibration sources for micro-systems applications [J]. Measurement science and technology, Vol. 17, no. 12, pp. R175–R195, 2006.
[6] Tom J.Kazmierki, Leran Wang, Bashir M. Al-Hashimi and Geoff V. Merrett, An explocit linearized state-space technique for accelerated simulation of electromagnetic vibration energy harvesters Transactions in computer-aided design of integrated circuits and system, Vol. 31,NO.4
[7] S. Kulkarni, E. Koukharenko, R. Torah, J. Tudor, S. Beeby, T.O' Donnell, and S. Roy, Design, fabrication and test of integrated micro scale vibration-based electromagnetic generator, Sensors and Actuators A, vol. 145-146, pp. 336-342, July-August, 2008.

[8] Arnold DP. Review of micro scale magnetic power generation [J].IEEE Trans. Magnetics (2007), 43(11):3940-3951.
[9] C .B. Williams, and R. B. Yates, Analysis of a micro electric generator for micro-systems, Sensors and Actuators A, vol. 52, pp. 8-11, 1996.
[10] D. Spreemann, D. Hoffmann, B. Folkmer, Y. Manoli. Numerical optimization approach for resonant electromagnetic vibration transducer designed for random vibration [J]. Micromechanics and Micro-engineering, 2008, 104001(8):46-57.
[11] C.Cepnik, O. Radler, S.Rosenbaum, T. Strohla, U. wallrabe. Effective optimization of electromagnetic energy harvesters through direct computation of the electromagnetic coupling[J]. Sensors and Actuators A: Physical, 2011, 416-421.

Key Engineering Materials Vols 645-646 (2015) pp 1223-1232
© (2015) Trans Tech Publications, Switzerland
doi:10.4028/www.scientific.net/KEM.645-646.1223

Submitted: 2014-12-02
Accepted: 2014-12-23

Design and Comparison of micro electromagnetic vibration energy harvesters

Yiming Lei[1,2,a] Zhiyu Wen[1,2,b] Li Chen[1,2,c]

[1]Key Laboratory of Fundamental Science on Micro/Nano-Device and System Technology, Chongqing University

[2]Microsystem Research Center of Chongqing University, Chongqing 400030, CHINA

[a]cqulym@sohu.com (corresponding author), [b]wzy@cqu.edu.cn, [c]cl2009@cqu.edu.cn

Key words: vibration energy harvesting, electromagnetic induction, micro energy harvester

Abstract: This paper presents two electromagnetic vibration energy harvesters based on micro-electro-mechanical (MEMS) technology. Two prototypes with different vibration structures were designed and fabricated. The energy harvester includes a permanent magnet attached on vibration structure (resonator) made by Si and a fixed wire-wound coil, with the total volume of 0.9 cm^3. Two energy harvesters with different resonator are tested and compared. Experiments show that: in the same acceleration and a load resistance, the resonant frequency of prototype B is approximately 95% of prototype A; The peak-peak voltage and the maximum power of prototype B is 1.6 times and 2.7 times of prototype A respectively. The test results was analyzed simply and it indicated that the electromagnetic energy harvesting with the spring B has better performance; also proved that the potential ability of the non-linear spring could extend the frequency bandwidth and improve output voltage.

1. Introduction

In order to make miniature sensors and actuators can be self-powered and avoid replacement power frequently, energy harvesters or micro power generators have become increasingly significant in recent years. Harvesting energy form environment has received great attention due to the availability of such sources as outdoor light, human motion, mechanical vibration or thermal energy *etc*. Among the potential environmental energy source, it has been shown that mechanical vibrations are available in many applications [1]. So vibration energy harvesters have become a hot spot in the self-sustaining power field. The transduction from kinetic energy to electrical energy usually includes electromagnetic, piezoelectric, or electrostatic techniques. Electromagnetic energy conversion gains the advantage of no need to have a separate voltage source and high output current due to low internal impedance [2]. Many early reported devices worked at frequency of several kHz [3], because a higher induction electromotive force can be generated at higher frequency. Such as, Santosh Kulkarni *et al* [4] developed a micro-generator for energy harvesting, which consists of four magnets coupled to a moving coil attached to a cantilever beam. The harvester of 106 mm^3 in size which can be able to harvest 148 nW power under 3.9 ms^{-2} and 8.08kHz excitation. However, the majority of ambient vibration sources are "low level" vibration, which have low frequency (<500Hz), small displacement (several μm) and low acceleration (<2g) [5]. In recent years, many research groups carried on working at nonlinear characteristics of the vibration energy harvester to improve energy harvesters' performance [6]-[10].

In this paper, our reports focus on design and fabrication of two electromagnetic vibration energy harvesters which have different vibrating structure and working frequency at about 300Hz. The different shapes of vibrating structure led to vary greatly in output voltage and power of the electromagnetic vibration energy harvester. Two planar springs with different beam structure were fabricated by MEMS technology. Two prototypes were assembled with the different vibrating spring and the wire-wound coil. Two vibration energy harvesters were tested. By compared and analyzed, testing results show that the electromagnetic vibration energy harvester with the nonlinear-vibrating spring B has a higher output voltage and power under the same experimental conditions.

2. Modeling and Design

2.1 Modeling

Micro vibration energy harvesters at a resonance frequency are conventionally modeled as a second-order mass-spring-damper system [2]. When the external vibration is a sinusoidal signal $y=Y_0\sin(\omega t)$, the dynamic behavior of the energy harvester is described as:

$$mz'' + d_t z' + kz = -m\omega^2 Y_0 \sin(\omega t) \tag{1}$$

Where z is the relative displacement, ω the external vibratory frequency, m the mass of the resonator, k the stiffness, the total damping d_t that is composed of the electromechanical produced (d_e) and the parasitic part (d_m). Depending on the deflections of the resonance structure and the amplitude of mechanical stimulus, the model can be linear or nonlinear. When the resonator has only a linear behavior, the spring force is equal to the elasticity constant k multiplied by the amplitude. For electromagnetic vibration energy harvesters, their work principle is Faraday's law.
According to Faraday's law any time change in the magnetic field linking a coil will cause a voltage to be induced in the coil. The principle of Faraday's law is that the voltage, induced in a circuit is proportional to the time rate of change of the magnetic flux linkage of that circuit. The voltage induced in an N turn coil is given by [5]:

$$V_{emf} = -\frac{d\Phi}{dt} = -\frac{d\Phi}{dz}\cdot\frac{dz}{dt} = -\frac{d\Phi}{dz}\cdot v \tag{2}$$

The voltage induced in the coil can be expressed as the product of a flux linkage gradient and the velocity. dΦ/dz is also called the electromagnetic coupling factor[7].
The ζ_e is called electromagnetic damping ratio which is shown in the equation (3):

$$\zeta_e = \frac{d_e}{2m\omega} = \frac{(d\Phi/dz)^2}{2(R_L + R_c + j\omega L_c)m\omega} \tag{3}$$

R_L and R_c are load and coil resistances, respectively. L_c is the coil inductance and m is the effective mass. When the vibration frequency matches the natural resonant frequency ($\omega_r=1$), the load voltage and the output power across the load may be expressed as functions of the input acceleration:

$$V_{load} = -\left(\frac{d\Phi}{dz}\right)\frac{a\cdot R_l}{2\omega\zeta_t(R_c + R_l)} \tag{4}$$

$$P_{load} = \frac{V_{load}^2}{R_l} = \left(\frac{d\Phi}{dz}\right)^2\cdot\frac{a^2 R_l}{4\omega\zeta_t^2(R_c + R_l)^2} = \frac{m\zeta_e a^2}{2\omega\zeta_t^2}\cdot\frac{R_l}{R_c + R_l} \tag{5}$$

Where *'a'* is the acceleration amplitude of the system and expressed as $a=\omega^2 Y_o$. According to formula (4) and (5), when amplitude of acceleration is unchanged, the load voltage is proportional to the magnetic flux linkage gradient and is inversely proportional to the input frequency, the total

damping ratio. Moreover, the output power depends on the input frequency, the effective oscillating mass and the damping ratio. The optimum load resistance can be found from the equation (6) [4]:

$$R_{l,opt} = R_c + \frac{(d\Phi/dz)^2}{d_m} \tag{6}$$

The efficiency of the electromagnetic vibration energy harvester can be expressed as equation (7) [10]:

$$\eta = \eta_e \cdot \eta_m = \frac{d_e}{d_e + d_m} \cdot \frac{R_l}{(R_l + R_c)} \tag{7}$$

For the resonator with nonlinear, it has been modeled as the mass-spring-damper system in which there is a damper and a nonlinear spring, the equation of the nonlinear spring as:

$$F_s = kz + k_3 z^3 \tag{8}$$

Consequently, the behavior equation of the vibration energy harvester takes the form:

$$mz'' + d_t z'' + kz + k_3 z^3 = -m\omega^2 Y_0 \sin(\omega t) \tag{9}$$

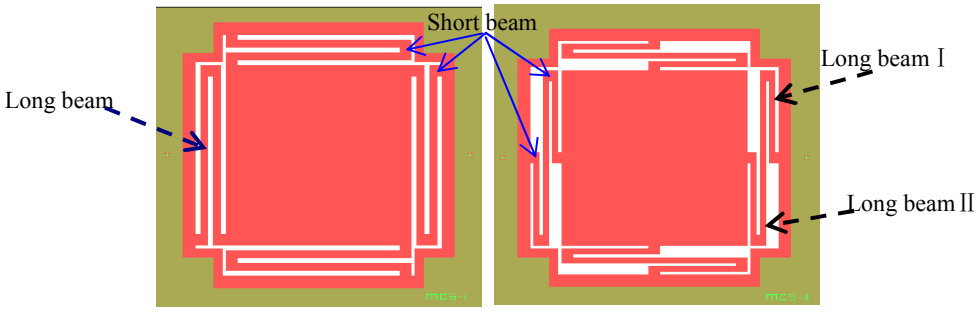
Dividing both sides by m and the equation (3) can be expressed in non-dimensional form as:

$$u'' + 2\zeta_t u' + u + \alpha u^3 = -\Omega^2 \sin(\Omega\tau + \phi) \tag{10}$$

Where $\Omega = \frac{\omega}{\omega_n}, u = \frac{z}{Y_0}, \alpha = \frac{k_3}{k_1} Y_0^2, \tau = \omega_n t, \zeta_t = \frac{d_t}{2m\omega_n}, \omega_n = \sqrt{\frac{k_1}{m}}$, and ϕ is the phase angle between the excitation and the response. The degree of non-linearity of the system α depends on both the physical properties of the system, k_1 and k_3, and the level of the input displacement, Y_0.

2.2 Resonator Design and Simulation

Two resonator structures based on MEMS technology were designed for the realization of harvesting energy by environmental vibration. The two resonator described in this paper were mentioned as A and B respectively. Both shapes A and B have four folded beams and a center platform. Their detailed shapes are showed in Figure 1.



(a) (b)

Figure 1 (a) Schematic of resonant structure A and (b) Schematic of resonant structure B

Figure 1 (a) and (b) shows different structure of resonators A and B with center platform sizes of 5×5 mm^2. The folded beams were adopted to increase the vibratory amplitude and get a lower mechanical resonant frequency. The total size of the resonator chip is 9×9 mm^2. The central platform of spring for fixed magnet, surrounded by folded beams. The main difference between A

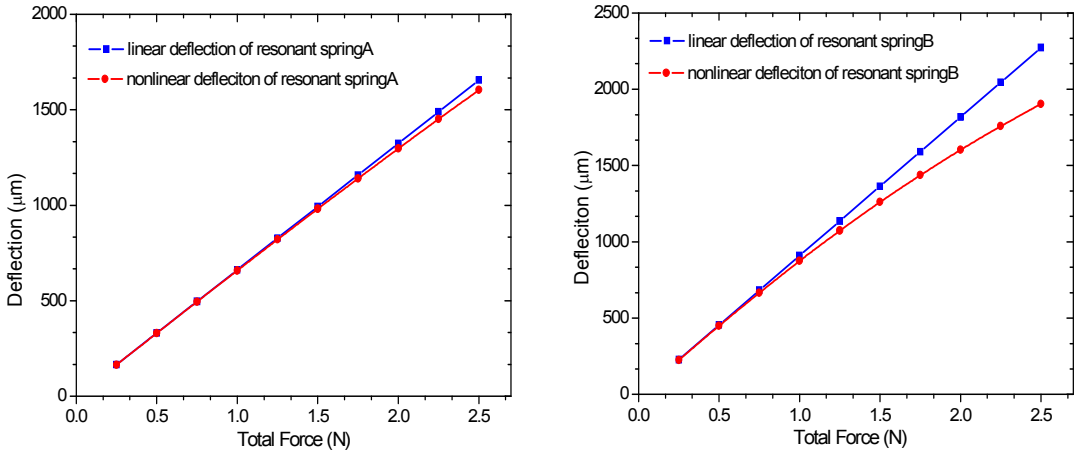
and B is the folded beams with different shapes and sizes. The U-shape beams was adopt for resonator A and S-shape beams for resonator B. The folded beams parameters of two resonators are shown in Table 1. The software ANSYS was used to simulate the resonant frequencies with corresponding vibration modes of resonators.

Table1.Primary parameters of the resonant spring

Parameters	Prototype A	Prototype B
Length of short beam (μm)	300	300
Width of short beam (μm)	150	100
Length of long beam I/Ⅱ (μm)	5000	2500/5000
Width of long beam (μm)	200	150
Thickness of beam (μm)	150	150
Young's modulus of the spring	130Gpa	130Gpa
Poisson's ration of the spring	0.278	0.278
Density of the spring	2.33g/cm^3	2.33g/cm^3
Magnet size	4×4×3.54mm^3	4×4×3.54mm^3
Young's modulus of the magnet	170 Gpa	170 Gpa
Density of the magnet	7.66g/cm^3	7.66g/cm^3

The vibration picking system of energy harvesters consist of a neodymium iron boron (NdFeB35) permanent magnet and a resonant spring. The mode simulation results shows: The main movement direction of the resonator A and B are perpendicular to the spring plane. The first mode frequency of vibration picking system with structure A is 296.16Hz and which of the resonator B is 269.52 Hz. When the resonant structure are attached on a 80 thickness SU-8 layer, the first mode frequency of resonator A is changed into 306.16Hz, which of the resonator B is 281.04Hz.

The deflections of the resonant springs at different loading were also calculated by software ANSYS. The linear and nonlinear results were got at 'Small Displacement Static' and 'Large Displacement Static' mode, respectively. Figure 2 is the curve of the deflections at the center of the resonant springs versus loading condition. As shown in Figure 2(a), the difference between the linear deflection and nonlinear deflection are very small, that means the nonlinearity of the resonator A is small. Whilst, the deflection of spring B is larger than which of spring A at the same loading, so the spring B has obvious nonlinear characteristics.



(a) (b)

Figure 2 (a) Simulated linear and nonlinear deflection of resonant spring A with load (b) Simulated linear and nonlinear deflection of spring B with load

3. Fabrication

3.1 Resonator structure fabrication

Two different resonators were fabricated directly using Si substrate，of which the schematic resonant shapes were shown in Figure 1. Typical micromachining was used to fabricate resonators' microstructure (resonant planar spring）.The chosen materials decreased the production cost and simplified the fabrication process. The fabrication processes of the resonant springs are shown in Figure 4.

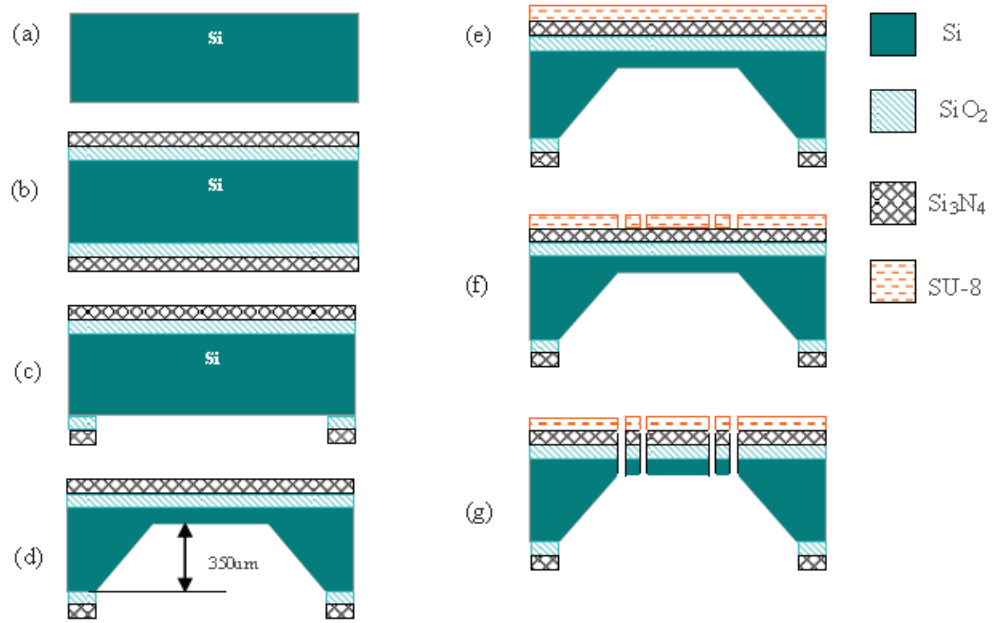


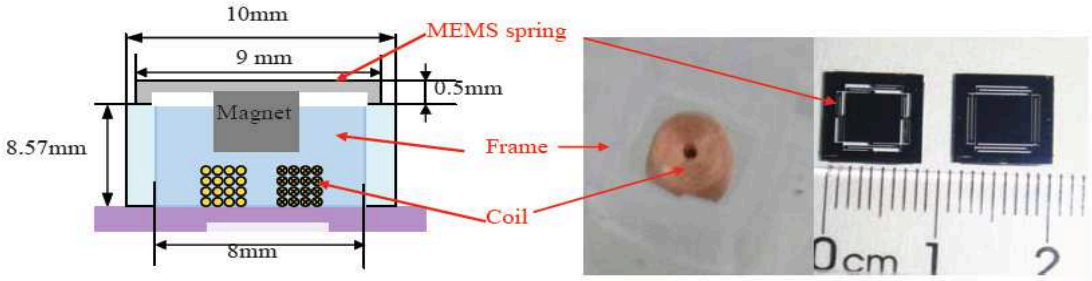
Figure 3 Fabrication processes of the suspension micro structure. (a) A 4-inch <100> silicon wafer; (b) Deposition of Si_3N_4 and SiO_2 on the both side of the silicon wafer; (c) Patterning of the backside; (d) Wet etching; (e) SU-8 photoresist is spun on the front side; (f) Patterning of SU-8 photoresist; (g)Dry etch on the front side to release the device.

The fabrication processes of the suspension microstructure begun with a 500um thick, 4-inch <100> silicon wafer (shown in Figure 3(a)). The first step, 0.2μm-thick wet thermal oxide layer was grown on the both sides of silicon substrate. The second step is to deposit 0.12μm-thick Si_3N_4 layer (Figure 3(b)). The backside oxide layer and the Si_3N_4 were patterned by photolithography and then removed

by RIE (Figure 3(c)). Then the exposed regions of silicon were etched by KOH solution. Under the temperature of 80℃ and KOH concentration of 33%, the etched depth was 350um after about 4.5 hours. (Figure 3(d)). As follows, the 80 μm thickness of the photo resist SU-8 was spun and patterned by photolithography to define the shape of the cantilever (Figure 3(e) and Figure 3(f)). Finally, the microstructure was released by inductively coupled plasma (ICP) as Figure 3(g). From the ANSYS simulation, we found that reservation the photo resist (SU-8) can reduce the beam deformation in static and had little impact on the resonant frequency. The ANSYS simulation results show that the increased resonance frequency was less than 5% to attach the photo resist (SU-8). So we kept the SU-8 on the spring structure.

3.2 Assembled of electromagnetic vibration energy harvesters

The electromagnetic vibration energy harvester was assembled by the resonator and wire-wound coil, it with resonant spring A is called Prototype A and it with resonant spring B is called prototype B. A permanent magnet was fixed on the bottom of resonant spring and suspended above the coil. The rectangle Neodymium (NdFeB 35) magnet was employed and the dimension of the magnet is $4\times4\times3.54mm^3$, which was attached on the platform of the planar spring. Then, the resonant spring with the magnet was fixed by its external edge at the frame case which is made of plexiglass and suspended above the coil. The frame's area is 10×10 mm^2. The distance between the magnet and coil was determined by the height of frames. The frame height was 8.57 mm corresponding to the distance between the magnet and coil was 1.02 mm. Prototype A and B use conventionally a wound-coils with 3000 turns. The coil was fixed on the bottom. The coil's dimension is as below: the internal diameter is 0.74 mm, external diameter is 5mm, and thickness is 4.12mm. The fill factor of the coil is 78.5%. The measured resistance of the coil was 405Ω. The schematic diagram of the energy harvester is shown in Figure 4(a) and (b).



(a) (b)

Figure 4 (a) Schematic of Configuration and dimensions of prototype and (b) Photo of resonant Si-spring and wire-wound coil

4. Experiment and results comparison

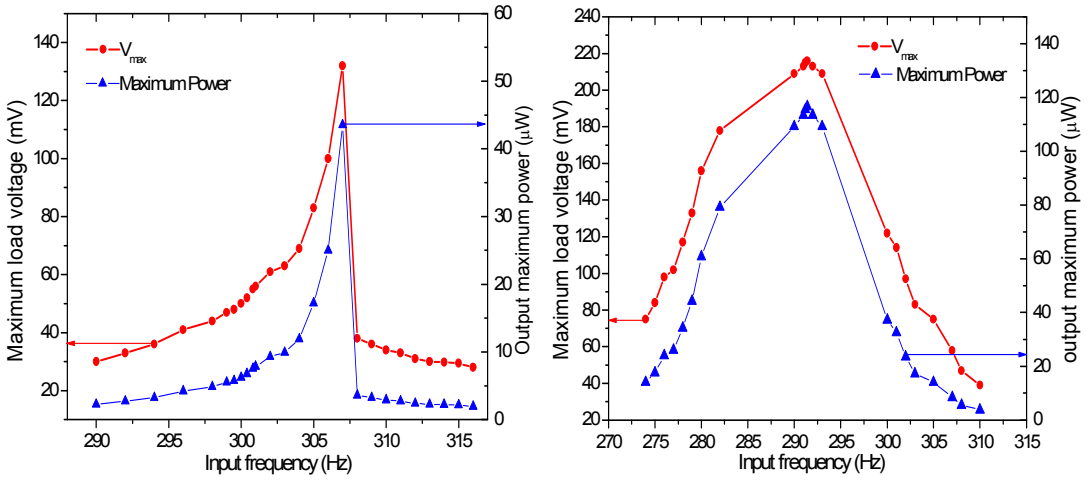
4.1 Experiment

The prototypes were tested from the experimental setup shown in Figure 5. The setup consists of an electromagnetic shaker, a signal generator, an accelerometer, a computer and an oscilloscope. The micro electromagnetic energy harvester was immobilized in a Perspex frame. Then, the frame with the harvester was fixed on the vibration table. The Perspex frame is used to reduce the impact of magnetic field generated by the vibration table.



Figure 5 Photograph of the experimental instruments

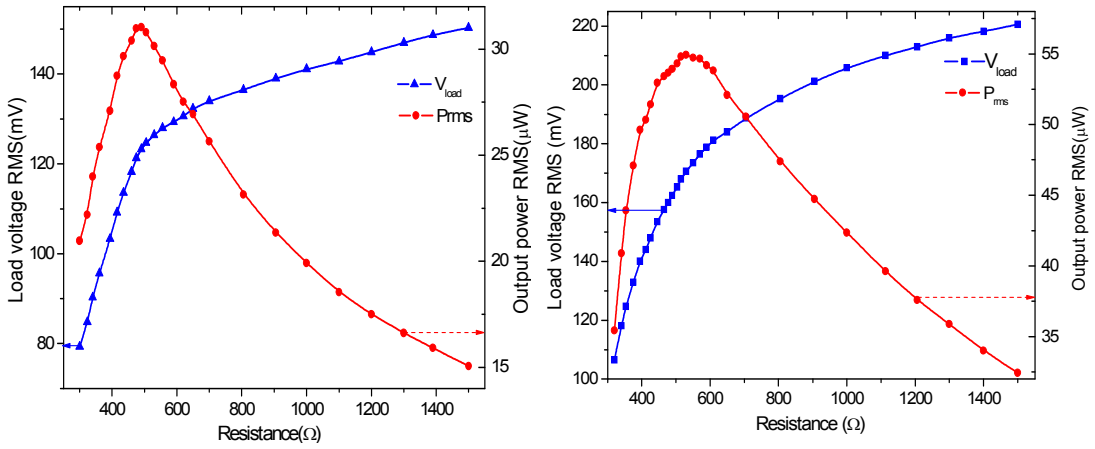
When the waveform generator supplies a sinusoidal signal to the vibrator, forced vibration is applied on the prototype and then the voltage is induced in the coil. The oscilloscope can obtain the voltage generated on the load resistance. The measured voltage at resonance of prototype A and B are shown in Figure 6. In these experiments, the acceleration of input vibration is 0.5g ($g=9.8m/s^2$). The variation of voltage with frequency of prototype energy harvesters are presented in Figure 6 and the load power can be calculated.



(a) (b)

Figure 6 (a) Variation of the load voltage and maximum power versus frequency for prototype A and (b) Variation of the load voltage and maximum power versus frequency for prototype B.

As shown in Figure 6(a), the load voltage of Prototype A was measured at different frequency under the 405Ω load resistance and the maximum value of voltage 132mV at 307Hz resonant frequency and 0.5g($g=9.8$ m/s^2) acceleration. The maximum power was 43.02 μW. Figure 6(b) shows the variation of output power and voltage as a function of frequency of prototype B. For Prototype B, the resonant frequency was observed at 291.4Hz. At the same acceleration and load resistance, the maximum load voltage and power of prototype B were 216 mV and 115.20 μW respectively.



(a) (b)

Figure 7 (a) Output voltage and power of the prototype A versus the resistive load. (b) Output voltage and power of the prototype B versus the resistive load

Figure 7 shows the output voltage and power of electromagnetic vibration energy harvesters with various load resistances at 0.6g acceleration and the resonant frequency. The output voltage increased with the load resistance. As shown in Figure 7(a), the output power of the prototype A was 31.04 μW when the optimized load resistance is 490 Ω. In Figure 7(b), the maximum output power of the prototype B was 54.91 μW across the optimized load of 530 Ω.

4.2 Measurement results comparison

In table 2, a comparison of the measured characteristics of two energy harvesters is given. The maximum voltage and power of prototype B is 1.6 times and 2.67 times of prototype A respectively. The quality factor for the energy harvesters was calculated considering that the ration of the resonant frequency and the difference between the 3dB frequencies at each side of the resonance. The measured results of two electromagnetic vibration energy harvesters which were assembled by two different shape planar springs with the same kind of material and the testing coil are different.

Table 2.Comparsion of characteristics of energy harvesters

Parameters	Prototype A	Prototype B
attach on the photoresist SU-8 (Hz)	306.16(the first mode)	281.04(the first mode)
Actual measurement results (Hz)	307	291.4
The maximum load voltage (mV)	132	216
Maximum power at resonance	43.02 μW	115.20 μW
Quality factor Q	170.6	19.3
Power density rms ($\mu W/cm^3g^{-2}$)	95.6	248.9
Optimum load (Ω)	490	530
3dB bandwidth of harvesters (Hz)	1.7	15
The efficiency of harvesters	4.24 %	6.68%

There are three possible reasons for different test results. Firstly, the resonant frequency of prototype A is greater than prototype B's. The harmonic responses show that: the magnet's vibratory amplitude of prototype B is a larger than which of prototype A. It means that Prototype B captured energy from the same excitation source more than the energy harvested by prototype A. Secondly, as shown in Figure 6 (b), the prototype B has a working band around 15Hz. This bandwidth generated due to the nonlinearity of the spring B. However, the nonlinearity performance of spring A is not obvious. i.e., the nonlinearity of the vibration energy harvester depends on vibrating structures (spring shape) and has a great effect on the output voltage. Thirdly, the slight difference between the magnetic flux gradient was ignored, we can consider the prototype A and prototype B have the same electromagnetic coupling factor, according to the equation (6), we can get the mechanical damping of prototype A is larger than prototype B. The efficiency of prototype A is smaller than the prototype B.

5. Conclusion

This paper describes the design, fabrication and the experimental results of two micro electromagnetic energy harvesters. The energy harvesters have a volume of 0.9cm^3. The dynamic characteristics of different structures were simulated by soft ANSYS and experiments were guided by FEA simulation results. Prototype A generated a maximum load power of 43.02 μW across load of 405 Ω at 307Hz and Prototype B generated a maximum load power of 115.20 μW at 291.4 Hz with an acceleration of 0.5g. Prototype B has a higher output voltage and a working bandwidth. In the similar experimental conditions, the performance of prototype B is better than the prototype A. It indicates that the output voltage of the electromagnetic vibration energy harvester is limited by the resonant frequency and the damping ratio. Using the nonlinear characteristics of vibrating structure (vibratory spring) can effectively extend the working frequency and improve the performance of the vibration energy harvester. The electromagnetic vibration energy harvester with a higher voltage and better performance can be got by optimizing vibratory structure design. The experimental data for the micro-MEMS technology laid the foundation for the development of electromagnetic vibration energy harvester.

Acknowledgments

This work was supported by the Higher school specialized research fund for the doctoral program (No. 20090191110009).

Reference

[1] S.P. Beeby, M.J. Tudor, N.M. White, Energy harvesting vibration sources for microsystems applications, Meas. Sci. Technol. 17 (2006) R175–R195.

[2] S.P. Beeby, R.N. Torah, M.J. Tudor, P. Glynne-Jones, T. O'Donnell, C.R.Saha, S. Roy, Micro electromganetic generator for vibration energy harvesting, J. Micromech. Microeng. 17 (7) (2007) 1257–1265.

[3] S. Roundy, P. K. Wright, and J. Rabaey, A study of low level vibrations as a power source for wireless sensor nodes, Comput. Commun, vol. 26, pp. 1130-1144, 2003.

[4] S. Roundy, On the effectiveness of vibration-based energy harvesting, Journal of intelligent material systems and structures, vol. 16, pp. 809-823, 2005.

[5] C.T. Pan, Y.J. Chen et. al. Application of low temperature co-fire ceramics on in-plane micro-generator [J], Sensors and Actuators A, 2008 144:144–153.
[6] E. Arroyo, A. Badel, F. Formosa, Y. Wu, J. Qiu, Comparison of electromagnetic and piezoelectric vibration energy harvesters: Model and experiments,[J]. Sensors and Actuators A 183(2012) 148-156.
[7] B. Yang, C. Lee, W. Xiang, J. Xie, J.H. He, R.K. Kotlanka, S.P. Low, H. Feng, Electromagnetic energy harvesting from vibrations of multiple frequencies [J]. Micromechanics and Microengineeting, 2009, 035001(19):8pp.
[8] Edwar Romero-Ramirez, Energy harvesting from Body motion using rotational micro-generation, 2010, 33-34.
[9] R. Torah, P. Glynne-Jones, M. Tudor, T. O'Donnell, S. Roy, S. Beeby, Self-powered autonomous wireless sensor node using vibration energy harvesting[J], Measurement Science and Technology, 2008,19(12),125202.
[10] Emmanuel Bouendeu. Printed Circuit Board-Based Electromagnetic Vibration Energy Harvesters [D]. Albert Ludwig University of Freiburg im Breisgau. June 2010.
[11] Tom J. Kazmierski, Steve Beeby, Energy harvesting systerms pinciples, modeling and applications.
[12] S. Kulkarni, E. Koukharenko, R. Torah, J. Tudor, S. Beeby, T.O'Donnell, and S. Roy, Design, fabrication and test of integrated microscale vibration-based electromagnetic generator, Sensors and Actuators A, vol. 145-146, pp. 336-342, July-August, 2008.
[13] D. Spreemann, D. Hoffmann, B. Folkmer, Y. Manoli. Numerical optimization approach for resonant electromagnetic vibration transducer designed for random vibration [J]. Micromechanics and Microengineering, 2008, 104001(8):46-57.
[14] E. Koukharenko, S. P. Beeby, M. J. Tudor, N. M. white, T. O'Donnell, C. R. Saha, S. Kulkarni, and S. Roy, Microelectromechanical systems vibration powered electromagnetic generator for wireless sensorapplications, Microsystem Technologies, vol. 12, no. 10-11, pp. 1071-1077, 2006.
[15] S. P. Beeby, R. N. Torah, M. J, Tudor, P. Glynne-Jones, T. O'Donnell, C. R. Saha, and S. Roy, A micro electromagnetic generator for vibration energy harvesting, Journal of Micromechanics and Microengineering, vol. 17, pp. 1257-1265, 2007.
[16] Byung-Chul Lee, Md Ataur Rahman, Seung-Ho Hyun and Gwiy-Sang Chung, Low frequency driven electromagnetic harvester for self-power system [J]. Smart Mater. Struct. 21 (2012) 125024(7pp).
[17] Santosh Kulkarni, Elena Koukharenko, Russell Torah, John Tudor, Steve Beeby, Terence O'Dnnell and Saibal Roy, Design, fabrication and test of integrated micro-scale vibrtion-based electromagnetic generator [J]. Sensors and Actuators A 145-146 (2008) 336-342.

Key Engineering Materials Vols 645-646 (2015) pp 1233-1243
Submitted: 2014-11-14
© (2015) Trans Tech Publications, Switzerland
Accepted: 2014-12-23
doi:10.4028/www.scientific.net/KEM.645-646.1233

Corrosion behavior of SAMs modified silver-coated 316LSS as PEMFC bipolar plates

Xiaojun Yan[1a], Jianbo Zhuang[2b], Naibao Huang[3c*], Chenghao Liang[3d], Hongtao Wang[4e], Lishuang Xu[5f]

[1]Business School of Central South University, Changsha, Hunan, CHINA

[2]new energy and technology management department, SAIC Motor, Shanghai, CNINA

[3]Department of Materials Science & Engineering, Dalian Maritime University, Dalian,Liaoning, CHINA

[4]Department of Marine Engineering, Jiangsu Maritime Institute, Nanjing, Jiangsu, CHINA

[5]Sunrise Power Co. Ltd., Dalian, Liaoning, CHINA

[a]xj_yan@chalco.com.cn,[b]zhuangjianbo@saicmotor.com,
[c]hnaibao@163.com (corresponding author),
[d]lchenghao@126.com,[e]wanght@163.com,[f]xlishuang@gmail.com

* Corresponding Author：Naibao Huang, Associate Professor, Transportation Equipments & Ocean Engineering College, Dalian Maritime University, Tel: 86-411-84723280, FAX: 86-411-84723280, email: nbhuang@dlmu.edu.cn hnaibao@dlmu.edu.cn

Keywords: SAM, Contact angle, PEMFC, bipolar plate

Abstract：In order to improve the anti-corrosion characteristic of Ag-coated 316SS bipolar plates in PEMFC environment, self-assembled monolayer (SAM) was prepared on its surface by chemical methods. The electrochemical characteristic of modified bipolar plate was also investigated. The results indicated that the SAM was composed of dodecyl thioalcohol. After forming SAM, the bipolar plate's contact angle increased from 58° to 102°. In addition, its double layer capacitance (Cd) was decreased and charge transfer resistance was increased. The homogeneous SAM, which acted as a protective barrier, inhibited the corrosive ion from corroding. SAM may provide significant protection against corrosion in PEMFC environment.

Introduction

Owing to the advantages of high efficiency, high power density, low temperature operation, fast and easy start up, etc., proton exchange membrane fuel cell (PEMFC) is gaining worldwide interest [1, 2]. However, expensive cost restricts its using in the large scale market [3]. Bipolar plate is one of the key components in PEMFC system. In PEMFC stacks, the widely used bipolar plate materials are graphite or graphite compounds [4-6]. High cost and brittleness of graphite bipolar plate limit them to the widespread use. Therefore, many researchers aim to substitute them with carbon composite materials, light metal materials [7-10], Fe-based alloys, stainless steels [11, 12], and Ni-based materials [13-15], etc. Among these alternative materials, stainless steel (SS) is a promising candidate due to its high mechanical strength, low cost, easy mass production.

Davies et al [16] proved that the fuel cell's performance improved with chromium and nickel contents of bipolar plates increasing. Brady et al [17] proposed using Cr nitride layer to decrease the

corrosion of stainless steel bipolar plate, and obtained promising results [18, 19]. Based on these results, many researchers had investigated the performance of stainless steel bipolar plates with chromium or chromium compound coatings [13, 20-27]. Although it seemed that stainless steel with chromium based film or carbide [28, 29] coatings had become promising materials for PEMFC bipolar plates, a few of companies used them as bipolar plates in fuel cell stack until now. On the contrary, stainless steel bipolar plates with noble metal coatings were still the most suitable materials by considering the corrosion resistance and conductivity. For example, Wind et al. [30] had shown that the performance of 316L bipolar plate with gold coating was similar to that of graphite. Wang et al. also confirmed that fuel cell performance of gold-plated titanium bipolar plate was close to and even better than that of graphite and pure titanium bipolar plates [9]. The characteristics of titanium bipolar plates with iridium oxide and platinum coatings were close to that of graphite bipolar plate [31]. Yoon et al [32] evaluated the characteristics of 304SS, 310SS, and 316SS with different coatings, which included gold (2nm, 10nm, and 1 m), Titanium, Zirconium, Zirconium Nitride (ZrN), Zirconium Niobium (ZrNb), and Zirconium Nitride with a gold top layer (ZrNAu). The results showed that a relatively thick gold coating (>10 nm) on Zr coated samples satisfied the USA Department of Energy (USA DOE) target for contact resistance and corrosion resistance. However, the high cost of noble metal coatings confines its application. Although electrodepositing Ag is suitable for protecting PEMFC stainless steel bipolar plates, the coatings have not been sufficiently viable due to pinhole defects, which are prone to corrosion and thus destroy the whole protecting film. To make defect-free coatings, Adopting suitable Method to diminish the presence of pinhole defects is necessary.

In this paper, self-assembled monolayer (SAM) is formed on the surface of Ag-coated 316SS (initial BP) to reduce its defects. In order to reveal the protecting performance and mechanism, corrosion resistance, contact angle, contact resistance and surface topography of initial BP with SAM (SAM BP) are investigated.

1 Experimental

1.1 Self-assembled monolayer preparation

Initial BP (100×450×1mm) were supplied by Sunrise Power Co., Ltd. (Dalian, China). The samples were cut into 20×20×1mm slices. The sample was ultrasonic degreased in acetone for 12 min, dried with nitrogen, and then etched with 10% sulphuric acid for 5 min. After that, it was immersed in isopropanol solvent containing 0.15 mol·L^{-1} dodecyl thioalcohol and 40g ·L^{-1} hexadecyl trimethyl ammonium bromide at 60℃ for 5min. At last, it was rinsed with isopropanol and dried with nitrogen.

1.2 Surface morphology of SAM

IR spectra were obtained in a single reflection mode with EQUINOX55 Fourier transform infrared spectrometer containing a universal reflectance attachment. The micrography of SAM BP was observed using Atomic force microscopy (AFM, Nano Scope IIIa, Digital Instruments). Contact angles were measured using the sessile drop method (Dataphysics OCA 20).

1.3 Electrochemical tests

Electrochemical measurements were carried out on VMP3 eletrochemical workstation (EG&G company). The procedure was controlled by EC-Lab software. Princeton flatcell was used for the electrochemical experiments. The working electrodes were initial BP and SAM BP with 1cm^2 exposed area. A platinum grid was used as counter-electrode and the reference electrode was

saturated calomel electrode (SCE, saturated KCl). Solutions used in electrochemical tests were 0.5 mol·L^{-1} H_2SO_4 + 2 ppm F^- solution. In order to simulate the anodic and the cathodic environments of PEMFC, the test coupon was put in the solution after it was bubbled with pure hydrogen gas (H_2) for 2 h and with air for 1h, respectively. Electrochemical impedance spectroscopy (EIS) was made at the open circuit potential with a 5 mV ac perturbation, and the frequency was controlled between 100 kHz and 0.01 Hz. The sample was stabilized at OCP for 1 h and then was polarized from OCP to positive direction with a scan rate of 1mV·s^{-1}. In order to investigate the stability of SAM BP under PEMFC operation condition, potentiostatic tests were conducted at simulated anodic and cathodic condition, respectively. The corresponding potential was -0.1V purged with H_2 and 0.6V purged with air, respectively. All tests were conducted at 80℃.

2. Results and discussion

2.1 Surface morphology

Infrared spectrum (IR) data of SAM are often quantitative analyzed and correlated with the film structure [33]. Fig.1 shows the C-H stretching region of reflectance infrared spectra for SAM BP. The position of asymmetric methylene [ν_a (CH_2)] stretching mode is at 2918cm^{-1} [34]. For SAM BP, The position is increased from 2918cm^{-1} to 2965 cm^{-1} and the line widths of the asymmetric methyl peaks is about 9cm^{-1}. The position increase is consistent with an increased content of gauche conformers [35]. At the same time, line widths increase implies homogeneous surface structure of methyl groups has formed on the surface of initial BP, which not only decreases the bipolar plate's roughness but also reduces its pin-hole defects.

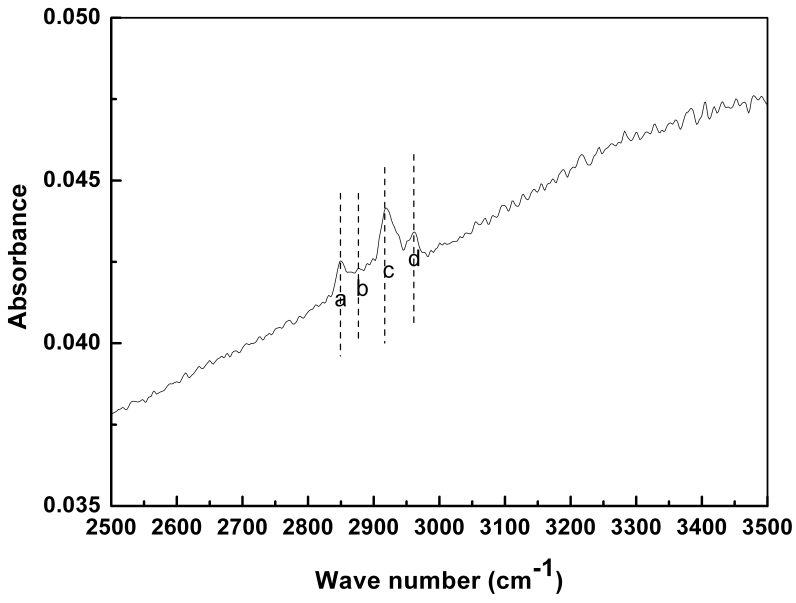
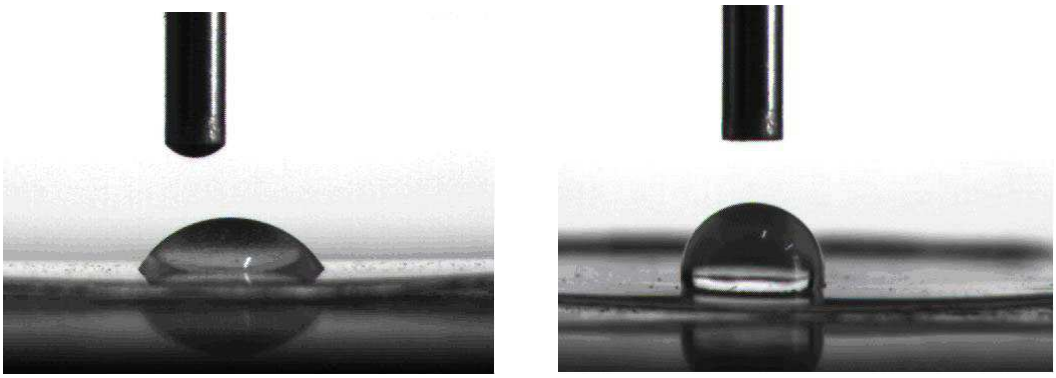


Fig.1 Infrared reflection spectra of octadecanethiol adsorbed onto Ag-coated 316SS bipolar plate in the high frequency region a: the in-plane symmetric methylene stretch, $\nu_s(CH_2)$=2851cm^{-1}; b: the symmetric methyl stretch, $\nu_s(CH_3)$=2879cm^{-1}; c: the in-plane asymmetric methylene stretch, $\nu_a(CH_2)$=2918cm^{-1}; d: the asymmetric methyl stretch, $\nu_a(CH_3)$=2965cm^{-1}

3.2 Contact angle and contact resistance

Contact angles of initial BP an SAM BP are shown in Fig.2. Contact angles for the former and the latter are 58° and 102°, respectively. Initial BP changes from hydrophilicity to hydrophobicity

after forming SAM on its surface. That is, bipolar plate's surface energy is decreased. In PEMFC system, in order to prevent proton exchange membrane from dehydration, the inlet gases need to be humidified. At the same time, electrochemical reaction could produce water. So, there exit many water and liquid-solid two-phase fluids in PEMFC system. For maintaining high power output, the liquid water including humidified and produced water, which would flood membrane electrode assembly (MEA), must be removed in time. Obviously, a partially hydrophobic surface of the plate material might be more beneficial for removing water from gas diffusion layer (GDL) and decreasing corrosion from the weak acid solution.



(a) (b)

Fig.2 Contact angle of the Ag-coated 316SS with and without SAM with water
(a) Ag-coated 316SS without SAM (b) Ag-coated 316SS with SAM

PEMFC's output power has something to do with its internal resistance. Contact resistance between bipolar plate and MEA plays an important role in the internal resistance. Fig.3 illustrates contact resistance of initial BP and SAM BP with Toray carbon paper. Nowadays, the range of 0.8-1.2MPa compact pressure is often applied to the PEMFC stack. So, the data of contact resistance between 0.8-1.2MPa are recorded. From Fig.4, contact resistances of initial BP and SAM BP are in the range of 6.20×10^{-3}-5.64×10^{-3} $\Omega.cm^{-2}$ and 6.32×10^{-3}-5.84×10^{-3} $\Omega.cm^{-2}$, respectively. SAM BP's contact resistance is a little bigger than that of initial BP when the compact pressure is over 1.0MPa. Since the increased contact resistance is only 1.20×10^{-4} -2.00×10^{-4} $\Omega.cm^{-2}$, the SAM coating on initial BP may not lead to the output power decreasing.

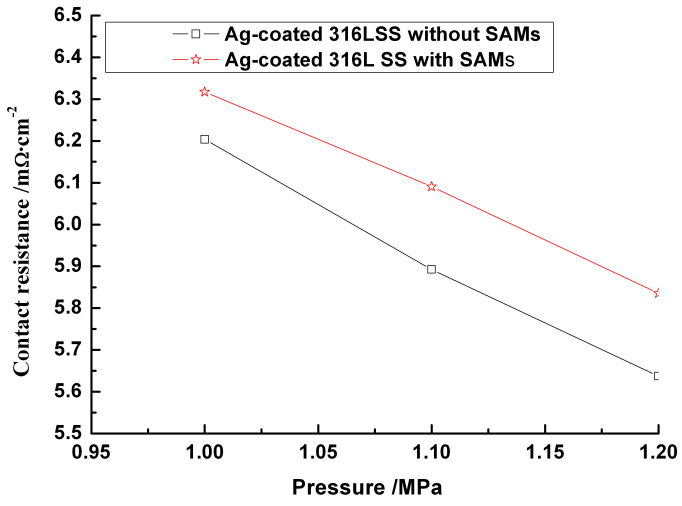
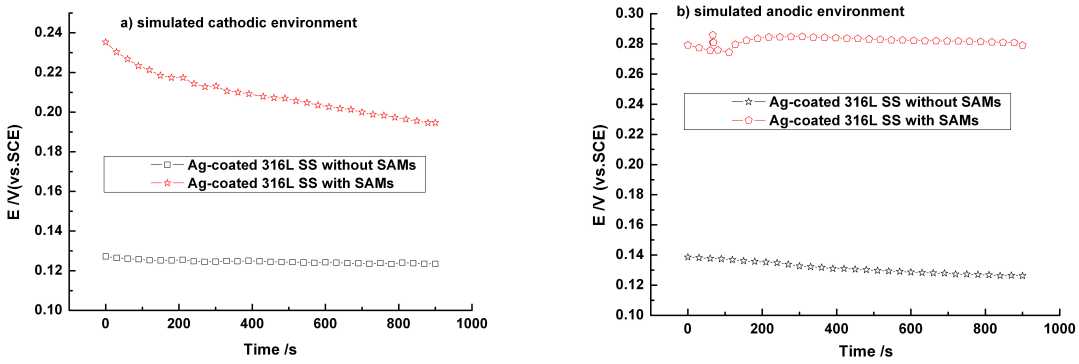


Fig.3 The contact resistance of Ag-coated 316SS with and without SAM

2.3 Electrochemical characteristic

2.3.1 Open circuit potential (OCP)

Figure 4 illustrates the curves of OCP versus time of initial BP and SAM BP in simulated PEMFC environment. In simulated cathodic environment, OCP increases from 0.12V to 0.20V after initial BP is treated with SAM. The stabilized value for SAM BP, about 0.20V, is obtained after immersed in test solution for 30 min While, it increases from 0.13V to 0.28V in anodic environment. Since the homogeneous SAM forms on initial BP surface (see Fig.3), which acts as a barrier layer between bipolar plate and the solution, OCP is improved. The impurity such as H_2S, SO_2, etc. in the air is inevitable, which is considered to be a bad influence on SAM's protecting effect. So, the OCP of SAM BP in simulated cathodic environment is worse than that in simulated anodic environment.

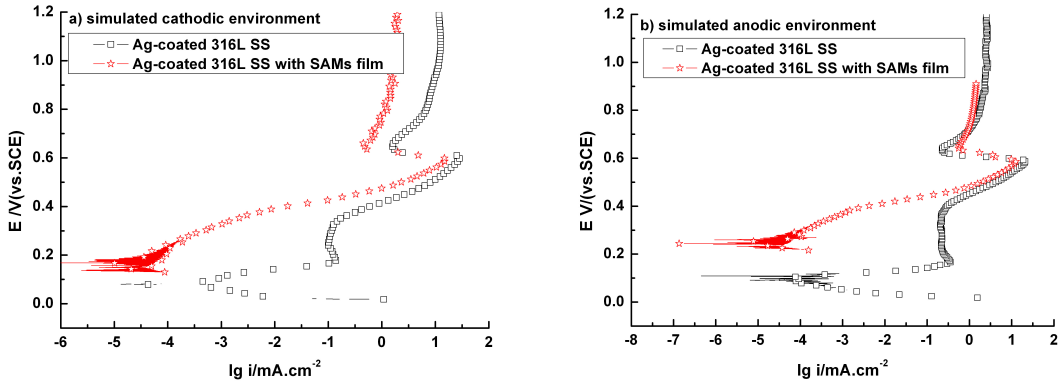


(a) (b)

Fig. 4 Plot of E_{OCP} versus time for Ag-coated 316SS with and without SAM in simulated PEMFC environment (a) simulated cathodic environment (b) simulated anodic environment

2.3.2 Potentiodynamic polarization curves and EIS

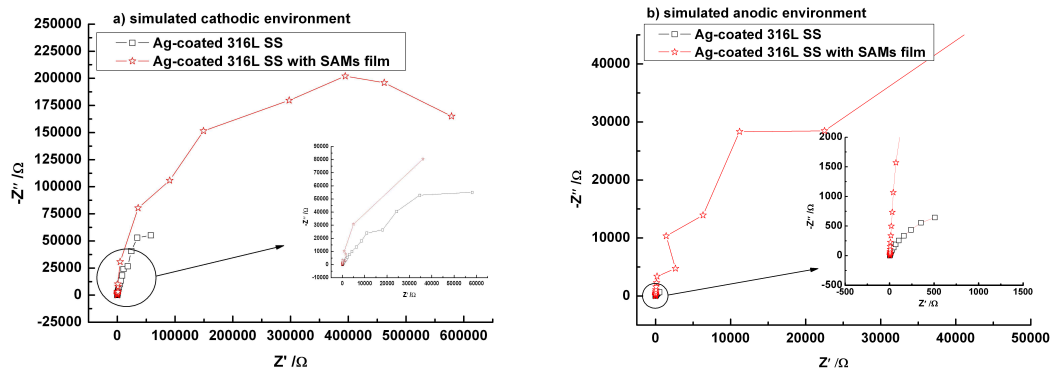
Potentiodynamic polarization curves of initial BP and SAM BP are given in Fig.5. Whether in anodic environment or cathodic environment, the current density of SAM BP is smaller than that of initial BP. For example, when the polarization potential is 0.4V, in cathodic environment, the polarization current density for initial BP and SAM BP are 0.593mA cm^{-2} and 1.61×10^{-2}mA cm^{-2}, respectively. Bipolar plate's current density decreases about one order of magnitude. The corresponding values are 0.296mA cm^{-2} and 3.81×10^{-3}mA cm^{-2} in anodic environment, respectively. It decreases about two orders of magnitude. At the same time, SAM BP's OCP also moves to positive, which is consistent with the results in Fig.5. The results confirmed that SAM establishes a barrier between bipolar plate and corrosion solution. So, bipolar plate's corrosion resistance is improved.



(a) (b)

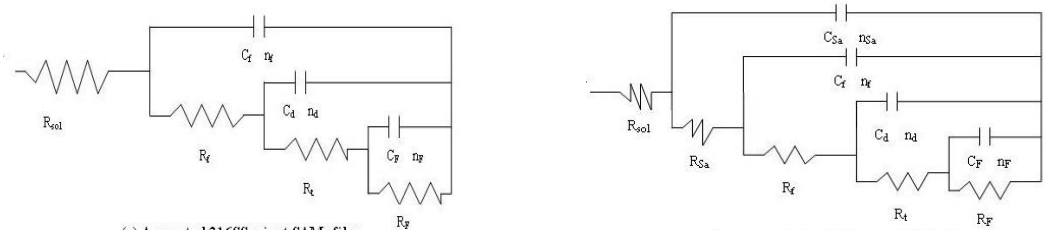
Fig.5 Polarization curves of Ag-coated 316SS with and without SAM in simulated PEMFC environment (a) simulated cathodic environment (b) simulated anodic environment

Fig.6 presents Nyquist plots of impedance spectra for initial BP and SAM BP. From fig.6, SAM BP's capacitance is greater than that of initial BP at high frequencies and intermediate frequencies region whether in anodic environment or in cathodic environment. Figure 7 shows the equivalent circuit model. The elements presented in the figure are shown as following. R_{sol} is the solution resistance between the reference electrode and the counter electrode; C_{Sa} and R_{Sa} denote the capacitance and electrical leakage through the SAM; C_F and R_F represent the capacitance and electrical leakage through ionic conduction of the Ag film, respectively. C_d and R_t correspond to the double layer capacitance and charge transfer resistance. Comparing to original BP, C_{Sa} and R_{Sa}, which attribute to SAM, appear in the equivalent circuit (Fig.7b). Since the same corrosion solution and initial BP are used, R_{sol} , C_F and R_F resemble each other for initial BP and SAM BP. So, the process of forming SAM on initial BP lead to remarkable effect the characteristic of electrical double layer. The results of parameter regression are summarized in Table 1. After initial BP is treated with SAM, its double layer capacitance (C_d) decreases from 6.82×10^{-4} F cm^{-2} to 2.9×10^{-6} F cm^{-2} in anodic environment, while its charge transfer resistance (R_t) increases from $2.75\times10^{3}\Omega$ cm^2 to $3.95\times10^{5}\Omega$ cm^2. In cathodic environment, the corresponding C_d value decreases from 5.32×10^{-5} F cm^{-2} to 9.90×10^{-6} F cm^{-2}, its R_t increases from $1.17\times10^{3}\Omega$ cm^2 to $4.73\times10^{4}\Omega$ cm^2. The decrease of Cd is due to forming close-packed interconnected structure film on the silver surface [36]. Since the increase of the charge transfer resistance is related to the electrode coverage [34], initial BP's surface is covered with organic film, which is chemically inert, and all the currents pass by the pinhole and defects in the electrode. Thus, R_t is increases two orders of magnitude in anodic environment and increases one order of magnitude in cathodic environment, respectively. The results all indicate that a close-packed interconnected structure film forms on the surface of initial BP, which implies the monolayer provides significant protection against corrosion.



(a) (b)

Fig.6 Nyquist curves of Ag-coated 316SS with and without SAM in simulated PEMFC environment (a) simulated cathodic environment (b) simulated anodic environment



(a) (b)

Fig.7 Equivalent circuit of Ag-coated 316SS with and without SAM in simulated PEMFC environment (a) Equivalent circuit for initial BP (b) Equivalent circuit for SAM BP

Table 1 Values of the elements of equivalent circuits

a) simulated cathodic environment

Parameter	R_{sol} /Ω·cm^2	C_d / F·cm^{-2}	R_t /Ω·cm^2
Sample without SAMs film	3.78	6.82×10^{-4}	2.75×10^{3}
Sample with SAMs film	3.91	2.94×10^{-6}	3.50×10^{5}

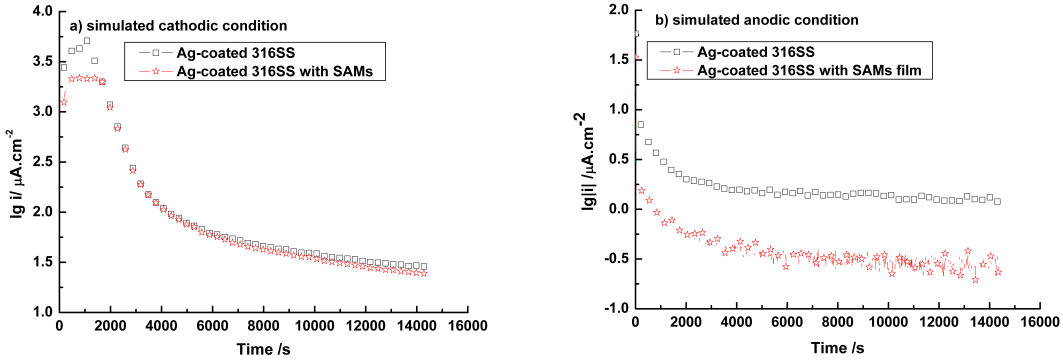
b) simulated anodic environment

Parameter	R_{sol}/Ω·cm^2	C_d / F·cm^{-2}	R_t /Ω·cm^2
Sample without SAMs film	2.37	5.32×10^{-5}	1.17×10^{3}
Sample with SAMs film	3.10	9.87×10^{-6}	4.73×10^{4}

2.3.3 Potentiostatic polarization curves

In PEMFC's operation environment, the major concern for the materials is its anti-corrosion characteristic and stability. Potentiostatic tests are conducted to study the corrosion behavior of the bipolar plate in simulated actual PEMFC working condition. The operating condition is as

followings: In simulated cathodic condition, the sample is polarized at 0.6V in the solution purged with air. While, in anodic environment, it is polarized at -0.1V in the solution purged with H_2. The results are illustrated in Fig.8. In cathodic condition, the current densities of initial BP and SAM BP decrease gradually with immersion time lengthening. After 12000s, the stabilized values for initial BP and SAM BP are about 3.16×10^{-2} mA cm^{-2} and 2.75×10^{-2} mA cm^{-2}, respectively. In anodic condition, the corresponding current densities stabilize quickly and stay at -0.30×10^{-3} mA cm^{-2} and -1.60×10^{-3} mA cm^{-2}, respectively. From fig.8, the polarized current density for SAM BP is smaller that of initial BP whether in cathodic or anodic condition. As a whole, we could conclude that SAM could improve the corrosion resistance of initial BP. Its long-term effect needs to be conducted in the coming work.



(a) (b)

Fig.8 Potentiostatic polarization curve of Ag-coated 316SS with and without SAM in simulated PEMFC operation condition

(a) simulated cathodic environment (b) simulated anodic environment

3. Summary

SAM is used to modify Ag-coated 316SS as bipolar plates of PEMFC. The homogeneous SAM, which is composed of dodecyl thioalcohol, has been obtained on the surface of Ag-coated 316SS bipolar plate. The obtained SAM could increase bipolar plate's contact angle, which is helpful to water management. At the same time, it not only decreases bipolar plate's roughness and but also reduces pin-hole defects of Ag film. Electrochemical tests confirm that SAM could reduce bipolar plate's double layer capacitance (C_d) and increase its charge transfer resistance. So, SAM may provide significant protection against corrosion in PEMFC environment.

Acknowledgements

This work is supported by the National Nature Science Foundation of China (No. 21276036), the Liaoning Provincial Nature Science Foundation of China (No.2014025018), the Foundation of Liaoning Educational Committee (L2014199), the Fundamental Research Funds for the Central Universities (No. 3132014323), Open Fund of Shanghai Key Laboratory of Digital Manufacture for Thin-walled Structures (No. 2014004).

References

[1] N. Rajalakshmi, S. Pandian, K.S. Dhathathreyan, Vibration tests on a PEM fuel cell stack usable in transportationapplication, Int J Hydrogen Energ 34 (2009) 3833-3837.

[2] S. Barrett, The European hydrogen and fuel cell Strategic Research Agenda and Deployment Strategy, Fuel Cells Bulletin 2005 (2005) 12-19.

[3] K. Jayakumar, S. Pandiyan, N. Rajalakshmi, K.S. Dhathathreyan, Cost-benefit analysis of commercial bipolar plates for PEMFC's, J Power Sources 161 (2006) 454-459.

[4] S.R. Dhakate, R.B. Mathur, B.K. Kakati, T.L. Dhami, Properties of graphite-composite bipolar plate prepared by compression molding technique for PEM fuel cell, Int J Hydrogen Energ 32 (2007) 4537-4543.

[5] C. Du, P.W. Ming, M. Hou, J. Fu, Q. Shen, D. Liang, Y.F. Fu, X.K. Luo, Z.G. Shao, B.L. Yi, Preparation and properties of thin epoxy/compressed expanded graphite composite bipolar plates for proton exchange membrane fuel cells, J Power Sources 195 (2010) 794-800.

[6] X.Q. Yan, M. Hou, H.F. Zhang, F.N. Jing, P.W. Ming, B.L. Yi, Performance of PEMFC stack using expanded graphite bipolar plates, J Power Sources 160 (2006) 252-257.

[7] C.H. Shen, M. Pan, Z.F. Hua, R.Z. Yuan, Aluminate cement/graphite conductive composite bipolar plate for proton exchange membrane fuel cells, J Power Sources 166 (2007) 419-423.

[8] N.F. Wan, C. Wang, Z.Q. Mao, Titanium substrate based micro-PEMFC operating under ambient conditions, Electrochem Commun 9 (2007) 511-516.

[9] S.H. Wang, J. Peng, W.B. Lui, J.S. Zhang, Performance of the gold-plated titanium bipolar plates for the light weight PEM fuel cells, J Power Sources 162 (2006) 486-491.

[10] S.H. Wang, J. Peng, W.B. Lui, Surface modification and development of titanium bipolar plates for PEM fuel cells, J Power Sources 160 (2006) 485-489.

[11] H.L. Wang, J.A. Turner, Ferritic stainless steels as bipolar plate material for polymer electrolyte membrane fuel cells, J Power Sources 128 (2004) 193-200.

[12] E. Fleury, J. Jayaraj, Y.C. Kim, H.K. Seok, K.Y. Kim, K.B. Kim, Fe-based amorphous alloys as bipolar plates for PEM fuel cell, J Power Sources 159 (2006) 34-37.

[13] M.P. Brady, H. Wang, B. Yang, J.A. Turner, M. Bordignon, R. Molins, M.A. Elhamid, L. Lipp, L.R. Walker, Growth of Cr-Nitrides on commercial Ni-Cr and Fe-Cr base alloys to protect PEMFC bipolar plates, Int J Hydrogen Energ 32 (2007) 3778-3788.

[14] R.J. Tian, J.C. Sun, Performance of a high Cr and Ni austenitic stainless steel bipolar plates in proton exchange membrane fuel cell working environments, J Power Sources 194 (2009) 981-984.

[15] M.P. Brady, K. Weisbrod, I. Paulauskas, R.A. Buchanan, K.L. More, H. Wang, M. Wilson, F. Garzon, L.R. Walker, Preferential thermal nitridation to form pin-hole free Cr-nitrides to protect proton exchange membrane fuel cell metallic bipolar plates, Scripta Mater 50 (2004) 1017-1022.

[16] D.P. Davies, P.L. Adcock, M. Turpin, S.J. Rowen, Stainless steel as a bipolar plate material for solid polymer fuel cells, J Power Sources 86 (2000) 237-242.

[17] M.P. Brady, K. Weisbrod, C. Zawodzinski, I. Paulauskas, R.A. Buchanan, L.R. Walker, Assessment of thermal nitridation to protect metal bipolar plates in polymer electrolyte membrane fuel cells, Electrochemical and Solid-State Letters 5 (2002) A245-A247.

[18] H. Wang, M.P. Brady, G. Teeter, J.A. Turner, Thermally nitrided stainless steels for polymer electrolyte membrane fuel cell bipolar plates part 1: Model Ni-50Cr and austenitic 349 alloys, J Power Sources 138 (2004) 86-93.

[19] H. Wang, M.P. Brady, K.L. More, H.M. Meyer III, J.A. Turner, Thermally nitrided stainless steels for polymer electrolyte membrane fuel cell bipolar plates Part 2: Beneficial modification of passive layer on AISI446, J Power Sources 138 (2004) 79-85.

[20] R.J. Tian, J.C. Sun, L. Wang, Plasma-nitrided austenitic stainless steel 316L as bipolar plate for PEMFC, Int J Hydrogen Energ 31 (2006) 1874-1878.

[21] Y. Fu, M. Hou, G.Q. Lin, J.B. Hou, Z.G. Shao, B.L. Yi, Coated 316L stainless steel with CrxN film as bipolar plate for PEMFC prepared by pulsed bias arc ion plating, J Power Sources 176 (2008) 282-286.

[22] K.H. Cho, W.G. Lee, S.B. Lee, H. Jang, Corrosion resistance of chromized 316L stainless steel for PEMFC bipolar plates, J Power Sources 178 (2008) 671-676.

[23] R.J. Tian, J.C. Sun, J.L. Wang, Study on behavior of plasma nitrided 316L in PEMFC working conditions, Int J Hydrogen Energ 33 (2008) 7507-7512.

[24] N.D. Nam, J.H. Han, J.G. Kim, P.H. Tai, D.H. Yoon, Electrochemical properties of TiNCrN-coated bipolar plates in polymer electrolyte membrane fuel cell environment, Thin Solid Films 518 (2010) 6598-6603.

[25] R. Tian, Chromium nitride/Cr coated 316L stainless steel as bipolar plate for proton exchange membrane fuel cell, In Press, Corrected Proof.

[26] B. Wu, Y. Fu, J. Xu, G.Q. Lin, M. Hou, Chromium nitride films on stainless steel as bipolar plate for proton exchange membrane fuel cell, J Power Sources 194 (2009) 976-980.

[27] K. Feng, Y. Shen, D.A. Liu, P.K. Chu, X. Cai, Ni-Cr Co-implanted 316L stainless steel as bipolar plate in polymer electrolyte membrane fuel cells, Int J Hydrogen Energ 35 (2010) 690-700.

[28] P.Y. Yi, L.F. Peng, L.Z. Feng, P. Gan, X.M. Lai, Performance of a proton exchange membrane fuel cell stack using conductive amorphous carbon-coated 304 stainless steel bipolar plates, J Power Sources 195 (2010) 7061-7066.

[29] K. Feng, Y. Shen, H.L. Sun, D.L. Liu, Q.Z. An, X. Cai, P.K. Chu, Conductive amorphous carbon-coated 316L stainless steel as bipolar plates in polymer electrolyte membrane fuel cells, Int J Hydrogen Energ 34 (2009) 6771-6777.

[30] R.S.H.W. J. Wind, Metallic bipolar plates for PEM fuel cel, J Power Sources 105 (2002) 256-260.

[31] J.P.A.W. Szu-Hua Wang, Surface modification and development of titanium bipolar plates for PEM fuel cells, J Power Sources 160 (2006) 485-489.

[32] W. Yoon, X.Y. Huang, P. Fazzino, K.L. Reifsnider, M.A. Akkaoui, Evaluation of coated metallic bipolar plates for polymer electrolyte membrane fuel cells, J Power Sources 179 (2008) 265-273.

[33] C.E.D. Chidsey, D.N. Loiacono, Chemical functionality in self-assembled monolayers. Structural and electrochemical properties, Langmuir 6 (1990) 682-691.

[34] F. Bensebaa, P. L'Ecuyer, K. Faid, C. Py, T.J. Tague, R.S. Jackson, Grazing angle infrared microspectroscopy of micropatterned self-assembled monolayers, Appl Surf Sci 243 (2005) 238-244.

[35] R.G. Nuzzo, L.H. Dubois, B.R. Zegarski, E.M. Korenic, D.L. Allara, Studies of small molecule and polymer adsorption on organic surfaces, Proceedings of the ACS Division of Polymeric Materials: Science and Engineering, April 1, 1990 - April 1, 1990, vol. 62, Publ by ACS, Boston, MA, USA, 1990, p. 852.

[36] M. Evesque, M. Keddam, H. Takenouti, The formation of self-assembling membrane of hexadecane-thiol on silver to prevent the tarnishing, Electrochemical Methods in Corrosion Research, May 4, 2003 - May 9, 2004, vol. 49, Elsevier Ltd, Nieuwpoort, Belgium, 2004, pp. 2937-2943.

CHAPTER 7:

Bioresearch and Biomedical Engineering

Key Engineering Materials Vols 645-646 (2015) pp 1247-1254
© (2015) Trans Tech Publications, Switzerland
doi:10.4028/www.scientific.net/KEM.645-646.1247

Submitted: 2014-10-28
Accepted: 2014-11-13

Stabilization of Pickering emulsions by bacterial cellulose nanofibrils

Wei Fu[2, a], Yang Liu[2, b], Chen Yang[2, c], Wenhua Wang[2, d], Man Wang[2, e], Yuanyuan Jia[1, 2, f *]

[1]Key Laboratory of Industrial Microbiology, Ministry of Education, Tianjin

University of Science and Technology, TEDA, Tianjin, 300457, P. R. China

[2]College of Material Science and Chemical Engineering, Tianjin University of Science and Technology, TEDA, Tianjin, 300457, P. R. China

[a]fuwei0012@gmail.com, [b]1121950566@qq.com, [c]1030289709@qq.com, [d]1278064722@qq.com
[e]wangman9005@hotmail.com, [f]jiayy@tust.edu.cn

Keywords: Pickering emulsion; Bacterial cellulose; Nanofibrils; Stability; Natural emulsifier; Contact angle of three-phase

Abstract. In order to develop safe and sustainable food and pharmaceutical emulsions, bacterial cellulose (BC) nanofibrils were prepared to stabilize maize oil/water Pickering emulsions. The influence of BC content and pH value on the emulsion stability was explored. Droplet diameters decreased with BC contents in emulsions. At pH 12, the emulsions were most stable among all tested pH values. The transformation of emulsion structure from liquid to gel-like at 8-15°C with BC content higher than 1.55 g/L is predominantly depended on the viscoelastic entangled BC network. These results can have meaningful inspiration of designing edible food and pharmaceutical emulsions.

1. Introduction

Emulsions are mixed systems consisting of a liquid dispersed in another partial miscible or immiscible liquid by the aid of emulsifier. Now they have been used widely in fields such as foods, cosmetics, pharmaceuticals and et al. Traditional emulsifiers are mainly surface-active components such as low molar mass surfactants, amphiphilic polymers or proteins [1, 2]. In the early 20th century, Ramsden found that solid particles of colloidal size can also stabilize emulsion and later then Pickering did systematic studies on it, so-called Pickering emulsion [3, 4]. By using solid particles as substitute for surfactants to stabilize emulsions, the increasing demands for non-toxic, environmental protective and eco-friendly products are more satisfied.

Irreversibly adsorbed particles at the interface were believed to be the essential element for stabilizing Pickering emulsion and its long stability [5, 6]. These particles usually can be partially wetted by both phases. Contact angle of three phase θ_{ow} is employed to describe this dual wettability [7]. An O/W emulsion is available when colloidal particles are relatively hydrophilic; while for hydrophobic particles, a W/O emulsion is produced.

Hard, smooth, and spherical particles, typically silica and latex spheres have been studied as model particles. Many biomass-based particles, for example rod-like or slim cellulose fibers and polyhedral starch granules, can also stabilize Pickering emulsions [8-10]. In the presence of these particles, many emulsions designed to be edible or natural can be improved. They are especially useful to manufacture cosmetics and pharmaceuticals, since they are nontoxic and safe. Similar to traditional emulsions, methods of emulsion preparation mainly include sonication [11, 12], homogenization [9, 13], and mechanical agitation [14, 15].

Cellulose is the most abundant, degradable and renewable bio-based polymer with partial crystalline structure existing primarily in plants. Some bacteria such as *Acetobacter*, can also produce cellulose, i.e. bacterial cellulose (BC), which has identical chemical formulation with plant cellulose but higher purity and free of accompanied compounds [16-19]. Bacterial cellulose is the main component of some traditional foods in Asia, such as Nata de coco and Kombucha for a long time [17, 20]. Recently, it has been applied in the field of medical and tissue engineering, thanks to its excellent biocompatibility [21-23]. Emulsifiers to produce pharmaceuticals, foods and biodegradable emulsions must be approved by Food and Drug Administration or Generally Recognized as Safe (GRAS). As a kind of bio-originated nanofiber, BC is qualified.

In present work, we prepared o/w Pickering emulsions stabilized with BC nanofibrils, taking edible maize oil as oil phase. The influence of fiber content and pH value on emulsion stability index (ESI) has been investigated. Emulsion gel transformation has been postulated from the points of network structure strength and oil-phase crystallization. The lower stability of maize-oil emulsions in comparison with liquid paraffin ones [24] has been explained from contact angle of three-phase. The results of this study help us to understand the mechanism of network strength to the stability of Pickering emulsions.

2. Materials

The Fulinmen® maize oil was a product of COFCO (China National Cereals, Oils and Foodstuffs Import and Export Corporation). The bacterial strain of *Glucose Acetobacter* CGMCC No.1.1812 (*Glucose xylinum*) was obtained from Key Laboratory of Industrial Microbiology, Tianjin University of Science and Technology.

3. Methods

3.1 Preparation and characterization of BC dispersions. *G. xylinum* was activated in the medium at 30 °C for 24 hours; the medium contains: 25 g/L anhydrous dextrose, 10 g/L yeast powder, 7.5 g/L peptone and 10 g/L disodium hydrogen phosphate, and the pH was adjusted to 5 by acetic acid. Then *G. xylinum* suspension was inoculated at 5% (v/v) in the same medium. BC pellicles were formed after 5-8 days. The harvested gel-like membranes were purified by washing with deionized water, and then by boiling in 0.1M NaOH to remove remaining medium and cells. Finally, they were washed till pH=7.

BC pellicles were dispersed preliminarily by a disintegrator (T-100, Adirondack Machine Corporation, USA) and then homogenized using a high pressure homogenizer (NS1001L Panda, GEA Process Engineering Inc.) for 10 times to obtain a nano-scale BC dispersion.

Scanning electron microscope (SEM) was used to visualize the morphology of BC nanofibrils. Freeze-dried BC dispersion was metalized with gold and visualized by a SEM (SU1510, Hitachi, Japan) operated at 5 kV to capture the morphology of cellulose.

3.2 Preparation and characterization of emulsions. The Pickering emulsions were prepared using maize oil and aqueous nano-scale BC dispersion at different pH and fiber contents (i.e. 0.25 g/L, 0.85 g/L, 1.55 g/L, referring to the weight of BC versus the volume of the emulsion system) with an oil/water ratio of 1:1. Equal volumes of maize oil and BC dispersion were sonicated with a high intensity ultrasonic vibracell processor (VCX150, SONICS & MATERIALS INC., USA) at a power of 40W for 5 min. The pH of BC dispersion was adjusted with 0.5 M NaOH or 0.5M HCl.
The emulsion stability was expressed by emulsion stability index (ESI), which was calculated as following:

$$\mathrm{ESI}(\%) = (H_E/H_T) \times 100 \quad (1)$$

where, H_E, the height of emulsified layer, and H_T, the total height of emulsion.

Emulsions were diluted on a haemocytometer cell (Weber Scientific) and viewed by a digital optical microscope (CX21, Olympus, Japan) fitted with a digital camera (C5050, Samsung, Korea). Droplet quantity-length mean diameters $D_{1,0}$ were determined by measuring the diameters of more than 100 droplets on several micrographs. The images were processed by ImageJ 1.45s software (National Institutes of Health Corporation, USA). Every sample was assayed in triplicate.

3.3 Measurement of contact angle. Dried BC membranes with smooth surface were prepared for testing contact angle. The contact angle of water or maize oil on BC membrane was determined at room temperature by using a dynamic contact angle tester (PGX 3.4a, Fibro System AB, Sweden) and the drop volume was set to 4 μL. Surface tensions of maize oil and deionized water and their interface tension were measured at the same room temperature by a digital interfacial tension measuring device (K9-MK1, Krüss, Germany). All the measurements were performed in triplicate.

4. Results and discussions

4.1 Wettability of BC fibrils at maize oil/water interface. Emulsions stabilized by particles are mainly attributed to their ability that partially wetted by both oil and water phase, resulting in particles accumulating and adsorbing at the oil-water interface [5]. Contact angle of three-phase θ_{ow}, the angle particles making at the interface, is widely used to describe the wettability. The difficulty to remove the particles from the interface is expressed by detachment energy *E,* which is given by Eq. 2, providing that the particles are small enough (typically less than a few microns in diameter) so that gravity effect is negligible [1]:

$$E = \pi r^2 \gamma_{ow} \left(1 \pm \cos\theta_{ow}\right)^2 \quad (2)$$

where r is the radius of particle, γ_{ow} is the oil-water interface tension and θ_{ow} is the contact angle of three-phase; For hydrophilic particle removing into the water phase, i.e. θ_{ow}<90°, the sign inside the bracket is negative; while for hydrophobic particles removing into the air or oil phase, i.e. θ_{ow}>90°, the sign inside the bracket is positive. When θ_{ow} is 90°, the detachment energy E is so large that the particles are most strongly held at the interface, and the emulsion is extremely stable; it is implied that closer to 90° the contact angle of three-phase, more stable the emulsion is. As we reported before [24], θ_{ow} is calculated by Eq. 2 [25], which is derived from the well-known Young's equation:

$$\cos\theta_{ow} = \frac{\gamma_w}{\gamma_{ow}}\cos\theta_w \quad \frac{\gamma_o}{\gamma_{ow}}\cos\theta_o \quad (2)$$

where γ_o and γ_w are the surface tensions of oil and water, respectively. θ_w and θ_o are the contact angles of water and oil on BC membrane, respectively. If θ_{ow}<20° or θ_{ow}>160°, the energy to remove particles away from the interface is so small that the emulsions cannot be stable enough [1]. The surface tensions of maize oil and deionized water at 25°C are 33.3 mN/m and 72.0 mN/m, respectively and their interface tension is 27.1 mN/m measured at the same temperature. The contact angles of deionized water and maize oil on BC membrane are respectively 59.4° and 56.7°. Hence, according to Eq. 2, the contact angle of three-phase θ_{ow} that BC nanofibers make at the interface of maize oil and water is 57.4°, indicating that BC is relatively hydrophilic and can be wetted by both maize oil and water. This hydrophilicity is believed to be originated from the four hydroxyl groups on every dextran monomer. [26] In our previous work [24], we prepared a series of

emulsions stabilized also with nano-BC taking liquid paraffin as oil phase, and the θ_{ow} that BC made at the liquid paraffin/water interface was 73.1°. This difference regarding θ_{ow} can probably be attributed to the discrepancy of polarity between maize oil and liquid paraffin, since ester groups are more hydrophilic than alkyl groups [27]. If an organic compound has a poor polarity, it will have a relatively high interfacial tension at the surface of water (the liquid paraffin/water interfacial tension is 40.83mN/m [24]). As a result, according to Eq. 1, presuming the same particle radius, the detachment energy of maize oil/water emulsion is smaller than that of liquid paraffin/water emulsion, which explains the relative poorer stability of maize oil emulsions.

4.2 Morphology of BC nanofibrils. It is shown in Fig. 4 that cellulose fibrils entangle with each other and several single fibrils combine into bundles; they pile up randomly to form a porous membrane. The average width of fibrils is around 50 nm. While it is difficult to know the length of fibrils since the ends of each fibril is hardly to distinguish. It is obvious that the nanofibrils have a large aspect ratio; their length is much bigger than their diameter. They twine with each other to form an interconnected network at the oil/water interface [12]. It was observed that BC nanofibrils were flexible enough to bend to adapt the curvature of the droplets. [24].

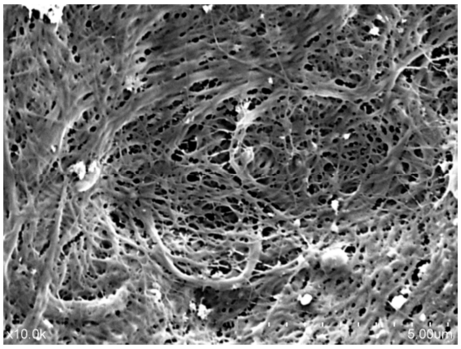


Fig.1 SEM image of nano-BC fibrils

4.3 Emulsion stability. All the emulsions creamed to some extent 5 min after preparation. 24 hours later, the emulsions tended to be stable, which was similar to the results of Ougiya et al. [28]. Fig. 2 shows the variation of ESI 30min and 24h after preparation at pH=12.

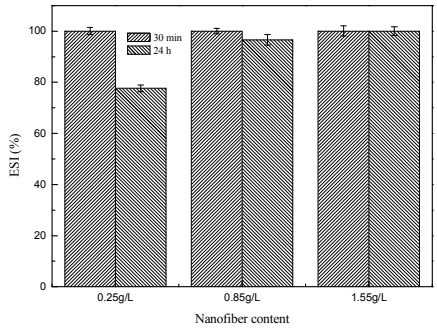


Fig.2 Variation of ESI 30min and 24h after preparation with 0.25, 0.85, and 1.55 g/L BC content at pH=12

When the BC concentration was 0.25 g/L, the decrease of ESI after 24 hours was significant. However, with increasing BC concentration, the ESI underwent slighter decline. The emulsion with 1.55 g/L BC didn't cream like other samples after 24 hours. It is shown in Fig. 3a that the emulsions with more BC had higher ESI at all tested pH values. The reason may be explained from two facets. More nanofibrils adsorb at the interface and provide stronger and denser single or multiple layers, preventing the contact and coalescence of oil phase between emulsion droplets, which accounts for the long term stability of Pickering emulsion. According to experiment and modeling calculation

[10-12], the surface coverage ratio increased with particle concentration. A higher surface coverage ratio may lead to a multiple-layer interface, which is advantageous to the emulsion stability. Tambe et al. [29] reported that the rheology property of oil/water interface changed to be viscoelastic when there were enough absorbed particles at the interface. Based on the model calculation, the viscoelastic nature could slow down the velocity that particle films gets thinner, which can enhance the detachment energy removing to water. The other point is that a three-dimensional array is formed between BC nanofibrils. Droplets were entrapped into the interconnected network composed of large-aspect-ratio fibers. The relationship between emulsion droplet diameter and BC concentration is shown in Fig. 4. The average droplet diameter $D_{1,0}$ decreased with the increasing fiber content, which is consistent with others' results [9, 10]. Smaller droplets have larger interfacial area, which can only be met by more particles.

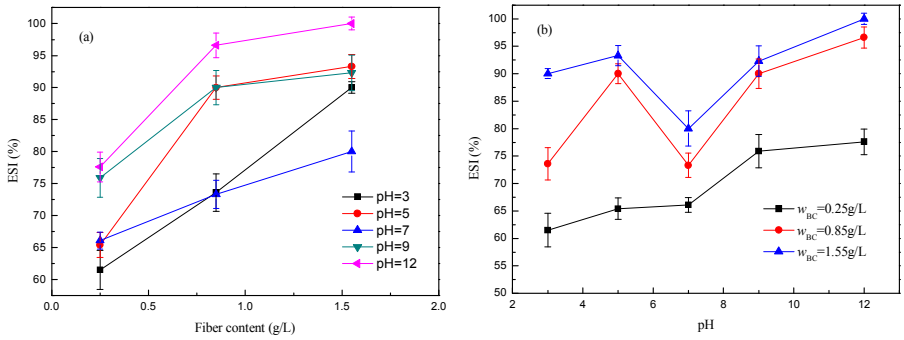


Fig.3 Effects of BC concentration (a) and pH value (b) on ESI (data taken at 24 hours after preparation)

When the pH was 12, the emulsions were the most stable at all tested BC concentrations and the ESI reached 100% when the BC content was 1.55 g/L (Fig. 3b). This might be referred to: (i) there were more negative charges on cellulose at higher pH, leading to enhanced electrostatic repulsion among droplets, and hence the coalescence of droplets was impeded, and (ii) in alkaline environment maize oil tended to be saponified and traces of bioactive component were formed.

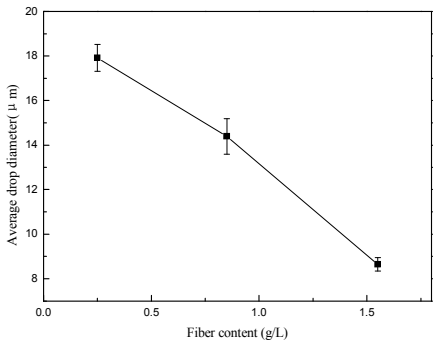


Fig.4 Relationship between $D_{1,0}$ and BC content at pH =12

Emulsions made with maize oil and liquid paraffin had good flowability at the early storage time. However, maize oil emulsion with 1.55 g/L BC concentration became gel-like after 2 months at 8-15°C environment (Fig. 5). Similar phenomenon was observed for Pickering emulsions stabilized by pregelatinized waxy maize starch [30]. At higher concentration, the individual cellulose chains began to overlap and more intermolecular hydrogen bonds formed, resulting in a stronger interlinked BC network, and consequently a higher emulsion viscosity [31]. It is imagined that the

droplets were ‘immobilized’ in the porous BC network in the gel-like emulsions. On the other hand, at low temperature, the crystallization of maize oil led to partial droplet coalescence, also contributing to the growth of emulsion viscosity [13, 32]. In this situation, the emulsion stability to creaming and coalescence was extremely well. Similarly, the liquid paraffin emulsion turned into a gel-like one when the BC concentration was higher than 1.55 g/L. However, at the same storage temperature, liquid paraffin did not crystallize as maize oil did. This fact suggests the importance of network strength to the formation of a jelly structure.



Fig. 5 Maize oil (left) and liquid paraffin (right) gel-like emulsion both with 1.55 g/L BC concentration at pH=12.

As a whole, the ESIs of maize oil emulsions were relatively lower than that of liquid paraffin emulsions [24]. Since the θ_{ow} at maize oil/water interface is 57.4°, lower than the θ_{ow} at liquid paraffin/water interface, 73.1°, it is easier to remove the nano-BC fibers from the maize oil-water interface, since the energy of detachment is lower.

Conclusions

The nano-BC fibrils with large aspect ratio overlap and interweave at the surface of emulsion droplets. There is a positive correlation between nano-BC concentration and emulsion stability. The average diameter $D_{1,0}$ decreased with fiber content. The maize oil emulsion was more stable at alkaline condition. Emulsions turned into gel-like system when BC concentration was higher than 1.55 g/L. The formation of emulsion gel was prominently due to the strong and interlinked BC network. According to contact angle of three-phase, BC fibrils were more susceptible to stabilize liquid paraffin emulsion than maize oil one. The presented results can have positive implication for designing and improving food emulsions.

Acknowledgment

The authors wish to thank the National Nature Science Foundation of China (Project No. 21106105) and 2014 National Training Programs of Innovation and Entrepreneurship for Undergraduates under the grant 201410057007.

References

[1]. B. P. Binks, Particles as surfactants similarities and differences, Curr. Opin. Colloid Interface Sci. 7 (2002) 21-41.
[2]. F. Leal-Calderon, V. Schmitt, Solid-stabilized emulsions, Curr. Opin. Colloid Interface Sci. 13 (2008) 217-227.
[3]. W. Ramsden, Separation of Solids in the Surface-layers of Solutions and 'Suspensions'. Proc. R. Soc. London: Series A. 72 (1903) 156-164.
[4]. S. U. Pickering, Emulsions, J. Chem. Soc. 91 (1907) 2001-2021.

[5]. Rayner Marilyn, Marku Diana, Eriksson Madeleine, et al., Biomass-based particles for the formulation of Pickering type emulsions in food and topical applications, Colloids Surf. A Physicochem. Eng. Asp. 458 (2014) 48-62.
[6]. Chevalier Yves, Bolzinger Marie-Alexandrine, Emulsions stabilized with solid nanoparticles: Pickering emulsions, Colloids Surf. A Physicochem. Eng. Asp. 439 (2013) 23-24.
[7]. J. Cayre Olivier, N. Paunov Vesselin, Contact angles of colloid silica and gold particles at air-water and oil-water interfaces determined with the gel trapping technique, Langmuir. 20 (2004) 9594-9599.
[8]. Frelichowska Justyna, Bolzinger Marie-Alexandrine, Chevalier Yves, Effects of solid particle content on properties of o/w Pickering emulsions, J. Colloid Interface Sci. 351(2010) 348-356.
[9]. Li Chen, Li, Yunxing, Sun, Peidong, et al., Pickering emulsions stabilized by native starch granules, Colloids Surf. A Physicochem. Eng. Asp. 431 (2013) 142-149.
[10]. Kalashnikova Irina, Bizot Herve, Cathala, Bernard, et al., New Pickering emulsions stabilized by bacterial cellulose nanocrystals, Langmuir. 27 (2011) 7471-7479.
[11]. Capron Isabelle, Cathala Bernard, Surfactant-free high internal phase emulsions stabilized by cellulose nanocrystals, Biomacromolecules. 14 (2013) 291-296.
[12]. Kalashnikova Irina, Bizot Herve, Bertoncini Patricia, et al., Cellulosic nanorods of various aspect ratios for oil in water Pickering emulsions, Soft Matter. 9 (2013) 952-959.
[13]. Marefati Ali, Rayner Marilyn, Timgren Anna, et al., Freezing and freeze-drying of Pickering emulsions stabilized by starch granules, Colloids Surf. A Physicochem. Eng. Asp. 436 (2013) 512-520.
[14]. J. Chen, R. Vogel, S. Werner, Influence of the particle type on the rheological behavior of Pickering emulsions, Colloids Surf. A Physicochem. Eng. Asp. 382 (2011) 238-245.
[15]. P. Thanasukarn, R. Pongsawatmanit, D. J. McClements, Impact of fat and water crystallization on the stability of hydrogenated palm oil-in-water emulsions stabilized by whey protein isolate, Colloids Surf. A Physicochem. Eng. Asp. 246 (2004) 49-59.
[16]. N. Tonouchi, T. Tsuchida, F. Yoshinaga, et al., Characterization of the biosynthetic pathway of cellulose from glucose and fructose in Acetobacter xylinum, Biosci. Biotechnol. Biochem. 60 (1996) 1377-1379
[17]. M. Iguchi, S. Yamanaka, A. Budhiono, Bacterial cellulose: A masterpiece of nature's arts. J Mater Sci. 35 (2000) 261-270.
[18]. Jonas R, Farah L F., Production and application of microbial cellulose, Polym. Degrad. Stab. 59 (1998) 101-106
[19]. Zaar K. Visulization of pores (export sites) correlated with cellulose production in the envelop of the gram-negative bacterium Acetobacter xylinum, J. Cell Biol. 80 (1979) 773-777.
[20]. Ashjaran Ali, Yazdanshenas Mohammad Esmail, Rashidi Abosaeed, et al., Overview of bio nanofabric from bacterial cellulose, Journal of the Textile Institute. 104 (2013) 121-131.
[21]. Cai Zhijiang, Kim Jaehwan, Bacterial cellulose/poly (ethylene glycol) composite: Characterization and first evaluation of biocompatibility, Cellulose. 17 (2010) 83-91.
[22]. Zhijiang Cai, Chengwei Hou, Guang Yang, Poly (3-hydroxubutyrate-co-4-hydroxubutyrate)/bacterial cellulose composite porous scaffold: Preparation, characterization and biocompatibility evaluation, Carbohydr. Polym. 87 (2012) 1073-1080.
[23]. Huang Yang, Zhu Chunlin, Yang Jiazhi, et al., Recent advances in bacterial cellulose, Cellulose. 21 (2014) 1-30.

[24]. Jia Yuan-Yuan, Wan Tong, Huo Ming-Ming, et al., Stabilization of Oil/Water Emulsions by Microfibrillized Bacterial Cellulose, Chemical Journal of Chinese Universities-Chinese. 34 (2013) 1475-1482.
[25] Jun Zhou, Preparation and stability investigations of the magnetic Pickering emulsions stabilized by Fe_3O_4 nanoparticles. D. Shanghai, China: Shanghai Jiaotong University. 2011.
[26] B. Derakhshandeh, R. J. Kerekes, S. G. Hatzikiriakos, Rheology of pulp fibre suspensions: A critical review, Chem. Eng. Sci. 66 (2011) 3460-3470.
[27] M. El-Mahrab-Robert, V. Rosilio, M. A. Bolzinger, et al., Assessment of oil polarity: Comparison of evaluation methods, Int. J. Pharm. 348 (2008) 89-94.
[28] H. Ougiya, K. Watanabe, T. Matsumura, et al., Relationship between suspension properties and fibril structure of disintegrated bacterial cellulose, Biosci. Biotechnol. Biochem. 62 (1998) 1714-1719.
[29] D. E. Tambe, M. M. Sharma, Factors controlling the stability of colloid-stabilized emulsions II. A model for the rheological properties of colloid-laden interfaces, J. Colloid Interface Sci. 162 (1994) 1-10.
[30] Grazyna Bortnowska, Jerzy Balejko, Grzegorz Tokarczyk, et al., Effects of pregelatinized waxy maize starch on the physicochemical properties and stability of model low-fat oil-in-water food emulsions, Food Hydrocolloids. 36 (2014) 229-237.
[31] F. Freitas, V. D. Alves, M. Carvalheira, et al., Emulsifying behaviour and rheological properties of the extracellular polysaccharide produced by Pseudomonas oleovorans grown on glycerol byproduct, Carbohydr. Polym. 78 (2009) 549-556.
[32] Fredrick Eveline, Walstra Pieter, Dewettinck Koen, Factors governing partial coalescence in oil-in-water emulsions, Adv. Colloid Interface Sci. 153 (2010) 30-42.

Key Engineering Materials Vols 645-646 (2015) pp 1255-1260
© (2015) Trans Tech Publications, Switzerland
doi:10.4028/www.scientific.net/KEM.645-646.1255

Submitted: 2014-10-30
Accepted: 2014-12-23

Enrichment Efficiency Optimization of Dielectrophoresis Cell Chip based on Interdigitated Microelectrodes Array

Wenwen Gu[1,2,a *] and Jie Huang[1,b]

[1]Department of Electronic and Control Engineering, College of Engineering and Technology, Southwest University, Chongqing 400715, P. R. China

[2]National Key Laboratory of Fundamental Science of Micro/Nano-Device and System Technology, Chongqing University, Chongqing 400030, P. R. China

[a]guww1983@163.com, [b]jiehuang@swu.edu.cn

Keywords: dielectrophoresis chip; interdigitated microelectrodes array; force simulation; cell enrichment efficiency; HepG2 hepatoma carcinoma cells

Abstract. At present, the majority dielectrophoresis chip designs optimize their performance by electric simulation and fluid field simulation. The lack of further cells force analysis and movement prediction results in a limited cell dielectrophoresis enrichment efficiency. The HepG2 hepatoma carcinoma cell movement under the action of dielectrophoresis force, fluid force and gravity was analyzed respectively by Comsol Multiphysics software. The preliminary optimization conditions for the cell enrichment were obtained. According to the simulation results, the experiments were carried out to investigate the enrichment effect of the HepG2 hepatoma carcinoma cells. The experiment result demonstrated the enrichment efficiency of HepG2 hepatoma carcinoma cells was reached to 88.89% under the 5 V amplitude and 4 MHz frequency sinusoidal signal excitation.

Introduction

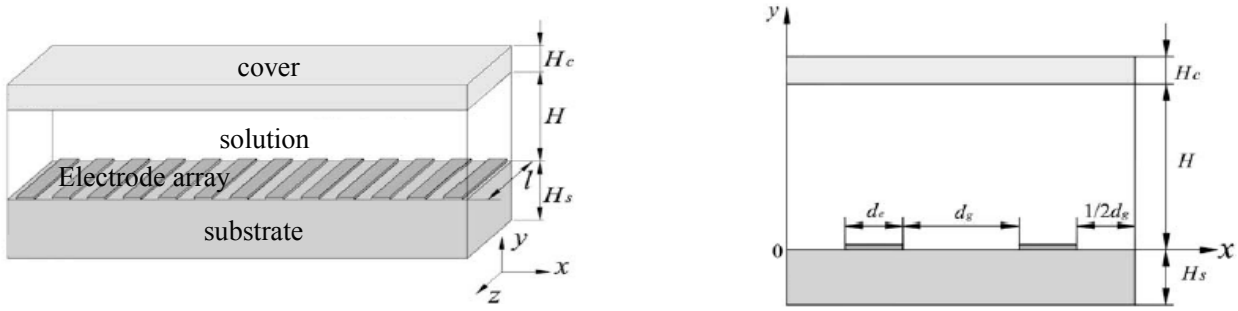
Dielectrophoresis chip is a kind of micro device which has appeared along with the development of Micro Total Analysis System (μ-TAS) and micro electro mechanical system (MEMS) [1]. By fabricating micro electrodes and micro channel network in the silicon, glass or high-molecular polymer based substrate, the process of dielectrophoresis enrichment and separation can be carried out in a substrate with the size of only square centimeters [2, 3]. Based on the different dielectric properties of samples, the dielectrophoresis technology can directly enrich and separate samples without pretreatment, which can maximize the retention of the physiological activity of the sample. In recent years, it has already achieved the separation of death and living cells [4, 5], the separation and enrichment of many kinds of biological particles, such as bacteria [6, 7], tumor cells[8–10]. The electrophoresis chip has the advantages of high efficiency, non-invasive, low reagent consumption, etc., which makes it have very important practical value and research significance in the field of cell analysis.

Reviewing the present research status at home and abroad, the design of the dielectrophoresis chip is based on the electric field and fluid field simulation to optimize the parameters of the chip [11–15]. However, in the actual samples, cells are heterogeneous system, which there are inevitable interaction with electric field and fluid field. Therefore, it is believed that it's lack of future analysis for cell force analysis and cell movement in the chip during the process of chip design. This paper was aimed to analysis and predict cell movement, and further increase the enrichment efficiency of the dielectrophoresis chip. This paper involved the HepG2 hepatoma carcinoma cells and the dielectrophoresis chip which had interdigitated microelectrodes array. It analyzed the single cell movement under the dielectrophoresis force, fluid force and gravity respectively by Comsol Multiphysiscs software, and further optimized the experimental condition for cell enrichment by dielectrophoresis effect.

1 Cell Force Analysis in Dielectrophoresis Chip

1.1 Modeling

The interdigitated microelectrodes array is used to build the model of dielectrophoresis chip, and the Comsol Multiphysics (Comsol), which is a multi-physics field coupling numerical analysis software, is used to solve the model and analyze the forces applied on the cell in the chip. Fig. 1 (a) illustrates the three-dimensional structure schematic. The direction of the X, Y and Z axis represents along the direction of electrode width (d_e), electrode thickness and electrode length (l), respectively. The interdigitated microelectrodes array is fabricated on the surface of the substrate, which the thickness of the substrate is expressed as H_s. The micro channel of the dielectrophoresis chip is fabricated on the surface of the cover material, which the depth of the micro channel is expressed as H and the thickness of the cover material is expressed as H_c. The cover material and the substrate are bonded to form dielectrophoresis chip. Because the length of the interdigitated microelectrodes array (feature sizes from 2 to 10 mm) is considerably larger than that of the electrode width (d_e), electrode spacing (d_g) and the micro channel depth (H), the three-dimensional structure can be simplified as X-Y plane two-dimensional model, shown as Fig.1 (b). Meanwhile, since the electric field distribution is periodic, it only chooses one or two pairs of electrodes to do simulation analysis.



(a) (b)

Fig. 1 Structure schematic of the dielectrophoresis chip based on interdigitated microelectrodes array: (a) 3D; (b) 2D.

Parameter setting: the thickness of the substrate and the cover are set to be 500μm and 1mm, respectively. The depth of the micro channel is set to be 100μm. The width, spacing and the thickness of the interdigitated microelectrodes array are set to be 20μm, 20μm and 0.2μm, respectively. KCl electrolyte solution is chosen to be the micro fluid through the micro channel of the dielectrophoresis chip, which the viscosity is set to be 0.001 Pa·s, density 1050 kg/m^3, conductivity 0.2 mS/m and relative permittivity 2.55ε_0.

1.2 The dielectrophoresis force applied to the cell

Fig. 2 indicates the simulation calculated distribution of logarithm dielectrophoresis force $\lg(F_{DEP})$ above the microelectrodes in the micro channel.

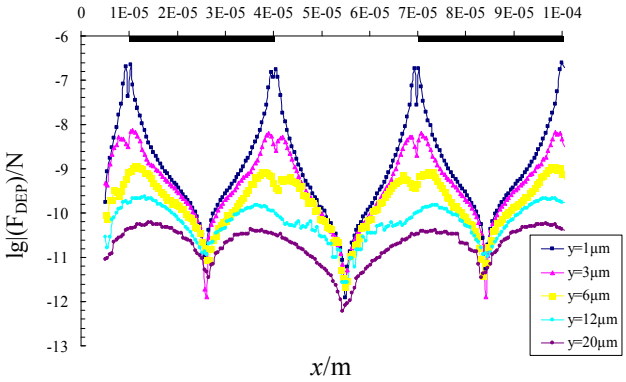


Fig. 2 Distribution of $\lg(F_{DEP})$ above the microelectrodes in the micro channel by Comsol.

With the increase of distance away from the surface of the microelectrodes (the value of Y axis increasing), the dielectrophoresis force decay rapidly. When at the same height, the maximum $\lg(F_{DEP})$ appears on the edge of the microelectrodes, while the minimum $\lg(F_{DEP})$ appears in the middle and the spacing center of the microelectrodes. Meanwhile the more close to the microelectrodes, the more obvious tendency that the maximum and minimum values appear. Thus, it is inferred that when the negative dielectrophoresis force is applied on the cell, the cell where it lies at the edge of the microelectrodes will move far away from the microelectrodes, while the cell where it lies in the middle and the spacing center of the microelectrodes will move toward to the surface of the microelectrodes.

1.3 The fluid force applied to the cell

Fig. 3 presents the fluid force changing in the direction of micro channel depth in the middle and the spacing center of the microelectrodes. The fluid forces both in the middle and the spacing center of the microelectrodes increase with the increase of distance from the surface of the microelectrodes. They reach the maximum values when the distance is 10μm from the surface of the microelectrodes. After that the fluid forces decrease with the increase of the distance. The positive fluid forces appear in the spacing center of the microelectrodes, while the positive fluid forces appear in the middle of the microelectrodes. Both the negative and the positive fluid force approach to zero when the distance from the microelectrodes is larger than 40μm.

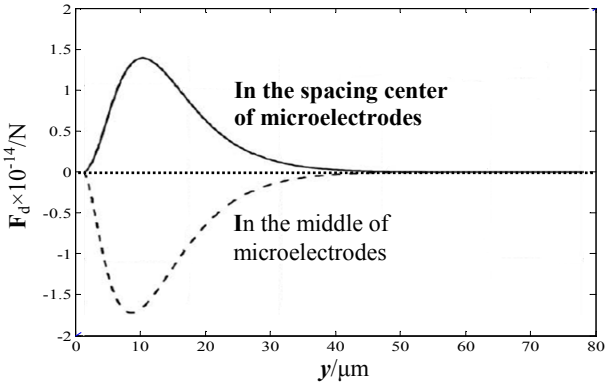


Fig. 3 Distribution of fluid force changing in the direction of micro channel depth in the middle and the spacing center of the microelectrodes by Comsol.

1.4 The gravity applied to the cell

The cell which is applied by negative dielectrophoresis force will be balanced under the action of dielectrophoresis force, fluid force and gravity. The cell satisfies the force balanced equation in the perpendicular direction,

$$F_{DEPy} = | F_d + F_g | \tag{1}$$

where F_{DEPy} represents the dielectrophoresis force in the perpendicular direction, F_d represents the fluid force and F_g represents the gravity of its own. By solving the Eq. 1, the cell's balanced position in the micro channel can be obtained.

The voltage amplitude can not only affect the dielectrophoresis force, but also the fluid force by electrothermal effect. It analyzes and calculates the balanced height in the micro channel when the cell is in the middle and the spacing center of the microelectrodes when it is applied by difference voltage amplitude. The result is shown as Fig. 4. It is revealed that under the action of the same voltage amplitude, the balanced height when the cell is in the middle of the microelectrodes is lower than that of the cell in the middle of the spacing center of the microelectrodes. Meanwhile, the balanced height difference increases as the voltage amplitude increases. Since the depth of the micro channel is usually set to be 30μm, considering the relation between the balanced height and the

applied voltage amplitude showed in Fig. 4, it is believed that the voltage amplitude for the cell dielectrophoresis manipulation should be limited within 10V.

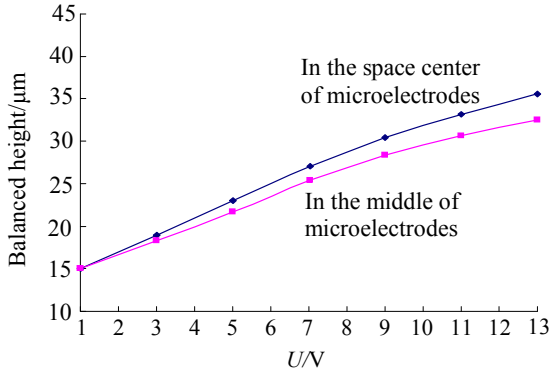


Fig. 4 The balanced height changing with the applied voltage amplitude in the middle and the spacing center of the microelectrodes by Comsol.

2 Experiment

Reagent and instrument: The HepG2 hepatoma carcinoma cells were provided by the First Affiliated Hospital of Chongqing Medical University; PBS buffer; Home made dielectrophoresis chip with interdigitated microelectrodes array (glass substrate with 30 pairs of interdigitated microelectrodes array, both the spacing and the width of the microelectrodes were 20μm; PDMS cover with micro channel of the width of 150μm and the depth of 30μm); micro injection pump (Harvard 55-2226， HARVARD APPARATUS, USA); fluorescent inverted microscope and matched Qcapture Pro image processing software (IX71, Olympus).

During the experiment, the concentration of 10^4 cell/L cell suspension was chosen. The cell suspension was injected into the micro channel of the dielectrophoresis chip by micro injection pump. After the cell suspension full filled the micro channel, change the experiment condition of dielectrophoresis enrichment and observe the results by Qcapture Pro image processing software.

1) Alternating voltage amplitude effects cell dielectrophoresis enrichment: when the frequency of the sinusoidal alternating voltage is fixed to 10MHz, the cell dielectrophoresis enrichment changes with the peak to peak voltage amplitude changing continuously from 1V to 10V;

2) Alternating voltage frequency effects cell dielectrophoresis enrichment: when the amplitude of the sinusoidal alternating voltage is fixed to 5V, the cell dielectrophoresis enrichment changes with the voltage frequency changing;

3) The measurement of enrichment efficiency for HepG2 hepatoma carcinoma cells: count the cell number in the sample reservoir of the dielectrophoresis chip, expressed as M_1; count the cell number where the cells are on the surface of the interdigitated microelectrodes array when the process of dielectrophoresis enrichment is over, expressed as M_2; calculate the enrichment efficiency of HepG2 hepatoma carcinoma cells by $M = M_2 / M_1 \times 100\%$.

3 Results & Discuss

3.1 Voltage amplitude effects cell dielectrophoresis enrichment

The enrichment time T is defined as a period of time from the alternating voltage beginning applying to the process of dielectrophoresis enrichment over and the cells on long moving. Fig. 5 gave the enrichment time T changes with the peak to peak voltage amplitude ($V_{p\text{-}p}$). It indicated that the T decreased as $V_{p\text{-}p}$ increases. When the $V_{p\text{-}p}$ was 7V, the HepG2 hepatoma carcinoma cells move like vortex disturbance between the interdigitated microelectrodes array. When the $V_{p\text{-}p}$ was small, the dielectrophoresis force can manipulate the cells for dielectrophoresis enrichment. As the $V_{p\text{-}p}$ increases, both the dielectrophoresis force and fluid force were increased. However, when the $V_{p\text{-}p}$ was much too large, the dielectrophoresis force applied on the cells was not large enough to overcome

the fluid force, leading to the cells cannot stay in the same place. Overall considered the enrichment time and efficiency, the V_{p-p} was set to 5V.

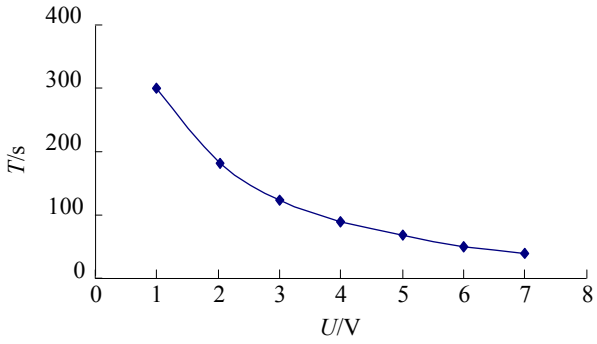


Fig. 5 The enrichment time changing with the peak to peak voltage amplitude for the HepG2 cells.

3.2 Frequency effects cell dielectrophoresis enrichment

Based on the simulation results, the maximum electric field intensity appears on the edge of the microelectrodes, where the cell is applied by positive dielectrophoresis force, while the minimum electric field intensity appears in the spacing center of the microelectrodes, where the cell is applied by negative dielectrophoresis force. Since there is an obvious difference between the position of positive and negative dielectrophoresis enrichment, it can achieve the dielectrophoresis enrichment and separation manipulation for the cells. By observing the moving direction of cells in the micro channel, it can judge the type of dielectrophoresis force (negative or positive) applied on the cells. If there is no obvious movement, it indicates that the dielectrophoresis force applied on the cells is zero, and the frequency of alternating voltage applied is the critical frequency of the cells.

Table 1 Experimental results of types of dielectrophoresis force changing with frequency applied on the cells

Frequency/MHz	0.5	1	2	3	5	7	9	10
Type of dielectrophoresis force	－	－	－	－	O	＋	＋	＋

Notes: "－" represents negative diectrophoresis force; " ＋" represents positive diectrophoresis force; " O" represents critical frequency

Table 1 showed the experimental results of the types of dielectrophoresis force changing with frequency applied on the cells. When the frequency is less than 3MHz, the cells were under the action of negative dielectrophoresis force, and enriched in the spacing center of the microelectrodes. When the frequency is 5MHz, there is not an obvious movement for the cells, which meant it was the critical frequency of the cells. When the frequency is greater than 5MHz, the cells were under the action of positive dielectrophoresis force, and enriched at the edge of the microelectrodes.

3.3 Measurement of cell's enrichment efficiency

Measure the cells' enrichment efficiency of applied alternating voltage with voltage amplitude V_{p-p} 5V and frequency 4MHz. The cell number M_1 in the sample reservoir of the dielectrophoresis chip was counted to be 360. The cell number on the 2 pairs of the interdigitated microelectrodes array was counted to be 21. Then it calculated the cell number on all the surface of the interdigitated microelectrodes array was $M_2 = (21/2) \times 30 = 315$ (30 pairs of microelectrodes array). Finally, the enrichment efficiency of HepG2 hepatoma carcinoma cells was $M = M_2 / M_1 \times 100\% = 87.5\%$.

4 Summary

This paper is aimed to analysis and predict cell movement under dielectrophoresis force, and further increase the enrichment efficiency of the dielectrophoresis chip. Based on the interdigitated microelectrodes array dielectrophoresis chip, it was analyzed the HepG2 hepatoma carcinoma cell movement under the dielectrophoresis force, fluid force and gravity respectively by Comsol

Multiphysiscs software. After that the preliminary optimal parameters and conditions for cell enrichment were obtained. The experiments were carried out to investigate the enrichment effect of the cells under the sinusoidal alternating voltage amplitude and frequency changes. Finally, the enrichment efficiency of 87.5% for HepG2 hepatoma carcinoma cells was obtained under the action of alternating voltage amplitude peak to peak of 5V and frequency of 4MHz.

Acknowledgement

The author acknowledges Foundational Research Founds for the Central Universities (No.XDJK2013C011), the financial support of Chongqing Natural Science Foundation (cstc2014jcyjA40038), National Key Laboratory of Fundamental Science of Micro/Nano-Device and System Technology, Chongqing University (No.2013MS05), and the Young Scientists Fund of the National Natural Science Foundation of China under Grant 61401373

References

[1] T.Z. Jubery, S.K. Srivastava and P. Dutta, Dielectrophoretic separation of bioparticles in microdevices: A review, ELECTROPHORESIS 35 (2014) 691-713.
[2] M. Li, W.H. Li, J. Zhang, G. Alici and W. Wen, A review of microfabrication techniques and dielectrophoretic microdevices for particle manipulation and separation, J. Phys. D: Appl. Phys. 47 (2014) 63001.
[3] Y. Demircan, E. Özgür and H. Külah, Dielectrophoresis: Applications and future outlook in point of care, ELECTROPHORESIS 34 (2013) 1008-1027.
[4] S. Patel, D. Showers, P. Vedantam, T.-R. Tzeng, S. Qian and X. Xuan, Microfluidic separation of live and dead yeast cells using reservoir-based dielectrophoresis, Biomicrofluidics 6 (2012) 34102.
[5] H. Shafiee, M.B. Sano, E.A. Henslee, J.L. Caldwell and R.V. Davalos, Selective isolation of live/dead cells using contactless dielectrophoresis (cDEP), Lab Chip. 10 (2010) 438-445.
[6] L. Yang, A REVIEW OF MULTIFUNCTIONS OF DIELECTROPHORESIS IN BIOSENSORS AND BIOCHIPS FOR BACTERIA DETECTION, Analytical Letters 45 (2012) 187-201.
[7] X. He, C. Hu, Q. Guo, K. Wang, Y. Li and J. Shangguan, Rapid and ultrasensitive Salmonella Typhimurium quantification using positive dielectrophoresis driven on-line enrichment and fluorescent nanoparticles label, BIOSENS. BIOELECTRON. 42 (2013) 460-466.
[8] F. Yang, X. Yang, H. Jiang, W.M. Butler and G. Wang, Dielectrophoretic Separation of Prostate Cancer Cells, Technol. Cancer Res. Treat. 12 (2013) 61-70.
[9] M. Alshareef, N. Metrakos, E. Juarez Perez, F. Azer, F. Yang, X. Yang and G. Wang, Separation of tumor cells with dielectrophoresis-based microfluidic chip, Biomicrofluidics 7 (2013) 11803.
[10] H.J. Mulhall, F.H. Labeed, B. Kazmi, D.E. Costea, M.P. Hughes and M.P. Lewis, Cancer, pre-cancer and normal oral cells distinguished by dielectrophoresis, Anal Bioanal Chem. 401 (2011) 2455-2463.
[11] X. Zeng, Y. Xu, Q. Cao, D. Hao, Y. Wu, Development of Structural Design and SimulationAnalysis for Dielectrophoresis Microchips, Micronanoelectronic Technology 46 (2009) 34-40.
[12] J. Cao, F. Hong, X. Chen, P. Zhen, Simulation and Experimental Study of Dielectrophoresis in a Microfluidic Chip with Interdigitated Electrodes, Micronanoelectronic Technology 45 (2008) 397-402.
[13] Y. Xu, Q. Cao, X. Zeng, Y. Wu, W. Zhang, Research of Cell Concentration and Separation on the Dielectrophoretic Chip with Arrayed Opposite Electrodes, Chemical Journal of Chinese Universities 30 (2009) 876-881.
[14] Z. Zhao, D. Zhao, H. Zeng, P, Yu, W. Wang, Z. Li,Study on Leukemia-cell Dielectrophoresis Microchip Based on MEMS, Piezoelectrics & Acoustooptics 33 (2001) 1002-1005.
[15] Y. Ren, H. Wu, G. Feng, L. Hou and H. Jiang: Chin. J. Effects of Chip Geometries on Dielectrophoresis and Electrorotation Investigation Mech. Eng. 27 (2014) 103-110.

Key Engineering Materials Vols 645-646 (2015) pp 1261-1266
Submitted: 2014-10-30
© (2015) Trans Tech Publications, Switzerland
Accepted: 2014-12-23
doi:10.4028/www.scientific.net/KEM.645-646.1261

Functionalization of mesoporous SBA-15 with APTES by co-condensation and its effect on immolibization of *Candida rugosa* lipase

Xiuyan Li[1, a], Yunqiang Xu[2,b] and Guowei Zhou*[2,c]

[1]School of Chemical Engineering and Environment, Weifang University of Science and Technology, Weifang 262700, Shandong, CHINA

[2]Key Laboratory of Fine Chemicals in Universities of Shandong, School of Chemistry and Pharmaceutical Engineering, Qilu University of Technology, Jinan 250353, Shandong, CHINA

[a]imlixiuyan@126.com, [b]xuyq163@163.com, [c]guoweizhou@hotmail.com

Keywords: Mesoporous SBA-15; co-condensation; (3-aminopropyl)triethoxysilane; *Candida rugosa* lipase; immobilization

Abstract. Functionalized SBA-15 with mesoscopic pore channels was synthesized by co-condensation of tetraethoxysilane and (3-aminopropyl)triethoxysilane (APTES) via hydrothermal process. Small-angle X-ray powder diffraction, scanning electron microscopy and transmission electron microscopy were used to monitor the effect of surface functionalization on the structural and textural features of the SBA-15. The results suggested that the structural ordering of functionalized SBA-15, as well as pore diameters, pore volumes and surface areas, were decreased with increasing the APTES molar ratio. *Candida rugosa* lipase (CRL) was used as a model enzyme for studying the effect of amino-functionalized on loading amount and enzymatic activity. The effects of pH and temperature on catalytic hydrolysis of tributyrin by immobilized CRL were investigated. The results showed that immobilized CRL had a well adaptability in a wide pH and temperature region, and CRL immobilized on functionalized SBA-15 exhibited much higher enzymatic activity than free CRL, especially, 5 mol% APTES functionalized SBA-15 immobilized CRL displayed the highest activity.

Introduction

In recent years, mesoporous silica materials, which have several advantages such as highly regular porous structure, high surface area and pore volume, low cytotoxicity and good biocompatibility [1], high thermal and hydrothermal stability [2], have been widely used in biochemistry as immobilization supports for enzymes [3]. Enzymes immobilized on mesoporous silica maybe exhibit higher activity than native enzymes [4]. It is believed that the free enzyme is more prone to misfolding, however, the immobilization leads to dispersion of the enzyme over a large surface area and maintains its native structural integrity. And the immobilization improves the enzymatic activity and operational stability by preventing its aggregation and enhancing the mass transfer of substrates in the mesochannel. Mesoporous SBA-15 has attracted more attention because of the well-ordered parallel mesochannel, variable pore size, chemically inert and mechanically stable. In addition, compared to short and straight mesopores, the bent and long channels of fiber-like SBA-15 with a high aspect ratio would place a serious resistance against the leaching of immobilized enzyme molecules [5], thus improve the operational stability and reusability of immobilized enzyme even under rigorous shaking condition.

Basically, three traditional methods of enzyme immobilization can be distinguished, binding to a support, entrapment (encapsulation) and cross-linking [6]. However, physical bonding (physical adsorption) is generally too weak to keep the enzyme fixed to the carrier, thus leading to the poor stability because of the leaching of adsorbed enzymes. Ionic binding and covalent binding (chemical adsorption) of the enzyme to the support are usually stronger, which preventing leaching of enzyme from the surface. Mesoporous silica materials can be functionalized easily due to the large amount of free silanol groups (Si–OH) in the silica wall. Two methods, which are so-called post-synthesis-grafting and co-condensation synthesis methods, are widely applied for the surface

functionalization. Especially the co-condensation method is the only way to enable a higher and more homogeneous surface coverage of organosilane functionalities [7]. In addition, the co-condensation method enables a better control of pore size, and the stability of the co-condensation synthesized mesoporous materials is better than those synthesized by post-synthesis-grafting method. Surface modification using (3-aminopropyl)triethoxysilane (APTES), which could produce terminal amine groups ($-NH_2$), has showed a potential use in the immobilization of enzymes. It is reported that amine groups grafted onto silica surface are stable under experimental conditions [8], and they can enhance the interactions of guest molecules with the support hosts by physical forces (hydrogen bonding, hydrophobic and electrostatic force) and covalent coupling.

In this study, functionalized mesoporous SBA-15 was prepared by co-condensation of tetraethoxysilane (TEOS) with APTES in a range of molar ratios of APTES/TEOS. results analysis provide strong evidence that morphological structure of functionalized SBA-15 became disordered with increasing the APTES molar ratio, as well as the further decreasing in pore diameters, pore volumes and surface areas of the samples. The *Candida rugosa* lipase (CRL, ~4 nm), one of the most industrially used microbial lipases in biotransformations because of its use in a variety of processes due to its high activity, both in hydrolysis and synthesis, had been physically absorbed onto SBA-15 and covalently anchored onto functionalized SBA-15, then the optimum catalysis condition, thermal stability and reusability of immobilized CRL were studied in details.

Experimental

Chemicals. Triblock copolymer P123 ($EO_{20}PO_{70}EO_{20}$, M_n = 5800), (3-Aminopropyl)triethoxysilane (98%), Triacetin (99%, $C_9H_{14}O_6$), and *Candida rugosa* lipase (CRL) were purchased from Aldrich. Tetraethoxysilane (TEOS) and other chemicals (AR) were all obtained from Tianjin Chemical Agent Company (China).

Preparation of pure mesoporous SBA-15 sample. Pure SBA-15 material was prepared following the literature procedure reported previously [9].

Co-condensation synthesis of functionalized SBA-15 samples. The synthesis of various APTES functionalized SBA-15 was essentially similar to that of the pure SBA-15 sample, except that different amount of APTES was added after the addition of TEOS. The final white solid materials were obtained after drying at atmosphere overnight, and denoted as NH-5/SBA-15, NH-10/SBA-15 and NH-15/SBA-15, respectively.

Preparation of enzyme immobilized in mesoporous supports. The immobilization of the lipase was carried out using a procedure described as follows: 40 mg of the support was immersed into 20 ml of CRL phosphate buffer (2 mg ml^{-1}, pH 6.0) in a vessel covered to prevent evaporation, and then stirred magnetically at 25 ^oC for 6 h to finish immobilization of CRL. The supernatant was separated from the solid by centrifugation for 10 min at 6000 rpm and 4 ^oC. The CRL solution concentration of the supernatant was measured using UV spectrophotometer at 258 nm, and then recalculated the CRL content of the supernatant.

All of the pure and functionalized supports were used in the same way for CRL immobilization. Samples after immobilization of CRL were designated as SBA-15-CRL, NH-5/SBA-15-CRL, NH-10/SBA-15-CRL and NH-15/SBA-15-CRL, respectively.

Activity assays. The activities of free and immobilized lipase were measured by titrating (with NaOH) the acetic acid produced in the hydrolysis of triacetin. Activity assay procedure was carried out as reported by Ma et al [10]. A mixture of triacetin (1.0 g), deionized water (25 ml) and pH 7.0 phosphate buffer (12 ml) was vigorously stirred for about 10 min to prepare a triacetin emulsion. When the pH stabilized, CRL was added. The mixture was continuously titrated with 0.02 M NaOH solution for 10 min to maintain a constant pH value. The volume of NaOH solution consumed was recorded and the activity of CRL was calculated in the standard way. The unit of CRL activity was denoted with U g^{-1} (one lipase activity unit (1 U) is defined as the amount of enzyme that hydrolyzes triacetin produces 1 μmol of acetic acid per min at 35 ^oC).The activity of immobilized CRL was assayed by the same method.

The optimum pH and reaction temperature of free and immobilized CRL were determined via the procedure as described above. The optimum pH of free and immobilized CRL was compared in buffer with the pH range of 5.0–9.0 (0.02 M K_2HPO_4–$C_6H_8O_7$ buffer solution for pH 5.0, 0.02 M phosphate buffer solution for pH 6.0–8.0 and 0.02 M Na_2CO_3–$NaHCO_3$ buffer solution for pH 9.0) at 35 ^oC. Thermal inactivation experiments were performed in phosphate buffer (pH 7.0) at the temperature range from 30 to 70 ^oC. The enzymatic performances of the free and immobilized CRL were calculated as activity recovery (R_e).

Characterization. Scanning electron microscopy (SEM) was conducted using a Quanta200 ESEM Felco-Holland microscope operating at accelerating voltage of 20 kV. Sample powder was placed on the surface of a silicon wafer and coated with a thin layer of gold before inserted into the microscope. Transmission electron microscopy (TEM) was performed using a JEM-100CX II electron microscope at an acceleration voltage of 100 kV. Before examination, the sample powder was dispersed in ethanol by sonication and deposited on a copper grid and dried in air. Small-angle powder X-ray diffraction (SAXRD) measurements were performed on a Bruker D8 advance diffractometer with Cu K_α radiation (25 kV, 20 mA) and a step size of 0.02^o from 0.5^o to 5^o.

Results and discussion

SAXRD. Fig. 1 depicts SAXRD patterns of pure SBA-15 and amine-functionalized SBA-15 with different APTES concentrations. It can be seen that the sample of pure SBA-15 (curve a) clearly shows three well-resolved peaks indexed to (100), (110) and (200) diffractions, indicating 2θ values of 0.91, 1.56, and 1.80, the ratio of which is about $1:\sqrt{3}:2$. This result is characteristic of highly ordered, two-dimensional hexagonal *p6mm* mesostructure. However, for samples synthesized with various molar ratios of APTES, the three peaks gradually become weakened by increasing the amount of APTES. Higher order (100), (110) and (200) peaks of NH-5/SBA-15 are still clearly observed, indicating that the ordered mesostructure of the material is well maintained when the molar ratios of APTES precursor is 5%; the (100) and (200) peak intensity decreases and the higher order (110) diffractions become ill-resolved when the APTES molar contents is 10%, indicating a relatively poor mesostructured ordering of NH-10/SBA-15 material. Specifically, only one wide and low-intensity peak (100) is observed in the XRD patterns of NH-15/SBA-15 material, which suggests a poor ordered mesostructure of NH-15/SBA-15. The above results show that varying the molar ratio of TEOS/APTES can lead to great changes in the mesostructure of the samples.

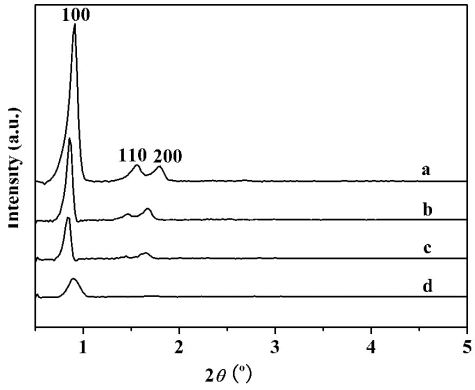


Fig. 1 SAXRD patterns of (a) SBA-15, (b) NH-5/SBA-15, (c) NH-10/SBA-15, (d) NH-15/SBA-15.

SEM. The morphologies of SBA-15, NH-5/SBA-15, NH-10/SBA-15 and NH-15/SBA-15 materials are examined by SEM and the images are shown in Fig. 2. The SEM images reveal that NH-5/SBA-15(Fig. 2B) has typical morphologies as commonly observed in the pure SBA-15(Fig. 2A) type material, which can be featured as wheat-like macrostructures consisting of many rope-like domains with relatively uniform sizes of 0.5–1.0 μm, indicating that minimal changes occur after the functionalization procedure with 5 mol% APTES. This type of morphology has been proven to have long-range channels with the 2D-hexagonal structure directions parallel to the long axis [11]. The

macroscopic morphologies of NH-10/SBA-15 (Fig. 2C) and NH-15/SBA-15 (Fig. 2D) are found to vary with the addition of APTES. The wheat-like macrostructures are disintegrated and single rod units are obtained in Fig. 2C. The morphology of NH-15/SBA-15 is obviously different from others; debris is formed instead of rod units, and the debris is more densely packed, suggesting that there is a significant change by 15 mol% APTES added into the pre-hydrolyzed silica mixture.

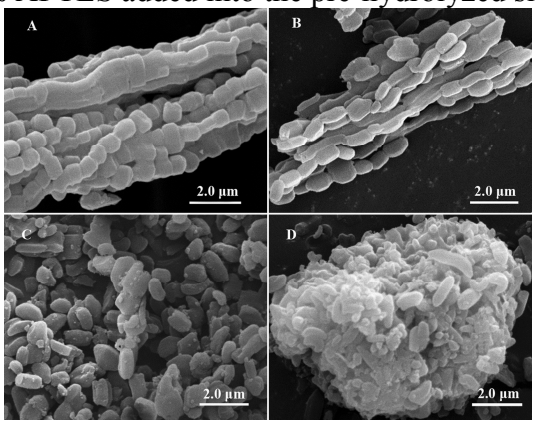


Fig. 2 SEM images of (A) SBA-15, (B) NH-5/SBA-15, (C) NH-10/SBA-15 and (D) NH-15/SBA-15

TEM. The TEM images of the pure SBA-15 and APTES functionalized samples are compared in Fig. 3. It has been observed in TEM investigations that SBA-15 (Fig. 3A), NH-5/SBA-15(Fig. 3B) and NH-10/SBA-15 (Fig. 3C) all show well-ordered arrays of long-range mesopore channels. This is clear evidence that a hexagonal structure is maintained during the functionalization procedure, suggesting that the APTES complex is embedded uniformly within the mesopores. It seems that NH-15/SBA-15 (Fig. 3D) has the poorest-ordered long range structure. There is partial collapse of the ordered mesoporous arrangement inside the sample, which can be regarded as worm-like structure pore; but still there are some domains with hexagonal structure at the channel opening. This resulting material always shows amorphous phase, which is in good agreement with that estimated from the XRD results.

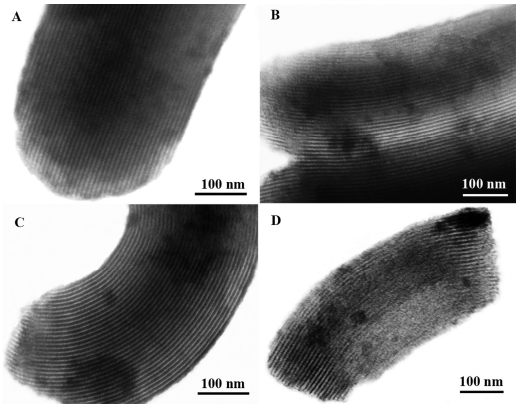


Fig. 3 TEM images of (A) SBA-15, (B) NH-5/SBA-15, (C) NH-10/SBA-15 and (D) NH-15/SBA-15

Effect of pH on corresponding enzymatic activity of free and immobilized CRL. Free and variously immobilized CRL activities are investigated in terms of pH. The effect of pH on free and immobilized CRL activities are studied in the pH range from 5.0 to 9.0 and the results are described in Fig. 4. The optimum pH of free CRL is 7.0, and that of immobilized CRL is shifted to 8.0, which is 1.0 pH unit higher than that of free CRL. This shift in pH optimum can be attributed to additional interaction of the supports with enzyme, which may reduce the sensitivity of enzyme to high pH. As for the immobilized enzyme on functionalized mesoporous silica hosts, the activity recoveries (R_e) are much higher than SBA-15-CRL, these improvements are associated with enhanced surface hydrophobicity. It can be explained that the hydrophobic groups (aminopropyl) of the functionalized mesoporous silica surface are involved in activating interactions with the hydrophobic domains of the lipase, which activate the catalytic centre of lipase [12]. However, the R_e of immobilized CRL is in

the order: NH-5/SBA-15-CRL > NH-15/SBA-15-CRL > NH-10/SBA-15-CRL > SBA-15-CRL, suggesting that NH-5/SBA-15-CRL has the highest activity, this may be due to the diffusional limitation of the substrate within the minor mesoporous of NH-10/SBA-15 and the poorest-ordered mesoporous of NH-15/SBA-15. Moreover, the pH profile of the NH-15/SBA-15-CRL is broader than that of others, indicating that this immobilized enzyme preserve the activity over a wide pH range.

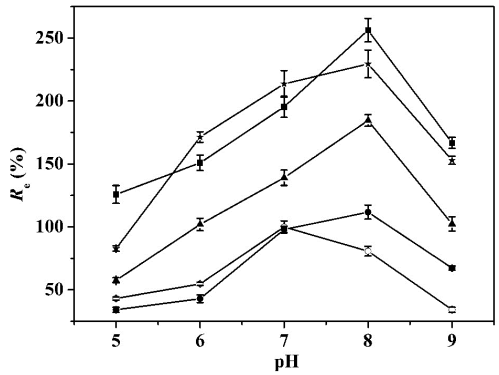


Fig. 4 Activity recovery of (○) free CRL, (●) SBA-15-CRL, (■) NH-5/SBA-15-CRL, (▲) NH-10/SBA-15-CRL, (★) NH-15/SBA-15-CRL as a function of medium pH.

Effect of reaction temperature on corresponding enzymatic activity of free and immobilized CRL. The effect of temperature on the catalytic behaviour of immobilized CRL is studied from 20 to 70 ^{o}C and the profiles are shown in Fig. 5. It shows that the optimal temperature of reaction is around 35 ^{o}C for free CRL, whereas the activities of the immobilized CRL increase with an increasing temperature from 30 to 50 ^{o}C, but beyond 50 ^{o}C the activities of immobilized CRL show a decrease except for the NH-15/SBA-15-CRL sample, which shows the maximum activity at 60 ^{o}C. However, the immobilized CRL keep higher activity recovery (R_e) within a range of temperature from 60 to 70 ^{o}C, suggesting that immobilized CRL could retain high enzyme activity and more stable at high temperature.

In particular, the R_e of SBA-15-CRL NH-5/SBA-15-CRL, NH-10/SBA-15-CRL and NH-15/SBA-15-CRL determined at optimal temperature are 162.92%, 384.64%, 315.24% and 328.25%, respectively, which are higher than that determined at optimum pH. It is probably due to the high temperature that enhances the activated molecule and diffusion rate of substrate, resulting in high enzymatic activity. In summary, mesoporous SBA-15 functionalized by co-condensation is the appropriate host for immobilization of CRL, and the immobilized CRL exhibits much higher catalytic activity, while immobilized CRL on post-grafted mesoporous SBA-15 shows inversely lower catalytic activity as compared with that of immobilized on pure SBA-15 [13], such functionalized SBA-15 promises potential applications in enzyme adsorption and catalysis.

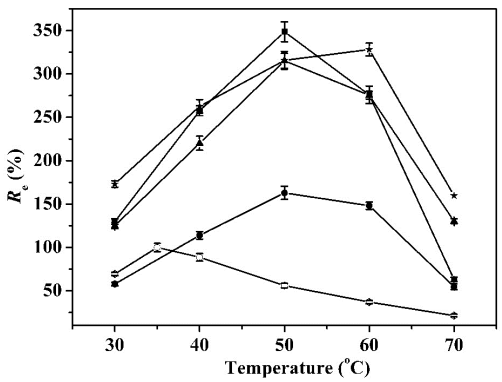


Fig. 5 Activity recovery of (○) free CRL, (●) SBA-15-CRL, (■) NH-5/SBA-15-CRL, (▲) NH-10/SBA-15-CRL, (★) NH-15/SBA-15-CRL as a function of incubation temperature.

Summary

Ordered mesoporous SBA-15 and amino-functionalized mesoporous NH-5/SBA-15, NH-10/SBA-15 and NH-15/SBA-15 are synthesized by co-condensation of TEOS and APTES, and characterized by SAXRD, SEM and TEM. The results show that the amino groups are condensed as the part of the silica framework, and the ordering of the mesostructure decrease with the increasing content of APTES. The mesoporous silica materials are used for the immobilization of CRL. The optimum catalytic pH of immobilized CRL is 8.0, which is 1.0 pH unit higher than that of free CRL. The optimum temperature of SBA-15-CRL, NH-5/SBA-15-CRL and NH-10/SBA-15-CRL is 50 ^{o}C, while it is 60 ^{o}C for NH-15/SBA-15-CRL.

Corresponding Author

Guowei Zhou; E-mail address: guoweizhou@hotmail.com; Tel: +86 531 89631696.

References

[1] S.P. Hudson, R.F. Padera, R. Langer, D.S. Kohane, Biomaterials 29 (2008) 4045–4055.

[2] Z.A. AlOthman, A.W. Apblett, Appl. Surf. Sci. 256 (2010) 3573–3580.

[3] G.W. Zhou, Y.J. Chen, S.H. Yang, Micropor. Mesopor. Mater. 119 (2009) 223–229.

[4] L.F. Giraldo, B.L. López, L. Pérez, S. Urrego, L. Sierra, M. Mesa, Macromol. Symp. 258 (2007) 129–141.

[5] M.II Kim, J. Kim, J. Lee, S. Shin, H.B. Na, T. Hyeon, H.G. Park, H.N. Chang, Micropor. Mesopor. Mater. 111 (2008) 18–23.

[6] R.A. Sheldon, Adv. Synth. Catal. 349 (2007) 1289–1307.

[7] X.A. Zhang, W.J. Wu, J.F. Wang, X.Z. Tian, Appl. Surf. Sci. 254 (2008) 2893–2899.

[8] X.H. Zhang, W.Y. Zhang, J.P. Li, N. Zhao, W. Wei, Y.H. Sun, Catal. Commun. 8 (2007) 437–441.

[9] A. Sayari, B.H. Han, Y. Yang, J. Am. Chem. Soc. 126 (2004) 14348–14349.

[10] H. Ma, J. He, D.G. Evans, X. Duan, J. Mol. Catal. B: Enzym. 30 (2004) 209–217.

[11] H. Zhang, J.M. Sun, D. Ma, X.H. Bao, A. Klein-Hoffmann, G. Weinberg, D.S. Su, R. Schlögl, J. Am. Chem. Soc. 126 (2004) 7440–7441.

[12] A. Macario, M. Moliner, A. Corma, G. Giordano, Micropor. Mesopor. Mater. 118 (2009) 334–340.

[13] A.Z. Abdullah, N.S. Sulaiman, A.H. Kamaruddin, Biochem. Eng. J. 44 (2009) 263–270.

Key Engineering Materials Vols 645-646 (2015) pp 1267-1272
© (2015) Trans Tech Publications, Switzerland
doi:10.4028/www.scientific.net/KEM.645-646.1267

Submitted: 2014-11-03
Accepted: 2014-12-23

Fabrication of a Pendulous Resonant Micro-machined Biosensor for Direct liquid detection

Gang Huang[1], Yuxin Li[2], Li Qian[2], Qi Li[2]

[1]Electronic Materials Research Laboratory, Xi'an Jiaotong University, Xi'an China

[2] China Astronaut Research and Training Center, Beijing, China

[a]liyuxin_85@126.com, [b]huanggang1971@sina.com, [c]ql_windedge@163.com

Keywords: pendulous resonant MEMS biosensor, direct liquid detection, SOI- MEMS, resonant paddle

Abstract. This paper presents a pendulous resonant MEMS biosensor for liquid detection based on SOI-MEMS technology. The biosensor consists of two electromagnetically driven and sensed resonant paddles working in the torsional mode. The differential output consisted by the two paddles provides the sensor reading. 1um thick SiNx is deposited on the electrodes by plasma enhanced chemical vapor deposition (PECVD), making the biosensor capable of working in liquid directly. In device fabrication, SOI-MEMS fabrication processes were utilized, where a new modified buffered hydrofluoric acid (BHF) solution was used to remove the buried oxide layer and release the paddles. High-current drive circuit and energy compensation circuit are designed to improve the Q-factor of the paddle in liquid. Experimental experiments show that the biosensor can distinguish the density of some liquid effectively.

Introduction

Biosensor based on micro-machined resonator is a new bio-chemical analysis method, which relates to the MEMS, Materials, Bio-chemistry, Mechanical and other cross-disciplinary subjects. Compared with traditional piezoresistive micro cantilevers, micro-machined resonant biosensor, with the advantages of ultrahigh sensitivity, fluorescent-labeling free, in-situ detection and low-cost fabrication, has been widely used in recent years [1-3]. However, the Q-factor is rapidly decayed in liquid due to the large damping, which makes some resonant structure not suitable to work in liquid. As it is a key step to achieve high performance in direct liquid detection, how to improve the resonator quality factor in the liquid phase has received increasing focus.

This paper presents a paddle structure working in the torsional mode, by which the resonator can achieve higher Q-factor. The paddle is electromagnetic excited, which can effectively improve the SNR (signal to noise ratio) of the sensor. To enhance the Q-factor, high-current drive circuit is designed to match the required large driving force in liquid, and an energy compensation circuit is designed according to the feature that the resonator output is related to resonant speed, moreover, two paddles are integrated in one chip as a differential system to improve the precision and stability of biosensor.

Structural design

The resonant elements consist of two crossed beams (called pendulous resonator), and the schematic diagram of the resonant torsional paddle is shown in Fig.1. The beam which is double-clamped and organized symmetrically along the diagonal direction suspended on a silicon square diaphragm is named support beam, and the beam swings around the support beam is named torsional beam.

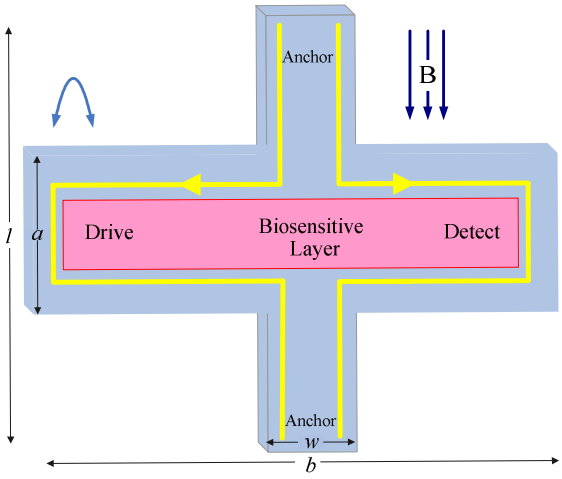


Fig. 1 Schematic of the resonant torsional paddle

The single-crystal silicon paddles used as resonators work in a torsional mode, which are actuated and detected electromagnetically by Au film electrodes located on the upper surface of the paddle. When an AC current applies through the drive port, the paddle swings around the support beam by Lorentz force, making the paddle resonant at its natural resonant frequency in torsional mode. At the same time, an AC voltage with the same frequency will be induced on the both end of the detect port according to the movement. When immerged in a liquid, the effective mass of the paddle will change, making the resonant frequency of the paddle shift.

This design is featured with a differential output, which effectively counterbalances the influence of the corresponding frequency drift of the resonant paddles due to ambient temperature variations, damping and other properties of the liquid, enhancing device stability and sensitivity. The micro-machined biosensor consisted by two resonant torsional paddles, which are utilized to enable differential. When the bio-chemical reaction happens, the detecting paddle is used to detect the bio/chemical change in the liquid, and the other one is used as a reference to lower the noise.

Simulation

The design of the sensor is verified by theoretical analysis and Finite Element Analysis (FEA) simulations. According to the mechanical theory of torsional, the fundamental frequency of a resonator can be expressed as:

$$f_t = \frac{1}{2} p \sqrt{K_t / I_t}, \quad I_t = h(2cw^3 + ab^3)/12 \tag{1}$$

Where f_t is the resonant frequency, K_t is the torsional rigidity, $K_t = 2K_l G w h^3 / c$, I_t is the inertial moment of the paddle, G is the shear modulus, ρ is the density of the paddle, and K_l varies with the variation of w/h. Assuming the mass placed on the paddle is even, the sensor sensitivity can be expressed as:

$$\Delta f_t / \Delta m = (2p)^{-1} (54 K_l G w b^4 / c)^{1/2} [r(2cw^3 + ab^3]^{-3/2} \tag{2}$$

Parameters of the paddle are optimized by (FEA) simulations using ANSYS software. FEM results show that the sensitivity of the sensor decreases with the increase of length and width of the paddle, and is irrelevant with the thickness, which accords with formula (2). Improving the Q-factor of the drive and sense mode is an available way to improve the performance of the sensor.[4] Considering the FEM results and the feasibility of MEMS processes, the structural parameters of the paddle are

optimized to achieve high Q-factor. Fig. 2 shows the FEM simulation results of resonant frequency shifts of the paddle with applied mass with the optimal parameters. The torsional frequency of the paddle is approximately 70 kHz and the sensitivity of the sensor is about 0.16Hz/pg.

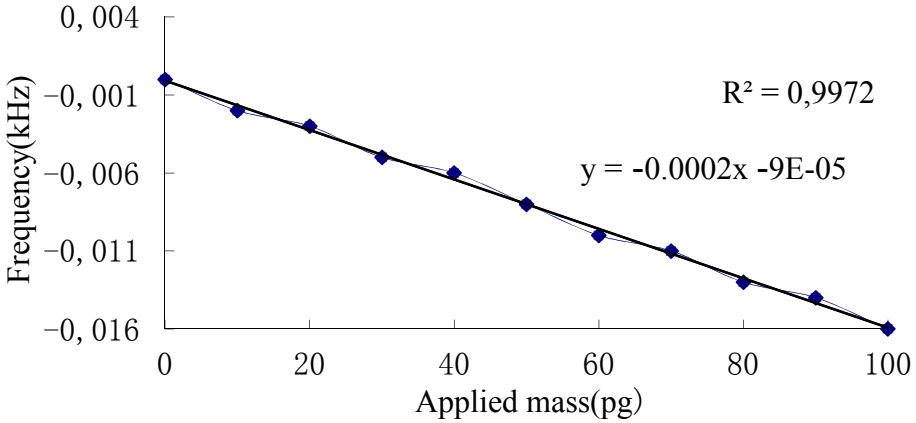


Fig. 2 Plot of the FEM simulated resonant frequency versus applied mass

Fabrication

Based on standard bulk MEMS processes, the sensor samples were fabricated using deep reactive ion etching technique (DRIE), photolithography, sacrificial layer release technique and thick SiNx filmdeposition technique. MEMS bulk-silicon processes proceed on a 3 inch SOI wafer (the thicknesses of the device layer, sacrificial layer and handle layer were 5μm, 2 μm and 350 μm, respectively). In this fabrication, a new modified BHF solution is used to remove the buried oxide layer and release the suspended resonator. The 5μm Si covered low-stressed SiNx layer with 2um in thickness by PECVD is used as the paddle of the sensor.

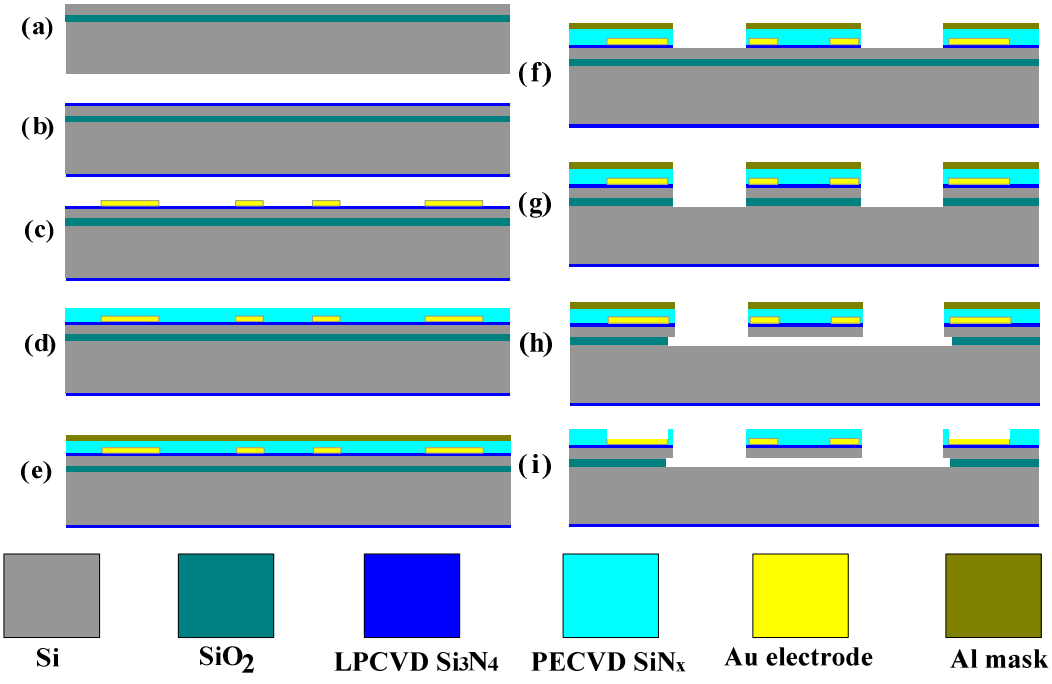
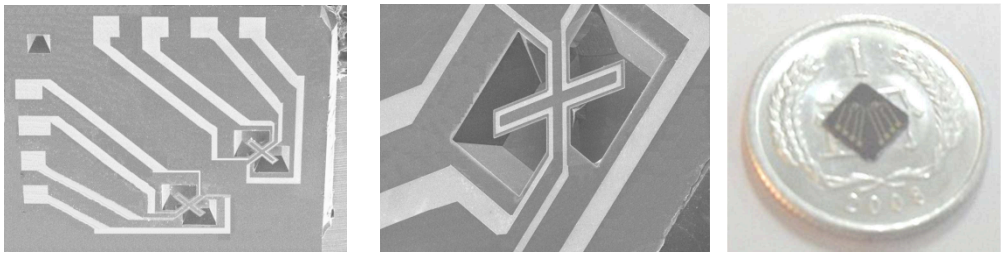


Fig. 3 The fabrication procedure for the sensor, relying on SOI-MEMS fabrication processes: (a) SOI wafer; (b) Si_3N_4 deposition by LPCVD; (c) patterning and sputtering of the Au electrodes; (d) thick SiN_x film deposition by PECVD; (e) sputtering of the Aluminum film as mask layer; (f) patterning and DRIE for the paddles and diaphragm area (g) releasing of the SiO_2 layer of the SOI wafer; (j) removing Aluminum mask layer and SiNx etching by RIE to expose the electrode pads

According to step (g), conventional BHF solution was used as the wet etchant firstly. The SiN_x film deposition by PECVD was directly exposed to the etchant, which makes the film seriously damaged, even partially stripped from the Si handle layer[5]. To address this issue, a modified BHF solution with addition of glycerol at 60°C is used to increase the etch selectivity between the SiO_2 sacrificial layer and the Aluminum mask layer. After using the new BHF solution, it takes effect to release resonant paddles while no significant damage can be noticed, which leads to a production yield higher than 95% with a good uniformity. Fig.4 shows the SEM photo of the fabricated sensor.



(a) (b) (c)

Fig.4 (a) SEM photo of the sensor chip; (b) SEM photo of the paddle; (c) photo of the sensor chip

Experiments and results

Two pieces of semicircular SmCo permanent magnet are placed in opposite position along the diagonal direction of the sensor chip to provide a horizontal magnetic field of 0.1 T for the actuation and sensing of the paddles. The sensor chip and the magnets setup are assembled together and then packaged on the Kovar substrate with epoxy resin.

An E5061B network analyzer is used to measure the frequency response of the paddle in an open-loop scanning manner with fixed amplitude of 50 mV. Resonant frequency of the paddle at 1 atmosphere air is 67.25 kHz with corresponding Q-factor 920. When it comes to the direct liquid detection, mass placed on the paddle caused by big damping makes the resonant frequency decrease to about 16 kHz and the Q-factor 4.9. To enhance the Q-factor, a high-current drive circuit and an energy compensation circuit (shown in fig.5) are designed to increase driving force and provide positive-feedback [6]. Experiments show that the circuit can effectively compensate the energy loss, and the Q-factor in pure water is improved from 4.9 to approximately 60.The charateristics tests for the sensor in pure water and ethanol are shown in fig.6.

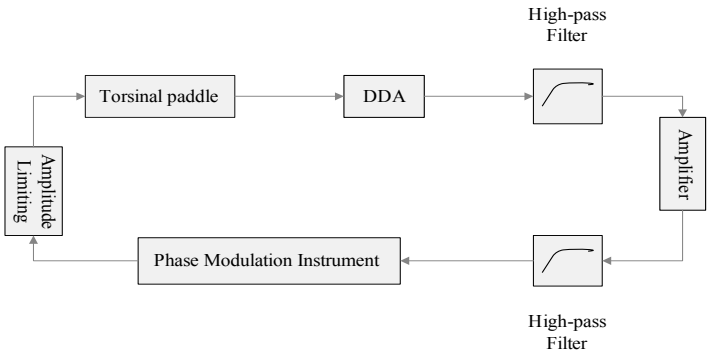


Fig.5. Block diagram of the system circuitry

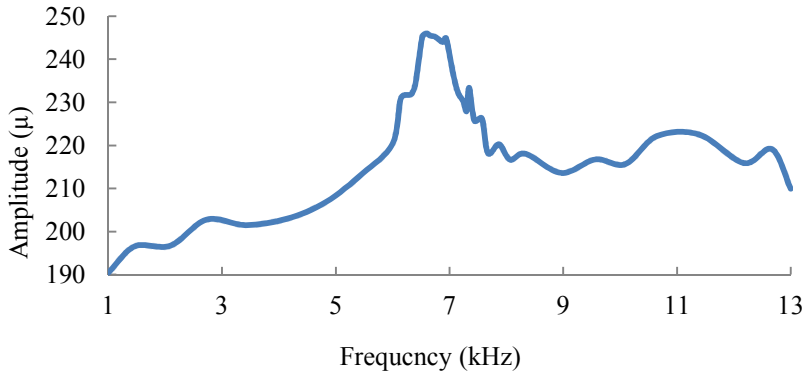


Fig.6 (a) output of the sensor in pure water

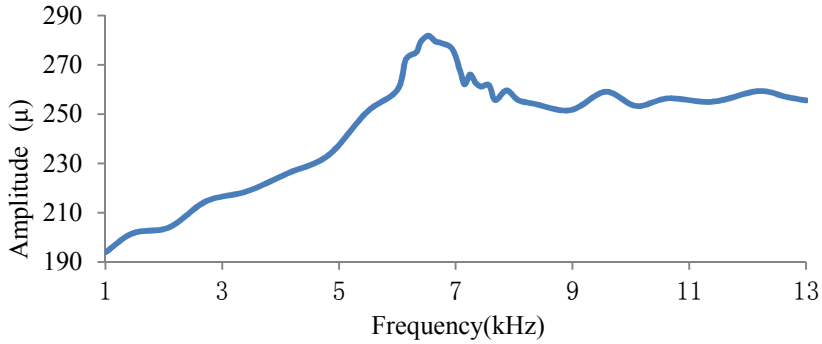


Fig.6 (b) output of the sensor in pure ethanol

Conclusions

A pendulous resonant MEMS biosensor for liquid detection with differential structures is presented with several key design aspects analyzed. The proposed sensor chip was successfully fabricated by SOI-MEMS micromachining processes and a modified BHF solution. The paddle works in a torsional mode, and the frequency is approximately 70 kHz with the sensitivity of the sensor is about 0.16Hz/pg. Open-loop electrical measurements of the beams revealed a quality factor of 980 in the air and 4.9 in pure water. In order to improve the Q-factor of the sensor in liquid, a closed-loop self-oscillating circuit with high-current drive and energy compensation is conducted to increase driving force and provide positive-feedback. Closed-loop tests show that the Q-factor is improved to 60 in pure water, and the sensor can distinguish liquids by different amplitude outputs.

Acknowledgment

This work is sponsored by NSFC (Natural Science Foundation of China) with project NO.21175121.

References

[1] L. B. Sharos, A. Raman, S. Crittenden, R. Reifenberger, Enhanced mass sensing using torsional and lateral resonances in microcantilevers, Applied Physics Letters. 84(2004) 4638-4640.

[2] C.Vancura, Y. Li, J. Lichtenberg, K. Kirstein, A. Hierlemann, Liquid-phase chemical and biochemical detection using fully integrated magnetically actuated complementary metal oxide semiconductor resonant cantilever sensor systems, Analytical Chemistry. 79(2007) 1646-1654.

[3] Sader, John E., Larson, Ian, Mulvaney, Paul White, Lee R., Method for the calibration of atomic force microscope cantilevers, Review of Scientific Instruments. 66(1995) 3789-3798.

[4] F.M.Battiston et al, A chemical sensor based on a microfabricated cantilever array with simultaneous resonance-frequency and bending readout, Sensors and Actuators, B 77 (2001)122-131.

[5] V.L.Vaganov, Construction Problems in Sensors, Sensors and Actuators. A28 (1991)161–172.

[6] US Lindholm, DD Kana, WH Chu and HN Abramson, Elastic vibration characteristics of cantilever plates in water, Journal of Ship Research. 9 (1965) 11–22.

Key Engineering Materials Vols 645-646 (2015) pp 1273-1278
Submitted: 2014-11-04
© (2015) Trans Tech Publications, Switzerland
Accepted: 2014-12-23
doi:10.4028/www.scientific.net/KEM.645-646.1273

In-Situ Synthesis of the Hollow Silica Microspheres with Porous Surface by Using Chemical Modified Pollen Grains as Biotemplate

Cao Feng[1, a *], Li Dongxu[2, b] and Wu Zhengying[1,c]

[1]School of Chemistry Biology and Material Engineering, Suzhou University of Science and Technology, Jiangsu Suzhou 215009, People's Republic of China

[2] College of Materials Science and Engineering, Nanjing Tech University, Jiangsu Nanjing 210009, People's Republic of China

[a]caofeng@mail.usts.edu.cn, [b]dongxuli@njut.edu.cn, [c]zywu@mail.usts.edu.cn

Keywords: Hollow microspheres; biotemplate synthesis; in-situ reaction; surface modification;

Abstract. Hollow silica microspheres with porous surface were synthesized by using the pollen grains as biotemplate through an in-situ synthesis process, in which the pollen grains were surface modified by ammonium oleate. Scanning electron microscopy, Fourier transform infrared spectroscopy and nitrogen adsorption-desorption porosimetry analyzer were applied to investigate the as-prepared microspheres. Bovine serum albumin was used as the model drug to estimate the adsorption property. And the effect of the different amount of tetraethoxysilane during the synthesis process were discussed in this paper. Results indicated that the hierarchical network of the pollen wall could be well replicated through this method, in which the hydrophobic interaction between the pollen wall and surfactant as well as the electrostatic interaction between the surfactant and the hydrolysate of tetraethoxysilane were considered as the key factors for the replication. The hollow silica microspheres have loading capacity for the model drug, and the adsorption property of this microsphere could be easily adjusted by changing the amount of tetraethoxysilane.

Introduction

Currently the microspheres with hollow structure and well-defined architectures attract plenty of attentions due to their high surface area, low density, permeability and large capacity of guest chemicals. These microspheres have extensive application prospects in a lot of fields such as catalysis[1], selective separation[2], micro-gas sensor[3-4], and control-released drug delivery system[5]. However the constitution of the hollow structure and the surface morphology in the microspheres is still a challenge for the researchers.

Biotemplate synthesis which means applying the biological tissues as templates and replicating the natural structure onto the materials is a new pathway to prepare the nano/micro materials with special structure and morphology. So far several biological tissues including lotus leaf[6-7], rose petal[8], butterfly wings[9-10] and pollen grains[11-13] have been applied in materials preparation. For the synthesis of microspheres pollen grain is a promising biotemplate since its regular shape, uniform particle size and natural fascinating surface morphology[14-15]. Despite there are many advantages, only a few progress was achieved and the desired replication of the pollen grains was barely reported.

Herein we reported a new method to synthesize the hollow silica (SiO_2) microspheres with pollen-like structure, which based on the surface modification and in-situ reaction. In this method the ammonium oleate, a surfactant was used as the surface modifying agent and the hydrophobic property of the pollen wall was applied. As a result, the hollow SiO_2 microspheres with hierarchical network surface were prepared successfully. The structure and morphology of this microsphere were characterized and the formation mechanism was discussed. Bovine serum albumin (BSA) was used as the model drug to investigate the adsorption property of the as-prepared microspheres.

Experimental Section

Materials. Tetraethoxysilane (TEOS), oleic acid, aqueous ammonia, and isopropyl alcohol were obtained from Sinopharm Chemical Reagent Co., Ltd. All reagents were of analytical grade and used as received. The rapeseed pollen grains (*Brassica napus*) collected by bees were purchased from a local apiculture company. A necessary purification was carried out before their using in synthesis. Briefly, the pollen grains were thoroughly ground, washed with absolute alcohol in an ultrasonic cleaner and then filtered. This process was repeated several times until a clear filtrate was observed. Finally, the pollen grains were dried at 50 °C overnight.

Synthesis of Hollow SiO_2 Microspheres. Firstly, 5 g pollen grains, 20 mL oleic acid and 120 mL isopropyl alcohol were mixed together in a 500 mL flask, followed by 10 mL aqueous ammonia. This mixed solution was magnetic stirred for 1 h at room temperature. Then 1.9 mL TEOS was added dropwise into the mixture under constant stirring. After TEOS injection the mixture was stirred for another 24 h to synthesize the pollen/SiO_2 microspheres. When the reaction ended the white powder was filtered from the mixture. The collected pollen/SiO_2 microspheres were rinsed with distilled water and absolute alcohol for several times respectively and put into a convection oven at 70 °C to dry overnight. Finally the pollen/SiO_2 microspheres were sintered at 600 °C to remove the pollen grains and fabricate the hollow SiO_2 microspheres. The heat treatment was performed under the atmosphere and a slow heating rate of 8 °C/min and furnace cooling were applied for preventing damage from heat stress. In the two control groups, same synthesis process were applied, but the amounts of the TEOS were adjusted to 1 mL and 3.8 mL. The microspheres synthesized with 1, 1.9, and 3.8 mL TEOS were labeled as A, B, and C respectively.

Characterization. The morphology and structure of the pollen grains, pollen/SiO_2 microspheres and hollow SiO_2 microspheres were characterized by the scanning electron microscope (SEM, FEI Quanta 200 and JEOL JSM-5900). All samples were coated with a thin gold layer before characterization, and an accelerating voltage of 15 kV was used. The Fourier transform infrared spectra (FT-IR) analysis was performed on a Nicolet Nexus 670 FT-IR spectrometer with the KBr pellet method. The scanning range is 400-4000 cm^{-1} and the resolution is 2 cm^{-1}. The nitrogen adsorption-desorption isotherm was measured on a surface area and porosimetry analyzer (Micromeritics ASAP2020) in which the hollow SiO_2 microspheres were first degassed at 300 °C in a vacuum for 2 h. The surface area and the pore size distribution were calculated by the Brunauer-Emmett-Teller (BET) method and Battet-Joyner-Halenda (BJH) respectively.

Drug Loading Test. To estimate the drug loading property of the as-prepared hollow SiO_2 microspheres, bovine serum albumin (BSA) was selected as the model drug. BSA was dissolved in an acetic buffer solution at pH 4.5 and the concentration of this solution was diluted to 3 mg/mL. As much as 25 mg hollow SiO_2 microspheres was then mixed with 20 mL of BSA solution. The mixtures were incubated in a water shaker for 12 h at 200 rpm and room temperature. At different periods of time, the mixtures were centrifuged at 5000 rpm for 5 min and the concentrations of BSA in solution were measured with a UV-Vis spectrometer by standard curve method.

Results and Discussion

Structure and Morphology of the Pollen Grains. Fig. 1 shows the SEM images of the pollen grains used in this study. As shown in Fig.1b, the pollen grain is a microsphere with porous surface of 20 μm in diameter. It could be found at low magnification that the regularity and uniformity of the pollen grains are comparable to the most used artificial microspheres (Fig. 1a). While at the high magnification, the porous surface of pollen grain which formed by a hierarchical network is much more attractive than any artificial microspheres (Fig. 1c). Since these structural features noted above, pollen grain is considered as the most desirable and promising template for the synthesis of microspheres. In addition, the natural core/shell structure of the pollen grains could be clearly observed through some broken ones (Fig. 1d). The core known as protoplasm takes most inner space of the pollen grains and consist of protein, amino acid, vitamins, and nucleic acids which easy to break down under thermal treatment[16-17]. The shell with porous surface usually called pollen wall is

made of a biopolymer named sporopollenin which has the high temperature stability and chemical resistance[18]. Due to the tender core and tough shell, pollen grain shows great potentiality in synthesis of the microspheres with hollow structure and special surface morphology. The core would be easy to remove by heat treatment and the shell would provide a stable template for the morphology replication. However the common methods in biotemplate synthesis like chemical and physical vapor deposition, lay-by-lay self-assembly and coprecipitation are not available for pollen grains, since the chemical inertness of the sporopollenin and the complicated morphology of the pollen wall.

Considering the characteristic of the pollen grains, an in-situ synthesis method based on chemical modification of the pollen wall was applied and the hollow SiO_2 microspheres with porous surface were prepared successfully in this study. The oleic acid played an important role during the in-situ synthesis process. Firstly, the oleic acid reacted with aqueous ammonia to give ammonium oleate, in which the ammonium is hydrophilic and the long-chain alkane is hydrophobic. Then, when the pollen grains were added, the synthesized ammonium oleate entirely covered the pollen grain through the hydrophobic interaction due to the hydrophobicity of the pollen wall. Furthermore the ammonium stretched toward the solution made the pollen grains being positively charged. As the TEOS was added, a typical sol-gel process under alkaline condition started and the hydrolysate being negatively charged was generated. As a result, the pollen grain was covered by the hydrolysate through the electrostatic interaction and followed by the in-situ polycondensation which turned hydrolysate coating into SiO_2.

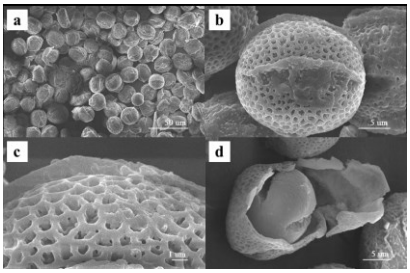


Fig. 1 SEM images of pollen grains (a-overview of pollen grains, b-an individual pollen grain, c-surface detail of the pollen wall, d-core/shell structure of the pollen grain)

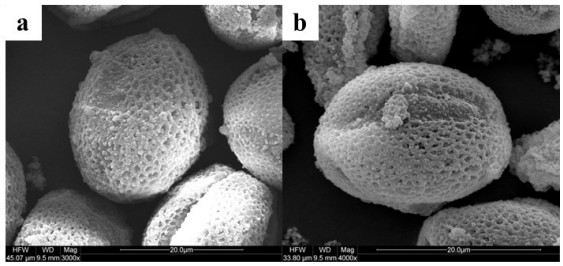


Fig. 2 SEM images of pollen/SiO_2 microspheres (a) and hollow SiO_2 microspheres (b)

Characterization of the Hollow SiO_2 Microspheres. As shown in Fig. 2, after the in-situ synthesis process the pollen grains were totally covered by SiO_2 nanoparticles and the morphology of the pollen wall were well kept (Fig. 2a). More importantly, even when the templates were removed, the final microspheres prepared by calcinations looked almost exactly like the pollen grains. When the single microspheres and pollen grain were compared, little change could be found except a bit of ovalization caused by shrinkage (Fig. 2b).

For further investigation of the structure of the SiO_2 microspheres, more SEM images of the different parts of the microspheres were taken. As shown in Fig. 3a, the as-prepared SiO_2 microspheres are well monodispersed and homogeneous shaped. The regularity and uniformity of these microspheres exhibit high similarity to the pollen grains. The common flaws in similar study like broken or deformation could be hardly found in this sample. At high magnification, it could be found that the porous morphology of the pollen wall was replicated because of the nano SiO_2 particles deposited along the framework of the pollen wall, which was attributed to the in-situ synthesis process (Fig. 3b). All these results indicate that the surface modification of the pollen grain is a helpful strategy for replication of its delicate microstructure. The hollow structure of the SiO_2 microsphere was investigated through some broken ones. As shown in Fig. 3c, pollen grain was totally removed after the heat treatment and a huge cavity was left. From the cross section of the shell of the microsphere, it could be found that the pores on the shell are connected to the inner cavity (Fig. 3d). These structures suggest that this microsphere is available in adsorption and preservation which would make it a desirable candidate for plenty of application.

The transition from the pollen grain to the hollow SiO_2 microspheres were also investigated by the FT-IR spectrum. As shown in Fig. 4a, there is a series of characteristic absorption peaks in the

FT-IR spectrum of the pollen grains. The peak at 2930 cm^{-1} and the shoulder peak nearby correspond to the asymmetric stretching vibration of methylene. The peaks at 1650 and 1550 cm^{-1} correspond to the vibration of amide I and amide II in the protein. And the peaks at 1406, 1240 and 1078 cm^{-1} correspond to the lignin, carboxylic acid and polysaccharide respectively[19-20]. All of these characteristic absorption peaks are weaken in the FT-IR spectrum of the pollen/SiO_2 microspheres shown in Fig. 4b, which may be caused by the coating of the silica. Besides, some new peaks appeared at 1100, 800, and 465 cm^{-1} which correspond to the asymmetric stretching vibration, symmetrical stretching vibration and bending vibration of the Si-O-Si indicate the existence of the silica on the pollen grains. While in the FT-IR spectrum shown in Fig. 4c, all the absorption peaks corresponding to organic component in the pollen grains disappear and only the absorption peaks corresponding to silica could be observed. This obvious conversion has proved that the pollen grains have been removed through the calcinations and the hollow SiO_2 microspheres have been synthesized.

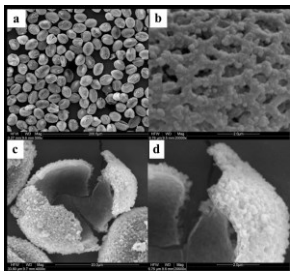


Fig. 3 SEM images of hollow SiO_2 microspheres (a-overview of hollow SiO_2 microspheres, b-surface detail, c-hollow structure, d-cross section of shell)

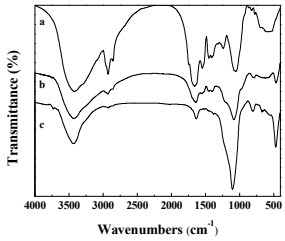


Fig. 4 FT-IR spectra of pollen grain (a), pollen/SiO_2 microsphere (b), hollow SiO_2 microsphere (c)

Effect of the Different TEOS Amount. From the SEM images shown in Fig. 5 it could be found that there are obvious differences in structure and morphology between the microspheres prepared with different TEOS amount. As shown in Fig. 5a, when 1 mL TEOS is used, more shrinkage is found in the as-prepared microsphere. In contrast, the microsphere synthesized with 3.8 mL TEOS is more close to spherical in shape (Fig. 5d). Suggested by the observation of the cross section of these two kinds of microspheres in which the shell of sample A (Fig. 5c) is much thinner than the shell of sample C (Fig. 5f), the amount of the deposited SiO_2 nanoparticles is thought to be the main reason for this difference. The more TEOS was used in the synthesis process, the thicker shell and the rounder shape of the microspheres were achieved. Furthermore the pore structure of the microspheres could also be affected by the amount of the TEOS. As shown in Fig. 5b and 5e, when less TEOS was used, the pores were larger and clear, and when the more TEOS was used, the pores were replaced by the closely packed nanoparticles.

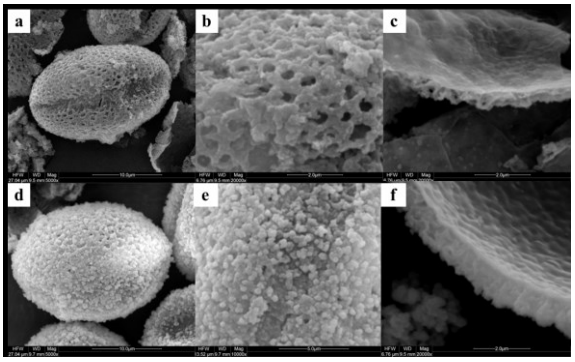


Fig. 5 SEM images of hollow SiO_2 microspheres prepared from different amount of TEOS(a, b, c-1 mL TEOS, d, e, f-3.8 mL TEOS)

The detailed pore structure of the different kinds of microspheres were characterized by N_2 adsorption-desorption measurement and the results were shown in Fig. 6 and Table 1. The N_2 adsorption-desorption isotherm of all the hollow SiO_2 microspheres exhibited the type IV isotherm with type H3 hysteresis loop, which suggested these microspheres were mesoporous, containing interconnected network of irregular pores. Meanwhile, the stretch of these hysteresis loop at high

relative pressure indicated the existence of marcopores. However, it is worth noting that the relative pressure of the stretch decreased with the increasing amount of TEOS, which suggests an increasing proportion of the mesoporous. This result was proved by the pore size analysis, in which sample A exhibited the widest distribution of pore size and largest average pore size while the pore size of sample C was much concentrated. The effects from the amount of TEOS indicate that the pore structure of the microspheres prepared through this in-situ synthesis process could be easily adjusted, which is the important for the application in adsorption and separation.

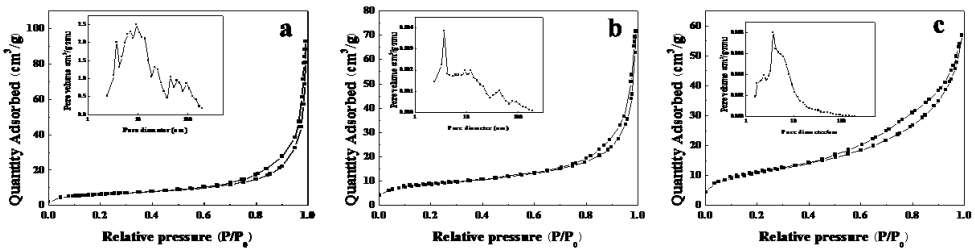


Fig. 6 N_2 adsorption-desorption isotherms and pore size distribution of hollow SiO_2 microspheres prepared from different amount of TEOS (a-1 mL b-1.9 mL, c-3.8 mL)

Table 1 The BET specific surface areas, pore volume and average pore diameter of the hollow SiO2 microspheres prepared from different amount of TEOS

Sample	S_{BET}(m^2/g)	Pore volume(cm^3/g)	Pore diameter(nm)
A	22.56	0.12	22.28
B	30.24	0.098	13.06
C	38.80	0.087	8.95

The adsorption curve of the BSA on the different kinds of hollow SiO_2 microspheres are shown in Fig. 7, and the drug loading, loading capacity (LC) and encapsulation efficiency (EE) of these microspheres are listed in Table 2. Although all three samples exhibit the adsorption capacity of BSA, the comparison of these samples indicates that there is a connection between the pore structure and adsorption properties. As shown in Table 2, the drug loading, loading capacity and encapsulation efficiency are all improved with the increasing amount of TEOS. Since the effect of the TEOS on the pore structure of microsphere, the adsorption of the microsphere is consider to be controllable by adjusting the synthesis process.

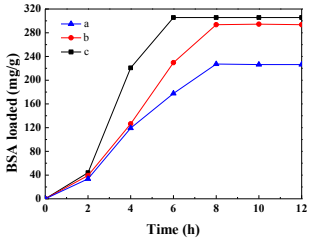


Fig. 7 BSA adsorption of the hollow SiO_2 microspheres prepared from different amount of TEOS (a-1mL, b-1.9 mL, c-3.8 mL)

Table 2 Drug loaded, loading capacity and encapsulation efficiency of the hollow SiO_2 microspheres prepared from different amount of TEOS

Sample	Drug loaded(mg)	LC(%)	EE(%)
A	5.67	22.68	9.45
B	7.34	29.37	12.23
C	7.64	30.59	12.73

Summary

In this paper an in-situ synthesis method based on the chemical modification of the pollen grains was used to prepare hollow SiO_2 microsphere from the natural pollen grain. In this method the hydrophobic pollen wall was coated by the surfactant through hydrophobic interaction, and the in-situ synthesis process took place by the electrostatic interactions between surfactant and TEOS. As a result, the hollow microspheres prepared by this method exhibited a high similarity to the pollen grain in both of appearance and pore structure. Furthermore, the structure and morphology of the microspheres synthesized through this method could be easily adjusted by changing the amount of added TEOS. The adsorption properties of the microspheres with different pore structures were studied. All samples exhibited the adsorption capacity to the model drug. And the drug loaded,

loading capacity and encapsulation efficiency of these microspheres could also be affect by the amount of added TEOS.

Acknowledgement

This work is financially supported by the National Natural Science Foundation of China (No. 21103119), and University Science Research Program of Jiangsu Province (No. 11KJB430012).

References

[1] S L Wang, P G Li, H W Zhu, et al, Controllable synthesis and photocatalytic property of uniform CuO/Cu2O composite hollow microspheres. Powder technology. 230 (2012) 48-53
[2] G Cheng, Z G Wang, Y L Liu, et al, Magnetic affinity microspheres with meso-/macroporous shells for selective enrichment and fast separation of phosphorylated biomolecules. Applied Materials and Interfaces. 5(8) 3182-3190
[3] H G Zhang, Q S Zhu, Z Yang, et al, One-pot synthesis and hierarchical assembly of hollow Cu_2O microspheres with nanocrystrals-composed porous multishell and their gas-sensing properties, Advanced Functional Materials. 17(2007) 2766-2771
[4] Z Chen, M H Cao, C W Hu, Novel Zn_2SnO_4 hierarchical nanostructures and their gas sensing properties toward ethanol, The Journal of Physical Chemistry C. 115(2011) 5522-5529
[5] Y Boonsongrit, H Abe, K Sato, et al, Controlled release of bovine serum albumin from hydroxyapatite microspheres for protein delivery system, Materials Science and Engineering B. 148 (2008) 162-165
[6] K C Chang, H Lu, C W Peng, et al. Nanocasting technique to prepare Lotus-leaf-like superhydrophobic electroactive plyimide as advanced anticorrosive coatings, Applied Materials and Interfaces, 5 (2013) 1460-1467
[7] M H Sun, C X Luo, L P Xu, et al, Artificial lotus leaf by nanocasting, Langmuir. 21 (2005) 8978-8981
[8] J C Qian, F Chen, Z G Chen, et al. China rose petal as biotemplate to produce two-dimensional ceria nanosheets, Journal of Nanoparticles Research. 13 (2011) 7149-7158
[9] W Zhang, D Zhang, T X,Fan et al, Novel photoanode structure templated from butterfly wing scales, Chemistry of Materials. 21 (2009) 33-40
[10] J Y Huang, X D Wang, Z L Wang, et al, Controlled replication of butterfly wings for achieving tunable photonic properties, Nano Letter. 6 (2006): 2325-2331
[11] S Fang, H L Su, H Jie, et al, Bioinspired hierarchical tin oxide scaffolds for enhanced gas sensing properties, The Journal of Physical Chemistry C. 116 (2012) 10274-11028
[12] B R Thio, K K Clark, A A Keller, Magnetic pollen grains as sorbents for facile removal of organic pollutants in aqueous media, Journal of Hazardous Materials. 194 (2011) 53-61
[13] F Cao, D X Li, Biotemplate synthesis of monodispersed iron phosphate hollow microspheres, Bioinspiration and Biomimetics. 5 (2010) 16005-16010
[14] Z S Guan, Y Zhang, Z Z Xu, et al, Morphology-controlled synthesis of SiO_2 hierarchical structures using pollen grains as templates, Chinese Journal of Chemistry. 26 (2008) 467-470
[15] F Cao, D X Li, Morphology-controlled synthesis of SiO_2 hollow microspheres using pollen grain as biotemplate, Biomedical Materials. 4 (2009) 25009-25013
[16] N Tanaka, K Uehara, J Murata, Correlation between pollen morphology and pollination mechanisms in the hydrocharitaceae, Journal of Plant Research. 117 (2004) 265-276
[17] J R Rowley, J J Skvarla, B Walles, Microsporogenesis in pinus sylvestris. VI. exine and tapetal development during the tetrad period, Nordic Journal of Botany. 20 (2000) 67-87
[18] T C Chambers, H Godwin, The fine structure of the pollen wall of Tilia Platrphrllos, New Phytologist. 60 (1961) 393-399
[19] F Schulte, J Lingott, U Pane, et al, Chemical characterization and classification of pollen, Analytical Chemistry. 80 (2008) 9551-9556
[20] K F Fang, Y N Wang, T Q Yu, et al, Isolation of de-exined pollen and cytological studies of the pollen initines of pinus bungeana zucc. ex endl. and picea wilsonii mast. Flora, 203 (2008) 332-340

Key Engineering Materials Vols 645-646 (2015) pp 1279-1284
© (2015) Trans Tech Publications, Switzerland
doi:10.4028/www.scientific.net/KEM.645-646.1279

Submitted: 2014-11-04
Accepted: 2014-12-23

CMOS Amplifier for neural signal Recording Applications

ZHANG Zhang[2,3,a] , CHENG Zhengxi [1,2,b*], ZHUANG Yiwei[1]

[1] Key Laboratory of Infrared Imaging Materials and Detectors, Shanghai Institute of Technical Physics, Chinese Academy of Sciences, Shanghai 200083,China

[2] State Key Laboratory of ASIC & System, Fudan University, Shanghai 200433, China

[3]School of Electronic Science & Applied Physics, Hefei University of Technology, Hefei, Anhui 230009, China

[a]zhangzhang@hfut.edu.cn, [b]czx@mail.sitp.ac.cn

Keywords: CMOS amplifier, neural signal, neural probe

Abstract. A low power low noise CMOS amplifier with integrated filter for neural signal recording is designed and fabricated with CSMC 0.5 μm CMOS process. DC offsets introduced by electrode-tissue interface are rejected through a feedback low-pass filter. The bandwidth of the amplifier is in 3.5Hz-5.5KHz range, and the gain is about 48dB in the midband. AC input differential mode voltage range is 10mV, and DC input differential mode voltage range is 180mV. The amplifier can accommodate 180mV DC offsets drift and 10mV neural spikes. The neural probe array is integrated directly on the surface of the amplifier array chip, and is tested in saline solution, and also is implanted in rats *in vivo* , the results of the experiments show that the amplifier is suitable for neural signal recording. The power dissipation is about 14μW while consuming 0.16 mm^2 of chip area, which satisfies implantable devices requirements.

Introduction

After more than 40 years development, micro neural probe arrays fabricated through MEMS technologies nowadays has a scale more than 100 microelectrodes, and integrates with amplifier, AD, and even wireless transmission circuits[1]. Micro neural probe array is used to detect multisite neural signals simultaneously in high temporal resolution and spatial resolution, which are widely applied in neuroscience laboratories for scientists to observe actives of neurons. And Micro neural probe array is also a prominent device for brain-machine interface, which is necessary for many fantastic applications, such as neural prosthetic for the disabled and the blind, action-as-thought unmanned fighter planes.

Toward the aim of a fully implanted device for chronic application in vivo, there is a strong need for low power low noise amplifier with small chip area for recording neural signals. To avoid the surrounding tissues damaged by the heat generated by the amplifiers, the power of each amplifier should be limited to no more than 0.128mW[2,3]. And to integrate the amplifier array directly with probe arrays, the dimension of each amplifier should be limited to the center-to-center distance of the probes, which is about 400 μm[4].

There are three parts of the voltage signal that the neural probe picks up: spikes , local field potentials(LFP) and DC offsets present at the electrode-tissue interface. Spikes or LFPs are as large as 1–2 mV in amplitude. Spikes are in 300 Hz–5 kHz, while LFPs are in 10 Hz –200 Hz. And DC offsets are about 0.3-1V in amplitude according to differential recording electrodes[2,3]. In order to amplify spikes and LFPs, DC offsets must be blocked firstly to prevent the amplifier from being saturated . There are two basic ways to block DC offsets. The first way is to use a MOS-bipolar pseudo-resistor to shunt off DC offsets. The advantage of shunt-off resistor is that it consumes very small chip area which is important for implant applications, while the disadvantage is that the resistor value must be controlled in a range according to the issue-electrode interface properties[5]. The second one is to use a high pass RC filter to restrain DC offsets. The advantage is that can be adopted to many different kinds of probes regardless the impedance of the issue-electrode interface, while the disadvantage is

that capacitors in the RC filter usually takes a large chip area which is not suitable for implantable devices[2,3].
This paper reports the design and testing of a low power low noise CMOS amplifier for neural signal recording. The bandwidth of the amplifier is in 3.5Hz-5.5KHz range, and the gain is about 48dB in the bandwidth. DC offsets are rejected through a low-pass filter in the feedback loop. Though blocked DC offsets voltage range is limited on the order 200mV, it satisfies many neural recording applications while consuming very small chip area [6].

Neural Amplifier Design

The basic circuit structure of the amplifier is adopted from Jin Ji[6], and some modifications are made. The amplifier is redesigned and fabricated with CSMC 0.5 μm CMOS process.
Block diagram of amplifier. Fig.1 shows the components of the amplifier. The high frequency small signal is amplified through a simple two stage operational amplifier. The first stage amplifier is a differential amplifier with dynamic load which is controlled by the DC feedback signal V_{adjust}. The second stage is a signal transistor amplifier with a current mirror as load. The output is amplified through a feedback amplifier, and filtered through a low pass filter to get the DC feedback signal V_{adjust} which is proportional to the DC part of the inputs. Then V_{adjust} controls the dynamic load of the first stage amplifier, and adjusts the DC operation points of the first stage, thus prevents the amplifier from saturation due to the input DC offsets and drifts.

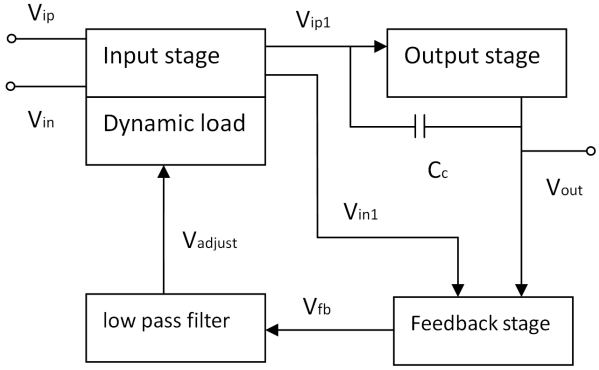


Fig. 1 Block diagram of the amplifier

Schematic of amplifier. Fig.2 shows the schematic of the amplifier. In the first stage, a PMOS differential pair including M_1 and M_2, is used at the input stage to reduce 1/f noise. M_{13} and M_{14} form the second stage with the gain G_2, which is the output stage. C_c is the compensate capacitor. The load of the first stage contains two parts, including M_{3a}, M_{4a}, M_{3b} and M_{4b}. M_{3a} and M_{4a} form a current mirror pair, to convert double inputs into single output. Since M_{3b} is in diode-connected form, it dominates the output impedance of the first stage, and sets the gain of the first stage, which is G_{1p}. High frequency signals are amplified by the input stage and the output stage, and higher cutoff frequency is determined by C_L.
M_8-M_{12} form the feedback amplifier with the gain G_3. C_1, C_2, C_3 and D_1, D_2, D_3 form a three stage low pass filter. D_1, D_2, D_3 are forward biased with equivalent resistance R_d . The capacitance of C_1, C_2, C_3 and the resistance of D_1, D_2, D_3 set lower cutoff frequency. So only low frequency signals can be feedback, and high frequency signals are filtered out in the feedback loop. M_{4a} and M_{4b} form a folded common source amplifier with the gain G_{m4}, and so do M_{3a} and M_{3b} with the gain G_{m3}. The two folded common source amplifier are connected in series to form the dynamic loads of the first stage. The DC feedback signal V_{adjust} controls the two folded common source amplifiers, thus adjusts the DC operation points of the first stage. If the DC offset in V_{ip} goes up, then $V_{ip}\uparrow \rightarrow V_{ip1}\downarrow \rightarrow V_{out}\uparrow \rightarrow V_{fb}\uparrow \rightarrow V_{adjust}\uparrow \rightarrow V_{in1}\downarrow \rightarrow V_{ip1}\uparrow$. This is a negative feedback, and stabilizes Vip1, thus prevent the amplifier from saturation. The similar process goes with V_{in}.

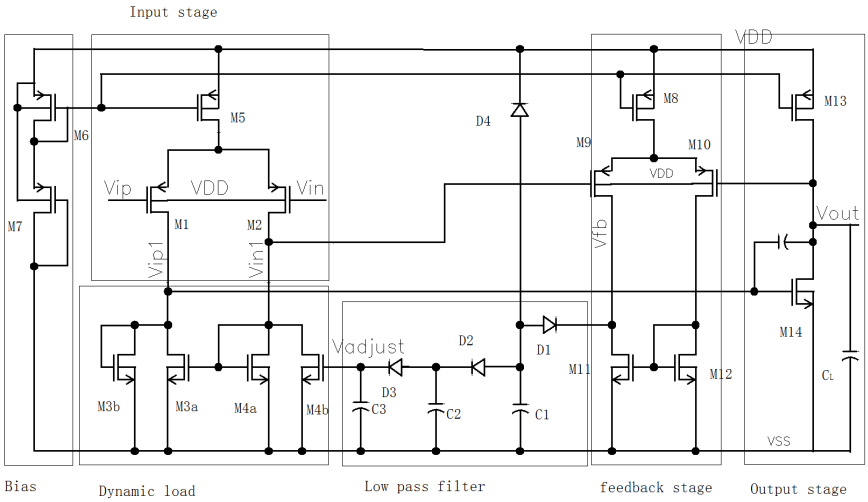


Fig. 2 Schematic of the amplifier

Experiment results

The amplifier was fabricated with CSMC 0.5 μm CMOS process. Fig.3 is the layout of amplifier. And Fig.4 is a photograph of the chip, which contains a sparse matrix of 20 amplifiers. The amplifiers was characterized first, then a three-dimension neural probe array was integrated on the top of the amplifiers[7,8], which is shown in Fig. 5. Performance of the neural probe array integrated with amplifier array was evaluated then.

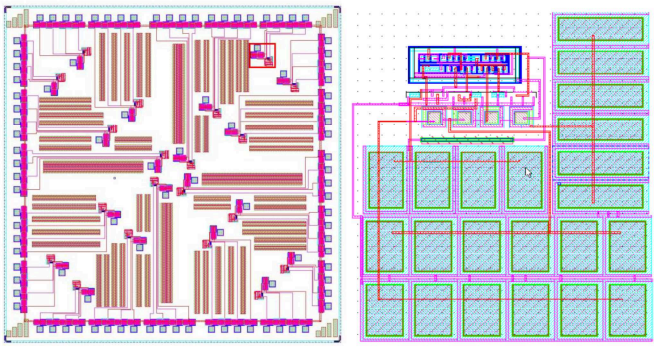


Fig. 3 The layout of the amplifier(a)sparse matrix of 20 amplifiers (b)a single amplifier

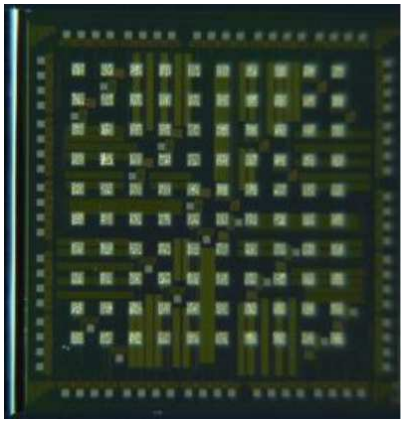


Fig. 4 The chip

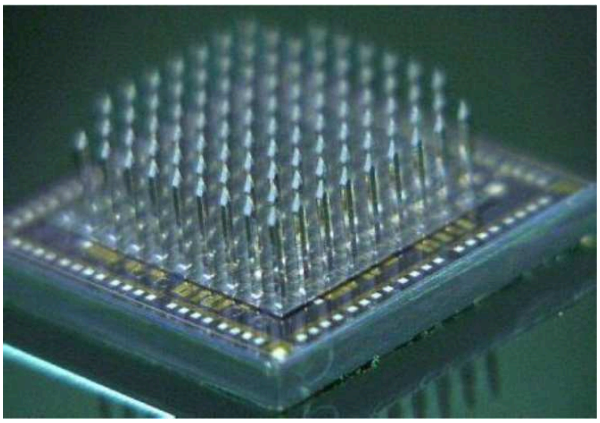
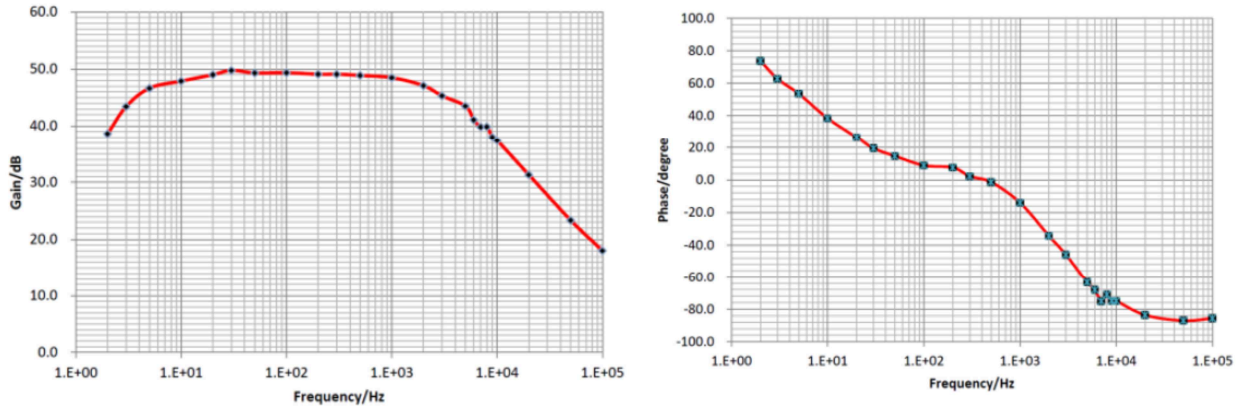


Fig. 5 Neural probe array integrated with amplifier array

Characterization. Fig.6 shows the measured amplifier transfer function from 2Hz to 100kHz. The midband gain is 48 dB. And the bandwidth is 3.5Hz-5.5kHz, which is a little smaller than the

designed aim, but is suitable for most neural spikes and LFPs. Table 1 summaries simulation results and measured results. Actually the amplifier was designed with 5V voltage supply, but used with 3.3V voltage supply to reduce power. AC input differential mode voltage range is 10mV, so the amplifier can accommodate neural spikes. The simulated DC input differential mode voltage range is 210mV, which is enough for DC offset block in many applications. And the measured result is 180mV. The amplifier can accommodate 180mV DC drift and 10mV neural spikes.



(a) (b)

Fig. 6 Measured transfer function of amplifier

Table 1 Simulated and measured characteristics of the amplifier

Parameter	Simulation	Measured
Supply voltage	3.3[V]	3.3[V]
Gain	≥50[dB]	48[dB]
Low-frequency cutoff	25[Hz]	3.5[Hz]
High-frequency cutoff	6.3k[Hz]	5.5k[Hz]
PSRR	80[dB]	52[dB]
CMRR	68[dB]	67[dB]
Input common mode voltage range(DC)	2[V]	1.8[V]
Input differential mode voltage range (DC)	210[mV]	180[mV]
Input differential mode voltage range(AC)	7[mV]	10[mV]
Input-referred noise	3.5[μV_{rms}]	0.35[μV_{rms}]
Power	20.4[μW]	14[μW]
Area	125 ×150 [μm^2]	125 ×150 [μm^2]

Performance evaluation of neural probe array integrated with amplifier array. The integrated probe array was evaluated by immersing the probe array into a 0.9%wt NaCl solution. An Pt electrode with 0.5 cm^2 area was placed 1 cm away from the probe array as the reference electrode. And an Ag electrode placed near the probe array acted as the simulation electrode. A periodic bipolar pulse signal by tektronix AFG3102 Dual Channel Arbitray/Funtion generator was inducted into the solution through Ag electrode, and was picked up by the probe array, and then was amplified by the amplifier, and shown and recorded by LeCroy oscillocsope (waverunner 6050). The neural probe and Pt reference electrode were connected to the positive and negative input end respectively. Different frequencies signal with the same amplitude 50mV were generated. A typical result is shown in Fig. 7, the frequency is 1kHz. Due to the attenuated by saline solution, the signal picked up at neural probe is smaller than 10mV, which is much smaller than signal picked up the simulation electrode. And many high frequency noises were also induced in saline solution, but filtered out by the amplifier.

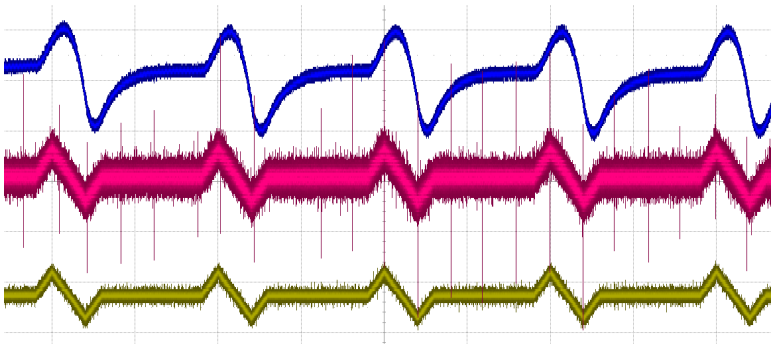


Fig. 7 Typical bipolar pulse signal: the blue line on the top is the signal picked up at output of the amplifier, the red line in the middle is the signal picked up at neural probe, the yellow line at the bottom is the signal picked at the simulation electrode

In a second set of proof-of-concept experiments, neural probe was implanted in primary motor cortex of SD rats *in vivo* under anasthesia. After anasthesia with intraperitoneal injection of urethane , the rat was fixed at stereofixture. The scalp was removed and a windows with 6mm × 6mm was opened on skull, and then dura mater was removed there. The neural probe array was carefully was inserted into the cerebral cortex. A typical signal is shown in Fig. 8.



Fig. 8 Typical neural signal

Summary

A low power low noise CMOS amplifier for neural signal recording is designed and fabricated with CSMC 0.5 μm CMOS process. DC offsets are blocked through a feedback low-pass filter. The bandwidth of the amplifier is in 3.5Hz-5.5kHz range, and the gain is about 48dB in the midband. DC input common mode voltage range is 1.8V. AC input differential mode voltage range is 10mV, and DC input differential mode voltage range is 180mV. The amplifier can accommodate 180mV DC drift and 10mV neural spikes. Neural probe array integrated amplifier array was tested in saline solution, and also was implanted in rats *in vivo* , the results of these experiments showed that the amplifier is suitable for neural signal recording. The power dissipation is about 14 μW while consuming 0.16 mm^2 of chip area, which satisfies the implantable devices requirements.

Acknowledgement

This work is supported by National Natural Science Foundation of China (No. 60906057) , Innovation projects of Shanghai Institute of Technical Physics(Q-ZY-86), and open projects of State Key Laboratory of ASIC & System(12KF002). The circuit is redesigned by ZHANG Zhang.

References

[1] K. D. WISE, D. J. ANDERSON, J. F. HETKE, D. R. KIPKE, AND K. NAJAFI, Wireless Implantable Microsystems: High-Density Electronic Interfaces to the Nervous System, IEEE PROCEEDINGS OF THE IEEE. 92,(2004)76-97.

[2] Reid R. Harrison, the design of integrated circuits to observe brain activity, Proceedings of the IEEE. 96, (2008) 1203-1216.

[3]Reid R. Harrison, Cameron Charles, a low-power low-noise CMOS amplifier for neural recording applications, IEEE journal of solid-state circuits. 38(2003)958-965.

[4]Yoon-Kyu Song, William R. Patterson, Christopher W. Bull, et al, Development of a chipscale Integrated Microelectrode/Microelectronic device for Brain Implantable Neuroengineering Applications. 13, (2005)220-226.
[5]Qing Bai, Kensall D. Wise, single-unit neural recording with active microelectrode arrays, IEEE transactions on biomedical engineering. 48, (2001) 911-920.
[6]Jin Ji, Kensall D. Wise, An Implantable CMOS Circuit Interface for Multiplexed Microelectrode Recording Arrays, IEEE Journal of solid-state circuits. 27(1992)433-443.
[7]Zhuang Yiwei, Cheng Zhengxi, Zhang Xueming, Yuan Honghui, Fabricaiton of the silicon-based three-dimension neural probe arrays, Key Engineering Materials. 609-610(2014)758-768.
[8] Cheng Zhengxi, Zhuang Yiwei, et al, Fabrication of Hybrid Three Dimension Neural Probe Arrays, Chinese Journal of sensors and actuators. 26(2013)150-156.

Key Engineering Materials Vols 645-646 (2015) pp 1285-1289
© (2015) Trans Tech Publications, Switzerland
doi:10.4028/www.scientific.net/KEM.645-646.1285

Submitted: 2014-11-16
Accepted: 2014-12-23

Analysis and simulation of a planar microelectrode structure for dielectrophoretic manipulation of a single cell and cell cluster

Ping Chen[1,a], Xueliang Ma[1,b], Hua Zhang[1,c], Meijie Han[1,d], Yongcun Wang[1,e], Binbin Li[1,f] and Haixin Zhu[1,g*]

[1] School of Electrical Engineering, Shanghai Dianji University, Shanghai 200240, P. R. China

[a]chenp@sdju.edu.cn, [b]maxl@sdju.edu.cn, [c]zhanghua@sdju.edu.cn, [d]hanmj@sdju.edu.cn, [e]ag43@163.com, [f]libb@sdju.edu.cn, [g]hzhu2012@gmail.com (corresponding author)

Keywords: Dielectrophoresis, finite element analysis, single cell manipulation, cancer diagnosis.

Abstract. In this paper, we proposed a four-electrode microdevice for precise isolating and trapping of a single cell using negative dielectrophoresis (nDEP) forces. To generate appropriate nDEP forces, sinusoidal alternating currents (AC) signals with various phase shifting were applied to the microelectrodes, and the finite element analysis (FEA) techniques were used to analyze the resulted electric field distribution. The simulation results implied that effective trapping and rotation forces can be realized by the proposed device structure under specific excitation condition. The geometry effect on the electric field distributions of electrodes was further studied in details. For the electrodes with 50 μm width, the maximum value of the gradient of the squared field strength could reach 10^6 V^2/m^3, which is higher than that for electrodes with 20 μm width. The influences of applied voltage to electric field gradient were also simulated and the result shows that the dielectrophoresis (DEP) force increased significantly with the magnitude of applied voltage. These preliminary results may provide useful insight and design guidelines for the future DEP microstructure design and fabrication.

1. Introduction

Precise manipulation of a single cell or cell cluster has been the most important focus during the development of single cell analysis which is aimed to study cellomics for the early diagnosis of diseases like cancer. There are several kinds of techniques to manipulate a cell or cell cluster, such as ultrasound [1, 2], optical tweezers [3, 4], magnetic force [5], electrophoresis, electroosmosis [6, 7] and dielectrophoresis. However, the electrophoresis requires the cell to be charged, while the magnetic force acts on the magnetic particle. The manipulation efficiency of ultrasound, optical tweezers and electroosmosis is not satisfactory. Among the above techniques, the dielectrophoresis-based (DEP) live cell manipulation technique shows the promise of providing high throughput, long-term analysis with minimized potential cell damage. The DEP technology has been widely used for cell trapping, separation and enrichment [8-15].

Dielectrophoresis is an electrokinetic movement of uncharged particle which induced by the polarization in the non-uniform electric field. The theoretically design of electrode is critical in the DEP cellular experiments which is related to the electric field distribution. In the present work, a four-electrodes electrorotation chip was proposed and the electric field distribution were analyzed by using the finite element method. The results demonstrated that the designed device could produce effective trapping and rotation electric field, which can be used for the single cell manipulation.

2. Theory and Methods

The dielectrophoresis force is occurred in the interface of cell and medium. For a spherical particle, the time-averaged DEP force can be calculated from the following equation [16]:

$$F_{DEP} = 2\pi\varepsilon_m r^3 \,\mathrm{Re}[f_{CM}]\nabla\left|E\right|^2 . \quad (1)$$

Where the ε_m, r, $\nabla|E|^2$ and f_{CM} is the permittivity of the suspending medium, the radius of the particle, the local electric field gradient and the Clausius-Mossotti (CM) factor, respectively.

The CM factor can be expressed as:

$$f_{CM} = \frac{\overline{\varepsilon_p} - \overline{\varepsilon_m}}{\overline{\varepsilon_p} + 2\overline{\varepsilon_m}}. \quad (2)$$

Where the $\overline{\varepsilon_p}$ and $\overline{\varepsilon_m}$ are the complex permittivities of particle and medium, respectively. According to the equations (1) and (2), it is found that the direction of DEP force is depending on the electric properties of particle and the medium. Depending on whether the force is in the direction of higher or lower electric filed, the positive DEP (pDEP, then $\mathrm{Re}[f_{CM}] > 0$) or negative DEP (nDEP, then $\mathrm{Re}[f_{CM}] < 0$) can be induced. In order to effectively trap and rotate a cell, a larger DEP force is demanded. Considering that the DEP force is proportional to the square electrical gradient, the effects of microelectrode structural sizes and applied alternating currents (AC) power on the electric field distribution were studied in details.

The electric field distribution was calculated by using the finite element numerical method. The electric field as the function of position was computed from the Laplace's equation $\nabla^2 V = 0$.

3. Results and discussion

A quadruple planar microelectrodes configuration was designed and shown in Fig. 1. The total space is 180 μm. Two electrode models with different widths (50 μm and 20 μm, respectively) were constructed to investigate the effect of electrode size on the electric field distribution. The distance between the opposite electrodes is 60 μm. The electrical conductivity of gold electrode and suspending medium is 45.6 S/m and 0.01 S/m, respectively. In all simulations, the phase of AC power which applied on the left electrode was selected as a reference, and the phase shift on adjacent electrodes is 90 degrees (around the anticlockwise direction).

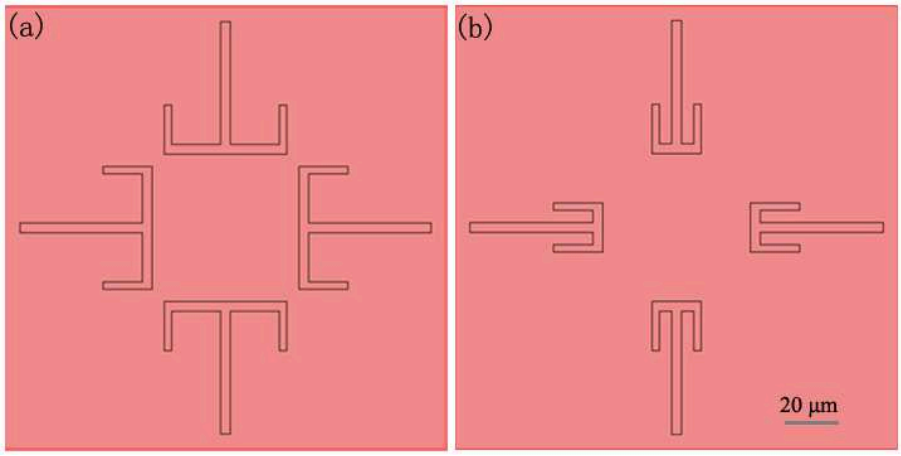


Fig. 1. The proposed planar microelectrodes model with different sizes. The width of gold electrodes in (a) and (b) is 50 μm and 20 μm, respectively.

Based on the above models, the electric field strength distribution and absolute values of the gradient of the squared field strength around the electrodes were calculated. The simulation results of the 50 μm electrode (Fig. 1(a)) were shown in Fig. 2. It indicated that the lowest electric field position located in the midpoint of microelectrodes. The cell or cell cluster can be trapped in this lower electric filed region by the n-DEP force. In contrast, for the 20 μm electrode, the effective trapping region is difficult to establish due to the constraint of electrode space (the results were not shown). For the electrodes with 50 μm width, the maximum value of the gradient of the squared field strength could reach 10^6 V^2/m^3, which is higher than that for electrodes with 20 μm width. These results implied that the electrode size is a key factor to the formation of suitable trapping region.

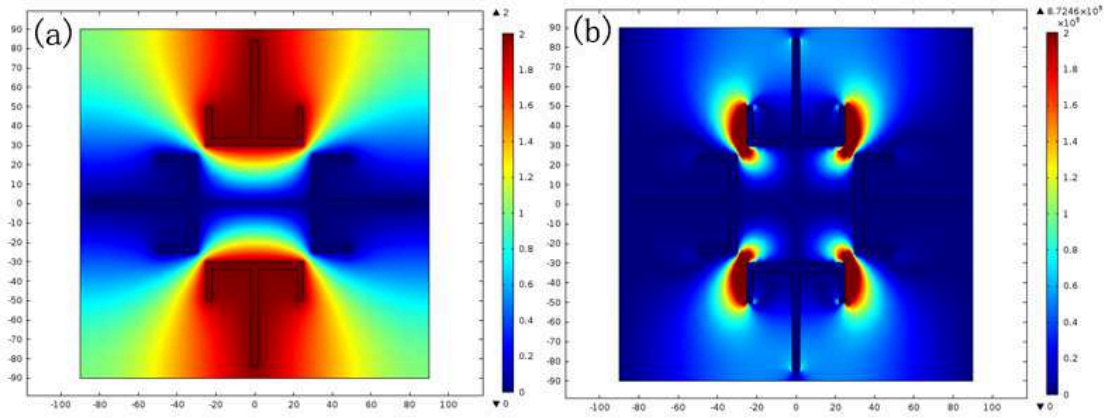


Fig. 2. The calculated electric field strength distribution (a) and absolute values of the gradient of the squared field strength (b) around the electrodes with 50 μm width.

Fig. 3 showed the absolute values of the gradient of the squared field strength distribution as the applied power for electrodes with different initial phase angles. The peak-peak value of the power (Vpp) is set to 2 V on each electrode. As can be seen from these pictures, the rotation electric field was formed. The minimum electrice field strength point which located in the centre was maintained as the changes of initial phase angle. Now, we can conclude that the present microelectrodes system is an effective trapping and rotation system. It is worthwhile to note that more than one minimum point was formed as the changes of initial phase angle. For example, two new minimum points were located at the joints of two electrodes while the applied power for electrodes with initial 30 degrees phase angle. In the accurate cellular experiment, the presence of new minimum points would lead to the oscillation of the trapped cell. In the future research, we will take more attention on how to eliminate this drawback by the design of novel devices. Of course, the theoretically predicted results should be examined by the future experimental work.

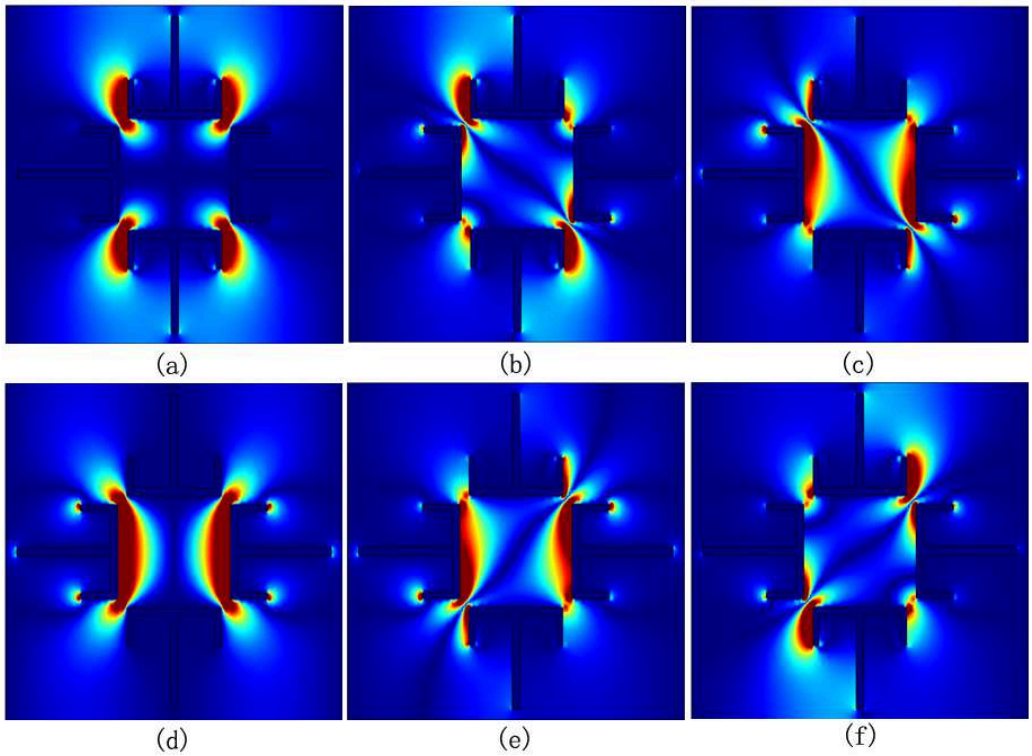


Fig. 3. The absolute values of the gradient of the squared field strength distribution as the applied power for electrodes with initial phase angle of (a) 0 degrees, (b)30 degrees,(c)60 degrees,(d)90 degrees,(e)120 degrees and (f)150 degrees. The power is set to 2 Vpp on each electrode with phase shift of 90 degrees.

Fig. 4 showed the absolute values of the gradient of the squared field strength distribution with different applied power. The applied voltage (Vpp) is selected as 2 V, 4 V, 6 V and 8 V, respectively. The results clearly showed the region with higher field strength increased significantly as the increase of applied voltage. The maximum value of gradient of the squared field strength was 8.7×10^5 V^2/m^3 while the applied voltage was 2 V. When the voltage was 8 V, the maximum value was increased to 1.4×10^7 V^2/m^3. The absolute values of the gradient of the squared field strength along the y=-x direction (through the centre of the trapping region) with different voltage magnitudes were shown in Fig. 5. The one dimension data showed that the value of gradient of the squared field strength was dependent on the magnitudes of voltage. The highest gradient of the squared field strength occurred at the edges of electrodes. In the midpoint of trapping region, the gradient of the squared field strength was already nearly zero. While a live cell was trapped in the central region, it would be less harmful to it because of the decrease of Joule-heat.

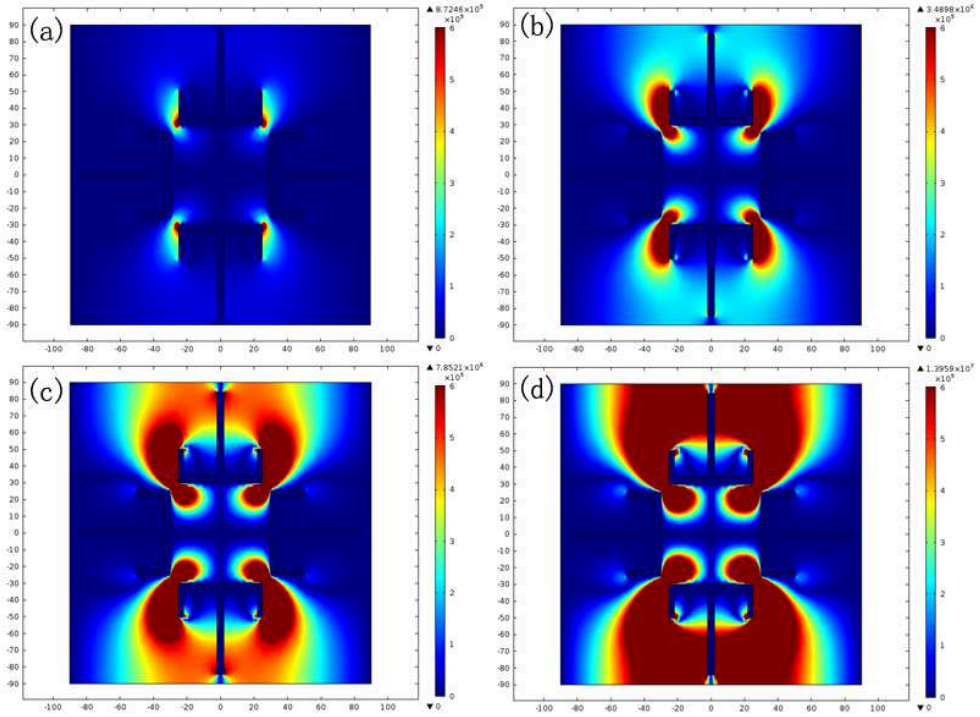


Fig. 4. The absolute values of the gradient of the squared field strength distribution with the applied power. The applied power is selected as (a) 2 V, (b) 4 V, (c) 6 V and (d) 8 V, respectively.

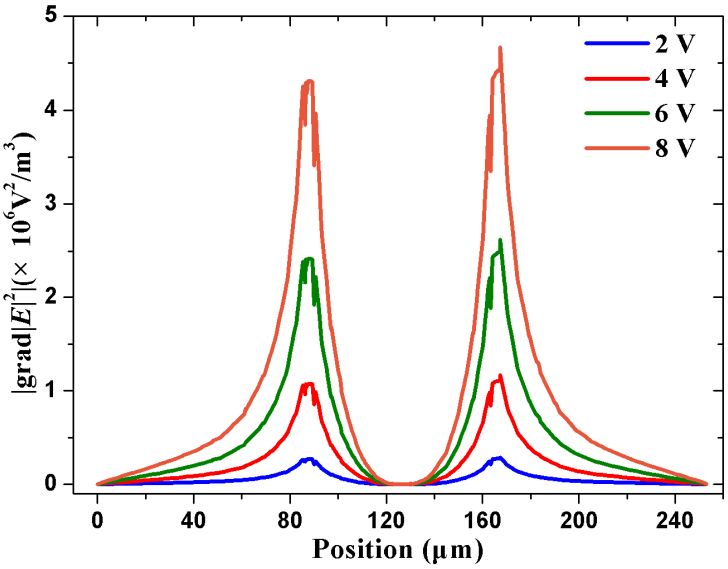


Fig. 5. The absolute value of the gradient of the squared field strength along the y = -x direction (through the centre of the trapping region) with different voltage magnitudes.

4. Conclusions

In summary, a planar four-microelectrode structure for the dielectrophoretic trapping and rotation of a single cell and cell cluster was proposed. The electric field distributions were calculated by using the finite element techniques. The effects of geometry sizes and applied AC powers on the electric field distributions were discussed in details. The obtained theoretical results indicated that the proposed device can produce effective trapping and rotation electric field, and which may provide meaningful guidance for the future theoretical design and device fabrication.

Acknowledgement

This research was supported by the start-up fund for Lingang Scholars in Shanghai Dianji University (13C414) and initial funding of Shanghai Dianji University (14QD22, 14QD23, 14QD24, 14QD25).

References

[1] J. Hultström, O. Manneberg, K. Dopf, H.M. Hertz, H. Brismar, M. Wiklund, Proliferation and viability of adherent cells manipulated by standing-wave ultrasound in a microfluidic chip, Ultrasound med. bio., 33 (2007) 145-151.

[2] J.J. Hawkes, R.W. Barber, D.R. Emerson, W.T. Coakley, Continuous cell washing and mixing driven by an ultrasound standing wave within a microfluidic channel, Lab Chip, 4 (2004) 446-452.

[3] A. Ashkin, J. Dziedzic, T. Yamane, Optical trapping and manipulation of single cells using infrared laser beams, Nature, 330 (1987) 769-771.

[4] S.M. Block, D.F. Blair, H.C. Berg, Compliance of bacterial flagella measured with optical tweezers, Nature, 338 (1989) 514-518.

[5] J. Dobson, Remote control of cellular behaviour with magnetic nanoparticles, Nature nanotech., 3 (2008) 139-143.

[6] P.C. Li, D.J. Harrison, Transport, manipulation, and reaction of biological cells on-chip using electrokinetic effects, Anal. chem., 69 (1997) 1564-1568.

[7] J. Voldman, Electrical forces for microscale cell manipulation, Annu. Rev. Biomed. Eng., 8 (2006) 425-454.

[8] N. Mittal, A. Rosenthal, J. Voldman, nDEP microwells for single-cell patterning in physiological media, Lab Chip, 7 (2007) 1146-1153.

[9] M. Şen, K. Ino, J. Ramón-Azcón, H. Shiku, T. Matsue, Cell pairing using a dielectrophoresis-based device with interdigitated array electrodes, Lab Chip, 13 (2013) 3650-3652.

[10] L. C. Hsiung, C.H. Yang, C.L. Chiu, C.L. Chen, Y. Wang, H. Lee, J.Y. Cheng, M.C. Ho, A.M. Wo, A planar interdigitated ring electrode array via dielectrophoresis for uniform patterning of cells, Biosens. Bioelectron., 24 (2008) 869-875.

[11] C. Huang, C. Liu, J. Loo, T. Stakenborg, L. Lagae, Single cell viability observation in cell dielectrophoretic trapping on a microchip, Appl. Phys. Lett., 104 (2014) 013703.

[12] M. Talary, K. Mills, T. Hoy, A. Burnett, R. Pethig, Dielectrophoretic separation and enrichment of CD34+ cell subpopulation from bone marrow and peripheral blood stem cells, Med. Biol. Eng. Comput., 33 (1995) 235-237.

[13] Y. Huang, S. Joo, M. Duhon, M. Heller, B. Wallace, X. Xu, Dielectrophoretic cell separation and gene expression profiling on microelectronic chip arrays, Anal. Chem., 74 (2002) 3362-3371.

[14] J. Vykoukal, D.M. Vykoukal, S. Freyberg, E.U. Alt, P.R. Gascoyne, Enrichment of putative stem cells from adipose tissue using dielectrophoretic field-flow fractionation, Lab Chip, 8 (2008) 1386-1393.

[15] M. Alshareef, N. Metrakos, E.J. Perez, F. Azer, F. Yang, X. Yang, G. Wang, Separation of tumor cells with dielectrophoresis-based microfluidic chip, Biomicrofluidics, 7 (2013) 011803.

[16] H.A. Pohl, The motion and precipitation of suspensoids in divergent electric fields, J. Appl. Phy., 22 (1951) 869-871.

Key Engineering Materials Vols 645-646 (2015) pp 1290-1297
Submitted: 2014-11-26
Accepted: 2014-12-23
© (2015) Trans Tech Publications, Switzerland
doi:10.4028/www.scientific.net/KEM.645-646.1290

A Biological 3D Printer for the Preparation of Tissue Engineering Micro-channel Scaffold

Zhang YaNan[1, a], Liu Yuanyuan[1, b *], Li Yu[1, c], Li Shuai[1, d] and Hu Qingxi[1, e]

[1]Rapid Manufacturing Engineering Center, Shanghai University, Shanghai 200444, China

[a] email: zhangyanan0501@163.com, [b] email: yuanyuan_liu@shu.edu.cn

[c] email: liyu_shu@shu.edu.cn, [d] email: allenle1991@shu.edu.cn,

[e]email: huqingxi@shu.edu.cn

Keywords: 3D printing; coaxial nozzle; micro-channel; vascularization; hydrogel scaffold

Abstract. The clinical applications of tissue engineering are still limited by the lack of a functional vascular supply in tissue-engineered constructs. In order to improve the pre-vascularization of tissue-engineered scaffold during in vitro culture, in this study, based on three-dimensional (3D) printing technology, using the crosslinking effect of coaxial fluids (sodium alginate and $CaCl_2$) to prepare vessel-like hollow gel fibers, then layer by layer overlapping into 3D scaffold. The biological 3D printing platform was successfully developed and a coaxial nozzle module was introduced to generate a $CaCl_2$-in-Alginate coaxial microfluidic. The inner core diameters of the prepared hollow gel fibers were 220~380 micrometers. In addition, the influence of materials concentration and dispensing rates on hollow fiber dimension were investigated, the cell-encapsulated in the printed hollow fibers was realized and the viability of endothelial cells (ECs) was studied with Laser scanning confocal microscopy (LSCM) and Live-Dead cell staining. The 3D scaffold built by hollow fibers could improve the phenomenon of diffusion constrain and enhance the survival rate of those ECs growing at a greater depth in the construct. This study provides a new theoretical basis for the vascularization of bone scaffold.

Introduction

Tissue engineering (TE) has been a promising field of research for several decades. However, the clinical applications of TE scaffolds still face many challenges, due mainly to its inability to provide sufficient blood supply in the initial phase after implantation. Most tissues and organs in the body rely on blood vessels to supply cells with nutrients and oxygen, so cells are always found no more than 100~200μm from the nearest capillary [1-4]. Due to the limited diffusion capability of hydrogels, when a complex and thick engineered tissue construct without sufficient vascularization is implanted, the seeded cells will have a limited capacity to uptake enough nutrients (glucose, amino acids), exchange oxygen gas and clear byproducts of metabolism (CO_2, lactate, and urea).These limitations impair cell viability, results in cell death and necrotic core, which hinders the success of the engineered tissue [5-7]. So it is critical that a tissue be prevascularized before implantation.

Many approaches to vascularization have been undertaken by researchers, including material functionalization, bioreactor development, microfabrication, scaffolds design, endothelial cell seeding and so on [8-14]. However, the manufacturing and integration of vascular networks is still a challenge. In order to solve the problem, some researchers tried to embed microfluidic networks in thick tissues or used hollow fiber instead the classic solid fiber to build tissue engineering scaffold, which can greatly enhance mass transport in hydrogels and spatiotemporally control the chemical microenvironment of cells, mimicking the function of native microvessels [15]. Moronie *et al*.[16] used viscous encapsulation technology to extrude coaxial bi-layer fiber. The bi-layer solid fiber turned to a hollow one by selectively dissolution. But the problem was that cells cannot be embedded in the fiber to realize integrated manufacturing. Min Hu *et al*.[17] reported a method that can produce cell-seeded solid and hollow hydrogel fibers by enzymatically crosslinking with a coaxial

triple-orifice microfluidic platform. This fiber's formation process was mild enough to retain the cell viability.

3D printing technology, using a layer-by-layer additive process through a computer controlled system can realized the production of complex engineered tissue construct, and has obvious advantages in the construction of microfluidic channel when compared to traditional manufacturing methods [18-21]. In this study, based on 3D printing platform, a new coaxial nozzle module was developed. The coaxial nozzle module can realize the simultaneous extrusion of different materials, can be used for material modification, drug loading, cell encapsulation and hollow fiber preparation etc [22-25]. Different from other research methods, in this study the hollow fiber formed by using the cross-linking effect of coaxial fluids materials. Sodium alginate as matrix material due to its structural similarities to the ECM of living tissues, low toxicity, excellent biocompatibility, and easy gelation via the addition of divalent cations such as Ca^{2+} [26-28]. As shown in Fig.1, the preparation process can be separated to three regions (α-γ). α region: The sodium alginate solution is dispensed through the sheath section of the coaxial spinneret, while the calcium chloride ($CaCl_2$) solution is dispensed through the core section of the coaxial spinneret; β region: Two solutions are dispensed out of the spinneret, crosslinking occurred while the two solutions contacting. And along with the diffusion of calcium ions (Ca^{2+}) in radial direction from inner to outer, the shell solution gradually becomes completely gelation along the flow direction; γ region: The gelled hollow fibers would be deposited on the receiving plate, then layer by layer overlapping into a 3D scaffold under the control of the motion platform.

In this study, we developed a 3D printing platform and a coaxial nozzle module. The hollow gel fiber and a certain shape scaffold were successfully prepared. In addition, the influence of materials concentration and dispensing rates on hollow fiber dimension were investigated and the cell-encapsulated in hollow fibers was realized. More detailed experimental contents would be showed in the following text.

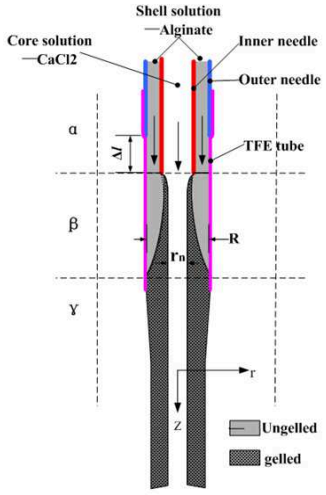


Fig.1 The schematic illustration of 3D printing hollow hydrogel fiber

Experimental Section

The Biological 3D printing platform. The Biological 3D printing platform (home-built equipment, Rapid Manufacturing Engineering Center, Shanghai University), as shown in Fig.2, which consisted of five main parts: variable management module (A in Fig.2), triaxial motion mechanism (B in Fig.2), multimode feed unit (C in Fig.2), forming platform (D in Fig.2) and a coaxial nozzle (E in Fig.2).

The coaxial nozzle assembly was introduced to generate a $CaCl_2$-in-alginate coaxial microfluidic. It mainly consisted of a tee coupling, an outer tube and an inner tube, as shown in Fig.2 (c, d) and Fig.3a. The alginate solution through the feed inlet was fed into the cavity formed between the outer and inner tubes, while $CaCl_2$ solution as cross-linking agent was fed through the inner tube to create hollow fiber. Both the two fluid materials were dispensed by syringe pumps (LongerPump, TJ-3A/W0109-1B) which can precisely control their dispensing rates. According to the upstream

distance of crosslinking agent, the outer needle was about 5 mm shorter than the inner one; a certain length tetrafluoroethylene (TFE) tube (Fig.2c) was equipped, its inner diameter was comparable to the out needle's outer diameter, and its length should exceed the inner needle orifice with a distance. The coaxial nozzle assembly has many benefits: the structure is simple, easy to manufacture, and could be conveniently changed inner and outer needles; the hydrogel clogged in the orifice could be removed conveniently through the detachable TFE tube; the TFE tube could convert the swelling of hydrogel in radius direction to axial direction fiber and uniform the outer diameter of the hollow fiber; the disturbance of environment factors to the coaxial jet were eliminated at the utmost.

The forming process of 3D scaffold containing microfluidic channels was shown in Fig.3b. With the two fluids contacting at the end of the nozzle, the filament with hollow structure was formed and printed immediately. The gelled hydrogel fibers deposited on the receiving plate, then layer by layer overlapping into a 3D scaffold under the control of the motion platform, alternating layers were oriented at 90° to each other.

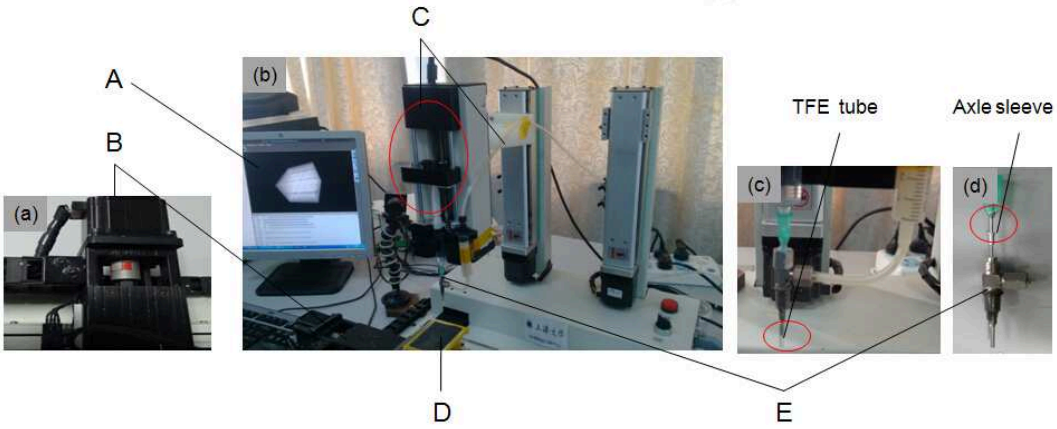


Fig.2 The biological 3D printing platform: A—variable management module (computer modeling); B—triaxial motion mechanism; C—multimode feed unit (syringe pump); D—forming platform (receiving plate); E—the coaxial nozzle.

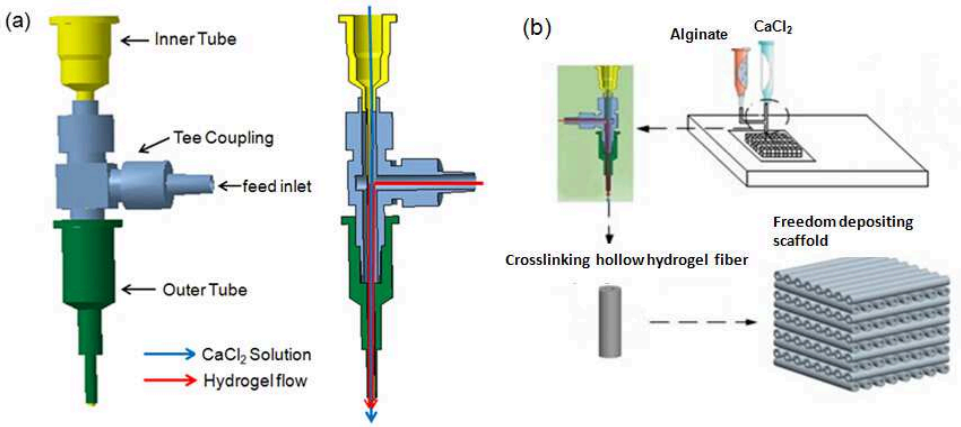


Fig.3 (a) 3D model and the cross-sectional view of the coaxial nozzle. (b) The forming process of the 3D micro-channel scaffold.

Materials. Sodium alginate (Chemical pure, molecular weight [9005-38-3]) and calcium chloride ($CaCl_2$, Analytically pure, molecular weight 110.8) were purchased from Sinopharm Chemical Reagent Co. China. 3~5% (w /v) sodium alginate was dissolved in deionized water and placed in a shaker for 10h at 120 rpm at room temperature. Similarly, 2~5% (w/v) calcium chloride solutions were prepared using deionized water.

Observation and measurement. The macro-morphology of hollow fiber was observed by optical microscope (EV3020, EASSON, shanghai university), fiber dimensions could also be measured.

The morphological characterization of scaffolds and hollow fibers were analyzed by the scanning electron microscope (SEM, SU1510, shanghai university). Hollow hydrogel fiber samples need extraction dehydration with hexamethyldisilazane (HMDS) and anhydrous ethanol, and pre-coated with a conductive layer of sputtered gold before observation and measurement.

Cell viability analysis. In the sterile clean bench (SW-CJ-2F, JingHua), the passage 3 endothelial cells (ECs), provided by Shanghai tissue engineering and research center, were uniformly mixed with alginate solution (disinfected by solid high pressure steam), and the final cell concentration was 5×10^6/mL; Then the cell-laden hollow fibers were printed in accordance with the forming method above. Put these cell-laden fibers in culture dishes and added some Dulbecco's Modified Eagle's Medium (DMEM) with 10% fetal bovine serum (FBS) medium into culture dishes, and co-cultured in an atmosphere of 5% CO_2 at 37°C. Culture medium was changed every other day.

For cell viability assay, the cell-laden fibers were stained with calcein acetoxymethylester (calcein AM) and ethidiumhomodimer-2 (Invitrogen) at a concentration of 1.0 mm each. Then these specimens were observed via Laser scanning confocal microscopy (LSM710, Occult International Ltd, shanghai university). ECs were underwent confocal imaging studies at day 1, day 4 and day 7. Image J (National Institutes of Health, Bethesda, MD) was used for the automated counting of red- and green stained ECs in z-axis projections, and percentages of viable cells were calculated.

Results and Discussion

Hollow filament formation and scaffold fabrication. During the process of preparation, process parameters were set as follow: the coaxial assembly had a 18 gauge (840μm inner diameter (I.D.), 1060μm outer diameter (O.D.)) inner needle and a 16 gauge (1190μm I.D., 1370μm O.D.) outer needle; the TFE tube's inner diameter was 1180μm; the receiving plate's moving speed was set at 14 mm/s. The single-layer scaffold (Fig.4a) and the four-layer micro-channel scaffold paved by hollow fibers were shown as Fig.4.

Hollow filaments samples and 3D scaffold were observed and measured by optical microscope and scanning electron microscope, as shown in Fig.5. Due to the different crosslinking degree in the radial direction, the transparent degree had a certain distinction, and the tubular wall and lumen can be clearly seen, as shown in Fig.5a, the average inner diameter of the hollow filaments was 320μm and the average wall thickness was about 280μm which within the scope of the hydrogel diffusion limited and basically met the diffusion of nutrients and metabolites. Fig.5b showed the SEM image of the hollow filament cross section, the lumen of the hollow filament had an acceptable cylindricity. After dehydration, the outer diameter shrank about 50%, while only a little changed on inner diameter. The optical microscope image of the scaffold's cross-section (Fig.5c) showed the structural integrity of the scaffold containing micro-channels, and the tubular wall and lumen could be clearly observed. However, due to the improper cutting method and compression, it had some deformation.

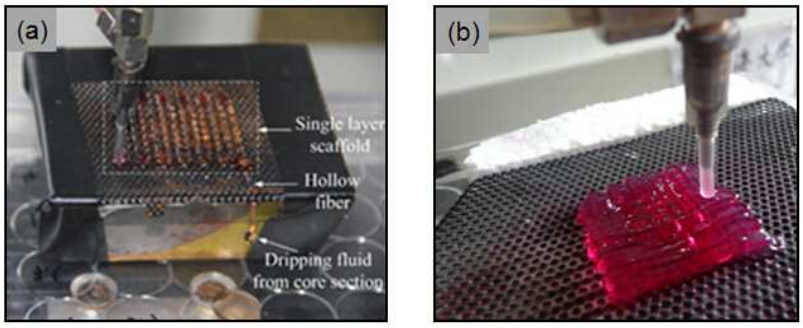


Fig.4 (a) The single-layer scaffold paved by hollow fiber. (b) The four-layer micro-channel scaffold

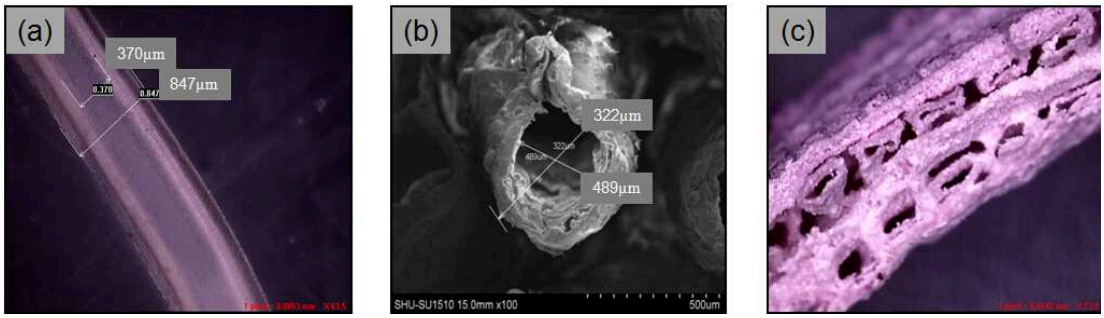


Fig.5 (a) Optical micrograph of the hollow fiber axis projection, the inner diameter is 370μm and the outer diameter is about 847μm, ×63.5; (b) SEM micrographs of the dehydrated fiber cross section, ×100; (c) Optical micrographs of 3D micro-channel scaffold.

Effect of material concentration on hollow fiber dimensions. Gelation of alginate occurred through the crosslinking mechanism, and it depends on alginate and $CaCl_2$ concentrations as well as their dispensing rates. In this section, effects of alginate and the crosslinker concentration on hollow filament dimensions were presented.

Alginate and $CaCl_2$ dispensing rate were fixed at 0.4 ml/min. As shown in Fig.6a, the results were obtained from an experiment conducted with 3~5% alginate cross-linked with 3% $CaCl_2$. It showed that the mean filament diameter increases with increasing of alginate concentration, whereas the mean inner core diameter decreases. It was due to that alginate's viscosity increased with the increasing of its concentration, which hindered the diffusion of Ca^{2+}, and made the crosslinking degree decrease. When alginate concentration was fixed at 4%, as shown in Fig.6b, the change of $CaCl_2$ concentration had no big impact on filament dimension, the variation amplitude of filament dimensions was no more than 100μm. The best dimension for tissue engineering was obtained at 4%Alginate-3%$CaCl_2$, where the mean filament diameter was 880μm, with a filament wall thickness of 280μm.

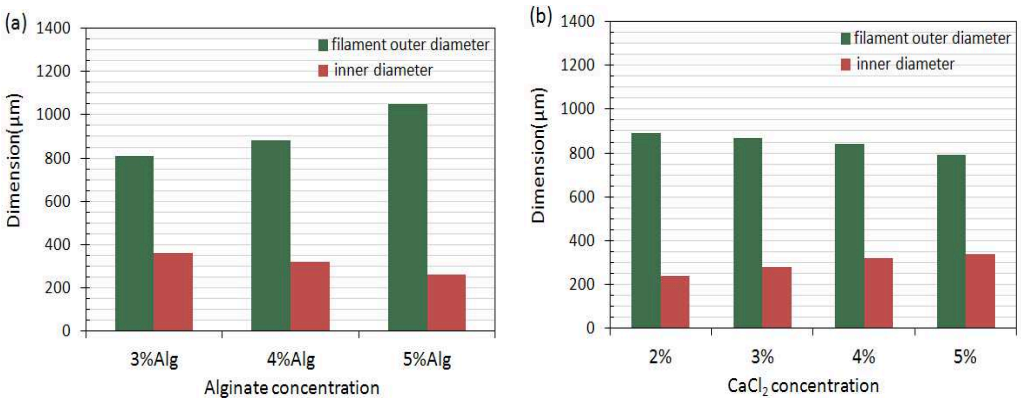


Fig. 6 (a) Effect of alginate concentration on hollow filament diameter and its inner core diameter, (3~5% alginate cross-linked with 3% $CaCl_2$); (b) Effect of $CaCl_2$ concentration on hollow filament diameter and its inner core diameter, (4% alginate cross-linked with 2~5% $CaCl_2$).

Effect of dispensing rate on hollow fiber dimensions. In this experiment, 4%Alginate-3%$CaCl_2$ was used. Their dispensing rates were controlled by syringe pump. As shown in Fig.7a, the alginate dispensing rate was set at 0.4ml/min, three feeding rates of $CaCl_2$ as 0.2, 0.4 and 0.6 ml/min were provided. As expected, with increasing of $CaCl_2$ dispensing rate, the inner core diameter increased, whereas the mean filament diameter decreased. Fig.7b showed the result of an experiment conducted with the $CaCl_2$ dispensing rate fixed at 0.4ml/min and the alginate dispensing pressure set at 0.3, 0.4 and 0.5 ml/min. Filament outer diameter increased as the alginate dispensing rate increased, but the inner core diameters were almost same and there was no distinct trend.

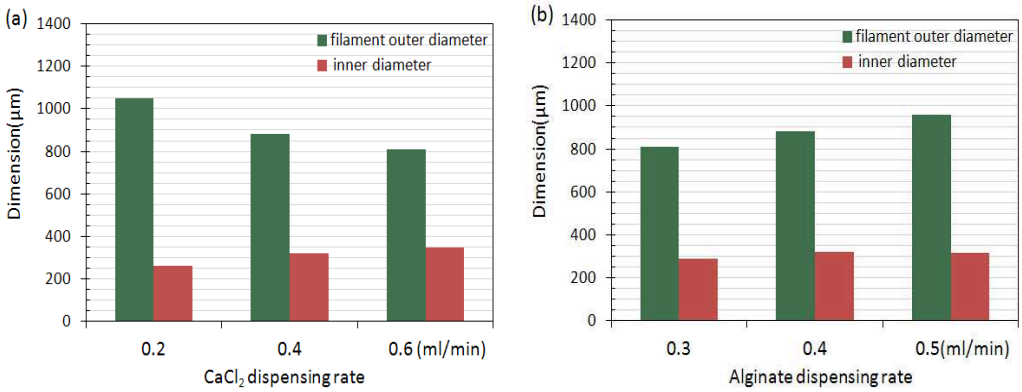


Fig.7 (a) Effect of $CaCl_2$ dispensing rate on filament dimensions, (0.4ml/min alginate cross-linked with 0.2, 0.4 and 0.6 ml/min $CaCl_2$); (b) Effect of alginate dispensing rate on filament dimensions, (0.3, 0.4 and 0.5 ml/min alginate cross-linked with 0.4ml/min $CaCl_2$).

Viability analysis of encapsulated ECs. Cells were evenly distributed in alginate solution before printing and were successfully encapsulated into solid fiber and hollow fiber during the fabrication process. For better visualization of embedded cells, we stained the ECs with red and green fluorescent dyes and observed with 3D scanning confocal laser microscopy. A z-axis stack of confocal images from top to center with 50μm intervals were shown in Fig.8 (a-c), demonstrating live/dead cells and their distribution in printed hollow fiber. These images indicated the presence of a perfectly formed 3D vessel with ECs which can be used for the future technologies for creating biomimetic microenvironments.

The viability was calculated by averaging three representative live/dead confocal images for each sample. Quantitative viability assays are presented in Fig.8d. The results indicated that there had no significant changes during 7 days of cell culture. The initial cell viability was about 85.4±1.16% 1 day post encapsulation within hollow filaments and maintained a high cell viability on day 3 (90.7±1.23%) and day 7 (89.3±1.67%).

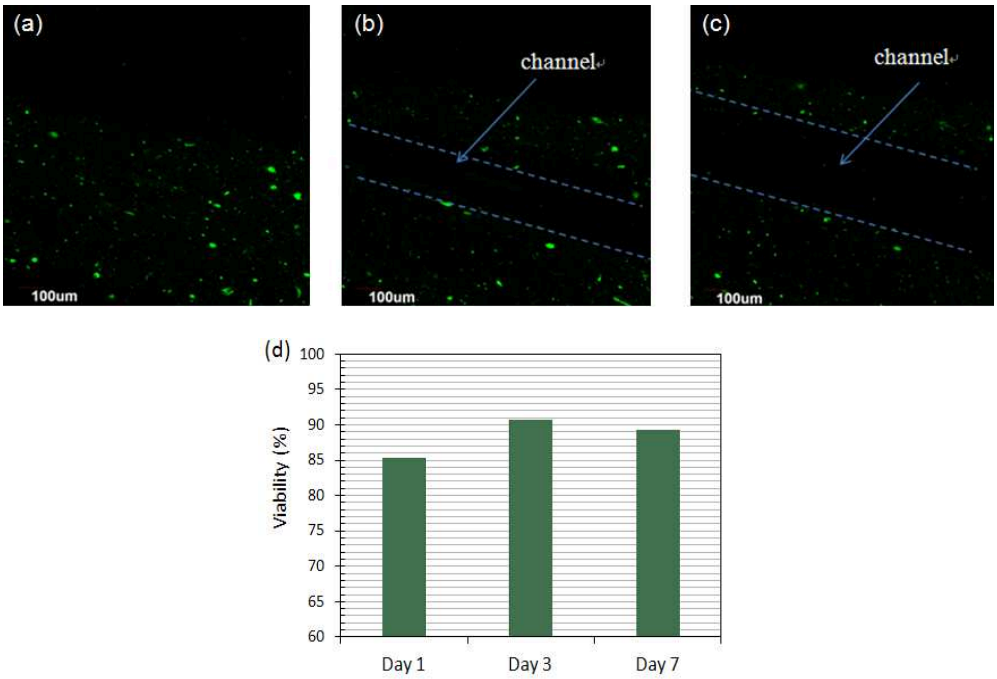


Fig.8 (a) Confocal image of cell-laden solid fiber; (b-c) Confocal images of cell-laden hollow fiber: (live cells showed fluorescent green); (d) cell viability over 7 days.

Conclusions

In this paper, we reported a biological 3D printer for the preparation of tissue engineering micro-channel scaffold and introduced a coaxial nozzle module to form hollow gel fibers by using sodium alginate solution cross-linked with $CaCl_2$. As expected, 3D micro-channel scaffold was successfully prepared by the method and the cell-encapsulated in hollow fibers was realized. The result showed that the hollow fiber had good interconnectivity and ECs could maintain high cell viability in the hollow fiber. It also showed that manipulation of the hollow fiber dimensions can be achieved by optimizing material components and the dispensing rate. Compared to traditional scaffold, 3D scaffolds made by hollow fibers could not only promote the transport of nutrients, but also reduce the adverse effects caused by biomaterial degradation. This approach provides a new theory and technique to achieve vascularization in tissue engineering scaffold and shows great potential to be used in thick tissue or living organs fabrication in the future.

Acknowledgments

This work was financially supported by the National Natural Science Foundation of China (No. 51475281 and No. 51375292), and the National Youth Foundation of China (No. 51105239).

References and Notes

[1] Luo, Y.C.; Bai, J.Q.; Li, Q.J.; Research progress of tissue engineered bone vascularization, J. China Journal of Coal Industry Medicine. 12 (2009) 501-503.

[2] Dong, Q.S.; Mao, T.Q. Construction ideas of bone tissue engineering vascularization, J. International Journal of Stomatology. 35 (2008) 321-324.

[3] Liu, Y.; Lim, J.; Teoh, S.H. Review: Development of clinically relevant scaffolds for vascularised bone tissue engineering, J. Biotechnology Advances. 31 (2013) 688-705.

[4] Muschler, G.F.; Nakamoto, C.; Griffith, L.G. Engineering principles of clinical cell-based tissue engineering, J. J Bone Joint Surg Am. 86 (2004) 1541-1558.

[5] Santos, M.I.; Reis, R.L. Vascularization in Bone Tissue Engineering: Physiology, Current Strategies, Major Hurdles and Future Challenges, J. Macromolecular Bioscience. 10 (2010) 12-27.

[6] Landman K.A.; Cai A.Q. Cell proliferation and oxygen diffusion in a vascularising scaffold, J. Bull Math Biol. 69 (2007) 2405-2428.

[7] Rouwkema, J.; Rivron, N.C.; van Blitterswijk, C.A. Vascularization in tissue engineering, J. Trends in Bio-technology. 26 (2008) 434-441.

[8] Lovett, M.; Lee, K.; Edwards, A.; Kaplan, D.L. Vascularization Strategies for Tissue Engineering, J. Tissue Engineering: Part B. 15 (2009) 353-370.

[9] Wang, J.L.; Yang, M.Y.; Zhu, Y.; Wang, L.; Tomsia, A.P.; Mao, C.B. Phage Nanofibers Induce Vascularized Osteogenesis in 3D Printed Bone Scaffolds, J. Advanced Materials. 26 (2014) 4961-4966.

[10] Krishnan, L.; Willett, N.J.; Guldberg, R.E. Vascularization Strategies for Bone Regeneration, J. Annals of Biomedical Engineering. 42(2014) 432-44.

[11] Volkmer, E.; Drosse, I.; Otto, S.; Stangelmayer, A.; Stengele, M.; Kallukalam, B.C.; Mutschler, W.; Schieker, M. Hypoxia in static and dynamic 3D culture systems for tissue engineering of bone, J. Tissue Engineer. Part A. 14 (2008) 1331-1340.

[12] Xiaohong Wang, Yongnian Yan, Renji Zhang. Recent trends and challenges in complex organ manufacturing, J. Tissue Engineering Part B. 16 (2010) 189-197.

[13] Yan, Y.N.; Zhang, T.; Zhang, R.J. Forming and Manufacturing Technique for Cells and Biological Materials, J. Journal of mechanical engineering. 46 (2010) 80-87.

[14] Yu, H.Y.; VandeVord, P.J.; Li, M.; Matthew, H.W.; Wooley, P.H.; Yang, S.Y. Improved tissue engineered bone regeneration by endothelial cell mediated vascularization, J. Biomaterials. 30 (2009) 508-17

[15] Huang, G.Y.; Zhou, Y.H.; Zhang, Q.C. Microfluidic hydrogels for tissue engineering, J. Biofabrication. 3 (2011) 1-13.

[16] Moroni, L.; Schotel, R.; Sohier, J. Polymer hollow fiber three-dimensional matrices with controllable cavity and shell thickness, J. Biomaterials .27 (2006) 5918-5926.

[17] Hu, M.; Kurisawa, M.; Deng, R.; Teo, C.M.; Schumacher, A. Cell immobilization in gelatin hydroxyphenylpropionic acid hydrogel fibers, J. Biomaterials. 30 (2009) 3523-3531.

[18] Zhang, J.M.; Zhang, X.Z.; Li, R.X. Preparation of tissue engineering scaffolds using rapid prototyping, J. Chinese Journal of Tissue Engineering Research. 17 (2013) 1435-1440.

[19] Whiteskles, G.M.; Grzybowski, B. Self-assembly at all scales, J. Science. 295 (2002) 2418-2421.

[20] Pfister, A.; Landers, R.; Laib, A.; Hübner, U.; Schmelzeisen, R.; Mülhaupt, R. Biofunctional rapid prototyping for tissue-engineering applications: 3D bioplotting versus 3D printing, J. Journal of Polymer Science Part A: Polymer Chemistry. 42(2004) 624-638.

[21] Bose, S.; Vahabzadeh, S. Bone tissue engineering using 3D printing, J. Materials Today. 16 (2013) 496-504.

[22] Cornock, R.; Beirne, S.; Thompson, B.; Wallace, G.G. Coaxial additive manufacture of biomaterial composite scaffolds for tissue engineering, J. Biofabrication. 6 (2014) 025002.

[23] Lewinska, D.; Chwojnowski, A.; Wojciechowski, C.; Kupikowska-Stobba, B; Grzeczkowicz, M. Electrostatic Droplet Generator with 3-Coaxial-Nozzle Head for Microencapsulation of Living Cells in Hydrogel Covered by Synthetic Polymer Membranes, J. Separation science and technology. 47 (2012) 463-469.

[24] Perez, R.A.; Kim, H.W. Core–shell designed scaffolds of alginate/alpha-tricalcium phosphate for the loading and delivery of biological proteins, J. Journal of Biomedical Materials Research Part A. 101A (2013) 1103-1112.

[25] Zhang, Y.; Yu, Y.; Chen, H.; Ozbolat, I.T. Characterization of printable cellular micro-fluidic channels for tissue engineering, J. Biofabrication. 5 (2013) 1-11.

[26] Ahn, S.H.; Lee, H.J.; Bonassar, L.J. Cells (MC3T3-E1)-Laden Alginate Scaffolds Fabricated by a Modified Solid-Freeform Fabrication Process Supplemented with an Aerosol Spraying, J. Biomacromolecules. 13 (2012) 2997-3003.

[27] Yang, C.H; Huang, K.S.; Wang, C.Y. Microfluidic-assisted synthesis of hemispherical and discoidal chitosan microparticles at an oil/water interface, J. Electrophoresis. 33 (2012) 3173-3180.

[28] He, S.L.; Yin, Y.J; Zhang, M. Research Advances on Sodium Alginate Hydrogels for Tissue Engineering, J. Chemical industry and engineering progress. 23 (2004) 1174-1177.

Key Engineering Materials Vols 645-646 (2015) pp 1298-1302
© (2015) Trans Tech Publications, Switzerland
doi:10.4028/www.scientific.net/KEM.645-646.1298

Submitted: 2014-11-26
Accepted: 2014-12-23

Specific Detection of Staphylococcus Enterotoxin B in Milk Using Piezoresistive Cantilever Aptasensor

Rui Zhao, Yongzheng Wen, Wei Ma, Jiancheng Yang and Xiaomei Yu [a]

National Key Laboratory of Science and Technology on Micro/Nano Fabrication, Institute of Microelectronics, Peking University, Beijing, 100871, CHINA

[a] yuxm@pku.edu.cn

Keywords: Aptasensor; Staphylococcus enterotoxin B (SEB); Piezoresistive cantilevers; Aptamers

Abstract. In this paper, an aptasensor with high sensitivity and rapid response was developed for the detection of staphylococcus enterotoxin B (SEB) by using thiol-modified piezoresistive cantilever. Thiol-modified aptamers, acting as the functionalized sensing elements, were immobilized on the nanogold-coated surface of the sensing cantilever as agents for detecting SEB. By using the functionalized aptasensors, different concentrations of SEB were detected with a wide detection range of 6-100 ng/mL and a quick response in milk. The experimental results indicated that the cantilever-based aptasensors had sufficient sensitivity for the detection of SEB in real food commodities and might provide an economical platform for on-site detections of different toxicants with the advantages of portability, high sensitivity, and rapid response.

Introduction

Staphylococcus enterotoxin B (SEB), a small monomeric protein (28.336 kDa) produced by the Gram-positive Staphylococcus aureus bacterium [1], is a pathogen with high thermal and proteolytic stability. There are some reports to prove from human volunteers exposed aerosols that the lethal dose of SEB reaches up to 0.02 μg/kg, but it can induce an emetic response at as low as 0.4 ng/kg [2]. These indicate that the clear need for developing toxin sensors with high sensitivity, rapid response, and reliability detection of SEB in food matrixes, especially from the standpoint of prominent and frequent cause of food poisoning and anti-bioterrorism.

Some researchers have concentrated on developing highly selective and sensitive tools to detect SEB, including electrical sensors, surface plasmon resonance (SPR), fluorescence labels or excited natural fluorescence, and chemiluminescence [3-7], all of which have exhibited high capability as a powerful tool for detecting SEB, but are performed by utilizing immunological assays, in which antibodies were crucial tools for bonding targets. Admittedly, antibodies have lots of advantages in biosensor applications, but they also have their limitations, such as time consuming, high cost, low stabilization, and ethical problems [8]. All of these attract intense interest of researchers to find out new recognition elements in biosensing applications. Aptamers, synthesized oligonucleotides that can bind tightly to a broad range of target molecules, have been demonstrated to overcome the negative factors of antibodies [9]. In particular, the conformation of aptamers often undergoes significant changes, which can offer remarkable flexibility in the design of novel biosensors. A few researches have demonstrated that highly sensitive and selective detections of SEB can be realized by utilizing aptamers [8, 10]. However, these detecting methods, which rely on expensively external instrumentations for measurement, are only suitable for detection in the laboratory.

Microfabricated piezoresistive (PZR) cantilevers, as the typical of the surface stress-based cantilevers, are highly attractive as transducers for their low cost, low power, and real-time measurement. Furthermore, PZR cantilevers, unlike optical cantilevers, have some incomparable advantages, including the simpler readout, measurement in opaque liquid phase or gas phase environments, and more easily being integrated in handle devices [11]. All these make PZR cantilevers be promisingly sensing platforms in bio/chemical on-site detections.

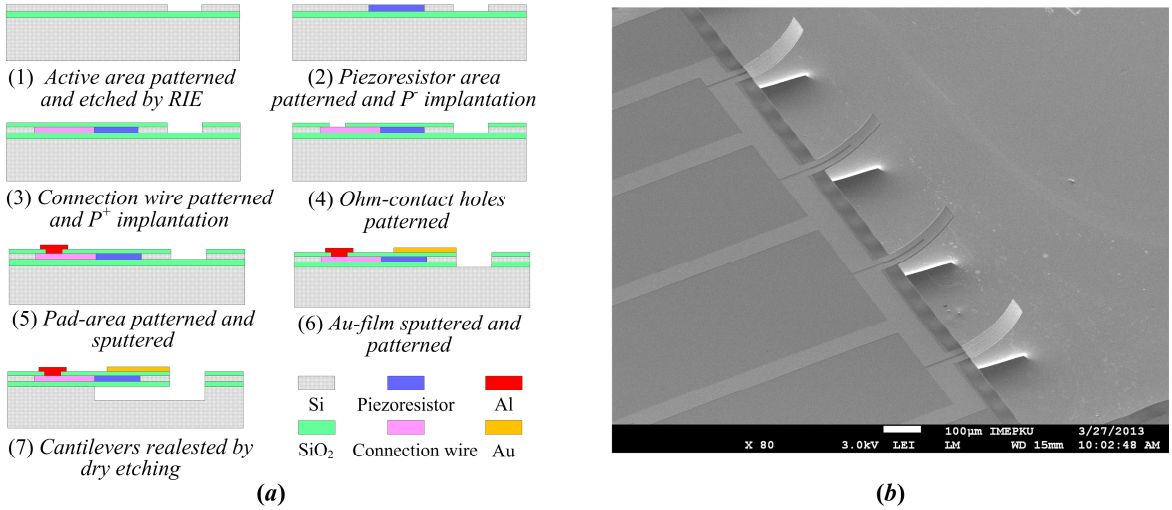
In this work, we combine PZR cantilevers with aptamer for a rapid, sensitive, and specific detection of SEB. A thiol-modified DNA aptamer, which serves as the active elements revealed by

Jeffrey A. DeGrasse in 2012 [12], was immobilized on the surface of PZR cantilevers for the detecting. Meanwhile, by using the functionalized aptasensors, different concentrations of SEB were detected with a wide detection range of 6-100 ng/mL and a quick response in milk.

Design and fabrication of PZR cantilever

In our design, each of the cantilevers was designed to be rectangular with the dimension of 200 μm×50 μm×1 μm and a piezoresistor's leg dimension of 100 μm×15 μm. Four piezoresistors with two of them located on measurement cantilevers and the other two on reference cantilevers form a Wheatstone bridge. Due to the four cantilevers with the identical mechanical structure, this design has a better suppression and counteraction on mechanical and external environmental noise.

The process used to fabricate the PZR cantilevers is shown in Fig. 1(a). Smart-cut SOI wafers with the device layer thickness of 0.34 μm, p-type, in [100] orientation were used. The processes can be summarized as follows: firstly, the device layer was implanted with phosphorus ions with a dosage of $5\times10^{13}cm^{-2}$ and energy 100 keV to form N^+ rings for the piezoresistors after a 30 nm silicon oxide layer was deposited by low pressure chemical vapor deposition (LPCVD) on the top of SOI wafer as the doping protective layer, with that the active areas were patterned by photolithography and reactive ion etching (RIE). Then the piezoresistors were formed by implanting boron ion at 50 keV with a dosage of $4\times10^{14}cm^{-2}$, which correspond a resistance of 7 kΩ for the designed piezoresistors. In the third step, electrical connection wires between the piezoresistors and pads were achieved by the heavy doped silicon of boron ion with a dosage of 1×10^{16} cm^{-2}. The forth was depositing another 300 nm SiO_2 layer by LPCVD as a passivation layer to fully encapsulate the piezoresistors and connection wires together with the buried oxide layer. After the contact holes were opened, an 800 nm aluminum layer was sputtered, patterned and alloyed to realize the ohm-contact. The penultimate step was sputtering a 10/50 nm Cr/Au composite nanofilm, which was patterned to cover the measurement cantilevers surface. Finally, the cantilevers were released by a hybrid process of SF_6 anisotropic and isotropic dry etching with thick photoresist as the mask. Fig. 1(b) shows a Scanning Electron Microscopic (SEM) image of a fabricated cantilever array.



(*a*) (*b*)

Fig. 1 Schematic diagram of (a) fabrication process of piezoresistive cantilever sensor array and (b) SEM image of the fabricated piezoresistive cantilever sensor

Reagent and materials

The SEB used in our experiments was purchased from Dianotech Science and Technology Co., Ltd. (Beijing, China). Bovine serum albumin (BSA, ≥ 98%) was obtained from Sigma-Aldrich Co. LLC. (Beijing, China). Phosphate buffered saline (PBS) solution (0.01 M, pH 7.4) and ethanolamine were acquired from Solarbio Ltd. (Beijing, China). SEB binding aptamer (anti-SEB) was synthesized by solid-phase peptide synthesis with thiol-labeled at the 5'-terminal and purified more than 95% purity by polyacrylamide gel electrophoresis (PAGE) method (AuGCT Ltd., Beijing, China). The

detailed sequence of the anti-SEB was 5'-HS-$(CH_2)_6$- GGT ATT GAG GGT CGC ATC CAC TGG TCG TTG TTG TCT GTT GTC TGT TAT GTT GTT TCG TGA TGG CTC TAA CTC TCC TCT -3', which was reported by J. A. DeGrasse [12]. Concentrated sulfuric acid (≥ 95% - 98%, guaranteed reagent ≥ 99.8%) and hydrogen peroxide (≥ 30%, guaranteed reagent ≥ 99.8%) were received from Beijing Chemical Works (Beijing, China). All aqueous solutions were prepared with double-distilled water.

Experiments and results

Immobilization of anti-SEB. The functionalization of sensing anti-SEB layer on cantilever surface was implemented with thiol-modified aptamers on nano-Au surface via Au-S bond. Prior to probe immobilization, the gold-coated PZR cantilevers were first pretreated with oxygen plasma (250 W, 20 sccm) for 5 min, followed by entirely cleaning with piranha solution (concentrated sulfuric acid and hydrogen peroxide mixture, 3:1, v/v) to remove any organic contamination for 20 min. The cantilevers were then rinsed in double-distilled water and dried with nitrogen gas.

Because of the impact of static electricity and airflow, the anti-SEB, supplied as lyophilized powder by the manufacturer, was centrifuged at 3000 rpm for 1 min at room temperature primarily. Then the anti-SEB was dissolved and diluted with double-distilled water to a final concentration of 20 μM. After that the anti-SEB solution was stored at 4 °C.

For anti-SEB immobilization, the cantilevers were immersed in 20 μM anti-SEB solution at 4 °C for 24 h allowing the formation of a self-assembled monolayer (SAM) through covalent bond of the thiol-group with the gold film, as shown in Fig. 2. When the probe immobilization of SEB was finished on the gold surface, the cantilevers were washed three times with PBS to remove unbound and weakly bound probes. Finally, the gold-coated surfaces of cantilevers were blocked with 1M ethanolamine solution, which was used to eliminate the nonspecific adsorption on the surface of cantilevers. After washing to remove unbound ethanolamine with PBS solution, the cantilevers were connected to the measuring instrument to obtain a stable baseline of the output signal.

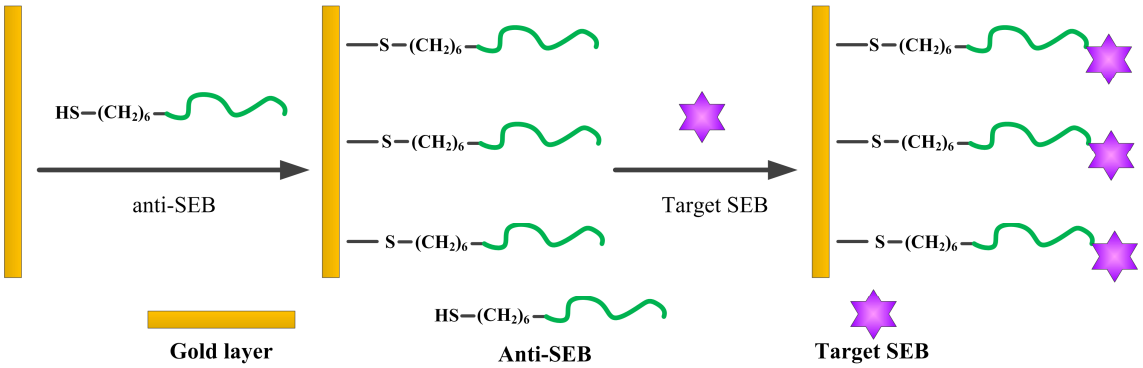


Fig. 2 Schematic diagram of the probe and target immobilization processes of SEB

Detection of SEB in milk. In order to evaluate the feasibility of the aptasensor for the detection of SEB in contaminated food samples, a 150 μL original and standard SEB concentration of 100 μg/mL was added to 1.35 mL of milk (bought from supermarket), which corresponded to the concentration of 10 μg/mL. After that, the skim milk sample (10 μg/mL) was further diluted to obtain five different concentrations solutions of SEB (3.3 μg/mL, 1.67 μg/mL, 1 μg/mL, 500 ng/mL, 200 ng/mL) with original milk. Then all solutions were stored at 4 °C for the contrast tests and recovery experiments.

A DC voltage of 3.0 V was applied to the bridge and the sensor output voltage was directly measured by a high-precision 6 1/2 digital multimeter (Aglilent, 34401A). Prior to the detections of SEB, all cantilever aptasensors were immersed in a 480 μL PBS solution separately in order to obtain a stable base line of the induced voltage. When the induced voltage of the cantilever aptasensor reached dynamic equilibrium, 15 μL different concentrations of SEB (without antigen, 200 ng/mL, 500 ng/mL, 1 μg/mL, 1.67 μg/mL, 3.3 μg/mL) were injected into each PBS solution separately, the corresponding concentrations of SEB were 0 ng/mL, 6 ng/mL, 15 ng/mL, 30 ng/mL, 50 ng/mL and 100 ng/mL respectively. Here, the added milk without SEB was used to ensure that there was no

adsorption to induce static deflection of the cantilevers resulting in the output voltage change. All the experimental conditions, including temperature (room temperature, 23 °C), probe concentration, PBS solution concentration and pH, and incubation time, were kept constant in the experiments.

Once the SEB solution was added, the target SEB adsorbed and bonded with the anti-SEB on the surface of the sensing PZR cantilevers immediately, which made the conformation of anti-SEB undergo significant change. This change brought to the rupture and generation of molecular hydrogen bond, which caused the sensing cantilever bended and the induced voltage changed. Fig. 3 shows the response curves of the PZR cantilevers after adding the five concentration target SEBs separately as previously described. We can see that the induced voltage signals reach saturation states for all curves but with different time. The voltage variations were 3 μV, 8.5 μV, 18 μV, 28 μV and 55 μV for the five concentrations of SEB respectively and the relationship of SEB concentration and voltage variation is shown in inset of Fig. 3. It is obvious that the higher of the target SEB concentration is, the larger of the voltage varies. This is because that more SEB molecules are able to adsorb and bond with the anti-SEB for the higher concentration test and hence induced larger voltage variation. It can also be noticed that the relation of concentrations and saturation voltage variation is approximately linear, which means that the aptasensor can provide a quantitative basis for applications.

We can also observe that the aptasensors have rapid response for the detection of SEB in milk. It can be noticed that the induced signals achieve saturation state for all response curves, but the saturation time is relatively longer for the higher concentration detections. It is obviously caused by the initially out of chemical equilibrium of system. On the other hand, in the case of no SEB, there was no prominent variation of output voltage. These results fully indicated that the static deflection of the cantilever and the induced voltage variation are indeed caused by the adsorption and bonding between the probe anti-SEB and the target SEB.

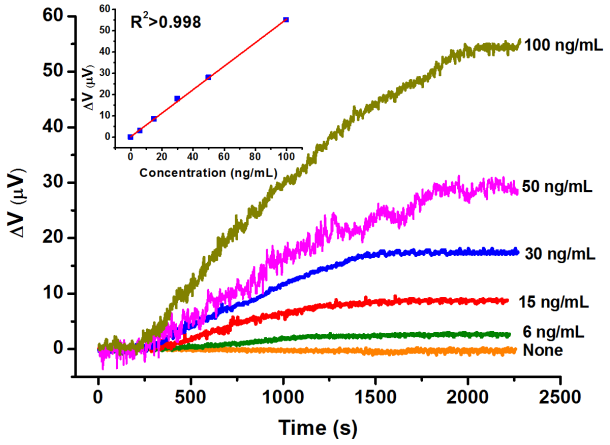


Fig. 3 Real-time monitoring of the aptasensor detected response for different concentrations SEB in trace levels (inset presents linear range of detection of SEB)

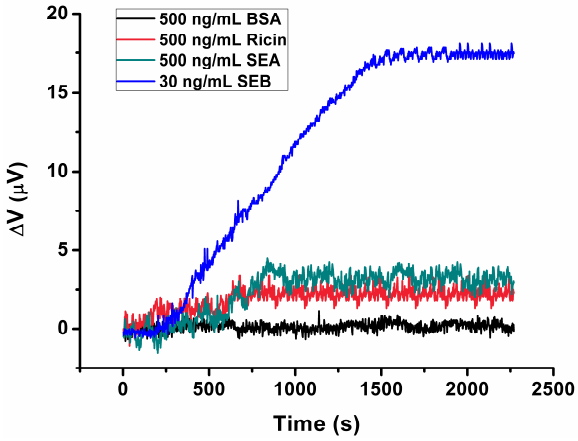


Fig. 4 Real-time monitoring of the aptasensor detected response for specific detection by utilizing three analogs at high concentrations (500 ng/mL)

Specificity test of aptasensor. The specificity of the aptasensor was tested with the same experimental procedure by utilizing the reaction of anti-SEB on the gold coated cantilever surface with different targets as analogs, including Staphylococcus enterotoxin A (SEA), BSA and ricin. In the experiments, the original and standard analogs of SEA and ricin were obtained from Dianotech Science and Technology Co., Ltd. (Beijing, China), and the finally detected concentrations were 500 ng/mL. The comparison test results are shown in Fig. 4. It is obviously that these three analogs failed to induce any significant changes on output voltage at high concentrations, which indicates these analogs cannot interact with the anti-SEB to generate conformation deformation of anti-SEB. These experimental results demonstrate that the anti-SEB has the excellently inherent specificity with SEB.

Summary

We have developed a piezoresistive cantilever aptasensor for a fast and sensitive detection of SEB in milk by using 5'-thiol-labeled aptamers as the detection probe. The experimental results have

shown that the cantilever aptasensors have sufficient sensitivity to detect SEB as low as a few nanograms in milk and a wide detected range. We also demonstrate that the aptasensors respond rapidly to SEB with the saturation time of approximate 10-15 min, and the output voltage of the aptasensor is proportional to the SEB concentration in milk. Although a lower limit of detection value of SEB can be obtained by using immunological or optical methods, the piezoresistive cantilever aptasensor provide a miniaturized, stable, and economical sensing platform for the on-site SEB detection in food stuffs. Furthermore, by using different aptamers, the piezoresistive cantilever sensors can also be applied for the detection of a variety of toxins and food contaminants.

Acknowledgement

The work was funded by the National Natural Science Foundation of China (grants No. 61275104 and 61036006).

References

[1] E. J. Schantz, W. G. Roessler, J. Wagman, L. Spero, D. A. Dunnery, and M. S. Bergdoll, Purification of Staphylococcal Enterotoxin B, Biochemistry, vol. 4, no. 6, pp. 1011-1016, 1965.

[2] G. A. Campbell, M. B. Medina, and R. Mutharasan, Detection of Staphylococcus enterotoxin B at picogram levels using piezoelectric-excited millimeter-sized cantilever sensors, Sens. Actuators B, Chem., vol. 126, no. 2, pp. 354-360, 2007.

[3] L. Wu, B. Gao, F. Zhang, X. Sun, Y. Zhang, and Z. Li, A novel electrochemical immunosensor based on magnetosomes for detection of staphylococcal enterotoxin B in milk, Talanta, vol. 106, pp. 360-366, Mar. 2013.

[4] D. Maraldo and R. Mutharasan, Detection and Confirmation of Staphylococcal Enterotoxin B in Apple Juice and Milk Using Piezoelectric-Excited Millimeter-Sized Cantilever Sensors at 2.5 fg/mL, Anal. Chem., vol. 79, no. 20, pp. 7636-7643, 2007.

[5] T. Alefantis, P. Grewal, J. Ashton, A. S. Khan, J. J. Valdes, and V. G. Del Vecchio, A rapid and sensitive magnetic bead-based immunoassay for the detection of staphylococcal enterotoxin B for high-through put screening, Molecular Cell Probes, vol. 18, no.6, pp. 379-382, Dec. 2004.

[6] K. E. Sapsford, J. Francis, S. Sun, Y. Kostov, and A. Rasooly, Miniaturized 96-well ELISA chips for staphylococcal enterotoxin B detection using portable colorimetric detector, Anal. Bioanal. Chem., vol. 394, no. 2, pp. 499-505, May 2009.

[7] J.-H. Han, H.-J. Kim, L. Sudheendra, S. J. Gee, B. D. Hammock, and I. M. Kennedy, Photonic crystal lab-on-a-chip for detecting staphylococcal enterotoxin B at low attomolar concentration, Anal. Chem., vol. 85, no. 6, pp. 3104-3109, Mar. 2013.

[8] E. Temur, A. Zengin, I. H. Boyaci, F. C. Dudak, H. Torul, and U. Tamer, Attomole sensitivity of staphylococcal enterotoxin B detection using an aptamer-modified surface-enhanced Raman scattering probe, Anal. Chem., vol. 84, no. 24, pp. 10600-10606, Dec. 2012.

[9] Y. Du, B. Li, and E. Wang, "Fitting" Makes "Sensing" Simple: Label-Free Detection Strategies Based on Nucleic Acid Aptamers, Accounts. Chem. Res., vol. 46, pp. 203-213, Nov. 2013.

[10] S. Wu, N. Duan, X. Ma, Y. Xia, H. Wang, and Z. Wang, A highly sensitive fluorescence resonance energy transfer aptasensor for staphylococcal enterotoxin B detection based on exonuclease-catalyzed target recycling strategy, Anal. Chim. Acta., vol. 782, pp. 59-66, Jun. 2013.

[11] J. Fritz, Cantilever biosensors, Analyst, vol. 133, no. 7, pp. 855-863, Jul. 2008.

[12] J. A. DeGrasse, A Single-Stranded DNA Aptamer That Selectively Binds to Staphylococcus aureus Enterotoxin B, PLoS One, vol. 7, no. 3, p. e33410, 2012.

Key Engineering Materials Vols 645-646 (2015) pp 1303-1307
© (2015) Trans Tech Publications, Switzerland
doi:10.4028/www.scientific.net/KEM.645-646.1303

Submitted: 2014-11-28
Accepted: 2014-12-23

Biological CAD/CAM/3D printing integrated molding platform and system building

Yun-Min Ma [1, a], Yuan-Yuan Liu [1, b *], Hai-Ping Chen [1,c] and Qing-Xi HU [1,d]

[1] Rapid Manufacturing Engineering Center, Shanghai University, Shanghai 200444, China

[a]mayunmin891206@163.com, [b]yuanyuan_liu@shu.edu.cn, [c]519673062@qq.com, [d]huqingxi@mail.shu.edu.cn

Keywords: CAD/CAM/3D printing; Electro-spinning; Integrated system

Abstract. The defective repairing and restructuring of some tissues and organs is becoming a livelihood issue which need settling urgently at present. Using polytechnics to design and prepare regenerated biological scaffolds is now facing a big bottleneck. In this paper, by the study and analyzing of CAD/CAM technology, 3D printing and electro-spinning technology, a new bionic CAD/CAM/3D printing integrated molding platform is expressed to meet the reunification of design and manufacture of regenerated bone scaffolds. Using the integrated molding platform, the Gelatin/chitosan – PVA scaffold were prepared with macro to micro structure. This molding method will help to develop the bio-manufacturing, biological 3D printing and their equipment, and has a realistic significance on pushing human health.

Introduction

At present, the most research and applications of preparing regenerated scaffolds focus on three different categories: The first is single forming process based on the existing mature 3D printing or electro-spinning technology; The second type is the composite forming technology combining 3D printing and electrostatic spinning technology to prepare regenerated bone scaffold; The third kind is the combination of mechanical CAD/CAM/NC, the theory and method of 3D printing, as well as the integrated forming method to realize the reunification of design and manufacture of tissue engineering regenerated scaffolds.

Albino Martins et al. in Minho University in Portugal has proposed a new three-dimensional bone scaffold manufacturing method, which has well solved the applying difficulties into three dimensional scaffolds of electrostatic spinning technology, when preparation the macrostructure through 3D printing, and joining a layer of nan-fiber between two layers of the macro-scaffolds through electro-spinning [1]. Carlos Mota in Pisa University in Italy has formed the tissue scaffolds with two scale pore structure separately at micron and micro level using PCL as the laminated materials and PLGA as the electrostatic spinning materials [2]. The Singapore National University, Li Geng et al made the layering and filling processing on skull 3D model by RPBOD and Mimics software, and created a silhouette chitosan engineering scaffold using the developed robot system and double nozzle direct writing process [3]. Cornell University, Daniel L Cohen et al developed a rapid prototyping equipment which could repair cartilage in situ [4].

Qingxi Hu et al from Shanghai University prepared a regenerated bone scaffold with a multi-scale internal pore structure using the low-temperature deposited shaping process and electro-spinning technology. And then by freeze-drying treatment, the scaffold would be full of micro-pore during the low temperature deposition process as the solvent distillation; three diverse scales of internal micro-porous structure could be formed through this preparing method [5-9]. Yongnian yan in Tsinghua University developed a low-temperature deposition manufacturing system, its digital model and discrete processing for the model is through the independent design of biological modeling software, it could be driven to prepare scaffold according to the machining path after sent the programmed data into this low-temperature deposition system [10]. Taiwan ming-yi li et al in Chang Gung University developed a laser sintering rapid prototyping machine based on the galil motion

control card, realized the Solidworks software modeling, the layered slice and path planning using the independent design software, and ultimately, completed the whole process from the scaffold model to the entity forming. And by utilizing the bone cement as material, a variety of different structure forms of scaffolds have been produced [11].

Given all that, on the one hand, although the domestic and foreign scholars have started to try to develop specialized 3D printing devices for the preparation of regenerated bone scaffold, similar to the mature 3D printing devices forming bone scaffold, they all need to rely on third-party software to complete medical image reconstruction, repair and processing work, without introduce the mechanical CAD/CAM/NC to realize the integration and automation of biological CAD/CAM/3d printing integrated forming system. The decoupling problem scaffold design and manufacture should be solved urgently through the effective combination of biological scaffold modeling and forming. As a result, the combination of biological modeling technology, medical image processing technology, computer aided manufacturing technology, 3D printing, electrostatic spinning technology to the integration design and comprehensive forming of tissue engineering scaffold has already started to get the attention of scholars both at home and abroad, and this has provided technical support for the design and manufacturing of macro/microstructure of regenerative bone scaffold, as well as developing the composite forming equipment.

2 Biological 3D printing synthetic molding

The biological 3d printing synthetic forming included the bone scaffold macro structure shaping with 3D printing, micro structure shaping with electro-spinning, and the multi-scale structure composite forming. Among them, the macrostructure formation is mainly for fiber diameter and dimension requirement in more than 300 um, the process path based on 3D printing is as shown in figure 1. Each layer structure is formed by nozzle, layer upon layer, to form the target regenerated bone scaffolds.

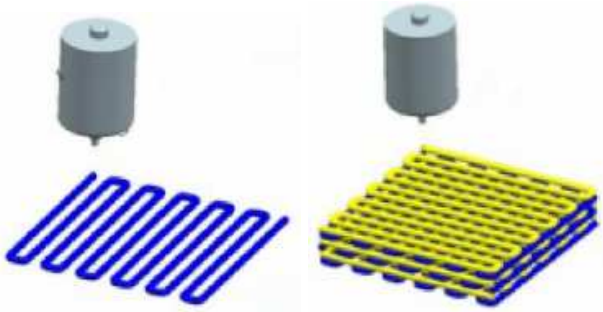


Fig. 1 Regenerative bone scaffold macrostructure forming with 3D print

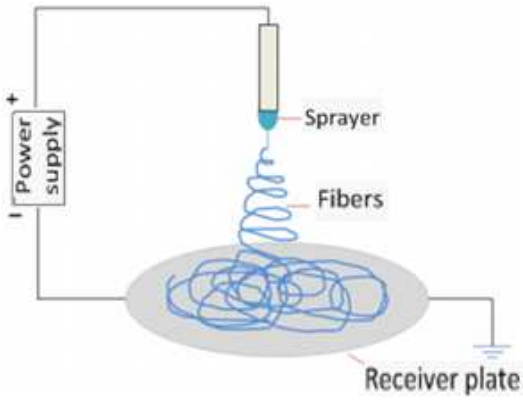
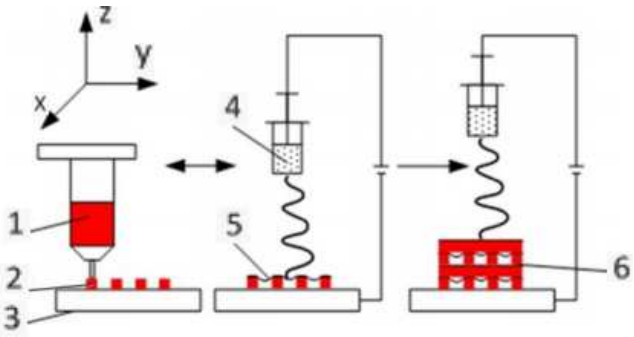


Fig.2 Regenerative bone scaffold microscopic structure forming with electros-spinning

On the flip side, the microstructure process of bone scaffold is faced for fiber diameter and dimension requirement under 300 microns, and its electrostatic spinning process shown in figure 2 is used to form nan-fibers in the form of non-woven fabrics. Regeneration bone scaffold multi-scale

structure composite molding combined with 3D printing and electrostatic spinning technology, to complete the integration of external macro structure and internal microstructure, which is shown in figure 3.



1.Piston extrusion feed nozzle; 2.Macro Scaffold layer; 3.The motion platform; 4.Electrospinning nozzle; 5.Nanofibers; 6.Composite forming stents.

Fig.3 Multi-scale regeneration scaffold composite molding process

Biological CAD/CAM / 3D printing integrated forming process is shown in figure 4, bio-CAD was used to reverse reconstruct, build of medical image, and output STL model of defect bone scaffold; Bio-CAM use the STL model or other executable STL file from CAD to complete regenerate bone scaffold forming path planning and post processing, and finally, output the driver files; After the driver file received by biological 3D printing integrated molding process, the general control module determined the implementation strategy to drive the corresponding upper desktop module download forming process parameters, then the control unit began to deal with the upper machine signal, output motion commands, which accused corresponding action of lower machine, ultimately, the regeneration bone scaffold was printed completely.

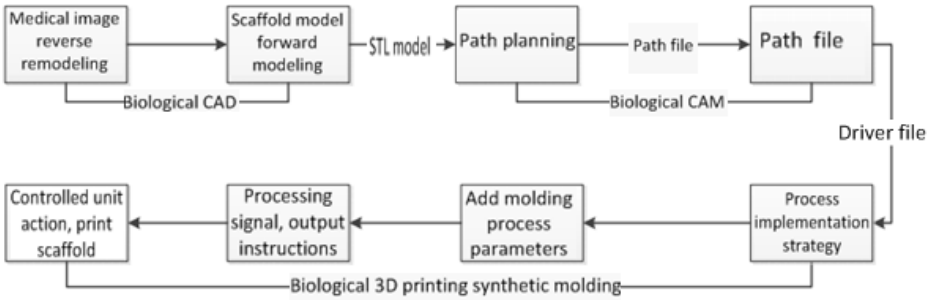


Fig.4 Biological CAD/CAM / 3D printing integrated molding system

3 Experiments

3.1 Experiment platform architecture

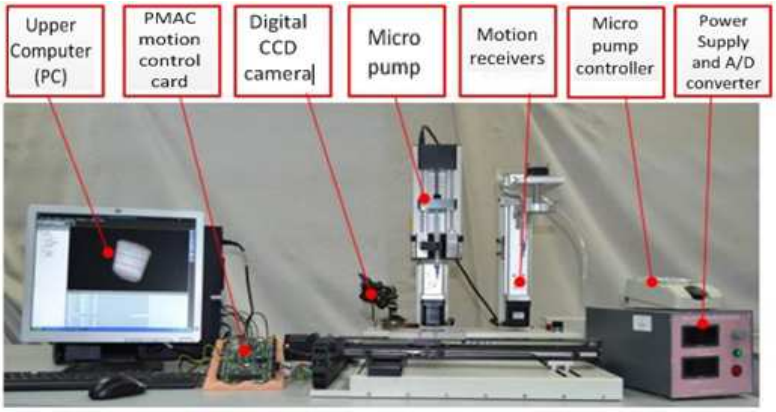


Fig.5 Integration platform architecture

Integration platform architecture was shown in figure 5 .

CAD/CAM software and 3D printing integrated forming system PC interface were used for path planning, post processing and process control; Firstly, biological modeling and path planning interface were used to set up the STL model of target tissue and generate planning path coordinates. Secondly, post processing and process control interface were used to post-process path coordinates, to generate code path and download into PMAC motion control card, as well as to add related process parameters.

3.2 Experimental materials

Materials of bone scaffold macro structure were the gelatin, chitosan mixture (gelatin, the Sigma Company; chitosan, Qingdao institute of medicine; acetic acid, Shanghai Lushi chemical industry co., LTD.). The gelatin dissolved in 60 ℃ deionized water made up 20% gelatin solution; The Chitosan soluble in 1% acetic acid made up 1% Chitosan solution. Materials selection of bone scaffold micro structure was the mixture of chitosan and PVA, by respectively dissolved in acetate and water to prepare PVA and chitosan mixed solution.

3.3 Experimental method

Make use of CAD/CAM to complete scaffold model path planning, post processing and process parameters adding. With the electro-spinning time setting to 10 s and voltage size setting to 12 KV, the integration platform started to prepare bone scaffold.

3.4 Results and analysis

Regenerated bone scaffolds prepared by integration platform was shown in figure 6, after freeze drying the electro spinning nan fibers has formed the scaffold microstructure observed by scanning electron microscope. The pore size of micro structure ranged from 55 ~ 80 microns, as shown in figure 7. As a result of the electrostatic spinning composite, regeneration of bone scaffold has obtained multi-scale structure.

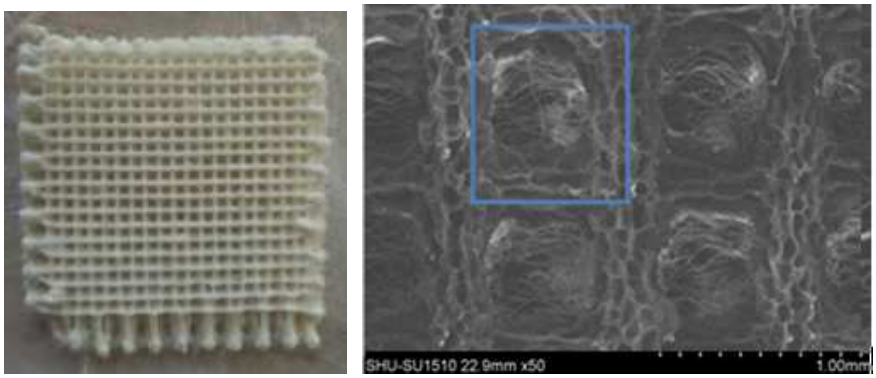


Fig. 6 Regenerative bone scaffold and its scanning electron microscopy (SEM)

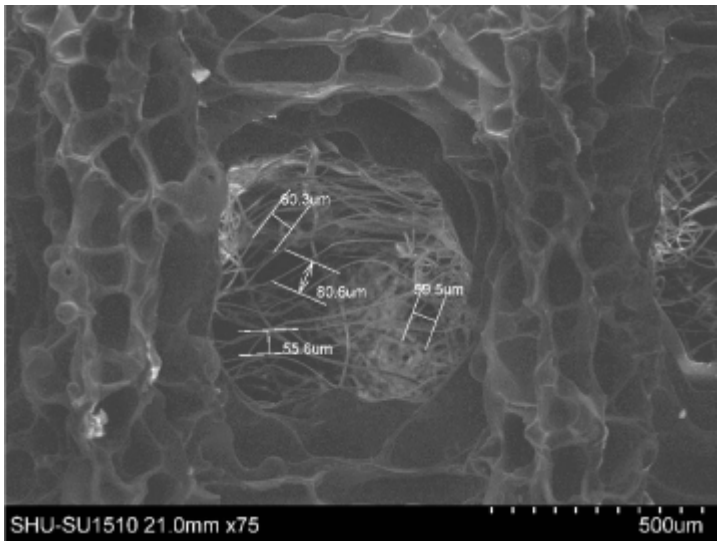


Fig.7 Regeneration of bone scaffold microstructure

4 Conclusions

On the basis of intensive study of CAD/CAM technology, 3D printing and electro-spinning process, this paper developed a set of integrated platform, which facing the more technology, multi-scale, more diversified regeneration scaffold preparation, can accomplish integration process from scaffold model input to scaffold printing output. In addition, the regeneration of bone scaffold composite molding based on the integration platform has been completed successfully, and the experimental results verified the macro and micro structure, indicating that forming morphology of regeneration scaffold was better.

The technological process of biological CAD/CAM/3D printing integrated molding and its integrated platform building provided important guarantee for developing biological 3D printing equipment, which also promoted the advancement of the BM technology. This article only preliminary realized based testing platform, however, there were still large gaps to fill the mature application. The functions of this integrated platform system still need further expansion and perfect.

Acknowledgement

This study is partly supported by National Natural Science Foundation of China (No.51375292, NO.51475281), National Youth Foundation of China (No.51105239).

References

[1] Martins A, Chung S, Pedro AJ, et al. Hierarchical starch-based fibrous scaffold for bone tissue engineering applications, J. Journal of tissue engineering and regenerative medicine. 3 (2009) 37-42.

[2] Schumann Detlef, Ekaputra Andrew K, Lam Christopher X F. Design of bioactive, multiphasic PCL/collagen type I and type II-PCL-TCP/collagen composite scaffolds for functional tissue engineering of osteochondral repair tissue by using electro spinning and FDM techniques, J. Methods in molecular medicine. 140 (2007) 101-24.

[3] Li G, Wei Diemar W, Hutmacher. Direct wiring of chitosan scaffold using the robotic system, J. Rapid Prototyping Journal. 11(2005) 90-97.

[4] Qianggao Wang, Yuanyuan Liu, Dali Liu et al. A new feeding device of electro spinning design for the micro-structure of bone scaffold prototyping, J. Advanced Materials Research. 211(2011) 1041-1045.

[5] LIU D L, GUO J, Fang SH H. A nan fibers manufacturing on-line monitoring system using the multi-target identification, J. Optical precision engineering. 20 (2012) 360-369. (in Chinese)

[6] Liu D L, Liu Y Y, Hu Q X, et al. Study on processing and model building of composite structure forming for 3-D regenerative bone scaffold, J. Applied Mechanics and Materials. 33 (2010) 518-522.

[7] Liu D L, Zhao X Y, Zhang H G, et al. Studying on auxiliary gradient rings for the collecting area of electro spinning, J. Advanced Materials Research. 203 (2011) 726-729.

[8] Liu D L, Jing CH J, Liu Y Y, et al. Algorithm Research of Pattern Recognition for Process Control of Electro spinning, J. Advanced Materials Research. 32 (2011) 314-315.

[9] Daniel L Cohen, Jeffrey I lipton, Lawrence J Bonassar, Additive manufacturing for in situ repair of osteochondral defects, J. Biofabrication. 2 (2010) 1-12.

[10] LIU L, XIONG ZH, YAN Y N, et al. Porous morphology, porosity, mechanical properties of poly(alpha-hydroxy acid)-tricalcium phosphate composite scaffolds fabricated by low-temperature deposition, J. Journal of Biomedical Materials Research, Part A. 82 (2007) 618-629.

[11] LI M Y, LI W D. Laser sintering rapid prototyping system development and application research on tissue engineering, D. Changqing University, 2005. (in Chinese)

Key Engineering Materials Vols 645-646 (2015) pp 1308-1313
© (2015) Trans Tech Publications, Switzerland
doi:10.4028/www.scientific.net/KEM.645-646.1308
Submitted: 2014-12-08
Accepted: 2014-12-23

A CMOS Automatic Gain Control Circuit for Biomedical Applications

Zhiqiang Gao[1,a], Fuxiang Huang[1], Jing Li[1], Liang Yin[1,b], and Xiaowei Liu[1]

[1]Department of Microelectronics, Harbin Institute of Technology, Harbin City, China 150080

[a]Email: gao_zhiqiang@hit.edu.cn, [b]Email: yinliang2003@126.com

Keywords: Exponential Approximation Function; Automatic Gain Control (AGC); Variable Gain Amplifier (VGA); CMOS Process.

Abstract. In this paper, a low-voltage automatic gain control (AGC) circuits is presented. The proposed circuit uses a novel approximated exponential function to increase the dB-linear output range. The three-stage AGC is fabricated in 0.18μm CMOS technology and shows the maximum gain variation of more than 100dB and a 67dB linear range with linearity error of less than ±1dB. The range of gain variation can be controlled from 34 to 101dB. The AGC dissipates less than 2.3mA under 1.8V supply voltage while occupying 0.4mm^2 of chip area.

I. Introduction

Nowadays, many scientists are interested to create an interface between the brain and artificial devices in order to help patients having severe diseases such as amyotrophic lateral sclerosis, spinal cord injury stroke, Parkinson's disease and other disorders and disabilities that can affect human bodies. Such interfaces (i.e. Brain Machine Interface (BMI)) can help humans to behave as normal human beings, since through these interfaces patients are going to be able to interact with the environment and to control external devices such as upper limb prostheses not only by manual control but also by mere thinking. These neural interfaces typically consist of Multi-Electrode-Array (MEA) for capturing the neural activity, followed by a bank of low-noise amplifiers (LNAs), band-pass filters, and programmable gain amplifiers or automatic gain control amplifiers (PGAs or AGCs) for signal conditioning. Then, a set of data converters follows in order to digitize the acquired data. The advances in the CMOS VLSI technology and the market demands for portable and mobile electronic equipment lead to increasing reductions on the power consumption.

Among the mostly used circuits in mixed signal VLSI circuits are VGA or AGC, which play an important role in neural interface systems. The key component for the design of VGAs and AGCs is the exponential function generator. The circuit is not available in CMOS technology since CMOS transistors follow a square-law characteristic in strong inversion. However, it is easily obtained in bipolar technology. Unfortunately, the bipolar techniques for VGAs and AGCs are not compatible for monolithic low-voltage CMOS based analog and mixed-signal circuits. Moreover, good performance bipolar transistors are not readily available in the conventional technology, while BiCMOS solution may not be cost-effective solution.

Since there is no intrinsic logarithmic MOS device operating in the saturation region for CMOS technologies, the exponential characteristics can be implemented by using "pseudo-exponential" generator, or the Taylor series expansion for realizing the exponential characteristics. However, these previously reported approaches show very small dB-linear output ranges less than 20dB. Though reported higher dB-linear range (30dB) by implementing the square of pseudo-exponential function, the dB-linear range is still restricted.

This paper proposes a novel exponential approximation function that can extend the dB-linear range up to very high value. The proposed circuit provides a 58dB range and a 67dB with the linearity error less than 1dB, while consumes low power (less than 4mW) at low-voltage applications.

II. The proposed principle of exponential approximation-function circuit

According to the Taylor series expansion, a general exponential function can be expressed as

$$e^{ax} = 1 + \frac{a}{1!}x + \frac{a^2}{2!}x^2 + \cdots \frac{a^n}{n!}x^n + \cdots \tag{1}$$

Where a and x are the coefficient and independent variables, respectively. For |ax|<<1, the Eq.1 can be approximated as

$$e^{ax} \approx 1 + \frac{a}{1!}x + \frac{a^2}{2!}x^2 = \frac{1}{2}[1 + (1+ax)^2] \tag{2}$$

The "pseudo-exponential" approximation function is also given as

$$e^{2\alpha x} = \frac{e^{\alpha x}}{e^{-\alpha x}} \cong \frac{[k + (1+\alpha x)^2]}{[k + (1-\alpha x)^2]} \tag{3}$$

To implement the Eq.3, the Taylor series expansion approximation function is needed. This section presents a novel very compact circuit for realizing the Taylor approximation as shown in Fig. 1. In the circuit, all transistors are operated in saturation region.

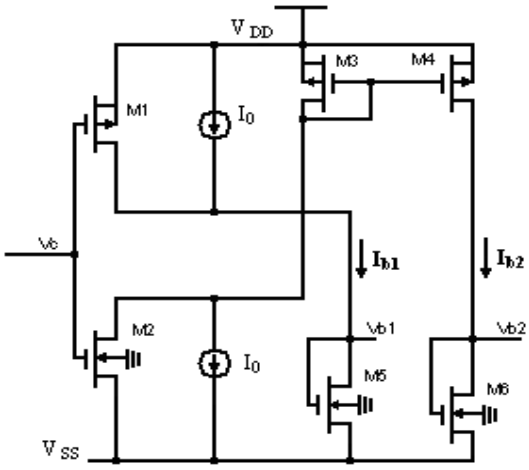


Fig. 1 A novel exponential gain control circuit

The control voltage Vc is applied the gate of PMOS transistor M1 and the gate of NMOS transistor M2. Then the drain current of transistor M1 and M2 is given as

$$I_{D1} = K_p(V_C - V_{DD} + |V_{thp}|)^2 \tag{5}$$

$$I_{D2} = K_n(V_C - V_{SS} - V_{thn})^2 \tag{6}$$

Where kp and kn are the coefficient of MOS transistor M1 and M2, respectively. Vthp and Vthn are threshold voltage of MOS transistor M1 and M2, respectively. In Figure 1, the bias current Ib1 and Ib2 can be expressed as

$$I_{b1} = I_{D1} + I_0 = K_p(V_{DD} - |V_{thp}|)^2 \times \left[\frac{I_0}{K_p(V_{DD} - V_{thp})^2} + (1 - \frac{V_C}{V_{DD} - |V_{thp}|})^2 \right] \tag{7}$$

$$I_{b2} = I_{D2} + I_0 = K_n(V_{SS} + V_{thn})^2 \times \left[\frac{I_0}{K_n(V_{SS} + V_{thn})^2} + (1 - \frac{V_C}{V_{SS} + V_{thn}})^2 \right] \tag{8}$$

Assume the coefficient $K_p = K_n = K$, $V_{DD} = -V_{SS}$, $V_{thn} = |V_{thp}| = V_{th}$, then the ratio between the bias current Ib2 and the bias current Ib1 can be expressed as

$$\frac{I_{b2}}{I_{b1}} = \frac{\frac{I_0}{K(V_{DD}-V_{th})^2} + (1+\frac{V_C}{V_{DD}-V_{th}})^2}{\frac{I_0}{K(V_{DD}-V_{th})^2} + (1-\frac{V_C}{V_{DD}-V_{th}})^2} = \frac{[k+(1+\alpha x)^2]}{[k+(1-\alpha x)^2]} \quad (9)$$

Where the coefficient $k = I_0 / K(V_{DD}-V_{th})^2$, $\alpha = 1/(V_{DD}-V_{th})$, and $x = V_C$. Eq.9 shows the numerator and denominator is exponential approximation function. The value of coefficient k can be changed by the current I0, so the ratio of Ib2 and Ib1 in dB is changed linearly.

When supply voltage $V_{DD} = 1.8V, V_{SS} = 0V$, and control voltage Vc is changed from 0.5~1.3V, the simulation of Ib2/Ib1 is given as shown in Fig. 2. Ib2/Ib1 is linearly changed from 0.5 to 1.3V.

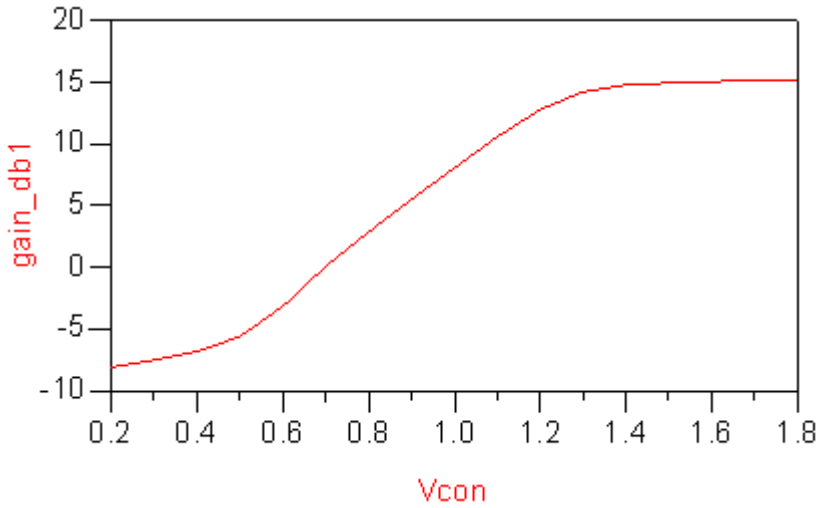


Fig. 2 The simulation of I_{b2}/ I_{b1}

III. The proposed AGC circuits

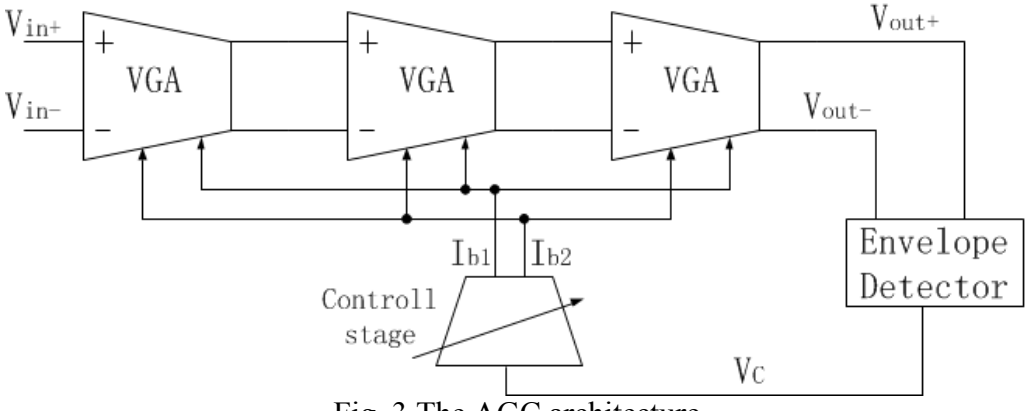


Fig. 3 The AGC architecture

Fig. 3 shows a block diagram of the overall AGC architecture. The AGC contains three stage VGAs, envelope detector, and control stage. The VGA adopts three amplifying blocks in cascade so that more than 120dB of gain variation can be achieved. In Fig. 3, all the stage VGAs are the same circuits as shown in Fig. 4. In Fig. 4, the amplifier consists of an input source-coupled pair (M9 and M12) and diode-connected loads (M10 and M11). The sizes of M9 and M12 are equal to M10 and M11, respectively. The two currents Ib1 and Ib2 from the control block in Fig. 3 are mirrored to M13 and M14. Therefore, the differential gain of the VGA shown in Fig. 4 can be expressed as

$$A_V = \frac{g_{m-input}}{g_{m-load}} = \sqrt{\frac{(W/L)_{input} I_{b2}}{(W/L)_{load} I_{b1}}} \tag{10}$$

Where gm-input is the transconductance of the input transistors (M9 and M12) and gm-load the transconductance of the diode connected transistors (M10 and M11), respectively. W and L is the width and length of the input transistors (M9 and M12) and load transistors (M10 and M11), respectively.

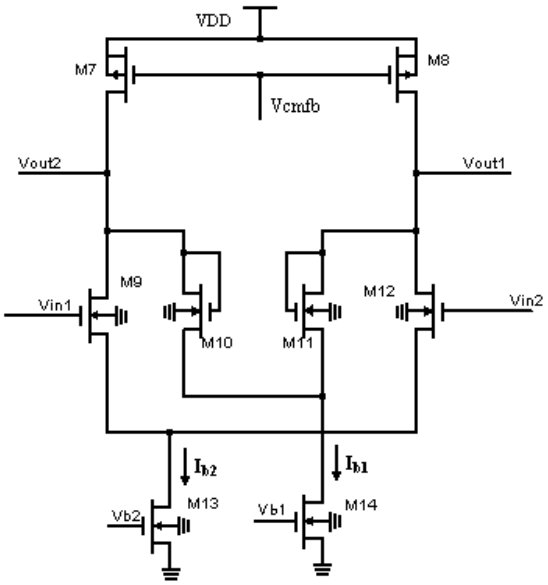


Fig. 4 Variable Gain Amplifier

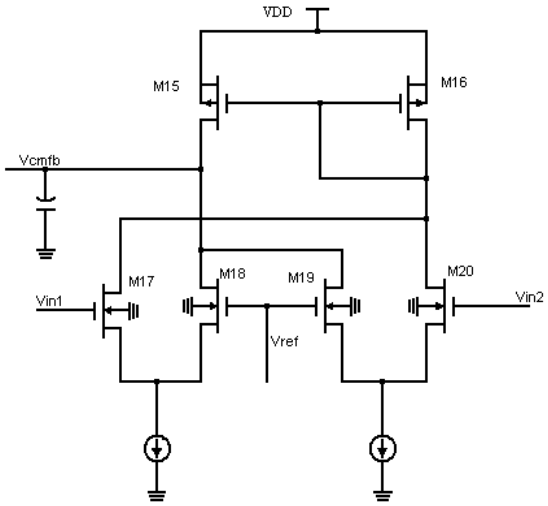


Fig. 5 The common-mode feedback circuit

From Fig. 5, the amplifier gain can be varied by controlling the current through transistors M13 and M14. Since the amplifier adopts current sources as active loads, the current through transistors M7 and M8. As a result, the drain currents through transistors M7 and M8 vary as a function of gain variation. Therefore, the strong common-mode feedback circuit shown in Fig. 5 is required in order to prevent any of the transistors from entering linear mode operation and to maintain a specific dc value for the biasing of the next stage. Regarding to the frequency response, the bandwidth of VGA is dominated by the pole at the input and the inter-stage node between amplifiers. The input pole is a function of the input capacitance and resistance. The output pole is proportional to the output capacitance and resistance. Since the resistance from the inter-stage node to the ac ground is dominated by the diode-connected transistors M10 and M11, which vary as a function of gain and

bandwidth. At higher gains, the current flowing through the diode-connected transistors is reduced leading to narrower bandwidth.

IV. The experiment of the circuit

The whole AGC circuit, shown in Fig. 3 is fabricated in 0.18μm CMOS technology with the supply voltage 1.8V. The microphotograph of the layout of the proposed AGC is shown in Fig. 6. The core of chip occupies less than 0.4mm^2. Fig. 7 shows the simulated gain versus control voltage. As shown in Fig. 7, the control voltage Vcont can vary from 0.5 to 1.3V. The gain of AGC can be changed from 34 to 101dB linearly. At the same time, the transient response of the proposed AGC circuit is shown in Fig. 8. The amplitude of the output voltage is controlled from 0.8 to 1.2V. The overall AGC circuit performance is summarized in Table I.

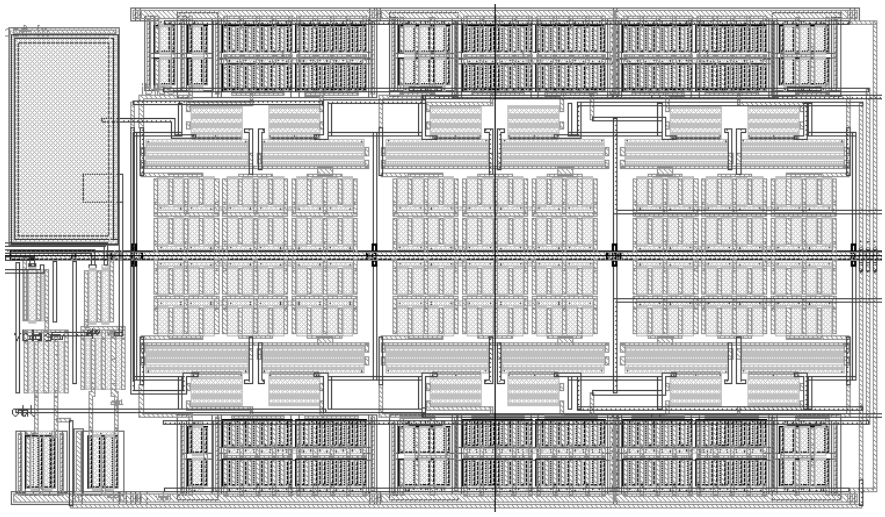


Fig. 6 Layout of the proposed AGC

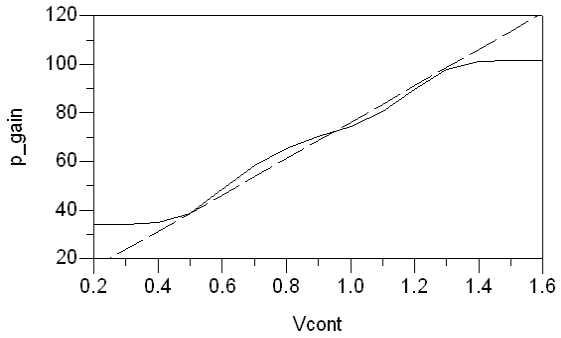


Fig. 7 The gain of AGC Vs control voltage

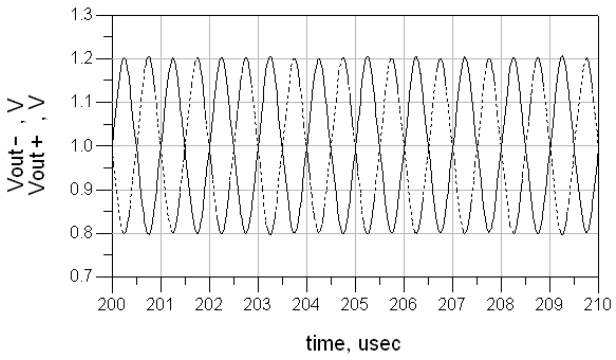


Fig. 8 Transient response of the proposed AGC

Table I The performance summarization of the circuit

Technology	0.18μm CMOS
Voltage supply VDD	1.8 V
Max Gain	101 dB
Gain control range	34dB~101dB
Gain Error	±1dB
Output voltage	0.8V~1.2V
IM3(0.4Vpp output)	<-60dBc

V. Summary

The CMOS AGC circuits with a wide range of gain variation, and low-power consumption is proposed. The novel exponential approximation function with wide decibel linear control range is utilized. The proposed AGC circuits is implemented in 0.18μm CMOS technology and shows linear gain variation of 67dB. The whole circuit dissipates an average current of 2.2mA from a 1.8V supply.

References

[1] W. M. Christopher. A variable gain CMOS amplifier with exponential gain control. Dig. Tech. papers IEEE Symp. VLSI Circuits. (2000) 146-149.

[2] P. Huang, L. Y. Chiou, and C. K. Wang. A 3.3V CMOS wideband exponential control variable gain amplifier. In proc. IEEE Int. Symp. Circuits Systems. (1998) 285-288.

[3] Q. H. Duong and S. G. Lee. CMOS exponential current-to-voltage circuit based on newly proposed approximation method. In proc. IEEE Int. Symp. Circuits Systems. (2004) 866-868.

[4] C.Qian, J. Parramon, and E. S. Sinencio. A micropower low-noise neural recording front-end circuit for epileptic seizure detection. IEEE J. Solid-State Circuits. 46 (2011) 1392-1405.

[5] M. Elguindy, and A. H. Madian. Low voltage digitally programmable gain and bandwidth fully differential CMOS neural amplifier. IEEE RAS/EMBS Int. Conf. on Biomed. Robotics and Biomech. (2012) 477-481.

Key Engineering Materials Vols 645-646 (2015) pp 1314-1319
© (2015) Trans Tech Publications, Switzerland
doi:10.4028/www.scientific.net/KEM.645-646.1314

Submitted: 2014-12-09
Accepted: 2014-12-23

Facile Preparation of Cu/TiO_2 Nanocomposite via Photocatalysis and Their Antibacterial Performance

Boxi She [1,a], Junbiao Long[1,b], Yuanming Deng [1,c], Xuejuan Wan[1,d], Kejun Zhu[2,e], Jiaoning Tang*[,1,f]

[1]Shenzhen Key Laboratory of Special Functional Materials, College of Materials Science and Engineering, Shenzhen University, Shenzhen 518060, P. R. China.
[2]Guangzhou Mente Nanometer Technology Co., Ltd,Guangzhou 511400,P. R. China.

[a]147080505@qq.com, [b]cbill.long@gmail.com, [c]ymdeng@szu.edu.cn, [d]wanxj@szu.edu.cn, [e]keke5501@126.com, [f]tjn@szu.edu.cn

Keywords: photocatalysis; hydrophilic aluminum foil; Cu/TiO_2 nanocomposite; antibacterial properties.

Abstract. Cu/TiO_2 nanocomposite was first prepared by photocatalytic reduction according to optimal processing condition selected via orthogonal test: 2.0% of glucose, 0.25% of TiO_2, 0.3% of $CuCl_2$ and reaction time of 12 h. Multiple characterization methods were utilized to confirm the structure of Cu/TiO_2 nanocomposite, and its antibacterial property against *Escherichia coli* (*E.coli*) was then investigated in detail. The obtained Cu/TiO_2 (*ca.* 50 nm) was composed of elemental copper, TiO_2 and a small amount of unreacted $CuCl_2$. EDTA titration and XRF indicated that solid content of Cu was about 61.68%. Antibacterial test showed that the inhibition zone diameter of Cu/TiO_2 with 1% solid content is 15.77 mm and the minimum bactericidal concentration (MBC) of which is 5 mg/mL. Furthermore, Cu/TiO_2 (1.0 wt%) was added into a super-hydrophilic coating for the aluminum cooling fin of air conditioner. The antibacterial ability of the fin can be significantly improved without obvious changes of hydrophilicity, which can reach the national standard (grade I).

Introduction

As a representative photocatalytic nano-antibacterial agent, TiO_2 nanoparticles [1] possesses advantages such as broad spectrum antibacterial property, good antibacterial endurance and safety, high stability and good adsorbability, which endows it with tremendous application potential [2,3,4,5]. Though TiO_2 nanoparticles has plenty of merits, there are obvious shortcomings and deficiencies as well. Photocatalytic reactive oxygen has a relatively short time, and meanwhile, photocatalytic antibacterial material will lose the bacteriostatic and bactericidal capacity in the dark because the photocatalytic reaction can not occur without the stimuli of UV-light. To solve these problems, two-component antibacterial complexes which combine TiO_2 with silver, copper and other antimicrobial metal ions have been widely studied [6,7,8]. Based on the great development prospect of these kinds of antibacterial materials, a nano-antibacterial composite Cu/TiO_2 was prepared to prevent the breeding of bacteria and molding in air conditioning heat exchanger. The application of Cu/TiO_2 nano-antibacterial agents in the heat exchanger cooling films can not only achieve the purification of air, but also maintain the hydrophilicity of the super-hydrophilic acrylic coatings, which may prevent mildewing and reproduction of germs. By combining the advantages of the metal iron antibacterial and photocatalytic antibacterial property, the antibacterial and mould proof effect can be well- improved[9], and the cost is low. Besides, the slow release of Cu^{2+} ion from the nano-scale Cu/TiO_2 composite can guarantee the long-lasting antibacterial capacity and low side effect. What's more, the TiO_2 substrate can effectively increase the surface area of copper particles, thus the utilization rate of copper can be significantly improved. The gradual formation of Cu_2O oxidation layer on the nanocomposite can further enhance the contact-antibacterial properties. In this paper, Cu/TiO_2 nanocomposite was added into a super-hydrophilic acrylic coating and coated uniformly onto an aluminum cooling fins. The obtained fins exhibited significantly improved antibacterial capacity and well-maintained hydrophilicity.

Experimental Section

Materials and measurements. Cupric chloride ($CuCl_2 \cdot 2H_2O$, AR), and glucose (AR) were purchased from Sinopharm Chemical Reagent Company and used as received. Titanium dioxide (TiO_2) of ca. 20-65 nm was prepared as literature reported [10]. The surface morphology and particle sizes of the Cu/TiO_2 nanocomposite were observed using a scanning electron microscope (SEM) and laser particle analyzer. The component of Cu/TiO_2 was carried out using an X-ray diffractometer (XRD). The solid content of Cu was analyzed via EDTA titration test and X-ray fluorescence spectrometer (XRF).

Synthesis of Cu/TiO_2 nanocomposites. Certain amount of $CuCl_2 \cdot 2H_2O$, TiO_2 nanoparticle and glucose were respectively dissolved with 300 mL deionized water. $CuCl_2$ solution was added slowly into TiO_2 suspension with magnetic stirring, followed by the addition of glucose solution. The reaction mixture was then diluted to 1 L with deionized water, and then placed in a self-made photocatalytic reaction workstation (Fig. 1) in a specified period of time.

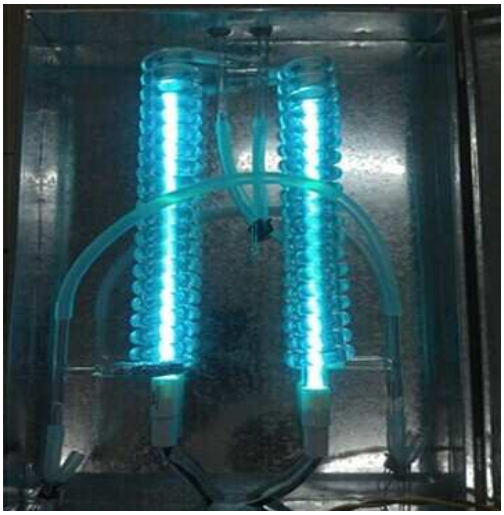


Fig. 1 Photocatalytic reaction workstation.

Antibacterial test. Inhibition zone qualitative test and minimum bactericidal concentration (MBC) quantitative test against *Escherichia coli* (*E.coli*) were adopted. Typical procedure of inhibition zone test can be described as follows: 1 mL bacterium suspension (~10^6 CFU/mL) was dropped onto the surface of a nutrient agar medium in a Petri dish, and then coated equably. Sample wafers of ca. 6mm were immersed into Cu/TiO_2 suspension (1.0 wt%) and glued onto the medium dispersedly. Blank control was prepared. The diameter of inhibition zone of samples was measured using vernier calipers for three times after being incubated at 37 for 24 h. MBC test was carried out as follows: five sample solutions were prepared by mixing 95 mL phosphate buffer (PB), 5 mL bacterium suspension and varied qualities of Cu/TiO_2(1.0 wt%). Blank control sample was prepared by replacing 5 mL bacterium suspension with 5 mL saline. The obtained sample solutions were incubated using bed temperature incubator at a sharking rate of 150 r/min at 37 ^oC for 24 h. 0.1 mL mixture of the above six samples was diluted to a certain concentration before being coated onto a plate (with about 20 mL solid medium) separately, and then incubated at 37 ^oC for another 24 h so as to figure up sterilizing efficiency by plate counting method. The lowest concentration of nanoparticles that killed 99.9% of the bacteria was the MBC.

Antibacterial test of the hydrophilic coating on aluminum foil. Different mass fractions of Cu/TiO_2(1.0 wt%) were added into super-hydrophilic acrylic coating, and dispersed by a high-speed homogenizer. The coating obtained was coated uniformly on an aluminum foil, and the antibacterial performance of which was evaluated according to GB/T 21866－2008.

Results and Discussion

Orthogonal test is the main method to screen out the optimal parameters when there are multiple factors influence the result. Representative four points and three levels for the preparation of Cu/TiO_2 nanocomposite were selected (factor 1: glucose with various qualities of 0, 2.0 and 4.0 wt%; factor 2: reaction time for 6, 12 and 18 h; factor 3: mass fractions of TiO_2: 0.1, 0.25 and 0.5 %; factor 4: concentration of $CuCl_2$ 0.1, 0.3 and 0.6 wt%).

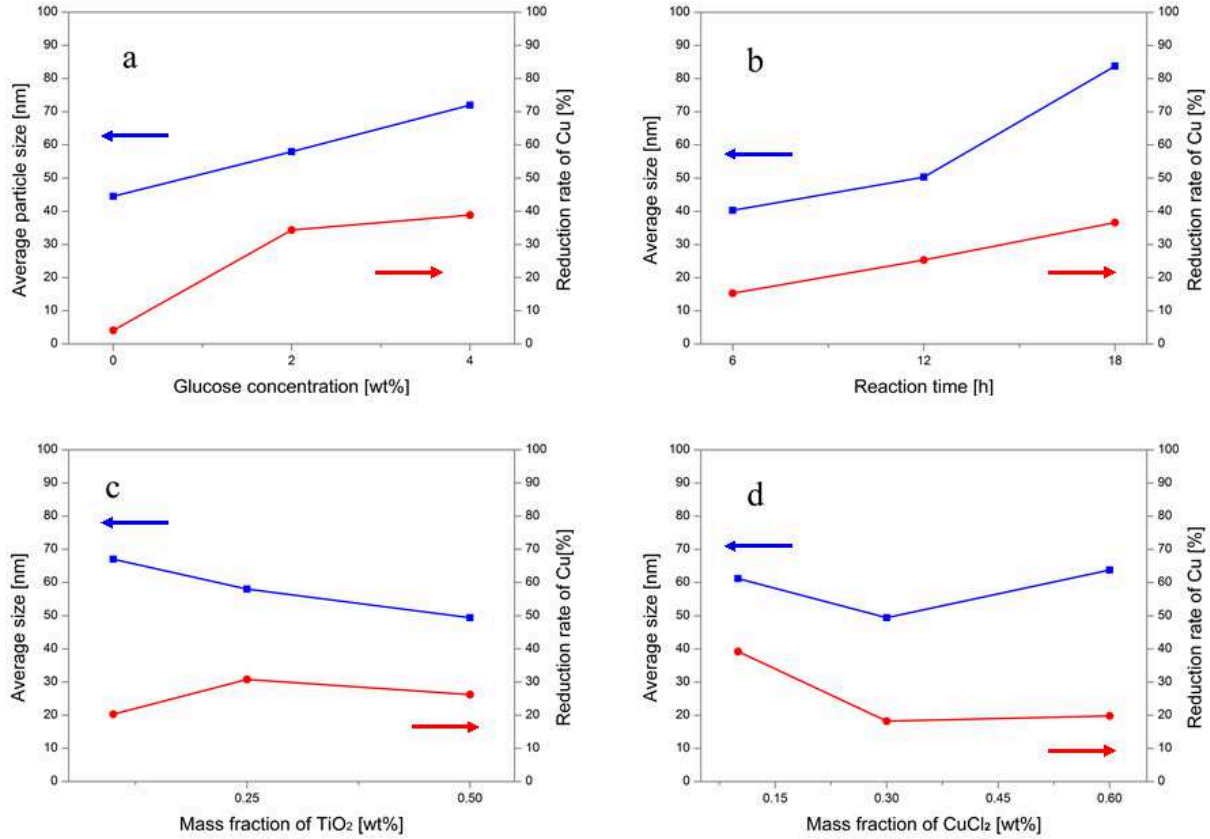


Fig. 2 The effect of glucose (a), reaction time (b), TiO_2 (c) and $CuCl_2$ (d) concentration on particle size of Cu/TiO_2 and the reduction rate of copper.

Orthogonal table $L_9(3^4)$ was studied to determine the preparation process of Cu/TiO_2 nanocomposite. The integrated average particle size and copper reduction rate of each factors and levels were described as Fig. 2. Particle size of Cu/TiO_2 and reduction rate of Cu increased with increasing concentration of glucose (Fig. 2a), as gradually enhanced impairment ability for free radical ·OH in photocatalytic reduction process could effectively inhibit oxidation reaction, resulting in improved reduction efficiency of Cu^{2+} and enlarged particle size. Considering the economic factors, the concentration of glucose is located at 2.0%. Fig. 2b indicated that copper reduction rate and particle size also increased with prolonged reaction time, ascribing to the growth in reduction quantity of copper on the surface of TiO_2 nanoparticles. In order to guarantee a certain reduction rate of Cu and simultaneously smaller particle size, 12 h was adopted as the optimum reaction time. In Fig. 2c, the reduction rate of Cu exhibited a tendency to decline with the increasing concentration of TiO_2, as too much TiO_2 solution would lead to lower pH value of the reaction mixture, thereby reducing the copper reduction rate and simultaneously decreasing the particle size of Cu/TiO_2 nanocomposite. Considering to obtain smaller particle size and relatively higher Cu reduction rate, mass fraction of TiO_2 was chosen as 0.25%. Fig. 2d demonstrated that Cu reduction rate fell with increasing concentration of $CuCl_2$ and then gradually stabilized. However, increasing $CuCl_2$ will bring increasing amount of Cu in solution, resulting in the larger composite site, which indicated that quality fraction of 0.3% was favorable in the preparation process. Thus, the optimum synthesis

condition was carried out as follows: quality fraction of glucose, TiO_2 and $CuCl_2$ were 2.0 wt% , 0.25 wt% and 0.3 wt% respectively, and reaction time was chosen as 12 h.

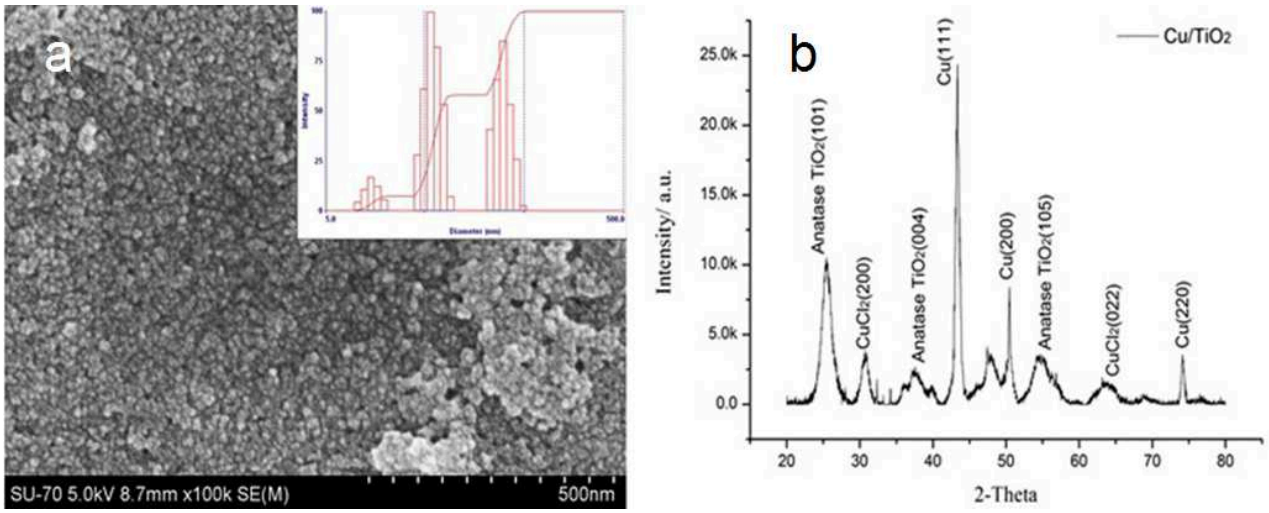


Fig. 3 SEM image,diameter distribution(a) and XRD spectrum(b) of Cu/TiO_2 nanocomposite .

The morphology of the obtained Cu/TiO_2 nanocomposite was studied by SEM analysis, and the granularity of it was also measured by laser granularity analyzer. It showed that the sample is featured of homogeneous distribution and regular shape with average size about 50 nm (Fig. 3a). The X-ray diffraction in Fig. 3b indicated that this sample is composed of elemental Cu, TiO_2 and unreacted $CuCl_2$ by comparison with the standard card. To characterize copper reduction rate of Cu/TiO_2 obtained under optimum technological condition, EDTA titration method was adopted to test upper clear liquid and X-ray fluorescence (XRF) measurement was used to determine lower sediment after centrifugation of the reaction mixture, and the results were shown in Table 1. The final reduction rate of Cu reached 61.8%, which is ideal.

Table 1 Reduction rate of copper.

EDTA titration[%]	XRF[%]	Average rate[%]
60.85	62.51	61.68

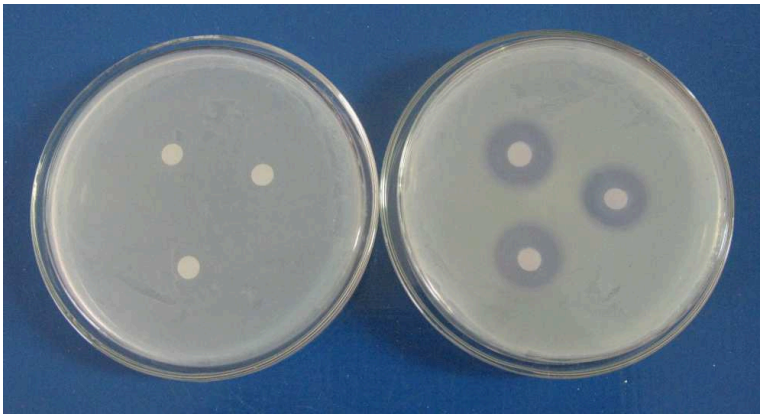


Fig. 4 Result of inhibition zone test of blank control (left) and Cu/TiO_2 (1.0 wt%, right).

Antibacterial activities of Cu/TiO_2 nanocomposite (1.0 wt%) were investigated via inhibition zone and minimum bactericidal concentration (MBC) tests. Digital image of the inhibition zone result was shown in Fig. 4. Average diameter of the three inhibition zones was measured to be 15.77 mm which was much larger than control filter paper (6 mm). Therefore, we can qualitatively determine that the obtained Cu/TiO_2 nanocomposite have excellent bactericidal and bacteriostatic performance.

For MBC test, a series of different concentration (1, 2, 3, 5, 10 mg/mL) of Cu/TiO_2 (1.0 wt%) samples were mixed with bacterial suspension and cultivated for 24 h. After that, 0.1 mL of the cultivation mixture was transferred into a plate, and cultivated for another 24 h. The number of viable bacteria of samples was compared with the blank control sample in order to calculate the bactericidal rate, and the result was shown in Table 2. As the concentration of Cu/TiO_2 nanocomposite exceeds 5 mg/mL, the sterilization rate was more than 99.9%. Thus, the MBC of Cu/TiO_2 is determined to be 5 mg/mL.

Table 2 Antibacterial rate of Cu/TiO_2 nanocomposite with various concentrations.

	Concentration of TiO_2 [mg/mL]				
	1	2	3	5	10
Number of colony of control sample [CFU]	5.2×10^8	1.6×10^9	3.4×10^8	1.1×10^9	4.2×10^8
Number of colony of Cu/TiO2 [CFU]	1.2×10^8	3.1×10^8	2.6×10^7	6.2×10^5	3.4×10^4
Antibacterial rate [%]	77.71	80.89	92.22	99.94	99.99

Various amount (0%, 2%, 4%, 6%) of Cu/TiO_2 (1 wt%) antibacterial agent were then added into a hydrophilic coating and further coated onto hydrophilic aluminum foil. The sterilization rate of the foil was investigated against *E.coli*. According to the national standard, the antibacterial agent was supposed to reach grade 1 when the sterilization rate exceeds 99%, while 90% for grade 2. The antibacterial effect of the as-prepared hydrophilic aluminum foil coated with Cu/TiO_2 nanocomposite could meet the first-grade as the quality fraction of Cu/TiO_2 was more than 4%, while meet the secondary-grade when the fraction was more than 2% (Fig. 5), suggesting that the antibacterial capacity of the Cu/TiO_2 nanocomposite can be well-retained in the hydrophilic coatings and endow the hydrophilic aluminum foil with outstanding antibacterial performance.

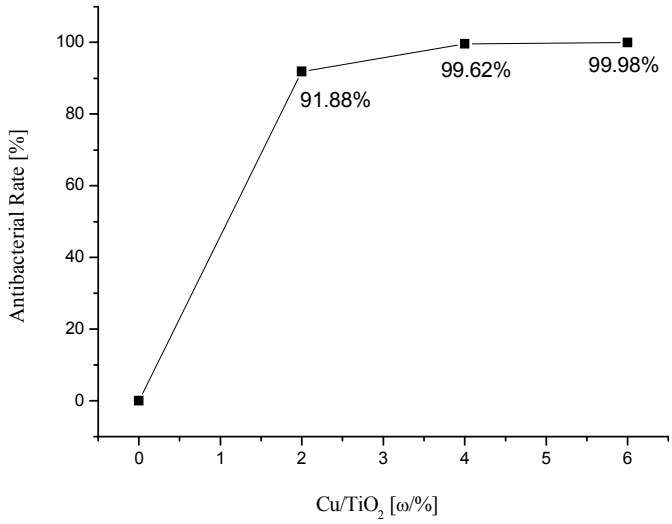


Fig. 5 Antibacterial activities of hydrophilic coating added with various Cu/TiO_2.

Table 3 Hydrophilic angle test results of the coating with different concentrations of Cu/TiO_2.

	Addition of Cu/TiO_2			
	0%	2%	4%	6%
1 [º]	<1	<1	<1	<1
2 [º]	<1	<1	<1	<2
3 [º]	<1	<1	<1	<1
average [º]	<1	<1	<1	<2

The hydrophilicity of the obtained antibacterial hydrophilic aluminum foil was determined and the results of hydrophilic angle test were shown in Table 3. Parallel experiments (three samples) were

conducted simultaneously, and average value was given. The results suggested that all the samples performed high hydrophilicity, indicating the addition of Cu/TiO_2 nanocomposite exhibited negligible interference of the hydrophilicity of the coating.

Conclusion

In conclusion, Cu/TiO_2 nanocomposite was prepared by photocatalytic reduction and its antibacterial ability was investigated in detail. The optimal preparation process of Cu/TiO_2 nanocomposite was first chosen by orthogonal test and the parameters were shown as followed: 2.0% of glucose, 0.25% of TiO_2, 0.3% of $CuCl_2$ and 12 h of reaction time. Antibacterial tests on Cu/TiO_2 indicate that the obtained samples have good antibacterial ability against *E.coli*. The inhibition zone diameter of Cu/TiO_2 (1.0 wt%) is about 15.77 mm and the minimum bactericidal concentration is 5 mg/mL. Subsequently, nanocomposite Cu/TiO_2 (1.0 wt%) was added into a super-hydrophilic coating and then coated on a aluminum cooling fin. The antibacterial ability of the fin can be significantly improved without obvious changes of hydrophilicity, which can reach the national standard (grade I).

Acknowledgements

The authors gratefully acknowledge financial support from National High-Tech Research and Development Program of China (863 Program, No. 2012AA030312).

References

Reference an article:

[1] J. Sund, J. Palomäki, N. Ahonen, K. Savolainen, et al, Phagocytosis of nano-sized titanium dioxide triggers changes in protein acetylation, J. Proteomics. 108 (2014) 469-483.

[2] E. Huerta-García, et al, Titanium dioxide nanoparticles induc strong oxidative stress and mitochondrial damage in glial cells, J. Free. Radical. Bio. Med. 73 (2014) 84-94.

[3] S. Rtimi, et al, Innovative transparent non-scattering TiO2 bactericide thin films inducing increased *E.coli* cell wall fluidity, J. Surf. Coat. Tech. 254 (2014) 333-343.

[4] Z.C. Yan, L. Liu, J.L. Tan, Q. Zhou, Z.F. Huang, D.D. Xia, H.G. Shu, X.K. Yang, X.Y. Wang, One-pot synthesis of bicrystalline titanium dioxide spheres with a core-shell structure as anode materials for lithium and sodium ion batteries, J. Power. Sources. 269 (2014) 37-45.

[5] M.S. Kim, K.M. Hong, J.G. Chung, Removal of Cu(II) from aqueous solutions by adsorption process with anatase-type titanium dioxide, J. Water. Res. 37 (2003) 3524-3529.

[6] B.S. Necula, I. Apachitei, F.D. Tichelaar, L.E. Fratila-Apachitei, J. Duszczyk, An electron microscopical study on the growth of TiO2-Ag antibacterial coatings on Ti6Al7Nb biomedical alloy, J. Acta. Biomater. 7 (2011) 2751-2757.

[7] B.S. Necula, I. Apachitei, F.D. Tichelaar, L.E. Fratila-Apachitei, J. Duszczyk, Antibacterial property and characterization of cotton fabric treater with chitosan/AgCl-TiO2 colloid, J. Carbohyd. Polym. 96 (2013) 326-331.

[8] J. Mungkalasiri, L. Bedel, F. Emieux, A.V.D. Cara, J. Freney, F. Maury, F.N.R. Renaud, Antibacterial properties of TiO2-Cu composite thin films grown by a one step DLICVD process, J. Surf. Coat. Tech. 242 (2014) 187-194.

[9] S.G. Chen, Y.J. Guo, H.Q. Zhong, S.J. Chen, J.N. Li, Z.C. Ge, J.N. Tang, Synergistic antibacterial mechanism and coating application of copper/titanium dioxide nanoparticles, J. Chem. Eng. J. 256 (2014) 238-246.

[10] Y.F. You, C.H. Xu, S.S. Xu, S. Cao, J.P. Wang, Y.B. Huang, S.Q. Shi, Structural characterization and optical property of TiO2 powders prepared by the sol-gel method, J. Ceram. Int. 40 (2014) 8659-8666.

Key Engineering Materials Vols 645-646 (2015) pp 1320-1325
© (2015) Trans Tech Publications, Switzerland
doi:10.4028/www.scientific.net/KEM.645-646.1320

Submitted: 2014-12-30
Accepted: 2015-01-07

Design of a microfluidic chip for enrichment of circulating tumor cells

X. X. Ling[1], D. H. Ren[1, a*], Z. You[1]

[1]Department of Precision Instrument, Tsinghua University, Beijing, 100084, P. R. China

[a]E-mail: rendh@tsinghua.edu.cn (corresponding author)

Keywords: Circulating tumor cell (CTC), Microfluidic, Enrichment, DLD, Negative enrichment

Abstract. Identification and characterization of CTCs can be used as a tool for the study of cancer metastases. A novel design of microfluidic chip used for enrichment of circulating tumor cells is presented in this paper. An integration of DLD method and negative enrichment method were designed to improve the throughput and recovery rate while getting intact CTCs. The DLD stage is used to separate CTCs from blood cells preliminarily, and the negative enrichment stage is used to acquire purified CTCs. Both of them were simulated with COMSOL Multiphysics. Simulation results showed that triangular micro-posts have better performance in DLD stage, and wave structures could generate better disturbance effect than herringbone structures. This chip provides a potential approach with high throughput and purity for the enrichment of CTCs.

Introduction

Cancer is a major killer of human beings, and about 90% cancer deaths result from metastasis [1]. A latent important cause of metastasis is the diffusion and transfer of circulating tumor cells (CTCs). CTCs are cells that shed from cancerous tumors, enter the circulatory system, and then migrate with the system, generating new metastases in distant organs. Identification and characterization of CTCs can be used as a tool for judging the metastases of cancers, estimating the prognosis and survival time, and even may be available for personalized medicine, drug screening, therapeutic effect monitoring, and development of new drugs for cancers[2]. The major challenge of applying CTCs in therapy is their rarity, approximately only one CTC in 10^9 whole blood cells[3]. Thus the enrichment plays an important role in detection of CTCs. So far, various methods, based on microfluidic technology, have been developed to separate CTCs from blood cells and enrich them, including positive enrichment depending on Epithelial Cell Adhesion Molecule (EpCAM)[4,5,6,7], negative enrichment depending on CD45[8,9], size based separation[10,11], dielectrophoresis (DEP)-based separation[12], and hydrodynamic separation[13,14,15,16]. Affinity based method, which includes positive enrichment and negative enrichment ways, is by far the most commonly used technology to enrich CTCs. In this method, enrichment is based on interaction of antigens and antibodies, which are either at the surfaces of CTCs (positive enrichment depending on EpCAM) or other cells (negative enrichment depending on CD45). The disadvantage of positive enrichment lies in the heterogeneity of CTCs, with low expression of EpCAM due to Epithelial Mesenchymal Transition (EMT). As leukocytes have much more quantity than CTCs, negative enrichment method cannot get a high-purity CTCs. In general, CTCs are bigger than erythrocytes and leukocytes. That difference can be used to separate them by size-based methods. However, the overlap of size among them decreases the performance of enrichment. DEP-based separation is stuck for the distinction of dielectric properties between CTCs and blood cells is not conspicuous, and there also may be harm to CTCs when utilizing dielectric field. Hydrodynamic separation, taking advantage of different streamlines of CTCs and blood cells in fluid field, is a high-throughput way for enriching CTCs. Nevertheless, the weakness of low-purity produce exists in this method. Considering shortcomings of each method, a combination of different methods is a developing trend to improve the performance.

In this paper, deterministic lateral displacement (DLD) method and negative enrichment method are combined for the purpose of improving the throughput and recovery rate simultaneously. Through this combined method, intact CTCs can be acquired, benefiting the subsequent study of CTCs.

Design of device

Microfluidic devices that integrated DLD and negative enrichment methods, with one inlet and three outlets for cancer cell separation, were designed, as shown in Figure 1. For DLD part, three shapes of micro-posts, which were circle, triangle and water-drop, were considered and compared. The chamber in this area is 42 mm long, 3 mm wide and 50μm high. The circular micro-posts have radius of 25μm and 25μm gaps. There is a tilted angle 2.28° of the microarray to the fluid flow direction. A critical particle size of 6μm can be calculated according to the theory developed by Inglis[17]. The triangular micro-posts have 25μm side length, 25μm gaps, and the tilted angle is 4.77 °, while the micro-posts of water-drop shape are with 25μm waist wide, 45μm high, and the tilted angle is 2.15°. The tilted angles above, by which all the DLD array got the same critical particle size of 6μm, were calculated by theoretical model raised by Loutherback[18].

In the DLD area, larger cells, including cancer cells and part of leukocytes, flow in a bumping mode, concentrating to the center of the chamber, while smaller cells, most of leukocytes, flow along the streamline direction. In this way, most of leukocytes are separated in the DLD area and flow out through outlets at the end of the DLD area. Meanwhile, cancer cells and part of leukocytes follow the center flow channel and then reach the negative enrichment area. In this area, the channels are coated by anti-CD45, a sort of antibody for leukocytes' surface antigen CD45, for the purpose of capturing leukocytes by means of immune reaction. Passing the negative enrichment area, leukocytes are captured and cancer cells are purified. Structures of wave shape were designed in order to make disturbance to the fluid, creating more chances for leukocytes to interact with channel surface. Lastly, purified cancer cells are collected from the outlet at the end of the microdevice.

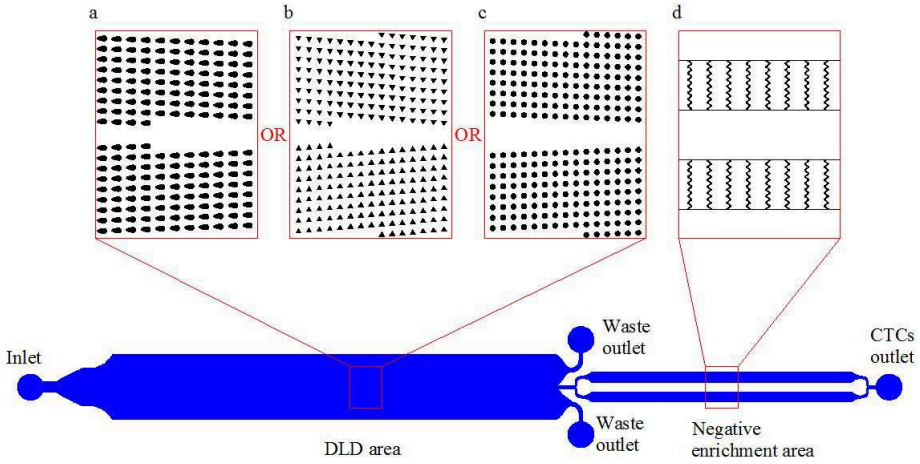


Figure 1. Schematic diagram of the microfluidic chip

Simulation

Simulation of DLD area. Three different shapes of DLD micro-posts were designed, namely circle, triangle and water-drop shapes. We used COMSOL Multiphysics 4.3a to simulate the fluid field of DLD array with shapes of triangle, circular, and water-drop shape, and compared them.

The fluid is defined, which should be pretreated blood in fact, as incompressible. The density of it is $1000\,kg/m^3$, and the dynamic viscosity is 0.005, assumed to be laminar flow in the channel. The velocity of fluid is set at inlet as 0.0001m/s, and the pressure at outlet is 0, with no viscous stress. The boundary condition is no slip. The velocity field is simulated, as shown in Figure 2, by which a comparison can be made between DLD array with circular micro-posts and that with triangular micro-posts (a), as well as triangular micro-posts and water-drop shaped micro-posts (b). Comparing the velocity field of these arrays, we can see that the velocity between triangular micro-posts is lower than that between circular micro-posts, and lower than that between water-drop shaped micro-posts as well. Thus the obstruction generated by the triangular micro-posts is the smallest among these

three shapes of micro-posts. As a result, the driving force exerted on cells in the fluid with triangular micro-posts is smaller than that with circular ones and water-drop shaped ones. The cell deformation, which will decrease the effective size of a cell, is related to the force it suffers. When the effective size of a cell becomes smaller than the critical size of the DLD array, the cell would not be separated effectively. Therefore, the DLD array with triangular micro-posts, which may generate smallest cell deformation, could have the best performance among these three shapes, according to the simulation results above. It has been reported that DLD array with a shape of triangle has better performance than that of circular shape[18], which fits well with our simulation results, and certifies the credibility of this simulation.

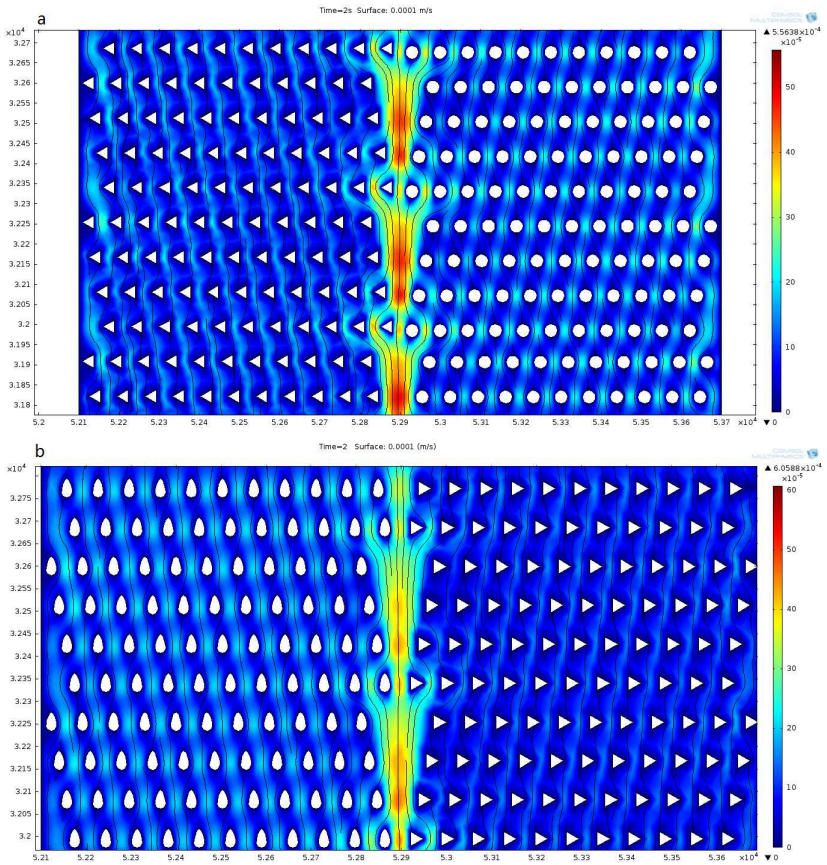


Figure 2. Contrasting simulation of fluid in DLD array with different shapes: (a) comparison of fluid among circular micro-posts and triangular micro-posts, (b) comparison of fluid among water-drop shaped micro-posts and triangular micro-posts.

Simulation of negative enrichment area. In negative enrichment area, antigens CD45 on the surface of leukocytes interact specifically with the anti-CD45 antibody pre-coated on the channel, and part of leukocytes which are omitted in the DLD stage would be captured on the channel, and then more purified CTCs would be released. The channel in this stage should be designed to generate more interaction between fluid and the channel surface, promoting the interplay between leukocytes and the channel surface and bringing more possibilities leukocytes being captured. Three channel forms are shown and compared, as illustrated by Figure 3. Figure 3(a) is a straight and plain channel without disturbance. Figure 3(b) is a channel with herringbone structures on the top of it, which was first developed by Stott[5]. Figure 3(c) is a channel with wave structures on the top, proposed by us. It is obvious that streamlines in (a) are straight, thus only cells at the edge of fluid can touch the channel surface, which is not favorable for the interaction of leukocytes and channel surface. Streamlines in (b) are disturbed by the herringbone structures, and more chances of interaction can be created. As shown in Figure 3, compared with streamlines in (b), streamlines are more complex and chaotic in (c), as a result of wave structures. From this perspective, it is more favorable for the interaction between cells and the channel when using channels with wave structures. Therefore, this form of channel is employed for the negative enrichment of CTCs.

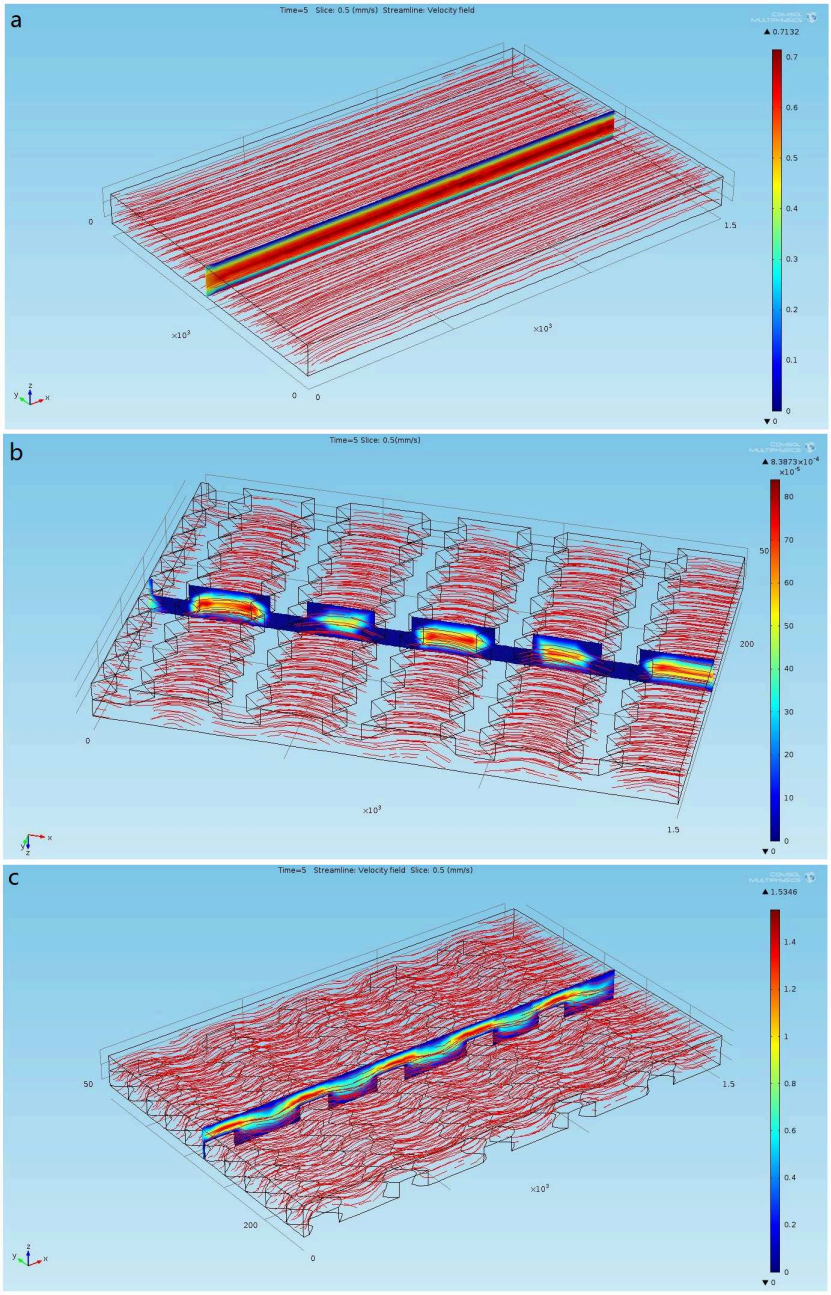


Figure 3. Simulation of negative enrichment channel with different disturbance structures: (a) straight and plain channel, (b) herringbone structures, and (c) wave structures.

Summary

We proposed a microfluidic chip used for the enrichment of circulating tumor cells. Into this design we integrated DLD method and negative enrichment method to improve the throughput and recovery rate at the same time, while getting intact CTCs. DLD was used to separate CTCs from blood cells preliminarily, and negative enrichment structures was used to acquire purified CTCs. Both of them were simulated with COMSOL Multiphysics 4.3a. Simulation results showed that triangular micro-posts have better performance in DLD stage, and wave structures proposed in this paper could generate better disturbance effect than herringbone structures. Further experiments will be done to test the performance of this microfluidic chip. It provides a potential approach for the high-throughput and high-purity enrichment of CTCs.

Acknowledgement

This work is supported by the National Natural Science Foundation of China (No. 61071002), National Program for Significant Scientific Instruments Development of China (No. 2011YQ030134), Funds for State Key Laboratory of China, Scientific Research Foundation for Returned Overseas Chinese Scholars and the Fund for Beijing Laboratory of Biomedical Detection Technology and Instrument.

References

[1] J.E. Butler, L. Ni, R. Nessler, K.S. Joshi, M. Suter, B. Rosenberg, J. Chang, W.R. Brown, L.A. Cantarero, The physical and functional behavior of capture antibodies adsorbed on polystyrene, J. Immunol. Methods. 1(1992)77-90.
[2] M. Cristofanilli, D.F. Hayes, G.T. Budd, M.J. Ellis, A. Stopeck, J.M. Reuben, G.V. Doyle, J. Matera, W.J. Allard, M.C. Miller, Others, Circulating tumor cells: A novel prognostic factor for newly diagnosed metastatic breast cancer, J. Clin. Oncol. 7(2005)1420-1430.
[3] H.J. Kahn, A. Presta, L. Yang, J. Blondal, M. Trudeau, L. Lickley, C. Holloway, D.R. McCready, D. Maclean, A. Marks, Enumeration of circulating tumor cells in the blood of breast cancer patients after filtration enrichment: Correlation with disease stage, Breast Cancer Res. Tr. 3(2004)237-247.
[4] S. Nagrath, L.V. Sequist, S. Maheswaran, D.W. Bell, D. Irimia, L. Ulkus, M.R. Smith, E.L. Kwak, S. Digumarthy, A. Muzikansky, P. Ryan, U.J. Balis, R.G. Tompkins, D.A. Haber, M. Toner, Isolation of rare circulating tumour cells in cancer patients by microchip technology, Nature. 7173(2007)1235-1239.
[5] S.L. Stott, C.H. Hsu, D.I. Tsukrov, M. Yu, D.T. Miyamoto, B.A. Waltman, S.M. Rothenberg, A.M. Shah, M.E. Smas, G.K. Korir, F.J. Floyd, A.J. Gilman, J.B. Lord, D. Winokur, S. Springer, D. Irimia, S. Nagrath, L.V. Sequist, R.J. Lee, K.J. Isselbacher, S. Maheswaran, D.A. Haber, M. Toner, Isolation of circulating tumor cells using a microvortex-generating herringbone-chip, Proc Natl Acad Sci U S A. 43(2010)18392-18397.
[6] H.J. Yoon, T.H. Kim, Z. Zhang, E. Azizi, T.M. Pham, C. Paoletti, J. Lin, N. Ramnath, M.S. Wicha, D.F. Hayes, Others, Sensitive capture of circulating tumour cells by functionalized graphene oxide nanosheets, Nature nanotechnology. 10(2013)735-741.
[7] U. Dharmasiri, S. Balamurugan, A.A. Adams, P.I. Okagbare, A. Obubuafo, S.A. Soper, Highly efficient capture and enumeration of low abundance prostate cancer cells using prostate-specific membrane antigen aptamers immobilized to a polymeric microfluidic device, Electrophoresis. 18(2009)3289-3300.
[8] Z. Liu, A. Fusi, E. Klopocki, A. Schmittel, I. Tinhofer, A. Nonnenmacher, U. Keilholz, Negative enrichment by immunomagnetic nanobeads for unbiased characterization of circulating tumor cells from peripheral blood of cancer patients, J Transl Med. 2011)70.
[9] K.A. Hyun, T.Y. Lee, H.I. Jung, Negative enrichment of circulating tumor cells using a geometrically activated surface interaction chip, Anal. Chem. 9(2013)4439-4445.
[10] S.W. Lee, J.Y. Kang, H.I. Jung, K.A. Hyun, Microfluidic dection of circulating tumor cells(CTC) using side filtration-based capture, 2013)
[11] T. Masuda, Y. Sun, M. Niimi, A. Yusa, H. Nakanishi, F. Arai, Cell layouter label-free cell isoation and aspiration system of circulating tumor cells, 2013)
[12] A. Alazzam, I. Stiharu, R. Bhat, A.N. Meguerditchian, Interdigitated comb-like electrodes for continuous separation of malignant cells from blood using dielectrophoresis, Electrophoresis. 11(2011)1327-1336.
[13] J.S. Park, S.H. Song, H.I. Jung, Continuous focusing of microparticles using inertial lift force and vorticity via multi-orifice microfluidic channels, Lab Chip. 7(2009)939-948.
[14] H.W. Hou, M.E. Warkiani, B.L. Khoo, Z.R. Li, R.A. Soo, D.S. Tan, W. Lim, J. Han, A.A.S. Bhagat, C.T. Lim, Isolation and retrieval of circulating tumor cells using centrifugal forces, Scientific reports. 2013)

[15] K. Loutherback, J. D'Silva, L. Liu, A. Wu, R.H. Austin, J.C. Sturm, Deterministic separation of cancer cells from blood at 10 mL/min, AIP Adv. 4(2012)42107.
[16]J. Sun, M. Li, C. Liu, Y. Zhang, D. Liu, W. Liu, G. Hu, X. Jiang, Double spiral microchannel for label-free tumor cell separation and enrichment, Lab Chip. 20(2012)3952-3960.
[17]D.W. Inglis, J.A. Davis, R.H. Austin, J.C. Sturm, Critical particle size for fractionation by deterministic lateral displacement, Lab Chip. 5(2006)655-658.
[18]K. Loutherback, K.S. Chou, J. Newman, J. Puchalla, R.H. Austin, J.C. Sturm, Improved performance of deterministic lateral displacement arrays with triangular posts, MICROFLUIDICS AND NANOFLUIDICS. 6(2010)1143-1149.

Key Engineering Materials Vols 645-646 (2015) pp 1326-1332
© (2015) Trans Tech Publications, Switzerland
doi:10.4028/www.scientific.net/KEM.645-646.1326

Submitted: 2015-01-15
Accepted: 2015-01-19

Biological Effect of Single Wall Carbon Nanotubes on *Skeletonema costatum* and *Prorocentrum donghaiense* in seawaters

Fangfang Li[1,a], Jiangtao Wang[1,b] and Liju Tan[1,c]

[1] Key Laboratory of Marine Chemistry Theory and Technology, Ministry of Education, Ocean University of China, 238 Songling Road, Qingdao 266100, PR China

[1] lifangfyc@163.com

[2]jtwang@ouc.edu.cn (corresponding author)Tel.:+86-0532-66782506

[3]lijutan@ouc.edu.cn

Keywords: single-walled carbon nanotubes; *Skeletonema costatum*; *Prorocentrum donghaiense*; biological effect

Abstract: Carbon nanotubes (CNTs) have been used in a variety of industrial areas as a kinds of new nanometer materials. Algal growth test was developed to determine the biological effect of single-walled carbon nanotubes (SWNTs) on *Skeletonema costatum* and *Prorocentrum donghaiense*. The results showed that SWNTs stimulated the growth of *S. costatum* within 72 h and 24 h as theirs concentrations were smaller than 0.5 mg/L and 10 mg/L respectively, While the growth of *S. costatum* was inhibited within 48 h and 96 h as theirs concentrations were higher than 10 mg/L and 0.5mg/L respectively ($p<0.05$). The concentrations of chlorophyll were the same as the density of phytoplankton cells. The growth of *P. donghaiense* was inhibited as SWNTs concentrations were higher than 100 mg/L within 72 h, while SWNTs promoted the growth of *P. donghaiense* within 48 h after SWNTs were added as their concentrations were smaller than 5 mg/L（$p<0.05$). The results of chlorophyll were similar to the density of *P. donghaiense* cells. The roles of SWNTs on the growth of algae were suggested to be associated with the active of some enzymes and the physical properties, such as agglomeration and shading.

1. Introduction

Carbon nanotubes (CNTs) as a kinds of new and important nanomaterials, also known as Pakistan tubules, have attracted much attention in many areas since their discovery two decades ago because of the special physical and chemical properties. As a kinds of almighty nanomaterials, carbon nanotubes (CNTs) are increasingly produced and used in a variety of industrial areas[1,2]. In every process of production and use, CNTs inevitably enter the aquatic environment and cause harm and even produce toxicity to the plant and animal. The wide range of application of CNTs have led to increased concerns on their possible contamination on the natural aquatic environment among the environmental community[3]. Previous research showed that both the aquatic environment and the physicochemical properties of CNTs, including the shape of CNTs [4], the presence of organics [5], the speed of pore water [6], played significant roles in the transport of CNTs.

CNTs were divided into single-walled carbon nanotubes (SWNTs), double-walled carbon nanotubes (DWNTs) and multi-walled carbon nanotubes (MWNTs) according to the arrangement of carbon atoms. Single-walled carbon nanotubes were widely produced and used in electronic, energy devices, nanomedicine，mechanical and biological fields. They were winded into lungs of organisms easily and were eventually harm in pulmonary accumulation over time because of their smaller size and lighter. Lam et al.[7] found that the lung was infected after 7 days when the mouse were

exposure to SWNTs. The damage effects were always there and more remarkable with time. Their toxicity was even higher than graphite and black carbon. Zhu[8]found the toxicity of SWNTs was more significant than MWNTs and C_{60} for *Daphnia magna*. Hyunguarded[9] and Roberts[10] showed that CTNs which got into water environment had better dispersion and stability with the role of organic matter and were likely harmful to aquatic organisms.

Algae, which are primary producers for aquatic environments, are easy to culture and sensitive to pollutants. Algae not only occupy an important position in the entire water ecosystems, but also maintain ecological balance and system stability. Algae are widely used as the tested material in various aspects of water safety evaluation, environmental pollution and poison detection in recent years. The uptake and accumulation of CNTs by algae is a new research field in recent years because CNTs can enter plant cells under certain conditions and cause plant toxicity at higher doses. For example, Schwab et al.[11] found that CNTs caused algae cell aggregation and had a shading effect on algae and then affected the growth of algae. One research showed that residual metal catalysts retained in the SWNTs even after prolonged washing with nitric acid[12].

At present, the reports about biological effects of CNTs in aquatic environment especially for marine algae, were still relatively less and the specific mechanisms of toxicity remained unclearly. *S. costatum* and *P. donghaiense* are the common species of algae in the coastal sea of China. An algal growth test was developed to determine the biological effect of single-walled carbon nanotubes (SWNTs) on *S. costatum* and *P. donghaiense*.

2. Experimental Section

2.1 Chemicals and Materials

S. costatum and *P. donghaiense* strains were from Ocean University of China. SWNTs were purchased from Beijing Deco Island Gold Ltd. The length is 5-30μm, diameter is 1-2nm and purity> 95%. The bbe Moldaenke was purchased from Germany.

2.2 Algae Cultivation

S. costatum and *P. donghaiense* strains were cultured in pasteurized seawater with f/2 medium in acid-cleaned 2 L Erlenmeyer flasks in a growth chamber with 12 h:12 h light-dark cycle at 21±0.1℃. All of the flasks were shaken two times per day on time by hand. The seawater and glass vessels were treated 20 mins at 120℃ high temperature and high pressure sterilization. Algae cells were counted daily, using a hemocytometer chamber by at least six times for every sample.

2.3 Algal Growth Assays

100 mL algae solution and different concentrations of SWNTs were added to each Erlenmeyer flask as *S. costatum* and *P. donghaiense* grew to exponential phase. The concentration gradient of SWNTs was 0, 0.5, 5, 10, 50, 100, 200 mg/L respectively. Three parallel groups were set and cultivated in growth chamber and the incubation time was 96 h. Density of algal cells and chlorophyll were measured every day. SWNTs suspensions were treated by sonication for 10 mins to make the uniform dispersion before using. Algae solution was treated in dark environment for 20 mins before measuring chlorophyll. Chlorophyll was measured by bbe Moldaenke every day.

2.4 Statistical Analysis

All of the experimental results were shown by $\bar{x} \pm s$. Each of the experimental data sets was compared with the corresponding control. All of the results were reported by the One-Way ANOVA of SPSS 16.0. Statistical significance (*) was accepted when the probability of the result assuming the null hypothesis (p) was less than 0.05[13].

3. Results and discussion

3.1 The effects of SWNTs on S. costatum

The change of cell density of *S. costatum* with time in different SWNTs concentrations was shown in Figure 1. The results showed that SWNTs stimulated the growth of *S. costatum* within 72 h and 24 h as theirs concentrations were smaller than 0.5 mg/L and 10mg/L respectively（$p<0.05$). While the growth of *S. costatum* was inhibited within 48 h and 96 h as SWNTs concentrations were higher than 10 mg/L and 0.5 mg/L respectively（$p<0.05$). The inhibition ratio of *S. costatum* was 0.053, 0.079, 0.099, 0.106, 0.240 and 0.516 respectively in different SWNTs concentrations in 96h. It was found that the inhibition effect in higher SWNTs concentrations groups was more significant than others, especially for SWNTs concentrations over 100 mg/L.

The changes of chlorophyll content was shown in Figure 2. The concentrations of chlorophyll were the same as the density of cells. Chlorophyll concentration was greater than that of control group when SWNTs were smaller than 0.5 mg/L within 72h, but the chlorophyll value was always below the control group as SWNTs concentrations were higher than 100 mg/L within 96h. The chlorophyll in high SWNTs concentration groups was below than that of control group at the first 24h of experiment, which suggested that SWNTs in high concentration had a shading effect on the algae and inhibited the growth of *S. costatum*. It was identical with the change of cell density.

The results of One-Way ANOVA of algal density and chlorophyll was shown in table 1. It was very good to match the two figures. There was a significant difference（$p<0.05$) between all experimental groups and control groups in 96 h.

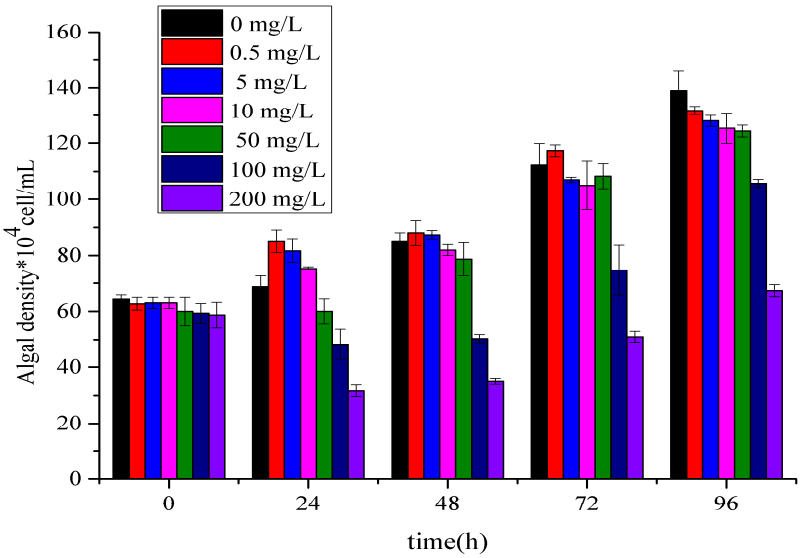


Figure 1. The algal density of *S. costatum* in different time and different SWNTs concentrations

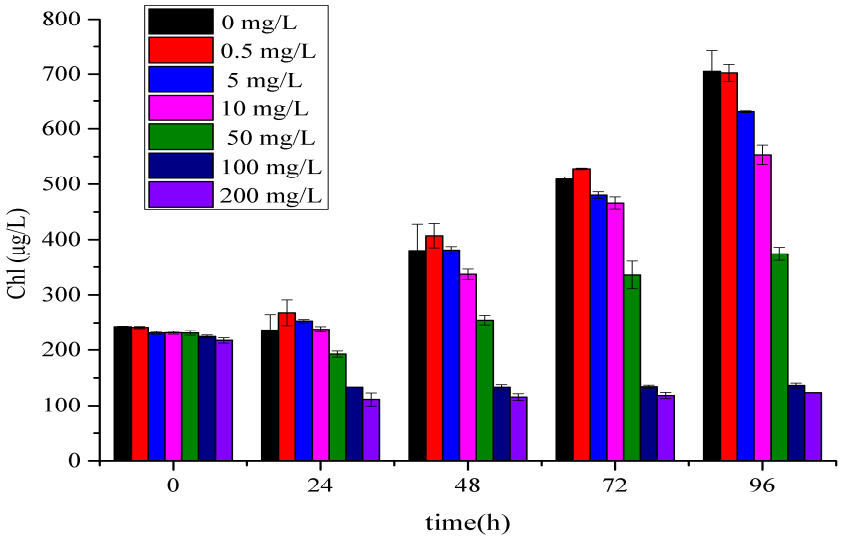


Figure 2. The chlorophyll of *S. costatum* in different time and different SWNTs concentrations

Table 1. The results of cell density and chlorophyll of *S. costatum* by One-Way ANOVA in 96h （1,2,3, 4,5,6,7 is represent for 0,0.5,5,10,50,100,200 mg/L）

Dependent Variable	(I) group	(J) group	Mean Difference (I-J)	Std. Error	Sig.(p)	95% Confidence Interval	
						Lower Bound	Upper Bound
Cell density	1	2	7.33333*	3.03420	.030	.8256	13.8410
		3	11.00000*	3.03420	.003	4.4923	17.5077
		4	13.66667*	3.03420	.000	7.1590	20.1744
		5	14.66667*	3.03420	.000	8.1590	21.1744
		6	33.333333*	3.03420	.000	26.8256	39.8410
		7	71.66667*	3.03420	.000	65.1590	78.1744
Chlorophyll	1	2	2.56667	14.24289	.860	-27.9813	33.1146
		3	74.16667*	14.24289	.000	43.6187	104.7146
		4	151.53333*	14.24289	.000	120.9854	182.0813
		5	330.70000*	14.24289	.000	300.1520	361.2480
		6	568.34667*	14.24289	.000	537.7987	598.8946
		7	581.39667*	14.24289	.000	550.8487	611.9446

*. The mean difference is significant at the 0.05 level. The group 1 is control group and others are experimental groups.

3.2 The effects of SWNTs on P. donghaiense

The change of cell density of *P. donghaiense* in different SWNTs concentrations was shown in Figure 3. The results showed that the growth of *P. donghaiense* was inhibited as SWNTs concentrations were higher than 100 mg/L, while SWNTs promoted the growth of *P. donghaiense* as SWNTs concentrations smaller than 5 mg/L（$p<0.05$) within 48 h. All experimental groups showed that the growth of *P. donghaiense* was inhibited by SWNTs between 72-96h, especially in 96h. The inhibition ratio was 0.171, 0.176, 0.179, 0.207, 0.247 and 0.591 respectively in 96h.

The changes of chlorophyll content was shown in Figure 4. The values of experiment groups were value was below than that of the control group as theirs concentrations were higher than 50 mg/L in all experimental process, which results were similar to the density of algae cells.

The results of One-Way ANOVA of algal density and chlorophyll was shown in table 2. It was very good to match the two figures. There was a significant difference（$p<0.05$) between experimental groups and control groups in 96 h.

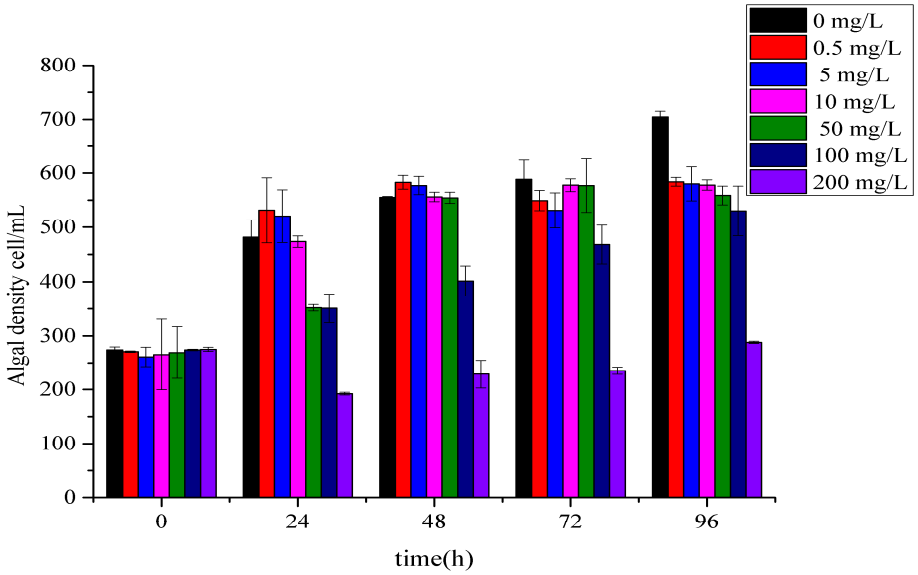


Figure 3. The algal density of *P. donghaiense* in different time and different SWNTs concentrations

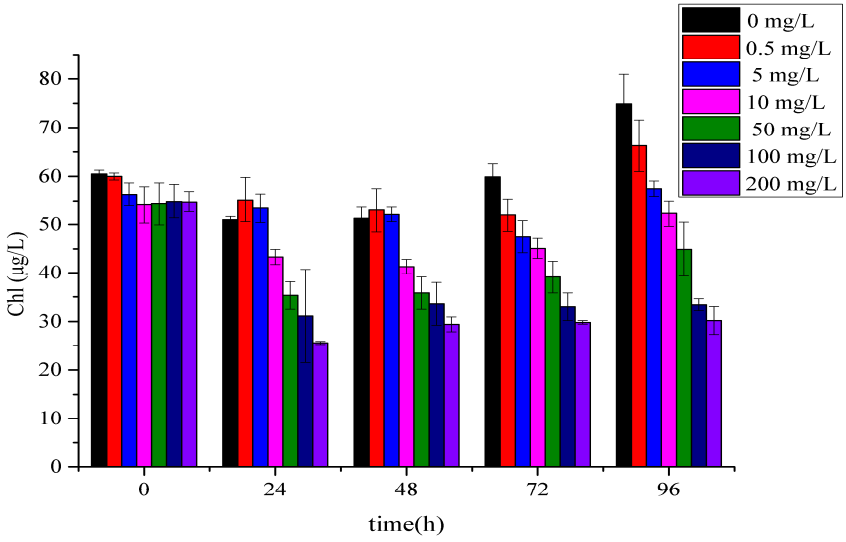


Figure 4. The chlorophyll of *P. donghaiense* in different time and different SWNTs concentrations

Table 2. The results of cell density and chlorophyll of *P. donghaiense* by One-Way ANOVA in 96h
（1,2,3, 4,5,6,7 is represent for 0,0.5,5,10,50,100,200 mg/L）

Dependent Variable	(I) group	(J) group	Mean Difference (I-J)	Std. Error	Sig.	95% Confidence Interval	
						Lower Bound	Upper Bound
Cell density	1	2	120.33333*	18.74135	.000	80.1371	160.5295
		3	124.00000*	18.74135	.000	80.1371	160.5295
		4	126.33333*	18.74135	.000	83.8038	166.5295
		5	145.66667*	18.74135	.000	86.1371	185.8629
		6	174.33333*	18.74135	.000	105.4705	214.5295
		7	416.33333*	18.74135	.000	376.1371	456.5295

Chlorophyll	1	2	8.51667*	3.29346	.022	1.4529	15.5804
		3	17.31667*	3.29346	.000	10.2529	24.3804
		4	22.52333*	3.29346	.000	15.4596	29.5871
		5	29.99667*	3.29346	.000	22.9329	37.0604
		6	41.47667*	3.29346	.000	34.4129	48.5404
		7	44.67000*	3.29346	.000	37.6062	51.7338

*. The mean difference is significant at the 0.05 level. The group 1 is control group and others are experimental groups.

3.3 Microscopical observation of S. costatum and P. donghaiense in SWNTs

The effects of SWNTs on the two algae were observed under optical microscope. The shape of *S. costatum* was cylindrical and *P. donghaiense* was oval, and they are well dispersed while no SWNTs added. Added SWNTs adsorbed a lot of algal cells around and formed a larger particles. This may be the main reason for the inhibition of SWNTs on the growth of algae. In addition, the physical damage and the shading of SWNTs on the algae also affected their growth[11].

SWNTs, which have a larger surface area, may lead to damage to cell structure, dysfunction and even necrosis because of theirs unique surface chemistry and electrical transport properties[14]. Previous research reproted that CNTs were more toxic to daphnid than that of fullerenes. Both core structure and surface chemistry influence theirs toxicity[15]. In addition, pulmonary toxicity tests of SWCNTs in mice showed an increasingly harmful trend with metal catalysts which remained in the process of production[7].

4. Conclusions

This research showed that the algal density in low SWNTs concentration was larger than that of the control group in the earlier stages of the experiment, while the algal density was lower than the control group in the last period. When the concentration of SWNTs was higher than 50 mg/L, they always inhibited growth of the two kinds of algae in the whole experiment. In addition, the effect of inhibition of *P. donghaiense* was higher than that of *S. costatum* in 96h. It was concluded that SWNTs can promote the growth of algae in low concentration and inhibit the growth of algae in high concentration. The possible mechanism was that SWNTs was absorbed by algae as carbon sources in the low concentration group, while the large number of SWNTs rally around the algal cells affected light absorption of algal cells and even influenced the efficiency of metabolic in high SWNTs concentrations group (> 50 mg/L). SWNTs also affected the active of some enzymes and increased the value of reactive oxygen species[16]. One of the most authoritative statement was that SWNTs attenuated electron transfer and conformational change of Cyt c, which consequently changed mitochondrial respiration of SWNTs-treated cells[17].

Acknowledgments

We would like to thank CSMNT2014 for the invitation to write this paper. We thank the College of Chemistry and Chemical Engineering of Ocean University of China, who provided the *S. costatum* and *P. donghaiense* strains and made the laboratory available for us.

References

[1] Baughman, R.H.; Zakhidov, A. A.; de Heer, W.A. Carbon nanotubes-The route toward applications. Sci. 2002, 297 (5582) 787−792.

[2] Mauter, M. S.; Elimelech, M. Environmental applications of carbon-based nanomaterials. *Environ.* Sci. 2008, 42 (16) 5843−5859.

[3] Klaine, S.J.; Alvarez, P.J.J.; Batley, G.E.; Fernandes, T.F.; Handy, R.D.; Lyon, D.Y.; Mahendra, S.; McLaughlin, M.J.; Lead, J.R. Nanomaterials in the environment: behavior, late, bioavailability and effects, Sci.2008,27(9) 1825-1851.

[4] Jaisi, D. P.; Elimelech, M. Single-walled carbon nanotubes exhibit limited transport in soil columns. *Environ.* Sci. Technol. 2009, 43 (24) 9161-9166.

[5] Saleh, N. B.; Pfefferle, L. D.; Elimelech, M. Influence of biomacromolecules and humic acid on the aggregation kinetics of single-walled carbon nanotubes. *Environ.* Sci. Technol. 2010, 44 (7) 2412−2418.

[6] Liu, X.; O'Carroll, D. M.; Petersen, E. J.; Huang, Q.; Anderson, C. L. Mobility of multiwalled carbon nanotubes in porous media. *Environ.* Sci. Technol.2009, 43 (21) 8153−8158.

[7] Chiu-Wing Lam, John T. James, Richard McCluskey, Robert L. Hunter, Pulmonary Toxicity of Single-Walled Carbon Nanotubes in Mice 7 and 90Days after intratracheal instillation, Toxicological Sciences.2004, 77(1) 126-134.

[8] Xiaoshan Zhu, Lin Zhu. Three kinds of the toxic effects of carbon nanomaterials on aquatic organisms. China Environmental Science.2008, 28(3) 269−273.

[9] Hyung H. Fortner J.D.; Hughes J.B. Natural organic matter stabilizes carbon nanotubes in the aqueous phase,Science.2007,41(1) 179-184.

[10] Roberts, A.P.; Mount, A.S.; Seda, B,et al. In vivo biomodification of lipid-coated carbon nanotubes by Daphnia magna, Sci. 2007,41(8) 3025-3029.

[11] Fabienne Schwab. Thomas D.Bucheli, Lungile P. Lukhele et al.. Are Carbon Nanotube Effects on Green Algae Caused by Shading and Agglomeration, Sci. 2011,45(14) 6136-6144.

[12] Pumera, M. Carbon nanotubes contain residual metal catalyst nanoparticles even after washing with nitric acid at elevated temperature because these metal nanoparticles are sheathed by several graphene sheets. Langmuir. 2007, 23 (11) 6453−6458.

[13] Zhifeng Long, Jing Ji. Systematic and Quantitative Investigation of the Mechanism of Carbon Nanotubes' Toxicity toward Algae. Environ. Sci. Technol.2012, 46(15) 8458−8466.

[14] Sivaram Arepalli. Chiu-wing Lam, John T. James, and Robert L. Hunter, A review of carbon nanotube toxicity and assessment of potential occupational and environmental health risks, Critical Reviews in Toxicology2006, 36, 189-217.

[15] Devrah A. Arndt, Maika Moua. Core Structure and Surface Functionalization of Carbon Nanomaterials Alter Impacts to Daphnid Mortality, Reproduction, and Growth: Acute Assays Do Not Predict Chronic Exposure ImpactsEnviron. Sci. Technol. 2013, 47, 9444−9452.

[16] Nel A, Xia T, Madler L, Li N.. Toxic potential of materials at the nanolevel. Science.2006,311(5761) 622-627

[17] Xiaowei Ma , Li-Hua Zhang .Single-Walled Carbon Nanotubes Alter Cytochrome c Electron Transfer and Modulate Mitochondrial Function, Sci. 2012,6(12) 10486–10496.

Key Engineering Materials Vols 645-646 (2015) pp 1333-1338
Submitted: 2014-11-07
© (2015) Trans Tech Publications, Switzerland
Accepted: 2014-12-23
doi:10.4028/www.scientific.net/KEM.645-646.1333

Expansion Performance of Novel Balloon-expandable Stent for Tapered Vessel

SHEN Xiang [a *], SUN Yang Yang[b] and WU Bo Bo[c]

School of Mechanical Engineering, Jiangsu University, Zhenjiang 212013, China

[a]sx@ujs.edu.cn, [b]hnhnsyy@163.com, [c]18352861825@163.com

Keywords: Balloon-expandable stent, tapered vessel, mechanical properties, finite element method

Abstract. In-stent restenosis still remains an obsession to cardiologist, especially in tapered vessels. In this paper, we designed a novel balloon-expandable stent for tapered vessel and proposed a finite element method (FEM) to study the expansion of the novel stent. The effect of stent design parameters on stent tapering and foreshortening were also researched. Results show that the radial displacement of stent proximal end was always larger than that of stent distal end during stent expansion, and the stent had a tapered shape as a whole after expansion. The degree of stent tapering observed increased with the expansion pressure increase. Besides, increasing the gradient of ring amplitude not only could increase the tapering degree of stent after expansion, but also could decrease stent foreshortening, improving the positioning accuracy after stent implantation. In conclusion, FEM can quantify expansion performance of novel balloon-expandable stents and help designers to devise and assess new stent designs for tapered vessel.

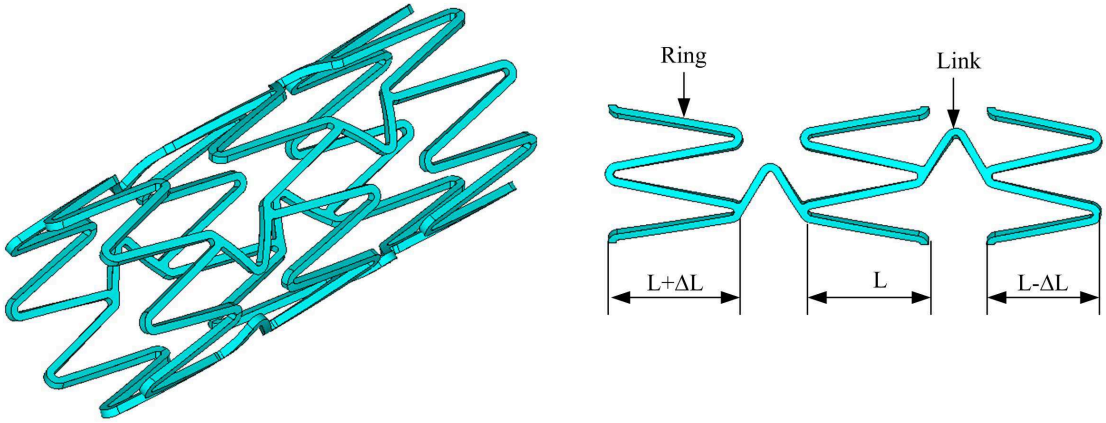
Introduction

The field of stent intervention has witnessed many advances over the last few decades that served to make it a safe and effective treatment for patients with coronary artery disease due to vessel stenosis [1]. Stents are medical devices used in cardiovascular intervention for unblocking the diseased arteries and restoring blood flow [2]. Balloon-expandable stents are widely used because of its strong radial supporting performance [3,4,5,6]. The characteristics of such conventional stents are that original shape of stent is cylindrical and stent diameter after expansion remains constant value in the longitudinal direction. However, vessel diameter of human varies along the length direction and the change of diameter is sometimes significant [7,8]. For instance, the diameter of carotid artery, femoral artery and the left anterior descending of the coronary artery are reduced along the length direction of vessels, i.e. their geometry structure is a taper. Those traditional stents with constant diameter are usually implanted into tapered vessels in clinical practice [9]. In addition to resulting in the undesired stent conformity to vessel, it will also overextended distal end of taped vessel, causing the injure of vessel wall and inducing in-stent restenosis (ISR) [10,11]. In order to improve the match of stent with tapered vessel and further reduce the occurrence of ISR after stent implantation, we designed a novel balloon-expandable stent for tapered vessel and proposed a finite element method (FEM) to study expansion process of the stent. The effect of stent design parameters on tapering degree and foreshortening of stent were also researched.

Materials and Methods

Geometry model. Geometry model of stent was generated on Pro-Engineer, and then exported to ANSYS for pre-treatment and calculations. A three-dimensional geometrical model of stent and its design parameters were shown in Fig.1. Stent usually consists of two parts: links and rings. The ring length of traditional stents remain unchanged in the axial direction, while that of novel stents have a decreasing trend from proximal end to distal end. The stent was modeled with a length of 5.1 mm and an original outer diameter 2 mm. To reduce computation, only a quarter of stent model was used to simulate the stent expansion process due to the circumferential symmetry condition. In order to study the effect of the gradient of ring amplitude (GORA) on stent tapering and axial shortening after stent expansion, five types of stent models were modeled and their design parameters were as shown in

Table 1, where the stent S with the GORA of 0 mm corresponded to the traditional stent with circular and straight structure after expansion.



(a) (b)

Fig. 1 Geometrical model and design parameters of stent: (a) Geometrical model; (b) Design parameters

Table 1 Design parameter of stents

Stent model	GORA ΔL (mm)	Proximal amplitude (mm)	Middle amplitude (mm)	Distal amplitude (mm)	Original diameter (mm)	Original length (mm)
S	0	1.3	1.3	1.3	2	5.1
T1	0.05	1.35	1.3	1.25	2	5.1
T2	0.1	1.4	1.3	1.2	2	5.1
T3	0.15	1.45	1.3	1.15	2	5.1
T4	0.2	1.5	1.3	1.1	2	5.1

Finite element model. The stent was assumed to be made of 316L stainless steel. Since the stent large deformation mainly depended on the plastic deformation and its material characteristic had been at the nonlinear phase, the Von Mises yield creation and bi-linear isotropic hardening rule were adopted here. The general mechanical properties of this material are as follows [6]: Yang's modulus, 200 GPa; Poisson's ratio, 0.35; tangent modulus, 1 GPa; yield strength, 315 MPa. The stent was meshed with SOLID186. There are at least two elements in stent thickness and width direction to meet the requirements of solution accuracy. The meshed stent was demonstrated in Fig. 2.

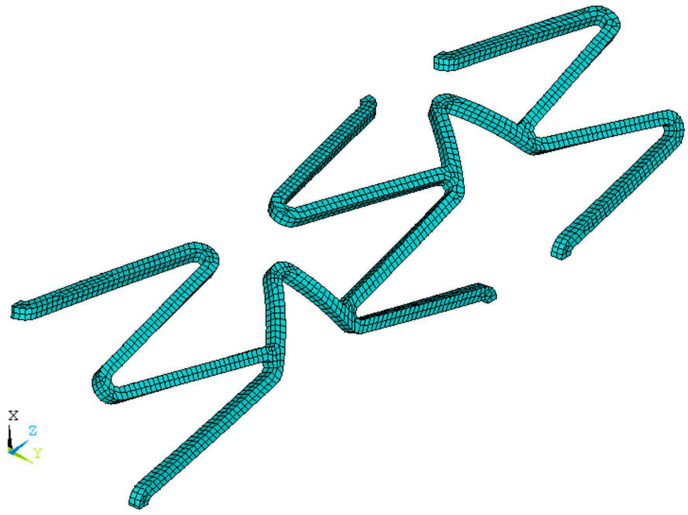


Fig. 2 Finite element model of novel stent

Boundary conditions and loading. Symmetrical boundary conditions were constrained to ensure the free radial expansion of stents. In order to prevent the occurrence of stent rigid movement, the

nodes of stent proximal end were constrained in axial direction and were not constrained in the radial direction. Rotation of stent was inhibited. An internal pressure on the inner surface of stent was used to expand the stent. The expansion process began from the original diameter of the stent. When the maximum radial displacement of 1 mm of the stent central nodes was reached, the internal pressure was removed to simulate balloon retraction.

The tapering and foreshortening were calculated by the following quantities:

• the transient tapering of stent, defined as

$$\text{Tapering} = \frac{D_{\text{proximal}} - D_{\text{distal}}}{D_{\text{proximal}}} \times 100\% \quad (1)$$

Where D_{proximal} and D_{distal} is the stent proximal and distal diameter, respectively.

• the transient foreshortening of stent, defined as

$$\text{Foreshortening} = \frac{L_{\text{original}} - L_{\text{load}}}{L_{\text{original}}} \times 100\% \quad (2)$$

Where L_{original} and L_{load} is the stent original length and final length, respectively.

Results and discussion

Free expansion of novel stent. Radial displacement of the stent T1 proximal and distal node in dependence of pressure was shown in Fig. 3. The radial displacement of stent proximal end was always larger than that of stent distal end during expansion process of the novel stent. Thus, the stent had a tapered shape as a whole after expansion, and it had a good match with a tapered vessel, increasing the conformity of the stent to the tapered vessel and reducing the likelihood of ISR in tapered vessel distal end. Moreover, the degree of stent tapering observed increased with the expansion pressure increase. Therefore, the appropriate expansion pressure should be selected according to the vessel shape and tapering in the clinical application. Fig. 4 showed that Von Mises stress distribution in stent T1 when it was expanded to the maximum diameter. The regions of high stresses in stent after expansion were concentrated in the junction between ring and link.

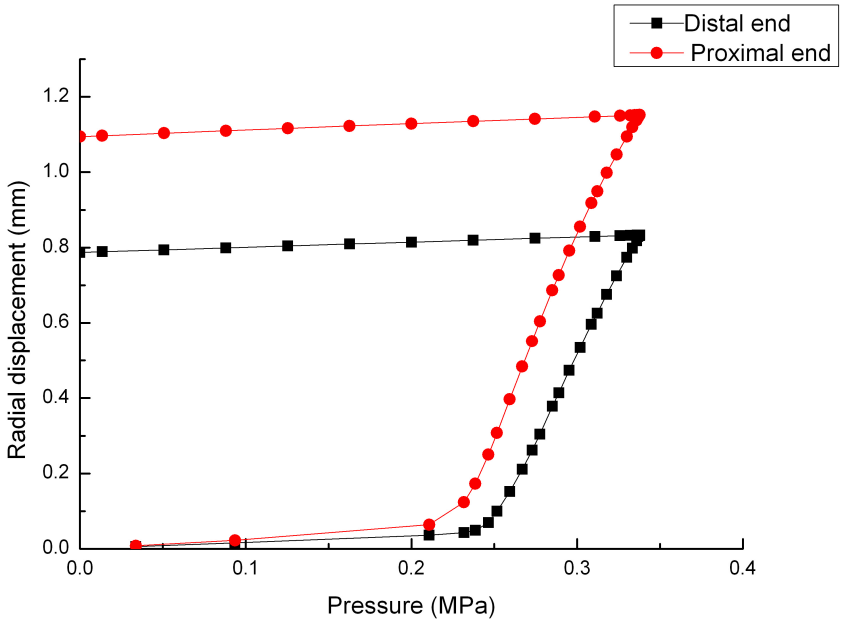


Fig. 3 Radial displacement of the stent T1 proximal and distal node in dependence of pressure

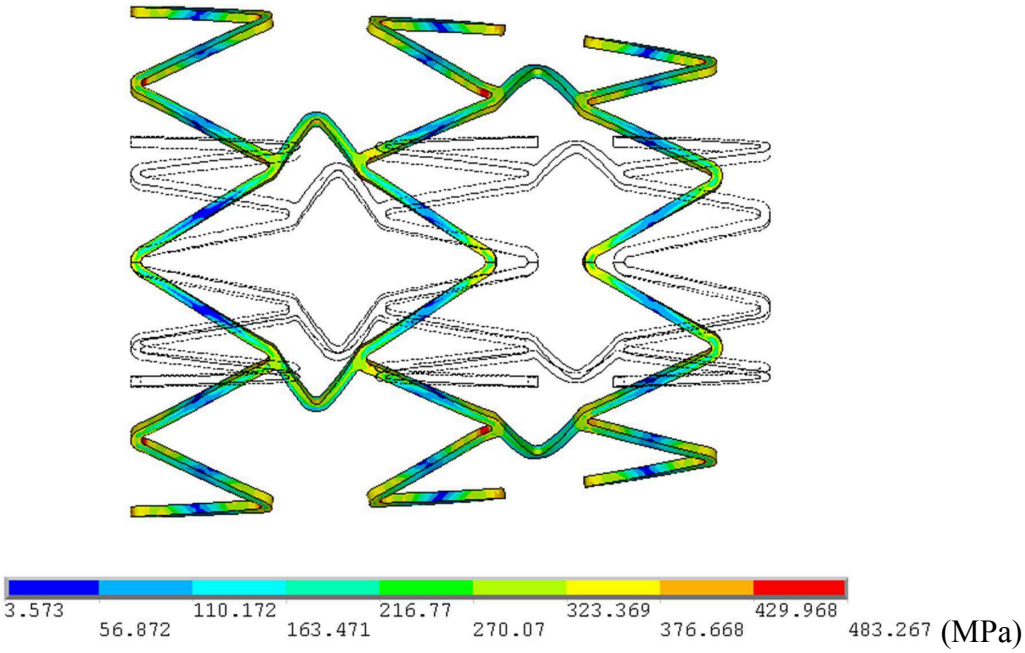


Fig. 4 Von Mises stress distribution in stent T1 when it was expanded to maximum diameter

The effect of GORA on maximum tapering of stent. The effect of GORA on the maximum tapering of stent after expansion was shown in Fig. 5. Five types of stents had the same design parameters except for the GORA. The maximum tapering of stent after expansion was proportional to the GORA. For example, in comparing stent S and stent T1, the increase in GORA from 0 mm to 0.05 mm resulted in an increase in maximum tapering of stent from 0 to 14.82%. A further increase in GORA from 0.05 mm (stent T1) to 0.2 mm (stent T4) resulted in a significant increase in maximum tapering of stent from 14.82% to 45.7%. The increase ratio was about 208.4%. Therefore, stents with larger GORA should be chosen when stents with large tapering are needed in clinical practice.

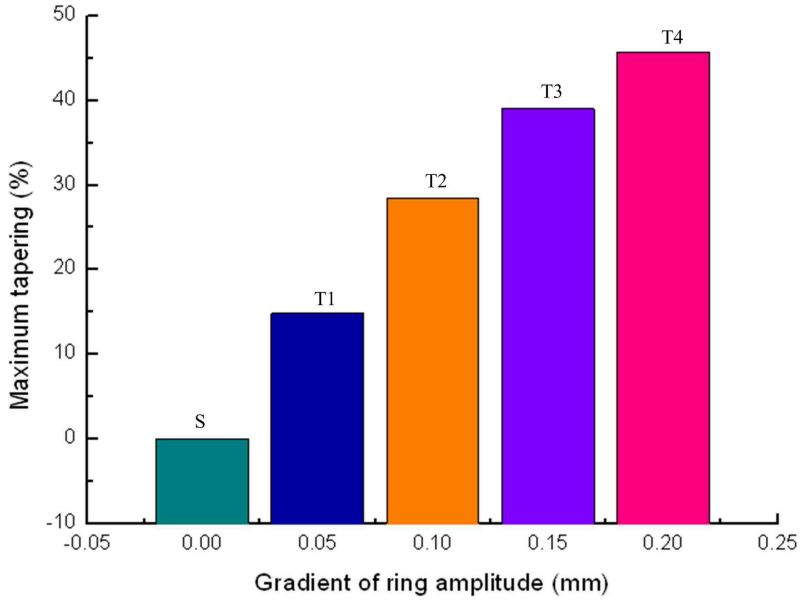


Fig. 5 The effect of GORA on maximum tapering of stent

The effect of GORA on foreshortening of stent. The effect of GORA on foreshortening of stent was shown in Fig. 6. Increasing the GORA resulted in smaller foreshortening of stent. For example, in comparing stent S and stent T1, the increase in GORA from 0 mm to 0.05 mm resulted in a reduction in foreshortening of stent from 8.81% to 7.71%. A further increase in GORA from 0.05 mm (stent T1) to 0.2 mm (stent T4) resulted in a reduction in foreshortening of stent from 7.71% to 6.81%.

The reduction ratio was about 11.7%. Therefore, in order to reduce foreshortening for improving the positioning accuracy after stent implantation, increasing the GORA should be considered when designing or selecting stents.

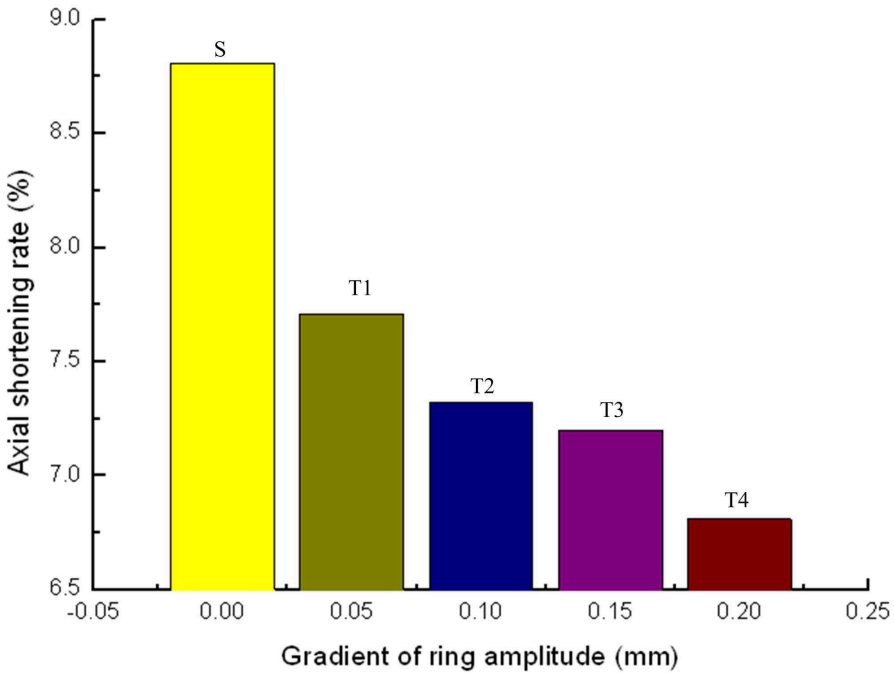


Fig. 6 The effect of GORA on foreshortening of stent

Conclusions

The finite element method is a formidable tool that can be used to analyze the expansion performance of novel balloon-expandable stent for tapered vessel. It was found that the novel stent had a tapered shape as a whole after expansion, increasing the conformity of the stent to the tapered vessel. Moreover, the degree of stent tapering observed increased with the expansion pressure increase. Besides, increasing GORA not only could increase the degree of stent tapering after expansion, but also could decrease stent foreshortening, improving the positioning accuracy after stent implantation. In conclusion, FEM provide a general tool for designers to study mechanical characteristics of novel stents and help designers to devise and assess new stent designs for tapered vessel.

Acknowledgements

This project is supported by National Natural Science Foundation of China (51305171), Natural Science Foundation of Jiangsu Province (BK20130525), Natural Science Foundation of the Higher Education Institutions of Jiangsu Province (13KJB460006) and Foundation of Jiangsu University (10JDG123, 13A608).

References

[1] W.M. Wilson, N.L.M. Cruden, Advances in coronary stent technology: current expectations and new developments, Research Reports in Clinical Cardiology 4 (2013) 85-96.

[2] R.T. Higashida, P.M. Meyers, C. C. Phatouros, J.J. Connors, J.D. Barr, Reporting standards for carotid artery angioplasty and stent placement, J Vasc Interv Radiol 15 (2004) E1-E24.

[3] G.R. Douglas, A.S. Phani, J. Gagnon, Analyses and design of expansion mechanisms of balloon expandable vascular stents, Journal of Biomechanics 47 (2014) 1438-1446.

[4] S. Zhao, L. Gu, S.R. Froemming, On the importance of modeling stent procedure for predicting arterial mechanics, Journal of Biomechanical Engineering 134 (2012) 121005.

[5] H. Li, T. Qiu, B. Zhu, J. Wu, X. Wang, Design optimization of coronary stent based on finite element models, The Scientific World Journal 2013 (2013) 630243.
[6] K. Takashima, T. Kitou, K. Mori, Simulation and experimental observation of contact conditions between stents and artery models, Medical Engineering & Physics 29 (2007) 326-335.
[7] M. Zubaid, C. Bullr, G.J. Mancini, Normal angiographic tapering of the coronary arteries, Canadian Journal of Cardiology 18 (2002) 973-980.
[8] P. Datir, A.Y. Lee, S.D.Lamm, H.C. Han, Effects of geometric variations of the buckling of arteries, International Journal of Applied Mechanics 3 (2011) 385-406.
[9] L.H. Timmins, C.A. Meyer, M.R. Moreno, J.E. Moore, Mechanical modeling of stents deployed in tapered arteries. Ann Biomed Eng 36 (2008) 2042-2050.
[10] L.H. Timmins, M.W. Miller, F.J. Clubb, Increased artery wall stress post-stenting leads to greater intimal thickening, Laboratory Investigation 91 (2011) 955-967.
[11] M.S. Kim, L.S. Dean, In-stent restenosis, Cardiovascular Therapeutics 29 (2011) 190-198.

Key Engineering Materials Vols 645-646 (2015) pp 1339-1344
© (2015) Trans Tech Publications, Switzerland
doi:10.4028/www.scientific.net/KEM.645-646.1339

Submitted: 2015-01-14
Accepted: 2015-01-15

Synthesis of Silica Modified Large-sized Hydroxyapatite Whiskers By a Hydrothermal Co-precipitation Method

Yin Yanting[1] , Chen qinghua[2], Yan Tingting, Chen qinghua*

Department of Materials Science and Engineering, Kunming University of Science and Technology, Kunming, Yunnan, China

* Corresponding Author：Chen Qinghua, Professor, Department of Materials Science and Engineering, Kunming University of Science and Technology,
Mobile:+86-13888013957, FAX: 0871-5192067, email: chenqinghua_yn1@163.com

Key words: hydroxyapatite, hydrothermal co-precipitation, surface modified, whiskers

Abstract. The objective of this study was to develop a novel silica modified large-sized hydroxyapatite whiskers with improved properties for use in bone repair applications. Large-sized whiskers with a mean length of 250μm were obtained by a hydrothermal co-precipitation method at 150°C, 7.5Mpa in high-pressure reactor. Silica modified hydroxyapatite whiskers were prepared by dissolving TEOS in ethanol solution, then sintering with hydroxyapatite. The compositional and morphological properties of prepared whiskers were studied by means of x-ray diffraction(XRD), Fouier transform infrared(FT-IR), scanning electron microscopy(SEM). The results indicated the evidence of nano-silicon dioxide particles on the surface of HAP whiskers. The size of nano-silicon dioxide particles depends on dropping and stirring rate. Hence, this new type of silica modified large-sized hydroxyapatite whiskers is a valuable candidate for biomedical applications.

1. Introduction

Hydroxyapatite(HAP), as the main tissue engineering materials, is an ideal biological material due to its excellent bioactivity, biocompatibility and high osteo-conductive[1-2]. HAP has been widely used in dental and orthopedic surgery and other clinical areas due to their close similarity in composition with natural bone[3]. However, the fracture toughness of HAP powders are poor have restricted to load bearing applications[4-5].

HAP whiskers can absorb energy and eliminate concentrated stress of crack tip through bridging, crack deflection and pulling effect to reduce the stress suffered by surrounding material[6]. So, HAP whiskers effectively improve the mechanical properties of materials, reaching the purpose of enhancing the toughness of biological material.

Silicon(Si) plays an important role in bones and found to be essential for bone generation, cartilage growth and increasing the rate of biomineralization[7]. Using silica to modify hydroxyapatite in the surface not only prevents whiskers form being pulled out, but also increases the retention of whiskers. Herein, comparing with traditional whisker, the silica surface modified HAP whiskers might possess excellent mechanical and biological properties.

HAP whiskers can be prepared by a variety of techniques, including high-temperature solid state reaction[8], dissolution reprecipitation of calcium phosphate gels[9], hydrothermal processes[10].Among them, the hydrothermal method could fabricate HA with good crystallinity. But, simple hydrothermal growth method have lower synthesis rate. In this study, we use hydrothermal-copricipiration method, add HAP seed crystal as nucleation agent, sorbitol as template, significantly improve the yield of HAP whiskers. High length-diameter ratio and

large-sized whiskers with good crystallinity have been prepared. The crystal structure and morphologies of the as-prepared samples were characterized by XRD, FT-IR and SEM.

2. Materials and methods

2.1 Materials

Calcium nitrate($Ca(NO_3)_2$•$4H_2O$), Urea(H_2NCONH_2), Ethanol（C_2H_5OH）were purchased form Tianjing Chemical Reagent Factory(China). Diammonium hydrogen phosphate($(NH_4)_2HPO_4$), concentrated nitric acid(HNO_3) were obtained form XilongChemicalCo.,Ltd.(China). Tetraethyl orthosilicate (TEOS), D-Sorbitol were supplied Sinopharm Chemical Reagent Co.,Ltd. Self-made HAP seed. All chemicals used for the synthesis were of analytical grade and were used as received without any further purification.

2.2 Systhesis of large-sized hydroxyapatite whiskers

Weighting 40L distilled water in high-pressure reactor, calcium nitrate, diammonium phosphate, urea, D-Sorbitol were added according to certain ratio to dissolve. The initial pH of the solution was adjusted and maintained about 2.5 by addition of concentrated nitric acid. The white precipitate was then stirred for 10 minutes followed by adding HAP seed crystal. Set the high-pressure reactor temperature at 150 ^oC, 7.5Mpa. Time of heat preservation was 90 minutes after reached the settled temperature. The heating rate was 3^oC /min. After the reaction, the product was filtered and washed with deionized water several times, and freeze for 12h at -20^oC. The frozen samples were lyophilized within a freeze-dryer at -50^oC for 48h to obtain large-sized hydroxyapatite whiskers.

2.3 Systhesis of silica surface modified hydroxyapatite whiskers

30ml of concentrated aqueous ammonia was dissolved in 150ml ethanol to obtain solution A. Weighing 3g large-sized hydroxyapatite whiskers added into the A solution, then ultrasonic dispersed for two minutes. 15ml of TEOS was dissolved in 100ml ethanol to obtain solution B. Solution A was slowly added dropwise to the solution B and stirred at 40^oC after the dropwise addition. After drying at room temperature, the mixture was stirred at 800 ^oC for 2h in furnace. Silica surface modified hydroxyapatite whiskers were prepared after cooling with furnace.

2.4 Characterization

The phase composition of all samples was characterized by X-ray diffraction using D8 ADVANCE diffractmeter with Cu Kα radiation at room temperature. The experiments were done at a scan rate of 20°-80°. The characteristic functional groups of all materials were carried out using an FT-IR spectrometer(Bruker, Tensor27 spectrophotometer, Germany) with spectral resolution of 4cm^{-1} and analyzed at range of 400-4000cm^{-1}. The morphologies of the synthesized materials were observed by scanning electron mnicroscope(SEM)(QUANTA200, American). Samples were analyzed at 25KV.

3. Results and discussion

3.1 XRD analysis

XRD patterns of two different whiskers are shown in Fig.1. All peaks are well matched with those of standard values of HAP (JCPDS:No.09–0432) both in terms of d-spacings and 2θ-positions, which suggesting the whiskers were HAP. The characteristic reflections of HAP, such as (002), (102), (210), (211), (112), (300) and (310) have appeared in Fig.1.

Comparing the patterns of sample A with standard spectrum, these sharp and strong XRD peaks indicate the samples are well crystallized with no secondary phase. However, the peak intensities of three strong reflections (211), (112), (300) are higher than standard values because HAP crystal selectively produce strong hydrogen bonds and electrostatic interactions owing to the template agent, resulting in preferential growth of HAP whiskers.

The diffraction peak intensity of (300) are significantly higher than (211) in sample A attributed to peaks of SiO_2 overlap with (300) reflections of HAP around $2\theta = 32°$. At $2\theta = 24°$ shows the characteristic peaks group of SiO_2. From the XRD analysis, it can be preliminary confirm the formation of SiO_2 in HAP whiskers.

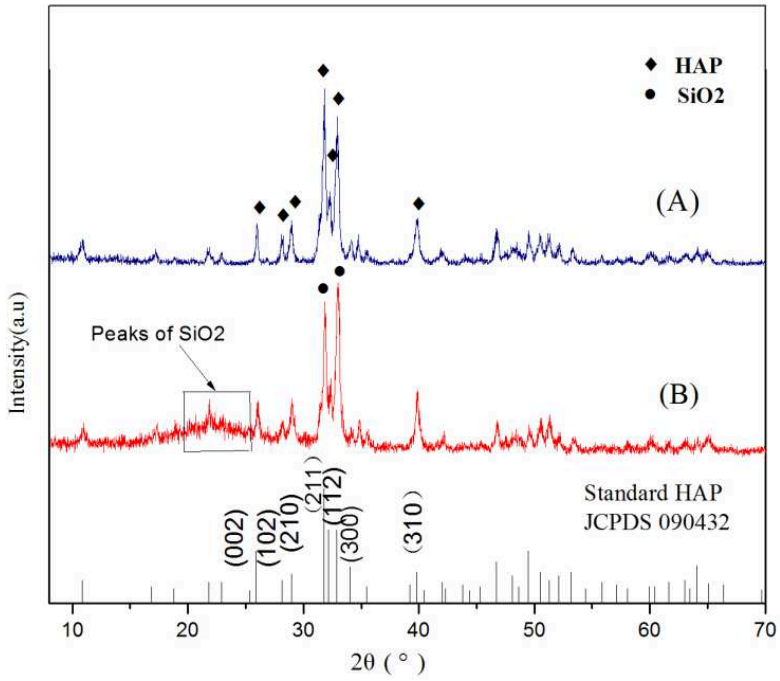


Fig.1 Sample A:large-sized hydroxyapatite whisker sample B:silica modified hydroxyapatite whisker

3.2 FT-IR analysis

Fig.2 shows the FT-IR spectrum of the samples. Large-sized HAP whiskers have the same absorption peaks with HAP powders indicating that they contain the same functional groups. The peaks at $1641cm^{-1}$ were the bending mode of the absorbed water, while the peaks at around $3430cm^{-1}$ were assigned to the stretching vibration of the lattice OH^- group of HAP. The characteristic bands for PO_4^{3-} appeared at $604cm^{-1}$, $561cm^{-1}$, $1111cm^{-1}$, $1030cm^{-1}$. Bonds at $870cm^{-1}$, $1455cm^{-1}$ and $1420cm^{-1}$ correspond to CO_3^{2-} demonstrating that the material contained traces of carbonate which similar to composition of natural bone apatite. However, the absorption intensity of large-sized HAP whiskers was significantly stronger than those of the HAP powders.

In the FT-IR spectra of silica modified hydroxyapatite whiskers bands appeared at 1089 cm^{-1} attributed to asymmetric stretch vibration of Si-O-Si bond. The bands at 804 cm^{-1} and 478 cm^{-1} assigned to stretch vibration of Si-O bond. Peaks at $474cm^{-1}$, $812cm^{-1}$, $1111cm^{-1}$ and $3431cm^{-1}$ increase in intensity because similarities in vibration between SiO^{4-} and PO^{3-} [11]. These changes indicate SiO_2 has generated in sample 3 consistent with the conclusions in XRD patterns.

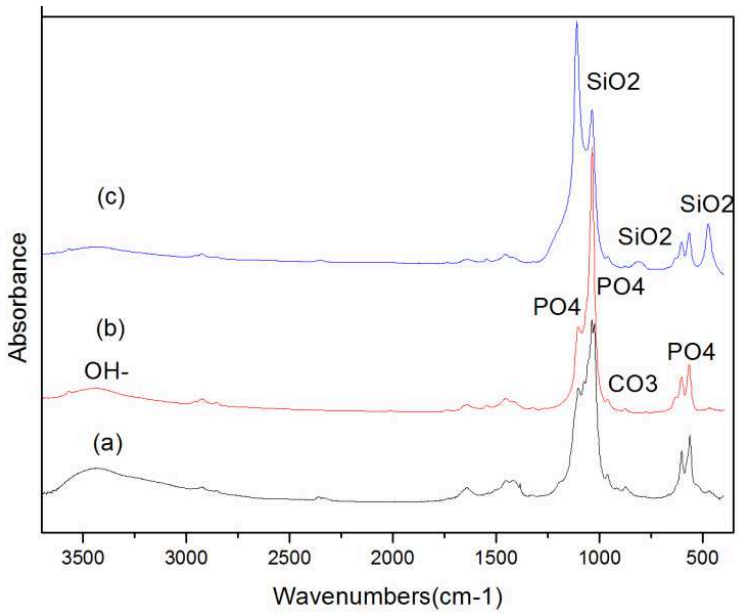


Fig.2 FT-IR spectrum for (a) HAP (b) Large-sized HAP whiskers (c) Silica modified hydroxyapatite whisker

3.3 SEM observation

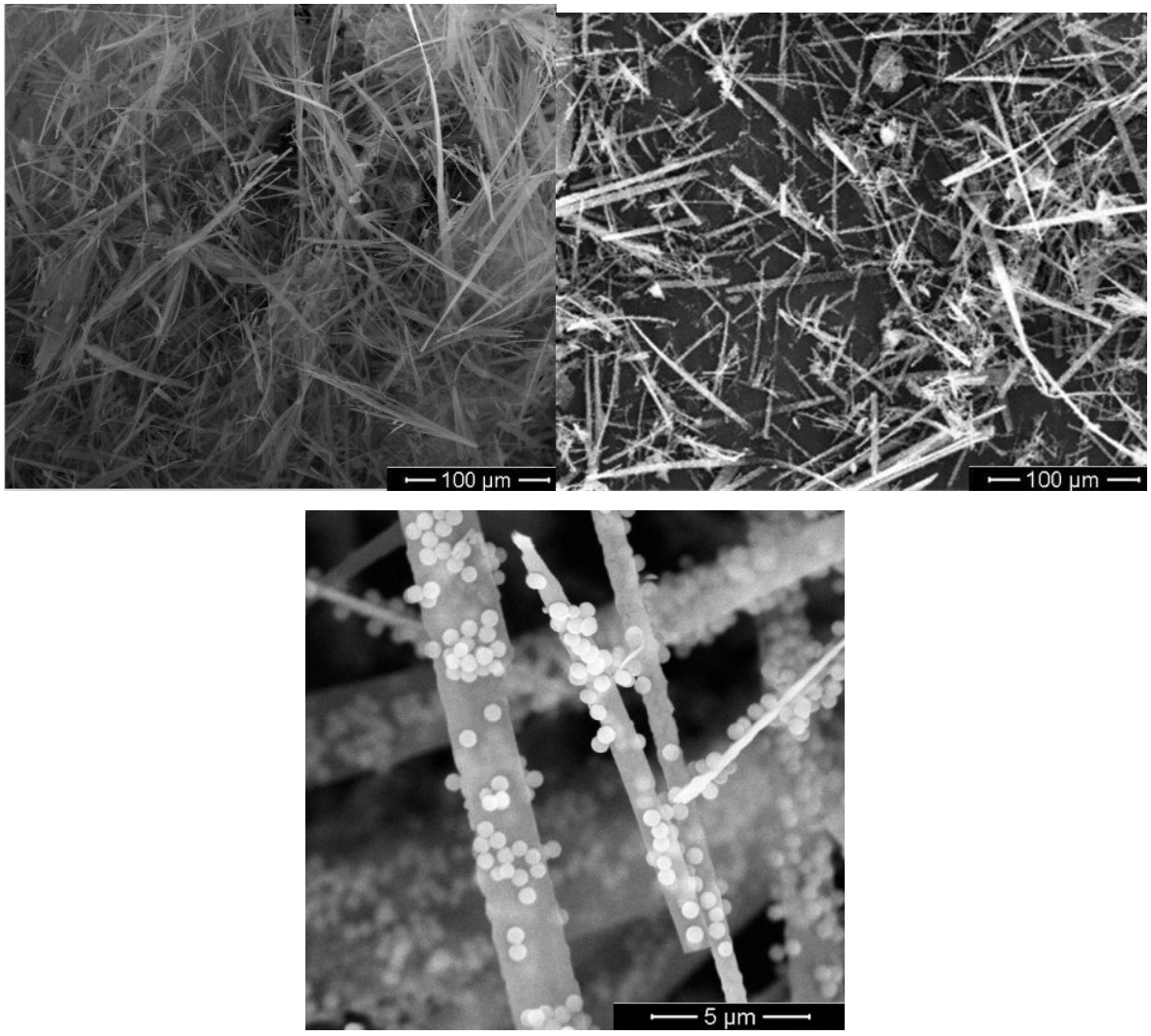


Fig.3 Shows the SEM images of the prepared large-sized HAP whiskers and silica modified hydroxyapatite whiskers.

It can be seen that both of the samples showed whisker-like morphology with mean length of 250μm and 800μm in maximum. Using sorbitol as a template can guide hydroxyapatite preferential growth along the C axis leading to whisker-like morphology. The addition of HAP seed crystal provides the nucleation for whiskers to grow, reduce the driving force required for nucleation, so that the yield of whisker improved. The surface of large-sized HAP whiskers was smooth and with good homogeneity because there is no particles formed on the surface. However, the surface of silica modified hydroxyapatite whisker was rough and covered by uniform spherical SiO_2 nano particles with diameter of 600nm. Based on the special structure of silica modified hydroxyapatite whiskers, it can produce a so-called "rebar effect" used as reinforced material compared to pure HAP whiskers[12]. When it combined with the material, large frictional force is produced which can furtherly improve the strength of the material. The size of nano-silicon dioxide particles depends on dropping and stirring rate.

4. Conclusion

Large-sized HAP whiskers and silica modified hydroxyapatite whiskers have been successfully synthesized by a hydrothermal co-precipitation method. This method has advantaged on its convenience, well crystallinity, less agglomeration in products and high yield The XRD and FT-IR analyses proved the formation of SiO_2 in HAP whiskers. SEM images shows that the samples in whisker-like morphology with mean length of 250μm and uniform spherical SiO_2 nano particles with diameter of 600nm on the surface of HAP whiskers. This new type of silica modified large-sized hydroxyapatite whiskers can enhance the mechanical properties of materials. Hence, these whiskers could be applied as a suitable biocompatible and mechanical reinforcement material for biomedical applications.

5. Acknowledgement

The authors are grateful to the the National Natural Science Foundation of China (Grant No. 31260228) and Joint Research Program of China and Italy(Grant No.2011IA008) for kindly funds to carry out this researchwork.

References

[1] Hongquan Zhang, Ming Zhang. Characterization and thermal behavior of calcium deficient hydroxyapatite whiskers with various Ca/P ratios[J]. Materials Chemistry and Physics, 2011, 126: 642-648.

[2] Ruixue Sun, Kezheng Chen, Zhongmiao Liao, et al. Controlled synthesis and thermal stability of hydroxyapatite hierarchical microstructures[J]. Materials Research Bulletin, 2013, 48: 1143-1147.

[3] Lin KL, Chen L, Chang J. Fabrication of dense hydroxyapatite nanobioceramics with enhanced mechanical properties via two-step sintering process[J]. Int J Appl Ceram Technol, 2012, 9(3): 479-485.

[4] Bojan Jokic, Miodrag Mitric, Velimir Radmilovic, et al. Synthesis and characterization of monetite and hydroxyapatite whiskers obtained by a hydrothermal method[J]. Ceramics International, 2011, 37: 167-173.

[5] Suchanek W, Yashima M, Kakihana M, et al. Processing and mechanical preperties of hydroxyapatite reinforced with hydroxyapatite whiskersf[J]. Biomaterials, 1996, 17(17): 1715.

[6] Wei G.C., Becher P.F. Toughening behavior in Sic-whisker-reinforced alumina[J]. J. Am. Ceram.Soc., 1994, 67(12): 267-269.

[7] Alieh Aminian, Mehran Solati-Hashjin, Ali Samadikuchaksaraei, et al. Synthesis of silicon-substituted hydroxyapatite by a hydrothermal method with two different phosphorous sources[J]. Ceramics International, 2011, 37: 1219-1229.
[8] Teshima K, Lee SH, Sakurai M, et al. Well formed one-dimensional hydroxyapatite crystals grown by an environmentally friendly flux method[J]. Cryst Growth Des, 2009, 9:2937-40.
[9] Ramanan SR, Venkatesh R. A study of hydroxyapatite fibers prepared via sol-gel route[J]. Mater Lett, 2004, 58:3320-3.
[10] Li-Xia Yang, Jia-Jun Yin, Lu-Lu Wang,et al. Hydrothermal synthesis of hierarchical hydroxyapatite:Preparation, growth mechanism and drug release property[J]. Ceramics International, 2012, 38: 495–502.
[11] Soderhohn K.J.M Shang S.W. Molecular orientation of silane the surface of colloidal sillica[J]. J Dent Res, 1993, 72: 1050-1054.

Key Engineering Materials Vols 645-646 (2015) pp 1345-1350
© (2015) Trans Tech Publications, Switzerland
doi:10.4028/www.scientific.net/KEM.645-646.1345

Submitted: 2014-10-29
Accepted: 2014-12-23

Flow Field Analysis for Plant Vessel and Bionic Structural Microfluidic Chip

Chong Zheng[1, a], Cuiyan Guo[1,b], Jingwei Xue[1,c], Shibing Liu[1,d] and Tao Chen[1,e]

[1] Institute of Laser Engineering, Beijing University of Technology, Beijing 100124, P. R. China

[a]zhengchong@emails.bjut.edu.cn, [b]30871021@qq.com, [c]xuejingwei03@163.com, [d]sbliu@bjut.edu.cn, [e]chentao@bjut.edu.cn (corresponding author)

Keywords: Vessel Element, Pits, Water Transport, Numerical Simulation.

Abstract. Microfluidic chips have been widely used in various of areas, such as biology, chemistry, medical science and so on. As one of the key techniques of microfluidic chips, the technique of micro driven of the water has been studied by experts all around the world for years. Of all kinds of the driven methods, the power costed by bionic driven is lowest. Moreover, as xylem is the main channel to transport the water in a tree, the mechanism of water transportation has been always an important issue in the study of physiological plant ecology. In this paper, the models of a single vessel element with different pit numbers (5 pits, 10 pits and 20 pits) or diameters(4μm and 7μm) were established according to the xylem and the pits' structure. The 3-dimensional flow distribution was analyzed by ANSYS 12.0 calculating by realizable κ-ε algorithm. The pressure distribution contours and the velocity distribution contours of a single vessel element could be obtained after calculated by the software. According to the results, the flow field in a single vessel element of the xylem was studied. In addition, the influence of pits on the pressure and velocity were analyzed. The results showed that the influence on pressure and velocity is less when the diameter is smaller. As the number of pits on the vessel increased, the influence on the distribution of pressure and velocity is greater. Based on the result of numerical simulation of vessel element, a bionic structural microfluidic chip was designed and then analyzed by ANSYS 12.0.

Introduction

As is known to all, the figure of *arbor*s are usually higher than other plants. The transport channel of water in a tree which starts from the root to its crown may always includes a xylem about several meters, even more than 100 meters in length. *Sequoia sempervirens* which distributed in the forest on the north part of California, U.S.A., is the highest tree specie in the world whose top height is 112.7 meter according to the report [1]. The mechanism of the long distance water transportation in a tree has always been a hot topic among plant physiology scientists for nearly a centry. It is known that the *vessel* which is the main channel to transport water in a tree is composed of a string of highly specialized hollow tubular cells, whose *end wall*s are connected by *perforation*. The diameter of the tube is about several micrometers, which is similar to a microfluidic device in dimension. Despite the diameter of each *vessel element* is very small, the total capability of water transportation and absorption of a tree is unimaginably powerful. Inspired by the phenomenon of water transportation, we analyzed the flow pattern in xylem based on the theory of fluid dynamics and the result of *phytotomy* experiment.

In this paper, we focus on the influence taken by *pit*s which are the passages of water and nutrient. It has already been certified that xylem embolism has close connection with the *permeability*, diameter and numbers of pits of a vessel element [2]. The *vulnerability* of xylem embolism raises when the permeability and diameter of pits increased. We presume that the pits are not only the connection between vessels, but also combined with cells so that the cells could absorb water and nutrition directly from the vessels (though it has not been proved by experiment). Thus, the velocity may increased by the total suction of pits. Numerical simulation of the water transportation process in xylem is studied based on Ansys 12.0/fluent. A microfluidic chip with a string of microholes on the

bottom of a microchannel was designed inspired by this structure. Flow field of designed microfluidic chip was also analyzed in Ansys 12.0 [3,4].

Analysis of Vessel Element

Physical model and ideal model. The ideal models (Fig.1a) of vessel element were built according to the image of its resin casts by scanning electron microscope (Fig.1 b). In this study, we mainly focus on the influence of pits' number and diameters on the flow field of vessel element, thus models with different pit numbers (5 pits, 10 pits and 20 pits) or diameters (4μm and 7μm) were established with Solidworks 2010. The length and diameter of vessel element were 345μm and 65μm, respectively. In addition, the thickness of pit structure was 1.5μm.

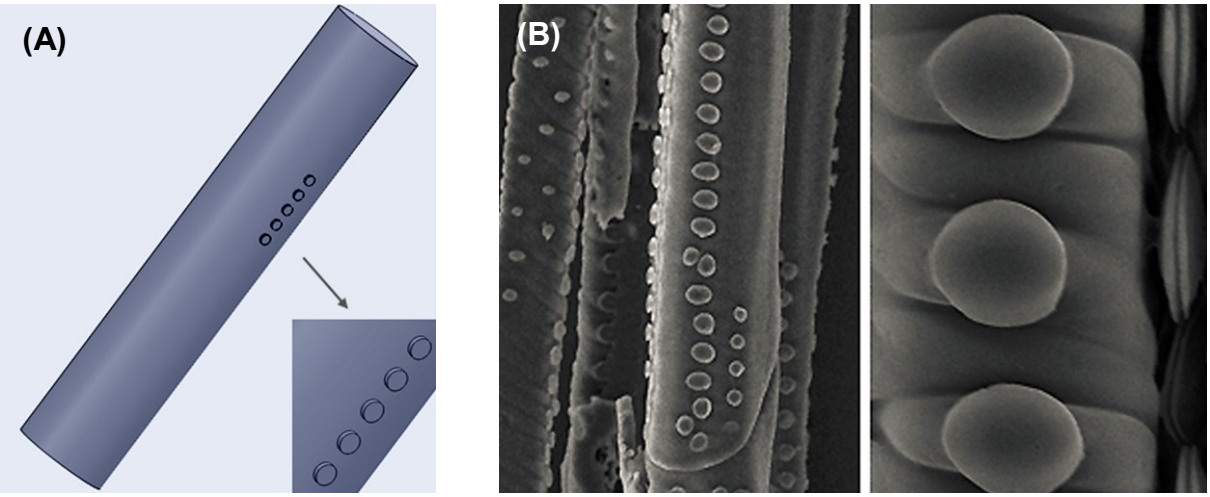


Fig.1. (A) The ideal model of vessel element with 5 pits (B) Resin casts of vessel element (*Ulmus pumila L.*)

Boundary conditions setup and fluid properties. There are two types flow patterns in real fluid which are laminar flow and turbulent flow. The flow pattern is characterized according to Reynolds number (**Re**) which is defined as (Eq.1):

$$\mathrm{Re} = \frac{VL}{v} \tag{1}$$

where, V denotes the average velocity of section, L is the characteristic length (for the flow in tube, the characteristic length L equals to the diameter of tube d) and v is the viscosity of flow. When Reynolds number (**Re**) is lower than critical Reynolds number ($\mathbf{Re_c}$), the flow state is laminar flow; While Re is larger than $\mathrm{Re_c}$, the flow is turbulent flow; If Re equals to $\mathrm{Re_c}$, the flow is critical flow. As Reynolds number is lower than 10 when water flows in the vessel element, the flow in vessel element is laminar flow [4]. A 3-dimensional model for the flow field was then established, and the steady state flow was simulated with the computational fluid dynamics (CFD) software based on Navier-Stokes equations.

Simulation of 5 pits vessel element with different pits' diameters. After meshing geometry models of vessel element, we simulated the model in realizable κ-ε method [5,6]. The inlet boundary condition was chosen as velocity-inlet boundary with the entrance speed of 7×10^{-5} m/s, the outlet boundary was setted as 0 Pa. As the entrance velocity of water is assumed to be in a low speed, the pressure of pits could be given as -0.1 Pa pressure-outlet condition. The pressure contours of vessel with 5 pits, the diameter of 7μm and 4μm respectively as shown in Fig.2 (A) and (C). Pressure gradually weaken from the inlet to the outlet. A pressure fluctuation was observed near the pits region. Pressure loss grows faster in this region and uniformly decreased after that. Pressure loss of 7μm pits

in vessel element is 19%, while pressure loss of 4μm pits vessel is decreased to 10%, which indicated 4μm pits have less influence on pressure distribution than 7μm pits in vessel element.

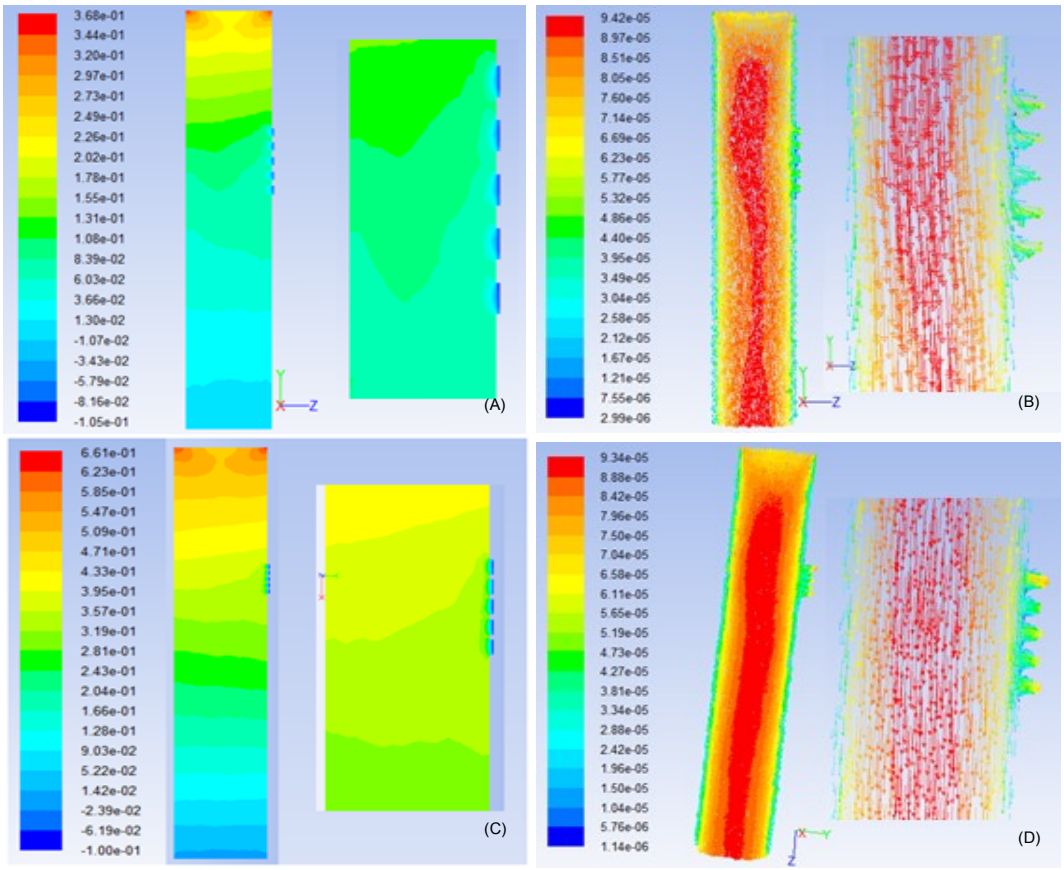


Fig.2. The pressure distribution contour (A), (C) and the velocity distribution vectorgraph (B), (D) of the five pits vessel(X=0) (In (A) and (B), the diameter of pits are 7μm,while (C) and (D) are 4μm.)

The velocity contours were shown as Fig.2 (B) and (D). The velocity in the center of vessel is 9.0×10^{-5} m/s in both of the two kinds of vessel elements which is larger than the velocity at boundary. The laminar flow in 4μm pits vessel flows steady than that of 7μm pits vessel. The central velocity in 4μm vessel has little influence by pits. The central velocity decreased when water flows past by the pits, and then the velocity recovered after passing the region.

Simulation of 10 pits vessel element. The pressure contour of 10 pits vessel is shown as Fig.3 (A). Pressure keeps losing from the inlet to the outlet. Pressure drops faster in the pits side than the other side and the loss of pressure is up to 20%. Pressure loss of the 23μm diameter vessel drops very fast. The pressure lost 80% at the second pit. The velocity vectorgraph is shown as Fig.3 (B). The central velocity is larger than that of boundary, appears to be a laminar flow. Decrease of velocity is 14.8% when flow passes by pits. The flow recover to stable state after passing the pits region as the similar situation when water flows over the 5 pits vessel element.

Simulation of 20 pits vessel element. The result of simulation by analysis the 20 pits vessel element shows that the pits region has similar results as that of 5 and 10 pits vessel element. Pressure drops from inlet to outlet and the loss increases faster at pits region. The velocity returned after the region and the loss of velocity up to 15%. The central velocity is between 1.0×10^{-4}~10.8×10^{-4} m/s.

The results above illustrated that pits with larger diameter (7μm pits) has greater pressure loss than the smaller one (4μm pits). Water flows in the vessel element with smaller pit's diameter(4μm) is more stable. Besides, when the number of pits of vessel increased, the influence on the pressure and velocity distribution is more obvious. The pits region can cause a fluctuation on pressure and velocity

field. Among some kinds of *angiosperms* and *gymnosperms*, pits has distinct resistance to water transportation up to 12% ~70% [7].This result is partly proved in our simulations.

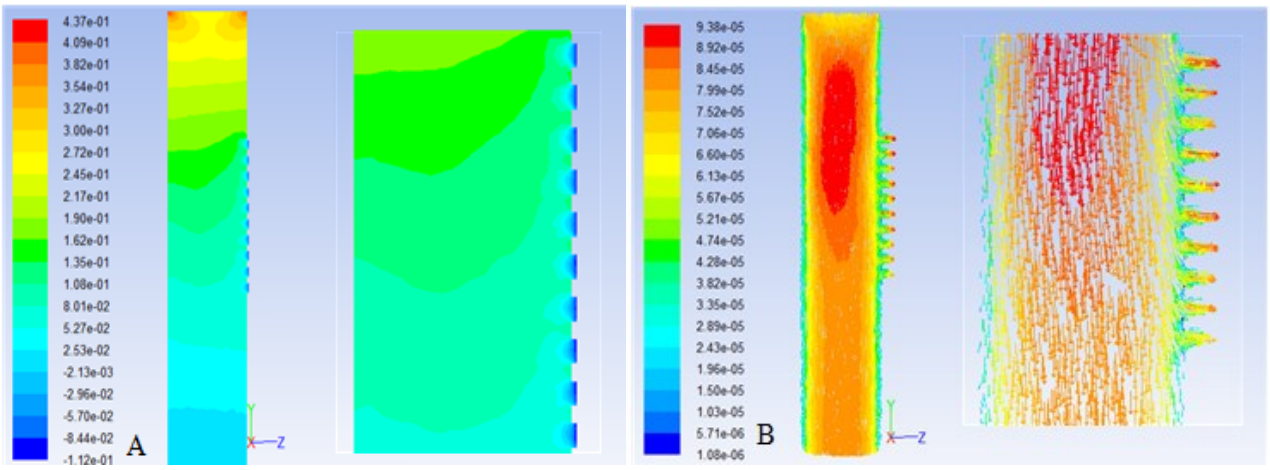


Fig.3. The pressure distribution contour (A) and the velocity distribution vectorgraph (B) of the ten pits vessel element(X=0)

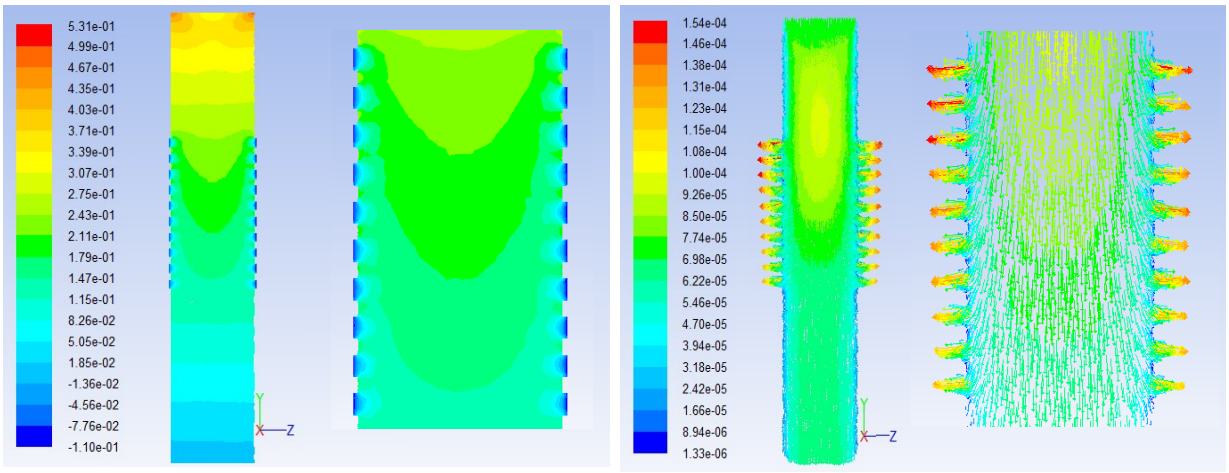


Fig.4. The pressure distribution contour (A) and the velocity distribution vectorgraph (B) of the twenty pits vessel element(X=0)

Analysis of Designed Microfluidic Chip

Design of Microfluidic Chip. According to the above analysis,we designed a microfluidic chip with 10 microholes whose diameter was 5μm (in order to reduce the fluctuation) on the bottom of the channel. Microholes connected with water absorbable material which offers suction force to drive the water flow. Center distance of microholes was 10μm. The size of the channel was 195μm× 50μm× 50μm and the microfluidic chip could be manufactured on a planar substrate (Fig.5.).

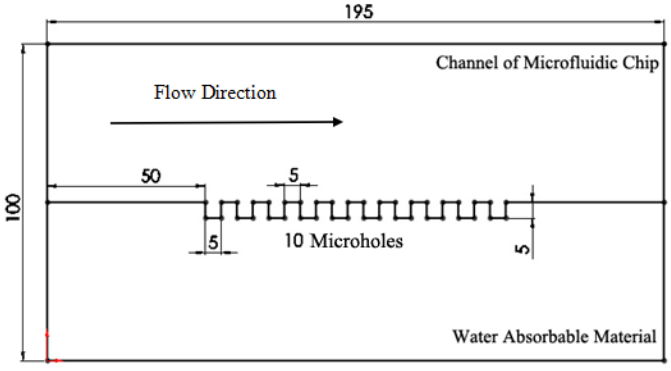


Fig.5. The structure of designed microfluidic chip. Dimensions in the figure are in micrometers.

Fluid properties. A 3D model of microfluidic chip was built in Solidworks 2010 and then analyzed by ANSYS 12.0 (Fig.6). In this model, water flows from the inlet, flows through the microchannel, and finally flows out from outlet. Because microfluidic chips were always driven by micropumps, the inlet boundary condition was selected as 'pressure-inlet'. Its gauge total pressure, turbulent intensity and turbulent length scale were set at 3000 Pa, 0.01% and 1μm, respectively. Outlet's gauge total pressure was set at 0 Pa. In the purpose to compare the structure with microholes to normal channel, boundary condition of microholes and normal channel were regarded as a 'wall' and -5000 Pa pressure-outlet.The velocity and pressure contour and vectorgraph were shown in Fig.6. According to the contour and vectorgraph, the velocity increment at the outlet is due to the microholes structure combined with water absorbable material.

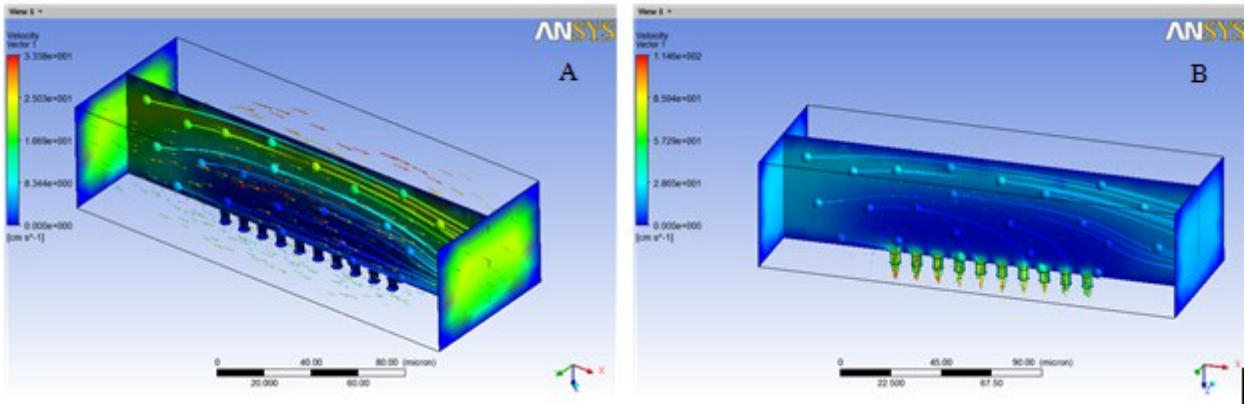
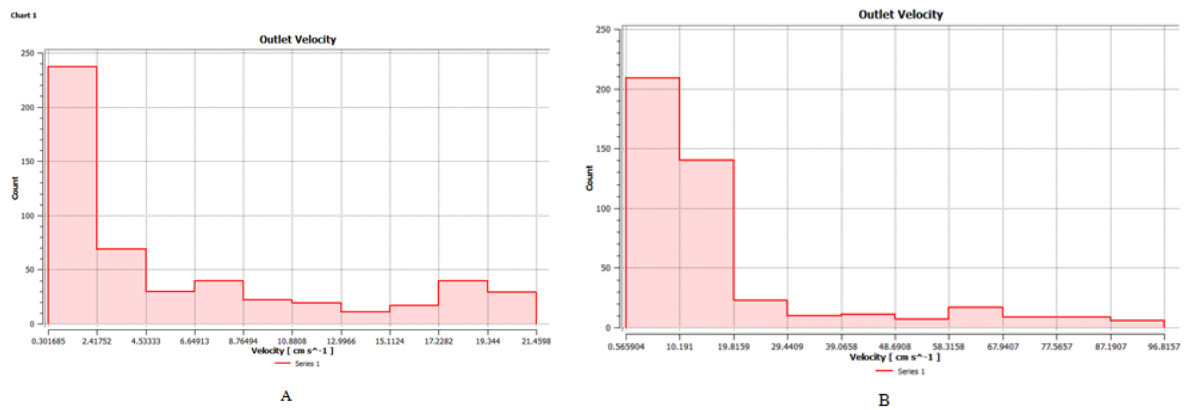


Fig.6. The velocity contours of the normal channel (A) and designed channel (B).

The velocity increased 4-5 times than the normal channel. Detailed data as shown in the outlet velocity diagrams (Fig.7.). From the outlet velocity counting diagram, we could find that the main part of velocity of the normal microfluidic chip is during 0.302~2.418 cm/s, the numbers of the velocity points is about 240.While the velocity region of structured one is among 0.566~10.191 cm/s. The numbers of this region is about 210. However, the number of velocity points among the second region (10.191-19.816 cm/s) is much larger than that of normal one.



A B

Fig.7. The outlet velocity counting diagram of normal microfluidic chip (A) and designed microfluidic chip (B)

The pressure gradient varied slowly benefited by the structure. The pressure of channel without microholes drops 3000 Pa, while structured channel lost pressure 2000 Pa. However, water flows more stable in the normal microfluidic chip (because there are no open microholes).

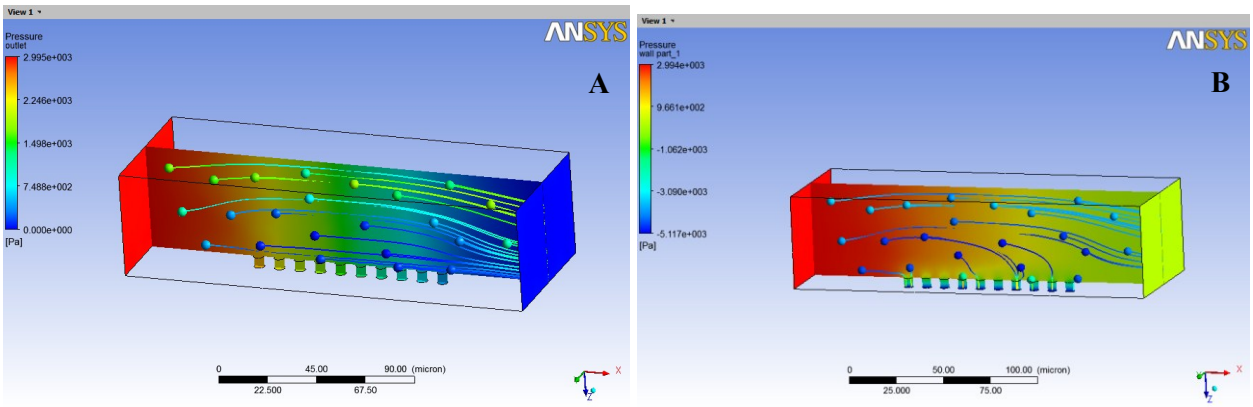


Fig.8 The pressure contours of the normal channel(A) and designed channel(B).

Summary

An ideal model of vessel element was built.The flow fields with different pits' diameters or numbers were analyzed by software ANSYS 12.0. The results illustrated that pits with larger diameter has greater pressure loss than the smaller one. When water flows in the vessel element with smaller pit's diameter, the flow field is more stable. Meanwhile, when the number of pits increased, the influence on the pressure and velocity distribution is more distinct. Besides, the pits region can cause a fluctuation on pressure and velocity field. Based on these conclusions, we designed a new type of microfluidic chip with microholes on the bottom of channel. Water absorbable material is bonded on the bottom of the substrate so that it could offer suction force to the flow. The simulations of both normal microfluidic chip and designed chip showed that channel with microholes and water absorbable material can increase the central velocity of flow. This phenomenon can be utilized and further developed into a new method of micro driven in the future.

Acknowledgments

The authors gratefully acknowledge the financial support by National Natural Science Foundation of China (Grant 50875007), Ministry of Science and Technology of China Major Project of Scientific Instruments and Equipment Development (Grant 2011YQ030112), Key Project of Science and Technology Plan of Beijing Municipal Commission of Education (Grant KZ201210005009) and Beijing Natural Science Foundation (Grant 4132017).

References

[1] A.R. Ambrose, S.C. Sillett, et al. Effects of height on treetop transpiration and stomatal conductance in coast redwood (Sequoiasempervirens), Tree Physiol. 30 (2010) 1260-1272.

[2] Y.H. Tang. Several supplementary on the embolism forming and repairing in xylem of woody plants. J. of Anhui Agri. 37 (2009) 7283-7286.

[3] X. Xue, M. K. Patel, M. Kersaudy-Kerhoas, et al. Analysis of fluid separation in microfluidic T-channels. Appl. Math. Model. 36 (2012) 743-755.

[4] W. Shumi, S.H. Kim, J. Lim, et al. Shear stress tolerance of Streptococcus mutans aggregates determined by microfluidic funnel device (μFFD), J. Microbiol. Meth. 93 (2013) 85-89.

[5] B.E. Launder, D.B. Spalding. Lectures in Mathematical Models of Turbulence. Academic Press, London, 1972.

[6] B.E. Launder, D.B. Spalding. The numerical computation of turbulent flows. Comput. Method. Appl. M. 3 (1974): 269-289.

[7] P.J. Schulte, A.C. Gibson. Hydraulic conductance and tracheid anatomy in six species of extant seed plants. Can. J. Bot. 66 (1988): 1073-1079.

Key Engineering Materials Vols 645-646 (2015) pp 1351-1356
© (2015) Trans Tech Publications, Switzerland
doi:10.4028/www.scientific.net/KEM.645-646.1351
Submitted: 2014-12-04
Accepted: 2014-12-23

The application of Micro-flow extrusion forming technology in the denture preparation

Jing ZHOU[1,a],Guolin DUAN[1,b *], Dongbin ZHU[1,c],Jin CAI[1,d]

[1]School of Mechanical Engineering, Hebei University of Technology,TianJin300130,China
[a]email:zhoujing0807@126.com, [b]email:glduan@hebut.edu.cn,[c]email:jzhou989@163.com
[d]email: caijinyy@126.com

Keywords: micro-flow extrusion forming, denture, rheology, simulation

Abstract: The forming process of denture preparation based micro-flow extrusion was researched. The dental ceramic materials having health care function was preparation. Through analysis and calculation, the rheological properties of the ceramic slurry confirmed to be pseudo-plastic fluid . The extrusion head as a key part was designed. The pressure distribution and velocity distribution of the internal flow field of extrusion head were simulated by using START- CD software ,the analysis result can used to guide the optimal design of extrusion head.

Introduction

Along with the improvement of living conditions, the people's consciousness to dental health increasingly strengthen, and also has a higher request for your beautiful teeth. Dental restoration is the only way to solve these problems currently. The traditional manual processing can't guarantee the product's precision and the stability of quality. The rapid prototyping technology in the application of dental restorations research has become a hot spot, more and more scholars apply this technology to the metal crowns, porcelain full crown, removable partial denture, the full denture, oral and maxillofacial region turns complex design and production aspects[1-5].

In the last ten years,Lewis produced ceramic artifacts by using microspheres injection molding in the zirconia ceramic powder rapid prototyping, and the preliminary research was conducted on the structure and performance. Ebert, etc. with the help of the droplet spray forming technology produced the whole porcelain crown sample, its strength and compressive strength can meet the requirements of clinical repair. Su tested the strength and microstructure of ceramic artifacts prepared by rapid prototyping technology, and direct sintering alumina porcelain powder to produce porcelain crown. Wang produced ceramic restoration mode using droplet spray technology and sintered the mold, finally the appearance of the restoration, strength and microstructure were accord with the requirement of clinical[6-15]. Ceramic restoration's rapid prototyping are mostly about the configuration of ceramic suspension sulrry (including the use of dispersants and solid phase ratio control, etc.) and the control of the forming process.

1. The preparation of dental ceramic materials

The preparation of dental ceramic material has always been the research hot spot , the main research is focus on improving the mechanical properties of denture ,aesthetic properties and processing convenience on the basis of meet the biocompatibility ,physical and chemical properties. In this paper, the prepared denture ceramic materials in addition to can satisfy the mechanical properties which the oral environment required, physical and chemical properties, biocompatibility, aesthetic performance, that can also satisfy the need of the human body health through the unique features .It has a higher level of health care function. The concrete operation process : At first ,it make rare earth material, far infrared emission material, surface energy adjust material, flux material mixed and ball mill 5-10 hours, then add tourmaline powder to ball mill 10-20 hours , using precipitation method prepared bioactive functional powder, after that make functional powder mixed with dental materials, ball mill about 20 hours, after vacuum stirring extraction for 30 minutes, get the high quality ceramic slurry with far infrared emission properties. By micro-flow extrusion forming process to print out denture crowns model, and then drying, high temperature sintering molding under 1450-1500 degrees Celsius , at last artificial buffing. The process flow is shown in figure 1:

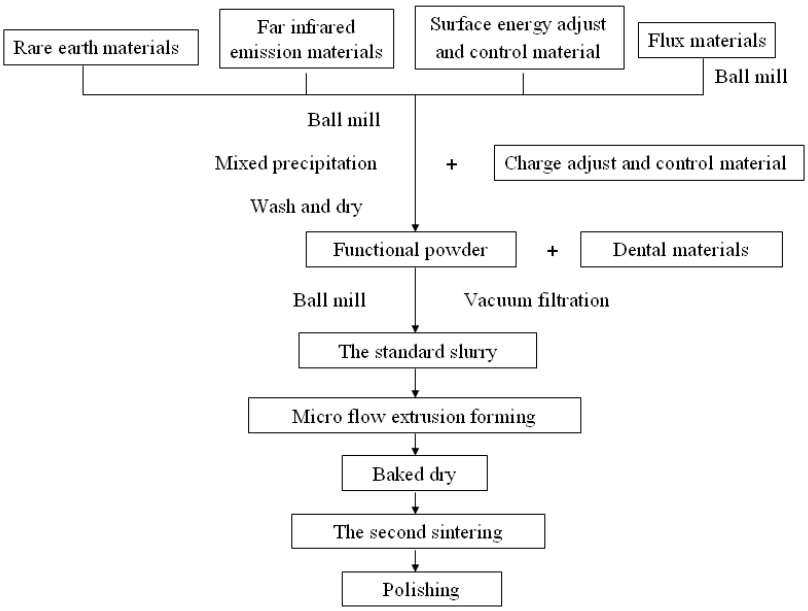


Figure1 The process flow diagram

2The rheological model of ceramic slurry and the mathematical description of sulrry flow

2.1 The rheological model of ceramic slurry

By NDJ - 9S viscometer to measure the viscosity value of ceramic slurry prepared as a function of the shear rate is shown in figure 2.

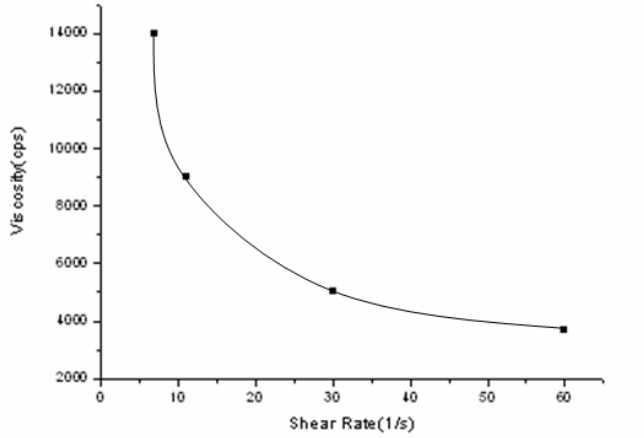


Figure 2 Viscosity of ceramic slurry as a function of the shear rate

The prepared ceramic slurry conform to the characteristics of pseudoplastic fluid in non-Newtonian fluid, which belongs to the power law model. The viscosity equation of the power-law model can be represented as shown in equations (1) :

$$\eta = K \cdot \dot{\gamma}^{n-1} \tag{1}$$

Where, K is consistency coefficient, which show the viscosity when $\dot{\gamma} = 1/s$, n is the viscosity index, $\dot{\gamma}$ is shearing rate.

2.2 Mathematical description of slurry flow in the extrusion process

In process of micro-flow extrusion forming, the required technological conditions and the rheological properties of paste depend on three basic equations of fluid mechanics, including continuous equation, energy equation, and motion equation, the key flow control of extrusion forming process is derived by above basis equations. It can derive the flow control equation of slurry

in the extrusion head. The three equations and constitutive equations constitute the basic equations set, under specific boundary conditions, which can accurately describe the ceramic slurry flow state in extrusion forming.

Fluid continuous equation, motion equation and the constitutive equation as shown in equations (2) :

$$\begin{cases} \dfrac{\partial v_x}{\partial x}+\dfrac{\partial v_y}{\partial y}+\dfrac{\partial v_z}{\partial z}=0 \\ \dfrac{\partial p}{\partial x}=\eta\left(\dfrac{\partial^2 v_x}{\partial x^2}+\dfrac{\partial^2 v_x}{\partial y^2}+\dfrac{\partial^2 v_x}{\partial z^2}\right) \\ \dfrac{\partial p}{\partial y}=\eta\left(\dfrac{\partial^2 v_y}{\partial x^2}+\dfrac{\partial^2 v_y}{\partial y^2}+\dfrac{\partial^2 v_y}{\partial z^2}\right) \\ \dfrac{\partial p}{\partial z}=\eta\left(\dfrac{\partial^2 v_z}{\partial x^2}+\dfrac{\partial^2 v_z}{\partial y^2}+\dfrac{\partial^2 v_z}{\partial z^2}\right) \\ \tau=\eta\left(\dot{\gamma}\right)\cdot\dot{\gamma}=k\cdot\dot{\gamma}^{n-1}\cdot\dot{\gamma} \end{cases} \tag{2}$$

Where P is static pressure, η is viscosity, τ is shear stress, $\dot{\gamma}$ is shearing rate, n is power law index

3. The structure and internal flow field analysis of extrusion head

3.1 The structure of extrusion head

Extrusion head is the key component in the process of micro-flow extrusion forming, ceramic slurry extrusion amount and extrusion diameter can be adjusted by changing the extrusion head. So when a micro-flow extruded ceramic slurry forming, extrusion effect of ceramic slurry, traffic, extrusion diameter all by extrusion head geometry, aperture size and the manufacturing precision of the decision[16]. The main structures of extrusion head in micro-flow extrusion forming are the pore size and shape of the nozzle. The pore diameter of nozzle determines the size of the ceramic slurry flow rate, and the shape of the nozzle determines the critical height of extrusion nozzle. The model and the structure of the nozzle as shown in figure 3 and figure 4.The entry diameter is 2 mm,and the exit diameter is 0.4mm.

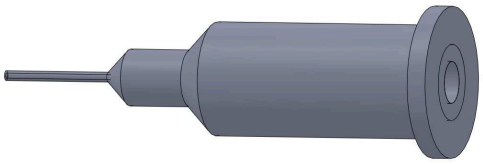


Figure3. 3D model for the extrusion head

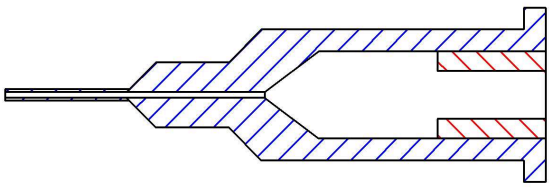


Figure4. Extrusion head structure diagram

The role of the extrusion head compression section is to form a strong convergence flow, in favour of prepared the high density and mechanical stable products. At the same time due to the existence of this section, which making the back pressure of extrusion head is produced and conducive to well forming of ceramic slurry.

3.2 slurry flow rate calculation

The flow rate of forming slurry reflects the volume flow rate of the slurry flow through the extrusion head, pressure drop and the relationship between material properties and geometric structure, any non-Newtonian fluid can be written as shown in equation (3)

$$Q'=K_Q\frac{\Delta p}{\eta_k} \tag{3}$$

For circular aperture type extrusion flow channel, its mouth mold coefficient of extrusion flow rate is shown in equation (4) :

$$K_Q = \frac{\pi R^{\frac{3n+1}{n}}}{2^{\frac{1}{n}}\left(\frac{3n+1}{n}\right)}\left(\frac{1}{L}\right)^{\frac{1}{n}} \tag{4}$$

Where the KQ is mouth mold coefficient, only related to the flow channel size and shape, n is the rheological constants; ηk is the material viscosity of extrusion head mouth area.

The outlet flow of extrusion head (the relationship between fluid flow Q and pressure drop P of power law laminar flow) calculated as shown in equation (5),

$$Q = \frac{\pi n R^3}{3n+1}\left(\frac{pR}{2LK}\right)^{\frac{1}{n}} \tag{5}$$

By type (4) the section average flow velocity can be further obtained as shown in equation (6),

$$\upsilon = \frac{Q}{\pi R^2} = \frac{nR}{3n+1}\left(\frac{pR}{2LK}\right)^{\frac{1}{n}} = \left(\frac{p}{2LK}\right)^{\frac{1}{n}}\left(\frac{n}{3n+1}\right)R^{\frac{n+1}{n}} \tag{6}$$

3.3 Internal flow field analysis of extrusion head

The internal structure of extrusion head influence the change of the internal flow field in the process of ceramic slurry extrusion , which will also have important influence on final extrusion effect. Through the virtual analysis of internal flow field in the extrusion head, the outlet flow of ceramic slurry through extrusion head can be calculated, which provide parameters for further carry out denture crown three-dimensional forming[17,18]. In the first place, setting related parameters of extrusion head in order to meet the constraint conditions, and the extrusion head made some necessary simplification to convenient for calculation and analysis. Setting the parameters is shown in table 1.

Table 1 Extrusion head related parameters set table

Material	Viscosity	Density	Radius entry	Radius exit	Entrance pressure	Outlet pressure
Dental ceramic slurry	14Pa·S	1285kg/m^3	0.001m	0.0002m	0.2 MPa	atmospheric environment

Actual internal structure of extrusion head is more complex. In order to facilitate the simulation analysis using START - CD software, the internal flow field area of extrusion head will simplified into cylindrical model. Due to the axial symmetry of the cylindrical model, it used the two dimensional model to replace the three-dimensional stereogram. The pressure distribution is shown in figure 5.

By the pressure distribution result it can be seen that extrusion head cavity formed high pressure area, the highest pressure is 35.21 MPa. From the extrusion head cavity to the export, pressure decrease until the normal atmospheric pressure. The highest stress puts forward a certain requirement on the material and the structure of the extrusion head, also provides a certain basis for the intensity of extrusion head and its safety inspection.

The internal flow velocity distribution of extrusion head and internal fluid flow state is shown in figure 6 and figure 7. Seen from the velocity distribution and flow state analysis result, ceramic slurry flowed in extrusion head is uniform, the velocity of extrusion head at the exit is the largest, the maximum speed is about 0.07 m/s, outlet flow is about 0.013g/s, which can satisfy the requirement of the denture crown three-dimensional forming, ceramic slurry can be stacked uniform and rapid ,that insure the accuracy and the uniformity of extrusion ceramic slurry.

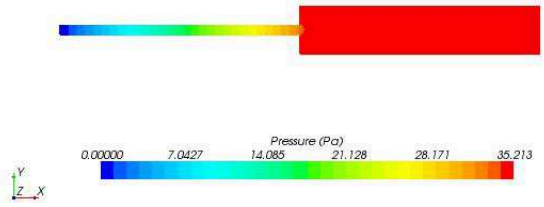


Figure5.The pressure distribution inside of the extrusion head

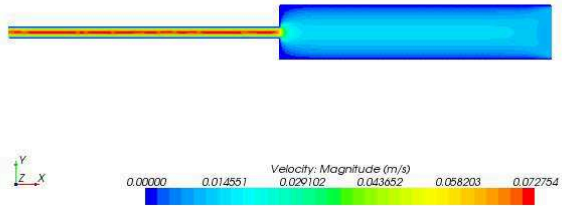


Figure6. The velocity distribution inside of the extrusion head

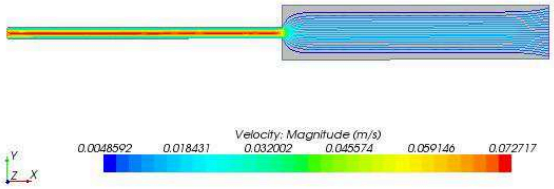


Figure7.The fluid flow state inside of the extrusion head

4. Conclusion

The micro-flow extrusion forming technology for denture manufacture was researched, which is used for restoring human oral tooth. Through analysis and calculation, the rheological properties of the ceramic slurry prepared confirmed to be pseudo-plastic fluid theoretically. According to the extruding process of micro-flow, it conducts modeling and simulation applying START- CD software. By the analysis of the internal fluid condition of extrusion head, the pressure distribution inside of the extrusion head, the slurry velocity distribution and the fluid flow state inside of the extrusion head were simulated, and the outlet flow is calculated about 0.013 g/s. This flow rate is easy to form the extrusion flow having good surface quality, thereby it verify the rationality of the structure design of the extrusion head. It can save dosage of ceramic slurry in the actual application, reduce denture crowns manufacture cost, and provide reference data to find the best extrusion status in the future actual production.

Acknowledgement

Supported by “The natural science foundation of Hebei Province ”under Grant Numbers:E2011508003.

References

[1] Anoop N. Samant, Narendra B. Dahotre . Laser machining of structural ceramics—A review. Journal of the European Ceramic Society 29 (2009): 969–993

[2] R.K. Kamboj, S. Dhara, P. Bhargava. Machining behaviour of green gelcast ceramics. Journal of the European Ceramic Society 23 (2003): 1005–1011

[3] Qingbin Liu , Ming C. Leu, Stephen M. Schmitt. Rapid prototyping in dentistry: technology and application. Int J Adv Manuf Technol (2006) 29: 317–335

[4] Abbas Azari , Sakineh Nikzad. The evolution of rapid prototyping in dentistry: a review. Rapid Prototyping Journal 15/3 (2009) :216–225

[5] Paolo Francesco Manicone, Pierfrancesco Rossi Iommetti , Luca Raffaelli. An overview of zirconia ceramics: Basic properties and clinical applications. Journal of dentistry 35 (2007): 819 – 826

[6] Jiwen Wang, Leon L. Shaw. Materials Science and Engineering A 397 (2005) 314–321

[7] Emre Özkol, Wen Zhang, Jörg Ebert, Rainer Telle. Journal of the European Ceramic Society 32 (2012) 2193–2201

[8]Jiwen Wang. Solid Freeform Fabrication of Biological Materials[D]. Graduate University of Connecticut, 2006

[9] J. Benbow, J. Bridgwater, Paste Flow and Extrusion Oxford Serieson Advanced Manufacturing, Clarendon Press, Oxford, 1993

[10] Williams. Use of CAD/CAM technology to fabricate a removable partial denture framework[J]. J Prosthet Dent, 2006, 96 (2): 96-99

[11] Lewis .Direct ink writing of three-dimensional ceramic structures[J]. J Am Ceram Soc, 2006, 89 (12): 3599-3609.

[12]Su B.Green ceramic machining:A top-down approach for the rapid fabrication of complexshaped ceramics [J]. J Eur Ceram Soc, 2008, 28（11）: 2109-2115.

[13]Leon L. Shaw .Solid freeform fabrication of permanent dental restorations via slurry micro-extrusion[J].J Am Ceram Soc, 2006, 89（1）: 346-349

[14] J. Ebert, E. Özkol, A. Zeichner,K. Uibel, Ö. Weiss, U. Koops,R. Telle, and H. Fischer. Direct Inkjet Printing of Dental Prostheses Made of Zirconia. Journal of Dental Research. 2009 ,88(7): 673-676

[15] L. Yin , H.X. Peng , L. Yang, B. Su. Fabrication of three-dimensional inter-connective porous ceramics via ceramic green machining and bonding.Journal of the European Ceramic Society 28 (2008): 531–537

[16] Gilberto Antonio Borges, Mario Fernando deGoes, Jeffrey A. Platt, Keith Moore, Fernando Hueb de Menezes,Euripedes Vedovato. Extrusion shear strength between an alumina-based ceramic and three different cements. The Journal of Prosthetic Dentistry. September 2007:208-214

[17] Chenxu Yu, Sundaram Gunasekaran. Modeling of melt conveying in a deep-channel single-screw cheese stretcher. Journal of Food Engineering 61 (2004) 241–251

[18] Daiquan Zhang, Guoping Chen. The Numerical Simulation for Extrusion Forming of Magnesium Alloy Pipes. Physics Procedia 25 (2012) 125 – 129

Key Engineering Materials Vols 645-646 (2015) pp 1357-1362
Submitted: 2015-01-09
© (2015) Trans Tech Publications, Switzerland
Accepted: 2015-01-13
doi:10.4028/www.scientific.net/KEM.645-646.1357

Yeast cells immobilization in microfluidic channels based on a self-polymerized nano-film of poly(dopamine)

Xing Chen*, Lulu Zhang, Jianhai Sun, Hui Li, Dafu Cui*

State Key Laboratory of Transducer Technology, Institute of Electronics, Chinese Academy of Sciences, Beijing, 100090, China
*xchen@mail.ie.ac.cn (corresponding author), *dfcui@mail.ie.ac.cn (corresponding author)

Keywords: Nano-film, self-polymerization, cell immobilization, surface plasmon resonance (SPR), Micro Electro Mechanical Systems technology (MEMS)

Abstract. In this paper, an effective, simple and universal method for cell immobilization was developed. A self-polymerization nano-film of poly(dopamine) was used to fix yeast cells in microfluidic channels. The surface morphology of the poly(dopamine) film was characterized by scanning electron microscopy (SEM) and atomic force microscopy (AFM) techniques. Water contact angles (WCA) was also used to characterize the surface property of the poly(dopamine) nano-film. The WCA on the PDMS substrates rapidly decreased from 105° to 59.8° with an increase in poly(dopamine) coating time. The interfacial process of dopamine self-polymerization and the cell immobilization were measured in a label-free and real-time mode by a surface plasmon resonance (SPR) instrument. Finally the immobilized yeast cells were observed by using a light microscope. From the experimental results, the yeast cells can be easily immobilized on the microfluidic channels modified with the nano-film of poly(dopamine), which will hold great potential for the immobilization, detection and further analysis of other suspension cells, such as blood cells.

Introduction

Mussel adhesive proteins excreted by marine mussels can form strong adhesive interaction with various substrates [1]. Dopamine, found in high concentration in mussel adhesive proteins, can self-polymerize to form adherent poly(dopamine) films and self-assembled on various materials, which open a new route to the modification of various substrates by the simple chemistry [2]. Previous researches [3] also showed that the composition of the poly(dopamine) film was independent of the substrate composition. Based on the self-polymerization and strong adhesion characteristics of dopamine, the poly(dopamine) coating was found to be an extremely versatile method of surface treatment for secondary reactions [4]. However to the author's knowledge, there is some lack of knowledge about the immobilization of cells by using the poly(dopamine) film.

Cell immobilization is essential not only for cell sensors but also for the other applications, e.g. biotransformation [5]. Gorazd Stojkovič [6, 7] reported a chemical method to immobilize yeast cells within microchannels of different materials. The various materials encompass glass, silica, polydimethylsiloxane (PDMS), polymethyl methacrylate (PMMA), and polystyrene (PS) [8]. The immobilization efficiency was evaluated by image analysis, after the microchannels fixed with cells were observed and photographed using a microscope. However the process of the surface modification is complicated and different materials usually require different modification methods. Moreover it is difficult to monitor the interfacial processes of the surface modification and the cell immobilization.

In this paper, a self-polymerization poly(dopamine) film was used to fix yeast cells, which will be developed a simple and universal technology for immobilizing suspension cells on various materials. At first, the nano-films of poly(dopamine) were easily fabricated on the microfluidic PDMS channels and SPR bare Au chips by only pumping the dopamine coating solution into the channels and chips. The nano-film was characterized by SEM, AFM and WCA techniques. And then yeast cells were pumped into microfluidic channels, which were detected off-line by using a

microscope. The self-assemble process of the nano poly(dopamine) film on the SPR chip and the cell immobilization process were measured on-line by using a home-made SPR instrument in turn.

Experimental

Chemicals and reagents Tris(hydroxymethyl)aminomethane (Tris) was purchased from Xinjingke (Beijing, China). Dopamine hydrochloride was purchased from Sigma-Aldrich (St. Louis, MO, USA). Sylgard 184 silicone elastomer and curing agent (PDMS) were purchased from Dow Corning (Midland, MI, USA). Deionized water was used to prepare10mM Tris-HCl buffer (pH 8.5). Instant dry yeast was purchased from Angel Yeast Co. LTD. The yeast cells were washed twice with deionized water and then resuspended in deionized water. This cell suspension solution was later used for the immobilization experiments.

Fabrication and characterization of poly(dopamine) film We prepared a nano poly(dopamine) coating onto the PDMS microfluidic channel and SPR bare Au chip based on the self-polymerization and self-assembly of dopamine. The dopamine coating solution (2g/L dopamine-HCl in a Tris-HCl buffer, pH 8.5) was pumped into the PDMS microfluidic channel and SPR bare Au chip, respectively. Then they were washed with the deionized water to remove the un-reacted chemicals.

The surface morphology of the poly(dopamine) film on the PDMS substrate was characterized by scanning electron microscopy (SEM) (HITACHI, S-4800) and that on the SPR Au chip was characterized by atomic force microscopy (AFM) (Bruker, Multimode 8), respectively.

Static contact angle measurements were implemented by using water droplets. 1μL water was dropped on microfluidic PDMS substrates modified with the nano poly(dopamine) film. And then the images of the droplet were photographed. The contact angle formed at the boundary of the droplet was measured based on the photographs.

Detection of self-polymerization and cell immobilization We used the surface plasmon resonance (SPR) technology to study the interfacial process of the dopamine self-polymerization and the yeast cell immobilization in a label-free and real-time mode. A home-made SPR instrument (Fig. S1) based on the Kretschmann configuration to achieve the total internal reflection resonant condition was used for the online detection [9]. The SPR bare Au chip was mounted on the SPR instrument. Then the dopamine coating solution (2g/L dopamine-HCl in a Tris-HCl buffer, pH 8.5), the deionized water and the solution of yeast cells was pumped sequentially into the SPR chip. Finally the deionized water was pumping into the chips to remove the unfixed yeast cells.

We used a microscope microscope (9XB-PC, Shanghai optical instrument factory, Shanghai, China) to study the yeast cells fixed on the microfluidic PDMS channels modified with a poly(dopamine) nano-film, after washing the microfluidic PDMS channels.

Results and discussion

Characterization of poly(dopamine) film The morphology of the poly(dopamine) films were characterized by SEM and AFM. The SEM image of the poly(dopamine) film on the PDMS substrate and the AFM image of that on the SPR bare Au chip are shown in Fig. 1. From the results of SEM and AFM, the morphology of the nano poly(dopamine) films is very uniform, which is consistent with the observation by Chien [10]. And it was very simple and easily to form a nano poly(dopamine) film on the microfluidic channels and SPR chips by only pumping the dopamine coating solution into the channels and chips.

Water contact angles (WCA) was also used to characterize the surface property of the poly(dopamine) film. WCA on the PDMS substrates modified with and without poly(dopamine) films were measured and calculated. As shown in Fig. 2, WCA on the PDMS substrates were measured and calculated at the different dip-coating time. From Fig. 2, an increase in poly(dopamine)

coating time results in a rapid decrease in WCA from 105° to 59.8°, which is consistent with the observation by Chien [10].

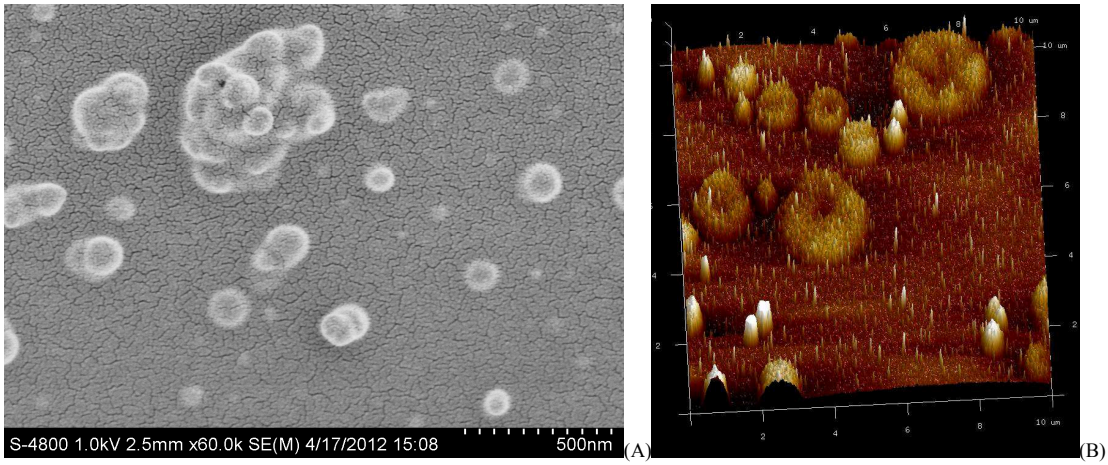


Figure 1. SEM (A) and AFM (B)of the poly(dopamine) film

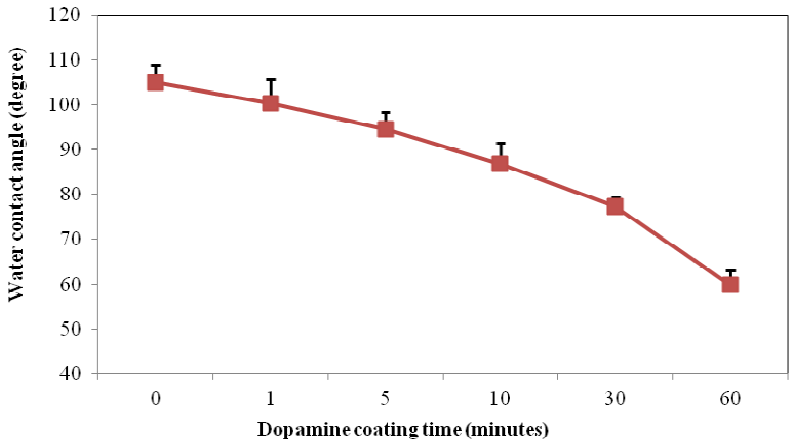


Figure 2. Water contact angles on PDMS substrates in the 2g/L dopamine solution for different time.

On-line detection of dopamine self-polymerization and cell immobilization Surface plasmon resonance (SPR) is the basis of many standard tools for measuring adsorption of material onto planar metal (typically gold and silver) surfaces [11]. One of the common applications of SPR is the measurement of the adsorbed self-assembled nano-film on Au chips. The resonance curves shift to higher angles as the thickness or density of the adsorbed film increases. In our previous research [12], we used the home-made SPR instrument (Fig. S1) to monitor the process of self-polymerization and self-assembly of dopamine.

In this paper, we firstly used the SPR technology to characterize the poly(dopamine) film's properties at the different dopamine coating time. The curves of SPR absorption peak were detected at the different coating time. As shown in Fig. 3A, the SPR absorption peaks shift from low angle to high angle with the prolonger dopamine coating time, meanwhile the depth of SPR absorption peak decreases. That means the thickness and density of the self-assembled poly(dopamine) film increases with the increasing exposure time in the dopamine solution.

And then the interfacial process of the dopamine self-polymerization and the yeast cell immobilization was monitored on real time by using the home-made SPR instrument at a fixed incidence angle. The detection curves are shown in Fig. 3B. The SPR signal during the process of dopamine self-polymerization is strongly increased. When the yeast cell solution is introduced, the SPR signal increases slowly. After washing the SPR chip by pumping the deionized water, the change of response units (ΔRU) is about 1700 for cell immobilization, while it is about 6000 for dopamine

self-polymerization. The possible reason could be that the refractive index of the poly(dompamine) film is quite different and the refractive index of yeast cell is relatively close to the water.

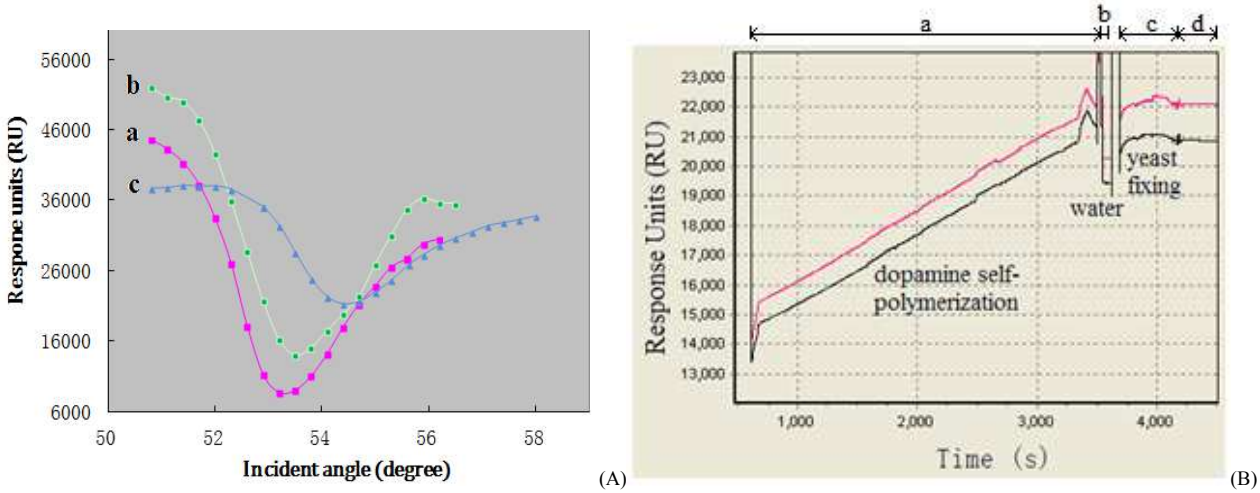


Figure 3 (A) SPR peak curves for Au chips exposed in the dopamine coating solution for 0 min ("a"), 5min ("b") and 60min ("c"). (B) SPR detection curves for the dopamine self-polymerization and yeast fixing (two curves represent different surface area). The dopamine coating solution ("a") and the yeast cell solution ("c") were pumped into the chip, respectively. The deionized water ("b" , "d") was pumped into the chip to remove the unfixed molecules and cells.

Off-line detection of cell immobilization PDMS substrates with the poly(dopamine) nano-film at the different dopamine coating time were used to immobilize yeast cells, which were characterized by a microscope. As shown in Fig. 4, small amounts of immobilized yeast cells are fixed on the PDMS substrate immersed in the dopamine coating solution for a short coating time, while the yeast cells were immobilized much more when the PDMS substrate was immersed in the dopamine coating solution for a longer coating time. From these experimental results, the yeast cells could be easily fixed on the PDMS substrates modified with a poly(dopamine) nano-film.

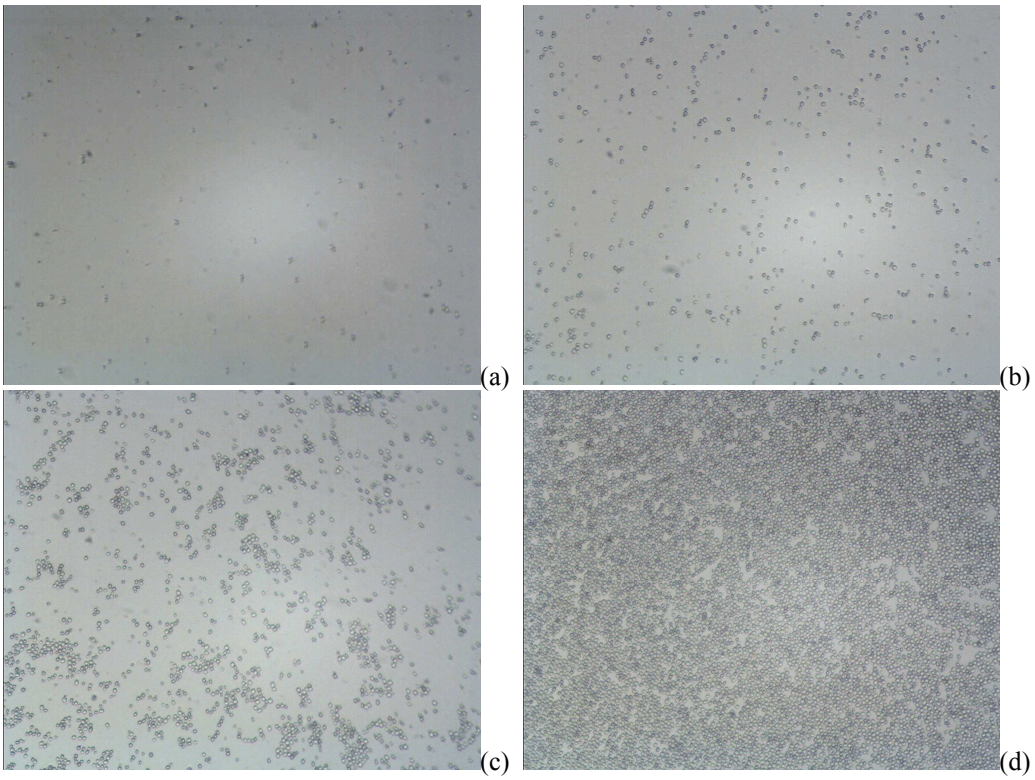


Figure 4. The microscope photos of the fixed yeast cells on the PDMS substrates when they were immersed in the dopamine coating solution for 0 min (a), 5 min (b), 30min (c) and (d)60min, respectively.

As shown in Fig. 5, the yeast cells fixed on the PDMS substrates are still alive and grow up after the fixed yeast were immersed in water over night.

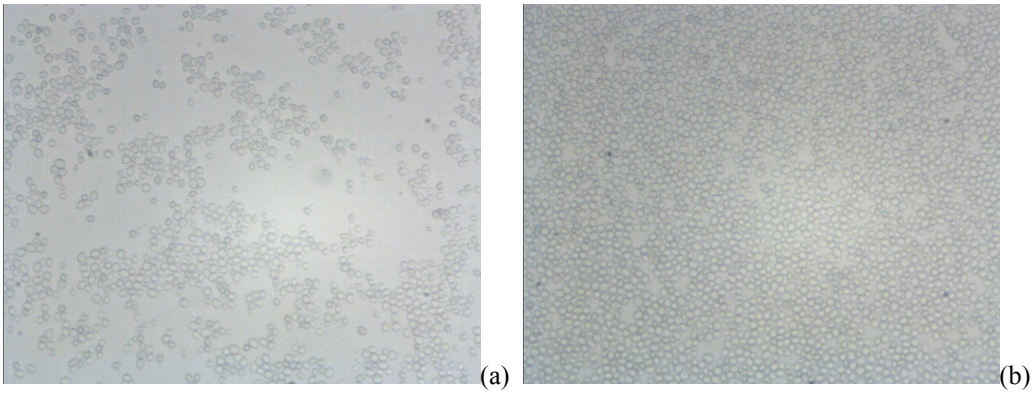


Figure 5. The microscope photos of the fixed yeast cells on the PDMS substrates immersed in the dopamine coating solution for 30 min (a) and 60 min (b), respectively, after the fixed yeast cell were in water over night.

Conclusions

A simple method for cell immobilization was developed with only a few solutions flowing through the microfluidic channels in this paper. Here a self-polymerization poly(dopamine) film was successfully used to fix yeast cells on the PDMS substrates or SPR Au chips by only pumping the dopamine coating solution and the cell solution into the channels. Moreover the fixed yeast cells were alive and grow up. The surface morphology and property of the poly(dopamine) film was studied by various technologies (SEM, AFM, WCA and SPR). With the increasing coating time of dopamine, the poly(dopamine) film became thicker and much more yeast cell can be fixed. At the same time, the cell growth state were independent of the poly(dopamine) film with different coating time. Base on above experimental results and the characteristic of the dopamine self-polymerization, we can conclude that this surface modification method would be a universal method for cell immobilization on various materials. This effective, simple and universal method has a great potential to be applied to cell transducers, whole cell micro-reactors, and so on.

Acknowledgments

The authors greatly acknowledge the financial support from the National Program on Key Basic Research Project (973 Program) under the grant numbers of 2014CB744600 and 2011CB933202. This work is also sponsored by National High-tech R&D Program of China (863 Program) under the grant number of 2014 AA 022303 and the National Science Foundation of China under the grant numbers of 61372055, 61201079, 31100820 and 8137171.

Supporting Figure

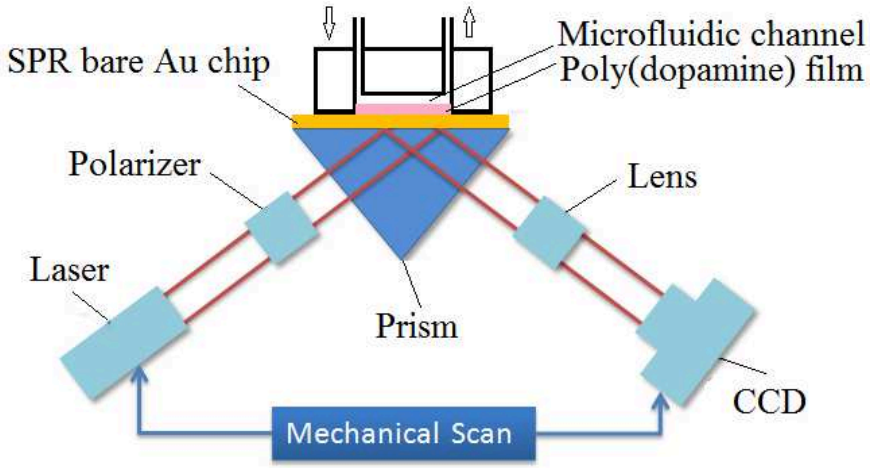


Figure S1. Schematic of a SPR chip with a poly(dopamine) nano-film on the SPR instrument.

References

[1] J. H. Waite, Mussel-designed protective coatings for compliant substrates [J]. Nature Materials 7(2008) 8-9.

[2] V. V. Papov, T. V. Diamond, K. Biemann, J. H. Waite, Hydroxyarginine-containing polyphenolic proteins in the adhesive plaques of the marine mussel Mytilus edulis [J]. J Biol Chem. 270(1995) 20183-21092.

[3] H. Lee, S. M. Dellatore, W. M. Miller and P. B. Messersmith, Mussel-inspired surface chemistry for multifunctional coatings [J] Science. 318 (2007) 426-430.

[4] J. H. Jiang, L. P. Zhu, X. L. Li, et al., Surface modification of PE porous membranes based on the strong adhesion of polydopamine and covalent immobilization of heparin [J]. J Membr Sci, 364(2010) 194-202.

[5] C.Y. Li, W. Yuan, H. Jiang, J.S. Li, F.J. Xu, W.T. Yang, J. Ma, PCL Film Surfaces Conjugated with P(DMAEMA)/Gelatin Complexes for Improving Cell Immobilization and Gene Transfection [J] Bioconjugate Chem. 22(2011) 1842-1851.

[6] G. Stojkovič, P. Žnidaršič-Plazl, Immobilization of yeast cells within microchannels of different materials [J]. Acta Chim Slov, 57(2010) 144-149.

[7] G. Stojkovič, P. Žnidaršič-Plazl, Continuous synthesis of L-malic acid using whole-cell microreactor [J]. Process Biochemistry. 47(2012) 1102-1107.

[8] A. Muck, A. Svatoš, Chemical modification of polymeric microchip devices [J]. Talanta. 74(2007) 333-341.

[9] D.F. Cui, H.Y. Cai, J.B. Wang, et al., Chinese Patent Appl. No. CN 200610066542.4, (2006). [P]

[10] H. Chien, W. Kuo, M. Wang, S. Tsai and W Tsai, Tunable Micropatterned Substrates Based on Poly(dopamine) Deposition via Microcontact Printing [J]. Langmuir. 28(2012) 5775-5782.

[11] J. Homola, S. S. Yee, G. Gauglitz, Surface plasmon resonance sensors: review [J]. Sens. Actua. B, 54(1999) 3-15.

[12] H. Li, D. Cui, H. Cai, L. Zhang, X. Chen, J. Sun and Y. Chao, Use of surface plasmon resonance to investigate lateral wall deposition kinetics and properties of polydopamine films [J]. Biosensors and Bioelectronics. 41(2013) 809-814.

Key Engineering Materials Vols 645-646 (2015) pp 1363-1367
© (2015) Trans Tech Publications, Switzerland
doi:10.4028/www.scientific.net/KEM.645-646.1363

Submitted: 2014-12-20
Accepted: 2014-12-29

An Ultrasonic Micro Knife Based on Triangular Silicon Horn Chip

Ting-ting Wang[1,2,a], Jing Wu[1,2], Ke-man Ying[3], Wen-gang Li[3], Hang Guo[1,2,b]

[1]Pentung Sah Institute of Micro-Nano Science and Technology, Xiamen University, China

[2]Department of Mechanical and Electrical Engineering, Xiamen University, China

[3]The Affiliated Chenggong Hospital of Xiamen University, Xiamen, Fujian, China

[a]821475212@qq.com, [b]hangguo@xmu.edu.cn

Keywords: ultrasonic scalpel, MEMS, silicon, triangular horn

Abstract: This paper presents a silicon-based ultrasonic scalpel for minimally invasive surgery. Starting from the fundamental theory, the micro ultrasonic scalpel using triangular silicon horn chip is designed and fabricated in detail. It is found that the magnification of the composed horn keeps 5.8 when size changes. A micro scalpel has been fabricated by MEMS technology. The test results show that a good performance in vibration and fit for puncturing biological tissues at the micro/nano scale are obtained in the micro ultrasonic scalpel.

Introduction

Since 1990s, the ultrasonic scalpels have been used as a routine tool in surgery due to its precise and effective cutting, less bleeding and thermal spread, low risk of burn and short operation period compared with electrosurgical scalpels [1-2]. MEMS technology developed so quickly during the past 20 years, and the silicon-based ultrasonic microsurgical tools have been proposed and developed [3-4], especially for minimally invasive surgery. As shown in Fig.1 (a), restricted by materials and processing technology, the traditional ultrasonic scalpel is using the structure of circular cross section, and the piezoelectric plates vertically arranged to transform the electrical energy into mechanical energy for surgery. For the silicon-based ultrasonic microsurgical tools, the piezoelectric plates are bonded to the micro-machined silicon horn chip on both sides. There are some different shapes for ultrasonic scalpels, such as exponential type, catenary type and ladder type. Each kind of scalpel has its own operation in minimally invasive surgery, since the characteristics and performance are different. The ultrasonic scalpel based on exponential silicon horn has been studied [5], and in this paper, a silicon-based ultrasonic micro scalpel based on triangular-type silicon horn chip for energy focusing and mechanical cutting is proposed, as shown in Fig.1 (b). Theory is studied in great detail for designing the micro scalpel and tested performance are also presented in the paper.

Theoretical analysis

The wave equation of longitudinal vibration of a variable section beam is written as

$$\frac{\partial^2 \zeta}{\partial x^2} + \frac{1}{s} \cdot \frac{\partial s}{\partial x} \cdot \frac{\partial \zeta}{\partial x} + k^2 \zeta = 0. \quad (1)$$

Where $s = s(x)$ is cross-section area, $\zeta = \zeta(x)$ is displacement, ρ is density, and E is Young's modulus, k is circular wavenumber, and $k^2 = \omega^2/c^2$ in which ω is circular frequency, $c = \sqrt{E/\rho}$ is velocity of longitudinal wave [4].

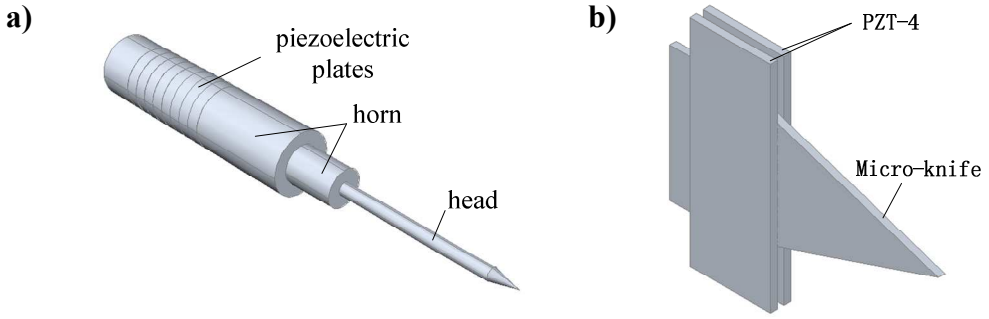


Fig.1 Schematic diagram of ultrasonic scalpels. (a) A traditional ultrasonic scalpel; (b) A micro ultrasonic scalpel.

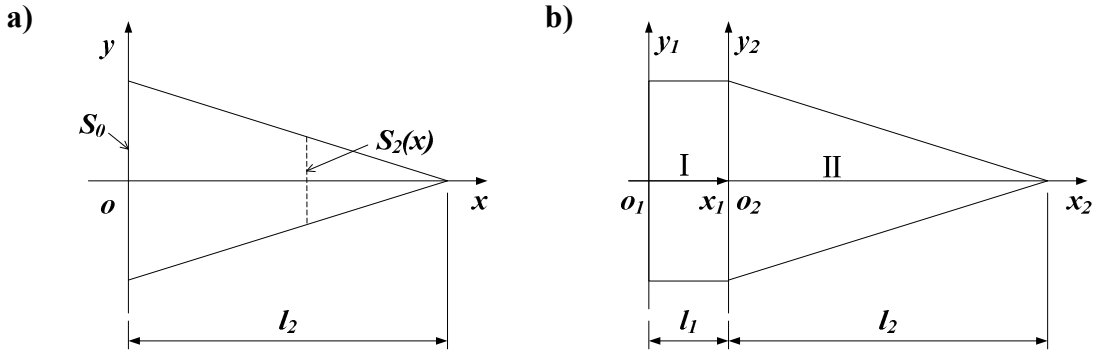


Fig.2 Models of silicon horn chips. (a) An triangular horn chip; (b) A composed horn chip.

Fig.2 (a) shows the schematic diagram of an exponential horn, with thickness of 0.45mm. Note that its cross-section areas at $x_2 = 0$ and $x_2 = x$ are S_0 and $S_2(x)$, and the function of area can be written as

$$S_2(x) = S_0 \cdot \frac{l_2 - x}{l_2}. \tag{2}$$

It supposes that the stress and the vibration velocity at $x_2 = x$ are $F_2(x)$ and $\dot{\zeta}_2(x)$ respectively and v_f is the velocity at the tip of triangular horn. By solving Eq. (1) under shape conditions of Eq. (2) according to the zero order Bessel equation, the particle displacement in triangular part can be obtained as

$$\zeta_2(x) = -jv_f J_0[k(x - l_2)]/\omega. \tag{3}$$

The vibration velocity is written as

$$\dot{\zeta}_2(x) = v_f J_0[k(x - l_2)]. \tag{4}$$

And the stress can be obtained as

$$F_2(x) = -jv_f \rho c S_2(x) J_1[k(x - l_2)]. \tag{5}$$

Where $J_m(\rho) = \sum_{n=0}^{\infty}(-1)^n \frac{1}{n!(m+n)!}(\frac{\rho}{2})^{m+2n}$.

The horn is used for gathering and transferring the energy, with its sharp tip for mechanical cutting. Therefore it is important to have a stable combination between ultrasonic vibration system and piezoelectric plates. In our study, a composed horn is adopted in which there are two parts in the horn: triangular single horn chip and square cross-section handle. Fig.2 (b) shows the schematic diagram of a composed horn chip.

For the square cross-section handle, its area equation is $S_1(x) = S_0$ and *t* is thickness, and S_0 is the border area of the horn.

At the handle, the wave equation is $\frac{\partial^2\zeta}{\partial x^2}+k^2\zeta=0$, under the condition of harmonic excitation, its general solutions at $x_1=l_1$ are

$$\zeta_1(l_1)=-jv_b\cos(kl_1)/\omega. \tag{6}$$

$$\dot{\zeta}_1(l_1)=v_b\cos(kl_1). \tag{7}$$

$$F_1(l_1)=j\rho cS_0v_b\sin(kl_1). \tag{8}$$

Where v_b is the velocity at $x_1=0$.

By considering the continuity of stress and velocity, the condition at border is written as

$$\begin{cases}\dot{\zeta}_1(l_1)=\dot{\zeta}_2(0)\\ F_1(l_1)=F_2(0)\end{cases}. \tag{9}$$

Than the frequency equation of the composed horn is deduced that

$$\frac{\sin(2\pi fl_1/\sqrt{E/\rho})}{J_1(2\pi fl_2/\sqrt{E/\rho})}=\frac{\cos(2\pi fl_1/\sqrt{E/\rho})}{J_0(2\pi fl_2/\sqrt{E/\rho})}. \tag{10}$$

The function of nodal plane position is obtained as

$$J_0[2\pi f(x-l_2)]=0. \tag{11}$$

Thus, the function of magnification can be written as

$$M_p=\frac{2}{J_0[2\pi f(x_T-l_2)]}. \tag{12}$$

Where x_T is the coordinate of the PZT equivalent output side.

With theoretical analysis, the micro ultrasonic scalpel can be designed. Parameters like resonance frequency, node displacement, and magnification are the primary factors for design.

It can be shown form Eq. (12) that the magnification of the composed horn is related to resonance frequency, location of equivalent output side and the length of triangular part. Meanwhile Eq. (10) shows the length of the handle can influence the resonance frequency of the horn, which should match with free frequency of PZT to gain the best performance. Then $w\approx c_{pzt}/4f$, where *w* is the half-width of PZT. Thus, the change of resonance frequency of horn can cause change of location of equivalent output side. These mean there are only two independent factors to influence the magnification, the length of the triangular part and the handle.

First, how l_2 influences the magnification as $l_1=4mm$ is studied. Table 1 shows the relative parameters under different values of l_2. The curves of displacement distribution are shown in Fig.3.

Table 1 Values of relevant parameters at different l_2

l_2[mm]	f[KHz]	$w_{PZT}/2$[mm]	x_0[mm]	M_p
7.0	505	1.7	0.34	5.80
10.0	394	2.2	1.47	5.78
12.5	332	2.6	2.39	5.76
15.0	287	3.0	3.28	5.78
17.5	253	3.4	4.20	5.78
20.0	226	3.8	5.12	5.78
22.5	204	4.2	6.04	5.78
25.0	186	4.6	6.96	5.78

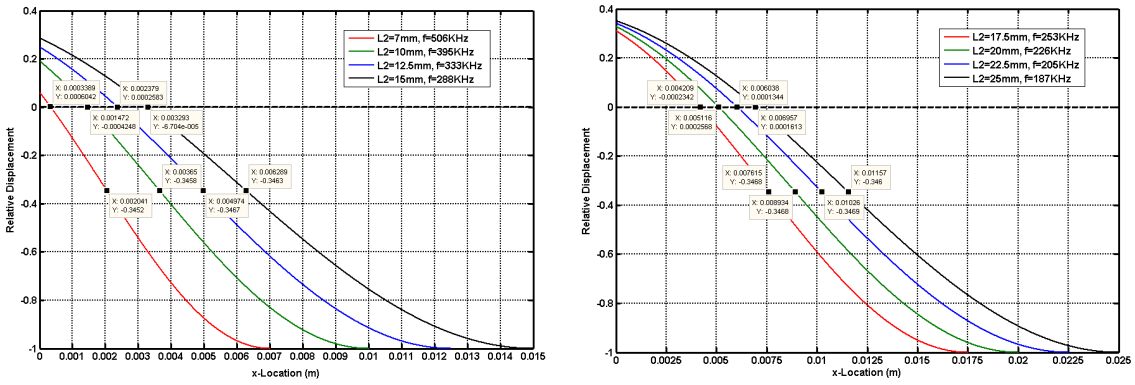


Fig.3 Curves of displacement distribution at different l_2

Next, it analysis how l_1 influences the magnification as $l_2 = 15mm$. Table 2 shows the relative parameters under different values of l_1. The curves of displacement distribution are shown in Fig.4.

Table 2 Values of relevant parameters at different l_1

l_1[mm]	f[KHz]	$w_{PZT}/2$[mm]	x_0[mm]	M_p
2.0	505.7	1.7	0.34	5.80
4.0	394.7	2.2	1.47	5.78
6.0	332.7	2.6	2.39	5.76
8.0	287.6	3.0	3.28	5.78

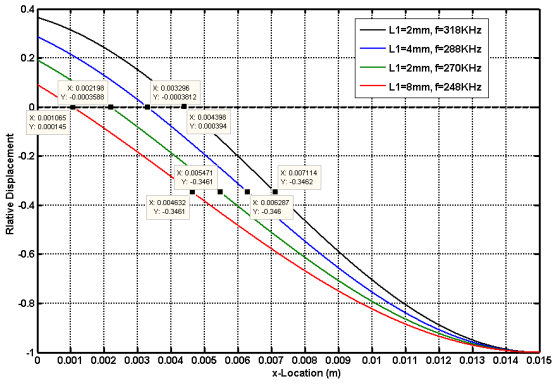


Fig.4 Curves of displacement distribution at different l_1

It can be seen from Table 1, Table 2, Fig.3 and Fig.4 that since the factors are correlated with each other, the slope of displacement curve and the location of equivalent side will change along with different sizes of composed horns. But the magnification keeps constant as 5.8, which is much higher than that of general ultrasonic micro knives. It also means that composed triangular horns can work at any ultrasonic frequency with same performance under constant output voltage.

Experiments

Based on the theoretical analysis above, a micro ultrasonic scalpel has been designed and fabricated, as shown in fig.5. The length of the single silicon horn part and the handle are 15mm and 4mm respectively. MATLAB is used to calculate the resonance frequency and magnification of the composed horn chip with Eq. (10), Eq. (11) and Eq. (12), while the results are 287KHz and 5.8. The impedance analyzer, Agilent 4294A, is used to test the resonance frequency of micro ultrasonic

scalpels, and a platform with CCD optical microscopic vision detection system is set up to test its magnification. The tested resonance frequency and magnification are 286KHz and 5.2, respectively, demonstrating that the theoretical calculation and testing results match with each other, and furthermore, the theoretical method developed in this paper can be effectively used in developing micro ultrasonic scalpels. The tested tip displacements are 4.41μm and 12.56μm when the applied voltages on PZT plates are $40V_{p-p}$ and $100V_{p-p}$. Thus, the vibration performance of the micro ultrasonic scalpels has been proved. With the vibration amplitude in the micrometer scale, the micro ultrasonic scalpels are suitable for minimally invasive surgery.

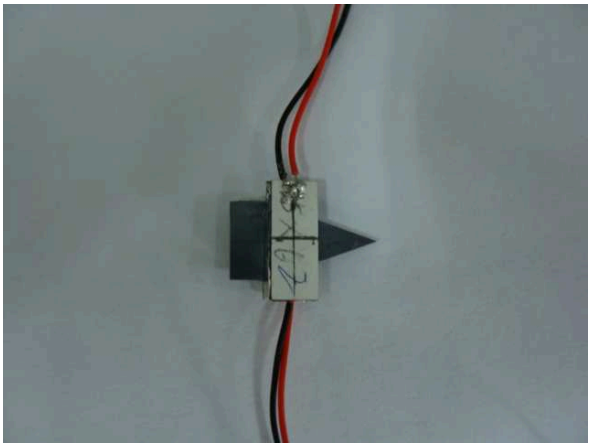


Fig.5 A micro ultrasonic scalpel

Summary

A triangular ultrasonic scalpel based on micro-fabricated silicon chip is proposed and investigated, with detailed theoretical analysis discussed in the paper. The micro-fabricated ultrasonic scalpels are tested and results proved the proposed micro ultrasonic scalpel has good vibration performance and can be used for minimally invasive surgery.

Acknowledgments

This work is financially supported by the New Century Talent Support Plan of the Ministry of Education of China (2007NCET-07-0723)and the Scientific Research and Development Program of City of Xiamen(3502Z20124036).

References

[1] Paul N. Afrooz, Jason N. Pozner and Barry E. DiBernardo, Noninvasive and Minimally Invasive Techniques in Body Contouring, Clinics in Plastic Surgery. 41 (2014), 789-804.
[2] D.M.Herron, M.Gagner, T.L.Kenyon, et al, The Minimally Invasive Surgical Suite Enters the 21st Century, Srug Endosc. 15 (2001), 415-422.
[3] A.Lal and R.M.White, Silicon microfabricated horns for power ultrasonics, Sensors and Actuators. 54 (1996), 542-546.
[4] H.Guo, H.Yang and L.M.Zou, Design and Fabrication of A Micro Knife for Minimally Invasive Surgery, Proceeding of the 2008 Micro Nano International Conference. (2008),169-171.
[5] T.T.Wang, J.Y.Wang, W.Q.Zhang, H.Guo, An Ultrasonic Micro Knife Based on Exponential Silicon Horn Chip, Applied Mechanics and Materials. 496-500(2014), 1464-1467.

Key Engineering Materials Vols 645-646 (2015) pp 1368-1373
© (2015) Trans Tech Publications, Switzerland
doi:10.4028/www.scientific.net/KEM.645-646.1368

Submitted: 2015-01-09
Accepted: 2015-01-15

Preparation and characterization of tissue engineering scaffolds by composite molding of 3D printing and electrospinning

Yun-Min Ma [1, a], Yuan-Yuan Liu [1, b *], Hai-Ping Chen [1,c] and Qing-Xi HU [1,d]

[1] Rapid Manufacturing Engineering Center, Shanghai University, Shanghai 200444, China

[a]mayunmin891206@163.com, [b]yuanyuan_liu@shu.edu.cn, [c]wfchp2003@aliyun.com.cn, [d]huqingxi@mail.shu.edu.cn

Keywords: Electrospinning; 3D printing; Tissue engineering scaffolds

Abstract. Currently, the developed electrospinning technique is capable of producing sub-micron diameter fibers, has better bionic of the extracellular matrix (ECM) on the size and morphology. Joining the nanofiber network into the porous macro scaffolds by the association of electrospinning with 3D printing technology can effectively support bionic microenvironment and improve the cell compatibility of scaffolds. We prepared the GE/CA-PCL scaffold by the composite approach, and characterized the morphology, cell compatibility and mechanical properties of scaffolds compared to the GE/CA scaffold prepared by single 3D printing technology. The composite molding process of 3D printing and electrospinning is a promising technique used for preparing scaffolds for tissue engineering and clinical medicine.

Introduction

Scaffolds for tissue engineering are the key to repair the defect of human tissues and organs. Among the methods of preparing scaffolds, 3D printing technology is developing rapidly which has achieved the precise control of the internal porous structure and complex shape of the tissue engineering scaffolds [1], but the porosity of the prepared scaffolds is low, usually less than 80% [2], and in addition the problem of the cells doing not readily adhere to the scaffold is still existing.

Electrospinning prepare nanoscale structures by high voltage electric field, close to the natural extracellular matrix, has a distinct advantage in constructing suitable cell survival microenvironment. Tens to thousands of volts were applied between the nozzle equipped with polymer solution or melt and the receiving device, making the produce of static electricity force opposite to the surface tension of the solution or melt under high voltage electrostatic field, which driving to be stretched into a Taylor at the end of the capillary. When the electric force is large enough, the polymer droplet could form jetting trickle with the surface tension being overcame [3]. One big feature of electrospinning is to fabricate nanofiber topology structure with high porosity and high surface area and the flexible controllable parameters is providing full space for the preparing of the scaffold containing cells in it.

This paper presents combining the electrospinning with 3D printing to prepare biological scaffold, making the scaffold have simultaneously macro, micro-structure characteristics, and effectively overcame the limitation of large aperture and small porosity existed in single 3D printing technology.

1 Materials and methods

1.1 Materials

Type B gelatin (American Biotechnology Co., Ltd) and Sodium alginate, Calcium chloride solution (cross-linking agent), polycaprolactone (PCL, average molecular weight is 73000). Human adipose stem cells were provided by the Shanghai Ninth People's Hospital.

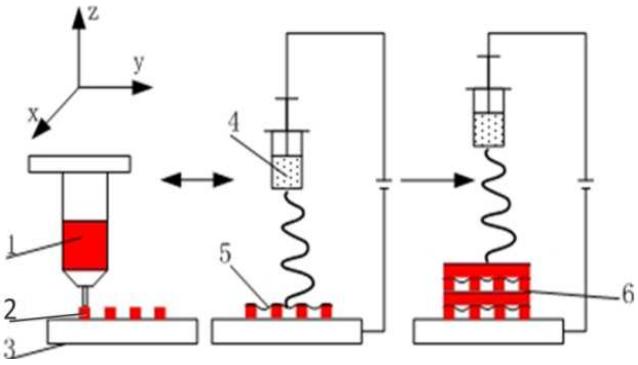
1.2 Solution preparation

20% gelatin solution and 4% sodium alginate solution, prepared by deionized water, were mixed at 1:1 with quality, then modified by the 25% Calcium chloride solution and stirred for 2 hours,

prepared the gelatin/calcium alginate solution(GE/CA). The PCL was dissolved in the mixed solution of chloroform / ethanol (3:1) to prepare the electrospinning solution with concentration of 7%.

1.3 Scaffold preparation

The prepared GE/CA solution and PCL solution were loaded in piston extruder nozzles and electrospinning sprinklers respectively. As shown in Fig.1, the motion platform first moved to the piston extrusion nozzle, then the receiving platform moved regularly along the X, Y direction according to the desired macroscopic structure of forming scaffold, after one layer was completed, the receiving platform moved to electrospinning nozzle to deposit a layer of nan web according to the desired microstructure under the electrostatic field. The receiving platform reciprocated between the two stations to complete the preparation of integrated scaffold.



1.Piston extrusion feed nozzle; 2.Macro Scaffold layer; 3.The motion platform; 4.Electrospinning nozzle; 5.Nanofibers; 6.Composite forming stents.

Fig. 1 Schematic of composite forming technology route

Preparation parameters of macro scaffold by 3D printing technology were selected and optimized based on many experiments and drawn as follows: pneumatic fast feed nozzles are optioned, the nozzle diameter is 0.5mm, feed rate is 0.4ml/min, the average speed of the receiving platform is 12mm/s; Forming parameters of electro spun fiber web were: 1ml/h of feed rate, 13KV of voltage, 10cm of the distance between needle and receiving plate, the ambient temperature is room temperature, and humidity of 30% -40% .

The preparation of the GE/CA scaffold through 3D printing is the same as above with removing the part of receiving electrospinning.

2 Characterization of scaffold

2.1 Scanning electron microscope (SEM)

Cut the scaffold prepared by composite approach into small pieces and placed in 24-well plates. Measured the aperture size of the scaffolds through Scanning electron microscopy (Zeiss Auriga crossbeam system, Germany).

2.2 Mechanical Properties Testing

Compressive strength of the scaffold was tested by electronic universal testing machine with loading direction of perpendicular to the deposition plane at 1mm/min loading rate.

2.3 Cell Culture

2.3.1 Cell – scaffolds

The scaffolds were washed with Phosphate buffer solution (PBS) for three times after sterilized and added the culture medium overnight to prepare for seeding cells. 1ml, $1X10^5$/ml of the third generation of the fat stem cell suspension were dropped uniformly on the scaffold and changing the medium every other day.

2.3.2 Cell morphology

The two kinds of cell-containing scaffolds were incubated for 3 days, then evaluated the cell morphology through the SEM. The specific steps are washing the scaffolds with PBS for 2-3 times and then gradient dehydration with 25 %, 50%, 75%, 85%, 95%, 100% alcohol solution in turns

soaking for every five minutes, and gradienting off alcohol using different ratios of ethanol/hexamethyl diamine alkyl mixed solution (ethanol: hexamethyl diamine alkyl = 3:1,1:1,1:3,0:1) in sequence soaking for every ten minutes. Finally, observed the morphology of scaffold by scanning electron microscope.

The scaffold materials were removed into a small centrifuge, added 1ml of PBS solution, 1ul of Stainning A and 1ul of Stainning B and observed the liability of ADSCs with inverted fluorescence microscope.

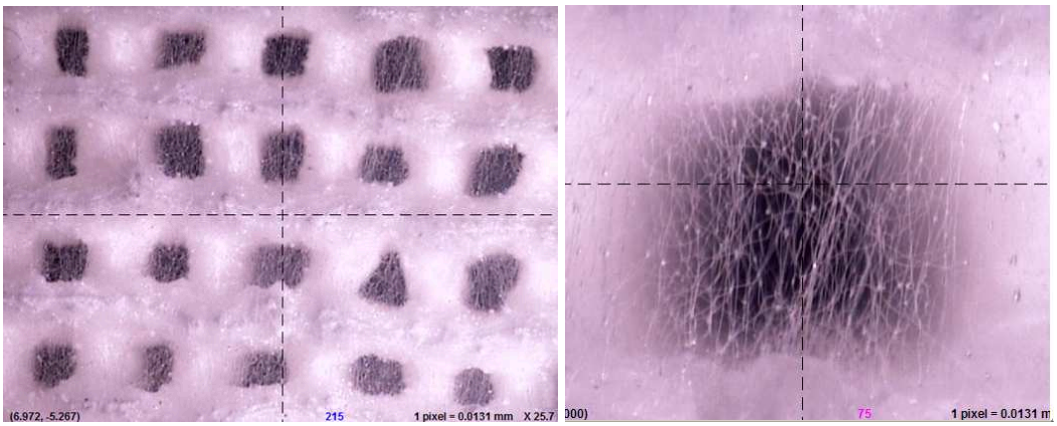
2.3.3 Cell proliferation assay

Cell proliferation was measured using MTS test. Cells were cultured on GE/CA-PCL scaffold for 1,3,5,7,9,11,13 days, added the MEM medium, and then added 40 μl of MTT solution (5mg/ml) into each sample a. After 4 hours of culturing and 10 minutes of oscillation, 100uL culture medium was suctioned to each hole of 96 -well plate. Then the absorbance of cells was measured with a TECAN plate reader at a wavelength of 550nm. This study is using multiple measurements to obtain average.

3 Results and Discussion

3.1 Macro and micro structure of scaffold

The characterization of the scaffold with macro and micro structure was shown in Fig.2. From the microscope figure which is enlarged 100 times, we can see that the microstructure of electrospinning PCL adhered uniformly on the macro- porous structure prepared by 3D printing technology.

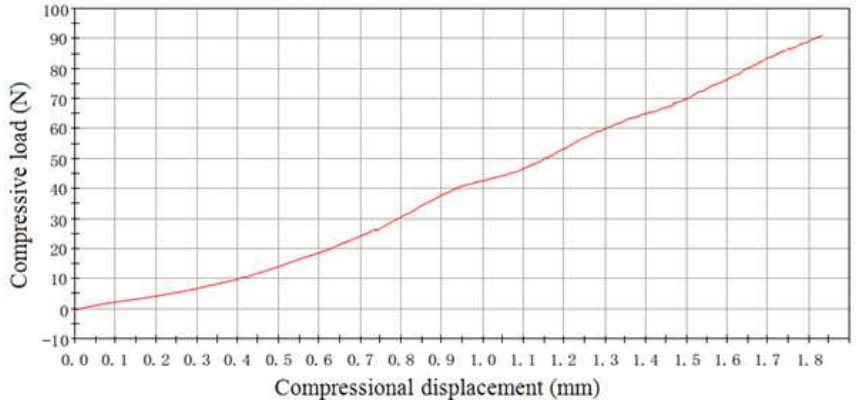


(a) X25.7 (b) X100

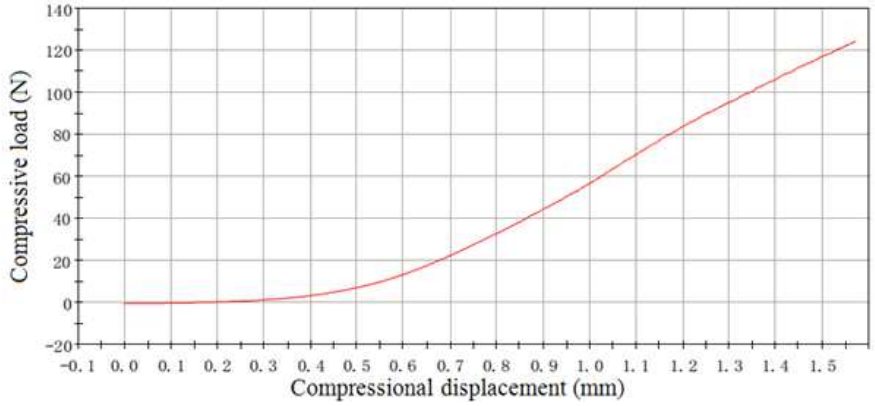
Fig.2 Structure enlargement of the composite scaffold

3.2 Mechanical properties of scaffold

Scaffolds needed to have certain mechanical strength to support the new organization and maintain the environment for the growth of cells. As shown in Fig.3, the maximum compressive load increased from -91.05N to -124.30N after adding the PCL nanofibers, which moaned that the joining of nanofibers would not affect the mechanical properties of scaffolds and contrary improved the mechanical properties to some extent.



(a)



(b)

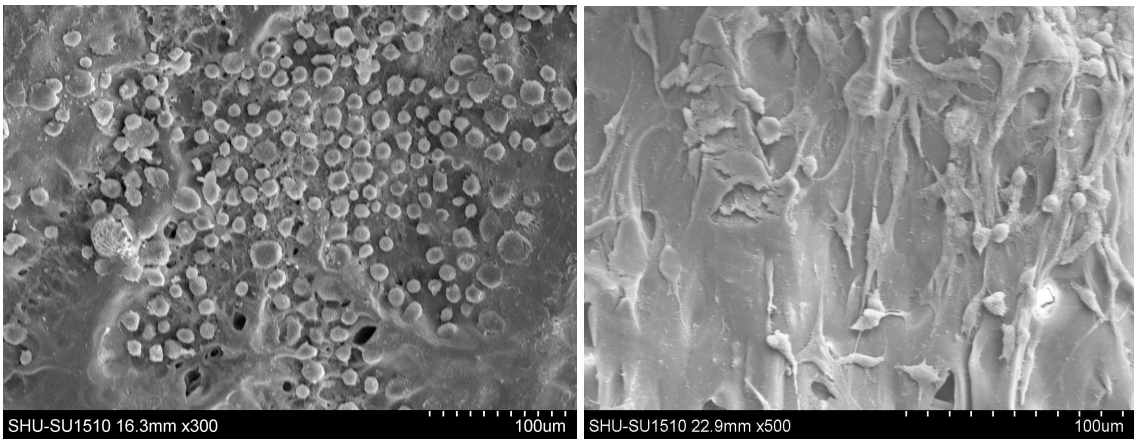
Fig.3 Pressure - displacement curve of two kinds of scaffolds. (a) GE/CA scaffold, (b) GE/CA-PCL scaffold.

3.3 Analysis of cell morphology

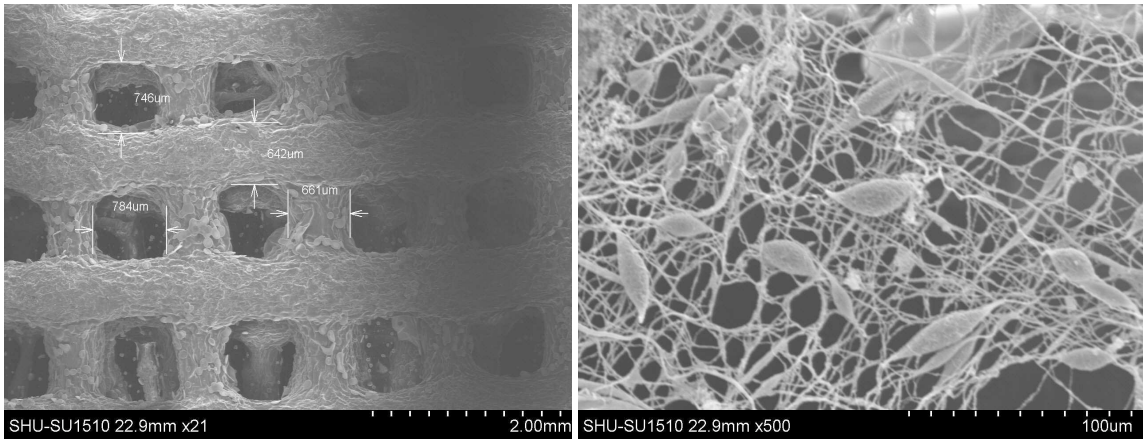
As shown in Fig.4, most cells in the control group were mainly spherical, and did not adhere to the scaffold. According to the theory of interaction between cells and materials, wherein the adhesion of cells and material is a base [4], the suitable adhesion must occur before the migration, differentiation and proliferation [5]. In Fig.4 (c) and (d), ADSCs stretched on the scaffold, and began to secrete extracellular matrix, interconnected into a film, pore size of scaffold was about 600-800um. Observed by confocal microscopy in Fig.5, most ADSCs cells on the control scaffolds were dead, while on the experimental group, they were mostly survival, rounded, uniform shape and arranged closed.

3.4 Cell proliferation assay

The same amounts of ADSCs were seeded in the two kinds of scaffolds for 1, 3, 5, 7, 9, 11, 13 days to analyze cell proliferation (Fig.6). In the initial period of culturing (three days ago), there was no significant difference of cell proliferation in two scaffolds, however by later (three days later), cell proliferation rate on experimental scaffolds was significantly higher than the control group, indicating that the scaffold made from composite molding process was more suitable for the growth and proliferation of cells and had better cell compatibility.

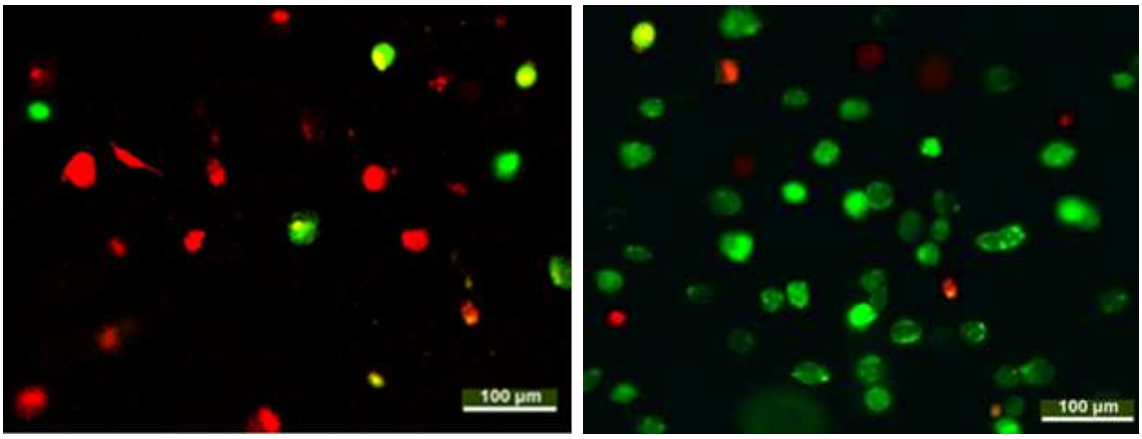


(a) (b)



(c) (d)

Fig.4 SEM images of cell morphology. (a), (b) GE/CA scaffolds. (c), (d) GE/CA-PCL scaffolds.



(e) (f)

Fig.5 Live/dead staining results: (e) cells grown in GE/CA scaffold; (f) cells grown in GE/CA -PCL scaffold.

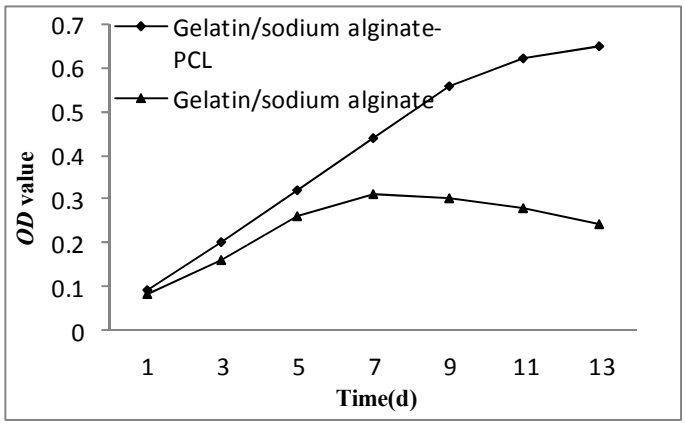


Fig.6 MTS proliferation assay of ADSCs cells cultured for 1, 3, 5, 7, 9,11and 13d.

4 Conclusions and Outlook

Comparing to other preparation methods, nanofibers fabricated by electrospinning technology has larger specific surface area, strong mechanical properties and high porosity, so is more closer to the structure of extracellular matrix [6] .

The experiment successfully prepared GE/CA-PCL scaffold through the combination of 3D printing and electrospinning technology. The observation showed that microstructure of PCL electrospinning attached uniformly on the macroscopic porous structure, the composite scaffold had certain strength and the joining of nanofibers could enhance the mechanical properties of scaffold to a certain extent. In addition, ADSCs in GE/CA scaffold prepared by single 3D printing technology were spherical, did not realize adherent growth, cell liability is lower with most cells died; However, the ADSCs in the GE/CA-PCL scaffold prepared by composite process attached well with three-dimensional growth and proliferation, mostly for long spindle-shaped with significant protrusions. The GE/CA-PCL scaffold is an ideal scaffold used for bone tissue engineering.

Through the combination of 3D printing and electrospinning technology, the nanofiber network was added into the macro-porous scaffolds, which has effectively overcome the defects of large aperture and low porosity faced by single 3D printing technology preparing scaffolds and could provide for the growth of cells with more three-dimensional space and adhesion sites [7], and thus to better simulate the extracellular matrix.

Acknowledgements

This study is partly supported by National Natural Science Foundation of China (No.51375292, NO.51475281), National Youth Foundation of China (No.51105239).

References

[1] Li X, Wang CT. Current progress of fabricating tissue engineering scaffold using rapid prototyping techniques, J. Chin J Biotech. 24(2008): 1321−1326.

[2] Wu LB, Ding JD. Advances in fabrication methodology and technology of three-dimensional porous scaffolds for tissue engineering, J. Funct Polym. 161(2007): 91−96.

[3] Yang DY, Jiang XY. Study progress of orderly nanofibers prepared by the electrospinning, J. Fibers. 602(2008): 1-5.

[4]Gumbiner,BM.Celladhesion: The molecular basis of tissue architecture and morphogenesis, J. Cell.98(1996):84:345.

[5] Boyan BD,Hummert,Dean DD, etal.Role of material surfaces in regulating bone and cartilage cell response, J.Biomaterials.323(1996):17-37.

[6] Liu ZR, Chen DL, Application progress of polycaprolactone in tissue engineering, J. Progress in Modern Biomedicine. 16 (2012):3182 -3184.

[7] Liu JJ, Wei YY, Cai ZD, Wang JG, Wang CY, Fan CY. Biocompatibility studies of coaxial electrospinning poly-L- lactic acid-caprolactone copolymer/bovine serum albumin nanofibers, J. Chinese Journal of orthopaedic Trauma.12 (2010):471 -475.

Key Engineering Materials Vols 645-646 (2015) pp 1374-1382
Submitted: 2014-11-02
Accepted: 2015-01-08
© (2015) Trans Tech Publications, Switzerland
doi:10.4028/www.scientific.net/KEM.645-646.1374

Pretreatment with Huperzine A-loaded poly(lactide-co-glycolide) nanoparticles protects against lethal effects of Soman-induced in mice

ZHANG Rui-hua, LI Li-qin*, WANG Chen, LU Xiao-jing, SHI Tong,

XU Jian-fu , SONG Liang-cai, WANG Hui-fang

（State Key Laboratory of NBC Protection for Civilian, Chemical Defense Research Institute of PLA, Beijing,China）

First Author: 15201517118@163.com Corresponding author: llq969696@163.com

Key words: Huperzine A, acetylcholinesterase, nerve agent, soman, nanoparticle

ABSTRACT

Huperzine A (HupA), an alkaloid isolated from the *Chinese club moss*, is a reversible inhibitor of cholinesterases which cross the blood-brain barrier and show high specificity for acetylcholinesterase (AChE). However, HupA induces unwanted side effects in an effective dose against nerve agent poisoning. In the present study, HupA–loaded poly(lactide-co-glycolide) nanoparticles (HupA-PLGA-NP) were prepared using the O/W emulsion solvent evaporation method. The results of SEM demonstrated that HupA-PLGA-NP had an spherical shape and a smooth surface without pores. It's mean diameter and PDI were 208.5±3.6nm and 0.09±0.01 respectively. The Zeta potential was -35.3±1.8mV and the drug loading was 2.86±0.6%. *In vitro* drug release studies showed that HupA-PLGA-NP had a sustained-release behavior in phosphate buffer solution, The accumulated amount of HupA was about 72.1% at 48h with a low burst release within 30min. The LD_{50} values of HupA and HupA-PLGA-NP were 1.40 and 4.85mg/kg respectively, showing that the toxicity of HupA was reduced by 3.5 times. We evaluated the protective efficacy for different doses of HupA or HupA-PLGA-NP against $1.0\times LD_{95}$（143.0μg/kg）soman toxicity. The results confirmed that HupA (0.3～0.5mg/kg) or HupA-PLGA-NP (0.5～1.5mg/kg) could ensure animals survive. However, about 10% of the animals injected with HupA (0.8mg/kg) died, while no animals died when injected with HupA-PLGA-NP (1.5mg/kg). Aim to 100% survival rate, the effective protective time (12h) of HupA-PLGA-NP (0.5mg/kg,iv) against $1.0\times LD_{95}$ soman toxicity in mice was significantly prolonged compared with that of HupA (4h). The study of AChE activity showed that whole-blood and supernatant of brain diluted by 80-fold and 10-fold respectively were optimum in this study. AChE inhibition after administration of HupA and HupA-PLGA-NP (0.5mg/kg,iv) was recorded and analyzed, The peak values of AChE inhibition in whole-blood and brain by HupA-PLGA-NP (17.6% and 21.8%) were lower than those by HupA (33.7% and 31.9%) and AChE inhibition time by HupA-PLGA-NP was longer than that by HupA. These data confirmed that HupA-PLGA-NP had less toxic and more longer time than HupA against $1.0\times LD_{95}$ soman poisoning and warrant further development as a potent medical countermeasure against chemical warfare nerve agents (CWNAs) poisoning.

1 Introduction

Organophosphorus nerve agents (OPNA) are extremely toxic materials used as chemical weapons, which continue to concern military personnel and civilians as potential battlefield and

terrorist threats [1,2]. The current antidotal therapy for nerve agent poisoning is pretreatment before poisoning along with post-exposure treatment [3-5]. A chemical attack provides a very stressful situation, where many victims should be treated. Timely administration of antidotes will then become a considerable problem. This holds in particular for soman poisoning because of its rapid entrance into the brain, and fast "aging" (within minutes) of soman-inhibited AChE, excluding further enzyme reactivation by an oxime. Therefore, effective pretreatment countermeasures of nerve agent poisoning are essential.

Current pretreatment against nerve agent poisoning includes reversible AChE inhibitors, such as pyridostigmine bromide (PB) and stoichiometric or catalytic bioscavenger zenymes like butyrylcholinesterase (BChE) and paraoxonase1, respectively. PB was introduced years ago for the pretreatment of nerve agent poisoning in western countries. However, pyridostigmine does not cross the blood brain barrier (BBB), and therefore, it can not protect central AChE and the central nervous system (CNS) against seizures and subsequent neuropathological states induced by nerve agent exposure [6-8].

Huperzine A (Hup A) is an alkaloid isolated from the *Chinese club moss*. *Huperzia serrata*, is a reversible and selective inhibitor of AChE [9,10]. Compared with carbamates, Hup A has a higher affinity for AChE than that for the other cholinesterases and a slower rate of dissociation. Moreover, Hup A can cross the blood-brain barrier to protect against nerve agents-induced CNS injuries [11-13]. In addition, Hup A exerts an anti-NMDA neuroprotective action [14]. Hup A has been approved for human use for the treatment of Alzheimer's disease and is currently in use in clinic. In previous studies, Hup A (0.5mg/kg) was shown to prevent soman-induced seizures and protect against CNS neuropathology. In addition, AChE activity in whole-blood and brain obtained protection to some extent [15-17]. However, Hup A appeared to unwanted toxic side effects such as chewing and salivation, which probably arised from its strong AChE inhibition that restricts the utility of its vital neuroprotective effects.

Nanoparticle-based drug delivery system is a rapidly developing area within nanotechnology, which has attracted increasing attention in the last decade. The important technological advantages of nanoparticles (NPs) used as drug carriers are increasing drug solubility under physiological conditions, sustained and controlled release, minimizing drug toxicity and targeted drug delivery. Biodegradable polymers are most commonly used to prepare nanoparticles for drug delivery. PLGA is used in a host of Food and Drug Administration (FDA) -approved therapeutic devices and has a long safety record [18,19]. A wide variety of biodegradable PLGA particles generated in various ways are utilized for sustained delivery of bioactive molecules as an injectable depot formulation due to their biocompatibility and low toxicity.

In this report, HupA-PLGA-NP was prepared to evaluate the protective efficacy of HupA-PLGA-NP pretreatment against soman lethal effect. Multiple lines of evidence including survival rate, inhibition of whole blood and brain AChE activity and behavioral signs are presented to demonstrate the efficacy of HupA-PLGA-NP pretreatment for protection against soman toxicity. In addition, the protective efficacy of pristine HupA was conducted simultaneously. As far as we know, this is the first study assessing HupA-PLGA-NP-pretreated animals against the lethal effects of soman in comparison to animals pretreated with HupA.

2 Materials and methods

2.1 Chemicals and reagents

Huperzine A with a chemical and chiral purity greater than 99% was obtained from Tianjin yifang technology Co,Ltd. Soman (O-pinacolyl methylphosphonofluoridate or GD, purity >98.8%) was synthesized in our laboratory. PLGA (75:25, MW20,000, with one acid as an end group) was purchased from Shandong Institute of Medical Instrument. polyvinyl alcohol (PVA,

MW30,000-50,000) was obtained from Sigma-Adlrich. Trifluoroacetic acid (purity > 97%) was from Fisher scientific.

ICR mice were obtained from Hua fukang biology technology Co,Ltd. The Laboratory animals weighed between 20.0±2.0g. The animals were kept in cages at room temperature under a 12h light/dark cycle and food and water were freely available.

2.2 Preparation of HupA-PLGA-NP

HupA-PLGA-NP was prepared by oil in water emulsion solvent evaporation method as described previously [20]. In brief, PLGA (80mg) and HupA (2mg) were dissolved in 2ml of dichloromethane (DCM) under moderately ultrasonic. The polymer solution was then added to 1% (w/v) PVA solution, and then the mixture was sonicated for 40 seconds at 200W on ice (Sonics VC750, America). The obtained emulsion was managed by Rotavapor (Büchi R-200, Switzerland), under vacuum at 40℃, in order to evaporate the organic solvent. The obtained PLGA nanoparticles were collected by centrifugation at 16,000rpm for 25 min (Sigma 3K-30, America) and washed twice with 10ml of distilled water in order to remove the weakly adsorbed (or simply mechanically adhered) HupA. Finally, nanoparticles containing 0.5% mannitol were frozen in liquid nitrogen and lyophilized (Christ Alpha 1-4, German).

2.3 Measurement of size, morphology and Zeta-potentials

The size of HupA-PLGA-NPs was measured by dynamic light scatter method. The mean particle diameter, size distribution, and Zeta potential of HupA-PLGA-NP were detected by Zetasizer Nano ZS (Malvern instruments, UK). Nanoparticle samples were diluted with deionized water not excessing to 0.4mg/ml (W/V) before measurement. The data were obtained as the average of three measurements.

The surface morphology of HupA-PLGA-NP was observed by scanning electron microscope (SEM) (Hitachi s4800, Japan). The SEM samples were prepared by mounting dried nanoparticles on metal stubs using double-sided adhesive tape with conductive effect, sputter coated with a thin layer of gold and analyzed with SEM at an accelerating voltage of 5 kV.

2.4 Determination of drug loading by HPLC

Drug content in the HupA-PLGA-NP was assayed by HPLC (Agilent 1200, Califormia). Briefly, 5mg dried nanoparticles were dissolved in 1ml of methyl alcohol under vigorous vortexing. The resulting solution was then centrifuged at 14000rpm for15min. The suspension was transferred to 5ml glass tubes. The methyl alcohol was evaporated in nitrogen atmosphere at 60℃ with a nitrogen evaporation system. Mobile phase was added to the glass tube and vibrated vigorously. Then the solution was transferred into a HPLC vial after filtering through an 0.22μm type membrane filter for HPLC analysis. Inertsil ODS-3 column (4.6mm×150mm, 5μm, Agilent Technologies, Inc., USA) was utilized for drug separation. The column effluent was detected at 308nm with a UV detector, while a methanol-1‰Trifluoroacetic acid (TFA) (40:60, v/v) was used as the mobile phase. The flow rate was set at 0.5ml/min. The chromatography was carried out at 25℃ and the injection volume was 20μl. The drug loading percentage was calculated as the following formula:

Drug loading (%) =[(Drug amounts determined by HPLC) / (Nanoparticles amounts)]×100%

2.5 *In vitro* release of HupA-PLGA-NPs

A dialysis method was used for the drug release determinations. In short, about 50mg of HupA-PLGA-NPs were placed in a dialysis tube and immersed in 40ml phosphate buffer solution (PBS, pH7.4, containing 0.02%KCl, 0.8%NaCl, 0.12% Na_2HPO_4 and 0.02% KH_2PO_4). The dialysis process was carried out using a D-Tube™ Dialyzer Mega MWCO 10kDa at 37℃ and under magnetic stirring (150rpm). This membrane was pretreated during 1h with the same buffer solution

to ensure its wetting and sealing. At specified times aliquots 0.5ml were withdrawn and the amount of HupA released was determined by means of HPLC system as previously described. An equal volume of buffer, maintained at the same temperature, was added after sampling to ensue sink conditions. All the experiments were carried out in triplicate.

2.6 Dose-toxicity relations of soman, HupA and HupA-PLGA-NPs

Soman (100,110,120, 130,140, 150μg/kg) was injected intramuscularly in a hind limb in volumes not exceeding 0.5ml/kg, in order to obtain optimal dosage of mice exposure to soman, and then lethality and symptoms was recorded.

Nanoparticle drug delivery system can alter biodistribution and reduce side effects. Therefore, HupA (0.8,1.0,1.2,1.5,2,3mg/kg) and HupA-PLGA-NPs (2,3,4,5,6,7mg/kg) were administered via tail vein in volumes not exceeding 0.5ml/kg, comparing the toxicity of HupA with the toxicity of HupA-PLGA-NPs. The lethality and signs were observed within 24h.

2.7 Pretreatment lethal effect of HupA and HupA-PLGA-NPs in mice exposed to soman

Several studies have examined the efficacy of an acutely administered 0.5mg/kg HupA against nerve agent intoxication. The results showed that HupA afforded a protection for animals intoxicated by soman, but it induced unwanted side effects. The effects of HupA pretreatment were closely related to varied routes of administration and species-dependent response to antidotal drugs. Hence, HupA (0.3, 0.5, 0.8mg/kg, iv) and HupA-PLGA-NPs (0.5, 1.0, 1.5mg/kg, iv) were administered at 30min before exposure to $1.0\times LD_{95}$ (143μg/kg,im) soman to determine appropriate pretreatment dose. While the dose of HupA-PLGA-NPs was used in this study due to the slow and sustained drug release from nanodrugs.

Based on the results, a dose of 0.5mg/kg HupA or HupA-PLGA-NPs was selected for further studies on evaluating the lethal efficacy against 143μg/kg soman exposure. The experiments were conducted in three groups including saline, HupA and HupA-PLGA-NPs. Soman was injected at designated time points after mice were pretreated with saline, HupA or HupA-PLGA-NPs. Survival rate was calculated and signs were recorded.

2.8 Measurement of AChE activity after administration of HupA and HupA-PLGA-NP

AChE activity assay of whole blood and brain tissue was conducted at designated time points after administration of HupA and HupA-PLGA-NP (0.5mg/kg,iv). AChE activity was measured using modified DTNB method as described previously [21]. AChE activity was normalized to the optical density (OD) measured at 412nm. All spectrophotometric reading was taken using a SpectraMax190 plate reader with Softmax Pro5.3 software (SpectraMax190, USA). Optimum dilution ratio of whole blood was selected by measuring the optical density of diluted whole blood (40, 60, 80, 100 and 120-fold) with 1/15mmol/L phosphate buffer (pH7.4).

The brain tissue was homogenized on ice in 1:4 ratio (W/V) of 0.9% physiological saline. The homogenate was centrifuged at 14,000 rpm for 15min at 4℃. Optimum dilution ratio was determined by diluting supernatant (5, 10 and 15-fold).

2.9 Statistics analyses methods

Statistics analyses were performed using OriginPro 8.0 software. Each value is the mean± SD of five mice in each group in AChE activity assay tests.The LD_{50} values of soman, HupA and HupA-PLGA-NPs were obtained by Bliss Method.

3 Results and discussion

3.1 Characterization of HupA-PLGA-NPs

HupA-PLGA-NPs were characterized according to their morphology, average particle diameter, size distribution, zeta potential and drug loading. The surface morphology of

HupA-PLGA-NPs was observed by SEM (Fig.1). The nanoparticles were spherical in shape with a smooth surface and the size was uniform.

The average particle diameter and polydispersity of prepared HupA-PLGA-NPs were 208.5±3.6nm and 0.09±0.01 respectively (Fig.2), suggesting an uniformity of the particle size distribution. It's zeta potential was -35.3±1.8mV (Fig.3).

The amount of incorporated HupA in nanoparticles was detected by HPLC. The results showed that the drug loading was 2.86±0.6%. Because the solubility of Huperzine A in pure water is about 1 mg/ml, the drug loading of HupA in nanoparticles is lower than lipophilic drug, but it was sufficient for subsequent animal experiments.

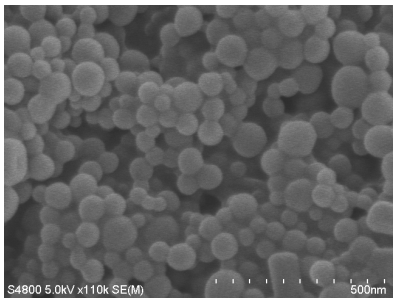


Fig.1 SEM of HupA-PLGA-NP

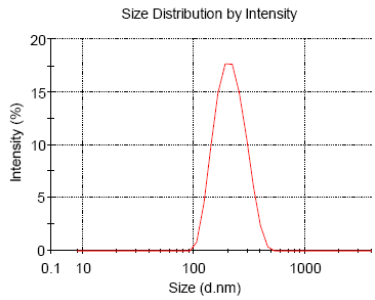


Fig.2 Size distribution of HupA-PLGA-NP

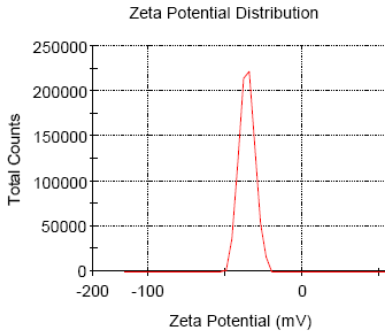


Fig.3 Zeta potential of HupA-PLGA-NP

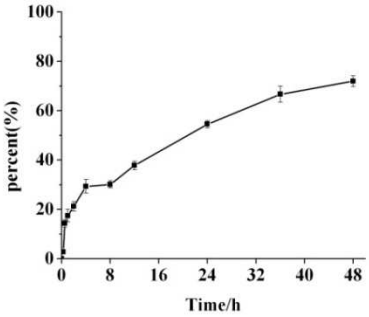


Fig.4 Release of HupA-PLGA-NP *in vitro*

3.2 *In vitro* release experiment of HupA-PLGA-NP

Drug release profiles from PLGA particles reported in the literature are quite controversial and a general trend has not been stated. Different PLGA properties, such as size, molecular weight,

hydrophobicity/hydrophilicity of drugs and the nature of the polymer used have been reported to influence the drug release.

Drug release test *in vitro* indicated that HupA release follows a biphasic profile probably due to diffusion-cum-degradation-mediated processes. HupA-PLGA-NPs showed a sustained release behavior in phosphate buffer solution. Although "burst release" was measured within 30min,the accumulated amount of HupA *in vitro* released from HupA-PLGA-NPs was about 72.1% in 48 h (Fig.4). Drug burst release occurs mainly by the loss of the surface-associated drug and by drug diffusion in the polymeric matrix. With respect to the release during the slower phase, it may result from polymer degradation, drug diffusion through the polymeric matrix, or both [22].

3.3 Acute toxicity of soman in ICR mice

Animals presented a clear cholinergic crisis characterized by chewing, hypersecretion, muscle fasciculations, tremors and convulsions after soman exposure. Only mild toxicity signs were observed in mice at lower dose and the survival rate was high. Animals died quickly within 30min at high dose presenting severe symptoms of intoxication, such as convulsions and seizures. Soman acts by irreversibly inhibiting AChE and rapid 'aging'of the inhibited AChE. Therefore, animals

died few if they could survive within 30min of soman exposure. The half of lethal dose (LD_{50}) and the ninty-five of lethal dose (LD_{95}) were 115.9μg/kg and 143.0μg/kg respectively. So In subsequent experiments, 143.0μg/kg of soman was selected as poisoning dose in this study.

3.4 Dose-response relations of HupA and HupA-PLGA-NP in mice

Survival rate and symptoms were recorded after animals were injected with HupA and HupA-PLGA-NP (*i.v* injection) within 24h. HupA and HupA-PLGA-NP have toxic effect in animals at higher concentrations. The LD_{50} values of HupA and HupA-PLGA-NP were 1.40 and 4.85 mg/kg respectively. Their LD_{95} values were 2.42 and 9.63 mg/kg respectively. The results showed that the toxicity of HupA-PLGA-NP was significantly reduced by 3.5 times compared to HupA.

3.5 Protective efficacy of different dose of Hup A and HupA-PLGA-NP against 143μg/kg soman

As shown in Fig.5, the survival rates of animals pretreated with different dose of HupA or HupA-PLGA-NP were significantly increased. No animals survived only injected 143.0μg/kg soman. However, HupA and HupA-PLGA-NP have toxic effect in animals at higher concentrations. For instance, HupA (0.8mg/kg) and HupA-PLGA-NP (1.5mg/kg) can induce chewing and salivation. However, about 10% of the animals injected with HupA (0.8mg/kg) died, while no animals died when injected with HupA-PLGA-NP (1.5mg/kg).

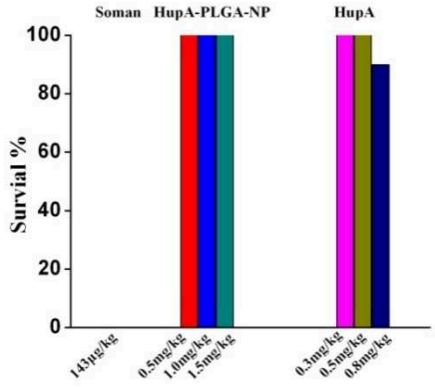


Fig.5 Protective efficacy of HupA and HupA-PLGA-NP pretreatment in mice against 143μg/kg soman

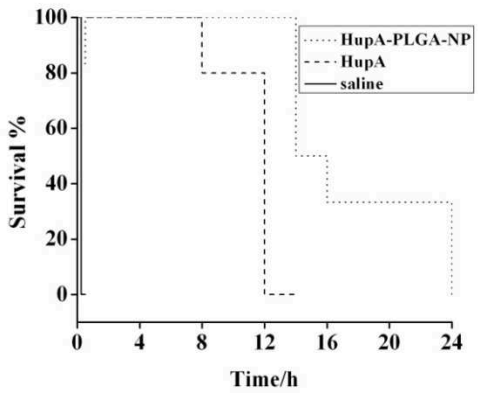


Fig.6 Survival rates of mice pretreated with HupA and HupA-PLGA-NP at different time after exposure to 143μg/kg soman

3.6 Effective pretreatment time of mice pretreated with HupA and HupA-PLGA-NP against soman

Without HupA or HupA-PLGA-NP pretreatment, only a few of animals pretreated with saline died in minutes after injection of 143μg/kg soman. Survival rate at different time after exposure to soman was shown in Fig.6. Pretreatment with 0.5mg/kg of HupA ensured animals survival rate 100% within 4h and 80% at 8h, No animal survived at 12h. Survival rate was 100% at 12 h when animals were treated with 0.5mg/kg of HupA-PLGA-NP and 33.3% of animals survived up to 16h. Aim to 100% survival rate, the effective protective time (12h) of HupA-PLGA-NP (0.5mg/kg,iv) against 1.0×LD_{95} soman toxicity in mice was prolonged significantly comparing to HupA (4h). The results showed that HupA-PLGA-NP significantly prolonged the effective pretreatment time against soman poisoning compared with HupA.

3.7 AChE activity in animals treated with HupA and HupA-PLGA-NP

Samples of diluted whole blood and brain were measured by modified DTNB method. As shown in Fig.7 and Fig.8, there was a good correlation between OD and diluted ratio of whole blood and brain tissue samples. Moreover, 80-fold and 10-fold dilutions were suitable for whole blood and brain tissue samples respectively.

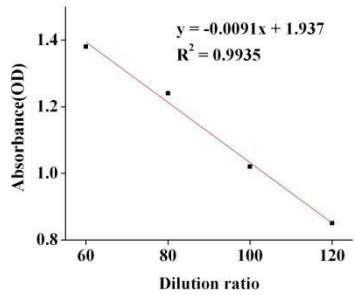


Fig.7 Measurement of whole blood AChE activity

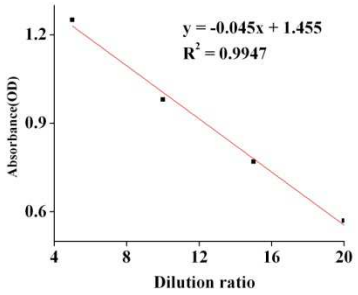


Fig.8 Measurement of brain AChE activity

The percentage of AChE activitiy in whole-blood or brain after HupA and HupA-PLGA-NP was analyzed by comparing to the normal blood level or an average of brains respectively. The inhibition of AChE activity by HupA in whole-blood rapidly reached to the peak value at 5 min (33.7%), while the peak (17.6%) of HupA-PLGA-NP appeared at 2h (Fig.9). The curve of inhibition of AChE activity in brain by HupA and HupA-PLGA-NP was similar to the blood: the peak value was 31.9% and 21.8% respectively (Fig.10). In summary, the maximum inhibition of AChE activity after treated with HupA-PLGA-NP was decreased and right shift compared with HupA, which is related to sustained release effect of nanodrugs. The results were in completely accord with pretreatment efficacy of soman posioning.

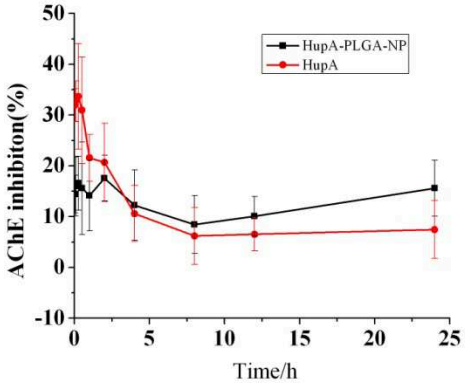


Fig.9 Time course of inhibition of whole-blood AChE in mice pretreatment with HupA and HupA-PLGA-NP

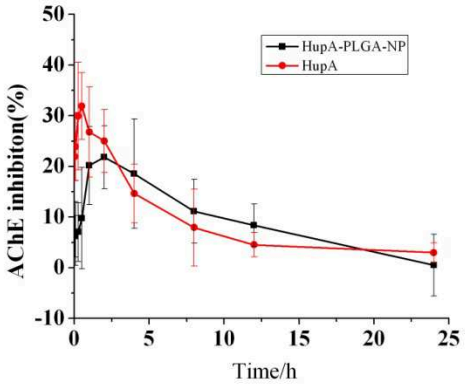


Fig.10 Time course of inhibition of brain tissue AChE in mice pretreatment with HupA and HupA-PLGA-NP

4 Conclusions

In the current study, HupA-PLGA-NP was prepared by oil in water emulsion solvent evaporation method and characterized. Results demonstrated that HupA-PLGA-NP had a spherical shape and a smooth surface without pores. It's drug loading was 2.86±0.6%, which was suitable for animal experiments. The *in vitro* release tests revealed that HupA-PLGA-NP had a low initial burst followed by a prolonged release. Study from dose-response of HupA and HupA-PLGA-NP confirmed that the toxicity of HupA-PLGA-NP was reduced about 3.5 times compared with HupA. Maximum inhibition of AChE activity by HupA-PLGA-NP in whole blood and brain were lower than those of HupA. More importantly, HupA-PLGA-NP afforded more opportunities for antidotal therapy of nerve agent exposure. Notably, the data showed that the advantage of the nanoparticle formulation over the pristine drug. Compared with HupA, the lower toxicity and prolonged prophylaxis time of the HupA-PLGA-NP can be contributed to the slow and sustained drug release manner. In a word, these findings confirm that protective efficacy of HupA-PLGA-NP against 143.0μg/kg soman was better than that of HupA.

Acknowledgments:

We would like to thank Prof. Chunying Chen and her colleagues, National Center for Nanoscience and Technology of China, for their help in the charcateration of HupA-PLGA-NP. This work was supported by National Natural Science Found of China(Grant NO. 81301187).

References

[1] M. Nagao, T. Takatori, Y. Matsuda, M. Nakajima, H. Iwase, K. Iwadate, Definitive evidence for the acute sarin poisoning diagnosis in the Tokyo subway, Toxicol. Appl. Pharmacol. 144 (1997) 198-203.

[2] N.M. Herkert, S. Schulz, T. Wille, H. Thiermann, R.A. Hatz, F. Worek, Pre- and post-treatment effect of physostigmine on soman-inhibited human erythrocyte and muscle acetylcholinesterase in vitro, Toxicol. Appl. Pharmacol. 253 (2011) 7–13.

[3] K. Cannard, The acute treatment of nerve agent exposure, J. Neurol. Sci. 249 (2006):86–94.

[4] J. Bajgar, Organophosphates/nerve agent poisoning: mechanism of action, diagnosis, prophylaxis, and treatment, Adv. Clin. Chem. 38 (2004):151–216.

[5] H.P.M. van Helden, M.J.A. Joosen, I.H.C. Philippens, Non-enzymatic pretreatment of nerve agent(soman)poisoning: A brief state-of-the-art review, Toxicol. Lett. 206 (2011)35-40.

[6] J.R. Haigh, S.R. Johnston, A. Peppernay, P.J. Mattern, G.E. Garcia, B.P. Doctor, R.K. Gordon, P.S. Aisen, Protection of red blood cell acetylcholinerterase by oral huperzineA against ex vivo soman exposure: Next generation prophylaxis and sequestering of acetylcholinerterase over butyrylcholinesterase, Chem. Bio. Interact. 175 (2008)380-386.

[7] Y. Wang, Y.L. Wei, S. Oguntayo, N. Jensen, B.P. Doctor ,M.P. Nambiar, [+]-Huperzine A Protects Against Soman Toxicity in Guinea Pigs, Neurochem. Res. 36 (2011)2381–2390.

[8] P. Masson, Evolution of and perspectives on therapeutic approaches to nerve agent poisoning.Toxicol. Lett. 206 (2011)5-13.

[9] Y.Q. Liang, X.C. Tang, Comparative effects of huperzine A, donepezil and rivastigmine on cortical acetylcholine level and acetylcholinesterase activity in rats, Neurosci. Lett. 361 (2004) 56–59.

[10] Y. Ashani, J.O. Peggins, B.P. Doctor, Mechanism of inhibition of cholinesterases by HUP A, Biochem. Biophys. Res. Commun. 30 (1992)719-726.

[11] E.X. Albuquerque, E.F.R. Pereira, Y. Aracava, W.P.F. Fawcett, M. Oliveira, W.R. Randall, Effective countermeasure against poisoning by organophosphorus insecticedes and nerve agents, Proc. Natl. Acad. Sci. 103 (2006)13220-13225.

[12] G. Lallement, V. Baille, D. Baubichon, P. Carpentier, J.M. Collombet, P. Filliat, A. Foquin, Review of the value of Huperzine as pretreatment of organophosphate poisoning, Neurotoxicology. 23 (2002) 1–5.

[13] L.S. Tonduli, G. Testylier, C. Masqueliez, G. Lallement, P. Monmaur, Effects of Huperzine used as pre-treatment against soman induced seizures. Neurotoxicology. 22 (2001)29–37.

[14] B.R. Coleman, R.H. Ratcliffe, S.A. Oguntayo, X. Shi, B.P. Doctor, R.K. Gordon, M.P. Nambiar, [+]-Huperzine A treatment protects against N-methyl-D-aspartate-induced seizure/status epilepticus in rats, Chem. Bio. Interact. 175 (2008)387–395.

[15] J. Grunwald, L. Raveh, B.P. Doctor, Y. Ashani, Huperzine A as a pretreatment candidate drug against nerve agent toxicity, Life. Sci, 54 (1994) 991–997.

[16] R.K. Gordon a, J.R. Haigha, G.E. Garcia, S.R. Feaster, M.A. Riel, D.E. Lenz, P.S. Aisen, B.P. Doctor, Oral administration of pyridostigmine bromide and huperzine A protects human whole blood cholinesterases from ex vivo exposure to soman, Chem. Bio. Interact. 157–158 (2005) 239–246.

[17] G. Lallement, J. Veyret, C. Masqueliez, S. Aubriot, M.F. Burckhart, D. Baubichon, Efficacy of huperzine in preventing soman-induced seizures, neuropathological changes and lethality. Fund. Clin. Pharmacol. 11 (1997) 387–394.

[18] T.M. Fahmy, S.L. Demento, M.J. Caplan, I. Mellman, W.M. Saltzman, Design opportunities for actively targeted nanoparticle vaccines, Nanomed. 3 (2008)343–355.

[19] Kohei Tahara, Yuta Miyazaki, Yoshiaki Kawashima , Hiromitsu Yamamoto, Brain targeting with surface-modified poly(D,L-lactic-co-glycolic acid) nanoparticles delivered via carotid artery administration, Eur. J. Pharm. Biopharm. 77 (2011) 84–88.

[20] F.Y. Sun, C. Sui, L.S. Teng, X.M. Liu, L.R. Teng, Q.F. Meng, Y.X. Li, Studies on the preparation, characterization and pharmacological evaluation of tolterodine PLGA microspheres

Int. J. Pharmaceu. 397 (2010) 44–49.

[21] R.H. Zhang, L.Q. Li, T. Shi, C. Wang, J.F. Xu, A blood cholinesterase assay method for organophosphorus compounds in vitro, Mil. Med. Sci. 36 (2012)424–426.

[22] G. Mittal, D.K. Sahana, V. Bhardwaj, M.N.V. Ravi Kumar, Estradiol loaded PLGA nanoparticles for oral administration: effect of polymer molecular weight and copolymer composition on release behavior in vitro and in vivo, J. Control. Rel.119 (2007) 77–85.

Keywords Index

(3-Aminopropyl)Triethoxysilane 1261
3D Indoor Positioning System 498
3D Printing 1290, 1368
3D Thin Film Microbattery 1170
4H-SiC 325

A

Abbe Error 1064
Absorption 126
Acceleration 896
Accelerometer 841
Acetylcholinesterase 1374
Activated Carbon 1150
Activation Energy 110
Active Disturbance Rejection Control 670
Adaptive Filter 957
ADC 548
Adhesion 381
Adsorption 40, 75
AFM 287, 817, 1093
AFM Probe 1054
Agglomeration 145
Al/Fe_2O_3 347
Al_2O_3 26
Alkalinity 352
Allan Variance 640, 888
Aluminum Nitride Film 1133
Ammonia 269
Analytical Potential Energy Function 313
Angle Measurement 906
Annealing Treatment 368
Anodic Oxidation 201, 303
ANSYS 555
Ansys Simulation 184
Antibacterial Properties 1314
Aptamers 1298
Aptasensor 1298
Arming Device 796, 968, 986
Asynchronous Communication 583
Atmosphere Pressure Sensor 504
Atomic Force Microscopy 670
Automatic Gain Control (AGC) 1308
Automatic Mass Measuring System 693
Automobile 444

B

Backside Exposure 853
Bacterial Cellulose 1247
Balloon-Expandable Stent 1333
Band Structure 98
Bandwidth Expansion 483
Bead Encapsulation 1009
Bernoulli Equation 462
Bi-Material Micro-Cantilever 951
Bi_2Te_3 32
Bias Instability 640
Biochemical Sensor 777
Biological Effect 1326
Biotemplate Synthesis 1273
Bipolar Plate 1233
Bistable 995
BN Nanowires 990
Bonding Strength 741
Boot Process 492
Boron Etch-Stop Technique 341
Bottom Electrode Position 706
Buckling Simulation 796
Butterfly Gyroscope 600

C

C-MBUS 806
CAD/CAM/3D Printing 1303
Calibration 817
Calibration of Weights 693
Cancer Diagnosis 1285
Candida rugosa Lipase 1261
Cantilever 817
Cantilever Beam 1189
Cantilever Bending Method 912
Capacitance Detection 538
Capacitance Measurement 824
Capacitive Membrane 577
Capillary Force 730
Capillary Pore 335
Carbon Dioxide 1111
Carbon Nanotube (CN) 92, 265

Carbon Nanotubes 681
Catalyst-Coated Membrtane 1156
Cathode 1145
Cell Enrichment Efficiency 1255
Cell Immobilization 1357
Cement Hydration 335
Central Composite Experimental Method 462
Centripetal Test 455
Ceria 394
Channel Shape 132
Characteristic Curve 830
Characterization Method 881
Charged Jet 281
Chemical Mechanical Planarization 291, 462
Chemical Synthesis 104
Chip-Scale Atomic Clocks 509
Chiral Sculptured Thin Films 9
Circuit Connection 841
Circulating Tumor Cell (CTC) 1320
Citrate Copper Plating System 783
CL-20 64
Closed-Loop 771
Closed-Loop Driving 543
Closed-Loop MEMS Accelerometer 640
Cloud 942
CMOS Amplifier 1279
CMOS-Compatible 836
CMOS Integrated Circuit 538
CMOS Process 1308
CMOS Technology 132
CMUT 577
Co-Condensation 1261
Coating 115
Coaxial Nozzle 1290
Colloidal Templates 347
Comb Accelerometer Sensor 824
Compensation Method 492
Composite Anodic Bonding 356
Composite Material 869
Composite N Precursor 368
Composite Structure 736
Compressive Stress 178
Computational Fluid Dynamics 761
COMSOL 449
Concentration Factor 681
Connectivity 900
Consistency of Polishing Rate 291
Constant Current 698
Contact Angle 208, 1233
Contact Angle of Three-Phase 1247
Contact Pair 830
Content 756
Control Strategy 1016
Control System 522
Controlling Flow Time 730
Convex Corner 58
Convex Plate-Shaped Micro Electrode 1043
Convolutional Encoder 1078
Copper Bulk Slurry 352
Copper Pillars 208
Corrugation 951
Counting of Small Particles 687
Coupling Inductors 583
Cracking 912
Cross Section 151, 1004
Cross Sensitivity 630
Crystal Growth 104
Cu/TiO_2 Nanocomposite 1314
Curing Kinetics 416
Current Collectors 1181
Current Density 319

D

DAC 605
Damping Material 931
Data-Translating 806
Defect 151
Deformation 533
Delamination 226, 912
Delay-Time Microchip 806
Density Functional Theory 40, 275
Density of States 325
Denture 1351
Detection 687
Detonating System 806
DFAFC 724
Diatomic Molecules 313
Die-Attach Adhesives 533
Dielectric Barrier Discharge 356
Dielectrophoresis 1285
Dielectrophoresis Chip 1255
Different-Height Resonant Beams 488
Differential Capacitance 630
Diffraction 853
Digital Demodulation 561

Digitally-Programmable 806
Diluted Magnetic Semiconductor (DMS) 15
Direct Digital Synthesis 561
Direct Liquid Detection 1267
Direct-Writing Technology 45
Discrimination 469
Dislocation Density 405
Dislocation Theory 405
Dispersion Behavior 394
Dispersity 145
Displacement Characteristic 920
Dissimilar Materials 388
Distributed Bragg Reflector 1087
DLD 1320
Double Hetero-Junction Phototransistor 1105
Droplet Microfluidics 1009
Dry Etching 163, 216
Dual Band 1059
DWA 657
Dynamic Characteristic 963
Dynamic Pull-In Parameter 706

E

Edible Oil 469
Effective Field Emitting Angle 1038
Effective Heat of Formation 421
Effective Thermal Conductivity 1032
Electric Field Microsensor 800
Electrical Property 157, 297
Electro-Osmotic 736
Electro-Spinning 375, 1303
Electro-Thermal Model 836
Electrochemical 1150
Electrochemical Behavior 388
Electrochemical Micromachining 1043
Electrochemical Vibration Sensor 483
Electrode 1150
Electroformed Nickel 259
Electrohydrodynamic Atomization 1156
Electrohydrodynamic Atomization (EHDA) 1175
Electrohydrodynamic Printing 45
Electromagnetic Damping Coefficient 1214
Electromagnetic Induction 1223
Electromagnetic Wave 126
Electronic Properties 990
Electronic Structures 325
Electroplating 783
Electrospinning 281, 1207, 1368
Electrospun 1201
Electrostatic Discharge 190
Electrostatically Actuated 1115
Electrostatically Actuated Cantilever 706
Elliptical Dimple 474
Energetic Composites 64
Energy Harvesting 995, 1189
Engine Coolant 444
Enrichment 1320
Epoxy Resin 362
Equal Channel Angular Pressing (ECAP) 427
Equivalent Electric Model 528
Error Analysis 972
Error Correction 761
Etching Rate 58
Eutectic Alloy 184
Eutectic Bonding 184, 504
Evaluation 444
Experiment 942
Exponential Approximation Function 1308
Extended Kalman Filter 498

F

Fabrication 1054
Failure 900
Fast Scan 670
Fault Diagnosis 687
Ferrite 126
FFT 771
Field Emission 265, 1038
Filament 169
Filling Ratio 1032
Film 1156
Film Bulk Acoustic Wave Resonator 509
Finite Element Analysis 319
Finite Element Analysis (FEA) 533, 1285
Finite Element Method 1072
Finite Element Method (FEM) 577, 951, 1333
First Principles 990
First-Principles Theory 15
Flake Absorbent 246
Flexible Film 195
Flexural Properties 411

Flexure Stage 810
Flip Chip 319
Flow Distribution 3
Fly Velocity 766
Footing Effects 522
Force Control 1016
Force Simulation 1255
Formaldehyde 719
Formic Acid 724
Forward Luminance 1087
FPGA 572
Frequency 859
Frequency Characteristics 120
Frequency Compensation 483
Frequency Quadrupler 80
Fuel-Air-Explosive 942
Fuel Cell 1156
Fuze 259
FWHM 1133

G

Gallium 1163
Gas Sensor 1111
GCC 517
Geometric Compensation 777
Geometry Shape Error 859
Geometry Size Deviation 859
GFET 139
GFET Frequency Multipliers 139
GFET Subharmonic Mixers 139
Giant Piezoresistive Effect 881
Graphene 40, 1207
Graphene Nanomesh 98
Graphene Oxide (GO) 110
Guidance Logic 653
Gyroscope 538
Gyroscopes 771

H

Hall Effect 595
Hall Output Probe Shape 595
Hardness 675
HDS 1163
Heading Drift 498
Heat Resistance 416
Heated Sheath Gas 45
Heavily Boron Doped Layers 341
HepG2 Hepatoma Carcinoma Cells 1255
Heterogeneity of Polishing Rate 462
Heterogeneity of Step Height Difference 462
HfO_x 169
Hierarchically Ordered Porous Carbon 64
High-Efficiency Preparation 368
High Enrichment 291
High Temperature Methanol Fuel Cell (HTMFC) 1175
High Temperature Proton Exchange Membrane (HTPEM) 1175
HMX 110
Hole Taper 1043
Hollow Microspheres 1273
Hollow Nanospheres 126
Host-Guest Chemistry 64
Hot-Filament Vacuum Gauge 836
Huperzine A 1374
Hybrid Fibers 411
Hydraulic Oil 756
Hydrodynamic Lubrication 474
Hydrogel Scaffold 1290
Hydrophilic 26
Hydrophilic Aluminum Foil 1314
Hydrophobic 26, 195
Hydrophobic Nano-Film 201
Hydrophobic Polytetrafluoroethylene 115
Hydrothermal Co-Precipitation 1339
Hydrothermal Method 32
Hydroxyapatite 1339
Hysteresis 957, 972

I

ICP 216
Image Edge Detection 810
Immobilization 1261
Impedance Analyze 790
Impregnation 64
Impurity Levels 325
In Situ Reaction 1273
Inclination Angle 474
Inductively Coupled Plasma 362
Inertial Sensors 875
Integral Drift 498
Integrated Sensor 610
Integrated System 1303
Interdigitated 513
Interdigitated Microelectrodes Array 1255

Interface 169, 912
Interface Circuit 605, 624, 1127
Interface Pretreatment 356
Interference Fit 1016
Intermediate Alloy 221
Intermolecular Interaction 252
Internal Stress 178, 405
Inverted Pyramid 1170
Ion Assisted Deposition 381
Ions 313
IOT 1111
Iron Wear Particle 756

J

Joule Heat 319

L

Lag 522
Large Area 195
Large Travel 1064
Laser 1054
Laser Damage Threshold 381
Laser Interferometer 810, 920
Laser Ranging 1099
Lateral Control Law 653
Line Width Measurement 810
Linear Sweep Voltammetry 783
Lithium-Ion Microbattery 1145
Load Modulation 583
Lock-Releasing Mechanism 986
Loss Factor 931
Low-Frequency Filters 875
Low-Grade Oil 469
Low Power Consumption 896
LPCVD 3
LPO 957

M

Machining Locality 1043
Magnetic Field Sensor 610
Magnetic Fileld Sensor 595
Magnetic Filter Technology 888
Magnetic Flux Linkage Gradient 1214
Magnetic Generator 1195
Magnetic Materials 104
Magnetic Sensitivity 595
Magnetic Sensitivity Characteristics 132
Magnetron Sputtering 566, 1133, 1145, 1170
Majority-Based Convolutional Encoder 1078
Marine Hydraulic Oil 687
Martensite Phase Transformation 427
Mask Process 21
Mass Transport 1181
Material Properties 259
Mathematical Modeling 995
MATLAB 853
Measurement Device 869
Mechanical Anisotropy 9
Mechanical Properties 926, 1072
Mechanical Property 287, 400, 1333
Mechanical Testing 1072
Mechanism of Phase Forming 421
Melt Electrospinning 45
Membrane Electrode Assembly (MEA) 1175
MEMS 178, 259, 455, 483, 513, 555, 616, 630, 636, 724, 796, 824, 859, 865, 968, 986, 1111, 1139, 1363
MEMS Accelerometer 533
MEMS-Based Solid Propellant Microthrusters 184
MEMS Capacitance Sensor 528
MEMS Devices 589
MEMS Humidity Sensor 761
MEMS Microphone 517
MEMS Mirror 1120
MEMS Nickle Material 926
MEMS Process 766
MEMS Sensor 942
MEMS Switch Series 572
MEMS Technology 120, 610
MEMS Vector Hydrophone 931
Mesoporous SBA-15 1261
Metal Bridge 865
Metal Particle 790
Metamaterials Absorber 1059
MHPs 208
Micro-Accelerometer 616
Micro Air Vehicle (MAV) 653
Micro-Assembly 1016
Micro-Channel 1290
Micro Channel - Inductive Method 756

Micro-Deformation 869
Micro Direct Methanol Fuel Cell (μDMFC) 1181
Micro-Electro Mechanical System (MEMS) 653
Micro Electro Mechanical Systems Technology (MEMS) 1357
Micro Electroforming 178
Micro-Electrostatic Vibration Energy Harvester 1127
Micro Energy Harvester 1223
Micro Fabrication 195
Micro Flat Heat Pipe 1032
Micro-Flow Extrusion Forming 1351
Micro-Flow Injection 746, 972
Micro-Fluidic Chip 449
Micro-Fluidic Inertial Switch 455
Micro Generator 1195
Micro-Gram Weights 693
Micro-Gyroscope 657
Micro Hotplate 698
Micro Inductor 783
Micro Laser Welding 388
Micro Molding 195
Micro-Nozzle 1009
Micro Pre-Concentrator 681
Micro-Scale 9, 942
Micro-Spring 830
Micro/Nanostructures 45
Micro/Nanosystems 190, 865
MicroBlaze 771
Microcavity Organic Light-Emitting Diodes 1087
Microfabrication 1170
Microfluidic 736, 1320
Microfluidic Chip 741, 790
Microfluidic Detection Chip 687
Microfluidic Device 469
Microfluidic Systems 730
Micromachining 455
Micromirror 1115
Microneedle 853
Microscopic Vision 1016
Microstructure 221, 1049
Mid-Infrared 1059
Millimeter Wave 80
Miniaturization 896
Mn-Zn Ferrite 246
Model Fuels 1163
Modeling 957
Modified Surfaces 75
Modulated Feedback 640
Modulator 657
Moisture 226
Molecular Dynamics 151, 1004
Molecular Dynamics (MD) 252
Mononitrotoluenes (MNs)-Plasticizer 252
Monte Carlo Method 589
Morphology 269
MoS_2 15
Motion Simulation 281
MS3110 528
Multi-Bit Quantization 548
Multi-Chip Module 636
Multi-Jet 281
Multi-Layer Mask Etching Process 488
Multi-Parameter 583
Multi-Physics 190
Multi-Regulated Cascode 646
Multi-Step Diffusion Method 341
Multiphysics Simulation 963
Multiscale Simulation 98
Multiwalled Carbon Nanotubes (MCWNTs) 719

N

N-Doped TiO_2 368
Nano-Film 1357
Nano-SiO_2 411
Nano-TiO_2 Fiber 375
Nano α-Fe_2O_3 232
Nanofibrils 1247
Nanofluid 444
Nanofluids 437
Nanoindentation 400
Nanoparticle 394, 1374
Nanopolysilicon TFTs 132
Nanoporous Copper 238
Nanopositioning Stage 1064
Nanoscale 912
Nanosecond Laser 1049
Nanosized TiN 221
Nanostructure 1054
Nanowire Polarizer 906
Nanowires Arrays 347
NaOH 303
Natural Emulsifier 1247
Near Boiling Point 58
Negative Enrichment 1320

Negative Resistance Oscillations 120
Nerve Agent 1374
Neural Probe 1279
Neural Signal 1279
Ni^+ Implantation 421
NiCr Alloy 566
Noise Analysis 624
Non-Linearity 980
Non-Photosensitive Polyimide 163
Nonlinear Vibration 995
Nonlinearity 972
Novel Wind Energy Harvesting Device 1139
Numerical Simulation 1345

O

Oleic Acid 437
One-Arm Bridge Type 1064
Optical Responsivity 1105
Optical Transition Frequency 1105
Optical Waveguide 777
Out-of-Plane Accelerometer 488
Output Characteristics 995
Overload Interference 888
Oxalic Acid Precipitation Method 145
Oxidant-Free 847
Oxygen Vacancy 169

P

Packaging Structure 931
Passive 583
Passive Acoustic Localization 517
PDMS 724
Peak Intensity 1087, 1133
PEMFC 1233
Pendulous Resonant MEMS Biosensor 1267
Phase Shift Method 1099, 1120
Photo-Catalysis 232
Photo Lithography 1093
Photocatalysis 1314
Photoresist Desquamation 777
PI 26
Pickering Emulsion 1247
PID System 681
Piezoelectric 86, 800, 1189
Piezoelectric Actuator 957, 1009
Piezoelectric Ceramics 746
Piezoelectric Coefficient d_{33} 920
Piezoelectric Generator 995
Piezoelectricity 275
Piezoresistance Effect 610
Piezoresistive Cantilevers 1298
Piezoresistive Detection 881
Pits 1345
Pizeoresistive Pressure Sensor 636
Planarization 330
Plasma Activation 356
Plastic Packaging 226
Plastic Strain 675
PMAC 1049
PMMA 1201
Polarization Imaging Sensor 906
Polarization Navigation 906
Polarizing Beam-Splitting Film 381
Polycrystalline Cubic Boron Nitride (PCBN) 52
Polycrystalline Diamond (PCD) 52
Polydimethylsiloxane 741
Polyhedral Oligomeric Silsesquioxane 416
Polymer Separator 1201
Polypyrrole 1150
Polyvinyl Pyrrolidone (PVP) 719
Pore Size 238
Porosity 900
Power 806
Power-Combining 80
Power MEMS 1195
Pre-Annealing 21
Pre-Stress Comb-Drive Actuator (PCA) 1115
Preferred Orientation 1133
Preparation Process 238
Pressure Sensor 610
Process Parameters 238
Process Variation 589
Processing Quality 52
Progressive Multi-Cycle Nanoindentation 675
Prorocentrum donghaiense 1326
PSG Thickness Uniformity 3
PVDF 1201
PVDF Membrane 269
Pyrex 7740 21
PZT Driven 800

Q

Q- Compensation 646

Q- Enhancement 646
Q-Factor 509
Quadrature Signal Generator 561
Quantitative Charges 92
Quantum-Chemical (QC) Method 252
Quantum-Dot Cellular Automata 1078
Quartz Crystal Microbalance (QCM) 719

R

Rare-Earth Atom 40
Rayleigh-Ritz Method 706
RDX 252
Reflectivity 1087
Reflow Soldering 226
Relaxation Oscillator 583
Reliability 226, 319
Residual Gas 504
Resistive Switching 169
Resonant Paddle 1267
Resonantor 1059
Rheological Properties 394
Rheology 1351
RKR Method 313
RLC 543

S

Sacrificial Layer 330
Sacrificial Process 616
Safety 986
Safety Device 796, 968
Sage–Husa Adaptive Filter 888
SAM 1233
Scalable Model 1024
Scanning 1099, 1120
Scanning Electron Microscope 810
Schottky Diode 80
Second Convergence 675
Selectivity Ratio 362
Self-Polymerization 1357
Self-Reactive Spray Forming Technology 246
Self-Sensing 746
Self-Sensing Actuator 972
Semi-Analytical Regression Model 455
Sensor Data Fusion 498
Sensors 719
Separation 269
Severe Plastic Deformation 427
Shape Measurement 1120
SiGe 70
Sigma-Delta 548, 605, 657
Sigma-Delta Modulator 980
Silicon 58, 1363
Silicon Cantilever 1093
Silicon Carbide (SiC) 287, 362, 400
Silicon Flyer 766
Silicon Gyroscope 548, 605
Silicon Magnetic Sensitivity Transistor 120
Silicon Microgyroscope 543, 624
Silicon Micromechanical Gyroscope on a Chip 492
Silicon Nanocantilevers 1072
Silicon Nanowire 881, 1004
Silicon Nanowires 151
Silicon-on-Glass 488
Silicon-on-Insulator (SOI) 777
Silicon Substrate 347
Silver Nanoparticle 75, 157, 297
Simulation 513, 543, 841, 1351
Simulation Modeling 942
Single Cell Manipulation 1285
Single-Loop 980
Single Proof Mass 630
Single-Walled Carbon Nanotubes 1326
Sintering Behavior 157, 297
SiO_2 26, 1201
SiO_2 Film 509
Size 1004
Size Effects 275
Skeletonema costatum 1326
Slapper Detonator 766
Slender Ratio 474
SnO_2 1207
SOI 616
SOI-MEMS 522, 1267
Sol-Gel 232
Solar Radiation 761
Solid Fuel Dispersion 942
Solvothermal 126
Soman 1374
Space Detection 1099
Space Environments 869
Spectroscopic Parameters of Molecules 313
Spindt Cathode 1038
Split-Drain MAGFET 132

Split-Ring 1059
Spray-On Waterproof Material 900
Square Thin Films 287
Stability 352, 1247
Stability Analysis 335
Staphylococcus Enterotoxin B (SEB) 1298
Statistical Analysis 589
Step Height 291
Stiffness 817
Stiffness Convexity Spring 830
Stiffness Factor 951
Stiffness Increase Spring 830
STM32 896
Strain Engineering 70
Stress 533
Stress Concentration 555
Structure Design 1064
Structure of Oxide Film 303
SU-8 577, 853
Subdivision Method 693
Super-Capacitor (SC) 1127
Supercapacitor 513, 1150
Surface Micromachined 1115
Surface Modification 1273
Surface Modified 1339
Surface Morphology 58
Surface Plasmon Resonance (SPR) 1357
Surface Roughness 291, 330
Surface Silicon Process 963
Surface Texturing 474
Surface Treatment 157, 297
Surface Velocity Uniformity 3
Suspended Rotor 538

T

Taguchi Method 238
Tapered Vessel 1333
TC4 Titanium Alloy 303
TCAD Simulation 70
TDOA 517
Temperature Characteristic 504
Temperature Control 600
Temperature-Related 926
Temperature Response Sensitivity 951
Temperature/Humidity 896
Test 942
Test Equipment System 572
Testing Algorithms 572
THD 980
Theotetical Analysis 841
Thermal Accumulation 265
Thermal Behavior 208
Thermal Conduction 1032
Thermal Conductivity 698
Thermal Decomposition 110
Thermomechanical Stress 630
Thin Film 381, 400, 912, 1145
Thin Film Pressure Sensor 566
Three-Component Magnetic Vector 888
Three-Dimensional Hydrodynamic Focusing 449
Three Dimensional System in Package (3D SIP) 1024
Threshold Value Judging Mechanism 968
Through Silicon via (TSV) 1024
Ti4Al6V 421
Time Division Multiplexing 583
Time Gate 730
Tin Oxide Water Contact Angle 115
TiNi Shape Memory Alloy 388
TiO_2 Nano-Tube 201
Tissue Engineering Scaffolds 1368
TMAH 58
TNT 252
Topological Insulator 32
Total Phosphorus 375
Total Phosphorus (TP) Digestion 847
Transconductance Reduction Techniques 875
Transimpedance 624
Transport 98
Tri-Axis Accelerometer 630
Triangular Horn 1363
Tribological Properities 437
Trichel Pulses 92
Triton X-100 58
TSV 190
TSV Technology 216
Tunable Active Resistor 646
Tuning Center Frequency 646
Turn-On Time 492

U

UHTCC 411
Ultra-Fined Grain 427
Ultrafine Nanofiber 281

Ultrasonic 178, 405
Ultrasonic Scalpel 1363
Ultraviolet Photocatalytic Oxidation 375
Undercut 1072
Uni-Traveling-Carrier 1105
Uniaxial Tension 926
Universal Capacitive Readout Integrated Circuit 528
UV Adhesive 86
UVC 847

V

V-Shaped Electrothermal Actuator 963
Vacuum Gauge 698, 836
Vapor Chamber 208
Variable Gain Amplifier (VGA) 1308
Variable Resistor 865
Variable Stiffness 830
Vascularization 1290
VCu_xO_y 1145
Vector Hydrophone 555
Verilog-A 139
Vertical Embedded Electrodes 736
Vessel Element 1345
Vibrating Ring Gyroscope 522
Vibration 859, 1189
Vibration Energy Harvesting 1214, 1223
Vibration Frequency 1004
Vibration-Isolation 931
Vibration Testing 9

W

W-Form Micro-Spring 796
Wafer Bonding 86
Water Crossover 1181
Water Transport 1345
Wear Resistance 221
Welded Joint 388
Wet Etching 21, 163
Whiskers 1339
Wire Electric Discharge Machining (WEDM) 52
Wireless 583

X

XRM 900

Y

YBCO Powder 145
Yield Enhancement 589
Young's Modulus 151

Z

Zener-Holloman 427
Zeolite 1163
Zero-Rate Output 600
Zeta Potential 394
ZnO Nanoparticles 437
ZnO Nanowires 275
ZnO Piezoelectric Thin Films Array 1139

Authors Index

B

Bai, Y.N. 132
Ban, C.C. 990
Bao, H. 869
Bi, R.K. 783
Bian, C. 375, 847
Bian, Y. 492
Bo, Z. 756, 790

C

Cai, C.L. 163, 362
Cai, H.Q. 64
Cai, J. 1351
Cai, J.F. 21, 341
Cai, L. 1078
Cai, X.D. 246
Cai, Y. 653
Cao, F. 1273
Cao, J.M. 15
Cao, X.R. 888
Cao, X.T. 653
Cao, Y.J. 15
Chang, H.L. 888
Chang, S. 98, 139
Chang, S.K. 706
Chen, D.H. 561
Chen, D.P. 951, 1111
Chen, D.X. 670, 810
Chen, D.Y. 483, 522
Chen, G.D. 352
Chen, H.B. 1004
Chen, H.L. 1181
Chen, H.P. 1303, 1368
Chen, H.Q. 687, 756, 790
Chen, J. 64, 347
Chen, J.M. 444
Chen, L. 265, 561, 1223
Chen, L.G. 356, 630
Chen, M.X. 238
Chen, P. 1285
Chen, Q.H. 1339, 1339
Chen, Q.S. 963
Chen, Q.W. 104
Chen, S. 1127
Chen, S.L. 853
Chen, S.M. 70
Chen, T. 356, 630, 1345
Chen, W. 741
Chen, W.P. 605, 771
Chen, X. 1357
Chen, X.R. 169
Chen, Y. 238
Chen, Y.H. 388, 616
Chen, Y.M. 287
Chen, Z.H. 600
Chen, Z.X. 1115
Cheng, B. 1054
Cheng, Z.X. 1279
Chu, J.K. 906
Cui, D.F. 1357
Cui, F.Y. 687
Cui, H.J. 600
Cui, H.Q. 1078
Cui, W.W. 26, 269
Cui, Y. 906

D

Dai, J. 184
Dai, J.Y. 1038
Dai, K.R. 513
Dai, T. 736
Dai, X.M. 517, 942
Dai, Z.D. 1009
Deng, F.C. 92
Deng, X.J. 80
Deng, Y.J. 1016
Deng, Y.M. 1314
Ding, L. 394
Ding, X.R. 190, 806, 865
Ding, Z.Q. 528
Dong, J.X. 488
Dong, L. 693
Dong, P.T. 287
Dong, Y. 777
Du, H.Y. 636
Du, L. 1195
Du, L.D. 504, 1139
Du, L.M. 528, 533, 824

Du, L.Q. 178, 405, 853
Du, X.H. 3
Duan, G.L. 1351

F

Fan, B. 1115
Fan, J.H. 416
Fan, S.D. 990
Fan, S.Y. 462
Fan, W. 1064
Fang, H. 9
Fang, K. 347
Fang, Z. 504, 1139
Feng, J. 169
Feng, J.H. 444
Feng, K. 800
Feng, S.J. 449, 469
Feng, X.Y. 572
Fu, Q. 657
Fu, Q.B. 766
Fu, Q.S. 951
Fu, W. 1247
Fu, W.Y. 498
Fu, X. 817, 1049
Fu, X.H. 381
Fu, Y.H. 474
Fu, Z.B. 40, 104

G

Gan, L. 730
Gao, C. 75
Gao, H.T. 246
Gao, L.L. 589, 859
Gao, S.Q. 1189
Gao, S.T. 810
Gao, W. 394
Gao, X. 411
Gao, Z.Q. 269, 548, 1308
Ge, Y.X. 881, 1072
Gong, W.H. 388
Gu, F. 151, 881, 1072
Gu, W.W. 1255
Gu, Y.S. 275
Guan, H.Y. 132
Guan, L. 906
Guan, P. 963
Guo, C.Y. 1345
Guo, F. 766
Guo, H. 195, 724, 783, 841, 1145, 1170, 1201, 1207, 1363
Guo, J.L. 1145, 1170
Guo, K.P. 1087
Guo, M.R. 517, 896, 942
Guo, N. 931
Guo, T. 75
Guo, X.D. 126
Guo, X.H. 796, 830, 986
Guo, X.P. 368
Guo, Y. 330
Guo, Y.L. 865
Guo, Z. 32

H

Han, H.H. 145
Han, L. 810
Han, M.J. 1285
Han, X.W. 736
Hang, J.X. 319
Hao, Q.L. 64
He, C.D. 577
He, G. 926
He, J. 98, 139
He, J.G. 394
He, L.B. 920
He, Q. 995
He, S.M. 64, 347
He, X.P. 528, 533, 824
He, Y. 80, 341
He, Y.F. 719
He, Z.W. 1043
Hong, J. 291
Hong, X. 1163
Hou, W.T. 427
Hou, Y.S. 246
Hu, D.P. 566
Hu, J. 362
Hu, Q.X. 1290, 1303, 1368
Hu, S. 362
Hu, Y.L. 368
Huang, F.X. 548, 1308
Huang, G. 522, 1267
Huang, H. 64, 1099
Huang, H.J. 252
Huang, J. 746, 1255

Huang, J.Q. 662
Huang, J.X. 226
Huang, N.B. 1233
Huang, Q. 139
Huang, Q.A. 583, 589, 636, 662
Huang, Q.J. 98
Huang, R.J. 1087
Huang, T.T. 995
Huang, X. 646

J

Ji, J.H. 474
Ji, L. 509
Jia, Y.Y. 1247
Jiang, G.Q. 216
Jiang, S.Y. 1064
Jiang, W.N. 980
Jiang, Y.D. 719
Jiang, Y.J. 900
Jiang, Z.Y. 1105
Jiao, B.B. 951
Jiao, Z.L. 400
Jin, D.Z. 265, 1038
Jin, L. 1189
Jin, X. 517, 942
Jin, Z.H. 640
Jing, B. 201
Jing, H. 416
Jing, Y.L. 1087

K

Kitamura, T. 9
Kong, D.Y. 1139
Kong, Y.M. 951
Kuang, L. 216

L

Lan, L. 15
Lei, D.J. 675
Lei, R. 86, 163
Lei, Y.M. 1214, 1223
Leng, G.J. 444
Li, B. 906
Li, B.B. 1285
Li, C. 275
Li, C.M. 1032
Li, D.L. 1133
Li, D.X. 1273
Li, F. 330
Li, F.F. 1326
Li, G. 610
Li, G.Z. 259, 926
Li, H. 670, 847, 1357
Li, H.B. 291
Li, J. 1308
Li, J.M. 730
Li, J.S. 252, 347
Li, K.C. 238
Li, L. 847, 990
Li, L.Q. 1374
Li, M. 70, 145, 151, 761, 881, 1072
Li, M.Q. 1175
Li, N.N. 265, 1038
Li, Q. 522, 875, 1267
Li, Q.F. 178
Li, Q.H. 411
Li, S. 1290
Li, S.Y. 906
Li, T. 730
Li, T.J. 777
Li, W. 810
Li, W.G. 1363
Li, W.H. 589, 859
Li, W.P. 670
Li, W.W. 281
Li, X.Y. 394, 675, 1261
Li, Y. 126, 291, 462, 1156, 1290
Li, Y.A. 483
Li, Y.F. 120
Li, Y.P. 577
Li, Y.X. 522, 1267
Li, Y.Y. 26, 269
Li, Z.L. 869
Li, Z.S. 1024, 1064
Liang, C.H. 1233
Liang, J.S. 1156, 1175
Lin, C.M. 110
Lin, J. 1145, 1170, 1201, 1207
Lin, Q.R. 595
Lin, Y.H. 45
Lin, Y.S. 810

Ling, C.D. 498
Ling, X.X. 1320
Liu, C. 52, 730, 1145, 1156, 1170, 1175
Liu, D.B. 252
Liu, D.M. 381
Liu, E.C. 687, 756
Liu, F.B. 201
Liu, F.Y. 190, 796, 968, 986
Liu, G.H. 830
Liu, H. 86, 330
Liu, H.C. 356
Liu, H.F. 368
Liu, H.N. 75
Liu, H.P. 1189
Liu, J. 1009
Liu, J.B. 670
Liu, J.G. 208
Liu, J.H. 681
Liu, J.Q. 269
Liu, J.Z. 297, 356
Liu, L.L. 600
Liu, L.Y. 151
Liu, L.Z. 26, 269
Liu, M. 449, 469
Liu, P. 572
Liu, P.S. 226, 319
Liu, Q.Q. 761, 881
Liu, R.W. 951
Liu, S. 221
Liu, S.B. 1345
Liu, T.T. 455
Liu, W.G. 86, 163, 330, 362
Liu, W.J. 291
Liu, X.D. 957
Liu, X.G. 238
Liu, X.W. 115, 538, 548, 605, 657, 736, 875, 980, 990, 1181, 1308
Liu, Y. 52, 1247
Liu, Y.D. 640
Liu, Y.F. 341, 488
Liu, Y.J. 777
Liu, Y.L. 291, 462
Liu, Y.Y. 771, 1290, 1303, 1368
Liu, Z.T. 605
Long, J.B. 1314
Lou, H.F. 246
Lou, W.Z. 190, 517, 572, 796, 806, 865, 896, 942, 968, 986
Lu, B. 80
Lu, D.K. 951
Lu, J. 796, 986
Lu, L. 32, 427
Lü, W.L. 3
Lu, X.J. 1374
Lu, Y. 226, 319
Lu, Y.F. 572, 806, 896
Lu, Y.X. 1127
Luo, J. 139
Luo, L. 405
Luo, Y. 208, 1032, 1156
Luo, Z.W. 281
Lv, M.W. 120, 132
Lv, Q.Y. 657
Lv, W.S. 513
Lv, Y.W. 98

M

Ma, D.Q. 145, 221
Ma, M.J. 640
Ma, Q. 252
Ma, T.J. 681
Ma, W. 1059, 1298
Ma, X.L. 1285
Ma, Y.H. 730
Ma, Y.M. 1303, 1368
Ma, Z.Z. 1181
Mao, H.Y. 1111
Mao, J. 741
Mao, X.H. 995
Mao, X.L. 761, 1072
Mao, Z.G. 538
Matsumoto, K. 9
Meng, H. 657
Miao, M. 1024
Ming, A.J. 1111
Mo, B. 498
Mu, A.L. 595

N

Nie, J. 163
Nie, M. 636

Ning, Z.W. 681

O

Ou, W. 1111

P

Pan , M.Q. 356
Pan, Y.G. 381
Pang, S.C. 1038
Peng, B. 528, 533, 616, 824
Peng, C.Y. 1087
Peng, P. 533
Peng, W. 1043
Peng, Y. 449, 469

Q

Qian, L. 1267
Qiao, X.J. 126
Qiao, Z.Q. 347
Qin, C.Q. 275
Qin, W.Z. 766
Qiu, A.P. 543, 624
Qiu, C.K. 1115
Qiu, Y.L. 1150
Qu, H. 528, 824

R

Ran, X. 437
Ren, D.H. 1320
Ren, M.Y. 538
Ren, Q.G. 126
Ren, Q.Y. 662
Ren, T.Q. 1156, 1175
Ren, X.P. 693
Ren, Y.H. 1111
Ru, C.B. 184
Ruan, X.P. 853

S

Shan, F.M. 957
Shan, Q. 208, 853, 1032
Shang, Z.G. 1133
Shao, Q. 657, 771
Shao, X.H. 221
She, B.X. 1314
Shen, F. 1016
Shen, R.Q. 184
Shen, X. 1333
Shen, Y.Y. 963
Shi, G.C. 259, 830, 1195
Shi, H. 26
Shi, L.P. 746, 972
Shi, Q. 492
Shi, T. 1374
Shi, X.Q. 449, 469
Shi, Z. 303
Shi, Z.G. 616
Song, C. 178, 405
Song, J.L. 577
Song, K.C. 92
Song, L.C. 1374
Song, M.C. 52
Song, R.C. 963
Song, Y.P. 817
Su, J. 151
Su, W. 58, 455, 616, 698
Su, Y. 543, 624
Sui, L. 259, 830
Sumigawa, T. 9
Sun, D.H. 3, 21, 45, 281
Sun, J.H. 681, 1357
Sun, L.L. 45
Sun, L.N. 356, 630
Sun, M. 462
Sun, P. 771
Sun, X. 275
Sun, X.Y. 444
Sun, Y.Q. 790
Sun, Y.Y. 1333
Sun, Z.G. 126

T

Tai, H.L. 719
Tan, G. 58
Tan, L.J. 1326
Tan, Q.L. 1111
Tan, Z.C. 178
Tan, Z.X. 1111
Tang, B. 58, 616, 698
Tang, C.Z. 1093
Tang, D. 583
Tang, G.P. 394
Tang, H.M. 963

Tang, J.L. 325
Tang, J.N. 1314
Tang, J.Y. 462
Tang, K. 1163
Tang, L. 509
Tang, W.F. 543, 624
Tang, W.X. 303
Tang, Y.J. 40
Tang, Z. 698
Tao, S.Q. 980
Tao, Y.S. 405
Tian, L. 736
Tian, Y. 561
Tong, J.H. 375, 800, 847

W

Wan, X.J. 1314
Wang, A.C. 291, 462
Wang, A.Q. 145, 221
Wang, B. 259
Wang, C. 80, 394, 455, 1049, 1374
Wang, C.Y. 40, 104
Wang, D.K. 796, 968, 986
Wang, D.Z. 1156, 1175
Wang, F. 896
Wang, F.F. 517, 796, 968, 986
Wang, F.M. 221
Wang, H. 98, 139, 474, 859
Wang, H.C. 1009
Wang, H.F. 1374
Wang, H.T. 1233
Wang, J. 352, 693
Wang, J.B. 483
Wang, J.J. 246
Wang, J.M. 427
Wang, J.Q. 836
Wang, J.T. 1326
Wang, J.Y. 32, 195, 841, 1201, 1207
Wang, L. 730
Wang, L.F. 583, 662
Wang, L.J. 45
Wang, L.Y. 3, 21, 341
Wang, M. 766, 1247
Wang, M.H. 1043
Wang, M.J. 52
Wang, P. 888
Wang, Q. 1115
Wang, Q.G. 900
Wang, R. 352
Wang, S.B. 232
Wang, S.Q. 1133
Wang, T.T. 195, 724, 841, 1363
Wang, W. 45
Wang, W.H. 1247
Wang, W.M. 1115
Wang, X. 281
Wang, X.D. 208, 1032, 1156
Wang, X.F. 513
Wang, X.H. 600, 1127
Wang, X.J. 381
Wang, X.L. 566
Wang, X.Y. 86, 163, 912
Wang, Y. 115, 421, 437, 766, 800, 1054
Wang, Y.B. 190, 806, 865
Wang, Y.C. 1285
Wang, Y.H. 157, 297
Wang, Y.J. 356
Wang, Z.C. 1078
Wang, Z.Z. 853
Wei, B. 1087
Wei, M.J. 1087
Wei, Q.L. 394, 675
Wei, X.W. 746
Wei, X.Y. 783
Wei, Y.B. 746, 972
Wen, C. 325
Wen, D.Z. 120, 132, 595, 610
Wen, M.P. 252
Wen, Y.Z. 1059, 1298
Wen, Z.Y. 1214, 1223
Weng, L. 26
Wilson, O. 693
Wu, B.B. 1333
Wu, H. 920
Wu, J. 796, 986, 1363
Wu, J.L. 783
Wu, J.Y. 416
Wu, L. 330, 335
Wu, L.Q. 670
Wu, Q.J. 145
Wu, S. 817

Wu, S.H. 504, 1139
Wu, T. 610
Wu, W.R. 1016
Wu, X.L. 1201
Wu, X.Z. 287
Wu, Y.F. 303
Wu, Y.L. 287, 1207
Wu, Z.J. 75
Wu, Z.Y. 1273
Wu, Z.Z. 469

X

Xia, G.M. 492, 543, 624
Xia, S. 1150
Xia, S.H. 375, 800, 847
Xiang, W. 265, 1038
Xiao, D.B. 600
Xiao, S.R. 761
Xiao, Z. 437
Xie, G.Z. 719
Xie, H. 157, 297
Xie, H.Y. 646, 1105
Xie, J.B. 888
Xie, J.L. 388
Xie, J.P. 145, 221
Xing, Y.J. 32
Xiong, J.J. 1111
Xiong, N. 335
Xiong, N.N. 157, 297
Xiong, R. 957
Xiong, W. 653
Xiong, Z. 616
Xu, C.G. 968
Xu, D. 1049
Xu, D.S. 15
Xu, H. 869
Xu, J.B. 184
Xu, J.F. 1374
Xu, J.H. 1150
Xu, L.S. 1233
Xu, S.L. 411
Xu, T. 1087
Xu, W.H. 269
Xu, Y.Q. 1261
Xue, C.Y. 577
Xue, H. 810
Xue, J.W. 1345

Y

Yan, D. 980
Yan, F. 265, 1038
Yan, J.K. 303
Yan, S.M. 1115
Yan, T.T. 1339
Yan, X.J. 1233
Yan, Y.B. 912
Yang, C. 1247
Yang, D.C. 1024
Yang, G. 303
Yang, H.L. 421
Yang, J. 900, 980
Yang, J.C. 1298
Yang, L.J. 1009, 1054
Yang, L.L. 226, 319
Yang, L.X. 741
Yang, M. 881
Yang, P. 920
Yang, Q.X. 900
Yang, S.C. 1024
Yang, T. 405, 455
Yang, W.Y. 1150
Yang, X. 40, 104
Yang, X.H. 610
Yang, X.K. 1078
Yang, Y.J. 1150
Yao, G.X. 636
Yao, M.Q. 58
Yao, Y. 1049
Ye, L.Y. 92
Ye, X.S. 75
Ye, Y.H. 184
Yi, F.T. 259
Yin, B.H. 670, 810
Yin, L. 605, 875, 980, 1308
Yin, P.H. 178
Yin, Y.T. 1339
Ying, K.M. 1363
You, Z. 513, 706, 1320
Yu, B.K. 208
Yu, C. 52
Yu, C.F. 313
Yu, F.Y. 335
Yu, H. 1004
Yu, H.J. 528, 533, 824

Yu, J. 836
Yu, L.K. 21
Yu, X.H. 421
Yu, X.M. 1059, 1298
Yu, X.Y. 437
Yu, Z.H. 98
Yu, Z.J. 45
Yuan, D.P. 777
Yuan, F. 630
Yuan, G.M. 888
Yuan, L. 40, 104
Yuan, S.S. 926
Yuan, W.T. 1150
Yuan, Y. 869
Yue, X.B. 675

Z

Zen, Y.A. 232
Zeng, B.Q. 1038
Zeng, G.Y. 110
Zeng, J. 449
Zeng, L. 687
Zeng, S.H. 70
Zeng, Y.B. 195, 724
Zha, W. 1156, 1175
Zhan, Z. 3, 21
Zhang, B.Z. 741
Zhang, C. 1099, 1120
Zhang, D. 1038
Zhang, F.T. 698
Zhang, G.F. 706
Zhang, G.J. 555, 931
Zhang, H. 730, 736, 1285
Zhang, H.E. 3
Zhang, H.F. 75, 115, 538
Zhang, H.P. 687, 756, 790
Zhang, H.Q. 120, 595
Zhang, J. 381, 1016
Zhang, J.H. 151, 761, 881, 1072
Zhang, J.L. 52
Zhang, J.T. 577
Zhang, L. 1043, 1111
Zhang, L.H. 646, 1105
Zhang, L.L. 1357
Zhang, M. 926
Zhang, M.L. 1078
Zhang, M.R. 968
Zhang, N.Y.S. 232
Zhang, P. 1004
Zhang, Q. 375
Zhang, R.H. 1374
Zhang, S.B. 1181
Zhang, S.Z. 126
Zhang, W. 70
Zhang, W.B. 1111
Zhang, W.D. 555, 577, 931
Zhang, W.R. 646, 1105
Zhang, X. 405
Zhang, X.D. 368
Zhang, X.L. 1072
Zhang, X.M. 756, 790
Zhang, Y. 139, 275, 1111
Zhang, Y.F. 1181
Zhang, Y.N. 681, 1290
Zhang, Z. 796, 986, 1279
Zhang, Z.S. 509
Zhang, Z.Y. 483, 616
Zhao, J.J. 1195
Zhao, L. 741
Zhao, P. 555
Zhao, R. 1059, 1298
Zhao, S.M. 488
Zhao, X.F. 120, 132, 595, 610
Zhao, Y.H. 70
Zhao, Y.K. 605
Zhao, Y.M. 888
Zhao, Y.W. 817
Zhao, Y.X. 646
Zhao, Y.Z. 157, 297
Zhao, Z. 178, 504, 1139
Zhao, Z.G. 724
Zheng, B.H. 252
Zheng, C. 21, 341, 1345
Zheng, G.F. 45, 281
Zheng, J.Y. 281
Zheng, Y.B. 698
Zhong, J.N. 325
Zhong, M. 70
Zhou, C.P. 1032
Zhou, G.W. 1261
Zhou, H. 561, 972
Zhou, H.M. 746
Zhou, J. 15, 1351

Zhou, J.H. 110
Zhou, J.J. 875
Zhou, J.L. 920
Zhou, L.J. 730
Zhou, Q.X. 40
Zhou, R.H. 3, 341
Zhou, S. 163, 330, 362
Zhou, W. 528, 533, 824
Zhou, Z.Y. 653
Zhu, B. 232
Zhu, D.B. 1351
Zhu, E.C. 951
Zhu, H.X. 1285
Zhu, J. 216, 400
Zhu, J.L. 498
Zhu, K.J. 1314
Zhu, P. 184
Zhu, R. 139
Zhu, X.F. 681
Zhu, X.H. 1156, 1175
Zhu, Y.F. 362
Zhuang, C.C. 990
Zhuang, J.B. 1233
Zhuang, Y.W. 1279
Zou, L.L. 208, 1032
Zou, Z.Y. 184